Cover Picture



Zhaoxiang Deng and Chengde Mao*

Designed DNA nanostructures can be accurately replicated into metal nanostructures by a molecular and a classic lithographic approach. The rational design and self-assembly of DNA motifs allows masks with sophisticated structures to be constructed. The cover picture shows one example, a gold film containing periodic, two-dimensional features that is replicated from a self-assembled, tetragonal DNA 2D array (repeating unit about 18 nm). More details can be found in the Communication by C. Mao and Z. Deng on page 4068 ff.

Contents

Angewandte EarlyView

The following Communications are available online (in Wiley InterScience). You can find them, as well as forthcoming Reviews, Highlights, and Essays, at www.angewandte.org, under Early View.

M. Tanaka, Y. Demizu, M. Doi, M. Kurihara, H. Suemune*:*
Chiral Centers in the Side Chains of α-Amino Acids Control the Helical Screw Sense of Peptides
DOI: 10.1002/anie.200460420
Published online: July 7, 2004

M. Finze, E. Bernhardt, H. Willner, C. W. Lehmann:*
$[(CF_3)_3BCP]^-$ and $[(CF_3)_3BCAs]^-$: Thermally Stable Phosphaethynyl and Arsaethynyl Complexes
DOI: 10.1002/anie.200454034
Published online: July 14, 2004

Articles judged by the referees or the editor as being either very important or very urgent are immediately edited, proof-read, and electronically published once the manuscript has arrived in the editorial office in its final form. As long as there is no page number available these articles should be cited in the following manner:

Author(s), *Angew. Chem. Int. Ed.*, online publication date, DOI.

News

Crystallographers Honor W. Saenger ____ **3994**

Novartis Award to R. Micura ____ **3994**

J. S. Miller Receives Utah Award of the ACS ____ **3994**

Books

Reactive Intermediate Chemistry ____ **3995**
Robert A. Moss, Matthew S. Platz, Maitland Jones, Jr.
reviewed by G. Bucher

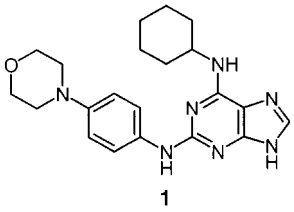
Carbohydrate-Based Drug Discovery ____ **3995**
Chi-Huey Wong
reviewed by O. Plettenburg, U. Stilz

Highlights

Dedifferentiation

C. Gey, A. Giannis* ____ **3998 – 4000**

Small Molecules, Big Plans—Can Low-Molecular-Weight Compounds Control Human Regeneration?



1

The name is the game. Reversine (**1**) is a low-molecular-weight compound that reverses the process of cell differentiation in mammals. Specialized muscle cells can be transformed into multipotent progenitor cells. This approach may have potential for targeted regeneration processes in humans.

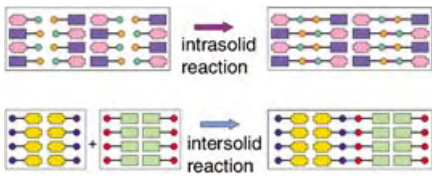
Minireviews

Solventless Reactions

D. Braga,* F. Grepioni ____ **4002 – 4011**

Reactions Between or Within Molecular Crystals

Weaning chemistry onto solids: reactions between solids (see picture) are often regarded as oddities and mechanical synthetic methods are felt to be fundamentally "nonchemical". This attitude is changing as solvent-free conditions become more important in environmentally friendly processes. In addition, solid-state synthetic procedures are often viable



alternative routes to known products and also to new compounds not obtainable by traditional solution chemistry.

© 2004 Wiley-VCH Verlag GmbH & Co. KGaA, Weinheim

Reviews



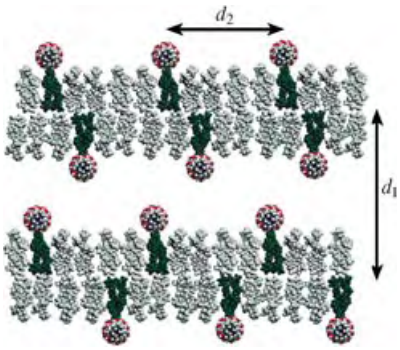
Through the membrane: The antigen transporter complex TAP plays a pivotal role in the translocation machinery which pumps antigenic peptides from the cytosol into the ER, a requirement for entry into the secretory pathway and subsequent display on the cell surface. Structural and mechanistic aspects of this ABC transporter are of great interest in membrane biology, immunology, virology, and cell biology. The picture shows the nucleotide binding domain of human TAP1.

Immunology

S. Beismann-Driemeyer, R. Tampé* ——— **4014 – 4031**

Function of the Antigen Transport Complex TAP in Cellular Immunity

Communications



Peptides sandwiched to order: Genetic engineering can be used to prepare charged polypeptides that self-assemble with oppositely charged surfactants into highly ordered multilayers (see diagram). Nanoscale order on three separate length scales can be controlled in the polyelectrolyte–surfactant self-assemblies by changing the peptide length, charge, and surfactant composition.

Nanostructures

I. Koltover,* S. Sahu, N. Davis ——— **4034 – 4037**

Genetic Engineering of the Nanoscale Structure in Polyelectrolyte–Lipid Self-Assembled Systems



Three complexes from one reaction: The reaction of *N*-(2-hydroxyethyl)iminodiacetic acid with $Ga(NO_3)_3$ yields an alkoxo-bridged dimer, a Ga_8 cluster (see picture), and a Ga_{13} cluster. The structures of these complexes and the structural relationships between them are reported, and the insight they may shed on the general mechanism of cluster formation is discussed.

Gallium Clusters

J. C. Goodwin, S. J. Teat, S. L. Heath* ——— **4037 – 4041**

How Do Clusters Grow? The Synthesis and Structure of Polynuclear Hydroxide Gallium(III) Clusters

For the USA and Canada:
ANGEWANDTE CHEMIE International Edition (ISSN 1433-7851) is published weekly by Wiley-VCH PO Box 191161, D 69451 Weinheim, Germany. Air freight and mailing in the USA by Publications Expediting Inc. 200 Meacham Ave., Elmont, NY 11003. Periodicals postage paid at Jamaica NY 11431. US POSTMASTER: send address changes to *Angewandte Chemie*, Wiley-VCH, 111 River Street, Hoboken, NJ 07030. Annual subscription price for institutions: Europe € 3430.00/3118.00; outside Europe US$ 4499.00/4090.00 (valid for print and electronic/print or electronic delivery); for individuals who are personal members of a national chemical society, or whose institution already subscribes, or who are retired or self-employed consultants, print only: Europe € 248.00/outside Europe US$ 378.00. Postage and handling charges included. All Wiley-VCH prices are exclusive VAT.

 © 2004 Wiley-VCH Verlag GmbH & Co. KGaA, Weinheim

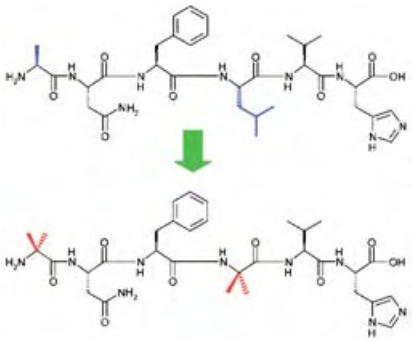
Contents

Inhibitor Design

S. Gilead, E. Gazit* ——— **4041 – 4044**

Inhibition of Amyloid Fibril Formation by Peptide Analogues Modified with α-Aminoisobutyric Acid

Breaking up is not hard to do with an α-aminoisobutyric (Aib) acid β-breaker, which has a remarkably restricted conformation. A novel approach to the inhibition of amyloid formation was developed that uses peptides modified with Aib (see figure). The similarity of Aib to hydrophobic amino acids, often found in amyloidogenic sequences, allows its integration into recognition motifs.

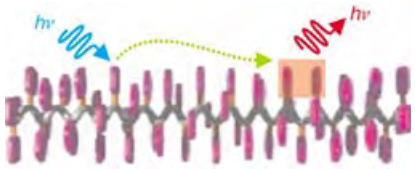


Multichromophoric Polymers

J. Hernando, P. A. J. de Witte, E. M. H. van Dijk, J. Korterik, R. J. M. Nolte, A. E. Rowan, M. F. García-Parajó,* N. F. van Hulst ——— **4045 – 4049**

Investigation of Perylene Photonic Wires by Combined Single-Molecule Fluorescence and Atomic Force Microscopy

Heterogeneous optical behavior of perylene polyisocyanides, which arises from different structures of the polymer backbone, is revealed by the combination of single-molecule fluorescence spectroscopy and atomic force microscopy. Short nonhelical perylene oligomers exhibit monomer-like fluorescence properties, whereas long helical perylene fiber emission arises from excimer sites after



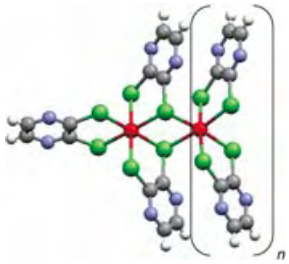
delocalization of the excitation along the polymer backbone (see picture).

Chiral Oligomers

X. Ribas, J. C. Dias, J. Morgado, K. Wurst, M. Almeida, T. Parella, J. Veciana, C. Rovira* ——— **4049 – 4052**

Stepwise Construction of Oligomeric 1,2-Diselenolene Platinum(IV) Complexes

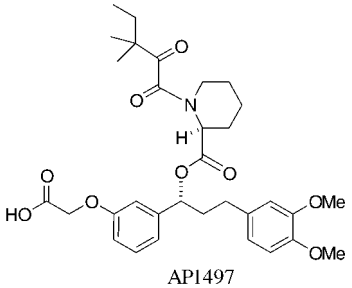
Surrounded by selenium: Pulse field gradient spin-echo (PGSE) NMR diffusion studies of a mixture of oligomeric 1,2-diselenolene Pt^{IV} complexes are performed to characterize the species in solution (see structure: $n=0$ (**1**), $n=1$ (**2**), $n=2$ (**3**); red Pt, green Se, blue N, gray C). The results are in accord with the single-crystal X-ray diffraction structures obtained for the chiral complexes $\{Pt^{IV}Se_6\}$ (**1**) and $\{Pt^{IV}_2Se_{10}\}$ (**2**).



Complementary-DNA Phage Display

K. M. McKenzie, E. J. Videlock, U. Splittgerber, D. J. Austin* ——— **4052 – 4055**

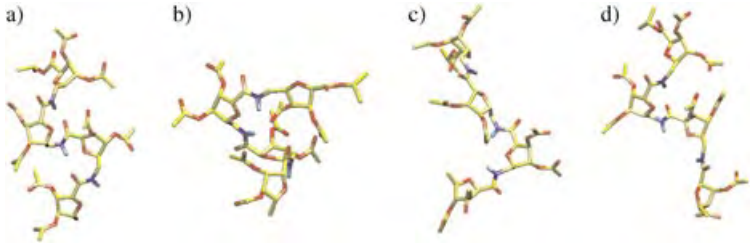
Simultaneous Identification of Multiple Protein Targets by Using Complementary-DNA Phage Display and a Natural-Product-Mimetic Probe



AP1497

Putting on a good display: A novel selection protocol was devised for the simultaneous display cloning of three homologues of the FK506-binding protein (FKBP12, FKBP12.6, and FKBP13) by using AP1497 (see structure), a mimetic of FK506, and a T7 complementary-DNA phage-display library. A quantitative on-phage binding assay was also performed to evaluate the affinity of the isolated proteins.

 © 2004 Wiley-VCH Verlag GmbH & Co. KGaA, Weinheim



Shaping up nicely: Carbopeptoids with THF rings in their backbone show distinct folding behavior depending on chain length, configuration, and solvent polarity. Molecular dynamics simulations of the folding yield averaged proton–proton distances in good agreement with experimental NOE data. They show, however, that a number of folds are important (b–d), whereas NOE data are usually interpreted in terms of single structures (a).

Conformation Analysis

R. Baron, D. Bakowies, W. F. van Gunsteren* ——— **4055 – 4059**

Carbopeptoid Folding: Effects of Stereochemistry, Chain Length, and Solvent

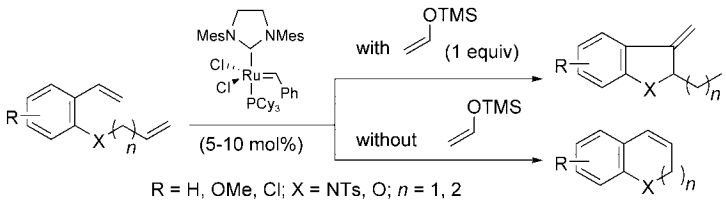


Dye hard: Strong intermolecular interactions of stilbazolium-like dyes with different structures and conformations seem to act as the main driving force for the formation of nanostructures with distinct morphological and spectral properties. Nanorods and nanospheres (see picture) with well-defined shapes and uniform sizes are formed by changing the solvent quality during synthesis.

Organic Nanostructures

Z. Tian, Y. Chen, W. Yang, J. Yao,* L. Zhu, Z. Shuai ——— **4060 – 4063**

Low-Dimensional Aggregates from Stilbazolium-Like Dyes



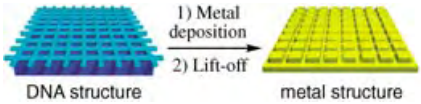
Substituted N and O heterocycles have been synthesized by the cycloisomerization of dienes using a ruthenium-carbene catalyst**.** The products obtained with and without trimethylsilyl vinyl ether differ (see scheme, Cy = cyclohexyl, Mes = 2,4,6-trimethylphenyl, Ts = *p*-toluenesulfonyl).

Heterocycle Synthesis

Y. Terada, M. Arisawa,* A. Nishida* ——— **4063 – 4067**

Cycloisomerization Promoted by the Combination of a Ruthenium–Carbene Catalyst and Trimethylsilyl Vinyl Ether, and its Application in The Synthesis of Heterocyclic Compounds: 3-Methylene-2,3-dihydroindoles and 3-Methylene-2,3-dihydrobenzofurans

Unmasking the potential: A DNA-templated nanofabrication approach is reported in which various 1D and 2D DNA nanostructures were assembled, and then these structures transformed into corresponding metal nanostructures through metal deposition (see schematic representation). The ease and flexibility of this technique offers a route to overcome the inabilities faced by traditional lithographic techniques.



Metallic Nanostructures

Z. Deng, C. Mao* ——— **4068 – 4070**

Molecular Lithography with DNA Nanostructures

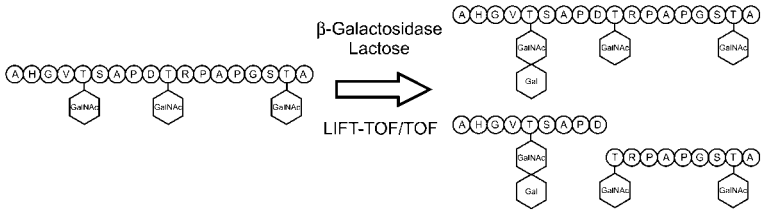
 © 2004 Wiley-VCH Verlag GmbH & Co. KGaA, Weinheim

Contents

Proteomics Research

M. Kurogochi, T. Matsushita, S.-I. Nishimura* ——— **4071 – 4075**

Post-Translational Modifications on Proteins: Facile and Efficient Procedure for the Identification of O-Glycosylation Sites by MALDI-LIFT-TOF/TOF Mass Spectrometry

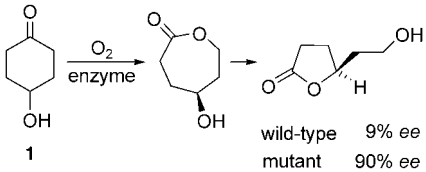


We have LIFT-TOF! Transglycosylation of glycopeptides by β-galactosidase in the presence of lactose combined with tandem mass spectrometry using a 2,5-dihydroxybenzoic acid matrix enables the O-glycosylation sites to be identified (see scheme). The highly sensitive and ideal fragmentation patterns generated from glycopeptide precursor ion peaks can be readily used for precise and reliable structure analyses.

Asymmetric Catalysis

M. T. Reetz,* B. Brunner, T. Schneider, F. Schulz, C. M. Clouthier, M. M. Kayser ——— **4075 – 4078**

Directed Evolution as a Method To Create Enantioselective Cyclohexanone Monooxygenases for Catalysis in Baeyer–Villiger Reactions

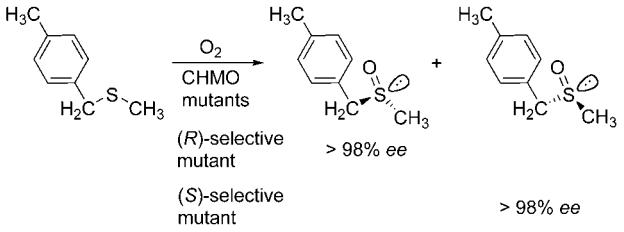


The direction and degree of enantioselectivity in the cyclohexanone monooxygenase catalyzed air-mediated Baeyer–Villiger reactions, such as the desymmetrization of **1**, can be controlled by directed evolution.

Asymmetric Catalysis

M. T. Reetz,* F. Daligault, B. Brunner, H. Hinrichs, A. Deege ——— **4078 – 4081**

Directed Evolution of Cyclohexanone Monooxygenases: Enantioselective Biocatalysts for the Oxidation of Prochiral Thioethers

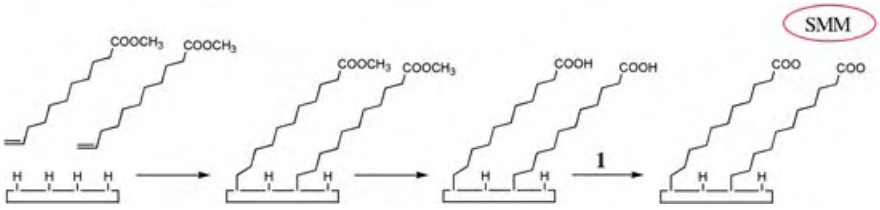


Mutational changes in cyclohexanone monooxygenases (CHMOs), for example the introduction of serine at position 432, lead to surprisingly versatile enantioselective biocatalysts that perform particularly well in the air-mediated partial oxidation of prochiral thioethers (see scheme).

Single-Molecule Magnets on Silicon

G. G. Condorelli, A. Motta, I. L. Fragalà,* F. Giannazzo, V. Raineri, A. Caneschi, D. Gatteschi ——— **4081 – 4084**

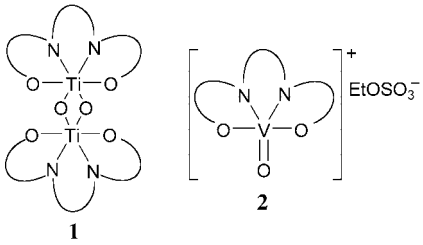
Anchoring Molecular Magnets on the Si(100) Surface



Hydrosilylation by H-terminated silicon of the double bond of methyl 10-undecenoate with formation of a robust Si–C bond is the first step in a three-step procedure (see scheme) for anchoring the single-molecule magnet (SMM) $[Mn_{12}O_{12}(OAc)_{16}(H_2O)_4]$ (**1**) on the Si(100) surface.

 © 2004 Wiley-VCH Verlag GmbH & Co. KGaA, Weinheim

A mixed complex which results from two salen-derived V^{V} and Ti^{IV} complexes (**1** and **2**), catalyzes the trimethylsilylcyanation of aldehydes. The reaction kinetics are largely determined by the titanium-derived portion, whereas the configuration of the mandelonitrile trimethylsilyl ether products is determined by the slower vanadium part of the catalyst. salen = *N*,*N*′-bis(salicylaldehydo)ethylenediamine.

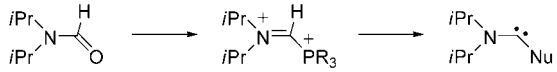


1 **2**

Homogeneous Catalysis

Yu. N. Belokon,* M. North, V. I. Maleev, N. V. Voskoboev, M. A. Moskalenko, A. S. Peregudov, A. V. Dmitriev, N. S. Ikonnikov, H. B. Kagan* ——— **4085 – 4089**

In Situ Formation of a Heterobimetallic Chiral [(Salen)Ti^{IV}]/[(Salen)V^{V}] Catalyst for the Asymmetric Addition of TMSCN to Benzaldehyde

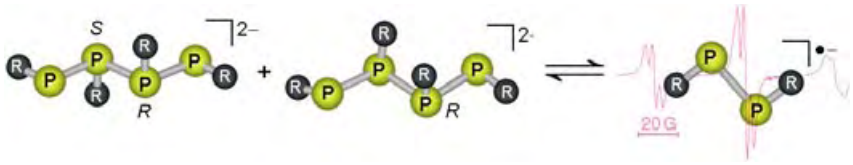


From amides to carbenes: Phosphonio-substituted iminium salts are readily available from the corresponding amides in a one-pot reaction. Deprotonation followed by substitution reactions affords a variety of transient and stable amino carbenes (see scheme).

Carbenes

S. Conejero, Y. Canac, F. S. Tham, G. Bertrand* ——— **4089 – 4093**

Readily Available Onio-Substituted Methyleneiminium Salts: Single Precursors for a Variety of Aminocarbenes



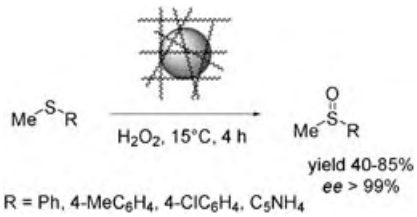
Encapsulation of the Na^{+} ions of the $[Na_2(P_4R_4)]$ ion triple with a *R*,*R* or *S*,*S* configuration at the inner phosphorus atoms by cryptands has enabled cation-separated dianions to be obtained in a crystalline form. Fragmentation of the $\{Na([2.2.2]cryptand)\}_2(P_4R_4)$ into radical anions $(P_2R_2)^{\bullet-}$ occurs in solution (see scheme), as determined by EPR spectroscopy.

Phosphorus Radicals

J. Geier, J. Harmer, H. Grützmacher* ——— **4093 – 4097**

"Naked" Phosphanediide Chains and their Fragmentation into Diphosphene Radical Anions

Bound to do the job: Sol–gel methods have been used to encapsulate chloroperoxidase (CPO) in microporous silica. The encapsulated CPO can then be used as an enantioselective catalyst for the oxidation of organic sulfides (see scheme) and can be recycled without appreciable loss of activity and enantioselectivity.



Enzymatic Oxidation

V. Trevisan, M. Signoretto, S. Colonna, V. Pironti, G. Strukul* ——— **4097 – 4099**

Microencapsulated Chloroperoxidase as a Recyclable Catalyst for the Enantioselective Oxidation of Sulfides with Hydrogen Peroxide

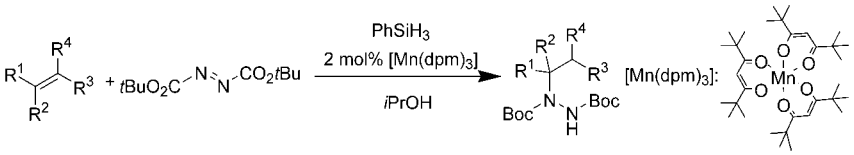
 © 2004 Wiley-VCH Verlag GmbH & Co. KGaA, Weinheim

Contents

Alkene Hydrazination

J. Waser, E. M. Carreira* ____ **4099 – 4102**

Catalytic Hydrohydrazination of a Wide Range of Alkenes with a Simple Mn Complex



Enhanced activity, lower catalyst loading, shorter reaction times, and expanded substrate scope are the advantages of $[Mn(dpm)_3]$ over Co catalysts in the hydrohydrazination reaction of alkenes (see scheme). Thus, sterically hindered alkenes, including tetrasubstituted alkenes, can now also readily undergo this reaction.

VIP Communications labeled with this symbol have been judged by two referees as being "very important papers".

Looking for outstanding employees?

Do you need another expert for your excellent team?
... Chemists, PhD Students, Managers, Professors, Sales Representatives...

Place an advert in the printed version and have it made available online for 1 month, free of charge!

Angewandte Chemie International Edition
Advertising Sales Department: Marion Schulz
Phone: 0 62 01 - 60 65 65
Fax: 0 62 01 - 60 65 50
E-Mail: MSchulz@wiley-vch.de

Service

Keywords ____ ***4104***

Authors ____ ***4105***

Angewandte's Sister Journals ____ ***4106 – 4107***

Preview ____ ***4109***



Crystallographers Honor W. Saenger

The Deutsche Gesellschaft für Kristallographie (German Society for Crystallography) has awarded Wolfram Saenger (Freie Universität Berlin, Germany) the Carl Hermann Medal in recognition of his lifework in the field of the crystal-structure analysis of biological macromolecules and the elucidation of their underlying fundamental chemical principles. Saenger's research includes the study of hydrogen bonding, cyclodextrin inclusion compounds, enzymes, nucleic acids, proteins, and photosynthesis. His Review on the tetracycline repressor as a paradigm for a biological switch appeared in 2000 in *Angewandte Chemie*.[1]



W. Saenger

After completing his PhD in 1965 with F. Cramer in Darmstadt (Germany) on the kinetics of cyclodextrin inclusion compounds, Saenger carried out postdoctoral research with J. Z. Gougoutas at Harvard University (USA). He then worked at the Max-Planck-Institut für Experimentelle Medizin in Göttingen (Germany), where he completed his habilitation in 1971. In 1981 he became a professor at the Institut für Kristallographie of the Freie Universität Berlin. Saenger was a member of the Editorial Board of *Angewandte Chemie* from 1994 until 2003.

Novartis Award to R. Micura

Ronald Micura (Universität Innsbruck, Austria) has been awarded the 2003 Novartis Award for chemistry for his work on the chemistry of modified RNA, in particular that of ribosomal translation and RNA folding. Micura studied chemistry at the Universität Linz (Austria) and completed his PhD there in 1995 with K. Grubmayr on model compounds for chromophore–protein interactions. He was awarded a prize by the Gesellschaft Österreichischer Chemiker (Austrian Chemical Society) for his PhD research. He began studying RNA during a postdoctoral period with Albert Eschenmoser, first at the ETH Zürich, then later at The Scripps Research Institute in La Jolla (California). At the end of 2000 he returned to Austria, and he completed his habilitation at the Universität Innsbruck in 2002. He has been a Professor of Organic Chemistry there since 2004.



R. Micura

Micura's research group focuses on the chemical biology of nucleic acids, in particular the synthesis of chemically modified RNA as a tool for investigations into the influence of natural and nonnatural modified nucleotides on the structure and function of RNA. In 2002 his Highlight on "Short Interfering RNAs and Their Chemical Synthesis" was published by *Angewandte Chemie*; recently a Communication appeared on the "Triggering of RNA Secondary Structures by a Functionalized Nucleobase".[2]

J. S. Miller Receives Utah Award of the ACS

In recognition of his achievements in the development, characterization, and application of new ferromagnetic materials,[3a,b] and the investigation of unusual carbon–carbon bonds,[3c] Joel S. Miller (University of Utah, Salt Lake City, USA) has been awarded the Utah Award by the ACS (American Chemical Society) Central Utah and Salt Lake Sections. The very first organic magnet and the first to work above room temperature were both synthesized by his research group.

Miller studied at Wayne State University in Detroit (USA) and completed his PhD in 1971 at the University of California in Los Angeles. He carried out postdoctoral research in 1972 at Stanford University (USA), then worked at the Xerox Webster Research Center and from 1978 at the Occidental Research Corporation. From 1983 until 1993 he was head of central solid-state research at DuPont. Miller has been a guest professor at the Technische Universität München (Germany), the Weizmann Institute (Rehovot, Israel), and the Université Paris-Sud (France). Since 1993 he has been a Professor of Chemistry at the University of Utah. Miller is a member of the Editorial Boards of *Chemistry—A European Journal* and *Advanced Materials*. Together with Marc Drillon (Strasbourg, France) he edited the four-volume work "Magnetism: Molecules to Materials" (Wiley-VCH, **2002**).



J. S. Miller

[1] W. Saenger, P. Orth, C. Kisker, W. Hillen, W. Hinrichs, *Angew. Chem.* **2000**, *112*, 2122; *Angew. Chem. Int. Ed.* **2000**, *39*, 2042.

[2] a) R. Micura, *Angew. Chem.* **2002**, *114*, 2369; *Angew. Chem. Int. Ed.* **2002**, *41*, 2265; b) C. Höbartner, H. Mittendorfer, K. Breuker, R. Micura, *Angew. Chem.* **2004**, *116*, 4012; *Angew. Chem. Int. Ed.* **2004**, *43*, 3922.

[3] a) J. S. Miller, A. J. Epstein, *Angew. Chem.* **1994**, *106*, 399; *Angew. Chem. Int. Ed. Engl.* **1994**, *33*, 385; b) J. S. Miller, *Adv. Mater.* **2002**, *14*, 1105; c) R. E. Del Sesto, J. S. Miller, P. Lafuente, J. J. Novoa, *Chem. Eur. J.* **2002**, *8*, 4894.

 © 2004 Wiley-VCH Verlag GmbH & Co. KGaA, Weinheim DOI: 10.1002/anie.200461287

Dedifferentiation

Small Molecules, Big Plans—Can Low-Molecular-Weight Compounds Control Human Regeneration?

*Claudia Gey and Athanassios Giannis**

Keywords:
regeneration processes · biological activity · cell cycle · dedifferentiation · reversine

Aristotle's statement that the salamander is able to pass through fire unharmed and extinguishes the flames at the same time is surely incorrect and unproved.[1] However, the capability of the salamander to regenerate its tail has been known for 235 years. In the middle of the 18th century the Italian scientist Lazarro Spallanzani wrote about the remarkable property of the adult animal to regenerate limbs, tail, and jaw lost after injury.[2] Even today the salamander provides the best example of regeneration in animals.

Unlike lower-order animals, vertebrates have limited capability to regenerate injured, dead, or lost body parts, since increased tissue specialization is accompanied by reduced regeneration capability. There are few examples for reparative regeneration in mammals (fingertips of children, repair of a hole in the ear of a rabbit).[3]

The human liver is considered to be a special case of regeneration. Removed tissue is replaced by both enlargement of the remaining tissue (hypertrophia) and increased cell number (hyperplasia). Concerning the latter, it is still not known if fully differentiated cells or hepatic stem cells divide.[4] Therefore, much research has been aimed at understanding the biochemical and molecular mechanisms of regeneration and improving regeneration capability in mammals.

[*] Dipl.-Biochem. C. Gey, Prof. Dr. A. Giannis
Institut for Organic Chemistry
University of Leipzig
Johannisallee 29
04103 Leipzig (Germany)
Fax: (+49) 0341-973-6599
E-mail: giannis@chemie.uni-leipzig.de

The unusual regeneration capability of the salamander is based on a process called dedifferentiation. This kind of regeneration is marked by cell proliferation at the edge of the wound preceding the development of a new part (epimorphosis). Cells of different tissues disassemble their specific structures in the area of the wound and regain the properties of progenitor cells. Such reembryonalized cells form the blastema and start to proliferate. Controlled by the environment, blastema cells can differentiate again and form different tissues and body parts, for example, limbs, tail, or jaw.

First scientific evidence for the dedifferentiation of amphibian cells was obtained in 1938. Shortly thereafter, electron-microscopic images showed that the muscle cells of newts next to an amputation site had lost their myofibrillar structure and that mononucleated cells formed the blastema. More recently, experiments using ^{3}H-labeled thymidine indicated DNA synthesis occurring at the same time.[5] In transplantation studies with muscle cells labeled with rhodamine–dextran conjugates, the dedifferentiation process was observed over time. In these studies the multinucleated myotubes of newts were cultivated in vitro and labeled permanently with the dye conjugate. One week after implantation of the multinucleated and size-selected myotubes into a regenerating newt limb, rhodamine-labeled, mononucleated cells could be detected. In addition, the number of mononucleated cells increased over time, suggesting that cell division took place.[6]

Echeverri et al. provided evidence that endogenous muscle cells are capable of dedifferentiating. They injected fluorescent tracers into single muscle fibers of the transparent axolotl (Mexican salamander) and performed amputations afterwards. By in vivo labeling and DIC (differential interference contrast) imaging they could show that all nuclei "budded off" from a single multinucleated muscle cell to form mononucleate cells and the blastema.[7]

Only little is known about the molecular mechanism of dedifferentiation. The lack of contact to neighboring cells at the amputation site is necessary but not sufficient to induce fragmentation into mononucleated cells and reentry into the cell cycle. To elucidate the intracellular signals in this process muscle fibers of several strains of mice were stimulated with a proliferation-inducing serum. Myocytes of mice (like most mammalian cells) are considered to be terminally differentiated and withdrawn from the cell cycle. In contrast, muscle cells of newts reenter the S-phase after serum stimulation. In 1994 Schneider et al. showed that multinucleated myotubes from mouse cells deficient in the retinoblastoma (Rb) gene were able to reenter the cell cycle when stimulated by serum.[8] Hence the Rb protein was supposed to regulate the cell cycle by blocking the G1–S transition; this was supported by the detection of phosphorylated, inactive Rb in stimulated myofibrils of newts.[9] In contrast, the Rb of wild-type murine myotubes remained unphosphorylated and active after serum stimulation. Mouse myotubes in which the expression of cyclin D and CDK4 was induced could overcome the G1–S block when cultivated in serum-rich conditions.[10] Thus the kinase pathway with Rb as a target as well as factors

 © 2004 Wiley-VCH Verlag GmbH & Co. KGaA, Weinheim DOI: 10.1002/anie.200460346

from the serum seem to be important for inducing dedifferentiation (Figure 1).

Recently P. G. Schultz, S. Ding, and their research groups screened a library of small heterocyclic compounds including 2,6-disubstituted purines for their ability to induce dedifferentiation in somatic mammalian cells.[11] Lineage-committed progenitor cells of mouse myotubes (myoblasts, C2C12 cells) were treated with the small molecules (5 μM) and then analyzed for subsequent dedifferentiation and transformation into multipotent cells. Specifically, after the compounds were removed, the cells were cultured under either osteoblast-inducing conditions or adipocyte-inducing conditions. Osteoblasts were identified by testing for alkaline phosphatase activity as a bone-specific marker; adipocytes were identified by staining with oil red O. Because this screen could also identify molecules that directly induce transdifferentiation of myogenic cells into osteogenic cells, the compounds were tested in the absence of osteogenesis-inducing medium and then tested for alkaline phosphatase activity.

In the second approach the C2C12 cells were tested to determine whether they can differentiate into adipocytes under adipogenesis-inducing conditions.

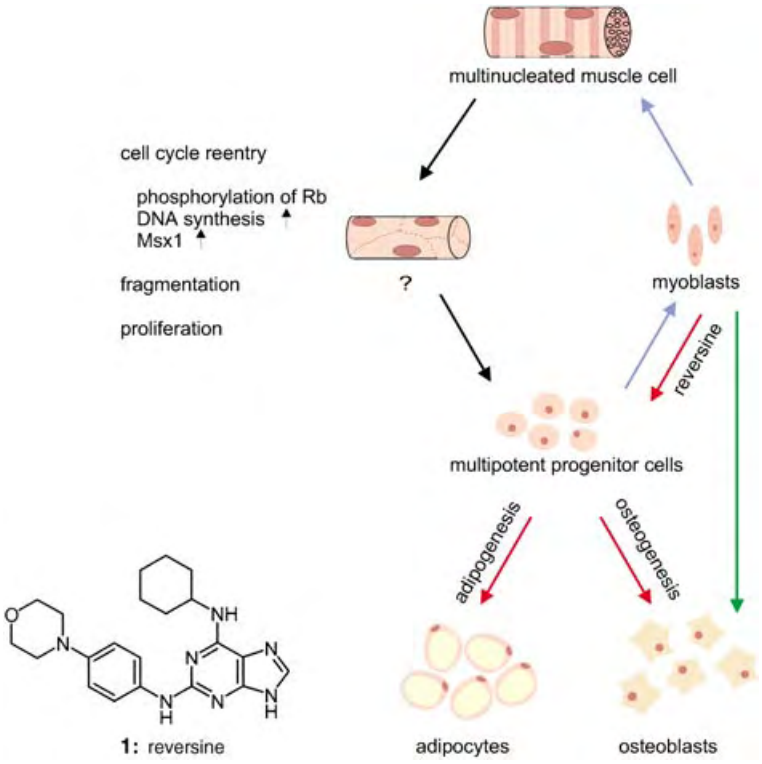


Figure 1. Dedifferentiation of myoblasts induced by reversine (**1**). Black arrows denote the dedifferentiation process, blue arrows ontogenesis. Molecular events during dedifferentiation are added as keywords on the left. Red arrows represent the experiment of Schultz and Ding et al.; an example of transdifferentiation is given by the green arrow. This diagram is based on refs.[11] and [15].

Of the library of 50000 discrete small molecules, 2-(4-morpholinoanilino)-6-cyclohexylaminopurine (**1**, Figure 1) was most active. Incubation with **1** and subsequent cultivation of the cells in osteogenesis-inducing medium led to a sevenfold increase in activity of alkaline phosphatase relative to the control (treatment with DMSO). Incubation with compound **1**, referred to as reversine, prevented myoblasts from forming multinucleated myotubes while the number of mononucleated cells increased. In the second approach 40% of the cells treated with reversine had the characteristic morphology of fat cells (oil droplets) and stained positive with oil red O.

Mouse myoblasts effected by reversine did not differentiate into myotubes but formed osteoblasts or adipocytes when treated with the appropriate medium. Control experiments without osteogenesis- or adipogenesis-inducing media did not cause differentiation; mononucleated cells were obtained. Therefore, a transdifferentiation effect of reversine was excluded. Reversine-treated lineage-committed myoblasts regained multipotency and were able to proliferate and redifferentiate like mesenchymal progenitor cells when exposed to appropriate growth conditions. So far, reversine is the first low-molecular-weight compound that can act as an external signal and induce lineage-committed mammalian cells to become multipotent progenitor cells.

If it is possible to induce dedifferentiation with small molecules, more complex animals like mammals may be able to replace lost parts by epimorphic regeneration. Clinical application of small molecules like reversine is still quite speculative. Nevertheless, reversine can be a useful tool to understand dedifferentiation on a molecular level. Analysis of structure–activity relationships may provide information about cellular targets, and affinity experiments with reversine could help to elucidate them. Whether reversine regulates the activity of a enzyme, for example, a kinase that directly or indirectly phosphorylates Rb and thus counteracts the G1–S block, is still not known. This explanation would be relevant for only one subprocess of dedifferentiation.

Schultz and Ding et al. used myoblasts in their experiments. These mononucleated cells are lineage committed in embryogenesis to become myotubes but still have characteristics of progenitor cells. It is unlikely that reversine alone can induce dedifferentiation of fully differentiated muscle cells. The signals triggering fragmentation of the multinucleated muscle cells of amphibians into mononucleated cells have not yet been identified. Myotubes of newts in which S-phase reentry was blocked by irradiation with X-rays or inhibition with CDK4 could still form mononucleated cells after transplantation into regenerating newt-limb blastemas. Thus, these cells could not have been formed by mitosis.[12] Dedifferentiation can be divided into two steps: fragmentation and reentry into the cell cycle and

 © 2004 Wiley-VCH Verlag GmbH & Co. KGaA, Weinheim

subsequent proliferation. Kinases are important regulators in activating cell division, and reversine probably interferes with them. The factors responsible for cell fragmentation, however, are still not known.

Many questions regarding dedifferentiation remain unanswered. Are fragmentation and cell division distinct processes, or are they mutually dependent? Which factors in serum cancel the cell cycle block? How important are the Msx genes? During embryogenesis members of this gene family prevent differentiation processes in order to promote proliferation of progenitor cells. Myotubes of mice forced to express Msx1 were able to dedifferentiate into multipotent cells.[13] Results obtained to date point out the complexity of the dedifferentiation process.

We can only anticipate the importance of dedifferentiation in regeneration in mammals. The latest results in the field of stem cell research indicate that the potential of regeneration in humans has been underestimated. So far adult stem cells have been found in more than 20 tissues including the brain. Moreover, some adult stem cells are thought not to be specialized for only one tissue; they may also have the capability to differentiate into cells of another tissue (plasticity). The mechanisms that lead to this plasticity are not fully understood, but dedifferentiation seems to be one possibility.[14] A single molecule like reversine cannot induce or control dedifferentiation, but it is a helpful tool in elucidating the basic molecular mechanisms.

Glossary

blastema	undifferentiated animal cells
CDK4	cyclin-dependent kinase 4; one of the kinases regulating the cell cycle
Cyclin D	protein that controls activity of CDK4
myoblast	progenitor cells of skeletal muscle cells
reparative regeneration	the regrowth of an organ, tissue, or part of the body that has been lost or damaged
retinoblastoma	malignant tumor of the retina. The Rb protein is not found in these cells, leading to a loss of proliferation control. Deficiency of the Rb gene (tumor suppressor gene) is associated with several malignant diseases
rhodamine–dextran	polymer tagged with the fluorescent dye rhodamine; because of its size it is used as a impermeable marker for cells.
transdifferentiation	reprogramming of tissue-specific stem cells to form differentiated cells of a different tissue type.

Published Online: July 8, 2004

[1] Aristotele (384–322 BC), *Historia animalium* (Ed.: I. Bekker), 552b, 10–17: Η σαλαμάνδρα ποιεί φανερόν: αυτη γάρ, ως φασί, διά του πυρός βαδίζουσα κατασβένυσι το πύρ. ("Now the salamander is a clear case in point… for this creature, so the story goes, not only walks through the fire but puts it out in doing so.")

[2] L. Spallanzani, *An Essay on Animal Reproductions* (translated from Italian by M. Maty), Becket & de Hondt, London, **1769**.
[3] D. Freudig in *Lexikon der Biologie* (Ed.: R. Sauermost), Spektrum, Heidelberg, **1999–2004**, 462–463.
[4] D. Palmes, H.-U. Spiegel, *Biomaterials* **2004**, *25*, 1601–1611.
[5] K. Echeverri, E. M. Tanaka, *Semin. Cell Dev. Biol.* **2002**, *13*, 353–360.
[6] D. C. Lo, F. Allen, J. P. Brockes, *Proc. Natl. Acad. Sci. USA* **1993**, *90*, 7230–7234.
[7] K. Echeverri, J. D. Clarke, E. Tanaka, *Dev. Biol.* **2001**, *236*, 151–164.
[8] J. W. Schneider, W. Gu, L. Zhu, V. Mahdavi, G. B. Nadal, *Science* **1994**, *264*, 1467–1471.
[9] E. M. Tanaka, A. A. F. Gann, P. B. Gates, J. P. Brockes, *J. Cell Biol.* **1997**, *136*, 155–165.
[10] L. Latella, A. Sacco, D. Pajalungra, M. Tianinen, D. Macera, M. D'Angelo, A. Felici, A. Sacchi, M. Crescenzi, *Mol. Cell Biol.* **2001**, *21*, 5631–5643.
[11] S. Chen, Q. Zhang, X. Wu, P. G. Schultz, S. Ding, *J. Am. Chem. Soc.* **2004**, *126*, 410–411.
[12] C. P. Velloso, A. Kumar, E. M. Tanaka, J. P. Brockes, *Differentiation* **2000**, *66*, 239–246.
[13] S. J. Odelberg, A. Kollhoff, M. T. Keating, *Cell* **2000**, *103*, 1099–1109.
[14] A. J. Wagers, I. L. Weissman, *Cell* **2004**, *116*, 639–648.
[15] S. J. Odelberg, *Semin. Cell Dev. Biol.* **2002**, *13*, 335–343.

 © 2004 Wiley-VCH Verlag GmbH & Co. KGaA, Weinheim

Solventless Reactions

Reactions Between or Within Molecular Crystals

Dario Braga and Fabrizia Grepioni*

Keywords:
crystal engineering · mechanochemistry · solid-state reactivity · solventless reactions · supramolecular chemistry

Reactions that occur within or between molecular crystals, in particular those reactions that are activated by mechanical methods, are reviewed. The focus is on processes (whether intrasolid or intersolid) that are controlled primarily by supramolecular bonding, such as template cycloadditions, formation of inclusion compounds, reactions between molecular crystals by the reassembling of noncovalent bonds, and the formation of complexes and coordination compounds. It is proposed that solvent-free mechanochemical methods, for example, cogrinding, milling, and kneading, represent viable "green" routes for the preparation of novel molecular and supramolecular solids.

1. Introduction

Herein we focus on recent developments in the synthesis of molecular and supramolecular compounds by means of reactions occurring in the solid state,[1] in particular on those activated mechanically. Reactions between or within solid reactants to yield a solid product are prototypical solvent-free reactions.[2] Since these reactions do not require recovery, storage, and disposal of solvents, they are attracting interest as a result of environmental and sustainability issues.[3] Besides being advantageous through the absence of solvents, solid–solid reactions often lead to very pure products and reduce the formation of solvate species.[4] Solid-state reactions activated by grinding or milling are known as mechanochemical reactions. To date, mechanochemical processes, and more generally solid-state reactions, have been little exploited in academic research, while they are commonly used industrially, mainly with inorganic solids and materials.[5]

Herein we will concentrate on solid-state preparatory methods used in basic research work on molecular systems where reactivity control is still largely based on trial and error. This is particularly true when product formation requires the breaking and forming of weak interactions between molecules (e.g. hydrogen bonds, donor–acceptor, and van der Waals host–guest interactions) or when packing effects are explicitly required to organize reactants into a suitable position for reactions that are controlled by the relative positions of the reactants in the solid. This latter type of processes can often be explained with the reaction-cavity concept, that is, reactivity takes place in a constrained environment generated by the surrounding molecules.[6] Solid-state reactions can also provide stereocontrolled access to molecules otherwise difficult or impossible to obtain from reactions in solution.[7]

The very concept of chemical reactivity between solids (and often within solids) is difficult to define. Indeed, it has been argued[2] that many solid-state syntheses, which occur with an intermediary liquid phase, such as a eutectic phase or a melt, cannot be regarded as genuine solid–solid reactions. The same applies to processes where destruction of the crystals is likely to take place prior to the reaction. This is the case, for instance, for reactions activated by cogrinding, since the heat generated in the course of the mechanochemical process can induce local melting at the interface between the different crystals, and also for reactions that require kneading of the reactants with small amounts of solvent (see Section 3.1.1). Although we agree that one has to be wary of the mechanistic implications of the different types of solid-state processes,[1–5] in the context of this review we have adopted a more utilitarian view: we will consider as solid-state reactions all solventless processes leading from a solid reactant to a solid product. We will, however, distinguish between two processes, intrasolid reactions, that is, reactions taking place between molecules within a crystal, and intersolid reactions, that is, reactions between different molecular crystals (see

[*] Prof. D. Braga
Dipartimento di Chimica
G. Ciamician
Università di Bologna
Via F. Selmi 2, 40126 Bologna (Italy)
Fax: (+39) 51-209-9456
E-mail: dario.braga@unibo.it
Prof. F. Grepioni
Dipartimento di Chimica
Università di Sassari
Via Vienna 2, 07100 Sassari (Italy)

 © 2004 Wiley-VCH Verlag GmbH & Co. KGaA, Weinheim DOI: 10.1002/anie.200301721

Figure 1). This distinction is, admittedly, artificial and only serves to aid the organization of the material in this article. A third, important, category of processes involving solids is represented by reactions between a crystalline solid and a

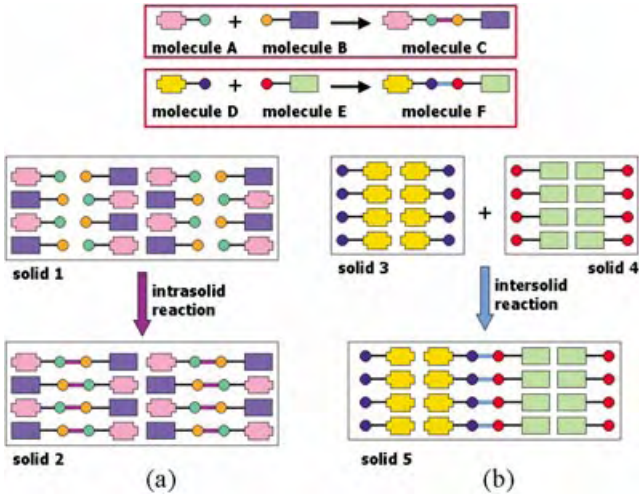


Figure 1. a) Intrasolid reactions take place between molecules within a crystal; b) intersolid reactions take place between different molecular crystals.

vapor to yield a new crystalline solid. Even though gas–solid reactions were among the first solventless processes to be studied (in 1884 the Italian scientist Pellizzari reported a study of the reaction of dry ammonia vapors with dried and pulverized phenols and carboxylic acids[8]) a systematic exploration of this field was only undertaken by Paul and Curtin in a series of elegant studies in the early 1970s.[8b]

Gas–solid reactions bear a close conceptual relationship to solid–solid reactions, but for reasons of space, they will only be briefly mentioned herein. For the same reason, we will not cover the classical reaction categories (thermal, oxidation, reduction, condensation, isomerization, etc.) but will focus mainly on those reactions activated by mechanical treatment of the reagents.



Dario Braga is Professor of Chemistry and Director of the Collegio Superiore of the University of Bologna. His awards include the Raffaello Nasini Prize from the Italian Society of Chemistry and the Federchimica Prize for his research on the intermolecular interactions in organometallic systems. His current research interests are in the crystal engineering exploitation of hydrogen-bonding interaction between ions and in solvent-free gas–solid and solid–solid reactions. He has published more than 300 papers and reviews and organized several international conferences on crystal engineering.

Fabrizia Grepioni is Associate Professor of General and Inorganic Chemistry at the University of Sassari. She received a Ph.D. from the University of Bologna. She was awarded the 1997 Raffaello Nasini Prize from the Italian Society of Chemistry for her studies on intermolecular interactions in organometallic solids. Her scientific interests are in the fields of crystal engineering and polymorphism.

The main disadvantage of solid-state studies is often the characterization of the structure of the reaction product, which is usually in the form of a polycrystalline powder whose characterization requires solid-state techniques,[9] such as, differential scanning calorimetry (DSC), thermogravimetric analysis (TGA), solid-state NMR spectroscopy (SSNMR), and X-ray powder diffraction (XPD), which are not always available. Moreover, the polycrystalline nature of the mechanochemical products prevents the use of single-crystal X-ray diffraction, while ab initio structure determination from powder diffraction is not yet amenable to routine work.[10] The lack of structural information can be overcome by finding a way to grow single crystals from the powdered material or to obtain single crystals of the same material by a different route.[11] When single crystals are available, comparison between calculated and measured powder diffraction patterns is possible.

On the other hand, carrying out solid–solid reactions usually only requires simple equipment. For most solid-state photochemically activated processes (such as, cyclizations and cycloadditions) a UV lamp, is often sufficient, while thermal treatment of reaction mixtures can be easily performed. We should not forget that the sun can be used as a source of UV energy, and making use of it is another example of green chemistry. In the case of mechanochemical reactions, a mortar and a pestle can often suffice, however ball-milling may be required and this technique also allows the use of inert or reactive gases or vacuum.[12]

2. Intrasolid Reactions

The basis of intrasolid reactions lies in two principal and too some extent contrasting ideas: molecular topochemistry and molecular mobility within the lattice. The topochemical approach began earlier and somewhat conditioned the development of the solid-state molecular (organic) chemistry that followed. About a century ago, Kohlschütter proposed that reactions in crystals had to proceed with the minimum atomic and molecular motion.[13] This idea led to the topochemical postulate that constituted the basis of Schmidt and co-workers work on solid-state [2+2] photochemically activated cycloaddition reactions.[14]

It is now clear that the topochemical postulate only accounts for part of the story: it works well in the cases of most cycloaddition reactions but cannot explain many solid–gas and solid–solid reactions that require molecules to travel through the reactant crystal. It has also been argued that crystal homogeneity (for example, the absence of amorphous material) could be much more relevant for the success of a solid-state process than the existence of suitable intermolecular separations in the crystal.[15]

After Schmidt and co-workers' pioneering attempts in the 1970s to apply reactions without solvents in preparative quantities,[14] Toda[16] and Kaupp and co-workers[17] were among the first to investigate in a systematic manner non-photochemical organic solid-state reactions for preparative purposes. Many solid-state reactions give a near quantitative yield of a single product and require high molecular mobility,

 © 2004 Wiley-VCH Verlag GmbH & Co. KGaA, Weinheim

so that the product phase forms at a reasonable rate. On the other hand, solid-state cycloaddition reactions can often be explained equally well on a topochemical basis. Since this subject has been recently reviewed,[18] we will confine our survey to examples of cycloaddition reactions controlled by supramolecular interactions or investigated directly on single crystals.

2.1. Solid-State Topochemical Reactions Driven by Supramolecular Interactions

Even though the investigation of cycloaddition reactions in the solid state dates back to Schmidt's work in the 1970s,[14a] it is in more recent times that the possibility of using noncovalent interactions to control the relative orientation of reactants has begun to be considered systematically. For instance, the participation of stacking interactions which are able to orientate the olefinic moieties in a geometry suitable for photochemical cycloaddition reactions, has been invoked by Coates et al. to explain the photodimerization and photopolymerization of mono- and di-olefins carrying phenyl and perfluorophenyl groups.[19]

Matsumoto et al. have reported the photodimerization of 2-pyridone in cocrystals with naphthalene-substituted monocarboxylic acids.[20] The reaction exploits the stacking effect of the naphthalene rings, which provides (as in the case for photopolymerization of mono- and di-olefins), a carbon–-carbon separation appropriate for [4+4] cycloaddition.[20a] Analogous methods have been used to for the photochemical polymerization of 1,3-diene monomers in *transoid* conformation.[20b]

An early development of the strategy based on the exploitation of directional supramolecular interactions to preassemble molecules for reaction in the solid state was by Feldman and Campbell, who exploited hydrogen-bonding interactions to enforce a particular stereo- and regiochemical outcome of the solid-state photo-cycloaddition of a naphthoic acid-derived cinnamic acid.[21]

In a conceptually similar approach Scheffer and coworkers have demonstrated that diamines can form double salts with a variety of *trans*-cinnamic acid derivatives. The locking in place of the double bonds steers the solid-state [2+2] photodimerization.[22]

MacGillivray's group has employed rigid bifunctional molecules,[23] such as 1,3-dihydroxybenzene[23a] and 1,8-naphthalenedicarboxylic acid,[23a] that function as linear templates to organize reactants, such as *trans*-1,2-bis(4-pyridyl)ethylene, through hydrogen bonds for single and multiple photoinduced [2+2] cycloadditions for the template-controlled synthesis of a 1,2,3,4-[(4-pyridyl)cyclobutane][23b] and also of paracyclophanes.[23a] Very recently, [*n*]ladderanes ($n=2$, 3) have been synthesized in the solid state by the UV irradiation of 2(5-methoxyresorcinol)·2(4-pyr-poly-*m*-ene) (where 4-pyr-poly-*m*-ene = *all-trans*-bis(4-pyridyl)poly-*m*-ene; $m=2$, 3; Figure 2).[23e]

Photodimerization reactions have been studied not only for crystalline powders but also (in fewer cases) in single crystals.

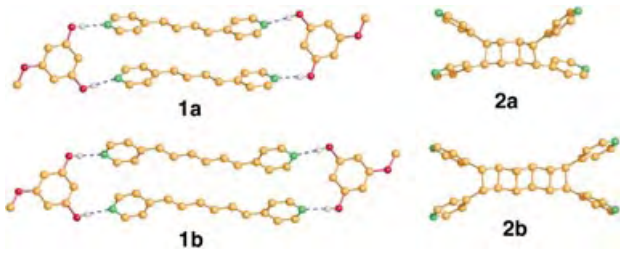


Figure 2. A recent example of template approach to solid-state cycloaddition reactions: 2(5-methoxyresorcinol)·2(4-pyr-poly-2-ene) (**1a**) and 2(5-methoxyresorcinol)·2(4-pyr-poly-3-ene) (**1b**) react in the solid-state to give [*n*]ladderanes ($n=3$, 5 for **2a** and **2b**, respectively).[23e]

Novak, Enkelman, and co-workers investigated the single-crystal-to-single-crystal (SC–SC) photodimerization of cinnamic acid and its thermally induced reverse reaction.[24] While in general, photodimerization reactions with irradiation in the range of the absorption maximum of the chromophore lead to the destruction of the single-crystalline nature of the sample, this is not so if the sample is irradiated with a wavelength corresponding to the tail of the chromophore absorption.[24b]

Irie et al. have shown that alternate irradiation (with UV and visible light) of single crystals of the diarylethene 1,2-bis(2,4-dimethyl-5-phenyl-3-thienyl)perfluorocyclopentene causes a photochemically reversible color change (from colorless to blue) associated with a reversible, intramolecular, photocyclization reaction.[25a] Upon irradiation with UV light, new steps appeared on the surface of the single-crystal and disappeared upon irradiation with visible light. These morphological changes of the surface were explained by changes in the molecular structure of the diarylethene molecules that are regularly packed in the single crystal. Irie's approach is reminiscent of Kaupp's earlier studies of the (albeit irreversible) morphological changes of photoreactive single-crystals of *trans*-cinnamic acids and anthracenes.[26]

More recently,[25b] single crystals of up to four different polymorphic modifications of another diarylethene compound, 1,2-bis(2-methyl-5-*p*-methoxyphenyl-3-thienyl)perfluorocyclopentene, were subjected to alternate UV and visible photoirradiation. It was shown that, although all the crystals undergo intramolecular photocyclization reactions with very similar photocyclization quantum yields (close to unity), the photocycloreversion quantum yields were different by as much as four times depending on the conformation of the closed-ring isomers in the crystals. With the same approach[25c] it has also been possible to achieve absolute asymmetric photocyclization of the achiral diarylethene derivative 1,2-bis(5*m*-formylphenyl-2-methyl-3-thienyl)perfluorocyclopentene in its chiral ($P2_1$) crystals with formation of either of the chiral closed-ring isomers depending on the absolute configuration of the crystals.

An example of a topotactic (topochemical) reaction that takes place without significant molecular rearrangements is provided by the enantioselective SC–SC photodimerization of coumarin or thiocumarin molecules in single crystals was reported by Toda and co-workers.[27]

 © 2004 Wiley-VCH Verlag GmbH & Co. KGaA, Weinheim

Molecular motion has been invoked to explain the SC–SC photochemically activated cycloaddition reaction of 2-benzyl-5-benzylidenecyclopentanone. The dimer molecules, once formed, move smoothly in the reactant crystal to generate the product crystal. The observations were substantiated by measuring eleven data sets (from single-crystal X-ray diffraction) on the same crystal undergoing the SC–SC transformation.[28]

The reactivity of 10-hydroxy-10,9-boroxophenanthrene in the solid state has been investigated and the mechanism of the solid-state reaction characterized by both X-ray diffraction and thermal analysis.[29] The reaction in which 10-hydroxy-10,9-boroxophenanthrene undergoes dimerization and dehydration to form a monohydride derivative, is different from that in solution.

Expanding on earlier results on the polymerization of preassembled triacetylene and triene monomers in the solid state,[30a,b] SC–SC topochemical polymerization of a terminal diacetylene has been exploited by Fowler and Lauher to obtain the corresponding conjugated polymer.[30c] The reaction is activated thermally by heating the single crystals at 150 °C for 24 h and the results imply that substantial molecular motion occurs.

In the context of solid-state polymerization in crystals the beautiful experiments recently reported by Lahav et al. must be mentioned.[31] Oligopeptides of 10–17 repeat units in length with homochiral sequences were generated by a topochemical reaction within racemic crystals of phenylalanine-*N*-carboxyanhydride. The polymerization reaction took place in crystals suspended in hexane and was initiated by *n*-butylammine. The combined X-ray diffraction study allowed a mechanistic hypothesis to account for the formation of the homochiral oligopeptide mixture (whose composition was determined by MALDI-TOF mass spectrometry) to be tested.

Recently, Scheffer has reported a method for asymmetric synthesis by organic photochemistry that is reminiscent of the Pasteur procedure for resolving racemic carboxylic acids and organic amines.[32] The method relies on the use of crystalline organic salts in which the enantioselectivity of a photochemical reaction of an achiral organic ion (for example, a carboxylate anion) is governed in the solid state by the presence of an optically pure counterion (for example, an optically active ammonium ion). Such optically pure counterions are termed "ionic chiral auxiliaries". Salts containing ionic chiral auxiliaries crystallize in chiral space groups, thus, providing the asymmetric environment necessary for chiral induction (Figure 3). Using this method, enantiomeric excess values approaching 100 % have been obtained in a wide variety of photochemical reactions.[32]

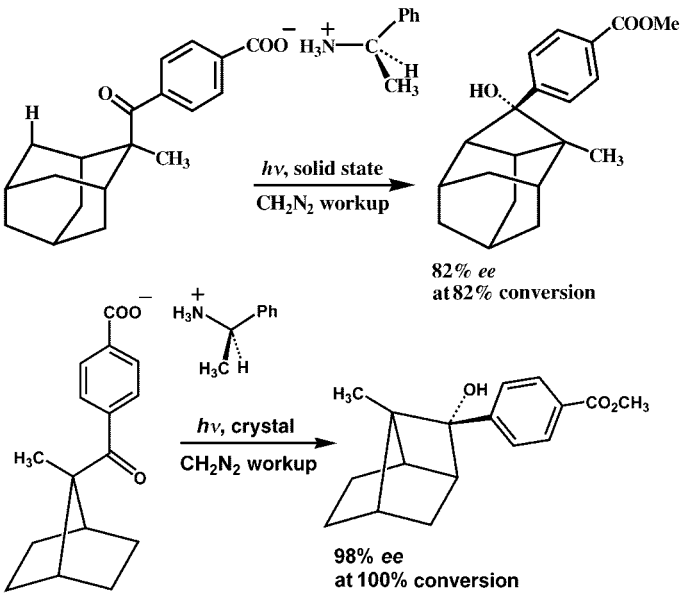


Figure 3. Schematic representation of the utilization of chiral auxiliaries to provide an asymmetric environment necessary for chiral induction.

3. Intersolid Reactions

For ease of presentation, this section has been organized into classes of intersolid processes that appear to be attracting the attention of an increasing number of groups.

Amongst the earliest pioneering investigations of intersolid reactions are those carried out by Rastogi et al. on reactions between naphthalene, phenanthrene, anthracene, naphthols, and other substituted hydrocarbons and picric acid in the solid state.[33] The kinetic studies showed that these reactions were diffusion controlled and that diffusion takes place by surface migration which favors small molecules of regular shape.

Etter et al. also carried out relevant earlier studies.[34–36] They investigated reactions between solids that could establish hydrogen-bonding interactions, thus demonstrating that cocrystals of hydrogen-bonded systems could be prepared not only by evaporation of a solution containing stoichiometric amounts of the components, but also by grinding the solid components together.[34] For example, 9-methyladenine and 1-methylthymine were shown to form cocrystals containing intermolecular hydrogen-bonded pairs in the solid state after the two pure components were simply ground together. Importantly, it was also shown that the cocrystals could form also in the presence of a third solid component.[35] In the case of 2-aminobenzoic acid, it was shown that polymorph interconversion could also be achieved by grinding.[36] The subjects of polymorphism and polymorph interconversion are covered in a recent book by Bernstein.[37]

As in the case of gas–solid reactions,[8b] Curtin and Paul also extensively studied reactions between crystals.[38] They showed, for instance, that a "mortar and pestle" technique applied to mixtures of quinone and hydroquinone allowed the preparation of unsymmetrical substituted quinhydrones, too unstable with respect to oxidation to be prepared in solution.

3.1. Mechanochemical Preparation of Cyclodextrin Inclusion Compounds

Cyclodextrins are natural molecules that have a remarkable capacity to form "host–guest" compounds thanks to their

 © 2004 Wiley-VCH Verlag GmbH & Co. KGaA, Weinheim

bowl-like structure,[39,40] and are amenable to treatment with guest molecules in solution as well as in the solid state.[41,42]

3.1.1. Inclusion Compounds Prepared by Cogrinding or Kneading

The 1:1 inclusion compound of tri-*O*-methyl-β-cyclodextrin and benzoic acid has been reported to be obtained by "shaking and grinding" an equimolar solid mixture of guest and host for about 3 h. Prolonged grinding transforms the inclusion crystals into an amorphous solid.[43]

The irradiation of *N*-methyl pyridone and *N*-ethyl pyridone that has been included in β-cyclodextrin yields the photocyclized product, chiral 2-azabicyclo-[2.2.0]-hex-5-en-3-ones, in almost 60% enantiomeric excess. The inclusion complex is readily made by mechanically mixing the solid host β-cyclodextrin and the solid guest pyridone.[44] The reaction can be regarded as a conceptual link between solid-state photocycloaddition discussed in the Section 2 and the mechanochemical preparation of cyclodextrins. A similar process has been described for the inclusion compound formed between β-cyclodextrin and coumarin. In this case the β-cyclodextrin dimer forms a "reaction nanotube" (Figure 4) in which the coumarin molecules undergo a photodimerization reaction in the solid state.[45]

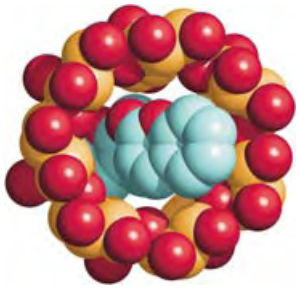


Figure 4. A space-filling representation of the inclusion compound between β-cyclodextrin (orange and red) and coumarin (predominantly turquoise).[45] Water molecules are not shown for clarity.

A very common method for the preparation of cyclodextrin inclusion compounds is the so-called kneading, that is, the grinding of powdered reactants in the presence of a minimal amount of solvent. Studies on kneading and on the development of laboratory/industrial "kneaders" (mainly of pharmaceutical powders) have been carried out.[46,47]

The binary β-cyclodextrin–bifonazole compounds of composition $(\beta\text{-cyclodextrin})_x$–bifonazole ($x = 1, 2,$ or 4) are made on a preparatory scale by kneading.[48] In a similar manner, β-cyclodextrin inclusion compounds of ketoprofen,[49] ketoconazole,[50] and carbaryl[50] have been obtained by a solid-state reaction at room temperature in the presence of saturated water vapor.

It is reasonable to suggest that the preparation of inclusion compounds by kneading cannot be regarded as a genuine solid–solid process, since solvent, though in a trace amount, is involved. We would argue in favor of it being a solid–solid reaction owing to the catalytic function of this solvent and in view of the fact that it is not retained within the crystalline products (but see also Section 3.3).

3.2. Mechanochemical Reactions Between Molecular Crystals

Useful introductions into the recent literature of organic solid-state reactions, including those activated mechanochemically have been published.[1c,51]

In an early study Toda and Miyamoto investigated the formation of charge-transfer complexes by grinding tetracyanoquinodimethane and tetrathiafulvalene or tetrathianaphthacene powders. The resulting complexes showed similar electrical conductivity to those prepared by conventional recrystallization methods suggesting that the donor and acceptor molecules can move freely in the solid state to form the charge-transfer stacks.[52a] An example of a charge-transfer complex that can be obtained by both solution crystallization[52b] and by cogrinding[52a] is shown in Figure 5.

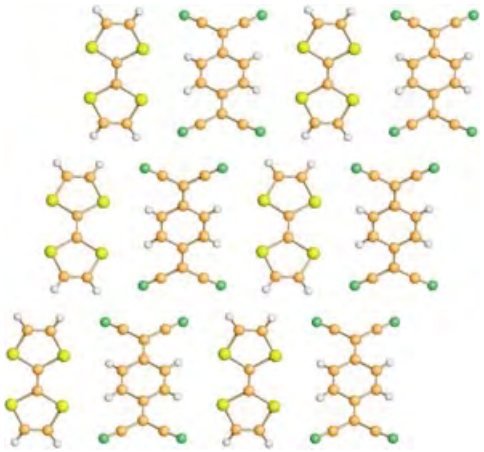


Figure 5. The crystal packing of the charge-transfer compound between tetrathiafulvalene and tetracyanoquinodimethane.[52b] The same compound was obtained by grinding together the two components.[52a] C orange, N green, S yellow, H gray.

More recently, Toda et al. have reported the photoirradiation of a 2:1 inclusion crystal of 2-pyridone and biphenyl-2,2′-dicarboxylic acid in the solid state. The inclusion crystallization of host and guest molecules is achieved mechanochemically. The subsequent photoirradiation gave the *trans-anti*-dimer of 2-pyridone in quantitative yield.[53] Since photodimerization follows the inclusion complexation of the two components, the host compound is functioning as a catalyst.[53]

Combining mechanochemistry with distillation techniques allows enantiomers to be separated by distillation, provided a chiral host compound is present. On mixing a powdered chiral host and a volatile racemic guest compound, one enantiomer forms a complex with the chiral host while the other does not. Upon heating the mixture in vacuo, the not-complexed enantiomer distils at a lower temperature than the enantiomer which is included by the host, thus allowing easy separation of enantiomers of various racemic guest compounds.[54]

Kuroda et al. have shown that cogrinding of crystals of racemic bis-β-naphthol and benzoquinone produces a novel crystal adduct that is structurally distinct from adducts obtained from solution or melt techniques.[55a] Chiral recog-

 © 2004 Wiley-VCH Verlag GmbH & Co. KGaA, Weinheim

nition was found to operate during this process demonstrating that molecules can exert chiral discrimination in the solid state by changing their relative location and hydrogen-bonding partners.[55b] Three-component adduct crystals of chiral 6,6′-dibromo-1,1′-bi-2-naphthol, benzoquinone, and biphenyl, were also produced from both solid-grinding and solution crystallization.[55c]

The mechanochemical formation of hydrogen-bonded cocrystals between sulfonamide (4-amino-*N*-(4,6-dimethylpyrimidin-2-yl)benzenesulfonamide) and aromatic carboxylic acids was investigated by Caira et al.[56] The kinetics of the solid-state reactions were measured by powder diffraction, and it was shown that sulfonamide selectively reacts with 2-aminobenzoic acid even when this compound is part of a binary mixture with other acids. The molecular recognition towards 2-aminobenzoic acid is so efficient that it is possible to replace 2-hydroxybenzoic acid from a cocrystal.

We have reported[57] that the manual grinding of the organometallic dicarboxylic acid complex $[Fe(\eta^5\text{-}C_5H_4COOH)_2]$ with a variety of solid bases, such as 1,4-diazabicyclo[2.2.2]octane, 1,4-phenylenediamine, piperazine, *trans*-1,4-cyclohexanediamine, and guanidinium carbonate, generates the corresponding organic–organometallic adducts quantitatively. In the case of the adduct $[HC_6N_2H_{12}][Fe(\eta^5\text{-}C_5H_4COOH)(\eta^5\text{-}C_5H_4COO)]$, not only is it possible to remove the base by a mild thermal treatment and thus regenerate the structure of the starting dicarboxylic acid, but the same organic–organometallic adduct can also be obtained by a (much slower) vapor uptake process (Figure 6).[58] The results imply the that the process involves breaking and reassembling hydrogen-bonded networks, conformational change from *cis* to *trans* of the COO/COOH groups on the ferrocene diacid, and proton transfer from acid to base.

The mechanical mixing of solid dicarboxylic acids of various chain lengths $HOOC(CH_2)_nCOOH$ ($n = 1$–7) with solid 1,4-diazabicyclo[2.2.2]octane, $C_6H_{12}N_2$, to generate the corresponding salts or cocrystals of formula $\{N(CH_2CH_2)_3N\}\text{-}H\text{-}\{OOC(CH_2)_nCOOH\}$ ($n = 1$–7) has been investigated. The reactions implied transformation of interacid O–H···O bonds into hydrogen bonds of the form O–H···N between acid and base. The nature (whether neutral O–H···N or charged $^-O\cdots H\text{–}N^+$) of the hydrogen bond was established by means of solid state NMR measurements.[66]

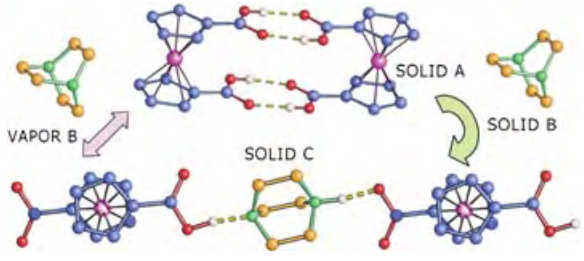


Figure 6. In $[HC_6H_{12}N_2][Fe(\eta^5\text{-}C_5H_4COOH)(\eta^5\text{-}C_5H_4COO)]$ the $[HC_6H_{12}N_2]^+$ ions act as bridges between acid sandwich molecular anions in *transoid* conformation. The adduct can be prepared both by cogrinding of the crystalline base $C_6H_{12}N_2$ and acid $[Fe(\eta^5\text{-}C_5H_4COOH)_2]$ or by vapor uptake. The formation is reversible. C blue or orange, O red, N green, Fe purple.

3.2.1. Seeding

The use of preformed microcrystals of the desired phase, that is, seeding, has been instrumental in the growth of crystals of suitable size for single-crystal X-ray diffraction in order to confirm, by a comparison of calculated and observed powder diffraction patterns, that the same phase obtained from solution crystallization and that yielded by solid–solid mixing processes has been obtained (Figure 7).[59]

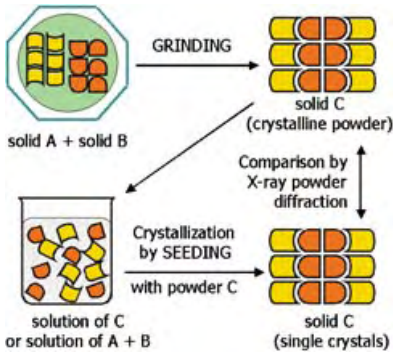


Figure 7. Schematic representation of the procedure adopted to characterize products of mechanochemical treatments. The solid yielded by grinding reactants in a mortar is compared by X-ray powder diffraction with the solids obtained through crystallization by seeding of a solution of the ground powder of the adduct.

Seeding procedures are commonly employed in the pharmaceutical industry to make sure that the desired crystal form is always obtained from a preparative process.[60] It is important to appreciate that seeding often prevents the formation of kinetically favored products.

Seeding can also be exploited to induce crystallization of an otherwise uncrystallizable material by using "seeds" of isostructural or quasi-isostructural species that crystallize well.[61] Seeding has been used in experiments on shape mimicry[62] and on heteromolecular seeding[63] in which near isostructural compounds can be used to template crystallization in less-accessible, elusive, or desired crystal forms. For instance, chiral cocrystals of tryptamine and hydrocinnamic acid have also been prepared by crystallization in the presence of seeds of different chiral crystals.[64] Of course, unintentional seeding may also alter the crystallization process in an undesired manner.[65,37]

3.3. Making Metal–Ligand Bonds by Mechanochemical Methods

There are not many examples of the utilization of mechanochemical procedures in coordination chemistry. Balema et al. have shown that the *cis*-platinum complexes *cis*-$[(Ph_3P)_2PtCl_2]$ and *cis*-$[(Ph_3P)_2PtCO_3]$ can be prepared mechanochemically from solid reactants in the absence of solvent. *cis*-$[(Ph_3P)_2PtCl_2]$ was obtained in 98% yield after ball-milling of polycrystalline $PtCl_2$ and Ph_3P, while the mechanically induced solid-state reaction of *cis*-$[(Ph_3P)_2PtCl_2]$ with an excess of anhydrous K_2CO_3 produced

 © 2004 Wiley-VCH Verlag GmbH & Co. KGaA, Weinheim

cis-$[(Ph_3P)_2PtCO_3]$ in 70% yield.[67] The same group has also investigated, by means of solid-state ^{31}P NMR spectroscopy and XPD, the formation of phosphonium salts during the high-energy ball-milling of triphenylphosphane with solid organic bromides.[68] In the case of 2-bromo-2-phenylacetophenone the solvent-free, mechanically induced transformation results in the formation of the thermodynamically favorable C-phosphorylated product, which in solution, is only obtained together with other products.[68] The mechanical preparation of phosphorus ylides has also been reported.[69]

Steed, Nichols, and Raston have explored the use of mechanochemistry in the synthesis of extended supramolecular arrays.[70a] Grinding of $Ni(NO_3)_2$ with 1,10-phenanthroline (phen) resulted in the facile preparation of $[Ni(phen)_3]^{2+}$ accompanied by a dramatic and rapid color change. Addition of the solid sodium salt of tetrasulfonatocalix[4]arene (tsc) gives two porous π-stacked supramolecular arrays $[Ni(phen)_3]_2[tsc^{4-}]\cdot n H_2O$ and the related $[Na(H_2O)_4(phen)][Ni(phen)_3]_4[tsc^{4-}][tsc^{5-}]\cdot n H_2O$ depending on stoichiometry (Figure 8).[70a]

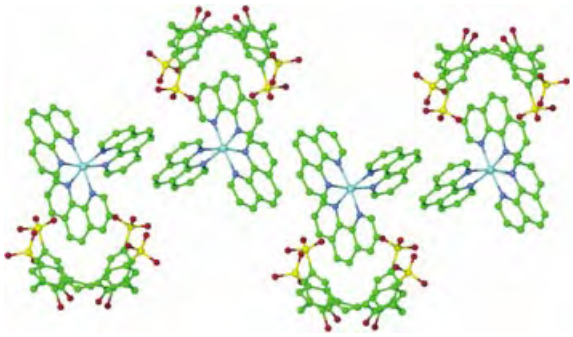


Figure 8. An infinite π-stacked chain in $[Ni(phen)_3]_2[tsc^{4-}]\cdot n H_2O$ showing the inclusion of one of the two $[Ni(phen)_3]^{2+}$ ions within the cavity of a *p*-sulfonatocalix[4]arene^{4-} ion. Ni turquoise, N blue, C green, S yellow, O red. Reproduced with permission from ref. [70a]

Grinding copper(II) acetate hydrate with 1,3-di(4-pyridyl)propane (dpp) gives a gradual color change from blue to blue-green over about 15 min. The resulting material was shown by solid-state NMR spectroscopy to comprise a 1D coordination polymer with water-filled pores. The same host structure, $[\{Cu(OAc)_2\}_2(\mu\text{-dpp})]_n$ could be obtained from a solution containing methanol, acetic acid or ethylene glycol as guest species.[70b]

In a recent study, Otera and co-workers have shown that the supramolecular self-assembly of a number of complexes is dramatically accelerated under solvent-free conditions leading to the formation of two- or three-dimensional structures and even double helicates.[71] For instance, reaction of $[(ethylendiamine)Pt(NO_3)_2]$ with 4,4′-bipyridine to form molecular squares takes more than 4 weeks at 100 °C, while the reaction is brought to completion within 10 min at room temperature by mixing the reactants without solvents.[71] Double-helix formation under solvent-free conditions has also been achieved by treating chiral oligo(bipyridine) copper complexes with $[(CH_3CN)_4Cu]PF_6$. The progress of the reaction was monitored by measuring solid-state CD-spectra, which showed that after grinding for 5 min the desired helicate had been obtained. These results are particularly valuable because not only do they show that solvent-free complexation can be easily achieved, even with relatively complex systems, but also that the reactions are much faster than in solution.

We have shown that the organometallic zwitterion $[Co^{III}(\eta^5\text{-}C_5H_4COOH)(\eta^5\text{-}C_5H_4COO)]$ (which forms hydrogen-bonded chains in the solid state) reacts quantitatively in the solid state with a number of crystalline alkali salts MX ($M = K^+$, Rb^+, Cs^+, NH_4^+; $X = Cl^-$, Br^-, I^-, PF_6^- though not in all permutations of cations and anions) with formation of supramolecular networks of formula $[\{Co^{III}(\eta^5\text{-}C_5H_4COOH)(\eta^5\text{-}C_5H_4COO)\}_2]\cdot M^+X^-$.[72] The fundamental repeating unit of the network $[Co^{III}(\eta^5\text{-}C_5H_4COOH)(\eta^5\text{-}C_5H_4COO)]_2\cdot K^+Br^-$, results from the encapsulation of the K^+ ions within a cage of zwitterion molecules, which are held together as pairs of dimers by the formation of O–H···O hydrogen bonds, with the Br^- ions forming layers in between the cationic complexes. The reactions imply an extensive solid-state rearrangement and the breaking and forming of O–H···O hydrogen-bonding interactions between the organometallic molecules. The solid-state complexation of alkali cations by the organometallic zwitterion has been described as a special kind of solvation process taking place in the solid state (see Figure 9). For some of the alkali salts the

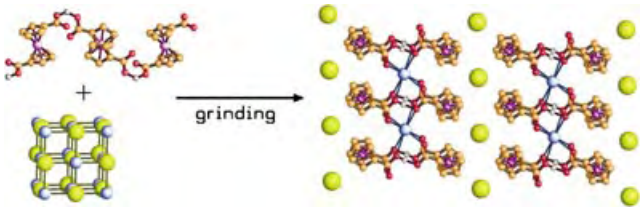


Figure 9. The organometallic zwitterion $[Co^{III}(\eta^5\text{-}C_5H_4COOH)(\eta^5\text{-}C_5H_4COO)]$ reacts quantitatively on grinding as a solid polycrystalline phase with a number of crystalline alkali salts MX ($M = K^+$, Rb^+, Cs^+, NH_4^+; $X = Cl^-$, Br^-, I^-, PF_6^- forming supramolecular complexes of formula $[\{Co^{III}(\eta^5\text{-}C_5H_4COOH)(\eta^5\text{-}C_5H_4COO)\}_2]\cdot M^+X^-$. Blue M^+, yellow X^+, purple Co, orange C.

mechanochemical complexation was speeded up by kneading, that is, by grinding the salts in the presence of a catalytic amount of water. Toda and co-workers demonstrated that the kinetics of cocrystal formation by grinding could be significantly improved by the addition of small amounts of appropriate solvent.[73]

The (serendipitous) discovery of our solid–solid reaction occurred while preparing KBr pellets of $[Co^{III}(\eta^5\text{-}C_5H_4COOH)(\eta^5\text{-}C_5H_4COO)]$ for IR spectroscopy.[73] This process brings about a well known—and possibly overlooked—class of mechanochemical reactions, those between the alkaline halogenides, such as KBr, CsI, used for IR pellets, and species, such as molecules carrying COOH groups, which may cause an alteration of the absorption frequencies with respect to those measured in solution or Nujol.[74] The mechanochemical reactions that take place when milling and pressing analites with KBr to form disks for IR experiments has been recently reviewed by Fernandez-Bertran and

 © 2004 Wiley-VCH Verlag GmbH & Co. KGaA, Weinheim

Reguera.[75a] The same group has extensively studied the interaction of alkali salts with inorganic and organic acids.[75] In the case of alkali fluorides it has been shown that milling leads to proton transfer and to formation of KHF_2, while the reactivity of fluorides follows the order $KF > NH_4F > NaF > LiF–CaF_2$.[75b,c]

3.4. Making Covalent Bonds by Mechanochemical Methods

The formation of covalent bonds can also be achieved by mechanochemical methods. Kaupp et al. have reported the quantitative preparation of hydrated azomethines by grinding together solid anilines with solid benzaldehydes without passing through liquid phases.[76] The solid-state mechanisms have been elucidated by atomic force microscopy (AFM) and in part by scanning near-field optical microscopy (SNOM). The results indicate long-distance migration of the aldehydes into the lattice of the aniline derivatives.[76]

Komatsu et al. have demonstrated that mechanochemical solvent-free techniques are particularly advantageous when applied to fullerenes, as the poor solubility of these compounds usually requires large quantities of solvent for reaction in solution.[77] Moreover, the possibility of direct contact between the nonsolvated reactants affords reaction pathways that are not accessible, or difficult to attain, in solution. In the cases of the reaction of fullerene with KCN, KOAc, and K_2CO_3, the solid-state process selectively gives the [2+2] dumbbell-shaped dimer C_{120},[77] whereas in the solution-phase reaction with KCN, C_{60} is simply cyanated.

In other examples, the soild-state reaction of pentacene with C_{60} gives a 2:1 adduct while the same reaction in solution only gives the 1:1 adduct,[78a] and in the reaction of C_{60} with phthalazine (2,3-diazanaphthalene), a new fullerene dimer with a bicyclic framework is formed under the mechanochemical solid-state reaction conditions.[78b] Various types of fullerene dimers (and even trimers) obtained "only" by the solid state mechanochemical reactions[79,80] are shown in Figure 10.

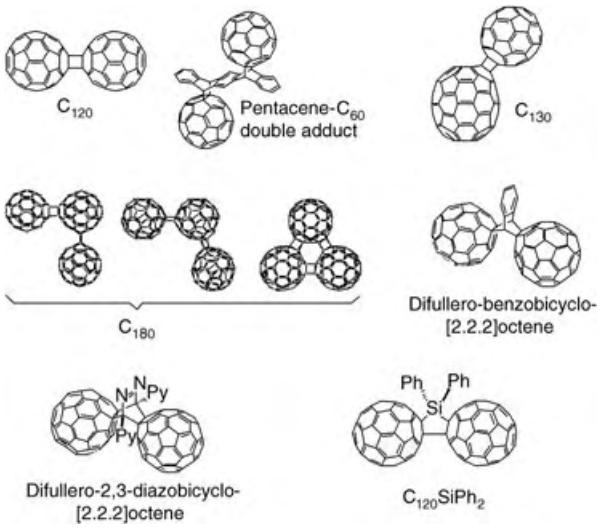


Figure 10. Fullerene dimers and trimers obtained by mechanochemical solid-state treatment of fullerenes.[78–80]

4. Conclusions and Outlook

Thirty years ago, Paul and Curtin wrote: "almost all organic compounds can be prepared in the crystalline state, and the majority are crystalline under ambient conditions. It is surprising, therefore, that although organic reactions in the solid state have been reported regularly since before the turn of the century [the 20th century] solid-state chemistry has frequently been regarded as a specialty of little interest to the practicing organic chemist"[38]

Although research work in this area has never stopped, it has also lacked popularity and has remained confined to a few connoisseurs. The reasons are practical and cultural. The structural characterization of solid products is more difficult than in solution, and it is only recently that powder diffraction methods have become widely accessible outside the crystallographic community. Similar considerations apply to solid-state NMR spectroscopic techniques. The cultural aspect goes back to the "chemistry in solution principle": organic synthesis (hence organometallic and much of coordination chemistry) takes place in solution. This is what has been taught for decades (and still is) in undergraduate chemistry courses. In molecular chemistry, reactions between solids, or between solids and gases are often mentioned as oddities or curiosities, while mechanical methods are felt as fundamentally "nonchemical".

The results discussed herein demonstrate that this attitude is rapidly changing and alternative solid-state preparative routes to both new and old compounds are becoming increasingly important. This is not to say that solid-state reactions are, or will ever be, of equal importance as those in solution for large scale preparations, but rather that solvent-free conditions should be systematically explored, which is even more important now that chemists are (more actively than in the past) seeking environmentally friendly, and possibly cheaper, processes. Furthermore, solid-state synthetic procedures are often viable alternative routes to the bottom-up construction of molecular materials from molecular or ionic building blocks, which is at the core of molecular crystal engineering.[81]

We have confined our survey to two classes of solid-state reactions, those taking place between molecules within a crystal (intrasolid reactions) and those taking place between different molecules in different crystals (intersolid reactions). The distinction is purely practical and carries no general implications for the reaction mechanisms (which we have not discussed). However, it can be argued that, while intrasolid reactions, for example, cycloadditions, are molecular reactions involving covalent bond breaking/forming that occur in a confined environment, in intersolid reactions the mechanical stress produced by grinding or milling together two distinct molecular solids fractures the crystals, increases surface area, and facilitates interpenetration and reaction depending on the ability of molecules to diffuse through the crystal surfaces. From this viewpoint, intersolid reactions between molecular crystals can be conceptually related to the

 © 2004 Wiley-VCH Verlag GmbH & Co. KGaA, Weinheim

uptake of a vapor from a molecular solid to form a new crystalline solid.

On approaching the types of processes described herein, it is essential to keep in mind that intersolid reactions are not necessarily reactions in the solid state, as mechanical stress may cause local melting, cogrinding may form an intermediate eutectic phase, and kneading probably generates locally hypersaturated solutions from which crystals of the new phase nucleate. In all these cases the crystal lattice is destroyed and reformed through recrystallization.

Our survey criterion has been an utilitarian one: we have chosen examples of solid-state reactions involving molecular crystals that lead from a solid reactant (or a mixture of solid reactants) to a molecular crystal product. In such processes hydrogen bonds, π-stacking, van der Waals, and ion-pairing interactions are either exploited to assemble molecules in the desired geometry (e.g. template cycloaddition or chiral induction) or broken and formed through the reaction process leading to the formation of supramolecular compounds, such as inclusion compounds, or hybrid molecular crystals. This latter class of reactions also comprises solid-state complexations, such as the formation of charge-transfer and coordination compounds.

It is unquestionable that solvent-free conditions are cheaper (owing to the savings in solvents, resources, energy, waste disposal, and of time) and are highly preferable in the quest for environmentally sustainable processes, that is, for green chemistry applications. It is tempting to consider solvent-free reactions, between molecular crystals or within molecular crystals, which occur exclusively by breaking and forming of noncovalent intermolecular bonding interactions as belonging to an expanding new area of supramolecular green chemistry.

Financial support by MIUR (FIRB and COFIN) and by the Universities of Bologna and Sassari is acknowledged. We wish to thank K. Komatsu, L. MacGillivray, J. Scheffer, F. Toda, J. Steed, L. Nassimbeni, M. Caira, G. Kaupp, L. Maini, and M. Polito for many useful suggestions at various levels and at various occasions during the preparation of this review.

Received: October 10, 2003 [M1721]
Published Online: June 21, 2004

[1] a) D. Bradley, *Chem. Br.* **2002**, 12, September, 42; b) K. Tanaka, F. Toda, *Chem. Rev.* **2000**, *100*, 1025; c) K. Tanaka, *Solvent-free Organic Synthesis*, Wiley-VCH, Weinheim, **2003**.

[2] a) G. W. V. Cave, C. L. Raston, J. L. Scott, *Chem. Commun.* **2001**, 2159; b) G. Rothenberg, A. P. Downie, C. L. Raston, J. L. Scott, *J. Am. Chem. Soc.* **2001**, *123*, 8701.

[3] P. T. Anastas, J. C. Warner, *Green Chemistry: Theory and Practice*, Oxford University Press, New York, **1998**.

[4] G. Kaupp, *CrystEngComm* **2003**, *5*, 117.

[5] a) V. V. Boldyrev, K. Tkacova, *J. Mater. Synth. Process.* **2000**, *8*, 121; b) J. F. Fernandez-Bertran, *Pure Appl. Chem.* **1999**, *71*, 581.

[6] a) T. Luty, C. J. Eckhardt, *J. Am. Chem. Soc.* **1995**, *117*, 2441; b) Y. Ohashi, *Acc. Chem. Res.* **1988**, *21*, 268; c) N. J. Coville, D. C. Levendis, *Eur. J. Inorg. Chem.* **2002**, 3067.

[7] See for example: a) S. Ariel, S. Askari, J. R. Scheffer, J. Trotter, *J. Org. Chem.* **1989**, *54*, 4324; b) P. R. Pokkuluri, J. R. Scheffer, J. Trotter, M. Yap, *J. Org. Chem.* **1992**, *57*, 1486; c) E. Cheung, T. Kanf, J. R. Scheffer, J. Trotter, *Chem. Commun.* **2000**, 2309.

[8] a) G. Pellizzari, *Gazz. Chim. Ital.* **1884**, *14*, 362; b) I. C. Paul, D. Y. Curtin, *Science* **1975**, *187*, 19.

[9] A. K. Cheetham, P. Day, *Solid State Chemistry Techniques*, Clarendon, Oxford, **1987**.

[10] a) K. D. M. Harris, M. Tremayne, *Chem. Mater.* **1996**, *8*, 2554; b) K. D. M. Harris, M. Tremayne, B. M. Kariuki, *Angew. Chem.* **2001**, *113*, 1674; *Angew. Chem. Int. Ed.* **2001**, *40*, 1626.

[11] a) D. Braga, F. Grepioni, *Chem. Soc. Rev.* **2000**, *29*, 229; b) D. Braga, F. Grepioni in *Crystal Design*, *Structure and Function. Perspectives in Supramolecular Chemistry*, *Vol. 7* (Ed. G. R. Desiraju), Whiley, Chichester, UK, **2003**.

[12] a) G. Kaupp, J. Schmeyers, *Chem. Eng. Sci.* **2002**, *57*, 763; b) G. Kaupp, M. R. Naimi-Jamal, H. Ren, H. Zoz, *Chem. Tech.* **2002**, *31*, 206.

[13] V. Kohlschütter, *Z. Anorg. Allg. Chem.* **1918**, *105*, 121.

[14] a) G. M. J. Schmidt, *Pure Appl. Chem.* **1971**, *43*, 647; b) M. D. Cohen, *Angew. Chem.* **1975**, *87*, 439; *Angew. Chem. Int. Ed. Engl.* **1975**, *14*, 386; c) M. D. Cohen, G. M. J. Schmidt, *J. Chem. Soc.* **1964**, 1996; d) G. A. Elgavi, B. S. Green, G. M. J. Schmidt, *J. Am. Chem. Soc.* **1973**, *95*, 2058.

[15] M. A. Garcia-Garibay, *Acc. Chem. Res.* **2003**, *36*, 491.

[16] F. Toda, *Top. Curr. Chem.* **1987**, *140*, 43.

[17] a) G. Kaupp, D. Matthies, *Chem. Ber.* **1986**, *119*, 2387; b) G. Kaupp, J. Schmeyers, J. Boy, *Chemosphere* **2001**, *43*, 55; c) G. Kaupp, J. Schmeyers, J. Boy, *Tetrahedron* **2000**, *56*, 6899; d) G. Kaupp in *Comprehensive Supramolecular Chemistry*, *Vol. 8* (Ed. J. E. D. Davies), Elsevier, Oxford, **1996**, pp. 381–423.

[18] L. R. MacGillivray, *CrystEngComm* **2002**, *4*, 37.

[19] G. W. Coates, A. R. Dunn, L. M. Henling, J. W. Ziller, E. B. Lobkovsky, R. H. Grubbs, *J. Am. Chem. Soc.* **1998**, *120*, 3641.

[20] a) T. Odani, A. Matsumoto, *CrystEngComm* **2002**, *4*, 467; b) A. Matsumoto, K. Sada, K. Tashiro, M. Miyata, T. Tsubouchi, T. Tanaka, T. Odani, S. Nagahama, T. Tanaka, K. Inoue, S. Saraghi, S. Nakamoto, *Angew. Chem.* **2002**, *114*, 2612; *Angew. Chem. Int. Ed.* **2002**, *41*, 2502.

[21] K. S. Feldman, R. F. Campbell, *J. Org. Chem.* **1995**, *60*, 1924.

[22] a) Y. Ito, B. Borecka, J. Trotter, J. R. Scheffer, *Tetrahedron Lett.* **1995**, *36*, 6083; b) Y. Ito, B. Borecka, G. Olovsson, J. Trotter, J. R. Scheffer, *Tetrahedron Lett.* **1995**, *36*, 6087.

[23] a) L. R. MacGillivray, J. L. Reid, J. A. Ripmeester, *J. Am. Chem. Soc.* **2000**, *122*, 7817; b) G. S. Papaefstathiou, A. J. Kipp, L. R. MacGillivray, *Chem. Commun.* **2001**, 2462; c) D. B. Varshney, G. S. Papaefstathiou, L. R. MacGillivray, *Chem. Commun.* **2002**, 1964; d) T. Friščić, L. R. MacGillivray, *Chem. Commun.* **2003**, 1306; e) X. Gao, T. Friščić, L. MacGillivray, *Angew. Chem.* **2004**, *116*, 234; *Angew. Chem. Int. Ed.* **2004**, *43*, 232.

[24] a) K. Novak, V. Enkelmann, G. Wegner, K. B. Wagener, *Angew. Chem.* **1993**, *105*, 1678; *Angew. Chem. Int. Ed. Engl.* **1993**, *32*, 1614; b) V. Enkelmann, G. Wegner, K. Novak, K. B. Wagener, *J. Am. Chem. Soc.* **1993**, *115*, 10390.

[25] a) M. Irie, S. Kobatake, M. Horichi, *Science* **2001**, *291*, 1769; b) M. Morimoto, S. Kobatake, M. Irie, *Chem. Eur. J.* **2003**, *9*, 621; c) S. Yamamoto, K. Matsuda, M. Irie, *Angew. Chem.* **2003**, *115*, 1674; *Angew. Chem. Int. Ed.* **2003**, *42*, 1636.

[26] a) G. Kaupp, *Angew. Chem.* **1992**, *104*, 606; *Angew. Chem. Int. Ed. Engl.* **1992**, *31*, 592; b) G. Kaupp, *Angew. Chem.* **1992**, *104*, 609; *Angew. Chem. Int. Ed. Engl.* **1992**, *31*, 595.

[27] K. Tanaka, F. Toda, E. Mochizuki, N. Yasui, Y. Kai, I. Miyahara, K. Hirotsu, *Angew. Chem.* **1999**, *111*, 3733; *Angew. Chem. Int. Ed.* **1999**, *38*, 3523.

[28] I. Turowska-Tyrk, *Chem. Eur. J.* **2001**, *7*, 3401.

[29] L. M. Greig, B. M. Kariuki, S. Habershon, N. Spencer, R. L. Johnston, K. D. M. Harris, D. Philp, *New J. Chem.* **2002**, *26*, 701.

[30] a) J. Xiao, M. Yang, J. W. Lauher, F. W. Fowler, *Angew. Chem.* **2000**, *112*, 2216; *Angew. Chem. Int. Ed.* **2000**, *39*, 2132; b) F. W.

 © 2004 Wiley-VCH Verlag GmbH & Co. KGaA, Weinheim

Fowler, J. W. Lauher, *J. Phys. Org. Chem.* **2000**, *13*, 850; c) X. Ouyang, F. W. Fowler, J. W. Lauher, *J. Am. Chem. Soc.* **2003**, *125*, 12400.
[31] J. G. Nery, G. Bolbach, I. Weissbuch, M. Lahav, *Angew. Chem.* **2003**, *115*, 2207; *Angew. Chem. Int. Ed.* **2003**, *42*, 2157.
[32] a) J. R. Scheffer, *Can. J. Chem.* **2001**, *79*, 349; b) B. O. Patrick, J. R. Scheffer, C. Scott, *Angew. Chem.* **2003**, *115*, 3905; *Angew. Chem. Int. Ed.* **2003**, *42*, 3775.
[33] a) R. P. Rastogi, P. S. Bassi, S. L. Chadha, *J. Phys. Chem.* **1963**, *67*, 2569; b) R. P. Rastogi, N. B. Singh, *J. Phys. Chem.* **1966**, *70*, 3315; c) R. P. Rastogi, N. B. Singh, *J. Phys. Chem.* **1968**, *72*, 4446.
[34] M. C. Etter, *J. Phys Chem.* **1991**, *95*, 4601.
[35] M. C. Etter, S. M. Reutzel, C. G. Choo, *J. Am. Chem. Soc.* **1993**, *115*, 4411.
[36] W. H. Ojala, M. C. Etter, *J. Am. Chem. Soc.* **1992**, *114*, 10228.
[37] J. Bernstein, *Polymorphism in Molecular Crystals*, Oxford University Press, Oxford, **2002**; see also J. Bernstein, R. J. Davey, J.-O. Henck, *Angew. Chem.* **1999**, *111*, 3646; *Angew. Chem. Int. Ed.* **1999**, *38*, 3440.
[38] a) D. Y. Curtin, I. C. Paul, *Acc. Chem. Res.* **1973**, *7*, 217; b) C. C. Chiang, C. T. Lin, A. H. J. Wang, D. Y. Curtin, I. C. Paul, *J. Am. Chem. Soc.* **1977**, *99*, 6303; c) A. O. Patil, D. Y. Curtin, I. C. Paul, *J. Am. Chem. Soc.* **1984**, *106*, 348.
[39] G. Crini, M. Morcellet, N. Morin, *Actual. Chim.* **2001**, *11*, 18.
[40] a) M. R. Caira, D. R. Dodds, L. R. Nassimbeni, *J. Therm. Anal. Calorim.* **2002**, *68*, 647; b) L. R. Nassimbeni, *Acc. Chem. Res.* **2003**, *36*, 631; c) S. Apel, M. Lennartz, L. R. Nassimbeni, E. Weber, *Chem. Eur. J.* **2002**, *8*, 67849.
[41] a) L. R. Nassimbeni, *CrystEngComm* **2002**, *5*, 200; b) S. J. Cantrill, G. J. Youn, J. F. Stoddart, D. J. Williams, *J. Org. Chem.* **2001**, *66*, 6857.
[42] a) K. Uekama, F. Hirayama, T. Irie, *Chem. Rev.* **1998**, *98*, 2045; b) S. A. Nepogodiev, J. F. Stoddart, *Chem. Rev.* **1998**, *98*, 1959; c) A. Harada, *Acc. Chem. Res.* **2001**, *34*, 456; d) S. Polarz, M. Antonietti, *Chem. Commun.* **2002**, 2593.
[43] I. Tsukushi, O. Yamamuro, H. Suga, *Thermochim. Acta* **1992**, *200*, 71.
[44] J. Shailaja, S. Karthikeyan, V. Ramamurthy, *Tetrahedron Lett.* **2002**, *43*, 9335.
[45] T. J. Brett, J. M. Alexander, J. L. Clark, C. R. Ross II, G. S. Harbison, J. J. Stezowski, *Chem. Commun.* **1999**, 1275.
[46] S. Watano, T. Okamoto, M. Tsuhari, I. Koizumi, Y. Osako, *Chem. Pharm. Bull.* **2002**, *50*, 341.
[47] S. Watano, J. Furukawa, K. Miyanami, Y. Osako, *Adv. Powder Technol.* **2001**, *12*, 427.
[48] N. Morin, A. Chilouet, J. Millet, J. C. Rouland, *J. Therm. Anal. Calorim.* **2000**, *62*, 187.
[49] G. Bruni, A. Marini, V. Berbenni, R. Riccardi, R. M. Villa, *J. Inclusion Phenom. Macrocyclic Chem.* **1999**, *35*, 517.
[50] a) F. Taneri, T. Guneri, Z. Aigner, M. Kata, *J. Inclusion Phenom. Macrocyclic Chem.* **2002**, *44*, 257; b) R. Saikosin, T. Limpaseni, P. Pongsawadsi, *J. Inclusion Phenom. Macrocyclic Chem.* **2002**, *44*, 191.
[51] *Organic Solid-State Reactions* (Ed.: F. Toda), Kluwer, Amsterdam, **2002**.
[52] a) F. Toda, H. Miyamoto, *Chem. Lett.* **1995**, 861; b) A. J. Schultz, G. D. Stucky, R. H. Blessing, P. Coppens, *J. Am. Chem. Soc.* **1976**, *98*, 3194, this paper reports the last X-ray determination of the structure of the tetrathiafulvalene with tetracyanoquinodimethane.
[53] M. Yagi, S. Hirano, S. Toyota, F. Toda, P. Giastas, I. M. Mavridis, *Heterocycles* **2003**, *59*, 735.
[54] F. Toda, H. Takumi, *Enantiomer* **1996**, *1*, 29.
[55] a) R. Kuroda, Y. Imai, N. Tajima, *Chem. Commun.* **2002**, 2848; b) R. Kuroda, Y. Imai, T. Sato, *Chirality* **2001**, *13*, 588; c) Y. Imai, N. Tajima, T. Sato, R. Kuroda, *Chirality* **2002**, *14*, 604.
[56] M. R. Caira, L. R. Nassimbeni, A. F. Wildervanck, *J. Chem. Soc. Perkin Trans. 2* **1995**, 2213.
[57] a) D. Braga, L. Maini, M. Polito, L. Mirolo, F. Grepioni, *Chem. Commun.* **2002**, *24*, 2960; b) D. Braga, L. Maini, M. Polito, L. Mirolo, F. Grepioni, *Chem. Eur. J.* **2003**, *9*, 4362.
[58] a) F. Takusagawa, T. F. Koetzle, *Acta Crystallogr. Sect. B* **1979**, *35*, 2888; b) G. J. Palenik, *Inorg. Chem.* **1969**, *8*, 2744.
[59] D. Braga, G. Cojazzi, L. Maini, M. Polito, F. Grepioni, *Chem. Commun.* **1999**, 1949.
[60] a) T. L. Threlfall, *Analyst* **1995**, *120*, 2435; b) N. Kubota, N. Doki, M. Yokota, D. Jagadesh, *J. Chem. Eng. Jpn.* **2002**, *35*, 1063.
[61] P. Seiler, J. D. Dunitz, *Acta Crystallogr. Sect. B* **1982**, *38*, 1741.
[62] R. J. Davey, N. Blagden, G. D. Potts, R. Docherty, *J. Am. Chem. Soc.* **1997**, *119*, 1767.
[63] D. Braga, G. Cojazzi, D. Paolucci, F. Grepioni, *CrystEngComm* **2001**, 1.
[64] H. Koshima, M. Miyauchi, *Cryst. Growth Des.* **2001**, *1*, 355.
[65] J. Dunitz, J. Bernstein, *Acc. Chem. Res.* **1995**, *28*, 193.
[66] D. Braga, L. Maini, G. de Sanctis, K. Rubini, F. Grepioni, M. R. Chierotti, R. Gobetto, *Chem. Eur. J.* **2003**, *9*, 5538.
[67] V. P. Balema, J. W. Wiench, M. Pruski, V. K. Pecharsky, *Chem. Commun.* **2002**, 1606.
[68] V. P. Balema, J. W. Wiench, M. Pruski, V. K. Pecharsky, *Chem. Commun.* **2002**, 724.
[69] V. P. Balema, J. W. Wiench, M. Pruski, V. K. Pecharsky, *J. Am. Chem. Soc.* **2002**, *124*, 6244.
[70] a) P. J. Nichols, C. L. Raston, J. W. Steed, *Chem. Commun.* **2001**, 1062; b) W. J. Belcher, C. A. Longstaff, M. R. Neckenig, J. W. Steed, *Chem. Commun.* **2002**, 1602.
[71] A. Orita, L. S. Jiang, T. Nakano, N. C. Ma, J. Otera, *Chem. Commun.* **2002**, 1362.
[72] D. Braga, L, Maini, M. Polito, F. Grepioni, *Chem. Commun.* **2002**, 2302.
[73] N. Shan, F. Toda, W. Jones, *Chem. Commun.* **2002**, 2372.
[74] a) H. Günzler, H.-U. Gremlich, *IR Spectroscopy*, Wiley-VCH, Weinheim, **2002**, chap. 4; b) M. Falk, *Vib. Spectrosc.* **1990**, *1*, 69.
[75] a) J. Fernandez-Bertran, E. Reguera, *Solid State Ionics* **1997**, *93*, 139; b) A. Valor, J. Fernandez-Bertran, J. Radilla, *J. Fluorine Chem.* **2001**, *107*, 137; c) J. Fernandez-Bertran, E. Reguera, *Solid State Ionics* **1997**, *93*, 139; d) J. Fernandez-Bertran, E. Reguera, A. Paneque, H. Yee-Madeira, A. Gordillo-Sol, *J. Fluorine Chem.* **2002**, *113*, 93; e) J. Fernandez-Bertran, J. Blanco Pascual, M. Hernandez, R. Rodriguez, *React. Solids* **1988**, *5*, 95; f) J. Fernandez-Bertran, *Solid State Ionics* **1998**, *112*, 351.
[76] J. Schmeyers, F. Toda, J. Boy, G. Kaupp, *J. Chem. Soc. Perkin Trans. 2* **1998**, 989.
[77] a) G.-W. Wang, K. Komatsu, Y. Murata, M. Shiro, *Nature* **1997**, *387*, 583; b) K. Komatsu, G.-W. Wang, Y. Murata, T. Tanaka, K. Fujiwara, K. Yamamoto, M. Saunders, *J. Org. Chem.* **1998**, *63*, 9358.
[78] a) Y. Murata, N. Kato, K. Fujiwara, K. Komatsu, *J. Org. Chem.* **1999**, *64*, 3483; b) Y. Murata, N. Kato, K. Komatsu, *J. Org. Chem.* **2001**, *66*, 7235.
[79] a) K. Komatsu, K. Fujiwara, Y. Murata, T. Braun, *J. Chem. Soc. Perkin Trans. 1* **1999**, 2963; b) K. Komatsu, K. Fujiwara, T. Tanaka, Y. Murata, *Carbon* **2000**, *38*, 1529; c) K. Komatsu, K. Fujiwara, Y. Murata, *Chem. Commun.* **2000**, 1583.
[80] a) K. Komatsu, K. Fujiwara, Y. Murata, *Chem. Lett.* **2000**, 1016; b) Y. Murata, M. Suzuki, K. Komatsu, *Chem. Commun.* **2001**, 2338c) M. Kunitake, S. Uemura, O. Ito, K. Fujiwara, Y. Murata, K. Komatsu, *Angew. Chem.* **2002**, *41*, 1011; *Angew. Chem. Int. Ed.* **2002**, *41*, 969; d) K. Fujiwara, K. Komatsu, *Org. Lett.* **2002**, *4*, 1039.
[81] see for example D. Braga, G. R. Desiraju, J. Miller, A. G. Orpen, S. Price, *CrystEngComm* **2002**, *4*, 500.

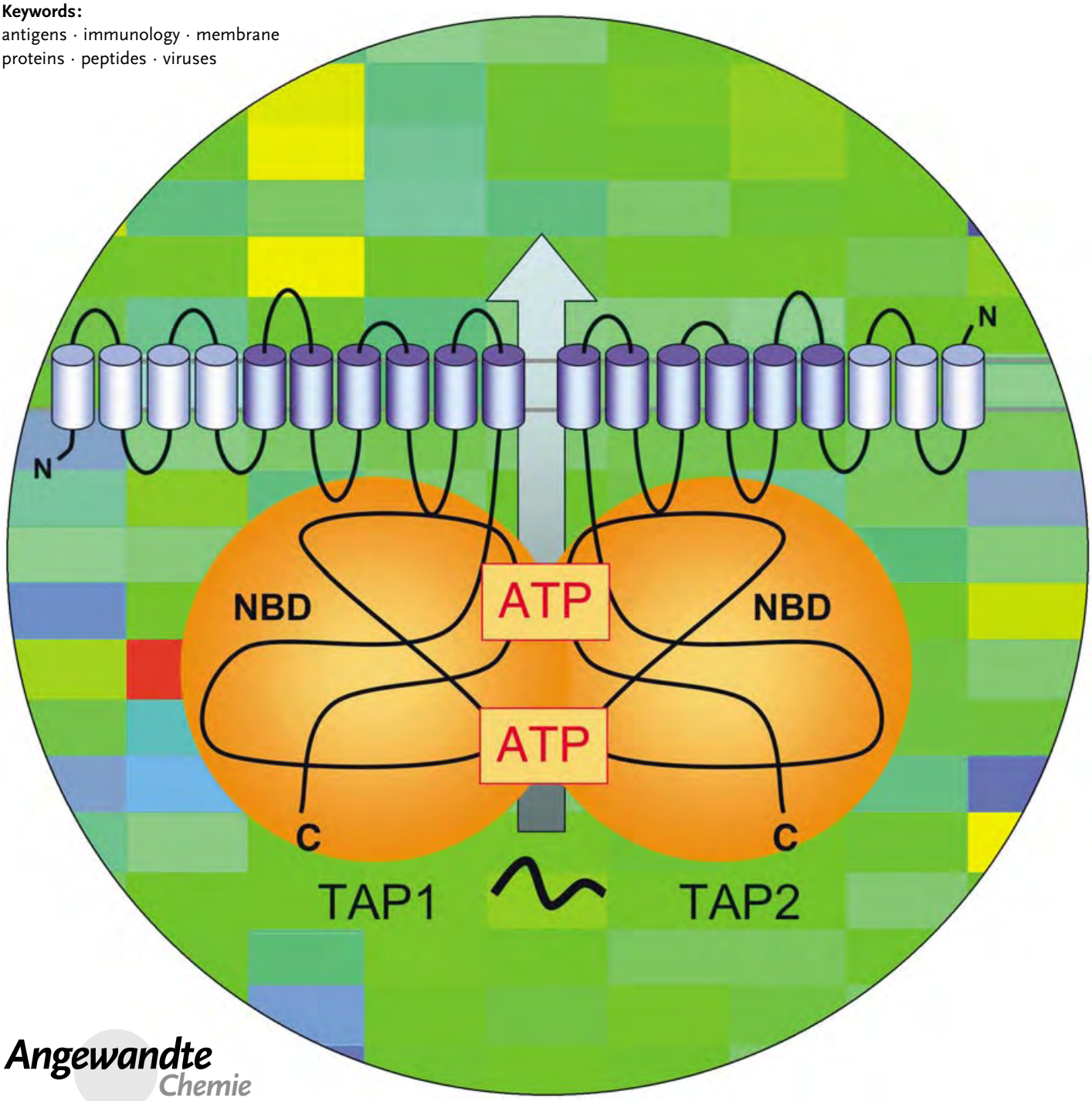
 © 2004 Wiley-VCH Verlag GmbH & Co. KGaA, Weinheim

Immunology

Function of the Antigen Transport Complex TAP in Cellular Immunity

*Silke Beismann-Driemeyer and Robert Tampé**

Keywords:
antigens · immunology · membrane proteins · peptides · viruses



 © 2004 Wiley-VCH Verlag GmbH & Co. KGaA, Weinheim DOI: 10.1002/anie.200300642

The immune system consists of several kinds of cells and molecules whose complex interactions form an efficient system for the protection of an individual from outside invaders and its own transformed cells. Innate immunity refers to the immediate antimicrobial response that occurs regardless of the nature of the invader. The adaptive immune system, on the other hand, mounts specialized immune responses to protect the individual against foreign cells from specific invaders or even tumorigenic cells, and provides long-term protection from subsequent exposure to these foreign cells. Antibody production and cell-mediated responses are the two interconnected branches of the adaptive immune system. Antigenic peptides displayed on the cell surface usually activate the cellular immune response. The transporter associated with antigen processing (TAP) plays a key role in the peptide-processing and -presentation pathway. This Review discusses the latest progress in the structure and mechanism as well as the diseases arising from dysfunction of the TAP complex.

From the Contents

1. Introduction 4015
2. The MHC I Antigen Processing and Presentation 4016
3. TAP Is a Member of the ABC Superfamily 4017
4. Structural Organization of the TAP Complex 4021
5. TAP Functions as a Peptide Transporter 4023
6. Transporters Related to TAP 4025
7. TAP Dysfunction in Human Diseases 4025
8. Summary and Outlook 4027

1. Introduction

The immune system is designed to defend the vertebrate organism against the numerous bacteria, viruses, toxins, and parasites with which it is confronted on a daily basis. The key players within the adaptive immune system are B and T lymphocytes: B lymphocytes produce antibodies, which circulate in the blood and lymph, and attach to foreign antigens to mark them for destruction by other immune cells, while T lymphocytes can be divided into two types that contribute to the immune defense in different ways. T-helper cells ($CD4^+$) are vital for orchestrating the overall immune response. Cytotoxic T cells ($CD8^+$), on the other hand, directly kill infected or malignant cells (for an overview see Ref. [1–4]).

The transporter associated with antigen processing (TAP)[+] plays a pivotal role in the adaptive immune response by translocating peptides derived from endogenous proteins from the cytosol into the endoplasmic reticulum (ER). This transport is required for subsequent presentation of peptides on the cell surface by major histocompatibility complex I molecules (MHC I).[5,6] "Foreign" peptides derived from viral and tumor-specific proteins can be recognized by $CD8^+$ cells, which subsequently kill the infected or tumorigenic cells. However, viruses have evolved sophisticated mechanisms to escape recognition by the immune system by impairing antigen presentation. Several viruses target the TAP and thus block the antigen-presentation pathway (for an overview see Ref. [7–9]).

Tumors can down-regulate MHC I expression on the cell surface, for example, by inhibiting TAP expression. In addition, mutations in TAP which lead to nonfunctional proteins can be associated with the development of cancer or can cause a severe immunodeficiency disease—the Bare Lymphocyte Syndrome.[10–12] Since the loss of TAP function is associated with serious disturbance of the immune system, it is important to understand the TAP structure and function as well as the mechanism of peptide transport in detail.

TAP belongs to the large family of ABC transporters, a number of which are associated with serious human diseases, for example, cystic fibrosis, Stargadt's disease, Tangier disease, and adrenoleukodystrophy.[13,14] ABC transporters have a common architecture of two transmembrane domains (TMDs), which are thought to build the substrate translocation pore, and two nucleotide-binding domains (NBDs), which hydrolyze ATP to provide the energy required for translocation of the solute. Although a number of ABC transporters from different organisms have been thoroughly examined, several questions concerning functional principles are still under debate, for example, how many ATP molecules are consumed per transport cycle and how the action of both NBDs is synchronized. Another challenge is to understand how the subunits within ABC transporters "talk to each other" during the substrate translocation cycle.

TAP is one of the most intensely studied ABC transporters and may constitute a suitable model for many other members of the ABC transporter family.[15–17] This Review

[+] A list of the most commonly used abbreviations can be found at the end of this review.

[*] Dr. S. Beismann-Driemeyer, Prof. Dr. R. Tampé
Institut für Biochemie, Biozentrum Frankfurt
Johann Wolfgang Goethe-Universität
Marie-Curie-Strasse 9, 60439 Frankfurt am Main (Germany)
Fax: (+49) 69-798-29495
E-mail: tampe@em.uni-frankfurt.de

 DOI: 10.1002/anie.200300642 © 2004 Wiley-VCH Verlag GmbH & Co. KGaA, Weinheim

summarizes the latest progress on this topic and addresses the points that have not yet been treated satisfactorily.

2. The MHC I Antigen Processing and Presentation

2.1. Overview

Antigens are defined as substances which elicit either an innate or an adaptive immune response. The main classes of antigens are polypeptides and polysaccharides. They are recognized by antibodies (immunoglobulins) secreted by B lymphocytes or by antigen-specific receptors on T lymphocytes. Immunoglobulins bind antigens in the extracellular space. T-cell receptors recognize intracellularly processed antigens bound to MHC I or MHC II molecules on the cell surface.

MHC II molecules, which are found only on professional antigen-presenting cells such as macrophages and dendritic cells, usually present peptides from ingested pathogens that reside extracellularly. Subsequently, the MHC II/peptide complex interacts with $CD4^+$ T lymphocytes through the T-cell receptor (TCR) and $CD4^+$. This leads to activation and secretion of cytokines, which mediate both humoral (antibody dependent) and cell-mediated immunity. MHC I molecules, on the other hand, present peptides from viruses, intracellularly replicating bacteria, or from tumor-specific proteins. $CD8^+$ T lymphocytes recognize the complex of MHC I molecules and an intracellular peptide on the cell surface through their TCR and $CD8^+$ molecules. The infected cells are subsequently lysed or undergo programmed cell death (apoptosis).

In addition to antigenic peptides, MHC I molecules constantly display peptides from normal cellular proteins, a process that is critical for the selection of T lymphocytes in the thymus. T lymphocytes whose antigen receptors recognize "self" peptides with high affinity and which would therefore be autoreactive are eliminated, whilst those recognizing "non-self" peptides survive (negative and positive selection; for an overview see Ref. [18–20]). The complex MHC I dependent antigen processing and presentation is constitutively active in nearly all nucleated cells but is up-regulated by inflammatory cytokines such as interferon-γ (IFN-γ). Cells display millions of different peptide epitopes for inspection by $CD8^+$ cells.[21,22] This is analogous to gene chips, which, for example, display thousands of cDNA fragments for the detection of complementary RNA transcripts in a sample.[23]

The MHC I pathway is divided into an antigen-processing part located in the cytosol, the formation of a multi-subunit peptide-loading complex (PLC) in the ER, and the transport of peptide-loaded MHC I molecules to the cell surface. The essential roles of TAP are to translocate peptides across the ER membrane and to facilitate loading of MHC I molecules, thereby connecting the cytosolic with the ER resident part of the peptide presentation pathway (Figure 1).

2.2. Antigen Processing

Protein degradation in the cytosol occurs mainly by the proteasome, a multicatalytic protease complex found in organisms of all three domains of life (eukarya, bacteria, and archaea).[24,25] The proteasome contains a 20S (ca. 700 kDa) core composed of 28 subunits, which are arranged in four stacks of heptameric rings.[26,27] The catalytic β subunits form the inner rings while the regulatory outer rings are composed of the α subunits responsible for structural and regulatory tasks. A specific form of the proteasome, the so-called immunoproteasome, has acquired the additional function in vertebrates of promoting the supply of peptide for MHC-dependent presentation on the cell surface. IFN-γ causes the replacement of the catalytically active β subunits, namely of LMP2 (low-molecular-weight protein), LMP7, and MECL-1 (multicatalytic endopeptidase complexlike protein-1) into the proteasome.[28–30] Moreover, the addition of the 19S regulatory subunits to the 20S complex leads to formation of the 26S (ca. 1500 kDa) proteasome.[25,31,32] While the 20S proteasome degrades proteins in an ATP-independent manner, the 26S proteasome complex is ATP-dependent. The 26S proteasome cleaves ubiquitinylated and some non-ubiquitinylated proteins into peptides of 3 to 30 residues with an optimum of 8 to 11 residues.[33–37] The size distribution of peptides generated by the proteasome overlaps with the size distribution of peptides bound by TAP and MHC I molecules.

The immunoproteasome preferentially generates peptides with hydrophobic and basic C termini, which are favored both



Silke Beismann-Driemeyer, born in 1970, studied biology at the Universities of Göttingen and Dublin. After completing a diploma in plant physiology with D. G. Robinson, she joined the group of R. Sterner at the University of Köln. She received her PhD in biochemistry in 2001 with a thesis on the structure and function of an enzyme complex of the thermophilic bacterium Thermotoga maritima. After an interim at the German Cancer Research Center in the Department of Immunochemistry with W. Dröge, she joined the group of R. Tampé, where she is currently working on the expression and biochemical characterization of human ABC transporters.



Robert Tampé, born in 1961, studied chemistry at the TU Darmstadt, where he received his PhD in biochemistry in 1989 working with H.-J. Galla on lipid–protein interactions. He worked with H. M. McConnell (Stanford University) on the structure and function of MHC II complexes. From 1992 to 1998 he was research group leader at the Max-Planck-Institute for Biochemistry in Martinsried and head of a research group at the Department of Biophysics at the TU Munich, where he completed his habilitation in biochemistry in 1996. In 1998 he became C4 professor of the Institute of Physiological Chemistry (Medicine) at the University Marburg. In 2001 he became C4 professor and director of the Institute of Biochemistry at the Biocenter Frankfurt.

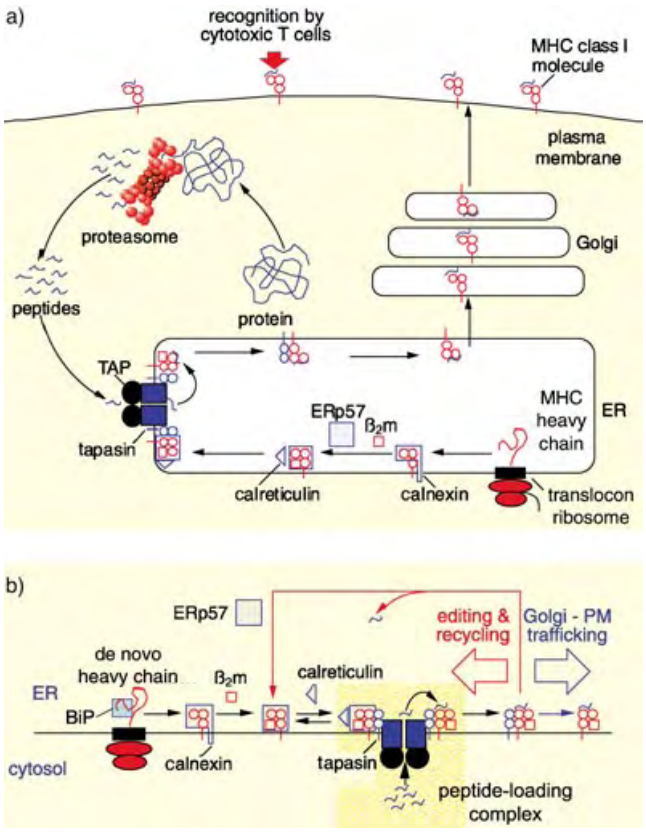


Figure 1. a) The mechanism for antigen processing and presentation by MHC I molecules. Proteins are generated in the cytoplasm by proteasomal degradation and then transported into the ER by TAP. The peptides are subsequently loaded onto MHC I molecules within the TAP/tapasin/MHC complex. Peptide/MHC complexes are transported to the cell surface where they display their antigenic cargo to T-cell receptors of $CD8^+$ cells. b) Schematic illustration of the assembly of MHC I molecules within the ER. Various chaperones orchestrate the assembly of the peptide-loading complex. See text for details.

by TAP and MHC I molecules.[38–40] Thus, the generated peptides already have suitable C termini for the subsequent steps within the processing and presentation pathway. They may be trimmed at the N terminus by amino peptidases in the cytosol and in the ER to gain a suitable length and N-terminus for loading onto MHC I.[41–45]

2.3. MHC I Loading and Antigen Presentation

Antigenic peptides generated in the cytosol have to be transferred by TAP into the ER lumen. Peptide association with TAP seems to primarily depend on diffusion, one problem being that free peptides are rapidly degraded by cytosolic peptidases such as thimet oligopeptidase.[46,47] It has been suggested that some peptides may escape cytosolic degradation by binding to cytosolic chaperones for delivery to TAP.[48–50] Nevertheless, cytosolic peptidases will probably remove the majority of peptides and leave only a small fraction for TAP-mediated transport into the ER and subsequent loading onto newly synthesized MHC I molecules.[51,52]

Loading of MHC I requires the assembly of a macromolecular peptide-loading complex (PLC). MHC I molecules consist of a polymorphic heavy chain (HC) of approximately 46 kDa, which is responsible for peptide specificity, an invariant light chain called β_2-microglobulin (β_2m) of 12 kDa, and a peptide necessary for stabilization.[53,54] Newly synthesized but unfolded MHC I HCs assemble with the chaperone BiP prior to or simultaneously with a second chaperone, calnexin.[55,56] The thiol oxidoreductase ERp57, which seems to aid proper folding and formation of intracellular disulfide bridges within the heavy chains, associates with the HC.[57,58] Calnexin is exchanged for another chaperone, calreticulin, and the calreticulin-bound HC binds to β_2m to form a MHC I heterodimer (HC/β_2m). Subsequently, tapasin (a 48-kDa TAP-associated transmembrane glycoprotein) and TAP join the preformed complex to build the final PLC (Figure 1b).[59,60]

Tapasin has been proposed to play several important roles in the peptide-loading process: 1) stabilization of the TAP1/TAP2 complex by binding to the transmembrane domains of both TAP1 and TAP2,[61–63] 2) bridging TAP to the HC/β_2m dimer to ensure proximity of the peptide donor and peptide receptor,[64–66] 3) stabilization of the not yet loaded HC/β_2m complexes,[64] and 4) optimization of the peptides bound in a kinetically stable manner to the HC/β_2m complex ("peptide editing").[62,67,68] MHC I heterodimers are loaded with peptides within the PLC. MHC I heterodimers bind peptides through their free N and C termini and one or two "anchor residues", which are usually hydrophobic. Proteasomal cleavage produced the hydrophobic or basic anchor residue at the C terminus of the peptide, and this residue also made the peptide an attractive substrate for TAP (see Section 5.1). Tapasin may exert its proposed editing function if a suboptimal peptide binds to HC/β_2m.[62,65,67] Thereby, bound peptides are either trimmed or exchanged for other peptides, which finally leads to a repertoire of high-affinity peptides. The resulting kinetically stable MHC I/peptide complexes enter the secretory pathway and traffic to the plasma membrane, where they present their antigenic cargo to cytotoxic T cells.

3. TAP Is a Member of the ABC Superfamily

ABC proteins are the largest family of paralogous proteins in many organisms.[69] The human genome, for example, contains at least 49 members of this protein family (http://www.humanabc.org). The human ABC transporters are classified by sequence homology into seven subfamilies, designated ABCA to ABCG. TAP1 and TAP2 are two of the eleven members of the ABCB subfamily (ABCB2, ABCB3).[70]

The family of ABC proteins is defined by their homology within the ATP-binding cassette (ABC) region.[71] This region contains three highly conserved motifs called Walker A and B motifs as well as the C loop (also known as the ABC signature motif). The Walker A and B motifs are present in many ATP-binding proteins,[71] while the C loop is specific for ABC proteins.[72] ABC proteins are found in all organisms from archaea and bacteria to eukaryotes. They are involved in

 © 2004 Wiley-VCH Verlag GmbH & Co. KGaA, Weinheim

numerous cellular functions, for example, nutrient uptake, lipid trafficking, ion and osmotic homeostasis, and antigen processing. Most of them act as ATP-dependent transporters which transfer substrates across cellular membranes, but several members of the ABC protein family lack a transport function. ABC transporters can translocate a huge variety of chemically different substrates, including ions, carbohydrates, antibiotics, lipids, peptides, and even large proteins (for example, hemolysin A, 110 kDa). The importance of ABC proteins in humans is illustrated by the fact that mutations in ABC transporter genes are so far associated with 14 genetic diseases.[13,70] At least eight human ABC transporters are capable of extruding amphipathic compounds, including anticancer drugs, out of the cell and severely impairing cancer chemotherapy (for an overview see Ref. [73]). In addition, ABC transporters of the human pathogenic fungus *Candida albicans*, which commonly infects immunocompromised individuals, such as AIDS patients, confer resistance to azole-based antifungal agents.[74,75]

All ABC transporters share a common architecture, and it is proposed that there are only one or a few mechanisms for energizing the substrate translocation across membranes. We will, therefore, first summarize some general aspects of ABC transporters before discussing the structure and function of TAP in more detail.

3.1. Architecture of ABC Transporters

3.1.1. General Aspects of the Architecture

ABC proteins without transport function, such as the ubiquitous RNAse L inhibitor (ABCE1) or the bacterial Rad50 protein, are soluble proteins which play different roles in cell metabolism, such as regulation of protein biosynthesis, DNA maintenance, or DNA repair. The human immunodeficiency virus (HIV) also recruits the host ABCE1 protein for capsid assembly.[76] In addition to optional extra functional units, all ABC proteins consist of two highly conserved NBDs that comprise the classical ABC motifs. ABC transporters have a minimum composition of two NBDs plus two poorly conserved TMDs, which anchor them either in the plasma membrane or in intracellular membranes (ER, mitochondria, lysosomes, peroxisomes, vacuoles). Two to four genes in prokaryotes encode the NBDs and TMDs. Fusions may occur between the NBDs, the TMDs, or between one NBD and one TMD (Figure 2). Bacterial importers are further associated with a periplasmic substrate-binding protein, which has a high affinity for the substrate and interacts with the transmembrane domains to regulate substrate import.[77] Bacterial export systems, on the other hand, are often accompanied by membrane-fusion proteins and/or outer-membrane factors.[78] The ABC transporters of eukaryotes are built up of either one $(TMD\text{-}NBD)_2$ fusion protein ("full-length transporters") or two TMD-NBD fusion proteins ("half transporters"). Additional domains may be present within the transport complex. In addition, there are some ABC proteins with transporter-like architecture (two NBDs plus two TMDs) which act as channels or regulators and, therefore, do not exhibit any direct transport function. An example is

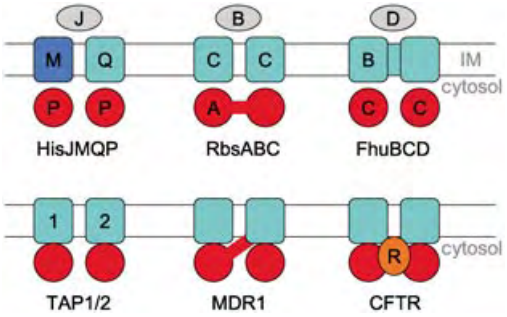


Figure 2. Domain organization of ABC transporters. Transmembrane domains (TMDs) are shown in blue and nucleotide-binding domains (NBDs) in red. Selected examples are depicted to illustrate the diverse organization of the domains in ABC transporters from bacteria (top row) and mammals (bottom row). HisJMPQ, RbsABC, and FhuBCD are bacterial import systems which are responsible for the uptake of histidine, ribose, and ferric hydroxamate, respectively. These importers work in concert with a periplasmic substrate-binding protein (gray). TAP, Pgp, and CFTR are eukaryotic exporters, which are responsible for the transport of peptides, hydrophobic drugs, and chloride ions, respectively. The regulatory domain (R) of CFTR is shown in orange.

the chloride-channel protein, the cystic fibrosis protein (cystic fibrosis transmembrane conductance regulator, CFTR). Mutations within the CFTR gene result in cystic fibrosis, one of the most common lethal genetic diseases in caucasians.[79,80] Another example is the sulfonylurea receptor (SUR), which is a subunit of the ATP-sensitive potassium channel (K_{ATP} channel) in pancreatic β cells. Within this channel complex, SUR1, SUR2A, or SUR2B are thought to operate as the ATP sensitizer, whereas the other subunit, $K_{IR}6.1$ or $K_{IR}6.2$, is the actual potassium channel.[81]

3.1.2. Nucleotide-Binding Domains

The hydrophilic NBDs of ABC transporters are highly conserved: there is over 25 % sequence homology irrespective of whether the sequence is of prokaryotic or eukaryotic origin. The NBDs act as "motor domains", since they convert the chemical energy of ATP hydrolysis into mechanical work, which is realized in conformational changes within the TMDs. The NBDs consist of approximately 250 amino acids and contain several characteristic motifs found in all ABC proteins. The most prominent motifs are the Walker A and B motifs as well as the C loop (ABC signature, Figure 3). The Walker A motif has the consensus sequence GX_4GKS/T (X: any amino acid in the single letter code) and the Walker B motif the consensus sequence Φ_4D (Φ: hydrophobic amino acid). The C loop is located between the Walker A and B motifs and has the consensus sequence LSGGQ. In contrast to the Walker A and B motifs, which are also present in other ATP- and GTP-binding proteins, the C loop is exclusively found in ABC proteins, though G proteins contain a related motif (GGQR/K/Q).[82] The D loop is located on the C-terminal side of the Walker B motif and has the consensus sequence SALD. The other loop "motifs" only contain a single conserved residue (Q, P, H, or G) but they are nevertheless characteristic features of the ABC family (for details see Ref. [83]).

 © 2004 Wiley-VCH Verlag GmbH & Co. KGaA, Weinheim

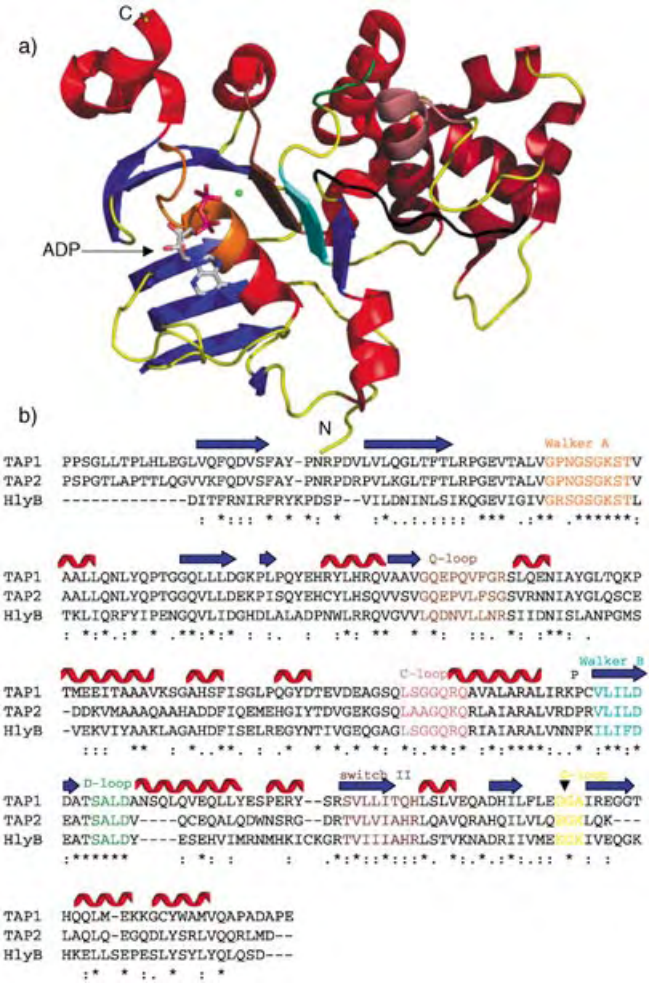


Figure 3. a) Structure of the nucleotide-binding domain (NBD) of human TAP1 (PDB code: 1JJ7).[91] Helices are drawn in red, β sheets in blue, and loops and turns in yellow. Bound ADP is shown in detail, with nitrogen atoms in blue, oxygen atoms in red, phosphorus atoms in magenta, and the magnesium ion in green. Characteristic motifs (Walker A and B; Q, C, P(Pro), D, and G loops; and switch II region) are color-coded as indicated in Figure 3b. This Figure and Figures 4a,b, 5, and 9b were produced with PyMOL (http://pymol.sourceforge.net/). b) Sequence alignment of the NBDs of human TAP1 and TAP2 as well as hemolysin B of *E. coli*. The secondary structure elements refer to the structure of TAP1/NBD. Alignments were performed using ClustalW.[222]

To date (October 2003), the crystal structures of nine NBDs of ABC proteins with transport function have been solved.[84–93] All NBDs adopt a similar fold that consists of two subdomains (also called arms). Arm I is an F1-ATPase-like domain and contains the Walker A and B motifs. The α-helical arm II, which is specific to ABC proteins, is thought to act as the signaling domain. Arm II lies perpendicular to the catalytic arm I and contains the C loop. The hinge region connecting arm I and arm II is located between the Q loop and the P(Pro) loop.[89,94] Figure 3 shows the structure of the TAP1 NBD as an example.[91]

All ABC proteins contain two NBDs which can form dimers in the absence of the membrane components.[95–97] Dimerization of the two NBDs of Rad50, a bacterial ABC ATPase involved in DNA double-strand repair, is induced upon ATP binding and causes a movement of arm II relative to arm I and a rearrangement of the linker P(Pro)- and Q-loop regions.[98] The Rad50 dimer is structurally similar to the dimer of MJ0796, an ABC transporter of the archaeon *Methanococcus jannaschii*.[87] The NBDs are arranged in a "head-to-tail" orientation (Figure 4a).[87,93,98] Previously

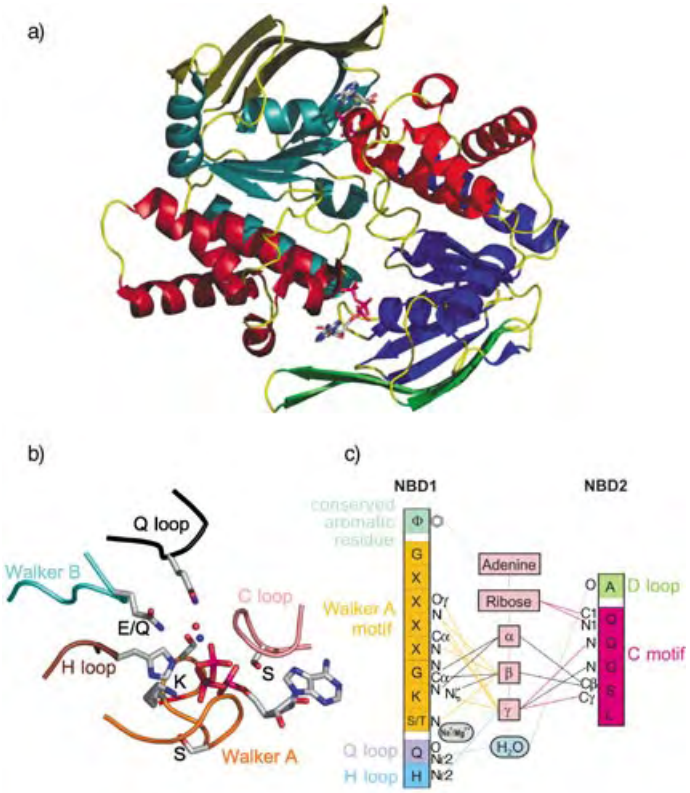


Figure 4. ATP-binding drives the formation of a nucleotide sandwich dimer. a) Dimeric structure of MJ0796 (PDB code: 1L2T).[87] The ATP-binding-core subdomain (arm I, F_1-ATPase-like domain) is illustrated in blue, the α subdomain (arm II, signaling domain) in red, and the antiparallel β subdomain in green. b) The catalytic site of ATPase hydrolysis. Amino acid side chains and the ATP are shown in detail with oxygen atoms in red, nitrogen atoms in blue, and phosphorus atoms in magenta. The α-carbon backbone of the Walker A loop (with two serines and one lysine) is colored yellow, the C loop (with one serine) of the opposite monomer is colored pink, the Q loop dark brown, the H loop brown, and the Walker B motif (with its mutated E171Q residue) cyan. The sodium ion is shown as a red dot and the coordinating water molecule as a blue dot. c) Interactions stabilizing the ATP and its Mg^{2+} (or Na^{+}) counterion. Black lines represent van der Waals contacts and colored lines the H bonds. The contacts to the ATP counterion are shown as gray lines, and the aromatic π–π stacking interaction between an aromatic amino acid near the N terminus and the adenine base are represented through a dashed green line.

described structures of NBD "dimers" in which the NBDs are either associated in a back-to-back or in an interlocking fashion are now considered to be only crystallographic dimers.[89,90]

Bound nucleotides were found both in monomeric and in dimeric NBD structures. Unlike in other ATPases, the bound nucleotide is strongly exposed to solvent within monomeric

 © 2004 Wiley-VCH Verlag GmbH & Co. KGaA, Weinheim

NBD structures.[86,88,91] Within an NBD/NBD dimer, the binding of a single ATP molecule is mainly accomplished by residues from the Walker A motif, the Q loop, and the H loop of one NBD and of residues from the C loop of the second NBD (Figure 4b,c). The alanine residue of the D loop of the second NBD contributes indirectly (through a water molecule) to ATP binding. In addition, the purine base of ATP is held in place by π-π interactions between a conserved aromatic residue near the N terminus (Y572 in human TAP1) and the adenine ring, which explains why ATP, GTP, and UTP can be taken as the energy source. The NBD–NBD interface is mainly formed by residues from the Walker A motif and loops C, D, and H (also referred to as switch II, see Figures 3 and 4).[93] Since the ATPase site of each NBD is complemented by residues from the second NBD within an NBD dimer, the function of the second NBD is to shield the nucleotide from solvent and to fix the γ-phosphate of the ATP. The ATP counterion (usually Mg^{2+}, Na^{+} in the MJ0796(E171Q) mutant) interacts with the conserved S/T residue from the Walker A motif, the Q-loop glutamine, and the β- and γ-phosphates of ATP. These interactions are proposed to help tether the two NBDs together.[87]

3.1.3. *Transmembrane Domains*

The TMDs are much more diverse in terms of sequence and length than the NBDs. This is probably a consequence of the requirement for the binding and transporting substrates of different size and shape by distinct pathways through different cellular membranes. For most ABC transporters, 6 + 6 transmembrane helices (TMs) were predicted. The crystal structures of the homodimeric lipid A exporter MsbA of *E. coli* and *V. cholera* also revealed six helices per monomer.[84,85] Larger numbers of TMs were predicted for some ABC transporters, and the recently solved structure of the *E. coli* vitamin B_{12} importer BtuCD shows ten transmembrane helices for each of the two TMDs.[93] Therefore, the TMDs of different ABC transporters probably also adopt distinct membrane topologies.

The ligand-free MsbA and BtuCD structures are currently the only available structures of complete ABC transporters. There are considerable differences between these structures in the NBDs, the TMDs, and the NBD–TMD interface (Figure 5). The TMD of MsbA is formed by a bundle of six helices. The two TMDs of the *E. coli* lipid A transporter dimer form a conelike structure with a 25-Å-large opening facing the cytoplasm ("open" conformation). The only intermolecular contact is made by the TMD part in the outer leaflet of the membrane and the extracellular loops. Within the lipid A transporter structures, an α-helical intracellular domain has been identified, which connects the NBDs and the TMDs. The TMDs and the intracellular domains together form a putative lipid A binding site.[99] This site is accessible from the inner leaflet of the plasma membrane. Thus, lipid A could be recruited in a fashion that resembles the proposed recruitment of lipophilic drugs to the multidrug resistance proteins, Pgp and LmrA.[100,101]

The NBDs of *E. coli* MsbA were only partially resolved: they lacked arm I with the Walker A and B motifs. If arm I of another NBD is included in the "open" conformation of MsbA by molecular modeling studies, the NBDs are about 50 Å apart. The C loop and the Walker A motif face away from each other and, thus, the formation of an NBD dimer as seen in MJ0796, Rad50, and BtuCD would require substantial rotation of the NBDs relative to each other.

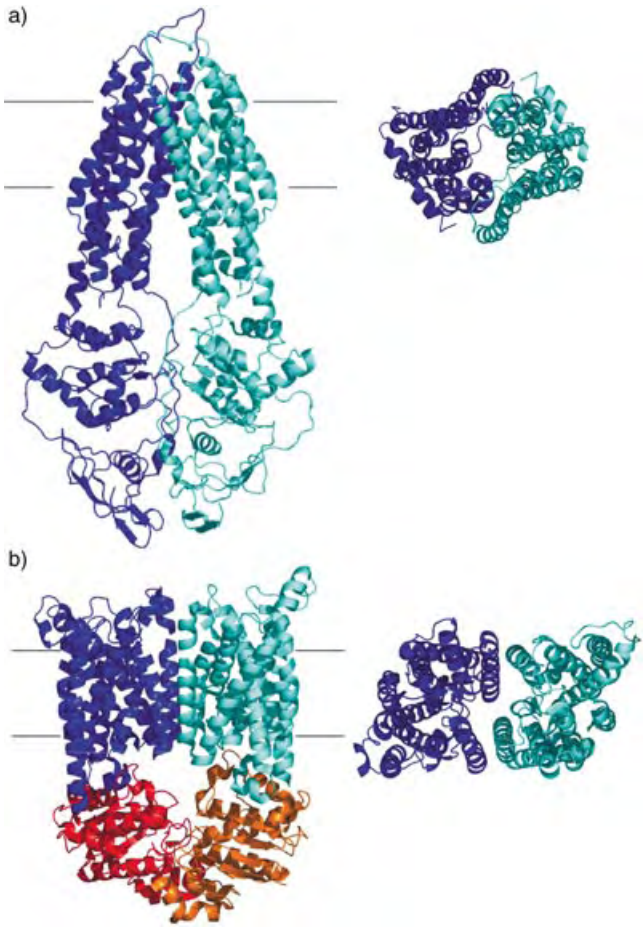


Figure 5. Structures of the ABC transporter MsbA and BtuCD. a) Lipid A flippase (MsbA) of *V. cholera* (PDB code: 1PF4).[85] Each subunit of the homodimer is illustrated in light and dark blue. b) Vitamin B_{12} importer (BtuCD) of *E. coli* (PDB code: 1L7V).[93] The two TMDs (BtuC) are illustrated in light and dark blue, and the two NBDs (BtuD) in orange and dark red. In the views from the top (right pictures), the NBDs have been omitted to highlight the organization of the transmembrane helices.

The lipid A transporter structure from *V. cholera* differs from that of *E. coli* in that the two helical bundles are in close contact and form a transmembrane channel, which is inaccessible from the cytosolic face (Figure 5a). This structure thus represents a "closed" conformation. Each monomer is rotated counterclockwise by approximately 90° relative to the monomers within the *E. coli* MsbA structure. As a consequence of this rotation, the NBD–NBD interface of *V. cholera* MsbA resembles that observed in other dimeric NBD structures.

The third structure of a complete ABC transporter, the vitamin B_{12} transporter, contains 10 transmembrane helices per monomer (Figure 5b). The helices are not parallel, as in the lipid A transporter, but packed in an intricate fashion.

Within the dimeric structure they form the predicted translocation channel for vitamin B_{12}, which is locked at the cytosolic surface by two loops connecting the transmembrane helices.

In the structure of the vitamin B_{12} importer BtuCD, intracellular domains as observed in MsbA are absent and the NBDs and TMDs are in direct contact. The contact between the NBDs and the TMDs is mainly made by the so-called L loop. This cytosolic region consists of two short helices connected by a glycine residue, which allows a sharp bend, thus resembling an "L". The L-loop sequence is moderately conserved in ABC transporters, which leads the authors to speculate that the L loop may also be generally involved in formation of the NBD–TMD interface in ABC transporters. Residues of the Q loop and of the region from helix 2 to helix 3 and helix 4, that is the connection between arm I and arm II, are mainly involved in the NBD–TMD interaction with the cytosolic BtuD subunit (NBD). Since all resolved structures of NBDs are very similar, it can be proposed that this region generally participates in the NBD–TMD interface of ABC transporters and may be involved in signal transduction from the TMDs to the NBDs upon substrate binding.

The larger distances between the NBD dimers of the vitamin B_{12} importer differentiates them from other NBD dimers. The NBD–NBD interface is consistent with a head-to-tail orientation, in which two ATP molecules can be sandwiched between the C loop of one NBD and the Walker A motif of the other NBD. It is reasonable to assume that ATP binding could force the NBDs together to form a close dimer as seen in the ATP-bound Rad50 and MJ0796 dimers.[87,98]

3.1.4. Function of ABC Transporters

ABC transporters transfer a broad spectrum of substrates across biological membranes. Bacterial importers are usually highly specific and accept only a single or a few structurally similar substrates. In contrast to this, export systems are usually more promiscuous. For example, the multidrug resistance protein Pgp and its bacterial homologue LmrA are able to expel nearly every known anticancer drug, and TAP transfers peptides of a large range of sizes and different sequences (see Section 5.1). As expected, there is no common substrate-binding site in the TMDs of all ABC transporters. Even the number of substrate-binding sites (one or two) is not clear. In contrast to this, the nucleotide-binding sites within the NBDs are very similar in all ABC transporters. The binding of ATP was shown to drive the NBDs together to build the catalytically competent NBD dimer.[87,97] Complete ABC transporters usually show a low basal ATPase activity, which can be stimulated by their substrates. The transport activity of an ABC transporter depends on specific interactions between the two NBDs and between the two TMDs as well as on signals sent between the TMDs and the NBDs. How exactly ATP hydrolysis is coupled to substrate transfer is not clear at the moment. There may be a common mechanism for all transporters or several distinct ones.

For most ABC transporters, the ATP-to-substrate stoichiometry has not yet been determined accurately. Nevertheless, recent biochemical studies demonstrated hydrolysis of two ATP molecules per transport cycle of OpuA, a bacterial importer of osmoprotectants, and of Mdl1, a homodimeric yeast peptide transporter located in the inner mitochondrial membrane (see Section 6).[97,102] It was shown that the two nucleotides (two ATP, one ATP plus one ADP, or two ADP) are present within the Mdl1/NBD dimer during distinct steps of the ATPase cycle. These findings lead to the following model of the ATPase cycle: The binding of two ATP molecules to two NBD monomers induces dimer formation. Dimerization of the NBDs is assumed to be the "power stroke".[87,98] ATP is hydrolyzed at one site and one inorganic phosphate is subsequently released, thereby creating an instable ATP/ADP bound state. The remaining ATP is hydrolyzed and the inorganic phosphate released. Electrostatic repulsion drives the dimer apart. ADP leaves the nucleotide-binding site and resets the NBDs for a new ATPase cycle. Thus, the NBDs may work in a sequential processive, rather than in an alternating, fashion as proposed in other models ("alternating site models").[85,103,104] One question remaining unanswered is what determines the sequence of ATP hydrolysis in the two identical motor domains of homodimeric transporters such as Mdl1. Nevertheless, this model may also be applicable to ABC transporters with functionally distinct NBDs such as SUR1, CFTR, or TAP.[105–107]

4. Structural Organization of the TAP Complex

The TAP transporter is composed of two polypeptide subunits, TAP1 and TAP2, each consisting of one NBD and one TMD. The overall sequence identity between the TAP1 and TAP2 amounts to approximately 40%. As generally found between ABC transporters, the NBDs are much closely related than the TMDs (around 60% versus 30% sequence identity). Human TAP1 is a protein with a calculated molecular mass of 81 kDa (748 amino acids), while human TAP2 has a calculated molecular mass of 75 kDa (686 amino acids). The TMD and NBD comprise the N- and the C-terminal halves, respectively, in both proteins.

When TAP-deficient cell lines were transfected with either one or both TAP genes (depending on whether the defect was in one or both TAP genes), MHC I dependent antigen presentation was restored.[108,109] TAP1 and TAP2 also proved to be necessary and, when expressed in otherwise TAP-deficient yeast or insect cells, sufficient for peptide transport into the ER.[108,110,111] These results, together with immunoprecipitation experiments, indicate that TAP1 and TAP2 form a heteromeric transport complex. Cross-linking studies and low-resolution single-particle electron microscopy analysis indicated that TAP is organized as a heterodimer.[112,113] Immunoelectron and immunofluorescence microscopy studies showed that the transport complex is located in the ER and the cis-Golgi membrane, although an ER retention signal could not be identified.[110,114]

 © 2004 Wiley-VCH Verlag GmbH & Co. KGaA, Weinheim

4.1. Nucleotide-Binding Domains

The NBDs of the TAP proteins comprise the amino acids 489–748 and 454–686 in TAP1 and TAP2, respectively (see Figure 3). The structure of the TAP1/NBD represents the only high-resolution structure of a mammalian ABC-transporter NBD reported so far.[91] The TAP1/NBD was crystallized in the presence of ATP and Mg^{2+}, but contained ADP within the structure. This is probably a result of either spontaneous hydrolysis or the activity of contaminating ATPases, since a (slightly different) TAP1/NBD construct shows no ATPase activity.[115] The structure shows the NBD in the monomeric form. The NBD has the same overall fold as the previously solved NBD structures consisting of the F1-ATPase-like arm I and the α-helical arm II. Arm II has a higher average B factor than arm I, therefore, arm II might be more flexible than arm I. This proposal is consistent with crystallographic data from MJ1276.[116] In addition, mutational studies on MalK indicated that arm II might act as a signaling domain, which undergoes conformational changes upon ATP binding and dimerization and, together with the other NBD, enables the TMDs to translocate peptides.[117,118] Walker A residues form extensive contacts to the α- and β-phosphate of the bound ADP in TAP1 as well as in HisP, MJ0796, and GlcV.[86,87,89,91]

The NBDs of TAP1 and TAP2 contain all the conserved motifs characteristic of ABC transporters (see Figure 3). Nevertheless, some variations within the conserved motifs in either TAP1 or TAP2 seem to be of functional importance. One interesting feature is the "degenerated" C loop of TAP2. Human and gorilla TAP2 have the sequence LAAGQ instead of LSGGQ. The rodent (hamster, mouse, rat) TAP2 C loop is LAVGQ, and animals from different orders have other TAP2 C loops. The only residue strictly conserved among all published TAP2 sequences is the fourth residue (glycine), which—like the serine in the consensus motif LSGGQ—forms hydrogen bonds to the γ-phosphate of ATP in the MJ0796 dimer (Figure 4b,c).[87] The exact role of the distinct C loops of human TAP1 and TAP2 is currently not clear. The mutations S644A/G646A in the TAP1 C loop and/or G610A in the TAP2 C loop abolished the peptide transport activity of the TAP complex without affecting the peptide- and ATP-binding ability.[119] Mutational studies on other ABC transporters showed that the strictly conserved second glycine residue was an absolute requirement for ATP hydrolysis, and thus for transport, while ATP binding is not impaired.[117,120,121] Exchange of the TAP2 C loop to the canonical LSGGQ motif results in a TAP complex with higher transport activity than wild-type TAP (M. Chen, R. Abele, R. Tampé, unpublished results). TAP mutants containing LAAGQ in the TAP1/NBD and LSGGQ in the TAP2/NBD exhibit wild-type transport activity, whereas peptide transport is reduced by 70% in TAP complexes with two LAAGQ motifs. Together, these studies of C-loop mutants give evidence that the second position of the C loop, which is either serine or alanine in all known TAP sequences, influences the rate of ATP hydrolysis and peptide transport of TAP and possibly also of other ABC transporters.

Interestingly, all the published mammalian TAP1 sequences have a glutamine residue (Q701 in human TAP1) in place of the histidine in the H loop, while fish (shark, salmon, trout) have the canonical histidine residue and Japanese quail has a glycine residue. Since the H loop (switch II) is involved in ATP binding and hydrolysis (see Section 3.1.2, Figures 3 and 4), it is likely that the difference in this motif also contributes to the functional nonequivalence of the human TAP1/ and TAP2/NBDs (see discussion in Section 5.2). In addition, the glutamate directly downstream of the Walker B motif, which is strongly conserved in ABC transporters, is exchanged to an aspartate residue (D686 in human TAP1) in all currently known TAP1 sequences. This latter residue is assumed to be the catalytic base in ATP hydrolysis; variation of this residue could thus account for differences in ATPase activity of TAP1 and TAP2.

Binding of ATP or other nucleotides leads to stabilization of the heterodimeric TAP complex, which is indicative of an induced conformational rearrangement.[122] This effect may be prevented by the human cytomegalovirus protein US6, which blocks ATP binding to TAP, thus leading to destabilization of the dimeric complex (see Section 7.3).[123,124]

4.2. Transmembrane Domains

The TMDs comprise the 488 residues at the N terminus of human TAP1 and the 453 residues at the N terminus in human TAP2. The numbers of transmembrane helices (TMs) predicted for TAP1 and TAP2 depend on the algorithm used. Ten TMs were proposed for TAP1 and nine for TAP2 on the basis of sequence alignments and hydrophobicity plots.[15,125] A comparison between the experimentally determined TMDs of Pgp (also a member of the ABCB subfamily) and the TAP protein sequences leads to the prediction of six "canonical" TMs plus additional N-terminal segments in TAP1 and TAP2 without counterparts in Pgp or any other ABC transporter except ABCB9 (Figure 6). These N-terminal stretches (residues 1–175 in TAP1 and 1–140 in TAP2) are predicted to

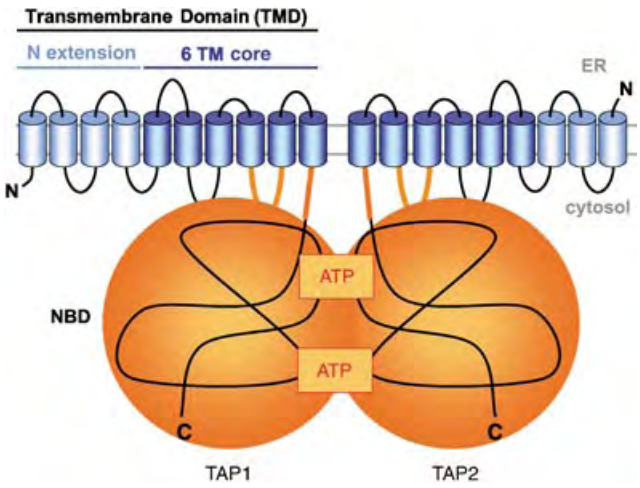


Figure 6. Structural organization of the TAP complex. Putative TMs of the N-terminal extensions are shown in light blue, while the six "canonical" TMs proposed to form the translocation pore (TM1-6) are shown in blue. The peptide-binding region is indicated in orange. See text for details.

contain four and three TMs in TAP1 and TAP2, respectively, which also results overall in ten membrane-spanning helices in TAP1 and nine in TAP2. Truncation studies indicate that the N-terminal domains are not essential for ER targeting and dimerization or TAP-dependent peptide transport but are essential for the binding of tapasin.[126]

Recently, functional cysteine-less TAP1 and TAP2 were constructed.[127] Introduction of single cysteine residues in predicted loops and probing their accessibility by membrane-impermeable thiol-specific probes will help to elucidate the membrane topology of a functional TAP complex and the possible conformational changes within the undisturbed complex.

The peptide-binding site was mapped by deletion studies and by peptide cross-linking followed by enzymatic and chemical cleavage of TAP and immunological probing for different epitopes in TAP1 and TAP2.[128,129] According to the topology model, the regions involved in peptide binding are located in the loop connecting the core helices TM4 and TM5 and in a C-terminal stretch of approximately 15 amino acids connecting TM6 with the NBD (Figure 6). In addition, parts of TM4 and TM6 themselves seem to contribute to peptide binding. It has been shown that peptide binding leads to a stabilization of the TAP complex.[122]

The results of kinetic and equilibrium binding studies (Scatchard analysis) are consistent with a single peptide-binding site in TAP, although the existence of a second peptide-binding site with very low affinity cannot be formally excluded.[40,130] Photo-cross-linking studies of peptides revealed that both TAP1 and TAP2 contribute to formation of the peptide-binding site.[131]

5. TAP Functions as a Peptide Transporter

Each human expresses a set of three to six different MHC I molecules which are capable of presenting almost every protein fragment of eight to ten amino acids. The human *tap1* and *tap2* genes show only limited polymorphism.[132,133] However, this polymorphism does not seem to influence the substrate specificity of TAP1 or TAP2.[134,135] So, how can TAP recognize and transport a large pool of peptides differing in length and sequence, and how is the required flexibility linked to specificity?

5.1. Specificity and Flexibility of the Peptide-Binding Pocket

The specificity of the peptide-binding pocket of TAP has been intensely investigated. Peptides with 8–16 residues were found to be optimal for binding to TAP.[136] Application of peptide libraries sharing one defined amino acid position enabled the elucidation of the effect of individual residues at a given position, independently of the sequence context.[39,40,137] A selectivity for basic and hydrophobic amino acids at the C terminus was found, which was consistent with earlier studies based on in vitro translocation assays with either semipermeabilized cells or microsomal membranes.[110,138] The three N-terminal residues also significantly influence the binding affinity (Figure 7). The strongest destabilizing effect was found in peptides with a proline in the second position, which almost completely abolished the binding of peptides to human TAP. This result leads to the conclusion that the peptide backbone at this position contributes to binding affinity.[40]

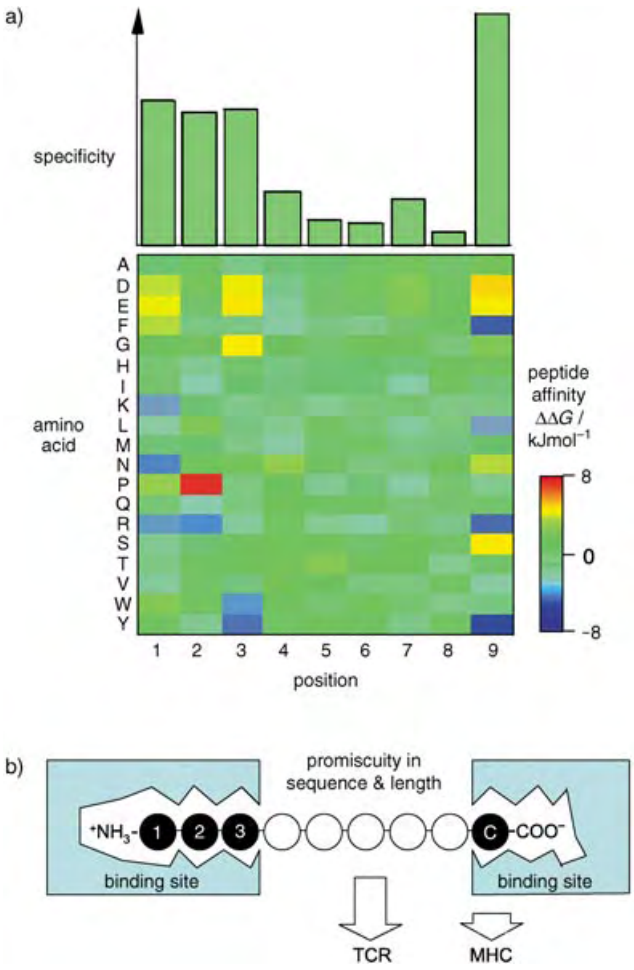


Figure 7. Peptide specificity of human TAP. a) By using combinatorial peptide libraries and statistical analysis, human TAP was found to be most specific for the three N-terminal and C-terminal residues of the peptide.[40,139] Favored and disfavored amino acids at a given peptide position are shown in blue (negative $\Delta\Delta G$ values) and red (positive $\Delta\Delta G$ values), respectively. b) Model of the peptide-binding pocket including residues utilized for MHC I binding and TCR recognition.

The influence of the peptide backbone was also studied by a "positional scanning" approach.[40] D-amino acids were placed at each position in peptides of different length. Interestingly, D-amino acids at positions 2 and 3 or, to a lesser extent, at position 1 and at the C terminus had a destabilizing effect, while D-amino acids at internal positions hardly influenced binding affinity. Therefore, these experiments also show the involvement of the peptide backbone at these positions. In addition, the peptides were fixed through hydrogen bonds at their free C and N termini.[139]

Interestingly, peptides which are sterically restricted by long and bulky side chains or even labeled with large

 © 2004 Wiley-VCH Verlag GmbH & Co. KGaA, Weinheim

fluorophors such as fluorescein are bound and even transported by TAP.[39,130,140,141] This result indicates there is a very flexible peptide-binding groove and translocation pore.

By taking these results together it was shown that peptides are hydrogen bonded to TAP through their free N and C termini and that the backbone residues and the side chains of the three N-terminal amino acids and of the C-terminal one contribute to the overall binding affinity (Figure 7b). The internal amino acid residues appear to form only minor contacts to the binding site, and they may even protrude into the solvent in the case of long or sterically restricted peptides. Thereby, flexibility of the peptide size and structure is combined with specificity obtained by constrictions of the N- and C-terminal anchor residues. The TCR, on the other hand, contacts mainly residues 5–8 of a MHC I associated nonapeptide in which TAP is promiscuous; therefore, the peptide pool is not restricted with respect to those residues which may be in direct contact with the TCR.[142]

5.2. Peptide Transport Is Coupled to ATP Hydrolysis

Although the TAP transporter has been the subject of numerous studies, it proves very difficult to assess the sequence of events during the peptide transport cycle. Studies with TAP mutants, in which conserved residues within the Walker A motifs of TAP1 and TAP2 were exchanged, only gave indirect evidence and partially contradictory results concerning the question as to whether nucleotide binding is a prerequisite for peptide association.[143–146] However, several research groups observed nucleotide-independent peptide binding to wild-type TAP under different assay conditions.[39,130,131] Studies with the viral protein ICP47, which inhibits the binding of the peptide to TAP (see Section 7.3), gave direct evidence that peptide binding is no prerequisite for nucleotide association.[147] Therefore, it seems that peptides and nucleotides bind to TAP in a random manner.

ATP binding induces the formation of a tight NBD sandwich dimer (see Section 3.1.2). This step could represent the "power stroke" because the binding energy of ATP could be transformed into mechanical work.[87,93,98] Kinetic studies revealed that peptides bind to TAP through a two-step mechanism in which a fast association step is followed by a slow isomerization of the TAP complex.[130] The isomerization is associated with large conformational changes within TAP during which approximately one-quarter of all TAP residues are rearranged.[148] The structural reorganization possibly resembles a molecular switch which activates the ATPase activity. ATP hydrolysis is a requirement for (ongoing) peptide transfer,[138,149] and interestingly, the stimulation of ATPase activity is correlated to peptide binding.[150] Importantly, sterically restricted peptides, which bind to TAP but are not transported, do not stimulate ATP hydrolysis.[150]

In a recent study, photolabeling with 8-azido-[α^{32}P]-ATP was combined with BeF_4^{2-} trapping.[151] $BeF_n^{(n-2)-}$ acts as an ATPase inhibitor by inducing formation of a stable Mg·ADP·-BeF_4^{2-} complex, which mimics the ATP-bound ground state.[152] It was shown that this complex is formed in a peptide-dependent manner in TAP and hydrolysis of ATP occurs at both subunits. These results indicate that ATP hydrolysis only takes place after peptide transfer. The function of ATP hydrolysis might therefore be to reset the transporter for further translocation cycles. At present, it is unclear how exactly the transfer of peptides through a proposed pore constructed by the TMDs is accomplished.

It has been shown that both NBDs hydrolyze ATP in the peptide transfer cycle.[151] A vanadate-trapping assay was performed in which orthovanadate (V_i) within the inhibitory Mg·ADP·V_i complex mimics the γ-phosphate during the transition state of ATP hydrolysis.[153,154] This assay revealed that ADP predominantly binds to TAP2, whereas the non-hydrolyzable ATP-analogue ATP·γ-biotin was only associated with TAP1.[144] This phenomenon, whereby the two subunits are differentially labeled, is also seen in other ABC transporters.[155–157] Together with results obtained from Walker A mutations and studies of chimeras with exchanged NBDs, this shows a nonequivalence of both NBDs during the catalytic cycle.[107,143–146,158,159] The reason for the requirement of two distinct NBDs in TAP is not understood. Although it has been shown that both NBDs hydrolyze ATP, mutational analysis indicated that ATP hydrolysis at TAP1 might not be essential (M. Chen, R. Abele, R. Tampé, unpublished results).[144]

The following hypothetical model of the peptide translocation cycle can be built from the available data (Figure 8): ATP and the peptide bind independently to TAP and both

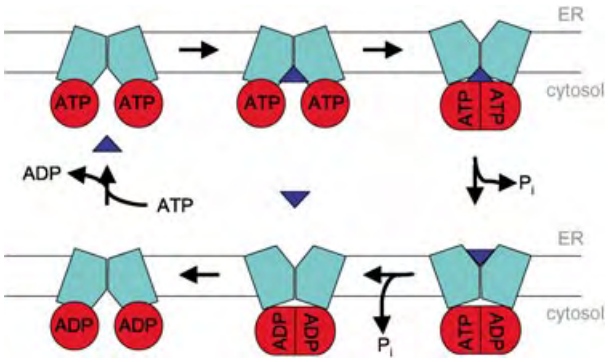


Figure 8. Model for the peptide translocation cycle of TAP. ATP and peptide (blue triangle) bind independently to TAP and both drive the formation of the NBD dimers. The TMDs rearrange to form a translocation pore through which the peptide is transferred into the ER lumen. One molecule of ATP is hydrolyzed at each NBD. The hydrolysis may occur in a processive, sequential mode as found for Mdl1, a close homologue of TAP.[97] Finally, ADP and inorganic phosphate are released and the NBDs are driven apart from each other. The transporter is then ready for the next peptide translocation cycle.

binding steps are associated with conformational changes within the NBDs and TMDs. As a consequence, the peptide-binding groove may approach the (possibly newly formed) transfer pore through which the peptide is then channeled into the ER lumen. ATP is hydrolyzed at both NBDs, in a sequential processive mode. After hydrolysis of both ATP molecules, the resulting ADP and inorganic phosphate are released. Considering the high cellular ATP concentrations

(3–8 mM), it can be assumed that TAP immediately gets reloaded with ATP after release of ADP, and is thus ready for the next peptide translocation cycle. The TAP model presented is speculative, and alternative models cannot be excluded.[160,161]

6. Transporters Related to TAP

MHC I molecules display intracellular peptides to cytotoxic T cells for immune surveillance. Most peptides are "self" peptides derived from endogenous cytosolic or organellar proteins, which usually do not elucidate an immune response.[162–164] The discrimination between "self" and "non-self" peptides is rather strict: the substitution of a single amino acid in endogenous peptides can trigger a T-cell response. As a result, the organism can rapidly eliminate cells with erroneous translation products, which might accumulate, for example, after exposure to mutagenic agents and/or malignant transformation. On the other hand, this very strict distinction between "self" and "non-self" peptides causes severe problems in transplantation medicine, since many human genes show considerable natural polymorphism. Thus, proteins that differ in a single amino acid between the graft and the host can produce so-called "minor histocompatibility antigens", which provoke rejection of the transplant. Interestingly, some minor histocompatibility antigens have been found to stem from mitochondrially encoded proteins which, like bacterial proteins, differ from nuclearly encoded proteins in that they are formylated at their N-terminal methionine residue.[165,166] It has been shown that the presentation of an *N*-formylated peptide derived from the mitochondrial NADH dehydrogenase (ND1) is at least partially TAP-dependent.[167]

Presentation of *N*-formylated peptides is an exception to the rule that TAP and MHC I reject peptides with substitution at their N or C termini. The means by which peptides translocate from the mitochondria to the cytoplasm for transport by TAP and subsequent MHC I presentation is unknown. One possibility is that they are translocated by the ABC transporters ABCB10 or ABCB8, which are located in the inner mitochondrial membrane. Both share significant sequence identity to TAP1 and TAP2 ($>30\,\%$).[168,169] The function of the yeast ABCB10 homologue Mdl1 has been elucidated recently.[78] This half-transporter forms a homodimer, which exports peptides from the mitochondrial matrix into the intermembrane space. Interestingly, Mdl1 transports peptides with 6–20 amino acids, thereby matching the range of peptides transported by TAP. Mdl1-mediated peptide release into the cytosol could also be involved in communication between the cellular and mitochondrial genome and/or metabolism. In addition, there is evidence for a role in the regulation of resistance to oxidative stress.[170] It is likely that the human homologue ABCB10 serves the same functions as Mdl1. An additional role in supplying peptides for antigen presentation seems possible but has not been established yet. The function of yeast Mdl2 and the human homologue ABCB8 is currently unknown.

The protein with the highest sequence identity to TAP (36.2 % and 37.1 % to TAP1 and TAP2, respectively) is ABCB9, also called TAPL (TAP-like protein).[171] ABCB9 and the TAP genes have probably evolved by gene duplication, but they are located on different chromosomes.[172] The high homology to TAP may enable ABCB9 to also serve as a peptide transporter. The location of the TAP-like protein is currently not clear. It has been proposed to be present in either the ER or the lysosomal membrane.[173,174] Furthermore, it is unknown whether ABCB9 forms a homodimer or a heterodimer with another half-transporter such as TAP1 or TAP2.

7. TAP Dysfunction in Human Diseases

Any defect that affects the delivery of the peptide into the ER will result in decreased expression of MHC I molecules on the cell surface. MHC I molecules are unstable without bound peptides and are degraded in the cytosol, thereby preventing presentation on the surface. Since the transport of peptides into the ER by TAP represents a bottleneck within the MHC I pathway, disruption of its function has a severe impact on the immune response to viral invaders and tumor-associated antigens. TAP function may be impaired through effects that act at different levels. First, mutations in the TAP genes may lead to inactive proteins. Loss of function may be a consequence of mutations in either TAP1 or TAP2, thus proving the requirement of a heterodimeric TAP1/TAP2 complex. Mutations may cause an immunodeficiency disorder, the Bare Lymphocyte Syndrome of type I, which represents the only known inherited disease connected with TAP. Second, the transcription of the TAP genes may be repressed as a result of the malfunction of one or more regulatory mechanisms of TAP expression. This has been found to be the case in several tumors.[175–177] Moreover, some viruses, for example, the Epstein–Barr virus, encode proteins that down-regulate expression of the TAP genes.[178] Third, function of the TAP complex can be impeded posttranslationally through inhibitory proteins. Different viruses use this strategy to evade immune recognition by their host.

7.1. Genetic Defects of TAP Cause an Immunodeficiency Disorder

Bare Lymphocyte Syndrome (BLS) is a rare, autosomal-recessive disorder first described by Touraine et al.[179] Three types of BLS can be distinguished: Patients with BLS type I, II, and III have MHC I, II, and combined MHC I and II deficiency, respectively.[180] In contrast to patients with BLS type II or III, who suffer from a complete lack of cellular and humoral immune responses to antigens and usually die within the first 3–4 years of life, most BLS type I patients survive into adulthood but may then die from progressive lung damage.[181,182] Patients with BLS type I suffer from down-regulation of MHC I surface expression as a result of mutations in either TAP1 or TAP2, which usually leads to a premature stop of translation.[11,12,183,184]

Typical symptoms of BLS type I are recurrent and chronic bacterial infections and necrotizing granulomatous skin lesions. Surprisingly, viral infections do not contribute to the

 © 2004 Wiley-VCH Verlag GmbH & Co. KGaA, Weinheim

disease pattern of BLS type I. Also, a person deficient in TAP as a result of a TAP2 mutation is completely asymptomatic.[185] Therefore, the cell-mediated immune response seems to work at least to some extent. Cells lacking MHC I molecules on the surface are usually killed by natural killer (NK) cells. NK cells may be involved in the development of the skin lesions, since upon sustained activation during bacterial infections they are capable of promoting inflammatory responses. An increase in the number of NK cells was found in the peripheral blood lymphocytes of patients with BLS type I. Nevertheless, the NK cells were unable to kill the cells deficient in MHC I. The reason for this could be an enhanced expression of inhibitory NK cell receptors.[186]

7.2. TAP Function in Tumor Development

Many tumor cells have lost the ability to present antigens and are therefore invisible to patrolling cytotoxic T cells. Tumor cells lacking MHC I at the cell surface are often also "ignored" by NK cells.[187] The reason is not fully understood, but may involve MHC I surrogates such as the UL18 protein of the ubiquitous human cytomegalovirus.[188]

There are several reasons for the loss of antigen presentation in tumor cells. A single point mutation in TAP1 was found in a small cell lung cancer cell line which led to the amino acid exchange R659Q within the P(Pro) loop.[189] The mutated TAP protein was expressed but was unable to mediate surface expression of peptide-loaded MHC I. A variety of tumors have reduced amounts of TAP complexes because of a malfunction of regulatory mechanisms of TAP expression.[175–177,190] One mechanism of TAP down-regulation could act through the inactive tumor suppressor protein p53, which normally induces TAP1 expression.[191] More than 50% of human tumors exhibit mutations in the p53 gene, and the resulting malfunctional protein may be unable to induce TAP1 and, therefore, diminish the overall amount of TAP complexes within the cell. Impaired TAP expression could be overcome in small cell lung carcinoma cell-culture models by transfection of the TAP1 gene or transfection of the TAP1, TAP2, and MHC I genes in human melanoma cell lines.[192–194] Additionally, defects in the regulation of TAP expression can often be corrected by application of IFN-γ.[194–196]

7.3. Viruses Undermine TAP-Dependent Antigen Presentation

Viruses have invented elaborated means to evade the host's immune response over their millions of years of coevolution and cause acute, chronic, or latent infections and, in some instances, also facilitating tumor development.[7] Most viruses do not concentrate on a single immune-evasion strategy but utilize several strategies in parallel. The blocking of antigen presentation is one strategy employed by different DNA viruses, and several of them have chosen TAP as the target.

Viral proteins can prevent MHC I presentation on the cell surface by directly or indirectly inhibiting TAP-mediated peptide transport into the ER. Adenoviruses cause mild infections of the upper respiratory tract in immunocompetent children, but lead to severe infections in immunocompromised patients. The adenovirus of homology group E inhibits expression of MHC I on the cell surface because of the association of MHC I with the 19K protein present in the ER.[197–199] The E3/19K protein can bind to both MHC I and TAP, but—unlike tapasin—not simultaneously. Binding to either TAP or MHC I prevents their interaction and thereby decreases association between the MHC I/TAP and the protein. The unstable free MHC I is degraded in the cytosol.[200]

Several members of the herpes virus family (Epstein–Barr virus, herpes simplex virus, human cytomegalovirus, human herpes virus 8) also inhibit antigen presentation on the level of TAP.[178,201–211]

The Epstein–Barr virus (EBV) infects B lymphocytes. The primary infection of immunocompromised hosts can cause infectious mononucleosis, a disease associated with fever, sore throat, and swollen lymph glands. The infection leads to a T-cell response, which EBV sustains by establishing a latency state, in which one specific protein, the latent membrane protein 1 (LMP-1), is not expressed. Later on, by expression of several "latent" genes, EBV contributes to the development of malignant diseases, for example Hodgkin's disease, Burkitt's lymphoma, and nasopharyngeal carcinoma.[178] During the acute phase of an EBV infection the expression of LMP-1 induces expression of TAP2, while that of TAP1 is down-regulated. This disequilibrium of TAP1 and TAP2 leads to the formation of only a few functional TAP complexes and, therefore, disturbance of peptide presentation and immune reaction.[178,200] The expression of TAP is also affected by the BCRF1 gene product of EBV. BCRF1 encodes a viral interleukin-10 homologue (vIL-10), which down-regulates TAP1 expression without influencing that of TAP2.[212] vIL-10 does not completely abolish MHC I dependent antigen presentation; indeed, even a signal sequence epitope of vIL-10 is presented on the cell surface and induces a T-cell response. The ongoing antigen presentation probably arises from a TAP-independent pathway.[213,214]

The herpes simplex virus and the human cytomegalovirus both encode proteins which interfere with peptide presentation by binding directly to TAP, thereby eliminating the supply of peptide for MHC I (Figure 9).[215] ICP47 and US6 are valuable tools to elucidate TAP function (see Sections 4.1, 4.2, and 5.2). Herpes simplex virus (HSV) occurs as two different serotypes. HSV-I infects facial epithelia while HSV-2, which is commonly referred to as genital herpes, produces lesions on the genitals, urethra, and bladder. Both serotypes lead to persistent infections.

TAP is the target of ICP47 of HSV-1 and HSV-2. Although the ICP47 proteins of both serotypes (88 and 86 amino acids, respectively, ca. 10 kDa) share an overall sequence identity of only 42%, they do not differ significantly in their effect on TAP.[204] The sequence similarity is strongest in the N-terminal part of the proteins, and it was shown that amino acids 3–34 are sufficient for TAP inhibition.[205] This active domain of ICP47 appears to be mainly unstructured in aqueous solution.[216] After membrane adsorption, an α-helical structure is induced, which is composed of two helical

 © 2004 Wiley-VCH Verlag GmbH & Co. KGaA, Weinheim

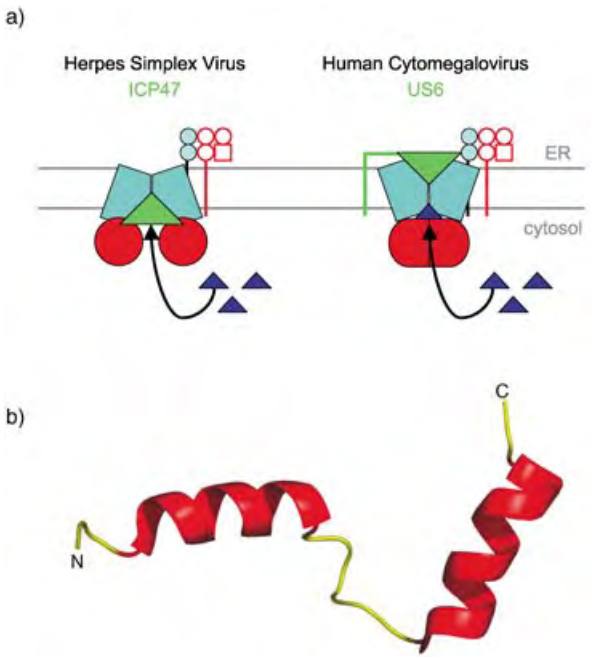


Figure 9. Immune evasion strategies of herpes simplex virus (HSV) and human cytomegalovirus (HCMV) using TAP as a target. a) ICP47 of HSV binds to TAP from the cytosolic side, thereby preventing peptide binding and translocation. The type I glycoprotein US6 of HCMV binds to ER-luminal regions of TAP and inhibits peptide translocation by blocking ATP binding to TAP. b) NMR structure of the active domain of ICP47(2-34) (PDB code: 1QL0).[217]

regions (amino acids 4–15 and 22–32) connected by a flexible loop (Figure 9b).[217]

ICP47 blocks the peptide-binding site of TAP, thereby preventing peptide association and transport into the ER.[147,206,218,219] In addition, binding of ICP47 seems to result in conformational changes, which lead to destabilization of the TAP1/TAP2 heterodimer.[112] However, ATP and ADP binding are not affected by ICP47.[218] The high-affinity association of ICP47 with TAP (K_D = ca. 50 nM) is reversible and can be competitively inhibited by peptides. Nevertheless, ICP47 does not seem to occupy the binding groove in the same way as substrate peptides, since peptides of the same size bind with very low affinity and N-terminal modification prevents peptide but not ICP47 binding.[39,40,207] At present, it is unknown which regions of ICP47 and TAP interact with each other.

Another protein, which circumvents MHC I surface presentation by direct inhibition of TAP, is encoded by the human cytomegalovirus (HCMV). The primary infection with HCMV is usually asymptomatic or mild, but can lead to complex diseases such as retinitis, pneumonitis, enterocolitis, and hepatitis in immunocompromized individuals. In infants the infection can cause a cytomegalovirus-associated disease (cytomegalic inclusion disease, CID), which is often associated with deafness and neurological damages. Following primary infection, HCMV can establish a life-long persistence in a latent state without causing any disease. In the activated state HCMV can escape the host immune response by inhibiting surface expression of MHC I (for an overview see Refs. [7,9,208,215,220]). Several viral gene products are involved in this process and they act at different points in the antigen-processing pathway. TAP is the target of the early gene product US6, a type I membrane glycoprotein consisting of 183 amino acids (23 kDa).[210,211,221] US6 consists of an N-terminal leader sequence followed by an ER-luminal domain, one transmembrane helix, and a short cytosolic tail. Truncation studies proved that the ER-luminal domain (amino acids 20–139) is essential and sufficient for TAP inhibition.[124,211] Glycosylation is not necessary for US6 function.[124] Binding of US6 to the ER-luminal part of TAP prevents peptide translocation, but—unlike ICP47—it does not adversely affect peptide binding.[211,221] Instead, by binding to ER-luminal regions of TAP, US6 stabilizes a conformation that blocks ATP binding and the peptide-stimulated ATPase activity of TAP.[123,124]

8. Summary and Outlook

The peptide transporter TAP constitutes a bottleneck within the antigen-processing and -presentation pathway. Peptide-binding studies showed that the two TMDs cooperate to recognize peptides of 8–30 residues mainly by their N- and C-terminal amino acids, while the internal amino acid residues have only minor contacts to the binding site. Basic and hydrophobic amino acids are preferred at the C terminus, and the three N-terminal residues were also shown to be determinants of binding affinity. Therefore, MHC I and TAP have overlapping peptide-binding specificities. Since the TCR binds to the internal amino acids of peptides, TAP does not restrict the pool of peptides available for presentation by the T-cell receptor. This fine-tuning of binding specificities indicates a long history of coevolution of TAP, MHC I, and TCR which enables the immune system to effectively detect and destroy infected cells.

Viruses have developed several mechanisms to block antigen presentation. The two viral inhibitors ICP47 and US6 have been studied in detail. Both hinder peptide transport into the ER by direct interaction with TAP. The residues involved in binding are not yet determined. Nevertheless, these viral inhibitors have been successfully used to explore the transport mechanism of TAP. On the basis of these viral inhibitors, therapeutic drugs could be designed that are potent immune suppressors or that are applicable in novel therapeutic strategies against viruses, thus restoring the ability of our immune system to recognize infected cells.

ATP binding and hydrolysis at the NBDs are required to facilitate ongoing peptide transport across the ER membrane. There is evidence for the requirement of one ATP molecule per NBD for translocation of one peptide molecule, but the exact stoichiometry of ATP to peptide has still to be determined. The peptide is thought to be translocated through a pore formed by the TMDs. The architecture of this proposed pore is currently unknown and can probably only be determined by high-resolution crystal structures of the TAP complex during different phases of the transport cycle. Crystal structures as well as further kinetic studies are required to decipher the communication between both NBDs

 © 2004 Wiley-VCH Verlag GmbH & Co. KGaA, Weinheim

and between the NBDs and the TMDs as well as to elucidate the nature of the conformational changes associated with intramolecular signal transduction. Other unanswered questions concerning the translocation mechanism are whether ATP is hydrolyzed in a sequential processive or in a parallel mode at both NBDs, as well as the nature of the actual "power stroke".

Other interesting questions that can be addressed in the era of proteomics are: what is the exact composition of the PLC, and how do the different protein components within the PLC communicate with each other for a coordinated peptide loading? Besides intensive research of the antigen processing and presentation pathway during the last decade, these and many other questions have so far remained open. In contrast, viruses have studied antigen presentation for millions of years, which has resulted in elusive mechanisms to evade immune recognition. We now have the chance to make use of the immense "knowledge" of viruses to get further insights into the fascinating field of antigen processing and presentation.

Abbreviations

ABC	ATP binding cassette
BLS	Bare Lymphocyte Syndrome
$CD4^+$	T-helper cells
$CD8^+$	cyctotoxic T cells
ER	endoplasmic reticulum
HC	heavy chain
HCMV	human cytomegalovirus
HSV	herpes simplex virus
ICD	intracellular domain
IM	inner membrane
MHC I	major histocompatibility complex I
NBD	nucleotide-binding domain
NK	natural killer
PLC	peptide-loading complex
TAP	transporter associated with antigen processing
TCR	T-cell receptor
TM	transmembrane helix
TMD	transmembrane domain

We are indebted to all current and former group members and collaborators. Without their enthusiasm, many insights into TAP function would not exist. We also thank Dr. Lutz Schmitt for help with the PyMOL presentations and Dr. Rupert Abele for helpful discussions and careful reading of the manuscript. The Deutsche Forschungsgemeinschaft (SFB 628: Functional Membrane Proteomics) supported this work.

Received: December 1, 2003 [A642]
Published Online: June 30, 2004

[1] C. A. Janeway, P. Travers, M. Walport, M. Shlomchik, *Immunobiology: The Immune System in Health and Disease*, 5. ed., Garland, New York, **2001**.
[2] P. C. Doherty, *Angew. Chem.* **1997**, *109*, 2014; *Angew. Chem. Int. Ed. Engl.* **1997**, *36*, 1926.
[3] R. M. Zinkernagel, *Angew. Chem.* **1997**, *109*, 2026; *Angew. Chem. Int. Ed. Engl.* **1997**, *36*, 1938.
[4] K. Eichmann, *Angew. Chem.* **1993**, *105*, 56; *Angew. Chem. Int. Ed. Engl.* **1993**, *32*, 54.
[5] K. Falk, O. Rötzschke, S. Stevanović, G. Jung, H. G. Rammensee, *Nature* **1991**, *351*, 290.
[6] K. Udaka, K. H. Wiesmüller, S. Kienle, G. Jung, P. Walden, *J. Exp. Med.* **1995**, *181*, 2097.
[7] H. L. Ploegh, *Science* **1998**, *280*, 248.
[8] J. W. Yewdell, A. B. Hill, *Nat. Immunol.* **2002**, *3*, 1019.
[9] E. W. Hewitt, *Immunology* **2003**, *110*, 163.
[10] H. L. Chen, D. Gabrilovich, R. Tampé, K. R. Girgis, S. Nadaf, D. P. Carbone, *Nat. Genet.* **1997**, *13*, 210.
[11] H. de la Salle, D. Hanau, D. Fricker, A. Urlacher, A. Kelly, J. Salamero, S. H. Powis, L. Donato, H. Bausinger, M. Laforet, M. Jeras, D. Spehner, T. Bieber, A. Falkenrodt, J.-P. Cazenave, J. Trowsdale, M. M. Tongio, *Science* **1994**, *265*, 237.
[12] H. Teisserenc, W. Schmitt, N. Blake, R. Dunbar, S. Gadola, W. L. Gross, A. Exley, V. Cerundolo, *Immunol. Lett.* **1997**, *57*, 183.
[13] M. M. Gottesman, S. V. Ambudkar, *J. Bioenerg. Biomembr.* **2001**, *33*, 453.
[14] P. Borst, R. O. Elferink, *Annu. Rev. Biochem.* **2002**, *71*, 537.
[15] R. Abele, R. Tampé, *Biochim. Biophys. Acta.* **1999**, *1461*, 405.
[16] L. Schmitt, R. Tampé, *ChemBioChem* **2000**, *1*, 16.
[17] B. Lankat-Buttgereit, R. Tampé, *Physiol. Rev.* **2002**, *82*, 187.
[18] J. Sprent, D. Lo, E. K. Gao, Y. Ron, *Immunol. Rev.* **1988**, *101*, 173.
[19] P. S. Ohashi, *Curr. Opin. Immunol.* **1996**, *8*, 808.
[20] J. Sprent, H. Kishimoto, *Philos. Trans. R. Soc. London Ser. B* **2001**, *356*, 609.
[21] K. Falk, O. Rötzschke, H.-G. Rammensee, *Nature* **1990**, *348*, 248.
[22] H.-G. Rammensee, K. Falk, O. Rötzschke, *Annu. Rev. Immunol.* **1993**, *11*, 213.
[23] N. Shastri, S. Schwab, T. Serwold, *Annu. Rev. Immunol.* **2002**, *20*, 463.
[24] W. Baumeister, J. Walz, F. Zuhl, E. Seemuller, *Cell* **1998**, *92*, 367.
[25] A. L. Goldberg, P. Cascio, T. Saric, K. L. Rock, *Mol. Immunol.* **2002**, *39*, 147.
[26] J. Löwe, D. Stock, B. Jap, P. Zwickl, W. Baumeister, R. Huber, *Science* **1995**, *268*, 533.
[27] M. Groll, L. Ditzel, J. Löwe, D. Stock, M. Bochtler, H. D. Bartunik, R. Huber, *Nature* **1997**, *386*, 463.
[28] M. P. Belich, R. J. Glynne, G. Senger, D. Sheer, J. Trowsdale, *Curr. Biol.* **1994**, *4*, 769.
[29] D. Nandi, H. Jiang, J. J. Monaco, *J. Immunol.* **1996**, *156*, 2361.
[30] M. Groettrup, R. Kraft, S. Kostka, S. Standera, R. Stohwasser, P. M. Kloetzel, *Eur. J. Immunol.* **1996**, *27*, 863.
[31] M. Rechsteiner, C. Realini, V. Ustrell, *Biochem. J.* **2000**, *345*, 1.
[32] P. M. Kloetzel, *Nat. Rev. Mol. Cell Biol.* **2001**, *2*, 179.
[33] B. Ehring, T. H. Meyer, C. Eckerskorn, F. Lottspeich, R. Tampé, *Eur. J. Biochem.* **1996**, *235*, 404.
[34] A. F. Kisselev, T. N. Akopian, K. M. Woo, A. L. Goldberg, *J. Biol. Chem.* **1999**, *274*, 3363.
[35] R. E. Toes, A. K. Nussbaum, S. Degermann, M. Schirle, N. P. Emmerich, M. Kraft, C. Laplace, A. Zwinderman, T. P. Dick, J. Müller, B. Schonfisch, C. Schmid, H. J. Fehling, S. Stevanovic, H. G. Rammensee, H. Schild, *J. Exp. Med.* **2001**, *194*, 1.
[36] G. Niedermann, E. Geier, M. Lucchiari-Hartz, N. Hitziger, A. Ramsperger, K. Eichmann, *Immunol. Rev.* **1999**, *172*, 29.
[37] G. Niedermann, *Curr. Top. Microbiol. Immunol.* **2002**, *268*, 91.
[38] J. Driscoll, M. G. Brown, D. Finley, J. J. Monaco, *Nature* **1993**, *365*, 262.

 © 2004 Wiley-VCH Verlag GmbH & Co. KGaA, Weinheim

[39] S. Uebel, T. H. Meyer, W. Kraas, S. Kienle, G. Jung, K. H. Wiesmüller, R. Tampé, *J. Biol. Chem.* **1995**, *270*, 18512.
[40] S. Uebel, W. Kraas, S. Kienle, K. H. Wiesmüller, G. Jung, R. Tampé, *Proc. Natl. Acad. Sci. USA* **1997**, *94*, 8976.
[41] J. Beninga, K. L. Rock, A. L. Goldberg, *J. Biol. Chem.* **1998**, *273*, 18734.
[42] L. Stoltze, M. Schirle, G. Schwarz, C. Schröter, M. W. Thompson, L. B. Hersh, H. Kalbacher, S. Stevanovic, H. G. Rammensee, H. Schild, *Nat. Immunol.* **2000**, *1*, 413.
[43] T. Serwold, S. Gaw, N. Shastri, *Nat. Immunol.* **2001**, *2*, 644.
[44] T. Saric, S. C. Chang, A. Hattori, I. A. York, S. Markant, K. L. Rock, M. Tsujimoto, A. L. Goldberg, *Nat. Immunol.* **2002**, *3*, 1169.
[45] K. Falk, O. Rötzschke, *Nat. Immunol.* **2002**, *3*, 1121.
[46] I. A. York, A. X. Mo, K. Lemerise, W. Zeng, Y. Shen, C. R. Abraham, T. Saric, A. L. Goldberg, K. L. Rock, *Immunity* **2003**, *18*, 429.
[47] T. Saric, J. Beninga, C. I. Graef, T. N. Akopian, K. L. Rock, A. L. Goldberg, *J. Biol. Chem.* **2001**, *276*, 36474.
[48] R. J. Binder, N. E. Blachere, P. K. Srivastava, *J. Biol. Chem.* **2001**, *276*, 17163.
[49] P. Srivastava, *Annu. Rev. Immunol.* **2002**, *20*, 395.
[50] J. Kunisawa, N. Shastri, *Mol. Cell* **2003**, *12*, 565.
[51] J. W. Yewdell, *Trends Cell Biol.* **2001**, *11*, 294.
[52] E. Reits, A. Griekspoor, J. Neijssen, T. Groothuis, K. Jalink, P. van Veelen, H. Janssen, J. Calafat, J. W. Drijfhout, J. Neefjes, *Immunity* **2003**, *18*, 97.
[53] A. Townsend, C. Ohlen, J. Bastin, H. G. Ljunggren, L. Foster, K. Karre, *Nature* **1989**, *340*, 443.
[54] A. Townsend, T. Elliott, V. Cerundolo, L. Foster, B. Barber, A. Tse, *Cell* **1990**, *62*, 285.
[55] K. M. Paulsson, P. Wang, P. O. Anderson, S. Chen, R. F. Pettersson, S. Li, *Int. Immunol.* **2001**, *13*, 1063.
[56] K. Paulsson, P. Wang, *Biochim. Biophys. Acta* **2003**, *1641*, 1.
[57] M. R. Farmery, S. Allen, A. J. Allen, N. J. Bulleid, *J. Biol. Chem.* **2000**, *275*, 14933.
[58] S. J. Kang, P. Cresswell, *J. Biol. Chem.* **2002**, *277*, 44838.
[59] B. Sadasivan, P. J. Lehner, B. Ortmann, T. Spies, P. Cresswell, *Immunity* **1996**, *5*, 103.
[60] B. Ortmann, J. Copeman, P. J. Lehner, B. Sadasivan, J. A. Herberg, A. G. Grandea, S. R. Riddell, R. Tampé, T. Spies, J. Trowsdale, P. Cresswell, *Science* **1997**, *277*, 1306.
[61] G. Raghuraman, P. E. Lapinski, M. Raghavan, *J. Biol. Chem.* **2002**, *277*, 41786.
[62] N. Garbi, N. Tiwari, F. Momburg, G. J. Hämmerling, *Eur. J. Immunol.* **2003**, *34*, 264.
[63] S. Li, K. M. Paulsson, S. Chen, H. O. Sjogren, P. Wang, *J. Biol. Chem.* **2000**, *275*, 1581.
[64] C. A. Peh, N. Laham, S. R. Burrows, Y. Zhu, J. McCluskey, *J. Immunol.* **2000**, *164*, 292.
[65] M. J. Barnden, A. W. Purcell, J. J. Gorman, J. McCluskey, *J. Immunol.* **2000**, *165*, 322.
[66] M. E. Paquet, D. B. Williams, *Int. Immunol.* **2002**, *14*, 347.
[67] A. P. Williams, C. A. Peh, A. W. Purcell, J. McCluskey, T. Elliott, *Immunity* **2002**, *16*, 509.
[68] B. Park, K. Ahn, *J. Biol. Chem.* **2003**, *278*, 14337.
[69] C. F. Higgins, *Annu. Rev. Cell Biol.* **1992**, *8*, 67.
[70] M. Dean, A. Rzhetsky, R. Allikmets, *Genome Res.* **2001**, *11*, 1156.
[71] J. E. Walker, M. Saraste, M. J. Runswick, N. J. Gay, *EMBO J.* **1982**, *1*, 945.
[72] S. C. Hyde, P. Emsley, M. J. Hartshorn, M. M. Mimmack, U. Gileadi, S. R. Pearce, M. P. Gallagher, D. R. Gill, R. E. Hubbard, C. F. Higgins, *Nature* **1990**, *346*, 362.
[73] M. M. Gottesman, T. Fojo, S. E. Bates, *Nat. Rev. Cancer* **2002**, *2*, 48.
[74] D. Sanglard, K. Kuchler, F. Ischer, J. L. Pagani, M. Monod, J. Bille, *Antimicrob. Agents Chemother.* **1995**, *39*, 2378.
[75] S. Perea, J. L. Lopez-Ribot, W. R. Kirkpatrick, R. K. McAtee, R. A. Santillan, M. Martinez, D. Calabrese, D. Sanglard, T. F. Patterson, *Antimicrob. Agents Chemother.* **2001**, *45*, 2676.
[76] C. Zimmerman, K. C. Klein, P. K. Kiser, A. R. Singh, B. L. Firestein, S. C. Riba, J. R. Lingappa, *Nature* **2002**, *415*, 88.
[77] M. Ehrmann, R. Ehrle, E. Hofmann, W. Boos, A. Schlosser, *Mol. Microbiol.* **1998**, *29*, 685.
[78] J. Young, I. B. Holland, *Biochim. Biophys. Acta* **1999**, *1416*, 177.
[79] M. J. Welsh, A. E. Smith, *Cell* **1993**, *73*, 1251.
[80] J. M. Pilewski, R. A. Frizzell, *Physiol. Rev.* **1999**, *79*, S215.
[81] A. P. Babenko, L. Aguilar-Bryan, J. Bryan, *Annu. Rev. Physiol.* **1998**, *60*, 667.
[82] P. Manavalan, D. G. Dearborn, J. M. McPherson, A. E. Smith, *FEBS Lett.* **1995**, *366*, 87.
[83] L. Schmitt, R. Tampé, *Curr. Opin. Struct. Biol.* **2002**, *12*, 754.
[84] G. Chang, C. B. Roth, *Science* **2001**, *293*, 1793.
[85] G. Chang, *J. Mol. Biol.* **2003**, *330*, 419.
[86] G. Verdon, S. V. Albers, B. W. Dijkstra, A. J. Driessen, A. M. Thunnissen, *J. Mol. Biol.* **2003**, *330*, 343.
[87] P. C. Smith, N. Karpowich, L. Millen, J. E. Moody, J. Rosen, P. J. Thomas, J. F. Hunt, *Mol. Cell* **2002**, *10*, 139.
[88] N. Karpowich, O. Martsinkevich, L. Millen, Y. R. Yuan, P. L. Dai, K. MacVey, P. J. Thomas, J. F. Hunt, *Structure* **2001**, *9*, 571.
[89] L. W. Hung, I. X. Wang, K. Nikaido, P. Q. Liu, G. F. Ames, S. H. Kim, *Nature* **1998**, *396*, 703.
[90] K. Diederichs, J. Diez, G. Greller, C. Müller, J. Breed, C. Schnell, C. Vonrhein, W. Boos, W. Welte, *EMBO J.* **2000**, *19*, 5951.
[91] R. Gaudet, D. C. Wiley, *EMBO J.* **2001**, *20*, 4964.
[92] Y. R. Yuan, S. Blecker, O. Martsinkevich, L. Millen, P. J. Thomas, J. F. Hunt, *J. Biol. Chem.* **2001**, *276*, 32313.
[93] K. P. Locher, A. T. Lee, D. C. Rees, *Science* **2002**, *296*, 1091.
[94] L. Schmitt, H. Benabdelhak, M. A. Blight, I. B. Holland, M. T. Stubbs, *J. Mol. Biol.* **2003**, *330*, 333.
[95] K. Nikaido, P. Q. Liu, G. F. Ames, *J. Biol. Chem.* **1997**, *272*, 27745.
[96] K. A. Kennedy, B. Traxler, *J. Biol. Chem.* **1999**, *274*, 6259.
[97] E. Janas, M. Hofacker, M. Chen, S. Gompf, C. van der Does, R. Tampé, *J. Biol. Chem.* **2003**, *278*, 26862.
[98] K. P. Hopfner, A. Karcher, D. S. Shin, L. Craig, L. M. Arthur, J. P. Carney, J. A. Tainer, *Cell* **2000**, *101*, 789.
[99] R. A. Shilling, L. Balakrishnan, S. Shahi, H. Venter, H. W. van Veen, *Int. J. Antimicrob. Agents* **2003**, *22*, 200.
[100] L. Homolya, Z. Holl, U. A. Germann, L. Pastan, M. M. Gottesman, B. Sarkadi, *J. Biol. Chem.* **1993**, *268*, 21493.
[101] H. Bolhuis, H. W. van Veen, D. Molenaar, B. Poolman, A. J. Driessen, W. N. Konings, *EMBO J.* **1996**, *15*, 4239.
[102] J. S. Patzlaff, T. van der Heide, B. Poolman, *J. Biol. Chem.* **2003**, *278*, 29546.
[103] A. E. Senior, M. K. al-Shawi, I. L. Urbatsch, *FEBS Lett.* **1995**, *377*, 285.
[104] A. E. Senior, D. C. Gadsby, *Semin. Cancer Biol.* **1997**, *8*, 143.
[105] M. Matsuo, N. Kioka, T. Amachi, K. Ueda, *J. Biol. Chem.* **1999**, *274*, 37479.
[106] L. Aleksandrov, A. A. Aleksandrov, X. B. Chang, J. R. Riordan, *J. Biol. Chem.* **2002**, *277*, 15419.
[107] P. Alberts, O. Daumke, E. V. Deverson, J. C. Howard, M. R. Knittler, *Curr. Biol.* **2001**, *11*, 242.
[108] T. Spies, R. DeMars, *Nature* **1991**, *351*, 323.
[109] S. J. Powis, A. R. Townsend, E. V. Deverson, J. Bastin, G. W. Butcher, J. C. Howard, *Nature* **1991**, *354*, 528.
[110] T. H. Meyer, P. M. van Endert, S. Uebel, B. Ehring, R. Tampé, *FEBS Lett.* **1994**, *351*, 443.
[111] S. Urlinger, K. Kuchler, T. H. Meyer, S. Uebel, R. Tampé, *Eur. J. Biochem.* **1997**, *245*, 266.

 © 2004 Wiley-VCH Verlag GmbH & Co. KGaA, Weinheim

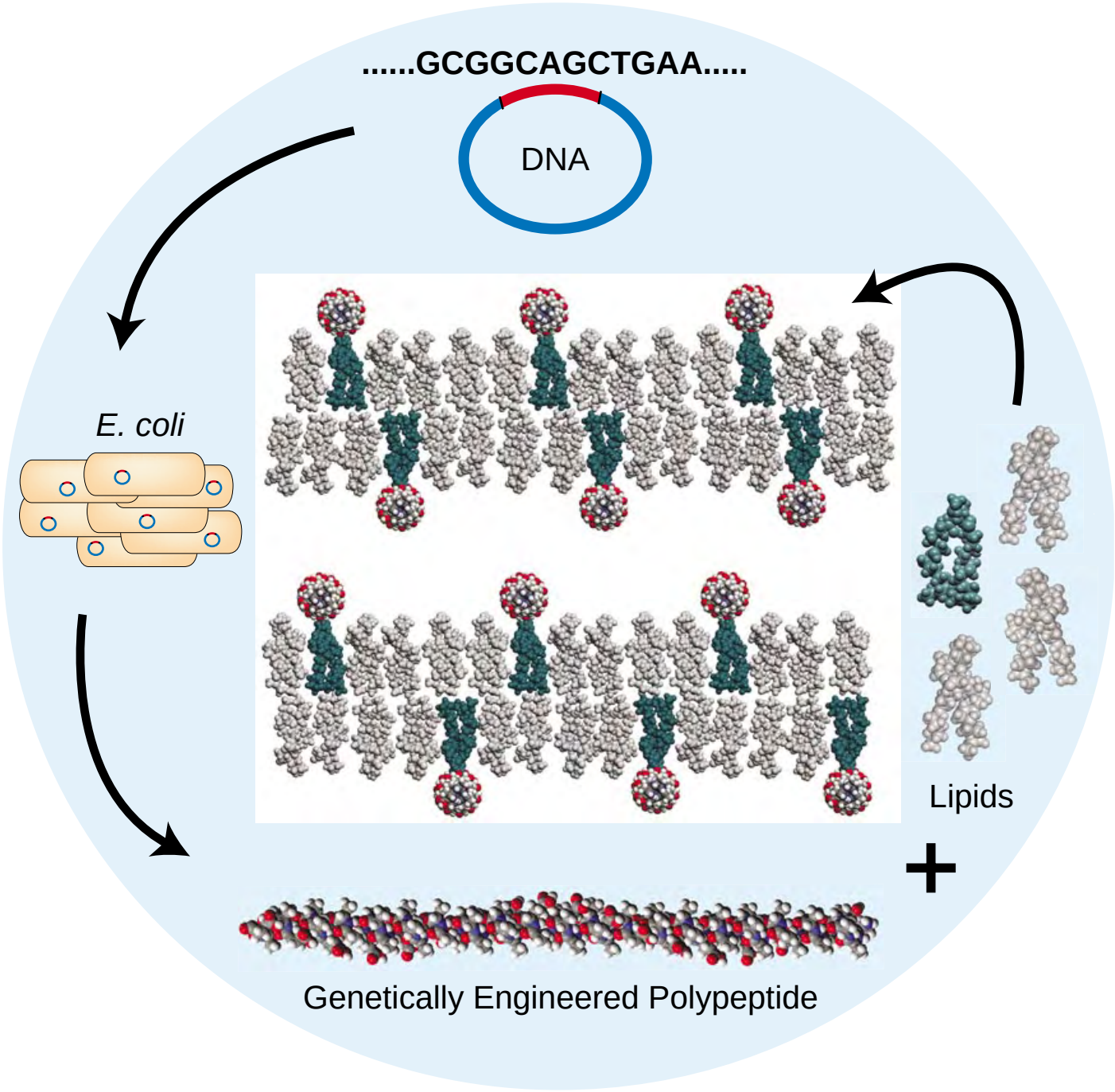
[112] V. G. Lacaille, M. J. Androlewicz, *J. Biol. Chem.* **1998**, *273*, 17386.
[113] G. Velarde, R. C. Ford, M. F. Rosenberg, S. J. Powis, *J. Biol. Chem.* **2001**, *276*, 46054.
[114] M. J. Kleijmeer, A. Kelly, H. J. Geuze, J. W. Slot, A. Townsend, J. Trowsdale, *Nature* **1992**, *357*, 342.
[115] K. M. Müller, C. Ebensperger, R. Tampé, *J. Biol. Chem.* **1994**, *269*, 14032.
[116] Y. R. Yuan, O. Martsinkevich, J. F. Hunt, *Acta Crystallogr. Sect. D* **2003**, *59*, 225.
[117] G. Schmees, A. Stein, S. Hunke, H. Landmesser, E. Schneider, *Eur. J. Biochem.* **1999**, *266*, 420.
[118] S. Hunke, M. Mourez, M. Jehanno, E. Dassa, E. Schneider, *J. Biol. Chem.* **2000**, *275*, 15526.
[119] E. W. Hewitt, P. J. Lehner, *Eur. J. Immunol.* **2003**, *34*, 422.
[120] E. Bakos, I. Klein, E. Welker, K. Szabo, M. Müller, B. Sarkadi, A. Varadi, *Biochem. J.* **1997**, *323*, 777.
[121] G. Szakacs, C. Ozvegy, E. Bakos, B. Sarkadi, A. Varadi, *Biochem. J.* **2001**, *356*, 71.
[122] P. M. van Endert, *J. Biol. Chem.* **1999**, *274*, 14632.
[123] E. W. Hewitt, S. S. Gupta, P. J. Lehner, *EMBO J.* **2001**, *20*, 387.
[124] C. Kyritsis, S. Gorbulev, S. Hutschenreiter, K. Pawlitschko, R. Abele, R. Tampé, *J. Biol. Chem.* **2001**, *276*, 48031.
[125] B. Lankat-Buttgereit, R. Tampé, *FEBS Lett.* **1999**, *464*, 108.
[126] J. Koch, R. Guntrum, S. Heintke, C. Kyritsis, R. Tampé, *J. Biol. Chem.* **2004**, *279*, 10142.
[127] S. Heintke, M. Chen, U. Ritz, B. Lankat-Buttgereit, J. Koch, R. Abele, B. Seliger, R. Tampé, *FEBS Lett.* **2003**, *533*, 42.
[128] U. Ritz, F. Momburg, H. P. Pircher, D. Strand, C. Huber, B. Seliger, *Int. Immunol.* **2001**, *13*, 31.
[129] M. Nijenhuis, S. Schmitt, E. A. Armandola, R. Obst, J. Brunner, G. J. Hämmerling, *J. Immunol.* **1996**, *156*, 2186.
[130] L. Neumann, R. Tampé, *J. Mol. Biol.* **1999**, *294*, 1203.
[131] M. J. Androlewicz, P. Cresswell, *Immunity* **1994**, *1*, 7.
[132] M. Colonna, M. Bresnahan, S. Bahram, J. L. Strominger, T. Spies, *Proc. Natl. Acad. Sci. USA* **1992**, *89*, 3932.
[133] S. H. Powis, I. Mockridge, A. Kelly, L. A. Kerr, R. Glynne, U. Gileadi, S. Beck, J. Trowsdale, *Proc. Natl. Acad. Sci. USA* **1992**, *89*, 1463.
[134] R. Obst, E. A. Armandola, M. Nijenhuis, F. Momburg, G. J. Hammerling, *Eur. J. Immunol.* **1995**, *26*, 2170.
[135] S. Daniel, S. Caillat-Zucman, J. Hammer, J. F. Bach, P. M. van Endert, *J. Immunol.* **1997**, *159*, 2350.
[136] P. M. van Endert, R. Tampé, T. H. Meyer, R. Tisch, J. F. Bach, H. O. McDevitt, *Immunity* **1994**, *1*, 491.
[137] G. E. Jung, *Combinatorial Peptide and Nonpeptide Libraries*, Wiley-VCH, Weinheim, **1996**.
[138] J. C. Shepherd, T. N. Schumacher, P. G. Ashton-Rickardt, S. Imaeda, H. L. Ploegh, C. A. Janeway, Jr., S. Tonegawa, *Cell* **1993**, *74*, 577.
[139] S. Uebel, R. Tampé, *Curr. Opin. Immunol.* **1999**, *11*, 203.
[140] I. Bačík, H. L. Snyder, L. C. Antón, G. Russ, W. Chen, J. R. Bennink, L. Urge, L. Otvos, B. Dudkowska, L. Eisenlohr, J. W. Yewdell, *J. Exp. Med.* **1997**, *186*, 479.
[141] M. Gromme, R. van der Valk, K. Sliedregt, L. Vernie, R. Liskamp, G. Hämmerling, J. O. Koopmann, F. Momburg, J. Neefjes, *Eur. J. Immunol.* **1997**, *28*, 898.
[142] D. N. Garboczi, P. Ghosh, U. Utz, Q. R. Fan, W. E. Biddison, D. C. Wiley, *Nature* **1996**, *384*, 134.
[143] S. Arora, P. E. Lapinski, M. Raghavan, *Proc. Natl. Acad. Sci. USA* **2001**, *98*, 7241.
[144] J. T. Karttunen, P. J. Lehner, S. S. Gupta, E. W. Hewitt, P. Cresswell, *Proc. Natl. Acad. Sci. USA* **2001**, *98*, 7431.
[145] M. R. Knittler, P. Alberts, E. V. Deverson, J. C. Howard, *Curr. Biol.* **1999**, *9*, 999.
[146] L. Saveanu, S. Daniel, P. M. van Endert, *J. Biol. Chem.* **2001**, *276*, 22107.
[147] R. Tomazin, A. B. Hill, P. Jugovic, I. York, P. van Endert, H. L. Ploegh, D. W. Andrews, D. C. Johnson, *EMBO J.* **1996**, *15*, 3256.
[148] L. Neumann, R. Abele, R. Tampé, *J. Mol. Biol.* **2002**, *324*, 965.
[149] J. J. Neefjes, F. Momburg, G. J. Hämmerling, *Science* **1993**, *261*, 769.
[150] S. Gorbulev, R. Abele, R. Tampé, *Proc. Natl. Acad. Sci. USA* **2001**, *98*, 3732.
[151] M. Chen, R. Abele, R. Tampé, *J. Biol. Chem.* **2003**, *278*, 29686.
[152] A. J. Fisher, C. A. Smith, J. B. Thoden, R. Smith, K. Sutoh, H. M. Holden, I. Rayment, *Biochemistry* **1995**, *34*, 8960.
[153] C. A. Smith, I. Rayment, *Biochemistry* **1996**, *35*, 5404.
[154] S. Sharma, A. L. Davidson, *J. Bacteriol.* **2000**, *182*, 6570.
[155] K. Szabo, G. Szakacs, T. Hegeds, B. Sarkadi, *J. Biol. Chem.* **1999**, *274*, 12209.
[156] K. Ueda, N. Inagaki, S. Seino, *J. Biol. Chem.* **1997**, *272*, 22983.
[157] Y. Hou, L. Cui, J. R. Riordan, X. Chang, *J. Biol. Chem.* **2000**, *275*, 20280.
[158] S. Arora, P. E. Lapinski, M. Raghavan, *Proc. Natl. Acad. Sci. USA* **2001**, *98*, 7241.
[159] O. Daumke, M. R. Knittler, *Eur. J. Biochem.* **2001**, *268*, 4776.
[160] E. A. Reits, A. C. Griekspoor, J. Neefjes, *Immunol. Today* **2000**, *21*, 598.
[161] P. M. van Endert, L. Saveanu, E. W. Hewitt, P. Lehner, *Trends Biochem. Sci.* **2002**, *27*, 454.
[162] A. Rudensky, S. Rath, P. Preston-Hurlburt, D. B. Murphy, C. A. Janeway, Jr., *Nature* **1991**, *353*, 660.
[163] R. M. Chicz, R. G. Urban, J. C. Gorga, D. A. Vignali, W. S. Lane, J. L. Strominger, *J. Exp. Med.* **1993**, *178*, 27.
[164] H. G. Rammensee, *Curr. Opin. Immunol.* **1995**, *7*, 85.
[165] S. M. Shawar, J. M. Vyas, J. R. Rodgers, R. G. Cook, R. R. Rich, *J. Exp. Med.* **1991**, *174*, 941.
[166] S. M. Shawar, J. R. Rodgers, R. G. Cook, R. R. Rich, *Immunol. Res.* **1991**, *10*, 365.
[167] E. Hermel, E. Grigorenko, K. F. Lindahl, *Int. Immunol.* **1991**, *3*, 407.
[168] D. L. Hogue, L. Liu, V. Ling, *J. Mol. Biol.* **1999**, *285*, 379.
[169] F. Zhang, D. L. Hogue, L. Liu, C. L. Fisher, D. Hui, S. Childs, V. Ling, *FEBS Lett.* **2000**, *478*, 89.
[170] M. Chloupkova, L. S. LeBard, D. M. Koeller, *J. Mol. Biol.* **2003**, *331*, 155.
[171] Y. Yamaguchi, M. Kasano, T. Terada, R. Sato, M. Maeda, *FEBS Lett.* **1999**, *457*, 231.
[172] R. Allikmets, B. Gerrard, A. Hutchinson, M. Dean, *Hum. Mol. Genet.* **1996**, *5*, 1649.
[173] F. Zhang, W. Zhang, L. Liu, C. L. Fisher, D. Hui, S. Childs, K. Dorovini-Zis, V. Ling, *J. Biol. Chem.* **2000**, *275*, 23287.
[174] A. Kobayashi, M. Kasano, T. Maeda, S. Hori, K. Motojima, M. Suzuki, T. Fujiwara, E. Takahashi, T. Yabe, K. Tanaka, M. Kasahara, Y. Yamaguchi, M. Maeda, *J. Biochem.* **2000**, *128*, 711.
[175] N. P. Restifo, F. Esquivel, Y. Kawakami, J. W. Yewdell, J. J. Mule, S. A. Rosenberg, J. R. Bennink, *J. Exp. Med.* **1993**, *177*, 265.
[176] D. P. Singal, M. Ye, J. Ni, D. P. Snider, *Immunol. Lett.* **1996**, *50*, 149.
[177] T. Kageshita, S. Hirai, T. Ono, D. J. Hicklin, S. Ferrone, *Am. J. Pathol.* **1999**, *154*, 745.
[178] L. Zhang, J. S. Pagano, *J. Virol.* **2001**, *75*, 341.
[179] J. L. Touraine, H. Betuel, G. Souillet, M. Jeune, *J. Pediatr.* **1978**, *93*, 47.
[180] A. Bernaerts, J. E. Vandevenne, J. Lambert, L. S. De Clerck, A. M. De Schepper, *Eur. J. Radiol.* **2001**, *11*, 815.
[181] C. Klein, B. Lisowska-Grospierre, F. LeDeist, A. Fischer, C. Griscelli, *J. Pediatr.* **1993**, *123*, 921.
[182] S. D. Gadola, H. T. Moins-Teisserenc, J. Trowsdale, W. L. Gross, V. Cerundolo, *Clin. Exp. Immunol.* **2000**, *121*, 173.

 © 2004 Wiley-VCH Verlag GmbH & Co. KGaA, Weinheim

[183] H. Furukawa, S. Murata, T. Yabe, N. Shimbara, N. Keicho, K. Kashiwase, K. Watanabe, Y. Ishikawa, T. Akaza, K. Tadokoro, S. Tohma, T. Inoue, K. Tokunaga, K. Yamamoto, K. Tanaka, T. Juji, *J. Clin. Invest.* **1999**, *103*, 755.
[184] H. de la Salle, J. Zimmer, D. Fricker, C. Angenieux, J. P. Cazenave, M. Okubo, H. Maeda, A. Plebani, M. M. Tongio, A. Dormoy, D. Hanau, *J. Clin. Invest.* **1999**, *103*, R9.
[185] H. de la Salle, X. Saulquin, I. Mansour, S. Klayme, D. Fricker, J. Zimmer, J. P. Cazenave, D. Hanau, M. Bonneville, E. Houssaint, G. Lefranc, R. Naman, *Clin. Exp. Immunol.* **2002**, *128*, 525.
[186] M. Vitale, J. Zimmer, R. Castriconi, D. Hanau, L. Donato, C. Bottino, L. Moretta, H. de la Salle, A. Moretta, *Blood* **2002**, *99*, 1723.
[187] A. K. Johnsen, D. J. Templeton, M. Sy, C. V. Harding, *J. Immunol.* **1999**, *163*, 4224.
[188] H. E. Farrell, H. Vally, D. M. Lynch, P. Fleming, G. R. Shellam, A. A. Scalzo, N. J. Davis-Poynter, *Nature* **1997**, *386*, 510.
[189] Ref. [10].
[190] B. Seliger, T. Cabrera, F. Garrido, S. Ferrone, *Semin. Cancer Biol.* **2002**, *12*, 3.
[191] K. Zhu, J. Wang, J. Zhu, J. Jiang, J. Shou, X. Chen, *Oncogene* **1999**, *18*, 7740.
[192] D. P. Singal, M. Ye, D. Bienzle, *Int. J. Cancer* **1998**, *75*, 112.
[193] J. Alimonti, Q. J. Zhang, R. Gabathuler, G. Reid, S. S. Chen, W. A. Jefferies, *Nat. Biotechnol.* **2000**, *18*, 515.
[194] C. A. White, S. A. Thomson, L. Cooper, P. M. van Endert, R. Tampé, B. Coupar, L. Qiu, P. G. Parsons, D. J. Moss, R. Khanna, *Int. J. Cancer* **1998**, *75*, 590.
[195] M. J. Maeurer, S. M. Gollin, D. Martin, W. Swaney, J. Bryant, C. Castelli, P. Robbins, G. Parmiani, W. J. Storkus, M. T. Lotze, *J. Clin. Invest.* **1996**, *98*, 1633.
[196] M. V. Corrias, M. Occhino, M. Croce, A. De Ambrosis, M. P. Pistillo, P. Bocca, V. Pistoia, S. Ferrini, *Tissue Antigens* **2001**, *57*, 110.
[197] M. Andersson, S. Paabo, T. Nilsson, P. A. Peterson, *Cell* **1985**, *43*, 215.
[198] H. G. Burgert, S. Kvist, *Cell* **1985**, *41*, 987.
[199] H. G. Burgert, S. Kvist, *EMBO J.* **1987**, *6*, 2019.
[200] E. M. Bennett, J. R. Bennink, J. W. Yewdell, F. M. Brodsky, *J. Immunol.* **1999**, *162*, 5049.
[201] C. Brander, T. Suscovich, Y. Lee, P. T. Nguyen, P. O'Connor, J. Seebach, N. G. Jones, M. van Gorder, B. D. Walker, D. T. Scadden, *J. Immunol.* **2000**, *165*, 2077.
[202] M. H. Furman, H. L. Ploegh, *J. Clin. Invest.* **2002**, *110*, 875.
[203] L. Lybarger, X. Wang, M. R. Harris, H. W. Virgin IV, T. H. Hansen, *Immunity* **2003**, *18*, 121.
[204] R. Tomazin, N. E. van Schoot, K. Goldsmith, P. Jugovic, P. Sempé, K. Früh, D. C. Johnson, *J. Virol.* **1998**, *72*, 2560.
[205] L. Neumann, W. Kraas, S. Uebel, G. Jung, R. Tampé, *J. Mol. Biol.* **1997**, *272*, 484.
[206] A. Hill, P. Jugovic, I. York, G. Russ, J. Bennink, J. Yewdell, H. Ploegh, D. Johnson, *Nature* **1995**, *375*, 411.
[207] B. Galocha, A. Hill, B. C. Barnett, A. Dolan, A. Raimondi, R. F. Cook, J. Brunner, D. J. McGeoch, H. L. Ploegh, *J. Exp. Med.* **1997**, *185*, 1565.
[208] E. Wiertz, A. Hill, D. Tortorella, H. Ploegh, *Immunol. Lett.* **1997**, *57*, 213.
[209] T. R. Jones, E. J. Wiertz, L. Sun, K. N. Fish, J. A. Nelson, H. L. Ploegh, *Proc. Natl. Acad. Sci. USA* **1996**, *93*, 11327.
[210] P. J. Lehner, J. T. Karttunen, G. W. Wilkinson, P. Cresswell, *Proc. Natl. Acad. Sci. USA* **1997**, *94*, 6904.
[211] K. Ahn, A. Gruhler, B. Galocha, T. R. Jones, E. J. Wiertz, H. L. Ploegh, P. A. Peterson, Y. Yang, K. Früh, *Immunity* **1997**, *6*, 613.
[212] R. Zeidler, G. Eissner, P. Meissner, S. Uebel, R. Tampé, S. Lazis, W. Hammerschmidt, *Blood* **1997**, *90*, 2390.
[213] X. Saulquin, M. Bodinier, M. A. Peyrat, A. Hislop, E. Scotet, F. Lang, M. Bonneville, E. Houssaint, *Eur. J. Immunol.* **2001**, *32*, 708.
[214] G. Lautscham, A. Rickinson, N. Blake, *Microbes Infect.* **2003**, *5*, 291.
[215] D. Bauer, R. Tampé, *Curr. Top. Microbiol. Immunol.* **2002**, *269*, 87.
[216] D. Beinert, L. Neumann, S. Uebel, R. Tampé, *Biochemistry* **1997**, *36*, 4694.
[217] R. Pfänder, L. Neumann, M. Zweckstetter, C. Seger, T. A. Holak, R. Tampé, *Biochemistry* **1999**, *38*, 13692.
[218] K. Ahn, T. H. Meyer, S. Uebel, P. Sempé, H. Djaballah, Y. Yang, P. A. Peterson, K. Früh, R. Tampé, *EMBO J.* **1996**, *15*, 3247.
[219] K. Früh, K. Ahn, H. Djaballah, P. Sempé, P. M. van Endert, R. Tampé, P. A. Peterson, Y. Yang, *Nature* **1995**, *375*, 415.
[220] H. Hengel, U. H. Koszinowski, *Curr Opin Immunol* **1997**, *9*, 470.
[221] H. Hengel, J. O. Koopmann, T. Flohr, W. Muranyi, E. Goulmy, G. J. Hämmerling, U. H. Koszinowski, F. Momburg, *Immunity* **1997**, *6*, 623.
[222] J. D. Thompson, D. G. Higgins, T. J. Gibson, *Comput. Appl. Biosci.* **1994**, *10*, 19.

 © 2004 Wiley-VCH Verlag GmbH & Co. KGaA, Weinheim

Communications



Genetically engineered polypeptides can self-assemble with oppositely charged lipids to form materials with nanoscale ordering on multiple controlled length scales. For more information see the Communication by I. Koltover et al. on the following pages.

DOI: 10.1002/anie.200460164
© 2004 Wiley-VCH Verlag GmbH & Co. KGaA, Weinheim

Nanostructures

Genetic Engineering of the Nanoscale Structure in Polyelectrolyte–Lipid Self-Assembled Systems**

Ilya Koltover, Sanjukta Sahu, and Nicolynn Davis*

The concept of molecular self-assembly has attracted interest in recent years as a route towards materials with structural order controlled on length scales from Ångstroms to micrometers. The assembly of macromolecules into ordered structures through noncovalent interactions has promise as an alternative to chemical synthesis; electrostatic, hydrophobic, and hydrogen-bonding interactions can be used to make equilibrium molecular structures with well-defined orientational and positional molecular order at the nanoscale without the need for complicated preparative procedures. An example of noncovalent self-assembly is the spontaneous formation of polyelectrolyte–lipid (PL) complexes in dilute solutions of polyelectrolytes and low-molecular-weight lipids,[1] with assembly driven by release of counterions from oppositely charged polymers and lipid head groups, as well as the hydrophobic association of the lipids. The resulting complexes usually have lamellar structures that consist of alternating lipid bilayers and adsorbed polyelecrolytes, although other mesophases can be obtained by tailoring the architecture of the surfactants.[2]

The utility of electrostatic self-assembly for making ordered nanomaterials is currently limited. Most known PL complexes have relatively disordered structures, with a small number of correlated polyelectrolyte/lipid layers (domain size) and no order among the polyelectrolyte chains sandwiched between membranes. Cationic lipid–DNA (CL–DNA) complexes are a notable exception, often having well-defined spacing among the DNA chains intercalated between the charged lipid membranes.[3] Thus, it is important to elucidate the requirements of polyelectrolyte architecture that are necessary to obtain a high degree of order in the PL complex. Herein, we report the formation of highly ordered PL complexes comprising cationic lipids and anionic polypeptides specifically designed and expressed in the bacterial host *Escherichia coli*. We demonstrate that when peptides have stable α-helical conformations with charge density matched to that of the cationic lipid membranes they form ordered PL complexes consisting of membrane stacks with peptide layers adsorbed on both surfaces of the membrane bilayers (Figure 1a). Furthermore, the peptide helices in the adsorbed monolayers form two-dimensional stripes, with the stripe thickness equal to the length of the monodisperse α helices, and well-defined interhelical spacing that can be varied by changing the composition of lipid membranes (Figure 1c, d). We demonstrate that control of polyelectrolyte molecular architecture opens a route to noncovalent self-assemblies with order on multiple length scales (Figure 1): lipid–polyelectrolyte stacking and two-dimensional order of the adsorbed polyelectrolytes.

DNA molecules have two distinctive features that may promote formation of the uniquely ordered CL–DNA structures. First, DNA has a well-defined double-helical fold that gives it rodlike shape and rigidity. Second, the area per anionic phosphate group of DNA is $\sigma^- = 68$ Å^2, with two helical lines of phosphate groups running along opposite sides of the DNA double helix.[4] This value is closely matched to the head-group size $\sigma^+ = 65$ Å^2 of the cationic lipid dioleoyl trimethylammonium propane (DOTAP), a fact contributing to the stability of a CL–DNA structure with layers of DNA binding together lipid bilayers in a stack. We hypothesized that a polypeptide with rigid shape and anionic charge density of $\sigma^- = 65$ Å^2 could also form ordered complexes with DOTAP-containing membranes. An α helix is the simplest rodlike peptide fold, and polypeptides with repetitive alanine-rich amino acid sequences are known to adopt stable helical conformations in aqueous solutions.[5] Hence, we chose to make PL complexes by using peptides with the sequence $(A_3E)_n$ (A = alanine, E = glutamic acid, n = integer). Molecular modeling studies of these peptides in α-helical conformation shows that the anionic glutamic acid residues are spaced at 6.5-Å intervals and are arranged on a helical line along the molecule axis;[6] with an α-helix diameter of 10 Å, this gives σ^- = ca. 65 Å^2, which is close to the desired charge density.

Helical folds of short (20–30 residue) peptides are unstable; they denature at temperatures of approximately 10 °C.[7] Therefore, we have used the methods of genetic engineering to prepare peptides of high molecular weight. DNA sequences (genes) encoding two polypeptides $(A_3E)_n$ with $n = 36$ and 48 were assembled from shorter synthetic oligonucleotides and inserted into bacterial expression plasmids in *E. coli* cells. Overexpression of these genes afforded two monodisperse polypeptides with precisely the expected molecular weights of 12.45 and 16.52 kDa.[8] The PL complexes precipitated as macroscopic globular aggregates from mixed solutions of these anionic peptides with cationic lipid vesicles. The vesicles comprised the cationic lipid DOTAP and the neutral lipid dioleoyl phosphatidylcholine (DOPC), and variation of the DOPC fraction (ϕ_{PC}) in the mixture was used to adjust the overall density of cationic lipids in the membrane bilayers. Stoichiometrically charge-neutral complexes were obtained by keeping the weight ratio of cationic DOTAP to anionic peptide at $\rho = 2$, since the molecular weight of DOTAP is twice that of the anionic A_3E repeat unit.[9]

The peptide conformations in solution and in the PL complexes were examined by using circular dichroism (CD)

[*] Prof. Dr. I. Koltover, S. Sahu, N. Davis
Department of Materials Science and Engineering
Northwestern University
Evanston, IL 60208 (USA)
Fax: (+1) 847-491-7820
E-mail: ilya@northwestern.edu

[**] Financial support for this research was provided by the National Sciences Foundation (grant no.: DMR-0134874) and the Petroleum Research Fund (grant no.: 37669-G7). X-ray experiments were carried out at the DND-CAT beam line of the Advanced Photon Source (ANL) facility supported by the DOE contract no. W-31-102-Eng-38.

Supporting information for this article is available on the WWW under http://www.angewandte.org or from the author.

 © 2004 Wiley-VCH Verlag GmbH & Co. KGaA, Weinheim DOI: 10.1002/anie.200460164

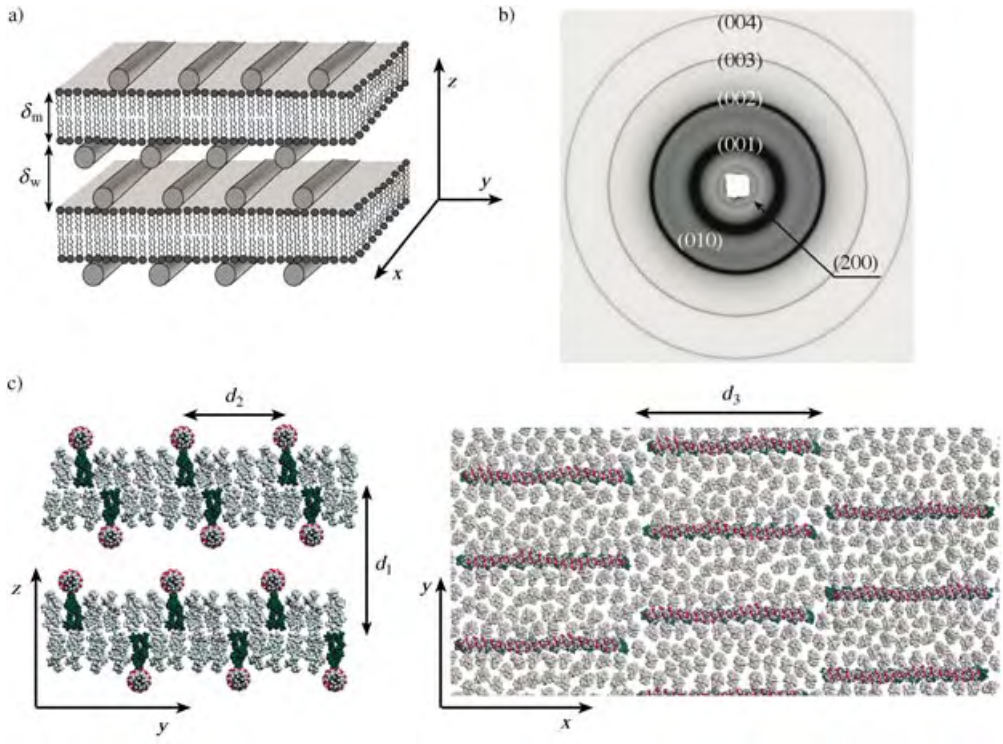


Figure 1. a) Schematic representation of the structure of the PL complex. b) SAXD pattern of the $(A_3E)_{48}$, $\rho = 2$, $\phi_{PC} = 0.75$ sample. c) and d) Molecular models of two projections of the structure of the PL complex; glutamic acid residues along the $(A_3E)_n$ α helices are shown in red, cationic DOTAP lipids are green, and neutral DOPC lipids are gray. For simplicity, $n = 18$ peptides were used to build the models.

spectroscopy (Figure 2). The CD spectra of pure peptides in solution show two minima at 208 and 223 nm and a maximum at 191 nm, a pattern characteristic of α-helical conformations. The peptides remained helical at room temperature (25 °C) and denatured into a random coil conformation above 40 °C. The CD spectra of dilute solutions of the PL complexes are nearly identical to those of pure peptides, a result indicating that they maintain a α-helical conformation inside the complexes.[10] Remarkably, the helical conformation of the peptides was stabilized in association with the cationic lipids, with strong helical CD signals for the PL complexes persisting at up to 70 °C.

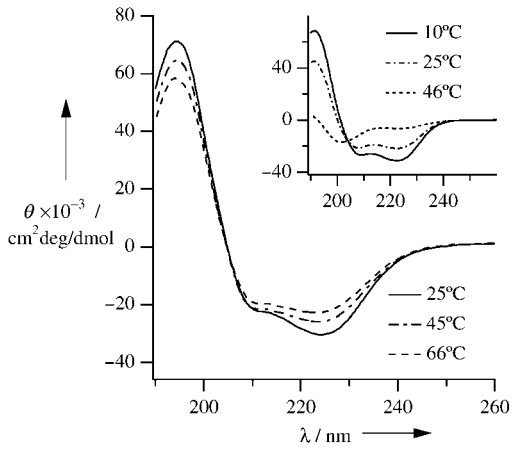


Figure 2. CD spectra of the $(A_3E)_{36}$, $\phi_{PC} = 0.7$, $\rho = 2$ complexes as a function of temperature in 10 mM sodium phosphate buffer (pH 6.5). The inset shows the CD spectra of pure $(A_3E)_{36}$ peptide solutions.

The nanoscale structure of the PL complexes was examined by using small-angle X-ray diffraction (SAXD) from concentrated aqueous suspensions of the complexes sealed in quartz capillaries.[10] Figure 1b shows a typical powder X-ray diffraction pattern of the PL complex with $n = 48$, $\rho = 2$, and $\phi_{PC} = 0.75$. Immediately apparent are the sharp periodically spaced (00l) rings, indicative of a highly periodic layered structure. Also visible is a diffuse (010) ring located between the first and second harmonics of the lamellar structure. Both the (00l) rings and the (010) ring were present in freshly prepared $\rho = 2$ complexes of either the $n = 36$ or $n = 48$ peptides with lipids for $\phi_{PC} > 0.5$, while only one or two rings at (00l) positions were visible in SAXD patterns of complexes with $\phi_{PC} < 0.5$.[11] Ordered complexes aged for several weeks yielded SAXD patterns with additional (h00) sharp reflections at very small angles, while the (00l) and (010) reflections remained unchanged.

To assign the three sets of X-ray diffraction peaks, we examined complexes with varying ϕ_{PC} and n (36 or 48) values. Figure 3a shows radially averaged plots of scattered X-ray intensity $I(q)$ for $(A_3E)_{36}$ samples with $\rho = 2$. The sharp (00l) peaks correspond to a PL complex with a highly periodic structure with stacked membrane and peptide/water layers along the z-axis (Figure 1). The stack periodicity $d_1 = 2\pi l/q_{00l}$ (where q = scattering vector) is equal to the sum of the membrane (δ_m) and peptide/water (δ_w) layer thicknesses. For a sample with $d_1 = 74.5$ Å and $\delta_m = 42$ Å ($\phi_{PC} = 0.8$),[3] the peptides occupy a space between the bilayers that is 32.5 Å

 © 2004 Wiley-VCH Verlag GmbH & Co. KGaA, Weinheim

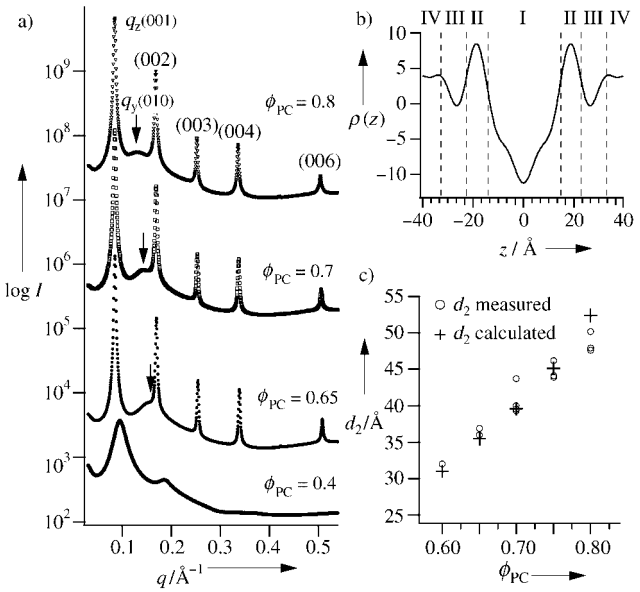


Figure 3. a) Radially averaged SAXD scans of $(A_3E)_{36}$, $\rho = 2$ samples; arrows indicate the shifting position of the interhelix-peptide correlation peak. Note the dramatic change in the data between the disordered ($\phi_{PC} < 0.5$) and ordered ($\phi_{PC} > 0.5$) samples. b) Electron density profile reconstructed from the SAXD scan for $\phi_{PC} = 0.8$. c) Variation of the interhelix-peptide spacing d_2 with the membrane composition ϕ_{PC} for all examined $(A_3E)_{36}$ and $(A_3E)_{48}$ samples; crosses indicate the d_2 values calculated with no adjustable parameters by using the space-filling model of PL complex shown in Figure 1.

thick. This is large enough to accommodate two layers of peptides with a diameter of 10 Å, with a water layer between them. Inversion of the X-ray data reveals a projected electron-density profile $\rho(z)$ with four distinct electron-density regions I–IV (Figure 3b).[12] Region I has a $\rho(z)$ profile characteristic of a hydrophobic lipid-bilayer interior, with an adjacent higher density layer (II) that corresponds to the lipid head groups. Peptides are adsorbed on both surfaces of the lipid bilayer, thereby giving rise to region III with a reduced $\rho(z)$ value because the carbon/nitrogen composition of the peptide results in electron density that is somewhat lower than that of the water layer (IV). The measured $\rho(z)$ pattern exactly corresponds to the repeating bilayer/peptide unit of the PL stacked structure shown in Figure 1.

The observed stack structure is different from the CL–DNA complexes, where DNA molecules bridge the neighboring membrane layers. However, DNA has two sets of anionic groups running along its double strand, while the helical (A_3E) peptides have a single row of charges that can efficiently neutralize only a single membrane surface. Furthermore, since at most half of the peptide charged groups face towards the membrane surface and interact directly with cationic lipid head groups, efficient charge neutralization can only occur for membranes with average charge density $\sigma^+ = 2 \times 65$ Å^2, which is two times lower than the expected geometric value. Thus, complexes with $\phi_{PC} < 0.5$ have disordered structures (bottom curve in Figure 3a) because of inefficient screening of the membrane charges by the adsorbed anionic peptides.

The average distance between the adsorbed peptide helices can be estimated from the ratio of peptide to membrane charge densities as $d_2 = (1\,e^-$ per 6.5 Å$)/(1\,e^+$ per 65 Å$^2 \times \phi_{TAP}) = 10/(1-\phi_{PC})$, which corresponds to $d_2 =$ ca. 50 Å for $\phi_{PC} = 0.8$. This value is close to the measured value of $d_2 = 2\pi/q_{010} = 48$ Å, a result suggesting that the broader (010) reflection arises from well-defined side-by-side ordering of the polypeptide chains. As expected, the (010) peak moves to smaller angles for samples with increasing ϕ_{PC} values (Figure 3a, c). A better estimate of $d_2(\phi_{PC})$ values can be obtained by matching the volumes occupied by membranes and peptides in the structure shown in Figure 1b (see the Supporting Information). Figure 3c shows the remarkable agreement between calculated d_2 values and the measured data. This further verifies the proposed structure of the PL complex and also shows that the well-defined ordering of adsorbed peptide helices can be experimentally controlled by adjusting the membrane composition.

The origin of the additional $(h00)$ reflections in aged samples of the PL complex was investigated by comparing the diffraction patterns in samples of peptides with different n values; these patterns were obtained by using a diffraction set-up capable of accessing smaller scattering angles. Figure 4 shows a set of radially averaged SAXD scans in the small-angle region for three $(A_3E)_{48}$ and two $(A_3E)_{36}$ samples with varying ϕ_{PC} values. It is clear that the positions of the $(h00)$ harmonics change dramatically for the samples with different peptide lengths. The expected lengths of α helices with 36 and 48 residues are 216 and 288 Å (1.5 Å $\times n$), respectively. Thus, the period d_3 of $(h00)$ reflections is essentially equal to the

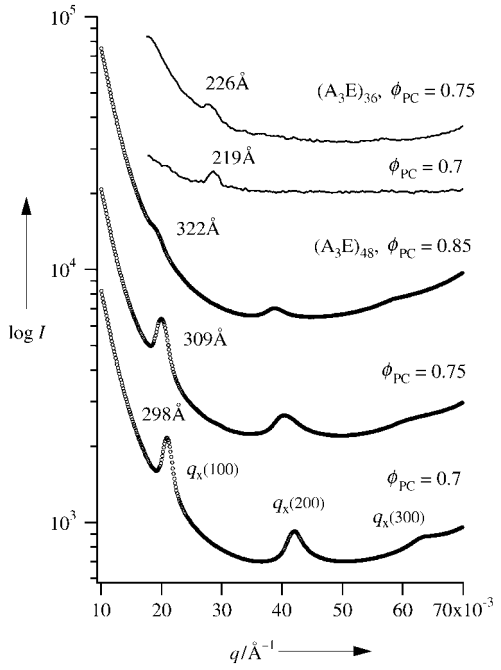


Figure 4. Small-angle diffraction region of aged samples of the PL complex. The bottom three scans are for $(A_3E)_{48}$, $\rho = 2$ samples; the top two scans are for $(A_3E)_{36}$, $\rho = 2$ samples. The noisier $(A_3E)_{36}$ data were recorded on a lower-resolution diffraction set-up. Numbers above the diffraction curves indicate the periodicity $d_3 = 2\pi/q_{100}$ of the corresponding data.

 © 2004 Wiley-VCH Verlag GmbH & Co. KGaA, Weinheim

peptide length. This means that the helical peptides slowly separate into two-dimensional stripes on the surfaces of lipid membranes. The stripe period d_3 is proportional to the helix length, and there is well-defined spacing (d_2) between helices in each stripe (Figure 1c). The small increase in the d_3 distance with increasing ϕ_{PC} value indicates that the stripes move slightly apart as the membrane charge density decreases.

It is likely that the separation of monodisperse peptides and associated cationic lipids into stripes reduces the thickness perturbation and elastic energy of the lipid membranes compared to a random peptide distribution along the *x*-axis. The X-ray peaks with a striped pattern appear in aged samples because two-dimenional diffusion of lipids with adsorbed peptides is slow. SAXD measurements show no correlations between peptide arrays on different membrane surfaces or between peptide positions in neighboring stripes. Importantly, the observed two-dimensional ordering of peptide chains is possible only as a consequence of the perfect monodispersity and uniform conformation of the genetically engineered polypeptide chains.

In summary, we have shown that highly ordered noncovalent self-assemblies can be prepared from cationic lipids and genetically engineered polypeptides. Our results demonstrate that polyelectrolyte conformation and charge density are the key design parameters for engineering order in PL self-assembled systems. It is important to note that the structure of the PL complex is essentially encoded in the DNA sequences, which prescribe the α-helical fold, charge density, and length of the molecules by establishing the sequence and length of the biosynthetic peptides. This synthetic strategy mimics the way that nature guides self-assembly through the use of genetically encoded, well-defined macromolecules.

Received: March 31, 2004 [Z460164]
Published Online: July 28, 2004

Keywords: amphiphiles · lipids · nanostructures · polyelectrolytes · self-assembly

[1] a) M. Antonietti, J. Conrad, A. Thunemann, *Macromolecules* **1994**, *27*, 6007; b) M. Antonietti, J. Conrad, *Angew. Chem.* **1994**, *106*, 1927; *Angew. Chem. Int. Ed. Engl.* **1994**, *33*, 1869; c) E. A. Ponomarenko, A. J. Waddon, K. N. Bakeev, D. A. Tirrell, W. J. MacKnight, *Macromolecules* **1996**, *29*, 4340; d) J. O. Radler, I. Koltover, T. Salditt, C. R. Safinya, *Science* **1997**, *275*, 810; e) G. Subramanian, R. P. Hjelm, T. J. Deming, G. S. Smith, Y. Li, C. R. Safinya, *J. Am. Chem. Soc.* **2000**, *122*, 26; f) G. C. L. Wong, J. X. Tang, A. Lin, Y. L. Li, P. A. Janmey, C. R. Safinya, *Science* **2000**, *288*, 2035.

[2] a) I. Koltover, T. Salditt, J. O. Radler, C. R. Safinya, *Science* **1998**, *281*, 78; b) S. Zhou, F. Yeh, C. Burger, B. Chu, *J. Phys. Chem. B* **1999**, *103*, 2107; c) R. Krishnaswamy, P. Mitra, V. A. Raghunathan, A. K. Sood, *Europhys. Lett.* **2003**, *62*, 357.

[3] I. Koltover, T. Salditt, C. R. Safinya, *Biophys. J.* **1999**, *77*, 915.

[4] D. Voet, J. G. Voet, *Biochemistry*, Wiley, New York, **1995**, p. 852.

[5] S. Marqusee, V. H. Robbins, R. L. Baldwin, *Proc. Natl. Acad. Sci. USA* **1989**, *86*, 5286.

[6] Molecular models of peptides and lipid/peptide assemblies were built by using the Materials Studio (Accelrys) package. Peptides were constructed by using conventional 18/5 α-helix dihedral angles. The structures were not minimized and were used as a guide for molecule design and structure visualization.

[7] J. M. Sholtz, H. Qiang, E. J. York, J. A. Stewart, R. L. Baldwin, *Biopolymers* **1991**, *31*, 1463.

[8] Details of peptide gene cloning, peptide expression and purification, and sample preparation can be found in the Supporting Information.

[9] All experiments performed with complexes prepared in water and 10 mM sodium acetate or sodium phosphate buffers (pH 6.5) yielded identical results. Furthermore, CD and SAXD data were identical for $(A_3E)_{36}$ and $(A_3E)_{48}$ samples, except the (*h*00) reflections in the very-small-angle diffraction region.

[10] Samples for CD experiments were prepared from dilute solutions of peptides ($0.25\,mg\,mL^{-1}$) and liposomes ($0.5\,mg\,mL^{-1}$). SAXD samples were prepared directly in 2 mm diameter quartz X-ray capillaries from peptide ($50\,mg\,mL^{-1}$) and liposome ($100\,mg\,mL^{-1}$) stock solutions.

[11] The difference between the $\phi_{PC} < 0.5$ (disordered) and $\phi_{PC} > 0.5$ (ordered) samples was also evident from their visual appearance: ordered samples consisted of compact, strongly birefringent globules, while the disordered ones had faint, weakly birefringent aggregates. See the Supporting Information for an example.

[12] a) H. Richardsen, U. Vierl, G. Cevc, W. Fenzl, *Europhys. Lett.* **1996**, *34*, 543; b) N. P. Franks, W. R. Lieb, *J. Mol. Biol.* **1979**, *133*, 469; intensities of the first six (00*l*) peaks were used for the reconstruction; the phases (−1, −1, −1, 1, −1, −1) were chosen based on the known reconstructions of pure lipid structures, with rejection of unphysical electron density profiles.

 © 2004 Wiley-VCH Verlag GmbH & Co. KGaA, Weinheim

Gallium Clusters

How Do Clusters Grow? The Synthesis and Structure of Polynuclear Hydroxide Gallium(III) Clusters**

*Jeremy C. Goodwin, Simon J. Teat, and Sarah L. Heath**

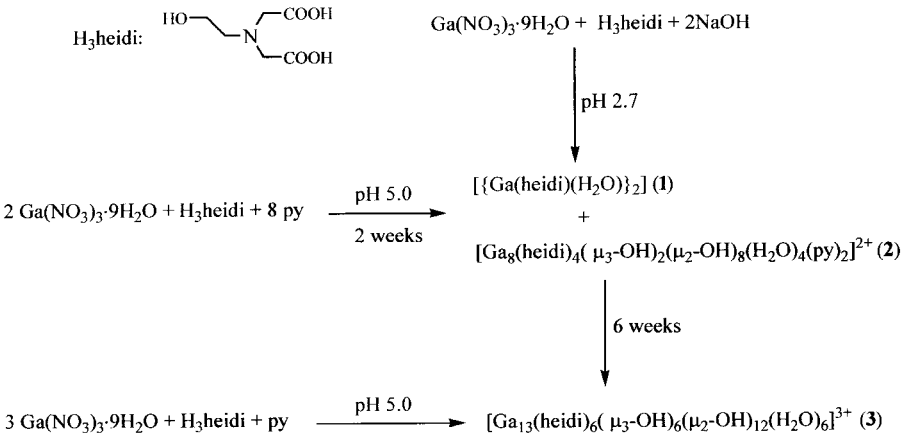
How metal–oxide and metal–oxo–hydroxide structures form in the early stages of nucleation is of importance in areas as diverse as biology, for example, the formation of ferritin from apoferritin,[1–3] and materials science, for example, the synthesis of metal–oxide particles for use in information stor-

[*] Dr. S. L. Heath
Department of Chemistry
University of Manchester
Oxford Road, Manchester M13 9PL (UK)
Fax: (+44) 161-274-4598
E-mail: sarah.l.heath@man.ac.uk
J. C. Goodwin
Department of Chemistry
University of York
Heslington, York YO10 5DD (UK)
S. J. Teat
Daresbury Laboratory
Daresbury, Warrington, Cheshire WA4 4AD (UK)

[**] This work was supported by the Royal Society (SLH) and the EPSRC (JCG).

 DOI: 10.1002/anie.200353542 © 2004 Wiley-VCH Verlag GmbH & Co. KGaA, Weinheim

age.[4] If we could understand this process it may help to control nucleation, and therefore, in the longer term, to make particles of a controlled size and morphology. To this end we prepared polynuclear metal hydroxide clusters by hydrolysing Lewis acidic metal ions (Fe^{3+} and Al^{3+}). Thus far we have only been able to isolate one fragment or cluster type for any combination of metal and ligand, and therefore conclusions about how the cluster grows are difficult to draw, that is, we see no "intermediates". However, by using the slightly less acidic metal ion Ga^{3+} we could isolate three distinct, but structurally related clusters from one reaction mixture.



Scheme 1. Synthesis of **1**, **2**, and **3**.

The reaction of hydrated $Ga(NO_3)_3$ with H_3heidi and pyridine in a 2:1:8 ratio in water[5] gives a colorless solution with a pH value of 5.01. Slow evaporation of this solution yields square blocks of **1** after two weeks, followed by large hexagonal blocks of **2**. On standing, **2** redissolves, and within six weeks **3** crystallizes as small needles. **1** and **3** can also be prepared as analytically pure materials,[5] by adjusting the metal:ligand ratios to 1:1 and 3:1, respectively. In the case of **1**, two equivalents of sodium hydroxide are added to give a resultant pH value of 2.7, whereas, to prepare **3**, pyridine is added until the pH value reaches 5.0 (Scheme 1).

X-ray analysis shows **1** to be an alkoxo-bridged dimer (Figure 1a and Experimental Section).[6] The heidi ligand is fully deprotonated and coordinates to each gallium atom in a tetradentate manner, and the alcoholate functionality additionally bridges the two gallium centers. The distorted octahedral coordination geometry is completed by a coordinated water molecule. Dimer **1** is isostructural with the iron(III)– and aluminum(III)–heidi dimers reported previously.[7,8]

The second product isolated from the reaction is an octanuclear alkoxo- and hydroxy-bridged cluster, $[Ga_8(heidi)_4(\mu_3\text{-}OH)_2(\mu_2\text{-}OH)_8(H_2O)_4(C_5H_5N)_2]^{2+}$ (**2**; Figure 1b and Experimental Section).[6] This cluster consists of a $[Ga_4(\mu_3\text{-}OH)_2(\mu_2\text{-}OH)_4]^{6+}$ core surrounded by four Ga–heidi–H_2O units. Each gallium atom is surrounded by six ligands in a distorted octahedral arrangement. The four gallium(III) ions of the core (Ga1, Ga1A, Ga2, Ga2A) lie in a plane and are linked by two μ_3-hydroxide ions (O1, O1A) and four μ_2-hydroxide ions (O2, O2A, O2B, O2C). The pyridine ligands complete the octahedral coordination spheres of Ga2 and Ga2A. The heidi ligands on the periphery coordinate in a tetradentate manner, and the alcoholate function of the ligand and a μ_2-hydroxide ion link each of the four outer gallium atoms to the core. The ligand coordination mode gives rise to two pairs of peripheral ligand units, in which the oxygen atoms of the bridging alkoxo ligands are coordinated *cis* and hence point towards one another.

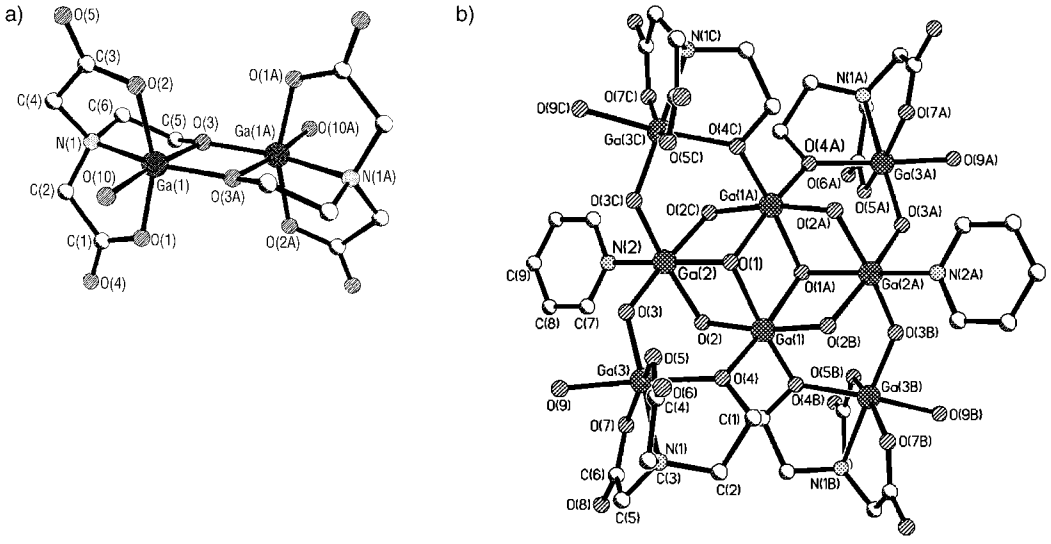


Figure 1. a) Structure of **1**. Symmetry equivalent: A: $-x$, $-y$, $-z$. b) Structure of **2**. Symmetry equivalents: A: $-x$, $-y+1$, $-z$; B: $-x$, $-y+1$, z; C: x, y, $-z$.

 © 2004 Wiley-VCH Verlag GmbH & Co. KGaA, Weinheim

The third product isolated from the reaction mixture is the tridecanuclear oxo- and hydroxy-bridged cluster **3.** X-ray analysis shows the presence of two isomeric Ga_{13} cluster species, **3A** and **3B** (Figure 2 and Experimental Section).[6] The ratio **3A**:**3B** is 1:2. Each cluster has a $[Ga_7(\mu_3\text{-}OH)_6(\mu_2\text{-}OH)_6]^{9+}$ core, which corresponds to a portion of a hexagonally close-packed hydroxide layer structure (brucite) with the gallium ions located in the octahedral holes. In **3A** and **3B**, the seven gallium ions of the core lie in a plane, and the six outer gallium ions are located alternatingly above and below it.

The gallium core is encapsulated by a shell of six gallium–heidi–H_2O units, which are connected to the core by μ_2-hydroxide bridges and μ_2-alkoxo bridges from the ligand. In **3A**, Ga(1) sits on a $\bar{3}$ axis and the ligands are arranged such that the μ_2-bridging alkoxo oxygen atoms coordinate *cis* to a μ_2-hydroxide ligand, and hence are all orientated in the same direction. This cluster is isostructural with the previously reported Al_{13}–heidi cluster.[4] In **3B**, the central gallium ion, Ga4, sits on a threefold axis and the ligands are arranged in pairs such that bridging μ_2-alkoxo ligands coordinate *cis* to each other. The arrangement of the ligands in **3B** is analogous to that observed in the Ga_8 cluster **2**.

The Ga_8 and Ga_{13} clusters are clearly structurally related, and Ga_8 may be considered to be part of a Ga_{13} cluster and hence a smaller fragment of the brucite lattice. This aspect, together with the fact that the Ga_8 cluster is only ever isolated in extremely low yield and always in the presence of the Ga_{13} cluster, suggests that the former cluster may be an intermediate in the formation of the latter. Such behavior provides tantalizing insight into cluster aggregation, and has led us to look more closely at the previously reported metal–oxo and metal–oxo–hydroxide clusters. A common feature of these clusters is the presence of a central $[M_7(OH)_{12}]^{n+}$ core, in which the central metal ion is surrounded by six metal ions in what may be regarded as a "first shell" (Figure 3). It is generally assumed that this shell is formed before extra metal atoms are added as a second shell of the lattice. The isolation of the M_8 cluster **2**, in which two metal atoms, Ga(3) and Ga(3A), have been added to the "second shell" before the first shell is complete, breaks this pattern.

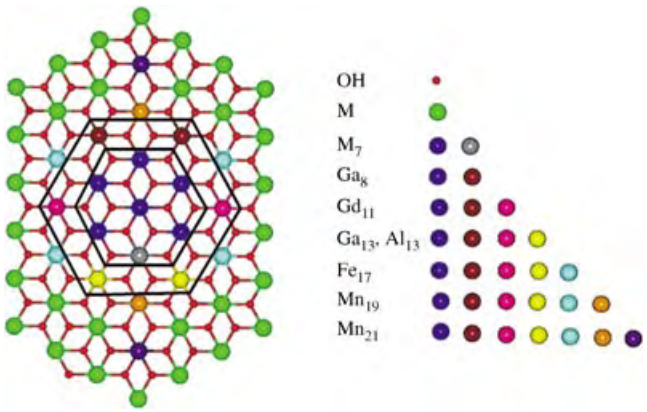


Figure 3. The brucite lattice with the first and second growth shells marked.

From the method of preparation it seems probable that **2** is a precursor of **3A** and **3B** in a reaction for which the formation of a complete M_7 first shell is not an essential first step. Figure 3 shows a portion of the brucite lattice with the two clusters discussed herein highlighted. However, we can also pick out many other metal–oxo–hydroxide clusters that have been previously reported: M_7,[9–12] Cd_{11},[13] Al_{13},[8] Fe_{17},[7,14,15] Fe_{19},[14,15] Mn_{19},[16] and Mn_{21}.[17] An implication of this observation is that clusters grow by the addition of metal ions into the brucite lattice, but that this addition does not necessarily involve the sequential completion of shells. For example, only M_7, M_{13}, and M_{19} clusters could have complete shells, and although these are observed, there are others—**2**, Ni_{21},[18] and Co_{24}—,[19] which begin new growth shells before

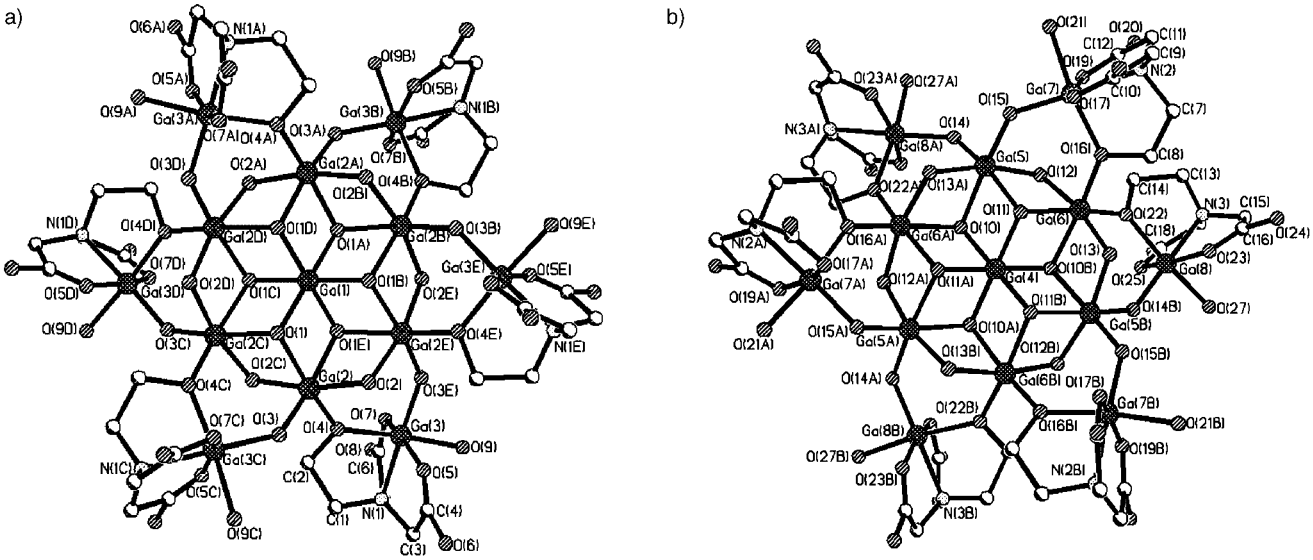


Figure 2. Structures of the Ga_{13} clusters **3A** (a) and **3B** (b). Symmetry equivalents for **3A**: A: $-x, -y, -z$; B: $-y, x-y, z$; C: $y, -x+y, -z$; D: $-x+y, -x, z$; E: $x-y, x, -z$.; for **3B**: A: $-y+1, x-y+1, z$; B: $-x+y, -x+1, z$.

 © 2004 Wiley-VCH Verlag GmbH & Co. KGaA, Weinheim

the inner shells are complete. In fact, it would seem that a regular structure is only maintained for smaller clusters, and thereafter the large number of potential growth points allows irregularities to appear.

The role of the ligand in the cluster aggregation is far from clear: the fact that **2** forms and redissolves before **3** is formed suggests that the heidi ligand might coordinate to the lower-nuclearity cage, dissociate and then recoordinate to the higher-nuclearity species. If this is the case, it may be possible to control the extent of cluster aggregation by controlling the binding strength of the ligand with suitable ligands, and a large number of irregular cluster species might be obtained.[20] We are currently undertaking solution-state studies on the interconversion of the gallium clusters in an attempt to investigate this hypothesis.

Experimental Section

Crystal data for **1**: $C_{12}H_{20}N_2O_{12}Ga_2$, $M = 523.74$, $T = 293(2)$ K. White block, $0.15 \times 0.15 \times 0.15$ mm. Triclinic, space group $P\bar{1}$, $a = 6.970(2)$, $b = 9.655(3)$, $c = 6.7520(10)$ Å, $\alpha = 97.08(2)$, $\beta = 99.38(2)$, $\gamma = 100.69(2)°$, $U = 435.0(2)$ Å^3, $Z = 1$, $\mu = 3.168$ mm^{-1}, $\rho_{cald} = 1.999$ Mg m^{-3}, $F(000) = 264$, $2\theta_{max} = 50°$, 1535 reflections collected, 1535 unique (R(int) = 0.0), all were used in the calculations. R indices [$I > 2\sigma(I)$]: $R1 = 0.0341$, $wR2 = 0.0843$, $S = 1.031$ for 1535 reflections with 168 parameters. R indices (all data): $R1 = 0.0525$, $wR2 = 0.0918$.[6]

Crystal data for **2**: $C_{45}H_{111}N_8O_{54.50}Ga_8$, $M = 2194.18$, $T = 150(2)$ K. Colorless block, $0.31 \times 0.22 \times 0.18$ mm. Orthorhombic, space group $Pnnm$, $a = 21.1675(12)$, $b = 11.7041(6)$, $c = 16.8350(9)$ Å, $U = 4170.8(4)$ Å^3, $Z = 2$, $\mu = 2.652$ mm^{-1}, $\rho_{cald} = 1.747$ Mg m^{-3}, $F(000) = 2242$, $2\theta_{max} = 57°$, 15144 reflections collected, 4761 unique (R(int) = 0.0695), all were used in the calculations. R indices [$I > 2\sigma(I)$]: $R1 = 0.0665$, $wR2 = 0.1799$, $S = 1.035$ for 3347 reflections with 332 parameters. R indices (all data): $R1 = 0.0892$, $wR2 = 0.1957$.[6]

Crystal data for **3**: $C_{36}H_{110.20}N_9O_{79.10}Ga_{13}$, $M = 2841.49$, $T = 150(2)$ K. Colorless plate, $0.18 \times 0.04 \times 0.02$ mm. Trigonal, space group $R\bar{3}c$, $a = b = 32.681(4)$, $c = 62.558(15)$ Å, $U = 57865(18)$ Å^3, $Z = 18$, $\mu = 2.769$ mm^{-1}, $\rho_{cald} = 1.468$ Mg m^{-3}, $F(000) = 25650$, $2\theta_{max} = 45°$, 36341 reflections collected, 8212 unique (R(int) = 0.1092), all were used in the calculations. R indices [$I > 2\sigma(I)$]: $R1 = 0.1256$, $wR2 = 0.3555$, $S = 1.177$ for 3321 reflections with 362 parameters. R indices (all data): $R1 = 0.2058$, $wR2 = 0.4086$.[6] Data for **3** were collected on Station 9.8 at the Daresbury Laboratory on a Bruker SMART 1K CCD diffractometer, equipped with an Oxford Cryostreams low-temperature attachment by using silicon-111 monochromated synchrotron radiation ($\lambda = 0.6942$ Å). A number of crystals of **3** were tried, the best of which decayed over a period of two hours in the nitrogen stream. Only the first 700 frames of the data collection could be used for structure solution and refinement. The diffraction intensities were also weak, with a maximum 2θ angle of 45°. To retain a reasonable data-to-parameter ratio of 9:1, only the gallium ions and core oxygen atoms could be refined anisotropically. The structures were solved with direct methods and refined by full-matrix-least-squares refinement of F^2 with SHELX 97 software.[21] From all data, the unit cell for crystals of **3** was determined to be the trigonal cell (see above). However, a careful analysis of the intensity distribution of the diffraction data showed that all the strong reflections belonged to a hexagonal subcell with $a = b = 18.7951(14)$, $c = 10.3224(11)$ Å, $U = 3158(4)$ Å^3. This seems to indicate that the majority of the structure in the trigonal and in the hexagonal cell is identical but that the ordering of a small part of the structure gives rise to the weak supercell reflections, which produce the larger cell. In the smaller subcell these groups would appear disordered. The unit cell superstructure that we observe is caused by a subtle difference in ligand orientation in **3A** and **3B**; therefore the diffraction effect is small and produces extremely weak reflections. Careful analysis of the Ga positions in the two independent molecules reveals a Ga-dominated subcell that is entirely consistent with the subcell observed for the crystals of **3**. The refinement of the data in this subcell resulted in a single molecule with a Ga_{13} core identical to that of the supercell, but with every other ligand molecule disordered in a ratio of 2:1. Furthermore, the single crystals obtained for compound **3** were extremely small and weakly diffracting and the data were not of sufficient quality to allow complete analysis of the structure. Each Ga_{13} cluster carries a +3 charge, so three counterions per cluster are expected. However, discrete nitrate ions could not be located in the Fourier difference map because of the weak reflections, the high symmetry of the space group, and the problems with solvent loss and crystal decay. The microanalytical data for **3** reveal a C:N ratio of 4.2:1, which compares well with the expected ratio of 4:1. An alternative formulation with bridging oxo ligands in place of hydroxide ligands would require the presence of positive counterions and would not be in agreement with the formulation based upon the previously reported analogous Al^{III} and Fe^{III} clusters.[7,8,14,15]

Received: December 16, 2003
Revised: May 17, 2004 [Z53542]

Keywords: aggregation · cluster compounds · cluster formation · gallium

[1] A. K. Powell, *Met. Ions Biol. Syst.* **1998**, *35*, 515.
[2] N. D. Chasteen, P. M. Harrison, *J. Struct. Biol.* **1999**, *126*, 182.
[3] S. M. Gorun, S. J. Lippard, *Nature* **1986**, *319*, 666.
[4] T. Hyeon, *Chem. Commun.* **2003**, 927.
[5] Preparation of **1**: H_3heidi (0.44 g, 2.5 mmol) and sodium hydroxide (0.20 g, 5 mmol) in H_2O (10 mL) were added to $Ga(NO_3)_3$ (0.64 g, 2.5 mmol) in H_2O (10 mL), pH 2.78. Crystals suitable for X-ray diffraction formed within two weeks. Yield 0.34 g, 52%. Anal. calcd. (found) for **1**, $C_{12}H_{20}N_2O_{12}Ga_2$: C 27.52 (27.43); H 3.85; N 5.35 (5.29). Preparation of **2**: H_3heidi (0.44 g, 2.5 mmol) and pyridine (1.62 mL, 20 mmol) were added to $Ga(NO_3)_3$ (1.27 g, 5 mmol) in H_2O (10 mL), pH 5.01. Crystals suitable for X-ray diffraction were obtained by layering with ethanol after eight weeks. This product always co-crystallizes as a minor product with **3**, and it was not possible to collect sufficient pure material for microanalysis. **3**: H_3heidi (0.44 g, 2.5 mmol) and pyridine (1.0 mL, 12 mmol) were added to $Ga(NO_3)_3$ (1.92 g, 7.5 mmol) in H_2O (10 mL). The pH value was adjusted to 5.0 by dropwise addition of pyridine. Colorless needles suitable for single-crystal X-ray diffraction formed within ten weeks. Yield 0.44 g, 10%. Anal. calcd. (found) for **3**, $C_{36}H_{110.20}N_9O_{79.10}Ga_{13}$: C 15.77 (15.57); H 4.60 (4.04); N 4.60 (4.36). IR (KBr disk): $\tilde{\nu} = 1384$ (sharp, $\nu_3(NO_3^-)$), 832 cm^{-1} (NO_3^-, out of plane).
[6] CCDC-226692–226694 contain the supplementary crystallographic data for compounds **1**–**3**. These data can be obtained free of charge via www.ccdc.cam.ac.uk/conts/retrieving.html (or from the Cambridge Crystallographic Data Centre, 12, Union Road, Cambridge CB2 1EZ, UK; fax: (+44) 1223-336-033; or deposit@ccdc.cam.ac.uk).
[7] S. L. Heath, A. K. Powell, *Angew. Chem.* **1992**, *104*, 191; *Angew. Chem. Int. Ed. Engl.* **1992**, *31*, 191.
[8] S. L. Heath, P. A. Jordan, I. D. Johnson, G. R. Moore, A. K. Powell, M. Helliwell, *J. Inorg. Biochem.* **1995**, *59*, 785.
[9] M. A. Bolcar, S. M. J. Aubin, K. Folting, D. N. Hendrickson, G. Christou, *Chem. Commun.* **1997**, 1485.
[10] M. Tesmer, B. Müller, H. Vahrenkamp, *Chem. Commun.* **1997**, 721.
[11] G. L. Abbati, A. Cornia, A. C. Fabretti, A. Caneschi, D. Gatteschi, *Inorg. Chem.* **1998**, *37*, 3759.

 © 2004 Wiley-VCH Verlag GmbH & Co. KGaA, Weinheim

[12] H. Oshio, N. Hoshino, T. Ito, M. Nakano, F. Renz, P. Gütlich, *Angew. Chem.* **2003**, *115*, 233; *Angew. Chem. Int. Ed.* **2003**, *42*, 223.
[13] S. Boulmaaz, R. Papiernik, L. G. Hubertpfalzgraf, J. Vaissermann, J. C. Daran, *Polyhedron* **1992**, *11*, 1331.
[14] A. K. Powell, S. L. Heath, D. Gatteschi, L. Pardi, R. Sessoli, G. Spina, F. Delgiallo, F. Pieralli, *J. Am. Chem. Soc.* **1995**, *117*, 2491.
[15] J. C. Goodwin, R. Sessoli, D. Gatteschi, W. Wernsdorfer, A. K. Powell, S. L. Heath, *J. Chem. Soc. Dalton Trans.* **2000**, 1835.
[16] I. A. M. Pohl, L. G. Westin, M. Kritikos, *Chem. Eur. J.* **2001**, *7*, 3438.
[17] J. T. Brockman, J. C. Huffman, G. Christou, *Angew. Chem.* **2002**, *114*, 2616; *Angew. Chem. Int. Ed.* **2002**, *41*, 2506.
[18] M. Murrie, H. Stoeckli-Evans, H. U. Güdel, *Angew. Chem.* **2001**, *113*, 2011; *Angew. Chem. Int. Ed.* **2001**, *40*, 1957.
[19] E. K. Brechin, S. G. Harris, A. Harrison, S. Parsons, A. G. Whittaker, R. E. P. Winpenny, *Chem. Commun.* **1997**, 653.
[20] R. E. Winpenny, *Comprehensive Coordination Chemistry II*, *Vol. 7* (Eds.: T. J. Meyer, J. A. McCleverty, C. Creutz), Elsevier, Dordrecht, **2004**, p. 125.
[21] G. M.Sheldrick, SHELXL97, an integrated system for solving and refining crystal structures from diffraction data, University of Göttingen, Germany, **1997**.

 © 2004 Wiley-VCH Verlag GmbH & Co. KGaA, Weinheim

Inhibitor Design

Inhibition of Amyloid Fibril Formation by Peptide Analogues Modified with α-Aminoisobutyric Acid**

*Sharon Gilead and Ehud Gazit**

The accumulation of amyloid deposits is observed in diseases of unrelated origin, such as Alzheimer's disease, Parkinson's disease, type II diabetes, and prion disorders.[1] An increasing body of evidence supports the hypothesis that the assembly of amyloid fibrils is a central factor in the development of the clinical symptoms of these diseases. A key step in amyloid formation is the transition of a protein from its native structure to a β-sheet arrangement.[1] Upon formation of amyloid fibrils, the protein molecules that compose the fibrils lose their native conformation and adopt ordered, stacked β-sheet structures. This observation suggests that prevention of the ability of amyloidogenic proteins to adopt a β-sheet conformation would be useful as a way to interfere with the amyloid self-assembly process.[2,3] The use of β-breaker elements is a promising approach to the development of fibrillization inhibitory drugs. A milestone in the search for proof of this concept was provided by Soto et al., who demonstrated that incorporation of β-breaker elements into short peptides composed of the recognition sequence of the amyloidogenic protein results in inhibition of amyloid formation.[1e,2b,2d] The proline residue is widely used in such research since it has greater β-breaking potential than the other natural amino acids. Another approach involves N-methylation of peptide inhibitors that prevent β-sheet stacking by interfering with the intermolecular backbone hydrogen bonds needed to form the structure.[2g]

α-Aminoisobutyric acid (Aib) is a unique β-sheet breaker. This achiral amino acid has two methyl residues attached to the C_α atom and strongly favors helical conformations.[4] The presence of a methyl group instead of the hydrogen atom found in the natural amino acids greatly affects the steric properties of the residue. Alanine has a wide range of allowed ϕ, ψ torsion angles, but Aib, which is α-methylated alanine, has an extremely limited conformational space. The conformational map of Aib is derived by superposing the Ramachandran plots of L-alanine and D-alanine (Figure 1).[4b,c] As shown in the figure, the allowed angles are restricted to small regions that are clearly much more suitable for an α-helical conformation than for a β-strand structure. Comparison of the map for Aib with that for proline clearly demonstrates that Aib has the potential to be a better β-breaker than proline (Figure 1).

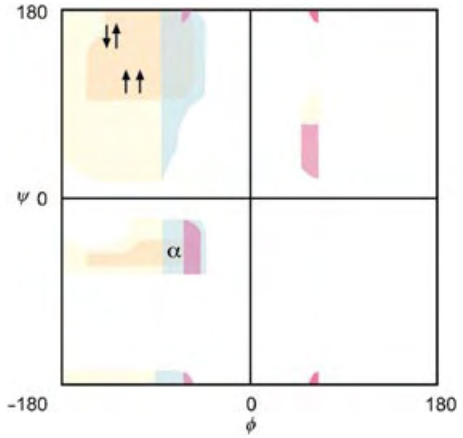


Figure 1. Conformational restriction of Aib. The Ramachandran plot shows the sterically allowed regions for all natural amino acids (yellow for fully allowed, orange for partially allowed), for L-proline (blue), and for the achiral Aib residue (magenta). ↑↓: antiparallel β sheet, ↑↑: parallel β sheet, α: α helix. The figure was prepared by merging separate plots from ref. [4c].

The effect of Aib incorporation on the conformation of short peptides has been studied extensively over the last two decades. The Aib residue has been shown to have a very high tendency to induce helical conformations and to disrupt β-sheet structures in a large number of peptides.[4] A study independent from that described herein recently demonstrated that the incorporation of an Aib residue into a fully protected Alzheimer's β-amyloid fragment ($A\beta_{17-21}$) induces

[*] S. Gilead, Dr. E. Gazit
Department of Molecular Microbiology and Biotechnology
Tel Aviv University, Tel Aviv 69978 (Israel)
Fax: (+972) 3-640-9407
E-mail: ehudg@post.tau.ac.il

[**] We thank Yaacov Delarea for help with the electron microscopy experiments, Faybia Margolin for manuscript preparation, and members of the Gazit laboratory for helpful discussions. Support from the Israel Science Foundation (Bikura Program) is gratefully acknowledged.

 DOI: 10.1002/anie.200353565 © 2004 Wiley-VCH Verlag GmbH & Co. KGaA, Weinheim

helical structure in the fragment in organic solvents.[5] We previously suggested the use of Aib as a conjugated β-breaker element for the inhibition of amyloid fibril formation.[3] To test this concept experimentally, we assayed the ability of Aib-containing peptide analogues to inhibit amyloid formation by human islet amyloid polypeptide (hIAPP). This 37 amino acid hormone peptide accumulates in amyloid deposits in the pancreas of individuals with type II diabetes.[6,7]

A growing body of evidence suggests that hIAPP amyloid fibril formation may play an important role in the loss of β-cell mass and the progressive decline in insulin secretion characteristic of type II diabetes.[6] We recently reported the use of a nonbiased peptide array scan to identify a novel region within hIAPP that appears to mediate the molecular recogntion processes that lead to amyloid fibril self-assembly.[7] Peptide fragments of the $hIAPP_{14-20}$ domain are highly amyloidogenic and have greater affinity for full-length hIAPP than does the widely studied $IAPP_{20-29}$ peptide. Herein, we use the $hIAPP_{14-20}$ domain as a target for the inhibition of hIAPP fibrillization by designed peptide-based inhibitors. We used the native peptide as a template and introduced small chemical modifications that maintain the recognition properties of the fragment but abolish its ability to assemble into amyloid fibrils. When added to hIAPP, the new peptides bind to the recognition domain, block it, and prevent its assembly into amyloid fibrils.

We designed three peptide inhibitors by substituting hydrophobic alanine and leucine residues in the sequences ANFLVHSS, ANFLVH, and ANFLV (corresponding to residues 13–17, 13–18, and 13–20 of hIAPP) with Aib residues. The resulting potential inhibitors have the sequences Aib-NF-Aib-VHSS, Aib-NF-Aib-VH, and Aib-NF-Aib-V, respectively. Since these changes are quite conservative in terms of the chemical properties of the recognition surface, the breakage elements can be integrated into the molecular recognition sequence. Conjugation of disturbing residues to molecular recognition motifs produces larger peptides, which have reduced potential as drug leads.

We first examined the ability of the Aib-modified peptides to form amyloid fibrils, compared to that of native peptides. Although the overall changes in the chemical structures are minor, we observed critical differences between the abilities of the native and modified peptides to form amyloid fibrils. The amyloidogenic nature of the peptides was determined by using electron microscopy (EM), Congo red (CR) birefringence, and FTIR spectroscopy assays. All the native peptides, ANFLVHSS, ANFLVH, and ANFLV, formed fibrillar structures that could be seen under the electron microscope. The ANFLVH peptide formed dense bundles of long, coiling fibrils that closely resemble the amyloid fibrils formed by full-length hIAPP. No fibrillar structures were observed for the Aib-containing peptides Aib-NF-Aib-VHSS, Aib-NF-Aib-VH, and Aib-NF-Aib-V. Even after a longer period of incubation, only a small amount of amorphous aggregates was detected (Figure 2a). The abundance of the amorphous material on the microscope grid was extremely low compared to the high abundance of ordered fibrillar structures observed with the unmodified peptides.

Upon staining with Congo red, the ANFLVH and ANFLV peptides exhibited a typical yellow-green birefringence. The ANFLVHSS peptide exhibited less intense birefringence. The Aib-NF-Aib-VHSS, Aib-NF-Aib-VH, and Aib-NF-Aib-V peptides exhibited no birefringence and thus appear to have no potential to form amyloid fibrils, which is in agreement with the results of the EM studies (Figure 2a). FTIR spectra were recorded to determine the internal conformation of the observed ultrastructures. Modification of the native peptides to form Aib-containing peptides produced a significant change in the infrared spectra. The ANFLVHSS, ANFLVH, and ANFLV peptides have spectra typical of β-sheet structures, with minima at 1631–1633 cm^{-1}. The ANFLVHSS peptide has a second band at 1678 cm^{-1}, which might indicate

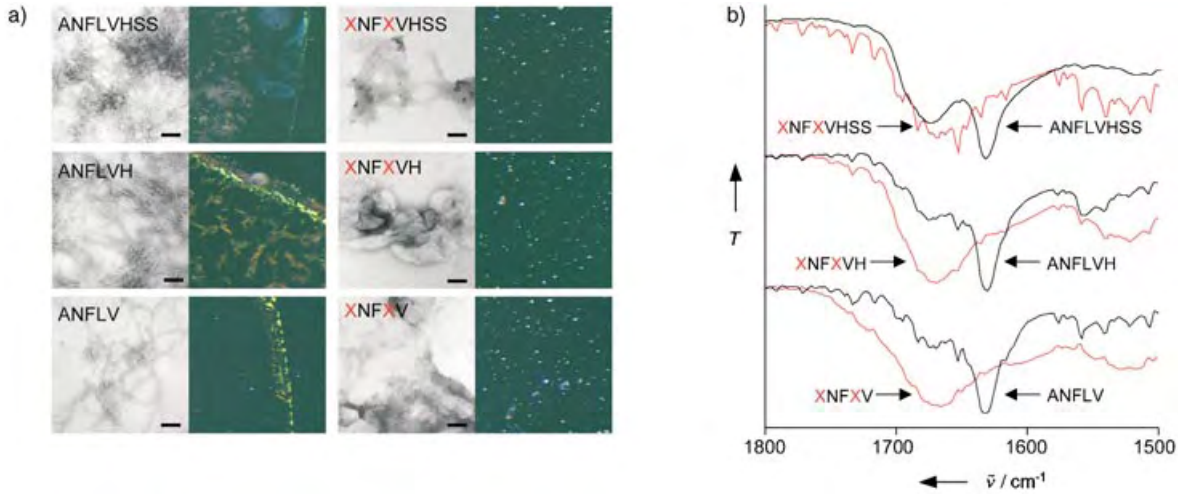


Figure 2. Amyloidogenic properties of native and Aib-modified peptides. a) The studied peptides were examined with an electron microscope and with a light microscope under cross-polarizers after staining with Congo red. The corresponding EM (left) and CR (right) photographs of each peptide are shown. b) Analysis of the secondary conformation of insoluble structures formed in aged solutions, as assessed by FTIR spectroscopy (*T*: Transmittance). The arrows show which spectrum corresponds to each peptide. Peptide solutions were aged for various periods of time, as described in the Experimental Section. X: Aib.

 © 2004 Wiley-VCH Verlag GmbH & Co. KGaA, Weinheim

the presence of non-β elements. The Aib-NF-Aib-VHSS, Aib-NF-Aib-VH, and Aib-NF-Aib-V peptides have minima at 1666–1670 cm^{-1}. These band frequencies are typical for Aib-containing peptides and indicate the presence of 3_{10} helices (Figure 2b).[8] We conclude that there is a fundamental difference between native peptides and their Aib-containing analogues. Native peptides are highly amyloidogenic, whereas their Aib-modified analogues are unable to form amyloid fibrils. The observation that this very minor chemical modification results in such a dramatic effect on the amyloidogenic potential of the peptide is consistent with structural models of the effect of Aib incorporation on conformational flexibility.[4]

The modified peptides display a recognition surface that is almost identical to that of the native sequence but lacks any amyloidogenic potential. These peptides are thus excellent candidates for the inhibition of amyloid self-assembly. We investigated the ability of the modified peptides to inhibit full-length hIAPP amyloid fibril formation by using the thioflavin-T (ThT) binding assay. This method provides quantitative information on amyloid fibril growth. hIAPP was allowed to form amyloid fibrils either in the presence of a 10-fold excess of peptide inhibitor or with no inhibitor. The fibrillization process was monitored and when a plateau was reached, the fluorescence intensity was recorded. The formation of amyloid fibrils was significantly reduced in the presence of the various Aib-containing peptides, as shown by the observed fluorescence intensities (Figure 3a). In contrast, when hIAPP was incubated in the presence of a 10-fold excess of the wild-type peptide ANFLVH in a control experiment, no significant inhibition was observed; the average ThT fluorescence was $97.1 \pm 7.4\%$ (four independent repeats) relative to that observed upon incubation of hIAPP in the absence of added peptides. These results clearly indicate that Aib-containing peptides have great potential as inhibitors of hIAPP amyloid fibril formation.

Since the Aib-NF-Aib-VH peptide exhibited the strongest inhibitory effect, we investigated the kinetics of hIAPP fibrillization in the presence and absence of this inhibiting peptide. In both cases, hIAPP fibrillization followed a typical nucleation-dependent path.[9] However, fibrillization occurred with strong exponential growth in the absence of inhibitor, whilst the fluorescence plot corresponding to fibrillization in the presence of inhibitor has only a small slope. The fluorescence intensity observed when the process had reached a plateau was dramatically lower for fibrillization under inhibitory conditions than in the absence of inhibitor (Figure 3b), as in the experiment described above. A clear difference was also observed upon staining with Congo red. Without inhibition, intense gold-green birefringence was observed; in the presence of the Aib-NF-Aib-VH peptide, only weak green birefringence was seen (Figure 3c).

Taken together, the results of our study suggest a new direction for the development of amyloid formation inhibitors: use of an Aib moiety as a β-breaker. Incorporation of such elements within a recognition motif rather than adjacent to it appears to be a powerful tool for the design of peptide inhibitors. This approach allows the creation of a wide range of molecules with highly specific chemical properties. In the last two years we have used a variety of experimental and theoretical techniques to demonstrate the key role of aromatic residues in self-assembly processes such as amyloid formation.[10] Herein, we have shown that the combination of an Aib modification and a native aromatic residue in a short

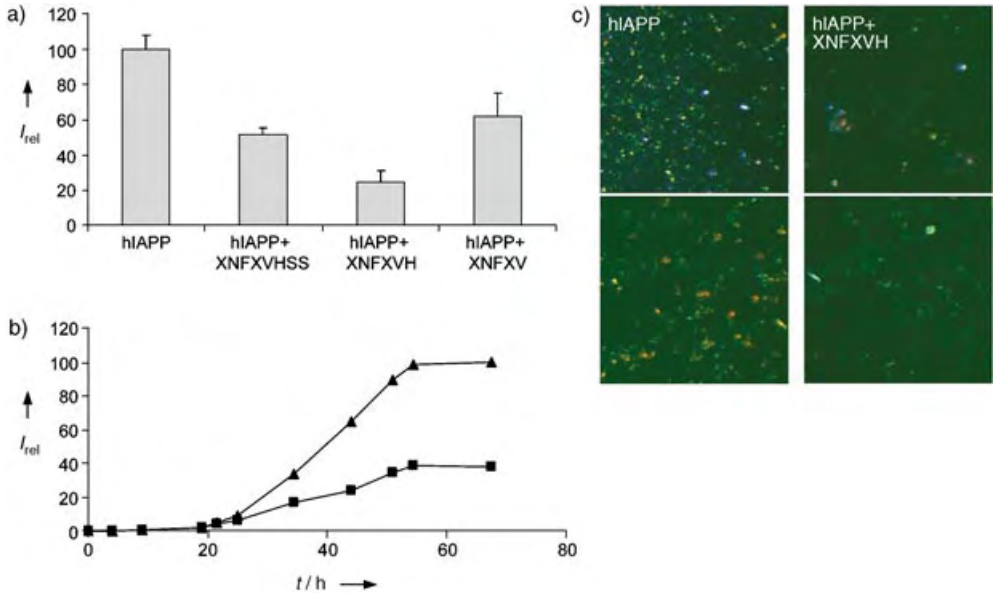


Figure 3. Inhibition of hIAPP amyloid formation. Quantitative representation of amyloid fibril formation by hIAPP in the absence and in the presence of Aib-containing peptide inhibitors, as assessed by the ThT binding assay. Peptide inhibitors were added in 10-fold excess. a) Relative fluorescence intensity I_{rel} of ThT added to hIAPP solutions aged for 3 days. Four independent repeat experiments were conducted. b) The kinetics of fibril formation by hIAPP alone (▲) and by hIAPP in the presence of the Aib-NF-Aib-VH peptide inhibitor (■). ThT was added to aliquots of hIAPP solutions over a period of 3 days, as described in the Experimental Section. c) Congo red staining and birefringence of hIAPP alone and in the presence of the Aib-NF-Aib-VH peptide inhibitor. Staining was performed after incubation for two (upper panel) and four days (bottom panel).

 © 2004 Wiley-VCH Verlag GmbH & Co. KGaA, Weinheim

recognition motif generates the molecular basis for significant inhibition properties, which include prevention of β-sheet formation and a high affinity for the hIAPP molecule.

Experimental Section

Peptide synthesis and solutions: Peptide synthesis was performed by Peptron, Inc. (Taejeon) using solid-phase methods. The identities of the peptides were confirmed by ion-spray mass spectrometry on a HP 1100 series LC/MSD instrument. The purity of the peptides was confirmed by reverse-phase high-pressure liquid chromatography on a C_{18} Vydac column. Lyophilized peptides were dissolved in dimethyl sulfoxide (DMSO) at a concentration of 100 mM. To avoid pre-aggregation, fresh stock solutions were prepared for each experiment. Peptide stock solutions were diluted with tris(hydroxymethyl)amino-methane buffer (10 mM, pH 7.2) to a final concentration of 5 mM (5% DMSO).

Congo red staining and birefringence: A suspension (10 μL) of peptide solution (5 mM) aged for 10 days was allowed to dry overnight on a glass microscope slide. A sample (100 μL) from the ThT assay, aged for 2 or 4 days, was used for hIAPP. Staining was performed by adding a suspension of saturated Congo red (10 μL) and NaCl in 80% ethanol (v/v) to the sample. Birefringence was determined with a SZX-12 stereoscope (Olympus) equipped with cross polarizers.

Transmission electron microscopy: A sample (10 μL) aged for 4 (native peptides) or 10 days (modified peptides) was placed on a 400-mesh copper grid (SPI supplies) covered with carbon-stabilized formvar film. After 1 minute, excess fluid was removed and the grid was negatively stained by treatment with 2% uranyl acetate in water for 2 minutes. Samples were viewed in a JEOL 1200EX electron microscope operating at 80 kV.

Fourier transform infrared spectroscopy: A sample (30 μL) of peptide solution aged for 2 weeks was suspended on a CaF_2 plate and dried in vacuo. The peptide deposit was resuspended in D_2O then dried. The resuspension procedure was repeated twice to ensure maximal hydrogen/deuterium exchange. Infrared spectra were recorded on a Nicolet Nexus 470 FT-IR spectrometer with a DTGS detector.

Thioflavin T binding fluorescence: Lyophilized synthetic hIAPP (Calbiochem) was dissolved in 1,1,1,3,3,3-hexafluoro-2-propanol to produce a 400-μM stock solution. This stock solution was added to solutions of the inhibiting peptides (40 μM) in sodium acetate buffer (20 mM, pH 6.5; 10-fold excess of inhibiting peptide), or to sodium acetate buffer (20 mM) alone to a final concentration of 4 μM. Immediately after dilution, the samples were centrifuged for 20 minutes at 18000 rpm in an Optima LE 70 ultracentrifuge (Beckman) equipped with a Ti 70.1 rotor at 4 °C. After centrifugation, the pellet was removed. 500-μL aliquots of the reaction solutions were added to sodium acetate buffer (500 μL) containing ThT (3 μM). Fluorescence values were measured with excitation at 450 nm and emission at 480 nm. The end-point experiment was repeated four times. Figure 3 shows average values with bars indicating standard deviations.

Received: December 18, 2003
Revised: May 10, 2004 [Z53565]

Keywords: amyloid fibrils · islet amyloid polypeptide · peptides · protein folding · self-assembly

[1] a) M. Sunde, C. C. F. Blake, *Q. Rev. Biophys.* **1998**, *31*, 1–39; b) J. C. Rochet, P. T. Lansbury, Jr., *Curr. Opin. Struct. Biol.* **2000**, *10*, 60–68; c) J. C. Sacchettini, J. W. Kelly, *Nat. Rev. Drug Discovery* **2002**, *1*, 267–275; d) E. Gazit, *Angew. Chem.* **2002**, *114*, 267–269; *Angew. Chem. Int. Ed.* **2002**, *41*, 257–259; e) C. Soto, *Nat. Rev.* **2003**, *4*, 49–60; f) M. Stefani, C. M. Dobson, *J. Mol. Med.* **2003**, *81*, 678–699.

[2] a) L. O. Tjernberg, J. Näslund, F. Lindqvist, J. Johansson, A. R. Karlström, J. Thyberg, L. Terenius, C. Nordstedt, *J. Biol. Chem.* **1996**, *271*, 8545–8548; b) C. Soto, E. M. Sigurdsson, L. Morelli, R. A. Kumar, E. M. Castano, B. Frangione, *Nat. Med.* **1998**, *4*, 822–826; c) M. A. Findeis, G. M. Musso, C. C. Arico-Muendel, H. W. Benjamin, A. M. Hundal, J. J. Lee, J. Chin, M. Kelley, J. Wakefield, N. J. Hayward, S. M. Molineaux, *Biochemistry* **1999**, *38*, 6791–6800; d) C. Soto, *FEBS lett.* **2001**, *498*, 204–207; e) T. L. Lowe, A. Strzelec, L. L. Kiessling, R. M. Murphy, *Biochemistry* **2001**, *40*, 7882–7889; f) L. A. Scrocchi, Y. Chen, S. Waschuk, F. Wang, S. Cheung, A. A. Darabie, J. McLaurin, P. E. Fraser, *J. Mol. Biol.* **2002**, *318*, 697–706; g) A. Kapurniotu, A. Schmauder, K. Tenidis, *J. Mol. Biol.* **2002**, *315*, 339–350.

[3] E. Gazit, *Curr. Med. Chem.* **2002**, *9*, 1725–1735.

[4] a) I. L. Karle, P. Balaram, *Biochemistry* **1990**, *29*, 6747–6756; b) R. Kaul, P. Balaram, *Bioorg. Med. Chem.* **1999**, *7*, 105–117; c) J. Venkatraman, C. S. Shankaramma, P. Balaram, *Chem. Rev.* **2001**, *101*, 3131–3152; d) S. Aravinda, N. Shamala, C. Das, A. Sriranjini, I. L. Karle, P. Balaram, *J. Am. Chem. Soc.* **2003**, *125*, 5308–5315.

[5] F. Formaggio, A. Bettio, V. Moretto, M. Crisma, C. Toniolo, Q. B. Broxterman, *J. Pept. Sci.* **2003**, *9*, 461–466.

[6] a) P. Westermark, U. Engström, K. H. Johnson, G. T. Westermark, C. Betsholtz, *Proc. Natl. Acad. Sci. USA* **1990**, *13*, 5036–5040; b) A. Lorenzo, B. Razzaboni, G. C. Weir, B. A. Yankner, *Nature* **1994**, *368*, 756–760; c) E. T. A. S. Jaikaran, A. Clark, *Biochim. Biophys. Acta* **2001**, *1573*, 179–203; d) S. Seino, *Diabetologia* **2001**, *44*, 906–909; e) R. Azriel, E. Gazit, *J. Biol. Chem.* **2001**, *276*, 34156–34161; f) A. Kapurniotu, *Biopolymers* **2001**, *60*, 438–459.

[7] Y. Mazor, S. Gilead, I. Benhar, E. Gazit, *J. Mol. Biol.* **2002**, *322*, 1013–1024.

[8] P. I. Haris, D. Chapman, *Biopolymers* **1995**, *37*, 251–263.

[9] J. D. Harper, P. T. Lansbury, Jr., *Annu. Rev. Biochem.* **1997**, *66*, 385–407.

[10] a) M. Reches, Y. Porat, E. Gazit, *J. Biol. Chem.* **2002**, *277*, 35475–5480; b) E. Gazit, *FASEB J.* **2002**, *16*, 77–83; c) E. Gazit, *Bioinformatics* **2002**, *18*, 880–883; d) M. Reches, E. Gazit, *Science* **2003**, *300*, 625–627; e) M. Reches, E. Gazit, *Amyloid* **2004**, in press.

 © 2004 Wiley-VCH Verlag GmbH & Co. KGaA, Weinheim

Multichromophoric Polymers

Investigation of Perylene Photonic Wires by Combined Single-Molecule Fluorescence and Atomic Force Microscopy**

Jordi Hernando, Pieter A. J. de Witte, Erik M. H.P van Dijk, Jeroen Korterik, Roeland J. M. Nolte, Alan E. Rowan, María F. García-Parajó, and Niek F. van Hulst*

Multichromophoric systems can exhibit interesting optical and electronic properties due to excitonic interactions between dye units that are near to each other.[1] An exquisite example found in nature is the light-harvesting antenna system in photosynthetic bacteria, which allow for efficient light absorption and unidirectional transfer of energy to the reaction center during photosynthesis.[2] The design of artificial multichromophoric arrays that mimic these properties is a great challenge, the ultimate goal being the construction of molecular photonic and electronic devices.

A unique insight into the physical behavior of multichromophoric systems is obtained with the help of single-molecule-detection techniques. Single-molecule force microscopy not only provides information on the dimensions of the aggregates but also on the internal organization of the chromophores,[1a,3] a crucial issue that governs their excitonic behavior. Single-molecule optical spectroscopy reveals characteristic features arising from exciton coupling, such as single-emitter behavior and collective fluorescent/nonfluorescent states, properties that otherwise remain hidden when probing the average behavior of ensembles of molecules.[4–6] In this work we have combined force and optical microscopy to investigate at the single-molecule level the properties of a new class of rigid multichromophoric polymers intended to act as synthetic antennas.

To attain optimal excitonic behavior in multichromophoric assemblies, a well-defined close packing of the chromophores is required. Recently, we have used intrinsically rigid and helical polymers of isocyanopeptides,[7] which have a persistence length of 76 nm,[8] as scaffolds to anchor porphyrin molecules. In this way long well-ordered porphyrin arrays with an average length of 87 nm were obtained.[9] In the work presented herein, we have used a similar approach to prepare perylene isocyano amino acid polymers. Perylene was chosen because of its: 1) high absorptivity and fluorescence quantum yield; 2) high thermal and high photochemical stability; 3) high electron affinity. Perylene-based chromophoric arrays[10] are promising components for the construction of optical and electronic molecular devices, for instance as n-type semiconductor material in organic photovoltaic cells.[11]

Figure 1 shows the structure of the perylene polyisocyanide **2**, as well as of the precursor perylene monomer **1**. A detailed description of the synthesis and characterization of **2**

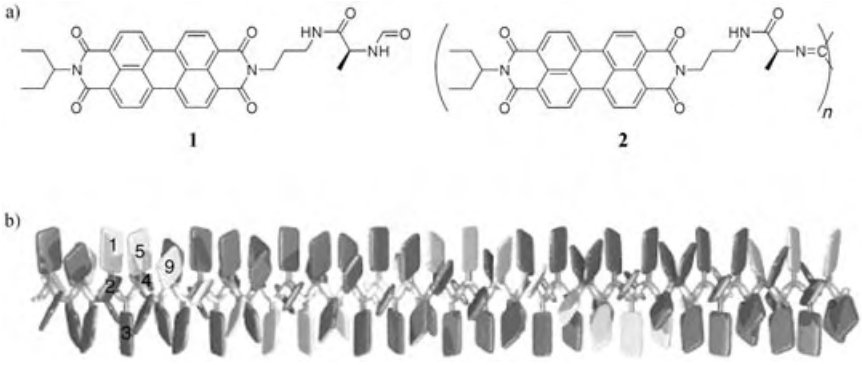


Figure 1. a) Structures of the perylene monomer (**1**) and the perylene polyisocyanide polymer (**2**); b) schematic 3D drawing of a molecule of polymer **2**. One perylene column is shown in light grey for clarity. Perylene units 1,5,9, and so on, belong to the same column.

[*] Dr. J. Hernando, Ir. E. M. H. van Dijk, Ing. J. Korterik, Dr. M. F. García-Parajó, Prof. Dr. N. F. van Hulst
Applied Optics group
Faculty of Science and Technology
University of Twente and MESA+ Research Institute
P.O. Box 217, 7500AE Enschede (The Netherlands)
Fax: (+31) 53-489-3511
E-mail: m.f.garciaparajo@tnw.utwente.nl
P. A. J. de Witte, Prof. Dr. R. J. M. Nolte, Dr. A. E. Rowan
Department of Organic Chemistry, NSRIM
University of Nijmegen
Toernooiveld 1, 6525ED Nijmegen (The Netherlands)
Fax: (+31) 24-365-2929

[**] The authors thank E. E. Neuteboom, S. C. J. Meskers and R. A. J. Janssen for providing with the monomer precursor for the perylene polymer synthesis and their help with the ensemble fluorescence lifetime measurements. Financial support from the EC SMARTON network is gratefully acknowledged. J.H. thanks the EC Program IHP-99 for a Marie Curie Fellowship (HPMF-CT-2002-01698). E.M.H.P.v.D. thanks the support by Dutch Foundation for Fundamental Research of Matter (FOM). M.F.G.P. acknowledges support from KNAW.

will be given elsewhere.[12] Briefly, a monoamino perylene was coupled to Boc-L-alanine by using standard peptide coupling reagents. The resulting perylene-L-alanine product was formylated to yield product **1**, whose terminal *N*-formyl group was subsequently converted into an isocyanide. Polymerization of the latter species yielded perylene polyisocyanide **2**. Fractionation by the successive precipitation of redissolved polymer samples was used to purify perylene polyisocyanides from nonreacted monomers in the reaction mixture. This process was repeated until no changes in the bulk absorption and emission spectra of **2** were observed. The rodlike nature of the purified polymer **2** (see below) prevented us from obtaining information about its molecular weight and polydispersity by means of the usual techniques, such as MALDI-TOF, MS, or GPC.

The circular dichroism spectrum of **2** in $CHCl_3$ shows Cotton effects in the absorption region of perylene, as well as for the imine groups of the polyisocyanide backbone.[12] The latter Cotton effect is observed for polyisocyanides with

 DOI: 10.1002/anie.200453745 © 2004 Wiley-VCH Verlag GmbH & Co. KGaA, Weinheim

alanine dipeptide sidegroups that form hydrogen-bonding arrays along the polymer.[13] This provides us with a clear signature indicating that polymer **2** has a rigid helical backbone, which is stabilized through a hydrogen-bonding network between the amino acid side chains, as shown schematically in Figure 1b. The perylene chromophores are attached to this backbone in four parallel stacks. For the previously synthesized porphyrin polyisocyanides,[9] the adjacent dye molecules in one stack were found to be 4.2 Å apart with a twist angle of 22°. Similar values are expected for the perylene polyisocyanide **2**. For such a chromophoric close-packing, an optical behavior governed by excitonic interactions is anticipated. This is demonstrated by the bulk absorption and fluorescence emission spectra of **1** and **2** in $CHCl_3$ (Figure 2). Compared to the monomer, the peak

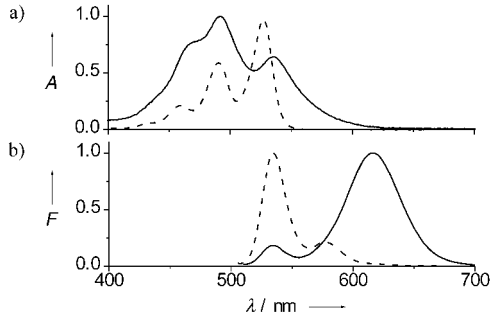


Figure 2. a) Absorption (*A*, arbitrary units) and b) fluorescence (*F*, arbitrary units) emission spectra of monomer **1** (dashed line) and polymer **2** (continuous line) in $CHCl_3$.

positions in the absorption spectrum of the polymer and their relative intensities have changed. These differences indicate that interaction between the perylene units in **2** already occurs in the ground state, pointing to the existence of excitonic effects. According to exciton theory[14] we assign the blue-shifted peak at $\lambda = 492$ nm to the interaction, parallel to the axis of the system, between the nearly face-to-face 1st, 5th, 9th, etc. perylene units, while the slightly red-shifted band at $\lambda = 536$ nm is ascribed to coupling between the 1st, 2nd, 3rd, and 4th dyes in the plane perpendicular to the axis of the polymer. The overlay of these two exciton bands and their vibronic peaks explains the broadening and apparent loss of structure of the polymer absorption spectrum. The fluorescence properties of the polymer are even more distinct: a broad structureless red-shifted band is visible, the quantum yield has decreased ($\Phi = 0.11$) and the fluorescence decay is multiexponential, with a minor contribution from a decay time equal to that of **1** ($\tau_1 = 3.9$ ns) and a major contribution from a much longer decay time ($\tau_2 = 19.9$ ns).[12] These features demonstrate that emission mainly arises from intramolecular excimer-like species in the polymer, a phenomenon known to occur in stacks of perylene molecules.[6,15] Although interaction in the ground state may also contribute to the formation of excimer-like species in the polymer,[16] this process essentially occurs upon irradiation of proximal chromophores, whose conjugation paths fully or partially overlap, as perylene units 1, 5, 9, etc. do in polymer **2**.

Diluted solutions of **2** in $CHCl_3$ were investigated by atomic force microscopy (AFM) after spin-coating on mica. Isolated single perylene polyisocyanide polymer molecules of different lengths were observed in the AFM images as shown in Figure 3. Fibers up to a few hundreds of nanometers in

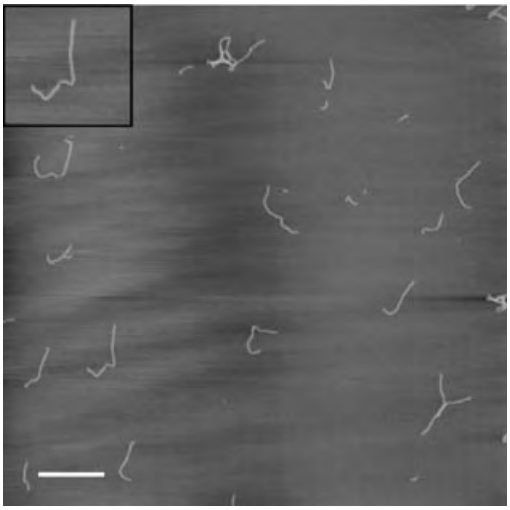


Figure 3. AFM image of a diluted solution of polymer **2** spin-coated on mica. Inset: enlargement of an individual fiber (bar = 500 nm).

length and about 2.5 nm in height are present, consistent with single helical perylene polyisocyanide polymer fibers being probed. In the absence of well-defined helical structure the height of the polymers should be much lower and thus not resolvable with AFM.

Detailed insight into the photophysical properties of individual perylene polyisocyanides was obtained by performing single-molecule fluorescence imaging of diluted solution of **2** in $CHCl_3$ after spin-coating on glass. Subsequently, the evolution of the emission intensity and fluorescence spectra of individual polymer fibers was recorded as a function of time. Two different species with distinct emissive behaviors were distinguished in the polymer sample. In the following discussion, we refer to these two types of molecules as green and red species owing to their different fluorescence spectra. The intensity time trajectories for two typical green and red species are shown in Figure 4 together with their fluorescence spectra integrated over the whole $t = 0$–25 s time window. A decrease in the fluorescence intensity with time was observed for both species, a process known to occur for multichromophoric systems due to successive photodegradation of the multiple emitting sites in the aggregate.[4–6] However, whereas a continuous decrease in fluorescence was measured for the red species, distinct and discrete intensity levels occurred for the green-fluorescent spot. These observations indicate that the latter species consisted of a few emitting units, while the former species contained a large number of independent fluorescent sites, as observed in conjugated polymers.[5b] The occurrence of a collective nonfluorescent state ($t = 3.5$–7.5 s) for the highest intensity level of the green species may arise from the photodriven generation of a long-lived trapped species fully quenching the fluorescence of the system, a

 © 2004 Wiley-VCH Verlag GmbH & Co. KGaA, Weinheim

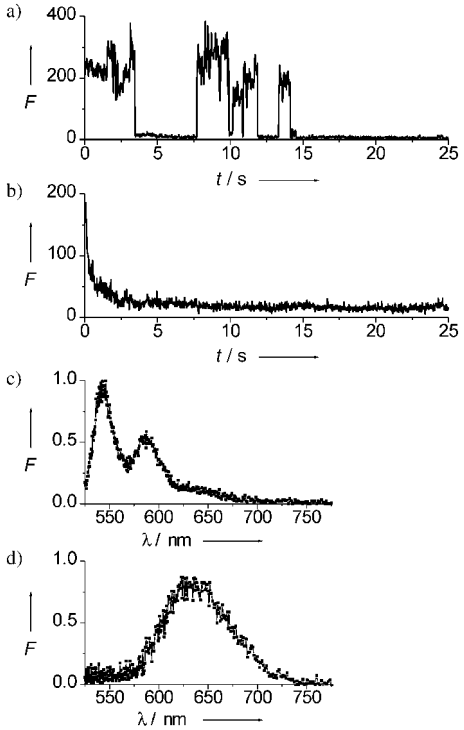


Figure 4. Fluorescence intensity trajectory for green (a) and red (b) single molecules; their emission spectra integrated over the whole $t = 0$–25 s time window are given in plots c) and d), respectively.

behavior usually ascribed to radical formation in perylene aggregates.[6,17] Spectral measurements were found to cast some light on the nature of these two types of fluorescent compounds. For the green species, the fluorescence spectrum resembled that of monomer **1**, which display the characteristic vibronic peaks for perylene emission. The red species, however, showed a broader red-shifted fluorescence spectrum indicating that the emission mainly arose from excimer-like sites, as observed for polymer **2** in solution. No significant spectral changes were observed during the emission period of both molecules.

The spread in fiber lengths as shown in Figure 3 suggests that the two emissive behaviors may arise from heterogeneity in the polymer structure. To investigate such a situation, simultaneous topographical and optical measurements on individual perylene polyisocyanides were performed. Figure 5 shows AFM and fluorescence images recorded on the same area of a spin-coated sample **2** on glass. Single polymer fibers with helical backbones (height ≈ 2.5 nm) are observed in the AFM picture; the length of these fibers vary between 20 to 120 nm. The emission arising from single fluorescent species is displayed in the fluorescence image. Green and red spots correspond to species emitting at $\lambda < 590$ nm and $\lambda > 590$ nm, respectively, which allowed us to distinguish between green ($\lambda < 590$ nm) and red species ($\lambda > 590$ nm). Clearly, a correlation between topography and fluorescence signal is only observed for those molecules emitting in the red, while green-fluorescent species do not show any counterpart feature in the AFM image.

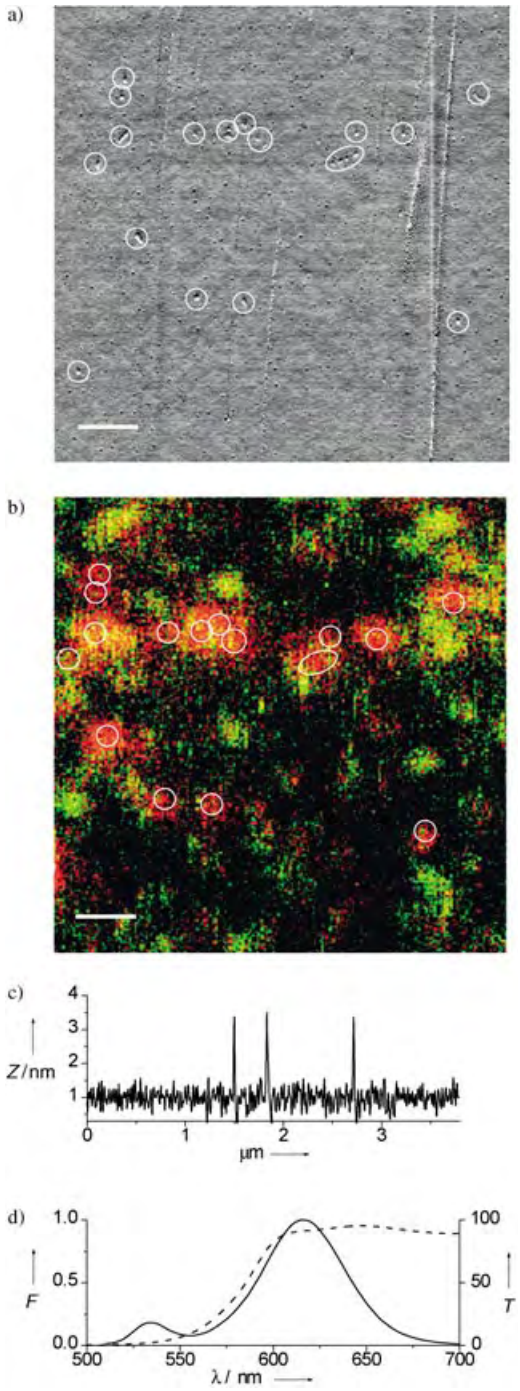


Figure 5. a) AFM and b) confocal fluorescence images from the same $3.8 \times 3.8\ \mu m^2$ area of a diluted solution of polymer **2** spin-coated on glass (bar = 500 nm); c) height profile (Z) for a line section of the AFM image; d) bulk fluorescence emission spectrum of polymer **2** in $CHCl_3$ (continuous line) and transmitance spectrum of the dichroic beam splitter used to distinguish between green ($\lambda < 590$ nm) and red ($\lambda > 590$ nm) fluorescent molecules (dashed line).

As the red emission originates from the single polymer fibers visualized in the topography image, we conclude that the helical perylene polyisocyanides emit through multiple independent excimer-like sites created along the fiber. After excitation of the polymer, we expect strong coupling between

 © 2004 Wiley-VCH Verlag GmbH & Co. KGaA, Weinheim

proximal perylene units, thus allowing exciton delocalization.[18] However, this process would be rapidly quenched by the formation of excimer-like species caused by the interaction between two or a few nearly cofacial perylenes. These perylenes act as a sink for the exciton, thus limiting the extent of the delocalization of the electronic excitation, and ultimately they are responsible for the polymer emission. Exploiting our combined single-molecule topography and fluorescence technique, we investigated the correlation between polymer length and emission intensity. The results obtained are presented in Figure 6, which shows the dependence of the fluorescence intensity (at $t=0$) arising from helical perylene polysisocyanides as a function of the polymer length. A clear linear correlation between these two parameters is found, which indicates that the longer the polymer, the higher the absorption and the number of excimer-like sites susceptible to be formed and, therefore, the stronger the polymer emission. Furthermore, the linear trend found in Figure 6 demonstrates that there are no saturation effects at the power density used to excite the molecules.

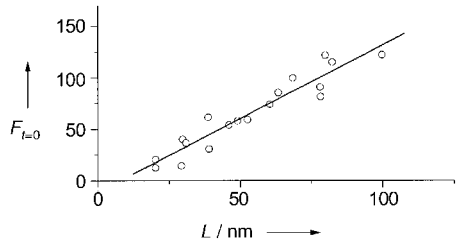


Figure 6. Plot of the fluorescence intensity (taken at $t=0$) versus the polymer length (L) for 18 single perylene polyisocyanide molecules. The values plotted in the length axis do not correspond to the actual length of the polymers but to the convolution between their length and the tip size, which explains why the line fit does not go through the origin.

On the other hand, we assign the green emission to short polyisocyanides oligomers consisting of only a few perylene units.[19] For these species, no helical structure of the polymer backbone is expected.[20] Accordingly, their height is much lower than the height of the helical polyisocyanides and therefore below the sensitivity of our AFM head (≈ 1 nm[21]), thus explaining why no correlated topography signal is obtained.[22] As there is an absence of a helical conformation, the interchromophoric distances between adjacent perylene units in polymer **2** will be much longer; consequently weaker (if any) excitonic effects without formation of excimer-like species are expected. This accounts for the fact that their fluorescence spectrum is the same as that of monomer **1**. The quantum yield of fluorescence for the short perylene oligomers undergoing weak excitonic interactions is expected to be similar to that of the monomer; however, the quantum yield of perylene excimer-like species is known to be much lower.[15] This partially explains why the overall fluorescence count rate arising from helical perylene polyisocyanides that contains hundreds to thousands chromophore units is in the same order of magnitude as that for the few-perylene nonhelical oligomers, as observed for the green and red species in Figure 4. In addition, the low fluorescence yield of the long helical polymers may also be due to charge separation and intramolecular electron transfer upon optical excitation, as recently suggested for perylene dimers with short interchromophoric distances.[17]

In summary, we have combined single-molecule confocal fluorescence and atomic force microscopy to unambiguously characterize a new class of multichromophoric polymers, namely perylene polyisocyanides. Our single-molecule measurements show that the synthesized perylene arrays are heterogeneous in nature, which we ascribe to distinct structures of the polymer backbone. Thus, short nonhelical perylene oligomers display monomer-like fluorescence properties, whereas long helical perylene polymer emission arises from multiple and independent excimer-like sites. Although the formation of the latter species prevents delocalization of the excitation energy along the polymer backbone over large distances, its long fluorescence decay time may favor the use of the polymers as n-type semiconductor in bulk-heterojunction solar cells.

Experimental Section

Atomic force microscopy**:** AFM experiments were performed by using a Nanoscope IIIa instrument from Digital Instruments. All images were recorded in tapping mode in air at room temperature.

Combined confocal fluorescence and atomic force microscopy: Fluorescence from single molecules was detected by means of a confocal scanning fluorescence microscope, as described elsewhere.[5c] Circularly polarized excitation light at $\lambda = 488$ nm with a power density at the sample 1–2 kW cm^{-2} was used. The fluorescence signal was detected by two avalanche photodiodes (APD, SPCM-AQ-14, EG&G Electro Optics) and a CCD camera (Andor, DV437-BV). A dichroic beam splitter (Omega, 590DRLP) in front of the APDs splitted the fluorescence into two distinct spectral windows (APD1: $\lambda < 590$ nm; APD2: $\lambda > 590$ nm; see Figure 5). A direct vision prism in front of the CCD camera spread the emission light over its wavelength components. Fluorescence spectra were collected by using an integration time of 1 s. A home-made AFM head[23] was placed on top of the confocal microscope to perform combined topography and fluorescence measurements for single molecules. All images were recorded in tapping mode in air at room temperature.

Received: January 13, 2004
Revised: April 30, 2004 [Z53745]

Keywords: fluorescence spectroscopy · nanotechnology · photochromism · scanning probe microscopy · single-molecule studies

[1] a) D. A. Higgins, J. Kerimo, D. A. Vanden Bout, P. F. Barbara, *J. Am. Chem. Soc.* **1996**, *118*, 4049–4058; b) V. Balzani, F. Scandola in *Comprehensive Supramolecular Chemistry: Supramolecular Technology, Vol. 10* (Eds.: J. L. Atwood, J. E. D. Davies, D. D. Macnicol, F. Vögtle, D. N. Reinhoudt), Pergamon, Oxford, **1996**, p. 687.

[2] T. Pullerits, V. Sundström, *Acc. Chem. Res.* **1996**, *29*, 381–389; X. Hu, A. Damjanović, T. Ritz, K. Schulten, *Proc. Natl. Acad. Sci. USA* **1998**, *95*, 5935–5941.

[3] S. Scheuring, F. Reiss-Husson, A. Engel, J. L. Rigaud, J. L. Ranck, *EMBO J.* **2001**, *20*, 3029–3035; A. Stamouli, S. Kafi, D. C. G. Klein, T. H. Oosterkamp, J. W. M. Frenken, R. J. Cogdell, T. J. Aartsma, *Biophys. J.* **2003**, *84*, 2483–2491.

 © 2004 Wiley-VCH Verlag GmbH & Co. KGaA, Weinheim

[4] M. Wu, P. M. Goodwin, W. P. Ambrose, R. A. Keller, *J. Phys. Chem.* **1996**, *100*, 17406 – 17409; M. A. Bopp, Y. W. Jia, L. Q. Li, R. J. Cogdell, R. M. Hochstrasser, *Proc. Natl. Acad. Sci. USA* **1997**, *94*, 10630 – 10635; L. Ying, X. S. Xie, *J. Phys. Chem. B* **1998**, *102*, 10399 – 10409; M. F. García-Parajó, M. Koopman, E. M. H. P. van Dijk, V. Subramaniam, N. F. van Hulst, *Proc. Natl. Acad. Sci. USA* **2001**, *98*, 14392 – 14397, and references therein.

[5] a) D. A. Vanden Bout, W.-T. Yip, D. Hu, D.-K. Fu, T. M. Swager, P. F. Barbara, *Science* **1997**, *277*, 1074 – 1077; D. Hu, J. Yu, P. F. Barbara, *J. Am. Chem. Soc.* **1999**, *121*, 6936 – 6937; J. Hofkens, W. Schroeyers, D. Loos, M. Cotlet, F. Köhn, T. Vosch, M. Maus, A. Herrmann, K. Müllen, T. Gensch, F. C. De Schryver, *Spectrochim. Acta Part A* **2001**, *57*, 2093 – 2107; C. Hettich, C. Schmitt, J. Zitzmann, S. Kühn, I. Gerhardt, V. Sandoghdar, *Science* **2002**, *298*, 385 – 389; P. Tinnefeld, K. D. Weston, T. Vosch, M. Cotlet, T. Weil, J. Hofkens, K. Mullen, F. C. De Schryver, M. Sauer, *J. Am. Chem. Soc.* **2002**, *124*, 14310 – 14311; C. G. Hubner, G. Zumofen, A. Renn, A. Herrmann, K. Mullen, T. Basché, *Phys. Rev. Lett.* **2003**, *91*, 093903; T. Vosch, M. Cotlet, J. Hofkens, K. Van Der Biest, M. Lor, K. Weston, P. Tinnefeld, M. Sauer, L. Latterini, K. Mullen, F. C. De Schryver, *J. Phys. Chem. A* **2003**, *107*, 6920 – 6931; b) T. Huser, M. Yan, L. J. Rothberg, *Proc. Natl. Acad. Sci. USA* **2000**, *97*, 11187 – 11191; c) J. Hernando, M. van der Schaaf, E. M. H. P. van Dijk, M. Sauer, M. F. García-Parajó, N. F. van Hulst, *J. Phys. Chem. A* **2003**, *107*, 43 – 52.

[6] J. Hofkens, M. Maus, T. Gensch, T. Vosch, M. Cotlet, F. Köhn, A. Herrmann, K. Müllen, F. C. De Schryver, *J. Am. Chem. Soc.* **2000**, *122*, 9278 – 9288; T. Vosch, J. Hofkens, M. Cotlet, F. Köhn, H. Fujiwara, R. Groenheid, K. van der Biest, T. Weil, A. Herrmann, K. Müllen, S. Mukamel, M. van der Auweraer, F. C. De Schryver, *Angew. Chem.* **2001**, *113*, 4779 – 4784; *Angew. Chem. Int. Ed.* **2001**, *40*, 4643 – 4648.

[7] J. J. L. M. Cornelissen, J. J. J. M. Donners, R. de Gelder, W. S. Graswinckel, G. A. Metselaar, A. E. Rowan, N. A. J. M. Sommerdijk, R. J. M. Nolte, *Science* **2001**, *293*, 676 – 680.

[8] P. Samori, C. Ecker, I. Gossl, P. A. J. de Witte, J. J. L. M. Cornelissen, G. A. Metselaar, M. B. J. Otten, A. E. Rowan, R. J. M. Nolte, J. P. Rabe, *Macromolecules* **2002**, *35*, 5290 – 5294.

[9] P. A. J. de Witte, M. Castriciano, J. J. L. M. Cornelissen, L. Monsû-Scolaro, R. J. M. Nolte, A. E. Rowan, *Chem. Eur. J.* **2003**, *9*, 1775 – 1781.

[10] H. Langhals, W. Jona, *Angew. Chem.* **1998**, *110*, 998 – 1001; *Angew. Chem. Int. Ed.* **1998**, *37*, 952 – 955; L. H. Gade, C. H. R. M. Williams, L. De Cola, M. McPartlin, B. Dong, L. Chi, *Angew. Chem.* **2003**, *115*, 2781 – 2785; *Angew. Chem. Int. Ed.* **2003**, *42*, 2677 – 2681.

[11] N. Noma, T. Tsuzuki, Y. Shirota, *Adv. Mater.* **1995**, *7*, 647 – 648; T. Toshimitsu, N. Hirota, N. Noma, *Thin Solid Films* **1996**, *273*, 177 – 180.

[12] P. A. J.de Witte, J. Hernando, E. E. Neuteboom, S. C. J. Meskers, R. A. J. Janssen, M. F. García-Parajó, N. F. van Hulst, R. J. M. Nolte, A. E. Rowan, *J. Am. Chem. Soc.*, submitted.

[13] J. J. L. M. Cornelissen, W. S. Graswinckel, P. J. H. M. Adams, G. H. Nachtegaal, A. P. M. Kentgens, N. A. J. M. Sommerdijk, R. J. M. Nolte, *J. Polym. Sci. Part A* **2001**, *39*, 4255 – 4264.

[14] M. Kasha, H. R. Rawls, M. Ashaf El-Bayoumi, *Pure Appl. Chem.* **1965**, *37*, 371; M. Bednarz, J. Knoester, *J. Phys. Chem. B* **2001**, *105*, 12913 – 12923.

[15] W. E. Ford, P. V. Kamat, *J. Phys. Chem.* **1987**, *91*, 6373 – 6380; P. B. Bisht, K. Fukuda, S. Hirayama, *Chem. Phys. Lett.* **1996**, *258*, 71 – 79; S. Akimoto, A. Ohmori, I. Yamazaki, *J. Phys. Chem. B* **1997**, *101*, 3753 – 3758, and references therein.

[16] P. Reynders, W. Kuhnle, K. A. Zachariasse, *J. Phys. Chem.* **1990**, *94*, 4073 – 4082.

[17] R. Liu, M. W. Holman, L. Zang, D. M. Adams, *J. Phys. Chem. B* **2003**, *107*, 6522 – 6526.

[18] For the related porphyrin polymer, excitonic interaction extends over domains larger than 25 dye units (see reference [9]).

[19] The same sort of behavior will be observed for the unconverted monomer molecules left in the purified polymer sample as well.

[20] Studies on polyisocyanides have proven that at least 10–15 repeat units are necessary for the helical structure to be stable.

[21] This is the average noise level in our AFM images (see Figure 4c). Two main factors are limiting our sensitivity: 1) the roughness of the substrate (O_2 plasma cleaned cover glass, which shows much better optical properties than mica) and 2) the vibrations induced by the immersion oil underneath the coverglass.

[22] Repetitive fluorescence scans on the same area before and after AFM detection allows us to rule out the possibility of spontaneous and tip-induced movement of the green species as the origin for their nonobservance in the topography image.

[23] K. O. van der Werf, C. A. Putman, B. G. de Grooth, F. B. Segerink, E. H. Schipper, N. F. van Hulst, J. Greve, *Rev. Sci. Instrum.* **1993**, *64*, 2892 – 2897.

 © 2004 Wiley-VCH Verlag GmbH & Co. KGaA, Weinheim

Chiral Oligomers

Stepwise Construction of Oligomeric 1,2-Diselenolene Platinum(IV) Complexes**

*Xavi Ribas, João C. Dias, Jorge Morgado, Klaus Wurst, Manuel Almeida, Teodor Parella, Jaume Veciana, and Concepció Rovira**

The chemistry of selenium-containing ligands has been increasingly studied in the last decade owing to the different properties these ligands have compared to the more common

[*] Dr. X. Ribas, Prof. J. Veciana, Prof. C. Rovira
Institut de Ciencia de Materials de Barcelona, CSIC
Campus de la UAB, 08193 Bellaterra (Spain)
Fax: (+34) 93-580-5729
E-mail: cun@icmab.es

J. C. Dias, Prof. J. Morgado, Prof. M. Almeida
Departamento de Química
Instituto Tecnológico e Nuclear
2686-953 Sacavém (Portugal)

Prof. J. Morgado
Departamento de Engenharia Química
Instituto Superior Tecnico
Av. Rovisco Pais, 1049-001 Lisboa (Portugal)

Dr. K. Wurst
Institut für Allgemeine Anorganische und Theoretische Chemie
Universiat Innsbruck, Innrain 52a, Innsbruck (Austria)

Dr. T. Parella
Servei de RMN, Universitat Autònoma de Barcelona
Bellaterra, 08193 Barcelona (Spain)

[**] This research has been supported by DGI Spain (Projects BQU2003-00760 and BQU2003-01677), DGR Catalonia (Project 2001SGR00362), FCT Portugal (Contract POCTI/35342/QUI/2000), and the ICCT-CSIC bilateral agreement which also benefited from COST D14. The authors thank D. Amabilino for fruitful discussions.

Supporting information for this article is available on the WWW under http://www.angewandte.org or from the author.

 DOI: 10.1002/anie.200453761 © 2004 Wiley-VCH Verlag GmbH & Co. KGaA, Weinheim

sulfur-containing analogues and their potential in various applications.[1] In the field of molecular conductors, although square-planar transition-metal bis(dithiolene) complexes are widely used as building blocks,[2–4] bis(diselenolene) analogues are much more scarce, and only recently some examples of Cu^{III} [5] and Au^{III} complexes[6] with pyrazine-1,2-diselenolene (pds) ligands,[6,7] as well as Ni^{II} , Pd^{II}, and Pt^{II} complexes with the maleonitrilediselenolene ligand,[8,9] were reported. In the complexes with the pds ligand, the redox behavior exhibited is mainly confined to the MSe_4 (M = metal center) units not extending to the ligands.[5] Thus, it is very attractive to compare complexes of the third-row transition-metal platinum and the pds ligand with the related known complexes. Herein we describe the results obtained following this approach that, in contrast to the well-known square-planar dichalcogenene species, leads to an unprecedented series of tris-, penta-, and hepta-1,2-diselenolene oligomeric complexes of which the mononuclear chiral $\{Pt^{IV}Se_6\}$ complex **1** and the dinuclear racemic $\{Pt^{IV}{}_2Se_{10}\}$ complex **2** have been isolated as single crystals.

Complex $[Pt^{IV}(pds)_3]Na_2{\cdot}6H_2O$ (**1**) was synthesized by the reaction of pds^{2-} ligand with $Pt^{II}Cl_2$ (in a 3:1 molar ratio). Single-crystal X-ray diffraction[10] shows the metal center in an octahedral coordination environment (see Figure 1 a),[11] with typical Pt^{IV}-Se separations of around 2.46 Å.[12] Complex **1** crystallizes in the orthorhombic chiral $P2_12_12_1$ space group owing to a spontaneous resolution phenomena leading to a conglomerate of crystalline enantiomers.[13] The three-blade propeller-like structure of **1** in the crystal studied is the anticlockwise *Λ* enantiomer. Noteworthy, the octahedral geometry around the metal center imposes an arrangement among the blades of the complex that yields a crystal packing of **1** with an orthogonal 3D offset face-to-face (OFF) π stacking (ring intercentroid separations ranging from 3.38 to 3.82 Å). The C-H···π(ring centroid) separations are over 3.70 Å and therefore, an edge-to-face (EF) motif is not considered (typical distances <2.9 Å).[14] Interestingly, a 8_2 helix type (following the disposition of the platinum centers) is formed in each orthogonal direction, with all the stacked aromatic moieties lying inside the helix (see Figure 2). It should be emphasized that the 8_2 helix type structure is rare as "strictly" 8-fold symmetry cannot exist in the crystal lattice. The efficient packing of **1** may be the driving force leading to the spontaneous resolution observed. The coordination of sodium ions to one nitrogen center of a pyrazine residue and to water molecules of crystallization may also play an important role in preventing a concerted OFF and EF structure.[5]

When the pds^{2-}:$Pt^{II}Cl_2$ molar ratio was decreased from 3:1 to 2:1 the crystalline product obtained contains a mixture of complex **1**, the dinuclear platinum complex $[Pt^{IV}{}_2(pds)_5]$-$Na_2{\cdot}7H_2O$ (**2**), and a minor amount of another species that has been ascribed to a trinuclear Pt^{IV} species (**3**, see below). Most of the crystals obtained were dark-red prisms of the three cocrystallized species,[15] but a few black-plate good quality single crystals of pure **2** were isolated allowing its structure to be solved by X-ray diffraction.[10] Complex **2** crystallizes in the orthorhombic space group *Pbca* as a racemate. The molecular structure is a dinuclear species with two Pt^{IV} centers in

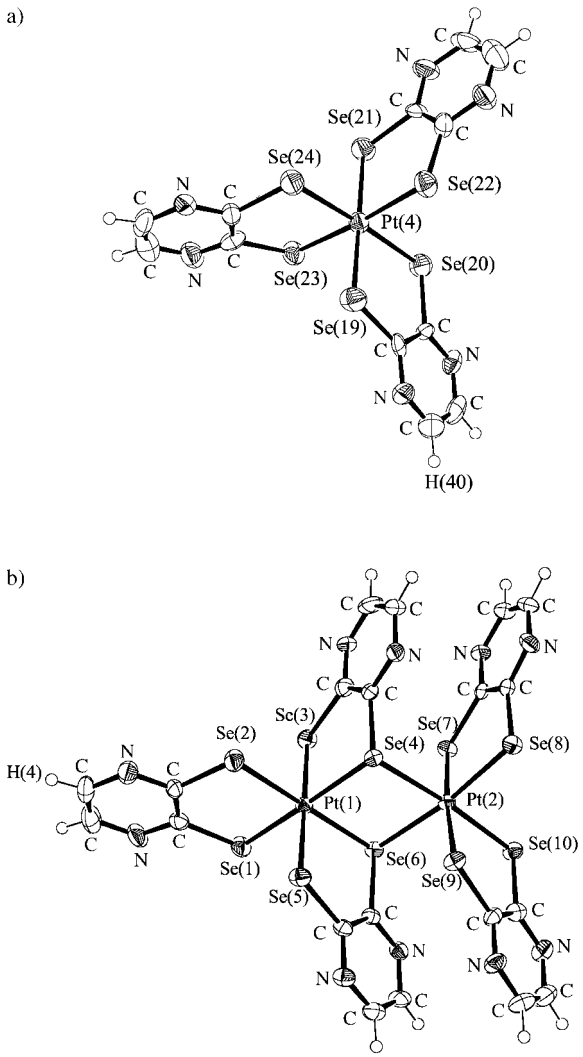


Figure 1. ORTEP structural representation (thermal ellipsoids set at 50 % probability) of the a) monomeric $[Pt^{IV}(pds)_3]^{2-}$ (**1**) and b) dimeric $[Pt^{IV}{}_2(pds)_5]^{2-}$ (**2**). Selected bond lengths [Å] and angles [°]: a) Pt(4)-Se(19) 2.4514(13), Pt(4)-Se(20) 2.4652(13), Pt(4)-Se(21) 2.4567(13), Pt(4)-Se(22) 2.4618(13), Pt(4)-Se(23) 2.4690(13), Pt(4)-Se(24) 2.4457(13); Se-Pt(4)-Se(*cis*) 86–94 (for Se in *trans*, 176–179); b) Pt(1)-Se(1) 2.4661(6), Pt(1)-Se(2) 2.4598(6), Pt(1)-Se(3) 2.4632(6), Pt(1)-Se(4) 2.4872(6), Pt(1)-Se(5) 2.4708(6), Pt(1)-Se(6) 2.4808(6), Pt(2)-Se(4) 2.5451(6), Pt(2)-Se(6) 2.5539(6), Pt(2)-Se(7) 2.4798(6), Pt(2)-Se(8) 2.4514(6), Pt(2)-Se(9) 2.4599(6), Pt(2)-Se(10) 2.4551(6), Pt(1)···Pt(2) 3.705(1); Pt(1)-Se(4)-Pt(2) 94.819(18), Pt(1)-Se(6)-Pt(2) 94.754(18), Se(4)-Pt(1)-Se(6) 86.559(18), Se(4)-Pt(2)-Se(6) 83.819(18).

octahedral coordination environments and bridged by two selenium atoms. This complex can be considered as the first member of an oligomeric series of compounds constructed by the addition of a $Pt(pds)_2$ moiety through its coordination to two selenium atoms (which bridge the Pt centers), and which can be generally described as $[\{Pt^{IV}(pds)_3\}\{Pt^{IV}(pds)_2\}_n]$ di-anions. In the case of **2**, the addition of a $Pt(pds)_2$ moiety yields a five-bladed binuclear structure (Figure 1 b). Indeed, whereas the coordination environment of Pt(1) in **2** is almost unchanged compared to that of the platinum center in **1**, the average Pt(2)-$Se_{bridging}$ bond lengths are longer than those of Pt(1)-$Se_{bridging}$ (2.55 Å versus 2.48 Å) leading to the distorted

 © 2004 Wiley-VCH Verlag GmbH & Co. KGaA, Weinheim

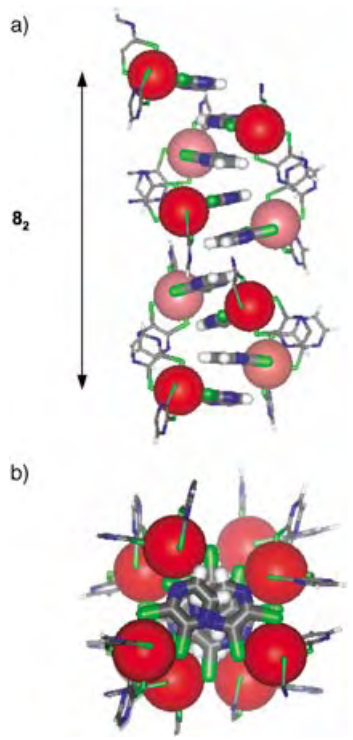


Figure 2. Views of the 8_2 helix-type secondary structure of **1**, a) along its main axis and b) perpendicular to the stacked aromatic rings. Red Pt, green Se, blue N, gray C.

rhombic $\{Pt_2Se_2\}$ core of **2**. The enantiomer shown in Figure 1b has *Λ* and *Λ* helicities for each platinum stereogenic center (or alternatively *M*,*M*). Both *M*,*M* and *P*,*P* enantiomers are placed in a tail-to-tail fashion within the crystal structure. No significant intermolecular π–π stacking is found (ring intercentroid separations >4.1 Å), in contrast to the enantiopure **1**. On the other hand, the dimer is further stabilized by the intradimer π–π stacking with intercentroid separations in the range 3.6–3.8 Å. A supramolecular network of 14 water molecules and 4 Na atoms is encapsulated between dimer molecules in a sphere of approximately 10 Å diameter.

The crystalline material isolated using a pds^{2-}:$Pt^{II}Cl_2$ molar ratio of 2:1 was fully characterized by ESI-MS, traditional 1D, 2D, and multinuclear NMR spectroscopy.[15] ESI-MS spectra identify two of the components in the crystalline mixture as **1** and **2** since the peaks with the correct isotopic pattern for the $[\{Pt^{IV}(pds)_3\}Na]^-$ and $[\{Pt^{IV}_2(pds)_5\}H]^-$ ions at $m/z=927$ and 1571, respectively, were observed. Multinuclear NMR spectroscopy studies reveal that the principal component of the crystalline material is the monomer **1** (≈72%, one singlet, symmetrical molecule in solution) followed by the dimer **2** (≈20%, five pairs of AB independent spin systems), showing also the presence of a third compound (**3**) (≈8%, seven pairs of AB systems).[16]

To characterize compound **3**, pulse field gradient spin-echo (PGSE) NMR diffusion experiments in solution were performed.[17–19] The PGSE methods specifically study the correlation between the molecular size of the species (strongly related to friction factors for translational motion) and their nuclear relaxation rates. Therefore, the decay of signal intensities of each compound can be related to the diffusion rates that in turn, enable the determination of the molecular dimensions in solution. Using CD_3CN as solvent, a quantitative analysis was accomplished by linear regression of the Stejskal–Tanner equation $(\ln(I/I_o)=-\gamma^2g^2\delta^2(\Delta-\delta/3)D)$,[20] affording self-diffusion coefficient (D) values of $1.070(6)\times10^{-9}$ for **1**, $0.942(6)\times10^{-9}$ for **2**, and $0.843(6)\times10^{-9}\,m^2s^{-1}$ for **3** (Figure 3). According to the Stokes–Einstein

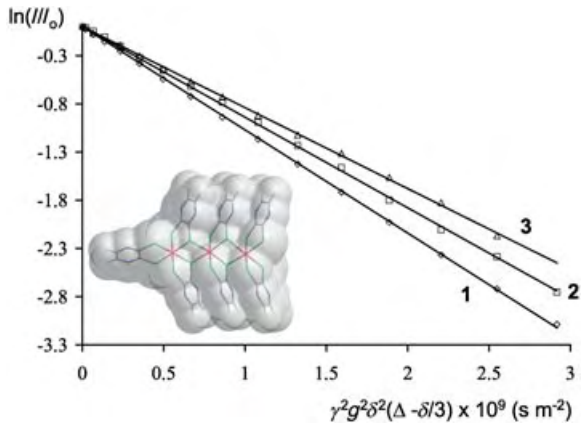


Figure 3. Plot of $\ln(I/I_0)$ versus $\gamma^2g^2\delta^2(\Delta-\delta/3)$ for the mixture of oligomers **1** (◇), **2** (□) and **3** (△) in CD_3CN at 298 K (I = signal intensity at a given pulsed-field gradient (PFG), I_0 = signal intensity in absence of PFG, γ = gyromagnetic ratio, g = strength of diffusion gradient, δ = length of the diffusion gradient, Δ = time separation between the leading edges of the two diffusion pulsed gradients). The inset shows the solvent accessible surface of the modeled structure of **3**. Red Pt, green Se, blue N, gray C.

equation ($D=kT/6\pi\eta r_H$; where k = Boltzmann constant, T = temperature, and η = solvent viscosity) D is inversely proportional to the hydrodynamic radius (r_H) of the diffusing molecules. Thus, the hydrodynamic radii (r_H) for the hypothetical spheres of **1**, **2**, and **3** are 5.82, 6.61, and 7.40 Å, respectively, yielding the ratios $r_H(\mathbf{2})/r_H(\mathbf{1})=1.14$ and $r_H(\mathbf{3})/r_H(\mathbf{1})=1.27$. On the other hand, the estimated radii from the X-ray or modeled structures are $r_{STR}(\mathbf{1})=6.50$ Å, $r_{STR}(\mathbf{2})=7.70$ Å and $r_{STR}(\mathbf{3})=8.49$ Å,[21] affording the ratios $r_{STR}(\mathbf{2})/r_{STR}(\mathbf{1})=1.18$ and $r_{STR}(\mathbf{3})/r_{STR}(\mathbf{1})=1.30$. Although the calculated r_H values are smaller than r_{STR} (owing to the assumption of the unrealistic spherical model, since the species have an ellipsoidal disk-like shape), the ratios between them are in excellent agreement. Based on the agreement between NMR PGSE experiments and the X-ray structures, the experimental results point towards a seven-bladed trinuclear structure for compound **3**, $[\{Pt^{IV}(pds)_3\}\{Pt^{IV}(pds)_2\}_n]$ ($n=2$), resulting from the addition of a $Pt(pds)_2$ moiety to **2**. This conclusion is further supported by the seven AB systems seen in the ^1H NMR spectrum.

It should be emphasized that, to our knowledge, no trimeric Pt^{IV} octahedral diselenolene complex has been reported. The compounds $[\{Pt^{IV}(pds)_3\}\{Pt^{IV}(pds)_2\}_n]$ **1** ($n=0$) and **2** ($n=1$) are the first tris- and penta-1,2-diselenolene monomeric and dimeric Pt^{IV} complexes reported. Only one similar mononuclear $\{Pt^{IV}Se_6\}$ octahedral structure has been

 © 2004 Wiley-VCH Verlag GmbH & Co. KGaA, Weinheim

reported bearing $(Se_4)^{2-}$ bidentate ligands.[12] In regard to compound **2**, only a dimeric $[Pt^{IV}{}_2Se_4C_2Cl_2]$ compound is known,[22] with a $\{Pt^{IV}{}_2Se_2\}$ core have two short and two long equivalent Pt–Se bonds of 2.42 and 2.62 Å, in sharp contrast to the inequivalently distorted rhombic $\{Pt^{IV}{}_2Se_2\}$ core found in **2**.

Besides the novelty of the selenium-containing Pt^{IV} complexes reported, a successful use of PGSE studies to characterize oligomeric structures of coordination compounds in solution has been demonstrated, which reveals the PGSE technique to be a powerful alternative when soft characterization by ESI-MS are not applicable, as for complex **3**. The excellent agreement between X-ray diffraction and PGSE in compounds **1** and **2** validates this method, and provides one of the few examples in which this comparison can be made.[19] These results prompt the application of the PGSE methods to series of supramolecular compounds differing only on size, which opens new possibilities to study the supramolecular interactions in solution. Work is underway to understand the parameters that control the formation of the different five-bladed and seven-bladed oligomers, such as temperature and ligand:metal ratios, and efforts are currently in progress to obtain 1D helical screw-like chiral polymers.

Received: January 15, 2004 [Z53761]

Keywords: Se ligands · chiral oligomers · NMR spectroscopy · platinum · structure elucidation

[1] E. G. Hope, W. Levason, *Coord. Chem. Rev.* **1993**, *122*, 171 – 225.
[2] N. Robertson, L. Cronin, *Coord. Chem. Rev.* **2002**, *227*, 93 – 127.
[3] H. Tanaka, Y. Okano, H. Kobayashi, W. Suzuki, A. Kobayashi, *Science* **2001**, *291*, 285 – 287.
[4] W. Suzuki, E. Fujiwara, A. Kobayashi, Y. Fujishiro, E. Nishibori, M. Takata, M. Sakata, H. Fujiwara, H. Kobayashi, *J. Am. Chem. Soc.* **2003**, *125*, 1486 – 1487.
[5] a) X. Ribas, J. Dias, J. Morgado, K. Wurst, M. Almeida, J. Veciana, C. Rovira, *Cryst. Struct. Commun.* **2002**, *4*, 564 – 567; b) X. Ribas, J. C. Dias, J. Morgado, K. Wurst, E. Molins, E. Ruiz, M. Almeida, J. Veciana, C. Rovira, *Chem. Eur. J.* **2004**, *10*, 1691 – 1704.
[6] J. Morgado, M. T. Duarte, L. Alcácer, I. C. Santos, R. T. Henriques, M. Almeida, *Synth. Met.* **1997**, *86*, 2187 – 2188.
[7] G. C. Papavassiliou, S. Y. Yiannopoulos, J. S. Zambounis, *Chem. Scr.* **1987**, *27*, 265 – 268.
[8] J. Morgado, I. C. Santos, M. T. Duarte, L. Alcázer, M. Almeida, *Chem. Commun.* **1996**, 1837 – 1838.
[9] C. C. McLauchlan, S. D. Robowski, J. A. Ibers, *Inorg. Chem.* **2001**, *40*, 1372 – 1375.
[10] Crystal data for **1**: $C_{12}H_{18}N_6Na_2O_6PtSe_6$, $M_r = 1057.15$, orthorhombic $P2_12_12_1$, $a = 19.0770(4)$, $b = 20.7610(3)$, $c = 26.5668(5)$ Å, $V = 10522.0(3)$ Å^3, $Z = 16$, $\rho_{calcd} = 2.669$ mg m^{-3}, $T = 233(2)$ K, $R = 0.0361$; $wR2 = 0.0670$, GOF = 1.055 ($I > 2.0\sigma(I)$). Crystal data for **2**: $C_{20}H_{24}N_{10}Na_2O_7Pt_2Se_{10}$, $M_r = 1742.25$, orthorhombic *Pbca*, $a = 14.2358(2)$, $b = 22.9014(3)$, $c = 23.7175(4)$ Å, $V = 7732.4(2)$ Å^3, $Z = 8$, $\rho_{calcd} = 2.993$ mg m^{-3}, $T = 233(2)$ K, $R = 0.0275$, $wR2 = 0.0512$, GOF = 1.049 ($I > 2.0\sigma(I)$). CCDC-228631 (**1**) and CCDC-228630 (**2**) contain the supplementary crystallographic data for this paper. These data can be obtained free of charge via www.ccdc.cam.ac.uk/conts/retrieving.html (or from the Cambridge Crystallographic Data Centre, 12, Union Road, Cambridge CB2 1EZ, UK; fax: (+44) 1223-336-033; or deposit@ccdc.cam.ac.uk).
[11] The final Pt^{IV} oxidation state is achieved by an air-mediated oxidation process affording the octahedral compound **1**, which is very stable as denoted by the lack of any reduction wave above −1.5 V in the cyclic voltammetry experiment.
[12] J. M. McConnachie, M. A. Ansari, J. A. Ibers, *Inorg. Chem.* **1993**, *32*, 3250 – 3255.
[13] L. Pérez-García, D. Amabilino, *Chem. Soc. Rev.* **2002**, *31*, 342 – 356.
[14] I. Dance, *Cryst. Struct. Commun.* **2003**, *5*, 208 – 221.
[15] Several crystals were studied by NMR spectroscopy (^{1}H, ^{13}C, ^{77}Se, ^{195}Pt) and ESI-MS. All data can be found in the Supporting Information.
[16] Content percentages were extracted from the integration of the ^{1}H NMR spectra.
[17] W. S. Price, *Concepts Magn. Reson.* **1997**, *9*, 299 – 336.
[18] W. S. Price, *Concepts Magn. Reson.* **1998**, *10*, 197 – 237.
[19] M. Valentini, H. Rüegger, P. S. Pregosin, *Helv. Chim. Acta* **2001**, *84*, 2833 – 2853.
[20] E. O. Stejskal, J. E. Tanner, *J. Chem. Phys.* **1965**, *42*, 282 – 292.
[21] r_{STR}(**1**): Pt(4)···H(40) separation; r_{STR}(**2**): distance from the centroid formed by Pt(1)-Se(4)-Se(6) to H(4) in the X-ray structure of **2**; r_{STR}(**3**): distance from the centroid formed by Pt(1)-Pt(2) to H(4) in the modeled structure of **3**.
[22] C. M. Bates, P. K. Khama, C. P. Morley, M. Di Vaira, *Chem. Commun.* **1997**, 913 – 914.

 © 2004 Wiley-VCH Verlag GmbH & Co. KGaA, Weinheim

Complementary-DNA Phage Display

Simultaneous Identification of Multiple Protein Targets by Using Complementary-DNA Phage Display and a Natural-Product-Mimetic Probe**

*Kathleen M. McKenzie, Elizabeth J. Videlock, Ute Splittgerber, and David J. Austin**

Both natural-product and cofactor affinity chromatography have long played a crucial role in the elucidation of biological mechanisms. More recent advances have shown that small-

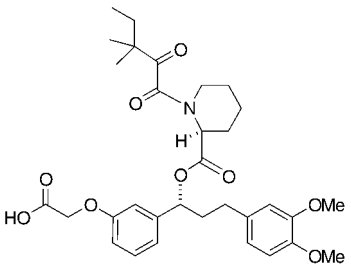
[*] K. M. McKenzie, E. J. Videlock, Prof. D. J. Austin
Department of Chemistry, Yale University
225 Prospect Street, New Haven, CT 06520 (USA)
Fax: (+1) 203-432-6144
E-mail: david.austin@yale.edu
Dr. U. Splittgerber
Targegen, Inc.
9393 Towne Centre Drive, San Diego, CA 92121 (USA)

[**] The authors thank Craig Crews (Yale University) for the donation of AP1497, Michael A. Tainsky and Fatima Nahhas (Karmanos Cancer Institute, Wayne State University School of Medicine) for the T7Forward and T7Reverse primer sequences, Viet-Anh Nguyen and Ruben M. Savizky (Yale University) for helpful discussions, and the National Institutes of Health (grant no. R01 GM59673) for financial support. D.J.A. is the recipient of an Alfred P. Sloan Foundation Fellowship.

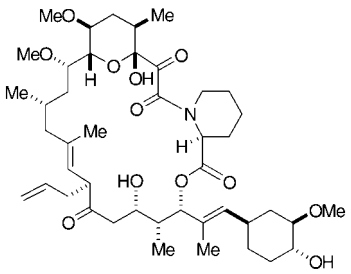
Supporting information for this article is available on the WWW under http://www.angewandte.org or from the author.

 © 2004 Wiley-VCH Verlag GmbH & Co. KGaA, Weinheim DOI: 10.1002/anie.200454004

molecule affinity-based techniques have the potential to play a major role in functional proteomics.[1] Toward this end we, and others, have employed T7 complementary-DNA (cDNA) phage display with affinity chromatography in order to clone genes encoding protein cellular targets (display cloning).[2] It remains a challenge, however, to develop a selection protocol that is capable of isolating more than one protein homologue from a native cDNA library, especially when there is a disparity in the relative abundance and affinity among family members. In this paper we describe the simultaneous cloning of three homologues of the FK506 binding protein (FKBP) from a T7 phage-display cDNA library by using novel elution conditions and a biotinylated form of AP1497, a structural mimetic of the natural product FK506.[3] Furthermore, we describe an on-phage titer binding assay, which can be used to rapidly determine relative binding affinities of isolated cDNA phage clones.



AP1497



FK506

Display cloning is a technique that involves the capture of bacteriophage, displaying cDNA-derived proteins on their outer coat, by using biotinylated molecules on an avidin-coated surface. After elution of bound phage, clones are amplified and either resubjected to selection conditions or analyzed. During optimization of the experimental protocol, we discovered that FK506 affinity selections, when performed using *Escherichia coli* to rescue phage between selection rounds, provided a homologue of FKBP (FKBP13) that was different from the FKBP12 homologue isolated in a previous study.[2a] This finding was intriguing, since FKBP13 has a markedly lower-affinity than FKBP12 for FK506,[4] a fact making it an unlikely victor in an affinity-based selection process. Furthermore, it has been reported that *E. coli* infection is a less efficient method for phage rescue than specific elution conditions.[5] We postulated that the appearance of the lower-affinity homologue, observed with *E. coli* elution, may be due to the reinfection process itself. At equilibrium, a higher proportion of a lower-affinity phage would be expected to be in solution at any given time. If the disparity between phage-binding affinities is large enough, the lower-affinity phage would have a larger representation in solution and, therefore, a distinct advantage for reinfection.

We therefore sought to develop a selection protocol that takes advantage of this observation. By using an *E. coli* elution, lower-affinity homologues may be amplified in greater ratios, relative to higher-affinity homologues. Combined with clone screening at an earlier stage in the selection process, before the population reaches homogeneity, we may also increase the number of different genes that can be isolated from a single cDNA library. In addition to improving the number of homologues we can isolate, we were also interested in evaluating molecules with lower affinity for their target proteins as potential probes in this assay. The FKBP-binding pipecolyl α-keto amides[6] were viewed as optimal for this endeavor, since their synthesis has been described[3] and these molecules have a lower affinity[1b,7] for the FKBP family of proteins than FK506.[3]

Functionalization of AP1497 was achieved by activation of the carboxylic acid with *N*-hydroxysuccinimide, followed by coupling with a polyethylene-linked amine containing biotin (biotin-PEO-LC-NH_2) in dimethyl sulfoxide to provide biotinylated AP1497 (bio-AP1497). A single well of an avidin-coated 96-well plate was treated with 10 μM bio-AP1497, and this was followed by blocking with 1 mM biotin. This secondary biotin incubation greatly reduces the amount of background binding by blocking unoccupied binding sites on the avidin plate that would otherwise provide a pocket for peptide affinity.[8] A 100-μL aliquot of a human-brain T7 cDNA phage library[2a] was precleared by incubation with an untreated avidin plate, in order to remove any avidin-binding proteins in the cDNA library, before it was transfered to the plate treated with bio-AP1497. After incubation and removal of the unbound phage, the remaining phage were amplified by addition of a log-phase culture of *E. coli* (100 μL). The resulting phage lysate was used directly in the next selection round, and this cycle was repeated for a total of three rounds. After the third round, the bound phage were eluted by using 1% sodium dodecylsulfate (SDS; in tris-buffered saline), diluted, and applied to Luria–Bertani top agarose plates in order to obtain spatially separated phage plaques.

Ninety-six randomly selected clones from the third round were amplified and tested individually for their ability to bind a 96-well plate treated with bio-AP1497. The phage clones were then ranked, based on elution titer, from highest to lowest, and the cDNA inserts from the top 30 bio-AP1497-binding clones were sequenced. Each of the top 22 clones were found to contain one of three different genes, which encode either FKBP12,[9] FKBP12.6,[10] or FKBP13,[11] all of which are known binders of the natural product FK506. In these clones, all three genes are in-frame with the T7 coat protein (cp10). The FKBP12 and FKBP12.6 clones contain the entire coding portion of the gene, while for FKBP13, only the FK506-binding region of the gene was isolated; this result suggests the potential of this affinity-based cloning method to

 © 2004 Wiley-VCH Verlag GmbH & Co. KGaA, Weinheim



Figure 1. Protein sequence alignment of translated FKBP12 (top), FKBP 12.6 (middle), and FKBP13 (bottom) isolated cDNA phage clones.

identify not only a target protein but also the minimal binding domain. The alignment of the translated peptide sequences for the three isolated genes is shown in Figure 1.[12]

In order to establish the probe dependence of phage binding, and to develop a quantitative binding assay that can be performed directly by using the protein expressed on the phage particle, the FKBP phage were subjected to affinity analysis in the presence of varying concentrations of the probe. Figure 2 shows the rescued phage titer (1% SDS

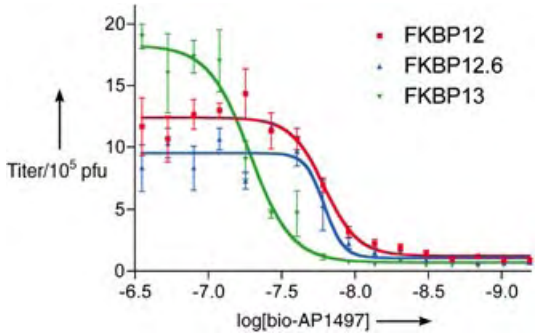


Figure 2. Titer binding assays at multiple probe concentrations for FKBP12-, FKBP12.6-, and FKBP13-displaying phage. pfu = plaque-forming units.

elution), as a function of log[bio-AP1497], for FKBP12, FKBP12.6, and FKBP13 phage. In each case, phage binding is probe dependent and can be fitted to a sigmoidal dose–response curve by using nonlinear regression analysis.[13] The calculated phage-binding EC_{50} values of bio-AP1497 for FKBP12 and FKBP12.6 are essentially identical at 16 nM (14–19 nM), while the EC_{50} value for FKBP13 is somewhat higher, 52 nM (44–62 nM), which is consistent with literature values.[3,4]

This on-phage binding assay is useful since phage clones can be analyzed within hours of affinity selection without the need for subcloning or additional instrumentation. Methods for quantitative phage-binding analysis at single probe concentrations have been described;[14] however, multiple-concentration titer data are a more accurate measure of relative protein affinity than single-concentration titer data, unless the relative protein display on the phage particle is taken into account.[15] As seen in Figure 2, the EC_{50} values observed for phage binding more accurately reflect the affinity of these phage-displayed proteins than the absolute titer observed at maximal probe concentrations does.

The utilization of small molecules in order to affinity purify phage-displayed proteins from cDNA libraries has great potential for the rapid identification of cellular protein targets; however, several factors must be taken into account when the appropriateness of this approach is evaluated for a particular molecule. A major factor that must be considered is whether a cDNA library actually contains the gene of interest. Protein expression can vary from cell to cell, and library quality can also vary, based on the mRNA source and the method used to construct the library. By their very nature, cDNA phage libraries are an enormous mixture of genes and gene fragments, some in-frame and some out-of-frame with the phage coat proteins. Therefore, particular care must also be taken in choosing the conditions employed for affinity selection, as evidenced by the results described above. Another consideration is the type of protein that can be isolated with this technique. To date, reports utilizing this protocol have primarily described the isolation of cytosolic single-domain proteins or single domains from large multi-domain proteins.[2] It is not clear at this time whether this trend suggests a limitation of the overall approach or is a result of the tendency for genetic-based selection techniques to provide the most efficient member of a given population. Rather conspicuously missing from the array of successes are integral membrane proteins or proteins that bind as either homo- or heterodimers. However, a recent paper describing the use of T7 cDNA phage display for the isolation of mRNA-binding proteins, which was not achievable without modification of the *E. coli* expression system,[2h] suggests that attention to details concerning protein expression may facilitate the isolation of more varied protein families.

In conclusion, the *E. coli* reinfection of affinity-captured cDNA phage provided selection conditions that allowed the isolation of a low-affinity FKBP homologue (FKBP13). A 96-well phage-based affinity binding screen, performed before the phage population reached homogeneity, allowed for the identification of a low-copy, yet high-affinity FKBP homologue (FKBP12.6). Neither of these modifications obviated the isolation of FKBP12, a high-copy, high-affinity FKBP homologue, and they resulted in a direct and rapidly verifiable method for the simultaneous isolation and identification of target genes. Development of a concentration-dependent on-phage binding assay allowed for the rapid assessment of relative binding affinities for each of the isolated clones. Furthermore, we have shown that a natural-product structural mimetic can be used as an effective affinity probe, with a T7 cDNA phage-display library, for the cloning of multiple homologues of human genes corresponding to the natural-product protein target. Efforts to expand this methodology for general use in small-molecule-based proteomic studies are currently underway.

Received: February 12, 2004
Revised: April 1, 2004 [Z54004]

Keywords: natural products · biomimetics · bioorganic chemistry · DNA · proteins

 © 2004 Wiley-VCH Verlag GmbH & Co. KGaA, Weinheim

[1] a) G. MacBeath, A. N. Koehler, S. L. Schreiber, *J. Am. Chem. Soc.* **1999**, *121*, 7967 – 7968; b) P. J. Hergenrother, K. M. Depew, S. L. Schreiber, *J. Am. Chem. Soc.* **2000**, *122*, 7849 – 7850; c) G. C. Adam, B. F. Cravatt, E. J. Sorensen, *Chem. Biol.* **2001**, *8*, 81 – 95; d) M. McPherson, Y. Yang, P. W. Hammond, B. L. Kreider, *Chem. Biol.* **2002**, *9*, 691 – 698; e) G. Chen, A. Heim, D. Reither, D. Yee, Y. Milgrom, M. A. Gawinowicz, D. Sames, *J. Am. Chem. Soc.* **2003**, *125*, 8130 – 8133.

[2] a) P. P. Sche, K. M. McKenzie, J. D. White, D. J. Austin, *Chem. Biol.* **1999**, *6*, 707 – 716; P. P. Sche, K. M. McKenzie, J. D. White, D. J. Austin, *Chem. Biol.* **2001**, *8*, 399 – 400; b) S. Zozulya, M. Lioubin, R. J. Hill, C. Abram, M. L. Gishizky, *Nat. Biotechnol.* **1999**, *17*, 1193 – 1198; c) M. Yamamoto, Y. Kominato, F. Yamamoto, *Biochem. Biophys. Res. Commun.* **1999**, *255*, 194 – 199; d) S. N. Savinov, D. J. Austin, *Comb. Chem. High Throughput Screening* **2001**, *4*, 593 – 597; e) M. H. Hansen, B. Ostenstad, M. Sioud, *Int. J. Oncol.* **2001**, *19*, 1303 – 1309; f) A. Zucconi, L. Dente, E. Santonico, L. Castagnoli, G. Cesareni, *J. Mol. Biol.* **2001**, *307*, 1329 – 1339; g) M. P. Burgoon, G. P. Owens, S. Carlson, A. L. Maybach, D. H. Gilden, *J. Immunol.* **2001**, *167*, 6009 – 6014; h) S. Danner, J. G. Belasco, *Proc. Natl. Acad. Sci. USA* **2001**, *98*, 12954 – 12959; i) Y. Jin, J. Yu, Y. G. Yu, *Chem. Biol.* **2002**, *9*, 157 – 162; j) E. J. Videlock, V. K. Chung, M. A. Mohan, T. M. Strok, D. J. Austin, *J. Am. Chem. Soc.* **2004**, *126*, 3730 – 3731.

[3] T. Keenan, D. R. Yaeger, N. L. Courage, C. T. Rollins, M. E. Pavone, V. M. Rivera, W. Yang, T. Guo, J. F. Amara, T. Clackson, M. Gilman, D. A. Holt, *Bioorg. Med. Chem.* **1998**, *6*, 1309 – 1335.

[4] O. Futer, M. T. DeCenzo, R. A. Aldape, D. J. Livingston, *J. Biol. Chem.* **1995**, *270*, 18935 – 18940.

[5] Y. G. Mikawa, I. N. Maruyama, S. Brenner, *J. Mol. Biol.* **1996**, *262*, 21 – 30.

[6] D. A. Holt, J. I. Luengo, D. S. Yamashita, H. J. Oh, A. L. Konialian, H. K. Yen, L. W. Rozamus, M. Brandt, M. J. Bossard, M. A. Levy, D. S. Eggleston, J. Liang, L. W. Schultz, T. J. Stout, J. Clardy, *J. Am. Chem. Soc.* **1993**, *115*, 9925 – 9938.

[7] a) J. F. Amara, T. Clackson, V. M. Rivera, T. Guo, T. Keenan, S. Natesan, R. Pollock, W. Yang, N. L. Courage, D. A. Holt, M. Gilman, *Proc. Natl. Acad. Sci. USA* **1997**, *94*, 10618 – 10623; b) G. MacBeath, S. L. Schreiber, *Science* **2000**, *289*, 1760 – 1763; c) E. A. Althoff, V. W. Cornish, *Angew. Chem.* **2002**, *114*, 2433 – 2436; *Angew. Chem. Int. Ed.* **2002**, *41*, 2327 – 2330.

[8] B. A. Katz, *Biochemistry* **1995**, *34*, 15421 – 15429.

[9] a) J. J. Siekierka, S. H. Y. Hung, M. Poe, C. S. Lin, N. H. Sigal, *Nature* **1989**, *341*, 755 – 757; b) M. W. Harding, A. Galat, D. E. Uehling, S. L. Schreiber, *Nature* **1989**, *341*, 758 – 760.

[10] H. Arakawa, H. Nagase, N. Hayashi, T. Fujiwara, M. Ogawa, S. Shin, Y. Nakamura, *Biochem. Biophys. Res. Commun.* **1994**, *200*, 836 – 843.

[11] Y.-J. Jin, M. W. Albers, W. S. Lane, B. E. Bierer, S. L. Schreiber, S. J. Burakoff, *Proc. Natl. Acad. Sci. USA* **1991**, *88*, 6677 – 6681.

[12] F. Jeanmougin, J. D. Thompson, M. Gouy, D. G. Higgins, T. J. Gibson, *Trends Biochem. Sci.* **1998**, *23*, 403 – 405.

[13] Nonlinear regression analysis with a four-parameter logistic equation was performed by using GraphPad Prism, version 4.0a for Mac OS X, GraphPad Software, San Diego, CA, USA.

[14] A. B. Sparks, N. B. Adey, S. Cwirla, B. K. Kay in *Phage Display of Peptides and Proteins. A Laboratory Manual* (Eds.: B. K. Kay, J. Winter, J. McCafferty), Academic Press, San Diego, **1996**, pp. 248 – 250.

[15] S. Rossenu, S. Leyman, D. Dewitte, D. Peelaers, V. Jonckheere, M. Van Troys, J. Vandekerckhove, C. Ampe, *J. Biol. Chem.* **2003**, *278*, 16642 – 16650.

 © 2004 Wiley-VCH Verlag GmbH & Co. KGaA, Weinheim

Conformation Analysis

Carbopeptoid Folding: Effects of Stereochemistry, Chain Length, and Solvent**

*Riccardo Baron, Dirk Bakowies, and Wilfred F. van Gunsteren**

The folding of a polypeptide chain into the stable three-dimensional structure of a biologically active protein is still not understood in atomic detail. However, several research groups have recently reported successful atomistic simulations of secondary-structure formation, including the formation of helices of different types, β turns and β sheets of α- and β-peptides.[1–23] Insight into the nature of both the folding process[24,25] and the unfolded state[15,26,27] has been obtained from various studies simulating the reversible folding of peptides. This development is encouraging and indicates that the biomolecular force fields in use are approaching the accuracy required to predict folding equilibria, although this has so far been demonstrated only for short polypeptides.

Experimentally, significant progress has been made in the design and synthesis of peptide analogues that mimic secondary-structure elements of proteins, such as α helices, turns, and β sheets.[28–30] For example, carbopeptoids, homo-oligomers of sugar-containing amino acids, have been prepared with both furanose[31] and pyranose[32] residues. These carbopeptoids are members of the family of δ-peptides which may formally be constructed from α-peptides by replacement of every second peptide fragment with a substituted tetrahydrofuran (THF) or tetrahydropyran ring.[33] These molecules have potential applications as drugs that block protein–protein interactions and inhibit enzyme catalysis.[34–36]

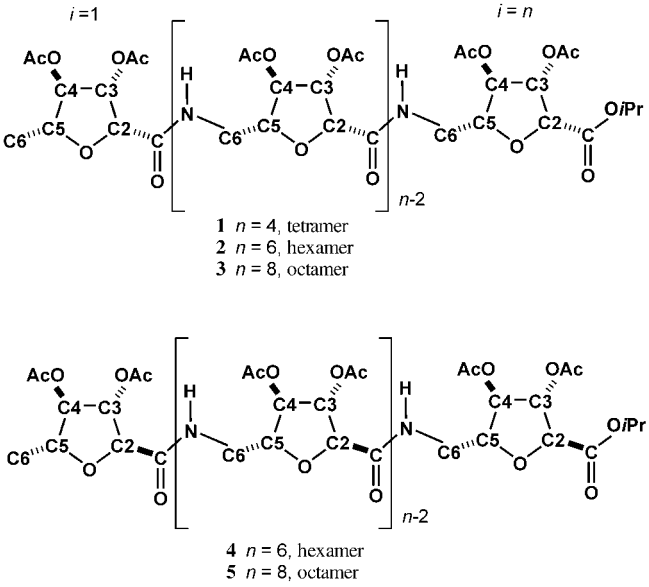
Structural preferences have been investigated in nuclear magnetic resonance (NMR) experiments.[31,37–40] Various oligomers with *cis* configurations at the C2 and C5 atoms of the THF ring (Scheme 1) tend to form conformations reminiscent of a conventional β turn.[41] The characteristic NH(i)–O(i–2) hydrogen-bonding pattern has been observed for tetramer **1** in both chloroform and dimethylsulfoxide (DMSO).[37] Chain extension to six or eight residues does not alter the preferred secondary structure. Apparently, hexamer **2** and octamer **3** show the hydrogen-bonding pattern of tetramer **1**, extended to six and eight residues, respectively. The *trans*-linked tetramers appear to have no conformational

[*] R. Baron, Dr. D. Bakowies, Prof. Dr. W. F. van Gunsteren
Laboratorium für Physikalische Chemie, ETH Zürich
8093 Zürich (Switzerland)
Fax: (+41) 1-632-1039
E-mail: wfvgn@igc.phys.chem.ethz.ch

[**] Financial support from the Schweizerischer Nationalfonds (Project no.: 2000-063590) and from the National Center of Competence in Research (NCCR), Structural Biology, of the Swiss National Science Foundation (SNSF) is gratefully acknowledged. We thank Dr. Tim Claridge for providing us with NMR spectroscopic data for the *cis*-tetramer **1**.

Supporting information for this article is available on the WWW under http://www.angewandte.org or from the author.

 DOI: 10.1002/anie.200454114 © 2004 Wiley-VCH Verlag GmbH & Co. KGaA, Weinheim



Scheme 1. Chemical formulas of the peptides studied. The numbering referred to in the text is indicated.

preferences or to adopt other types of structure, depending on the substituents at the C3 and C4 positions.[31] The *trans* octamer **5** with ketal protecting groups at the C3 and C4 positions is reported to form a rare type of left-handed helix, stabilized by interresidue NH(*i*)–O(*i*–3) hydrogen bonds.[31,40]

The apparent dependence of structural motifs on chain length and stereochemistry prompted us to carry out molecular dynamics (MD) simulations to supplement the indirect experimental observations with a more detailed atomistic picture. Scheme 1 shows the peptides considered in the present study. Tetramer **1**, hexamer **2**, and octamer **3** are all based upon a *cis*-linked β-D-*arabino*-furanose scaffold. Hexamer **4** and octamer **5** are the corresponding *trans*-linked stereoisomers. All simulations were performed with chloroform as solvent. An additional simulation of tetramer **1** in DMSO was performed to assess the effect of solvent on secondary-structure formation.

The accuracy of MD simulations may be assessed by comparison to results from nuclear Overhauser effect (NOE) experiments. Qualitative NOE intensities have been reported for tetramer **1** in chloroform.[37] Table 1 lists these data and compares them with $\langle r^{-3}\rangle^{-1/3}$ averages of proton–proton r distances computed from the MD trajectory and with the corresponding distances of a structure modeled to satisfy all NOE distance limits. Generally, proton pairs showing an NOE signal are expected to have an average distance of 0.5 nm or less, and strong signals indicate shorter distances. Inspection of Table 1 shows that the MD simulation satisfies all experimentally derived distance limits, except those for N(4)–C3(2), N(3)–C3(1), and C6(3)-*pro*-S–C3(1). However, all of these three proton pairs show weak signals experimentally. The distance analysis has also been performed separately for the three most populated clusters of structures, subsets of the MD trajectory that contain only structures that are very similar to each other. Clusters 1 and 3 show N(3)–C3(1) and N(4)–C3(2) proton-pair distances, respectively, which are within experimental limits. Likewise, the average distance of the proton pair C6(3)-*pro-S*–C3(1) is noticeably smaller for cluster 1 than it is for the entire trajectory. These observations indicate that all experimentally derived proton–proton contacts are reproduced by the MD simulation, although the distribution of distances for three proton–proton pairs may be inaccurate. It is interesting to note, moreover, that the remaining distance limits are not only satisfied by the ensemble of all trajectory structures but also by each of the subsets of structures discussed above. This may appear surprising because structures representative of these three sets look quite different from each other (see Figure 2a). In fact, this observation points to the general problem of interpreting experimentally measured NOE intensities in terms of a single three-dimen-

Table 1: NOE proton-pair distance [nm] analysis for the *cis* tetramer **1** in $CHCl_3$.[a]

Proton pair	NOE intensity	Model structure	⟨Trajectory⟩	⟨1st cluster⟩	⟨2nd cluster⟩	⟨3rd cluster⟩
N(4)–C6(3)-*pro-R*	w	0.325	0.422	0.432	0.423	0.361
N(4)–C5(4)	m	0.196	0.285	0.292	0.276	0.271
N(4)–C2(3)	w	0.352	0.320	0.316	0.325	0.336
N(4)–C4(4)	w	0.418	0.393	0.363	0.422	0.391
N(4)–C3(2)	w	0.441	0.743	0.732	0.888	0.498
N(3)–C6(3)-*pro-S*	s	0.227	0.262	0.280	0.248	0.241
N(3)–C6(3)-*pro-R*	m	0.285	0.267	0.252	0.281	0.284
N(3)–C6(2)-*pro-R*	m	0.280	0.400	0.355	0.408	0.407
N(3)–C5(3)	m	0.271	0.285	0.287	0.287	0.263
N(3)–C2(2)	w	0.340	0.325	0.332	0.327	0.332
N(3)–C4(3)	w	0.428	0.372	0.430	0.257	0.437
N(3)–C3(1)	w	0.427	0.654	0.507	0.687	0.715
N(2)–C6(2)-*pro-S*	s	0.230	0.253	0.240	0.265	0.257
N(2)–C5(1)	w	0.435	0.430	0.432	0.430	0.428
N(2)–C2(1)	w	0.328	0.321	0.328	0.317	0.319
N(2)–C4(2)	w	0.417	0.395	0.433	0.406	0.370
C4(3)–C6(3)-*pro-R*	m	0.250	0.283	0.249	0.349	0.256
C4(3)–C6(3)-*pro-S*	s	0.232	0.257	0.261	0.246	0.244
C6(3)-*pro-S*–C3(1)	w	0.407	0.830	0.703	0.854	0.868
C6(3)-*pro-S*–C5(3)	s	0.245	0.253	0.236	0.285	0.241

[a] The first column shows the pairs of protons for which experimentally determined NOE data are available. Residue sequence numbers are given in parentheses (see Scheme 1 for reference). The NOE intensities in the second column are only classified as weak (w), medium (m), or strong (s), (Tim Claridge, private communication). The distances in the third column refer to a structure modeled to satisfy all experimental NOE limits. The fourth column reports the distances averaged ($\langle r^{-3}\rangle^{-1/3}$)over the whole ensemble of structures generated in the 100-ns simulation. The following three columns show distances, calculated in analogy from structures in the first, second, and third most populated conformational clusters.

 © 2004 Wiley-VCH Verlag GmbH & Co. KGaA, Weinheim

sional structure, as they reflect an averaging over geometries biased ($\langle r^{-3}\rangle^{-1/3}$) towards short proton–proton distances r.[42–44] Clearly this problem is more severe for peptides that show a high degree of conformational flexibility.

Figure 1 shows, as a function of time, the atom-positional root-mean-square deviation (RMSD) of trajectory structures

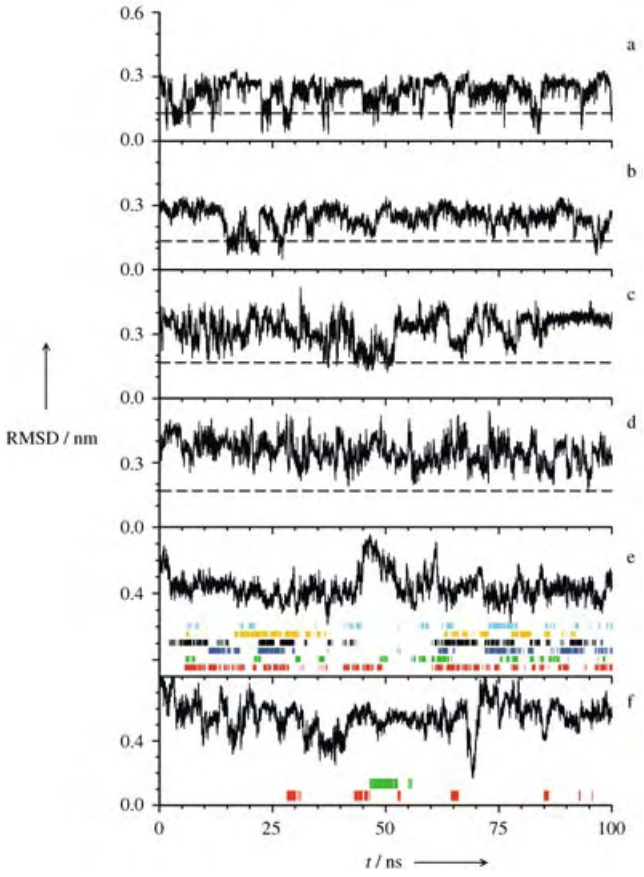


Figure 1. Panels a–e show backbone atom-positional root-mean-square-deviations (RMSD) of trajectory structures from model structures as a function of time. The *cis*-linked tetramer **1** in chloroform and in DMSO (a, b), the *cis* hexamer **2** (c), the *trans* hexamer **4** (d), and the *cis* octamer **3** (e) are compared to hypothetical model structures derived from qualitative NOE data for the *cis* tetramer **1**. The *trans* octamer **5** (f) is compared to a model structure inferred from ref. [31]. Dashed lines indicate the backbone RMSD similarity criterion chosen to define the folded structures. For the *cis* octamer **3** (e), the formation of NH(3)–O(1) (red), NH(4)–O(2) (green), NH(5)–O(3) (blue), NH(6)–O(4) (black), NH(7)–O(5) (orange), and NH(8)–O(6) (cyan) hydrogen bonds is shown as a function of time. For the *trans* octamer **5** (f), we show the formation of hydrogen bonds NH(4)–O(6) (red) and NH(7)–O(3) (green), which characterize, respectively, a 20- and 22-membered hydrogen-bonded ring.

from idealized model structures (see the Experimental Section). We have used all backbone atoms (N, C6, C5, O, C2, C) for this analysis, but excluded the C6, C5, and O atoms of the first residue and the C atom of the last residue (compare with Scheme 1). Single trajectory structures are considered folded if their RMSD from the reference model structure is less than 0.13 (tetramer), 0.17 (hexamers), or 0.28 nm (octamers).

The *cis* tetramer **1** experiences several folding and unfolding events during 100 ns of simulation. With chloroform as solvent, the molecule frequently adopts conformations close to the repeating β-turn right-handed helical model structure (Figure 1 a). This conformation is less often visited when the solvent is DMSO (Figure 1 b). The stronger hydrogen-bonding character of DMSO clearly disfavors formation of intramolecular hydrogen bonds in the peptide. While the hydrogen bonds NH(3)–O(1) and NH(4)–O(2) are, respectively, formed for 11 and 6 % of the simulation with chloroform, they occur for only 1 and 3 % of the simulation with DMSO as solvent (see the Supporting Information). Analysis of temperature coefficients and chemical shifts leads to similar conclusions.[37]

The folded *cis* hexamer **2** forms four hydrogen bonds of type NH(i)–O($i-2$) with $i = 3$, 4, 5, and 6. Figure 1 c shows the RMSD time series calculated for our MD simulation with chloroform as the solvent. Several folding and unfolding events are observed after about 35 ns. We have not attempted to build a model structure for the *trans* hexamer **4**, as no experimental data have been reported. Figure 1 d shows that it assumes a conformation similar (RMSD < 0.17 nm) to the model of the *cis* isomer only once during the 100 ns of simulation. The *trans* substitution at the THF ring clearly disfavors the formation of the β turn found for the series of *cis*-linked carbopeptoids. Clustering trajectory snapshots into batches of highly similar configurations (see the Experimental Section) generally shows the dominant configurations sampled in an MD simulation. In the case of the *cis* hexamer **3**, we find 11 % of all snapshots in the first cluster and a total of 20 significantly (> 1 % each) populated clusters, which sums up to 76 % of all configurations. These results indicate that the ensemble of *cis*-hexamer configurations is dominated by a fairly small number of different types of structure. The trajectory generated for the *trans* hexamer, however, clusters into significantly more batches. Only 5 % of all snapshots are found in the first cluster and a total of 30 significantly populated clusters cover only 62 % of all configurations. We conclude that the *trans* hexamer shows a much lower tendency to form any preferred type of secondary structure than the *cis* hexamer. This observation is in line with the experimentally claimed[39] absence of stable secondary structures for short *trans*-linked peptides of the type studied here.

The *cis* octamer **3** folds to a stable structure that shows the same hydrogen-bonding pattern, NH(i)–O($i-2$), as the smaller *cis* oligomers. These hydrogen bonds are observed in our 100-ns-long simulation with chloroform as solvent (Figure 1 e and the Supporting Information). Again, the *trans* octamer **5** shows very different behavior. NH(i)–O($i-2$) hydrogen bonds are not formed at all, a result pointing to the steric constraints imposed by the different stereochemistry. However, other hydrogen bonds, NH(i)–O($i+k$), occur with significant frequency (Figure 1 f and the Supporting Information) to form rings of size 20 ($k = 2$), 22 ($k = -4$), 26 ($k = 3$), 28 ($k = -5$), 32 ($k = 4$), and 38 ($k = 5$). Reflecting their size, these rings are rather flexible and give rise to fairly large RMSD variations (Figure 1 f). A left-handed helix composed of 16-membered rings ($k = -3$) was suggested in experimental NMR studies for a similar *trans* octamer,[40] but this is

 © 2004 Wiley-VCH Verlag GmbH & Co. KGaA, Weinheim

observed only once in our simulation (at 69 ns, Figure 1 f). Unfortunately, the experimental paper provides only vague information about the measured NOE values, thereby precluding a direct comparison between NOE and MD data. We note, however, that our analysis of the MD trajectory does not give any indication of long-range contacts of type NH(i)–H5($i-2$), NH(i)–H3($i-3$), H2(i)–H4($i-2$), or H2(i)–H3($i-2$), mentioned in ref. [40] as the calculated values of $\langle r^{-3}\rangle^{-1/3}$ range from 0.7 to 1.2 nm (data not shown).

Figure 2 shows the dominant conformations of the *cis* tetramer **1** and of both the octamers **3** and **5**, together with the corresponding model structures. For the *cis* tetramer, there are 11 clusters populated by at least 1%, which totals 94% of the entire ensemble. The helical model structure falls into the third cluster, whose central member structure shows a similar backbone configuration. For the *cis* and *trans* octamers, we find a larger number of significantly (>1%) populated clusters (27 and 28, respectively), which totals 82 and 87% of the entire ensemble, respectively. The larger diversity of structures reflects the increased conformational flexibility of longer peptide chains. In the case of *cis* octamer **3**, the central member structure of the third cluster displays three examples of the characteristic NH(i)–O($i-2$) hydrogen bonds ($i=3$, 4, and 6) discussed above. One hydrogen bond of this type is also present in the central member structures of the first and second clusters ($i=6$ and 3, respectively).

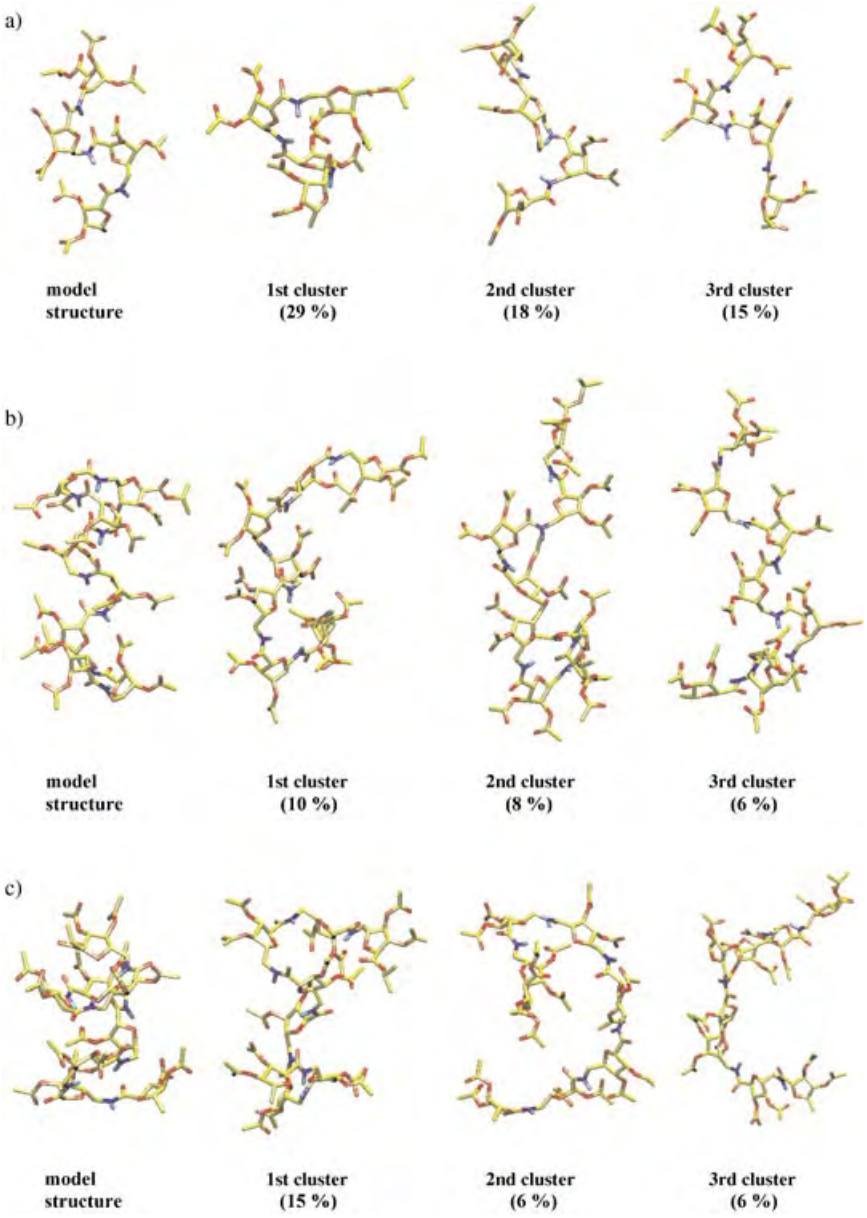


Figure 2. Dominant conformations found for the *cis* tetramer **1** (a), the *cis* octamer **3** (b), and the *trans* octamer **5** (c) in chloroform. Reference model structures are presented to the left, and central member structures of the three most populated clusters are shown on the right. Central member structures are displayed in orientations similar to those chosen for the model structures (superposition of backbone atoms). Populations are given in parentheses.

Carbopeptoids containing THF moieties in their backbone show distinct folding behavior depending on chain length and absolute configuration at the THF–peptide link. The simulations presented herein show good agreement with the, admittedly limited, experimental data available. Sets of NOE data were published only for the tetramer, and they are in good agreement with the simulation. More qualitative conclusions drawn in experimental work are confirmed in the simulations as well. It is important to note that we have not undertaken any attempt to calibrate the force-field parameters specifically for carbopeptoid simulations. Instead we have used a well-calibrated general biomolecular force field which apparently captures the folding behavior of carbopeptoids. Once the agreement with experimental data is established, MD simulations of peptides can be used with some confidence to interpret experimental results in terms of conformational distributions and to explore the various types of secondary structure involved.

Two other major conclusions are apparent from our study: first, it seems misleading to interpret experimentally obtained NOE distance limits in terms of a single dominant structure. In fact, a variety of stable conformations (clusters of structures) is found. Second, the total number of conformations prevailing in the ensemble is still fairly small. This supports a conclusion previously drawn for β-peptides,[15,26] namely that the accessible portion of the unfolded state consists of significantly fewer conformations than expected from simple combinatorial counts of low-energy conformers.

 © 2004 Wiley-VCH Verlag GmbH & Co. KGaA, Weinheim

Experimental Section

With the fully extended structures as a starting point, the carbopeptoids **1**–**5** were simulated in (explicit) chloroform and DMSO (only molecule **1**) at 298 K and 1 atm by using the GROMOS96 simulation package[45,46] and the GROMOS biomolecular force field (version 45A3[46,47]). For simulation and analysis details, see the Supporting Information and ref. [48].

The reference (right-handed helical) model structure of the *cis* tetramer **1** was generated by using MD simulations with all available NOE distance limits implemented as additional restraints. This structure is indeed confirmed to satisfy all distance limits (see Table 1). Model structures of the *cis* hexamer **2** and *cis* octamer **3** were constructed in analogy, by assuming the NOE distance limits of the tetramer and augmenting them with the corresponding H–H contacts for the additional residues. This procedure seemed justified, as no experimental data were available to us except for qualitative statements that all *cis* oligomers share analogous NOE patterns. The left-handed helical model structure for the *trans* octamer **5** was built by using qualitative information given in ref. [31].

Received: February 26, 2004 [Z54114]
Published Online: July 19, 2004

Keywords: computer chemistry · conformation analysis · molecular dynamics · peptide folding · tetrahydrofurans

[1] M. Prevost, I. Ortmans, *Proteins Struct. Funct. Genet.* **1997**, *29*, 212 – 227.
[2] X. Daura, B. Jaun, D. Seebach, W. F. van Gunsteren, A. E. Mark, *J. Mol. Biol.* **1998**, *280*, 925 – 932.
[3] Y. Duan, P. A. Kollman, *Science* **1998**, *282*, 740 – 744.
[4] M. Schäfer, C. Bartels, M. Karplus, *J. Mol. Biol.* **1998**, *284*, 835 – 848.
[5] X. Daura, K. Gademann, B. Jaun, D. Seebach, W. F. van Gunsteren, A. E. Mark, *Angew. Chem.* **1999**, *111*, 249 – 253; *Angew. Chem. Int. Ed.* **1999**, *38*, 236 – 240.
[6] M. Takano, T. Yamato, J. Higo, A. Suyama, K. Nagayama, *J. Am. Chem. Soc.* **1999**, *121*, 605 – 612.
[7] A. R. Dinner, T. Lazaridis, M. Karplus, *Proc. Natl. Acad. Sci. USA* **1999**, *96*, 9068 – 9073.
[8] V. S. Pande, D. S. Rokhsar, *Proc. Natl. Acad. Sci. USA* **1999**, *96*, 9062 – 9067.
[9] D. Roccatano, A. Amadei, A. Di Nola, H. J. C. Berendsen, *Protein Sci.* **1999**, *8*, 2130 – 2143.
[10] A. M. J. J. Bonvin, W. F. van Gunsteren, *J. Mol. Biol.* **2000**, *296*, 255 – 268.
[11] P. Ferrara, A. Caflisch, *Proc. Natl. Acad. Sci. USA* **2000**, *97*, 10780 – 10785.
[12] B. Y. Ma, R. Nussinov, *J. Mol. Biol.* **2000**, *296*, 1091 – 1104.
[13] H. W. Wang, S. S. Sung, *J. Am. Chem. Soc.* **2000**, *122*, 1999 – 2009.
[14] X. Daura, K. Gademann, H. Schäfer, B. Jaun, D. Seebach, W. F. van Gunsteren, *J. Am. Chem. Soc.* **2001**, *123*, 2393 – 2404.
[15] W. F. van Gunsteren, R. Bürgi, C. Peter, X. Daura, *Angew. Chem.* **2001**, *113*, 363 – 367; *Angew. Chem. Int. Ed.* **2001**, *40*, 351 – 355.
[16] J. Higo, O. V. Galzitskaya, S. Ono, H. Nakamura, *Chem. Phys. Lett.* **2001**, *337*, 169 – 175.
[17] G. Hummer, A. E. Garcia, S. Garde, *Proteins Struct. Funct. Genet.* **2001**, *42*, 77 – 84.
[18] R. Bürgi, X. Daura, A. E. Mark, M. Bellanda, S. Mammi, E. Peggion, W. F. van Gunsteren, *J. Pept. Res.* **2001**, *57*, 107 – 118.
[19] C. Simmerling, B. Strockbine, A. E. Roitberg, *J. Am. Chem. Soc.* **2002**, *124*, 11258 – 11259.
[20] C. D. Snow, H. Nguyen, V. S. Pande, M. Gruebele, *Nature* **2002**, *420*, 102 – 106.
[21] A. Glättli, X. Daura, D. Seebach, W. F. van Gunsteren, *J. Am. Chem. Soc.* **2002**, *124*, 12972 – 12978.
[22] G. Colombo, D. Roccatano, A. E. Mark, *Proteins Struct. Funct. Genet.* **2002**, *46*, 380 – 392.
[23] H. W. Wu, S. M. Wang, B. R. Brooks, *J. Am. Chem. Soc.* **2002**, *124*, 5282 – 5283.
[24] X. Daura, W. F. van Gunsteren, A. E. Mark, *Proteins Struct. Funct. Genet.* **1999**, *34*, 269 – 280.
[25] H. Schäfer, X. Daura, A. E. Mark, W. F. van Gunsteren, *Proteins Struct. Funct. Genet.* **2001**, *43*, 45 – 56.
[26] X. Daura, A. Glättli, P. Gee, C. Peter, W. F. van Gunsteren, *Adv. Protein Chem.* **2002**, *62*, 341 – 360.
[27] R. Baron, D. Bakowies, W. F. van Gunsteren, X. Daura, *Helv. Chim. Acta* **2002**, *85*, 3872 – 3882.
[28] K. D. Stigers, M. J. Soth, J. S. Nowick, *Curr. Opin. Chem. Biol.* **1999**, *3*, 714 – 723.
[29] M. S. Cubberley, B. L. Iverson, *Curr. Opin. Chem. Biol.* **2001**, *5*, 650 – 653.
[30] D. J. Hill, M. J. Mio, R. B. Prince, T. S. Hughes, J. S. Moore, *Chem. Rev.* **2001**, *101*, 3893 – 4011.
[31] M. D. Smith, G. W. J. Fleet, *J. Pept. Sci.* **1999**, *5*, 425 – 441.
[32] L. Szabo, B. L. Smith, K. D. McReynolds, A. L. Parrill, E. R. Morris, J. Gervay, *J. Org. Chem.* **1998**, *63*, 1074 – 1078.
[33] J. A. Smith, L. G. Pease, *Crit. Rev. Biochem.* **1980**, *8*, 315 – 412.
[34] F. Schweizer, *Angew. Chem.* **2001**, *113*, 240 – 264; *Angew. Chem. Int. Ed.* **2001**, *40*, 230 – 253.
[35] S. A. W. Gruner, E. Locardi, E. Lohof, H. Kessler, *Chem. Rev.* **2002**, *102*, 491 – 514.
[36] T. K. Chakraborty, S. Ghosh, S. Jayaprakash, *Curr. Med. Chem.* **2002**, *9*, 421 – 435.
[37] M. D. Smith, T. D. W. Claridge, G. E. Tranter, M. S. P. Sansom, G. W. J. Fleet, *Chem. Commun.* **1998**, 2041 – 2042.
[38] N. L. Hungerford, T. D. W. Claridge, M. P. Watterson, R. T. Aplin, A. Moreno, G. W. J. Fleet, *J. Chem. Soc. Perkin Trans. 1* **2000**, 3666 – 3679.
[39] M. D. Smith, D. D. Long, A. Martin, D. G. Marquess, T. D. W. Claridge, G. W. J. Fleet, *Tetrahedron Lett.* **1999**, *40*, 2191 – 2194.
[40] T. D. W. Claridge, D. D. Long, N. L. Hungerford, R. T. Aplin, M. D. Smith, D. G. Marquess, G. W. J. Fleet, *Tetrahedron Lett.* **1999**, *40*, 2199 – 2202.
[41] V. P. B. Di Blasio, M. Saviano, A. Lombardi, F. Nastri, C. Pedone, E. Benedetti, M. Crisma, M. Anzolin, C. Toniolo, *J. Am. Chem. Soc.* **1992**, *114*, 6273 – 6278.
[42] X. Daura, I. Antes, W. F. van Gunsteren, W. Thiel, A. E. Mark, *Proteins Struct. Funct. Genet.* **1999**, *36*, 542 – 555.
[43] C. Peter, X. Daura, W. F. van Gunsteren, *J. Biomol. NMR* **2001**, *20*, 297 – 310.
[44] C. Peter, M. Rueping, H. J. Wörner, B. Jaun, D. Seebach, W. F. van Gunsteren, *Chem. Eur. J.* **2003**, *9*, 5838 – 5849.
[45] W. R. P. Scott, P. H. Hünenberger, I. G. Tironi, A. E. Mark, S. R. Billeter, J. Fennen, A. E. Torda, T. Huber, P. Krüger, W. F. van Gunsteren, *J. Phys. Chem. A* **1999**, *103*, 3596 – 3607.
[46] W. F. van Gunsteren, S. R. Billeter, A. A. Eising, P. H. Hünenberger, P. Krüger, A. E. Mark, W. R. P. Scott, I. G. Tironi, *The GROMOS96 Manual and User Guide*, Vdf Hochschulverlag AG, Zürich, **1996**.
[47] L. D. Schuler, X. Daura, W. F. van Gunsteren, *J. Comput. Chem.* **2001**, *22*, 1205 – 1218.
[48] R. Baron, D. Bakowies, W. F. van Gunsteren, *J. Peptide Sci.*, in press.

 © 2004 Wiley-VCH Verlag GmbH & Co. KGaA, Weinheim

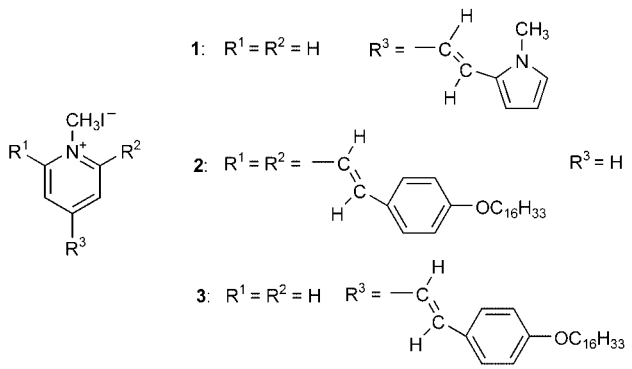
Organic Nanostructures

Low-Dimensional Aggregates from Stilbazolium-Like Dyes**

Zhiyuan Tian, Yu Chen, Wensheng Yang, Jiannian Yao, Lingyun Zhu, and Zhigang Shuai*

Organic low-dimensional nanostructures used as nanoscale building blocks have attracted considerable research interest in the development of novel nanodevices.[1] This interest is driven by the fact that organic nanostructures may exhibit a wide range of electrical and optical properties that depend sensitively on both their shapes and sizes, and thus is likely to provide a new method for modifying the optical and electronic properties of organic functional materials.[2] From this standpoint, an important challenge in the discovery of novel mesoscopic properties and the development of nanotechnology is to fabricate organic nanomaterials with the desired shape and size. Although extensive studies on the size-dependent optical and electronic properties of organic nanostructures such as particles,[2a–d] wires,[2e] and tubes[2f] have been performed recently, the ability to understand and predict the final structures of nanomaterials, which is critical to guide the rational fabrication of nanoscale materials with a desired shape, size, and therefore function, is still limited.[2a,3]

Herein, we report the facile fabrication of organic nanostructures with well-defined shapes and uniform sizes from stilbazolium-like dyes (Scheme 1). Compounds **1**–**3** were synthesized with the original intention of exploring the possible influence of the substituents on the shape, and therefore the optical properties, of the resulting nanostructures. Low-dimensional nanorods and nanospheres with high monodispersities in both shape and size were prepared by the self-aggregation of compounds **1** and **2**, respectively. The concomitant property changes upon formation of nanorods with intermolecular charge-transfer (inter-CT) characteristics, as well as highly monodisperse nanospheres with size-dependent spectral features, may be exploited in many fields.[1b]



Scheme 1. Structures of model compounds **1**–**3**.

The aggregation of molecule **1** was induced by injecting a certain amount of stock solution of compound **1** in ethanol into a 1:1 mixed solvent of hexane and methylcyclohexane (MCH) with vigorous stirring. Ethanol is a good solvent but the mixed solvent is a poor one for compound **1**, so aggregation of molecule **1** occurred as a consequence of the change in the solvent quality. The size of nanostructures of **1** was controlled by varying the concentration of the stock solution. For example, nanorod sizes of 110 and 80 nm were obtained when 60 μL of the 1.0×10^{-3} M stock solution and 120 μL of the 5.0×10^{-4} M stock solution were injected, respectively. Water was used as the poor solvent for the aggregation of compound **2** to obtain the colloids. The average size of nanostructures of **2** was controlled through a ripening process by variation of the aging time, that is, by changing the time intervals after injection of the stock solution. For example, aging times of 15 and 30 minutes gave nanospheres with diameters of 60 and 100 nm, respectively. The nanorods obtained from compound **1** and the nanospheres from compound **2** were very uniform in size, as indicated by the scanning (SEM) and tunneling electron microscopy (TEM) images (Figure 1). It can be seen that the sample derived from **1** consists of rather straight nanorods

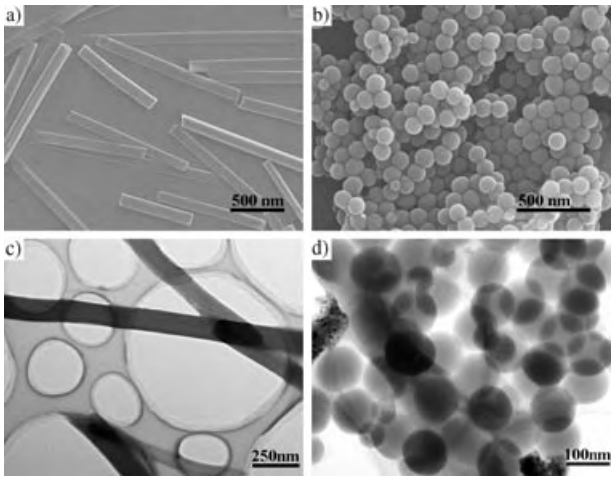


Figure 1. a) Medium-magnification SEM images of the nanorods formed from **1**. b) Low-magnification SEM images showing a large quantity of the nanospheres formed from **2**. c) TEM image of the nanorods. d) TEM image of the nanospheres.

[*] Dr. Z. Tian, Y. Chen, W. Yang, Prof. J. Yao
Key Laboratory of Photochemistry
Center for Molecular Science
Institute of Chemistry, Chinese Academy of Sciences
Beijing 100080 (P. R. China)
Fax: (+86) 10-8261-6517
E-mail: jnyao@mail.iccas.ac.cn
Dr. L. Zhu, Prof. Z. Shuai
Key Laboratory of Organic Solids
Center for Molecular Science
Institute of Chemistry, Chinese Academy of Sciences
Beijing 100080 (P. R. China)

[**] This work was supported by the National Natural Science Foundation of China, the Chinese Academy of Sciences, and the National Research Fund for Fundamental Key Projects No.973 (G19990330).

Supporting information for this article is available on the WWW under http://www.angewandte.org or from the author.

 © 2004 Wiley-VCH Verlag GmbH & Co. KGaA, Weinheim DOI: 10.1002/anie.200454131

with lengths up to the micrometer range that have a uniform size along the entire length. In addition, the surfaces of the nanorods are clean and smooth. The product from **2** consists of a large quantity of perfect nanospheres with very high monodispersity in terms of size, and some nanospheres are assembled into regular hexagonal arrays in a small domain (see Supporting Information). We note that there are scarcely any previous examples of nanostructures with such high monodispersity from small organic molecules without the use of templates. Furthermore, the distinct morphological features as well as the high monodispersity in size of the nanostructures of **1** and **2** lead us to assume that there would, most probably, be specific driving forces involved in the formation of these nanostructures.

It is known that the spectra of the nanostructures can give information about the formation process.[2a–e] Figure 2 displays the absorption spectra of the colloidal dispersions of the as-prepared nanorods and nanospheres. The monomer of **1** in ethanol exhibits an intensive intramolecular charge-transfer (intra-CT) absorption band at about 446 nm (2.77 eV), which is assigned to the transition from the HOMO of the donor to the LUMO of the acceptor (that is, π_D–π_A^*).[4] In the spectra of nanorods of **1**, the intra-CT band shows a slight gradual red shift with increasing nanorod size and simultaneously an additional band centered at approximately 500 nm (2.48 eV) emerges and gradually becomes predominant at the expense of the intra-CT band. This new band is attributed to an inter-CT transition between neighboring molecules in the nanorods.[1a] The spectrum of dilute **2** in ethanol solution also exhibits an intensive π–π* band at about 409 nm (3.03 eV), while the spectra of the nanospheres shift gradually to shorter wavelengths on increasing the particle size. In addition, both the excitation and emission fluorescence spectra of the nanospheres show similar hypsochromic shifts as the absorption spectra (see Supporting Information). However, only very weak fluorescence emission was detected for the nanorods of **1**, which indicates that strong quenching occurred in the aggregates of model molecule **1**.

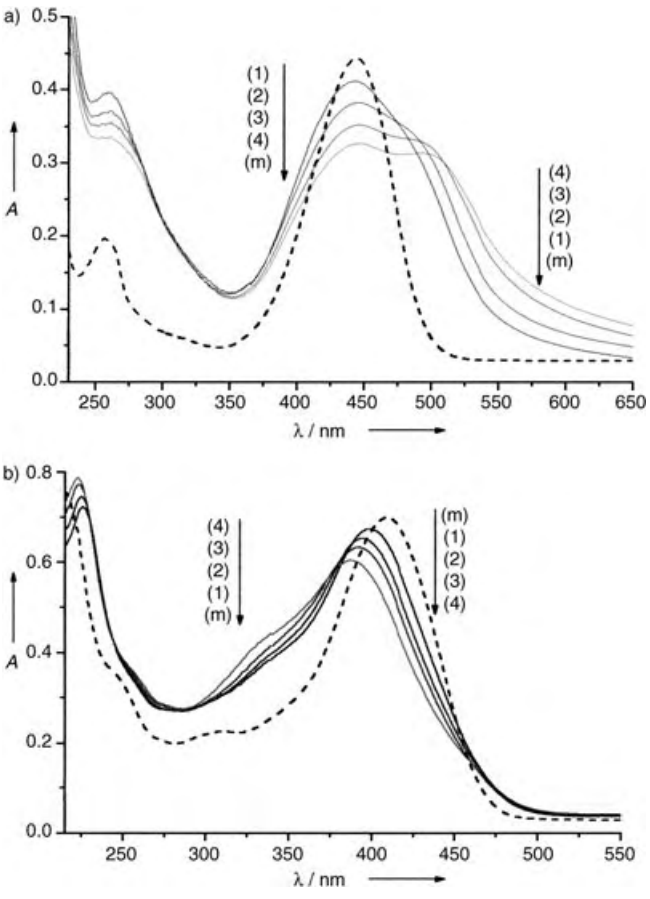


Figure 2. a) Absorption spectra of dispersions of nanorods with different diameters: 1) 40 nm, 2) 80 nm, 3) 110 nm, 4) 150 nm. b) Absorption spectra of dispersions of nanospheres with different sizes: 1) 30 nm, 2) 60 nm, 3) 100 nm, 4) 130 nm. For comparison, the spectra of the corresponding monomers in ethanol are also shown as (m) in (a) and (b) (dashed lines). *A* = absorbance (arbitrary units).

Molecule **1** consists of a strong electron-withdrawing moiety *N*-methylpyridinium (Nmpd) and a strong electron-releasing moiety *N*-methylpyrrole (Nmpr) connected by a conjugated system.[5] For molecule **2**, two weak electron-releasing 4-hexadecyloxyphenyl (4Hop) moieties, relative to Nmpr, are symmetrically connected to the Nmpd moiety through a conjugated ethylene group. One noteworthy conformational difference between molecules **1** and **2** is the planarity: the dihedral angles θ between the π systems of the donor and acceptor groups are nearly 0° for molecule **1** but 33° for molecule **2**, as indicated by the molecular mechanics optimizations of single molecules of **1** and **2** (Figure 3 a,b). It can also be seen from Figure 3 that molecule **1** has a linear D–π–A structure, while this is not the case for **2.** These molecular structural and conformational differences are expected to be responsible for the different spectral features, such as the 0.26 eV difference in the π–π* transition energy between monomers **1** and **2** that reflects the different extent of π-electron delocalization between the donor and acceptor moieties in the molecules.

SEM and TEM observations, along with the analysis of the molecular structural features and spectroscopic data, provide a clue for the understanding of the possible formation mechanism of the structurally distinct shapes of the nanostructures formed from **1** and **2**. It is well-documented that the spatial configuration of organic molecules plays an important role in determining their stacking mode and therefore the properties of the resulting aggregates.[2e,6] For example, an approximately face-to-face arrangement of the donor–acceptor (D–A) pair, which gives the largest orbital overlap, is necessary for the formation of inter-CT complexes. For compounds having the typical molecular structural characteristics of a strong D–A pair, a linear D–π–A structure, and a more planar conformation, strong D–A interactions[7] are known to act as the main driving force for the aggregation of molecules and the formation of one-dimensional (1D) nanostructures.[7c] The molecular structural characteristics of compound **1** discussed above enabled a similar mechanism to be proposed for the aggregation of molecule **1**, that is, by a donor-to-acceptor growth process (Figure 3 c) with eventual formation of rodlike nanostructures. Inter-CT processes[7c] and the extended delocalization of π electrons are expected as concomitant spectral features of the strong D–A interactions between adjacent molecules in the nanorods. In fact,

 © 2004 Wiley-VCH Verlag GmbH & Co. KGaA, Weinheim

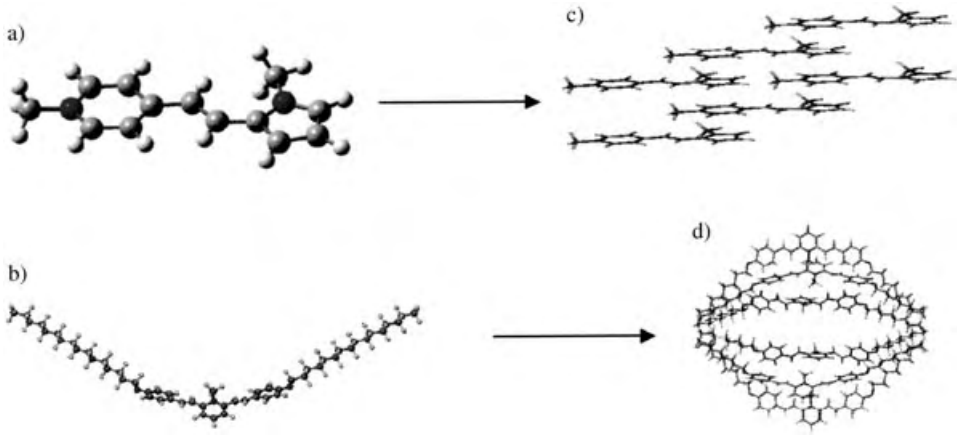


Figure 3. Energy-optimized single molecules of **1** (a) and **2** (b); computer-generated 1D aggregates of **1** (c) and 0D aggregates of **2** (d). In Figure 3d, the length of the hydrocarbon chains was shortened to eight carbon atoms for simplification.

the gradual appearance of a CT band and the slight bathochromic shift of the π–π* band in the spectra are consistent with the proposed mechanism for the formation of the nanorods. In addition, the quenching of the nanorod fluorescence emission can also be attributed to the presence of low-lying CT states in the nanorods.[8] XRD measurements show that the nanorods grow preferentially along the crystallographic [011] direction (see Supporting Information). This kind of preferential growth along a specific crystallographic direction is prone to forming 1D structures.

In the case of **2**, however, the possibility of D–A interaction acting as the dominating driving force for the aggregation of molecules was excluded because of the weak D–A pair, nonlinear molecular structure, and nonplanar configuration, as discussed above. Molecule **2** has two long flexible alkyl side chains substituted on the ionized pyridine ring, and therefore is a typical amphiphilic molecule bearing a hydrophilic "head" (ionized pyridine ring) and two long and flexible hydrophobic "arms" (alkyl chains), as shown in Figure 3b. The gradually blue-shifted spectral characteristics of the nanospheres compared with the monomer suggest the formation of H-type aggregates[9] in which the pyridine units are arranged in an almost parallel manner (see Figure 3d). Apparently, this type of aggregation is energetically favorable because it maximizes favorable stacking interactions between pyridine units and minimizes the unfavorable interactions between the molecule and the solvent. Subsequently, these H-type aggregates are presumed to attract each other—this is the so-called collective behavior generally observed in biology and chemistry that originates from interactions between units with the same shape,[10] and which is expected to be followed by a process involving fusion and then rearrangement. Nearly the same spectral features (UV/Vis absorption, fluorescence emission and excitation) as those discussed above, as well as spherical nanostructures, were observed when the mixed solvent of 1:1 hexane/MCH was used as the poor solvent during the aggregation of **2**. This finding indicates that it is mainly the difference between the compatibility of the two moieties (4Hop and Nmpd) of molecule **2** with the poor solvent, as well as the specific molecular structural features, that eventually lead to the aggregation of molecule **2** in a manner different from that of molecule **1**. Somewhat surprisingly, the nanospheres obtained after the ripening process are very monodisperse both in terms of shape and size (Figure 1b and Supporting Information). Similar results were also obtained in our previous work concerning organic nanostructures derived from pyrazoline derivatives.[2c,d] As discussed above, the growth of the nanospheres appears to be involved in the process consisting of the attraction, fusion, and rearrangement of relatively small particles, which suggests that the Ostwald ripening mechanism most probably does not apply to the present case. The relatively small particles are expected to aggregate preferentially through solvophobic interactions and then fuse as a result of their relatively large surface areas, eventually giving the focused size distribution of the nanospheres produced.[11] The underlying basis of the narrow size distribution of the as-prepared nanostructures is still under investigation.

Molecular modeling studies also provide a coherent picture of the process by which the resulting nanostructures are formed. The spectral features generated from the proposed aggregation models, namely the slight red shift of the intra-CT band and the inter-CT process between adjacent molecules in nanorods of **1**, as well as the blue-shifted intra-CT transition in the nanospheres of **2**, agree well with our experimental results. In particular, the calculated results clearly show the charge-transfer process from the donor to acceptor units between neighboring molecules in the case of nanorods (see Supporting Information).

The morphological and spectral features of the nanostructures formed by reference model compound **3** were also investigated. Molecule **3** is found to aggregate into rodlike nanostructures, as indicated by SEM studies (see Supporting Information). Although molecule **3** has a linear structure, it has a weak D–A interaction between the Nmpr and 4Hop moieties compared to molecule **1**, and thus may aggregate in a head-to-tail fashion through intermolecular D–A interactions, which should be much weaker than those occurring within the rods. However, molecule **3** bears only one long flexible alkyl chain while two are present in molecule **2**. Thus, the solvophobic interaction is unlikely to result in the formation of H-type aggregates with a nearly parallel

 © 2004 Wiley-VCH Verlag GmbH & Co. KGaA, Weinheim

arrangement of the pyridine ring moieties of molecule **3**. As a result, neither the apparent inter-CT feature similar to that observed in the spectra of the nanorods nor the gradually blue-shifted spectral feature on increasing the particle size, seen in the spectra of the nanospheres, is observed for the rodlike nanostructures in our experiments (see Supporting Information). The morphology of aggregates from **3** is relatively undefined compared to that of the rods and particles as a result of competition between the two relatively weaker D–A and solvophobic interactions.

In conclusion, we have successfully prepared stilbazolium-like dye nanorods and nanospheres by changing the solvent quality during the synthesis of model compounds. Sufficiently strong interactions between the constituent molecules allow the formation of nanostructures with well-defined shape and highly monodisperse size. Furthermore, different dominant intermolecular interactions, based on molecular components with different structural and conformational characteristics, are likely to be responsible for the formation of organic nanostructures with distinct shapes. This work provides specific examples and, therefore, the possibility of constructing nanomaterials that are expected to be useful in the development of photoelectronic nanodevices.

Received: February 27, 2004 [Z54131]

Keywords: aggregation · charge transfer · donor–acceptor systems · nanostructures · solvophobic interaction

[1] a) S. R. Forrest, *Chem. Rev.* **1997**, *97*, 1793; b) *Handbook of Advanced Electronic and Photonic Materials and Devices*, *Vol. 6* (Ed.: H. S. Nalwa), Academic Press, San Diego, **2001**.

[2] a) H. Kasai, H. Kamatani, S. Okada, H. Oikawa, H. Matsuda, H. Nakanishi, *Jpn. J. Appl. Phys.* **1996**, *35*, L221; b) H. B. Fu, J. N. Yao, *J. Am. Chem. Soc.* **2001**, *123*, 1434; c) H. B. Fu, B. H. Loo, D. B. Xiao, R. M. Xie, X. H. Ji, J. N. Yao, B. W. Zhang, L. Q. Zhang, *Angew. Chem.* **2002**, *114*, 1004; *Angew. Chem. Int. Ed.* **2002**, *41*, 962; d) D. B. Xiao, L. Xi, W. S. Yang, H. B. Fu, Z. G. Shuai, Y. Fang, J. N. Yao, *J. Am. Chem. Soc.* **2003**, *125*, 6740; e) H. B. Fu, D. B. Xiao, J. N. Yao, G. Q. Yang, *Angew. Chem.* **2003**, *115*, 2989; *Angew. Chem. Int. Ed.* **2003**, *42*, 2883; f) L. Y. Zhao, W. S. Yang, Y. Ma, J. N. Yao, Y. L. Li, H. B. Liu, *Chem. Commun.* **2003**, 2442.

[3] a) H. Nakanishi, H. Katagi, *Supramol. Sci.* **1998**, *5*, 289; b) A. Ibanez, S. Maximov, A. Guiu, C. Chaillout, P. L. Baldeck, *Adv. Mater.* **1998**, *10*, 1540; c) J. A. A. W. Elemans, A. E. Rowan, R. J. M. Nolte, *J. Am. Chem. Soc.* **2002**, *124*, 1532.

[4] M. M. Habashy, F. El-Zawawi, M. S. Antonious, A. K. Sheriff, M. S. A. Abdel-Mottaleb, *Indian J. Chem. Sect. A* **1985**, *24*, 908.

[5] a) A. Albert, *Heterocyclic Chemistry*, Oxford University Press, New York, **1968**; b) I. D. L. Albert, T. J. Marks, M. A. Ratner, *J. Am. Chem. Soc.* **1997**, *119*, 6575.

[6] a) M. Pope, C. E. Swenberg, *Electronic Processes in Organic Crystals*, Oxford University Press, Oxford, **1982**; b) C. A. Hunter, J. K. M. Sanders, *J. Am. Chem. Soc.* **1990**. *112*, 5525; c) C. A. Hunter, *Angew. Chem.* **1993**, *105*, 1653; *Angew. Chem. Int. Ed. Engl.* **1993**, *32*, 1584; d) B. K. An, S. K. Kwon, S. D. Jung, S. Y. Park, *J. Am. Chem. Soc.* **2002**, *124*, 14410.

[7] a) D. B. Amabilino, P. R. Anelli, P. R. Ashton, G. R. Brown, E. Córdova, L. A. Godinez, W. Hanes, A. E. Kaifer, D. Philp, A. M. Z. Slawin, N. Spencer, J. F. Stoddart, M. S. Tolley, D. J. Williams, *J. Am. Chem. Soc.* **1995**, *117*, 11142; b) B. Cabezon, J. G. Cao, F. M. Raymo, J. F. Stoddart, A. J. P. White, D. J. Williams, *Chem. Eur. J.* **2000**, *6*, 2262; c) A. D. L. Escosura, M. V. Martinez-Diaz, P. Thordarson, A. E. Rowan, R. J. M. Nolte, T. Torres, *J. Am. Chem. Soc.* **2003**, *125*, 12300.

[8] U. Hofstra, R. B. M. Koehorst, T. J. Schaafsma, *Chem. Phys. Lett.* **1986**, *130*, 555.

[9] E. S. Emerson, M. A. Colin, A. E. Rosenoff, K. S. Norland, H. Rodriguez, D. Chin, G. R. Bird, *J. Phys. Chem.* **1967**, *71*, 2396.

[10] a) M. Adams, Z. Dogic, S. L. Keller, S. Fraden, *Nature* **1998**, *393*, 349; b) V. J. Anderson, H. N. W. Lekkerkerker, *Nature* **2002**, *416*, 810; c) Z. Y. Tang, N. A. Kotov, M. Giersig, *Science* **2002**, *297*, 237.

[11] a) X. G. Peng, J. Wickham, A. P. Alivisatos, *J. Am. Chem. Soc.* **1998**, *120*, 5343; b) Z. A. Peng, X. G. Peng, *J. Am. Chem. Soc.* **2001**, *123*, 1389.

 © 2004 Wiley-VCH Verlag GmbH & Co. KGaA, Weinheim

Heterocycle Synthesis

Cycloisomerization Promoted by the Combination of a Ruthenium–Carbene Catalyst and Trimethylsilyl Vinyl Ether, and its Application in The Synthesis of Heterocyclic Compounds: 3-Methylene-2,3-dihydroindoles and 3-Methylene-2,3-dihydrobenzofurans**

Yukiyoshi Terada, Mitsuhiro Arisawa, and Atsushi Nishida**

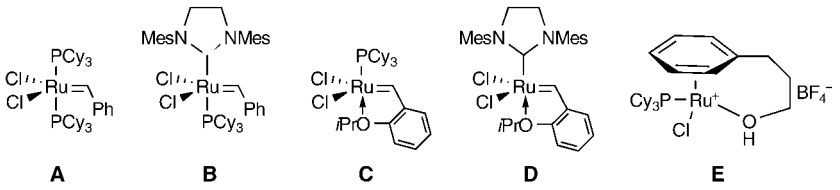
Transition-metal-catalyzed cyclization of α,ω-dienes is an efficient method for the construction of carbo- and heterocycles. One particularly interesting cyclization is olefin metathesis,[1] in which significant progress was made after the development of well-defined ruthenium–carbene catalysts, such as **A** and **B** (Scheme 1). In particular, the commercially available ruthenium–carbene catalyst **B** has shown enhanced activity in ring-closing metathesis (RCM), ring-opening metathesis polymerization (ROMP), and cross metathesis (CM).[1c,2] On the other hand, the nonmetathetic behaviors of ruthenium–carbene catalysts have been demonstrated in recent studies of olefin metatheses.[3] When a substrate cannot give a product by metathesis, nonmetathetic reactions, such as the Kharasch addition,[4] olefin isomerization,[5] and hydro-

[*] Y. Terada, Dr. M. Arisawa, Prof. Dr. A. Nishida
Graduate School of Pharmaceutical Sciences
Chiba University, 1-33 Yayoi-cho, Inage-ku
Chiba 263-8522 (Japan)
Fax: (+81) 43-290-2909
E-mail: arisawa@p.chiba-u.ac.jp
nishida@p.chiba-u.ac.jp

[**] This research was supported by a Grant-in-Aid for Scientific Research on Priority Areas (A) "Exploitation of Multi-Element Cyclic Molecules" and a Grant-in-Aid for Exploratory Research from the Ministry of Education, Culture, Sports, Science, and Technology, Japan.

Supporting Information for this article is available on the WWW under http://www.angewandte.org or from the author.

 DOI: 10.1002/anie.200454157 © 2004 Wiley-VCH Verlag GmbH & Co. KGaA, Weinheim



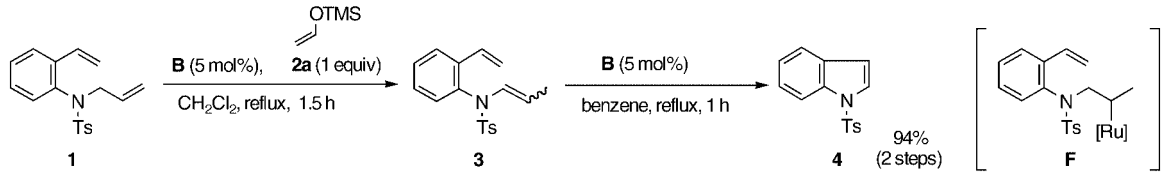
Scheme 1. Ruthenium catalysts. Cy = cyclohexyl, Mes = 2,4,6-trimethylphenyl.

genation, either proceed efficiently or complete recovery of the starting materials is observed. These discoveries have expanded the synthetic utility of these catalysts beyond olefin metathesis. For example, olefin isomerization can be used in the deprotection of allyl ethers and amines,[5a–e] the synthesis of cyclic enol ethers,[5f,g] and the formation of dienamide from allenamide.[5h]

Another method that can be used to prepare cyclic compounds from α,ω-dienes is cycloisomerization.[6] In comparison to RCM, in which the carbon–carbon double bond is formed with the release of a stoichiometric amount of ethene, cycloisomerization proceeds without the loss of carbon units. Therefore, selective and catalytic cycloisomerization can be considered a highly atom-economic reaction. Recently, it has been shown that these reactions can be catalyzed by various transition metals, such as palladium,[7a–d,f] nickel,[7a] titanium,[7e] rhodium,[7f] and ruthenium.[8,9] Although ruthenium species that induce cycloisomerization, such as **E**[8a] and $[\{RuCl_2(p\text{-cymene})\}_2]$, (*p*-cymene = *p*-isopropyltoluene)[8b,c] have been identified, there are few successful reports. A highly selective cycloisomerization using a ruthenium catalyst was established by Itoh and co-workers, who used $[\{Ru(cod)Cl_2\}_n]$ (cod = 1,5-cyclooctadiene).[9]

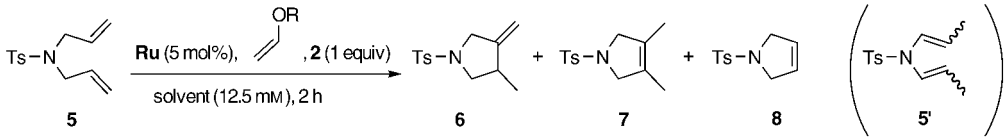
We have been studying the syntheses of nitrogen-containing heterocycles using ruthenium–carbene catalysts,[10] and have recently demonstrated the facile and selective isomerization of the terminal olefin by a combination of **B** and trimethylsilyl vinyl ether (**2a**). The aromatic enamides **3** that were obtained were subjected to standard RCM to give the corresponding indole **4** in excellent yield. The combination of these transformations established a novel synthesis for substituted indoles (Scheme 2).[11] Although the active ruthenium species for our isomerization was not characterized, we postulated that a low-valent ruthenium species, such as a ruthenium hydride, which might be generated by the reaction of **B** and **2a**, catalyzed the isomerization of an olefin via intermediate **F**. Based on our hypothesis, it is possible that **F**, which has another olefin at an appropriate position in the substrate, may undergo intramolecular olefin insertion into the Ru–C bond, followed by a *syn* β-H elimination to produce the cycloisomerized product. Herein, the cycloisomerization of α,ω-dienes using ruthenium–carbene catalyst **B** and **2a** is reported together with its application to the synthesis of heterocycles.

First, we examined the reaction of *N*,*N*-diallyl-*p*-toluenesulfonamide (**5**), which is widely used for RCM and cycloisomerization. When diene **5** was stirred with catalyst **B** (5 mol%) in dichloromethane at room temperature for two hours, the RCM product **8** was obtained quantitatively. In marked contrast, when **5** was stirred with **B** (5 mol%) and one equivalent of **2a** under the same conditions, the expected cycloisomerized product **6** was isolated in 65% yield, along with 21% of **8** (Table 1, entry 1). The same reaction at an elevated temperature (40°C) led to higher yields of **6** and **7** (86 and 14%, respectively; entry 2). The amount of **7** formed increased at a higher temperature in toluene (entry 3). In fact, the isomerization of **6** to **7** proceeded under the same conditions. The use of **A** or **C** (entries 4 and 5) or ethyl



Scheme 2. Selective isomerization of a terminal olefin: the synthesis of an indole through RCM. Ts = *p*-toluenesulfonyl, TMS = trimethylsilyl.

Table 1: Reaction of *N*,*N*-diallyl-*p*-toluenesulfonamide (**5**). [a]



Entry	Ru		R	Solvent	*T* [°C]	Yield [%][b]			
						5	**6**	**7**	**8**
1	**B**	**2a**	TMS	CH_2Cl_2	RT	0	65	0	21
2	**B**	**2a**	TMS	CH_2Cl_2	40	0	86	(14)	0
3	**B**	**2a**	TMS	toluene	110	0	(22)	78	0
4	**A**	**2a**	TMS	CH_2Cl_2	40	28	10	0	59
5	**C**	**2a**	TMS	CH_2Cl_2	40	0	29	0	64
6	**D**	**2a**	TMS	CH_2Cl_2	40	0	71	24	0
7	**B**	**2b**	Et	CH_2Cl_2	40	58	37	0	5

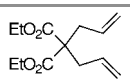
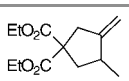
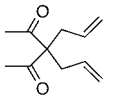
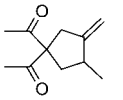
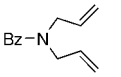
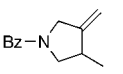
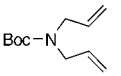
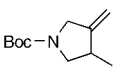
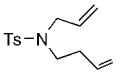
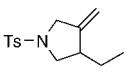
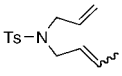
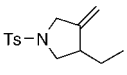
[a] RT = Room temperature, TMS = trimethylsilyl. [b] Yields in parenthesis were estimated by ^1H NMR spectroscopy.

 © 2004 Wiley-VCH Verlag GmbH & Co. KGaA, Weinheim

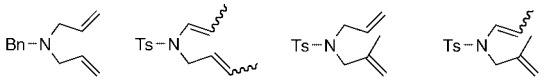
vinyl ether (**2b**) (entry 7) was less effective for the reaction, while **D** showed a high activity that was comparable to that of **B** (entry 6). Thus, the *N*-heterocyclic carbene (NHC) ligand of a ruthenium catalyst has been shown from these results to be important for highly efficient cycloisomerizations, in terms of regio- and chemoselectivity. The ruthenium complex $[RuCl(H)(CO)(PPh_3)_3]$,[12] which is known to catalyze cyclizations of enynes[12a] and isomerization of terminal olefins,[12b,c] did not promote the cycloisomerization of **5**, and isomerized compounds **5′** were obtained quantitatively instead of **6** or **7**. To the best of our knowledge, this is the first example of cycloisomerization with a α,ω-diene using a ruthenium–carbene catalyst as a precursor to the active species. By employing our conditions, a cycloisomerized compound can be selectively prepared even when the substrate can readily yield a RCM product.

The scope and limitations of this reaction are further shown in Table 2. Reactions of **9** and **10** gave the corresponding products **17** and **18** in respective yields of 83 and 87%. *N*-Benzoyldiallylamine (**11**) also gave **19** in good yield, although *N*-*tert*-butoxycarbonyldiallylamine (**12**) gave **20** in only 47% yield. The reaction of **12** heated in toluene to reflux did not increase the yield of **20**. In the case of **13**, neither cycloisomerization nor olefin migration occurred, perhaps because of an electron-donating effect. Both **14** and **15** gave **21** in low yields, along with **14′** (59 and 81%, respectively), while the reaction of **16**, which has a methallyl group, only gave isomerized products **16′**. Although the substituents at the nitrogen center and the terminal olefin functionality are very important, we thought that this reaction could have potential for the construction of nitrogen-containing heterocycles as well as carbocycles.

Table 2: Cycloisomerization of dienes.[a]

Entry	Substrate		Product		Yield [%][b]
1		**9**		**17**	83
2		**10**		**18**	87
3		**11**		**19**	75
4		**12**		**20**	47
5		**14**		**21**	18
6		**15**		**21**	13

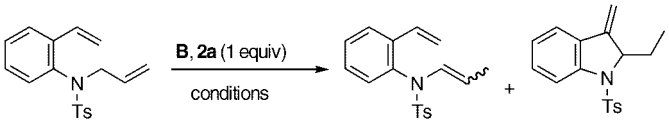
[a] Conditions: **B** (5 mol%), **2a** (1 equiv), CH_2Cl_2 (12.5 mM), heated to reflux, 2 h. [b] Yield of isolated product. Bn = benzyl.



13 **14′** **16** **16′**

Next, we investigated the application of this cycloisomerization to the synthesis of *N*- and *O*-benzo-fused heterocycles, which are important structures in many pharmacologically active compounds. Although the reaction of **1** with **2a** and **B** in dichloromethane heated to reflux gave enamides **3** in quantitative yields (Table 3, entry 1), the reaction of **1** to prepare the corresponding cycloisomerized product was investigated further. As a result, when the reaction of **1** was performed in toluene at 40 °C, the cycloisomerized indolidene **22** was obtained, albeit in low yield (entry 2). When the same reaction was carried out in either toluene or xylene heated to reflux, **22** was obtained in respective yields of 35 and 68% (entries 3 and 4). Finally, it was found that a higher temperature (in xylene at reflux) and greater amount of catalyst (10 mol%) were necessary to obtain **22** in excellent yield (entry 5). Initial isomerization of **1** converted it into **3**, which after cyclization led to the formation of **22**. This reaction pathway is indicated as the reaction of **3** under the optimized conditions (in xylene at reflux) yielded **22** in moderate yield with recovered **3** (62 and 38%, respectively). It is noteworthy that the reaction of **3** with $[\{Ru(cod)Cl_2\}_n]$ in isopropanol for 24 hours, which is the typical procedure reported by Itoh and co-workers,[9] did not produce **22** at all.

Table 3: Isomerization and cycloisomerization of α,ω-diene **1**.



1 **3** **22**

Entry	**B** [mol%]	Conditions	Yield [%][a]	
			3	**22**
1	5	CH_2Cl_2, reflux, 1.5 h	quant.	0
2	5	toluene, 40 °C, 2 h	97	3
3	5	toluene, reflux, 2 h	65	35
4	5	xylene, reflux, 2 h	30	68
5	10	xylene, reflux, 2 h	12	81

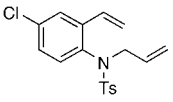
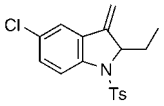
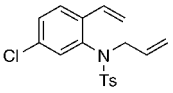
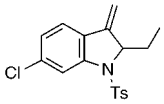
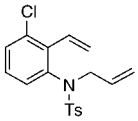
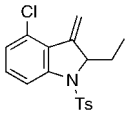
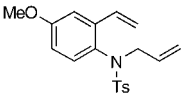
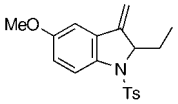
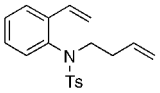
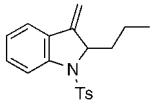
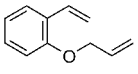
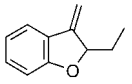
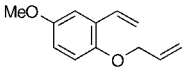
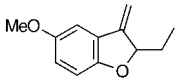
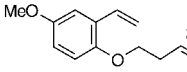
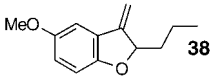
[a] Yields were estimated by ^{1}H NMR spectroscopy.

Several substituted *N*- and *O*-benzo-fused heterocycles were synthesized under our cycloisomerization conditions (Table 4). Compounds **23**–**25**, which have a chloro-substituted benzene ring, gave the corresponding indolidenes **31**–**33** in respective yields of 84, 78, and 78%. On the other hand, the reaction of **26**, which has a methoxy-substituted benzene ring, gave **34** in only 24% yield. The reaction of **27**, which has a butenyl group at the nitrogen center, also gave the cyclized product **35** in good yield. In contrast to the reactions of the nitrogen-containing substrates (**1**, **23**–**27**), the oxygen-containing substrates **28**–**30** readily cyclized to give the corresponding heterocycles **36**–**38** in good yields. The 3-methylene-2,3-dihydrobenzofurans **36**–**38** readily isomerized to the corresponding 3-methylbenzofurans **39**–**41** under acidic conditions, such as in HCl (1M) and trifluoroacetic acid.

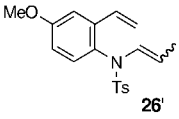
To obtain more detailed information on the cycloisomerization the reaction of **5** with **B** and **2** in $[D_8]$toluene was monitored by spectroscopic analysis. The relative amounts of **5** and the cyclized products **6** and **7** were analyzed by ^{1}H NMR

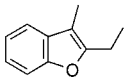
 © 2004 Wiley-VCH Verlag GmbH & Co. KGaA, Weinheim

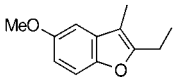
Table 4: Synthesis of 3-methylene-2,3-dihydroindoles and 3-methylene-2,3-dihydrobenzofurans.[a]

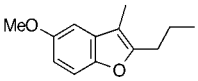
Entry	Substrate		Solvent	Product		Yield [%][b]
1		**23**	xylene		**31**	84
2		**24**	xylene		**32**	78
3		**25**	xylene		**33**	78
4		**26**	xylene		**34**	24[c]
5		**27**	xylene		**35**	58
6		**28**	toluene		**36**	78
7		**29**	toluene		**37**	76
8		**30**	toluene		**38**	73

[a] Conditions: **B** (10 mol% for entries 1–5; 5 mol% for entries 6–8), **2a** (1 equiv), solvent (12.5 mM), heated to reflux, 2 h. [b] Yield of isolated product unless otherwise noted. [c] Determined by ^{1}H NMR spectroscopy. Enamides **26′** were also obtained in 76% yield.


26′


39


40


41

spectroscopy, and the relative amounts of ruthenium complexes, including **B** and **G**,[13] were analyzed by ^{1}H and ^{31}P NMR spectroscopy. First, we periodically monitored the reaction of **5** with **B** in the presence of **2a** in [D_8]toluene (0.17 M) at 50 °C. The reaction was complete within 10 minutes and both **5** and **B** were consumed. Since the reaction rate under the above conditions was too fast to monitor, **2b** was used instead of **2a** to decrease the rate of the reaction, and the results are summarized in Figure 1. After 15 minutes of heating, ^{31}P NMR spectroscopy showed the disappearance of a signal at $\delta = 29.8$ ppm in the spectrum of **B**, accompanied by the emergence of a new signal at $\delta = 30.6$ ppm. Similarly, ^{1}H NMR spectroscopic analysis showed the disappearance of a signal at $\delta = 19.7$ ppm from the spectrum of **B**, while a new signal appeared at $\delta = 14.2$ ppm. These observations show the rapid formation of Fischer-type carbene **G** from the reaction between **B** and **2b**. After 29 minutes, ^{31}P NMR spectroscopic analysis showed that **G** had partially decomposed to other unidentified ruthenium compounds ($\delta = 46.7$, 32.5 ppm). In contrast to the reaction of **B**, the conversion of **5** to **6** proceeded gradually under these conditions and was complete after 45 minutes. The formation of **7** was not observed.

As demonstrated in the ^{1}H and ^{31}P NMR spectroscopic analyses, catalyst **G** appears to play an important role in the cycloisomerization process. According to Louie and Grubbs, **G** shows high reactivity for metathesis processes, such as ROMP and RCM.[13] Therefore, we synthesized **G** and confirmed that it efficiently catalyzes the RCM reaction of **5** in toluene at 50 °C to give **8** in 79% yield along with recovered **5** (21%). However, the reaction of **5** in the presence of both **G** (5 mol%) and one equivalent of **2b** gave **6** in 98% yield.

Although it is unclear which ruthenium species participate in this cycloisomerization, the ruthenium hydride species is a

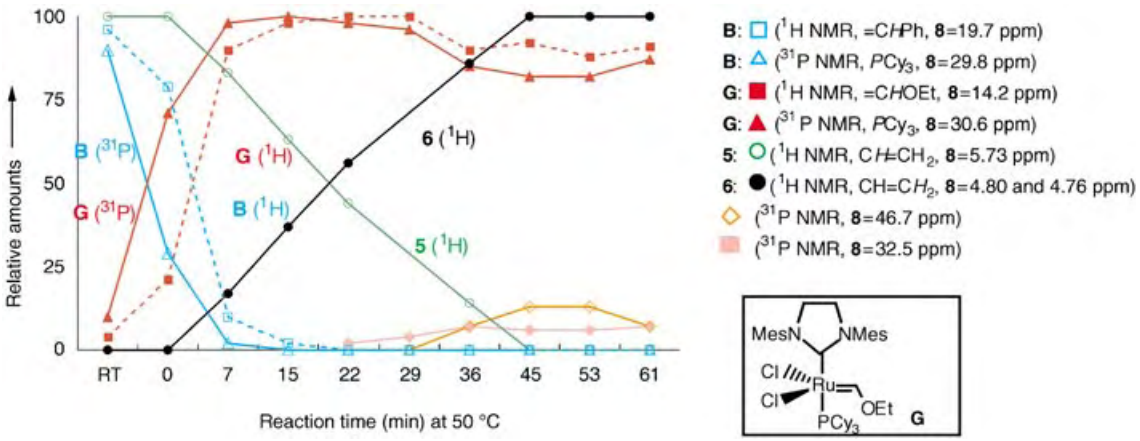


Figure 1. Cycloisomerization of *N*,*N*-diallyl-*p*-toluenesulfonamide (**5**) in [D_8]toluene (0.17 M) at 50 °C in the presence of **B** (5 mol%) and **2b** (1 equiv). The relative amounts of **B**, **G**, and decomposition products were estimated by ^{31}P NMR spectroscopic analysis using H_3PO_4 (85%) as the external standard and ^{1}H NMR spectroscopic analysis using 1,2;5,6-dibenzanthracene (5 mol%) as the internal standard. The relative amounts of **5** and **6** were estimated by ^{1}H NMR spectroscopy.

 © 2004 Wiley-VCH Verlag GmbH & Co. KGaA, Weinheim

possibility according to the mechanism proposed by Itoh and co-workers.[9a] Moreover, it has been reported that the ruthenium–hydride species[14] are generated from the Grubbs carbene complex through the formation of the ruthenium Fischer carbene.[15] However, the following findings allow an increased insight into ruthenium catalysis: 1) The experimental results show that $[RuCl(H)(CO)(PPh_3)_3]$[12] or reaction conditions using ruthenium–carbene catalysts without NHC ligands **A** and **C** were less effective for cycloisomerization. Also ruthenium catalysts **B** and **D** gave cycloisomerized products in good to excellent yields, which indicate that the presence of NHC ligands in the ruthenium–carbene catalyst is a key component for cycloisomerization. 2) Our cycloisomerization conditions can be used to prepare indolidenes, *N*-benzo-fused heterocycles. The preparation of which have not been reported using the most successful ruthenium catalyst $[\{Ru(cod)Cl_2\}_n]$. Further studies on the ruthenium species involved in the cycloisomerization process and an investigation of the reaction mechanism are currently in progress.

In conclusion, a new methodology for the cycloisomerization of dienes using a Grubbs carbene complex and trimethylsilyl vinyl ether has been established. The utility of this reaction was demonstrated in the synthesis of *exo*-methylene heterocyclic compounds, which could act as key intermediates for pharmacologically active compounds. We believe that these results offer a further insight into the chemistry of ruthenium–carbene complexes.

Received: March 2, 2004
Revised: May 5, 2004 [Z54157]

Keywords: cyclization · heterocycles · isomerization · metathesis · ruthenium

[1] For recent reviews of olefin metathesis, see: a) A. Fürstner, *Angew. Chem.* **2000**, *112*, 3140–3172; *Angew. Chem. Int. Ed.* **2000**, *39*, 3012–3043; b) T. M. Trnka, R. H. Grubbs, *Acc. Chem. Res.* **2001**, *34*, 18–29; c) S. J. Connon, S. Blechert, *Angew. Chem.* **2003**, *115*, 1944–1968; *Angew. Chem. Int. Ed.* **2003**, *42*, 1900–1923.

[2] a) M. Scholl, S. Ding, C. W. Lee, R. H. Grubbs, *Org. Lett.* **1999**, *1*, 953–956; b) A. K. Chatterjee, T.-L. Choi, D. P. Sanders, R. H. Grubbs, *J. Am. Chem. Soc.* **2003**, *125*, 11360–11370.

[3] a) B. Alcaide, P. Almendros, *Chem. Eur. J.* **2003**, *9*, 1259–1262; b) B. Schmidt, *Eur. J. Org. Chem.* **2004**, *9*, 1865–1880.

[4] J. A. Tallarico, L. A. Malnick, M. L. Snapper, *J. Org. Chem.* **1999**, *64*, 344–345.

[5] a) B. Alcaide, P. Almendros, J. M. Alonso, *Tetrahedron Lett.* **2003**, *44*, 8693–8695; b) B. Alcaide, P. Almendros, J. M. Alonso, *Chem. Eur. J.* **2003**, *9*, 5793–5799; c) B. Alcaide, P. Almendros, J. M. Alonso, M. F. Aly, *Org. Lett.* **2001**, *3*, 3781–3784; d) C. Cadot, P. I. Dalco, J. Cossy, *Tetrahedron Lett.* **2002**, *43*, 1839–1841; e) Y.-J. Hu, R. Dominique, S. K. Das, R. Roy, *Can. J. Chem.* **2000**, *78*, 838–845; f) B. Schmidt, *Eur. J. Org. Chem.* **2003**, 816–819; g) A. E. Sutton, B. A. Seigal, D. F. Finnegan, M. L. Snapper, *J. Am. Chem. Soc.* **2002**, *124*, 13390–13391; h) S. S. Kinderman, J. H. van Maarseveen, H. E. Schoemaker, H. Hiemstra, F. P. J. T. Rutjes, *Org. Lett.* **2001**, *3*, 2045–2048; i) T. R. Hoye, H. Zhao, *Org. Lett.* **1999**, *1*, 1123–1125; j) A. Fürstner, O. R. Thiel, L. Ackermann, H.-J. Schanz, S. P. Nolan, *J. Org. Chem.* **2000**, *65*, 2204–2207; k) D. Bourgeois, A. Pancrazi, S. P. Nolan, J. Prunet, *J. Organomet. Chem.* **2002**, *643–644*, 247–252; l) J. C. Sworen, J. H. Pawlow, W. Case, J. Lever, K. B. Wagener, *J. Mol. Catal. A* **2003**, *194*, 69–78.

[6] a) G. C. Lloyd-Jones, *Org. Biomol. Chem.* **2003**, *1*, 215–236; b) B. M. Trost, M. J. Krische, *Synlett* **1998**, 1–16.

[7] a) B. Radetich, T. V. RajanBabu, *J. Am. Chem. Soc.* **1998**, *120*, 8007–8008; b) P. Kisanga, R. A. Widenhoefer, *J. Am. Chem. Soc.* **2000**, *122*, 10017–10026; c) L. A. Goj, R. A. Widenhoefer, *J. Am. Chem. Soc.* **2001**, *123*, 11133–11147; d) R. A. Widenhoefer, *Acc. Chem. Res.* **2002**, *35*, 905–913; e) S. Okamoto, T. Livinghouse, *J. Am. Chem. Soc.* **2000**, *122*, 1223–1224; f) R. Grigg, J. F. Malone, T. R. B. Mitchell, A. Ramasubbu, R. M. Scott, *J. Chem. Soc. Perkin Trans. 1* **1984**, 1745–1754.

[8] a) Y. Miyaki, T. Onishi, S. Ogoshi, H. Kurosawa, *J. Organomet. Chem.* **2000**, *616*, 135–139; b) D. Séméril, C. Bruneau, P. H. Dixneuf, *Helv. Chim. Acta* **2001**, *84*, 3335–3341; c) B. Çetinkaya, S. Demir, I. Özdemir, L. Toupet, D. Séméril, C. Bruneau, P. H. Dixneuf, *New J. Chem.* **2001**, *25*, 519–521; d) M. Michaut, M. Santelli, J.-L. Parrain. *Tetrahedron Lett.* **2003**, *44*, 2157–2159; e) S. J. Connon, S. Blechert, *Bioorg. Med. Chem. Lett.* **2002**, *12*, 1873–1876; f) A. Fürstner, M. Liebl, C. W. Lehmann, M. Picquet, R. Kunz, C. Bruneau, D. Touchard, P. H. Dixneuf, *Chem. Eur. J.* **2000**, *6*, 1847–1857; g) M. Bassetti, F. Centola, D. Séméril, C. Bruneau, P. H. Dixneuf, *Organometallics* **2003**, *22*, 4459–4466; h) B. Çetinkaya, S. Demir, I. Özdemir, L. Toupet, D. Séméril, C. Bruneau, P. H. Dixneuf, *Chem. Eur. J.* **2003**, *9*, 2323–2330; i) I. Özdemir, E. Çetinkaya, B. Çetinkaya, M. Çiçek, D. Séméril, C. Bruneau, P. H. Dixneuf, *Eur. J. Inorg. Chem.* **2004**, 418–422.

[9] a) Y. Yamamoto, Y. Nakagai, N. Ohkoshi, K. Itoh, *J. Am. Chem. Soc.* **2001**, *123*, 6372–6380; b) Y. Yamamoto, N. Ohkoshi, M. Kameda, K. Itoh, *J. Org. Chem.* **1999**, *64*. 2178–2179. Very recently, Itoh and co-workers developed the ruthenium-catalyzed one-pot double allylation/cycloisomerization of 1,3-dicarbonyl compounds, see: Y. Yamamoto, Y. Nakagai, K. Itoh, *Chem. Eur. J.* **2004**, *10*, 231–236.

[10] a) M. Arisawa, E. Takezawa, A. Nishida, M. Mori, M. Nakagawa, *Synlett* **1997**, 1179–1180; b) M. Arisawa, C. Kato, H. Kaneko, A. Nishida, M. Nakagawa, *J. Chem. Soc. Perkin Trans. 1* **2000**, 1873–1876; c) M. Arisawa, H. Kaneko, A. Nishida, M. Nakagawa, *J. Chem. Soc. Perkin Trans. 1* **2002**, 959–964; d) M. Arisawa, C. Theeraladanon, A. Nishida, M. Nakagawa, *Tetrahedron Lett.* **2001**, *42*, 8029–8033; e) C. Theeraladanon, M. Arisawa, A. Nishida, M. Nakagawa, *Tetrahedron* **2004**, *60*, 3017–3035.

[11] M. Arisawa, Y. Terada, M. Nakagawa, A. Nishida, *Angew. Chem.* **2002**, *114*, 4926–4928; *Angew. Chem. Int. Ed.* **2002**, *41*, 4732–4734.

[12] a) M. Nishida, N. Adachi, K. Onozuka, H. Matsumura, M. Mori, *J. Org. Chem.* **1998**, *63*, 9158–9159; b) W. A. L. van Otterlo, E. L. Ngidi, C. B. de Koning, *Tetrahedron Lett.* **2003**, *44*, 6483–6486; c) W. A. L. van Otterlo, R. Pathak, C. B. de Koning, *Synlett* **2003**, *12*, 1859–1861.

[13] J. Louie, R. H. Grubbs, *Organometallics* **2002**, *21*, 2153–2164.

[14] For studies on ruthenium–hydride complexes, see: a) C. S. Yi, D. W. Lee, Y. Chen, *Organometallics* **1999**, *18*, 2043–2045; b) C. S. Yi, D. W. Lee, *Organometallics* **1999**, *18*, 5152–5156; c) H. M. Lee, D. C. Smith, Jr., Z. He, E. D. Stevens, C. S. Yi, S. P. Nolan, *Organometallics* **2001**, *20*, 794–797.

[15] For studies on the decomposition of ruthenium–carbene complexes to ruthenium–hydride complexes, see: a) Z. Wu, S. T. Nguyen, R. H. Grubbs, J. W. Ziller, *J. Am. Chem. Soc.* **1995**, *117*, 5503–5511; b) T. M. Trnka, J. P. Morgan, M. S. Sanford, T. E. Wilhelm, M. Scholl, T.-L. Choi, S. Ding, M. W. Day, R. H. Grubbs, *J. Am. Chem. Soc.* **2003**, *125*, 2546–2558; c) M. B. Dinger, J. C. Mol, *Organometallics* **2003**, *22*, 1089–1095; and ref [13].

 © 2004 Wiley-VCH Verlag GmbH & Co. KGaA, Weinheim

Metallic Nanostructures

Molecular Lithography with DNA Nanostructures**

*Zhaoxiang Deng and Chengde Mao**

The great success of photolithography results from its ability to accurately control the produced patterns. An alternative, bottom-up approach to build ordered patterns by self-assembly is promising and may supersede the traditional top-down lithography-based techniques for the preparation of nanoscaled patterns.[1–9] Among the many challenges in developing parallel and bottom-up techniques, the capabilities of controlling pattern topography and to scale-down feature dimensions are two central issues concerning their practical applications. One possible solution is to use tunable, self-assembled, supramolecular structures as lithography masks; DNA nanostructures appear to be ideal for this purpose.[10–16] Here we demonstrate that DNA nanostructures can be used as masks for molecular lithography. DNA nanostructures could be accurately replicated into metal nanostructures by metal evaporation followed by lifting off of the mask. The ease and flexibility of this reported technique make it suitable for producing defined and integrated nanopatterns, which represents a novel route to overcome the inabilities faced by traditional lithographic techniques.

DNA has found many applications beyond its original genetic interest.[7,8,10–20] DNA metalization to fabricate metallic or semiconductive nanowires is one example of how long DNA duplexes can be replicated. However, the metalization process results in a loss of the structural details of the DNA molecules. The resulting nanowires are at least 10-times thicker than the DNA templates.[17–19] More seriously, the resulting structures are exclusively linear structures, which is far removed from the structural complexities required for technological applications. The emergence and fast development of DNA nanotechnology makes it possible to construct complicated DNA structures through bottom-up self-assembly of engineered DNA motifs. The resulting DNA structures have been explored for performing molecular computations,[10] crafting nanomechanical devices,[13] and organizing other functional units.[15,20] These DNA structures would also provide an ideal means to meet the complexity requirement. It is conceivable that well-defined nanopatterns with designed DNA structures could be produced as masks for direct replication. Since it is possible to overcome the feature-size limitation of current lithographic techniques by the use of suitable molecules/macromolecules as masks, research on this topic may have fundamental influence on both nanoscience and nanotechnology. The molecular lithographic method we report here is a general and parallel method. The process consists of four steps (Figure 1), and can generate 1D and 2D metallic nanopatterns with feature sizes down to about 10 nm. With further elaborations, this method might be promising for making functional circuits, sensors, and display panels with highly controllable topography at the nanometer scale.

We assembled DNA arrays by slowly cooling equimolar mixtures of the corresponding component DNA strands from 95 °C to 22 °C, and depositing them onto freshly cleaved mica substrates. A 20-nm-thick gold film was then thermally evaporated onto the mica substrate. At the end of the evaporation, a drop of epoxy mixture was sandwiched and solidified between the gold film and a glass slide. The glass slide together with the gold film was then separated from the mica surface. The side contacting the DNA samples were exposed to air and contained the negative replica of the DNA structures. We analyzed the DNA structures and their metallic replicas by tapping mode atomic force microscopy (AFM).

We first demonstrated the principle with a one-dimensional (1D) DNA double crossover (DX)[14] array (Figure 2 and Supporting Information). There is an even number of half turns between any two crossovers in the 1D DX array (Figure 2a). Linear DX arrays could be easily resolved by AFM imaging. Section analysis indicated that the height of the 1D DX arrays was about 0.9 nm. Replication worked very well for this DNA structure. The gold film appeared to be an exact negative replica of the DNA molecules on the mica surfaces. The depth of the replicated grooves was about 0.6 nm. This lower value compared to the DNA masks was presumably a result of imaging artifacts. The 1D DX arrays were 4-nm wide and smaller than the radius of the AFM tip (10 nm). Thus, an AFM tip could not fully track down to the negative replicas. The apparent widths (measured as full-width at half maximum) of the DX arrays and their replicas were 13 nm and 11 nm, respectively.

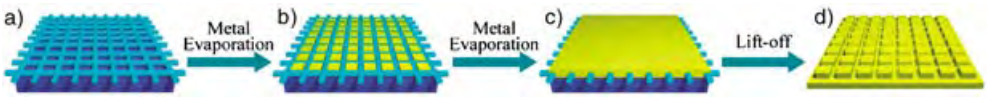


Figure 1. Schematic representation of the process of molecular lithography. a) DNA nanostructues are self-assembled in solution and deposited on mica. b) and c) Metal evaporates until a continuous metal film forms and covers the DNA mask on the mica surface. d) The metal film, after removal from the DNA/mica, exhibits a negative replica of the DNA mask.

[*] Z. Deng, Prof. C. Mao
Department of Chemistry
Purdue University
West Lafayette, IN 47907 (USA)
Fax: (+1) 765-494-0239
E-mail: mao@purdue.edu

[**] This work was supported by the NSF (EIA-0323452), DARPA/DSO (MDA 972-03-1-0020), and Purdue University (a start-up fund). We thank Dr. A. Ribbe and Dr. D. Liu for help with AFM imaging.

Supporting information for this article is available on the WWW under http://www.angewandte.org or from the author.

 © 2004 Wiley-VCH Verlag GmbH & Co. KGaA, Weinheim DOI: 10.1002/anie.200460257

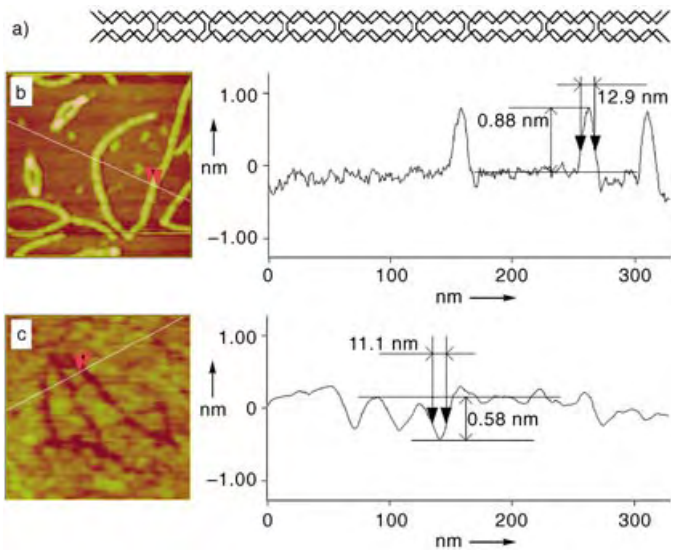


Figure 2. AFM analysis of the replication of DX 1D arrays. a) Schematic representation of a 1D DNA double crossover (DX) array. AFM images and section analysis of: b) the DNA arrays and c) their negative gold replica.

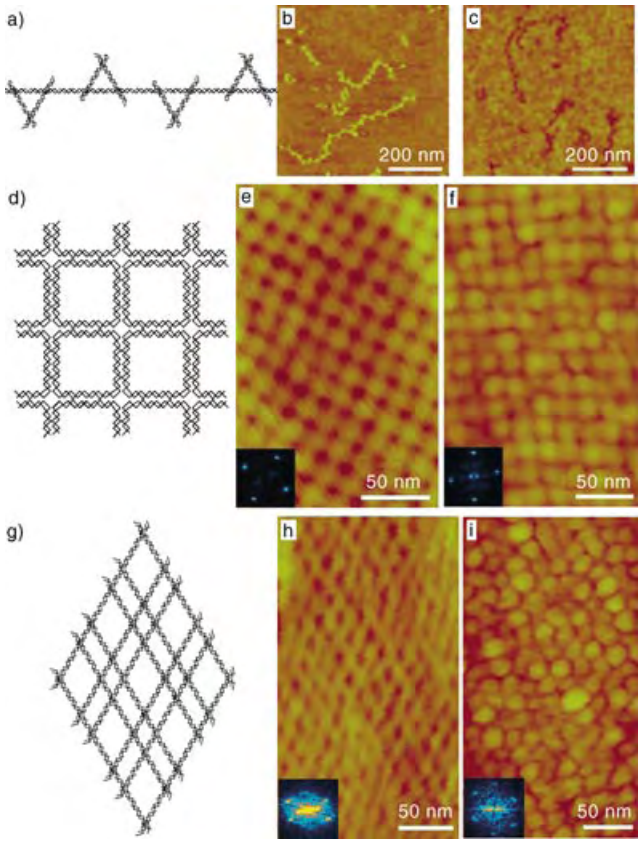


Figure 3. AFM images showing replications of three DNA nanostructures. a)–c) Replication of 1D DNA triangle arrays; d)–f) replication of a tetragonal 2D DNA array; g)–i) replication of a pseudohexagonal 2D array. a), d), and g) Schematic representations of DNA structures; b), e), and h) AFM images of DNA arrays; c), f), and i) AFM images of gold replicas of DNA arrays. The insets show the 2D Fourier transforms of the corresponding AFM images, which clearly show symmetry similarities between the DNA samples and their gold replicas. Height scales in all images are 5 nm.

We further analyzed the mica surface after the gold film had been peeled off. To our surprise, the DNA molecules remained on the mica surface and were intact (see the Supporting Information). We noticed that the height of the DNA samples became higher and could reach 3–4 nm. We suspected that this phenomenon was caused by heating during the evaporation stage, which could partially denature DNA molecules, especially the hydrogen bonds between sticky ends, and cause the spread DNA to contract into discontinuous, high bumps. However, this would not prevent DNA from serving as a mask for pattern replication, since the gold pattern layer of about 1 nm in thickness was formed at the very beginning of the evaporation process when no significant heat accumulated.

A 1D DNA triangle array[16] was also used as a template for molecular lithography. AFM images of the DNA samples and their replicas are shown in Figure 3a–c and in the Supporting Information. The DNA structure was an array of pearled-up DNA triangles with a regular spacing (27 nm) between all adjacent triangles. The vertex-to-vertex distance within each triangle was only about 12 nm, and our results showed an impressive resemblance between the DNA arrays and their negative replicas, which implies the great potential of this molecular lithography technique when dealing with extremely small lateral dimensions of around 10 nm.

The first two-dimensional (2D) DNA array that we chose to replicate was a tetragonal array (Figure 3d–f and Supporting Information).[15] A basic unit of the array had a cross-shaped structure, which contained four four-armed junctions pointing in four orthogonal directions. Figure 3e shows an image of the tetragonal 2D DNA array. The pitch of the DNA grids was measured to be about 18.0 nm, which is in good agreement with the estimated (17.6 nm) and the reported value.[15] The gold replicas showed negative patterns that were consistent with the DNA masks (Figure 3f). Since the DNA mask had a square grid structure, we would expect that the replicas would be an array of pillars with the same symmetry and periodicity as the mask. This expectation was verified by measuring the average distance between neighboring pillars. This distance was shown to be about 18.0 nm, which is almost identical to the periodicity of the corresponding DNA structure. The grid structure of the DNA mask and the pillarlike gold replica were more clearly represented by a 3D surface view of the AFM images (see the Supporting Information), which, together with the consistency in the periodicities and the similarity in the overall platelike shapes between the DNA arrays and their replicas (Figure 3e and f), unambiguously proved the high fidelity of our replication process.

A very appealing aspect of DNA nanostructures is that it is relatively easy to vary their structures: patterns with different symmetries are achievable. As a demonstration we have chosen a pseudohexagonal 2D DNA array formed by Holliday junctions (Figure 3g–i).[12] The basic unit of the array is a rhombus with an inner angle of approximately 62°. Thus, the DNA arrays have a pseudohexagonal symmetry. Con-

 © 2004 Wiley-VCH Verlag GmbH & Co. KGaA, Weinheim

sequently, a hexagonal symmetry would be expected for their gold replicas. Figure 3h and i are AFM images of the Holliday junction array and its gold replica, respectively. The experimental results have clearly showed that self-assembled DNA nanostructures are suitable masks for making well-defined surface patterns.

In conclusion, we have successfully demonstrated that it is possible to use designed DNA nanostructures as molecular masks for the preparation of nanoscaled patterns. Masks with more sophisticated structures could be constructed by rational design and self-assembly of DNA motifs.[11] Following this approach and benefiting from the ease and accuracy of synthesizing and manipulating DNA, the wealth of enzyme tools for modifying DNA structures, and the availability of other evaporation materials besides metals as replication matrices, the construction of highly structured patterns for more realistic applications such as nanocircuits, nanosensors, nanofluidics, information storage, and super high resolution display panels with nanoscale pixels should be possible after further elaboration of the technique. Although the cost of preparing long DNA oligomers may become a concern, this technique is a cost-effective lithographic method because it doesn't require any special and expensive chemicals and facilities such as clean rooms and photoresists. It is very likely that this technique will merge with soft lithography[5,6] through the development of patterns on polymer substrates to obtain soft stamps, since the state-of-the-art soft lithographic technique can transfer patterns with vertical features as small as 2 nm, which can facilitate transfer and duplication of the replicated patterns.

Experimental Section

Construction of DNA structures: The design and construction of all DNA structures were reported previously.[12,14–16] DNA single strands were purchased from Integrated DNA technologies, Inc., and purified by denaturing polyacrylamide gel electrophoresis (PAGE). DNA nanostructures were formed by annealing equimolar mixtures of component DNA strands from 95 °C to 22 °C over 2 to 48 h.

Replication of DNA patterns: All the metal evaporations were carried out using a thermal evaporator (Turbo Vacuum Evaporator-EFFA). The evaporation speed was adjusted to 0.2 nm s^{-1}. After metal evaporation, a drop of premixed epoxy adhesive was then put on the gold film and immediately covered by a glass slide. After the epoxy was completely solidified, the metal replicas could be easily lifted off from the mica surfaces.

AFM imaging: A drop of DNA sample solution (2 μL) was spotted onto a freshly cleaved mica surface, and left for 10 s to allow strong adsorption to occur. The sample drop was then washed off with 10 mM $Mg(OAc)_2$ solution (30 μL) and dried with compressed air. DNA samples and their metal replicas were imaged by a tapping-mode atomic force microscopy on a Nanoscope IIIa microscope (Digital Instruments) with NSC15 tips (silicon cantilever, Mikro-Masch). For large area scans ($> 5 \times 5$ μm^2), the tip velocity was kept at 10 μm s^{-1}, otherwise a scan frequency of 1 or 1.5 Hz was used. The tip–surface interaction was minimized by optimizing the scan set-point.

Received: April 7, 2004 [Z460257]

Keywords: DNA · lithography · nanofabrication · nanostructures · self-assembly

[1] H. Huang, X. F. Duan, Q. Q. Wei, C. M. Lieber, *Science* **2001**, *291*, 630–633.
[2] P. A. Smith, C. D. Nordquist, T. N. Jackson, T. S. Mayer, B. R. Martin, J. Mbindyo, T. E. Mallouk, *Appl. Phys. Lett.* **2000**, *77*, 1399–1401.
[3] B. Messer, J. H. Song, P. D. Yang, *J. Am. Chem. Soc.* **2000**, *122*, 10232–10233.
[4] S. M. Huang, X. Y. Cai, J. J. Liu, *J. Am. Chem. Soc.* **2003**, *125*, 5636–5637.
[5] B. D. Gates, G. M. Whitesides, *J. Am. Chem. Soc.* **2003**, *125*, 14986–14987.
[6] Y. Xia, J. J. McClelland, R. Gupta, D. Qin, X.-M. Zhao, L. L. Sohn, R. J. Celotta, G. M. Whitesides, *Adv. Mater.* **1997**, *9*, 147–149.
[7] A. P. Alivisatos, K. P. Johnsson, X. Peng, T. E. Wilson, C. J. Loweth, M. P. Bruchez, Jr., P. G. Schultz, *Nature* **1996**, *382*, 609–611.
[8] C. A. Mirkin, R. L. Letsinger, R. C. Mucic, J. J. A. Storhoff, *Nature* **1996**, *382*, 607–609.
[9] S. Wong, V. Kitaev, G. A. Ozin, *J. Am. Chem. Soc.* **2003**, *125*, 15589–15598.
[10] N. C. Seeman, *Nature* **2003**, *421*, 427–431.
[11] C. D. Mao, T. H. LaBean, J. H. Reif, N. C. Seeman, *Nature* **2000**, *407*, 493–496.
[12] C. D. Mao, W. Q. Sun, N. C. Seeman, *J. Am. Chem. Soc.* **1999**, *121*, 5437–5443.
[13] a) C. M. Niemeyer, *Angew. Chem.* **2002**, *114*, 3933–3937; *Angew. Chem. Int. Ed.* **2002**, *41*, 3779–3783; b) C. D. Mao, W. Q. Sun, Z. Y. Shen, N. C. Seeman, *Nature* **1999**, *397*, 144–146; c) B. Yurke, A. J. Turberfield, A. P. Mills, F. C. Simmel, J. L. Neumann, *Nature* **2000**, *406*, 605–608; d) H. Yan, X. Zhang, Z. Shen, N. C. Seeman, *Nature* **2002**, *415*, 62–65.
[14] E. Winfree, F. R. Liu, L. A. Wenzler, N. C. Seeman, *Nature* **1998**, *394*, 539–544.
[15] H. Yan, S. H. Park, G. Finkelstein, J. H. Reif, T. H. LaBean, *Science* **2003**, *301*, 1882–1884.
[16] D. G. Liu, M. S. Wang, Z. X. Deng, R. Walulu, C. D. Mao, *J. Am. Chem. Soc.* **2004**, *126*, 2324–2425.
[17] a) K. Keren, R. S. Berman, E. Buchstab, U. Sivan, E. Braun, *Science* **2002**, *297*, 72–75; b) E. Braun, Y. Eichen, U. Sivan, G. Ben-Yoseph, *Nature* **1998**, *391*, 775–778; c) K. Keren, R. S. Berman, E. Buchstab, U. Sivan, E. Braun, *Science* **2003**, *302*, 1380–1382.
[18] J. Richter, R. Seidel, R. Kirsch, M. Mertig, W. Pompe, J. Plaschke, H. K. Schackert, *Adv. Mater.* **2000**, *12*, 507–510.
[19] Z. X. Deng, C. D. Mao, *Nano Lett.* **2003**, *3*, 1545–1548.
[20] C. M. Niemeyer, T. Sano, C. L. Smith, C. R. Cantor, *Nucleic Acids Res.* **1994**, *22*, 5530–5539.

 © 2004 Wiley-VCH Verlag GmbH & Co. KGaA, Weinheim

Proteomics Research

Post-Translational Modifications on Proteins: Facile and Efficient Procedure for the Identification of O-Glycosylation Sites by MALDI-LIFT-TOF/TOF Mass Spectrometry

*Masaki Kurogochi, Takahiko Matsushita, and Shin-Ichiro Nishimura**

Mass spectrometry has become one of the most important and powerful methods for the rapid identification of proteins in recent post-genome science and technology.[1] In addition to phosphorylation, a variety of post-translational modifications such as sulfation, acylations, methylation, and glycosylations were recently recognized to regulate the structures and functions of proteins.[2] Therefore, advent of an efficient and general strategy for identifying sites of post-translational modifications on proteins is highly awaited in proteomics research. Although glycosylations of proteins are basically classified into two major types, N-glycosylation and O-glycosylation, post-translational modification by glycosylation has been studied extensively in the case of *N*-linked-type glycans.[3] It has been known from studies of the *N*-glycans that *N*-acetyl-D-glucosamine links to an asparagine residue of the tripeptide sequence Asn-X-Ser(Thr) through formation of a stable amide bond. In contrast to N-glycosylation, there is no consensus sequence directing the initial incorporation of the sugar into mucin peptides by UDP-GalNAc, a polypeptide *N*-acetyl-D-galactosaminyltransferase (GalNAc-transferase). The difficulty in identifying O-glycosylation sites of mucins is a result of the instability of O-glycosidic bonds between GalNAc (GlcNAc) and Ser/Thr in these compounds. It has also been suggested that direct observation of O-glycosylation sites during collision-induced dissociation in mass spectrometry has proved difficult because the glycosidic linkages are labile and easily cleaved, thus resulting in very little fragmentation of the glycopeptides.[4] As a result, an alternative way for direct observation has been used: β-elimination followed by Michael addition of some nucleophiles to the dehydroalanine residue.[5] At present, it seems that NMR spectroscopy is virtually the only effective and reliable method for the structural elucidation of mucin-type glycopeptides with unstable O-glycosidic bonds, even though milligram-scale samples are required.[6]

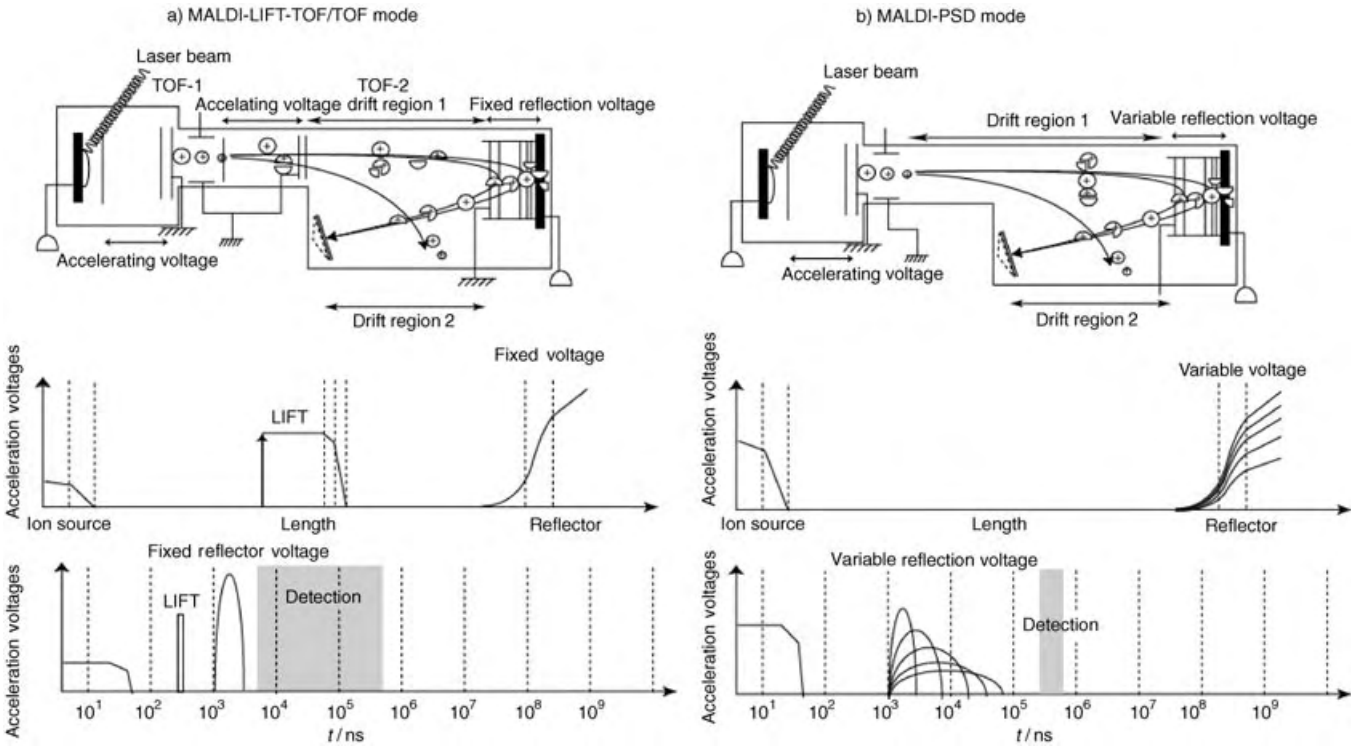


Figure 1. Schematic diagrams of LIFT-TOF/TOF (a) and PSD (b) in MALDI mass instruments.

In the course of our synthetic studies on functional glycopeptides and proteomics of modified β-galactosidases,[6b,7] we found that MALDI-TOF and MALDI-LIFT-TOF/TOF mass spectra measured in the presence of 2,5-dihydroxybenzoic acid (DHB) as the matrix often gave observable peaks corresponding to the target (glyco)peptides

[*] M. Kurogochi, T. Matsushita, Prof. S.-I. Nishimura
Division of Biological Sciences, Graduate School of Science
Frontier Research Center for the
Post-Genomic Science and Technology
Hokkaido University, N21, W11, Sapporo 001–0021 (Japan)
Fax: (+81) 11-706-9042
E-mail: shin@glyco.sci.hokudai.ac.jp

Supporting information for this article is available on the WWW under http://www.angewandte.org or from the author.

 DOI: 10.1002/anie.200460020 © 2004 Wiley-VCH Verlag GmbH & Co. KGaA, Weinheim

and glycoproteins. The artificial glyco-insulin carrying a sialooligosaccharide branch could also be detected as a single ion peak without any degradation of the sugar moiety,[7b] thus suggesting that the use of DHB might help in the ionization of unstable O-glycopeptides bearing α-sialosides. In addition, Schnaible et al. recently reported that peptide fragment ions having unstable S–S bonds can be clearly detected by mass spectrometry using a MALDI-LIFT-TOF/TOF instrument.[8] We thought that these interesting features of MALDI-TOF mass spectra must depend on the collision process used in the LIFT-TOF/TOF method having a significant affect on the intramolecular relaxation of the fragment ions.[9] Although a post source decay (PSD) as well as a collision-induced dissociation (CID) mode is used for MS/MS of glycopeptides,[10] precise analysis of fragment ion peaks often seems to be difficult because of preferential and fast deglycosylation.

As illustrated in Figure 1a, the LIFT-TOF/TOF instruments are characterized by a colinear arrangement of two TOF mass analyzers (TOF-1 and TOF-2), each equipped with an ion source that allows control over the acceleration and focusing of the ions. In TOF-1, the analyte ions are accelerated, and precursor ions are selected and fragmented. Then, fragment ions are selected to proceed to the source of TOF-2, where they are again accelerated and analyzed by the detector. As shown in the schematic diagram, interpretation of the LIFT-TOF/TOF method is straightforward as only one assignment must be verified,[9] while the PSD or CID mode requires several trials to control the reflectron voltage and enable separation and detection of each product ion (Figure 1b). As a result, the collision process in the MALDI-LIFT-TOF/TOF mass spectrometer under a mild and very fast experimental process seemed to offer much faster analysis and higher sensitivity than that of CID or PSD mode, even in cases of some unstable fragment ions. The merit of LIFT-TOF/TOF mass spectrometry in the peptide fragmentation studies prompted us to investigate the high-throughput identification of O-glycosylation sites of glycopeptides by MALDI-TOF mass spectrometry. Herein, we report that the MS/MS spectra of some synthetic O-glycopeptides measured on a MALDI-LIFT-TOF/TOF instrument in the presence of DHB as a matrix gave ideal fragmentation patterns and high sensitivity of structure-specific fragment ions that were suitable for identifying O-glycosylation sites of mucin-type glycoproteins.

Figure 2 shows MALDI-LIFT-TOF/TOF spectra of a peptide Ac-AHGVTSAPDTRPAPGSTA-NH_2 (**1**), and seven synthetic glycopeptide isomers having GalNAc residue at the position(s) T5, T10, or/and T17 (**2**)-(**8**). It was suggested that the DHB matrix produced much more reasonable and

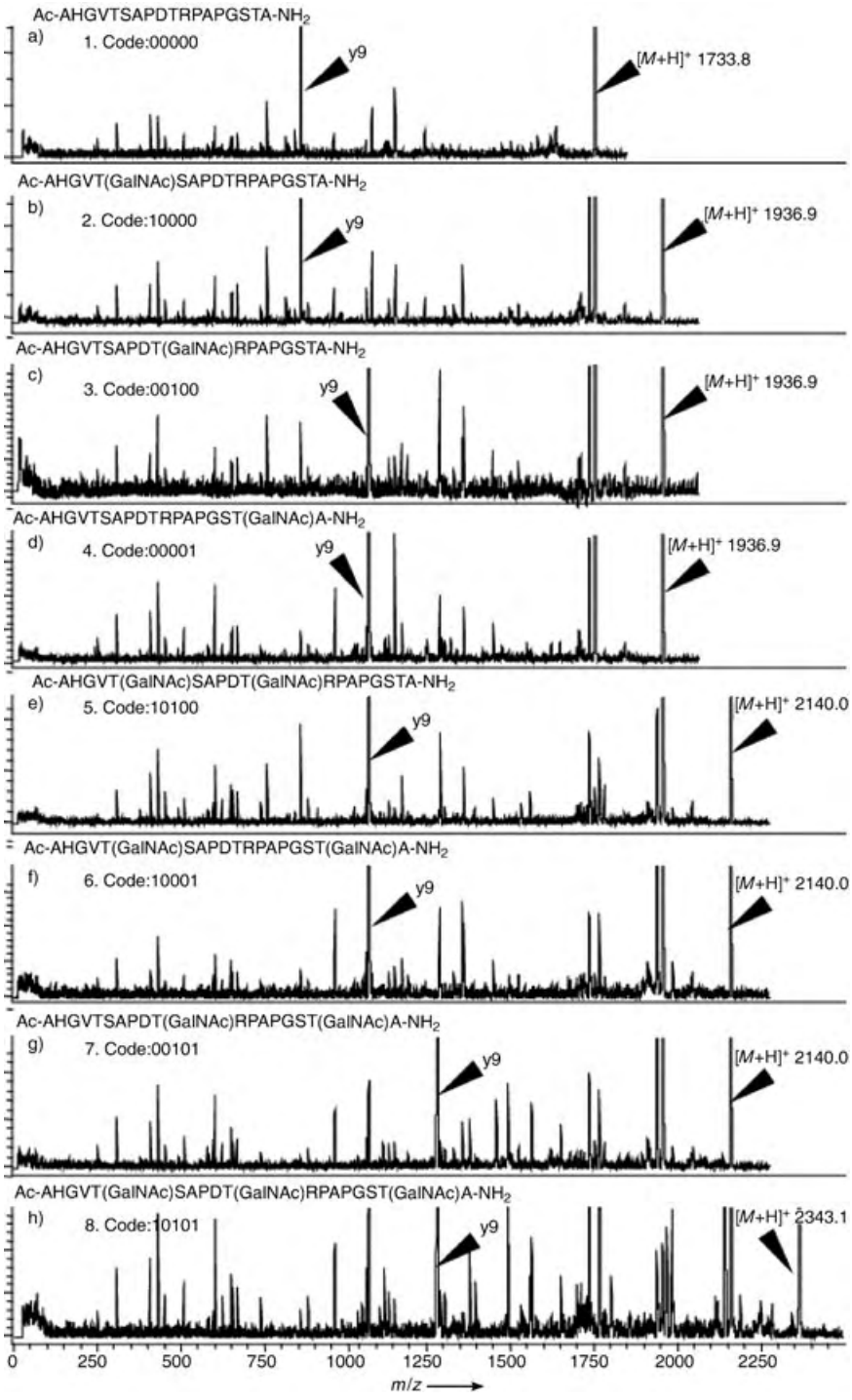


Figure 2. Fragmentations of peptide (**1**) and glycopeptides (**2**–**8**) by LIFT-TOF/TOF MS.

 © 2004 Wiley-VCH Verlag GmbH & Co. KGaA, Weinheim

sensitive fragment ion peaks (b and y fragment ion series) bearing GalNAc residue(s) for the structural elucidation than α-cyano-4-hydroxycinnamic acid (CHCA) or sinapinic acid (SA; see the Supporting Information). In addition, we found that a major fragment ion peak (y9) of each glycopeptide generated by LIFT-TOF/TOF MS significantly sifted in accordance with the O-glycosylation site(s). These results greatly facilitated high-throughput identification of the O-glycosylation site by assignment of the fragment ions with Biotool 2.2 software (Bruker Daltonik GmbH). For example, a glycopeptide isomer bearing GalNAc residues at the three positions (**8**, code: 10101) gave important fragment peaks such as b4, b5, b8, b10, b16, y2, y3, y8, y9, y13, and y14 thus indicating the exact mass of the GalNAc residues attached to positions T5, T10, and T17 (Figure 3). In addition, significant fragment ions at *m*/*z* 1733, 1936, and 2140 corresponding to losses of neutral carbohydrate units also supported the reliability in the assignment of this compound. It was suggested that use of a MS/MS scoring method such as molecular weight search (MOWSE) with some selected query fragment ion peaks would greatly accelerate high-throughput identification of the O-glycosylation site(s) of mucin-type glycopeptides. Although MOWSE scoring predicted two plausible candidates (code: 10110 and code: 10101), further precise analysis of important ion peaks of the b and y series, such as b16, y2, and y3 gave a reasonable structure of compound **8** coded as 10101.

The versatility of the present method was preliminarily demonstrated by monitoring a transglycosylation reaction catalyzed by β-galactosidase as illustrated in Scheme 1. Transglycosylation by β-galactosidase was carried out according to the conditions reported by Vliegenthart et al.[4d] using a glycopeptide **8** (code: 10101) as an acceptor substrate and lactose as a donor substrate. It is known that this galactosylation reaction may proceed in moderate or relatively low yield and give Galβ(1→3)GalNAc derivatives as the main products. As anticipated, transglycosylation of **8** provided a new ion peak at *m*/*z* 2509.1 in addition to a peak corresponding to the starting material (*m*/*z* 2343.1; Figure 4). Although MOWSE scoring predicted three plausible candidates of the product, it was concluded from precise analysis of the y and b series of fragment ions that this peak involves two galactosylated isomers coded as 20101 and 10201.

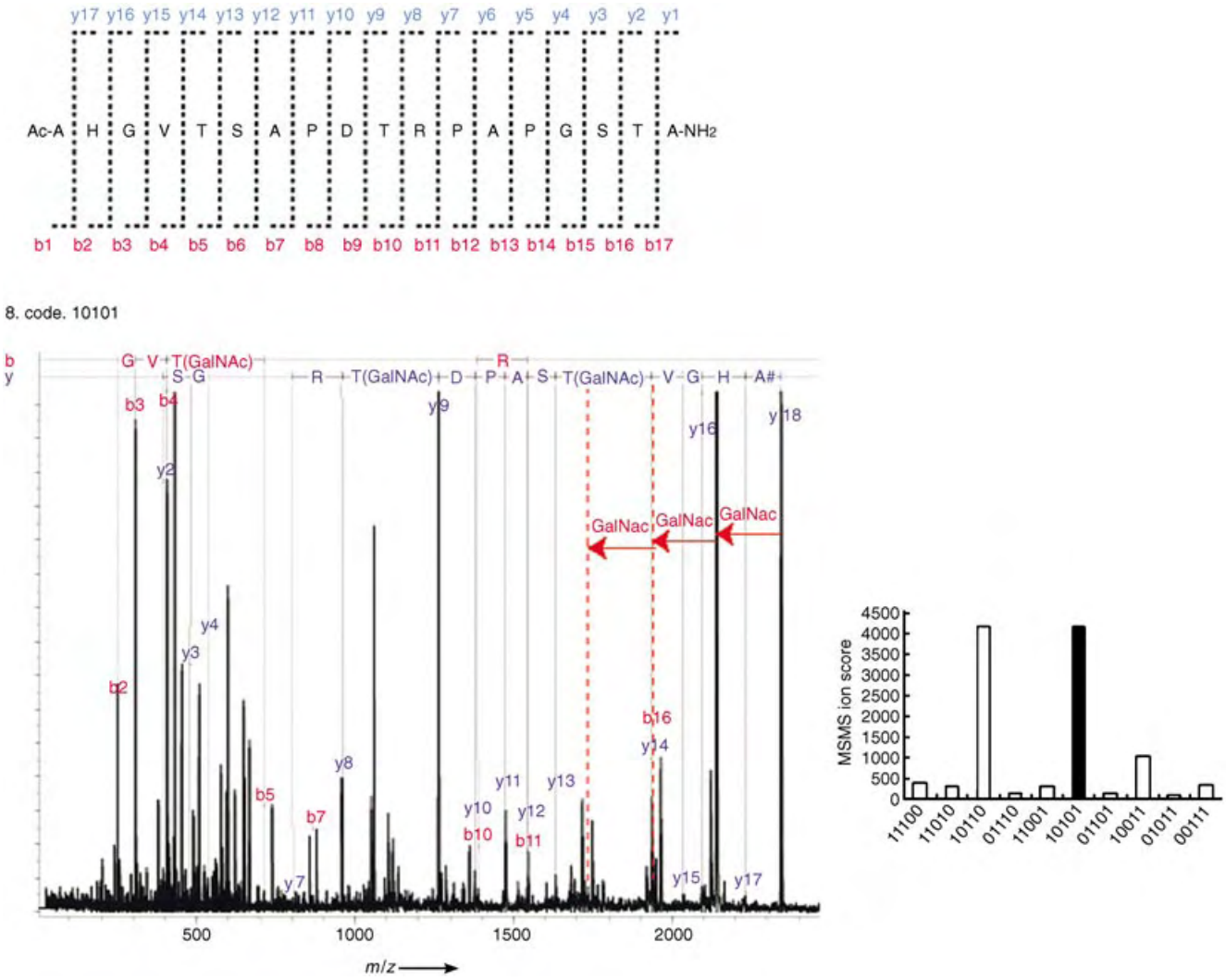
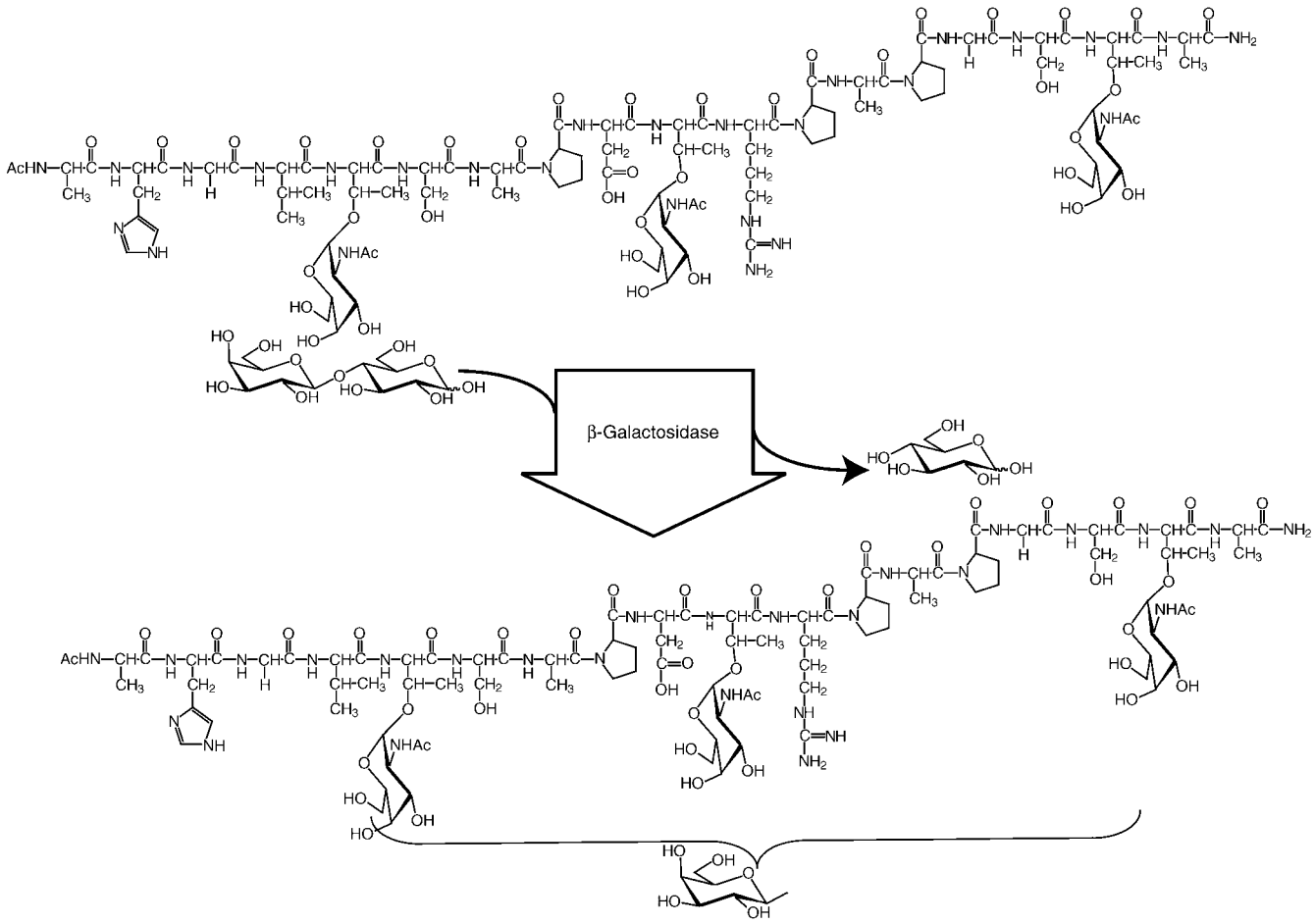


Figure 3. Precise analysis of LIFT-TOF/TOF spectra and MOWSE scoring for compound **8**.

 © 2004 Wiley-VCH Verlag GmbH & Co. KGaA, Weinheim



Scheme 1. The transglycosylation reaction of compound **8** catalyzed by β-galactosidase in the presence of lactose as a glycosyl donor.

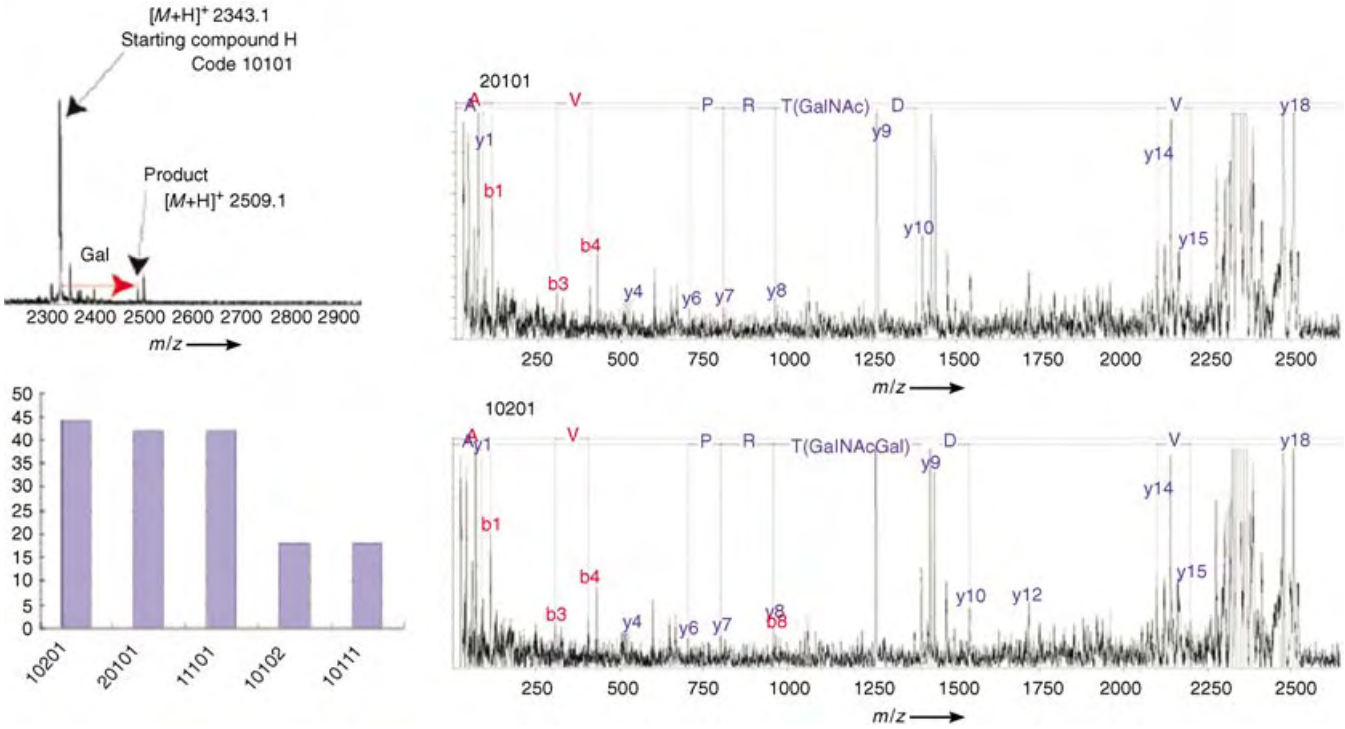


Figure 4. Transglycosylation reaction catalyzed by β-galactosidase with glycopeptide **8** and identification of sugar elongation site(s) by LIFT-TOF/TOF MS.

 © 2004 Wiley-VCH Verlag GmbH & Co. KGaA, Weinheim

In conclusion, we have found that MALDI-LIFT-TOF/TOF spectrometry in the presence of a DHB matrix gives highly sensitive and ideal fragmentation patterns (b and y series of ions) generated from glycopeptide precursor ion peaks and they can be readily used for precise and reliable structure analyses including the identification of O-glycosylation sites of mucin-type glycopeptide derivatives. The merit of the present strategy is that the combined use of the fragmentation behavior of unknown glycopeptides and database searching of peptide mass fingerprints will greatly contribute to high-throughput proteomics research in terms of the post-translational modifications on functional proteins. In addition, this method could also be applied for screening systems of chemical and enzymatic synthesis of glycopeptides and glycoproteins in a combinatorial synthetic manner as preliminarily demonstrated in Figure 4.

Received: March 17, 2004 [Z460020]

Keywords: glycosylation · high-throughput screening · mass spectrometry · protein modifications · proteomics

[1] T. Keough, R. S. Youngquist, M. P. Lacey, *Anal. Chem.* **2003**, *75*, 156–165.
[2] a) T. Kouzarides, *EMBO. J.* **2000**, *19*, 1176–1179; b) A. E. McBridge, P. A. Silver, *Cell* **2001**, *106*, 5–8; c) L, Wells, K. Vosseller, G. W. Hart, *Science* **2001**, *291*, 2376–2378.
[3] a) K. Hankansson, H. J. Cooper, M. R. Emmett, C. E. Costello, A. G. Marshall, C. L. Nilsson, *Anal. Chem.* **2001**, *73*, 4530–4536; b) K. Hankansson, M. J. Chalmers, J. P. Quinn, M. A. McFarland, C. L. Hendrickson, A. G. Marshall, *Anal. Chem.* **2003**, *75*, 3256–3262.
[4] a) S. Muller, S. Goletz, N. Packer, A. Gooley, A. M. Lawson, F.-G. Hanisch, *J. Biol. Chem.* **1997**, *272*, 24780–24793; b) S. Goletz, B. Thiede, F.-G. Hanisch, M. Schultz, J. Peter-Katalinic, S. Muller, O. Seitz, U. Karsten, *Glycobiology* **1997**, *7*, 881–896; c) F.-G. Hanisch, B. N. Green, R. Bateman, J. Peter-Katalinic, *J. Mass Spectrom.* **1998**, *33*, 358–362; d) R. G. Gallego, G. Dudziak, U. Kragl, C. Wandrey, J. P. Kamerling, J. F. G. Vliegenthart, *Biochimie* **2003**, *85*, 275–286.
[5] a) K. D. Greis, B. K. Hayes, F. I. Comer, M. Kirk, S. Barnes, T. L. Lowary, G. W. Hart, *Anal. Biochem.* **1996**, *234*, 38–49; b) L. Wells, K. Vosseller, R. N. Cole, J. M. Cronshaw, M. J. Matunis, G. W. Hart, *Mol. Cell. Proteomics* **2002**, *1*, 791–804.
[6] a) D. M. Coltart, A. K. Royyuru, L. J. Williams, P. W. Glunz, D. Sames, S. D. Kuduk, J. B. Schwarz, X.-T. Chen, S. J. Danishefsky, D. H. Live, *J. Am. Chem. Soc.* **2002**, *124*, 9833–9844; b) Y. Tachibana, G. L. Fletcher, N. Fujitani, S. Tsuda, K. Monde, S.-I. Nishimura, *Angew. Chem.* **2004**, *116*, 874–880; *Angew. Chem. Int. Ed.* **2004**, *43*, 856–862.
[7] a) T. Ohta, N. Miura, N. Fujitani, F. Nakajima, K. Niikura, R. Sadamoto, C.-T. Guo, T. Suzuki, K. Monde, S.-I. Nishimura, *Angew. Chem.* **2003**, *115*, 5344–5347; *Angew. Chem. Int. Ed.* **2003**, *42*, 5186–5189; b) M. Sato, R. Sadamoto, K. Niikura, K. Monde, H. Kondo, S.-I. Nishimura, *Angew. Chem.* **2004**, *116*, 1542–1546; *Angew. Chem. Int. Ed.* **2004**, *43*, 1516–1520; c) M. Kurogochi, S.-I. Nishimura, Y. C. Lee, *J. Biol. Chem.* **2004**, submitted.
[8] V. Schnaible, S. Wefing, A. Resemann, D. Suckau, A. Bucker, S. Wolf-Kummeth, D. Hoffmann, *Anal. Chem.* **2002**, *74*, 4980–4988.
[9] D. Suckau, A. Resemann, M. Schuerenberg, P. Hufnagel, J. Franzen, A. Holle, *Anal. Bioanal. Chem.* **2003**, *376*, 952–965.
[10] a) N. Xu, Z.-H. Huang, B. L. M. de Jonge, D. A. Gage, *Anal. Chem.* **1997**, *248*, 7–14; b) A. Tsarbopoulos, U. Bahr, B. N. Pramanik, M. Karas, *Int. J. Mass Spectrom. Ion Processes* **1997**, *169*/170, 251–261; c) R. J. Chalkley, A. L. Burlingame, *J. Am. Soc. Mass Spectrom.* **2001**, *12*, 1106–1113; d) R. J. Chalkley, A. L. Burlingame, *Mol. Cell. Proteomics* **2003**, *2*, 182–190.

 © 2004 Wiley-VCH Verlag GmbH & Co. KGaA, Weinheim

Asymmetric Catalysis

Directed Evolution as a Method To Create Enantioselective Cyclohexanone Monooxygenases for Catalysis in Baeyer–Villiger Reactions**

Manfred T. Reetz, Birgit Brunner, Toni Schneider, Frank Schulz, Christopher M. Clouthier, and Margaret M. Kayser*

Dedicated to Professor Jean-Marie Lehn on the occasion of his 65th birthday

The Baeyer–Villiger (BV) reaction of ketones with hydroperoxides affords the corresponding esters or lactones.[1] The reaction is accelerated by acids, bases, or metal complexes, and enantioselective catalysis is possible in certain cases.[1,2] Alternatively, flavin-dependent enzymes such as cyclohexanone monooxygenases (CHMOs) can be used as biocatalysts in asymmetric BV reactions.[3,4] In this enzymatic process dioxygen (air) reacts with the enzyme-bound flavin (FAD) to form an intermediate hydroperoxide, which in the deprotonated form initiates the BV reaction by transferring one oxygen atom originating from O_2 to the substrate (ketone), the other being ultimately reduced to water.[3–6] This means that the flavin co-factor needs to be recycled by reduction, the second co-factor NADPH taking over this function. Consequently, when employing the isolated CHMOs, NADPH has to be recycled. Although NADPH recycling systems are well known,[3] it is currently more convenient to use whole cells expressing CHMO. This process has been employed successfully for a number of enantioselective BV reactions, such as kinetic resolution and desymmetrization of prochiral substrates.[4,6] Of course, many ketones fail to react with accept-

[*] Prof. Dr. M. T. Reetz, B. Brunner, T. Schneider, F. Schulz
Max-Planck-Institut für Kohlenforschung
Kaiser-Wilhelm-Platz 1, 45470 Mülheim/Ruhr (Germany)
Fax: (+49) 208-306-2985
E-mail: reetz@mpi-muelheim.mpg.de

C. M. Clouthier, Prof. Dr. M. M. Kayser
Department of Physical Sciences
The University of New Brunswick
Post Office Box 5050, Saint John, NB, E2L4L5 (Canada)

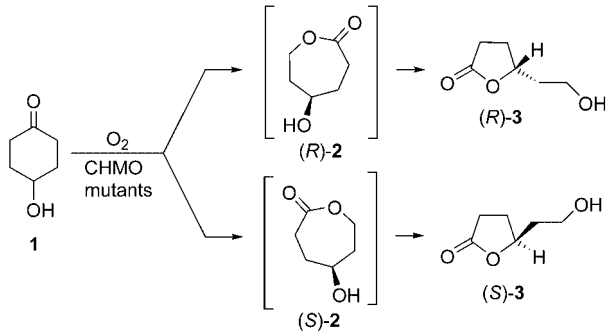
[**] We thank the Fonds der Chemischen Industrie for generous support.

Supporting information for this article is available on the WWW under http://www.angewandte.org or from the author.

 DOI: 10.1002/anie.200460272 © 2004 Wiley-VCH Verlag GmbH & Co. KGaA, Weinheim

able levels of enantioselectivity. Here we show that the methods of directed evolution[7] encompassing repetitive cycles of gene mutagenesis, expression, and screening are ideally suited to solve this problem. Previously we demonstrated that this new approach to asymmetric catalysis can be used to evolve enantioselective lipases[8] and epoxide hydrolases,[9] and that the lessons learned from directed evolution following appropriate theoretical analysis provide valuable structural and mechanistic insights.[10]

For our study we chose the desymmetrization of 4-hydroxycyclohexanone (**1**) as the model reaction and the CHMO from *Acinetobacter* sp. NCIMB 9871 (EC 1.14.13.22)[5b] as the "Baeyer–Villigerase", specifically whole-cell preparations of *E. coli* expressing this recombinant enzyme.[11] The BV reaction of ketone **1** leads to the lactone (*R*)/(*S*)-**2**, which spontaneously rearranges to (*R*)/(*S*)-**3** without change in stereochemistry. The primary process provides an enantiomeric excess (9% *ee*; wild-type) of (*R*)-**3**, which is opposite to the usual *S* selectivity that is generally observed for 4-substituted cyclohexanone derivatives using this enzyme as a catalyst.[3–6]



As in our previous studies on directed evolution of enantioselective enzymes,[8,9] we began exploring protein sequence space by applying the error-prone polymerase chain reaction (epPCR) as the mutagenesis method.[7,12] Accordingly, several libraries of mutant CHMO genes were produced under different epPCR conditions. In doing so the $MgCl_2$ concentration and other parameters were varied which led to different mutagenesis rates.[12] After insertion of the genes into the *E. coli* host,[11] plating on agar plates, and harvesting the bacterial colonies with the help of a colony picker, the whole cells were placed in the deep wells of 96-format microtiter plates and used as biocatalysts in the model reaction. The product was extracted with ethyl acetate by using robotic equipment followed by analysis by using an adapted form of our previously described medium-throughput GC-based screening system,[13] which allows about 800 *ee*-determinations per day.

Upon screening a total of 10000 mutants, at least two dozen hits showed enhanced *R* selectivity, while about one dozen mutants displayed reversal of enantioselectivity in favor of (*S*)-**3**. A total of eight mutants were sequenced (Table 1), in which between one and three amino acids were exchanged.

Table 1: Altered CHMO mutants identified in the first round of epPCR (reaction time: 24 h; 23–25 °C; >95% conversion).

Mutant	Amino acid exchanges	Favored enantiomer of **3**	*ee* [%]
wild-type	–	*R*	9
1-C2-B7	F432Y, K500R	*R*	34
1-F1-F5	L143F	*R*	40
1-E12-B5	F432I	*R*	49
1-H7-F4	L426P, A541V	*R*	54
1-H3-C9	L220Q, P428S, T433A	*S*	18
1-F4-B9	D41N, F505Y	*S*	46
1-K6-G2	K78E, F432S	*S*	78
1-K2-F5	F432S	*S*	79

Evolutionary optimization of *R* selectivity was then attempted by using the genes of some of the *R*-selective mutants as starting points for a second round of epPCR. In each case about 1600 mutants were screened. Although a systematic search was not strived for at this stage, this strategy turned out to be successful. In the case of 1-F1-F5 (40% *ee*), which is characterized by a single mutation L143F, a second round of epPCR led to a markedly improved mutant (2-D19-E6). The latter catalyzes the BV reaction with an *ee* value of 90% in favor of (*R*)-**3**. Sequencing revealed that three new amino acid exchange events have occurred (E292G, L435Q, T464A) in addition to the already existing L143F mutation.

Previous research has shown that the mechanism of the CHMO-catalyzed BV reaction is similar to that of the classical synthetic process under basic conditions[1] in that the hydroperoxide anion adds nucleophilically to the carbonyl moiety followed by σ-bond migration.[3–6] The fundamental difference is that in the enzymatic reaction the process occurs in the protein environment (Figure 1). As stereoselective σ-bond migration proceeds, a geometric change can be anticipated that accompanies ring expansion. One factor that will

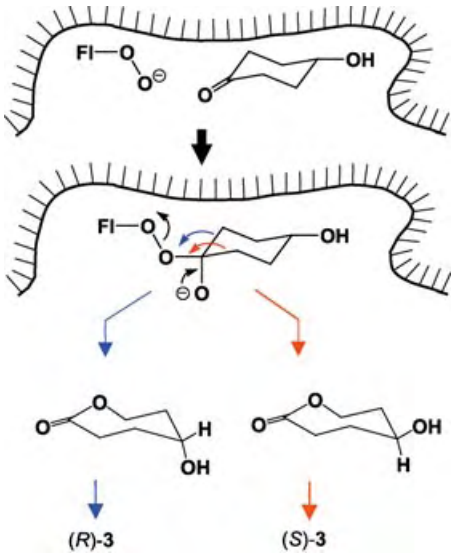
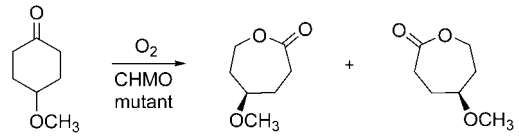


Figure 1. Scheme for the CHMO-catalyzed Baeyer–Villiger reaction of 4-hydroxycyclohexanone (Fl = flavin). Migration of the enantiotopic σ-bond indicated by the blue arrow leads to (*R*)-**3**, whereas migration of the other σ-bond (red arrow) initiates the formation of (*S*)-**3**.

 © 2004 Wiley-VCH Verlag GmbH & Co. KGaA, Weinheim

influence enantioselectivity in the present case is the fact that the two ring expansion modes place the 4-hydroxy moiety with its potential H-bond donor capability in two different protein environments prior to rearrangement. Since crystallographic data on the wild-type CHMO is not available at this time, we refrain from more detailed speculations regarding models that have been proposed in other CHMO-catalyzed BV reactions.[14] We do not yet have kinetic data concerning the catalytic activity of the various mutants, although all of them induce >95% conversion under the standard conditions (24 h, 23–25 °C).

Directed evolution of an enantioselective enzyme for a given substrate does not necessarily mean narrow substrate acceptance.[8] To study this important aspect, the catalytic performance of some of the evolved mutants was examined in the BV reaction of various 4-substituted cyclohexanone derivatives that lead to the corresponding seven-membered lactones. We regarded 4-methoxycyclohexanone (**4**) to be of particular interest, because the methoxy group can function as a hydrogen acceptor, but not as a hydrogen donor.



4 (*R*)-**5** (*S*)-**5**

The wild-type CHMO from *Acinetobacter* sp. NCIMB 9871 catalyzes the BV reaction of ketone **4** with *S* selectivity (78% *ee*), similar to certain 4-alkyl derivatives of cyclohexanone.[11] This means that all of these substrates show the opposite enantioselectivity relative to that of the hydroxy substrate **1**. Mutant 2-D19-E6, which had previously been shown to be highly *R* selective in the reaction of hydroxy ketone **1** (90% *ee*), leads to a low degree of enantioselectivity in the reaction of the methoxy ketone **4** (25% *ee* in favor of (*R*)-**5**). In contrast, the most *S*-selective mutant (1-K2-F5) in the reaction of **1** (Table 1) shows essentially complete enantioselectivity when catalyzing the BV reaction of **4** (98.6% *ee* in favor of (*S*)-**5**). These observations suggest that this mutant has undergone an amino acid substitution as a consequence of which an additional hydrogen bond is formed to the methoxy moiety in the transition state of the reaction of **4** and/or shape complementarity is allowed. Indeed, 1-K2-F5 is characterized by a single amino acid substitution at position 432, serine replacing phenylalanine (F432S).

We then studied the catalytic performance of mutant 1-K2-F5 in the BV reaction of other 4-substituted cyclohexanone derivatives, such as the methyl, ethyl, chloro, bromo, and iodo compounds that are known to be converted by the wild-type CHMO with 95–99% *ee*.[15] In no case did we observe any substantial reduction in enantioselectivity. Thus, this mutant accepts a relatively wide range of substrates and catalyzes conversion with 95–99% *ee*.

Since amino acid number 432 seems to be a particularly sensitive "hot spot", hosting a mutation in four different CHMO variants (Table 1), we performed saturation mutagenesis at this position. We expect all of the theoretically possible 20 mutants to be present in the 300–400 bacterial colonies studied. This mini-library was then screened in the BV reaction of **1**. Several mutants displaying altered enantioselectivity were identified and sequenced, including two *R*-selective variants, 1-D10 (F432Y; 17% *ee*) and 4-D11 (F432P; 72% *ee*), and two *S*-selective counterparts, 1-C8(F432G; 17% *ee*) and 1-D5 (F432S; 79% *ee*). 1-D5 is identical to 1-K2-F5 that had been created and identified in the first cycle of epPCR. As shown in the following paper in this issue, this mutant also catalyzes the enantioselective oxidation of prochiral thioethers.[16]

In summary, we have demonstrated that the methods of directed evolution can be applied successfully to the creation of enantioselective cyclohexanone monooxygenases as catalysts in Baeyer–Villiger reactions of several different substrates, for which the enantioselectivity ranges between 90% and 99%.[17] This was accomplished without any knowledge of the three-dimensional structure of the enzyme, which would not be possible in a traditional approach based on "rational design".[3] So far only a small portion of protein sequence space has been explored, the total number of mutants screened being less than 20000. Crystallographic data of the wild-type CHMO and of the enantioselective mutants would be of great interest for a sound theoretical analysis.

Received: April 8, 2004 [Z460272]

Keywords: asymmetric catalysis · Baeyer–Villiger reactions · directed evolution · enzyme catalysis · protein engineering

[1] a) G. R. Krow, *Org. React. (N. Y.)* **1993**, *43*, 251–798; b) M. Renz, B. Meunier, *Eur. J. Org. Chem.* **1999**, 737–750; c) G. Strukul, *Angew. Chem.* **1998**, *110*, 1256–1267; *Angew. Chem. Int. Ed.* **1998**, *37*, 1198–1209.

[2] a) C. Bolm, G. Schlingloff, K. Weickhardt, *Angew. Chem.* **1994**, *106*, 1944–1946; *Angew. Chem. Int. Ed. Engl.* **1994**, *33*, 1848–1849; b) A. Gusso, C. Baccin, F. Pinna, G. Strukul, *Organometallics* **1994**, *13*, 3442–3451; c) C. Bolm, G. Schlingloff, *J. Chem. Soc. Chem. Commun.* **1995**, 1247–1248; d) C. Bolm, G. Schlingloff, F. Bienewald, *J. Mol. Catal. A: Chem.* **1997**, *117*, 347–350; e) C. Bolm, T. K. K. Luong, G. Schlingloff, *Synlett* **1997**, 1151–1152; f) G. Strukul, A. Varagnolo, F. Pinna, *J. Mol. Catal. A: Chem.* **1997**, *117*, 413–423; g) C. Bolm, O. Beckmann, T. Kühn, C. Palazzi, W. Adam, P. B. Rao, C. R. Saha-Möller, *Tetrahedron: Asymmetry* **2001**, *12*, 2441–2446; h) T. Uchida, T. Katsuki, *Tetrahedron Lett.* **2001**, *42*, 6911–6914; i) C. Bolm, O. Beckmann, A. Cosp, C. Palazzi, *Synlett* **2001**, 1461–1463; j) C. Bolm, O. Beckmann, C. Palazzi, *Can. J. Chem.* **2001**, *79*, 1593–1597; k) T. Uchida, T. Katsuki, K. Ito, S. Akashi, A. Ishii, T. Kuroda, *Helv. Chim. Acta* **2002**, *85*, 3078–3089; l) K. Ito, A. Ishii, T. Kuroda, T. Katsuki, *Synlett* **2003**, 643–646.

[3] a) K. Drauz, H. Waldmann, *Enzyme Catalysis in Organic Synthesis: A Comprehensive Handbook*, Vol. *I*-III, 2nd ed., VCH, Weinheim, **2002**; b) K. Faber, *Biotransformations in Organic Chemistry*, 4th ed., Springer, Berlin, **2000**.

[4] Reviews of enzymatic BV reactions: a) M. D. Mihovilovic, B. Müller, P. Stanetty, *Eur. J. Org. Chem.* **2002**, 3711–3730; b) J. D. Stewart, *Curr. Org. Chem.* **1998**, *2*, 195–216; c) A. Willetts, *Trends Biotechnol.* **1997**, *15*, 55–62; d) S. D. Doig, L. M. O'Sullivan, S. Patel, J. M. Ward, J. M. Woodley, *Enzyme Microb. Technol.* **2001**, *28*, 265–274; e) J. D. Stewart, *Curr.*

 © 2004 Wiley-VCH Verlag GmbH & Co. KGaA, Weinheim

Org. Chem. **1998**, *2*, 195 – 216; f) S. Flitsch, G. Grogan in *Enzyme Catalysis in Organic Synthesis: A Comprehensive Handbook*, Vol. *III*, 2nd ed. (Eds.: K. Drauz, H. Waldmann) VCH, Weinheim, **2002**, p. 1202; g) N. M. Kamerbeek, D. B. Janssen, W. J. H. van Berkel, M. W. Fraaije, *Adv. Synth. Catal.* **2003**, *345*, 667-668.

[5] Isolation, characterization and/or mechanistic studies of CHMOs as whole cells or isolated enzymes: a) G. E. Turfitt, *Biochem. J.* **1948**, *42*, 376 – 383; b) N. A. Donoghue, D. B. Norris, P. W. Trudgill, *Eur. J. Biochem.* **1976**, *63*, 175 – 192; c) J. M. Schwab, W. B. Li, L. P. Thomas, *J. Am. Chem. Soc.* **1983**, *105*, 4800 – 4808; d) C. T. Walsh, Y.-C. J. Chen, *Angew. Chem.* **1988**, *100*, 342 – 352; *Angew. Chem. Int. Ed. Engl.* **1988**, *27*, 333 – 343; e) P. C. Brzostowicz, D. M. Walters, S. M. Thomas, V. Nagarajan, P. E. Rouvière, *Appl. Environ. Microbiol.* **2003**, 334 – 342.

[6] Synthetic applications of CHMOs in BV reactions:[4,5] a) M. J. Taschner, D. J. Black, *J. Am. Chem. Soc.* **1988**, *110*, 6892 – 6893; b) V. Alphand, R. Furstoss, S. Pedragosa-Moreau, S. M. Roberts, A. J. Willetts, *J. Chem. Soc. Perkin Trans. 1* **1996**, 1867 – 1872; c) J. D. Stewart, K. W. Reed, J. Zhu, G. Chen, M. M. Kayser, *J. Org. Chem.* **1996**, *61*, 7652 – 7653; d) M. D. Mihovilovic, B. Müller, A. Schulze, P. Stanetty, M. M. Kayser, *Eur. J. Org. Chem.* **2003**, 2243 – 2249.

[7] a) F. H. Arnold, *Nature* **2001**, *409*, 253 – 257; b) K. A. Powell, S. W. Ramer, S. B. del Cardayré, W. P. C. Stemmer, M. B. Tobin, P. F. Longchamp, G. W. Huisman, *Angew. Chem.* **2001**, *113*, 4068 – 4080; *Angew. Chem. Int. Ed.* **2001**, *40*, 3948 – 3959; c) S. Brakmann, K. Johnsson, *Directed Molecular Evolution of Proteins (or How to Improve Enzymes for Biocatalysis)*, Wiley-VCH, Weinheim, **2002**; d) F. H. Arnold, G. Georgiou, *Directed Enzyme Evolution: Screening and Selection Methods, in Methods and Molecular Biology, Vol. 230*, Humana, Totowa, **2003**.

[8] a) M. T. Reetz, A. Zonta, K. Schimossek, K. Liebeton, K.-E. Jaeger, *Angew. Chem.* **1997**, *109*, 2961 – 2963; *Angew. Chem. Int. Ed. Engl.* **1997**, *36*, 2830 – 2832; b) M. T. Reetz, S. Wilensek, D. Zha, K.-E. Jaeger, *Angew. Chem.* **2001**, *113*, 3701 – 3703; *Angew. Chem. Int. Ed.* **2001**, *40*, 3589 – 3591; c) M. T. Reetz, *Tetrahedron* **2002**, *58*, 6595 – 6602; d) M. T. Reetz, *Proc. Natl. Acad. Sci.* **2004**, *101*, 5716 – 5722.

[9] a) F. Cedrone, S. Niel, S. Roca, T. Bhatnagar, N. Ait-Abdelkader, C. Torre, H. Krumm, A. Maichele, M. T. Reetz, J. C. Baratti, *Biocatal. Biotransform.* **2003**, *21*, 357 – 364; b) M. T. Reetz, C. Torre, A. Eipper, R. Lohmer, M. Hermes, B. Brunner, A. Maichele, M. Bocola, M. Arand, A. Cronin, Y. Genzel, A. Archelas, R. Furstoss, *Org. Lett.* **2004**, *6*, 177 – 180.

[10] M. Bocola, N. Otte, K.-E. Jaeger, M. T. Reetz, W. Thiel, *ChemBioChem* **2004**, *5*, 214 – 223.

[11] a) J. D. Stewart, K. W. Reed, C. A. Martinez, J. Zhu, G. Chen, M. M. Kayser, *J. Am. Chem. Soc.* **1998**, *120*, 3541 – 3548; b) G. Chen, M. M. Kayser, M. D. Mihovilovic, M. E. Mrstik, C. A. Martinez, J. D. Stewart, *New J. Chem.* **1999**, *23*, 827 – 832.

[12] a) D. W. Leung, E. Chen, D. V. Goeddel, *Technique (Philadelphia)* **1989**, *1*, 11 – 15; b) R. C. Cadwell, G. F. Joyce, *PCR Methods Appl.* **1992**, *2*, 28 – 33.

[13] a) M. T. Reetz, K. M. Kühling, S. Wilensek, H. Husmann, U. W. Häusig, M. Hermes, *Catal. Today* **2001**, *67*, 389 – 396; b) Review of high-throughput *ee*-assays: M. T. Reetz, *Angew. Chem.* **2001**, *113*, 292 – 320; *Angew. Chem. Int. Ed.* **2001**, *40*, 284 – 310.

[14] a) S. Wang, M. M. Kayser, V. Jurkauskas, *J. Org. Chem.* **2003**, *68*, 6222 – 6228; b) D. R. Kelly, C. J. Knowles, J. G. Mahdi, I. N. Taylor, M. A. Wright, *J. Chem. Soc. Chem. Commun.* **1995**, 729 – 730; c) R. Furstoss in *Microbial Reagents* in *Organic Synthesis* (Ed.: S. Servi) Kluwer, Dordrecht, **1992**, p. 333; d) M. J. Taschner, L. Peddada, P. Cyr, Q. Z. Chen, D. J. Black in *Microbial Reagents in Organic Synthesis* (Ed.: S. Servi)) Kluwer, Dordrecht, **1992**, p. 347; e) G. Ottolina, P. Pasta, G. Carrea, S. Colonna, S. Dallavalle, H. L. Holland, *Tetrahedron: Asymmetry* **1995**, *6*, 1375 – 1386; f) G. Ottolina, G. Carrea, S. Colonna, A. Rückemann, *Tetrahedron: Asymmetry* **1996**, *7*, 1123 – 1136.

[15] a) M. D. Mihovilovic, G. Chen, S. Wang, B. Kyte, F. Rochon, M. M. Kayser, J. D. Stewart, *J. Org. Chem.* **2001**, *66*, 733 – 738; b) S. Wang, Dissertation, University of New Brunswick, **2003**.

[16] M. T. Reetz, F. Daligault, B. Brunner, H. Hinrichs, A. Deege, *Angew. Chem.* **2004**, *116*, DOI: 10.1002/ange.200460311; *Angew. Chem. Int. Ed.* **2004**, *43*, DOI: 10.1002/anie.200460311.

[17] Other examples of directed evolution of enantioselective enzymes (although in some cases only a single round of epPCR was performed which is not an evolutionary process):[9] a) G. W. Matcham, A. R. S. Bowen, *Chim. Oggi* **1996**, *14(6)*, 20 – 24; b) S. Fong, T. D. Machajewski, C. C. Mak, C.-H. Wong, *Chem. Biol.* **2000**, *7*, 873 – 883; c) E. Henke, U. T. Bornscheuer, *Biol. Chem.* **1999**, *380*, 1029 – 1033; d) O. May, P. T. Nguyen, F. H. Arnold, *Nat. Biotechnol.* **2000**, *18*, 317 – 320; e) G. P. Horsman, A. M. F. Liu, E. Henke, U. T. Bornscheuer, R. J. Kazlauskas, *Chem. Eur. J.* **2003**, *9*, 1933 – 1939; f) G. DeSantis, K. Wong, B. Farwell, K. Chatman, Z. Zhu, G. Tomlinson, H. Huang, X. Tan, L. Bibbs, P. Chen, K. Kretz, M. J. Burk, *J. Am. Chem. Soc.* **2003**, *125*, 11476 – 11477; g) M. W. Peters, P. Meinhold, A. Glieder, F. H. Arnold, *J. Am. Chem. Soc.* **2003**, *125*, 13442 – 13450; h) R. Carr, M. Alexeeva, A. Enright, T. S. C. Eve, M. J. Dawson, N. J. Turner, *Angew. Chem.* **2003**, *115*, 4955 – 4958; *Angew. Chem. Int. Ed.* **2003**, *42*, 4807 – 4810.

 © 2004 Wiley-VCH Verlag GmbH & Co. KGaA, Weinheim

Asymmetric Catalysis

Directed Evolution of Cyclohexanone Monooxygenases: Enantioselective Biocatalysts for the Oxidation of Prochiral Thioethers**

Manfred T. Reetz, Franck Daligault, Birgit Brunner, Heike Hinrichs, and Alfred Deege*

In the preceding communication in this issue we reported that the methods of directed evolution can be used to evolve enantioselective mutants of the cyclohexanone monooxygenase (CHMO) from *Acinetobacter* sp. NCIMB 9871 (EC 1.14.13.22)[1] as catalysts in the Baeyer–Villiger (BV) reaction of 4-hydroxycyclohexanone and other 4-substituted cyclohexanone derivatives.[2] Since the isolated form of this flavin-dependent enzyme requires co-factor regeneration, we preferred to use whole cells, dioxygen from air serving as the oxidant. In view of the well-known fact that CHMOs can also

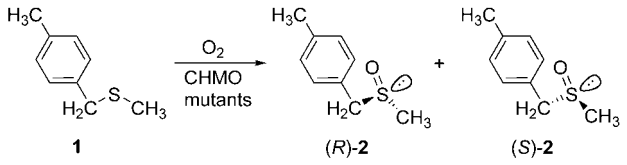
[*] Prof. Dr. M. T. Reetz, Dr. F. Daligault, B. Brunner, H. Hinrichs, A. Deege
Max-Planck-Institut für Kohlenforschung
Kaiser-Wilhelm-Platz 1, 45470 Mülheim/Ruhr (Germany)
Fax: (+49) 208-306-2985
E-mail: reetz@mpi-muelheim.mpg.de

[**] We thank the Fonds der Chemischen Industrie for generous support and the EU for a Marie Curie Stipend ("Improving Human Potential", HPMF-CT-2002-01975). Support from the "Conseil Régional de Bretagne is also acknowledged.

Supporting information for this article is available on the WWW under http://www.angewandte.org or from the author.

 © 2004 Wiley-VCH Verlag GmbH & Co. KGaA, Weinheim DOI: 10.1002/anie.200460311

be used as a catalyst in the enantioselective air-oxidation of certain prochiral thioethers with formation of chiral sulfoxides,[1,3] we posed the question whether directed evolution can be applied in the quest to enhance enantioselectivity in "difficult" cases of this reaction type, that is, when the wild-type enzyme results in poor *ee* values. As an example, we chose the oxidation of methyl-*p*-methylbenzyl thioether (**1**) with formation of the chiral sulfoxide **2**, the wild-type CHMO from *Acinetobacter* sp. NCIMB 9871 leading to an *ee* of only 14% in favor of (*R*)-**2**.[3b] It was of practical and theoretical interest to evolve both *S*- and *R*-selective CHMOs, because this allows for enantiodivergence on an optional basis.



As in our previous studies on the directed evolution of enantioselective enzymes,[2,4] we started the exploration of protein sequence space by applying error-prone polymerase reaction (epPCR).[5] However, since the first round of epPCR has no evolutionary character, new mutagenesis experiments were not necessary, that is, we initially used the mutant CHMOs produced previously.[2]

The development of an appropriate *ee* assay was not a trivial task, because previously devised high-throughput screening systems[6] were not easily adaptable in the present case. We finally modified a commercially available HPLC instrument equipped with a sample manager and the appropriate software to handle 96- (or 384-)well microtiter plates. Since enantiomeric separation of (*R*)-**2**/(*S*)-**2** has to be fast and efficient, exploratory experiments were performed by using a variety of different chiral stationary phases, solvents, and conditions. An efficient system turned out to be benzoylated cellulose as the stationary phase with a mixture of *n*-heptane and ethanol as the mobile phase. For rapid analysis short columns 50 mm in length and 4.5 mm in diameter were used. This system allows at least 800 *ee*-determinations per day. Unfortunately, the *E. coli*-based expression system[7] produces small amounts of indole,[8] which leads to an overlap with the HPLC peak of (*S*)-**2**. Although this can be considered in the quantitative evaluation, the *ee* values accessible under these conditions are not precise and were consequently used only to identify hits. These were subsequently analyzed by a similar HPLC setup using a longer column (250 mm) that allows about 40 precise *ee*-determinations per day.

There was no reason to believe that the most enantioselective CHMO mutants evolved in our previous study concerning the BV reaction of cyclohexanone derivatives[2] should also function well as biocatalysts in a completely different reaction type involving a thioether that has no structural similarity with the previously used cyclohexanone-derived substrates. Therefore we did not focus on the original hits,[2] but rather screened the complete 10000-membered library.[2] This led to the discovery of at least 20 mutants having *ee* values in the range 85%–99%, some being *R*- and others being *S*-selective. Five mutants resulting in *ee* values of $>95\%$ were sequenced (Table 1).[3c]

Table 1: Selected mutant CHMOs from *Acinetobacter* sp. NCIMB 9871 for the enantioselective air-oxidation of thioether **1** (24 h; 23–25 °C) using whole cells.

Mutant	Amino acid exchanges	Yield of **2** [%]	Configuration	*ee* [%]	Sulfone **3** as side product [%]
wild-type	–	75	*R*	14.0[a]	<1
1-D10-F6	D384H	75	*R*	98.9	7.9
1-K15-C1	F432S	55	*R*	98.7	20.0
1-C5-H3	K229I, L248P	77	*S*	98.1	5.6
1-H8-A1	Y132C, F246I, V361A, T415A	52	*S*	99.7	26.6
1-J8-C5	F16L, F277S	84	*S*	95.2	5.6

[a] Only 5% *ee* was obtained when the enzyme extract was used.

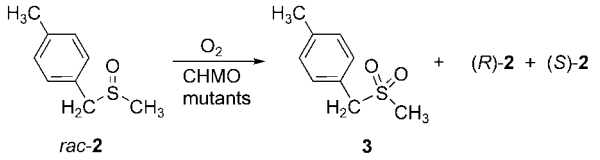
It can be seen that two mutants (1-D10-F6 and 1-K15-C1) are *R*-selective, while the other three variants (1-C5-H3, 1-H8-A1 and 1-J8-C5) induce the opposite enantioselectivity in favor of (*S*)-**2**. Sequencing studies show that between one and four amino acid exchanges have occurred. In four cases the mutants are different from those that were previously identified as hits in the BV reaction of prochiral cyclohexanone derivatives.[2] In contrast, we were surprised to learn that mutant 1-K15-C1, which leads to 98.7% *ee* in favor of (*R*)-**2**, is characterized by amino acid exchange F432S and is therefore identical to mutant 1-K2-F5 previously identified as a highly enantioselective biocatalyst in the asymmetric BV reaction of a wide range of 4-substituted cyclohexanone derivatives.[2] Thus, one and the same single mutational change at position 432, namely the introduction of serine, leads to a surprisingly versatile biocatalyst. It was identified twice by screening the same 10000-membered library in two different reaction types.

We conclude that directed evolution provides mutant CHMOs that would hardly have been obtained by traditional methods based on rational design and site-specific mutagenesis, especially because the crystal structure of the wild-type is not (yet) available.[1–3] In view of the lack of structural data it is too early to discuss the origin of enantioselectivity of 1-K15-C1 (1-K2-F5) or of the other mutants.

Careful analysis of all products formed under the conditions revealed another notable effect. In all cases small amounts of over-oxidation with formation of achiral methyl-*p*-methylbenzyl sulfone (**3**) were observed (Table 1), which could influence the degree of enantioselectivity either in a positive or a negative manner. This effect is known to occur in CHMO-catalyzed and other microbial oxidations of prochiral thioethers,[1,3,9] although it is usually small due to the low rate of over-oxidation. Depending upon the particular system, the effect can increase or decrease the final measured enantiopurity of the primary product **2**. Similar effects (positive or negative) have been reported in the titanium-catalyzed oxidation of thioethers using the Sharpless/Kagan/Modena

 © 2004 Wiley-VCH Verlag GmbH & Co. KGaA, Weinheim

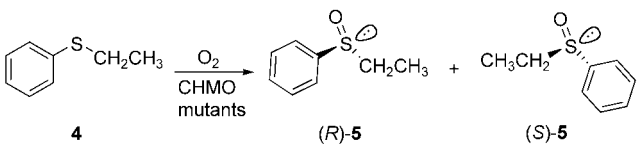
systems.[10] We therefore prepared racemic sulfoxide **2** and performed the kinetic resolution[11] using the *R*- and *S*-selective mutants 1-D10-F6 and 1-H8-A1, respectively. In both cases the usual conditions were applied (24 h; 23–25 °C), each reaction being carried out three times.



In the case of mutant 1-D10-F6 the reaction after 24 h led to 43% conversion to the sulfone **3** with concomitant enrichment of (*R*)-**2** (98.7% *ee*).[12] This means that (*S*)-**2** is consumed preferentially. Thus, in the original desymmetrization of prochiral sulfoxide **1** mutant 1-D10-F6 functions *cooperatively* in two different catalytic reactions, namely in the highly favored formation of (*R*)-**2** and in the enantioselective oxidative destruction of the opposite enantiomer (*S*)-**2**. An analogous effect was observed in the case of mutant 1-H8-A1, which after a 24 h reaction of *rac*-**2** leads to 62% formation of sulfone **3** with concomitant enrichment of (*S*)-**2** (98.9% *ee*). Thus, the process of random mutagenesis/screening leads to the evolution of highly enantioselective biocatalysts for two different oxidative processes, in both cases *R*- and *S*-selectivity being possible on an optional basis. In contrast, the wild-type is not only a poor catalyst in the desymmetrization of **1** (Table 1), but also fails in the oxidative kinetic resolution of *rac*-**2** (after 24 h about 18% sulfone **3** and 6% *ee* in slight favor of (*R*)-**2**).

We then attempted to apply directed evolution to reduce the amount of sulfone formation while maintaining high enantioselectivity in the desymmetrization of thioether **1**. After performing epPCR with the gene encoding mutant 1-H8-A1 and screening a library of 1600 clones for high *S* selectivity *and* low sulfone-formation, mutant 2-K11-F11 was identified. It is characterized by three of the four mutations of the parent mutant (Y132C, V361A, and T415A) and by three new amino acid exchanges Q92R, F246N, and P169 L. This mutant leads to 99.8% *ee* in favor of (*S*)-**2**, the amount of undesired sulfone **3** being almost negligible (< 5%).

Finally, to test whether the best mutant CHMOs evolved for substrate **1** are also efficient biocatalysts in the oxidation of structurally different thioethers, ethylphenyl thioether **4** was used as the substrate. The wild-type CHMO leads to an *ee* of only 47% in favor of (*R*)-**5**.[3b] Mutant 1-J8-C5 results in a pronounced enhancement of *R* selectivity (88% *ee*), whereas mutant 1-C5-H3 catalyzes the complete reversal of enantioselectivity in favor of (*S*)-**5** (98.9% *ee*).



In summary, directed evolution is ideally suited to control the direction and degree of enantioselectivity in the CHMO-catalyzed air-oxidation of prochiral thioethers. The evolved mutants showing highest enantioselectivity for the reaction of a given substrate can also be used as catalysts for other substrates. Finally, the methods of directed evolution not only provide biocatalysts for the enantioselective oxidation of thioethers, but also for the efficient kinetic resolution of racemic sulfoxides. We are currently expanding the range of substrates and reaction types catalyzed by mutant CHMOs.

Received: April 13, 2004 [Z460311]
Published Online: July 28, 2004

Keywords: asymmetric catalysis · directed evolution · enzyme catalysis · protein engineering · sulfoxides

[1] a) N. A. Donoghue, D. B. Norris, P. W. Trudgill, *Eur. J. Biochem.* **1976**, *63*, 175–192; b) C. T. Walsh, Y.-C. J. Chen, *Angew. Chem.* **1988**, *100*, 342–352; *Angew. Chem. Int. Ed. Engl.* **1988**, *27*, 333–343; c) M. D. Mihovilovic, B. Müller, P. Stanetty, *Eur. J. Org. Chem.* **2002**, 3711–3730; d) J. D. Stewart, *Curr. Org. Chem.* **1998**, *2*, 195–216; e) S. Flitsch, G. Grogan in *Enzyme Catalysis in Organic Synthesis: A Comprehensive Handbook*, Vol. *III*, 2nd ed. (Eds.: K. Drauz, H. Waldmann) VCH, Weinheim, **2002**, p. 1202.

[2] M. T. Reetz, B. Brunner, T. Schneider, F. Schulz, C. M. Clouthier, M. M. Kayser, *Angew. Chem.* **2004**, *116*, DOI: 10.1002/ange.200460311; *Angew. Chem. Int. Ed.* **2004**, *43*, DOI: 10.1002/anie.200460311.

[3] a) D. R. Light, D. J. Waxman, C. Walsh, *Biochemistry* **1982**, *21*, 2490–2498; b) G. Carrea, B. Redigolo, S. Riva, S. Colonna, N. Gaggero, E. Battistel, D. Bianchi, *Tetrahedron: Asymmetry* **1992**, *3*, 1063–1068; c) P. Pasta, G. Carrea, H. L. Holland, S. Dallavalle, *Tetrahedron: Asymmetry* **1995**, *6*, 933–936; d) V. Alphand, N. Gaggero, S. Colonna, R. Furstoss, *Tetrahedron Lett.* **1996**, *37*, 6117–6120; e) V. Alphand, N. Gaggero, S. Colonna, P. Pasta, R. Furstoss, *Tetrahedron* **1997**, *53*, 9695–9706; f) H. L. Holland, J.-X. Gu, A. Kerridge, A. Willetts, *Biocatal. Biotransform.* **1999**, *17*, 305–317; g) F. Secundo, G. Carrea, S. Dallavalle, G. Franzosi, *Tetrahedron: Asymmetry* **1993**, *4*, 1981–1982; h) G. Chen, M. M. Kayser, M. D. Mihovilovic, M. E. Mrstik, C. A. Martinez, J. D. Stewart, *New J. Chem.* **1999**, *23*, 827–832.

[4] a) M. T. Reetz, A. Zonta, K. Schimossek, K. Liebeton, K.-E. Jaeger, *Angew. Chem.* **1997**, *109*, 2961–2963; *Angew. Chem. Int. Ed. Engl.* **1997**, *36*, 2830–2832; b) M. T. Reetz, S. Wilensek, D. Zha, K.-E. Jaeger, *Angew. Chem.* **2001**, *113*, 3701–3703; *Angew. Chem. Int. Ed.* **2001**, *40*, 3589–3591; c) M. T. Reetz, *Tetrahedron* **2002**, *58*, 6595–6602; d) M. T. Reetz, *Proc. Natl. Acad. Sci. USA* **2004**, *101*, 5716–5722.

[5] a) D. W. Leung, E. Chen, D. V. Goeddel, *Technique (Philadelphia)* **1989**, *1*, 11–15; b) R. C. Cadwell, G. F. Joyce, *PCR Methods Appl.* **1992**, *2*, 28–33.

[6] a) M. T. Reetz, *Angew. Chem.* **2001**, *113*, 292–320; *Angew. Chem. Int. Ed.* **2001**, *40*, 284–310; b) M. T. Reetz, *Angew. Chem.* **2002**, *114*, 1391–1394; *Angew. Chem. Int. Ed.* **2002**, *41*, 1335–1338.

[7] J. D. Stewart, K. W. Reed, C. A. Martinez, J. Zhu, G. Chen, M. M. Kayser, *J. Am. Chem. Soc.* **1998**, *120*, 3541–3548.

[8] D. Wang, X. Ding, P. N. Rather, *J. Bacteriol.* **2001**, *183*, 4210–4216.

[9] a) B. J. Auret, D. R. Boyd, H. B. Henbest, C. G. Watson, K. Balenovic, V. Polak, V. Johanides, S. Divjak, *Phytochemistry* **1974**, *13*, 65–68; b) B. J. Auret, D. R. Boyd, F. Breen, R. M. E. Greene, P. M. Robinson, *J. Chem. Soc. Perkin Trans. 1* **1981**, 930–933; c) A. Lattanzi, P. Iannece, A. Scettri, *Tetrahedron: Asymmetry* **2004**, *15*, 413–418.

 © 2004 Wiley-VCH Verlag GmbH & Co. KGaA, Weinheim

[10] a) P. Pitchen, E. Duñach, M. N. Deshmukh, H. B. Kagan, *J. Am. Chem. Soc.* **1984**, *106*, 8188 – 8193; b) F. Di Furia, G. Modena, R. Seraglia, *Synthesis* **1984**, 325 – 327; c) H. B. Kagan, in *Catalytic Asymmetric Synthesis, 2nd Ed.* (Ed.: I. Ojima) Wiley-VCH, New York, **2000**, p. 327; d) K. P. Volcho, N. F. Salakhutdinov, A. G. Tolstikov, *Russ. J. Org. Chem.* **2003**, *39*, 1537 – 1552; e) W. Adam, F. Heckel, C. R. Saha-Möller, M. Taupp, P. Schreier, *Tetrahedron: Asymmetry* **2004**, *15*, 983 – 985.

[11] a) C.-S. Chen, Y. Fujimoto, G. Girdaukas, C. J. Sih, *J. Am. Chem. Soc.* **1982**, *104*, 7294 – 7299; b) H. B. Kagan, J. C. Fiaud, *Top. Stereochem.* **1988**, *18*, 249 – 330.

[12] We noticed some variation when computing the selectivity factor *E* according to the formula of Sih[11a] even in the conversion range of 25–45 %. Therefore, we refrain from reporting *E* values in this whole-cell system and provide conversion data and *ee* values following reactions under standard conditions (24 h at 23–25 °C).

 © 2004 Wiley-VCH Verlag GmbH & Co. KGaA, Weinheim

Single-Molecule Magnets on Silicon

Anchoring Molecular Magnets on the Si(100) Surface**

Guglielmo G. Condorelli, Alessandro Motta, Ignazio L. Fragalà, Filippo Giannazzo, Vito Raineri, Andrea Caneschi, and Dante Gatteschi*

The continuous scaling down of device size in integrated circuits (ICs) has led to many questions about the limitations (lithographic, physical, or economic) of top-down developments of microelectronic devices. On the other hand, bottom-up technologies using molecules as single data-processing devices are enormously promising in terms of storage and data-handling density, and there are reports on molecular wires, switches, rectifiers, and storage elements which, in principle, could form the basis of future molecular electronics.[1] Nevertheless any synthetic strategy towards such molecules remains useless for molecular devices unless they are ordered in a suitable and accessible way so that their state can be probed. The most promising architecture in molecular electronics is a hybrid system in which a dense array of molecular devices is hosted on a silicon-based microelectronic circuit.[2]

In the last decade, it was discovered that single molecules can be used to store magnetic information. The prototype of this class of materials, referred to as single-molecule magnets (SMMs), is the dodecamanganese(III,IV) cluster $[Mn_{12}O_{12}(OAc)_{16}(H_2O)_4]\cdot 4H_2O\cdot 2AcOH$ ($\mathbf{1}\cdot 4H_2O\cdot 2AcOH$).[3] A recent paper showed the possibility of anchoring a thiol-substituted Mn_{12} cluster on a gold substrate.[4] However, no reports have appeared to date on the possibility of anchoring the Mn_{12} cluster on a surface of technological importance, such as Si(100). Very recently, patterned Mn_{12} aggregates were deposited from solution on a silicon oxidized surface, but no indication of suitable bonding between the Si surface and the Mn_{12} cluster was reported.[5]

The Mn_{12} cluster **1** itself is not suited for direct anchoring on silicon, and therefore two different strategies can be adopted, based either on modification of the cluster with suitable functionalities capable of surface binding, or on modification of the surface with a layer capable of cluster coordination. The first approach has severe drawbacks due to the thermal instability of the Mn_{12} core, which is not well suited to classical protocols for silicon grafting.[6] In contrast, preliminary modification of the silicon surface allows anchoring of the cluster under mild conditions and thus precludes degradation of the core.

Herein we report on the anchoring of Mn_{12} SMMs on silicon by using undecanoic acid grafted on H-terminated Si(100) surfaces. Hydrosilylation of the double bond with formation of a robust Si–C bond is well documented.[6] We describe a three-step process (Scheme 1) consisting of 1) grafting of the methyl ester of 10-undecenoic acid on the silicon surface, 2) hydrolysis of the ester group, and 3) ligand exchange between $\mathbf{1}\cdot 4H_2O\cdot 2AcOH$ and the grafted undecanoic acid to anchor the Mn_{12} SMMs to the organic layer. The presence of free COOH groups atop the grafted monolayer is the key to successful anchoring of the Mn_{12} clusters.

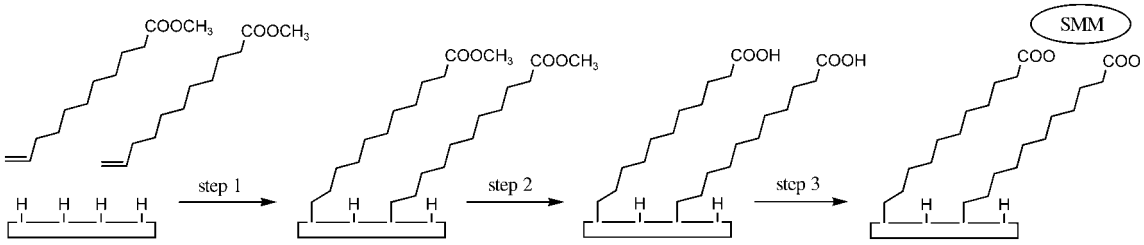
X-ray photoelectron spectroscopy (XPS), especially in angle-resolved mode, proved to be an ideal tool for characterization of the nanoscale layer and probing the depth distribution of elements and their bonding states. Therefore, each reaction step was monitored by XPS, and in all cases it provided evidence for all the expected elements in the grafted layers with associated binding energies (BEs) in excellent agreement with the expected bonding states. An XPS BE scale was calibrated by centering the Si $2p_{3/2}$ peak at 99.0 eV.[7] Thus, the weak C 1s signal of the adventitious carbon observed on the freshly HF etched Si(100) surface has a BE value of 284.5 eV, in close agreement with 284.6–285.0 eV commonly reported in the literature.[8] The Si 2p region of the samples grafted with methyl 10-undecenoate is a reliable indicator of the grafting efficiency. There is evidence of the well-resolved Si $2p_{3/2,1/2}$ spin–orbit doublet of elemental silicon, and the absence of any signal around BE = 103 eV for oxidized Si, even after several days of exposure to air, points unequivocally to efficient passivation of the surface by the ester monolayer.

Spectral features due to Si 2p after hydrolysis of the ester (step 2) and anchoring of the Mn cluster (step 3), do not

[*] Dr. G. G. Condorelli, Dr. A. Motta, Prof. I. L. Fragalà
Dipartimento di Scienze Chimiche
Università degli Studi di Catania and INSTM UdR di Catania
viale A. Doria 6, 95125 Catania (Italy)
Fax: (+39) 095-580-138
E-mail: lfragala@dipchi.unict.it
Dr. F. Giannazzo, Dr. V. Raineri
IMM, sezione di Catania, CNR
stradale Primosole 50, 95121 Catania (Italy)
Prof. A. Caneschi, Prof. D. Gatteschi
Dipartimento di Chimica
Università di Firenze and INSTM UdR di Firenze
via della Lastruccia 3, 50019 Sesto Fiorentino (Italy)

[**] The authors thank Dr. A. Cornia for stimulating discussions and the MIUR (FIRB 2001 and PRIN 2003 research programs) for financial support.

 DOI: 10.1002/anie.200453933 © 2004 Wiley-VCH Verlag GmbH & Co. KGaA, Weinheim



Scheme 1. Three-step process used for anchoring SMMs on Si(100). Conditions: step 1) mesitylene, 200 °C; step 2) H^+, H_2O, 100 °C; step 3) **1**·4 H_2O·2 AcOH, toluene, 60 °C, 100 mm Hg.

reveal appreciable surface oxidation, even though the hydrolysis reaction (step 2) requires a highly oxidizing environment (boiling water).

The relative intensity of the C 1s signal in the grafted ester is strongly enhanced relative to the freshly HF-etched surface (Figure 1 a and b), and thus corresponds to the increased

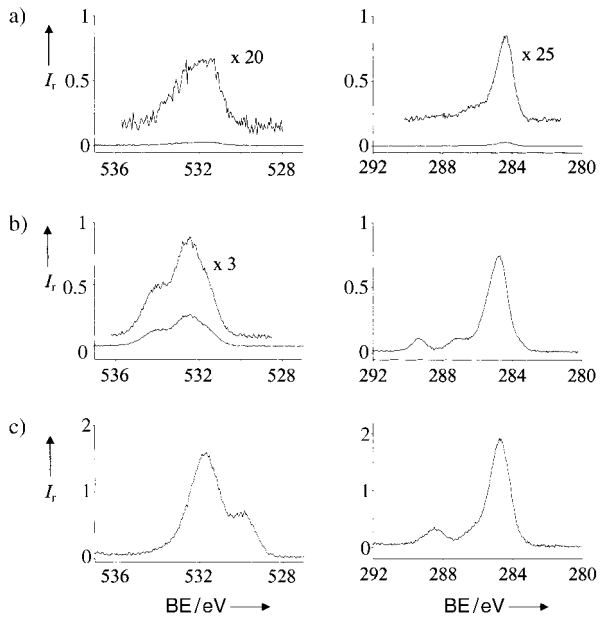


Figure 1. High-resolution XPS spectra of a) HF-etched Si(100) substrate, b) after grafting of 10-methyl undecenoate on the silicon surface, c) after hydrolysis of the ester groups followed by anchoring of Mn_{12} SMMs. Left: O 1s; Right: C 1s. The relative intensities I_r are normalized to the total Si signal.

amount of carbon due to the organic layer. Moreover, the spectrum shows a rich structure, clearly due to the presence of several bonding states. It consists of four main components, centered at 283.5 eV (the carbide Si–C bond), 284.8 eV (the aliphatic backbone), 287.2 eV (the OCH_3 groups), and 289.4 eV (the C=O groups). All these features are entirely consistent with an Si–C-grafted monolayer of methyl undecanoate. A further component at 285.8 eV is due to slightly oxidized carbon surface contaminants. This feature is apparent in all the recorded spectra and it is likely due to the chemical manipulations. The contribution of adventitious carbon to the component centred at 284.8 eV can be neglected, since it is present in small amounts on freshly HF-etched surfaces and is usually of even less relevance on organic compounds.[9]

Anchoring of the Mn cluster causes remarkable changes to the C 1s spectral region (Figure 1 c) relative to the grafted ester layer. The C 1s band has an increased intensity and shows a clear shift of the carboxy component (289.4 eV) toward lower binding energies (288.5 eV), as expected for the COO^- groups present both in coordinated acetate and undecanoate ligands. However, broadening of this band might hide any low-intensity component at 289.4 eV still present because of partial ligand exchange. Finally the shoulder at 283.6 eV is no longer visible because of the increased thickness of the grafted layer.

Similar to the C 1s peaks, the intensity of the O 1s envelope is markedly higher in the grafted layer compared to the freshly HF-etched Si(100) surface (Figure 1). In particular, in the grafted ester (Figure 1 b) the O 1s band consists of three overlapping signals. The two main components, centered at 532.7 and 534.1 eV, represent C=O and $COCH_3$ groups, respectively. Their intensity ratio is 1:1, as expected for the grafted ester. A low-intensity shoulder at 531.6 eV is due to oxygen in Si–O bonds.

In the SMM layer, the O 1s feature is resolved into three components. The bands centered at 530.1 and 531.7 eV are assigned to the $Mn_{12}O_{12}$ core and to the remaining 36 O atoms of the ligand framework.[4] Their intensity ratio of 1:3 is in agreement with the expected efficiency of substitution. The third component (at 531.6 eV) is associated with oxidized silicon.

The O:Mn atomic ratio inferred from the O 1s (530.1 eV) and Mn $2p_{3/2}$ (641.7 eV) signals, evaluated by using Wagner sensitivity factors[10] and corrected for the instrument transmission function, is 1:1, as required for the $Mn_{12}O_{12}$ core.

Moreover, the valence state of manganese in the SMM layer was obtained from the Mn 3s spectral region. The Mn 3s band splitting that originates from exchange coupling between the 3s hole and the 3d electrons is the best indicator for the Mn valence state.[11] The observed value of 5.1 eV is consistent with a formal valency of 3+ to 3.3+, as expected for complex **1**.

Deeper insight into the structure of the grafted layer was obtained by angle-resolved XPS spectra measured at takeoff angles of 10, 45, and 80° (relative to the surface), which provide information on the depth distribution of elements in the grafted layers (Figure 2 and Table 1).

In the case of the ester monolayer, these data are of great relevance, since it acts as the bridge between the silicon

 © 2004 Wiley-VCH Verlag GmbH & Co. KGaA, Weinheim

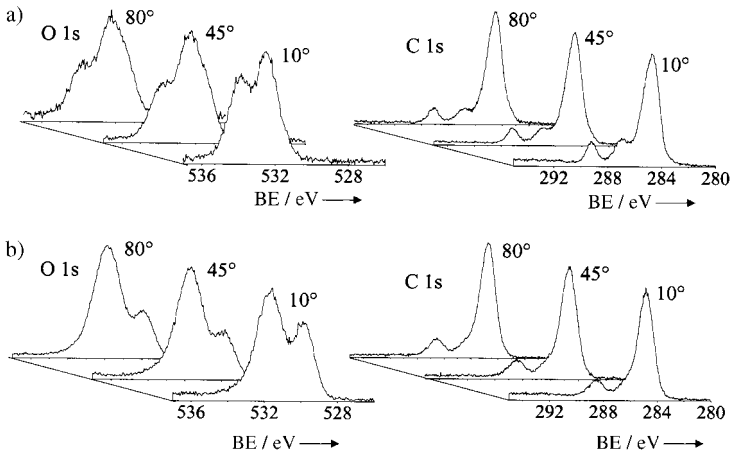


Figure 2. Spectra determined at takeoff angles between 10 and 80° for samples obtained a) after grafting of methyl 10-undecenoate on the silicon surface, and b) after anchoring of the Mn_{12} cluster.

Table 1: Dependence of elemental composition on takeoff angle for grafted methyl 10-undecenoate before and after anchoring of the Mn_{12} cluster.

Takeoff angle	Atomic fraction [%] before Mn_{12} anchoring			
	Si	C	O	Mn
80°	60.7	29.2	10.1	–
45°	49.7	37.2	13.1	–
10°	13.4	66.3	20.3	–
Takeoff angle	Atomic fraction [%] after Mn_{12} anchoring			
	Si	C	O	Mn
80°	29.8	33.8	32.6	3.7
45°	20.7	41.0	33.0	5.3
10°	4.0	33.0	35.8	9.9

substrate and the magnetic cluster. The C 1s spectral region (Figure 2a) shows a progressive increase in the components at 289.4 and 287.2 eV upon decreasing the takeoff angle (i.e., for shorter sampling depths). By contrast, the component associated with the Si–C carbon (283.5 eV) almost disappears at lower angles. These results are consistent both with Si–C bond grafting and with terminal ester groups atop the layer.

At smaller takeoff angles, the O 1s features have reduced intensity of the band at 531.6 (SiO_x) relative to components at 532.7 and 534.1 eV due to C=O and OCH_3. This observation is compatible with carboxylic termination on the topmost region of the layer.

The anchored Mn_{12} cluster does not show significant changes in the C 1s feature at different takeoff angles (Figure 2b). This is a consequence of the approximately spherical distribution of the alkanecarboxylato ligands (undecanoato and acetato).

By contrast, in the O 1s region the observed increased intensity at lower grazing angle of the signal due to Mn-bonded oxygen (530.1 eV) points to the Mn_{12} cluster lying atop the layer.

In addition, as expected for an Mn-containing overlayer homogeneously distributed on the substrate, the Mn:Si atomic ratio progressively increases with decreasing takeoff angle (Table 1). The Mn:C atomic ratio is slightly higher for smaller takeoff angles, as expected for an Mn-containing layer mainly located above the grafted carbon chains.

To show the importance of the coordination bond between the grafted undecanoic acid and Mn_{12} cluster **1**, some experiments were performed to determine whether **1** could stick to surfaces on which no ligand exchange takes place. The acetato ligands in the cluster form a slightly hydrophobic sphere around the $Mn_{12}O_{12}$ core, as suggested by the insolubility of the cluster in water and its solubility in organic solvents such as acetonitrile. Therefore, a hydrophobic methyl-terminated monolayer (1-decene grafted on Si) and a less hydrophobic methyl ketone-terminated monolayer (5-hexen-2-one grafted on Si) were chosen to evaluate the physisorption of cluster **1**.[12]

Negligible cluster sticking was detected in XPS spectra on both 1-decene and 5-hexen-2-one monolayers (<0.1 and 0.8% Mn, respectively) subjected to the same treatment for cluster anchoring as the acid-terminated surface. These results indicate that significant irreversible physisorption does not occur, and cluster anchoring requires acid-terminated compounds to exchange with acetato ligands and coordinate the $Mn_{12}O_{12}$ core.

The roughness and homogeneity of the Mn-containing layer were determined by AFM analysis. Figure 3 compares the AFM images of the ester layer before and after anchoring the Mn_{12} cluster. The layer before cluster anchoring appears very flat and homogeneous with a roughness of less than 0.1 nm, comparable to that of a freshly etched Si(100) surface. The thickness of the grafted layer was estimated by atomic force lithography using the AFM tip. Thus, grafted molecules

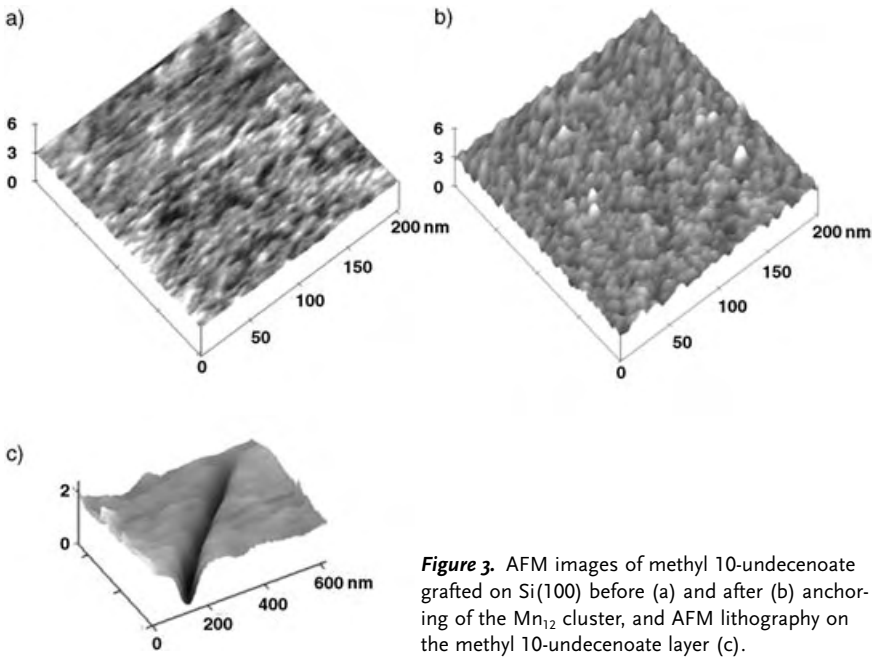


Figure 3. AFM images of methyl 10-undecenoate grafted on Si(100) before (a) and after (b) anchoring of the Mn_{12} cluster, and AFM lithography on the methyl 10-undecenoate layer (c).

 © 2004 Wiley-VCH Verlag GmbH & Co. KGaA, Weinheim

were removed along a straight line by rastering the AFM tip on the surface under a suitable constant force. The depth of the scratch obtained in the ester layer was about 1.1 nm, a value slightly lower than the total length (ca. 1.5 nm) of the linear chain of methyl 10-undecenoate. Therefore, an inclined (ca. 45°) grafting geometry must be assumed to account for the observed value. After grafting of the Mn_{12} clusters, the surface is much more structured than that of the host surface. The typical vertical size of the observed features of about 1 nm is consistent with the expected height of cluster **1**. There is evidence of poorly ordered particles, almost homogeneously distributed over the surface. Their apparent lateral size is about 5–15 nm, which is greater than the expected value for isolated Mn_{12} clusters. This difference could be explained by the limited lateral resolution of the AFM analysis, but also by possible cluster aggregates not resolved by AFM. Similarly to what was observed for Mn_{12} SMMs anchored on Au,[4] the disordered arrangement might be due to the long alkyl chains of the grafting units, whose conformational flexibility prevents the formation of regular arrangements.

In conclusion, this study has shown a viable route for anchoring Mn_{12} SMMs on Si(100), that is, on surfaces suited to integration with well-established silicon technologies. This novel bottom-up approach represents a promising perspective for information storage with SMMs.

Experimental Section

1·4 H_2O·2 AcOH was synthesized according to the literature procedure[3a] and crystallized by diffusion in acetone/acetic acid solution. Elemental analysis (%) calcd for $C_{36}H_{72}O_{56}Mn_{12}$: C 20.97, H 3.52; found: C 21.01, H 3.24. ^{1}H NMR (500 MHz, CD_3CN, 25 °C, TMS): $\delta =$ 47 (12 H, axial $Mn^{III}Mn^{III}$), 40 (24 H, equatorial $Mn^{III}Mn^{III}$), 14 ppm (12 H, axial $Mn^{III}Mn^{IV}$).

Methyl 10-undecenoate was synthesized according to the method reported by Sieval et al.[6a] Briefly, a mixture of 10-undecenoic acid (10 g, 54 mmol), methanol (65 mL), and sulfuric acid (0.14 mL) was refluxed for 3 h. The excess methanol was removed in vacuum, and the resulting material was dissolved in diethyl ether. The product was distilled under vacuum to obtain a transparent liquid. ^{1}H NMR (500 MHz, $CDCl_3$, 25 °C, TMS): $\delta = 5.83–5.78$ (m, 1 H), 5.00–4.91 (m, 2 H), 3.66 (s, 3 H), 3.31–2.84 (m, 2 H), 2.06–2.01 (m, 2 H), $\delta = 1.63–1.9$ (m, 2 H), 1.38–1.29 ppm (m, 10 H).

Monolayer preparation: 10 mL of alkene solution (60 % v/v) in mesitylene was placed in a small, three-necked flask fitted with a nitrogen inlet and a condenser. The solution was deoxygenated with dry nitrogen for at least 1 h. Subsequently, a Si(100) substrate was etched in 2.5 % hydrofluoric acid for 2 min and immediately placed in the solution. The solution was then refluxed at 200 °C for 2 h with slow N_2 bubbling to prevent bumping. After cooling to room temperature, the sample was removed from the solution and sonicated in dichloromethane for 10 min.

The methyl ester was hydrolyzed by boiling according to a modification of the method reported by Sieval et al.[6a]

The Mn_{12}-funtionalized silicon surface was synthesized by a modified ligand-exchange method.[13] The silicon surface was rinsed in a slurry of freshly prepared **1**·4 H_2O·2 AcOH in anhydrous toluene, and the solvent was distilled under reduced pressure (100–150 mbar). Additional azeotropic distillations were performed with toluene (3 × 10 mL, 100–150 mbar). The modified substrate was removed from the solution and sonicated in acetonitrile and dichloromethane for 10 min to remove unanchored Mn_{12} clusters.

1-decene and 5-hexen-2-one monolayers were prepared and characterized by XPS similarly to the methyl 10-undecenoate monolayer. In both cases, the Si 2p XPS region showed only the Si $2p_{3/2-1/2}$ spin–orbit doublet of elemental silicon. The absence of significant signals around BE = 103 eV due to oxidized Si pointed to efficiently passivated surfaces. Similarly, the C 1s region was consistent with the presence of organic monolayers. The C 1s region of grafted 1-decene consisted of two main components centered at 283.5 (carbide Si–C bond) and 284.8 eV (aliphatic backbone). The C 1s region of grafted 5-hexen-2-one also showed a third main component centered at 286.1 eV (C=O group).

The XPS spectra were recorded on a PHI ESCA/SAM 5600 Multy technique spectrometer equipped with a monochromated $Al_{K\alpha}$ X-ray source. The analyses were carried out at various photoelectron angles (relative to the sample surface) in the range 10–80° with an acceptance angle of ±7°.

AFM images were obtained in high-amplitude mode (tapping mode) by a Digital Instrument Multimode apparatus. The noise level before and after each measurement was 0.01 nm. AFM lithography was performed with an NT-MTD instrument.

Received: February 4, 2004
Revised: April 20, 2004 [Z53933]

Keywords: cluster compounds · monolayers · photoelectron spectroscopy · single-molecule magnets · surface chemistry

[1] G. P. Lopinsky, D. D. M. Wayner, R. A. Wolkow, *Nature* **2000**, *406*, 48.
[2] G. F. Cerofolini, G. Ferla, *J. Nanopart. Res.* **2002**, *4*, 185.
[3] a) T. Lis, *Acta Crystallogr. Sect. B* **1980**, *36*, 2042; b) R. Sessoli, D. Gatteschi, A. Caneschi, M. A. Novak, *Nature* **1993**, *365*, 141; c) G. Christou, D. Gatteschi, D. N. Hendrickson, R. Sessoli, *Mater. Res. Bull.* **2000**, *35*, 66.
[4] A. Cornia, A. C. Fabretti, M. Pacchioni, L. Zobbi, D. Bonacchi, A. Caneschi, D. Gatteschi, R. Biagi, U. del Pennino, V. De Renzi, L. Gurevich, H. S. J. Van der Zant, *Angew. Chem.* **2003**, *115*, 1683; *Angew. Chem. Int. Ed.* **2003**, *42*, 1645.
[5] M. Cavallini, F. Biscarini, J. Gomez-Segura, D. Ruiz, J. Veciana, *Nano Lett.* **2003**, *3*, 1527.
[6] a) A. B. Sieval, A. L. Demirel, J. M. Nissink, M. R. Linford, J. H. van der Maas, W. H. de Jeu, H. Zuilhof, E. J. R. Sudhölter, *Langmuir* **1998**, *14*, 1759; b) G. F. Cerofolini, C. Galati, S. Reina, L. Renna, *Mater. Sci. Eng. C* **2003**, *23*, 253.
[7] G. F. Cerofolini, C. Galati, S. Lorenti, L. Renna, O. Viscuso, C. Bongiorno, V. Raineri, C. Spinella, G. G. Condorelli, I. L. Fragalà, A. Terrasi, *Appl. Phys. A* **2003**, *77*, 403.
[8] I. L. Swift, *Surf. Interface Anal.* **1982**, *4*, 47.
[9] D. Briggs in *Practical Surfaces Analysis*, *Vol. 1*, 2nd ed. (Eds.: D. Briggs, M. P. Seah), Wiley, New York, **1995**, p. 440.
[10] C. D. Wagner, L. E. Davis, M. V. Zeller, J. A. Taylor, R. H. Raymond, L. H. Gale, *Surf. Interface Anal.* **1981**, *4*, 211.
[11] a) V. R. Galakhov, M. Demeter, S. Bartkowski, M. Neumann, N. A. Ovechkina, E. Z. Kurmaev, N. I. Lobachevskaya, Ya. M. Mukovskii, J. Mitchell, D. L. Ederer, *Phys. Rev. B* **2002**, *65*, 113102; b) V. Di Castro, G. Polzonetti, *J. Electron Spectrosc. Relat. Phenom.* **1989**, *48*, 117.
[12] Note that the methyl ketone-terminated surface is expected to have comparable hydrophobicity to that grafted with methyl 10-undecenoate, but the latter monolayer was not suited to evaluate cluster physisorption since it is partially hydrolyzed during the anchoring process due to the presence of water and acetic acid in the starting material **1**·4 H_2O·2 AcOH.
[13] H. J. Eppley, H.-L. Tsai, N. de Vries, K. Folting, G. Christou, D. N. Hendrickson, *J. Am. Chem. Soc.* **1995**, *117*, 301.

 © 2004 Wiley-VCH Verlag GmbH & Co. KGaA, Weinheim

Homogeneous Catalysis

In Situ Formation of a Heterobimetallic Chiral [(Salen)Ti^{IV}]/[(Salen)V^{V}] Catalyst for the Asymmetric Addition of TMSCN to Benzaldehyde**

Yuri N. Belokon, Michael North, Victor I. Maleev, Nikolay V. Voskoboev, Margarita A. Moskalenko, Alexander S. Peregudov, Andrey V. Dmitriev, Nikolai S. Ikonnikov, and Henri B. Kagan**

The wide potential of molecules with multiple (multidentate) Lewis acid sites that bind and chemically activate small organic molecules has been recognized for some time.[1] Quite recently, several groups made significant progress towards the design and use of chiral homo- and heterobimetallic complexes for asymmetric catalysis, with particularly important contributions reported by Shibasaki et al.[2] and Trost et al.[3] The former group developed an effective chiral bimetallic catalyst based on an alkali metal/lanthanoid complex for asymmetric Michael addition reactions, whereas the latter group elaborated on dinuclear zinc complexes of a chiral pentadentate ligand for asymmetric Henry and aldol condensation reactions. In the case of the asymmetric opening of epoxides catalyzed by chiral [(salen)Co] complexes (salen = *N,N'*-bis(salicylaldehydo)ethylenediamine),[4] the reaction involved two separate chiral salen–metal species in the rate-limiting step of the reaction, and subsequently, very efficient oligomeric catalysts were developed based on this principle.[5] It is reasonable to propose that many other established catalysts may operate via unrecognized polymetallic intermediates lying on the reaction coordinate; a large number of nonlinear effects observed in asymmetric catalytic reactions seem to indicate such a possibility.[6]

[*] Prof. Dr. Y. N. Belokon, Dr. V. I. Maleev, Dr. M. A. Moskalenko, Prof. Dr. A. S. Peregudov, A. V. Dmitriev, Dr. N. S. Ikonnikov
A. N. Nesmeyanov Institute of Organo-Element Compounds
Russian Academy of Sciences
Vavilov 28, 119991 Moscow (Russian Federation)
Fax: (+95) 135-5085
E-mail: yubel@ineos.ac.ru
Prof. Dr. H. B. Kagan
Institut de Chimie Moléculaire et des Matériaux d'Orsay,
Laboratoire de Synthèse Asymétrique (UMR 8075)
Université de Paris-Sud
Bâtiment 420, 91405 Orsay Cedex (France)
Fax: (+33) 169-157-895
E-mail: kagan@icmo.u-psud.fr
Prof. M. North
Department of Chemistry, King's College
Strand, WC2R 2LS London (UK)
N. V. Voskoboev
Higher Chemical College, Russian Academy of Sciences
Miusskaya pl. 9, 125 047 Moscow (Russian Federation)

[**] We thank the Russian Foundation for Basic Research (Project Nos. 02-03-32091 and 03-03-06461) and the EU (Descartes Prize research fund) for financial support of this work. TMSCN = trimethylsilyl cyanide.

Homo- or heterobimetallic complexes have enormous potential to revolutionize asymmetric catalysis. They can activate both components of a bimolecular reaction simultaneously, overcome entropy barriers associated with bringing the two reagents together, minimize the energy barrier that arises from solvent–shell rearrangements during the reaction, and recognize prochiral faces or groups within the reagents through predetermination of the reaction trajectory.

Belokon', North and co-workers have developed an efficient catalyst based on dinuclear, chiral [{(salen)Ti^{IV}-(μ-O)}$_2$] precatalysts for the asymmetric addition of trimethylsilyl cyanide to aldehydes.[7] Kinetic studies indicated that two Ti^{IV} complexes were involved in the rate-limiting step of this reaction.[8] Subsequently, monomeric chiral ionic [(salen)V^{V}(O)]$^{+}EtOSO_3^{-}$ complexes were shown to be even more enantioselective in the same reaction, although the rate was almost two orders of magnitude slower than that with the analogous Ti^{IV} catalysts.[9] Kinetic studies indicated that two cationic V^{V} complexes were again involved in the rate-limiting step of the reaction.[9a]

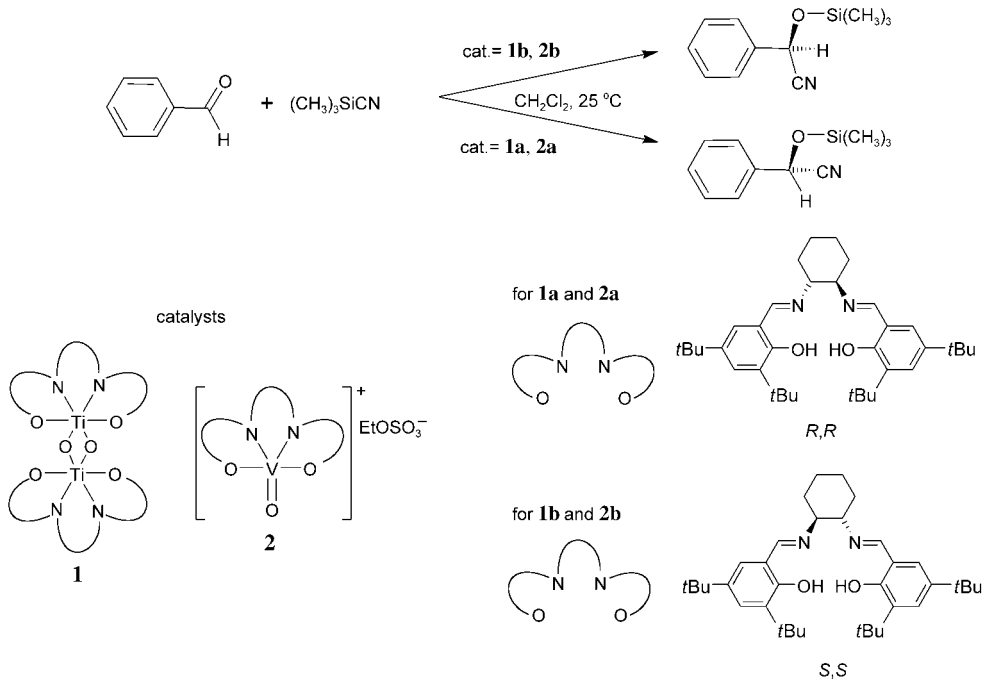
Based on these results, we thought that a mixed-metal complex derived from Ti^{IV} and V^{V} might form an even better catalyst, which would exhibit the asymmetric induction associated with V^{V} complexes and the faster rates of reaction associated with Ti^{IV} catalysts. Furthermore, we considered complexes derived from enantiomeric ligands to study the interactions between the complexes, as mixed species could give rise to anomalies with respect to the independent metal catalysts. Herein, we report the performance of mixtures of [{((*R*,*R*)-salen)Ti^{IV}(μ-O)}$_2$] or [{((*S*,*S*)-salen)Ti^{IV}(μ-O)}$_2$], and ionic [((*S*,*S*)-salen)V^{V}(O)]$^{+}EtOSO_3^{-}$ or [((*R*,*R*)-salen)-V^{V}(O)]$^{+}EtOSO_3^{-}$ in the asymmetric addition of trimethylsilyl cyanide to benzaldehyde at different molar ratios of Ti/V.

The [{((*R*,*R*)-salen)Ti^{IV}(μ-O)}$_2$] **1a** (or [{((*S*,*S*)-salen)-Ti^{IV}(μ-O)}$_2$], **1b**), and [((*R*,*R*)-salen)V^{V}(O)]$^{+}EtOSO_3^{-}$ **2a** (or [((*S*,*S*)-salen)V^{V}(O)]$^{+}EtOSO_3^{-}$, **2b**) catalysts (Scheme 1) were synthesized as described previously.[9b] The asymmetric addition of trimethylsilyl cyanide to benzaldehyde (Scheme 1) was catalyzed by **1a** or **2a** to give (*S*)-*O*-(trimethylsilyl)mandelonitrile (80 and 90% *ee*, respectively).[7,9] Use of **1b** or **2b** similarly led to (*R*)-*O*-(trimethylsilyl)mandelonitrile.

Use of a mixture of **1b** and **2a** as a catalyst in the reaction at a 1:1 molar ratio of Ti/V may be expected to result in: 1) Completely racemic product if a fast exchange of ligands between the two metal centers takes place. 2) Almost exclusive (*R*)-mandelonitrile formation at this ratio (and up to a 1:4 molar ratio of Ti/V) if **1b** and **2a** were independent. Above a 1:4 molar ratio of Ti/V, the enantiomeric excess of the product would decrease and at a 1:11 ratio of Ti/V, racemic product would be formed (see Figure 1, curve a). Accordingly, exclusive formation of (*S*)-mandelonitrile would be observed if a 1:1 mixture of **1a** and **2b** were used as a catalyst. 3) Formation of a mixed complex with novel catalytic properties, which could not be predicted in advance.

As the [(salen)Ti] catalyst is almost two orders of magnitude faster than the [(salen)V]$^{+}$ catalyst, one could expect the Ti catalyst to determine the absolute configuration

 DOI: 10.1002/anie.200454031 © 2004 Wiley-VCH Verlag GmbH & Co. KGaA, Weinheim



Scheme 1. The asymmetric addition of trimethylsilyl cyanide to benzaldehyde.

of the resulting mandelonitrile. Theoretically, a mixture of **1b** and **2a** in a ratio of 1:2 should give (*R*)-mandelonitrile and a mixture of **1a** and **2b** should produce (*S*)-mandelonitrile. Unexpectedly, it was predominantly (*R*)-mandelonitrile that was formed in 82% *ee* when a 1:2 mixture of **1a** and **2b** was employed as catalyst, and the *S* product that was formed from a mixture of **1b** and **2a** as catalyst. These results are not consistent with either a fast exchange of ligands or with the independent function of the catalysts with respect to one another. The absolute configuration of the product appeared to be determined by the slower vanadium catalyst rather than by the faster titanium catalyst.

Figure 1 illustrates the variation of the enantiomeric excess and absolute configuration of the mandelonitrile trimethylsilyl ether as the mol% of a mixture of **1a** and **2b** (curve b) or **1b** and **2a** (curve c) was progressively varied from 100% of the titanium catalyst to 100% of the vanadium catalyst (calculated as a ratio of the metal ions and not the complexes; the total catalyst concentration was maintained at 3.1×10^{-4} M and assumes that both Ti and V catalysts are calculated as monomers). The results indicate that catalysis by titanium complexes was predominant only when the mol% of vanadium in the mixture was very low. Introduction of just 10 mol% of vanadium into the catalyst results in the formation of racemic product, and at a catalyst composition of 35% vanadium and 65% titanium, the vanadium appears already to determine the absolute configuration of the product.

There are at least two interpretations of these results: One is the formation of a catalytically active, mixed titanium–vanadium complex, which overrides the original titanium- and vanadium-based catalysts; the vanadium-based portion of the mixed catalyst is then responsible for the determination of the configuration of the mandelonitrile. The second possibility is that the vanadium precatalyst **2** is involved in the deactivation of the titanium precatalyst **1** by catalyzing a side reaction. Such a side reaction might result from the attack of trimethylsilyl cyanide at the remaining oxygen bridge of a bimetallic [(salen)Ti] complex that forms during the catalytic cycle[8] to result in the formation of inactive mononuclear complexes (Scheme 2).[9b]

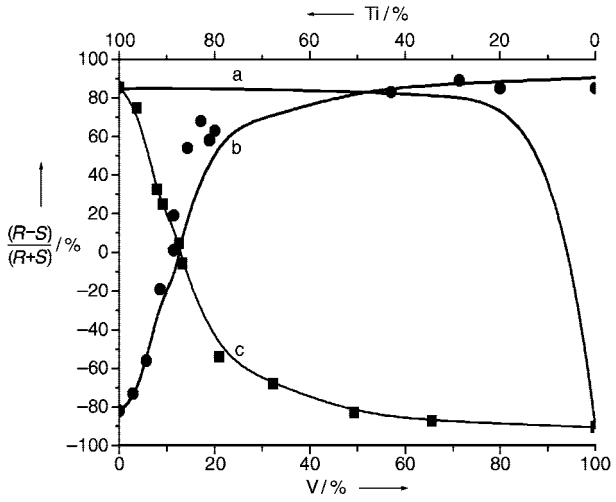
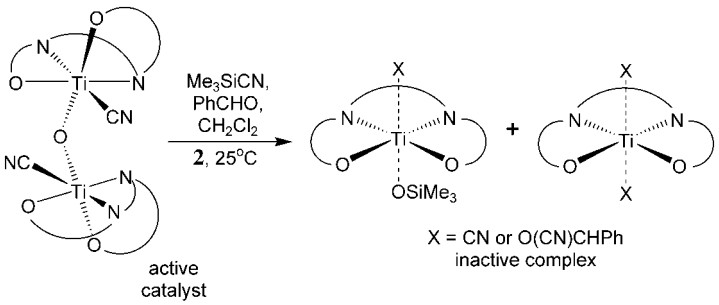


Figure 1. a) The calculated enantiomeric excess of the product if catalysts **1b** and **2a** work independently of one another (the sum of the total catalyst concentration is maintained at 3.1×10^{-4} M, and the relative reactivities of the two catalysts are taken into account); b) and c) The variation of enantiomeric excess and absolute configuration of mandelonitrile as the mol% of a mixture of **1a** and **2b** (curve b) or **1b** and **2a** (curve c) is varied from 100% of titanium-based catalyst to 100% of vanadium-based catalyst (calculated as a ratio of metal ions).

 © 2004 Wiley-VCH Verlag GmbH & Co. KGaA, Weinheim



Scheme 2. Formation of inactive mononuclear complexes.

To distinguish between these two possibilities, we studied the variation in the enantiomeric excess of the product during the course of the reaction and measured the reaction kinetics at various ratios of Ti/V. The formation of a mixed complex (once complete) would result in the formation of the product with a constant enantiomeric excess throughout the reaction. In contrast, the destruction of the titanium catalyst mediated by complex **2** should result in a change in the enantiomeric excess (and even the absolute configuration) of the mandelonitrile trimethylsilyl ether during the reaction. Furthermore, there should be a significant decrease in the rate of the reaction relative to the reaction catalyzed by pure **1** at the same initial concentration.

Figure 2 shows the variation of the enantiomeric excess of mandelonitrile trimethylsilyl ether with the reaction yield for **1a**, **2b**, and mixtures of **1a** and **2b**. There was no observed variation in the enantiomeric excess with the reaction yield (or time) for either of the pure catalysts (Figure 2, curves a and b). In contrast, very significant changes were observed for a mixture composed of 90% titanium and 10% vanadium (calculated as a ratio of metal ions; Figure 2, curve e). At 75% conversion, (*S*)-mandelonitrile trimethylsilyl ether was formed. Extrapolation of the curve to the beginning of the reaction leads to approximately 60–70% *ee* of the *S* product. At 80% conversion the product became a racemic mixture

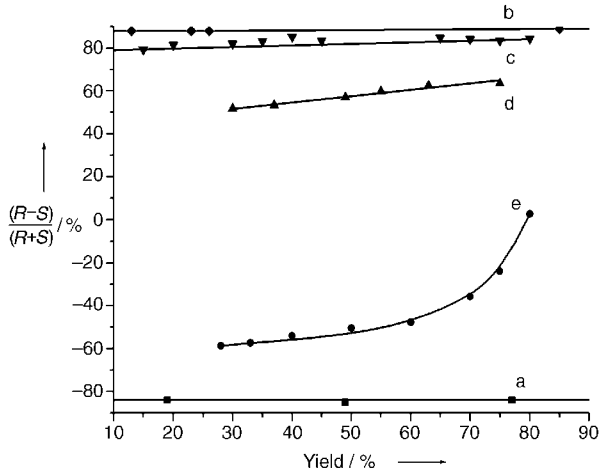


Figure 2. Variation of the enantiomeric excess of mandelonitrile trimethylsilyl ether with yield at different ratios of Ti/V: a) pure **1a**; b) pure **2b**; c) a mixture of **1a** and **2b** with Ti/V = 1:1; d) a mixture of **1a** and **2b** with Ti/V = 4:1; e) a mixture of **1a** and **2b** with Ti/V = 10:1.

and predominantly *R* product was formed, albeit with a very low enantiomeric excess (see also Figure 1). The rate of the reaction was significantly diminished (Figure 3), in line with the removal of the more-active titanium-based catalyst from the reaction mixture. These results seem to be consistent with the suppression of the activity of complex **1** by the complex **2**.

It can also be seen that the *R* product is formed even during the first 20% of the reaction as the amount of vanadium in the catalytic mixture increased from 10 to 20% (Figure 2, curve d) and then to 50%

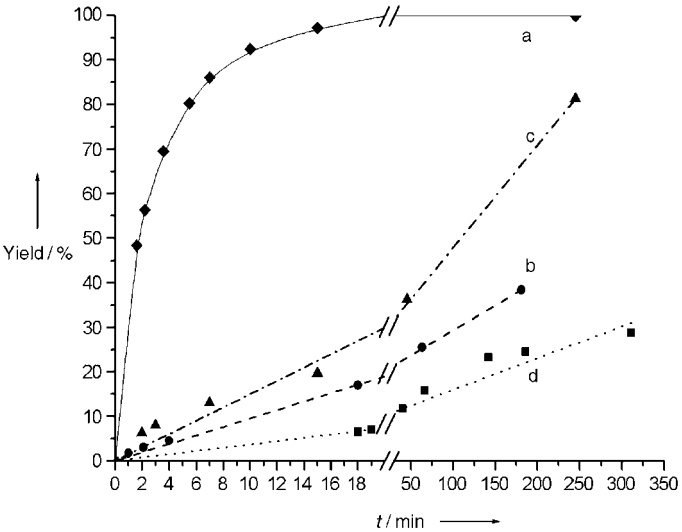


Figure 3. Variation of the yield of mandelonitrile with time as monitored by ^{1}H NMR spectroscopy at 25°C (CD_2Cl_2 solutions) for the reaction catalyzed by: a) pure **1a**, b) pure **2b**, c) a mixture of **1a** and **2b** with Ti/V = 1:1, d) a mixture of **1a** and **2b** Ti/V = 10:1.

(Figure 2, curve c). The variation of the enantiomeric excess with the yield diminished as the percentage of vanadium increased, and at a ratio of 1:1 Ti/V, the enantiomeric excess remained constant throughout the reaction.

The rate of the reaction catalyzed by pure **1a** or **2b** or by a 1:1 mixture of the two catalysts was monitored by ^{1}H NMR spectroscopy (CD_2Cl_2 solutions, Figure 3). Both the disappearance of benzaldehyde and the appearance of the reaction product lead to identical results. The rate of the reaction obeyed second-order kinetics with reasonable correlation coefficients of 0.99 for **1a** and 0.98 for each of the other three cases (**2b**, and 1:1 and 10:1 mixtures of Ti/V). Rate constants (k) were calculated for reactions catalyzed by pure **1a**, pure **2b**, a 1:1 mixture of Ti and V, and a 10:1 mixture of Ti and V ($k = 1.62 \times 10^{-2}$, 3.21×10^{-4}, 5.86×10^{-4}, and 2.79×10^{-4} $M^{-1} s^{-1}$, respectively).

The variation of the apparent initial zero-order rate constant with the composition of the catalyst follows a bell-shaped profile, provided that at least 10% vanadium-based catalyst was present (monitored by UV/Vis spectroscopy of CH_2Cl_2 solutions, Figure 4). The maximum rate constant was observed at a Ti/V ratio of 1:1, which corresponded to 33 mol% of **1b** and 67 mol% of **2a**. Thus it appears that a new

 © 2004 Wiley-VCH Verlag GmbH & Co. KGaA, Weinheim

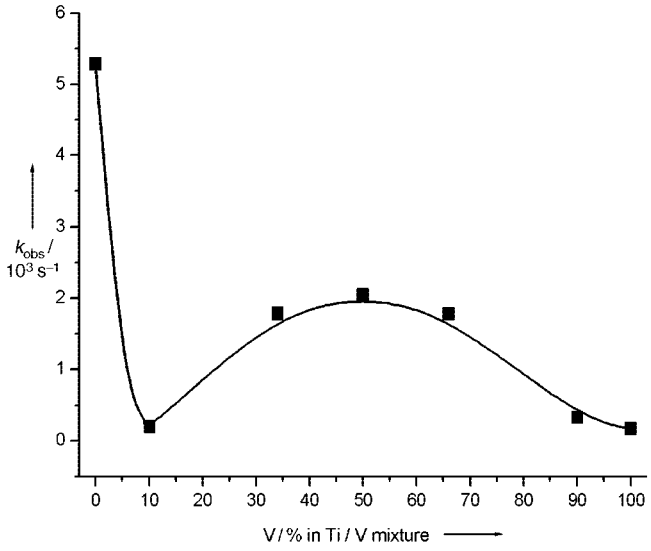


Figure 4. Observed zero-order rate constants of the reaction in CH_2Cl_2 at 20 °C catalyzed by complexes **1a** and **2b** with different ratios of titanium and vanadium.

catalyst was formed from **1b** and **2a** (or **1a** and **2b**) in the reaction mixture, which consisted of one V^V ion and one Ti^{IV} ion, with the resultant stereochemistry determined by the vanadium part of the catalyst and its kinetic behavior largely determined by its titanium-derived portion.

The variation in the *ee* observed in the early stages of the reaction with large ratios of up to 4:1 Ti/V can be explained by the mixed catalyst being formed slowly during this time. Hence, in the early stages of the reaction some titanium-based catalyst **1b** (or **1a**) is still present and catalyzes the formation of (*R*)-mandelonitrile trimethylsilyl ether (or the *S* product in the case of **1a**). However, once all of the titanium catalyst has been either inactivated or converted into a mixed catalyst, only the *S* product is formed. Thus, the enantiomeric excess varies in the early stages of the reaction and then remains almost constant.

With a mixture of catalysts **1b** and **2b** (i.e. both derived from (*S*,*S*)-cyclohexanediamine) in a 1:1 ratio of Ti/V, (*R*)-mandelonitrile trimethylsilyl ether was obtained in 95 % yield with 89 % *ee* after 30 min at 25 °C. A mixture of **1b** and **2a** under the same conditions gave (*S*)-mandelonitrile in 30 % yield (Figure 3) with 82 % *ee* (Figure 2). This is also consistent with the formation of a mixed complex, as pure **2b** would have produced only 20 % of the product under these conditions. As the formation of the mixed complex would be expected to take place at any titanium/vanadium ratio, it is most likely that this complex, rather than the vanadium complex **2**, catalyzes the decomposition of the titanium-based catalyst **1** by the route shown in Scheme 2 or in some other way.

In summary, we have shown that a mixture of two salen-derived V^V and Ti^{IV} complexes results in the formation of a mixed complex, which exhibits catalytic properties derived from both homometallic species. The mixed complex, besides its ability to catalyze asymmetric trimethylsilylcyanation reactions, appears to induce the inactivation (by TMSCN) of any remaining [(salen)Ti] catalyst (Scheme 2). We believe that this behavior is unique to a mixture of chiral catalysts and we are currently trying to extend this concept to some other classes of organometallic catalysts.

Experimental Section

General. Dichloromethane or CD_2Cl_2 were purified as described earlier.[10] Trimethylsilyl cyanide was purchased from Aldrich and freshly distilled before use. Catalysts **1a**,**b** and **2a**,**b** were prepared as described previously.[9b] Kinetics experiments were run in oven-dried glassware under an argon atmosphere. Kinetics measurements were conducted on a "Specord M40" spectrophotometer. Enantiomeric excesses were determined with chiral GC: DP-TFA-γ-CD, fused-silica capillary column (25 m × 0.23 mm), He as the carrier gas (T = 110 °C).

Kinetic experiments were carried out in a flask under thermostat control at 21 ± 0.5 °C. Standard solutions of **1** (2.46×10^{-6} mol) and **2** (4.75×10^{-6} mol) dissolved in dichloromethane (14 mL and 13.5 mL, respectively) were employed to give the initial concentration of the catalysts (3.52×10^{-4} M, calculated as the concentration of the metal ions). Solutions of catalysts were freshly prepared before use and were left for 20 min before samples (1.75 mL) of either the solutions of pure complexes or mixtures of **1** and **2** in the desired ratio (maintaining the total volume 1.75 mL) were mixed under argon and stirred for 15 min. The solution of the catalyst was then added to benzaldehyde (0.1 mL). After 2 min, TMSCN (0.15 mL) was added to the mixture. The resultant total concentration of the metal ions was 3.1×10^{-4} M. Samples (0.01 mL) were taken at appropriate intervals as the reaction progressed and diluted with dry CH_2Cl_2 (5 mL) to quench the reaction. The resulting solution was then analyzed by UV/Vis spectrophotometry at the maximum absorption band for benzaldehyde (246 nm in CH_2Cl_2). The absorption data were used to determine the concentration of benzaldehyde.

^{1}H NMR spectroscopy experiments were run in a similar manner in CD_2Cl_2, and the kinetics of the reaction in NMR tubes were monitored by the disappearance of the benzaldehyde resonances at $\delta = 10.01$ (s, CHO) or 7.65 ppm (t, *p*-Ph). The formation of mandelonitrile was monitored by the increase in the signal at δ = 5.54 ppm (s, CH), which is attributed to the CH group of the reaction product. The rate law was calculated from the second-order reaction rates:

$$k = \frac{1}{t}\frac{1}{(a-b)}\ln\frac{b(a-x)}{a(b-x)}$$

For enantiomeric excess analyses, samples were taken in the same manner; the only variation was a dilution of the sample with hexane (5 mL) followed by filtration through a small silica-filled column (2 × 0.5 cm; hexane/EtOAc 5:1) to remove the catalysts.

Received: February 16, 2004
Revised: May 7, 2004 [Z54031]

Keywords: asymmetric catalysis · cooperative effects · heterobimetallic complexes · titanium · vanadium

[1] J. D. Wuest, *Acc. Chem. Res.* **1999**, *32*, 81 – 89.
[2] a) M. Shibasaki, M. Kanai, K. Funabashi, *Chem. Commun.* **2002**, 1989 – 1999, and references therein; b) R. Takita, T. Ohshima, M. Shibasaki, *Tetrahedron Lett.* **2002**, *43*, 4661 – 4665.
[3] a) B. Trost, V. S. C. Yeh, *Angew. Chem.* **2002**, *114*, 889 – 891; *Angew. Chem. Int. Ed.* **2002**, *41*, 861 – 863, and references therein; b) B. M. Trost, J. L. Gunzner, T. Yasukata, *Tetrahedron Lett.* **2001**, *42*, 3775 – 3778.

 © 2004 Wiley-VCH Verlag GmbH & Co. KGaA, Weinheim

[4] a) M. Ready, E. N. Jacobsen, *J. Am. Chem. Soc.* **2001**, *123*, 2687 – 2688; b) D. E. White, E. N. Jacobsen, *Tetrahedron: Asymmetry* **2003**, *14*, 3633 – 3638.
[5] J. M. Ready, E. N. Jacobsen, *Angew. Chem.* **2002**, *114*, 1432 – 1435; *Angew. Chem. Int. Ed.* **2002**, *41*, 1374 – 1377.
[6] C. Girard, H. B. Kagan, *Angew. Chem.* **1998**, *110*, 3088 – 3127; *Angew. Chem. Int. Ed.* **1998**, *37*, 2922 – 2959.
[7] Yu. N. Belokon', S. Caveda-Cepas, B. Green, N. S. Ikonnikov, V. N. Krustalev, V. S. Larichev, M. A. Moscalenko, M. North, C. Orizu, V. I. Tararov, M. Tasinazzo, G. I. Timofeeva, L. V. Yashkina, *J. Am. Chem. Soc.* **1999**, *121*, 3968 – 3973.
[8] Yu. N. Belokon', B. Green, N. S. Ikonnikov, V. S. Larichev, B. V. Lokshin, M. A. Moskalenko, M. North, C. Orizu, A. S. Peregudov, G. I. Timofeeva, *Eur. J. Org. Chem.* **2000**, 2655 – 2661.
[9] a) Yu. N. Belokon', M. North, T. Parsons, *Org. Lett.* **2000**, *11*, 1617 – 1619; b) Yu. N. Belokon', A. V. Gutnov, M. A. Moskalenko, L. V. Yashkina, N. S. Ikonnikov, N. V. Voskoboev, V. N. Khrustalev, M. North, *Helv. Chim. Acta* **2002**, *85*, 3301 – 3312.
[10] A. J. Gordon, R. A. Ford, *The Chemist's Companion: A Handbook of Practical Data*, *Techniques*, *and References*, Wiley, New York **1972**, p. 437.

 © 2004 Wiley-VCH Verlag GmbH & Co. KGaA, Weinheim

Carbenes

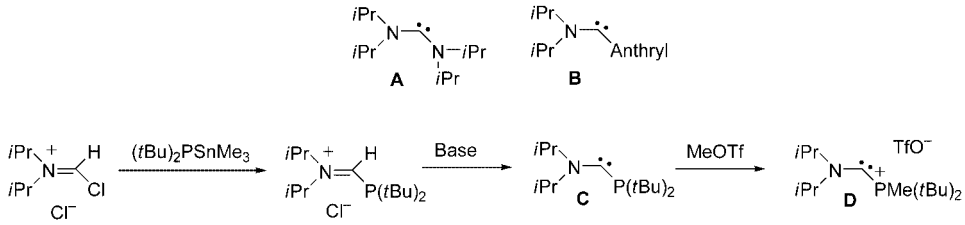
Readily Available Onio-Substituted Methyleneiminium Salts: Single Precursors for a Variety of Aminocarbenes**

*Salvador Conejero, Yves Canac, Fook S. Tham, and Guy Bertrand**

Due to their strong σ-donor properties, N-heterocyclic-carbenes (NHCs) have found numerous applications as ligands for transition-metal catalysts.[1] More recently, it has been found that acyclic diaminocarbenes **A** (see Scheme 1)[2] or even amino aryl carbenes **B**[3] also behave as strong-σ-donor weak-π-acceptor ligands and therefore could be considered as alternative ligands for catalysts;[4,5] to date, **A** is the most basic carbene ligand known.[4c] However, the range of acyclic amino carbenes (AAC) known is far surpassed by that of their NHCs counterparts. Obstacles to extending the range of available AACs reside in their supposed inherent instability,[6] but also in the lack of a general and convenient synthetic route for their preparation. We have recently reported that substitution reactions occur at the carbene center of the phosphonio-substituted carbene **D**, thus giving rise to new stable carbenes.[7] However, the synthesis of **D** requires several steps, which includes the preparation of a stannyl phosphane; a very fragile carbene intermediate **C**;[8] and most importantly, is limited to (methyl)di(*tert*-butyl)-phosphane as a leaving group. Indeed, to assure the stability of carbene **C**, bulky groups at phosphorus are required, and the addition of an organic group to the phosphane to form a quaternary P center is limited to methylation. (Methyl)di(*tert*-butyl)phosphane is 1) very basic, therefore not the perfect leaving group; 2) bulky, thus preventing the substitution reaction with sterically hindered nucleophiles; 3) features acidic methyl protons, which often react with the nucleophile (base) to afford undesirable products.

Herein, we report an easy entry to amino(phosphonio)-carbenes by using simple phosphanes and readily available reagents, and the subsequent substitution reactions at the carbene center.

As one of the most common synthetic routes to stable carbenes is based on the deprotonation of the corresponding iminium salt,[1] phosphonio iminium salts **3** were the obvious precursors to amino(phosphonio)carbenes. Based on the elegant work by Weiss and co-workers, we predicted that dications such as **3** should be accessible and stable as compounds that feature bis(onio)substituted sp^3- and even sp^2-carbon atoms have been isolated.[9] Indeed, we have found that Alder's dimer **1**[2,10] cleanly reacts at room temperature with the basic tricyclohexylphosphane, but also with very simple phosphanes such as triphenylphosphane, thus leading to the formation of the desired dications **3a,b** in 94 and 93% yield, respectively (Scheme 2). Although **3a,b** are water sensitive, giving back diisopropylamide when exposed to moisture, they are highly thermally stable (m.p.: **3a**: 217°C; **3b**: 172°C). Importantly, although the trifluoromethane sulfonate salts **3a,b** are barely soluble in most classical organic solvents, they are soluble in acetonitrile; thus, their purification is quite easy and large quantities can be prepared in a one-pot reaction from the amide (it is not necessary to isolate Alder's dimer **1**). However, in this reaction, half of the

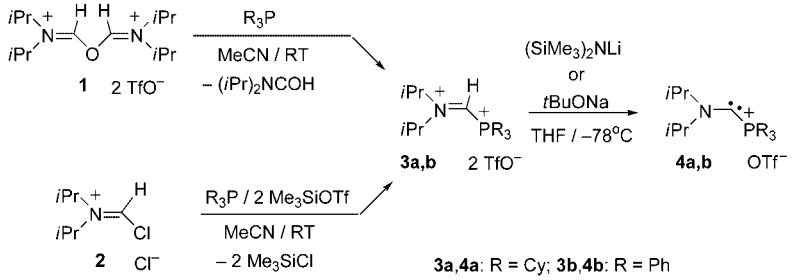


Scheme 1. Carbenes **A** and **B**, and the synthesis of carbenes **C** and **D**.

[*] Dr. S. Conejero, Dr. Y. Canac, Dr. F. S. Tham, Prof. G. Bertrand
UCR–CNRS Joint Research Chemistry Laboratory (UMR 2282)
Department of Chemistry
University of California
Riverside, CA 92521-0403 (USA)
Fax: (+1) 909-787-2725
E-mail: gbertran@mail.ucr.edu

[**] We are grateful to the ACS/PRF (38192-AC4) and RHODIA for financial support of this work, and to the Spanish Ministerio de Educacion, Cultura y Deporte for a postdoctoral fellowship (S C).

 DOI: 10.1002/anie.200460045 © 2004 Wiley-VCH Verlag GmbH & Co. KGaA, Weinheim



Scheme 2. Synthesis of **3a,b** and **4a,b**.

starting amide is lost. This is not significant when simple amides are used, but may become an important issue with more sophisticated amides. A way to bypass this obstacle is to treat an adduct of phosphane and trimethylsilyl triflate, generated in situ,[11] with the iminium chloride **2**. Using this route, we isolated **3a,b** in 89 and 94 % yield, respectively, from the amide.

The acidity of the iminium protons of **3a,b** is indicated by the low field ^{1}H NMR chemical shifts (**3a**: 9.33 ppm, $J_{HP} = 19.3$ Hz **3b**: 9.66 ppm, $J_{HP} = 24.6$ Hz). Thus, the addition of one equivalent of sodium *tert*-butoxide and lithium bis(trimethylsilyl)amide to suspensions of dications **3a** and **3b** in tetrahydrofuran cleanly led to the formation of the corresponding amino(phosphonio)carbenes **4a** and **4b**, respectively. They have been isolated as air-sensitive orange–yellow crystals indefinitely stable in solution and in the solid state (m.p.: **4a**: 164 °C; **4b** 178 °C; Scheme 2).

The ^{13}C NMR signals for the carbene carbon atoms (**4a**: $\delta = 304.52$ ppm, $J_{CP} = 109.0$ Hz; **4b**: $\delta = 292.4$ ppm, $J_{CP} = 110.5$ Hz) are shifted considerably downfield relative to the resonances observed for their protonated precursors **3a,b** (**3a**: $\delta = 172.3$ ppm, $J_{CP} = 37.3$ Hz; **3b**: $\delta = 169.9$ ppm, $J_{CP} = 64.1$ Hz). In contrast, single-crystal X-ray diffraction studies[12] show very similar features for all four compounds **3a,b** and **4a,b** (Figure 1): no interaction with the counterion, a

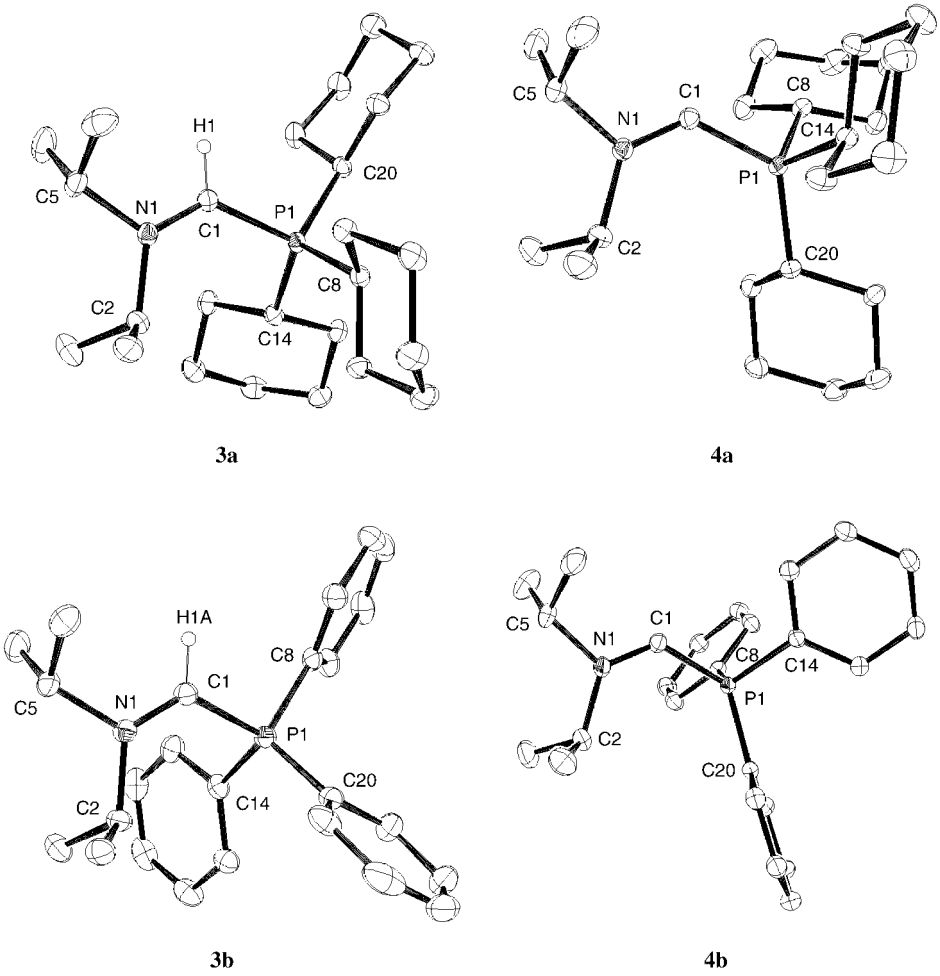
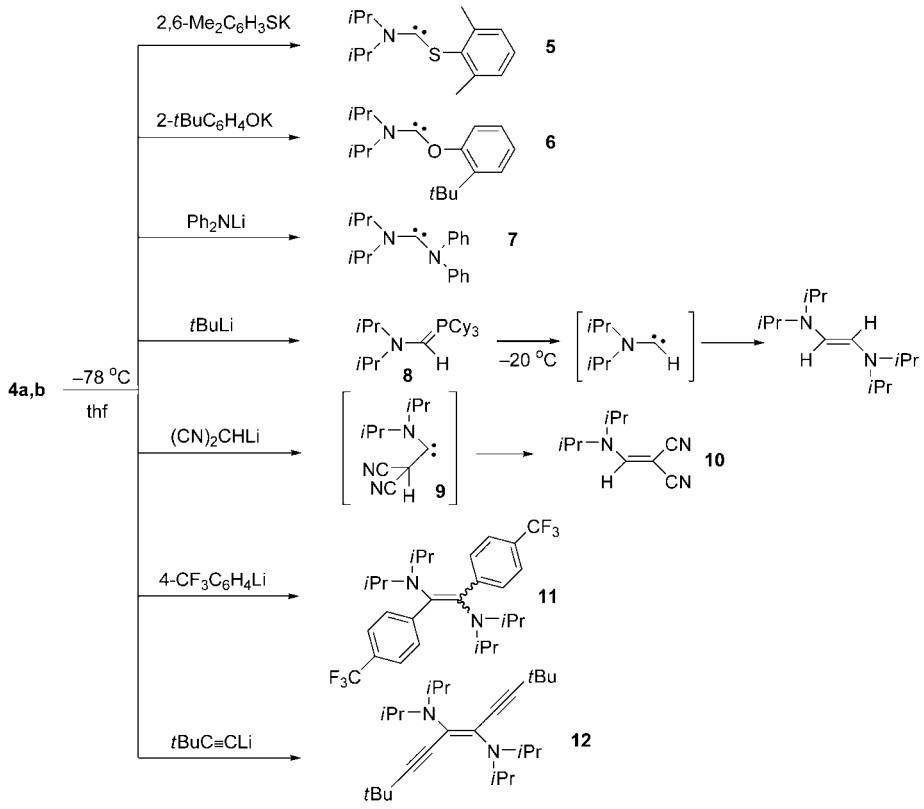


Figure 1. Selected bond distances [Å] and bond angles [°]: **3a**: N(1)-C(1) 1.283, P(1)-C(1) 1.849; N(1)-C(1)-P(1) 129.64, C(1)-N(1)-C(5) 119.1, C(1)-N(1)-C(2) 125.41, C(2)-N(1)-C(5) 115.48, C(14)-P(1)-(C8) 112.02, C(20)-P(1)-C(8) 108.92, C(20)-P(1)-C(14) 111.43. **4a**: N(1)-C(1) 1.281, P(1)-C(1) 1.792; N(1)-C(1)-P(1) 129.3, C(1)-N(1)-C(5) 115.4, C(1)-N(1)-C(2) 129.1, C(2)-N(1)-C(5) 115.5, C(8)-P(1)-C(14) 107.18, C(1)-P(1)-C(20) 126.01, C(8)-P(1)-C(20) 113.17. **3b**: N(1)-C(1) 1.275, P(1)-C(1) 1.844; N(1)-C(1)-P(1) 125.64, C(1)-N(1)-C(2) 124.00, C(1)-N(1)-C(5) 119.94, C(2)-N(1)-C(5): 116.05, C(20)-P(1)-C(8) 111.20, C(20)-P(1)-C(14) 111.65, C(8)-P(1)-C(14) 110.52. **4b**: N(1)-C(1) 1.282, P(1)-C(1) 1.775; N(1)-C(1)-P(1) 129.14, C(1)-N(1)-C(2): 128.05, C(1)-N(1)-C(5): 115.97, C(2)-N(1)-C(5): 115.98, C(14)-P(1)-C(8): 108.42, C(14)-P(1)-C(20): 105.63, C(8)-P1)-C(20): 109.06.

 © 2004 Wiley-VCH Verlag GmbH & Co. KGaA, Weinheim

short CN bond (**3a**: 1.283; **4a**: 1.281; **3b**: 1.275; **4b**: 1.282 Å), a long CP bond (**3a**: 1.849; **4a**: 1.792; **3b**: 1.844; **4b**: 1.775 Å), and an acute angle about the iminium and carbene centers (**3a**: 129.6; **4a**: 129.3; **3b**: 125.6; **4b**: 129.4°). Notably, the similarities observed between the carbenes **4a,b**, which feature two phosphanes that are very different in nature, suggest that there is only a slight, if any, interaction between the phosphonio group and the carbene center.

Since large quantities of amino(phosphonio)carbenes **4a,b** were now available, we were able to investigate the scope of the substitution reaction at the carbene center. As already observed with the previously reported onio–carbene **D**, the potassium salts of 2,6-dimethylthiophenol and 2-*tert*-butylphenol react cleanly with **4a,b** in THF at −78 °C; multinuclear NMR spectroscopy showed the quantitative formation of carbenes **5**[7] and **6**,[10b] along with the corresponding phosphane (Scheme 3). As Ph_2NLi is too basic to promote substitution with **D**, a study of its reactivity was of interest. Again, the reaction of Ph_2NLi with **4a,b** at −78 °C, yields exclusively the unsymmetrical diamino carbene **7** that has been fully characterized in solution by multinuclear NMR spectroscopy (m.p.: 75 °C). To define the limit of the method, carbenes **4a,b** were then treated with *tert*-butyl lithium. Although in the case of **4b**, a complex mixture was obtained, for **4a** the corresponding phosphorus ylide **8** was formed quantitatively (^{31}P NMR: $\delta = 14.9$ ppm, d, $^2J_{CP} = 50$ Hz). Not surprisingly, the latter is unstable[13] and dissociates at −20 °C within ten minutes into the phosphane and the diisopropylaminocarbene, which dimerizes.[14] To prevent this reduction reaction, the use of a secondary alkyl lithium was explored.



Scheme 3. Reactivity of **4a,b**.

Addition of the lithium salt of malonitrile to **4a,b** cleanly afforded enamine **10**, which demonstrates that the desired substitution reaction occurred, and that the primary formed carbene **9** is unstable towards a 1,2-hydrogen shift.[15,16] Substitution reactions also take place with aryl and alkynyl lithium salts, thus leading to transient carbenes, which dimerize into alkenes **11** and **12**, respectively.

In summary, we have developed a new route for the synthesis of amino(phosphonio)carbenes, by deprotonation of readily available dicationic precursors. The onio–carbenes are excellent building blocks for the synthesis of new stable and transient acyclic monoamino carbenes. The only limitation observed for this route is with tertiary alkyl carbenes, which remain unknown and constitute an exciting synthetic challenge.

Experimental Section

All manipulations were performed under argon by using standard Schlenk techniques. Dry, oxygen-free solvents were employed.

Synthesis of C-phosphonio iminium salts **3a,b**: R_3P (20 mmol), was added at room temperature to an acetonitrile solution (120 mL) of **1** (20 mmol) and the mixture was stirred for 1 h. Alternatively, an acetonitrile solution (30 mL) of trimethylsilyltrifluoromethane sulfonate (8.9 g, 40 mmol) and R_3P (20 mmol) was added, at room temperature to an acetonitrile solution (50 mL) of iminum chloride **2**[17] (3.7 g, 20 mmol) and the reaction mixture stirred for 1 hour. The solvent was evaporated under vacuum, and the residue was washed with THF (150 mL) affording white microcrystalline solids. **3a**: $^{31}P\{^1H\}$ NMR (CD_3CN): $\delta = 43.86$ ppm; ^{1}H NMR (CD_3CN): $\delta = 1.64$–2.20 (m, 30 H, CH_2), 1.83 and 1.86 (d, 6 H, J(H,H) = 6.5 Hz, CH_3CH), 3.50 (m, 3 H, Cy-C*H*), 4.70 (sept, 1 H, J(H,H) = 6.5 Hz, C*H*N), 5.09 (sept d, 1 H, J(H,H) = 6.5 Hz, J(H,P) = 2.9 Hz, C*H*N), 9.33 ppm (d, 1 H, J(P,H) = 19.3 Hz, =C*H*); $^{13}C\{^1H\}$ NMR (CD_3CN): $\delta = 21.26$ and 24.90 (s, *C*H$_3$CH), 25.86 (s, CH_2), 27.21 (d, J(C,P) = 14.5 Hz, CH_2), 28.81 (br, CH_2), 35.40 (d, J(C,P) = 29.0 Hz, Cy-*C*H), 66.00 (br, *C*HN), 69.67 (s, *C*HN), 123.31 (q, J(C,F) = 319.4 Hz, CF_3), 172.29 ppm (d, J(C,P) = 37.3 Hz, =*C*H). **3b**: $^{31}P\{^1H\}$ NMR (CD_3CN): $\delta = 21.50$ ppm; ^{1}H NMR (CD_3CN) $\delta = 1.25$ and 1.72 (d, 6 H, J(H,H) = 6.7 Hz, CH_3CH), 4.52 (sept, 1 H, J(H,H) = 6.7 Hz, C*H*N), 4.87 (sept d, 1 H, J(H,H) = 6.7 Hz, J(H,P) = 3.1 Hz, C*H*N), 7.85–8.09 (m, 15 H, Ph), 9.66 ppm (d, 1 H, J(P,H) = 24.6 Hz, =C*H*); $^{13}C\{^1H\}$ NMR (CD_3CN): $\delta =$ 24.04 and 26.29 (s, *C*H$_3$CH), 68.00 (d, J(C,P) = 3.2 Hz, CHN), 67.45 (d, J(C,P) = 6.7 Hz, *C*HN), 121.89 (q, J(C,F) = 320.7 Hz, CF_3), 114.04 (d, J(C,P) = 88.2 Hz, C_{ipso}), 132.50 (d, J(C,P) = 13.4 Hz, C_{meta}), 136.08 (d, J(C,P) = 12.0 Hz, C_{ortho}), 138.54 (s, C_{para}),

 © 2004 Wiley-VCH Verlag GmbH & Co. KGaA, Weinheim

169.93 ppm (d, J(C,P) = 64.1 Hz, =*C*H).

Synthesis of phosphonio carbenes **4a,b**: A 1/1 mixture of *t*BuONa and **3a**, or $(Me_3Si)_2NLi$ and **3b** (1.2 mmol) was cooled to −78 °C, and THF (6 mL) was added. The suspension was brought to room temperature and stirred for 30 min. The solvent was removed under vacuum and the residue was washed with Et_2O (2 mL). Orange solids, containing NaOTf or LiOTf, were obtained (quantitative reaction by ^{31}P NMR) and used for the substitution reactions without purification. Single crystals were grown by slow diffusion of a THF solution of the solids in ether. **4a**: $^{31}P\{^1H\}$ NMR ([D$_8$]THF): δ = 15.16 ppm; ^{1}H NMR ([D$_8$]THF): δ = 1.14–1.89 (m, 30 H, CH_2), 1.38 and 1.45 (d, 6 H, J(H,H) = 6.7 Hz, CH_3CH), 2.76 (m, 3 H, Cy-C*H*), 4.31 ppm (br, 2 H, C*H*N); $^{13}C\{^1H\}$ NMR ([D$_8$]THF): δ = 20.70 and 23.29 (s, *C*H$_3$CH), 26.84 (s, CH_2), 27.47 (d, J(C,P) = 11.7 Hz, CH_2), 28.59 (d, J(C,P) = 3.4 Hz, CH_2), 34.62 (d, J(C,P) = 36.9 Hz, CH), 44.74 and 48.10 (br, CH_3CH), 122.33 (q, J(C,F) = 321.9 Hz, CF_3), 304.52 ppm (d, J(C,P) = 109.0 Hz, $C_{carbene}$); **4b**: $^{31}P\{^1H\}$ NMR ([D$_8$]THF): δ = −2.46 ppm; ^{1}H NMR ([D$_8$]THF): δ = 1.37 (d, 12 H, J(H,H) = 6.5 Hz, CH_3CH), 4.46 (br, 2 H, C*H*N), 7.63–7.76 ppm (m, 15 H, Ph); $^{13}C\{^1H\}$ NMR ([D$_8$]THF, 220 K): δ = 21.51 (s, *C*H$_3$CH), 59.31 (br. CH_3CH), 73.52 (br. CH_3CH), 122.00 (q, J(C,F) = 321.1 Hz, CF_3), 123.14 (d, J(C,P) = 81.1 Hz, C_{ipso}), 132.00 (d, J(C,P) = 10.4 Hz, C_{meta}), 134.72 (d, J(C,P) = 10.4 Hz, C_{ortho}), 135.37 (s, C_{para}), 292.40 ppm (d, J(C,P) = 110.5 Hz, $C_{carbene}$); at room temperature, the signals of the isopropyl carbon are too broad to be observed.

General procedure for the substitution reactions**:** A THF solution (2 mL) of the nucleophile (1.2 mmol) was added to a suspension of carbene **4a** or **4b** (1.2 mmol) in 2 mL of THF at −78 °C. The mixture was warmed to room temperature and stirred for 30 minutes. According to NMR spectroscopy, all the reactions are quantitative. Carbene **7**: ^{1}H NMR ([D$_8$]THF): δ = 0.84 and 1.42 (d, 6 H, J(H,H) = 6.4 Hz, CH_3CH), 3.71 and 3.75 (sept, 1 H, J(H,H) = 6.4 Hz, C*H*N), 7.07–7.27 ppm (m, 10 H, Ph); $^{13}C\{^1H\}$ NMR ([D$_8$]THF): δ = 20.94 and 26.41 (s, *C*H$_3$CH), 49.42 and 50.78 (s, *C*HN), 125.27, 125.55, 129.47 and 151.27 (s, Ph), 258.20 ppm (s, $C_{carbene}$). Enamine **10**: ^{1}H NMR ($CDCl_3$): δ = 1.30 and 1.32 (d, 6 H, J(H,H) = 6.5 Hz, CH_3CHN), 3.75 and 4.77 (sept, 1 H, J(H,H) = 6.5 Hz, CH_3CH*N*), 7.03 ppm (s, 1 H, =CH); $^{13}C\{^1H\}$ NMR ($CDCl_3$): δ = 20.49 and 23.88 (s, *C*H$_3$CHN), 48.88 and 50.85 (s, CH_3*C*HN), 49.02 (s, =*C*$(CN)_2$), 115.78 and 118.22 (s, CN), 153.19 ppm (s, =CH). Dimer **11**: *E*/*Z* = 3/1; ^{1}H NMR (C_6D_6): δ(*E*) = 0.69 (d, 24 H, J(H,H) = 6.4 Hz, CH_3CHN), 3.05 (sept, 4 H, J(H,H) = 6.4 Hz, CH_3C*H*N), 7.42 and 7.45 ppm (d, 4 H, J(H,H) = 9.4 Hz, H_{arom}); δ(*Z*) = 1.07 (d, 24 H, J(H,H) = 7.0 Hz, CH_3CHN), 3.73 (sept, 4 H, J(H,H) = 7.0 Hz, CH_3C*H*N), 7.03 and 7.07 ppm (d, 4 H, J(H,H) = 9.4 Hz, H_{arom}); $^{13}C\{^1H\}$ NMR (C_6D_6): δ(*E*) = 23.62 (s, *C*H$_3$CHN), 52.16 (s, CH_3*C*HN), 125.15 (s, C_{ortho}), 125.58 (q, J(C,F) = 272.8 Hz, CF_3), 129.29 (q, J(C,F) = 31.1 Hz, C_{para}), 132.12 (s, C_{meta}), 140.37 (s, =C), 149.02 ppm (s, C_{ipso}); δ(*Z*) = 24.46 (s, *C*H$_3$CHN), 48.21 (s, CH_3*C*HN), 124.35 (s, C_{ortho}), 133.66 (s, C_{meta}), 134.86 (s, =C), 147.95 ppm (s, C_{ipso}); $^{19}F\{^1H\}$ NMR (C_6D_6): δ(*E*) = 1.09; (*Z*): 1.37 ppm. Dimer **12**: ^{1}H NMR (C_6D_6): δ = 1.23 (s, 18 H, CH_3C), 1.31 (d, 24 H, J(H,H) = 6.4 Hz, CH_3CHN), 3.50 ppm (sept, 4 H, J(H,H) = 6.4 Hz, CH_3C*H*N); $^{13}C\{^1H\}$ NMR (C_6D_6): δ = 22.50 (s, *C*H$_3$CHN), 28.91 (s, CH_3*C*), 31.36 (s, *C*H$_3$C), 50.62 (s, CH_3*C*HN), 80.55 (s, C≡C), 106.60 (s, C≡C), 134.53 ppm (s, C=C).

Received: March 19, 2004 [Z460045]

Keywords: carbenes · cations · iminium salts · phosphanes · substitution reactions

[1] a) M. C. Perry, K. Burgess, *Tetrahedron: Asymmetry* **2003**, *14*, 951; b) W. A. Herrmann, *Angew. Chem.* **2002**, *114*, 1342; *Angew. Chem. Int. Ed.* **2002**, *41*, 1290; c) T. M. Trnka, R. H. Grubbs *Acc. Chem. Res.* **2001**, *34*, 18; d) L. Jafarpour, S. P. Nolan, *Adv. Organomet. Chem.* **2001**, *46*, 181; e) D. Enders, H. Gielen, *J. Organomet. Chem.* **2001**, *617*, 70; f) A. Fürstner, *Angew. Chem.* **2000**, *112*, 3140; *Angew. Chem. Int. Ed.* **2000**, *39*, 3012; g) D. Bourissou, O. Guerret, F. P. Gabbaï, G. Bertrand, *Chem. Rev.* **2000**, *100*, 39.

[2] a) R. W. Alder in *Carbene Chemistry: From Fleeting Intermediates to Powerful Reagents* (Ed.: G. Bertrand), Marcel Dekker, New York, **2002**, pp. 153–204; b) R. W. Alder, P. R. Allen, M. Murray, A. G. Orpen, *Angew. Chem.* **1996**, *108*, 1211; *Angew. Chem. Int. Ed. Engl.* **1996**, *35*, 1121.

[3] S. Solé, H. Gornitzka, W. W. Schoeller, D. Bourissou, G. Bertrand, *Science* **2001**, *292*, 1901.

[4] a) M.-T. Lee, C.-H. Hu, *Organometallics*, **2004**, *23*, 976; b) W. A. Herrmann, K. Öfele, D. von Preysing, E. Herdtweck, *J. Organomet. Chem.* **2003**, *684*, 235; c) K. Denk, P. Sirsch, W. A. Herrmann, *J. Organomet. Chem.* **2002**, *649*, 219; d) M. Tafipolsky, M. Scherer, K. Öfele, G. Artus, B. Pedersen, W. A. Herrmann, G. S. McGrady, *J. Am. Chem. Soc.* **2002**, *124*, 5865.

[5] X. Cattoën, H. Gornitzka, D. Bourissou, G. Bertrand, *J. Am. Chem. Soc.* **2004**, *126*, 1342.

[6] M. Jones, Jr. in *Reactive Intermediate Chemistry* (Eds.: R. A. Moss, M. S. Platz, M. Jones, Jr.), Wiley-Interscience, Hoboken, NJ, **2004**, pp. 273–328.

[7] N. Merceron-Saffon, A. Baceiredo, H. Gornitzka, G. Bertrand, *Science* **2003**, *301*, 1223.

[8] N. Merceron, K. Miqueu, A. Baceiredo, G. Bertrand, *J. Am. Chem. Soc.* **2002**, *124*, 6806.

[9] a) R. Weiss, R. Roth, *Z. Naturforsch. B* **1998**, *53*, 599; b) R. Weiss, S. Reichel, M. Handke, F. Hampel, *Angew. Chem.* **1998**, *110*, 352; *Angew. Chem. Int. Ed.* **1998**, *37*, 344; c) R. Weiss, R. Roth, *Synthesis* **1987**, 870.

[10] a) R. W. Alder, M. E. Blake, S. Bufali, C. P. Butts, A. G. Orpen, J. Schütz, S. J. Williams *J. Chem. Soc. Perkin Trans. 1* **2001**, 1586; b) R. W. Alder, C. P. Butts, A. G. Orpen, *J. Am. Chem. Soc.* **1998**, *120*, 11526.

[11] a) R. Weiss, R. May, B. Pomrehn, *Angew. Chem.* **1996**, *108*, 1319; *Angew. Chem. Int. Ed. Engl.* **1996**, *35*, 1232; b) R. Weiss, B. Pomrehn, F. Hampel, W. Bauer, *Angew. Chem.* **1995**, *107*, 1446; *Angew. Chem. Int. Ed. Engl.* **1995**, *34*, 1319; c) R. Weiss, N. J. Salomon, G. E. Miess, R. Roth, *Angew. Chem.* **1986**, *98*, 925; *Angew. Chem. Int. Ed. Engl.* **1986**, *25*, 917.

[12] The Bruker SMART-1000[18a] X-ray diffraction instrument with Mo radiation was used for data collection of compounds **3a**, **3b**, **4a**, and **4b.** All data frames were collected by using ω-scan mode (−0.3° ω-scan width, hemisphere of reflections) and integrated by using the Bruker SAINTPLUS program.[18b] The intensity data were corrected for Lorentzian polarization and absorption corrections were performed by using the SADABS program incorporated in the SAINTPLUS program. The Bruker SHELXTL program[18c] was used for direct methods of phase determination and structure refinement. Atomic coordinates, isotropic and anisotropic displacement parameters of all the non-hydrogen atoms of the four compounds were refined by means of a full-matrix least-squares procedure on F^2. All H atoms were included in the refinement in calculated positions riding on the atoms to which they were attached. Crystal data for **3a:** size 0.56 × 0.44 × 0.28 mm^3, orthorhombic, space group *Pbca*, a = 14.709(3) Å, b = 15.705(4) Å, c = 28.878(6) Å, $\alpha = \beta = \gamma$ = 90°, V = 6671(3) Å^3, ρ_{calcd} = 1.378 g cm^{-3}, $2\theta_{max}$ = 56.56°, Mo radiation (λ = 0.71073 Å), low temperature = 223(2) K, total reflections collected = 69549, independent reflections = 8276 (R_{int} = 0.0377, R_{sig} = 0.0203), 6571 (79.4%) reflections were greater than $2\sigma(I)$, index ranges $-19 \le h \le 19$, $-20 \le k \le 20$, $-36 \le l \le 38$, absorption coefficient μ = 0.280 mm^{-1}; max/min transmission = 0.9256/0.8588, 513 parameters were refined and converged at $R1$ = 0.0460, $wR2$ = 0.1131, with intensity $I > 2\sigma(I)$, the final difference map was 0.538/−0.327 e Å^{-3}. **3b:** size 0.51 × 0.30 × 0.13 mm^3, monoclinic, space group $P2(1)/c$, a =

8.4220(12) Å, $b = 19.597(3)$ Å, $c = 18.867(3)$ Å, $\beta = 101.212(3)°$, $V = 3054.5(8)$ Å^3, $\rho_{calcd} = 1.465$ g cm^{-3}, $2\theta_{max} = 52.74°$, Mo-radiation ($\lambda = 0.71073$ Å), low temperature = 223(2) K, total reflections collected = 17766, independent reflections = 6234 ($R_{int} = 0.0274$, $R_{sig} = 0.0303$), 4972 (79.8 %) reflections were greater than $2\sigma(I)$, index ranges $-10 \le h \le 10$, $-23 \le k \le 24$, $-20 \le l \le 23$, absorption coefficient $\mu = 0.305$ mm^{-1}; max/min transmission = 0.9615/0.8601, 422 parameters were refined and converged at $R1 = 0.0387$, $wR2 = 0.0960$, with intensity $I > 2\sigma(I)$, the final difference map was 0.402/−0.306 e Å^{-3}. **4a:** size $0.48 \times 0.14 \times 0.08$ mm^3, monoclinic, space group $P2(1)/n$, $a = 10.4384(14)$ Å, $b = 9.7257(10)$ Å, $c = 28.325(4)$ Å, $\beta = 91.238(2)°$, $V = 2874.9(6)$ Å^3, $\rho_{calcd} = 1.251$ g cm^{-3}, $2\theta_{max} = 52.74°$, Mo-radiation ($\lambda = 0.71073$ Å), low temperature = 223(2) K, total reflections collected = 26302, independent reflections = 5865 ($R_{int} = 0.0589$, $R_{sig} = 0.0486$), 4157 (70.9 %) reflections were greater than $2\sigma(I)$, index ranges $-13 \le h \le 12$, $-12 \le k \le 12$, $-35 \le l \le 35$, absorption coefficient $\mu = 0.215$ mm^{-1}; max/min transmission = 0.9830/0.9040, 367 parameters were refined and converged at $R1 = 0.0574$, $wR2 = 0.1479$, with intensity $I > 2\sigma(I)$, the final difference map was 1.043/−0.611 e Å^{-3}. **4b:** size $0.68 \times 0.42 \times 0.41$ mm^3, monoclinic, space group $P2(1)/n$, $a = 8.3940(11)$ Å, $b = 10.5726(14)$ Å, $c = 29.903(4)$ Å, $\beta = 97.160(3)°$, $V = 2633.1(6)$ Å^3, $\rho_{calcd} = 1.321$ g cm^{-3}, $2\theta_{max} = 56.56°$, Mo-radiation ($\lambda = 0.71073$ Å), low temperature = 228(2) K, total reflections collected = 19642, independent reflections = 6509 ($R_{int} = 0.0263$, $R_{sig} = 0.0273$), 5494 (84.4 %) reflections were greater than $2\sigma(I)$, index ranges $-11 \le h \le 10$, $-14 \le k \le 14$, $-22 \le l \le 39$, absorption coefficient $\mu = 0.233$ mm^{-1}; max/min transmission = 0.9056/0.7309, 320 parameters were refined and converged at $R1 = 0.0470$, $wR2 = 0.1251$, with intensity $I > 2\sigma(I)$, the final difference map was 0.501/−0.541 e Å^{-3}. CCDC-233824 (**3a**), CCDC-233825 (**3b**), CCDC-233826 (**4a**) and CCDC-233827 (**4b**) contain the supplementary crystallographic data for this paper. These data can be obtained free of charge via www.ccdc.cam.ac.uk/conts/retrieving.html (or from the Cambridge Crystallographic Data Centre, 12, Union Road, Cambridge CB2 1EZ, UK; fax: (+44) 1223-336-033; or deposit@ccdc.cam.ac.uk).

[13] The dissociation energy for the parent compound $H_3PCH(NH_2)$ has been calculated to be only 8.1 kcal mol^{-1}. H. J. Bestmann, A. Kos, K. Witsgall, P. von R. Schleyer, *Chem. Ber.* **1986**, *119*, 1331.

[14] M. Otto, S. Conejero, Y. Canac, V. D. Romanenko, V. Rudzevitch, G. Bertrand, *J. Am. Chem. Soc.* **2004**, *126*, 1016.

[15] a) The activation energies for 1,2-hydrogen shifts[16a] are essentially zero for simple alkylcarbenes but increase significantly for heteroatom-substituted alkylcarbenes.[16b,c]

[16] a) R. Bonneau, M. T. H. Liu in *Advances in Carbene Chemistry*, *Vol. 2* (Ed.: U. H. Brinker), Jai Press, Stamford, **1998**, p. 1; b) J. D. Evanseck, K. N. Houk, *J. Phys. Chem.* **1990**, *94*, 5518; c) E. Despagnet, H. Gornitzka, A. B. Rozhenko, W. W. Schoeller, D. Bourissou, G. Bertrand, *Angew. Chem.* **2002**, *114*, 925; *Angew. Chem. Int. Ed.* **2002**, *41*, 2959.

[17] G. Wieland, G. Simchen, *Liebigs Ann. Chem.* **1985**, 2178.

[18] a) SMART Software Reference Manual, Version 5.054, Bruker Analytical X-Ray System, Inc., Madison, WI **1997–1998**; b) SAINTPLUS Software Reference Manual, Version 6.02A, Bruker Analytical X-Ray System, Inc., Madison, WI **1997–1998**; c) SHELXTL Software Reference Manual, Version 6.10, Dec. 5th, **2000**, Bruker Analytical X-Ray System, Inc., Madison, WI.

 © 2004 Wiley-VCH Verlag GmbH & Co. KGaA, Weinheim

Phosphorus Radicals

"Naked" Phosphanediide Chains and their Fragmentation into Diphosphene Radical Anions**

*Jens Geier, Jeffrey Harmer, and Hansjörg Grützmacher**

Most multiple charged molecules are unstable in the absence of a stabilizing environment of opposite charge and decompose either under "Coulomb explosion", that is, under bond cleavage, and/or by electron detachment.[1] The latter process occurs easily in the case of polyanions because electrons are readily lost by tunneling through the barrier at the intersection of the X^{n-} and $X^{(n-1)-} + e^-$ (X = molecular fragment) potential energy surfaces. Numerous polyanions with phosphorus are found in the solid state as Zintl phases (M_nP_m), which generally show tight anion–cation contacts.[2] For example, in Ca_2P_2[3] or $[Cs_2P_4(NH_3)_2]$,[4] which contain the small $(P_2)^{4-}$ or the 6π aromatic $(P_4)^{2-}$ ions, the high concentration of negative charge is stabilized by the formation of bicyclobutane-type arrangements such as **A** in Figure 1. Such

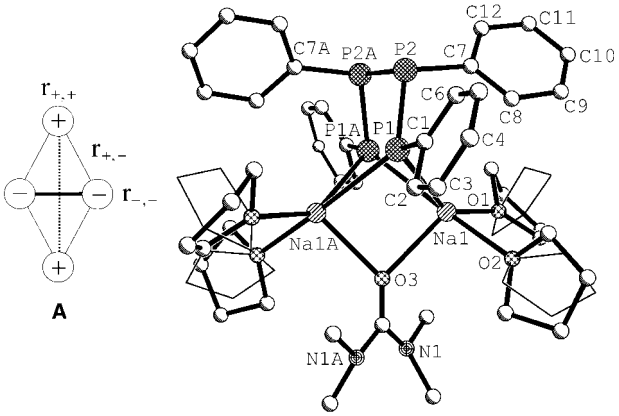


Figure 1. Bicyclobutane-shaped fragment **A** characteristic for $[(M^+)_2(X^{2-})]$ ion triples and structure of *rac*-[**1a**$(thf)_4$(tmu)]. Hydrogen atoms are omitted for clarity and the second orientation of the disordered THF molecules is shown in thin lines. Selected distances [Å] and angles [°]: Na1-P1 2.974(2), Na1-P1A 2.918(2), Na1-Na1A 3.491(4), Na1-O1 2.405(4), Na1-O2 2.326(4), Na1-O3 2.453(4), P1-P2 2.163(2), P2-P2A 2.206(2), P1-C1 1.809(4), P2-C7 1.850(5); C1-P1-P2 102.0(1), P1-P2-P2A 104.4(1), P1-P2-C7 107.4(1), C7-P2-P2A 98.8(2), C2-C1-C6 115.7(4), C8-C7-C12 117.3(4), P1-P2-P2A-P1A −31.9(1), C1-P1-P2-C7 88.8(2), C7-P2-P2A-C7A −170.6(3), normal angle (Na1,P1,P1A)/(Na1A,P1,P1A): 85.7(1).

[*] Dr. J. Geier, Dr. J. Harmer, Prof. Dr. H. Grützmacher
Department of Chemistry, HCI
ETH Hönggerberg
8093 Zürich (Switzerland)
Fax: (+41) 1-63-1032
E-mail: gruetzmacher@inorg.chem.ethz.ch

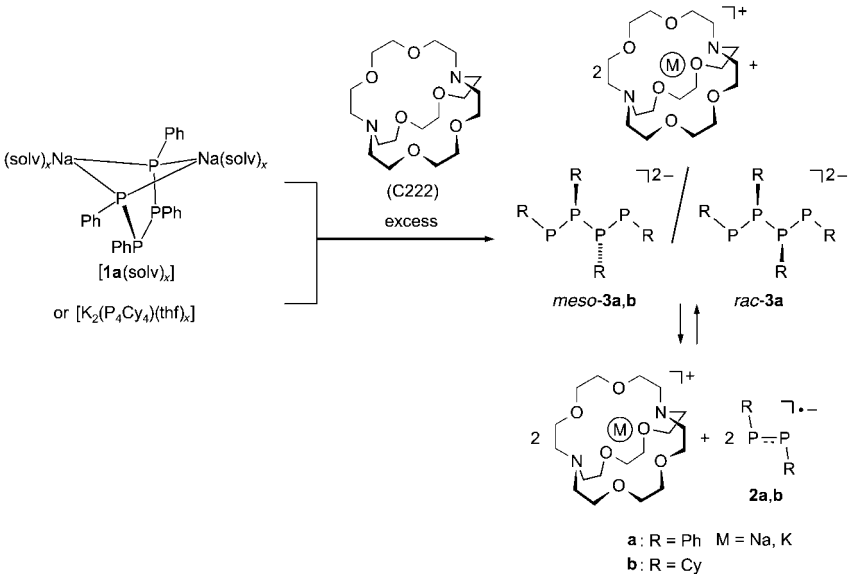
[**] This work was supported by the ETH Zürich and Ciba Speciality Chemicals.

Supporting information for this article is available on the WWW under http://www.angewandte.org or from the author.

 DOI: 10.1002/anie.200460130 © 2004 Wiley-VCH Verlag GmbH & Co. KGaA, Weinheim

arrangements are typical for ion triples[5] and are favored because they contain four attractive Coulombic interactions ($r_{+,-}$) but only two repulsive ones ($r_{-,-}$ and $r_{+,+}$), respectively. Exceptions are $[(BnMe_3N)^+_2(P_{11}H)^{2-}]$ and $[(EtMe_3N)^+_3(P_{11})^{3-}]$[6] which contain weakly coordinating large cations and the negative charges are delocalized over the σ framework of the P_{11} cage. Geminal dianions $(RP)^{2-}$ could be isolated in organophosphorus chemistry as cage compounds through intimate contacts with the countercations.[7] In the solid-state structures of bis(alkali metal)-*catena*-oligophosphane-α,ω-diides $[M_2(P_mR_m)(solv)_x]$ (M = Li, Na, K; $m = 2$, 3, 4; solv = M-bonded solvent molecules) ion triples with a M_2P_2-bicyclobutane-type arrangement were observed.[8,9] An example of such an ion triple is the C_2-symmetric disodium 1,2,3,4-tetraphenyltetraphosphane-1,4-diide $[Na_2(P_4Ph_4)(thf)_4(tmu)]$ (*rac*-[**1a**$(thf)_4$-(tmu)], tmu = tetramethylurea; Figure 1).[10] This compound was obtained by reduction of phenylphosphonous acid dichloride with sodium metal in toluene/tetramethylethylenediamine (tmeda)[8a] and recrystallization of the product $[Na_2(P_4Ph_4)(tmeda)_2]$ from THF in the presence of tetramethylurea. The folding along the (P1,P1A) vector, caused by the bridging carbonyl oxygen atom of the strong tmu ligand, is particularly acute ($\Phi = 85.7°$), and consequently the Na···Na distance (3.491(4) Å) is relatively short compared with other $[Na_2P_nR_n]$ bicyclic structures ($n = 3$, 4). All other structural parameters lie within the typical range (Figure 1).[8,9] The terminal phenyl rings are only slightly tilted with respect to the adjacent P1–P2/P1A–P2A bonds (12.6°), and the terminal P–C bonds are shorter (P1–C1 1.809(4) Å) than the internal ones (P2–C7 1.850(5) Å), thus indicating charge delocalization from the formally negatively charged terminal phosphorus centers into the phenyl rings. The phosphorus centers at the central P–P unit of the P_4 chain in the $[M_2(P_4R_4)]$ ion triples has the *R*,*R*(*S*,*S*) configuration, that is, the P_4 chain is made of the sterically favored racemic *threo* isomer.

Would "naked" $(P_4R_4)^{2-}$ dianionic chains be stable? To answer this question we added an excess of the bicyclic sodium/potassium-complexing agent [2.2.2]cryptand (C222)[11] to (EPR-silent) solutions of *rac*-[**1a**(solv)] (solv = tmeda, dimethoxyethane (dme), thf; Scheme 1). A color change from yellow to red-orange occurred immediately and was accompanied by the precipitation of most of the phosphorus-containing species (> 90 %), firstly as a red oil which soon crystallized to give red and yellow crystals. Freshly prepared, inhomogeneous samples of the *rac*-[**1a**(solv)]/cryptand mixture gave a strong EPR signal ($g = 2.0089$) which appeared as a triplet ($a_{iso}[P] = 115$ MHz) as a result of hyperfine coupling with two identical ^{31}P nuclei. The signal is further split by smaller ^1H couplings to two nonequivalent *ortho* protons on each benzene ring ($a_{iso}[H] = 8.5$ MHz and $a_{iso}[H'] = 4.0$ MHz; Figure 2a).



Scheme 1. Syntheses of **2a**,**b** and *rac*-**3a**/*meso*-**3a**,**b**.

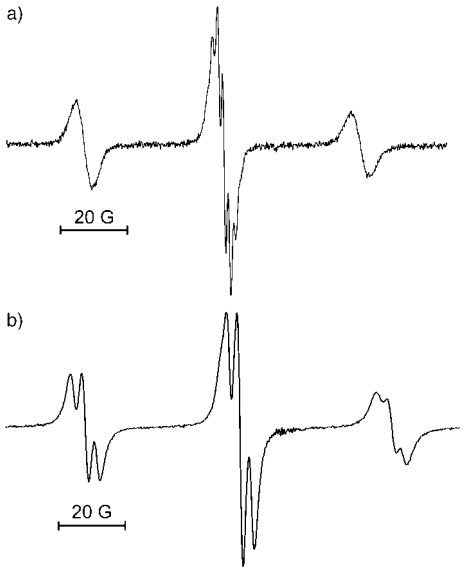


Figure 2. X-band EPR spectra of **2a** (a) and **2b** (b) in THF at room temperature. Spectra were measured with a microwave frequency of 9.7 GHz, a modulation amplitude of 0.05 mT, and a modulation frequency of 100 kHz.

This EPR spectrum is assigned to the free diphenyldiphosphene radical anion $(P_2Ph_2)^{\bullet-}$ (**2a**) formed by homolytic cleavage of the central P–P bond in the $(P_4Ph_4)^{2-}$ dianion upon removal of its charge-stabilizing contacts to the positive sodium counterions.[12] Dilute solutions of **2a** are remarkable stable, however, the same crystalline solids as formed in the reaction of *rac*-[**1a**(solv)] with (C222) were obtained upon concentration. These crystals were carefully washed with small portions of THF and then suspended in THF, which became slightly orange, thus indicating the complex was slightly soluble.

 © 2004 Wiley-VCH Verlag GmbH & Co. KGaA, Weinheim

However, no ^{31}P NMR signal could be recorded; instead, **2a** was again detected by EPR spectroscopy. X-ray structure analyses were performed on both the red and yellow crystals. The red crystals, which are formed in a smaller amount, contain the 2*R*,3*S* diastereomer (*meso* or *erythro* isomer) of the "naked" $(P_4Ph_4)^{2-}$ chain (*meso*-**3a**)[10] (Figure 3a) and the yellow ones the (2*R*,3*R*)/(2*S*,3*S*)-configured diastereomer *rac*-**3a**[10] (not shown here because the crystals of *rac*-**3a** were of poor quality and although the gross structural features could be unambiguously determined, a sufficient refinement of the data sets was impossible, see the Supporting Information for details and structure plots).

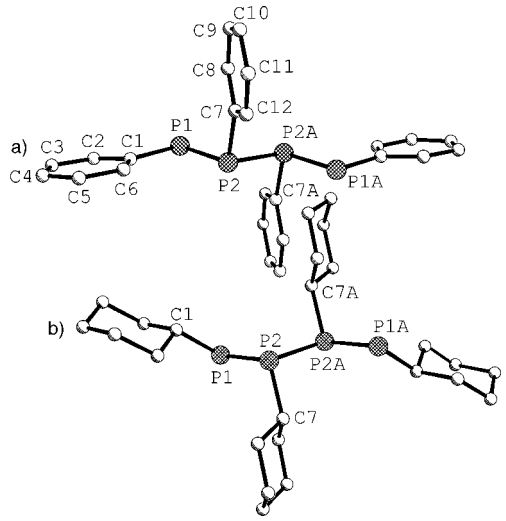


Figure 3. Solid-state structures of *meso*-**3a** (a) and *meso*-**3b** (b). Hydrogen atoms and countercations (*meso*-**3a**: $[Na(C222)]^+$, *meso*-**3b**: $[K(C222)]^+$) are omitted for clarity. Selected distances [Å] and angles [°]: a) P1-P2 2.178(1), P2-P2A 2.224(2), P1-C1 1.811(3), P2-C7 1.863(3); C1-P1-P2 99.8(1), P1-P2-P2A 97.4(1), P1-P2-C7 105.4 (1), C7-P2-P2A 97.7(1), C2-C1-C6 115.9(3), C8-C7-C12 117.3(3), P1-P2-P2A-P1A 180.0(0), C1-P1-P2-C7 −86.5(1), C7-P2-P2A-C7A 180.0(0); b) P1-P2 2.147(3), P2-P2A 2.210(4), P1-C1 1.866(7), P2-C7 1.876(8); C1-P1-P2 102.1(3), P1-P2-P2A 104.2(2), P2-P2-C7 106.2(3), C7-P2-P2A 96.3(3), P1-P2-P2A-P1A 180.0(0), C1-P1-P2-C7 121.7(4), C7-P2-P2A-C7A 180.0(0).

We also examined the reaction of the cyclohexyl (Cy) analogue $[K_2(P_4Cy_4)(thf)_x]$ [**1b**$(thf)_x$][13] (of unknown structure) with an excess of the [2.2.2]cryptand. As with *rac*-[**1a**(solv)], a strong EPR signal was observed ($g = 2.0099$) which indicates the formation of the radical anion $(P_2Cy_2)^{\bullet-}$ **2b** (Figure 2b). In addition to the ^{31}P hyperfine couplings of $a_{iso}[P] = 127$ MHz, which are slightly larger than the ones in **2a**, couplings with the protons at the C1 atom were observed ($a_{iso}[H] = 10$ MHz). One sort of crystals precipitated from the THF solution and was subjected to X-ray structure analysis. The result (Figure 3b) shows them to be composed of $[\{K(C222)\}_2^+](P_4Cy_4)^{2-}$. The "naked" $[P_4Cy_4]^{2-}$ chain corresponds to the 2*R*,3*S* diastereomer, that is, $[\{K(C222)\}_2^+](P_4Cy_4)^{2-}$ is denoted as *meso*-**3b**.

The centrosymmetric dianions in *meso*-**3a** and *meso*-**3b** provide the first structures for "naked" α,ω-dianions of chains made from main-group IV/V elements. The sodium ions in *meso*-**3a** and the potassium ions in *meso*-**3b** are completely encapsulated in the internal cavity of the cryptand. The shortest contacts between the formally negatively charged terminal phosphorus atoms P1 and P1A and the hydrogen atoms at the outside of the $[M(C222)]^+$ ions (M = Na, K) are about 2.88–3.05 Å. With exception of the C1-P1-P2-P2A torsion angles (*meso*-**3a**: −173.4(3)° , *meso*-**3b**: −137.2(3)°) the structural features of both P_4 chains are quite similar. For electrostatic reasons they adopt a planar 1,4-*anti* conformation to maximize the P1···P1A distance (5.139(2) Å in *meso*-**3a**, 5.289(2) Å in *meso*-**3b**) which is much shorter in the ion triple *rac*-[**1a**$(thf)_4(tmu)$] (3.475(2) Å). As in this latter complex, the terminal phenyl groups in *meso*-**3a** are almost coplanar with the P_4 chain (tilt angle 8.7°), and the distinctly shorter terminal P–C bonds (P1–C1: 1.811(3) Å versus P2–C7: 1.863(3) Å) may indicate some charge delocalization. This proposal is consistent with the observation of hindered rotation of the phenyl groups in the planar $(P_2Ph_2)^{\bullet-}$ radical anion[14] on the EPR time scale, that is, **2a** also profits from some π-type charge delocalization. Evidently, such effects are absent in the cyclohexyl-substituted analogues and the P–C bonds in *meso*-**3b** are almost identical (P1–C1: 1.866(7) Å and P2–C7: 1.876(8) Å). The most notable structural feature in *meso*-**3a**,**b** is that the stereochemistry at one of the central phosphorus atoms has been inverted when compared to the ion triples *rac*-[**1a**(solv)]. In view of the sizable inversion barriers at σ^3,λ^3-phosphorus centers in phosphanes (PR_3)[15] and the typical sum of bond angles at P2/P2A (*meso*-**3a**: 300.5°, *meso*-**3b**: 306.7°), it is reasonable to assume that the 2*R*,3*S*-configured P_4 chains in *meso*-**3a**,**b** result from a cleavage of the central P–P bond of the P_4 units in the ion triples into two $(P_2R_2)^{\bullet-}$ radical anions **2a**,**b** upon removal of the stabilizing anion–cation interactions. Subsequently, the radicals recombine to give the P_4 chains with the sterically favored *anti* arrangement of the internal substituents at P2 and P2A.[16] This process is reversible, that is, the ion triple *rac*-**1a** with its *R*,*R*(*S*,*S*)-configured P_4 units is reformed when crystals of *meso*/*rac*-**3a** are dissolved in a solution of sodium triflate (NaO_3SCF_3) in THF. No unusual P–P bond lengths are observed in *meso*-**3a**,**b**, and thus neither strain nor an especially weak central P–P bond is responsible for the dissociation process. The central P–P bond in the ion triple $[Na_2(P_4Ph_4)(thf)_4(tmu)]$ (*rac*-[**1a**$(thf)_4(tmu)$]) and the P_4 chains in *meso*-**3a**,**b** (*rac*-[**1a**$(thf)_4(tmu)$]: 2.206(2) Å; *meso*-**3a**: 2.224(2) Å; *meso*-**3b**: 2.210(4) Å) is only slightly longer than the terminal ones (*rac*-[**1a**$(thf)_4(tmu)$]: 2.163(2) Å; *meso*-**3a**: 2.178(1) Å; *meso*-**3b**: 2.147(3) Å). In contrast, the sterically overcrowded diphosphane $[(Me_3Si)_2CH]_2P–P[CH(SiMe_3)_2]_2$, which is cleaved into two $[(Me_3Si)_2CH]_2P^{\bullet}$ radicals upon melting, dissolution, or vaporization, shows a modestly elongated P–P bond (2.3103(7) Å) and considerable distortions in the geometry of the ligands.[17] The destabilizing energy which causes the dissociation of the "naked" $(P_4R_4)^{2-}$ chains in solution must have its origin mainly in the Coulombic repulsion between the negative charges. On the other hand, the electrostatic field in the crystals of *meso*-**3a**,**b** is clearly capable of allowing these weakly bonded or even unstable dianions to form quite normal oligophosphanes. While the neutral "phosphoben-

 © 2004 Wiley-VCH Verlag GmbH & Co. KGaA, Weinheim

zene" PhP=PPh is unstable,[18] the phenomena described here allow the synthesis of the persistent free-radical anion $(P_2Ph_2)^{\bullet-}$ with partial P,P multiple bond character in solution. Such species must be considered in the chemistry of organophosphanides.[19]

Experimental Section

Inert conditions were maintained throughout all procedures. *rac*/*meso*-**3a**: Vacuum-distilled [2.2.2]cryptand (28 mg, 0.074 mmol) was added at room temperature in one portion to a solution of *rac*-[**1a**(tmeda)$_2$][8a] (25 mg, 0.035 mmol) in THF (0.5 mL) contained in a narrow (5 mm diameter) glass tube. The yellow solution became cloudy red-orange and a deep red oil separated which subsequently solidified over several hours to form a mixture of red, irregular-shaped (*meso*-**3a**) and yellow, needlelike (*rac*-**3a**) crystals (combined yield: $>90\%$). The ratio of *rac*-**3a** to *meso*-**3a** was approximately 3:1—4:1 and increased further on using more dilute solutions. The orange-colored solution contained the radical **2a**, which was also observed in a lower concentration upon re-suspending the isolated (namely, rigorously THF-washed), sparingly soluble crystals of *meso*/*rac*-**3a** in THF. Addition of sodium triflate to *meso*/*rac*-**3a** in THF gave a clear yellow solution. The ^{1}H, ^{13}C, and ^{31}P NMR spectra for the $(P_4Ph_4)^{2-}$ section were identical to those of the starting material *rac*-[**1a**(tmeda)$_2$]. *Meso*-**3b** was prepared by addition of [2.2.2]cryptand (100 mg, 0.266 mmol) to a suspension of $[K_2(P_4Cy_4)(thf)_x]$[13] (70 mg, <0.13 mmol) in THF (20 mL). A clear red solution formed upon sonification and short (30 s) warming to 45 °C. Yellow crystals of *meso*-**3b** deposited on storing overnight (ca. 70%). M.p. 135 °C (decomp); IR (neat): $\tilde{\nu}$ = 2962w, 2886m, 2835m, 2824m, 2800m, 1479m, 1456w, 1445m, 1356m, 1295m, 1258m, 1166w, 1133m, 1095s, 1081s, 986w, 944s, 932s, 875w, 845w, 830m, 819w, 750w, 699w cm^{-1}. The solution contained the radical **2b**, which was also observed (in lower concentration) upon suspending the sparingly soluble, carefully washed crystals of *meso*-**3b** in THF. *rac*-[**1a**(thf)$_4$(tmu)]: Tetramethylurea (25 mg, 0.22 mmol) was added to *rac*-[**1a**(tmeda)$_2$] (150 mg, 0.21 mmol) in THF (10 mL). Large yellow crystals were isolated after concentration to 1/5 of the original volume and storing for one day at room temperature (47%; for spectroscopic data see the Supporting Information), m.p. 95 °C.

Received: March 26, 2004 [Z460130]

Keywords: EPR spectroscopy · ion pairs · phosphorus · radicals

[1] For a recent short review, see D. Schröder, *Angew. Chem.* **2004**, *116*, 1351; *Angew. Chem. Int. Ed.* **2004**, *43*, 1329.
[2] H.-G. von Schnering, W. Hönle, *Chem. Rev.* **1988**, *88*, 243.
[3] J. Getzschmann, P. Boettcher, W. Katurza, *Z. Kristallogr.* **1996**, *211*, 90.
[4] F. Kraus, J. C. Aschenbrenner, N. Korber, *Angew. Chem.* **2003**, *115*, 4162; *Angew. Chem. Int. Ed.* **2003**, *42*, 4030.
[5] A. Streitwieser, Jr., *Acc. Chem. Res.* **1984**, *17*, 353.
[6] N. Korber, J. Daniels, H.-G. von Schnering, *Angew. Chem.* **1996**, *108*, 1188; *Angew. Chem. Int. Ed. Engl.* **1996**, *35*, 1107.
[7] Reviews: a) K. Izod, *Adv. Inorg. Chem.* **2000**, *50*, 33; b) M. Driess, *Adv. Inorg. Chem.* **2000**, *50*, 236; c) M. Driess, *Acc. Chem. Res.* **1999**, *32*, 1017; [Mg(PR)] compounds: d) M. Westerhausen, M. Krofta, A. Pfitzner, *Inorg. Chem.* **1999**, *38*, 598; e) M. Westerhausen, S. Schneiderbauer, J. Knizek, H. Nöth, A. Pfitzner, *Eur. J. Inorg. Chem.* **1999**, 2215.
[8] a) J. Geier, H. Rüegger, M. Wörle, H. Grützmacher, *Angew. Chem.* **2003**, *115*, 4081; *Angew. Chem. Int. Ed.* **2003**, *42*, 3951; b) lithium compounds: D. Stein, M. Scherer, H. Grützmacher, unpublished results.
[9] R. Wolf, E. Hey-Hawkins, "Alkali Metal Salts of Catenated Oligophosphanes—Corresponding Structures in the Solid State and in Solution?", lecture presented by R. Wolf at ALKCHEM-3, Würzburg, Germany, 30.09.2003.
[10] The data were collected on a Bruker AXS Smart Platform (*rac*-[**1a**(thf)$_4$(tmu)]) or an Apex (*meso*/*rac*-**3a**,**b**) CCD diffractometer and were corrected with the program SADABS version 2.03 (Bruker AXS). The structures were solved by direct methods and all atoms except hydrogen were refined anisotropically (SHELXTL version 6.12, Bruker AXS). *rac*-[**1a**(thf)$_4$(tmu)]: $C_{45}H_{64}N_2Na_2O_5P_4$; yellow cuboid, crystal size $0.63\times0.59\times0.51$ mm; monoclinic, space group $C2/c$, a = 13.785(4), b = 16.245(5), c = 21.955(6) Å, β = 90.695(4)°, V = 4916(2) Å^3, Z = 4, μ = 0.21 mm^{-1}; $\lambda(Mo_{K\alpha})$ = 0.71073 Å, T = 293 K, $2\theta_{max}$ = 52.74°, collected (independent) reflections = 18872 (5036), R_{int} = 0.0289; 259 refined parameters, R_1 = 0.0823 for 3021 reflections with $I>2\sigma$, wR_2 = 0.2790 for all data, GOF on F^2 = 1.036, max./min. residual electron density = 0.53/−0.28 e Å^{-3}. Two orientations were refined for each of the disordered THF molecules with occupancies of 0.45/0.55 and 0.33/0.67 respectively. *Meso*-**3a:** $C_{60}H_{92}N_4Na_2O_{12}P_4$; red irregular crystal, crystal size $0.40\times0.32\times0.15$ mm; triclinic, space group $P\bar{1}$, a = 11.254(1), b = 12.674(1), c = 14.259(1) Å, α = 98.248(1), β = 112.408(1), γ = 112.302(1)°, V = 1637.9(2) Å^3, Z = 1, μ = 0.19 mm^{-1}; $\lambda(Mo_{K\alpha})$ = 0.71073 Å, T = 293 K, $2\theta_{max}$ = 52.74°, collected (independent) reflections = 13289 (6630), R_{int} = 0.0181; 370 refined parameters, R_1 = 0.0631 for 4720 reflections with $I>2\sigma$, wR_2 = 0.1877 for all data, GOF on F^2 = 1.039, max./min. residual electron density = 1.24/−0.36 e Å^{-3}. *Meso*-**3b**: $C_{60}H_{116}K_2N_4O_{12}P_4$; yellow irregular crystal, crystal size $0.19\times0.18\times0.15$ mm; triclinic, space group $P\bar{1}$, a = 11.420(5), b = 12.218(6), c = 13.391(6) Å, α = 92.041(8), β = 104.659(8), γ = 106.041(7)°, V = 1726(1) Å^3, Z = 1, μ = 0.29 mm^{-1}; $\lambda(Mo_{K\alpha})$ = 0.71073 Å, T = 293 K, $2\theta_{max}$ = 43.92°, collected (independent) reflections = 9153 (4160), R_{int} = 0.1125; 370 refined parameters, R_1 = 0.0916 for 1936 reflections with $I>2\sigma$, wR_2 = 0.2259 for all data, GOF on F^2 = 0.893, max./min. residual electron density = 1.53/−0.62 e Å^{-3}. The structure of *rac*-**3a** could not be refined: $C_{60}H_{92}N_4Na_2O_{12}P_4$; yellow needle, crystal size $0.18\times0.06\times0.05$, triclinic, space group $P\bar{1}$, a = 12.975(6), b = 13.023(6), c = 22.72(1) Å, α = 95.25(1), β = 95.12(1), γ = 95.54(1)°, V = 3786(3) Å^3, Z = 2.
[11] 4,7,13,16,21,24-Hexaoxa-1,10-diazabicyclo[8.8.8]hexacosane: B. Dietrich, J.-M. Lehn, J.-P. Sauvage, J. Blanzat, *Tetrahedron* **1973**, *29*, 1629.
[12] Other persistent radical anions have been reported; $[P_2(2,4,6\text{-}tBu_3Ph)_2]^{\bullet-}$: a) B. Cetinkaya, P. B. Hitchcock, M. F. Lappert, A. J. Thorne, H. Goldwhite, *J. Chem. Soc. Chem. Commun.* **1982**, 691; $[P_2\{(Me_3Si)_3C\}_2]^{\bullet-}$: b) A. J. Bard, A. H. Cowley, J. E. Kilduff, J. K. Leland, N. C. Norman, M. Pakulski, G. A. Heath, *J. Chem. Soc. Dalton Trans.* **1987**, 249; c) M. Culcasi, G. Gronchi, J. Escudié, C. Cuoret, L. Pujol, P. Tordo, *J. Am. Chem. Soc.* **1986**, *108*, 3130; $[P_2(2,6\text{-}Mes_2Ph)_2]^{\bullet-}$: d) S. Shaw, S. C. Burdette, S. Swavey, F. L. Urbach, J. D. Protasiewicz, *Organometallics* **1997**, *16*, 3395; $[P_2tBu_2]^{\bullet-}$: e) H. Binder, B. Riegel, G. Heckmann, M. Moscherosch, W. Kaim, H.-G. von Schnering, W. Hönle, H.-J. Flad, A. Savin, *Inorg. Chem.* **1996**, *35*, 2119.
[13] a) This THF-insoluble compound was prepared in the reaction of P_4Cy_4 (from $CyPCl_2$ and $CyPH_2$[13b]) with potassium in THF according to: K. Issleib, K. Krech, *Chem. Ber.* **1965**, *98*, 2545; b) W. A. Henderson, Jr., M. Epstein, F. S. Seichter, *J. Am. Chem. Soc.* **1963**, *85*, 2462.
[14] A planar structure is also predicted by DFT calculations, which show that the planar *trans* isomer is preferred by about 8 kcal mol^{-1} over the *gauche* isomer: J. Geier, unpublished results; see also ref. [12d].

 © 2004 Wiley-VCH Verlag GmbH & Co. KGaA, Weinheim

[15] Inversion barriers lie around 30–36 kcal mol^{-1}: R. D. Baechler, K. Mislow, *J. Am. Chem. Soc.* **1970**, *92*, 3090.

[16] Although the structure is not known, we assume that the $(P_4Cy_4)^{2-}$ chain in the ion triple $[K_2(P_4Cy_4)(thf)_x]$ ([**1b**(thf)$_x$]) has, like the $(P_4Ph_4)^{2-}$ chains in *rac*-[**1a**(solv)], the sterically favored *R*,*R*(*S*,*S*) configuration. We cannot definitively say that the intact $(P_4R_4)^{2-}$ chains are not present in solution together with the radical anions $(P_2R_2)^{\bullet-}$, although we have no spectroscopic indication that they are present. The observation that the racemic "naked" $(P_4Ph_4)^{2-}$ chain can be isolated as $[\{Na(C222)\}_2^+](P_4Ph_4)^{2-}$ (*rac*-**3a**) from *rac*-[**1a**(solv)] indicates that such a species may also have a short lifetime in solution. In this case, nucleophilic substitution reactions, that is for example, 2 *rac*-$(P_4Ph_4)^{2-} \rightarrow (P_6Ph_6)^{2-} + (P_2Ph_2)^{2-} \rightarrow 2$ *meso*/*rac*-$(P_4Ph_4)^{2-}$, or elimination processes involving neutral cyclooligophosphanes (in simplified form for example, *rac*-$(P_4Ph_4)^{2-} \rightarrow (PPh)_n^{2-} + (4-n)/m\ (PPh)_m \rightarrow$ *meso*/*rac*-$(P_4Ph_4)^{2-}$, $1 < n < 4$ and $3 \leq m \leq 6$) might also operate but $(PPh)_n^{2-}$ dianions with $n > 4$ have never been observed.

[17] a) S. L. Hinchley, C. A. Morrison, D. W. H. Rankin, C. L. B. Macdonald, R. J. Wiacek, A. Voigt, A. H. Cowley, M. F. Lappert, G. Gundersen, J. A. C. Clyburne, P. P. Power, *J. Am. Chem. Soc.* **2001**, *123*, 9045; b) S. L. Hinchley, C. A. Morrison, D. W. H. Rankin, C. L. B. Macdonald, R. J. Wiacek, A. H. Cowley, M. F. Lappert, G. Gundersen, J. A. C. Clyburne, P. P. Power, *Chem. Commun.* **2000**, 2045.

[18] This compound as originally formulated by Michaelis and Köhler in 1877 was shown to be $(PhP)_n$ ($n = 3$—6) in the 1960s. The first genuine diphosphene was prepared in 1981 and needed bulky substituents for kinetic stabilization: a) M. Yoshifuji, I. Shima, N. Inamoto, K. Hirotsu, T. Higushi, *J. Am. Chem. Soc.* **1981**, *103*, 4587; this reference also cites older work; PhP=PPh itself could only be stabilized by transition-metal complexation, see for example: b) J. Borm, L. Zolnai, G. Huttner, *Angew. Chem.* **1983**, *95*, 1018; *Angew. Chem. Int. Ed. Engl.* **1983**, *22*, 977.

[19] Chainlike tetraphosphanediides M-PPh-PPh-PPh-PPh-M (M = Li, K) in solution were proposed by: a) P. R. Hoffman, K. G. Caulton, *J. Am. Chem. Soc.* **1975**, *97*, 6370; however, these results were differently interpreted by: b) M. Baudler, D. Koch, E. Tolls, K. M. Diedrich, B. Kloth, *Z. Anorg. Allg. Chem.* **1976**, *420*, 146; c) M. Baudler, D. Koch, *Z. Anorg. Allg. Chem.* **1976**, *425*, 227.

 © 2004 Wiley-VCH Verlag GmbH & Co. KGaA, Weinheim

Enzymatic Oxidation

Microencapsulated Chloroperoxidase as a Recyclable Catalyst for the Enantioselective Oxidation of Sulfides with Hydrogen Peroxide**

*Valentina Trevisan, Michela Signoretto, Stefano Colonna, Vincenza Pironti, and Giorgio Strukul**

Microencapsulation of enzymes is a technique that was developed about ten years ago to increase their stability, their ease of recovery, and facilitate their use as catalysts in organic synthesis.[1] Chloroperoxidase (CPO, EC 1.11.1.10) from *Caldariomyces fumago* is a rather versatile heme enzyme that has been extensively studied in recent years.[2,3] Among the wide range of biotransformations carried out by CPO, enantioselective oxidations of olefins and sulfides proved to be very useful for the preparation of important intermediates in organic synthesis.[4] Major drawbacks to the large-scale use of CPO are its high cost, instability at moderate temperatures, and deactivation when using high concentrations of the oxidant hydrogen peroxide. To date, attempts to incorporate CPO into a solid matrix have met with only moderate success, but the enzyme has been adsorbed on mesoporous solids such as MCM-48, SBA-15 and SBA 16,[5] and on microporous solids such as talc.[6] However, adsorption on preformed materials implies there is also a possible desorption process and, in fact, the enzyme was rapidly released into solution during subsequent use of such materials as catalysts. More recently,[7] CPO has been covalently bound to silica gel, thus ensuring a better stability towards leaching, but the catalytic activity of the material has so far not been reported.

Herein we report our successful attempt to apply a different strategy, that is, to build a microporous silica gel cage around CPO and its subsequent use as an enantioselective catalyst in the oxidation of sulfides to sulfoxides.

Tetramethylorthosilicate (TMOS) was prehydrolyzed by addition of a diluted ammonia solution (pH 10) and sonicated for 15 minutes. Either 183 or 3360 CPO units buffered at pH 3.75 were then added and the mixtures stirred for three hours at room temperature until gelation was attained. This yielded two different samples containing 13 units/gram of gel (sample **A**) and 425 units/gram of gel (sample **B**) respectively. The gels were thoroughly washed with acetate buffer

[*] Dr. V. Trevisan, Dr. M. Signoretto, Prof. Dr. G. Strukul
Dipartimento di Chimica
Università di Venezia
Dorsoduro 2137, 30123 Venezia (Italy)
Fax: (+39) 041-234-8517
E-mail: strukul@unive.it
Prof. Dr. S. Colonna, Dr. V. Pironti
Istituto di Chimica Organica "Alessandro Marchesini"
Facoltà di Farmacia
Università di Milano
via Venezian 21, 20133 Milano (Italy)

[**] We thank MIUR (PRIN funds) for financial support of this work.

 DOI: 10.1002/anie.200460365 © 2004 Wiley-VCH Verlag GmbH & Co. KGaA, Weinheim

(pH 3.75) and aged, to complete reticulation, for 2 weeks at 4 °C while covered with buffer (3 mL). This was removed daily and changed with a fresh amount. The xerogels obtained after this time were stored under acetate buffer and used for catalytic studies. The buffer solution aliquots recovered during the preparation were analyzed for their CPO content. The amount of enzyme units lost was calculated using the Morris–Hager assay.[8] As shown in Figure 1, there is a slow

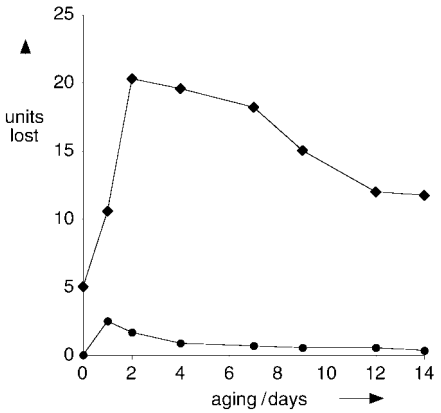


Figure 1. Units of CPO lost during the aging. ●: sample **A**, ◆: sample **B**.

release of CPO from the encapsulated samples that shows a maximum after one–two days and becomes practically negligible with respect to the original amount introduced after two weeks (sample **A**: 1/183 total units introduced; sample **B**: 12/3360 total units introduced). After aging the gels for two weeks the total loss of CPO was $<5\%$ with respect to the original amount and new CPO concentrations are: **A** 12.5 units/gram of gel, **B** 410 units/gram of gel.

Appropriate amounts of xerogels **A** and **B** were dried in vacuo at room temperature and their N_2 adsorption isotherms were analyzed. These indicated that both samples were $>90\%$ microporous (pore diameter <2 nm) with BET surface areas of 700–750 $m^2 g^{-1}$. Microporosity is an essential prerequisite to ensure that CPO remains encapsulated within the silica matrix. However, the presence of a small amount of mesopores could easily explain the loss of approximately 4% of the initially present units during the aging time.

Catalytic reactions using encapsulated CPO (0.3 g) were initially carried out in the oxidation of methylphenylsulfide (MPS) with 0.1M H_2O_2 in 0.1M acetate buffer (pH 3.75) at 15 °C in the absence of solvent. The procedure by which H_2O_2 is added to the system is very important, since it is known that H_2O_2 deactivates CPO.[2,3,4c,5a,6,9] The oxidant solution was added in different aliquots, so that the concentration of the oxidant in the reaction medium never exceeded 10% of the amount of substrate initially present. Some blank tests were also carried out to check the effect of the spontaneous oxidation of MPS in the absence of catalyst and the possible effect of the silica matrix. To this end a pure silica gel sample was prepared using the procedure described above without addition of CPO. The curves obtained are shown in Figure 2, together with the result obtained with free CPO. As expected

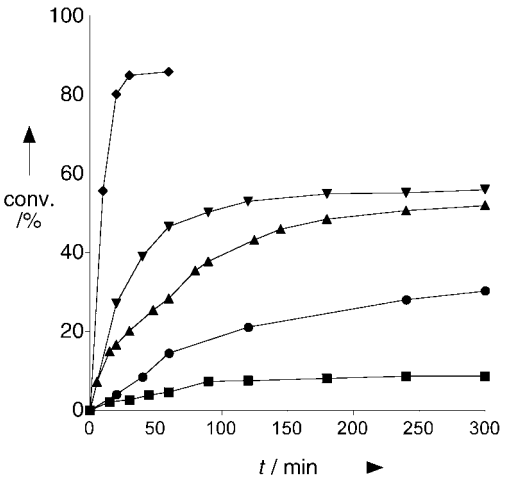


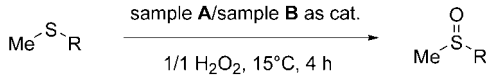
Figure 2. Plots of the conversion of MPS versus time for different catalysts. ■: spontaneous reaction, ●: silica gel, ▲: sample **A**, ◆: sample **B**, ▼: free CPO.

B (123 CPO units in 0.3 g catalyst) is much more active than **A** (3.7 CPO units in 0.3 g catalyst). A small amount of spontaneous oxidation of MPS to sulfoxide is evident as well as some catalysis by the silica gel. The latter reactions are clearly non-enantioselective and hence they will influence the possible overall enantioselectivity observed with **A** as catalyst, while with **B** their effect will be practically negligible.

Figure 2 shows also that 3.7 units of free CPO display a higher conversion rate than the same amount encapsulated in silica (**A**), thus indicating that diffusion through the microporous gel structure may be a limitation. Significantly, however, the maximum conversion attained is the same in both cases.

Samples **A** and **B** were tested also in the oxidation of a series of methylsulfides and a summary of their catalytic properties is reported in Table 1. Formation of sulfones was never observed. Conversions in the range 40–85% and with *ee* $>99\%$ were achieved in all cases with **B** as the catalyst, while the lower conversions and *ee* values observed with **A**

Table 1: Oxidation of different sulfides to sulfoxides with hydrogen peroxide in the presence of encapsulated CPO.[a]



R = Ph, 4-MeC_6H_4, 4-ClC_6H_4, C_5NH_4

Entry	R	Catalyst sample	*t* [min]	Conversion [%][b]	*ee* [%][b]
1	Ph	**A**	240	52	87
2	4-MeC_6H_4	**A**	240	48	76
3	4-ClC_6H_4	**A**	240	40	73
4	[c]	**A**	240	49	92
5	Ph	**B**	30	85	>99
6	4-MeC_6H_4	**B**	30	62	>99
7	4-ClC_6H_4	**B**	30	57	>99
8	[c]	**B**	30	40	>99

[a] Reaction conditions: catalyst 0.3 g; sulfide 12.5 μmol; H_2O_2 12.5 μmol; $T=15$ °C. [b] Determined by GC. [c] 2-pyridyl.

 © 2004 Wiley-VCH Verlag GmbH & Co. KGaA, Weinheim

can be attributed to the blank reactions reported in Figure 2, but also to CPO deactivation after the indicated reaction time. In fact, only a slow formation of sulfoxide and a decrease in the *ee* value of the product are observed if the reaction is run for a longer time. For example, if the reaction described in entry 1 is performed for 1440 min the conversion increases to 81 % while the overall *ee* value decreases to 56 %, thus indicating that all the new sulfoxide produced after 240 min is racemic and what is observed is just a dilution effect on the *ee* value of the sulfoxide already present after 240 min. In agreement with this view is the observation that **A** is almost inactive if recycled for a second run (about 15 % methylphenylsulfoxide, 7–8 % *ee*).

The possible recycling of **B** was tested in the oxidation of MPS. Interestingly, this catalyst could be recycled up to four times with only moderate loss of activity, but retaining its enantioselectivity (Table 2). Recycling of the solution adding fresh amounts of sulfide and hydrogen peroxide resulted in no activity, thereby demonstrating that the reaction is truly heterogeneous and that the amount of CPO realeased from the matrix is negligible.

Table 2: Oxidation of methylphenylsulfide with hydrogen peroxide using sample **B** as the catalyst: Effect of catalyst recycling.[a]

Recycle	*t* [min]	Conversion [%][b]	*ee* [%][b]
fresh	30	85	>99
1st	35	82	>99
2nd	50	78	>99
3rd	40	80	>99

[a] Reaction conditions: catalyst 0.3 g; sulfide 12.5 μmol; H_2O_2 12.5 μmol; $T = 15\,^{\circ}C$. [b] Determined by GC.

In conclusion, the protocol reported in this work seems a reliable method for encapsulating CPO and ensure a sufficient stability in the presence of hydrogen peroxide for carrying out the oxidation of a number of organic sulfides with high activity and enantioselectivity. Oxidation reactions are performed using only substrate and hydrogen peroxide with no solvents, in the presence of a catalyst that can be easily separated and recycled. These characteristics taken together make the process described here particularly attractive also for the "greening" of these oxidation reactions.

Received: April 19, 2004 [Z460365]

Keywords: enantioselectivity · enzymes · hydrogen peroxide · oxidation · sulfides

[1] See seminal works by: a) L. M. Ellerby, C. R. Nishida, F. Nishida, S. A. Yamanaka, B. Dunn, J. S. Valentine, J. I. Zink, *Science* **1992**, *255*, 1113; b) M. T. Reetz, A. Zonta, J. Simpelkamp, *Angew. Chem.* **1995**, *107*, 373; *Angew. Chem. Int. Ed. Engl.* **1995**, *34*, 301; c) B. C. Dave, B. Dunn, J. S. Valentine, J. I. Zink, *Anal. Chem.* **1994**, *66*, 1120A; d) D. Avnir, S. Braun, O. Lev, M. Ottolenghi, *Chem. Mater.* **1994**, *6*, 1605; e) S. A. Yamanaka, F. Nishida, L. M. Ellerby, C. R. Nishida, B. Dunn, J. S. Valentine, J. I. Zink, *Chem. Mater.* **1992**, *4*, 495; f) S. Braun, S. Shtelzer, S. Rappoport, D. Avnir, M. Ottolenghi, *J. Non-Cryst. Solids* **1992**, *147–148*, 739.

[2] F. van Rantwijk, R. A. Sheldon, *Curr. Opin. Biotechnol.* **2000**, *11*, 554.

[3] S. Colonna, N. Gaggero, C. Richelmi, P. Pasta in *Enzymes in Action* (Eds.: B. Zwanenburg, M. Mikolajczyk, P. Kielbasinshi), Kluwer, Dordrecht, **2000**, p. 133.

[4] a) S. Kobayashi, M. Nakano, T. Kimura, A. P. Schaap, *Biochemistry* **1987**, *26*, 5019; b) S. Colonna, S. Del Sordo, N. Gaggero, G. Carrea, P. Pasta, *Heteroat. Chem.* **2002**, *13*, 467; c) M. P. J. van Deurzen, F. van Rantwijk, R. A. Sheldon, *Tetrahedron* **1997**, *53*, 13183; d) A. Zaks, D. R. Dodds, *J. Am. Chem. Soc.* **1995**, *117*, 10419; e) L. P. Hager, F. J. Lakner, A. Basavapathruni, *J. Mol. Catal. B* **1998**, *5*, 95.

[5] a) Y. J. Han, J. T. Watson, G. D. Stucky, A. Butler, *J. Mol. Catal. B* **2002**, *17*, 1; b) F. van de Velde, M. Bakker, F. van Rantwijk, G. P. Rai, L. P. Hager, R. A. Sheldon, *J. Mol. Catal. B* **2001**, *11*, 765; c) W. A. Loughlin, D. B. Hawkes, *Bioresour. Technol.* **2000**, *71*, 167; d) J. Fan, J. Lei, L. Wang, C. Yu, B. Tu, D. Zhao, *Chem. Commun.* **2003**, 2140.

[6] S. Aoun, M. Baboulene, *J. Mol. Catal. B* **1998**, *4*, 101.

[7] A. Petri, T. Gambicorti, P. Salvadori, *J. Mol. Catal. B* **2004**, *27*, 103.

[8] D. R. Morris, R. P. Hager, *J. Biol. Chem.* **1966**, *241*, 1763.

[9] a) S. Colonna, N. Gaggero, L. Casella, G. Carrea, P. Pasta, *Tetrahedron: Asymmetry* **1992**, *3*, 95; b) S. Hu, L. P. Hager, *J. Am. Chem. Soc.* **1999**, *121*, 872; c) K. M. Manoj, L. P. Hager, *Biochim. Biophys. Acta* **2001**, *1547*, 408; d) M. P. J. van Deurzen, I. J. Remkes, F. van Rantwijk, R. A. Sheldon, *J. Mol. Catal. A* **1997**, *117*, 329; e) F. van de Velde, F. van Rantwijk, R. A. Sheldon, *J. Mol. Catal. B* **1999**, *6*, 453; f) K. Seelbach, M. P. J. van Deurzen, F. van Rantwijk, R. A. Sheldon, U. Kragl, *Biotechnol. Bioeng.* **1997**, *55*, 283; g) E. Kiljunen, L. T. Kanerva, *J. Mol. Catal. B* **2000**, *9*, 163.

 © 2004 Wiley-VCH Verlag GmbH & Co. KGaA, Weinheim

Alkene Hydrazination

Catalytic Hydrohydrazination of a Wide Range of Alkenes with a Simple Mn Complex**

*Jérôme Waser and Erick M. Carreira**

Heterofunctionalization reactions of olefins are highly desirable processes as they convert readily available starting materials into value-added building blocks for chemical synthesis.[1–4] In this respect, the best illustration is the role played by epoxides and diols in chemical synthesis which arises from the availability of a plethora of epoxidation reagents and catalysts[2,5,6] and advances in olefin dihydroxylation.[7] However, despite the numerous processes for the

[*] J. Waser, Prof. Dr. E. M. Carreira
Laboratorium für Organische Chemie
ETH Hönggerberg, HCI H335
8093 Zürich (Switzerland)
Fax: (+41) 1-632-1328
E-mail: carreira@org.chem.ethz.ch

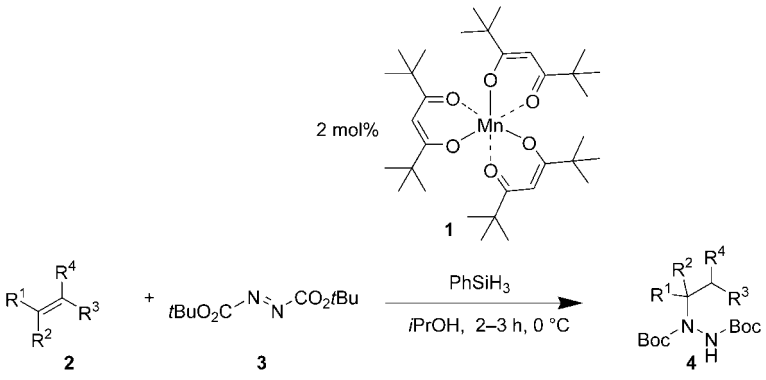
[**] This research was supported by a Swiss National Science Foundation Grant.

Supporting information for this article is available on the WWW under http://www.angewandte.org or from the author.

 DOI: 10.1002/anie.200460811 © 2004 Wiley-VCH Verlag GmbH & Co. KGaA, Weinheim

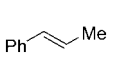
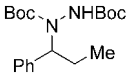
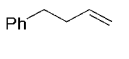
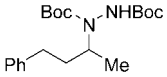
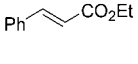
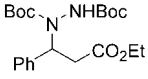
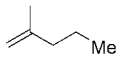
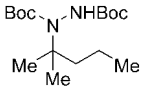
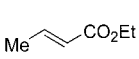
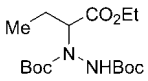
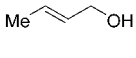
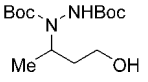
introduction of oxygen functions, there are relatively few methods available for the introduction of nitrogen-containing functional groups.[8–13] We have recently reported a Co complex[14] that mediates the conversion of simple olefins into the corresponding hydrazides with azodicarboxylates as the nitrogen source.[15] The hydrohydrazination reaction complements existing methods that involve azodicarboxylates to access hydrazine derivatives,[16–24] which are useful building blocks and precursors to free amines.[25,26] In our continuing interest in discovery and development of additional new catalysts for such a process we have identified a simple Mn^{III} complex, namely [Mn(dpm)$_3$] (**1**),[27,28] which catalyzes the reaction of azodicarboxylates and alkenes [Eq. (1)] (Boc = *tert*-butoxycarbonyl) with much higher activity and larger scope than the known Co catalysts we had previously studied. The introduction of a new catalytic system that differs both in metal and ligand to carry out the hydrohydrazination reaction sets the stage for further investigations of the process, including the development of its stereoselective counterpart.

In the earlier study involving the use of a Co catalyst for olefin hydrohydrazination we noted that substrates such as cyclohexene, crotyl alcohol, and tetrasubstituted alkenes were not sufficiently reactive to lead to product formation in useful yields; moreover, full conversion of the starting material was observed only with $PhSiH_3$ as reductant, even with the most reactive substrates. We subsequently focused our efforts in identifying improved conditions and catalysts, with particular attention on enhanced reactivity in order to expand the scope.



A broad-based study of numerous metal salts and complexes led us to examine [Mn(dpm)$_3$] (**1**).[29] This complex has been studied in the hydration of α,β-unsaturated ketones and esters to give α-hydroxyketones and -esters, respectively,[27,28,30] as well as for epoxidation of alkenes,[31] reduction of ketones,[32] and conjugate reduction of α,β-unsaturated ketones.[33] Based on our speculations regarding the similarities between the metal-catalyzed functionalization of alkenes using oxygen and phenylsilane[27,28,34] and the hydrohydrazination reaction, we hypothesized that this complex could also catalyze the reaction of alkenes and azodicarboxylates. Indeed, as shown in Table 1, a selection of olefins that serve well in the Co-catalyzed reactions (catalyst (5 mol%), $PhSiH_3$ (1.0 equiv), di-*tert*-butyl azodicarboxylate (1.5 equiv), ethanol, 23 °C) also afford hydrazide adducts when [Mn(dpm)$_3$] (2 mol%) together with $PhSiH_3$ (1.0 equiv) and di-*tert*-butyl azodicarboxylate (**3**; 1.5 equiv) are employed at 0 °C in 2-propanol.[35] The adducts are obtained for 1,2- along with 1,1-disubstituted alkenes and α,β-unsaturated esters in 86–94% yield (Table 1, entries 1–5), which is comparable with the Co system (66–92%) but with shorter reaction times (2–3 h at 0 °C instead of 5–20 h at 23 °C). Interestingly, crotyl alcohol (Table 1, entry 6), which had proven to be a rather poor substrate with the Co system (25% yield, 3:1 mixture of regioisomers) furnished a 1.8:1 mixture of the bis-*N*-Boc-protected 3- and 2-hydrazinobutan-1-ol in 90% combined yield.

Table 1: Hydrohydrazination reactions of simple alkenes with [Mn(dpm)$_3$] (**1**).

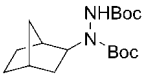
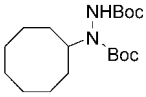
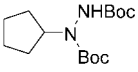
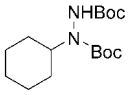
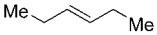
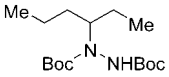
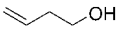
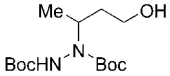
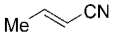
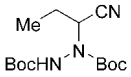
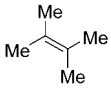
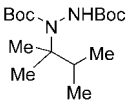
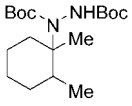
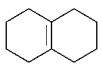
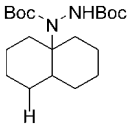
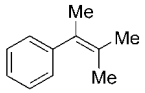
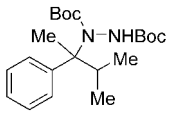
Entry	Alkene	Product[a]	Regioselectivity[b]	Yield [%][c]
1			>20:1	94
2			5.5:1	94
3			9:1	87
4			>20:1	86
5			>20:1	88
6			1.8:1	90

[a] Major product shown. [b] With the Co catalyst, the regioselectivity was generally higher than 20:1, except for entry 6 (3:1). [c] Standard conditions: alkene (0.5 mmol), $PhSiH_3$ (0.5 mmol), **3** (0.75 mmol), catalyst **1** (2 mol%), 2-propanol (2.5 mL), N_2, 0 °C.

The initial set of reactions described above proved revealing in a number of important ways: 1) wider scope; 2) higher yields; and, perhaps most importantly, 3) the rate of product formation with 5 mol% of [Mn(dpm)$_3$] (**1**) was considerably higher (5 min, 23 °C)[35] than that observed for the Co catalyst (5 mol%, 6–20 h, 23 °C) under otherwise identical conditions. These observations led us to reexamine specifically other olefins that furnished lower yields in the earlier study. Table 2 illustrates the hydrohydrazination reaction of additional substrates for the Mn-catalyzed reaction along with a head-to-head comparison with the results for the Co-catalyzed reaction. Interestingly, for those cases that had given products in 62–74% yield with the Co catalyst (cyclopentene, norbornene, cyclooctene), the hydrazides could now be isolated in >94% yield and it was never necessary to use more than 1.5 equivalents of di-*tert*-butyl

 © 2004 Wiley-VCH Verlag GmbH & Co. KGaA, Weinheim

Table 2: Hydrohydrazination reactions of more-challenging alkenes.

Entry	Alkene	Product	Yield [%] Co[a]	Mn[b]
1			66	98
2			62	95
3			74	94
4			24	90
5			16	66
6			22[c]	72[c]
7			44[c]	45[c]
8			16	78
9			18	79
10			10	74
11			13[c]	51[c]

[a] Standard conditions: alkene (0.5 mmol), $PhSiH_3$ (0.5 mmol), **3** (0.75 mmol), Co catalyst[14] (5 mol%), ethanol (2.5 mL), N_2, 23 °C. [b] Standard conditions: alkene (0.5 mmol), $PhSiH_3$ (0.5 mmol), **3** (0.75 mmol), catalyst **1** (2 mol%), 2-propanol (2.5 mL), N_2, 0 °C. [c] Only one regioisomer was observed.

azodicarboxylate (**3**) as was the case of cobalt (Table 2, entries 1–3). The advantages of the Mn-catalyzed process are best appreciated, however, upon comparing substrates such as cyclohexene, 3-hexene, and buten-3-ol (Table 2, entries 4–6), which had previously afforded products in only 16–24% yield with the Co catalyst. Under catalysis with $[Mn(dpm)_3]$ (**1**) the corresponding adducts can now be isolated in much higher yields (72–90%). Only acrylonitrile proved recalcitrant to improvement (44% with Co and 45% with Mn) (Table 2, entry 7). Given the promising results, we decided to examine the sterically most challenging substrates for heterofunctionalization, namely tetrasubstituted olefins, which under Co catalysis afford products in 10–16% yield. Remarkably, for the tetrasubstituted alkenes examined (2,3-dimethyl-2-butene, 1,2-dimethylcyclohexene, 9,10-dehydrodecalin, and 3-methyl-2-phenyl-2-butene) the highly substituted hydrohydrazination adducts could be isolated in useful yields (51–79%; Table 2, entries 8–11).

In the studies conducted to date, we have examined the use of $PhSiH_3$ as the reductant, because it had proven most convenient and effective in the Co-catalyzed process. Given the observation of unique reactivity for the Mn complex, we proceeded to investigate whether this catalyst would permit the use of other silanes. We were pleased to note that in the hydrohydrazination reaction of 4-phenylbutene with $[Mn(dpm)_3]$ (2 mol%) the hydrazide adduct is obtained when using PMHS (poly(methylhydrosiloxane)), a considerably less-expensive and more-stable silane, in 88% yield in 12 h at 23 °C, whereas the Co system showed less than 20% conversion after 24 h when using this silane.

In summary, with $[Mn(dpm)_3]$ (**1**) we have identified a new catalyst class for the hydrohydrazination reaction of alkenes. The salient features of this catalyst system are the broad substrate scope of the process (to include tetrasubstituted alkenes), faster reaction rates (minutes), higher yields, and the compatibility with the less-expensive PMHS reductant. In this expanded scope, the hydrohydrazination process allows access to a wider range of structurally diverse building blocks, which should find use for drug synthesis. The availability of another class of complexes that catalyzes this process also offers several new avenues for the development of versatile and improved transformations that may be amenable to development into the corresponding asymmetric transformations. Studies in this respect are ongoing and their results will be reported as they become available.

Received: May 27, 2004 [Z460811]

Keywords: alkenes · homogeneous catalysis · hydrazination · manganese · silanes

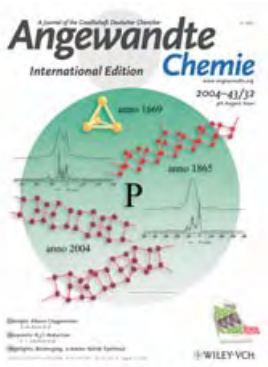
[1] S. Patai, Z. Rappoport, *The Chemistry of Double-Bonded Chemical Groups*, Wiley, New York, **1997**.
[2] A. S. Rao, R. A. Johnson, K. B. Sharpless, A. H. Haines, J. Tsuji, J. E. G. Kemp, K. A. Swiss, D. C. Liotta, S. Torii, T. Inokuchi, D. G. Lee, T. Chen in *Comprehensive Organic Synthesis*, *Vol. 7* (Eds.: B. M. Trost, I. Fleming, S. V. Ley), Pergamon, Oxford, **1991**, p. 357.
[3] A. Togni, H. Grützmacher, *Catalytic Heterofunctionalization. From Hydroamination to Hydrozirconation*, Wiley-VCH, Weinheim, **2001**.
[4] *Comprehensive Organic Synthesis*, *Vol. 4* (Eds.: B. M. Trost, I. Fleming, M. F. Semmelhack), Pergamon, Oxford, **1991**.
[5] R. A. Johnson, K. B. Sharpless, in *Catalytic Asymmetric Synthesis* (Ed.: I. Ojima), Wiley-VCH, Weinheim, **2000**, p. 231.

 © 2004 Wiley-VCH Verlag GmbH & Co. KGaA, Weinheim

[6] T. Katsuki in *Catalytic Asymmetric Synthesis* (Ed.: I. Ojima), Wiley-VCH, Weinheim, **2000**, p. 287.
[7] R. A. Johnson, K. B. Sharpless in *Catalytic Asymmetric Synthesis* (Ed.: I. Ojima), Wiley-VCH, Weinheim, **2000**, p. 357.
[8] A. Ricci, *Modern Amination Methods*, Wiley-VCH, Weinheim, **2000**.
[9] B. R. Brown, *The Organic Chemistry of Aliphatic Nitrogen Compounds*, Oxford University Press, New York, **1994**.
[10] D. Enders, U. Reinhold, *Tetrahedron: Asymmetry* **1997**, *8*, 1895.
[11] S. Kobayashi, H. Ishitani, *Chem. Rev.* **1999**, *99*, 1069.
[12] P. W. Roesky, T. E. Müller, *Angew. Chem.* **2003**, *115*, 2812; *Angew. Chem. Int. Ed.* **2003**, *42*, 2708.
[13] M. Nobis, B. Drießen-Hölscher, *Angew. Chem.* **2001**, *113*, 4105; *Angew. Chem. Int. Ed.* **2001**, *40*, 3983.
[14] Sodium-bis-[*N*-salicylidene-2-amino-isobutyrato]-cobaltate(III).
[15] J. Waser, E. M. Carreira, *J. Am. Chem. Soc.* **2004**, *126*, 5676.
[16] P. S. Baran, C. A. Guerrero, E. J. Corey, *Org. Lett.* **2003**, *5*, 1999.
[17] M. A. Brimble, C. H. Heathcock, *J. Org. Chem.* **1993**, *58*, 5261.
[18] D. A. Evans, T. C. Britton, R. L. Dorow, J. F. Dellaria, *J. Am. Chem. Soc.* **1986**, *108*, 6395.
[19] D. A. Evans, T. C. Britton, R. L. Dorow, J. F. Dellaria, *Tetrahedron* **1988**, *44*, 5525.
[20] D. A. Evans, S. G. Nelson, *J. Am. Chem. Soc.* **1997**, *119*, 6452.
[21] D. A. Evans, D. S. Johnson, *Org. Lett.* **1999**, *1*, 595.
[22] C. Gennari, L. Colombo, G. Bertolini, *J. Am. Chem. Soc.* **1986**, *108*, 6394.
[23] L. A. Trimble, J. C. Vederas, *J. Am. Chem. Soc.* **1986**, *108*, 6397.
[24] B. List, *J. Am. Chem. Soc.* **2002**, *124*, 5656.
[25] E. W. Schmidt, *Hydrazine and Its Derivatives*, *Preparation, Properties, Applications*, 2nd ed., Wiley-Interscience, New York, **2001**.
[26] U. Ragnarsson, *Chem. Soc. Rev.* **2001**, *30*, 205.
[27] S. Inoki, K. Kato, S. Isayama, T. Mukaiyama, *Chem. Lett.* **1990**, 1869.
[28] P. Magnus, A. H. Payne, M. J. Waring, D. A. Scott, V. Lynch, *Tetrahedron Lett.* **2000**, *41*, 9725.
[29] dpm = dipivaloylmethanato. Both $[Mn(dpm)_2]$ and $[Mn(dpm)_3]$ proved equally active in the hydrohydrazination reaction, but as the former is very air sensitive, the more-stable $[Mn(dpm)_3]$ complex was preferentially used.
[30] P. Magnus, D. A. Scott, M. R. Fielding, *Tetrahedron Lett.* **2001**, *42*, 4127.
[31] T. Yamada, K. Imagawa, T. Mukaiyama, *Chem. Lett.* **1992**, 2109.
[32] P. Magnus, M. R. Fielding, *Tetrahedron Lett.* **2001**, *42*, 6633.
[33] P. Magnus, M. J. Waring, D. A. Scott, *Tetrahedron Lett.* **2000**, *41*, 9731.
[34] S. Isayama, T. Mukaiyama, *Chem. Lett.* **1989**, 1071.
[35] Conducting the reaction with 5 mol% catalyst at 23°C gave full conversion after 5 min, but the regioselectivity was lower in certain cases (e.g. 4-phenylbutene give a 3:1 mixture of secondary/primary hydrazide at 23°C versus a 5.5:1 mixture at 0°C).

 © 2004 Wiley-VCH Verlag GmbH & Co. KGaA, Weinheim

Cover Picture



Arno Pfitzner,* Michael F. Bräu, Josef Zweck, Gunther Brunklaus, and Hellmut Eckert*

Alternatives to the structure of Hittorf phosphorus were predicted a few years ago, and these have now been confirmed experimentally as phosphorus nanorods. A. Pfitzner, H. Eckert, and co-workers report on page 4228 ff. that these new allotropic forms of phosphorus can be isolated from the adduct compounds $(CuI)_8P_{12}$ and $(CuI)_3P_{12}$ by extraction with an aqueous cyanide solution. The nanorods have been characterized by high-resolution TEM and ^{31}P magic-angle spinning NMR spectroscopy.

Contents

Angewandte EarlyView

The following Communications are available online (in Wiley InterScience). You can find them, as well as forthcoming Reviews, Highlights, and Essays, at www.angewandte.org, under Early View.

J. M. J. Paulusse, R. P. Sijbesma:*
Reversible Mechanochemistry of a Pd^{II} Coordination Polymer
DOI: 10.1002/anie.200460040
Published online: July 28, 2004

N. Pinna, G. Neri, M. Antonietti, M. Niederberger*:*
Nonaqueous Synthesis of Nanocrystalline Semiconducting Metal Oxides for Gas Sensing
DOI: 10.1002/anie.200460610
Published online: July 28, 2004

Articles judged by the referees or the editor as being either very important or very urgent are immediately edited, proof-read, and electronically published once the manuscript has arrived in the editorial office in its final form. As long as there is no page number available these articles should be cited in the following manner:

Author(s), *Angew. Chem. Int. Ed.*, online publication date, DOI.

Obituary

Orville L. Chapman (1932–2004): Organic Chemistry and Education ——— **4122** R. J. McMahon

Books

Experimental Design for Combinatorial and High Throughput Materials Development ——— **4123** James N. Cawse *reviewed by U. S. Schubert*

Organosilanes in Radical Chemistry ——— **4124** Chryssostomos Chatgilialoglu *reviewed by D. L. J. Clive*

Highlights

Synthesis of α-Amino Nitriles

M. North* ——— **4126 – 4128**

Oxidative Synthesis of α-Amino Nitriles from Tertiary Amines

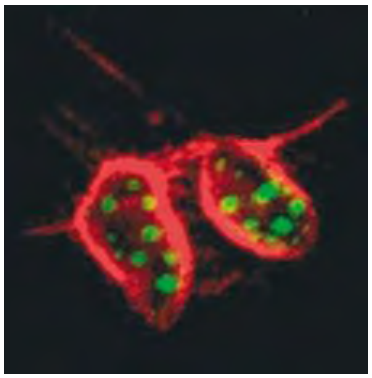


A catalytic option: Tertiary amines are converted into the corresponding α-amino nitriles in the presence of hydrated ruthenium trichloride (5 mol%), sodium cyanide (1.2 equiv), and molecular oxygen (see scheme). This is a valuable alternative to the Strecker synthesis of α-amino nitriles and can be used to prepare *N*-aryl glycine derivatives and unsymmetrical 1,2-diamines.

Imaging Agents

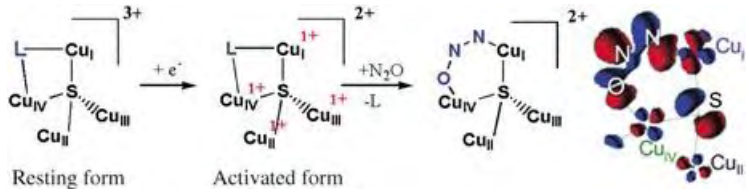
M. Green* ——— **4129 – 4131**

Semiconductor Quantum Dots as Biological Imaging Agents



Dots in cells: Recent advances in the use of functionalized semiconductor quantum dots in bioimaging, from cancer studies to blood-flow monitoring, are described. The image shows a mouse fibroplast labeled with two different sizes (and therefore two different colors) of CdSe/ZnS quantum dots.

Minireviews



A spectrum of unusual features: N_2O reduction is accomplished in biology by an active site consisting of a μ_4-sulfide-bridged tetranuclear copper cluster (the Cu_Z center), which has many unusual spectroscopic features. Recent studies have led to electronic-structure descriptions of resting Cu_Z, its catalytically relevant form, and elucidated the role of Cu_Z in N_2O activation and reduction (see scheme).

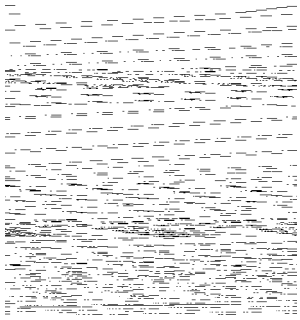
Metalloenzymes

P. Chen, S. I. Gorelsky, S. Ghosh, E. I. Solomon* ——— **4132 – 4140**

N_2O Reduction by the μ_4-Sulfide-Bridged Tetranuclear Cu_Z Cluster Active Site

Reviews

A rational improvement of rhodium/iridium-catalyzed olefin oxygenation by dioxygen or hydrogen peroxide requires more detailed insight into underlying mechanisms and ligand effects (see scheme). In this Review, results from model studies are related to known catalytic systems, and differences between rhodium/iridium- and palladium-catalyzed olefin oxidation are discussed.

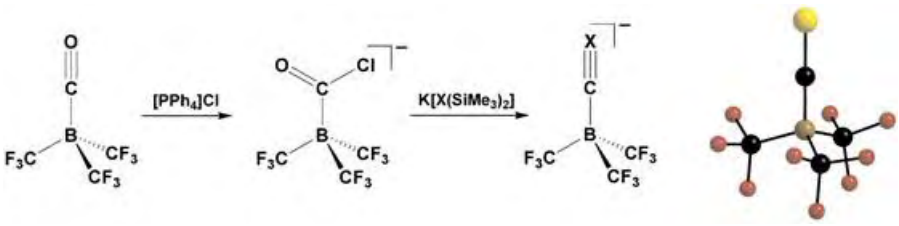


Alkene Oxygenation

B. de Bruin,* P. H. M. Budzelaar, A. W. Gal ——— **4142 – 4157**

Functional Models for Rhodium-Mediated Olefin-Oxygenation Catalysis

Communications



Make mine a triple: The tetraphenyl phosphonium salts of $[(CF_3)_3BCX]^-$ (X = P, As) are stable even well above room temperature. The synthesis of these first phospha- and arsaethynyl complexes of boron from $(CF_3)_3BCO$ is carried out in two steps (see scheme). The complex $[(CF_3)_3BCAs]^-$ is the first stable anionic arsaalkyne.

C≡P and C≡As Bonds

M. Finze, E. Bernhardt, H. Willner,* C. W. Lehmann ——— **4160 – 4163**

$[(CF_3)_3BCP]^-$ and $[(CF_3)_3BCAs]^-$: Thermally Stable Phosphaethynyl and Arsaethynyl Complexes

For the USA and Canada:
ANGEWANDTE CHEMIE International Edition (ISSN 1433-7851) is published weekly by Wiley-VCH PO Box 191161, D 69451 Weinheim, Germany. Air freight and mailing in the USA by Publications Expediting Inc. 200 Meacham Ave., Elmont, NY 11003. Periodicals postage paid at Jamaica NY 11431. US POSTMASTER: send address changes to *Angewandte Chemie*, Wiley-VCH, 111 River Street, Hoboken, NJ 07030. Annual subscription price for institutions: Europe € 3430.00/3118.00; outside Europe US$ 4499.00/4090.00 (valid for print and electronic/print or electronic delivery); for individuals who are personal members of a national chemical society, or whose institution already subscribes, or who are retired or self-employed consultants, print only: Europe € 248.00/outside Europe US$ 378.00. Postage and handling charges included. All Wiley-VCH prices are exclusive VAT.

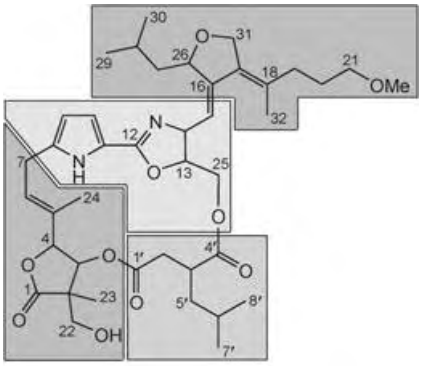
 © 2004 Wiley-VCH Verlag GmbH & Co. KGaA, Weinheim

Contents

Biosynthesis

H. B. Bode, S. C. Wenzel, H. Irschik, G. Höfle, R. Müller* ——— **4163 – 4167**

Unusual Biosynthesis of Leupyrrins in the Myxobacterium *Sorangium cellulosum*



1

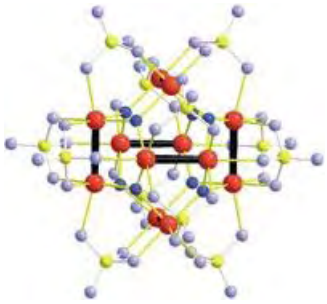
Classical feeding experiments indicate involvement of nonribosomal peptide, polyketide, and isoprenoid biosynthesis in the formation of the myxobacterial antibiotic leupyrrin (**1**). The resulting structural elements are modified further (e.g. by a semipinacol-like rearrangement and oxidative formation of a methylene bridge) to yield the unique leupyrrin framework.

Cluster Compounds

M. Pley, M. S. Wickleder* ——— **4168 – 4170**

The Cluster Ion $[Pt_{12}O_8(SO_4)_{12}]^{4-}$

Platinum dumbbells: The reaction of platinum nitrate with concentrated sulfuric acid at 350 °C leads to the deep red oxide–sulfate $(NH_4)Pt_3O_2(SO_4)_3$, in which six $[Pt_2]^{6+}$ dumbbells are linked by oxide ions and sulfate groups to the novel cluster anion $[Pt_{12}O_8(SO_4)_{12}]^{4-}$ (see picture). The structure of the core of this anion matches exactly the recent prediction for dodecanuclear complexes built from six metal dumbbells.

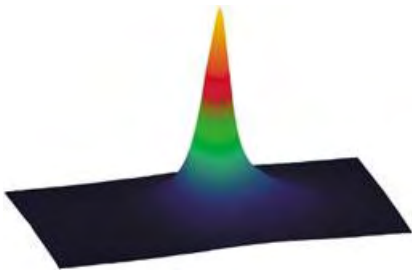


Scanning Electrochemical Microscopy

C. Zhao, G. Wittstock* ——— **4170 – 4172**

An SECM Detection Scheme with Improved Sensitivity and Lateral Resolution: Detection of Galactosidase Activity with Signal Amplification by Glucose Dehydrogenase

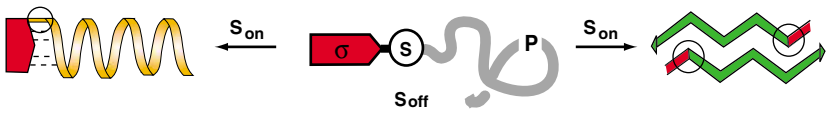
An enzymatic amplification cycle is used in a novel detection scheme for scanning electrochemical microscopy (SECM). An immobilized enzyme system comprising galactosidase and PQQ-dependent glucose dehydrogenase was imaged by SECM with high sensitivity and high lateral resolution.
PQQ = pyrroloquinolinequinone.



Protein Folding

M. Mutter,* A. Chandravarkar, C. Boyat, J. Lopez, S. Dos Santos, B. Mandal, R. Mimna, K. Murat, L. Patiny, L. Saucède, G. Tuchscherer ——— **4172 – 4178**

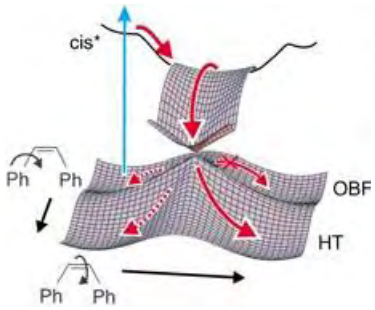
Switch Peptides In Statu Nascendi: Induction of Conformational Transitions Relevant to Degenerative Diseases



A novel concept for triggering conformational transitions, and thus changes in structure and function, in peptides with a switching element **S** provides intriguing perspectives for studying molecular processes (see scheme) that play a key role, for example, in early events of Alzheimer's disease.

 © 2004 Wiley-VCH Verlag GmbH & Co. KGaA, Weinheim

A motion breaking with tradition: The *cis–trans* isomerization of nonpolar conjugated π systems does not proceed simply by the 180° twist of a C=C bond ("one-bond flip", OBF), but by the rotation of a central CH group out of the plane ("hula twist", HT). The hula-twist motion does not require any external constraint but is driven by an internal force: the slope on the way through a conical intersection.

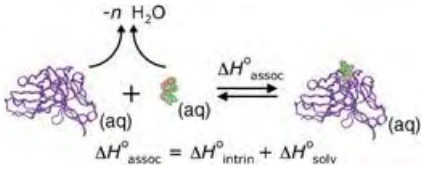


Gas-Phase Reactions

W. Fuß,* C. Kosmidis, W. E. Schmid, S. A. Trushin ——— **4178 – 4182**

The Photochemical *cis–trans* Isomerization of Free Stilbene Molecules Follows a Hula-Twist Pathway

Divide and conquer: A novel approach was used to separate solvent effects from the intrinsic interactions involved in the association of biological complexes (see figure). The enthalpy of solvent reorganization for the formation of an intermolecular hydrogen bond in a biomolecular complex was determined by comparing the solution and gas-phase stabilities of structurally related complexes.

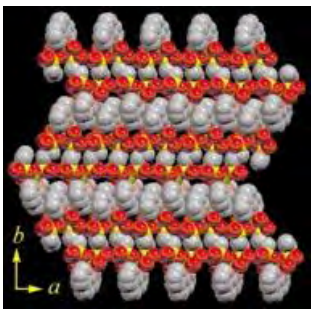


Biological Complexes

E. N. Kitova, D. R. Bundle, J. S. Klassen* ——— **4183 – 4186**

Partitioning of Solvent Effects and Intrinsic Interactions in Biological Recognition

Robo copper: A mechanically robust corrugated sheet, 1 DOP-Cu, is composed of mats of individual chain-bundles joined by π–π interactive forces (see structure). Upon electrochemical charge injection into 1 DOP-Cu, the variations of the cell parameters of the Li-inserted phase were observed by X-ray diffraction. The mechanical deformation of the whole sheet is produced by a Cu^{II}/Cu^{I} redox process.

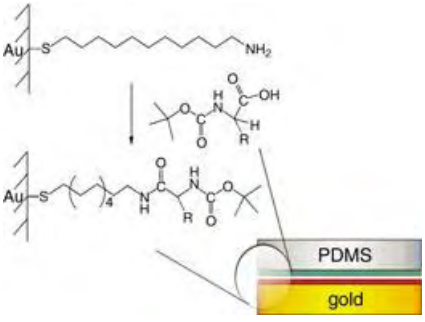


Supramolecular Machines

K.-J. Lin,* S.-J. Fu, C.-Y. Cheng, W.-H. Chen, H.-M. Kao ——— **4186 – 4189**

Towards Electrochemical Artificial Muscles: A Supramolecular Machine Based on a One-Dimensional Copper-Containing Organophosphonate System

Pressing a rubber stamp inked with carboxylic acids onto an amine-terminated surface leads to the formation of amide bonds at room temperature (see scheme). Oligopeptides were created on the surface in this way from a monolayer. This rapid and uncatalyzed formation of amide bonds is attributed to the nanoscale confinement of the molecules between the stamp and the preorganized monolayer substrate.
PDMS = poly(dimethylsiloxane).



Contact Printing

T. P. Sullivan, M. L. van Poll, P. Y. W. Dankers, W. T. S. Huck* ——— **4190 – 4193**

Forced Peptide Synthesis in Nanoscale Confinement under Elastomeric Stamps

 © 2004 Wiley-VCH Verlag GmbH & Co. KGaA, Weinheim

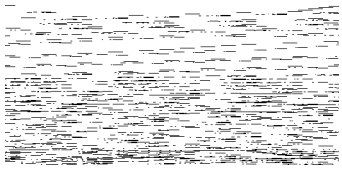
Contents

Cysteine Protease Inhibitors

P. M. O'Neill,* P. A. Stocks, M. D. Pugh, N. C. Araujo, E. E. Korshin, J. F. Bickley, S. A. Ward, P. G. Bray, E. Pasini, J. Davies, E. Verissimo, M. D. Bachi* ... **4193 – 4197**

Design and Synthesis of Endoperoxide Antimalarial Prodrug Models

A masked combination chemotherapy which relies on the embedding of a number of active components, in a latent form, within a single endoperoxidic chemical entity is the aim of the research presented. The approach is illustrated by means of purposely designed bicyclic endoperoxide prodrug prototypes **1** and subsequently validated through the study

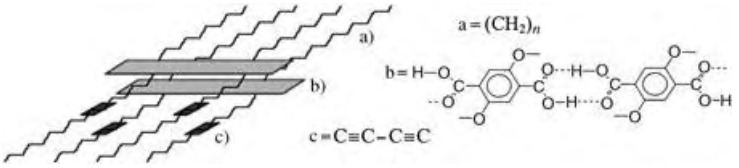


of model compounds **2** (Ar = Ph, *p*-FC_6H_4, *p*-ClC_6H_4).

Thermochromism

Z. Yuan, C.-W. Lee, S.-H. Lee* ... **4197 – 4200**

Reversible Thermochromism in Hydrogen-Bonded Polymers Containing Polydiacetylenes

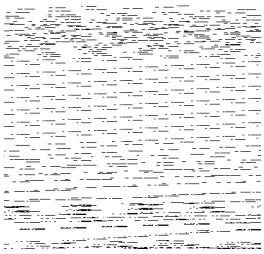


Out of the blue: A reversible temperature-dependent change in the absorption characteristics of spin-coated terephthalic acid/diacetylene polymers is observed. The polymer is prepared by topochemical photopolymerization of the diacetylene side chains of the stacked terephthalic acid units (see picture). The absorption bands of the polymeric product move reversibly from 640 nm (blue form of the polymer) to 580 nm (red form) during heating–cooling cycles.

Annulenes

C. S. Wannere, K. W. Sattelmeyer, H. F. Schaefer III, P. v. R. Schleyer* ... **4200 – 4206**

Aromaticity: The Alternating C–C Bond Length Structures of [14]-, [18]-, and [22]Annulene

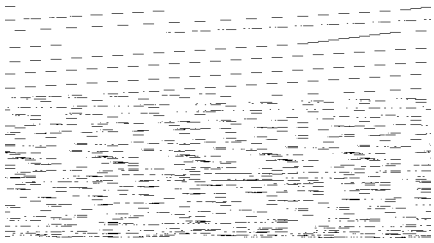


First among unequals: Equal C–C bond lengths, as found in benzene, are not necessary for aromaticity. [18]Annulene is the next Hückel monocycle where D_{6h} symmetry is possible topologically (see picture). However, this widely accepted structure of [18]annulene is not correct. The ^1H NMR chemical shifts and energy computations show that [18]annulene prefers C–C bond-length alternation and C_2 symmetry.

Natural Products Synthesis

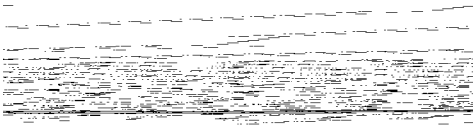
M. Inoue, W. Yokota, M. G. Murugesh, T. Izuhara, T. Katoh* ... **4207 – 4209**

Total Synthesis of (+)-Scyphostatin, a Potent and Specific Inhibitor of Neutral Sphingomyelinase



The five crucial steps in the first total synthesis of (+)-scyphostatin from D-arabinose involve (see picture): a) stereoselective aldol coupling to form a quaternary stereocenter, b) ring-closing metathesis (RCM) to construct the cyclohexene ring, c) Negishi coupling for the preparation of the fatty acid side chain, d) amide formation to connect the cyclohexene and fatty acid segments, e) stereospecific epoxide-ring formation.

 © 2004 Wiley-VCH Verlag GmbH & Co. KGaA, Weinheim



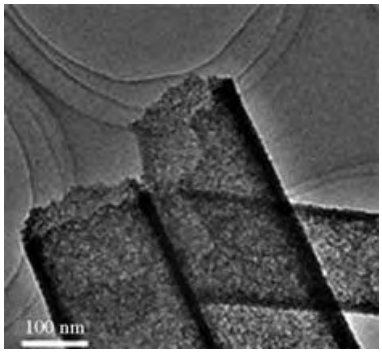
Opportunities with silver: A dinuclear silver(I) compound was found to efficiently catalyze the intramolecular amidation of saturated C–H bonds of carbamates and sulfamates (see scheme). This highly regioselective, stereospecific reaction offers a practical method for the construction of cyclic nitrogen-containing organic molecules.

C–H Activation

Y. Cui, C. He* ——— **4210 – 4212**

A Silver-Catalyzed Intramolecular Amidation of Saturated C–H Bonds

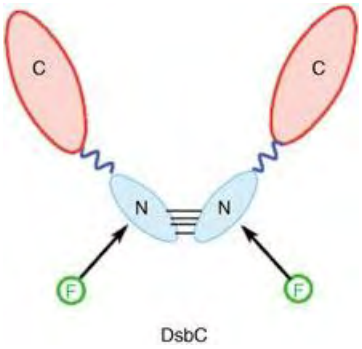
Higher capacity rechargeable batteries can be constructed by using mesoscale nickel hydroxide tubes as the positive-electrode material. The tubes were prepared by deposition of nickel ions and aqueous ammonia in an anodic alumina membrane as the template. The picture shows a high-resolution TEM image of the tubes.



Nickel Hydroxide Tubes

F.-S. Cai, G.-Y. Zhang, J. Chen,* X.-L. Gou, H.-K. Liu, S.-X. Dou ——— **4212 – 4216**

$Ni(OH)_2$ Tubes with Mesoscale Dimensions as Positive-Electrode Materials of Alkaline Rechargeable Batteries

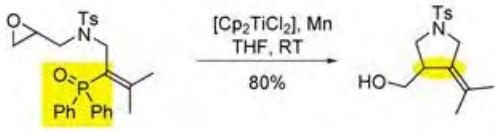


The folding/unfolding of a protein structure has been studied through measuring the donor–donor energy migration between two fluorescent probes (F) coupled selectively to the N termini of the homodimeric DsbC protein (see picture). The fluorometric strategy provides a convenient and reliable method to investigate conformational changes in dimeric proteins.

Fluorescence Spectroscopy

X. Duan, Z. Zhao, J. Ye, H. Ma,* A. Xia,* G. Yang, C.-C. Wang* ——— **4216 – 4219**

Donor–Donor Energy-Migration Measurements of Dimeric DsbC Labeled at Its N-Terminal Amines with Fluorescent Probes: A Study of Protein Unfolding



A phosphinoyl radical leaving group in the β position is a key feature of a new Ti^{III}-mediated domino radical cyclization/β elimination reaction of vinylic phosphine oxides, which affords alkylidenepyrrolidines in good yields (see scheme).

Domino Radical Cyclization

D. Leca, L. Fensterbank,* E. Lacôte,* M. Malacria* ——— **4220 – 4222**

Titanium-Mediated Domino Radical Cyclization/β Elimination of Phosphine Oxides

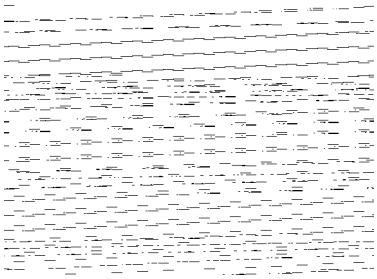
 © 2004 Wiley-VCH Verlag GmbH & Co. KGaA, Weinheim

Contents

Natural Products Synthesis

X. Pu, D. Ma* ——— **4222 – 4225**

Total Synthesis of Lepadins B, D, E, and H; Determination of the Configuration of the Latter Three Alkaloids



A common bicyclic intermediate was used in an efficient strategy towards lepadins B, D, E, and H shown. These alkaloids are members of a family of natural products with diverse biological activity. The described total syntheses of lepadins D, E, and H enabled the full elucidation of their configuration.

Asymmetric Oxidations

J. Legros, C. Bolm* ——— **4225 – 4228**

Highly Enantioselective Iron-Catalyzed Sulfide Oxidation with Aqueous Hydrogen Peroxide under Simple Reaction Conditions

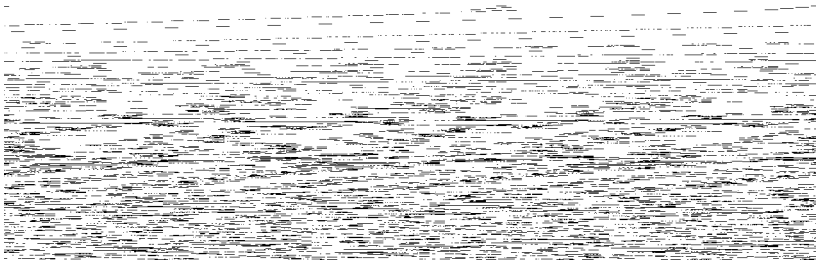


An attractive alternative to the currently existing methods for the metal-catalyzed oxidation of sulfides to sulfoxides is asymmetric iron-catalyzed oxidation with hydrogen peroxide as the terminal oxidant (see scheme). In the presence of a benzoic acid derivative, this simple process provides sulfoxides with up to 96% *ee* in moderate to good yields (up to 78%).

Phosphorus Nanorods

A. Pfitzner,* M. F. Bräu, J. Zweck, G. Brunklaus, H. Eckert* — **4228 – 4231**

Phosphorus Nanorods—Two Allotropic Modifications of a Long-Known Element

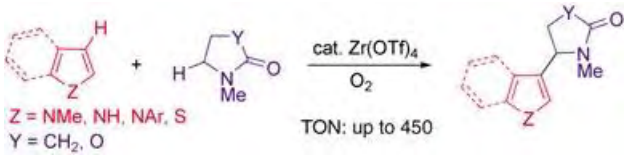


Extracting the P: Two novel amorphous allotropes of elemental phosphorus that consist of polymeric chains (see example depicted) were obtained in a pure form by extraction from their copper iodide adducts with an aqueous solution of potassium cyanide. ^{31}P NMR spectra and high-resolution TEM images suggest that the structure of these phosphorus nanorods is unchanged after extraction.

Coupling Reactions

T. Tsuchimoto,* Y. Ozawa, R. Negoro, E. Shirakawa,* Y. Kawakami **4231 – 4233**

Zirconium Triflate Catalyzed Direct Coupling Reaction of Lactams with Heterocyclic Arenes under Atmospheric Oxygen



Exclusive coupling: High turnover numbers were attained in the dehydrogenative coupling reaction between C(sp^2) and C(sp^3) atoms. A zirconium catalyst mediates the coupling reactions of heterocyclic arenes and lactams exclusively at the carbon atom adjacent to the nitrogen atom of the latter under an oxygen atmosphere (see scheme).

VIP Communications labeled with this symbol have been judged by two referees as being "very important papers".

 © 2004 Wiley-VCH Verlag GmbH & Co. KGaA, Weinheim

WILEY InterScience®
DISCOVER SOMETHING GREAT

"Hot Papers" are chosen by the Editors for their importance in a rapidly evolving field of high current interest. A preview with the graphical abstracts of these articles can be found on the *Angewandte Chemie* homepage in Wiley InterScience at www.angewandte.org.

"VIPs" are Communications which are identified by two referees as being very important. They are published online up to several weeks ahead of print. A preview with short summaries of these articles can also be found on the journal's homepage.

Service

Keywords ____ 4234

Authors ____ 4235

Preview ____ 4237



ISBN 3-527-30542-4

Prices per volume:
€ 259.– / £ 200.– / US$ 370.–

Publication dates:

volumes 1–5	Feb 2004
volumes 6–10	Aug 2004
volumes 11–16	May 2005

The Nucleus of Knowledge

Robert A. Meyers (Ed.), Ramtech Ltd., Tarzana, CA, USA

Encyclopedia of Molecular Cell Biology and Molecular Medicine

2nd Edition, 16 Volume Set

Highly acclaimed and referenced by the scientific community, the *Encyclopedia of Molecular Biology and Molecular Medicine* is now entering its second edition. The new edition features extensive new material on the molecular aspects of cell biology, which is reflected in its new title: *Encyclopedia of Molecular Cell Biology and Molecular Medicine*. With new articles on functional genomics, proteomics, and bioinformatics, there is no better, cutting-edge reference in the field.

"This series is a classic..."
Molecular Medicine Today / Trends in Molecular Medicine

http://meyers-emcbmm.de



John Wiley & Sons, Inc., Customer Care,
Fax: +1 800-597-3299, e-mail:custserv@wiley.com, www.wiley.com
Wiley-VCH, Customer Service Department,
Fax: +49 (0) 6201-606-184, e-mail: service@wiley-vch.de, www.wiley-vch.de
John Wiley & Sons, Ltd, Customer Services Department,
Fax: +44 (0) 1243-843-296, e-mail: cs-books@wiley.co.uk, www.wileyeurope.com

68313072_ba

 © 2004 Wiley-VCH Verlag GmbH & Co. KGaA, Weinheim

Orville L. Chapman (1932–2004): Organic Chemistry and Education

Orville L. Chapman died on January 22, 2004 at the age of 71 from complications associated with pulmonary fibrosis. He was born on June 26, 1932 in New London (CT, USA). The son of a naval officer, he grew up in several cities in the United States and Central America.. He attended elementary school in Washington, DC while his father served as chief engineer on F. D. Roosevelt's yacht. During this time the young Chapman and his mother visited many museums in Washington, stimulating a lifelong interest in art, symmetry, and structure. Chapman received his undergraduate degree from Virginia Polytechnic Institute in Blacksburg with a double major in chemistry and English and completed his PhD with Jerrold Meinwald at Cornell University (NY) in 1957. He began his independent career at Iowa State University, where he rose quickly through the ranks to become full professor in 1964.



Orville L. Chapman

Chapman was a pioneer in the field of organic photochemistry. His selection of this research area was characteristically bold, especially in view of his lack of prior experience in mechanistic chemistry. Chapman credited his colleagues Chuck DePuy and Glen Russell with teaching him physical organic chemistry. His early work focused on enone photochemistry and the mechanism of photocycloaddition reactions.[1] At a time when NMR spectroscopy remained in the domain of physical chemistry, Chapman recognized the potential of this technique for structure determination, and published widely cited contributions in this area. In collaboration with entomologist Jerry Klun, Chapman pursued research on insect sex pheromones.[2]

Chapman's interest in reaction mechanisms and theoretically interesting molecules led him to adopt techniques that allowed direct experimental detection of reactive species. Early efforts involved IR spectroscopy of intermediates generated upon photolysis of neat precursors at 77 K. A critical advance came in the early 1970s when he was introduced to rare-gas matrix isolation spectroscopy by Jake Pacansky. They adapted this technique to study reactive intermediates in organic chemistry, including the classic cases of cyclobutadiene and *o*-benzyne.[3]

Chapman accepted a position at the University of California, Los Angeles (UCLA) in 1974. The years 1975–88 brought the investigation of a wide variety of intermediates, such as carbenes, nitrenes, propadienones, silenes, carbonyl oxides, and strained alkynes.[4] In 1981 Chapman initiated work directed at the chemical synthesis of the novel molecule C_{60}, as part of a broader program which involved the synthesis and characterization of various types of strained, nonplanar aromatic compounds.[5] In retrospect, these efforts are recognized as pioneering contributions to materials chemistry. Chapman's understanding of C_{60}, C_{70}, C_{84}, and curved polyacenes anticipated discoveries that revolutionized chemistry.

Throughout his career, Chapman's intellect, creativity, and personality attracted tremendously talented students and postdoctoral fellows to his research group. He was a fountain of ideas and inspiration. He gave his students wide latitude, but abundant support and encouragement, in their efforts to reduce these ideas to practice. He graciously and generously distributed praise, and he took great pride in the accomplishments of his co-workers.

In 1984, Chapman and his colleague Arlene Russell formed a company that offered in-house short courses in technical writing. They also produced a laser videodisc for teaching NMR spectroscopy and pioneered the use of ^{13}C NMR spectroscopy to teach symmetry and structure in introductory chemistry courses. From 1989 until his death he was Associate Dean for Educational Innovation at UCLA. In 1995, he spearheaded a project for systemic reform of the undergraduate curriculum, which led to a widely adopted instructional software program for developing writing and critical-thinking skills in large undergraduate classes, known as "Calibrated Peer Review (CPR)".[6]

Chapman received many national and international awards, including the ACS Award in Pure Chemistry and the Arthur C. Cope Award from the ACS (American Chemical Society), the Havinga Medal from the Stichtung Havinga (Leiden, The Netherlands), and the Texas Instruments Foundation Founders' Prize. He was elected to the US National Academy of Sciences in 1974. In 1995 he received the Computer-World Smithsonian Institute Award for the best use of computers in education and academia.

Orville Chapman was a man of extraordinary talents: a scholar, a scientist, an author, a poet, a man of indefatigable spirit. Creativity burst from him in every manifestation. He was a trailblazer and innovator in photochemistry, matrix isolation spectroscopy, reactive intermediates, chemical communication, olfactory perception, and materials chemistry. As a long-term consultant for Mobil Chemical, he participated in the invention of many of their industrial processes. He achieved a worldwide reputation for bringing the best of information technology to higher education.

Chapman is survived by his mother, his wife, two sons, and three grandsons. He will be remembered for his warmth, generosity, and great creativity.

Robert J. McMahon
University of Wisconsin, Madison (USA)

[1] O. L. Chapman, *Pure Appl. Chem. (Supplement)* **1971**, 311.
[2] J. A. Klun, O. L. Chapman, K. C. Mattes, P. W. Wojtkowski, M. Beroza, P. E. Sonnet, *Science* **1973**, *181*, 661.
[3] O. L. Chapman, *Pure Appl. Chem.* **1974**, *40*, 511.
[4] a) O. L. Chapman, *Pure Appl. Chem.* **1979**, *51*, 331; b) O. L. Chapman, J. W. Johnson, R. J. McMahon, P. R. West, *J. Am. Chem. Soc.* **1988**, *110*, 501.
[5] S. Kivelson, O. L. Chapman, *Phys. Rev. B* **1983**, *28*, 7236.
[6] http://cpr.molsci.ucla.edu/

 © 2004 Wiley-VCH Verlag GmbH & Co. KGaA, Weinheim DOI: 10.1002/anie.200460954

Synthesis of α-Amino Nitriles

Oxidative Synthesis of α-Amino Nitriles from Tertiary Amines

*Michael North**

Keywords:
amines · cyanides · homogeneous catalysis · oxidation · ruthenium

Compounds with versatile functional groups in close proximity such as α-amino nitriles are extremely useful synthetic intermediates; the nitrile functionality can be hydrolyzed easily to produce α-amino acids, and nucleophilic additions to the nitrile group provide access to α-amino aldehydes, α-amino ketones, α-amino alcohols, and 1,2-diamines. The synthesis of α-amino nitriles is almost always achieved by the Strecker reaction—a three-component condensation of a carbonyl compound, an amine, and cyanide.[1] This can be carried out either as a one-pot process or by adding cyanide to a preformed imine. The Strecker synthesis usually works very well with aldehyde substrates, giving high yields of the α-amino nitrile under mild conditions. However, with ketone substrates, the traditional, achiral Strecker reaction often gives low yields of α-amino nitriles, especially if the amine is also sterically hindered. Asymmetric versions of the Strecker reaction that employ a chiral auxiliary on the amine are well established,[1–3] and recently catalytic, asymmetric variations of the Strecker reaction have been developed.[3–5]

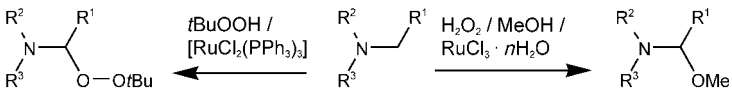
An alternative route to α-amino nitriles involves the oxidation of a secondary amine to an imine, or the oxidation of a tertiary amine to an iminium ion, and in situ trapping of the imine/iminium ion with cyanide. In the case of secondary amines, this can be achieved by the use of phenylseleninic anhydride as the oxidizing agent to form an isolable imine to which cyanide can then be added under anhydrous conditions.[6] An alternative route in the case of secondary amines involves N-chlorination followed by dehydrochlorination to form an imine to which hydrogen cyanide can be added.[7]

Tertiary amines can be converted into α-amino nitriles by oxidation with chlorine dioxide in the presence of sodium cyanide.[8] Alternatively, conversion of a tertiary amine to an N-oxide by treatment with hydrogen peroxide or *meta*-chloroperbenzoic acid followed by iminium ion formation with trifluoroacetic anhydride and trapping with potassium cyanide accomplishes the same transformation.[9] Mercuric acetate will oxidize a tertiary amine to an enamine, and subsequent reaction with hydrogen cyanide then results in formation of an α-amino nitrile.[10] It is also known that electrolysis of tertiary amines in methanol in the presence of sodium cyanide leads to α-amino nitriles, presumably via an intermediate iminium ion.[11] *N*,*N*-Dimethylarylamines react with 1-cyano-3-(1*H*)-1,2-benziodoxols,[12] benzoyl cyanide, and oxygen in the presence of iron(III) chloride,[13] tetracyanoethylene in the presence of heat and light,[14] or rat liver microsomes[15] to form *N*-cyanomethyl-*N*-methyl-arylamines.

In 1988 Murahashi et al. reported that ruthenium catalysts catalyze the α-oxidation of tertiary amines by *tert*-butyl hydroperoxide to form α-amino peroxyethers (Scheme 1). Best results were obtained with 3 mol% of $[RuCl_2(PPh_3)_3]$ as the catalyst.[16,17] Subsequently, the authors showed that if the *tert*-butyl hydroperoxide was replaced by aqueous hydrogen peroxide and methanol, then α-aminoalkyl methyl ethers could be obtained. In this case, hydrated ruthenium trichloride (5 mol%) was found to be the most effective catalyst (Scheme 1).[18] The purpose behind this work was to prepare a synthetic mimic of cytochrome P450.[19]

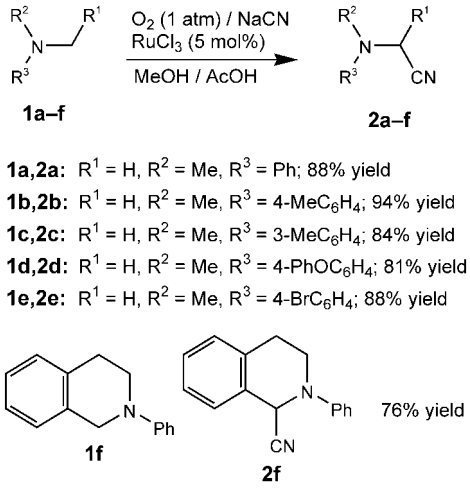
Recently, Murahashi and his coworkers have extended this work with a new synthesis of α-amino nitriles from tertiary amines.[20] Thus, treatment of a tertiary amine with sodium cyanide in the presence of catalytic ruthenium trichloride in the presence of molecular oxygen resulted in the formation of α-amino nitriles (Scheme 2). The solvent system for this reaction was chosen with care, and the presence of acetic acid was found to be essential. Best results were obtained with 5 mol% of the catalyst in a methanol/acetic acid solvent system at 60 °C. Under these conditions, *N*,*N*-dimethylanilines were converted into *N*-cyanomethyl-*N*-methyl anilines in >80% yield, and *N*-phenyl tetrahydroisoquinoline **1f** gave amino nitrile **2f** in 76% yield. It is particularly notable that this conversion utilizes molecular oxygen as the oxidant rather than the

[*] Prof. M. North
Department of Chemistry
King's College London
Strand, London, WC2R 2LS (UK)
Fax: (+44) 870-1313-783
E-mail: michael.north@kcl.ac.uk



Scheme 1. α-Oxidation of tertiary amines.

 © 2004 Wiley-VCH Verlag GmbH & Co. KGaA, Weinheim DOI: 10.1002/anie.200301750



Scheme 2. Ruthenium-catalyzed amino nitrile synthesis.

peroxides used in Murahashi's previous work.[16,18]

To determine the mechanism of the reaction shown in Scheme 2, Murahashi et al. constructed a Hammett plot. The relative reaction rates of *para*-substituted *N*,*N*-dimethylanilines were found to correlate with σ and gave a ρ value of -3.35. This suggests that electron transfer away from the amine occurs in or before the rate-determining step of the mechanism. The authors also studied the deuterium isotope effect by the use of *para*-substituted *N*-methyl-*N*-trideuteromethyl anilines. The observed deuterium isotope effects (k_H/k_D) were found to be dependent on the value of σ, with electron-donating substituents giving the highest isotope effects and electron-withdrawing substituents the lowest. Finally, the authors were able to show that each molecule of oxygen consumed during the reaction resulted in the conversion of two molecules of amine into the corresponding α-amino nitrile.

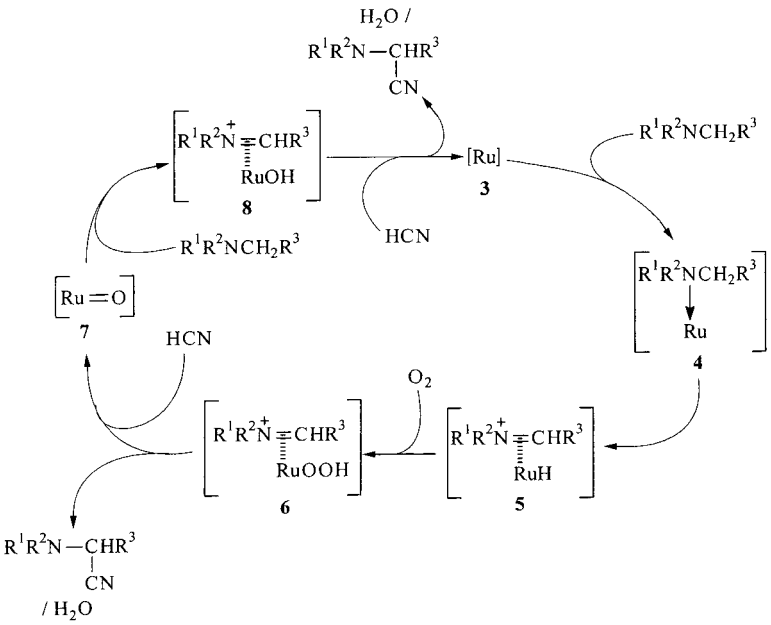
These results are consistent with the catalytic cycle shown in Scheme 3, which is also consistent with previous work on the catalytic oxidation of tertiary amines.[19] The mechanism starts with a ruthenium complex **3** and the tertiary amine. Complexation of the ruthenium to the lone pair of the amine generates complex **4**. Transfer of a hydrogen atom from the coordinated amine to the ruthenium then forms a ruthenium-complexed iminium ion **5**. Insertion of oxygen into ruthenium hydride **5** gives a ruthenium peroxide complex **6**. Reaction of complex **6** with hydrogen cyanide (generated in situ from sodium cyanide and acetic acid) produces one molecule of amino nitrile product along with water and a ruthenium oxo species **7**. Complex **7** can coordinate to a second molecule of amine, and transfer of a hydrogen atom from the coordinated amine to Ru=O generates complex **8**. The catalytic cycle can then be completed by addition of hydrogen cyanide to the coordinated iminium ion of complex **8** with formation of the second molecule of amino nitrile and water and regeneration of ruthenium complex **3**.

One consequence of this catalytic cycle is that the stereocenter of the amino nitrile is created by the addition of cyanide to a ruthenium-coordinated iminium ion (complexes **6** and **8**). Thus, by use of chiral ligands attached to the ruthenium it may be possible to develop a catalytic, asymmetric synthesis of α-amino nitriles using this chemistry. This is further supported by the use of $[RuCl_2(PPh_3)_3]$ to catalyze a related process[16] and would be valuable as catalytic, asymmetric Strecker reactions are not yet well developed.[3–4]

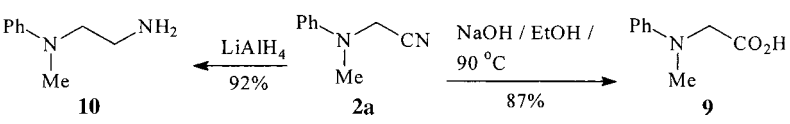
To illustrate the utility of this chemistry, compound **2a** was hydrolyzed to the corresponding glycine derivative **9** by treatment with sodium hydroxide as shown in Scheme 4. Compound **2a** was also reduced to unsymmetrical diamine **10** by treatment with lithium aluminium hydride.

In summary, the ruthenium-based system shown in Scheme 2 is a biomimetic system capable of converting tertiary amines into α-amino nitriles using molecular oxygen as the oxidizing agent. The synthetic system utilizes a Ru=O species to mimic the Fe=O porphyrin complex found in cytochrome P450. There is potential for further development of this chemistry to produce an asymmetric catalyst capable of converting tertiary amines into nonracemic α-amino nitriles and hence α-amino acids.

Published Online: July 15, 2004



Scheme 3. Proposed mechanism for ruthenium-catalyzed amino nitrile synthesis.



Scheme 4. Applications of α-amino nitriles.

 © 2004 Wiley-VCH Verlag GmbH & Co. KGaA, Weinheim

[1] For a review see: M. North in *Comprehensive Organic Functional Group Transformations, Vol. 3* (Eds.: A. R. Katritzky, O. Meth-Cohn, C. W. Rees, G. Pattenden), Pergamon, Oxford, **1995**, pp. 611 – 617.

[2] For reviews of this area see: a) C. Cativiela, M. D. Díaz-de-Villegas, *Tetrahedron: Asymmetry* **2000**, *11*, 645 – 732; b) C. Cativiela, M. D. Díaz-de-Villegas, *Tetrahedron: Asymmetry* **1998**, *9*, 3517 – 3599.

[3] For reviews of this area see: a) H. Gröger, *Chem. Rev.* **2003**, *103*, 2795 – 2828; b) D. Enders, J. P. Shilvock, *Chem. Soc. Rev.* **2000**, *29*, 359 – 373; c) S. Kobayashi, H. Ishitani, *Chem. Rev.* **1999**, *99*, 1069 – 1094.

[4] For more recent work in this area see: a) S. Masumoto, H. Usuda, M. Suzuki, M. Kanai, M. Shibasaki, *J. Am. Chem. Soc.* **2003**, *125*, 5634; b) P. Vachal, E. N. Jacobsen, *J. Am. Chem. Soc.* **2002**, *124*, 10012 – 10014; c) B. Liu, X. Feng, F. Chen, G. Zhang, X. Cui, Y. Jiang, *Synlett* **2001**, 1551 – 1554; d) H. Nogami, S. Matsunaga, M. Kanai, M. Shibasaki, *Tetrahedron Lett.* **2001**, *42*, 279 – 283; e) M. Chavarot, J. J. Byrne, P. Y. Chavant, Y. Vallée, *Tetrahedron: Asymmetry* **2001**, *12*, 1147 – 1150.

[5] For a recent report of the related asymmetric addition of hydrogen cyanide to hydrazones see: J. M. Keith, E. N. Jacobsen, *Org. Lett.* **2004**, *6*, 153 – 155.

[6] D. H. R. Barton, A. Billion, J. Boivin, *Tetrahedron Lett.* **1985**, *26*, 1229 – 1232, and references therein.

[7] G. Stork, R. M. Jacobsen, R. Levitz, *Tetrahedron Lett.* **1979**, 771 – 774.

[8] C.-K. Chen, A. G. Hortmann, M. R. Marzabadi, *J. Am. Chem. Soc.* **1988**, *110*, 4829 – 4831.

[9] a) W. C. Groutas, M. Essawi, P. S. Portoghese, *Synth. Commun.* **1980**, *10*, 495 – 502; b) M. Lounasmaa, A. Koskinen, *Heterocycles* **1982**, *19*, 2115 – 2117.

[10] N. J. Leonard, A. S. Hay, *J. Am. Chem. Soc.* **1956**, *78*, 1984 – 1987.

[11] a) S. Andreades, E. W. Zahnow, *J. Am. Chem. Soc.* **1969**, *91*, 4181 – 4190; b) T. Chiba, Y. Takata, *J. Org. Chem.* **1977**, *42*, 2973 – 2977; c) E. Le Gall, J.-P. Hurvois, T. Renaud, C. Moinet, A. Tallec, P. Uriac, S. Sinbandhit, L. Toupet, *Liebigs Ann. Chem.* **1997**, 2089 – 2101.

[12] V. V. Zhdankin, C. J. Kuehl, A. P. Krasutsky, J. T. Bolz, B. Mismash, J. K. Woodward, A. J. Simonsen, *Tetrahedron Lett.* **1995**, *36*, 7975 – 7978.

[13] S. Murata, K. Teramoto, M. Miura, M. Nomura, *Bull. Chem. Soc. Jpn.* **1993**, *66*, 1297 – 1298.

[14] M. Ohashi, S. Suwa, Y. Osawa, K. Tsujimoto, *J. Chem. Soc. Perkin Trans. 1* **1979**, 2219 – 2223.

[15] J. Iley, R. Tolando, *J. Chem. Soc. Perkin Trans. 2* **2000**, 2328 – 2336.

[16] S.-i. Murahashi, T. Naota, K. Yonemura, *J. Am. Chem. Soc.* **1988**, *110*, 8256 – 8258.

[17] For related work on ruthenium-catalyzed oxidations of primary and secondary amines see: K. Yamaguchi, N. Mizuno, *Angew. Chem.* **2003**, *115*, 1518 – 1521; *Angew. Chem. Int. Ed.* **2003**, *42*, 1480 – 1483, and references therein.

[18] S.-i. Murahashi, T. Naota, N. Miyaguchi, T. Nakato, *Tetrahedron Lett.* **1992**, *33*, 6991 – 6994.

[19] For a review see: S.-i. Murahashi, *Angew. Chem.* **1995**, *107*, 2670 – 2693; *Angew. Chem. Int. Ed. Engl.* **1995**, *34*, 2443 – 2465.

[20] S.-i. Murahashi, N. Komiya, H. Terai, T. Nakae, *J. Am. Chem. Soc.* **2003**, *125*, 15312 – 15313.

Imaging Agents

Semiconductor Quantum Dots as Biological Imaging Agents**

*Mark Green**

Keywords:
bioinorganic chemistry · cadmium · imaging agents · luminescence · quantum dots

The advent of high-quality, solution-grown nanomaterials that may be manipulated as a typical reagent whilst still maintaining their photoluminescent properties has allowed new applications, notably in biology. Organometallic chemistry has provided synthetic pathways to robust, monodispersed, highly emissive nanomaterials, such as CdSe, which can be further capped with a shell of ZnS to electronically passify the surface. The correct choice of structure, capping agent, and growth temperature can yield materials with quantum yields as high as 90%. Tuning the color of emission through the visible spectrum can be routinely achieved by altering the particle size during growth. The emission profile can be narrowed by selective precipitation procedures, ensuring no cross-coupling of signals during multicolor applications. Numerous colors can be excited by a single source, allowing for multiplexing (obtaining multiple streams of data from a single excition source), and the materials are extremely photostable, unlike conventional dyes. The long luminescent life times allow imaging of living cells without interference from background autofluorescence.

Recently, Kim et al. have reported a key advance in cancer imaging.[1] Despite the efficiency of CdSe/ZnS core–shell materials in imaging, other similar structures can be used. CdTe/CdSe nanoparticles, referred to as type II quantum dots have a different core–shell energy mismatch and emit in the near infrared region of the spectrum. The particles were prepared by an organometallic chemistry route and the surface-capping agent deposited during synthesis was exchanged for an oligomeric water-soluble phosphane. Dots observed to have solid-state core of 10 nm (as determined by TEM), were found to have a hydrodynamic diameter of between 15 and 20 nm. This feature makes the particles ideal for retention in sentinel lymph nodes (SLN).[1] Incubation of the dots in serum at 37°C for 30 minutes resulted in only a small drop off in emission intensity, which suggests the IR emitting materials were suitable for labeling applications. The dots were used in lymph mapping, a major procedure in cancer surgery. Following intradermal injection of dots into the paw of a mouse, the near-IR-emitting dots could be detected in the lymphatic system within minutes using an intraoperative imaging system. When injected into a larger animal (400 pmol into a 35 kg pig), a surgeon could follow the dots in real time to the SLN, approximately 1 cm below the skin. Because the dots allowed image guidance through the procedure, the size of any required incision was reduced. Analysis of the procedure demonstrated that the dots were localized in the SLN, at the outermost rim of the nodes. The imaging of SLN in real time without the need of a traditional blue dye or radioactive marker is a significant breakthrough. Owing to the stability of the dots over traditionally unstable IR-emitting dyes, the surgeon can examine any site even after surgery to ensure the successful removal of the lymph nodes. Despite the low doses of dots used, it was estimated that at least a hundred-fold lower dose could be used owing to their stability.

Chan and Nie, and Bruchez et al. published the seminal papers on quantum-dot (QD) bioimaging.[2,3] The key factor in using dots grown in organic solvents was the successful phase transfer to water with minimal loss of emission, whilst maintaining a bioactive surface. Bruchez et al. approached the problem by growing a silica (SiO_2) shell around CdSe/ZnS nanoparticles and used silica chemistry to couple ligands to the shell which were utilized in coupling reactions. The resulting materials (which could be engineered to have a maximum quantum yield of 21%) were used to label mouse fibroplasts (Figure 1). The labels appeared photostable when compared to conventional dyes. Constant excitation of bioactive QDs over 4 h with a 488 nm Ar+ laser resulted in constant emission, unlike

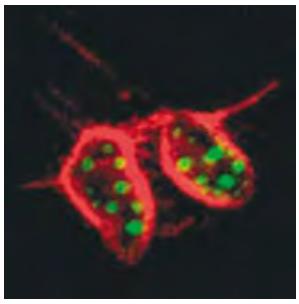


Figure 1. Mouse 3T3 fibroplast labeled with quantum dots.[2] Red particles label the F-actin filaments, whilst green particles stain the cell nucleus. Reproduced with permission from ref. [2].

[*] Dr. M. Green
Department of Physics
King's College London
The Strand, London WC2R 2LS (UK)
Fax: (+44) 20 7451 2692
E-mail: mark.a.green@kcl.ac.uk

[**] The author thanks *Science* for permission to use Figure 1 and Figure 2, and *Nature Biotechnology* for permission to use Figure 3.

DOI: 10.1002/anie.200301758
© 2004 Wiley-VCH Verlag GmbH & Co. KGaA, Weinheim

Rhodamine 6G dyes which bleached in 10 mins.[2]

Chan and Nie used a simpler method for making CdSe/ZnS particles water soluble and bioactive. Solution exchange of the organic ligands on the QD surface for mercaptoacetic acid resulted in soluble particles that have a pendant carboxylic acid group for coupling. They also reported the observation of receptor-mediated endocytosis of the luminescent particles when incubated with HeLa Cells. Further experiments with immunoglobulin G-QD conjugates incubated with bovine serum albumin (BSA) and a specific polyclonal antibody demonstrated a tendency for the dots to aggregate when the antibody recognized the so called fab fragment of the immunoglobulin G.[3] These two papers have been the basis of numerous studies.

Work has not been confined to static imaging. Phagokinetic track studies into the motility of human mammary epithelial tumor cells and nontumor cells has been undertaken.[4] Thin layers of silica capped CdSe/ZnS were deposited on collagen coated substrates, followed by the plating of cells. Traditional dyes cannot be used owing to photobleaching, and large submicrometer gold particles used previously interfered with cell motility. As a cell passed through the substrate, the uptake of the luminescent cells was observed over time by confocal fluorescence microscopy. In less than 3 h, the tumor cells engulfed nanocrystals, which then clustered in the cytoplasm, presumably in the vesicles. Further experiments revealed the nanoparticles were restricted to the cytoplasm and had not entered the nucleus. The migratory pathways of the tumor cells could be observed by imaging the substrate and observing areas free of nanocrystals, as a result of the uptake. Imaging of substrates plated with noncancer cells (non-migratory) revealed an intact layer with little evidence of motility. These results confirmed cancer cells are both invasive and migratory, whilst noncancer cells are non-invasive and relatively immotile.

One of the first papers describing in vivo studies using QDs used mercaptoacetic acid capped CdSe/ZnS, which were incubated with thiolated peptides, which passivated the QD surface.[5] Three specific peptides were used in the studies, peptide CGFECVRQCPERC (GFE), which binds to a membrane dipeptidase on the endothelial cells in lung blood vessels; F3, which binds to blood vessels and tumor cells in certain tumors; and LyP-1, which binds to lymphatic vessels and tumor cells in certain tumors. QDs coupled to F3 alone displayed a tendency to aggregate, which was overcome by co-passivating with thiolated polyethylene glycol (PEG), which is known to minimize molecular interactions, improve colloidal stability, and inhibit nonspecific binding. The QDs were then injected into the tail veins of specifically xenografted mice and left to circulate for up to 20 minutes before the relevant tissues were harvested. As hypothesized, dots passivated with GFE were found in the lungs, and dots capped with F3 and LyP-1 were found in the targeted tumors, whilst the subcellular fluorescence pattern suggested the dots were internalized into the cells. GFE capped dots were not detected in tumors. The dots were not found in the brain, heart, kidney, or skin, but were observed in the liver and spleen regardless of the peptide used, except when co-passivated with PEG, which reduced co-adsorption by 95 %.[5]

Despite the above applications, there are still problems using specifically capped QDs as biolabels. Simple surface-capping-agent exchange as described by Chan and Nie[2] results in a material with decreased emission efficiency and poor colloidal stability. Growing a silica shell on the particles as described by Bruchez et al.[3] results in a stable material, but is difficult to do, hard to control and time consuming, resulting in a material with a decreased quantum yield. A more important problem for QD biolabels prepared by either method is the tendency to absorb nonspecifically or aggregate when taken up by cells. Various researchers have addressed these issues, and methods include the addition of small polymeric species on the surface of silica capped QDs, or the use of electrostatic interactions to absorb a protein on the QD surface which can act as a bridging agent.

Dubertret et al. has investigated a simple way of making bioactive quantum dots that overcome the issues, such as nonspecific binding, by encapsulating the nanoparticles in phospholipid micelles, the outer layer of which is repellent to biomolecules.[6] DNA was coupled to the end of the outer-layer of the micelle, providing a binding point for bioconjugation by hybridization. Ideally, the dots need to be slightly bigger than the core, stabilizing the micelle. If the particles are too small, the stability of the micelle is affected and multiple dots can inhabit a single cavity. Simple QD micelles were injected into *Xenopus* embryos and used in in vivo studies. The micelles appeared to be cell autonomous, had little toxic effect on the cells and were stable in vivo showing no signs of aggregation after 4 days. The micelles were used to successfully label numerous cell types, and remained luminescent throughout embryonic development despite pigmentation and background fluorescence.

Deep tissue in vivo imaging and blood-flow monitoring studies were also carried out using CdSe/ZnS capped with an octylamine modified polyacrylic acid.[7] The probes were determined to have two-photon action cross sections (a measure of brightness for imaging) of up to 47000 Goeppert–Mayer (GM) units, an order of magnitude higher than organic molecules designed for similar biological functions and close to the theoretical maximum for CdSe dots, estimated at 50000 GM. The dots appeared stable for months and the action cross-section remained constant, however, a large fraction of nonfluorescent dots were also observed. No evidence for blinking (fluctuation of radiation intensity) was observed and it is suggested that this phenomenon averages out and is unlikely to be an issue in nanoparticle imaging applications. It was observed that the sizes of the quantum dots are similar to fluorescent dextrans, which make them ideal for angiography. Intravenous injection in live mice was carried out to examine skin and adipose tissues, both of which are highly scattering and have a high refractive index mismatch. The vasculature system was clearly observed through unbroken skin up to 250 μm deep. Compared to similar imaging agents such as fluorescent dextrans (compare Figure 2a and d), quantum

 © 2004 Wiley-VCH Verlag GmbH & Co. KGaA, Weinheim

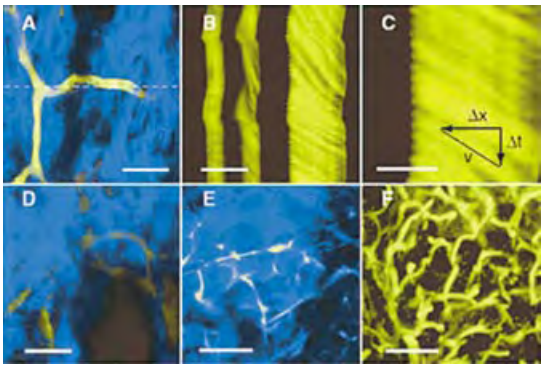


Figure 2. Deep tissue imaging of a vasculature system.[7] A) CdSe dots in capillaries at the base of the dermis (100 μm deep); B) line scan used to measure blood velocity; C) magnification of image (B); D) fluorescent dextrans under same conditions as image (A); E) image of adipose tissue surrounding the ovary; F) capillary structure of adipose tissue (250 μm deep). Scale bars: A,B,D = 20 μm, C = 10 μm, E,F = 50 μm. Reproduced with permission from ref. [7].

dots shows significantly more detail with less power, attributable to the high action cross-section. Figure 2 shows images obtained from the study, highlighting various structures (the blue color is collagen autofluorescence). The mice used in the study showed no ill effects from the cadmium-containing labels and investigations are ongoing as to the suitability of heavy-metal containing labels.

Semiconductor quantum dots are becoming highly efficient tools for biological imaging and have numerous demonstrated advantages over conventional dyes. Other studies of note include the imaging of the cancer marker Her2,[8] and the development of quantum-dot-doped polystyrene beads designed for assays[9] (Figure 3). The beads are particularly note worthy as they are internalized into the bead core without requiring surface exchange, thus maintaining their luminescent efficiency. The controlled manner in which this was achieved allowed for the development of a quantum-dot bar based assay.

Despite the numerous advances, initial investigation into CdSe QD toxicity using primary hepatocytes rich in metallothionein as a model for the liver clearly displayed that under certain conditions, the QDs were cytotoxic. This property was attributed to the liberation of Cd^{2+} ions during oxidation.[10] However, further toxicity studies are required, and clearly the use of QDs in imaging is an exciting application that is yet to realize its full potential.

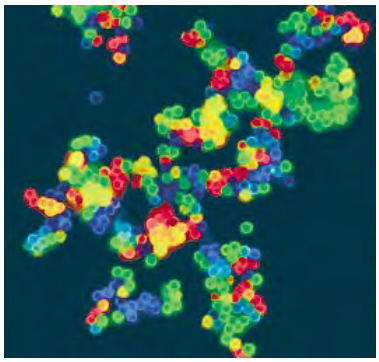


Figure 3. Microbeads containing various levels of CdSe/ZnS quantum dots. Reproduced with permission from ref. [9].

Published Online: July 20, 2004

[1] S. Kim, Y. T. Lim, E. G. Soltesz, A. M. De Grand, J. Lee, A. Nakayama, J. A. Parker, T. Mihaljevic, R. G. Laurence, D. M. Dor, L. H. Cohn, M. G. Bawendi, J. V. Frangioni, *Nat. Biotechnol.* **2004**, *22*, 93.
[2] M. Bruchez, M. Moronne, P. Gin, S. Weiss, A. P. Alivisatos, *Science* **1998**, *281*, 2013.
[3] W. C. W. Chan, S. Nie, *Science* **1998**, *281*, 2016.
[4] W. J. Parak, R. Boudreau, M. Le Gros, D. Gerion, D. Zanchet, C. M. Micheel, S. C. Williams, A. P. Alivisatos, C. Larabell, *Adv. Mater.* **2002**, *14*, 882.
[5] M. E. Åkerman, W. C. W. Chan, P. Laakkonen, S. N. Bhatia, E. Ruoslahti, *Proc. Natl. Acad. Sci. USA* **2002**, *99*, 12617.
[6] B. Dubertret, P. Skourides, D. J. Norris, V. Noireaux, A. H. Brivanlou, A. Libchaber, *Science* **2002**, *298*, 1759.
[7] D. R. Larson, W. R. Zipfel, R. M. Williams, S. W. Clark, M. P. Bruchez, F. W. Wise, W. W. Webb, *Science* **2003**, *300*, 1434.
[8] X. Wu, H. Liu, J. Liu, K. N. Haley, J. A. Treadway, J. P. Larson, N. Ge, F. Peale, M. P. Bruchez, *Nat. Biotechnol.* **2003**, *21*, 41.
[9] M. Han, X. Gao, J. Z. Su, S. Nie, *Nat. Biotechnol.* **2001**, *19*, 631.
[10] A. M. Derfus, W. C. W. Chan, S. N. Bhatia, *Nano Lett.* **2004**, *4*, 11.

 © 2004 Wiley-VCH Verlag GmbH & Co. KGaA, Weinheim

Metalloenzymes

N_2O Reduction by the μ_4-Sulfide-Bridged Tetranuclear Cu_Z Cluster Active Site**

*Peng Chen, Serge I. Gorelsky, Somdatta Ghosh, and Edward I. Solomon**

Keywords:
bioinorganic chemistry · copper · electronic structure · metalloenzymes · structure–activity relationships

Nitrous oxide (N_2O) reduction is a chemical challenge both in the selective oxidation of organic substrates by N_2O and in the removal of N_2O as a green-house gas. The reduction of N_2O is thermodynamically favorable but kinetically inert, and requires activating transition-metal centers. In biological systems, N_2O reduction is the last step in the denitrification process of the bacterial nitrogen cycle and is accomplished by the enzyme nitrous oxide reductase, whose active site consists of a μ_4-sulfide-bridged tetranuclear Cu_Z cluster which has many unusual spectroscopic features. Recent studies have developed a detailed electronic-structure description of the resting Cu_Z cluster, determined its catalytically relevant state, and provided insight into the role of this tetranuclear copper cluster in N_2O activation and reduction.

1. Introduction

Selective oxidation of organic substrates is a significant challenge.[1] Reagents energetically capable of performing useful oxidations are often so reactive that they offer no substrate selectivity; others produce byproducts that lead to undesirable side reactions. A potentially attractive oxo-transfer reagent to oxidize organic substrates is nitrous oxide ($N_2O + 2H^+ + 2e^- \rightarrow N_2 + H_2O$, $E^\circ = 1.76$ V),[2] which provides a clean reaction since the sole byproduct is N_2. However, N_2O is a kinetically inert molecule, which is reflected in the approximately 59 kcal mol^{-1} activation barrier for its thermal decomposition (a unimolecular, spin-forbidden process).[3] Reduction of N_2O in homogenous systems normally requires transition metals, such as Ti, V, Ni, Zr, Ru, Hf,[4–9] as activation centers, where the required two electrons are either derived from the metal centers, which results in terminal[10,11] or bridged[4] metal-oxide products, or from the ligands through insertion of the oxygen atom into the metal–ligand bond.[5–7,12] To date, none of the reported metal/N_2O complexes has been structurally determined crystallographically. The N_2O unit in the $[(NH_3)_5Ru(N_2O)]^{2+}$ complex has been found from spectroscopy to coordinate to the ruthenium atom in a linear end-on mode by its terminal nitrogen atom.[13] Additional terminal oxygen coordination to metal sites has also been implicated in the formation of the $\{Ru(N_2O)Ru\}$ dimer[10,14] and has been spectroscopically identified in N_2O adsorption on α-Cr_2O_3.[15]

The reduction of N_2O in biological systems is accomplished by the multicopper-center containing enzyme nitrous oxide reductase (N_2OR). This reaction is the last step of the denitrification process, where the denitrifying organisms utilize oxidized forms of nitrogen in place of oxygen as the terminal electron acceptors for anaerobic respiration (Figure 1) that is coupled to ATP synthesis.[16] The reduction of N_2O is also environmentally important because N_2O is a green-house gas (third only to CO_2 and CH_4) and largely generated from artificial fertilizers used in farming and from the burning of fossil fuels.[3,16] The enzyme N_2OR contains two types of copper active sites, Cu_A and Cu_Z.[16–18] The Cu_A center is a well-characterized electron-transfer site with two copper atoms bridged by two cysteine ligands.[19,20] The structure of

[*] P. Chen, Dr. S. I. Gorelsky, S. Ghosh, Prof. Dr. E. I. Solomon
Department of Chemistry
Stanford University
Stanford, California 94305 (USA)
Fax: (+1) 650-725-0259
E-mail: Edward.Solomon@Stanford.Edu

[**] This research is supported by NIH grant DK-31450 (E.I.S.). The S K-edge data were collected by Dr. S. DeBeer George (Stanford Synchrotron Radiation Laboratory). We thank Profs. I. Moura (Portugal), D. Dooley (Montana State University), K. Hodgson and B. Hedman (Stanford Synchrotron Radiation Laboratory), and W. E. Antholine (Wisconsin Medical College) for collaborations on different parts of this research. P.C. was supported by a Gerhard Casper Stanford Graduate Fellowship and a Franklin Veatch Memorial Fellowship. S.I.G. has been supported by a NSERC (Ottawa) postdoctoral fellowship.

 © 2004 Wiley-VCH Verlag GmbH & Co. KGaA, Weinheim DOI: 10.1002/anie.200301734

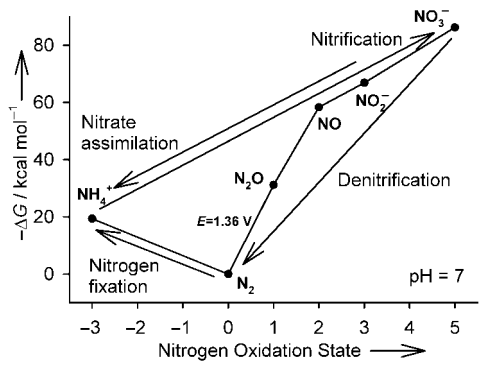


Figure 1. Bacterial nitrogen cycle and its thermochemistry (aqueous solution at pH 7). The values of ΔG (ox + $ne^- \rightarrow$red) refer to N_2 as standard (zero) but are quoted per mol of N atoms.

the catalytic Cu_Z site, however, was elusive and was originally assigned as a binuclear copper center based on some initial spectroscopic results.[21,22] A low-resolution crystal structure (2.4 Å) was later solved for N_2OR from *Pseudomonas nautica* (*Pn*),[23] and indicated that the Cu_Z center has a strikingly new structural motif composed of a bridged tetranuclear copper cluster and is located in the N-terminal domain in each subunit of the dimeric protein, while the Cu_A center is located in the C-terminal domain of each subunit. The neighboring Cu_A and Cu_Z centers are from different subunits in the dimeric protein (Figure 2). Quantitative elemental analysis combined with spectroscopic arguments soon indicated that the Cu_Z center is in fact a μ_4-sulfide bridged tetranuclear copper cluster.[24] This was later confirmed by the high-resolution crystal structure of N_2OR from *Paracoccus denitrificans* (*Pd*) (1.6 Å), and the original *Pn* N_2OR structure was then revised.[25,26]

The Cu_4S core of the Cu_Z structure has approximate C_s symmetry with Cu_I-S-Cu_{II} defining the mirror plane (see Figure 2). The Cu_I-S-Cu_{II} angle is approximately 160°, and the other Cu-S-Cu angles are close to orthogonal. All the Cu–S bond lengths are approximately the same, about 2.3 Å. However, the Cu–Cu separations are very different, with the three copper centers, Cu_{II}, Cu_{III}, Cu_{IV} (Figure 2), closer to each other and Cu_I more distant (Cu_I–Cu_{III}/Cu_I–$Cu_{IV} \approx 3.4$ Å, Cu_{II}–Cu_{III}/Cu_{II}–$Cu_{IV} \approx 2.6$ Å, Cu_{III}–$Cu_{IV} \approx 2.9$ Å). The whole {Cu_4S} cluster is coordinated to the protein backbone by seven histidine ligands, and there is an additional ligand L at the Cu_I/Cu_{IV} edge. This Cu_I/Cu_{IV} edge is believed to be the substrate binding site.[23] To date the exact nature of this ligand (O^{2-}, OH^-, H_2O) is unclear from the crystal-structure studies.

Much spectroscopic data have been published on the resting Cu_Z center,[27] including its absorption spectrum (Figure 3a, solid line) which shows an intense charge-transfer (CT) band at about 640 nm ($\approx 15\,650$ cm^{-1}), and the low-temperature magnetic circular dichroism (MCD) spectrum (Figure 3a, broken line) which has an intense feature in this 640 nm region.[21,22,24,28] The EPR spectrum of resting Cu_Z has also been reported, it exhibits a very small $g_\parallel$ value and complicated hyperfine-coupling pattern.[18,21,28] However, because of the lack of accurate quantification of the number of copper atoms in the enzyme, their oxidation states, and



Peng Chen received his B.S. from Nanjing University, China in 1997. After spending a year at University of California at San Diego with Prof. Yitzhak Tor, he moved to Stanford University to work with Prof. Edward I. Solomon. There he did his Ph.D. on the electronic structure studies of biologically relavent Cu sites involved in O_2 and N_2O activation. He was supported by a Gerhard Casper Stanford Graduate Fellowship and a Franklin Veatch Memorial Fellowship. He recently started his postdoctoral research with Prof. Sunney Xie at Harvard University.



Serge Gorelsky received his B.S. and M.S. from Moscow State University. He completed his Ph.D. under the supervision of Prof. A. Barry P. Lever at York University, Toronto, on electronic spectroscopy of ruthenium complexes. In 2002, he joined Prof. Edward I. Solomon's group at Stanford University as an NSERC Postdoctoral Fellow. His research focuses on electronic-structure and spectroscopic studies of copper-containing proteins. He is a recipient of Governor General of Canada's Gold Medal for academic excellence (2002).



Somdatta Ghosh was born in Kolkata, India. She received her B.S. degree from Presidency College, Calcutta University, and M.S. degree from the Indian Institute of Technology, Kanpur. She moved to Stanford University as a graduate student in 2002, and joined the research group of Prof. Edward I. Solomon. Her research focuses on spectroscopic, kinetic, and computational studies aimed at elucidating the mechanism of N_2O reduction and substrate oxygenation by copper containing enzymes.



Edward I. Solomon grew up in North Miami Beach, Florida, received his Ph.D. from Princeton University (with D. S. McClure), and was a postdoctoral fellow at the H. C. Ørsted Institute (with C. J. Ballhausen) and then at Caltech (with H. B. Gray). He was a professor at MIT until 1982. He then moved to Stanford University where he is now a Monroe E. Spaght Professor of Humanities and Sciences. His research is in the fields of physical–inorganic and bioinorganic chemistry with emphasis on the elucidation of electronic structures and their contributions to the physical properties and reactivity of transition-metal complexes.

 © 2004 Wiley-VCH Verlag GmbH & Co. KGaA, Weinheim

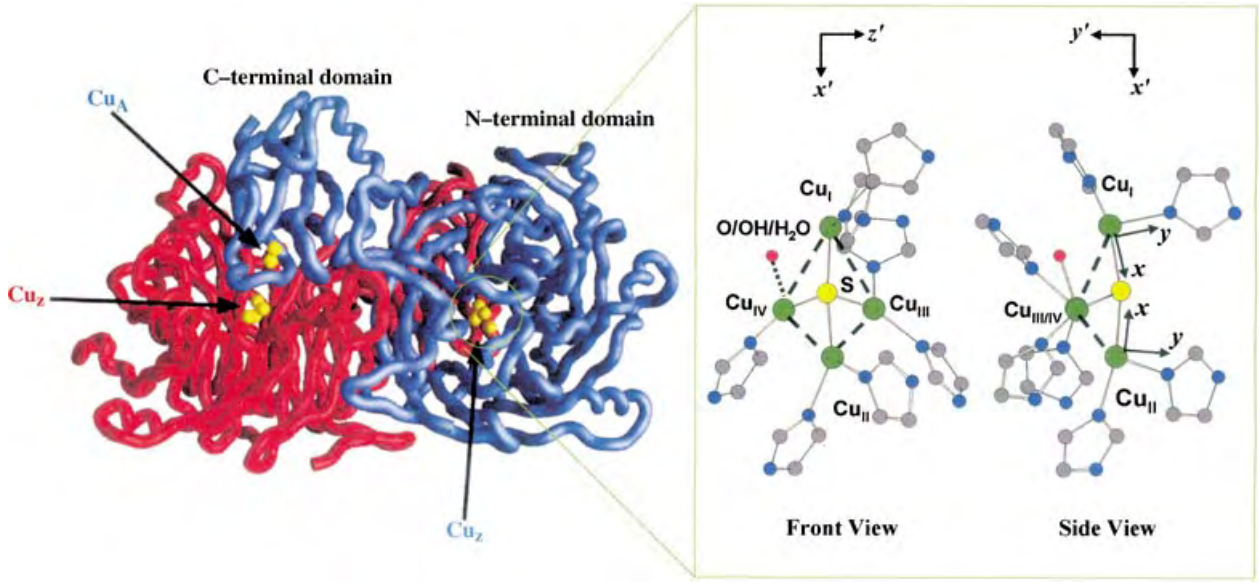


Figure 2. Crystal structure of the Cu_Z site from *Pn*. The two subunits in the homodimeric protein are indicated in red and blue. The Cu_4S cluster has approximate C_s symmetry with Cu_I-S-Cu_{II} defining the mirror plane. $r(Cu–S) \approx 2.3$ Å, $r(Cu_I–Cu_{III})$ and $r(Cu_I–Cu_{IV}) \approx 3.4$ Å, $r(Cu_{II}–Cu_{III})$ and $r(Cu_{II}–Cu_{IV}) \approx 2.6$ Å, $r(Cu_{III}–Cu_{IV}) \approx 2.9$ Å; Cu_I-S-$Cu_{II} \approx 160°$, all other Cu-S-Cu angles are close to 90°. The water-derived ligand L (O^{2-}, OH^-, H_2O) is weakly bound according to the higher resolution structure of *Pd* (1.6 Å resolution) with $r(Cu_{IV}–O) \approx 2.6$ Å and $r(Cu_I–O) \approx 2.8$ Å, however its nature has not been assigned. Molecular (x',y',z') and local (x,y,z) coordinate systems are indicated, which are used for labeling orbitals.

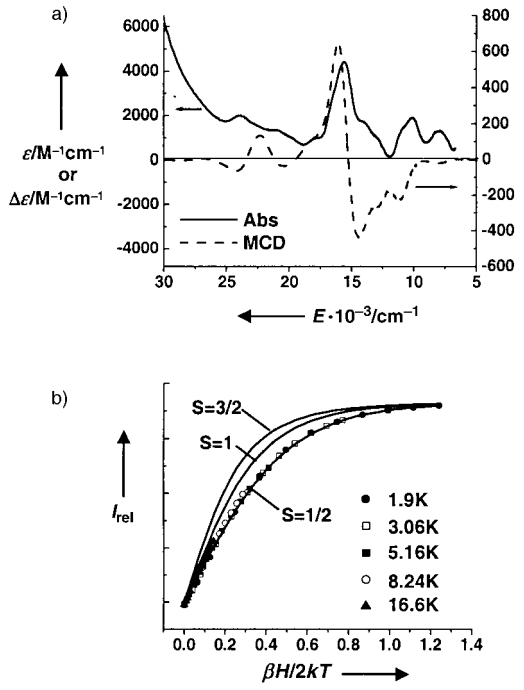


Figure 3. a) absorption spectrum of resting Cu_Z from *Pn* N_2OR at 10 K and the corresponding 7 T MCD spectrum at 5 K. b) VTVH saturation MCD (points) at 620 nm of resting Cu_Z along with simulated saturation curves (solid lines).

structural information, a reasonable understanding of these spectral features and the enzymatic mechanism had not been possible. Herein, we focus on our recent efforts to understand these spectroscopic features and develop an electronic-structure description of the Cu_Z site of the N_2OR enzyme.[29–31] Insight into the contribution of the electronic structure to N_2O reduction and the possible mechanism for this reaction by the Cu_Z center are also presented.

2. The Electronic Structure of the Cu_Z Center

The intensity of the MCD signals shown in Figure 3a are temperature and magnetic-field dependent (contribution of the MCD C-term) and increases with lower temperature and higher magnetic field. The MCD intensity will eventually saturate at high field (≈ 7 T) and low temperature (≈ 2 K). Different spin-state systems have different saturation behaviors.[32] Variable temperature, variable field (VTVH) saturation MCD can thus determine the spin state of the resting Cu_Z center, which is the state of the crystallographically defined Cu_Z cluster. The VTVH MCD saturation of resting Cu_Z is shown in Figure 3b along with theoretically calculated saturation curves for $S = {}^1/_2$, 1, and ${}^3/_2$ systems, which show that the resting Cu_Z center has an $S_{total} = {}^1/_2$ ground state.[29]

Since the Cu_Z center is a tetranuclear copper cluster, there are two possibilities for the copper oxidation states to give $S_{total} = {}^1/_2$, either $1\,Cu^{II}/3\,Cu^I$ or $3\,Cu^{II}/1\,Cu^I$ (Cu^{II}, d^9, oxidized; Cu^I, d^{10}, reduced). In the latter case, two of the oxidized copper atoms would have to be antiferromagnetically coupled. Cu K-edge X-ray absorption spectroscopy (XAS) was used to distinguish between these two possibilities. Cu^I complexes have an intense characteristic absorption feature at approximately 8984 eV, which is the electric-dipole-allowed Cu 1s→4p transition, while Cu^{II} complexes have no intense feature below 8985 eV. Instead they have a very weak transition at about 8979 eV, which is the electric-dipole-forbidden Cu 1s→3d transition.[33] The copper K-edge X-ray

 © 2004 Wiley-VCH Verlag GmbH & Co. KGaA, Weinheim

absorption spectrum of resting Cu_Z is given in Figure 4, along with simulated spectra for the $1Cu^{II}/3Cu^{I}$ and $3Cu^{II}/1Cu^{I}$ configurations. The simulations show that the $1Cu^{II}/3Cu^{I}$ model is far better than the $3Cu^{II}/1Cu^{I}$ alternative, which

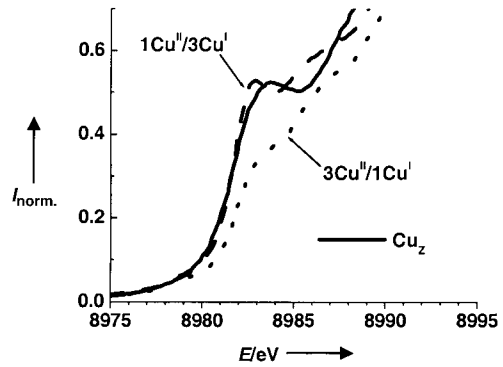


Figure 4. Cu K-edge XAS spectrum of resting Cu_Z from *Pn* N_2OR and simulated spectra assuming $1Cu^{II}/3Cu^{I}$ and $3Cu^{II}/1Cu^{I}$ oxidation state configurations.

indicates that there is only one oxidized Cu^{II} in the Cu_Z cluster with a single spin (a single Cu d-hole).[29]

EPR spectroscopy was used to determine the distribution of the single spin (from one Cu^{II} center) over the Cu_Z center. The Q-band ($\nu \approx 35$ GHz) EPR spectrum of resting Cu_Z (Figure 5a) shows an axial pattern with $g_{\parallel} \approx 2.16 > g_{\perp} \approx 2.04 > 2.0$, indicating that the single spin resides in a Cu $d_{x^2-y^2}$

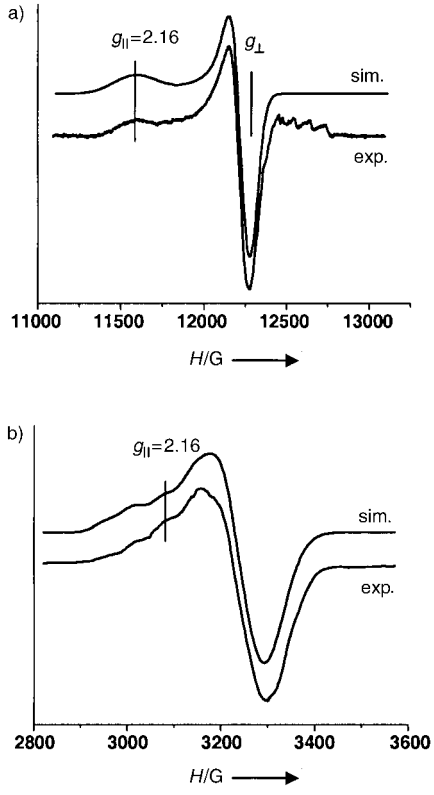


Figure 5. Experimental and simulated EPR spectra of resting Cu_Z from *Pn* N_2OR at a) Q-band and b) X-band.

orbital.[34] The $g_{\parallel}$ value of resting Cu_Z is very small as compared to the approximately 2.3–2.4 for normal tetragonal Cu^{II} complexes (e.g. $CuSO_4$).[35] This could be due to extensive covalent character in the metal–ligand bonding or high d–d transition energies.[35] High transition energies affect the *g* values as the spin-orbit coupling of these excited states with the ground state leads to the *g* values deviating from 2.0023, and this deviation will decrease as the energies of these excited states increase. In correlating the Q-band to the lower frequency X-band ($\nu \approx 9.3$ GHz) EPR spectrum of resting Cu_Z, metal hyperfine coupling is resolved in the $g_{\parallel}$ region (Figure 5b). Mapping the *g* values determined from the Q-band EPR onto the X-band EPR spectrum, the $g_{\parallel}$ value (≈ 2.16) coincides with a hyperfine feature indicating metal hyperfine pattern with an odd number of lines (Figure 5b). This is in contrast to the EPR hyperfine pattern of normal mononuclear Cu^{II} complexes, which is a four-line pattern (Cu nuclear spin $= {}^3/_2$).[35] To account for the X-band metal hyperfine pattern, two copper centers are required for the hyperfine coupling. One copper center dominates the hyperfine splitting ($A_{\parallel} = 61 \times 10^{-4}$ cm^{-1}) and a second copper center contributes somewhat less with $A_{\parallel} = 24 \times 10^{-4}$ cm^{-1}. The ratio of the hyperfine coupling constants gives the approximate ratio of spin densities on the two copper atoms, approximately 5:2. Therefore, resting Cu_Z in *Pn* N_2OR can be described as a partially delocalized mix-valent system with the single spin predominantly in a $d_{x^2-y^2}$ orbital on one copper atom.[29]

XAS at the Cu K-edge was used to determine the copper oxidation states of resting Cu_Z. XAS at the sulfur K-edge (S K-edge) was also used to determine the bridging-sulfide covalency in the ground state of resting Cu_Z.[36] The pre-edge transition at the S K-edge is the S 1s→ground state SOMO transition, where the SOMO is a linear combination of Cu 3d and S 3p orbitals (Figure 6a). The intensity of this pre-edge transition is directly proportional to the sulfide covalency α^2 in the ground-state wave function (see Equation in Figure 6a).[36] Figure 6b presents the S K-edge spectrum of resting Cu_Z,[37] where the S pre-edge transition occurs at approximately 2469 eV and its weak intensity corresponds to around 15–22% sulfur character in the ground-state wave function. For comparison, the S K-edge spectrum of the Cu_A center (also given in Figure 6b) has a much stronger pre-edge feature at about 2470 eV. The intensity of this Cu_A pre-edge transition corresponds to approximately 46% S character in the ground state, which is well documented.

Density functional theory (DFT) calculations were used to obtain a detailed description of the resting Cu_Z ground-state wave function. Figure 7 and Table 1 give the optimized structures and atomic spin densities of the spin-doublet state of the Cu_Z cluster with different Cu_I/Cu_{IV}-edge ligands. These calculations indicate that the ground-state wave function and the spin-density distribution of the Cu_Z cluster are sensitive to the nature of the ligand at the Cu_I/Cu_{IV} edge. In general, Cu_I is the predominantly oxidized copper center (Table 1). This situation is consistent with Cu_I having a four-coordinate structure and the other copper atoms having lower coordination numbers (see Figures 2 and 7). The spin distribution between the Cu_I and Cu_{II} atoms in the cluster with $L = H_2O$ and the spin distribution between the Cu_I and Cu_{IV} atoms in

 © 2004 Wiley-VCH Verlag GmbH & Co. KGaA, Weinheim

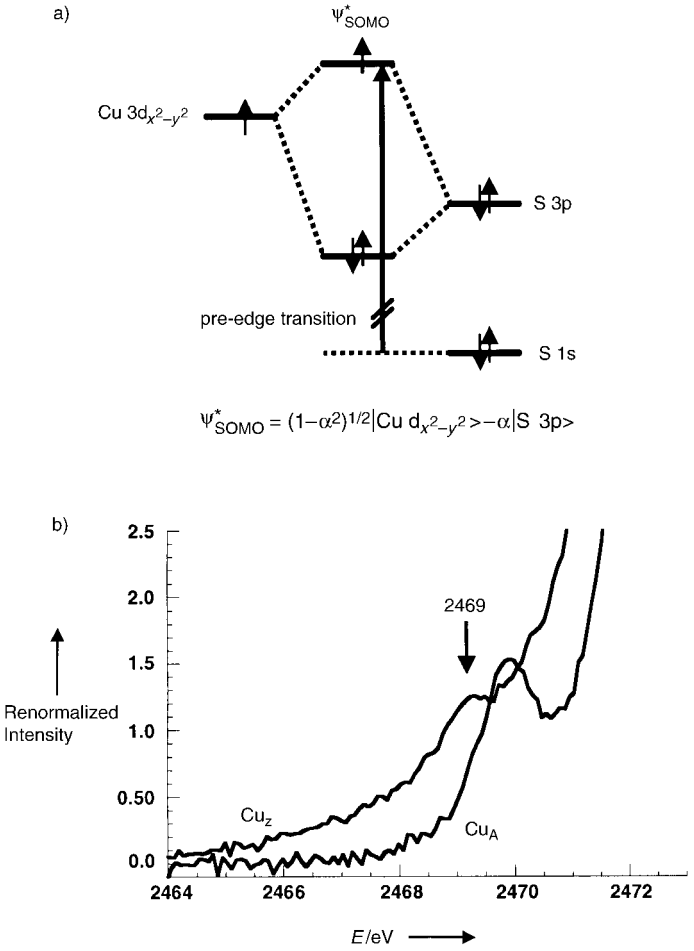


Figure 6. a) Methodology of S K-edge XAS. SOMO: singly occupied molecular orbital. b) Sulfur K-edge spectra of resting Cu_Z from *Achromobacter cycloclastes* N_2OR and Cu_A center.

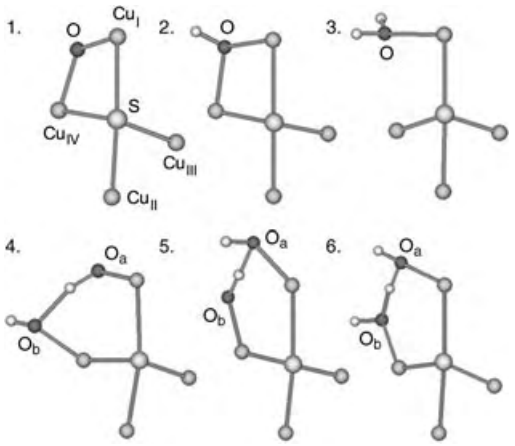


Figure 7. The optimized structures of the Cu_Z cluster with different Cu_I/Cu_{IV} edge ligands L from spin unrestricted calculations at the BP86/LanL2DZ level. The Cu_4S core and the ligand L coordinates of Cu_Z were optimized while the histidine ligand (modeled as imidazole, not shown here for clarity) positions were kept frozen to those from the crystal structure of *Pd* N_2OR; L ligands: 1) O^{2-}, 2) OH^-, 3) H_2O, 4) and 5) two OH^-, and 6) H_2O and OH^-; other L = $H_3O_2^-$, L = $O_2H_2^{2-}$ species were considered. These results will be reported elsewhere. The complex with two H_2O ligands was considered as well, however, the calculations showed that such a structure is not stable. O_a and O_b refer to Table 1.

the cluster with L = HO-H-OH^- have an approximately 2:1 ratio. This ratio is in agreement with the Q/X-band EPR results which indicate an approximately 5:2 ratio. The complexes with other water-derived ligands show a spin distribution different from 5:2. This observation suggests H_2O or the HO-H-OH^- ion as the edge ligand in the resting form of the Cu_Z cluster. In these species, the μ_4-bridging sulfide group contributes around 13–16% to the ground-state wave function, which is also consistent with the S covalency determined from the S K-edge results (Figure 6b). The electron delocalization in the Cu_Z cluster is very important because it contributes to a low reorganization energy during redox processes of the Cu_Z center and leads to stabilization of the oxidized form of Cu_Z after N_2O reduction.

The description obtained from the ground-state wave function greatly facilitates the understanding of other characteristic spectroscopic features of resting Cu_Z cluster. Figure 8a presents the resonance Raman spectrum of resting Cu_Z clusters excited at 624.4 nm.[30] Three dominant features are observed, at 366, 386, and 415 cm^{-1}, all of which shift to lower frequencies upon ^{34}S isotope labeling.[39] Based on the frequencies and ^{34}S isotope shifts, these three vibrations can be assigned as Cu–S based stretching vibrations. The vibration modes observed can be understood by using a Cu_4S cluster model, which has an approximate C_s symmetry with Cu_I-S-Cu_{II} defining the mirror plane (Figure 2).[25] There are four Cu–S bonds in this cluster and thus a total of four Cu–S based stretching modes: two symmetric (A′ symmetry in the C_s point group) in-plane modes from Cu_I–S/Cu_{II}–S vibrations and two out-of-plane modes, one the symmetric (plus)

Table 1: Atomic spin densities[a] of the Cu_Z cluster with different ligands on the Cu_I/Cu_{IV} edge (see Figure 7 for structures).

Ligand	Ratio[b]	Cu_I	Cu_{II}	Cu_{III}	Cu_{IV}	S	O_a	O_b
O^{2-}	5.7 (19)	0.31 (0.40)	0.02 (0.01)	0.01 (0.01)	0.06 (0.02)	0.11 (0.13)	0.48 (0.42)	–
OH^-	3.4 (5.2)	0.41 (0.45)	0.07 (0.08)	0.05 (0.07)	0.12 (0.01)	0.22 (0.26)	0.07 (0.06)	–
H_2O[38]	2.4 (2.0)	0.42 (0.39)	0.18 (0.19)	0.07 (0.07)	0.04 (0.05)	0.15 (0.16)	0.01 (0.01)	–
O-H-OH^{2-}	5.1	0.47	0.00	0.01	0.09	0.11	0.28	0.01
HO-H-O^{2-}	1.4	0.24	0.00	0.00	0.34	0.08	0.04	0.28
HO-H-OH^-	1.7 (3.6)	0.41 (0.51)	0.06 (0.06)	0.02 (0.02)	0.24 (0.14)	0.13 (0.11)	0.02 (0.05)	0.04 (0.01)

[a] The calculations were performed for the spin-doublet ground state at the spin unrestricted B3LYP/6-311G** level of theory using the BP86/LANL2DZ and B3LYP/6-311G** optimized structures. The spin densities obtained using the B3LYP/6-311G** optimized structures are shown in parenthesis. [b] Ratio of the atomic spin density between the copper atoms with the largest and second-largest values.

 © 2004 Wiley-VCH Verlag GmbH & Co. KGaA, Weinheim

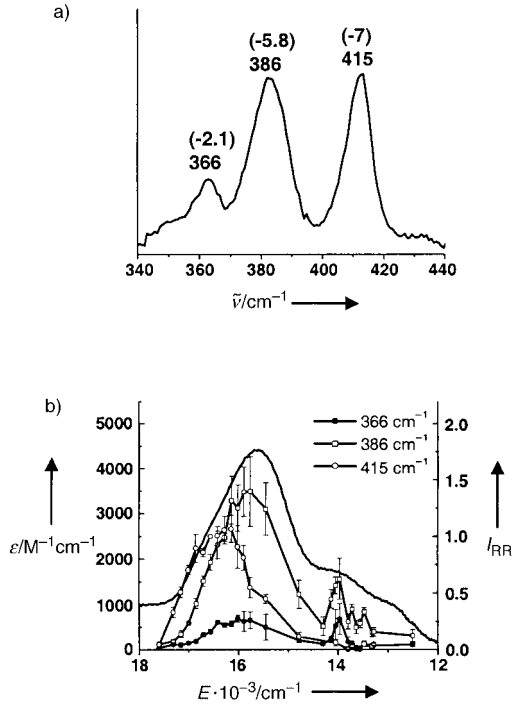


Figure 8. a) Resonance Raman spectrum of resting Cu_Z excited at $\lambda = 624.4$ nm. Numbers in parentheses are ^{34}S isotope shifts. b) Excitation profiles of the resonance Raman (RR) modes (points)of resting Cu_Z overlaid on its low-temperature absorption spectrum (solid line).

combination of Cu_{III}–S/Cu_{IV}–S, and the other the antisymmetric (minus, A″ symmetry) combination of Cu_{III}–S/Cu_{IV}–S. The antisymmetric mode should not be resonance enhanced.[40] Therefore, only three symmetric resonance Raman modes are expected and experimentally observed (Figure 8a). Using the observed vibrational frequencies and ^{34}S isotope shifts, individual Cu–S bond strengths can be determined from a normal coordinate analysis.[30] The Cu_I–S bond is the strongest (ca. 3.3 mdyn Å^{-1}), the Cu_{II}–S bond is next in strength (ca. 3.1 mdyn Å^{-1}), and the Cu_{III}–S/Cu_{IV}–S bonds are the weakest (ca. 1.3 mdyn Å^{-1}). The bond-strength pattern of the four Cu–S bonds reflects the electronic structure description of the resting Cu_Z site with L = H_2O, where Cu_I is the predominantly oxidized center, Cu_{II} gains some oxidized character through electron delocalization from Cu_I through the bridging sulfide, and Cu_{III} and Cu_{IV} are mostly reduced.

The excitation profiles of the observed resonance Raman modes are shown in Figure 8b, overlaid on the absorption spectrum of resting Cu_Z.[30] All three Cu–S based vibrations are resonance enhanced by excitation in the region of the broad CT absorption envelope centered at approximately 640 nm (≈15650 cm^{-1}), which indicates their S→Cu CT nature. Importantly, three individual electronic transitions are resolved in the resonance Raman excitation profiles, at about 14300, 15700, and 16500 cm^{-1}. These three transitions can be associated with excitations from the three p orbitals of the μ_4-bridging sulfide.

Returning to the absorption and MCD spectra of resting Cu_Z, mentioned in the Introduction (Figure 3a), a number of transitions can be experimentally resolved by a Gaussian analysis of the bands (Figure 9).[30] The ground-state wave function (spin-down LUMO) is the σ-antibonding combination of mainly the Cu_I $d_{x^2-y^2}$ and S p_x' orbitals and is the acceptor orbital for all the electronic transitions. Three S→Cu CT bands have been identified in the resonance Raman excitation profiles (Figure 8b, and bands 5, 6, 7 in Figure 9). Band 6 is the strongest among the three transitions in the absorption spectrum and can be assigned as the S p_x'→spin-down LUMO transition. In this transition, the donor orbital is the direct bonding counterpart to the acceptor orbital and thus this transition has the largest donor–acceptor orbital overlap and is the most intense in the absorption spectrum. Band 5 is the weakest S→Cu CT transition and can be assigned to the transition from the S p_z' donor orbital. This S p_z' orbital is out of the Cu_I $d_{x^2-y^2}$ plane and orthogonal to this acceptor orbital (i.e. poor donor–acceptor overlap), which leads to its low intensity in the absorption spectrum. Band 7 is intermediate in intensity in the absorption spectrum and can be assigned to the CT transition out of the S p_y' orbital. Since only Cu_I is dominantly oxidized in resting Cu_Z, only this center exhibits d–d transitions (Bands 1, 3, 4, and 8, Figure 9).

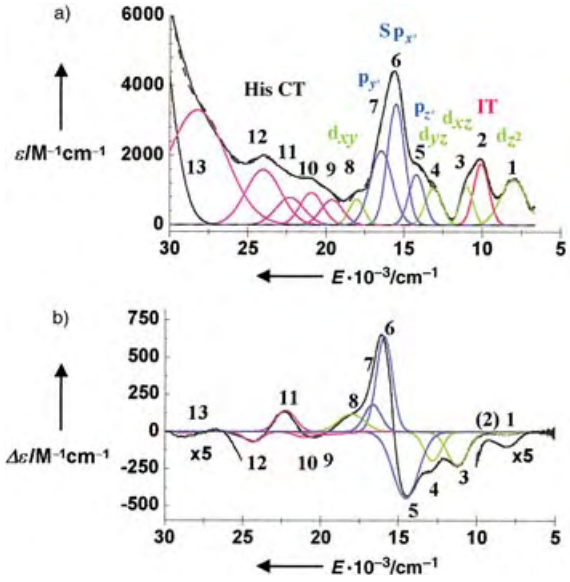


Figure 9. a) 10 K absorption and b) 5 K 7 T MCD spectra of resting Cu_Z with Gaussian-fitting-resolved electronic transitions.

These d–d transitions have a large MCD/absorption intensity ratio, which is due to the large spin-orbit coupling on the copper center ($\xi(Cu^{II}) \approx -830$ cm^{-1}).[41] Interestingly, the d_{xy}→spin-down LUMO transition is high in energy at approximately 18000 cm^{-1}, relative to its position in normal tetragonal Cu^{II} complexes.[42] Its high energy comes from the ligand geometry of the Cu_I center which has two histidine and one sulfide ligand forming a T-shaped environment with one histidine distorted out of the molecular plane.[30] The high energy of the d_{xy} transition is the reason for the small $g_\parallel$ value (ca. 2.16) observed for the resting Cu_Z cluster, since the covalency of the bridging sulfide is low (ca. 15–22% S char-

 © 2004 Wiley-VCH Verlag GmbH & Co. KGaA, Weinheim

acter in the ground state, Figure 6b) and can not account for the observed $g_{\|}$ value. Additionally, band 2 in the absorption spectrum of the resting Cu_Z cluster has been identified as an intervalence charge transfer (IT) transition.[30] This IT transition is unidirectional and thus does not give rise to MCD intensity at low-temperature (Figure 9b).[43] It formally corresponds to an electron transfer $Cu^{I}(d^{10})\rightarrow Cu^{II}(d^{9})$, and reflects the electronic coupling and electron delocalization between the copper atoms mediated by the bridging sulfide unit. The higher energy bands (9–13, Figure 9) can be assigned as histidine→Cu CT transitions. They are in fact low in energy relative to CT transitions in tetragonal copper–imidazole model complexes.[42] This is due to the low coordination number (three-coordinate) of the Cu_I center in the Cu_Z cluster.

3. Catalytically Relevant State of the Cu_Z Center

Past studies indicate that N_2OR can be activated in vitro to reduce N_2O by incubation with dithionite-reduced methyl viologen, and prolonged pre-incubation can result in higher enzyme activity.[28,44–47] To identify the catalytically relevant form of Cu_Z, the X-band EPR spectrum of N_2OR was measured after different incubation times in excess methyl viologen and dithionite solution (Figure 10a).[31] At time zero, the spectrum shows the characteristic EPR signal of resting Cu_Z with $g_{\|}=2.16$. The signal intensity decreases gradually with increasing incubation time. Since resting Cu_Z is at the $1\,Cu^{II}/3\,Cu^{I}$ state with only one electron hole, the loss of the Cu_Z EPR signal in this reducing environment indicates that the Cu_Z cluster is reduced to the $4\,Cu^{I}$ form. Parallel activity measurements at similar incubation times show that the enzyme activity increases with increasing incubation time and the increase of activity is directly correlated to the decrease of the resting Cu_Z EPR signal (Figure 10b).[31] This direct correlation of enzyme activity and reduction of resting Cu_Z indicates that the catalytically relevant form of Cu_Z is the fully reduced $4\,Cu^{I}$ state.[48] Recent measurements using absorption and nitrogen labeling are consistent with these findings.[49]

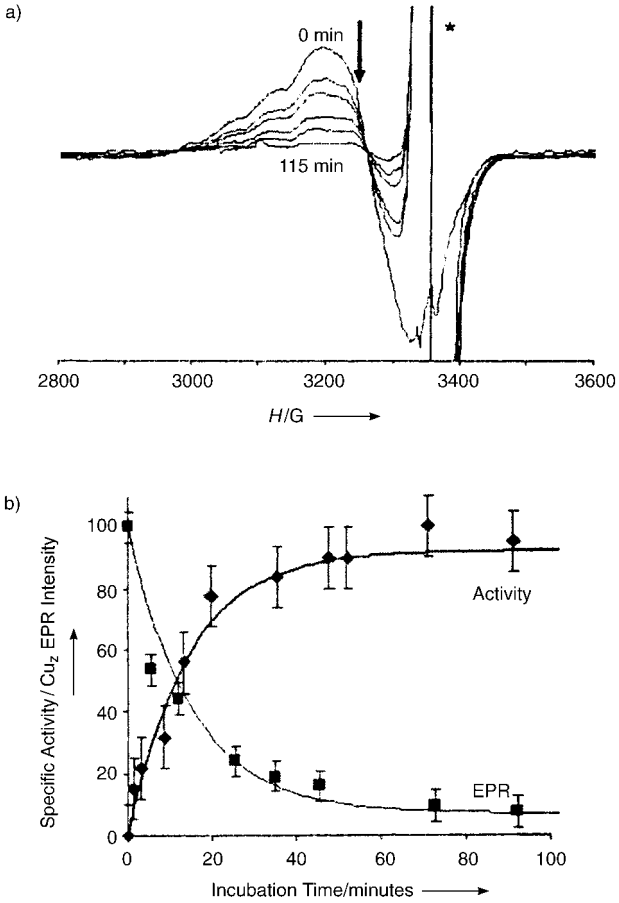


Figure 10. a) Time dependence of Cu_Z EPR signal; $*$ = methyl viologen radical signal. b) Time correlation between *Pn* N_2OR activity (100% corresponds to the reduction of 275 μmols N_2O min^{-1} (mg of enzyme)$^{-1}$) and Cu_Z EPR signal (100% corresponds to the $1\,Cu^{II}/3\,Cu^{I}$ resting form of Cu_Z).

4. N_2O Activation and the Role of the Tetranuclear Cu_4S Cluster

Having developed a description of the electronic structure of the resting Cu_Z center and determined the catalytically relevant form of Cu_Z, we could gain insight into the reaction catalyzed by this cluster, which is the two-electron reduction of N_2O to N_2. The catalytically relevant form of Cu_Z is an electron-rich site with four reduced Cu^{I} centers. At the substrate-binding Cu_I/Cu_{IV} edge (Figure 2), the N_2O substrate could interact with both Cu_I and Cu_{IV}, possibly in a bridged binding mode (Figure 11). Two electrons could be simultaneously donated from Cu_I and Cu_{IV} to overcome the reaction barrier for N_2O reduction. Additionally, there are good electron-transfer pathways from the neighboring Cu_A center in the second subunit of the dimeric N_2OR protein to Cu_{II} and Cu_{IV}.[29] Together with the delocalized electronic structure of

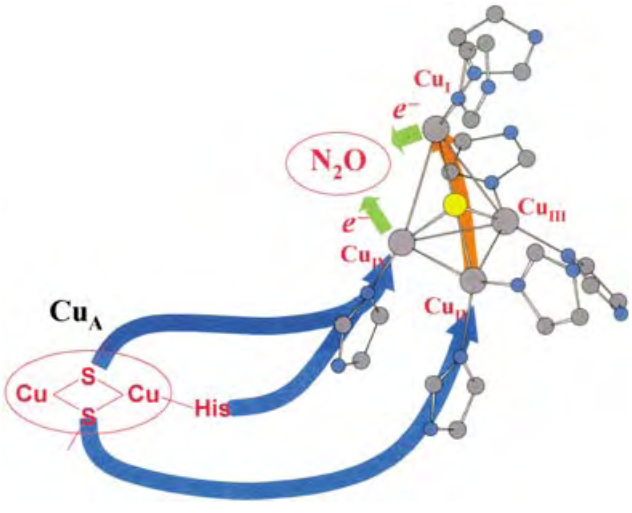


Figure 11. Reduction of N_2O at the Cu_Z Site.

the Cu_Z cluster, these could allow rapid re-reduction of the Cu_Z center during enzymatic turnover. The electron delocalization over the bridging sulfide contributes to a low

© 2004 Wiley-VCH Verlag GmbH & Co. KGaA, Weinheim

reorganization energy during redox processes and stabilization of the oxidized form of the Cu_Z center after N_2O reduction.

Computational methods were used to investigate the possible interaction of the N_2O substrate with the catalytic $4\,Cu^I$ form of the Cu_Z center.[31] The lowest energy structure of the $Cu_Z(4\,Cu^I)$–N_2O complex is shown in Figure 12, where

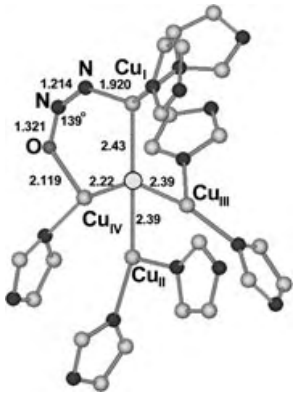


Figure 12. DFT optimized geometry of the N_2O complex with the $4\,Cu^I$ form of Cu_Z.[31]

N_2O binds at the Cu_I/Cu_{IV} edge in a bent μ-1,3 bridging mode ($\sphericalangle$N-N-O = 139°) with the terminal nitrogen atom coordinating to Cu_I. (Other binding modes of N_2O to the Cu_Z cluster are higher in energy.) The bending of the bound N_2O unit in the $Cu_Z(4\,Cu^I)$–N_2O complex results in a 2 eV splitting of the doubly degenerate LUMO of free N_2O into two nondegenerate π^* orbitals. The π^* LUMO in the N-N-O plane is stabilized by approximately 3 eV owing to its loss in antibonding character (Figure 13b). This change shifts the π^* orbital of N_2O close to the fully occupied d orbitals of the

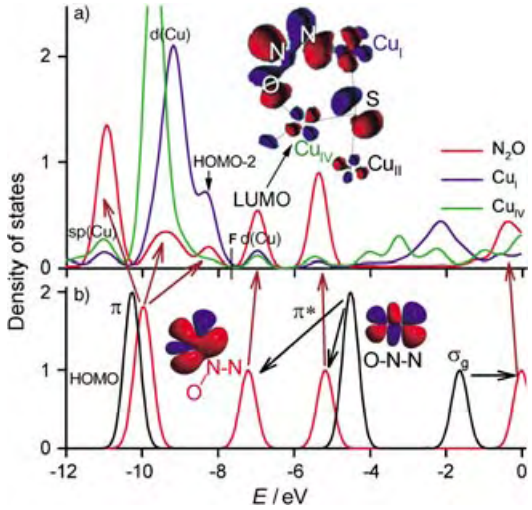
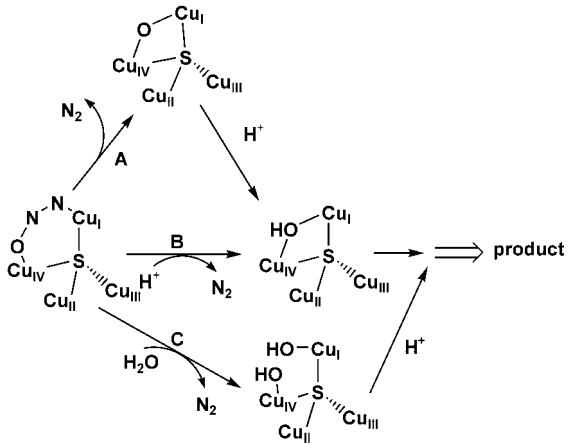


Figure 13. a) Contributions of N_2O, Cu_I, and Cu_{IV} to the density of states of the $Cu_Z(4\,Cu^I)$-N_2O complex. The Fermi level is indicated by F. Inset: LUMO of $Cu_Z(4\,Cu^I)$-N_2O. b) Density of states of the N_2O molecule with a linear geometry (black line) and with the bent N_2O geometry (red line) in the same Coulomb potential as in the $Cu_Z(4\,Cu^I)$-N_2O complex. Inset: the LUMO of bent (left) and linear (right) N_2O.

$Cu_Z(4\,Cu^I)$ cluster and makes the N_2O ligand a very good electron acceptor.

The LUMO of the $Cu_Z(4\,Cu^I)$–N_2O complex (Figure 13a) has mostly N_2O π^* character (54%) with d orbital contributions of 12% from Cu_I and 10% from Cu_{IV}, which indicates significant backbonding interactions from the fully reduced Cu_Z center to the bound N_2O. This substantial Cu d→N_2O π^* backbonding interaction is reflected in the −0.53 charge of the bound N_2O ligand and the elongation of the N–N and N–O bonds (+0.03 and +0.07 Å, respectively). This strong $Cu_Z(4\,Cu^I)$-to-N_2O back donation is only present when N_2O binds at the Cu_I/Cu_{IV} edge in a bent μ-1,3 bridging mode. Other binding modes of N_2O exhibit much weaker back donation (4–5 times samller).

The electronic interactions between the fully reduced Cu_Z cluster and the bound N_2O ligand play a crucial role in N_2O activation and reduction which leads to N–O bond cleavage. The Cu d→N_2O π^* backbonding interaction significantly weakens the N–O bond which may facilitate the direct N–O bond cleavage through simultaneous transfer of two electrons from Cu_Z to the μ-1,3 bridged N_2O (Scheme 1



Scheme 1. Possible Channels for N_2O Reduction at the Cu_Z Site.

path A). This backbonding interaction also increases the electron density on the oxygen atom of the bound N_2O molecule (oxygen charge = −0.5), and would activate it for electrophilic attack by a proton (Scheme 1 path B). The HOMO-2 of the $Cu_Z(4\,Cu^I)$–N_2O complex, which lies close to HOMO and has significant O character (Figure 13a), can serve as the donor frontier molecular orbital for protonation. This and other possible reaction channels (Scheme 1 path C) leading to the reductive cleavage of the N–O bond in N_2O are presently being evaluated. Our DFT calculations[50] indicate that path B is a very favorable reaction channel: oxygen-atom protonation of the coordinated N_2O causes the barrierless N–O bond cleavage.

5. Summary

Spectroscopic methods combined with density functional calculations have been used to define the spin state, copper

 © 2004 Wiley-VCH Verlag GmbH & Co. KGaA, Weinheim

oxidation state, spin distribution, and ground-state wave function of the resting Cu_Z center, and to understand its unusual vibrational and optical spectral features. The electronic-structure description developed for the resting Cu_Z cluster and the determination that the catalytically relevant form of Cu_Z is the fully reduced state provide the basis for understanding the role of the μ_4-sulfide bridged tetranuclear copper cluster in the activation of N_2O for two-electron reduction. Strong back donation into the N_2O ligand in the $Cu_Z(4\,Cu^I)$-N_2O complex where N_2O binds in as bent μ-1,3 bridging mode activates the reductive cleavage of the $O-N_2$ bond.

Received: December 19, 2003 [M1734]
Published Online: June 30, 2004

[1] R. A. Sheldon, J. K. Kochi in *Metal-Catalyzed Oxidations of Organic Compounds*, Academic Press, New York, **1981**.
[2] D. R. Lide, *CRC Handbook of Chemistry and Physics*, 76th ed., CRC, New York, **1996**.
[3] W. L. Jolly in *The Inorganic Chemistry of Nitrogen*, Benjamin, New York, **1964**.
[4] F. Bottomley, I. J. B. Lin, M. Mukaida, *J. Am. Chem. Soc.* **1980**, *102*, 5238.
[5] G. A. Vaughan, G. L. Hillhouse, R. T. Lum, S. L. Buchwald, A. L. Rheingold, *J. Am. Chem. Soc.* **1988**, *110*, 7215.
[6] G. A. Vaughan, P. B. Rupert, G. L. Hillhouse, *J. Am. Chem. Soc.* **1987**, *109*, 5538.
[7] P. T. Matsunaga, G. L. Hillhouse, *J. Am. Chem. Soc.* **1993**, *115*, 2075.
[8] F. Bottomley, J. Darkwa, *J. Chem. Soc. Dalton Trans.* **1983**, 399.
[9] J. N. Armor, H. Taube, *J. Am. Chem. Soc.* **1969**, *91*, 6874.
[10] J. T. Groves, J. S. Roman, *J. Am. Chem. Soc.* **1995**, *117*, 5594.
[11] M. R. Smith, III. , P. T. Matsunaga, R. A. Anderson, *J. Am. Chem. Soc.* **1993**, *115*, 7049.
[12] K. Koo, G. L. Hillhouse, A. L. Rheingold, *Organometallics* **1995**, *14*, 456.
[13] F. Bottomley, W. V. F. Brooks, *Inorg. Chem.* **1976**, *15*, 501.
[14] J. N. Armor, H. Taube, *Chem. Commun.* **1971**, 287.
[15] A. Zecchina, L. Cerruti, E. Borello, *J. Catal.* **1972**, *25*, 55.
[16] W. G. Zumft, *Microbiol. Mol. Biol. Rev.* **1997**, *61*, 533.
[17] W. G. Zumft, P. M. H. Kroneck in *Mechanisms of Metallocenter Assembly* (Eds.: R. P. Hausinger, G. L. Eichhorn, L. G. Marzilli), Wiley-VCH, Weinhein, **1996**, p. 193.
[18] F. Neese, Ph.D. thesis, Universitat Konstanz, **1996**.
[19] F. Neese, W. G. Zumft, W. E. Antholine, P. M. H. Kroneck, *J. Am. Chem. Soc.* **1996**, *118*, 8692.
[20] D. R. Gamelin, D. W. Randall, M. T. Hay, R. P. Houser, T. C. Mulder, G. W. Canters, S. D. Vries, W. B. Tolman, Y. Lu, E. I. Solomon, *J. Am. Chem. Soc.* **1998**, *120*, 5246.
[21] J. A. Farrar, A. J. Thomson, M. R. Cheesman, D. M. Dooley, W. G. Zumft, *FEBS Lett.* **1991**, *294*, 11.
[22] J. A. Farrar, W. G. Zumft, A. J. Thomson, *Proc. Natl. Acad. Sci. USA* **1998**, *95*, 9891.
[23] K. Brown, M. Tegoni, M. Prudencio, A. S. Pereira, S. Besson, J. J. Moura, I. Moura, C. Cambillau, *Nat. Struct. Biol.* **2000**, *7*, 191.
[24] T. Rasmussen, B. C. Berks, J. Sanders-Loehr, D. M. Dooley, W. G. Zumft, A. J. Thomson, *Biochemistry* **2000**, *39*, 12753.
[25] K. Brown, K. Djinovic-Carugo, T. Haltia, I. Cabrito, M. Saraste, J. J. G. Moura, I. Moura, M. Tegoni, C. Cambillau, *J. Biol. Chem.* **2000**, *275*, 41133.
[26] T. Haltia, K. Brown, M. Tegoni, C. Cambillau, M. Saraste, K. Mattila, K. Djinovic-Carugo, *Biochem. J.* **2003**, *369*, 77.
[27] Resting Cu_Z was prepared by treating the isolated N_2OR enzyme with excess dithionite solution, the Cu_A center in the enzyme is thus reduced to the spectroscopically silent Cu^I/Cu^I state and does not contribute to absorption, MCD, and EPR signals. See refs. [28,30].
[28] M. Prudêncio, A. S. Pereira, P. Tavares, S. Besson, I. Cabrito, K. Brown, B. Samyn, B. Devreese, J. VanBeeumen, F. Rusnak, G. Fauque, J. J. G. Moura, M. Tegoni, C. Cambillau, I. Moura, *Biochemistry* **2000**, *39*, 3899.
[29] P. Chen, S. D. George, I. Cabrito, W. E. Antholine, J. J. G. Moura, I. Moura, B. Hedman, K. O. Hodgson, E. I. Solomon, *J. Am. Chem. Soc.* **2002**, *124*, 744.
[30] P. Chen, I. Cabrito, J. J. G. Moura, I. Moura, E. I. Solomon, *J. Am. Chem. Soc.* **2002**, *124*, 10497.
[31] S. Ghosh, S. I. Gorelsky, P. Chen, I. Cabrito, J. J. G. Moura, I. Moura, E. I. Solomon, *J. Am. Chem. Soc.* **2003**, *125*, 15708.
[32] F. Neese, E. I. Solomon, *Inorg. Chem.* **1999**, *38*, 1847.
[33] L. S. Kau, D. J. Spira-Solomon, J. E. Penner-Hahn, K. O. Hodgson, E. I. Solomon, *J. Am. Chem. Soc.* **1987**, *109*, 6433.
[34] E. I. Solomon, *Comments Inorg. Chem.* **1984**, *3*, 227.
[35] B. R. McGarvey in *Transition Metal Chemistry*, *Vol. 3* (Ed.: R. L. Carlin), Dekker, New York, **1966**, p. 89.
[36] F. Neese, B. Hedman, K. O. Hodgson, E. I. Solomon, *Inorg. Chem.* **1999**, *38*, 4854.
[37] S. Debeer George, S. Ghosh, S. I. Gorelsky, J. M. Chan, D. M. Dooley, E. I. Solomon, unpublished results.
[38] Previous calculations of Cu_Z with $L = H_2O$ were performed on a simplified model where the histidine ligands were modeled as NH_3 (see refs. [29,30]). The results for the $L = H_2O$ species presented here are similar to the previous values.
[39] M. L. Alvarez, J. Y. Ai, W. Zumft, J. Sanders-Loehr, D. M. Dooley, *J. Am. Chem. Soc.* **2001**, *123*, 576.
[40] R. S. Czernuszewicz, T. G. Spiro in *Inorganic Electronic Structure and Spectroscopy*, *Vol. 1* (Eds.: E. I. Solomon, A. B. P. Lever), Wiley, New York, **1999**, p. 353.
[41] A. A. Gewirth, E. I. Solomon, *J. Am. Chem. Soc.* **1988**, *110*, 3811.
[42] A. B. P. Lever in *Inorganic Electronic Spectroscopy* (2nd ed.), Elsevier, Amsterdam, **1984**.
[43] E. I. Solomon, E. G. Pavel, K. E. Loeb, C. Campochiaro, *Coord. Chem. Rev.* **1995**, *144*, 369.
[44] S. Ferretti, J. G. Grossmann, S. S. Hasnain, R. R. Eady, B. E. Smith, *Eur. J. Biochem.* **1999**, *259*, 651.
[45] J. K. Kristjansson, T. C. Hollocher, *J. Biol. Chem.* **1980**, *255*, 704.
[46] S. W. Snyder, T. C. Hollocher, *J. Biol. Chem.* **1987**, *262*, 6515.
[47] B. C. Berks, D. Baratta, D. J. Richardson, S. J. Ferguson, *Eur. J. Biochem.* **1993**, *212*, 467.
[48] Note that the slow rate of reduction of the resting Cu_Z center ($1\,Cu^{II}/3\,Cu^I$) indicates that this species can not take part in the catalytic cycle, and the rate of re-reduction of the N_2O-oxidized Cu_Z center must be fast in enzymatic turnover.
[49] J. M. Chan, J. A. Bollinger, C. L. Grewell, D. M. Dooley, *J. Am. Chem. Soc.* **2004**, *126*, 3030..
[50] S. I. Gorelsky, S. Ghosh, E. I. Solomon, unpublished results.

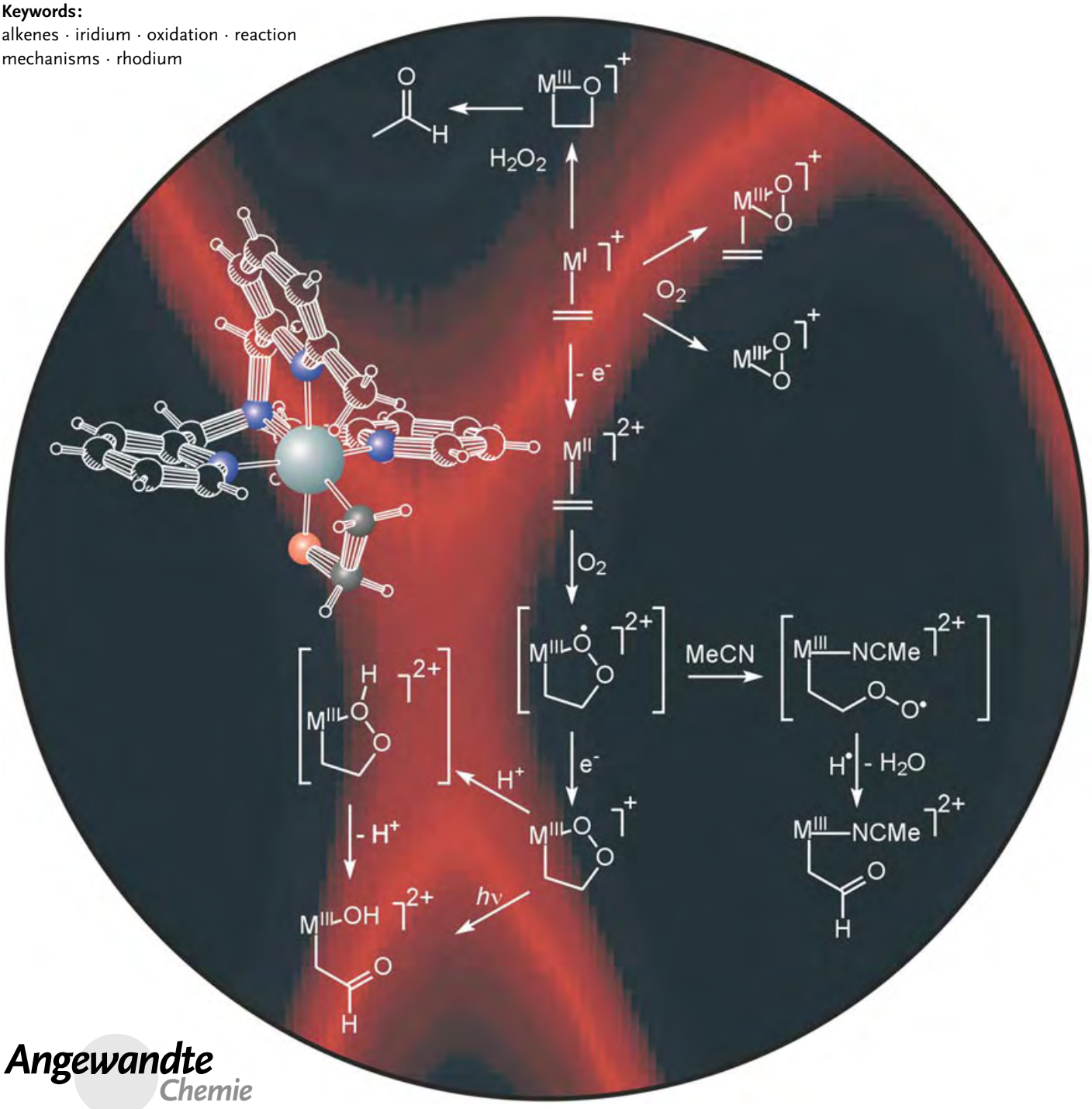
 © 2004 Wiley-VCH Verlag GmbH & Co. KGaA, Weinheim

Alkene Oxygenation

Functional Models for Rhodium-Mediated Olefin-Oxygenation Catalysis

Bas de Bruin, Peter H. M. Budzelaar, and Anton W. Gal*

Keywords:
alkenes · iridium · oxidation · reaction mechanisms · rhodium



Angewandte Chemie

 © 2004 Wiley-VCH Verlag GmbH & Co. KGaA, Weinheim DOI: 10.1002/anie.200300629

Oxygenation of C–H and C=C bonds of hydrocarbons with H_2O_2 and O_2 is an important industrial method to convert mineral oil into useful chemicals. Despite their enormous economic impact, these reactions are still not fully understood. In the early 1970s, the potential of Rh and Ir complexes for olefin oxygenation was investigated intensively. Simple inorganic salts of these metals proved to be rather useless for industrial application when compared with the traditional Wacker system. However, the appropriate choice of ligands allows the stepwise oxidation of olefins at Rh and Ir. These systems are therefore useful to study mechanistic details of substrate binding and C–O bond formation at the catalytic metal center. Insight from these model studies helps in understanding the catalytic reactions at these (and possibly other) metal centers. Further insight into the differences between the Rh system and traditional Wacker-type oxidation at Pd may lead to useful applications.

From the Contents

1. Introduction 4143
2. Metal-Catalyzed Olefin Oxidation 4143
3. Stoichiometric Models for Oxidation Catalysis 4147
4. Implications for Real Catalytic Systems 4152
5. Conclusion 4154

1. Introduction

Oil supplies us with a tremendous feedstock of cheap starting materials. At present, however, most of this feedstock is burnt as fuel for cars and aeroplanes. Oxidation of olefins provides a way to turn mineral oil into higher added-value chemicals such as epoxides, ketones, aldehydes, etc. In fact, oxidation of hydrocarbons is one of the most important methods for converting these common starting materials into bulk chemicals. Oxidative functionalization of C–H and C=C bonds is also an important transformation in the production of fine chemicals. Clearly, oxygen (from air) would be the most attractive oxidant as it is cheap and abundant. However, oxidation with oxygen is notoriously difficult to control. Therefore, alternative oxidants, themselves produced from O_2, are often used. Hydrogen peroxide is probably the most attractive and most environmentally friendly alternative to O_2.[1–4] Other oxidants such as periodate and chromate are also still in use, despite their higher cost and environmental impact, because in some cases they are more effective or selective. Recycling of these oxidants can reduce their environmental impact, but this increases process complexity and cost. Therefore, there is a clear case for shifting to catalytic oxidation with O_2 or its best alternative, H_2O_2, wherever possible.

For this to happen, more insight is required into the mechanisms by which H_2O_2 and in particular O_2 oxidize hydrocarbons. Oxidation reactions are extremely exothermic. An initial, difficult step is often followed by a cascade of fast reactions, leading to one or more final products, with little opportunity for detecting intermediates. As a consequence, metal-catalyzed oxidation is still largely an empirical art.

In this Review, we focus on the oxidation of olefins coordinated to a metal, primarily rhodium and iridium. Catalytic olefin oxidation at these metals was studied extensively in the 1970s and 1980s, but has since then received much less attention than the related (Wacker) oxidation at palladium. During the last decade, however, it has become clear that—with the appropriate choice of ligands—it is possible to follow the oxidation of olefins at Rh and Ir step by step. The detection and isolation of stable analogues of species previously proposed as intermediates in catalytic cycles makes it possible to reevaluate mechanisms proposed in the past. This may eventually lead to improved oxidation catalysts. To put the work in perspective, we first present a brief overview of catalytic olefin oxidation in general, and at Rh and Ir in particular. We then summarize the recent results on stoichiometric oxidation reactions. Finally, we discuss the implications of this model work for "real" catalysis.

2. Metal-Catalyzed Olefin Oxidation

2.1. Catalysts and Products

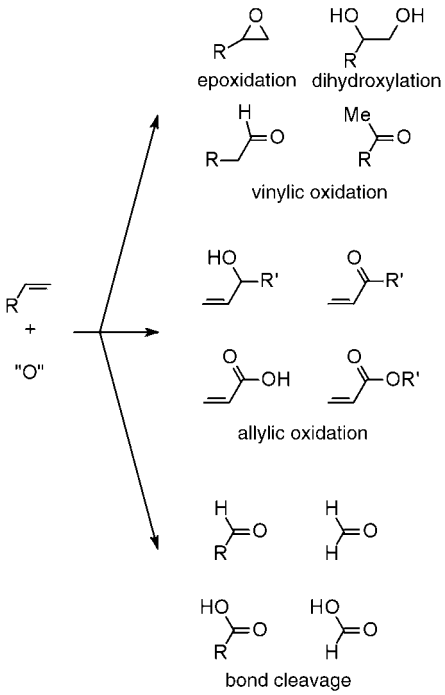
Metal-catalyzed oxidation of olefins can give rise to a whole variety of organic products, as illustrated for terminal olefins in Scheme 1. Cleavage of the double bond results in aldehydes or carboxylic acids. In the absence of bond cleavage, either vinylic oxidation (to epoxides, aldehydes, ketones, or glycols) or allylic oxidation (to α,β-unsaturated alcohols, ketones, esters or acids) occurs.

It would be impractical to give a full description of the tremendous amount of literature that has appeared on metal-catalyzed olefin oxidation. For detailed overviews we refer to books and review articles on this topic.[5–20] To illustrate the importance of the field, we briefly review some of the well-known olefin-oxidation reactions.

One of the most important oxidation reactions is epoxidation. Epoxidation of ethene is relatively easy. The industrial process uses oxygen (as the oxidant) and a heterogeneous silver catalyst.[21–23] Butadiene can be oxidized in a

[*] Dr. B. de Bruin, Dr. P. H. M. Budzelaar, Prof. A. W. Gal
Metal-Organic Chemistry
University of Nijmegen
Toernooiveld 1, 6525 ED Nijmegen (The Netherlands)
Fax: (+31)-24-355-3450
E-mail: bdebruin@sci.kun.nl

 DOI: 10.1002/anie.200300629 © 2004 Wiley-VCH Verlag GmbH & Co. KGaA, Weinheim



Scheme 1. Products from metal-catalyzed oxidation of terminal alkenes.

similar manner.[24,25] Unfortunately, most other olefins cannot be oxidized selectively in this way, presumably because allylic oxidation prevails.[4,25–28] Industrially, such olefins are epoxidized with hydrogen peroxide or organic hydroperoxides in the presence of a molybdenum[29] or (supported) titanium[30–34] catalyst. The most important developments in laboratory-scale epoxidation are probably asymmetric variations such as the Ti-catalyzed Sharpless epoxidation of allylic alcohols with *t*BuOOH[35–38] and the Kochi–Jacobsen–Katsuki [Mn(salen)]-based catalysts for enantioselective epoxidation of other olefins with PhIO, NaOCl, or MCPBA (*m*-chloroperoxybenzoic acid).[39–44] Laboratory-scale (achiral) epoxidation with air and a Ru catalyst was also reported.[45]

Industrially, one of the most important applications of epoxides is in the production of (substituted) glycols. It is also possible to produce glycols directly from olefins, for example, with high-valent Os or Ru complexes.[46,47] The use of O_2 or (hydro)peroxides as the terminal oxidant in these systems is possible[48,49] but not easy, and this has prevented large-scale applications. Asymmetric variations (mostly based on Os, a chiral amine auxiliary ligand, and $[Fe(CN)_6]^{3-}$ as the oxidant[50,51]) have attracted considerable attention because of possible applications in the synthesis of pharmaceuticals, in which oxidant cost and environmental impact are less of an issue.

The Pd/Cu-catalyzed oxidation of ethene by O_2 to acetaldehyde, known as the Wacker process,[52,53] is probably the most intensively studied catalytic olefin-oxidation reaction. Unfortunately, when applied to higher olefins this reaction produces mainly ketones. Several systems based on Rh or Ir (see below) instead of Pd yield similar products, although lower rates and faster deactivation make them less attractive for industrial applications.

Allylic oxidation is usually associated with radical chain mechanisms. These may be *initiated* by a metal species, but then usually *propagate* far from the metal center. This type of oxidation is often unselective and occurs frequently as an unwanted side reaction.

Finally, olefin oxidation by a variety of terminal oxidants and high-valent Ru catalysts (e.g. RuO_4) almost invariably results in cleavage of the double bond.[54–56] Products can be either aldehydes, ketones, or carboxylic acids, depending on the degree of substitution of the alkene. Cleavage has also been observed for some Rh and Ir catalysts.[57,58]

2.2. General Overview of Mechanisms

Metal-catalyzed olefin-oxidation mechanisms can—at least in principle—be divided into three classes:

1) Autoxidations: These are *initiated* at the metal center, but then *propagate* far from the metal species through a radical chain mechanism.
2) Oxygen transfer from the oxidant to the olefin, without any direct metal–olefin interaction: Oxidation reactions at early- and middle-transition-metal centers are increasingly believed to belong to this category (examples include Mo-[59–62] and Ti-catalyzed[63–65] epoxidation as well as dihydroxylation with OsO_4).[66–68]
3) Oxygenation of an olefin coordinated to a metal center: This class of mechanism is especially likely for late-



Bas de Bruin was born in Arnhem in 1971. He studied chemistry at the University of Nijmegen (1989–1994). His PhD research (1994–1999) at the University of Nijmegen with Prof. Anton W. Gal involved oxygenation of rhodium–olefin complexes. As an Alexander-von-Humboldt postdoctoral fellow (1999–2000), he studied transition-metal complexes containing pyridine-2,6-diimine ligands in the group of Prof. Karl Wieghardt at the Max-Planck Institut für Strahlenchemie, Mülheim an der Ruhr (Germany). After his postdoctoral research he returned to the University of Nijmegen.



Peter H. M. Budzelaar studied chemistry in Utrecht and obtained his PhD in the group of Prof. G. J. M. van der Kerk in 1983. After postdoctoral research with Prof. Paul von Ragué Schleyer in Erlangen and a year at the University of Eindhoven, he moved to the Homogeneous Catalysis group of Piet van Leeuwen at Shell Research, Amsterdam, where he worked for 10 years. In 1996, he joined the Inorganic Chemistry research group of Prof. Anton W. Gal in Nijmegen.

 © 2004 Wiley-VCH Verlag GmbH & Co. KGaA, Weinheim

transition metals, which can form relatively strong bonds to olefins; the Wacker oxidation certainly falls into this category.

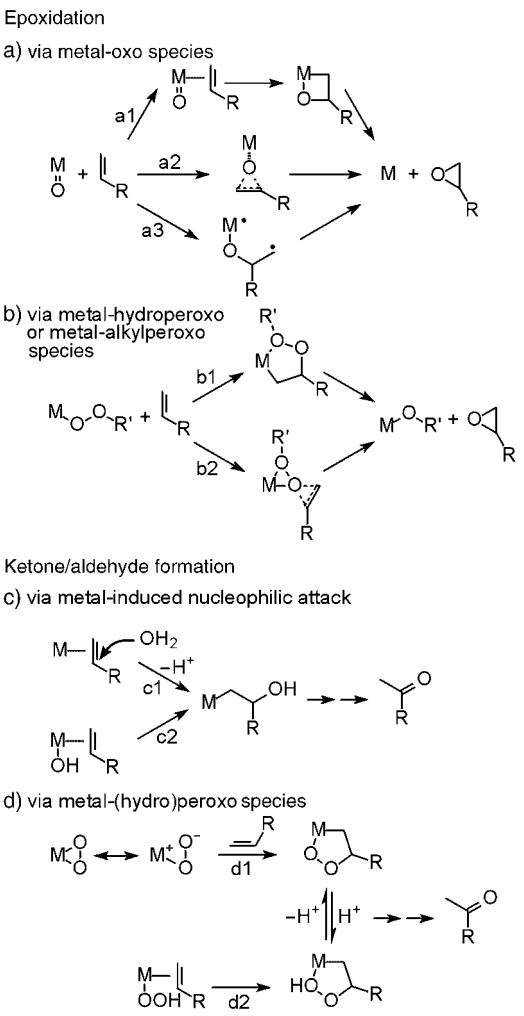
The involvement of radical chain mechanisms can often be deduced from the selectivity (or lack thereof) of the reaction. Distinguishing between the other two classes is often more complicated, as noted below.

Alternative mechanistic formulations of the various steps are summarized in Scheme 2 for two important reactions, epoxidation and ketone formation. Epoxidation at Mn has been interpreted in terms of metalla-oxetanes (i.e., class 3; Scheme 2, step a1)[69] and direct transfer (class 2; Scheme 2, step a2 or a3);[70] the mechanism is still controversial.[71,72] For early-transition-metal catalysts in high oxidation states (acidic metal centers), epoxidations have been proposed to proceed by olefin insertion into the metal–oxygen bond of the alkylperoxo or hydroperoxo complex[15] (route b1) or through oxygen transfer by nucleophilic attack of the olefin at the electron-poor peroxide species[16] (route b2, analogous to epoxidation with organic peroxyacids). Theoretical calculations and spectroscopic studies are clearly in favor of route b2.[59–65] The mechanisms of late-transition-metal-catalyzed olefin oxygenations are likely to be different. For example, Pt-catalyzed epoxidation of olefins with hydrogen peroxide has been proposed to proceed by activation of both the alkene and the oxidant. Coordination increases the electrophilic character of the alkene, and deprotonation increases the nucleophilic character of hydrogen peroxide (Scheme 2, path d2).[13]

In the present Review, we concentrate on stoichiometric models for class 3 reactions, primarily ketone formation. Wacker-type chemistry is always formulated in terms of class 3 reactions. The classical Wacker catalysis involves *inter*molecular nucleophilic attack of water (or hydroxide) at a coordinated alkene (Scheme 2, step c1) as the key C–O bond-forming step. However, *intra*molecular nucleophilic attack (step c2) is also well-documented,[73] and in some cases the two types of attack compete. The term Wacker reaction is also used in a more general sense to denote nucleophilic attack at an alkene activated by coordination to a transition metal. The rhodium- and iridium-catalyzed reactions described in Section 2.3 have been proposed to proceed mainly through steps b1, c2, d1, and d2 (Scheme 2) and thus also belong to class 3.



Anton W. Gal was born in 1950. He studied chemistry at the University of Nijmegen, where he received his PhD in 1977 under Prof. J. J. Steggerda. He then worked at Shell (1978–1994) as project leader and technical director on alkene and alkyne metathesis at early-transition-metal centers, high-purity early-transition-metal salts, submicron noble metal and metal oxide powders, and electronic-grade metal–alkyl complexes. Since 1994 he holds the chair in Inorganic Chemistry at the University of Nijmegen, where he researches oxygenation, polymerization, and hydrogenation of olefins.



Scheme 2. Proposed mechanisms for olefin oxidation to epoxides (a, b) and ketones (c, d).

2.3. Catalytic Oxidation at Rh and Ir Centers

Though less well known than Pd, both Rh and Ir are able to catalyze the oxidation of olefins with O_2 and H_2O_2;[11,15,74–76] Rh is generally more effective than Ir. Most of these reactions are homogeneous and occur in organic solvents, but a few rhodium catalysts supported on alumina and silica have also been reported.[77–79] The oxidation of terminal alkenes almost invariably results in the formation of methyl ketones. The oxidation of internal alkenes leads to epoxides, allylic alcohols, ethers, or ketones. The mechanistic picture of rhodium-catalyzed oxidations is complex, and several mechanisms were proposed for various catalysts under different conditions: Wacker-type reactivity,[80] reaction of a metal peroxide with the alkene to give a peroxymetallacycle,[81–86] formation of an intermediate hydroperoxo or alkylperoxo complex, which reacts with the olefin,[87–90] and initial formation of a π-allyl complex.[81] Some early work on

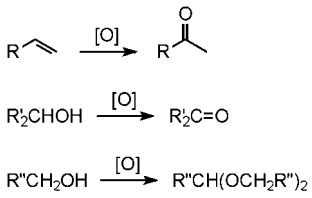
 © 2004 Wiley-VCH Verlag GmbH & Co. KGaA, Weinheim

olefin oxidation with Rh– and Ir–peroxo complexes was shown to proceed through free-radical pathways.[91–93] It is useful to distinguish between oxidations carried out in alcohols (the most efficient and commonly applied variation) and those carried out in completely aprotic solvents.[89]

2.3.1. Olefin Oxidation in Alcohols

In oxidizable alcohols, Rh complexes (with or without cocatalysts) are able to oxidize ethene to acetaldehyde and terminal alkenes to ketones with O_2. The simplest and most frequently used catalyst precursor is $RhCl_3 \cdot x H_2O$, but other sources of Rh may be used. Initiation seems to involve reduction to Rh^I (or, equivalently, a Rh^{III} hydride), usually by the solvent. The rate of the reaction depends critically on the chloride concentration, a Cl:Rh ratio of about 2 being optimal. At least one of the roles of the frequently used copper cocatalyst is the removal of excess chloride as insoluble Cu^ICl. Excess water inhibits the reaction.[98] Possibly, both chloride and water can block coordination sites at the Rh^{III} center at some point in the reaction.

The oxidation of ethene to acetaldehyde is usually not accompanied by solvent cooxidation[94] and can even be carried out in water.[80] However, most mechanistic studies of Rh-catalyzed olefin oxidation have been carried out on higher olefins, typically 1-hexene or 1-octene. For these higher olefins, ketone formation in the Rh-only system is accompanied by an approximately equivalent amount of solvent cooxidation (Scheme 3); together, these account for the

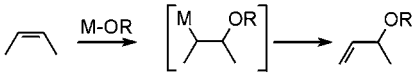


Scheme 3. Olefin oxidation to ketones and alcohol (solvent) cooxidation.[90]

amount of O_2 consumed.[87,95–97] Interestingly, in the presence of a Cu cocatalyst *both* oxidizing equivalents of O_2 can be used for olefin oxidation, and solvent oxidation is suppressed.[87,98] Also, the reaction is strongly accelerated. Turnovers up to ≈ 100 (4 hr) with selectivities $> 98\%$ can be achieved.

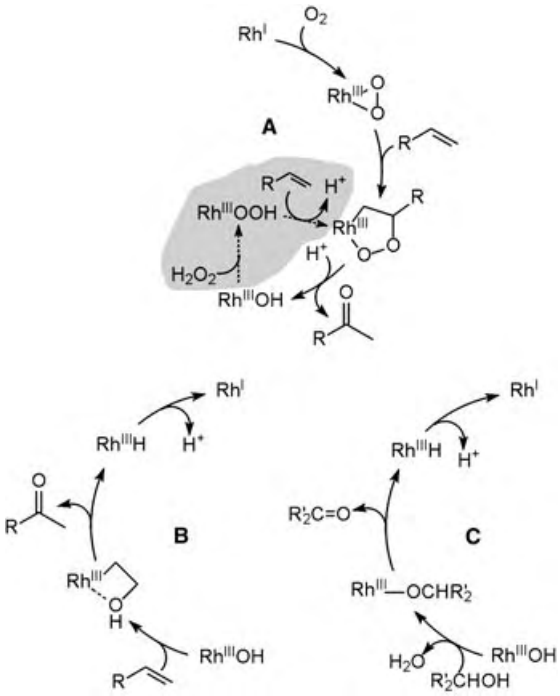
Oxidation of 1,5-cyclooctadiene gives mainly the monooxygenation product 4-cycloocten-1-one.[89] Internal monoalkenes are much less reactive than terminal alkenes, and give rise not only to ketones but also to allylic ethers or alcohols. These have been proposed to arise through allylic activation,[98] but labeling studies (for *aprotic* systems) and observed product distributions agree better with oxygen attack at a vinylic carbon atom, followed by β-elimination (Scheme 4).[99]

From the original literature, no clear single mechanistic picture emerges. Mimoun et al. originally proposed a catalytic cycle consisting of two parts, a "peroxide" part (**A**) and a "Wacker" part (**B**), based on his observation that (in the presence of a Cu cocatalyst) both oxygen atoms of O_2 can be



Scheme 4. Formation of allylic alcohols/ethers from internal alkenes.[99]

used to generate the ketone product (Scheme 5).[98] Taken together, these constitute a complete catalytic cycle. Unfortunately, Rh alone (i.e. without the Cu cocatalyst) does *not*



Scheme 5. Schematic representation[100] of partial cycles in Rh-catalyzed olefin oxidation. **A**: peroxide formation, **B**: Wacker oxidation, **C**: solvent cooxidation. The mechanisms are based on proposals by Mimoun et al.[98] and Drago et al.[87]). The shaded area in part A is the H_2O_2 "shunt" proposed by Drago et al.

actually use both oxygen atoms for oxidation of terminal olefins, but instead uses one of them to oxidize the alcohol solvent, so it cannot follow the **A** + **B** cycle. To accommodate this, Drago et al.[87] replaced part **B** of the cycle by a solvent cooxidation step (**C**, Scheme 5), so that the overall reaction now follows an **A** + **C** cycle. To explain the lack of solvent cooxidation in the Rh/Cu system, he then suggested that part **B** would somehow be assisted by Cu, so that *with* Cu an **A** + **B** cycle is followed instead of an **A** + **C** cycle. Drago et al. also suggested that the Rh/Cu system involved free H_2O_2 as an intermediate (possibly formed at the Cu^I center) based on the similarity in rates between O_2 and H_2O_2 oxidation with the Rh/Cu catalyst; this is the "H_2O_2 shunt" included in part **A** (shaded gray in Scheme 5). However, Bregeault and co-workers observed much lower rates with H_2O_2[89] and concluded that free H_2O_2 was not involved. Apart from this, Bregeault and co-workers proposed a mechanism very similar to the **A** + **B**/**A** + **C** cycles; the role of the Cu cocatalyst in promoting half-cycle **B** over half-cycle **C** remains unclear.

 © 2004 Wiley-VCH Verlag GmbH & Co. KGaA, Weinheim

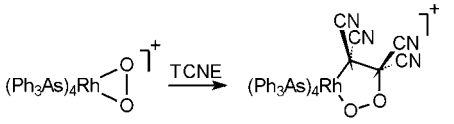
2.3.2. Aprotic Systems

Rhodium/iridium-catalyzed oxidation of olefins by O_2 generally requires a sacrificial reductant. The Rh/Cu cocatalyst systems described above are the only exceptions to this requirement. Alcohols are particularly suitable as coreductants. Cooxidation of olefins and phosphanes[84,85,101] or H_2[88] has also been reported.

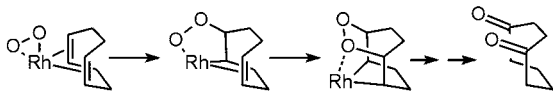
Olefin oxidation by O_2 in aprotic media (e.g., benzene) has mostly been studied with phosphane and arsane complexes. The oxidation can be catalytic in Rh, but in the absence of a suitable coreductant the reaction is always accompanied by ligand oxidation (typically, 1–3 molecules of ligand per molecule of olefin). It is not always clear whether olefin and ligand oxidation are really coupled or simply competitive. Turnovers are generally low, much lower than in alcohols: these reactions are "barely" catalytic. The ketone oxygen atom has been shown to be derived from dioxygen[102] and not from adventitious water, as would be expected for Wacker oxidation.

Remarkably, catalytic oxidation of 1,5-cyclooctadiene produces 1,4-cyclooctanedione selectively, whereas the monooxygenation products are obtained in alcohols (see Section 2.3.1). Moreover, both oxygen atoms in the product were shown to be derived from the *same* O_2 molecule, and the intermediacy of free 4-cycloocten-1-one could be ruled out.[86,103] Thus, this is a rare case of direct alkene *dioxygenation*. Unfortunately, the reaction is rather slow and is still accompanied by ligand oxidation, which in this case must be competitive.

Metalladioxolanes have been proposed as intermediates in these aprotic oxidations. Some support for the intermediacy of such species comes from the isolation of a metalladioxolane from the reaction of $[Rh(AsPh_3)_4(O_2)]^+$ and the (rather atypical) olefin tetracyanoethylene (Scheme 6).[104] The above-mentioned 1,4-cyclooctanedione formation could also be explained on the basis of a metalladioxolane intermediate (Scheme 7).[86]



Scheme 6. Metalladioxolane formation from O_2 complex and TCNE.[104]



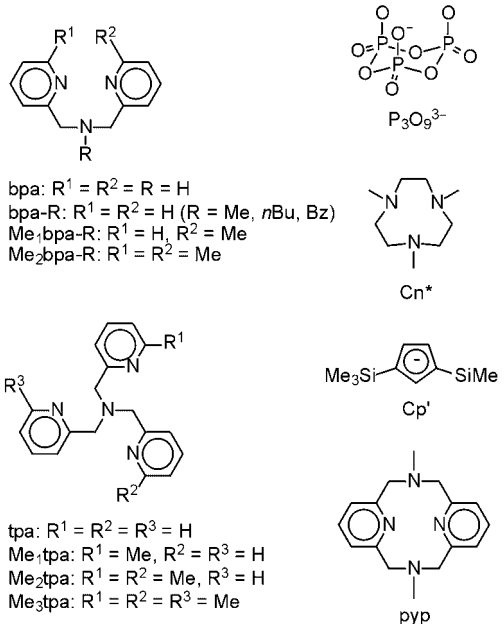
Scheme 7. Proposed mechanism for cod dioxygenation.[86]

3. Stoichiometric Models for Oxidation Catalysis

From the previous sections, it appears that rhodium- and iridium-catalyzed olefin oxygenation has mainly been described in terms of alkene insertions into metal–peroxo bonds and/or Wacker-type reactivity. This means that dioxygen/peroxide *and* the olefin are activated by the metal. Thus, one may expect stoichiometric reactions of well-defined olefin *complexes* of rhodium and iridium with O_2 and H_2O_2 to yield valuable information on the catalytic Rh/Ir systems. In the following sections we focus on model reactions for the oxygenation of olefin complexes. We should mention here that several rhodium–peroxo[106,107] and –hydroperoxo[108–111] complexes have been reported, including a crystallographically characterized hydroperoxo–rhodium(III) complex obtained by the reaction of a rhodium(I) complex with O_2 and H^+.[108] A related topic, dioxygen binding and activation at cobalt, was reviewed by Bianchini and Zoellner.[105]

3.1. Oxygenation of Cyclooctadiene Complexes

Oxygenation of M^I–cod (cod = cyclooctadiene) complexes with multidentate, oxidation-resistant ("innocent") ligands (Scheme 8) has led to a number of well-characterized



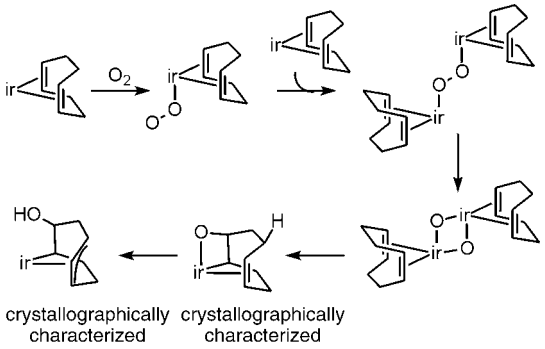
Scheme 8. Ligands used in stoichiometric oxidation reactions.

products. Oxygenation of the M^I(cod) fragment is substantially influenced by the ligand environment. For example, the oxidation of the complexes $[\{(cod)M^I(\mu\text{-}Cl)\}_2]$ by air does not result in oxygenation of cod. The rhodium compound is stable towards air, whereas the iridium analogue converts slowly into the dinuclear oxo-hydroxo complex $[Ir^{III}_2Cl_2(cod)_2(\mu\text{-}OH)_2(\mu\text{-}O)]$.[112] In contrast, $[\{(cod)Ir^{III}(H)(Cl)(\mu\text{-}Cl)\}_2]$, the HCl adduct of $[\{(cod)Ir^I(\mu\text{-}Cl)\}_2]$, has been reported to eliminate 4-cyclooctenone upon reaction with O_2, after which the complex becomes a catalyst for the oxidation of cyclooctene by O_2/H_2.[88] A $[(cod)Ir^{III}(OOH)]$ species was postulated as intermediate.

A crystallographically characterized 2-iridaoxetane was obtained by Klemperer and co-workers in the stoichiometric

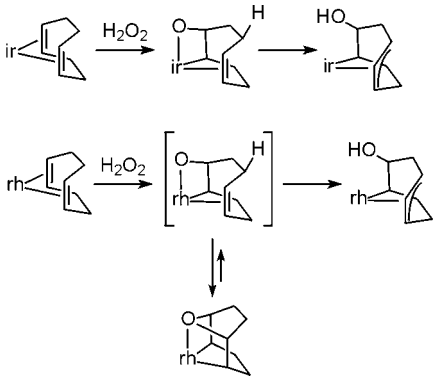
 © 2004 Wiley-VCH Verlag GmbH & Co. KGaA, Weinheim

oxidation of the trimetaphosphate complex $[(P_3O_9)Ir^I(cod)]^{2-}$ by O_2.[113] The 2-iridaoxetane proved to be unstable, and was converted into a hydroxy alkyl allyl compound. The mechanism proposed for the formation of the intermediate 2-iridaoxetane, mainly on the basis of volumetric gas-uptake measurements, involves dinuclear activation of O_2 by two Ir^I centers (Scheme 9).



Scheme 9. Proposed mechanism for the oxygenation of $[(P_3O_9)Ir(cod)]^{2-}$ through dinuclear activation of O_2; ir = $[(P_3O_9)Ir]^{2-}$.[113]

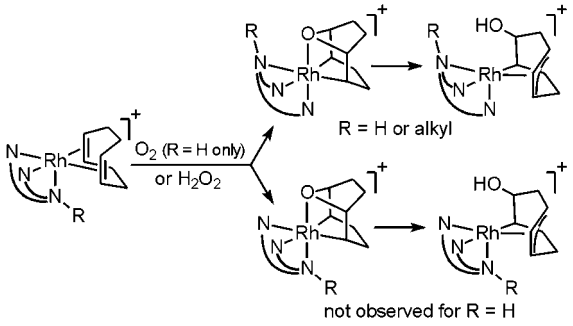
Rhodium and iridium compounds similar to those of Klemperer and co-workers were obtained by our group and by Flood et al. upon oxygenation of complexes $[(N_3\text{-ligand})M^I(cod)]^+$ with H_2O_2 (Scheme 10).[114–116] For rhodium, the



Scheme 10. Oxygenation of $[Cn^*M^I(cod)]^+$ by H_2O_2; ir = $[Cn^*Ir]^+$, rh = $[Cn^*Rh]^+$.[114–116]

presumed 2-metallaoxetane intermediates undergo rapid insertion of the second double bond of cod into the Rh–O bond, yielding substituted tetrahydrofuran derivatives (compare with the second insertion in Scheme 7). Apparently this reaction is reversible; formation of hydroxy alkyl allyl compounds probably proceeds through abstraction of an allylic proton by the intermediate 2-rhodaoxetane oxygen. The analogous 2-iridaoxetanes are stable at room temperature, but are converted into hydroxy alkyl allyl compounds upon heating.

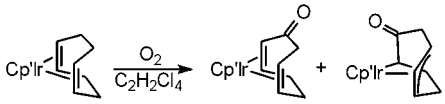
The oxidation of $[(Cn^*)M^I(cod)]^+$ produces only a single metallaoxetane or THF derivative. However, oxidation of $[(bpa\text{-}R)Rh^I(cod)]^+$ produces two isomeric THF derivatives, each of which decomposes into a single hydroxy alkyl allyl complex (Scheme 11).[115] Oxidation of $[(bpa\text{-}R)Ir^I(cod)]^+$ could produce three isomeric oxetanes, two of which have actually been observed; they decompose into the expected hydroxy alkyl allyl derivatives.[117]



Scheme 11. Oxygenation of $[(bpa\text{-}R)Rh^I(cod)]^+$ by H_2O_2 and O_2.[115]

Interestingly, the reaction of $[(bpa)Rh(cod)]^+$ with O_2 leads to the same products as that with H_2O_2.[115] Oxidation of the Rh complex is catalyzed by acid. According to ^1H NMR spectroscopic analysis, the diamagnetic products shown in Scheme 11 account for only 75% of the total starting material; the remainder is converted into NMR- and EPR-silent by-products. Volumetric measurements indicate the uptake of 1 mol of O_2 per mol of starting material,[115] compared with 0.5 mol for the Ir complex studied by Klemperer and co-workers.[113] For Rh, the fate of the second O atom remains obscure. It may have been incorporated in the by-products. The solvent (CH_2Cl_2) may also be involved; in other solvents (MeCN, acetone) the reaction is less selective.

Possibly related to this, Klemperer and co-workers reported an example in which the solvent plays a crucial role in the oxygenation of $[M^I(cod)]$ complexes by O_2. The reaction of $[Cp'Ir^I(cod)]$ ($Cp' = \eta^5\text{-}1,3\text{-}C_5H_3(Si(CH_3)_3)_2$) with O_2 in 1,1,2,2-tetrachloroethane (TCE) at 75 °C leads to a mixture of an oxocyclooctadiene and an oxoalkyl allyl species (Scheme 12).[118] In this solvent, addition of *t*BuOOH signifi-



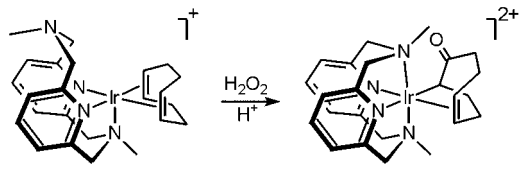
Scheme 12. Oxygenation of $[Cp'Ir^I(cod)]$ by O_2 in 1,1,2,2-tetrachloroethane.[118]

cantly increases the reaction rate, whereas in other solvents *t*BuOOH does not react with $[Cp'Ir^I(cod)]$. Klemperer and co-workers attributed the rate increase to the generation of solvent radicals from the reaction of *t*BuOOH and TCE. They proposed a radical (autoxidation) mechanism involving the formation of $CHCl_2CCl_2^{\bullet}$, $CHCl_2CCl_2O^{\bullet}$, and $Cl^{\bullet}$ radicals, which can abstract allylic hydrogen atoms from the $[Ir^I(cod)]$ complex. Such allylic radicals could react with O_2 and

 © 2004 Wiley-VCH Verlag GmbH & Co. KGaA, Weinheim

subsequently abstract a hydrogen atom from the solvent, thus completing a chain reaction for oxidation. The observed products of a (partial) allylic oxidation indeed suggest that radical-type reactions occur. However, as the observed products could also have been formed by vinylic oxidation and double-bond shifts (see Scheme 4), labeling experiments would be required to establish the position of the attack by oxygen. Most other model reactions in this Review exclusively show vinylic oxidation products.

Oxidation of $[(pyp)Ir^{I}(cod)]^{+}$ with excess H_2O_2 in the presence of HBF_4 (1 equiv) yields a oxocyclooctenyl complex (Scheme 13). Although this is a vinylic oxidation product, it

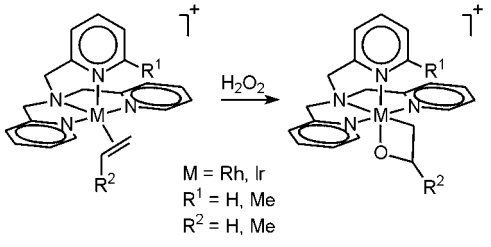


Scheme 13. Oxygenation of $[(pyp)Ir^{I}(cod)]^{+}$ by H_2O_2.[119]

bears some resemblance to the allylic oxocyclooctadiene and oxoalkyl allyl oxidation products observed by Klemperer and co-workers. However, the oxidation of $[(pyp)Ir^{I}(cod)]^{+}$ by H_2O_2 occurs under milder conditions (MeOH, room temperature), making solvent-derived radicals unlikely in this case. A mechanism involving further oxidation of an intermediate 2-iridaoxetane by H_2O_2 was proposed in this case (see Section 3.2).[119]

3.2. Monooxygenation of Rhodium(I) and Iridium(I) Complexes of Ethene and Propene by H_2O_2

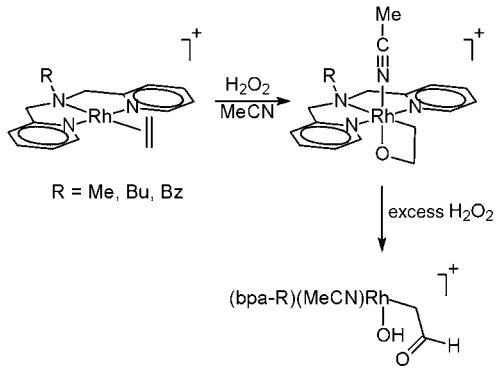
Complexes of the type $[(N_4\text{-ligand})M^{I}(ethene)]^{+}$ can be oxidized cleanly by H_2O_2 to unsubstituted 2-metalla(III)–oxetanes, provided that the ligand is not too bulky (Scheme 14).[114,120,121] Thus, the reaction works well for tpa and Me_1tpa, but not for Me_2tpa and Me_3tpa; in the latter cases, mixtures of many different products, some of them paramagnetic, are obtained. Likewise, oxidation of $[(Me_n\text{-tpa})M^{I}(propene]^{+}$ produces 4-methyl-2-metallaoxetanes. However this reaction is now only selective for tpa complexes.[121] Selectivity decreases with an increase in n, with almost no formation of metallaoxetanes for $n=2$ or 3. Propene coordination is much weaker than ethene coordination, which might lead to easier loss of olefin early in the



Scheme 14. Oxygenation of $[(tpa)M^{I}(olefin)]^{+}$ by H_2O_2.[114,120,121]

oxidation. In all cases only the geometric isomer with the oxetane oxygen atom *cis* to the amine nitrogen atom is obtained.

It is also possible to oxidize square-planar complexes $[(N_3\text{-ligand})Rh^{I}(C_2H_4)]^{+}$ in the presence of a donor solvent (MeCN), again provided that the N_3-ligand is not too bulky (bpa-R reacts, but Me_2bpa-R does not). These reactions yield $[(bpa\text{-}R)(MeCN)Rh^{III}(CH_2CH_2O)]^{+}$, which contains a labile MeCN ligand (Scheme 15).[122]



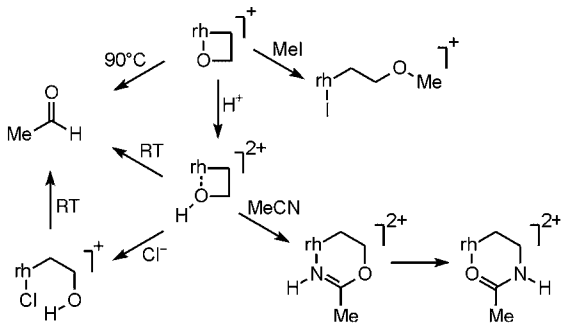
Scheme 15. Oxygenation of $[(bpa\text{-}R)M^{I}(olefin)]^{+}$ by H_2O_2 in the presence of acetonitrile.[122]

The results of a theoretical study[123] support the earlier suggestion[115] that the most plausible path for oxygenation is heterolytic cleavage of the peroxide O–O bond on approach to the metal center, that is, formation of $Rh^{III}(OH)$ by net transfer of OH^{+} to Rh^{I}. This would then be followed by intramolecular nucleophilic attack of the metal-bound OH group at the coordinated olefin. The O–O cleavage process was found to be strongly assisted by hydrogen bonding (of a water solvent molecule or a ligand NH group if present) to the nascent OH^{-} ion. This mechanism was preferred over variations involving concerted transfer of the distal OH group of coordinated H_2O_2 to the olefin or deprotonation of the metal-bound OH group to a terminal oxo group before oxetane formation.

The N_4-ligand-coordinated metallaoxetanes are remarkably stable; $[(tpa)Rh^{III}(CH_2CH_2O)]^{+}$ only decomposes through elimination of acetaldehyde upon heating to 90 °C. The Ir analogue is even less reactive, decomposing at around 150 °C in DMSO (dimethyl sulfoxide). The complex ion $[(tpa)Rh^{III}(CH_2CH(Me)O)]^{+}$ eliminates acetone upon heating (80 °C, DMSO). Weakening of the Rh–O bond by protonation or alkylation of the 2-rhodaoxetane oxygen atom provides a way to activate these unexpectedly stable four-membered-ring compounds. Protonation leads to elimination of acetaldehyde or capture of other substrates (Scheme 16).[120,124]

The presence of a labile ligand lowers the stability of the oxetane; the complexes $[(bpa\text{-}R)(MeCN)Rh^{III}(CH_2CH_2O)]^{+}$ (R = Me, Bu, Bz) decompose into acetaldehyde already at room temperature. Presumably, dissociation of the MeCN ligand initiates the decomposition. Elimination of acetaldehyde involves a reductive elimination step. The decomposi-

 © 2004 Wiley-VCH Verlag GmbH & Co. KGaA, Weinheim



Scheme 16. Activation of 2-metallaoxetanes by protonation and alkylation of the oxygen atom; Rh = (tpa)Rh.[120,124]

tion of $[(bpa\text{-}R)(MeCN)Rh^{III}(CH_2CH_2O)]^+$ in CH_2Cl_2 in the presence of ethene results in nearly quantitative recovery of $[(bpa\text{-}R)(MeCN)Rh^{I}(ethene)]^+$.[122] The system thus completes one catalytic turnover, albeit that oxygenation and product elimination take place in different solvents. Attempts to use $[(bpa\text{-}R)(MeCN)Rh^{I}(ethene)]^+$ to mediate "one-pot" oxygenation of ethene to acetaldehyde by H_2O_2 in MeCN has not yet led to any true catalytic activity.

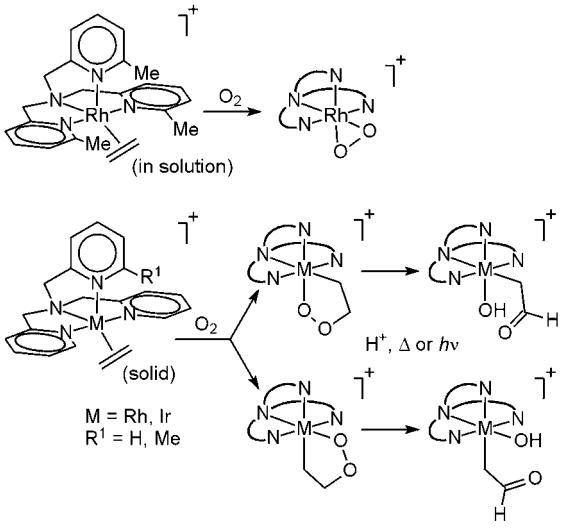
Treatment of $[(bpa\text{-}Bz)(MeCN)Rh^{III}(CH_2CH_2O)]^+$ with excess H_2O_2 results in further oxidation to a transient β-oxoethyl complex $[(bpa\text{-}Bz)(MeCN)Rh^{III}(OH)(CH_2\text{-}C(O)H)]^+$ (see Scheme 15).[122] Such "over-oxidation" of 2-metallaoxetanes by H_2O_2 is probably closely related to the oxocyclooctenyl complex obtained by oxidation of $[(pyp)Ir^{I}\text{-}(cod)]^+$ with excess H_2O_2 (Scheme 13).[119]

3.3. Dioxygenation of Rhodium(I)– and Iridium(I)–Ethene Complexes by O_2

From the previous section it is clear that oxygenation of Rh– and Ir–olefin (cod, ethene, propene) complexes by H_2O_2 in most cases leads to (selective) formation of 2-metallaoxetanes, regardless of the olefinic substrate or the supporting σ-donor ligand. In the cases in which oxygenation of $[M^{I}(cod)]$ can be performed with O_2 (that is, $[(P_3O_9)Ir^{I}(cod)]^{2-}$ and $[(bpa)Rh^{I}(cod)]^+$), the reaction also leads to the formation of 2-metallaoxetanes. The outcome of oxygenation reactions of $[(N\text{-ligand})M^{I}(ethene)]^+$ (M = Rh, Ir) complexes by O_2 depends strongly on both the metal and the N-ligand.

In most cases, oxygenation of Rh– and Ir–ethene complexes by O_2 results in dioxygenation products, and thus does *not* result in the formation of 2-metallaoxetanes. There is one exception: oxygenation of $[(Me_1tpa)Ir^{I}(ethene)]^+$ by O_2 in CH_2Cl_2 yields a 2-iridaoxetane identical to that obtained with H_2O_2 (Scheme 14) albeit in very low yield (~14%, other products are unidentified, some of them paramagnetic).[117,125] It is tempting to assume that this reaction as well as the reaction of $[(bpa\text{-}R)Rh^{I}(cod)]^+$ with O_2 (Scheme 11) proceed via (hydro)peroxides generated in situ.[115,116,126]

In solution, all $[(N\text{-ligand})Rh^{I}(ethene)]^+$ complexes lose ethene upon contact with O_2, as observed with NMR spectroscopic analysis. Presumably, ethene is substituted by O_2, but in most cases the resulting peroxide species are quite reactive. The subsequent reactions are unselective and therefore products could not be identified. However, $[(Me_3tpa)\text{-}Rh^{I}(ethene)]^+$ is selectively converted into $[(Me_3tpa)\text{-}Rh^{III}(O_2)]^+$ upon reaction with O_2 (Scheme 17).[126] Apparently, steric shielding of the peroxo fragment by the methyl groups of the Me_3tpa ligand prevents further reactions.



Scheme 17. Dioxygenation of $[(tpa)M^{I}(C_2H_4)]^+$ by O_2: difference between solution and solid–gas reactivity.[127,128]

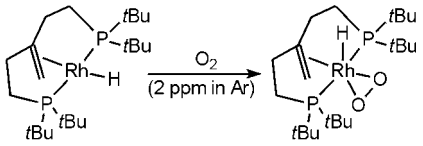
As a solid, however, $[(N_4\text{-ligand})Rh^{I}(ethene)]^+$ complexes are converted selectively into the 3-rhodadioxolanes $[(N_4\text{-ligand})Rh^{III}(CH_2CH_2OO)]^+$ without the loss of ethene (Scheme 17);[127,128] the formation of the product is accompanied by the appearance of a persistent EPR signal.[125] Depending on the counterion (and thereby, crystal packing) different ratios of the two possible isomers are observed. As for the H_2O_2 reactions in solution, the solid–gas reaction works well only for the sterically less-demanding N_4 ligands pyp, tpa and Me_1tpa, but not for Me_2tpa and Me_3tpa; in the latter cases, the reaction simply does not proceed. Similar solid–gas reactions were observed for the corresponding tpa– and Me_1-tpa–iridium(I)–ethene complexes, leading to similar 3-irida-1,2-dioxolanes.

Thermal or photochemical activation or protonation of these 3-metalla(III)-1,2-dioxolanes does not result in elimination of oxygenated organic products. Instead, stable hydroxy-β-oxoethyl species are formed[128,129] which do not eliminate any organic fragment upon (moderate) heating. Prolonged photoillumination of these species results in unselective decomposition. Treatment of these hydroxy-β-oxoethyl species with additional acid did not result in elimination of acetaldehyde, but only in protonation of the hydroxo ligand to give an aqua ligand. The hydroxy- or aqua-β-oxoethyl complexes did not react with olefins.

Ethene dissociation in the solution-phase reaction of rhodium–ethene complexes with O_2 must be related to the weak affinity of Rh^{III} for olefins. Olefin displacement can be prevented by the chelate effect, allowing selective oxygenation of some rhodium–cod complexes (see Section 3.1).

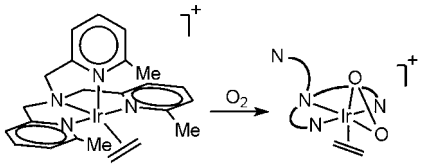
 © 2004 Wiley-VCH Verlag GmbH & Co. KGaA, Weinheim

Related to this, the neutral square-planar hydrido–rhodium(I) complex $[(CH_2{=}C(CH_2CH_2P\mathit{t}Bu_2)_2)Rh^{I}(H)]$ is converted into a hydrido–olefin–peroxo complex with O_2 (Scheme 18).[130] Selective conversion requires prolonged exposure to a very dilute mixture (2 ppm) of O_2 in Ar; direct exposure to concentrated O_2 leads to unselective decomposition reactions.



Scheme 18. Dioxygenation of $[(CH_2{=}C(CH_2CH_2P\mathit{t}Bu_2)_2)Rh^{I}(H)]$ by *diluted* O_2.[124]

Ethene binds more strongly to Ir^{III} than to Rh^{III}, and upon reaction of $[Ir^{I}(ethene)]$ complexes with O_2 in solution, several peroxo–ethene complexes have been isolated. In 1973, van der Ent and Onderdelinden proposed (on the basis of spectroscopic studies) the formation of $[(PPh_3)_2(Cl)Ir^{III}(O_2)(ethene)]$ from $[(PPh_3)_2(Cl)Ir^{I}(ethene)_2]$ and O_2.[131,132] In 2002, $[(Me_2bpa\text{-}Me)Ir^{III}(O_2)(ethene)]^+$ (crystallographically characterized) and $[(\kappa^3\text{-}Me_3tpa)Ir^{III}(O_2)(ethene)]^+$ were prepared by reaction of tetracoordinate $[(Me_2\text{-}bpa\text{-}Me)Ir^{I}(ethene)]^+$ and pentacoordinate $[(Me_3tpa)\text{-}Ir^{I}(ethene)]^+$, respectively, with O_2 in CH_2Cl_2



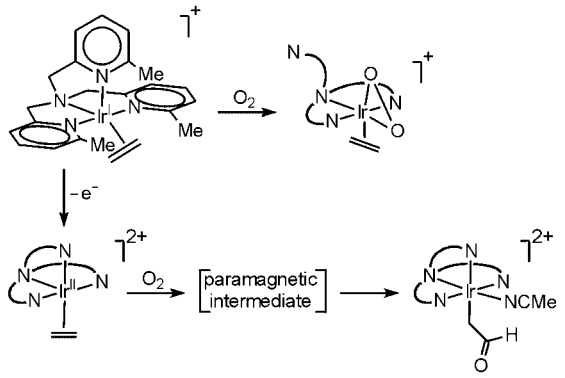
Scheme 19. Dioxygenation of $[(Me_3tpa)Ir^{I}(C_2H_4)]^+$ by O_2.[126]

(Scheme 19).[126] The yield of these reactions was only 25%, the remainder being unidentified (EPR-silent) paramagnetic material. Solution-phase reactivity of O_2 towards iridium(I)–ethene complexes with sterically less-hindered ligands (tpa, Me_1tpa) is even less selective.

3.4. Reaction of Paramagnetic Iridium(II)–Ethene Complexes with O_2

Even though nearly all oxidation reactions mentioned so far can be described as closed-shell reactions, with the metal switching between low-spin M^{I} and M^{III} states, we have frequently observed paramagnetism in O_2 oxidation reactions. This prompted us to consider involvement of odd-electron species in C–O coupling reactions.

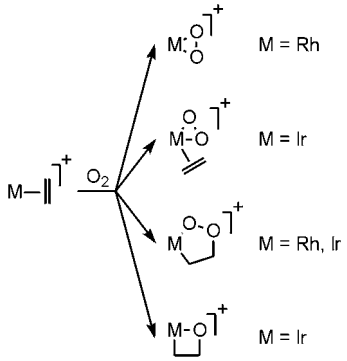
Stable, mononuclear $[(Me_3tpa)Ir^{II}(ethene)]^{2+}$ was obtained by oxidation of $[(Me_3tpa)Ir^{I}(ethene)]^+$ by ferrocenium.[133] Its reactivity towards O_2 turned out to be completely different from that of its Ir^{I} precursor, which simply gave the olefin–peroxo complex $[(\kappa^3\text{-}Me_3tpa)Ir(ethene)(O_2)]^+$ (Scheme 20). The Ir^{II} complex instead gave mainly the C–O coupled product $[(Me_3tpa)Ir^{III}(MeCN)(CH_2C(O)H)]^{2+}$ ($\approx$70% of the observed diamagnetic products). The reaction proceeds via a paramagnetic intermediate, detectable by



Scheme 20. O_2 binds to $[(Me_3tpa)Ir^{I}(C_2H_4)]^+$ (top) but forms a C–O bond with $[(Me_3tpa)Ir^{II}(C_2H_4)]^{2+}$ (bottom).[133]

EPR, which is presumably a superoxo species $[Ir^{III}(ethene)(O_2^{\bullet-})]$ or a superoxoethyl species $[Ir^{III}(CH_2CH_2OO^{\bullet})]$. Whatever the precise details of this reaction are, it seems clear that paramagnetic intermediates may indeed play a role in C–O coupling between olefins and O_2, starting from diamagnetic complexes.

We now consider the variety of products that can be obtained from Rh/Ir–olefin complexes and O_2 (Scheme 21).



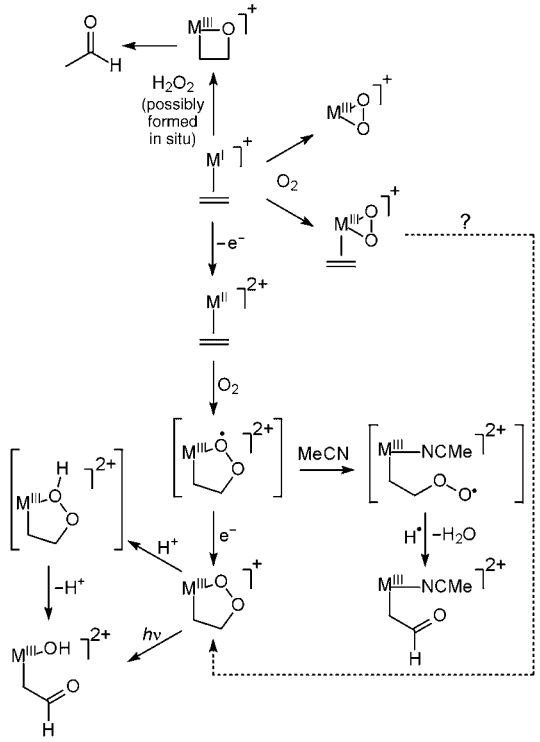
Scheme 21. Diversity in oxygenation of M^{I}–ethene complexes by O_2.

The formation of peroxo complexes (ethene displacement by O_2) and peroxo–olefin complexes (tpa arm displacement by O_2) does not seem to require more than the spin flip needed to produce diamagnetic products from triplet O_2. The formation of metallaoxetanes is most easily explained with H_2O_2 or (hydro)peroxide intermediates and again does not require odd-electron intermediates. Metalladioxolane formation, however, is more likely to involve M^{II} intermediates. Preliminary calculations[121] suggest that in diamagnetic *mer*-$[(bpa)M(C_2H_4)(O_2)]^+$ complexes, C–O coupling is difficult, and indeed such complexes do not seem to undergo C–O coupling spontaneously.[126] If $[(tpa)M(C_2H_4)]^+$ were to be oxidized in the solid state by simple tpa arm detachment

 © 2004 Wiley-VCH Verlag GmbH & Co. KGaA, Weinheim

followed by O_2 coordination, the basal ligand arm should detach first,[134] leading to stable *mer*-[(κ^3-tpa)M(C_2H_4)(O_2)]$^+$. Calculations also suggest that C–O coupling would be much easier in *fac*-[(κ^3-tpa)M(C_2H_4)(O_2)]$^+$, but this would first require the much less favorable dissociation of an apical tpa arm.

As these diamagnetic pathways appear less likely, and olefin–O_2 coupling occurs easily at Ir^{II}, one has to at least consider the possibility of M^{II} intermediates in the solid–gas reactions. One possible path would involve initial formation of a trace of the M^{II} complex, for example, by oxidation at the crystal surface. This could bind O_2, undergo C–O coupling, and then oxidize the next molecule of M^I complex, leading to a solid-state chain reaction. This mechanism is, as yet, purely speculative. Scheme 22 summarizes how the different reactions of Scheme 21 might be connected.

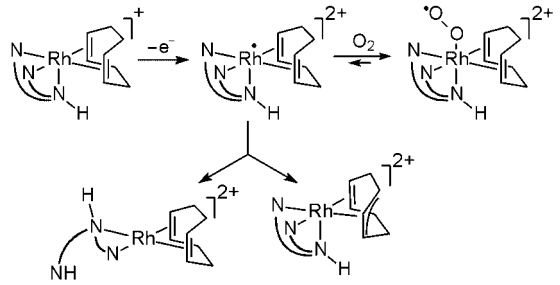


Scheme 22. Proposed connections between species formed from Rh/Ir–olefin complexes and O_2. Species shown in parentheses have not been isolated.

Odd-electron species do not always readily undergo C–O coupling. Isolated [(bpa)Rh^{II}(cod)]$^{2+}$ binds O_2 in acetone, but the resulting superoxo–Rh^{III} complex decomposes into the same mixture of nonoxygenated products as obtained by disproportionation of [(bpa)Rh^{II}(cod)]$^{2+}$ in the *absence* of O_2 (Scheme 23).[135] Apparently, O_2 uptake by Rh^{II} is reversible and nonproductive; C–O bond formation is too slow to compete with disproportionation.

3.5. Lessons from the Stoichiometric Model Reactions

The main results from the stoichiometric reactions described above are summarized below; we hope they are general and thus relevant to the discussion of catalytic oxidation in the next section.



Scheme 23. Reversible oxygenation and irreversible disproportionation of [(bpa)Rh^{II}(cod)]$^{2+}$.[135]

- Oxidation of M^I–alkene fragments with H_2O_2 often results in the rapid formation of 2-metalla(III)-oxetanes. These readily undergo elimination of $CH_3C(O)R$ upon protonation or ligand dissociation, which is similar to reductive elimination from palladium(II)–β-hydroxoalkyl species in the Wacker oxidation of olefins.
- Although formation of a C–O bond through coupling of a hydroxo ligand and an alkene coordinated at a M^{III} center seems easy, coordinatively saturated M^{III}–hydroxo species (such as hydroxy-β-oxoethyl complexes in Scheme 17) do not react with added olefin.
- Coordinatively saturated κ^2-peroxo complexes do not react with free olefins. Even for κ^2-peroxo–olefin complexes, it can be difficult to overcome the barrier for C–O coupling.
- Metal ions M^{III}, in particular Rh^{III}, have a very low affinity for olefins. Upon exposure of Rh^I–olefin complexes to O_2, the olefin tends to dissociate before C–O coupling occurs. Oxygenation of M^I–olefin complexes via odd-electron M^{II}–olefin species might be a way to circumvent this problem.
- So far, 3-metalla-1,2-dioxolanes have only been obtained in solid–gas reactions. Our failure to observe their formation in solution may be due to the factors mentioned above. Thermal, photochemical, or proton-assisted decomposition of model 3-metalla-1,2-dioxolane complexes results in stable β-oxoethyl species [M^{III}(OH)(CH_2-C(O)H)], which so far seem reluctant to liberate acetaldehyde. Co^{III} enolates have been reported to yield the free ketone upon protolysis,[136] but Rh–C bonds are generally stronger than Co–C bonds.

4. Implications for Real Catalytic Systems

4.1. Rh-Catalyzed Oxidations

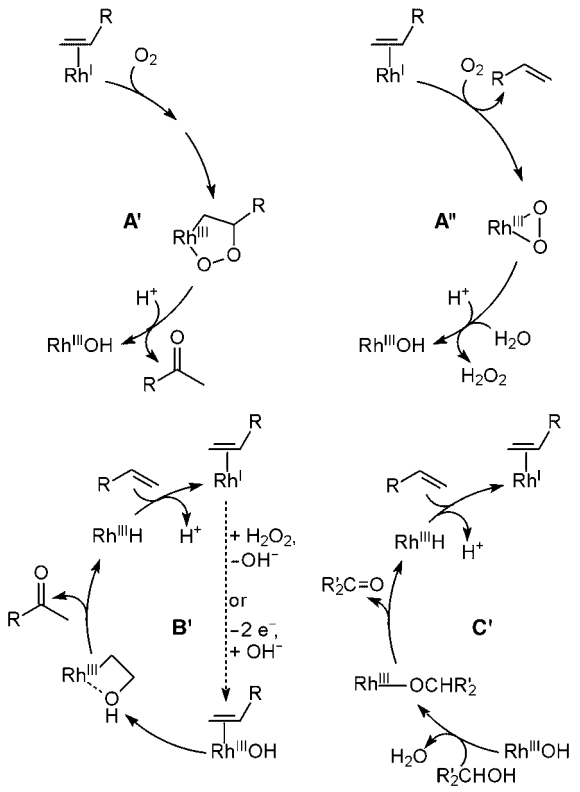
In Section 3, we saw many species closely related to those proposed in catalytic oxidations (parts **A**, **B**, **C** of Scheme 5 and variations on this theme). We will now try to integrate the stoichiometric chemistry and the catalysis. Much of this section is necessarily speculative; we hope it will fuel new research in catalytic oxidation.

 © 2004 Wiley-VCH Verlag GmbH & Co. KGaA, Weinheim

4.1.1. *"Wacker" Steps*

According to experimental and theoretical results of investigations into the oxidation of $[(N_4\text{-ligand})M(C_2H_4)]^+$ complexes, intramolecular attack of OH^- at olefins is fast and easy. The resulting (protonated) M^{III} oxetane can easily decompose into aldehyde and M^I ions. Therefore, intramolecular Wacker oxidation is a very reasonable step for catalytic oxidation. The only "problem" is that the olefin must somehow enter the coordination sphere of the metal. Given the low affinity of M^{III} for olefins and the inertness of the M^{III} octahedral arrangement, olefin entry at $M^{III}(OH)$ should be difficult.[137] Wacker oxidation of the most strongly coordinating and easily oxidizable olefin ethene in the presence of oxidation-resistant solvents H_2O and MeOH does occur, but is rather slow;[80,94] one could expect this reaction to be slower still for higher olefins. In the stoichiometric model processes, this problem is "solved" by generating $M^{III}(OH)$ species in situ in the presence of coordinated olefin, through oxidation of the M^I–olefin complex. If this interpretation is correct, it would explain why "Wacker" part **B** (Scheme 5) does not normally work, whereas H_2O_2 oxidation of olefin complexes, thought to involve the same type of nucleophilic attack, *does* work (Scheme 24, part **B′**).

In a bimetallic variation of "Wacker" attack, ethene complex $[Cp^*Ir(Ph)(PMe_3)(C_2H_4)]^+$ has been reported to react with hydroxide $[Cp^*Ir(Ph)(PMe_3)(OH)]$ to give $[Cp^*Ir(Ph)(PMe_3)(CH_2CH_2OH)]$.[138] Although the possibility of bimetallic catalysis is certainly intriguing and should be kept in mind, this route is essentially equivalent to external attack of free hydroxide onto coordinated olefin.



Scheme 24. Proposed modification for the mechanism of Rh-catalyzed olefin oxygenations. Rh-only catalysis: either **A′**+**C′** or **A″**+**B′**+**C′**. Rh/Cu cocatalysis: **B′** only (Cu^I generates H_2O_2 (analogous to Rh^I in **A″**) to oxidize the first molecule of Rh^I–olefin (**B′**, H_2O_2 variation), and Cu^{II} oxidizes the second molecule (**B′**, $-2\,e^-$ variation).[100]

4.1.2. *"Peroxide" Steps*

The stoichiometric processes summarized herein suggest that C–O bond formation between a coordinated olefin and a coordinated peroxide may not always be straightforward. The possibility of paramagnetic intermediates should at least be considered. It is clear both from the stoichiometric studies and from the catalytic processes in aprotic media that, regardless of the mechanism, such a coupling *can* occur. However, experimental work also shows that olefin displacement by oxygen is a competing reaction and that clean C–O coupling is difficult to achieve unless special precautions are taken (e.g., solid–gas reactions). Based on the assumption for the moment that olefin–O_2 coupling occurs within the coordination sphere, the resulting metalladioxolanes (Scheme 24, part **A′**) will easily undergo O–O bond cleavage, leading to hydroxy-β-oxoalkyl species. In stoichiometric reactions, these have been found to be rather stable, possibly as a result of the rigid N_4-ligand framework employed; this might not apply to the complexes used in real catalysis. It might also be that they decompose through a more complicated route, for example, reduction to a hydrido-β-oxoalkyl complex (possibly formed through solvent oxidation) followed by reductive elimination of ketone. Reductive ketone elimination from $[(P_4\text{-ligand})Rh^{III}(H)(CH_2C(O)R)]^+$ (obtained by the reaction of Rh^I with epoxides) has been reported.[139] In any case, methyl ketones appear to be the most logical organic end-products from such β-oxoalkyls (C enolates).

Formal protonolysis of the enolate Rh–C bond would produce the ketone but leave the metal center in the M^{III} state. Because at this point there will be no olefin left in the coordination sphere of the metal atom, the Rh^{III} center needs to be reduced to Rh^I by the solvent (Scheme 24, part **C′**). This could explain solvent cooxidation in Rh-only catalysis (i.e. in the absence of cocatalyst).

In protic media, protonation of the peroxo ligand to a hydroperoxo group seems likely. Like OH^-, OOH^- should easily attack any olefin present within the coordination sphere, thus leading to protonated metalladioxolanes (protonated version of part **A′** in Scheme 24), which would in turn rearrange quickly to β-oxoalkyl derivatives.

These considerations lead to a catalytic cycle for Rh-only oxidation consisting of parts **A′** (olefin oxygenation) and **C′** (solvent cooxidation). One could, however, also imagine an alternative in which O_2 *displaces* the olefin at Rh^I, leading to a Rh^{III}–peroxide complex without any coordinated olefin. This would eventually generate an olefin-free Rh^{III} species (which would oxidize a solvent molecule) and H_2O_2, which would oxidize a *second* Rh^I–olefin complex to an aldehyde. This alternative cycle thus consists of parts **A″** (H_2O_2 generation), **B′** (H_2O_2 use), and **C′** (solvent cooxidation). In view of the complicated nature of the C–O coupling step necessary for **A′** and our failure to obtain acetaldehyde from $[M^{III}(OH)(CH_2$-

 © 2004 Wiley-VCH Verlag GmbH & Co. KGaA, Weinheim

CHO)] complexes, we currently favor this alternative formulation.

4.1.3. Cu Cocatalysis

As mentioned before, the current picture of Cu cocatalysis is unsatisfactory because it does not explain how Cu would promote Wacker oxidation (Scheme 5, **B**) over solvent oxidation (Scheme 5, **C**). We propose an admittedly speculative explanation,[140] in part based on the suggestion by Drago et al.[87] that Cu^{I} is more effective than Rh^{I} in generating H_2O_2. Thus, Cu^{I} ions would generate H_2O_2, which would oxidize a Rh^{I}–olefin complex to an oxetane and water, analogous to the stoichiometric reactions (Scheme 24, **B′**, H_2O_2 variant). Decomposition of the oxetane leads to ketone and eventual re-formation of the Rh^{I}–olefin complex. This complex is oxidized by Cu^{II}, captures OH^- from water, and oxidizes a second molecule of olefin to oxetane and hence to ketone (**B′**, $-2e^-$ variant). The important difference from earlier proposals is our emphasis on the requirement that the olefin must be coordinated to the metal *before* it is oxidized to M^{III}, because of the inertness and low olefin affinity of the metal ions in the oxidation state $+3$. This is where the main difference lies with Pd/Cu Wacker, in which Pd^{II} easily exchanges ligands and has a fair affinity for olefins.

Drago et al. reported that H_2O_2 was about as effective as O_2 in olefin oxidation,[87] whereas Bregeault and co-workers observed much lower rates with H_2O_2.[89] This discrepancy might be due to the use of different reaction conditions. Drago et al. used H_2O_2 in low concentration and a high olefin/H_2O_2 ratio. Under these conditions, regeneration of the Rh^{I} olefin complex in part **B′** (Scheme 24) seems reasonable. At higher H_2O_2 concentrations, Rh^{I} would be reoxidized to Rh^{III} before it could capture an olefin, thus preventing olefin oxidation. This might explain the results of Bregeault and coworkers (unfortunately, no experimental details were provided). It might also explain our own failure to observe true catalysis with $[(bpa\text{-}R)(MeCN)Rh^{I}(ethene)]^+$ and H_2O_2 (Section 3.2). Generation of low concentrations of H_2O_2 in situ might be an important feature of this catalytic process.

Even if this idea is correct, it is certainly not the last word on Rh-catalyzed olefin oxidation. For example, the precise roles of Cu in generating H_2O_2 (possibly in concert with Rh) and in Rh^{I}/Rh^{III} redox chemistry (possibly via Rh^{II}) clearly warrant further attention. Also, the model studies have suggested that the C–O coupling step in part **A′**, if it occurs at all, might not be straightforward and might involve Rh^{II} intermediates.

4.2. Metallaoxetanes and Metalladioxolanes

The stoichiometric chemistry described in this Review demonstrates that metallaoxetanes can be stable species and should be considered as viable intermediates in catalytic reactions. Their involvement in intramolecular Wacker-type chemistry seems likely or at least possible. However, metallaoxetanes have more often been proposed as intermediates in epoxidation catalysis. We have never found any evidence for the formation of epoxides from metallaoxetanes. Epoxides are highly strained species, metallaoxetanes much less so. Thus, it would require a metal in an abnormally high oxidation state to make reductive elimination of an epoxide thermodynamically favorable; Rh^{III} and Ir^{III} probably do not qualify in this respect. Indeed, oxidative addition of an epoxide to Rh^{I} has been shown to result in the formation a 2-rhoda(III)–oxetane,[142] indicating that reductive elimination (the microscopic reverse step) requires more energy in this case.

Metalla-oxetanes are not only intermediates to ketones; they also exhibit interesting reactivities themselves. The oxygen atom is very nucleophilic, as is expected of an alkoxide. After attack by an electrophile, the ring opens readily, which can lead to decomposition to an aldehyde through a β-elimination process. The few other metallaoxetanes that have been reported are all stabilized either by geometric constraints or by lack of β-hydrogen atoms.[141–152] However, the acetonitrile chemistry shown in Scheme 16 demonstrates that more complicated transformations are possible. Thus, there might be prospects for organic syntheses via metallaoxetanes. Their easy formation by nucleophilic attack within the coordination sphere of Rh and Ir suggests that they could also form easily at other metal centers; indeed, a platinaoxetane species was recently obtained from a Pt^{II}–μ^3-oxo complex and norbornene.[152]

The requirements for metalladioxolane formation, on the other hand, appear to be much more critical. The fact that the formation of this species has not yet been observed in solution seems to indicate that it involves one or more highly reactive intermediates. Also, metalladioxolanes seem to only decompose into β-oxoalkyl species. Thus, they might be intermediates in the formation of ketones from olefins, but prospects for using or deliberately synthesizing them for other purposes seem slim.

5. Conclusion

The chemistry of oxidation remains as exciting as ever. Stoichiometric reactions have produced functional models for almost all steps of the oxidation catalysis, although none of the models mentioned supports a full catalytic cycle (yet). This might be due to the rigidity of the ligands used, which decreases the number of reaction paths available and hence leads to more-stable and less-reactive intermediates. The interaction between model chemistry and catalysis leads to new ideas, which clearly require further testing. In particular, the possibility that paramagnetic species may be important in reactions that one would typically regard as simple closed-shell steps is fascinating. Solid–gas reactions seem to offer new opportunities for reactions involving highly reactive intermediates. Finally, the idea that in order to oxidize an olefin it may be necessary to oxidize a complex with the olefin already coordinated to the metal center may lead to new catalytic applications.

Received: August 26, 2003 [A629]
Published Online: July 7, 2004

 © 2004 Wiley-VCH Verlag GmbH & Co. KGaA, Weinheim

[1] R. Noyori, M. Aoki, K. Sato, *Chem. Commun.* **2003**, 1977.
[2] C. W. Jones, *Application of Hydrogen Peroxide and Derivatives*, Royal Society of Chemistry, Cambridge, **1999**.
[3] *Catalytic Oxidations with Hydrogen Peroxide* (Ed.: G. Strukul), Kluwer, Dordrecht, **1992**.
[4] In certain cases, ozone (O_3) should also be considered as a possible alternative: T. Berndt, O. Böge, J. Heintzenberg, *Ind. Eng. Chem. Res.* **2003**, *42*, 2870.
[5] D. H. R. Barton, *The Activation of Dioxygen and Homogeneous Catalytic Oxidation*, Plenum, New York, **1993**.
[6] R. H. Holm, *Chem. Rev.* **1987**, *87*, 1401.
[7] R. S. Drago, *Coord. Chem. Rev.* **1992**, *117*, 185.
[8] R. A. Sheldon, J. Dakka, *Catal. Today* **1994**, *19*, 215.
[9] R. S. Drago, R. H. Beer, *Inorg. Chim. Acta* **1992**, *198–200*, 359.
[10] T. G. Spiro, *Metal Ion Activation of Dioxygen*, Wiley, New York, **1980**.
[11] R. A. Sheldon, J. K. Kochi, *Metal Catalyzed Oxidations of Organic Compounds*, Academic Press, New York, **1981**.
[12] I. I. Moiseev, *J. Mol. Catal. A* **1997**, *127*, 1.
[13] G. Strukul, *Angew. Chem.* **1998**, *110*, 1256; *Angew. Chem. Int. Ed.* **1998**, *37*, 1198.
[14] E. I. Becker, M. Tsutsui, *Organometallic Reactions*, *Vol. 3*, Wiley, New York, **1972**.
[15] H. Mimoun in *Comprehensive Coordination Chemistry*, *Vol. 6* (Ed.: G. Wilkinson), Elsevier, Amsterdam, **1987**, chap. 61.3.
[16] K. A. Jørgensen, *Chem. Rev.* **1989**, *89*, 431.
[17] J. A. Moulijn, P. W. N. M. van Leeuwen, R. A. van Santen, *Stud. Surf. Sci. Catal.* **1993**, *79* (*Catalysis: An Integrated Approach to Homogeneous, Heterogeneous, and Industrial Catalysis*).
[18] Z. Li, C. G. Xia, *Prog. Chem.* **2002**, *14*, 384.
[19] I. C. W. E. Arends, R. A. Sheldon, *Top. Catal.* **2002**, *19*, 133.
[20] J. M. Takacs, X. T. Jiang, *Curr. Org. Chem.* **2003**, *7*, 369.
[21] M. A. Barteau, R. J. Madix in *The Chemical Physics of Solid Surfaces and Heterogeneous Catalysis* (Eds.: D. A. King, D. P. Woodruff), Elsevier, Amsterdam, **1982**, p. 95.
[22] R. A. van Santen, H. P. C. E. Kuipers, *Adv. Catal.* **1987**, *35*, 265.
[23] W. M. H. Sachtler, C. Backx, R. A. van Santen, *Catal. Rev.* **1981**, *23*, 127.
[24] M. A. Barteau, *Top. Catal.* **2003**, *22*, 3.
[25] J. R. Monnier, *Appl. Catal. A* **2001**, *221*, 73.
[26] Direct evidence for allylic hydrogen abstraction: W. X. Huan, J. M. White, *Catal. Lett.* **2002**, *84*, 143.
[27] Selectivities of up $\approx$30% to propylene oxide have been observed for oxidation of propene over silver-based catalysts: J. Q. Lu, M. F. Luo, H. Lei, C. Li, *Appl. Catal. A* **2002**, *237*, 11.
[28] Epoxidation of propene by O_2/H_2 mixtures over heterogeneous Au catalysts has been reported; this involves the formation of H_2O_2 in situ; see, for example: A. K. Sinha, S. Seelan, T. Akita, S. Tsubota, M. Haruta, *Appl. Catal. A* **2003**, *240*, 243.
[29] R. Landau, G. A. Sullivan, D. Brown, *CHEMTECH* **1979**, 602.
[30] R. A. Sheldon, *J. Mol. Catal.* **1980**, *7*, 107.
[31] M. Taramasso, G. Perego, B. Notari (Enichem), US Pat. 4410501, **1983** [*Chem. Abstr.* **1981**, *95*, 206272k].
[32] B. Notari, *Catal. Today* **1993**, *18*, 163.
[33] B. Notari, *Stud. Surf. Sci. Catal.* **1987**, *37*, 413.
[34] For a highlight, see: R. Murugavel, H. W. Roesky, *Angew. Chem.* **1997**, *109*, 491; *Angew. Chem. Int. Ed. Engl.* **1997**, *36*, 477.
[35] T. Katsuki, K. B. Sharpless, *J. Am. Chem. Soc.* **1980**, *102*, 5974.
[36] R. A. Johnson, K. B. Sharpless in *Comprehensive Organic Synthesis*, *Vol. 7* (Eds.: B. M. Trost, I. Fleming), Pergamon, New York, **1991**, p. 389.
[37] R. A. Johnson, K. B. Sharpless, *Catalytic Asymmetric Synthesis* (Ed.: I. Ojima), VCH, Weinheim, **1993**, p. 103.
[38] T. Katsuki, V. S. Martin, *Org. React.* **1996**, *48*, 1.
[39] K. Srinivasan, P. Michaud, J. K. Kochi, *J. Am. Chem. Soc.* **1986**, *108*, 2309.
[40] R. Irie, K. Noda, Y. Ito, T. Katsuki, *Tetrahedron Lett.* **1991**, *32*, 1055.
[41] W. Zhang, J. L. Loebach, S. R. Wilson, E. N. Jacobsen, *J. Am. Chem. Soc.* **1990**, *112*, 2801.
[42] E. N. Jacobsen in *Catalytic Asymmetric Synthesis* (Ed.: I. Ojima), VCH, Weinheim, **1993**, p. 159.
[43] T. Katsuki, *J. Mol. Catal. A: Chem.* **1996**, *113*, 87.
[44] P. J. Pospisil, W. Zhang, E. N. Jacobsen, *Chem. Eur. J.* **1996**, *2*, 974.
[45] J. T. Groves, R. Quinn, *J. Am. Chem. Soc.* **1985**, *107*, 5790.
[46] T. K. M. Shing, E. K. W. Tam, V. W.-F. Tai, I. H. F. Chung, Q. Jiang, *Chem. Eur. J.* **1996**, *2*, 50.
[47] T. K. M. Shing, V. W.-F. Tai, E. K. W. Tam, *Angew. Chem.* **1994**, *106*, 2408; *Angew. Chem. Int. Ed. Engl.* **1994**, *33*, 2312.
[48] C. Döbler, G. Mehltretter, M. Beller, *Angew. Chem.* **1999**, *111*, 3211; *Angew. Chem. Int. Ed.* **1999**, *38*, 3026.
[49] C. Döbler, G. Mehltretter, U. Sundermeier, M. Beller, *J. Am. Chem. Soc.* **2000**, *122*, 10289.
[50] M. Schröder, *Chem. Rev.* **1980**, *80*, 187.
[51] H. C. Kolb, M. S. van Nieuwenhuize, K. B. Sharpless, *Chem. Rev.* **1994**, *94*, 2483.
[52] R. Jira, W. Blay, G. Grimm, *Hydrocarbon Process.* **1976**, *55*, 97.
[53] J. March, *Advanced Organic Chemistry: Reactions, Mechanisms, and Structure*, 4th ed., Wiley, New York, **1992**, p. 1196, and references therein.
[54] R. Rappo, A. Becker, *Isr. Res. Counc. Bull. A* **1956**, *5*, 300.
[55] D. G. Lee, V. S. Chang, S. Helliwell, *J. Org. Chem.* **1976**, *41*, 3644.
[56] D. G. Lee, S. Helliwell, V. S. Chang, *J. Org. Chem.* **1976**, *41*, 3646.
[57] K. Takao, Y. Fujiwara, T. Imanaka, S. Teranishi, *Bull. Chem. Soc. Jpn.* **1970**, *43*, 1153.
[58] K. Takao, M. Wayaku, Y. Fujiwara, T. Imanaka, S. Teranishi, *Bull. Chem. Soc. Jpn.* **1970**, *43*, 3898.
[59] I. V. Yudanov, C. Di Valentin, P. Gisdakis, N. Rösch, *J. Mol. Catal. A: Chem.* **2000**, *158*, 189.
[60] D. V. Deubel, J. Sundermeyer, G. Frenking, *J. Am. Chem. Soc.* **2000**, *122*, 10101.
[61] D. V. Deubel, J. Sundermeyer, G. Frenking, *Inorg. Chem.* **2000**, *39*, 2314.
[62] D. V. Deubel, J. Sundermeyer, G. Frenking, *Eur. J. Inorg. Chem.* **2001**, 1819.
[63] a) Y.-D. Wu, D. K. W. Lai, *J. Org. Chem.* **1995**, *60*, 673; b) Y.-D. Wu, D. K. W. Lai, *J. Am. Chem. Soc.* **1995**, *117*, 11327.
[64] I. V. Yudanov, P. Gisdakis, C. Di Valentin, N. Rösch, *Eur. J. Inorg. Chem.* **1999**, 2135.
[65] For a selection of experimental evidence for early transition-metal-catalyzed olefin epoxidation through step b2 in Scheme 2, see: a) A. M. Al-Aljouni, J. H. Espenson, *J. Am. Chem. Soc.* **1995**, *117*, 9243; b) A. M. Al-Aljouni, J. H. Espenson, *J. Org. Chem.* **1996**, ***61***, 3969; c) H. Tan, J. H. Espenson, *Inorg. Chem.* **1998**, *37*, 467; d) F. E. Kühn, A. M. Santos, P. W. Roesky, E. Herdtweck, S. Scherer, P. Gisdakis, I. V. Yudanov, C. Di Valentin, N. Rösch, *Chem. Eur. J.* **1999**, *5*, 3603.
[66] U. Pidun, C. Boehme, G. Frenking, *Angew. Chem.* **1996**, *108*, 3008; *Angew. Chem. Int. Ed. Engl.* **1996**, *35*, 2817.
[67] S. Dapprich, G. Ujaque, F. Maseras, A. Lledós, D. G. Musaev, K. Morokuma, *J. Am. Chem. Soc.* **1996**, *118*, 11660.
[68] M. Torrent, L. Q. Deng, M. Duran, M. Sola, T. Ziegler, *Organometallics* **1997**, *16*, 13.
[69] C. Linde, M. Arnold, P.-O. Norrby, B. Åckermark, *Angew. Chem.* **1997**, *109*, 1802; *Angew. Chem. Int. Ed. Engl.* **1997**, *36*, 1723.

 © 2004 Wiley-VCH Verlag GmbH & Co. KGaA, Weinheim

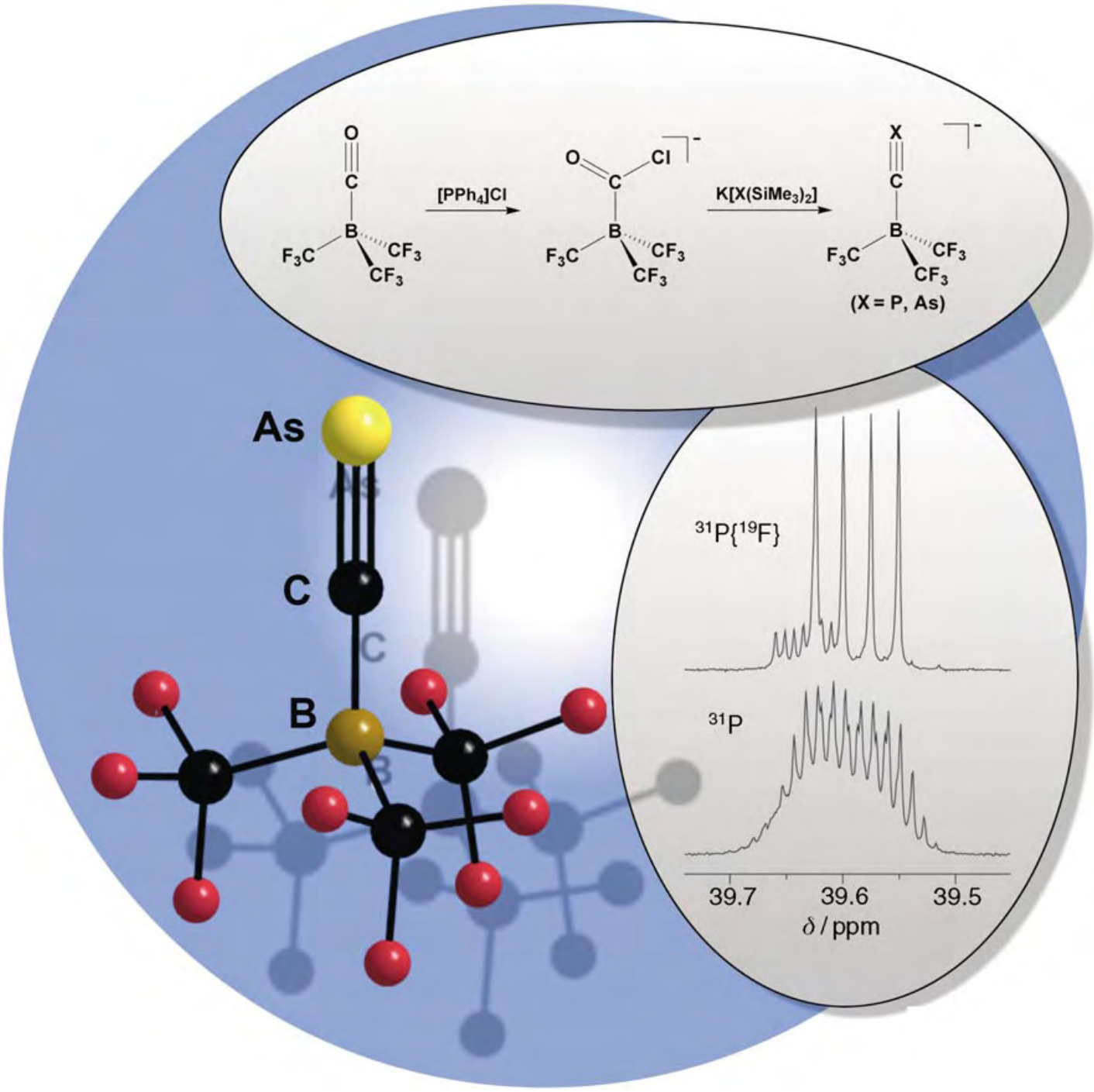
[70] N. S. Finney, P. J. Pospisil, S. Chang, M. Palucki, R. G. Konsler, K. B. Hansen, E. N. Jacobsen, *Angew. Chem.* **1997**, *109*, 1798; *Angew. Chem. Int. Ed. Engl.* **1997**, *36*, 1720.
[71] T. Linker, *Angew. Chem.* **1997**, *109*, 2150; *Angew. Chem. Int. Ed. Engl.* **1997**, *36*, 2060.
[72] For a recent computational study, see: L. Cavallo, H. Jacobsen, *Eur. J. Inorg. Chem.* **2003**, 892.
[73] See, for example "Monoolefin and Acetylene Complexes of Palladium": P. M. Maitlis, P. Espinet, M. J. H. Russell in *Comprehensive Organometallic Chemistry, Vol. 6* (Ed.: G. Wilkinson, Pergamon, Oxford, **1982**, p. 357.
[74] R. S. Dickson, *Homogeneous catalysis with Compounds of Rhodium and Iridium*, Reidel, Dordrecht, **1985**, chap. 5.
[75] E. S. Gore, *Stud. Inorg. Chem.* **1991**, *11* (*Chemistry of the Platinum Group Metals: Recent Developments*).
[76] J. T. Groves in *Metal Ion Activation of Dioxygen* (Ed.: T. G. Spiro), Wiley, New York, **1980**.
[77] J. W. McMillan, H. E. Fischer, J. Schwartz, *J. Am. Chem. Soc.* **1991**, *113*, 4014.
[78] J. Schwartz, J. W. McMillan, H. E. Fischer, *J. Mol. Catal.* **1992**, *74*, 443.
[79] K. Takahashi, M. Yamaguchi, T. Shido, H. Ohtani, K. Isobe, M. Ichikawa, *J. Chem. Soc. Chem. Commun.* **1995**, 1301.
[80] B. R. James, M. Kastner, *Can. J. Chem.* **1972**, *50*, 1698.
[81] H. Mimoun, *Pure Appl. Chem.* **1981**, *53*, 2389.
[82] F. di Furia, G. Modena, *Pure Appl. Chem. Chem.* **1982**, *54*, 1853.
[83] O. Bortolini, F. di Furia, G. Modena, R. Seraglia, *J. Mol. Catal.* **1984**, *22*, 313.
[84] C. Dudley, G. Read, *Tetrahedron Lett.* **1972**, 5273.
[85] G. Read, P. J. C. Walker, *J. Chem. Soc. Dalton Trans.* **1977**, 883.
[86] G. Read, M. Urgelles, *J. Chem. Soc. Dalton Trans.* **1985**, 1591.
[87] R. S. Drago, A. Zuzich, E. D. Nyberg, *J. Am. Chem. Soc.* **1985**, *107*, 2898.
[88] M. A. Atlay, M. Preece, G. Strukul, B. R. James, *J. Chem. Soc. Chem. Commun.* **1982**, 406.
[89] M. Faraj, J. Martin, C. Martin, J.-M. Bregeault, *J. Mol. Catal.* **1985**, *31*, 57.
[90] M. Bressan, F. Morandini, A. Morvillo, P. Rigo, *J. Organomet. Chem.* **1985**, *280*, 139.
[91] J. E. Lyons, J. O. Turner, *Tetrahedron Lett.* **1972**, 2903.
[92] J. E. Lyons, J. O. Turner, *J. Org. Chem.* **1972**, *37*, 2881.
[93] A. Fusi, R. Ugo, F. Fox, A. Pasini, S. Cenini, *J. Organomet. Chem.* **1971**, *26*, 417.
[94] R. Cramer, *Inorg. Chem.* **1962**, *1*, 722.
[95] M. Bressan, F. Morandini, P. Rigo, *J. Organomet. Chem.* **1983**, *247*, C8.
[96] A. Morvillo, M. Bressan, *J. Mol. Catal.* **1986**, *37*, 63.
[97] C. Martin, M. Faraj, J. Martin, J.-M. Bregeault, J. Mercier, J. Fillaux, P. Dizabo, *J. Mol. Catal.* **1986**, *37*, 201.
[98] H. Mimoun, M. M. P. Machirant, I. S. de Roch, *J. Am. Chem. Soc.* **1978**, *100*, 5437.
[99] G. Read, J. Shaw, *J. Chem. Soc. Chem. Commun.* **1984**, 1313.
[100] The peroxide and metalladioxolane species in part **A** of Scheme 5 and parts **A′**, **A″** of Scheme 24 are depicted in an unprotonated state for simplicity. Mechanistic proposals in the literature contain both protonated and unprotonated variations. Our schemes are not intended to express any preference for the unprotonated variation.
[101] L. Carlton, G. Read, *J. Mol. Catal.* **1981**, *10*, 133.
[102] R. Tang, F. Mares, N. Neary, D. E. Smith, *J. Chem. Soc. Chem. Commun.* **1979**, 274.
[103] L. Carlton, G. Read, M. Urgelles, *J. Chem. Soc. Chem. Commun.* **1983**, 586.
[104] F. Igersheim, H. Mimoun, *J. Chem. Soc. Chem. Commun.* **1978**, 559.
[105] C. Bianchini, R. W. Zoellner, *Adv. Inorg. Chem.* **1997**, *44*, 263.
[106] See, for example: C. A. Ghilardi, S. Midollini, S. Moneti, A. Orlandini, G. Scapacci, *J. Chem. Soc. Dalton Trans.* **1992**, 3371.
[107] M. Aresta, I. Tommassi, E. Quaranta, C. Fragale, J. Mascetti, M. Tranquille, F. Galan, M. Fouassier, *Inorg. Chem.* **1996**, *35*, 4254.
[108] D. Carmona, M. P. Lamata, J. Ferrer, J. Modrego, M. Perales, F. J. Lahoz, R. Atencio, L. A. Oro, *J. Chem. Soc. Chem. Commun.* **1994**, 575.
[109] H. L. Roberts, W. R. Symes, *J. Chem. Soc. A* **1968**, 1450.
[110] H. Suzuki, S. Matsuura, Y. Moro-Oka, T. Ikawa, *J. Organomet. Chem.* **1985**, *286*, 247.
[111] A. Morvillo, M. Bressan, *J. Organomet. Chem.* **1987**, *332*, 337.
[112] F. A. Cotton, P. Lahuerta, M. Sanau, W. Schwotzer, *Inorg. Chim. Acta* **1986**, *120*, 153.
[113] V. W. Day, W. G. Klemperer, S. P. Lockledge, D. J. Main, *J. Am. Chem. Soc.* **1990**, *112*, 2031.
[114] B. de Bruin, M. J. Boerakker, J. J. J. M. Donners, B. E. C. Christiaans, P. P. J. Schlebos, R. de Gelder, J. M. M. Smits, A. L. Spek, A. W. Gal, *Angew. Chem.* **1997**, *109*, 2154; *Angew. Chem. Int. Ed. Engl.* **1997**, *36*, 2064.
[115] B. de Bruin, J. A. Brands, J. J. J. M. Donners, M. P. J. Donners, R. de Gelder, J. M. M. Smits, A. W. Gal, A. L. Spek, *Chem. Eur. J.* **1999**, *5*, 2921.
[116] T. C. Flood, M. Iimura, J. M. Perotti, A. L. Rheingold, T. E. Concolino, *Chem. Commun.* **2000**, 1681.
[117] R. J. N. A. M. Kicken, PhD Thesis, University of Nijmegen, **2001**.
[118] V. W. Day, T. A. Eberspacher, W. G. Klemperer, B. Zhong, *J. Am. Chem. Soc.* **1994**, *116*, 3119.
[119] T. Sciarone, J. Hoogboom, P. P. J. Schlebos, P. H. M. Budzelaar, R. de Gelder, J. M. M. Smits, A. W. Gal, *Eur. J. Inorg. Chem.* **2002**, 457.
[120] B. de Bruin, M. J. Boerakker, J. A. W. Verhagen, R. de Gelder, J. M. M. Smits, A. W. Gal, *Chem. Eur. J.* **2000**, *6*, 298.
[121] M. Krom, PhD Thesis, University of Nijmegen, **2003**.
[122] B. de Bruin, J. A. W. Verhagen, C. H. J. Schouten, A. W. Gal, D. Feichtinger, D. A. Plattner, *Chem. Eur. J.* **2001**, *7*, 416. The configuration of the bpa-R ligand (*mer* or *fac*) in the over-oxidation product could not be established.
[123] P. H. M. Budzelaar, A. N. J. Blok, *Eur. J. Inorg. Chem.* **2004**, 2385.
[124] B. de Bruin, M. J. Boerakker, R. de Gelder, J. M. M. Smits, A. W. Gal, *Angew. Chem.* **1999**, *111*, 118; *Angew. Chem. Int. Ed.* **1999**, *38*, 219.
[125] B. de Bruin, T. P. J. Peters, unpublished results.
[126] B. de Bruin, T. P. J. Peters, J. B. M. Wilting, S. Thewissen, J. M. M. Smits, A. W. Gal, *Eur. J. Inorg. Chem.* **2002**, 2671.
[127] M. Krom, R. G. E. Coumans, J. M. M. Smits, A. W. Gal, *Angew. Chem.* **2001**, *113*, 2164; *Angew. Chem. Int. Ed.* **2001**, *40*, 2106.
[128] M. Krom, T. P. J. Peters, R. G. E. Coumans, T. J. J. Sciarone, J. Hoogboom, S. I. ter Beek, P. P. J. Schlebos, J. M. M. Smits, R. de Gelder, A. W. Gal, *Eur. J. Inorg. Chem.* **2003**, 1072.
[129] M. Krom, R. G. E. Coumans, J. M. M. Smits, A. W. Gal, *Angew. Chem.* **2002**, *114*, 595; *Angew. Chem. Int. Ed.* **2002**, *41*, 576.
[130] A. Vigalok, L. J. W. Shimon, D. Milstein, *Chem. Commun.* **1996**, 1773.
[131] H. van Gaal, H. G. A. M. Cuppers, A. van der Ent, *Chem. Commun.* **1970**, 1694.
[132] A. van der Ent, A. L. Onderdelinden, *Inorg. Chim. Acta* **1973**, *7*, 203.
[133] B. de Bruin, T. P. J. Peters, S. Thewissen, A. N. J. Blok, J. B. M. Wilting, R. de Gelder, J. M. M. Smits, A. W. Gal, *Angew. Chem.* **2002**, *114*, 2239; *Angew. Chem. Int. Ed.* **2002**, *41*, 2138.
[134] A. R. Rossi, R. Hoffmann, *Inorg. Chem.* **1975**, *14*, 365.
[135] D. G. H. Hetterscheid, B. de Bruin, J. M. M Smits, A. W. Gal, *Organometallics* **2003**, *22*, 3022.

 © 2004 Wiley-VCH Verlag GmbH & Co. KGaA, Weinheim

[136] T. M. Vickrey, R. N. Katz, G. N. Schrauzer, *J. Am. Chem. Soc.* **1975**, *97*, 7248.
[137] This is an important difference to the typical "Wacker" metals Pd^{II} and Pt^{II}, which have a more labile coordination environment and a higher affinity for olefins, so that mechanisms involving entry of the olefin at the M^{II} oxidation state *after* formation of the M–O bond are more likely. For an example, see reference [152].
[138] J. C. M. Rittner, R. G. Bergman, *J. Am. Chem. Soc.* **1997**, *119*, 2580.
[139] D. Milstein, *Acc. Chem. Res.* **1984**, *17*, 221.
[140] Although a "unified" mechanism of Rh-only and Rh/Cu catalysis is certainly attractive, we realize that the products may also be formed through different mechanisms, which happen to arrive at the same products. Ketones are the almost inevitable products of olefin oxidation and can be formed through a variety of routes.
[141] A. A. Zlota, F. Frolow, D. Milstein, *J. Am. Chem. Soc.* **1990**, *112*, 6411.
[142] M. J. Calhorda, A. M. Galvão, C. Ünaleroglu, A. A. Zlota, F. Frolow, D. Milstein, *Organometallics* **1993**, *12*, 3316.
[143] J. Bakos, Á. Orosz, S. Cscrépi, I. Tóth, D. Sinou, *J. Mol. Catal. A: Chem.* **1997**, *116*, 85.
[144] R. Schlodder, J. A. Ibers, M. Lenarda, M. Graziani, *J. Am. Chem. Soc.* **1974**, *96*, 6893.
[145] M. Lenarda, N. B. Pahor, M. Calligaris, M. Graziani, L. Randaccio, *J. Chem. Soc. Dalton Trans.* **1978**, 279.
[146] D. P. Klein, J. C. Hayes, R. G. Bergman, *J. Am. Chem. Soc.* **1988**, *110*, 2031.
[147] J. C. Hartwig, R. G. Bergman, R. A. Andersen, *J. Am. Chem. Soc.* **1990**, *112*, 3234.
[148] J. C. Hartwig, R. G. Bergman, R. A. Andersen, *Organometallics* **1991**, *10*, 3344.
[149] S. Baba, T. Ogura, S. Kawaguchi, H. Tokunan, Y. Kai, N. Kashi, *J. Chem. Soc. Chem. Commun.* **1972**, 910.
[150] L. Pandolfo, G. Paiaro, G. Valle, P. Ganis, *Gazz. Chim. Ital.* **1985**, *115*, 65.
[151] W. A. Herrmann, U. Küsthardt, A. Schäfer, E. Herdtweck, *Angew. Chem.* **1986**, *98*, 818; *Angew. Chem. Int. Ed. Engl.* **1986**, *25*, 817.
[152] E. Szuromi, H. Shan, P. R. Sharp, *J. Am. Chem. Soc.*, **2003**, *125*, 10522.

 © 2004 Wiley-VCH Verlag GmbH & Co. KGaA, Weinheim

Communications



The conversion of the CO group of $(CF_3)_3BCO$ into a phospha- or arsaethynyl moiety gives the first borane compounds with these ligands. The $[(CF_3)_3BCAs]^-$ ion is the first example of an anionic arsaalkyne. The synthesis, structure, and spectroscopic properties of these thermally stable products are described by H. Willner and co-workers on the following pages.

DOI: 10.1002/anie.200454034
© 2004 Wiley-VCH Verlag GmbH & Co. KGaA, Weinheim

C≡P and C≡As Bonds

$[(CF_3)_3BCP]^-$ and $[(CF_3)_3BCAs]^-$: Thermally Stable Phosphaethynyl and Arsaethynyl Complexes**

Maik Finze, Eduard Bernhardt, Helge Willner, and Christian W. Lehmann*

Dedicated to Professor Gerd-Volker Röschenthaler on the occasion of his 60th birthday.

After discovery of the first phosphaalkyne, HC≡P,[1] in 1961, there was a gap of 20 more years until the synthesis of a room-temperature stable phosphaalkyne, *t*BuCP,[2] was successful. Since these pioneering studies, syntheses of other phosphaalkynes have been reviewed several times.[3–7] Stabilization of the phosphaalkyne group is achieved in most cases by steric shielding using large substituents, for example, the *tert*-butyl group,[2] otherwise the unstable C–P triple bond polymerizes.[6] By using transition-metal catalysts tetramerizations are possible, which yield cubane analogous compounds.[6,7] The anionic derivatives $[OCP]^-$,[8] $[SCP]^-$,[9] and $[i\text{PrNCP}]^-$[10] are resonance stabilized [Eq. (1)] and in addition the relatively high stability is due to the negative charge, which makes polymerization to highly charged anionic products more difficult. The interaction of the lone pair(s) at the heteroatom with the π system of the C–P triple bond is clearly shown by ab initio calculations,[11] NMR spectroscopy,[10] and structural studies.[9]

$$^-\text{X}-\text{C}\equiv\text{P} \leftrightarrow \text{X}=\text{C}=\text{P}^- \quad (\text{X} = i\text{PrN, O, S}) \tag{1}$$

Twenty-five years after the discovery of HCP, the first arsaalkyne, Mes*CAs (Mes* = 2,4,6-tri-*tert*-butylphenyl) was reported.[12] The thermal stability of Mes*CAs is mainly due to the bulky Mes* group. A further stabilizing effect may be the interaction of the aryl π systems with the C–As triple bond, as found in anionic phosphaalkynes. The only other known arsaalkyne, CH_3CAs,[13] is unstable at room temperature and the parent compound, HCAs, is still unknown. The much lower number of known arsaalkynes in comparison to phosphaalkynes is on account of their much lower stability and makes all the failed syntheses of *t*BuCAs understandable.[14]

[*] Dipl.-Chem. M. Finze, Dr. E. Bernhardt, Prof. Dr. H. Willner
Fachbereich C—Anorganische Chemie
Bergische Universität Wuppertal
Gaußstrasse 20, 47097 Wuppertal (Germany)
Fax: (+49) 202-439-3052
E-mail: willner@uni-wuppertal.de
Dr. C. W. Lehmann
Max-Planck-Institut für Kohlenforschung
Kaiser-Wilhelm-Platz 1, 45470 Mülheim an der Ruhr (Germany)

[**] Financial support by the Deutsche Forschungsgemeinschaft and the Merck KGaA Company, Darmstadt, is gratefully acknowledged.

Supporting information for this article is available on the WWW under http://www.angewandte.org or from the author.

The borates $[(CF_3)_3BCP]^-$ and $[(CF_3)_3BCAs]^-$ reported herein are the first complexes with the phosphaethynyl or arsaethynyl ligand. They are the higher homologues of the cyanoborate anion, $[(CF_3)_3BCN]^-$.[15] In contrast to the above mentioned anionic phosphaalkynes, there is no stabilization possible by π back-bonding in $[(CF_3)_3BCX]^-$ (X = N, P, As) as in the related boron carbonyl, $(CF_3)_3BCO$.[16,17] The stabilization of the CX^- ligand is due to the steric shielding of the $(CF_3)_3B$ group and the negative charge of the complex. $[(CF_3)_3BCAs]^-$ is the second example of a kinetic stable arsaalkyne and the first example of an anionic complex with the arsaalkynyl ligand.

The synthesis of the new borates is by treatment of the acyl halide complexes $[(CF_3)_3BC(O)Hal]^-$ Hal = Cl, Br[18] with a mixture of $K[X(SiMe_3)_2]$ and $X(SiMe_3)_3$ X = N, P, As in dry THF or dimethoxyethane [Eq. (2), 91% yield].

$$[(CF_3)_3BC(O)Hal]^- + K[X(SiMe_3)_2] \xrightarrow[-25\,^\circ C \rightarrow RT]{X(SiMe_3)_3} [(CF_3)_3BCX]^- + KHal + (Me_3Si)_2O \tag{2}$$

This synthetic method has been employed for the synthesis of Mes*CAs,[12] and is similar to methods used for the synthesis of kinetically stable phosphaalkynes.[2,7] The reagent $K[X(SiMe_3)_2]$ is formed in situ by treating $X(SiMe_3)_3$ (X = P, As) with KO*t*Bu. While the formation of the phosphide $K[P(SiMe_3)_2]$ by using KO*t*Bu has been reported,[19] to our knowledge the analogous reaction to the arsenide $K[As(SiMe_3)_2]$ is unknown. It is important to run the reaction with excess $X(SiMe_3)_3$ to scavenge the intermediate $[Me_3SiO]^-$ ion. Otherwise $[Me_3SiO]^-$ ions react with the acyl halide borate anions or the desired product.

Both CX^- complexes are stable for days in wet $[D_3]$acetonitrile solution. The attempted metathesis between $[PPh_4][(CF_3)_3BCP]$ with $K[BPh_4]$ in such solutions failed; the product of this reaction, $K[(CF_3)_3BCH_2P(O)(OH)H]$ has been detected by NMR spectroscopy (Table 1). The addition of two water molecules to the CP ligand [Eq. (3)] indicates a negative charge at the carbon atom and a positive charge at the phosphorus atom.

$$[(CF_3)_3BCP] + 2\,H_2O \rightarrow [(CF_3)_3BCH_2P(O)(OH)H]^- \tag{3}$$

This charge distribution is consistent with the results of calculations of other phosphaalkynes.[11] In the homologous cyanoborate ion, $[(CF_3)_3BCN]^-$, the charge distribution is inverted. Correspondingly, after activation of the cyano ligand by methylation, the anion hydrolyses to $[(CF_3)_3BC(O)NHMe]^-$ [Eq. (4)].[15]

$$[(CF_3)_3BCN] \xrightarrow[-CF_3SO_3^-]{+CF_3SO_3Me} [(CF_3)_3BCNMe] \xrightarrow{+H_2O} [(CF_3)_3BC(O)NHMe]^- \tag{4}$$

$[PPh_4][(CF_3)_3BCP]$ and $[PPh_4][(CF_3)_3BCAs]$ are colorless solids and both melt at 125 °C. According to differential scanning calorimetry (DSC) measurements $[PPh_4][(CF_3)_3BCP]$ decomposes at a surprisingly high temperature of 290 °C. As expected $[PPh_4][(CF_3)_3BCAs]$ is of lower stability and decomposes at 173 °C.

 © 2004 Wiley-VCH Verlag GmbH & Co. KGaA, Weinheim DOI: 10.1002/anie.200454034

Table 1: NMR spectroscopy data of $[(CF_3)_3BCX]^-$ (X = N, P, As) and related species.[a]

Parameter	$[(CF_3)_3BCN]^-$	$[(CF_3)_3BCP]^-$	$[(CF_3)_3BCAs]^-$	$(CF_3)_3BCO$	$[B(CF_3)_4]^-$	$[(CF_3)_3BCH_2P(O)(OH)H]^-$[b]
$\delta(^{11}B)$	−22.3	−19.8	−17.3	−17.9	−18.9	−18.8
$\delta(^{13}C)$ (CF_3)	132.4	133.4	133.1	130.1	132.9	n.o.[c]
$\delta(^{13}C)$ (BCX)	127.5	202.3	233.9	188.9	–	n.o.
$\delta(BC^nX)$ (^{15}N, ^{17}O, ^{31}P)	−103.3	39.6	n.o.	342	–	45.4
$\delta(^{19}F)$	−62.1	−61.9	−61.8	−58.7	−61.6	−62.3
$^1J(^{13}CX,C^nX)$	14.7	27.6	–	–	–	–
$^1J(^{11}B,^{13}CF_3)$	76.2	73.5	73.6	73.1	73.4	n.o.
$^1J(^{11}B,^{13}CX)$	64.0	59.5	57.7	66.6	–	–
$^1J(^{13}CF_3,C^{19}F_3)$	303.2	306.7	308.0	298.9	304.3	306.0
$^2J(^{11}B,C^{19}F_3)$	29.0	27.4	27.3	36 ± 2	25.9	26.0
$^2J(^{11}B,^{31}P)$	–	3.0	–	–	–	n.o.
$^3J(^{13}CF_3,C^{19}F_3)$	3.6	3.5	3.4	n.o.	3.9	n.o.
$^3J(^{13}CX,C^{19}F_3)$	3.5	2.9	2.9	–	–	–
$^3J(^{13}CF_3,^{31}P)$	–	8.4	–	–	–	n.o.
$^4J(^{12}C^{19}F_3,^{13}C^{19}F_3)$	6.3	6.3	6.3	6.1	5.8	
$^4J(C^{19}F_3,^{31}P)$	–	1.3	–	–	–	2.5
Ref.	[15]	[d]	[d]	[16]	[21]	[d]

[a] δ in ppm and ^nJ in Hz. [b] $\delta(^1H)$ (PH) = 7.1 ppm; $\delta(^1H)$ (CH_2) = 1.0 ppm; $^1J(^1H,^{31}P) = 552.0$ Hz; $^2J(C^1H_2,^{11}B) = 5.6$ Hz; $^2J(C^1H_2,^{31}P) = 23.2$ Hz; $^5J(C^{19}F_3,P^1H) = 1.1$ Hz. [c] n.o. = not observed. [d] This work.

$[(CF_3)_3BCP]^-$ and $[(CF_3)_3BCAs]^-$ have been characterized by ^{11}B, ^{19}F, and ^{13}C NMR spectroscopy, and $[(CF_3)_3BCP]^-$ in addition to ^{31}P NMR spectroscopy (Table 1). The ^{11}B and ^{19}F NMR chemical shifts and coupling constants of both anions are similar and comparable with those of other tris(trifluormethyl)boron derivatives (Table 1).[16,20,21] In addition the ^{11}B and ^{19}F NMR resonance signals of the phosphaethynyl borate anion are split into doublets by the ^{31}P nucleus.

The ^{13}C NMR spectra of the $[(CF_3)_3BCP]^-$ and $[(CF_3)_3BCAs]^-$ ions are depicted in Figure 1 and Figure 2. In both spectra there are two resonance signals in an intensity ratio of 1:3, assigned to the CX^- ligands and the CF_3 groups, respectively. The position and coupling pattern of the ^{13}C NMR signal of the CF_3 groups in $[(CF_3)_3BCP]^-$ (δ = 133.4 ppm) and in $[(CF_3)_3BCAs]^-$ (δ = 133.1 ppm) are comparable to those of similar compounds.[16,20,21] The ^{13}C NMR signal of the CP ligand (δ = 202.3 ppm) is shifted to lower frequency in comparison to that of the CAs ligand (δ = 233.9 ppm). This trend is in accordance with the data of CH_3CP[22] and CH_3CAs.[13] Both ^{13}C signals are split into quartets by coupling with ^{11}B and in decets by coupling with ^{19}F. In addition, both ^{13}C NMR signals of $[(CF_3)_3BCP]^-$ show the coupling with ^{31}P. To make this coupling clearer in Figure 1 the $^{13}C\{^{19}F\}$ NMR spectrum of $[(CF_3)_3BCP]^-$ is also depicted.

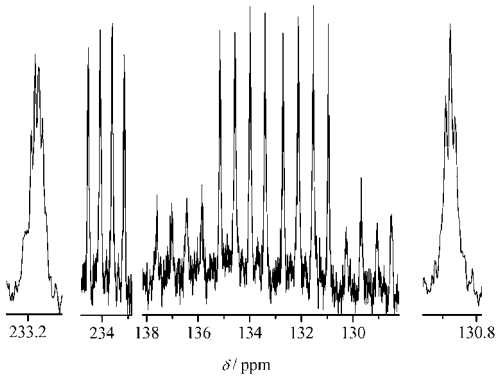


Figure 2. ^{13}C NMR spectrum of $[(CF_3)_3BCAs]^-$ in CD_3CN solution.

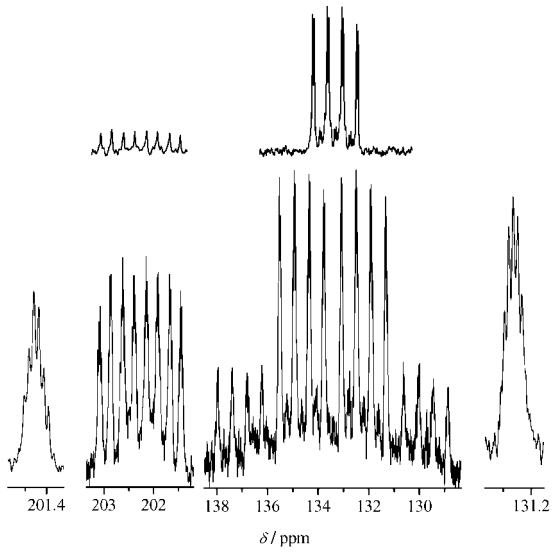


Figure 1. $^{13}C\{^{19}F\}$ NMR spectrum (top) and ^{13}C NMR spectrum (bottom) of $[(CF_3)_3BCP]^-$ in CD_3CN solution.

Figure 3 shows the ^{31}P and $^{31}P\{^{19}F\}$ NMR spectra of $[(CF_3)_3BCP]^-$. The position of the ^{31}P signal (δ = 39.6 ppm) is not characteristic because CP groups can have chemical shifts in the region $\delta = -384$ to 96 ppm.[3–7] However, an unambiguous assignment is made pos-

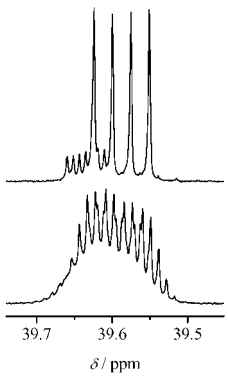


Figure 3. $^{31}P\{^{19}F\}$ NMR spectrum (top) and the ^{31}P NMR spectrum (bottom) of $[(CF_3)_3BCP]^-$ in CD_3CN solution.

 © 2004 Wiley-VCH Verlag GmbH & Co. KGaA, Weinheim

sible by the couplings. The signal is split into a quartet by interaction with the ^{11}B nucleus and in a decet by coupling with the nine equivalent F atoms. In the $^{31}P\{^{19}F\}$ NMR spectrum, the ^{10}B satellites are visible.

The Raman spectra of $[PPh_4][(CF_3)_3BCP]$ and $[PPh_4][(CF_3)_3BCAs]$ are dominated by the bands from the cations. However, it is possible to assign the strong bands of the stretching modes of the CP^- (1468 cm^{-1}) and CAs^- (1325 cm^{-1}) ligands. In comparison to the CP-stretching vibrations in phosphaalkynes ν(CP) is shifted by about 100 cm^{-1} to lower wavenumber in the (negatively charged) borate complex (Table 2).[4] There are no vibrational data available for arsaalkynes and hence ν(CAs) in $[(CF_3)_3BCAs]^-$ is the first example.

Table 2: Characteristic data of $[(CF_3)_3BCX]^-$ (X = P, As) and related species.

Compound	$\tilde{\nu}$(CX) [cm^{-1}]	$\delta(^{13}CX)$ [ppm]	$\delta(C^{31}P)$ [ppm]	$^1J(^{13}C,^{31}P)$ [Hz]	d(Y-C) [Å]	d(C-X) [Å]	Ref.
$[(CF_3)_3BCP]^-$	1468	202.3	39.6	27.6	[a]	1.563(10)	[b]
$[(CF_3)_3BCAs]^-$	1325	233.9			1.597(14)	1.675(12)	[b]
CH_3CP	1559	170.8	−61	49.0	1.465	1.5438(4)	[22–24]
*t*BuCP	1533	184.8	−69.2	38.5	1.473(1)	1.548(1)	[2, 27]
OCP^-[c]	1763	166.5	−382.8	41.4	1.198(4)	1.555(3)	[8, 11, 25]
CH_3CAs	n.o.[e]	196.4			1.463(1)	1.661(1)	[13]
Mes*CAs[d]	n.o.[e]	191.9			1.441(9)	1.657(7)	[12, 26]

[a] No exact value available. [b] This work. [c] Values for $Li^+OPC^-\cdot 2\,DME$. [d] Mes* = 2,4,6-tri-*tert*-butylphenyl. [e] n.o. = not observed.

Further proof of the existence of the new phospha- and arsaaethynyl borate anions comes from the crystal structures of the tetraphenyl phosphonium salts (Figure 4).[28] The salts $[PPh_4][(CF_3)_3BCP]$ and $[PPh_4][(CF_3)_3BCAs]$ crystallize in the

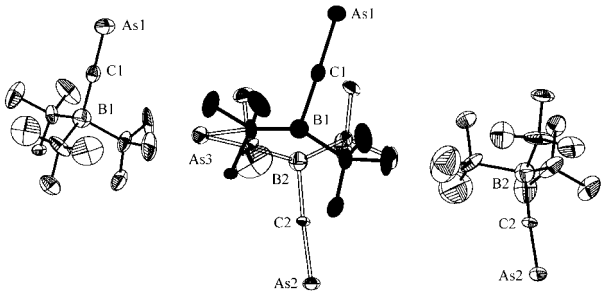


Figure 4. The $[(CF_3)_3BCAs]^-$ ions in $[PPh_4][(CF_3)_3BCAs]$ (thermal ellipsoids set at 25% probability). Selected bond lengths [Å] and angles [°]: C-As 1.675(12), B-C 1.597; B-C-As 177.5(9).

orthorhombic space group *Ama*2. The anions lie on crystallographic mirror planes and are disordered. The phosphorus atoms of the cations are located on the twofold axis and form stacks of cations in the crystal. The anions are placed between the stacks (see Supporting Information, Figures S1, S2). The disorder of the anions can be described by parallel *a*,*b* layers with all the BCAs groups pointing in the same direction; through the twofold symmetry axis antiparallel orientated layers are generated. This arrangement leads to overlapped $(CF_3)_3B$ groups, unrealistic As–As contacts, and uncertain B–C and C–As bond lengths (Table 2). The bonding parameters of the disordered anions are very similar. The C–As bond length of 1.675(12) Å is in agreement with that of Mes*CAs (1.657(7) Å)[26] and CH_3CAs (1.661(1) Å).[13]

The structure of $[PPh_4][(CF_3)_3BCP]$ was refined in a similar way to that of $[PPh_4][(CF_3)_3BCAs]$ but is of lower quality.[29] Because the BCP group is largely unaffected, an approximate value of 1.563(10) Å for the CP bond length can be given. Crystals of the potassium salts have also been investigated, however, it appears that they are X-ray amorphous.

In conclusion, through the synthesis, spectroscopic, and structural characterization of the new borate anions $[(CF_3)_3BCP]^-$ and $[(CF_3)_3BCAs]^-$ as their tetraphenyl phosphonium salts, unexpected, stable CP and CAs compounds have been discovered. In addition the results demonstrate the high synthetic potential of $(CF_3)_3BCO$[16] and its derivatives for example, $[(CF_3)_3BC(O)Hal]^-$ (Hal = Cl, Br).[18] A comprehensive discussion of the syntheses, spectroscopic properties and quantum chemical calculations of both anions $[(CF_3)_3BCP]^-$ and $[(CF_3)_3BCAs]^-$ as well as attempts to gain improved structural data from other salts will be presented in a forthcoming study.

Received: February 16, 2004 [Z54034]
Published Online: July 14, 2004

Keywords: NMR spectroscopy · arsenic · boron · multiple bonds · phosphorus · structure elucidation

[1] T. E. Gier, *J. Am. Chem. Soc.* **1961**, *83*, 1769.
[2] G. Becker, G. Gresser, W. Uhl, *Z. Naturforsch. B* **1981**, *36*, 16.
[3] M. Regitz, P. Binger, *Angew. Chem.* **1988**, *100*, 1541; *Angew. Chem. Int. Ed. Engl.* **1988**, *27*, 1484.
[4] A. C. Gaumont, J. M. Denis, *Chem. Rev.* **1994**, *94*, 1413.
[5] J. F. Nixon, *Coord. Chem. Rev.* **1995**, *145*.
[6] M. Regitz, *Chem. Rev.* **1990**, *90*, 191.
[7] F. Mathey, *Angew. Chem.* **2003**, *115*, 1616; *Angew. Chem. Int. Ed.* **2003**, *42*, 1578.
[8] G. Becker, W. Schwarz, N. Seidler, M. Westerhausen, *Z. Anorg. Allg. Chem.* **1992**, *612*, 72.
[9] G. Becker, K. Hübler, *Z. Anorg. Allg. Chem.* **1994**, *620*, 405.
[10] G. Heckmann, G. Becker, S. Horner, H. Richard, H. Kraft, P. Dvortsak, *Z. Naturforsch. B* **2001**, *56*, 146.
[11] K. Hübler, P. Schwerdtfeger, *Inorg. Chem.* **1999**, *38*, 157.
[12] G. Märkl, H. Sejpka, *Angew. Chem.* **1986**, *98*, 286; *Angew. Chem. Int. Ed. Engl.* **1986**, *25*, 264.
[13] J.-C. Guillemin, L. Lassalle, P. Dréan, G. Wlodarczak, J. Demaison, *J. Am. Chem. Soc.* **1994**, *116*, 8930.
[14] P. B. Hitchcock, J. A. Johnson, J. F. Nixon, *Angew. Chem.* **1993**, *105*, 86; *Angew. Chem. Int. Ed. Engl.* **1993**, *32*, 103.
[15] M. Finze, E. Bernhardt, C. W. Lehmann, H. Willner, unpublished results.
[16] M. Finze, E. Bernhardt, A. Terheiden, M. Berkei, H. Willner, D. Christen, H. Oberhammer, F. Aubke, *J. Am. Chem. Soc.* **2002**, *124*, 15385.
[17] A. Terheiden, E. Bernhardt, H. Willner, F. Aubke, *Angew. Chem.* **2002**, *114*, 823; *Angew. Chem. Int. Ed.* **2002**, *41*, 799.

 © 2004 Wiley-VCH Verlag GmbH & Co. KGaA, Weinheim

[18] M. Finze, E. Bernhardt, C. W. Lehmann, H. Willner, unpublished results.
[19] F. Uhlig, R. Hummeltenberg, *J. Organomet. Chem.* **1993**, *452*, C9.
[20] M. Finze, E. Bernhardt, H. Willner, C. W. Lehmann, *Angew. Chem.* **2003**, *115*, 1082; *Angew. Chem. Int. Ed.* **2003**, *42*, 1052.
[21] E. Bernhardt, G. Henkel, H. Willner, G. Pawelke, H. Bürger, *Chem. Eur. J.* **2001**, *7*, 4696.
[22] J.-C. Guillemin, T. Janati, T. Guenot, P. Savignac, J. M. Denis, *Angew. Chem.* **1991**, *103*, 191; *Angew. Chem. Int. Ed. Engl.* **1991**, *30*, 196.
[23] K. Ohno, H. Matsuura, D. McNaughton, H. W. Kroto, *J. Mol. Spectrosc.* **1985**, *111*, 415.
[24] H. W. Kroto, J. F. Nixon, N. P. C. Simmons, *J. Mol. Spectrosc.* **1979**, *77*, 270.
[25] G. Heckmann, G. Becker, H. Kraft, *Magn. Reson. Chem.* **1999**, *37*, 667.
[26] P. B. Hitchcock, C. Jones, J. F. Nixon, *J. Chem. Soc. Chem. Commun.* **1994**, 2061.
[27] M. Y. Antipin, A. N. Chernega, K. A. Lysenko, Y. T. Struchkov, J. F. Nixon, *J. Chem. Soc. Chem. Commun.* **1995**, 505.
[28] Crystal structure analysis of $[PPh_4][(CF_3)_3BCAs]$: $C_{28}H_{20}AsBF_9P$, KappaCCD-diffractometer (Bruker AXS); $Mo_{K\alpha}$ radiation ($\lambda = 0.71073$ Å, graphite monochromator); measurement temperature 100 K. Colorless crystals ($0.07 \times 0.06 \times 0.30$ mm^3), obtained from CH_2Cl_2/pentane, orthorhombic, space group *Ama*2 (no. 40), $a = 22.0967(5)$, $b = 16.7199(3)$, $c = 7.3510(1)$ Å, $V = 2715.86(9)$ Å^3, $Z = 4$, $\rho_{calcd} = 1.575$ Mg m^{-3}, $\mu(Mo_{K\alpha}) = 1.390$ mm^{-1}, $F(000) = 1288$, 16036 measured reflections ($3.03 < \Theta < 33.20°$) Integration and empirical absorption corrections (DENZO scalepack)[32] are applied to obtain a structure solution by direct methods and crystal structure refinement against F^2 with 5022 independent reflections (4075 independent reflections with $I > 2\sigma(I)$), 261 variables and 201 restraints (SHELXS-97).[30,31] All atoms are refined anisotropically. $R_1 = 0.0970$ ($I > 2\sigma(I)$). CCDC-230926 ($[PPh_4][(CF_3)_3BCAs]$) contains the supplementary crystallographic data for this paper. These data can be obtained free of charge via www.ccdc.cam.ac.uk/conts/retrieving.html (or from the Cambridge Crystallographic Data Centre, 12 Union Road, Cambridge CB2 1EZ, UK; fax: (+44) 1223-336-033; or deposit@ccdc.cam.ac.uk).
[29] Crystal structure analysis of $[PPh_4][(CF_3)_3BCP]$: $C_{28}H_{20}BF_9P_2$, KappaCCD-diffractometer (Bruker AXS); $Mo_{K\alpha}$ radiation ($\lambda = 0.71073$ Å, graphite monochromator); measurement temperature 100 K. Colorless crystals ($0.08 \times 0.03 \times 0.02$ mm^3) obtained from CH_2Cl_2/pentane, orthorhombic, space group *Ama*2 (no. 40), $a = 22.1201(5)$, $b = 16.7427(3)$, $c = 7.3933(2)$ Å, $V = 2738.12(11)$ Å^3, $Z = 4$, $\rho_{calcd} = 1.495$ Mg m^{-3}, $\mu(Mo_{K\alpha}) = 0.242$ mm^{-1}, $F(000) = 1248$, 14814 measured reflections ($10.29 < \Theta < 27.72°$). Structure solution by direct methods and crystal structure refinement against F^2 with 3076 independent reflections (2679 independent reflections with $I > 2\sigma(I)$), 199 variables and 109 restraints (SHELXS-97).[30,31] Only phosphorus and carbon atoms of the cations are refined anisotropically. $R_1 = 0.114$ $I > 2\sigma(I)$.
[30] G. M. Sheldrick, SHELXS-97, Program for Crystal Structure Solution, University of Göttingen, Germany, **1997**.
[31] G. M. Sheldrick, SHELXL-97, Program for Crystal Structure Refinement, University of Göttingen, Germany, **1997**.
[32] Z. Otwinowski, W. Minor, *Methods Enzymol.* **1997**, *276*, 307.

 © 2004 Wiley-VCH Verlag GmbH & Co. KGaA, Weinheim

Biosynthesis

Unusual Biosynthesis of Leupyrrins in the Myxobacterium *Sorangium cellulosum***

*Helge Björn Bode, Silke C. Wenzel, Herbert Irschik, Gerhard Höfle, and Rolf Müller**

Dedicated to Professor A. Zeeck on the occasion of his 65th birthday

The Gram-negative myxobacteria are a rich source of structurally novel secondary metabolites with remarkable biological activities.[1] These natural products often reveal unusual biosyntheses producing rare structural elements, for example, cinnamate and methoxymalonate moieties.[2,3] Myxobacterial secondary metabolites are frequently hybrid structures derived from carboxylic acids and amino acids, which corresponds well with the high number of hybrid polyketide synthase (PKS)/nonribosomal peptide synthetase (NRPS) biosynthetic gene clusters in the genomes of the producing strains.[4] Another typical feature of myxobacterial secondary metabolism is the low frequency of post-PKS or post-NRPS modifications (e.g. methylations, oxidations/reductions, glycosylations), which are usually found in other secondary metabolites, for example, from actinomycetes. In myxobacteria most of these modifications are catalyzed by domains located within the PKS or PKS/NRPS proteins.[5–7] Therefore, genes from the myxobacterial secondary metabolism can be used in combinatorial biochemistry[8] to produce specific

[*] Dr. H. B. Bode,[+] Dipl.-Chem. S. C. Wenzel, Prof. Dr. R. Müller[+]
Abteilung Molekularbiologie der Myxobakterien
Gesellschaft für Biotechnologische Forschung
Mascheroder Weg 1, 38124 Braunschweig (Germany)
Fax: (+49) 681-302-5473
E-mail: rom@mx.uni-saarland.de

Dr. H. Irschik
Abteilung Naturstoffbiologie
Gesellschaft für Biotechnologische Forschung
Braunschweig (Germany)

Prof. Dr. G. Höfle
Abteilung Naturstoffchemie
Gesellschaft für Biotechnologische Forschung
Braunschweig (Germany)

[+] Present address:
Pharmazeutische Biotechnologie
Universität des Saarlandes
Gebäude 8.1, Postfach 151150, 66123 Saarbrücken (Germany)

[**] The authors would like to thank Dr. V. Wray and co-workers from the Department of Structural Research at the GBF for recording NMR spectra and Prof. H. G. Floss (University of Washington), Prof. T. Mahmud (Oregon State University), and Priv.-Doz. Dr. M. Müller (Forschungszentrum Jülich) for critically reading the manuscript. Financial support for H.B.B. (DFG, Forschungsstipendium Bo 1834/1-1), S.C.W. and R.M. (Fonds der Chemischen Industrie (FCI), Kekulé fellowship) and G.H. (FCI) is acknowledged.

Supporting information for this article is available on the WWW under http://www.angewandte.org or from the author.

 DOI: 10.1002/anie.200454240 © 2004 Wiley-VCH Verlag GmbH & Co. KGaA, Weinheim

structural elements not accessible through genes from other sources.

We became interested in the biosynthesis of the recently described leupyrrin family of secondary metabolites (see Figure 1) since these compounds show an unusually substituted γ-butyrolactone fragment as well as pyrrole and dehydrofuran ring structures that cannot be explained by typical PKS and NRPS biosynthesis mechanisms.[9] These findings encouraged us to perform feeding studies with putative precursors of the leupyrrins (in singly and multiply ^{13}C-labeled form) and to determine their incorporation into leupyrrin A_1 (**1**), the main component of the leupyrrin family from the myxobacterium *Sorangium cellulosum* So ce690. Because of the complexity of the observed labeling pattern in almost all experiments, we will discuss our findings and the implications for the biosynthesis of **1** according to defined structural elements, which turn out to be distinct biosynthetic units.

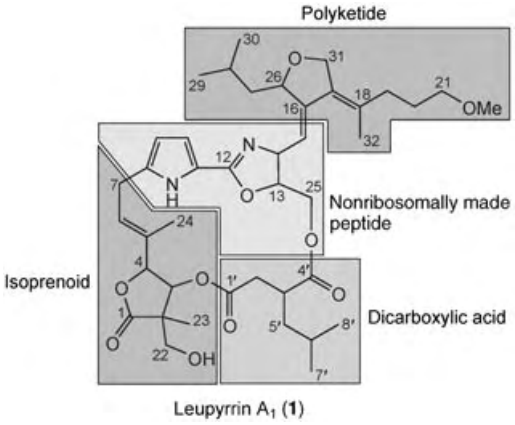


Figure 1. Structure and biosynthetic origin of leupyrrin A_1 (**1**).

Nonribosomal peptide biosynthesis: The biosynthesis of **1** most likely starts with the formation of the pyrrole carboxylic acid (fragment C8–C12), which in turn is presumably derived from proline.[10] Incorporation of two intact acetate units (C8/C9 and C11/C12, Figure 2a[11]) and an additional intact C_5 fragment from a feeding experiment with a uniformly ^{13}C-labeled protein mixture confirm this hypothesis (Figure 2b). The observed incorporation matches the expected labeling pattern of proline derived from α-ketoglutarate and glutamate.[12] The unexpected incorporation of label from [2-^{13}C]acetate at C8 and C12 (Table 1) is the result of a very active intermediary metabolism.[13]

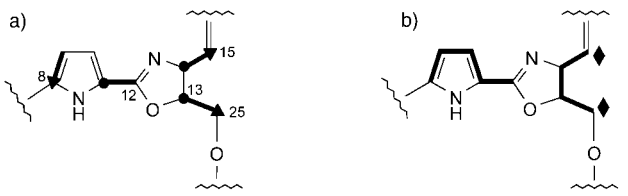


Figure 2. Labeling pattern of the peptide part of leupyrrin A_1 (**1**). a) Labeling from [1-^{13}C]acetate (▲), [2-^{13}C]acetate (●), and [1,2-$^{13}C_2$]acetate (bold lines). b) Labeling from [1-+^{13}C]propionate (◆) and from a [U-^{13}C]protein extract (bold lines). For additional isotopomers see the Supporting Information.

Table 1: ^{13}C abundance and coupling constants in leupyrrin A_1 (**1**) after feeding of [1-^{13}C]acetate (A), [2-^{13}C]acetate (B), [2-^{13}C]malonate (C), [1,2-$^{13}C_2$]acetate (D), and a [U-^{13}C]protein extract (E).

Atom	δ [ppm]	A	B	C	D	E[a]
		^{13}C Enrichment [b]			$J_{C,C}$ [Hz]	
C1	179.3	–[c]	6.3	8.7	6	6; 6/50
C2	51.1	1.7	1.8	5.5	33	33; 33/39/50; 33/39/40/50
C3	75.4	2.4	1.7	1.6	6	6; 6/39
C4	85.5	1.2	2.6	1.8	–	50
C5	135.1	2.3	1.9	4.1	43	43; 43/75; 43/50/75
C6	128.4	1.2	2.4	1.7	43	43; 43/75
C7	26.9	1.6	1.0	1.0	43	43
C8	136.5	3.1	2.5	4.9	65	65
C9	109.6	1.2	2.0	1.3	65	65; 50/65
C10	115.2	1.2	1.7	1.0	50	50/69
C11	119.3	–	7.5	7.4	88	88; 69/88
C12	160.6	–	4.2	–	88	88
C13	84.5	1.2	1.8	1.0	42	42; 33/42
C14	68.8	1.2	1.9	1.0	47	47; 33/47
C15	123.0	2.0	1.4	1.2	47	47; 33/47
C16	144.9	1.4	7.0	12.5	56	56
C17	131.2	2.8	2.5	5.3	56	56
C18	134.0	2.7	5.7	11.1	42	42
C19	34.9	3.4	1.0	1.4	42	42
C20	28.3	1.2	3.1	4.0	39	39
C21	72.8	3.1	1.3	1.9	39	39
C22	65.7	1.5	2.8	1.6	–	40
C23	14.6	1.1	2.9	1.8	33	33
C24	11.4	1.1	5.0	3.4	43	43
C25	65.9	2.3	1.6	1.5	42	42
C26	80.5	1.3	2.4	1.5	–	36
C27	44.3	1.3	1.2	1.6	–	34; 36/34
C28	26.1	1.3	1.2	1.7	–	34/34/34
C29	24.1	1.0	1.3	2.0	–	34
C30	22.0	1.1	1.7	2.4	–	34
C31	70.1	1.1	1.0	1.5	–	–
C32	20.2	1.1	1.7	3.2	–	–
C1′	172.1	3.4	2.4	5.3	58	58
C2′	36.4	1.3	3.1	3.8	58	58
C3′	39.8	1.2	2.3	1.5	58	58
C4′	175.4	3.1	3.2	7.4	58	58
C5′	40.1	1.3	1.4	1.7	–	35; 35/35
C6′	26.9[d]	–	–	–	–	35/35/35
C7′	22.9	1.1	1.3	2.0	–	35
C8′	22.7	1.0	1.3	2.1	–	35
OCH_3	58.8	1.2	1.7	5.2	–	–

[a] Coupling constants for the different isotopomers are separated by semicolons. [b] In comparison to natural abundance: 1.0 = no enrichment. [c] – = not detected. [d] ^{13}C enrichments could not be observed due to overlap of the signals for C7 and C6′, but it should be similar to C28.

The next step in the biosynthesis is an NRPS-like condensation (for a recent review on NRPSs see ref. [14]) of a presumed acyl-carrier-protein-bound pyrrole carboxylic acid with either hydroxythreonine or threonine that is later on oxidized to hydroxythreonine (C13–C15, C25). This can be concluded from the bidirectional incorporation of two acetate units (Figure 2a), the incorporation of one C_4 and two C_2

 © 2004 Wiley-VCH Verlag GmbH & Co. KGaA, Weinheim

fragments in the feeding experiment with the labeled protein mixture (Figure 2b), and the incorporation of [1,4-$^{13}C_2$]succinate into C15 and C25 (see the Supporting Information). This is exactly what one would expect to find assuming classic threonine biosynthesis to take place in *S. cellulosum* with oxaloacetate and aspartate as central intermediates.[12] An NRPS-encoded cyclization domain is supposed to finally form the oxazoline ring.[15] The threefold enrichment of label from [1-^{13}C]propionate into C15 and C25 (Figure 2b) additionally indicates the presence of a methylmalonyl-CoA/succinyl-CoA mutase activity as was described previously for several streptomycetes.[16]

Polyketide biosynthesis: The biosynthesis of **1** proceeds with the condensation of the threonine carboxylate carbon

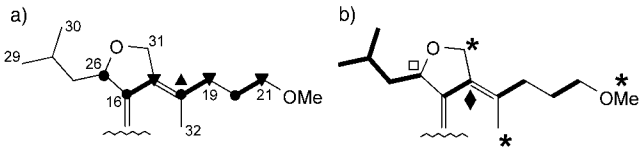


Figure 3. Labeling pattern of the polyketide part of leupyrrin A_1 (**1**). For explanations of symbols see Figure 2. Additional labeling from [*methyl*-^{13}C]methionine (*) and [2-^{13}C]leucine (□). For additional isotopomers see the Supporting Information.

(C15) with an unusual extender unit (C16, C17, C26–C30; Figures 3 and 4), which is labeled by [2-^{13}C]leucine and the protein mixture at C26 and C26–C30, respectively (Figure 3).[17] This indicates the biosynthesis of the extender unit to result from elongation of isovaleryl-CoA (**6**) with a C_2 extender unit (see Figure 4). Isovaleryl-CoA is derived from leucine degradation by the branched-chain keto acid dehydrogenase (BKD) complex, a multienzyme system essential for the degradation of valine, leucine, and isoleucine, as previously shown in myxobacteria and other organisms.[12,18,19] The acetate labeling pattern of C16 and C17 indicates a condensation of isovaleryl-CoA (**6**) with malonyl-CoA (**10**) (or acetyl-CoA (**9**) followed by carboxylation to activate the whole extender unit for further extension) to yield intermediate **7**. This is further modified to give extender unit **8**, whose biosynthesis is discussed in more detail below. In contrast to other malonyl-CoA/acetyl-CoA extender units in **1**, C17 was labeled weakly by [1-^{13}C]propionate, indicating a more complex biosynthesis of the overall extender unit **7**. Consecutive elongation of C17 with two malonyl-CoA extender units, C-methylation with *S*-adenosyl methionine (SAM), a reductive chain termination as described in the myxochelin and myxalamid biosyntheses,[6,20] and O-methylation of the resulting hydroxy group would result in the final PKS/NRPS part of **1** (Figure 3). The isolation of leupyrrins with a C19/C20 double bond indicates an additional enoyl reductase that reduces the unsaturated compounds[19] or a separate oxidase that acts vice versa. In both cases the enzyme might be unspecific or not very efficient, thus generating mixtures of reduced and nonreduced leupyrrins.[9] However, the incorporation of [1-^{13}C]acetate into C18 cannot be explained by standard biochemical transformations and thus indicates a so-far unknown difference in the nature of the C_2 extender units C18/C19 and C20/C21.

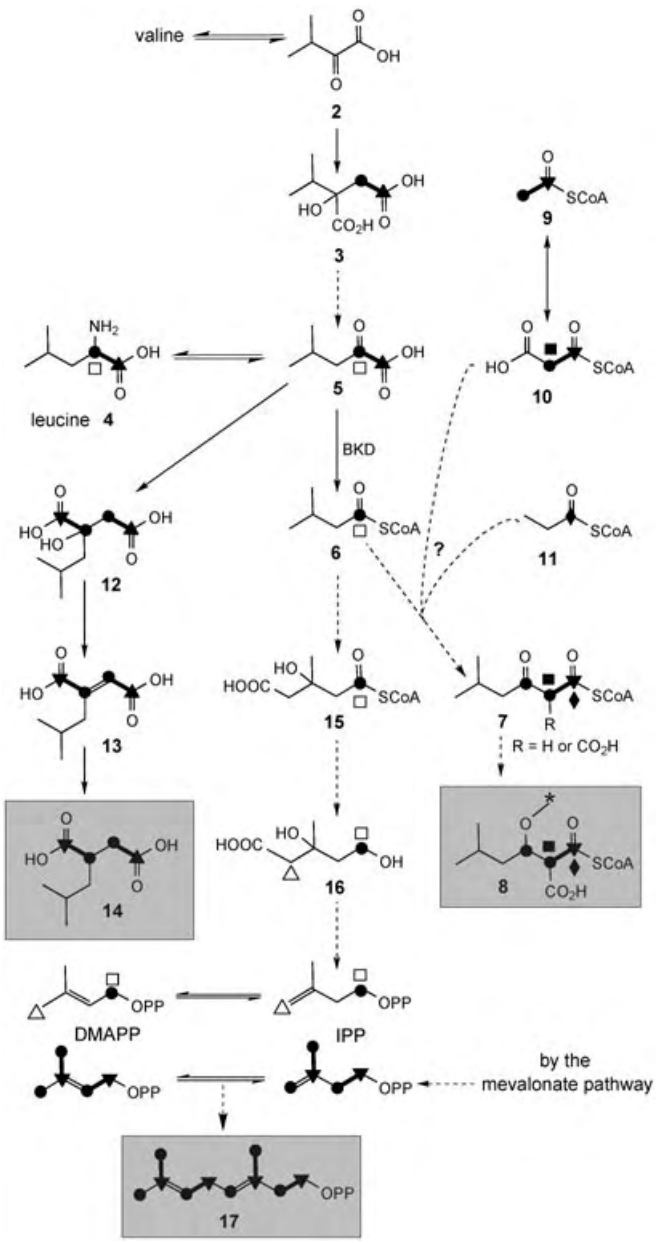


Figure 4. Postulated biosynthesis of the unusual extender unit **8** and the dicarboxylic acid moiety **14**. Isopentenyl pyrophosphate (IPP) and dimethylallyl pyrophosphate (DMAPP) are shown as observed in leupyrrin A_1 (**1**) from *S. cellulosum* So ce690. For simplicity, not all observed isotopomers are shown. For symbol assignment see Figures 2 and 3; labeling from [2-^{13}C]malonate (■) and [2-^{13}C]mevalonolactone (△). Compounds in gray boxes are putative direct precursors of **1**. Broken arrows indicate multistep reactions.

Methylation and formation of the furan ring: C-methylations are usually observed at the α-position of the newly elongated carboxyl ester (e.g. C18), whereas methylations of β-positions (e.g. C17) are presumed to result from a condensation with acetyl-CoA similar to the biosynthesis of hydroxymethylglutaryl-CoA (HMG-CoA) in mevalonate biosynthesis.[12] Consequently, HMG-CoA synthase type proteins are encoded within the biosynthetic gene clusters of some secondary metabolites (e.g. mupirocin from *Pseudo-*

 © 2004 Wiley-VCH Verlag GmbH & Co. KGaA, Weinheim

monas fluorescens).[21] However, the presence of two SAM-derived methyl groups at adjacent carbon atoms indicates a novel biosynthetic mechanism. This is corroborated by the 88-, 55-, and 36-fold enrichments found in the methoxy group, C32, and C31, respectively, in a [*methyl*-^{13}C]methionine feeding experiment. Our current hypothesis to explain both the unusual methylation pattern and the biosynthesis of the furan ring is the extension of the C15 carboxylate with the extender unit **8** derived from reduction and O-methylation of **7** (Figure 4). After or during biosynthesis of the final PKS/NRPS product (see above) the furan ring is formed most likely in analogy to the methylene bridge in the berberine biosynthesis in plants (Figure 5).[22,23] The lesser enrichment

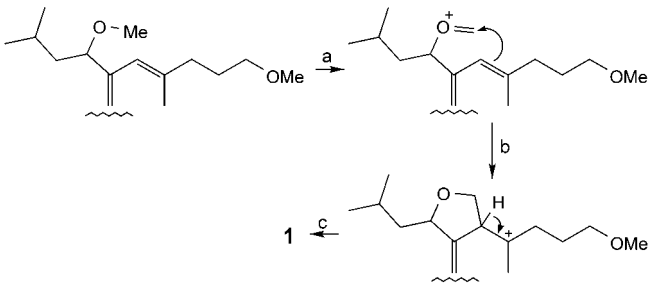


Figure 5. Postulated furan ring biosynthesis in leupyrrin A_1 (**1**). a) Oxidation of the methyl group; b) cyclization; c) deprotonation. The first two steps might be catalyzed by a single enzyme similar to the berberine bridge enzyme in the biosynthesis of berberine.[22,23]

of C-31 compared to C-32 and the methoxy group in the [*methyl*-^{13}C-]methionine feeding experiment might result from a dilution of label due to biosynthesis of **8** prior to the addition of labeled methionine. Feeding experiments with ^{13}C- and ^{18}O-labeled putative extender units are in progress to shed some light on this part of the biosynthesis.

Isoprenoid and dicarboxylic acid linker biosynthesis: The C1–C7/C22–C24 structural element was labeled completely by acetate (Figure 6a). Due to the acetate-derived methyl branches, mevalonate-dependent isoprenoid biosynthesis was thought to be involved in its biosynthesis which was confirmed by the tenfold enrichment of label at C4 and C22 after feeding [2-^{13}C]mevalonolactone (Figure 6b). Unexpectedly, feeding of [2-^{13}C]leucine resulted in the incorporation of label at C3 (18-fold) and C7 (6-fold), which was supported by the presence of two leucine-derived C_5 isotopomers after feeding

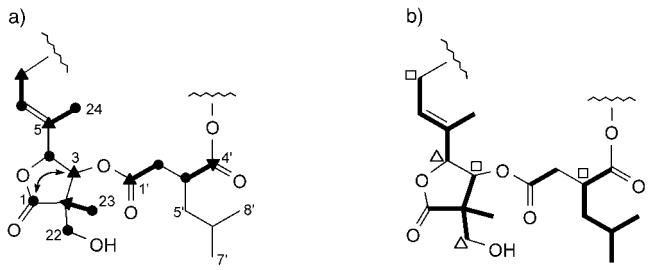


Figure 6. Labeling pattern of the dicarboxylic acid moiety and the isoprenoid part of leupyrrin A_1 (**1**). For explanations see Figures 2, 3, and 4. The observed ^2J coupling between C1 and C3 is indicated by a double-headed arrow.

the [U-^{13}C]protein mixture (Figure 6b). This unexpected observation might be explained by leucine degradation to isovaleryl-CoA (**6**) and subsequent formation of HMG-CoA (**15**), the central intermediate in mevalonate-dependent isoprenoid biosynthesis, which is normally generated from acetyl-CoA (Figure 4).[12,24] Similar results were obtained previously for the biosynthesis of the steroid cycloartenol in the myxobacterium *Stigmatella aurantiaca*.[25] Furthermore, the saprophytic lifestyle of most myxobacteria could argue for employing an effective mevalonate biosynthesis predominantly from leucine, which was also found in the parasite *Leishmania mexicana*.[26]

Feeding of [2-^{13}C]leucine also results in enrichment of C3′ (Figure 6b). Together with results from further feeding experiments, this indicates the biosynthesis of the dicarboxylic acid (C1′–C8′) **14** to take place by means of condensation of leucine-derived 2-ketoisocaproate (**5**) and acetyl-CoA (**9**) (Figure 4), thus giving rise to a similar isotopic pattern as described for the extender unit **8**.

The data suggest the prenylation of the pyrrole moiety with a geranylpyrophosphate (**17**) (Figure 4), which is desaturated in analogy to carotenoid biosynthesis and hydroxylated in a cytochrome P-450 dependent manner (Figure 7). A

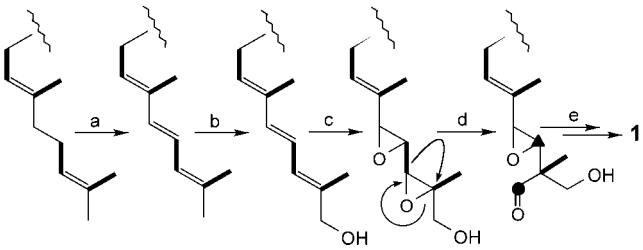


Figure 7. Postulated biosynthesis of the isoprenoid moiety (C1–C7/C-22–C24) of leupyrrin A_1 (**1**). Intact acetyl units from the mevalonate-dependent isoprenoid biosynthesis are shown in bold. The cleaved acetyl-CoA unit is indicated (● and ▲). a) Desaturation, b) hydroxylation, c) epoxidation, d) semipinacol-like rearrangement, e) oxidation of the resulting aldehyde and opening of the remaining epoxide by the C1 carboxylate.[29]

similar hydroxylation is described for geraniol itself in the biosynthesis of loganin and secologanin from various plants.[27] Epoxidation of the double bonds and a semipinacol-like rearrangement[28] indicated by a small coupling constant of $^2J = 6.0$ Hz between C1 and C3 in the feeding experiment with doubly labeled acetate (Figure 6a) would generate the carbon skeleton of the γ-butyrolactone ring as it is found in **1**. Opening of the remaining epoxide by the carboxylate groups of C1 (after oxidation of the aldehyde) might result in the direct formation of the butyrolactone ring.[29]

Our studies on the structure and biosynthesis of leupyrrin A_1 (**1**) show it to be a most exiting secondary metabolite. The biosynthesis involves the condensation of amino acids, carboxylic acids, and an isoprenoid moiety, all of which are further modified to form the unique macrodiolide structure. Furthermore, the labeling studies have revealed unusual biosyntheses of some of the underlying precursors (e.g. isoprenoid biosynthesis from leucine degradation and by the

 © 2004 Wiley-VCH Verlag GmbH & Co. KGaA, Weinheim

mevalonate pathway). Understanding the mechanisms involved is the prerequisite for optimizing production and yield of these and other secondary metabolites biosynthesized from similar precursors. Identification and analysis of the gene cluster for leupyrrin biosynthesis and a more detailed analysis of the metabolic network present in myxobacteria are currently in progress in our group.

Experimental Section

Labeled precursors (160 mg [1-^{13}C]acetate, 160 mg [2-^{13}C]acetate, 200 mg [1,2-$^{13}C_2$]acetate, 120 mg [*methyl*-^{13}C]methionine, 185 mg [1-^{13}C]propionate (all dissolved in 5 mL H_2O and 99% ^{13}C at the indicated positions; 600 mg [2-^{13}C]malonic acid, 200 mg [2-^{13}C]leucine, 100 mg D,L-[2-^{13}C]mevalonolactone, 500 mg [1,4-$^{13}C_2$]succinic acid, 500 mg [U-^{13}C]algal crude protein extract (all dissolved in 10 mL H_2O and 99% ^{13}C at the indicated positions) were obtained from Campro Scientific or Cambridge Isotopes. *Sorangium cellulosum* So ce690 and its cultivation were described previously.[9] All feeding experiments were conducted in 2-L Erlenmeyer flasks containing 800 mL of production medium with 1% of XAD-16, and labeled precursors were added in four to seven portions between the 103rd and 168th hour after inoculation. The cultures were harvested after 192 or 240 h, dependent on the glucose and starch consumption.

Isolation and purification of **1** followed the previously published procedure.[9] Briefly, wet cells and XAD-16 were extracted with MeOH (4 × 200 mL). After removal of the MeOH by evaporation, the resulting aqueous layer was adjusted to pH 10 with aqueous NH_3. Extraction with diethyl ether (4 × 100 mL) and evaporation of the solvent yielded an oily residue, which was dissolved in 3 mL MeOH and extracted with *n*-heptane (4 × 4 mL). Evaporation of the remaining MeOH solution resulted in an orange solid, which was subjected to sequential preparative RP-HPLC as described previously (yielding 6–10 mg L^{-1} of pure **1**).

NMR spectra were recorded at 300 K on a Bruker AMX400 or ADVANCE DMX 600 NMR spectrometer with CD_3OD as solvent and internal standard. For determinations of relative ^{13}C enrichments, either the peak integral or the peak height of the signal from the enriched sample was compared with that of a control sample of natural abundance.

Received: March 11, 2004 [Z54240]

Keywords: antibiotics · biosynthesis · labeling studies · leupyrrins · myxobacteria

[1] K. Gerth, S. Pradella, O. Perlova, S. Beyer, R. Müller, *J. Biotechnol.* **2003**, *106*, 233.
[2] H. B. Bode, R. Müller, *Plant Physiol.* **2003**, *132*, 1153.
[3] J. Ligon, S. Hill, J. Beck, R. Zirkle, I. Molnar, J. Zawodny, S. Money, T. Schupp, *Gene* **2002**, *285*, 257.
[4] B. Silakowski, B. Kunze, R. Müller, *Gene* **2001**, *275*, 233.
[5] N. Gaitatzis, B. Silakowski, B. Kunze, G. Nordsiek, H. Blöcker, G. Höfle, R. Müller, *J. Biol. Chem.* **2002**, *277*, 13082.
[6] N. Gaitatzis, B. Kunze, R. Müller, *Proc. Natl. Acad. Sci. USA* **2001**, *98*, 11136.
[7] S. Weinig, H. J. Hecht, T. Mahmud, R. Müller, *Chem. Biol.* **2003**, *10*, 939.
[8] C. R. Hutchinson, R. McDaniel, *Curr. Opin. Investig. Drugs* **2001**, *2*, 1681.
[9] H. B. Bode, H. Irschik, S. C. Wenzel, H. Reichenbach, R. Müller, G. Höfle, *J. Nat. Prod.* **2003**, *66*, 1203.
[10] M. G. Thomas, M. D. Burkart, C. T. Walsh, *Chem. Biol.* **2002**, *9*, 171.
[11] Due to the broad and small ^{13}C signal of C12, no enrichment can be observed after feeding [1-^{13}C]acetate (see also Table 1 and Figure 2).
[12] G. Michal, *Biochemical Pathways*, Spektrum, Heidelberg, **1999**.
[13] The incorporation of [2-^{13}C]acetate into carbon atoms expected to be labeled by [1-^{13}C]acetate can be observed throughout the molecule (C8, C12, C17, C1′, C4′). Due to a highly active tricarboxylic acid cycle in the producing organism, [2-^{13}C]acetate is converted efficiently into [2-^{13}C]oxaloacetate, which itself can be decarboxylated to yield [2-^{13}C]pyruvate.[12] Pyruvate is one of the major sources of acetyl-CoA and one of the best carbon sources known for the model myxobacterium *Myxococcus xanthus*. Thus, [1-^{13}C]acetate could be generated in a few steps from [2-^{13}C]acetate or [2-^{13}C]malonate. After feeding of [1,2-$^{13}C_2$]succinate, almost all carbon atoms were labeled (see the Supporting Information), also indicating a highly active intermediary metabolism whose complex network cannot be resolved at this point. In additional feeding experiments with unlabeled glyoxylate and labeled acetate, the incorporation of labeled acetate into **1** was very low compared to a control (data not shown), which shows the presence of a very active glyoxylate shunt as well.
[14] D. Schwarzer, R. Finking, M. A. Marahiel, *Nat. Prod. Rep.* **2003**, *20*, 275.
[15] T. A. Keating, C. G. Marshall, C. T. Walsh, *Biochemistry* **2000**, *39*, 15522.
[16] W. Zhang, K. A. Reynolds, *J. Bacteriol.* **2001**, *183*, 2071.
[17] A second isotopomer resulting from the incorporation of [U-^{13}C]valine-derived 2-ketoisovalerate (**2**) (the biosynthetic precursor of leucine) can be detected in C27 as an additional doublet (Table 1 and the Supporting Information).
[18] T. Mahmud, H. B. Bode, B. Silakowski, R. M. Kroppenstedt, M. Xu, S. Nordhoff, G. Höfle, R. Müller, *J. Biol. Chem.* **2002**, *277*, 32768.
[19] The de novo biosynthesis of leucine is confirmed by the incorporation of [2-^{13}C]acetate in C26 (Figure 3a), as one would expect for the formation of 3-carboxy-3-hydroxy-isocaproate (**3**) and 2-ketoisocaproate (**5**) from **2** and acetyl-CoA (Figure 4).[12]
[20] B. Silakowski, G. Nordsiek, B. Kunze, H. Blöcker, R. Müller, *Chem. Biol.* **2001**, *8*, 59.
[21] A. K. El-Sayed, J. Hothersall, S. M. Cooper, E. Stephens, T. J. Simpson, C. M. Thomas, *Chem. Biol.* **2003**, *10*, 419.
[22] T. M. Kutchan, H. Dittrich, *J. Biol. Chem.* **1995**, *270*, 24475.
[23] J. A. Bjorklund, T. Frenzel, M. Rueffer, M. Kobayashi, U. Mocek, C. Fox, J. M. Beale, S. Groger, M. H. Zenk, H. G. Floss, *J. Am. Chem. Soc.* **1995**, *117*, 1533.
[24] The four- to sixfold enrichment of C2, C5, C1′, and C4′ after feeding [2-^{13}C]leucine shows leucine degradation due to the formation of [1-^{13}C]acetate, which would result from the cleavage of acetoacetate, the final HMG-CoA degradation product. In the biosynthesis of mevalonate **16** and isoprenoids derived thereof, acetoacetate serves as direct precursor for HMG-CoA (**15**).[12] As a result of this degradation–biosynthesis network, three isotopomers (from acetyl-CoA, acetoacetyl-CoA, and leucine-derived HMG-CoA) can be observed for C2 and C5 after feeding of the ^{13}C-labeled protein mixture (Table 1 and the Supporting Information).
[25] H. B. Bode, B. Zeggel, B. Silakowski, S. C. Wenzel, H. Reichenbach, R. Müller, *Mol. Microbiol.* **2003**, *47*, 471.
[26] M. L. Ginger, M. L. Chance, I. H. Sadler, L. J. Goad, *J. Biol. Chem.* **2001**, *276*, 11674.
[27] G. Collu, N. Unver, A. M. Peltenburg-Looman, R. van der Heijden, R. Verpoorte, J. Memelink, *FEBS Lett.* **2001**, *508*, 215.
[28] M. B. Smith, J. March, *Advanced Organic Chemistry: Reactions, Mechanisms, and Structure*, 5th ed., Wiley-Interscience, New York, **2001**.
[29] Alternatively, the epoxide might be opened by the C1′ carboxylate.

 © 2004 Wiley-VCH Verlag GmbH & Co. KGaA, Weinheim

Cluster Compounds

The Cluster Ion $[Pt_{12}O_8(SO_4)_{12}]^{4-}$**

*Martin Pley and Mathias S. Wickleder**

The connection of two Pt^{3+} ions to dinuclear $[Pt_2]^{6+}$ dumbbells was observed for the first time in the sulfate $K_2[Pt_2(SO_4)_4(H_2O)_2]$.[1] Within the ion $[Pt_2(SO_4)_4(H_2O)_2]^{2-}$ the four sulfate groups act as chelating ligands, and the H_2O molecules occupy the terminal positions of the $[Pt_2]^{6+}$ dumbbell. Subsequently, this motive, occasionally called the "lantern type structure", has been extensively varied, for example, by the replacement of the $[SO_4]^{2-}$ ions by phosphate ligands, or by substitution of the terminal H_2O molecules for other donors.[2] The investigation of these compounds was motivated by both theoretical aspects of the chemical bonding,[3] and the luminescence properties of the $[Pt_2]^{6+}$ ion.[4] To date, extended structures with the linkage of several metal dumbbells to larger building units have not been reported. On the other hand, there is a report on the potential structure of a building unit constructed by the connection of six dumbbells by eight oxide ions. According to topological considerations by Bucknum[5] and theoretical calculations by Hoffmann et al.,[6] which have been carried out on a hypothetical tungsten compound with W–W quadruple bonds, the twelve metal atoms should be arranged in the form of a distorted icosahedron. In course of our investigations of precious metals with complex anions[7] and their potential as precursors for the synthesis of metal nanoparticles we started to prepare thermally labile platinum compounds. These efforts led now to the first oxide–sulfate of platinum, $(NH_4)Pt_3O_2(SO_4)_3$. Of note is that in the crystal structure of this compound the predicted building unit is observed for the first time, although the metal atoms are connected only by single bonds in the present case.

The oxide–sulfate $(NH_4)Pt_3O_2(SO_4)_3$ was obtained as dark red single crystals in the reaction of $Pt(NO_3)_2$ with concentrated sulfuric acid at 350 °C in sealed glass ampoules.[8] As a side product yellow single crystals of $(NH_4)_2[Pt_2(SO_4)_4(H_2O)_2]$, which is isotypic with the corresponding potassium compound,[1] could be isolated. It is noteworthy that the $[NH_4]^+$ ions originate from the reduction of the platinum nitrate. The presence of the ammonium ion is demonstrated by IR spectroscopy (ν(N-H) = 3221 cm^{-1}, $\delta(NH_4)$ = 1402 cm^{-1}) and is further supported by the fact that the isotypic potassium compound can be prepared.[9] However, details of this complicated redox reaction are not known. $(NH_4)Pt_3O_2(SO_4)_3$ crystallizes in the trigonal–rhombohedral system (space group $R\bar{3}$) and contains as a characteristic structural feature the unprecedented cluster ion $[Pt_{12}O_8(SO_4)_{12}]^{4-}$. To emphasize this building unit of the oxide–sulfate we rewrite its formula as $(NH_4)_4[Pt_{12}O_8(SO_4)_{12}]$. Within the anion the twelve platinum(III) ions are arranged in form of an icosahedron which is remarkably distorted owing to the formation of six Pt_2 dumbbells (Figure 1). The distance

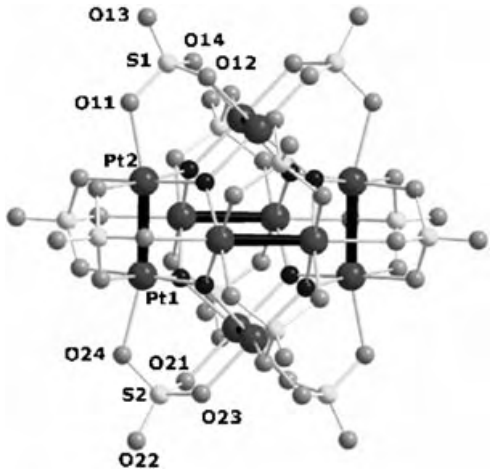


Figure 1. Perspective view of the cluster ion $[Pt_{12}O_8(SO_4)_{12}]^{4-}$. The anion contains two crystallographically different platinum atoms and two crystallographically different sulfate groups. The oxide ions are situated on the Wyckoff sites 6*c* (O1) and 18*f* (O2), and occur in a ratio of 1:3 in the anion. Selected bond lengths [pm] and angles [°]: Pt1-Pt2 253.18(9), S1-O11 148(1), S1-O12 152(1), S1-O14 153(1), S1-O13 142(1), S2-O21 153(1), S2-O23 152(1), S2-O24 146(1), S2-O22 144(1), Pt1-O24 216(1), Pt2-O11 214(1); O11-Pt2-Pt1 167.9(3), O24-Pt1-Pt2 169.2(3).

between the platinum centers in the dumbbells is 253.18(9) pm and thus significantly longer than in $K_2[Pt_2(SO_4)_4(H_2O)_2]$[1] (246.6 pm) and $(NH_4)_2[Pt_2(SO_4)_4(H_2O)_2]$ (247.1 pm). Accordingly, the distances to the other neighboring platinum atoms are enlarged and range from 344 to 346 pm. The six Pt_2 dumbbells of the icosahedron are linked by eight O^{2-} ions so that an almost perfect trigonal-planar coordination of the oxide ions by three platinum atoms results. Within the standard deviations the Pt–O separations are found to be 200 pm, and the angles are 120°. This arrangement results in eight of the twenty triangular faces of the icosahedron being centered by oxide ions. Above the remaining twelve triangular faces tridentate coordinating $[SO_4]^{2-}$ groups are situated. Each sulfate ion acts as a bidentate chelating ligand to one Pt_2 dumbbell and as monodentate ligand to the next. Thus, one oxygen atom of the sulfate tetrahedron is not attached to a platinum atom. The different environments of the oxygen atoms is reflected by the S–O separations: They are found to be around 152 pm for the "chelating" oxygen atoms, 142 and 144 pm for the noncoordinating oxygen atoms, and the "monodentate" oxygen atoms which occupy the terminal positions of the dumbbell have S–O bonds of 146 and 148 pm. In this way each platinum atom is in a distorted octahedral coordination

[*] Dipl.-Chem. M. Pley, Priv.-Doz. Dr. M. S. Wickleder
Universität zu Köln
Institut für Anorganische Chemie
Greinstrasse 6, 50939 Köln (Germany)
Fax: (+49) 221-470-5083
E-mail: mathias.wickleder@uni-koeln.de

[**] This work was financially supported by the Deutsche Forschungsgemeinschaft as part of the Graduiertenkolleg 549. We thank Prof. G. Meyer for his valuable support.

 © 2004 Wiley-VCH Verlag GmbH & Co. KGaA, Weinheim DOI: 10.1002/anie.200454257

environment of five oxygen atoms and one further platinum atom. The Pt–O separations are 214 and 216 pm for the oxygen atoms which are in *trans* orientation with respect to the Pt–Pt axis (O11 and O24), while for the remaining four oxygen atoms the Pt–O separations are about 200 pm. The angles O11-Pt2-Pt1 and O24-Pt1-Pt2 are 167.9(3) and 169.2(3)°, respectively, and demonstrate severe deviation from the linearity observed for $K_2[Pt_2(SO_4)_4(H_2O)_2]$.[1]

The $[Pt_{12}O_8(SO_4)_{12}]^{4-}$ clusters are arranged in the trigonal body-centered unit cell in a way that their centers are situated in the origin of the cell (Wyckoff site 3*a*) leading to S_6 symmetry for the anions. Charge balance is achieved by two crystallographically different $[NH_4]^+$ ions both located on the Wyckoff sites 6*c*. One of the ammonium ions is coordinated by nine oxygen atoms with separations between 292 and 334 pm, and the coordination number increases to 15 if separations up to 401 pm are taken into account. The second $[NH_4]^+$ ion is coordinated by thirteen oxygen atoms at distances between 281 and 331 pm (Figure 2).

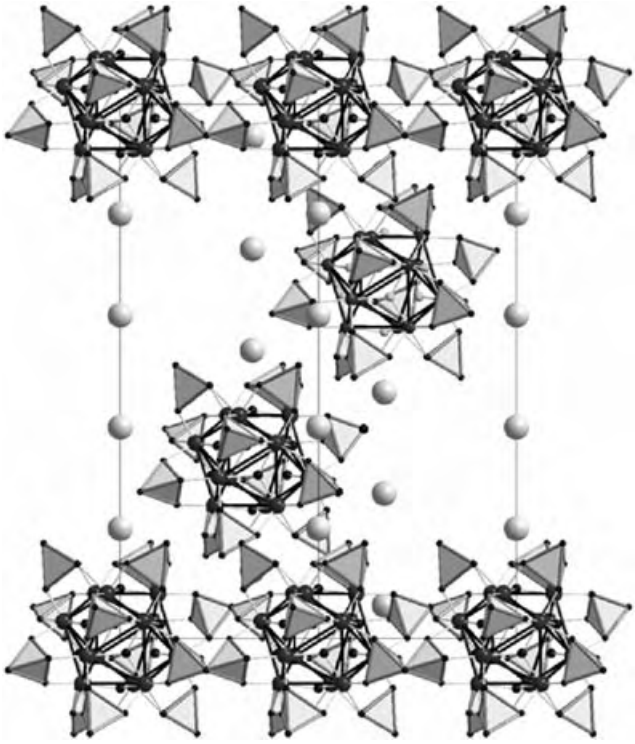


Figure 2. Perspective presentation of the crystal structure of $(NH_4)_4[Pt_{12}O_8(SO_4)_{12}]$. For clarity only the N atoms of the ammonium ions are shown, the positions of the H atoms have not been determined.

In conclusion we have described, for the first time, an oxide–sulfate of platinum, $(NH_4)_4[Pt_{12}O_8(SO_4)_{12}]$. It contains the unprecedented cluster anion $[Pt_{12}O_8(SO_4)_{12}]^{4-}$, which is formed by the linking of six dumbbell shaped $[Pt_2]^{6+}$ ions. The motive of this connection has been predicted theoretically for a hypothetical tungsten compound. Thus, this cluster anion is the first experimental example for such a building unit. Further investigation must show if the observed stability is due to electronic reasons, analogous to the findings for the hypothetical compound. Moreover, we hope that it is possible to find a solvent in which $(NH_4)_4[Pt_{12}O_8(SO_4)_{12}]$ can be dissolved without destruction of the cluster, this would allow the structure of this complex cluster anion to be studied in solution by means of NMR spectroscopic methods.

Experimental Section

$(NH_4)_4[Pt_{12}O_8(SO_4)_{12}]$: $Pt(NO_3)_2$ (0.7 g, 2.19 mmol) and concentrated sulfuric acid (2 mL, 37.31 mmol) were placed in a glass ampoule ($\varnothing$ = 10 mm, l = 100 mm, thickness of the wall = 2 mm). The sealed ampoule was placed in a resistance furnace and kept at 350 °C for three days followed by slow cooling. The product contained deep red and remarkably hygroscopic single crystals of the title compound as well as yellow plate-like single crystals of $(NH_4)_2[Pt_2(SO_4)_4(H_2O)_2]$. $(NH_4)_4[Pt_{12}O_8(SO_4)_{12}]$ is the main product of the reaction (approximately 70% with respect to the initial nitrate). Several of the red crystals were selected for the X-ray investigations and mounted in glass capillaries. For the best specimen intensity data were collected.[8] IR (KBr): 3221 (s), 1402 (m), 1285 (w), 1242 (m), 1172 (s), 1070 (s), 1010 (m), 696 (w), 657 (vw), 614 (w), 576 (m), 504 cm^{-1} (s). Reliable Raman spectra could not be obtained owing to the decomposition of $(NH_4)_4[Pt_{12}O_8(SO_4)_{12}]$ in the laser beam (Nd:YAG, 1064 nm).

Received: March 13, 2004 [Z54257]

Keywords: metal–metal bonds · cluster compounds · crystal structures · platinum · sulfates

[1] G. S. Muraveiskaya, V. S. Orlova, O. N. Evstaf'eva, *Russ. J. Inorg. Chem.* **1974**, *19*, 1030; G. S. Muraveiskaya, G. A. Kukina, V. S. Orlova, O. N. Evstaf'eva, M. A. Porai-Koshits, *Dokl. Akad. Nauk SSSR* **1976**, *226*, 596.

[2] D. P. Bancroft, F. A. Cotton, L. R. Falvello, S. Han, W. Schwotzer, *Inorg. Chim. Acta* **1984**, *87*, 147; F. A. Cotton, L. R. Falvello, S. Han, *Inorg. Chem.* **1982**, *21*, 2889; H. L. Conder, F. A. Cotton, L. R. Falvello, S. Han, R. A. Walton, *Inorg. Chem.* **1983**, *22*, 1887; A. Zipp, *Coord. Chem. Rev.* **1988**, *84*, 47; J. D. Woollins, P. F. Kelly, *Coord. Chem. Rev.* **1985**, *65*, 115; D. M. Roundhill, H. B. Gray, C.-M. Che, *Acc. Chem. Res.* **1989**, *22*, 55; R. El-Mehdawi, F. R. Fronczek, D. M. Roundhill, *Inorg. Chem.* **1986**, *25*, 1155; R. J. H. Clark, *Chem. Soc. Rev.* **1990**, *19*, 107.

[3] F. A. Cotton, R. A. Walton, *Multiple Bonds Between Metal Atoms*, Wiley, New York, **1982**.

[4] D. M. Roundhill, *Photochemistry and Photophysics of Metal Complexes*, Plenum, New York, **1994**.

[5] M. J. Bucknum, *Chemistry Preprint Server (CPS)*, **2002**, Physchem/0204007.

[6] M. M. Balakrishnarajan, P. Kroll, M. J. Bucknum, R. Hoffmann, *New J. Chem.* **2004**, *28*, 185.

[7] M. S. Wickleder, *Z. Anorg. Allg. Chem.* **2001**, *627*, 2112; M. S. Wickleder, O. Büchner, *Z. Naturforsch. B* **2001**, *56*, 1340; M. S. Wickleder, K. Esser, *Z. Anorg. Allg. Chem.* **2002**, *628*, 911; M. S. Wickleder, *Z. Anorg. Allg. Chem.* **2002**, *628*, 2151.

[8] Crystallographic data for $(NH_4)_4[Pt_{12}O_8(SO_4)_{12}]$: Prismatic (0.1 × 0.1 × 0.06 mm), trigonal–rhombohedral, $R\bar{3}$, $Z = 3$, $a = 1189.7(1)$, $c = 2796.5(5)$ pm, $V_{UC} = 3428(1)$ Å^3, $\rho_{calcd} = 5.345$ g cm^{-3}, $2\theta_{max} = 56°$, $\lambda(Mo_{K\alpha}) = 0.71073$ Å, ω-scan (2°/image) at $\varphi = 0°$ and 90° (STOE IPDS II), 170 K, 16198 measured and 1845 unique reflections ($R_{int} = 0.1848$, $R_\sigma = 0.0667$), numerical absorption correction ($\mu = 37.270$ mm^{-1}, min/max transmission factors = 0.0138/0.0643, programs X-Red and X-Shape: STOE, Darmstadt 1998), structure solution by direct methods, full-matrix-least-square refinement (128 parameters) on $|F^2|$, no treatment of H

 © 2004 Wiley-VCH Verlag GmbH & Co. KGaA, Weinheim

atoms (programs SHELXS-86 and SHELXL-97: G. M. Sheldrick, programs for the solution and refinement of crystal structures, Göttingen 1986 and 1997), $R1 = 0.0451$, $wR2 = 0.1006$ for 1494 reflections with $I > 2\sigma(I)$ and $R1 = 0.0587$, $wR2 = 0.1081$ for all data, max/min residual electron density = 2.512/−2.844. Further details on the crystal structure investigation may be obtained from the Fachinformationszentrum Karlsruhe, 76344 Eggenstein-Leopoldshafen, Germany (fax: (+49) 7247-808-666; e-mail: crysdata@fiz-karlsruhe.de), on quoting the depository number CSD-413807.

[9] Lattice parameters for $K_4[Pt_{12}O_8(SO_4)_{12}]$: Trigonal-rhombohedral, $R\bar{3}$, $Z = 3$, $a = 1192.5(1)$, $c = 2789.3(5)$ pm, $V_{UC} = 3435.1(1)$ Å^3 (M. Pley, M. S. Wickleder, unpublished results).

 © 2004 Wiley-VCH Verlag GmbH & Co. KGaA, Weinheim

Scanning Electrochemical Microscopy

An SECM Detection Scheme with Improved Sensitivity and Lateral Resolution: Detection of Galactosidase Activity with Signal Amplification by Glucose Dehydrogenase**

*Chuan Zhao and Gunther Wittstock**

Scanning electrochemical microscopy (SECM) has grown to be a powerful technique for the study of heterogeneous electron-transfer reactions, charge-transfer at liquid–liquid interfaces, and molecular transport across membranes.[1] Since the inception of SECM, a major application has been the study of biological systems, for example, the metabolic activity of cells, whole organisms, subcellular particles, and enzymes.[2] In particular, much attention has been devoted to imaging the activity of immobilized enzymes on patterned interfaces because of the practical significance of these structures for the prototyping of integrated and miniaturized biosensors and chip-based assays.[3] SECM can be used in the feedback (FB) and generation collection (GC) modes, and both modes have been applied successfully for imaging enzyme activity at interfaces.

In the FB mode, an ultramicroelectrode (UME) probe is used to oxidize or reduce a reversible electron mediator. The feedback process occurs when the mediator diffuses to the sample and is restored to its original oxidation state through an electrochemical, chemical, or enzymatic reaction. The FB mode provides better lateral resolution than GC imaging because the regeneration of the mediator only occurs in close proximity to the UME. The sensitivity of the feedback mode is, however, very limited because the flux generated by the enzymatic reaction at the interface must be detected against the strong background signal resulting from the hindered diffusion of the mediator from the bulk phase to the UME. When imaging enzymatic activity the FB mode can only be applied to oxidoreductases, as the immobilized enzyme requires the mediator as a redox-active cofactor.

In the GC mode, the UME detects the concentration of a species generated at the surface of the sample. Ideally, the UME acts only as a passive sensor to produce concentration maps of a particular chemical species near the sample surface. The GC mode is more sensitive because the background signal is very weak. However, lateral resolution in the GC mode is rather limited as a result of the diffusion of detected species from their source at the sample surface. GC imaging can also be used for enzymes other than oxidoreductases if the enzyme converts a substrate into a redox-active product that is detected at the UME.[4]

Herein we introduce a new detection scheme which combines the advantages of the FB and GC modes and allows high sensitivity and lateral resolution in SECM imaging. The method is demonstrated with a multienzyme system composed of immobilized galactosidase (Gal) and PQQ-dependent glucose dehydrogenase (GDH) (PQQ = pyrroloquinoline quinone). Gal, one of most commonly used labeling enzymes,[5] is not an oxidoreductase and can not be imaged in the conventional FB mode. GDH is an extremely useful quinoprotein for biosensor applications owing to its insensitivity to dissolved oxygen and its very high activity.[6] Both enzymes have been studied individually by SECM in the GC mode and GDH has also been studied in the FB mode.[7] In conventional GC imaging of Gal, *p*-aminophenyl-β-D-galactopyranoside (PAPG) is added to the solution; *p*-aminophenol (PAP) is then generated from PAPG (Figure 1a). The potential of the UME is set to $E_T = 400$ mV (Ag | AgCl), so that PAP, but not PAPG, can be oxidized under diffusion-controlled conditions at the UME to *p*-quinoneimine (PQI).[7a]

In the new detection mode, the electrochemically produced PQI, which is an efficient cofactor of GDH,[8] diffuses to the microspot, where it is reconverted into PAP by immobilized GDH in the presence of D-glucose (Figure 1b). PAP then diffuses back to the UME and thus closes the SECM feedback loop. The UME current, i_T, therefore arises from the oxidation of PAP formed at Gal-modified surfaces from PAPG (GC mode) and at GDH-modified surfaces from PQI (FB mode). Unlike in the conventional GC mode, the signal amplification by the FB contribution only occurs in a small region defined by the location of the GDH coupled to the sample.

Gal and GDH were immobilized on separate batches of paramagnetic microbeads. A mound of a 1:1 mixture of Gal- and GDH-modified beads was deposited on a hydrophobic surface by a procedure developed in our laboratory.[4] The optical microphotograph in Figure 2a shows the bead spot with a diameter of 100 μm. In the corresponding SECM image from the combined detection scheme a well-defined, sharp peak is observed above the microspot with the immobilized

[*] Dr. C. Zhao, Prof. Dr. G. Wittstock
Carl von Ossietzky Universität Oldenburg
Faculty of Mathematics and Natural Sciences
26111 Oldenburg (Germany)
Fax: (+49) 441-798-3684
E-mail: gunther.wittstock@uni-oldenburg.de

[**] This work was supported by the Deutsche Forschungsgemeinschaft (DFG, grant Wi1617/1-4). SECM = scanning electrochemical microscopy.

 © 2004 Wiley-VCH Verlag GmbH & Co. KGaA, Weinheim DOI: 10.1002/anie.200454261

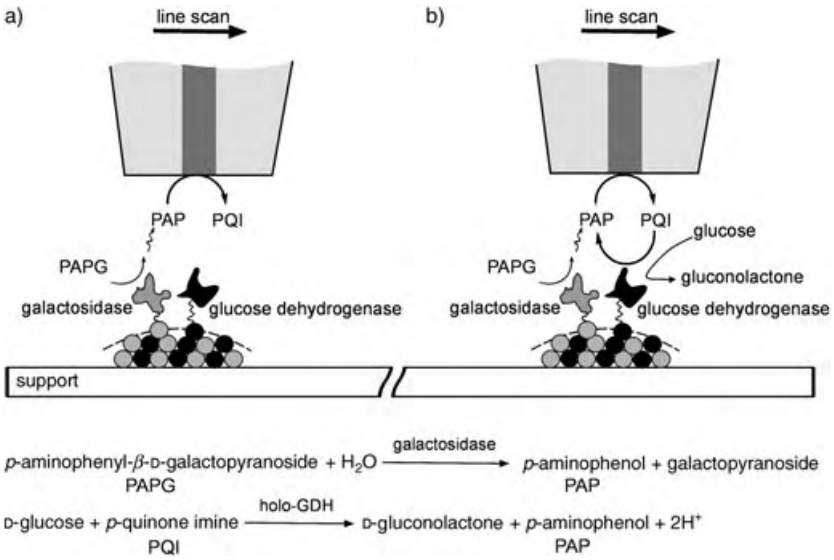


Figure 1. Schematic representation of the combined detection principle for SECM in the immobilized Gal–GDH multienzyme system: a) conventional GC mode for Gal in the absence of glucose; b) signal amplification in the presence of glucose. PAPG = *p*-aminophenyl-β-D-galactopyranoside, PAP = *p*-aminophenol, PQI = *p*-quinoneimine. The diagram is not drawn to scale.

Gal–GDH system (Figure 2b). The peak is characterized by an extremely small background current and a very steep increase in the signal above the spot as a result of the enzymatic feedback amplification. Such sharply defined signals are not observed in conventional GC experiments.

To differentiate between the contributions of Gal and GDH to the observed electrode current, separate line scans were performed across the center of the spot with activated and deactivated GDH. GDH catalysis was switched off by using a D-glucose-free assay solution (peak a in Figure 3). The peak corresponds to the detection of PAP released through the Gal-catalyzed reaction in the conventional GC mode (Figure 1a). After the addition of glucose to the assay solution, a clear increase in the current strength was observed above the spot (peak b in Figure 3) as a result of the additional GDH-mediated feedback loop. Thus, in the combined mode i_T is caused by the GC contribution from Gal and the feedback amplification by GDH. The peak current observed in the combined mode is about 1.8 times stronger than that observed in the conventional GC mode. The enhancement factor is distance-dependent and increases with decreasing operating distance. A further decrease in the operating distance was not attempted because of the risk of displacing the bead agglomerate mechanically with the UME.

The full width at half maximum (FWHM) of the signal is about 140 μm for peak a (Figure 3) but only about 100 μm for peak b. Evidently, the lateral resolution is also superior in the combined detection scheme. The FWHM of peak b in Figure 3 is in perfect agreement with the diameter of the agglomerate in the optical microphotograph in Figure 2a. The combined mode enables the detection of Gal with a resolution

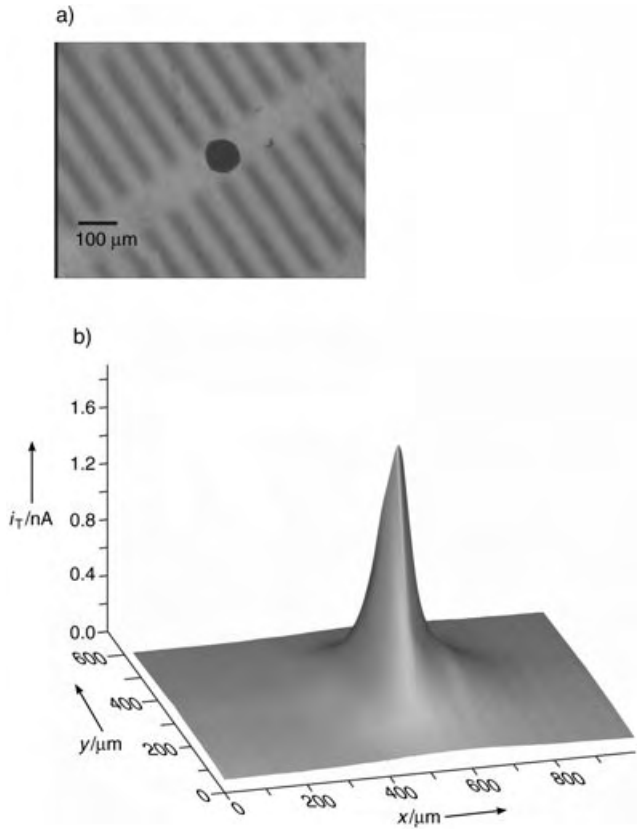


Figure 2. a) Optical microscopic and b) SECM images of the bead microspot. The unsharp lines in (a) are from a microscopic rule and have a periodicity of 100 μm. SECM conditions: HEPES buffer (20 mM) containing KCl (30 mM), $CaCl_2$ (1.0 mM), $MgCl_2$ (1.0 mM), PAPG (2.0 mM), and glucose (50 mM); $r_{UME} = 25$ μm, $r_{spot} = 50$ μm, $E_T = 400$ mV, $d = 40$ μm, translation speed = 10 μm s^{-1}.

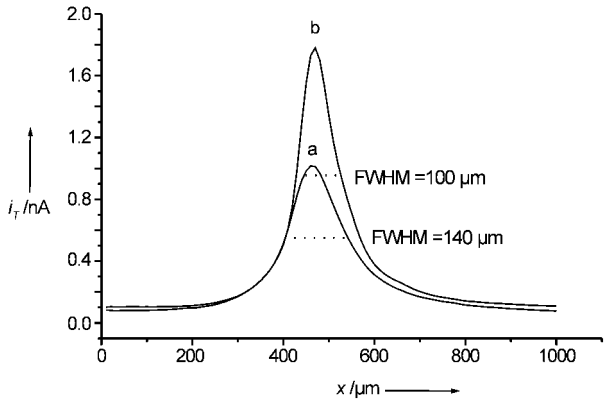


Figure 3. SECM line scans across the center of the microspot: a) conventional GC mode; b) combined mode. Curve (a) was obtained for the assay solution without glucose, and curve (b) was obtained after adding glucose (50 mM) to the solution. The conditions were otherwise the same as those described for Figure 2.

 © 2004 Wiley-VCH Verlag GmbH & Co. KGaA, Weinheim

usually possible only in FB experiments, which can not be used for Gal. This high resolution is a major advantage of the new method. The principle can be applied directly to all enzymes that produce PAP. The activity of alkaline phosphatase, which is another widely used labeling enzyme, has already been imaged in the conventional GC mode through the detection of PAP.[9] In this case the sensitivity was also improved and a very low background current maintained by using the new detection scheme.

In conclusion, a new combined detection scheme for SECM was proposed and tested in the multienzyme system Gal–GDH. The approach is a new SECM method for the investigation and control of interactions between microstructured enzyme layers. The new detection scheme can be used for the design and characterization of enzyme-based biochips and biosensors and of immunoassays, for the detection of enzyme labels, and for other SECM imaging experiments. Further work is in progress towards the quantitative description of the detection scheme by digital simulations and its development into a general detection principle for SECM.

Experimental Section

Biotinylated Gal was bound to streptavidin-coated microbeads as described previously.[7] Apo-GDH (PQQ-dependent, from *Escherichia coli*, EC 1.1.99.17) was biotinylated, and then a Lowry protein assay was performed to determine the concentration of the enzyme.[10] Biotinylated GDH was treated similarly.[7] To reconstitute the holo-GDH from apo-GDH, PQQ (0.5 mg mL^{-1}, 50 μL) and $CaCl_2$ (0.1 M, 10 μL) were added to a suspension of the beads (40 μL), and the mixture was incubated at room temperature for 30 min. The Gal-coated microbeads were then mixed with the GDH-coated microbeads in a 1:1 ratio, and the mixture was resuspended in HEPES buffer (20 mM, 100 μL, pH 7.5; HEPES = (*N*-(2-hydroxylethyl)piperazine-*N*′-(2-ethanesulfonic acid)). A microspot of Gal–GDH-coated beads was deposited on parafilm-coated glass slides (Figure 2a) according to a procedure described previously,[4] and then bathed in a buffered assay solution of HEPES (20 mM) with KCl (30 mM), $CaCl_2$ (1.0 mM), $MgCl_2$ (1.0 mM), D-glucose (50 mM), and PAPG (2.0 mM).

The SECM measurements were performed with a self-built instrument described previously.[3] An UME with a diameter of 50 μm (RG ≈ 5) was made according to the method developed by Kranz et al.[11] and was used throughout the SECM measurements at an operating distance $d = 40$ μm.

Received: March 14, 2004 [Z54261]

Keywords: electrochemistry · enzyme catalysis · interfaces · scanning probe microscopy · SECM

[1] a) *Scanning Electrochemical Microscopy* (Eds.: A. J. Bard, M. V. Mirkin), Marcel Dekker, New York, **2001**; b) A. J. Bard, F.-R. F. Fan, D. T. Pierce, P. R. Unwin, D. O. Wipf, F. Zhou, *Science* **1991**, *254*, 68–74; c) A. L. Barker, M. Gonsalves, J. V. Macpherson, C. J. Slevin, P. R. Unwin, *Anal. Chim. Acta* **1999**, *385*, 223–240.

[2] a) B. R. Horrocks, G. Wittstock in reference [1a], pp. 445–519; b) D. T. Pierce, P. R. Unwin, A. J. Bard, *Anal. Chem.* **1992**, *64*, 1795–1804; c) G. Wittstock, W. Schuhmann, *Anal. Chem.* **1997**, *69*, 5059–5066; d) S. Gaspar, M. Mosbach, L. Wallman, T. Laurell, E. Csöregi, W. Schuhmann, *Anal. Chem.* **2001**, *73*, 4254–4255.

[3] a) T. Wilhelm, G. Wittstock, *Langmuir* **2002**, *18*, 9485–9493; b) T. Wilhelm, G. Wittstock, *Angew. Chem.* **2003**, *115*, 2350–2353; *Angew. Chem. Int. Ed. Engl.* **2003**, *42*, 2247–2250.

[4] C. A. Wijayawardhana, G. Wittstock, H. B. Halsall, W. R. Heineman, *Anal. Chem.* **2000**, *72*, 333–338.

[5] E. Burestedt, C. Nistor, U. Schagerlöf, J. Emneus, *Anal. Chem.* **2000**, *72*, 4171–4177.

[6] a) J. A. Duine, *J. Biosci. Bioeng.* **1999**, *88*, 231–236; b) C. Anthony, *Biochem. J.* **1996**, *320*, 697–711; c) A. Oubrie, H. J. Rozeboom, K. H. Kalk, A. J. J. Olsthoorn, J. A. Duine, B. W. Dijkstra, *EMBO J.* **1999**, *18*, 5187–5194; d) L. Ye, M. Hämmerle, A. J. J. Olsthoorn, W. Schuhmann, H. L. Schmidt, J. A. Duine, A. Heller, *Anal. Chem.* **1993**, *65*, 238–241.

[7] a) C. Zhao, J. K. Sinha, C. A. Wijayawardhana, G. Wittstock, *J. Electroanal. Chem.* **2004**, *561*, 83–91; b) C. Zhao, G. Wittstock, *Anal. Chem.* **2004**, *76*, 3145–3154.

[8] A. Rose, F. W. Scheller, U. Wollenberger, D. Pfeiffer, *Fresenius J. Anal. Chem.* **2001**, *369*, 145–152.

[9] G. Wittstock, K. Yu, H. B. Halsall, T. H. Ridgway, W. R. Heineman, *Anal. Chem.* **1995**, *67*, 3578–3582.

[10] a) D. J. Hnatowich, F. Virzi, *J. Nucl. Med.* **1987**, *28*, 1294–1302; b) O. H. Lowry, N. J. Rosebrough, A. L. Farr, R. J. Randall, *J. Biol. Chem.* **1951**, *193*, 265–275.

[11] C. Kranz, M. Ludwig, H. E. Gaub, W. Schuhmann, *Adv. Mater.* **1995**, *7*, 38–40.

 © 2004 Wiley-VCH Verlag GmbH & Co. KGaA, Weinheim

Protein Folding

Switch Peptides In Statu Nascendi: Induction of Conformational Transitions Relevant to Degenerative Diseases**

Manfred Mutter, Arunan Chandravarkar, Christine Boyat, John Lopez, Sonia Dos Santos, Bhubaneswar Mandal, Richard Mimna, Karine Murat, Luc Patiny, Lydiane Saucède, and Gabriele Tuchscherer*

Aspects of conformational transitions, folding, and misfolding of peptides and proteins have moved into the center of interest in various domains of research at the interface of chemistry, biology, and medicine because of their impact on neurodegenerative diseases.[1] For example, recent research suggests that conformational transitions of soluble amyloid β precursor molecules into aggregated, β-sheet-type forms play a key role in the deposition of cerebral amyloid plaques

[*] Prof. M. Mutter, Dr. A. Chandravarkar, Dr. C. Boyat, Dr. J. Lopez, Dipl.-Chem. S. Dos Santos, Dipl.-Chem. B. Mandal, Dipl.-Chem. R. Mimna, Dipl.-Chem. K. Murat, Dr. L. Patiny, Dipl.-Chem. L. Saucède, Dr. G. Tuchscherer
Institute of Chemical Sciences and Engineering (ISIC)
Swiss Federal Institute of Technology, EPFL-BCH
1015 Lausanne (Switzerland)
Fax: (+41) 21-693-9415
E-mail: manfred.mutter@epfl.ch

[**] This work was supported by the Swiss National Science Foundation. The Ncap peptidomimetic was a generous gift from Prof. Klaus Müller, Hoffman-La Roche, Basel, Switzerland.

 © 2004 Wiley-VCH Verlag GmbH & Co. KGaA, Weinheim DOI: 10.1002/anie.200454045

characteristic of Alzheimer's disease.[2] Similarly, α-helix-to-β-sheet transitions are thought to be at the molecular origin of the transformation of the physiological PrP^c form of the prion protein into pathological PrP^{sc}.[3] Due to the intimate relationship between sequence, secondary structure, and physicochemical properties, studies on oligo- and polypeptides[4] exhibiting high propensity for β-sheet formation are severely limited by the intrinsic tendency of peptides for self-association and irreversible aggregation.[1] Consequently, β-sheet- and fibril-forming processes related to degenerative diseases remain elusive, as delineation of structure nucleation or inhibition is a formidable task, often yielding contradictory observations.

Based on concepts for inducing and disrupting peptide structure and function,[5–7] we describe here a novel class of switch peptides.[8] With these compounds we can study folding events in the dynamic process of structure onset and evolution, that is, "in statu nascendi" (ISN) of the molecule. We used chemical synthesis to construct modular switch peptides (Figure 1) consisting of three segments: a conformation induction unit (**σ**), a switch element (**S**) and a target peptide (**P**, depending on its function also termed as host, ligand, or native peptide). A major conceptual feature here is that the conformational impact of **σ** on the target peptide **P** is switched on by the intramolecular X→N migration (X = O, S) of an acyl residue.

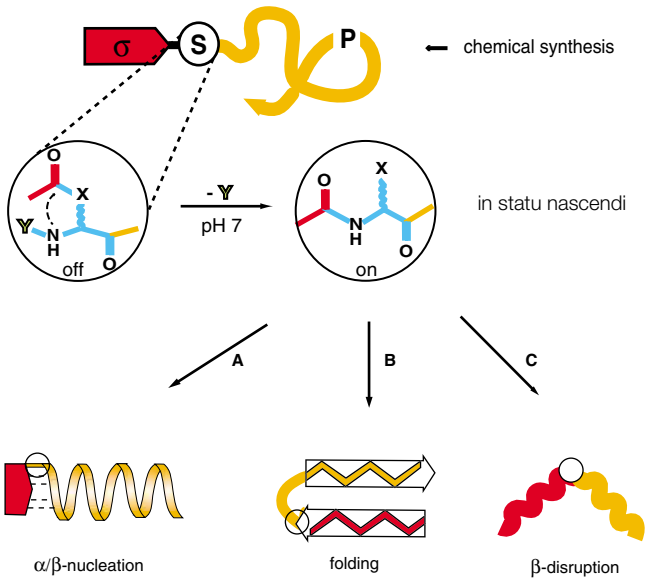


Figure 1. ISN-induced conformational transitions. By removal of Y (enzymatic or by change of pH), X→N acyl migration is triggered. This leads to the formation of a regular peptide bond between **σ** and **P** and results in a change in conformation, typically from a flexible random-coil ($\mathbf{S}_{off}$) to a folded ($\mathbf{S}_{on}$) state. By application of peptidomimetics and templating effects, these conformation changes can be used to study the **σ**-induced nucleation (A), onset (B), and disruption (C) of secondary and tertiary structures.

Acyl-transfer reactions have been the subject of extensive mechanistic studies,[9,10] and their role in protein biosynthesis and splicing,[9,11] peptide synthesis and solubilization,[12] prodrug design,[13] and native chemoselective ligation strategies[9,14] has attracted considerable attention recently. For the purpose at hand, induced intramolecular X→N acyl-transfer reactions as the key step for the onset of structure and function offer several appealing features:

a) The precursor molecules ("switch peptides"), structurally corresponding to N(Y)-protected *O/S*-acyl isopeptides (also termed O/S-peptides[15]) are readily accessible by chemical synthesis[16] and show appropriate stability and solubility in aqueous buffers (presence of a polar or charged group in element **S**), facilitating purification steps prior to acyl migration.
b) The insertion of an **S** element exhibiting a flexible nonpeptidic linkage interrupts the hydrogen-bonding pattern of the regular amide backbone and deactivates the conformational effects of the inducer **σ** upon peptide **P**.[17] Depending on the state of **S** ("on" or "off") the peptide assumes one of two distinct conformational states ($\mathbf{S}_{on}$ and $\mathbf{S}_{off}$) which have different properties.
c) For triggering the X→N acyl migration reaction in situ, a broad palette of methodologies can be envisioned.[18] We developed enzymatically cleavable N-protecting groups (**Y**) as prototypes for in vitro and in vivo applications. Alternatively, we also apply pH-induced acyl-transfer reactions as a well-established procedure.[11a,13]
d) The native peptide bond is formed very fast by acyl migration following first-order kinetics,[9] setting off structure and function.

We demonstrate the concept outlined in Figure 1 for the nucleation, disruption, and onset of secondary and tertiary structures of designed and native peptides of therapeutic relevance.

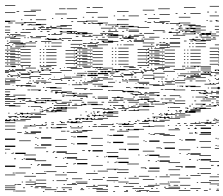
In strategy A, synthetic building blocks[5,19] and peptidomimetics designed to overcome the entropically unfavorable nucleation energy for polypeptide folding[4a] may serve as the induction unit **σ** for the ISN nucleation of secondary structures.

In our first studies we assembled a highly constrained peptidomimetic (Ncap[19e]) as the induction unit **σ** on a parent peptide **P** (**Ia**, Table 1). In the absence of the nucleation effect ($\mathbf{S}_{off}$), **Ia** adopts predominantly a random-coil conformation (CD spectrum, Figure 2a). When the pH is adjusted to 7, the O→N acyl migration is triggered (migration half-life $t_{1/2} \sim$ 25 min, inset Figure 2a), and the helix nucleating property of the Ncap unit is set off (ISN, $\mathbf{S}_{on}$). This results in a spontaneous conformational transition to an α-helical structure (percentage of the helix content corresponding to degree of migration), which is evident from characteristic Cotton effects in the CD spectra. For comparison we assembled **Ib** which features an acetyl group as the induction unit **σ** in an otherwise identical peptide sequence. In contrast to **Ia**, switch peptide **Ib** shows upon acyl migration ($t_{1/2} < 5$ min) a conformational transition from a random-coil ($\mathbf{S}_{off}$) to a β-sheet structure ($\mathbf{S}_{on}$) (Figure 2b). This points out the intrinsic conformational preference of the amphiphilic oligopeptide $(Ser\text{-}Leu)_n$[20] and the pronounced helix-nucleation power of the Ncap in **Ia**. In view of the large pool of synthetic units such as topological templates, scaffolds, and peptidomimetics at

 © 2004 Wiley-VCH Verlag GmbH & Co. KGaA, Weinheim

Table 1: Switch peptides prepared by the assembly of modules **P** and **σ** by switch element **S** (Scheme 1) according to Figure 1.

		Y–Ser[a] (σ)–P	
Switch peptide	**Y**	σ	**P**
Ia	H_2^+	Ncap[b]-A	$(LS)_3LG\text{-}NH_2$
Ib	H_2^+	Ac-A	$(LS)_3LG\text{-}NH_2$
IIa	H_2^+	Ac-$(SL)_2$	$(LS)_2L\text{-}NH_2$
IIb	Acoeoc[c]	Ac-$(SL)_2$	$(LS)_2L\text{-}NH_2$
IIc	pGlu	Ac-$(SL)_2$	$(LS)_2L\text{-}NH_2$
IId	Arg	Ac-$(SL)_2$	$(LS)_2L\text{-}NH_2$
IIIa	H_2^+	Ac-$(SL)_2$-Aβ (14–20)	Aβ (21–24)-SLG-NH_2[d]
IIIb	H_2^+	Ac-LSL	NFGAIL-SLSG-NH_2
IVa	H_2^+	Ac-SLSΨPro[e]L	$(LS)_2LG\text{-}NH_2$
IVb	H_2^+	Ac-ΨPro	$FFD\text{-}NH_2$
IVc	H_2^+	Ac-βAΨPro	$FFD\text{-}NH_2$
V	H_2^+	Ac-NPY (21–31)[f]	NPY (33–36)[g]

[a] Cys (**IVc**), Thr (**V**). [b]  [c]  .

[d] HQKLVFFAEDV. [e]  . [f] YSALRHYINLI. [g] RQRY.

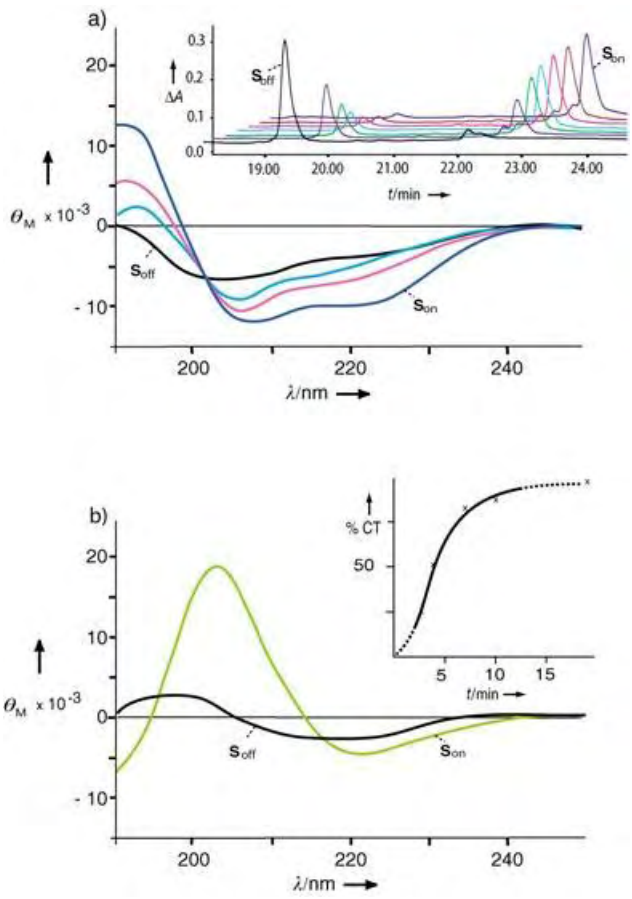


Figure 2. ISN-induced conformational transitions monitored by CD spectroscopy. a) Upon pH-induced acyl migration, switch peptide **Ia** transforms (inset: time course of migration monitored by HPLC) from a random-coil ($\mathbf{S}_{off}$) to an α-helical state ($\mathbf{S}_{on}$). b) In contrast, **Ib** shows under identical experimental conditions the transition from a random-coil ($\mathbf{S}_{off}$) to a β-sheet ($\mathbf{S}_{on}$) (inset: time course (best fit to experimental data points) of conformational transition (CT) taking the normalized Θ_M values at $\lambda = 218$ nm for $\mathbf{S}_{off}$ (0%) and $\mathbf{S}_{on}$ (100%) as reference.

hand today,[5,19] their use as induction units for the in situ transformation of conformational states, for example, potentially β-sheet-forming oligopeptides to helical structures as shown above may offer a powerful tool for reversing processes relevant in degenerative diseases.

When individual peptide blocks **σ** and **P** are used having a chain length n below the critical value for the formation of helix (n_c, α) or β-sheet (n_c, β) structures,[4,20] the resulting switch peptide inherently adopts a nonfolded flexible conformation ($\mathbf{S}_{off}$). When a regular peptide bond is established between **σ** and **P** upon acyl migration ($\mathbf{S}_{on}$), the peptide attains the critical chain length for secondary-structure formation, thus initiating sequence-dependent conformational transitions.

To further test this concept, we assembled oligopeptides $(Leu\text{-}Ser)_n$ (**II** in Table 1)[20a] and amyloid-derived sequences (**III**),[2,6] both exhibiting high potential for β-sheet and fibril formation as switch peptides. As revealed by CD, IR, and EM studies, the insertion of a switch element **S** results in the disruption of ordered structures. When the pH is adjusted to trigger the acyl-transfer reaction, ISN-induced conformational transitions from random-coil to β-sheet structures are observed, which are accompanied by a significant decrease in peptide solubility (Figure 3a, Figure 4a).[5,19] A reference peptide of **IIa** with irreversible N-protection (**Y** = Ac) shows pH-independent random-coil conformations, confirming that the observed transition originates exclusively from the **σ** induction by acyl migration.

Since acyl migration can be initiated in various ways, the rate of structure transition can be modulated over a broad timescale ($t_{1/2} < 1$ min to several hours). Correlating $t_{1/2}$ values of migration (monitored by HPLC) and onset of secondary structure (monitored by CD or other spectroscopic methods) provides access to quantitative data on the kinetics and experimental parameters of β-sheet formation.[27] For switch peptide **IIa** formation of the β-sheet structure has a $t_{1/2}$ value of 38 min at a given starting concentration (7.2×10^{-6} M) and pH (6.6, curve 3 in Figure 3b). In contrast, at physiological pH, the corresponding $t_{1/2}$ value shifts to ≈ 10 min (Figure 3c). For tailoring the onset of conformational transitions in vitro, the use of enzymatically cleavable N-protecting groups (**Y**) is a versatile alternative as exemplified for trypsin-, esterase-, and pyroglutamate aminopeptidase-induced acyl migrations (E1–E3, Figure 3d). Most notably, all enzymes used here showed high specificity for the cleavage site at the N-terminus of parent peptide **P** (Arg-Ser, E1; acetyl ester bond in Acoeoc, E2; pGlu-Ser, E3).[21]

We applied host–guest techniques[4e] for mimicking the structural environment of peptides "excised" from their native polypeptide. For example, after incorporation into a

 © 2004 Wiley-VCH Verlag GmbH & Co. KGaA, Weinheim

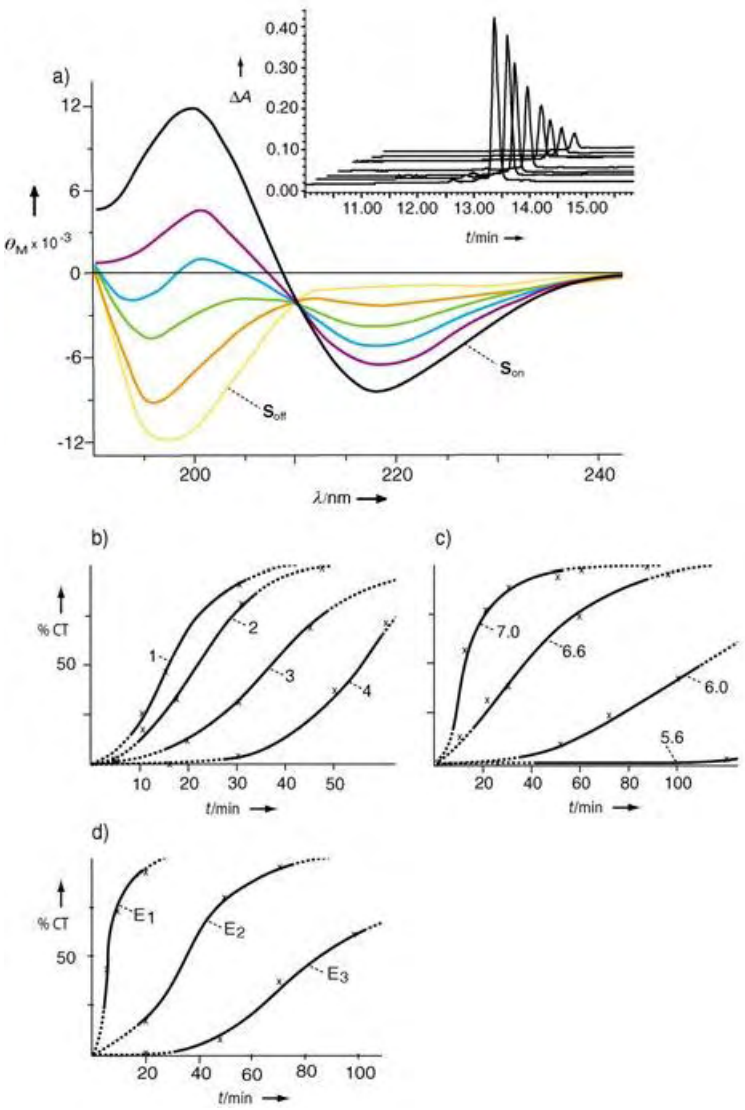


Figure 3. The onset of β-sheet structure in statu nascendi of **IIa**. a) CD monitoring of the conformational transition upon acyl migration (inset: HPLC) from a random-coil (S_{off}) to a β-sheet (S_{on}) conformation at pH 6.6 ($c = 7.2 \times 10^{-6}$ M). Dependence of CT (see legend to Figure 2) on b) concentration at pH 6.6 (1: $c = 2.9 \times 10^{-5}$ M; 2: $c = 1.45 \times 10^{-5}$ M; 3: $c = 7.2 \times 10^{-6}$ M; 4: $= 3.6 \times 10^{-6}$ M); c) pH (concentration of **IIa** in S_{off} state: $c = 8 \times 10^{-6}$ M); d) type of enzymatic cleavage site (**IId** (trypsin, E1), **IIb** (esterase, E2), **IIc** (pyroglutamate aminopeptidase, E3)).

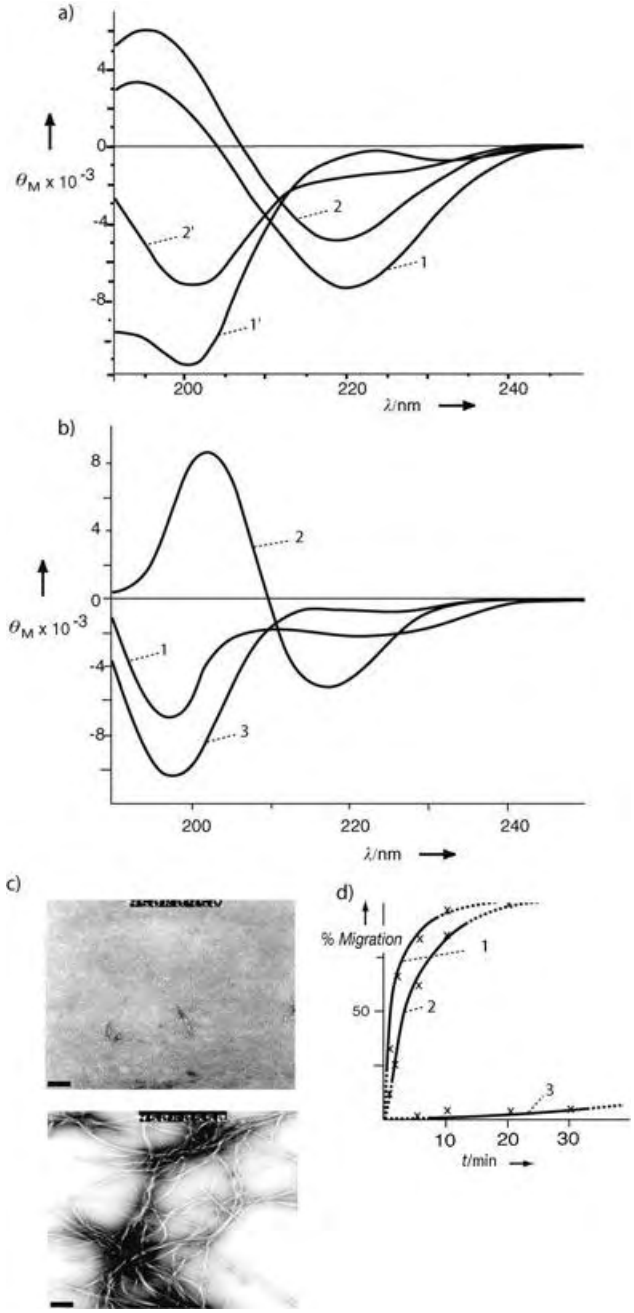


Figure 4. Host–guest techniques for studying conformational transitions. a) CD of the ISN-induced conformational transition from random-coil (S_{off}, pH 4.4) to β-sheet (S_{on}, pH 7) for **IIIa** (1′, 1) and **IIIb** (2′, 2). b) CD spectrum of **IVa** in the absence (1) and presence (2) of a template β-sheet (1:1 mixture of **IVa** (S_{off}) and **IIa** (S_{on})) and (3) of **IIa** (S_{on}) in the presence of **IVa** (S_{on}). c) Electron microscopic images of peptide **IIa** in the S_{off} (top) and S_{on} state after 2 d. d) Kinetics of the acyl migration of **IVa** (1), **IVc** (2), **IVb** (3).

β-sheet-promoting host peptide (switch peptides **IIIa**, **b**), the amyloid β(14–24) peptide and islet-protein-derived sequence NFGAIL,[1,6] undergo upon acyl migration a conformational transition from random-coil to β-sheet structure, paralleled by the onset of fibril formation (Figure 4a). In the evaluation of the impact of external factors (e.g. inhibitors, β-sheet breakers) upon the critical concentration for the evolution of β-sheet structures (Figure 3b–d) as nuclei for fibril formation,[2,6,22] host–guest switch peptides may serve as a diagnostic kit system of considerable therapeutic potential.

For the design of potentially amyloid-fibril-inhibiting or -disrupting compounds, the concept of "separating" recognition (**σ** inactivated) and functional (**σ** activated) states appears of particular relevance. With this objective in mind, we assembled pseudoproline (ΨPro)-containing building blocks as induction units **σ** for β-sheet breaking and ligands **P** (strategy C, Figure 1, switch peptides **IVa–c**). Due to the conformational decoupling (S_{off}) of **σ** and **P**, the intrinsic β-sheet potential of peptides **P** should promote their association to host β-sheets or fibrils in a first step. For example, the amphiphilic oligopeptide **P** in **IVa** with $n < n_c$, β adopts a

 © 2004 Wiley-VCH Verlag GmbH & Co. KGaA, Weinheim

random-coil conformation at pH 7 but is transformed into a β-sheet in the presence of a host oligopeptide ($n > n_c$, β) serving as template (Figure 4b). Similarly, the amyloid-derived peptides **P** (**IVb**, **c**) may serve as ligands for amyloid-template recognition. In triggering the acyl migration, that is, in establishing the regular peptide backbone, the well-known structure disrupting ("β-breaking") effect of the ΨPro system (featuring a *cis*-amide bond)[6a,7b,23] is set off, as revealed by the presence of random-coil conformations in peptides **IVa–c** ($\mathbf{S}_{on}$, Figure 4b).

Interestingly, the ΨPro-containing switch peptides undergo migration at significantly different rates (Figure 4d). The cysteine-containing peptide **IVc** has a stronger tendency for intramolecular acyl migration than the serine-containing **IVb**. Preliminary in vitro studies on the amyloid-fibril-disrupting potential[6a,24] of these peptides point to some interesting therapeutic applications.[25]

Finally, we apply the ISN induction of conformational transitions for the onset of biological function, making use of structure–activity relationship studies on neuropeptide Y (NPY) and its shorter analogues.[26] As shown previously, the C-terminal peptide NPY (21–36) has the minimum chain length for retaining significant binding capacity to NPY receptor Y2, notably in a helical state as the bioactive conformation. When the two peptide blocks NPY (21–31) and NPY (33–36), both with $n < n_c$,α, are conformationally decoupled by insertion of switch element **S** (derived from Thr[32]), the resulting switch peptide **V** adopts a random-coil conformation and shows no binding to Y2 ($IC_{50} \gg 10$ mM[21]). When native NPY (21–36) is triggered by O→N acyl migration ($t_{1/2} = 20$ min at pH 5.8, $t_{1/2} < 2$ min at physiological pH), a random-coil-to-helix transition is observed (typical CD curves, Figure 5), paralleled by the onset of biological function ($IC_{50} = 0.8$ nM).

We expanded this strategy to polypeptides of higher complexity. Native amyloid β (1–42),[22a] assembled as switch peptide (featuring multiple **S** elements), exhibits a random-coil structure and excellent solubility during peptide synthesis and purification, in contrast to the native molecule.[27]

In conclusion, the in statu nascendi (ISN) induction of structure and function provides a novel tool for the study of major conformational transitions observed in native peptides and proteins. Through application of alternative methodologies for monitoring conformational transitions on variable timescales, the molecular origin of dynamic conformational processes leading to self-association, polymerization, and irreversible aggregation as early events in degenerative diseases becomes accessible. This opens challenging perspectives in molecular recognition, biosensor technology, and drug design.

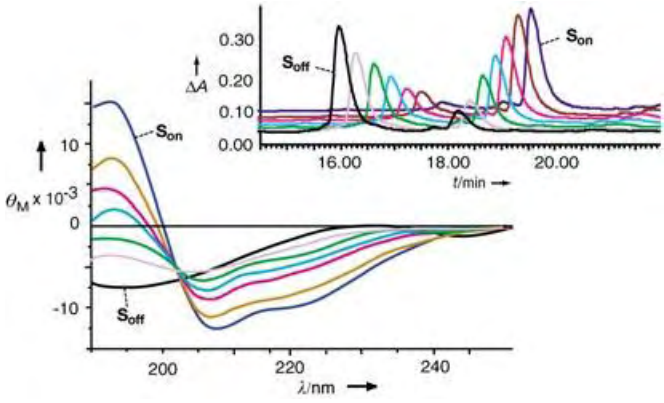
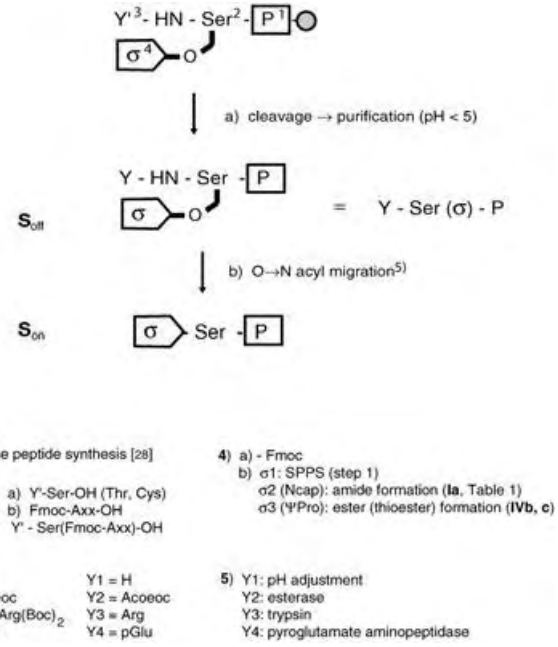


Figure 5. ISN induction of structure and function. CD spectrum of the course of α-helix formation of **V**. Inset: HPLC monitoring of the acyl migration.

Experimental Section

Peptide synthesis: Switch peptides **I**–**V** were synthesized according to standard procedures of solid-phase peptide synthesis (SPPS)[28] following the Fmoc/*t*Bu strategy on Rink-4-methylbenzhydrylamine) (MBHA) resin (step 1 in Scheme 1).[28c] After removal of the N-terminal Fmoc protection with 20% piperidine in DMF, amino acid coupling (2 equiv) was mediated by PyBOP or DIC/HOBT activation in the presence of DIPEA and repeated if necessary. After cleavage of the peptides from the resin with TFA/TIS/H_2O (95/2.5/2.5), all peptides were subjected to RP-HPLC purification and characterized by amino acid analysis and ESI-MS. DIC = diisopropylcarbodiimide, DIPEA = diisopropylethylamine, DMF = dimethylformamide, HOBt = 1-hydroxybenzotriazole, PyBOP = 1-benzotriazolyloxy-tris(pyrrolidino)phosphonium hexafluorophosphate, TFA = trifluoroacetic acid, TIS = triisopropylsilane.



Scheme 1. Strategy for the chemical synthesis of switch peptides (see Figure 1 and Table 1).

The N-terminal Ser residue of target peptide **P** (switch element **S**, steps 2–4 in Scheme 1, variant A) was coupled as an α-Boc-protected residue (2 equiv Boc-Ser-OH, PyBOP, DIPEA in DMF). For side-chain esterification of Ser, a Nα-Fmoc-protected amino acid (3 equiv) was coupled with DIC (3 equiv) and DMAP (0.1 equiv) in anhydrous dichloromethane. Alternatively, the switch element **S** was introduced as an N(Y′)-protected O-acyl isodipeptide[16a,21] and incorporated as a building block in SPPS according to Scheme 1 (variant B). DMAP = dimethylaminopyridine.

 © 2004 Wiley-VCH Verlag GmbH & Co. KGaA, Weinheim

Triggering O→N acyl migrations (step 5 in Scheme 1): pH Induction (**Y1**): Stock solutions of switch peptides were prepared (10^{-3} M in doubly distilled water, pH < 5). An aliquot was removed and the pH adjusted by addition of sodium phosphate buffer (100 mmol). To monitor O→N acyl migration by HPLC, 20-μL aliquots were removed at regular time intervals, quenched by adding 0.2 N HCl, and injected.

Enzymatic triggering (**Y2**–**4**): The corresponding peptide (1 mg) was dissolved in 500 μL sodium phosphate buffer (pH 7.4) at 37 °C and the appropriate enzyme added (0.1 mg trypsin (**Y3**); 50 μL pyroglutamate aminopeptidase (**Y4**); few beads of immobilized esterase (**Y2**)). The reaction was monitored by HPLC as described above.

CD spectra were recorded on a Jasco J-810 spectropolarimeter with a Jasco–Peltier-type temperature controller (model PFD-425S) at a concentration of 10^{-5} M in quartz cells (Hellma, QS, strain-free suprasil; path length 0.1 cm). Data were collected as an average of three scans of 2.0-nm bandwidth.

ESI-mass analysis was carried out on a Finnigan MAT SSQ 710C spectrometer equipped with an IBM PS/295 XP86 (software Technivent Vector II) in positive ionization mode.

Received: February 17, 2004 [Z54045]

Keywords: Alzheimer's disease · circular dichroism · protein folding · protein structures · switch peptides

[1] *Self-Assembling Peptide Systems in Biology, Medicine and Engineering* (Eds.: A. Aggeli, N. Boden, S. Zhang), Kluwer, Dordrecht, **2001**, and references therein.

[2] a) B. Sommer, *Curr. Opin. Pharmacol.* **2002**, *2*, 87–92; b) C. Soto, *Mol. Med. Today* **1999**, *5*, 343–350; c) L. C. Serpell, *Biochim. Biophys. Acta* **2000**, *1502*, 16–30; d) P. Hammerström, R. L. Wiseman, E. T. Powers, J. W. Kelly, *Science* **2003**, *299*, 713–716; e) J. Hardy, D. J. Selkoe, *Science* **2002**, *297*, 353–356.

[3] a) J. P. Taylor, J. Hardy, K. H. Fischbeck, *Science* **2002**, *296*, 1991–1995; b) C. Soto, *Nat. Rev. Neurosci.* **2003**, *4*, 49–60; c) S. W. Liebman, *Proc. Natl. Acad. Sci. USA* **2002**, *99*, 9098–9100.

[4] a) T. E. Creighton, *Proteins*, 2nd ed., Freeman, New York, **1993**; b) C. L. Nesloney, J. W. Kelly, *Bioorg. Med. Chem.* **1996**, *4*, 739–766; c) M. J. I. Andrews, A. B. Tabor, *Tetrahedron* **1999**, *55*, 11711–11734; d) C. Toniolo, M. Crisma, F. Formaggio, C. Peggion, *Biopolymers* **2001**, 60, 396–419; e) M. Mutter, *Angew. Chem.* **1985**, *97*, 639–653; *Angew. Chem. Int. Ed. Engl.* **1985**, *24*, 639–653.

[5] a) S. Vuilleumier, M. Mutter, *Angew. Chem.* **1989**, *101*, 551–692; *Angew. Chem. Int. Ed. Engl.* **1989**, *28*, 535–554; b) J. P. Schneider, J. W. Kelly, *Chem. Rev.* **1995**, *95*, 2169–2187; c) M. S. Searle, *J. Chem. Soc. Perkin Trans. 1* **2001**, *2*, 1011–1020; d) M. P. Glenn, D. P. Fairlie, *Mini-Rev. Med. Chem.* **2002**, *2*, 433–445; d) X. Li, J. Chmielewski, *Org. Biomol. Chem.* **2003**, *1*, 901–904.

[6] a) C. Adessi, M.-J. Frossard, C. Boissard, S. Fraga, S. Bieler, T. Rueckle, F. Vilbois, S. M. Robinson, M. Mutter, W. A. Banks, C. Soto, *J. Biol. Chem.* **2003**, *278*, 13905–13911; b) K. Tenidis, M. , Waldner, J. Berhagen, W. Fischle, M. Bergmann, M. Weber, M.-L. Merkle, W. Voelter, H. Brunner, A. Kapurniotu, *J. Mol. Biol.* **2000**, *295*, 1055–1071.

[7] a) C. Toniolo, M. Bonora, M. Mutter, V. N. R. Pillai, *Makromol. Chem.* **1981**, 182, 1997–2005; b) M. Mutter, A. Nefzi, T. Sato, X. Sun, F. Wahl, T. Wöhr, *Pept. Res.* **1995**, *8*, 145–153.

[8] a) M. Mutter, R. Hersperger, *Angew. Chem.* **1990**, *102*, 195–197; *Angew. Chem. Int. Ed. Engl.* **1990**, *29*, 185–187; b) M. Mutter, R. Gassmann, U. Buttkus, K.-H. Altmann, *Angew. Chem.* **1991**, *103*, 1504–1506; *Angew. Chem. Int. Ed. Engl.* **1991**, *30*, 1514–1516; c) H. Mihara, Y. Takaheshi, I. Obataya, S. Sakamoto in *Self-Assembling Peptide Systems in Biology, Medicine and Engineering* (Eds.: A. Aggeli, N. Boden, S. Zhang), Kluwer, Dordrecht, **2001**, chap. 14, pp. 187–205; d) R. S. Signarvic, W. F. DeGrado, *J. Mol. Biol.* **2003**, *334*, 1–12; e) O. Hénin, B. Barbier, F. Boillot, A. Brack, *Chem. Eur. J.* **1999**, *5*, 218–226.

[9] D. M. Coltart, *Tetrahedron* **2000**, *56*, 3449–3491.

[10] a) D. S. Kemp, D. J. Kerkman, S.-L. Leung, G. Hanson, *J. Org. Chem.* **1981**, *46*, 490–498; b) M. Brenner, W. Hofer, *Helv. Chim. Acta* **1961**, *44*, 1794–1801.

[11] a) Y. Shao, H. Paulus, *J. Pept. Res.* **1997**, *50*, 193–198; b) I. Giriat, T. W. Muir, *J. Am. Chem. Soc.* **2003**, *125*, 7180–7181; c) H. D. Mootz, T. W. Muir, *J. Am. Chem. Soc.* **2002**, *124*, 9044–9045.

[12] a) T. Johnson, M. Quibell, R. C. Sheppard, *J. Pept. Sci.* **1995**, *1*, 11–25; b) L. P. Miranda, W. D. F. Meutermans, M. L. Smythe, P. F. Alewood, *J. Org. Chem.* **2000**, *65*, 5460–5468; c) Y. Sohma, M. Sasaki, Y. Hayashi, T. Kimura, Y. Kiso, *Chem. Commun.* **2004**, 124–125; d) J. Offer, C. N. Boddy, P. E. Dawson, *J. Am. Chem. Soc.* **2002**, *124*, 4642–4646.

[13] a) R. Oliyai, V. J. Stella, *Bioorg. Med. Chem. Lett.* **1995**, *5*, 2735–2740; b) T. R. Hurley, C. E. Colson, G. Hicks, M. J. Ryan, *J. Med. Chem.* **1993**, *36*, 1496–1498; c) Y. Hamada, H. Matsumoto, S. Yamaguchi, T. Kimura, Y. Hayashi, Y. Kiso, *Bioorg. Med. Chem.* **2004**, *12*, 159–170; Y. Hamada, H. Matsumoto, S. Yamaguchi, T. Kimura, Y. Hayashi, Y. Kiso, *Bioorg. Med. Chem.* **2002**, *10*, 4155–4167; d) W. M. Kazmierski, P. Bevans, E. Furfine, A. Spaltenstein, H. Yang, *Bioorg. Med. Chem. Lett.* **2003**, *13*, 2523–2526.

[14] a) J. P. Tam, J. Xu, K. D. Eom, *Biopolymers* **2001**, *60*, 194–205; b) P. E. Dawson, B. H. Kent, *Annu. Rev. Biochem.* **2000**, *69*, 923–960; c) S. Kent, *J. Pept. Sci.* **2003**, *9*, 574–593; d) K. D. Eom, Z. Miao, J.-L. Yang, J. P. Tam, *J. Am. Chem. Soc.* **2003**, *125*, 73–82.

[15] N. Sewald, H.-D. Jakubke, *Peptides: Chemistry and Biology*, Wiley-VCH, Weinheim, **2002**.

[16] a) *Methods in Org. Chem. (Houben-Weyl)*, *Vol. E 22d*, **2003**, pp. 7–67; b) O. Kuisle, E. Quiñoa, R. Riguera, *J. Org. Chem.* **1999**, *64*, 8063–8075; c) B. L. Nilsson, R. J. Hondal, M. B. Soellner, R. T. Raines, *J. Am. Chem. Soc.* **2003**, *125*, 5268–5269; d) *Synthetic Peptides* (Ed.: G. A. Grant), 2nd ed., Oxford University Press, Oxford, **2002**.

[17] a) P. J. Flory, *Statistical Mechanics of Chain Molecules*, Hanser, New York, **1988**; b) I. L. Karle, C. Das, P. Balaram, *Biopolymers* **2001**, *59*, 276–289.

[18] a) D. Kadereit, H. Waldmann, *Chem. Rev.* **2001**, *101*, 3367–3396; b) A. R. Hamel, F. Hubler, A. Carrupt, R. Wenger, M. Mutter, *J. Pept. Res.* **2004**, *63*, 1–8; c) H. Bundgaard, *Adv. Drug Delivery Rev.* **1989**, *3*, 39–65; d) X. Sung, C. R. Xu, H. T. He, T. J. Siahaan, *Bioorg. Chem.* **2002**, *31*, 285–301; e) J. Mozdzanowski, J. Bongers, K. Anumula, *Anal. Biochem.* **1998**, *260*, 183–187; f) C. J. Bosques, B. Imperiali, *J. Am. Chem. Soc.* **2003**, *125*, 7530–7531.

[19] a) J. S. Nowick, J. O. Brower, *J. Am. Chem. Soc.* **2003**, *125*, 876–877; b) R. Aurora, G. D. Rose, *Protein Sci.* **1998**, *7*, 21–38; c) W. Maison, E. Arce, P. Renold, R. J. Kennedy, D. S. Kemp, *J. Am. Chem. Soc.* **2001**, *123*, 10245–10254; d) D. Obrecht, M. Altorfer, J. A. Robinson, *Adv. Med. Chem.* **1999**, *4*, 1–68; e) K. Müller, D. Obrecht, A. Knierzinger, C. Stankovic, C. Spiegler, W. Bannwarth, A. Trzeciak, G. Englert, A. M. Labhard, P. Schönholzer in *Perspectives in Medicinal Chemistry* (Eds.: B. Testa, E. Kyburz, W. Fuhrer, R. Giger), Verlag Helvetica Chimica Acta, Basel, **1993**, pp. 513–533; f) F. Formaggio, A. Bettio, V. Moretto, M. Crisma, C. Toniolo, Q. B. Broxterman, *J. Pept. Sci.* **2003**, *9*, 461–466.

[20] a) K.-H. Altman, A. Flörsheimer, M. Mutter, *Int. J. Pept. Protein Res.* **1986**, *27*, 314–319; b) C. Toniolo, G. M. Bonora, M. Mutter, *J. Am. Chem. Soc.* **1979**, *101*, 450–454.

 © 2004 Wiley-VCH Verlag GmbH & Co. KGaA, Weinheim

[21] S. Dos Santos, K. Murat, E. Grouzmann, M. Mutter, in preparation.
[22] a) P. M. Gorman, A. Chakrabartty, *Biopolymers* **2001**, *60*, 381–394; b) C. Hetényi, T. Körtvélyesi, B. Penke, *Bioorg. Med. Chem.* **2002**, *10*, 1587–1593.
[23] T. Wöhr, F. Wahl, A. Nefzi, B. Rohwedder, T. Sato, X. Sun, M. Mutter, *J. Am. Chem. Soc.* **1996**, *118*, 9218–9227.
[24] a) B. Permanne, C. Adessi, G. P. Saborio, S. Fraga, M.-J. Frossard, I. Dewachter, J. Van Dorpe, W. A. Banks, F. Van Leuven, C. Soto, *FASEB J.* **2002**, *16*, 860–862; b) T. Oishi, K. Hagiwara, T. Kinumi, Y. Yamakawa, M. Nishijiama, K. Nakamura, H. Arimoto, *Org. Biomol. Chem.* **2003**, *1*, 2626–2629; c) S. J. Wood, R. Wetzel, J. D. Martin, M. R. Hurle, *Biochemistry* **1995**, *34*, 724–730; d) Y. Kuroda, Y. Maeda, H. Hanaoka, K. Miyamoto, T. Nakagawa, *J. Pept. Sci.* **2004**, *10*, 8–17; e) L. O. Tjernberg, D. J. E. Callaway, A. Tjernberg, S. Hahne, C. Lilliehöök, L. Terenius, J. Thyberg, C. Nordstedt, *J. Biol. Chem.* **1999**, *274*, 12619–12625; f) D. J. Gordon, K. L. Sciarretta, S. C. Meredith, *Biochemistry* **2001**, *40*, 8237–8245; g) M. Lopez de la Paz, K. Goldie, J. Zurdo, E. Lacroix, C. M. Dobson, A. Hoenger, L. Serrano, *Proc. Natl. Acad. Sci. USA* **2002**, *99*, 16052–16057.
[25] M. Mutter, J. Dubochet, M. Adrian, E. Grouzmann, C. Soto, in preparation.
[26] a) A. Beck-Sickinger, G. Jung, *Biopolymers* **1995**, *37*, 123–142; b) D.-D. Malis, E. Grouzmann, D. R. Morel, M. Mutter, J.-S. Lacroix, *Br. J. Pharmacol.* **1999**, *126*, 1–8.
[27] C. Arunan, M. Mutter, in preparation.
[28] a) J. M. Stewart, J. D. Young, *Solid Phase Peptide Synthesis*, Pierce Chemical, Rockford, IL, **1984**; b) G. A. Grant, *Synthetic Peptides*, 2nd ed., Oxford University Press, Oxford, **2002**; c) H. Rink, *Tetrahedron Lett.* **1987**, *28*, 3787.

 © 2004 Wiley-VCH Verlag GmbH & Co. KGaA, Weinheim

Gas-Phase Reactions

The Photochemical *cis–trans* Isomerization of Free Stilbene Molecules Follows a Hula-Twist Pathway**

Werner Fuß, Constantine Kosmidis, Wolfram E. Schmid, and Sergei A. Trushin*

The hula-twist mechanism was suggested by Liu et al. in 1985 to explain how the retinal chromophore can undergo *cis–trans* isomerization within the limited volume of the opsin matrix.[1] Whereas in the conventional one-bond flip (OBF) mechanism the substituents of the C=C bond move along the surface of a cone, in the hula-twist (HT) mechanism only the CH group of the double bond rotates out of plane and the other parts reorient within the plane. An equivalent description says that a double bond and an adjacent single bond both rotate by 180°. In 1998 we found experimental support for the HT mechanism in the photoisomerization of a steroid triene, previtamin D, in a matrix at 90 K.[2] We also pointed out that the highly twisted geometries calculated for the S_1/S_0 conical intersection (CI) of polyenes[3] are fully compatible with an HT pathway and concluded that there is an internal driving force, namely the slope on the potential energy surfaces through the CI, that guides at least the nonpolar polyenes along this way. This view was also explained in detail on a quantum-chemical basis.[4]

In the meantime, more observations of HT have been presented[5] (a possible case also in ref. [6]), and in several reviews Liu and Hammond have reinterpreted many previous findings in terms of this mechanism.[7] Because the conformers expected from HT were observed only in a matrix or with suitable steric hindering, Liu and Hammond suggested that HT is a higher-energy path, taking place only in the presence of an external or internal constraint. This would be in contrast to our claim that there is an internal driving force preferring HT.

In this communication we compare the rates of *cis–trans* isomerization for *cis*-stilbene (**1**) and a ring-fused analogue (*trans*-1,1′-bis(indanylidene), "stiff stilbene", **2**) in the gas phase (Figure 1). The difference found is readily understood, if in the unhindered **1** the lower-energy CI is of the HT type. HT also explains the relative orientation of the *trans*-stilbene produced photochemically from *cis*-stilbene, which was previously observed but not understood.

After excitation of *cis*- and *trans*-stilbene in the first UV band, the ethylenic double bond twists by 90°, and an S_1 minimum (p*) is reached that is common to both isomers.[8] For leaving the fluorescent region (cis* and trans*) towards p*, the molecules must overcome a small barrier which is, however, barely detectable for cis*. In the interpretation of refs. [9–11] this barrier results from an avoided crossing with another excited state of the same symmetry (B_2). In the gas phase, the lifetime for trans* is 10 to >100 ps depending on the excess energy,[12] and 300 fs for cis*.[13,14] The lifetime in the perpendicular minimum (p*) has only recently been measured and found to be 135–160 fs.[14] This short lifetime implies that the path leads through an easily accessible CI, as pointed out previously.[15–18] After the C=C twist, the path hence changes direction. According to calculations, the new coordinate either involves a twist of the adjacent single bond (leading to a CI of HT type)[15] or pyramidalization (rehybridization) of one ethylenic C atom[17,18] (OBF-type CI). The single bonds are fixed in the stiff stilbene **2**. The hula-twist mechanism is hence hindered in it, whereas pyramidalization is actually favored by the five-membered ring. Therefore, if HT is the lower-energy path in the parent stilbene **1**, the departure from p* should be slower in **2**, whereas it should be faster, if one-bond flip is the lower-energy channel. We

[*] Dr. W. Fuß, Dr. W. E. Schmid, Dr. S. A. Trushin
Max-Planck-Institut für Quantenoptik
85741 Garching (Germany)
Fax: (+49) 89-32905-200
E-mail: w.fuss@mpq.mpg.de
Dr. C. Kosmidis
Department of Physics
University of Ioannina
45110 Ioannina (Greece)

[**] This work was supported by the Deutsche Forschungsgemeinschaft. We are indebted to René Lapouyade for a sample of **2** and to Jörg Schroeder for helpful discussions.

Supporting information for this article is available on the WWW under http://www.angewandte.org or from the author.

 © 2004 Wiley-VCH Verlag GmbH & Co. KGaA, Weinheim DOI: 10.1002/anie.200454221

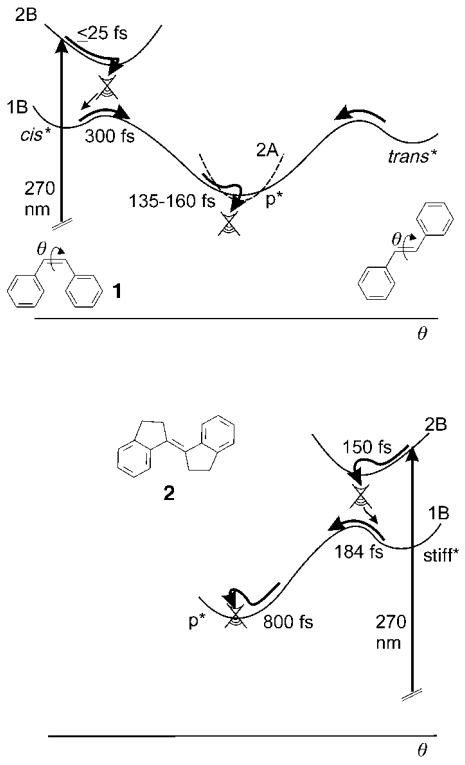


Figure 1. Suggested potential energy surfaces and pathways for the isomerization of **1** and **2**. θ is the C=C twist angle. The initial motion on the 2B surface and through the first conical intersection (CI) is not time-resolved in **1**. The CI is outside the drawing plane. Entering from there into the 1B valley can stimulate a vibration.[14] The last CI, which is reached from p*, is displaced towards hula twist (in φ direction, Scheme 1) for **1**, but for stiff stilbene **2** probably involves pyramidalization of an ethylenic C.

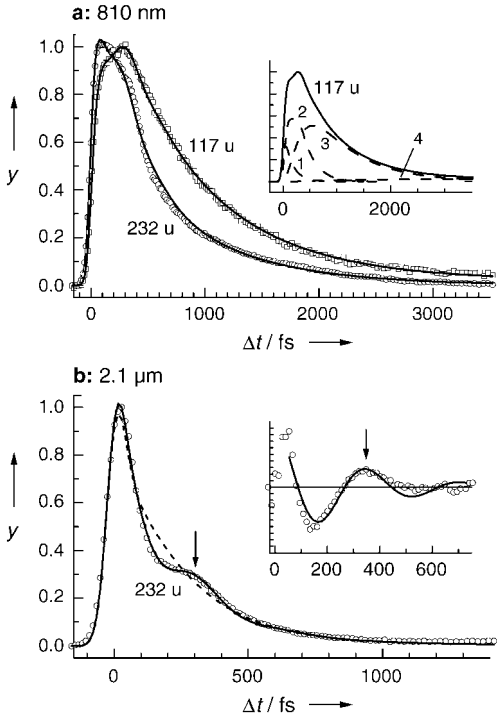


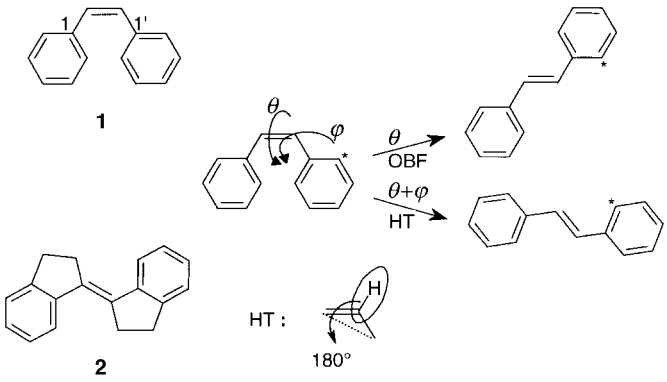
Figure 2. Normalized transient ion yields y of the parent (232 u, circles) and a fragment ion (117 u, squares, about 10% of the parent) versus pump–probe delay Δt; probe wavelengths are indicated. The broken lines in the inset of (a) show the contributions (sums of exponentials, convoluted with the instrumental function) of the different observation windows to the 117-u signal. The broken line in (b) shows the sum of such nonperiodic contributions. The bold lines also comprise an oscillatory component, and the latter is separately displayed (after subtraction of the nonperiodic part, i.e. the broken line, and dividing by the time-dependent L_2 population) in the inset of (b). The fit parameters are given in the Supporting Information.

compared the ultrafast dynamics of **2** with that of **1**. (Note that from p* the further development is the same for the *cis* and *trans* isomers, as evidenced by the same *cis*/*trans* branching ratio for the two isomers.[8])

Following the same procedures used with *cis*-stilbene,[14] we excited stiff stilbene[19] in the gas phase ($\approx 10^{-7}$ mbar, 130°) with a pulse ($\approx$60 fs) at 270 nm in the short-wavelength wing of the first absorption band[20,21] and then probed it by ionization at 810 nm (50 fs, $\approx 10^{13}$ W cm^{-2}) or at 2.1 μm (40 fs, $\approx 10^{13}$ W cm^{-2}). The ion yields were measured mass-selectively as a function of the pump–probe delay time. As the molecule (the wave packet) slides down the potential energy surfaces, the ionization probability decreases and the degree of fragmentation grows. This increase is due to conversion of electronic to vibrational energy, giving rise to a hot molecule; ionization then produces a hot ion, and this ion has sufficient time (nanoseconds) to dissociate. These features help in assigning the signals and time constants.[14] Some time-dependent signals of the parent ion and a fragment ion are shown in Figure 2. All signals were simulated (details in the Supporting Information) by a sum of exponentials with one set of time constants τ_i, convoluted with the pump and probe pulses. This nonperiodic part is subtracted from the signals leaving as a residual a strongly damped coherent oscillation (Figure 2b inset), certainly caused by a vibration. The τ_i correspond to lifetimes of consecutive locations on the potential surfaces. We assign them (details in the Supporting Information) on the basis of the changing fragmentation pattern and ionization probability, by extrapolation of previous data in solvents of different viscosity and in direct analogy to **1**, where the τ_i values were identified by independent measurements of the fluorescence lifetime.[14] The potential surfaces of **1** and **2** with the τ_i are compared to each other in Figure 1.

Initial excitation populates the 2B state.[21] Relaxation from there within $\tau_1 = 150$ fs leads to the fluorescent region (stiff*) of 1B; the corresponding process is too fast ($\leq$25 fs) to be resolved in *cis*-stilbene.[14] Hence it must pass through an easily accessible CI between the two surfaces, as indicated in Figure 1. This relaxation stimulates vibrations in the 1B valley (detected as oscillations in the parent-ion signal), which are perpendicular to the drawing plane of Figure 1 (see Figure 5 in ref. [14]) and involve a bend in the molecular plane and single-bond twist (φ) in **1**. Both the bend and the twist can be understood by the 1,3 interaction between p orbitals,[4] as indicated in Scheme 1. The oscillation in **2** corresponds to a comparable wavenumber (94 cm^{-1}). Obviously the 2B/1B CI is displaced along these coordinates. The hindering of the φ twist in **2** explains why τ_1 is longer than in **1**. From stiff*, the

 © 2004 Wiley-VCH Verlag GmbH & Co. KGaA, Weinheim



Scheme 1. *cis*-Stilbene (**1**), "stiff stilbene" **2**, and the two isomerization pathways, "one-bond flip" (OBF, θ) and "hula twist" (HT, $\theta + \varphi$). The asterisk shows that in substituted stilbenes different conformers would result from the two paths. φ and θ indicate the rotation of the substituents attached to a space-fixed CH group. Alternatively, one can also rotate this CH group around an axis indicated by the broken line (bottom), and its substituents thereby reorient within the plane. The broken line also indicates an attractive 1,3 interaction between p orbitals that causes the disrotatory motion of the substituents.[4]

wave packet leaves in a time ($\tau_2 = 184$ fs) that is not only shorter than for trans* but even for cis*. That is, the activation energy is smaller in **2**, as was previously found in solution.[20,22] This is not unexpected: Since the barrier results from avoided crossing, its height depends on the 2B–1B gap, and polarizable substituents (such as the five-membered rings) tend to lower 2B more than 1B.[14] In fact, the UV absorption maximum (reflecting 2B) is at lower energy in **2** than in **1**.[20,21]

The most interesting difference between **1** and **2** is the p* lifetime, which is five to six times longer in **2** ($\tau_3 = 800$ fs) than in **1**. This means that an activation energy must be met in order to reach a CI from p*(**2**), but much less from p*(**1**). In the gas phase the excess energy released on the relaxation path will help to overcome the barrier. A solvent, however, will absorb part of the excess energy by cooling and thus prolong the p*(**2**) lifetime. In fact, it was found to be 10 ps in hydrocarbon solutions,[23] thus confirming the idea of an activation barrier in **2**. A natural interpretation of such a barrier is the assumption that the lowest-energy CI in **1** involves a twist of a single bond, which is blocked in **2**, so that a higher point of the intersection space must be used by **2** to leave from S_1. Hence our comparison of **1** and **2** supports for the former the HT-type CI predicted by molecular mechanics valence bond (MMVB) calculations.[15] This type of CI is generally expected if the S_1 state is covalent,[4] as the 2A state is. We therefore set the 2A surface (broken line) in Figure 1 at slightly lower energies than those calculated in ref. [9]. The alternative type of CI, which is predicted for stilbene if its S_1 minimum (p*) is ionic like the 1B state, mainly involves pyramidalization (rehybridization) of one ethylenic C atom and the beginning of an H migration.[18] This is probably the path taken in **2**. The five-membered rings in **2** facilitate such a distortion but apparently not enough to reduce the activation energy to a value comparable to that in **1**. It is worth mentioning that also **1** requires a given activation energy for leaving S_1, since τ_3 (≥ 135 fs) is clearly longer than the time for reaching the corresponding CI in butadiene (≈ 20 fs[24]). Furthermore, it is remarkable that *cis*-stilbene has some momentum in the right direction already long before leaving p* towards the HT-type CI: The two vibrations detected in the cis* region both have a φ component.[14]

Only half the rotation of a full hula twist is accomplished at an HT-type CI. In principle, the molecule can also turn to the OBF direction on the lower cone of the CI[4] (Figure 3). It would therefore be desirable to know whether HT is really completed in free stilbene as well. Indeed this idea finds supported in an observation made by Hochstrasser et al., which was previously not understood. By laser-induced fluorescence this group determined the orientation of *trans*-stilbene produced from *cis*-stilbene excited by a polarized laser in hexadecane.[25–27] The transition moment in both molecules is very near the line connecting the center of the two benzene rings.[9,10] This line would be expected to turn by $\approx 60°$ (Scheme 1), if only the ethylenic double bond twisted by 180° (also if both benzene rings turn by $\pm 90°$, thus conserving the center of mass). However, the authors found a reorientation angle ρ of only 35°[27] and concluded that "the reaction coordinate is more intricate".[25] Indeed, this ρ is just consistent with the asynchronous hula-twist mechanism postulated above (Figure 4): The initial C=C twist by 90° changes ρ just by 34°. For the CI to be reached from this perpendicular minimum, one phenyl group has to rotate by 90°, which does not change ρ and the position of the benzene ring. To complete the hula twist, one CH group must rotate around the axis (dotted in Figure 4) connecting its two neighboring atoms; this again does not change ρ. (If the molecule followed the HT path from the beginning, that is, if double and single bonds rotated synchronously, then ρ could stay at 0°; the rotation axis (the dotted line in Scheme 1) would then be fixed in space and the process would be space-

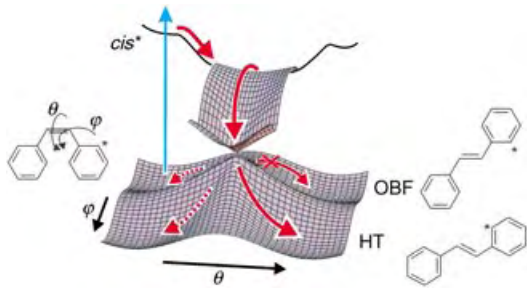


Figure 3. Suggested surfaces and topology of the S_1/S_0 conical intersection, showing the possible branchings. The energy is not to scale: The activation energies for C=C and C–C isomerization in S_0 are much more different than shown, and the CI lies higher. The structures correspond to the minima of the lower surface. Our results provides evidence for the HT product and against the OBF product. The experiment does not differentiate between the two arrows on the left; however, a photochemical single-bond isomerization has been suggested,[29] consistent with the arrow front left. For a departure from p* with opposite change of φ (motion into the plane of the drawing, conrotatory instead of disrotatory) we must postulate a higher activation energy, because only the disrotatory path is consistent with HT.

 © 2004 Wiley-VCH Verlag GmbH & Co. KGaA, Weinheim

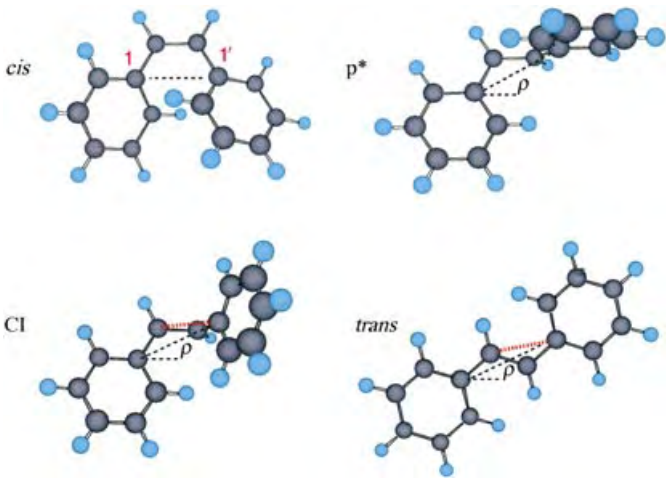


Figure 4. Reorientation of the two benzene rings (angle ρ, indicated by the broken lines connecting C^1 with $C^{1'}$). In the initial *cis* structure, the two benzene rings are twisted out of plane due to steric hindering. In the perpendicular minimum (p*), probably two planar benzylic groups are perpendicular to each other. To reach the HT-type CI, a phenyl group rotates so that its $C^{1'}$ p orbital can interact with the p orbital of the other benzylic group; actually this (weak) 1,3 bond (dotted red line) is much shorter than shown and the enclosed CH group is pyramidalized (rehybridized).[15] Although asynchronous, the θ and φ twists are concerted and disrotatory (θ and φ arrows in Scheme 1), if the sign of the interacting p orbitals is preserved as in polyenes.[4] This is strongly supported by the disrotatory (concerted) continuation of the process, namely the completion of hula twist by which we explained the observed ρ.

saving. Such a synchronous HT can be assumed for stilbenes in highly viscous media.)

We conclude that hula twist can also take place in free molecules without any constraint and that it is therefore the lowest-energy pathway for *cis–trans* isomerization. It is an example how a CI can control the stereochemistrical course of a reaction. Quantum-chemical calculations generalize the HT-type CI (or "kink-type" CI[3]) for all double-bond systems (at least three adjacent pπ orbitals are needed), which have a covalent S_1 minimum;[3,4] in particular, these systems comprise nonpolar and not too strongly polar conjugated polyenes. There is now one experimental example to support this claim, but no evidence has ever been found for the opposite (that C=C twist would be the lower-energy path), except in monoolefins and in cases with constraints such as in **2**. The fact that many documented examples of hula twist were found in matrixes[7] does not necessarily point to the action of any volume constraint: The matrix may have simply served for freezing the primary conformer, which was necessary for the hula twist to be recognized. Furthermore, the cryogenic temperatures in these experiments imply that HT has an activation energy near zero and is thus the lowest-energy path.[2]

It is still worth noting that the isomerization of stilbene is not a prototypical photochemical *cis–trans* isomerization but a limiting case. On UV excitation, monoolefins twist their double bond by 90° and leave from this S_1 minimum through a CI with pyramidalization and partial H migration towards the product(s) and back to the reactant.[28] Polyenes have planar S_1 states; from the minimum they leave by synchronous C=C and C–C twisting through an HT-type CI towards products and reactant.[3,4] Stilbene reaches the same type of CI by an asynchronous hula twist.

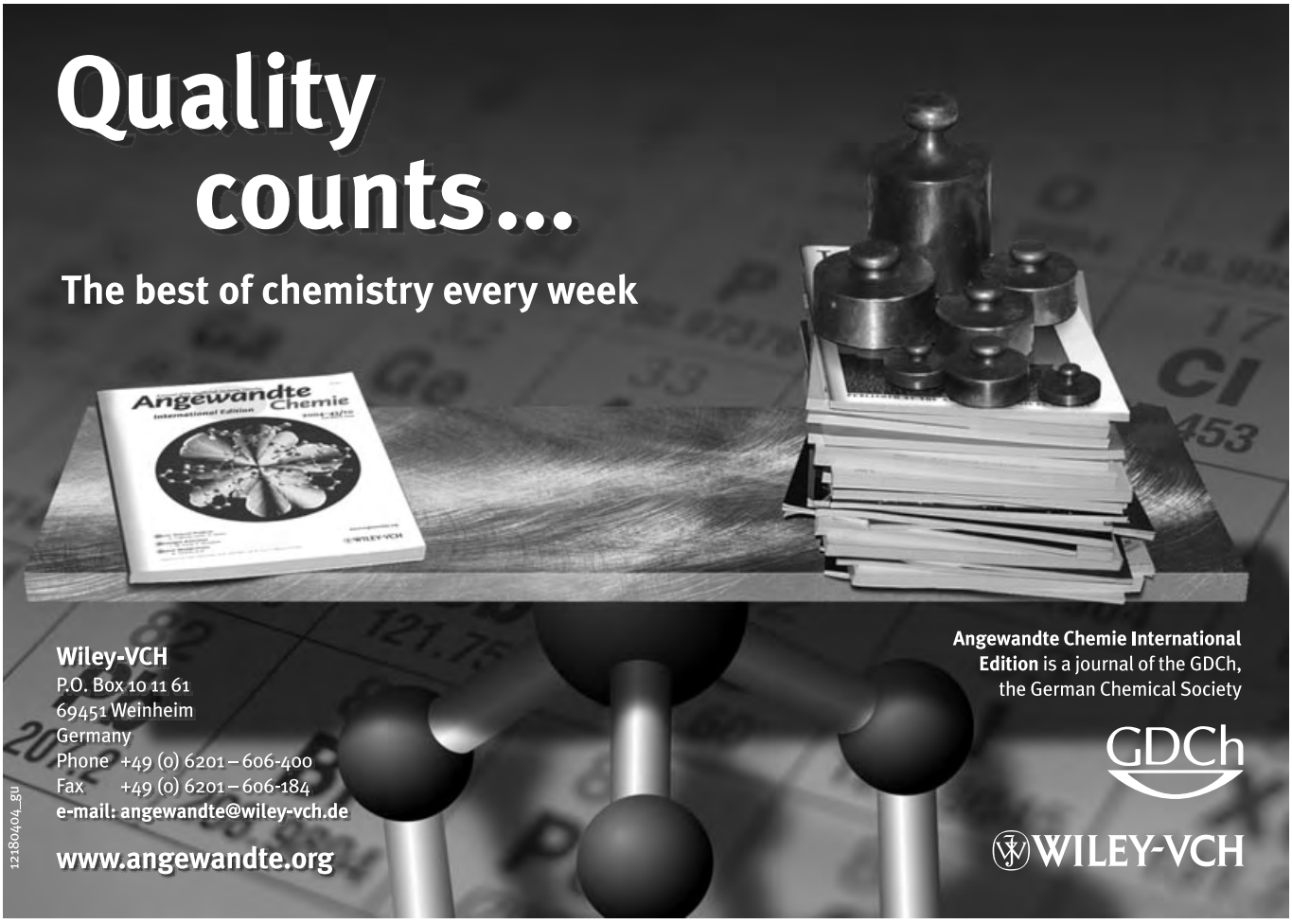
Received: March 9, 2004
Revised: May 5, 2004 [Z54221]

Keywords: femtochemistry · isomerization · photochemistry · polyenes · potential energy surfaces

[1] R. S. H. Liu, D. T. Browne, *Acc. Chem. Res.* **1986**, *19*, 42–48; R. S. H. Liu, A. E. Asato, *Proc. Natl. Acad. Sci. USA* **1985**, *82*, 259–263.
[2] A. M. Müller, S. Lochbrunner, W. E. Schmid, W. Fuß, *Angew. Chem.* **1998**, *110*, 520–522; *Angew. Chem. Int. Ed.* **1998**, *37*, 505–507.
[3] P. Celani, M. Garavelli, S. Ottani, F. Bernardi, M. A. Robb, M. Olivucci, *J. Am. Chem. Soc.* **1995**, *117*, 11584–11585.
[4] D. Sampedro Ruiz, A. Cembran, M. Garavelli, M. Olivucci, W. Fuß, *Photochem. Photobiol.* **2002**, *76*, 622–633.
[5] M. Uda, T. Mizutani, J. Hayakawa, A. Momotake, M. Ikegami, R. Nagahata, T. Arai, *Photochem. Photobiol.* **2002**, *76*, 596–605; Y. Imamoto, T. Kuroda, Kataoka, S. Shevyakov, G. Krishnamoorthy, R. S. H. Liu, *Angew. Chem.* **2003**, *115*, 3758–3761; *Angew. Chem. Int. Ed.* **2003**, *42*, 3630–3633; G. Kaupp, *Photochem. Photobiol.* **2002**, *76*, 590–595; M. Squillacote, T. Semple, J. W. Chen, F. Liang, *Photochem. Photobiol.* **2002**, *76*, 634–639.
[6] T. Hirano, I. T. Lim, D. M. Kim, X. G. Zheng, K. Yoshihara, Y. Oyama, H. Imai, Y. Shichida, M. Ishiguro, *Photochem. Photobiol.* **2002**, *76*, 606–615.
[7] R. S. H. Liu, *Acc. Chem. Res.* **2001**, *34*, 555–562; R. S. H. Liu, G. S. Hammond, *Proc. Natl. Acad. Sci. USA* **2000**, *97*, 11153–11158; R. S. H. Liu, G. S. Hammond, *Chem. Eur. J.* **2001**, *7*, 4536–4544; R. S. H. Liu, *Photogr. Sci. Photochem.* **2002**, *80*, 81–87.
[8] D. H. Waldeck, *Chem. Rev.* **1991**, *91*, 415–496; H. Görner, H. J. Kuhn, *Adv. Photochem.* **1995**, *19*, 1–117; J. Saltiel, Y. P. Sun in *Photochromism—Molecules and Systems* (Eds.: H. Dürr, H. Bouas-Laurent), Elsevier, Amsterdam, **1990**, pp. 64–164.
[9] V. Molina, M. Merchán, B. O. Roos, *Spectrochim. Acta Part A* **1999**, *55*, 433–446.
[10] V. Molina, M. Merchán, B. O. Roos, *J. Phys. Chem. A* **1997**, *101*, 3478–3487.
[11] L. Gagliardi, G. Orlandi, V. Molina, P. A. Malmqvist, B. O. Roos, *J. Phys. Chem. A* **2002**, *106*, 7355–7361; R. Improta, F. Santoro, C. Dietl, E. Papastathopoulos, G. Gerber, *Chem. Phys. Lett.* **2004**, *387*, 509–516.
[12] J. S. Baskin, L. Bañares, S. Pedersen, A. H. Zewail, *J. Phys. Chem.* **1996**, *100*, 11920–11933; J. A. Syage, W. R. Lambert, P. M. Felker, A. H. Zewail, *Chem. Phys. Lett.* **1982**, *88*, 266–270.
[13] S. Pedersen, L. Bañares, A. H. Zewail, *J. Chem. Phys.* **1992**, *97*, 8801–8804; B. I. Greene, R. C. Farrow, *J. Chem. Phys.* **1983**, *78*, 3336–3338; T. Baumert, T. Frohnmeyer, B. Kiefer, P. Niklaus, M. Strehle, G. Gerber, A. H. Zewail, *Appl. Phys. B* **2001**, *72*, 105–108.
[14] W. Fuß, C. Kosmidis, W. E. Schmid, S. A. Trushin, *Chem. Phys. Lett.* **2004**, *385*, 423–430.
[15] M. J. Bearpark, F. Bernardi, S. Clifford, M. Olivucci, M. A. Robb, T. Vreven, *J. Phys. Chem. A* **1997**, *101*, 3841–3845.
[16] W. Fuß, S. Lochbrunner, A. M. Müller, T. Schikarski, W. E. Schmid, S. A. Trushin, *Chem. Phys.* **1998**, *232*, 161–174.
[17] Y. Amatatsu, *Chem. Phys. Lett.* **1999**, *314*, 364–368.
[18] J. Quenneville, T. J. Martínez, *J. Phys. Chem. A* **2003**, *107*, 829–837.

 © 2004 Wiley-VCH Verlag GmbH & Co. KGaA, Weinheim

[19] Stiff stilbene **2** was synthesized by R. Lapouyade. Gas-chromatographic analysis showed no *cis* isomer or other impurity.
[20] J. Saltiel, J. T. D'Agostino, *J. Am. Chem. Soc.* **1972**, *94*, 6445 – 6456.
[21] G. Hohlneicher, R. Wrzal, D. Lenoir, R. Frank, *J. Phys. Chem. A* **1999**, *103*, 8969 – 8975; M. Oelgemöller, B. Brem, R. Frank, S. Schneider, D. Lenoir, N. Hertkorn, Y. Origane, P. Lemmen, J. Lex, Y. Inoue, *J. Chem. Soc. Perkin Trans. 2* **2002**, 1760 – 1771.
[22] G. Rothenberger, D. K. Negus, R. M. Hochstrasser, *J. Chem. Phys.* **1983**, *79*, 5360 – 5367.
[23] F. E. Doany, E. J. Heilweil, R. Moore, R. M. Hochstrasser, *J. Chem. Phys.* **1984**, *80*, 201 – 206.
[24] W. Fuß, W. E. Schmid, S. A. Trushin, *Chem. Phys. Lett.* **2001**, *342*, 91 – 98.
[25] S. Abrash, S. Repinec, R. M. Hochstrasser, *J. Chem. Phys.* **1990**, *93*, 1041 – 1053.
[26] R. J. Sension, S. T. Repinec, R. M. Hochstrasser, *J. Phys. Chem.* **1991**, *95*, 2946 – 2948.
[27] R. J. Sension, S. T. Repinec, A. Z. Szarka, R. M. Hochstrasser, *J. Chem. Phys.* **1993**, *98*, 6291 – 6315.
[28] I. Ohmine, *J. Chem. Phys.* **1985**, *83*, 2348 – 2362; M. Klessinger, J. Michl, *Excited States and Photochemistry of Organic Molecules*, VCH, New York, **1995**; M. Ben-Nun, T. J. Martínez, *Chem. Phys.* **2000**, *259*, 237 – 248; R. P. Krawczyk, A. Viel, U. Manthe, W. Domcke, *J. Chem. Phys.* **2003**, *119*, 1397 – 1411; M. Ben-Nun, T. J. Martínez, *Chem. Phys. Lett.* **1998**, *298*, 57 – 65.
[29] A. M. Brouwer, H. J. C. Jacobs, *Recl. Trav. Chim. Pays-Bas* **1995**, *114*, 449 – 458.



 © 2004 Wiley-VCH Verlag GmbH & Co. KGaA, Weinheim

Biological Complexes

Partitioning of Solvent Effects and Intrinsic Interactions in Biological Recognition**

*Elena N. Kitova, David R. Bundle, and John S. Klassen**

The association of molecules to form specific, noncovalent complexes is central to many biological processes. The strength and specificity of binding is governed both by the formation of selective solute–solute interactions and by solvent effects.[1–4] Although the structures and association thermochemistry of many biological complexes in solution have been determined, these data do not provide a complete description of the recognition process.[5] The challenge for researchers aiming to achieve a more complete understanding of the molecular recognition process is the separation of solvent effects from solute–solute interactions, something never-before accomplished for a biomolecular complex. Herein, we describe a novel methodology to perform this task. Our approach involves comparison of the energetic stabilities of solvated complexes with those of their desolvated (gaseous) counterparts.

The enthalpy of association in solution (ΔH_{assoc}) can be expressed as the sum of the enthalpic contributions made by intrinsic solute–solute interactions (ΔH_{intrin}) and solvent effects (ΔH_{solv}), as shown in Equation (1).

$$\Delta H_{assoc} = \Delta H_{intrin} + \Delta H_{solv} \quad (1)$$

The ΔH_{assoc} term can be determined directly by isothermal titration calorimetry (ITC)[6] or from a van't Hoff analysis of the temperature dependence of the association constant.[7] The strength of the solute–solute interactions is most reliably determined in the absence of solvent, that is, in vacuo. In principle, ΔH_{intrin} can be determined from the temperature dependence of the equilibrium constant for the association of the complex in the gas phase, that is, from the slope of a van't Hoff plot. This slope corresponds to $\Delta H_{assoc,g}$, the association enthalpy of the gaseous complex. However, such measurements are generally not possible for biologically relevant molecules because of their extremely low vapor pressures. Furthermore, measurements of this kind probably would not provide the desired thermodynamic information since the structure of the complex formed in the gas phase is unlikely to resemble the structure in solution.[8] A more useful quantity is the energetic stability of the biomolecular complex formed initially in solution and then dehydrated such that it retains the essential aspects of its solution structure. Transfer of biomolecular complexes from the aqueous phase to the gas phase by electrospray or nanoelectrospray ionization readily affords the desolvated species. The value of $\Delta H_{assoc,g}$ cannot be determined directly but can be estimated from the Arrhenius activation energy (E_a) for the dissociation of the desolvated complex at thermal equilibrium. The value E_a is related to the enthalpy of activation for the dissociation of the complex, $\Delta H^{\ddagger}_{diss,g}$ ($E_a = \Delta H^{\ddagger}_{diss,g} + RT$),[9] which can provide a good approximation of the magnitude of $\Delta H_{assoc,g}$ (opposite sign to that of $\Delta H^{\ddagger}_{diss,g}$) if the reaction is assumed to be barrierless (that is, no reverse activation energy).[10] If the reaction is not barrierless, determination of $\Delta H^{\ddagger}_{diss,g}$ yields an overestimation of $\Delta H_{assoc,g}$. Providing that the solution structure is preserved in the gas phase, the contribution of ΔH_{solv} to the formation of a complex is simply the sum of the experimentally determined ΔH_{assoc} and $\Delta H^{\ddagger}_{diss,g}$ values [Eq. (2)].

$$\Delta H_{assoc} = \Delta H_{intrin} + \Delta H_{solv} = \Delta H_{assoc,g} + \Delta H_{solv} \approx -\Delta H^{\ddagger}_{diss,g} + \Delta H_{solv} \quad (2)$$

NMR spectroscopy and X-ray crystallography can be used to gain an insight into the structures of biomolecular complexes in solution. However, no techniques are available that allow direct characterization of the structure of large gaseous ions, so identification of the individual intermolecular interactions in gaseous biological complexes has not been possible. Our research group recently developed a novel reactivity-based approach that employs blackbody infrared radiative dissociation (BIRD),[10,11] a thermal dissociation technique implemented with a Fourier-transform ion cyclotron resonance mass spectrometer. We used a combination of BIRD and functional group replacement (FGR) to identify and quantify individual interactions in gaseous biomolecular complexes.[12,13] The main features of this approach are described below.

The potential energy surface for the dissociation of a gaseous biomolecular complex stabilized by multiple noncovalent interactions typically has a "staircase" appearance (Figure 1). Each step corresponds to the cleavage of an intermolecular interaction.[12] Dissociation of the complex proceeds by sequential cleavage of the intermolecular interactions. The transition state (TS) corresponds to the structure

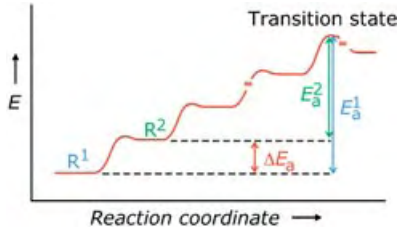


Figure 1. Energy diagram for the sequential cleavage of the intermolecular hydrogen bonds stabilizing two noncovalent complexes, R^1 and R^2, which differ by a single interaction. The strength of this interaction is equal to the difference in dissociation activation energy (E_a) between R^1 and R^2, that is, $\Delta E_a = E_a^1 - E_a^2$.

[*] Dr. E. N. Kitova, Dr. D. R. Bundle, Dr. J. S. Klassen
Department of Chemistry
University of Alberta
Edmonton, Alberta, T6G 2G2 (Canada)
Fax: (+1) 780-492-8231
E-mail: john.klassen@ualberta.ca

[**] The authors acknowledge the Natural Sciences and Engineering Research Council of Canada and the Alberta Ingenuity Centre for Carbohydrate Science for generous funding, and S. Marcus for assistance with the protein cloning.

Supporting information for this article is available on the WWW under http://www.angewandte.org or from the author.

 DOI: 10.1002/anie.200353051 © 2004 Wiley-VCH Verlag GmbH & Co. KGaA, Weinheim

formed during cleavage of the last remaining interaction. The thermodynamic formulation of transition-state theory states that the unimolecular reaction rate constant (k) reflects the enthalpy (or energy) difference between the TS and the reactant (R), in which all interactions are present [Eq. (3a,b); k_B is the Boltzmann constant, h is Planck's constant, and $\Delta S^{\neq}$ is the entropy of activation].

$$k = (k_B T/h)\exp(\Delta S^{\neq}/R)\exp(-\Delta H^{\neq}/RT) \quad (3a)$$

$$k = (k_B T/h)\exp(1+\Delta S^{\neq}/R)\exp(-E_a/RT) \quad (3b)$$

In the absence of extensive intramolecular solvation of groups originally involved in intermolecular interactions, E_a (determined from the temperature dependence of k) reflects the sum of *all* individual interactions in the reactant. The contribution of individual functional groups to the stability of the complex can be determined from the difference between the E_a values of structurally related complexes that differ by a single interaction. A change (decrease) in E_a coinciding with a structural modification (that is, $\Delta E_a = E_a$(unmodified complex)$-E_a$(modified complex)$\neq 0$) indicates that the modified group was involved in stabilizing the complex. If the structural modification eliminates a particular intermolecular interaction, ΔE_a provides a measure of the strength of the lost interaction.

A limited number of structural studies on gaseous noncovalent protein–ligand complexes have provided us with evidence that nonspecific interactions (interactions not present in solution that form during the desolvation process) can influence stability.[12,14] A modified methodology that focuses on the energies of individual interactions rather than on the overall energy of the entire collection of interactions is therefore more appropriate. Such a *single interaction* approach, while experimentally labor intensive, has the important advantage that it minimizes the influence of systematic error upon measurements (both solution and gas phase) because the quantities of interest are derived directly from the difference between two experimental values.

The contribution of a given solution-specific intermolecular interaction to the overall ΔH_{assoc} value can be determined by measuring the change in ΔH_{assoc} that results from the loss of the interaction, that is, $\Delta\Delta H_{assoc} = \Delta H_{assoc}$(unmodified complex)$-\Delta H_{assoc}$(modified complex). This approach is rigorously correct only when the individual interactions operate in an additive fashion but should provide a good approximation of the enthalpic contribution of specific interactions and is widely used in association thermochemistry to assess the contributions of particular functional groups or residues.[15] As outlined above, the strength of individual interactions in the gaseous complex is readily established from the ΔE_a values determined with the BIRD/FGR method. The enthalpy change resulting from solvent reorganization upon formation of a specific solute–solute interaction ($\Delta\Delta H_{solv}$) can be estimated as the difference between the change in binding enthalpy (energy) upon loss of the interaction in solution ($\Delta\Delta H_{assoc}$) and that in the gas phase ($-\Delta E_a$), as shown in Equation (4).

$$\Delta\Delta H_{assoc} = \Delta\Delta H_{intrin} + \Delta\Delta H_{solv} \approx -\Delta E_a + \Delta\Delta H_{solv} \quad (4)$$

We used this methodology to determine $\Delta\Delta H_{solv}$ for one of the specific hydrogen bonds in the complex formed by a single-chain variable domain fragment (scFv) from the carbohydrate-binding IgG antibody Se155-4 with its native trisaccharide ligand, Galα[Abe]Man (**1**). The complex of **1** with the Se155-4 antibody was the focus of a comprehensive study on carbohydrate recognition by proteins in aqueous solution. The crystal structure of the related scFv·**1** complex has been solved[16] (Figure 2) and the association thermochemistry of the complexation of this IgG with **1**, as well as with several monodeoxy congeners, has been determined by ITC.[17] The scFv·**1** complex is among the biomolecular

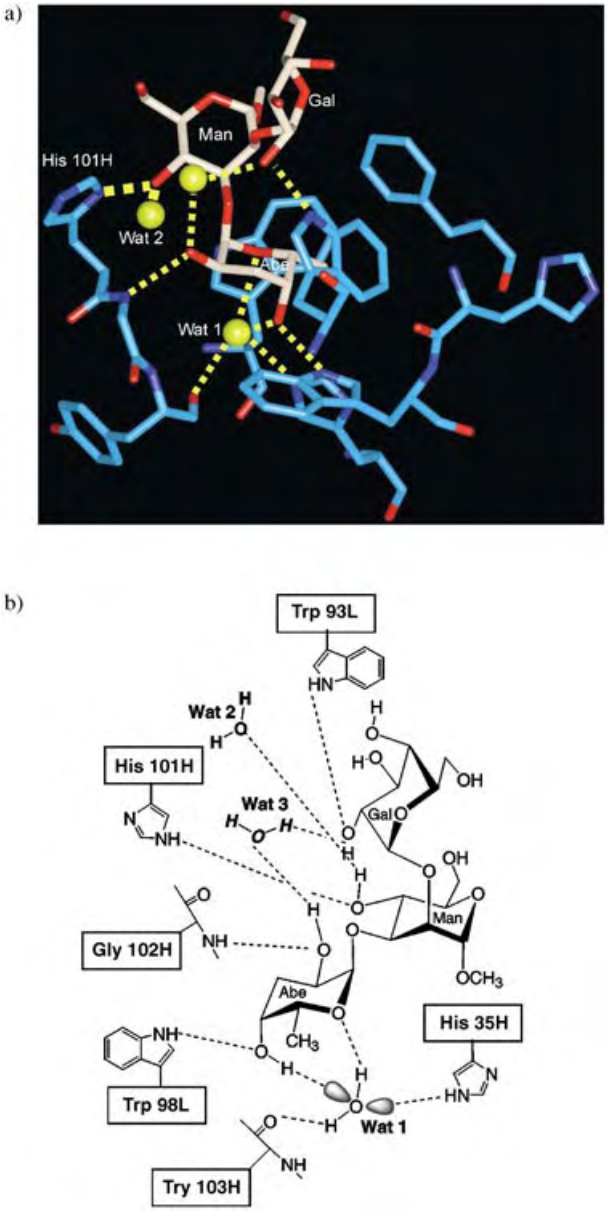


Figure 2. Crystal structure of the scFv·Galα[Abe]Man complex (scFv·**1**). a) Structure of the complex formed by the single-chain antibody fragment and the trisaccharide ligand Galα[Abe]Man. The H_{His101}–OH_{ManC4} hydrogen bond and the solvent-exposed nature of the mannose (Man) residue compared to the buried abequose (Abe) residue are shown. b) Detailed hydrogen-bonding map for scFv·**1**. Wat: water molecule.

 © 2004 Wiley-VCH Verlag GmbH & Co. KGaA, Weinheim

complexes most extensively investigated in the gas phase.[8,12,13,18] A previous gas-phase study of the scFv·**1** complex and complexes of structural analogues (produced by nanoelectrospray ionization) showed that the specific hydrogen bond H_{His101}–OH_{ManC4} present in solution (Figure 2) is preserved in the gas phase.[13] This is the first and, at present, only example of the preservation of a specific intermolecular interaction in a gaseous biomolecular complex.

The ΔH_{assoc} values of the complexes formed by scFv with **1** and with the Man C4 monodeoxy congener **2**, in which the H_{His101}–OH_{ManC4} hydrogen bond is absent, were determined by ITC. From these values, we calculated that $\Delta\Delta H_{assoc} = 1.7 \pm 0.3$ kcal mol^{-1} for the H_{His101}–OH_{ManC4} interaction.[16] In principle, the energy of the H_{His101}–OH_{ManC4} hydrogen bond determined for a single charge state of the scFv·**1** complex could be used in conjunction with the $\Delta\Delta H_{assoc}$ value to arrive at a value for $\Delta\Delta H_{solv}$. However, it is possible that electrostatic effects arising from the multiple charges on the gaseous complex influence the interaction. To establish that charge effects are not significant, we applied the BIRD/FGR approach to evaluate the H_{His101}–OH_{ManC4} interaction energy over a range of charge states (+6 to +10 and −8). The strength of the interaction was determined in three ways for each charge state: 1) by using functional group modification, whereby the interaction energy is determined from the difference between the E_a value of the scFv complex with **1** and that of the complex with the monodeoxy congener **2** (that is, ΔE_a), 2) active site mutation, whereby the interaction energy is determined from the ΔE_a value for the complexes formed by **1** with scFv and with a His101Ala mutant in which the His101 residue is replaced with alanine, and 3) pair-wise modification, whereby the interaction energy is determined from the ΔE_a value for the complex formed by scFv with **1** and that formed by the His101Ala mutant with **2**. Table 1 shows that we determined the same hydrogen-bond strength for each of the six charge states with all three modification strategies, within the precision of the measurements. The fact that the hydrogen-bond strength remains the same for all of the protonated and deprotonated ions implies that electrostatic effects do not significantly influence the interaction, at least at these low charge states. The average interaction energy determined for the six charge states by using the three modification strategies is 3.6 ± 1.2 kcal mol^{-1}. This value is lower than that calculated for a single hydrogen bond in an imidazole–H_2O complex (6 kcal mol^{-1}), which is the best available model for the H_{His101}–OH_{ManC4} interaction.[19] The lower energy calculated for the H_{His101}–OH_{ManC4} interaction may reflect the effect of steric or conformational structural constraints, which prevent optimal bonding.

Table 1: The differences between the Arrhenius activation energies [kcal mol^{-1}] measured upon loss of a neutral ligand from gaseous protonated and deprotonated scFv·**1** (I), His101Ala·**1** (II), scFv·**2** (III), and His101Ala·**2** (IV) in six charge states.

Charge state	ΔE_a (I)−(II)[a]	ΔE_a (I)−(III)[a]	ΔE_a (I)−(IV)[a]
+6	2.7±1.8	4.9±1.4	3.9±1.9
+7	4.1±1.1	4.0±2.1	3.0±1.6
+8	2.8±1.8	1.8±1.7	2.9±1.6
+9	4.7±1.7	1.9±1.6	2.7±1.0
+10	4.3±1.0	5.2±1.6	4.6±1.2
−8	3.1±1.3	3.8±1.0	3.9±1.4
Average ΔE_a[b]	3.6±1.0	3.6±1.5	3.5±1.0
$\Delta\Delta H_{solv}$[c,d]	5.3±1.3	5.3±1.7	5.2±1.3

[a] Errors were calculated by propagation of one standard deviation of the corresponding E_a values. [b] Mean values ± standard deviations for the six measurements. [c] $\Delta\Delta H_{solv}$ values [kcal mol^{-1}] calculated for the H_{His101}–OH_{ManC4} interaction from the ΔE_a and ΔH_{assoc} values determined for I and III by ITC: $\Delta\Delta H_{solv} = \Delta\Delta H_{assoc} + \Delta E_a$, where $\Delta\Delta H_{assoc} = 1.7 \pm 0.3$ kcal mol^{-1}.[14] [d] Errors were calculated by propagating one standard deviation of the $\Delta\Delta H_{assoc}$ and ΔE_a values.

The energetic data obtained in solution ($\Delta\Delta H_{assoc} = 1.7 \pm 0.3$ kcal mol^{-1}) and in the gas phase ($\Delta E_a = 3.6 \pm 1.2$ kcal mol^{-1}) were combined by using Equation (4) to give $\Delta\Delta H_{solv} = 5.3 \pm 1.4$ kcal mol^{-1} for the formation of the H_{His101}–OH_{ManC4} hydrogen bond. We believe that the magnitude of $\Delta\Delta H_{solv}$ corresponds to the net enthalpy change arising from the displacement of water molecules from the Man C4 hydroxy group and the His101 imidazole NH group, and the return of these water molecules to the bulk solution. Since our measurement is the first of its kind, it is not possible to compare our result with other measurements. However, the enthalpies of hydration of small model compounds have been determined calorimetrically and used to evaluate the enthalpies of hydration of various functional groups.[20] These values provide an estimate of the hydration enthalpy of polar and nonpolar groups associated with protein unfolding[20] and it is of interest to compare them with the $\Delta\Delta H_{solv}$ value determined in the study reported herein. The average enthalpies of hydration for OH and NH groups in small, linear molecules are −9.5 and −9.2 kcal mol^{-1}, respectively. The enthalpic penalty for completely dehydrating both an NH and an OH group is approximately 19 kcal mol^{-1}, a value roughly four times larger than our calculated $\Delta\Delta H_{solv}$ value. We believe the difference in these values has two origins: 1) The scFv·**1** crystal structure shows that the C4 OH group of Man is not fully dehydrated but remains associated with a single water molecule; 2) the chemical environments of the NH and OH groups in the protein and trisaccharide ligand are different from those in the small model systems. In the protein and trisaccharide, neighboring group effects may alter and reduce the strength of interactions between the NH and OH groups and solvent molecules. Consequently, 19 kcal mol^{-1} represents an upper limit for the dehydration enthalpy. This analysis highlights the dangers associated with the use of thermochemical parameters established for small, model systems to predict parameters for large, complex biological molecules.

The methodology described herein may be applied to other classes of biomolecular complexes and will allow the determination of solvent effects according to type of interaction and chemical environment. This information is imperative for the development of a molecular model of biological recognition. Such models could, in turn, lead to a paradigm shift in rational drug design and may aid the development of predictive models for protein folding.

Received: October 9, 2003
Revised: May 14, 2004 [Z53051]

 © 2004 Wiley-VCH Verlag GmbH & Co. KGaA, Weinheim

Keywords: mass spectrometry · molecular recognition · oligosaccharides · proteins · solvent effects

[1] a) R. P. Rand, *Science* **1992**, *256*, 618; b) M. F. Colombo, D. C. Rau, V. A. Parsegian, *Science* **1992**, *256*, 655 – 659.
[2] J. Israelachvili, H. Wennerström, *Nature* **1996**, *379*, 219 – 225.
[3] H. Gohlke, G. Klebe, *Angew. Chem.* **2002**, *114*, 2764 – 2798; *Angew. Chem. Int. Ed.* **2002**, *41*, 2644 – 2676.
[4] a) R. U. Lemieux, *Acc. Chem. Res.* **1996**, *29*, 373 – 380; b) M. C. Chervenac, E. J. Toone, *J. Am. Chem. Soc.* **1994**, *116*, 10533 – 10539.
[5] *Protein–Ligand Interactions. From Molecular Recognition to Drug Design* (Eds.: H.-J. Böhm, G. Schneider), Wiley-VCH, Weinheim, **2003**.
[6] J. J. Lundquist, E. J. Toone, *Chem. Rev.* **2002**, *102*, 555 – 578.
[7] O. Exner, *Prog. Phys. Org. Chem.* **1973**, *10*, 411 – 482.
[8] W. Wang, E. N. Kitova, J. S. Klassen, *J. Am. Chem. Soc.* **2003**, *125*, 13630 – 13631.
[9] J. F. Steinfeld, J. S. Francisco, W. L. Hase, *Chemical Kinetics and Dynamics*, Prentice Hall, New Jersey, **1998**.
[10] R. C. Dunbar, T. B. McMahon, *Science* **1998**, *279*, 194 – 197.
[11] W. D. Price, P. D. Schnier, R. A. Jockush, E. F. Strittmatter, E. R. Williams, *J. Am. Chem. Soc.* **1996**, *118*, 10640 – 10644.
[12] E. N. Kitova, D. R. Bundle, J. S. Klassen, *J. Am. Chem. Soc.* **2002**, *124*, 5902 – 5913.
[13] E. N. Kitova, D. R. Bundle, J. S. Klassen, *J. Am. Chem. Soc.* **2002**, *124*, 9340 – 9341.
[14] Q. Wu, J. Gao, D. Joseph-McCarthy, G. B. Sigal, J. E. Bruce, G. M. Whitesides, R. D. Smith, *J. Am. Chem. Soc.* **1997**, *119*, 1157 – 1158.
[15] F. A. Quiocho, N. K. Vyas in *Carbohydrates* (Ed.: S. Hecht), Oxford University Press, Oxford, **1998**, pp. 441 – 457; A. R. Fersht, J.-P. Shi, J. Knill-Jones, D. M. Lowe, A. J. Wilkinson, D. M. Blow, P. Brick, P. Carter, M. M. Y. Waye, G. Winter, *Nature* **1985**, *314*, 235 – 238.
[16] A. Zdanov, D. R. Bundle, S.-J. Deng, C. R. MacKenzie, S. A. Narang, M. N. Young, M. Cygler, *Proc. Natl. Acad. Sci. USA* **1994**, *91*, 6423 – 6427.
[17] D. R. Bundle, E. Eichler, M. A. J. Gidney, M. Meldal, A. Ragauskas, B. W. Sigurskjold, B. Sinnot, D. C. Watson, M. Yaguchi, N. M. Young, *Biochemistry* **1994**, *33*, 5172 – 5182.
[18] E. N. Kitova, W. Wang, D. R. Bundle, J. S. Klassen, *J. Am. Chem. Soc.* **2002**, *124*, 13980 – 13981.
[19] S. Scheiner, T. Kar, J. Pattanayak, *J. Am. Chem. Soc.* **2002**, *124*, 13257 – 13264.
[20] G. I. Makhatadze, P. L. Privalov, *J. Mol. Biol.* **1993**, *232*, 639 – 659.

 © 2004 Wiley-VCH Verlag GmbH & Co. KGaA, Weinheim

Supramolecular Machines

Towards Electrochemical Artificial Muscles: A Supramolecular Machine Based on a One-Dimensional Copper-Containing Organophosphonate System**

Kuan-Jiuh Lin, Shu-Juan Fu, Ching-Yuan Cheng, Wei-Hung Chen, and Hsien-Ming Kao*

Protein motors, such as myosin (from skeletal muscle) or kinesin (from the brain) are composed of mats of bipolar one-dimensional (1D) filaments. These filaments are set into motion either by an electrochemical reaction or by a chemical signal, which initiates a reversible contraction/stretched process.[1] To mimic the motions taking place in biological motors is very challenging. The mimetic nanofilaments should have mixed copper(II/I) centers and phosphate ligands and be self-assembled by much weaker π–π interactions. It is therefore of interest to explore the kind of supramolecular filaments that may be reversibly tuned simply by inserting and extracting ion species with an applied voltage. Such biomimetic concepts could lead to a new class of the battery-like actuations.[2–5]

Many inorganic 1D fibers, such as carbon nanotubes and conducting polymer, have been reported and investigated in the construction of smart actuator materials,[6,7] however, to date, relatively few examples of coordination-polymer-based artificial machines are known.[8] To maximize the potential of such supramolecular machines, we propose that the following are required: 1) the construction of a 1D supramolecular chain structure with redox active metal centers, especially mixed copper(II/I) centers,[9] 2) the introduction of metal-ion intercalation into the crystal at an arbitrary position, and 3) the introduction of crystal-volume change through an applied voltage.

Encouraged by our success in using ethylenediphosphate as a building block unit for the construction of extra-large molecular sieves under hydrothermal conditions,[10] we have turned our attention to the introduction of 1,10-phenanthroline (phen) units into the metal–organophosphate phases to

[*] Prof. Dr. K.-J. Lin, S.-J. Fu, C.-Y. Cheng, W.-H. Chen
Department of Chemistry
Center of Nanoscience and Nanotechnology
National Chung-Hsing University
Taichung 402 (Taiwan)
Fax: (+886) 4-2286-2547
E-mail: kjlin@dragon.nchu.edu.tw
Prof. Dr. H.-M. Kao
Department of Chemistry
National Central University, Chung-Li 32054 (Taiwan)

[**] We thank H. S. Sheu at Synchrotron radiation research center for technical assistance with XRD and XANES data. This work was supported by the National Science Council of Taiwan (NSC 92-2113-M005-028; NSC-92-2120-M-007-002) and the Institute of Chemistry, Academia Sinica.

Supporting information for this article is available on the WWW under http://www.angewandte.org or from the author.

 © 2004 Wiley-VCH Verlag GmbH & Co. KGaA, Weinheim DOI: 10.1002/anie.200454159

create 1D chain structures (Figure 1a). Green crystals of 1DOP-Cu (Figure 1) were grown from a reaction mixture of $CuCl_2 \cdot 2H_2O$, ethylenediphosphate, phen, and water in molar ratios of 2:1:1:1778 that was heated at 180 °C for 48 h in an

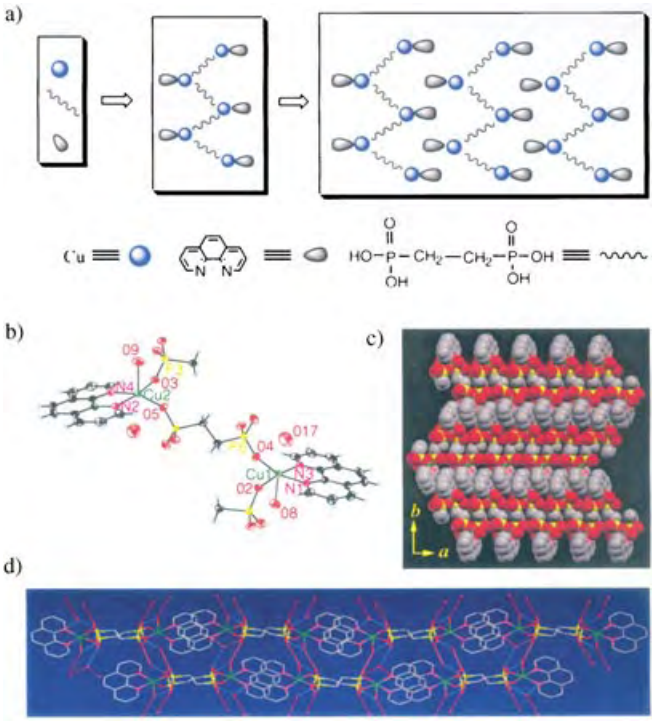


Figure 1. a) Schematic illustration of a macroscopic sheet generated by 1D chains. b) An ORTEP plot of a section of an infinite chain in 1DOP-Cu (thermal ellipsoids set at 50% probability). Selected bond lengths [Å]: Cu1–O2 1.934(3), Cu1–O4 1.936(4), Cu1–N1 2.002(4), Cu1–N3 2.020(4), Cu1–O8 2.391(4), Cu2–O3 1.945(3), Cu2–O5 1.940(3), Cu2–N2 2.011(3), Cu2–N4 2.025(4), Cu2–O9 2.277(4). c) Space-filling view of the *ab* plane showing the corrugated π–π network constructed from copper–ethylenediphosphate chains incorporating phen molecules. d) Perspective view of crystal packing along the *a* axis, showing adjacent layers are stacked on top of each other along the *c* axis and are held together by the hydrogen bonds. Green Cu, red O, pink N, yellow P, gray C.

autoclave. This hydrothermal synthesis gives a yield of 48% and is highly reproducible. The structure of 1DOP-Cu was determined by single-crystal X-ray analysis (Figure 1b–d). The structure reveals infinite 1D inorganic zigzag chains, [-Cu^{II}-O_3P-$(CH_2)_2$-PO_3-Cu^{II}-], in which the phen ligands are bound to the metal centers. The chain structure of 1DOP-Cu has three intriguing features. First, the backbone of 1DOP-Cu consists of phosphonate groups, at which acid-functionalized groups may serve as carriers of protons, the phosphonate groups can also serve as a solid-state matrix for metal-ion transport. Second, the incorporated phen ligands play an important role in the construction of a π-stacked layer structure between adjacent crystallographically symmetry-related chains, which makes the layered framework conducting. Like natural muscle fibers, the corrugated sheets are composed of mats of individual chain-bundles joined by π–π interactions along the crystallographic *a* axis. Third, both the two crystallographically distinct Cu^{II} atoms have square-pyramidal coordination geometries, chelated by two nitrogen atoms of the phen ligands, two oxygen atoms from two distinct ethylenediphosphate groups, and one coordinated water molecule. The triggering signals of actuator of 1DOP-Cu could be envisaged to be an electrochemical signal that initiates a redox process converting Cu^{II} into Cu^{I}. The proposed principle of the redox motion is shown in Figure 2.

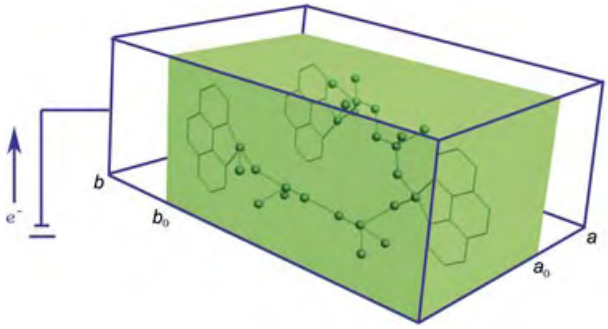


Figure 2. Schematic illustration of the increasing thickness of the sheet when it is charged negatively (green box 1DOP-Cu, blue box Li@1DOP-Cu). The strains, relative length change $\varepsilon_a = (a-a_0)/a_0 = \Delta a/a_0$, $\varepsilon_b = (b-b_0)/b_0 = \Delta b/b_0$, and the volume change $\varepsilon_V = (V-V_0)/V_0 = \Delta V/V_0$, are relative to the lattice parameters of 1DOP-Cu. The electrochemical actuator is based on materials that change in shape and dimension when a potential is applied. Water molecules and Li^+ ions can be intercalated between the layers by applying a negative voltage to the organophosphonate sheet. We proposed that the electrochemical intercalation of Li^+ ions must be compensated by some reduction of Cu^{II} ions in the sheet. Thus, to maintain electroneutrality, partial Cu^{I} ions are formed, which are much larger than Cu^{II} ions (0.91 Å instead of 0.71 Å). Fundamentally, Cu^{I} prefers four-coordinate binding mode whereas Cu^{II} prefers five-coordinate square-pyramidal geometry. Therefore, the reduction of Cu^{II} ions leads to a strong deformation of the chain structure, leading to the mechanical deformation of the whole sheet.

To achieve a new battery actuator, a mechanically robust framework is necessary. The stability of the layered structure was therefore assessed by thermogravimetric analysis (TGA) and in situ synchrotron powder X-ray diffraction (XRD) studies. The results show that the phosphonate groups are stable up to 300 °C in the presence of air or nitrogen.

Because the phosphonate groups can act as a solid-state matrix for lithium ions to make crystalline phases with fast ion conduction, the insertion or doping of a lithium compound in 1DOP-Cu was studied. Insertion was achieved by the recharge battery methodology[10] in the ionic liquid, $LiClO_4$, to give Li@1DOP-Cu. Electrochemical studies show that the charge-state of 1DOP-Cu was stable over a potential window of approximately 5 V, and especially a remarkable cyclabilty was traced between 3 and 5 volts (Figure 3). The electromechanical cycling of a battery shows an actuator response that can be detected during cyclic voltammetry, there are also concomitant changes in volume. It is evident from TGA analysis that the weight loss (9.8%) of the Li-inserted phase (Li@1DOP-Cu) is significantly larger than that (4.4%) of 1DOP-Cu upon heating up to 220 °C (Figure 4, inset). It is also of interest to compare the change in unit-cell volume.

 © 2004 Wiley-VCH Verlag GmbH & Co. KGaA, Weinheim

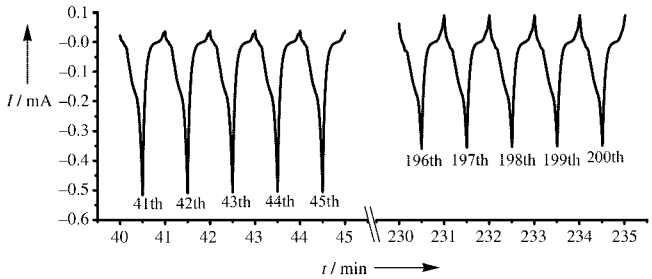


Figure 3. Current versus time plot for cyclic voltage changes in the range of 3–5 V for an anode graphite/cathode 1 DOP-Cu (**C** | 1 DOP-Cu) cell employing 1 M $LiClO_4$ in an electrolyte mixture of ethylene carbonate, dimethyl carbonate, and methyl formate ($T = 30\,°C$, scan rate 100 $mV s^{-1}$). The cyclability of 1 DOP-Cu by intercalating/de-intercalating lithium ions is shown (the numbers next to the peaks indicate the number of the cycle).

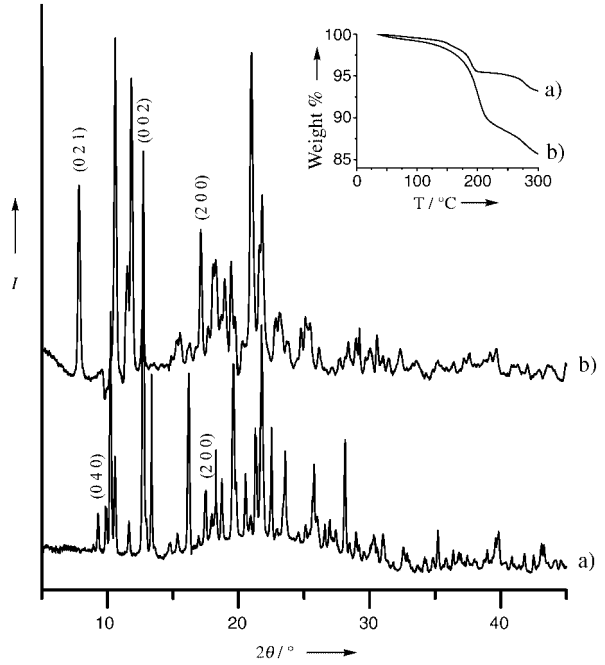


Figure 4. The XRD patterns (synchrotron radiation, $\lambda = 1.32633$ Å) of a) 1 DOP-Cu and b) Li@1 DOP-Cu. *I* is the X-ray intensity (arbitrary units). It is noteworthy that the simulated diffraction patterns based on the analysis of a single-crystal X-ray structure is in good agreement with the XRD patterns obtained for 1 DOP-Cu samples, which indicates that 1 DOP-Cu is a pure phase. (Li@1 DOP-Cu still has a monoclinic structure with the lattice constants $a = 9.51$, $b = 32.84$, $c = 12.88$ Å, $\beta = 110.5$, $V = 3767$ Å^3). The inset shows the corresponding weight loss of a) 1 DOP-Cu and b) Li@1 DOP-Cu, by TGA analysis.

According to the XRD patterns, the cell-volume strain $\Delta V/V_0$ change is 10.2%. Phenomenologically, the actuator must produce the observed volume change by a change in the basal-plane dimension rather than in the distance between layers. The corresponding XRD spectra are presented in Figure 4. It is worth noting that the distance between layers (d_{002}) remains constant whereas the dimension of the unit cell of the corrugated sheets changes, which is caused by the uneven stress along the *a* and *b* axes. The variation of the strain $\Delta a/a_0$ and $\Delta b/b_0$ is 3.8% and 6.2%, respectively. The larger strain in the *b* axis direction during actuation could be due to the weakness of the π–π repulsions between chains. The whole thickness within the framework sheet increases owing to the strong deformation of the redox chain structure when it is charged negatively (see the Supporting Information movie file). This result may be similar to the battery-like actuation mechanism of conducting polymers where a redox reaction must occur to enable the flux of ionic dopant.[7,11]

Elucidating the mechanism of the deformation of the chain structure upon lithium insertion into crystals of 1 DOP-Cu is interesting for developing supramolecular machines. To address this problem, solid-state nuclear magnetic resonance (SSNMR) and X-ray absorption spectroscopy were used to elucidate the lithium-inserted state of 1 DOP-Cu. In ^{7}Li NMR spectrum, a chemical shift of $\delta = +1.8$ ppm for the Li^+ ion is small enough to assign the lithium residing in the phosphoric matrix as being in a highly ionic state rather than a metallic state. Moreover, it appears that the narrow line width (full width at half height, ≈400 Hz) offers a conclusive evidence for lithium-ion motion in crystalline Li@1 DOP-Cu.[12,13] Lithium-ion coordination contributes to the reversible charge–discharge reaction which takes place at the bonding orbitals of the Cu-O-P-O units. Evidence for the partial electronic reduction of Cu^{II} in Li@1 DOP-Cu was provided by ^{31}P-{^{1}H} MAS (magic-angle spinning) NMR data (Figure 5a). Owing to the paramagnetic character of the bonding orbital of $Cu^{II}(d^9)$-O-P-O in 1 DOP-Cu, the ^{31}P NMR spectrum reveals a significant downfield chemical shift with associated spinning sidebands in the range $\delta = 200$–1000 ppm, whereas in the lithium-inserted state, Li@1 DOP-Cu ($Cu^{I}(d^{10})$-O-P-O···Li^+)

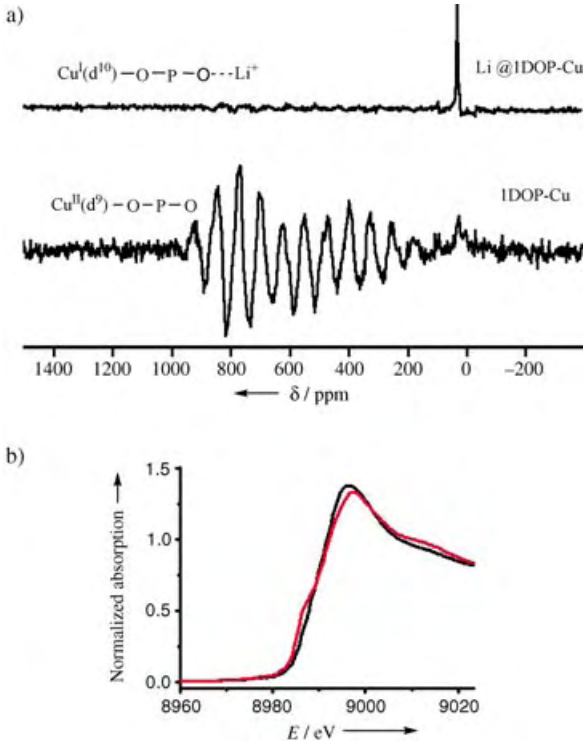


Figure 5. Monitoring the redox process in solid actuator by a) ^{31}P-{^{1}H} MAS NMR and b) XANES spectra. Red Li@1 DOP-Cu, black 1 DOP-Cu.

 © 2004 Wiley-VCH Verlag GmbH & Co. KGaA, Weinheim

the chemical shift is $\delta = 31$ ppm. Finally, it is necessary to examine whether the coordination geometry of Cu^{II} or Cu^{I} is changed in the redox process, a key concept of artificial machines postulated by Sauvage.[9] X-ray absorption near edge spectra (XANES) is often used as a probe for the ligand-field geometry, electronic structure, and oxidation state of the metal center.[14] The synchrotron radiation XANES spectra for lithium (de)insertion states are shown in Figure 5b. A comparison of the XANES spectra reveals that the lithium-inserted state has a shoulder or partially resolved peak on the rising edge at 8985.4 eV in addition to 1s→3d pre-edge transition at 8991.8 eV, which suggests different environments in the geometry around the metal ions. It is observed that only a pre-edge peak from a 1s→3d transition is found in the XANES spectra of square-pyramidal copper-based 1DOP-Cu. For Li@1DOP-Cu the significant shoulder on the low-energy side of the edge was assigned to a $1s \rightarrow 4p_z$ transition in accordance with the destabilization of $4p_z$ metal orbital (z being the elongation axis), suggesting distortion from square-pyramidal into a square-planar geometry. It is reasonable to assume that 1DOP-Cu could afford machines that are electrochemically muscle-like, with basal planes that allow the conversion of the five-coordinate (Cu^{II}) geometry into the four-coordinate (Cu^{I}) arrangement and vice versa.

The electrochemical actuator process presented herein provides an approach for studying the actuating mechanism of natural molecular motor, this being one of the key goals for the progress of molecular motor technology. Not only could this work lead to the development of all-solid-state rechargeable lithium batteries, but also our approach could open the route for the design of new ionic-switched electrochemical artificial muscle systems.

Experimental Section

Synthesis of 1DOP-Cu: The reaction was carried out in a 23-mL teflon-lined acid digestion bomb (Parr), heated in a programmable electric furnace (Lindberg/Blue). A reaction mixture of $CuCl_2 \cdot 2H_2O$ (0.0850 g, 0.5 mmol), ethylenediphosphate (0.2850 g, 0.24 mmol), 1,10-phenanthroline monohydrate (0.0493 g, 0.24 mmol), and H_2O (8 mL) was sealed in a 23 mL teflon-lined stainless autoclave, heated at 100 °C for 2 h at 120 °C h^{-1}, then heated at 180 °C for 48 h, then cooled to 70 °C at 9 °C h^{-1} and then allowed to cool to room temperatue. The resulting blue-green crystals were collected by filtration, and washed with deionized water. Yield 48 %.

The X-ray diffraction data were collected on a CCD Bruker AXS SMART-1000 diffractometer with monochromated $Mo_{K\alpha}$ radiation ($\lambda = 0.71069$ Å) in the $\omega/2\theta$ scan. Crystal size $0.211 \times 0.277 \times 0.278$ mm, monoclinic, space group $P2(1)/n$, $a_0 = 9.1579(18)$, $b_0 = 30.916(6)$, $c_0 = 12.882(3)$ Å, $\beta_0 = 110.52(3)$; $V_0 = 3415.7(12)$ Å^3, $Z = 4$, $F(000) = 1864$, $\sigma = 1.796$ Mg m^{-3}, $2\theta max = 55^o$; $R1 = 0.0778$, $wR_2(F^2) = 0.2586$, and $GOF = 1.086$; residual electron density between 2.499 and -1.353 e Å^{-3}. CCDC-228650 contains the supplementary crystallographic data for this paper. These data can be obtained free of charge via www.ccdc.cam.ac.uk/conts/retrieving.html (or from the Cambridge Crystallographic Data Centre, 12 Union Road, Cambridge CB21EZ, UK; fax(+44)1223–336–033; or deposit@ccdc.cam.ac.uk).

All solid-state NMR spectra were recorded on a Bruker AVANCE-400 spectrometer with a standard Bruker double-tuned 4 mm probe; ^{31}P 161.73 mHz and ^{7}Li 155.45 MHz. A $\pi/2$ pulse length of 4 μs and a recycle delay of 10 s were used to acquire all the NMR spectra. ^{31}P MAS spectra were obtained under conditions of high-power proton decoupling. Chemical shifts of ^{31}P and ^{7}Li were externally referenced to 85 % H_3PO_4 and 1 M LiCl(aq), respectively.

Received: March 2, 2004 [Z54159]

Keywords: actuators · biomimetic chemistry · copper · lithium · supramolecular chemistry

[1] I. Fujiwara, S. Takahashi, H. Tadakuma, T. Funatsu, S. Ishiwata, *Nat. Cell Biol.* **2002**, *4*, 666–673.
[2] G. Gu, M. Schmid, P. W. Chiu, A. Minett, J. Fraysse, G. T. Kim, S. Roth, M. Kozlov, E. Muñoz, R. H. Baughman, *Nat. Mater.* **2003**, *2*, 316–319.
[3] J. Weissmüller, R. N. Viswanath, D. Kramer, P. Zimmer, R. Würschum, H. Gleiter, *Science* **2003**, *300*, 312–315.
[4] W. Lu, A. G. Fadeev, B. Qi, E. Smela, B. R. Mattes, J. Ding, G. M. Spinks, J. Mazurkiewicz, D. Zhou, G. G. Wallace, D. R. MacFarlane, S. A. Forsyth, M. Forsyth, *Science* **2002**, *297*, 983–987.
[5] T. F. Otero, M. T. Cortés, *Adv. Mater.* **2003**, *15*, 279–282.
[6] R. H. Baughman, C. Cui, A. A. Zakhidov, Z. Iqbal, J. N. Barisci, G. M. Spinks, G. G. Wallace, A. Mazzoldi, D. D. Rossi, A. G. Rinzler, O. Jaschinski, S. Roth, M. Kertesz, *Science* **1999**, *284*, 1340–1344.
[7] E. W. H. Jager, E. Smela, O. lnganäs, *Science* **2000**, *290*, 1540–1545.
[8] J. P. Collin, C. Dietrich-Buchecker, P. Gaviña, M. C. Jimenez-Molero, J. P. Sauvage, *Acc. Chem. Res.* **2001**, *34*, 477–487.
[9] M. C. Jimenez-Molero, C. Dietrich-Buchecker, J. P. Sauvage, *Chem. Commun.* **2003**, *14*, 1613–1616.
[10] C.-Y. Cheng, S.-J. Fu, C.-J. Yang, W.-H. Chen, K.-J. Lin, G.-H. Lee, Y. Wang, *Angew. Chem.* **2003**, *115*, 1981–1984; *Angew. Chem. Int. Ed.* **2003**, *42*, 1937–1940.
[11] E. Smela, *Adv. Mater.* **2003**, *15*, 481–494.
[12] Z. Gadjourova, Y. G. Andreev, D. P. Tunstall, P. G. Bruce, *Nature* **2001**, *412*, 520–523.
[13] T. Nakamura, T. Akutagawa, K. Honda, A. E. Underhill, A. T. Coomber, R. H. Friend, *Nature* **1998**, *394*, 159–162.
[14] T. A. Smith, J. E. Penner-Hahn, M. A. Berding, S. Doniach, K. O. Hodgson, *J. Am. Chem. Soc.* **1985**, *107*, 5945–5955.

 © 2004 Wiley-VCH Verlag GmbH & Co. KGaA, Weinheim

Contact Printing

Forced Peptide Synthesis in Nanoscale Confinement under Elastomeric Stamps**

*Terena P. Sullivan, Maaike L. van Poll, Patricia Y. W. Dankers, and Wilhelm T. S. Huck**

In solution, only collisions between molecules of sufficient energy to overcome the activation barrier lead to the formation of reaction products. The rate of the reaction is influenced by the temperature, concentration of the reactants, solvent, orientation of the reactants, and structure of the molecules. Catalysts or enzymes lower the activation energy by making available alternative reaction pathways and preorganize the reactant molecules in close proximity, which leads to an increase in the effective concentration of the reactants.[1] Herein, we report the first example in which a reaction (amide-bond formation) is made possible because the reactant molecules are physically pushed together. An elastomeric stamp (as used in microcontact printing[2]) comes into conformal (van der Waals) contact with a functionalized surface,[3] thus forcing "ink" molecules very close to the surface. We speculate that the nanoscale confinement of the ink at the interface between the stamp and the self-assembled monolayer (SAM), in combination with the preorganization of the reactants in the monolayer, facilitates the formation of covalent bonds.

The on-chip synthesis of single-strand DNA molecules has revolutionized genotyping research. Fodor and co-workers[4,5] developed photolithographic techniques in combination with wet surface chemistry to attain >99% yield in coupling steps for the preparation of libraries of peptides or oligonucleotides. Usually, a range of catalysts and activated substrates are required for efficient covalent-bond formation on surfaces. In our research on patterned self-assembled monolayers, we were intrigued by the rapid and efficient formation of SAMs on gold or Si/SiO_2 through the use of microcontact printing (μCP).[2] When an elastomeric stamp inked with trichloroalkyl silanes is placed on a clean Si/SiO_2 surface, the formation of the polysiloxane network is essentially complete within minutes, whereas this process could take hours in solution. Microcontact printing has previously been used to couple molecules to a reactive surface, but in all cases a catalyst or activated substrate was used to induce covalent-bond formation.[6–9] Herein we report the formation of new bonds solely as a result of the nanoscale confinement of molecules between stamp and surface.

Amide-bond formation is a suitably challenging test case, as such reactions require catalysts (4-(dimethylamino)pyridine (DMAP), *N*-hydroxybenzotriazole (HOBT), or dicyclohexylcarbodiimide (DCC)) or elevated temperatures and long reaction times when performed in solution. In a typical reaction (Figure 1), we prepared a clean amine-terminated SAM surface on gold. To ensure all amines were deprotonated, we washed the surface with a saturated solution of K_2CO_3. A flat hydrophilic stamp (treated for 30 s with an oxygen plasma and stored under millipore water) was inked with a solution of an appropriate Boc-protected amino acid (1 mM) in ethanol, dried under a stream of nitrogen, and placed on this surface. If necessary the sample was heated with the stamp on a hotplate (to approximately 40 °C). After a certain reaction time, the stamp was lifted off and the substrate washed vigorously with ethanol and water to remove all noncovalently bound molecules. The surfaces were then characterized by ellipsometry, FTIR spectroscopy, and contact angle goniometry.

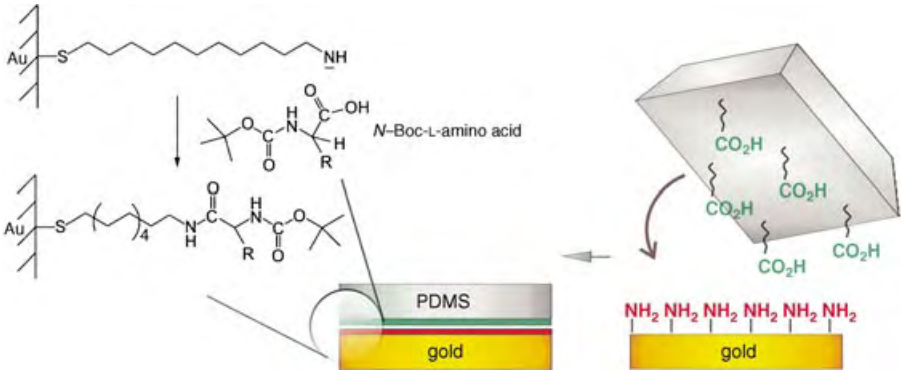


Figure 1. Printing a Boc-protected amino acid onto a reactive amine SAM. A plasma-oxidized flat PDMS stamp inked with an *N*-Boc-L-amino acid is pressed into contact with an amine monolayer on gold for a series of reaction times and temperatures. After the stamp has been lifted off, the substrate is rinsed thoroughly to remove any noncovalently bound molecules. Boc = *tert*-butoxycarbonyl, PDMS = poly(dimethylsiloxane).

In Figure 2 a typical results of the ellipsometry measurements are shown for three different amino acids. We found that Boc-protected proline (Boc-proline) was the most reactive amino acid with a maximum thickness increase observed after only 10 s. Fmoc-protected alanine (Fmoc-alanine) was also reactive at room temperature but a reaction

[*] T. P. Sullivan, M. L. van Poll, Dr. W. T. S. Huck
Melville Laboratory for Polymer Synthesis
Department of Chemistry, Cambridge University
Lensfield Road, Cambridge CB2 1EW (UK)
Fax: (+44) 1223-334-866
E-mail: wtsh2@cam.ac.uk
Dr. P. Y. W. Dankers
Eindhoven University of Technology
Chemical Engineering and Chemistry
PO Box 513, Helix STO 4.36
5600 MB Eindhoven (The Netherlands)

[**] This work was funded in part by the BBSRC and Biorobotics. We thank Prof. E. W. Meijer and Prof. A. J. Kirby for valuable discussions.

 © 2004 Wiley-VCH Verlag GmbH & Co. KGaA, Weinheim DOI: 10.1002/anie.200460271

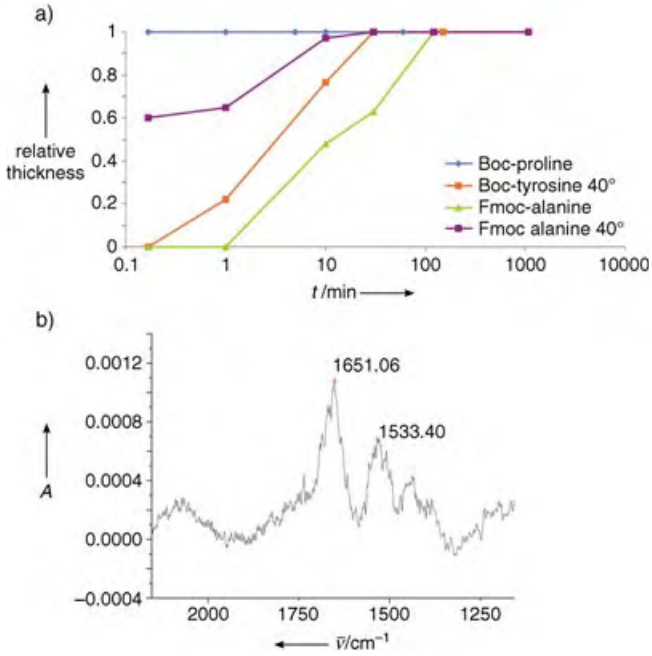


Figure 2. a) Ellipsometry data showing the thickness increase versus contact time for a series of amino acids; b) FTIR spectrum of proline covalently attached to an amine SAM. Fmoc = 9-fluorenylmethoxycarbonyl.

time of 30 mins was required for a maximum thickness to be reached. However, Boc-protected tyrosine (Boc-tyrosine) required a reaction temperature of 40 °C and a printing time of 30 min. The different reactivities of the various amino acids indicate that a chemical reaction takes place. After removal of the Boc protecting group under acidic conditions (25 % trifluoroacetic acid in dichloromethane, 10 min), we measured the FTIR spectrum of the proline bound to the amine-terminated SAM (Figure 2b). The bands at $\tilde{\nu} = 1651$ and 1533 cm^{-1} are characteristic for amide I and amide II absorptions. The only source for these absorptions is the formation of amide bonds between printed amino acids and amine-terminated SAMs. We also observed changes in the advancing contact angles from 61° for the free amine to 74° for Boc-tyrosine, 82° for Boc-proline, and 83° for Fmoc-alanine, which changed to 76° after deprotection.

As a control, a flat oxidized PDMS stamp was immersed in ethanol with no reagent; the stamp was dried as before and printed onto an amine monolayer for 30 min at room temperature**.** Ellipsometry showed an increase in thickness of 0.2 nm, but this is within the error of ellipsometry measurements on gold and consistent with the findings of Glasmastar et al.[10] The experiment was repeated with a 10 mM solution of Boc-proline in ethanol and a non-oxidized stamp. The ethanolic solution did not ink the hydrophobic PDMS stamp in a homogeneous way, and only a patchy increase of < 0.3 nm was observed. The silica layer of the oxidized PDMS can act as an acid catalyst,[11] and to show that this did not influence our reactions under the stamp, we prepared permanently hydrophilic PEG-coated stamps according to Delamarche et al.[12] When we repeated the chemistry with the modified stamp, our result was consistent with the results with our nonmodified stamps, thus indicating that there is no acid effect on the PDMS. Finally we attempted the reaction without the use of a stamp. A drop of the solution of Boc-proline was placed on the surface of an amine SAM, and the solvent was allowed to evaporate. The surface was left overnight, and ellipsometry showed no evidence of a reaction having taken place. Again the thickness increase was 0.2 nm, which is within the error limits of the instrument.

The tripeptide arginine–glycine–aspartate (RGD) is involved in the interactions between extracellular matrix proteins, such as fibronectin, and the integrin proteins located in the cell membranes of most human cells. The immobilization of RGD peptides on a surface enhances the adhesion of tissue-forming cells.[13–15] To further support our hypothesis we decided to synthesize the tripeptide RGD on the surface through multiple stamping steps. The first step involved printing a {2-[2-(Fmoc-amino)ethoxy]ethoxy}acetic acid (Fmoc-AEEA-OH) linker onto an aminopropyltrimethoxysilane (APTS) SAM on silicon. Subsequent removal of the Fmoc group was followed by printing Boc-aspartate (D), Boc-glycine (G), and Boc-arginine (R) (to allow for the correct N–C coupling direction). 3T3 mouse cells were seeded in cell-culture medium without fetal bovine serum (FBS) on top of treated surfaces; under these conditions no nonspecific cell spreading was observed. Cell attachment was evident, however, on the printed surfaces, thus indicating that the RGD was present on the surface, and that a multistep sequence can be carried out by repetitive stamping (Figure 3).

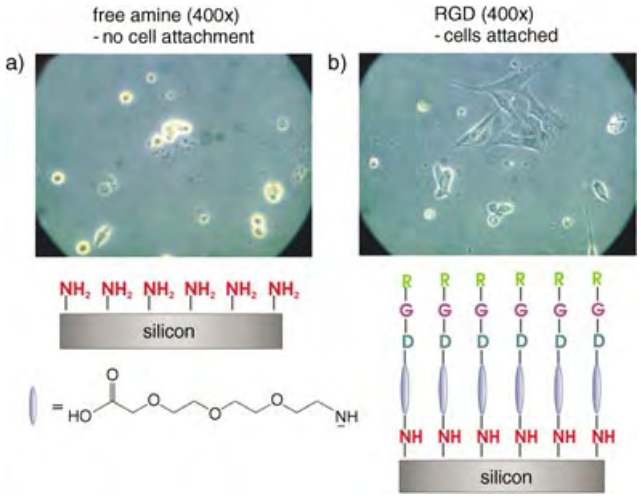


Figure 3. Microscope images to illustrate cell growth on an RGD surface: a) On amine surfaces, the cells are still round and not stretched, as the cells do not attach in the absence of proteins in solution; b) cells are attached and stretched as a result of the presence of the tripeptide RGD on the surface.

To demonstrate the viability of this approach, a 20-mer peptide nucleic acid (PNA) strand was synthesized step by step on the surface. First the Fmoc-AEEA-OH spacer was printed onto the APTS monolayer. Unreacted amines were acylated with a capping solution (acetic anhydride/2,6-lutidine/*N*,*N*-dimethylformamide (DMF)) to prevent further unwanted reactions. The Fmoc protecting groups were

 © 2004 Wiley-VCH Verlag GmbH & Co. KGaA, Weinheim

subsequently removed with DMF/piperidine. By using the same printing activation cycle and commercially available nucleotides the sequence CACTGAACCTGCCTACCTAA-Fmoc was printed in 20 steps. Ellipsometry measurements showed a steady increase in thickness with each base that was added, and a slight decrease for each Fmoc group removed (Figure 4). The ellipsometry data show a fairly linear increase in thickness for the first five bases (Figure 4c), but deviation from the initial slope seems to indicate a decrease in "yield", that is, thickness increase per base. The final thickness of the PNA 20-mer is roughly half that which could be expected from extrapolation of the initial increases. However, per printing step, this would still mean an average of well over 90% efficiency.

The PNA chip was also analyzed by FTIR spectroscopy (Figure 4d). The spectrum shows clear evidence of amide bonds in the PNA chain at $\tilde{\nu} = 1650\ cm^{-1}$. There is also evidence for phenyl-ring stretching vibrations at $\tilde{\nu} = 1550\ cm^{-1}$. The peak at $\tilde{\nu} = 1745\ cm^{-1}$ is due to the urethane groups of the benzhydryloxycarbonyl (Bhoc) protecting groups. A band of peaks at around $2950\ cm^{-1}$ (not shown) result from the different types of CH stretching. The peak at $1465\ cm^{-1}$ might arise from the conjugated C–N double bonds in the purine and pyrimidine molecules.

Prior to hybridization, the terminal Fmoc group was removed, followed by the Bhoc groups along the PNA backbone (50% trifluoroacetic acid, 2 h). The PNA on the surface was hybridized with a DNA 16-mer that was complementary to the 16 top-most bases with a hexaethylene glycol–Cy3 fluorophore attached. The hybridization was visualized by using a laser fluorescence scanner (Figure 4b). There was a clear increase in fluorescence on the PNA-modified surfaces after removal of the Bhoc protecting groups. On another section of the silicon chip two other non-complementary PNA sequences were prepared, one with a 6-base and the other with a 20-base mismatch. The DNA probe described earlier did not hybridize with these sequences, thus demonstrating a lack of nonspecific binding and that all fluorescence intensity is due to the presence of the PNA 20-mer.

We have demonstrated that a covalent amide bond is formed in the absence of catalysts or activated substrates in the nanoscale confinement between stamp and surface. The interaction of DNA molecules and cells with these surfaces provides further proof of the viability of our approach. This rapid method of forming covalent bonds is now being investigated for its ability to promote reactions that normally require high temperatures, pressures, or catalysts. We are also carrying out kinetic studies to determine the actual rate enhancement in this system. We believe this printing method has enormous potential for applications in the field of peptide arrays for protein studies. The formation of new covalent bonds can be combined with nanocontact printing[16] as a means to synthesize molecules on the sub-50-nm scale.

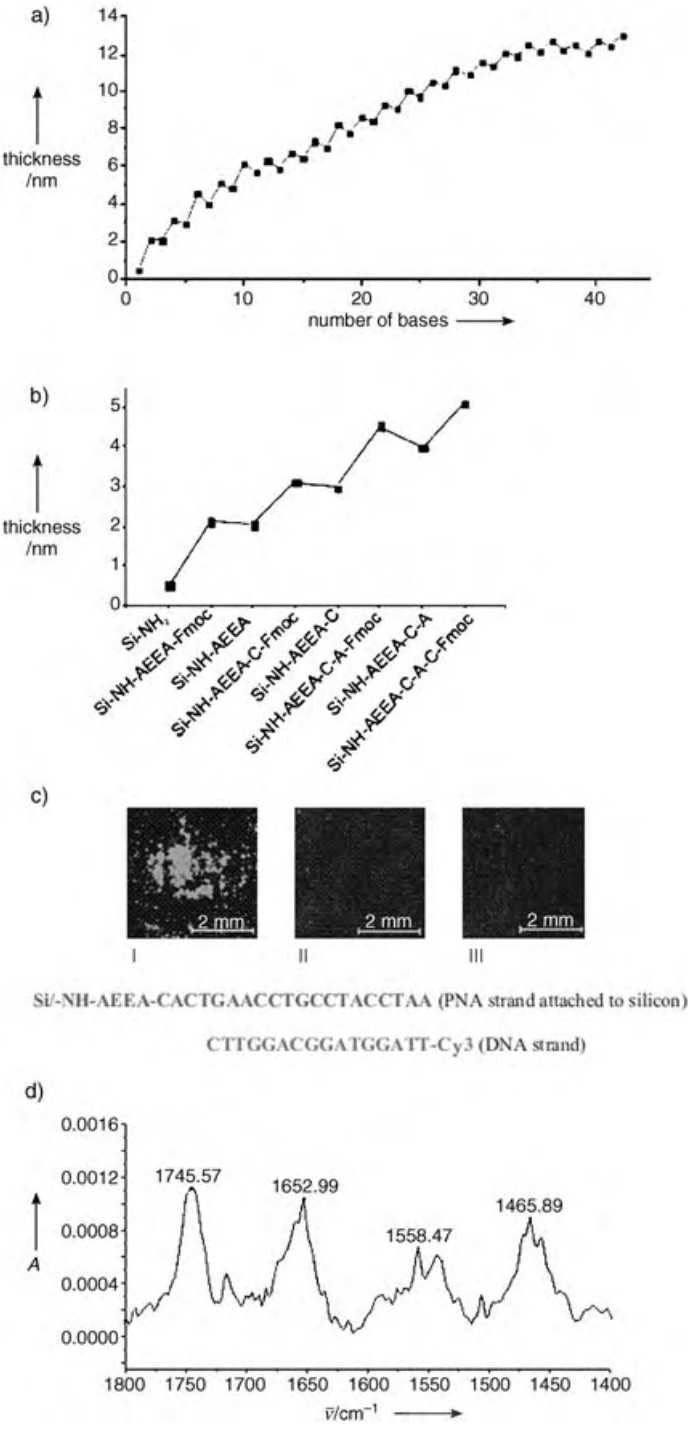


Figure 4. a), b) Ellipsometry data showing the increase in thickness with increasing number of PNA bases. c) I) Positive hybridization with a complementary DNA–Cy3 probe; II) negative hybridization with a 6-base (consecutive, mid-chain) mismatch; III) negative hybridization with a 16-base mismatch. d) FTIR spectrum of the PNA chains on the silicon wafer. Cy3 = indocarbocyanine.

Experimental Section

All Boc-protected amino acids were purchased from Novabiochem with >98% purity and checked in-house by mass spectrometry for Fmoc acid and Boc residues. PNA monomers, the AEEA linker, and deblocking reagents were purchased from Applied Biosystems. 11-

 © 2004 Wiley-VCH Verlag GmbH & Co. KGaA, Weinheim

sulfanylundecylammonium chloride was synthesized according to a procedure described elsewhere.[17] The Cy3 fluorescence DNA probe was obtained from Amersham Biosciences. All other materials were used as received from Aldrich. Ethanol was obtained as AR grade 100% and all water used was obtained from a Milli-Q water purification system at 18.2 MΩ. All substrates were stored under nitrogen gas. Ellipsometry measurements were carried out on a DRE ELX-02C ellipsometer with a 632.8-nm laser at 70° from the normal. A refractive index of 1.5 was assumed for all monolayers used. FTIR transmittance FTIR spectra were recorded on a BioRad FTS 6000 spectrometer. The gold was evaporated by using a BOC Edwards Auto500 Thermal Evaporator & RF Sputter Coater (NXE-141-000) in thermal deposition mode. Contact angle goniometry was performed by using a homemade stage comprised of a computer-controlled micro syringe and digital camera. The fluorescent probe was made visible on an Axon instruments Genepix personal 4100A scanner. Poly(dimethylsiloxane) (PDMS) elastomeric stamps were made as described in the literature. All PDMS stamps were freshly oxidized by using an Emitech K1050X plasma asher for 30 s.

Received: April 4, 2004 [Z460271]

Keywords: cell adhesion · contact printing · nanotechnology · peptides · surface chemistry

[1] S. J. Benkovic, S. Hammes-Schiffer, *Science* **2003**, *301*, 1196.
[2] Y. Xia, G. M. Whitesides, *Angew. Chem.* **1998**, *110*, 568; *Angew. Chem. Int. Ed.* **1998**, *37*, 551.
[3] A. K. Geim, S. V. Dubonos, I. V Grigorieva, K. S. Novoselov, A. A. Zhukov, S. Y. Shapoval, *Nat. Mater.* **2003**, *2*, 461.
[4] S. P. A. Fodor, J. L. Read, M. C. Pirrung, L. Stryer, A. T. Lu, D. Solas, *Science* **1991**, *251*, 767.
[5] A. C. Pease, D. Solas, E. J. Sullivan, M. T. Cronin, C. P. Holmes, S. P. A. Fodor, *Proc. Natl. Acad. Sci. USA* **1997**, *94*, 5022.
[6] P. F. Xiao, N. Y. He, Z. C. Liu, Q. G. He, X. Sun, Z. H. Lu, *Nanotechnology* **2002**, *13*, 756.
[7] L. Yan, C. Marzolin, A. Terfort, G. M. Whitesides, *Langmuir* **1997**, *13*, 6704.
[8] L. Yan, W. T. S. Huck, X. M. Zhao, G. M. Whitesides, *Langmuir* **1999**, *15*, 1208.
[9] T. P. Sullivan, W. T. S. Huck, *Eur. J. Org. Chem.* **2003**, *1*, 17.
[10] K. Glasmastar, J. Gold, A. S. Andersson, D. S. Sutherland, B. Kasemo, *Langmuir* **2003**, *19*, 5475.
[11] X.-M. Li, M. Péter, J. Huskens, D. N. Reinhoudt, *Nano Lett.* **2003**, *3*, 1449.
[12] E. Delamarche, M. Geissler, A. Bernard, H. Wolf, B. Michel, J. Hilborn, C. Donzel, *Adv. Mater.* **2001**, *13*, 1164.
[13] B. T. Houseman, M. Mrksich, *Biomaterials* **2001**, *22*, 943.
[14] M. N. Yousaf, B. T. Houseman, M. Mrksich, *Angew. Chem.* **2001**, *113*, 1127; *Angew. Chem. Int. Ed.* **2001**, *40*, 1093.
[15] M. Mrksich, *Chem. Soc. Rev.* **2000**, *29*, 267.
[16] H. W. Li, B. V. O. Muir, G. Fichet, W. T. S. Huck, *Langmuir* **2003**, *19*, 1963.
[17] J. Tien, A. Terfort, G. M. Whitesides, *Langmuir* **1997**, *13*, 5349.

 © 2004 Wiley-VCH Verlag GmbH & Co. KGaA, Weinheim

Cysteine Protease Inhibitors

Design and Synthesis of Endoperoxide Antimalarial Prodrug Models**

Paul M. O'Neill, Paul A. Stocks, Matthew D. Pugh, Nuna C. Araujo, Edward E. Korshin, Jamie F. Bickley, Stephen A. Ward, Patrick G. Bray, Erica Pasini, Jill Davies, Edite Verissimo, and Mario D. Bachi**

There has been an increase in support for combination chemotherapy as a rational strategy to combat malaria.[1] It is anticipated that, in addition to pharmacodynamic benefits such as the synergistic effect of drugs, combination therapy will delay the development of drug resistance in the malaria parasite *P. falciparum*. For malaria chemotherapy it was suggested that one component of such a drug combination should be a 1,2,4-trioxane-containing artemisinin derivative, as these compounds show fast antiparasitic action.[2,3] Very recently, an extension of this approach resulted in the elaboration of new potent modular antimalarial agents. These active compounds each contain two antimalarial pharmacophores, such as 1,2,4-trioxane and aminoquinoline[4,5] or an aliphatic diamine,[6] within the same molecule.

Herein, we describe a paradigm for a masked combination chemotherapy which relies on the embedding of a number of active components, in a latent form, within a single endoperoxidic chemical entity. Following penetration as a "Trojan horse" into the ferrous-rich food vacuole (FV) of the malaria parasite, these endoperoxidic prodrugs will be unmasked by in situ iron(II)-mediated fragmentation thus releasing multiple parasiticidal entities.[7]

Our approach is illustrated by means of the purposely designed bicyclic endoperoxide prodrug prototypes **1** and subsequently proved through the study of model compounds **2**. The substituents at position 4 in **1** should secure the in situ generation of chalcones of type **3** alongside additional noxious species as shown in Scheme 1. Some of these active

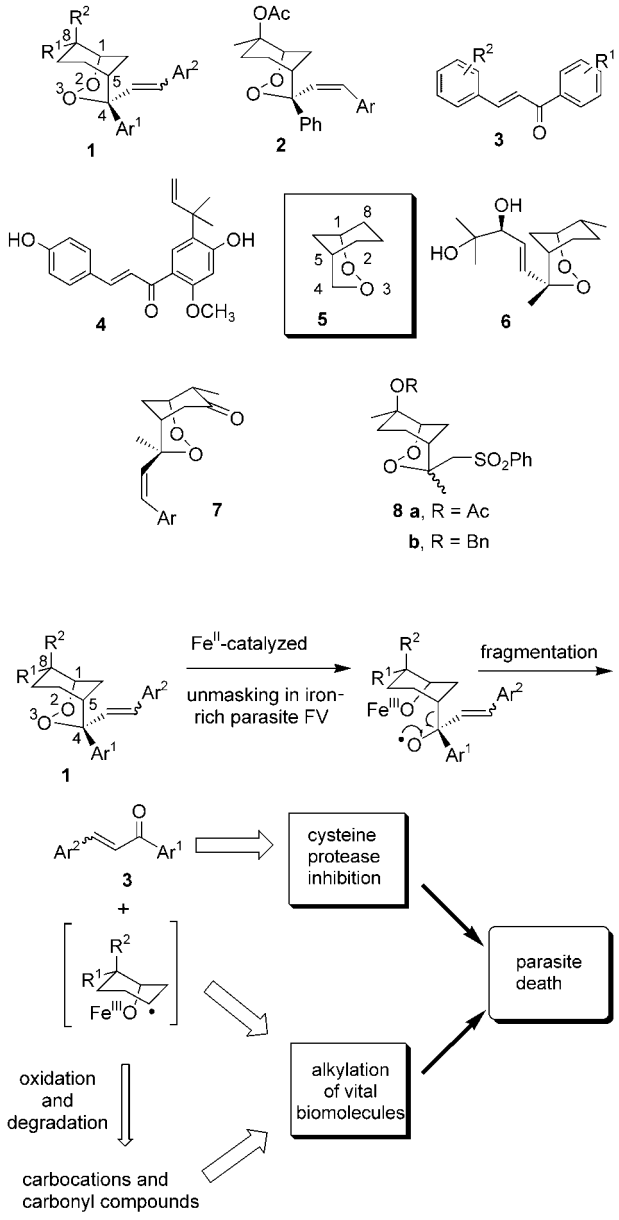
[*] Dr. P. M. O'Neill, Dr. P. A. Stocks, Dr. M. D. Pugh, N. C. Araujo, J. F. Bickley, J. Davies, E. Verissimo
Department of Chemistry
The Robert Robinson Laboratories
University of Liverpool
Liverpool L69 7ZD (UK)
Fax: (+44) 151-794-3588
E-mail: p.m.oneill01@liv.ac.uk

Dr. E. E. Korshin, Prof. Dr. M. D. Bachi
Department of Organic Chemistry
The Weizmann Institute of Science
Rehovot 76100 (Israel)
Fax: (+972) 8-934 4142
E-mail: mario.bachi@weizmann.ac.il

Prof. Dr. S. A. Ward, Dr. P. G. Bray, E. Pasini
Liverpool School of Tropical Medicine
Pembroke Place, Liverpool L3 5QA (UK)

[**] This work was supported by grants from the BBSRC (UK) for P.A.S., P.O'N., and S.A.W. (26/B13581) and from the EPSRC (UK) for M.D.P.

 DOI: 10.1002/anie.200453859 © 2004 Wiley-VCH Verlag GmbH & Co. KGaA, Weinheim

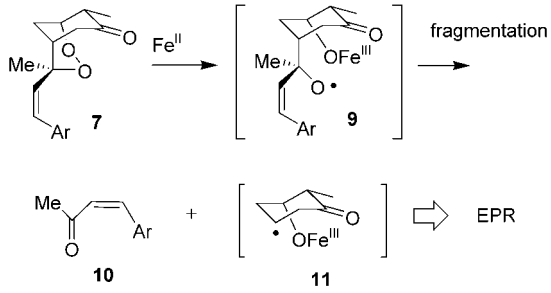


Scheme 1. The designed ferrous-catalyzed degradation of the generic prodrug **1**.

species are reminiscent of those generated by artemisinin and related trioxanes and presumably kill the parasite through a similar mode of action.[7–9] In contrast, chalcones **3** cannot be formed by ferrous-mediated degradation of the currently known 1,2,4-trioxanes. On the other hand, a series of chalcones have been found to be effective antimalarial cysteine protease (CP) inhibitors.[10] Moreover, natural licochalcone A (**4**) was reported to provide efficacious protection against *P. berghei* malaria in mice.[11] Falcipain 2, a CP of the papain family, is a *P. falciparum* FV hemoglobinase; it acts in concert with some aspartic proteases to degrade hemoglobin, thus enabling the malaria parasite to acquire amino acids for its protein biosynthesis.[12] Therefore, plasmodium CPs constitute an attractive target for antimalarial drug research.[1,12,13]

The designed prodrugs **1** are new representatives of an emerging class of promising antimalarial endoperoxides which contain the 2,3-dioxabicyclo[3.3.1]nonane framework **5** and are structurally related to naturally occurring yingzhaosu A (**6**).[14,15] Synthetic endoperoxides, such as arteflene (**7**, Ar = 2,4-bis(trifluoromethyl)phenyl) and its analogues,[16] as well as the β-sulfonyl endoperoxides **8a** and **8b** and related compounds,[15,17,18] were found to be potent and nontoxic antimalarial agents in vivo. In vitro antimalarial activity was reported for 4-acetal, 1,4-diacetal, and 1- or 4-iodomethyl derivatives of **8**.[19–21]

Biomimetic Fe^{II}-induced degradation reactions of arteflene (**7**) provided some clues on the mode of action of these endoperoxides.[22,23] Thus, on being subjected to ferrous-mediated fragmentation in water/MeCN, arteflene (**7**) gave the stable enone **10** and the transient carbon-centered cyclohexyl radical **11** (Scheme 2).[22] This latter species was



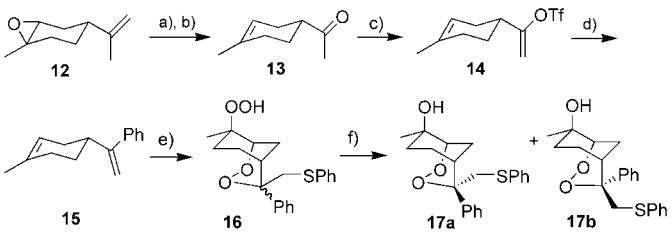
Scheme 2. Fe^{II}-catalyzed degradation of arteflene (**7**).

directly detected by EPR[23] and trapped with TEMPO (2,2,6,6-tetramethylpiperidinyloxy) in a degradation induced by Mn^{II}–tetraphenylporphyrin (TPP).[24] (Parallel biomimetic studies with the sulfonyl endoperoxide **8a** demonstrated that secondary C-centred radicals, related to **11**, can also readily undergo oxidation by Fe^{III} to potentially toxic carbocations.[25]) Whereas the enone **10** liberated from arteflene is inactive against *Plasmodium falciparum*,[22] the prodrugs described herein have the capacity to liberate an enone of the chalcone class with antimalarial activity.[10,11,26]

The synthesis of the model endoperoxides **2** is depicted in Schemes 3 and 5. Ozonolysis of commercially available (*R*)-limonene oxide (**12**) followed by in situ reduction and transformation of the internal epoxide into the corresponding alkene[27] afforded the unsaturated ketone **13** (50%; Scheme 3). The subsequent formation of the kinetic enol triflate **14** was initially attempted with trifluoromethanesulfonic anhydride. However, the unsatisfactory yield (8%) prompted us to use $PhNTf_2$[28] as the triflating agent and KHMDS as the base, which provided the triflate **14** in 64% yield. The triflate **14** was then subjected to a nickel-catalyzed cross-coupling[29] with phenyl magnesium bromide to give **15**, a phenyl analogue of (*R*)-limonene (75%; Scheme 3).

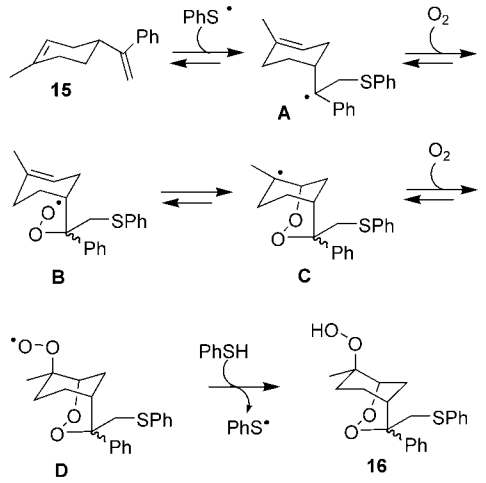
Recently we applied the free-radical, four-component, sequential thiol–olefin co-oxygenation (TOCO) reaction to limonene and similar monoterpenes, thus providing an efficient tool for the construction of the 2,3-dioxabicyclo[3.3.1]nonane system **5**.[30,31] This reaction was found to

 © 2004 Wiley-VCH Verlag GmbH & Co. KGaA, Weinheim



Scheme 3. a) O_3, −78 °C, CH_2Cl_2; b) NaI, AcOH, AcONa, Zn (50% from **12**); c) KHMDS (1.5 equiv, 1.0 M in THF), $PhNTf_2$ (1.5 equiv), THF, −78 → −40 °C, 64%; d) PhMgBr (2 equiv), $[Ni(acac)_2]$ (0.1 equiv), Et_2O, room temperature, 75%; e) PhSH (1.2 equiv), AIBN (0.07 equiv), O_2 (excess), *hν*, 0 °C, CH_3CN; f) Ph_3P (1.6 equiv), CH_3CN, CH_2Cl_2, 0 °C to room temperature (70% from **16**; **17a**/**17b** ca. 4:3). KHMDS = potassium hexamethyldisilazane; $PhNTf_2$ = *N*-phenyltrifluoromethanesulfonimide; acac = acetylacetonate; AIBN = azabisisobutyronitrile.

be particularly suitable for the formation of the bicyclic endoperoxidic backbone of model compounds **2**. Optimization of this reaction led to the following protocol: a solution of PhSH was added during 30 min to a solution of the 1,5-diene **15** and AIBN in acetonitrile at 0 °C under small positive pressure of pure oxygen and under UV irradiation, to afford the hydroperoxy endoperoxides **16**. The reactive hydroperoxy group was reduced selectively in the same vessel with Ph_3P to give the rather stable hydroxy endoperoxides **17**. The diastereomeric compounds **17a**,**b** (**a**/**b** ca. 4:3) were isolated after flash chromatography in 70% yield (average yield per newly formed bond: > 93%). The mechanism of the sequential TOCO reaction is illustrated in Scheme 4.



Scheme 4. Mechanism of the TOCO reaction.

It has been noted for the case of the parent limonene that it is necessary to maintain a low concentration of PhSH and a high monoterpene/PhSH ratio throughout the TOCO reaction to obtain the bridged bicyclic endoperoxides in good yield.[31] However, because of the supporting effect of the phenyl group in the phenyl analogue **15**, addition of the sulfanyl radical to the terminus of the exocyclic C=C bond in **15** to generate radical **A** is faster (Scheme 4). The phenyl group stabilizes radical **A**, thus shifting the equilibrium **15** ⇄ **A** to the right and accelerating the whole chain process. As a result, the TOCO reaction gave the hydroperoxy endoperoxides **16** in high yield, even in a more concentrated solution, in shorter reaction times, and with close to stochiometric ratios of the reagents.

The configuration of the diastereomeric sulfides **17a** and **17b** was assigned based on their NMR spectra in accordance with the previously formulated empirical rules.[30,31] Some relevant ^{1}H NMR data are shown in Figure 1. The assignment for **17a** by NMR spectroscopy was corroborated by the crystal structure of the corresponding crystalline acetoxy sulfone **17c** (Figure 1),[32] which was obtained in a silylation, acetylation, and oxidation process.[18,31]

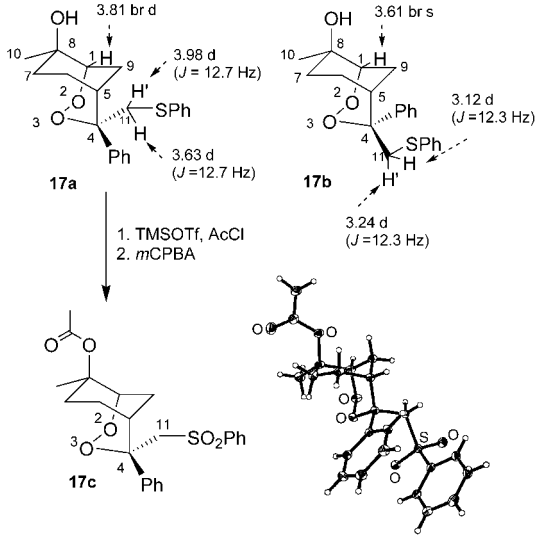


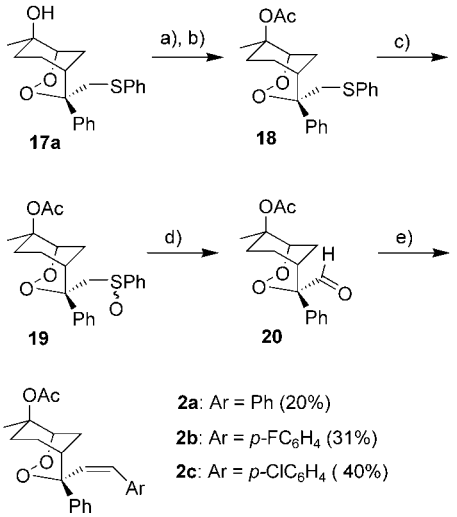
Figure 1. Distinctive ^{1}H NMR data for sulfides **17a** and **17b**, and synthesis and X-ray crystal structure of the sulfone **17c** (ORTEP).[32]

The completion of the synthesis of the model prodrugs **2** is described in Scheme 5. The acetylation of the sterically hindered tertiary hydroxy group in **17a** to give the sulfide **18** was achieved by 1) silylation with TMSOTf, and 2) acylation of the crude TMS derivative with neat AcCl.[18,31] The key aldehyde intermediate **20** was obtained by a Pummerer-type oxidative desulfurization as reported for similar endoperoxidic sulfoxides:[15] selective oxidation of **18** with *m*CPBA afforded a mixture of the epimeric sulfoxides **19**; treatment of **19** with TFAA[33] afforded the desired aldehyde **20** (40%). Finally, this aldehyde was converted into the prototypic prodrugs **2a–c** through a Wittig *cis* olefination.[16a,b]

The endoperoxidic prodrug prototypes **2a–c** were assayed for in vitro antimalarial activity against the chloroquine-resistant K1 strain of *Plasmodium falciparum* (Table 1). The data are encouraging in the sense that all of the prepared analogues **2** have superior activity to the Hoffmann LaRoche antimalarial drug candidate arteflene (**7**).

A biomimetic Fe^{II}-mediated degradation of the model endoperoxide **2a** in H_2O/MeCN at room temperature according to the previously described protocol[22,23] afforded the expected *trans* chalcone **3a** (45%) as the major product (Scheme 6),[34] along with a smaller amount of the diol **21**

 © 2004 Wiley-VCH Verlag GmbH & Co. KGaA, Weinheim

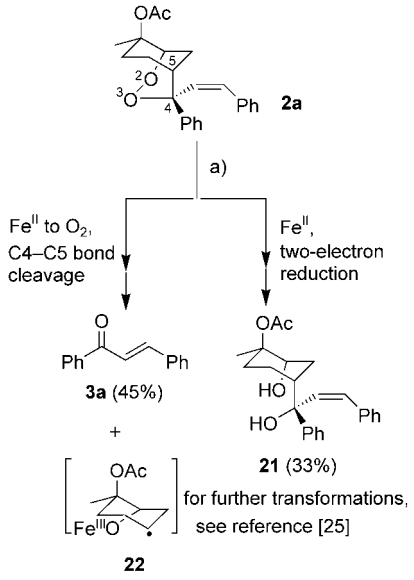


Scheme 5. a) TMSOTf (2 equiv), 2,6-lutidine (2.75 equiv), CH_2Cl_2, 95%; b) neat AcCl (60% from **17a**); c) *m*CPBA (1.1 equiv), CH_2Cl_2, 0°C, 85%; d) TFAA (2 equiv), morpholine, CH_3CN, 40%; e) $(ArCH_2)Ph_3P^+Br^-$ (1.4 equiv), KHMDS (1.4 equiv), THF, −10→25°C, 2 h. TMSOTf = trimethylsilyl triflate; TFAA = trifluoroacetic anhydride.

Table 1: In vitro antimalarial activity of prototype endoperoxides **2a–c** against the K1 strain of *P. falciparum*.

Compound	IC_{50} [nM]	SD ±
2a	34	4
2b	29	5
2c	23	4
arteflene (**7**)	47	8
artemisinin	15	4

(33%), the product of a two-electron reduction.[22] (The chalcone **3a** is a surrogate marker for the generation of the secondary C-centered radical **22**.) More significantly, LC–MS analysis of ethyl acetate extracts of isolated FVs of mid-term trophozoites exposed to 50 μM prodrug clearly demonstrated the presence of parent chalcone **3a**. Quantification was achieved by LC–MS monitoring of $[M+H]$ at m/z 209.3. The chalcone **3a** was identified by matching the MS/MS spectrum of the parent ion and by comparing the retention times with those of an authentic sample.



Scheme 6. a) $FeCl_2 \cdot 4H_2O$ (1 equiv), CH_3CN/H_2O (1:1), room temperature.

In conclusion, we have developed a general synthetic route for the preparation of a promising class of antimalarial prodrug candidates of the general structure **1**. Compound **2a** was chosen as a prototype. It was expected that for a variety of substituents R^1 and R^2 at C8 of the bridged bicyclic framework **5**, different compounds of type **1** ($Ar^1 = Ar^2 = Ph$) would act as precursors to the chalcone **3a**, which is the prototype of the known CP inhibitors **3** and **4**. Indeed, it was proved that the endoperoxide **2a** liberates, through iron(II) mediation, the chalcone **3a** and additional potential parasiticidal species. Not only did all three model compounds **2** exhibit significant antimalarial activity but definitive proof that these systems are capable of liberating a chalcone in the living parasite was provided by LC–MS analysis of prodrug-exposed parasites. It is planned to extend the present work by studying compounds of type **1** with masked chalcone units endowed with varying CP-inhibition potential and antimalarial potencies.

Received: January 27, 2004 [Z53859]

Keywords: antimalarial agents · chalcones · combination chemotherapy · cysteine protease inhibitors · endoperoxides

[1] P. J. Guerin, P. Olliaro, F. Nosten, P. Druilhe, R. Laxminarayan, F. Binka, W. L. Kilama, N. Ford, N. J. White, *Lancet Infect. Dis.* **2002**, *2*, 564–573.
[2] M. Frederich, J. M. Dogne, L. Angenot, P. De Mol, *Curr. Med. Chem.* **2002**, *9*, 1435–1456.
[3] S. Pukrittayakamee, N. J. White, *Pharm. News* **2001**, *8*, 21–26.
[4] a) A. Robert, O. Dechy-Cabaret, J. Cazelles, B. Meunier, *Acc. Chem. Res.* **2002**, *35*, 167–174; b) O. Dechy-Cabaret, F. Benoit-Vical, A. Robert, B. Meunier, *ChemBioChem* **2000**, *1*, 281–283; c) L. K. Basco, O. Dechy-Cabaret, M. Ndounga, F. S. Meche, A. Robert, B. Meunier, *Antimicrob. Agents Chemother.* **2001**, *45*, 1886–1888.
[5] O. Dechy-Cabaret, A. Robert, B. Meunier, *C. R. Chim.* **2002**, *5*, 297–302.
[6] S. Hindley, S. A. Ward, R. C. Storr, N. L. Searle, P. G. Bray, B. K. Park, J. Davies, P. M. O'Neill, *J. Med. Chem.* **2002**, *45*, 1052–1063.
[7] a) G. H. Posner, S. B. Park, L. Gonzalez, D. Wang, J. N. Cumming, D. Klinedinst, T. A. Shapiro, M. D. Bachi, *J. Am. Chem. Soc.* **1996**, *118*, 3537–3538; b) J. N. Cumming, P. Ploypradith, G. H. Posner, *Adv. Pharmacol.* **1997**, *37*, 253–297; c) G. H. Posner, J. N. Cumming, M. Krasavin in *Biomedicinal Chemistry: Applying Chemical Principles to the Understanding and Treatment of Disease* (Ed.: P. F. Torrence), Wiley-Interscience, New York, **2000**, pp. 289–309; d) K. Borstnik, I.-H. Paik, G. H. Posner, *Mini-Rev. Med. Chem.* **2002**, *2*, 573–583.
[8] a) A. Robert, J. Cazelles, B. Meunier, *Angew. Chem.* **2001**, *113*, 2008–2011; *Angew. Chem. Int. Ed.* **2001**, *40*, 1954–1957; b) A. Robert, B. Meunier, *J. Am. Chem. Soc.* **1997**, *119*, 5968–5969; c) Y. Wu, *Acc. Chem. Res.* **2002**, *35*, 255–259; d) Y. Wu, Z.-Y. Yue, Y.-L. Wu, *Angew. Chem.* **1999**, *111*, 2730–2733; *Angew.*

 © 2004 Wiley-VCH Verlag GmbH & Co. KGaA, Weinheim

Chem. Int. Ed. **1999**, *38*, 2580 – 2583; e) C. W. Jefford, *Curr. Med. Chem.* **2001**, *8*, 1803 – 1826.

[9] a) S. R. Meshnick, T. E. Taylor, S. Kamchonwongpaisan, *Microbiol. Rev.* **1996**, *60*, 301 – 315; b) S. R. Meshnick, *Int. J. Parasitol.* **2002**, *32*, 1655 – 1660; c) Y.-L. Hong, Y.-Z. Yang, S. R. Meshnick, *Mol. Biochem. Parasitol.* **1994**, *63*, 121 – 128; d) W. Asawamahasakda, I. Ittarat, Y.-M. Pu, H. Ziffer, S. R. Meshnick, *Antimicrob. Agents Chemother.* **1994**, *38*, 1854 – 1858; e) J. Bhisutthibhan, X.-Q. Pan, P. A. Hossler, D. J. Walker, C. A. Yowell, J. Carlton, J. B. Dame, S. R. Meshnick, *J. Biol. Chem.* **1998**, *273*, 16192 – 16198; f) A. V. Pandey, B. L. Tekwani, R. L. Singh, V. S. Chauhan, *J. Biol. Chem.* **1999**, *274*, 19383 – 19388; g) U. Eckstein-Ludwig, R. J. Webb, I. D. A. van Goethem, J. M. East, A. G. Lee, M. Kimura, P. M. O'Neill, P. G. Bray, S. A. Ward, S. Krishna, *Nature* **2003**, *424*, 957 – 961.

[10] R. Li, G. L. Kenyon, F. E. Cohen, X. Chen, B. Gong, J. N. Dominguez, E. Davidson, G. Kurzban, R. E. Miller, E. O. Nuzum, P. J. Rosenthal, J. H. McKerrow, *J. Med. Chem.* **1995**, *38*, 5031 – 5037.

[11] a) M. Chen, T. G. Theander, S. B. Christensen, L. Hviid, L. Zhai, A. Kharazmi, *Antimicrob. Agents Chemother.* **1994**, *38*, 1470 – 1475; b) L. Nadelmann, J. Tjornelund, S. H. Hanse, C. Cornetti, U. G. Sidelmann, *Xenobiotica* **1997**, *27*, 667 – 680.

[12] a) P. J. Rosenthal, *Emerging Infect. Dis.* **1998**, *4*, 49 – 57; b) P. J. Rosenthal, *Adv. Parasitol.* **1999**, *43*, 105 – 159; c) P. J. Rosenthal, J. H. McKerrow, M. Aikawa, H. Nagasawa, J. H. Leech, *J. Clin. Invest.* **1988**, *82*, 1560 – 1566; d) D. E. Goldberg, A. F. G. Slater, R. Beavis, B. Chait, A. Cerami, G. B. Henderson, *J. Exp. Med.* **1991**, 173, 961 – 969; e) N. D. Gamboa de Dominguez, P. J. Rosenthal, *Blood* **1996**, *87*, 4448 – 4454; f) M. Dua, P. Raphael, P. S. Sijwali, P. J. Rosenthal, M. Hanspal, *Mol. Biochem. Parasitol.* **2001**, *116*, 95 – 99.

[13] a) R. G. Ridley, *Nature* **2002**, *415*, 686 – 693; b) G. H. Coombs, D. E. Goldberg, M. Klemba, C. Berry, J. Kay, J. Mottram, *Trends Parasitol.* **2001**, *17*, 532 – 537; c) P. Olliaro, J. Cattani, D. Wirth, *JAMA* **1996**, *275*, 230 – 233.

[14] a) X. T. Liang, D. Q. Yu, W. L. Wu, H. C. Deng, *Acta Chim. Sin. (Engl. Ed.)* **1979**, *37*, 215 – 230; b) X. Liang in *Advances in Chinese Medicinal Materials* (Eds.: H. M. Chang, H. W. Yeung, W. W. Tso, A. Koo), World Scientific, Singapore, **1985**, pp. 427 – 432; c) X. X. Xu, J. Zhu, D.-Z. Huang, W.-S. Zhou, *Tetrahedron Lett.* **1991**, *32*, 5785 – 5788.

[15] M. D. Bachi, E. E. Korshin, R. Hoos, A. M. Szpilman, *J. Heterocycl. Chem.* **2000**, *37*, 639 – 646.

[16] a) W. Hofheinz, G. Schmid, H. Stohler, Eur. Pat. Appl. 311955, **1989** [*Chem. Abstr.* **1990**, *112*, 20999]; b) W. Hofheinz, H. Burgin, E. Gocke, C. Jaquet, R. Masciadri, G. Schmid, H. Stohler, H. Urwyler, *Trop. Med. Parasitol.* **1994**, *45*, 261 – 265; c) C. Jaquet, H. R. Stohler, J. Chollet, W. Peters, *Trop. Med. Parasitol.* **1994**, *45*, 266 – 271.

[17] M. D. Bachi, E. E. Korshin, P. Ploypradith, J. N. Cumming, S. J. Xie, T. A. Shapiro, G. H. Posner, *Bioorg. Med. Chem. Lett.* **1998**, *8*, 903 – 908.

[18] M. D. Bachi, E. E. Korshin, R. Hoos, A. M. Szpilman, P. Ploypradith, S. Xie, T. A. Shapiro, G. H. Posner, *J. Med. Chem.* **2003**, *46*, 2516 – 2533.

[19] P. M. O'Neill, N. L. Searle, K. J. Raynes, J. L. Maggs, S. A. Ward, R. C. Storr, B. K. Park, G. H. Posner, *Tetrahedron Lett.* **1998**, *39*, 6065 – 6068.

[20] a) T. Tokuyasu, A. Masuyama, M. Nojima, H.-S. Kim, Y. Wataya, *Tetrahedron Lett.* **2000**, *41*, 3145 – 3148; b) T. Tokuyasu, A. Masuyama, M. Nojima, K. J. McCullough, H.-S. Kim, Y. Wataya, *Tetrahedron* **2001**, *57*, 5979 – 5989.

[21] H.-S. Kim, K. Begum, N. Ogura, Y. Wataya, T. Tokuyasu, A. Masuyama, M. Nojima, K. J. McCullough, *J. Med. Chem.* **2002**, *45*, 4732 – 4736.

[22] P. M. O'Neill, L. P. Bishop, N. L. Searle, J. L. Maggs, S. A. Ward, P. G. Bray, R. C. Storr, B. K. Park, *Tetrahedron Lett.* **1997**, *38*, 4263 – 4266.

[23] P. M. O'Neill, L. P. Bishop, N. L. Searle, J. L. Maggs, R. C. Storr, S. A. Ward, B. K. Park, F. Mabbs, *J. Org. Chem.* **2000**, *65*, 1578 – 1582.

[24] J. Cazelles, A. Robert, B. Meunier, *J. Org. Chem.* **1999**, *64*, 6776 – 6781.

[25] A. M. Szpilman, E. E. Korshin, R. Hoos, G. H. Posner, M. D. Bachi, *J. Org. Chem.* **2001**, *66*, 6531 – 6540.

[26] A variety of peptidyl aldehydes are also potent in vitro inhibitors of protozoan CP; see: K. A. Scheidt, W. R. Roush, J. H. McKerrow, P. M. Selzer, E. Hansell, P. J. Rosenthal, *Bioorg. Med. Chem.* **1998**, *6*, 2477 – 2494, and references therein.

[27] H. Takikawa, Y. Yamazaki, K. Mori, *Eur. J. Org. Chem.* **1998**, 229.

[28] T. Hayashi, Y. Katsuro, M. Kumada, *Tetrahedron Lett.* **1980**, *21*, 3915.

[29] P. M. O'Neill, M. D. Pugh, A. V. Stachulski, S. A. Ward, J. Davies, B. K. Park, *J. Chem. Soc. Perkin Trans. 1* **2001**, 2682.

[30] M. D. Bachi, E. E. Korshin, *Synlett* **1998**, 122 – 124.

[31] E. E. Korshin, R. Hoos, A. M. Szpilman, L. Konstantinovski, G. H. Posner, M. D. Bachi, *Tetrahedron* **2002**, *58*, 2449 – 2469.

[32] CCDC 228984 (**17c**) contains the supplementary crystallographic data for this paper. These data can be obtained free of charge via www.ccdc.cam.ac.uk/conts/retrieving.html (or from the Cambridge Crystallographic Data Centre, 12, Union Road, Cambridge CB2 1EZ, UK; fax: (+44) 1223-336-033; or deposit@ccdc.cam.ac.uk).

[33] For these modified Pummerer reaction conditions, see: Y. Arroyo-Gomez, J. F. Rodriguez-Amo, M. Santos-Garcia, M. A. Sanz-Tejedor, *Tetrahedron: Asymmetry* **2000**, *11*, 789 – 796.

[34] A partial *cis*-to-*trans* isomerization of enone **10** upon Mn^{III}TPP-induced fragmentation of arteflene (**7**) has been reported in reference [24].

 © 2004 Wiley-VCH Verlag GmbH & Co. KGaA, Weinheim

Thermochromism

Reversible Thermochromism in Hydrogen-Bonded Polymers Containing Polydiacetylenes**

*Zhongzhe Yuan, Chan-Woo Lee, and Suck-Hyun Lee**

Numerous diacetylene (DA) derivatives have been synthesized and incorporated into polymerized assemblies for their potential applications as optoelectronic devices and biosen-

[*] Z. Yuan, C.-W. Lee, S.-H. Lee
Department of Molecular Science and Technology
Ajou University
Suwon 443-749 (Korea)
Fax: (+82) 31-219-1592
E-mail: hyja@madang.ajou.ac.kr

[**] We thank the financial support by Korea Science and Engineering Foundation through the Hyper-Structured Organic Materials Research Center at the Seoul National University. We thank Professor Zin at POSTECH for helpful discussions with X-ray characterization.

Supporting information for this article is available on the WWW under http://www.angewandte.org or from the author.

 DOI: 10.1002/anie.200453995 © 2004 Wiley-VCH Verlag GmbH & Co. KGaA, Weinheim

sors.[1] The most extensively studied systems are self-assembled or surface-attached layers (vesicles and Langmuir–Blodgett films) containing polydiacetylenes (PDAs).[2] Much less explored systems include large molecules containing dyes or other functional units bridged by a DA group.[3] With these materials substantial progress has been made in understanding the nature of the polymerization of DA moiety, the spectral changes, and the thermochromic transitions of PDAs. The rationale behind our work is that by choosing the appropriate substituents the supramolecular polymeric system will provide a specific order of the reactive groups and promote a certain degree of flexibility to accommodate structural changes during the polymerization and subsequent color changes of the PDA. In the construction of supramolecular polymers hydrogen bonding plays a prominent role because of its directionality and versatility. However, hydrogen bonds between aromatic dicarboxylic acids have rarely been used to form supramolecular polymers.[4] Recently we have been able to construct very stable dispersions of supramolecular polymers from the doubly hydrogen-bonded compounds of long dialkoxy substituted terephthalic acids.[5] The phase separation resulting from the presence of the apolar side-chain groups stabilizes the terephthalic acid core through the formation of self-assembled layers of molecules. Herein we report a novel class of similar supramolecular polymers containing DA moieties in the side chains. Using these hydrogen-bonded terephthalic acid DA compounds allows the easy preparation of PDAs with characteristics, such as thermoreversible color switching, which differ significantly from those of conventional systems.

The structures of our materials and their synthesis are schematically shown in Figure 1 and Scheme 1. The powder

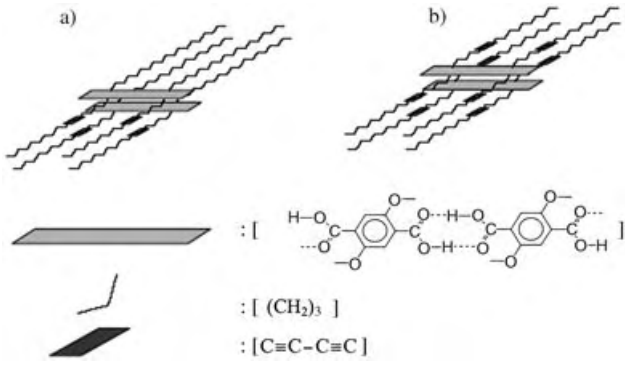
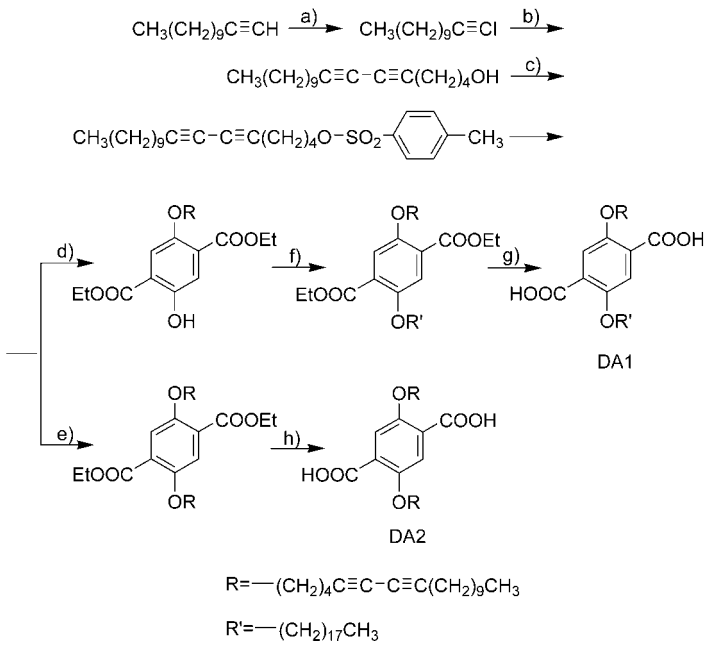


Figure 1. Stacking structures of the compounds a) DA1 and b) DA2.

X-ray diffraction results were not sufficient to allow a complete indexing of all the reflections but confirmed that during the photopolymerization process the highly ordered layer structure is preserved with slightly decreased interlayer spacings and side-chain crystallinities (Figure 2). These DA compounds DA1 and DA2 (Scheme 1) are soluble in common organic solvents, can be deposited by casting or spin coating, and even before polymerization display some typical poly-



Scheme 1. Preparation of the compounds DA1 and DA2. a) I_2, b) $HO(CH_2)_nC{\equiv}CH$, c) *p*-toluenesulfonyl chloride, d) and e) diethyl-2,5-dihydroxyterephthalate, f) $CH_3(CH_2)_{17}Br$, g) KOH, h) KOH.

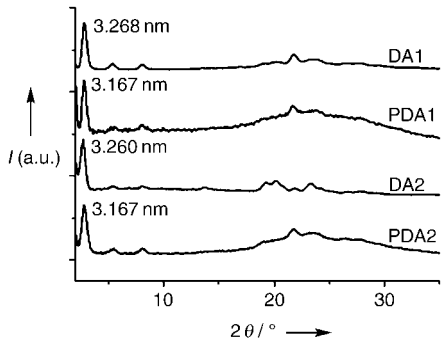


Figure 2. Powder X-ray diffractograms of DA1, PDA1, DA2, and PDA2 at 25 °C. Polymers prepared in dispersion ($CHCl_3$/hexane).

meric properties, such as high solution viscosities. To understand the influence of the DA content and its specific molecular packing within the side chains on the layer structure and thermochromism of the PDAs (PDA1 and PDA2), we examined the polymerization behavior for the two compounds DA1 and DA2 upon exposure to UV light. The polymerization of DA groups, which is a topochemical (or topotactic) polymerization, requires specific molecular position and orientation in the solid-state, which gives rise to a lot of barriers to their production. In our materials the DA groups could be polymerized either in a simple dispersion medium of chloroform/hexane or in spin-coated films. Figure 3 presents the comparison of the UV/Vis spectra for DA1 in various sample forms before and after UV exposure. The spectra for DA2 are omitted because the spectra of DA1 and DA2 are nearly identical except the relative intensity ratio I_{PDA}/I_{DA}. The not-polymerized sample in a $CHCl_3$

 © 2004 Wiley-VCH Verlag GmbH & Co. KGaA, Weinheim

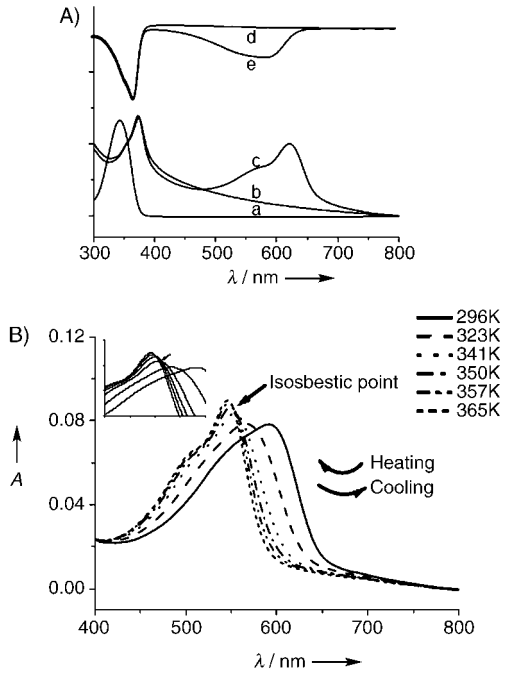


Figure 3. A) UV/Vis absorption (a,b,c) and transmission spectra (d,e) of: a) DA1 in $CHCl_3$ solution, b) a dispersion of DA1 in $CHCl_3$/hexane (0.5% *v*/*v*) unexposed and c) exposed to UV irradiation (254 nm, 23 mW cm^{-2}) for 20 min, d) a spin-coated film of DA1 on quartz unexposed and e) exposed to UV irradiation for 1 min. B) Reversible colorimetric transitions of a spin-coated film made from PDA1 as thermal stimulus was imposed and removed at the indicated temperatures.

solution, in a dispersion of $CHCl_3$/hexane, and as a film show no absorption peaks in the region from 400 to 720 nm and all these probes fluoresce when irradiated with UV/Vis light. A characteristic absorption band of the dispersed phase with λ_{max} around 370 nm is red-shifted by 25 nm relative to the corresponding band in solution. A similar absorption band is also observed for the spin-coated film. This excitonic absorption shift can be understood as an indication that under the given experimental conditions supramolecular polymers form an aggregate by parallel stacking of the aromatic rings of the terephthalic acid cores and the side chains (Figure 1).[6] The assembly of the aromatic groups into a rigid core by stacking is a prerequisite for the formation of the layered architecture which is required for the DA units to react topochemically. As shown in Figure 3, the absorption spectrum for the dispersion sample has a distinct maximum at 640 nm with a shoulder around 580 nm after UV irradiation, which is characteristic for PDAs. When the irradiation time is extended to 20 min, the absorption intensity of the so-called blue form of the polymer at 640 nm increased and the maximum only shifted slightly towards shorter wavelengths. Continuing irradiation for an hour results in a weak blue-form absorption band, leaving the red form at 580 nm dominant. The transmission spectrum for the spin-coated PDA sample is similar but has a blue-shifted absorption at 600 nm and another at 540 nm ascribable to the red form, which indicates the formation of a mixture of red and blue forms. Note that a fractional monomer conversion after photopolymerization for spin-coated films (≈23%) determined by isolating the polymeric insoluble part (from the soluble monomer part owing to incomplete polymerization) was also much lower than for the dispersion specimen (79%). We think that the localized shear stresses and the accompanying changes in samples and molecular dimensions produced during the spinning process drives the films to a more disordered "red" film as a result of the perturbation of the π-conjugation system. It is also of note that the topochemical polymerization observed for DA1 provides evidence for the spontaneous association of like–like side chains, a macroscopic expression of molecular DA recognition. As this compound has asymmetric side chains attached to the terephthalic acid units it seems unlikely that DA chains that are just held in position geometrically will be able to overcome thermal fluctuations and pack in a stable enough way for the topochemical reaction to occur in the liquid state.

To investigate the thermochromic transition of the spin-coated films, we measured absorption spectra against temperature based on the results of differential scanning calorimetry (DSC) measurements (Figure 4). These materials exhibit

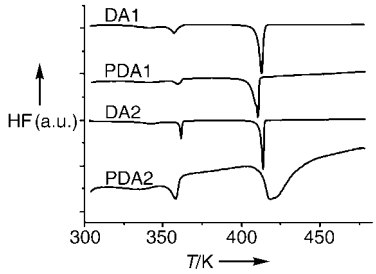


Figure 4. DSC traces of compounds DA1, PDA1, DA2, and PDA2.

structural and thermal behaviors similar to the side-chain polymers based on a rigid backbone (see Supporting Information).[7] Their general architecture can be described in terms of hydrogen-bonded aromatic rigid backbones separated by layers composed of relatively well packed side chains. The two endothermic transitions observed by DSC before melting of the whole sample indicate that the properties of the rigid-backbone layers are considerably different from the properties of the side-chain layers. The low-temperature transition is attributed to the onset of disordering processes in the side-chain region, while the layered structure and thus the ordered arrangement of the backbones is maintained, the higher transition temperature is associated with motion of the rigid-core. As illustrated in Figure 3B, polymer PDA1 shows completely reversible spectroscopic changes during the thermal cycles. The blue form which gives rise to the band at 600 nm progressively disappears and the red form appears as the temperature increases. The absorptions of the red form appear at 540 and 500 nm at 350 K and then grow in intensity up to the melting temperature of 408 K even though the film was not fully blue to begin with. Upon cooling to room temperature the blue form reappears in a completely reversible manner. This remarkable thermochromic behavior is not usually observed in PDAs. To our knowledge, only a few examples have been reported to date.[8]

 © 2004 Wiley-VCH Verlag GmbH & Co. KGaA, Weinheim

A more detailed investigation of the spectra reveals that there appears to be an isosbestic point above the transition temperature of 352 K. It shows that increasing temperature merely increases the amount of the red form without passing through any observable new intermediate form. DSC data suggest that the spectral change above the transition temperature of 352 K is triggered by strain coming from the side-chain layers existing in a liquid state. Thermal stimulus gives the side chains enough energy to impose mechanical strain on the PDAs by rotation around the single bonds between the methylene units although such movement of the side chains must be restricted so that the necessary crystal integrity for reversibility is maintained. Theoretical calculations revealed that such a side-group motion could induce a change in the electronic structure of PDAs.[9] Thus, the origin of this chromism remains unclear but our data support a mechanism in which the red form, a form which indicates a diminished conjugation length, is merely a thermally equilibrated molecular fluctuation of the blue form. The observed reversibility in PDA2 (see Supporting Information) corroborates that the layer integrity is retained at higher annealing temperatures. In fact, polymerization of DA2 produces the unusual rigid ladder-type bonding in the layer structures (see Figure 1) and such sterically controlled systems have no degree of freedom to respond to intralayer strain that causes structural modifications. Thus up to the backbone melting temperature the thermochromic transitions for our material are dominated by the flexibility of the side-chain packing between supramolecular polymers.

The experimental data presented herein do not allow a conclusive molecular model to be constructed for the spatial arrangement of the PDA chains with respect to each other and the terephthalic acid plane. We can, however, conclude that the combination of double hydrogen-bonds between the hard terephthalic acid cores and a molecular recognition of DA moieties in the side chains, which enables topochemical polymerization to occur, allowed us to prepare PDAs in dispersed solutions or even in spin-coated films. The formation of stable, ultrathin polymer films is crucial for the envisaged application of PDAs as sensors for biological detection or coatings for optoelectronic applications. These materials also have thermochromic properties which allow a reversible color switching, thus expanding the scope of potential applications for polydiacetylenes.

Received: February 11, 2004
Revised: May 5, 2004 [Z53995]

Keywords: alkynes · hydrogen bonds · layered compounds · polymers · thermochromism

[1] a) S. Y. Okada, R. Jelinek, D. Charych, *Angew. Chem.* **1999**, *111*, 678 – 682; *Angew. Chem. Int. Ed.* **1999**, *38*, 655 – 659; b) D. T. McQuade, A. E. Pullen, T. M. Swager, *Chem. Rev.* **2000**, *100*, 2537 – 2574; c) K. Morigaki, T. Baumgart, A. Offenhausser, W. Knoll, *Angew. Chem.* **2001**, *113*, 184 – 186; *Angew. Chem. Int. Ed.* **2001**, *40*, 172 – 174; d) D. W. Britt, U. G. Hofman, D. Mobius, S. W. Hell, *Langmuir* **2001**, *17*, 3757 – 3765; e) S. A. Yamanaka, D. H. Charych, D. A. Loy, D. Y. Sasaki, *Langmuir* **1997**, *13*, 5049 – 5053.

[2] a) S. Okada, S. Peng, W. Spevak, D. Charych, *Acc. Chem. Res.* **1998**, *31*, 229 – 239; b) R. W. Carpick, T. M. Mayer, D. Y. Sasaki, A. R. Burns, *Langmuir* **2000**, *16*, 4639 – 4647; c) Y. Lu, Y. Yang, A. Sellinger, M. Lu, J. Huang, H. Fan, R. Haddad, G. Lopez, A. R. Burns, D. Y. Sasaki, J. Shelnutt, J. Brinker, *Nature* **2001**, *410*, 913 – 917; d) Y. Yang, Y. Lu, M. Lu, J. Huang, R. Haddad, G. Xomeritakis, N. Liu, A. P. Malanoski, D. Sturmayr, H. Fan, D. Y. Sasaki, R. A. Assink, J. A. Shelnutt, F. v. Swol, G. P. Lopez, A. R. Burns, C. J. Brinker, *J. Am. Chem. Soc.* **2003**, *125*, 1269 – 1277.

[3] H. M. Barentsen, M. v. Dijk, P. Kimkes, H. Zuihof, E. J. R. Sudholter, *Macromolecules* **1999**, *32*, 1753 – 1762.

[4] L. Brunsveld, B. J. B. Folmer, E. W. Meijer, R. P. Sijbesma, *Chem. Rev.* **2001**, *101*, 4071 – 4097.

[5] Z. Yuan, C.-W. Lee, S.-H. Lee, *Polym. Mater. Sci. Eng.* **2003**, *88*, 378 – 379.

[6] R. B. M. Koehorst, R. G. Fokkink, M. C. Stuart, H. Zuihof, E. J. R. Sudholter, *Macromolecules* **2002**, *35*, 4226 – 4228.

[7] a) O. P. Kwon, S.-H. Lee, G. Montemezzani, P. Gunter, *Adv. Funct. Mater.* **2003**, *13*, 434 – 438; b) M. Ballauff, *Angew. Chem.* **1989**, *101*, 261; *Angew. Chem. Int. Ed. Engl.* **1989**, *28*, 253.

[8] a) U. Jonas, K. Shah, S. Norvez, D. H. Charych, *J. Am. Chem. Soc.* **1999**, *121*, 4580 – 4588; b) D. J. Ahn, E.-H. Chae, G. S. Lee, H.-Y. Shim, T.-E. Chang, K.-D. Ahn, J. M. Kim, *J. Am. Chem. Soc.* **2003**, *125*, 8976 – 8977; c) A. Singh, R. B. Thompson, J. M. Schnur, *J. Am. Chem. Soc.* **1986**, *108*, 2785 – 2787.

[9] H. Eckert, D. S. Boudreaux, R. R. Chance, *J. Chem. Phys.* **1986**, *85*, 4116.

 © 2004 Wiley-VCH Verlag GmbH & Co. KGaA, Weinheim

Annulenes

Aromaticity: The Alternating C–C Bond Length Structures of [14]-, [18]-, and [22]Annulene**

*Chaitanya S. Wannere, Kurt W. Sattelmeyer, Henry F. Schaefer III, and Paul von Ragué Schleyer**

Dedicated to Professor Kurt Mislow

[18]Annulene ($C_{18}H_{18}$)[1] is the critical signpost along the $4n+2$ π electron Hückel[2] route from benzene to the larger aromatic $(CH)_k$ rings. Although Mislow[1a] pointed out the steric problems of the planar D_{6h} form very early, [18]annu-

[*] Dr. C. S. Wannere, Dr. K. W. Sattelmeyer, Prof. Dr. H. F. Schaefer III, Prof. Dr. P. v. R. Schleyer
Center for Computational Chemistry
Department of Chemistry
The University of Georgia
Athens, Georgia 30602-2525 (USA)
Fax: (+1) 706-542-7514
E-mail: schleyer@chem.uga.edu

[**] This work was supported by National Science Foundation Grant CHE-0209857. The authors thank N. L. Allinger, C. D. Stevenson, N. Handy, G. Robinson, M. Kertesz, S. Shaik, W. Allen, H. Rzepa, S. Grimme, C. Musgrave, and A. T. Balaban for helpful discussions.

Supporting information for this article is available on the WWW under http://www.angewandte.org or from the author.

 © 2004 Wiley-VCH Verlag GmbH & Co. KGaA, Weinheim DOI: 10.1002/anie.200454188

lene has been assigned[1b] the same essential D_{6h} symmetry as benzene—"the bonds do *not* alternate in length"—for over four decades. However, geometries with nearly equal C–C bond lengths are not expected for the very large [4*n*+2]annulenes. Since the aromatic stabilization energy per carbon decreases with increasing size,[3,4] very large annulenes should approach the behavior of polyolefins. This was first predicted[5] in 1959 by Longuet-Higgins and Salem, who guessed that C–C bond-length alternation might begin with [30]annulene. Indeed, this result was obtained at the DFT-B3LYP and MP2 theoretical levels in the comprehensive computational annulene survey of Choi and Kertesz (CK) in 1998.[4] In contrast, herein we show that this crossover point occurs much earlier, at [14]annulene, which, along with [18]annulene, has alternating rather than equalized C–C bond lengths.

As stressed by Shaik, Hiberty et al., the σ framework of aromatic compounds favors regular geometries, but the π components prefer bond alternation owing to greater overlap of adjacent p orbitals when they are closer together.[6–8] The π system has two competing tendencies: the preference for pair-wise interactions when C–C separations are shorter (as in double bonds) competes with the gain in aromatic stabilization energy when the C–C separations are equalized, but longer (as in benzene). However, this equalization tendency is the weaker of these two π effects and cyclic electron delocalization is not eliminated, but only reduced slightly, by bond alternation.[3] Thus, benzene, rather than being the aromatic prototype in this sense, is the exception! Benzene favors the highly symmetric D_{6h} structure[9] solely due to its σ skeleton.[6] Naphthalene and virtually all other polybenzenoid hydrocarbons, even in corronene (over 0.05 Å) which has D_{6h} symmetry, exhibit appreciable C–C bond-length differences. This partial localization is fully consistent with their aromatic character. In the larger annulenes, the preference for either a bond alternating or a higher symmetry structure depends on the Shaik–Hiberty[8] "fine balance of σ resistance and π distortivity."

Hence, it is important to ascertain[3–5,10,11] the point in the annulene progression at which the σ skeleton ceases to be the dominating influence and is replaced by the inherent predilection for double-bond localization. We establish herein that the preference for bond-alternating structures along the 4*n*+2 Hückel π-electron series begins at [14]annulene. Additionally, we also show that the next higher homologue, [18]annulene also shows remarkable C–C bond alternation. Benzene is not the aromatic paradigm!

[18]Annulene: The structure of [18]annulene, the most extensively[11–15] investigated higher Hückel monocycle, is of critical importance in this context. But the seemingly secure and currently accepted experimental[14,15] and theoretical conclusion[4,13] that [18]annulene ($C_{18}H_{18}$) has a D_{6h} structure cannot be correct. Like benzene, [18]annulene belongs to the [4*n*+2]aromatic subgroup with $6(2p+1)$ π electrons (where "*p*" is an integer), which permits but does not require the highly symmetrical D_{6h} point group. Although well established to be aromatic, the $C_{18}H_{18}$ chemistry differs markedly from that of benzene: [18]annulene undergoes reactions typical of localized π systems. The 1965 X-ray structure determination at 80 K favored D_{6h} symmetry[15] with somewhat different (but not alternating) 1.382 and 1.419 Å lengths for the 12 inner and the six outer C–C bonds, respectively. The 1995 X-ray reinvestigation at 111 K revealed some disorder in the [18]annulene crystal[14] but gave C–C bond lengths of 1.385 and 1.405 Å and confirmed the essential D_{6h} symmetry.[16] Electron correlated MP2 and various DFT computations[4,13,17] reproduced the X-ray structure well and supported the experimental conclusions that $C_{18}H_{18}$ has a "highly delocalized D_{6h} structure." Other indirect evidence based on IR, UV/Vis, fluorescence, and photoelectron spectroscopy[18,19] also was consistent with a D_{6h} structure. However, data from such methods are not sensitive to geometry changes. In sharp contrast, the proton chemical shifts respond markedly even to slight variations in structure.[3,20]

Bühl and Schleyer established and validated the use of ab initio/GIAO/NMR methods for structural determinations.[21,22] Based on the comparison of experimental and computed chemical shifts for a large number of boranes, carboranes, and nonclassical carbocation systems, Bühl and Schleyer found excellent agreement between the experimental and computed chemical shifts only when the geometries were correct,[21] and revealed many errors in experimental structures. Likewise, the ^{1}H NMR chemical shifts of many arenes computed by GIAO-B3LYP/6-311 + G** are generally within 0.2 to 0.5 ppm of the experimental values.[23,24] Hence, accurate structures of [*n*]annulenes may be established by comparing computed with experimental chemical shifts. Excellent agreement is expected only when the geometries are correct. The results obtained by using this procedure demonstrate that [18]annulene cannot have a D_{6h} structure. The evidence is decisive: the proton chemical shifts computed using the X-ray geometry[25] are in gross disagreement with those measured[26,27] experimentally.

This large disagreement has been found before, but its importance was not appreciated.[3,4,13b] CK[4] noted that the inner–outer proton chemical shift differences for all the higher aromatic annulenes, computed using the B3LYP/6-31G* geometries, were far from the available experimental NMR spectroscopic data, and stated that "the origin of this discrepancy is not clear." Baldridge and Siegel (BS)[13b] reported the chemical shifts of the inner and outer protons for D_{6h}, D_{3h}, and D_3 [18]annulene geometries; the later two were obtained at HF levels, but only a D_{6h} minimum was found at MP2 and all the DFT levels employed. None of these geometries gave δ ^{1}H values that agreed acceptably with the experimental values. But according to BS, the single D_{6h} minimum obtained at MP2 and various DFT levels (e.g. BPW91/dz(d), B3PW91/dz(d,p), and B3PW91/dz(2df,2p)) and the agreement with the X-ray geometry, were decisive in supporting the D_{6h} [18]annulene structure. BS speculated that the large discrepancy (12.3 ppm) between the observed and computed ^{1}H NMR chemical shifts of the inner protons in the D_{6h} structure might be due to the "strong temperature dependence" or to the deficiencies in the theory, stating that "the ring current is over-estimated at these computational levels." However, Stevenson and Kurth subsequently found only a small temperature dependence of the δ values of the inner protons of [18]annulene.[27] What then is the cause of the

 © 2004 Wiley-VCH Verlag GmbH & Co. KGaA, Weinheim

discrepancy? Our explanation is simple: neither the X-ray nor the electron-correlated geometries are correct. [18]Annulene does not have a D_{6h} structure.

The ^{1}H NMR chemical shifts computed with numerous methods on D_{6h} geometries, optimized at various HF, MP2, or various DFT levels by imposing D_{6h} symmetry, failed completely in reproducing the experimental results (Figure 1 and Table 1). The solution of the disagreement is not the level of theory employed, but rather in the use of the lower symmetry geometries. Although D_{3h} and D_3 structures gave results in closer agreement with the experimental values, as BS noted, these results are still unsatisfactory. We find that *only* the C_2 geometry gave acceptable computed chemical shifts (Table 1). These findings exclude the "highly delocalized" D_{6h} structure for [18]annulene, as well as the D_{3h} and D_3 alternatives.

While the degree of delocalization is overestimated by various DFT and MP2 methods, the HF level underestimates the delocalization in aromatic molecules.[3] Consequently, a hybrid density functional that has a larger HF component should give an intermediate structure on optimization. Indeed at the KMLYP and BHLYP levels, which include approximately 50% HF, reduced symmetry (D_{3h}, D_3, and C_2) [18]annulene structures are lower in energy than the D_{6h}. However, the C_2 geometry is the only minimum (Table 1). While the computed δH values of the outer protons of D_{3h} and D_3 structures are acceptable compared with experiment (Table 1), the chemical shifts of the inner protons of the D_3 ($\delta H_{inner} = -4$ ppm) and D_{3h} ($\delta H_{inner} = -5$ ppm) forms differ by 1 and 2 ppm, respectively. In contrast, the bond-length alternating C_2 KMLYP and BHLYP minima gives[28] outer and inner proton chemical shifts (average: 8.9 and −2.5 ppm

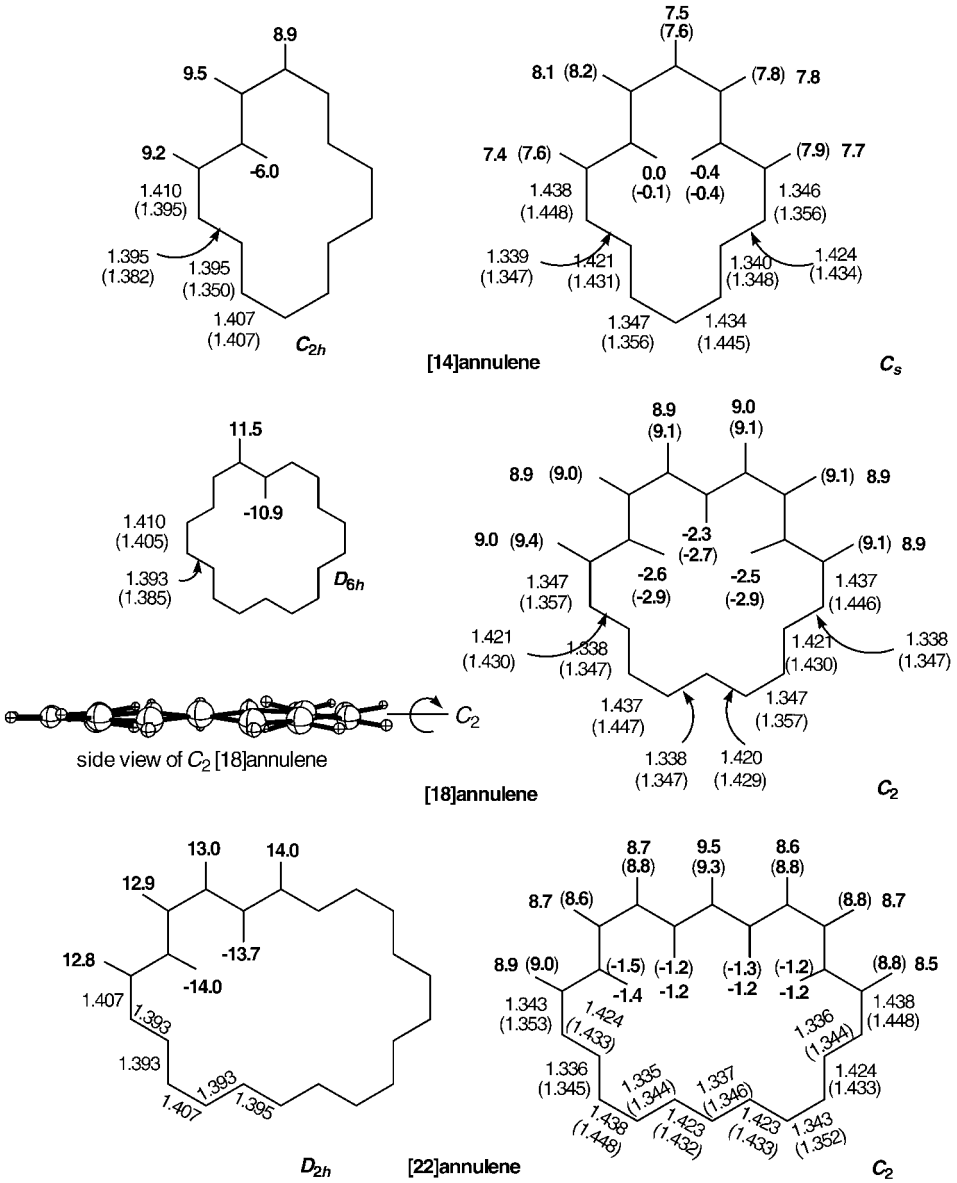


Figure 1. Optimized geometries and chemical shifts (bold) of [14]-, [18]-, and [22]annulenes. The high symmetry structures on the left were optimized at B3LYP/6-311+G** (the numbers in parenthesis are the X-ray distances in Å) and the corresponding lower symmetry structures on right at KMLYP/6-311+G** and BHLYP/6-311+G** (in parenthesis). The ^{1}H chemical shifts (in ppm) were computed on these geometries at GIAO-B3LYP/6-311+G**//. The experimental NMR values are given in Table 1.

 © 2004 Wiley-VCH Verlag GmbH & Co. KGaA, Weinheim

Table 1: Theoretical results[41] for the [4*n*+2]π annulenes, Figure 1.[a]

[N]	PG	Level	Δr	E_{rel}	$\tilde{\nu}$	δH_{inner}	δH_{outer}
[14]	D_2	B3LYP	0.015	2.6	102.7	−6.7	9.0 to 9.7
	C_{2h}	B3LYP	0.015	0.0	97.8	−6.0	8.9 to 9.5
	D_2	KMLYP	0.013	5.3	741.0*i*	−7.0	8.7 to 9.4
	C_2	KMLYP	0.105	1.7	97.8	0.4 to 1.0	7.3 to 7.9
	C_{2h}	KMLYP	0.013	2.5	664.3*i*	−6.1	8.6 to 9.3
	C_s	KMLYP	0.098	0.0	103.8	0.0 to −0.4	7.4 to 8.1
	D_2	BHLYP	0.014	5.0	680.5*i*	−7.0	8.8 to 9.5
	C_2	BHLYP	0.109	1.9	98.1	0.4 to 1.0	7.4 to 8.0
	C_{2h}	BHLYP	0.014	2.2	608.0*i*	−6.1	8.7 to 9.4
	C_s	BHLYP	0.101	0.0	104.0	−0.1 to −0.4	7.6 to 8.2
	C_{2h}	Experiment[26]	0.057			0.0	7.6
[18]	D_{6h}	B3LYP	0.017	0.0	72.3	−10.9 to −11.0	11.5 to 11.6
	D_{6h}	KMLYP	0.015	3.2	1218.3*i*	−11.3 to −11.5	11.2 to 11.4
	D_{3h}	KMLYP	0.095	0.6	97.5*i*, 95.4*i*, 45.8*i*	−4.9 to −5.0	9.3 to 9.8
	D_3	KMLYP	0.095	0.4	74.9*i*	−4.2 to −4.5	9.4 to 9.5
	C_2	KMLYP	0.099	0.0	73.0	−2.3 to −2.6	8.9 to 9.0
	D_{6h}	BHLYP	0.015	2.6	1073.0*i*	−11.2 to −11.4	11.2 to 11.5
	D_{3h}	BHLYP	0.094	0.4	100.0*i*, 89.4*i*, 56.2*i*	−4.9 to −5.1	9.6 to 9.8
	D_3	BHLYP	0.095	0.4	23.7*i*, 22.6*i*	−4.3 to −4.6	9.5 to 9.7
	C_2	BHLYP	0.100	0.0	74.0	−2.7 to −2.9	9.0 to 9.4
		Experiment[26,27]	0.042			−2.99	9.3
[22]	D_{2h}	B3LYP	0.014		48.3	−13.7 to −14.0	12.8 to 14.0
	D_{2h}	KMLYP	0.013	6.4	1840.0*i*	−14.0 to −14.6	12.4 to 13.9
	C_{2v}	KMLYP	0.100	0.2	22.0	−3.1 to −3.4	9.2 to 10.1
	C_2	KMLYP	0.103	0.0	46.6	−1.2 to −1.4	8.5 to 9.5
	D_{2h}	BHLYP	0.014	5.4	1605.8*i*	−13.9 to −14.5	12.5 to 13.9
	C_{2v}	BHLYP	0.101	0.2	104.7*i*	−3.0 to −3.3	9.3 to 10.1
	C_2	BHLYP	0.104	0.0	97.8	−1.2 to −1.5	8.6 to 9.3
		Experiment[37]			−0.4 to −1.2	8.5 to 9.7	

[a] The 6-311+G** basis set was used throughout for optimization of the structures. [N] indicates the number of carbon atoms in the annulene ring. PG is the point group. Δr [Å] is the difference between the shortest and the longest C–C bond length. E_{rel} [kcal mol^{-1}] is the relative energy[41] with respect to the energetically most stable structure, at various levels of theory. $\tilde{\nu}$ gives the imaginary (indicated with *i*) or the smallest real vibrational frequency. δH_{inner} and δH_{outer} [ppm] are the GIAO-B3LYP/6-311+G** ^{1}H NMR chemical shifts evaluated relative to TMS (with a computed proton shielding of 31.98).

KMLYP; 9.2 and −2.8 ppm BHLYP, Figure 1) remarkably close to the experimental data, 9.3 and −3.0.

In addition to this NMR spectroscopic evidence, C_2 [18]annulene is appreciably lower in energy than the D_{6h} form at KMLYP and BHLYP as well as at MPW1PW91 (Table 2). The same is true at the current cutting edge of theory: single-point energy comparisons using the highly correlated CCSD(T) method (with DZP(C)+DZ(H)) also predict the C_2 form to be more stable than the D_{6h} structure. The different energy ordering at B3LYP and at MP2 (Table 2) is suspect: Schaefer and co-workers[29] have stressed that these methods "overestimate the delocalization." While the KMLYP and BHLYP energy differences between the C_2 and the D_3 and D_{3h} geometries are small (Table 1), the D_3 and D_{3h} forms are higher order saddle points rather than minima. D_{6h} [18]annulene is a transition structure, rather than a minimum. The eigenvectors of the sizable imaginary frequencies, 1218*i* at KMLYP and 1073*i* cm^{-1} at BHLYP (Table 1), indicate the strong preference for C–C bond alternation. Hence, we conclude that [18]annulene prefers a bond alternating C_2 (or closely related) geometry over the currently accepted bond equalized D_{6h} (or slightly nonplanar) structure. Grimme's newly introduced SCS-MP2 method overcomes the delocalization overestimation problem of MP2[30] and yields similar results for [18]annulene as CCSD(T): the C_2 form is favored over D_{6h} by 1.2 kcal mol^{-1} at SCS-MP2/TZV(d,p)//SCS-MP2/TZV(d,p).[31]

Why does [18]annulene prefer the C_2 structure? In 1952, Mislow predicted that the higher annulenes should not be planar owing to the steric repulsion between the inner hydrogen atoms.[1a] As Mislow foresaw, the average 1.88 Å H···H nonbonded distance in the D_3 structure is 0.03 Å larger than that in the D_{6h} form (1.85 Å). However, the average H···H separation in the C_2 form is appreciably larger (1.94 Å) and this helps explain the preference for lower symmetry C_2 form for [18]annulene.

Table 2: Single-point energy C_2 versus D_{6h} [18]annulene energy differences, E_{rel} [kcal mol^{-1}].

Level	C_2	D_{6h}	E_{rel}[a]
HF/6-311+G**//KMLYP/6-311+G**	−692.11092	−692.07832	20.45
KMLYP/6-311+G**//KMLYP/6-311+G**	−695.38249	−695.37735	3.22
CCSD(T)/DZP(C)+DZ(H)(fc)//KMLYP/6-311+G**	−694.47008	−694.46674	2.10
CCSD(T)/DZ(fc)//KMLYP/6-311+G**	−693.44243	−693.43812	2.70
BHLYP/6-311+G**//KMLYP/6-311+G**	−696.34217	−696.33821	2.49
MPW1PW91/6-311+G**//KMLYP/6-311+G**	−696.61875	−696.61819	0.35
B3LYP/6-311+G**//KMLYP/6-311+G**	−696.80933	−696.81557	−3.91
BLYP/6-311+G**//KMLYP/6-311+G**	−696.48006	−696.49043	−6.51
BP86/6-311+G**//KMLYP/6-311+G**	−696.78056	−696.79173	−7.00
MP2/6-31G*//KMLYP/6-311+G**	−694.23195	−694.25595	−15.06

Positive values of E_{rel} indicate that the C_2 structure is more stable whereas negative E_{rel} values signify the greater stability of D_{6h}.

Why did the X-ray structure determination fail to find the correct geometry? Both static and dynamic disorders are possible reasons. Static disorder is due to a superposition of a lower symmetry structure leading to apparent higher symmetry. According to Gorter et al.,[14] the diameters determined by X-ray analysis for [18]annulene excluded the possibility of a 50:50 inversion disorder model of bond alternating D_{3h} structures. However, their reference model was based on an early[32] HF/6-31G* geometry, which had "calculated ring diameters up to 0.20 Å

 © 2004 Wiley-VCH Verlag GmbH & Co. KGaA, Weinheim

too large" (Table 3). In contradiction, the data in Table 3 demonstrate that the 50:50 inversion disorder C_2 (or D_{3h}) model of [18]annulene cannot be excluded, since the computed major and minor ring diameters for the C_2, D_{3h}, as well as the D_{6h} structures have deviations less than 0.06 Å from the experimental values. Furthermore, the 50:50 C_2 [18]annulene superposition shown in Figure 2 also yields an averaged "D_{6h} structure" with internal (1.379 Å) and external (1.392 Å) C–C bond lengths close to the reputed X-ray separations,[14] 1.385 and 1.405 Å, respectively. Consequently we believe that the X-ray evidence does not forbid 50:50 inversion disorder for a bond alternating C_2 (or D_{3h}) [18]annulene structure.[9,16]

Table 3: Comparison of C–C major and minor interatomic distances [Å] across the ring for the X-ray [18]annulene structure[14] with those computed[41] at different levels of theory.

		C···C across the ring		Deviations from X-ray	
		Minor [Å]	Major [Å]	Minor [Å]	Major [Å]
X-ray	D_{6h}	5.91	7.54	0.00	0.00
//HF/6-31G*	D_{6h}	5.93	7.56	+0.02	+0.02
//B3LYP/6-311+G**	D_{6h}	5.96	7.60	+0.05	+0.06
//KMLYP/6-311+G**	D_{6h}	5.86	7.48	−0.05	−0.06
50:50 Distortion models:					
//HF/6–31G*	D_{3h}	5.95	7.60	+0.04	+0.06
//KMLYP/6-311+G**	D_{3h}	5.86	7.49	−0.05	−0.05
//KMLYP/6-311+G**	C_2	5.86	7.48	−0.05	−0.06
//BHLYP/6-311+G**	C_2	5.92	7.54	+0.01	0.00

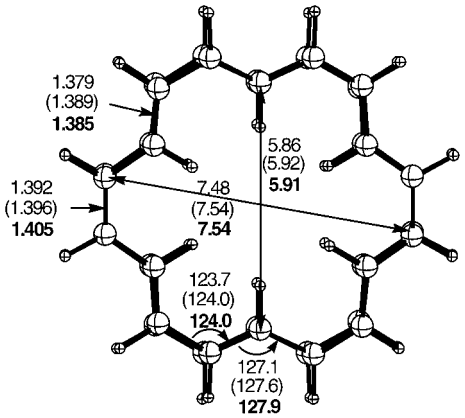


Figure 2. 50:50 Inversion disorder (superposition) of KMLYP and BHLYP optimized C_2 [18]annulene. The values in parentheses are the corresponding BHLYP geometries while those in bold are from the X-ray data (1995)[14] measured at 111 K.

Dynamic disorder is a further complication. D_{6h} [18]annulene is a transition state joining the two C_2 structures with an interconversion barrier of only about 3 kcal mol^{-1} at KMLYP and BHLYP (2.1 kcal mol^{-1} at our highest CCSD(T) level, Table 2). Hence, the symmetrization of [18]annulene takes place rapidly even at 111 K (the temperature of the 1995 X-ray investigation) which should result in a time-averaged D_{6h} structure and compromises the interpretation of the experimental data. Haddon[16] also pointed out that "unfortunately the X-ray study cannot be regarded as definitive in the present case" since the "C–C distances are averaged over time and over a large number of unit cells by the diffraction process."

Unlike the NMR spectroscopic data, the presently available low-resolution experimental IR spectrum[1b] does not permit differentiation among the geometrical alternatives. Although the agreement between the experimental[1b] and computed[17] IR spectra (BLYP/6-311G*) for D_{6h} [18]annulene was said to lend "further support to the delocalized structure," not only the D_{6h}, but also the D_{3h}, D_3, and particularly the C_2 optimized [18]annulene structures all give computed IR frequencies in the same range. For example, on average, corresponding frequencies for all these structures differ by merely 2.3 %, which is in marked contrast to the large variation (> 200 % for inner protons and > 25 % for outer protons, Table 1) for the δ values. The same relative insensitivity to structural changes (and the lack of high resolution data) characterizes other spectroscopic methods which have been applied to [18]annulene.[18,19]

[14]Annulene: Although the highest possible symmetry of [14]annulene is D_{2h}, this lower homologue of $C_{18}H_{18}$ suffers from having more severe nonbonded repulsions among the intra-annular hydrogen atoms. These are ameliorated in nonplanar geometries. The X-ray structure determination[33] at 283–303 K found C_{2h} symmetry and moderate C–C bond alternation ($\Delta r = R_{\text{single}} - R_{\text{double}} = 0.057$ Å, the same alternation as in the naphthalene perimeter). However, the ^{1}H NMR chemical shifts of the inner hydrogen atoms ($\delta H_{\text{inner}} = -5.4$ to -7.0 ppm), computed using the X-ray geometry,[25] are far from the measured $\delta = 0.0$ ppm value.[26] Hence, the experimental structure of [14]annulene also requires revision.

While all the DFT levels (Table 1) find the C_{2h} form to be slightly more stable (2.5 kcal mol^{-1}) than the D_2, the local C_{2h} B3LYP/6-311+G** minimum gives computed proton chemical shifts far from the experimental values. The C_{2h} form is a transition state at both the BHLYP and KMLYP levels; the single imaginary frequency ($> 600i$ cm^{-1}) leads to the most stable C_s structure. The computed ^{1}H NMR chemical shifts of the C_s inner ($\delta = 0.0$ to -0.4 ppm) and outer ($\delta = 7.4$ to 8.2 ppm) protons are in good agreement with experiment (Table 1). Note that the substantial ($\Delta r = 0.10$ Å) C–C bond alternation in the optimized C_s structure (Table 1 and Figure 1) is nearly twice as large as the X-ray finding. We conclude that the currently accepted bond-length equalized C_{2h} structure of [14]annulene is not correct; instead, a bond-length alternating C_s geometry is favored.

[10]Annulene: The second member of the neutral aromatic hydrocarbon series after benzene, [10]annulene, cannot adopt D_{10h} symmetry owing to ring strain. No X-ray structure[34] of [10]annulene is available, but computational studies reveal many possible (azulene-like, naphthalene-like, twist, boat, and heart) conformations all of which are nonplanar. Employing the "cutting edge" CCSD(T) method, two investigations concluded that the non-aromatic twist C_2 form is best.[29,35] Schaefer and co-workers demonstrated that HF underestimates, whereas MP2, B3LYP, and several other DFT

 © 2004 Wiley-VCH Verlag GmbH & Co. KGaA, Weinheim

levels overestimate the degree of delocalization in the minimally nonplanar aromatic conformations.[29] In contrast, we find that the KMLYP and BHLYP methods, which have a larger HF component than B3LYP, give optimized geometries and relative energies of [10]annulene isomers which agree well[36] with the much more computational-resource demanding CCSD(T). This result further supports our use of KMLYP and BHLYP to optimize the [14]-, [18]-, and [22]annulene geometries, since this is not feasible at CCSD(T).

[22]Annulene: Although [22]annulene was prepared by Sondheimer and co-workers[37] in 1971, its X-ray structure is not known. The NMR ^{1}H chemical shifts of the inner and outer protons are $\delta = -0.4$ to -1.2 and 8.5 to 9.7 ppm, respectively. CK reported[4] a bond-length equalized D_{2h} structure at B3LYP/6-31G*, but the very large disagreement between the computed and experimental ^{1}H NMR chemical shifts (Table 1) clearly excludes such high symmetries for [22]annulene. The eigenvector of the large imaginary vibrational frequency of the D_{2h} form ($\tilde{\nu}_i > 1600i\ \mathrm{cm}^{-1}$ at KMLYP and BHLYP) points towards bond-alternating structures.

The computed ^{1}H NMR chemical shifts (Table 1) of the C_2 [22]annulene outer ($\delta_{\mathrm{outer}} = 8.4$ to 9.5 ppm) and inner ($\delta_{\mathrm{inner}} = -1.2$ to -1.4 ppm) protons agree with the experimental[37] NMR spectroscopy values; those computed for the higher-energy C_{2v} forms differ by 2 ppm. Hence, we predict that [22]annulene favors a bond-alternating structure. By implication, this should be true of all the higher annulenes.

Bridged annulenes: The inner hydrogen repulsion and conformational flexibility problems in larger annulenes, as in Vogel and Roth's 1,6-methano[10]annulene,[38] have been overcome in bridged structures. Both X-ray data and DFT computations[39] show various bridged [10]annulenes to have C–C bond-equalized structures. The same is true for many of the bridged [14]annulenes. The X-ray geometries of both bis(methano)[14]annulene conformers, *syn* and *anti*, are reproduced by B3LYP/6-31G* computations.[40] While the *syn* form is aromatic, the small C–C bond-length range (1.427 to 1.389 Å) may be due, at least in part, to the restraints of the bridging CH_2 groups. Conversely, the non-aromatic behavior (1.486 to 1.356 Å C–C range) of the *anti* conformer is partly due to the steric constraints of the bridges. KMLYP and BHLYP give geometries in equally good agreement with the X-ray data. *trans*-Dihydropyrene, another bridged [14]annulene, favors C_{2h} symmetry at B3LYP (the C–C bond-length range is only 1.393 to 1.401 Å) but a lower symmetry C_2 form (1.364 to 1.394 Å) at KMLYP.

In contrast, the bridged [18]annulene, hexahydrocoronene, behaves distinctly differently at B3LYP than at KMLYP and BHLYP. While the B3LYP structure is highly C–C bond equalized at the $D_{3\mathrm{d}}$ minimum, this D_{3d} geometry is a transition state ($\tilde{\nu} = 1069i\ \mathrm{cm}^{-1}$) at KMLYP and BHLYP. Instead, the D_3 form, with moderate bond alternation ($\Delta r = 0.077$ Å), is a minimum at KMLYP and BHLYP. The inner six-membered ring in hexahydrocoronene has essentially equal C–C bond lengths owing to the tendency of the σ framework to favor regular geometries.

In summary, our evidence establishes that the crossover point from the more symmetrical to bond-alternating Hückel monocycles occurs at [14]annulene. The currently accepted highest possible symmetry structures of [14]-, [18]-, and [22]annulene can be ruled out as they give computed ^{1}H chemical shifts which disagree grossly with the experimental values. The correct structures, which can be obtained by optimization at the KMLYP and BHLYP DFT levels, give excellent δ ^{1}H chemical shift agreement. All three annulenes have lower symmetries and exhibit considerable C–C bond-length alternation ($\Delta r = 0.1$ Å, Table 1). Nonetheless, they are clearly aromatic, judging from their abnormal inner and outer proton chemical shifts as well as their appreciable aromatic stabilization energies.[3,4] Equal C–C bond lengths in $[4n+2]\pi$ systems are not required for aromaticity, and actually reduce the stability of the [14]-, [18]-, and [22]annulenes by about 2.0, 2.8, and 5.8 kcal mol^{-1}, respectively (Table 1). As we have noted herein and earlier,[3,20] changes in geometry have much greater effects on the magnetic properties, which appear to be the most sensitive measures of the degree of cyclic electron delocalization. The commonly used descriptive terms, "localized, " for bond alternating,[3] and "delocalized," for bond equalized, are deceptive and misleading; they should be abandoned in the context of aromaticity or specified explicitly. The structures of fully conjugated $4n+2$ π-electron systems may have appreciable bond alternation and still be delocalized and aromatic.[3] Shaik, Hiberty, and co-workers have emphasized the strong global distortive tendency of π components towards localized bonding.[6–8] This tendency is not overcome in the most symmetrical geometries of the [14]-, [18]-, and [22]annulenes by the modest gain in delocalization energy resulting from bond-length equalization, even when combined with the preference of the σ C–C bonds to have the same length.

Received: March 4, 2004 [Z54188]

Keywords: annulenes · aromaticity · density functional calculations · NMR spectroscopy · structure elucidation

[1] a) K. Mislow, *J. Chem. Phys.* **1952**, *20*, 1489; b) F. Sondheimer, R. Wolovsky, Y. Amiel, *J. Am. Chem. Soc.* **1962**, *84*, 274.
[2] E. Hückel, *Z. Phys.* **1931**, *70*, 204.
[3] C. S. Wannere, P. von R. Schleyer, *Org. Lett.* **2003**, *5*, 865.
[4] C. H. Choi, M. Kertesz, *J. Chem. Phys.* **1998**, *108*, 6681.
[5] H. C. Longuet-Higgins, L. Salem, *Proc. R. Soc. London* **1959**, *251*, 172.
[6] S. Shaik, A. Shurki, D. Danovich, P. C. Hiberty, *Chem. Rev.* **2001**, *101*, 1501.
[7] K. Jug, P. C. Hiberty, S. Shaik, *Chem. Rev.* **2001**, *101*, 1477.
[8] P. C. Hiberty, S. Shaik, *Phys. Chem. Chem. Phys.* **2004**, *6*, 224.
[9] O. Ermer, *Angew. Chem.* **1987**, *99*, 791; *Angew. Chem. Int. Ed. Engl.* **1987**, *26*, 782. Ermer has pointed out that X-ray diffraction studies are indecisive not only in differentiating D_{3h} and D_{6h} symmetries in benzene but also in solving the structures of higher [*n*]annulenes, bridged annulenes, etc.
[10] X. Li, J. Paldus, *Int. J. Quantum Chem.* **1996**, *60*, 513.
[11] F. Sondheimer, *Acc. Chem. Res.* **1972**, *3*, 81.
[12] Reviews: a) F. A. Van Catledge, N. L. Allinger, *J. Am. Chem. Soc.* **1969**, *91*, 2582; b) A. T. Balaban, M. Banciu, V. Ciorba, *Annulenes, Benzo-Hetero-, Homo- Derivatives, and Their Valence Isomers*, *Vol. 1–3*, CRC, Boca Raton, **1987**; c) R. D. Kennedy, D. Lloyd, H. McNab, *J. Chem. Soc. Perkin Trans. 1* **2002**, 1601.

 © 2004 Wiley-VCH Verlag GmbH & Co. KGaA, Weinheim

[13] a) H. Jiao, P. von R. Schleyer, *Angew. Chem.* **1996**, *108*, 2548; *Angew. Chem. Int. Ed. Engl.* **1996**, *35*, 2383; b) K. K. Baldridge, J. S. Siegel, *Angew. Chem.* **1997**, *109*, 765; *Angew. Chem. Int. Ed. Engl.* **1997**, *36*, 745.

[14] S. Gorter, E. Rutten-Keulemans, M. Krever, C. Romers, D. W. J. Cruickshank, *Acta Crystallogr. Sect. B* **1995**, *51*, 1036.

[15] J. Bregman, F. L. Hirshfeld, D. Rabinovich, G. M. J. Schmidt, *Acta Crystallogr.* **1965**, *19*, 227.

[16] In 1980, Haddon noted that the 1965 X-ray study of [18]annulene "cannot not be regarded as definitive" as the C–C separations are averaged over time. R. C. Haddon, *Chem. Phys. Lett.* **1980**, *70*, 210.

[17] a) C. H. Choi, M. Kertesz, A. Karpfen, *J. Am. Chem. Soc.* **1997**, *119*, 11994; b) the annulene survey at the semi-empirical electron correlated MNDOC level by Yoshizawa et al. also found [18]annulene to prefer D_{6h} symmetry, K. Yoshizawa, T. Kato, T. Yamabe, *J. Phys. Chem.* **1996**, *100*, 5697.

[18] H. Baumann, J. F. M. Oth, *Helv. Chim. Acta* **1982**, *65*, 1885.

[19] H. Baumann, J.-C. Bünzli, J. F. M. Oth, *Helv. Chim. Acta* **1982**, *65*, 582.

[20] C. S. Wannere, D. Moran, N. L. Allinger, B. A. Hess, Jr., L. J. Schaad, P. von R. Schleyer, *Org. Lett.* **2003**, *5*, 2983.

[21] M. Bühl, P. von R. Schleyer, *J. Am. Chem. Soc.* **1992**, *114*, 477.

[22] P. von R. Schleyer, C. Maerker, *Pure Appl. Chem.* **1995**, *67*, 755.

[23] P. R. Rablen, S. A. Pearlman, J. J. Finkbiner, *J. Phys. Chem. A* **1999**, *103*, 7357.

[24] B. Wang, U. Fleischer, J. F. Hinton, P. Pulay, *J. Comput. Chem.* **2001**, *22*, 1887.

[25] The X-ray structures of [14]- and [18]annulene were retrieved from the Cambridge Crystallographic Data Center (www.ccdc.cam.ac.uk/conts/retrieving.html (the Cambridge Crystallographic Data Centre, 12, Union Road, Cambridge CB21EZ, UK; fax: (+44) 1223-336-033; or deposit@ccdc.cam.ac.uk)).

[26] J. F. M. Oth, *Pure Appl. Chem.* **1971**, *25*, 573.

[27] a) C. D. Stevenson, T. L. Kurth, *J. Am. Chem. Soc.* **2000**, *122*, 722, b) C. D. Stevenson, personal communication to P. von R. Schleyer.

[28] a) The upfield and the downfield chemical shift of the inner and the outer protons, respectively, document the strong diatropic ring currents of [18]annulene.[3] In a closely related but non-aromatic structure, the outer as well as the inner protons are in the vinylic proton region (δ^1H = 6.0 to 7.4 ppm); see C. S. Wannere, P. von R. Schleyer, *Org. Lett.* **2003**, *5*, 605; b) We have analyzed the 2 ppm ^{1}H NMR chemical shift differences between the D_3 and C_2 structures in detail using LMO-dissection and find that these are due about half to the local shielding influences of the nearby bonds and the other half are due to the sum of small remote effects.

[29] R. A. King, D. T. Crawford, J. F. Stanton, H. F. Schaefer III, *J. Am. Chem. Soc.* **1999**, *121*, 10788.

[30] a) S. Grimme, *J. Chem. Phys.* **2003**, *118*, 9095; b) S. Grimme, *J. Comput. Chem.* **2003**, *24*, 1529.

[31] S. Grimme, personal communication to P. von R. Schleyer.

[32] J. M. Schulman, R. L. Disch, *J. Mol. Struct. (Theochem)* **1991**, *234*, 213.

[33] C. C. Chiang, I. C. Paul, *J. Am. Chem. Soc.* **1972**, *94*, 4741.

[34] S. Masamune, N. Darby, *Acc. Chem. Res.* **1972**, *5*, 272.

[35] D. R. Price, J. F. Stanton, *Org. Lett.* **2002**, *4*, 2809, reported excellent agreement between the computed and experimental ^{13}C NMR chemical shifts only for the lowest energy C_2 structure of [10]annulene.

[36] Structures and energies of all [10]annulene conformations employing various density functional methods with the 6-311+G** basis set are reported in the Supporting Information.

[37] R. M. Mcquilki, B. W. Metcalf, F. Sondheimer, *Chem. Commun.* **1971**, 338.

[38] E. Vogel, H. D. Roth, *Angew. Chem.* **1964**, *76*, 145; *Angew. Chem. Int. Ed. Engl.* **1964**, *3*, 228.

[39] 1,6-Methano- (C_{2v}) and 1,5-methano-[10]annulenes (C_1) both have delocalized structures but with moderate C–C bond-length differences ($\Delta r = 0.039$ and 0.061 Å, respectively, at KMLYP). Optimized geometries of various bridged annulenes are reported in the Supporting Information.

[40] M. Nendel, K. N. Houk, L. M. Tolbert, E. Vogel, H. J. Jiao, P. von R. Schleyer, *J. Phys. Chem. A* **1998**, *102*, 7191.

[41] *Methods*: All the structures were fully optimized both using lower as well as higher (imposed) symmetries at the B3LYP, KMLYP,[42] and BHLYP DFT methods with 6-311+G** basis set using the Gaussian 98 suite[43] of programs. The frequencies were computed at the same level; the ground-state structures, transition states, and higher order saddle-point structures were confirmed by the presence of imaginary (or real) vibrational frequencies. Single-point energies of D_{6h} and C_2 [18]annulene structures were computed using CCSD augmented by a perturbative treatment of triple excitations, CCSD(T),[44] with the DZP(C)+DZ(H) (fc) and the DZ (fc) basis sets using the local version of the ACESII program.[45] The rest of the data in Table 2 were obtained using the Gaussian 98. The ^{1}H NMR chemical shifts were computed at GIAO[46]-B3LYP/6-311+G**//using the DFT/6-311+G** geometry. The expected absolute proton shieldings, σ, were converted into chemical shifts, δ, as the difference from the proton shieldings of TMS, 31.98 ppm.

[42] J. K. Kang, C. B. Musgrave, *J. Chem. Phys.* **2001**, *115*, 11040.

[43] Gaussian 98 (Revision A.7), M. J. Frisch, G. W. Trucks, H. B. Schlegel, G. E. Scuseria, M. A. Robb, J. R. Cheeseman, V. G. Zakrzewski, J. A. Montgomery, R. E. Stratmann, J. C. Burant, S. Dapprich, J. M. Millam, A. D. Daniels, K. N. Kudin, M. C. Strain, O. Farkas, J. Tomasi, V. Barone, M. Cossi, R. Cammi, B. Mennucci, C. Pomelli, C. Adamo, S. Clifford, J. Ochterski, G. A. Petersson, P. Y. Ayala, Q. Cui, K. Morokuma, D. K. Malick, A. D. Rabuck, K. Raghavachari, J. B. Foresman, J. Cioslowski, J. V. Ortiz, B. B. Stefanov, G. Liu, A. Liashenko, P. Piskorz, I. Komaromi, R. Gomperts, R. L. Martin, D. J. Fox, T. Keith, M. A. Al-Laham, C. Y. Peng, A. Nanayakkara, C. Gonzalez, M. Challacombe, P. M. W. Gill, B. G. Johnson, W. Chen, M. W. Wong, J. L. Andres, M. Head-Gordon, E. S. Replogle, J. A. Pople, Gaussian, Inc., Pittsburgh, PA, **1998**.

[44] a) K. Raghavachari, G. W. Trucks, J. A. Pople, M. Head-Gordon, *Chem. Phys. Lett.* **1989**, *157*, 479; b) R. J. Bartlett, J. D. Watts, S. A. Kucharski, J. Noga, *Chem. Phys. Lett.* **1990**, *165*, 513.

[45] J. F. Stanton, J. Gauss, J. D. Watts, W. J. Lauderdale, R. J. Bartlett, *Int. J. Quantum Chem.* **1992**, *S26*, 879.

[46] K. Wolinski, J. F. Hinton, P. Pulay, *J. Am. Chem. Soc.* **1990**, *112*, 8251.

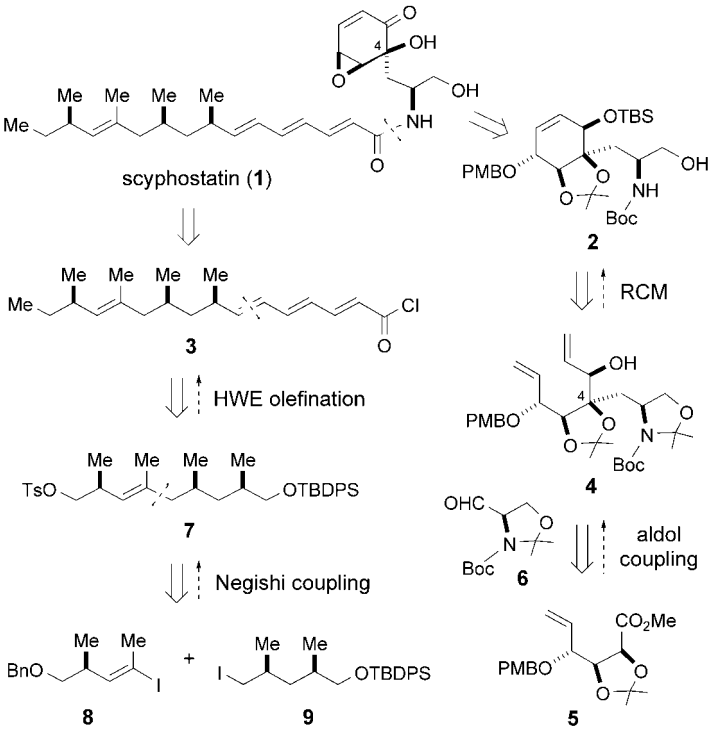
 © 2004 Wiley-VCH Verlag GmbH & Co. KGaA, Weinheim

Natural Products Synthesis

Total Synthesis of (+)-Scyphostatin, a Potent and Specific Inhibitor of Neutral Sphingomyelinase**

*Munenori Inoue, Wakako Yokota, Modachur G. Murugesh, Takashi Izuhara, and Tadashi Katoh**

Scyphostatin (**1**, Scheme 1), isolated from a culture broth of *Dasyscyphus mollissimus* SANK-13892 by Ogita and co-workers in 1997,[1] is a powerful and specific inhibitor of neutral sphingomyelinase (N-SMase). It has been reported that **1** inhibits N-SMase and acidic SMase (A-SMase) with IC_{50} values of 1.0 μM and 49.3 μM, respectively.[2] Although a large number of N-SMase inhibitors have been reported to date,[3] **1** is still the most potent inhibitor of the enzyme.[1,2] N-SMase inhibitors regulate the level of ceramide, the hydrolysis product of sphingomyelin, in a wide variety of mammalian cells. Therefore, **1** is expected to be a promising new agent for the treatment of ceramide-mediated pathogenic states such as AIDS,[4] inflammation, and immunological and neurological disorders.[2] Structurally, **1** features a novel, highly oxygenated cyclohexene ring and an aminopropanol side chain linked to a C_{20} unsaturated fatty acid moiety. The significant biological properties coupled with the unique structural features make **1** an exceptionally intriguing and timely target for total synthesis. Although several synthetic approaches, including ours,[5] have appeared recently,[6] no total synthesis has been reported to date. We have already prepared the fully functionalized cyclohexene segment with the *N*,*O*-protected aminopropanol side chain and the correct stereogenic centers;[5b] however, all attempts to remove the *N*,*O*-protecting group (the cyclic carbonate moiety) from the cyclohexene segment met with failure.[5c] Herein we disclose an alternative and more reliable synthetic strategy that led to the completion of the total synthesis of **1**.



Scheme 1. Retrosynthetic plan for scyphostatin (**1**). TBS = *tert*-butyldimethylsilyl, PMB = 4-methoxybenzyl, Boc = *tert*-butoxycarbonyl, Ts = *p*-toluenesulfonyl, TBDPS = *tert*-butyldiphenylsilyl, Bn = benzyl.

The retrosynthetic plan for scyphostatin (**1**) is outlined in Scheme 1. Our preliminary model studies[5a,b] suggested that the labile epoxycyclohexenone moiety should be elaborated at a late stage of the synthesis. We envisaged that the cyclohexene segment **2** would be produced through ring-closing metathesis (RCM) of diene **4**. The RCM substrate **4** would be prepared through aldol coupling of ester **5** with the Garner aldehyde (**6**),[7] which would establish the requisite quaternary stereocenter C4. During the course of our studies, Hoye and Tennakoon reported that the fatty acid side chain (the ethyl ester variant of **3**) can be synthesized from tosylate **7** through Horner–Wadsworth–Emmons (HWE) olefination.[8] Therefore, we planned to employ **7** as a key intermediate in our synthesis and explored an alternative approach to **7**, which features Negishi coupling of vinyl iodide **8** and alkyl iodide **9**.[23]

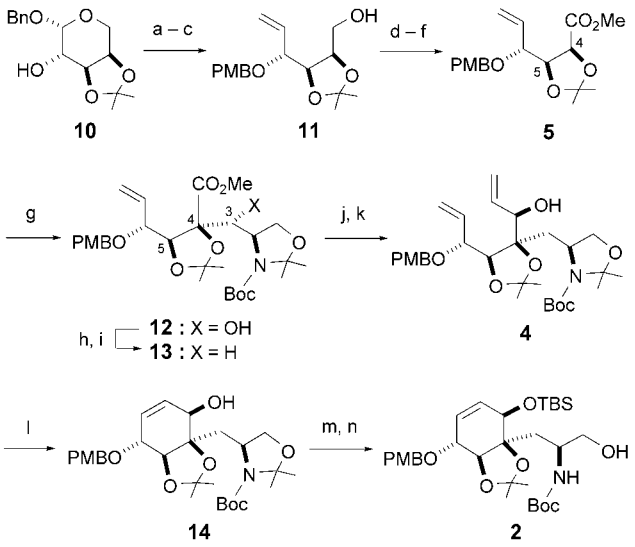
The synthesis of the cyclohexene segment **2** started from the known compound **10**[9] (Scheme 2), readily prepared from D-arabinose by *O*-benzylglycosylation and acetonide formation. PMB protection of **10** followed by debenzylation and Wittig methylenation provided alcohol **11**, which was subsequently converted into methyl ester **5** through a three-step sequence involving twofold oxidation and methyl esterification. The crucial aldol coupling of **5** with **6** was effected by treatment of **5** with $NaN(SiMe_3)_2$ (1.3 equiv) followed by addition of **6** (1.1 equiv), which led to the desired product **12** as a single diastereomer in 69% yield.[10] The stereochemistry at C4 in **12** was deduced by NOE studies[11] of the deoxygenated compound **13**, which was obtained by applying the procedure reported by Barton and McCombie.[12] The

[*] Dr. M. Inoue, W. Yokota, Dr. M. G. Murugesh, Prof. Dr. T. Katoh[+]
Sagami Chemical Research Center
2743-1 Hayakawa, Ayase, Kanagawa 252-1193 (Japan)
E-mail: katoh@tohoku-pharm.ac.jp
Dr. T. Izuhara
Department of Electronic Chemistry
Tokyo Institute of Technology
Nagatsuta, Yokohama 226-8502 (Japan)
[+] Address correspondence to this author at
Tohoku Pharmaceutical University
4-4-1 Komatsushima, Aoba-ku, Sendai 981-8558 (Japan)
Fax: (+81) 22-275-2013

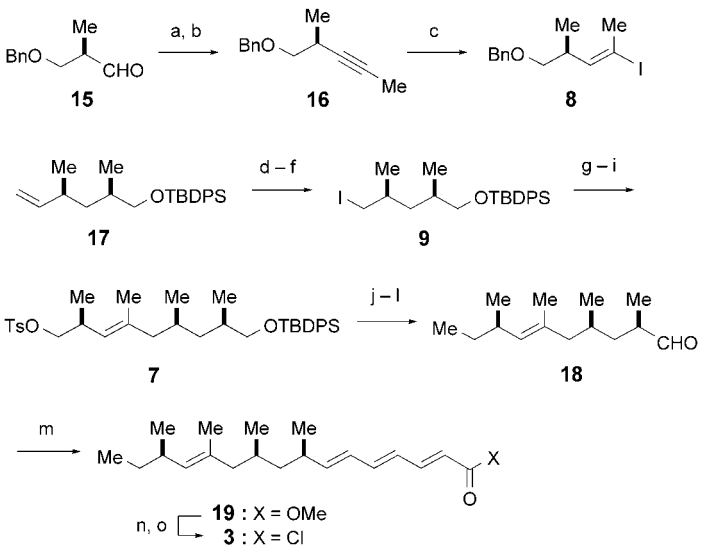
[**] We are grateful to Dr. H. Kogen, Dr. T. Ogita, and Dr. T. Akiyama (Sankyo Co., Ltd.) for fruitful discussions and a generous gift of natural (+)-scyphostatin (**1**). We also thank Dr. N. Sugimoto and Dr. N. Kawahara (National Institute of Health Sciences) for measurements of HRMS and assistance with NMR spectroscopy experiments. M.G.M thanks JST for an STA fellowship.

Supporting information for this article is available on the WWW under http://www.angewandte.org or from the author.

 DOI: 10.1002/anie.200454192 © 2004 Wiley-VCH Verlag GmbH & Co. KGaA, Weinheim



Scheme 2. Synthesis of the cyclohexene segment **2**. a) PMBCl, NaH, DMSO, room temperature, 70%; b) H_2, Raney Ni, EtOH, room temperature, 86%; c) $Ph_3P^+CH_3Br^-$, *t*BuOK, benzene, reflux, 86%; d) DMSO, $(COCl)_2$, CH_2Cl_2, −78 °C; *i*Pr_2NEt, −78→0 °C, 95%; e) $NaClO_2$, NaH_2PO_4, DMSO/H_2O, room temperature; f) CH_2N_2, Et_2O/MeOH, 0 °C, 78% (two steps); g) $NaN(SiMe_3)_2$, THF, −78 °C; Garner aldehyde (**6**), −78 °C, 69%; h) $NaN(SiMe_3)_2$, THF, 0 °C; CS_2; MeI, 0 °C→RT; i) *n*Bu_3SnH, AIBN, toluene, reflux, 53% (two steps); j) DIBAL, CH_2Cl_2, −100 °C, 88%; k) vinylmagnesium bromide, THF, 0 °C, 93%; l) $(Cy_3P)_2RuCl_2$(=CHPh) (10 mol%), CH_2Cl_2, reflux, 96%; m) TBSOTf, 2,6-lutidine, CH_2Cl_2, room temperature, 93%; n) PPTS, EtOH, 60 °C, 57%. DMSO = dimethyl sulfoxide, AIBN = 2,2′-azobisisobutyronitrile, DIBAL = diisobutylaluminum hydride, TBS = *tert*-butyldimethylsilyl, Tf = trifluoromethanesulfonyl, Cy = cyclohexyl, PPTS = pyridinium *p*-toluenesulfonate.



Scheme 3. Synthesis of the fatty acid segment **3**. a) PPh_3, CBr_4, CH_2Cl_2, 0 °C; b) *n*BuLi, THF, −78 °C; MeI, 94%, (two steps); c) Cp_2ZrHCl, benzene, 40 °C; I_2, RT, 63%; d) O_3, CH_2Cl_2/MeOH, −78 °C; $NaBH_4$, room temperature , 84%; e) MsCl, Et_3N, CH_2Cl_2, room temperature; f) NaI, acetone, reflux, 95% (two steps); g) *t*BuLi, $ZnCl_2$, Et_2O, −78→0 °C; **8**, $[Pd(PPh_3)_4]$, THF, 81%; h) lithium 4,4′-di-*tert*-butylbiphenylide, THF, −78 °C, 90%; i) TsCl, Et_3N, DMAP, CH_2Cl_2, RT; j) MeLi, CuI, Et_2O, −40 °C, 97% (two steps); k) TBAF, THF, room temperature, 91%; l) $(nPr)_4NRuO_4$, NMO, CH_2Cl_2, room temperature; m) $(MeO)_2P(O)CH_2CH{=}CH{-}CH{=}CH{-}CO_2Me$, LDA, THF, −78→−30 °C, 46% (two steps); n) KOH (2 M), MeOH/THF, room temperature; o) $(COCl)_2$, DMF, CH_2Cl_2, room temperature. Ms = methanesulfonyl, DMAP = 4-dimethylaminopyridine, TBAF = tetrabutylammonium fluoride, NMO = 4-methylmorpholine *N*-oxide, LDA = lithium diisopropylamide, DMF = *N*,*N*-dimethylformamide.

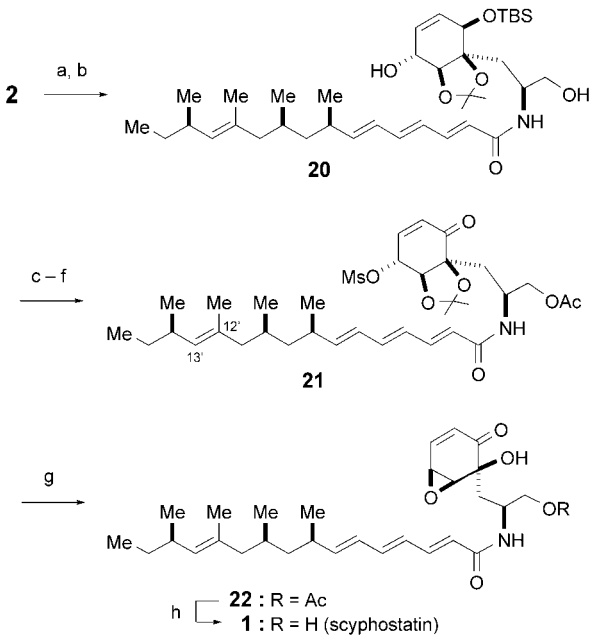
remarkable stereoselectivity at C4 observed in this coupling reaction seems to be induced by the adjacent C5 stereocenter. Reduction of **13** with DIBAL followed by vinylation of the resulting aldehyde furnished diene **4**. The critical RCM reaction of **4** in the presence of the Grubbs catalyst[13] proceeded smoothly and cleanly to give cyclohexenol **14** in 96% yield. Finally, **14** was converted into **2** by *O*-silylation and selective acetonide cleavage.

The synthesis of the fatty acid segment **3** was next investigated (Scheme 3). Vinyl iodide **8** was prepared from the known aldehyde **15**[14] via alkyne **16** by a Corey–Fuchs reaction[15] and subsequent hydrozirconation/iodination.[16] Alkyl iodide **9**, the coupling partner of **8**, was derived from the known olefin **17**[17] by ozonolysis with reductive workup followed by mesylation and iodination. The key Negishi coupling of **9** and **8** was carried out successfully by employing the modified conditions of Smith et al.[18] to give the desired coupling product (81% yield), which was converted into the Hoye intermediate **7** by debenzylation and tosylation. According to the Hoye protocol,[8] **7** was transformed into aldehyde **18** in a three-step sequence. Aldehyde **18** was then subjected to HWE olefination[19] to yield methyl ester **19**. Spectral data (^1H and ^{13}C NMR, MS) of **19** were in good agreement with those reported.[20] Finally, the desired acid chloride **3** was derived from **19** in two steps.

The projected synthesis was completed as shown in Scheme 4. The Boc and PMB groups of the cyclohexene segment **2** were simultaneously removed with TMSOTf[21] to produce the corresponding amino diol, which was immediately treated with the fatty acid segment **3** to give, after treatment of aqueous AcOH, the desired amide **20** in 73%. Enone **21** was elaborated from **20** by selective acetylation, mesylation, desilylation, and Dess–Martin oxidation. In our previous work,[5a,b] the requisite epoxide moiety was successfully installed by hydrolysis of the acetonide with aqueous CF_3CO_2H, followed by treatment with base. However, upon applying these conditions to **21**, partial isomerization of the C12′-C13′ double bond in the side chain was observed during the acid hydrolysis. Eventually, we overcame this problem by using aqueous CCl_3CO_2H instead of CF_3CO_2H; subsequent treatment with NaOH afforded the desired epoxide **22** without appreciable isomerization of the double bond. The final step was to remove the acetyl group of **22**; deprotection was best brought about by exposure of **22** to lipase PS in phosphate buffer,[22] furnishing (+)-scyphostatin (**1**) in 60% yield, which was identical to natural (+)-**1** in all respects (^1H and ^{13}C NMR, HRMS, and $[\alpha]_D$).[1,2]

In conclusion, we completed the first total synthesis of (+)-scyphostatin (**1**) in an efficient and flexible way. Impor-

 © 2004 Wiley-VCH Verlag GmbH & Co. KGaA, Weinheim



Scheme 4. Total synthesis of scyphostatin (**1**). a) TMSOTf, 2,6-lutidine, CH_2Cl_2, room temperature; MeOH; b) **3**, Et_3N, CH_2Cl_2, room temperature; AcOH (aq.), 73% (two steps); c) Ac_2O, pyridine, DMAP, CH_2Cl_2, room temperature, 72%; d) MsCl, Et_3N, CH_2Cl_2, room temperature, 93%; e) TBAF, THF, room temperature; f) Dess–Martin periodinane, CH_2Cl_2, room temperature, 98% (two steps); g) CCl_3CO_2H, CH_2Cl_2/H_2O, reflux; NaOH (2 M), room temperature, 45%; h) lipase PS, pH 7 phosphate buffer/acetone, room temperature, 60%. TMS = trimethylsilyl.

tantly, the synthesis has the potential for producing scyphostatin analogues with a wide variety of fatty acid side chains.

Received: March 5, 2004 [Z54192]

Keywords: aldol reaction · inhibitors · natural products · ring-closing metathesis · total synthesis

[1] M. Tanaka, F. Nara, K. Suzuki-Konagai, T. Hosoya, T. Ogita, *J. Am. Chem. Soc.* **1997**, *119*, 7871.

[2] a) F. Nara, M. Tanaka, T. Hosoya, K. Suzuki-Konagai, T. Ogita, *J. Antibiot.* **1999**, *52*, 525; b) F. Nara, M. Tanaka, S. Masuda-Inoue, Y. Yamasato, H. Doi-Yoshioka, K. Suzuki-Konagai, S. Kumakura, T. Ogita, *J. Antibiot.* **1999**, *52*, 531.

[3] a) R. Uchida, H. Tomoda, Y. Dong, S. Omura, *J. Antibiot.* **1999**, *52*, 572; b) M. Tanaka, F. Nara, Y. Yamasato, S. Masuda-Inoue, H. Doi-Yoshioka, S. Kumakura, R. Enokita, T. Ogita, *J. Antibiot.* **1999**, *52*, 670; c) M. Tanaka, F. Nara, Y. Yamasato, Y. Ono, T. Ogita, *J. Antibiot.* **1999**, *52*, 827; d) C. Arenz, A. Giannis, *Angew. Chem.* **2000**, *112*, 1498; *Angew. Chem. Int. Ed.* **2000**, *39*, 1440; e) C. Arenz, A. Giannis, *Eur. J. Org. Chem.* **2001**, 137; f) C. Arenz, M. Thutewohl, O. Block, H.-J. Altenbach, H. Waldmann, A. Giannis, *ChemBioChem* **2001**, *2*, 141; g) C. Arenz, M. Gartner, V. Waschowlowski, A. Giannis, *Bioorg. Med. Chem.* **2001**, *9*, 2901; h) T. Yokomatsu, H. Takechi, T. Akiyama, S. Shibuya, T. Kominato, S. Soeda, H. Shimeno, *Bioorg. Med. Chem. Lett.* **2001**, *11*, 1277; i) T. Hakogi, Y. Monden, M. Taichi, S. Iwama, S. Fujii, K. Ikeda, S. Katsumura, *J. Org. Chem.* **2002**, *67*, 4839; j) C. C. Lindsey, C. Gómez-Díza, J. M. Villalba, T. R. R. Pettus, *Tetrahedron* **2002**, *58*, 4559; k) T. Yokomatsu, T. Murano, T. Akiyama, J. Koizumi, S. Shibuya, Y. Tsuji, S. Soeda, H. Shimeno, *Bioorg. Med. Chem. Lett.* **2003**, *13*, 229; l) M. Taguchi, K. Sugimoto, K. Goda, T. Akama, K. Yamamoto, T. Suzuki, Y. Tomishima, M. Nishiguchi, K. Arai, K. Takahashi, T. Kobori, *Bioorg. Med. Chem. Lett.* **2003**, *13*, 1963; m) M. Taguchi, K. Goda, K. Sugimoto, T. Akama, K. Yamamoto, T. Suzuki, Y. Tomishima, M. Nishiguchi, K. Arai, K. Takahashi, T. Kobori, *Bioorg. Med. Chem. Lett.* **2003**, *13*, 3681.

[4] S. Chatterjee, *Arterioscler. Thromb. Vasc. Biol.* **1998**, *18*, 1523.

[5] a) T. Izuhara, T. Katoh, *Tetrahedron Lett.* **2000**, *41*, 7651; b) T. Izuhara, T. Katoh, *Org. Lett.* **2001**, *3*, 1653; c) T. Izuhara, W. Yokota, M. Inoue, T. Katoh, *Heterocycles* **2002**, *56*, 553.

[6] a) M. K. Gurjar, S. Hotha, *Heterocycles,* **2000**, *53*, 1885; b) K. A. Runcie, R. J. K. Taylor, *Org. Lett.* **2001**, *3*, 3237; c) H. Fujioka, N. Kotoku, Y. Sawama, Y. Nagatomi, Y. Kita, *Tetrahedron Lett.* **2002**, *43*, 4825; d) R. Takagi, W. Miyanaga, Y. Tamura, K. Ohkata, *Chem. Commun.* **2002**, 2096; e) L. M. Murray, P. O'Brien, R. J. K. Taylor, *Org. Lett.* **2003**, *5*, 1943; f) M. Eipert, C. M. Mössmer, M. E. Maier, *Tetrahedron* **2003**, *59*, 7949.

[7] a) P. Garner, J. M. Park, *J. Org. Chem.* **1987**, *52*, 2361; b) A. Dondoni, D. Perrone, *Synthesis* **1997**, 527; c) A. Dondoni, D. Perrone, *Org. Synth.* **1997**, *77*, 64.

[8] T. R. Hoye, M. A. Tennakoon, *Org. Lett.* **2000**, *2*, 1481.

[9] C. E. Ballou, *J. Am. Chem. Soc.* **1957**, *79*, 165.

[10] The stereochemistry at C3 in the coupling product **12** was tentatively assigned based on the usual Felkin–Anh model.

[11] An NOE interaction between 3-H and 5-H was observed.

[12] D. H. R. Barton, S. W. McCombie, *J. Chem. Soc. Perkin Trans. 1* **1975**, 1574.

[13] a) P. Schwab, M. B. France, J. W. Ziller, R. H. Grubbs, *Angew. Chem.* **1995**, *107*, 2179; *Angew. Chem. Int. Ed. Engl.* **1995**, *34*, 2039; for a recent review, see: b) T. M. Trnka, R. H. Grubbs, *Acc. Chem. Res.* **2001**, *34*, 18.

[14] T. F. Walsh, R. B. Toupence, F. Ujjainwalla, J. R. Young, M. T. Goulet, *Tetrahedron* **2001**, *57*, 5233.

[15] E. J. Corey, P. L. Fuchs, *Tetrahedron Lett.* **1972**, 3769.

[16] D. W. Hart, T. F. Blackburn, J. Schwartz, *J. Am. Chem. Soc.* **1975**, *97*, 679.

[17] W. R. Roush, A. D. Palkowitz, K. Ando, *J. Am. Chem. Soc.* **1990**, *112*, 6348.

[18] A. B. Smith III, T. J. Beauchamp, M. J. LaMarche, M. D. Kaufman, Y. Qiu, H. Arimoto, D. R. Jones, K. Kobayashi, *J. Am. Chem. Soc.* **2000**, *122*, 8654.

[19] M. Kinoshita, H. Takami, M. Taniguchi, T. Tamai, *Bull. Chem. Soc. Jpn.* **1987**, *60*, 2151.

[20] S. Saito, N. Tanaka, K. Fujimoto, H. Kogen, *Org. Lett.* **2000**, *2*, 505.

[21] M. Sakaitani, Y. Ohfune, *J. Org. Chem.* **1990**, *55*, 870.

[22] All attempts at deacetylation of **22** under a various conditions (e.g. K_2CO_3, NaOMe, or KOH in MeOH; aqueous KOH in THF or CH_2Cl_2; DBU or NH_3 in THF) met with failure; presumably, the epoxycyclohexenone moiety present in **22** and/or **1** is sensitive to these basic conditions. Detailed results and discussions will be presented in a full account.

[23] Note added in proof: After submission of this manuscript, we learnt of independent syntheses of the scyphostatin side chain in which similar Negishi-type cross-coupling reactions were employed: a) Z. Tan, E.-i. Negishi, *Angew. Chem.* **2004**, *116*, 2971; *Angew. Chem. Int. Ed.* **2004**, *43*, 2911; b) G. D. McAllister, R. J. K. Taylor, *Tetrahedron Lett.* **2004**, *45*, 2551; we are grateful to Professor Ei-ichi Negishi for kindly providing us with a preprint of his paper prior to publication.

 © 2004 Wiley-VCH Verlag GmbH & Co. KGaA, Weinheim

C–H Activation

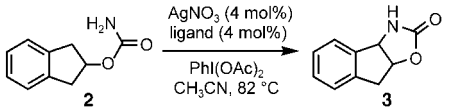
A Silver-Catalyzed Intramolecular Amidation of Saturated C–H Bonds**

*Yong Cui and Chuan He**

Oxidative insertion reactions into saturated C–H bonds to form amines and amine derivatives under transition-metal catalysis are attractive synthetic methodologies.[1–14] Besides providing facile access to various organic structures, these reactions also offer opportunities to study the fundamental mechanism of C–H activation. It has been demonstrated that Rh- and Ru-based compounds mediate C–H amidation reactions particularly well.[2,4,14–19] A dirhodium(II) tetracarboxylate system was shown to catalyze the intramolecular amidation of C–H bonds of carbamates and sulfamates with high regioselectivity and good to excellent diastereoselectivity.[14–16] It is thought that a metal-bound nitrene species might be formed which then inserts oxidatively into saturated C–H bonds in these reactions. Despite extensive studies of metal-catalyzed amidations of C–H bonds, efficient and practical examples of such processes are limited. We report herein an efficient amidation reaction of saturated C–H bonds catalyzed by silver(I).

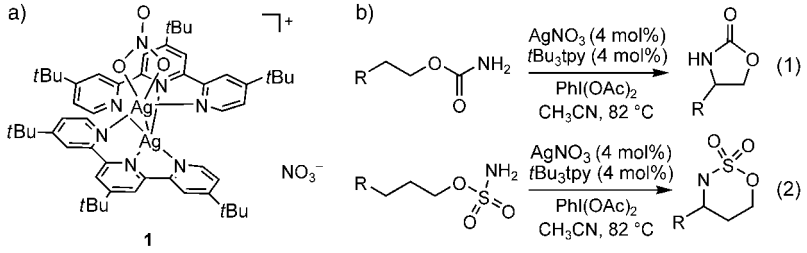
Silver complexes exhibit interesting activity, and silver-catalyzed organic transformations have attracted attention recently.[20–23] In particular, several nonradical oxidative group-transfer reactions catalyzed by silver were discovered.[24–27] We reported a disilver(I) compound (**1**, Scheme 1a) that efficiently catalyzes the aziridination of olefins.[26] Surprisingly, subsequent studies showed that only this disilver complex gave clean aziridine products in the silver-mediated reactions tested with a variety of different ligands. This led us to propose that the disilver structure may be important for the unique activity of this complex, and that the same compound may catalyze other reactions, such as the activation of saturated C–H bonds. After several experiments we found that **1** generated in situ catalyzed the efficient intramolecular amidation of saturated C–H bonds, as shown in Scheme 1b. With the indanol-derived carbamate **2** as the substrate, $AgNO_3$ (4 mol%) with 4,4′,4″-tri-*tert*-butyl-2,2′:6′,2″terpyridine (tBu$_3$tpy, 4 mol%) as the catalyst, and $PhI(OAc)_2$ (2.0 equiv) as the oxidant, the cyclized product indanooxazolidin-2-one (**3**) was isolated from the reaction in acetonitrile in 83% yield (Table 1 and entry 2 of Table 2). A color change from pale yellow to deep brown was observed during the course of the reaction, which may suggest the involvement of high-valent silver species.

Table 1: Conditions for the oxidative cyclization of a carbamate.[a]



Ligand	Yield [%]
pyridine	–[b]
4-*tert*-butylpyridine	–[b]
bipyridine	22
4,4′-di-*tert*-butylbipyridine	35
2,2′:6′,2″-terpyridine (tpy)	41
4,4′,4″-tBu$_3$tpy	89
4-*tert*-butylbis(oxazoline)	–[b]
4-phenylbis(oxazoline)pyridine	–[b]

[a] All reactions were conducted at 82 °C in CH_3CN with 2.0 equivalents of $PhI(OAc)_2$. The reported yields were determined by NMR spectroscopy by using mesitylene as an internal standard. [b] Product **3** was not observed.



Scheme 1. a) A unique disilver(I) catalyst $[Ag_2(t\text{Bu}_3\text{tpy})_2(NO_3)](NO_3)$ (**1**). b) Oxidative cyclization of carbamates [Eq. (1)] and sulfamates [Eq. (2)].

Although different types of ligands were tested (Table 1), a clean reaction was observed and the product was obtained in high yield only when tBu$_3$tpy was used, as had also been observed for the olefin aziridination reaction.[26] Combinations of other ligands with silver(I) salts were either completely inactive or led to a low yield of the product. Sulfamate substrates were also tested, and very similar results were obtained. Although both silver and copper can catalyze olefin aziridination in the presence of tBu$_3$tpy,[26] copper, unlike silver, is not able to catalyze insertion into C–H bonds. It was reported that copper ions can mediate the amidation of saturated C–H bonds when an electron-deficient ligand is used.[6] In this case a reactive electrophilic copper nitrene species may form. In the system described herein, it appears that the silver nitrene species are more oxidative than analogous copper species. The high oxidation potential often observed for silver complexes supports this notion.[28]

A range of carbamates and sulfamates were tested, as shown in Table 2. Five-membered-ring and six-membered-ring insertion products were generated preferentially from

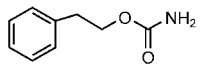
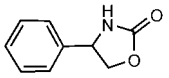
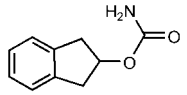
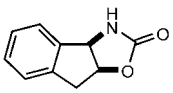
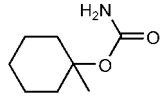
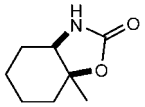
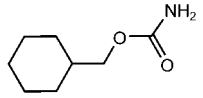
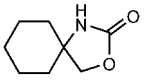
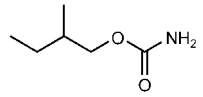
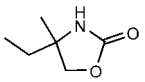
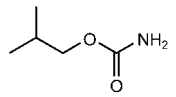
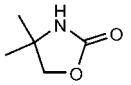
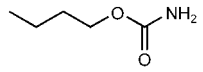
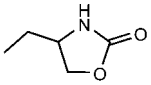
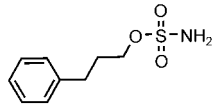
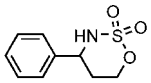
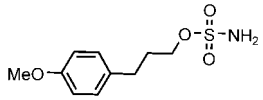
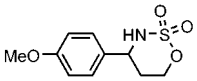
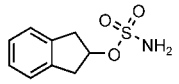
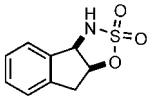
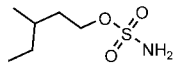
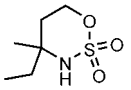
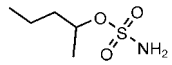
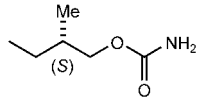
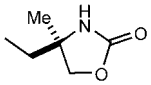
[*] Dr. Y. Cui, Prof. C. He
Department of Chemistry
University of Chicago
5735 S. Ellis Avenue, Chicago, IL 60637 (USA)
Fax: (+1) 773-702-0805
E-mail: chuanhe@uchicago.edu

[**] This research was supported by the University of Chicago. We acknowledge the donors of the American Chemical Society Petroleum Research Fund for support of this research (PRF 38848-G3). C.H. is also a recipient of a Research Innovation Award (RI1179) from Research Corporation.

Supporting information for this article is available on the WWW under http://www.angewandte.org or from the author.

 © 2004 Wiley-VCH Verlag GmbH & Co. KGaA, Weinheim DOI: 10.1002/anie.200454243

Table 2: Disilver(I)-catalyzed oxidative cyclization.[a]

Entry	Substrate	Product	Yield [%]
1			81
2			83[b]
3			85[b]
4			85
5			76 (68)[c]
6			74 (70)[c]
7			58
8			87
9			78
10			65 (57)[b,c]
11			90
12			53[c,d]
13			73

[a] All reactions were conducted at 82 °C in CH_3CN in the presence of $AgNO_3$, tBu$_3$tpy (4 mol%), and PhI(OAc)$_2$ (1.4 equiv for sulfamates and 2.0 equiv for carbamates). The yield of the isolated product is reported. [b] The *cis* product was obtained. [c] The reaction was carried out with 4-*tert*-butylpyridine (2 mol%; the yield determined by NMR spectroscopy for the reaction in the absence of 4-*tert*-butylpyridine is reported in parenthesis). [d] *syn*/*anti* = 2.2:1.0.

carbamates and sulfamates, respectively (in particular, see entries 7 and 12 of Table 2). Good to excellent yields comparable to or better than those found with other catalytic systems[14–16] were observed with our silver catalyst. The addition of a stoichiometric amount of a base was not necessary. The addition of 2 mol% of 4-*tert*-butylpyridine led to better yields and cleaner products in several cases (Table 2, entries 5, 6, 10, and 12). However, excess amounts of the monodentate ligand 4-*tert*-butylpyridine (10 equiv with respect to the silver catalyst) had a deleterious effect on the reaction. The exact role played by 4-*tert*-butylpyridine is not clear. Perhaps the binding of a monodentate ligand to one terminal side of disilver influences the activity on the other end. We also employed several amides as potential substrates. However, no product was observed under the various reaction conditions tested so far. Efforts to use catalyst **1** or other silver compounds to mediate insertion reactions of amides and other substrates are in progress.

A substrate derived from (*S*)-2-methyl-1-butanol was employed to probe the mechanism of this reaction and determine its stereoselectivity (Table 2, entry 13).[14] A mixture of enantiomers would be expected as the product if a discrete radical species is the reactive intermediate. Retention of configuration should occur if a nitrene intermediate is produced and inserts directly into the C–H bond. The product of this reaction has the same optical rotation as an enantiomerically pure sample of the oxazolidinone[14] shown in entry 13 of Table 2.[29] The product obtained from the corresponding racemic starting material in a control experiment showed no optical rotation (Table 2, entry 5). This result indicates that the silver-catalyzed reaction is stereospecific. It also provides support for the involvement of a nitrene-type oxidant in the reaction, although the involvement of a short-lived radical as the reactive intermediate can not be excluded completely.

The disilver(I) catalyst **1** was probed by electrospray mass spectrometry (MS(ESI)) in acetonitrile. The molecular peak for the disilver(I) cation core $[Ag_2(t\text{Bu}_3\text{tpy})_2NO_3]^+$ is clearly visible in the spectrum (Figure 1). Mononuclear silver(I)

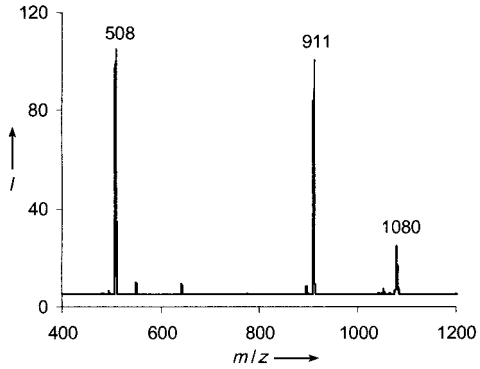


Figure 1. The MS(ESI) spectrum of complex **1** in CH_3CN. MS(ESI$^+$): calcd for $[Ag_2(t\text{Bu}_3\text{tpy})_2NO_3]^+$: 1080, $[Ag(t\text{Bu}_3\text{tpy})_2]^+$: 911, $[Ag(t\text{Bu}_3\text{tpy})]^+$: 508.

species were also observed. These species perhaps result from the decomposition of **1** under the conditions of mass spectrometry; our previous NMR spectroscopic studies suggest that **1** remains a dimer in acetonitrile.[26] The peak for the disilver cation core remained in the spectrum after compound **1** was treated with PhI=NTs (Ts = *p*-toluenesulfonyl) for 2 h at room temperature. A color change from pale yellow to brown occurred during the course of the reaction. A weak peak corresponding to a molecular weight of 1189 was

 © 2004 Wiley-VCH Verlag GmbH & Co. KGaA, Weinheim

also observed, and assigned as the molecular peak of the disilver complex associated with the nitrenoid moiety =NTs. (The molecular weight of $Ag_2(t\mathrm{Bu}_3\mathrm{tpy})_2$ with the nitrenoid =NTs is 1188.) When PhI=NSO_2Ph was used, this peak shifted to 1175 as expected, which corresponds to the removal of a methyl group.[30] There is no direct evidence to indicate that this species is a silver–nitrene intermediate. However, the results seem to suggest that the disilver structure can remain intact when in contact with the nitrenoid group. Evidently further mechanistic studies are required to fully elucidate the mechanism. We did not observe similar species upon the treatment of complex **1** with $PhI(OAc)_2$ and carbamates. No color change occurred at room temperature after complex **1** was mixed with $PhI(OAc)_2$ and a carbamate. In this case, the reaction intermediates may not be stable to analysis by mass spectrometry.

In summary, we have reported an efficient amidation reaction of saturated C–H bonds catalyzed by a unique disilver(I) complex. The results suggest the involvement of a silver–nitrene intermediate. The reaction is stereospecific and practical for constructing amine-containing organic molecules. Both the ligand $t\mathrm{Bu}_3$tpy and the silver salt are commercially available. With their inherent high oxidation potential, we believe silver ions are good oxidation catalysts that could exhibit other unique activities.

Received: March 11, 2004
Revised: June 7, 2004 [Z54243]

Keywords: amidation · C–H activation · homogeneous catalysis · silver · synthetic methods

[1] R. Breslow, S. H. Gellman, *J. Chem. Soc. Chem. Commun.* **1982**, 1400.
[2] R. Breslow, S. H. Gellman, *J. Am. Chem. Soc.* **1983**, *105*, 6728.
[3] I. Nägeli, G. Baud, G. Bernardinelli, Y. Jacquier, M. Moran, P. Müller, *Helv. Chim. Acta* **1997**, *80*, 1087.
[4] S. M. Au, J. S. Huang, W. Y. Yu, W. H. Fung, C. M. Che, *J. Am. Chem. Soc.* **1999**, *121*, 9120.
[5] P. Dauban, L. Sanière, A. Tarrade, R. H. Dodd, *J. Am. Chem. Soc.* **2001**, *123*, 7707.
[6] M. M. Díaz-Requejo, T. R. Belderraín, M. C. Nicasio, S. Trofimenko, P. J. Pérez, *J. Am. Chem. Soc.* **2003**, *125*, 12078.
[7] F. Ragaini, A. Penoni, E. Gallo, S. Tollari, C. L. Gotti, M. Lapadula, E. Mangioni, S. Cenini, *Chem. Eur. J.* **2003**, *9*, 249.
[8] D. P. Albone, P. S. Aujla, P. S. Taylor, S. Challenger, A. M. Derrick, *J. Org. Chem.* **1998**, *63*, 9569.
[9] J. P. Mahy, G. Bedi, P. Battioni, D. Mansuy, *Tetrahedron Lett.* **1988**, *29*, 1927.
[10] Y. Kohmura, K.-i. Kawasaki, T. Katsuki, *Synlett* **1997**, 1456.
[11] A. Hinman, J. Du Bois, *J. Am. Chem. Soc.* **2003**, *125*, 11510.
[12] J. J. Fleming, K. W. Fiori, J. Du Bois, *J. Am. Chem. Soc.* **2003**, *125*, 2028.
[13] P. M. Wehn, J. Du Bois, *J. Am. Chem. Soc.* **2002**, *124*, 12950.
[14] C. G. Espino, J. Du Bois, *Angew. Chem.* **2001**, *113*, 618; *Angew. Chem. Int. Ed.* **2001**, *40*, 598.
[15] C. G. Espino, P. M. Wehn, J. Chow, J. Du Bois, *J. Am. Chem. Soc.* **2001**, *123*, 6935.
[16] P. M. Wehn, J. Lee, J. Du Bois, *Org. Lett.* **2003**, *5*, 4823.
[17] J. L. Liang, S. X. Yuan, P. W. H. Chan, C. M. Che, *Org. Lett.* **2002**, *4*, 4507.
[18] J. L. Liang, J. S. Huang, X. Q. Yu, N. Y. Zhu, C. M. Che, *Chem. Eur. J.* **2002**, *8*, 1563.
[19] J. L. Liang, S. X. Yuan, J. S. Huang, W. Y. Yu, C. M. Che, *Angew. Chem.* **2002**, *114*, 3615; *Angew. Chem. Int. Ed.* **2002**, *41*, 3465.
[20] J. Cirakovic, T. G. Driver, K. A. Woerpel, *J. Am. Chem. Soc.* **2002**, *124*, 9370.
[21] N. S. Josephsohn, M. L. Snapper, A. H. Hoveyda, *J. Am. Chem. Soc.* **2003**, *125*, 4018.
[22] N. Momiyama, H. Yamamoto, *J. Am. Chem. Soc.* **2003**, *125*, 6038.
[23] C. M. Wei, Z. G. Li, C. J. Li, *Org. Lett.* **2003**, *5*, 4473.
[24] K. Burgess, H. J. Lim, A. M. Porte, G. A. Sulikowski, *Angew. Chem.* **1996**, *108*, 192; *Angew. Chem. Int. Ed. Engl.* **1996**, *35*, 220.
[25] H. V. R. Dias, R. G. Browning, S. A. Polach, H. V. K. Diyabalanage, C. J. Lovely, *J. Am. Chem. Soc.* **2003**, *125*, 9270.
[26] Y. Cui, C. He, *J. Am. Chem. Soc.* **2003**, *125*, 16202. A copper-catalyzed olefin aziridination is described in the Supporting Information.
[27] H. V. R. Dias, R. G. Browning, S. A. Richey, C. J. Lovely, *Organometallics* **2004**, *23*, 1200.
[28] H. N. Po, *Coord. Chem. Rev.* **1976**, *20*, 171.
[29] The value of the optical rotation of the product ($[\alpha]_{29}^{D} = +5.2$; $c = 0.5$, $CHCl_3$) compares well with that of a reference sample ($[\alpha]_{29}^{D} = +5.0$; $c = 0.5$, $CHCl_3$).
[30] The mass spectra are shown in the Supporting Information.

 © 2004 Wiley-VCH Verlag GmbH & Co. KGaA, Weinheim

Nickel Hydroxide Tubes

$Ni(OH)_2$ Tubes with Mesoscale Dimensions as Positive-Electrode Materials of Alkaline Rechargeable Batteries**

Feng-Shi Cai, Guo-Ying Zhang, Jun Chen, Xing-Long Gou, Hua-Kun Liu, and Shi-Xue Dou*

Rechargeable batteries are becoming more and more important in everyday life, especially in consumer electronic devices such as cellular telephones, notebook computers, compact camcorders, and electric vehicles.[1–3] The nickel hydroxide/nickel oxyhydroxide couple $Ni(OH)_2/NiOOH$ is the primary redox system used as the positive electrode of alkaline rechargeable batteries including nickel/cadmium (Ni/Cd), nickel/iron (Ni/Fe), nickel/metal hydride (Ni/MH), and nickel/zinc (Ni/Zn).[4,5] These batteries are usually positive-

[*] Dr. F.-S. Cai, Dr. G.-Y. Zhang, Prof. Dr. J. Chen, Dr. X.-L. Gou
Institute of New Energy Materials Chemistry
Nankai University, Tianjin 300071
and National Center for Nanoscience and Nanotechnology
Beijing 100084 (P. R. China)
Fax: (+86) 22-2350-9118
E-mail: chenabc@nankai.edu.cn
Prof. H.-K. Liu, Prof. Dr. S.-X. Dou
Institute for Superconducting & Electronic Materials
University of Wollongong, NSW 2522 (Australia)

[**] This work was supported by the National NSFC (20325102), TCTPF (200248)—Key Project (104055), and 973 Program (2003CB211800 and 2003CB). F.S.C. and G.Y.Z. contributed equally to this work. We thank two referees for pertinent comments.

 © 2004 Wiley-VCH Verlag GmbH & Co. KGaA, Weinheim DOI: 10.1002/anie.200460053

electrode-limited for reasons of proper recombination reactions and battery safety. It follows that increasing the energy density of the nickel hydroxide electrode is essential for raising the energy density of such batteries.

The reversible nickel electrode reaction may be briefly described by Equation (1).

$$\beta\text{-Ni(OH)}_2 + OH^- \rightleftharpoons \beta\text{-NiOOH} + H_2O + e^- \quad (1)$$

That is, nickel hydroxide $Ni(OH)_2$ is oxidized on charging to nickel oxyhydroxide (NiOOH). Thus, one mole of $Ni(OH)_2$ (92.7 g) can theoretically yield a capacity of 289(26800/92.7) mA h g^{-1}. However, the charge/discharge reactions which take place in the nickel hydroxide electrode are much more complex. Four phases are reported to be produced over the lifetime of a nickel hydroxide electrode, namely, β-$Ni(OH)_2$, β-NiOOH, γ-NiOOH, and α-$Ni(OH)_2$.[6,7] α-$Ni(OH)_2$ can also be oxidized to γ-NiOOH at a lower potential than the corresponding oxidation state compared with β-$Ni(OH)_2$, with a higher discharge capacity than β-$Ni(OH)_2$/β-NiOOH, since the nickel oxidation state in γ-NiOOH is known to exceed 3 because of Ni^{4+} defects.[8] The formation of these phases is associated with volume expansion or swelling of the nickel hydroxide electrode, which interferes with effective contact between particles of the active material, and this increases the resistance of the electrode reaction, especially at high-rate or high-temperature charge/discharge.[9] To improve the characteristics of the nickel hydroxide electrode, much work has focused on the development of spherical $Ni(OH)_2$ powder and related composite materials.[10–14] Nickel hydroxide particles with nanostructural multiphase exhibit superior electrochemical behavior and higher proton diffusion coefficients.[15,16] On the one hand, spherical nickel hydroxide powder, which suppresses the development of inner-pore volume, makes it possible to increase the density of the active material itself. On the other hand, the core of spherical nickel hydroxide powder is still inactive at high-rate and high-temperature charge/discharge due to the diffusion barrier.

Recently, single-crystal $Ni(OH)_2$ nanorods[17] and β-$Ni(OH)_2$ nanosheets[18] have been prepared by the hydrothermal method. However, no attempt has been made to fabricate $Ni(OH)_2$ micro- and/or nanotubes and test their electrochemical activity. Here we report that $Ni(OH)_2$ tubes with mesoscale dimensions, produced by chemical deposition of nickel ions and ammonia within anodic alumina membranes, have superior capacity and good cycling reversibility, and are promising positive-electrode materials for alkaline rechargeable batteries.

$Ni(OH)_2$ tubes were synthesized by a template method,[19–22] as shown schematically in Figure 1. The preparation process mainly involves 1) impregnating nickel ions in the pore walls of the alumina template; 2) dripping ammonia solution through the alumina membrane to precipitate nickel hydroxide; 3) dissolving the alumina membrane in NaOH solution to obtain tube bundles.

The homogeneity and crystallinity of the product was examined by powder XRD (Figure 2). All the diffraction peaks can be indexed as a hexagonal β-$Ni(OH)_2$ structure

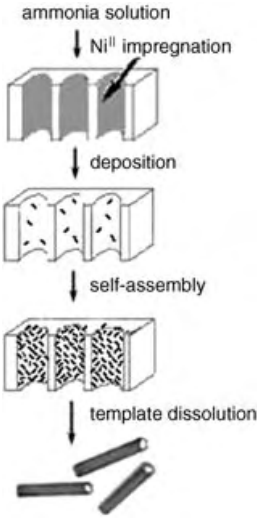


Figure 1. Schematic diagram showing the template preparation of $Ni(OH)_2$ tubes.

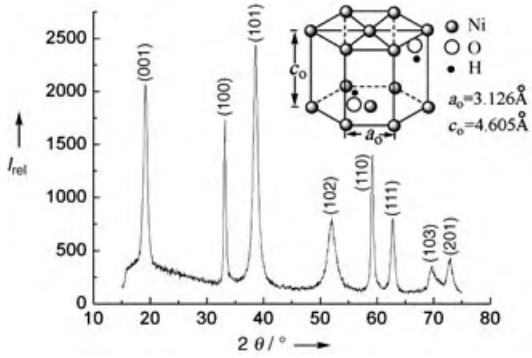


Figure 2. XRD pattern of the as-prepared β-$Ni(OH)_2$.

with the lattice constants $a = 3.127$ Å and $c = 4.606$ Å, in good agreement with that of the standard values (ICDD-JCPDS card No. 14-0117). The broadening of peaks in the XRD pattern indicates that the component crystallites are of nanoscale character. No peaks from other phases were found, that is, the as-synthesized β-$Ni(OH)_2$ is of high purity. The contents of Ni and Al in the product, analyzed by inductively coupled plasma (ICP) emission spectroscopy (Model P-5200 from Hitachi), were 62 and 0.1 %, respectively, that is, traces of alumina remain.

Figure 3 shows SEM images of the as-prepared sample at different magnifications. Figure 3a is an overall view of the product, from which it can be seen that a large quantity of filament bundles were obtained. The length of the bundles is approximately 60 μm, which corresponds to the thickness of the template membrane employed in the synthesis process. Figure 3b shows an SEM image of one bundle at a higher magnification. This shows that the $Ni(OH)_2$ tubes are arranged roughly parallel to one another with a smooth-surface alignment. This might be due to the remaining trace of the alumina matrix rather than a kind of self-organization. Figure 3c is a typical SEM image with end-on view, showing the open ends of a tube bundle. The tubes are not all 200 nm

 © 2004 Wiley-VCH Verlag GmbH & Co. KGaA, Weinheim

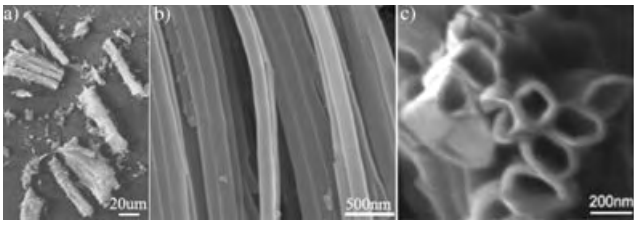


Figure 3. Typical SEM images of as-synthesized β-$Ni(OH)_2$. a) Overall view at low magnification. b) Walls of the tube bundles. c) Tube-bundle tips at high magnification.

in diameter, because of the pore-diameter distribution of the template around 200 nm. The tubes are cylinders with a wall thickness of 20–30 nm.

To further understand the detailed structure of the tubes, TEM and HRTEM were performed (Figure 4). Figure 4a is

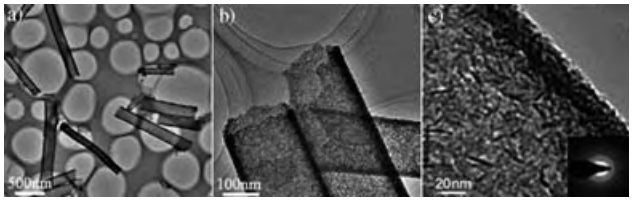


Figure 4. Representative TEM (a, b) and HRTEM (c) images of the as-prepared $Ni(OH)_2$ tubes. The inset in c) is the corresponding electron diffraction pattern.

the TEM image of a group of $Ni(OH)_2$ tubes scattered on the copper mesh. The central parts of the mesostructures are bright in contrast to their edges, confirming their hollow-tube nature. However, the tubes are only several micrometers long, much shorter than those observed in SEM images (ca. 60 μm). This phenomenon arises from the strong supersonic vibrations prior to the sample preparation for TEM analysis, that is, the long tubes were broken into shorter ones. The open-ended walls surrounding the central hollow core with an average outer diameter of 200 nm and a smooth surface are clearly visible in the TEM image of Figure 4b. The wall is complete and is composed of an array of needlelike and multilayered nanoparticles (Figure 4c). This was confirmed by the electron diffraction pattern of the tube (inset of Figure 4c), which shows the coexistence of nanocrystallites and amorphous structures. This result indicates that the crystallites have no preferred orientation. The mechanism of formation presumably resembles that of the noble-metal nanoparticle nanotubes reported by Rubinstein et al.[22] Note that under our synthesis conditions, the homogeneity of the $Ni(OH)_2$ tubes is high (> 98% based on the SEM and TEM observations). Therefore, the lengths and diameters of the tubes are definitely of mesoscale dimensions.

Figure 5 shows the cyclic voltammograms of the two spherical-powder and tube $Ni(OH)_2$ electrodes in the first cycle. Similarly shaped voltammograms were also obtained for five-potential cycling. Reversible peaks are observed for the spherical-powder and tube electrodes, but their characteristics are different. The features of the voltammograms are

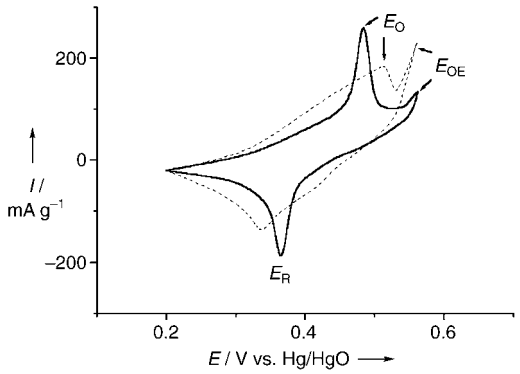


Figure 5. Cyclic voltammograms of $Ni(OH)_2$ tube (solid line) and spherical-powder (dotted line) electrodes at 20 °C and a scan rate of 0.5 mV s^{-1}.

summarized in Table 1: 1) When the electrodes were scanned cathodically, two peaks, for the oxidation potential E_O and oxygen-evolution potential E_{OE}, appeared; during the following anodic polarization, only one peak was observed, which was assigned to the reduction potential E_R. 2) The difference $E_O - E_R$ between the oxidation potential and the reduction potential is taken as a measure of the reversibility of the electrode reaction. The smaller this value, the more reversible the electrode reaction. 3) The intensities of E_O and E_R for the tube electrode were much larger than those of the spherical-powder electrode, that is, the energy density in the tube electrode is higher. 4) The difference between the oxygen-evolution potential and the oxidation potential $E_{OE} - E_O$, is also an important parameter for judging the performance of the nickel electrode. The value of $E_{OE} - E_O$ increased from 25 mV for the spherical-powder electrode to 77 mV for the tube electrode. This allows the tube electrode to be charged fully (i.e., complete oxidation of Ni^{2+} to Ni^{3+}) before oxygen evolution. Consequently, it demonstrates that the tube electrode exhibits much better electrochemical-cyclic properties than the spherical-powder electrode.

Table 1: Reduction potential E_R, oxidation potential E_O, oxygen-evolution potential E_{OE}, $E_O - E_R$, and $E_{OE} - E_O$ for the nickel hydroxide tube and spherical-powder electrodes at 20 °C.

Electrode	Potentials [mV]				
	E_R	E_O	E_{OE}	$E_O - E_R$	$E_{OE} - E_O$
Tube	365	485	562	120	77
Spherical powder	335	515	540	180	25

Figure 6 shows the charge–discharge curves of the tube and spherical-powder electrodes in the tenth cycle. The discharge curve of the tube electrode displays a higher discharge voltage and a longer plateau than that of the spherical-powder electrode, while its charge curve has a lower plateau. The highest discharge capacity of 315 mA h g^{-1} for the tube electrode, achieved at 50 mA g^{-1} and 20 °C, illustrates that in addition to the phase transformation of β-$Ni(OH)_2$ to β-NiOOH, partial formation of γ-NiOOH occurred.

 © 2004 Wiley-VCH Verlag GmbH & Co. KGaA, Weinheim

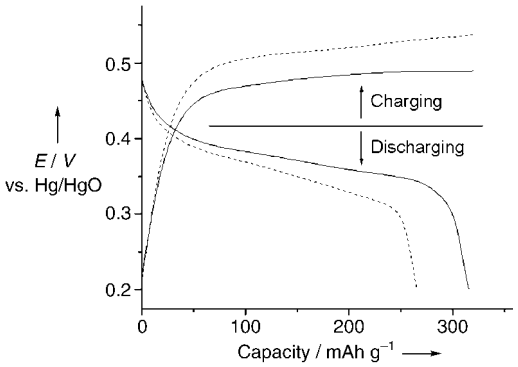


Figure 6. Charge/discharge curves as a function of capacity for nickel hydroxide tube (solid line) and spherical-powder (dotted line) electrodes at 20 °C.

Table 2 summarizes the effect of the working temperature and the discharge current density on the electrode capacity. At 20 °C and 150 mA g^{-1}, the tube electrode still retained 265 mA h g^{-1}, corresponding to about 84.1 % of the electrode capacity at 50 mA g^{-1}, while the spherical-powder electrode only showed 203 mA h g^{-1} (about 76.6 % of its capacity at 50 mA g^{-1}). Furthermore, it can also be seen that as the working temperature increases, the tube electrode has much higher capacities than the spherical-powder electrode. The tube electrode shows improved high-rate and high-temperature discharge ability due to the faster diffusion processes in the hollow tubes than in the dense spherical powder. This feature is critical for alkaline rechargeable batteries for high-power output at high temperatures.

Table 2: Effect of temperature and discharge current density on the discharge capacity of nickel hydroxide tube and spherical-powder electrodes.

Electrode	T [°C]	Current density [mA g^{-1}]	Discharge capacity [mA h g^{-1}]
Tube	20	50	315
		100	289
		150	265
	40	50	281
		100	257
		150	232
	60	50	251
		100	229
		150	205
Spherical powder	20	50	265
		100	235
		150	203
	40	50	233
		100	182
		150	154
	60	50	198
		100	155
		150	123

After a preliminary test of 50 charging/discharging cycles at 150 mA g^{-1} with 100 % depth of charge and discharge, the capacity of the tube electrode decreased by only about 4 %, that is, an average capacity fading of 0.2 mA h g^{-1} per cycle. Therefore, the hollow structure of the nickel hydroxide tube, which allows diffusion and oxidation/reduction to occur easily, contributes to superior capacity, reversibility, high-rate discharge, high-temperature performance, and cycling stability.

In summary, $Ni(OH)_2$ tubes prepared by a template method under ambient conditions can be used as the positive-electrode materials of alkaline rechargeable batteries showing important advantages in terms of capacity, high-rate discharge, and high-temperature performance.

Experimental Section

Anodic aluminum oxide membranes (Whatman, Φ47 mm with 0.2 μm pores and 60 μm thickness) were used as the templates. $NiCl_2{\cdot}6H_2O$, ammonia, and other reagents were all of analytical grade and used without further purification.

The $Ni(OH)_2$ tubes were prepared by chemical deposition within the alumina membranes. In a typical synthesis, an alumina template was gently immersed in 0.4 M aqueous solutions of $NiCl_2{\cdot}6H_2O$ for 30 min to fully impregnate the pore walls of the membrane with nickel ions. After removing the alumina membrane from the nickel solution, 2 M ammonia was slowly dripped onto it, so that the ammonia solution penetrated the template slowly under gravity and adhesive driving force. The white membrane gradually took on the light green color of nickel hydroxide. This solution filling and nickel hydroxide precipitation procedure was repeated several times at regular intervals to form tubes in the template pores. After five cycles, the membrane was rinsed with deionized water several times, and dissolved by 2 M NaOH solution. Then the solid was collected by filtration, washed with deionized water and absolute ethanol, and dried at 60 °C in vacuum for 2 h to obtain the product. The precipitation reaction of the nickel hydroxide can be expressed as Equation (2).

$$NiCl_2 \cdot 6H_2O + 2NH_4OH \rightarrow Ni(OH)_2 + 2NH_4Cl + 6H_2O \qquad (2)$$

The as-prepared samples were characterized by powder XRD (Rigaku INT-2000 X-ray generator, $Cu_{K\alpha}$ radiation), SEM (Philips XL-30, 20 kV), TEM, and high-resolution TEM (HRTEM; Philips Tecnai F20, 200 kV).

Nickel hydroxide electrodes were prepared by inserting an active paste into a nickel foam substrate. A paste containing 85 wt % nickel hydroxide tubes or spherical powder (Tanaka Chemical, Japan), 10 wt % carbon black, and 5 wt % polytetrafluoroethylene (PTFE) was used. The electrode was dried at 80 °C for 1 h and cut into a disk (1.2 × 1.2 cm), which was pressed at a pressure of 100 kg cm^{-2} to a thickness of 0.4 mm. Then the electrode was spot-welded to a nickel sheet for electrical connection. Electrochemical performance was measured with a Solartron SI 1260 Potentionstat Analyzer with 1287 Interface and an Arbin charge/discharge unit at controlled temperatures in an electrochemical cell, which contained the nickel hydroxide working electrode, a metal hydride electrode, a Hg/HgO reference electrode, and 6 M KOH solution as the electrolyte. The discharge capacity of the nickel hydroxide in the positive electrode was based on the amount of active material ($Ni(OH)_2$) excluding the weight of carbon black and PTFE in the electrode. The discharge capacity of each electrode was expressed in mA h per gram of active material.

Received: March 19, 2004 [Z460053]

Keywords: electrochemistry · nanotubes · nickel · rechargeable batteries · template synthesis

 © 2004 Wiley-VCH Verlag GmbH & Co. KGaA, Weinheim

[1] S. R. Ovshinsky, M. A. Fetcenko, J. Ross, *Science* **1993**, *260*, 176.
[2] M. S. Dresselhaus, I. L. Thomas, *Nature* **2001**, *414*, 332.
[3] J. M. Tarascon, M. Armand, *Nature* **2001**, *414*, 359.
[4] J. McBreen in *Modern Aspects of Electrochemistry*, *Vol. 21* (Eds.: R. E. White, J. O'M. Bockris, B. E. Conway), Plenum, New York, **1990**, p. 29.
[5] D. Linden, *Handbook of Batteries*, 3rd ed., McGraw-Hill, New York, **2002**.
[6] H. Bode, K. Dehmelt, J. Witte, *Electrochim. Acta* **1966**, *11*, 1079.
[7] G. Halpert in *Nickel Hydroxide Electrodes*, *Vols. 90–94* (Eds.: D. A. Corrigan, A. H. Zimmerman), The Electrochemistry Society, Pennington, NJ, **1990**, p. 1.
[8] R. Barnard, C. F. Randell, F. L. Tye, *J. Appl. Electrochem.* **1980**, *10*, 109.
[9] D. Singh, *J. Electrochem. Soc.* **1998**, *145*, 116.
[10] M. Oshitani, M. Watada, T. Tanaka, T. Iida in *Hydrogen and Metal Hydride Batteries*, *Vol. 94* (Eds.: P. D. Bennett, T. Sakai), The Electrochemistry Society, Pennington, NJ, **1994**, p. 303.
[11] J. Chen, D. H. Bradhurst, S. X. Dou, H. K. Liu, *J. Electrochem. Soc.* **1999**, *146*, 3606.
[12] B. Liu, X. Y. Wang, H. T. Yuan, Y. S. Zhang, D. Y. Song, Z. X. Zhou, *J. Appl. Electrochem.* **1999**, *29*, 855.
[13] A. M. Fojas, E. Murphy, P. Stroeve, *Ind. Eng. Chem. Res.* **2002**, *41*, 2662.
[14] I. Zhitomirsky, *J. Appl. Electrochem.* **2004**, *34*, 235.
[15] E. David, J. Alvin, R. Peter, T. Xiao, *J. Power Sources* **1997**, *65*, 231.
[16] X. Wang, H. Luo, P. V. Parkhutik, A. C. Millan, E. Matveeva, *J. Power Sources* **2003**, *115*, 153.
[17] M. Keitaro, K. Takashi, T. Akira, *Adv. Mater.* **2002**, *14*, 1216.
[18] Z. H. Liang, Y. J. Zhou, X. L. Hu, *J. Phys. Chem. B* **2004**, *108*, 3488.
[19] C. R. Martin, *Science* **1994**, *266*, 1961.
[20] E. D. Sone, E. R. Zubarev, S. I. Stupp, *Angew. Chem.* **2002**, *114*, 1781; *Angew. Chem. Int. Ed.* **2002**, *41*, 1706.
[21] F. Schüth, *Angew. Chem.* **2003**, *115*, 3730; *Angew. Chem. Int. Ed.* **2003**, *42*, 3604.
[22] M. Lahav, T. Sehayek, A. Vaskeich, I. Rubinstein, *Angew. Chem.* **2003**, *42*, 5734; *Angew. Chem. Int. Ed.* **2003**, *42*, 5576.

 © 2004 Wiley-VCH Verlag GmbH & Co. KGaA, Weinheim

Fluorescence Spectroscopy

Donor–Donor Energy-Migration Measurements of Dimeric DsbC Labeled at Its N-Terminal Amines with Fluorescent Probes: A Study of Protein Unfolding**

Xuejun Duan, Zhen Zhao, Jianping Ye, Huimin Ma, Andong Xia,* Guoqiang Yang, and Chih-Chen Wang**

Fluorescence resonance energy transfer (FRET) is a powerful technique for the determination of distances between two fluorophores. The overall geometry of protein structures[1–4] and the conformational changes of a molecule under different conditions can be studied by this method if appropriate sites of the molecule are labeled with fluorescence donor and acceptor probes. Nevertheless, it is rather difficult to specifically introduce two different fluorophore groups into one molecule,[2] especially into a homodimeric biomacromolecule that has two identical reactive sites. Different from the conventional FRET technique, donor–donor energy migration (DDEM) takes advantage of certain fluorescence probes that display an overlap of their absorption and emission spectra and are therefore able to transfer energy between themselves.[2–4] Energy transfer in this case is a reversible process and can be measured through analysis of the time-resolved depolarization of the fluorescence emission (as donor–donor energy migration results in additional depolarization). As only one type of probe is required, DDEM simplifies greatly not only the labeling operation but also the theoretical analysis and the time-resolved measurements and has been widely used to study the steady-state conformational changes of biomacromolecules.

DsbC (**1**), a member of the Dsb family in the periplasm of Gram-negative bacteria, is a thiol-protein oxidoreductase that displays molecular chaperone activity.[5–7] The DsbC molecule is a V-shaped homodimer consisting of two 23.4-kDa subunits.[8] Each subunit is composed of a C-terminal thiore-

[*] X. Duan, Dr. J. Ye, Prof. Dr. H. Ma, Prof. Dr. A. Xia, Prof. Dr. G. Yang
Center for Molecular Sciences, Institute of Chemistry
Chinese Academy of Sciences, Beijing 100080 (China)
Fax: (+86) 106-255-9373
E-mail: mahm@iccas.ac.cn
andong@iccas.ac.cn

Z. Zhao, Prof. C.-C. Wang
National Laboratory of Biomacromolecules
Institute of Biophysics, Chinese Academy of Sciences
Beijing 100101 (China)
Fax: (+86) 106-487-2026
E-mail: chihwang@sun5.ibp.ac.cn

[**] This work was supported by the National Natural Science Foundation of China (Grant no. 20375044), the Ministry of Science and Technology of China, and the Chinese Academy of Sciences. We thank Dr. Rudi Glockshuber (Eidgenössische Technische Hochschule, Hönggerberg, Switzerland) for the generous gift of *p*DsbC plasmid.

Supporting information for this article is available on the WWW under http://www.angewandte.org or from the author.

 © 2004 Wiley-VCH Verlag GmbH & Co. KGaA, Weinheim DOI: 10.1002/anie.200460072

doxin-like domain and a N-terminal domain, which is responsible for dimerization and is essential for the chaperone activity of the molecule.[8,9]

The V-shaped structure of homodimeric DsbC led us to apply the DDEM method to explore its unfolding and dissociation behavior and to understand further its structure–function relationship. In this context, the two N-terminal amino groups of DsbC are the sites of choice at which to link two identical probes; however, the labeling of other amino groups, such as ε-amino groups of lysine residues, and the nonspecific modification of groups other than amino groups could also occur. Several new methods for the introduction of fluorescent probes into proteins have recently been developed to improve the specificity of labeling.[10–12] The most common approach is to engineer a pair of reactive cysteine residues to provide two thiol handles for conjugation.[2,13] Alternatively, a ketone handle, produced through the introduction of an unnatural keto-containing amino acid, can be labeled with hydrazide-functionalized fluorophores with no observed cross-reactivity.[1,13]

Herein, we describe a general method for the specific labeling of N-terminal groups through a transamination reaction, in which the N-terminal amino group of a protein molecule is converted into a reactive carbonyl group, which is then treated with a hydrazide-containing fluorophore. As the intermediate in transamination reactions involves the participation of an adjacent peptide bond, only the conversion of the terminal amino group occurs without modification of the internal amino groups on lysine residues.[14–17] Subsequently, the conformational changes of dimeric DsbC during unfolding (induced by guanidine hydrochloride (GuHCl)) were studied by DDEM.

The fluorescent dye BODIPY FL (shown as the hydrazide derivative **2** in Figure 1) was employed as the probe owing to its high fluorescence quantum yield, its insensitivity to solvent polarity and pH, and its Förster radius of 57 Å.[2,13,18] The N-terminal amino groups of **1** were modified as shown in Figure 1 by a) a transamination reaction in the presence of glyoxylate and $CuSO_4$,[14,17] b) coupling of the product **3** with BODIPY FL hydrazide (**2**), and c) reduction of the imine groups to the more stable amine form **4** of the labeled product. Sodium cyanoborohydride instead of borane-pyridine was used as the reducing agent owing to its better selectivity for imines[19] and the absence of quenching effects on the fluorescence from the BODIPY dye (data not shown).

In a similar procedure, **1** was also labeled by following the transamination step carried out in the absence of glyoxylate. As shown in Figure 2, the absorption spectrum of the protein modified in the *presence* of glyoxylate exhibits a main peak at 280 nm characteristic of native protein and a less intense band at 505 nm for the BODIPY moiety,[13] whereas the absorption profile for the protein modified in the *absence* of glyoxylate shows only one band for native protein; this indicates that the BODIPY-labeled DsbC **4** can be prepared only through a transamination process carried out in the presence of glyoxylate.

To confirm further that the DsbC molecule had been specifically labeled with BODIPY, **4** was also examined by MALDI TOF mass spectrometry. A peak at m/z 47300, in agreement with the theoretical value of m/z 47410 expected for DsbC with two N-terminal BODIPY labels **4**, was detected with a mass error $< 0.3\,\%$.[20] Although the presence of a small amount of DsbC modified on only one N-terminal amino group cannot be ruled out, it should not affect the DDEM measurements, especially in dilute solution. The efficiency with which fluorophores are incorporated into DsbC is about 9%, which is ascribed to the limited accessibility of the N termini of the DsbC molecule.

The fluorescence spectra of **4** display an excitation band at 505 nm and an emission band at 510 nm (see Figure 2 inset),

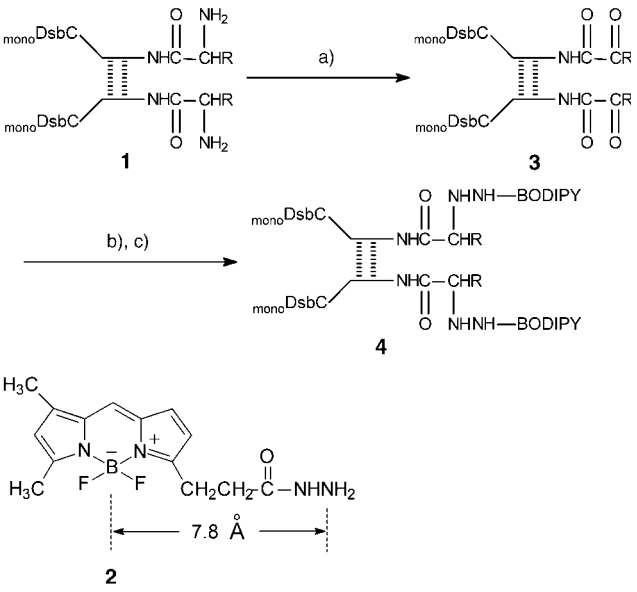


Figure 1. Specific modification of the N-terminal amino groups of dimeric DsbC (**1**): a) transamination reaction with glyoxylate; b) coupling with **2**; c) reduction with sodium cyanoborohydride. The separation between the central B atom of the BODIPY FL dye and the terminal N atom of the hydrazide group of the linker arm in **2** is 7.8 Å (calculated with CS Chem 3D software). BODIPY FL = 4,4-difluoro-5,7-dimethyl-4-bora-3a,4a-diaza-*s*-indacene-3-propionic acid.

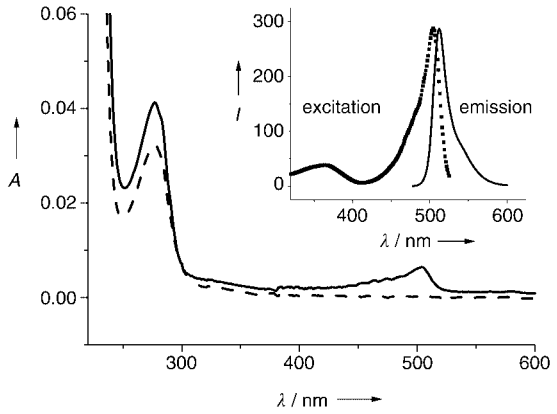


Figure 2. Absorption spectra of DsbC labeled with BODIPY. DsbC (**1**) was modified in the presence (solid line, **4**, 1.2 μM) and absence (dashed line, 1.0 μM) of glyoxylate. The inset shows the excitation ($\lambda_{em} = 535$ nm) and emission ($\lambda_{ex} = 467$ nm) spectra of **4** (4.1 μM); 5-nm excitation and emission slits were used.

 © 2004 Wiley-VCH Verlag GmbH & Co. KGaA, Weinheim

which are almost the same as that for the free BODIPY dye[13] and indicate that the attachment of the fluorophore to DsbC does not alter its spectral properties. On the other hand, **4** shows the same circular dichroism spectrum as that of the native DsbC,[20] which suggests that the introduction of BODIPY does not affect the secondary structure of the protein. The native DsbC, the partially denatured DsbC formed in the presence of GuHCl (1.5 M), and the fully denatured DsbC formed in the presence of GuHCl (6 M) and dithiothreitol (0.1 M), all labeled with BODIPY, displayed near-identical fluorescence-decay profiles,[20] which were fitted to a single exponential function with a satisfactory low value of χ^2 in the range of 1.17–1.38. The fluorescence lifetime (τ) in each of the three cases was about 6.7 ns (calculated based on $I(t) = A\,e^{(-t/\tau)}$) and indicate that the fluorescence lifetime of BODIPY in BODIPY-labeled DsbC is unaffected by the extent of denaturing of the protein (Table 1).On the other hand, the decay rates of fluorescence anisotropy $r(t)$ show a variation with different extents of denaturing of DsbC (Figure 3). The initial decay of $r(t)$ of the fully denatured DsbC is much slower than that of the native DsbC. The fast decay of the fluorescence anisotropy from the native DsbC suggests that the observed emission is not from the originally excited BODIPY fluorophore. The other adjacent fluorophore in the same DsbC molecule could contribute to the observed emission by an energy-transfer mechanism and thereby lead to the fast depolarization. This is an experimental hallmark of donor–donor energy-migration processes.[4]

The interfluorophore distance R is defined as the distance between the centers of two fluorophores and can be estimated based on energy-transfer measurements.[2–4,21] The rate ω of energy transfer between two interacting fluorophores is expressed by Equation (1) according to the Förster energy-transfer mechanism:[2,3,21]

$$\omega = \frac{3}{2}\langle\kappa^2\rangle\frac{1}{\tau}\left(\frac{R_0}{R}\right)^6 \quad (1)$$

(τ = fluorescence lifetime, R_0 = Förster radius (57 ± 1 Å for BODIPY),[2,18] and $\langle\kappa^2\rangle$ = orientation factor, for which an average value of $^2/_3$ is usually taken; the parameter ω obtained from DDEM measurements and the values of R estimated by Equation (1) are summarized in Table 1).

Table 1: Results from DDEM measurements[a]

DsbC	ω [ns^{-1}]	τ [ns]	R [Å]	R_c [Å]
Native	0.569	6.7	46	35
Partially denatured	0.141	6.7	58	47
Fully denatured	–	6.6	–	–

[a] The parameter ω was obtained from the best-fit curves based on $r(t) = A\exp(-2\omega t) + B$; the value of χ^2 for each fitting was in the range of 1.077–1.422. The interfluorophore distance R in **4** denatured to different extents was calculated according to Equation (1). R_c is the corrected value of R. The data quoted are the average of two independent experiments.

The calculated interfluorophore distances in the native and partially denatured DsbC are 46 and 58 Å, respectively, and contain a contribution from the length of the linker group of the BODIPY dye (Figure 1). Moreover, it is reasonable to

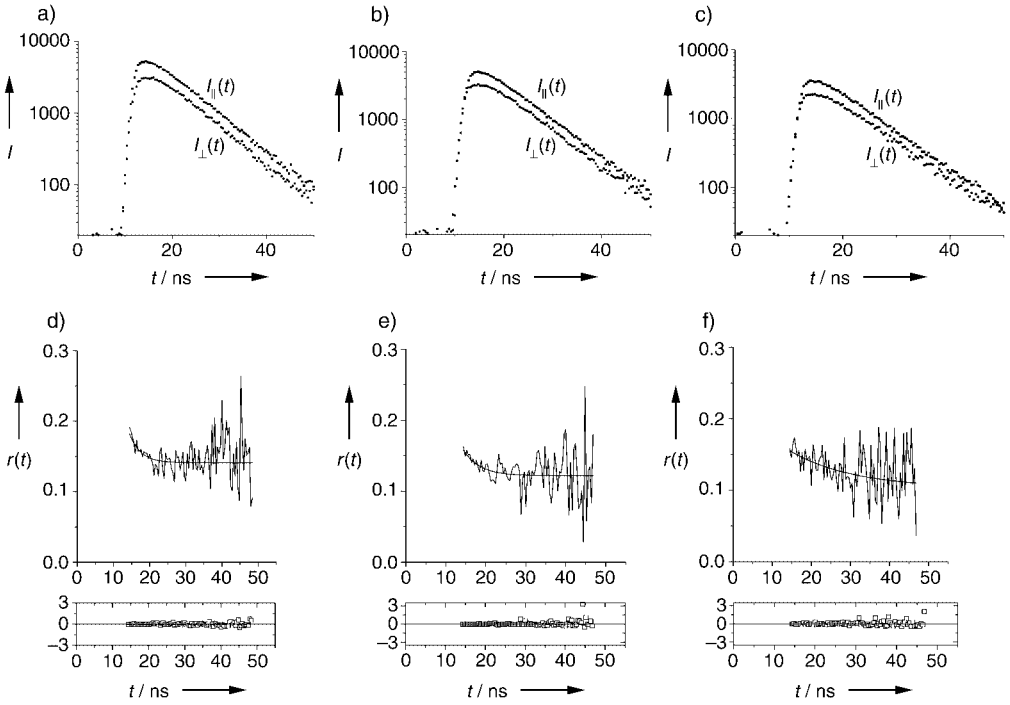


Figure 3. a)–c) Polarized fluorescence decays of $I_\parallel(t)$ and $I_\perp(t)$ and d)–f) anisotropy decays (along with the best-fit curves and the weighted residuals) of **4** (4.1 μM) at various extents of denaturing of the DsbC protein; a), d) native DsbC; b), e) denatured in GuHCl (1.5 M); c), f) denatured in GuHCl (6 M) with dithiothreitol (DTT, 0.1 M). $I_\parallel(t)$ and $I_\perp(t)$ represent the intensities of the fluorescence observed with the emission polarizer orientated parallel and perpendicular, respectively, to the excitation polarizer. All measurements were carried out at 273 K.

 © 2004 Wiley-VCH Verlag GmbH & Co. KGaA, Weinheim

assume an averaged right-angled geometry between the two linker groups attached to the N termini of DsbC.[21] The corrected value R_c for the native DsbC is thus 35 Å (Table 1), which is in agreement with the value of 29 Å measured from the crystal structure of the protein.[8] Similarly, the corrected distance between the two N termini in the partially denatured DsbC is 47 Å, which is markedly longer than 35 Å in the native protein. The much longer distance measured between the two N termini in a partially denatured molecule indicates that the unfolding of DsbC in the presence of GuHCl (1.5 M) renders the molecule more loose and flexible but not dissociated (Table 1). The very slow decay of the fluorescence anisotropy of the fully denatured DsbC could only arise from the rotation of the probe molecule together with the fluctuation of the conformation of DsbC rather than from DDEM processes. The interfluorophore distance in this case, which is far longer than the critical distance R_0 of BODIPY and could not be determined by DDEM measurements, implies the dissociation of the dimeric molecule in the fully denatured protein.

In summary, we have developed a valuable method, which consists of N-terminal-specific fluorescence labeling through a transamination reaction followed by DDEM measurements, to study the unfolding/folding processes of a dimeric protein. The transamination step provides a general approach for the selective attachment of a fluorophore to N-terminal amino acid residues, and the dimeric structure of DsbC allows the introduction of two identical fluorophores so that the DDEM method can be used to trace its unfolding behavior. This combined strategy is useful to investigate conformational changes of other dimeric proteins under variable conditions. An important development would be to combine the specific labeling method with DDEM measurement at the single-molecule level. Furthermore, this labeling approach could also be extended to nondimeric protein molecules and would therefore broaden the scope of application of fluorescence spectroscopy.

Experimental Section

General: DsbC (**1**) was prepared as reported previously[7,9] from plasmid *p*DsbC, which contains the full-length DsbC precursor gene. Glyoxylate was purchased from Acros. BODIPY FL hydrazide was purchased from Molecular Probes, Inc. MALDI TOF mass spectrometry was performed on a Bruker BIFLEX III instrument.

3: DsbC (**1**; 1 mg) was dissolved in an aqueous solution of sodium acetate (2 mL; 1 M, pH 5.5) containing glyoxylate (0.1 M) and $CuSO_4$ (5 mM) and was stirred for 1 h at 296 K. The reaction was quenched through the addition of ethylenediaminetetraacetic acid diammonium salt to a final concentration of 20 mM followed by dialysis against sodium phosphate buffer (0.1 M, pH 7.4).

4: BODIPY FL hydrazide (**2**; 200 μL; 1.96 mM in MeOH) and concentrated HCl (to a final concentration of 0.5 M) were consecutively added to **3**, and the mixture was stirred for 1 h at 296 K in the dark. Sodium cyanoborohydride (5 equiv relative to the protein; Sigma) was then added and the solution was incubated overnight at 277 K. The mixture was applied onto a Sephadex G-25 column to remove any remaining free BODIPY dye and the excess reducing reagent. The protein fraction **4**, which displays an absorbance at both 280 and 505 nm, was collected and then thoroughly dialyzed against phosphate buffer. The efficiency of labeling was calculated from the absorption spectra/molar absorptivities of the fluorescent probe **2** ($\varepsilon = 80000\,M^{-1}cm^{-1}$ at 505 nm)[2] and the dimeric protein **1** ($\varepsilon = 32340\,M^{-1}cm^{-1}$ at 280 nm).[22] As a control, the same procedure was performed with DsbC in the absence of glyoxylate.

Received: March 22, 2004
Revised: May 10, 2004 [Z460072]

Keywords: amines · analytical methods · energy transfer · fluorescent probes · protein folding

[1] S. Weiss, *Science* **1999**, *283*, 1676 – 1683.
[2] J. Karolin, M. Fa, M. Wilczynska, T. Ny, L. B.-Å. Johansson, *Biophys. J.* **1998**, *74*, 11 – 21.
[3] T. Ikeda, B. Lee, S. Kurihara, S. Tazuke, S. Ito, M. Yamamoto, *J. Am. Chem. Soc.* **1988**, *110*, 8299 – 8304.
[4] H. Otto, T. Lamparter, B. Borucki, J. Hughes, M. P. Heyn, *Biochemistry* **2003**, *42*, 5885 – 5895.
[5] D. Missiakas, S. Raina, *J. Bacteriol.* **1997**, *179*, 2465 – 2471.
[6] D. Missiakas, C. Georgopoulos, S. Raina, *EMBO J.* **1994**, *13*, 2013 – 2020.
[7] J. Chen, J. L. Song, S. Zhang, Y. Wang, D. F. Cui, C. C. Wang, *J. Biol. Chem.* **1999**, *274*, 19601 – 19605.
[8] A. A. McCarthy, P. W. Haebel, A. Törrönen, V. Rybin, E. N. Baker, P. Metcalf, *Nat. Struct. Biol.* **2000**, *7*, 196 – 199.
[9] X. X. Sun, C. C. Wang, *J. Biol. Chem.* **2000**, *275*, 22743 – 22749.
[10] V. W. Cornish, D. R. Benson, C. A. Altenbach, K. Hideg, W. L. Hubbell, P. G. Schultz, *Proc. Natl. Acad. Sci. USA* **1994**, *91*, 2910 – 2914.
[11] R. L. Lundblad, *Chemical Reagents for Protein Modification*, 2nd ed., CRC Press, Boca Raton, **1991**.
[12] T. J. Tolbert, C. H. Wong, *Angew. Chem.* **2002**, *114*, 2275 – 2278; *Angew. Chem. Int. Ed.* **2002**, *41*, 2171 – 2174.
[13] R. P. Haugland, *Handbook of Fluorescent Probes and Research Products*, 9th ed., Molecular Probes, Inc., Eugene, **2002**, pp. 104 – 110.
[14] P. Wu, L. Brand, *Methods Enzymol.* **1997**, *278*. 321 – 330.
[15] R. Q. He, C. L. Tsou, *Biochem. J.* **1992**, *287*, 1001 – 1005.
[16] B. Hammack, S. Godbole, B. E. Bowler, *J. Mol. Biol.* **1998**, *275*, 719 – 724.
[17] H. B. F. Dixon, R. Fields, *Methods Enzymol.* **1972**, *25*, 409 – 419.
[18] J. Karolin, L. B.-Å. Johansson, L. Strandberg, T. Ny, *J. Am. Chem. Soc.* **1994**, *116*, 7801 – 7806.
[19] R. F. Borch, M. D. Bernstein, H. D. Durst, *J. Am. Chem. Soc.* **1971**, *93*, 2897 – 2904.
[20] See Supporting Information.
[21] A. A. Deniz, T. A. Laurence, G. S. Beligere, M. Dahan, A. B. Martin, D. S. Chemla, P. E. Dawson, P. G. Schultz, S. Weiss, *Proc. Natl. Acad. Sci. USA* **2000**, *97*, 5179 – 5184.
[22] A. Zapun, D. Missiakas, S. Raina, T. E. Creighton, *Biochemistry* **1995**, *34*, 5075 – 5089.

 © 2004 Wiley-VCH Verlag GmbH & Co. KGaA, Weinheim

Domino Radical Cyclization

Titanium-Mediated Domino Radical Cyclization/ β Elimination of Phosphine Oxides**

Dominique Leca, Louis Fensterbank, Emmanuel Lacôte,* and Max Malacria**

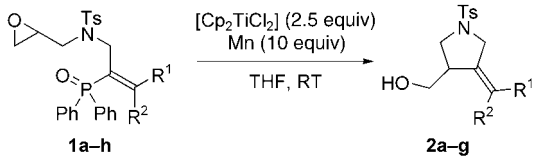
Radical reactions involving organophosphorus radicals have a long history.[1] In particular, the stability of P-centered radicals has facilitated the use of phosphorus hydrides as surrogates for tin hydrides.[2–6] Furthermore, the addition of phosphinyl,[7] phosphinoyl,[8–12] and phosphonyl[13,14] radicals, as well as their sulfur-containing counterparts,[15–17] to alkenes is a widely used method for the preparation of organophosphorus compounds and polymers.

In contrast, little is known about the β elimination of P-centered radicals, and the use of such pathways in synthesis. It has been shown that phosphinyl radical additions are reversible.[18] Radicals derived from phosphinates have been exploited for the preparation of aromatic compounds,[19] and phosphonyl radical eliminations for the synthesis of ketones,[20] although in both cases the systems were significantly biased to favor the elimination pathway. The first case was a rearomatization, and the second involved a highly reactive acyl phosphonate, with restoration of a C=O bond. To the best of our knowledge, this process has yet to afford simple olefinic compounds.

In the course of previous work, we observed a by-product arising from a radical addition/β elimination domino reaction on a vinylic phosphine oxide.[21] As far as we could tell, this was the first example of such a process. In the meantime, we had developed an efficient method allowing the preparation of enantiopure alkylidenecyclopentanes from sulfoxides through a formal asymmetric intramolecular vinylation of a prochiral radical.[22] Because sulfinyl radicals are very special β-eliminating moieties, the elimination rate of which is close to the diffusion limit,[23] the observed side reaction led us to speculate that a phosphine oxide might be a viable, kinetically different alternative to a sulfoxide and afford a novel reaction sequence. Intermolecular (but achiral),[24,25] and semi-intermolecular[26] versions involving sulfones and sulfides as leaving groups have also been reported, but none involving phosphine oxides.

In 1988, Nugent and RajanBabu reported that [Cp_2TiCl] was able to transfer one electron to oxiranes with formation of β-titanoxy radicals, which could be used further in syntheses.[27] This seminal work was made even more useful when Gansäuer et al. rendered this reaction catalytic,[28] and soon thereafter asymmetric.[29] Since then, a few titanium-mediated domino reactions have been reported,[30] but as far as we are aware, no vinylation protocol relying on the inter- or intramolecular addition/elimination sequence has been reported. Furthermore, the mediator is not an hydride-transfer agent, and we felt this would be advantageous. Thus, because the radical β elimination of phosphinoyl radicals was still uncharted territory, we decided to investigate it more closely, and report herein our preliminary results.

We first carried out the reaction with substrates derived from dimethyl malonate and the preformed titanium(III) complex, but encountered problems with lactonization. We then replaced the *gem*-diester group with a tosyl-protected nitrogen atom (**1a**), and obtained the desired domino product *exo*-isopropylidenepyrrolidine **2a** at room temperature as the sole product in good yield (Scheme 1; Table 1, entry 1).



Scheme 1. Titanium-mediated preparation of alkylidenepyrrolidines. Ts = toluenesulfonyl.

The reaction exhibits good versatility, affording access to tetrasubstituted (entries 1 and 4–8) and trisubstitued (entries 2 and 3) *exo*-alkylidenepyrrolidines. In the case of the trisubstituted olefins **2b** and **2c**, β elimination proceeds with retention of configuration, as evidenced by NOE studies (entry 2). However, in the case of oxirane **1c**, 25% of the *Z* isomer was also observed. At this time we do not understand this result. Vinyl phosphine oxide **1g** led either to **2g** or to **3**, depending on the workup conditions: stronger acidic hydrolysis deprotected the ketal.

Since the titanium(III) reagent is an organometallic compound, we wanted to confirm that the observed products were being formed via a domino radical reaction pathway. The reaction of cyclopropyl-substituted precursor **1h** led to the ring-opened product **4** as a single diastereomer, the relative configuration of which was determined by X-ray crystallography. It is derived from pseudo-chair cyclization transition state **A**, which leads to opening of the cyclopropyl ring (Scheme 2). This strongly suggests that the cyclization is radical in nature. While there is no reason for totally stereoselective ring opening, we did not observe any *Z*-olefinic product by NMR spectroscopy.[31]

To gather data on the elimination step, we designed several experiments. First, we carried out the tin-mediated

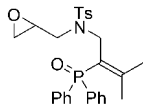
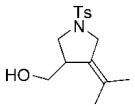
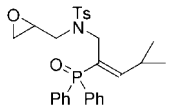
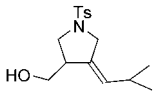
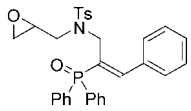
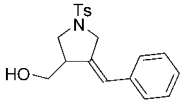
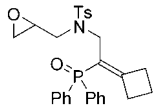
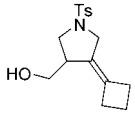
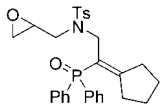
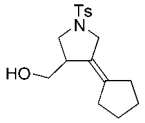
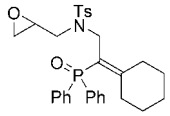
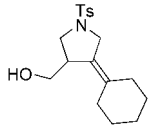
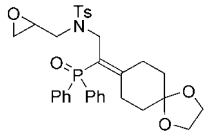
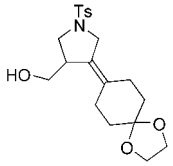
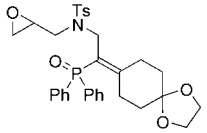
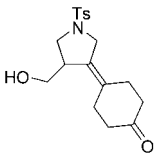
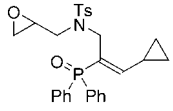
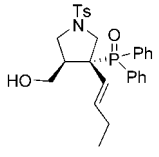
[*] D. Leca, Prof. L. Fensterbank, Dr. E. Lacôte, Prof. M. Malacria
Laboratoire de Chimie Organique
UMR CNRS 7611
Université Pierre et Marie Curie, Case 229
4, place Jussieu, 75005 Paris (France)
Fax: (+33)1-4427-7360
E-mail: fensterb@ccr.jussieu.fr
lacote@ccr.jussieu.fr
malacria@ccr.jussieu.fr

[**] This work was supported by the Université Pierre et Marie Curie and the CNRS. D.L. thanks the Ministère de la Recherche for a grant. We thank Prof. Michael E. Jung (UCLA) for his valuable suggestions, Dr. Mihaela Gulea (CNRS, Caen) for helpful discussions, and Matthew L. Maddess (University of Toronto) for proofreading this manuscript.

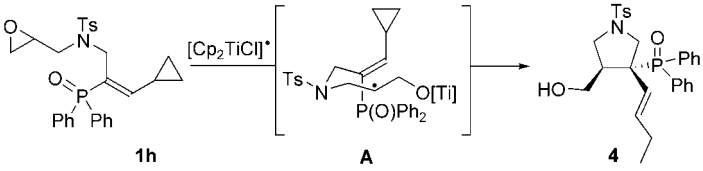
Supporting information for this article is available on the WWW under http://www.angewandte.org or from the author.

 © 2004 Wiley-VCH Verlag GmbH & Co. KGaA, Weinheim DOI: 10.1002/anie.200460099

Table 1: Titanium-mediated preparation of alkylidenepyrrolidines.

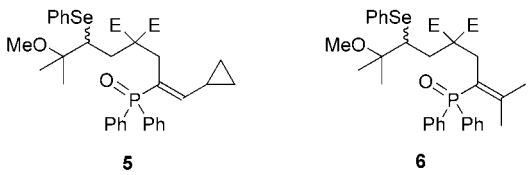
Entry	Substrate	Product	Yield [%]
1	 **1a**	 **2a**	80
2	 **1b**	 **2b**	60
3	 **1c**	 **2c**	71[a]
4	 **1d**	 **2d**	57
5	 **1e**	 **2e**	58
6	 **1f**	 **2f**	82
7	 **1g**	 **2g**	57[b]
8	 **1g**	 **3**	60[c]
9	 **1h**	 **4**	70

[a] *E*/*Z* ratio 3:1. [b] Hydrolysis with a saturated solution of NH_4Cl. [c] Hydrolysis with aqueous 1 M HCl.

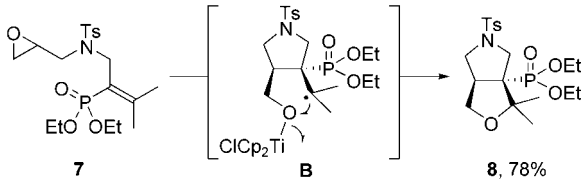


Scheme 2. Cyclization of cyclopropyl-substituted vinylic phosphine oxides.

cyclization of substrates **5** and **6** (E = CO_2Me) with triethylborane/oxygen as initiator. Diester **5** gave a cyclopropyl-ring-opened cyclopentane adduct in 75% yield as a single diastereomer. The relative configuration was assumed to be similar to that of **4**, which was further confirmed by NOE studies. This again indicates that a radical cyclization, but also that the rate of elimination of β-phosphinoyl radical is considerably slower than that of the sulfinyl leaving group, for in that case we observed no opening of the strained ring. In the case of **6**, the domino product was accompanied by roughly an equimolar amount of directly reduced material. This behavior was different from that of its sulfoxide counterpart, and can be rationalized by the increased steric bulk around the heteroatom.



We next carried out our titanium-mediated process on phosphonate derivative **7** and obtained the bicyclic product **8** (Scheme 3). Previously, we had subjected the corresponding



Scheme 3. Reaction of a vinyl phosphonate.

malonate to the classical tin-mediated reaction and observed the overwhelming formation of cyclopentane products (i.e., cyclized but not eliminated), along with a minimal (5%) amount of desired product. More interestingly, the radical termination step was not a bimolecular reduction by the tin hydride, but a dismutation of the intermediate radical. This seemed to indicate that the tertiary β-phosphono radical is rather long-lived. A similar outcome to the production of **8** was described recently by Gansäuer et al. and Trost et al.[32,33] It originates from a Ti–O bond breaking 5-*exo*-*tet* radical cyclization on the oxygen atom of intermediate **B**. Gansäuer et al. took advantage of the "relative persistence under reducing conditions [of tertiary radicals] through exclusion

 © 2004 Wiley-VCH Verlag GmbH & Co. KGaA, Weinheim

of competing radical pathways". Together with our previous observations, this is important circumstantial evidence that no rapid reduction by a second equivalent of Ti^{III} reagent takes place, and that in the case of β-phosphinoyl radicals, radical elimination is observed. If this were not the case, we would much more likely have observed formation of structures like **8**, especially in the case of tetrasubstituted olefins.

In conclusion, we were able to observe for the first time a titanium-mediated intramolecular vinylation based upon the previously unknown elimination of β-phosphinoyl radicals.[34] Work to examine the full scope and limitations of this method, as well as the development of an asymmetric version, is currently underway.

Received: March 23, 2004
Revised: May 25, 2004 [Z460099]

Keywords: cyclization · domino reactions · phosphorus · radical reactions · titanium

[1] M. S. Kharasch, E. V. Jensen, W. H. Urry, *J. Am. Chem. Soc.* **1945**, *67*, 1864 – 1865.
[2] D. H. R. Barton, D. O. Jang, J. C. Jaszberenyi, *J. Org. Chem.* **1993**, *58*, 6838 – 6842.
[3] C. Chatgilialoglu, V. I. Timokhin, M. Ballestri, *J. Org. Chem.* **1998**, *63*, 1327 – 1329.
[4] S. R. Graham, J. A. Murphy, A. R. Kennedy, *J. Chem. Soc. Perkin Trans. 1* **1999**, 3071 – 3073.
[5] T. A. Khan, R. Tripoli, J. J. Crawford, C. G. Martin, J. A. Murphy, *Org. Lett.* **2003**, *5*, 2971 – 2974.
[6] C. M. Jessop, A. F. Parsons, A. Routledge, D. J. Irvine, *Tetrahedron: Asymmetry* **2003**, *14*, 2849 – 2851.
[7] A. R. Stiles, F. F. Rust, W. E. Vaughan, *J. Am. Chem. Soc.* **1952**, *74*, 3282 – 3284.
[8] T. Sumiyoshi, W. Schnabel, *Makromol. Chem.* **1985**, *186*, 1811 – 1823.
[9] A. Kajiwara, Y. Konishi, Y. Morishima, W. Schnabel, K. Kuwata, M. Kamachi, *Macromolecules* **1993**, *26*, 1656 – 1658.
[10] M. Kamachi, A. Kajiwara, K. Saegusa, Y. Morishima, *Macromolecules* **1993**, *26*, 7369 – 7371.
[11] G. W. Sluggett, P. F. McGarry, I. V. Koptyug, N. J. Turro, *J. Am. Chem. Soc.* **1996**, *118*, 7367 – 7372.
[12] S. Jockusch, N. J. Turro, *J. Am. Chem. Soc.* **1998**, *120*, 11773 – 11777.
[13] A. N. Pudovik, I. V. Konovalova, *Zh. Obshch. Khim.* **1959**, *29*, 3342 – 3346 [*Chem. Abstr.* **1960**, *54*, 15224b].
[14] R. L. Kenney, G. S. Fisher, *J. Org. Chem.* **1974**, *39*, 682 – 686.
[15] M. Finke, H. J. Kleiner, *Liebigs Ann. Chem.* **1974**, 741 – 750.
[16] J. G. Dingwall, B. Tuck, *J. Chem. Soc. Perkin Trans. 1* **1986**, 2081 – 2090.
[17] C. Lopin, G. Gouhier, A. Gautier, S. R. Piettre, *J. Org. Chem.* **2003**, *68*, 9916 – 9923.
[18] J. Pellon, *J. Am. Chem. Soc.* **1961**, *83*, 1915 – 1916.
[19] D. L. J. Clive, S. Kang, *J. Org. Chem.* **2001**, *66*, 6083 – 6091.
[20] S. Kim, C. H. Cho, C. J. Lim, *J. Am. Chem. Soc.* **2003**, *125*, 9574 – 9575.
[21] S. Bogen, M. Gulea, L. Fensterbank, M. Malacria, *J. Org. Chem.* **1999**, *64*, 4920 – 4925.
[22] B. Delouvrié, L. Fensterbank, E. Lacôte, M. Malacria, *J. Am. Chem. Soc.* **1999**, *121*, 11395 – 11401.
[23] P. J. Wagner, J. H. Sedon, M. J. Lindstrom, *J. Am. Chem. Soc.* **1978**, *100*, 2579 – 2580.
[24] J. Xiang, W. Jiang, J. Gong, P. L. Fuchs, *J. Am. Chem. Soc.* **1997**, *119*, 4123 – 4129.
[25] F. Bertrand, B. Quiclet-Sire, S. Z. Zard, *Angew. Chem.* **1999**, *111*, 2135 – 2138; *Angew. Chem. Int. Ed.* **1999**, *38*, 1943 – 1946. .
[26] E. E. Korshin, Y. V. Bilokin, H. Zheng, M. D. Bachi, *J. Am. Chem. Soc.* **2004**, *126*, 2708 – 2709.
[27] W. A. Nugent, T. V. RajanBabu, *J. Am. Chem. Soc.* **1988**, *110*, 8561 – 8562.
[28] A. Gansäuer, H. Bluhm, M. Pierobon, *J. Am. Chem. Soc.* **1998**, *120*, 12849 – 12859.
[29] A. Gansäuer, H. Bluhm, B. Rinker, S. Narayan, M. Schick, T. Lauterbach, M. Pierobon, *Chem. Eur. J.* **2003**, *9*, 531 – 542.
[30] J. Justicia, A. Rosales, E. Buñuel, J. L. Oller-López, M. Valdivia, A. Haïdour, J. E. Oltra, A. F. Barrero, D. J. Cárdenas, J. M. Cuerva, *Chem. Eur. J.* **2004**, *10*, 1778 – 1788, and references therein.
[31] For a recent example, see A. Ogawa, I. Ogawa, R. Obayashi, K. Umezu, M. Doi, T. Hirao, *J. Org. Chem.* **1999**, *64*, 86 – 92.
[32] A. Gansäuer, B. Rinker, M. Pierobon, S. Grimme, M. Gerenkamp, C. Mück-Lichtenfeld, *Angew. Chem.* **2003**, *115*, 3815 – 3818; *Angew. Chem. Int. Ed.* **2003**, *42*, 3687 – 3690.
[33] B. M. Trost, H. C. Shen, J.-P. Surivet, *Angew. Chem.* **2003**, *115*, 4073 – 4077; *Angew. Chem. Int. Ed.* **2003**, *42*, 3943 – 3947.
[34] Note that phosphinoyl derivatives have one additional advantage: when subjected to the titanium-mediated sequence, sulfoxides lead to both low yields and reduction to the corresponding sulfides. We did not study this further, but to some extent this precludes part of the asymmetric version, since initial reduction would eliminate any stereochemical information present on the sulfur atom.

 © 2004 Wiley-VCH Verlag GmbH & Co. KGaA, Weinheim

Natural Products Synthesis

Total Synthesis of Lepadins B, D, E, and H; Determination of the Configuration of the Latter Three Alkaloids**

*Xiaotao Pu and Dawei Ma**

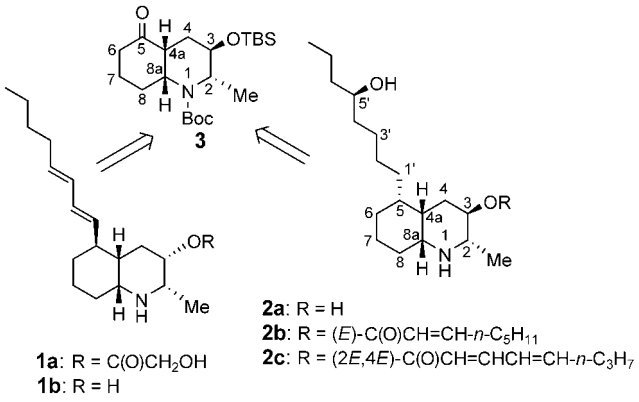
Lepadins are a growing family of alkaloids with a *cis*-fused decahydroquinoline ring. Its first member, lepadin A (**1a**, Scheme 1), was isolated in 1991 by Steffan from the tunicate *Clavelina lepadiformis* in the North Sea.[1] Two other members, lepadins B (**1b**) and C, were isolated from the same

[*] X. Pu, Prof. Dr. D. Ma
State Key Laboratory of Bioorganic and
Natural Products Chemistry
Shanghai Institute of Organic Chemistry
Chinese Academy of Sciences
354 Fenglin Lu, Shanghai 200032 (China)
Fax: (+86) 21-6416-6128
E-mail: madw@mail.sioc.ac.cn

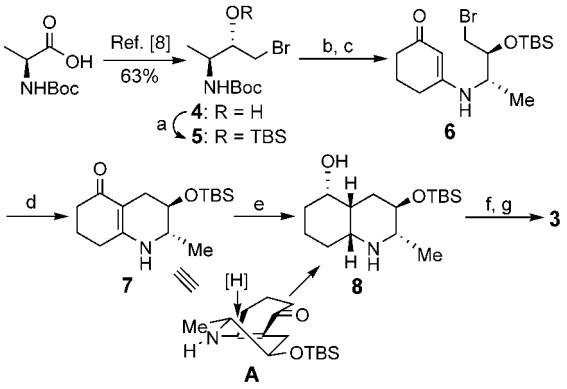
[**] The authors are grateful to the Chinese Academy of Sciences, the National Natural Science Foundation of China (grant 20321202), and the Science and Technology Commission of Shanghai Municipality (grants 02JC14032 and 03XD14001) for their financial support.

Supporting information for this article is available on the WWW under http://www.angewandte.org or from the author.

 © 2004 Wiley-VCH Verlag GmbH & Co. KGaA, Weinheim DOI: 10.1002/anie.200460128



Scheme 1. Structures and retrosynthetic analysis of lepadins A (**1a**), B (**1b**), D (**2a**), E (**2b**), and H (**2c**). Boc = *tert*-butoxycarbonyl, TBS = *tert*-butyldimethylsilyl.



Scheme 2. a) TBSCl, imidazole, DMF; b) HCO_2H/CH_2Cl_2, then aqueous $NaHCO_3$, 80% from **4**; c) 1,3-cyclohexandione, benzene, reflux, 65%; d) NEt_3, NaI, DMF, 110°C, 98%; e) Pt/C, 80 atm H_2, dry AcOH, 50°C, 85%; f) $(Boc)_2O$, benzene, 90%; g) Dess–Martin oxidation, 92%. DMF = *N*,*N*-dimethylformamide.

species and other sources four years later.[2] These compounds have been found to possess significant in vitro cytotoxicity against several human cancer cell lines.[2] Very recently, Wright et al. reported the isolation of lepadins D–F from a new *Didemnum* species collected from the Great Barrier Reef,[3] whereas Carroll and co-workers described their discovery of lepadins F–H in *Aplidium tabascum* Kott.[4] Interestingly, lepadins D–F showed low cytotoxicity but significant and selective antiplasmodinium and antitrypanosomal activity and therefore may serve as lead structures for the development of novel antimalarial drugs.[3]

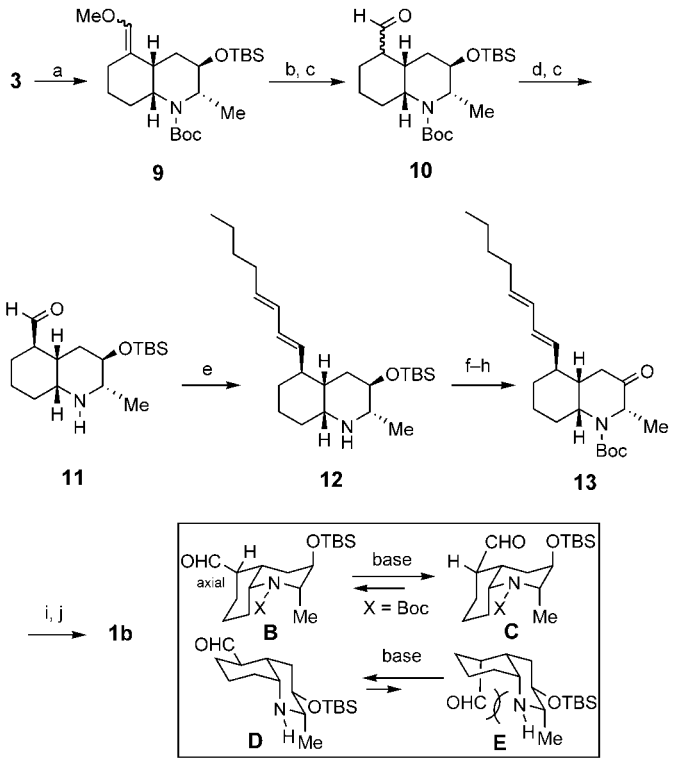
During the past five years, considerable effort has been directed towards the total synthesis of lepadins, and two successful protocols have resulted.[5,6] However, the requirement by both routes of lengthy reaction sequences to construct the left cyclohexane ring greatly diminished their synthetic efficiency. In 2002 Zard and co-workers described a short formal synthesis of racemic lepadin B,[7] but many more steps would evidently be necessary if this strategy was applied in an enantioselective synthesis. Herein we wish to describe a very efficient and general entry into the lepadin family. The key elements include a concise synthesis of the bicyclic ketone **3** (Scheme 1) and subsequent stereoselective introduction of both α- and β-oriented side chains at C5 of this intermediate. Furthermore, the configuration of lepadins D (**2a**), E (**2b**), and H (**2c**) was established fully through this study; in previous reports the absolute configuration of these three compounds and their configuration at C5′ were undefined.

The assembly of the bicyclic ketone **3** from *N*-Boc-L-alanine is outlined in Scheme 2. *N*-Boc-L-alanine was converted in three steps by a literature procedure into the α-amino alcohol **4** (63% overall yield),[8] which was protected as the silyl ether **5**. After selective cleavage of the Boc group of **5** with formic acid, the resulting amine was condensed with 1,3-cyclohexandione in benzene at reflux to give the enamine **6.** Subsequent alkylative cyclization of **6** mediated by Et_3N at 110°C in DMF produced the enone **7**. The next planned step was the diastereoselective hydrogenation of the C–C double bond in **7**. Based on a previous observation,[9] we envisaged that a stereoelectronically controlled axial addition of hydrogen would occur at the *Re* face of the more stable conformation **A**, thus leading to the desired configuration at C4a and C8a for the synthesis of lepadins A, B, D, E, and H. As expected, this reaction worked well under the catalysis of Pt/C in dry acetic acid at 80 atm and 50°C to afford **8** as a single isomer with the 4a*R*,8a*R* configuration, as established by NOESY studies. Other catalysts, such as Raney-Ni, Pd/C, and $Pd(OH)_2/C$, failed to promote the reaction. Finally, the protection of **8** with a Boc group followed by a Dess–Martin oxidation provided **3**.

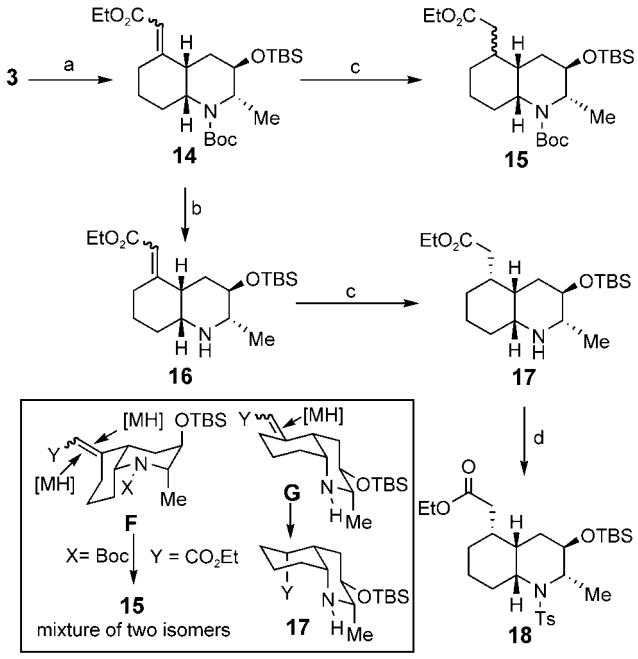
The stage was now set for the installation of the β-oriented side chain at C5 of the ketone **3** to complete the synthesis of lepadin B. Accordingly, **3** was successfully transformed into the olefin **9** through a Wittig reaction (Scheme 3). Selective hydrolysis of the enol ether moiety of **9** with trichloroacetic acid in dichloromethane containing a trace of water gave the aldehyde **10**.[10] By ^{1}H NMR spectroscopic analysis it was found that an inseparable mixture of diastereomers were present in a ratio of 1:1.3. After failure to enhance the ratio by treatment of this mixture with K_2CO_3 in methanol, we realized that the two isomers might have similar stability and occupy the favored conformations **B** and **C**, respectively. Further conformational analysis based on the studies of Booth and co-workers[11] showed that if the *N*-Boc group was removed, the favored conformations would be **D** and **E** for the two possible aldehydes. The more pronounced 1,5-strain in **E** would make conformer **D** more stable, and thus compound **11** with the aldehyde substituent in the β orientation would be afforded exclusively. Indeed, after selective cleavage of the Boc group in **10** with trifluoroacetic acid (TFA) and subsequent treatment with K_2CO_3 in methanol, the aldehyde **11** was isolated as a single isomer.

The C1′–C8′ side chain was installed by a Horner–Wadsworth–Emmons reaction,[12] and the desired *E*,*E* diene **12** was obtained with greater than 95% selectivity. (Several methods for a modified Julia olefination gave a mixture in favor of the *E*,*Z* diene.[13]) The remaining task for completion of the synthesis was the inversion of the C3 stereocenter, for which we employed an oxidation/reduction strategy. Thus, after protection of the N atom with a Boc group, desilyation with TBAF and a subsequent Dess–Martin oxidation pro-

 © 2004 Wiley-VCH Verlag GmbH & Co. KGaA, Weinheim



Scheme 3. a) $Ph_3P{=}CHOMe$, −40 °C→RT, 75 %; b) CCl_3CO_2H, CH_2Cl_2, H_2O (trace); c) K_2CO_3, MeOH, 79 % for **10** and 76 % for **11** from **9**; d) CF_3CO_2H, CH_2Cl_2; e) diethyl (2*E*)-heptenylphosphonate, KHMDS, THF, 95 %; f) $(Boc)_2O$, benzene, reflux; g) TBAF, THF; h) Dess–Martin oxidation, 60 % for 3 steps; i) $NaBH_4$, MeOH, −78 °C, 90 %; j) CF_3CO_2H (5 %), CH_2Cl_2, 80 %. HMDS = hexamethyldisilazide, TBAF = tetrabutylammonium fluoride.

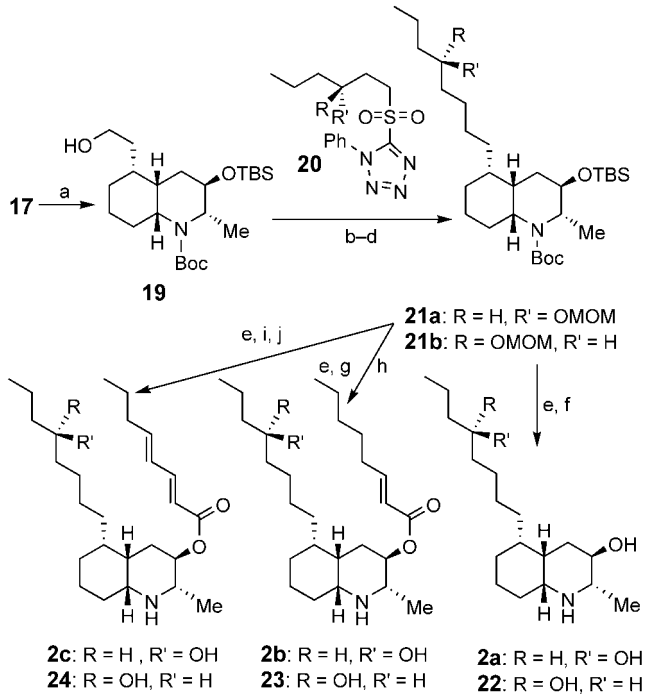


Scheme 4. a) $TMSCH_2CO_2Et$, LDA, −78 °C→RT, 98 %; b) CF_3CO_2H, CH_2Cl_2, 100 %; c) Pt/C, H_2 (1 atm), dry AcOH, 50 °C, 95 %; d) TsCl, Et_3N, CH_2Cl_2, 80 %. LDA = lithium diisopropylamide, TMS = trimethylsilyl, Ts = *p*-toluenesulfonyl.

vided the ketone **13**. The reduction of **13** with $NaBH_4$ gave a single diastereomer, which was treated with TFA to furnish lepadin B as its TFA salt, whose analytical data were identical to those reported.[2] The overall yield was about 5.3 % over 20 linear steps from *N*-Boc-L-alanine.

To introduce the α-oriented side chain at C5 of the ketone **3**, a Peterson reaction[14] was employed to provide the olefin **14** (Scheme 4). Direct Pt/C-catalyzed hydrogenation of **14** in dry acetic acid gave **15** with a diastereomeric ratio of 3:1. However, we were pleased to observe that the hydrogenation of **16**, a derivative of **14** without the *N*-Boc group, produced **17** in a highly diastereoselective manner (d.r. > 97:3). X-ray crystal-structure analysis of **18**, a tosylation product of **17**, confirmed that the side chain at C5 was in the α orientation. These two stereochemical courses might be rationalized by the difference in steric hindrance towards hydrogen attack in the two favored conformations **F** and **G**, as depicted in Scheme 4.

The completion of lepadins D, E, and H is depicted in Scheme 5. The protection of **17** by treatment with $(Boc)_2O$, followed by reduction with DIBAL, afforded the alcohol **19**, which was oxidized to the aldehyde, coupled with the sulfone **20**, and hydrogenated over Pd/C to produce **21**. Since the sulfones **20** could be constructed by a Sharpless epoxidation/reductive ring opening sequence and subsequent transforma-



Scheme 5. a) $(Boc)_2O$, DMAP, then DIBAL, −40 °C, 95 %; b) Swern oxidation; c) **20**, NaHMDS, THF; d) Pd/C, H_2, 90 %; e) TBAF, THF, room temperature, 100 %; f) HCl, *i*PrOH/MeOH, 85 %; g) (2*E*)-octenoic acid, $Cl_3C_6H_2COCl$, iPr_2NEt, DMAP, 64 %; h) CF_3CO_2H, CH_2Cl_2, 87 %; i) (2*E*,4*E*)-octadienoic acid, EDCI, DMAP, CH_2Cl_2, 73 %; j) CF_3CO_2H, CH_2Cl_2, 90 %. DIBAL = diisobutylaluminum hydride, DMAP = 4-dimethylaminopyridine, EDCI = 1-[3-(dimethylamino)propyl]-3-ethylcarbodiimide hydrochloride, MOM = methoxymethyl.

 © 2004 Wiley-VCH Verlag GmbH & Co. KGaA, Weinheim

tions,[15] both (*R*)-**20** and (*S*)-**20** were readily accessible by tuning the ligands in the Sharpless epoxidation, thus providing a chance to establish the configuration at C5′. The complete deprotection of **21** led to both **2a** and its C5′ epimer **22**. The cleavage of just the silyl ether in **21** yielded two alcohols, which were acylated with (2*E*)-octenoic acid ($Cl_3C_6H_2COCl/i$PrNEt$_2$)[16] or (2*E*,4*E*)-octadienoic acid (EDCI/DMAP),[17] and then deprotected to furnish **2b** and **23**, and **2c** and **24**, respectively. Although both the NMR spectra and the optical rotation for **2a** and **22**, **2b** and **23**, and **2c** and **24** were very similar, a marked difference in the ^{1}H NMR spectra of **2c** and **24** at $\delta = 1.2$–1.5 ppm clearly showed that the data for **2c**, but not for **24**, were identical to those reported for lepadin H. Furthermore, the value $[\alpha]_D^{20} = -12$ ($c = 1.0$ MeOH) observed for the hydrochloride salt of **2a** is close to that reported for the hydrochloride salt of lepadin D ($[\alpha]_D^{20} = -14$ ($c = 0.2$ MeOH)[3]), whereas the value for the optical rotation of the hydrochloride salt of **22** was significantly lower ($[\alpha]_D^{20} = -5.7$ ($c = 0.9$ MeOH)). Therefore, we concluded that lepadins D, E, and H have the absolute configuration 2*S*,3*R*,4a*S*,5*S*,8a*R*,5′*R*.

In summary, we have developed an efficient and divergent strategy towards the lepadins, including a concise synthesis of lepadin B, as well as the first total synthesis of lepadins D, E, and H, which enabled us to fully determine their configuration. These results should prompt further studies on the synthesis and biological activity of these compounds and their analogues.

Received: March 26, 2004 [Z460128]

Keywords: alkaloids · configuration determination · hydrogenation · olefination · total synthesis

[1] B. Steffan, *Tetrahedron* **1991**, *47*, 8729.
[2] J. Kubanek, D. E. Williams, E. D. de Silva, T. Allen, R. J. Anderson, *Tetrahedron Lett.* **1995**, *36*, 6189.
[3] A. D. Wright, E. Goclik, G. M. König, R. Kaminsky, *J. Med. Chem.* **2002**, *45*, 3067.
[4] R. A. Davis, A. R. Carroll, R. J. Quinn, *J. Nat. Prod.* **2002**, *65*, 454.
[5] a) N. Toyooka, M. Okumura, H. Takahatam, *J. Org. Chem.* **1999**, *64*, 2182; b) N. Toyooka, M. Okumura, H. Takahatam, H. Nemoto, *Tetrahedron* **1999**, *55*, 10673.
[6] a) T. Ozawa, S. Aoyagi, C. Kobayashi, *Org. Lett.* **2000**, *2*, 2955; b) T. Ozawa, S. Aoyagi, C. Kobayashi, *J. Org. Chem.* **2001**, *66*, 3338.
[7] C. Kalai, E. Tate, S. Z. Zard, *Chem. Commun.* **2002**, 1430.
[8] P. D. Rotella, *Tetrahedron Lett.* **1995**, *36*, 5453.
[9] X. Pu, D. Ma, *J. Org. Chem.* **2003**, *68*, 4400.
[10] P. E. Harrington, I. A. Stergiades, J. Erickson, A. Makriyannis, M. A. Tius, *J. Org. Chem.* **2000**, *65*, 6576.
[11] a) H. Booth, A. H. Bostock, *J. Chem. Soc. Perkin Trans. 2* **1972**, 615; b) H. Booth D. V. Griffiths, *J. Chem. Soc. Perkin Trans. 2* **1975**, 111.
[12] a) B. M. Trost, J. L. Gunzner, O. Dirat, Y. H. Rhee, *J. Am. Chem. Soc.* **2002**, *124*, 10396; b) R. K. Boeckman, Jr., C. H. Weinder, R. B. Perni, J. J. Napier, *J. Am. Chem. Soc.* **1989**, *111*, 8036.
[13] A. B. Smith III, I. G. Safonov, R. M. Corbett, *J. Am. Chem. Soc.* **2002**, *124*, 11102.
[14] K. Shimoji, H. Taguchi, K. Oshima, H. Yamamoto, H. Nozaki, *J. Am. Chem. Soc.* **1974**, *96*, 1620.
[15] a) L. J. D'Souza, S. C. Sinha, S. Lu, E. Keinan, S. C. Sinha, *Tetrahedron* **2001**, *57*, 5255; b) P. A. Blackemore, W. J. Cole, P. J. Kocienski, A. Morley, *Synlett* **1998**, 26.
[16] C. Gaul, J. T. Njardarson, S. J. Danishefsky, *J. Am. Chem. Soc.* **2003**, *125*, 6042.
[17] D. A. Evans, P. H. Carter, E. M. Carreira, J. A. Prunet, A. B. Charette, M. Lautens, *Angew. Chem.* **1998**, *37*, 2526; *Angew. Chem. Int. Ed. Engl.* **1998**, *37*, 2354.

 © 2004 Wiley-VCH Verlag GmbH & Co. KGaA, Weinheim

Asymmetric Oxidations

Highly Enantioselective Iron-Catalyzed Sulfide Oxidation with Aqueous Hydrogen Peroxide under Simple Reaction Conditions**

*Julien Legros and Carsten Bolm**

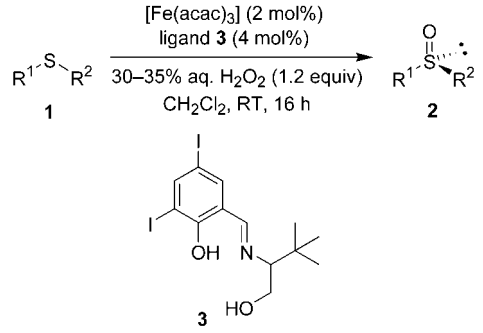
Iron is one of the most abundant metals in the universe.[1] It is inexpensive, environmentally benign, and relatively nontoxic in comparison to other metals. For oxidation reactions the application of iron catalysts[2] in combination with aqueous hydrogen peroxide[3] would be most desirable. Asymmetric oxidations could then be achieved by the use of chiral iron complexes. In this context we recently reported a new enantioselective sulfide oxidation,[4–6] which provides optically active sulfoxides with up to 90% *ee*.[7] The catalysis proceeds under very simple reaction conditions (at room temperature in a capped flask) and utilizes a readily available iron complex generated in situ from $[Fe(acac)_3]$ and Schiff base **3**.[8] Inexpensive and safe 30–35% aqueous hydrogen peroxide serves as terminal oxidant (Scheme 1).

Although the asymmetric induction in this iron-catalyzed sulfoxidation was remarkable, the practicability of the process was limited owing to the low conversion of **1**. Thus, under the conditions required for high enantioselectivities, large amounts of unconverted sulfides remained, and the best yield of sulfoxide **2** was only 44%. We now report on a significant improvement in this iron-catalyzed sulfide oxidation, leading to both higher enantioselectivities (up to 96% *ee*) and better yields (up to 78%).

[*] Dr. J. Legros, Prof. Dr. C. Bolm
Institut für Organische Chemie der RWTH Aachen
Professor-Pirlet-Strasse 1, 52056 Aachen (Germany)
Fax: (+49) 241-809-2391
E-mail: carsten.bolm@oc.rwth-aachen.de

[**] We are grateful to the Fonds der Chemischen Industrie and to the Deutsche Forschungsgemeinschaft (DFG) within the SFB 380 "Asymmetric Synthesis by Chemical and Biological Methods" for financial support. We thank the Alexander von Humboldt Foundation for a postdoctoral fellowship (J.L.). Degussa is acknowledged for gifts of (*S*)- and (*R*)-*tert*-leucine. J.-C. Frison and Dr. Y. Yuan are thanked for fruitful discussions.

 DOI: 10.1002/anie.200460236 © 2004 Wiley-VCH Verlag GmbH & Co. KGaA, Weinheim



Scheme 1. Iron-catalyzed enantioselective sulfoxidation.

The use of additives is a common and convenient method for the enhancement of the efficiency of metal-catalyzed reactions,[9] as it allows the fine-tuning of the catalyst system without redesigning the ligand.[10] Recently, Jacobsen and co-workers reported the beneficial effects of the presence of substoichiometric amounts of a carboxylic acid in epoxidation reactions with H_2O_2 and the iron complex $[Fe^{II}(mep)(CH_3CN)_2](SbF_6)_2$ (mep = *N*,*N*′-dimethyl-*N*,*N*′-bis(2-pyridylmethyl)-ethylene 1,2-diamine).[11] Motivated by these observations we began to investigate the influence of benzoic acid (**AH1**) on the enantioselectivity and the yield of methyl phenyl sulfoxide (**2a**) obtained in the iron-catalyzed oxidation of methyl phenyl sulfide (**1a**). As shown in Figure 1 the

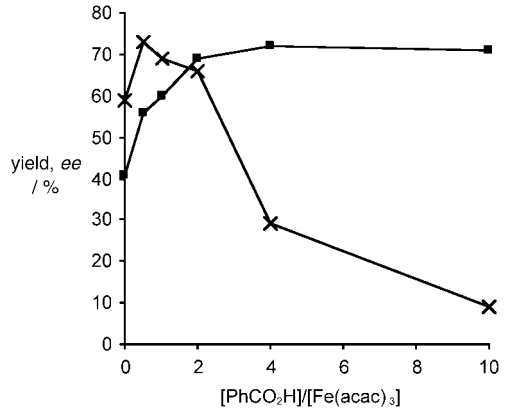
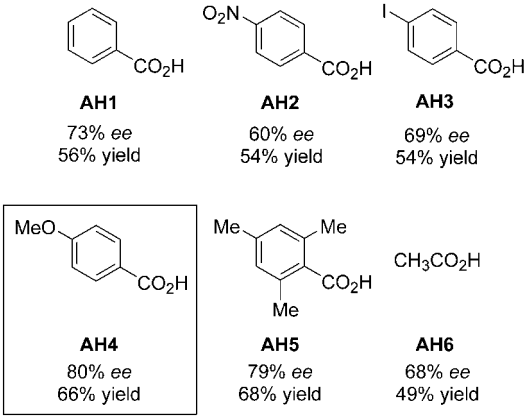


Figure 1. Effect of benzoic acid (**AH1**) on the *ee* value (×; measured by HPLC on the crude product) and the yield (■; determined by NMR spectroscopic analysis) of (*S*)-**2a** obtained in the asymmetric oxidation of **1a** with H_2O_2 (35%; 1.2 equiv) catalyzed by $[Fe(acac)_3]$ (2 mol%) and (*S*)-**3** (4 mol%).

effect of the acid was remarkable. Its presence improved both the asymmetric induction as well as the yield. The best enantioselectivity was obtained with an **AH1**/$[Fe(acac)_3]$ ratio of 0.5:1. Under those conditions (see footnote in Figure 1), the enantiomeric excess of sulfoxide **2a** increased from 59% *ee* (no additive) to 73% *ee*. Furthermore, the yield of **2a** rose from 41% (no additive) to 56%. The use of larger quantities of benzoic acid afforded **2a** with lower *ee* values, albeit in good yield [for example, an **AH1**/$[Fe(acac)_3]$ ratio of 10:1 gave **2a** with 9% *ee* in 71% yield)].

Next, several other carboxylic acids (**AH2**–**AH6**), which varied in their electronic and steric properties, were applied (Scheme 2). Apparently, the nature of the carboxylic acid and the position of its substituents has a major effect on the sulfide



Scheme 2. Effect of various carboxylic acids (**AH1**–**AH6**, 1 mol%) on the yield (determined by NMR spectroscopic analysis) and the *ee* value (measured on the crude product) of (*S*)-**2a** obtained in the asymmetric oxidation of **1a** with H_2O_2 (35%; 1.2 equiv) catalyzed by $[Fe(acac)_3]$ (2 mol%) and (*S*)-**3** (4 mol%).

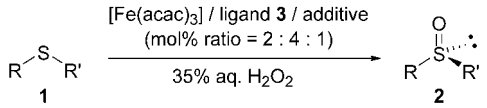
oxidation. Thus, use of acids with electron-withdrawing substituents (NO_2: **AH2**; I: **AH3**) led to a decrease in the efficiency of the catalysis (relative to the reaction with benzoic acid, **AH1**). In contrast, electron-rich benzoic acids **AH4** and **AH5** (with *p*-MeO-phenyl and mesityl groups) gave very good results and afforded **2a** with 80 and 79% *ee*, respectively. The yields were slightly better as well (56% for **AH1**, 66% for **AH4**, and 68% for **AH5**). Also the presence of acetic acid (**AH6**) resulted in an improvement (with respect to the original conditions), giving **2a** with 68% *ee*.

The fact that the electron-rich carboxylic acids **AH4** and **AH5** led to the best results suggested that the additives acted as coligands, and that the essential characteristic was their chelating properties, not their acidity. Carboxylate salts were therefore expected to increase the efficiency of the reaction further. To our delight we found that this hypothesis was correct. Thus, the use of lithium 4-methoxybenzoate (**ALi4**) in the oxidation of thioanisole **1a** resulted in the formation of sulfoxide **2a** with 90% *ee* (Table 1, entry 1).[12] As shown in Table 1, the effect of the carboxylate in the oxidation of other substrates was similar.

Relative to the original protocol (without any additive), both the enantioselectivity and the yield increased when the sulfide oxidation was performed in the presence of either acid **AH4** or carboxylate **ALi4**. In most cases the latter additive proved to be superior with respect to the former. The best results were observed with *para*-substituted substrates (Table 1, entries 11, 15, 17 and 21), leading to sulfoxides with >92% *ee* (ee_{max} = 96%) in moderate to good yields (up to 78%). Remarkable enantioselectivities were also attained in the oxidation of more-challenging substrates such as phenyl ethyl sulfide (**1b**) and phenyl benzyl sulfide (**1c**), which gave the corresponding sulfoxides with 82 and 79% *ee*, respectively

 © 2004 Wiley-VCH Verlag GmbH & Co. KGaA, Weinheim

Table 1: Catalytic enantioselective oxidation of sulfides **1** to sulfoxides **2** with H_2O_2 and a chiral iron complex in the presence of an additive.[a]



Entry	Config. of **3**	**1**	Additive	**2**	Yield [%][b]	*ee* [%][c,d]	Config. of **2**[e]
1	(*S*)	Ph-S-Me (**1a**)	**ALi4**	**2a**	**63**	**90**	(*S*)-(−)
2	(*R*)	Ph-S-Me (**1a**)	**AH4**	**2a**	61	77	(*R*)-(+)
3	(*R*)	Ph-S-Me (**1a**)	**ALi4**	**2a**	**64**	**88**	(*R*)-(+)
4	(*S*)	Ph-S-Et (**1b**)	–	**2b**	30	44	(*S*)-(−)
5	(*S*)	Ph-S-Et (**1b**)	**AH4**	**2b**	51	71	(*S*)-(−)
6	(*S*)	Ph-S-Et (**1b**)	**ALi4**	**2b**	**56**	**82**	(*S*)-(−)
7	(*S*)	Ph-S-Bn (**1c**)	–	**2c**	40	27	(*S*)-(−)
8	(*S*)	Ph-S-Bn (**1c**)	**AH4**	**2c**	**73**	**79**	(*S*)-(−)
9	(*S*)	Ph-S-Bn (**1c**)	**ALi4**	**2c**	64	78	(*S*)-(−)
10	(*S*)	4-MeC_6H_4-S-Me (**1d**)	**AH4**	**2d**	68	78	(*S*)-(−)
11	(*S*)	4-MeC_6H_4-S-Me (**1d**)	**ALi4**	**2d**	**78**	**92**	(*S*)-(−)
12	(*S*)	2-BrC_6H_4-S-Me (**1e**)	**ALi4**	**2e**	48	**66**	(−)
13	(*S*)	4-BrC_6H_4-S-Me (**1f**)	–	**2f**	41	78	(*S*)-(−)
14	(*S*)	4-BrC_6H_4-S-Me (**1f**)	**AH4**	**2f**	55	91	(*S*)-(−)
15	(*S*)	4-BrC_6H_4-S-Me (**1f**)	**ALi4**	**2f**	**59**	**94**	(*S*)-(−)
16	(*S*)	4-ClC_6H_4-S-Me (**1g**)	–	**2g**	32	65	(*S*)-(−)
17	(*S*)	4-ClC_6H_4-S-Me (**1g**)	**AH4**	**2g**	**60**	**92**	(*S*)-(−)
18	(*S*)	4-ClC_6H_4-S-Me (**1g**)	**ALi4**	**2g**	53	92	(*S*)-(−)
19	(*S*)	4-$NO_2C_6H_4$-S-Me (**1h**)	–	**2h**	21	90	(*S*)-(−)
20	(*S*)	4-$NO_2C_6H_4$-S-Me (**1h**)	**AH4**	**2h**	41	91	(*S*)-(−)
21	(*S*)	4-$NO_2C_6H_4$-S-Me (**1h**)	**ALi4**	**2h**	**36**	**96**	(*S*)-(−)
22	(*S*)	2-Naphthyl-S-Me (**1i**)	–	**2i**	44	70	(*S*)-(−)
23	(*S*)	2-Naphthyl-S-Me (**1i**)	**AH4**	**2i**	**67**	**95**	(*S*)-(−)
24	(*S*)	2-Naphthyl-S-Me (**1i**)	**ALi4**	**2i**	63	93	(*S*)-(−)
25	(*S*)	$PhCH_2$-S-Me (**1j**)	**ALi4**	**2j**	64	23	(+)

[a] Reaction conditions: $[Fe(acac)_3]$ (0.02 mmol), ligand **1** (0.04 mmol), **AH4** or **ALi4** (0.01 mmol), sulfide (1 mmol) and aqueous H_2O_2 (35%; 1.2 mmol) in CH_2Cl_2 at room temperature for 16 h. [b] After column chromatography. [c] The *ee* values were measured on the isolated product and determined by HPLC analysis on a chiral stationary phase. [d] In cases in which the *ee* value was $\geq 90\%$, the formation of sulfone (10–15%) was observed; see also comment in reference [13]. [e] The absolute configurations were assigned by comparing optical rotations and/or HPLC elution order with known literature data.

(Table 1, entries 6 and 8). The last result is particularly impressive, as the product was obtained with only 27% *ee* in the absence of an additive. Furthermore, the yield of **2c** increased from 44% (no additive) to 73% (with **AH4**).[13]

Although it is difficult to provide a mechanistic rational for the observed improvements at the present stage, the fact that the best results were obtained with 0.5 equivalents of the carboxylic acid (and/or the carboxylate salt) relative to iron suggests that monocarboxylate-bridged diiron(III) complexes similar to those investigated as functional models able to mimic non-heme metalloproteins[2,14] could be involved. Attempts to isolate and to characterize those species formed in situ under the conditions described herein are currently in progress.

In summary, we developed an asymmetric iron-catalyzed sulfide oxidation with hydrogen peroxide as terminal oxidant, which provides sulfoxides with up to 96% *ee* in moderate to good yields (up to 78%). The simplicity of the process (room temperature, aerobic atmosphere) and the high enantioselectivities render this process an attractive alternative to the currently existing methods for metal-catalyzed asymmetric sulfide oxidations.

Experimental Section

$[Fe(acac)_3]$ (7.1 mg, 0.02 mmol) and ligand **3** (18.9 mg, 0.04 mmol) were dissolved in dichloromethane (0.7 mL), and the clear red solution was stirred until it turned clear brown (15 min). This solution was then transferred into a 10-mL flask containing a suspension of either 4-methoxybenzoic acid (**AH4**; 1.5 mg, 0.01 mmol) or lithium salt **ALi4** (1.6 mg, 0.01 mmol) in dichloromethane (0.5 mL), and the resulting mixture was stirred for 10 min. A solution of the sulfide **1** (1 mmol) in dichloromethane (0.8 mL) was then added to the previous solution, followed by the dropwise addition of aqueous H_2O_2 (35%; 1.2 mmol). The flask was then capped, and the reaction mixture was slowly stirred at room temperature (approximately 150 rpm). After 16 h, the aqueous layer was separated, the organic layer was dried over $MgSO_4$, filtered, and the solvent was removed in vacuo. The product was then purified by chromatography on silica gel (pentane/Et_2O 1:2, then ethyl acetate). The *ee* values were determined by HPLC on a chiral stationary phase (Gynkotek apparatus; UV detector UVD 170S (254 nm); 20°C; flow rate 0.5 mL min^{-1}). Retention times [min]: (*R*)-**2a** 26.5, (*S*)-**2a** 31.2 (Chiralcel OD; heptane/*i*PrOH, 9:1); (*R*)-**2b** 22.0, (*S*)-**2b** 27.2 (Chiralcel OD; heptane/*i*PrOH, 9:1); (*R*)-**2c** 28.8, (*S*)-**2c** 36.1 (Chiralcel OD; heptane/*i*PrOH, 9:1); (*R*)-**2d** 24.0, (*S*)-**2d** 26.2 min (Chiralcel OD; heptane/*i*PrOH, 9:1); (−)-**2e** 19.3, (+)-**2e** 28.9 (Chiralcel OB; heptane/*i*PrOH, 8:2); (*S*)-**2f** 25.8, (*R*)-**2f** 35.9 (Chiralcel OB; flow rate, heptane/*i*PrOH, 8:2); (*S*)-**2g** 19.9, (*R*)-**2g** 30.0 (Chiralcel OB; heptane/*i*PrOH, 8:2); (*R*)-**2h** 42.9, (*S*)-**2h** 47.5 (Chiralcel OJ; heptane/*i*PrOH, 7:3); (*R*)-**2i** 37.2, (*S*)-**2i** 40.8 (Chiralcel OD; heptane/*i*PrOH, 9:1); (+)-**2j** = 22.8, (−)-**2j** = 28.4 (Chiralcel OB; heptane/*i*PrOH, 8:2).

Received: April 6, 2004 [Z460236]

Keywords: asymmetric catalysis · iron · oxidation · peroxides · sulfoxides

 © 2004 Wiley-VCH Verlag GmbH & Co. KGaA, Weinheim

[1] F. A. Cotton, G. Wilkinson, *Anorganische Chemie*, 4th ed., Verlag Chemie, Weinheim, **1982**, p. 767.

[2] For reviews on non-heme iron catalysts in oxidation reactions, see: a) M. Fontecave, S. Ménage, C. Duboc-Toia, *Coord. Chem. Rev.* **1998**, *178–180*, 1555 – 1572; b) M. Costas, K. Chen, L. Que, Jr., *Coord. Chem. Rev.* **2000**, *200–202*, 517 – 544, and references therein.

[3] For overviews on the use of hydrogen peroxide in oxidation reactions, see: a) *Catalytic Oxidations with Hydrogen Peroxide as Oxidant* (Ed.: G. Strukul), Kluwer Academic, Dordrecht, **1992**; b) C. W. Jones, *Applications of Hydrogen Peroxides and Derivatives*, Royal Society of Chemistry, Cambridge, **1999**; c) B. S. Lane, K. Burgess, *Chem. Rev.* **2003**, *103*, 2457 – 2473; d) R. Noyori, M. Aoki, K. Sato, *Chem. Commun.* **2003**, 1977 – 1986.

[4] For reviews on asymmetric sulfoxidations, see: a) H. B. Kagan, T. Luukas in *Transition Metals for Organic Synthesis* (Eds.: M. Beller, C. Bolm), Wiley-VCH, Weinheim, **1998**, pp. 361 – 373; b) H. B. Kagan in *Catalytic Asymmetric Synthesis*, 2nd ed. (Ed.: I. Ojima), Wiley-VCH, New York, **2000**, pp. 327 – 356; c) C. Bolm, K. Muñiz, J. P. Hildebrand in *Comprehensive Asymmetric Catalysis* (Eds.: E. N. Jacobsen, A. Pfaltz, H. Yamamoto), Springer, Berlin, **1999**, pp. 697 – 713; d) for a recent review on chiral sulfoxides, see: I. Fernández, N. Khiar, *Chem. Rev.* **2003**, *103*, 3651 – 3705.

[5] One of the most widely sold drugs in the world (with total sales in 2002 of US$ 6.6 billion) is the chiral sulfoxide omeprazole. Its enantioselective synthesis involves an asymmetric sulfide oxidation. For a summary of recent developments and data, see: A. M. Rouhi, *Chem. Eng. News* **2003**, *81*(19), 56 – 61.

[6] For other iron-catalyzed sulfoxidations, see: a) J. T. Groves, P. Viski, *J. Org. Chem.* **1990**, *55*, 3628 – 3634; b) Y. Naruta, F. Tani, K. Maruyama, *J. Chem. Soc. Chem. Commun.* **1990**, 1378 – 1380; c) Y. Naruta, F. Tani, K. Maruyama, *Tetrahedron: Asymmetry* **1991**, *2*, 533 – 542; d) L.-C. Chiang, K. Konishi, T. Aida, S. Inoue, *J. Chem. Soc. Chem. Commun.* **1992**, 254 – 256; e) Q. L. Zhou, K. C. Chen, Z. H. Zhu, *J. Mol. Catal.* **1992**, *72*, 59 – 65; f) C. Duboc-Toia, S. Ménage, C. Lambeaux, M. Fontecave, *Tetrahedron Lett.* **1997**, *38*, 3727 – 3730; g) C. Duboc-Toia, S. Ménage, R. Y. N. Ho, L. Que, Jr., M. Fontecave, *Inorg. Chem.* **1999**, *38*, 1261 – 1268; h) Y. Mekmouche, H. Hummel, R. Y. N. Ho, L. Que, Jr., V. Schünemann, F. Thomas, A. X. Trautwein, C. Lebrun, K. Gorgy, J.-C. Leprêtre, M.-N. Collomb, A. Deronzier, M. Fontecave, S. Ménage, *Chem. Eur. J.* **2002**, *8*, 1196 – 1204.

[7] J. Legros, C. Bolm, *Angew. Chem.* **2003**, *115*, 5645 – 5647; *Angew. Chem. Int. Ed.* **2003**, *42*, 5487 – 5489.

[8] Schiff bases of this type have also been used in vanadium-catalyzed asymmetric sulfide oxidations with H_2O_2. Most interestingly, the same ligand **3** (derived from 3,5-di-iodosalicyladehyde) that is optimal for the V-catalyzed asymmetric sulfur oxidation is also optimal in the iron-promoted process. For the vanadium-catalyzed reaction, see: a) C. Bolm, F. Bienewald, *Angew. Chem.* **1995**, *107*, 2883 – 2885; *Angew. Chem. Int. Ed. Engl.* **1995**, *34*, 2640 – 2642; b) C. Bolm, G. Schlingloff, F. Bienewald, *J. Mol. Catal. A* **1997**, *117*, 347 – 350; c) C. Bolm, F. Bienewald, *Synlett* **1998**, *34*, 1327 – 1328; d) B. Pelotier, M. S. Anson, I. B. Campbell, S. J. F. Macdonald, G. Priem, R. F. W. Jackson, *Synlett* **2002**, 1055 – 1060; e) S. A. Blum, R. G. Bergman, J. A. Ellman, *J. Org. Chem.* **2003**, *68*, 150 – 155; f) D. J. Weix, J. A. Ellman, *Org. Lett.* **2003**, *5*, 1317 – 1320; g) for a review, see: C. Bolm, *Coord. Chem. Rev.* **2003**, *237*, 245 – 256, and references therein.

[9] For an interesting list of additives used in metal-catalyzed epoxidation with hydrogen peroxide, see reference [3c]; for a general review on additive effects in catalysis, see: E. M. Vogl, H. Gröger, M. Shibasaki, *Angew. Chem.* **1999**, *111*, 1672 – 1680; *Angew. Chem. Int. Ed.* **1999**, *38*, 1570 – 1577.

[10] This strategy has already been demonstrated in asymmetric sulfoxidations: Maruyama and co-workers used 1-methylimidazole with iron porphyrin catalysts,[6b,c] and Katsuki and co-workers added methanol to Bolm's vanadium catalyst (C. Ohta, H. Shimizu, A. Kondo, T. Katsuki, *Synlett* **2002**, 161 – 163). In both cases improvements in enantioselectivities were observed, whereas turnovers and yields did not increase. The use of those additives in the iron-catalyzed reaction shown in Scheme 1 had a negative effect.

[11] M. C. White, A. G. Doyle, E. N. Jacobsen, *J. Am. Chem. Soc.* **2001**, *123*, 7194 – 7195.

[12] Sodium, potassium, cesium and tetrabutyl ammonium salts have also been assessed in the oxidation of **2a**: **ANa4**, 90% *ee*; **AK4**, 88% *ee*; **ACs4**, 87% *ee*; **ABu$_4$N4**, 82% *ee*.

[13] In oxidations that give sulfoxides with high *ee* values ($\geq$ 90%) significant amounts of sulfone (ca. 15%) were detected in the crude product. Preliminary studies revealed the existence of a kinetic resolution process that enhances the inherent *ee* value of the sulfoxide. This behavior contrasts that found in the original process (without an additive[7]). Details of these findings will be reported in due course.

[14] For a review on models for non-heme carboxylate-bridged diiron metalloproteins, see: E. Y. Tshuva, S. J. Lippard, *Chem. Rev.* **2004**, *104*, 987 – 1012, and references therein.

 © 2004 Wiley-VCH Verlag GmbH & Co. KGaA, Weinheim

Phosphorus Nanorods

Phosphorus Nanorods—Two Allotropic Modifications of a Long-Known Element

Arno Pfitzner, Michael F. Bräu, Josef Zweck, Gunther Brunklaus, and Hellmut Eckert**

Dedicated to Professor H. G. von Schnering

Elemental phosphorus has been known for about 350 years. As a result of huge scientific interest, numerous textbooks are filled with information about this element, its different allotropes, and its compounds.[1] Like boron and carbon, the element features tremendous structural variability, resulting in great diversity of physical properties and chemical reactivity: White phosphorus, P_4, forms three crystal struc-

[*] Prof. Dr. A. Pfitzner, M. F. Bräu
Institut für Anorganische Chemie
Universität Regensburg, 93040 Regensburg (Germany)
Fax: (+49) 941-943-4983
E-mail: arno.pfitzner@chemie.uni-regensburg.de
Dr. G. Brunklaus, Prof. H. Eckert
Institut für Physikalische Chemie
Westfälische Wilhelms-Universität, 48149 Münster (Germany)
Fax: (+49) 251-832-9159
E-mail: eckerth@uni-muenster.de
Prof. Dr. J. Zweck
Institut für Experimentelle und Angewandte Physik
Universität Regensburg, 93040 Regensburg (Germany)

 © 2004 Wiley-VCH Verlag GmbH & Co. KGaA, Weinheim DOI: 10.1002/anie.200460244

tures,[2] including a plastic phase at room temperature, and is highly reactive with air. Violet (Hittorf's) phosphorus forms layers of chain polymers[3] and is less reactive, whereas black phosphorus, the conducting high-pressure modification,[4] has full 2D connectivity and is, comparably, chemically inert. Theoretical investigations by Häser and Böcker showed that alternative molecular and polymeric structures can be expected for the pure element.[5] However, due to difficulties in obtaining crystalline material no more allotropic forms, such as red phosphorus have yet been structurally well-characterized.

Recent research has shown that copper halides can be used as a unique synthetic tool towards the formation of compounds with new phosphorus-based architectures, such as low-charged phosphorus polyanions and phosphorus chalcogenide cage molecules.[6–11] Furthermore, polymeric phosphorus strands are readily formed as their copper iodide adducts by treating stoichiometric mixtures of CuX (X = Br, I) with elemental P. Compounds of this kind include two different $^1_\infty[P_{12}]$ polymers in $(CuI)_8P_{12}$[12] and in $(CuI)_3P_{12}$,[13] respectively, and a $^1_\infty[P_{14}]$ polymer in $(CuI)_2P_{14}$.[14] The separation of the pure phosphorus strands from the copper halide matrix represents an intriguing chemical challenge and should help to verify the theoretical investigations. Herein, we report the isolation and characterization of the $^1_\infty[P_{12}]$ polymers which are present in $(CuI)_8P_{12}$—$^1_\infty$[P8]P4(4)[(**1**)—and in $(CuI)_3P_{12}$—$^1_\infty$[P10]P2[(**2**; Figure 1)—by a low-temperature route.[15]

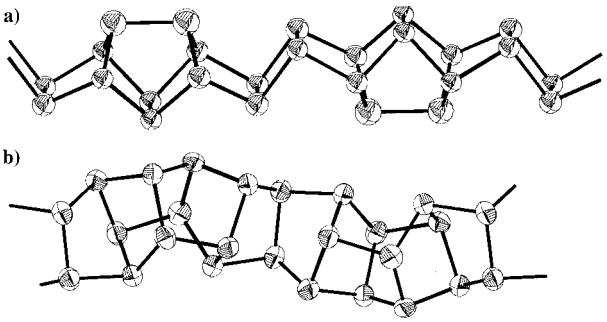


Figure 1. Structure of a) **1** and b) **2** as observed in their adducts to copper iodide. Data for **1** are taken from reference [12].

The copper iodide adducts were obtained by a typical high-temperature synthesis and the resulting crystalline materials were subsequently treated with an aqueous solution of potassium cyanide at room temperature. For both crystalline $(CuI)_8P_{12}$ and crystalline $(CuI)_3P_{12}$, the surfaces of the crystals were destroyed and dark-red/brown fibrous products were obtained. The yields were about 99% based on phosphorus and no elements other than phosphorus were detected in the isolated products by energy dispersive X-ray analysis. The colors of the two resulting products were quite similar and differ significantly from that of amorphous red phosphorus. Powder X-ray diffraction showed that the reaction products were amorphous. Structural information on **1** and **2** was obtained by high-resolution transmission electron microscopy (HRTEM), see Figure 2. The HRTEM images can be interpreted as showing the parallel orientation

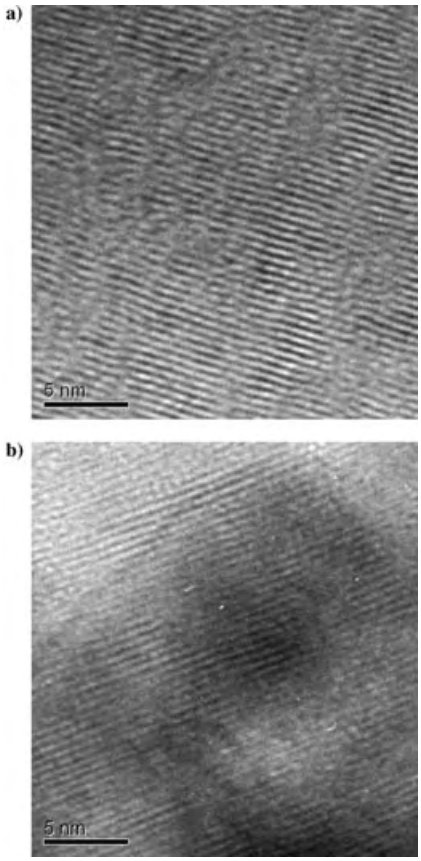


Figure 2. HRTEM images of a) **1** and b) **2**. The parallel arrangement of the phosphorus nanorods is clear.

of the isolated phosphorus nanorods over a range of at least 30 nm. However, the stacking periods of the rods can be determined by means of line scans perpendicular to the polymers. Thus, we obtained a period of 5.0 Å for **1** and of 5.4 Å for **2**. The diameters present in the crystalline CuI adducts are 3.3 Å (**1**) and 4.7 Å (2). To obtain structural information on a local level, ^{31}P MAS NMR spectra (MAS is magic angle spinning) of the crystalline starting materials and of the amorphous phosphorus allotropes derived from these starting materials were recorded (Figure 3). The parent compounds $(CuI)_8P_{12}$ and $(CuI)_3P_{12}$ are easily distinguished, thus reflecting the differences in the local environments of the 12 distinct phosphorus sites found in each polymer. However, in $(CuI)_3P_{12}$, the situation is a bit more complicated. Due to the packing in the crystal structure, two different polymers are present with a different number of copper atoms coordinating the phosphorus strands. When the metal halide is removed from the compound, both strands become equivalent. One has to assume that the strands show some relaxation, especially of the bond angles, upon extraction of the metal halide from the starting material. Compared to their starting materials, the spectra of **1** and **2** are significantly broadened, thus reflecting the loss of long-range periodicity in these amorphous samples. However, the spectra obtained for **1** and **2** differ from each other, each exhibiting principally the shape of the signal envelope of its respective starting material. These results suggest that the individual nanorods remain

 © 2004 Wiley-VCH Verlag GmbH & Co. KGaA, Weinheim

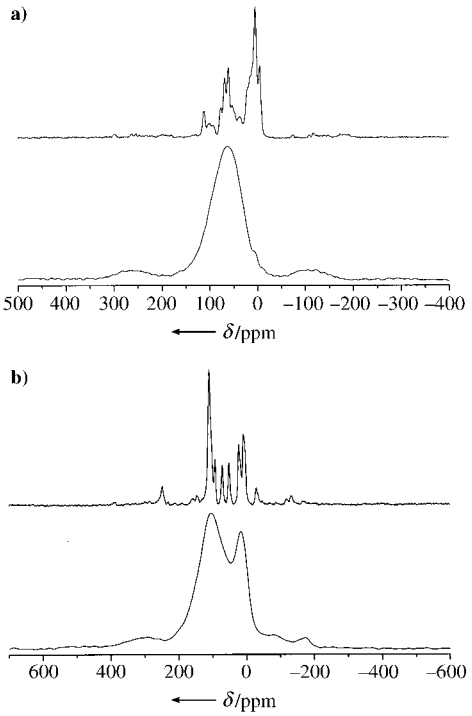


Figure 3. a) 162.05 MHz ^{31}P MASNMR spectra of $(CuI)_3P_{12}$ (top) and **2** (bottom), at a rotor speed of 30 kHz; b) ^{31}P MAS NMR spectra of $(CuI)_8P_{12}$ recorded at 202.46 MHz at a rotor speed of 28 kHz (top), and **1**, recorded at 81.01 MHz at a rotor speed of 15 kHz (bottom)

unchanged when they are extracted from the adducts by an aqueous cyanide solution. Due to the existence of two crystallographically different strands in $(CuI)_3P_{12}$ that become equivalent in the pure element, it is quite reasonable that the NMR spectra of $(CuI)_3P_{12}$ and of **2** are not as closely related as those of $(CuI)_8P_{12}$ and **1**.

We conclude that copper(I) halides can be used as an synthetic tool,[6] not only for the synthesis of unknown molecules and polymers, but also for the phosphorus polymers $^1_\infty$[P8]P4(4)[and $^1_\infty$[P10]P2[, which can readily be extracted from the adduct compounds. By following this approach, two novel allotropic modifications of this long known element are established. Further investigations dealing with the chemical and physical characterization of these polymers as well as the isolation of the [P12(4)]P2[nanorod are in progress.

Experimental Section

The starting materials $(CuI)_8P_{12}$ and $(CuI)_3P_{12}$ were obtained by treating stoichiometric mixtures of CuI (> 98%, Merck) with red phosphorus (99.999%, Hoechst) as formerly described.[13,16] CuI was purified by recrystallization from aqueous HI prior to use.[6] The purity of the adduct compounds was checked by X-ray powder diffraction (STOE STADI P, Ge monochromator, $Cu_{K\alpha 1}$). Pure $(CuI)_8P_{12}$ or $(CuI)_3P_{12}$ (1 to 5 g) was dissolved in a 1 mol L^{-1} aqueous solution of KCN under an atmosphere of nitrogen. The reaction mixtures were stirred for three days at room temperature. The dark-red/brown residue was isolated by filtration under an inert atmosphere and subsequently dried by washing with aqueous KCN and water. After the products had been dried in a vacuum, a yield of about 99% based on phosphorus was obtained in both cases. By means of chemical analyses the corresponding amounts of copper (nearly 100% in each case) were determined in the aqueous solution. This means the extraction process is quantitative and only traces are lost during the isolation process. The pure and dry phosphorus nanorods are fairly air-stable over a period of several weeks. However, the chemical reactivity of the phosphorus nanorods under discussion has to be elucidated in future experiments. Solid-state NMR spectroscopy measurements were conducted on Bruker DSX-400 and 500 spectrometers equipped with high-speed MASNMR probes. Spectra were recorded with rotor-synchronized spin echoes and relaxation delays ranging from 60 to 300 seconds. $(CuI)_8P_{12}$: ^{31}P NMR (202.44 MHz, 85% H_3PO_4): $\delta = 109.0, 102.8, 92.0, 20.7, 50.4, 21.7, 16.5, 8.0, 3.3$ ppm. $(CuI)_3P_{12}$: ^{31}P NMR (162.05 MHz, 85% H_3PO_4): $\delta = 112.1, 102.8, 99.5, 68.4, 60.4, 52.7, 47.0, 37.1, 20.3, 14.8, 4.4, -5.3$ ppm. **1**: ^{31}P NMR (81.01 MHz, 85% H_3PO_4): $\delta = 101$, 15 ppm. **2**: ^{31}P NMR (162.05 MHz, 85% H_3PO_4): $\delta = 65$ ppm.

A more detailed investigation of different phosphorus polymorphs, especially red phosphorus from different sources, is in progress to provide more detailed structural information and the influence of the preparation techniques on the molecular structure.

For the HRTEM measurements, the powdery materials were suspended in distilled water and small amounts of the suspension were transferred onto a specimen microgrid, which has previously been coated with a thin electron-transparent carbon film. The investigations were carried out on particles protruding over the edge of holes in the carbon film, thus ensuring that no additional phase blur arising from the amorphous film decreased the contrast. The microscope used was a Philips CM 30 equipped with a TWIN objective lens which allows a resolution of 0.23 nm to be achieved. The microscope was operated at 300 kV for the investigations. During the investigations one could observe a slight tendency of the electron beam to induce structure degradation.

Received: April 6, 2004 [Z460244]

Keywords: element modification · nanorods · NMR spectroscopy · phosphorus

[1] For example: D. E. C. Corbridge, *Phosphorus 2000*, Elsevier, Amsterdam, **2000**.
[2] A. Simon, H. Borrmann, J. Horakh, *Chem. Ber.* **1997**, *130*, 1235.
[3] H. Thurn, H. Krebs, *Acta Crystallogr. Sect. B* **1969**, *25*, 125.
[4] R. Hultgren, N. S. Gingrich, B. E. Warren, *J. Chem. Phys.* **1935**, *3*, 351.
[5] S. Böcker, M. Häser, *Z. Anorg. Allg. Chem.* **1995**, *621*, 258.
[6] A. Pfitzner, *Chem. Eur. J.* **2000**, *6*, 1891.
[7] A. Pfitzner, S. Reiser, T. Nilges, *Angew. Chem.* **2000**, *112*, 4328; *Angew. Chem. Int. Ed.* **2000**, *39*, 4160.
[8] S. Reiser, G. Brunklaus, J. H. Hong, J. C. C. Chan, H. Eckert, A. Pfitzner, *Chem. Eur. J.* **2002**, *8*, 4228.
[9] T. Nilges, S. Reiser, A. Pfitzner, *Z. Anorg. Allg. Chem.* **2003**, *629*, 563.
[10] G. Brunklaus, J. C. C. Chan, H. Eckert, S. Reiser, T. Nilges, A. Pfitzner, *Phys. Chem. Chem. Phys.* **2003**, *5*, 3768.
[11] S. Nilges, T. Nilges, H. Haeuseler, A. Pfitzner, *J. Mol. Struc.* **2004**, in press.
[12] M. H. Möller, W. J. Jeitschko, *J. Solid State Chem.* **1986**, *65*, 178.
[13] A. Pfitzner, E. Freudenthaler, *Angew. Chem.* **1995**, *107*, 1784; *Angew. Chem. Int. Ed. Engl.* **1995**, *34*, 1647.
[14] A. Pfitzner, E. Freudenthaler, *Z. Naturforsch. B* **1997**, *52*, 199.
[15] The nomenclature used here was developed by Häser et al., for example [5]. The advantage is that this systematic description of phosphorus molecules enables the user to describe such structures in terms of small fragments or cages, which are combined to form bigger molecular units. In case of the polymers

 © 2004 Wiley-VCH Verlag GmbH & Co. KGaA, Weinheim

1 and **2**, the advantage becomes immediately obvious: both have P_{12} as repeating units. Compound **1** consists of P_8 cages connected by P_4 rings—$^{1}_{\infty}$[P8]P4(4)[—, and **2** exhibits P_{10} cages which are linked by P_2 fragments—$^{1}_{\infty}$[P10]P2[.

[16] E. Freudenthaler, A. Pfitzner, D. C. Sinclair, *Mater. Res. Bull.* **1996**, *31(2)*, 171.

 © 2004 Wiley-VCH Verlag GmbH & Co. KGaA, Weinheim

Coupling Reactions

Zirconium Triflate Catalyzed Direct Coupling Reaction of Lactams with Heterocyclic Arenes under Atmospheric Oxygen

Teruhisa Tsuchimoto, Yoshitaka Ozawa, Ryoju Negoro, Eiji Shirakawa,* and Yusuke Kawakami*

The alkylation of aromatic rings by the Friedel–Crafts reaction has become the focus of extensive research.[1] Alkyl halides or alkenes have been the substrates of choice for Friedel–Crafts reactions, even though a carbon–halide or a carbon–carbon double bond has to be introduced prior to the alkylation. Furthermore, hydrogen halides that cause environmental problems are co-produced in the use of alkyl halides. In contrast, direct use of a C(sp^3)–H bond of alkanes for the alkylation of arenes is apparently useful because intricate introduction of reactive functional groups can be omitted and no accompanying harmful waste is produced. Although Lewis acid mediated or catalyzed dehydrogenative coupling reactions of arenes with alkanes are also known,[2,3] poor regioselectivity with alkanes and turnover numbers (TON) of Lewis acids have so far diminished the advantages of the methodology. Herein we report the first dehydrogenative coupling reaction between lactams and heterocyclic arenes which affords lactams that are arylated exclusively at the carbon atoms adjacent to the nitrogen atom in the presence of $Zr(OTf)_4$ catalyst under atmospheric oxygen.

First, we investigated suitable conditions for direct coupling reaction of 1-methylindole (**1a**: R = Me, Y = H) with 1-methylpyrrolidin-2-one (**2a**) ([Eq. 1], Table 1). Treatment of **1a** (1.0 mmol) and **2a** (2.0 mL, 20.7 mmol) with $Zr(OTf)_4$ (0.5 mol %) at 130 °C for 5 h under O_2 (1 atm) gave a 97:3 mixture of 1-methyl-5-(1-methylindol-3-yl)pyrrolidin-2-one (**3a**) and 1-(1-methylindol-3-ylmethyl)pyrrolidin-2-one (**4a**) in 54 % yield (Table 1, entry 1),[4,5] in which the carbon atoms next to the nitrogen atom in **2a** exclusively form bonds with C3 of **1a**. Notably, the TON of $Zr(OTf)_4$ was 108, which so far is the highest known for the Lewis acid catalyzed arylation of alkanes: to the best of our knowledge, the maximum TON reported is 20.3.[2h] Prolonged reaction time slightly increased the yield (Table 1, entry 2). The TON was improved up to 450 with lower catalyst loading (Table 1, entry 3). Unexpectedly, higher loading of $Zr(OTf)_4$ reduced the yield (Table 1, entry 4). Dilution of oxygen with argon retarded the coupling reaction, whereas the reaction hardly proceeded in the presence of nitrogen (Table 1, entries 5 and 6). Almost no coupling product was formed without oxygen (Table 1, entries 7 and 8). Other metal triflates also catalyzed the reaction albeit less efficiently (Table 1, entries 9–11), whereas the use of metal halides or the absence of a Lewis acid lowered the yield and the selectivity (Table 1, entries 12–14). Although triflic acid (TfOH) also effected the reaction, the TON was, unfortunately, low (Table 1, entries 15 and 16). Thus, use of $Zr(OTf)_4$ as a catalyst under O_2 was found to be important.

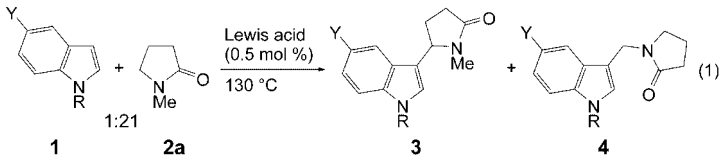


Table 1: Lewis acid catalyzed oxidative coupling reaction of 1-methylindole (R = Me, Y = H) with 1-methylpyrrolidin-2-one.[a]

Entry	Lewis acid	Atmosphere	Conv. [%][b]	Yield [%][b]	**3a**/**4a**[c]	TON
1	$Zr(OTf)_4$	O_2	76	54	97:3	108
2[d]	$Zr(OTf)_4$	O_2	99	58	97:3	116
3	$Zr(OTf)_4$[e]	O_2	64	45	96:4	450
4	$Zr(OTf)_4$[f]	O_2	57	31	97:3	31
5	$Zr(OTf)_4$	Ar/O_2 (4:1)	45	29	98:2	58
6	$Zr(OTf)_4$	air	19	1	99:1	2
7	$Zr(OTf)_4$	Ar	15	<1	–	<1
8	$Zr(OTf)_4$	N_2	16	1	83:17	2
9	$In(OTf)_3$	O_2	63	38	96:4	76
10	$Sc(OTf)_3$	O_2	47	31	96:4	62
11	$Zn(OTf)_2$	O_2	49	27	95:5	54
12	$ZrCl_4$	O_2	48	16	92:8	32
13	$InCl_3$	O_2	36	8	85:15	16
14	none	O_2	53	7	92:8	–
15	TfOH	O_2	14	4	99:1	8
16	TfOH[g]	O_2	39	24	98:2	12

[a] The reaction was carried out at 130 °C for 5 h with **1a** (1.0 mmol) and **2a** (2.00 mL, 20.7 mmol) using a Lewis acid or TfOH (5.0 μmol) under a certain gas atmosphere (1 atm). [b] Determined by GC using chlorobenzene as an internal standard. [c] Determined by GC. [d] The reaction was carried out for 24 h. [e] $Zr(OTf)_4$ (1.0 μmol) was used. [f] $Zr(OTf)_4$ (10.0 μmol) was used. [g] TfOH (20.0 μmol) was used.

[*] Dr. T. Tsuchimoto, Y. Ozawa, R. Negoro, Prof. Dr. E. Shirakawa,[+] Prof. Dr. Y. Kawakami
Graduate School of Materials Science
Japan Advanced Institute of Science and Technology
Asahidai, Tatsunokuchi, Ishikawa 923-1292 (Japan)
Fax: (+81) 761-51-1635
E-mail: tsuchimo@jaist.ac.jp
shirakawa@kuchem.kyoto-u.ac.jp

[+] Present address:
Department of Chemistry, Graduate School of Science
Kyoto University
Sakyo-ku, Kyoto 606-8502 (Japan)
Fax: (+81) 75-753-3988

Supporting information for this article is available on the WWW under http://www.angewandte.org or from the author.

 DOI: 10.1002/anie.200460429 © 2004 Wiley-VCH Verlag GmbH & Co. KGaA, Weinheim

We next investigated the scope of the reaction (Table 2, [Eq. (1–4)]). Substituted 1-methylindoles reacted with **2a** with a similar high regioselectivity (Table 2, entries 1 and 2). A more-electron-rich aryl group contributed to higher yields

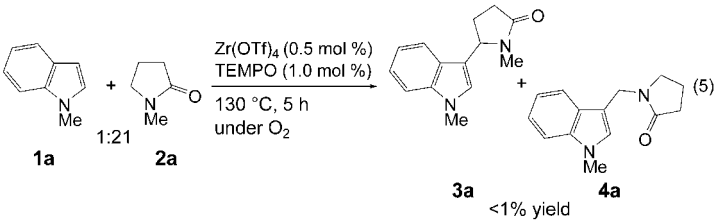
Table 2: $Zr(OTf)_4$-catalyzed oxidative coupling reaction of indole derivatives with 1-methylpyrrolidin-2-one.[a]

Entry	R	Y	*t* [h]	Yield [%][b]	**3**:**4**[c]	TON
1	Me	MeO	10	28	>99:1	56
2	Me	Br	3	30	96:4	60
3	4-$MeOC_6H_4$	H	20	40	93:7	80
4	2-$MeOC_6H_4$	H	50	44	96:4	88
5	Ph	H	80	24	95:5	48
6	4-$EtOCOC_6H_4$	H	120	9	89:11	18
7	H	H	10	21	>99:1	42

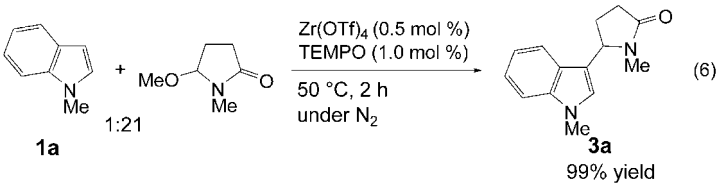
[a] The reaction was carried out at 130 °C with **1** (1.0 mmol) and **2a** (2.00 mL, 20.7 mmol) in the presence of $Zr(OTf)_4$ (5.0 μmol) under atmospheric oxygen (1 atm). [b] Yield of the isolated product based on the indole. [c] Determined by GC.

and selectivities for **3** in the reactions of 1-aryl indoles (Table 2, entries 3–6). In the case of indole, only a single regioisomer **3** was produced (Table 2, entry 7). Indoles with an aminomethyl group at C3 are interesting in view of their biological activity.[6] A pyrrole and a thiophene also coupled oxidatively with **2a** [Eq. (2,3)]. Although 3-methyloxazolidin-2-one reacted also with **1a** exclusively at the carbon atom adjacent to the nitrogen atom but not the oxygen atom [Eq. (4)], an acyclic amide such as *N*,*N*-diethylacetamide unfortunately gave no coupling product under similar conditions.

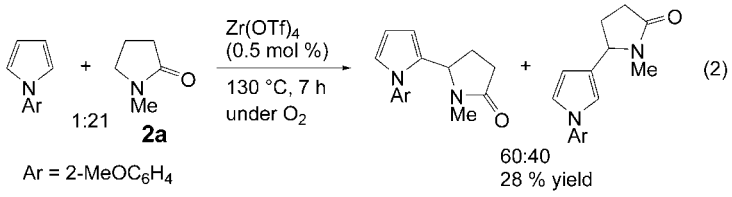
Some evidence is available to allow a discussion of the reaction mechanism. Treatment of **1a** and **2a** with $Zr(OTf)_4$ (0.5 mol %) and 2,2,6,6-tetramethylpiperidine 1-oxyl (TEMPO; 1.0 mol %)[7] gave no coupling product, in contrast to the reaction without TEMPO ([Eq. (5)]; Table 1, entry 1). As $Zr(OTf)_4$ quantitatively catalyzed the reaction of **1a** with 5-methoxy-1-methylpyrrolidin-2-one in the presence of TEMPO [Eq. (6)],[8,9] the inability of $Zr(OTf)_4$ in the oxidative coupling reaction should not be ascribed to repression of its Lewis acidity by TEMPO. Thus, some radical species probably exist in the oxidative coupling reaction. However, the exclusive C3 selectivity of indoles observed in this case implies that the radical species is not concerned directly with the carbon–carbon bond formation because radical species are known to attack C2 of indoles.[10] On the other hand, similar preference for C3 between the oxidative coupling reaction and the reaction of the α-methoxyamide may possibly show that nucleophilic attack of an indole to an *N*-acyliminium cation is involved also in the oxidative coupling reaction.[11] Thus, it may be reasonable to consider that a possible mechanism includes stepwise single electron oxidation to give an *N*-acyliminium cation via a cation radical of **2a**. The result that treatment of **2a** (20.7 mmol) with $Zr(OTf)_4$ (5.0 μmol) at 130 °C for 10 h in the absence of **1a** under O_2 gave 0.42 mmol of an oxidized compound, 1-methylsuccinimide, might support the mechanism that includes the oxidation of **2a**.



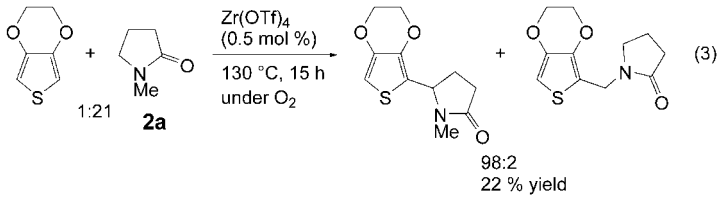
(5)



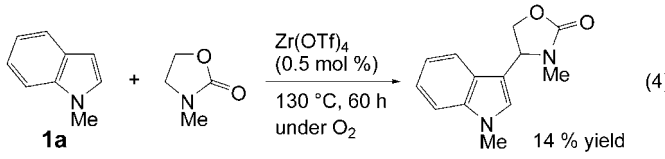
(6)



(2)



(3)



(4)

In summary, we have disclosed the first example of a Lewis acid catalyzed oxidative coupling reaction of lactams with heterocyclic arenes. Zirconium catalyzes the coupling reaction under atmospheric oxygen, scoring the highest TON with quite high regioselectivity. Studies on the improvement of the yield of products and details of the mechanism as well as the application of the reaction to other substrates are in progress.

Experimental Section

General procedure: $Zr(OTf)_4$ (3.4 mg, 5.0 μmol) was placed in a 20-mL Schlenk tube, which was heated at 150 °C in vacuo for 2 h. The tube was cooled to room temperature and filled with oxygen. To this were added successively **2a** (2.00 mL, 20.7 mmol) or 3-methyloxazolidin-2-one (2.00 mL, 23.1 mmol) and a heterocyclic arene (1.0 mmol), and the resulting mixture was stirred at 130 °C. After the time specified in Table 2 and [Eq. (2–4)], the mixture was diluted with diethyl ether (100 mL) and washed successively with water (3 × 10 mL), saturated aqueous $NaHCO_3$ (5 mL), and brine (5 mL), and

 © 2004 Wiley-VCH Verlag GmbH & Co. KGaA, Weinheim

then dried over anhydrous magnesium sulfate. Filtration through a pad of celite and evaporation of the solvent followed by column chromatography on silica gel gave the corresponding coupling products as a mixture of isomers. Further isolation was performed with preparative recycling column chromatography on silica gel.

Received: April 23, 2004 [Z460429]

Keywords: C–C coupling · heteroarenes · lactams · Lewis acids · zirconium

[1] For reviews, see: a) G. A. Olah in *Friedel–Crafts and Related Reactions*, Wiley-Interscience, New York, **1964**; b) G. A. Olah, R. Krishshnamurit, G. K. S. Prakash in *Comprehensive Organic Synthesis*, *Vol. 3* (Eds.: B. M. Trost, I. Fleming, G. Pattenden), Pergamon, Oxford, **1991**, chap. 1.8, pp. 293–339; c) M. Bandini, A. Melloni, A. Umani-Ronchi, *Angew. Chem.* **2004**, *116*, 560–566; *Angew. Chem. Int. Ed.* **2004**, *43*, 550–556.

[2] a) L. Schmerling, J. A. Vesely, *J. Org. Chem.* **1973**, *38*, 312–315; b) G. A. Olah, P. Schilling, J. S. Staral, Y. Halpern, J. A. Olah, *J. Am. Chem. Soc.* **1975**, *97*, 6807–6810; c) R. Miethchen, C.-F. Kröger, *Z. Chem.* **1975**, *15*, 135–141; d) R. Miethchen, A. Gärtner, U. Roth, K. Miechert, C. F. Kröger, *J. Prakt. Chem.* **1977**, *319*, 383–390; e) R. Miethchen, S. Steege, C.-F. Kröger, *J. Prakt. Chem.* **1983**, *325*, 823–834; f) S. Chalais, A. Cornélis, A. Gerstmans, W. Kolodziejski, P. Laszlo, A. Mathy, P. Métra, *Helv. Chim. Acta* **1985**, *68*, 1196–1203; g) F. Yonehara, Y. Kido, S. Morita, M. Yamaguchi, *J. Am. Chem. Soc.* **2001**, *123*, 11310–11311; h) F. Yonehara, Y. Kido, H. Sugimoto, S. Morita, M. Yamaguchi, *J. Org. Chem.* **2003**, *68*, 6752–6759.

[3] Late transition metals such as Pd, Ru, and Rh are known to catalyze the dehydrogenative coupling reaction between two $C(sp^2)$–H bonds effectively; for reviews, see: a) C. Jia, T. Kitamura, Y. Fujiwara, *Acc. Chem. Res.* **2001**, *34*, 633–639; b) V. Ritleng, C. Sinlin, M. Pfeffer, *Chem. Rev.* **2002**, *102*, 1731–1770; c) F. Kakiuchi, N. Chatani, *Adv. Synth. Catal.* **2003**, *345*, 1077–1101.

[4] All new compounds were characterized by ^1H and ^{13}C NMR spectroscopy and HRMS. For details, see supporting information.

[5] By-products based on **1a** were detected by GC–MS analysis as 1-methylisatin (1-methylindole-2,3-dione), a dimer of **1a**, and a trimer of **1a** that bears a carbonyl function.

[6] a) R. J. Sundberg in *Comprehensive Heterocyclic Chemistry II*, *Vol. 2* (Eds.: A. R. Katritzky, C. W. Rees, E. F. V. Scriven, C. W. Bird), Pergamon, Oxford, **1996**, chap. 2.03, pp. 119–206; b) G. W. Gribble in *Comprehensive Heterocyclic Chemistry II*, *Vol. 2* (Eds.: A. R. Katritzky, C. W. Rees, E. F. V. Scriven, C. W. Bird), Pergamon, Oxford, **1996**, chap. 2.04, pp. 207–258.

[7] TEMPO has been reportedly used as a radical scavenger; for example, see: a) I. Pallagi, A. Toró, G. Horváth, *J. Org. Chem.* **1999**, *64*, 6530–6540; b) S. Mikami, K. Fujita, T. Nakamura, H. Yorimitsu, H. Shinokubo, S. Matsubara, K. Oshima, *Org. Lett.* **2001**, *3*, 1853–1855.

[8] It is well known that treatment of α-methoxyamides with Lewis acids generates cations stabilized by the lone pair of the nitrogen atom, *N*-acyliminium cations, to react with various nucleophiles: H. Hiemstra, W. N. Speckamp in *Comprehensive Organic Synthesis*, *Vol. 2* (Eds.: B. M. Trost, I. Fleming, C. H. Heathcock), Pergamon Press, Oxford, **1991**, chap. 4.5, pp. 1047–1082.

[9] C. Kleber, Z. Andeade, R. A. F. Matos, *Synlett* **2003**, 1189–1191.

[10] a) E. Baciocchi, E. Muraglia, G. Sleiter, *J. Org. Chem.* **1992**, *57*, 6817–6820; b) D. R. Artis, I.-S. Cho, S. Jaime-Figueroa, J. M. Muchowski, *J. Org. Chem.* **1994**, *59*, 2456–2466; c) J. H. Byers, J. E. Campbell, F. H. Knapp, J. G. Thissell, *Tetrahedron Lett.* **1999**, *40*, 2677–2680; d) Y. M. Osornio, R. Cruz-Almanza, V. Jiménez-Montaño, L. D. Miranda, *Chem. Commun.* **2003**, 2316–2317.

[11] Electrophilic substitution of indoles is well known to take place at C3: J. A. Joule, K. Mills in *Heterocyclic Chemistry*, Blackwell Science, Oxford, **2000**, pp. 324–379.

 © 2004 Wiley-VCH Verlag GmbH & Co. KGaA, Weinheim

Cover Picture



K. C. Nicolaou,* Stepan Vyskocil, Theocharis V. Koftis, Yoichi M. A. Yamada, Taotao Ling, David Y.-K. Chen, Wenjun Tang, Goran Petrovic, Michael O. Frederick, Yiwei Li, and Masayuki Satake*

The mussel toxin azaspiracid-1, which was isolated from *Mytilus edulis*, has baffled chemists for quite some time, as the originally proposed structure was incorrect. In their Communications on pages 4312 ff. and 4318 ff., Nicolaou and co-workers describe how they determined the structure and absolute configuration of the molecule through degradation studies and total synthesis. The synthesis should render this valuable, but scarce, substance available for much-needed biotoxin assays and biological investigations.

Contents

Angewandte EarlyView

The following Communications are available online (in Wiley InterScience). You can find them, as well as forthcoming Reviews, Highlights, and Essays, at www.angewandte.org, under Early View.

C. Ochsenfeld, J. Kussmann, F. Koziol:*
Ab Initio NMR Spectra for Molecular Systems with One Thousand and More Atoms: A Linear-Scaling Method
DOI: 10.1002/anie.200460336
Published online: August 11, 2004

C. Yang, L.-M. Fu, Y. Wang, J.-P. Zhang,* W.-T. Wong,* X.-C. Ai, Y.-F. Qiao, B.-S. Zou, L.-L. Gui:*
A Highly Luminescent Europium Complex Showing Visible-Light-Sensitized Red Emission: Direct Observation of the Singlet Pathway
DOI: 10.1002/anie.200454141
Published online: July 14, 2004

N. Giuseppone, J.-L. Schmitt, J.-M. Lehn:*
Generation of Dynamic Constitutional Diversity and Driven Evolution in Helical Molecular Strands under Lewis Acid Catalyzed Component Exchange
DOI: 10.1002/anie.200460343
Published online: July 14, 2004

Articles judged by the referees or the editor as being either very important or very urgent are immediately edited, proof-read, and electronically published once the manuscript has arrived in the editorial office in its final form. As long as there is no page number available these articles should be cited in the following manner:

Author(s), *Angew. Chem. Int. Ed.*, online publication date, DOI.

News

J. F. Hartwig Receives Thieme–IUPAC Prize — **4250**

Honorary Doctorate to H. Ringsdorf — **4250**

Nagoya Medal to J. F. Stoddart — **4250**

Books

Host–Guest Systems Based on Nanoporous Crystals — **4251**
Franco Laeri, Ferdi Schüth, Ulrich Simon, Michael Wark
reviewed by K. S. W. Sing

Chiral Separations—Methods and Protocols — **4252**
Gerald Gübitz, Martin G. Schmid
reviewed by U. J. Meierhenrich

Essays

Paul Ehrlich

F. Stern* — **4254 – 4261**

Paul Ehrlich: The Founder of Chemotherapy



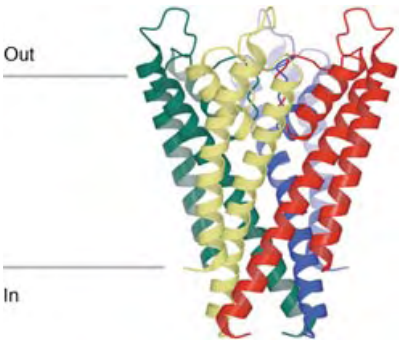
150 years of Ehrlich: He was the founder of chemotherapy and established the basis for modern immunology. This year sees the 150th anniversary of Paul Ehrlich's birth. Prize-winning writer Fritz Stern sketches a portrait of a man born into a world of progress, a brilliant researcher, who through his achievements, became a target for hostility.

Reviews

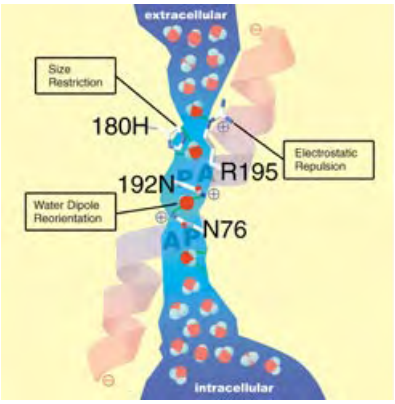
Ion Channels

R. MacKinnon* — **4265 – 4277**

Potassium Channels and the Atomic Basis of Selective Ion Conduction (Nobel Lecture)



Closing in on the facts: The key to understanding the transport of K^+ ions through the cell membrane lay in the structure elucidation of a K^+ ion channel (see picture). The studies of Roderick MacKinnon and co-workers have contributed significantly to the understanding of this research area. In his Nobel Lecture, he describes the structural characteristics of K^+ ion channels as well as a possible mechanism for ion conduction.



Water is the most important component of all organisms and is the basis of all life. That water can pass through cell membranes has long been known—but how is the selective transport of water molecules achieved without concommitent diffusion of H_3O^+ ions? Peter Agre received the 2003 Nobel Prize in Chemistry for the discovery and investigation of the membrane proteins responsible, namely, the aquaproteins.

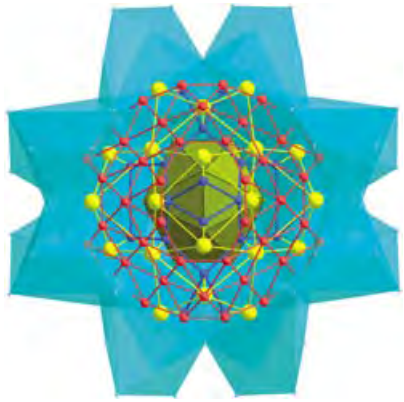
Membrane Proteins

P. Agre* _____ **4278 – 4290**

Aquaporin Water Channels (Nobel Lecture)

Communications

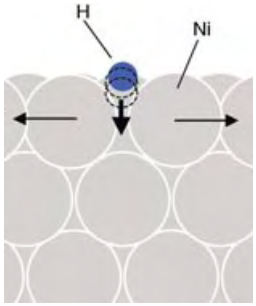
The peeling of an onion: Embedded in the voids of an infinite cationic $[Te_{32}Ni_{30}X_3O_{90}]^{5+}$ network lies an icosahedral $[Ni_4X_{13}]^{5-}$ anionic guest cluster (ochre). It may be considered wrapped and trapped in a successive series of concentric skins made from the lone pairs of Te atoms (blue), the Te (yellow), O (red), and Ni atoms (light blue polyhedra). But are there any other guests?



Host–Guest Systems

M. Johnsson,* S. Lidin, K. W. Törnroos, H.-B. Bürgi, P. Millet _____ **4292 – 4295**

Host–Guest Compounds in the Family of Tellurium–Nickel Oxohalogenides



Expansive surface strain facilitates the formation of subsurface heteroatoms in transition metals. Density functional calculations show that subsurface hydrogen atoms form more rapidly, as depicted schematically in the picture, and are thermodynamically stable at much lower pressures and higher temperatures in stretched (as opposed to unstretched) nickel surfaces.

Surface Chemistry

J. Greeley, W. P. Krekelberg, M. Mavrikakis* _____ **4296 – 4300**

Strain-Induced Formation of Subsurface Species in Transition Metals

For the USA and Canada:
ANGEWANDTE CHEMIE International Edition (ISSN 1433-7851) is published weekly by Wiley-VCH PO Box 191161, D 69451 Weinheim, Germany. Air freight and mailing in the USA by Publications Expediting Inc. 200 Meacham Ave., Elmont, NY 11003. Periodicals postage paid at Jamaica NY 11431. US POSTMASTER: send address changes to *Angewandte Chemie*, Wiley-VCH, 111 River Street, Hoboken, NJ 07030. Annual subscription price for institutions: Europe € 3430.00/3118.00; outside Europe US$ 4499.00/4090.00 (valid for print and electronic/print or electronic delivery); for individuals who are personal members of a national chemical society, or whose institution already subscribes, or who are retired or self-employed consultants, print only: Europe € 248.00/outside Europe US$ 378.00. Postage and handling charges included. All Wiley-VCH prices are exclusive VAT.

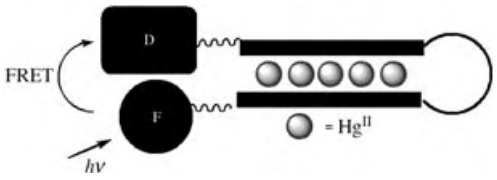
 © 2004 Wiley-VCH Verlag GmbH & Co. KGaA, Weinheim

Contents

Molecular Sensors

A. Ono,* H. Togashi ——— **4300 – 4302**

Highly Selective Oligonucleotide-Based Sensor for Mercury(II) in Aqueous Solutions

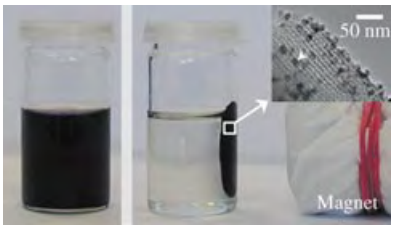


Mercury gauge: An oligodeoxyribonucleotide(ODN)-based sensor, which carries energy-donor and -acceptor moieties (fluorescein, F, and dabcyl, D, respectively), selectively detects Hg^{II} ions in aqueous solution. Upon binding Hg^{II} ions, the ODN takes on a hairpin structure (see picture); this results in a decrease in the fluorescence emission through enhanced FRET (fluorescence resonance energy transfer) from F to D.

Magnetic Carbon

A.-H. Lu, W. Schmidt, N. Matoussevitch, H. Bönnemann, B. Spliethoff, B. Tesche, E. Bill, W. Kiefer, F. Schüth* **4303 – 4306**

Nanoengineering of a Magnetically Separable Hydrogenation Catalyst

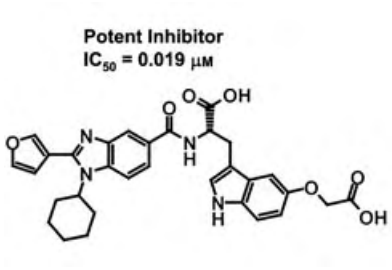


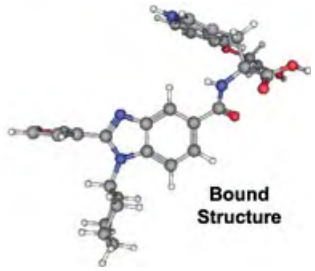
Magnetic, highly porous ordered carbon of the CMK-3 and CMK-5 type and with pure carbon or carbon–nitrogen framework were nanoengineered by a sequence of bulk manipulation steps. The materials can be used as efficient magnetic adsorbents (see picture) or catalysts, but applications going far beyond these can be envisaged.

Drug Design

S. R. LaPlante,* A. Jakalian, N. Aubry, Y. Bousquet, J.-M. Ferland, J. Gillard, S. Lefebvre, M. Poirier, Y. S. Tsantrizos, G. Kukolj, P. L. Beaulieu ——— **4306 – 4311**

Binding Mode Determination of Benzimidazole Inhibitors of the Hepatitis C Virus RNA Polymerase by a Structure and Dynamics Strategy





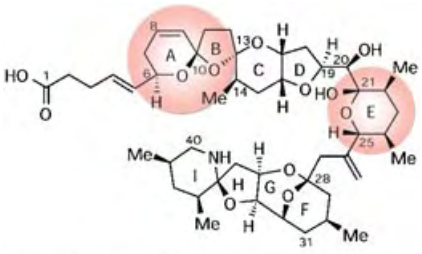
A novel strategy involving NMR, medicinal chemistry, and molecular modeling is described for determining the binding mode of ligands and the binding roles of their substituents. The first solution structure of an inhibitor bound to hepatitis C virus (HCV) polymerase (see picture) provides practical information for the rational design of potential therapeutics against HCV infections.

Natural Products Synthesis

K. C. Nicolaou,* S. Vyskocil, T. V. Koftis, Y. M. A. Yamada, T. Ling, D. Y.-K. Chen, W. Tang, G. Petrovic, M. O. Frederick, Y. Li, M. Satake* ——— **4312 – 4318**

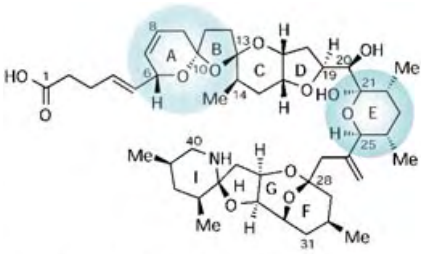
Structural Revision and Total Synthesis of Azaspiracid-1, Part 1: Intelligence Gathering and Tentative Proposal

Phantom molecules from Nature: Degradation studies of azaspiracid-1 (see originally proposed, incorrect structure), the notorious marine neurotoxin isolated from contaminated mussels, revealed that the double bond of ring A was located at C7–C8 and not at C8–C9 and also provided further information on the overall stereochemistry of the molecule.



Azaspiracid-1: originally proposed structure

 © 2004 Wiley-VCH Verlag GmbH & Co. KGaA, Weinheim



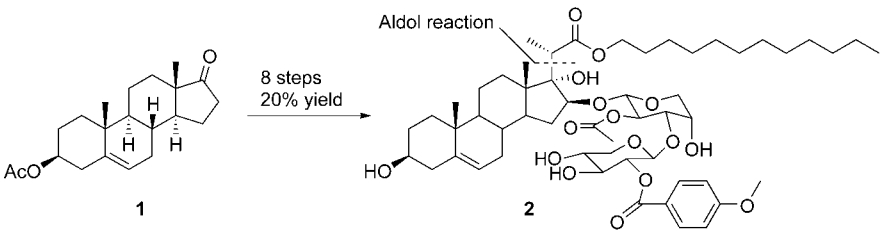
Azaspiracid-1: revised structure confirmed by total synthesis

The chase for the structure of azaspiracid-1 has ended with a revised structure (see picture). The total synthesis of this challenging target has closed another chapter in this intriguing chemical detective story and allowed the assignment of the relative and absolute configuration of the molecule.

Natural Products Synthesis

K. C. Nicolaou,* T. V. Koftis, S. Vyskocil, G. Petrovic, T. Ling, Y. M. A. Yamada, W. Tang, M. O. Frederick — **4318 – 4324**

Structural Revision and Total Synthesis of Azaspiracid-1, Part 2: Definition of the ABCD Domain and Total Synthesis

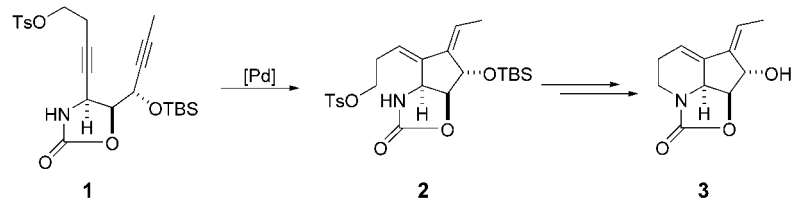


An aldol condensation is the key to the eight-step linear synthesis of 23-oxa analogues of OSW-1 (e.g. **2**) in more than 20% overall yield from the industrially produced steroid **1**. Compound **2** is up to 2000 times more potent than cisplatin as an inhibitor of tumor cell growth.

Medicinal Chemistry

B. Shi, H. Wu, B. Yu,* J. Wu **4324 – 4327**

23-Oxa-Analogues of OSW-1: Efficient Synthesis and Extremely Potent Antitumor Activity



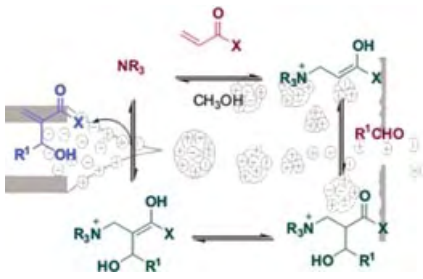
(+)-Streptazolin synthesis revisited: The key reaction in the 11-step total synthesis of (+)-streptazolin (**3**), which starts from D-mannitol diacetonide, is the palladium-catalyzed reductive cyclization of two alkyne arms in **1** to provide the desired 1,3-diene **2** with the correct defined geometry. TBS = *tert*-butyldimethylsilyl.

Natural Products Synthesis

B. M. Trost,* C. K. Chung, A. B. Pinkerton — **4327 – 4329**

Stereocontrolled Total Synthesis of (+)-Streptazolin by a Palladium-Catalyzed Reductive Diyne Cyclization

"Ion fishing": Protonated intermediates in the catalytic cycle of the Baylis–Hillman reaction between an activated alkene and an electrophile have been intercepted and characterized by electrospray ionization tandem mass spectrometry. This approach provides direct evidence for the currently accepted mechanism (see scheme).



Reaction Mechanisms

L. S. Santos, C. H. Pavam, W. P. Almeida, F. Coelho,* M. N. Eberlin* **4330 – 4333**

Probing the Mechanism of the Baylis–Hillman Reaction by Electrospray Ionization Mass and Tandem Mass Spectrometry

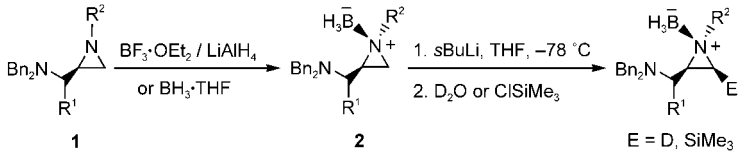
 © 2004 Wiley-VCH Verlag GmbH & Co. KGaA, Weinheim

Contents

Enantioselective Reactions

J. M. Concellón,* J. R. Suárez, S. García-Granda, M. R. Díaz ——— **4333 – 4336**

Synthesis and Stereoselective Lithiation of Enantiopure 2-(1-Aminoalkyl)aziridine–Borane Complexes

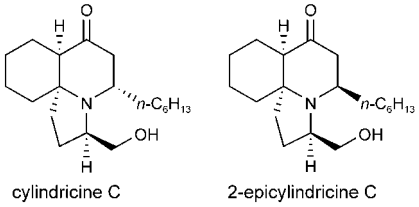


Two alternative methodologies can be used to obtain enantiopure aziridine–borane complexes **2**: successive treatment of 2-(1-aminoalkyl)aziridines **1** with $BF_3{\cdot}Et_2O$ and $LiAlH_4$ or by direct reaction with $BH_3{\cdot}THF$ (see scheme, Bn = benzyl). The complexes **2** can be deuterated or silylated highly stereoselectively at C3 by reaction with *s*BuLi and subsequent treatment with D_2O or $ClSiMe_3$, respectively.

Natural Products Synthesis

S. Canesi, D. Bouchu, M. A. Ciufolini* ——— **4336 – 4338**

Fully Stereocontrolled Total Syntheses of (−)-Cylindricine C and (−)-2-Epicylindricine C: A Departure in Sulfonamide Chemistry



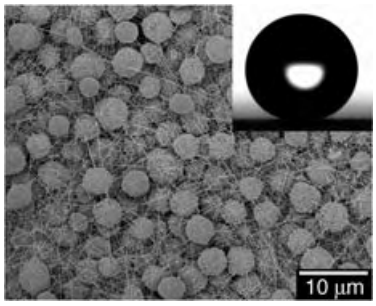
A common intermediate was used in the total syntheses of (−)-cylindricine C and (−)-2-epicylindricine C (see picture) in a process that involves the initial oxidative spirocyclization of a phenolic sulfonamide. The remainder of the molecules is constructed through interesting sulfonamide chemistry.

Superhydrophobic Surface

Y. Zhao, J. Zhai, L. Jiang* — **4338 – 4341**

A Lotus-Leaf-like Superhydrophobic Surface: A Porous Microsphere/Nanofiber Composite Film Prepared by Electrohydrodynamics

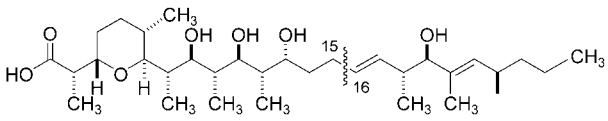
A hierarchical micro/nanostructure and low surface energy result in superhydrophobicity in a polystyrene film prepared by the electrohydrodynamics method. The composite film consists of porous microspheres, which contribute to superhydrophobicity by increasing the surface roughness, and interwoven nanofibers, which reinforce the film (see the SEM image). A water droplet resides on the film with a contact angle of about 160° (see inset).



Natural Products Synthesis

K. Komatsu, K. Tanino, M. Miyashita* ——— **4341 – 4345**

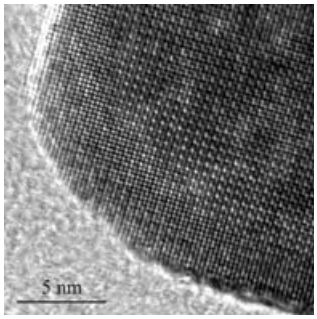
Stereoselective Total Synthesis of the Ionophore Antibiotic Zincophorin



zincophorin (**1**)

Acyclic stereocontrol is the basis of an original strategy adopted for the first, highly stereoselective total synthesis of the free acid zincophorin (**1**), a unique ionophore antibiotic. The stereoselective synthesis of the trisubstituted tetrahydropyran moiety and the construction of the eight contiguous stereogenic centers were key challenges in the synthesis.

 © 2004 Wiley-VCH Verlag GmbH & Co. KGaA, Weinheim



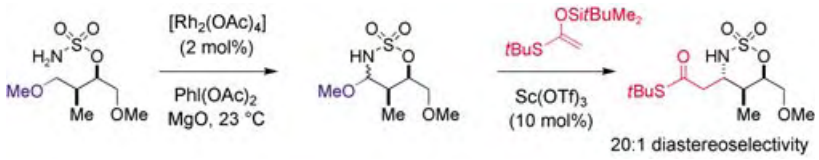
Superior crystallinity and good yields are found for SnO_2 and In_2O_3 (see HRTEM image) semi-conducting metal oxide nanocrystals prepared by a non-aqueous approach involving the reaction of a metal alkoxide with benzyl alcohol. The sensor devices fabricated just by deposition of the as-synthesized nanoparticles showed the high sensitivity and good recovery time required for technological applications.

Gas Sensors

N. Pinna,* G. Neri, M. Antonietti, M. Niederberger* ——— 4345 – 4349

Nonaqueous Synthesis of Nanocrystalline Semiconducting Metal Oxides for Gas Sensing

---



Intramolecular C–H insertion with sulfamates catalyzed by rhodium complexes offers an effective method for the preparation of N,O-acetals, which function as iminium ion precursors and undergo smooth diastereoselective coupling with nucleophiles under Lewis acidic conditions (see scheme). These findings advance the versatility of catalytic C–H amination for the assembly of structurally complex nitrogen-containing products. Tf = trifluoromethanesulfonyl.

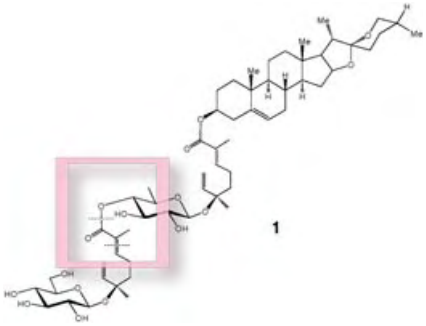
N,O-Acetals

K. Williams Fiori, J. J. Fleming, J. Du Bois* ——— 4349 – 4352

Rh-Catalyzed Amination of Ethereal C^{α}–H Bonds: A Versatile Strategy for the Synthesis of Complex Amines

---

A bottleneck in the synthesis of the model compound **1**, which bears a dimeric terpenoyl glycoside side chain from cytotoxic saponins, was overcome by the stepwise construction of the terpene part by regioselective acylation of the sugar with a functionalized phosphonate followed by a Horner–Wadsworth–Emmons olefination.

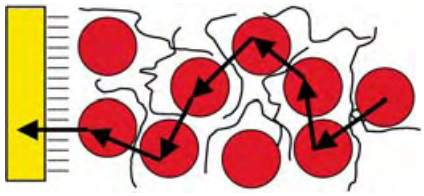


Glycoside Synthesis

S. Reicheneder, C. Unverzagt* ——— 4353 – 4357

Synthesis of Dimeric Terpenoyl Glycoside Side Chains from Cytotoxic Saponins

---



Strata pack: Electroactive cytochrome *c* multilayer assemblies were constructed within a polyelectrolyte network on a gold electrode. Up to 15 layers were electroactive, with a linear increase in redoxactive protein per layer. Evidence for a protein–protein electron transfer through the assembly was found (pathway marked by arrows in the picture).

Multilayer Electrodes

M. K. Beissenhirtz, F. W. Scheller, W. F. M. Stöcklein, D. G. Kurth, H. Möhwald, F. Lisdat* ——— 4357 – 4360

Electroactive Cytochrome *c* Multilayers within a Polyelectrolyte Assembly

 © 2004 Wiley-VCH Verlag GmbH & Co. KGaA, Weinheim

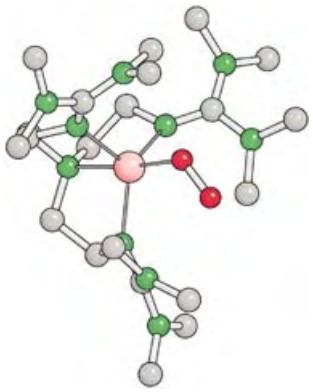
Contents

Dioxygen Complexes

M. Schatz, V. Raab, S. P. Foxon, G. Brehm, S. Schneider, M. Reiher, M. C. Holthausen,* J. Sundermeyer,* S. Schindler* _____ **4360 – 4363**

Combined Spectroscopic and Theoretical Evidence for a Persistent End-On Copper Superoxo Complex

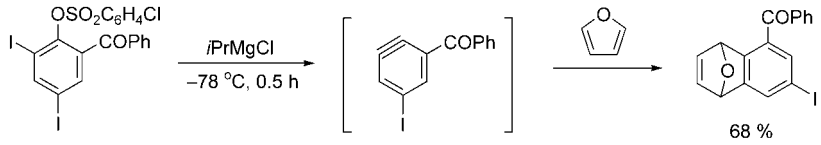
A tale of two modes: An end-on copper superoxo complex was identified in a combined experimental and theoretical study. Theory clearly discloses the presence of an end-on complex (see picture, O red, Cu pink, N green) with a minute isotopic resonance Raman splitting below experimental resolution. The results cast doubts on the uncritical use of $^{16}O,^{18}O$ isotopic-labeling Raman experiments to discriminate end-on from side-on bonding modes in $M(O_2)$ complexes.



Functionalized Arynes

I. Sapountzis, W. Lin, M. Fischer, P. Knochel* _____ **4364 – 4366**

Preparation of Polyfunctional Arynes via 2-Magnesiated Diaryl Sulfonates



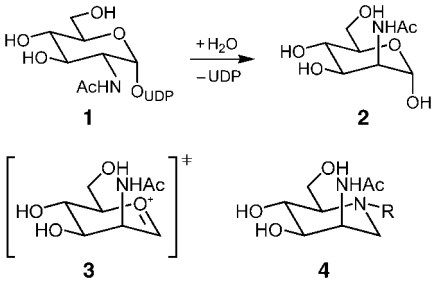
The synthetic potential of arynes can be exploited through a new method for their generation from functionalized aryl magnesium reagents and controlled reaction. Arynes with functional groups such as ester, nitrile, ketone, or nitro groups, or with a quinolyl skeleton, can be formed from polyfunctionalized 2-iodo aryl 4-chlorobenezenesulfonates and trapped in 68–93% yield with furan (see scheme).

Sialic Acids

S. Al-Rawi, S. Hinderlich,* W. Reutter, A. Giannis* _____ **4366 – 4370**

Synthesis and Biochemical Properties of Reversible Inhibitors of UDP-*N*-Acetylglucosamine 2-Epimerase

Sialic acids have important biochemical functions in healthy organisms, for example, in embryogenesis, as well as in the spread of diseases like influenza. A key step in the biosynthesis of the sialic acid *N*-acetylneuraminic acid is the epimerization of **1** to give **2** (see scheme, UDP = uridine diphosphate). Transition-state analogues (e.g. **4**) of this enzyme-catalyzed reaction were made and tested for their inhibitory action.



VIP Communications labeled with this symbol have been judged by two referees as being "very important papers".

Sources

Product and Company Directory

You can start the entry for your company in "Sources" in any issue of *Angewandte Chemie*.

If you would like more information, please do not hesitate to contact us.

Wiley-VCH Verlag – Advertising Department
Tel.: 0 62 01 - 60 65 65
Fax: 0 62 01 - 60 65 50
E-Mail: MSchulz@wiley-vch.de

Service

Keywords _____ *4372*

Authors _____ *4373*

Angewandte's Sister Journals _____ *4374 – 4375*

Sources _____ *A51*

Preview _____ *4377*



J. F. Hartwig Receives Thieme–IUPAC Prize

John F. Hartwig is the recipient of the 2004 Thieme–IUPAC Prize for his outstanding achievements in the field of organic synthesis. The prize, awarded during the ICOS-15 conference in Nagoya (Japan), is reserved for chemists under the age of 40. The prize recognizes Hartwig's contributions towards the development of palladium-catalyzed transformations of aryl halides into aryl amines. This methodology, which was the subject of his Review in *Angewandte Chemie* in 1998,[1] is of considerable importance for the synthesis of pharmacologically active compounds. He also developed a method for the catalytic α arylation of carbonyl compounds.



J. F. Hartwig

Hartwig studied in Princeton (USA) and completed his PhD at the University of California, Berkeley under the supervision of R. G. Bergman and R. A. Andersen. He then worked as a fellow of the American Cancer Society with S. J. Lippard at the Massachusetts Institute of Technology (USA). In 1992 he moved to Yale University (USA), where he is now professor of chemistry. His research focuses on the development of new transition-metal-catalyzed reactions and the elucidation of their mechanisms. Two Communications on iridium-catalyzed etherification and allylation reactions are due to appear soon in *Angewandte Chemie*.

Photo: M. Marsdale (Yale Univ.)

Honorary Doctorate to H. Ringsdorf

French universities have awarded honorary doctorates since 1918 to foreign individuals for eminent services rendered to science, literature, or art, France, or the awarding university. Helmut Ringsdorf (Universität Mainz, Germany) received this distinction from the Université Louis Pasteur in Strasbourg in June. He was honored for his scientific work, as well as for his interaction with French research establishments and dedication to his role (since 1998) as a foreign member of the national scientific advisory board to the French Ministry of Education and Research. Ringsdorf has also received honorary doctorates from the Université Paris-Sud, Trinity College Dublin (Ireland), and the ETH Zürich (Switzerland).



H. Ringsdorf

Ringsdorf studied chemistry in Frankfurt, Darmstadt, and Freiburg (Germany), where he completed his PhD in 1958 as the last student of the Nobel laureate in chemistry Hermann Staudinger.[2] He undertook postdoctoral research with C. G. Overberger and H. F. Mark at Brooklyn Polytechnic Institute (USA), then completed his habilitation at the Universität Marburg (Germany), and accepted a position at the Institut für Organische Chemie at the Universität Mainz (Germany) in 1971. Since his "retirement" in 1994 he has spent time as a guest professor in Jilin (China), Los Angeles (USA), London (UK), and Cardiff (UK). Ringsdorf is recognized as one of the pioneers of research in the fields of polymers, functional supramolecular systems, and liquid crystals (the synthesis of a mesogen in the form of the coat of arms of the city of Mainz was featured on the cover of issue 12/1987 of *Angewandte Chemie*). Biomembranes played a fundamental role in his research.[3] Many of his numerous and widely cited publications contain caricatures in the reference section.

Nagoya Medal to J. F. Stoddart

The Nagoya Medal (Gold) has been presented annually since 1995 for outstanding achievements in organic chemistry. This year J. Fraser Stoddart is the recipient, with the award presentation taking place during the IUPAC ICOS-15 conference. His award lecture is entitled "The Nature of the Mechanical Bond". A focal point of his research is molecular machines based on switchable catenanes and rotaxanes, which are synthesized by his research groups by covalent, supramolecular, and noncovalent methods. His research is also centered on the connection of molecular machines with the macroscopic world through self-organization.[4]



J. F. Stoddart

Stoddart studied chemistry in Edinburgh (UK) and completed his PhD there in 1966. After a postdoctoral period at Queen's University in Kingston (Canada) he moved to the University of Sheffield (UK) in 1970 and became a professor at Birmingham University (UK) in 1990. He succeeded Donald J. Cram in 1997 at the University of California, Los Angeles. Stoddart has been a member of the international advisory board of *Angewandte Chemie* since 1995.

[1] J. F. Hartwig, *Angew. Chem.* **1998**, *110*, 2154; *Angew. Chem. Int. Ed.* **1998**, *37*, 2046.

[2] a) R. Mülhaupt, *Angew. Chem.* **2004**, *116*, 1072; *Angew. Chem. Int. Ed.* **2004**, *43*, 1054; b) H. Ringsdorf, *Angew. Chem.* **2004**, *116*, 1082; *Angew. Chem.* **2004**, *43*, 1064.

[3] a) H. Ringsdorf, B. Schlarb, J. Venzmer, *Angew. Chem.* **1988**, *100*, 117; *Angew. Chem. Int. Ed. Engl.* **1988**, *27*, 113; b) M. Ahlers, W. Müller, A. Reichert, H. Ringsdorf, J. Venzmer, *Angew. Chem.* **1990**, 102, 1310; *Angew. Chem. Int. Ed. Engl.* **1990**, *29*, 1269.

[4] a) V. Balzani, A. Credi, F. M. Raymo, J. F. Stoddart, *Angew. Chem.* **2000**, *112*, 3484; *Angew. Chem. Int. Ed.* **2000**, *39*, 3348; b) S. J. Rowan, S. J. Cantrill, G. R. L. Cousins, J. K. M. Sanders, J. F. Stoddart, *Angew. Chem.* **2002**, *114*, 938; *Angew. Chem. Int. Ed.* **2002**, *41*, 898.

 © 2004 Wiley-VCH Verlag GmbH & Co. KGaA, Weinheim DOI: 10.1002/anie.200461423

Paul Ehrlich

Paul Ehrlich: The Founder of Chemotherapy**,+

*Fritz Stern**

Keywords:
Ehrlich, Paul · history of science · immunology

> *"A natural scientist must be at once a general and a spy."*
> Richard Willstätter, 1913[1]

I am a historian with but a limited knowledge of the natural sciences. Still, I have been trying to understand certain aspects of the history of science in the decades preceding and following the First World War, chancing into this area as a result of my research on Fritz Haber and Albert Einstein, their circle of friends, and the political–scientific ambience they worked in. I was fascinated by these figures, and especially intrigued by their devotion to a science that then still seemed to be innocent, untainted. One could sense the passion that inspired their great accomplishments. What, we may ask, were the prerequisites for their commitment and success? What was the scientific ethos of the era? What factors lay behind that burst of creativity which propelled German scientists to such prodigious and pioneering achievements?

The life of an individual scientist, such as Paul Ehrlich, may help to shed light on the wellsprings of scientific progress. He was both genius and a representative figure. Though he was totally centered on and committed to his research, with little interest in the world about him, that world—and his friends and rivals—helped to shape his life. His biography shows how external factors both impeded and facilitated his creativity. Perhaps there is a certain gap in our understanding of these interrelations: literature in the natural sciences often neglects the human–historical dimension, while historians until recently have paid too little attention to the sociopolitical importance of natural scientists.

I realize that the historical guild may view my fascination with the human side of natural scientists as old-fashioned at best. The great physiologist Hermann von Helmholtz once spoke about the "inner psychological history" of science; even Einstein stressed the "reciprocity between scientific accomplishment and greatness of character." Though one can be intrigued by that "inner" history, one must not lose sight of the close connections in earlier eras between scientists and the intellectual, political, and economic world.

Sheer energy and fortitude, disciplined intuition and stamina, appear to be determinative in the life of the scientist, despite the dangers and disappointments they experience. And in Germany during the early years of the twentieth century, there were geniuses of research. The word "genius" in German has a special overtone, even a tinge of the demonic, a mysterious power and energy; a genius—whether artist or scientist—is considered to have a special vulnerability, a precariousness, a life of constant risk and often close to troubled turmoil. It was precisely in the same era that Thomas Mann embarked on his lifelong preoccupation with and analysis of the vulnerability of the artist. Artists and great scientists have a certain affinity. Someone observed that although Ehrlich "never created works of art in the strict sense, he had qualities closely akin to those of the artist." There are also many differences: the artist is commonly an isolate, living in a kind of permanent jeopardy; the scientist, by contrast, usually has an institutional home, a cluster of collegiality and even friendship that makes bearable the inevitable frictions and occasional meanspiritedness of colleagues. Ehrlich had his full taste of the good and the bad—the latter perhaps more clearly discernible in the private correspondence.

In writings by and about Ehrlich, certain words recur: "genius", "leader", "warrior-hero". This is also true of Rudolf Virchow, Louis Pasteur, Robert Koch, and many others. It was how they were characterized, and it was the tone of public praise. Theirs was a historical moment in which often heroic individual researchers, putting their very lives at risk, forged a new world. Ehrlich's generation stood on the threshold of what the theologian Adolf Harnack termed in 1905 "science as a large-scale enterprise." And perhaps more than anyone else, Paul Ehrlich proved just

[*] Prof. Dr. F. Stern
Columbia University
15 Claremont Avenue, New York, NY 10027 (USA)
Fax: (+1) 212-316-0370
E-mail: fs20@columbia.edu

[**] This essay is based on a lecture by Fritz Stern given on the occasion of the opening of the Paul Ehrlich Institute in Langen. The text was published in the essay collection "Einstein's German World", Fritz Stern, Princeton University Press, 1999. We thank Princeton University Press for permission to print the essay. The graphical material was kindly made available to us by the Paul Ehrlich Institute, Langen.

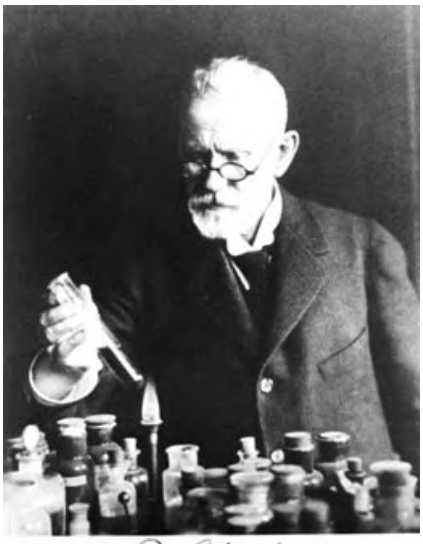
[+] In May 1990 I gave the opening lecture at the dedication of the new Paul Ehrlich Institute in Langen, near Frankfurt am Main. The lecture, a historical–biographical portrait, was followed by a scientific symposium. Subsequently, my friend Günther Schwerin, Paul Ehrlich's grandson, presented Rockefeller University with the complete Ehrlich Archive, which he had ingeniously retrieved after the Second World War. To make use of these materials proved irresistible, and I revised the previously unpublished lecture utilizing these new and untapped sources. I am indebted to the Rockefeller Archive Center in Tarrytown, New York, for their friendly assistance.

 © 2004 Wiley-VCH Verlag GmbH & Co. KGaA, Weinheim DOI: 10.1002/anie.200460632

how much one individual could accomplish: thanks to his discoveries in the laboratory, clinicians were able to save countless lives. The later historian Felix Gilbert was correct in observing that "in the intellectual life of the modern era, natural scientists became the new heroes."

I believe that Paul Ehrlich, born in 1854, was part of a second Age of Genius in Germany, indeed one of its key representatives. Only recently have we recognized this era for what it was, an era of pioneering discovery and invention when scientific and experimental medicine was making its first huge strides. In Germany the enormous advances made in the chemical industry during the nineteenth century, and the invention of synthetic dyes, became the foundation for progress in biological and virological research. There was widespread, unbounded faith in the perfection of empirical or positivistic science—a conviction that humans could comprehend nature and control its forces. Rudolf Virchow, physician, research scientist, and a fierce champion of liberalism against Bismarck, speaking in 1865 at the fortieth Congress of German Natural Scientists and Physicians, observed: "For us, science has become a religion." And in 1873: "We too have a creed: faith in the progress of our knowledge of the truth". Emil Du Bois-Reymond spoke of "natural science as the world conqueror in our day". Until the First World War, this was the predominant tone in the world of science and industry. At the founding convention of the Kaiser-Wilhelm-Society in January 1911, the renowned chemist Emil Fischer—in Ehrlich's presence and alluding to his work—declared that the future did not lie in the conquest of colonial empires; rather, "chemistry and with it, more generally, all of natural science is the true land of boundless opportunities". And there was solid evidence to back up this faith: practical knowledge was triumphing in the struggles against infection, against epidemic diseases, against the scourge of infant mortality.

In public, many scientists averred their trust in the progress and potential of science, yet in numerous unpublished documents—private letters from Ehrlich, Einstein, Haber, and Willstätter,



for example—one can sense their unpretentiousness, their doubts, their dissatisfaction with their own work. This was precisely because they were animated by such a powerful faith in science: the more lofty the aspirations of science as a collective enterprise, the more understandable the modesty of the individual researcher. Certainly there were also human frailties: ambition, jealousy, desire for fame. But Willstätter's plea to Ehrlich in 1903 was characteristic: "Please lower very greatly the scientific assessment you so generously accord me. I find it depressing to be overestimated by a research scientist for whom I have such great admiration. I feel I'm just a beginner.[2]

The advance of natural science also had critics and opponents—Nietzsche, for example, and, in an analogous but different way, Max Weber—who sensed the profound hazards lurking in the unqualified faith in science. There were also groups of people who thought that science endangered their interests, who imagined that positivistic science threatened their monopoly on morals in education and religion. We know that various church and religious leaders opposed the claims of science. Distortions and misunderstandings abounded. Many of the great scientists experienced in themselves a sense of the mystery of the universe; they hoped to serve and aid humanity without destroying its faith in the abiding mystery of the universe.

Paul Ehrlich was born into this world of progress, which he came to enrich with singular success. He was born in 1854 in Strehlen (now a Polish town, Strzelin), near Breslau (Wroclaw), the son of a prosperous Silesian–Jewish family. His scientific interests were awakened by his mother's cousin, the distinguished pathologist Carl Weigert. Already as a medical student he was fascinated by physiological research and recognized the huge potential for physiological experimentation that industrially manufactured dyes made possible. He had a special "love," as Willstätter noted, for the new dyes, especially methylene blue and its potential as a biological reagent. And he had an intuitive grasp of the bond linking chemistry, biology, and medicine. His earliest investigations led him to the concept that governed his future work: "that chemical affinities govern all biological processes." It was "the dawn of that great age in which medicine and chemistry forged their alliance for the benefit of all mankind," as Otto Warburg wrote.

Ehrlich's path as a scientist was not an easy one. He was a loner: though a physician, he was unwilling to enter clinical practice; though a researcher, he was devoid of ambition to teach. There had already been renowned successes in biomedical research, such as Pasteur developing a vaccine for rabies. Ehrlich worked in the developing field of immunology, convinced that the body's natural immune system could be fortified by chemical means. Finally, it was he who invented chemotherapy, indeed coined the term. But neither his passion for independence nor his work plans fitted the structure of scientific research at the time. Only the support given him by three exceptional personalities gave him the chance to develop his brilliant gifts to the full.

In 1878, the famous internist Theodor Frerichs, for a time Bismarck's personal physician, brought the young Ehrlich to the famed Charité Hospital in Berlin. Frerichs himself was convinced that the exactitude of physics and chemistry should have its analogue in medicine; under his sympathetic aegis, Ehrlich was able to dedicate himself totally to research. Frerichs recognized the young genius, of whom these lines by

 © 2004 Wiley-VCH Verlag GmbH & Co. KGaA, Weinheim

Theodor Fontane, written at the time, serve as a fitting description:
Gifts, who is without them?
Talents—mere toys for children.
Seriousness makes the man,
*application the genius.**

For even then, the young Ehrlich was distinguished by seriousness, unswerving commitment, by his impassioned, iron concentration, and his sublime forgetfulness regarding all trivialities. In 1882, Robert Koch delivered his lecture "On Tuberculosis," in which he set forth his discovery of the rod-shaped tubercle bacilli responsible for what he insisted was the infectious disease of tuberculosis. Ehrlich later wrote: "Everyone in attendance was deeply moved, and for me that evening has remained etched in my mind as my greatest scientific event." Soon thereafter Ehrlich developed an improved method of staining tubercle bacilli—and he and Koch became friends.

In fact, Frerichs and Koch became models for Ehrlich, and at the same time important promoters of his work. When Koch, only eleven years Ehrlich's senior, died in 1910. Ehrlich wrote a long obituary that reveals a good deal about his own life; the unconscious autobiographical elements of such eulogies should be listened to. He spoke of the "epoch-making work of the young doctor from Wollstein, Robert Koch," who demonstrated the "specificity of bacterial strains and their sole responsibility in the genesis of infectious diseases." Then he went on to the external circumstances that had helped Koch:

"Unknown and far removed from centers of scientific research … he was deeply engrossed in problems which the foremost scientists had struggled in vain to solve. By astute and unflagging application, he was able to provide answers so authoritative as to earn him the admiration and unqualified recognition of his contemporaries. And perhaps it was propitious that his genius and energy were given free rein to pursue his trailblazing ideas, undisturbed and unimpeded—a genius and an energy that in so exceptional a way combined to form his personality."

Was this not an apt description of Ehrlich himself?

He went on:

"It seems only natural that upon such a man—champion of science, bold and victorious leader in the battle against the deadliest common epidemics, universally acclaimed cultural celebrity—the highest honors were bestowed. … All of us who knew him will always admire his masterful genius as a researcher, his superior intellect, his inexhaustible capacity for work, his prodigious energy, and, last but not least, his heroic courage. That courage enabled him to defy the greatest dangers. Through it he became the great figure he was for us all and will remain for future generations: a defender of the common welfare, a victorious commander and leader in the fight against its fiercest foes."

Commemorating the memory of a paragon, Ehrlich did not realize the extent to which he himself had come to emulate his model, but posterity is well aware of it.

Ehrlich sounded a military note, jarring perhaps today, but normal in Wilhelmine Germany and in the developing field of bacteriology; Koch himself had often invoked similar metaphors, especially in his successful struggle to put bacteriological research and knowledge at the service of German public health, improving sanitary conditions in overcrowded cities. It was also an era when the "chief" was deemed almighty, the embodiment of scientific authority, surrounded in clinic and laboratory by a retinue of subalterns. Since Ehrlich's career was also shaped by strife, his use of these military metaphors seems all the more understandable.

In March 1885, Frerichs died suddenly; his successor did not properly appreciate Ehrlich's worth and had him transferred to clinical duty—this at the cost of his scientific work. That marked the beginning of an unhappy period at the Charité for Ehrlich and his wife, Hedwig Pinkus, whom he had wed a short time before. Her love and understanding, not to mention her private wealth, were to prove enduring sources of solace and comfort for him (Figure 1.*



Figure 1. Paul Ehrlich with his wife Hedwig. Source: Paul Ehrlich Institute, Langen.

In 1890, Koch announced that he had successfully created tuberculin, the sterile liquid containing substances extracted from the tubercle bacillus, which could be used in the diagnosis and cure of tuberculosis. This internationally acclaimed success led in Germany to the establishment in 1892 of a state Institute for Infectious Diseases, which was deemed a necessity in the globally competitive world of medicine. (The fact that in the same year, Bismarck's banker Gerson von Bleichröder, acting anonymously, made a million marks available for a hospital where patients would be treated in accordance with Koch's methods, has not been noted, not even in a standard biography of Koch.) In 1892, Koch brought Ehrlich, whom he held in

* Gaben, wer hätte sie nicht?
Talente—Spielzeug für die Kinder.
Erst der Ernst macht den Mann,
erst der Fleiss das Genie.
Theodor Fontane, "Unter der Bildnis Adolf Menzels," Gedichte (Stuttgart und Berlin, 1908),p. 325.

* Ehrlich's love letters to his nineteen-year-old fiancée overflow with affection and candor; their style well expresses his personality, even as they seem characteristic of the prevailing notions of the special decency and nobility inherent in womankind. He thanks her for having rekindled his "enthusiasm for the Good and Beautiful," but "it's such a shame that life's ordinary demands and impediments are so importune that I can scarcely find the time ... to hint to you in a few words what I feel." Ehrlich to Pinkus, July 28 and February 2, 1883, Paul Ehrlich Collection. Ehrlich practiced his own parsimonious orthography: he defied German convention by not capitalizing nouns and was indifferent to the rules of punctuation. Rockefeller Archive Center, Pocantino Hills, N.Y.

 © 2004 Wiley-VCH Verlag GmbH & Co. KGaA, Weinheim

high esteem, to the institute as "research associate". The institute was intended to deal with all infectious diseases, not just tuberculosis, particularly after tuberculin proved a failure in therapy.

Ehrlich now began to work with Emil von Behring at the Koch institute. The Koch institute in general and Behring and Ehrlich in particular benefited from the growing eagerness of the German chemical industry, Farbwerke-Hoechst especially, to support academic research that would produce practical and profitable results—in this instance involving the production of immunizing serum. Behring and Ehrlich were markedly different in personality: Behring rather authoritarian and contentious, Ehrlich vulnerable and yet stubborn, reticent and even reclusive. Together they concentrated their work on fighting diphtheria: at the time, some 45,000 children in Germany alone contracted the disease every year, and half of these died agonizing deaths. Behring discovered an antitoxin, but it was Ehrlich who learned how to develop the serum in live horses by slowly increased injections and then to standardize the required dosage for humans. With the help of August Laubenheimer, research director of the chemical company Farbwerke-Hoechst, that plant was commissioned to produce the substance: "Every vial of diphtheria serum from Farbwerke-Hoechst bears the label: manufactured according to Behring–Ehrlich."[3] Behring and Ehrlich had come to an agreement in 1892 regulating the distribution of profits between them, and their joint labors liberated humankind from a horrible scourge. Their initially successful cooperation alternated with bitter disputes. Ehrlich was convinced that Behring had taken advantage of him financially, while denigrating his superior scientific achievement.

At this point in his career, Ehrlich needed help, and he found it in the person of Friedrich Althoff, a department head in the Prussian Ministry of Education from 1882 to 1907, he was the commanding figure in Prussia's academic life. He was controversial in his time and remains so today: his achievements were great, his methods questionable. His ambition was to make Prussia's universities and research centers the best in the world, even against the will of opinionated professors with their insistence on autonomy, and in the teeth of prevailing religious biases. Althoff knew that in the battle against infectious diseases, Ehrlich was one of the most brilliant scientists anywhere—and, ultimately, one of the most successful. Soon a genuine friendship developed between the two, a bond that brought professional benefits to both men.

Althoff recognized that Ehrlich was unhappy with his subordinate position in Koch's institute, so in 1896 he set up a new state Institute for Serum Research and Serum Testing in Steglitz, a suburb of Berlin, and named Ehrlich its director. But that, too, was to prove only a temporary solution. Althoff succeeded in convincing the mayor of Frankfurt am Main, Franz Adickes, that his city's fame would be enhanced by establishing a Royal Institute for Experimental Therapy there, headed by Ehrlich and jointly financed by the city and the Prussian state, with contributions from industry and private donors—a further example of the emergence of an industrial–scientific-state complex that gave German science its all-important social setting. Ehrlich moved to Frankfurt, where the institute was inaugurated in 1899.

In 1906, a dream long cherished by Althoff and Ehrlich finally came true: the widow of the Jewish banker Georg Speyer donated an additional building to Ehrlich for his biomedical research and experimental chemotherapy, and the Speyer Foundation provided generous funding for his work. The Georg-Speyer House, as it was called, was interdisciplinary from the outset and had close ties with industry. Ehrlich was working with modest, even primitive facilities and equipment, but the institute grew, and even though operations were always kept on a tight budget, new tasks were taken on, new staff appointed. Scarce funds restricted research, and Althoff, knowing how fierce the foreign competition was and adept at raising private money, complained to Ehrlich, "It is truly lamentable that we in Germany don't also have wealthy people who can provide for our institutes along the lines of the largesse given the Pasteur Institute [in Paris]. … Why can't the tycoons in Frankfurt like B. Metzler … etc., donate millions for your institute!"[4]

It was in Frankfurt that Ehrlich made his great theoretical and practical discoveries. Here he conducted his celebrated research on immunity, here he proved that antibody formation could be stimulated, and therefore that substances protecting against infection could be produced in strengths that made their use in medical treatment possible. In 1906 Ehrlich defined his hopes dramatically; he thought that "in the chemist's retort" substances would be created that would "be able to exert their full action exclusively on the parasite harbored within the organism and would represent … magic bullets which seek their target of their own accord." Ehrlich's English friend and colleague, the Nobel laureate Sir Henry Dale, noted in 1950 that "Ehrlich's imaginative genius" led him to develop his side-chain theory of the formation of antibodies, which is still today the basis of chemotherapy. He searched for "substances which, by virtue of their chemical structure and combining properties, would directly attach themselves to, and be able thus to kill or weaken, the infecting organisms, but would leave the tissues of the infected patient unharmed."

Ehrlich's private letters attest to his close bonds of friendship with Althoff and report on his vexing difficulties. Althoff was his friend, benefactor, and go-between, but the main troublemaker was Behring, another protégé of Althoff's. As early as 1900, Althoff had to assure Ehrlich, "We shall never launch any campaigns against you. … In your mutual interest, the constant feuding [with Behring] must not be allowed to become a permanent fixture."[5] Money was one problem here, as well as Behring's limited regard for Ehrlich's merits. Six years later, Ehrlich complained that Behring had been unfair to him over the diphtheria serum, and was now making new demands that would gravely injure the work of Ehrlich's institute: "A feeling of deep bitterness still wells up in me when I recall that time—not because of the material losses I suffered and have forgotten, but because of the enormous ruthlessness with which von Behring began the game and played it out. It was only thanks to my help that he could

 © 2004 Wiley-VCH Verlag GmbH & Co. KGaA, Weinheim

mount the saddle and his first act was to kick the man who had aided him, and whose assistance, however uncongenial, was indispensable."

But any further harm to his institute Ehrlich found intolerable: "Without being immodest, I think I can say that the Institute has everywhere won full recognition and even emulation in the development of modern research on immunity—and that not only as an Institute for testing new products—but that also my work and that of my associates have contributed importantly to the advance of modern science."[6]

Ehrlich had wanted to dedicate his most important work to Althoff, who, understandably gratified, accepted the honor: "I have been deeply moved by your intention to dedicate the publication of your path-breaking studies on side-chain theory to me. I feel in no way deserving of such a great honor, but since in the past I have endured so many and in part truly undeserved attacks, I shall now gratefully accept this honor, equally undeserved, bestowed on me by such an outstanding friend."[7]

And when in 1907 Althoff for reasons of health resigned from his post, Ehrlich wrote him an official letter, the text of which so pleased Althoff that he copied it out and distributed it to friends:

"You have done more to further the advance of science in all fields than anyone else, and I believe we have you to thank above all others for the fact that we are still today in the leading position. May the future keep this primacy from slipping from us. I myself own you both my entire career and the chance I had to bring my ideas to practical fruition. Shunted about as an assistant, forced into impossible conditions, totally ignored by the university, I thought myself quite useless. I never received a call to even the most minor position and was regarded as a person without a field—i.e., as totally useless. If you, with your strong hand and brilliant initiative, had not come to my aid and, in your untiring zeal and benevolent friendship, had not arranged a place where I might work, I would have been left to wither away entirely."[8]

This generous appraisal was typical of Ehrlich, though somewhat unfair to Frerichs and the others who had earlier supported him.

Althoff died in 1908—shortly before his protégé was awarded the Nobel Prize (shared jointly with Élie Metchnikoff) for his work on immunology. Ehrlich had earned earlier distinctions, and others followed: honorary doctorates from Oxford and elsewhere, medals and honors, an honorary professorship and an imperial appointment to the rank of Privy Councillor (with the address Your Excellency, a rare high honor). Ehrlich was a founding member of the executive board of the Kaiser-Wilhelm-Society. He was nominated for a second Nobel after inventing Salvarsan, but his early death prevented his receiving this very rare double distinction.

All this recognition and success came with repeated strife and animosity. For example, Ehrlich had to defend himself against attacks by the Swedish scientist Svante Arrhenius, for whom a Nobel Institute for Physical Chemistry had been founded in 1905. Commenting in a letter to his old friend and colleague Albert Neisser on this feud, Ehrlich noted, "Physical chemists comprise one of the best-organized cliques anywhere in the world, acting in unison to push each other forward."[9]

Ehrlich's ties were international, his fame widespread throughout the scientific community. In medicine, there already emerged something like "globalization," albeit dominated by the West. In 1904, he lectured in the United States, later in England and across Europe; his often improvised talks, as he himself described them, gained him close friends in the Anglo–American world, some of whom induced John D. Rockefeller to donate $10000 for the support of Ehrlich's institute. He cultivated contacts with colleagues everywhere: he asked for snake venom from Africa, studied tropical diseases such as sleeping sickness, maintained close ties with Japanese and, of course, with European scientists. The major (and for a time last) international medical congress in London in 1913 feted Ehrlich as the most eminent research scientist in the world.

In 1911, Ehrlich gave a paper on Salvarsan at the Congress of Natural Scientists in Karlsruhe, the gathering, where Fritz Haber and Albert Einstein first met; a year later, he delivered the principal lecture, "Modern Initiatives in Therapy," at Haber's Kaiser-Wilhelm-Institute. Ehrlich, Haber, and Einstein: two generations of German–Jewish scientists who intellectually and materially enriched their country and enhanced its worldwide prestige. A triumvirate of diverse personalities, all three outstanding representatives of the second Age of Genius.

Ehrlich's institute—the equal and rival of the Institut Pasteur and the Rockefeller Institute—investigated the etiology of and possible therapy for various diseases and was among the fist to undertake cancer research. But Ehrlich's greatest triumph—after years of experimentation—was his discovery of Salvarsan, the "magic bullet" also known as 606—605 earlier solutions having proved ineffectual. The trade name alluded to one of its ingredients, arsenic, which he, together with his Japanese colleague Sahachiro Hata, had developed as a chemotherapeutic agent against the syphilis spirochete (Figure 2). It made possible the most effective treatment to date for syphilis, which at the turn of the century was claiming more and more victims; its third stage—paresis—ended in wretched and painful death. The great dramas of the time, such as Ibsen's, alluded to the tragedy of syphilis, even if decorum dictated that its name be unmentioned. Only a few decades earlier, the famous English doctor Samuel Solly had praised syphilis as God's retribution for sinners, admonishing people to live a moral life (not unlike the situation today, where the battle against AIDS is waged with extremely limited funding and against similar moralizing). Through Ehrlich's work, humanity was largely freed from this scourge—a fact that the sanctimonious hypocrites of the day greeted critically.

Ehrlich himself had other worries. At the 1910 Congress of Internists in Wiesbaden, he had distributed 65000 units of Salvarsan gratis to colleagues and was extraordinarily meticulous in following up on the results. A "Salvarsan war" erupted: countless complaints alleged adverse side effects or unsuccessful treatment. "But the most unpleasant thing," he wrote in 1910, "is that there is a marked contrast between my own personality, which is anything

 © 2004 Wiley-VCH Verlag GmbH & Co. KGaA, Weinheim

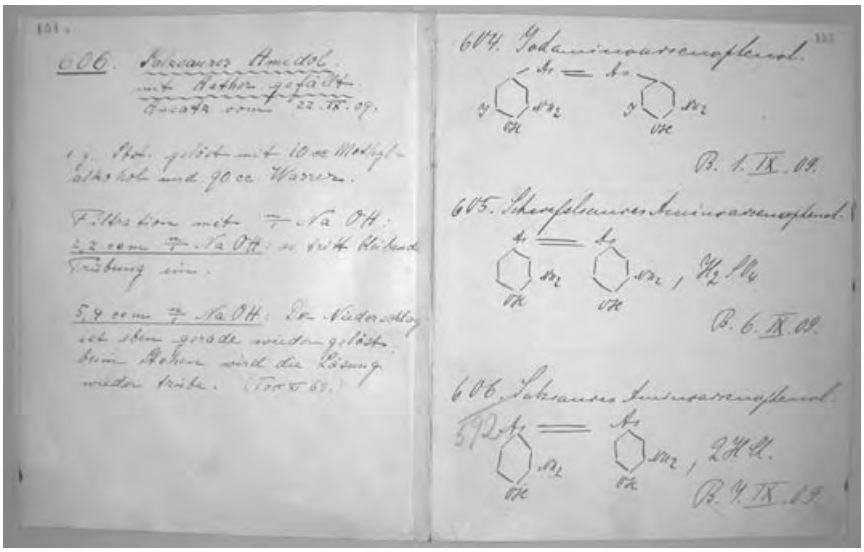


Figure 2. Page of Paul Ehrlich's laboratory book with the formula for the preparation 606 (Salvarsan). Source: Paul Ehrlich Institute, Langen.

but bold, and my scientific conviction that the disease ought to be vanquished by one mighty, possibly hazardous, blow, rather than to apply a mild but ineffective therapy, leaving the patients to their fate."

Ehrlich's enemies gleefully made his setbacks known, and his wife noted in her diary: "Paul is in very low spirits. … He says a Brazilian told him that Professor Finger [in] Vienna had two cases of deafness in his clinic as a result of 606, considered the drug poisonous and would campaign against it."[10] There was even a legal suit involving Salvarsan therapy, and Ehrlich had to appear in court. But Ehrlich himself unceasingly tracked the results of his cure, concerned about the effectiveness of Salvarsan, worried about improper applications of it. He knew that "the step from the laboratory to the patient's bedside … is extraordinarily arduous and fraught with danger." Correctly sensing enemies lurking in the field, in early 1911 he wrote to his friend Simon Flexner at the Rockefeller Institute: "The past year was a very hard one for me and I really feel how nervously exhausted I am. I must also say that I could have become old and have died without having had any notion of the meanness of mankind, which I now have had to experience." Constant conflicts exacerbated the burden of a furious work schedule. But Salvarsan proved a success: Ehrlich cured countless sufferers from what had once been all too often a fatal affliction. His labors, however, did grave harm to his own health.

In 1914, on the occasion of his sixtieth birthday, Ehrlich's unique standing was internationally celebrated. A comprehensive commemorative volume offered a "description of his scientific contributions." Despite his motto, "Work hard, publish little," he had some 212 publications to his name by then, the first having appeared when he was only twenty-three. His colleagues admired him not just for his successful results, but for the masterly methods he employed in achieving them, which in turn expressed his unfailing sense for science's proper tasks and potential: "We are not masters of nature, but its pupils." The guiding principle at his institute was "a unified direction in research, while allowing the individual the greatest possible scope for independent work." To another American friend, Samuel Meltzer, he wrote, "I was always particularly proud of the art of 'marching off' [Die Kunst des Abmarsches]"—by which he meant his ability to leave a field that had become barren. And it is true that he lost no time with matters that gave him no pleasure, leaving it to others to reap the harvest of many of his ingenious ideas. Most scientists praised his exemplary ethical attitude, and the enormous care he took in introducing new medicines. Ever self-critical, he resented the unfair denigrating criticisms of some colleagues.

In the volume honoring Ehrlich's sixtieth birthday, Richard Willstätter wrote: "Before our eyes the images of the great thinkers and artists of the past rise up … when we admire the universality of Paul Ehrlich's work, and recognize how versatile was his work as a chemist and how deeply, the breadth notwithstanding, he penetrated into the problems of organic chemistry. … As a chemist, Ehrlich is the pupil of no other master; he is not borne along, or even influenced, by any tide of his time; by his intuition and the power of his personality, vast new fields are being opened up for us." A genius originated the field of modern chemotherapy—a field of incomparable medical importance for our century.*

Renowned for his passion for work and his scintillating spontaneous monologues about scientific questions, Ehrlich was also a loving husband and the happy father of two daughters, whose weddings he lived to see. Unlike Haber or Einstein, his family life was tranquil and happy. Prodigiously well-read in science (though not in literature), Ehrlich developed what he dubbed the technique of "diagonal reading," rapidly scanning a page from top left to bottom right, pausing only for what was important to him. He was always pressed for time. His wife commented: "Paul can only work at the very last moment."[11] Like Haber, he relaxed by reading

* Perhaps Ehrlich could be described as one of those rare individuals who was both hedgehog and fox: he had one great idea—that all biological processes are chemical in nature—and he tirelessly pursued many therapeutic means to provide immunity to or cure for various diseases. Yet another American friend of Ehrlich's Dr. Christian A. Herter, in a celebrated Columbia lecture in 1909, said: "The imagination of a Darwin or Pasteur, for example, is as high and productive a form of imagination as that of Dante, or Goethe, or even Shakespear [sic] if we regard the human uses which result from the exercise of imaginative powers and mean by human uses not merely meat and drink, clothes and shelter, but also the satisfaction of mental and spiritual needs." Columbia University Quarterly, 1909–1910, p. 19.

 © 2004 Wiley-VCH Verlag GmbH & Co. KGaA, Weinheim

detective novels. Arthur Conan Doyle's portrait hung on the wall of his study, and the author sent him some of his books as presents. Perhaps he had a kind of elective affinity with Sherlock Holmes: his motto, "We have to learn how to take aim," also applied to Holmes' practiced knack for discovery. Both unearthed deadly secrets.

Ehrlich had no regard for his own health. He lived for his work, and from our perspective he seemed unwise: it was said that his absolute staples were mineral water and an all-day diet of the strongest cigars. He tended to view vacations and regular meals as disagreeable interruptions that he tolerated out of love for his family. In the winter of 1914–15, he collapsed from exhaustion and in August 1915 succumbed to a second stroke. By then, science had lost its innocence in the Great War, and Ehrlich's world lay in ruins.

Emil von Behring spoke at his open grave, lauding Ehrlich as a *"magister mundi"* in medical science, his personality an *"anima candida"*: "In our harsh era of a ruthless struggle for existence, you [Du] always remained so pure and untainted in your disposition, so tender in your sentiments, that any who knew you had to sense sharp pangs of conscience if ever they dared to treat you harshly." Were these belated pangs of Behring's own conscience, a graveside confession? Nonetheless, the friend–foe had understood him.

Ehrlich scarcely had time for or interest in politics, yet we know of two somewhat contrary instances when he was a participant in historical events. In 1913, Chaim Weizmann visited Ehrlich in his laboratory and persuaded him to join the project of establishing a Jewish university in Jerusalem; Weizmann regarded Ehrlich's support as uniquely important. After a trip to Paris in February 1914, Ehrlich reported his impressions of the possible French assistance that would come for the planned university, to be financed by Edmond de Rothschild. Weizmann hoped that Ehrlich would work out a plan for a research institute at the university in Jerusalem, a project to be presented to Baron Rothschild for additional support. The outbreak of war put a quick end to the projected venture, but it is clear that Ehrlich, unlike most German Jews, wanted to champion the "Jewish-national" cause. His report on a conversation with the physician and scientist Georges Widal provides insight into his own views: "Widal is rather indifferent when it comes to [Jewish] national questions. … One factor, partially affecting his case, is that although he is Jewish, he has never had any adverse personal experiences because of this and has enjoyed a brilliant career right from the start. Of course, he is a very outstanding and capable individual."[12]

But in consonance with the great majority of Jews in Germany, Ehrlich was also quite able to support the "German-national" side in the war. He too signed the ill-conceived Manifesto of the 93 in October 1914—undoubtedly much to the chagrin of his many friends and admirers in the Allied countries. The Ehrlich Archives offer no clue as to who might have solicited his signature, but, other great scientists, Planck, Haber, and Willstätter for example, signed as well.*

Paul Ehrlich was a Jew and remained so all his life, yet at the same time, his identity as a German was for him an absolute given. And it was as a German that he was celebrated abroad. In Germany, he suffered the disappointments that were the common lot there of all Jews. I doubt that any of the great Jewish scientists could escape the virtually unquestioned bias of the day; neither baptism nor outstanding achievement could shake society's fundamental outlook. Ehrlich triumphed after he had encountered hindrances and hostility; he was troubled by the far worse obstacles faced by fellow Jews who lacked genius. In his own case, and this was symptomatic of the times, the slights were mitigated by the personal engagement of colleagues and superiors who gave him practical and moral support—Frerichs, Koch, Althoff, and others. At its higher levels, Germany was distinguished by harmonious creativity. Yet prejudice—and I intentionally avoid the term anti-Semitism, due to its racist and populist overtones—was practically universal.

This *ressentiment* of Jews had a certain seductive force for Germans, and it may have also brought them some advantage, permitting them a sense of moral superiority while categorizing certain specific traits—ruthless ambition, dogged self-assertion, a desire for power and money—as typically Jewish. That prejudice expressed a sense of one's own uprightness. At the same time, it masked a double anxiety: fear of possible contamination by those very traits that one maligned or might already be infected with; anxiety that Jews, by these very same qualities, might effectively challenge the position and intellectual patrimony of their Christian colleagues.

So German Jews encountered both animosity and friendship. The obstacles that prejudice put in their way often had a contrary effect: anti-Semitism served as the sting that spurred Jews on to overachievement, to maintain their own in often subliminal competition. The biographies of Ehrlich and his colleagues suggest that the widespread antipathy to Jews in a society marked by a high degree of assimilation proved an unintended impetus for success. Thus Wilhelmine society derived several benefits from its legacy of prejudice: Christians could enjoy the psychic satisfaction of moral superiority and society at large could benefit from the fortuitously enhanced capacity and austere dedication of Jewish scientists. Ehrlich's and Haber's achievements were an immeasurable boon to Imperial Germany, to German industry, to Germany's international prestige. Shulamit Volkov has investigated this pattern of Jewish success in medicine and the natural sciences: the talented young Jewish researcher was initially often placed at a disadvantage and appointed to less demanding posts; he was frequently passed over and condemned to the limbo of a non-tenured lectureship (Privatdozent) for longer than others; yet this allowed him time to pursue his own research and develop as a specialist.[13] Ehrlich was spared having to witness the destruction on this unique bond of Christian–Jewish

* There is a certain irony that one of the best-known German pacifists, Friedrich Wilhelm Foerster, wrote Ehrlich's long-time secretary, thanking her for her reminiscences of Ehrlich: "Yes, he is the kind of German as God had willed him." Foerster to Martha Marquardt, Paris, September 17, 1929, Paul Ehrlich Collection.

 © 2004 Wiley-VCH Verlag GmbH & Co. KGaA, Weinheim

cooperation, or to suffer the abominations of later years.*

This newly established Paul Ehrlich Institute is living proof of historic change. Ehrlich had once commented that if he had to, he could work in a barn, and the institute named for him today is a far cry from a barn. But change also brings new hazards. Today the value of the natural sciences is generally allowed, as are their enormous costs, but science has lost its former innocence, and the technology it helped to create, in all its ambiguity about human life, is a source of concern. The person in the white coat is no longer quite the god he or she once was—true still in my childhood; they too have been demythologized. They too are measured by the degree to which they act responsibly. Increasingly, current science has become "big science," and is dominated less by individual geniuses or giants like Koch, Ehrlich, or, more recently, perhaps, Robert Oppenheimer.

The name of Paul Ehrlich recalls an illustrious era and remains an admonition, a specific summons to moral and civic responsibly. The German catastrophe in part made possible by German science enfeebled its scientific community. German scientists committed terrible atrocities or kept silent in the face of crimes that violated all human decency. German science and the nation as a whole have been offered something grand and rare in human history and life: a second chance, an open door to a new beginning in a new Europe. I wish the Paul Ehrlich Institute every success in realizing this opportunity and this promise. To conclude with a variation on a favorite phrase of Ehrlich, I wish it "the four essentials—money, patience, skill, and luck."

* His family was not spared. His daughter Stephanie, married to a great industrialist Ernst Schwerin, presided over a splendid salon in Breslau, which the writer Gerhart Hauptmann much liked to attend—until 1933. In 1937, Ernst Schwerin was warned of his impending arrest and emigrated with his family to the United States. In 1938 he was deprived of his German citizenship and dispossessed—a term that had a fateful double meaning for German Jews. Paul Ehrlich's widow emigrated only after the *Kristallnacht* pogrom of November 1938. My mother's family was related to Ernst Schwerin's family. I vividly remember the close friendship in Breslau and in the United States between my parents and Stephanie Schwerin. (I studied at the same gymnasium in Breslau that Paul Ehrlich attended—at a time when he had become an "unperson," and I can still recall addressing his widow as "Your Excellency" in her American exile.) When I spoke at Stephanie Schwerin's funeral in New York in 1966, I said that she exuded not only great benevolence but a quiet, grave authority; she was a true representative of the German *Bürgertum*. In 1989 the Bundesbank issued a new 200 deutschmark bill with Paul Ehrlich's portrait and a microscope on it—a curious form of restitution.

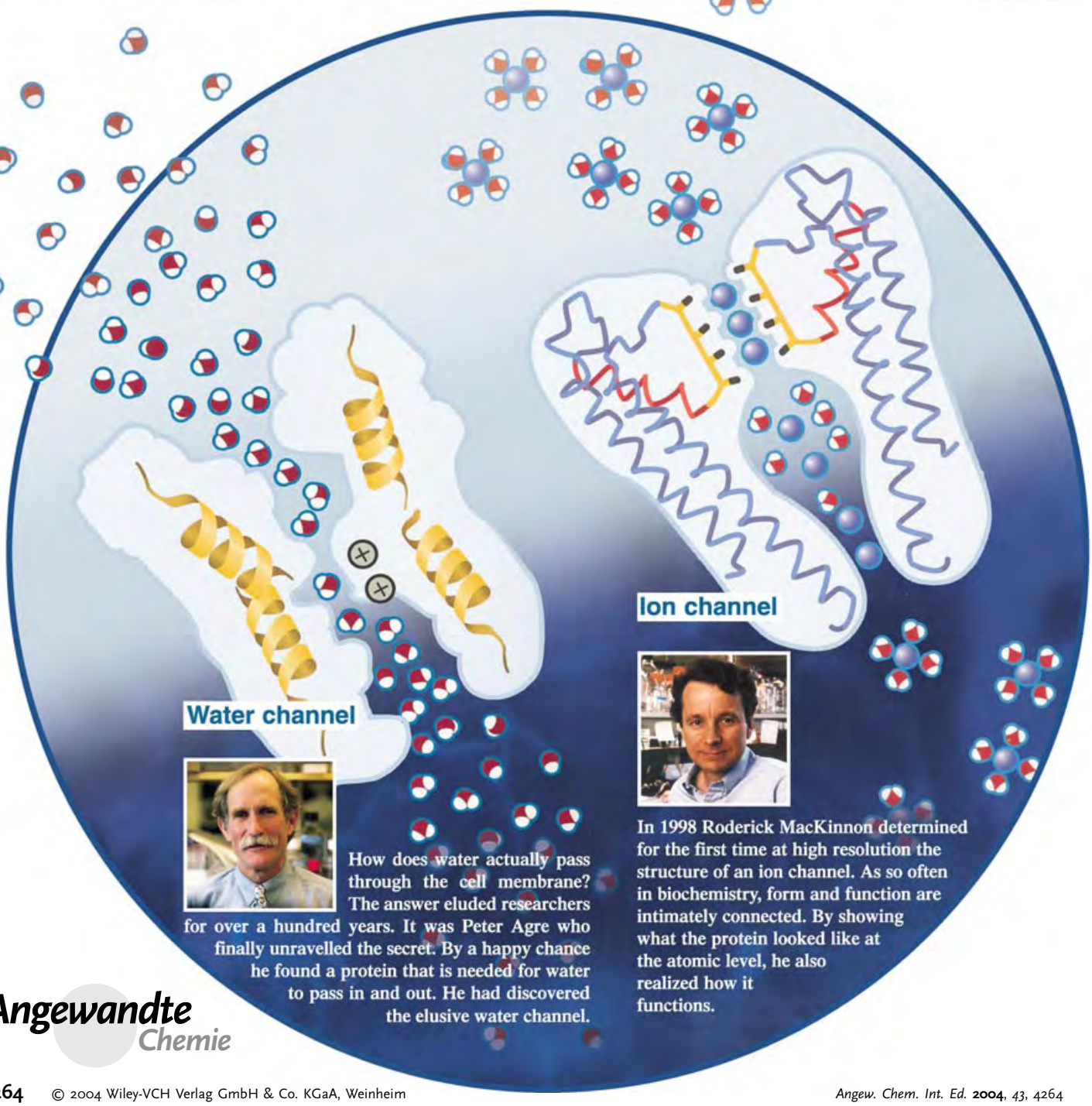
[1] Hebrew University Archive, Jerusalem
[2] Willstätter to Ehrlich, October 7, 1903, Paul Ehrlich Collection in the Rockefeller Archive Center. In publishing this Essay I have limited myself to providing references to quotations from the Ehrlich Archive. The scientific literature about Ehrlich is vast; the biographical studies are scant and rather unsatisfactory. I found especially valuable Timothy Lenoir, "A Magic Bullet: Research for Profit and the Growth of Knowledge in Germany aound 1900," *Minerva* 26, 1 (spring 1988), pp. 66–88.
[3] Ehrlich to Friedrich Althoff, November 1, 1906, Paul Ehrlich Collection.
[4] Althoff to Ehrlich, April 14, 1907, Paul Ehrlich Collection.
[5] Althoff to Ehrlich, February 25, 1900, Paul Ehrlich Collection.
[6] Ehrlich to Althoff, November 1, 1906, Paul Ehrlich Collection.
[7] Althoff to Ehrlich, August 31, 1902, Paul Ehrlich Collection.
[8] Ehrlich to Althoff, July 27, 1907, Paul Ehrlich Collection.
[9] Ehrlich to Albert Neisser, April 15, 1904, Paul Ehrlich Collection.
[10] Hedwig Ehrlich, diary entry, November 10, 1910, Paul Ehrlich Collection.
[11] Paul Ehrlich Collection., December 9, 1910.
[12] Ehrlich to Chaim Weizmann, February 13, 1914, and Weizmann to Ehrlich, February 16, 1914, Paul Ehrlich Collection.
[13] Shulamit Volkov, *Jüdisches Leben und Antisemitismus im 19. und 20. Jahrhundert* (Munich, 1990), pp. 146–180. Also see her reconsiderations "Juden als wissenschaftliche 'Mandarine' im Kaiserreich und in der Weimarer Republik," *Archiv für Sozialgeschichte* 27 (1997), pp. 1–18.

 © 2004 Wiley-VCH Verlag GmbH & Co. KGaA, Weinheim

THE NOBEL PRIZE IN CHEMISTRY 2003



Unravelling the secrets of cell channels



How does water actually pass through the cell membrane? The answer eluded researchers for over a hundred years. It was Peter Agre who finally unravelled the secret. By a happy chance he found a protein that is needed for water to pass in and out. He had discovered the elusive water channel.

In 1998 Roderick MacKinnon determined for the first time at high resolution the structure of an ion channel. As so often in biochemistry, form and function are intimately connected. By showing what the protein looked like at the atomic level, he also realized how it functions.

 © 2004 Wiley-VCH Verlag GmbH & Co. KGaA, Weinheim

Ion Channels

Potassium Channels and the Atomic Basis of Selective Ion Conduction (Nobel Lecture)**

*Roderick MacKinnon**

Keywords:
ion channels · membranes · Nobel Lecture · protein structures · structure elucidation

From the Contents

Introduction	4267
Early Studies: The Signature Sequence of the K^+Channel	4268
The KcsA Structure And Selective K^+Conduction	4269
Common Structural Principles Underlie K^+ And Cl^- Selectivity	4272
Trying to See a K^+Channel Open and Close	4273
Concluding Remarks	4275

I was born on February 19, 1956 in the middle of a snowstorm. It remains one of those humorous family stories that my mother likes to tell. My father, the planner, had rehearsed the way to the hospital but apparently things looked a lot different at night in a blizzard. Eventually they made it and so did I, the fourth of seven children. My father was a postal worker when I was very young but studied computers and became a programmer on the big IBM main frames. My mother worked as a part-time schoolteacher, but mostly took care of the children at home. Thinking back on it now, I know we did not have much money but I never knew that growing up. My parents provided a happy environment and made their expectations clear to us. Television is bad for you, reading is good for you, and you better get an A for effort in school. What you end up doing in life is up to you. Just make sure you enjoy what you do because then you will do it well. We all pursued completely different walks of life. I became the scientist.

I suppose there were some early indications of my tendency to a life of curiosity. Apparently from a very young age I had a habit of asking lots of questions: "what would happen if ...?" was a favorite. I also liked having facts straight and knowing how things worked, and did not hesitate to give explanations to those around me, apparently to an annoying degree sometimes. I remember one day my father, at the end of his patience, commenting that I was a "compendium of useless information". I certainly can understand his plight with one of the seven having way too many questions and answers all the time. On the positive side, I learned a new word that day when I looked up compendium in the dictionary.

There were probably even indications that my curiosity might be scientific. Burlington Massachusetts was rural when I was young and I loved to roam and explore. I had rock collections and read children's books on geology and the history of the Earth. I made little volcanoes out of plaster of paris and added baking soda and vinegar to the craters to simulate volcanic eruptions. I had an accident one day that made my mother laugh, to my utter frustration: at that young age I failed to appreciate the humor in a little boy telling his mother he had dropped a volcano on his toe! In the summer I collected butterflies, turtles, snakes, and other living things. One summer my mother enrolled me in a science-enrichment class for elementary school students and I was allowed to take home a microscope. I used it to look at everything I could find: microorganisms from the nearby pond, leaves, and blades of grass. I spent hour after hour alone, mesmerized by the tiny little things that I could see. My scientific curiosity took a back seat to athletics through junior-high and high school. Gymnastics was a good match to my small build and to my solitary nature. I was a member of a team, but gymnastics is an individual sport. You learn a technique, then a "move", and then a "routine". Then you perfect it through practice, working mostly alone. I had a very good no-nonsense teacher, coach Hayes, who really instilled in me the idea of perfection through practice. I was actually not all that bad, particularly at floor exercise and high bar. I even considered pursuing gymnastics in college, but during my final year of high school I began to wonder what I should pursue for a career. I attended the University of Massachusetts in Boston for one year and then transferred to Brandeis University. Brandeis was an eye-opening experience for me. For the first time in my life I was in a seriously intellectual environment. The classes tended to be small, intense, and stimulating. I discovered that I had a passion for science, and that I was very good at it. I chose Biochemistry as a major and a newly arrived assistant professor named Chris Miller for my honors thesis advisor. He had a little laboratory with big windows and

[*] Prof. Dr. R. MacKinnon
Howard Hughes Medical Institute
Laboratory of Molecular Neurobiology and Biophysics
Rockefeller University
1230 York Avenue, New York, NY 10021 (USA)
Fax: (+1) 212-327-7289
E-mail: mackinn@mail.rockefeller.edu

[**] Copyright© The Nobel Foundation 2003. We thank the Nobel Foundation, Stockholm, for permission to print this lecture.

 DOI: 10.1002/anie.200400662 © 2004 Wiley-VCH Verlag GmbH & Co. KGaA, Weinheim

lots of light shining in. I studied calcium transport and learned about the cell membrane as an electrode. I could see that Chris Miller was a man having lots of fun in his daily life and it was inspiring to me, and the memory of this stayed with me. But the biggest influence Brandeis had on my life happened in Physics class. There I met my future wife Alice Lee, whose sparkling eyes and sharp mind caught my attention. Against Chris Miller's advice I went to medical school after Brandeis. I studied at Tufts University School of Medicine and then at Beth Israel Hospital Boston for house-officer training in Internal Medicine. I learned a lot, but in the end I should have taken Chris' advice to pursue science. Medicine required a lot of memorization and little analytical problem solving. To keep a certain part of my brain active I began to study mathematics, and continue this even today, learning new methods and solving problems with the same disciplined approach I had learned in gymnastics. I started back to science near the end of house-officer training when I worked with Jim Morgan studying calcium in cardiac muscle contractility, which was very enjoyable and kept me connected to medicine. But I had a yearning to work on a very basic science problem, which meant I would have to break my medical ties. This was a difficult decision because I had invested so many years in medical education; to abandon it was to admit to myself that I had misspent a big piece of my life. There were practical considerations as well. It was time finally to get a permanent job; after all, my wife Alice had supported me through years of training. Not to mention I was nearly 30 years old with no real basic science training beyond my Brandeis undergraduate education: would I even be able to make it as a scientist?



Two factors had the greatest influence on my decision. Back in my first year of medical school I lost my sister Elley, an artist only two years my senior. Diagnosed with leukemia during my hematology clerkship as I learned about the dreaded disease, she lasted only two months. This horrifying event impressed upon me how fragile and precious life is, and how important it is to seize the moment and enjoy what you do while you can. I remember thinking when I look back upon my life at the age of seventy, thirty will seem young: just go for it. The second factor was Alice. She had complete faith in my ability to succeed. Never mind that postdoctoral studies meant a reduction of my already piddling house-officer salary. She simply said you have no choice; we will manage somehow.Memories of Chris Miller's laboratory beckoned so I returned for postdoctoral studies. Of course I will never out-live his reminding me that I should have listened to him in the first place. Feeling far behind in my knowledge, I approached my postdoctoral studies with intensity, learning techniques and theory. I felt I should be an expert in electrochemistry, stochastic processes, linear systems theory, and many more subjects. I read books, solved the problem sets, mastered the subjects, and carried out experiments. I had the very good fortune of a co-worker Jacques Neyton, a postdoctoral scientist from France. Jacques is a very critical thinker who would brood on a problem. We exchanged ideas often. When I would tell him one of my ideas he had



Alice Lee, 1986, at the time of my decision to leave medicine for science.

a tendency just to listen quietly. Then, after a while, if his response started with "Hey Roddy, there's something I don't understand" I knew I was in trouble—my idea was probably no good!After I completed a series of biophysical studies on K^+ channels, it came time to apply for an academic position. During the late 1980s physiology departments were more interested in hiring channel gene cloners than biophysicists. But Peter Hess convinced his colleagues at Harvard that my work showed promise and I was offered an assistant professorship there. My laboratory made good progress on K^+ channels. It was exciting for a while but in just a few years I began to feel that the return on what we could learn from studying the functional effects of mutations was diminishing. We had identified the signature sequence of the K^+ channel, but without knowing its structure we never would understand the chemical principles of ion selectivity in K^+ channels. I decided at that point to learn X-ray crystallography to someday see a K^+ channel.

I began to learn methods of protein purification and X-ray crystallography while still at Harvard, initially working with channel toxins and a small soluble protein called a PDZ domain. However, I thought it best to move away from my familiar environment at Harvard to pursue channel structure. There were really two reasons motivating me to move. First was the practical issue of obtaining funding to work in an area in which I had no background: start-up funds associated with moving to a new university would be useful for this purpose. The second, and far more important, reason was that moving would enable me to immerse myself completely in the new endeavor. A change of environment would remove the distractions of everyday life, isolate me from the temptation to fall back on channel physiology studies that I was already good at, and allow me to focus with singular purpose on the structural studies. I needed this to become an expert in membrane protein biochemistry and X-ray crystallography, and to develop a "feel" for protein structure. When the president of Rockefeller University Torsten Wiesel heard about my scientific plans he suggested that I move to Rockefeller University and I did. Rockefeller provided a wonderful environment for concentrating on a difficult problem.

It has been said that giving up my already successful laboratory at Harvard to pursue the structure of a K^+ channel was a risky thing to do. At the time I was told that my aspirations were altogether unrealistic. From my perspective I had little choice because I wanted to understand K^+ selectivity and I knew that the atomic structure provided the only path to understanding. I would rather fail trying than never try at all. It helped that I was accustomed to making transitions and had become good at teaching myself new subjects. I have to admit that few people working with me at the time wanted much to do with the new endeavor—only one new postdoctoral scientist Declan Doyle was enthusiastic. My wife Alice, an organic

 © 2004 Wiley-VCH Verlag GmbH & Co. KGaA, Weinheim



A recent photograph of Rod and Alice.

chemist, saw that I was going to be pretty lonely and decided to join me in the lab. And to my good fortune she has worked with me since. I have learned that most people do not like change, but I do. For me change is challenging, good for creativity, and it definitely keeps life interesting. I think of the past eight years of my life in New York at Rockefeller University as a personal odyssey. The new laboratory started out very small, with only Declan, Alice, and me. But it grew in the first year with the addition of other enthusiastic postdoctoral scientists, including João Morais Cabral, and John Imredy. Working with membrane proteins was very difficult, as expected. We had our periods of despair, but every time we felt left without options something good happened and despair gave way to excitement. Persistence and dedication eventually paid off. The atomic structure of the K^+ selectivity filter was more informative and more beautiful than I ever could have imagined. My laboratory now is an incredible place, over-flowing with excitement and ideas sustained by the continual infusion of bright young scientists who come from around the world to work with me. It gives me great satisfaction to know that these young scientists who are sophisticated in their knowledge of protein chemistry and structure will lead the field of ion-channel research into the future. This has been a wonderful adventure.

I owe thanks for the life I have: to Alice, to all my loving family of MacKinnons and Lees, to my scientific family of students, postdoctoral researchers, and colleagues, to senior colleagues who have helped me along my way to pursue my passion, and to the Rockefeller University, the Howard Hughes Medical Institute, and the National Institutes of Health for their support. I am very thankful for my life as a scientist, for the opportunity to understand in some small way the world around me. I hope my best experiment and scientific ideas are yet to come. This hope keeps me going.

Introduction

All living cells are surrounded by a thin, approximately 40-Å-thick lipid bilayer called the cell membrane. The cell membrane holds the contents of a cell in one place so that the chemistry of life can occur, but it is a barrier to the movement of certain essential ingredients including the ions Na^+, K^+, Ca^{2+}, and Cl^-. The barrier to ion flow across the membrane—known as the dielectric barrier—can be understood at an intuitive level: the interior of the cell membrane comprises an oily substance and ions are more stable in water than in oil. The energetic preference of an ion for water arises from the electric field around the ion and its interaction with neighboring molecules. Water is an electrically polarizable substance, which means that its molecules rearrange in an ion's electric field so that negative oxygen atoms point in the direction of cations and positive hydrogen atoms point toward anions. These electrically stabilizing interactions are much weaker in a less-polarizable substance such as oil. Thus, an ion will tend to stay in the water on either side of a cell membrane rather than enter and cross the membrane. Yet numerous cellular processes, ranging from electrolyte transport across epithelia to electrical signal production in neurons, depend on the flow of ions across the membrane. To mediate the flow, specific protein catalysts known as ion channels exist in the cell membrane. Ion channels exhibit the following three essential properties: 1) they conduct ions rapidly, 2) many ion channels are highly selective, which means only certain ion species flow while others are excluded, 3) their function is regulated by processes known as gating, that is, ion conduction is turned on and off in response to specific environmental stimuli. Figure 1 summarizes these properties.

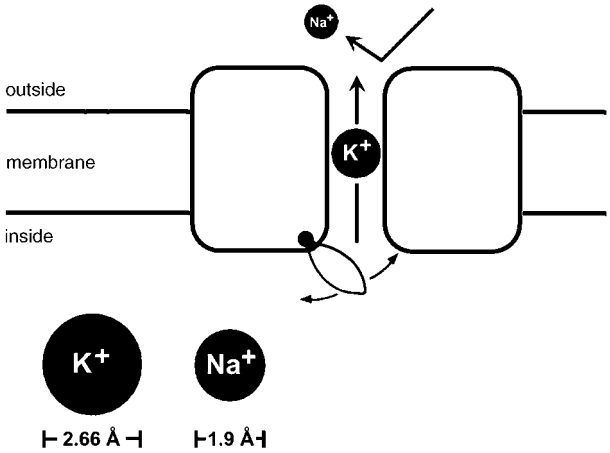


Figure 1. Ion channels exhibit three basic properties: 1) They conduct specific ions at high rates: for example, 10^7–10^8 K^+ ions per second flow through a K^+ channel, 2) they are selective (a K^+ channel essentially excludes Na^+ ions), and 3) conduction is turned on and off by opening and closing a gate, which can be regulated by an external stimulus such as ligand binding or membrane voltage. The relative size of K^+ and Na^+ ions is shown.

The modern history of ion channels began in 1952 when Hodgkin and Huxley published their seminal papers on the theory of the action potential in the squid giant axon.[1–4] A fundamental element of their theory was that the axon membrane undergoes changes in its permeability to Na^+ and K^+ ions. The Hodgkin–Huxley theory did not address the mechanism by which changes in the membrane permeability occur: ions could potentially cross the membrane through

 © 2004 Wiley-VCH Verlag GmbH & Co. KGaA, Weinheim

channels or by a carrier-mediated mechanism. In their words "*Details of the mechanism will probably not be settled for some time*".[1] It is fair to say that the pursuit of this statement has accounted for much research on ion channels over the past fifty years.

As early as 1955 experimental evidence for channel-mediated ion flow was obtained when Hodgkin and Keynes measured the directional flow of K^+ ions across axon membranes using the isotope $^{42}K^+$.[5] They observed that the flow of K^+ ions in one direction across the membrane depends on the flow in the opposite direction, and suggested that "*the ions should be constrained to move in single file and that there should, on average, be several ions in a channel at any moment*". Over the following two decades Armstrong and Hille used electrophysiological methods to demonstrate that Na^+ and K^+ ions cross cell membranes through unique protein pores—Na^+ channels and K^+ channels—and developed the concepts of selectivity filters for ion discrimination and gates for regulating ion flow.[6–12] The patch recording technique invented by Neher and Sakmann then revealed the electrical signals from individual ion channels, as well as the extraordinary diversity of ion channels in living cells throughout nature.[13]

The past twenty years have been the era of molecular biology for ion channels. The ability to manipulate amino acid sequences and express ion channels at high levels opened up entirely new possibilities for analysis. The advancement of techniques for protein-structure determination and the development of synchrotron facilities also created new possibilities. For me, a scientist who became fascinated with understanding the atomic basis of life's electrical system, there could not have been a more opportune time to enter the field.

Early Studies: The Signature Sequence of the K^+ Channel

The cloning of the Shaker K^+ channel gene from *Drosophila melanogaster* by Jan, Tanouye, and Pongs revealed for the first time the amino acid sequence of a K^+ channel and stimulated efforts in many laboratories to discover which of these amino acids form the pore, selectivity filter, and gate.[14–16] In Chris Miller's laboratory at Brandeis University I developed an approach to find the pore amino acids. Chris and I had just completed a study showing that charybdotoxin, a small protein from scorpion venom, inhibits a K^+ channel isolated from skeletal muscle cells by plugging the pore and obstructing the flow of ions.[17] In one of those late night "let's see what happens if" experiments while taking a molecular biology course at Cold Spring Harbor I found that the toxin—or what turned out to be a variant of it present in the charybdotoxin preparation—inhibited the Shaker K^+ channel.[18,19] This observation meant I could use the toxin to find the pore, and it did not take very long to identify the first site-directed mutants of the Shaker K^+ channel with altered binding of the toxin.[20] I continued these experiments at Harvard Medical School where I had become assistant professor in 1989. Working with my small group at Harvard, including Tatiana Abramson, Lise Heginbotham, and Zhe Lu, and sometimes with Gary Yellen at Johns Hopkins University, we reached several interesting conclusions concerning the architecture of K^+ channels. They had to be tetramers in which four subunits encircle a central ion pathway.[21] This conclusion was not terribly surprising but the experiments and analysis to reach it gave me great pleasure since they required only simple measurements and clear reasoning with binomial statistics. We also deduced that each subunit presents a "pore loop" to the central ion pathway (Figure 2).[22] This "loop" formed the binding sites for scorpion toxins[20,23,24] as well as

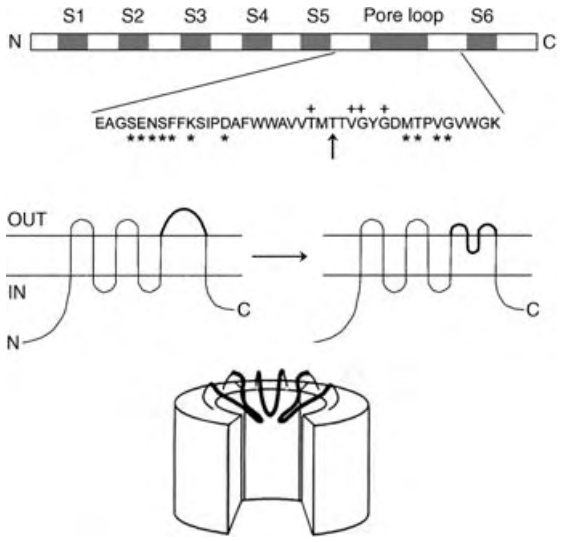


Figure 2. One of the first pictures of a tetrameric K^+ channel with a selectivity filter made of pore loops. A linear representation of a Shaker K^+ channel subunit on top shows shaded hydrophobic segments S1 to S6 and a region designated the pore loop. A partial amino acid sequence from the Shaker K^+ channel pore loop highlights amino acids shown to interact with extracellular scorpion toxins (*), intracellular tetraethylammonium (↑), and K^+ ions (+). The pore loop was proposed to reach into the membrane (middle) and form a selectivity filter at the center of four subunits (bottom).

the small-molecule inhibitor the tetraethylammonium ion,[25,26] which had been used by Armstrong and Hille decades earlier in their pioneering analysis of K^+ channels.[9,27] Most important to my thinking was that mutations of certain amino acids within the "loop" affected the channel's ability to discriminate between K^+ and Na^+ ions, the selectivity hallmark of K^+ channels.[28,29] Meanwhile, new K^+ channel genes were discovered and they all had one clear feature in common: the very amino acids that we had found to be important for K^+ selectivity were conserved (Figure 3). We called these amino acids the signature sequence of the K^+ channel, and imagined four pore loops somehow forming a selectivity filter with the signature sequence amino acids inside the pore.[22,29]

When you consider the single-channel conductance of many K^+ channels found in cells you realize just how incredible these molecular devices are. With typical cellular electrochemical gradients, K^+ ions conduct at a rate of 10^7 to 10^8 ions per second. That rate approaches the expected collision frequency of K^+ ions from solution with the entrance

 © 2004 Wiley-VCH Verlag GmbH & Co. KGaA, Weinheim

Bacteria	2TM :	TATTVGYG
Archea	6TM :	TATTVGYG
Plant	6TM :	TLTTVGYG
Fruitfly	6TM :	TMTTVGYG
Worm	6TM :	TMTTVGYG
Mouse	6TM :	SMTTVGYG
Human	2TM :	TQTTIGYG
Human	6TM :	TMTTVGYG

Figure 3. The signature sequence of the K^+ channel (shown as single letter amino acid code) is highly conserved in organisms throughout the tree of life. Some K^+ channels contain six membrane-spanning segments per subunit (6TM) while others contain only two (2TM). The 2TM K^+ channels correspond to 6TM K^+ channels without the first four membrane-spanning segments (S1–S4 in Figure 2).

to the pore. This means that K^+ ions flow through the pore almost as fast as they diffuse up to it. For this to occur the energetic barriers in the channel have to be very low, something like those encountered by K^+ ions diffusing through water. All the more remarkable is that the high rates are achieved in the setting of exquisite selectivity: the K^+ channel conducts K^+ ions, a monovalent cation of Pauling radius 1.33 Å, while essentially excluding Na^+ ions, a monovalent cation of Pauling radius 0.95 Å—this ion selectivity is critical to the survival of a cell. How does nature accomplish high conduction rates and high selectivity at the same time? The answer to this question would require knowing the atomic structure formed by the amino acids forming the signature sequence, that much was clear. The conservation of the signature sequence amino acids in K^+ channels throughout the tree of life, from bacteria[30] to higher eukaryotic cells, implied that nature had settled upon a very special solution to achieve rapid, selective K^+ conduction across the cell membrane. For me, this realization provided inspiration to want to directly visualize a K^+ channel and its selectivity filter.

The KcsA Structure And Selective K^+ Conduction

I began to study crystallography, and although I had no idea how I would obtain funding for this endeavor, I have always believed that if you really want to do something then you will find a way.

By happenstance I explained my plan to Torsten Wiesel, then president of Rockefeller University. He suggested that I come to Rockefeller where I would be able to concentrate on the problem. I accepted his offer and moved there in 1996. In the beginning I was joined by Declan Doyle and my wife Alice Lee MacKinnon and within a year others joined, including João Morais Cabral, John Imredy, Sabine Mann, and Richard Pfuetzner. We had to learn as we went along, and what we may have lacked in size and skill we more than compensated for with enthusiasm. It was a very special time. At first I did not know how we would ever reach the point of obtaining enough K^+-channel protein to attempt crystallization, but the signature sequence of the K^+ channel continued to appear in a growing number of prokaryotic genes, thus making expression in *Escherichia coli* possible. We focused our effort on a bacterial K^+ channel called KcsA from *Streptomyces lividans*, discovered by Schrempf et al.[31] The KcsA channel has a simple topology with only two membrane-spanning segments per subunit that corresponds to the Shaker K^+ channel without segments S1–S4 (Figure 2). Despite its prokaryotic origin, KcsA closely resembled the amino acid sequence of the Shaker K^+ channel's pore, and even exhibited many of its pharmacological properties, including inhibition by scorpion toxins.[32] This surprised us from an evolutionary standpoint, because why should a scorpion want to inhibit a bacterial K^+ channel? However, from the utilitarian point of view of protein biophysicists we knew exactly what the scorpion toxin sensitivity meant, KcsA had to be very similar in structure to the Shaker K^+ channel.

The KcsA channel produced crystals but they were poorly ordered and not very useful in the X-ray beam. After we struggled for quite a while I began to wonder whether some part of the channel was intrinsically disordered and interfering with crystallization. Fortunately my neighbor Brian Chait and his postdoctoral colleague Steve Cohen were experts in the analysis of soluble proteins by limited proteolysis and mass spectrometry, and their techniques applied beautifully to a membrane protein. We found that KcsA was as solid as a rock, except for its C-terminus. After removing the disordered amino acids from the C-terminus with chymotrypsin, the crystals improved dramatically and we were able to solve an initial structure at a resolution of 3.2 Å.[33] We could not clearly see K^+ ions in the pore at this resolution, but my years of work on K^+-channel function told me that Rb^+ and Cs^+ ions should be valuable electron-dense substitutes for K^+ ions, and they were. Difference Fourier maps with Rb^+ and Cs^+ ions showed these ions lined up in the pore—as Hodgkin and Keynes might have imagined in 1955.[5]

The KcsA structure was altogether illuminating, but before I describe it, I will depart from chronology to explain the next important technical step. A very accurate description of the ion-coordination chemistry inside the selectivity filter would require a higher-resolution structure. From the results of the 3.2-Å data we could infer the positions of the main-chain carbonyl oxygen atoms by applying our knowledge of small-molecule structures, that is, our chemical intuition, but we needed to see the selectivity filter atoms in detail. A high-resolution structure was actually quite difficult to obtain. After more than three additional years of work by João and then Yufeng (Fenny) Zhou, we finally managed to produce high-quality crystals by attaching monoclonal Fab fragments to KcsA. These crystals provided the information we needed, a structure at a resolution of 2.0 Å in which K^+ ions could be visualized in the grasp of selectivity filter protein atoms (Figure 4).[34] What did the structure of the K^+ channel tell us and why did nature conserve the signature sequence of amino acids in the K^+ channel?

Not all protein structures speak to you in an understandable language, but the KcsA K^+ channel does. Four subunits surround a central ion pathway that crosses the membrane (Figure 5a). Two of the four subunits are shown in Figure 5b together with electron density from K^+ ions and water along the pore. Near the center of the membrane the ion pathway is very wide, forming a cavity about 10 Å in diameter with a hydrated K^+ ion at its center. Each subunit directs the C-terminal end of a "pore helix" (shown in red)

 © 2004 Wiley-VCH Verlag GmbH & Co. KGaA, Weinheim

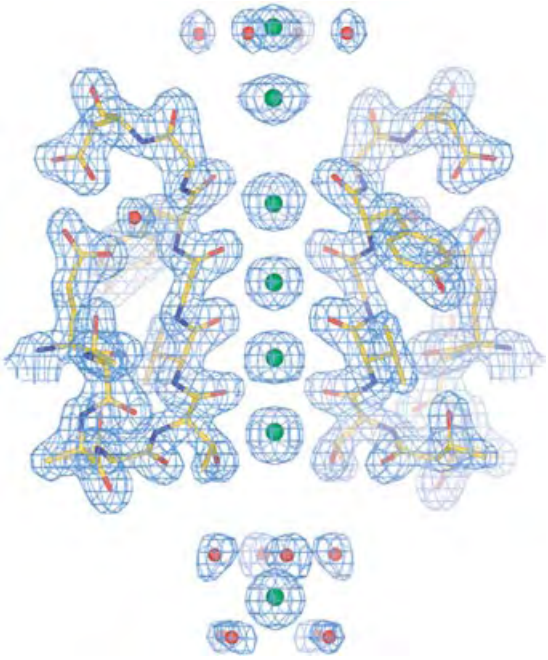


Figure 4. Electron density ($2F_o-F_c$ contoured at 2σ) derived from a high-resolution structure of the KcsA K^+ channel. This region of the channel features the selectivity filter with K^+ ions and water molecules along the ion pathway. The refined atomic model is shown in the electron-density representation. Adapted from ref. [34].

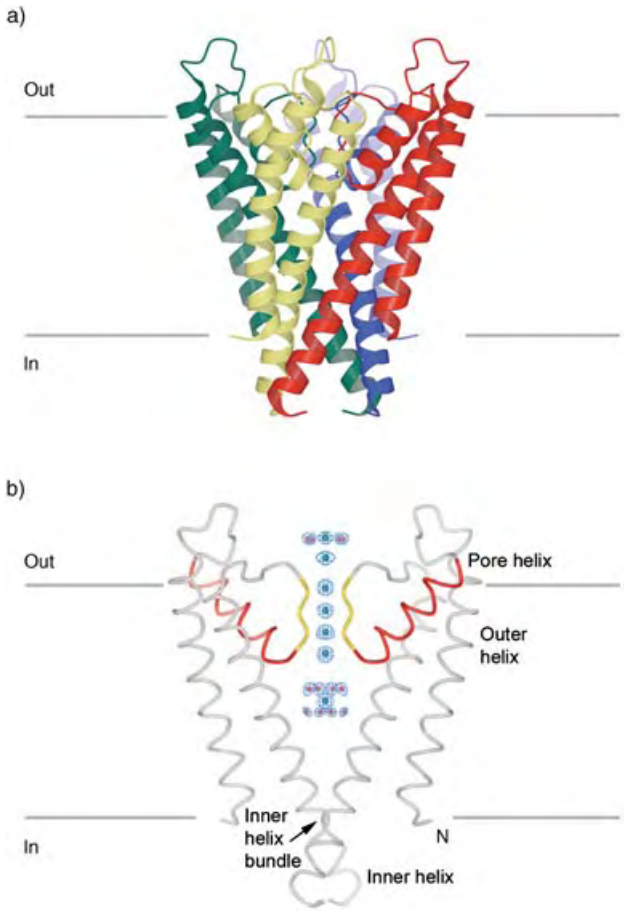


Figure 5. a) A ribbon representation of the KcsA K^+ channel with its four subunits colored differently. The channel is oriented with the extracellular solution on top. b) The KcsA K^+ channel with front and back subunits removed. The pore helices are shown in red and selectivity filter in yellow; the electron density along the ion pathway is shown in a blue mesh. The outer and inner helices correspond to S5 and S6 in Figure 2.

toward the ion. The C-terminal end of an α-helix is associated with a negative "end charge" as a result of carbonyl oxygen atoms that do not participate in secondary-structure hydrogen bonding, so the pore helices are directed as if to stabilize the K^+ ion in the cavity. At the beginning of this lecture I raised the fundamental issue of the cell membrane being an energetic barrier to ion flow because of its oily interior. KcsA allows us to intuit a simple logic encoded in its structure, and electrostatic calculations support the intuition:[35] the K^+ channel lowers the membrane dielectric barrier by hydrating a K^+ ion deep inside the membrane, and by stabilizing it with charges at the ends of the α-helix.

How does the K^+ channel distinguish K^+ from Na^+ ions? Our earlier mutagenesis studies had indicated that the amino acids of the signature sequence would be responsible for this most basic function of a K^+ channel. Figure 6 shows the structure formed by the signature sequence—the selectivity filter—located in the extracellular third of the ion pathway. The glycine amino acids in the sequence TVGYG have dihedral angles in or near the left-handed helical region of the Ramachandran plot, as does the threonine residue, thus allowing the main-chain carbonyl oxygen atoms to point in one direction, toward the ions along the pore. It is easy to understand why this sequence is so conserved among K^+ channels: the alternating glycine amino acids permit the required dihedral angles, the threonine hydroxy oxygen atom coordinates to a K^+ ion, and the side-chains of valine and tyrosine are directed into the protein core surrounding the filter to impose geometric constraint. The end result when the subunits come together is a narrow tube consisting of four

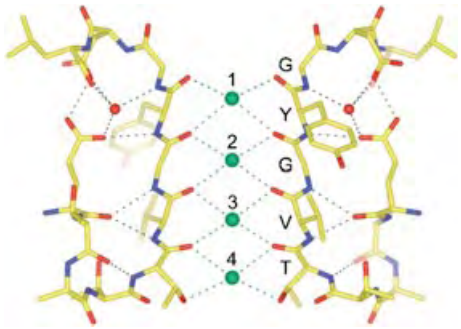


Figure 6. Detailed structure of the K^+-selectivity filter (two subunits). Oxygen atoms (red) coordinate K^+ ions (green spheres) at positions 1 to 4 from the extracellular side. Single letter amino acid code identifies select amino acids of the signature sequence (yellow: carbon, blue: nitrogen, and red: oxygen). Green and gray dashed lines show O···K^+ and hydrogen-bonding interactions, respectively.

equally spaced K^+-binding sites, labeled 1 to 4 from the extracellular side. Each binding site is a cage formed by eight oxygen atoms on the vertices of a cube, or a twisted cube

 © 2004 Wiley-VCH Verlag GmbH & Co. KGaA, Weinheim

called a square antiprism (Figure 7). The binding sites are very similar to the single alkali-metal site in nonactin, a K^+-selective antibiotic with nearly identical $K^+\cdots O$ distances.[36,37] The principle of K^+ selectivity is implied in a subtle feature of

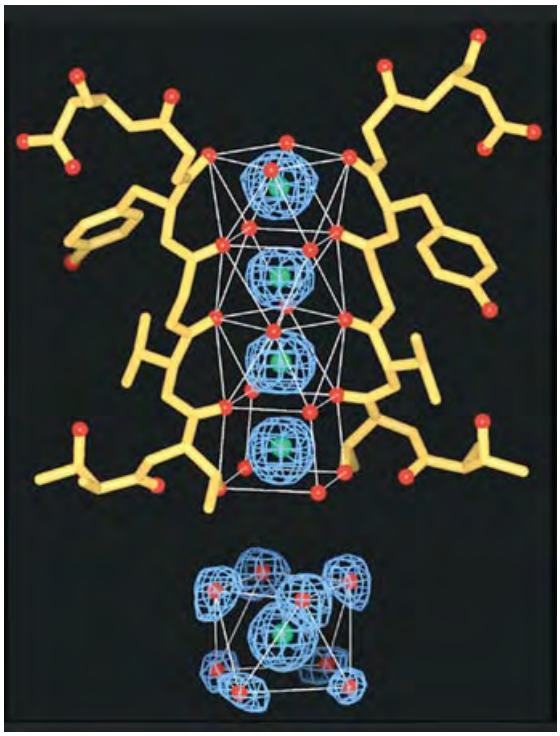


Figure 7. A K^+ channel mimics the hydration shell surrounding a K^+ ion. The electron density (blue mesh) for K^+ ions in the filter and for a K^+ ion and water molecules in the central cavity are shown. White lines highlight the coordination geometry of K^+ ions in the filter and in water. Adapted from ref. [34].

the KcsA crystal structure. The oxygen atoms surrounding the K^+ ions in the selectivity filter are arranged in a similar manner to the water molecules surrounding the hydrated K^+ ion in the cavity. This comparison conveys a visual impression of binding sites in the filter paying for the energetic cost of the dehydration of the K^+ ions. The Na^+ ion is apparently too small for these K^+-sized binding sites, so its dehydration energy is not compensated.

The question that compelled us most after seeing the structure was exactly how many ions are in the selectivity filter at a given time? To begin to understand how ions move through the filter we needed to know the stoichiometry of the ion-conduction reaction, and that meant knowing how many ions can occupy the filter. Four binding sites were apparent, but are they all occupied at once? Four K^+ ions in a row separated by an average center-to-center distance of 3.3 Å seemed unlikely for electrostatic reasons. From an early stage we suspected that the correct number would be closer to two, because two ions more easily explained the electron density we observed for the larger alkali-metal ions Rb^+ and Cs^+.[33,38] Quantitative evidence for the precise number of ions came with the high-resolution structure and with the analysis of Tl^+ ions.[40] Thallium is the most ideally suited "K^+ analogue" because it flows through K^+ channels, has a radius and dehydration energy very close to K^+, and has the favorable crystallographic attributes of high electron density and an anomalous signal. The one serious difficulty in working with Tl^+ ions is the formation of the insoluble TlCl in the presence of Cl^-. Fenny meticulously worked out the experimental conditions and determined that on average there are between two and two and a half conducting ions in the filter at one time, with an occupancy at each position of around one half.

We also observed that if the concentration of K^+ (or Tl^+) ions bathing the crystals is lowered sufficiently (below normal intracellular levels), then a reduction in the number of ions from two to one occurs and is associated with a structural change to a "collapsed" filter conformation, which is pinched closed in the middle.[34,40] At concentrations above 20 mM the entry of a second K^+ ion drives the filter to a "conductive" conformation, as shown in Figure 8. Sodium, on the other hand, does not drive the filter to a "conductive" conformation, even at concentrations up to 500 mM.

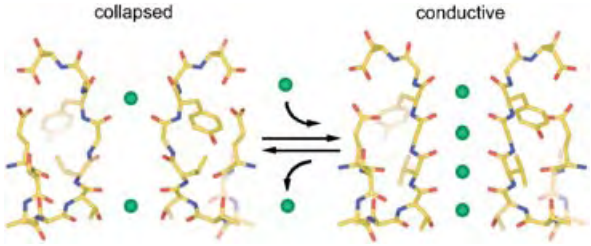


Figure 8. The selectivity filter can adopt two conformations. At low concentrations of K^+ ions, one K^+ ion resides on average at either of two sites near the ends of the filter, which is collapsed in the middle. At high concentrations of K^+ ions, a second ion enters the filter as it changes to a conductive conformation. On average, two K^+ ions in the conductive filter reside at four sites, each with about half occupancy.

The K^+-induced conformational change has thermodynamic consequences for the affinity of two K^+ ions in the "conductive" filter. It implies that a fraction of the second ion's binding energy must be expended as work to bring about the filter's conformational change, and as a result the two ions will bind with reduced affinity. To understand this statement at an intuitive level, it must be recognized that for two ions to reside in the filter they must oppose its tendency to collapse and force one of them out, that is, the two-ion "conductive" conformation is under some tension, which will tend to lower the affinity for K^+ ions. This is a desirable property for an ion channel because weak binding favors high conduction rates. The same principle, referred to as the "induced fit" hypothesis, had been proposed decades earlier by enzymologists to explain high specificity with low substrate affinity in enzyme catalysis.[39]

If two K^+ ions were randomly distributed in the "conductive" filter then they would occupy four sites in six possible ways. But several lines of evidence hinted to us that the ion positions are not random. For example, Rb^+ and Cs^+ ions exhibit preferred positions with clearly low occupancy at position 2.[38,40] With K^+, we observed an unusual

 © 2004 Wiley-VCH Verlag GmbH & Co. KGaA, Weinheim

doublet peak of electron density at the extracellular entrance to the selectivity filter (see Figure 9).[34] We could explain this density if the K^+ ion is attracted from solution by the negative protein surface charge near the entrance and at the same time repelled by K^+ ions inside the filter. Two discrete peaks implied two distributions of ions in the filter. If K^+ ions are separated by a water molecule for electrostatic reasons then the two dominant configurations would be 1,3 (K^+ ions in positions 1 and 3 with a water molecule in between) and 2,4 (K^+ ions in positions 2 and 4 with a water molecule in between). A mutation at position 4 (threonine to cysteine) was recently shown to influence K^+ occupancy at positions 2 and 4 but not at 1 and 3, thus providing strong evidence for specific 1,3 and 2,4 configurations of K^+ ions inside the selectivity filter.[69]

Discrete configurations of an ion pair suggested a mechanism for ion conduction (Figure 10a).[38] The K^+ ion pair could diffuse back and forth between 1,3 and 2,4 configurations (bottom pathway), or alternatively an ion could enter the filter from one side of the membrane as the ion–water queue moves and a K^+ ion exits at the opposite side (the top pathway). Movements would have to be concerted because the filter is no wider than a K^+ ion or water molecule. The two paths complete a cycle: in one complete cycle each ion moves only a fraction of the total distance through the filter, but the overall electrical effect is to move one charge all the way. As two K^+ ions are present in the filter throughout the cycle, we expect there should be electrostatic repulsion between them. Together with the filter conformational change that is required to achieve a "conductive" filter with two K^+ ions in it, electrostatic repulsion should favor high conduction rates by lowering K^+ affinity.

The absolute rates from 10^7 to 10^8 ions per second are truly impressive for a highly selective ion channel. One aspect of the crystallographic data suggests that very high conductance K^+ channels such as KcsA might operate near the maximum rate that the conduction mechanism will allow. All four positions in the filter have a K^+ occupancy close to one half, which implies that the 1,3 and 2,4 configurations are equally probable, or energetically equivalent, but there is no evident reason why this should be. A simulation of ions diffusing around the cycle offers a possible explanation: maximum flux is achieved when the energy difference between the 1,3 and 2,4 configurations is zero because that is the condition under which the "energy landscape" for the conduction cycle is smoothest (Figure 10b). The energetic balance between the configurations therefore might reflect the optimization of the conduction rate by natural selection.[38] It is not so easy to demonstrate this point experimentally, but it is certainly fascinating to ponder.

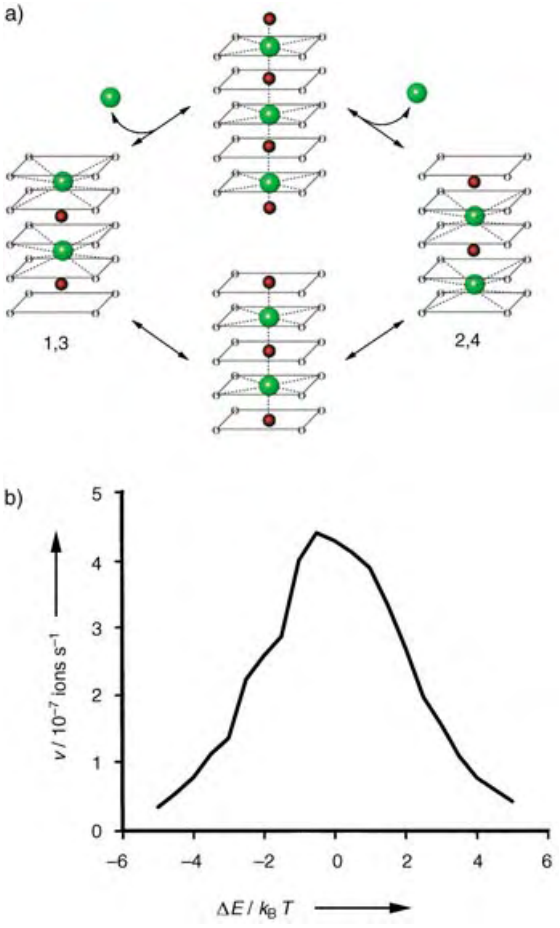


Figure 10. a) Throughput cycle for K^+ conduction invoking 1,3 and 2,4 configurations. The selectivity filter is represented as five square planes of oxygen atoms. K^+ ions and water are shown as green and red spheres, respectively. b) Simulated K^+ flux around the cycle is shown as a function of the energy difference between the 1,3 and 2,4 configurations. Adapted from ref. [38].

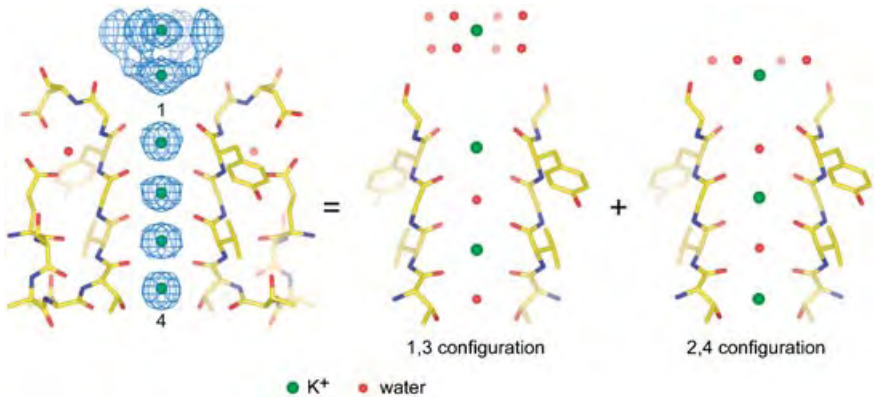


Figure 9. Two K^+ ions in the selectivity filter are hypothesized to exist predominantly in the two specific configurations 1,3 and 2,4. Adapted from ref. [34].

Common Structural Principles Underlie K^+ And Cl^- Selectivity

The focus of this lecture is K^+ channels, but for a brief inter-

lude I would like to show you a Cl^--selective transport protein. By comparing a K^+ channel and a Cl^- "channel" we can begin to appreciate familiar themes in nature's solutions to different problems: getting cations and anions across the cell membrane. ClC chloride channels are found in many different cell types and are associated with a number of physiological processes that require flow of Cl^- ions across lipid membranes.[41,42] As is the case for K^+ channels, genes of the ClC family are abundant in prokaryotes, which is a fortunate circumstance for protein expression and structural analysis. When Raimund Dutzler joined my laboratory he, Ernest Campbell, and I set out to address the structural basis of Cl^--ion selectivity. We determined crystal structures of two bacterial members of the ClC Cl^- channel family, one from *Escherichia coli* (EcClC) and another from *Salmonella typhimurium* (StClC).[43] Recent studies by Accardi and Miller on the function of EcClC have shown that it is actually a Cl^-–proton exchanger.[44] We do not yet know why certain members of this family of Cl^--transport proteins function as channels and others as exchangers, but the crystal structures are fascinating and give us a view of Cl^- selectivity. Architecturally the ClC proteins are unrelated to K^+ channels, but if we focus on the ion pathway certain features are similar (Figure 11). As we saw with the K^+ channels, the ClC proteins

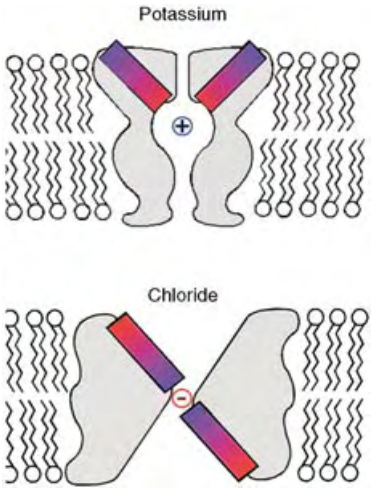


Figure 11. The overall architecture of K^+ channels and ClC Cl^--transport proteins is very different, but certain general features are similar. One similarity shown here is the direction of α-helix end charges toward the ion pathway. The negative C-terminal end charge (red) points to the K^+ ion. The positive N-terminal end charge (blue) points to the Cl^- ion.

have α-helices pointed at the ion pathway, but the direction is reversed, with the positive charge of the N-terminus close to the Cl^- ions. This makes perfect sense for lowering the dielectric barrier for a Cl^- ion. In ClC we see that ions in its selectivity filter tend to be coordinated by main-chain protein atoms, with amide nitrogen atoms surrounding the Cl^- ion instead of carbonyl oxygen atoms surrounding the K^+ ion (Figure 12). We also see that both the K^+ and Cl^- selectivity filters contain multiple close-spaced binding sites and appear to contain more than one ion, perhaps to exploit electrostatic

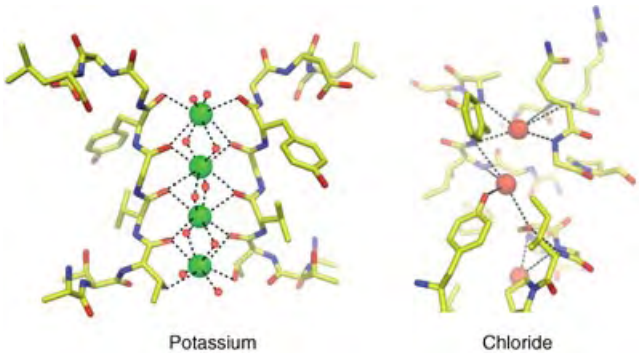


Figure 12. K^+- and Cl^--selectivity filters make use of main-chain atoms to coordinate ions: carbonyl oxygen atoms for K^+ ions (green) and amide nitrogen atoms for Cl^- ions (red). Both filters contain multiple close-spaced ion-binding sites. The Cl^--selectivity filter is that of a mutant ClC in which a glutamate amino acid was changed to glutamine.[64]

repulsion between ions in the pore. I find these similarities fascinating. They tell us that certain basic physical principles are important, such as the use of α-helix end charges to lower the dielectric barrier when ions cross the lipid membrane.

Trying to See a K^+ Channel Open and Close

Most ion channels conduct when called upon by a specific stimulus such as the binding of a ligand or a change in membrane voltage.[45] The processes by which ion conduction is turned on are called gating. The conduction of ions occurs on a time scale that is far too rapid to involve very large conformational changes of the proteins. That is undoubtedly one of the reasons why a single KcsA structure could tell us so much about ion selectivity and conduction. Gating on the other hand occurs on a much slower time scale and can involve large conformational changes of the proteins. The challenge for a structural description of gating is to capture a channel in both opened (on) and closed (off) conformations so that they can be compared.

Gating in the KcsA K^+ channel is controlled by intracellular pH values and the composition of the lipid membrane, but unfortunately the probability of the KcsA channel being open reaches a maximum value of only a few percent in functional assays.[46,47] At first we had no definitive way to know whether a gate was open or closed in the crystal structures. In the 1970s Armstrong had proposed the existence of a gate near the intracellular side of the membrane in voltage-dependent K^+ channels because he could "trap" large organic cations inside the pore between a selectivity filter near the extracellular side and a gate near the intracellular side.[9,48] Following these ideas, we crystallized KcsA with tetrabutylantimony (TBA), a heavy-atom version of one of his organic cations, and found that it binds inside the central cavity of KcsA.[49] This was very interesting because the approximately 10-Å diameter of TBA far exceeds the pore diameter leading up to the cavity: in KcsA the intracellular pore entrance is constricted to about 3.5 Å by the inner helix bundle (Figure 5b). Seeing TBA "trapped" in the cavity

 © 2004 Wiley-VCH Verlag GmbH & Co. KGaA, Weinheim

behind the inner helix bundle evoked Armstrong's classical view of K^+-channel gating, and implied that the inner helix bundle serves as a gate and is closed in KcsA. Mutational and spectroscopic studies in other laboratories also pointed to the inner helix bundle as a possible gate-forming structural element.[50,51]

Youxing Jiang and I hoped we could learn more about K^+-channel gating by determining the structures of new K^+ channels. From gene-sequence analysis we noticed that many prokaryotic K^+ channels contain a large C-terminus that encodes what we called RCK domains, and we suspected that these domains controlled pore opening, perhaps through binding of an ion or a small molecule. We determined the structure of isolated RCK domains from an *Escherichia coli* K^+ channel, but by themselves they were not very informative beyond hinting that a similar structure exists on the C-terminus of eukaryotic Ca^{2+}-dependent "BK" channels.[52] We subsequently determined the crystal structure of MthK, a complete K^+ channel containing RCK domains from *Methanobacterium thermoautotrophicus* (Figure 13).[53] This structure was extremely informative. The RCK domains form a "gating ring" on the intracellular side of the pore. In clefts between domains we could see what appeared to be divalent cation binding sites and the crystals had been grown in the presence of Ca^{2+} ions. In functional assays we discovered that the open probability of the MthK channel increased as the concentration of the Ca^{2+} or Mg^{2+} ions was raised, thus giving us good reason to believe that the crystal structure should represent the open conformation of a K^+ channel.

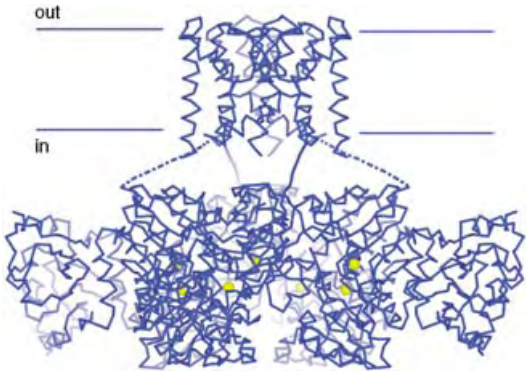


Figure 13. The MthK K^+ channel contains an intracellular gating ring (bottom) attached to its ion-conduction pore (top). Ca^{2+} ions (yellow) are bound to the gating ring in clefts in between domains. The connections between the gating ring and the pore, which were poorly ordered in the crystal, are shown as dashed lines.

In our MthK structure the inner helix bundle is opened like the aperture of a camera (Figure 14).[54] As a result, the pathway leading up to the selectivity filter from the intracellular side is about 10 Å wide, which explains how Armstrong's large organic cations can enter the cavity to block a K^+ channel, and how K^+ ions gain free access to the selectivity filter through aqueous diffusion. By comparing the KcsA and MthK channel structures it seemed that we were looking at examples of closed and opened K^+ channels, and could easily imagine the pore undergoing a conformational

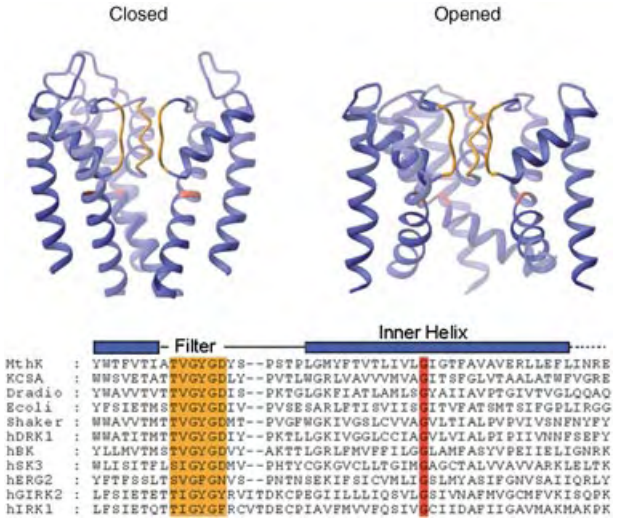


Figure 14. KcsA and MthK represent closed and opened K^+ channels. Three subunits of the closed KcsA K^+ channel (left) and opened MthK K^+ channel (right) are shown. The inner helices of MthK are bent at a glycine hinge (red), thus allowing the inner helix bundle to open. Partial amino acid sequences from a variety of K^+ channels with different gating domains are compared. Colors highlighting the selectivity filter sequence (orange) and inner helix glycine hinge (red) match colors used in the structures. Adapted from ref. [54].

change from closed to open. To open, the inner helices would have to bend at a point halfway across the membrane as their C-terminus is displaced laterally away from the pore axis by conformational changes in the gating ring. A glycine amino acid facilitates the bending in MthK by introducing a hinge point in the middle of the inner helix. Like MthK, KcsA and many other K^+ channels contain a glycine at the very same location; its conservation suggests that the inner helices move in a somewhat similar manner in many different K^+ channels (Figure 14).

Gating domains convert a stimulus into pore opening. Further studies are needed to understand how the free energy of Ca^{2+} binding is converted into pore opening in the MthK channel. The mechanistic details of ligand gating will vary from one channel type to the next because nature is very modular with ion channels, just like with other proteins. Gene sequences show us that a multitude of different domains can be found attached to the inner helices of different K^+ channels, thus allowing ions such as Ca^{2+} or Na^+, small organic molecules, and even regulatory proteins to control the conformational state of the pore and so gate the ion channel (http://www.ncbi.nlm.nih.gov/BLAST/).[55–58]

A fundamentally different kind of gating domain allows certain K^+, Na^+, Ca^{2+}, and nonselective cation channels to open in response to changes in the membrane voltage. Referred to as voltage sensors, these domains are connected to the outer helices of the pore and form a structural unit within the membrane. The basic principle of operation for a voltage sensor is the movement of protein charges through the membrane electric field coupled to pore opening.[59–61] Like transistors in an electronic device, voltage-dependent channels are electrical switches. They are a serious challenge for crystallographic analysis because of their conformational

 © 2004 Wiley-VCH Verlag GmbH & Co. KGaA, Weinheim

flexibility. Youxing Jiang and I working with Alice Lee and Jiayun Chen solved the structure of the voltage-dependent K^+ channel KvAP from the thermophilic Archea *Aeropyrum pernix* (Figure 15).[62,63] In the crystal of KvAP the voltage sensors, held by monoclonal Fab fragments, adopted a non-native conformation. This observation in itself is meaningful as it underscores the intrinsic flexibility of voltage sensors: in contrast Fab fragments had little effect on the more rigid KcsA K^+ channel and ClC Cl^- channel homologue, both of which we determined in the presence and absence of Fab fragments.[33,34,43,64] KvAP's voltage sensors contain a hydrophobic helix-turn-helix element with arginine residues beside the pore,[63] and functional experiments using tethered biotin and avidin show that this element moves relative to the plane of the membrane.[70] Additional structures revealing different channel conformations will be needed to better understand the mechanistic details of voltage-dependent gating. However, the KvAP structure and associated functional studies have provided a conceptual model for voltage-dependent gating processes—one in which the voltage sensors move at the protein–lipid interface in response to a balance between hydrophobic and electrostatic forces. Rees and colleagues at the California Institute of Technology determined the structure of a voltage-regulated mechanosensitive channel called MscS, and although it is unrelated to traditional voltage-dependent channels, it too contains hydrophobic helix-turn-helix elements with arginine residues apparently against the lipid membrane.[65] MscS and KvAP are fascinating membrane protein structures. They do not fit into the standard category of membrane proteins with rigid hydrophobic walls against the lipid membrane core. I find such proteins intruiging.

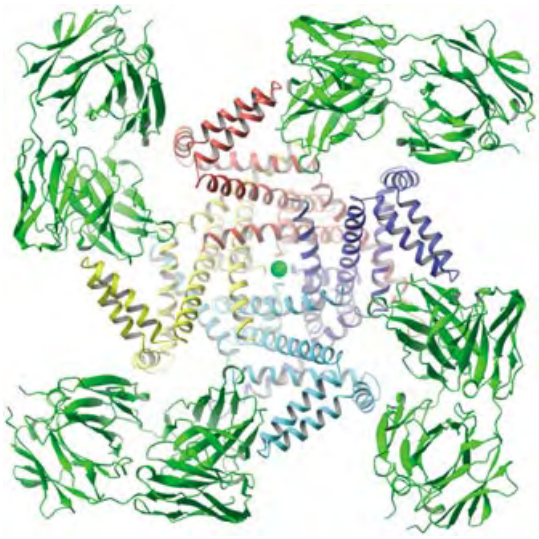


Figure 15. Crystal structure of the KvAP K^+ channel in a complex with monoclonal antibody Fab fragments. The channel is viewed along the pore axis from the intracellular side of the membrane, with α-helical subunits colored in blue, yellow, cyan, and red. One Fab fragment (green) is bound to the helix-turn-helix element of the voltage sensor on each subunit. Adapted from ref. [63].

We are only just beginning to understand the structural principles of ion-channel gating and regulation. Electrophysiological studies have uncovered a multitude of connections between cellular biochemical pathways and ion-channel function.[45] New protein structures are now beginning to do the same. The β subunits of certain eukaryotic voltage-dependent channels are structurally related to oxidoreductase enzymes.[66,67] PAS domains on other K^+ channels belong to a family of sensory molecules,[68] and a specialized structure on G-protein-gated channels forms a binding site for regulatory G-protein subunits.[71] The interconnectedness of ion-channel function with many aspects of cell function is beginning to reveal itself as complex and fascinating.

Concluding Remarks

I think the most exciting time in ion-channel studies is just beginning. So many of the important questions are waiting to be answered and we have the tools in hand to answer them. I am very optimistic about the future, and for the great possibilities awaiting young scientists who are now setting out to study ion channels and other membrane proteins. I consider myself very fortunate to have contributed to some small part of the knowledge we have today. Of course, my contributions would never have been possible without the

Table 1: MacKinnon laboratory from 1989 to 2003.

Postdoctoral researchers		Students	Staff scientists	Collaborators
Laura Escobar	Francis Valiyaveetil	Lise Heginbotham	Tatiana Abramson	Gary Yellen
Zhe Lu	Xiao-Dan Pfenninger-Li	Michael Root	John Lewis	Maria Garcia
Adrian Gross	Ming Zhou	Patricia Hidalgo	Alice Lee MacKinnon	Gerhard Wagner
Kenton Swartz	Ofer Yifrach	Sanjay Aggarwal	Sabine Mann	Andrzej Krezel
Chul-Seung Park	Yufeng Zhou	James Morrell	Richard Pfuetzner	Brian Chait
Rama Ranganathan	Sebastien Poget	Alexander Pico	Anling Kuo	Steve Cohen
Chinfei Chen	Motohiko Nishida	Vanessa Ruta	Minhui Long	Martine Cadene
Declan Doyle	Uta-Maria Ohndorf	Ian Berke	Amelia Kaufman	Benoit Roux
John Imredy	Steve Lockless		Ernest Campbell	Tom Muir
João Morais Cabral	Qiu-Xing Jiang		Jiayun Chen	
Youxing Jiang	Seok-Yong Lee			
Jacqueline Gulbis	Stephen Long			
Raimund Dutzler				

© 2004 Wiley-VCH Verlag GmbH & Co. KGaA, Weinheim

efforts and enthusiasm of the young scientists who have come from around the world to study ion channels with me (Table 1). I also owe thanks to the Rockefeller University, the Howard Hughes Medical Institute, and the National Institutes of Health for supporting my scientific research. I also thank the synchrotrons CHESS, NSLS, ALS, APS, and ESRF as well as my assistant Wendell Chin.

Received: March 1, 2004 [A662]

[1] "A quantitative description of membrane current and its application to conduction and excitation in nerve": A. L. Hodgkin, A. F. Huxley, *J. Physiol.* **1952**, *117*, 500 – 544.
[2] "Currents carried by sodium and potassium ions through the membrane of the giant axon of Loligo": A. L. Hodgkin, A. F. Huxley, *J. Physiol.* **1952**, *116*, 449 – 472.
[3] "The components of membrane conductance in the giant axon of Loligo": A. L. Hodgkin, A. F. Huxley, *J. Physiol.* **1952**, *116*, 473 – 496.
[4] "The dual effect of membrane potential on sodium conductance in the giant axon of Loligo": A. L. Hodgkin, A. F. Huxley, *J. Physiol.* **1952**, *116*, 497 – 506.
[5] "The potassium permeability of a giant nerve fibre": A. L. Hodgkin, R. D. Keynes, *J. Physiol.* **1955**, *128*, 61 – 88.
[6] "Ionic channels in nerve membranes": B. Hille, *Prog. Biophys. Mol. Biol.* **1970**, *21*, 1 – 32.
[7] "The permeability of the sodium channel to organic cations in myelinated nerve": B. Hille, *J. Gen. Physiol.* **1971**, *58*, 599 – 619.
[8] "Potassium channels in myelinated nerve. Selective permeability to small cations": B. Hille, *J. Gen. Physiol.* **1973**, *61*, 669 – 686.
[9] "Interaction of tetraethylammonium ion derivatives with the potassium channels of giant axons": C. M. Armstrong, *J. Gen. Physiol.* **1971**, *58*, 413 – 437.
[10] "Destruction of sodium conductance inactivation in squid axons perfused with pronase": C. M. Armstrong, F. Bezanilla, E. Rojas, *J. Gen. Physiol.* **1973**, *62*, 375 – 391.
[11] "Inactivation of the sodium channel. II. Gating current experiments": C. M. Armstrong, F. Bezanilla, *J. Gen. Physiol.* **1977**, *70*, 567 – 590.
[12] "Sodium channels and gating currents": C. M. Armstrong, *Physiol. Rev.* **1981**, *61*, 645 – 683.
[13] "Single-channel currents recorded from membrane of denervated frog muscle fibres": E. Neher, B. Sakmann, *Nature* **1976**, *260*, 799 – 802.
[14] "Sequence of a probable potassium channel component encoded at Shaker locus of Drosophila": B. L. Tempel, D. M. Papazian, T. L. Schwarz, Y. N. Jan, L. Y. Jan, *Science* **1987**, *237*, 770 – 775.
[15] "Molecular characterization of Shaker, a Drosophila gene that encodes a potassium channel": A. Kamb, L. E. Iverson, M. A. Tanouye, *Cell* **1987**, *50*, 405 – 413.
[16] "Shaker encodes a family of putative potassium channel proteins in the nervous system of Drosophila": O. Pongs, N. Kecskemethy, R. Muller, I. Krah-Jentgens, A. Baumann, H. H. Kiltz, I. Canal, S. Llamazares, A. Ferrus, *EMBO J.* **1988**, *7*, 1087 – 1096.
[17] "Mechanism of charybdotoxin block of the high-conductance, Ca^{2+}-activated K^+ channel": R. MacKinnon, C. Miller, *J. Gen. Physiol.* **1988**, *91*, 335 – 349.
[18] "Charybdotoxin block of Shaker K^+ channels suggests that different types of K^+ channels share common structural features": R. MacKinnon, P. H. Reinhart, M. M. White, *Neuron* **1988**, *1*, 997 – 1001.
[19] "Purification and characterization of three inhibitors of voltage-dependent K^+ channels from Leiurus quinquestriatus var. hebraeus venom": M. L. Garcia, M. Garcia-Calvo, P. Hidalgo, A. Lee, R. MacKinnon, *Biochemistry* **1994**, *33*, 6834 – 6839.
[20] "Mutant potassium channels with altered binding of charybdotoxin, a pore-blocking peptide inhibitor": R. MacKinnon, C. Miller, *Science* **1989**, *245*, 1382 – 1385.
[21] "Determination of the subunit stoichiometry of a voltage-activated potassium channel": R. MacKinnon, *Nature* **1991**, *350*, 232 – 235.
[22] "Pore loops: an emerging theme in ion channel structure": R. MacKinnon, *Neuron* **1995**, *14*, 889 – 892.
[23] "Revealing the architecture of a K^+ channel pore through mutant cycles with a peptide inhibitor": P. Hidalgo, R. MacKinnon, *Science* **1995**, *268*, 307 – 310.
[24] "Spatial localization of the K^+ channel selectivity filter by mutant cycle-based structure analysis": R. Ranganathan, J. H. Lewis, R. MacKinnon, *Neuron* **1996**, *16*, 131 – 139.
[25] "Mutations affecting TEA blockade and ion permeation in voltage-activated K^+ channels": R. MacKinnon, G. Yellen, *Science* **1990**, *250*, 276 – 279.
[26] "Mutations affecting internal TEA blockade identify the probable pore-forming region of a K^+ channel": G. Yellen, M. E. Jurman, T. Abramson, R. MacKinnon, *Science* **1991**, *251*, 939 – 942.
[27] "The inner quaternary ammonium ion receptor in potassium channels of the node of Ranvier": C. M. Armstrong, B. Hille, *J. Gen. Physiol.* **1972**, *59*, 388 – 400.
[28] "A functional connection between the pores of distantly related ion channels as revealed by mutant K^+ channels": L. Heginbotham, T. Abramson, R. MacKinnon, *Science* **1992**, *258*, 1152 – 1155.
[29] "Mutations in the K^+ channel signature sequence": L. Heginbotham, Z. Lu, T. Abramson, R. MacKinnon, *Biophys. J.* **1994**, *66*, 1061 – 1067.
[30] "An Escherichia coli homologue of eukaryotic potassium channel proteins": R. Milkman, *Proc. Natl. Acad. Sci. USA* **1994**, *91*, 3510 – 3514.
[31] "A prokaryotic potassium ion channel with two predicted transmembrane segments from Streptomyces lividans": H. Schrempf, O. Schmidt, R. Kummerlen, S. Hinnah, D. Muller, M. Betzler, T. Steinkamp, R. Wagner, *EMBO J.* **1995**, *14*, 5170 – 5178.
[32] "Structural conservation in prokaryotic and eukaryotic potassium channels": R. MacKinnon, S. L. Cohen, A. Kuo, A. Lee, B. T. Chait, *Science* **1998**, *280*, 106 – 109.
[33] "The structure of the potassium channel: molecular basis of K^+ conduction and selectivity": D. A. Doyle, J. H. Morais Cabral, R. A. Pfuetzner, A. Kuo, J. M. Gulbis, S. L. Cohen, B. T. Chait, R. MacKinnon, *Science* **1998**, *280*, 69 – 77.
[34] "Chemistry of ion coordination and hydration revealed by a K^+ channel–Fab complex at 2.0 Å resolution": Y. Zhou, J. H. Morais-Cabral, A. Kaufman, R. MacKinnon, *Nature* **2001**, *414*, 43 – 48.
[35] "The cavity and pore helices in the KcsA K^+ channel: electrostatic stabilization of monovalent cations": B. Roux, R. MacKinnon, *Science* **1999**, *285*, 100 – 102.
[36] "Die Struktur des KNCS-Komplexes von Nonactin": M. von Dobler, J. D. Dunitz, B. T. Kilbourn, *Helv. Chim. Acta* **1969**, *52*, 2573 – 2583.
[37] J. D. Dunitz, M. von Dobler, *Structural studies of ionophores and their ion-complexes. In Biological aspects of inorganic chemistry* (Eds.: A. W. Addison, W. R. Cullen, D. Dolphin, B. R. James, Wiley, New York, **1977**, pp. 113 – 140.
[38] "Energetic optimization of ion conduction rate by the K^+ selectivity filter": J. H. Morais-Cabral, Y. Zhou, R. MacKinnon, *Nature* **2001**, *414*, 37 – 42.
[39] W. P. Jencks, *Catalysis in chemistry and enzymology*, Dover Publications, **1987**..
[40] "The occupancy of ions in the K^+ selectivity filter: Charge balance and coupling of ion binding to a protein conformational

change underlie high conduction rates": Y. Zhou, R. MacKinnon, *J. Mol. Biol.* **2003**, *333*, 965 – 975.
[41] "The CLC chloride channel family": T. J. Jentsch, T. Friedrich, A. Schriever, H. Yamada, *Pfluegers Arch.* **1999**, *437*, 783 – 795.
[42] "A decade of CLC chloride channels: structure, mechanism, and many unsettled questions": M. Maduke, C. Miller, J. A. Mindell, *Annu. Rev. Biophys. Biomol. Struct.* **2000**, *29*, 411 – 438.
[43] "X-ray structure of a ClC chloride channel at 3.0 Å reveals the molecular basis of anion selectivity": R. Dutzler, E. B. Campbell, M. Cadene, B. T. Chait, R. MacKinnon, *Nature* **2002**, *415*, 287 – 294.
[44] "Proton-coupled chloride transport mediated by ClC-ec1, a bacterial homologue of the ClC chloride channels": A. Accardi, C. Miller, *Biophys. J.* **2004**, *86*, 286.
[45] B. Hille, *Ion Channels of Excitable Membranes*, Sinauer Associates, Sunderland, MA, **2001**.
[46] "pH-dependent gating in the Streptomyces lividans K^+ channel": L. G. Cuello, J. G. Romero, D. M. Cortes, E. Perozo, *Biochemistry* **1998**, *37*, 3229 – 3236.
[47] "Functional reconstitution of a prokaryotic K^+ channel": L. Heginbotham, L. Kolmakova-Partensky, C. Miller, *J. Gen. Physiol.* **1998**, *111*, 741 – 749.
[48] "Ionic pores, gates, and gating currents": C. M. Armstrong, *Q. Rev. Biophys.* **1974**, *7*, 179 – 210.
[49] "Potassium channel receptor site for the inactivation gate and quaternary amine inhibitors": M. Zhou, J. H. Morais-Cabral, S. Mann, R. MacKinnon, *Nature* **2001**, *411*, 657 – 661.
[50] "Structural rearrangements underlying K^+-channel activation gating": E. Perozo, D. M. Cortes, L. G. Cuello, *Science* **1999**, *285*, 73 – 78.
[51] "Blocker protection in the pore of a voltage-gated K^+ channel and its structural implications": D. del Camino, M. Holmgren, Y. Liu, G. Yellen, *Nature* **2000**, *403*, 321 – 325.
[52] "Structure of the RCK domain from the E. coli K^+ channel and demonstration of its presence in the human BK channel": Y. Jiang, A. Pico, M. Cadene, B. T. Chait, R. MacKinnon, *Neuron* **2001**, *29*, 593 – 601.
[53] "Crystal structure and mechanism of a calcium-gated potassium channel": Y. Jiang, A. Lee, J. Chen, M. Cadene, B. T. Chait, R. MacKinnon, *Nature* **2002**, *417*, 515 – 522.
[54] "The open pore conformation of potassium channels": Y. Jiang, A. Lee, J. Chen, M. Cadene, B. T. Chait, R. MacKinnon, *Nature* **2002**, *417*, 523 – 526.
[55] "A component of calcium-activated potassium channels encoded by the Drosophila slo locus": N. S. Atkinson, G. A. Robertson, B. Ganetzky, *Science* **1991**, *253*, 551 – 555.
[56] "Structure of the gating domain of a Ca^{2+}-activated K^+ channel complex with Ca^{2+}/calmodulin": M. A. Schumacher, A. F. Rivard, H. P. Bachinger, J. P. Adelman, *Nature* **2001**, *410*, 1120 – 1124.
[57] "The sodium-activated potassium channel is encoded by a member of the Slo gene family": A. Yuan, C. M. Santi, A. Wei, Z. W. Wang, K. Pollak, M. Nonet, L. Kaczmarek, C. M. Crowder, L. Salkoff, *Neuron* **2003**, *37*, 765 – 773.
[58] "Primary structure and functional expression of a rat G-protein-coupled muscarinic potassium channel": Y. Kubo, E. Reuveny, P. A. Slesinger, Y. N. Jan, L. Y. Jan, *Nature* **1993**, *364*, 802 – 806.
[59] "Charge movement associated with the opening and closing of the activation gates of the Na^+ channels": C. M. Armstrong, F. Bezanilla, *J. Gen. Physiol.* **1974**, *63*, 533 – 552.
[60] "Voltage gating of ion channels": F. J. Sigworth, *Q. Rev. Biophys.* **1994**, *27*, 1 – 40.
[61] "The voltage sensor in voltage-dependent ion channels": F. Bezanilla, *Physiol. Rev.* **2000**, *80*, 555 – 592.
[62] "Functional analysis of an archeabacterial voltage-dependent K^+ channel": V. Ruta, Y. Jiang, A. Lee, J. Chen, R. MacKinnon, *Nature* **2003**, *422*, 180 – 185.
[63] "X-ray structure of a voltage-dependent K^+ channel": Y. Jiang, A. Lee, J. Chen, V. Ruta, M. Cadene, B. Chait, R. MacKinnon, *Nature* **2003**, *423*, 33 – 41.
[64] "Gating the selectivity filter in ClC chloride channels": R. Dutzler, E. B. Campbell, R. MacKinnon, *Science* **2003**, *300*, 108 – 112.
[65] "Crystal structure of Escherichia coli MscS, a voltage-modulated and mechanosensitive channel": R. B. Bass, P. Strop, M. Barclay, D. C. Rees, *Science* **2002**, *298*, 1582 – 1587.
[66] "Structure of a voltage-dependent K^+ channel beta subunit": J. M. Gulbis, S. Mann, R. MacKinnon, *Cell* **1999**, *97*, 943 – 952.
[67] "Structure of the cytoplasmic β subunit-T1 assembly of voltage-dependent K^+ channels": J. M. Gulbis, M. Zhou, S. Mann, R. MacKinnon, *Science* **2000**, *289*, 123 – 127.
[68] "Crystal structure and functional analysis of the HERG potassium channel N-terminus: a eukaryotic PAS domain": J. H. Morais Cabral, A. Lee, S. L. Cohen, B. T. Chait, M. Li, R. MacKinnon, *Cell* **1998**, *95*, 649 – 655.
[69] "A mutant KcsA K^+ channel with altered conduction sp properties and selectivity filter ion distribution": M. Zhou, R. MacKinnon, *J. Mol. Biol.* **2004**, *338*, 839 – 846.
[70] "The principle of gating charge movement in a voltage-dependent K^+ channel": Y. Jiang, V. Ruta, J. Chen, A. Lee, R. MacKinnon, *Nature* **2003**, *423*, 42 – 48.
[71] "Structural Basis of Inward Rectification: Cytoplasmic Pore of the G Protein-Gated Inward Rectifier GIRK1 at 1.8 Å Resolution": M. Nishida, R. MacKinnon, *Cell* **2002**, *111*, 957 – 965.

 © 2004 Wiley-VCH Verlag GmbH & Co. KGaA, Weinheim

Membrane Proteins

Aquaporin Water Channels (Nobel Lecture)**

*Peter Agre**

Keywords:
aquaporins · medicinal chemistry · membrane proteins · Nobel lecture · protein structures

From the Contents

Introduction 4278

The Discovery of AQP1 4279

Structure of AQP1 4281

The Aquaporin and Aquaglyceroporin Protein Family 4282

AQP1 Proteins in Kidneys 4283

AQP1-null Phenotypes 4284

Other Aquaporins—AQP2 in the Collecting Ducts 4285

AQP6 in Acid Secretory Cells 4286

AQPo in Lenses 4286

AQP4 in the Brain 4286

AQP5 in Secretory Glands 4287

Aquaglyceroporins AQP7 and AQP9 4287

Nonhuman Aquaporins 4287

Conclusion 4288

Thank you very much. I am humbled, I am delighted; I am honored. It is every scientist's dream to give the Nobel Lecture in Stockholm. But I would not be honest if I did not tell you that I am having a little anxiety being on this platform. I have lectured a number of times in Sweden, and I thought I would share with you some events preceding a special lecture that I gave here a few years ago. Arriving at Arlanda Airport, I waited in line at the Passport Control behind a group of businessmen in suits with briefcases. I heard the first in line asked by the control officer to state the purpose of his visit to Sweden. When the man replied "business," the officer approved and stamped his passport. One at a time, each stepped forward and was asked the same thing; each answered "business" and was approved. Eventually it was my turn, and I was dressed in rumpled clothes after spending the night in the Economy Minus section of an SAS jetliner. The officer asked me the purpose of my visit, and I said "I am here to give the von Euler Lecture at Karolinska Institute." The officer immediately looked up, stared at me, and asked, "Are you nervous?" At that point I became intensely nervous and said "Yes, I am a little nervous." The officer looked up again and stated "Well, you should be!" So if the lecturers look a little nervous, the problem is at Arlanda.

Introduction

I am going to talk about aquaporin water channels. We have studied these proteins for several years, and we now understand that they explain how water crosses biological membranes. Water is commonly regarded as the "solvent of life", since our bodies are 70% water. All other vertebrates, invertebrates, microbes, and plants are also primarily water. The organization of water within biological compartments is fundamental to life, and the aquaporins serve as the plumbing systems for cells. Aquaporins explain how our brains secrete and absorb spinal fluid, how we can generate aqueous humor within our eyes, how we can secrete tears, saliva, sweat, and bile, and how our kidneys can concentrate urine so effectively. These proteins are fundamental to mammalian physiology, but they are also very important in the lives of microorganisms and plants.

I wish to discuss the background in order to give credit to the individuals who were in this field long before we joined. With the recognition of the lipid bilayer as the plasma membranes of cells back in the 1920s, it was correctly proposed that water could move through the membrane simply by diffusing through the lipid bilayer. The current view is that the lipid bilayer has a finite permeability for water, but, in addition, a set of proteins exists that we now refer to as

[*] Prof. Dr. P. Agre
The Johns Hopkins University
School of Medicine
Baltimore, MD 21205 (USA)
Fax: (+1) 410-955-3149
E-mail: pagre@jhmi.edu

[**] Copyright© The Nobel Foundation 2003. We thank the Nobel Foundation, Stockholm, for permission to print this lecture.

 © 2004 Wiley-VCH Verlag GmbH & Co. KGaA, Weinheim DOI: 10.1002/anie.200460804

"aquaporins." Their existence was suggested by a group of pioneers in the water transport field, such as Arthur K. Solomon in Boston, Alan Finkelstein in New York, Robert Macey in Berkeley, Gheorghe Benga in Romania, Guillermo Whittembury in Venezuela, and Mario Parisi in Argentina, who preceded us by decades. They predicted by biophysical methods that water channels must exist in certain cell types with high water permeability such as renal tubules, salivary glands, and red cells (see the review by Finkelstein[1]).

The difference between diffusional and channel-mediated water permeability is fairly remote. Diffusion is a low capacity, bidirectional movement of water that occurs in all cell membranes, whereas the membranes of a subset of cells with aquaporin proteins have a very high capacity for permeation by water. This permeability is selective, since water (H_2O) passes through the membranes with almost no resistance, while the hydronium ion (H_3O^+) does not permeate the proteins. This distinction is essential to life. As I will discuss later, our kidneys reabsorb 99% of the water from the primary filtrate to prevent us from becoming dehydrated. If our kidneys reabsorbed water *and* acid, we would develop systemic acidosis.

The movement of water is directed by osmotic gradients, and so aquaporins are not pumps or exchangers. They form a simple pore that allows water to rapidly pass through membranes by osmosis, a phenomenon that we all learned about in middle school. There are also other differences between diffusion and channel-mediated water transport. No inhibitors are known for simple diffusion. In contrast, mercury compounds were discovered by Robert Macey to inhibit water transport in red blood cells, but water permeability was restored by treatment with reducing agents.[2] These observations led to the prediction that water channels must be proteins with sulfanyl groups and characteristically low Arrhenius activation energy.

A number of investigators attempted to identify the water channel molecule by using very logical approaches, but identification proved a very difficult problem. Water is ubiquitous and cannot be modified to include photoactivated side chains. Attempts at expression cloning were unsuccessful. Isotopic mercury compounds were used to label several membrane proteins: the anion-exchanger protein (band 3) by Solomon and a group of several proteins (band 4.5) by Benga. Nevertheless, none of the proteins were isolated, reconstituted, and shown to transport water (see the review in Ref. [3]).



Peter Agre received his MD in 1974 from Johns Hopkins University (Baltimore, Maryland, USA). He was a post-doctoral researcher at Case Western Reserve University (1975–1978) and at the University of North Carolina at Chapel Hill (1980–1981). After research work in the group of V. Bennett (1981–1983) he became Assistant Professor at Johns Hopkins School of Medicine in 1984, and since 1993 he has been Professor of Biological Chemistry and Professor of Medicine. He was awarded the Nobel Prize for Chemistry in 2003 for his work on aquaporins.

The Discovery of AQP1

The field was essentially stuck, but following the well-known scientific approach known as "sheer blind luck", we stumbled upon the protein that is the answer to the question: Do water channels exist? Looking through our notebooks for the earliest studies that showed there was such a protein, I found an autoradiograph prepared by my first lab assistant Andy Asimos. I was at that time a hematologist, and we were studying the Rhesus (Rh) blood group antigens. We were attempting to raise antibodies in rabbits to the denatured partially purified Rh polypeptide. The rabbits vigorously produced antibodies that reacted with a polypeptide of approximately 30 kDa, and a series of higher-order oligomers and glycosylated proteins. We were very excited about this, but we failed to recognize initially that our antibody did not react with the core Rh polypeptide (32 kDa), as seen clearly by silver staining of sodium dodecyl sulfate polyacryamide electrophoresis gels (SDS-PAGE). Instead, our antibodies reacted only with a 28-kDa polypeptide that we had mistakenly believed to be a breakdown product of the larger Rh polypeptide. Thus, the 28 kDa was an unrelated protein that merely contaminated our Rh preparations.

A number of features about the 28-kDa protein created a large amount of interest. Postdoctoral fellow Brad Denker and laboratory assistant Barbara Smith isolated the protein by a simple approach based upon detergent solubility. Silver staining of the electrophoresis gels revealed a discrete band of 28 kDa in detergent-insoluble extracts. No one had seen this protein before, since it failed to stain with the conventional protein stains such as Coomassie blue. The protein was then purified in large amounts from the membranes of human red blood cells.[4,5]

The 28-kDa protein was strikingly abundant: With approximately 200000 copies per red blood cell, it was one of the major proteins in the membrane. In a way, this may be compared to the surprise one would have if, while driving along a road in northern Sweden, one came upon a town with 200000 people not on the map—it certainly got our attention. Moreover, the protein had features that suggested it was a tetrameric membrane-spanning protein and thus was a channel—but a channel for what? The purified protein also provided us with the N-terminal amino acid sequence that we used for cDNA cloning. Using our antibody, we looked at several other tissues and found the protein is also strikingly abundant in human kidney. We observed staining over the apical and basolateral membranes of proximal renal tubules and the descending thin limb of the loops of Henle, but we were still frustrated by our failure to recognize what the protein's function might be.

In science, one should use all available resources to solve difficult problems. One of our most powerful resources is the insight of our colleagues. I spoke to a dozen or more well-known biochemists and physiologists about this protein, but none could predict what its function might be. My clinical

 DOI: 10.1002/anie.200460804 © 2004 Wiley-VCH Verlag GmbH & Co. KGaA, Weinheim

mentor, John C. Parker (1935–1993) at the University of North Carolina at Chapel Hill was the first to suggest to me that red blood cells and renal tubules were exceedingly permeable to water. He recommended that we consider a role in water transport through membranes. While John did not live to see our later studies, he did live to see our initial discovery and we celebrated together.

Gregory Preston, then a postdoctoral fellow in my research group, cloned the cDNA from an erythroid library.[6] The coding region corresponded to a 269 amino acid polypeptide, which was predicted by hydropathy analysis to have six bilayer-spanning domains. Interestingly, the amino terminal half (repeat 1) and the carboxy terminal half of the molecule (repeat 2) were genetically about 20% identical. The two loops B and E were more highly related to each other, and each contained the signature motif: asparagine, proline, alanine (NPA, Figure 1). By examining the genetics database we recognized several sequence-related DNAs from diverse sources: lenses of cow eyes, brains of fruit flies, bacteria, and plants. Nevertheless, none was functionally defined.

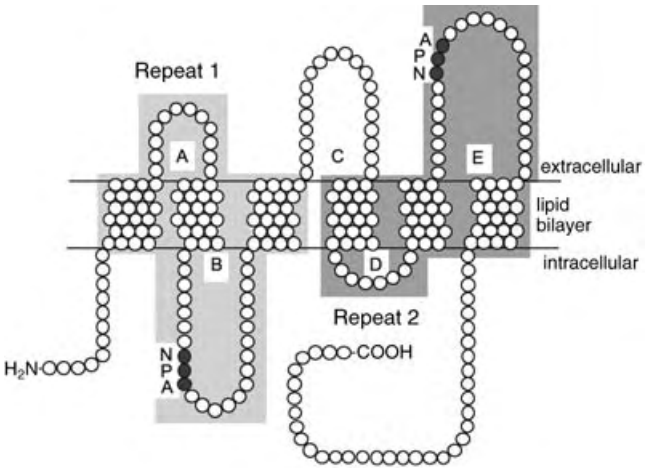


Figure 1. Membrane orientation of AQP1 predicted from primary amino acid sequence. Two tandem repeat units of the protein each have three bilayer-spanning domains and are oriented 180° with respect to each other. The loops B and E each contain the conserved motif Asn-Pro-Ala (NPA).

These clues heightened our suspicion that the 28-kDa protein was a water transporter, so we tested for possible water-transport function in collaboration with our colleague Bill Guggino at Johns Hopkins University. We used oocytes from the frog *Xenopus laevis*. This convenient expression system was particularly useful, since frog oocytes have very low water permeability and survive even in fresh-water ponds. Control oocytes were injected with water alone; test oocytes were injected with 2 ng of cRNA encoding our protein. After three days of protein synthesis, the oocytes appeared essentially identical. Then we stressed the oocytes by transferring them to distilled water, and an amazing difference was immediately apparent: The control oocytes, having exceedingly low water permeability, failed to swell, while the test oocytes were highly permeable to water and exploded like popcorn (Figure 2).[7] This result produced much celebration in the laboratory; the celebrations continue still. The protein was christened "aquaporin" and is now officially designated "AQP1," the first functionally defined water-channel protein.[8]

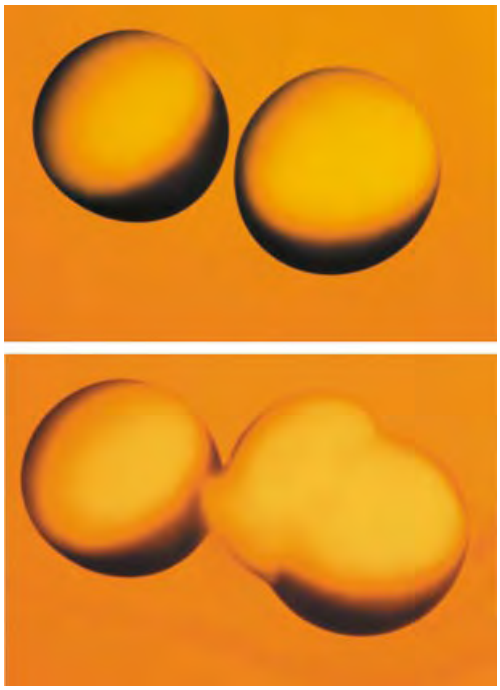


Figure 2. Functional expression of AQP1 water channels in *Xenopus laevis* oocytes. The control oocyte (left) was injected with water, the test oocyte (right) was injected with AQP1-coding cRNA. The oocytes were transferred to hypotonic buffer. After 30 s (top) the AQP1 oocyte has begun to swell and after 3 min (bottom) it has exploded. Modified and reprinted with permission from Ref. [7].

We confirmed the function of this protein by studying the purified AQP1 reconstituted into synthetic lipid vesicles with diameters of about 0.1 microns prepared by our colleague Suresh Ambudkar at Johns Hopkins University.[9] These simple membrane vesicles were examined by freeze-fracture electron microscopy by our colleague Arvid Maunsbach, from the University of Aarhus. When lipid was reconstituted without protein, the membrane surfaces were smooth; however, membranes reconstituted with AQP1 contained many intramembraneous particles with diameters of 0.01 microns.[10] We tested the membranes for water permeability in collaboration with Mark Zeidel at Harvard Medical School. The simple liposomes shrank on transfer to hypertonic buffer by using stopped-flow techniques, and reached equilibrium in about one half second; this is believed to represent the baseline water permeability. When membranes reconstituted with AQP1 were examined, the shrinking occurred much more rapidly, with equilibrium reached in about 20 ms. The channel-mediated flow of water was confirmed, since it was inhibited with mercury compounds. We calculated the Arrhenius activation energy (< 5 kcal mol^{-1}), and determined the unit permeability to be about $3\times$

 © 2004 Wiley-VCH Verlag GmbH & Co. KGaA, Weinheim

10^9 water molecules per subunit per second. Importantly, we attempted to measure proton permeation of AQP1, but despite massive water permeability, acid permeation was not detected. These studies verified that we had, in fact, isolated the long-sought water-channel protein.

Structure of AQP1

Subsequent efforts were devoted to identifying the binding site for the mercury inhibitors predicted by the studies of Macey. Mercury compounds react with free sulfanyl groups in cysteine. Four cysteine residues are found in the AQP1 polypeptide, but only the residue in loop E (Cys-189 proximal to the second NPA motif) is inhibited by mercury compounds. We altered the AQP1 sequence by site-directed mutagenesis and expressed the recombinants in oocytes for water permeability studies. Mutation of this residue to serine (Cys-189-Ser) resulted in full water permeability without inhibition by mercury compounds. When we then replaced the alanine residue in the corresponding position of loop B with a cysteine residue (Ala-73-Cys), the protein exhibited water permeability that was sensitive to the presence of mercury compounds.[11] Substitutions elsewhere in the AQP1 failed to produce this behavior. This result suggested to us that loops B and E in opposite parts of the molecule must somehow form the aqueous pore. The model that we concocted turned out to be schematically correct and was termed "the hourglass"—an ancient timepiece that allows sand to run from the upper chamber to lower chamber; if inverted, the sand will flow in the opposite direction.

Six bilayer-spanning domains were predicted to surround a central domain containing loop B, which dips into the membrane from the cytoplasmic surface, and loop E, which dips into the membrane from the extracellular surface (Figure 3). The overlap of loops B and E was predicted to form a single aqueous pore down through the center of the molecule with the NPA motifs juxtaposed and the binding site of the mercurial inhibitors alongside.[12] The AQP1 protein is a tetramer with a central pore in each subunit. Thus, AQP1 is structurally unlike ion-channel proteins where four subunits surround a single central pore.

We then sought to establish the high-resolution structure of AQP1 in collaboration with Andreas Engel and his research group at the Biozentrum in Basel. We were later joined by Yoshinori Fujiyoshi and his research group from Kyoto University. AQP1 protein from human red blood cells was purified by Barb Smith in our laboratory; Andreas's student Tom Walz reconstituted it into synthetic membranes at very high protein concentrations. Under these conditions the AQP1 protein forms remarkably symmetrical arrays that are referred to as membrane crystals. By measuring the water permeability, we confirmed that the function was 100% retained, thus giving us confidence that the structure we deduced would be the biologically relevant structure.[13]

By using the techniques of cryoelectron microscopy and atomic force microscopy, our colleagues in Basel and Kyoto undertook studies that provided an electron-density map of human AQP1 at a resolution of 3.8 Å. Models were developed using constraints established by our site-directed mutagenesis studies.[14] When a single AQP1 subunit is viewed in cross-section in the middle of the membrane bilayer, a single aqueous pore is visible with hydrophobic residues lining most

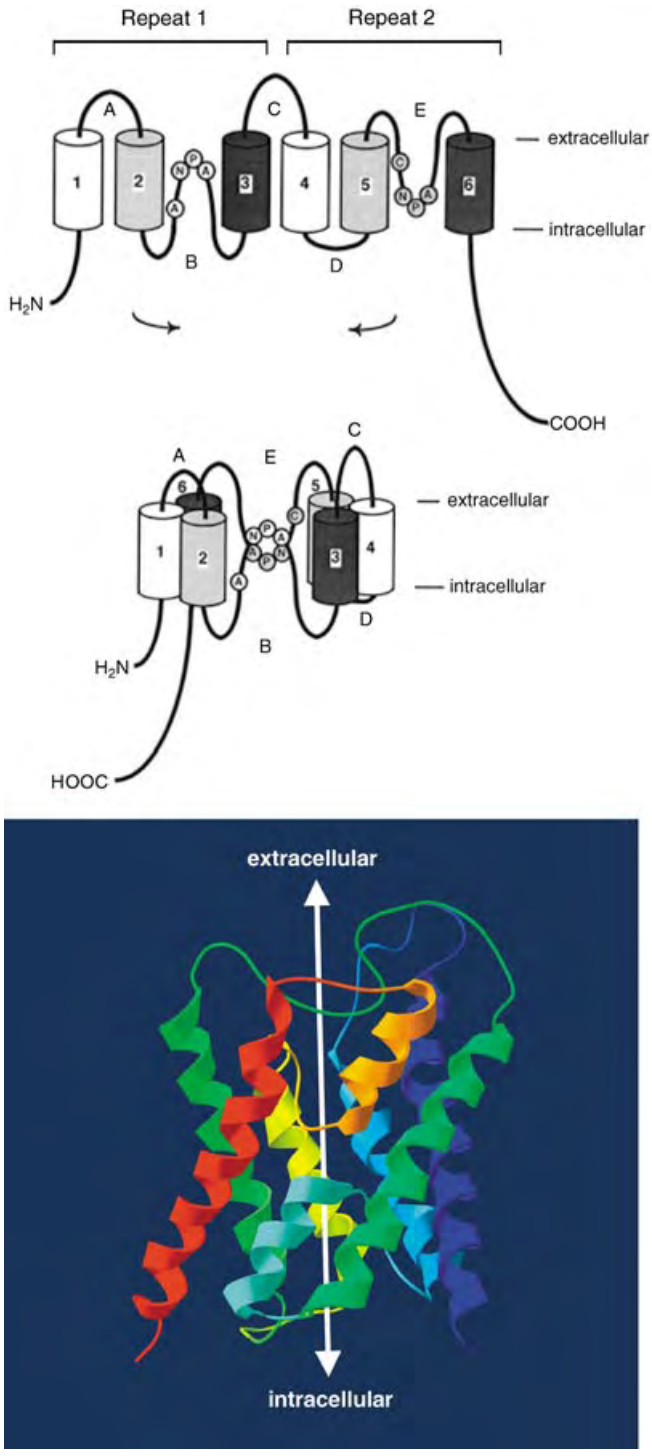


Figure 3. Hourglass model for the membrane topology of the AQP1 subunit. Top: Schematic representation of the folding of loops B and E; the loops overlap within the lipid bilayer to form a single aqueous pathway. Bottom: Ribbon model of the three-dimensional structure of the AQP1 subunit. Modified and reprinted with permission from Refs. [12] and [19].

 © 2004 Wiley-VCH Verlag GmbH & Co. KGaA, Weinheim

of the circumference of the wall, but the two highly conserved asparagine residues of the NPA motifs are aligned on the other wall. When viewed in longitudinal section, a narrow aqueous pore is visible with the two highly conserved asparagine residues.

We faced the question of how a simple pore with no moving parts could allow rapid transit of water with no movement of protons. Exciting contributions by X-ray crystallographers in the groups of Robert Stroud at UCSF and Bing Jap at Lawrence Berkeley Laboratory solved the atomic structures of the glycerol facilitator GlpF from *E. coli*,[15] and AQP1 from bovine red blood cells[16] at 2.2-Å resolution. These observations enabled molecular dynamics simulations to be performed by Bert de Groot and Helmut Grubmüller at the University of Göttingen[17] and the group of Klaus Schulten at University of Illinois at Urbana-Champaign.[18] We now understand how this protein facilitates the movement of water but not protons. If water were simply H_2O, it would be a gas (such as in steam), but water in a bulk solution exists as $(H_2O)_n$, with hydrogen-bonding interactions between adjacent water molecules causing it to be a liquid. If water existed as a column of aligned water molecules in contact with each other, protons would rapidly jump along by a mechanism known as the Grotthus effect ("proton wire").

The hourglass structure of the AQP1 molecule has an extracellular vestibule and an internal vestibule where water is in bulk solution. These vestibules are separated by a distance of approximately 20 Å, and linked through a channel which is so narrow that water moves through in single file while protons are reflected. Near the top of this bridge the channel reaches its narrowest constriction of 2.8 Å. Thus, the pore is just large enough to accommodate a single water molecule. At this site, the side chain of a perfectly conserved arginine residue following the NPA motif in loop E forms a fixed positive charge, and a conserved histidine residue on the other wall forms a partial positive charge; together they serve to repel protons. Further along, another barrier to protons exists where a single water molecule will transiently undergo a transient dipole reorientation as it simultaneously forms hydrogen bonds with the side chains of the two asparagine residues in the juxtaposed NPA motifs. In addition, the nonbilayer-spanning α-helices in the distal ends of loops B and E contribute partial positive charges that further serve to block proton conduction (Figure 4 left; see also the review by Kozono et al.[19]). The right-hand side of Figure 4 shows how mercury compounds inhibit water flow through AQP1. The side chain of Cys-189 lies along the pore, so if it is blocked by a mercury compound, the channel will be occluded.

The Aquaporin and Aquaglyceroporin Protein Family

While we were pursuing studies of AQP1, several other research groups from around the world became interested in

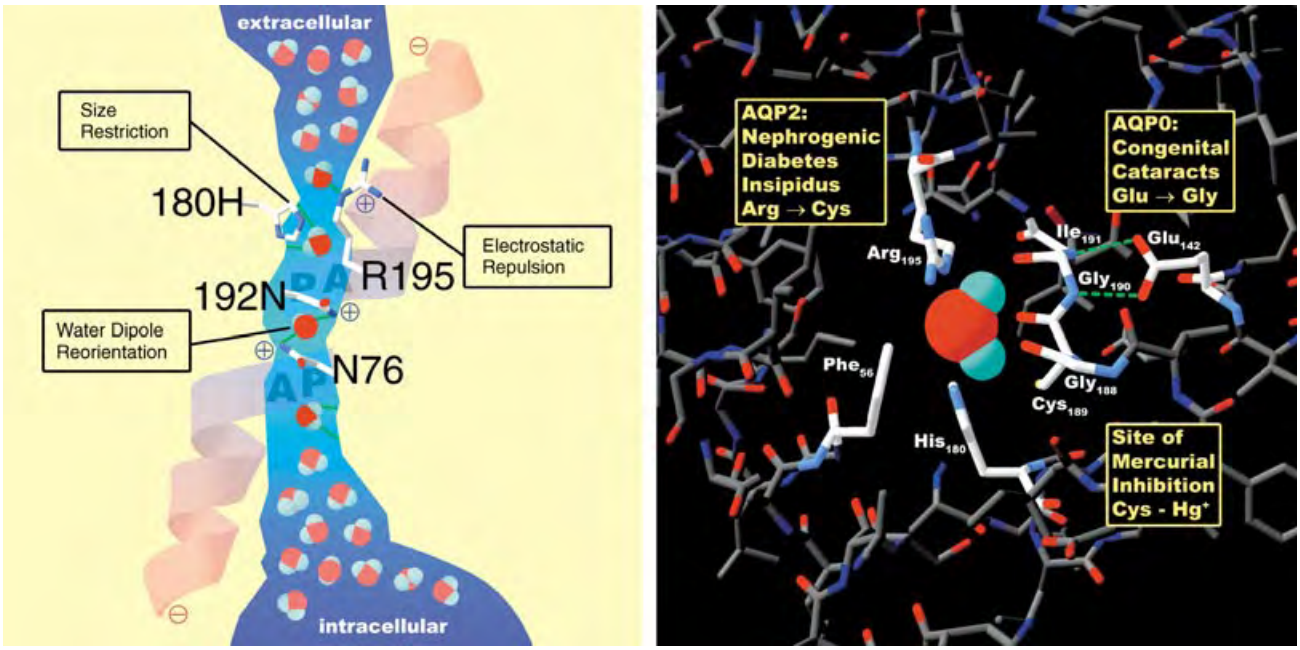


Figure 4. Schematic representation of the selective flow of water through the AQP1 subunit and residues involved in human disease. Left: The sagittal cross-section of AQP1 reveals bulk water in the extracellular and intracellular vestibules of the hourglass structure. These vestibules are separated by a 20-Å channel through which water passes in a single file with transient interactions with pore-lining residues that prevent the formation of hydrogen bonds between the water molecules. Two structural elements are believed to prevent permeation by protons (H_3O^+): 1) electrostatic repulsion is created by a fixed positive charge from the pore-lining arginine residue (R195) at a 2.8-Å narrowing in the channel; 2) reorientation of the water dipole occurs from the simultaneous hydrogen bonding of water molecule with the side chains of two asparagine residues in NPA motifs (N192 and N76). Two partial positive charges at the center of the channel result from the orientation of two nonmembrane-spanning α-helices distal to the NPA motifs. Right: Space-filling representation of a water molecule at the narrowest region of a pore (cross-section). The binding site of mercury inhibitors at cysteine residue Cys189 in AQP1; the AQP2 mutation in nephrogenic diabetes insipidus (Arg→Cys); and AQP0 mutation in congenital cataracts (Glu→Gly) are highlighted. Reprinted with permission from Ref. [19].

 © 2004 Wiley-VCH Verlag GmbH & Co. KGaA, Weinheim

what is now known to be a large family of related proteins. The combined efforts of these labs have led to the molecular identification of 12 mammalian aquaporin homologues, and several hundred related proteins have been recognized in other vertebrates as well as invertebrates, plants, and unicellular microorganisms. The mammalian homologues may be loosely clustered into two subsets (Figure 5). The first is referred to as "classical aquaporins", since they were initially considered to be exclusive water pores. The second is referred to as "aquaglyceroporins", since they are permeated by water and glycerol. Interestingly, *E. coli* has one member of each, AqpZ[20] and GlpF, isolated. Together, the mammalian aquaporins and aquaglyceroporins are now known to contribute to multiple physiological processes that occur during our daily lives.

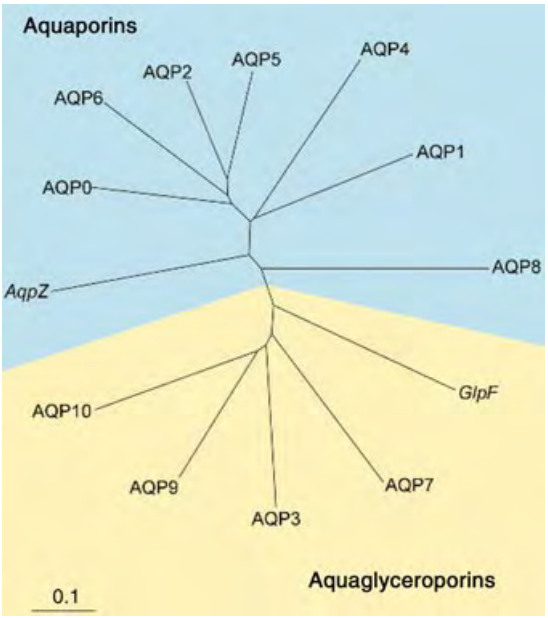


Figure 5. The human aquaporin gene family contains two subsets: Homologues freely permeated by water (classical aquaporins, blue) or water and glycerol (aquaglyceroporins, yellow). *E. coli* has one aquaporin (AqpZ) and one aquaglyceroporin (GlpF). The scale bar corresponds to the genetic distance between homologues. Reprinted with permission from Ref. [65].

AQP1 Proteins in Kidneys

We were very fortunate to collaborate with Søren Nielsen from the University of Aarhus, a superb microscopist with particular expertise in kidney physiology. Each of our two kidneys contains approximately one million nephron units working in concert to eliminate toxic wastes and provide the appropriate pH value and ionic composition of our circulating blood. Every day, approximately 180 L of plasma are filtered through the capillary tufts in the glomeruli. Water and certain solutes in this primary filtrate are then reabsorbed as the fluid makes its way through the tubules. The proximal convoluted tubules and descending thin limbs of the loop of Henle exhibit constitutively high water permeability and are responsible for the countercurrent mechanism for the concentration of urea in the kidneys. This coincides exactly with the sites where AQP1 is expressed. The ascending segments are permeated by certain ions and small molecules but lack the AQP1 protein and exhibit low water permeability. Multiple nephron units empty into collecting ducts which exhibit low water permeability in the unstimulated state. Collecting ducts are known to become highly permeable to water when stimulated by the antidiuretic hormone vasopressin, which is released from the brain in response to dehydration.

Immunohistological analysis of rat kidney by Søren Nielsen revealed an extremely strong labeling of the proximal tubules and descending thin limbs with our affinity purified anti-AQP1.[21] The apical brush border stains intensely; our analyses indicate that AQP1 comprises about 4% of the total brush border membranes. Immunogold electron microscopy showed that AQP1 is largely present at the apical brush border membrane surface, where water reabsorption is known to occur, but the protein is present at a minimal level within the cell body (Figure 6 left).

Thus, it became clear that AQP1 is not actively trafficking from intracellular sites to the plasma membrane and back to intracellular sites. AQP1 is also abundant in the basolateral membranes of these epithelial cells. Thus, water is reabsorbed in a transcellular route from the tubular lumen through the apical membrane of the tubular epithelium and out through the basolateral membrane into the interstitium where it is absorbed into capillaries and venules that are also rich in AQP1 protein (Figure 6 right). In normal circumstances, water does not flow between cells, since tight junctions form a barrier. The direction of the water flow through these

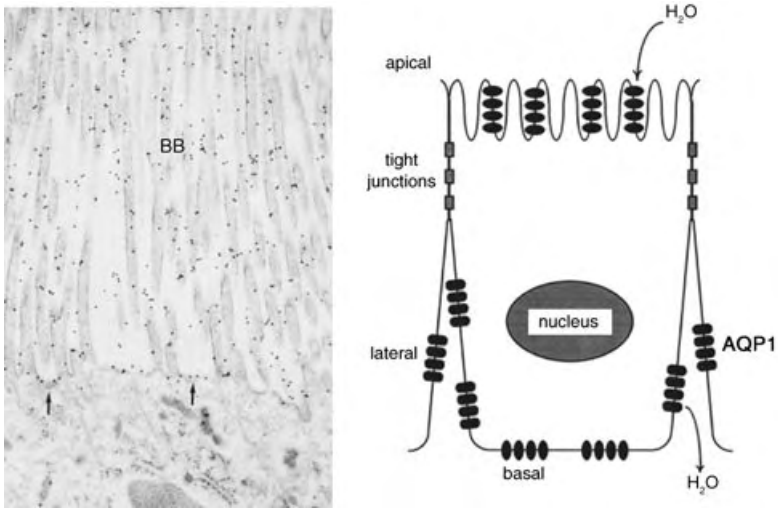


Figure 6. Subcellular localization of AQP1 in proximal tubules from rat kidney. Left: Anti-AQP1 labeling studies using immunogold electron microscopy reveals labeling of apical brush border (BB) but not cell body (25000×). Right: Schematic representation of the transcellular passage of water: entry through AQP1 in the apical brush border and exit through AQP1 in basolateral membranes. Reprinted with permission from Ref. [21].

© 2004 Wiley-VCH Verlag GmbH & Co. KGaA, Weinheim

epithelia, from the primary filtrate back into the vascular space, is determined by small, standing osmotic gradients created by the solute transporters, and water follows passively.

AQP1-null Phenotypes

Chulso Moon, one of our students in the Graduate Program in Human Genetics at Johns Hopkins University, was studying the structural gene encoding human AQP1 which we located on the short arm of human chromosome seven by fluorescence in situ hybridization (FISH).[22] We looked in Victor McKusick's atlas of human genetic linkages for similar gene sequences, and our friend Colvin Redman at the New York Blood Center pointed out that this location coincides with the site of an interesting blood group system: the Colton (Co) antigens. Being a hematologist, I am very much interested in blood group antigens. While hundreds of blood group antigens are known, they represent multiple polymorphisms in approximately 25 different blood group systems, with each system being a different genetic locus. So the coincidental localization of the *AQP1* gene and a human blood group antigen was a very strong clue that they correspond to the same molecule. The Co blood group antigens are not of large clinical significance, since most of us have the same Co blood type—approximately 90% of us are homozygous for Co^a, almost 10% are heterozygotes carrying both Co^a and Co^b, and only 0.3% are homozygous for Co^b. In collaboration with investigators from the International Blood Group Referencing Laboratory in Bristol, UK, we found the Co antigens correspond to an alanine–valine polymorphism at residue 45 which resides in an extracellular location of the AQP1 protein.[23]

Surprisingly the blood group referencing laboratories have identified only a handful of individuals in the entire world who lack both Co antigens. We turned our attention to the Co-null individuals, and, with the help of John Moulds and Jean Pierre Cartron, we obtained DNA, blood, and urine from three different Co-null kindreds. The probands were all women who apparently became sensitized to the Co antigens on the red cells of their babies during childbirth. We hypothesized that these individuals carried mutations in their genes encoding AQP1. We found that the probands from each kindred were homozygous for a unique disruption of the *AQP1* gene:[24] They do not express AQP1 in red blood cells, renal tubule cells, or presumably in choroid plexus, ciliary epithelium, or any other tissues where the protein is normally found—hence they are termed AQP1-null. The probands, however, did not show any clinical illness. Their unique blood types make it impossible for them to receive transfusions from any other individual, so each has cryopreserved blood in local blood banks for emergencies or if a transfusion is needed during surgery.

Their lack of clinical symptoms suggested that AQP1 is either not important in humans or is important only in certain physiological states or clinical settings. Studies of mice bearing targeted disruption of the gene encoding AQP1 by Alan Verkman at UCSF and collaborating scientists at NIH indicated that AQP1 is important for renal concentration.[25,26] Our colleague Landon King at Johns Hopkins University designed a series of clinical evaluations to probe for the importance of the human AQP1 protein. Two AQP1-null individuals were studied during inpatient evaluations at the General Clinical Research Center at Johns Hopkins Hospital. Water permeability is clearly reduced in AQP1-null red cells, but all baseline studies were found to be normal. Then Landon performed a simple test: he thirsted the patients. Every night during our sleep we become a little dehydrated; upon arising in the morning that first taste of orange juice is so delicious. To protect against dehydration, our kidneys respond by maximally concentrating our urine, and all normal individuals concentrate to approximately 1000 mosmol L^{-1}. The AQP1-null individuals were found to have urine concentrations reaching no higher than 450 mosmol L^{-1} after overnight thirsting, and prolonged thirsting to 24 h followed by administration of the antidiuretic hormone vasopressin and infusion of hypertonic sodium chloride yielded no further response.[27] In modern life, with free access to fluids and air conditioning, the need to concentrate above 450 mosmol L^{-1} is not essential; however, the AQP1-null individuals would be at a profound disadvantage if they were to reside in an environment with restricted access to fluids. Certainly during human evolution, our progenitors did not always have free access to water. The patients are described as having a mild form of nephrogenic diabetes insipidus that is usually subclinical but physiologically distinct.

Søren Nielsen also established that AQP1 protein is extremely abundant in human capillaries in both the luminal and abluminal endothelial membranes.[28,29] Landon King in collaboration with Robert Brown measured the capillary fluid permeability in AQP1-null humans.[30] By using a technique developed by Wayne Mitzner and Elias Zerhouni at Johns Hopkins University that employed the high-resolution computerized tomography of lung, they performed scans at a baseline level. By focusing upon small bronchioles of 2–3-mm diameter, the cross-sectional areas of the adjacent venules were measured and the wall thicknesses determined. The scans were repeated after rapid infusion of three liters of saline. All normal individuals and AQP1-null individuals exhibited comparable evidence of vascular engorgement following saline infusions. We then looked at the wall thickness of the small breathing tubules and found that all normal individuals developed an increase in the wall thickness, which represents a release of fluid from the venules and accumulation in the soft tissues surrounding the bronchioles—a situation referred to by clinicians as incipient pulmonary edema. The interstitial edema appears in the peribronchiolar soft tissues in all normal individuals, but the AQP1-null individuals are resistant to this, thus indicating to us that they have a very significant reduction in vascular water permeability. Whether this may be beneficial or deleterious will depend on the clinical setting. At the time of birth, lungs turn from a secretory organ to an absorptive organ. We hypothesize that the inability of newborn infants to move fluid from the pulmonary intersitium into the vascular space may be very harmful, possibly explaining why the AQP1-null state is such a rare phenotype.

 © 2004 Wiley-VCH Verlag GmbH & Co. KGaA, Weinheim

Other Aquaporins—AQP2 in the Collecting Ducts

Within weeks of our original studies, other research groups began to search for other aquaporins. Particular interest in renal collecting ducts led Sei Sasaki and his colleagues at Tokyo Medical and Dental University to the isolation of a cDNA encoding AQP2.[31] Søren Nielsen et al. established that AQP2 is primarily expressed in renal collecting ducts where regulated water permeability is known to occur.[32] Although my research group was not involved in the studies of AQP2, I wish to share exciting information published by several other investigators because I believe this has very large potential clinical significance.

In a definitive study, Søren Nielsen, Mark Knepper, and co-workers from NIH looked at AQP2 in collecting ducts isolated from rats.[33] The ducts were perfused while water permeability was measured. Some of the specimens were then sectioned and stained with anti-AQP2, and they found by immunogold electron microscopy that very little of the AQP2 protein was found in the apical plasma membrane of collecting duct principal cells, but most of the protein appeared to be in membranes of intracellular vesicles (Figure 7, upper left). When the isolated perfused tubules were pulsed with physiological concentrations of vasopressin (the physiological antidiuretic hormone released from the brain), the water permeability was increased approximately fivefold, which coincided with the expected physiological increase. Immunogold electron microscopy studies showed that the AQP2 protein had relocated to the apical plasma membrane (Figure 7, lower left). When vasopressin was removed, the AQP2 protein was re-internalized and the collecting duct water permeability decreased.

These observations closely reflect the known variations in the water permeability if the renal collecting duct occurring in our daily lives. On Friday afternoons, our students celebrate the end of the week at the departmental beer party (TGIF = Thank God it's Friday). A student drinking two liters of beer has excess fluid in his system and the alcohol inhibits release of vasopressin from brain. This causes AQP2 to remain in intracellular vesicles, so the apical membranes of renal collecting duct principal cells are not able to reabsorb water from the filtrate (the diuretic state). The first place the student visits following the TGIF party is the toilet where he empties his bladder of a large volume of dilute urine. The next morning, the student lies in bed in a moderately dehydrated state with high vasopressin levels in his circulation. This causes AQP2 to relocalize to the apical plasma membranes, facilitating maximal reabsorption of water from the urine. Thus, when he arises, his urine is maximally concentrated (the antidiuretic state). These cycles may be repeated multiple times even within a single day.

In summary, vasopressin binds to V2 receptors at the basolateral membrane of the renal collecting duct causing activation of a G-coupled adenylylcyclase cascade that results in phosphorylation of residue 256 on the C-terminus of AQP2 by protein kinase A. The protein is then inserted into the apical plasma membrane, as established by Nielsen and Knepper, the research groups of Deen in Nijmegen, Dennis Brown in Boston, Sasaki in Tokyo, Anita Aperia in Stockholm, and others. Water in the primary urine enters the apical membrane through AQP2 and exits from the basolateral membranes through other aquaporins (AQP3 or AQP4) following a transcellular pathway from the lumen into the vascular space (see the review by Nielsen et al.[34])

Inherited defects in AQP2 cause very rare but severe clinical problems, as found by Carel van Os, Peter Deen, and their colleagues in Nijmegen, The Netherlands.[35] These patients are profoundly affected, they make up to 20 L of urine per day in some cases. Acquired defects in the level of AQP2 expression are commonly found in clinical medicine. When AQP2 levels are too high, fluid retention occurs (as shown by the Nielsen and Knepper research group as well as by Robert Schrier and his colleagues at the University of Colorado). Presumably this is happening in patients sustaining myocardial infarctions; such patients often suffer fluid retention which causes inadequate pulmonary function. Similarly, some women during pregnancy experience pathological retention of fluid, which causes hypertension and neurological dysfunction. The opposite situation results when AQP2 levels are too low, resulting in inadequate concentration of urine. This result is found after reversal of urinary obstruction (by Jørgen Frøkiaer in Aarhus) and in patients with nocturnal enuresis (by

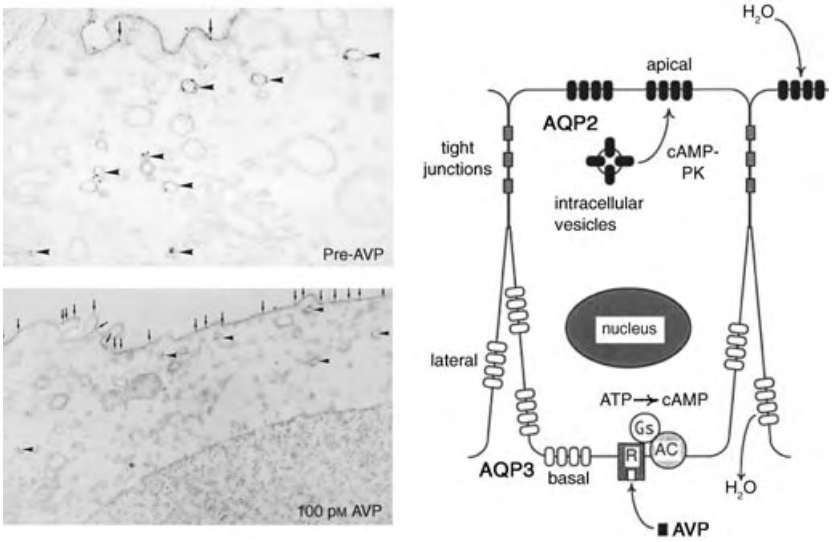


Figure 7. Subcellular localization of AQP2 in collecting duct principal cells from rat kidney. Left: Anti-AQP2-labeled immunogold electron microscopy of isolated collecting duct from rat kidney. Before vasopressin (AVP) stimulation, most labeling occurs at the intracellular vesicles (top, 25000×). After stimulation with 100 pM AVP, most labeling appears at the apical membrane (bottom, 15000×). Right: Schematic representation of the AVP-dependent exocytosis of AQP2 to the apical membrane of the principal cell: entry through AQP2 in apical membrane, exit through AQP3 (or AQP4) in the basolateral membranes. Modified and reprinted with permission from Refs. [33a] and [33b].

 © 2004 Wiley-VCH Verlag GmbH & Co. KGaA, Weinheim

Ivana Valenti in Bari). Thus, AQP2 is very important in clinical medicine (see the review by Nielsen et al.[33])

AQP6 in Acid Secretory Cells

At this point we thought we knew a lot about aquaporins, but then we were surprised. AQP6, a protein genetically closest to AQP2, was found to be a very poor water channel and is never present in the plasma membrane. Double-label immungold electron microscopy studies by Søren Nielsen and Tae-Hwan Kwon showed that AQP6 colocalizes with H^+-ATPase in intracellular vesicles of α-intercalated cells in the renal collecting duct. Upon stimulation of acid secretion, H^+-ATPase becomes exocytosed to the plasma membrane, but AQP6 is fully retained within the cell. A second surprise was that AQP6 is a very good anion channel with particularly high permeation by nitrate when activated by low pH values.[36] These cells control acid secretion, so while AQP6 is clearly a genetic member of the aquaporin family, it apparently has a very different physiological function, as proposed by our colleague Masato Yasui at Johns Hopkins University.

AQPo in Lenses

Another member of the aquaporin family is AQP0, which is expressed only in fiber cells of lenses. First recognized more than 30 years ago and termed MIP (major intrinsic protein), the physiological function was unknown. AQP0 has a fairly low water permeability, but the protein may have a second function as a cell-to-cell adhesion molecule, as proposed by Andreas Engel and co-workers.

Shomi Bhattacharya, from Moorefield's Eye Hospital in London, identified two large kindreds with congenital cataracts of dominant inheritance with complete penetrance. While cataracts are fairly common among elderly individuals, they are very rare in small children. Each family bore a missense mutation in a structurally important residue, and the physical nature of the opacities was quite different.[37] Members of the family with an arginine replacing an essential threonine residue (Thr-138-Arg) have numerous opacities throughout the lens. Members of the second family with a glycine replacing an essential glutamate residue (Glu-134-Gly) have a single lamellar opacity in the center of the lens. This distribution corresponds to the perimeter of the lens at the time of birth, thus indicating that the mutation is deleterious only at birth.[38] This example illustrates how human biology is so much more complicated than represented by simple gene disruption studies performed on mice. Lens fiber cells survive for decades, so it is plausible that subtle polymorphisms in the AQP0 protein may be a risk factor for the development of cataracts as individuals grow older.

AQP4 in the Brain

AQP4 is expressed in multiple tissues, including the brain.[39] Unlike peripheral capillaries that are quite leaky, capillaries in the brain are known to be much tighter because of the astroglial endfeet surrounding them in the brain. In studies undertaken with Ole Petter Ottersen and his research group at the University of Oslo, and including Søren Nielsen, the protein was shown by immunogold electron microscopy to reside at the blood–brain barrier, the site where vascular space and brain parenchyma are juxtaposed.[40,41] Brain capillaries are surrounded by a basement membrane that is surrounded by astroglial endfeet. The AQP4 resides almost entirely in the endfeet membranes, directly in contact with the basement membrane and is virtually absent in other astroglial membranes (Figure 8a, b).

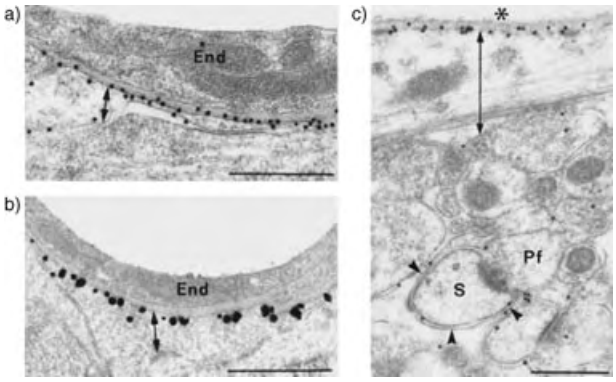


Figure 8. Polarized expression of AQP4 in rat brain visualized by anti-AQP4 immunogold electron microscopy. a, b) AQP4 in perivascular membranes of astroglial endfeet but not in membranes facing the neuropil. c) Labeling of pia on the brain surface. Scale bars: 0.5 μm. End = endothelium, Pf = parallel fibers, S = spike of a Purkinje cell, ✱ = pia surface. Reprinted with permission from Ref. [39].

Similarly, at the surface of the brain, AQP4 is abundant at the brain surface where liquid and brain are juxtaposed (Figure 8c). These locations strongly suggested that AQP4 would be important in the movement of water from blood or cerebrospinal fluid into the brain as well as in the reverse direction. AQP4 is extremely heavily expressed at these locations and generate microcrystalline forms referred to as "square arrays", with the size of the assembly determined by the N-terminus of AQP4.[42] Other workers, including Antonio Frigeri in Bari, also documented that movement of water in brain and skeletal muscle may be of pathophysiological significance.[43]

Our student John Neely recognized a protein-binding motif in the C-terminus of AQP4 that predicted that it would associate with dystrophin-associated proteins. In collaboration with Marv Adams and Stan Froehner in Seattle as well as with our colleagues in Oslo, we evaluated the localization of AQP4 in mice bearing targeted disruption in α-syntrophin (syn), a member of the dystrophin-associated proteins.[44] AQP4 was found by immunogold electron microscopy to be grossly mislocalized in syn-null animals. Interestingly, when stressed with brain injury resulting from middle cerebral artery occlusion, the control animals did much worse, having significantly larger areas of infarction and edema, while the syn-null animals did much better.[45] These studies suggest that

 © 2004 Wiley-VCH Verlag GmbH & Co. KGaA, Weinheim

if AQP4 could be selectively inhibited, patients sustaining brain injuries might be protected from some of the tragic consequences of brain swelling. Protection against hyponatremia-induced brain swelling was observed by Søren Nielsen and co-workers.[46] Geoff Manley and colleagues independently established the same conclusions with AQP4-null mice.[47]

AQP5 in Secretory Glands

AQP5 resides in the apical membrane of acini in salivary, lacrimal, sweat, and other secretory glands.[48,49] This is the last membrane water crosses during the generation of saliva, tears, and other secretions. It is known that these glands facilitate the release of large amounts of fluid. For example, any individual fasted for several hours will secrete massive amounts of saliva when he senses food is available.

AQP5 may be important in certain clinical disorders. In collaboration with Kazuo Tsubota from Tokyo and Chris Delporte from Brussels, we examined AQP5 distribution in gland biopsies from a small series of patients with Sjögren's Syndrome. This disorder affects women at midlife and causes dry eyes and a dry mouth, although the precise biological cause of the disorder is unknown. The normal apical staining is lost with our anti-AQP5 immunohistochemical labeling, and the protein appears to be mislocalized throughout the cytoplasm in the Sjögren's biopsies.[50,51] Other investigators led by Roland Jonsson in Bergen did not find AQP5 mislocalization in a larger series of Sjögren's patients; however, they noted decreased expression of AQP1 in the myoepithelia surrounding glandular acini.[52] Thus, while Sjögren's Syndrome may be heterogeneous, aquaporins have been implicated in these two series of patients.

AQP5 is also abundant in sweat glands. In another collaborative study with Søren Nielsen and his research group, the qualitative analysis of sweating was compared in wild-type mice and mice bearing targeted disruption of the the gene encoding AQP5 (prepared by Carissa Krane and Anil Menon at the University of Cincinnati). While the morphology of the sweat glands was preserved, the release of amylase in sweat after pilocarpine injection was found to be greatly diminished, thus indicating that AQP5 must be important for the ability to sweat.[53]

Aquaglyceroporins AQP7 and AQP9

AQP7 is expressed in adipocytes. During fasting, energy stored as triglycerides is provided by release of fatty acids, exported by special fatty acid transporters, and glycerol, exported through AQP7. The preferred gluconeogenic substrate, glycerol, passes through AQP9 in the hepatocyte plasma membranes. Glycerol is converted into glucose within the heptacytes. In the fasted state, AQP9 expression is greatly increased, as demonstrated in the work of Jennifer Carbrey and Dan Gorelick in our research group. Multiple research groups have reached the same conclusion that these two proteins (AQP7 and AQP9) form an axis for energy transfer, together maintaining blood-glucose levels during starvation.[54,55]

AQP7 and AQP9 have a very curious capacity to transport certain heavy metals, a discovery made by Barry Rosen and his colleagues at Wayne State University.[56] Measurement of arsenic trioxide uptake was performed with yeast expressing AQP7 or AQP9 as well as in oocytes expressing the proteins. Arsenic trioxide is uncharged at neutral pH values and is very toxic. Clinical features of greatest concern in arsenic poisoning include hepatocellular damage and hepatocellular carcinoma. The World Health Organization has established that an alarming epidemic of arsenic poisoning is now occurring in the Ganges Delta because of arsenic contamination of the groundwater. Tube wells were installed because the surface water is infested with *Vibrio cholera*, but heavy-metal determinations were apparently not performed. While our work explains why these unfortunate people are vulnerable to hepatocellular damage, it does not provide a useful antidote. Prevention of this poisoning requires access to pure drinking water, a basic right deserved by all persons on Earth.

Nonhuman Aquaporins

Aquaporins are also important in plants. *Arabidopsis thaliana*, a relative of the mustard plant, is frequently studied by plant physiologists (also known as "the green people"). Ralf Kaldenhoff at the University of Würzburg demonstrated this dramatically by comparing the gross morphology of a parental *Arabidopsis* to a plant modified to express the rootlet aquaporin group PIP1b at only 20% of the normal levels. Both plants exhibit similar foliage, but to maintain the same stem turgor, the modified plant sends out more greatly arborized rootlets (Figure 9).[57] Thus, the plants are keenly



Figure 9. Rootsystem of *Arabidopsis thaliana*. Reprinted with permission from Ref. [57].

aware of water balance. *Arabidopsis thaliana* has at least 35 different aquaporin genes, and these are presumed to participate in different physiological processes, including photosynthesis (in which carbon dioxide passes through leaf aquaporins)[58] and restriction of rootlet water uptake regulated by low pH values.[59] These observations may be relevant

 © 2004 Wiley-VCH Verlag GmbH & Co. KGaA, Weinheim

to human aquaporins, since similar observations have been reported for AQP1[60] and AQP3.[61]

Aquaporins are also expressed in all forms of microorganisms. *Escherichia coli* has two: AqpZ, a classic aquaporin, and GlpF, an aquaglyceroporin. The structures of the narrowest sections of the channels are somewhat different: narrower and more hydrophilic in aquaporins than in aquaglyceroporins. Archaea, the third kingdom of life, also carry a gene that encodes AqpM, which is homologous to aquaporins and aquaglyceroporins. AqpM may not exist for water transport but may facilitate hydrogen sulfide transport.[62] Whatever the function, their presence in all three kingdoms of life reinforces the fundamental importance of this family of proteins. *Sacharomyces cerevisiae* have two aquaporin genes and two aquaglyceroporin genes. Exciting studies by Stefan Hohmann at the University of Göteborg revealed interesting functions: yeast aquaporins confer resistance to freezing, whereas the aquaglyceroporin FPS1 protects the organisms against hypoosmotic shock.[63]

Conclusion

The discovery of the aquaporins has provided the explanation for the selective transport of water across the plasma membranes of cells without allowing protons to also cross the membrane. Some homologues have special permeation properties for glycerol, nitrate, or arsenic trioxide. The structural models of aquaporins provide remarkable insight into the biophysical functions. Aquaporins have been implicated in numerous clinical disorders and are clearly involved in some forms of renal vascular diseases, including nephrogenic diabetes insipidus. Roles in defense against thermal stress are expected. Last summer during the heat wave in France, 14000 people died when the temperature reached 40 °C. Many of these individuals were older, and it is likely that they manifested age-dependent diminution of physiological processes involving aquaporins (concentration of urine, sweating, and thirst mechanisms). While these deficiencies may be unimportant during normal life, they may cause severe problems when individuals are thermally stressed. Aquaporins have also been associated with problems of brain edema and loss of vision. Aquaglyceroporins are involved in the defense against starvation. These proteins are expressed throughout the natural world.

The advice given to his students by Santiago Ramón y Cajal, the father of neuroscience, "In summary, there are no small problems. Problems that appear small are large problems that are not understood"[64] also applies here: Certainly the issue of water permeation of membranes was initially assumed to be a small problem related to diffusion. Instead it has turned out to be a complex problem with large physiological and pathophysiological significance.

I thank the past and present members of my laboratory and the many individuals with whom we have collaborated in these studies. I particularly wish to thank my former chairmen, Victor McKusick, Department of Medicine, and M. Daniel Lane, Department of Biological Chemistry, for hiring me onto their faculty. I dedicate this lecture to the memory of John C. Parker, a friend and generous mentor.

Received: May 27, 2004

[1] A. Finkelstein, "Water movement through lipid bilayers, pores, and plasma membranes: Theory and reality", New York, Wiley, **1987**.
[2] "Inhibition of water and solute permeability in human red cells": R. I. Macey, R. E. L. Farmer, *Biochim. Biophys. Acta* **1970**, *211*, 104–106.
[3] "Aquaporin CHIP: the archetypal molecular water channel": P. Agre, G. M. Preston, B. L. Smith, J. S. Jung, S. Raina, C. Moon, W. B. Guggino, S. Nielsen, *Am. J. Physiol. Renal Physiol.* **1993**, *265*, F463–F476.
[4] "Identification, purification, and partial characterization of a novel Mr 28000 integral membrane protein from erythrocytes and renal tubules": B. M. Denker, B. L. Smith, F. P. Kuhajda, P. Agre, *J. Biol. Chem.* **1988**, *263*, 15634–15642.
[5] "Erythrocyte Mr 28000 transmembrane protein exists as a multisubunit oligomer similar to channel proteins": B. L. Smith, P. Agre, *J. Biol. Chem.* **1991**, *266*, 6407–6415.
[6] "Isolation of the cDNA for erythrocyte integral membrane protein of 28 kilodaltons: member of an ancient channel family": G. M. Preston, P. Agre, *Proc. Natl. Acad. Sci. USA* **1991**, *88*, 11110–11114.
[7] "Appearance of water channels in Xenopus oocytes expressing red cell CHIP28 protein": G. M. Preston, T. P. Carroll, W. B. Guggino, P. Agre, *Science* **1992**, *256*, 385–387.
[8] "Aquaporins: a family of water channel proteins": P. Agre, S. Sasaki, J. Chrispeels, *Am. J. Physiol. Renal Physiol.* **1993**, *265*, F461.
[9] "Reconstitution of functional water channels in liposomes containing purified red cell CHIP28 protein": M. L. Zeidel, S. V. Ambudkar, B. L. Smith, P. Agre, *Biochemistry* **1992**, *31*, 7436–7440.
[10] "Ultrastructure, pharmacologic inhibition, and transport selectivity of aquaporin channel-forming integral protein in proteoliposomes": M. L. Zeidel, S. Nielsen, B. L. Smith, S. V. Ambudkar, A. B. Maunsbach, P. Agre, *Biochemistry* **1994**, *33*, 1606–1615.
[11] "The mercury-sensitive residue at cysteine 189 in the CHIP28 water channel": G. M. Preston, J. S. Jung, W. B. Guggino, P. Agre, *J. Biol. Chem.* **1993**, *268*, 17–20.
[12] Molecular structure of the water channel through aquaporin CHIP. The hourglass model": J. S. Jung, G. M. Preston, B. L. Smith, W. B. Guggino, P. Agre, *J. Biol. Chem.* **1994**, *269*, 14648–14654
[13] "Biologically active two-dimensional crystals of aquaporin CHIP": T. Walz, B. L. Smith, M. L. Zeidel, A. Engel, P. Agre, *J. Biol. Chem.* **1994**, *269*, 1583–1586.
[14] "Structural determinants of water permeation through aquaporin-1": K. Murata, K. Mitsuoka, T. Hirai, T. Walz, P. Agre, J. B. Heymann, A. Engel, Y. Fujiyoshi, *Nature* **2000**, *407*, 599–605.
[15] "Structure of a glycerol-conducting channel and the basis for its selectivity": D. Fu, A. Libson, L. J. Miercke, C. Weitzman, P. Nollert, J. Krucinski, R. M. Stroud, *Science* **2000**, *290*, 481–486.
[16] "Structural basis of water-specific transport through the AQP1 water channel": H. Sui, B. G. Han, J. K. Lee, P. Walian, B. K. Jap, *Nature* **2001**, *414*, 872–878.
[17] "Water permeation across biological membranes: mechanism and dynamics of aquaporin-1 and GlpF": B. L. de Groot, H. Grubmüller, *Science* **2001**, *294*, 2353–2357.
[18] "Control of the selectivity of the aquaporin water channel family by global orientational tuning": E. Tajkhorshid, P. Nollert, M. O.

 © 2004 Wiley-VCH Verlag GmbH & Co. KGaA, Weinheim

Jensen, L. J. Miercke, H. O'Connell, R. M. Stroud, K. Schulten, *Science* **2002**, *296*, 525 – 530.

[19] "Aquaporin water channels: atomic structure and molecular dynamics meet clinical medicine": D. Kozono, M. Yasui, L. S. King, P. Agre, *J. Clin. Invest.* **2002**, *109*, 1395 – 1399.

[20] "Molecular cloning and characterization of AqpZ, a water channel from *Escherichia coli*": G. Calamita, W. R. Bishai, G. M. Preston, W. B. Guggino, P. Agre, *J. Biol. Chem.* **1995**, *270*, 29063 – 29066.

[21] "CHIP28 water channels are localized in constitutively water-permeable segments of the nephron": S. Nielsen, B. L. Smith, E. I. Christensen, M. A. Knepper, P. Agre, *J. Cell Biol.* **1993**, *120*, 371 – 383.

[22] "The human aquaporin-CHIP gene. Structure, organization, and chromosomal localization": C. Moon, G. M. Preston, C. A. Griffin, E. W. Jabs, P. Agre, *J. Biol. Chem.* **1993**, *268*, 15772 – 15778.

[23] "Human red cell aquaporin CHIP. I. Molecular characterization of ABH and Colton blood group antigens": B. L. Smith, G. M. Preston, F. A. Spring, D. J. Anstee, P. Agre, *J. Clin. Invest.* **1994**, *94*, 1043 – 1049.

[24] "Mutations in aquaporin-1 in phenotypically normal humans without functional CHIP water channels": G. M. Preston, B. L. Smith, M. L. Zeidel, J. J. Moulds, P. Agre, *Science* **1994**, *265*, 1585 – 1587.

[25] J. Schnermann, C. L. Chou, T. Ma, T. Traynor, M. A. Knepper, A. S. Verkman, *Proc. Natl. Acad. Sci. USA* **1998**, *95*, 9660 – 9664.

[26] "Reduced water permeability and altered ultrastructure in thin descending limb of Henle in aquaporin-1 null mice": C. L. Chou, M. A. Knepper, A. N. van Hoek, D. Brown, B. Yang, T. Ma, A. S. Verkman, *J. Clin. Invest.* **1999**, *103*, 491 – 496.

[27] "Defective urinary-concentrating ability due to a complete deficiency of aquaporin-1": L. S. King, M. Choi, P. C. Fernandez, J. P. Cartron, P. Agre, *N. Engl. J. Med.* **2001**, *345*, 175 – 179.

[28] "Distribution of the aquaporin CHIP in secretory and resorptive epithelia and capillary endothelia": S. Nielsen, B. L. Smith, E. I. Christensen, P. Agre, *Proc. Natl. Acad. Sci. USA* **1993**, *90*, 7275 – 7279.

[29] "Aquaporin-1 water channel protein in lung: ontogeny, steroid-induced expression, and distribution in rat": L. S. King, S. Nielsen, P. Agre, *J. Clin. Invest.* **1996**, *97*, 2183 – 2191.

[30] "Decreased pulmonary vascular permeability in aquaporin-1-null humans": L. S. King, S. Nielsen, P. Agre, R. H. Brown, *Proc. Natl. Acad. Sci. USA* **2002**, *99*, 1059 – 1063.

[31] "Cloning and expression of apical membrane water channel of rat kidney collecting tubule": K. Fushimi, S. Uchida, Y. Hara, Y. Hirata, F. Marumo, S. Sasaki, *Nature* **1993**, *361*, 549 – 552.

[32] "Cellular and subcellular immunolocalization of vasopressin-regulated water channel in rat kidney": S. Nielsen, S. R. DiGiovanni, E. I. Christensen, M. A. Knepper, H. W. Harris, *Proc. Natl. Acad. Sci. USA* **1993**, *90*, 11663 – 11667.

[33] "The aquaporin family of water channels in kidney": a) S. Nielsen, P. Agre, *Kidney Int.* **1995**, *48*, 1057 – 1068; b) "Vasopressin increases water permeability of kidney collecting duct by inducing translocation of aquaporin-CD water channels to plasma membrane": S. Nielsen, C. L. Chou, D. Marples, E. I. Christensen, B. K. Kishore, M. A. Knepper, *Proc. Natl. Acad. Sci. USA* **1995**, *92*, 1013 – 1017.

[34] S. Nielsen, J. Frokiaer, D. Marples, T. H. Kwon, P. Agre, M. A. Knepper, *Physiol. Rev.* **2002**, *82*, 205 – 244.

[35] "Requirement of human renal water channel aquaporin-2 for vasopressin-dependent concentration of urine": P. M. Deen, M. A. Verdijk, N. V. Knoers, B. Wieringa, L. A. Monnens, C. H. van Os, B. A. Van Oost, *Science* **1994**, *264*, 92 – 95.

[36] "Rapid gating and anion permeability of an intracellular aquaporin": M. Yasui, A. Hazama, T. H. Kwon, S. Nielsen, W. B. Guggino, P. Agre, *Nature* **1999**, *402*, 184 – 187.

[37] "Missense mutations in MIP underlie autosomal dominant 'polymorphic' and lamellar cataracts linked to 12q": V. Berry, P. Francis, S. Kaushal, A. Moore, S. Bhattacharya, *Nat. Genet.* **2000**, *25*, 15 – 17.

[38] "Functional impairment of lens aquaporin in two families with dominantly inherited cataracts": P. Francis, J. J. Chung, M. Yasui, V. Berry, A. Moore, M. K. Wyatt, G. Wistow, S. S. Bhattacharya, P. Agre, *Hum. Mol. Genet.* **2000**, *9*, 2329 – 2334.

[39] "Molecular characterization of an aquaporin cDNA from brain: candidate osmoreceptor and regulator of water balance": J. S. Jung, R. V. Bhat, G. M. Preston, W. B. Guggino, J. M. Baraban, P. Agre, *Proc. Natl. Acad. Sci. USA* **1994**, *91*, 13052 – 13056.

[40] "Specialized membrane domains for water transport in glial cells: high- resolution immunogold cytochemistry of aquaporin-4 in rat brain": S. Nielsen, E. A. Nagelhus, M. Amiry-Moghaddam, C. Bourque, P. Agre, O. P. Ottersen, *J. Neurosci.* **1997**, *17*, 171 – 180.

[41] "Aquaporin-4 water channel protein in the rat retina and optic nerve: polarized expression in Muller cells and fibrous astrocytes": E. A. Nagelhus, M. L. Veruki, R. Torp, F. M. Haug, J. H. Laake, S. Nielsen, P. Agre, O. P. Ottersen, *J. Neurosci.* **1998**, *18*, 2506 – 2519.

[42] "Aquaporin-4 square array assembly: opposing actions of M1 and M23 isoforms": C. S. Furman, D. A. Gorelick-Feldman, K. G. V. Davidson, T. Yasumura, J. D. Neely, P. Agre, J. E. Rash, *Proc. Natl. Acad. Sci. USA* **2003**, *100*, 13609 – 13614.

[43] "Aquaporin-4 deficiency in skeletal muscle and brain of dystrophic mdx mice": A. Frigeri, G. P. Nicchia, B. Nico, F. Quondamatteo, R. Herken, L. Roncali, M. Svelto, *FASEB J.* **2001**, *15*, 90 – 98.

[44] "Syntrophin-dependent expression and localization of Aquaporin-4 water channel protein": J. D. Neely, M. Amiry-Moghaddam, O. P. Ottersen, S. C. Froehner, P. Agre, M. E. Adams, *Proc. Natl. Acad. Sci. USA* **2001**, *98*, 14108 – 14113.

[45] "An alpha-syntropin-dependent pool of AQP4 in astroglial end-feet confers bidirectional water flow between blood and brain": M. Amiry-Moghaddam, T. Otsuka, P. D. Hurn, R. J. Traystman, H. Finn-Mogens, S. C. Froehner, M. E. Adams, J. D. Neely, P. Agre, O. P. Ottersen, A. Bhardwaj, *Proc. Natl. Acad. Sci. USA* **2003**, *100*, 2106 – 2111.

[46] Z. Vajda, M. Pedersen, E.-M. Fuchtbauer, K. Wert, H. Stodkilde-Jorgensen, E. Sulyok, T. Doczi, J. D. Neely, P. Agre, J. Frokiaer, S. Nielsen, *Proc. Natl. Acad. Sci. USA* **2002**, *99*, 13131 – 13136.

[47] "Aquaporin-4 deletion in mice reduces brain edema after acute water intoxication and ischemic stroke": G. T. Manley, M. Fujimura, T. Ma, N. Noshita, F. Filiz, A. W. Bollen, P. Chan, A. S. Verkman, *Nat. Med.* **2000**, *6*, 159 – 163.

[48] "Molecular cloning and characterization of an aquaporin cDNA from salivary, lacrimal, and respiratory tissues": S. Raina, G. M. Preston, W. B. Guggino, P. Agre, *J. Biol. Chem.* **1995**, *270*, 1908 – 1912.

[49] "Aquaporins in complex tissues. I. Developmental patterns in respiratory and glandular tissues of rat": L. S. King, S. Nielsen, P. Agre, *Am. J. Physiol.* **1997**, *273*, C1541 – C1548.

[50] "Defective cellular trafficking of lacrimal gland aquaporin-5 in Sjogren's syndrome": K. Tsubota, S. Hirai, L. S. King, P. Agre, N. Ishida, *Lancet* **2001**, *357*, 688 – 689.

[51] "Abnormal distribution of aquaporin-5 water channel protein in salivary glands from Sjogren's syndrome patients": S. Steinfeld, E. Cogan, L. S. King, P. Agre, R. Kiss, C. Delporte, *Lab. Invest.* **2001**, *81*, 143 – 148.

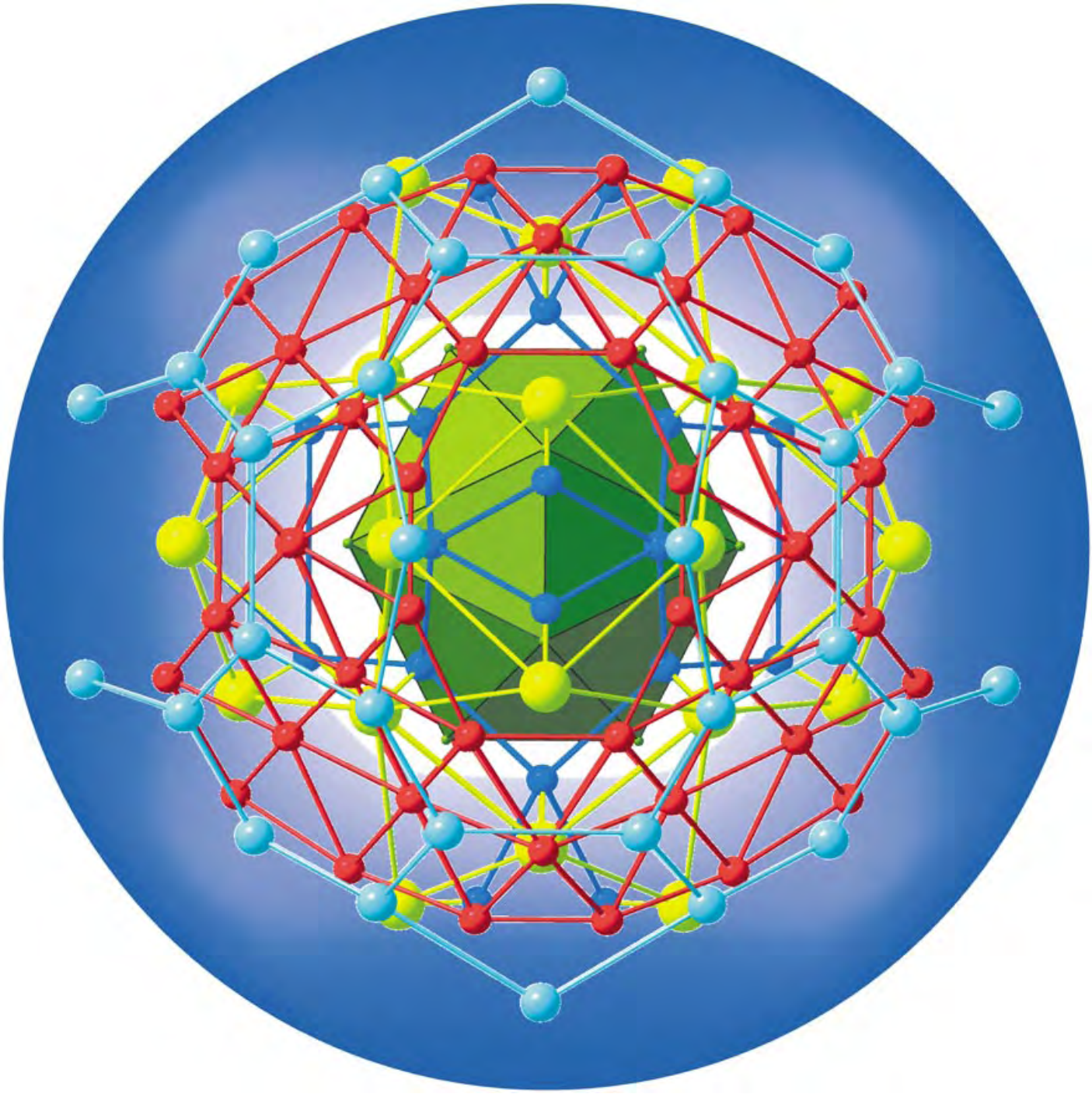
[52] "Selective down-regulation of aquaporin-1 in salivary glands in primary Sjogren's syndrome": D. Beroukas, J. Hiscock, B. J. Gannon, R. Jonsson, T. P. Gordon, S. A. Waterman, *Lab. Invest.* **2002**, *82*, 1547 – 1552.

 © 2004 Wiley-VCH Verlag GmbH & Co. KGaA, Weinheim

[53] "Functional requirement of aquaporin-5 in plasma membranes of sweat glands": L. N. Nejsum, T. H. Kwon, U. B. Jensen, O. Fumagalli, J. Frokiaer, C. M. Krane, A. G. Menon, L. S. King, P. C. Agre, S. Nielsen, *Proc. Natl. Acad. Sci. USA* **2002**, *99*, 511 – 516.
[54] "Coordinated regulation of fat-specific and liver-specific glycerol channels, aquaporin adipose, and aquaporin 9": H. Kuriyama, H. Shimomura, K. Kishida, H. Kondo, N. Furuyama, H. Nishizawa, N. Maeda, M. Matsuda, H. Nagaretani, S. Kihara, T. Nakamura, Y. Tochino, T. Funahashi, Y. Matsuzawa, *Diabetes* **2002**, *51*, 2915 – 2921.
[55] "Aquaglyceroporin AQP9: Solute permeation and metabolic control of expression in liver": J. M. Carbrey, Gorelick-D. A. Feldman, D. Kozono, J. Praetorius, S. Nielsen, P. Agre, *Proc. Natl. Acad. Sci. USA* **2003**, *100*, 2945 – 2950.
[56] "Arsenite transport by mammalian aquaglyceroporins AQP7 and AQP9": Z. Liu, J. Shen, J. M. Carbrey, R. Mukhopadhyay, P. Agre, B. Rosen, *Proc. Natl. Acad. Sci. USA* **2002**, *99*, 6053 – 6058.
[57] "Significance of plasma lemma aquaporins for water-transport in Arabidopsis thaliana": R. Kaldenhoff, K. Grote, J. J. Zhu, U. Zimmermann, *Plant J.* **1998**, *14*, 121 – 128.
[58] "The tobacco aquaporin NtAQP1 is a membrane CO2 pore with physiological functions": N. Uehlein, C. Lovisolo, F. Siefritz, R. Kaldenhoff, *Nature* **2003**, *425*, 734 – 737.
[59] "Cytosolic pH regulates root water transport during anoxic stress through gating of aquaporins": C. Tournaire-Roux, M. Sutka, H. Javot, E. Gout, P. Gerbeau, D. T. Luu, R. Bligny, C. Maurel, *Nature* **2003**, *425*, 393 – 397.
[60] "Effect of expressing the water channel aquaporin-1 on the CO2 permeability of Xenopus oocytes": N. L. Nakhoul, B. A. Davis, M. F. Romero, W. F. Boron, *Am. J. Physiol.* **1998**, *274*, C297 – C298.
[61] "Transport of water and glycerol in aquaporin 3 is gated by H(+)": T. Zeuthen, D. A. Klaerke, *J. Biol. Chem.* **1999**, *274*, 21 631 – 21 636.
[62] "Functional expression and characterization of an archaeal aquaporin: AqpM from *Methanothermobacter marburgensis*": D. Kozono, X. Ding, I. Iwasaki, X. Meng, Y. Kamagata, P. Agre, Y. Kitagawa, *J. Biol. Chem.* **2003**, *278*, 10 649 – 10 656.
[63] "Osmotic stress signaling and osmoadaptation in yeasts": S. Hohmann, *Microbiol. Mol. Biol. Rev.* **2002**, *66*, 300 – 372.
[64] S. Ramón y Cajal, *Advice to a Young Investigator* (1897), translated by N. Swanson, L. W. Swanson, Cambridge, MIT Press, **1999**.
[65] "Aquaporin water channels - from atomic structure to clinical medicine": P. Agre, L. S. King, M. Yasui, W. B. Guggino, O. P. Otterson, Y. Fujiyoshi, A. Engel, S. Nielsen, *J. Physiol.* **2002**, *278*, 3 – 16

 © 2004 Wiley-VCH Verlag GmbH & Co. KGaA, Weinheim

Communications



The depicted supramolecular compound comprises an infinite cation Te–Ni oxohalogenide mixture constructed from a sequence of covalently linked homoatomic onion-like skins. The outer Ni atoms (light blue) form a buckminsterfullerene-like cluster that packs in a bcc arrangement. For more details, see the Communication by M. Johnsson et al. on the following pages.

DOI: 10.1002/anie.200460001
© 2004 Wiley-VCH Verlag GmbH & Co. KGaA, Weinheim

Host–Guest Systems

Host–Guest Compounds in the Family of Tellurium–Nickel Oxohalogenides**

Mats Johnsson, Sven Lidin, Karl W. Törnroos, Hans-Beat Bürgi, and Patrice Millet*

Some elements with stereochemically active lone pairs show a strong propensity in their oxohalogenides to agglomerate with halogenide ions, thus forming clusters, rods or lamellar assemblies, to bond covalently to an oxidic matrix, and to spatially separate one from the other.[1] This behavior mimics that of water–amphiphile–oil systems not only structurally, but also in the sense that the oxohalogenides may be manipulated similarly by using chalcophile or halophile metals to swell the oxide or halide volume. We have recently described the planar layer structures of $[Ni_5(TeO_3)_4]Cl_2$ and $[Ni_5(TeO_3)_4]Br_2$, the first oxohalogenide phases that contain Te^{IV} ions in combination with Ni^{II} ions.[2] To our knowledge only three other oxide phases that contain Te^{IV} ions in combination with Ni^{II} ions have been described before, namely $NiTe_2O_5$, $Ni_2Te_3O_8$, and $Ni_3(OH)_2(TeO_3)_2$.[3–5]

Herein we present the synthesis of three products within this new family of compounds with the idealized composition $[Te_{32}Ni_{30}X_3O_{90}]^{5+}[Ni_4X_{13}]^{5-}$. The anionic part of the products discloses further dimensions of complexity and necessitates a division of the three structures into two types. The first type is represented by $[Te_{32}Ni_{30}Br_{2.64}O_{90}][Ni_{3.39}Br_{12.14}]$ (**1a**) and $[Te_{32}Ni_{30}Cl_{2.69}O_{90}][Ni_{3.10}Cl_{11.52}]$ (**1b**); the second type is represented by $[Te_{32}Ni_{30}Cl_{2.67}O_{90}][Ni_{4.48}Cl_{15.78}]$ (**2**). These new phases form only at relatively high temperatures, above 800 K. All attempts to produce the compounds as single phases have been unsuccessful, and the reaction product is always a mixture of the title compounds and a matrix of $[Ni_5(TeO_3)_4]X_2$.[2] Therefore all crystals subject to analyses were selected manually on the basis of color and morphology. All three compounds crystallize in the cubic system, space group $Im\bar{3}$ (no. 204). Results of stoichiometric analyses by energy-dispersive spectrometry (EDS) and X-ray diffraction (XRD) are compared in Table 1.

Table 1: Elemental analysis for **1a**, **1b**, and **2**.[a]

Compound	**1a (X = Br)**		**1b (X = Cl)**		**2 (X = Cl)**	
Elemental analysis	EDS	XRD	EDS	XRD	EDS	XRD
Te	40.6 ± 0.6	39.9	39.6 ± 0.7	40.4	39.0 ± 1.4	37.7
Ni	41.0 ± 0.7	41.7	41.1 ± 0.9	41.7	40.4 ± 1.7	40.6
X	18.4 ± 0.7	18.4	19.3 ± 0.7	17.9	20.5 ± 1.9	21.7

[a] Results of EDS analyses are averages of determinations on ten different crystals. XRD results were obtained from refined compositions (in %, O atoms not included).

Both types of compounds contain covalently bonded, cationic entities of approximate composition $[Te_{32}Ni_{30}X_3O_{90}]^{5+}$ (X = Br, Cl), which form an infinite porous network enclosing large cavities that contain guests of anionic clusters. The cationic network is effectively identical for all three compounds, whereas the anionic guest clusters differ from compound to compound.

The cationic clusters may be considered as being built from a sequence of homoatomic, concentric onion skins. The outermost shell is a Buckminster Fullerene-like polyhedron of 60 Ni atoms. It shares hexagons along the [111] direction and edges along the [100] direction with neighboring Ni_{60} units. The simultaneous contacts along [111] and [100] reduce the symmetry of the Fullerene-like shells from icosahedral to cubic. The Ni atoms may be considered as sitting on a P-type minimal surface that defines the interface between individual spheres of a *bcc* packing (Figure 1). The Ni atoms surrounded

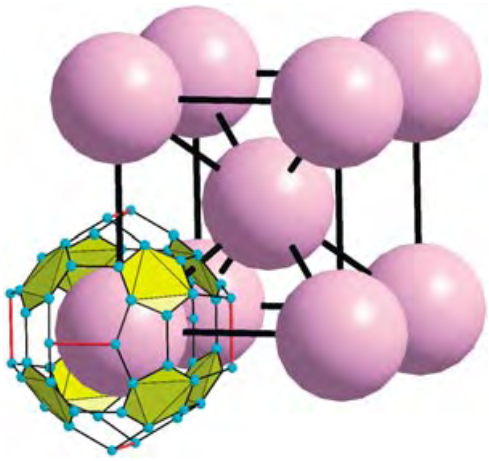


Figure 1. One Buckminster Fullerene-like Ni_{60}-cluster with violet skins indicating the subsequent inner shells of atoms (O and Te) and the innermost central anionic cluster. The *bcc* packing of the spherical shells is indicated by black lines.[6]

[*] Dr. M. Johnsson, Prof. Dr. S. Lidin
Department of Inorganic chemistry, Stockholm University
S-106 91 Stockholm (Sweden)
Fax: (+46) 8-152187
E-mail: matsj@inorg.su.se
Prof. K. W. Törnroos
Department of Chemistry, University of Bergen
Allégt. 41, 5007 Bergen (Norway)
Prof. Dr. H.-B. Bürgi
Laboratorium für Kristallographie, Universität Bern
Freiestr. 3, 3012 Bern (Switzerland)
Dr. P. Millet
Centre d'Elaboration de Matériaux et d'Etudes Structurales (CEMES/CNRS)
29 rue Jeanne Marvig, BP 4347, Toulouse Cedex 4 (France)

[**] We thank Mr. Marian Mikus at Sandvik Coromant AB for the microsond analyses and Dr. Javier Garcia-Garcia at Stockholm University for the TEM study. This work has been carried out in part through financial support from the Swedish Research Council and the European Union (HPHN-CT-2002-00193).

 © 2004 Wiley-VCH Verlag GmbH & Co. KGaA, Weinheim DOI: 10.1002/anie.200460001

by the coordinating O atoms are given in polyhedral representation in Figure 2. Each $\{NiO_6\}$ octahedron share edges with two other $\{NiO_6\}$ octahedra, six of which form a ring of composition $\{Ni_6O_{24}\}$. The $\{Ni_6O_{24}\}$ units also share corners with the $\{NiO_5X\}$ octahedra, which themselves are connected into dimers through a shared halide ion X. The distance between these two Ni atoms is much longer than between the other Ni atoms. This spherical arrangement of sixty coordinated Ni ions surrounds a shell of O atoms, which in turn envelopes the shell that contains Te atoms and the cavities hosting the anionic guest clusters.



Figure 2. The Ni shell together with the inner and outer O shells in a polyhedral representation. The ringlike $\{Ni_6O_{24}\}$ units built up from $\{NiO_6\}$ octahedra (green) share corners with the dimeric units $\{O_5Ni\text{-}X\text{-}NiO_5\}$; the two octahedra (red) of the dimer share a halogen atom (brown). Together the green and red polyhedra enclose the subsequent Te shell and the central anionic cluster, both indicated as a violet sphere.

The O atoms that line the inside of the Ni shell form an intriguing arrangement in itself, being close-packed on a curved surface (Figure 3). It may thus be considered as a 3D curved variant of the planar layer structures that figure so prominently among halide compounds with available lone pairs.[7]

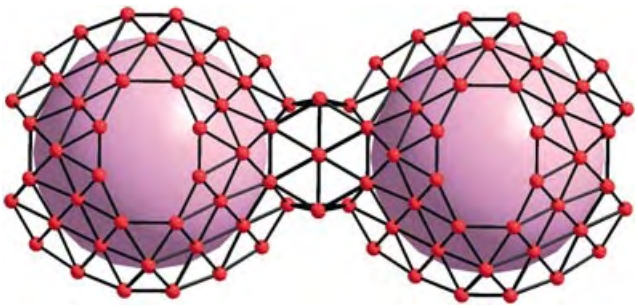


Figure 3. A close-packed layer of oxygen atoms envelopes both sides of the Ni substructure (See Figure 2). The innermost layer of O atoms is shown. The violet skins indicate the next shell of atoms, Te, and the anionic cavity inside of this O layer.

Thirty two Te atoms form the third shell of the structure and constitute the boundary of the cavity for the anionic guests. The Te atoms come in three groups with different center-to-vertex distances (Figure 4). The first group, which is closest to the center of the cavity with a center-to-vertices distance of 5.5 Å, forms a cube. The second shell at 6.5 Å forms a distorted icosahedron. These two groups of Te atoms have their lone pairs pointing towards the center of the cavity. The third group at 7.4 Å forms another icosahedron, but the lone pairs are clearly pointing away from the center (Figure 5a) and towards the bridging halogen atoms ($\{NiO_5X\text{-}NiO_5\}$; Figure 2 and Figure 4). The two groups with the longer distances may also be viewed as constituting the corners of a deformed truncated octahedron.

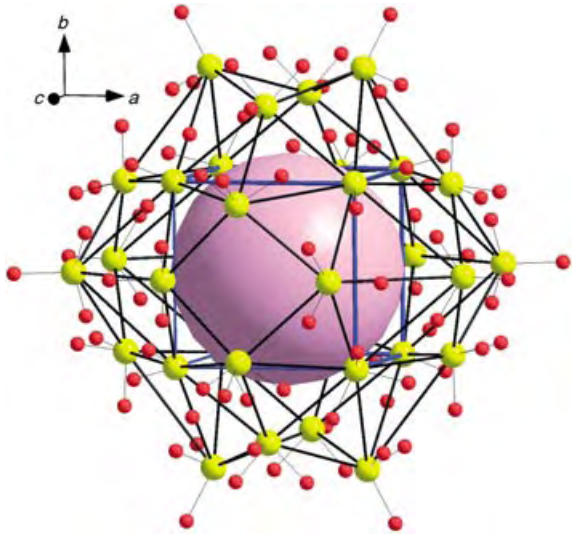


Figure 4. The Te shell (yellow) found inside the innermost layer of O atoms (red). The 24 Te atoms furthest away from the center of the onion form a distorted truncated octahedron, outlined with thick black lines. The eight innermost Te atoms form a cube emphasized by blue edges. The central cavity containing an anionic cluster is marked with a violet sphere.

The description above is, however, somewhat simplified. In fact, the population of the halogen X in the $\{O_5NiXNiO_5\}$ dimer is diminished so that the actual population of X is smaller than unity, 0.88 and 0.90 in **1a** and **1b**, respectively. Concurrently, the group of most-distant Te atoms from the center (Te3) are disordered over two positions of which the one with the larger population is shown in Figure 4. The minor Te site with a population between 0.10 and 0.12 is displaced towards the center of the cavity by 0.35 to 0.5 Å, depending on the compound. Disorder in the cationic cluster is thus modest.

The situation inside the cavities is both more complex and more variable than that in the host network. In compound **1a**, 12 Br atoms form an almost perfect icosahedron with crystallographic $m3$ (T_h) symmetry and surround a central Br ion reminiscent of the $\{Hg_5Cl_{13}\}$ arrangement in $Hg_{11}Ca_2Cl_{26}(H_2O)_{16}$.[8] The 20 triangular faces of the Br icosahedron are capped by the 8 lone pairs of the Te atoms forming a cube and 12 lone pairs of the closer of the two Te

 © 2004 Wiley-VCH Verlag GmbH & Co. KGaA, Weinheim

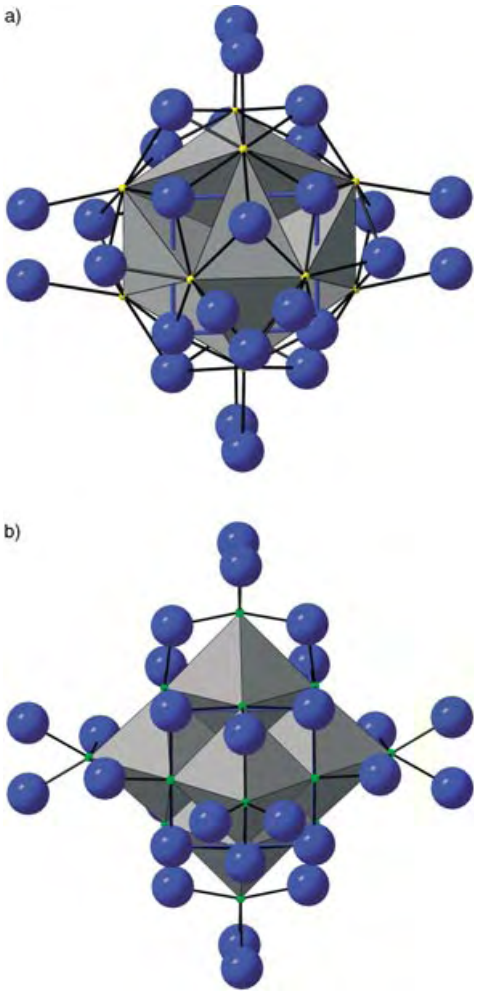


Figure 5. a) The icosahedral $\{X_{13}\}$ cluster found in **1a** and **1b**, surrounded by Te lone pairs (blue). The twelve closed tetrahedra (gray) host the Ni atoms, but only three or four tetrahedra are occupied in any given cavity. Note that the eight lone pairs forming an inner cube cap the faces of empty tetrahedra, while the lone pairs capping the filled tetrahedra are further away. X atoms (Br or Cl) in light brown. b) The $[Cl_{19}]$ cluster found in **2** surrounded by Te lone pairs (blue). The six closed octahedra (gray) host one Ni atom each. Note the eight lone pairs that form a cube cap the empty tetrahedra between the $\{NiCl_6\}$ octahedra. Twelve lone pairs sit over the edges of the octahedra and another 12 are further away. Cl atoms are in green.

icosahedra. The second set of Br triangles together with the central Br constitute 12 tetrahedral cavities that host Ni atoms (Figure 5a). The refined composition of the cavity is $[Ni_{3.39}Br_{12.14}]^{5.36-}$, thus implying that only three or four Ni atoms reside in any given cavity and that there is a slight deficit of Br ions (12.1 versus 13). It is, however, not possible to determine the exact local arrangements of atoms in this cluster from the X-ray diffraction data.

For the relatively large Br ion in **1a**, only the icosahedral guest cluster described above has been observed. For the smaller Cl^- ion, other configurations are allowed. Specifically in compound **2**, if the rock-salt structure is assumed, approximately half of the icosahedra clusters are replaced by a $\{Ni_6Cl_{19}\}$ fragment. A central Cl^- ion is surrounded by a Ni_6 octahedron, each of which is itself octahedrally coordinated by Cl^- ions (Figure 5b). An analogous $[V_6O_{19}]$ cluster has recently been observed in an alkoxo–oxovanadium compound.[9] The remaining half of the cavities is filled with a $[Ni_3Cl_{12.78}]$ cluster that is similar to the $[Ni_{3.39}Br_{12.14}]$ cluster described above for **1a**. The sum of the negative charges of these two clusters in **2** exceeds the positive charge of the surrounding cationic framework.

The anionic cluster in the chloride compound **1b**, synthesized from a flux containing KCl in addition to $NiCl_2$, has the composition $[Ni_{3.10}Cl_{11.52}]^{5.31-}$. Atomic positions as well as the Ni:Cl ratio are very similar to that in **1a** (0.28 versus 0.27), but the cluster occupies only about 90% of the cavities. Electron-density-difference maps show indications of the rock-salt-like $[Ni_6Cl_{19}]$ cluster, but its occupancy is too low to be included in a meaningful least-squares refinement of the X-ray data.

These complex disorder patterns raise questions about the exact composition of the compounds reported and the possibility of locally lowered crystal symmetry. Selected-area electron-diffraction studies, however, give no indication of locally lowered symmetry and it may be assumed that symmetry breaking in one cavity has negligible effect on neighboring cavities.

The EDS data in Table 1 agree within experimental uncertainties with the populations obtained by X-ray diffraction. For **1a** and **1b**, these populations were obtained with the constraint that the crystal be electroneutral resulting in final compositions of $[Te_{32}Ni_{30}Br_{2.64}O_{90}]^{5.36+}[Ni_{3.39}Br_{12.14}]^{5.36-}$ and $[Te_{32}Ni_{30}Cl_{2.69}O_{90}]^{5.31+}[Ni_{3.10}Cl_{11.52}]^{5.31-}$, respectively. Refinements without this constraint tend to increase the halogen content by about 0.7, thus implying excess negative charge. Improvement in the confidence factors is minor, typically $\approx 0.1\%$ in $\Delta R1$. The unconstrained charges in the cationic and anionic clusters of **2** clearly match less well, namely, $[Te_{32}Ni_{30}Cl_{2.67}O_{90}]^{5.33+}$ versus $[Ni_{4.48}Cl_{15.78}]^{6.82-}$. However, the imposition of an electroneutrality constraint on the crystallographic refinement of **2** results in an unreasonable increase in confidence factors, from $R1 = 2.8\%$ to 4.2%.

The consistent tendency towards excess negative charge in crystallographic refinements of all three compounds could be related to the pronounced disorder in the anionic cluster, which makes it difficult to model the electron density under the constraint of electroneutrality. Overestimation of halogen content coupled with an overestimation of thermal or disorder smearing is but one of the explanations of our observations; underestimation of the Ni population is another. In addition, the difficulty of doing an exact absorption correction in the presence of elements as heavy as Te also adds a degree of uncertainty with respect to the population factors of the lighter elements.

The coordination of the individual atoms in the host structure is standard and depends little on the halogen type. The two crystallographically different Ni sites in the $\{Ni_6O_{24}\}$ rings show nearly regular octahedral coordination to the O atoms. The coordination of the octahedra in the $\{O_5NiXNiO_5\}$ dimer is better described as square-planar with four normal Ni–O distances, 2.021(3)–2.031(4) Å, in a plane and long distances to the halogen (Cl, Br), 2.511(1)–2.567(2),

 © 2004 Wiley-VCH Verlag GmbH & Co. KGaA, Weinheim

2.629(2) Å, and O atoms, 2.44(1)–2.582(9) Å, perpendicular to that plane.

The Te atoms all exhibit a classical coordination polyhedron denoted {TeO_3E} formed by three O atoms and a lone pair E. The TeO_3 distances range from 1.880(5) to 1.916(3) Å and the bond angles from 82.9(2) to 101.4(1)°; individual values for specific Te atoms are similar within the statistical uncertainty among the three compounds. All O atoms of the {TeO_3E} tetrahedra are shared with the Ni-centered octahedra.

Given the variety of the observed structures and compositions of the central anionic clusters, compounds **1a**, **1b**, and **2** likely constitute the first members of a new family of inorganic supramolecular compounds,[10] in which the cavities of the peculiarly shelled covalent network could host various other anionic clusters consisting of, for example, Mo, Mn, Hg, or Cu atoms in combination with halogen atoms.

Experimental Section

All compounds were synthesized by chemical-transport reactions in sealed evacuated glass tubes. The starting materials were NiO (Avocado Research Chemicals Ltd.), $NiCl_2$ (Merck, >98% anhydrous), $NiBr_2$ (Strem Chemicals, 99+%), KCl (Merck, p.a.) and TeO_2 (Strem Chemicals, 99+%).

Compound **1a** was synthesized from a mixture of NiO:$NiBr_2$:TeO_2 in a molar ratio of 3:1:3 at 823 K for 65 h producing pale brown small cubic crystals. Compound **1b** was synthesized from a mixture of NiO:$NiCl_2$:TeO_2:KCl in a molar ratio of 2:2:3:2 kept at 873 K for 40 h yielding green cubic crystals. For compound **2**, a mixture of NiO:$NiCl_2$:TeO_2 in a molar ratio of 4:1:4 was kept at 873 K for 40 h yielding green cubic crystals. The products were characterized with a scanning electron microscope (SEM, JEOL 820) and with an energy-dispersive spectrometer (EDS, LINK AN10000). The latter confirmed the presence and stoichiometry of Ni, Te, Cl, and Br (Table 1). EDS and microprobe analysis (JEOL JXA8900R) at 10, 15, and 20 kV conclusively proved the absence of Na, Si or K contaminations.

The single crystal X-ray data were collected on a Bruker-AXS SMART 2 K CCD diffractometer equipped with an Oxford Cryostream series 600 crystal cooling system, $Mo_{K\alpha}$ radiation, λ = 0.71073 Å, graphite monochromator. A full reflection sphere was collected by means of 0.3° ω-scans by using SMART and reduced by using SAINT.[11,12] Gaussian face-indexing absorption correction, structure solution, and refinement were made with SHELXTL.[13] The lone-pair positions were calculated in geometrically idealized positions 1.25 Å away from the Te atoms.

1a: Crystal size: 0.074 × 0.074 × 0.064 mm, T = 100 K, cubic $Im\bar{3}$, a = 17.5077(9) Å, V = 5366.5(5) Å^3, Z = 2, ρ_{calc} = 5.45 g cm^{-3}, $2\theta_{max}$ = 54.22°, 33882 integrated reflections, 1093 unique, R_{int} = 0.0663, 104 parameters, μ = 20.40 mm^{-1}, $R1$ [$I > 2\sigma(I)$] = 0.0213, $wR2$ (all data) = 0.0512, S = 1.07, largest difference peaks 1.08/−1.46 e Å^{-3}.

1b: Crystal size: 0.104 × 0.125 × 0.154 mm, T = 123 K, cubic $Im\bar{3}$, a = 17.4549(8) Å, V = 5318.0(4) Å^3, Z = 2, ρ_{calc} = 4.75 g cm^{-3}, $2\theta_{max}$ = 65.08°, 47467 integrated reflections, 1762 unique, R_{int} = 0.0355, 104 parameters, μ = 14.11 mm^{-1}, $R1$ [$I > 2\sigma(I)$] = 0.0285, $wR2$ (all data) = 0.0573, S = 1.307, largest difference peaks 2.20/−1.99 e Å^{-3}.

2: Crystal size: 0.125 × 0.119 × 0.100 mm, T = 153 K, cubic $Im\bar{3}$, a = 17.5443(3) Å, V = 5400.2(2) Å^3, Z = 2, ρ_{calc} = 4.97 g cm^{-3}, $2\theta_{max}$ = 65.44°, 26545 integrated reflections, 1771 unique, R_{int} = 0.0358, 109 parameters, μ = 14.75 mm^{-1}, $R1$ [$I > 2\sigma(I)$] = 0.0278, $wR2$ (all data) = 0.0498, S = 1.21, largest difference peaks 1.25/−1.27 e Å^{-3}.

The unit cells and the space group were confirmed from X-ray powder diffraction patterns obtained in a Guinier–Hägg focusing camera with subtraction geometry and $Cu_{K\alpha1}$ radiation (λ = 1.54060 Å). Finely powdered Si [a = 5.43088(4) Å] was added as an internal standard. The recorded films were evaluated in an automatic film scanner. Unit cell parameters were refined with the program PIRUM.[14] . Illustrations have been produced by using the program DIAMOND.[15]

Further details on the crystal-structure investigation may be obtained from the Fachinformationszentrum Karlsruhe, 76344 Eggenstein-Leopoldshafen, Germany (fax: (+49) 7247-808-666; e-mail: crysdata@fiz-karlsruhe.de), on quoting the depository numbers CSD-413823, CSD-413824, and CSD-413825.

Received: March 15, 2004 [Z460001]
Published Online: June 23, 2004

Keywords: cluster compounds · host–guest systems · supramolecular chemistry · tellurium

[1] P. Millet, M. Johnsson, V. Pashchenko, Y. Ksari, A. Stepanov, F. Mila, *Solid State Ionics* **2001**, *141–142*, 559–565.
[2] M. Johnsson, K. W. Törnroos, P. Lemmens, P. Millet, *Chem. Mater.* **2003**, *15*, 68–73.
[3] C. Platte, M. Trömel, *Acta Crystallogr. Sect. B* **1981**, *37*, 1276–1278.
[4] C. R. Feger, G.L Schimek, J. W. Kolis, *J. Solid State Chem.* **1999**, *143, 246–253*.
[5] G. Perez, F. Lasserre, J. Moret, M. Maurin, *J. Solid State Chem.* **1976**, *17*, 143–149.
[6] Note that the ratio of the contact distances between the cages along the [111] and [100] directions is 0.887, the ratio between a cubic axis and half its body diagonal. This difference leads to two different center-to-vertex distances for the cage atoms. Distortions such as these invariably occur when icosahedral clusters pack densely with translational symmetry.
[7] T. F. Semenova, I. V. Rozhdestvenskaya, S. K. Filatov, L. P. Vergasova, *Mineral. Mag.* **1992**, *56*, 241–245.
[8] D. Putzas, H. W. Rotter, G. Thiele, K. Brodersen, G. Pezzei, *Z. Anorg. Allg. Chem.* **1991**, *595*, 193–202.
[9] J. Spandl, C. Daniel, I. Brüdgam, H. Hartl, *Angew. Chem.* **2003**, *115*, 1195–1198; *Angew. Chem. Int. Ed.* **2003**, *42*, 1163–1166.
[10] A. Müller, H. Reuter, S. Dillinger, *Angew. Chem.* **1995**, *107*, 2505–2539; *Angew. Chem. Int. Ed. Engl.* **1995**, *34*, 2328–2361.
[11] SMART, Version 5.054 Bruker AXS Inc., Madison, Wisconsin, USA, **1999**.
[12] SAINT, Version 6.28a Bruker AXS Inc., Madison, Wisconsin, USA, **2002**.
[13] SHELXTL, Version 6.12 Bruker AXS Inc., Madison, Wisconsin, USA, **2001**.
[14] P. E. Werner, PIRUM, *Ark. Kemi* **1969**, *31*, 513–516.
[15] K. Brandenburg, DIAMOND. Release 2.1e. Crystal Impact GbR, Bonn, Germany, **2000**.

 © 2004 Wiley-VCH Verlag GmbH & Co. KGaA, Weinheim

Surface Chemistry

Strain-Induced Formation of Subsurface Species in Transition Metals**

*Jeff Greeley, William P. Krekelberg, and Manos Mavrikakis**

Surface strain has recently been shown to have a significant effect on the reactivity of transition-metal surfaces,[1] and numerous examples of strain effects on both the thermochemistry and kinetics of surface reactions have been identified.[2–7] Several of these studies focused on strain induced by epitaxial metal overlayers, but recently it has been demonstrated that strain from another source, namely, dislocations that intersect crystal surfaces, likewise causes significant changes in surface reactivity.[8] This suggests that a careful study on the effect of strain on catalytic processes might yield substantial insights into the effect of defects on these processes. Defects, in turn, have been shown to dominate the reactivity of certain surface reactions.[9] In particular, an analysis of the manner in which strain influences the population of subsurface species in transition metals could contribute to an understanding of the more general problem of how dislocation-induced surface defects mediate the transfer of adsorbates to subsurface regions. Such an analysis could permit a comparison between the behavior of subsurface species on single-crystal and polycrystalline metals,[10,11] and it could have broad application to a number of technologically important problems, including the catalytic reactivity of subsurface oxygen and carbon in connection with corrosion, oxidation, or carbonylation processes,[12,13] subsurface hydrogen reactivity for hydrogenation and hydrogenolysis reactions,[14–19] hydrogen storage in and embrittlement of metals,[11,20,21] and the purification of hydrogen fuel streams with Pd-alloy membranes.[22,23]

Here we analyze the effect of strain on the creation of subsurface species in metals by focusing on the hydrogen/nickel system and using periodic, self-consistent density functional theory (DFT) calculations. As recent atomically resolved STM images of surface defects on Ru(0001) showed regions with lattice stretching of up to 10% in the immediate vicinity of these defects,[8] we focused our studies on Ni(111) slabs with 3 and 10% expansive strain. We show that, while very high H_2 pressures are required to produce subsurface hydrogen on perfect, unstretched Ni(111) surfaces,[24] only modest pressures (on the order of tens of bar) are required for subsurface hydrogen to form on the stretched Ni surfaces that might exist in the vicinity of defects. We also demonstrate that strain qualitatively changes both the site preferences of subsurface hydrogen and the character of the stable surface and subsurface phases of the H/Ni(111) system. We discuss these results in the context of defect-mediated penetration of hydrogen into subsurface regions of both single-crystal and polycrystalline nickel catalysts, and we comment on the implications of the results for other processes involving various subsurface species in transition metals.

A summary of the low-coverage ($\theta = 0.25$ ML (ML = monolayer), corresponding to one H atom per four surface Ni atoms) data for the lowest energy sites of surface, first-layer subsurface, and second-layer subsurface hydrogen at three strain levels is given in Table 1. A modest strain effect on the binding energy (BE_H) of surface hydrogen is found (an increase of 0.05 eV in the magnitude of BE_H is calculated between the unstretched and the 10%-stretched slabs), consistent with a calculated upshift of 0.24 eV in the nickel d-band center (see Ruban et al.[3] for a discussion of the relationship between this electronic structure parameter and the surface reactivity). This effect becomes more pronounced for hydrogen in the first and second subsurface layers (strain-related stabilizations of 0.14 and 0.32 eV are calculated in these cases), and this suggests that, at low hydrogen coverages, stretched slabs appear to stabilize subsurface H to a greater extent than surface H.

Table 1: Binding energies BE_H for surface and subsurface hydrogen on slabs with 0, 3, and 10% expansive lattice strain.[a]

Layer	Strain [%]	H site[b]	BE_H [eV][c]
Surface	0	fcc[d]	−2.89[e]
Surface	3	fcc[d]	−2.91[e]
Surface	10	fcc[d]	−2.94[e]
1st subsurface	0	octa	−2.18[e]
1st subsurface	3	octa	−2.28[e]
1st subsurface	10	tetra (under top)	−2.32[e]
2nd subsurface	0	octa	−2.11[f]
2nd subsurface	3	octa	−2.24[f]
2nd subsurface	10	tetra (under top)[d]	−2.43[f]

[a] Total coverage of 0.25 ML on a 2×2 surface unit cell. [b] octa = octahedral, tetra = tetrahedral. [c] The reference state for the hydrogen binding energies is gas-phase atomic H and a clean nickel slab at infinite separation. [d] One or more other sites have energies comparable to the energies of the indicated sites. [e] Four-layer Ni(111) slabs with the top two layers relaxed. [f] Five-layer Ni(111) slabs with the top three layers relaxed.

One-dimensional potential energy surfaces (PESs) for hydrogen diffusion from the surface to the first and second subsurface nickel layers at various strain levels are given in Figure 1. As the Ni(111) surface is stretched from 0 to 3%, the energy at all points along the PES is lowered, and the barriers E^* for hydrogen diffusion from the surface to the first subsurface layer and from the first to the second subsurface

[*] J. Greeley, W. P. Krekelberg, Prof. M. Mavrikakis
Department of Chemical and Biological Engineering
University of Wisconsin-Madison
1415 Engineering Drive, Madison, WI 53706 (USA)
Fax: (+1) 608-262-5434
E-mail: manos@engr.wisc.edu

[**] J.G. acknowledges partial financial support from an NSF predoctoral fellowship. This work was supported through an NSF-CAREER Award (CTS-0134561) and a DOE-BES Catalysis Science Grant (DE-FG02-03ER15469). We thank DOE-NERSC and NSF-NPACI for supercomputing time. Fruitful discussions on the atomic-scale aspects of defects on metal surfaces with Professor Joost Wintterlin are gratefully acknowledged.

 © 2004 Wiley-VCH Verlag GmbH & Co. KGaA, Weinheim DOI: 10.1002/anie.200454062

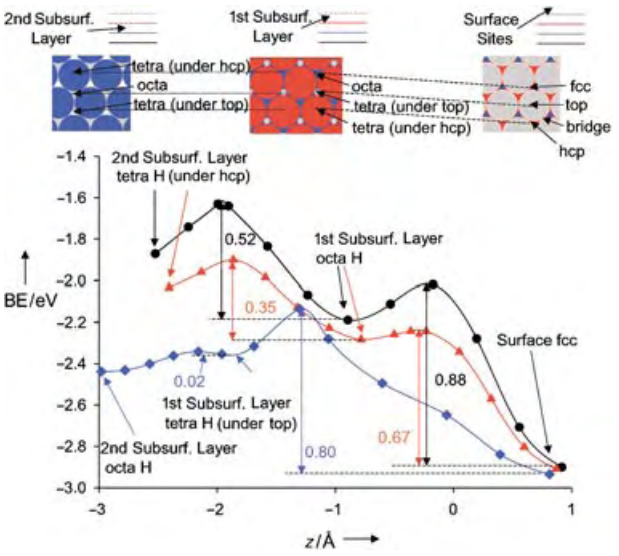


Figure 1. One-dimensional potential energy surface for the sequential diffusion of atomic hydrogen from the surface to the first and second subsurface layers in Ni(111). $\theta_{total} = 0.25$ ML. Diffusion coordinates on slabs with 0, 3, and 10% lattice strain are denoted by black circles, red triangles, and blue diamonds, respectively. $z = 0$ signifies the position of the first layer of nickel atoms on the respective clean, relaxed nickel slabs, and the z coordinate denotes the distance of the hydrogen atom from this reference point. For diffusion from the surface to the first subsurface layer, four-layer slabs (top two layers relaxed) were used. For diffusion from the first subsurface to the second subsurface layer, five-layer slabs (top three layers relaxed) were used. Data for four-layer slabs are given at the intersection of these regions. Tetra = tetrahedral, octa = octahedral. Insets describe the various surface and subsurface sites; the color of the Ni atoms indicates their location (gray = surface layer, red = first subsurface layer, blue = second subsurface layer). Numerical values represent E* [eV] values.

layer decrease from 0.88 and 0.52 eV to 0.67 and 0.35 eV, respectively. At the same time, the resurfacing barrier for subsurface H (corresponding to movement of hydrogen atoms from subsurface octahedral sites—the lowest energy sites at these strain levels—to surface fcc sites) decreases from 0.17 to 0.04 eV. As the surface is stretched still further, the resurfacing barrier drops to zero, and the octahedral sites become unstable. Thus, for Ni(111) slabs with 10% strain, hydrogen must diffuse to an under-top tetrahedral site to find a stable subsurface configuration. This additional diffusional requirement raises the surface-to-subsurface diffusion barrier to 0.80 eV; this value is greater than the corresponding barrier for 3%-stretched slabs, in which subsurface octahedral sites are still stable, but it is less than the corresponding value for the unstretched surface (0.88 eV). Hydrogen diffusion deeper into the 10%-stretched slab is facile; a barrier of only 0.02 eV exists between the first and second subsurface nickel layers. These kinetic results, in combination with the thermochemical comparison of the 0%- and 10%-stretched slabs described above, suggest that both the thermochemistry and the kinetics of subsurface hydrogen formation are enhanced by expansive strain, which might be present in the vicinity of surface defects.

Thermochemical data for hydrogen coverages up to 2.0 ML at various strain levels are given in Table 2 and

Table 2: Binding energies BE_H per hydrogen atom for low- and high-coverage surface and subsurface hydrogen on and in Ni(111) slabs with 0, 3, and 10% lattice stretching.[a]

Strain [%]	Total hydrogen coverage [ML]	Hydrogen surface and subsurface sites[b]	Average BE_H per hydrogen atom [eV][c]	Differential BE_H [eV][d]
0	0.25	fcc(1)	−2.89	−2.89
0	0.50	fcc(1) + hcp(1)	−2.91	−2.93
0	0.75	fcc(3)	−2.86	−2.77
0	1.00	fcc(4)	−2.86	−2.86
0	1.25	hcp(4) + octa(1)	−2.73	−2.20
0	1.50	hcp(4) + octa(2)	−2.65	−2.26
0	1.75	hcp(4) + octa(3)	−2.60	−2.28
0	2.00	hcp(4) + octa(4)	−2.56	−2.29
3	0.25	fcc(1)	−2.91	−2.91
3	0.50	fcc(2)	−2.90	−2.95
3	0.75	fcc(3)	−2.90	−2.85
3	1.00	fcc(4)	−2.91	−2.93
3	1.25	hcp(4) + octa(1)	−2.78	−2.27
3	1.50	hcp(4) + octa(2)	−2.71	−2.34
3	1.75	hcp(4) + octa(3)	−2.66	−2.36
3	2.00	hcp(4) + octa(4)	−2.62	−2.38
10	0.25	fcc(1)	−2.94	−2.94
10	0.50	fcc(2)	−2.95	−2.96
10	0.75	fcc(3)	−2.96	−2.98
10	1.00	fcc(4)	−2.97	−3.02
10	1.25	fcc(4) + tetra(1)	−2.87	−2.44
10	1.50	fcc(4) + tetra(2)	−2.80	−2.46
10	1.75	fcc(4) + tetra(3)	−2.75	−2.48
10	2.00	fcc(4) + tetra(4)	−2.72	−2.50

[a] All calculations were performed on 2×2×4 slabs with the top two layers relaxed. [b] octa = octahedral, tetra = tetrahedral under top (directly under a Ni atom). The numbers in parenthesis indicate how many of these sites are populated in the specific configuration. Only the lowest energy configurations calculated at each coverage are shown. [c] The reference state for the BE_H is gas-phase atomic H and a clean nickel slab at infinite separation. [d] The differential binding energy is the energy change for the reaction $H(g) + n\,H/Ni(111) \rightarrow (n+1)H/Ni(111)$.

Figure 2. For total coverages of 1.0 ML or less and for each strain, the average BE_H value per H atom remains practically constant (only surface sites are occupied at these coverages); the variations in the differential BE_H values are slightly larger. As subsurface sites become populated at higher coverages, and for all strain levels, the magnitude of the average BE_H level per hydrogen atom decreases steadily. At the same time, the magnitude of the differential BE_H value drops quickly (by 0.5–0.7 eV, characterizing the onset of subsurface site occupation) and then increases again (by 0.05–0.10 eV); the increase in the magnitude of the differential BE_H value at higher subsurface coverages may be due to substrate-mediated attraction between the subsurface H atoms. Although these general trends exist for all strain levels examined, certain features of the coverage dependence of the BE_H value are strain-dependent. For example, between 0 and 10% strain, the strength of hydrogen binding increases for all coverages. Interestingly, however, the magnitude of the increase is greater at higher coverages (both the average and

 © 2004 Wiley-VCH Verlag GmbH & Co. KGaA, Weinheim

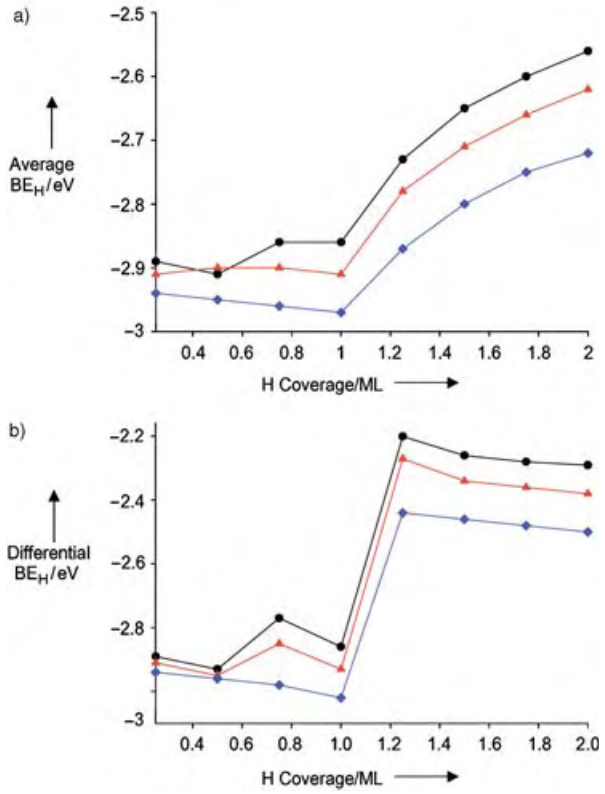


Figure 2. a) Average BE_H as a function of total hydrogen coverage. Black circles, red triangles, and blue diamonds denote BE_H on slabs with 0, 3, and 10% strain, respectively. b) Differential BE_H (defined in Table 2) as a function of total hydrogen coverage .

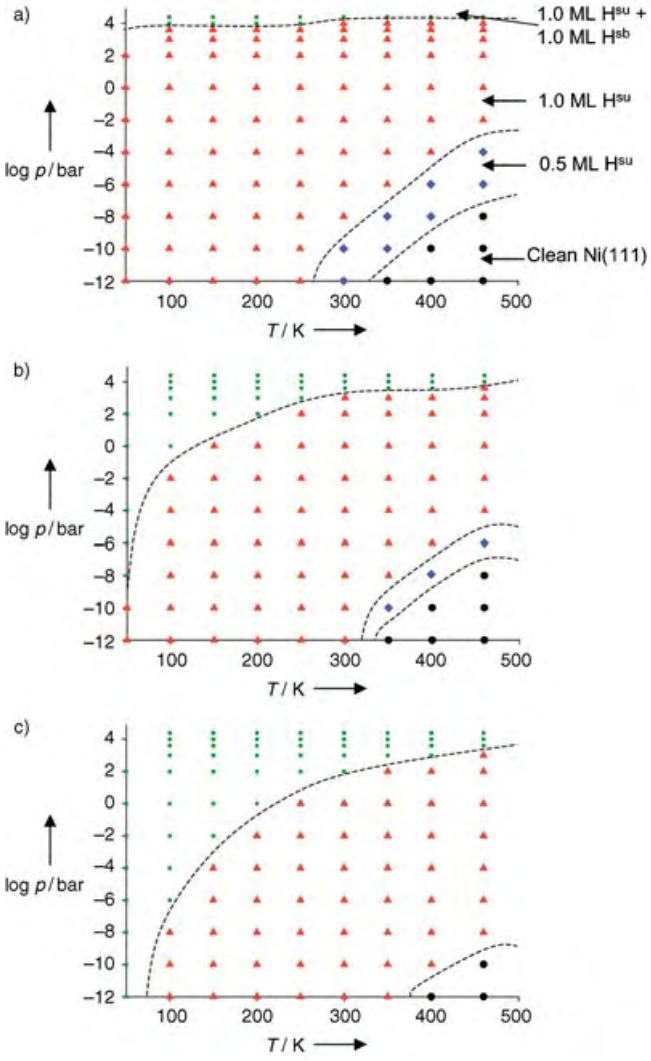


Figure 3. Phase diagrams for surface and subsurface hydrogen on Ni(111) slabs at a) 0, b) 3, and c) 10% lattice strain. See Table 2 for details of the corresponding configurations. Zero-point energy corrections are included for all coverages. The lines between different phases represent, in an approximate manner, the corresponding phase transitions. H^{su} = surface hydrogen, H^{sb} = subsurface hydrogen.

differential BE_H magnitudes increase by 0.05 eV between 0 and 10% strain at $\theta = 0.25$ ML, while the corresponding increases at a total coverage of 2.0 ML are 0.16 and 0.21 eV, respectively). This result demonstrates that the greater expansive-strain-induced stabilization of subsurface H over surface H, described above for hydrogen coverages of 0.25 ML, is even more pronounced at higher coverages. Thus, we suggest that expansive strain may facilitate the thermochemistry of subsurface species formation more dramatically at higher coverages than at lower coverages.

Phase diagrams for H on/in Ni(111) surfaces with 0, 3, and 10% strain (including approximate zero-point energy corrections) are given in Figure 3. The diagrams are constructed under the assumption that an effective equilibrium condition exists between the surface region (represented by our Ni(111) slabs with ad(b)sorbed hydrogen; see Theoretical Section) and both a gas-phase H_2 reservior and a bulk nickel reservoir. We note that a suitable nickel reservoir will be present provided that hydrogen is confined in a local energy minimum near the surface (this will be the case if the timescale for hydrogen transfer from the gas phase to the surface region is much shorter than that for hydrogen population of the bulk nickel reservoir; see Christensen et al.[25] for analogous discussions).[24,26,27] Although no experimental data are available with which to compare the stretched-slab results, the phase diagram on the unstretched slab has been shown to give good agreement with experiment.[24,28,29] The broad trends in each of the phase diagrams are similar; increasing pressure and decreasing temperature favor higher total coverages of hydrogen. Also, we note that, in each diagram, the phases that are present correspond to the minima in the differential BE_H values versus coverage graph (Figure 2b; the minima in the graph indicate stronger binding). However, the relative sizes of the various coverage regimes on the phase diagrams change significantly as a function of strain. As the surface is stretched, the 1.0 ML H phase (surface hydrogen only) and the clean surface phase become smaller, while the 0.5 ML H phase (surface only) is completely absent for the 10%-stretched slab. In contrast, as the surface is stretched, the 2.0 ML phase, where 1.0 ML of subsurface H is present, increases substantially in size. In consequence, whereas pressures on the order of thousands of bar are required to produce subsurface hydrogen from H_2(g) at room temperature on an unstretched Ni(111) surface, pressures of only

 © 2004 Wiley-VCH Verlag GmbH & Co. KGaA, Weinheim

tens of bar are required for production of subsurface H on slabs with 10% strain.

The above results demonstrate that subsurface hydrogen will form more readily in stretched regions of Ni surfaces than in unstretched regions. The kinetics of subsurface H formation are improved, as evidenced by the lower barrier for surface-to-subsurface diffusion on stretched surfaces, and this suggests that population of subsurface sites will occur more rapidly in stretched regions. For example, if differences in preexponential factors are neglected, the 0.21 eV difference in diffusion barriers between surface and first subsurface layers (Figure 1) suggests that the rate constant for hydrogen penetration to the first subsurface layer will be about 3500 times higher on 3%-stretched than on unstretched slabs at room temperature. Further, and more significantly, subsurface hydrogen will be thermodynamically stable at much lower pressures and/or at higher temperatures in stretched areas than in unstretched regions. This information, when combined with insights from recent work showing that large stretched areas are induced in crystal surfaces by dislocations that originate in the bulk,[8] implies that nickel crystals with such defects will absorb hydrogen more readily than perfect Ni(111) surfaces. This mechanism for strain-mediated formation of subsurface hydrogen around defects, possibly combined with previous proposals for subsurface H formation by grain-boundary diffusion and/or direct hydrogen penetration through steps and kinks,[11,30] could explain the observed higher solubility of hydrogen in polycrystalline, as opposed to single-crystal, nickel samples.[31] In turn, we suggest that, if subsurface species play a special role in catalytic surface chemistry, that role might be more pronounced on real catalytic particles, where defect density is much higher than on single crystal surfaces. We note that, for extremely small catalytic nanoparticles, bulk-induced defects will be less common, and compressive strain (a general characteristic of such small nanoparticles),[32,33] as opposed to the stretching described above, may dominate the characteristics of the particle. Thus, the changes in absorptive and catalytic properties of nickel described here will not apply to the very smallest nickel nanoparticles.

The relationship between strain and formation of subsurface species, described above for the particular case of subsurface hydrogen in nickel, may have important implications for other systems in which subsurface heteroatoms play a significant role. Corrosion, embrittlement, hydrogenation, hydrogen storage, and hydrogen purification processes may all be influenced by such effects. As such, in addition to providing insights into the differences between these processes on single-crystal and polycrystalline metals, a careful study of the effect of strain on these systems could provide novel, as-yet unanticipated, insights into the basic chemical and physical processes that underlie them.

Theoretical Section

To study the effect of strain on formation of subsurface hydrogen, we used DFT calculations. Many of the details of both the DFT calculations and the construction of the phase diagrams have been described previously,[24] and here we give only a brief summary. DACAPO, the periodic, self-consistent, DFT-based total energy code, was used for all calculations.[34,35] The GGA-PW91 functional was employed,[36,37] and four- or five-layer slabs (with the top two or three layers relaxed, respectively) with a 2×2 surface unit cell were used. Zero-point energies were included in the results only where explicitly specified. Both gas-phase atomic H and Ni(111) slabs (clean and hydrogen-covered) were treated with fully spin-polarized calculations. To simulate stretched nickel surfaces, the lattice constant d of the unit cell was increased from the unstretched value of 3.52 Å to 3.62 Å and then to 3.87 Å, corresponding to relative strain values $\Delta d/d_{eq}$ of about 3 and 10%, respectively, a range suggested by recent atomically resolved STM measurements on single-crystal transition metal surfaces.[8] For all calculations on stretched slabs, the Ni–Ni interlayer distance was kept at its unstretched value (although the top two or three layers were still allowed to relax according to the Hellman–Feynman forces) to simulate strain in directions parallel to the surface only. Phase diagrams for surface and subsurface hydrogen were constructed by determining the state with the lowest grand canonical potential (we note that the periodic boundary conditions employed in the calculations prevent the analysis of disordered phases); the temperature and pressure behavior was calculated by assuming chemical equilibrium between hydrogen on the surface and in the gas phase.

Received: February 20, 2004 [Z54062]

Keywords: density functional calculations · hydrogen · phase diagrams · strain effects · surface chemistry

[1] M. Gsell, P. Jakob, D. Menzel, *Science* **1998**, *280*, 717.
[2] A. Schlapka, M. Lischka, A. Groß, U. Käsberger, P. Jakob, *Phys. Rev. Lett.* **2003**, *91*, 016101.
[3] A. Ruban, B. Hammer, P. Stoltze, H. L. Skriver, J. K. Nørskov, *J. Mol. Catal. A* **1997**, *115*, 421.
[4] M. Mavrikakis, B. Hammer, J. K. Nørskov, *Phys. Rev. Lett.* **1998**, *81*, 2819.
[5] E. Kampshoff, E. Hahn, K. Kern, *Phys. Rev. Lett.* **1994**, *73*, 704.
[6] J. A. Rodriguez, D. W. Goodman, *Science* **1992**, *257*, 897.
[7] M. K. Rose, A. Borg, T. Mitsui, D. F. Ogletree, M. Salmeron, *J. Chem. Phys.* **2001**, *115*, 10927.
[8] J. Wintterlin, T. Zambelli, J. Trost, J. Greeley, M. Mavrikakis, *Angew. Chem.* **2003**, *115*, 2956; *Angew. Chem. Int. Ed.* **2003**, *42*, 2850.
[9] S. Dahl, A. Logadottir, R. C. Egeberg, J. H. Larsen, I. Chorkendorff, E. Törnqvist, J. K. Nørskov, *Phys. Rev. Lett.* **1999**, *83*, 1814.
[10] A. D. Johnson, K. J. Maynard, S. P. Daley, Q. Y. Yang, S. T. Ceyer, *Phys. Rev. Lett.* **1991**, *67*, 927.
[11] *Hydrogen in Metals II*, *Vol. 29* (Eds.: G. Alefeld, J. Völkl), Springer, Berlin, **1978**.
[12] A. Knop-Gericke, M. Hävecker, T. Schedel-Niedrig, R. Schlögl, *Top. Catal.* **2001**, *15*, 27.
[13] M. P. Ryan, D. E. Williams, R. J. Chater, B. M. Hutton, D. S. McPhail, *Nature* **2002**, *415*, 770.
[14] A. D. Johnson, S. P. Daley, A. L. Utz, S. T. Ceyer, *Science* **1992**, *257*, 223.
[15] S. T. Ceyer, *Acc. Chem. Res.* **2001**, *34*, 737.
[16] X. Sha, B. Jackson, *Chem. Phys. Lett.* **2002**, *357*, 389.
[17] A. Michaelides, P. Hu, A. Alavi, *J. Chem. Phys.* **1999**, *111*, 1343.
[18] V. Ledentu, W. Dong, P. Sautet, *J. Am. Chem. Soc.* **2000**, *122*, 1796.
[19] G. Henkelman, A. Arnaldsson, H. Jónsson, *Surf. Sci.*, submitted.
[20] W. Zhong, Y. Cai, D. Tomanek, *Nature* **1993**, *362*, 435.
[21] C. Elsässer, H. Krimmel, M. Fähnle, S. G. Louie, C. T. Chan, *J. Phys. Condens. Matter* **1998**, *10*, 5131.
[22] K. Hou, R. Hughes, *J. Membr. Sci.* **2003**, *214*, 43.
[23] D. R. Alfonso, A. V. Cugini, D. S. Sholl, *Surf. Sci.* **2003**, *546*, 12.

 © 2004 Wiley-VCH Verlag GmbH & Co. KGaA, Weinheim

[24] J. Greeley, M. Mavrikakis, *Surf. Sci.* **2003**, *540*, 215.
[25] A. Christensen, A. V. Ruban, P. Stoltze, K. W. Jacobsen, H. L. Skriver, J. K. Nørskov, F. Besenbacher, *Phys. Rev. B* **1997**, *56*, 5822.
[26] M. V. Bollinger, K. W. Jacobsen, J. K. Nørskov, *Phys. Rev. B* **2003**, *67*, 085410.
[27] N. Moll, A. Kley, E. Pehlke, M. Scheffler, *Phys. Rev. B* **1996**, *54*, 8844.
[28] K. Christmann, O. Schober, G. Ertl, M. Neumann, *J. Chem. Phys.* **1974**, *60*, 4528.
[29] K. Christmann, R. J. Behm, G. Ertl, M. A. Van Hove, W. H. Weinberg, *J. Chem. Phys.* **1979**, *70*, 4168.
[30] K. Haug, G. Raibeck, *J. Phys. Chem. B* **2003**, *107*, 11433.
[31] S. W. Stafford, R. B. McLellan, *Acta Metall.* **1974**, *22*, 1463.
[32] P. Nava, M. Sierka, R. Ahlrichs, *Phys. Chem. Chem. Phys.* **2003**, *5*, 3372.
[33] M. Klimenkov, S. Nepijko, H. Kuhlenbeck, M. Bäumer, R. Schlögl, H.-J. Freund, *Surf. Sci.* **1997**, *391*, 27.
[34] B. Hammer, L. B. Hansen, J. K. Nørskov, *Phys. Rev. B* **1999**, *59*, 7413.
[35] J. Greeley, J. K. Nørskov, M. Mavrikakis, *Annu. Rev. Phys. Chem.* **2002**, *53*, 319.
[36] J. P. Perdew, J. A. Chevary, S. H. Vosko, K. A. Jackson, M. R. Pederson, D. J. Singh, C. Fiolhais, *Phys. Rev. B* **1992**, *46*, 6671.
[37] J. A. White, D. M. Bird, *Phys. Rev. B* **1994**, *50*, 4954.

 © 2004 Wiley-VCH Verlag GmbH & Co. KGaA, Weinheim

Molecular Sensors

Highly Selective Oligonucleotide-Based Sensor for Mercury(II) in Aqueous Solutions**

Akira Ono and Humika Togashi*

Contamination with heavy metal ions may have severe effects on human health and the environment. Mercury contamination is widespread and arises from a variety of natural sources, such as oceanic and volcanic emissions,[1] as well as anthropogenic sources,[2] such as gold mining and the combustion of solid waste and fuels. Once introduced into the marine environment, bacteria convert inorganic mercury into methylmercury, which enters the food chain and accumulates in higher organisms, such as large edible fish.[3] Methylmercury is neurotoxic and has been implicated as a cause of mercury-pollution-related diseases.[4]

To increase our understanding of mercury pollution, efforts are being made to develop new mercury-sensing strategies that can detect mercury ions in the environment.[5] Such mercury sensors should display solubility in water and a high selectivity for mercury ions against a background of competing analytes. Small synthetic molecules offer one approach to such probes; many small-molecule sensors that rely on spectroscopic and colorimetric methods of detection have been prepared.[6] However, most of these molecules have limitations owing to interference from other metal ions, delayed response to mercury ions, and/or low water solubility. Only a few compounds have been reported to selectively detect Hg^{II} ions in aqueous solutions.[6n,o]

Herein, we report an oligodeoxyribonucleotide (ODN)-based sensing system that selectively detects Hg^{II} ions in aqueous solution. We recently observed the selective binding of Hg^{II} ions to thymine–thymine (T–T) base pairs in DNA duplexes.[7] As the binding of mercury by T–T pairs is strong and highly selective, duplexes that contain a T–T pair are thermally stabilized in the presence of Hg^{II} ions. In contrast, other heavy-metal ions, such as Cu^{II}, Ni^{II}, Pd^{II}, Co^{II}, Mn^{II}, Zn^{II}, Pb^{II}, Cd^{II}, Mg^{II}, Ca^{II}, Fe^{II}, Fe^{II}, and Ru^{II}, do not show any notable effects on duplex stability. Thus, a highly selective sensor for Hg^{II} ions that relies on the selective binding of Hg^{II} ions with a T–T pair could be envisaged.

The ODNs tested for the Hg^{II}-sensing system are shown in Figure 1. The sensor **D–ODN–F** consists of an ODN functionalized with a fluorophore (fluorescein, **F**) and a quencher moiety (dabcyl, **D**) at the 3′- and the 5′-termini, respectively.[8] Both the fluorescent and the quencher moieties are commercially available and are stable under the reaction conditions required for the chemical synthesis and deprotection of ODNs. The ODN sequence is divided into two parts: the thymine-rich mercury-binding sequence and the linker sequence. A mechanism for the detection of Hg^{II} ions by **D–ODN–F** is shown schematically in Figure 2. In the presence of Hg^{II} ions, mercury-mediated base pairs (T–Hg–T)

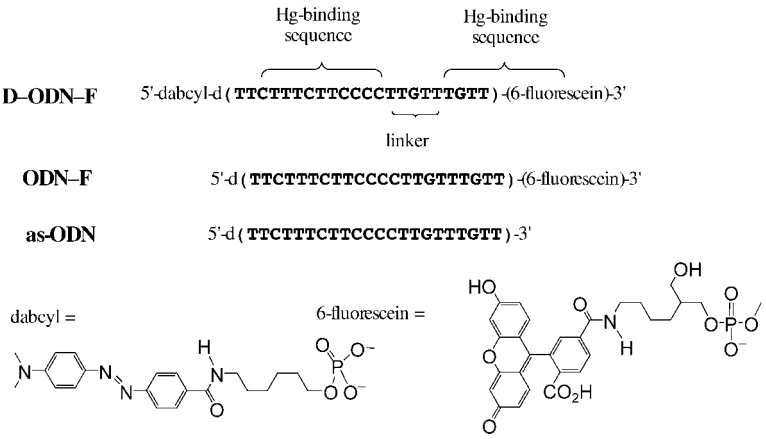


Figure 1. Structures of the ODN-based molecular sensors for mercury(II), **D–ODN–F**, **ODN–F**, and **as-ODN**.

[*] Prof. A. Ono, H. Togashi
Department of Chemistry
Graduate School of Science, Tokyo Metropolitan University
Minami-Ohsawa 1-1, Hachioji, Tokyo 192-0397 (Japan)
Fax: (+81) 426-77-2525
E-mail: akiraono@comp.metro-u.ac.jp

[**] This work was supported in part by the National Project on Protein Structural and Functional Analyses and by the Fund for Special Research Projects at Tokyo Metropolitan University. We thank Prof. W. S. Price for helpful discussions.

Supporting information for this article is available on the WWW under http://www.angewandte.org or from the author.

 © 2004 Wiley-VCH Verlag GmbH & Co. KGaA, Weinheim DOI: 10.1002/anie.200454172

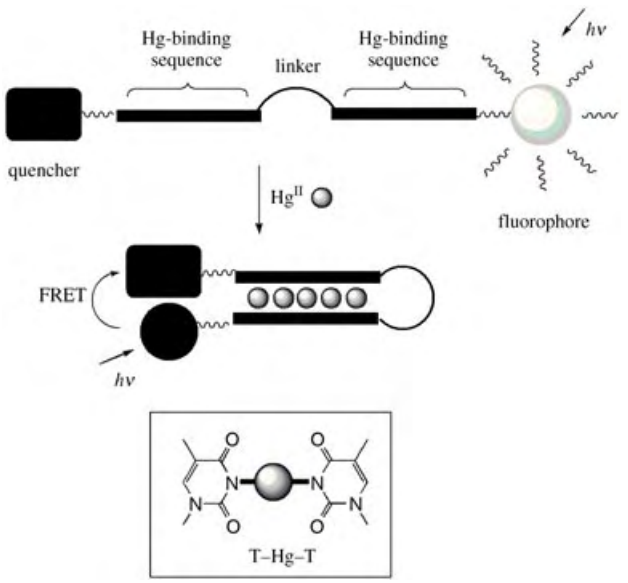


Figure 2. A schematic representation of the hairpin structure induced in **D–ODN–F** by Hg^{II} ion-mediated T–Hg–T pair formation, which results in the quenching of fluorescence from F.

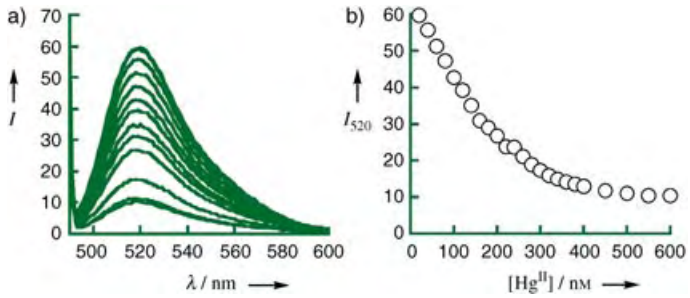


Figure 3. a) Fluorescence response of **D–ODN–F** (10 nM) upon addition of Hg^{II} ion (0, 20, 40, 60, 80, 100, 120, 140, 160, 200, 300, 400, 500, and 600 nM). The intensity of fluorescence emission decreased as the Hg^{II} ion concentration increased. b) Fluorescence emission intensity (520 nm) versus Hg^{II} concentration. A buffer solution of 3-(*N*-morpholino)propanesulfonic acid (10 mM, pH 7.0), NaCl (25 mM), $NaNO_3$ (500 mM), and ethylenediamine (0.1 mM) was used.

are formed between thymine residues from two Hg-binding sequences in the ODN to give rise to a hairpin structure. Both termini of the ODN are brought close to each other upon formation of the hairpin structure which leads to an enhanced fluorescence resonance energy transfer (FRET) process between the F and D moieties. Consequently, this results in significant quenching of the fluorescent emission relative to the random coil.

As shown in Figure 3a, the intensity of the fluorescence emission of **D–ODN–F** was sensitive to Hg^{II} ions and decreased as the concentration of Hg^{II} increased. A linear correlation between the emission intensity and the concentration of Hg^{II} ions was observed in the concentration range $40\ nM < [Hg^{II}] < 100\ nM$ (Figure 3b; detection limit = 40 nM, three times the standard deviation of the blank solution). The variation of the fluorescence intensity was not linear for Hg^{II} concentrations lower than 40 nM probably owing to the requirement of several Hg^{II} ions bound to one sensor molecule for formation of the hairpin structure. The sensitivity of this oligonucleotide-based sensor is greater than those of the previously reported small molecular sensors for Hg^{II}.[6n,o]

As well as high sensitivity, the sensing system requires high selectivity towards the Hg^{II} ion. Fluorescence spectra of **D–ODN–F** recorded in the absence and presence of heavy-metal ions are shown in Figure 4a. The addition of a mixture of other metal ions (Ca^{II} and Mg^{II} (both 1 mM), and Cu^{II}, Fe^{II}, Cd^{II}, Pb^{II}, Zn^{II}, Ni^{II}, Mn^{II}, and Co^{II} (each 1 μM)) did not alter the shape or the intensity of the fluorescence spectra (Figure 4a, +Mix). In contrast, the fluorescence emission spectrum was sensitive to the presence of Hg^{II} ions and its intensity decreased as the Hg^{II} concentration increased. The fluorescence spectra of a control oligodeoxyribonucleotide, **ODN–F**, which did not carry the quencher moiety D, were identical in both the absence and the presence of Hg^{II} ions (Figure 4b).

The reliability of the Hg^{II} sensing can be corroborated by reference to a control, which, in this case, uses an antisensor oligodeoxyribonucleotide (**as-ODN** in Figure 1) that has the same sequence as **D–ODN–F**, but does not carry the **F** and **D** residues. In the presence of excess **as-ODN**, the fluorescence spectrum of **D–ODN–F** changed only slightly upon addition

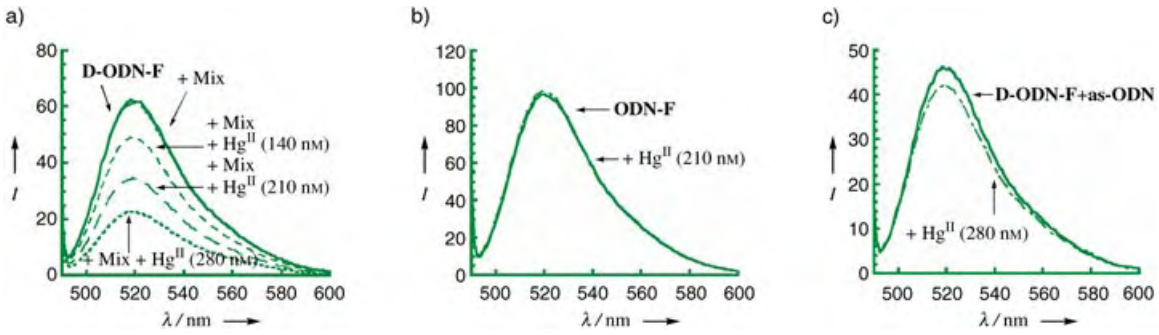


Figure 4. Fluorescence spectra. a) Solutions containing **D–ODN–F** (10 nM), a mixture of heavy metal ions (Mix; $CaCl_2$ and $MgCl_2$ (both 1 mM), and $CuCl_2$, $FeCl_2$, $CdCl_2$, $PbCl_2$, $ZnCl_2$, $NiCl_2$, $MnCl_2$, and $CoCl_2$ (each 1 μM)), and an appropriate concentration of $Hg(ClO_4)_2$. b) Solutions containing **ODN–F** (10 nM) in the absence or presence of $Hg(ClO_4)_2$. c) A solution containing **D–ODN–F** (10 nM) and **as-ODN** (1 μM) in the absence or presence of $Hg(ClO_4)_2$. The same buffer as described in Figure 3 was used.

 © 2004 Wiley-VCH Verlag GmbH & Co. KGaA, Weinheim

of Hg^{II}, as most of the Hg^{II} ions were taken up by **as-ODN** and the Hg^{II} ion concentration decreased substantially (Figure 4c). In the analysis of environmental samples, the fluorescence of sensors can be quenched through the direct interaction of the fluorophores with unexpected substances in the sample media. In the present system, this unexpected quenching can be distinguished from Hg^{II}-derived quenching by using **as-ODN** as a control. When the fluorescence of **D–ODN–F** is quenched in the absence of **as-ODN**, but maintained in the presence of **as-ODN**, the sample contains Hg^{II} ions. Conversely, when the fluorescence of **D–ODN–F** is quenched in the presence *and* the absence of **as-ODN**, the quenching is most likely caused by unexpected contaminants in the sample and the presence of Hg^{II} in the sample is uncertain.

Consequently, our ODN-based Hg^{II}-sensing system has several advantages. First, the sensitivity of the system to Hg^{II} ions is higher than those of existing small molecular sensors. Moreover, the ODN-based sensing system can selectively detect Hg^{II} ions in a solution that contains excess amounts of other heavy metal ions. The reliability of Hg^{II} sensing can be corroborated by performing control experiments using a properly designed antisensor oligodeoxyribonucleotide. Furthermore, the sensitivity of ODN-based sensors can be regulated easily by variation of the sequences of metal-ion-binding sites and linkers.[9] Another advantage of the system is that fluorescence emissions at various wavelengths can be used to indicate different metal ions through variation of the donor–acceptor combinations for FRET.[10]

We hope that our findings will help to improve the direct detection of Hg^{II} ions in the environment and in the presence of excess mono- and divalent ions and other contaminants. Furthermore, our results demonstrate the utility of the oligonucleotide-based molecular design strategy in the development of molecular sensors.[7,11,12]

Received: March 3, 2004
Revised: June 7, 2004 [Z54172]

Keywords: biosensors · fluorescence · FRET (fluorescence resonance energy transfer) · mercury · oligonucleotides

[1] a) A. Renzoni, F. Zino, E. Franchi, *Environ. Res.* **1998**, *77*, 68–72; b) O. Malm, *Environ. Res.* **1998**, *77*, 73–78.

[2] R. von Burg, R. M. Greenwood in *Metals and Their Compounds in the Environment* (Ed.: E. Merian), VCH, Weinheim, **1991**, pp. 1045–1088.

[3] a) F. M. M. Morel, A. M. L. Kraepiel, M. Amyot, *Annu. Rev. Ecol. Syst.* **1998**, *29*, 543–566; b) D. W. Boening, *Chemosphere* **2000**, *40*, 1335–1351; c) M. Nendza, T. Herbst, C. Kussatz, A. Gies, *Chemosphere* **1997**, *35*, 1875–1885; d) S. Hardy, P. Jones, *J. Chromatogr. A* **1997**, *791*, 333–338; e) H. H. Harris, I. J. P. Pickering, G. N. George, *Science* **2003**, *301*, 1203.

[4] a) G. E. McKeown-Eyssen, J. Ruedy, A. Neims, *Am. J. Epidemiol.* **1983**, *118*, 470–479; b) P. W. Davidson, G. J. Myers, C. Cox, C. F. Shamlaye, D. O. Marsh, M. A. Tanner, M. Berlin, J. Sloane-Reeves, E. Cernichiari, O. Choisy, A. Choi, T. W. Clarkson, *Neurotoxicology* **1995**, *16*, 677–688; c) P. Grandjean, P. Heihe, R. F. White, F. Debes, *Environ. Res.* **1998**, *77*, 165–172; d) T. Takeuchi, N. Morikawa, H. Matsumoto, Y. Shiraishi, *Acta Neuropathol.* **1962**, *2*, 40–57; e) H. Matsumoto, G. Koya, T. Takeuchi, *J. Neuropathol. Exp. Neurol.* **1965**, *24*, 563–574; f) M. Harada, *Crit. Rev. Toxicol.* **1995**, *25*, 1–24.

[5] a) I. Murkovic, O. S. Wolfbeis, *Sens. Actuators B* **1997**, *38–39*, 246–251; b) A. A. Vaughan, R. Narayanaswamy, *Sens. Actuators B* **1998**, *51*, 368–376; c) B. Kuswandi, R. Narayanaswamy, *Anal. Lett.* **1999**, *32*, 649–664; d) H. Prestel, A. Gahr, R. Niessner, *Fresenius J. Anal. Chem.* **2000**, *368*, 182–191; e) R. Yang, K. Wang, D. Xiao, K. Luo, X. Yang, *Fresenius J. Anal. Chem.* **2000**, *368*, 797–802; f) S. S. M. Hassan, M. B. Saleh, A. A. A Gaber, R. A. H. Mekheimer, N. A. A. Kream, *Talanta* **2000**, *53*, 285–293; g) W. H. Chan, R. H. Yang, K. M. Wang, *Anal. Chim. Acta* **2001**, *444*, 261–269; h) B. Kuswandi, R. Narayanaswamy, *Sens. Actuators B* **2001**, *74*, 131–137; i) X.-B. Zhang, C.-C. Guo, Z.-Z. Li, G.-L. Shen, R.-Q. Yu, *Anal. Chem.* **2002**, *74*, 821–825; j) L. Manganiello, A. Ríos, M. Valcárcel, *Anal. Chem.* **2002**, *74*, 921–925; k) X. Xu, T. G. Thundat, G. M. Brown, H.-F. Ji, *Anal. Chem.* **2002**, *74*, 3611–3615; l) M. H. Mashhadizadeh, I. Sheikhshoaie, *Talanta* **2003**, *60*, 73–80; m) S. Cherian, R. K. Gupta, B. C. Mullin, T. Thundat, *Biosens. Bioelectron.* **2003**, *19*, 411–416; n) V. Vyacheslav, N. Kim, *J. Microbiol. Biotechnol.* **2003**, *13*, 373–377; o) S. A. M. Marzouk, W. T. Al-Ariqui, S. S. M. Hassan, *Anal. Bioanal. Chem.* **2003**, *375*, 1186–1192; p) W. Yantasee, Y. Lin, T. S. Zemanian, G. E. Fryxell, *Analyst (Cambridge, UK)* **2003**, *128*, 467–472; q) A. T. Maghasi, S. D. Conklin, T. Shtoyko, A. Piruska, J. N. Richardson, C. J. Seliskar, W. R. Heineman, *Anal. Chem.* **2004**, *76*, 1458–1465; r) E. Palomares, R. Vilar, J. R. Durrant, *Chem. Commun.* **2004**, 362–363.

[6] a) M.-Y. Chae, A. W. Czarnik, *J. Am. Chem. Soc.* **1992**, *114*, 9704–9705; b) J. Yoon, N. E. Ohler, D. H. Vance, W. D. Aumiller, A. W. Czarnik, *Tetrahedron Lett.* **1997**, *38*, 3845–3848; c) J. D. Winkler, C. M. Bowen, V. Michelet, *J. Am. Chem. Soc.* **1998**, *120*, 3237–3242; d) G. Hennrich, H. Sonnenschein, U. Resch-Genger, *J. Am. Chem. Soc.* **1999**, *121*, 5073–5074; e) O. Brümmer, J. J. La Clair, K. D. Janda, *Org. Lett.* **1999**, *1*, 415–418; f) K. Rurack, M. Kollmannsberger, U. Resch-Genger, J. Daub, *J. Am. Chem. Soc.* **2000**, *122*, 968–969; g) L. Prodi, C. Bargossi, M. Montalti, N. Zaccheroni, N. Su, J. S. Bradshaw, R. M. Izatt, P. B. Savage, *J. Am. Chem. Soc.* **2000**, *122*, 6769–6770; h) K. Rurack, U. Resch-Genger, J. L. Bricks, M. Spieles, *Chem. Commun.* **2000**, 2103–2104; i) F. Szurdoki, D. Ren, D. R. Walt, *Anal. Chem.* **2000**, *72*, 5250–5257; j) M. J. Choi, M. Y. Kim, S.-K. Chang, *Chem. Commun.* **2001**, 1664–1665; k) F. Sancenón, R. Martínez-Máñez, J. Soto, *Chem. Commun.* **2001**, 2262–2263; l) G. Hennrich, W. Wolther, U. Resch-Genger, H. Sonnenschein, *Inorg. Chem.* **2001**, *40*, 641–644; m) P. N. W. Baxter, *Chem. Eur. J.* **2002**, *8*, 5250–5264; n) A. B. Descaloz, R. Martínez-Máñez, R. Radeglia, K. Rurack, J. Sato, *J. Am. Chem. Soc.* **2003**, *125*, 3418–3419; o) E. M. Nolan, S. J. Lippard, *J. Am. Chem. Soc.* **2003**, *125*, 14270–14271.

[7] A. Ono, H. Togashi, Y. Miyake, unpublished results.

[8] M. N. Stojanovic, P. de Prada, D. W. Landry, *J. Am. Chem. Soc.* **2001**, *123*, 4928–4931.

[9] Besides **D–ODN–F**, the ODN-based Hg sensors **D**–($\mathbf{T_{21}}$)–**F** and **D**–($\mathbf{T_4C_4T_4}$)–**F** were also synthesized. As with **D–ODN–F**, the fluorescence emission spectra of **D**–($\mathbf{T_{21}}$)–**F** and **D**–($\mathbf{T_4C_4T_4}$)–**F** were quenched by Hg^{II} ions. However, the sensitivities of these sensors for the Hg^{II} concentration varied (see Supporting Information).

[10] P. R. Selvin, *Methods Enzymol.* **1995**, *246*, 300–379.

[11] H. Ueyama, M. Takagi, S. Takenaka, *J. Am. Chem. Soc.* **2002**, *124*, 14286–14287.

[12] C. S. Chow, F. M. Bogdon, *Chem. Rev.* **1997**, *97*, 1489–1513.

 © 2004 Wiley-VCH Verlag GmbH & Co. KGaA, Weinheim

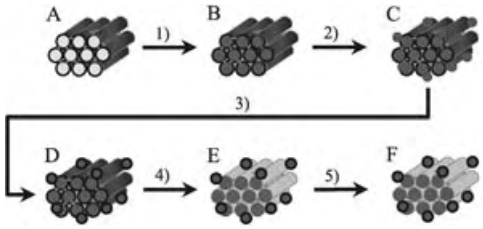
Magnetic Carbon

Nanoengineering of a Magnetically Separable Hydrogenation Catalyst**

*An-Hui Lu, Wolfgang Schmidt, Nina Matoussevitch, Helmut Bönnemann, Bernd Spliethoff, Bernd Tesche, Eckhard Bill, Wolfgang Kiefer, and Ferdi Schüth**

Mesoporous materials, with a variety of desired properties, are extensively used as absorbents, catalysts, and supports in the chemical and petrochemical industries. Very interesting members of this class of materials are ordered mesoporous carbons (OMC),[1] which are obtained by nanocasting from ordered mesoporous silica[2] as a mould. Porous carbon materials combine chemical inertness, biocompatibility, and thermal stability, and are thus suitable for many different applications. However, carbons are notoriously difficult to separate from solutions, and thus magnetic separation is an attractive alternative to filtration or centrifugation and therefore high on the wish list in catalysis for a long time.[3] Introduction of ferromagnetism in carbon particles while retaining their pore system is difficult, though: The commonly employed strategy to synthesize magnetic carbon materials is the condensation of divalent and trivalent iron salts in an activated carbon slurry in the presence of hydroxide with subsequent calcination.[4] Magnetic silica gel can be synthesized by entrapment of magnetite particles in the forming gel.[5] In the case of carbon, the resulting material has typically surface areas of around 600 $m^2 g^{-1}$ and a pore volume below 0.2 $cm^3 g^{-1}$.[4] Such synthetic procedures, however, lead to substantial blocking of the pore space, whereas the pore size distribution of the carbons is inherently broad. In addition, the materials are not stable against corrosive media or high temperature, which lead to dissolution of the magnetic component or coalescence of the particles, respectively, thus sacrificing most of the advantages of the carbon.

To overcome these limitation, we used a combination of nanocasting, spatially selective deposition of magnetic nanoparticles, protection of the nanoparticles by a nanometer-thick carbon layer,[6] and subsequent introduction of the catalytically active component to nanoengineer a magnetically separable catalyst characterized by various distinct features on the nanometer length scale. The overall synthetic strategy is shown in Scheme 1, which includes: 1) the use of



Scheme 1. Illustration of the synthesis procedure: A) ordered mesoporous silica SBA-15; B) carbon/SBA-15 composite; C) B with surface-deposited cobalt nanoparticles; D) protected cobalt nanoparticles on C; E) magnetic-ordered mesoporous carbon; F) Pd on E. 1) Carbonization of the carbon precursor in SBA-15; 2) incorporation of cobalt nanoparticles on B; 3) coating of carbon on cobalt nanoparticles; 4) dissolution of silica to create pore system; 5) loading of Pd in pores to introduce catalytic function.

the mesostructured SBA-15[2b] as template to synthesize a carbon/SBA-15 composite; 2) deposition of cobalt nanoparticles[7] selectively on the outer surface of the composite particle; 3) protection of the cobalt particles by a nanometer-thick carbon layer; 4) removal of the silica scaffold by an aqueous solution of hydrofluoric acid (HF); 5) loading the now-accessible pore system by an impregnation process with a catalytically active noble metal. A related process that involves reversible polymer protection of the pore system has been developed to produce magnetic ordered mesoporous silica.[8]

The success of this strategy can be recognized best when the material obtained after step 4 is analyzed. Transmission electron microscopy of these materials reveals the typical noodle-shaped morphology of SBA-15, which is the result of the nanocasting process (Figure 1a). The well-dispersed cobalt nanoparticles grafted on the mesoporous carbon can be clearly observed. Elemental analysis reveals a cobalt content close to the nominal amount adjusted in the impregnation step. The material, discussed in detail below, has a loading of 9 wt.%.

Higher resolution TEM analysis (Figure 1b) shows that the resulting mesoporous carbon exhibits an ordered structure with hexagonal symmetry, the typical characteristic of OMC templated from SBA-15.[9] The center-to-center distances of adjacent channels are about 7.8 nm. The cobalt particles, highly dispersed on the surface of the carbon particles, have a uniform diameter of about 11 ± 2 nm, while the original size of the cobalt nanoparticles was about 10 ± 1 nm. The increase in diameter is attributed to the coating with the carbon layer, the thickness of which roughly corresponds to three graphite layers. The formation of the carbon layer is preferentially induced on the cobalt particles as the carbonization of the furfuryl alcohol is strongly catalyzed by the cobalt. The pore system, on the other hand, remains accessible (see below). As the sample shown in

[*] Dr. A.-H. Lu, Dr. W. Schmidt, Dr. N. Matoussevitch, Prof. Dr. H. Bönnemann, B. Spliethoff, Dr. B. Tesche, Prof. Dr. F. Schüth
Max-Planck-Institut für Kohlenforschung
45470 Mülheim an der Ruhr (Germany)
Fax: (+49) 208-306-2395
E-mail: schueth@mpi-muelheim.mpg.de
Dr. E. Bill
Max-Planck-Institut für Bioanorganische Chemie
45470 Mülheim an der Ruhr (Germany)
Prof. Dr. W. Kiefer
Institut für Physikalische Chemie
Universität Würzburg
Am Hubland, 97074 Würzburg (Germany)

[**] A.-H. Lu, acknowledges the Alexander von Humboldt Foundation for a scholarship. The authors would like to thank the Leibniz-Program and the FCI for support in addition to the basic funding provided by the Institute.

 DOI: 10.1002/anie.200454222 © 2004 Wiley-VCH Verlag GmbH & Co. KGaA, Weinheim

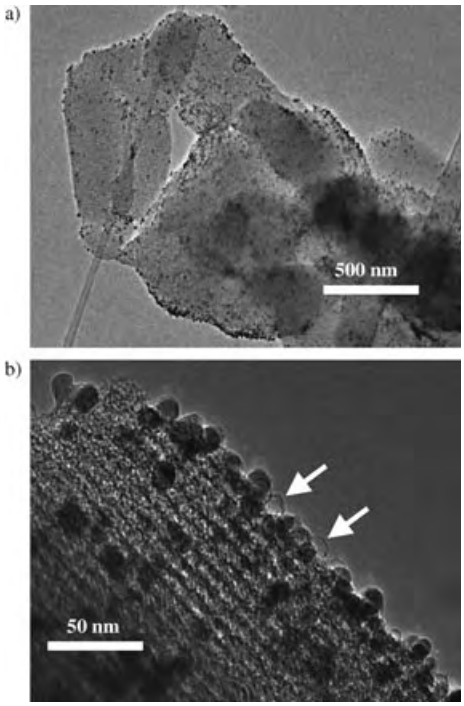


Figure 1. TEM images of Co–OMC at different magnification: a) low magnification; b) high magnification. Arrows indicate hollow carbon shells left after the leaching procedure.

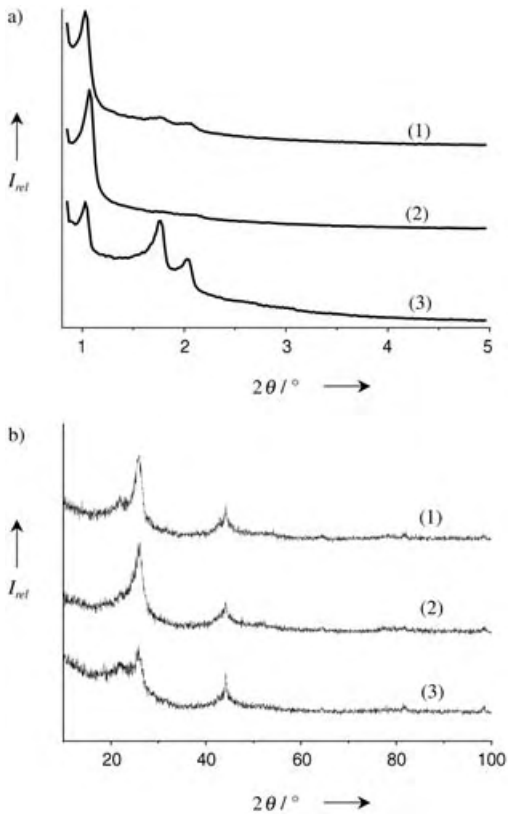


Figure 2. XRD patterns of different Co–OMC: a) low angle; b) wide angle. Types of mesoporous carbons shown in the Figure are: 1) magnetic CMK-3, 2) magnetic polyacrylonitrile-based OMC, and 3) magnetic CMK-5.

Figure 1 had been leached in HF for 72 h, one can infer that the coating of the cobalt nanoparticles is perfect in most cases and the particles are well protected against acid erosion. However, in addition to the intact particles, one can observe the existence of hollow carbon shells (arrows), which are the result of dissolution of the cobalt core by HF solution, while the imperfect shells remain. It is noteworthy that the cobalt nanoparticles do not sinter even after thermal treatment at temperatures up to 850 °C. This can be attributed to the passivation and stabilization of the cobalt nanoparticles by carbon layers through the decrease of the surface energy, and the strong interaction between the carbon coating of the cobalt particles and the bulk carbon material of the OMC.

The low-angle X-ray powder diffraction (XRD) pattern (Figure 2a) of the resultant Co–OMC shows well-resolved reflections, thus indicating an ordered structure. This is consistent with the TEM observation. The d (100) value is about 7.8 nm, from which a unit cell parameter of $a = 9.0$ nm (assuming space group *P6mm*) can be calculated, which is in reasonable agreement with the TEM analysis. The wide-angle XRD reflection (Figure 2b) matches the face-centered cubic (fcc) structure of cobalt. No indication of hexagonal close packing (hcp) cobalt was observed. The size of the cobalt particles, calculated with the Scherrer equation from the reflection broadening of the wide angle reflections, is around 10 nm, which is almost identical to the value estimated from the TEM analysis. Also shown in the Figure are the XRD patterns of two other ordered mesoporous magnetic carbons, which are either based on a different structure, that is, CMK-5,[1b,c] or on a different framework composition, that is, a carbon–nitrogen framework[10] derived from a polyacrylonitrile precursor. This observation demonstrates the general applicability of the pathway described.

The textural properties of Co–OMC were examined by nitrogen adsorption. The isotherm presented in Figure 3 is of

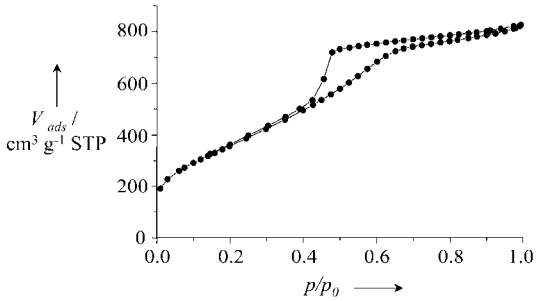


Figure 3. Nitrogen adsorption isotherm of Co–OMC.

type IV and exhibits a hysteresis loop in the relative pressure range of 0.45–0.60, thus indicating a narrow pore-size distribution in the mesopore range and proving the accessibility of the pore system. The pore-size distribution is mainly located around 3–4 nm, and the average pore size calculated by the BJH (Barrett-Joyner-Halenda) algorithm based on the adsorption branch is 3.8 nm (due to the closure of the hysteresis around $p/p_0 = 0.42$, the desorption branch was not used to avoid errors due to instability of the meniscus at this

 © 2004 Wiley-VCH Verlag GmbH & Co. KGaA, Weinheim

point).[11] The actual pore size may be slightly larger, as the BJH method is known to underestimate the pore size in this range.[11] The specific surface area and pore volume are as high as 1319 $m^2 g^{-1}$ and 1.25 $cm^3 g^{-1}$, respectively, which by far exceed the textural parameters of any other magnetic material reported so far.

These data indicate one potential application of unmodified Co–OMC, that is, its use as easily recoverable adsorbent. As an example, the adsorption of the dye Rhodamine 6G (Rh6G, $C_{28}H_{31}N_2O_3Cl$) from aqueous solutions, by using Co–OMC as adsorbent, was investigated. The concentration of the Rh6G solution was 0.1 $g L^{-1}$. After the addition of Co–OMC to the Rh6G-containing solution, there was a change from orange-red to colorless within minutes, thus indicating that the Rh6G dye is strongly adsorbed by Co–OMC. The dye-loaded Co–OMC was separated by placing a conventional laboratory magnet near the glass bottle. As shown in Figure 4, the black particles were attracted to the magnet, the

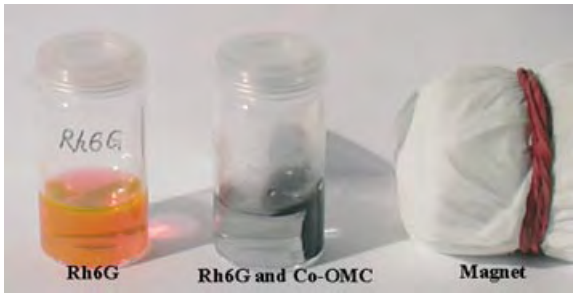


Figure 4. Rh6G aqueous solution (left) and after adsorption of the Rh6G on Co–OMC and separation of the dye loaded Co–OMC by a magnet (right).

clear solution could be decanted off or removed by pipette. This simple experiment demonstrates that the Co–OMC is magnetic and can potentially be used as a magnetic adsorbent to remove dyes or other large molecules in liquid-phase processes.

To study the magnetic properties of the materials in more detail, magnetization measurements of 9 wt.% Co–OMC were performed as a function of temperature from 2 K to 290 K in a magnetic field of $B = 1.0$ T. The magnetization (12.8 $emu g^{-1}$) of the cobalt nanoparticles is essentially temperature-independent, the effective magnetic moment increases following approximately a square-root dependence with increasing temperature. Saturation of magnetization at room temperature is reached with applied fields of about 1 T without observable hysteresis. The saturation magnetic moment (12.8 $emu g^{-1}$) corresponds to 1.5 spins per cobalt atom, which perfectly matches the value for bulk cobalt metal. This shows that the cobalt nanoparticles are in the ferromagnetic state. Oxidation would lead to the formation of antiferromagnetic spinel type oxide. The ferromagnetic properties thus demonstrate that the cobalt particles are still intact, even though this particular sample was stored under air for more than 5 months.

Magnetically separable carbon-catalyst supports are highly attractive for many applications, as carbon supports are often used in liquid-phase processes. For such applications, the particle sizes need to be small to avoid mass-transfer limitations. Small particles, however, create severe problems with respect to catalyst separation. To test the performance of the magnetic OMC as catalyst support, the hydrogenation of octene to octane was selected as a simple test reaction. Catalytic activity was introduced by loading the magnetically modified carbon with palladium. The catalyst was used as a slurry in a small, well-stirred reactor that had a continuous supply of hydrogen, and the hydrogen consumption was monitored as a measure of the progress of the reaction (Figure 5). The rate of hydrogen consumption stayed con-

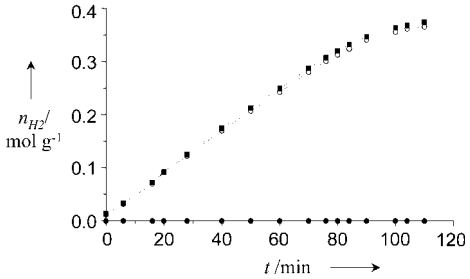


Figure 5. Hydrogenation of octene over 1% Pd-loaded Co–OMC. (■) Fist run, (○) second run after separation of catalyst and new addition of octene, (●) run to test how separable the catalyst is after magnetic removal of catalyst and readmission of hydrogen.

stant, thus indicating a continuous transformation of octene into octane until all octene had been converted. The reacted solution was removed by pipette after the magnetic carbon had been separated from the solution by applying a magnetic field to the reactor. The hydrogenation reaction was repeated by refilling fresh octene into the reactor. It was found that the reaction rate was almost identical to the initial run. This demonstrates the reproducibility of the octene hydrogenation catalyzed by Pd loaded Co–OMC.

More importantly from the point of view of an application, it is possible to remove the catalyst completely after the reaction. This aspect was checked by the following experiment: During the reaction, the catalyst was attracted to the bottom of the reactor by the application of a magnetic field. Subsequently, the partly reacted solution was transferred to a new reactor, which was once again exposed to hydrogen to carry out a new hydrogenation. However, as expected for full separation of the catalyst, no hydrogen consumption was detected. To exclude complete consumption of the octene prior to the separation, fresh octene was added. Again, no hydrogen was consumed. These experiments prove the that the catalyst can be completely separated from the reaction solution.

In summary, by using a sequence of well designed manipulation steps commonly employed in the synthesis of nanomaterials, ordered mesoporous carbons with surface-grafted magnetic particles was successfully synthesized. Such magnetic nanocomposites have very high surface area, a large pore volume, and uniform pore size. Applications of this Co–OMC as magnetically separable adsorbent and catalyst were demonstrated in this study. However, one may envisage also

 © 2004 Wiley-VCH Verlag GmbH & Co. KGaA, Weinheim

other applications, such as a magnetically directed drug carrier. If a drug were loaded onto the porous carbon, one could possibly accumulate the magnetic particles in the target area of the organism, and then induce release of the drug by magnetic heating of the particles. Experiments in progress will show whether such applications can be realized.

Experimental Section

The detailed synthesis of SBA-15 can be found elsewhere.[2b] In short, tetraethyl orthosilicate (TEOS) (8.5 g, 6.9 mmol; Aldrich) were hydrolyzed at 40 °C in an aqueous solution that contained surfactant P123 (4.0 g, mol; BASF), distilled water (105 g) and aqueous 37% HCl (20 mL; Fluka). The milky mixture was aged at 90 °C for 2 days. SBA-15 was obtained after calcination at 550 °C in air. Subsequently, diluted furfuryl alcohol (Fluka) in trimethylbenzene (Fluka) was infiltrated into SBA-15 in the presence of oxalic acid as catalyst by incipient wetness impregnation with a molar ratio of furfuryl alcohol to oxalic acid of 200. The concentration of furfuryl alcohol can be varied from 30 vol.% to 80 vol.%. After the polymerization of furfuryl alcohol first at 60 °C, then at 80 °C, the carbon/SBA-15 composite was obtained by carbonization at 850 °C for 4 h under argon.[1c]

Cobalt nanoparticles were synthesized by using $[Co_2(CO)_8]$ as the source of cobalt and toluene as solvent. The nanoparticles were stabilized with the surfactant Korantin SH.[7]

The obtained carbon/SBA-15 composite was contacted with the desired amount of cobalt nanoparticles dispersed in toluene. Subsequently, toluene was removed by evacuation. To encapsulate the cobalt particles with carbon, the dried sample was impregnated with furfuryl alcohol solution followed by polymerization and carbonization up to 850 °C for 4 h. OMC with surface-grated cobalt nanoparticles was obtained by dissolving the silica in an aqueous solution of hydrofluoric acid (40%, Fluka) for 72 h.

Pd-loaded magnetic carbon was prepared by incipient wetness impregnation of Co–OMC with an aqueous solution of $Pd[(NH_3)_4Cl_2]$. The loading amount of Pd over the sample described herein was determined as 1 wt.%, but samples with higher loading were also prepared. After drying, Pd was reduced under hydrogen at 400 °C for 2 h. For the octane hydrogenation, 6 mL of octene and 0.068 g Pd-containing Co–OMC were used.

TEM images of samples were obtained with an Hitachi HF2000 microscope equipped with a cold-field emission gun. The acceleration voltage was 200 kV. Samples were prepared dry on a lacey carbon grid. Low-angle X-ray diffraction patterns of samples were recorded with a Stoe Stadi P diffractometer in the Bragg-Brentano (reflection) geometry. The step width was 0.02° at an acquisition time of 8 s per step in the range of 2θ 0.85–5°. Nitrogen-adsorption isotherms were measured with an ASAP2010 adsorption analyzer (Micromeritics) at liquid-nitrogen temperature. Magnetic susceptibility measurements were performed on a SQUID susceptometer (Quantum Design, MPMS-7) with an applied magnetic field of 0–7 T. The powdered sample was immobilized in a hard gelation capsule during the measurement. Sample temperatures were varied from 2–290 K.

Received: March 9, 2004 [Z54222]

Keywords: carbon allotropes · heterogeneous catalysis · hydrogenation · magnetic carbon · mesoporous compounds

[1] a) R. Ryoo, S. H. Joo, S. Jun, *J. Phys. Chem. B* **1999**, *103*, 7743–7746; b) S. H. Joo, S. J. Choi, I. Oh, J. Kwak, Z. Liu, O. Terasaki, R. Ryoo, *Nature* **2001**, *412*, 169–172; c) A.-H. Lu, W. Li, W. Schmidt, W. Kiefer, F. Schüth, *Carbon*, accepted.

[2] a) C. T. Kresge, M. E. Leonowicz, W. J. Roth, J. C. Vartuli, J. S. Beck, *Nature* **1992**, *359*, 710–712; b) D. Zhao, J. Feng, Q. Huo, N. Melosh, G. H. Fredrickson, B. F. Chmelka, G. D. Stucky, *Science* **1998**, *279*, 548–552.

[3] W. Teunissen, F. M. F. de Groot, J. Geus, O. Stephan, M. Tence, C. Colliex, *J. Catal.* **2001**, *204*, 169–174.

[4] L. C. A. Olivera, R. V. R. A. Rios, J. D. Fabris, V. Garg, K. Sapag, R. M. Lago, *Carbon* **2002**, *40*, 2177–2183.

[5] M. T. Reetz, A. Zonta, V. Vijayakrishnan, K. Schimossek, *J. Mol. Catal. A* **998**, *134*, 251–258.

[6] R. S. Ruoff, D. C. Lorents, B. Chan, R. Malhotra, S. Subramoney, *Science* **1993**, *259*, 346–348.

[7] H. Bönnemann, W. Brijoux, R. Brinkmann, N. Matoussevitch, N. Waldöfner, N. Palina, H. Modrow, *Inorg. Chim. Act*a. **2003**, *350*, 617–624.

[8] A.-H- Lu, W. Li, A. Kiefer, W. Schmidt, E. Bill, G. Fink, F. Schüth, *J. Am. Chem. Soc.*, **2004**, *126*, 8616.

[9] R. Ryoo, S. H. Joo, M. Kruk, M. Jaroniec, *Adv. Mater.* **2001**, *13*, 677–681.

[10] A.-H. Lu, A. Kiefer, W. Schmidt, F. Schüth, *Chem. Mater.* **2004**, *16*, 100–103.

[11] M. Kruk, M. Jaroniec, *Chem. Mater.* **2001**, *13*, 3169–3183.

 © 2004 Wiley-VCH Verlag GmbH & Co. KGaA, Weinheim

Drug Design

Binding Mode Determination of Benzimidazole Inhibitors of the Hepatitis C Virus RNA Polymerase by a Structure and Dynamics Strategy**

Steven R. LaPlante, Araz Jakalian, Norman Aubry, Yves Bousquet, Jean-Marie Ferland, James Gillard, Sylvain Lefebvre, Martin Poirier, Youla S. Tsantrizos, George Kukolj, and Pierre L. Beaulieu*

Infection by the hepatitis C virus (HCV) is a serious cause of chronic liver disease worldwide, with more than 170 million infected individuals at significant risk of mortality.[1] Though an immunomodulator treatment of limited efficacy exists, there is an urgent need for potent drugs which can specifically target the viral proteins.[2] The HCV-encoded NS5B RNA-

[*] Dr. S. R. LaPlante, A. Jakalian, N. Aubry, Y. Bousquet, J.-M. Ferland, J. Gillard, S. Lefebvre, M. Poirier, Y. S. Tsantrizos, G. Kukolj, P. L. Beaulieu
Departments of Chemistry and Biological Sciences
Boehringer Ingelheim (Canada) Ltd., Research and Development
2100 Cunard St., Laval, Quebec (Canada) H7S2G5
Fax: (+1) 450-682-8434
E-mail: slaplante@lav.boehringer-ingelheim.com

[**] We are grateful to Dr. Michael Bös, Dr. Michael Cordingley, and Dr. Paul Anderson for encouragement and support. We also thank Dr. Timothy Stammers, Dr. Nathalie Goudreau, Dr. Marc-André Poupart, Dr. Dale Cameron, and Mr. Jeff O'Meara for comments or critical reading of the manuscript, as well as Ginette McKercher for determining inhibition constants.

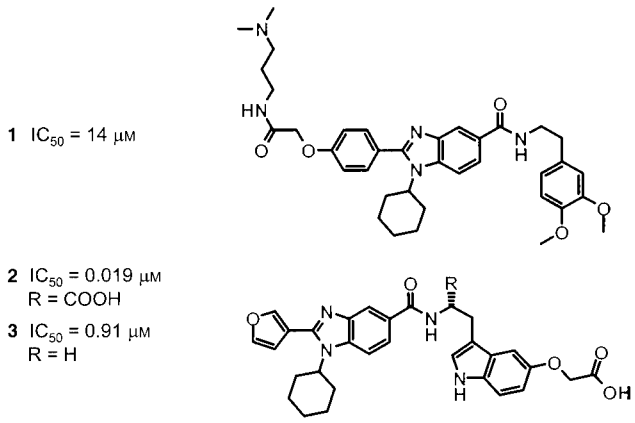
Supporting information for this article is available on the WWW under http://www.angewandte.org or from the author.

 © 2004 Wiley-VCH Verlag GmbH & Co. KGaA, Weinheim DOI: 10.1002/anie.200460326

dependent RNA polymerase is essential for viral replication and has long been considered an attractive target for therapeutic intervention in HCV-infected patients.[3]

Herein, we report the application of structure- and dynamics-based strategies for determining the binding mode of novel benzimidazole inhibitors of the HCV polymerase. We demonstrate that a screen-derived compound binds directly to NS5B, and determine the polymerase-bound structure of a potent analogand upon binding the polymerase, and elucidate the principle binding roles of each of the substituents. Besides providing medicinal chemists with practical information for designing HCV polymerase inhibitors, the methodology has general utility and can be applied to most ligand–macromolecule systems for studying molecular recognition processes.

Our search for potential leads for inhibitors of NS5B polymerase (HCV polymerase) began by using a high-throughput screen (HTS) of our compound collection, from which compound **1** was identified.[4] In addition to our



biochemical specificity assays,[4] differential line broadening (DLB) NMR experiments[5,6] played an important role in demonstrating that **1** binds directly to HCV polymerase and not to RNA, a substrate in the HTS screen and specificity assays. Figure 1a shows that a ^{1}H NMR resonance of free **1** (blue) incrementally broadened upon addition of HCV polymerase (red), whereas broadening was not detected in the presence of RNA (blue versus red, Figure 1b). The observed broadening is a result of fast-exchange binding (on the NMR timescale) to the polymerase and is an average of the linewidths and chemical shifts of the free and bound states. A higher stoichiometry of ligand was employed to simplify signal detection. Having identified compound **1** as a valid lead compound,[4,7] we subsequently synthesized numerous analogues and discovered potent compounds such as **2**,[7,8] which has a truncated left side and a more optimal right side that imparts a 738-fold improvement in potency. The discovery process for these compounds[4,7,8] involved the development of structure–activity relationships (SAR), assistance from combinatorial chemistry, and the elucidation of the binding role of each substituent.

As part of our inhibitor-optimization effort, several NMR spectroscopic methods were used to monitor direct binding to HCV polymerase. ^{1}H DLB experiments provided a straightforward and practical tool. Notably, specific resonances in the ^{1}H spectrum of free compound **2** and the related analogue **5** (blue spectra in Figure 1d,e, respectively) differentially broadened in the presence of relatively small amounts of HCV polymerase (red). ^{19}F NMR experiments also provided evidence of direct binding. The sharp trifluoromethyl resonance of free compound **4** (blue spectrum in Figure 1c) broadened and shifted upon binding to the HCV polymerase (red spectra). Unlike the ^{1}H DLB experiment which employed an excess of inhibitor, the ^{19}F NMR data were acquired at a 1:1 inhibitor:polymerase ratio and thus provided the additional advantage of potentially monitoring the number of binding sites. The observation of a single, bound ^{19}F resonance in Figure 1c (red) is consistent with a single binding site. Finally, a ^{1}H transferred NOESY experiment[5,6] was also applied to detect the binding of **1** (see Supporting Information) and **2**. The NOESY spectrum of free **2** (Figure 2a) lacks crosspeaks, as would be expected for a fast-tumbling small molecule. In the presence of HCV polymerase, multiple negative-sign crosspeaks appear as a result of fast-exchange binding to the slower tumbling HCV polymerase (Figure 2b).

The "transferred" NOESY crosspeaks in Figure 2b also reflect a fingerprint of short, intramolecular hydrogen bonds when compound **2** is bound to the polymerase. Overall, the ensemble of data was suggestive of a single, bound conformation with the exception of two potential orientations of the benzoic acid–amide bond. On the basis of the transferred NOESY crosspeaks, distance-restrained simulated-annealing calculations were applied to determine the bound structure of **2**. Two possible 3D structures, that differed only in the orientation of the benzoic acid–amide bond, were determined by calculations that varied only by the inclusion of an H15 to H4 restraint (herein defined as the "NH up" orientation, Figure 2c), or the inclusion of an H15 to H6 restraint (herein defined as the "NH down" orientation, Figure 2d). A definition of the atom numbering scheme is provided in Figure 1e.) Although both corresponding NOESY crosspeaks of equal intensity were observed and suggested a perpendicular amide–benzimidazole orientation, our ab initio calculations were more consistent with the existence of either or both energetically favorable coplanar orientations (see the Supporting Information). It is also possible and likely that one of the NOESY crosspeaks was an artifact of spin-diffusion contamination[6] and experimental attempts to resolve the problem were unsuccessful (that is, very short mixing times, QUIET-NOESY, etc.). Hence, we resorted to the design of azabenzimidazole **7** as a conformational probe in which the carbon atom at position Y was substituted by a nitrogen atom. This compound was predicted by ab initio calculations to preferentially adopt the coplanar NH up orientation of the benzoic acid–amide bond in the free state as a result of a favorable electrostatic interaction between the NH and lone-pair of electrons on the nitrogen atom. This preferential orientation in the free state was also observed by ROESY NMR experiments (see the Supporting Information), and is consistent with the bound structure in Figure 2c since compounds **6** (Y = CH) and **7** (Y = N) exhibit similar affinity

 © 2004 Wiley-VCH Verlag GmbH & Co. KGaA, Weinheim

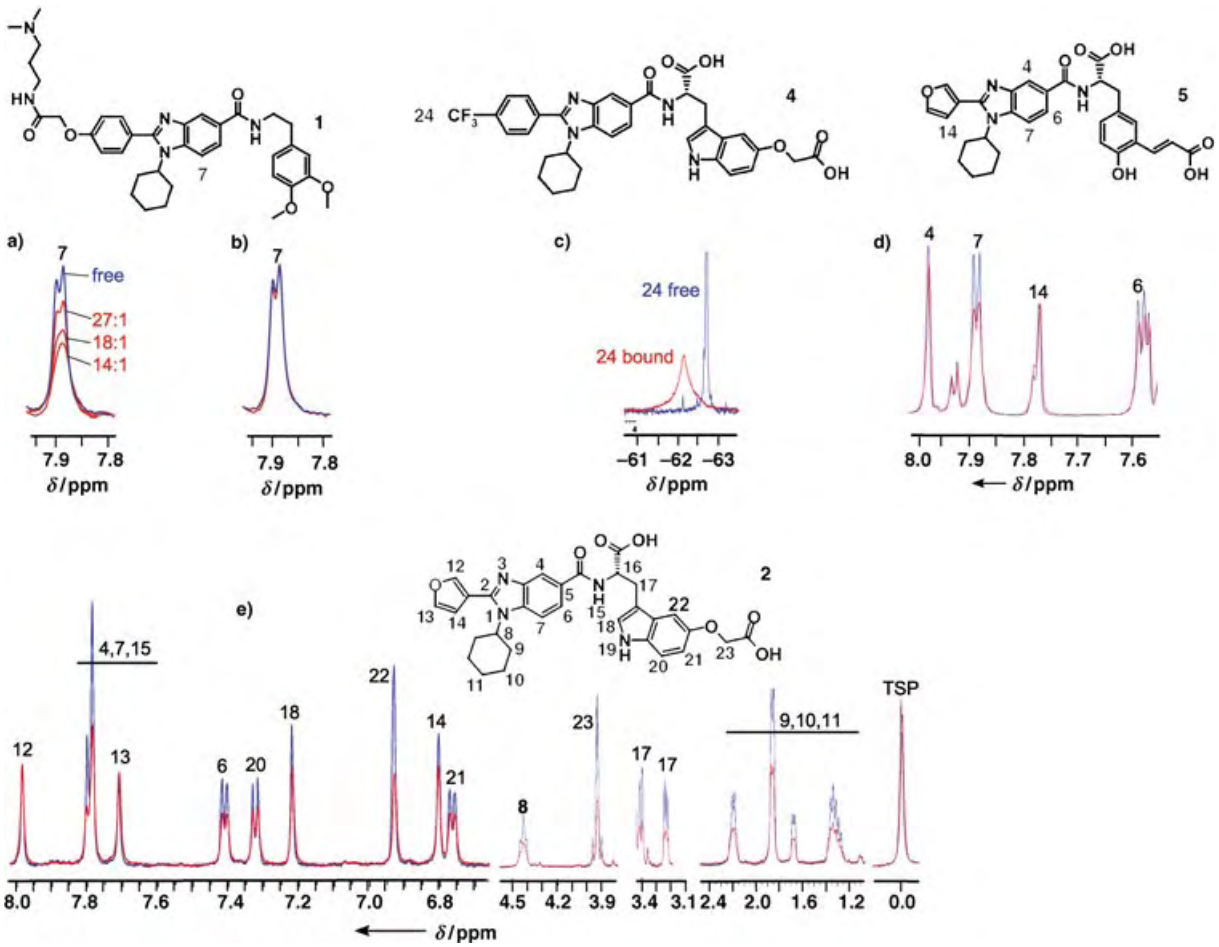
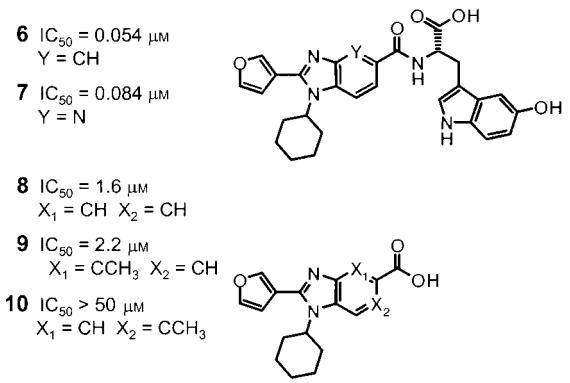


Figure 1. ^{1}H DLB and ^{19}F NMR resonance broadening for monitoring the binding to HCV polymerase. a) The ^{1}H resonance of H 7 of **1** in the absence (blue) and in the presence (red) of incremental amounts of HCV polymerase (at inhibitor to polymerase ratios of 27:0, 18:1, and 14:1). The NS5BΔ21C-HT polymerase construct was used for all NMR studies. b) The ^{1}H resonance of H 7 of **1** in the absence (blue) and in the presence (red) of tRNA (at an inhibitor to tRNA ratio of 14:1). c) ^{19}F NMR spectra (scaled as ppm) in the absence (blue) and in the presence (red) of HCV polymerase at an inhibitor to polymerase ratio of 1:1. An IC_{50} value of 0.5 μM was measured for compound **4**. d) A subregion of the ^{1}H spectra (scaled in ppm) of **5** in the absence (blue) and in the presence (red) of HCV polymerase at an inhibitor to polymerase ratio of 70:1. The hydrogen assignments are provided above each resonance. An IC_{50} value of 0.03 μM was measured for compound **5**. e) Subregions of the ^{1}H spectra (scaled in ppm) of **2** in the absence (blue) and in the presence (red) of HCV polymerase at an inhibitor to polymerase ratio of 70:1. The hydrogen assignments are provided above each resonance. The resonances of the spectator molecule [2,2,3,3-D_4]3-trimethylproprionic acid (TSP) were used to normalize the resonance intensities.



for the polymerase. In conclusion, the 3D bound structure in Figure 2c provided the first insight into the bioactive conformation of this class of compounds. Notably, the cyclohexyl and furan planes are perpendicular with respect to the benzimidazole scaffold, and the tryptophan residue on the right side extends above and perpendicular to the benzimidazole plane giving the molecule an overall L shape.

We also investigated the binding roles of the individual substituents of this class of compounds to support medicinal and combinatorial chemistry efforts. First, the importance of the cyclohexyl group became evident given that replacement with a hydrogen atom resulted in a greater than 116-fold loss in potency, and only very conservative replacements of the cyclohexyl group were tolerated.[7] We also observed significant DLB for the NMR resonances of the cyclohexyl ring (H8–H11) of compound **2** in the presence of the polymerase (red spectrum, Figure 1e). Thus, the data taken together is consistent with the cyclohexyl group having a direct role in binding, and it highlights the application of DLB as a tool for epitope mapping, as we reported elsewhere.[5]

 © 2004 Wiley-VCH Verlag GmbH & Co. KGaA, Weinheim

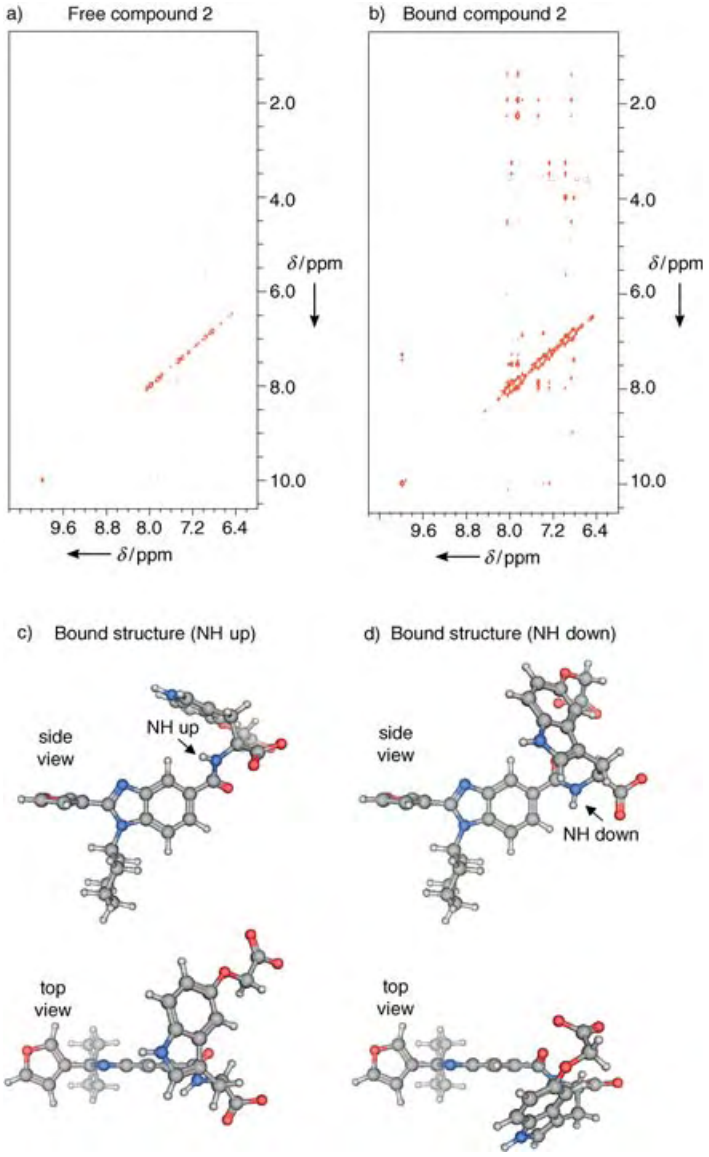


Figure 2. Monitoring of the binding and determination of the bound structures of compound **2**. a) The amide/aromatic (horizontal axis) to aliphatic (vertical axis) subregion of the ^{1}H NOESY spectrum of free compound **2** (75 msec mixing time). b) A subsequent NOESY experiment is shown after the addition of polymerase (NS5BΔ21-His$_6$ construct) to the NMR sample tube (transferred NOESY data were acquired at a 70:1 inhibitor to polymerase ratio). c) A representative structure of **2** when bound to HCV polymerase as determined by a simulated annealing calculation that employed restraints derived from transferred NOESY data. The calculations included a restraint between H15 and H4 (and none between H15 and H6, see the numbering scheme for the hydrogen atoms in Figure 1e). d) Another possible structure of **2** when bound to HCV polymerase for which the calculations included a restraint between H15 with H6 (and none between H15 with H4). The structures in (c) and (d) are colored by atom-type (oxygen: red, nitrogen: blue, carbon: gray, hydrogen: white). It must be kept in mind that determination of the 3D structures is limited by the inherent pseudosymmetry of the compound. Given the C_2 pseudosymmetry along the benzimidazole plane, the furan ring can adopt the bound conformations shown in (c) (top view) and/or an orientation rotated by approximately 180° along the carbon C_2-furan axis (see Figure 1e for a definition of the atom numbering scheme employed).

Elucidation of the principle role of the C2 substituent was also pursued. Initially, we observed the lack of DLB for the ^{1}H NMR resonances of the extended left side of compound **1**.[7] This observation suggested that these hydrogen atoms experienced insignificant changes in their magnetic environments upon binding, as one would expect if they were exposed to solvent in both the free and bound states. It was also consistent with our finding that partial truncation of the left side resulted in no significant change in the binding affinity for the polymerase.[7] Similarly, the lack of DLB observed for H12–H14 of the furan ring at position 2 of compound **2** (Figure 1e) also suggested that it experiences a minimal, direct contact with the polymerase, and it is consistent with our results obtained from studies of structure–activity relationships[7] which showed that the furan ring can be substituted by a variety of aromatic groups with little effect on potency. However, replacement of the furan ring by a hydrogen atom resulted in a 30-fold loss in potency.[7] One possible explanation is that the furan ring doesn't directly contact the polymerase, but instead influences the conformation of the critical cyclohexyl ring in the free state. We applied ab initio calculations to monitor the preferred orientations of the S_1 torsion angle (defined by the C8–N1 bond in Figure 3c) of compound **2** versus that of a model compound in which the furan ring is replaced by a hydrogen atom. The calculations determined that a single, lowest-energy torsion angle at approximately 0° was preferred for compound **2**, with high-energy barriers to rotation (Figure 3a). In contrast, the calculations involving the model compound (Figure 3b) exhibited two lowest-energy torsion angles at about 180 and 0° with much lower energy barriers to rotation. Thus, the furan ring apparently contributed to orienting the cyclohexyl ring of the free compound (ca. 0° for S_1) to a conformation that resembled the bound state (ca. 0° for S_1 in Figure 2c and d). As further validation, ROESY data on the free state of compound **2** and transferred NOESY data on the bound state exhibit similar crosspeak patterns that are indicative of a preference for a 0° torsion angle along S_1. Spectra in the Supporting Information show large crosspeaks between H8 with H14 and H12, as well as smaller crosspeaks between H8 and H7. Furthermore, a restricted rotation about the C8–N1 bond was also consistent with the relatively short ^{13}C spin-lattice relaxation times (^{13}C T_1) for the C8 and C11 atoms of the cyclohexyl ring of compound **2** (Figure 3c, numbers in round brackets). ^{13}C T_1 values are sensitive to motions on the pico- to nanosecond time scale and represent an excellent NMR parameter for monitoring the relative flexibility of C-H vectors. Shorter times are indicative of relatively slower segmental motion or flexibility. In summary, the conformational restriction induced by the furan ring results in a minimization of the overall entropic cost of binding.

The function of the benzimidazole ring was also investigated. Its role as a scaffold that orients the three appendages in 3D space is visible in Figure 2c and d. In addition, our DLB data also showed significant DLB for H6, which suggests that this portion of the ring contacts the

 © 2004 Wiley-VCH Verlag GmbH & Co. KGaA, Weinheim

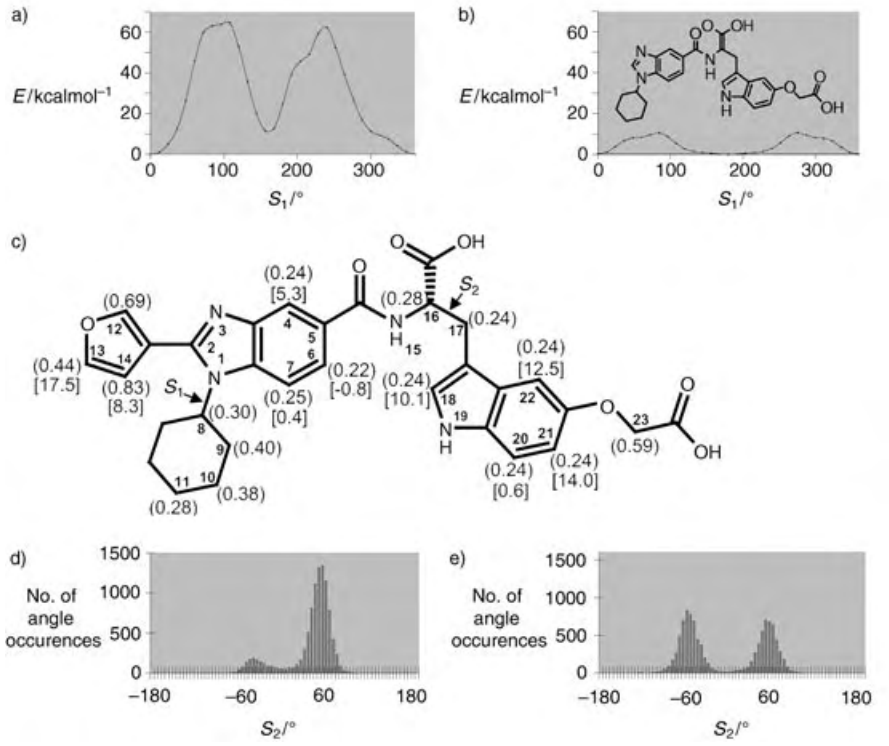


Figure 3. Monitoring the flexibility (dynamics) attributes of free and bound compound **2** and free compound **3**. a) ab initio RHF/6-31G** calculations of compound **2** in which the energy is determined for each torsion angle value of S_1 along the N1–C8 bond. The torsion angle is defined as the C2-N1-C8-H8 atoms. The atom numbering scheme is shown by the numbers with no brackets. b) Similar calculations are reported for a model compound that is similar to **2** with the exception that the furan ring is replaced by a hydrogen atom. c) ^{13}C NMR T_1 relaxation times (seconds) are displayed (round brackets) beside each carbon atom for compound **2** (data are derived from the compound in [D$_6$]DMSO). In the cases where two hydrogen atoms are attached to a single carbon atom, NT_1 data are given (the product of the number of attached protons and the longitudinal relaxation time). Transferred ^{13}C T_1 relaxation data are displayed within square brackets. The values displayed are the percentage change from free versus that after addition of the polymerase (NS5BΔ21-HT construct). Data were acquired using aqueous buffer (see Supporting Information). Transferred ^{13}C T_1 data were not acquired for the aliphatic carbon atoms. d) Histogram of torsion angle S_2 of compound **2** sampled during a 1 nsec molecular dynamics simulation. The S_2 torsion angle is defined by the indole atoms C-C17-C16-H16, see (c). e) A similar histogram as in (d) is shown except that compound **3** was studied.

polymerase (Figure 1e). The resonances of H4 and H7 were superimposed with H15 (Figure 1e), which unfortunately hindered interpretation. However, observations were possible for these hydrogen atoms in the closely related analogue **5** (Figure 1d), in which the resonances of H7 and H6 were line-broadened and H4 was relatively less affected, thus suggesting that the former were exposed to the polymerase pocket whereas the latter was exposed to the solvent in the bound state. These observations were further probed by monitoring changes in the binding affinity upon addition of bulky methyl groups at the C4 or the C6 positions in a related, truncated series (that is, **8**–**10**). It was noteworthy that **9** ($IC_{50} = 2.2$ μM), which is methylated at position C4 (defined as X_1), had similar potency relative to the unmethylated analogue (**8**, $IC_{50} = 1.6$ μM), thus suggesting that the methyl group was likely exposed to the solvent. In contrast, methylation at the C6 position (defined as X_2) resulted in a >31-fold loss in potency (**10**, $IC_{50} > 50$ μM), which suggests that it unfavorably bumped into the polymerase surface. Thus, it appeared that the lower part of the benzimidazole participated in direct binding to the polymerase pocket, whereas the upper part was exposed to the solvent.

Our studies also probed the binding role of the carboxylic acid at position C16 of compound **2**. Its importance was evident given that a 48-fold loss in potency was observed upon substituting the carboxylate group with a hydrogen atom (**2** versus **3**). This loss could not be attributed to the elimination of an ionic or hydrogen-bonding interaction with the polymerase, since esterification of the carboxylic acid to a methyl ester or replacement of the carboxylic acid with a methyl group in a related series resulted in equipotent compounds.[8,11] We therefore considered that the carboxylic acid contributed to a favorable rigidification of the indole and linker segment (C16 and C17). The relative flexibility of both compounds in the free state was thus monitored by NMR spectroscopic and molecular modeling methods. First, middle-range ^{1}H coupling constants were observed for **3** ($J_{NH,H16} = 5.6$, 5.6 Hz, $J_{H16,H17} = 7.1$, 7.1 Hz) which are indicative of an average of populated torsion angles, whereas more extreme values were observed for compound **2** ($J_{NH,H16} = 7.2$ Hz, $J_{H16,H17} = 10.1$, 4.5 Hz) which is consistent with a more defined conformation. Moreover, the ^{13}C T_1 values for the right-side segment of compound **2** were significantly shorter, thus suggesting a lower degree of flexibility relative to those of **3** (for example, 0.28 versus 0.82 for C16, 0.24 versus 0.38 for C17, and 0.59 versus 0.68 for C23; see the Supporting Information). Furthermore, our free-state molecular dynamics (MD) calculations determined that a boundlike torsion angle of approximately 50° along C16–C17 (S_2 as defined in Figure 3c) was preferentially populated for **2** (Figure 3d), whereas an additional torsion angle of −50° was also populated in **3** (Figure 3e). In summary, the presence of the acid at C16 rendered compound **2** less flexible than **3** which translates into a lower entropic cost for binding.

We previously reported a stepwise SAR that illustrated the importance of the indole and acetic acid groups to the affinity of compound **2** for the polymerase.[8] Line-broadening was observed for the resonances of H20–H22 (Figure 1e), which indicates the indole partially contacts the polymerase pocket. We also identified important differences between the free and bound states of the indole ring. The H6 of the benzimidazole is distal from the acetic acid H23 in the bound state based on the absence of the corresponding transferred NOESY peaks, whereas a ROESY crosspeak was observed between these hydrogen atoms in the free state (see the Supporting Information). We further probed this difference

 © 2004 Wiley-VCH Verlag GmbH & Co. KGaA, Weinheim

using the transferred ^{13}C T_1 experiment, which was developed particularly for the purpose of identifying ligand substituents that are flexible in the free state and which become rigidified in the bound state.[9] ^{13}C T_1 data were acquired for free compound **2** and were then compared to data acquired on the same sample after adding polymerase. The percentage difference for each carbon atom is shown in Figure 3c within square brackets. High percentage changes were observed for C18, C21, and C22 (namely, they were rigidified upon binding) and a low percentage change was observed for C20 (minimal flexibility changes upon binding). One would expect this pattern upon rigidifying a flexible C17–indole torsion angle in the free state to a single bound conformation, when it is considered that the C20 C-H vector experienced only minor percentage changes because it lies along the pivotal C17–indole axis.

In conclusion, we have described a concerted approach involving SAR and structure- and dynamics-based methods for elucidating important features of the binding mode of novel benzimidazole inhibitors of HCV polymerase. We have demonstrated the utility of these ligand-focused methods when applied early in the drug-discovery process, such as the validation of HTS hits for lead identification, thus providing an additional NMR screening strategy that can compliment STD[10] and SAR by NMR spectroscopic methods.[10] We have also demonstrated its utility as a medicinal chemistry tool for optimization of compound potency. In the examples described here, and in the design of HCV protease inhibitors reported elsewhere,[5,11] they have been particularly valuable in the absence of X-ray structural information of a complex, a dilemma frequently encountered at the early stages of drug discovery. Despite this situation, the information described here has further potential value for medicinal chemistry purposes, and several avenues are currently under evaluation.[12] For example, rigidified analogues could be designed that mimic the bioactive conformation and reduce entropic costs upon binding. Given that large percentage transferred ^{13}C T_1 values were observed for the indole and furan rings (Figure 3c, numbers within square brackets), analogues that rigidify the C17–indole and C2–furan torsion angles should improve potency. Also, a diversity of functional groups could replace the acid at C16 as long as the indole and linker segments are adequately rigidified. Finally, the 3D bound structures and DLB data of **2** may be useful in determining the first model of a complex using an apo crystal structure of HCV polymerase, as we have done successfully in our HCV protease inhibitor program.[5] This approach could be guided by the recently proposed polymerase binding site near Pro 495 for a related benzimidazole–cyclohexyl compound that was determined by cell culture resistance studies.[13] Notably, these resistance studies suggest that the benzimidazole inhibitors bind distal to the active-site tunnel and at a distinct site from other classes of inhibitors reported to date,[14] and thus further highlights the potential "drugability" of HCV polymerase.

Received: April 14, 2004 [Z460326]

Keywords: drug design · hepatitis C virus · molecular modeling · NMR spectroscopy · structure–activity relationships

[1] a) Q.-L. Choo, G. Kuo, A. J. Weiner, L. R. Overby, D. W. Bradley, M. Houghton, *Science* **1989**, *244*, 359; b) G. Kuo, Q.-L. Choo, H. J. Alter, G. L. Gitnick, A. G. Redeker, R. H. Purcell, T. Miyamura, J. L. Dienstag, M. J. Alter, C. E. Stevens, *Science* **1989**, *244*, 362; c) A. M. Di Bisceglie, *Lancet* **1998**, *351*, 351. d) World Health Organization, *J. Virol. Hepatol.* **1999**, *6*, 35.

[2] a) G. Chander, M. S. Sulkowski, M. W. Jenckes, M. S. Torbenson, H. F. Herlong, E. B. Bass, K. A. Gebo, H *epatology* **2002**, *36*, S135; b) S.-L. Tan, A. Pause, Y. Shi, N. Sonenberg, *Nat. Rev. Drug Discovery* **2002**, *1*, 867; c) A. M. Di Bisceglie, J. McHutchison, C. M. Rice, *Hepatology* **2002**, *35*, 224.

[3] a) S. E. Behrens, L. Tomei, R. De Francesco, *EMBO J.* **1996**, *15*, 12; b) A. A. Kolykhalov, K. Mihalik, S. M. Feinstone, C. M. Rice, *J. Virol.* **2000**, *74*, 2046; c) K. E. Reed, C. M. Rice, *Curr. Top. Microbiol. Immunol.* **2000**, *242*, 55.

[4] G. McKercher, P. Beaulieu, D. Lamarre, S. LaPlante, S. LeFebvre, C. Pellerin, L. Thauvette, G. Kukolj, *Nucleic Acids Res.* **2004**, *32*, 422.

[5] a) S. R. LaPlante, D. R. Cameron, N. Aubry, S. Lefebvre, G. Kukolj, R. Maurice, D. Thibeault, D. Lamarre, M. Llinàs-Brunet, *J. Biol. Chem.* **1999**, *274*, 18618; b) S. R. LaPlante, N. Aubry, P. Bonneau, G. Kukolj, D. Lamarre, S. Lefebvre, H. Li, M. Llinàs-Brunet, C. Plouffe, D. R. Cameron, *Bioorg. Med. Chem. Lett.* **2000**, *10*, 2271; c) Y. Tsantrizos, G. Bolger, P. Bonneau, D. R. Cameron, N. Goudreau, G. Kukolj, S. R. LaPlante, M. Llinàs-Brunet, H. Nar, D. Lamarre, *Angew. Chem.* **2003**, *115*, 1394; *Angew. Chem. Int. Ed.* **2003**, *42*, 1356.

[6] F. Ni, *Prog. Nucl. Magn. Reson. Spectrosc.* **1994**, *26*, 517.

[7] P. L. Beaulieu, M. Bös, Y. Bousquet, G. Fazal, J. Gauthier, J. Gillard, S. Goulet, S. LaPlante, M.-A. Poupart, S. Lefebvre, G. McKercher, C. Pellerin, V. Austel, G. Kukolj, *Bioorg. Med. Chem. Lett.* **2004**, *14*, 119.

[8] P. L. Beaulieu, M. Bös, Y. Bousquet, P. DeRoy, G. Fazal, J. Gauthier, J. Gillard, S. Goulet, M.-A. Poupart, S. Valois, G. McKercher, G. Kukolj, *Bioorg. Med. Chem. Lett.* **2004**, *14*, 967.

[9] S. R. LaPlante, N. Aubry, R. Deziel, F. Ni, P. Xu, *J. Am. Chem. Soc.* **2000**, *122*, 12530.

[10] a) B. Meyer, T. Peters, *Angew. Chem.* **2003**, *115*, 890; *Angew. Chem. Int. Ed.* **2003**, *42*, 864; b) S. B. Shuker, P. J. Hajduk, R. P. Meadows, S. W. Fesik, *Science* **1996**, *274*, 1531.

[11] D. Lamarre, P. C. Anderson, M. Bailey, P. Beaulieu, G. Bolger, P. Bonneau, M. Bös, D. R. Cameron, M. Cartier, M. G. Cordingley, A.-M. Faucher, N. Goudreau, S. H. Kawai, G. Kukolj, L. Lagacé, S. R. LaPlante, H. Narjes, M.-A. Poupart, J. Rancourt, R. E. Sentjens, R. St George, B. Simoneau, G. Stelnmann, D. Thibeault, Y. S. Tsantrizos, S. M. Weldon, C.-L. Yong, M. Llinàs-Brunet, *Nature* **2003**, *426*, 186.

[12] P. Beaulieu, M.-A. Poupart, unpublished results.

[13] L. Tomei, S. Altamura, L. Bartholomew, A. Biroccio, A. Cessacci, L. Pacini, F. Narjes, N. Gennari, M. Bisbocci. I. Incitti, L. Orsatti, S. Harper, I. Stansfield, M. Rowley, R. De Francesco, G. Migliaccio, *J. Virology* **2002**, *77*, 13225.

[14] a) D. Dhanak, K. J. Duffy, V. K. Johnston, J. Lin-Goerke, M. Darcy, A. N. Shaw, B. Gu, C. Silverman, A. T. Gates, M. R. Nonnemacher, D. L. Earnshaw, D. J. Casper, A. Kaura, A. Baker, C. Greenwood, L. L. Gutshall, D. Maley, A. DelVecchio, R. Macarron, G. A. Hofmann, A. Alnoah, H.-Y. Cheng, G. Chan, S. Khandekar, R. M. Keenan, R. T. Sarisky, *J. Biol. Chem.* **2002**, *277*, 38322; b) L. Chan, T. J. Reddy, M. Proulx, S. K. Das, O. Pereira, W. Wang, A. Siddiqui, C. G. Yannopoulos, C. Poisson, N. Turcotte, A. Drouin, M. H. Alaoui-Ismaili, R. Bethell, M. Hamel, L. L'Heureux, D. Bilimoria, N. Nguyen-Ba, *J. Med. Chem.* **2003**, *46*, 1283; c) M. Wang, K. K.-S. Ng, M. M. Cherney, M. Maia, L. Chan, C. G. Yannopoulos, J. Bedard, N. Morin, N. Nguyen-Ba, M. H. Alaoui-Ismaili, R. C. Bethell, M. N. G. James, *J. Biol. Chem.* **2003**, *278*, 9489.

 © 2004 Wiley-VCH Verlag GmbH & Co. KGaA, Weinheim

Natural Products Synthesis

Structural Revision and Total Synthesis of Azaspiracid-1, Part 1: Intelligence Gathering and Tentative Proposal**

K. C. Nicolaou, Stepan Vyskocil, Theocharis V. Koftis, Yoichi M. A. Yamada, Taotao Ling, David Y.-K. Chen, Wenjun Tang, Goran Petrovic, Michael O. Frederick, Yiwei Li, and Masayuki Satake**

In memory of D. John Faulkner

Structure **1-i** (Figure 1, absolute stereochemistry and relative stereochemistry between ABCDE and FGHI domains unknown) was proposed in 1998, on the basis of NMR spectroscopic analysis, for a poisonous substance called azaspiracid-1, which was isolated from the mussel family *Mytilus edulis*.[1] A recent total synthesis[2,3] of **1-i** and its FGHI epimer proved that this assignment was incorrect.[4] Herein we report synthetic and degradation studies that led to the revised structure **1-c** or ABCD-*epi*-**1-c** as the most likely depiction of the molecular architecture of this biotoxin (Figure 1). The only doubt that remained was the absolute configuration of the ABCD domain of the molecule, and this question was resolved by total synthesis, as is described in the following paper in this issue.[5]

Upon realizing that the originally proposed structure **1-i** of azaspiracid-1 was in error,[2,3] our plan for determining its true structure called for the degradation of the natural material into smaller fragments, whose chemical synthesis may narrow down the location of the structural discrepancy between the synthesized (originally proposed) and actual

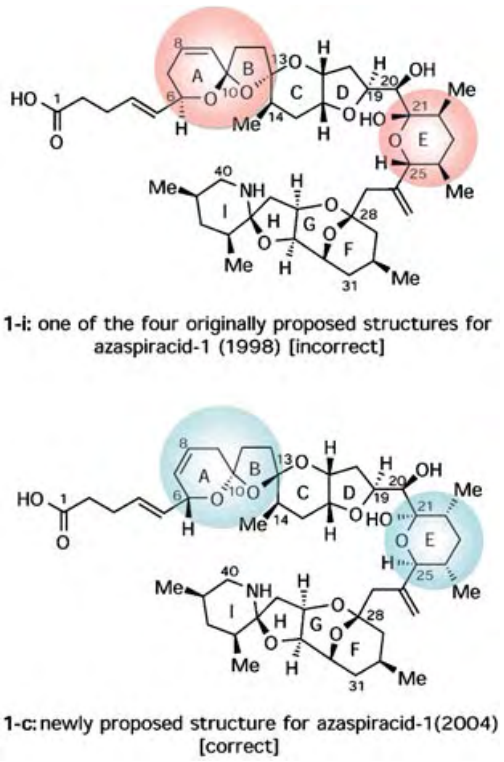


Figure 1. Originally proposed structure **1-i** (relative stereochemistry between ABCDE (C1–C27) and FGHI (C28–C40) domains and absolute stereochemistry unknown) and newly proposed structure **1-c** or ABCD-*epi*-**1-c** of azaspiracid-1.

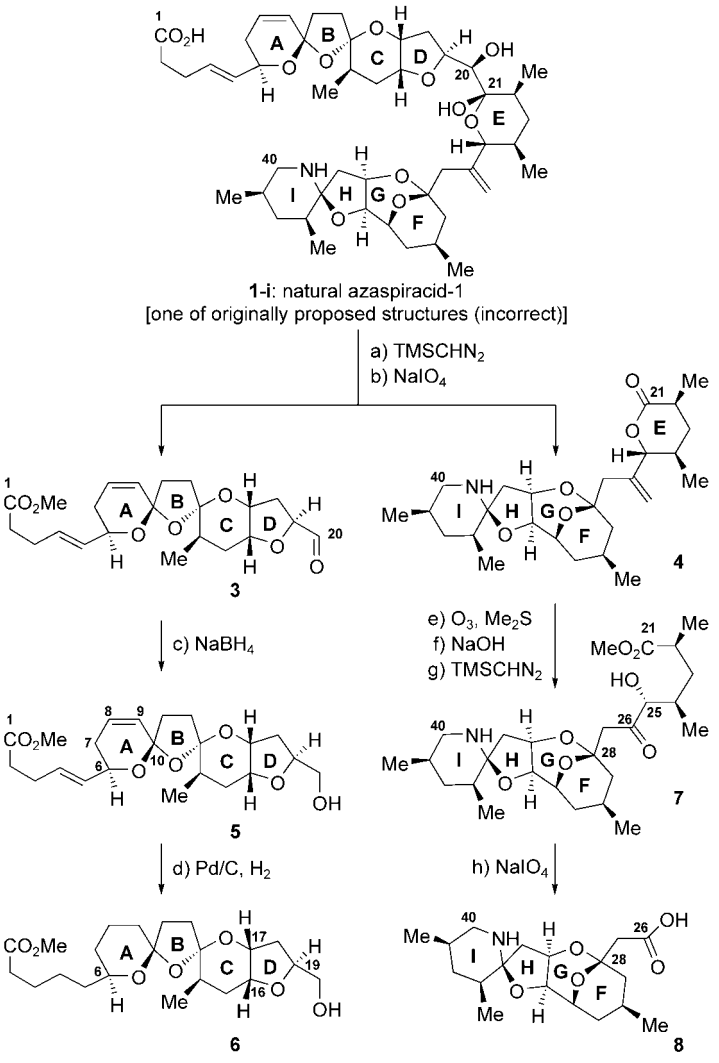
structures. To this end, azaspiracid-1 was derivatized by exposure to $TMSCHN_2$ in MeOH, and the methyl ester obtained was treated with $NaIO_4$ in aqueous MeOH at ambient temperature, resulting in the cleavage of its C20–C21 bond and in the formation of the corresponding aldehyde **3** (C1–C20 fragment) and lactone **4** (C21–C40 fragment) in quantitative yield (Scheme 1). Compound **3** was further elaborated by treatment with $NaBH_4$ to afford, supposedly, hydroxy methyl ester **5** (≈90% yield), followed by hydrogenation to give the fully saturated compound **6** (≈90% yield). On the other hand, cleavage of the exocyclic olefinic bond within **4** with O_3–Me_2S to the corresponding ketone, followed by saponification of the E-ring lactone with aqueous NaOH in MeOH and esterification of the resulting carboxylic acid with $TMSCHN_2$ gave methyl ester **7** (≈90% yield). Finally, treatment of compound **7** with $NaIO_4$ furnished amino acid **8** in high yield (≈90%). These degradatively derived intermediates (i.e. **4**–**6** and **8**, Scheme 1) were to serve several purposes. First, spectroscopic comparisons with synthetic materials would immediately pinpoint any errors in each domain of the molecule. Second, comparison of amino lactone **4** with the two synthetic FGHI epimers of the same structure (i.e. **4**) would clarify the relative stereochemistry between the ABCDE and FGHI domains of azaspiracid-1. Third, optical rotation comparisons of the degradative and synthetic samples may reveal the absolute configuration of each fragment and, consequently, of the entire structure.

One drawback of the adopted degradation scheme was the loss of stereochemical information regarding the C20 and

[*] Prof. Dr. K. C. Nicolaou, Dr. S. Vyskocil, Dr. T. V. Koftis, Dr. Y. M. A. Yamada, Dr. T. Ling, Dr. D. Y.-K. Chen, Dr. W. Tang, Dr. G. Petrovic, M. O. Frederick, Dr. Y. Li
Department of Chemistry and
The Skaggs Institute for Chemical Biology
The Scripps Research Institute
10550 North Torrey Pines Road, La Jolla, CA 92037 (USA)
Fax: (+1) 858-784-2469
and
Department of Chemistry and Biochemistry
University of California, San Diego
9500 Gilman Drive, La Jolla, CA 92093 (USA)
E-mail: kcn@scripps.edu
Prof. Dr. M. Satake
Graduate School of Agriculture
Tohoku University
Tsutsumi-dori Amamiya, Aoba-ku, Sendai 981-8555 (Japan)
Fax: (+81) 22-717-8817
E-mail: satake@biochem.tohoku.ac.jp

[**] We thank Dr. D. H. Huang and Dr. G. Siuzdak for NMR spectroscopic and mass spectrometric assistance, respectively. Financial support for this work was provided by grants from the National Institutes of Health (USA) and the Skaggs Institute for Chemical Biology, and fellowships from the Ernst Schering AG Foundation (to S.V.), the Japanese Society for the Advancement of Science (to Y.M.A.Y.), the National Science Foundation (to M.O.F.), and Eli Lilly (to Y.L.).

 © 2004 Wiley-VCH Verlag GmbH & Co. KGaA, Weinheim DOI: 10.1002/anie.200460695



Scheme 1. Chemical degradation and derivatization of azaspiracid-1 (**1-i**: originally proposed structure) to C1–C20 alcohol **6**, C21–C40 lactone **4**, and C26–C40 carboxylic acid **8**. Reagents and conditions: a) $TMSCHN_2$, MeOH, 25 °C, 1 h; b) $NaIO_4$, MeOH/H_2O (4:1), 25 °C, 1 h, ≈100% over two steps; c) $NaBH_4$, MeOH, 25 °C, ≈90%; d) Pd/C (5%), H_2, MeOH, 25 °C, ≈90%; e) O_3, Me_2S, MeOH, −78 °C; f) NaOH (0.1 N), MeOH/H_2O (4:1), 25 °C, 2 h; g) $TMSCHN_2$, MeOH, 25 °C, 15 min, ≈90% over three steps; h) $NaIO_4$, MeOH/H_2O (4:1), 25 °C, 30 min, ≈90%. TMS = trimethylsilyl.

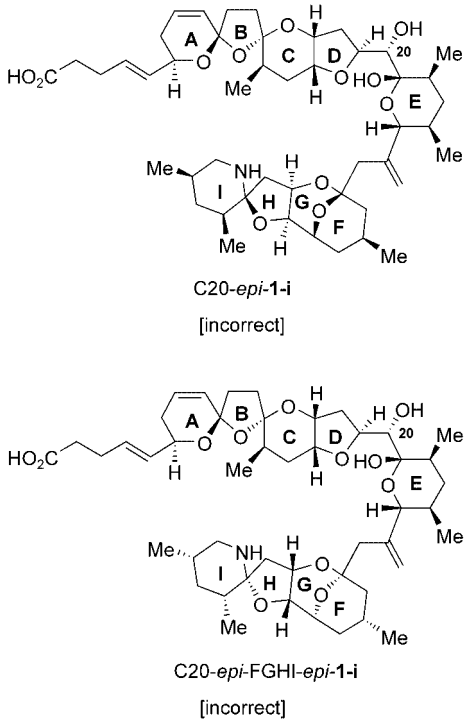


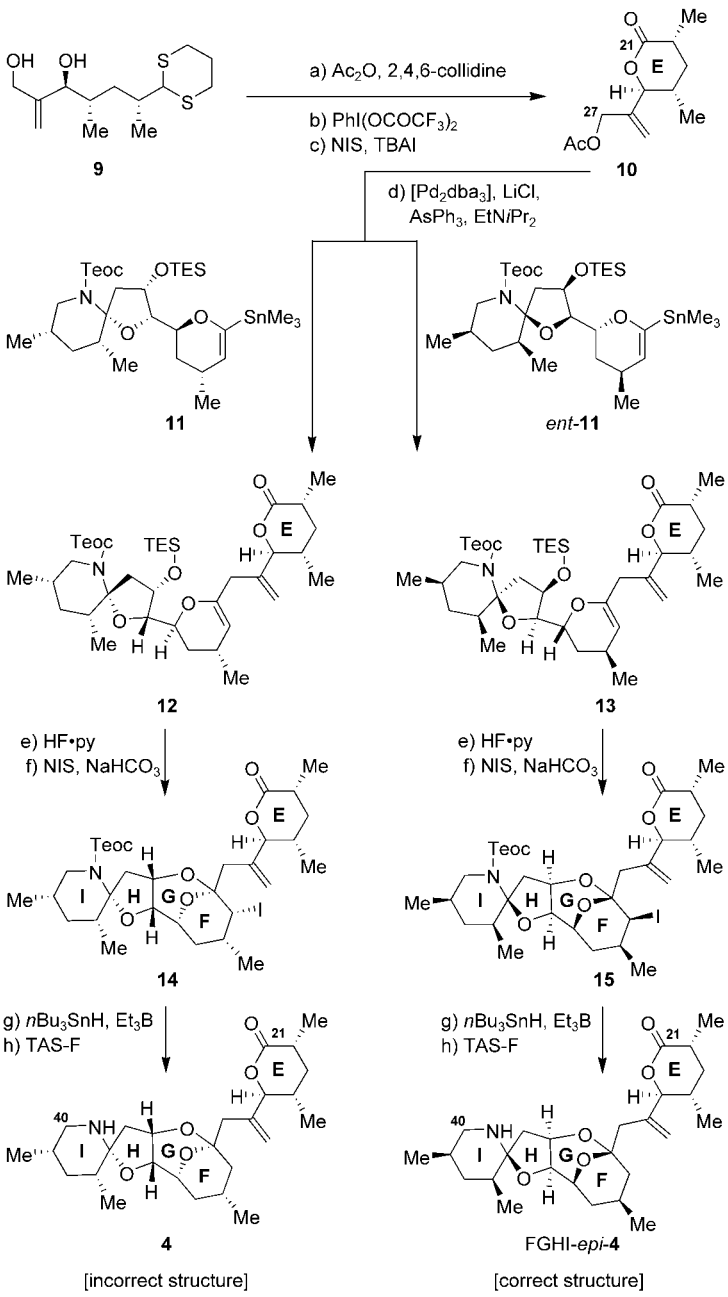
Figure 2. Structures of C20-*epi*-**1-i** and C20-FGHI-*epi*-**1-i** (synthesized and proven incorrect).

C21 hydroxy-bearing centers. However, if we assume that the C21 hemiketal functionality would rest in its thermodynamically most stable conformation, the only stereocenter in question would be that at C20. As **1-i** had already been eliminated as the true structure, the C20-*epi*-azaspiracid-1 (C20-*epi*-**1-i**) structure and its FGHI epimer (C20-*epi*-FGHI-*epi*-**1-i**) as logical targets moved to the front as possible alternatives (see Figure 2). Their total syntheses along the same lines as those described for **1-i**,[2,3] however, also proved them to be incorrect.[6]

Having established that the azaspiracid-1 structural problem did not reside exclusively at the C20 stereocenter, the focus of our investigation shifted next to the synthesis of the two diastereomeric EFGHI amino lactones **4** and FGHI-*epi*-**4** (Scheme 2). Thus, the previously synthesized dihydroxy dithiane **9**[2] was selectively monoacetylated (at the primary position) with Ac_2O in the presence of 2,4,6-collidine (85% yield), and the resulting hydroxy dithiane intermediate was deprotected by exposure to $PhI(OCOCF_3)_2$[7] to afford the corresponding lactol, whose oxidation with NIS–TBAI[8] completed the synthesis of the required allylic acetate lactone **10**. The latter compound, **10**, underwent Stille coupling with stannanes **11** and *ent*-**11** according to a previously described procedure[3] to afford compounds **12** and **13**, respectively. These substrates were then smoothly transformed into the targeted amino lactones **4** and FGHI-*epi*-**4**, respectively, via intermediate compounds **14** (for **4**) and **15** (for FGHI-*epi*-**4**) according to our previous sequence[3] and as summarized in Scheme 2: 1) HF·py-induced selective TES removal; 2) NIS-initiated ring closure; 3) nBu_3SnH–Et_3B-facilitated reductive deiodination; and 4) TAS-F-mediated desilylation. The only deviation from the previously employed sequence[3] was the use of TAS-F[9] instead of TBAF, as the former reagent afforded superior results in the final deprotection step. Most gratifyingly, the ^1H NMR spectral data of one of these synthetic materials, namely FGHI-*epi*-**4**, matched those of the sample derived from natural azaspiracid-1 (Scheme 1), whereas its diastereomeric amino lactone **4** exhibited slightly different and diagnostically distinct signals to those of the naturally derived substance. Based on these results, we concluded that the relative stereochemical arrangement for the EFGHI domain of azaspiracid-1 is that depicted by structure FGHI-*epi*-**4** (absolute stereochemistry unknown).[10]

The next goal was to establish the absolute stereochemistry of azaspiracid-1, and as we had confirmed the structural

 © 2004 Wiley-VCH Verlag GmbH & Co. KGaA, Weinheim

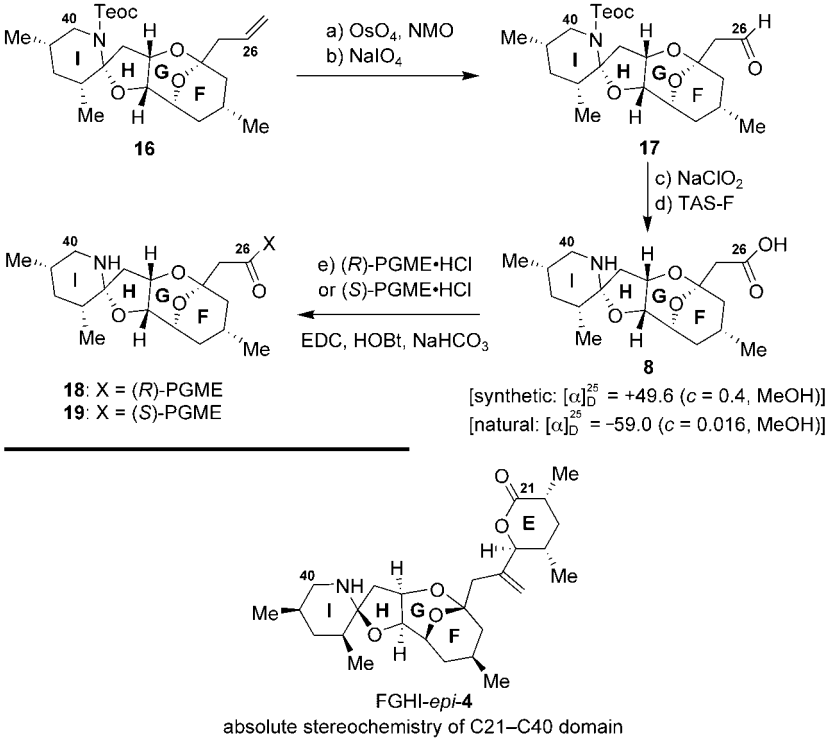


Scheme 2. Chemical synthesis of C21–C40 lactone **4** and its FGHI epimers, FGHI-*epi*-**4** and determination of the relative stereochemistry within the EFGHI domain. Reagents and conditions: a) Ac_2O (5.0 equiv), 2,4,6-collidine (10.0 equiv), CH_2Cl_2, 25 °C, 16 h, 85 %; b) $PhI(OCOCF_3)_2$ (1.5 equiv), MeCN/pH 7 buffer (4:1), 0 °C, 10 min, 81 %; c) NIS (10.0 equiv), TBAI (2.0 equiv), CH_2Cl_2, 25 °C, 40 min, 74 %; d) **10** (3.0 equiv), $[Pd_2dba_3]$ (0.9 equiv), $AsPh_3$ (0.9 equiv), LiCl (18 equiv), $EtNiPr_2$ (12 equiv); then **11** or *ent*-**11** (0.03 M in THF, syringe pump addition), NMP, 45 °C, 4 h; e) HF·py (excess), THF/py (1:1), 0→25 °C, 2 h; f) NIS (10.0 equiv), $NaHCO_3$ (30 equiv), THF, 0 °C, 16 h, 26 % for **14** and 38 % for **15** over three steps; g) Et_3B (1.0 M in hexanes, 0.2 equiv), nBu_3SnH/toluene (1:2), 0 °C, 5 min; h) TAS-F (5.0 equiv), DMF, 0 °C, 20 h, 70 % for **4** and 74 % for FGHI-*epi*-**4** over two steps. NIS = *N*-iodosuccinimide, NMP = *N*-methylpyrrolidinone, TBAI = tetra-*n*-butylammonium iodide, dba = dibenzylideneacetone, TAS-F = tris(dimethylamino)sulfur (trimethylsilyl)difluoride.

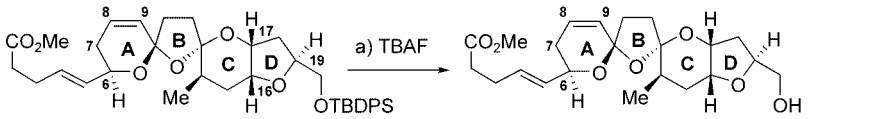
integrity of the FGHI domain **8** of the molecule and had secured its optical rotation from degradation studies (see Scheme 1), we decided to synthesize the carboxylic acid **8** for comparison purposes. This objective was met expeditiously, starting with the previously prepared intermediate **16**,[2] as shown in Scheme 3. Thus, a two-step oxidative protocol involving dihydroxylation (NMO–OsO_4 cat.) of the terminal olefin of **16**, followed by $NaIO_4$-induced cleavage of the resulting 1,2-diol, provided aldehyde **17** in 80 % overall yield. Oxidation of this aldehyde (**17**) with $NaClO_2$, followed by TAS-F-mediated desilylation resulted in the formation of the desired amino acid **8** in 35 % yield over the two steps. As expected, the NMR spectroscopic data of synthetic **8** matched those of the degradatively obtained material. Furthermore, the two samples exhibited comparable rotations, but with opposite signs (synthetic: $[\alpha]_D^{25} = +49.6$ ($c = 0.4$, MeOH); natural: $[\alpha]_D^{25} = -59.0$ ($c = 0.016$, MeOH)). Furthermore, the ^{1}H NMR spectrum of the (*R*)-PGME (phenyl glycine methyl ester) derivative **18** (see Scheme 3 for preparation of the PGME derivatives) of synthetic carboxylic acid **8** was identical to the (*S*)-PGME derivative of the naturally derived acid **8** (and (*S*)-PGME derivative **19** derived from synthetic **8** was identical to the (*R*)-PGME derivative of the naturally derived **8**), thereby establishing the absolute stereochemistry of the FGHI domain of azaspiracid-1 as the antipode of compound **8** that we had prepared as shown in Scheme 3. By virtue of the chemistry depicted in Scheme 2, the absolute stereochemistry of the entire EFGHI domain of azaspiracid-1 could now be shown as that in Scheme 3 (structure FGHI-*epi*-**4**).

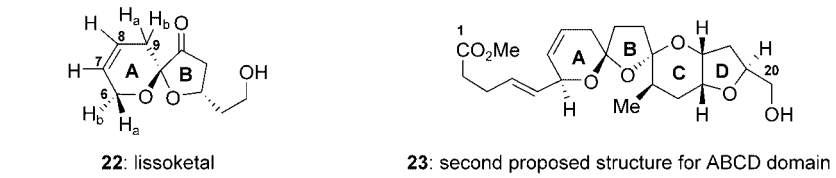
With the establishment of both the relative and absolute stereochemistries of the EFGHI domain of azaspiracid-1, our attention was then turned to the remaining segment, namely the ABCD (C1–C20) framework of the natural product, in which we had, by now, suspected the structural discrepancy to be embedded. As outlined in Scheme 4, a synthetic sample of **21**, a substance corresponding to the degradatively derived compound from the natural product (structure **5**, Scheme 1) was prepared from the previously synthesized intermediate **20**[2] by desilylation (TBAF, 88 % yield). The spectroscopic data for these two samples (**5** and **21**) differed significantly, thereby confirming our suspicions for the location of the structural discrepancy (see Table 1). Furthermore, the main differences between the two sets of spectra were associated with protons located on ring A, namely 6-H, 7-H, 8-H, and 9-H (see numbering on structure **21**, Scheme 4). Despite these clear differences, the final structural deconvolution of this region of azaspiracid-1 remained elusive, primarily as a result of the very similar 2D NMR spectral data for the naturally derived and synthetic materials whose comparison implied only subtle connectivity and spatial differences. Finally, it was a discovery by C. Hopmann and the late Professor D. John Faulkner that shed light on this issue. Indeed, the structural elucidation of lissoketal (**22**, see Scheme 4),[11] a marine natural product isolated by these workers in 1997, provided the first clue to the azaspiracid-1 puzzle. This secondary metabolite **22** bears a close resemblance to the proposed structure of azaspiracid-1 (**1-i**) except for the fact that the endocyclic double bond in ring A resides between C7 and C8, rather than between C8 and C9. Intriguingly, close examination of the ^{1}H NMR chemical shift values (see Table 1) and the 2D NMR correlation pattern reported for lissoketal (**22**)

 © 2004 Wiley-VCH Verlag GmbH & Co. KGaA, Weinheim



Scheme 3. Synthesis of FGHI amino acid **8** and determination of the absolute stereochemistry of EFGHI domain of azaspiracid-1. Reagents and conditions: a) OsO_4 (0.1 equiv), NMO (3.0 equiv), acetone/H_2O (3:1), 25 °C, 3 h, 92%; b) $NaIO_4$ (3.0 equiv), MeOH/pH 7 buffer (2.5:1), 25 °C, 1 h, 87%; c) $NaClO_2$ (10.0 equiv), NaH_2PO_4 (10.0 equiv), 2-methyl-2-butene (excess), *t*BuOH/H_2O (4:1), 25 °C, 30 min, 93%; d) TAS-F (5.0 equiv), DMF, 0 °C, 16 h, 38%; e) (*R*)-PGME or (*S*)-PGME (5.0 equiv), EDC (5.0 equiv), HOBt (5.0 equiv), $NaHCO_3$ (10 equiv), DMF, 25 °C, 16 h, 75% for **18** and 63% for **19**. NMO = *N*-methylmorpholine *N*-oxide, PGME = phenyl glycine methyl ester, EDC = 1-(3-dimethylaminopropyl)-3-ethylcarbodiimide, HOBt = 1-hydroxybenzotriazole.





Scheme 4. Chemical synthesis of C1–C20 alcohol **21** for comparison with naturally derived material, structure of lissoketal (**22**), and second proposed structure, **23**, for the ABCD domain of azaspiracid-1. Reagents and conditions: a) TBAF (2.0 equiv), THF, 25 °C, 2 h, 88%. TBAF = tetra-*n*-butyl ammonium fluoride.

showed remarkable similarities to those observed for natural azaspiracid-1.[1] In particular, a weak HMBC correlation between C10 and 7-H as well as a weak COSY correlation between 6-H and 9-H observed for the natural azaspiracid-1 are in line with observations reported by Hopmann and Faulkner[11] and, therefore, point to the lissoketal ring A structural arrangement. Furthermore, relocating the endocyclic double bond from C8–C9 to C7–C8, places the 6-H in a doubly allylic environment, thereby providing a possible explanation for the significant downfield shift for this proton exhibited in the ^{1}H NMR spectrum of the naturally derived intermediate **5** (δ = 4.79 ppm) relative to that observed for the synthetic material **21** (δ = 4.51 ppm).[12] With the NMR spectroscopic parameters associated with rings B, C, and D for the naturally derived (**5**) and synthetic (**21**) samples in good agreement, the alternative structure **23** (see Scheme 4) was proposed for the hydroxy methyl ester derived from the natural product through intermediate **3** (see Scheme 1). To test this hypothesis, a chemical synthesis of the newly proposed structure **23** was required.

The synthesis of the newly proposed structure **23** was initiated from the previously described compound **24**[2] and proceeded as outlined in Scheme 5. Thus, the free hydroxy group in **24** was protected as a TES ether (95% yield), the pivaloate ester was cleaved with DIBAL-H (96% yield), and the liberated primary alcohol was oxidized under Swern conditions to afford aldehyde **25** (95% yield). Addition of vinyl Grignard reagent to **25** (76% yield) followed by acetylation (85% yield) yielded allylic acetate **26** as a mixture of diastereoisomers (≈2:1). Ireland–Claisen rearrangement[13] of **26** followed by methylation of the resulting carboxylic acid with diazomethane gave methyl ester **27** in 52% overall yield. Selective removal of the TES group (HF·py, 85% yield) from **27**, Swern oxidation of the resulting alcohol (90% yield) followed by treatment with KHMDS–TMSCl led to TMS enol ether **28**, whose oxidation to the corresponding enone (55% overall yield), reduction with $NaBH_4$, and acetylation (71% overall yield) furnished allylic acetate **29**. Finally, exposure of **29** to catalytic amounts of $[Pd_2dba_3]\cdot CHCl_3$ in the presence of nBu$_3$P and $NaBH_4$,[14] followed by treatment with TBAF led to the targeted intermediate **23** (42% overall yield) through intermediate **30** (which was chromatographically separated from its $\Delta^{8,9}$ isomer that emerged as the minor product during the reduction step (≈2:1)).

Much to our disappointment, however, the spectral data of synthetic **23** did not match those of the degradatively

 © 2004 Wiley-VCH Verlag GmbH & Co. KGaA, Weinheim

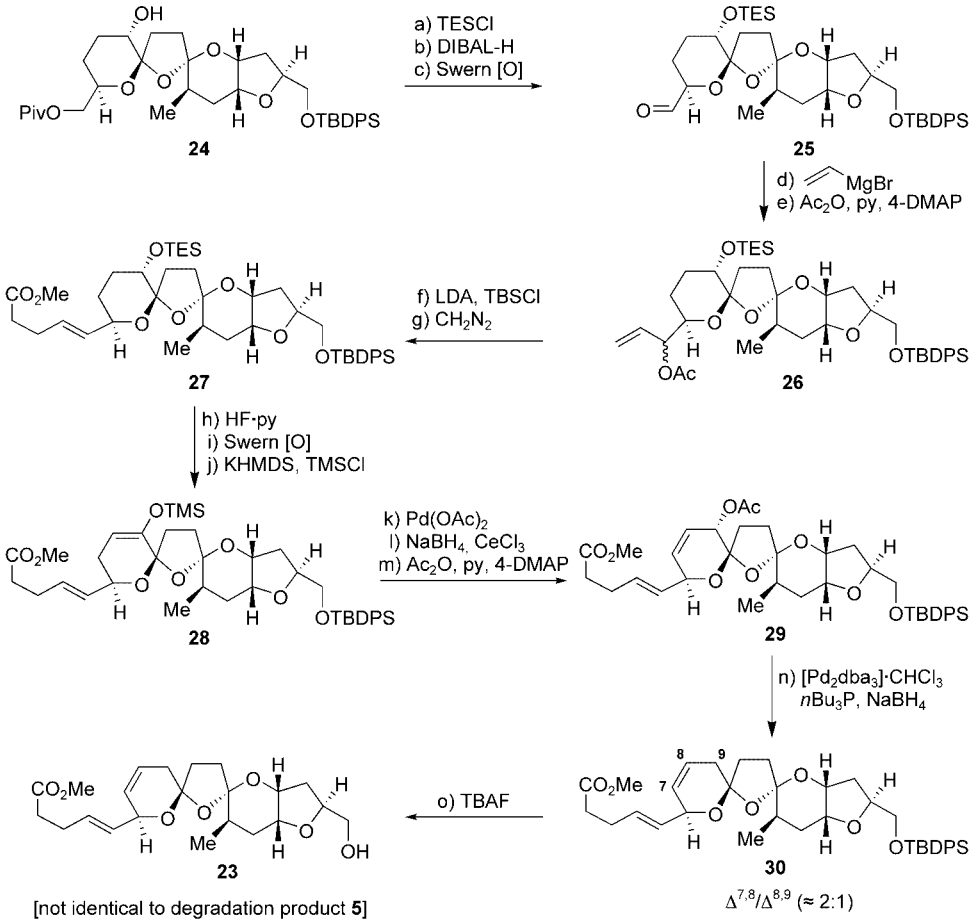
Table 1: Key ^{1}H NMR chemical shifts of compounds **5**, and **21**–**23**.

H	**5**[a] (natural)	**21**	**22**	**5**[b]	**23**
		$\delta(^1H)$ [ppm]			
6-H	4.79	4.50	4.34	4.79	4.81
7-H	2.48	2.06	5.80	5.62	5.61
	2.03	2.04			
8-H	5.74	6.07	5.80	5.74	5.77
9-H	5.62	5.79	2.57	2.48	2.51
			1.91	2.03	2.18
16-H	3.78	3.94	–	3.78	3.84
17-H	4.21	4.27	–	4.21	4.15
19-H	4.34	4.57	–	4.34	4.51
41-H	0.92	0.98	–	0.92	0.95

[a] Original incorrect assignments. [b] Revised (correct) assignments for the $\Delta^{7,8}$ isomer at **5** (note that structure was still incorrect).

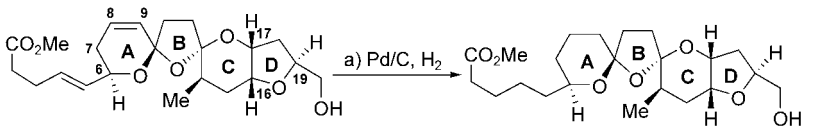
derived **5** (see Table 1), sending us, one more time, back to the drawing board. Apparently, the location of the double bond in ring A was not the only problem with the originally proposed structure (**1-i**) of azaspiracid-1. A more profound structural change, perhaps having to do with the skeletal stereochemistry, was needed to accommodate the structure of the natural product. Indeed, the fully hydrogenated synthetic product **31** (see Scheme 6) obtained from synthetic **21** (10% Pd/C, H_2, 95% yield) proved to be different from the corresponding hydrogenated fragment **6** obtained from **5**, which was derived by degradation and elaboration of the natural product as already described above (see Scheme 1).

At this juncture, and having pinned down the location of the double bond within ring A, we were still faced with 128 possible structures for the ABCD domain of azaspiracid-1 arising from its seven stereogenic centers. However, our intelligence gathering at this stage extended to an additional piece of information regarding the thermodynamic stability of the degradatively derived ABCD fragments (e.g. **5**) and of the natural product itself. Their ABC double spiroketal bridge



Scheme 5. Chemical synthesis of the second proposed structure **23** for the ABCD domain. Reagents and conditions: a) TESCl (1.5 equiv), imidazole (3.0 equiv), 4-DMAP (0.1 equiv), CH_2Cl_2, 0°C, 12 h, 95%; b) DIBAL (2.0 equiv), CH_2Cl_2, −78°C, 1 h, 96%; c) $(COCl)_2$ (5.0 equiv), DMSO (11 equiv), CH_2Cl_2, −78°C, 30 min, −60°C, 1 h; then Et_3N (22 equiv), −78→−25°C, 95%; d) CH_2=CHMgBr (1.6 equiv), Et_2O, 0→25°C, 1 h, 76%; e) Ac_2O (5.0 equiv), py (10.0 equiv), 4-DMAP (0.1 equiv), CH_2Cl_2, 0°C, 3 h, 85%; f) LDA (1.5 equiv), THF, −78°C, 10 min, TBSCl (1.5 equiv), HMPA (1.5 equiv), −78→25°C, 24 h; g) CH_2N_2 (excess), Et_2O, 25°C, 30 min, 52% over two steps; h) HF·py (10.0 equiv), py/THF (1:1), 0°C, 2 h, 85%; i) $(COCl)_2$ (10.0 equiv), DMSO (22 equiv), CH_2Cl_2, −78°C, 30 min, −60°C, 1 h; then Et_3N (44 equiv), −78→−25°C, 90%; j) KHMDS (1.5 equiv), THF, −78°C, 1 h, TMSCl (1.6 equiv), −78°C, 30 min; k) $Pd(OAc)_2$ (5.0 equiv), DMSO, 72 h, 55% over two steps; l) $NaBH_4$ (3.0 equiv), $CeCl_3 \cdot 7H_2O$ (1.0 equiv), MeOH, −50°C, 1 h; m) Ac_2O (20 equiv), py (40 equiv), 4-DMAP (0.1 equiv), CH_2Cl_2, 0→25°C, 12 h, 71% over two steps; n) $[Pd_2dba_3]\cdot CHCl_3$ (0.2 equiv), nBu_3P (0.4 equiv), $NaBH_4$ (10.0 equiv), dioxane/H_2O (9:1), 0→25°C, 12 h; o) TBAF (3.0 equiv), THF, 0→25°C, 3 h, $\Delta^{7,8}/\Delta^{8,9}$ (2:1), 42% over two steps. TES = triethylsilyl, DMSO = dimethyl sulfoxide, TBS = *tert*-butyldimethylsilyl, LDA = lithium diisopropylamide, KHMDS = potassium bis(trimethylsilyl)amide.

 © 2004 Wiley-VCH Verlag GmbH & Co. KGaA, Weinheim



(synthetic compound from L-malic acid)

Scheme 6. Preparation of fully saturated synthetic ABCD fragment **31**. Reagents and conditions: a) Pd/C (10%), H_2, CH_3CO_2Et, 25 °C, 1 h, 95%.

was noted to be stable under acidic conditions, whereas our corresponding synthetic materials so far revealed their fleeting nature under similar conditions. This intriguing observation, subtle as it was, proved to be crucial in shaping our next hypothesis for solving the mystery of azaspiracid-1, as we will describe in the following communication in this issue.[5]

Experimental Section

4: $R_f = 0.30$ (silica gel, EtOAc/MeOH 9:1); $[\alpha]_D^{25} = +36.4$ (MeOH, $c = 0.14$); IR (film): $\tilde{\nu}_{max} = 3416, 2954, 2919, 1727, 1430, 1261, 1096, 1044, 797, 673\ cm^{-1}$; ^1H NMR (600 MHz, CD_3OD/0.5% CD_3COOD): $\delta =$ 5.35 (s, 1H), 5.31 (s, 1H), 4.52 (d, $J = 10.1$ Hz, 1H), 4.26 (br s, 1H), 3.81 (d, $J = 1.8$ Hz, 1H), 2.85–2.70 (m, 2H), 2.64–2.56 (m, 1H), 2.49 (dd, $J = 14.5$, 4.8 Hz, 1H), 2.44–2.38 (m, 1H), 2.40 (d, $J = 14.5$ Hz, 1H), 2.32 (d, $J = 14.5$ Hz, 1H), 2.30–2.22 (m, 2H), 2.10–1.95 (m, 3H), 1.85–1.71 (m, 2H), 1.60 (d, $J = 12.7$ Hz, 1H), 1.56–1.49 (m, 1H), 1.46–1.39 (m, 2H), 1.27–1.23 (m, 2H), 1.23 (d, $J = 7.0$ Hz, 3H), 1.17–1.04 (m, 1H), 0.95 (d, $J = 6.6$ Hz, 3H), 0.93 (d, $J = 6.1$ Hz, 3H), 0.91 (d, $J =$ 7.0 Hz, 3H), 0.89 ppm (d, $J = 6.6$ Hz, 3H); ^{13}C NMR (125 MHz, CD_3OD): $\delta = 177.2, 143.1, 120.4, 97.9, 95.9, 92.0, 79.6, 75.8, 72.6, 45.5, 43.4, 43.1, 42.4, 40.0, 38.0, 37.6, 37.0, 35.4, 33.1, 31.8, 26.4, 23.8, 19.8, 18.0, 17.5, 16.2$ ppm; HRMS (MALDI): calcd for $C_{26}H_{41}NO_5H^+$ [M+H^+]: 448.3057; found: 448.3051.

FGHI-*epi*-**4**: $R_f = 0.29$ (silica gel, EtOAc/MeOH 9:1); $[\alpha]_D^{25} = -18.0$ (MeOH, $c = 0.30$); IR (film): $\tilde{\nu}_{max} = 3374, 2962, 2921, 2854, 1729, 1452, 1411, 1261, 1090, 1021, 865, 800, 701, 666\ cm^{-1}$; ^1H NMR (600 MHz, CD_3OD/0.5% CD_3COOD): $\delta = 5.40$ (s, 1H), 5.37 (s, 1H), 4.44 (d, $J = 9.6$ Hz, 1H), 4.37 (br s, 1H), 4.03 (d, $J = 2.6$ Hz, 1H), 3.25 (d, $J = 12.3$ Hz, 1H), 3.05 (t, $J = 12.3$ Hz, 1H), 2.72 (dd, $J = 14.9$, 4.4 Hz, 1H), 2.66–2.60 (m, 1H), 2.48 (d, $J = 14.5$ Hz, 1H), 2.40–2.30 (m, 1H), 2.32 (d, $J = 14.5$ Hz, 1H), 2.30–2.20 (m, 1H), 2.15–2.08 (m, 2H), 2.04–2.00 (m, 1H), 1.83 (dd, $J = 14.0$, 5.7 Hz, 1H), 1.73 (d, $J =$ 14.0 Hz, 1H), 1.58–1.51 (m, 1H), 1.46–1.39 (m, 2H), 1.35–1.25 (m, 3H), 1.25 (d, $J = 7.0$ Hz, 3H), 1.18–1.09 (m, 2H), 1.00 (d, $J = 6.6$ Hz, 3H), 0.98 (d, $J = 6.6$ Hz, 3H), 0.97 (d, $J = 6.2$ Hz, 3H), 0.95 ppm (d, $J = 6.1$ Hz, 3H); ^{13}C NMR (150 MHz, CD_3OD): $\delta = 177.1, 142.5, 121.0, 98.1, 95.9, 92.4, 79.5, 75.8, 72.7, 45.7, 43.3, 43.2, 41.8, 40.0, 37.9, 37.7, 37.4, 35.6, 32.6, 31.8, 26.3, 23.9, 19.8, 17.9, 17.4, 16.2$ ppm; HRMS (MALDI): calcd for $C_{26}H_{41}NO_5H^+$ [M+H^+]: 448.3057; found: 448.3057.

8: $R_f = 0.19$ (silica gel, $CHCl_3$/MeOH/H_2O 20:3:1); $[\alpha]_D^{25} = +49.6$ (MeOH, $c = 0.4$); IR (film): $\tilde{\nu}_{max} = 3359, 2922, 2948, 1700, 1575, 1455, 1393, 1257, 1116, 1064, 1043, 1012, 793, 621\ cm^{-1}$; ^1H NMR (600 MHz, C_5D_5N): $\delta = 4.71$ (br s, 1H), 4.46 (br s, 1H), 3.59 (br s, 1H), 2.95 (s, 2H), 2.92 (t, $J = 12.3$ Hz, 1H), 2.83–2.75 (m, 1H), 2.34–2.27 (m, 1H), 2.20–2.13 (m, 2H), 2.10–2.04 (m, 1H), 1.95–1.88 (m, 1H), 1.80–1.71 (m, 2H), 1.57–1.50 (m, 1H), 1.49–1.42 (m, 2H), 1.31–1.24 (m, 1H), 0.91 (d, $J = 5.7$ Hz, 3H), 0.78 (d, $J = 4.8$ Hz, 3H), 0.72 ppm (d, $J =$ 5.3 Hz, 3H); ^{13}C NMR (150 MHz, CD_3OD): $\delta = 177.4, 97.2, 95.7, 80.2, 75.3, 72.2, 52.0, 48.2, 43.1, 39.6, 37.7, 35.4, 31.2, 30.8, 26.5, 23.9, 19.6, 16.1$ ppm; HRMS (MALDI): calcd for $C_{18}H_{29}NO_5H^+$ [M+H^+]: 340.2118; found: 340.2122.

21: $R_f = 0.22$ (silica gel, EtOAc/hexanes 1:2); $[\alpha]_D^{25} = +45.0$ ($CHCl_3$, $c = 1.1$); IR (film): $\tilde{\nu}_{max} = 3439, 2924, 2360, 2320, 1739, 1450, 1378, 1320, 1235, 1155, 1091, 1049, 1020, 978, 855, 800, 667\ cm^{-1}$; ^1H NMR (500 MHz, $CDCl_3$): $\delta = 6.07$ (ddd, $J = 9.9$, 5.1, 2.2 Hz, 1H), 5.80–5.74 (m, 2H), 5.62 (dd, $J = 15.7$, 6.1 Hz, 1H), 4.60–4.55 (m, 1H), 4.52–4.48 (m, 1H), 4.28–4.26 (m, 1H), 3.94–3.93 (m, 1H), 3.83–3.81 (m, 1H), 3.75 (s, 3H), 3.58–3.53 (m, 1H), 2.49–2.42 (m, 4H), 2.31–2.25 (m, 1H), 2.21–1.97 (m, 9H), 1.89–1.87 (m, 1H), 1.58–1.51 (m, 1H), 0.98 ppm (d, $J = 6.6$ Hz, 3H); ^{13}C NMR (150 MHz, $CDCl_3$): $\delta = 173.4, 131.1, 130.1, 129.1, 128.5, 111.4, 104.2, 78.9, 76.3, 75.9, 68.6, 64.8, 51.5, 35.7, 33.9, 33.6, 31.0, 29.9, 29.7, 27.6, 23.4, 15.6$ ppm; HRMS (MALDI): calcd for $C_{22}H_{32}O_7Na^+$ [M+Na^+]: 431.2040; found: 431.2060.

Received: May 17, 2004 [Z460695]
Published Online: June 25, 2004

Keywords: degradation studies · natural products · neurotoxins · structure elucidation · total synthesis

[1] M. Satake, K. Ofuji, H. Naoki, K. J. James, A. Fruey, T. McMahon, J. Silke, T. Yasumoto, *J. Am. Chem. Soc.* **1998**, *120*, 9967–9968.

[2] K. C. Nicolaou, Y. Li, N. Uesaka, T. V. Koftis, S. Vyskocil, T. Ling, M. Govindasamy, W. Qian, F. Bernal, D. Y.-K. Chen, *Angew. Chem.* **2003**, *115*, 3777–3781; *Angew. Chem. Int. Ed.* **2003**, *42*, 3643–3648.

[3] K. C. Nicolaou, D. Y.-K. Chen, Y. Li, W. Qian, T. Ling, S. Vyskocil, T. V. Koftis, M. Govindasamy, N. Uesaka, *Angew. Chem.* **2003**, *115*, 3781–3783; *Angew. Chem. Int. Ed.* **2003**, *42*, 3649–3653.

[4] For synthetic studies directed toward azaspiracid-1, see: a) R. G. Carter, D. J. Weldon, *Org. Lett.* **2000**, *2*, 3913–3916; b) R. G. Carter, D. E. Graves, *Tetrahedron Lett.* **2001**, *42*, 6035–6039; c) R. G. Carter, T. C. Bourland, D. E. Graves, *Org. Lett.* **2002**, *4*, 2177–2179; d) C. J. Forsyth, J. Hao, J. Aiguade, *Angew. Chem.* **2001**, *113*, 3775–3779; *Angew. Chem. Int. Ed.* **2001**, *40*, 3663–3667; e) A. B. Dounay, C. J. Forsyth, *Org. Lett.* **2001**, *3*, 975–978; f) J. Hao, J. Aiguade, C. J. Forsyth, *Tetrahedron Lett.* **2001**, *42*, 817–820; g) J. Hao, J. Aiguade, C. J. Forsyth, *Tetrahedron Lett.* **2001**, *42*, 821–824; h) R. G. Carter, T. C. Bourland, D. E. Graves, *Org. Lett.* **2002**, *4*, 2177–2179; i) R. G. Carter, D. E. Graves, M. A. Gronemeyer, G. S. Tschumper, *Org. Lett.* **2002**, *4*, 2181–2184; j) M. Sasaki, Y. Iwamuro, J. Nemoto, M. Oikawa, *Tetrahedron Lett.* **2003**, *44*, 6199–6201; k) Y. Ishikawa, S. Nishiyama, *Tetrahedron Lett.* **2004**, *45*, 351–354; l) Y. Ishikawa, S. Nishiyama, *Heterocycles* **2004**, *63*, 539–565; m) Y. Ishikawa, S. Nishiyama, *Heterocycles* **2004**, *63*, 885–893.

[5] See following Communication in this issue: K. C. Nicolaou, T. V. Koftis, S. Vyskocil, G. Petrovic, T. Ling, Y. M. A. Yamada, W. Tang, M. O. Frederick, *Angew. Chem.* **2004**, *116*, 4418; *Angew. Chem. Int. Ed.* **2004**, *43*, 4318.

[6] As in the cases of synthetic **1-i** and FGHI-*epi*-**1-i**,[3] both C20-*epi*-**1-i** and C20-*epi*-FGHI-*epi*-**1-i** were found to exist as mixtures of inseparable compounds, and neither of the samples matched by TLC, HPLC, or ^1H NMR with the natural azaspiracid-1. Complete details will be discussed in the full account of this work.

[7] G. Stork, K. Zhao, *Tetrahedron Lett.* **1989**, *30*, 287–2902.

[8] S. Hanessian, D. H. Wong, M. Therien, *Synthesis* **1981**, 394–396.

[9] W. R. Roush, D. S. Coffey, D. J. Madar, *J. Am. Chem. Soc.* **1997**, *119*, 11331–11332.

[10] Both **4** and FGHI-*epi*-**4** were found to be labile upon prolonged standing in CD_3OD or CD_3OD/0.5% CD_3COOD at ambient temperature.

 © 2004 Wiley-VCH Verlag GmbH & Co. KGaA, Weinheim

[11] C. Hopmann, D. J. Faulkner, *Tetrahedron Lett.* **1997**, *38*, 169–170.
[12] For selected compounds with a doubly allylic oxymethine hydrogen atom attached to a 3-dihydropyran ring, see: a) P. A. Wender, S. G. Hedge, R. D. Hubbard, *J. Am. Chem. Soc.* **2002**, *124*, 4956–4957; b) C. Iwamoto, K. Minoura, T. Oka, T. Ohta, S. Hagishita, A. Numata, *Tetrahedron* **1999**, *55*, 14353–14368; c) L. V. Dunkerton, A. J. Serino, *J. Org. Chem.* **1992**, *57*, 2814–2816.
[13] R. E. Ireland, R. H. Mueller, *J. Am. Chem. Soc.* **1972**, *94*, 5897–5898.
[14] H. Nakamura, M. Ono, Y. Shida, H. Akita, *Tetrahedron: Asymmetry* **2002**, *13*, 705–713.

 © 2004 Wiley-VCH Verlag GmbH & Co. KGaA, Weinheim

Natural Products Synthesis

Structural Revision and Total Synthesis of Azaspiracid-1, Part 2: Definition of the ABCD Domain and Total Synthesis**

K. C. Nicolaou, Theocharis V. Koftis, Stepan Vyskocil, Goran Petrovic, Taotao Ling, Yoichi M. A. Yamada, Wenjun Tang, and Michael O. Frederick*

The preceding communication in this issue[1] detailed studies that led to the absolute structural definition of the EFGHI segment (C21–C40 domain) of azaspiracid-1 (see one of the four originally proposed structures, **1-i**, Figure 1), but left the final structural assignment for the ABCD framework (C1–C20 domain) as an open question, despite considerable effort to resolve this issue. Herein we present the remainder of the azaspiracid-1 saga that led to the complete definition of the ABCD ring framework. The total synthesis of azaspiracid-1 (**1-c**) has finally revealed the long-sought structure of this marine neurotoxin, rendering it readily available for biological investigations.

In recapping the studies on the ABCD domain of azaspiracid-1 described in the preceding paper,[1] we note that the degradatively derived fragment did not match either structure **2** ($\Delta^{8,9}$, Figure 1), which was designed on the basis of the originally proposed structure of azaspiracid-1 (**1-i**), or compound **3** ($\Delta^{7,8}$, Figure 1), whose adoption as possible candidate for the correct architecture was based on the structure of lissoketal. These findings still left us with a multiple choice as to which stereoisomer of structure **3** (which by now became our favorite representation of the coveted subtarget molecule) to pursue next. However, based on our knowledge at the time, we could decrease the reasonable isomer possibilities to a small number that included compound **4** (Figure 2). This isomer appeared to benefit from a double anomeric effect (based on manual molecular modeling) and to fulfil the crucial requirement for the NOE effect between 6-H and the methyl group at C14 (see Figure 2) observed for the natural product[2] and its ABCD-domain degradation product.[1] It was precisely because of this latter observation that compound **4** became our next priority target. Its attempted synthesis (Scheme 1) was met with unexpected, but nevertheless, path-pointing observations. Thus, substrate **9** was prepared from building blocks[3] **6**, **7**, and **8** according to our previously reported route,[3] with the appropriate modification of building block **7** to accommodate the new stereochemical requirement at C14 in subtarget **4**. The intermediate **9** was then subjected to deprotection–cyclization cascade conditions.[3] Interestingly, however, the major product formed in this double spiroketalization process (**9**→**10**) was that with the opposite stereochemistry at C13 from the one proposed in the C14-*epi* target intermediate **4**. This rather distressing signal became even more ominous four steps further along the sequence when an attempt was made to correct the stereochemistry at C13. Thus, when intermediate **11** (obtained from **10** by 1) pivaloate formation; 2) dithiane cleavage; and 3) reduction with sodium borohydride) was exposed to TFA, an equilibrium was reached in which the isomer **12** with the isomerized C13 center predominated (≈55:45). Although NOE studies revealed a strong effect between 6-H and the methyl group at C14 in **12**, the chemical shift of the latter signal differed significantly from the corresponding signal in the natural product, suggesting the axial orientation for this methyl substituent (C14). Indeed, the observed thermodynamic stability of azaspiracid-1 under acidic conditions[2] did not bode well for isomer **4** as the correct representation of the ABCD domain of the natural product. Its construction, therefore, was abandoned at this stage in favor of another synthesis, this time directed toward the next suspected structure, namely **5** (Figure 2). The latter structure, in which the C6 stereocenter is inverted, also enjoys the thermodynamic stability (manual molecular modeling) derived from two anomeric effects, provided that the two spirocenters are inverted into the opposite configurations as shown in Figure 2 (structure **5**).

Compound **5** was synthesized stereoselectively as shown in Scheme 2. Thus, starting with the ketophosphonate **6** derived from L-malic acid (natural), and following our

[*] Prof. Dr. K. C. Nicolaou, Dr. T. V. Koftis, Dr. S. Vyskocil, Dr. G. Petrovic, Dr. T. Ling, Dr. Y. M. A. Yamada, Dr. W. Tang, M. O. Frederick
Department of Chemistry and
The Skaggs Institute for Chemical Biology
The Scripps Research Institute
10550 North Torrey Pines Road, La Jolla, CA 92037 (USA)
Fax: (+1) 858-784-2469
and
Department of Chemistry and Biochemistry
University of California, San Diego
9500 Gilman Drive, La Jolla, CA 92093 (USA)
E-mail: kcn@scripps.edu

[**] We thank Dr. D. H. Huang and Dr. G. Siuzdak for NMR spectroscopic and mass spectrometric assistance, respectively. Financial support for this work was provided by grants from the National Institutes of Health (USA) and the Skaggs Institute for Chemical Biology, and fellowships from the Ernst Schering AG Foundation (to S.V.), the National Science Foundation (to M.O.F.), and the Japanese Society for the Advancement of Science (to Y.M.A.Y.).

 © 2004 Wiley-VCH Verlag GmbH & Co. KGaA, Weinheim DOI: 10.1002/anie.200460696

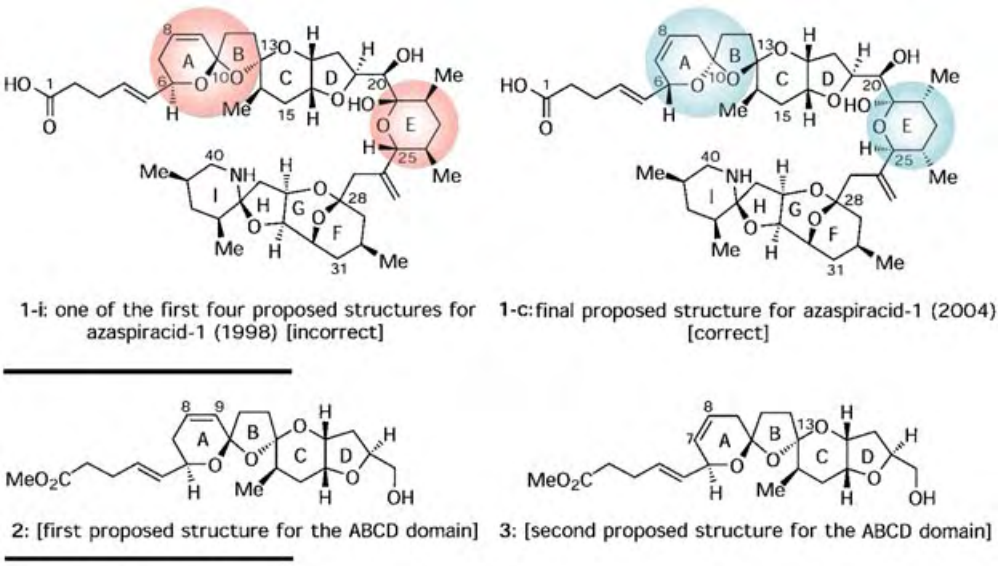


Figure 1. Originally (**1-i**) and newly (**1-c**) proposed structures of azaspiracid-1, and unsuccessful attempts to match synthetic materials (**2** and **3**) with naturally derived ABCD fragment.

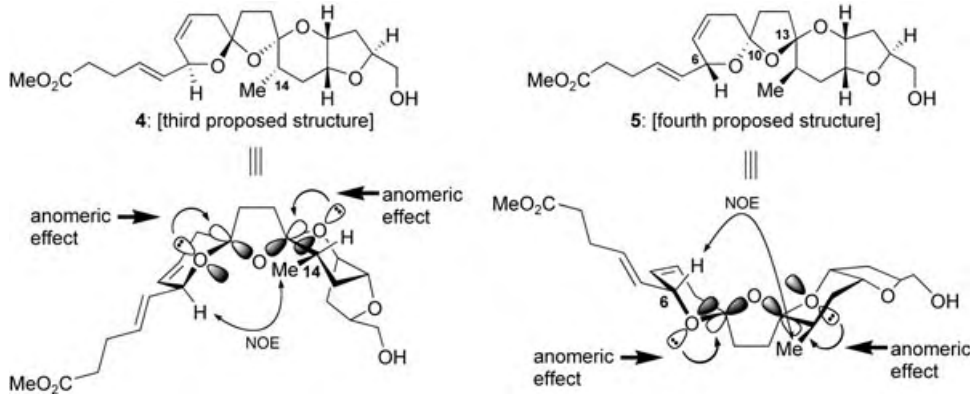
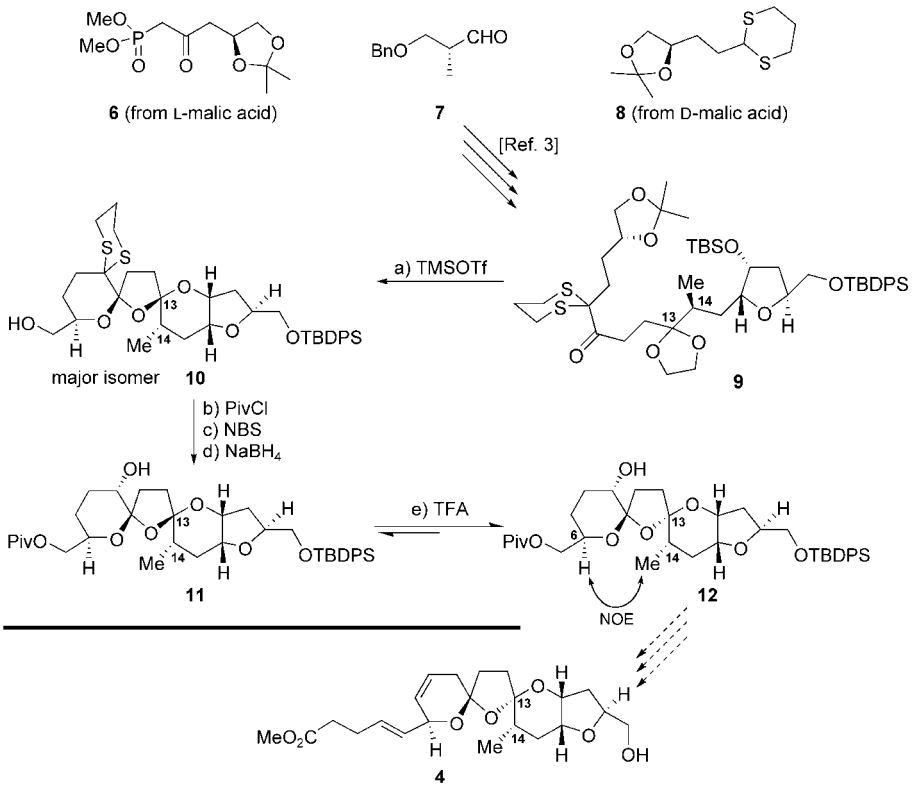


Figure 2. Third and fourth proposed structures (**4** and **5**) of the ABCD domain of azaspiracid-1 with expected anomeric effects and NOE interactions.

previously described route,[3] intermediate **13** was prepared in 12 steps in good overall yield. To accommodate the requirements of the new subtarget **5**, a substantially modified sequence from **13** to **5** had to be developed. To facilitate the pending cyclization to the ABCD tetracycle (see below), the TBS group of **13** was exchanged with a TES group, followed by cleavage of the double bond to give aldehyde **14** in excellent overall yield. Coupling of **14** with dithiane **15** (also derived from L-malic acid)[3] under the influence of *n*BuLi afforded the corresponding secondary alcohol as a mixture of diastereoisomers (≈1:1, 98% yield) whose oxidation with DMP transformed it into the required cyclization precursor **16** in 90% yield. The anticipated deprotection–double spirocyclization of **16** proceeded smoothly under the influence of TMSOTf in CH_2Cl_2 at −90 °C to furnish the desired polycycle **17** in 89% yield as a single stereoisomer. The observed NOE interaction between 6-H and C14-Me confirmed the anticipated structure **17** and provided support for our proposition of its thermodynamic stability. To decrease the number of steps required for the side-chain attachment, an olefin metathesis protocol was applied instead of the previously reported procedure.[1] Thus, Swern oxidation of alcohol **17** followed by Wittig olefination of the resulting aldehyde furnished the desired terminal olefin **19** in 81% overall yield. Cross-metathesis of **19** with olefin **21** was effected by the action of Grubbs catalyst **20**,[4] yielding the corresponding *E* olefin as the major product, from which the minor *Z* olefin was easily separated chromatographically (95% yield total after three cycles, ≈60% conversion in each cycle, $E/Z \approx 10{:}1$). The dithiane moiety was then removed from the resulting olefin by exposure to PhI-$(OCOCF_3)_2$, leading to ketone **22** in 90% yield. The introduction of the required α,β-unsaturation within **22** was successfully carried out by the Mukaiyama method (LDA–*t*BuN=SPhCl)[5] to afford **23** in 81% yield. Regio- and stereoselective reduction of the enone functionality of **23** with $NaBH_4$–$CeCl_3$, followed by exposure to $ClCO_2Me$ in the presence of pyridine, led to allylic carbonate **24** through the intermediacy of the corresponding alcohol in 70% overall yield. Compound **24** served well as a precursor to olefin **25**

 © 2004 Wiley-VCH Verlag GmbH & Co. KGaA, Weinheim



Scheme 1. On the way to proposed intermediate **4** (C14-*epi*): a) TMSOTf (4.0 equiv), CH_2Cl_2, −90 °C, 30 min, 89 %; b) PivCl (3.0 equiv), pyridine (10.0 equiv), 4-DMAP (0.1 equiv), CH_2Cl_2, 0→25 °C, 12 h; 95 %; c) NBS (8.0 equiv), 2,6-lutidine (16 equiv), MeCN/H_2O (4:1), 25 °C, 1 h, 80 %; d) $NaBH_4$ (1.1 equiv), MeOH, −78→−60 °C, 3 h, 92 %; e) TFA (2.0 equiv), CH_2Cl_2, 0 °C, 1.5 h, 98 % (**12**/**11** ≈ 55:45). TMS = trimethylsilyl, Piv = trimethylacetyl, 4-DMAP = 4-(dimethylamino)pyridine, NBS = *N*-bromosuccinimide, TFA = trifluoroacetic acid.

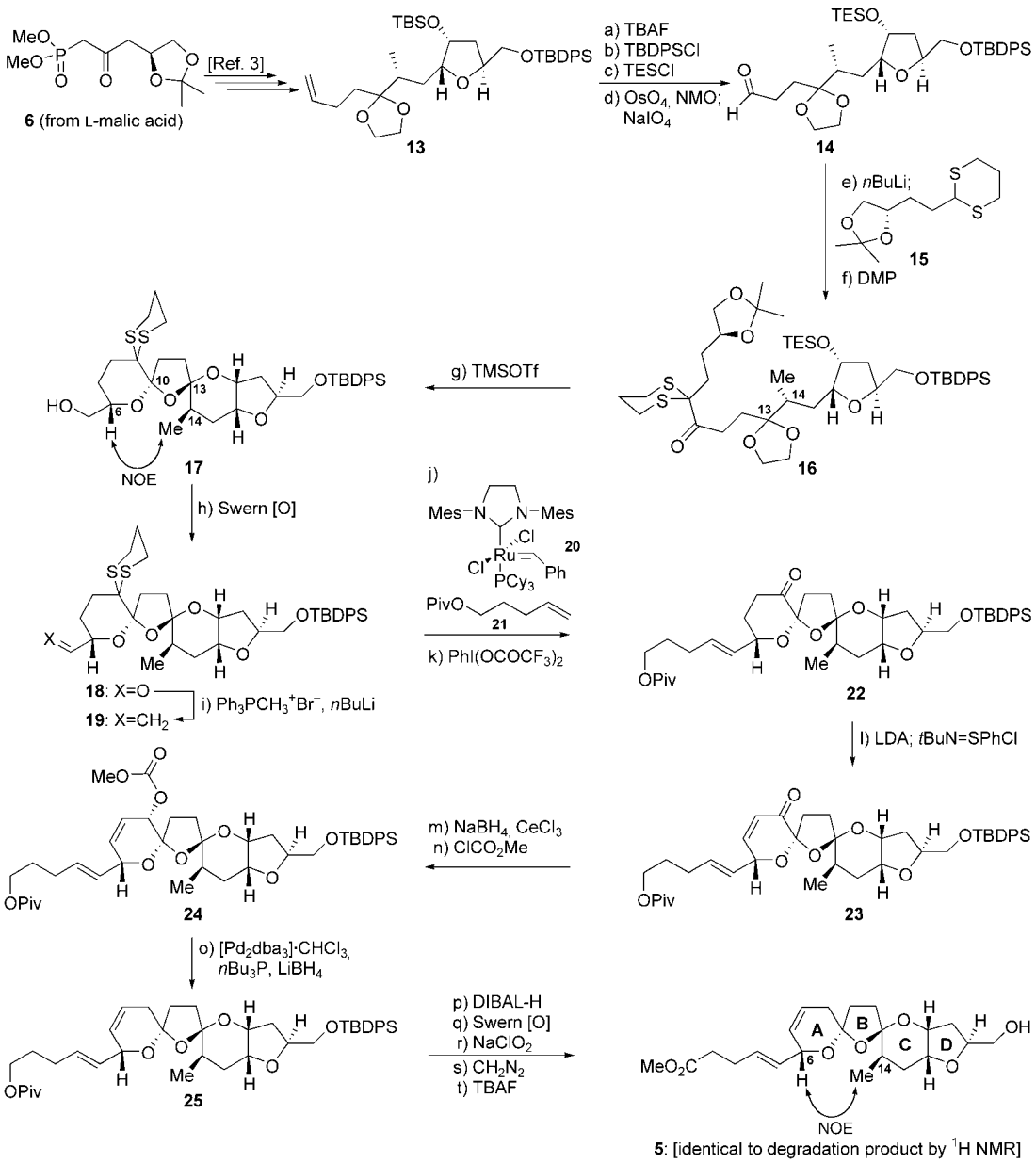
under a palladium-catalyzed reductive protocol ([Pd_2dba_3]·$CHCl_3$, nBu_3P, $LiBH_4$, DME),[6] furnishing the desired $\Delta^{7,8}$ olefinic compound **25** as the predominant product (82 % yield, $\Delta^{7,8}/\Delta^{8,9} \approx 7{:}1$; the undesired $\Delta^{8,9}$ isomer was chromatographically removed at this stage). The key intermediate **5** was then generated from **25** in 71 % overall yield by a five-step sequence: 1) DIBAL-induced cleavage of the pivaloate group; 2) Swern oxidation of the resulting alcohol to the aldehyde; 3) further oxidation to the corresponding carboxylic acid; 4) methylation with diazomethane; and 5) desilylation with TBAF (Scheme 2). Synthetic **5** matched the degradatively derived material by ^{1}H NMR spectroscopy.[7] This was indeed a pleasing moment in the azaspiracid-1 campaign, although the minute supplies of the degradation product did not permit optical rotation comparisons, and, therefore, the absolute stereochemistry of **5** still remained elusive. This gap in our intelligence gathering dictated the synthesis of the other enantiomer of **25** as well (*ent*-**25**, see Scheme 3), a task that was easily accomplished starting from the enantiomer of **6** (prepared from D-malic acid, see Scheme 2) and proceeding in the manner described above for **25**.

Having secured adequate supplies of both enantiomers of **25** and being assured that one of them corresponded to the ABCD domain of our target natural product, we set out to reach the final target. The first enantiomer to reach the end was that derived from non-natural D-malic acid (i.e. *ent*-**25**), only to find that it did not correspond to azaspiracid-1. The final drive toward azaspiracid-1 from enantiomer **25** (derived from L-malic acid) was then undertaken in earnest, following the convergent strategy previously employed in these laboratories for the synthesis of the originally proposed structure (**1-i**).

Owing to the problems that arose in the final deprotection step of our previous route[8] to azaspiracid-1, we opted to adopt a TBS protecting group for the hydroxy group of C25, as opposed to the originally employed acetate group. The new sequence toward advanced intermediate **32** (see Scheme 3), which was required for the planned palladium-catalyzed coupling reaction with the FHI segment, began with intermediate **25** and proceeded along the path delineated in Scheme 3. Thus, the TBDPS protecting group was removed from **25** by exposure to TBAF to reveal the primary alcohol (98 % yield), which was oxidized in a two-step procedure to carboxylic acid **26** in 90 % overall yield. Compound **26** was converted into its pentafluorophenyl ester **27** by DCC-facilitated coupling with pentafluorophenol in 84 % yield. The activated form of dithiane **28** (nBuLi–$n$$Bu_2Mg$) was then treated with **27** at −90 °C to generate the coupled product **29** in 50 % yield. A two-step sequence involving excess DIBAL-H followed by TBAF was then used to convert **29** into **30** in 44 % overall yield. The indicated stereochemistry at C20 was assigned to tetraol **30** by analogy to our previous results[8,9] in the synthesis of the originally proposed azaspiracid-1 structure. The activation–protection required for **30** prior to coupling with the FHI segment was introduced by selective acetylation of its primary hydroxy groups (90 % yield) and silylation of the C25-OH group (86 % yield) to afford intermediate **31**. Final unmasking of the keto group of **31** by treatment with $PhI(OCOCF_3)_2$ furnished the advanced C1–C27 fragment **32** (68 % yield) ready for further elaboration.

The second crucial coupling in the synthesis, that between the ABCD (C1–C27) and FHI (C28–C40) fragments **32** and **33**, was brought about by the action of [Pd_2dba_3] catalyst in the presence of LiCl, $AsPh_3$, and Et$Ni$$Pr_2$ and led to intermediate **34** (55 % yield), which contains all the carbon atoms required for azaspiracid-1, but lacks rings G and E (Scheme 4). Ring G was cast first through the intervention of TBAF to remove the TES group selectively followed by ring closure as induced by NIS and reductive removal of the residual iodine atom ($n$$Bu_3$SnH–$Et_3B$) to afford octacyclic compound **36** through intermediate iodide **35** in 43 % overall yield. The construction of ring E was left until last, and not before all the necessary functionality for the final target was in place. Thus, a TES group was called upon to temporarily

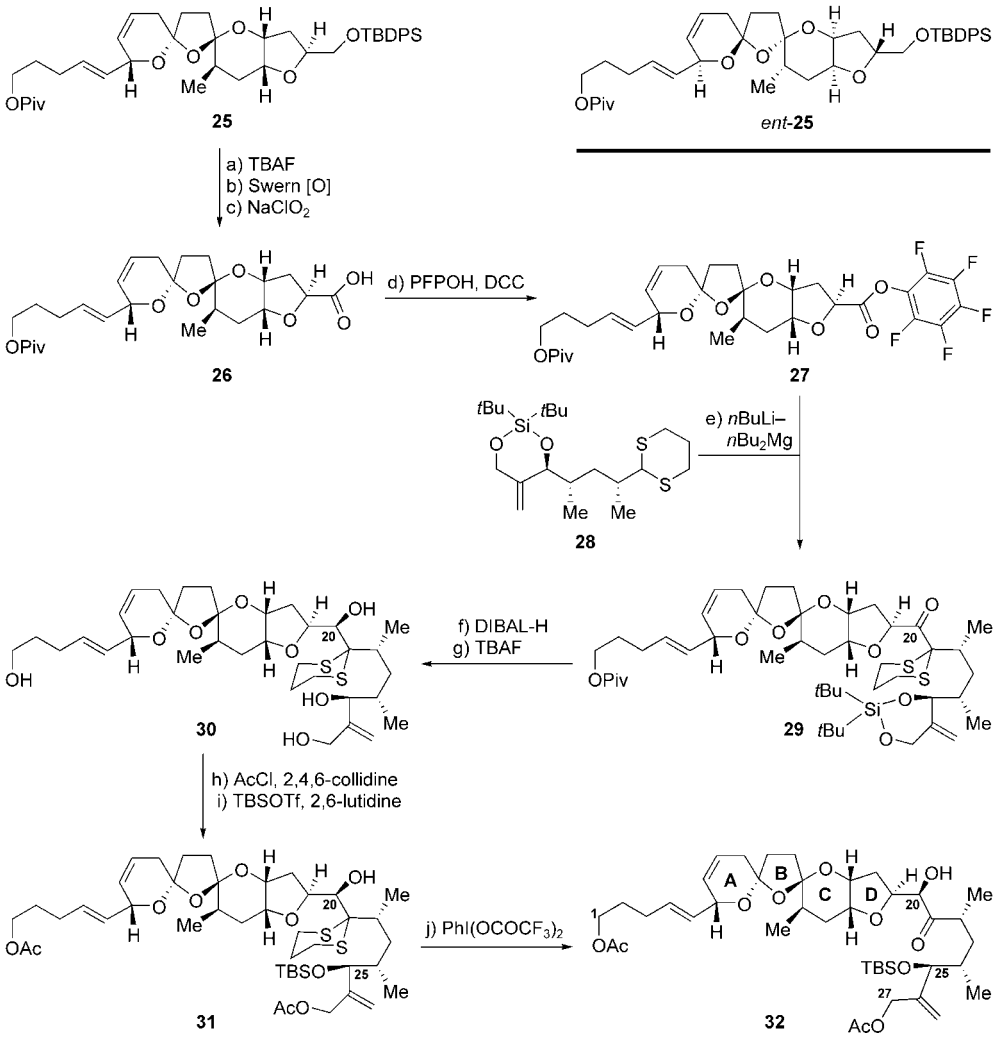
 © 2004 Wiley-VCH Verlag GmbH & Co. KGaA, Weinheim



Scheme 2. Synthesis of key intermediate **5** and confirmation of the structure of the ABCD domain. Reagents and conditions: a) TBAF (1.0 M in THF, 3.0 equiv), THF, 25 °C, 48 h, 99%; b) TBDPSCl (1.2 equiv), Et_3N (3.0 equiv), 4-DMAP (0.1 equiv), CH_2Cl_2, 0 °C, 12 h, 90%; c) TESCl (1.5 equiv), imidazole (3.0 equiv), 4-DMAP (0.1 equiv), CH_2Cl_2, 0 °C, 30 min, 95%; d) OsO_4 (0.03 equiv), NMO (2.0 equiv), *t*BuOH/THF/H_2O (10:2:1), 25 °C, 12 h; then $NaIO_4$ (5.0 equiv), pH 7 buffer, 25 °C, 5 h, 95%; e) *n*BuLi (1.6 M in hexanes, 3.5 equiv), **15** (3.5 equiv), THF, −30 °C, 30 min, 98%; f) DMP (1.2 equiv), py (10.0 equiv), CH_2Cl_2, 0 °C, 1 h, 90%; g) TMSOTf (4.0 equiv), CH_2Cl_2, −90 °C, 30 min, 89%; h) $(COCl)_2$ (5.0 equiv), DMSO (11 equiv), CH_2Cl_2, −78→−60 °C, 1.5 h; then Et_3N (22 equiv), −25 °C; i) $Ph_3PCH_3^+Br^-$ (5.0 equiv), *n*BuLi (4.0 equiv), THF, −78→0 °C, 1 h; then −78 °C; then **18**, −78→0 °C, 30 min, 81% from **17**; j) **21** (3.0 equiv), **20** (0.1 equiv), CH_2Cl_2, 40 °C, 12 h, 60%, $E/Z \approx 10:1$; k) $PhI(OCOCF_3)_2$ (3.0 equiv, slow addition), MeCN/pH 7 buffer (4:1), 0 °C, 30 min, 90%; l) LDA (1.5 equiv), *t*BuN=SPhCl (1.5 equiv), THF, −78 °C, 10 min, 81%; m) $NaBH_4$ (3.1 equiv), $CeCl_3 \cdot 7H_2O$ (1.0 equiv), MeOH, −65 °C, 40 min, 80%; n) $ClCO_2Me$ (25 equiv), 4-DMAP (1.0 equiv) CH_2Cl_2:py (2:1), −10 °C, 3 h, 87%; o) $[Pd_2dba_3]\cdot CHCl_3$ (0.125 equiv), nBu_3P (0.48 equiv), $LiBH_4$ (10.0 equiv), DME, 0 °C, 1 h, 82%, $\Delta^{7,8}/\Delta^{8,9} = 7:1$; p) DIBAL-H (1.0 M in CH_2Cl_2, 2.0 equiv), CH_2Cl_2, −78 °C, 15 min; q) $(COCl)_2$ (5.0 equiv), DMSO (11 equiv), CH_2Cl_2, −78→−60 °C, 1.5 h; then Et_3N (22 equiv), −25 °C; r) $NaClO_2$ (10.0 equiv), NaH_2PO_4 (10.0 equiv), 2-methyl-2-butene (excess), *t*BuOH/H_2O (4:1), 25 °C, 1 h; s) CH_2N_2 (excess), Et_2O, 25 °C; t) TBAF (1.0 M in THF, 2.0 equiv), THF, 25 °C, 1 h, 71% from **25**. TBAF = tetra-*n*-butylammonium fluoride, TBDPS = *tert*-butyldiphenylsilyl, TES = triethylsilyl, NMO = *N*-methylmorpholine *N*-oxide, DMP = Dess–Martin periodinane, Tf = trifluoromethanesulfonyl, DMSO = dimethyl sulfoxide, LDA = lithium diisopropylamide, dba = dibenzylideneacetone, DME = 1,2-dimethoxyethane, DIBAL-H = diisobutylaluminum hydride.

protect the C20-OH group of compound **36** (91% yield); removal of the acetate group from C1 with K_2CO_3 in MeOH furnished the corresponding primary alcohol (81% yield), which was sequentially oxidized, first to the aldehyde and then to the carboxylic acid, to afford the penultimate precursor, compound **37** (70% over two steps). Finally, all

 © 2004 Wiley-VCH Verlag GmbH & Co. KGaA, Weinheim



Scheme 3. Construction of key intermediate **32**. Reagents and conditions: a) TBAF (1.0 M in THF, 2.0 equiv), THF, 25 °C , 2 h, 98%; b) $(COCl)_2$ (5.0 equiv), DMSO (11 equiv), CH_2Cl_2, −78 °C, 30 min; then Et_3N (22 equiv), −78→0 °C; c) $NaClO_2$ (6.0 equiv), NaH_2PO_4 (6.0 equiv), 2-methyl-2-butene (excess), *t*BuOH/H_2O (4:1), 25 °C, 1 h, 90% over two steps; d) PFPOH (1.5 equiv), DCC (2.0 equiv), CH_2Cl_2, 25 °C, 2.0 h, 84%; e) **28** (7.0 equiv), *n*BuLi–nBu_2Mg (1.1 M in hexanes, 4.7 equiv), THF, 0→25 °C, 1.5 h; then −90 °C; then **27**, 30 min, 50%; f) DIBAL-H (1.0 M in CH_2Cl_2, 10.0 equiv), CH_2Cl_2, −90 °C, 1 h; g) TBAF (1.0 M in THF, 2.0 equiv), THF, 25 °C, 8 h, 44% over two steps; h) AcCl (20 equiv), 2,4,6-collidine (40 equiv), CH_2Cl_2, −78 °C, 6 h, 90%; i) TBSOTf (10.0 equiv), 2,6-lutidine (20 equiv), CH_2Cl_2, −78→0 °C, 30 min, 86%; j) $PhI(OCOCF_3)_2$ (2.0 equiv), MeCN/pH 7 buffer (4:1), 0 °C, 10 min, 68%. PFP = pentafluorophenyl, DCC = dicyclohexylcarbodiimide, TBS = *tert*-butyldimethylsilyl.

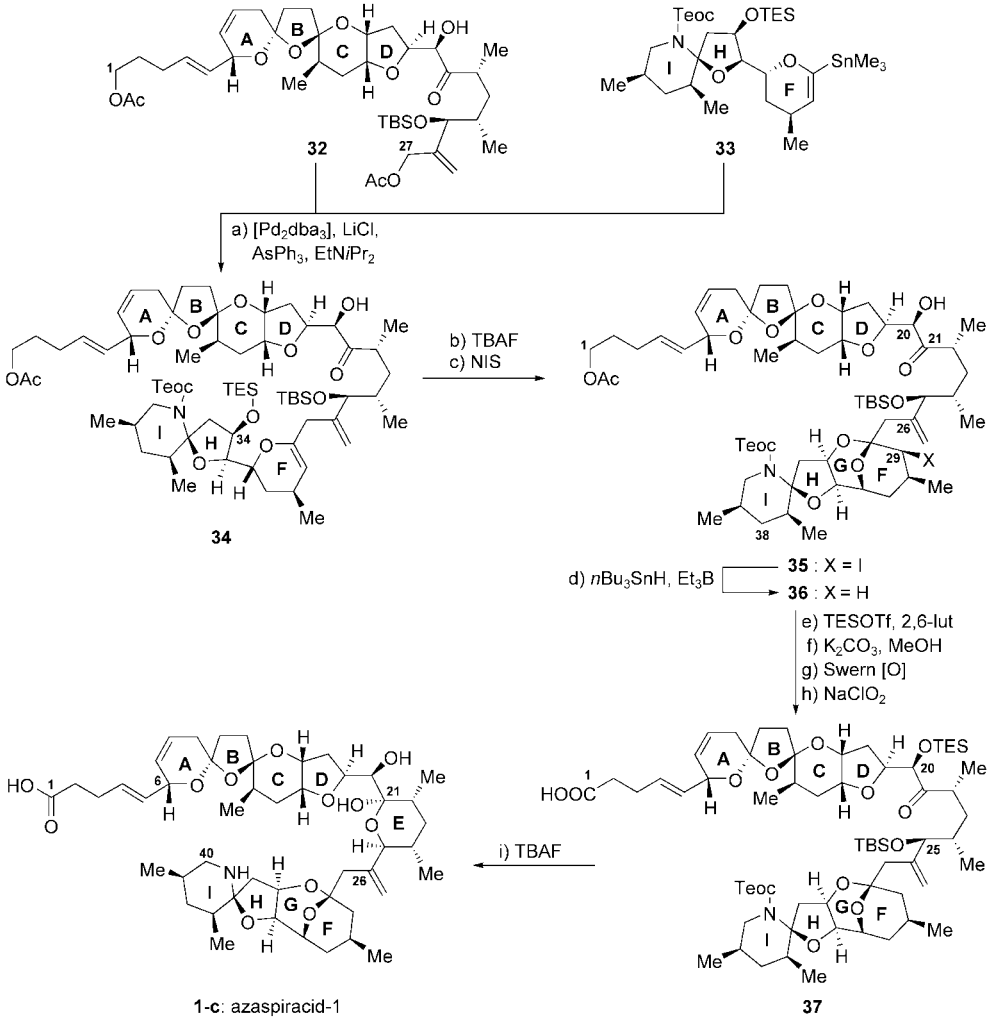
three remaining protecting groups on **37** (TES, TBS, and Teoc) were removed concurrently by exposure to excess TBAF in THF at ambient temperature to reveal the desired structure **1-c**, which was spontaneously formed upon collapse of the liberated C25-OH group onto the carbonyl functionality at C21 (Scheme 4). This time, the TLC profile of the synthetic material matched that of natural azaspiracid-1 obtained from the Yasumoto–Satake group.[7] More convincingly, and delightfully, all data (^{1}H NMR, ^{13}C NMR, MS, TLC, optical rotation) for the synthetic and natural samples of azaspiracid-1 were identical.[7]

Thus, the long-sought structural elucidation of azaspiracid-1, the notorious marine neurotoxin originally isolated from mussels (*Mytilus edulis*) collected in European waters, ended with its total synthesis, an accomplishment that also renders this valuable, but scarce, substance available for much-needed biological investigations. Among such investigations, those directed towards the development of assays for its detection and measurement in seafood and seawater and the elucidation of its mechanism of action must rank high on the list.

Experimental Section

5: $R_f = 0.24$ (silica gel, EtOAc/hexanes 2:1); $[\alpha]_D^{25} = -2.7$ ($CHCl_3$, $c = 0.45$); IR (film): $\tilde{\nu}_{max} = 3413, 2929, 2871, 1739, 1433\ cm^{-1}$; ^{1}H NMR (500 MHz, $CDCl_3$): $\delta = 5.77$–5.69 (m, 2H), 5.63 (dt, $J = 10.5$, 1.0 Hz, 1H), 5.49 (dd, $J = 15.5$, 7.5 Hz, 1H), 4.80 (br s, 1H), 4.35 (ddt, $J = 6.0$, 5.5, 3.0 Hz, 1H), 4.22 (m, 1H), 3.90 (m, 1H), 3.73 (dd, $J = 7.0$, 3.0 Hz, 1H), 3.67 (s, 3H), 3.49 (dd, $J = 7.0$, 5.5 Hz, 1H), 2.51 (dm, $J = 17.5$ Hz, 1H), 2.44–2.37 (m, 3H), 2.30 (dt, $J = 12.0$, 7.5 Hz, 1H), 2.15 (dt, $J = 12.0$, 7.0 Hz, 1H), 2.13–2.04 (m, 2H), 2.02 (dt, $J = 13.0$, 7.5 Hz, 1H), 1.92 (dd, $J = 13.0$, 6.5 Hz, 1H), 1.71–1.89 (m, 4H), 1.67 (dd, $J = 12.5$, 7.0 Hz, 1H), 0.93 ppm (d, $J = 7.0$ Hz, 3H); ^{13}C NMR (125 MHz, $CDCl_3$): $\delta = 173.1, 131.1, 130.4, 128.1, 122.6, 110.0, 105.7, 79.0, 76.7,$

 © 2004 Wiley-VCH Verlag GmbH & Co. KGaA, Weinheim



Scheme 4. Total synthesis of azaspiracid-1 (**1-c**). Reagents and conditions: a) **32**, $[Pd_2dba_3]$ (0.3 equiv), $AsPh_3$ (0.3 equiv), LiCl (6.0 equiv), $EtNiPr_2$ (12 equiv); then **33** (3.0 equiv, 0.03 M in THF, syringe pump addition), NMP, 40 °C, 1 h, 55%; b) TBAF (1.0 M in THF, 1.2 equiv), THF, 0 °C, 20 min, 80%; c) NIS (2.0 equiv), $NaHCO_3$ (10.0 equiv), THF, 0 °C, 12 h, 62%; d) Et_3B (1.0 M in hexanes, 0.2 equiv), nBu_3SnH/toluene (1:2), 0 °C, 5 min, 86%; e) TESOTf (10.0 equiv), 2,6-lutidine (20 equiv), CH_2Cl_2, −78→0 °C, 10 min, 91%; f) K_2CO_3 (2.0 equiv), MeOH, 25 °C, 1 h, 81%; g) $(COCl)_2$ (10.0 equiv), DMSO (20 equiv), CH_2Cl_2, −78 °C, 1 h; then Et_3N (50 equiv), −78→−20 °C, 30 min; h) $NaClO_2$ (10.0 equiv), NaH_2PO_4 (10.0 equiv), 2-methyl-2-butene (excess), *t*BuOH/H_2O (4:1), 25 °C, 30 min, 70% over two steps; i) TBAF (1.0 M in THF, 5.0 equiv), THF, 25 °C, 15 h, 60%. NIS = *N*-iodosuccinimide, Teoc = 2-(trimethylsilyl)ethoxycarbonyl, NMP = *N*-methylpyrrolidinone.

72.1, 70.8, 65.0, 51.6, 36.6, 35.3, 34.8, 33.4, 32.2, 31.4, 29.6, 27.6, 16.1 ppm; HRMS (MALDI): calcd for $C_{22}H_{32}O_7Na^+$ [M+Na^+]: 431.2040; found: 431.2047.

32: $R_f = 0.39$ (silica gel, EtOAc/hexanes 1:2); $[\alpha]_D^{25} = +11.25$ (CH_2Cl_2, $c = 2.40$); IR (film): $\tilde{\nu}_{max} = 3463, 2930, 2856, 1743, 1458, 1368, 1242, 1069, 1021, 987, 961, 839\ cm^{-1}$; ^1H NMR (500 MHz, CD_2Cl_2): $\delta = 5.74$ (m, 1H), 5.68 (dt, $J = 10.5$, 1.0 Hz, 1H), 5.63 (dt, $J = 10.5$, 1.0 Hz, 1H), 5.43 (ddt, $J = 15.5$, 7.0, 1.0 Hz, 1H), 5.16 (d, $J = 3.0$ Hz, 2H), 4.78 (br s, 1H), 4.57 (d, $J = 14.0$ Hz, 1H), 4.51 (d, $J = 14.0$ Hz, 1H), 4.38 (t, $J = 5.5$ Hz, 1H), 4.23 (dt, $J = 9.0$, 5.5 Hz, 1H), 4.17 (br s, 1H), 4.03 (t, $J = 6.5$ Hz, 2H), 3.98 (br s, 1H), 3.93 (d, $J = 5.5$ Hz, 1H), 3.35 (d, $J = 5.5$ Hz, 1H), 3.11 (ddq, $J = 17.5$, 7.5, 4.0 Hz, 1H), 2.47 (ddt $J = 17.5$, 4.5, 2.5 Hz, 1H), 2.25 (dt, $J = 12.0$, 7.5 Hz, 1H), 2.15–2.07 (m, 5H), 2.05 (s, 3H), 2.01 (s, 3H), 1.98–1.90 (m, 3H), 1.88–1.83 (m, 1H), 1.79 (dd, $J = 13.0$, 6.5 Hz, 1H), 1.75–1.67 (m, 3H), 1.62 (dd, $J = 12.0$, 7.0 Hz, 2H), 1.42 (br s, 1H), 1.10 (d, $J = 7.0$ Hz, 3H), 0.92 (s, 9H), 0.91 (d, $J = 7.0$ Hz, 3H), 0.87 (d, $J = 7.0$ Hz, 3H), 0.06 (s, 3H), −0.01 ppm (s, 3H); ^{13}C NMR (125 MHz, CD_2Cl_2): $\delta = 215.2$, 171.2, 170.7, 145.6, 132.0, 130.6, 128.6, 122.9, 113.9, 110.3, 106.0, 79.3, 78.9, 77.7, 77.5, 72.1, 71.1, 64.1, 64.1, 40.9, 37.0, 35.9, 35.7, 35.1, 34.1, 32.6, 31.7, 29.9, 29.0, 28.4, 26.0, 21.1, 19.4, 19.4, 18.5, 17.0, 16.3, −4.5, −5.0 ppm; HRMS (ESI-TOF): calcd for $C_{41}H_{66}O_{11}SiNa^+$ [M+Na^+]: 785.4266; found: 785.4245.

36: $R_f = 0.33$ (silica gel, EtOAc/hexanes 1:3); $[\alpha]_D^{25} = +2.4$ (CH_2Cl_2, $c = 0.9$); IR (film): $\tilde{\nu}_{max} = 3437, 2956, 2927, 2851, 1741, 1700, 1654, 1560, 1508, 1458, 1249, 1057, 837\ cm^{-1}$; ^1H NMR (600 MHz, CD_2Cl_2): $\delta = 5.75$–5.73 (m, 1H), 5.71–5.63 (m, 2H), 5.43 (dd, $J = 15.3$, 7.4 Hz, 1H), 5.18 (br s, 1H), 4.96 (br s, 1H), 4.79 (br s, 1H), 4.72 (m, 1H), 4.37–4.32 (m, 2H), 4.24 (d, $J = 4.9$ Hz, 1H), 4.20 (br s, 1H), 4.18–4.15 (m, 2H), 4.03 (t, $J = 6.6$ Hz, 2H), 4.02 (m, 1H), 3.92 (br s, 1H), 3.74 (br s, 1H), 3.73 (d, $J = 4.4$ Hz, 1H), 3.66 (d, $J = 14.0$ Hz, 1H), 3.20 (t, $J = 12.5$ Hz, 1H), 2.94–2.91 (m, 1H), 2.54–2.50 (m, 1H), 2.46 (m, 1H), 2.25 (dt, $J = 12.5$, 7.9, 1H), 2.15–2.08 (m, 7H), 2.01 (s, 3H), 1.99–1.95 (m, 2H), 1.94–1.92 (m, 1H), 1.90 (dd, $J = 8.8$, 4.8 Hz, 1H), 1.84 (m, 2H), 1.75–1.68 (m, 4H), 1.67–1.57 (m, 6H), 1.51 (q, $J = 13.2$ Hz, 2H), 1.40 (dt, $J = 13.6$, 5.2 Hz, 1H), 1.31 (q, $J = 12.2$ Hz, 2H), 1.04 (d, $J = 7.0$ Hz, 3H), 1.03–0.99 (m, 2H), 0.97 (d, $J = 7.0$ Hz, 3H), 0.92 (s, 9H), 0.91 (d, $J = 7.0$ Hz, 3H), 0.88 (d, $J = 6.1$ Hz, 3H), 0.82 (d, $J = 6.6$ Hz, 3H), 0.81 (d, $J = 6.1$ Hz, 3H), 0.04 (s, 9H), 0.03 (s, 3H), 0.00 ppm (s, 3H); ^{13}C NMR (125 MHz, CD_3OD):

 © 2004 Wiley-VCH Verlag GmbH & Co. KGaA, Weinheim

δ = 215.3, 171.2, 156.3, 146.9, 132.0, 130.7, 128.6, 122.9, 114.5, 110.3, 106.0, 97.4, 96.9, 79.1, 78.8, 78.5, 78.0, 77.6, 74.0, 72.4, 71.3, 71.1, 64.2, 63.2, 49.1, 45.8, 40.8, 40.0, 39.5, 37.0, 35.1, 34.9, 34.8, 33.6, 32.6, 31.7, 31.7, 30.1, 29.9, 29.0, 28.4, 26.2, 26.1, 24.9, 23.2, 21.1, 19.7, 18.9, 18.6, 18.5, 18.2, 18.2, 16.7, 16.3, −1.4, −3.8, −4.9 ppm; HRMS (ESI-TOF): calcd for $C_{61}H_{101}NO_{14}Si_2Na^+$ [M+Na^+]: 1150.6652; found: 1150.6662.

37: R_f = 0.2 (silica gel, EtOAc:hexanes 2:1); $[\alpha]_D^{25} = -6.2$ (CH_3OH, c = 0.13); IR (film): $\tilde{\nu}_{max}$ = 3383, 2955, 2921, 2874, 1698, 1674, 1568, 1555, 1411, 1252, 1170, 1259, 837 cm^{-1}; ^1H NMR (500 MHz, CD_3OD): δ = 5.76–5.70 (m, 2H), 5.62 (d, J = 10.5 Hz, 1H), 5.42 (dd, J = 15.5, 7.5 Hz, 1H), 5.21 (br s, 1H), 4.96 (br s, 1H), 4.79–4.77 (m, 2H), 4.59 (d, J = 3.0 Hz, 1H), 4.49–4.45 (m, 1H), 4.29 (br s, 1H), 4.23 (d, J = 6.0 Hz, 1H), 4.20 (dd, J = 10.5, 6.5 Hz, 1H), 4.16–4.15 (m, 1H), 4.10–4.04 (m, 1H), 3.88 (br s, 1H), 3.80 (d, J = 4.0 Hz, 1H), 3.79–3.77 (m, 1H), 3.71 (d, J = 13.0 Hz, 1H), 3.26 (d, J = 13.0 Hz, 1H), 2.79 (q, J = 7.0 Hz, 1H), 2.45 (m, 1H), 2.34–2.26 (m, 3H), 2.24–2.22 (m, 4H), 2.15–2.10 (m, 3H), 2.08–2.05 (m, 1H), 2.03–1.96 (m, 2H), 1.92 (dd, J = 12.1, 7.7 Hz, 1H), 1.86–1.83 (m, 1H), 1.82–1.78 (m, 1H), 1.76–1.69 (m, 3H), 1.68–1.63 (m, 2H), 1.62–1.52 (m, 3H), 1.44–1.34 (m, 2H), 1.33–1.28 (m, 4H), 1.05 (d, J = 6.6 Hz, 3H), 1.03 (ddd, J = 9.9, 6.2, 3.0 Hz, 2H), 0.99 (d, J = 7.0 Hz, 3H), 0.96 (t, J = 8.0 Hz, 9H), 0.94 (s, 9H), 0.93 (d, J = 7.0 Hz, 3H), 0.90 (d, J = 6.2 Hz, 3H), 0.86 (d, J = 6.6 Hz, 3H), 0.82 (d, J = 5.9 Hz, 3H), 0.62 (q, J = 8.0 Hz, 6H), 0.06 (s, 9H), 0.05 (s, 3H), 0.02 ppm (s, 3H); ^{13}C NMR (125 MHz, CD_3OD): δ = 215.6, 181.9, 157.6, 148.2, 133.9, 130.6, 129.4, 123.3, 115.3, 111.2, 107.1, 98.4, 97.8, 80.5, 80.2, 79.6, 78.8, 75.0, 73.4, 72.6, 72.1, 64.1, 50.0, 49.9, 47.0, 42.5, 41.7, 40.3, 38.7, 37.9, 37.6, 35.8, 35.4, 34.6, 34.5, 33.2, 32.9, 32.8, 32.5, 30.82, 30.78, 30.75, 30.5, 26.7, 25.8, 23.6, 20.9, 19.2, 19.1, 18.5, 16.8, 16.6, 7.2, 5.8, −1.3, −3.4, −4.7 ppm; HRMS (ESI-TOF): calcd for $C_{65}H_{111}NO_{14}Na^+$ [M+Na^+]: 1236.7204; found: 1236.7189.

Received: May 17, 2004 [Z460696]
Published Online: June 29, 2004

Keywords: degradation studies · natural products · neurotoxins · structure elucidation · total synthesis

[1] See preceding Communication in this issue: K. C. Nicolaou, S. Vyskocil, T. V. Koftis, Y. M. A. Yamada, T. Ling, D. Y.-K. Chen, W. Tang, G. Petrovic, M. O. Frederick, Y. Li, M. Satake, *Angew. Chem.* **2004**, *116*, 4412; *Angew. Chem. Int. Ed.* **2004**, *43*, 4312.
[2] M. Satake, K. Ofuji, H. Naoki, K. J. James, A. Fruey, T. McMahon, J. Silke, T. Yasumoto, *J. Am. Chem. Soc.* **1998**, *120*, 9967 – 9968.
[3] K. C. Nicolaou, W. Qian, F. Bernal, N. Uesaka, P. M. Pihko, J. Hinrichs, *Angew. Chem.* **2001**, *113*, 4192 – 4195; *Angew. Chem. Int. Ed.* **2001**, *40*, 4068 – 4071.
[4] A. K. Chatterjee, T.-L. Choi, D. P. Sanders, R. H. Grubbs, *J. Am. Chem. Soc.* **2003**, *125*, 11360 – 11370.
[5] T. Mukaiyama, J. Matsuo, H. Kitagawa, *Chem. Lett.* **2000**, 1250 – 1251.
[6] A modification from the originally reported method ($[Pd_2dba_3]\cdot CHCl_3$, $n$$Bu_3P$, $NaBH_4$, dioxane, H_2O): H. Nakamura, M. Ono, Y. Shida, H. Akita, *Tetrahedron: Asymmetry* **2002**, *13*, 705 – 713.
[7] We thank Prof. Dr. Masayuki Satake for providing us with a ^1H NMR spectrum of degradatively derived compound **5** and with an authentic sample of natural azaspiracid-1.
[8] K. C. Nicolaou, Y. Li, N. Uesaka, T. V. Koftis, S. Vyskocil, T. Ling, M. Govindasamy, W. Qian, F. Bernal, D. Y.-K. Chen, *Angew. Chem.* **2003**, *115*, 3777 – 3781; *Angew. Chem. Int. Ed.* **2003**, *42*, 3643 – 3648.
[9] K. C. Nicolaou, D. Y.-K. Chen, Y. Li, W. Qian, T. Ling, S. Vyskocil, T. V. Koftis, M. Govindasamy, N. Uesaka, *Angew. Chem.* **2003**, *115*, 3781 – 3783; *Angew. Chem. Int. Ed.* **2003**, *42*, 3649 – 3653.

 © 2004 Wiley-VCH Verlag GmbH & Co. KGaA, Weinheim

Medicinal Chemistry

23-Oxa-Analogues of OSW-1: Efficient Synthesis and Extremely Potent Antitumor Activity**

Bingfeng Shi, Hao Wu, Biao Yu, and Jiarui Wu*

Saponin OSW-1, which contains a novel 16β,17α-dihydroxycholest-22-one aglycone unit with an acylated disaccharide at the 16-OH group, was discovered by Sashida, Mimaki, and coworkers in 1992 in the bulbs of *Ornithogalum saudersiae*, a perennial garden plant of the lily family widely cultivated in southern Africa.[1] Tremendous attention has been given to this compound since its antitumor activity was tested in 1995: OSW-1 has a low toxicity for normal cells but inhibits the growth of a variety of malignant tumor cells and is 10–100 times more potent than clinically applied anticancer agents such as mitomycin C, adriamycin, cisplatin, camptothecin, and taxol.[2] Further research on *O. saudersiae* and taxonomically related plants has revealed a family of 16β,17α-dihydroxycholest-22-one saponins.[3] Considerable effort has been directed toward the synthesis of OSW-1, the first and most abundant member of the family having been isolated.[4–7] The aglycone was first synthesized by Fuchs and Guo in 1998.[4] Shortly afterwards, we coupled the aglycone with the disaccharide moiety to complete the total synthesis of OSW-1.[5] Jin and Yu recently greatly improved this synthesis.[6] However, studies on the structure–activity relationships (SAR) of this novel type of anticancer agent have so far been limited;[3,8] the ascertained structural requirements for the exceptionally strong antitumor activity of OSW-1 are the presence of Ac and MBz groups on the disaccharide moiety and β orientation of the 16-*O*-sugar unit.[3,8b] Detailed biological, toxicological, and pharmacokinetic studies await the outcome of attempts to overcome a new synthetic challenge: the preparation of a variety of analogues, derivatives, and hopefully a lead compound in multigram quantities. Herein we report a novel and efficient approach to the construction of the 16β,17α-dihydroxycholest-22-one structure. One of the

[*] B. Shi, Prof. B. Yu
State Key Laboratory of Bioorganic
and Natural Products Chemistry
Shanghai Institute of Organic Chemistry
Chinese Academy of Sciences
354 Fenglin Road, Shanghai 200032 (P.R. China)
Fax: (+86) 21-6416-6128
E-mail: byu@mail.sioc.ac.cn

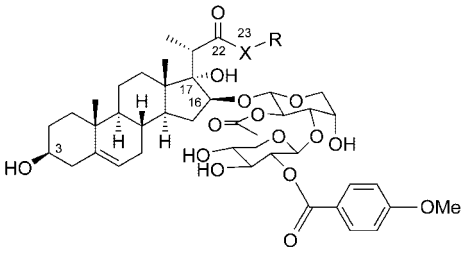
H. Wu, Prof. J. Wu
Institute of Biochemistry and Cell Biology
Shanghai Institute for Biological Sciences
Chinese Academy of Sciences
Shanghai 200031 (P.R. China)

[**] This work was supported by the National Natural Science Foundation of China (Grant nos. 20372070, 20321202, and 29925203) and the Chinese Academy of Sciences (Grant no. KGCX2-SW-209).

Supporting information for this article is available on the WWW under http://www.angewandte.org or from the author.

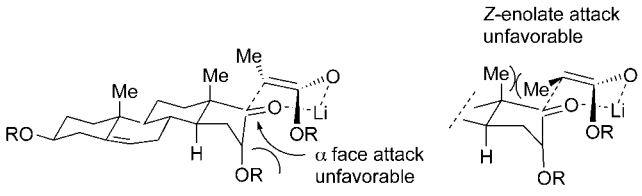
 © 2004 Wiley-VCH Verlag GmbH & Co. KGaA, Weinheim DOI: 10.1002/anie.200454237

23-oxa-analogues of OSW-1 (**1**–**3**) prepared by this method is a more potent inhibitor of the growth of tumor cells than OSW-1.



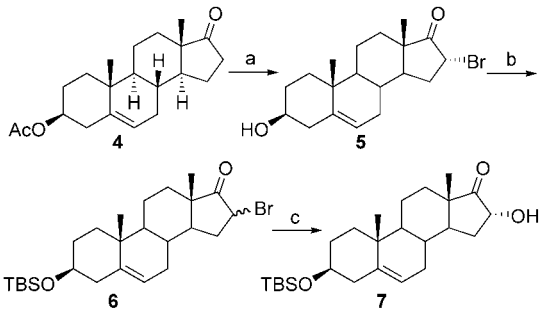
OSW-1: X = CH_2, R = $CH_2CH(CH_3)_2$
1: X = O, R = $CH_2CH(CH_3)_2$
2: X = O, R = CH_2CH_3
3: X = O, R = $(CH_2)_{11}CH_3$

A major challenge in the synthesis of OSW-1 is the elaboration of the 16β,17α-dihydroxycholest-22-one structure. Fuchs and Guo assembled the side chain on 5-androsten-3β-ol-17-one by a Wittig olefination and ene reaction sequence. The 16β,17α-diol was then introduced by dihydroxylation of the 16,17-ene group (1 equiv OsO_4) followed by inversion of the resulting 16α-OH group.[4] Jin and Yu developed a novel protocol for the synthesis of OSW-1 that involves 1,4-addition of an α-alkoxy vinyl cuprate to a 17(20)-en-16-one. The 17α-OH group was introduced to the resulting 16,17-enolate by treatment with Davis reagent.[6] Morzycki et al. used intramolecular ring opening of the 16α,17α-epoxide by the 22-carbonyl function as a starting point for further elaboration.[7a,b] We reanalyzed the characteristic 16β,17α-dihydroxycholest-22-one structure of OSW-1 saponins and envisioned the synthetic target as an α-methyl-β,γ-diol-one. This evaluation suggested that aldol condensation (between an α-hydroxy ketone and a propionate) would be the most direct approach to synthesis of the desired product.[9] We hoped to achieve stereocontrol by using a rigid 16α-hydroxy-17-oxo steroid as the ketone substrate, which would lead to the desired natural stereochemistry at C17 and C20 if the bulky 16α-OR group could force the enolate to approach from the β face (by nonchelation control,[10] Scheme 1, left). The chair transition state (Zimmerman–Traxler model)[10a] favors the *E* enolate over the *Z* enolate since the *E* conformation avoids steric interaction of the 18-methyl group with the methyl group of the propionate enolate (right).



Scheme 1. Proposed construction of the 21α-methyl-16α,17α-diol steroid structure by stereocontrolled aldol condensation.

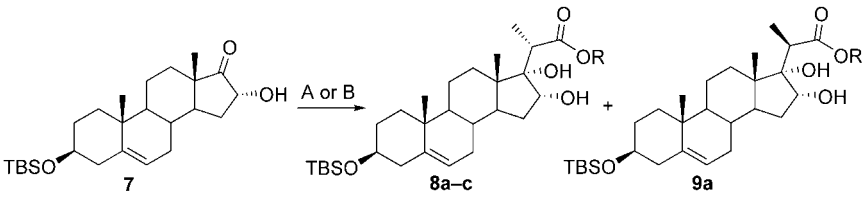
Encouragingly, Gros and Doller found that β-face attack of *tert*-butyl propionate by a lithium enolate leads to a 16α-acetoxy-17-oxo-androstane.[11]



Scheme 2. Introduction of the 16α-OH group. a) $CuBr_2$ (3.0 equiv), CH_3OH, reflux, 91%; b) TBSCl, imidazole, DMF, RT, overnight, 96%; c) NaOH (1.3 equiv), DMF/CH_2Cl_2/H_2O (3:2:1, v/v/v), RT, overnight, 95%. TBS = *tert*-butyldimethylsilyl, DMF = dimethylformamide.

The required 16α-hydroxy-5-androsten-17-one **7**, with the 3-OH group protected by a TBS ether, was readily prepared from the industrially produced acetate **4** by using a modified version of a literature procedure (Scheme 2).[12] Bromination of ketone **4** by treatment with $CuBr_2$ (3 equiv) in methanol under reflux provided 16α-bromide **5** in 91% yield (full cleavage of the 3-OAc group). Protection of the 3-OH group by treatment with TBSCl in the presence of imidazole in DMF gave **6**. Epimerization of the 16α-bromide and its 16β isomer took place readily. S_N2 displacement of the 16β-bromide by a hydroxide ion in DMF afforded the 16α-alcohol **7** in 95% yield.

The crucial aldol condensation of 16α-hydroxy-17-one **7** with propionate enolates was examined carefully (Scheme 3). The lithium *E* enolate of ethyl propionate was generated by



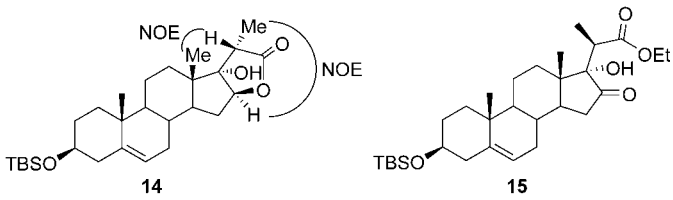
Scheme 3. Aldol condensation of 16α-hydroxy-17-one **7** with propionate enolates. Conditions: A) 1. iPr_2NH, *n*BuLi, −78°C, 15 min; 2. HMPA, THF, −78°C, then ethyl propionate, 0.5 h; 3. **7**, −78°C, 63% (for **8a**). B) 1. iPr_2NH, *n*BuLi, −78°C, 15 min; 2. propionates, THF, −78°C, 0.5 h; 3. **7**, −78°C, 75% (**8a**), 12% (**9a**), 78% (**8b**), 81% (**8c**). HMPA = hexamethyl phosphoramide, THF = tetrahydrofuran.

the method described by Ireland et al.[13] When **7** was treated with this enolate (A, Scheme 3), only the expected 17α-hydroxy-21α-methyl product **8a** was produced (in 63% yield). Without the use of stereocontrol to generate exclusively the *E* enolate of ethyl propionate (B, Scheme 3), the condensation reaction predominantly led to the desired 21α-methyl product **8a** (75% yield), but its 21β-methyl isomer **9a** was also isolated in 12% yield. Condensation with isobutyl

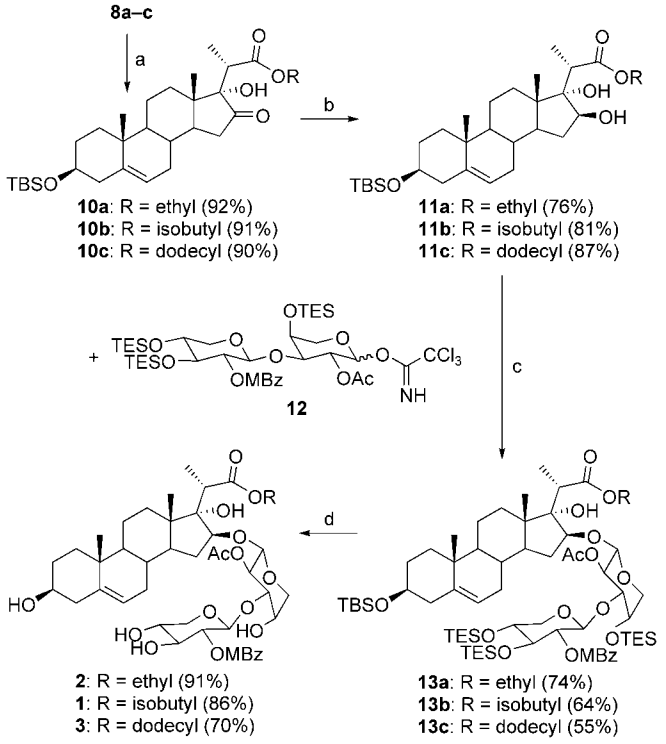
 © 2004 Wiley-VCH Verlag GmbH & Co. KGaA, Weinheim

and dodecyl propionate under conditions B gave predominantly the *E* enolates as a result of the greater size of the isobutyl and dodecyl groups compared to the ethyl group;[14] the desired 17α-hydroxy-21α-methyl compounds (**8b** and **8c**) were the only isolated products (78% and 81% yield, respectively).

The stereochemistry of the aldol products was confirmed by analysis of their reaction products **14** and **15**. Lactone **14**



was produced in the course of inversion of the 16α-OH group of **8** (**10**→**11**, Scheme 4) and was analyzed by NMR spectroscopy. NOE interactions were observed between the α-oriented protons at position 16 and on the 21-methyl group, and between the β-oriented protons at position 20 and on the 18-methyl group. Single-crystal X-ray diffraction analysis was performed on **15**,[15] which was prepared by oxidation of the 16-OH group of the minor aldol product **9a** (conditions similar to those for **8**→**10**, Scheme 4).



Scheme 4. Completion of the synthesis of 23-oxa-OSW-1 (**1**) and its congeners **2** and **3**. a) TPAP, NMO, 4-Å MS, CH_2Cl_2, RT, overnight. b) $NaBH_4$, $CeCl_3 \cdot 7H_2O$, THF, −10°C, then −40°C, MeOH, 15 min. c) TMSOTf (0.1 equiv), 4-Å MS, CH_2Cl_2, −20°C, 2 h. d) $[PdCl_2(MeCN)_2]$, acetone/water (20:1, v/v), RT, overnight. MBz = 4-methylbenzoyl, MS = molecular sieves, NMO = *N*-methylmorpholine *N*-oxide, TES = triethylsilyl, TMSOTf = trimethylsilyl trifluoromethanesulfonate, TPAP = tetrapropylammonium perruthenate.

Once the desired 17α-hydroxy-21α-methyl-22-one architecture had been constructed, synthesis of OSW-1 and its congeners was straightforward. However, we first turned our attention to the synthesis of the 23-oxa analogues of OSW-1, **1**–**3**, which we obtained from **8a–c** in four steps by employing transformations similar to those used in our previously described OSW-1 synthesis.[5] The results are shown in Scheme 4. Oxidation of the 16α-OH group of **8b** by treatment with TPAP/NMO[16] gave the 16-keto compound **10b** in 91% yield. Reduction of the resulting 16-ketone with $NaBH_4$ in the presence of $CeCl_3$ afforded 16β-ol **11b** stereoselectively in 81% yield. This reaction had to be quenched at −40°C, as higher temperatures resulted in the production of lactone **14**. The lactonization also took place in $CDCl_3$ during NMR measurement. Coupling of 16β,17α-diol **11b** with disaccharide imidate **12**[5] in the presence of TMSOTf (0.1 equiv) and 4-Å MS gave glycoside **13b** in a satisfactory yield (64%), without production of a significant amount of lactone **14**. Finally, deprotection of the silyl groups by treatment with $[PdCl_2(MeCN)_2]$[17] afforded the desired product **1** in 86% yield. The congeners **2** and **3**, which have a shorter or a longer side chain than **1**, were similarly prepared from **8a** and **8c**, respectively.

23-Oxa-OSW-1 (**1**) strongly suppressed the growth of the three types of malignant tumor cells tested. The concentration of **1** required for 50% inhibition (IC_{50}) was 0.031–3.1 μM, which indicates that this compound is as potent as OSW-1 and is 8–60 times more potent than the anticancer drug cisplatin in the assay we used (Table 1). The short congener **2** was slightly less potent than **1**. Interestingly, the longer congener **3** was considerably more potent than OSW-1 (as much as 25 times more potent against the human liver carcinoma cell line 7404).

Table 1: Cytotoxic activities of **1**–**3** and the controls OSW-1 and cisplatin against tumor cells.[a]

Tumor cells[b]	IC_{50} [μM]				
	1	**2**	**3**	OSW-1	cisplatin
AGS	3.10	11.82	0.40	1.42	24.1
7404	0.031	0.30	0.004	0.10	8.37
MCF-7	0.31	1.48	0.052	0.27	18.7

[a] The standard MTT assay was used (MTT = 3-(4,5-dimethylthiazol-2-yl)-2,5-diphenyltetrazolium bromide). The IC_{50} values determined for cisplatin against the three cell lines used in our assay are consistent with those determined by others.[15] [b] AGS = human stomach cancer cell line, 7404 = human liver carcinoma cell line, MCF-7 = human breast cancer cell line.

In summary, a novel and efficient approach to the construction of the 16β,17α-dihydroxycholest-22-one steroidal architecture characteristic of the saponin OSW-1 family was developed that uses an aldol condensation as the key reaction. Members of this family of compounds have exceptionally potent antitumor activities. The 23-oxa analogues of OSW-1 **1**–**3** were synthesized from the industrially produced steroid **4** in 26, 30, and 20% overall yield, respectively, by a

 © 2004 Wiley-VCH Verlag GmbH & Co. KGaA, Weinheim

linear eight-step procedure. The 23-oxa-OSW-1 (**1**) showed similar antitumor potency to that of OSW-1, while the longer congener **3** was even more potent. Progress toward an understanding of the SARs and antitumor mechanisms of OSW-1 saponins should be greatly accelerated by the development described herein. The results of our ongoing research will be reported in due course.

Received: March 11, 2004
Revised: June 2, 2004 [Z54237]

Keywords: aldol reaction · antitumor agents · OSW-1 analogues · saponins · synthetic methods

[1] S. Kubo, Y. Mimaki, M. Terao, Y. Sashida, T. Nikaido, T. Ohmoto, *Phytochemistry* **1992**, *31*, 3969.
[2] a) Y. Mimaki, M. Kuroda, A. Kameyama, Y. Sashida, T. Hirano, K. Oka, R. Maekawa, T. Wada, K. Sugita, J. A. Beutler, *Bioorg. Med. Chem. Lett.* **1997**, *7*, 633; b) A. M. Rouhi, *Chem. Eng. News* **1995**, *11*, 28.
[3] a) M. Kuroda, Y. Mimaki, A. Yokosuka, F. Hasegawa, Y. Sashida, *J. Nat. Prod.* **2002**, *65*, 1417; b) M. Kuroda, Y. Mimaki, A. Yokosuka, Y. Sashida, *Chem. Pharm. Bull.* **2001**, *49*, 1042; c) M. Kuroda, Y. Mimaki, A. Yokosuka, Y. Sashida, J. A. Beutler, *J. Nat. Prod.* **2001**, *64*, 88.
[4] C. Guo, P. L. Fuchs, *Tetrahedron Lett.* **1998**, *39*, 1099.
[5] S. Deng, B. Yu, Y. Lou, Y. Hui, *J. Org. Chem.* **1999**, *64*, 202.
[6] a) W. Yu, Z. Jin, *J. Am. Chem. Soc.* **2001**, *123*, 3369; b) W. Yu, Z. Jin, *J. Am. Chem. Soc.* **2002**, *124*, 6576.
[7] a) J. W. Morzycki, A. Gryszkiewicz, I. Jastrzebska, *Tetrahedron Lett.* **2000**, *41*, 3751; b) J. W. Morzycki, A. Wojtkielewicz, *Carbohydr. Res.* **2002**, *337*, 1269; c) Q. Xu, X. Peng, W. Tian, *Tetrahedron Lett.* **2003**, *44*, 9375.
[8] a) C. Guo, T. G. LaCour, P. L. Fuchs, *Bioorg. Med. Chem. Lett.* **1999**, *9*, 419; b) X. Ma, B. Yu, Y. Hui, Z. Miao, J. Ding, *Bioorg. Med. Chem. Lett.* **2001**, *11*, 2153; c) L. Deng, H. Wu, B. Yu, M. Jiang, J. Wu, *Bioorg. Med. Chem. Lett.* **2004**, *14*, 2781.
[9] M. T. Reetz, *Angew. Chem.* **1984**, *96*, 542; *Angew. Chem. Int. Ed. Engl.* **1984**, *23*, 556.
[10] a) H. E. Zimmerman, M. D. Traxler, *J. Am. Chem. Soc.* **1957**, *79*, 1920; b) W. A. Kleschick, C. T. Buse, C. H. Heathcock, *J. Am. Chem. Soc.* **1977**, *99*, 247; c) D. A. Evans, *Top. Stereochem.* **1982**, *13*, 1.
[11] D. Doller, E. G. Gros, *Synth. Commun.* **1990**, *20*, 3115.
[12] M. Numazawa, M. Nagaoka, Y. Osawa, *J. Org. Chem.* **1982**, *47*, 4024.
[13] a) R. E. Ireland, R. H. Mueller, *J. Am. Chem. Soc.* **1976**, *98*, 2891; b) R. E. Ireland, P. Wipf, J. D. Armstrong III, *J. Org. Chem.* **1991**, *56*, 650.
[14] J. Otera, Y. Fujita, S. Fukuzumi, *Synlett* **1994**, 213.
[15] See the Supporting Information.
[16] L. A. Paquette, H. Wang, Z. Su, M. Zhao, *J. Am. Chem. Soc.* **1998**, *121*, 5213.
[17] B. H. Lipshutz, D. Pollart, J. Monforte, H. Kotsuki, *Tetrahedron Lett.* **1985**, *26*, 705.

 © 2004 Wiley-VCH Verlag GmbH & Co. KGaA, Weinheim

Natural Products Synthesis

Stereocontrolled Total Synthesis of (+)-Streptazolin by a Palladium-Catalyzed Reductive Diyne Cyclization**

Barry M. Trost, Cheol K. Chung, and Anthony B. Pinkerton*

The palladium-catalyzed reductive diyne cyclization provides efficient access to dialkylidenecyclopentanes and -hexanes of defined geometry about the alkene.[1] Only one example of the synthetic utility of this atom-economic construction of dienes has recently been recorded with regard to a short synthesis of siccanin.[1b] To further demonstrate the efficiency of this approach, especially towards very sensitive 1,3-diene units, herein we describe the total synthesis of (+)-streptazolin, for which controlled generation of the delicate 1,3-diene constitutes a major challenge.

(+)-Streptazolin (**1**) is a lipophilic antibiotic, first isolated from cultures of *Streptomyces viridochromogenes* in 1981.[2] The tricyclic skeleton contains an internal urethane moiety, which is rarely found in natural products. Streptazolin exhibits only limited antimicrobial activities; however, structural variants such as 3,9-dihydrostreptazolin[2] and Diels–Alder adducts with naphthoquinones[3] show enhanced antimicrobial and cytotoxic activity. Owing to these biological properties as well as its interesting chemical structure, several studies have been reported aimed towards the synthesis of **1**[4–7] and related compounds.[8]

The first two reported syntheses of **1**[4,5] rely on Wittig reactions of a ketone to install the exocyclic ethylidene group which unfortunately gave a mixture of geometrical isomers and favored the undesired *E*-ethylidene stereoisomer. The third reported synthesis by Kibayashi and co-workers[6] utilizes an elegant enyne cycloisomerization[9] to construct the diene. This reaction, however, gave the 1,4-diene as the major product, which then had to be isomerized to the 1,3-diene by using an iron complex. A more recently reported synthesis[7] took advantage of another palladium-catalyzed reaction: an intramolecular reductive vinyl bromide–alkyne coupling reaction developed by Grigg.[10] This strategy, which required a number of functional-group modifications, suc-

[*] Prof. B. M. Trost, C. K. Chung, A. B. Pinkerton
Department of Chemistry, Stanford University
Stanford, CA 94305-5080 (USA)
Fax: (+1) 650-725-0002
E-mail: bmtrost@stanford.edu

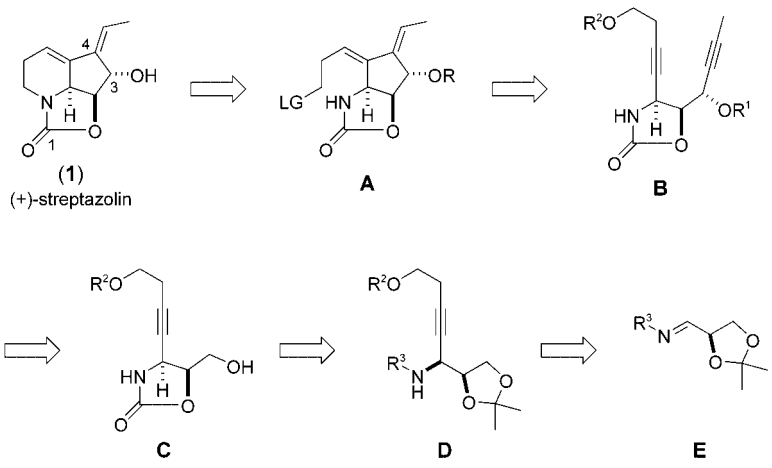
[**] We thank Professor D. L. Comins for kindly providing us with the spectroscopic data for **1**, and the National Institutes of Health (GM 033 049) and the National Science Foundation for their generous financial support. C.K.C. is a Stanford Graduate Fellow. Mass spectra were measured by the Mass Spectrometry Facility, University of San Francisco, supported by the NIH Division of Research Resources.

Supporting information for this article is available on the WWW under http://www.angewandte.org or from the author.

 DOI: 10.1002/anie.200460058 © 2004 Wiley-VCH Verlag GmbH & Co. KGaA, Weinheim

cessfully provided the desired 1,3-diene with the correct defined geometry.

Our goal was to provide a more efficient and atom-economical[11] approach to **1**, which is outlined in Scheme 1.



Scheme 1. Retrosynthetic analysis of (+)-streptazolin (**1**). LG = leaving group.

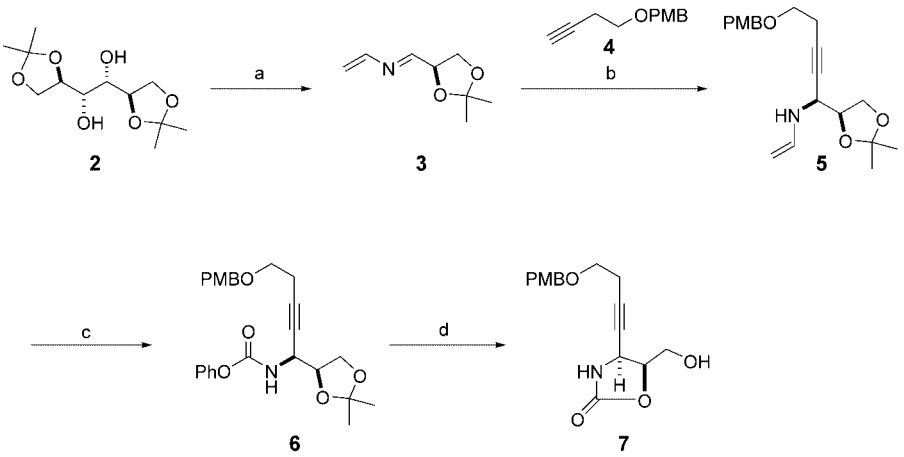
The target molecule **1** was envisioned to be obtained from the penultimate intermediate **A** through a cyclization of the oxazolidinone nitrogen center with an activated alcohol. The 1,3-diene **A** would come from the key palladium-catalyzed reductive diyne cyclization reaction of **B**, which itself results from the addition of an acetylide to an aldehyde derived from the alcohol **C**. The precursor of **C** would be a protected aminodiol **D**, which would come from the known imine derivative of D-glyceraldehyde acetonide **E**[12] in a series of straightforward steps.

The preparation of the oxazolidinone core of streptazolin is outlined in Scheme 2. Commercially available D-mannitol diacetonide (**2**) was subjected to oxidative cleavage with periodate followed by imine formation with allylamine.[13] The imine **3** was obtained in sufficiently pure form to be used in the subsequent reaction without further purification and was, therefore, treated directly with the metal alkynylide derived from the alkyne **4**.[14] Although the use of alkynyl Grignard reagents resulted in poor diastereofacial selection (< 2:1) and that of alkynyllithium trifluoroborate[15] showed rather capricious selectivity (2:1 ~ 12:1), the use of alkynyllithium trimethylaluminate[16] gave the desired Felkin–Anh adduct **5** with high diastereoselectivity and in good yield (13:1, 69%).

The protecting group of the amine (allyl group) needed to be removed at this stage because its cleavage would be problematic after the oxazolidinone was formed. The one-pot palladium-catalyzed removal of the allyl group[17] and formation of the carbamate gave **6** in nearly quantitative yield (Scheme 2). The carbamate **6** was, in turn, derivatized to the oxazolidinone compound **7** through sequential treatment with *p*-toluenesulfonic acid and potassium carbonate in methanol to give the oxazolidinone core in 88% yield after removal of the undesired diastereomer. These two sequences of one-pot procedures nicely circumvented the difficulty associated with the isolation of the polar compounds.

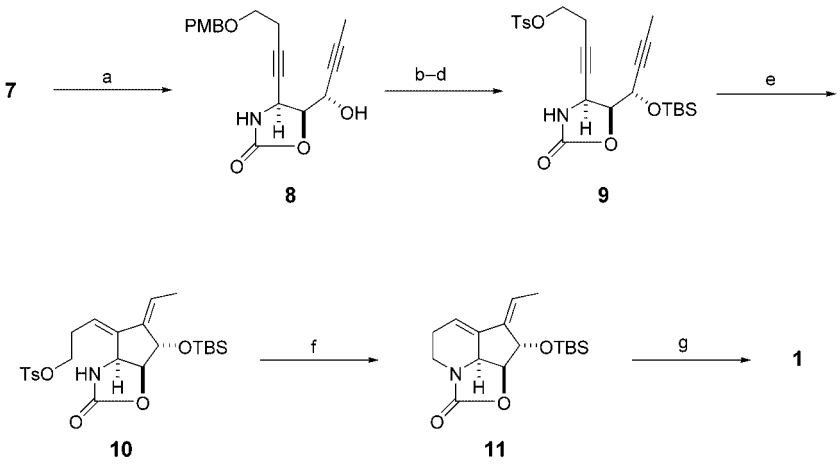
The alcohol **7** then needed to be oxidized to the corresponding aldehyde in the next step. Disappointingly, both Dess–Martin[18] and Moffatt–Swern[19] oxidation reactions were plagued with problems of epimerization and low yields after workup, presumably owing to the destabilization of the resultant aldehyde by the neighboring electronegative oxazolidinone group. The reaction mixture from the Moffatt–Swern oxidation reaction was treated directly with an excess amount of propynyl magnesium bromide in the presence of zinc chloride at low temperature to give a diastereomeric mixture (6:1) of the secondary alcohol **8** in 50% yield (Scheme 3).[20,8c] The two diastereomers were easily separated by flash chromatography after protection of the secondary alcohol as a silyl ether. The relative stereochemistry of the major diastereomer was unclear at this stage but was later confirmed (at the completion of the synthesis) to be the desired chelation-controlled product (Scheme 3). Interestingly, the use of an alkynyllithium–trimethylaluminate complex, which is known to favor Felkin–Anh addition, also gave the chelation-controlled product as the major diastereomer (≈4:1). This indicates that the Felkin–Anh mode of addition is unfavorable, even in the absence of a chelating metal species, owing to the steric hindrance by a neighboring substituent, which stretches along the trajectory of the incoming nucleophile (Scheme 4).

Deprotection of the PMB ether in **8**, followed by tosylation of the resultant primary alcohol, gave the diyne **9**, which set the stage for the crucial palladium-catalyzed reductive cyclization reaction (Scheme 3). Compound **9** was subjected to our standard

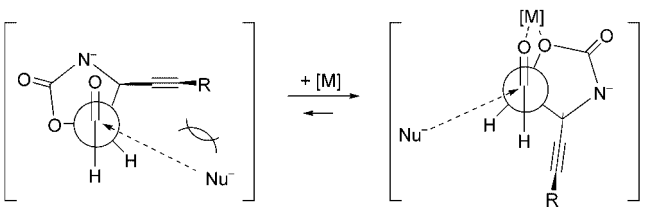


Scheme 2. Stereoselective construction of oxazolidinone core of **1**. Reagents and conditions: a) $NaIO_4$, H_2O, 0 °C; allylamine, 1,2-dichloroethane, 0 °C → RT, 95%; b) **4**, *n*BuLi, Me_3Al, toluene, −78 °C, then **3**, −78 °C → RT, 69%, d.r. = 13:1; c) $[Pd(dba)_2]$, dppb, 2-thiosalicylic acid, THF, 60 °C, then PhOCOCl, aqueous $NaHCO_3$, room temperature, 99%, d.r. = 13:1; d) *p*-TsOH, methanol, then K_2CO_3 (solid), room temperature, 88%. PMB = *p*-methoxybenzyl, dba = dibenzylideneacetone, dppb = 1,4-bis(diphenylphosphanyl)butane, Ts = *p*-toluenesulfonyl.

 © 2004 Wiley-VCH Verlag GmbH & Co. KGaA, Weinheim



Scheme 3. Total synthesis of (+)-streptazolin. Reagents and conditions: a) DMSO, $(COCl)_2$, Et_3N, CH_2Cl_2, −78 °C, then $ZnCl_2$, −78 °C, propynyl magnesium bromide, THF, −78 °C→RT, 50%, d.r. = 6:1; b) TBSCl, imidazole, CH_2Cl_2, room temperature, 75% (+13% C3 epimer); c) DDQ, aqueous CH_2Cl_2, 0 °C→RT, 93%; d) *p*-TsCl, pyridine, 0 °C→RT, 75%; e) $[Pd_2(dba)_3{\cdot}CHCl_3]$, HCO_2H, Et_3SiH, toluene, room temperature, 64%; f) NaH, THF, 0 °C→RT, 84%; g) TBAF, THF, 0 °C, 99%. DMSO = dimethylsulfoxide, TBSCl = *tert*-butyldimethylsilyl chloride, DDQ = 2,3-dichloro-5,6-dicyano-1,4-benzoquinone, TBAF = tetra-*n*-butylammonium fluoride.



Scheme 4. Proposed explanation for the stereoselectivity.

"ligandless" reductive cyclization conditions ($[Pd_2(dba)_3{\cdot}CHCl_3]$ 2.5%, HCO_2H, Et_3SiH, toluene, 80 °C) to provide the desired diene **10** in 61% yield. The nature of the primary alcohol group had a dramatic impact on the efficiency of the process. The reductive cyclization of the free alcohol or the mesylate, instead of the tosylate, yielded the corresponding diene products in only 15 and 41%, respectively. Lowering the reaction temperature to 23 °C gave a slightly higher yield of **10** (64%) along with some unconverted starting material **9** (7%).

Finally, an intramolecular cyclization through nucleophilic displacement of the tosylate **10** to form the third ring of the structure was required. The cyclization reaction took place smoothly in the presence of sodium hydride, and treatment of the resulting tricyclic compound **11** with TBAF gave the natural product (+)-streptazolin in near-quantitative yield. The spectroscopic data of the product prepared herein were indistinguishable from those reported in the literature,[6] and the specific rotation, $[\alpha]_D^{24} = +18.43$ ($c = 0.16$, $CHCl_3$), was also in good agreement ($[\alpha]_D^{23} = +22$ ($c = 2.8$, $CHCl_3$)).[2]

In conclusion, the total synthesis of (+)-streptazolin was performed in 11 steps starting from D-mannitol diacetonide. Our synthesis features a palladium-catalyzed reductive cyclization reaction of a diyne as the key step. The diyne precursor was constructed stereoselectively from the sequential additions of alkynylides to a chiral imine and aldehyde. The current strategy is atom economical and efficiently addresses the problems associated with the location and geometry of the double bonds. This synthesis also highlights the utility of the palladium-catalyzed cycloreduction reaction in the construction of complex and labile molecules.

Received: March 19, 2004
Revised: June 1, 2004 [Z460058]

Keywords: antibiotics · cyclization · natural products · palladium · total synthesis

[1] a) B. M. Trost, D. C. Lee, *J. Am. Chem. Soc.* **1988**, *110*, 7255; b) B. M. Trost, F. J. Fleitz, W. J. Watkins, *J. Am. Chem. Soc.* **1996**, *118*, 5146.
[2] H. Drautz, H. Zähner, E. Kupfer, W. Keller-Schierlein, *Helv. Chim. Acta* **1981**, *64*, 1752.
[3] S. Grabley, H. Kluge, H.-U. Hoppe, *Angew. Chem.* **1987**, *99*, 692; *Angew. Chem. Int. Ed. Engl.* **1987**, *26*, 664.
[4] A. Kozikowski, P. Park, *J. Am. Chem. Soc.* **1985**, *107*, 1763.
[5] C. Flann, L. E. Overman, *J. Am. Chem. Soc.* **1987**, *109*, 6115.
[6] H. Yamada, S. Aoyagi, C. Kibayashi, *J. Am. Chem. Soc.* **1996**, *118*, 1054.
[7] S. Huang, D. L. Comins, *Chem. Commun.* **2000**, 569.
[8] a) (±)-8α-Hydroxystreptazoline: I. Nomura, C. Mukai, *Org. Lett.* **2002**, *4*, 4301; b) (−)-4a,5-dihydrostreptazolin: H. Yamada, S. Aoyagi, C. Kibayashi, *Tetrahedron Lett.* **1996**, *37*, 8787; c) J. Cossy, I. Pevet, C. Meyer, *Synlett* **2000**, 122.
[9] a) B. M. Trost, *Acc. Chem. Res.* **1990**, *23*, 34; b) B. M. Trost, M. Krische, *Synlett* **1998**, 1.
[10] R. J. Grigg, *Heterocycl. Chem.* **1994**, *31*, 631.
[11] B. M. Trost, *Science* **1991**, *254*, 1471.
[12] R. Grigg, M. Thornton-Pett, J. Xu, L.-H. Xu, *Tetrahedron* **1999**, *55*, 13841.
[13] a) B. K. Banik, M. S. Manhas, Z. Kaluza, K. J. Barakat, A. K. Bose, *Tetrahedron Lett.* **1992**, *33*, 3603; b) D. R. Wagle, C. Garai, J. Chiang, M. G. Monteleone, B. E. Kurys, T. W. Strohmeyer, V. R. Hedge, M. S. Manhas, A. K. Bose, *J. Org. Chem.* **1988**, *53*, 4232.
[14] For a review, see: R. Bloch, *Chem. Rev.* **1998**, *98*, 1407.
[15] K. B. Aubrecht, M. D. Winemiller, D. B. Collum, *J. Am. Chem. Soc.* **2000**, *122*, 11084, and references therein.
[16] D. A. Cogan, J. A. Ellman, *J. Am. Chem. Soc.* **1999**, *121*, 268.
[17] S. Lemaire-Audoire, M. Savignac, J. P. Genet, *Tetrahedron Lett.* **1995**, *36*, 1267.
[18] D. B. Dess, J. C. Martin, *J. Org. Chem.* **1983**, *48*, 4155.
[19] A. J. Mancuso, D. Swern, *Synthesis* **1981**, 165.
[20] a) R. E. Ireland, D. W. Norbeck, *J. Org. Chem.* **1985**, *50*, 2198; b) M. D. Lewis, J. P. Duffy, J. V. Heck, R. Menes, *Tetrahedron Lett.* **1988**, *29*, 2279.

 © 2004 Wiley-VCH Verlag GmbH & Co. KGaA, Weinheim

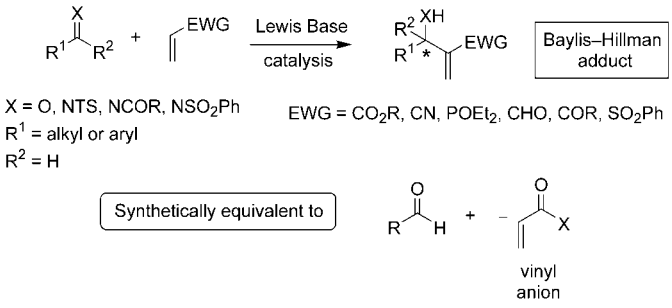
Reaction Mechanisms

Probing the Mechanism of the Baylis–Hillman Reaction by Electrospray Ionization Mass and Tandem Mass Spectrometry**

Leonardo Silva Santos, Cesar Henrique Pavam, Wanda P. Almeida, Fernando Coelho, and Marcos N. Eberlin**

The search for efficient methodologies to form C–C bonds continues to challenge chemists who face the construction of organic molecules of increasing complexity and functions. Multifaceted functional-group transformations and the creation and control of new asymmetric centers are key steps in the total synthesis of organic molecules, with special emphasis on catalytic activation.[1] Atom economy and high chemo-, regio-, and stereoselectivity are also essential requisites of new, efficient synthetic reactions.[2]

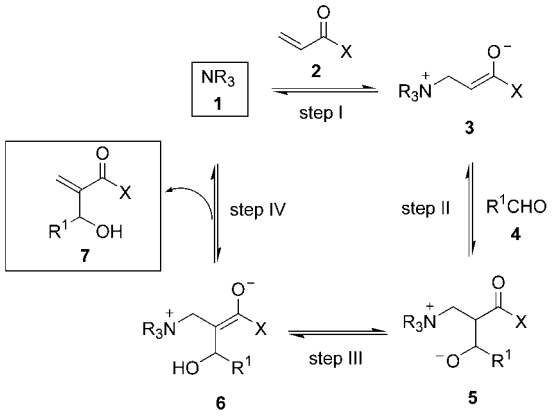
Within this scenario, the Baylis–Hillman reaction (Scheme 1) has recently experienced an enormous growth in importance and use.[3] This versatile multicomponent reaction was first described by Morita et al.[4] and later, in a German patent, by Baylis and Hillman.[5] The reaction leads to the straightforward formation of new σ C–C bonds in a single step, and yields densely functionalized molecules (α-methylene-β-hydroxy derivatives), which are then conveniently manipulated as key synthons in the synthesis of a variety of natural and nonnatural products.[6]



Scheme 1. General scope of the Baylis–Hillman reaction.

The Baylis–Hillman reaction can be broadly defined as a coupling reaction between an alkene activated by an electron-withdrawing group and an electrophile (Scheme 1) that occurs under Lewis base catalysis, with 1,4-diazabicyclo[2.2.2]octane (DABCO) normally used as the base.[3] Formally, the reaction is synthetically equivalent to the addition of a vinyl anion to an aldehyde.

Several mechanistic considerations and kinetic studies led to the general acceptance of the Baylis–Hillman catalytic cycle summarized in Scheme 2. This mechanism was initially proposed by Hill and Isaacs,[7a] and later refined by others.[7b–d]



Scheme 2. Currently accepted catalytic cycle for the Baylis–Hillman reaction.

According to Scheme 2, the first reaction step I consists of the 1,4-addition of the catalytic tertiary amine **1** to the activated alkene **2** (α,β-unsaturated carbonyl compounds), which generates the zwitterion intermediate **3**. In step II, **3** adds to aldehyde **4** by an aldolic addition reaction to yield intermediate **5**. Step III involves an intramolecular prototropic shift within **5** to form intermediate **6**, which in step IV forms the final Baylis–Hillman adduct **7** through E2 or E1cb elimination in the presence of a Lewis base. The last step IV returns catalyst **1** to the catalytic cycle. The reaction rate seems to be determined by step II because the dipole moment is increased by further charge separation.

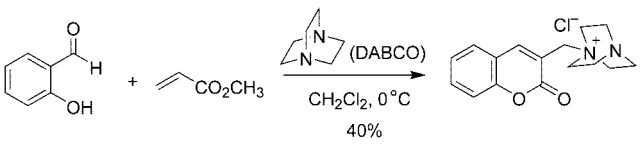
Despite its increasing importance and use, up to now only a single experimental study has collected evidence for the catalytic cycle of the Baylis–Hillman reaction. Drewes et al.[8] carried out the reaction of methyl acrylate with 2-hydroxybenzaldehyde in dichloromethane at 0 °C in the presence of DABCO (Scheme 3), isolated a type-**6** intermediate (Scheme 2) as a coumarin salt, and characterized the salt by X-ray crystallography.

Molecular analysis by mass spectrometry (MS) has greatly benefited from the development of electrospray ionization (ESI),[9] since molecules and supramolecules[10] of high polarity, molecular complexity, and/or mass can be easily ionized by ESI for investigation by MS. ESI is an interesting "ion-

[*] C. H. Pavam, Dr. F. Coelho
Laboratory of Synthesis of Natural Products and Drugs
Institute of Chemistry, State University of Campinas
UNICAMP, 13083-970 Campinas, SP (Brazil)
Fax: (+55) 19-3788-3023
E-mail: coelhp@iqm.unicamp.br
Dr. L. S. Santos, Dr. M. N. Eberlin
Thomson Mass Spectrometry Laboratory
Institute of Chemistry, State University of Campinas
UNICAMP, 13083-970 Campinas, SP (Brazil)
Fax: (+55) 19-3788-3073
E-mail: eberlin@iqm.unicamp.br
W. P. Almeida
Graduate Program in Cellular and Structural Biology
Institute of Biology, State University of Campinas
UNICAMP, 13083-970 Campinas, SP (Brazil)

[**] We thank the São Paulo State Research Foundation (FAPESP) and the Brazilian National Research Council (CNPq) for financial support. F.C. and M.N.E. thank CNPq, and C.H.P. and L.S.S. thank FAPESP for research fellowships.

 © 2004 Wiley-VCH Verlag GmbH & Co. KGaA, Weinheim DOI: 10.1002/anie.200460059



Scheme 3. The single Baylis–Hillman intermediate so far isolated and characterized by X-ray crystallography.

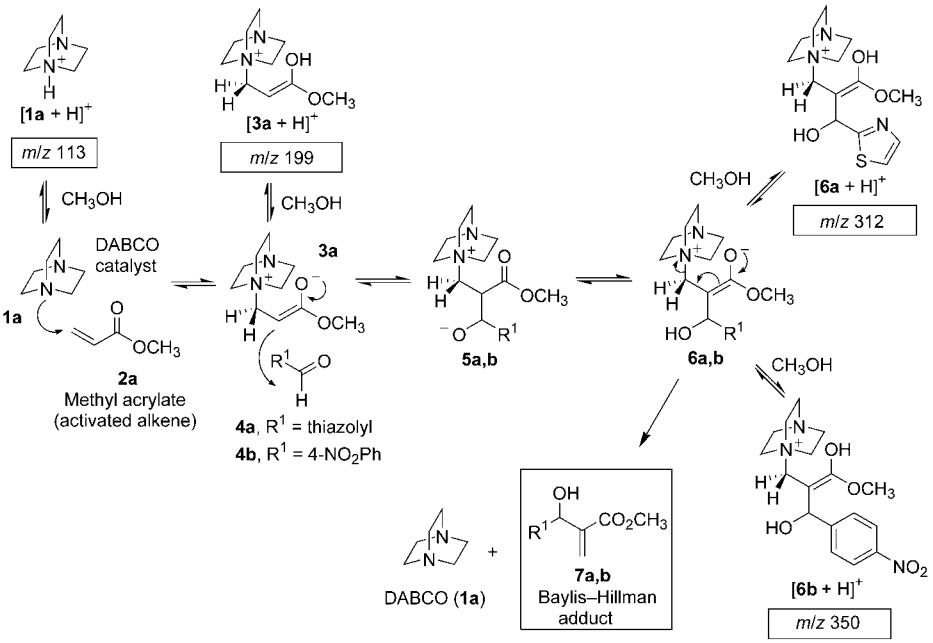
fishing" technique, since it gently transfers preformed ions directly from solution to the gas phase. ESI-MS (and its tandem version ESI-MS/MS) is rapidly becoming the technique of choice for solution mechanistic studies in chemistry and biochemistry[11], and in high-throughput screening of homogeneous catalysis reactions.[12]

Several neutral zwitterionic intermediates are involved in the currently accepted mechanism for the Baylis–Hillman reaction of acrylates with aldehydes catalyzed by DABCO (Scheme 2). However, these neutral species are expected to be in equilibrium with their protonated forms in methanolic solution. ESI-MS/MS appears therefore to be the ideal technique to probe the Baylis–Hillman reaction mechanism and catalytic cycle, since ESI could "fish" (with high sensitivity) such cationic intermediates directly from solution to the gas phase for their unprecedented MS interception, mass analysis, and MS/MS structural characterization. Herein, we describe the results of an ESI-MS/MS study aimed at detecting and structurally characterizing the putative intermediates of the Baylis–Hillman reaction.

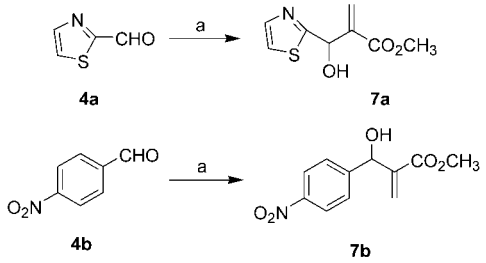
Our investigation began with the ESI-MS monitoring[13] of the reaction of methyl acrylate with two aldehydes (**4a** and **4b**, Scheme 4) catalyzed by DABCO in methanol.[14] The aim was to intercept the cationic species resulting from the proton-exchange equilibrium with methanol using ESI-MS in the positive-ion mode (Scheme 5). ESI is known for its ability to transfer ions to the gas phase without inducing undesirable side reactions,[9] and the composition of ESI-generated ions often closely reflects that in solution.[10,15] We then mixed DABCO (0.65 equiv), methyl acrylate (1.30 equiv), and the respective aldehyde (1.00 equiv) in methanol (2 mL), and monitored the reaction by ESI-MS using a microsyringe pump to deliver the methanol solution directly to the ESI source at flow rates of 0.01 mL min^{-1}.

The cationic reaction intermediates are likely to be in equilibrium with their respective neutral zwitterionic forms in methanolic solutions, and even disfavored equilibria could be useful because of the high sensitivity of ESI-MS analysis. Indeed, the ESI-MS spectra collected for such reactions are extraordinarily clean and mechanistically enlightening. Shortly after one to five minutes of reaction of aldehyde **4a**, three covalently bonded cationic species directly related to the proposed Baylis–Hillman catalytic cycle (Scheme 5) are detected as major ions (Figure 1a): [**1a**+H]$^+$ of *m*/*z* 113, [**3a**+H]$^+$ of *m*/*z* 199, and [**6a**+H]$^+$ of *m*/*z* 312. The ESI-MS spectrum for the reaction of aldehyde **4b** (Figure 1b) shows two of the same major ions, [**1a**+H]$^+$ of *m*/*z* 113 and [**3a**+H]$^+$ of *m*/*z* 199 but, as expected, [**6a**+H]$^+$ of *m*/*z* 312 from aldehyde **4a** was replaced by [**6b**+H]$^+$ of *m*/*z* 350 from aldehyde **4b** (Scheme 5). The formation of covalent species is indicated by the relatively high kinetic energy of gas-phase ions transferred from the ESI source into the mass spectrometer (acceleration cone voltage of 40–45 V), and the optimized declustering properties of the ESI source. Under such conditions, loosely bonded species should not survive.

All these intermediates, so gently transferred to the gas phase by ESI in their intact protonated forms, were then individually mass-selected by quadrupole Q1 for collision-induced dissociation (CID) with nitrogen in quadrupole q2, and were structurally characterized by tandem mass spectro-



Scheme 5. Baylis–Hillman reaction of methyl acrylate and aldehydes catalyzed by DABCO. The protonated species expected to be intercepted and structurally characterized by ESI(+)-MS/MS, with their respective *m*/*z* ratios.



Scheme 4. Baylis–Hillman reactions monitored by ESI(+)-MS/MS. Reagents and conditions: a) DABCO (**1a**), methyl acrylate (**2a**), MeOH, RT.

 © 2004 Wiley-VCH Verlag GmbH & Co. KGaA, Weinheim

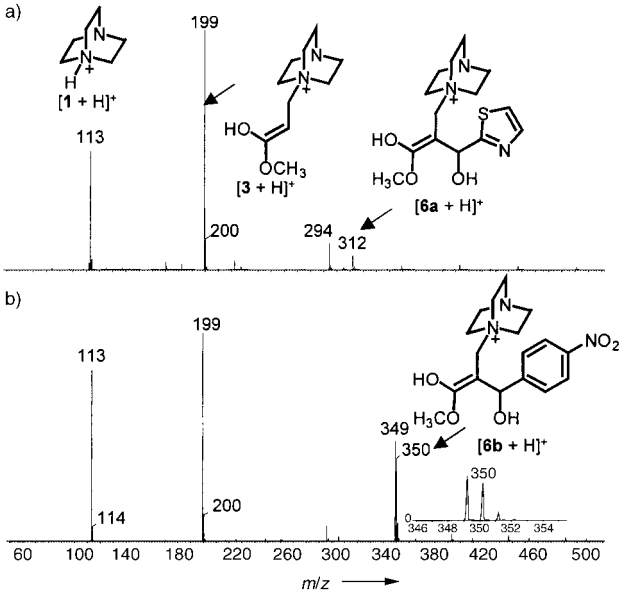


Figure 1. ESI(+)-MS spectra for the Baylis–Hillman reaction of methyl acrylate with aldehydes a) **4a** and b) **4b** catalyzed by DABCO. Other unidentified ions are likely to correspond to either impurities (favorably ionized under positive-ion ESI) or side-reaction products.

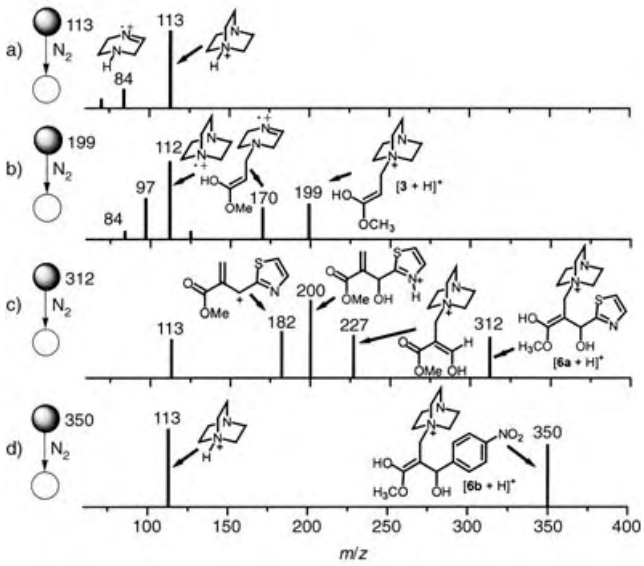


Figure 2. ESI(+)-MS/MS spectra of a) protonated DABCO $[\mathbf{1}+H]^+$ and intermediates, b) $[\mathbf{3}+H]^+$, c) $[\mathbf{6a}+H]^+$, and d) $[\mathbf{6b}+H]^+$. In the terminology used to describe the tandem mass spectrometric experiments, the circle represents a mass analyzer that transmits either an ion with a fixed *m*/*z* ratio (filled circle) or variable *m*/*z* ratio (open circle). The arrow indicates the ion course, with mass changes being caused by dissociative collisions with a neutral gas (N_2). For more details, see reference [19].

metric (MS/MS) analysis.[13] The relatively high resistance toward CID (15–30 eV collisions with nitrogen were needed to promote dissociation) and the diverse dissociation chemistry displayed by such ionic products cause loosely bonded adducts, such as proton-bonded dimers $[M_1\cdots H\cdots M_2]^+$, to be discarded. Noncovalently bonded adducts would dissociate exclusively or nearly exclusively to form either M_1H^+ or M_2H^+, or both.[16] The ESI-MS/MS spectra show that protonated DABCO $[\mathbf{1a}+H]^+$ of *m*/*z* 113 loses an ethyl radical to form the fragment ion of *m*/*z* 84 (Figure 2a). Intermediate $[\mathbf{3a}+H]^+$ of *m*/*z* 199 also loses an ethyl radical, probably from the DABCO moiety, to form the fragment ion of *m*/*z* 170 (Figure 2b). However, the main dissociation routes of $[\mathbf{3a}+H]^+$ lead to ionized DABCO of *m*/*z* 112, which dissociates in turn by the loss of a methyl radical to form the ion of *m*/*z* 97.

Intermediate $[\mathbf{6b}+H]^+$ of *m*/*z* 350 dissociates nearly exclusively by the loss of neutral **7b** to yield protonated DABCO $[\mathbf{1a}+H]^+$ of *m*/*z* 113 (Figure 2d). Therefore, there is an interesting close analogy between this CID process and the final Baylis–Hillman reaction step that affords **7b** by the release of neutral DABCO (Scheme 5). The analogue intermediate $[\mathbf{6b}+H]^+$ of *m*/*z* 312 also dissociates by the loss of neutral **7a** to yield $[\mathbf{1a}+H]^+$ of *m*/*z* 113 (Figure 2c), but several other dissociation channels are available to $[\mathbf{6a}+H]^+$ for which R^1 = thiazolyl. This ion can dissociate by the loss of neutral thiazole to form the fragment ion of *m*/*z* 227, which dissociates in turn by the loss of neutral DABCO and then water to give ions of *m*/*z* 200 and 182, respectively.

In conclusion, the proposed intermediates for the catalytic cycle of the Baylis–Hillman reaction (**3**–**5**/**6**, Schemes 2 and 5) have been successfully intercepted and structurally characterized for the first time using electrospray ionization with mass and tandem mass spectrometry. Strong evidence for the currently accepted mechanism has been collected, thus confirming the proposals initially made by Isaacs and Hill and refined later by others. Studies aimed at intercepting key cationic intermediates of Baylis–Hillman reactions catalyzed by Lewis acids, such as those described by Aggarwal et al.,[17] and of reactions performed in ionic liquids as solvents for which contradictory conclusions have been reached,[18] are under way.

Received: March 19, 2004 [Z460059]

Keywords: aldehydes · alkenes · electrophilic addition · mass spectrometry · reaction mechanisms

[1] a) K. C. Nicolaou, D. Vourloumis, N. Winssinger, P. S. Baran, *Angew. Chem.* **2000**, *112*, 46–126; *Angew. Chem. Int. Ed.* **2000**, *39*, 44–122; b) E. J. Corey, *Angew. Chem.* **1991**, *103*, 469–479; *Angew. Chem. Int. Ed. Engl.* **1991**, *30*, 455–465.

[2] B. M. Trost, *Angew. Chem.* **1995**, *107*, 285–307; *Angew. Chem. Int. Ed. Engl.* **1995**, *34*, 259–281, and references therein.

[3] For comprehensive reviews on the Baylis–Hillman reaction see: a) D. Basavaiah, A. J. Rao, T. Satyanarayama, *Chem. Rev.* **2003**, *103*, 811–891; b) W. P. Almeida, F. Coelho, *Quim. Nova* **2000**, *23*, 98–101 [*Chem. Abstr.* **2000**, *132*, 236562e]; c) E. Ciganek, *Org. React.* **1997**, *51*, 201–350; d) D. Basavaiah, P. D. Rao, R. S. Hyma, *Tetrahedron* **1996**, *52*, 8001–8062.

[4] K. Morita, Z. Suzuki, H. Hirose, *Bull. Chem. Soc. Jpn.* **1968**, *41*, 2815–2815.

[5] A. B. Baylis, M. E. D. Hillman, German Patent 2155113, **1972** [*Chem. Abstr.* **1972**, *77*, 34174q].

[6] For some examples see: a) W. P. Almeida, F. Coelho, *Tetrahedron Lett.* **2003**, *44*, 937–940; b) M. A. Feltrin, W. P. Almeida,

 © 2004 Wiley-VCH Verlag GmbH & Co. KGaA, Weinheim

Synth. Commun. **2003**, *33*, 1141 – 1146; c) R. C. Rossi, F. Coelho, *Tetrahedron Lett.* **2002**, *43*, 2797 – 2800; d) C. R. Mateus, M. P. Feltrin, A. M. Costa, F. Coelho, W. P. Almeida, *Tetrahedron* **2001**, *57*, 6901 – 6908; e) Y. Iwabuchi, M. Furukawa, T. Esumi, S. Hatakeyama, *Chem. Commun.* **2001**, 2030 – 2031; f) Y. Iwabuchi, T. Sugihara, T. Esumi, S. Hatakeyama, *Tetrahedron Lett.* **2001**, *42*, 7867 – 7871; g) A. Masunari, G. Trazzi, E. Ishida, F. Coelho, W. P. Almeida, *Synth. Commun.* **2001**, *31*, 2100 – 2109; h) F. Ameer, S. E. Drewes, M. S. Houston-McMillan, P. T. S. Kaye, *S. Afr. J. Chem.* **1986**, *39*, 57 – 63; i) H. M. R. Hofmann, J. Rabe, *Helv. Chim. Acta* **1984**, *67*, 413 – 415; j) H. M. R. Hofmann, J. Rabe, *J. Org. Chem.* **1985**, *50*, 3849 – 3859; k) S. E. Drewes, N. D. Emslie, *J. Chem. Soc. Perkin Trans. 1* **1982**, 2079 – 2083.

[7] a) J. S. Hill, N. S. Isaacs, *J. Phys. Org. Chem.* **1990**, *3*, 285 – 290; b) H. M. R. Hoffman, J. Rabe, *Angew. Chem.* **1983**, *95*, 795 – 796; *Angew. Chem. Int. Ed. Engl.* **1983**, *22*, 796 – 797; c) P. T. Kaye, M. L. Bode, *Tetrahedron Lett.* **1991**, *32*, 5611 – 5614; d) Y. Fort, M.-C. Berthe, P. Caubère, *Tetrahedron* **1992**, *48*, 6371 – 6384.

[8] S. E. Drewes, O. L. Njamela, N. D. Emslie, N. Ramesar, J. S. Field, *Synth. Commun.* **1993**, *23*, 2807 – 2815.

[9] a) C. M. Whitehouse, R. N. Dreyer, M. Yamashita, J. B. Fenn, *Anal. Chem.* **1985**, *57*, 675 – 679; b) J. B. Fenn, M. Mann, C. K. Meng, S. F. Wong, C. M. Whitehouse, *Science* **1989**, *246*, 64 – 71; c) R. B. Cole, *Electrospray Ionization Mass Spectroscopy*, Wiley, New York, **1997**.

[10] a) R. G. Cooks, D. X. Zhang, K. J. Koch, F. C. Gozzo, M. N. Eberlin, *Anal. Chem.* **2001**, *73*, 3646 – 3655; b) Z. Takats, S. C. Nanita, R. G. Cooks, *Angew. Chem.* **2003**, *115*, 3645 – 3647; *Angew. Chem. Int. Ed.* **2003**, *42*, 3521 – 3523; c) M. N. Eberlin, F. C. Gozzo, C. S. Consorti, J. Dupont, *Chem. Eur. J.* **2004**, in press.

[11] a) K. J. Koch, F. C. Gozzo, S. C. Nanita, Z. Takats, M. N. Eberlin, R. G. Cooks, *Angew. Chem.* **2002**, *114*, 1797 – 1800; *Angew. Chem. Int. Ed.* **2002**, *41*, 1721 – 1724; b) E. C. Meurer, A. A. Sabino, M. N. Eberlin, *Anal. Chem.* **2003**, *75*, 4701 – 4709; c) R. G. Cooks, D. X. Zhang, K. J. Koch, F. C. Gozzo, M. N. Eberlin, *Anal. Chem.* **2001**, *73*, 3646 – 3655; d) J. Griep-Raming, S. Meyer, T. Bruhn, J. O. Metzger, *Angew. Chem.* **2002**, *114*, 2863 – 2866; *Angew. Chem. Int. Ed.* **2002**, *41*, 2738 – 2742; e) A. A. Sabino, A. H. L. Machado, C. R. D. Correia, M. N. Eberlin, *Angew. Chem.* **2004**, *116*, 2568 – 2572; *Angew. Chem. Int. Ed.* **2004**, *43*, 2514 – 2518; f) S. Meyer, J. O. Metzger, *Anal. Bioanal. Chem.* **2003**, *377*, 1108 – 1114; g) M. N. Eberlin, J. B. Domingos, E. Longhinotti, T. A. S. Brandão, C. A. Bunton, L. S. Santos, F. Nome, *J. Org. Chem.* **2004**, in press.

[12] a) C. Hilderling, C. Adlhart, P. Chen, *Angew. Chem.* **1998**, *110*, 2831 – 2835; *Angew. Chem. Int. Ed.* **1998**, *37*, 2685 – 2689; b) P. Chen, *Angew. Chem.* **2003**, *115*, 2938 – 2954; *Angew. Chem. Int. Ed.* **2003**, *42*, 2832 – 2847.

[13] The mass spectrometer was a high-resolution hybrid double quadrupole (Qq) and orthogonal time-of-flight (TOF) mass spectrometer (QTOF, Micromass UK). The temperature of the nebulizer was 50 °C. The ESI source and the mass spectrometer were operated in the positive-ion mode. The cone and extractor potentials were set to 40–45 and 5–10 V, respectively. The scan range was m/z 50–1000.

[14] a) W. P. Almeida, F. Coelho, *Tetrahedron Lett.* **1998**, *39*, 8609 – 8612; b) F. Coelho, W. P. Almeida, C. R. Mateus, D. Veronese, E. C. S. Lopes, G. P. C. Silveira, R. C. Rossi, C. H. Pavam, *Tetrahedron* **2002**, *58*, 7437 – 7447; c) F. Coelho, E. C. S. Lopes, D. Veronese, R. C. Rossi, *Tetrahedron Lett.* **2003**, *44*, 5731 – 5735; d) F. Coelho, W. P. Almeida, C. R. Mateus, L. D. Furtado, J. C. F. Gouveia, *ARKIVOC* **2003**, *X*, 443 – 467.

[15] a) D. M. Tomazela, F. C. Gozzo, G. Eberling, J. Dupont, M. N. Eberlin, *Inorg. Chim. Acta* **2004**, *357*, 2349 – 2357; b) B. A. da Silveira Neto, G. Ebeling, R. S. Gonçalves, F. C. Gozzo, M. N. Ebelin, J. Dupont, *Syntheses* **2004**, 1155 – 1158; c) R. M. S. Pereira, V. I. Paula, R. Buffon, D. M. Tomazela, M. N. Eberlin, *Inorg. Chim. Acta* **2004**, *357*, 2100 – 2106.

[16] Cleavage of electrostatic ion/neutral interactions such as those operating in proton-bonded dimers has been shown to be invariably much more efficient than the breaking of stronger covalent bonds of gas-phase ions, see for example: a) R. G. Cooks, P. S. H. Wong, *Acc. Chem. Res.* **1998**, *31*, 379 – 386; b) M. N. Eberlin, T. Kotiaho, B. J. Shay, S. S. Yang, R. G. Cooks, *J. Am. Chem. Soc.* **1994**, *116*, 2457 – 2465.

[17] V. K. Aggarwal, A. Mereu, G. J. Tarver, R. McCague, *J. Org. Chem.* **1998**, *63*, 7183 – 7189.

[18] a) J. N. Rosa, C. A. M. Afonso, A. G. Santos, *Tetrahedron* **2001**, *57*, 4189 – 4193; b) V. K. Aggarwal, I. Emme, A. Mereu, *Chem. Commun.* **2002**, 1612 – 1613.

[19] M. N. Eberlin, *Mass Spectrom. Rev.* **1997**, *16*, 113 – 144.

 © 2004 Wiley-VCH Verlag GmbH & Co. KGaA, Weinheim

Enantioselective Reactions

Synthesis and Stereoselective Lithiation of Enantiopure 2-(1-Aminoalkyl)aziridine–Borane Complexes**

José M. Concellón, José Ramón Suárez, Santiago García-Granda, and M. Rosario Díaz*

Ammonium salts are an important class of organic compounds with useful synthetic applications.[1] A limited number of syntheses of enantiopure ammonium salts, in which the nitrogen atom is tetrasubstituted by four different groups, have been reported.[2] In addition, formation of amine–borane complexes is a useful strategy to efficiently carry out regioselective metalations, and other functionalizations, of amines when direct metalation is not possible.[3] Amine–borane complexes have also been used to perform reductive amination of aldehydes[4] and ketones,[4a,5] to reduce ketones and imines,[6] and in hydroboration of alkenes.[5]

We have previously described the synthesis of enantiopure 2-(1-aminoalkyl)aziridines **1** (Scheme 1).[7] Subsequently, we reported their ring opening by several nucleophiles[8] with total regio- and stereoselectivity. Now, we

[*] Dr. J. M. Concellón, J. R. Suárez
Departamento de Química Orgánica e Inorgánica
Facultad de Química, Universidad de Oviedo
33071 Oviedo (Spain)
Fax: (+34) 98-510-3446
E-mail: jmcg@fq.uniovi.es
Dr. S. García-Granda, Dr. M. R. Díaz
Departamento de Química Física y Analítica
Facultad de Química, Universidad de Oviedo
33071 Oviedo (Spain)

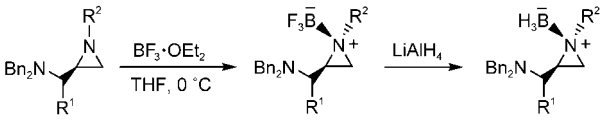
[**] We thank the Ministerio de Ciencia y Tecnología (BQU2001-3807) for financial support and J. S. Hartman for his assistance with the preparation of the manuscript. J.M.C. thanks Carmen Fernández-Flórez for her help.

Supporting information for this article is available on the WWW under http://www.angewandte.org or from the author.

 DOI: 10.1002/anie.200460120 © 2004 Wiley-VCH Verlag GmbH & Co. KGaA, Weinheim

describe the first method for the selective formation of the aziridine–borane complex **2** by treatment of (2*S*,1′*S*)-2-(1′-aminoalkyl)aziridines **1** with $BF_3{\cdot}Et_2O$ and subsequent reduction with $LiAlH_4$. Direct reaction of **1** with borane afforded the same (1*R*,2*S*,1′*S*)-2-(1′-dibenzylaminoalkyl)aziridine(N^1–B) boranes **2**. In both syntheses, only one diastereoisomer of complexes **2** was obtained in an enantiopure form. Subsequent lithiation, deuteration, or silylation and decomplexation of the obtained aziridinioborane complexes **2** afforded 3-deuterated or 3-silylated aminoaziridines **7b** or **8b** (Scheme 4) with total regio- and very high diastereoselectivity.

Treatment of a solution of aminoaziridines **1** in THF with one equivalent of $BF_3{\cdot}Et_2O$ at 0 °C for 5 minutes, followed by the addition of two equivalents of $LiAlH_4$, at the same temperature, for 30 minutes afforded, after hydrolysis, enantiopure (1*R*,2*S*,1′*S*)-2-(1′-dibenzylaminoalkyl)aziridine(N^1–B) boranes **2** as the sole product in high yield (Scheme 1 and Table 1). To the best of our knowledge, this method of obtaining amine–borane complexes is novel.



1 3 2

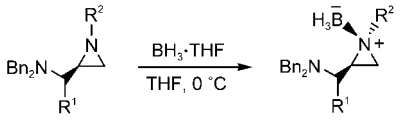
Scheme 1. Synthesis of aziridine–borane complexes **2** with $BF_3{\cdot}OEt_2$ and $LiAlH_4$. Bn = benzyl.

Table 1: Synthesis of aminoalkylaziridine–borane complexes **2**.

Entry	2	Method[a]	R^1	R^2	Yield [%][b]
1	**2a**	B	Me	propyl	79
2	**2b**	A	Me	allyl	76
3	**2b**	B	Me	allyl	80
4	**2c**	A	*i*Bu	allyl	75
5	**2d**	A	*i*Bu	Bn	81
6	**2d**	B	*i*Bu	Bn	77
7	**2e**	B	Bn	cyclohexyl	77
8	**2f**	A	Bn	Bn	83
9	**2f**	B	Bn	Bn	82

[a] Method A: $BF_3{\cdot}OEt_2$ and $LiAlH_4$. Method B: $BH_3{\cdot}THF$. [b] Yield of isolated product after column chromatography based on the starting aminoaziridine **1**.

When the complexation of aminoaziridines **1** was performed with a commercial $BH_3{\cdot}THF$ solution, the same borane complexes **2** were also isolated in high yield (Scheme 2 and Table 1).[3a] A similar yield and purity of complexes **2** (Table 1) was obtained with both methodologies and, consequently, the cheaper $BF_3{\cdot}Et_2O/LiAlH_4$ methodology is a valuable alternative to the use of $BH_3{\cdot}THF$ solution.



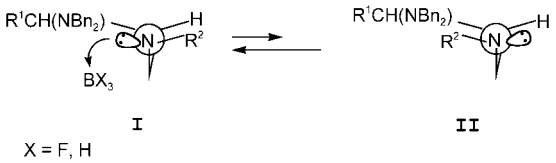
1 2

Scheme 2. Synthesis of aziridine–borane complexes **2** with $BH_3{\cdot}THF$.

Complexes **2** are surprisingly stable; they can be purified by column chromatography and stored for several weeks at room temperature. It is noteworthy that only one diastereoisomer of **2** was obtained, in an enantiopure form, with no apparent presence of any other diastereoisomers by NMR analysis of the crude reaction mixture (^1H NMR: 300 MHz, ^{13}C NMR: 75 MHz). It is clear that the level of diastereoisomeric purity of the borane–aziridine complexes **2** (> 97 %) was not affected by the size of R^1 and R^2 in the starting aminoaziridine (see Table 1). In contrast, previous work involving the reaction of tertiary amines with borane gave a mixture of diastereoisomers.[3d,9]

The orientations of the benzyl and the borane groups in **2d** were determined by a NOESY analysis. Positive NOESY interactions were observed between the methylene hydrogen atoms of the benzyl group and C2-H as well as with the C3-H, which is *cis* with respect to the aziridinium ring, thus confirming the *trans* relationship between the benzyl group and the 1-dibenzylaminoalkyl group. This configurational assignment of **2d**, as depicted in Schemes 1 and 2, was subsequently confirmed by single-crystal X-ray diffraction analysis.[10] The configuration of the other complexes **2** was assigned by analogy.

The described transformation and the observed stereochemistry of products **2** may be explained by assuming that coordination of either the Lewis acid ($BF_3{\cdot}Et_2O$) or BH_3 to the aziridine nitrogen atom is favored over coordination to the dibenzylamine nitrogen atom as a result of steric hindrance. The isolation of complexes **2** as a single diastereoisomer can be explained by taking into account the difference in stability between the two diastereoisomers **I** and **II** (Scheme 3): **I** predominates over **II** as a consequence of the steric hindrance involved, thus the reaction of **I** with $BF_3{\cdot}Et_2O$ or BH_3 is favored.[11]



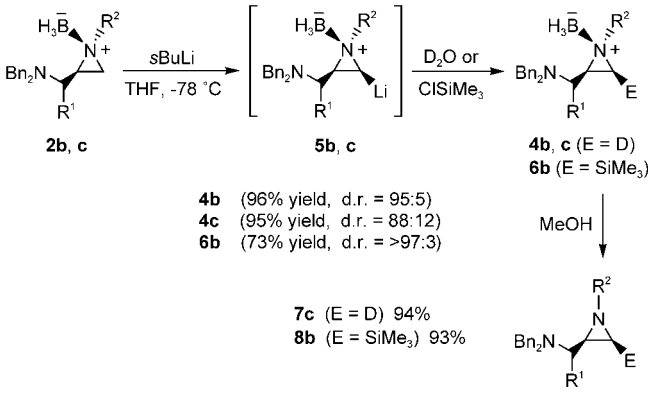
Scheme 3. Configurational equilibrium.

Aziridines are important building-blocks in organic synthesis,[12] and taking into account the usefulness of isotopically labeled compounds to establish the mechanism of organic reactions or the biosynthesis of many natural products,[13] the development of an effective general method for the stereoselective deuteration of aziridine would be of significant value. In addition, to the best of our knowledge only two papers describing the enantioselective lithiation of aziridines have been published previously.[3a,14] For this reason, preliminary attempts to deuterate complexes **2** were performed. Thus, lithiation experiments of complexes **2b,c** were carried out with *sec*-BuLi (45 min in THF at −78 °C), followed by deuterolysis with D_2O,[3a] to afford the corresponding 3-

 © 2004 Wiley-VCH Verlag GmbH & Co. KGaA, Weinheim

deuterioaziridine-borane complexes **4b,c** with total regioselectivity (^{1}H and ^{13}C NMR analysis), and with complete incorporation of deuterium (> 95 %, ^{1}H NMR). The lithiated aziridine **5b** was subsequently treated with $ClSiMe_3$.

The diastereoselectivity of both the deuteration and silylation reactions was either very high or total. Thus, 3-deuterioaziridine or 3-(trimethylsilyl)aziridine-borane complexes **4b**,**c** or **6b** were isolated with high diastereoselectivity from **2b**,**c** (d.r. = 95:5, 88:12, and > 97:3 % respectively),[15] as determined from the ^{1}H NMR spectrum of the crude reaction products. Assuming retention of configuration from the C-Li intermediate through the C-D or C-$SiMe_3$ bond-forming step to obtain **4** or **6**, initial lithiation occurs *syn* to the boron atom, giving the enantiopure *trans* aziridinium **5** (Scheme 4). This



Scheme 4. Synthesis of deuterated or silylated aminoaziridines **7c** or **8b**.

assignment is based on the coupling constants between C2-H and C3-H of **4b**,**c** and **6b** (8.5, 8.2 and 9.6 Hz, respectively), in agreement with a *cis* relative configuration. This *syn*-directing effect of N-BH_3 has been reported for the lithiation of other aziridine-borane complexes.[3a]

The 3-deuterioaziridine and 3-(trimethylsilyl)aziridine-borane complexes **4c** and **6b**, respectively, were easily decomplexed by treatment with methanol, to give the corresponding enantiopure (2*S*,3*S*,1′*S*)-3-deuterio-2-(1′-dibenzylaminoalkyl)aziridine (**7c**) or (2*S*,3*S*,1′*S*)-2-(1′-dibenzylaminoalkyl)-3-(trimethylsilyl)aziridine (**8b**) in high yield (94 and 93 %, respectively). Thus, the successive treatment of aminoaziridines with BH_3 or $BF_3{\cdot}Et_2O/LiAlH_4$, *sec*-BuLi, D_2O, or $ClSiMe_3$, followed by decomplexation, is an easy and effective method for enantioselective deuteration or silylation of aziridine.

In conclusion, the above studies show that the enantiopure 2-(1-aminoalkyl)aziridine–borane complexes **2** can easily be obtained by two alternative methodologies: either reaction with $BF_3{\cdot}Et_2O$ followed by reduction with $LiAlH_4$ or by direct reaction with a solution of BH_3 in THF. In addition, regio- and stereoselective C3 deuteration or silylation of 2-(1-aminoalkyl)aziridine **1** can be effected by deprotonation/deuteration or silylation/decomplexation of the corresponding borane complex **2**. Application of this methodology to functionalize 2-(1-aminoalkyl)aziridines with other different electrophiles is currently under investigation.

Experimental Section

2: $BF_3{\cdot}OEt_2$ (0.025 mL, 0.2 mmol) and $LiAlH_4$ (0.4 mL, 0.4 mmol, 1 M in THF) were added successively at 0 °C to a stirred solution of the corresponding aminoaziridine **1** (0.2 mmol) in THF (2 mL). After stirring the reaction at this temperature for 30 min, it was quenched by addition of a saturated aqueous solution of NH_4Cl (5 mL). Standard workup afforded the crude complexes **2**, which were purified by flash column chromatography on silica gel (hexane/EtOAc, 10:1). Yields are given in Table 1.

4 or **6**: A solution of *sec*-BuLi (0.54 mL, 1.4 M in cyclohexane) was added at −78 °C to a stirred solution of **2b** or **2c** (0.15 mmol) in THF (1 mL). After stirring the reaction mixture for 45 min at this temperature, it was quenched with D_2O (0.015 mL, 0.75 mmol) or with $ClSiMe_3$ (0.10 mL, 0.75 mmol). Standard workup afforded the crude complexes **4** or **6**. Treatment of **4c** or **6b** (0.10 mmol) with MeOH (1 mL) at room temperature for 24 h gave compound **7c** (94 %) or **8b** (93 %), respectively.

Received: March 25, 2004 [Z460120]

Keywords: boranes · deuteration · enantioselectivity · lithiation · small ring systems

[1] Reviews: a) M. Nabyl, *Synlett* **2003**, 1757 – 1758; b) J. R. Sceffer, *Can. J. Chem.* **2001**, *79*, 349 – 357.
[2] a) T. Ooi, E. Tayama, K. Maruoka, *Angew. Chem.* **2003**, *115*, 599 – 602; *Angew. Chem. Int. Ed.* **2003**, *42*, 579 – 582; b) F.-Y. Zhang, E. J. Corey, *Org. Lett.* **2000**, *2*, 1097 – 1100; c) E. J. Corey, F. Xu, M. C. Noe, *J. Am. Chem. Soc.* **1997**, *119*, 12414 – 12415.
[3] For recent examples see: a) E. Vedejs, S. Bhanu Prasad, J. T. Kendall, J. S. Russel, *Tetrahedron* **2003**, *59*, 9849 – 9856; b) E. Vedejs, S. C. Fields, R. Hayashi, S. R. Hitchcock, D. R. Powell, M. R. Schrimpf, *J. Am. Chem. Soc.* **1999**, *121*, 2460 – 2470; c) P. Bisseret, C. Bouix-Peter, O. Jacques, S. Henriot, J. Eustache, *Org. Lett.* **1999**, *1*, 1181 – 1182; d) M. R. Ebden, N. S. Simpkims, D. N. A. Fox, *Tetrahedron* **1998**, *54*, 12923 – 12952; e) A. J. Blake, M. R. Weden, D. N. A. Fox, W.-S. Li, N. S. Simpkins, *Synlett* **1998**, 189 – 191.
[4] a) A. E. Moormann, G. D. Searle, *Synth. Commun.* **1993**, *23*, 789 – 795; b) A. Pelter, R. M. Rosser, *J. Chem. Soc. Perkin Trans. 1* **1984**, 717 – 720.
[5] a) K. Otsuka, K. Ito, T. Katsuki, *Synlett* **1995**, 429 – 430; b) C. F. Lane, *Aldrichimica Acta* **1973**, *6*, 51 – 58.
[6] a) J. M. Brunel, G. Buono, *Synlett* **1996**, 177 – 178; b) J. A. Morley, L. Eirod, Jr., J. F. Bauer, *Anal. Chem.* **1994**, *66*, 4283 – 4287; c) C. R. Sarko, J. C. Gunch, H. Dimare, *J. Org. Chem.* **1994**, *59*, 705 – 706.
[7] J. M. Concellón, P. L. Bernad, E. Riego, S. García-Granda, A. Forcén-Acebal, *J. Org. Chem.* **2001**, *66*, 2764 – 2768.
[8] a) J. M. Concellón, P. L. Bernad, E. Riego, *J. Org. Chem.* **2003**, *68*, 6407 – 6410; b) J. M. Concellón, E. Riego, J. R. Suárez, *J. Org. Chem.* **2003**, *68*, 9242 – 9246.
[9] a) S. Drinkuth, S. Groetsch, E. M. Peters, K. Peters, M. Christl, *Eur. J. Org. Chem.* **2001**, 2665 – 2670; b) J. P. Alazard, A. Leboff, S. Labidalle, C. Thal, *Tetrahedron Lett.* **1988**, *29*, 4713 – 4716.
[10] CCDC-234474 (**2b**) contains the supplementary crystallographic data for this paper. These data can be obtained free of charge via www.ccdc.cam.ac.uk/conts/retrieving.html (or from the Cambridge Crystallographic Data Centre, 12, Union Road, Cambridge CB2 1EZ, UK; fax: (+44) 1223-336-033; or deposit@ccdc.cam.ac.uk).
[11] a) For a nitrogen-inversion process of aziridines, see: a) N. Mimura, Y. Miwa, T. Ibuka, Y. Yamamoto, *J. Org. Chem.* **2002**, *67*, 5796 – 5801; b) J. M. B. Nielsen, *J. Phys. Chem.* **1998**, *102*,

 © 2004 Wiley-VCH Verlag GmbH & Co. KGaA, Weinheim

3193 – 3201; c) D. Kost, M. Raban, *J. Am. Chem. Soc.* **1982**, *104*, 2960 – 2967.
[12] a) W. McCoull, F. A. Davis, *Synthesis* **2000**, 1347 – 1365; b) W. H. Pearson, B. W. Lian, B. W. Bergmeier in *Comprehensive Heterocyclic Chemistry II*, *Vol. 1A* (Ed.: A. Padwa), Pergamon, Oxford, **1996**, pp. 1 – 60; c) D. Tanner, *Angew. Chem.* **1994**, *106*, 625 – 646; *Angew. Chem. Int. Ed. Engl.* **1994**, *33*, 599 – 619; d) W. L. F. Armarego, *Stereochemistry of Heterocyclic Compounds*, Part 1, Wiley, New York, **1977**.
[13] a) J. Mann, R. S. Davidson, J. B. Hobbs, D. V. Banthorpe, J. B. Harborne, *Natural Products*, Addison Wesley, Essex, **1996**; b) for an example see: M. C. Pierre, C. Chèze, J. Vercauteren, *Tetrahedron Lett.* **1997**, *38*, 5639 – 5642.
[14] H. Quast, C. A. Weise Vélez, *Angew. Chem.* **1978**, *90*, 224 – 225; *Angew. Chem. Int. Ed. Engl.* **1978**, *17*, 213 – 214.
[15] The observed difference in diastereoselectivity in the deuteration of **2b** and **2c** (d.r. = 95:5 and 88:12) is probably a consequence of higher steric hindrance for the metalation of the hydrogen C_3-H *cis* with respect to the BH_3 group in **2c** than in **2b**.

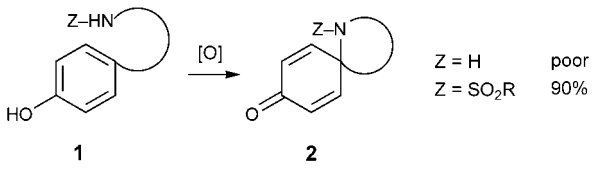
 © 2004 Wiley-VCH Verlag GmbH & Co. KGaA, Weinheim

Natural Products Synthesis

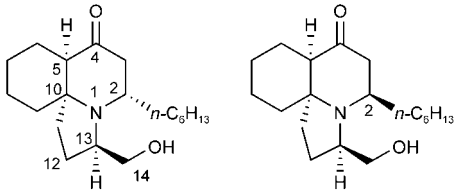
Fully Stereocontrolled Total Syntheses of (−)-Cylindricine C and (−)-2-Epicylindricine C: A Departure in Sulfonamide Chemistry**

*Sylvain Canesi, Denis Bouchu, and Marco A. Ciufolini**

The oxidative spirocyclization of phenolic primary amines (**1**→**2**; Z = H) holds considerable potential in the chemical syntheses of spirocyclic natural products and pharmaceutically interesting molecules. We recently disclosed that this hitherto problematic transformation may be carried out through the oxidation of sulfonamide derivatives of primary amines with $PhI(OAc)_2$ ((diacetoxyiodo)benzene, DIB) in excellent yield.[1] Further studies have revealed that the sulfonamide unit may function not only as a modulator of the reactivity of the primary amino group to allow an otherwise "impossible" transformation, but also (and especially so) as a useful implement for the subsequent elaboration of spirocycles **2** (Z = SO_2R) into more-complex synthetic goals. Herein, we describe the fully stereocontrolled total syntheses of (−)-cylindricine C (**3**) and its stereoisomer (−)-2-epicylindricine C (**4**), which has not yet been observed as a natural product, from a common precursor **14**, to illustrate some possibilities inherent to the combination of oxidative spirocyclization technology with such sulfonamide-based transformations.



1 **2**



3 **4**

Cylindricines are structurally unique alkaloids produced by the ascidian, *Clavelina cylindric*a.[2] Their unusual architecture and (moderate) cytotoxic activity have elicited substantial interest in the synthetic arena.[3,4] Research in this domain has shown that the series of 2-epi derivatives may result from a Michael-[5] or Mannich-type[3e] cyclization of suitable precursors. A synthesis capable of providing *either* **3** or **4** from a common intermediate, such as **14** in the present case, is clearly not subject to any stereochemical uncertainty.

Commercial D-homotyrosine[6] was elaborated into the sulfonamide **5** in a conventional fashion.[7] Subsequent oxidation of **5** by DIB in hexafluoro-2-propanol induced cyclization into **6** in excellent yield. The primary OH group was then protected as a bulky *tert*-butyldiphenylsilyl (TBDPS) ether prior to the desymmetrization of the locally symmetrical dienone in **7** through the regioselective base-promoted 1,4-addition of the anion of the sulfonamide group. It is apparent that the methyl group of the mesylamide is poised to become the carbonyl group of **3** and **4**. Conversion of **7** into **8** occurred with satisfactory diastereoselectivity (d.r. = 7:1) upon treatment of **7** with KHMDS at −100 °C.[8] The two regioisomers thus produced were not separable at this point, but the minor isomer was readily removed at the stage of compound **10**, which resulted upon treatment of **8** with PhSH and $BF_3{\cdot}OEt_2$ to form **9** diastereoselectively,[9] followed by the desulfurization of the latter with Raney Ni[10] (Scheme 1).

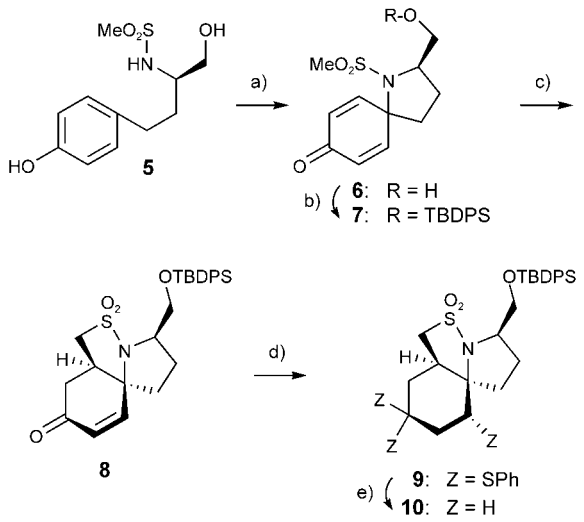
The importance of the sulfonamide function in the construction of the third and final ring of the molecule becomes fully apparent at this juncture. Deprotonation of **10** with *t*BuLi[11] and capture of the anion with racemic octene oxide activated by $BF_3{\cdot}OEt_2$[12] resulted in the formation of **11**,

[*] S. Canesi, Dr. D. Bouchu, Prof. Dr. M. A. Ciufolini
Laboratoire de Synthèse et Méthodologie Organiques, CNRS UMR 5181
Université Claude Bernard Lyon 1 and Ecole Supérieure de Chimie Physique Electronique de Lyon
43, Bd. du 11 Novembre 1918, 69622 Villeurbanne cedex (France)
Fax (+33) 472-432-963
E-mail: ciufi@cpe.fr

[**] We thank the MENRT (doctoral fellowship to S.C.), the CNRS, and the Région Rhône-Alpes for support of our research. We are grateful to Ms. Laurence Rousset for the mass spectral data, to Professor Monique Perrin for the X-ray crystallographic studies, and to Prof. Adrian J. Blackman for ^{1}H NMR spectra. M.A.C. is the recipient of a Merck & Co. Academic Development Award.

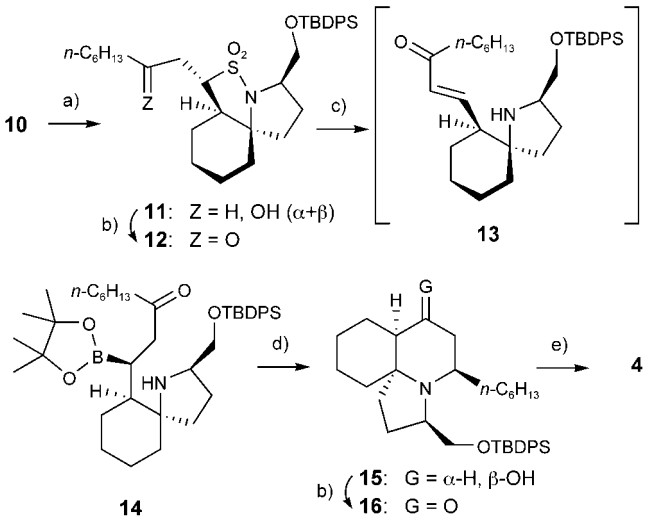
Supporting information for this article is available on the WWW under http://www.angewandte.org or from the author.

 © 2004 Wiley-VCH Verlag GmbH & Co. KGaA, Weinheim DOI: 10.1002/anie.200460178



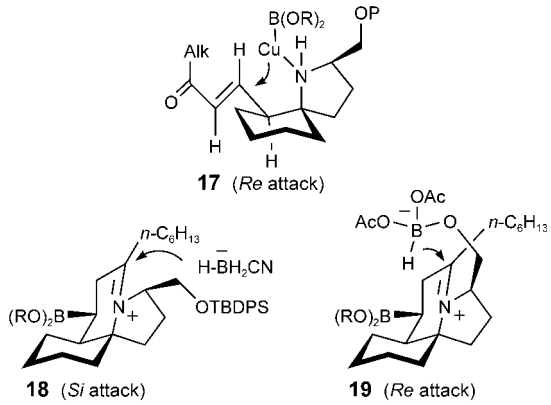
Scheme 1. a) $PhI(OAc)_2$, $(CF_3)_2CHOH$, room temperature; b) $tBuPh_2SiCl$, imidazole, DMF, room temperature, 82% over two steps; c) KHMDS, THF, −100°C, 89% (d.r. = 7:1); d) PhSH, $BF_3{\cdot}OEt_2$ (cat.), CH_2Cl_2, 0°C, 77%; e) Raney Ni, EtOH/THF, 77%. DMF = *N*,*N*-dimethylformamide, KHMDS = potassium hexamethyldisilazide

which was then subjected to a Dess–Martin oxidation[13] to give **12**. A one-pot sequence, which involved sequential β-elimination and Miyaura borylation[14] of the isolable intermediate **13**, resulted in the extremely rapid (20 min; the reaction normally requires > 15 h) and highly diastereoselective[15] formation of the boronic ester **14** (Scheme 2). Several pieces of evidence suggest that the unusually fast rate and the high degree of diastereoselectivity observed in the Miyaura reaction of **13** may be ascribed to a directing effect of



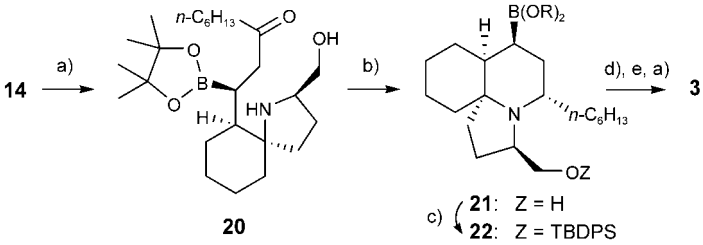
Scheme 2. a) *t*BuLi, THF, −78°C, (±)-1-octene oxide, BF_3OEt_2; b) Dess–Martin periodinane, CH_2Cl_2, room temperature, 88% over two steps for **12**; 94% for **16**; c) 1. DBU, DMF, then 2. bis(pinacolyl)diboronate, CuCl, KOAc, room temperature, 86%; d) 1. $NaBH_3CN$, AcOH, MeOH, 0°C, then 2. H_2O_2, NaOH, 80%; e) TBAF, THF, 96%. DBU = 1,8-diazabicyclo[5.4.0]undec-7-ene, TBAF = tetra-*n*-butylammonium fluoride

the nitrogen atom. We thus envision that the selective delivery of the copper(I) agent to the *Re* face of the double bond occurs from a complex such as **17**. Similar directed organocopper additions are documented.[16]



Intermediate **14** is then readily and diastereoselectively elaborated into either cylindricine C or into 2-epicylindricine C (Scheme 2). Compound (−)-**4** was prepared through an initial one-pot, sequential intramolecular reductive amination reaction (AcOH, $NaBH_3CN$)[17] and borane oxidation process (H_2O_2, NaOH). This resulted in the highly stereoselective[15] formation of **15**. A rationale for this elevated diastereoselectivity is proposed as follows: A MM+ force field study suggests that the configuration of the borylated stereogenic carbon center defines **18** as the most stable conformer of the presumed iminium ion intermediate. Reduction of **18** under stereoelectronic control (axial delivery of hydride)[18] yields **15**. Dess–Martin oxidation[13] of **15** and deprotection led to **4**.[19]

The total synthesis of (−)-cylindricine (Scheme 3) started with the desilylation of **14** followed by treatment of the



Scheme 3. a) TBAF, THF, 95% for **20**, 96% for **3**; b) $NaBH(OAc)_3$, AcOH (cat.), CH_2Cl_2, −78°C, 73%; c) $tBuPh_2SiCl$, imidazole, DMF, 95%; d) H_2O_2, NaOH, THF, 0°C 97%; e) Dess-Martin periodinane, CH_2Cl_2, room temperature, 94%.

resultant product **20** with $NaBH(OAc)_3$ and a catalytic quantity of AcOH. This induced a highly stereoselective[15] Evans-type directed reduction[20] of a presumed iminium ion intermediate **19**. Such a directed reduction of an iminium ion appears to be undocumented. The emerging product **21** was readily transformed into **3** as shown in Scheme 3.[21]

 © 2004 Wiley-VCH Verlag GmbH & Co. KGaA, Weinheim

The applicability of the new technology to other synthetic problems is currently under study and will constitute the subject of future reports.

Received: March 31, 2004 [Z460178]

Keywords: antitumor agents · cyclization · spiro compounds · sulfonamides · total synthesis

[1] S. Canesi, P. Belmont, D. Bouchu, L. Rousset, M. A. Ciufolini, *Tetrahedron Lett.* **2002**, *43*, 5193.
[2] a) A. J. Blackman, C. Li, D. C. R. Hockless, B. W. Skelton, A. H. White, *Tetrahedron* **1993**, *49*, 8645; b) C. Li, A. J. Blackman, *Aust. J. Chem.* **1994**, *47*, 1355; c) C. Li, A. J. Blackman, *Aust. J. Chem.* **1995**, *48*, 955.
[3] Total synthesis of (−)-cylindricine C: a) G. A. Molander, M. Roenn, *J. Org. Chem.* **1999**, *64*, 5183; total synthesis of (+)-cylindricines C, D, and E: b) B. M. Trost, M. T. Rudd, *Org. Lett.* **2003**, *5*, 4599; total synthesis of (±)-cylindricines A, D, and E: c) B. B. Snider, T. Liu, *J. Org. Chem.* **1997**, *62*, 5630; total synthesis of (±)-cylindricines A and B: d) J. F. Liu, C. H. Heathcock, *J. Org. Chem.* **1999**, *64*, 8263; synthesis of (±)-4-epicylindricine C: e) K. M. Werner, J. M. de los Santos, S. M. Weinreb, M. Shang, *J. Org. Chem.* **1999**, *64*, 4865; synthetic studies: f) W. Oppolzer, C. G. Bochet, *Tetrahedron: Asymmetry* **2000**, *11*, 4761; g) W. H. Pearson, N. S. Barta, J. W. Kamp, *Tetrahedron Lett.* **1997**, *38*, 3369.
[4] For synthetic studies on the structurally related alkaloids, fasicularin and lepadiformine, see: a) H. Abe, S. Aoyagi, C. Kibayashi, *J. Am. Chem. Soc.* **2000**, *122*, 4583; b) T. J. Greshock, R. L. Funk, *Org. Lett.* **2001**, *3*, 3511; c) J.-H. Maeng, R. L. Funk, *Org. Lett.* **2002**, *4*, 331; d) W. H. Pearson, *Pure Appl. Chem.* **2002**, *74*, 1339; e) H. Abe, S. Aoyagi, C. Kibayashi, *Angew. Chem.* **2002**, *114*, 3143, *Angew. Chem. Int. Ed.* **2002**, *41*, 3017; f) S. M. Weinreb, *Acc. Chem. Res.* **2003**, *36*, 59; g) R. Hunter, P. Richards, *Synlett* **2003**, 271; h) C. Kibayashi, S. Aoyagi, H. Abe, *Bull. Chem. Soc. Jpn.* **2003**, *76*, 2059; i) M. D. Fenster, G. R. Dake, *Org. Lett.* **2003**, *5*, 4313.
[5] Unpublished results from these laboratories; details will be provided in a forthcoming full paper.
[6] The absolute configuration of cylindricine C is unknown.[2] We chose to prepare (−)-**4** from D-homotyrosine for comparison purposes because at the beginning of our investigations the only enantioselective synthesis of (−)-**4** reported in the literature was that by Molander and Roenn.[3a]
[7] a) $SOCl_2$/MeOH; b) MsCl/TEA (excess), CH_2Cl_2, 0 °C, (formation of the *N*,*O*-dimesyl derivative), 91% over two steps; c) $NaBH_4$/EtOH/THF, 94%; d) NaOH/dioxane, 80 °C, 90%. Ms = methanesulfonyl, TEA = triethylamine.
[8] Under identical conditions, cyclization of the corresponding methyl ether proceeded with d.r. = 3.5:1 and that of the TBDMS ether with d.r. = 4.5:1.
[9] The structure of this material was confirmed by an X-ray crystallographic study of its desilylated analogue. The selectivity of the 1,4-addition of PhSH to **8** appears to be due to a Felkin–Anh-type stereoelectronic effect created by the strongly electronegative sulfonamide nitrogen atom. For examples, see: a) E. L. Eliel, S. H. Wilen, *Stereochemistry of Organic Compounds*, Wiley, New York, **1994**, p. 875; b) S. Bennabi, K. Narkunan, L. Rousset, D. Bouchu, M. A. Ciufolini, *Tetrahedron Lett.* **2000**, *41*, 8873, and references therein.
[10] R. Mozingo, D. E. Wolf, S. A. Harris, K. Folkers, *J. Am. Chem. Soc.* **1943**, *65*, 1013.
[11] Weaker bases were ineffective for deprotonation of **10**, in accord with: L. A. Paquette, S. C. Ra, J. D. Schloss, S. M. Leit, J. C. Gallucci, *J. Org. Chem.* **2001**, *66*, 3564.
[12] a) M. J. Eis, J. E. Wrobel, B. Ganem, *J. Am. Chem. Soc.* **1984**, *106*, 3693; b) B. Achmatowicz, S. Marczak, J. Wicha, *J. Chem. Soc. Chem. Commun.* **1987**, 1226.
[13] D. B. Dess, J. C. Martin, *J. Org. Chem.* **1983**, *48*, 4155–4156.
[14] K. Takahashi, T. Ishiyama, N. Miyaura, *J. Organomet. Chem.* **2001**, *625*, 47.
[15] Only one stereoisomer of the product was apparent within the limits of ^{1}H- (300 MHz) and ^{13}C NMR (75 MHz) spectrometry.
[16] For amine-directed organocuprate additions, see: a) D. K. Hutchinson, S. A. Hardinger, P. L. Fuchs, *Tetrahedron Lett.* **1986**, *27*, 1425; b) for an excellent bibliography on general directed organocuprate addition reactions,see: B. Breit, P. Demel, *Tetrahedron* **2000**, *56*, 2833.
[17] For related processes, see reference [3g].
[18] For a discussion, see: R. V. Stevens, *Acc. Chem. Res.* **1984**, *17*, 289.
[19] The ^{1}H NMR spectra of (−)-**4** synthesized herein ($[\alpha]_D^{25} = -39°$; $c = 0.5$ in CH_2Cl_2), could be superimposed on those of (±)-2-epicylindricine C published by Weinreb and co-workers[3e] (see Supporting Information).
[20] D. A. Evans, J. S. Clark, R. Metternich, V. J. Novack, G. S. Sheppard, *J. Am. Chem. Soc.* **1990**, *112*, 866.
[21] The ^{1}H NMR spectra of (−)-**3** synthesized herein could be superimposed on those of (−)-cylindricine C reported by Molander and Roenn[3a] (see Supporting Information), and the specific rotations were also essentially identical: $[\alpha]_D^{25} = -66°$ ($c = 0.5$ in CH_2Cl_2) for **3** versus $[\alpha]_D^{25} = -64°$ ($c = 0.2$ in CH_2Cl_2) for reference [3a].

 © 2004 Wiley-VCH Verlag GmbH & Co. KGaA, Weinheim

Superhydrophobic Surface

A Lotus-Leaf-like Superhydrophobic Surface: A Porous Microsphere/Nanofiber Composite Film Prepared by Electrohydrodynamics**

Lei Jiang, Yong Zhao, and Jin Zhai*

Inspired by self-cleaning lotus leaves, superhydrophobic surfaces with water contact angles (CA) larger than 150° have attracted great interest over the last few years for both fundamental research and practical applications. The fundamental mechanism of this phenomenon proposes that a combination of a hierarchical micro/nanostructure and low-

[*] Prof. Dr. L. Jiang, Dr. Y. Zhao, Prof. Dr. J. Zhai
Center of Molecular Sciences
Institute of Chemistry, Chinese Academy of Sciences
Beijing 100080 (P. R. China)
Dr. Y. Zhao
Graduate School of the Chinese Academy of Sciences (P. R. China)
Prof. Dr. L. Jiang
National Center for Nanoscience and Nanotechnology
Beijing 100080 (P. R. China)
Fax: (+86) 10-8262-7566
E-mail: jianglei@iccas.ac.cn

[**] The authors thank the State Key Project for Fundamental Research (G1999064504) and the Special Research Foundation of the National Nature Science Foundation of China (29992530) for continuing financial support. The Chinese Academy of Sciences is gratefully acknowledged.

 © 2004 Wiley-VCH Verlag GmbH & Co. KGaA, Weinheim DOI: 10.1002/anie.200460333

surface-energy materials are essential for superhydrophobicity.[1] To fabricate such surfaces, various methods have been proposed, such as the solution method,[2] the sol–gel method,[3] solidification of alkylketene dimer,[4] the plasma fluorination method,[5] and others.[6–9] We have already made some progress in this field. For example, we prepared superamphiphobic films of aligned carbon nanotubes with fluoroalkylsilane coating.[10] Furthermore, aligned polymer nanofiber films with superhydrophobic properties were fabricated by a template method.[11] Recently, several thermally or optically responsive smart interfacial materials that can switch between superhydrophilicity and superhydrophobicity were reported.[12]

The electrohydrodynamics (EHD) technique has proved to be a versatile and effective method for manufacturing micro- to nanoscale fibers or particles from a variety of materials, such as polymers,[13] inorganic,[14] and hybrid (organic/inorganic)[15] compounds, for a broad range of applications in membrane technology,[16] tissue engineering,[17] optical[18] and biosensors,[19] and drug delivery.[20] Here we report the preparation of a lotus-leaf-like porous microsphere/nanofiber composite film of polystyrene (PS), a cheap industrial polymer, by a simple EHD method, which for the first time afforded superhydrophobicity ($CA = 160.4°$) without any modification.

In a typical EHD process, a sample solution is pumped through a nozzle to which a high voltage is applied relative to a grounded metal plate (collector) to form an electrically charged jet of solution. The solution jet solidifies with accompanying evaporation of solvent and forms a film on the collector.[21] We prepared EHD films with different morphologies from PS/DMF solutions of different concentrations at a constant distance between the tip and collector of 14 cm and an applied voltage of 14 kV.

Nanofibrous film I was first fabricated from a 25 wt% solution of PS in DMF. Figure 1a and b show SEM images of film I. The nanofibers are randomly oriented on the substrate, and the individual fibers have high slenderness ratios. The average diameter of the fibers is 420 nm, and they are longer than several millimeters. Film I has a network structure because numerous fibers interweave integrally like a spider's web. The wetting properties of film I were investigated. Compared with a native PS surface prepared by spin coating (water $CA = 95.1 \pm 0.3°$, Figure 1c), film I has a much higher water CA of $139.1 \pm 1.8°$ (Figure 1d), that is, the hydrophobicity of film I is improved to some extent because of the network structure.

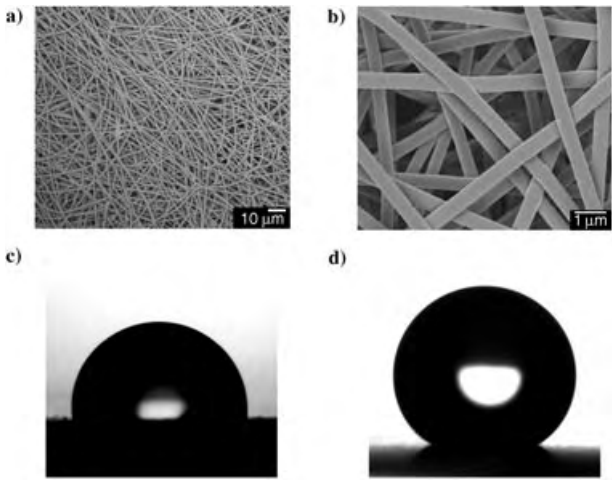


Figure 1. a) SEM image of film I prepared from a 25 wt% PS/DMF solution; b) magnified part of (a); water droplets on a spin-coated PS film (c) and on film I (d).

Next a dilute PS/DMF solution (5 wt%) was used to fabricate microparticle film II. The particles, diameters of which range from 2 to 7 μm, exhibit a hollow conical shape (Figure 2a), as a result of constringence and collapse during solidification of the solution droplets upon evaporation of solvent in the EHD process. A more highly magnified image shows that the microparticles are covered by nanopapilla of 50–70 nm (Figure 2b). Thus the surface roughness of film II is greater than that of film I. Since surface roughness is a very important factor in wetting,[1] it can be deduced that film II should be more hydrophobic than film I. Wettability measurements confirmed this hypothesis and showed that film II is superhydrophobic with a water CA of $162.1 \pm 1.0°$ (Figure 2c). However, during CA measurements, some clusters of microparticles separated from the substrate spontaneously and floated on water droplets (arrows in Figure 2c) because the density of porous PS microparticles is lower than that of water. This drawback prevents its further application.

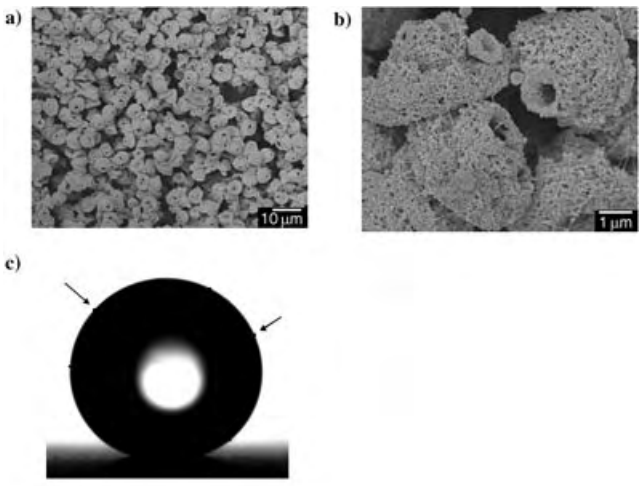


Figure 2. a) SEM image of film II fabricated from a 5 wt% PS/DMF solution; b) magnified image of porous microparticles; c) water droplet on film II (the dots on the droplet, indicated by arrows, are clusters of particles separated from the film).

Accordingly, a stable superhydrophobic EHD film should be realizable by building a composite structure of films I and II that has both the structural stability of nanofibers and the superhydrophobicity of porous microparticles. There have been a few reports on the formation of bead-fibers when uniform fibers are fabricated,[22–25] but most of them concentrate on preparing fibers while neglecting to investigate the properties of the bead-fibrous film. Here we pay more attention to investigating the porous microsphere/nanofiber

 © 2004 Wiley-VCH Verlag GmbH & Co. KGaA, Weinheim

composite film (PMNCF) with its unique structure, which was prepared from a 7 wt % PS/DMF solution. The SEM image of the as-prepared film (Figure 3 a) shows numerous microspheres and nanofibers distributed densely over the whole

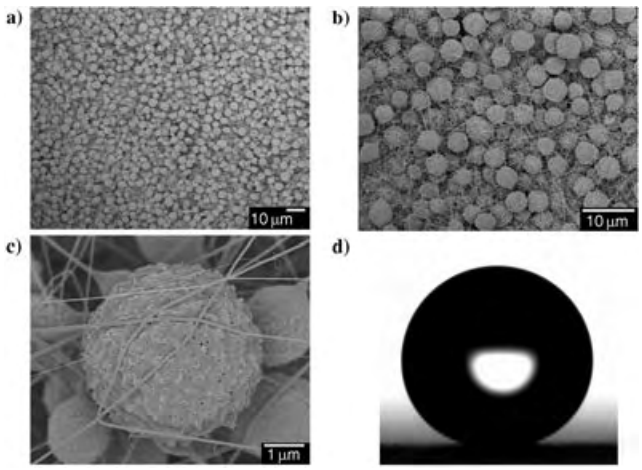


Figure 3. a) SEM image of PMNCF prepared from a 7 wt% PS/DMF solution; b) 3D network structure of PMNCF; c) surface nanostructure of a single porous microsphere; d) water droplet on PMNCF.

substrate. Almost every microsphere is interlinked with nanofibers, and the nanofibers are interwoven in a stable multilayer 3D network in which the microspheres are embedded (Figure 3 b). A more highly magnified image indicates the presence of many protuberances and cavities with dimensions of tens to hundreds of nanometers on the surfaces of the microspheres (Figure 3 c). The sizes of the microspheres and nanofibers are 3–7 μm and 60–140 nm, respectively. The water CA of the PMNCF is $160.4 \pm 1.2°$ (Figure 3 d), that is, it shows stable superhydrophobicity. In other words, PMNCF combines the advantages of films I and II while overcoming the disadvantages of both. Moreover, the morphologies of the EHD products could be easily controlled by merely adjusting the concentration of the solution.

The morphologies of the EHD products method are mainly influenced by the concentration of the solution, the solvent, the electric potential, and the nozzle-to-collector distance.[22] Of these, the solution concentration and solvent are crucial for the film morphology, while the electric potential and distance have less influence for a given solution. As a consequence of the effect of surface tension, the liquid jet prefers to shrink to spherical droplets to acquire the smallest surface area. In the EHD process, however, the solution jet is placed in a strong electric field, so competition between electrical force and surface tension decides the morphology of the product. When a concentrated solution (20–30 wt %) is used, the high viscosity and polymer content make the solution jet elongate and solidify quickly, and ultrafine fibers are formed. With dilute solutions (3–5 wt %), the very low viscosity does not suffice to sustain the elongation of the liquid jet, and therefore the thin jet of solution leaving the nozzle instantly shrinks to droplets and ultimately forms microparticles. The formation of PMNCF is a mesostate of these two conditions (6–10 wt %), in which one part of the liquid jet shrinks to spheres, and the other solidifies to fibers.

In PMNCF, the porous microspheres of PMNCF play the leading role in the superhydrophobicity, while nanofibers act as a skeleton that reinforces the composite film. It has long been known that lotus leaves show excellent water-repellent properties, and much attention has been paid to constructing biomimetic self-cleaning materials on the basis of the lotus-leaf effect. The superhydrophobicity of the lotus leaf is due to surface roughness caused by branchlike nanostructures on top of the micropapillae and the low surface energy epicuticular wax.[1b] Similarly, the surfaces of as-prepared PMNCF are composed of micro- and nanoscale structures. Additionally, PS is a low surface energy material because of its CH groups. The micro/nano hierarchical structures increase surface roughness dramatically, so that air can be trapped in the aperture of porous microspheres and nanofibers. It is known that the air trapped in the surface is very important to hydrophobicity, because the water CA of air is regarded to be 180°. Cassie and Baxter proposed Equation (1) to describe the relationship between the CA of a water droplet on a smooth surface (θ) and the CA on a heterogeneous surface (θ_{CB}) composed of a solid and air.[26]

$$\cos\theta_{CB} = f_1 \cos\theta - f_2 \quad (1)$$

Here, f_1 and f_2 are the fractions of solid surface and air in contact with liquid, respectively, that is, $f_1 + f_2 = 1$. Given the water CAs of a native PS surface and PMNCF, f_2 is calculated to be 0.934, which indicates that the achievement of superhydrophobicity by PMNCF is mainly a result of the air trapped in the rough surface by combining microstructures of spheres with nanostructures of protuberances and cavities.

In conclusion, a superhydrophobic PS film with a novel composite structure consisting of porous microspheres and nanofibers has been prepared by the versatile EHD method. The morphologies of EHD products could be controlled by adjusting the concentration of the starting solution. The porous microspheres contribute to the superhydrophobicity by increasing surface roughness, while nanofibers interweave to form a 3D network that reinforces the composite film. We believe that the EHD method described here could easily be extended to preparing stable superhydrophobic surfaces from a wide variety of materials.

Experimental Section

Preparation of PMNCF: PS (homopolymer, $M_w = 220000$, Beijing Yanshan Petrochemical Co., Ltd.) was dissolved in DMF (Beijing Yili Fine Chemical Co.) by stirring for 5 h to form a 7 wt % transparent solution. About 2 mL of the precursor solution was placed in a 5-mL syringe equipped with a blunt metal needle of 0.6 mm inner diameter. The syringe was placed in a syringe pump that maintained a solution feed rate of 0.5 mL h^{-1}. A stainless steel plate covered with a sheet of aluminum foil was employed as the collector. The distance between the needle tip and collector was 14 cm, and the voltage was set at 14 kV.

Preparations of films I and II were similar to that of PMNCF. A 25 wt % solution (film I) and a 5 wt % solution (film II) with feed

 © 2004 Wiley-VCH Verlag GmbH & Co. KGaA, Weinheim

rates of 2 and 0.5 mL h^{-1}, respectively, were processed at the same voltage and distance as PMNCF. The native PS film was prepared from a 20 wt % PS/DMF solution by spin coating on a cleaned silicon wafer.

FE-SEM images were obtained on a JEOL JSM-6700F (Japan) scanning electron microscope at 3.0 kV. Contact angles were measured on an OCA20 contact-angle system (Dataphysics Co., Germany) at ambient temperature.

Received: April 15, 2004 [Z460333]

Keywords: electrohydrodynamics · hydrophobic effect · nanostructures · polymers · surface chemistry

[1] a) L. Jiang, R. Wang, B. Yang, T. J. Li, D. A. Trigk, A. Fujishima, K. Hashimoto, D. Zhu, *Pure Appl. Chem.* **2000**, *72*, 73; b) L. Feng, S. Li, Y. Li, H. Li, L. Zhang, J. Zhai, Y. Song, B. Liu, L. Jiang, D. Zhu, *Adv. Mater.* **2002**, *14*, 1857.

[2] a) Q. Xie, J. Xu, L. Feng, L. Jiang, W. Tang, X. Luo, C. C. Han, *Adv. Mater.* **2004**, *16*, 302; b) H. Y. Erbil, A. L. Demirel, Y. Avci, O. Mert, *Science* **2003**, *299*, 1377.

[3] a) R. Wang, K. Hashimoto, A. Fujishima, M. Chikuni, E. Kojima, A. Kitamura, M. Shimohigoshi, T. Watanabe, *Nature* **1997**, *388*, 431; b) N. J. Shirtcliffe, G. Hale, M. I. Newton, C. C. Perry, *Langmuir* **2003**, *19*, 5626; c) K. Tadanaga, J. Morinaga, A. Matsuda, T. Minami, *Chem. Mater.* **2000**, *12*, 590.

[4] T. Onda, S. Shibuichi, N. Satoh, K. Tsujii, *Langmuir* **1996**, *12*, 2125.

[5] a) D. O. H. Teare, C. G. Spanos, P. Ridley, E. J. Kinmond, V. Roucoules, J. P. S. Badyal, S. A. Brewer, S. Coulson, C. Willis, *Chem. Mater.* **2002**, *14*, 4566; b) I. Woodward, W. C. E. Schofield, V. Roucoules, J. P. S. Badyal, *Langmuir* **2003**, *19*, 3432.

[6] J. Genzer, K. Efimenko, *Science* **2000**, *290*, 2130.

[7] A. Nakajima, A. Fujishima, K. Hashimoto, T. Watanabe, *Adv. Mater.* **1999**, *11*, 1365.

[8] A. Nakajima, K. Abe, K. Hashimoto, T. Watanabe, *Thin Solid Films* **2000**, *376*, 140.

[9] J. Bico, C. Marzolin, D. Quere, *Europhys. Lett.* **1999**, *47*, 220.

[10] a) H. Li, X. Wang, Y. Song, Y. Liu, Q. Li, L. Jiang, D. Zhu, *Angew. Chem.* **2001**, *113*, 1790; *Angew. Chem. Int. Ed.* **2001**, *40*, 1743; b) T. Sun, G. Wang, H. Liu, L. Feng, L. Jiang, D. Zhu, *J. Am. Chem. Soc.* **2003**, *125*, 14996; c) S. Li, H. Li, X. Wang, Y. Song, Y. Liu, L. Jiang, D. Zhu, *J. Phys. Chem. B* **2002**, *106*, 9274.

[11] a) L. Feng, Y. Song, J. Zhai, B. Liu, J. Xu, L. Jiang, D. Zhu, *Angew. Chem.* **2003**, *115*, 824; *Angew. Chem. Int. Ed.* **2003**, *42*, 800; b) L. Feng, S. Li, H. Li, J. Zhai, Y. Song, L. Jiang, D. Zhu, *Angew. Chem.* **2002**, *114*, 1269; *Angew. Chem. Int. Ed.* **2002**, *41*, 1221.

[12] a) T. Sun, G. Wang, L. Feng, B. Liu, Y. Ma, L. Jiang, D. Zhu, *Angew. Chem.* **2004**, *116*, 361; *Angew. Chem. Int. Ed.* **2004**, *43*, 357; b) X. Feng, L. Feng, M. Jin, J. Zhai, L. Jiang, D. Zhu, *J. Am. Chem. Soc.* **2004**, *126*, 62.

[13] a) C. L. Casper, J. S. Stephens, N. G. Tassi, D. B. Chase, J. F. Rabolt, *Macromolecules* **2004**, *37*, 573; b) M. S. Khil, H. Y. Kim, M. S. Kim, S. Y. Park, D. R. Lee, *Polymer* **2004**, *45*, 295; c) M. Bognitzki, W. Czado, T. Frese, A. Schaper, M. Hellwig, M. Steinhart, A. Greiner, J. H. Wendorff, *Adv. Mater.* **2001**, *13*, 70; d) S. Madhugiri, A. Dalton, J. Gutierrez, J. P. Ferraris, K. J. Balkus, Jr., *J. Am. Chem. Soc.* **2003**, *125*, 14531; e) L. Yao, T. W. Haas, A. Guiseppi-Elie, G. L. Bowlin, D. G. Simpson, G. E. Wnek, *Chem. Mater.* **2003**, *15*, 1860.

[14] a) F. Ko, Y. Gogotsi, A. Ali, N. Naguib, H. Ye, G. Yang, C. Li, P. Wills, *Adv. Mater.* **2003**, *15*, 1161; b) G. Larsen, R. Velarde-Ortiz, K. Minchow, A. Barrero, I. G. Loscertales, *J. Am. Chem. Soc.* **2003**, *125*, 1154; c) H. Q. Hou, D. H. Reneker, *Adv. Mater.* **2004**, *16*, 69; d) J. Y. Lu, K. A. Runnels, C. Norman, *Inorg. Chem.* **2001**, *40*, 4516.

[15] a) R. A. Caruso, J. H. Schattka, A. Greiner, *Adv. Mater.* **2001**, *13*, 1577; b) H. Dai, J. Gong, H. Kim, D. Lee, *Nanotechnology* **2002**, *13*, 674; c) B. Ding, H. Kim, C. Kim, M. Khil, S. Park, *Nanotechnology* **2003**, *14*, 532.

[16] X. H. Zong, S. F. Ran, K. S. Kim, D. F. Fang, B. S. Hsiao, B. Chu, *Biomacromolecules* **2003**, *4*, 416.

[17] G. E. Wnek, M. E. Carr, D. G. Simpson, G. L. Bowlin, *Nano Lett.* **2003**, *3*, 213.

[18] X. Y. Wang, C. Drew, S. H. Lee, K. J. Senecal, J. Kumar, L. A. Samuelson, *Nano Lett.* **2002**, *2*, 1273.

[19] X. Y. Wang, Y. G. Kim, C. Drew, B. C. Ku, J. Kumar, L. A. Samuelson, *Nano Lett.* **2004**, *4*, 331.

[20] E. H. Sanders, R. Kloefkorn, G. L. Bowlin, D. G. Simpson, G. E. Wnek, *Macromolecules* **2003**, *36*, 3803.

[21] D. H. Renker, I. Chun, *Nanotechnology* **1996**, *7*, 216.

[22] Z. M. Huang, Y. Z. Zhang, M. Kotaki, S. Ramakrishna, *Compos. Sci. Technol.* **2003**, *63*, 2223.

[23] K. H. Lee, H. Y. Kim, H. J. Bang, Y. H. Jung, S. G. Lee, *Polymer* **2003**, *44*, 4029.

[24] G. Larsen, R. Spretz, R. Velarde-Ortiz, *Adv. Mater.* **2004**, *16*, 166.

[25] H. Fong, I. Chun, D. H. Deneker, *Polymer* **1999**, *40*, 4585.

[26] A. B. D. Cassie, S. Baxter, *Trans. Faraday Soc.* **1944**, *40*, 546.

 © 2004 Wiley-VCH Verlag GmbH & Co. KGaA, Weinheim

Natural Products Synthesis

Stereoselective Total Synthesis of the Ionophore Antibiotic Zincophorin**

*Kei Komatsu, Keiji Tanino, and Masaaki Miyashita**

The ionophore antibiotics, often polyethers and peptides, are known to transport a specific metal ion or specific metal ions through membranes in organisms.[1,2] Ionophore antibiotics have also been shown to transport a specific metal cation by forming a metal chelate. Zincophorin (**1**), isolated from a strain of *Streptomyces griseus*, is a unique ionophore antibiotic with a very high affinity for Zn^{II} cations.[3,4] This affinity also extends to Mg^{II} ions.[3,4] Several novel structural features of zincophorin, as well as its strong antibacterial properties, render this ionophore a worthy target for synthetic exploration.[5] The Danishefsky group reported the first total synthesis of zincophorin methyl ester based on a hetero-

[*] K. Komatsu, Dr. K. Tanino, Prof. Dr. M. Miyashita
Division of Chemistry, Graduate School of Science
Hokkaido University
060-0810 Sapporo (Japan)
Fax: (+81) 11-706-4920
E-mail: miyasita@sci.hokudai.ac.jp

[**] Financial support from the Ministry of Education, Culture, Sports, Science, and Technology, Japan (a Grant-in-Aid for Scientific Research (A) (No. 12304042) and a Grant-in-Aid for Scientific Research on Priority Areas (A): "Exploitation of Multi-Element Cyclic Molecules" (No. 13029003)) is gratefully acknowledged.

Supporting information for this article is available on the WWW under http://www.angewandte.org or from the author.

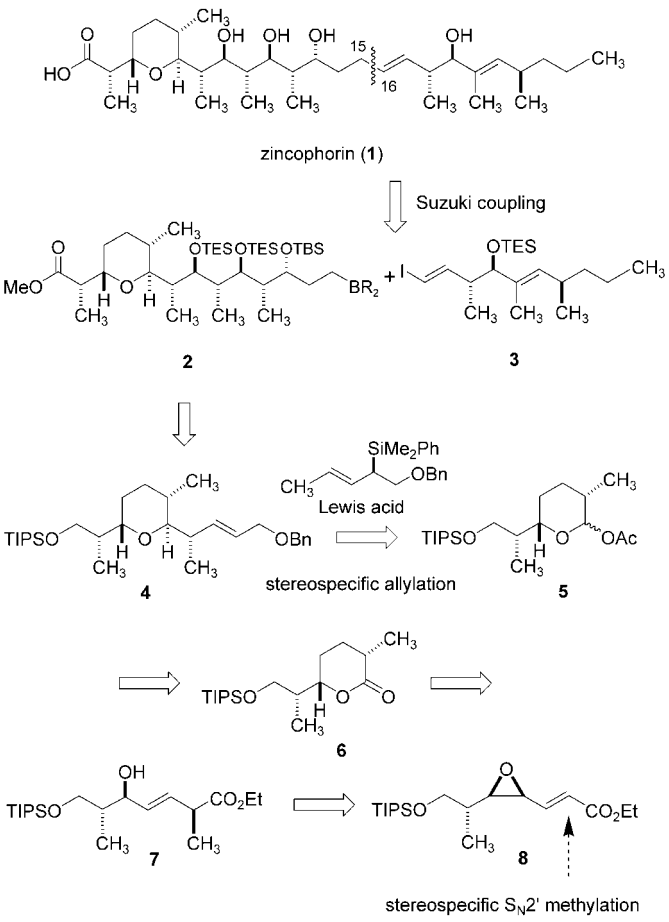
 DOI: 10.1002/anie.200460434 © 2004 Wiley-VCH Verlag GmbH & Co. KGaA, Weinheim

Diels–Alder strategy,[6] and very recently Cossy and coworkers also reported the successful synthesis of zincophorin methyl ester.[7] However, the total synthesis of zincophorin (**1**) itself has not been reported, probably because of the difficulty in characterizing the free acid.[6]

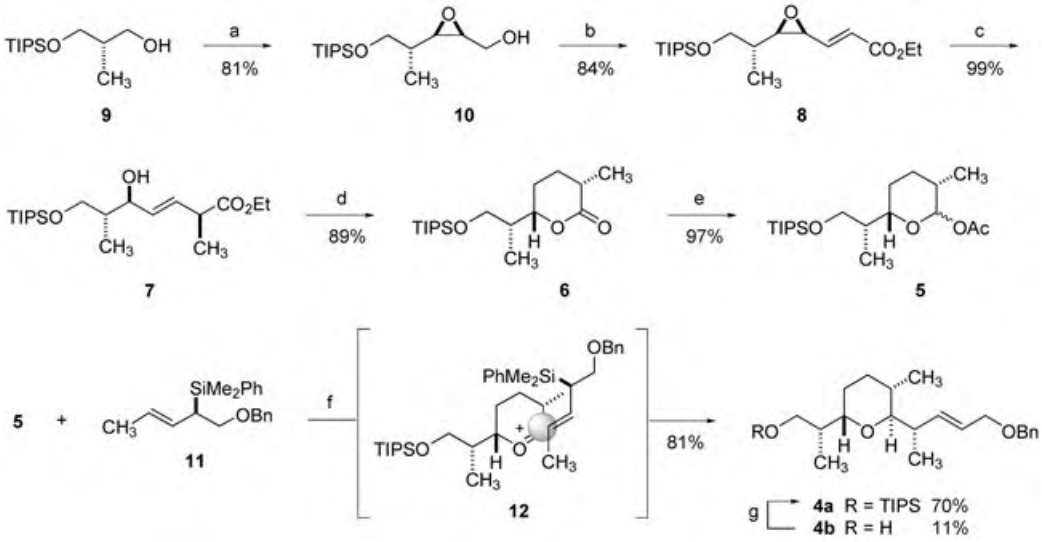
We report herein the first and highly stereoselective total synthesis of the free acid zincophorin based on our original strategy of acyclic stereocontrol (Scheme 1). Retrosynthetically, zincophorin (**1**) was disconnected at the C15–C16 bond and divided into the fragments **2**, which contains a terminal alkyl borane, and **3**, with a trisubstituted double bond and a terminal vinyl iodide. These two fragments could be connected by a Suzuki coupling.[8] Fragment **2**, which consists of the 2,5,6-trisubstituted tetrahydropyran moiety and a polypropionate-derived chain, contains eight contiguous asymmetric carbon atoms as well as two further stereogenic centers. Thus, the stereoselective synthesis of the trisubstituted tetrahydropyran moiety and construction of the contiguous stereogenic centers are the key points in the present synthesis.

To prepare the requisite trisubstituted tetrahydropyran **4** highly stereoselectively, we designed a synthetic route via the δ-lactone **6**. A stereospecific allylation reaction of the lactol **5** with a chiral allyl silane was envisaged. We planned to construct the crucial intermediate **6** stereoselectively by an S_N2' methylation reaction of the *cis*-epoxy unsaturated ester **8** to give **7**, since it has been reported that α methylation of δ-lactones that bear an alkyl substituent at the C5 position generally leads to a 1:1 mixture of stereoisomers.[9]

The trisubstituted tetrahydropyran **4** was synthesized highly stereoselectively according to Scheme 2. Thus, (*S*)-3-(triisopropylsilyloxy)-2-methylpropanol (**9**) was converted into the expected *Z* unsaturated ethyl ester by a Swern oxidation followed by a Horner–Emmons reaction with the



Scheme 1. Retrosynthetic analysis of zincophorin (**1**).



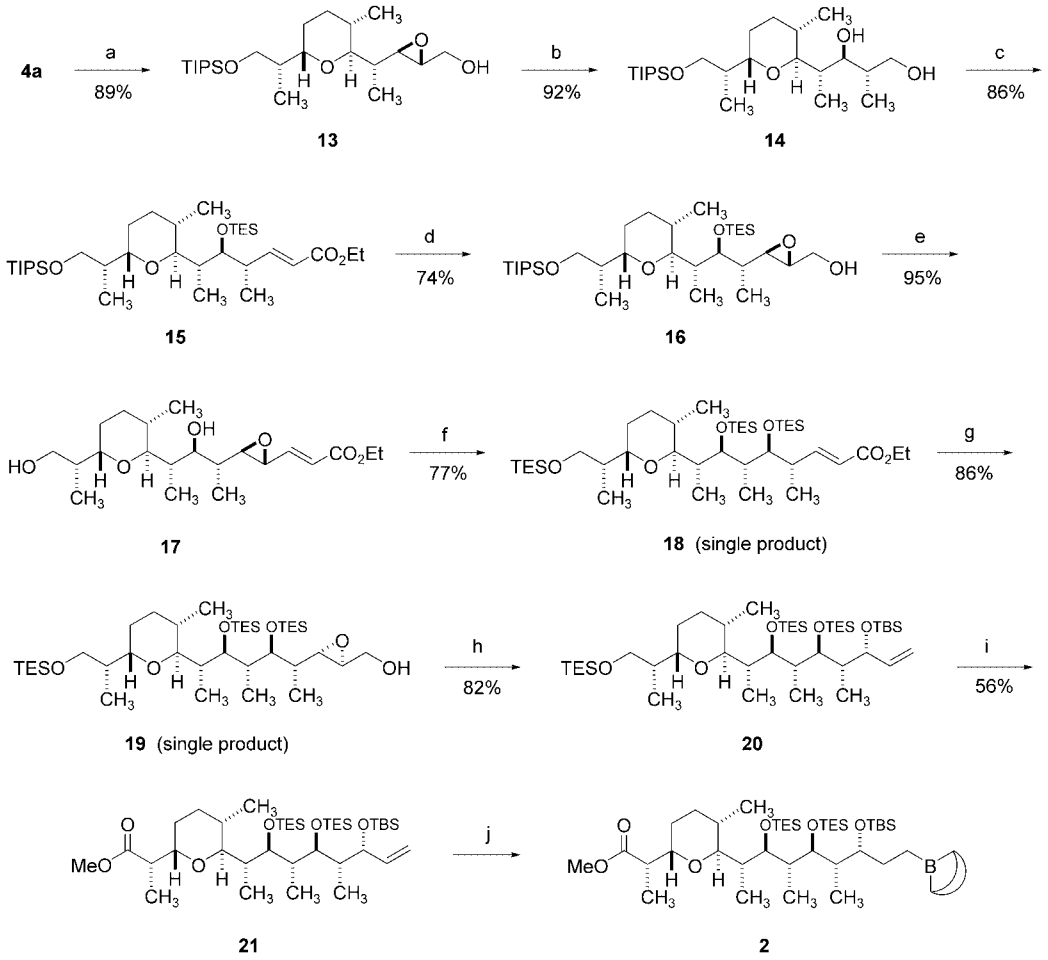
Scheme 2. Synthesis of the trisubstituted tetrahydropyran **4a**: a) 1. Swern oxidation; 2. $(o\text{-}CH_3C_6H_4O)_2P(O)CH_2CO_2Et$, NaH, THF, −78 °C, 92% (2 steps); 3. DIBAL-H, THF, −78→0 °C; 4. MCPBA, CH_2Cl_2, −78→−45 °C, 88% (2 steps); b) 1. Swern oxidation; 2. $(i\text{PrO})_2P(O)CH_2CO_2Et$, *t*BuOK, THF, −78 °C, 84% (2 steps); c) Me_2Zn–CuCN, DMF, 0 °C, 99% (α/γ = 97:3); d) 1. H_2, PtO_2, EtOH, room temperature; 2. $Ti(O\text{i}Pr)_4$, DMF, 100 °C, 89% (2 steps); e) DIBAL-H, CH_2Cl_2, −78 °C, then Ac_2O, pyridine, DMAP, −78 °C→RT, 97%; f) $TiCl_3(O\text{i}Pr)$, CH_2Cl_2, −78 °C, 81%; g) TIPSOTf, 2,6-lutidine, CH_2Cl_2, 0 °C, 100%. Bn = benzyl, DIBAL-H = diisobutylaluminium hydride, MCPBA = *m*-chloroperoxybenzoic acid, DMF = *N*,*N*-dimethylformamide, DMAP = 4-(dimethylamino)pyridine, RT = room temperature, TIPS = triisopropylsilyl, Tf = trifluoromethanesulfonyl.

 © 2004 Wiley-VCH Verlag GmbH & Co. KGaA, Weinheim

Ando reagent[10] in 92% yield ($Z/E = 93:7$). After reduction of the ester with DIBAL-H, the resulting Z allylic alcohol was oxidized stereoselectively with MCPBA to afford the β-epoxy alcohol **10** ($\alpha/\beta = 7:93$, 88% yield),[11] which was then transformed into the epoxy unsaturated ester **8** by a Swern oxidation followed by a Horner–Emmons reaction in 84% yield from **10**. The crucial S_N2' methylation reaction of **8** occurred highly stereoselectively in the presence of a new Me_2Zn–CuCN reagent in DMF recently discovered in our laboratory,[12] to give the product of S_N2' methylation **7** quantitatively. The *syn* product was obtained exclusively in this reaction and was readily converted into the key α-methyl-δ-lactone intermediate **6** by a two-step reaction sequence: 1) hydrogenation of the alkene double bond, and 2) lactonization with $Ti(OiPr)_4$ in DMF. The lactone was transformed routinely into the acetal **5** by reduction with DIBAL-H followed by acetylation of the resulting lactol in a one-pot operation.

The key allylation of **5** with the chiral allyl silane **11**[13] occurred stereospecifically in the presence of the Lewis acid $TiCl_3(OiPr)$ in CH_2Cl_2 at −78 °C to give **4a** and **4b**, each as a single stereoisomer, in 70 and 11% yield, respectively. The latter compound was readily converted quantitatively into the former by treatment with TIPSOTf. As expected, the allylation reaction of **5** proceeded highly stereoselectively, probably via the transition state **12** in which the double bond of the oxonium ion derived from **5** and that of the allyl silane occupy the favorable antiperiplanar conformation with maximum overlap of the π orbitals.[14]

Thus, the critical intermediate **4a** with five stereogenic centers was synthesized with complete stereoselectivity. Compound **4a** was then converted into the single α-epoxy alcohol **13** by removal of the benzyl group followed by asymmetric epoxidation (Scheme 3).[15] Upon the treatment of **13** with the Gilman reagent,[11b] compound **14** with seven stereogenic centers was obtained in 92% yield as the only

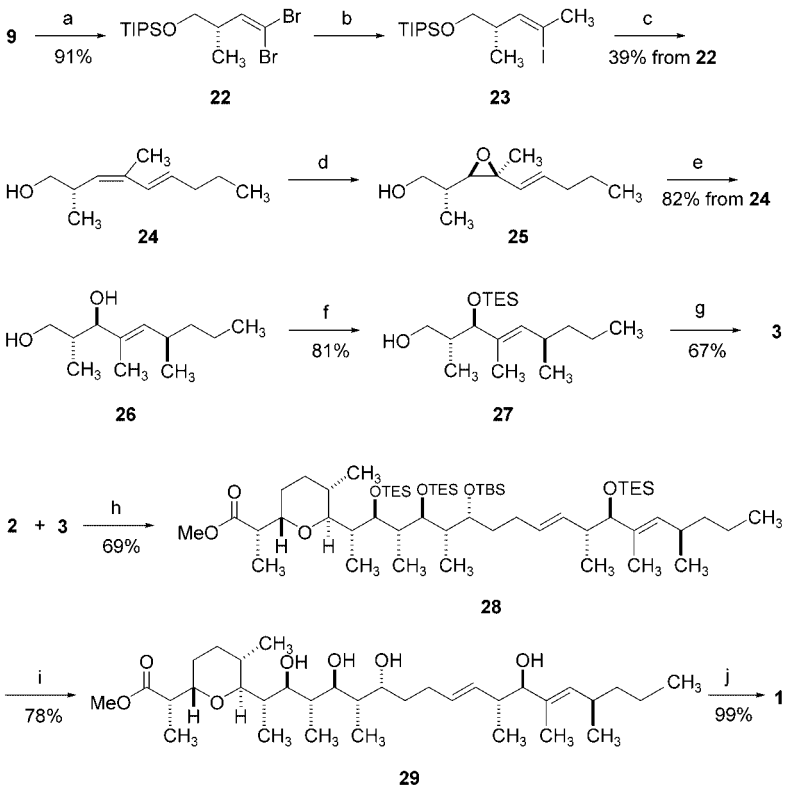


Scheme 3. Synthesis of **2**: a) 1. Ca, NH_3, THF, −78 °C; 2. $Ti(OiPr)_4$, D-(−)-DIPT, TBHP, MS (4 Å), CH_2Cl_2, −23 °C, 89% (2 steps); b) Me_2CuLi, Et_2O, −40→0 °C, 92%; c) 1. TESOTf, 2,6-lutidine, CH_2Cl_2, 0 °C; 2. Swern oxidation; 3. $(iPrO)_2P(O)CH_2CO_2Et$, *t*BuOK, THF, −78 °C, 86% (3 steps); d) 1. DIBAL-H, THF, −78→0 °C; 2. $Ti(OiPr)_4$, D-(−)-DET, TBHP, MS (4 Å), CH_2Cl_2, −23 °C, 74% (2 steps), ($\alpha/\beta = 5:95$); e) 1. Swern oxidation; 2. $(EtO)_2P(O)CH_2CO_2Et$, NaH, THF, 0 °C; 3. TBAF, THF, room temperature, 95% (3 steps); f) 1. Me_3Al–D_2O, CH_2Cl_2, −30 °C; 2. TESOTf, 2,6-lutidine, CH_2Cl_2, 0 °C, 77% (2 steps); g) 1. DIBAL-H, THF, −78→0 °C, 98%; 2. MCPBA, CH_2Cl_2, −78→0 °C, 88%; h) 1. PPh_3, I_2, imidazole, benzene, room temperature; 2. BuLi, THF, −78 °C, 92% (2 steps); 3. TBSCl, DMAP, DMF, room temperature, 89%; i) 1. Swern oxidation; 2. $NaClO_2$, NaH_2PO_4, 2-methyl-2-butene, *t*BuOH, H_2O, THF, room temperature, then $TMSCHN_2$, CH_2Cl_2, room temperature, 56% (3 steps); j) 9-BBN, THF, 60 °C. DIPT = diisopropyl tartrate, TBHP = *tert*-butyl hydroperoxide, MS = molecular sieves, TES = triethylsilyl, DET = diethyl tartrate, TBAF = tetrabutylammonium fluoride, TBS = *tert*-butyldimethylsilyl, TMS = trimethylsilyl, 9-BBN = 9-borabicyclo[3.3.1]nonane.

 © 2004 Wiley-VCH Verlag GmbH & Co. KGaA, Weinheim

product. It was transformed into the unsaturated ester **15** by a three-step reaction sequence: 1) protection of the hydroxy groups as TES ethers, 2) Swern oxidation by the Spur protocol,[16] and 3) Horner–Emmons reaction, in 86% overall yield. After the reduction of **15** with DIBAL-H, asymmetric epoxidation of the resulting allylic alcohol furnished the epoxy alcohol **16** stereoselectively. Compound **16** was subjected to another Swern oxidation/Horner–Emmons olefination sequence, followed by removal of the silyl protecting groups with TBAF, to afford the epoxy unsaturated ester **17** (95% for the three steps). The key methylation reaction of **17** proceeded stereospecifically with a Me_3Al–water system[17] to give a single product with nine asymmetric carbon atoms. The treatment of this compound with TESOTf then afforded **18** (77% yield over two steps). When **18** was treated with DIBAL-H in THF and then with MCPBA in CH_2Cl_2, the α-epoxy alcohol **19** was obtained as a single product in 86% yield.[18]

Compound **19** was transformed in turn into the terminal olefin **20** by a three-step reaction sequence: 1) conversion into an epoxy iodide, 2) treatment with BuLi to give an allylic alcohol,[19] and 3) protection of the secondary alcohol with TBSCl (82% yield over three steps). All that remained in the synthesis of fragment **2** was the oxidation of the TES-protected primary alcohol moiety to the carboxylic acid and subsequent hydroboration of the terminal olefin. These transformations were performed successfully by a Swern oxidation[16] followed by $NaClO_2$ oxidation of the resultant aldehyde to the carboxylic acid, esterification with $TMSCHN_2$ (56% for the three steps), and further treatment of the product **21** with 9-BBN in THF. Thus, fragment **2** with ten stereogenic centers was synthesized in a straightforward and highly stereoselective manner by our original strategy based on acyclic stereocontrol.



Scheme 4. Synthesis of **3** and total synthesis of zincophorin (**1**): a) 1. Swern oxidation; 2. CBr_4, PPh_3, pyridine, CH_2Cl_2, 0°C, 91% (2 steps); b) Me_2CuLi, Et_2O, −78°C, then I_2, −40°C; c) 1. (*E*)-$CH_3(CH_2)_2CH{=}CHZrCp_2Cl$, $ZnBr_2$, $[PdCl_2(PPh_3)_2]$, DIBAL-H, THF, room temperature; 2. HF, THF, room temperature, 39% from **22**; d) MCPBA, CH_2Cl_2, −60→−30°C, (α/β = 7:93); e) Me_2CuLi, Et_2O, −78°C, 82% from **24**; f) 1. TESOTf, 2,6-lutidine, CH_2Cl_2, 0°C, 96%; 2. HF–py, pyridine, THF, 0°C, 84%; g) 1. Dess–Martin periodinane; 2. $CrCl_2$, CHI_3, THF, 0°C, 67% (2 steps); h) aqueous Cs_2CO_3, $AsPh_3$, $[PdCl_2(dppf)]$, THF, DMF, room temperature, 69%; i) TEAF, DMF, room temperature, 78%; j) LiOH, H_2O, MeOH, THF, room temperature, then 1N HCl, 99%. py = pyridine, dppf = 1,1′-bis(diphenylphosphanyl)ferrocene, TEAF = tetraethylammonium fluoride.

We next focused on the synthesis of fragment **3**. Although we presumed that the synthesis of **3** would be difficult because of its densely functionalized stereostructure, we were able to synthesize **3** in a straightforward fashion according to Scheme 4. Thus, the dibromomethylene compound **22**, readily prepared from the same starting material **9** as used for the synthesis of fragment **2**, was treated with the Gilman reagent in Et_2O, and the *Z* vinyl copper species generated in situ was quenched with iodine to give the *Z* vinyl iodide **23**.[20] A Negishi coupling[21] with an (*E*)-1-pentenylzirconium reagent then furnished the desired *Z*,*E* conjugated diene **24** (39% yield over three steps). The homoallylic alcohol **24** was oxidized with MCPBA to produce the β-epoxy alcohol **25** stereoselectively (α/β = 7:93). The key S_N2' methylation reaction of **25** proceeded upon treatment with the Gilman reagent[22] in a highly stereoselective manner to afford the *syn* compound **26** as a single product in 82% yield from **24**. After protection of the secondary hydroxy group in **26** with a TES group in two steps, the product **27** was transformed into fragment **3** by Dess–Martin oxidation followed by the Takai reaction[23] in 67% yield.

With the segments **2** and **3** in hand, we had reached a critical stage in the total synthesis: the coupling of the two segments, removal of the protecting groups, and final hydrolysis of the methyl ester moiety. The key Suzuki coupling reaction[8,24] of **2** and **3** was performed under the conditions given in Scheme 4 and resulted in the formation of **28** in 69% yield. The removal of the four silyl groups in **28** with tetraethylammonium fluoride (TEAF) in DMF afforded zincophorin methyl ester (**29**) in 78% yield.

All spectral data of the synthetic compound **29** and its optical rotation value ($[\alpha]_D^{26} = +22$ ($c = 0.64$, $CHCl_3$)) were identical with those of the methyl ester derived from natural zincophorin ($[\alpha]_D^{24} = +21$ ($c = 2.0$, $CHCl_3$)).[4] Finally, hydrolysis of the methyl ester **29** with aqueous LiOH in MeOH and THF, followed by acidification with 1N HCl, provided zincophorin (**1**) in nearly quantitative yield.[25] The synthetic compound (free acid) was identical in all respects with naturally occurring zincophorin,[3] including spectroscopic

 © 2004 Wiley-VCH Verlag GmbH & Co. KGaA, Weinheim

characteristics (^{1}H and ^{13}C NMR, IR, and mass spectra), melting point (m.p. 65–69 °C; lit.:[3] m.p. 66–70 °C), and optical rotation ($[\alpha]_D^{24} = -1.9$ ($c = 0.59$, $CHCl_3$); lit.:[3] $[\alpha]_D^{25} = 0$ ($c = 1.0$, $CHCl_3$)).

In summary, we have reported the first, highly stereoselective total synthesis of zincophorin free acid through an original strategy based on acyclic stereocontrol without the use of aldol methodologies.

Received: April 24, 2004 [Z460434]

Keywords: allylation · antibiotics · natural products · stereoselectivity · total synthesis

[1] *Polyether Antibiotics*, *Vol. 1* and *2* (Ed.: J. W. Westley), Marcel Dekker, New York, **1982**.
[2] M. Dobler in *Ionophores and their Structures*, Wiley, New York, **1981**.
[3] a) U. Gräfe, W. Schade, M. Roth, L. Radics, M. Incze, K. Ujszaszy, *J. Antibiot.* **1984**, *37*, 836; b) L. Radics, *J. Chem. Soc. Chem. Commun.* **1984**, 599.
[4] H. A. Brooks, D. Gardner, J. P. Poyser, T. J. King, *J. Antibiot.* **1984**, *37*, 1501.
[5] a) M. Balestra, M. D. Wittman, J. Kallmerten, *Tetrahedron Lett.* **1988**, *29*, 6905; b) C. L. Cywin, J. Kallmerten, *Tetrahedron Lett.* **1993**, *34*, 1103; c) J. F. Booysen, C. W. Holzapfel, *Synth. Commun.* **1995**, *25*, 1473; d) J. A. Marshall, M. R. Palovich, *J. Org. Chem.* **1998**, *63*, 3701; e) S. R. Chemler, W. R. Roush, *J. Org. Chem.* **1998**, *63*, 3800; f) Y. Guindon, L. Murtagh, V. Caron, S. R. Landry, G. Jung, M. Bencheqroun, A.-M. Faucher, B. Guérin, *J. Org. Chem.* **2001**, *66*, 5427; g) J. Cossy, N. Blanchard, M. Defosseux, C. Meyer, *Angew. Chem.* **2002**, *114*, 2248; *Angew. Chem. Int. Ed.* **2002**, *41*, 2144.
[6] a) S. J. Danishefsky, H. G. Selnick, M. P. DeNinno, R. E. Zelle, *J. Am. Chem. Soc.* **1987**, *109*, 1572; b) S. J. Danishefsky, H. G. Selnick, R. E. Zelle, M. P. DeNinno, *J. Am. Chem. Soc.* **1988**, *110*, 4368.
[7] M. Defosseux, N. Blanchard, C. Meyer, J. Cossy, *Org. Lett.* **2003**, *5*, 4037.
[8] N. Miyaura, A. Suzuki, *Chem. Rev.* **1995**, *95*, 2457.
[9] H. Yamada, M. Nishizawa, *J. Org. Chem.* **1995**, *60*, 386.
[10] a) K. Ando, *J. Org. Chem.* **1997**, *62*, 1934; b) K. Ando, *J. Org. Chem.* **1999**, *64*, 6835.
[11] a) M. R. Johnson, T. Nakata, Y. Kishi, *Tetrahedron Lett.* **1979**, *20*, 4343; b) H. Nagaoka, Y. Kishi, *Tetrahedron* **1981**, *37*, 3873.
[12] A. Hirai, A. Matsui, K. Komatsu, K. Tanino, M. Miyashita, *Chem. Commun.* **2002**, 1970.
[13] Although the chiral allyl silane **11** was a new compound, we were able to prepare it by the Ito method: M. Suginome, A. Matsumoto, Y. Ito, *J. Am. Chem. Soc.* **1996**, *118*, 3061.
[14] a) I. Fleming, J. Dunoguès, R. Smithers, *Org. React.* **1989**, *37*, 2; b) C. E. Masse, J. S. Panek, *Chem. Rev.* **1995**, *95*, 1293.
[15] T. Katsuki, K. B. Sharpless, *J. Am. Chem. Soc.* **1980**, *102*, 5974.
[16] A. Rodríguez, M. Nomen, B. W. Spur, J. J. Godfroid, *Tetrahedron Lett.* **1999**, *40*, 5161.
[17] M. Miyashita, M. Hoshino, A. Yoshikoshi, *J. Org. Chem.* **1991**, *56*, 6483. We recently discovered that a Me_3Al–D_2O system is superior to the previously reported Me_3Al–H_2O system.
[18] K. Maruyama, M. Ueda, S. Sasaki, Y. Iwata, M. Miyazawa, M. Miyashita, *Tetrahedron Lett.* **1998**, *39*, 4517.
[19] J. A. Marshall, R. Sedrani, *J. Org. Chem.* **1991**, *56*, 5496.
[20] This as yet unpublished synthetic method was recently developed in our laboratory.
[21] a) E. Negishi, N. Okukado, A. O. King, D. E. Van Horn, B. I. Spiegel, *J. Am. Chem. Soc.* **1978**, *100*, 2254; b) J. Ichikawa, M. Fujiwara, H. Nawata, T. Okauchi, T. Minami, *Tetrahedron Lett.* **1996**, *37*, 8799; c) J. S. Panek, T. Hu, *J. Org. Chem.* **1997**, *62*, 4912.
[22] J. A. Marshall, J. D. Trometer, B. E. Blough, T. D. Crute, *J. Org. Chem.* **1988**, *53*, 4274.
[23] K. Takai, K. Nitta, K. Utimoto, *J. Am. Chem. Soc.* **1986**, *108*, 7408.
[24] S. R. Chemler, D. Trauner, S. J. Danishefsky, *Angew. Chem.* **2001**, *113*, 4676; *Angew. Chem. Int. Ed.* **2001**, *40*, 4544.
[25] To isolate zincophorin free acid, it is essential to protonate the lithium carboxylate by acidification and to isolate the resulting carboxylic acid by extraction, as purification by column chromatography on silica gel gives an inseparable mixture of zincophorin and zincophorin–metal (probably magnesium) complexes.

 © 2004 Wiley-VCH Verlag GmbH & Co. KGaA, Weinheim

Gas Sensors

Nonaqueous Synthesis of Nanocrystalline Semiconducting Metal Oxides for Gas Sensing**

Nicola Pinna, Giovanni Neri, Markus Antonietti, and Markus Niederberger**

Air pollution is one of the emerging problems in our society. The more and more strict regulations on the emission of toxic gases require fast and accurate detection at sub-ppm concentrations. Among these gases, carbon monoxide and nitrogen oxides are the major atmospheric pollutants. In Europe, for example, the alarm thresholds are about 10 ppm for CO and 0.1 ppm for NO_2. Sensing devices based on metal oxide semiconductors are mainly used for the detection of these gases. When a metal oxide is exposed to reducing or oxidizing gases, its resistance varies in accordance with the gas concentration. The theory for the operation of such sensors involves absorption/desorption phenomena and reactions at the surface of the metal oxide. Materials with high surface areas are advantageous for obtaining a good sensitivity in sensing applications. Indeed it was demonstrated that a decrease in the size of the crystallite in the sensing layer leads to a considerable increase in sensitivity.[1]

[*] Dr. N. Pinna, Prof. Dr. M. Antonietti, Dr. M. Niederberger
Max-Planck-Institute of Colloids and Interfaces
14424 Potsdam (Germany)
Fax: (+49) 331-567-9502
E-mail: pinna@mpikg-golm.mpg.de
markus.niederberger@mpikg-golm.mpg.de

Prof. Dr. G. Neri
University of Messina
Department of Industrial Chemistry and Materials Engineering
98166 Messina (Italy)

[**] Financial support by the Max-Planck Society is gratefully acknowledged. We thank the Fritz-Haber Institute and Prof. R. Schlögl for the use of the electron microscope, and Klaus Weiss for his technical assistance.

 DOI: 10.1002/anie.200460610 © 2004 Wiley-VCH Verlag GmbH & Co. KGaA, Weinheim

Sol–gel procedures based on the hydrolysis and condensation of metal halide or metal alkoxide precursors in aqueous solution have been applied extensively to prepare thin films suitable for sensing applications.[2,3] However, the approach involving direct deposition of preformed nanopowders onto the substrates of the micropatterned sensors has been less explored.[4–7] This latter approach is highly versatile because it permits the large-scale production of the sensor devices by simply depositing the prefabricated metal oxide particles onto the sensor substrates.

We reported recently a halide- and surfactant-free nonaqueous route to control the particle size, shape, and crystallinity of nanocrystalline perovskites and related compounds.[8] The successful preparation of V_2O_3, Nb_2O_5, Ta_2O_5, and HfO_2 nanoparticles gave further evidence for the wide applicability of this approach.[9–11]

Herein we present a nonaqueous synthesis of nanocrystalline SnO_2 and In_2O_3. The SnO_2, in particular, was obtained in a previously non-accessible small particle size and crystal quality. These two metal oxides are particularly interesting for sensing applications. SnO_2 shows good sensitivity to reducing gas (for example, CO)[12] and In_2O_3 to oxidizing ones (for example, NO_2)[13,14] depending, among other parameters, on the method of preparation and crystallite size.[15,16] To investigate the sensing characteristics of the as-synthesized nanocrystals, they were deposited without addition of any binder or activation layers on a micropatterned alumina substrate and tested for their ability to detect trace levels of NO_2, CO, and CH_4 in air.

The X-ray powder diffraction (XRD) patterns of the as-synthesized nanoparticles are shown in Figure 1. The XRD pattern of pure SnO_2 (Figure 1a) displays four main broad peaks arising from the very small cristallite size and can be attributed to the Cassiterite structure (JCPDS 41-1445). This assignment is further confirmed by diffraction patterns calculated from the Debye scattering equation[17,18] for spherical, monodisperse particles with diameters of 2.2 nm (Figure 1a dotted line). The calculated and experimental patterns are in good agreement. The XRD pattern of the In_2O_3 nanoparticles (Figure 1b) shows sharp peaks corresponding to the In_2O_3 cubic structure (JCPDS 6-416). The sharpness of the peaks indicates a much larger particle size compared to SnO_2.

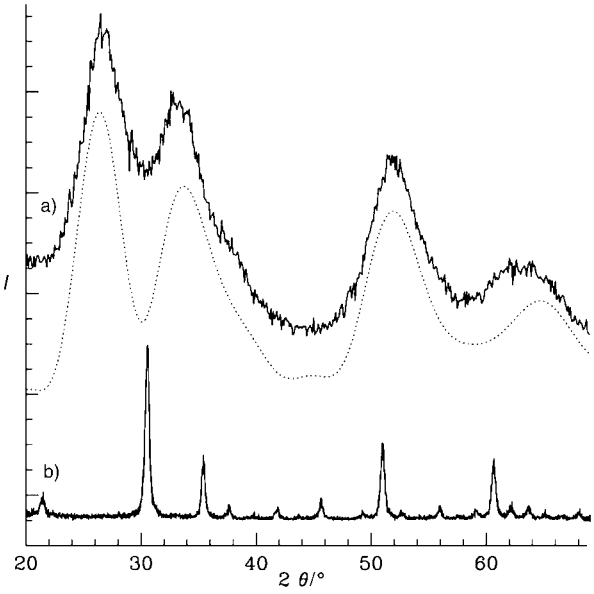


Figure 1. X-ray powder diffraction patterns of the as-synthesized SnO_2 (a), and In_2O_3 (b) nanoparticles. The Debye scattering equation calculated for 2.2-nm spherical SnO_2 nanoparticles is shown as a dotted line.

Figure 2a shows a high-resolution transmission electron micrograph (HRTEM) of an assembly of SnO_2 nanoparticles with an average size of 2–2.5 nm, which is in good agreement with the XRD data. Each particle presents well-defined lattice fringes which indicate that the particles are highly crystallized even at such a small size. The lack of any surface-protecting layers results in some agglomeration of the particles. The randomly oriented lattice fringes show the particles are neither coalesced nor do they show epitaxial aggegration. Figure 2b shows a selected-area electron diffraction (SAED) pattern. The lattice distances measured from the diffraction rings are in perfect agreement with the Cassiterite structure. Figure 2c shows the HRTEM image of an isolated particle oriented along the [110] direction. Its power spectrum (PS; Figure 2d) provides evidence that the particle is highly crystallized and does not present any structural defaults.

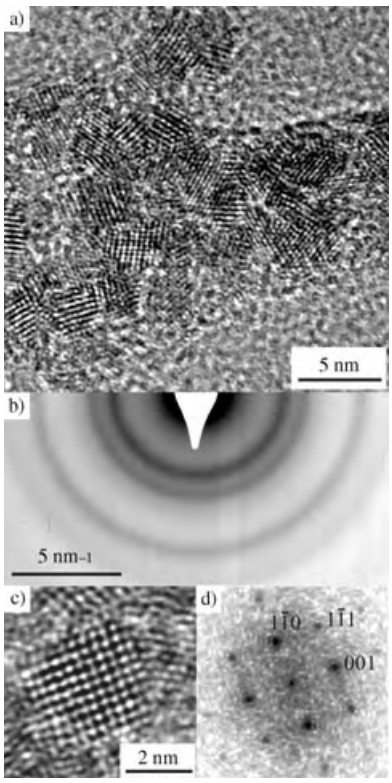


Figure 2. HRTEM image of an assembly of SnO_2 nanoparticles (a), selected-area electron diffraction (b), HRTEM image of an isolated nanoparticle (c), and its PS (d).

 © 2004 Wiley-VCH Verlag GmbH & Co. KGaA, Weinheim

Figure 3a shows a TEM image of the corresponding In_2O_3 nanoparticles. The particles have a cubelike shape with an average length of 20 nm. The SAED pattern of such an assembly (Figure 3b) shows rings, formed by many spots,

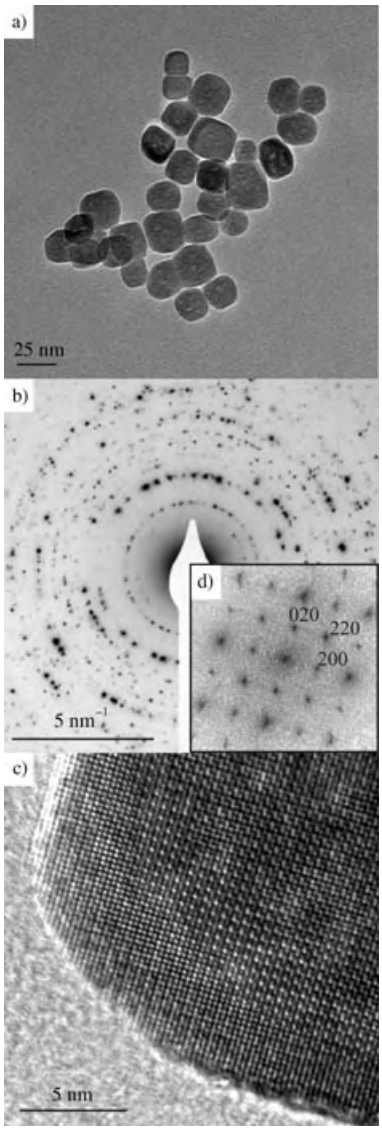


Figure 3. TEM image of an assembly of In_2O_3 nanoparticles (a), selected-area electron diffraction (b), HRTEM image of a part of a nanoparticle (c), and its PS (d).

which correspond to the In_2O_3 cubic structure. The HRTEM image (Figure 3c) of a part of one particle shows several lattice planes with perfect crystallinity. The sharp reflections of its PS can be unambiguously attributed to the In_2O_3 structure for a particle oriented along the [001] direction.

Sensors were realized from these SnO_2 and In_2O_3 nanoparticles by depositing thin films of the respective particles from an aqueous ink onto alumina substrates by a simple printing method. The mechanical and electrical properties of the deposited films were evaluated prior to the sensing tests. It is interesting to note that the sensing films without sintering are already mechanically resistant and adhere to the support. This observation is likely a consequence of the very fine particle size, which strongly improves the adhesion on the alumina surface. From an electrical point of view, the In_2O_3 sensor shows a substantially higher conductivity (around 1.8×10^{-4} A) compared to the SnO_2 sensor (3.6×10^{-9} A) in dry air at 300 °C. This result is likely related to the very small particle size of the tin dioxide, which is well below the critical grain size $d_c < 2L$ and a space-charge depth $L = 3$ nm for SnO_2, and results in the formation of an electron-depleted space charge layer extending over the whole crystallite.[19]

The sensing properties of the nanopowders towards trace levels of both oxidizing (NO_2) and reducing gases (CO, CH_4) were analyzed between 100 and 450 °C in dry air. The response of the In_2O_3 sensor to 2 ppm of NO_2 as a function of the operating temperature is shown in Figure 4a. The response to NO_2 increases with increasing temperature, with a maximum sensitivity $S = I_{air}/I_{2\,ppm\ NO_2} = 100$ around 200 °C. Figure 4b shows the dynamic response of the sensor at 250 °C to different and successive concentration pulses of NO_2 (2–20 ppm). NO_2 is an oxidizing gas and therefore causes a decrease in the conductance of n-type semiconductors. The output signals essentially recover to the initial level, thus indicating the reversibility of the interactions between the sensing elements and the gas to be detected, with a fast (less than 60 s) response time (that is, the time required to reach 90% of the full response). Figure 4c displays the calibration curve of the sensor at 250 °C for NO_2. The experimental data were fitted by using a power-law relation expressed as:

$$S = I_{air}/I_{gas} = (1 + k\,[NO_2])^m \qquad (1)$$

where k is the sensitivity coefficient and m the power-law exponent. From the straight line obtained, we calculated $m = 0.49 \pm 0.06$ ppm^{-1} and extrapolated a lower detection limit of about 1 ppb for NO_2 in air. Our results show a remarkable increase in sensitivity (between two and ten times) with respect to the In_2O_3-based NO_2 sensors reported in the recent literature.[13,14,16,20,21] However, in these cases the sensing layers were prepared by different methods.

An additional advantage of our sensor is that cross-sensitivity tests with CO and CH_4 have shown that it does not show an appreciable response to reducing gases between 100–300 °C, thus making it highly selective towards the detection of nitrogen dioxide.

A good response for the reducing gases was observed with both the In_2O_3 and SnO_2 sensors at temperatures higher than 400 °C. This behavior is typical for metal oxides, which generally require the presence of suitable metal promoters to decrease the operating temperature substantially.[22] As an example, Figure 5 reports the dynamic response of the SnO_2 sensor at 400 °C towards different CO concentrations (10–100 ppm) in dry air.

In conclusion the successful synthesis of semiconducting metal oxide nanocrystals of SnO_2 and In_2O_3 by using a nonaqueous approach involving the reaction of a metal alkoxide with benzyl alcohol is presented. The products were obtained in the form of fine nanocrystalline powders that had superior crystallinity and good yields which permits them to

 © 2004 Wiley-VCH Verlag GmbH & Co. KGaA, Weinheim

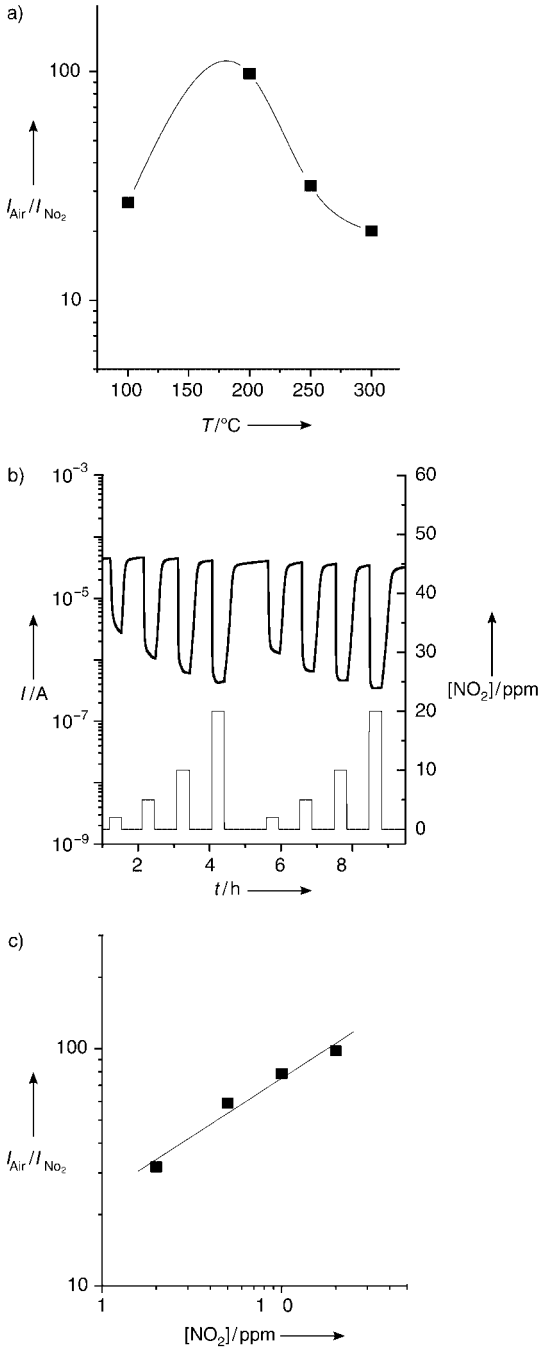


Figure 4. Response to 2 ppm of NO_2 versus operating temperature of the In_2O_3 sensor (a), its dynamic response at 250 °C (b), and calibration curve at 250 °C (c).

be used for sophisticated applications in customer-near devices, for example, as conducting glass coatings, for IR filters, or in sensors. The nanopowders can be used directly to fabricate sensor devices just by deposition of the as-synthesized nanoparticles onto micropatterned alumina substrates. Both metal oxides showed high sensitivity and good recovery time. Indium oxide, in particular, showed an unusual high sensitivity to NO_2 (namely, 1 ppb) at low temperature as well as the essential selectivity against CO and methane required by high technological applications.

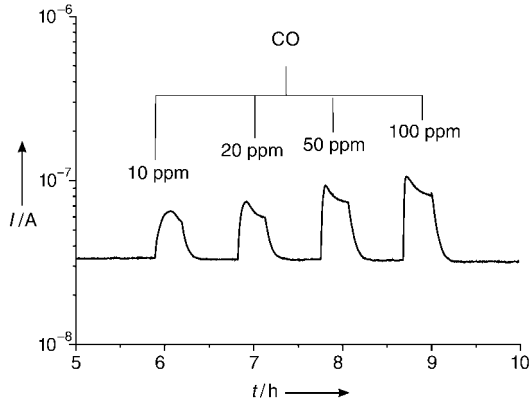


Figure 5. Dynamic response of the SnO_2 sensor at 400 °C to trace levels of CO in air.

Experimental Section

Synthesis: All the synthetic procedures were carried out in a glovebox (O_2 and $H_2O < 0.1$ ppm). In a typical synthesis of nanoparticles, tin(IV) *tert*-butoxide (500 mg, 1.216 mmol) or indium(III) isopropoxide (200 mg, 0.685 mmol) was added to benzyl alcohol (20 mL). The reaction mixture was transferred into a teflon cup of 45 mL inner volume, placed in a steel autoclave, and carefully sealed. The autoclave was taken out of the glovebox and heated in a furnace at 220 °C for 2 days. The resulting milky suspensions were centrifuged, the precipitates thoroughly washed with ethanol and dichloromethane, and subsequently dried in air at 60 °C.

Characterization: For TEM studies one or more drops of the solution of the nanoparticles dispersed in ethanol were deposited on the amorphous carbon film. A Philips CM200 FEG microscope, 200 kV, equipped with a field emission gun was used. The coefficient of spherical aberration was $C_s = 1.35$ mm. The X-ray powder diffraction (XRD) patterns of all samples were measured in reflection mode ($Cu_{K\alpha}$ radiation) on a Bruker D8 diffractometer equipped with a scintillation counter.

Sensing tests: These were carried out on sensors prepared by depositing thin films of the nanopowders dispersed in water onto alumina substrates (3×3 mm^2) at a thickness of around 1 μm. The substrates were fitted, on the front side, with gold interdigitated contacts and, on the backside, with a Pt heater. The sensors were bound as suspended devices onto TO-8 supports and introduced in a teflon test chamber for testing their sensitivity to CO, CH_4, and NO_2 in a controlled atmosphere. The gases coming from certified bottles were further diluted in air and their concentration was varied by a gas-mixing system (MKS mod. 647B) and different mass-flow controllers (MFCs). The experiments were carried out by measuring the electrical current of the sensor devices under a voltage of 1 V by an electrometer (Keithley mod. 6517A). A personal computer with LABview software controlled all the operations related to the gas protocol and to data acquisition, storage, and plotting in real time through a GPIB interface. The sensor response was defined as I_{air}/I_{gas} for NO_2 detection and I_{gas}/I_{air} for CO and CH_4 detection, where I_{air} is the electrical current of the film in air and I_{gas} is the electrical current under gas flow.

Received: May 10, 2004 [Z460610]
Published Online: June 28, 2004

Keywords: gas sensors · indium · nanoparticles · synthetic methods · tin

 © 2004 Wiley-VCH Verlag GmbH & Co. KGaA, Weinheim

[1] N. Yamazoe, *Sens. Actuators B* **1991**, *5*, 7.
[2] R. Rella, P. Siciliano, S. Capone, M. Epifani, L. Vasanelli, A. Licciulli, *Sens. Actuators B* **1999**, *58*, 283.
[3] S. Shukla, S. Seal, L. Ludwig, C. Parish, *Sens. Actuators B* **2004**, *97*, 256.
[4] P. Fau, M. Sauvan, S. Trautweiler, C. Nayral, L. Erades, A. Maissonat, B. Chaudret, *Sens. Actuators B* **2001**, *78*, 83.
[5] K. Soulantica, L. Erades, M. Sauvan, F. Senocq, A. Maissonat, B. Chaudret, *Adv. Funct. Mater.* **2003**, *13*, 553.
[6] Y. Wang, X. Jiang, Y. Xia, *J. Am. Chem. Soc.* **2003**, *125*, 16176.
[7] M. Law, H. Kind, B. Messer, F. Kim, P. Yang, *Angew. Chem.* **2002**, *114*, 2511; *Angew. Chem. Int. Ed.* **2002**, *41*, 2405.
[8] M. Niederberger, N. Pinna, J. Polleux, M. Antonietti, *Angew. Chem.* **2004**, *116*, 2320; *Angew. Chem. Int. Ed.* **2004**, *43*, 2270.
[9] N. Pinna, M. Antonietti, M. Niederberger, *Colloids Surf. A* **2004**, in press.
[10] N. Pinna, G. Garnweitner, M. Antonietti, M. Niederberger, *Adv. Mater.* **2004**, in press.
[11] M. Antonietti, M. Niederberger, N. Pinna, Deutsche Patentanmeldung Nr. 10 2004 016 131.3, **2004**.
[12] N. Yamazoe, Y. Kurokawa, T. Seiyama, *Sens. Actuators* **1983**, *4*, 283.
[13] A. Gurlo, N. Bârsan, M. Ivanovskaya, U. Weimar, W. Göpel, *Sens. Actuators B* **1998**, *47*, 92.
[14] M. Ivanovskaya, A. Gurlo, P. Bogdanov, *Sens. Actuators B* **2001**, *77*, 264.
[15] R. Dolbec, M. A. El Khakoni, A. M. Serventi, R. G. Saint-Jacques, *Sens. Actuators B* **2003**, *93*, 566.
[16] A. Gurlo, M. Ivanovshaya, N. Barsan, M. Schweizer-Berberich, U. Weimar, W. Gopel, A. Dieguez, *Sens. Actuators B* **1997**, *44*, 327.
[17] W. Vogel, *Cryst. Res. Technol.* **1998**, *33*, 1141.
[18] N. Pinna, U. Wild, J. Urban, R. Schlögl, *Adv. Mater.* **2003**, *15*, 329.
[19] Y. Shimizu, M. Egashira, *MRS Bull.* **1999**, *24*, 18.
[20] H. Steffes, C. Imawan, F. Solzbacher, E. Obermeier, *Sens. Actuators B* **2003**, *68*, 249.
[21] C. Cantalini, W. Wlodarski, H. T. Sun, M. Z. Atashbar, M. Passacantando, A. R. Phani, S. Santucci, *Thin Solid Films* **1999**, *350*, 276.
[22] D. Kohl, *Sens. Actuators B* **1990**, *1*, 158.

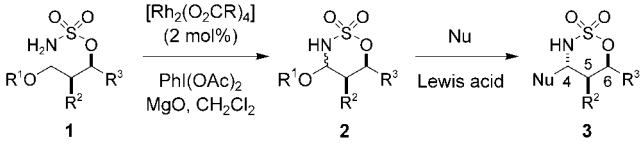
 © 2004 Wiley-VCH Verlag GmbH & Co. KGaA, Weinheim

N,O-Acetals

Rh-Catalyzed Amination of Ethereal C^{α}–H Bonds: A Versatile Strategy for the Synthesis of Complex Amines**

*Kristin Williams Fiori, James J. Fleming, and Justin Du Bois**

The recent advancement of highly selective catalytic methods for the amination of C–H bonds has inspired novel approaches to complex natural products.[1] Our efforts to expand this chemistry further have led to the identification of a distinct class of 1,2,3-oxathiazinane-2,2-dioxide heterocycles **2**, made accessible through sulfamate ester **1** insertion into ethereal C^{α}–H centers (Scheme 1).[2,3] Herein, we demonstrate a simple and effective method, which capitalizes on catalyst-controlled regioselective C–H oxidation, for assembling these unique N,O-acetals **2**. Such compounds display exceptional versatility as iminium ion equivalents, coupling smoothly and with high diasteroinduction to allyl silanes, enol ethers, silyl ketene acetals, and, as reported previously, alkynyl zinc reagents.[2] From these studies has evolved a broadly predictive stereochemical model for nucleophilic addition reactions with **2**. In all, the stereoselective assembly of functionalized oxathiazinanes through this efficient two-step sequence opens untapped possibilities for C–H amination in synthesis.[4]



Scheme 1. Oxathiazinane N,O-acetals as iminium ion equivalents.

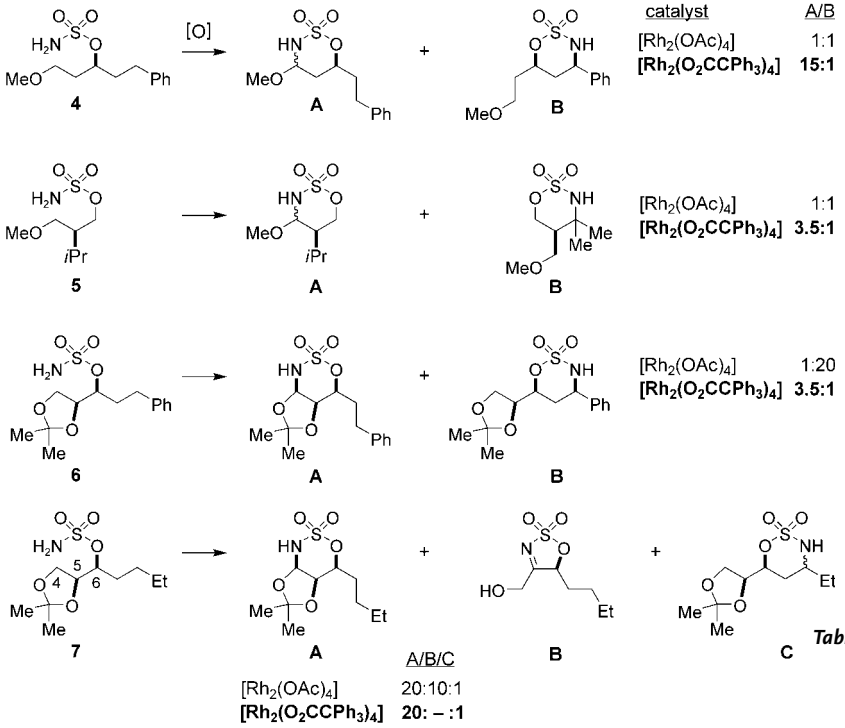
Metal–carbene and metal–nitrene oxidants display a high proclivity for insertion into ethereal C^{α}–H bonds.[5] In principle, this bias can be exploited to direct site selectivity in amination reactions of substrates that possess multiple reactive C–H centers. Such conjecture is readily tested with sulfamates **4**–**7** (Scheme 2). Each of these compounds can

[*] K. Williams Fiori, J. J. Fleming, Prof. Dr. J. Du Bois
Department of Chemistry
Stanford University
Stanford, CA 94305-5080 (USA)
Fax: (+1) 650-725-0259
E-mail: jdubois@stanford.edu

[**] We thank the National Institutes of Health (NINDS, R01 NS045684), Abbott Laboratories, Amgen, Boehringer Ingelheim, Bristol-Myers Squibb, Eli Lilly, GlaxoSmithKline, Merck, Pfizer, and Roche for support of our program. K.W.F. is the recipient of a National Science Foundation Predoctoral Fellowship. J.J.F. is grateful to Amgen for a Graduate Fellowship Award.

Supporting information for this article is available on the WWW under http://www.angewandte.org or from the author.

 DOI: 10.1002/anie.200460791 © 2004 Wiley-VCH Verlag GmbH & Co. KGaA, Weinheim



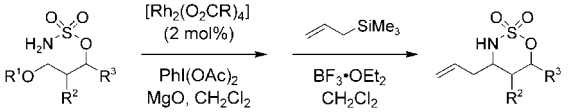
Scheme 2. Catalyst-controlled regioselectivity in C–H amination reactions.

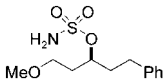
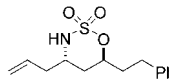
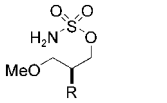
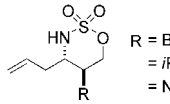
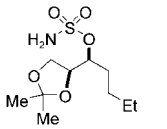
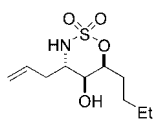
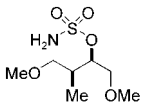
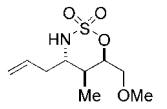
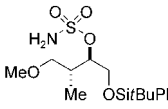
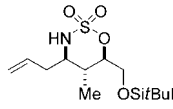
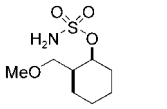
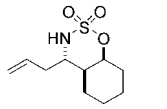
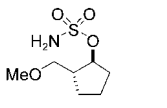
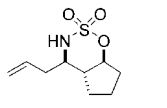
furnish two isomeric oxathiazinane products, as well as the smaller 5-membered ring sulfamidates. Under $[Rh_2(OAc)_4]$ catalysis, sulfamates **4** and **5** show only a slight preference for insertion into a C^{α}–H bond of the ether. These data indicate that the relative rates of ethereal, benzylic, and tertiary C–H amination are in fact comparable. Nonetheless, the regioselectivity is improved substantially when $[Rh_2(O_2CCPh_3)_4]$ is used in place of the tetraacetate complex.[6,7] As a general rule, we have found that the bulky Rh–triphenylacetate catalyst disfavors insertion into sterically crowded C–H bonds and is particularly disinclined towards reaction at benzylic sites. This latter conclusion is nicely illustrated with sulfamates **4** and **6**.[8] When more complex substrates, such as **7**, are employed, the choice of $[Rh_2(O_2CCPh_3)_4]$ also proves optimal, and formation of the undesired C5–H-insertion product is avoided. In contrast, the reaction of **7** with $[Rh_2(OAc)_4]$ is complicated by sulfamidate production. Collectively, these findings offer compelling support for a Rh-bound nitrene-type oxidant and provide an attractive strategy for the regioselective assembly of oxathiazinane N,O-acetals.

Access to structurally complex N,O-acetals has furthered our efforts to develop these compounds as iminium ion precursors.[9] Initially, this work was hampered by the instability of certain N,O-acetal derivatives towards silica gel, which often complicated their purification. The efficiency and high regioselectivity observed in the amination reaction have made it possible, however, to employ N,O-acetal products without recourse to chromatography. Following this new protocol, the reaction mixture is filtered after the oxidation to remove MgO, and the unpurified material is treated with $BF_3{\cdot}OEt_2$ and allyltrimethylsilane. The coupling of $Me_3SiCH_2CH{=}CH_2$ to a range of substituted heterocycles proceeds in high yield and in almost all cases with excellent diastereocontrol (Table 1).[10] These data constitute the first report of allyl additions to such starting materials.

The uniqueness and utility of the allylated oxathiazinane products (Table 1) merits discussion. Preparation of these compounds through the direct insertion of an appropriately substituted sulfamate is limited by aziridine formation and poor product yields [Eq. (1)]. As such, our two-step protocol involving ethereal C^{α}–H amination makes available functionalized oxathiazinanes that are otherwise difficult to access. Further manipulation of these structures is facilitated through nucleophilic ring opening of the oxathiazinane core and/or alkene functionalization.[11,12] Such compounds should thus find service for the assembly of stereochemically complex amines.

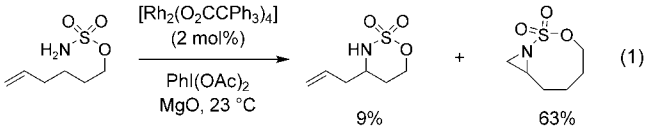
Table 1: Coupling of an allyl silane with heterocyclic N,O-acetals.[a]



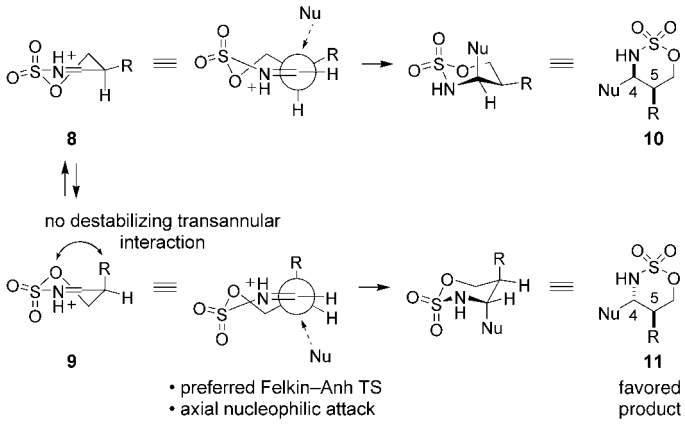
Entry	Substrate	Major product	d.r.[b]	Yield [%][c]
1			20:1	71[d]
2		 R = Bn = *i*Pr = NHP	20:1 10:1 20:1	75[d,e] 60 60[d,f]
3			20:1	78[d]
4			20:1	72
5			1.5:1	81
6			20:1	89
7			2.5:1	82

[a] Sulfamate oxidation: $[Rh_2(OAc)_4]$ (2 mol%), $PhI(OAc)_2$ (1.1 equiv), MgO (2.3 equiv); coupling reaction: $Me_3SiCH_2CH{=}CH_2$ (4 equiv), $BF_3{\cdot}OEt_2$ (1.5 equiv); $BF_3{\cdot}OEt_2$ was added dropwise over 75 min to a solution of the allylsilane and the oxathiazinane; see Supporting Information for details. [b] Diastereomeric ratios were determined by ^1H NMR spectroscopy. [c] Combined yield of the two diastereomers over two steps. [d] $[Rh_2(O_2CCPh_3)_4]$ was employed in place of $[Rh_2(OAc)_4]$. [e] Bn = benzyl. [f] NHP = $NHCO_2CH_2CCl_3$.

 © 2004 Wiley-VCH Verlag GmbH & Co. KGaA, Weinheim

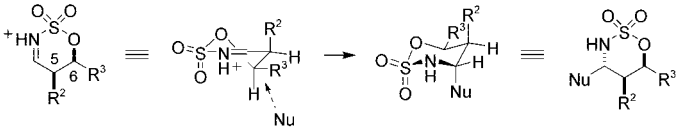


The addition of allylsilanes to oxathiazinane N,O-acetals **2** has proven highly diastereoselective and has enabled the refinement of a predictive transition-state model for this process. Our original investigations demonstrated that alkynyl zinc reagents couple to **2** with a strong bias for the formation of the 4,5-*syn* product **10** (Scheme 3).[2] To rationalize these data, the work of Stevens was considered.[13] In this context, the expected result of axial attack by the zinc reagent on the twist-chair form of iminium ion **8** was consistent with the observed stereochemical outcome. This proposal also accounts for the *anti* selectivity observed in allylsilane reactions with C6-branched N,O-acetals, as highlighted in entry 1 of Table 1. For C5-substituted oxathiazinanes (Table 1, entry 2), however, the analysis becomes more complex. Iminium intermediates generated from such starting materials can adopt either conformation **8** or **9** with minimal energetic cost, as 1,3-*trans* diaxial interactions are virtually absent in **9**. Observed formation of the 4,5-*anti* oxathiazinanes in entry 2 is consistent with allylsilane coupling along a pathway in which the substituent at C5 is aligned axially. Such a model parallels that of Felkin, Anh, and Eisenstein for nucleophilic additions to carbonyl groups.[14,15] Accordingly, the transition state (TS) leading from **9** minimizes steric and torsional strain in the developing product and, in certain cases (e.g. R = $NHCO_2CH_2CCl_3$, OH), profits from stereoelectronic stabilization.[16]

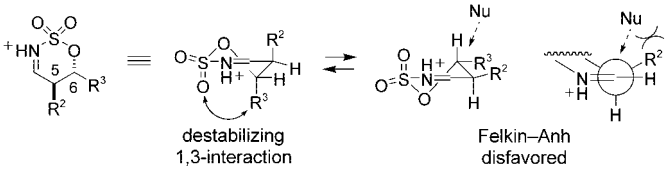


Scheme 3. Stereochemical models for iminium ion additions.

5,6-Disubstituted oxathiazinane acetals (Table 1, entries 3–7) were used to test further the proposed TS model. In these examples, the configuration of the vicinal C5,C6 centers can reinforce or oppose the Felkin–Anh preferred arrangement. Sulfamate esters with a 5,6-*syn* substitution pattern (Table 1, entries 3, 4, 6) are in consonance with both the Stevens and Felkin–Anh constructs, and thus the allylsilane adds with excellent selectivity (Scheme 4). Conversely, the *anti*-configured sulfamates (Table 1, entries 5, 7) can not adopt a conformation that satisfies both models simultaneously (Scheme 5). As a result, diastereoinduction is greatly diminished in the allylsilane coupling reaction. Although these TS designs are speculative, their predictive power should prove beneficial for synthesis development.



Scheme 4. Highly selective addition to 5,6-*syn*-substituted iminium ions.



Scheme 5. Selectivity erodes with 5,6-*anti*-configured substrates.

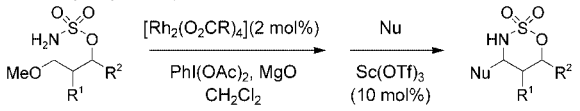
An interest in examining further the validity of the iminium ion stereochemical model combined with the successful addition of allyltrimethylsilane to N,O-acetals **2** prompted investigations with alternative nucleophiles (Scheme 6, Table 2). Reactions of **2** with silyl enol ethers and ketene acetals would furnish Mannich-type products conveniently disposed for an assortment of subsequent transformations.[17] These reagents, however, were unstable to stoichiometric amounts of $BF_3{\cdot}OEt_2$ at ambient temperature, conditions utilized previously for the allylsilane additions. Not surprisingly, initial test reactions to condense **12** with **13** afforded oxathiazinane **14** in poor yields (Scheme 6). Guided by notable reports of Mannich additions catalyzed by metal triflates, we identified $Sc(OTf)_3$ as an exceptionally effective agent.[18,19] An optimized protocol thus employs $Sc(OTf)_3$ (10 mol %) in CH_3CN to promote efficient and diastereoselective coupling of silyl enol ethers and ketene acetals with structurally disparate N,O-acetals (Table 2).[10,20] The procedure is straightforward and does not require purification of the intermediate oxathiazinane. Importantly, the sense and degree of induction recorded for these addition reactions is

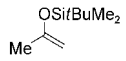
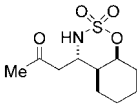
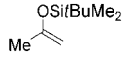
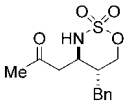
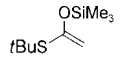
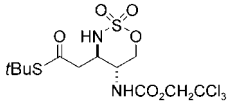
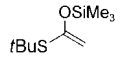
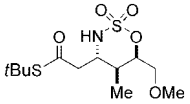
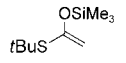
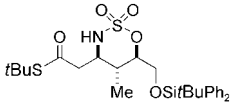
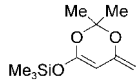
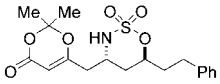


Scheme 6. Coupling with a silyl ketene O,S-acetal under catalytic conditions.

 © 2004 Wiley-VCH Verlag GmbH & Co. KGaA, Weinheim

Table 2: $Sc(OTf)_3$-catalyzed Mannich reactions of N,O-acetals.[a]



Entry	Nucleophile	Major product	d.r.[b]	Yield [%][c]
1			20:1	80
2			20:1	68[d]
3			20:1	60[d]
4			20:1	65
5			2.5:1	76
6			20:1	72[d]

[a] Sulfamate oxidation: $[Rh_2(OAc)_4]$ (2 mol%), $PhI(OAc)_2$ (1.1 equiv), MgO (2.3 equiv); coupling reaction: nucleophile (4 equiv), $Sc(OTf)_3$ (0.1 equiv); see Supporting Information for details. [b] Diastereomeric ratios determined by ^1H NMR spectroscopy. [c] Combined yield of the two diastereomers over two steps. [d] $[Rh_2(O_2CCPh_3)_4]$ was employed in place of $[Rh_2(OAc)_4]$. Tf = trifluoromethanesulfonyl.

entirely consistent with the Stevens/Felkin–Anh TS analysis outlined above.

Methods for the oxidation of C–H bonds are finding ever-increasing application to problems in synthesis. The continued evolution of such work is contingent upon the ability to functionalize with high precision specific C–H centers in structurally intricate substrates. We have shown that the architecture of the Rh catalyst and the reactivity of ethereal C^{α}–H bonds can be used in combination to direct the regioselective amination of substituted sulfamate starting materials. These findings make available a novel class of heterocyclic N,O-acetals that function proficiently as iminium ion equivalents. High-yielding nucleophilic addition to these latent electrophiles is now possible with allylsilanes, silyl enol ethers, and ketene acetals, as well as alkynyl zinc reagents.[2] Predictable and, in most cases, marked levels of diastereoselectivity underscore the addition process. Thus, with the ability to assemble an impressive range of chiral oxathiazinane derivatives, catalytic C–H amination appears as a forefront strategy for accessing nitrogen-containing products.

Received: May 26, 2004 [Z460791]

Keywords: amination · C–H insertion · N,O-acetals · rhodium · sulfamates

[1] a) P. M. Wehn, J. Du Bois, *J. Am. Chem. Soc.* **2002**, *124*, 12950; b) B. M. Trost, J. L. Gunzner, O. Dirat, Y. H. Rhee, *J. Am. Chem. Soc.* **2002**, *124*, 10396; c) H. Huang, J. S. Panek, *Org. Lett.* **2003**, *5*, 1991; d) K. A. Parker, W. Chang, *Org. Lett.* **2003**, *5*, 3891; e) A. Hinman, J. Du Bois, *J. Am. Chem. Soc.* **2003**, *125*, 11510.

[2] J. J. Fleming, K. Williams Fiori, J. Du Bois, *J. Am. Chem. Soc.* **2003**, *125*, 2028.

[3] Compounds **2** and **3** are known generally as 1,2,3-oxathiazinane-2,2-dioxides or as 2,2-dioxotetrahydro-1,2,3-oxathiazines. We refer to such structures as oxathiazinanes or oxathiazinane N,O-acetals for convenience.

[4] For recent reviews on C–H amination, see: a) P. Dauban, R. H. Dodd, *Synlett* **2003**, 1571; b) P. Müller, C. Fruit, *Chem. Rev.* **2003**, *103*, 2905.

[5] a) P. Wang, J. Adams, *J. Am. Chem. Soc.* **1994**, *116*, 3296; b) G. A. Sulikowski, S. Lee, *Tetrahedron Lett.* **1999**, *40*, 8035.

[6] For the original description of the use of $[Rh_2(OCCPh_3)_4]$, see: S.-i. Hashimoto, N. Watanabe, S. Ikegami, *Tetrahedron Lett.* **1992**, *33*, 2709.

[7] For excellent discussions on the influence of the metal catalyst on C–H insertion reactions of carbenes, see: a) A. Padwa, D. J. Austin, *Angew. Chem.* **1994**, *106*, 1881; *Angew. Chem. Int. Ed. Engl.* **1994**, *33*, 1797; b) M. P. Doyle, T. Ren, *Prog. Inorg. Chem.* **2001**, *49*, 113; c) D. F. Taber, P. V. Joshi, *J. Org. Chem.* **2004**, *69*, 4276.

[8] Benzylic C–H insertion in such substrates is highly diastereoselective ($\geq$10:1) under $[Rh_2(OAc)_4]$ catalysis. Interestingly, this selectivity is diminished in reactions conducted with $[Rh_2(O_2CCPh_3)_4]$. For a detailed account of amination reactions with chiral sulfamates, see: P. M. Wehn, J. Lee, J. Du Bois, *Org. Lett.* **2003**, *5*, 4823.

[9] For reviews on addition reactions to iminium ions, see: a) S. M. Weinreb, *Top. Curr. Chem.* **1997**, *190*, 131; b) D. Enders, U. Reinhold, *Tetrahedron: Asymmetry* **1997**, *8*, 1895; c) R. Bloch, *Chem. Rev.* **1998**, *98*, 1407.

[10] The stereochemistry of the product was determined by ^1H NMR spectroscopy (a combination of coupling-constant and NOE data); see the Supporting Information for details.

[11] C. G. Espino, P. M. Wehn, J. Chow, J. Du Bois, *J. Am. Chem. Soc.* **2001**, *123*, 6935.

[12] R. E. Meléndez, W. D. Lubell, *Tetrahedron* **2003**, *59*, 2581.

[13] R. V. Stevens, *Acc. Chem. Res.* **1984**, *17*, 289.

[14] a) N. T. Anh, O. Eisenstein, *Nouv. J. Chim.* **1977**, *1*, 61; b) N. T. Anh, *Top. Curr. Chem.* **1980**, *88*, 145.

[15] A. Mengel, O. Reiser, *Chem. Rev.* **1999**, *99*, 1191.

[16] Addition reactions to oxocarbenium ions derived from 1,3-dioxanes may also conform to this model; see: a) S. Uehira, Z. Han, H. Shinokubo, K. Oshima, *Org. Lett.* **1999**, *1*, 1383; b) N. A. Powell, S. D. Rychnovsky, *J. Org. Chem.* **1999**, *64*, 2026.

[17] Silyl enol ethers and ketene acetals were prepared following established protocols; see: a) D. A. Evans, T. Rovis, M. C. Kozlowski, C. W. Downey, J. S. Tedrow, *J. Am. Chem. Soc.* **2000**, *122*, 9134; b) A. Fettes, E. M. Carreira, *J. Org. Chem.* **2003**, *68*, 9274.

[18] S. Kobayashi, M. Sugiura, H. Kitagawa, W. W.-L. Lam, *Chem. Rev.* **2002**, *102*, 2227, and references therein.

[19] Although $Sc(OTf)_3$ will catalyze the addition of allyltrimethylsilane to N,O-acetals, reaction times are typically quite long (48 h), and product yields are diminished.

[20] Similar reaction conditions were described recently for the addition of silyl enol ethers to 2-methoxy- and 2-acyloxypiperidines; see: O. Okitsu, R. Suzuki, S. Kobayashi, *J. Org. Chem.* **2001**, *66*, 809; see also: M. Yamanaka, A. Nishida, M. Nakagawa, *J. Org. Chem.* **2003**, *68*, 3112.

 © 2004 Wiley-VCH Verlag GmbH & Co. KGaA, Weinheim

Glycoside Synthesis

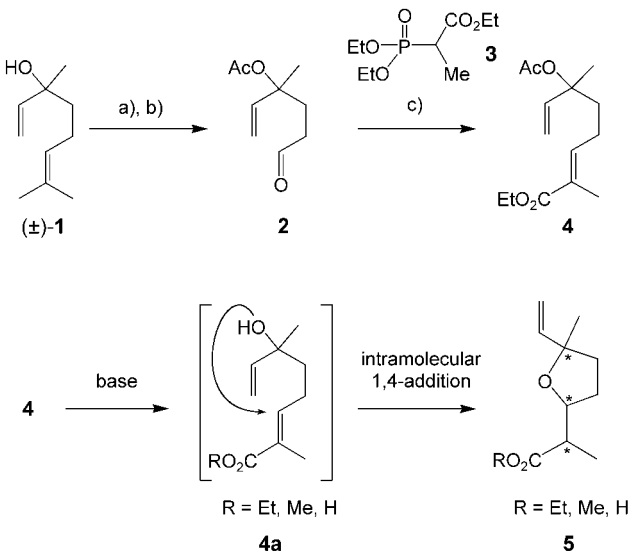
Synthesis of Dimeric Terpenoyl Glycoside Side Chains from Cytotoxic Saponins**

*Sabine Reicheneder and Carlo Unverzagt**

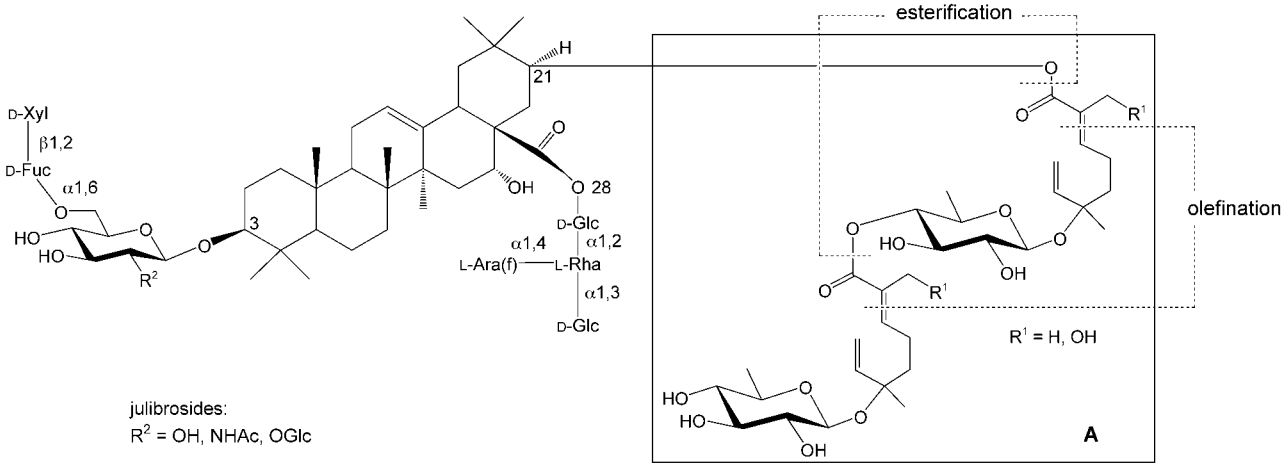
Dedicated to Professor Axel Zeeck on the occasion of his 65th birthday

Saponins are natural products from plants and marine organisms exhibiting a wide variety of biological activities, for example, anticancer properties.[1] Most saponins consist of a lipophilic steroid or triterpene core and hydrophilic oligosaccharide side chains. Despite their structural diversity, only few saponins contain an additional monoterpene glycoside side chain (**A**, Scheme 1) like that found in julibrosides,[2] elliptosides[3] and avicins.[4] These compounds selectively inhibit tumor cell growth by induction of apoptosis[4a,c] (IC_{50}: 0.2 μg mL^{-1} for Jurkat cells) and prevent chemically induced carcinogenesis in mice.[4d,e] The occurrence of the terpenoyl glycoside side chain **A** appears to enhance the cytotoxic effect,[2a] which encouraged us to develop a synthetic path to this unique motif for subsequent bioactivity studies.

Our initial approach to terpenoyl glycosides was to functionalize linalool **1** with a carboxylate followed by glycosylation (Scheme 2). The tertiary alcohol function of racemic linalool (±)-**1** was acetylated, and the more substituted double bond was selectively cleaved to give the aldehyde **2** by epoxidation with MCPBA, periodic-acid-catalyzed diol formation, and oxidative cleavage of the vicinal diol.[5] The volatile aldehyde **2** was extended to furnish the desired menthiafolic acid ethyl ester **4**[6] in a Horner–Wadsworth–Emmons (HWE) reaction[7] using phosphonate **3**.



Scheme 2. Functionalization of linalool: a) Ac_2O, NEt_3, DMAP (75%); b) 1. MCPBA, 0°C; 2. $HIO_4 \cdot 2H_2O$, THF/H_2O (b: 65%); c) **3**, NaH, THF (87%, *E*:*Z* = 95:5). DMAP = 4-dimethylaminopyridine, MCPBA = *m*-chloroperbenzoic acid.



Scheme 1. Retrosynthesis of terpenoyl glycoside side chain **A** from cytotoxic saponins.

However, the tertiary alcohol could not be deprotected without undesired side reactions. In the presence of base in methanol, the free hydroxy group participated in an intramolecular 1,4-addition, resulting in a mixture of eight possible diastereomers of the tetrahydrofuran derivative **5**. In addition transesterification to the methyl ester and hydrolysis to the free acid were observed.

In order to circumvent the use of a protective group for the OH function, the tertiary alcohol was glycosylated prior to

[*] S. Reicheneder, Prof. C. Unverzagt
Bioorganische Chemie, Gebäude NW1
Universität Bayreuth
95440 Bayreuth (Germany)
Fax: (+49) 921-555365
E-mail: carlo.unverzagt@uni-bayreuth.de

[**] This work was supported by the Fonds der Deutschen Chemischen Industrie.

Supporting information for this article is available on the WWW under http://www.angewandte.org or from the author.

 DOI: 10.1002/anie.200352895 © 2004 Wiley-VCH Verlag GmbH & Co. KGaA, Weinheim

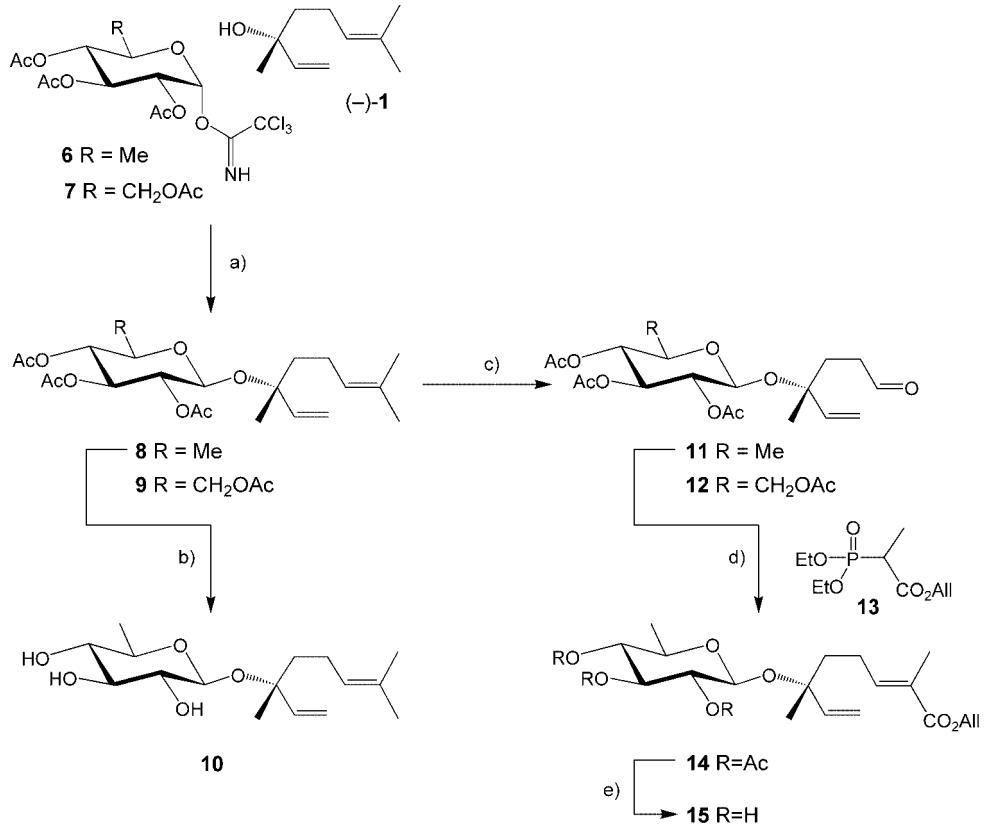
the construction of the α,β-unsaturated ester. Glycosylation[8] of linalool (−)-**1** with the trichloroacetimidates of D-quinovose (**6**[9]) and D-glucose (**7**[10]) gave the corresponding linalyl β-glycosides **8** and **9**[11] in satisfactory yields (Scheme 3). A general advantage of this strategy was the increased chemical stability of the terpene glycosides and their nonvolatility.

The linalyl glycosides **8** and **9** were conveniently converted into the aldehydes **11** (61%) and **12** (81%) by epoxidation and periodate cleavage. Subsequent HWE reaction of **11** with phosphonate **13**[12] led to the quinovoside **14** in 83% yield (E/Z = 85:15; isomers can be separated by repeated chromatography) without affecting the acetylated carbohydrate moieties. Selective deacetylation of compounds **9** and **14** (containing an allyl ester) was achieved by a variant of the Zemplén deacylation using catalytic sodium allylate in allyl alcohol. With the deprotected menthiafolyl quinovoside **15**, a monomeric building block for the side chain (**A**) of julibrosides was obtained.

To avoid the extensive use of protective groups for the sugar part we attempted the regioselective esterification of compound **15** at OH-4. However, acylation of the unprotected quinovosides **10** and **15** with a variety of anhydrides was found to proceed with good to excellent regioselectivity for OH-3. Previously, 3-monoacylated quinovosides were obtained only by enzymatic reactions,[13] whereas stannylene acetals yielded mixtures.[14] Following the observed regioselectivity, the esterification of quinovoside **10** with glucosyl menthiafolic acid **16**[15] gave the dimeric terpene glycoside **17** in 43% yield (Scheme 4), a 3-*O*-acylated regioisomer of the naturally occurring 4-*O*-acyl side chain **A**. Acyl groups tend to undergo migration to neighboring hydroxy groups under basic conditions; however, isolated **17** did not undergo rearrangement, presumably due to the bulky and deactivated (α,β-unsaturated) terpenoic acid moiety.

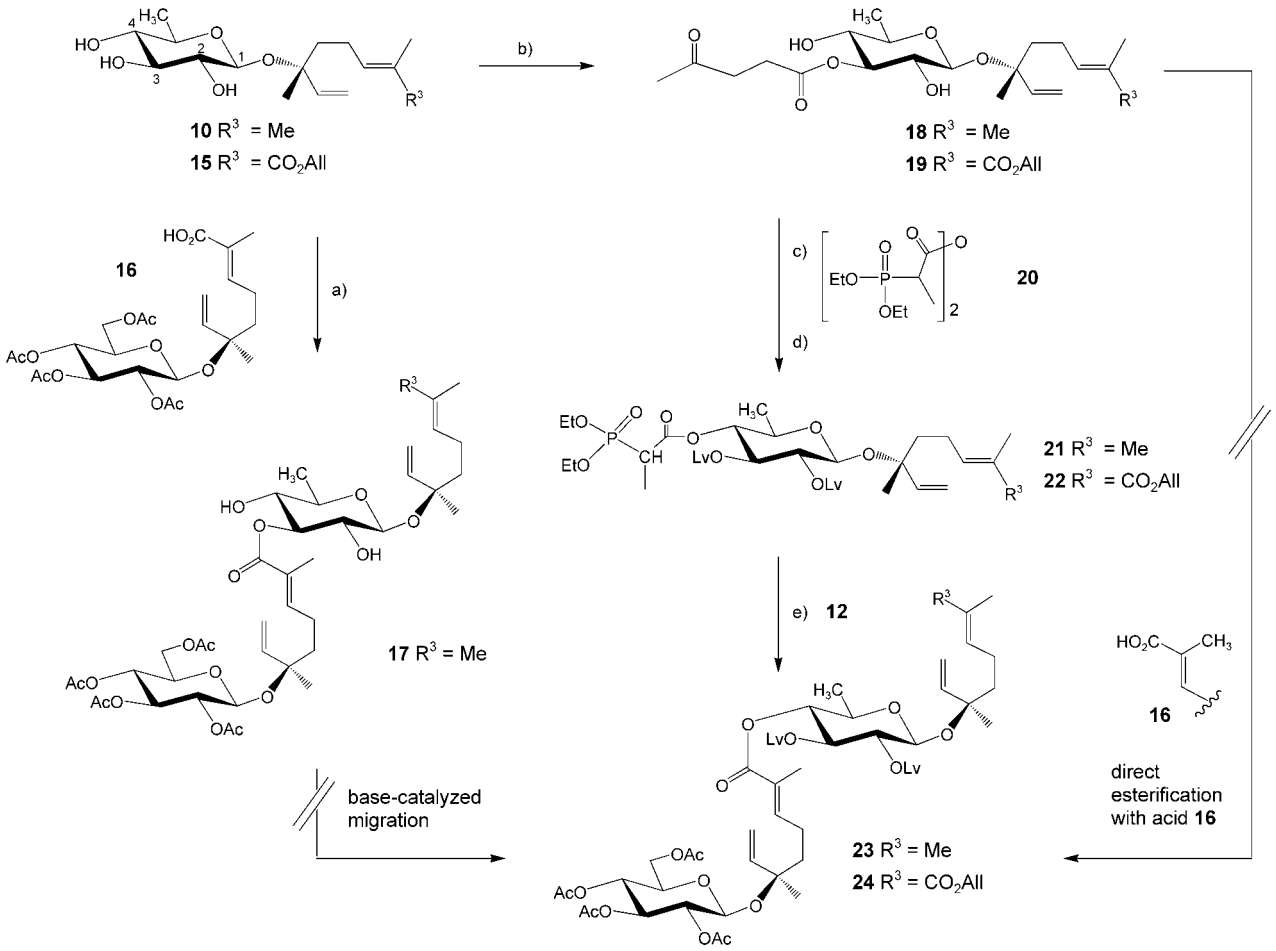
Thus, we developed a different strategy to 4-*O*-acylated quinovosides by first introducing levulinic acid at OH-3 as an orthogonal temporary protecting group (**18**, **19**) using levulinoic anhydride and DMAP catalysis. In contrast to previous acylation studies of β-quinovosides[16] OH-4 was more reactive than OH-2 of the menthiafolyl quinovosides **18** and **19**. By using optimized Yamaguchi conditions[17] we could couple the model compound tiglic acid (α-methyl crotonic acid) to OH-4 of compounds **18** and **19**, albeit in low yields and with concomitant overacylation. However, when we tried to attach the glucosylated acid **16**, only traces of regioisomeric products were detected, rendering this direct approach ineffective. This can be rationalized by the significantly reduced reactivity of α,β-unsaturated acids in esterifications compared with that of their saturated counterparts.[18] An additional α-methyl group decreases the reactivity (acidity) further and increases the steric hindrance. In the case of compounds **18** and **19**, the levulinoyl protection at O-3 limits the accessibility of OH-4 for the complex and unreactive acid **16**.

To overcome this bottleneck in the synthesis we anticipated that we could reduce the steric hindrance by assembling the terpenoic acid part stepwise from a sugar functionalized



Scheme 3. Functionalization of terpene glycosides: a) 5 equiv (−)-**1**, $BF_3{\cdot}OEt_2$, CH_2Cl_2, −40°C to RT (**8**: 64%, **9**: 55%); b) NaOMe, MeOH (91%); c) 1. MCPBA, 0°C; 2. $HIO_4{\cdot}2H_2O$, THF/H_2O (c: **11**: 61%, **12**: 81%); d) **13**, NaH, THF, E/Z = 85:15 (83%); e) NaOAll, AllOH/THF (99%). All = allyl.

 © 2004 Wiley-VCH Verlag GmbH & Co. KGaA, Weinheim



Scheme 4. Regioselective acylation and HWE elongation: a) **16**, EDCI, NEt_3, DMAP, CH_2Cl_2 (43%) b) Lv_2O, pyridine, DMAP, CH_2Cl_2, 0°C (**18**: 90%, **19**: 84%); c) **20**, pyridine, CH_2Cl_2, 0°C (R = Me: 54%, R = CO_2All: 53%); d) Lv_2O, pyridine, DMAP, CH_2Cl_2 (**21**: 87%, **22**: 93%); e) **12** (1 equiv), NaH, THF (**23**: 40%, **24**: 72%). EDCI = *N*-ethyl-*N*′-(-dimethylaminopropyl)carbodiimide, Lv = levulinoyl.

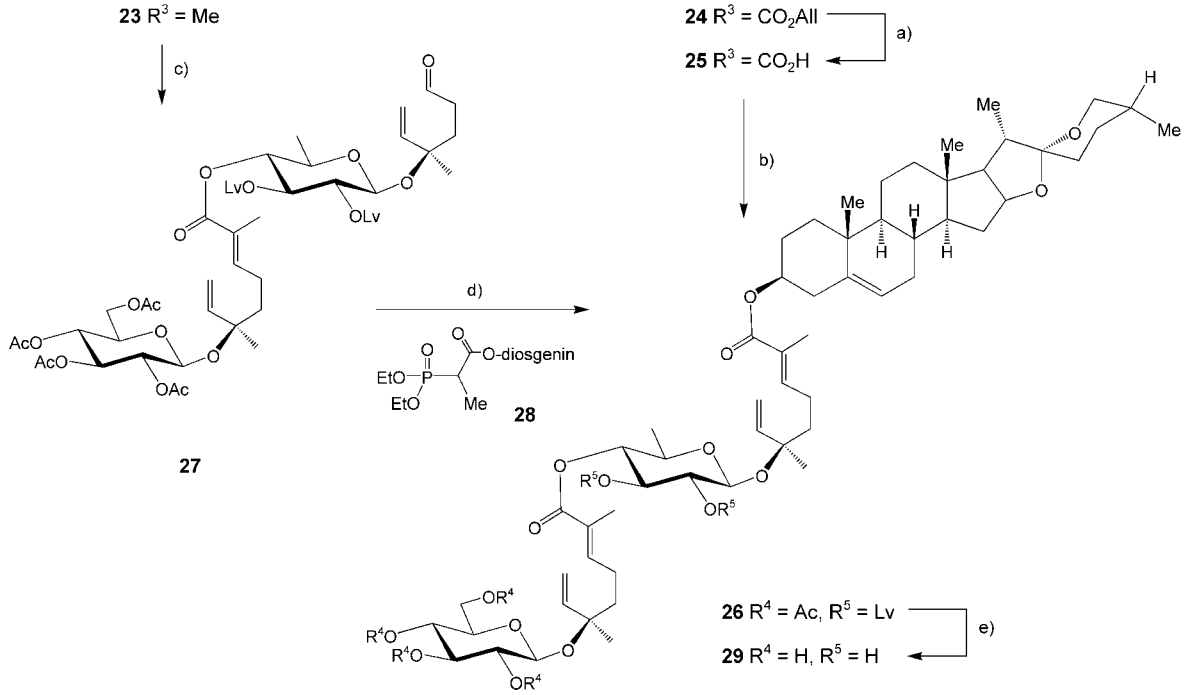
with a phosphonate group at O-4, which is then used in a HWE elongation. The required phosphonate functionality was selectively installed at OH-4 of compounds **18** and **19** by esterification with anhydride **20**. Some overreaction at OH-2 was observed but could be minimized when DMAP was omitted. Subsequently, OH-2 was blocked with levulinic acid to give the fully protected terpenoyl quinovoside phosphonates **21** and **22**. These compounds set the stage for the envisioned HWE olefination with aldehyde **12**. To our delight, the coupling of the two glycosylated building blocks in the presence of sodium hydride gave the desired dimeric terpene glycosides **23** and **24** in yields of 40% and 72%, respectively (*E* diastereomer only).

To obtain conjugates of the dimeric terpenoyl glycoside side chain **A** with other steroids, compound **24** was first deallylated by palladium(0) catalysis (Scheme 5).[19] The resulting carboxylic acid **25** was successfully coupled to diosgenin by means of a Yamaguchi esterification. However, the yield of the complex neosaponin conjugate **26** was moderate (37%), probably due to the intrinsically low reactivity of the α,β-unsaturated, α-branched carboxylic acid **25**. For this reason we attempted elongation by a HWE olefination. The required aldehyde **27** was obtained by regioselective epoxidation and periodate cleavage of the most activated double bond of the linalyl model compound **23**. The HWE olefination of diosgenyl phosphonate **28** (obtained from diosgenin and phosphonate **20**) and aldehyde **27** gave the complex neosaponin **26** with significantly higher yields in the coupling step (52%, *E* diastereomer only).

Finally, the deprotection of the glycoconjugate **26** was examined. Brief exposure to sodium methylate in methanol selectively removed the acetyl moieties without affecting the remaining ester bonds. The levulinates were cleaved with hydrazine acetate to furnish the deprotected neosaponin **29**[20] carrying a variant of the dimeric side chain (**A**) of julibrosides. With the accessibility of synthetic terpenoyl glycoside conjugates (**29**) the biological properties of these unusual side chains from cytotoxic saponins can be investigated.

The presented synthetic strategy provides the first chemical access to terpenoyl glycoside side chains from cytotoxic saponins. A Horner–Wadsworth–Emmons elongation of selectively phosphonate-functionalized glycosides with terpene-derived aldehydes was identified as a key step in the construction of the glycoconjugates.[21] The adaptation of this

 © 2004 Wiley-VCH Verlag GmbH & Co. KGaA, Weinheim



Scheme 5. Coupling of complex terpenoyl glycosides to diosgenin and deprotection: a) $[Pd(PPh_3)_4]$, dimedone, THF (74%); b) Yamaguchi esterification: 2,4,6-trichlorobenzoyl chloride, NEt_3, DMAP, diosgenin, 1,2-dichloroethane, reflux (37%); c) 1. MCPBA, 0°C; 2. $HIO_4 \cdot 2H_2O$, THF/H_2O (c: 46%); d) **28**, NaH, THF (52%); e) 1. NaOMe, MeOH/CH_2Cl_2, 5 min; 2. hydrazine acetate (e: 93%).

flexible strategy to the natural variations in stereochemistry and functionalization of the terpene moieties is in progress.

Received: September 17, 2003
Revised: April 2, 2004 [Z52895]

Keywords: antitumor agents · carbohydrates · natural products · olefination · saponins

[1] a) K. Hostettmann, A. Marston, *Saponins*, Cambridge University Press, **1995**; b) "Bioactive Natural Products (Part B)": M. A. Lacaille-Dubois, H. Wagner, *Stud. Nat. Prod. Chem.* **2000**, *21*, 633–687.

[2] a) T. Ikeda, S. Fujiwara, J. Kinjo, T. Nohara, Y. Ida, J. Shoji, T. Shingu, R. Isobe, T. Kajimoto, *Bull. Chem. Soc. Jpn.* **1995**, *68*, 3483–3490; b) T. Ikeda, S. Fujiwara, K. Araki, J. Kinjo, T. Nohara, T. Miyoshi, *J. Nat. Prod.* **1997**, *60*, 102–107; c) K. Zou, Y. Zhao, G. Tu, J. Cui, Z. Jia, R. Zhang, *Carbohydr. Res.* **2000**, *324*, 182–188.

[3] J. A. Beutler, Y. Kashman, L.K. Pannell, J. H. Cardellina II, M. R. A. Alexander, M. S. Balaschak, T. R. Prather, R. H. Shoemaker, M. R. Boyd, *Bioorg. Med. Chem.* **1997**, *5*, 1509–1517.

[4] a) V. Haridas, M. Higuchi, G. S. Jayatilake, D. Bailey, K. Mujoo, M. E. Blake, C. J. Arntzen, J. U. Gutterman, *Proc. Natl. Acad. Sci. USA* **2001**, *98*, 5821–5826; b) G. S. Jayatilake, D. R. Freeberg, Z. Liu, S. L. Richheimer, M. E. Blake (Nieto), D. T. Bailey, V. Haridas, J. U. Gutterman, *J. Nat. Prod.* **2003**, *66*, 779–783; c) K. Mujoo, V. Haridas, J. J. Hoffmann, G. A. Wachter, L.K. Hutter, Y. Lu, M. E. Blake, G. S. Jayatilake, D. Bailey, G. B. Mills, J. U. Gutterman, *Cancer Res.* **2001**, *61*, 5486–5490; d) M. Hanausek, P. Ganesh, Z. Walaszek, C. J. Arntzen, T. J. Slaga, J. U. Gutterman, *Proc. Natl. Acad. Sci. USA* **2001**, *98*, 11551–11556; e) V. Haridas, C. J. Arntzen, J. U. Gutterman, *Proc. Natl. Acad. Sci. USA* **2001**, *98*, 11557–11562.

[5] R. Croteau, D. M. Satterwhite, D. E. Cane, C. C. Chang, *J. Biol. Chem.* **1986**, *261*, 13438–13445.

[6] Y. Hiraga, S. Izumi, T. Hirata, T. Suga, *Chem. Lett.* **1991**, 49–52.

[7] L. Horner, H. Hoffmann, H. G. Wippel, *Chem. Ber.* **1958**, *91*, 61–63.

[8] O. Mbairarou, T. Ton-That, C. Tapiéro, *Carbohydr. Res.* **1994**, *253*, 79–99.

[9] Z.-H. Jiang, X.-B. Han, R. R. Schmidt, *Liebigs Ann. Chem.* **1993**, 1179–1184.

[10] R. R. Schmidt, W. Kinzy, *Adv. Carbohydr. Chem. Biochem.* **1994**, *50*, 21–123.

[11] H. Paulsen, B. Lê-Nguyên, V. Sinnwell, V. Heemann, F. Seehofer, *Liebigs Ann. Chem.* **1985**, 1513–1536.

[12] W. R. Roush, R. J. Sciotti, *J. Am. Chem. Soc.* **1998**, *120*, 7411–7419.

[13] B. Danieli, F. Peri, G. Roda, G. Carrea, S. Riva, *Tetrahedron* **1999**, *55*, 2045–2060.

[14] E. A. Khatuntseva, A. A. Sherman, A. S. Shashkov, J. Dabrowski, N. E. Nifant'ev, *Bioorg. Khim.* **1997**, *23*, 228–233; *Russ. J. Bioorg. Chem. (Eng. Trans.)* **1997**, *23*, 205–210.

[15] Compound **16** was obtained from aldehyde **12** by olefination with phosphonate **13** followed by Pd^0-catalyzed deallylation.[19]

[16] Y. Kondo, K. Miyahara, N. Kashimura, *Can. J. Chem.* **1973**, *51*, 3272–3276.

[17] a) J. Inanaga, K. Hirata, H. Saeki, T. Katsuki, M. Yamaguchi, *Bull. Chem. Soc. Jpn.* **1979**, *52*, 1989–1993; b) F. Scheufler, M. E. Maier, *Synlett* **2001**, 1221–1224.

[18] J. J. Sudborough, E. R. Thomas, *J. Chem. Soc.* **1911**, *99*, 2307–2319.

[19] H. Kunz, H. Waldmann, *Angew. Chem.* **1984**, *96*, 49–50; *Angew. Chem. Int. Ed. Engl.* **1984**, *23*, 71–72.

[20] **29**: $R_f = 0.34$ (silica gel, CH_2Cl_2/MeOH 10:1); $[\alpha]_D^{27} = -36.3$ ($c = 0.80$, CH_2Cl_2); ^1H NMR (500 MHz, [D_6]DMSO, D = diosgenin,

G = glucose, Q = quinovose, *T* = monoterpene): $\delta = 6.69$ (t, $J =$ 7 Hz, 1H, T-3), 6.66 (t, $J = 7$ Hz, 1H T-3′), 5.98 (dd, $J_{trans} = 17.6$, $J_{cis} = 11.0$ Hz, 1H, T-7), 5.92 (dd, $J_{trans} = 17.6$, $J_{cis} = 11.0$ Hz, 1H, T-7′), 5.37–5.30 (m, 1H, D-6), 5.22–5.02 (m, 6H, 2T-8, Q-OH-2, Q-OH-3), 4.87 (d, $J_{2,OH} = J_{3,OH} = 4.4$ Hz, 2H, G-OH-2, G-OH-3), 4.82 (d, $J_{4,OH} = 4.4$ Hz, 1H, G-OH-4), 4.52–4.45 (m, 1H, D-3), 4.42 (dd, $J_{3,4} = J_{4,5} = 9.3$ Hz, 1H, Q-4), 4.32–4.24 (m, 3H, D-16, Q-1, G-6OH), 4.17 (d, $J_{1,2} = 7.7$ Hz, 1H, G-1), 3.64–3.56 (m, 1H, G-6a), 3.44–3.34 (m, 4H, G-6b, D-26a, Q-5, Q-3), 3.19 (dd, $J_1 = J_2 = 11$ Hz, 1H, D-26b), 3.15–2.88 (m, 5H, G-3, Q-2, G-4, G-5, G-2), 2.32–2.16 (m, 6H, D-4, 2T-4), 2.03–1.71 (m, 11H, D-15a, D-7a, D-1a, D-20, D-2a, 2T-10), 1.71–1.43 (m, 14H, D-12a, D-17, 2T-5, D-8, D-24a, D-2b, D-7b, D-25, D-11a, D-23), 1.43–0.87 (m, 22H, D-11b, D-24b, 2T-9, D-15b, D-12b, D-14, D-1b, D-19, Q-6, D-9, D-21), 0.75–0.70 ppm (m, 6H, D-18, D-27); ^{13}C NMR (125.8 MHz, [D$_6$]DMSO): $\delta = 166.6$, 166.5 (2T-1), 143.5, 143.3, 142.9, 142.5 (2T-3, 2T-7), 139.5 (D-5), 127.0, 126.8 (2T-2), 121.9 (D-6), 114.1, 113.8 (2T-8), 108.4 (D-22), 97.70 (G-1), 97.56 (Q-1), 80.2 (D-16), 78.7, 78.6 (2T-6), 77.0 (G-3), 76.6 (G-5), 75.9 (Q-4), 73.8 (Q-3, Q-2), 73.5 (G-2), 73.2 (D-3), 70.1 (G-4), 68.8 (Q-5), 65.9 (D-26), 61.8 (D-17), 61.1 (G-6), 55.7 (D-14), 49.4 (D-9), 41.1 (D-20), 39.1 (D-12), 37.68, 37.64, 37.57 (2T-5, D-4), 37.1, 36.5 (D-10, D-13), 36.2 (D-1), 31.48, 31.43 (D-7, D-15), 30.92 (D-8), 30.90 (D-23), 29.8 (D-25), 28.5 (D-24), 27.4 (D-2), 24.05, 24.02 (2T-9), 22.79, 22.65 (2T-4), 20.3 (D-11), 19.0 (D-19), 17.7 (Q-6), 17.1 (D-27), 16.0 (D-18), 14.6 (D-21), 12.31, 12.21 ppm (2T-10); ESI-MS: *m*/*z* calcd for [$C_{59}H_{90}O_{16}$ + Na]: 1077.6, found: 1077.7 [*M*+Na].

[21] The esterification of phosphonate **20** with triterpene alcohols bearing a secondary neopentyl OH group has been demonstrated and subsequent HWE olefination is in progress.

 © 2004 Wiley-VCH Verlag GmbH & Co. KGaA, Weinheim

Multilayer Electrodes

Electroactive Cytochrome *c* Multilayers within a Polyelectrolyte Assembly**

*Moritz K. Beissenhirtz, Frieder W. Scheller, Walter F. M. Stöcklein, Dirk G. Kurth, Helmuth Möhwald, and Fred Lisdat**

The use of biological redox and recognition processes for the construction of sensors and bioelectronic functionalities[1] is most promising. One suitable component is cytochrome *c*, a model redox protein[2-4] of known function and high stability. Numerous attempts to arrange this protein on electrode surfaces have been successful,[5–9] but there is a need to increase the functional density and this can be achieved by going beyond the monolayer arrangement. However, in thicker films or multilayers, generally only protein molecules near the electrode surface are electroactive. Therefore it is necessary to construct stable films of protein multilayers in which the proteins can effectively exchange electrons with the electrode without the need of a mediator. Herein this construction is achieved by making use of the layer-by-layer adsorption technique which has been shown to be a useful tool in building up artificial architectures.[10–15]

Fully electroactive multilayer assemblies were built up by alternating incubation steps of a cytochrome *c* (cyt.*c*) monolayer electrode in solutions of anionic polyaniline sulfonate (PASA) and cationic cyt.*c*. The monolayer electrode was constructed using mixed alkanethiols (OH- and COOH-terminated) attached to a gold surface and cyt.*c* molecules which were adsorbed to this promoter layer. This monolayer arrangement has been shown to provide an efficient protein–electrode communication.[16,17]

Figure 1 shows the resulting protein assembly using PASA as a building block. The stepwise adsorption of cyt.*c* and polyelectrolyte was verified by surface plasmon resonance investigations. The technique was also used to determine optimal working conditions for the self-organizing process.

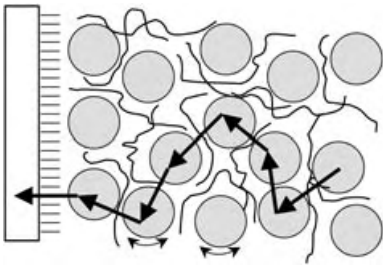


Figure 1. Schematic depiction of the multilayer electrode. Circles = cyt.*c*, wavy lines = PASA, rectangle = promoter-modified gold electrode. Arrows indicate suggested pathway for electron transfer through the cyt.*c* assembly with rotational flexibility of the protein.

Electrochemical studies using cyclic voltammetry showed that the increase in protein loading on the electrode corresponds to an increase in the electrode-addressable amount of cyt.*c* molecules. Repeated incubation steps resulted in an enhancement of the voltammetric peak area allowing for a quantification of the electroactive protein amount (Figure 2). Multilayers containing up to 15 protein layers showed a quasi-reversible electron transfer to the electrode, with a high reproducibility. Control experiments in which either the PASA or the cyt.*c* solution was replaced by buffer showed only the response of a monolayer electrode, which demonstrates that both compounds are necessary for a successful formation of the multilayer protein assembly.

The formal potential of the protein was determined to be -15 ± 7 mV (versus Ag/AgCl/1M KCl) and thus is within the experimental error of the value found for cyt.*c* monolayer electrodes (-19 ± 5 mV). An increase in the peak width at

[*] M. K. Beissenhirtz, Prof. F. W. Scheller, Dr. W. F. M. Stöcklein, Prof. Dr. F. Lisdat
Analytical Biochemistry
Institute for Biochemistry and Biology
University of Potsdam
Karl-Liebknecht-Strasse 24–25, H. 25, 14476 Golm (Germany)
Fax: (+49) 331-977-5053
E-mail: flisdat@rz.uni-potsdam.de
Dr. D. G. Kurth, Prof. H. Möhwald
Max-Planck-Institute for Colloids and Interfaces
Am Mühlenberg 1, 14476 Golm (Germany)

[**] The authors would like to thank the Bundesministerium für Bildung und Forschung Germany (0311487A) and the Ministerium für Forschung, Wissenschaft und Bildung Brandenburg (24#2598–04*327) for financial support.

Supporting information for this article is available on the WWW under http://www.angewandte.org or from the author.

 DOI: 10.1002/anie.200352804 © 2004 Wiley-VCH Verlag GmbH & Co. KGaA, Weinheim

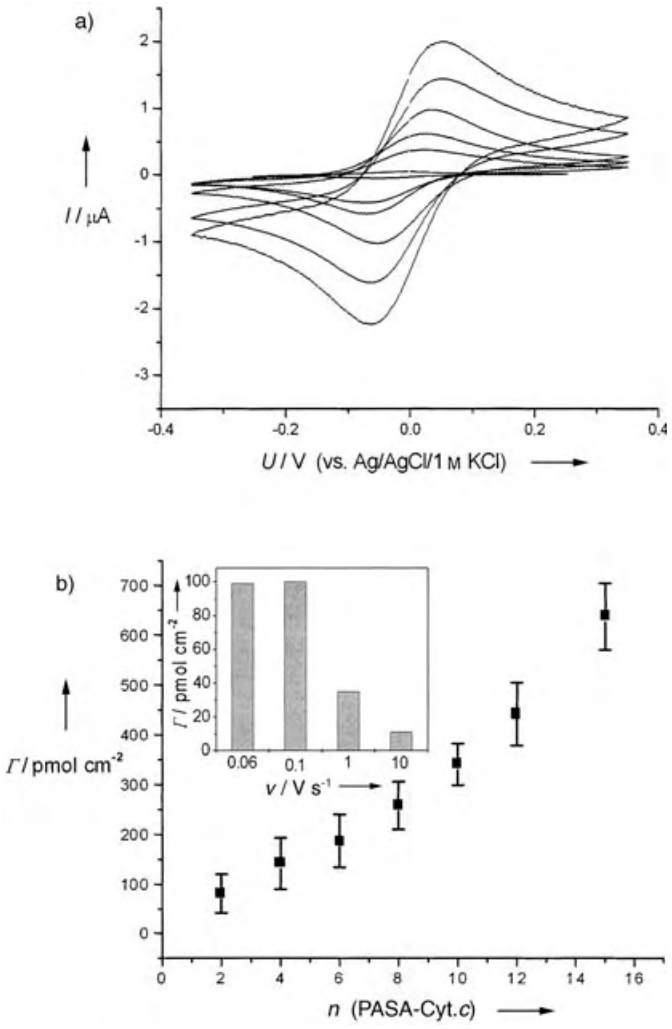


Figure 2. a) Cyclic voltammograms of multilayer electrodes of PASA and cyt.*c*. in order of increasing magnitude: monolayer, 4, 6, 8, 12, 15 layers of cyt.*c*. b) Surface density of electrode-addressable cyt.*c* immobilized in 2–15 layers of polyelectrolyte and cyt.*c*; n = number of double layers. Inset: surface density of electrode-addressable cyt.*c* at different scan rates (ν). Values are given in percent of the cyt.*c* amount detected at 100 mV s^{-1} for an eight-layer electrode.

half peak height confirmed the presence of different states of cyt.*c* within the assembly compared to in the monolayer (180 ± 9 mV for the multilayer assembly compared to 130 ± 5 mV for the monolayer electrode). This variation can be expected for protein molecules bound in slightly differing microenvironments within a polyelectrolyte matrix.

The mechanism behind the electron transport over longer distances is an interesting aspect of the system studied. Several experiments indicate a protein–protein electron transfer within the multilayer assembly as the main pathway. The cyt.*c* monolayer electrode is able to exchange electrons with cyt.*c* molecules in solution. Cyclic voltammograms of such an electrode showed an increased reduction peak in the presence of cyt.*c* in solution (5 mM phosphate buffer pH 7.0, 50 mV s^{-1}, see Supporting Information). Since the cyt.*c* in solution is mostly oxidized, the additional electrons in the reduction cycle must have been transferred to the protein in solution. An increase in scan rate eliminated this effect, as the scanning speed surpassed the interprotein electron-transfer rate (at about 1 V s^{-1}).

A somewhat similar behavior could be found for the multilayer assembly. While the cyt.*c* monolayer electrode exhibit quasi-reversible electron transfer with a k_s of 75 ± 5 s^{-1}, in which the amount of electroactive cyt.*c* is independent of the scan rate, the multilayer electrodes showed a drastic decrease in the amount of electroactive cyt.*c* with increasing scan rates (while the increase in peak separation with scan rate remained similar to that observed with the monolayer electrode). For instance, at 10 V s^{-1}, the amount of electrode-addressable protein in an eight-layer-electrode decreased to about 10% of the value determined at 0.1 V s^{-1}, which indicates that the scanning speed has exceeded the rate of electron transfer between the protein layers (see inset of Figure 2b). Clearly, the electron-exchange rate between the protein molecules in the network is significantly slower ($k_s = 1.5 \pm 0.3$ s^{-1} for 3–15 layers) than the reaction rate of the cyt.*c* monolayer and the electrode.

When the cross-linking agent 1-ethyl-3-(3-dimethyl-aminopropyl)carbodiimide (EDC) was added to a multilayer electrode, the electroactive cyt.*c* amount decreased and the peak separation increased profoundly. For example, electrodes containing six layers of PASA/cyt.*c* showed a peak separation of 280 mV after addition of EDC, compared to 80 mV without cross-linking (scan rate = 0.1 V s^{-1}). This finding indicates that the flexibility of the protein molecules plays a crucial role for an efficient and rapid electron transfer within the assembly.

PASA showed no redox activity of its own in the range between −0.5 and 0.5 Volt (vs. Ag/AgCl/1M KCl) at a cyt.*c* monolayer electrode, suggesting that the polyelectrolyte in the multilayer system is responsible for stabilizing the structure rather than for electrochemically wiring the protein to the electrode. The replacement of PASA by stronger polyanions, such as polystyrene sulfonic acid or polyacrylic acid, disturbed the multilayer formation and thus prevented generation of a fully electroactive cyt.*c* multilayer arrangement (see Supporting Information).

To further support the concept of protein–protein electron transfer, multilayer electrodes containing apo-cyt.*c* were constructed. Since apo-cyt.*c* was prepared by chemical removal of the heme moiety, it should act as a barrier to interprotein electron transport. Surface plasmon resonance (SPR) experiments verified the formation of apo-cyt.*c*/PASA multilayers. Table 1 summarizes three electrode designs. System 1 consists of a monolayer electrode in which cyt.*c* is replaced by apo-cyt.*c*. As expected, this electrode showed no electroactivity, owing to the absence of the heme group apo-cyt.*c* (the loss of the heme group which was confirmed independently by spectroscopic measurements). System 2

Table 1: Design of three different multilayer electrodes containing apo-cyt.*c* for the study of electron transfer mechanism.

System	Arrangement
System 1	MUA/MU-Apo
System 2	MUA/MU-cyt.*c*—(PASA/Apo) × 4—(PASA/cyt.*c*) × 4
System 3	MUA/MU-cyt.*c*—(PASA/Apo) × 12—(PASA/cyt.*c*) × 4

 © 2004 Wiley-VCH Verlag GmbH & Co. KGaA, Weinheim

contains an active cyt.*c* monolayer, four layers of apo-cyt.*c*, followed by four layers of cyt.*c*. Cyclic voltammograms showed that the heme-containing protein deposited in the last four incubation steps still communicated with the electrode. However, the addition of EDC to this electrode system resulted in a complete loss of electroactivity, which shows that the barrier of four apo-cyt.*c* layers combined with a restricted mobility of the protein prevented electron transfer between the electrode surface and the cyt.*c*. System 3 has 12 layers of apo-cyt.*c* between the electroactive cyt.*c* monolayer and the four layers of cyt.*c*. Cyclic voltammograms of this system showed no redox events. The increased thickness of the electrochemically inactive barrier effectively blocked any electron transfer between the electrode and the outer cyt.*c*. Cyclic voltammograms of systems 2 and 3 are depicted in Figure 3.

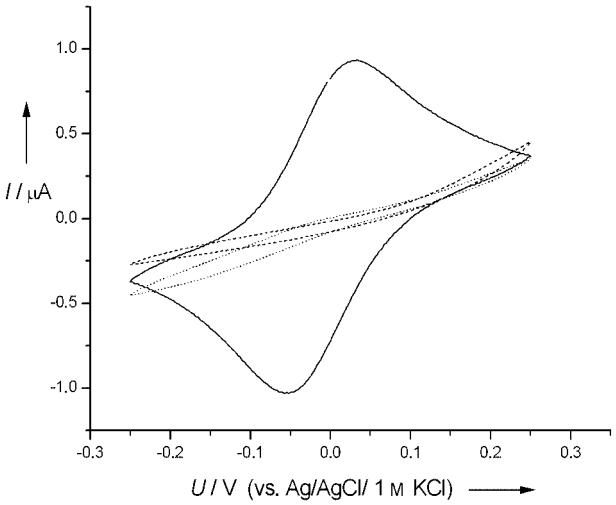


Figure 3. Cyclic voltammograms of multilayer electrodes containing apo-cyt.*c* (Apo). Solid line: MUA/MU-cyt.*c*-(PASA/Apo)$_4$-(PASA/cyt.*c*)$_4$, dashed line: MUA/MU-cyt.*c*-(PASA/Apo)$_4$-(PASA/cyt.*c*)$_4$ covalently immobilized with EDC, dotted line: MUA/MU-cyt.*c*-(PASA/Apo)$_{12}$-(PASA/cyt.*c*)$_4$; MUA = 11-sulfanyl-1-undecanoic acid, MU = 11-sulfanyl-1-undecanol.

These findings suggest that protein–protein electron transfer is the major contributor to the electrochemical communication between the electrode and the cyt.*c* layers, since electron transport by the polyelectrolyte should not be completely prevented by the inclusion of the electrochemically inactive apo-cyt.*c*. The successful electron transport over four layers of apo-cyt.*c* might be explained by the structure of the multilayer assembly, which can be understood to be not an architecture of flat layers on top of one another, but more of a complex protein network stabilized by the polyelectrolyte chains.[10–18] On the other hand the insulating effect of 12 apo-cyt.*c* layers between the electrode and the outer cyt.*c* was stable over several hours. Furthermore, no leakage of cyt.*c* into the protein-free buffer was observed within this period. Cyt.*c* is clearly an integral building block of the assembly. Therefore, it is unlikely that cyt.*c* can diffuse through the assembly to reach the electrode surface (thus making electron transport possible) within the time scale of the voltammetric experiments.

The most probable process for this protein–protein redox reaction is the electron exchange between face-to-face oriented cyt.*c* molecules through the exposed heme edge. This mechanism requires a certain degree of flexibility in the molecules to achieve the appropriate orientation to the successive reaction partners. Such rotational flexibility has been detected at cyt.*c* monolayer electrodes[19] and it might also be one reason for an increase of the electron-transfer rate found for cyt.*c* when its mobility is limited by complex formation with an appropriate modified electrode.[20]

Our results demonstrate a new system which allows the immobilization of cyt.*c* on electrodes as part of a polyelectrolyte–protein architecture. A nearly linear increase in the amount of electroactive protein was shown for up to 15 layers. To our knowledge, such a significant increase in the amount of electroactive protein with mediatorless electron transfer has not been reported for a system in which the protein was integral part of the multilayer structure. Other reported multilayer systems with myoglobin rely on rough surfaces, the use of nanoparticles, and a non-natural function of this transport protein (electron transfer instead of its transport function).[21,22]

Our system offers new possibilities particularly for biosensing, where cyt.*c* electrodes have been applied to the quantification of oxygen radicals.[17] For this purpose, the use of a multilayer sensor with higher amounts of electroactive cyt.*c* can be expected to yield a significantly enhanced sensitivity.

The efficient reproducible electron transfer through several layers also provides an opportunity to simulate biological electron transport systems with cyt.*c* shuttling electrons between reaction partners. The integration of cyt.*c* into multilayer architectures could open up the way to artificial models of biological redox systems leading to bioelectronic functionalities.

Received: September 5, 2003
Revised: May 26, 2004 [Z52804]

Keywords: cyclic voltammetry · cytochromes · electron transfer · heme proteins · surface plasmon resonance

[1] I. Willner, E. Katz, *Angew. Chem.* **2000**, *112*, 1230; *Angew. Chem. Int. Ed.* **2000**, *39*, 1180.
[2] T. Sagara, K. Niwa, A. Sone, C. Hinnen, K. Niki, *Langmuir* **1990**, *6*, 254.
[3] M. J. Eddowes, H. A. O. Hill, *J. Am. Chem. Soc.* **1979**, *101*, 4461.
[4] M. J. Tarlov, E. F. Bowden, *J. Am. Chem. Soc.* **1991**, *113*, 1847.
[5] M. Fedurco, *Coord. Chem. Rev.* **2000**, *209*, 263.
[6] S. Song, R. A. Clark, E. F. Bowden, M. J. Tarlov, *J. Phys. Chem.* **1993**, *97*, 6564.
[7] T. Daido, T. Akaike, *J. Electroanal. Chem.* **1993**, *344*, 91.
[8] P. Bianco, J. Haladin, *Electrochim. Acta* **1994**, *39*, 911.
[9] Z. Q. Feng, Sh. Imabayashi, T. Kakiuchi, K. Niki, *J. Electroanal. Chem.* **1995**, *394*, 149.
[10] G. Decher, *Science* **1997**, *277*, 1232.
[11] Y. Lvov, H. Möhwald, *Protein Architecture: Interfacing Molecular Assemblies and Immobilization Biotechnology*, Marcel Dekker, New York, **1999**.
[12] V. Panchagnula, C. V. Kumar, J. F. Rusling, *J. Am. Chem. Soc.* **2002**, *124*, 12515.
[13] Y. M. Lvov, Z. Q. Lu, J. B. Schenkman, X. L. Zu, J. F. Rusling, *J. Am. Chem. Soc.* **1998**, *120*, 4073.

 © 2004 Wiley-VCH Verlag GmbH & Co. KGaA, Weinheim

[14] P. Rilling, T. Walter, R. Pommersheim, W. Vogt, *J. Membr. Sci.* **1997**, *129*, 283.
[15] L. W. Wang, N. F. Hu, *Bioelectrochemistry* **2001**, *53*, 205.
[16] A. El Kasmi, J. M. Wallace, E. F. Bowden, S. M. Binet, R. J. Lindermann, *J. Am. Chem. Soc.* **1998**, *120*, 225.
[17] B. Ge, F. Lisdat, *Anal. Chim. Acta* **2002**, *454*, 53.
[18] Sh. Liu, D. G. Kurth, B. Bredenkoetter, D. Vollmer, *J. Am. Chem. Soc.* **2002**, *124*, 12279.
[19] A. Avila, B. W. Gregory, K. Niki, T. M. Cotton, *J. Phys. Chem. A* **2000**, *104*, 2759.
[20] J. Wei, H. Liu, A. R. Dick, H. Yamamoto, Y. He, D. H. Waldeck, *J. Am. Chem. Soc.* **2002**, *124*, 9591.
[21] H. Ma, N. Hu, J. F. Rusling, *Langmuir* **2000**, *16*, 4946.
[22] Y. Lvov, B. Munge, O. Giraldo, I. Ichinose, S. L. Suib, S. F. Rusling, *Langmuir* **2000**, *16*, 8850.

 © 2004 Wiley-VCH Verlag GmbH & Co. KGaA, Weinheim

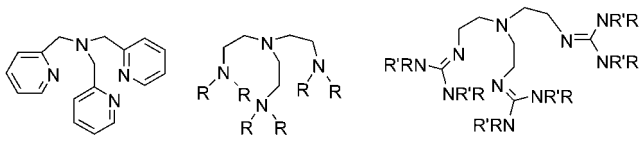
Dioxygen Complexes

Combined Spectroscopic and Theoretical Evidence for a Persistent End-On Copper Superoxo Complex**

Markus Schatz, Volker Raab, Simon P. Foxon, Georg Brehm, Siegfried Schneider, Markus Reiher, Max C. Holthausen, Jörg Sundermeyer,* and Siegfried Schindler**

Reactions of small synthetic copper(I) complexes with O_2 have been studied extensively to gain a better understanding of dioxygen activation at metal sites in biological and industrial catalytic systems.[1,2] Dinuclear 2:1 Cu/O_2 adducts have been proposed as reactive species in these systems, and both, side-on μ-η^2:η^2-peroxo and bis(μ-oxo) dicopper complexes have been characterized crystallographically.[3] Furthermore, using low-temperature stopped-flow and/or resonance Raman techniques, the initial formation of labile 1:1 Cu/O_2 adducts has been detected as a process which occurs prior to the rapid formation of dinuclear complexes.[2,4–7] This finding is particularly interesting as these 1:1 species are postulated to exist in copper enzymes (such as, dopamine β-monooxgenase, peptidyglycine α-amidating monooxygenase/peptidyglycine α-hydroxylating monooxygenase (PAM/PHM), or galactose oxidase) with mononuclear active sites that activate dioxygen.[8] To date, only two 1:1 Cu/O_2 adducts involving bi- and tridentate ligands were sufficiently stable for structural characterization, and they were identified as side-on (η^2) superoxo complexes.[9,10] There is an ongoing debate about the correct formal description of side-on dioxygen adduct complexes (see refs. [15,17]).An early report on a crystal structure of an end-on (η^1) superoxo copper(II) complex employing a modified tris(2-pyridylmethyl)amine (tmpa) ligand[11] was probably incorrect, and the species was claimed later to be a copper(II) hydroxo complex.[12] By using a closely related ligand environment, the X-ray characterization of an end-on hydroperoxo species stabilized by intramolecular hydrogen bonding was accomplished.[13] Indications for the existence of end-on superoxo coordination modes come from a combination of UV/Vis and FT-IR or resonance Raman spectroscopic measurements.[4,14,15] To date, however, no crystal structure or detailed theoretical characterization[16] of end-on copper(II) superoxo complexes has been reported.

Copper(I) complexes with tripodal tetradentate ligands, such as tmpa (Scheme 1) react with dioxygen to form end-on *trans*-μ-1,2-peroxo dicopper(II) complexes. This observation suggests an end-on (η^1) coordination mode of the superoxide ligand in the initially formed labile 1:1 Cu/O_2 adducts,[4,7] an assumption that is supported by the fact that these tripodal-ligand copper(II) complexes always have a trigonal bipyramidal geometry when coordinated to other ligands (such as Cl^-, OH^-, H_2O).[18–20] An octahedral geometry or the replacement of one ligand arm would be a prerequisite for a side-on superoxide coordination involving this ligand type, neither has been observed.



Scheme 1. Tetradentate tripod ligands.

Low-temperature stopped-flow studies recently revealed that the 1:1 Cu/O_2 adduct of Me_6tren is much more persistent than its tmpa analogue, which made it possible to obtain resonance Raman data for this type of complex for the first time ($[Cu(Me_6tren)O_2]^+$: $\tilde{\nu}(^{16}O\text{-}^{16}O) = 1122\ cm^{-1}$).[4] The sub-

[*] Dr. V. Raab, Dr. M. C. Holthausen, Prof. Dr. J. Sundermeyer
Fachbereich Chemie der Philipps-Universität Marburg
Hans-Meerwein-Strasse
35032 Marburg (Germany)
Fax: (+49) 6421-28-25566
E-mail: max.holthausen@chemie.uni-marburg.de
jsu@chemie.uni-marburg.de
Dr. M. Schatz, Dr. S. P. Foxon, Prof. Dr. S. Schindler
Institut für Anorganische und Analytische Chemie
Justus-Liebig-Universität Gießen
Heinrich-Buff-Ring 58, 35392 Gießen (Germany)
Fax: (+49) 641-993-4149
E-mail: siegfried.schindler@anorg.chemie.uni-giessen.de
Dr. G. Brehm, Prof. Dr. S. Schneider
Institut für Physikalische und Theoretische Chemie
Universität Erlangen-Nürnberg
Egerlandstrasse 3, 91058 Erlangen (Germany)
PD Dr. M. Reiher
Theoretische Chemie
Universität Bonn, Wegelerstrasse 12, 53115 Bonn (Germany)

[**] The authors gratefully acknowledge financial support from the Deutsche Forschungsgemeinschaft (Schwerpunktprogramm 1118). M.C.H. acknowledges support through a Liebig-Habilitation fellowship by the Fonds der Chemischen Industrie and S.P.F. is thanks the DAAD for a scholarship. Markus Weitzer is acknowledged for his assistance with the handling of the sample and we thank Prof. Rudi van Eldik (University of Erlangen-Nürnberg) for supporting this work.

 © 2004 Wiley-VCH Verlag GmbH & Co. KGaA, Weinheim DOI: 10.1002/anie.200454125

sequent formation of dinuclear peroxo complexes is suppressed, probably because of the increased steric hindrance caused by the tetradentate tripodal ligand systems. Strictly speaking, however, in this and related investigations the spectroscopic data on the transient superoxo species could not be correlated with the coordination mode, that is, end-on or side-on of the dioxygen ligand.[6,19,21]

Herein we present a combined experimental and theoretical study which associates spectroscopic properties with an end-on superoxo coordination mode. We anticipated that the stronger N-donor character of superbasic ligands, such as peralkyl guanidine ligands, would stabilize a $\{Cu(O_2)\}^+$ moiety more than the polydentate amines or azaaromatic ligands used in earlier work. With our recently designed ligand tris(tetramethylguanidino)tren (TMG_3tren,[22] Scheme 1) we were confident of having a sufficiently bulky ligand at hand to prevent subsequent formation of dinuclear peroxo and/or bis(μ-oxo) species. Indeed, at low temperatures we observed that the trigonal pyramidal ion $[Cu(TMG_3tren)]^+$[20] reacted with dioxygen to form exclusively a dark green 1:1 Cu/O_2 adduct, which was quite stable. Stopped-flow investigations in acetone or propionitrile showed the fast development of absorption bands at 442 and 690 nm. Formation of a 2:1 Cu/O_2 adduct was not detected. Furthermore, the reaction was found to be completely reversible: warming the solution to room temperature in a closed optical cell caused formation of the copper(I) complex and release of dioxygen, while cooling of the sample led again to formation of the superoxo species. The progress of this reaction can be readily followed by UV/Vis or resonance Raman spectroscopy (see below). We repeated the warming/cooling cycles several times without any detectable decomposition. With other tren-ligand derivatives, only irreversible oxidation reactions were observed upon warming to room temperature.[21] The observed stability of the superoxo complex formed should allow its isolation in solid form. To date, however, our attempts to obtain a pure solid sample of this complex have been unsuccessful.

Resonance Raman spectra of $[Cu(TMG_3tren)O_2]^+$ in acetone at −70 °C revealed an isotope-sensitive band at $\tilde{\nu}(^{16}O\text{-}^{16}O) = 1117\ cm^{-1}$ (Table 1, $\tilde{\nu}(^{18}O\text{-}^{18}O) = 1059\ cm^{-1}$) in

Table 1: Calculated (BP86/RI/TZVP) and experimental wave numbers for the O–O stretching modes in cm^{-1}.

Complex	$^{16}O\text{-}^{16}O$	$^{18}O\text{-}^{18}O$	$[Cu]\text{-}^{18}O\text{-}^{16}O$	$[Cu]\text{-}^{16}O\text{-}^{18}O$
1	1111.3	1054.2	1083.1	1082.9
2	1032.6	974.2	1003.7	1004.0
experiment	1117	1059	1089	

accordance with the data reported for $[Cu(Me_6tren)O_2]^+$ ($\tilde{\nu}(^{16}O\text{-}^{16}O) = 1122\ cm^{-1}$) and $[Cu(Bz_3Me_3tren)O_2]^+$ ($\tilde{\nu}(^{16}O\text{-}^{16}O) = 1120\ cm^{-1}$, $\tilde{\nu}(^{18}O\text{-}^{18}O) = 1059\ cm^{-1}$; Bz = benzyl).[4,6] In line with the UV/Vis measurements mentioned above this band disappeared when the sample was warmed to room temperature, and it reappeared upon cooling. With a mixture of $^{16}O_2$, $^{18}O_2$, and $^{16}O\text{-}^{18}O$ only one additional peak (at $1089\ cm^{-1}$) was observed (Figure 1), which implies the

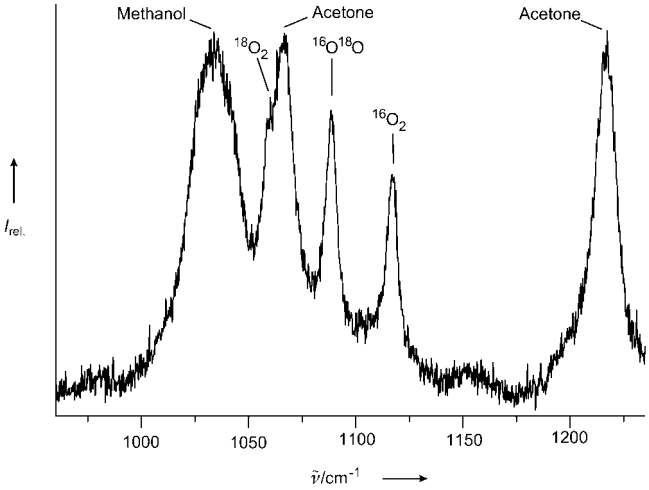


Figure 1. Resonance Raman spectrum of $[Cu(TMG_3tren)O_2]^+$ in acetone with a mixture of $^{16}O_2$, $^{18}O_2$, and $^{16}O\text{-}^{18}O$ at −70 °C.

formation of a side-on superoxo complex. An end-on (η^1) superoxide coordination should lead to two additional peaks corresponding to the two possible orientations of an end-on $^{16}O\text{-}^{18}O$ ligand at the metal center.[5,14,23]

As an alternative source of information on the structural properties of this superoxo complex, we performed DFT calculations.[24] We identified isomer **1** (Figure 2), which is

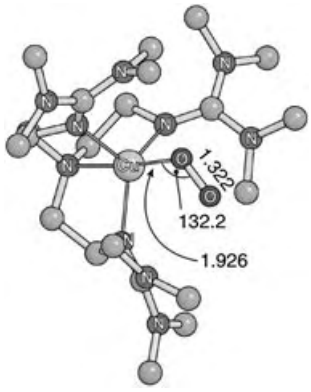


Figure 2. BP86/RI/TZVP optimized structure of the end-on complex **1** (hydrogen atoms are omitted for clarity, bond lengths [Å] and angles [°]).

characterized by a tetradentate N-coordination and an end-on dioxygen ligand. Several attempts to localize a corresponding side-on isomer lead directly back to **1** during unconstrained geometry optimizations. Some manipulations of the starting geometry, however, led instead to expulsion of one of the ligand arms from the copper coordination sphere and resulted in a second isomer (**2**, Figure 3) featuring a tridentate N-coordination and a side-on dioxygen coordination mode.[25] Both, **1** and **2**, were characterized as minima by analysis of the Hessian matrices, with **1** being 29.4 kJ mol^{-1} more stable than **2**.

 © 2004 Wiley-VCH Verlag GmbH & Co. KGaA, Weinheim

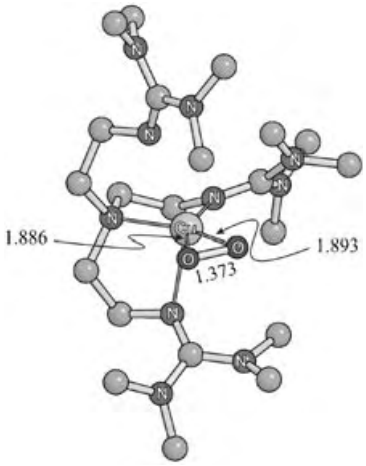


Figure 3. BP86/RI/TZVP optimized structure of the side-on complex **2** (hydrogen atoms are omitted for clarity, bond lengths [Å] and angles [°]).

The computed harmonic frequencies for **1** and **2** allow for an assignment of the observed resonance Raman signatures (Table 1): The almost perfect match between experiment and theory for **1**, and the fact that the computed O–O stretching frequency of **2** is 80 cm^{-1} lower than the experimentally observed vibration, reveals the end-on complex **1** as the experimentally observed isomer.[26] The finding of only a minute difference in the computed isotopic shifts for the two orientations of the mixed-isotope dioxygen is baffling ($\tilde{\nu}$([Cu]-^{18}O-^{16}O) = 1083.1 cm^{-1}, $\tilde{\nu}$([Cu]-^{16}O-^{18}O) = 1082.9 cm^{-1}). However, this result resolves the seeming contradiction between the clear theoretical evidence for an end-on superoxide being 29.4 kJ mol^{-1} more stable than the side-on isomer and the lack of the expected experimental isotopic splitting. Furthermore, the frequencies computed for **2** match perfectly well experimental data for the only fully characterized side-on complex described by Solomon and coworkers ($\tilde{\nu}$(^{16}O-^{16}O) = 1043 cm^{-1}, $\tilde{\nu}$(^{18}O-^{18}O) = 984 cm^{-1}) that also has a completely different UV/Vis spectrum to **1**.[15]

For the first time, our results provide clear evidence for the facile, reversible formation of an end-on superoxo copper complex, **1**, at low temperatures. Furthermore, the spectroscopic similarities imply that also the 1:1 Cu/O_2 adducts with related tetradentate tripodal ligands (such as tmpa, Me_6tren, and Bz_3Me_3tren, or other symmetrical tren derivatives) are of the end-on type. The possible existence of end-on superoxo species in such constrained tetradentate tripodal ligand complexes has recently been disputed by Tolman and coworkers on the basis of the lack of isotopic patterns in related resonance Raman investigations.[5] Our present findings, however, clearly show that the lack of isotopic splitting in resonance Raman spectra using a gas mixture of $^{16}O_2$, $^{18}O_2$, and ^{16}O-^{18}O is not sufficient to unambiguously assign the coordination mode for complexes of this type.[35] It appears, in fact, that a clear structural characterization and/or detailed quantum chemical calculations are indispensable for a definite assignment of O_2 coordination modes in the mononuclear copper complexes.

Experimental Section

The synthesis of [Cu(TMG_3tren)]ClO_4 was described elsewhere.[20] Handling of samples and low-temperature stopped-flow measurements were performed according to published procedures.[4] Resonance Raman spectra were obtained using a homebuilt Ti:sapphire laser pumped by an argon ion laser (Coherent Innova 90-6) with an excitation wavelength of 785 nm. The spectral line width of the laser system was less than 1 wave number. The detection system was combined with a glass Dewar flask in which the sample solution in a special optical cell could be cooled to −90 °C using a mixture of liquid nitrogen and methanol. As spectrograph a double-monochromator (Jobin-Yvon Model 1402) coupled with a nitrogen-cooled CCD (Jobin-Yvon 2000 × 800) was used. The entrance slit was set to 20 μm to achieve a theoretical resolution of 0.5 cm^{-1}. The sample solution was illuminated through the cooling liquid in a backscattering geometry. The laser power at the sample was around 250 mW and the spectra were averages of 25 accumulations (each with an exposure time of 15 seconds). Spectra were fitted (data max from Galactic Industries Corp.) to determine band position and band width. The spectrum scale was recalibrated with the band positions of the internal standard acetone.

Received: February 27, 2004
Revised: May 17, 2004 [Z54125]

Keywords: copper · density functional calculations · dioxygen ligands · Raman spectroscopy · tripod ligands

[1] a) K. D. Karlin, A. D. Zuberbühler in *Bioinorganic Catalysis, 2nd Ed.* (Eds.: J. Reedijk, E. Bouwman), Dekker, New York, **1999**, p. 469 – 534; b) S. Schindler, *Eur. J. Inorg. Chem.* **2000**, *11*, 2311 – 2326; c) A. G. Blackman, W. B. Tolman in *Structure & Bonding 97: Metal-Oxo and Metal-Peroxo Species in Catalytic Oxidations* (Ed.: B. Meunier), Springer, Berlin, **2000**, pp. 179 – 211; d) E. I. Solomon, P. Chen, M. Metz, S.-K. Lee, A. E. Palmer, *Angew. Chem.* **2001**, *113*, 4702 – 4724; *Angew. Chem. Int. Ed.* **2001**, *40*, 4570 – 4590.

[2] a) E. A. Lewis, W. B. Tolman, *Chem. Rev.* **2004**, *104*, 1047 – 1076; b) L. M. Mirica, X. Ottenwaelder, T. D. P. Stack, *Chem. Rev.* **2004**, *104*, 1013 – 1045.

[3] L. Que, Jr., W. B. Tolman, *Angew. Chem.* **2002**, *114*, 1160 – 1185; *Angew. Chem. Int. Ed.* **2002**, *41*, 1114 – 1137.

[4] M. Weitzer, S. Schindler, G. Brehm, S. Schneider, E. Hörmann, B. Jung, S. Kaderli, A. D. Zuberbühler, *Inorg. Chem.* **2003**, *42*, 1800 – 1806.

[5] B. A. Jazdzewski, A. M. Reynolds, P. L. Holland, V. G. Young, S. Kaderli, A. D. Zuberbühler, W. B. Tolman, *J. Biol. Inorg. Chem.* **2003**, *8*, 1432 – 1437.

[6] K. Komiyama, H. Furutachi, S. Nagatomo, A. Hashimoto, H. Hayashi, S. Fujinami, M. Suzuki, T. Kitagawa, *Bull. Chem. Soc. Jpn.* **2004**, *77*, 59 – 72.

[7] K. D. Karlin, N. Wei, B. Jung, S. Kaderli, P. Niklaus, A. D. Zuberbühler, *J. Am. Chem. Soc.* **1993**, *115*, 9506 – 9514.

[8] a) J. P. Klinman, *Chem. Rev.* **1996**, *96*, 2541 – 2561; b) J. W. Whittaker, *Chem. Rev.* **2003**, *103*, 2347 – 2363; c) S. T. Prigge, B. A. Eipper, R. E. Mains, L. M. Amzel, *Science* **2004**, *304*, 864 – 867

[9] K. Fujisawa, M. Tanaka, Y. Moro-oka, N. Kitajima, *J. Am. Chem. Soc.* **1994**, *116*, 12079 – 12080.

[10] a) N. W. Aboelella, E. A. Lewis, A. M. Reynolds, W. W. Brennessel, C. J. Cramer, W. B. Tolman, *J. Am. Chem. Soc.* **2002**, *124*, 10660 – 10661; b) D. J. E. Spencer, N. W. Aboelella, A. M. Reynolds, P. L. Holland, W. B. Tolman, *J. Am. Chem. Soc.* **2002**, *124*, 2108 – 2109.

 © 2004 Wiley-VCH Verlag GmbH & Co. KGaA, Weinheim

[11] M. Harata, K. Jitsukawa, H. Masuda, H. Einaga, *J. Am. Chem. Soc.* **1994**, *116*, 10817 – 10818.
[12] L. M. Berreau, S. Mahapatra, J. A. Halfen, V. G. Young, Jr., W. B. Tolman, *Inorg. Chem.* **1996**, *35*, 6339 – 6342.
[13] A. Wada, M. Harata, K. Hasegawa, K. Jitsukawa, H. Masuda, M. Mukai, T. Kitagawa, H. Einaga, *Angew. Chem.* **1998**, *110*, 874 – 875; *Angew. Chem. Int. Ed.* **1998**, *37*, 798 – 799.
[14] P. Chaudhuri, M. Hess, T. Weyhermüller, K. Wieghardt, *Angew. Chem.* **1999**, *111*, 1165 – 1168; *Angew. Chem. Int. Ed.* **1999**, *38*, 1095 – 1098.
[15] P. Chen, D. E. Root, C. Campochiaro, K. Fujisawa, E. I. Solomon, *J. Am. Chem. Soc.* **2003**, *125*, 466 – 474.
[16] For qualitative theoretical work see: A. Bérces, *Int. J. Quantum Chem.* **1997**, *65*, 1077 – 1086.
[17] a) C. J. Cramer, W. B. Tolman, K. H. Theopold, A. L. Rheingold, *Proc. Natl. Acad. Sci. USA* **2003**, *100*, 3635 – 3640; b) D. A. Pantazis, J. W. McGrady, *Inorg. Chem.* **2003**, *42*, 7734.
[18] S. C. Lee, R. H. Holm, *J. Am. Chem. Soc.* **1993**, *115*, 11789 – 11798; M. J. Scott, S. C. Lee, R. H. Holm, *Inorg. Chem.* **1994**, *33*, 4651 – 4662; M. Becker, F. W. Heinemann, S. Schindler, *Chem. Eur. J.* **1999**, *5*, 3124 – 3129.
[19] M. Schatz, M. Becker, O. Walter, G. Liehr, S. Schindler, *Inorg. Chim. Acta* **2001**, *324*, 173 – 179.
[20] V. Raab, J. Kipke, O. Burghaus, J. Sundermeyer, *Inorg. Chem.* **2001**, *40*, 6964 – 6971.
[21] S. Schindler, unpublished results.
[22] H. Wittmann, V. Raab, A. Schorm, J. Plackmeyer, J. Sundermeyer, *Eur. J. Inorg. Chem.* **2001**, 1937 – 1948.
[23] K. Nakamoto, *Infrared and Raman Spectra of Inorganic and Coordination Compounds, part B*, 5th ed., Wiley, New York, **1997**, p. 97 – 101.
[24] Density functional calculations were performed using the program Turbomole[27] employing the BP86 functional[28] in combination with the all-electron TZVP basis set of Ahlrichs and co-workers[29] and the resolution of identity (RI) approach.[30] A restricted Kohn–Sham formalism was used throughout. The SNF program package[31] was utilized for numerical evaluation of vibrational frequencies from analytic energy gradients. Starting structures for DFT calculations were generated at the semiempirical PM3(TM) level by means of the program Spartan, which was also used for conformational searching.[32]
[25] Conformational searching at the PM3(TM) level[32] revealed a few isoenergetic structures. Reoptimizations of the geometries of selected low-energy conformers at the DFT level resulted in **2** as the most stable conformer. An exhaustive coverage of the conformational space at this level of theory, however, is outside the scope of the present study.
[26] The BP86 functional has been identified as a reliable tool for the assessment of structural parameters and vibrational frequencies of transition-metal complexes.[33,34] Although an anharmonic treatment of complexes of the present size is not possible for us, it is generally found that computed harmonic frequencies at the BP86 level compare favorably to experimental fundamentals without scaling.[33] This has been substantiated recently: a) M. Reiher, J. Neugebauer, B. A. Hess, *Z. Phys. Chem. (Muenchen Ger.)* **2003**, *217*, 91 – 103; b) J. Neugebauer, B. A. Hess, *J. Chem. Phys.* **2003**, *118*, 7215 – 7225; c) G. Brehm, M. Reiher, S. Schneider, *J. Phys. Chem. A* **2002**, *106*, 12024 – 12034; d) M. Reiher, G. Brehm, S. Schneider, *J. Phys. Chem. A* **2004**, *108*, 734 – 742.
[27] a) R. Ahlrichs, M. Bär, H. P. Baron, R. Bauernschmitt, S. Böcker, M. Ehrig, K. Eichkorn, S. Elliott, F. Furche, F. Haase, M. Häser, C. Hättig, H. Horn, C. Huber, U. Huniar, M. Kattanek, A. Köhn, C. Kölmel, M. Kollwitz, K. May, C. Ochsenfeld, H. Öhm, A. Schäfer, U. Schneider, O. Treutler, K. Tsereteli, B. Unterreiner, M. v. Arnim, F. Weigend, P. Weis, H. Weiss, *Turbomole—Program System for ab initio Electronic Structure Calculations Version 5.6*, Universität Karlsruhe, Germany, **2002**; b) R. Ahlrichs in *Encyclopedia Computational Chemistry* (Ed.: P. v. R. Schleyer), Wiley, Chichester, **1998**, p. 3123 – 3129; c) R. Ahlrichs, M. Bär, M. Häser, H. Horn, C. Kölmel, *Chem. Phys. Lett.* **1989**, *162*, 165 – 169.
[28] a) A. D. Becke, *Phys. Rev. A* **1988**, *38*, 3098 – 3100; b) J. B. Perdew, *Phys. Rev. B* **1986**, *33*, 8822 – 8824.
[29] A. Schäfer, C. Huber, R. Ahlrichs, *J. Chem. Phys.* **1994**, *100*, 5829 – 5835.
[30] a) K. Eichkorn, O. Treutler, H. Öhm, M. Häser, R. Ahlrichs, *Chem. Phys. Lett.* **1995**, *240*, 283 – 289; b) K. Eichkorn, F. Weigend, O. Treutler, R. Ahlrichs, *Theor. Chem. Acc.* **1997**, *97*, 119 – 124; c) R. A. Kendall, H. A. Früchtl, *Theor. Chem. Acc.* **1997**, *97*, 158 – 163.
[31] J. Neugebauer, M. Reiher, C. Kind, B. A. Hess, *J. Comput. Chem.* **2002**, *23*, 895 – 910.
[32] Spartan, Pro, Wavefunction.
[33] W. Koch, M. C. Holthausen, *A Chemist's Guide to Density Functional Theory*, *2nd Ed.*, Wiley-VCH, Weinheim, **2001**.
[34] M. Reiher, O. Salomon, D. Sellmann, B. A. Hess, *Chem. Eur. J.* **2001**, *7*, 5195 – 5202.
[35] A referee criticized the lack of resonance Raman data for the Cu–O metal–ligand stretching region, which should also reveal significant isotopic shifts. While we were unsuccessful to date in obtaining experimental data for this region of the spectrum for technical reasons, we find indeed a significant splitting in the computed $\tilde{\nu}$Cu-O modes upon isotopic substitution: **1**: [M]-$^{16}O_2$: 437.8 cm^{-1}, [M]-^{18}O-^{16}O: 420.9 cm^{-1}, [M]-^{16}O-^{18}O: 436.7 cm^{-1}, [M]-$^{18}O_2$: 419.7 cm^{-1}, **2**: [M]-$^{16}O_2$: 463.5 cm^{-1} (asymmetric Cu-O_2 stretch, as), 471.4 cm^{-1} (symmetric stretch, s), [M]-^{18}O-^{16}O: 457.3 cm^{-1} (as), 468.9 cm^{-1} (s), [M]-^{16}O-^{18}O: 451.1 cm^{-1} (as), 468.6 (s), [M]-^{18}O-^{18}O: 448.6 cm^{-1} (as), 463.8 cm^{-1} (s). Hence, with a computed splitting of 15.8 cm^{-1} the Cu–O region for the mixed-isotope species we find indeed a significant splitting for the end-on complex **1**, which could be detectable within the experimental resolution. However, as the stretching modes for the pure $^{16}O_2$ and $^{18}O_2$ coincide with the modes identified for the mixed-isotope species, this splitting is unlikely to be of use as a unique signature for end-on complexes.

 © 2004 Wiley-VCH Verlag GmbH & Co. KGaA, Weinheim

Functionalized Arynes

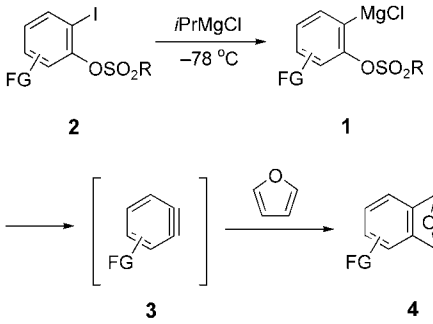
Preparation of Polyfunctional Arynes via 2-Magnesiated Diaryl Sulfonates**

*Ioannis Sapountzis, Wenwei Lin, Markus Fischer, and Paul Knochel**

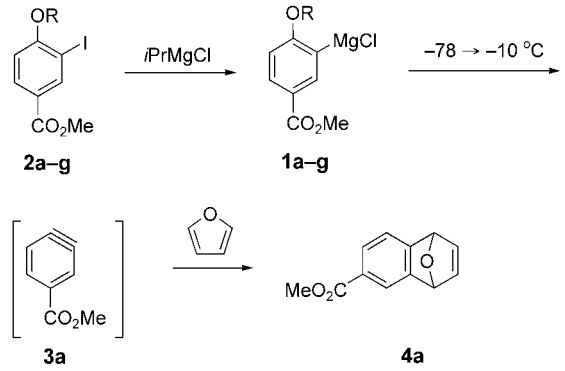
Dedicated to Professor Rolf Huisgen

Arynes are highly reactive intermediates which have found numerous applications in organic synthesis.[1] As a result of the strained nature of the ring (ca. 63 kcal mol^{-1}),[2] arynes react with a broad range of reagents (with nucleophiles in addition reactions, with alkenes in cycloadditions and ene reactions) and therefore have significant synthetic potential.[3] Whereas a number of methods for the generation of benzyne itself are known, the preparation of functionalized arynes is often incompatible with the harsh basic conditions necessary for their generation. Recently, we developed a new method for the synthesis of polyfunctionalized aryl magnesium compounds through an iodine–magnesium exchange.[4] This method can be used for the preparation of a variety of 2-magnesiated aryl sulfonates of type **1** from the corresponding 2-iodo derivates **2** (Scheme 1).

The leaving-group ability of the sulfonate group (RSO_2O^-) was found to be essential for the optimization of the reaction conditions and yield. Because of the strong metal-directing effect of the sulfonate moiety, the I/Mg exchange was complete at −78 °C within 15 min. Thus, we prepared the sulfonates **2a–g** derived from methyl 4-hydroxy-3-iodobenzoate and converted them into the corresponding Grignard reagents **1a–g**, which were in turn transformed into the products **4a** upon treatment with furan (Scheme 2 and Table 1).



Scheme 1. Generation and trapping of functionalized arynes **3**. FG = functional group.



Scheme 2. Tuning of the leaving group for the generation of the aryne **3a**; for R, see Table 1.

Table 1: Optimization of the leaving group for the generation of **3a**.

Entry	R (sulfonate)	*t* [h]	Yield of **4a** [%][a]
1	CF_3SO_2 (**2a**)	–	0
2	CH_3SO_2 (**2b**)	30[b]	72
3	$CF_3CH_2SO_2$ (**2c**)	–	0
4	4-$MeC_6H_4SO_2$ (**2d**)	30[b]	90
5	2,5-$Cl_2C_6H_3SO_2$ (**2e**)	1	87
6	3,5-$(CF_3)_2C_6H_3SO_2$ (**2f**)	1	78
7	4-$ClC_6H_4SO_2$ (**2g**)	4	93

[a] Yield of isolated, analytically pure compound. [b] The reaction mixture was warmed to 25 °C.

Because of the rapid decomposition of **2a** (R = SO_2CF_3) at −78 °C with immediate formation of the aryne, it was not possible to monitor the reaction. The product **4a** was not isolated in this case (Table 1, entry 1).[5] The corresponding mesylate **2b** required a reaction time of 30 h at 20 °C to undergo full conversion into the expected product **4a** in just 72 % yield (Table 1, entry 2). Thus, the mesylate group is only a moderate leaving group, and the rate of formation of the aryne **3a** is too slow in this case. We varied the electron-withdrawing ability of the sulfonate leaving group systematically. Although the tosylate **2d** afforded the product **4a** in 90 % yield, a reaction time of 30 h was still required. In the reactions of the 2,5-dichlorobenzenesulfonate **2e** and the 3,5-bis(trifluoromethyl)benzenesulfonate **2f** rapid formation of the aryne was observed, but **4a** was isolated in just 87 and 78 % yield, respectively (Table 1, entries 5 and 6). The best result was obtained with the 4-chlorobenzenesulfonate **2g**, from which **4a** was formed in 93 % yield after a reaction time of only 4 h at −10 °C.

This effective leaving group was used for the preparation of the functionalized arynes **3a–i** and the heteroaryne **3j**,

[*] Dipl.-Chem. I. Sapountzis, Dipl.-Chem. W. Lin, M. Fischer, Prof. Dr. P. Knochel
Department Chemie
Ludwig-Maximilians-Universität München
Butenandtstrasse 5–13, Haus F
81377 München (Germany)
Fax: (+49) 89-2180-77680
E-mail: paul.knochel@cup.uni-muenchen.de

[**] We thank the Fonds der Chemischen Industrie and Merck Research Laboratories (MSD) for financial support. I.S. thanks Aventis Pharma (Frankfurt) for a fellowship. We also thank Chemetall GmbH (Frankfurt), Wacker Chemie GmbH (München), BASF AG (Ludwigshafen), and Bayer Chemicals AG for the generous gift of chemicals.

Supporting information for this article is available on the WWW under http://www.angewandte.org or from the author.

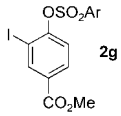
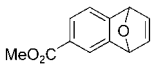
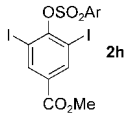
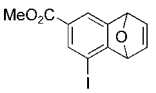
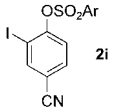
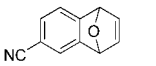
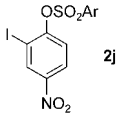
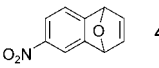
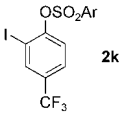
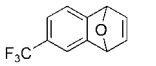
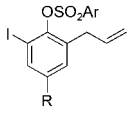
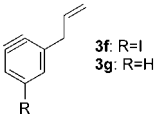
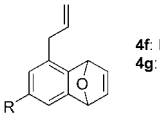
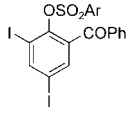
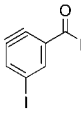
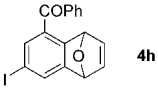
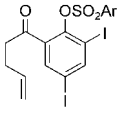
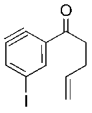
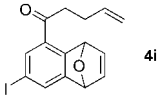
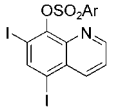
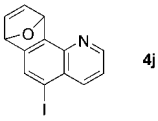
 © 2004 Wiley-VCH Verlag GmbH & Co. KGaA, Weinheim DOI: 10.1002/anie.200460417

which were trapped in the presence of an excess of furan to provide the expected products **4a–j** (Table 2). Thus, a variety of functionalities, such as an iodine (Table 2, entries 2, 6, 8, 9, and 10), ester (Table 2, entries 1 and 2), nitrile (Table 2, entry 3), and trifluoromethyl group (Table 2, entry 5), are tolerated in the aryne intermediates for the first time. Interestingly, even very sensitive functional groups, such as a nitro group (Table 2, entry 4)[6] and even a ketone function (Table 2, entries 8 and 9)[7] are compatible with our preparation method. The quinolinyl sulfonate **2p** was also readily converted into the corresponding Grignard reagent, which underwent transformation via the heterocyclic aryne **3j** into the desired product **4j** in 77% yield.

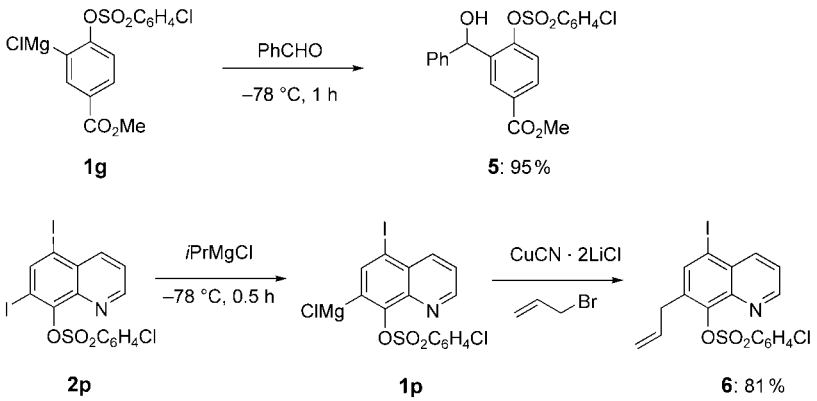
The I/Mg exchange with precursors of type **2** proceeds under very mild conditions, and is therefore compatible with many functional groups. Furthermore, the intermediate Grignard reagent of type **1** is stable at low temperatures and can be quenched with a variety of electrophiles. For example, the functionalized aryl magnesium chloride **1g** reacted at low temperature (−78 °C) within 1 h with benzaldehyde to give the corresponding benzylic alcohol **5** in 95% yield (Scheme 3). The transmetalation of this Grignard reagent led to stable copper or zinc organometallic reagents, which were not prone to undergo aryne formation, so that the reactions could be performed over a broad range of temperatures. Thus, the Grignard reagent **1p** formed from the heterocyclic sulfonate **2p** (*i*PrMgCl, −78 °C, 30 min) was transmetalated to the copper derivative with CuCN·2 LiCl (1 equiv, −78 °C→RT) and treated with allyl bromide (2 equiv) to give the product **6** in 81% yield (Scheme 3). Remarkably, the I/Mg exchange only occurred at the position α to the sulfonate group.

Our method allows the functionalization of the triiodoaryl sulfonate **2q**. Thus, the magnesiation of **2q** with *i*PrMgCl followed by transmetalation with CuCN·2 LiCl provides a copper intermediate, which could be acylated with 3-(2-furyl)propionyl chloride[8] (−78 °C→RT, 1 h) to give the iodoketone **2r** in 65% yield (Scheme 4). This compound underwent a further I/Mg exchange at −78 °C with *i*PrMgCl. Upon warming to ambient temperature, the resulting aryne underwent an intramolecular cyclization with the furan moiety to provide the polycyclic iodoketone **7** in 48% yield. We observed competitive protonation of the magnesium intermediate as a side reaction.[9]

Table 2: Generation of polyfunctionalized arynes **3** and their reaction with furan.

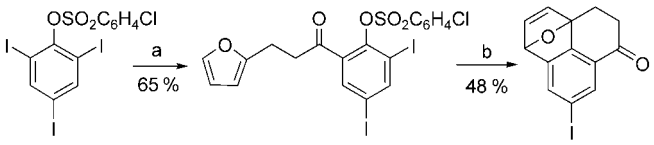
Entry	Precursor[a]	Aryne	Product	Yield [%][b]
1	 **2g**	 **3a**	 **4a**	93
2	 **2h**	 **3b**	 **4b**	71
3	 **2i**	 **3c**	 **4c**	78
4	 **2j**	 **3d**	 **4d**	78
5	 **2k**	 **3e**	 **4e**	75
6 7	 **2l**: R=I **2m**: R=H	 **3f**: R=I **3g**: R=H	 **4f**: R=I **4g**: R=H	88 83
8	 **2n**	 **3h**	 **4h**	68
9	 **2o**	 **3i**	 **4i**	71
10	 **2p**	 **3j**	 **4j**	77

[a] Ar = 4-ClC$_6$H$_4$. [b] Yield of isolated, analytically pure product.



Scheme 3. Reactions of the magnesium reagents **1g** and **1p** with electrophiles.

 © 2004 Wiley-VCH Verlag GmbH & Co. KGaA, Weinheim



2q **2r** **7**

Scheme 4. Intramolecular trapping of a functionalized aryne: a) *i*PrMgCl, −78 °C, 0.5 h, then CuCN·2 LiCl, −78 °C, 10 min, then 3-(2-furyl)propionyl chloride (2 equiv, −78 °C→RT, 1 h); b) *i*PrMgCl, −78 °C, 0.5 h,then −78 °C→RT, 1 h.

In summary, we have developed a new and general method for the preparation of functionalized arynes by the readily tunable elimination of 2-magnesiated aryl sulfonates. Further applications are under investigation in our laboratories.

Experimental Section

Typical procedure: **4a**: A dry, argon-flushed 10-mL Schlenk tube equipped with a magnetic stirring bar and a septum was charged with a solution of methyl iodobenzoate **2g** (452 mg, 1.00 mmol) in dry THF (5 mL) and cooled to −78 °C. *i*PrMgCl (0.920 mL, 1.05 mmol, 1.10 M in THF) was then added dropwise, and after 30 min furan (0.38 mL, 5.0 mmol) was added slowly at −78 °C. The resulting mixture was warmed to room temperature and stirred for a further 2 h. The reaction was quenched with a saturated solution of NH_4Cl, the mixture was extracted with CH_2Cl_2, and the organic extracts were dried over Na_2SO_4, filtered, and concentrated in vacuo. Purification by flash chromatography on silica gel (pentane/diethyl ether 2:1) furnished **4a** (188 mg, 93 %) as a colorless solid.

Received: April 22, 2004 [Z460417]

Keywords:
Grignard reagents · arynes · cycloaddition · elimination · metalation

[1] For excellent reviews, see: a) J. Sauer, R. Huisgen, *Angew. Chem.* **1960**, *72*, 294; b) R. W. Hoffmann, *Dehydrobenzene and Cycloalkynes*, Academic Press, New York, **1967**; c) L. Castedo, E. Guitian in *Studies in Natural Products Chemistry*, *Vol. 3*, Part B, (Ed.: A. U. Rahman), Elsevier, Amsterdam, **1989**, p. 417; d) S. V. Kessar in *Comprehensive Organic Synthesis*, *Vol. 4* (Eds.: B. M. Trost, I. Fleming, H. F. Semmelhack), Pergamon, Oxford, **1991**, p. 483; e) R. F. C. Brown, *Synlett* **1993**, 9; f) W. Sander, *Acc. Chem. Res.* **1999**, *32*, 669; g) H. Pelissier, M. Santelli, *Tetrahedron* **2003**, *59*, 701.

[2] C. Wentrup, *Reactive Molecules*, Wiley, New York, **1984**, p. 288.

[3] For some recent applications, see: a) T. Hamura, Y. Ibusuki, K. Sato, T. Matsumoto, Y. Osamura, K. Suzuki, *Org. Lett.* **2003**, *5*, 3551; b) T. Hosoya, T. Hamura, Y. Kuriyama, M. Miyamoto, T. Matsumoto, K. Suzuki, *Synlett* **2000**, 520; c) T. Hosoya, E. Takashiro, T. Matsumoto, K. Suzuki, *J. Am. Chem. Soc.* **1994**, *116*, 1004; d) M. Beller, C. Breindl, T. H. Riermeier, A. Tillack, *J. Org. Chem.* **2001**, *66*, 1403; e) P. Maurin, M. Ibrahim-Ouali, M. Santelli, *Tetrahedron Lett.* **2001**, *42*, 8147; f) Z. Liu, R. C. Larock, *Org. Lett.* **2003**, *5*, 4673; g) H. Yoshida, Y. Honda, E. Shirakawa, T. Hiyama, *Chem. Commun.* **2001**, 1880; h) H. Yoshida, E. Shirakawa, Y. Honda, T. Hiyama, *Angew. Chem.* **2002**, *114*, 3381; *Angew. Chem. Int. Ed.* **2002**, *41*, 3247; i) D. Peña, S. Escudero, D. Pérez, E. Guitián, L. Castedo, *Angew. Chem.* **1998**, *110*, 2804; *Angew. Chem. Int. Ed.* **1998**, *37*, 2659; j) J.-M. Becht, A. Gissot, A. Wagner, C. Mioskowski, *Chem. Eur. J.* **2003**, *9*, 3209.

[4] a) P. Knochel, W. Dohle, N. Gommermann, F. Kneisel, F. Kopp, T. Korn, I. Sapountzis, V. A. Vu, *Angew. Chem.* **2003**, *115*, 4438; *Angew. Chem. Int. Ed.* **2003**, *42*, 4302; b) A. Staubitz, W. Dohle, P. Knochel, *Synthesis* **2003**, 233; c) A. E. Jensen, W. Dohle, I. Sapountzis, D. M. Lindsay, V. A. Vu, P. Knochel, *Synthesis* **2002**, 565; d) N. Gommermann, C. Koradin, P. Knochel, *Synthesis* **2002**, 2143; e) I. Sapountzis, P. Knochel, *Angew. Chem.* **2004**, *116*, 915; *Angew. Chem. Int. Ed.* **2004**, *43*, 897.

[5] Interestingly, the magnesium derivative of methyl 4-pivaloxy-3-iodobenzoate is also unstable and rapidly decomposes at −78 °C.

[6] For the preparation of Grignard reagents that bear a nitro group, see: I. Sapountzis, P. Knochel, *Angew. Chem.* **2002**, *114*, 1680; *Angew. Chem. Int. Ed.* **2002**, *41*, 1610.

[7] For the preparation of Grignard reagents that contain a ketone function, see: F. F. Kneisel, P. Knochel, *Synlett* **2002**, 1799.

[8] For the preparation of 3-(2-furyl)propionyl chloride we used literature procedures starting from furfural: a) M. Takeuchi, T. Taniguchi, K. Ogasawara, *Synthesis* **1999**, 341; b) A. Robertson, D. Philip, N. Spencer, *Tetrahedron* **1999**, *55*, 11365; c) A. Padwa, T. J. Wisnieff, E. J. Walsh, *J. Org. Chem.* **1989**, *54*, 298.

[9] Besides **7** (48 % yield), we also isolated an iodoketone (2-[3-(2-furyl)propanoyl]-4-iodophenyl 4-chlorobenzenesulfonate), which probably formed through protonation of the corresponding Grignard reagent.

 © 2004 Wiley-VCH Verlag GmbH & Co. KGaA, Weinheim

Sialic Acids

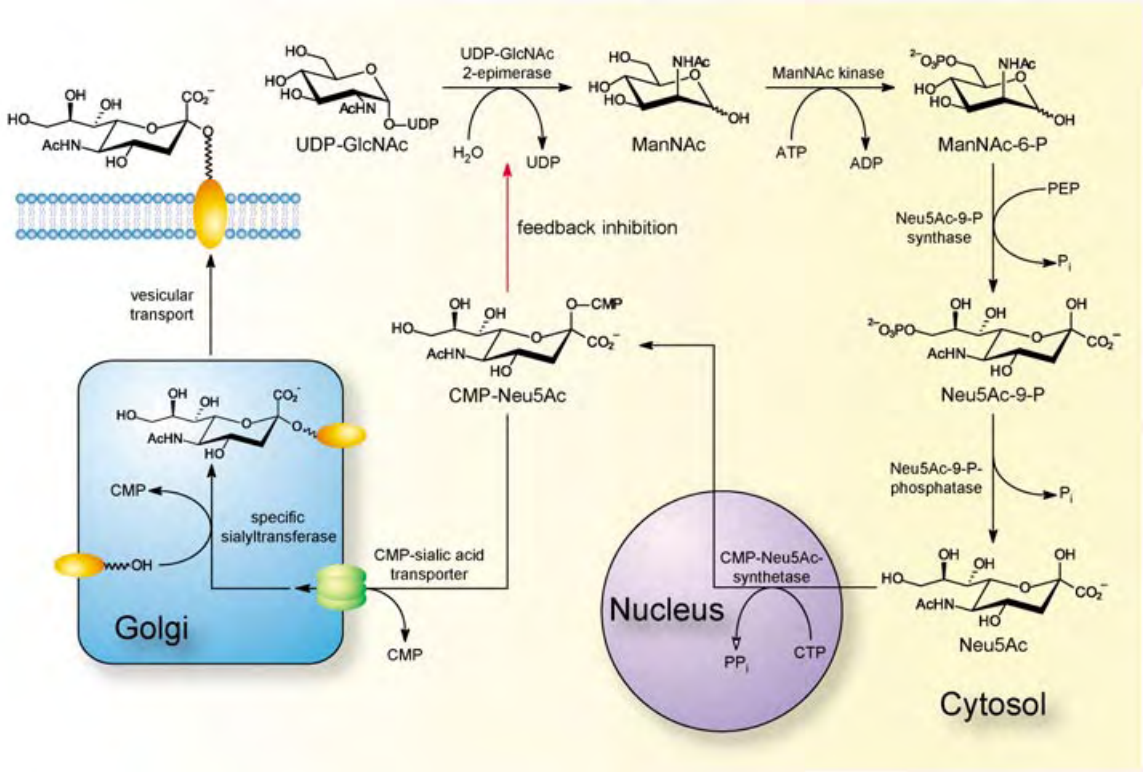
Synthesis and Biochemical Properties of Reversible Inhibitors of UDP-*N*-Acetylglucosamine 2-Epimerase

Samy Al-Rawi, Stephan Hinderlich, Werner Reutter, and Athanassios Giannis**

Sialic acids comprise a family of α-keto acids with a backbone skeleton consisting of nine carbon atoms. *N*-Acetylneuraminic acid (Neu5Ac or NANA; see Scheme 1) is the most common sialic acid and also the biosynthetic precursor of almost all known 50 members of this class.[1] Due to their exposed position at the distal end of oligosaccharide chains, sialic acids contribute to the biological properties of glyco-

[*] Dr. S. Hinderlich, Prof. Dr. W. Reutter
Charité – Universitätsmedizin Berlin
Campus Benjamin Franklin
Institut für Molekularbiologie und Biochemie
Arnimallee 22, 14195 Berlin-Dahlem (Germany)
Fax: (+49) 30-8445-1541
E-mail: stephan.hinderlich@charite.de
Dipl.-Chem. S. Al-Rawi, Prof. Dr. A. Giannis
Institut für Organische Chemie
Universität Leipzig
Johannisallee 29, 04103 Leipzig (Germany)
Fax: (+49) 341-973-6599
E-mail: giannis@chemie.uni-leipzig.de

 © 2004 Wiley-VCH Verlag GmbH & Co. KGaA, Weinheim DOI: 10.1002/anie.200453863



Scheme 1. Biosynthesis of Neu5Ac and incorporation on cell-surface glycoconjugates.

conjugate structures in a significant manner. Glycoconjugates containing sialic acid play an essential role in a variety of fundamental physiological and pathological processes,[2] for example, embryogenesis, organogenesis, immune defense, migration and homing of leucocytes, and metastasis of neoplastic cells as well as inflammation reactions and invasion of pathogens in cells. Many tumors bear a large amount of sialic acids like a protective shield on their cell surface. The most prominent example of sialic acid mediated cell–virus interaction is the infection by the influenza virus. The invasion of cells, as well as the release of newly formed viruses is mediated by sialic acid containing structures on the host cell surface. Inhibitors of influenza sialidase, the virus-releasing enzyme, are currently applied in antiviral therapy (Zanamivir, Oseltamivir).[3] Although all steps of Neu5Ac biosynthesis have been known for a long time,[4] only a limited number of inhibitors have been developed.[5,6] In this paper we report the conception, synthesis, and biochemical properties of a potent reversible inhibitor of UDP-*N*-acetylglucosamine (GlcNAc) 2-epimerase (UDP = uridinediphosphate, GlcNAc = *N*-acetylglucosamine), the key enzyme in Neu5Ac biosynthesis.

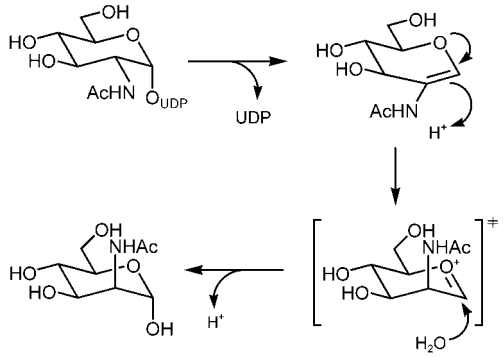
Biosynthesis of Neu5Ac begins with the epimerization of UDP-GlcNAc under concomitant release of UDP, followed by phosphorylation of the formed *N*-acetylmannosamine (ManNAc) at the 6-hydroxy functionality. Both steps are catalyzed by the bifunctional enzyme UDP-GlcNAc 2-epimerase/ManNac kinase (Scheme 1).[7,8] This key enzyme is regulated in a complex manner.[7–10] Lymphocytes that show a deficiency in activitiy of this enzyme are not capable of synthesizing sialic acids by themselves and show serious defects in sialic acid dependent functions.[11] Inactivation through targeted mutagenesis in mice causes hyposialylation of the embryos and induces early lethality on day 8.5 of embryonic development.[12] These results emphasize the importance of UDP-GlcNAc 2-epimerase in the biosynthesis of *N*-acetylneuraminic acid and make this enzyme an interesting target for the development of effective inhibitors.

The homologous mammalian UDP-GlcNAc 2-epimerase has recently become available in a recombinant form and does not differ in mechanism[13] from the bacterial[14] enzyme. Both enzymes first generate 2-acetamidoglucal as an intermediate after *anti*-elimination of UDP. Positional isotope exchange experiments showed that the reaction proceeds by C–O bond cleavage at the anomeric position. By monitoring the reaction with coupled NMR experiments, we were able to determine that the subsequent addition of water occurs from the bottom side of the 2-acetamidoglucal. Thus, the released ManNAc is the α-anomer (Scheme 2). The oxocarbenium intermediate might represent the transition state of the addition of water on the 2-acetamidoglucal.

Because stable analogues of the transition state are known to be bound much more tightly to the active site of the enzyme than analogues of the substrate in its ground state,[15] we considered the synthesis of iminosugars **2**–**4** (Figure 1) as potential inhibitors of UDP-GlcNAc 2-epimerase. At physiological pH such iminosugars are protonated and they should consequently be good analogues of the proposed transition state.

The bicyclic oxazolidinylpiperidine of type **9** (Scheme 3) served as the central, chiral building block in the preparation

 © 2004 Wiley-VCH Verlag GmbH & Co. KGaA, Weinheim



Scheme 2. Proposed reaction mechanism of mammalian UDP-GlcNAc 2-epimerase and postulated transition state for the *syn*-addition of water at the 2-acetamidoglucal.

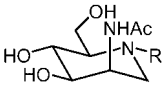
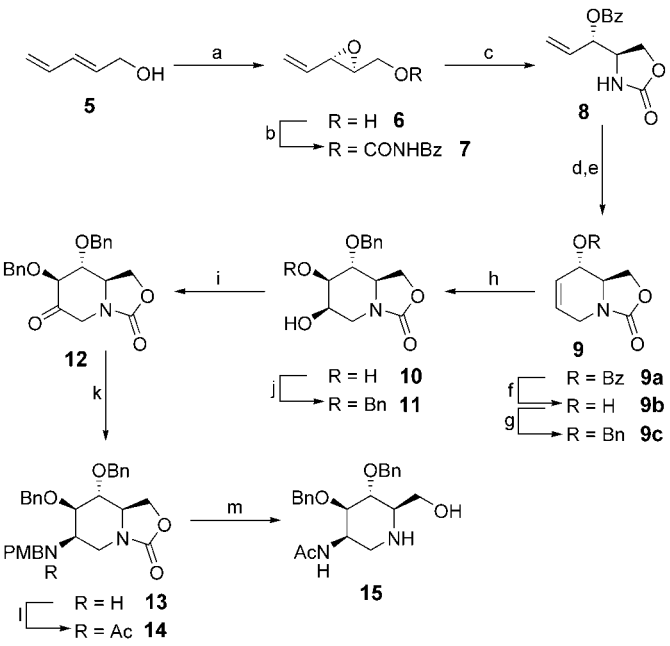


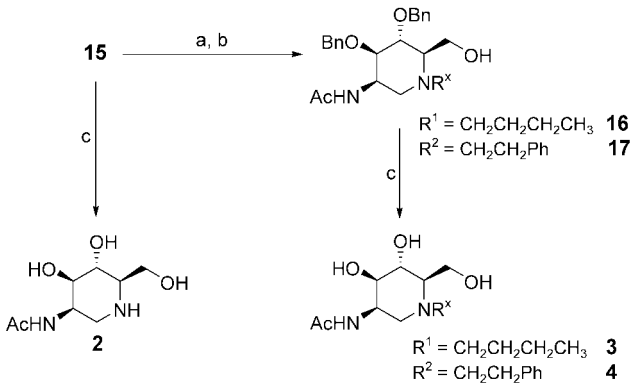
Figure 1. Transition-state analogues of UDP-GlcNAc 2-epimerase. **2**: R = H, **3**: R = *n*Bu, and **4**: R = CH_2CH_2Ph.

of the 1-deoxyiminosugar. According to the previous work by Martin et al.,[16] the doubly unsaturated alcohol **5** was stereoselectively epoxidized under Sharpless conditions.[17] Subsequent conversion of the (2*S*,3*S*)-epoxyalcohol **6** with benzoylisocyanate gave the benzoylcarbamate **7**. Regioselective opening of the epoxide under mild conditions in a biphasic system lead to an intramolecular migration of the benzoyl group to afford the substituted oxazolidinone **8**. The compound was first allylated at the ring nitrogen then subjected to a ring-closing metathesis to give the bicyclic derivate **9a** in almost quantitative yield. With regard to the following synthetic steps, it was necessary to convert the ester group of the piperidine ring into a benzyl ether. Compound **9c** was synthesized from **9a** in two steps. By using catalytic amounts of potassium osmate and *N*-methylmorpholine-*N*-oxide (NMMO) as the cooxidant in a mixture of *t*BuOH/water, we converted compound **9c** into the corresponding diol. In this reaction no acceptable diastereomeric excess could be achieved; however, with $(DHQD)_2Phal$ as chiral auxiliary[18] and $K_3[Fe(CN)_6]$ as cooxidant, bishydroxylation of compound **10** resulted with nearly complete diastereoselectivity in very good yields. The structure was determined by NOE and COSY experiments.

Reaction of compound **10** with dibutyltin oxide gave as intermediate the corresponding dibutyltin ketal, which was converted into compound **11** using benzyl bromide in the presence of tetrabutylammonium bromide[19] with a regioselectivity of 3.5:1. Swern oxidation of **11** yielded ketone **12**. Reductive amination of this derivative with *p*-methoxybenzylamine and sodium triacetoxyborohydride resulted in compound **13**. Acetylation of compound **13** gave the amide **14** in good yield. Oxidative cleavage of the *p*-methoxybenzyl group in the presence of cerium(IV) ammonium nitrate (CAN) followed by opening of the oxazolidinone ring with barium hydroxide afforded compound **15**. After cleavage of the protecting groups of compound **15** by hydrogenolysis, target structure **2** was finally formed (Scheme 4).[20] For subsequent application of the inhibitors in cellular systems and for the



Scheme 3. Synthesis of the protected iminosugar **15**: a) $Ti(O\mathit{i}Pr)_4$, L-(+)-DIPT, *t*BuOOH, CH_2Cl_2, 3-Å molecular sieves, −15 °C, 57%; b) BzNCO, Et_2O, RT, 84%; c) K_2CO_3, $(C_8H_{17})_3CH_3NCl$, CH_2Cl_2/H_2O, RT, 84%; d) NaH, allyl bromide, DMF, 0 °C→RT, 81%; e) Grubbs catalyst, toluene, RT, 99%; f) K_2CO_3, MeOH, RT, 85%; g) NaH, BnBr, DMF, 0 °C→RT, 91%; h) $(DHQD)_2Phal$, K_2OsO_4, K_2CO_3, $K_3[Fe(CN)_6]$, $CH_3SO_2NH_2$, *t*BuOH/H_2O, RT, 90%; i) 1. $n Bu_2SnO$, toluene, reflux; 2. BnBr, Bu_4NBr, 100 °C, 69%; j) DMSO, $(COCl)_2$, DIPEA, CH_2Cl_2, −70 °C→RT, 86%; k) 4-methoxybenzylamine, AcOH, $Na(OAc)_3BH$, 1,2-dichloroethane, RT, 78%; l) pyridine, DMAP, AcCl, 0 °C→RT, 86%; m) 1. CAN, CH_3CN/H_2O, RT; 2. $Ba(OH)_2\times 8H_2O$, EtOH/H_2O, reflux, 63%. Bz = benzoyl, Bn = benzyl, CAN = ceric ammonium nitrate, $(DHQD)_2Phal$ = dihydroquinidine 1,4-phthalazinediyl ether, DIPEA = *N*,*N*-diisopropylethylamine, DIPT = diisopropyl tartrate, DMAP = 4-dimethylaminopyridine, PMB = *p*-methoxybenzyl.



Scheme 4. Derivatization and deprotection: a) Butyraldehyde, AcOH, $Na(OAc)_3BH$, 1,2-dichloroethane, RT, 95%; b) phenylacetaldehyde, AcOH, $NaCNBH_3$, CH_3CN, RT, 85%; c) H_2, Pd/C, HCl, EtOH, RT, **2**: 87%, **3**: 90%, **4**: 90%.

determination of new structure–activity relationships, it could be helpful to synthesize more lipophilic N-alkylated derivatives like compounds **3** and **4**. The synthesis succeeded without any problems by reductive amination of **15** in the

 © 2004 Wiley-VCH Verlag GmbH & Co. KGaA, Weinheim

presence of the corresponding aldehydes and gave derivatives **16** and **17**, which provided compounds **3** and **4** after hydrogenolysis (Scheme 4).

In tests with standard enzyme preparations[21] compounds **2**–**4** did not show any inhibition of UDP-GlcNAc 2-epimerase activity in either concentrations equimolar to (1 mM) or in concentrations up to four times higher of that of the substrate UDP-GlcNAc. These results show that the 1,2-dideoxy-2-acetamidomannojirimycin derivatives, if they are effective inhibitors, are not able to reach the active site of the enzyme, perhaps because they are blocked by UDP-GlcNAc or UDP, which is used in standard preparations to stabilize the enzyme. Further experiments were then performed using enzyme preparations containing no UDP.[21] Preincubation of these samples in the presence of the inhibitors **2**–**4** led to clear inhibition of enzyme activity (up to 70%). When 0.1 mM UDP was added to the enzyme samples before addition of the inhibitors and then preincubation, no significant inhibition (under 10%) was observed. Furthermore, no inhibition was achieved when UDP-free enzyme preparations were used in the enzyme activity experiments without any preincubation, that is, enzyme, inhibitor, and UDP-GlcNAc were mixed simultaneously. These experiments show that the synthesized compounds are readily able to bind to the active site of the enzyme, if it is not blocked by UDP and/or by UDP-GlcNAc.

In order to compare the effectiveness of the inhibitors **2**–**4**, they were tested under various concentrations (Figure 2). All three compounds examined inhibited the activity of UDP-GlcNAc 2-epimerase in a concentration-dependent manner. Inhibition of 50% activity was observed at a concentration of 0.5 mM. Concentrations of **2** and **3** up to 2 mM in the preincubation sample induced almost complete inhibition, while treatment with **4** resulted in a remaining activity of nearly 10%. The presence of UDP in the preincubation samples prevented enzyme inhibition in almost all experiments. Addition of UDP and/or UDP-GlcNAc after an incubation of 20 min had nearly no effect on the inhibition by **2**–**4**. These data suggest that the inhibitors are bound very tightly by the enzyme as soon as they have reached the active site. This observation supports the hypothesis that transition-state analogues are bound much more tightly by the enzyme than the physiological substrate. Although the binding constants of the inhibitors were not determined in these experiments, they should be lower than the binding constants of UDP and UDP-GlcNAc, since the subsequent addition of both substrates does not displace the inhibitors.[22] The K_m values of UDP-GlcNAc and UDP are about 10 μM; thus the K_i values of the inhibitors should be lower.

The specificity of the inhibitors was determined by the lack of inhibition of the natural sugars ManNAc and GlcNAc, which were tested under the same conditions as the inhibitors. Neither the activity of the ManNAc kinase of the bifunctional UDP-GlcNAc 2-epimerase/ManNAc kinase was influenced by the inhibitors nor was its hexameric oligomeric structure affected, which serves as an indicator of structural integrity.[7] By comparing the inhibitors it seems to be noteworthy to mention that the ring nitrogen can be substituted with hydrophobic residues without affecting inhibitory potency. This might be important for subsequent applications in cellular systems, since hydrophobic compounds permeate the plasma membrane much more easily. The application of these inhibitors, for which we propose the name nanastatines, opens up the possibility of better understanding the role of *N*-acetylneuraminic acid containing conjugates in physiological and pathological processes.

Received: January 27, 2004
Revised: May 19, 2004 [Z53863]

Keywords: biosynthesis · carbohydrates · epimerases · inhibitors · sialic acids

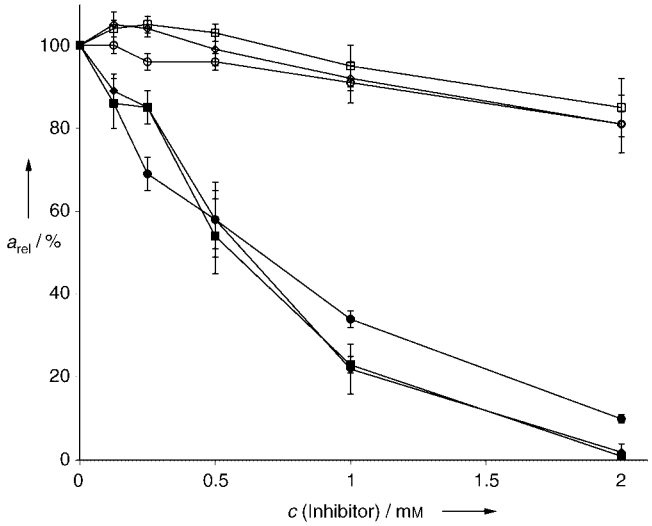


Figure 2. Inhibition of UDP-GlcNAc 2-epimerase by compounds **2**–**4**. ◆: **2**, ◇: **2** + UDP, ■: **3**, □: **3** + UDP, ●: **4**, ○: **4** + UDP. The enzyme was preincubated with the inhibitors for 20 min at 37°C in the absence or presence of 0.1 mM UDP and subsequently used in the activity assay. Noted concentrations refer to the final volume in the activity assay. Data shown above represent mean values ± standard deviation of three independent experiments.

[1] T. Angata, A. Varki, *Chem. Rev.* **2002**, *102*, 439.
[2] S. Kelm, R. Schauer, *Int. Rev. Cytol.* **1997**, *175*, 137.
[3] M. J. Kiefel, M. von Itzstein, *Chem. Rev.* **2002**, *102*, 471.
[4] a) A. P. Corfield, R. Schauer in *Sialic Acids—Chemistry, Metabolism and Function* (Ed.: R. Schauer), Springer, Vienna, **1982**, p. 195; b) A. Varki, *Glycobiology* **1993**, *3*, 97.
[5] R. Zeitler, A. Giannis, S. Danneschewski, E. Henk, T. Henk, C. Bauer, W. Reutter, K. Sandhoff, *Eur. J. Biochem.* **1992**, *204*, 1165.
[6] a) A. Blume, H. Chen, W. Reutter, R. R. Schmidt, S. Hinderlich, *FEBS Lett.* **2002**, *521*, 127; b) F. Stolz, M. Reiner, A. Blume, W. Reutter, R. R. Schmidt, *J. Org. Chem.* **2004**, *69*, 665–679.
[7] S. Hinderlich, R. Stäsche, R. Zeitler, W. Reutter, *J. Biol. Chem.* **1997**, *272*, 24313.
[8] R. Stäsche, S. Hinderlich, C. Weise, K. Effertz, L. Lucka, P. Moormann, W. Reutter, *J. Biol. Chem.* **1997**, *272*, 24319.
[9] S. Kornfeld, R. Kornfeld, E. F. Neufeld, P. J. O'Brien, *Proc. Natl. Acad. Sci. USA* **1964**, *61*, 371.
[10] R. Horstkorte, S. Nöhring, K. Danker, K. Effertz, W. Reutter, L. Lucka, *FEBS Lett.* **2000**, *470*, 315.
[11] O. T. Keppler, S. Hinderlich, J. Langner, R. Schwartz-Albiez, W. Reutter, M. Pawlita, *Science* **1999**, *284*, 1372.

 © 2004 Wiley-VCH Verlag GmbH & Co. KGaA, Weinheim

[12] M. Schwarzkopf, K.-P. Knobeloch, E. Rohde, S. Hinderlich, N. Wiechens, L. Lucka, I. Horak, W. Reutter, R. Horstkorte, *Proc. Natl. Acad. Sci. USA* **2002**, *99*, 5267.
[13] W. K. Chou, S. Hinderlich, W. Reutter, M. E. Tanner, *J. Am. Chem. Soc.* **2003**, *125*, 2455.
[14] P. M. Morgan, R. F. Sala, M. E. Tanner, *J. Am. Chem. Soc.* **1997**, *119*, 10269.
[15] L. Pauling, *Chem. Eng. News* **1946**, *24*, 1375.
[16] R. Martin, A. Moyano, M. A. Pericas, A. Riera, *Org. Lett.* **2000**, *2*, 93.
[17] Y. Gao, J. M. Klunder, R. M. Hanson, H. Masamune, S. Y. Ko, K. B. Sharpless, *J. Am. Chem. Soc.* **1987**, *109*, 5765.
[18] K. B. Sharpless, W. Amberg, Y. L. Bennani, G. A. Crispino, J. Hartung, K. S. Jeong, H. L. Kwong, K. Morikawa, Z. M. Wang, D. Xu, X. L. Zhang, *J. Org. Chem.* **1992**, *57*, 2768.
[19] H. Böshagen, F. R. Heiker, A. M. Schüller, *Carbohydr. Res.* **1987**, *164*, 141.
[20] Compound **2** was already synthesized earlier using a chemoenzymatic strategy as well as starting from suitable functionalized carbohydrate structures and tested as an inhibitor for a wide range of glycosidases. However, no inhibitory effect was detected. a) G. W. Fleet, L. E. Fellows, P. W. Smith, *Tetrahedron* **1987**, *43*, 979; b) T. Kajimoto, K. K. C. Liu, R. L. Pederson, Z. Zhong, Y. Ichikawa, J. A. Porco, Jr., C. H. Wong, *J. Am. Chem. Soc.* **1991**, *113*, 6187.
[21] Recombinant UDP-GlcNAc-2-epimerase from insect (Sf9) cells was purified as described by A. Blume, D. Ghaderi, V. Liebig, S. Hinderlich, P. Donner, W. Reutter, L. Lucka, *Protein Expression Purif.* **2004**, in press. For purification of UDP-free preparations the samples were applied to a PD-10 column (Amersham) and the column was eluted with 10 mM NaH_2PO_4 (pH 7.5), 100 mM NaCl, 1 mM EDTA, 1 mM dithiotreitol. UDP-GlcNAc 2-epimerase assays contained in a final volume 200 μL 45 mM NaH_2PO_4 (pH 7.5), 10 mM $MgCl_2$, 1 mM UDP-GlcNAc, 0.2 mM NADH, 2 mM phospho*enol*pyruvat, 2 U pyruvat kinase, 2 U lactate dehydrogenase, 5 μg purified UDP-GlcNAc 2-epimerase/ManNAc kinase, and indicated concentrations of inhibitors. The samples were incubated for 20 min at 37 °C and quenched by addition of 800 μL 10 mM EDTA. Subsequently the extinction was determined at 340 nm. Preincubation samples contained 5 μg purified UDP-GlcNAc 2-epimerase/ManNAc kinase and variable amounts of inhibitors in a final volume of 20 μL. The samples were incubated for 20 min at 37 °C, and enzyme reaction was started by addition of remaining components in a final volume of 200 μL. Inhibitor concentrations noted in the text refer to the final volume.
[22] In this context it might be interesting to use chimeric compounds, which consist of the iminosugars described here and specific parts of UDP-GlcNAc. Currently we are synthesizing such derivatives.

 © 2004 Wiley-VCH Verlag GmbH & Co. KGaA, Weinheim

Cover Picture



Christian Ochsenfeld,* Jörg Kussmann, and Felix Koziol

A missing link between theory and experiment for the difficult puzzle of assigning NMR spectra for molecules with more than a thousand atoms is provided by the calculation of ab initio NMR spectra, as symbolized in the cover picture. In their Communication on page 4485 ff., C. Ochsenfeld et al. describe how an approximate solution of the Schrödinger equation becomes possible by reducing the computational effort from cubic to linear.

Contents

Angewandte EarlyView

The following Communications are available online (in Wiley InterScience). You can find them, as well as forthcoming Reviews, Highlights, and Essays, at www.angewandte.org, under Early View.

F. E. Hahn, C. Schulze Isfort, T. Pape:*
A Dinuclear, Triple-Stranded Helicate with a Diamide-Bridged Catechol/Benzenedithiol Ligand
DOI: 10.1002/anie.200460188
Published online: August 9, 2004

M. B. Steffensen, E. E. Simanek:*
Synthesis and Manipulation of Orthogonally Protected Dendrimers: Building Blocks for Library Synthesis
DOI: 10.1002/anie.200460031
Published online: August 12, 2004

Articles judged by the referees or the editor as being either very important or very urgent are immediately edited, proof-read, and electronically published once the manuscript has arrived in the editorial office in its final form. As long as there is no page number available these articles should be cited in the following manner:

Author(s), *Angew. Chem. Int. Ed.*, online publication date, DOI.

Obituary

Cyril A. Grob (1917–2003): Fragmentation and Inductivity ——— **4392** P. Schiess

Books

Microsystem Engineering for Lab-on-a-Chip Devices ——— **4393** Oliver Geschke, Henning Klank, Pieter Tellemann *reviewed by J. Moorthy, D. T. Eddington, D. J. Beebe*

Industrial Organic Pigments ——— **4393** Willy Herbst, Klaus Hunger *reviewed by P. Erk*

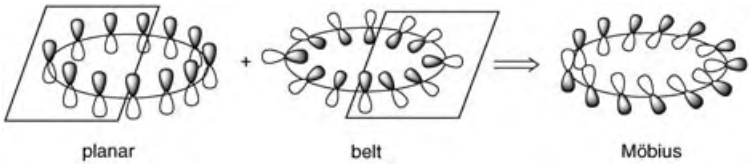
Metal–Ligand Bonding ——— **4394** Bob Janes, Elaine Moore *reviewed by S. Schindler*

Highlights

Aromaticity

T. Kawase,* M. Oda* ——— **4396 – 4398**

Möbius Aromatic Hydrocarbons: Challenges for Theory and Synthesis



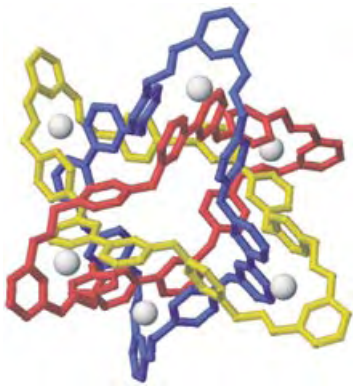
Twisting a belt-shaped loop of p orbitals results in a Möbius structure (see scheme). Only recently have synthetic chemists realized this idea first proposed by Heilbronner 40 years ago. The interaction of theory and synthesis, which has distinguished the concept of aromaticity since its inception, has opened a new chapter in this field.

Topochemistry

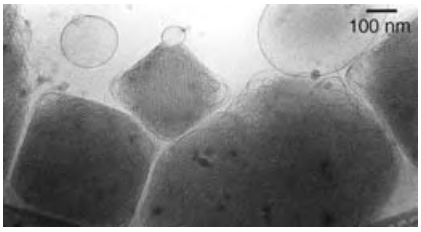
C. A. Schalley* ——— **4399 – 4401**

Borromean Rings: A One-Pot Synthesis

Elegance and precision are shown in the self-assembly strategy developed by Stoddart, Atwood, and co-workers for the synthesis of molecular Borromean rings. Metal-ion template effects direct the dynamic formation of covalent bonds, which result in the energetically favorable product having the highly symbolic ring motif (see picture).



Cubosomes, cubic liquid-crystalline nanoparticles (see cryo-TEM image), can be prepared from aqueous dispersions of cubic lipid–water phases and are stabilized in the presence of dispersing agents and through polymerization of reactive lipids in cubic lipid assemblies. These nanoparticles can incorporate and release lipophilic, amphiphilic, and water-soluble molecules in a controlled manner.

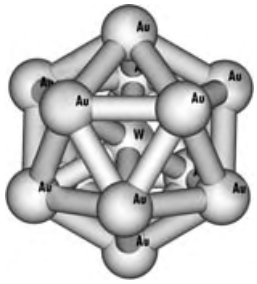


Minireviews

Nanostructures

D. Yang, B. Armitage, S. R. Marder* ——— **4402 – 4409**

Cubic Liquid-Crystalline Nanoparticles



A golden age for theoretical chemistry: From studies of small molecules to molecular dynamics simulations, including the aurophilic attraction and predictions for new species such as the those for the [WAu_{12}] cluster depicted, theoretical chemistry of gold has come of age. Certain aspects of the softness and the electronic plasmon oscillations may provide further challenges.

Reviews

Theoretical Chemistry

P. Pyykkö* ——— **4412 – 4456**

Theoretical chemistry of gold



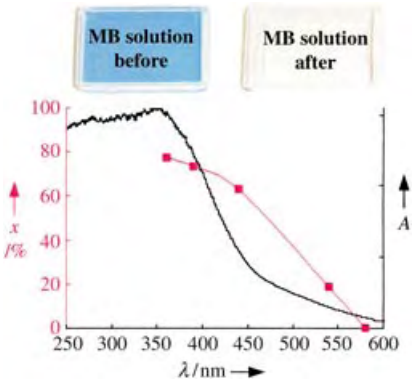
Breaking up and making up: The ultrasonic cleavage of high-molecular-weight linear coordination polymers of phosphane telechelic polytetrahydrofuran and palladium dichloride in dilute solution is a reversible process (see picture). Sonication for 1 h led to a decrease in the weight-averaged molecular weight of the polymer from 1.7×10^5 to 1.0×10^5 g mol^{-1}. Upon leaving the sample to stand for 24 h, the original molecular weight was completely restored.

Communications

Coordination Polymers

J. M. J. Paulusse, R. P. Sijbesma* ——— **4460 – 4462**

Reversible Mechanochemistry of a Pd^{II} Coordination Polymer



Green degradation: Organic contaminants such as volatile organic compounds and dyes (e.g. acetaldehyde and methylene blue (MB)) can be photocatalytically degraded over a novel $CaBi_2O_4$ catalyst. The reaction is environmentally friendly (O_2 oxidant) and proceeds at room temperature under visible-light irradiation of wide-ranging wavelength (see picture: x = conversion of CH_3CHO into CO_2, A = absorbance).

Photocatalysis

J. Tang, Z. Zou, J. Ye* ——— **4463 – 4466**

Efficient Photocatalytic Decomposition of Organic Contaminants over $CaBi_2O_4$ under Visible-Light Irradiation

For the USA and Canada:
ANGEWANDTE CHEMIE International Edition (ISSN 1433-7851) is published weekly by Wiley-VCH PO Box 191161, D 69451 Weinheim, Germany. Air freight and mailing in the USA by Publications Expediting Inc. 200 Meacham Ave., Elmont, NY 11003. Periodicals postage paid at Jamaica NY 11431. US POSTMASTER: send address changes to *Angewandte Chemie*, Wiley-VCH, 111 River Street, Hoboken, NJ 07030. Annual subscription price for institutions: Europe € 3430.00/3118.00; outside Europe US$ 4499.00/4090.00 (valid for print and electronic/print or electronic delivery); for individuals who are personal members of a national chemical society, or whose institution already subscribes, or who are retired or self-employed consultants, print only: Europe € 248.00/outside Europe US$ 378.00. Postage and handling charges included. All Wiley-VCH prices are exclusive VAT.

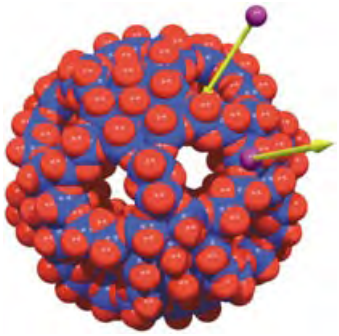
 © 2004 Wiley-VCH Verlag GmbH & Co. KGaA, Weinheim

Contents

Nanostructures

A. Müller,* D. Rehder,* E. T. K. Haupt, A. Merca, H. Bögge, M. Schmidtmann, G. Heinze-Brückner _____ **4466 – 4470**

Artificial Cells: Temperature-Dependent, Reversible Li^+-Ion Uptake/Release Equilibrium at Metal Oxide Nanocontainer Pores

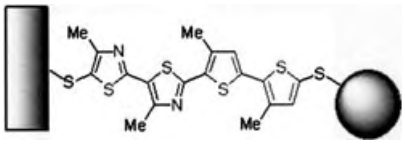


Lithium ion trafficking: Surprisingly stable and soluble spherical molybdenum oxide based porous nanocontainers/artificial cells (see graphic) interact specifically with their environment, for example, with cations abundant in solution, to incorporate them at well-defined internal cell positions. In the present case, the traffic of Li^+ ions between the "outside and inside" is in equilibrium (homeostasis) as measured by NMR spectroscopy. (Li purple, Mo blue, O red)

Molecular Electronics

P. Jiang, G. M. Morales, W. You, L. Yu* _____ **4471 – 4475**

Synthesis of Diode Molecules and Their Sequential Assembly to Control Electron Transport

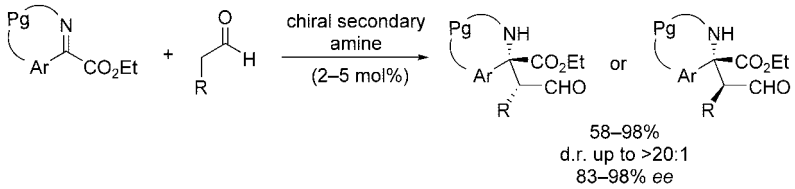


A sequential deprotection and immobilization procedure was enabled by the synthesis of two thiophene–thiazole diblock oligomers with two different thiol protection groups. Investigation of the *I*/*V* behaviors of these diblock molecules between two gold electrodes (see picture) showed that the rectifying direction was controlled by their orientation between the electrodes.

Asymmetric Organocatalysis

W. Zhuang, S. Saaby, K. A. Jørgensen* _____ **4476 – 4478**

Direct Organocatalytic Enantioselective Mannich Reactions of Ketimines: An Approach to Optically Active Quaternary α-Amino Acid Derivatives



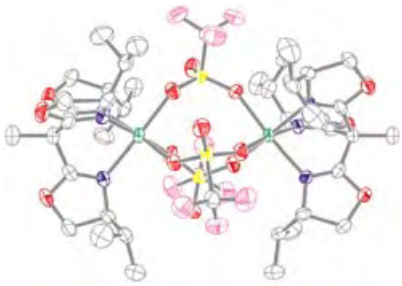
You're in control of which diastereomer of a quaternary α-amino acid derivative is formed in a direct organocatalytic diastereoselective and enantioselective Mannich reaction of ketimines with aldehydes (see scheme). The reactions are high yielding and can be controlled through the choice of the catalyst to give either diastereomer of the product with diastereomeric ratios as high as >20:1 and with 83–98% *ee*. Pg = protecting group.

Biomimetic Catalysis

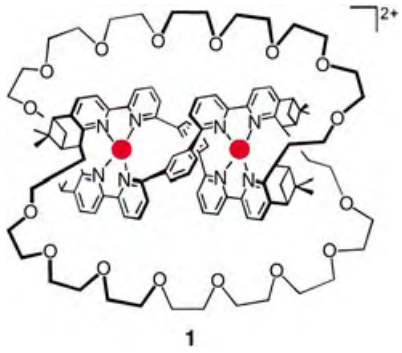
C. Dro, S. Bellemin-Laponnaz,* R. Welter, L. H. Gade* _____ **4479 – 4482**

A C_3-Symmetrical Chiral Trisoxazoline Zinc Complex as a Functional Model for Zinc Hydrolases: Kinetic Resolution of Racemic Chiral Esters by Transesterification

Mimicking the activity of tris(histidine)-zinc-based enzymes, chiral dinuclear tris-oxazolinezinc complexes such as the triflato cation (see picture) are the first non-enzymatic catalysts for the asymmetric transesterification of activated esters. First results of the kinetic resolution of amino acid phenolates establish the stereoselectivity for this reaction. (F pink, N blue, O red, S yellow, Zn cyan)



 © 2004 Wiley-VCH Verlag GmbH & Co. KGaA, Weinheim

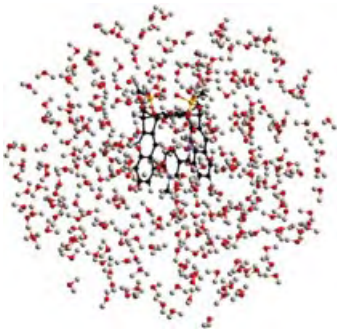


Tying nice neat knots is demonstrated on a molecular level with the stereoselective synthesis of a trefoil knot. The key reaction was the completely stereoselective formation of a double-stranded helical precursor from two pinene–bipyridine threads around two Cu^{I} centers (the pinene moieties contain stereogenic centers). The helix was then transformed through several steps into **1**; demetallation of the complex **1** yielded the configurationally predetermined free trefoil knot.

Supramolecular Chemistry

L.-E. Perret-Aebi, A. von Zelewsky,* C. Dietrich-Buchecker, J.-P. Sauvage ——— **4482 – 4485**

Stereoselective Synthesis of a Topologically Chiral Molecule: The Trefoil Knot

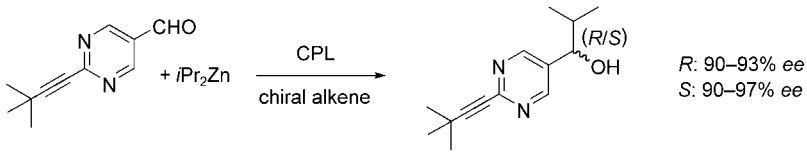


A method for the calculation of NMR shieldings is presented, which allows for the first time the study of molecular systems with one thousand and more atoms at the ab initio level (see picture), by reducing the computational scaling from cubic to linear. This opens new possibilities for the often difficult assignment of experimental NMR spectra.

Quantum Chemistry

C. Ochsenfeld,* J. Kussmann, F. Koziol ——— **4485 – 4489**

Ab Initio NMR Spectra for Molecular Systems with a Thousand and More Atoms: A Linear-Scaling Method

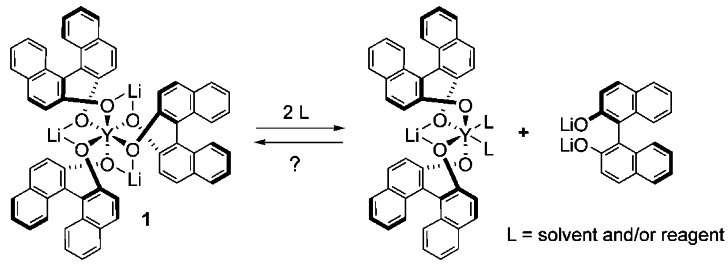


The light touch: Asymmetric photoequilibrium and autocatalysis act as sources of homochirality in a highly enantioselective preparation of chiral alcohols (see scheme). This process is initiated by left- and right-circularly polarized light (CPL) and exploits the resulting photoequilibrium between chiral olefin substrates to yield 2-alkynyl-5-pyrimidyl alkanols.

Enantioselective Synthesis

I. Sato, R. Sugie, Y. Matsueda, Y. Furumura, K. Soai* ——— **4490 – 4492**

Asymmetric Synthesis Utilizing Circularly Polarized Light Mediated by the Photoequilibrium of Chiral Olefins in Conjunction with Asymmetric Autocatalysis



The power of three: Mechanistic studies based on the kinetic profiles of the catalytic asymmetric 1,4-addition of an amine to chalcone revealed that all three binol ligands of the [YLi_3{tris(binaphthoxide)}] complex **1** are involved in the active species of the Y–Li heterobimetallic catalyst.

Reaction Mechanisms

N. Yamagiwa, S. Matsunaga, M. Shibasaki* ——— **4493 – 4497**

Mechanistic Studies of a Reaction Promoted by the [YLi_3{tris(binaphthoxide)}] Complex: Are Three 1,1′-Bi-2-naphthol Units in a Rare-Earth–Alkali-Metal Heterobimetallic Complex Necessary?

 © 2004 Wiley-VCH Verlag GmbH & Co. KGaA, Weinheim

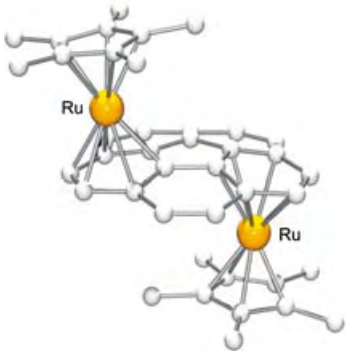
Contents

Buckybowls

P. A. Vecchi, C. M. Alvarez, A. Ellern, R. J. Angelici,* A. Sygula, R. Sygula, P. W. Rabideau _____ **4497 – 4500**

Synthesis and Structure of a Dimetallated Buckybowl: Coordination of One $\{Cp^*Ru\}^+$ Unit to Each Side of Corannulene

A significantly flattened corannulene, which is η^6-coordinated on each side by a $\{Cp^*Ru\}^+$ moiety, is revealed in the X-ray structure analysis of $[(Cp^*Ru)_2(\mu_2\text{-}\eta^6,\eta^6\text{-}C_{20}H_{10})][PF_6]_2$. The reaction of $[\{Cp^*Ru(\mu_3\text{-}Cl)\}_4]$ with Ag^+ ions and the curved-surface buckybowl corannulene ($C_{20}H_{10}$) in CD_3NO_2 solvent affords this dimetallated corannulene complex (see picture).

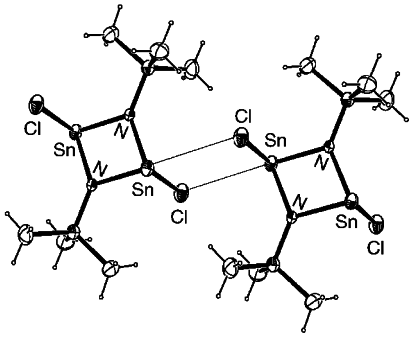


Main-Group Chemistry

H. Cox,* P. B. Hitchcock, M. F. Lappert,* L. J.-M. Pierssens _____ **4500 – 4504**

A 1,3-Diaza-2,4-distannacyclobutane-diide: Synthesis, Structure, and Bonding

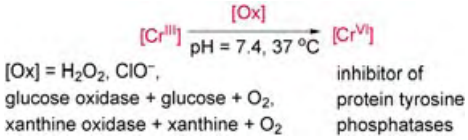
A combined experimental and computational study throws light on the structure and bonding of the diamagnetic $\{(SnN)_2\}$ compound $[\{Sn\{N(SiMe_3)\}Cl\}_2]$ (see picture), obtained from the reaction of $[Sn\{N(SiMe_3)_2\}(\mu\text{-}Cl)]_2$ with AgOCN.



Bioinorganic Chemistry

I. Mulyani, A. Levina, P. A. Lay* _____ **4504 – 4507**

Biomimetic Oxidation of Chromium(III): Does the Antidiabetic Activity of Chromium(III) Involve Carcinogenic Chromium(VI)?

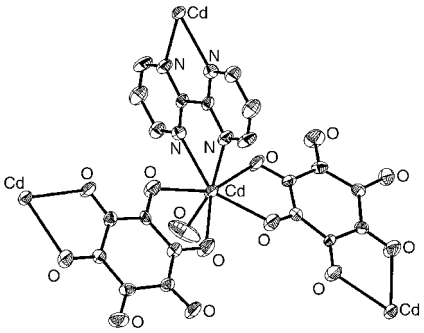


The insulin-enhancing activities of some Cr^{III} complexes, such as $[Cr_3O(OCOEt)_6(OH_2)_3]^+$ (**1**), previously attributed to specific interactions of Cr^{III} ions with cellular insulin receptors, are more likely to be caused by the formation of $[CrO_4]^{2-}$ (**2**). Oxidation of **1** to **2** by biologically relevant oxidants, including enzymes (see scheme), and inhibition of an isolated protein tyrosine phosphatase by a Cr^{VI} complex are reported.

Coordination Modes

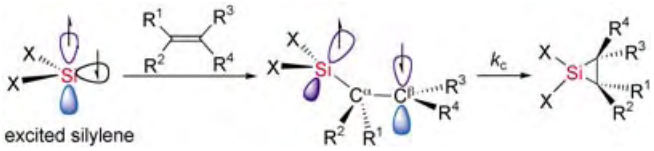
C.-C. Wang,* C.-T. Kuo, P.-T. Chou, G.-H. Lee _____ **4507 – 4510**

Rhodizonate Metal Complexes with a 2D Chairlike M_6 Metal–Organic Framework: $[M(C_6O_6)(bpym)(H_2O)]\cdot n\,H_2O$



Two transition-metal rhodizonate complexes, $[M(C_6O_6)(bpym)(H_2O)]\cdot n\,H_2O$ ($M = Cd$, $n = 1$; $M = Mn$, $n = 2$; bpym = 2,2′-bipyrimidine), are reported. Both the rhodizonate and bpym ligands are bis-bidentate ligands (see the Cd example depicted) which chelate the metal ions, thus forming a novel 2D chairlike M_6 metal–organic framework.

 © 2004 Wiley-VCH Verlag GmbH & Co. KGaA, Weinheim

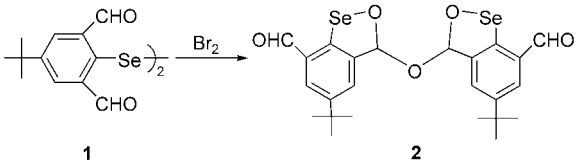


The singlet 1,1-diradical ($^1B_1$) state of a silylene plays a key role in its photoreactions with benzenes and alkenes, even though similar $^1B_1$ states are rarely encountered in carbene chemistry. The photochemical addition to alkenes should be stepwise and the ring closure of the intermediate singlet 1,3-diradicals was very facile with rates (k_c) of more than $10^9\ s^{-1}$ (see scheme).

Silylenes

M. Kira,* S. Ishida, T. Iwamoto, A. de Meijere, M. Fujitsuka, O. Ito ——— 4510 – 4512

The Singlet Excited State of a Stable Dialkylsilylene Is Responsible for Its Photoreactions

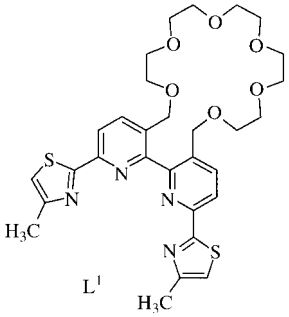


Enzyme mimicry: Halogenation of diselenide **1** affords the cyclic selenenate ester **2** (see scheme) through a highly unstable selenenic acid intermediate. Compound **2** exhibits a strong intramolecular nonbonding Se···O interaction. Both **1** and **2** show excellent glutathione peroxidase-like catalytic activity.

Selenium Compounds

S. S. Zade, H. B. Singh,* R. J. Butcher ——— 4513 – 4515

The Isolation and Crystal Structure of a Cyclic Selenenate Ester Derived from Bis(2,6-diformyl-4-*tert*-butylphenyl)diselenide and its Glutathione Peroxidase-Like Activity

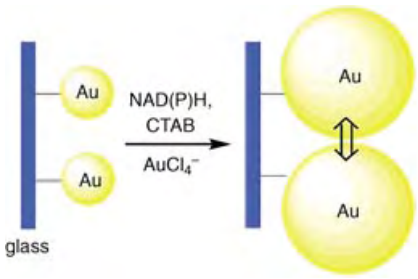


A potentially tetradentate pyridyl–thiazole ligand chain and an additional "external" crown ether binding site connect the two halves of a new ditopic ligand. The pyridyl-thiazole binding sites can be changed or "reprogrammed" by the addition of Ba^{2+}: In the presence of Hg^{2+} and Na^+ the ligand L^1 forms a dinuclear double helicate ($[Hg_2(L^1)_2Na_2]^{6+}$), whereas in the presence of Hg^{2+} and Ba^{2+} a mononuclear species is formed ($[Hg(L^1)Ba]^{4+}$).

Reprogrammable Ligands

C. J. Baylies, L. P. Harding, J. C. Jeffery, T. Riis-Johannessen, C. R. Rice* ——— 4515 – 4518

Allosteric and Electrostatic Reprogramming of a Ditopic Ligand



Gold-plated gold: NAD(P)H cofactors mediate the catalytic growth of Au nanoparticles in the presence of $AuCl_4^-$ and CTAB (cetyltrimethylammonium bromide; see picture). The process allows for the optical detection of the cofactors and the analysis of $NAD(P)^+$-dependent biocatalyzed transformations in solutions and on surfaces.

Nanotechnology

Y. Xiao, V. Pavlov, S. Levine, T. Niazov, G. Markovitch, I. Willner* ——— 4519 – 4522

Catalytic Growth of Au Nanoparticles by NAD(P)H Cofactors: Optical Sensors for $NAD(P)^+$-Dependent Biocatalyzed Transformations

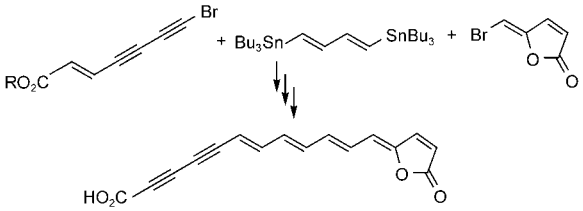
 © 2004 Wiley-VCH Verlag GmbH & Co. KGaA, Weinheim

Contents

Natural Products Synthesis

A. Sorg, R. Brückner* ——— **4523 – 4526**

Total Synthesis of Xerulinic Acid

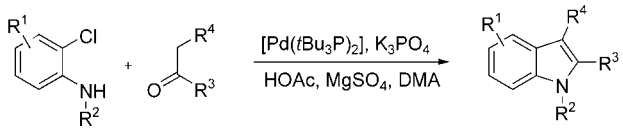


An inhibitor of the biosynthesis of cholesterol, xerulinic acid, has been synthesized for the first time. The convergent approach applied involves the palladium-catalyzed coupling of an enediynoic ester building block, a conjunctive C_6 bisstannane, and a bromine-containing methylenebutenolide (see scheme; $R = Me_3SiCH_2CH_2$).

Indole Synthesis

M. Nazaré,* C. Schneider, A. Lindenschmidt, D. W. Will ——— **4526 – 4528**

A Flexible, Palladium-Catalyzed Indole and Azaindole Synthesis by Direct Annulation of Chloroanilines and Chloroaminopyridines with Ketones



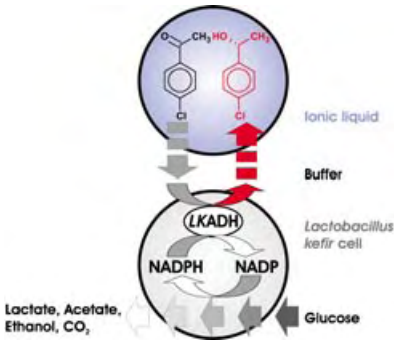
The "ringmaster" $[Pd(tBu_3P)_2]$ serves as the catalyst in the direct synthesis of indoles by annulation of *ortho*-chloroanilines with ketones (see picture). This versatile method can be used to synthesize a variety of functionalized indoles and azaindoles. DMA = dimethylacetamide.

Bioengineering

H. Pfruender,* M. Amidjojo, U. Kragl, D. Weuster-Botz* ——— **4529 – 4531**

Efficient Whole-Cell Biotransformation in a Biphasic Ionic Liquid/Water System

Biocompatible ionic liquids act as a substrate reservoir and an in situ extracting agent in biotransformations with whole cells (see scheme). In the reduction of 4-chloroacetophenone to (*R*)-1-(4-chlorophenyl)ethanol, high product concentration (82 g L^{-1}) and purity (99.6% *ee*) were achieved without the addition of cofactors and without damaging the biocatalyst.



VIP Communications labeled with this symbol have been judged by two referees as being "very important papers".

Deadline for recruitment adverts

35/2004	August 20	Publication date:	September 6
36/2004	August 27	Publication date:	September 13

Angewandte Chemie International Edition
Advertising Sales Department:
Marion Schulz
Phone: 0 62 01 – 60 65 65
Fax: 0 62 01 – 60 65 50
E-Mail: MSchulz@wiley-vch.de

Place an advert in the printed version and have it made available online for 1 month, free of charge!

Service

Keywords ——— *4532*

Authors ——— *4533*

Vacancies ——— *A55*

Preview ——— *4535*

It was reported that 1,N^6-etheno-2′-deoxyadenosine-3′-monophosphate (etheno-dAMP) elutes before 2′-deoxyadenosine-3′-monophosphate (dAMP). The authors have now found that etheno-dAMP elutes immediately after 2′-deoxythymidine-3′-monophosphate (dTMP). The assignment of the signals in the Communication relied on a commercially modified oligonucleotide standard thought to contain etheno-dAMP. As the synthesized 1,N^6-etheno-2′-deoxyadenosine-3′-monophosphates are now characterized unambiguously, the mistake must have been because of an improperly defined oligonucleotide standard or decomposition of the modified oligonucleotide. The authors apologize for the error.

Capillary Electrophoresis Analysis of DNA Adducts as Biomarkers for Carcinogenesis

O. J. Schmitz,* C. C. T. Wörth, D. Stach, M. Wießler

Angew. Chem. Int. Ed. **2002**, *41*, 445–448
DOI 10.1002/1521-3773(20020201)41:3<445::AID-ANIE445>3.0.CO;2-7

The reported physical data in reference [25] are from a by-product. The physical data for compound **3** are the following:
TLC (petroleum ether/ethyl acetate 1:1): $R_f = 0.20$; $[\alpha]_D = -13.8$ ($c = 1.1$, chloroform); ^{1}H NMR (250 MHz, $CDCl_3$): $\delta = 0.12$ (s, 3H), 0.15 (s, 3H), 0.83 (s, 6H), 0.85 (s, 3H), 0.88 (s, 3H), 1.61 (sept, 6.8 Hz, 1H), 1.96 (s, 3H), 3.21 (dt, $J = 10.3$, 7.8 Hz, 1H), 3.53 (m, 1H), 3.60 (dd, $J = 9.5$, 8.3 Hz, 1H), 3.70 (m, 2H), 3.81 (s, 3H), 3.90 (dd, $J = 10.3$, 8.3 Hz, 1H), 4.17 (dd, $J = 12.8$, 5.8 Hz, 1H), 4.27 (dd, $J = 12.8$, 9.5 Hz, 1H), 4.51 (s, 2H), 5.06 (d, $J = 8.0$ Hz, 1H), 5.19 (m, 2H), 5.65 (d, $J = 7.8$ Hz, 1H), 5.90 (m, 1H), 6.88 (d, $J = 8.5$ Hz, 2H), 7.26 ppm (d, $J = 8.5$ Hz, 2H); ^{13}C NMR (62.5 MHz, $CDCl_3$): $\delta = -3.53$, -1.82, 18.52, 20.04, 23.61, 24.77, 34.03, 55.26, 59.19, 70.61, 72.96, 73.19, 73.34, 73.62, 80.28, 94.89, 113.84, 116.94, 129.29, 129.95, 135.16, 159.28, 170.10 ppm. Furthermore, the desilylation step c in the transformation of compound **7** to **6** requires addition of acetic acid to be successful.

Stereoselective Synthesis of β-D-Mannopyranosides with Reactive Mannopyranosyl Donors Possessing a Neighboring Electron-Withdrawing Group

A. A.-H. Abdel-Rahman, S. Jonke, E. S. H. El Ashry,* R. R. Schmidt*

Angew. Chem. Int. Ed. **2002**, *41*, 2972–2974
DOI 10.1002/1521-3773(20020816)41:16<2972::AID-ANIE2972>3.0.CO;2-4

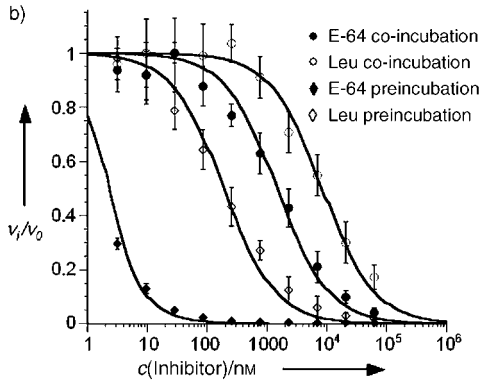
In this Communication C. R. D. Correia is also a correspondence author.
In addition, the structure for compound **18** is incorrectly depicted in Scheme 5; the correct structure for **18** is the one shown in Scheme 4, which corresponds to 2-(4-methoxyphenyl)-2,5-dihydrofuran. The first sentence of the third paragraph on page 2515 should read as follows: "Interestingly, the composition of the cationic intermediates changes drastically with time, as observed by continuous monitoring of these intermediates by ESIMS."

Probing the Mechanism of the Heck Reaction with Arene Diazonium Salts by Electrospray Mass and Tandem Mass Spectrometry

A. A. Sabino, A. H. L. Machado, C. R. D. Correia,* M. N. Eberlin*

Angew. Chem. Int. Ed. **2004**, *43*, 2514–2518
DOI 10.1002/anie.200353076

In this Communication, Figure 4b was incorrect. The correct graph is shown.



Enzyme Microarrays: On-Chip Determination of Inhibition Constants Based on Affinity-Label Detection of Enzymatic Activity

J. Eppinger,* D. P. Funeriu,* M. Miyake, L. Denizot, J. Miyake

Angew. Chem. Int. Ed. **2004**, *43*, 3806–3810
DOI 10.1002/anie.200353623

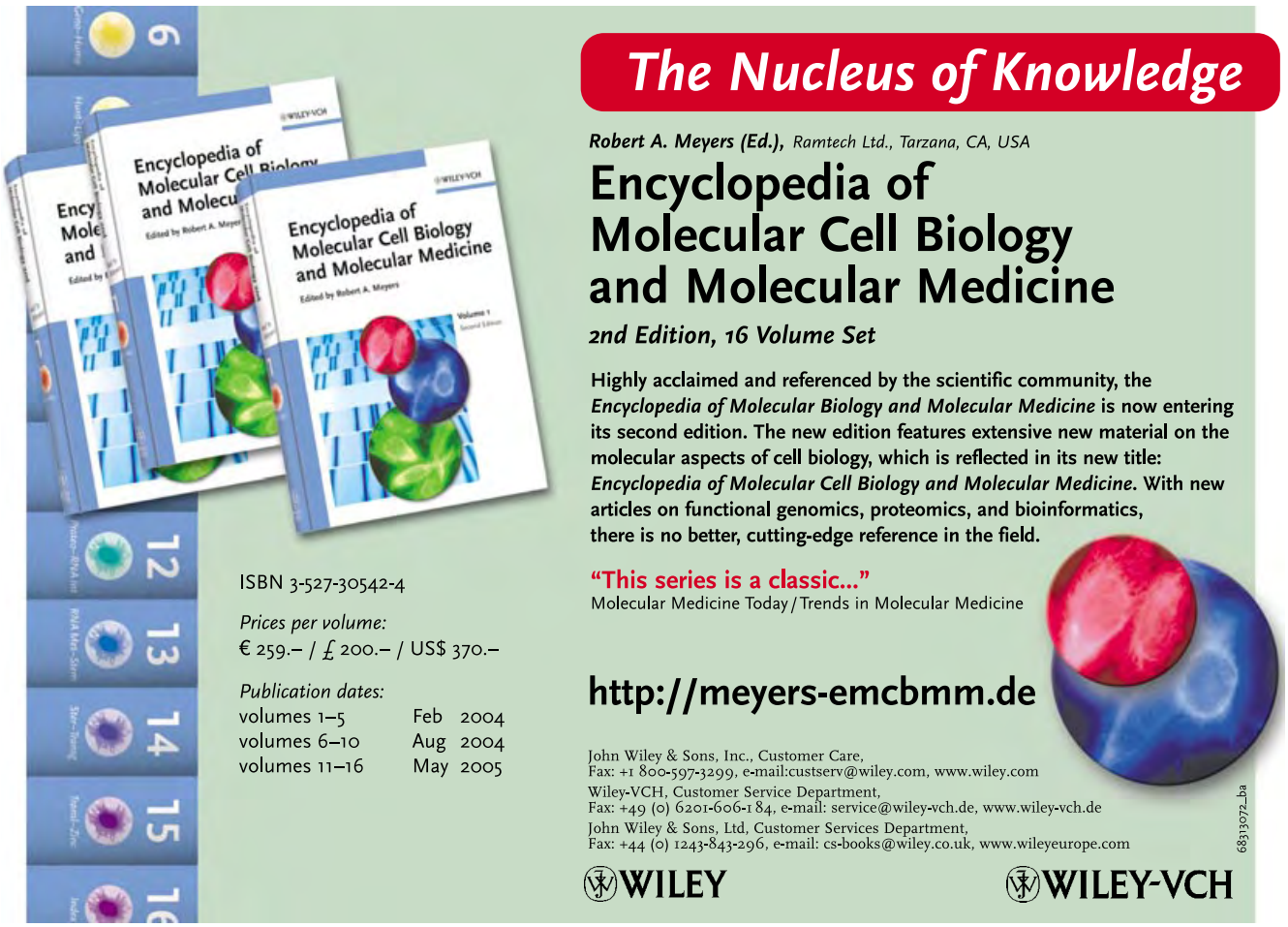
 © 2004 Wiley-VCH Verlag GmbH & Co. KGaA, Weinheim

A Dodecameric Water Cluster Built Around a Cyclic Quasiplanar Hexameric Core in an Organic Supramolecular Complex of a Cryptand

S. K. Ghosh, P. K. Bharadwaj*

Angew. Chem. Int. Ed. **2004**, *43*, 3577–3580
DOI 10.1002/anie.200454002

A relevant paper by O. Ermer and J. Neudoerfl in *Chem. Eur. J.* **2001**, *7*, 4961–4980 was not cited. The authors apologize for the omission.



 © 2004 Wiley-VCH Verlag GmbH & Co. KGaA, Weinheim

Cyril A. Grob (1917–2003): Fragmentation and Inductivity

Cyril A. Grob died in his home in Basel (Switzerland) on December 15, 2003 at the age of 86. He was born in London (UK) to Swiss parents, studied chemistry at the Eidgenössische Technische Hochschule Zürich (ETH Zürich), and completed his PhD in 1943 under the guidance of Leopold Ruzicka (Nobel Prize in Chemistry 1939) on artificial steroidal antigens. He then moved to Basel to work with Taddeus Reichstein first at the pharmaceutical institute and from 1947 at the organic chemistry institute of the university, where he moved up the academic career ladder to become the director of the institute and holder of the chair there as Reichstein's successor in 1960. He retained this function until he was given emeritus status in 1987.



Cyril A. Grob

Initially Grob's research focused mainly on natural products, with synthetic studies on biotin, lysergic acid, and the steroid framework. He also completed an elegant synthesis of sphingosin. A research stay with Saul Winstein at the University of California, Los Angeles (1951/52) gave him the critical impetus: After his return to Basel he dedicated himself more and more to the elucidation of reaction mechanisms and structure–reactivity relationships.

An investigation of the reductive elimination of bromine from 1,4-dibromides in the presence of zinc led in 1955 to the recognition of heterolytic fragmentation as a general reaction principle.[1] The structural and stereochemical prerequisites for a fragmentation to occur were investigated with model compounds, and the fundamental mechanisms of this reaction type were elucidated.[2] The heterolytic fragmentation has now entered textbooks under the name of its discoverer. These studies also led to the elucidation of the mechanism of the Beckmann rearrangement. Experimental evidence for vinyl cations as discrete reactive intermediates was also first provided by Grob.[3]

The inductive substituent effect occupied Grob for many years. Substituted quinuclidines were chosen as model compounds, as they bear the polar functional groups at a clearly defined distance from basic or protonated nitrogen atoms as a result of their rigid molecular framework. Through the exact measurement of protonation equilibria a large number of substituent inductivity constants were determined.[4]

In solvolytic reactions intermediate carbon-centered cations often undergo rearrangement of the carbon framework with the transfer of charge to neighboring centers. These reactions do proceed via a nonclassic intermediate or transition state, in which a carbon atom is formally bonded to five other atoms. Whether a charge transfer occurs prior to the complete displacement of the leaving group or in a subsequent elementary step was highly controversial for a long time. Grob saw an answer in the determination of the so-called inductivity; that is, the sensitivity of the rate of the ionization process on neighboring substituents. These substituents should influence the incipient charge transfer in the transition state through their inductive effect. A kinetic study showed that the nature of the transition depends on the individual reaction. Only in exceptional cases, for example, for the notorious norbornyl cation, does the nonclassic structure seem to be more stable than one with a localized charge.[5] This result was compared in 1983 in a "symposium in print" with the reports by H. C. Brown and G. A. Olah, who had approached this question from different angles with a similar result. As C. Walling, the "arbitrator", observed, this publication settled peacefully a long and intense controversy.[6]

Except in kinetic studies, Grob was a forerunner in the field of physical organic chemistry in continental Europe. Students and colleagues at the university and in his working environment profited considerably from this role of his. As a lecturer he had the ability to present complex concepts in a simple, clear, and precise way, and to convince his audience through well thought out arguments. He allowed his numerous co-workers much freedom, but always gave them good advice at the right time.

Cyril Grob never acted impulsively, but always calmly and deliberately. He never sought attention in public, but fulfilled his social duties efficiently, reliably, and without a fuss. In this way as dean he directed the affairs of the faculty for a year and presided over the Swiss Chemical Society during a two-year term. With his scientific success came frequent invitations to almost all countries in Europe, as well as the USA and other parts of the world. He always prized these trips very highly as recognition of his scientific achievements.

In public Cyril Grob was reserved and he did not particularly enjoy socializing. Only in intimate circles did he shine as a relaxed, witty, cultured, and kind person. However, his scientific interests always came first, not only in his professional but also in his private life.

Peter Schiess
Universität Basel

[1] C. A. Grob, W. Baumann, *Helv. Chim. Acta* **1955**, *38*, 94.
[2] C. A. Grob, *Angew. Chem.* **1969**, *81*, 543; *Angew. Chem. Int. Ed. Engl.* **1969**, *8*, 535.
[3] C. A. Grob, *Chimia* **1971**, *25*, 87.
[4] a) C. A. Grob, *Angew. Chem.* **1976**, *88*, 621; *Angew. Chem. Int. Ed. Engl.* **1976**, *15*, 569; b) C. A. Grob, *Helv. Chim. Acta* **1985**, *68*, 882.
[5] C. A. Grob, *Angew. Chem.* **1982**, *94*, 87; *Angew. Chem. Int. Ed. Engl.* **1982**, *21*, 87.
[6] C. Walling, *Acc. Chem. Res.* **1983**, *16*, 448.

 © 2004 Wiley-VCH Verlag GmbH & Co. KGaA, Weinheim DOI: 10.1002/anie.200461144

Aromaticity

Möbius Aromatic Hydrocarbons: Challenges for Theory and Synthesis

Takeshi Kawase and Masaji Oda**

Keywords:
annulenes · aromaticity · carbocycles · hydrocarbons

In memory of Masazumi Nakagawa

Since the beginnings of organic chemistry the concept of aromaticity has been studied by both theoretical and synthetic chemists, and their interaction has resulted in exciting developments in this field.[1] In the nineteenth century it was recognized that benzene exhibits unusual stability for a highly unsaturated hydrocarbon and that all six carbon atoms are equivalent. In 1865 Kekulé put forward the hexagonal formula now used and introduced the hypothesis of valence oscillation between two cyclohexatriene structures to explain the absence of double-bond isomers for 1,2- and 1,3-disubstituted benzenes. However, the unusually high stability of benzene was not explained satisfactorily for a long time.

In the 1930s Hückel published his detailed treatise on the theoretical foundations of aromaticity which led to the formulation of his now famous "4*n*+2" rule: for ground-state molecules with a cyclic array of p orbitals, (4*n*+2) π electrons, where *n* is zero or any positive number, lead to special stability based on the presence of a closed electronic shell. Calculations also predicted that systems having 4*n* π electrons are unstable, namely "antiaromatic" owing to open-shell electronic structures. The Hückel rule not only accounted for the unusual stability of benzene but it also stimulated synthetic organic chemists to construct various carbocyclic conjugated systems. Annulenes $(CH)_n$ were the main targets of synthesis. The scope and limitation of the Hückel rule have thus been established: the rule is applicable to planar or nearly planar cyclic systems without any apparent twist of the π frameworks interrupting the conjugation.

However, while the development of synthetic methodology has expanded the chemistry of conjugated systems, some difficulties have emerged. It is not easy to determine experimentally whether a compound is aromatic, particularly for non-benzenoid systems. In this context, computational analyses of bond-length equalization and magnetic properties such as the harmonic oscillator model of aromaticity (HOMA)[2] and nucleus-independent chemical shifts (NICS)[3] are now used as probes of aromaticity.

In 1964 Heilbronner conceived of "Möbius aromaticity" based on simple Hückel molecular orbital theory and predicted that [4*n*] Möbius systems would be stable because they possess a closed-shell structure in contrast to [4*n*] Hückel systems (Figure 1).[4] His idea was extended in the formulation of a selection rule for inferring the aromaticity of the transition states of pericyclic reactions: Zimmerman generalized the idea as the "Möbius–Hückel" concept.[5] However, Möbius annulenes conforming to Heilbronner's concept have not been realized up until recently, probably because it is difficult for even large macrocyclic annulenes to adopt Möbius geometries without any apparent angle or steric strain.

In 1998 Schleyer and co-workers reported that cyclononatetraenyl cation **1** with 8 π electrons is Möbius aromatic rather than nonaromatic on the basis of calculated NICS values (Figure 2). The cation **1** is formed easily in spite of the anticipated antiaromaticity of the planar structure.[6] According to calculations (B3LYP 6-311+G*), the Möbius conformation (C_2) **1a** is 21.6 kcal mol^{-1}

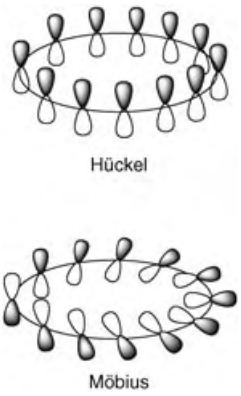


Figure 1. The π system labeled "Hückel" is a destabilized [4*n*] system, whereas that labeled "Möbius" is a stabilized [4*n*] system.

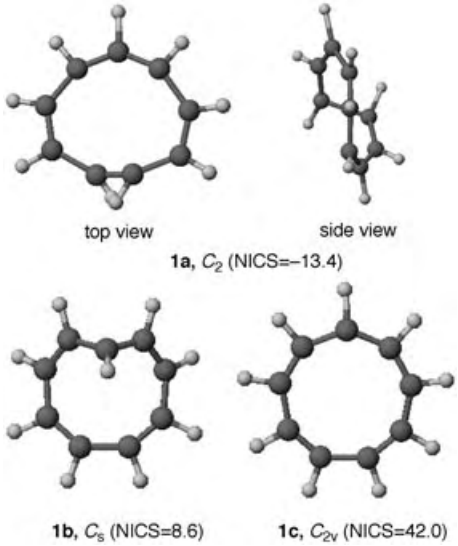
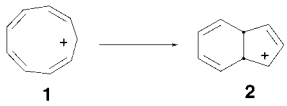


Figure 2. Conformations of $(CH)_9^+$.

[*] Prof. Dr. T. Kawase, Prof. Dr. M. Oda
Department of Chemistry
Graduate School of Science
Osaka University
Toyonaka, Osaka 560-0043 (Japan)
Fax: (+81) 6-6850-5387
E-mail: tkawase@chem.sci.osaka-u.ac.jp
moda@chem.sci.osaka-u.ac.jp

 © 2004 Wiley-VCH Verlag GmbH & Co. KGaA, Weinheim DOI: 10.1002/anie.200460050

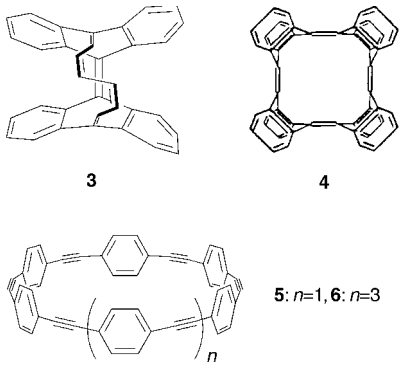
lower in energy than a second minimum conformation, **1b**, which has strong bond alternation. The energy difference between **1a** and the planar Hückel conformation (C_{2v}) **1c** is 26.3 kcal mol^{-1}. The NICS value of **1a** (−13.4) is more negative than that of **1b** (+8.6) and even than that of benzene (−9.7). Although formed easily, **1a** is a short-lived species; it isomerizes readily to the more stable bicyclo[4.3.0]nonatrienyl cation **2**, a bishomoaromatic cation (−11.8), through an electrocyclic ring closure (Scheme 1).



Scheme 1. Electrocyclization of **1** to **2**.

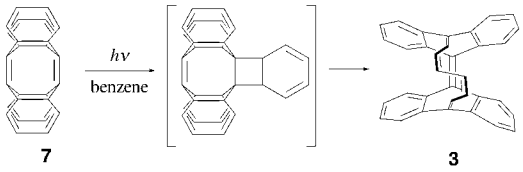
The electronic properties of small-ring compounds containing a strained allene bond or a *trans* double bond have also been discussed by theoreticians in connection with Möbius aromatic properties.[7] Although these computational studies predicted the importance of Möbius conjugation, the twisted cyclic molecules are destabilized by strong ring strain. In larger cyclic systems, however, ring strain is less pronounced. Rzepa's and Schleyer's groups have explored various isomers and conformations of [4*n*]annulenes ($n = 3$–5) computationally. These annulenes exist in equilibrium mixtures of geometrical isomers because of their structural flexibility. The calculations predict that some isomers of these systems adopt Möbius aromatic structures as energy minima, but the structures are very flexible and tend to flip back to the less strained Hückel structures with low activation energies.[8]

To display Möbius aromaticity, therefore, the target molecules should have rigid frameworks that enforce a smoothly twisted conjugation. Moreover, the molecular strain should be dispersed over the entire molecule. Almost the same concept was applied in the molecular design of "belt-shaped" conjugated systems.[9] The systems, in which the p orbitals are aligned horizontally on a rigid surface, have also been sought as attractive synthetic targets. Since the discovery of fullerenes and carbon nanotubes, these belt-shaped conjugated systems have been regarded as good models for the new carbon materials. The first examples, picotubes **3** and **4** and carbon nanorings **5** and **6**, were synthesized as relatively



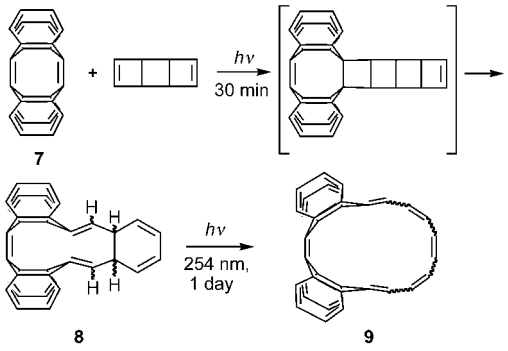
stable substances by Herges et al. and by our research group in 1996.[10,11] It is notable that a Möbius structure can be regarded as a combination of a "normal" aromatic structure and a belt-shaped aromatic structure as illustrated graphically in Scheme 2.[10]

Recently Herges and co-workers have synthesized the first stable Möbius molecule based on this consideration.[12] They found that tetradehydrodianthracene (TDDA, **7**) reacts with a number of alkenes upon photoirradiation to form rigid macrocyclic compounds by metathesis of the corresponding [2+2] cycloadducts. The twisted[14] annulene **3** was obtained from the [2+2] adduct of **7** with benzene (Scheme 3).[10a] The steric interaction of the inner *ortho* protons of



Scheme 3. Reaction of benzene with **7**.

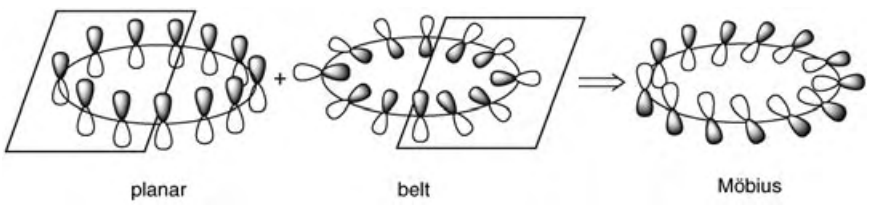
the anthracene units forces the molecule to assume a tubelike structure. This interesting synthetic strategy was also applied to the synthesis of the twisted [16]annulene **9** using *syn*-tricyclooctadiene, a valence-bond isomer of cyclooctatetraene, in place of benzene (Scheme 4). In this case, the first meta-



Scheme 4. Reaction of *syn*-tricyclooctadiene with **7**.

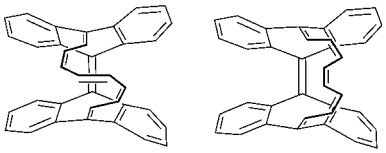
thesis proceeded thermally, but the second one proceeded photochemically. Although it contains rigid anthraquinodimethane moieties, annulene **9** has a number of geometrical and conformational isomers. According to calculations of all 108 isomers, the six most stable isomers, including the global minimum, possess Möbius-type structures.[12]

Five isomers were separated by HPLC and fully characterized by spectroscopic and crystallographic analysis. The orange crystalline *Z*,*E*,*Z* isomer **9a** (C_2) exhibits relatively little bond alternation (HOMA value = 0.50), whereas the colorless crystalline *Z*,*Z*,*Z* isomer **9b** exhibits strong bond alternation (HOMA value = 0.05) (Figure 3). The authors concluded that **9a** is Möbius



Scheme 2. Schematic construction of a Möbius structure.

 © 2004 Wiley-VCH Verlag GmbH & Co. KGaA, Weinheim



9a Möbius **9b** Hückel

Figure 3. Molecular structures of isomers of **9**.

aromatic and that **9b** is a Hückel structure but nonaromatic. The orange color of **9a** clearly indicates the extension of conjugation.

Schleyer's group have predicted that "[4*n*+2] trannulenes" having in-plane cyclic conjugation are aromatic like Hückel annulenes;[13] however, it is not yet clear how orbital pyramidalization can cause a change in cyclic conjugation. Moreover, it is well known that a benzene nucleus in polycyclic conjugated systems drastically reduces the peripheral conjugation in the molecules. Actually, the families of picotubes and carbon nanorings do not exhibit much effect of peripheral conjugation.[11b] Despite these disadvantages, the hydrocarbon prepared by the Herges group is the first stable molecule having a Möbius structure. Thus, synthetic organic chemists have now realized Heilbronner's idea about 40 years after it was proposed. Theoretical studies on other Möbius conjugated systems have been advanced recently, and the synthesis of such compounds will be a highly interesting subject.[14] Thus, the synthesis of aromatic compounds has now entered a new stage, and bent cyclophanes, twisted polycyclic aromatic hydrocarbons, and, notably, fullerenes are just some examples of new targets.

[1] For recent reviews, see: P. von R. Schleyer (special editor), *Chem. Rev.* **2001**, *101*, 1115 – 1566.

[2] T. M. Krygowski, *J. Chem. Inf. Comput. Sci.* **1993**, *33*, 70 – 78.

[3] P. von R. Schleyer, C. Maerker, A. Dransfield, H. Jiao, N. J. R. van Eikema Hommes, *J. Am. Chem. Soc.* **1996**, *118*, 6317 – 6318.

[4] E. Heilbronner, *Tetrahedron Lett.* **1964**, 1923 – 1926.

[5] H. E. Zimmerman, *Acc. Chem. Res.* **1971**, *4*, 272 – 280.

[6] M. Mauksch, V. Gogonea, H. Jiao, P. von R. Schleyer, *Angew. Chem.* **1998**, *110*, 2515 – 2517; *Angew. Chem. Int. Ed.* **1998**, *37*, 2395 – 2397.

[7] S. Martin-Santamaria, B. Lavan, H. S. Rzepa, *Chem. Commun.* **2000**, 1089 – 1090; S. Martin-Santamaria, H. S. Rzepa, *J. Chem. Soc. Perkin Trans. 2* **2000**, 2372 – 2377; C. J. Kastrup, S. P. Oldfield, H. S. Rzepa, *Chem. Commun.* **2002**, 642 – 643.

[8] S. Martin-Santamaria, B. Lavan, H. S. Rzepa, *J. Chem. Soc. Perkin Trans. 2* **2000**, 1415 – 1417; C. Castro, C. M. Isborn, W. L. Karney, M. Mauksch, P. von R. Schleyer, *Org. Lett.* **2002**, *4*, 3431 – 3434.

[9] L. T. Scott, *Angew. Chem.* **2003**, *115*, 4265 – 4267; *Angew. Chem. Int. Ed.* **2003**, *42*, 4133 – 4135, and references therein.

[10] a) S. Kammermeier, P. G. Jones, R. Herges, *Angew. Chem.* **1996**, *108*, 470 – 472; *Angew. Chem. Int. Ed. Engl.* **1996**, *35*, 417 – 419; b) S. Kammermeier, P. G. Jones, R. Herges, *Angew. Chem.* **1996**, *108*, 2834 – 2836; *Angew. Chem. Int. Ed. Engl.* **1996**, *35*, 2669 – 2671.

[11] a) T. Kawase, H. R. Darabi, M. Oda, *Angew. Chem.* **1996**, *108*, 2803 – 2805; *Angew. Chem. Int. Ed. Engl.* **1996**, *35*, 2664 – 2666; b) T. Kawase, N. Ueda, K. Tanaka, Y. Seirai, M. Oda, *Tetrahedron Lett.* **2001**, *42*, 5509 – 5511.

[12] D. Ajami, O. Oeckler, A. Simon, R. Herges, *Nature* **2003**, *426*, 819 – 821.

[13] A. A. Fokin, H. Jiao, P. von R. Schleyer, *J. Am. Chem. Soc.* **1998**, *120*, 9364 – 9365.

[14] Recent theoretical studies of a molecular Möbius strip with a figure-eight structure; J. Dobrowolski, *J. Chem. Inf. Comput. Sci.* **2002**, *42*, 490 – 499; A. T. Balaban, M. Randic, *J. Chem. Inf. Comput. Sci.* **2004**, *44*, 50 – 59.

 © 2004 Wiley-VCH Verlag GmbH & Co. KGaA, Weinheim

Topochemistry

Borromean Rings: A One-Pot Synthesis

*Christoph A. Schalley**

Keywords:
self-assembly · structure elucidation · template synthesis · topochemistry

The aesthetics of beautiful molecules has been, and still is, a strong motivation for many chemists. Complex interwoven structures[1] such as catenanes, rotaxanes, and knots are even nowadays appealing because of their interesting topological properties, although their functions as molecular machines[2] have become more and more of the focus of interest.



Figure 1. A small selection from the mathematical zoo of knots.

The ability of chemistry to realize the mathematical zoo of knots (Figure 1),[3] at the molecular level still suffers from narrow limitations, and it is thus well-justified to consider the synthesis of trefoil knots as a major achievement.[4] Borromean rings possess an even more complex topology than the trefoil knot, thus making them a challenging target for chemical synthesis. This is reflected in the fact that they have only so far[5] been realized at the molecular level through the DNA nanoassembly methodology developed by Seeman and co-workers.[6] Consequently, the first chemical synthesis of Borromean rings by Stoddart, Atwood, and their co-workers[7] is certainly a highlight in supramolecular chemistry.

Borromean rings consist of three rings which are entangled in a way which prevents separation of the rings just by changing their shape (Figure 2). Opening one of the rings, however, makes the whole assembly fall apart. It is this property which has made the

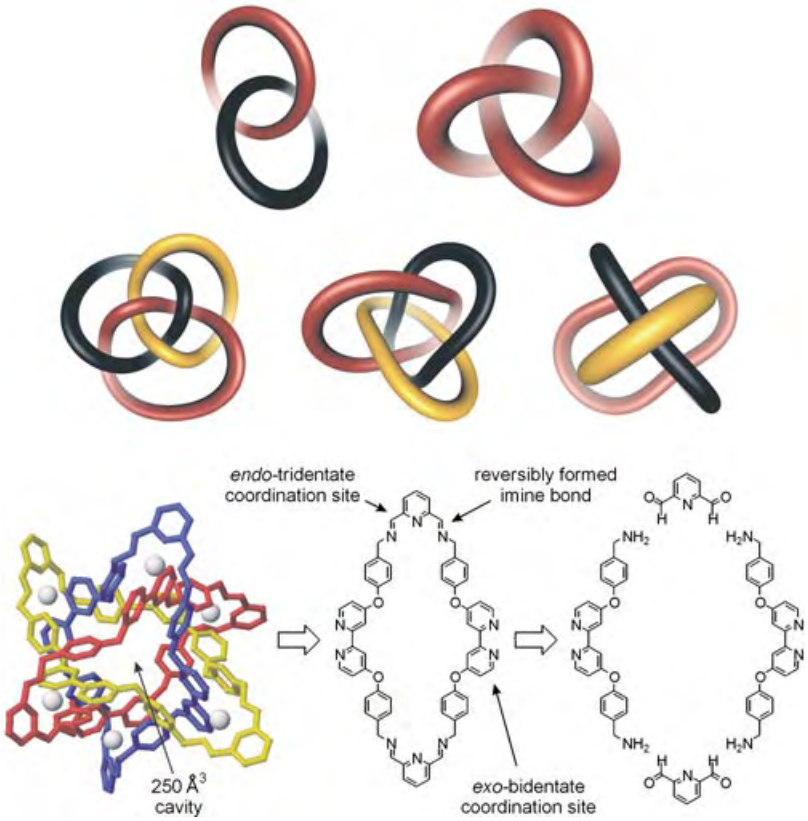


Figure 2. Top: Catenane (left) and trefoil knot (right). Center: Three views of Borromean rings. Bottom: Chemical realization of Borromean rings through self-organization.

[*] Priv.-Doz. Dr. C. A. Schalley
Kekulé-Institut für Organische Chemie und Biochemie
Universität Bonn
Gerhard-Domagk-Strasse 1
53121 Bonn (Germany)
Fax: (+49) 228-735-662
E-mail: c.schalley@uni-bonn.de

DOI: 10.1002/anie.200460583
© 2004 Wiley-VCH Verlag GmbH & Co. KGaA, Weinheim

Borromean rings important in historical terms as a symbol for strength in unity.

Borromean rings can be found throughout the history of mankind—from the vikings to christian iconography to far-East family emblems.[8] Their name originated from the inclusion of the rings in the fifteenth century crest of the Borromeo family from Milan. Figure 3 shows the rings on the entrance to the church San Sigismondo in Cremona in the dukedom of Milan.



Figure 3. The entrance door to San Sigismondo in Cremona, carved from walnut wood by Paolo and Giuseppe Sacca between 1536 and 1542. Reproduced with kind permission of Dr. Peter Cromwell.[8]

The fact that the Borromean rings fall apart if one of them is missing or cut was utilized as evidence for the topology of the DNA-based Borromean rings: enzymatic cleavage of one of the rings destroys the whole structure and results in the formation of three independent parts. What is an advantage for characterization is a problem for the synthesis of Borromean rings in the laboratory. Although precursors for catenanes and rotaxanes can be found relatively easily because they need to organize only two subunits into a suitable crossed arrangement, a total of six such crossing points need to be generated in the correct geometry for the synthesis of Borromean rings.

The latter can only be successful with a sophisticated template synthesis.[9] One possible synthetic strategy relies on the application of two different template effects and leads to a stepwise synthesis (Figure 4).[10] In the first step the second ring is moved into and bound by the first ring.[11] The second step involves the third ring being subsequently threaded into the complex by a second template effect in which all the geometric requirements necessary for the generation of Borromean rings are fulfilled. Such a strategy has the merit of structural variability: if two different templates are used successively, the three rings can be different from each other.

The other synthetic extreme, that is, an elegant one-pot synthesis utilizing self-assembly processes,[12] has now been used by Stoddart, Atwood, and coworkers.[7] Self-assembly requires reversible, multiple error-checking and error-correction steps that enable the system to reach its thermodynamic minimum. The retrosynthetic strategy and the building blocks used in this synthesis are shown in Figure 2. The condensation of the dialdehydes and diamines shown to form imines serves as the reversible bond-formation step in the macrocyclizations.[13] The resulting macrocycle bears two pairs of opposing *endo*-tridentate and *exo*-bidentate metal-coordination sites and has the overall oval shape required for the threading process.

Under template-free conditions, a complicated mixture of macrocyclic and linear oligomers would be expected to form from these building blocks. Therefore, the presence of transition-metal ions is required to form kinetically labile complexes with the coordination sites built into the macrocycles. Six zinc(II) ions are perfectly suited for this purpose; they template the formation of Borromean rings by binding to one of the exocyclic bipyridine units of one of the three macrocycles and to one of the tridentate endocyclic coordination sites of the next one, thus bridging one ring with the others and providing a way of threading the macrocycles into each other. After one macrocycle is encapsulated within another, nonsaturated coordination sites remain at the zinc ions, and these control the threading of the open-chain precursor of the third macrocycle. A final macrocyclization terminates the synthesis, with the product formed in a yield of about 90%.

The characterization was achieved by NMR spectroscopy, ESI mass spectrometry,[14] and crystal-structure analysis. In the solid state the Borromean rings have an S_6 symmetry. The Zn^{II} ions

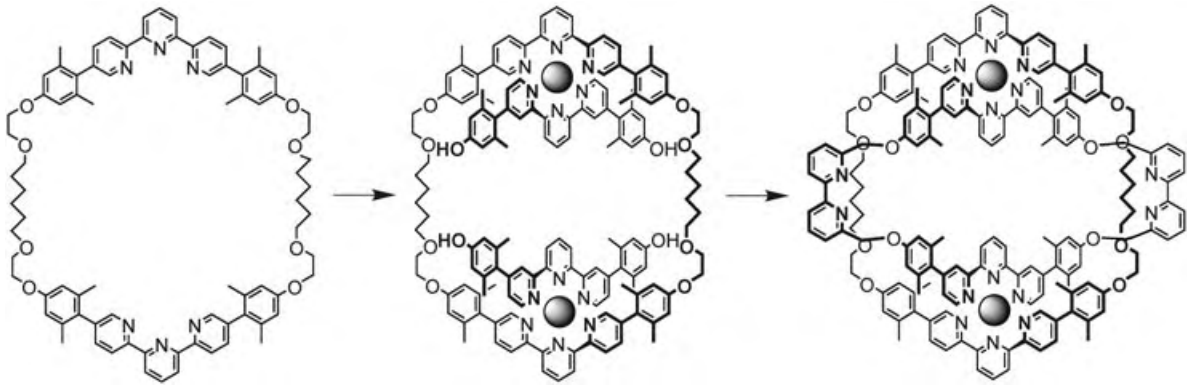


Figure 4. Stepwise synthesis of Borromean rings: Precursors and intermediates.

 © 2004 Wiley-VCH Verlag GmbH & Co. KGaA, Weinheim

are 12.7 Å apart and have an almost octahedral coordination environment consisting of five nitrogen atoms and one oxygen atom from one of the triflate counterions. In addition to all their special topological features, the Borromean rings have a particular property that is highly interesting for supramolecular chemistry: They possess a cavity in their center with a volume of about 250 $Å^3$ which is defined by twelve oxygen atoms. ESI mass spectrometry as well as ^1H NMR experiments indicate the presence of an additional $Zn(CF_3SO_3)_2$ ion triple as a guest inside the cavity.

In view of the cavity and the defined arrangement of six transition-metal ions, it will be interesting to follow the further development of the Borromean rings, which will likely take them far beyond their aesthetic structure into the world of functional materials.

Published Online: July 7, 2004

[1] a) G. Schill, *Catenanes, Rotaxanes and Knots*, Academic Press, New York, **1971**; b) *Molecular Catenanes, Rotaxanes, and Knots* (Eds.: J.-P. Sauvage, C. Dietrich-Buchecker), Wiley-VCH, Weinheim, **1999**.

[2] a) V. Balzani, A. Credi, F. M. Raymo, J. F. Stoddart, *Angew. Chem.* **2000**, *112*, 3484; *Angew. Chem. Int. Ed.* **2000**, *39*, 3348; b) C. A. Schalley, A. Lützen, M. Albrecht, *Chem. Eur. J.* **2004**, *10*, 1072.

[3] Pictures of the knots were generated with the shareware program Knotplot by Rob Scharein: http://www.cs.ubc.ca/nest/imager/contributions/scharein/KnotPlot.html.

[4] a) C. O. Dietrich-Buchecker, J.-P. Sauvage, *Angew. Chem.* **1989**, *101*, 192; *Angew. Chem. Int. Ed. Engl.* **1989**, *28*, 189; b) R. F. Carlina, C. Dietrich-Buchecker, J.-P. Sauvage, *J. Am. Chem. Soc.* **1996**, *118*, 9110; c) P. R. Ashton, O. A. Matthews, S. Menzer, F. M. Raymo, N. Spenzer, J. F. Stoddart, D. J. Williams, *Liebigs Ann.* **1997**, 2485; d) G. Rapenne, C. Dietrich-Buchecker, J.-P. Sauvage, *J. Am. Chem. Soc.* **1999**, *121*, 994; e) S. C. J. Meskers, H. P. J. M. Dekkers, G. Rapenne, J.-P. Sauvage, *Chem. Eur. J.* **2000**, *6*, 2129; f) O. Safarowsky, M. Nieger, R. Fröhlich, F. Vögtle, *Angew. Chem.* **2000**, *112*, 1699; *Angew. Chem. Int. Ed.* **2000**, *39*, 1616; g) H. Adams, E. Ashworth, G. A. Breault, J. Guo, C. A. Hunter, P. C. Mayers, *Nature* **2001**, *411*, 763; h) C. R. Woods, M. Benaglia, S. Toyota, K. Hardcastle, J. S. Siegel, *Angew. Chem.* **2001**, *113*, 771; *Angew. Chem. Int. Ed.* **2001**, *40*, 749; i) F. Vögtle, A. Hünten, E. Vogel, S. Buschbeck, O. Safarowsky, J. Recker, A. H. Parham, M. Knott, W. M. Müller, U. Müller, Y. Okamoto, T. Kubota, W. Lindner, E. Francotte, S. Grimme, *Angew. Chem.* **2001**, *113*, 2534; *Angew. Chem. Int. Ed.* **2001**, *40*, 2468; j) O. Lukin, W. M. Müller, U. Müller, A. Kaufmann, C. Schmidt, J. Leszczynski, F. Vögtle, *Chem. Eur. J.* **2003**, *9*, 3507.

[5] Metallic microknots and Borromean Rings have been generated on a micro- to millimeter scale by chemical means. Their fabrication relies on the electrodeposition of a metal on two suitably patterned cylinders, and finally producing a junction between the two cylinders at the right parts of their surfaces. Removing the cylinders finally yields the desired microknots: H. Wu, S. Brittain, J. Anderson, B. Grzybowski, S. Whitesides, G. M. Whitesides, *J. Am. Chem. Soc.* **2000**, *122*, 12691.

[6] a) C. Mao, W. Sun, N. C. Seeman, *Nature*, **1997**, *386*, 137; the synthesis of trefoil and figure-eight knots based on DNA and RNA have also been reported: b) S. M. Du, B. D. Stollar, N. C. Seeman, *J. Am. Chem. Soc.* **1995**, *117*, 1194; c) H. Wang, R. J. Di Gate, N. C. Seeman, *Proc. Natl. Acad. Sci. USA* **1996**, *93*, 9477.

[7] K. S. Chichak, S. J. Cantrill, A. R. Pease, S.-H. Chiu, G. W. V. Cave, J. L. Atwood, J. F. Stoddart, *Science* **2004**, *304*, 1308; for a report on this publication, see J. S. Siegel, *Science*, **2004**, *304*, 1256.

[8] P. R. Cromwell, E. Beltrami, M. Rampichini, *Mathematical Intelligencer* **1998**, *20*, 53.

[9] a) T. J. Hubin, A. G. Kolchinski, A. L. Vance, D. H. Busch, *Adv. Supramol. Chem.* **1999**, *5*, 237; b) *Templated Organic Synthesis* (Eds.: F. Diederich, P. J. Stang), Wiley-VCH, Weinheim **2000**; c) T. J. Hubin, D. H. Busch, *Coord. Chem. Rev.* **2000**, *200–202*, 5; d) M. Kogej, P. Ghosh, C. A. Schalley, *How to thread a string into the eye of a molecular needle: Template-directed synthesis of mechanically interlocked molecules* in *Strategies and Tactics in Organic Synthesis*, *Vol. 4* (Ed.: M. Harmata), Elsevier, Amsterdam, **2004**, p. 171.

[10] Precursors for the synthesis of Borromean rings have been reported previously: J. C. Loren, M. Yoshizawa, R. F. Haldimann, A. Linden, J. S. Siegel, *Angew. Chem.* **2003**, *115*, 5880; *Angew. Chem. Int. Ed.* **2003**, *42*, 5702.

[11] a) M. Schmittel, A. Ganz, D. Fenske, *Org. Lett.* **2002**, *4*, 2289; b) S.-H. Chiu, A. R. Pease, J. F. Stoddart, A. J. P. White, D. J. Williams, *Angew. Chem.* **2002**, *114*, 280; *Angew. Chem. Int. Ed.* **2002**, *41*, 270.

[12] a) G. M. Whitesides, J. P. Mathias, C. T. Seto, *Science* **1991**, *254*, 1312; b) D. Philp, J. F. Stoddart, *Angew. Chem.* **1996**, *108*, 1242; *Angew. Chem. Int. Ed. Engl.* **1996**, *35*, 1154; c) J.-M. Lehn, *Chem. Eur. J.* **2000**, *6*, 2097; d) M. Albrecht, *Chem. Rev.* **2001**, *101*, 3457.

[13] a) S. J. Rowan, S. J. Cantrill, G. R. L. Cousins, J. K. M. Sanders, J. F. Stoddart, *Angew. Chem.* **2002**, *114*, 938; *Angew. Chem. Int. Ed.* **2002**, *41*, 898; reviews: b) P. A. Brady, J. K. M. Sanders, *Chem. Soc. Rev.* **1997**, *26*, 327; c) J.-M. Lehn, *Chem. Eur. J.* **1999**, *5*, 2455.

[14] For MS studies aimed at the structural characterization of topologically interesting molecules, see also a) C. A. Schalley, *Int. J. Mass Spectrom.*, **2000**, *194*, 11; b) C. A. Schalley, *Mass Spectrom. Rev.* **2001**, *20*, 253.

 © 2004 Wiley-VCH Verlag GmbH & Co. KGaA, Weinheim

Nanostructures

Cubic Liquid-Crystalline Nanoparticles

*Da Yang, Bruce Armitage, and Seth R. Marder**

Keywords:
lipids · liquid crystals · nanostructures · nanotechnology · polymers

In memory of David O'Brien

Cubic liquid-crystalline nanoparticles prepared from aqueous dispersions of cubic lipid–water phases are kinetically stable in the presence of certain dispersing agents. The properties of cubic nanoparticles from monoolein–water and other lipid–water systems have been examined with a variety of experimental techniques. The cubic nanoparticles can be stabilized by polymerization of the reactive lipids in cubic lipid assemblies. Several low-energy-input methods have been developed to facilitate the production and application of cubic nanoparticles. The ability to incorporate and deliver lipophilic, amphiphilic, and water-soluble molecules in a controlled manner and the good biocompatibility of cubic nanoparticles make them excellent candidates for drug-delivery applications.

1. Introduction

The self-assembly of amphiphilic molecules into complex structures is a broad and active area of research. Amphiphiles are characterized by a hydrophilic headgroup attached to at least one hydrophobic tail. Amphiphile–water systems are known to form a variety of different lyotropic liquid-crystalline phases, such as lamellar, inverted hexagonal, and inverted cubic phases (Figure 1). The enthalpically unfavorable interfacial interactions between the hydrophobic tail(s) of the lipid with the polar water molecules induce the former to aggregate with the hydrophobic tails of other lipids, while the hydrophilic headgroup remain exposed to the aqueous environment. Inverted cubic phases, which are bicontinuous with respect to the aqueous and the lipid regions, can be considered as organic analogues of zeolites. A cubic-phase liquid-crystalline gel material is a temperature-stable, optically isotropic, viscous gel with an extremely high surface area (as much as 400 $m^2 g^{-1}$ of cubic gel).[1] A cubic lipid gel may solubilize both hydrophilic and hydrophobic substances, as well as amphiphilic molecules. The most popular application of cubic phases is as a delivery vehicle for materials that are solubilized in the cubic gel but diffuse out in a controlled-release manner.

Cubic gels in equilibrium with excess water can be dispersed into nanoparticles. In analogy with liposomes, which are formed from lamellar liquid-crystalline materials, these nanoparticles are termed cubosomes.[2] In this Minireview we briefly describe recent progress in the study of cubic

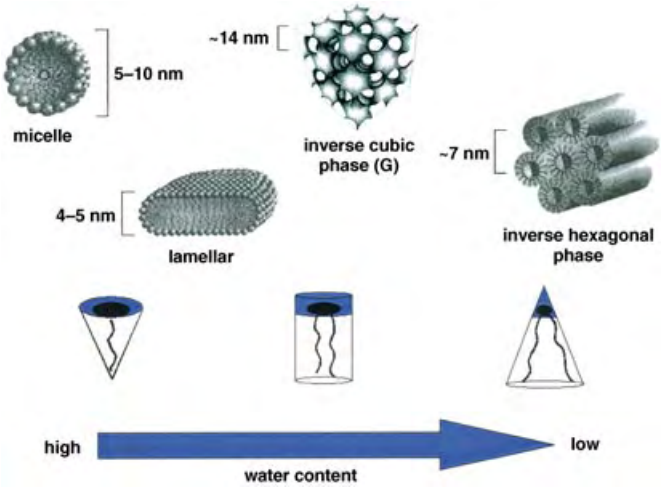


Figure 1. Some liquid-crystalline phases of hydrated lipids. From left to right, the phase changes from micellar to lamellar to bicontinuous cubic and to inverse hexagonal as the spontaneous curvature of the lipids changes from positive to negative and the water content of the sample decreases.

[*] Prof. S. R. Marder
School of Chemistry and Biochemistry
Georgia Institute of Technology
770 State Street, Atlanta, GA 30332-0400 (USA)
Fax: (+1) 404-385-6057
E-mail: seth.marder@chemistry.gatech.edu
Dr. D. Yang
Material Science and Engineering Department
Cornell University, Ithaca, NY 14853 (USA)
Prof. B. Armitage
Department of Chemistry, Carnegie Mellon University
Pittsburgh, PA 15213 (USA)

 © 2004 Wiley-VCH Verlag GmbH & Co. KGaA, Weinheim DOI: 10.1002/anie.200301683

liquid-crystalline nanoparticles derived from aqueous dispersions of cubic lipid–water phases.

2. Cubic Lipid–Water Phases

Bicontinuous cubic phases in membrane lipid–water systems were first reported by Luzzati et al.[3] in the 1960s, although detailed studies of these phases did not begin until the mid-1980s. Since then, these phases have been found in a wide range of lyotropic systems, including lipid–water systems and block copolymers. Scriven[4] first suggested that bicontinuous cubic phases have interface structures based on periodic minimal surfaces; this description is now generally held to be correct. A cubic liquid-crystalline lipid–water phase is one in which the lipid bilayers are arranged in periodic three-dimensional cubic-lattice structures. By contorting the bilayers into the shape of infinite periodic minimal surfaces, the mean curvature at any point on the surface is zero. The mean curvature H is defined as $^1/_2(\kappa_1 + \kappa_2)$, in which κ_1 and κ_2 are two principal curvatures. A minimal surface is a surface with $H = 0$ at all points, so that every point on the surface is a balanced saddle point. The three inverse bicontinuous phases currently known are the double-diamond (D), gyroid (G), and primitive (P) phases, which correspond to the *Pn*3*m*, *Ia*3*d*, and *Im*3*m* space-group symmetries, respectively (Figure 2).[5] Inspection of the minimal surfaces and the complementary three-dimensional labyrinth nets reveals the interpenetrating nature of two distinct water channels (Figure 3). The size of the aqueous channels, which is a function of the lipid composition and the phase, can range from $\approx$4 to 20 nm in diameter, sufficiently large to accommodate certain water-soluble macromolecules. The amount of water accommodated in the G, D, and P phases increases accordingly,[6] as does the size of the aqueous channels.

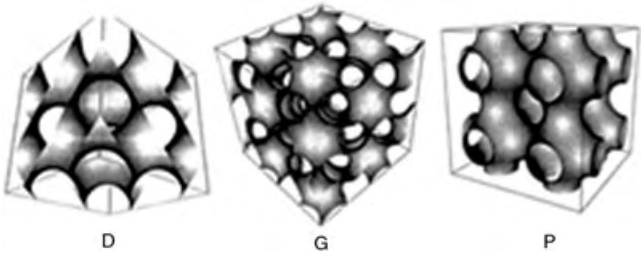


Figure 2. Mathematical representation of the three bicontinuous cubic morphologies associated with lipid water systems. These minimal surfaces (D, G, and P) correspond to the lipid portion of the respective phases.[5]

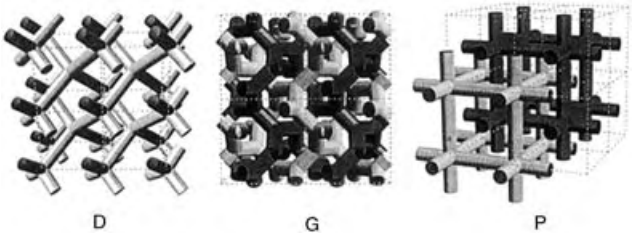


Figure 3. Representation of the three-dimensional networks complementary to the three bicontinuous cubic morphologies, D, G, and P. These labyrinths correspond to the water portion of the respective cubic phases.[5]

Among the various lyotropic liquid-crystalline phases, the lamellar phase with alternating stacked lipid bilayers and water is perhaps the most well known in biological systems. The inverted hexagonal liquid-crystalline phase consists of infinite water rods stacked into a two-dimensional hexagonal lattice separated by lipid bilayers. Generally, the inverted hexagonal phase is found at higher temperatures and lower water content than the lamellar phase, whereas the inverted bicontinuous cubic phase occurs at intermediate temperatures and concentrations. Like lamellar and hexagonal phases, cubic liquid-crystalline phases exhibit long-range order but have no short-range order, that is, the hydrophobic chains are disordered. Whereas lamellar and hexagonal phases are optically birefringent, cubic phases are optically isotropic, which makes a cubic-phase gel a clear, viscous, jellylike material (Figure 4).

One of the most well characterized lipid–water systems, GMO–water (GMO = glycerol monooleate), exhibits two types of bicontinuous cubic phases at water contents between 20 and 40 wt% at room temperature.[7] An increase in the water content results in a transition from the lamellar phase to the gyroid (G) cubic phase then to the double-diamond (D) cubic phase. These cubic phases can coexist in equilibrium with excess water. A very detailed phase diagram of the



Bruce Armitage received his PhD in 1993 under the supervision of Prof. David O'Brien (University of Arizona) and was a postdoctoral fellow with Prof. Gary B. Schuster (University of Illinois and Georgia Tech; 1995–1997). He then spent the summer of 1997 with Prof. Peter E. Nielsen and Prof. Henrik Nielsen (University of Copenhagen). He subsequently took up a position as Associate Professor of Chemistry at Carnegie Mellon University, where he studies biomolecular recognition in nucleic acid chemistry and biology, supramolecular photochemistry, and materials science.



Seth Marder is currently a Professor of Chemistry and the founding Director of the Center for Organic Photonics and Electronics (COPE) at the Georgia Institute of Technology. He is also a cofounder of Arizona Microsystems, and Focal Point Microsystems L.L.C. and an Associate Director and of the National Science Foundation Science and Technology Center: Materials and Device for Information Technology Research. Dr. Marder was the 1993 recipient of the JPL Lew Allen Award. He is a Fellow of the American Association for the Advancement of Science (2002) and of the Optical Society of America (2004).

© 2004 Wiley-VCH Verlag GmbH & Co. KGaA, Weinheim



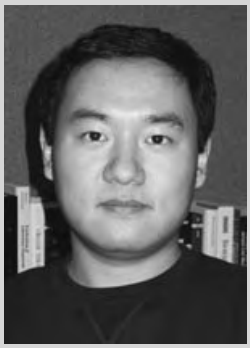
Figure 4. Photograph of a sample of a bulk cubic gel. The cubic-phase gel is a clear, viscous, jellylike material that is temperature-stable and highly biocompatible.[9]

GMO–water system was reported recently by Qiu and Caffrey.[8]

Although GMO–water is the most frequently studied lipid-water system for cubic phases, other lipids such as phosphatidylcholines, phosphatidylethanolamines, PEGylated phospholipids (PEG = poly(ethylene glycol)), and various monoglycerides have been shown to form bicontinuous cubic phases as well. Most common experimental methods for the characterization of cubic phases include X-ray diffraction, transmission and freeze–fracture electron microscopy, and nuclear magnetic resonance spectroscopy.[10] Some of the other techniques applied in the study of cubic lipid–water systems are time-resolved fluorescence,[11] neutron diffraction,[12] FTIR,[13] differential scanning calorimetry,[14] resonance Raman spectroscopy,[15] and atomic force microscopy.[16]

3. Cubic Liquid-Crystalline Nanoparticles Stabilized by Dispersing Agents

Although cubic gels have interesting and potentially useful properties, they are difficult to handle and process. Dispersion into smaller structures that retain at least some of the properties of the bulk material would facilitate the use of cubic materials for various applications. The desire to create such stable dispersions has motivated the preparation of cubic liquid-crystalline nanoparticles from aqueous dispersions of cubic lipid–water phases. It is well known that lamellar phases in coexisteance with water can be easily dispersed into stable vesicles termed liposomes. Dispersions of reversed amphiphilic liquid-crystalline phases are less commonly found owing to their limited stabilities in aqueous environments. Bicontinuous cubic phases do not form stable aqueous dispersions, as the resulting exposure of the hydrophobic domains to the aqueous medium surrounding the particles effectively disrupts the crystallinity of the inner structure.[2] However, if the unfavorable interaction between the hydrophobic domain and the aqueous media can be avoided without breaking the inner cubic structure, for example, by addition of amphiphilic dispersion agents, it is possible to form nanoparticles with a cubic liquid-crystalline inner structure. The correct choice of dispersing agent is the key, as the dispersing agent will participate in the lipid–water assembly, and needs to do so without disrupting the cubic liquid-crystalline structure.



Da Yang received his BS degree in polymer chemistry in 1997 from the University of Science and Technology of China. He obtained a PhD in organic chemistry from the University of Arizona in 2003 under the supervision of Prof. David F. O'Brien and Prof. Seth R. Marder. He is now a postdoctoral research associate with Prof. Christopher K. Ober at Cornell University.

The first fragmentized bilayer cubic-phase structure was observed approximately 20 years ago.[17] Aqueous dispersions of cubic phases have been prepared with bile salts, amphiphilic proteins, and amphiphilic block copolymers as the dispersing agents. The cubic phase formed from a monoglyceride–water mixture was dispersed in the presence of micellar solutions of bile salts.[18,19] The cubic phase was stabilized by the formation of a lamellar envelope composed of bile salt and monoglycerides shielding the inner cubic structure. Separately, casein, an amphiphilic protein and a very effective emulsifier, was used to disperse the monoglyceride–water cubic phase. In this strategy, the protein is believed to partition into the outer layer of the lipid, making it more hydrophilic and therefore easy to disperse.[20]

A third strategy for dispersing cubic phases utilizes poloxamer 407 (also called pluronic F127), a nonionic triblock copolymer composed of polyethylene oxide (PEO) and polypropylene oxide (PPO): $PEO_{98}PPO_{67}PEO_{98}$. This is by far the most widely used dispersing agent and is also used for the stabilization of a variety of colloids as well as in drug-delivery studies. While the hydrophobic PPO block is adsorbed onto or incorporated in the surface of the stabilized particle, the hydrophilic PEO blocks extend to cover the surface, providing steric shielding and stabilizing the colloid particles.[21] The ternary system composed of pine needle oil monoglycerides (89.5 wt% GMO)–poloxamer 407–water exhibits an extended inverted cubic-phase field in which four different cubic structures were detected by X-ray diffraction.[22]

This system was dispersed into submicron particles by first forming a coarse dispersion (by dropping the homogeneous melt of lipids and poloxamer 407 into water while stirring), then feeding into a microfluidizer for further size reduction.[23,24] A minimum of 4 wt% poloxamer 407 was required for stable dispersion of the cubic gel. The cubic nature of these particles was characterized by small-angle X-ray scattering (SAXS) and cryo-transmission electron microscopy (cryo-TEM). Line broadening was observed in the SAXS diffraction pattern of dispersed samples (compared to that of the nondispersed cubic gel) and was concluded to be a consequence of the submicron particle size. Cryo-TEM

 © 2004 Wiley-VCH Verlag GmbH & Co. KGaA, Weinheim

images revealed mostly square cubosomes with a clear inner periodicity (Figure 5).

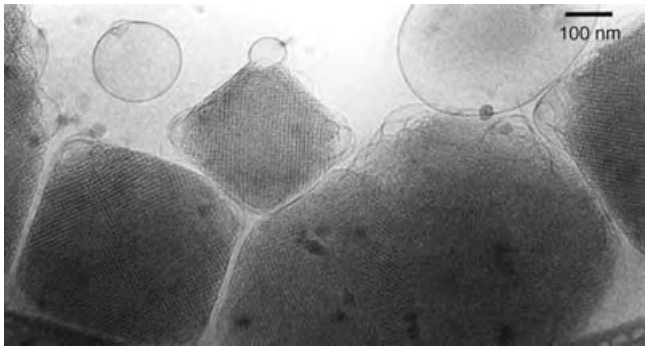


Figure 5. Cryo-TEM micrograph of the dispersed cubic particles from a cubic phase of monoolein–poloxamer 407–water (7.4 wt% polymer to lipid). The particles have a faceted shape with a clear inner periodicity.[24]

Smaller particles were observed for samples in which larger amounts of polymer were present. Handa and coworkers[25] also reported a decrease in particle size as the polymer/lipid weight ratio increased up to 10%. No further size decrease was observed when the amount of polymer was greater than 10%. Differential interference contrast micrographs (taken with and without crossed polarizers) of the cubic nanoparticles are shown in Figure 6.[9] The particles

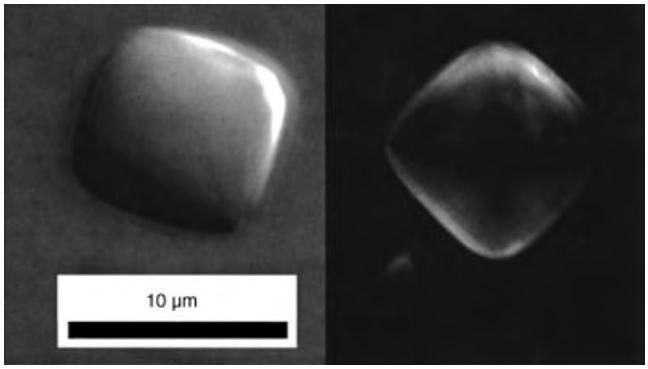


Figure 6. Optical micrograph of cubic particles from an aqueous dispersion of monoolein–poloxamer 407–water system, taken with (right) and without (left) crossed polarizers. The particles have a cubic inner morphology and an optically birefringent (probably lamellar) surface coating.[9]

adopt a distinct cubic shape despite their gel state and large scale relative to the cubic unit-cell dimensions, with edges terminated along the principal directions of the unit cell. Although the inner cubic morphology is optically isotropic, the existence of a birefringent surface structure suggests a noncubic coating, probably a lamellar phase, on the particles.

SAXS data revealed that two distinct cubic phases coexist for the inner structure of the cubic particles: double diamond (D) and primitive (P). The X-ray diffraction pattern revealed that the D cubic phase was dominant at low polymer content, whereas the P cubic phase appeared at higher polymer/lipid ratios.[24] Nakano et al.[25] suggested that poloxamer 407 was mostly adsorbed onto the surface of the particles at low polymer content, while the inner structure had a D cubic phase consisting mostly of hydrated monoolein. Once the polymer completely saturates the surface, it begins to insert into the monoolein bilayer and forms the P cubic phase (Figure 7). It is known that the P cubic phase has a less-

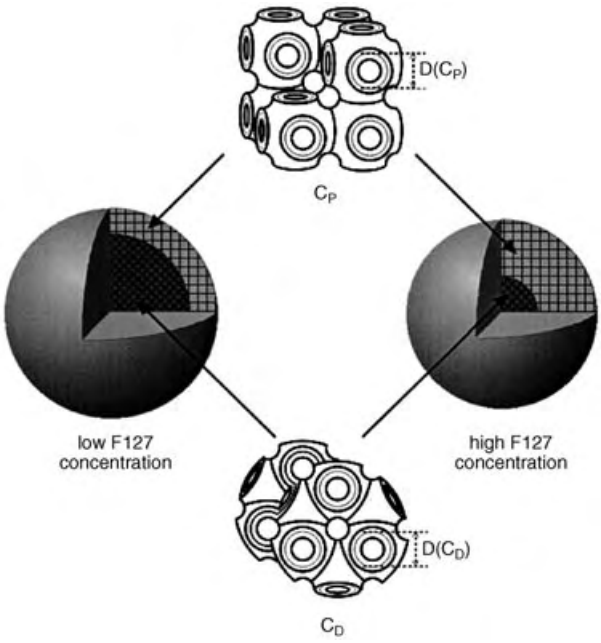


Figure 7. Internal structure change of the cubic particles relative to the amount of poloxamer 407 (F127) incorporated. a) At low polymer content, the D cubic phase (C_D) is the dominant structure. b) The P cubic phase (C_P) dominates at high polymer content.[25]

negative curvature than the D cubic phase.[26] The D–P transition can be attributed to the highly hydrophilic poloxamer 407 inducing a positive curvature in the lipid bilayer, which favors the formation of the less-negatively curved P cubic phase.

A similar behavior was observed when oleic acid (a fatty acid that has the same acyl chain as monoolein and a negative spontaneous curvature) was mixed in the lipid region of the cubic particles from a monoolein–water mixture. The X-ray diffraction pattern revealed a transformation from a bicontinuous cubic to an inverted hexagonal phase with increasing amounts of oleic acid.[27] The inner microstructure of these dispersed particles was also examined by ^{13}C NMR relaxation measurements.[28] A comparison of the ^{13}C NMR relaxation rates measured for monoolein in the dispersed particles with those measured for the corresponding nondispersed cubic samples indicated that the lipid organization and dynamic properties of the original cubic assemblies were retained. These dispersed samples were reported to be stable for up to six months.

Nakano et al. used ^{13}C NMR experiments with a paramagnetic ion as a probe to demonstrate the accessibility of

 © 2004 Wiley-VCH Verlag GmbH & Co. KGaA, Weinheim

metal ions to the water channels running through the cubic particles.[25] Upon addition of europium ion (Eu^{3+}), a shift was observed for the signal of the carbonyl carbon atom of the [1-^{13}C]oleic acid mixed in the lipid assembly. Steady-state fluorescence spectroscopy experiments suggested that there might be two different water compartments in the cubic particles: one is open to the outer water environment and one is closed.[29] The cubic colloidal particles were observed in situ by atomic force microscopy,[16] showing a narrow size distribution of about 300 nm (Figure 8). Size distribution

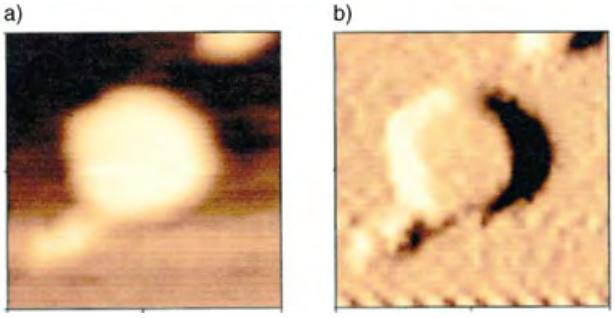


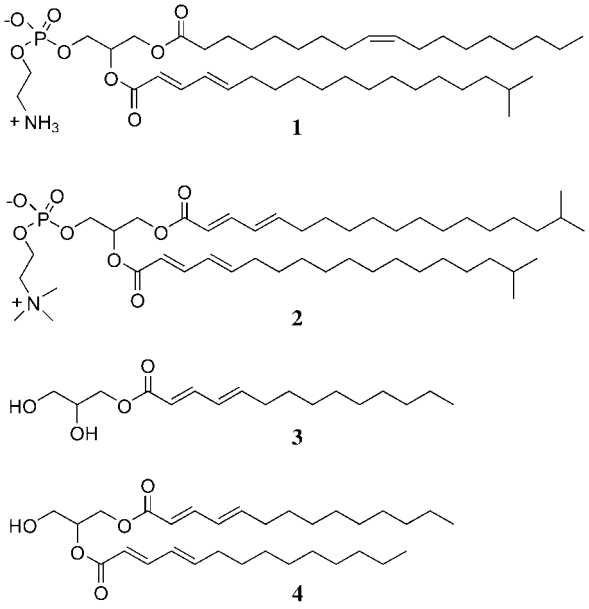
Figure 8. Noncontact AFM image of a dispersion of cubic particles on mica: a) topographic image, b) internal sensor image. The particle in these images is about $300\times300\times23$ nm^3 in dimensions.[16]

analysis of the same sample by quasi-elastic light scattering (QELS) revealed a mean particle diameter of 254 nm. The in situ observation technique allows the direct observation of modifications in the liquid-crystalline structure under different conditions such as addition and/or release of the solubilized molecules, variations in temperature or concentration, etc.

Cubic nanoparticles have also been prepared from aqueous dispersions of lipid–water systems other than monoolein–water. Johnsson and Edwards[30] reported cubic nanoparticles from aqueous dispersions of dioleoylphosphatidylethanolamine (DOPE)–PEG-derivatized phospholipids (PEG-lipid–water systems) with PEG-lipids as a dispersing agent. Cubic nanoparticles have also been made from synthetic reactive monoglycerides, as described in the next section.

4. Polymerized Cubic Liquid Crystalline Nanoparticles

As described in Section 2, the inverted bicontinuous cubic phase can be viewed as an intermediate phase between lamellar and inverted hexagonal phases. Lipid assemblies form cubic phases only within certain lipid concentration, temperature, and pressure ranges. The potential utility of liquid-crystalline lipid assemblies is partly dependent on the stabilization of these phases in order to expand their rather limited useful temperature and concentration ranges. One important approach to stabilized self-assembling materials is based on the polymerization of liquid-crystalline phases composed of reactive lipids.[31,32] During the past decade, polymerization has been utilized to modify the chemical and physical properties of lamellar[33,34] and nonlamellar[35,36] liquid-crystalline lipid assemblies. Lee et al. described the polymerization of a preformed inverted cubic phase as well as an inverted hexagonal phase from a pair of synthetic polymerizable lipids, a monodienoyl-substituted phosphatidylethanolamine **1** (mono-DenPE) and a bisdienoyl-substituted phosphatidylcholine **2** (bis-DenPC).[35] SAXS and cryo-



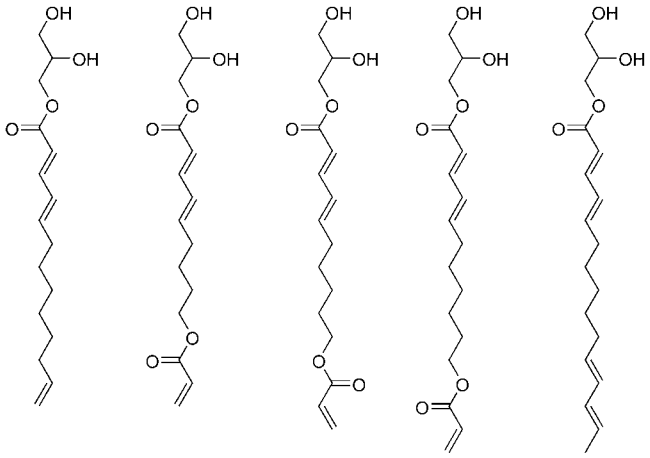
TEM data revealed that a lipid mixture (**1**/**2** = 3:1) formed a D cubic phase at temperatures above 60 °C. ^{31}P NMR experiments were also consistent with a cubic phase, based on the observation of a signal at 60 °C for an isotropic substance. Redox polymerization of the cubic phase at 65 °C led to broadening of the ^{31}P NMR signal, indicating that a nonlamellar phase was retained. Moreover, the signal persisted after cooling and extended incubation at room temperature, indicating that polymerization significantly stabilized the nonlamellar phase adopted by this mixture.

Polymerizable monoglycerides have also been synthesized for studies of cubic lipid assemblies.[37] Srisiri et al. have shown that when monodienoyl-substituted monoacylglycerol **3** was combined with bisdienoyl-substituted diacylglycerol **4** (9:1), an optically clear G cubic phase gel was formed.[38] Investigation of the lipid mixture by X-ray diffraction and by ^{2}H NMR spectroscopy of an analogue of **3** with a deuterated glycerol headgroup, and visualization with polarized light revealed a well-defined cubic phase between 5 and 45 °C. Polymerization of the reactive lipids increased the stability of the assembly with retention of the cubic phase. A signal for an isotropic compound was observed up to 70 °C, whereas the unpolymerized sample was only stable at temperatures below 45 °C. Furthermore, the diffusion coefficient of water within the polymerized cubic phase was determined by pulsed field gradient NMR spectroscopy as $1.2\pm0.2\times10^{-10}$ m^{2}s^{-1}, an order of magnitude smaller than that of pure water (2×10^{-9} m^{2}s^{-1}) but virtually identical to that in the unpolymer-

 © 2004 Wiley-VCH Verlag GmbH & Co. KGaA, Weinheim

ized cubic phase. Similar diffusion results were observed for cubic phases formed by the monoolein–water system.[39]

The lipid systems described above demonstrated the possibility of using polymerization to stabilize cubic phases. However, these systems either require complicated lipid synthesis (PE–PC system) or lack the required functionality to generate cross-linked lipid assemblies (monoacyl–diacyl glycerol systems), which are more beneficial than linear polymers for forming stable structures. To overcome these deficiencies, Yang et al. introduced a general strategy for the assembly of cross-linked cubic phases from reactive lipids. The phase behavior of a series of reactive monoglycerides, a group of readily synthesized lipids, has been studied.[40,41] Each of these monoglycerides has two reactive groups located on the same acyl chain (Scheme 1). Copolymerization with a



Scheme 1. Reactive monoglycerides for the polymerization of stabilized cubic nanoparticles. The dienoyl unit linked to the glycerol headgroup can be selectively polymerized by exposure to UV radiation (254 nm), while the acryloyl group at the terminus of the hydrophobic tail is polymerized in the presence of redox initiators.

small-molecule cross-linker led to the formation of a stable, cross-linked lipid assembly. The cross-linker also participates in the formation of cubic phases by increasing the hydrophobic portion of the system. This has an effect similar to having a more-negative spontaneous curvature, which in these cases is desirable for cubic-phase formation. A cubic-phase gel was formed when these lipids were hydrated in the presence of 10–15 mol% of cross-linker (divinylbenzene). The cubic gel was later dispersed into nanoparticles with poloxamer 407 as a stabilizing agent. Sequential UV-initiated and redox polymerization resulted in the reaction of the dienoyl and acryloyl groups, respectively, and gave cross-linked lipid assemblies, which were stable upon the addition of organic solvents and upon solubilization by surfactants. ^{2}H NMR spectroscopy showed a signal for the isotropic cubic nanoparticle samples prior to polymerization, which was progressively broadened after polymerization, an expected consequence of the decreased lateral diffusion of the polymerized lipids. These cross-linked cubic nanoparticles are expected to be as useful as the unpolymerized precursors and are potentially more suitable for applications under harsh conditions.

5. Processing Cubic Liquid-Crystalline Nanoparticles

A common method for processing cubic liquid-crystalline nanoparticles is by high-energy dispersion of bulk cubic gels. Cubic particles from monoolein–water systems are usually produced by mixing monoolein, dispersing agent, and water, followed by incubation for 24 h. The cubic-gel product is then dispersed into nanometer- and micron-scale particles by application of mechanical or ultrasonic energy. Homogenizers are often employed for the dispersion process, which requires high pressure and numerous cycles before homogeneous cubic-particle dispersions are produced.[42] The size can be reduced further in a high-pressure emulsifier.[25,27] One disadvantage of this process is the large amount of mechanical energy required for homogenization, which increases the risk of degrading the cubic lipid–water assembly. Furthermore, the viscous nature of the cubic gel intermediate makes scale-up very difficult. In this section, we describe several low-energy-input processes that have been developed to replace the current long hold time (incubation), viscous gel processing, and high-energy-input dispersion methods.

Spicer et al. reported the development of a "hydrotrope" process for producing cubic particles spontaneously by dilution of a monoolein–ethanol–water system.[9] In this case, a hydrotrope is defined as a molecule with both hydrophobic and hydrophilic character but incapable of displaying surfactant behavior. Hydrotropes are capable of disrupting liquid-crystalline phases, as well as functioning as facilitators of liquid-crystalline particle dispersions, although they do not form liquid crystals by themselves. However, when mixed in substantial quantities, they do help increase the solubility of water-insoluble lipids such as monoolein (monoolein solubility in water is $\approx 10^{-6}$ M). A hydrotrope process that produces lamellar liquid-crystalline vesicles by the dilution of a liquid precursor with water was previously reported by Friberg et al.[43,44]

Ethanol can be used as a hydrotrope in combination with monoolein to create a liquid precursor that forms cubic nanoparticles spontaneously when diluted with water, presumably by a homogeneous nucleation process. Dilution of monoolein–water–hydrotrope systems can produce particles as small as 50 nm or as large as 20 μm. The dilution process was found to produce smaller cubic nanoparticles more consistently than conventional methods. In principle, any lipid and hydrotrope combination that forms cubic liquid-crystalline phases can be dispersed by this simple method. Colloidally stabilized, controlled-release dispersions can be produced by this process by the direct inclusion of active ingredients and colloidal stabilizers into either of the two solutions. This process could be applied to applications that require the formation of cubic nanoparticles in situ.

Although the hydrotrope process provides the advantage of low-energy input and easier handling, for many applications it would be desirable to have dry powders or granular materials rather than liquid products. Freeze-drying is a well-

 © 2004 Wiley-VCH Verlag GmbH & Co. KGaA, Weinheim

known method for the production of liposomes for drug-delivery applications. Powdered precursors of drug-containing vesicles have been prepared by freeze-drying for the delivery of DNA and proteins by inhalation.[45] Kim et al. attempted to create powdered cubic-nanoparticle precursors by freeze-drying.[46] However, no cryo-TEM or SAXS data were reported, making it difficult to confirm the cubic nature of the particles that were produced. Another method for producing powdered precursors for lipid particles is spray-drying (Figure 9). Freitas and Müller reported the formation

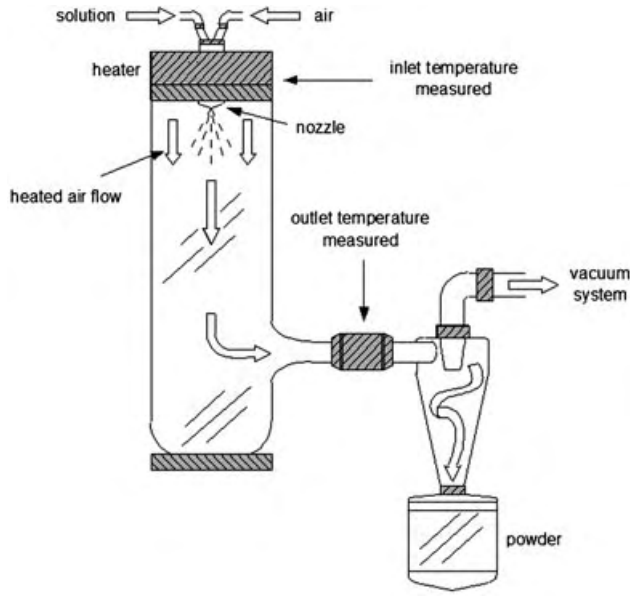


Figure 9. Spray-dryer apparatus for the production of cubic nanoparticle dry powder precursors.[48]

of lipid nanoparticle powders from non-liquid-crystalline lipids by spray-drying.[47] Spicer and co-workers applied this method in the production of two types of dry powder cubic-nanoparticle precursors: 1) a starch-encapsulated monoolein precursor from a dispersion of cubic liquid-crystalline particles in an aqueous starch solution, and 2) a dextran-encapsulated monoolein by spray-drying an emulsion from ethanol-dextran-monoolein-water system.[48] The encapsulants were introduced to decrease powder cohesion during spray-drying and to function as soluble colloidal stabilizers upon hydration of the powder precursors. Both powdered precursors were found to form 600-nm (volume-weighted average) colloidally stable cubic nanoparticles upon hydration of the powder. The dextran-stabilized system gave a narrower powder-size distribution as a result of the relative ease of dispersing and spraying an emulsion in contrast to a dispersion. The powder-precursor process widens the range and ease of applications for cubic nanoparticles by making their production and use in products convenient for manufacturing and formulation personnel instead of being limited to specialized researchers with access to sophisticated instruments. However, this process is limited to some degree by the large proportion of polymer required for encapsulation, that is, 75 wt% for starch and 60 wt% for dextran. The smaller proportion of lipids encapsulated means that only a limited amount of active ingredients can be incorporated for subsequent delivery. Therefore, the dry-powder-precursor process is more applicable for high-value-added materials such as pharmaceuticals, enzymes, vitamins, etc.

6. Summary and Outlook

Cubic liquid-crystalline nanoparticles have been prepared from aqueous dispersions of cubic lipid–water phases. These particles are kinetically stable in the presence of certain dispersing agents, and their properties have been studied with various experimental techniques. While most of the work has been done on monoolein–water systems, cubic nanoparticles from other lipid–water systems have also been studied. The cubic nanoparticles can be further stabilized by polymerization of the reactive lipids in cubic lipid assemblies. Several low-energy-input methods have been developed to facilitate the production and application of cubic nanoparticles.

We conclude this review by briefly discussing the potential uses of cubic nanoparticles from lipid assemblies. Bicontinuous cubic gels have been examined for drug-delivery applications since the 1990s.[49,50] The ability to incorporate and release a variety of drug additives in a controlled manner makes cubic gels more appealing as a universal carrier for drug delivery than liposomes and hydrogels. However, the high viscosity of cubic gels complicates their direct application, for example, for administration by injection. Cubic nanoparticles formed from aqueous dispersions of bulk cubic gels are more suitable as sustained-release delivery systems. The cubic-lipid assembly nanostructure that can be preserved in cubic nanoparticles offers advantages similar to those of bulk cubic gels, but the nanoparticles should be much easier to handle and process. One advantage of cubic nanoparticles over liposomes is the high bilayer area to particle volume ratio, which may increase the relative payload of lipophilic and amphiphilic additives. Additives can be loaded by direct addition to melted lipids and/or to the aqueous phase before cubic-phase formation, or by diffusion into the lipid–water structure after it is formed. Amphiphilic or lipophilic additives should be stable in the lipid matrix, and their release is also controlled by the structure. Loading of water-soluble additives is difficult owing to the open water channels in cubic phases. However, Lynch et al. have demonstrated the enhanced loading of negatively charged water-soluble additives by the inclusion of cationic surfactants into the liquid crystal.[51]

Received: July 15, 2003 [M1683]
Published Online: July 15, 2004

[1] M. J. Lawrence, *Chem. Soc. Rev.* **1994**, *23*, 417–423.
[2] K. Larsson, *J. Phys. Chem.* **1989**, *93*, 8453–8467.
[3] V. Luzzati, A. Tardieu, T. Gulik-kryzwicki, E. Rivas, F. Reiss-Husson, *Nature* **1968**, *220*, 485.
[4] L. E. Scriven, *Nature* **1976**, *263*, 123–125.
[5] A. D. Benedicto, D. F. O'Brien, *Macromolecules* **1997**, *30*, 3395–3402.

 © 2004 Wiley-VCH Verlag GmbH & Co. KGaA, Weinheim

[6] A. H. Schoen, *NASA Tech. Note* **1970**, *D-5541*, 1 – 98.
[7] S. T. Hyde, B. Ericsson, S. Andersson, K. Z. Larsson, *Z. Kristallogr.* **1984**, *168*, 213 – 219.
[8] H. Qiu, M. Caffrey, *Biomaterials* **2000**, *21*, 223 – 234.
[9] P. T. Spicer, K. L. Hayden, M. L. Lynch, A. Ofori-Boateng, J. L. Burns, *Langmuir* **2001**, *17*, 5748 – 5756.
[10] G. Lindblom, L. Rilfors, *Biochim. Biophys. Acta* **1989**, *988*, 221 – 256.
[11] L. B.-Å. Johansson, G. Lindblom, *J. Chem. Phys.* **1983**, *78*, 1519 – 1522.
[12] C. Czeslik, R. Winter, G. Rapp, K. Bartels, *Biophys. J.* **1995**, *68*, 1423 – 1429.
[13] A. Nilsson, A. Holmgren, G. Lindblom, *Biochemistry* **1991**, *30*, 2126 – 2133.
[14] H. Chung, M. Caffrey, *Biophys. J.* **1995**, *69*, 1951 – 1963.
[15] V. Razumas, Z. Talaikyte, J. Barauskas, K. Larsson, Y. Miezis, T. Nylander, *Chem. Phys. Lipids* **1996**, *84*, 155 – 164.
[16] C. Neto, G. Aloisi, P. Baglioni, K. Larsson, *J. Phys. Chem. B* **1999**, *103*, 3896 – 3899.
[17] J. S. Patton, M. C. Carrey, *Science* **1979**, *204*, 145 – 148.
[18] M. Lindström, H. Ljusberg-Wahren, K. Larsson, B. Borgström, *Lipids* **1981**, *16*, 749 – 754.
[19] J. Gustafsson, T. Nylander, M. Almgren, H. Ljusberg-Wahren, *J. Colloid Interface Sci.* **1999**, *211*, 326 – 335.
[20] W. Bucheim, K. Larsson, *J. Colloid Interface Sci.* **1987**, *117*, 582 – 583.
[21] P. Alexandridis, *Curr. Opin. Colloid Interface Sci.* **1997**, *1*, 490 – 501.
[22] T. Landh, *J. Phys. Chem.* **1994**, *98*, 8453 – 8467.
[23] J. Gustafsson, H. Ljusberg-Wahren, M. Almgren, K. Larsson, *Langmuir* **1996**, *12*, 4611 – 4613.
[24] J. Gustafsson, H. Ljusberg-Wahren, M. Almgren, K. Larsson, *Langmuir* **1997**, *13*, 6964 – 6971.
[25] M. Nakano, A. Sugita, H. Matsuoka, T. Handa, *Langmuir* **2001**, *17*, 3917 – 3922.
[26] P. Stroem, D. M. Anderson, *Langmuir* **1992**, *8*, 691 – 709.
[27] M. Nakano, T. Teshigawara, A. Sugita, W. Leesajakul, A. Taniguchi, T. Kamo, H. Matsuoka, T. Handa, *Langmuir* **2002**, *18*, 9283 – 9288.
[28] M. Monduzzi, H. Ljusberg-Wahren, K. Larsson, *Langmuir* **2000**, *16*, 7355 – 7358.
[29] L. Q. Zhang, J. Y. Um, H. Chung, I. C. Kwon, G. Z. Li, S. Y. Jeong, *J. Dispersion Sci. Technol.* **2003**, *24*, 123 – 128.
[30] M. Johnsson, K. Edwards, *Biophys. J.* **2001**, *80*, 313 – 323.
[31] D. F. O'Brien, B. Armitage, A. D. Benedicto, D. E. Bennett, H. G. Lamparski, Y.-S. Lee, W. Srisiri, T. M. Sisson, *Acc. Chem. Res.* **1998**, *31*, 861 – 868.
[32] A. Mueller, D. F. O'Brien, *Chem. Rev.* **2002**, *102*, 727 – 758.
[33] D. F. O'Brien, *Trends Polym. Sci.* **1994**, *2*, 183 – 188.
[34] H. Ringsdorf, B. Schlarb, J. Venzmer, *Angew. Chem.* **1988**, *100*, 113 – 162; *Angew. Chem. Int. Ed. Engl.* **1988**, *27*, 113 – 158.
[35] Y.-S. Lee, J. Yang, T. M. Sisson, D. A. Frankel, J. T. Gleeson, E. Aksay, S. L. Keller, S. M. Gruner, D. F. O'Brien, *J. Am. Chem. Soc.* **1995**, *117*, 5573 – 5578.
[36] W. Srisiri, T. M. Sisson, D. F. O'Brien, K. M. McGrath, Y. Han, S. M. Gruner, *J. Am. Chem. Soc.* **1997**, *119*, 4866 – 4873.
[37] W. Srisiri, H. G. Lamparski, D. F. O'Brien, *J. Org. Chem.* **1996**, *61*, 5911 – 5915.
[38] W. Srisiri, A. D. Benedicto, D. F. O'Brien, T. P. Trouard, G. Orädd, S. Persson, G. Lindblom, *Langmuir* **1998**, *14*, 1921 – 1926.
[39] G. Lindblom, K. Larsson, L. B.-Å. Johansson, K. Fontell, S. Forsén, *J. Am. Chem. Soc.* **1979**, *101*, 5465 – 5470.
[40] D. Yang, D. F. O'Brien, S. R. Marder, *J. Am. Chem. Soc.* **2002**, *124*, 13388 – 13389.
[41] D. Yang, S. Liu, D. F. O'Brien, S. R. Marder, *Polym. Mater. Sci. Eng.* **2003**, *88*, 100 – 101.
[42] H. Ljusberg-Wahren, L. Nyberg, K. Larsson, *Chim. Oggi* **1996**, *14*, 40 – 43.
[43] S. E. Friberg, S. Campell, L. Fei, H. Yang, R. Patel, P. A. Aikens, *Colloids Surf. A* **1997**, *129–130*, 167 – 174.
[44] S. E. Friberg, H. Yang, L. Fei, S. Sadasivan, D. H. Rasmussen, P. A. Aikens, *J. Dispersion Sci. Technol.* **1998**, *19*, 19 – 30.
[45] F. C. Szoka, A. Rolland, J. Wang, US Patent 5811406, **1998**.
[46] J. S. Kim, H. K. Kim, H. Chung, Y. Y. Sohn, I. C. Kwon, S. Y. Jeong, *Proc. Int. Symp. Controlled Release Bioact. Mater.* **2000**, *27*, 1118 – 1119.
[47] C. Freitas, R. H. Müller, *Eur. J. Pharm. Biopharm.* **1998**, *46*, 145 – 151.
[48] P. T. Spicer, W. B. Small, M. L. Lynch, J. L. Burns, *J. Nanopart. Res.* **2002**, *4*, 297 – 322.
[49] C. J. Drummond, C. Fong, *Curr. Opin. Colloid Interface Sci.* **2000**, *5*, 449 – 456.
[50] J. C. Shah, Y. Sadhale, D. M. Chilukuri, *Adv. Drug Delivery Rev.* **2001**, *47*, 229 – 250.
[51] M. L. Lynch, A. Ofori-Boateng, A. Hippe, K. Kochvar, P. T. Spicer, *J. Colloid Interface Sci.* **2003**, *260*, 404 – 413.

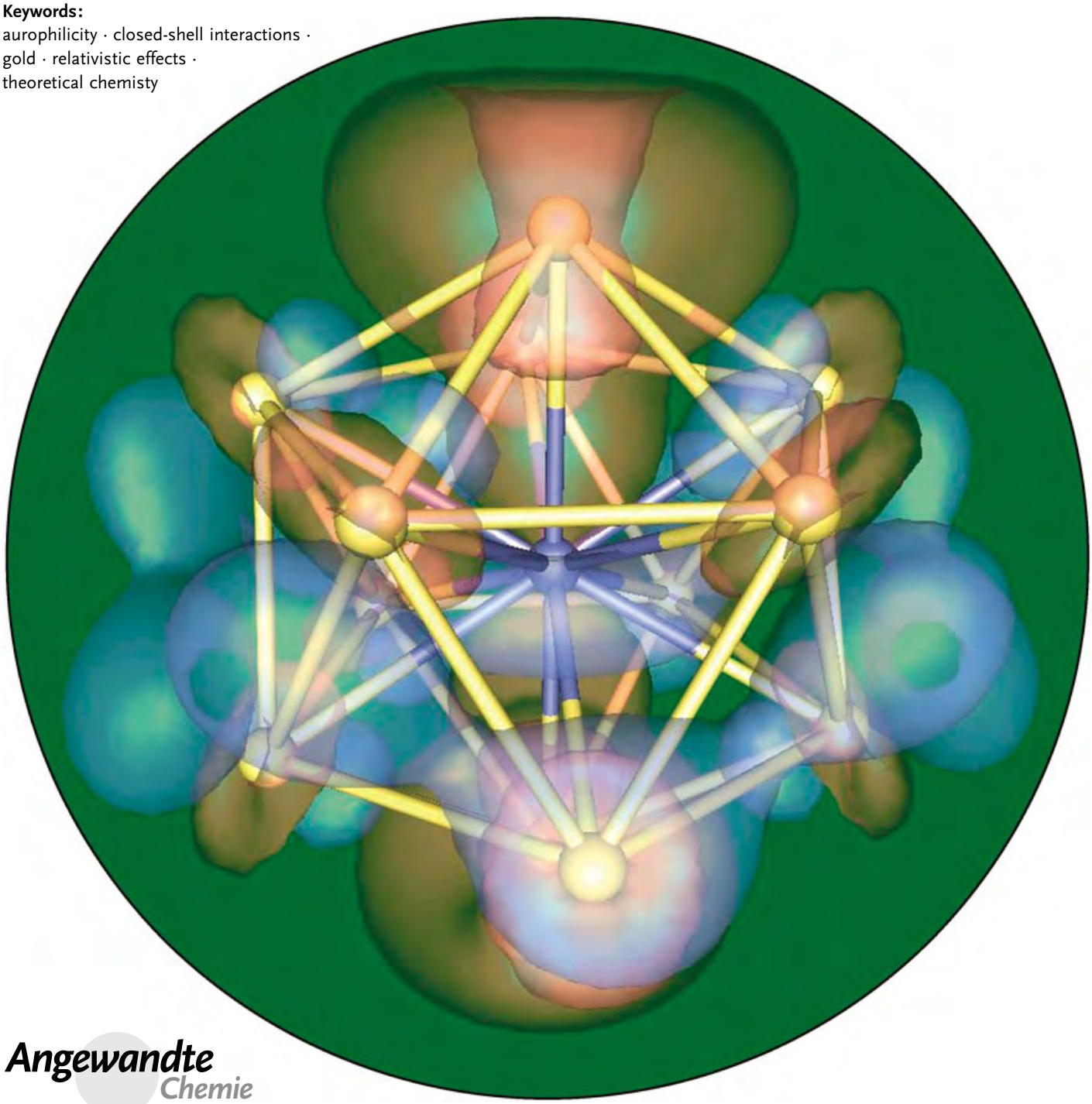
 © 2004 Wiley-VCH Verlag GmbH & Co. KGaA, Weinheim

Theoretical Chemistry

Theoretical Chemistry of Gold

*Pekka Pyykkö**

Keywords:
aurophilicity · closed-shell interactions · gold · relativistic effects · theoretical chemisty



Angewandte Chemie

 © 2004 Wiley-VCH Verlag GmbH & Co. KGaA, Weinheim DOI: 10.1002/anie.200300624

Angewandte Chemie

Gold is an element whose unique properties are strongly influenced by relativistic effects. A large body of appropriate calculations now exist and their main conclusions are summarized. The theoretical interpretation of the aurophilic attraction is discussed in detail.

From the Contents

1. Introduction	4413
2. Physical Principles and Computational Methods	4413
3. Results from Theoretical Calculations	4416
4. Further Aspects	4423
5. Catalysis	4440
6. Conclusions	4443

1. Introduction

The element gold has many "personalities", of which the image of a noble but soft, yellow metal would first across one's mind. The recently discovered nanoparticles and nanowires containing gold are a natural extension of this aspect, as are the uses of gold in electronics and decoration. Thought to be noble, gold actually has a rich chemistry.[1] For example, much of the extraction of gold in mining is done by using the gold(i)dicyanide anion. In the chemistry of gold, organic groups, phosphanes, thiolates, or halides are some common partners of the metal. Even the "noble" gas xenon forms surprisingly strong chemical bonds to gold cations. Fascinating in its complexity for academic chemists, this chemistry has potential applications in materials science, medicine and, recently, in both heterogeneous and homogeneous catalysis. Some fresh promises are related to the optical properties of certain gold compounds or to the possibility of forming new nanostructures based on gold.

In much of this chemistry, it was a puzzle that two or more closed-shell Au^{I} cations, having distances slightly above that in gold metal, often form aggregates, and the Au–Au binding energies are comparable to that of a strong hydrogen bond despite the fact that both atoms carry charges of the same sign and have no valence electrons to make covalent bonds. This phenomenon appears to be understood by now and the theoretical explanation is discussed below.

Two further "personalities" of gold deserve to be mentioned. Gold also is a psuedohalogen and forms an entire class of auride, Au^{-I}, compounds.[2,3] Its atomic electron affinity is not very far from that of iodine. Furthermore gold, or rather phosphanylgold, R_3P–Au, has some chemical resemblance with hydrogen, as noted by Lauher.[4] This similarity can be discussed by using the isolobality concept of Hoffmann.[5] All these aspects can be addressed theoretically and such theoretical discussions sometimes focus on a single suggested pet reason, such as relativistic effects on the valence orbitals.[3] Another such pet explanation is the attribution of the "bulk nobleness" of metallic gold to details of its band structure and surface adsorption by Hammer et al.[6,7]

Gold is, indeed, a unique element in that it has very large relativistic effects, larger than its neighbours, and larger than any other element with $Z < 100$. The exact size of these effects was recently reviewed[3] and only some main points will be recapitulated here.

Due to the particular properties of this element, the theoretical chemistry of gold merits its own review. A shorter review was recently published by Schwerdtfeger,[8] who also reviewed the chemistry of gold clusters.[9] A summary of the theoretical literature on gold compounds from 1993 to 1999 is available.[10] The gas-phase chemistry of gold has just been thoroughly reviewed by Schwarz.[11] There is also a review by Bartlett[12] on gold fluoride chemistry. For a general text on the science and technology of gold, see the treatise edited by Schmidbaur[1] or earlier reviews, notably by Puddephatt[13–16] or Schmidbaur.[17–19]

2. Physical Principles and Computational Methods

2.1. Relativity and Chemical Trends

Relativistic effects in chemistry can qualitatively be attributed to the high speeds of all electrons if they move near a heavy nucleus. The consequent mass increase will lead to an energetic stabilization and radial contraction.[20] For the s and p orbitals this will be the main effect. The contraction of those orbitals leads to a stronger screening of the nuclear attraction, and hence to a destabilization and expansion on the d and f orbitals, an effect of the opposite sign. These effects can be described by the Dirac equation, or some approximation to it. Small further corrections, beyond Dirac level, are the Breit correction to the electron–electron interaction and the quantum electrodynamical (QED) effects of vacuum polarization and self-energy (SE; vacuum fluctuation). These QED effects are of opposite sign, the vacuum polarization (VP) being smaller and attractive while SE is larger and repulsive. Their sum cancel each other out, for the binding energies of the valence s electrons of heavy elements ($Z > 50$), only about $-1\,\%$ of the Dirac-level relativistic

[*] Prof. P. Pyykkö
Lehrstuhl für Theoretische Chemie
Friedrich-Alexander-Universität Erlangen-Nürnberg
Egerlandstrasse 3, 91058 Erlangen (Deutschland)
and
Present and permanent address:
Department of Chemistry
University of Helsinki
P.O.B. 55 (A.I. Virtasen aukio 1), 00014 Helsinki (Finland)
Fax: (+358) 9-191-50169
E-mail: pekka.pyykko@helsinki.fi

 DOI: 10.1002/anie.200300624 © 2004 Wiley-VCH Verlag GmbH & Co. KGaA, Weinheim

effects remain.[21,22] Thus the pre-QED relativistic quantum chemistry was physically almost complete and the credibility of the currently available quantum chemical methods looks good.

Relativistic effects explain many of the differences and some of the similarities between the 5th and 6th row of the Periodic System. A well-known example is the difference between silver and gold, attributed to relativity in reference [23]; see also the later reviews.[3,24–26] The relativistic effects on valence-shell properties increase down a column of the periodic table roughly like Z^2, in which Z is the full nuclear charge, and become comparable in size with various shell-structure effects on the 6th row ($Z = 55$–86). As stated, in a many-electron atom they tend to contract and stabilize the s and p shells, and expand and destabilize the d and f shells.

The lanthanide contraction (the effect of filling the 4f shell on the subsequent 6s and 6p shells) works in the same direction as relativistic effects and is roughly comparable in size. If relativity is absent, it leads to a situation where the nonrelativistic (NR) 5d and 6s orbital energies of Au are similar to the 4d and 5s orbital energies of Ag, whereas the relativistic effects (R) are not (see Figure 1). This situation occurs both in the metal atoms M and their diatomic hydrides MH.[23–25] Thus the entire orbital-energy difference between silver and gold can be attributed to relativity. Note that both lanthanide contraction and relativity are needed to reproduce the experimental trends down a column (i.e., a group of the periodic table).

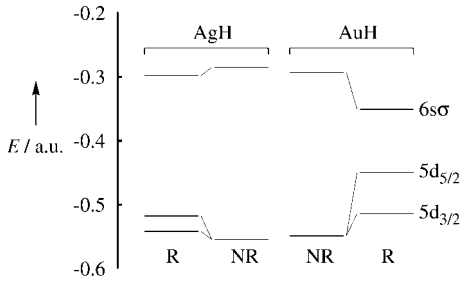


Figure 1. The relativistic (R) and nonrelativistic (NR) orbital energies of [AgH] and [AuH] molecules (a.u. is atomic units). From the data it was concluded that the chemical difference between silver and gold is mainly a relativistic effect.[23]



Pekka Pyykkö was born in 1941 in Hinnerjoki, Finland, and received his Ph.D. in 1967 at the University of Turku. After working at several institutes until 1974, he became Associate Professor of Quantum Chemistry at Åbo Akademi in Turku. Since 1984 he has held the Swedish Chair of Chemistry at the University of Helsinki, with a five-year stint (1995–2000) as Research Professor of The Academy of Finland. With Jean-Paul Desclaux, he identified the chemical differences between silver and gold as being a relativistic effect in 1976 and with Yongfang Zhao (and others) the aurophilic attraction as being a correlation effect in 1991. He predicted the existence of several gold-containing species, notably the covalently bonded $[AuXe]^+$ and $[XeAuXe]^+$, the triple-bonded $[C{\equiv}Au]^+$ (with Maria Barysz) and the goldfullerene $[WAu_{12}]$ (with Nino Runeberg), all of which were later synthesized.

It could be said that among the coinage metals (Cu, Ag, Au), only silver is "normal". As already said, gold is anomalous due to large relativistic effects. Copper is anomalous as is has a nodeless and therefore very compact d shell, with strong electron–electron repulsion; this repulsion may be related to the brown color and the existence of Cu^{II}.

There also exists a relativistic bond-length contraction, which also correlates roughly with Z^2.[25] This contraction is able to pull in the Au–L (L = ligand) single-bond lengths to lengths similar to or less than those of the corresponding Ag–L bonds, and to simultaneously make the Au–L bond strengths larger than those of the corresponding Ag–L bonds.[23,26]

It should be stated that in the field of solid-state physics it was noted even earlier that the nonrelativistic optical properties of metallic gold for the transitions from the top of the 5d-band to the Fermi level differ from experimental results, whereas the relativistic data correspond to the observations.[27] The R/NR Ag/Au comparison were first reported in reference [23] and the connection to visual appearances of the metal and the word "yellow" may appear for the first time in reference [25].

2.2. Methods of Quantum Chemical Calculations

The physical approximations, if any, and computational approaches are summarized in several books and reviews;[24,26,28,29] many others exist.

The four-component, one-electron Dirac equation can be solved without approximations or it can be transformed into various two-component equations, such as the Douglas–Kroll (DK) or zeroth-order regular approximation (ZORA) equations, both of which have stood the test of time. In them, the two-electron part of the Hamiltonian can also be transformed. The relativistic elimination of small components (RESC) may have difficulties at larger values of Z and is not recommended. A further step is to take a spin-orbit (SO) average. Such one-component methods are known as scalar relativistic (SR) or quasirelativistic (QR) approaches. (The various acronyms are collected and given in the appendix at the end of the Review.)

For a many-electron system, the exchange and correlation parts can be economically handled by density functional theory (DFT), or by wave-function-based methods. The latter can start from a single Slater determinant (corresponding to the Hartree–Fock (HF) model), or from a combination of many such determinants. These are called single-reference or multireference methods, respectively. From the simplest to the most complicated, common single-reference methods beyond HF are the nth-order Møller-Plesset (MPn, $n = 2$–4), coupled-clusters with single and double excitations (CCSD) or, adding perturbatively triplet excitations, the CCSD(T) methods.

For calculating the valence properties of molecules with heavy elements, large savings can be made by replacing the

 © 2004 Wiley-VCH Verlag GmbH & Co. KGaA, Weinheim

core orbitals by an effective core potential (ECP), also called pseudopotential (PP). The valence part is still treated ab initio. The inner nodes of the wavefunctions will then be smoothed out. By this device one avoids both the inner electrons and their basis functions. This PP approach has been thoroughly tested. The most popular pseudopotentials for gold are listed in Table 1.

Table 1: Some common pseudopotentials for Gaussian-basis calculations on the gold atom. For basis-set extensions, see the footnotes.[a] The "ultrasoft PP" for plane-wave basis are described in the original articles.

N	Authors	Year	Valence space	L_{max}	Comments
11	Hay and Wadt[434]	1985	5d6s	4	"LANL1DZ". No f basis.
19	Hay and Wadt[435]	1985	5s5p5d6s	4	"LANL2DZ". Double-zeta, without f basis.
	Schwerdtfeger et al.[67]	1989	5s5p5d6s	3	R/NR.
	Andrae et al.[436]	1990	5s5p5d6s	3	No f basis.
	Stevens et al.[437]	1992	5s5p5d6s	4	No f basis.

[a] The first column shows the number of explicitly treated valence electrons, *N*. L_{max} is the largest *L*-value in the potential. [b] An α_f of 1.19 recommended as polarization function of the 5d shell. The source is the CCSD(T) energy of the Au atom.[117] An α_f of 0.20 recommended for polarizabilities and aurophilicity. The source is the polarizability of the Au^+ ion.[116]

A particular way of using pseudopotentials is to use a plane-wave basis. For some examples from gold chemistry, see reference [30,31]. If even the nuclear motions are included by using a plane-wave basis, one arrives at the Car–Parrinello (CP) method, which also has been used in gold chemistry.[32,33].

There are "minority approaches" like the DFT-based scattered-wave (SW) approach, whose basis functions are numerical radial functions with various angular momenta at the various atoms, augmented with plane waves between atomic spheres. For simple diatomics, the Dirac equation can be solved by using two-dimensional numerical methods.[34]

It should be emphasized that fully relativistic, all-electron calculations up to CCSD(T) level are now possible for few-atom molecules containing even the heaviest elements. The more approximate ab initio methods can be and have been calibrated.

In addition to the ab initio methods above, it is possible to carry out relativistic semiempirical calculations.[35]. Such methods depend on adjusted input parameters and treat the valence electrons only, often by using a small basis. One well-known method is the extended Hückel theory (EHT). The various "neglect of differential overlap" (NDO) approaches include explicitly parts of the electron–electron repulsion. For INDO/S parameters for gold, see Shapley et al.[36]

2.3. Calibration on Atomic Systems

The best currently available theoretical results for gold are collected in Table 2. For the experimental first ionization potential, IP1(Au) of 9.22554(2) eV, it is seen that the best relativistic calculation deviates from the experimental value by only 0.0285 eV, whereas the corresponding nonrelativistic calculation lies 2.169 eV below the experimental value. For comparison, the QED effect on gold IP1 is calculated to be

Table 2: Latest relativistic benchmark results on atomic gold, [AuH], [Au_2] and Au(s). Note the agreement between all-electron (AE) and pseudopotential (PP) methods.

System	Property[a]	Exp.	R	NR	R–NR	Method	Ref.
Au(atom)	*IP*1 [eV]	9.22554(2)	9.197	7.057	2.140	CCSD	[446][b]
	EA [eV]	2.30863[c]	2.295	1.283	1.012	CCSD	[446][b]
	α	30(4)[d]	36.06			CCSD(T)	[447]
Au^+	α		12.75			CCSD(T)	[447]
AuH	R_e [pm]	152.4	152.5	175.0	-22.5	AE CCSD(T)	[48][b]
			152.7	174.7	-22.0	PP CCSD(T)	[49]
			151.0	–	0.0[e]	PP CCSD(T)	[50]
	ω_e [cm^{-1}]	2305	2288	1565	723	AE CCSD(T)	[48][b]
			2306	1575	731	PP CCSD(T)	[49]
			2330	–	6[e]	PP CCSD(T)	[50]
	D_e [eV]	2.302(8)	2.92	1.79	1.13	AE CCSD(T)	[48][b]
			3.124	2.086	1.038	PP CCSD(T)	[49]
			3.31	–	0.03[e]	PP CCSD(T)	[50]
Au_2	R_e	247.2[f]	248.8	–	–	AE cp-CCSD(T)	[51]
	ω_e [cm^{-1}]	191	187	–	–	AE cp-CCSD(T)	[51]
	D_e [eV]	2.302(8)	2.19	–	–	AE cp-CCSD(T)	[51]
			2.23	–	0.06[e]	PP CCSD(T)	[50]
Au(solid)	a_0 [pm]	408	407	429	−22		[448]
	E_{coh} [eV]	3.81	3.96	3.03	0.93		
	B_0 [GPa]	173.2	182	108	74		
	$E_{interband}$ [eV]	2.4	2.38	4	−1.62		[27,345]

[a] Dipole polarizability, α, in atomic units. Bond lengths R_e in pm, vibrational frequencies ω_e in cm^{-1}, and dissociation energies D_e in eV. For solids, a_0 is the lattice parameter, E_{coh} the cohesive energy and $E_{interband}$ the interband energy from the top of the 5d band to the Fermi level. R = relativistic, NR = nonrelativistic. [b] Including newer results from a private communication. [c] Reference [38] [d] Reference[449] [e] SO contribution. [f] Reference [450]

 © 2004 Wiley-VCH Verlag GmbH & Co. KGaA, Weinheim

−0.026 eV.[22] Only a small improvement in handling the electron correlation, which is the present bottleneck, would make it visible.

The experimental electron affinity, EA(Au) is 2.30863 eV and the best relativistic calculation is 0.014 eV below it. The NR EA is 1.012 eV below the experimental value. Thus almost half of the electron affinity of gold comes from relativity.[37] The experimental EA(Au) is not qualitatively different from that of iodine, 3.059037 eV.[38] As already mentioned, auride anions, Au^-, exist in several stable compounds.

For the record, the atomic energy levels of Au and Au^+ are given by Moore.[39] Further data are available[40–42] for Au^+ and for occasional states of highly-ionized systems up to Au^{10+},[43], or to about Au^{50+} in plasmas.[44] Even the hydrogen-like gold, Au^{78+}, has been experimentally studied and forms one of the test-benches for quantum electrodynamics.[45]

2.4. Further Principles and Methods

AuH and Au_2: In quantum chemistry the simple molecules AuH and Au_2 have become classical test cases for relativistic effects.[23,46,47] The most accurate benchmark results[48–51] for the bond lengths, vibrational frequencies and dissociation energies of these two molecules are also quoted in Table 2. One particularity is that although these two $^1\Sigma$ molecules have no first-order SO effects, the second-order SO effects lead to a small additional stabilization of the molecular ground state.[50,52] For a qualitative explanation, see chapter IV.A.8 of reference [53]: While the Au atom is spherical and has no SO effects at the dissociation limit, the AuH or Au_2 molecules can lower their energy by mixing in excited $^3\prod$ states through second-order SO effects, thus increasing D_e.

Solids: For the pure metals it is seen from Table 2 that relativistic effects compress gold to the experimentally determined interatomic distance. For the cohesive energy, or the bulk modulus of Au, a considerable relativistic increase takes place. Finally, the attribution of the yellow color of gold to relativity rests on the result that the relativistic interband energy between the top of the 5d band and the Fermi level in the half-filled 6s band, 2.4 eV, is close to the experimental value of 2.38 eV, whereas the NR interband energy would be much larger. Comparative R/NR calculations of the reflectivity do not seem to exist. Similarly it would seem that the exact roles of the bulk electronic-band structure and that of surface plasmons have not yet been worked out. For the experimental data, see the report by Saeger and Rodies.[54]

The nature of the "gold maximum" of relativistic effects in Group 11 (including Cu and Ag; see Figure 2) was thought to be related to the overlap between the valence *n*s shell which suffers a direct relativistic contraction, and the underlying $(n-1)$d shell. This qualitative idea has now been confirmed by Autschbach et al.[55]

Role of orthogonality: To be orthogonal against the 1s shell, the higher s shells would have to have a node inside it. Detailed investigations show that most of the relativistic energy contribution for the higher *n*s shells, including the valence 6s shell, arises from the resulting first half-wave inside the K-shell.[56,57]

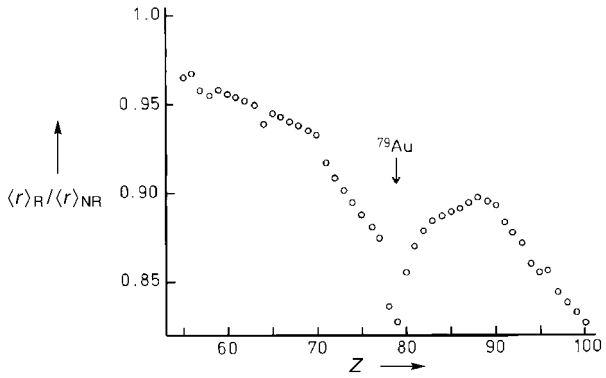


Figure 2. The ratio of relativistic and nonrelativistic 6s shell radii in the atomic ground states of the elements 55–100.[25]

Molecular dynamics: For treating very large systems, interatomic potentials are first developed and then molecular dynamics are carried out by using them. Some such potentials are shown in Table 3. All of them are many-body potentials; pure pair potentials are mainly of historical interest. An early example of the calculations, performed by Landman et al.[58] predicted the formation of nanowires between a nickel needle and a gold surface.

Table 3: Atom–atom potentials for molecular-dynamics calculations on gold-containing systems.

Authors	Year	Comments
Foiles et al.[438]	1986	Au and its dilute alloys.
Ercolessi et al.[285]	1988	The "glue model".
Oh and Johnson[439]	1988	Embedded atom model.
Ackland and Vitek[440]	1990	Gold alloys. Tested on phase diagrams.
Cleri and Rosato[441]	1993	Au and its alloys. Up to the 5th neighbor.
Kelchner et al.[442]	1994	Embedding functions, especially for small clusters.
Cai and Ye[443]	1996	Embedding atom potential with long-range forces.
Kallinteris et al.[444]	1997	Tight-binding potentials from total-energy calculations.
Avinc and Dimitrov[445]	1999	Effective Lennard–Jones potentials.

3. Results from Theoretical Calculations

In this section, we summarize some of the central theoretical conclusions that are expected to be of wide interest.

3.1. The Oxidation States of Gold

The common oxidation states of gold are +I and +III whereas +V is so far only observed in fluoro gold compounds.

 © 2004 Wiley-VCH Verlag GmbH & Co. KGaA, Weinheim

The local coordination in these three cases is in general linear (+I), quadratic planar (+III), and octahedral (+V). It was expected that the larger relativistic destabilization and expansion of the 5d shells on the third transition row would favor higher oxidation states for them, as compared to the corresponding 4d shells of the second transition row.[24] The role of relativity in the change of Au oxidation state from I to III[59,60] or from III to V[60] in halide complexes was explicitly demonstrated by Schwerdtfeger et al. In the particular case of $(AuX_2)^q$, X = Cl, Br, mass-spectroscopic experiments and related calculations show that gold can have the three oxidation states +I, +II, and +III corresponding to the total charges q of −1, 0, and +1, respectively.[61] The AuX_2^+ ion may have both linear, bent, and end-on geometries.

As to the Au^{II} atom, both open-shell, monomeric, paramagnetic Au^{II} compounds as well as closed-shell, dimeric compounds are known.[16] The bonding in the latter was discussed by Hoffmann's group[62] and similar conclusions were reached later after calculations were performed at the ab initio level.[63] When further ligands X exist on the X-Au^{II}-Au^{II}-X axis, the antibonding 5dσ* is oxidized away and actually a considerable 6sσ bonding character is reintroduced. Experimentally, one unbridged P-Au^{II}-Au^{II}–P bond with an Au–Au bond length of 261 pm was synthesized by Yam et al.[64] Recently, a doubly bridged system with an Au^{II}–Au^{II} distance of only 247 pm was reported by Fackler's group.[65]

One Au^{IV} compound is quoted by Puddephatt and Vittal.[16] Gimeno and Laguna[66] are not convinced of the existence of Au^{IV} atom. Note that some apparently divalent compounds have charge disproportionation; for instance AuO is $Au^{I}Au^{III}O_2$.

Examples of the oxidation state Au^0 exist, not only in solid gold or neutral clusters, but also in certain compounds, some of which would seem to contain a hidden Au_2 unit. Two examples are given in Section 4.2. Finally, the oxidation state Au^{-I} is discussed separately below in Setion 4.1.

3.2. Coordination to Gold

Au^+–L systems: The trends for the Au–X halides were considered by Schwerdtfeger et al.[67] While trying to make the predicted Au–Xe bond, Schröder et al.[68] wanted to determine the order of strength of various ligands, coordinated to an Au^+ center in the gas phase. The result of the combined experimental and calculated studies[69,70] became for the reaction $Au^+ + L \rightarrow AuL^+$:

$L = Xe < C_6F_6 < H_2O < CO < H_2S < CH_3CN \approx C_2H_4 \approx NH_3 \approx CH_3NC < CH_3SCH_3 < PH_3$.

A combination of DFT calculations[71] and experiments places ethene above ammonia in terms of bond strength. A closer analysis of $[Au^I(ethene)]^+$ at levels, up to CCSD(T), was presented by Hertwig et al.[72] About half of the bonding comes from relativity, σ donation is more important than π back donation, and the AuC_2 structure is symmetrical (C_{2v}). Analyses of covalent bonds exist for Au^+CH_3[73,74] and $AuNO_2$.[75] For multiple bonds to gold, see Section 4.3. The neutral $[Au(C_2H_4)]$ complex was studied by Nicolas and Spiegelmann[76] and by Mendizabal.[77]

L-Au-L systems: In contrast to the previous case ($[Au^I(ethene)]^+$), the Au 5d and 6p orbitals are now more important in bonding.[78] Electronegative ligands (σ acceptors) support d participation while electropositive ligands (σ donors) support p participation in the Au–L bond. The particular cases comprise L = CO,[79] $L = CN^-$, see also Table 6.[79] A particular issue is the existence of "nonclassical" carbonyl complexes, which have higher C–O stretching frequencies than that of the free molecule (2143 cm^{-1}).[80,81] For further cases see Table 6.

Gold in water: No $Au^I(aq)$ or $Au^{III}(aq)$ species is known. Against that background, it is interesting that in the gas phase $[Au(H_2O)_n]^+$ $n \leq 10$ ions have been experimentally observed by Poisson et al.[82] Evidence was obtained for both two or more closely coordinated water molecules. The results agreed with those of Feller et al.,[83] who studied the gas-phase hydration models $[Au^+(H_2O)]_n$; $n = 1$–4. The $n = 1$ case was nonplanar. The first two water molecules had an incremental binding enthalpy of about 167 kJ mol^{-1} (40 kcal mol^{-1}) each, the third and fourth molecules had less than half of that. Note that the latter molecules bound to the previous water molecules, not to the gold center. The hydrolysis of Au^I in aqueous acetonitrile solutions was experimentally studied by Kissner et al.[84] In the related $[Au(dimethyl\ ether)_n]^+$ complexes, the two first Au–O bonds ($n = 1,2$) are also stronger than the others.[85]

Aromatic rings: When coordinating to benzene, the Au^+ center is calculated to prefer an η^2 position.[86] Hertwig et al. find its position to be asymmetrical for both benzene and propene.[71] In contrast, in the case of an Au^+ center with pyridine, the lowest conformation has an in-plane Au–N bond.[87] For the vibrational frequencies, see reference [88].

In the chlorogold phosphane model $[AuCl(PH_2CH_2S(C_6H_5))]$, MP2-level calculations also gave preferential secondary bonding of that Au^I to the ipso and α carbons of the phenyl group at about 319 pm. At HF level these distances would be much larger.[89] This suggests a dispersion-type interaction between Au^I and an aromatic ring.

Comments on particular ligands**:** Phosphanes are among the most important ligands bound to gold. Schwerdtfeger et al. found a large relativistic increase of the bond energy for $[Au(PH_3)_2]^+$.[78] In the series $[Au(PH_3)_n]^+$ or $[ClAu(PH_3)_n]$, the two first, linearly coordinated ligands are more strongly bound than the third or fourth ligand.[90]

Comparing various substituted phosphanes PR_3, the group of Rösch found that in the series $[MeAuPR_3]$; R = H,Me,Ph, already a PH_3 group gave realistic structures, whereas to obtain information on the energy properties and the dipole moment, at least a PMe_3 group had to be used. They also found a large relativistic strengthening of the Au–P bond.[91] Scattered-wave calculations of the optical properties were presented by Larson et al.[92]

Experimentally, for the Au^{III} atom in $[Me_3Au–PPh_3]$, the *cis* Au–C bond lengths were 210 and 217 pm while the *trans* bond length is 192 pm, a trend characterized by Schmidbaur[18] as "trans influence" by the tertiary phosphane.

An accurate treatment for $[AuCO]^+$ was presented by Dargel et al. by using basis functions up to 3 g and electron correlation up to CCSD(T).[93] The best calculated D_0 was

 © 2004 Wiley-VCH Verlag GmbH & Co. KGaA, Weinheim

201(8) kJ mol^{-1}, compared to two experimental values of 209(21) and 188 kJ mol^{-1}. For earlier work, see Table 5.

The $[Au(CN)_2]^-$ ion is the most stable complex known in gold(I) chemistry. Its bonding has been analyzed.[78] Both a σ bond to the Au 6s and a π bond to the Au 5d were found. An accurate analysis of the bonding in the AuCN and AuNC monocyanides was presented by Dietz et al.[94]

The complexation of Au^I to biologically interesting molecules such as guanine and alanine,[95] or glycine, formate, and formamide[96] has been studied.

"T" for three? Let us define for a planar AuL_3 group the three possible geometries of a "Y" (quasi-C_{2v}, including the case of a side-on bonded L–L), a star shape (quasi-D_{3h}), and a "T" (C_{2v}, having one essentially linear L-Au-L axis and one side-on Au–L bond). The T shape could also be viewed as pseudo D_{4h}, with one empty coordination site. In this terminology, the $[Au(PR_3)_3]^+$ moieties are expected to adopt a star shape, with a trigonal planar $\{AuP_3\}$ arrangement. A quasi-planar $\{Au_3P_3Cr_6\}$ framework (but with four-coordinate gold atoms) was reported by Vogel et al.[97] It was surprising then that the valence isoelectronic $[Au(GeCl_3)_3]^{2-}$ was observed to be a "T". Schwerdtfeger and Schmidbaur[98] calculated that the free ions are indeed trigonal planar. The distortion was attributed to and reproduced by added counterions in a molecular model.

On the other hand, the AuH_3 distorts to a Y shape.[99–101] An approximate "T" is preferred when L = F and Cl.[60,102,103] In the case of L = I[104] there is a "soft intermediate" somewhere between a T and a Y shape.[102] Crawford and Klapötke have written a minireview on gold hydrides and iodides.[105] Gold hydrides are discussed below in Section 4.5.

3.3. Aurophilicity

An apparent attraction between two or more nominally monovalent Au^I ions in compounds has been known in structural chemistry for a long time. Some reviews on this phenomenon since 1961 are listed in Table 4. The typical observed Au–Au interatomic distances are in the order of 300(25) pm. Some strengths of interaction per pair of Au atoms have been measured by temperature-dependent NMR spectroscopy and are in the range of 29–46 kJ mol^{-1}, comparable with a good hydrogen bond (see Table 5 in reference [53]). The available experimental values are given as black triangles in Figure 3. Ab initio theoretical calculations support these data. Schmidbaur coined the name "aurophilic attraction" for this phenomenon.[106] An obvious generalization is metallophilic attraction".[107]

The earliest theoretical discussions of such a d^{10}–d^{10} attraction were the estimates of the (screened) van der Waals forces between the d^{10} cores in the bulk noble metals by the group of Kohn in 1975.[108] They concluded that about 17% of the cohesive energy of metallic gold or 0.105 eV/Au–Au pair comes from that source. For molecules, the earliest theoretical approaches were the EHT calculations by Hoffmann's group for Pt^0–Pt^0 interactions[109] and for Cu^I–Cu^I interactions[110] in 1978. The Au^I–Au^I case was considered later.[62,111,112] An attraction was indeed reproduced, and now attributed to hybridization between the formally filled $5d^{10}$ shell and the formally empty 6s and 6p shells of gold.

The dispersion nature of aurophilicity: In 1991 Pyykkö and Zhao[113] studied a $[(ClAuPH_3)_2]$ model dimer by varying the Au–Au distance at the HF and MP2 levels. The HF curve

Table 4: Articles reviewing closed-shell attractions involving heavier elements.

Year	Reference	Subject
1961	Hesse[451]	Coinage metal thiocarbamates
1976	Sadler[361]	The biological chemistry of Au
1980	Puddephatt[13]	Chemistry of Au
1981	Jones[452]	Au
1982	Puddephatt[14]	Au organometallics
1986	Melnik and Parish[453]	Au. Structure and Mössbauer
1987	Puddephatt[15]	Au coordination chemistry
	Jansen[454]	d^{10}–d^{10}, mostly Ag
1990	Schmidbaur[455]	Aurophilicity
	Cui and Kertesz[456]	Chains of d^{10} systems
1992	Krebs (ed.)[457]	All closed-shell cases
	Mingos and Watson[458]	Heteronuclear Au clusters
1992	Housecroft[459]	Coordination chemistry of Au
1993	Pathaneni and Desiraju[460]	Database analysis of 693 Au···Au pairs
	Welch and Chapman (ed.)[461]	Cu, Ag, Au
1994	Balch[462]	Trifunctional phosphane-based ligands
	Grandberg and Dyadchenko[463]	Au organometallics
	Sadler[362]	The biological chemistry of Au
1995	Grohmann and Schmidbaur[19]	Au organometallics
1996	Dance[464]	Supramolecular inorganic chemistry
	Mingos[263]	Cluster chemistry of Au
1997	Akrivos et al.[465]	Compounds with Group 15–17 donors
	Pyykkö[53]	Strong closed-shell interactions in inorganic chemistry
1998	Vicente[466]	Au^I
1999	Bardají and Laguna[467]	Aurophilicity
	Collinson and Bruce[468]	Metallic mesogens
	Schmidbaur (ed.)[1]	All aspects of gold
2000	Desiraju[469]	Includes aurophilicity
2002	Mingos et al.[470]	Alkynyl complexes of Au; Au^I–Hg^{II}
2003	Gimeno and Laguna[66]	Coordination chemistry of Ag and Au

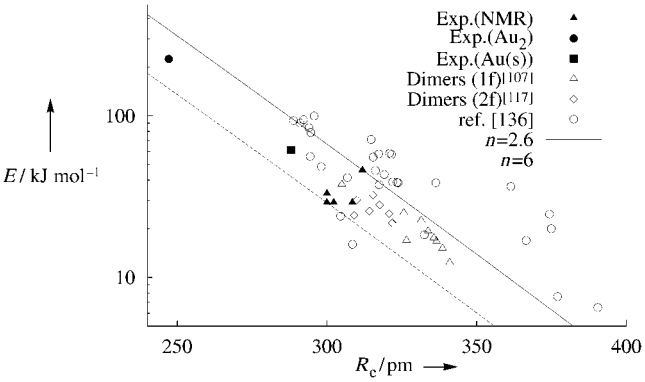


Figure 3. Various experimental (black triangles) and calculated estimates of the aurophilic energy, plotted against the Au–Au interatomic distance. The straight lines correspond to Equation (1).[136]

was purely repulsive. If hybridization would have been the reason for it, at least some attraction could be expected already at the HF level. Therefore it was concluded that the EHT calculations were correct only in an "allegorical sense". At the MP2 level the aurophilic attraction was recovered and therefore it was attributed to electron-correlation effects, tentatively to the dispersion or van der Waals part in them. All dispersion is correlation but all correlation is not dispersion. The only earlier hint of the importance of correlation effects for this interaction between coinage-metal atoms (Group 11) in molecules was from the calculations on the bridged copper complexes with supershort Cu–Cu interatomic distances,[114] such as $[\{Cu(RN_5R)\}_3]$ or $[\{Cu(RN_3R)\}_2]$, R = H, Ph. The case of an analogous Tl^I–Tl^I interaction was attributed to correlation effects by using a $[(TlH)_2]$ dimer model by Schwerdtfeger in 1991.[115] Furthermore it was noted that, if the Au 6p functions were omitted from the basis, over half of the aurophilic attraction disappeared.[113] Later it was found that if the Au 5d orbitals were omitted from the MP2 virtual excitations, the entire attraction disappeared.[107]

Methodological questions: Later work brought technical improvements, further confirmation, and many more examples. The basis-set superposition error (BSSE) can be substantial for such weak interactions and the "counterpoise correction" for it was included in all intermolecular calculations since 1992.[116] Concerning the Au basis, at least two f functions were found to be necessary. The diffuse function ($\alpha = 0.2$) maximizes the Au^+ static polarizability,[116] and hence approximately the dispersion interaction. The compact function ($\alpha = 1.19$) is an appropriate polarization function for describing the primary, covalent bonds to the gold. It optimizes the CCSD(T) energy of the Au atom.[117] The diffuse spd basis functions on Au were not found to be critical.[117] Magnko et al. increased the basis to 3f2g.[118] These localized-orbital MP2 (LMP2) calculations are the currently largest available for calibration. For soft ligand atoms, such as the P atom in phosphanes, a d function has a large effect.[119]

As to the method of calculation, the saw-tooth behavior exhibited in Figure 4 and 5 was found to be typical. The second-order Møller–Plesset model (MP2) gives, for large basis sets, a too strong closed-shell interaction and a too short distance.[120] The MP4 is closer to the right answer and is

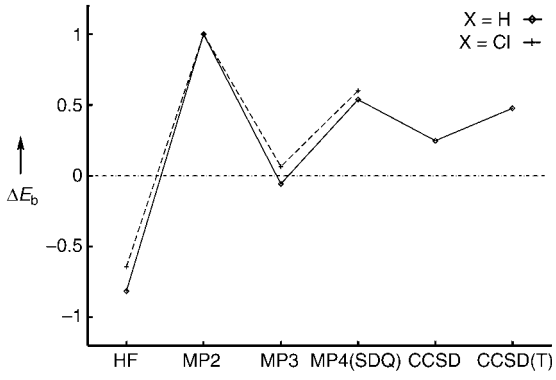


Figure 4. Influence of the level of treating electron correlation on the calculated interaction energy in $[(XAuPH_3)_2]$.[117]

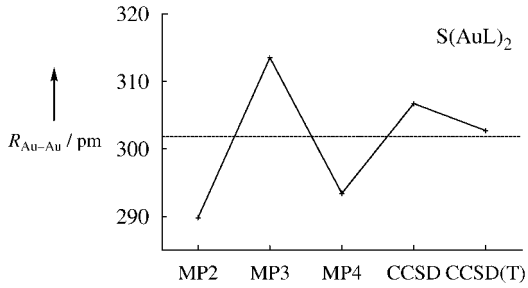


Figure 5. Influence of the level of treating electron correlation on the calculated Au–Au distance (R_{Au-Au}) of the A-frame molecule $[S(AuPH_3)_2]$. The horizontal line is the experimental value for $[S(AuPPh_3)_2]$.[136]

thought to be given by the coupled-cluster model with single and double excitations, including a perturbative triplet correction (CCSD(T)). That is the highest level used so far for this problem.

All calculations on aurophilicity presented herein use relativistic pseudopotentials. In these cases, the 11-valence-electron (11-VE) level gives attractions that are too strong.[117,121] This result can be attributed to the absence of node in the 6s and 6p pseudo-orbitals.[122,123] The 19-VE level seems to give the right result for the right reason. No major differences were found between the Andrae, Schwerdtfeger, or Stevens pseudopotentials in Table 1.[117] There is also a nonrelativistic reference pseudopotential and an appropriate basis set.

Further evidence for the dispersion character: A first, clear evidence for the dispersion character of the aurophilic attraction was its behavior as a function of R^{-6} at large distances (see Figure 6).[122]. The detailed contributions to this

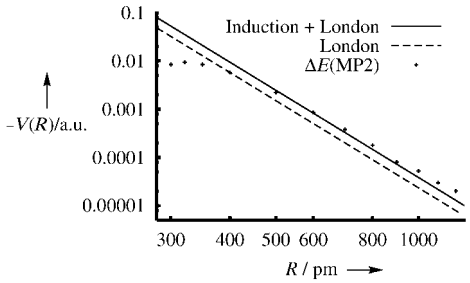


Figure 6. At large Au–Au distances (R) the aurophilic interaction in a perpendicular $[(XAuPH_3)_2]$ dimer decreases with R^{-6}.[122]

interactions could be analyzed by using the LMP2 method.[124] In addition to the classical dispersion mechanism, which corresponds to the virtual excitations A→A′, B→B′ for the two subsystems A and B, the "ionic" or virtual charge-transfer terms (see Figure 7; A→A′, B→A′) were also found to be important near the equilibrium Au–Au distance, R_e.[124,118] At large values of R these charge-transfer terms decay exponentially. The LMP2 method has the added advantage of minimizing the BSSE without any further corrections. It should be added that all of the four localized orbitals involved are not always located on the metal atoms for all of the

 © 2004 Wiley-VCH Verlag GmbH & Co. KGaA, Weinheim

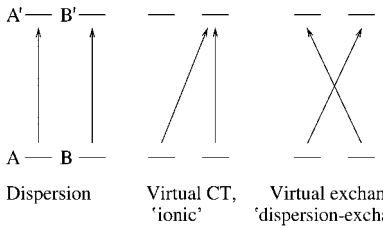


Figure 7. The types of virtual excitations between localized orbitals of the subsystems A and B for a) dispersion, b) virtual charge-transfer or "ionic" and c) virtual exchange or "dispersion–exchange" contributions.[118,124]

excitations.[118] The metallophilic attraction that is there should then be understood in diluted terms. One or more of the four orbitals A, A′, B, B′ may arise from ligands in certain contributions.

Aurophilicity in solids: The local-orbital method was applied to solid AuCl by Doll et al.[125] The starting point was a crystal-HF calculation. It was supplemented by correlated calculations at levels up to CCSD(T). Correlation effects were needed to obtain the experimental {-Cl-Au-Cl-} chain structure, instead of the cubic NaCl structure, adopted by AgCl. About half of the correlation energy arises from the Au^+–Cl^- pairs and roughly 40% from the van der Waals interaction between Au^+ ions. However, the latter part increases about threefold in the chain structure. The calculated value was about 0.2 eV (19 kJ mol^{-1}) per Au–Au pair at the experimental R(Au−Au) of 322 pm. Three-body interactions were found to be small.

DFT calculations: Concerning censity functional theory (DFT), treatment of the two molecules as a "supermolecule" does not even lead to an R^{-6} power law but rather to an exponential decay of the interaction at large R. Also the interaction energy—or even its sign—near the van der Waals minimum is unreliable because the specific form of correlation energy, related to two local dipole moments, is not properly described. Caution should be applied to the use of DFT for the aurophilic interaction. Certain functionals may be able to mimic the process near R_e.

Relativity: The relativistic effects on the aurophilic attraction of a perpendicular [$(ClAuPH_3)_2$] model system suggest a decrease of the $V(R_e)$ by −27% when passing from the relativistic to the nonrelativistic case for this system under these approximations.[117] Runeberg et al.[124] find for the same system a decrease of −22% at the LMP2 level, between the two minima. Interestingly, Schwerdtfeger et al.[90] find that the relativistic dimer [$(ClAuPH_3)_2$] prefers an antiparallel arrangement of monomers while at nonrelativistic level a doubly bridged [H_3P-Au(μ-Cl)$_2$Au-PH_3] arrangement is found.

Hard and soft ligands: A study of the perpendicular model systems [$(XAuPH_3)_2$] for X = F, H, Cl, -CH_3, -CN, Br, -CCH, I, -SCH_3 gave increasing interactions in that order and suggested that the softer ligands, X, would give stronger aurophilic attractions.[107,117] There are experimental observations supporting this prediction.[126–129]

A-frames and pyramids: In this case the aurophilic attraction forms the bar of the "A" in an [$S(AuPR_3)_2$] system, for instance, or the base plane of a trigonal or tetragonal pyramid. Its role is to sharpen the apical bond angle.[116,119,130] As an example, the HF-level Au-S-Au bond angle of [$S(AuPH_3)_2$] is 99.4° while the MP2-derived angle is 79.3°, and the experimental value (for PPh_3 groups) is 88.7°, see Figure 5. Rather similar bond angles were obtained for the naked $[SAu_3]^+$ system and for the more realistic $[S(AuPH_3)_3]^+$ case[130] and a similar result had been previously obtained by Li et al.[116]

This attraction can be strong enough to entirely change the geometry. While the "gilded ammonium" ion $[N(AuPR_3)_4]^+$ is approximately tetrahedral in the solid state (R = Ph)[131] and in the MP2 calculations (R = H),[119] the valence isoelectronic $[As(AuPPh_3)_4]^+$ was found to be a tetragonal pyramid both in the solid state[132] and in MP2 calculations.[119] For P, it was predicted that C_{4v} would lie below C_{3v}, which in turn is preferred over T_d. Such tetragonal $P[(AuL)_4]^+$ structures have been found with a fifth, apical gold atom by Schmidbaur et al.[133] and by Bachman and Schmidbaur.[134] Thus the aurophilicity between the Au atoms can be strong enough to override the tendency of the central E atom to form a tetrahedron and use its sp^3 hybridized orbitals.

A particularly striking example is the tetragonal pyramidal $[HC(AuPPh_3)_4]^+$, discovered experimentally by Schmidbaur's group.[135] An MP2 calculation gave a structure close to

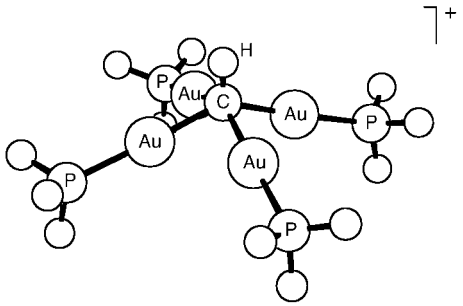


Figure 8. The calculated MP2 structure of $[HC(AuPH_3)_4]^+$.[136] It closely agrees with the experimental structure of $[HC(AuPPh_3)_4]^+$ from Schmidbaur.[135]

that found in the solid state (see Figure 8) and a proton affinity of the tetragonal species of 1213 kJ mol^{-1}.[136] This value explains why this system survives experimentally in the presence of a strong Lewis base, such as dimethylaniline, whose proton affinity is 941 kJ mol^{-1}. In this case it could be considered that aurophilicity prepares the pyramid, and the hybrid orbital at the apex yields this huge proton affinity.

Although the aurophilic aspects are hardly mentioned, we quote here the EHT-level analysis of mono- and dicarbido systems [$E(AuPH_3)_m$] (E = B,C,N) and [$C_2(AuPH_3)_m$] (m = 8, 10, 12), respectively.[137] It was concluded that the radial bonding is dominant. The work built on earlier calculations on empty or gold-centred clusters.[138]

Coupled A frames yield structures such as the [Au_5Ph_5] star, treated at the experimental geometry by DFT methods by Belanzoni et al.[139] A geometry optimization at MP2 or

higher level would be interesting to have an idea of the aurophilic contribution.

Element centred systems, general**:** Experimentally, structures of $[E(AuL)_n]^+$-type centred systems are known for E = C($n = 5$, 6), N($n = 4$, 5), O($n = 3$, 4), P and S($n = 2$, 3, 4) and Se($n = 3$, 4).[136,140] The A frames ($n = 2$) and pyramids ($n = 3$, 4) have been already discussed above. In all these cases the aurophilicity, roughly estimated as the difference between HF and MP2, pulls the gold atoms together. If the symmetry is broken, then one diminishes the Au-E-Au bond angle, where E is the central atom. If the higher symmetry is maintained, as for the tetrahedral $[N(AuPPh_3)_4]^+$, the angles are not changed.

The "gilded methane" $[C(AuL)_4]$ has only been obtained experimentally by using very bulky tertiary phosphanes as ligands.[141] Calculations suggest three minima, C_{3v}, T_d and C_{4v} at relative energies of 0, +0.5, and +46 kJ mol^{-1}, respectively.[136]

In the case $n = 5$, the local $[EAu_5]$ geometries of C_{4v} or D_{3h} are possible. For E = C, the latter is preferred by a small margin.[136] For $n = 6$, a cubic structure was found experimentally for E = C.[106] In DFT calculations, the group of Rösch finds that the phosphanes open up the Au 5d shell and that this leads to lateral Au–Au bonding.[142,143]

It should be noted that in addition to the AuL groups, other ligands can be present. An example[144] is $[(NC)_2C(AuL)_2]$, in which the calculated MP2 Au-C-Au bond angle is 91° (experimental 87.7° for R = Ph).[136] The HF angle is 105°, close to the tetrahedral angle.

Burdett et al.[111] considered $[AX_n(AuPR_3)_m]$ molecules at EHT level. They mainly focus on species such as $[(AuPR_3)_4I_2]$ or centred species. Orbital energies and overlap populations are used as the criterion for Au···Au bonding.

Doubly bridged L-Au-L systems**:** The doubly bridged, eight-ring systems, of the type $[Au_2(X(ZR_2)Y)_2]$, see Figure 9,

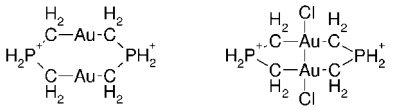


Figure 9. a) An example on a doubly bridged Au^{I}–Au^{I} system. b) Further oxidation will lead to a covalent Au^{II}–Au^{II} bond.

were studied at EHT level by Jiang et al.[62] Ab initio studies were reported by Pyykkö and Mendizabal.[63] Pan and Zhang[145] studied combinations of bis(diphosphino)methane (dpm), PH_2CH_2S, $SHCH_2S$, and SCH_2S ligands. At MP2 level, Au–Au interatomic distances of the order of 300 pm were reproduced.

If the system is oxidized by two halides at the ends of the {-Au-Au-} axis, the gold atoms become Au^{II} and the Au–Au bond shortens experimentally to 260 pm in $[\{Au(CH_2PH_2CH_2)\}_2]X_2$; X = Cl. This was closely reproduced by the MP2 calculation.[63]

Other rings: The smaller, doubly bridged $[Au_2X_4]^{2-}$ systems were compared at HF and MP2 levels by Pyykkö and Mendizabal.[63] When X = Cl, Br, the Au···Au distances were long. The MP2 value for X = I was short, 265 pm. It was suggested that this could qualitatively correspond to the experimental situation in the solid AuX monohalides. In them the chloride has an Au-X-Au angle of 92°, the iodide 72.6° and the bromide occurs in two modifications with an angle of 92.3 or 77°.

The calculated results for the six-membered $[Au_2Te_4]^{2-}$ systems also showed a large shortening of the central Au–Au distance from 318 to 279 pm between HF and MP2, respectively.[63]

The range of the aurophilic interaction**:** In the experimental literature, it is sometimes thought that the aurophilic attraction would exist inside some specific radius and vanish outside it. Actually the question is quantitative, not qualitative. Pyykkö[53] derived a simple expression: Equation (1) for

$$D_e = -(R_e\, b/n)\,[10^2\,\mathrm{N\,m^{-1}}]\,e^{(R_e - a)/b} \quad (1)$$

the aurophilic attraction energy D_e (here in J) as function of the equilibrium distance, R_e (in pm). In this case, n is a free parameter and a and b (both in pm) are so-called Herschbach–Laurie parameters in Equation (2) in which F is the Au–

$$R_e\,[\mathrm{pm}] = a + b\ln[\mathrm{F}/[10^2\,\mathrm{N\,m^{-1}}]] \quad (2)$$

Au stretching force constant. In other words, they can be obtained from Raman spectroscopy combined with crystallography. The used values for gold, $a = 268$ pm and $b = -29$ pm, are obtained from experimental data by Harvey.[146] (At MP2 19-VE 1f level the perpendicular $[(XAuPH_3)_2]$ model with X = F-I would give $a = 289$ pm and $b = -20.6$ pm.[107]) With D_e in kJ mol^{-1} one obtains Equation (3).

$$D_e = -(R_e\, b/n)\,(6.022 \times 10^{-2})\,e^{(R_e - a)/b} \quad (3)$$

Equations (1) and (3) are based on an assumed universal gold–gold repulsion $A\exp(-BR)$, which is overcome by a CR^{-n} attraction, in which n is a fitting parameter near R_e. In Figure 3, the trends of Equation (1) appear as straight lines.

A simple exponential equation was proposed by Schwerdtfeger et al. [Eq.(4)][147] with D_e in kJ mol^{-1} and R_e

$$D_e = 1.27 \times 10^6 \exp(-0.035\,R_e), \quad (4)$$

in pm. In Figure 10 Equation (3) (with $n = 3.95$) and Equation (4) are compared. This Figure could be taken as currently the best broad trend between the Au–Au distance and the aurophilic attraction energy. It equals 100 kJ mol^{-1} around an Au–Au distance, R_e, of 273 pm, decaying to about 10 kJ mol^{-1} around 348 pm, per Au–Au pair. Note that in the octahedral $[C(AuPPh_3)_6]^{2+}$ system, for instance, there are 12 pairs and the experimental Au–Au interatomic distance is 300.4 pm,[106] corresponding to about 45 kJ mol^{-1} pair^{-1}.

Electrostatic interactions: At this point it should be pointed out that the electrostatic multipole interactions between the components of the crystal are present. Some cases were analyzed by Pyykkö et al.[122] An example in which these interactions override the aurophilic attraction are the methylisocyanide halides, $[(MeNCAuX)_2]$; X = Cl,I.[148]

 © 2004 Wiley-VCH Verlag GmbH & Co. KGaA, Weinheim

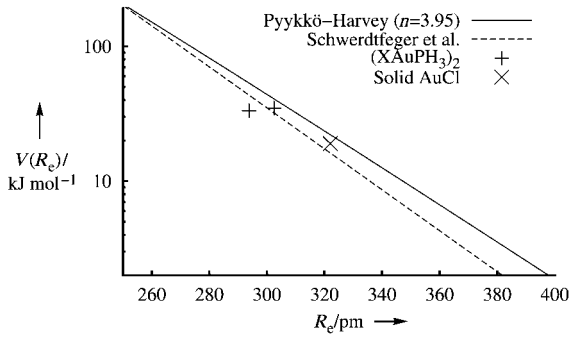


Figure 10. The best current estimates for the aurophilic interaction energy per Au^{I}–Au^{I} pair by using Equation (3)[53] (with $n = 3.95$ and the Harvey *a* and *b* parameters[146]) Equation (4).[147] The large-basis LMP2 results of Magnko et al.[118] for perpendicular $[\{XAuPH_3\}_2]$ models with X = H, Cl and the LCCSD(T) results for solid AuCl are included.[125]

Cation–cation and anion–anion interactions**:** It could be imagined that two [XAuL] molecules suffer a ligand redistribution to an $[LAuL]^+[XAuX]^-$ ion pair. Such systems are indeed known and then apparently paradoxical crystal structures are sometimes obtained in which the gold atoms of two cations or two anions make a short contact in the aurophilic range. The case with X = Cl, L = PH_3 was considered at MP2 level with a 2f basis.[149] The linear dimers of stiff dimers (−+)(+−), (+−) (−+) and (+−)(+−) as well as a cyclic tetramer were all found to have energy minima as a function of the central Au−Au distance, already without including the crystal Madelung potential in any way. One possible way to interpret the result was that the Au atom nonbonding orbital (NBO) populations of about +0.5 were comparable in the $[LAuL]^+$ cation and in the $[XAuX]^-$ anion and hence the nearest atom contact would be rather indifferent to the order of the actual charges.

In crystallography, linear equidistant anion chains of are known to occur, for instance in viologen·(AuI_2).[150]

Other oxidation states: Theoretical studies of the mixed $Au^{I}\cdots Au^{III}$, d^{10}–d^{8} case have appeared. Canales et al.[151] still found a correlation-induced shortening and obtained Au^{I}–Au^{III} interatomic distances of the order of 335–360 pm in the experimental range for trigonal Se-centred models. Mendizabal[152] found an interaction in the range 21–25 kJ mol^{-1} for cis-$[PH_3Au^{I}C(L)=C(L)Au^{III}(R)_2PH_3]$; L, R = H, CH_3.

Closed-shell interactions between gold and other metals: Among the coinage metals M, the calculated Au^{I}–M^{I} interaction energies for the perpendicular $[(ClAuPH_3)(ClMPH_3)]$ dimers with M = Cu,Ag were between the corresponding M–M and Au–Au dimers.[117] Across-ring M–M′ interactions for M = Cu–Au were studied in $[MM'(H_2PCH_2SH)_2]$ models by Fernández et al.[153] The various ligand choices (PAuP, PAuS and SAuS) were considered.

An Au^{I}–Pd^{II} interaction was experimentally discovered by Crespo et al.[89] In a monomolecular, theoretical $[AuPdCl_3(PH_2Ch_2SH)(SH_2)]$ model, it was found at MP2 level and absent at HF level. An LMP2 treatment of a *trans*-$[PdH_2(PH_3)_2][HAuPH_3]$ model, about two thirds of the interaction energy were found to be dispersion and about one-third virtual (i.e., ionic + exchange–dispersion). The ionic terms in the two directions Au→Pd and Pd→Au were comparable. Further examples on an attraction between Au^{I} and Pd^{II} or Pt^{II} were presented by Xia et al.[154]

Short Au^{I}–Tl^{I} distances of 303–308 pm were observed by Fernandez et al.[155] Quasirelativistic MP2-level calculations on a simplified $[Au(C_6H_5)_2][Tl(OPH_3)_2]$ model gave a closely comparable distance of 303 pm. In the case of Au–Tl, a strong ionic bonding contribution of about 80% was found, in addition to the dispersion part. Experimentally, a very short Au^{I}–Tl^{I} of 289 pm was observed in $[AuTl(C_6Cl_5)_2(toluene)_2$-(dioxane)].[155] For a review on interactions between Au^{I} and Group 11–13 metals, see Bardají and Laguna.[156]

Combination with other kinds of bonding: The aurophilic mechanism can coexist with covalent bonding. In the $[\{AuPH_3\}_4]^{2+}$ model system, Pyykkö and Runeberg[157] estimated that the two parts are comparable. The covalent part then is a two-electron four-center bond, made by the a_1 MO. One might recall here the estimate by Rehr et al.[108] that in metallic gold the van der Waals attraction would contribute 17% of the total cohesive energy (Section 3.3). In the diatomic Au_2, Hess and Kaldor[51] attribute a part of the cohesion in Au_2 to aurophilicity. A CNDO-level semiempirical study of various $[AuPR_3]_4^{2+}$ systems (R = H,Me,*t*Bu) was reported by Boca.[158]

Oxidative covalent bonds: As mentioned above (Section 3.3.10), further oxidation of the doubly bridged systems, such as that in Figure 9 by anions along the Au^{I}–Au^{I} axis, results in a covalent Au^{II}–Au^{II} bond. It was analyzed both by EHT and ab initio[63] methods. Considerable 6s–6s character was found in the bond. A five-atom gold chain results if two such dimers are coupled by an $[Au(C_6F_5)_2]^-$ unit. This case, formally Au^{II}-Au^{II}-Au^{I}-Au^{II}-Au^{II}, was modelled at EHT level by Calhorda and Veiros.[112] Bridged four- and three-atom chains are also mentioned.

There are systems that exhibit both aurophilic contacts and hydrogen bonding.[159] The first theoretical models for such systems have appeared.[160,161] One conclusion was that when an aurophilic attraction is present, the hydrogen bonding loses strength and directionality to retain the gold–gold interaction.[160]

Extremely strong $6s^2$–$6s^2$ attractions were found for the two diatomic systems $AuBa^-$ and $AuHg^-$ by Wesendrup and Schwerdtfeger.[162] The latter has a calculated bond length of about 300 pm, similar to the interauride distances below.[163] See Section 4.1 and the aurophilic part of Table 6.

3.4. Bond-Length Effects

The coinage-metal monohydrides were the second case in which a relativistic contraction of the length of a chemical bond was demonstrated by Desclaux and Pyykkö.[23] That result is still semiquantitatively valid (see Figure 11).

The relativistic bond-length effects on Au^{III} compounds are smaller than those on Au^{I} compounds. Furthermore, in a series of analogous systems, the Au^{I} center is found to be smaller than Ag^{I} by about 5–10 pm.[164–170] The discussion was opened by the emphatic statement "gold is smaller than

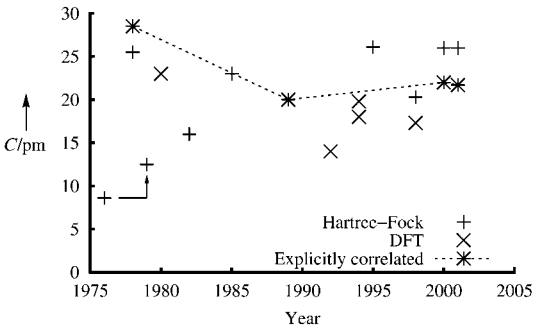


Figure 11. Obtained values for the relativistic bond-length contraction, $C = R_{NR} - R_R$, of the [AuH] molecule at HF,[23, 46, 49, 424–429] DFT[428, 430–432] and explicitly correlated level[46, 49, 429, 433] as a function of time. The year-2000 all-electron and pseudopotential values agree.[49]

silver" for two-coordinated diphosphane cations and a difference between Ag and Au of 8 pm was reported.[165] The later cases comprise bonds to phosphanes (about 10 pm from 14 compounds with coordination numbers (CNs) of 2, 3 and 4[167]), dithiolate anions (5.1 pm, CN = 2[168]), $[M(CN)_2]^-$ anions (6.8 pm, CN = 2[170]) and tetra-arsine cations (9 pm, CN = 4[166]).

Theoretical calculations on crystals containing $[SAuS]^{3-}$ anions reproduced the trend.[171] The calculated results for $[M(PR_3)_2]^+$ cations gave Au–P bonds, about 10 pm shorter than Ag–P bonds.[172] In $[PH_3MCl]$ systems, the calculated, relativistic M–P difference was 11.1 pm but the M–X difference only 2.9 pm.

4. Further Aspects

4.1. Gold as a Halogen: Auride Chemistry

Concerning first the atomic properties of the free Au^- ion, its experimental and calculated ionization potential (IP; the EA of Au) are quoted in Table 2. The electric dipole polarizability is calculated by Kellö et al. as 93 a.u. at DK-CCSD(T) level;[173] it is more than halved by relativity.

The solid compounds RbAu and CsAu were discovered in 1943 by Sommer.[174, 175] Even earlier it was noted that sodium alloys with gold dissolve to some extent in molten NaBr.[176] Another semiconducting auride, $BaAu_2$, was synthesized in 1938 by Biltz and Weibke;[177] for a review, see reference [3]. The available experimental data on aurides has been reviewed by Hensel,[178] Jansen and Mudring,[2] Zachwieja[179] and Pyykkö.[3] A particularly noteworthy example is the $CsAu{\cdot}NH_3$, studied both experimentally and theoretically by Mudring et al.[163] This compound is deep blue and, according to the Mössbauer isomer shift, not fully auridic. The auride ions form zig-zag chains with an Au–Au distance of 302 pm. For comparison, the intermetallic phase Na_2Au contains linear Au chains with Au–Au bond length of 276 pm.[179]

Band-structure calculations exist on CsAu. A R/NR comparison shows that without relativity the system would be a metal, instead of a semiconductor.[180–182] The available calculations on aurides, both in discrete molecules and in the condensed phases, are summarized in Table 5. At molecular-dynamics level, simulations have been published for liquid CsAu.[183, 184]

Table 5: Available ab initio calculations on solid or molecular aurides.

Authors	System	Comments
Solids		
Wood and Reitz[471]	CsAu	Band structure by using QDM; ionic.
Liu and Amar[472]	CsAu	Band structure by using QDM KKR.
Norris[473]	RbAu, CsAu	Exp. photoelectron spectra.
Hasegawa[180]	CsAu	R semiconductor, NR metal.
Overhof et al.[474]	RbAu, CsAu.	Photoelectron spectra.
Christensen[181]	CsAu	R/NR.
Robertson[475]	CsAu	Tigh-binding, Can *F* centres exist?
Wertheim et al.[476]	CsAu	Charge transfer.
Watson[182]	CsAu	R/NR.
Grosch[477]	MAu, M = alkali	
Grosch[478]	MAu_5, M = alkali	
Mudring[479]	$Rb_5Au_3O_2$	Contains both Au^{-I} and Au^{I}.
Mudring[163]	$CsAu{\cdot}NH_3$	Bonding analysis.
Molecules		
Saue[480]	[CsAu]	DF/HF.
Gagliardi[186]	$[MAu_4]$, M = Ti-Hf, Th, U	
Fossgaard et al.[481]	[CsM]; M = Cu-Au CsAu	D_e revised to 2.53 eV.

The optical excitations of a confined auride ion were considered by Kędziera et al.[185] They explained the lack of color in solid tetramethylammonium auride as a confinement effect, modeling the closed-shell nearest-neighbour hydrogen atoms as helium atoms. Madelung effects from the cation charge were found to be larger than the confinement effect, due to Pauli repulsion.

Further recent molecular auride species were predicted by Gagliardi.[186] In the series of tetrahedral molecules $[MAu_4]$ (M = Ti, Zr, Hf, Th, U), the auride anion was sizewise between Br and I but, concerning the strength of the bonds, weaker than any real halogen from F to I.

If Au is a "halogen", Au^+ (or the isoelectronic Pt) would then be "chalcogens".[187] The mass-spectroscopically observed $[CAu]^+$, $[CAu_2]^{2+}$, and $[CAu_3]^+$ were found to be good bonding analogues of CO, CO_2, and CO_3^{2-}, respectively. The $[Au{=}C{=}Au]^{2+}$ bonding system is of a new type for gold. In this "autogenic isolobality", no outside ligands are needed on the terminal metal atom.

4.2. The Chemical Analogy between Gold and Hydrogen

In 1978, in one of the first pseudopotential calculations by Hay et al. on diatomic gold hydride,[46] it was noticed that the Mulliken populations were almost equal ($Au^{0.02}H^{-0.02}$). The dipole moment of AuH is calculated to be 1.08 D at the GGA level[52] or 1.017 D at CCSD(T) level.[49] Including a vibra-

 © 2004 Wiley-VCH Verlag GmbH & Co. KGaA, Weinheim

tional correction, a value of (−)1.332 D was obtained by Avramopoulos et al.[188]

Lauher and Wald[4] noticed the closely similar structure types of several hydrides and an {AuPPh$_3$} group, despite the fact that the effective radius of the latter group is about 98 pm larger than that of the hydride. Some examples are the existence of the compounds [Co(CO)$_4$AuPPh$_3$] and [Co(CO)$_4$H] or the tetrahedral systems [HFeCo$_3$(CO)$_{12}$] and its analogue [(Ph$_3$P)Au−FeCo$_3$(CO)$_{12}$]. Further examples would be the pairs [O(AuPPh$_3$)$_3$]$^+$ and OH$_3^+$ or [N(AuPPh$_3$)$_4$]$^+$ and NH$_4^+$. Krüger et al.[189] point out that one can regard the moiety [AuPR$_3$]$^+$ as a σ acceptor in analogy to H$^+$.

The corresponding analogue of an H$_2$ molecule, [Ph$_3$PAu−AuPPh$_3$], was claimed by Mingos,[791] but the observation has not been verified. A calculation that compares [H$_3$PAu−AuPPH$_3$] with Au$_2$, has been presented by Schwerdtfeger and Boyd.[190] The calculated MP2-level Au−Au distance was 255 pm for an [Au$_2$(PH$_3$)$_2$] model. The calculated {P-Au-Au-P} part was linear. Substantial Au 5d and 6p character was present in the bonding.

Some "chemical approximations" to Mingos' proposal were synthesized by Hagen et al.[191] With two or three stannaborate, [SnB$_{11}$H$_{11}$]$^{2-}$, anions coordinated from the sides, the Au−Au distances were 262.5 or 259.0 pm, respectively. The electron correlation effects in the MP2 method were found to be important and the main excited MOs had Au 5d character. The calculated MP2-level Au Mulliken charges for these complexes were nearly zero, which suggests the Au atom has an oxidation state of zero (Au^0). Another approximate example of such an "H$_2$" species is the gold–indium compound of Gabbaï et al.[192] The observed Au−Au distance of 269.4 pm in the {CrAu$_2$} triangle of [*Cis*-η^2-(Ph$_3$PAu)$_2$Ph$_3$PCr(CO)$_4$]·THF could be regarded as a side-on bonded "H$_2$" species or as the shortest known aurophilic bond.[193]

Knowing that H$_2$ can form side-on complexes, Burdett et al.[111] considered the possibility that both its gold analogue and those of higher H$_n$ combinations could bind to a central main-group atom. The calculations were at EHT level, only. Examples on this thinking were the known [(AuPR$_3$)$_4$I$_2$] (containing an approximate Au$_4^{2+}$ tetrahedron) and [As(AuPR$_3$)$_4$] (which can be considered as containing an approximate side-on-bonded Au$_4^{4-}$ square, bound to an As^{5+} core) or a predicted [(AuPR$_3$)$_3$I]. Analogues of H$_3^+$ were also mentioned.

The aurated water molecule Au-O-H has a waterlike bond angle.[194] The X···Au-Y gold analogues of hydrogen bonds were studied.[194]

4.3. Multiple Bonds to Gold

Carbenes of gold are known. As discussed by Irikura and Goddard,[195] the Au=CH$_2^+$ double bond has one σ and one π component. The calculated Au=C bond energy was 393(8) kJ mol^{-1}. The bond had a strong π component. Hrušák[74] compared DFT and CCSD(T) results and obtained at the latter level 396 kJ mol^{-1}. A recent experimental upper limit[196] is 372(3) kJ mol^{-1}. Structures of carbenes in which the C atom is part of a five-membered ring were calculated at DFT level by Raubenheimer et al.[197] A study of the [ClAuM′R$_2$]; M′ = C-Ge series show strongly decreasing Au−M′ bond energies.[198] The Au=C bond has a calculated strength of 346 kJ mol^{-1}. The ionic and σ bonding were dominant, the π back donation less important.

Barysz and Pyykkö[199] predicted that Au≡C$^+$ should exist, and have a partial triple bond. The Au 5dπ orbitals delocalize to the empty 2pπ orbitals of the carbon. This species was produced mass-spectroscopically shortly afterwards and the experimental D_0 of 3.36(4) eV[196] was close to the calculated CCSD(T) value of 3.525 eV. The calculated D_0 of the valence isoelectronic AuTh$^+$ ion, 3.50 eV, was small compared to that of the multiply bonded isoelectronic PtTh.[200]

Drawing bond lines is not enough if they don't correspond to the actual molecular orbital structure. Satisfactory in itself, a formula like Au≡N does not correspond to reality: the two further electrons, after [AuC]$^+$, occupy an antibonding π* orbital and no chemical ways to put them somewhere else were found in a theoretical study.[201] Hence the bond order of AuN will be less than three. The gas-phase [AuN]$^{2+}$ ion has a similar calculated bond length of about 180 pm, as the AuC$^+$ ion.[201]

4.4. Bonds Between Rare Gases and Gold

Knowing that the [ClAuCl]$^-$ ion and the valence isoelectronic [SAuS]$^{3-}$ and [PAuP]$^{5-}$ ions exist in compounds, Pyykkö asked whether the isoelectronic ions [RgAuRg]$^+$ (Rg is a rare gas) could exist as a fourth member of the series.[202] Ab initio calculations produced reasonably strong and short covalent bonds. Qualitatively speaking, the 5pσ orbitals of Xe in [XeAuXe]$^+$ were found to donate charge to the originally empty Au$^+$ 6s orbital. Simpler, diatomic [AuRg]$^+$ species were also considered. Both of these systems, as well as [Xe−Au−C$_6$F$_6$]$^+$, were produced mass-spectroscopically by Schröder et al.[68] In the same paper, an improved D_e of 1.31 eV and R_e of 257.4 pm were calculated for [AuXe]$^+$ at CCSD(T) level, including a *g* function in the basis. These were the first chemical bonds between gold and a rare gas. Read and Buckingham[203] made an attempt to reinterpret the bond of the diatomic [AuRg]$^+$ species as a multipole expansion.

As an unexpected by-product, Seidel and Seppelt synthesized the bulk compound [AuXe$_4$]$^{2+}$[Sb$_2$F$_{11}$]$_2^-$, which contained a quasi-D_{4h} Au^{II} cation [AuXe$_4$]$^{2+}$.[204] The salt is formed from Au^{2+} dissolved in HF/SbF$_5$ in the presence of xenon. Under a slight overpressure of xenon, the ion was stable in solution almost to room temperature. A commentary was included in the same issue of *Science*.[205] There were calculated structures in the experimental paper[204] and improved calculations by Hu and Huang gave Au−Xe distances close to the experimental value.[206] The charge-density distribution of [AuRg$_4$]$^{2+}$; Rg = Ar–Xe was discussed by Berski et al.[207] Further compounds with Au−Xe bonds were reported by Seppelt's group[208] for Au^{2+} and also Au^{3+} centers, in *trans*-[AuXe$_2$F]$^{2+}$[SbF$_6$]$^-$[Sb$_2$F$_{11}$]$^-$. The latter compound has terminal Au−Xe bonds of 259 and 262 pm. Their

latest example is $[(F_3As)AuXe]^+[Sb_2F_{11}]^-$, whose calculated MP2 structure agrees well with the crystallographic structure.[209] The Au–Xe bond length is 261 pm.

Spectroscopically well-characterized [ArAuCl] and [KrAuCl],[210] as well as [ArAuF] and [ArAuBr][211] were produced by the group of Gerry. They were assessed to be at most weakly covalent.[205]

The rare-gas compound $[KrF][AuF_6]$ was synthesized by Lehmann and Schrobilgen.[212] Molecular calculations for that ion pair, having a F–Kr···F–Au fluorine bridge, simulated the experimental structure and helped to assign the vibrational frequencies.

4.5. Individual Spectroscopic Species

The following Table 6 contains production results for molecules. The acronyms for the methods of calculation are explained on at the end of this Review. The last column also gives the way of including relativistic effects. For searching ab initio results on a given species we recommend the Japanese QCLDB database.[213] Examples would be H_3AuClP (H_3PAuCl, 9 hits) or Au (any gold-containing species), 792 hits, or about 1 % of papers included. Many new species with gold come from matrix spectroscopy and most of these experimental papers have a concomitant theoretical analysis. We start with a discussion of binary compounds.

Hydrides: [AuH] is well characterized in the gas phase. In matrix spectroscopy, the higher gold hydride molecules $[AuH_3]$, having a $[(H_2)AuH]$ structure, and $[AuH_5]$, having a $[(H_2)AuH_3]$ structure, were observed by Wang and Andrews.[101,214] Their measurements and calculations agree with the predictions that $[AuH_3]$ is a planar "Y".[99,100] Recently the group of Andrews produced the linear anions $[AuAuH]^-$ and $[HAuH]^-$, and the tetragonal planar anion $[AuH_4]^-$.[215,216] The symmetrical $[AuHAu]^-$ species was also seen.[217]

Alkali-metal compounds: The diatomics [LiAu], [NaAu], [KAu][67,218] and CsAu have been considered, see Tables 5 and 6.

Alkaline earths: See Table 6 for the known diatomic examples AuM^q, q being the charge.

Group 3 metals: The diatomic species [AuLa] and [AuLu] have large experimental D_0 of 3.47(20) and 3.43(17) eV, respectively. Other spectroscopic data remain unknown. Schwerdtfeger and Dolg[219] summarized the situation for intermetallic diatomics of gold. A large relativistic increase of D_0 and change of the dipole moment were calculated for these molecules, and for $[Au_2Lu]$.

Group 4: As mentioned in Section 4.1, Gagliardi predicted the existence of the molecular species $[MAu_4]$, M = Ti–Hf; Th, or U.[186]

Group 11: The intermetallic [CuAu] and [AgAu] were calculated to have bond lengths between the pure dimers. The diatomic Au(E111) is a little longer and much more weakly bound than $[Au_2]$.[220] Note that the eka-gold atom has a different, d^9s^2 ground state. In Groups 10 and 12, the properties of the unknown molecules $AuPt^-$ and $AuHg^+$ were predicted.[221]

Group 13: The molecules BAu[199] and AlAu[222] had been calculated to have high dissociation energies, in agreement with experimental values. An extension to cations of Group 14 showed even higher D_0 for the valence isoelectronic $[AuC]^+$ and $[AuSi]^+$.[199]

Group 15: [AuN] has two electrons in an antibonding π orbital and has hence not an Au≡N triple bond.[201] That triple bond is found in $[AuN]^{2+}$.

Oxides: The group of Andrews saw in argon matrices AuO, OAuO and the side-on bonded $Au(O_2)$.[223] In neon matrices they saw the oxides $Au(O_2)$ and $Au(O_2)_2$.[214] The assignment was based on DFT calculations and isotope substitution.

For reactions of oxygen on gold clusters, see below. The solid Au_2O_3 is well-known and has been studied theoretically.[224] It is metastable up to about 150–170 °C; for a review on oxoaurates, see reference [225]. In the manufacturing of ruby glass, Mössbauer spectra suggest that the stage preceding the coagulation to colloidal gold consists of linear oxoaurates(I), dissolved in the glass.[226]

Halides: For calculations on molecular halides, see Table 6. [AuCl][46] was a classical example of concomitant relativistic shortening and weakening of a bond. While the bond contracts as usual, the relativistic increase of the IP of Au, from which a partial donation towards the ligand takes place, will decrease the D_e (see Figure 7 and 12 of Ref. [26]). For a detailed discussion on the properties of diatomic [AuF] and its ion, see the review on gas-phase ion chemistry by Schwarz.[11] Among the halides, the missing diatomic [AuF] was a bit of a puzzle. It was synthesized following theoretical predictions.[227,228] Later high-end calculations of its properties exist[229] and it has been used as a test case for theoretical methods.[230,231] The fluoride anions of gold were studied by Seth et al.[232] The vibrational frequencies of the $[AuF_n]^-$ series ($n = 2,4,6$) could be compared with experiments for $n = 4,6$. For a review on these ions, see Bartlett.[12] The crystal structure of dimeric $[(AuF_5)_2]$ and related calculations were published by Hwang and Seppelt.[233]

As to the chlorides, solid AuCl has a chain structure. It has been studied theoretically.[125] In that case the cubic and chainlike structures had otherwise comparable energies but the aurophilic interaction favoured the latter. The relative stability of cubic and chainlike structures of all [AuX]; X = F,Cl,Br,I was discussed by Söhnel and Schwerdtfeger[234] who attributed the preference for chains more generally to relativistic effects, which strengthen the chemical bonds of the chain. Their calculations were of DFT type.

$\{AuCl_3\}$(s,g) exists as a planar dimer $[Au_2Cl_6]$. Its structure obtained by electron diffraction was compared with ab initio calculations by Hargittai et al.[103] An augmented, correlation consistent polarized valence triple-zeta basis was necessary for agreement at MP2 level. Incidentally, mixed metal halides, such as $[AlAuCl_6]$(g) also exist[235] and spectroscopic evidence suggests a planar surrounding at Au and a tetrahedral one at Al.[236]

The stability of gold iodides in the gas phase and the solid state was studied by Söhnel et al.[104] The two ions $[AuI_2]^-$ and

Text continued on page 4433

 © 2004 Wiley-VCH Verlag GmbH & Co. KGaA, Weinheim

Table 6: Ab initio production results for molecules containing gold.

System and comments	Reference	Method
Diatomics, Groups 1–18		
[AuH]; bond-length contraction; orbital energy compared with [AgH]	[23, 424]	DF–OCE
[AuH]; potential-energy curve; R/NR	[46]	PP–HF
[AuH]; bond-length contraction obtained in 1st-order PT	[430, 482]	DFT + PT
[AuH]; confirm that bond-length contraction is not an orbital-contraction effect	[483]	DF–OCE
[AuH]; large STO basis with "kinetic balance"; potential energay curve; R/NR	[425, 484]	DF–LCAO
[AuH]; R/NR; μ almost halved; bonding analyzed	[485]	PP
[AuH]; ground state potential curve; R_e still too large; STO basis; R/NR	[426]	PP CI
[AuH]; numerical and STO radial functions	[486]	DF, + CI
For comments, see Balasubramanian et al.[487] and the reply by Malli et al.[488]		
$[AuH]^+$ by using the method of Malli and Pyper[486]	[489]	
[AuH]; origin of relativistic correlation effects on orbital energies	[490]	DF-LCAO
[AuH]; test of the DK approach	[433]	DK
$[AuH]^+$; bonding analyzed	[491, 492]	PP-GVB
[AuH]; quadrupole moment	[493]	QR-CC
[AuH]; dipole moment; later values are smaller	[494]	QR MBPT
[AuH]; Test of a GTO DK method; R/NR	[431]	DK-DFT-LCGTO
[AuH]	[495]	DK
[AuH]; test two-electron terms	[496]	DK
[AuH] as test of the ZORA approximation; R/NR	[432]	DFT
[AuH]	[48]	DK CC
[AuH]; dipole moments	[497]	PT
[AuH]; comparison between relativistic methods; R/NR	[427]	HF, MP2
[AuH] as test of DFT by DPT	[498]	DFT
[AuH]; dipole moments	[499, 500]	DK
[AuH]; SO effects through ZORA	[52]	DFT
[AuH]	[501]	DFT
[AuH]	[502]	SR DFT
[AuH]; test of DPT at HF, DFT, MP2 level. R/NR	[428]	DPT,PT
[AuH]; SO effects	[50]	PP
[AuH]; ZORA/PT or full Dirac with HF, MP2, DFT	[230, 220]	
[AuH]; test a new method	[503]	RESC
[AuH]; test RESC	[504, 505]	DFT + RESC
A[AuH]; compare PP and DK for DFT; potential-energy curve	[506]	
[AuH]; accurate; potential-energy curve	[49]	PP + CCSD(T)
[AuH]; ground and excited states	[507]	RESC + MRMP.
[AuH]; vibrational correlation to electric properties (μ, α, β)	[188]	DK CCSD(T)
[AuH]; test of DK3; R/NR	[429]	DK3 + CCSD(T)
[AuH]; test of new DF program	[508]	DF
[CsAu]; potential-energy curve; R/NR	[482]	DFT + PT
[CsAu]	[509]	QR-DFT
[CsAu]	[480]	DF/HF
[MAu]; M = Li–K; potential-energy curves	[218]	DFT, CCSD(T)
[CsAu]; Experimental D_e revised to 2.53 eV using theoretical data	[481]	Dirac DFT, CCSD(T)
Also [CsCu], [CsAg].		
$[AuM]^+$, M = Be,Mg	[199]	DK
$[AuBa]^q$, $q = -1,0,1$: very strong closed-shell interaction of 140 kJ mol^{-1} for $q = -1$	[162]	PP
[AuLa], [AuLu]; large D_0 reproduced	[219]	PP
$[AuTh]^+$. CASSCF, CASPT2	[200]	DK
MM′; M = Rh–Au	[510, 511]	PP
[AuPt], $[AuPt]^+$; electronic states	[512]	PP
$[AuPt]^-$	[221]	
$[Au_2]$, potential-energy curve; SO; ground and excited states	[513]	PP-MCSCF-CI
$[Au_2]$; potential-energy curve	[47]	PP-MCSCF
$[Au_2]$, [AgAu]; potentail-energy curves	[514]	PP-CI.
$[Au_2]$; bond-length contraction obtained in 1st-order PT	[430]	DFT + PT
$[Au_2]^+$; SO, uses PP of reference [47, 513, 515]	[516]	PP
$[Au_2]^+$; SO effects on potential curves	[517]	PP
$[Au_2]$; IP; s–d hybridization	[518]	D-SW
$[Au_2]$; ground-state properties	[509]	QR-DFT
$[Au_2]$, [AgAu]; ground-state potential curve; STO basis; R/NR	[426]	PP CI
$[Au_2]$; orbital and bond-length contractions within PP picture	[519]	PP
$[Au_2]$, $[Au_2]^+$, [AgAu]; still too large R_e	[426]	PP
$[Au_2]$; calibration for triatomics	[520]	PP + CPF

 © 2004 Wiley-VCH Verlag GmbH & Co. KGaA, Weinheim

Table 6: (Continued)

System and comments	Reference	Method
$[Au_2]$; excited states; SO	[521]	PP-CASSCF-RCI
$[Au_2]^q$, $q=-1,0,1$	[522]	PP + MCPF
$[Au_2]^{2+}$; metastable excited states in a tight-binding picture	[259]	EHT
$[Au_2]$; 1st-order PT R	[523]	PT + CPF
$[Au_2]$; test of new PP	[524]	
$[Au_2]^{2+}$; dissociative ground state	[525]	PP MCSCF
$[Au_2]$; best benchmark of that time	[526]	PP QCISD(T)
$[Au_2]$; test of new method	[431]	DK-DFT-LCGTO
$[Au_2]$; fully numerical, fully relativistic benchmark; Slater exchange	[34]	"DFT"
$[Au_2]$; test two-electron terms	[496]	DK
$[Au_2]$ as test of the ZORA approximation	[432]	DFT
$[Au_2]$ as test of DFT by DPT	[498]	DFT
$[Au_2]$; SO effects via ZORA	[52]	DFT
$[Au_2]$	[502]	SR DFT
$[Au_2]$	[501]	DFT
$[Au_2]$; SO effects	[50]	PP
$[Au_2]$; one-centre "AMFI" SO + spin-free DK	[527]	
$[Au_2]$; R/NR; various functionals, finite nuclei compared	[505]	SR DFT; RESC
$[Au_2]$; various functionals compared	[528]	DV DFT
$[Au_2]$; compare PP and DK for DFT; potential-energy curve	[506]	
$[Au_2]$; finite-nucleus effects on ground state; test of large-basis DK3; R/NR	[429, 529]	DK3-CCSD(T)
$[Au_2]$; test of new DF program	[508]	DF
$[Au_2]$; vertical excitations at B3LYP level.	[530]	DFT
$[Au_2]$; test of multipartitioning perturbation theory; five lowest excited states reproduced; transition dipole moment, lifetimes.	[531]	PP + "MPPT"
$[Au_2]$; polarizability tensor	[532]	R-RPA
$[Au_2]^{2+}$; ground-state repulsive, excited states bound.	[260]	
$[CuAu]^q$, $[AgAu]^q$, $q=-1,0,1$.	[522]	PP + MCPF
[CuAu], [AgAu]; electric properties.	[533]	PT
[CuAu], [AgAu]; ZORA/PT with DFT; R(Cu-Au) 233 pm = experiment	[230]	ZORA-DFT
[AuM], M = Au,(E111); bonding trends	[220]	Dirac or ZORA DFT
[AuM]; M = Hg,(E112); models for adsorption of M on a gold surface	[534]	R-DFT
$[AuZn]^+$; calculated D_e 3.67 eV	[359]	PP + MP2
$[AuHg]^+$; ground-state properties predicted	[221]	PP CCSD(T)
$[AuHg]^q$, $q=-1,0,1$; very-strong closed-shell attraction of 37 kJ mol^{-1} for $q=-1$	[162]	PP
[BAu]	[535]	DK
[AlAu]; electric properties; D_e 3.41 eV;	[222]	DK CCSD(T)
[InAu]	[536]	DFT
$[AuX]^+$, X = C, Si. An Au≡C$^+$ triple bond found	[199]	DK
[AuSi]; ground state $^2\Sigma$	[537, 538]	DK, CASPT2, CCSD(T)
$[AuSi]^q$, $q=-1,0,+1$	[539]	DK
[AuSi]; low-lying states	[540]	DK3 + CASPT2
[AuN]	[201]	PP
[AuO]; experimental + calcd	[223]	PP + DFT
[AuO]; ZORA or full Dirac DFT; μ	[220]	
[AuS]; X $^4\Sigma^-$ predicted	[541]	PP + MP2
[AuCl]; potential-energy curve; R/NR	[46]	PP-HF
[AuCl]; potential-energy curve; R/NR	[542]	PP
[AuCl]; potential-energy curve; R/NR with 1st-order PT	[482]	DFT + PT
[AuF], $[AuF]^+$; predicted; thermochemistry discussed.	[227, 228]	PP + MP, CCSD(T)
[AuF]	[543]	DF + MP2
[AuF]	[229]	DK + CCSD(T)
[AuCl]; test of new method	[431]	DK-DFT-LCGTO
[AuCl]; spectroscopically constants, μ, α	[544, 545]	PP + CCSD(T); R/NR
[AuCl]	[501]	DFT
[AuCl]	[502]	SR-DFT
[AuCl]; test new method	[504]	DFT + RESC
[AuCl]; compare PP and DK for DFT; potential-energy curve	[506]	
[AuCl]; electric-field gradients	[358]	DK
[AuI]	[546]	PP
[AuI]	[104]	PP + CCSD(T)
[AuX], X = F,Cl; ZORA/PT with DFT	[230]	DFT
[AuX], X = F-Br; ZORA or full Dirac with DFT; μ	[220]	

© 2004 Wiley-VCH Verlag GmbH & Co. KGaA, Weinheim

Table 6: (Continued)

System and comments	Reference	Method
[AuX], X = F-I	[231]	DF
[AuX], X = F-I, $[AuF]^+$, $[AuI]^+$; potential-energy curves	[547]	PP + CCSD(T)
[AuX], X = F-Br; potential-energy curves, electronic spectra, with SO	[548]	PP + MRCI, CC
$[RgAu]^+$, Rg = He–Xe; existence predicted	[202]	PP
$[ArAu]^+$, $[XeAu]^+$; bonding handled as polarization and dispersion	[203]	
$[XeAu]^+$; synthesized; improved CCSD(T) D_e 1.31 eV	[68]	PP
Diatomics [AuH], [AuCu], [AuAg], $[Au_2]$, [AuO], [AuS] in a DFT test set for five different functionals.	[549]	PP + DFT
Triatomic clusters		
$[Au_3]$	[550]	
$[Au_3]$; two minima, linear and isosceles triangle.	[551]	PP-MRSDCI
$[Au_3]$; EA.	[552]	
[MM"], $[MM'M'']^q$; $q = -1,0$, M = Cu–Au; anion linear, neutral C_{2v}; in triatomic anions, Au atom prefers terminal position	[553]	
$[Au_3]$	[522]	PP + MCPF
$[Au_3]$; excited states; SO	[554, 555]	PP-MRSDCI
$[Au_3]$; hyperfine properties	[355]	Dirac SW
$[Au_3]^q$, $q = 0, +1$	[192]	DFT
$[Au_3]^q$, $q = -1,0,+1$	[192, 556]	PP
$[Au_3]$; SO effects stabilize D_{3h}, give 0.2 eV splitting	[251]	PP + CAS/MRCI
$[Au_n]^q$, $n = 2,3$, $q = -1,0$.	[390]	DFT to CCSD(T)
Larger gold clusters		
$[Au_n]^q$, $n = 3,4$, $q = 1,2$; R/NR; *A* and *g* tensors; IP; s–d hybridization	[557]	D-SW
$[Au_4]$; geometry; excited states	[558]	PP-MRSDCI
$[Au_n]$, $n = 3,4$; comments on Balasubramanian's work	[559]	PP MCPF
For reply, see reference [560]	[560]	PP-MRSDCI
$[Au_4]^+$; planar D_{2h}; IP	[561]	PP-CAS-MCSCF
$[Au_4]$; EA	[562]	PP MRSDCI + Q
$[Au_4]^q$, $q = -1, 0, 1$; adiabatic dynamics	[563]	PP + CCSD
$[Au_n]$, $n = 2$–6; non-additive terms claimed important	[275, 276]	PP + MP2
$[Au_4]$; DFT calibration.	[564]	Dirac DFT
$[Au_n]^q$, $n = 1$–4, $q = 0,1$; IP	[565]	PP MRCI
$[Au_n]^q$; review by Balasubramanian	[566]	
$[Au_n]^q$, $n = 1$–4, $q = -1,0,+1$, missed D_{2h} for $[Au_4]$	[567]	PP + DFT
$[Au_n]^q$, $n = 4,5$, $q = -1,0$; Rhombus and "W"; EA, IP	[568]	PP MCPF
$[Au_n]^q$, $n = 2$–5, $q = -1, 0$	[569]	DFT
$[Au_n]$; $n = 2$–5; EA as test of Gaussian/PW method	[385]	PP + DFT, PW or GTO
$[Au_6]^{2+}$; bonding analysis	[570]	D-SW
$[Au_6]^q$; Jahn-Teller distortion at ZDO level	[571]	
$[Au_6]^q$, $q = -1,0$; lowest-energy for C_{5v}, not for a D_{6h} ring However, experimental ring observation is supported	[572]	PP-CAS-CI
$[Au_n]^q$, $n = 1$–6; $q = -1,0,1$	[573]	PP + DFT
$[Au_6]$, $[Au_6]^+$; capped pentagonal suggested	[574]	PP + MRCI
$[Au_6]^q$, $q = 0$–4	[91]	DFT
$[Au_6]$; octahedral	[575]	Dirac SW
$[Au_6]$; R/NR orbital energies	[576]	DFT
$[Au_6]$, $[Au_6]^{2+}$	[352]	
$[Au_7]^-$; R planar, NR not; also $n = 8$–13	[248]	PP, PW
$[Au_n]$, $n = 5,7$; *g* factors, hyperfine structure at ZORA level	[577]	DFT
$[Au_n]$, $[Au_n]^-$; $n = 2$–10	[578]	DFT + PW
$[Au_{13}]$ (I_h); bonding analysis; IP	[579, 580]	D-SW
$[Au_{13}]$; assumed cubo-octahedral; electronic structure	[581]	DFT(LDA)
$[Au_{13}]$; deisordered	[253]	DFT + PW
$[Au_n]^q$, $n = 1$–13, $q = -1,0$	[582]	PP-DFT, MP2, CCSD
$[Au_n]^q$, $n = 4$–14, $q = -1,0$	[583]	PP-DFT
$[Au_n]$, $n = 2$–20; near spherical for $n \geq 15$; IP calculated	[254]	DFT + Dmol.
$[Au_n]$, $n = 2$–20; 2D rafts only; polarizabilities	[584]	DFT + Dmol
$[Au_{13}]$ and $[Au_{19}]$ amorphous		
$[Au_n]$	[585]	SW
$[Au_{20}]$; tetrahedral; EA 2.741 eV; large HOMO–LUMO gap	[255]	PP + DFT

 © 2004 Wiley-VCH Verlag GmbH & Co. KGaA, Weinheim

Table 6: (Continued)

System and comments	Reference	Method
$[Au_{55}]$; structural transitions; both single-atom, local and collective processes occur	[586]	MD simulations
$[Au_n]$, $n=38,55,75$; amorphous	[252]	MD
$[Au_n]$, $n=2,6,55$; naked and PR_3-clad $[Au_6]^{m+}$	[587]	DFT
energy levels for $n=55$, I_h or O_h, related to a jellium model		
$[Au_n]$, $n\leq 147$; R_{av}, E_{coh}, B_0, IP, EA trends; 4f level shifts	[274, 588]	DFT
$[Au_\infty]$; infinite 1D ring (inifinite chain with periodic boundary conditions)	[589, 590]	PP + (U)HF
$[Au_\infty]$; infinite 1D chain	[303]	DFT + PP
Review on calculations on gold clusters	[591]	
Heteroatomic clusters		
$[AuCu_2]$	[520]	PP + CPF
$[CuAu_2]$, $[AgAu_2]$, $[Cu_2Au]$, $[Ag_2Au]$, [CuAgAu]	[522]	PP + MCPF
$[Ag_2Au]^q$, $q=-1,0,1$; adiabatic dynamics	[563]	PP + CCSD
$[Ag_mAu_n]^q$, $3\leq m+n\leq 5$, $q-1,0,1$. $[Ag_mAu_m]$, $m=3$–$5,10$; $[Ag_{12}Au_8]$	[396]	PP + DFT
Number of heterobonds and peripheral Au atoms maximized; Au "more s–d and planar" than Ag		
$[Pt_3Au]$; electronic states; ground state $^2A_2$ C_{3v}	[512]	PP
$[PdAu_n]$, $n=1$–4	[279]	PP
$[Au_nPd]^q$, $n=1$–4, $q=-1,0,1$; structures, IP	[592]	PP + DFT
$[Au_nH]^q$, $n=2$–6, $q=-1,0$	[593]	DFT
$[Au_5Zn]^+$; planar C_{2v}; "σ aromatic"; strong magnetic shielding inside	[359]	PP + MP2
$[Au_NZn]^q$, $N\leq 6$, $q=0,1$; all planar; IP	[594]	PP DFT
$[Au_mAg_n]^q$, $m+n=2$–7, $q=-1,0$; Ag inside, Au outside	[582]	PP DFT
$[MAu_{12}]$, M = Ta^-,W,Re^+	[266]	PP DFT, MP2
$[MAu_{12}]$, M = Mo, W. Geometries, EA studied; synthesized	[268]	PP DFT
$[Au_{12}Pd]$	[280]	MS
$[M_nAu]$, M = Na,Cs, $n\leq 9$	[262]	DFT
$[Au_nS]$; $n=1$–5, $[Au_nS]$, $n=1$–4; triangular or tetrahedral $[Au_n]$	[541]	PP + MP2
$[Ni_6Au_n]$; $n=0,8,32$; $[Ni_{13}Au_n]$; $n=0,6,8,14,24,30,42$; Au–Au relatively short, Ni–Ni relatively long; dependence of Ni-induced magnetism on n	[595]	DK DFT
Gold atoms in other substances		
Au/Rg	[596]	
Au/Rg	[597]	
Au/Si	[343, 344]	
Clusters with ligands or endohedral atoms		
$[XAu_n]^{m+}$ clusters; X = B–N, Al–S; $n=4$–6; HF only; bonding trends	[598]	PP-HF
$[AuAuH]^q$, $[AuHAu]^q$, $q=-1,0$; vibrational spectra	[217]	PP-DFT
$[Au_3(PH_3)_4L_n]$, $n=0$–3, L = $-InCl_2H_2O$.	[192]	DFT
Also $[Au_3]^q$, $[Au_3(PH_3)_4]^q$, $q=0,+1$; $[Au_3(PH_3)_3]^+$		
$[Au_4]^+$–Ar_n, $n=0$–4; photodissociation	[599]	PP + MP2, DFT
$[Au_5Ph_5]$; star; experimental geometry assumed	[139]	DFT
$[(H_3PAu)_nSH]^{(n-1)+}$, $n=1$–3; larger n strengthens Au–P, weakens Au–S bonds	[189]	DK + DFT
$[Au_4(AsH_3)_2(H_2PCH_2CH_2PH_2)_2]^{2+}$	[600]	PP + HF, MP2
$[Au_n(O_2)_m]^q$; $n=2$–5; $q=0,-1$, $m=1$–2	[385]	DFT + PW or GTO
$[Au_n(O_2)_m]^q$; $n=2,3$; $q=0,-1$, $m=1$–2	[390]	PP + DFT to CCSD(T)
O_2 bonds more strongly to odd-electron species. Second O_2 binds more weakly than first one.		
$[Au_6]^q$, $q=0$–4; $[Au_6X]^q$, X = B,C,N; $[(LAu)_nX]^q$, $n=4$–6	[91]	DFT
$[Au_n]/OH^-$, $[Au_n(O_2)OH]^-$, $n=2$–5; role of hydration in catalysis	[383]	PP + DFT
$[Au_n]/O_2$; $n=3$–6	[601]	PP + DFT
$[Au_8]$–$(OSO_3H)^-$; threefold site preferred; Au(111) model	[418]	DFT + PP
$[Au_9]$–SCH_3	[602]	PP
$[Au_{12}]/H_2S$, $HSCH_3$	[603]	PP
$[Au_{16}]/SH$, SCH_3	[604]	PP
$[Au_{38}(SCH_3)_{24}]$; capacitance 0.084 aF	[30]	PP
bimetallic clusters: $[Au_4\{Fe(CO)_4\}_4]^{4-}$	[282]	DFT
$[Au_n]$ wires between two gold electrodes	[31]	DFT
	[32]	DFT
	[33]	DFT
$[Au_n]$ wires between two gold electrodes;	[302]	DFT

 © 2004 Wiley-VCH Verlag GmbH & Co. KGaA, Weinheim

Table 6: (Continued)

System and comments	Reference	Method
gives forces, energies due to stretching; thiolates added		
$[Au_n]$ wires between two gold electrodes	[301]	DFT
gives forces due to stretching		
{Au-H-Au-H} nanowires	[306]	PP + DFT
$[Au_\infty]$ band structure for equidistant model wire	[605]	LMTO
Clusters on surfaces and cluster catalysis		
adsorption of Au on cluster models of NaCl(100).	[313]	PP
$[Au_n]^+/CH_3OH$, $n \leq 15$; Car–Parrinello study of adsorption	[414]	DFT + PP
$[Au_8]$ on MgO surface; catalyst for CO oxidation	[391]	PP
$[Au_3Sr]$, $[Au_n]$, $n = 4,8$ on MgO surface; catalyst for CO oxidation	[398]	PP + PW
C_{60} on Au(111); electron tunneling spectra	[420]	PP + DFT
Polyatomic Au–L systems		
[AuOH]; relativistic bond-angle decrease	[606]	DK3 CCSD(T).
[AuOH] "Au bonds", analogous to H-bonds	[194]	PP MP2
$[AuCH_3]$; R/NR	[607]	DFT + PT
[AuR]; R = Me,Ph	[608]	PP + MP2, CCSD(T)
$[AuBH_4]$	[609]	PP
AuCN, AuNC; accurate; ZORA-DFT, PP-CCSD(T)	[94]	
[AuCO]; bound due to relativity	[610]	PP
$[AuCO]^+$	[611]	PP
$[AuCO]^+$	[612]	PP
$[AuCO]^+$; accurate	[93]	PP
$[MCH_2]^+$, MCH^+, M = La–Au	[195]	PP
$[MCH_2]^+$, M = Fe–Au	[613]	PP
$[M=CH_2]^+$, $[M{-}CH_3]^+$, M = Au	[74]	PP
$[AuNH_3]$ as model for surface adsorption; Gaussian, Slater, PW basis	[614]	PP + DFT
$[Au\text{-}O_2]$, [OAuO]; experimental and calcd	[223]	PP + DFT
L-Au-L′ systems		
$[AuH_2]$; ground and excited states; SO	[615]	MRSD-CI
$[AuH_2]$; ground state	[214, 101, 215]	PP-DFT
$[AuH_2]^-$; Vibrational spectra	[216, 215]	DFT
$[Au(CH_3)_2]^-$	[616]	PP MP2
$[SAuS]^{3-}$	[617]	QR-SW
$[RgAuRg]^+$; Rg = He–Xe predicted	[202]	PP
$[XAuX]^{3-}$; X = O–Se in crystal field	[164, 171]	DFT
$[AuF_2]$	[227, 228]	PP + MP, CCSD(T)
$[AuF_2]^-$	[232]	PP + MP2,DFT
$[AuX_2]$, $[AuX_2]^-$; X = Cl–I; photoelectric spectra assigned	[618]	PP TD-DFT
$[MeAuPR_3]$, R = H,Me; photoelectric spectra interpreted, bonding analyzed	[619]	DFT + PT
$[MeAuPR_3]$, R = H,Me,Ph.	[620]	DFT
$[ClAuPH_3]$, $[ClAuPH_2Ph]$, $[ClAuPPh_3]$; eigenvalue spectrum	[92]	SR SW
[ClAu(CO)]	[621]	PP
[ClAu(CO)], $[\{ClAu(CO)\}_2]$	[622]	PP, ADF
[Rg-AuCl], Rg = Ar, Kr; structure and bonding	[210]	PP + MP2
[XAu(CO)], X = F–Br. Structure and bonding	[623]	PP + MP2
$[(PR_3)_2Au]^+$, $[PR_3AuCl]$, R = H,Me	[172]	DFT
$[Au(CO)_2]^+$	[80, 81]	PP
$[Au(CO)_n]$, $n = 1,2$; $[Au(CO)_n]^+$, $n = 1$–4; IR spectra interpreted	[624]	
[Au(SiO)], $[Au(SiO)_2]$; bent Au-Si-O	[625]	PP + DFT
$[AuNO]^q$, $[Au(NO)_2]^q$, $q = 0,1$; IR spectra interpreted	[626]	
$[Au{\equiv}C]^+$; do other Au≡L exist?	[201]	PP
$[Au(CN)_2]^-$, $[Au(CO)_2]^+$; DFT, MP2, CCSD(T)	[79]	PP +
$[Au(CNO)_2]^-$; structure, IR spectrum	[627]	PP + DFT
$[Au{=}C{=}Au]^{2+}$; bonding like OCO	[187]	PP DFT
$[AuI_n]^-$; $n = 2,4$; relation to II_n^- polyiodides; $[AuI_2]^-$ and I_3^- interchangeable	[628]	PP + MP2
$[AuO_n]$, n = 1–3; experimental and calcd	[223]	PP

 © 2004 Wiley-VCH Verlag GmbH & Co. KGaA, Weinheim

Table 6: (Continued)

System and comments	Reference	Method
Centred $[Au(L)_n]$ systems, $n>2$		
$[AuH_3]$; predicted to be a narrow "Y"; R/NR	[60]	PP+HF, MP2
$[AuH_3]$; predicted to be a narrow "Y"	[99,100]	PP CCSD(T)
$[(H_2)AuH]$, $[(H_2)AuH_3]$	[214,101,217]	PP-DFT
$[AuX_3]$, X=F–Cl; predicted to be a narrow "Y"; R/NR	[60]	PP+HF
$[AuH_4]^-$.Vibrational spectra	[216,215]	DFT
$[AuX_n]^-$, $n=2,4$, X=F–I; R/NR	[59]	PP CISD
$[AuX_n]^-$, $n=4$ and X=H, F–I, $n=6$, X=F; R/NR	[60]	PP+HF, MP2
$[AuF_n]^-$, $n=4,6$	[232]	PP+MP2, DFT
$[AuI_n]^-$, $n=2,4$	[628]	PP
$[AuI_n]^-$, $n=2,4$; AuI_3: "T"	[104]	PP+DFT
$[AuCl_4]^-$, $[AuI_4]^-$, $[AuI_4]^{2-}$; ligand binding energy	[206]	PP+DFT
$[AuF_3]$, $[AuCl_3]$, ("T"), $AuCl_4^-$	[103]	PP+DFT or MP2
$[AuX_3]$, X=F-I	[102]	PP CCSD(T)
$[AuF_6]^q$, $q=-3$ to 0. EA_n, geometries	[629]	PP CI
$[AuRg_4]^{q+}$, Rg=Ar–Xe, $q=2,3$; good bond-lengths obtained; 2f1g in basis	[206]	PP+CCSD(T)
$[AuRg_4]^{2+}$ Rg=Ar–Xe; charge-density analysis	[207]	PP+DFT
$[Au(CO)_n]$, $n=1,2$, $[Au(CO)_n]^+$, $n=1$–4; IR spectra interpreted	[624]	PP DFT
$[Au(CO)_n]$, $n=1$–3; dispersion important	[630]	PP+MP2, CCSD(T)
$[Au(CO)_n]^+$, $n=1$–4; $C_{\infty v}$, $D_{\infty h}$, D_{3h}, T_d, respectively	[631]	PP, B3LYP or CCSD(T)
Free $[Au(GeCl_3)_3]^{2-}$ is trigonal planar, like $[Au(PH_3)_3]^+$; counterions distort it into a "T", observed in crystals	[98]	PP+HF, MP2
$[Au(\text{dimethyl ether})_n]^+$, $n=1$–4; first two Au–O bonds are strong	[85]	PP+MP2, CCSD(T)
$[Au(PH_3)_n]^+$, $n=1$–4, $[AuCl(PH_3)_n]$, $n=1$–3; two-coordination preferred	[90]	PP
$[Au(ClO_4)_4]^-$; structure distorted D_{4h}	[632]	PP-DFT
Aurophilic dimer models		
Doubly bridged $[\{Au(H_2PCH_2PH_2)\}_2]^{2+}$; bonding discussed Nature of d^{10}–d^{10} interaction not understood	[633]	QR-SW
$[(ClAuPH_3)_2]$ model introduced	[113]	PP+HF, MP2
$[(XAuPH_3)_2]$; X=H,F-I,CH_3,-CCH,CN,-SCH_3. d^{10}–d^{10}	[107,117,122]	PP
$[(ClAuPH_3)_n]$ isomers, $n=2,4$	[149]	PP
$[H_2C\{P(Ph)_2AuX\}_2]$, $HC[P(Ph)_2AuX]_3$, X=Cl,I; d^{10}–d^{10}	[634]	PP+MP2
$[H_3PS\{Au(PH_3)_n\}]^{n+}$; $n=1$–3. $[H_2P(S)S\{Au(PH_3)\}_2]^+$; d^{10}–d^{10}	[635]	PP
$[(PR_3)_2Au]^+$, $[PR_3AuCl]$, R=H,Me	[172]	DFT
$[M_2Se]$, $[M_2I]^+$, M=Ag,Au	[636]	PP+MP2
$[Au_2I]^+$, $[I(AuCl)_2]^-$	[546]	PP+MP2,DFT
$[Au_2O]$; experimental and calcd	[223]	PP
$[Au_2As]^-$, $[Au_2Br]^+$; aurophilicity	[637]	PP+MP2-CCSD(T)
$[Au_2Te]$; correlation up to CCSD(T); basis unknown	[638]	PP
$[X(AuPH_3)_n]^{m+}$, X=C,N,O,P,S, $n=1$–6; $[HC(AuPH_3)_4]^+$; d^{10}–d^{10}	[136]	PP
cyclic $[Se_nAu_2]^{2-}$, $n=5,6$: d^{10}–d^{10}	[639]	PP
$[(Au_2S)_n]$, $n=1,2$: d^{10}-d^{10}.	[121]	PP+CCSD(T)
$[(XAuPH_3)_2]$, X=H,Cl; d^{10}–d^{10}.	[124]	PP
isocyanide models $[(H_3C\text{-}NC\text{-}AuX)_2]$, X=Cl,I; dominant long-range dipole–dipole interactions induce antiparallel position	[148]	PP+LMP2
Larger aurophilic systems		
$[SAu_3]^+$, $[S(AuPH_3)_3]^+$; d^{10}–d^{10}	[130]	PP
$[OAu_3]^+$, $[O(AuPH_3)_3]^+$, their dimers	[640]	DFT
$[X(AuPH_3)_n]^{m+}$, X=C,N,O,P,S, $n=1$–6; $[HC(AuPH_3)_4]^+$ d^{10}–d^{10}	[136]	PP
$[IAu_3]^{2+}$, $[IAu_4]^{3+}$, $[I(AuCl)_m]^-$, $m=1$–4	[546]	PP
$[E(AuPH_3)_4]^+$, E=N-As; d^{10}–d^{10}	[119]	PP
solid AuCl; chain structure due to d^{10}–d^{10}	[125]	PP
$[CH_2(PH_2AuPH_2)_2CH_2]^{2+}$	[641]	PP
$[M_2(H_2PCH_2SH)_2]^{2+}$, M=Au	[169]	PP
rings $[M_2(PH_2CH_2PH_2)_2]^{2+}$, $[M_2(NHCHNH)_2]$, $[M_2(SCHS)_2]$, $[M_2X_4]^{2-}$, M=Au; X=Cl–I		
$[\{Au_2(PH_2CH_2PH_2)_2\}Cl_2]$; $[Au_2Te_4]^{2-}$; d^{10}–d^{10}	[63]	PP
$[Au_2X_2C_2H_2(PH_2)_2]$; X=Cl–I; *cis* has d^{10}–d^{10}	[147]	PP
$[Se(AuPH_3)_n]^{(n-2)+}$; $n=2$–6; d^{10}–d^{10}	[642]	PP-HF/MP2

 © 2004 Wiley-VCH Verlag GmbH & Co. KGaA, Weinheim

Table 6: (Continued)

System and comments	Reference	Method
$[Au_2(PH_2CH_2S)_2]$and related systems	[145]	PP + MP2
ring $[Cp(CO)_2Cr_6(\mu\text{-}H)_6(\mu_4\text{-}P)_3Au_3]$; has Au–Cr bonds, Au···Au	[97]	PP + DFT
Other metallophilic systems		
$Au^{I}\cdots Au^{III}$ interactions modelled by $[S(AuPH_3)_n(AuH_3)_{3-n}]$	[643]	DFT
$Au^{I}\cdots Au^{III}$ interactions modelled by $[(L_3Au)\text{–}Se(AuPH_3)_2]$, L = H,Me, and similar systems	[151]	PP-HF/MP2
$[\{Ag(C_6F_5)_2\}py]$, $[Ag(NH_3)_3][Au(C_6F_5)_2]$, $[Ag(NH_3)_2(py)][Au(C_6F_5)_2]$. Ag···Au attraction.	[644]	PP + LMP2
$[PdH_2(PH_3)_2][HAuPH_3]$. $Au^{I}\cdots Pd^{II}$.	[89]	PP-LMP2
[*Trans*-$Pt(PH_3)_2(CN)_2$ – $Au(PH_3)_2^+$]. $Au^{I}\cdots Pd^{II}$ or Pt^{II} interactions.	[154]	PP-MP2
$[LTlL'][Au(C_6H_5)_2]$; L = py, H_2O. Tl-Au 301.6 pm assumed. Optical spectra calculated; also Tl.Au···Au···Tl tetramer spectra; intermetallic origin of luminescence	[349]	PP + TD-DFT
Further complexes		
$H_3PAuC{\equiv}CAuPH_3$ complex with $CHCl_3$	[645]	PP
$Au(CO)_2^+$, $[Au(CO)_2F_2]^-$. "Nonclassical" metal carbonyls.	[80]	PP
$[M(CO)_n]^{x+}$; $M^{x+} = Au^+$; $n = 1$–5.	[81]	PP
$[\{Au(CO)\}^+_n]$, AuCN, $Au(CN)_2^-$, $n = 1$–3	[646]	PP, MP2 to QCISD(T)
$[Au(CN)_2]^-$	[79]	PP
$[Au(CO)_2]^+$; DFT, MP2, CCSD(T)		
Other, larger inorganic, and organometallic systems		
$[AuO_3]$; experimental and calcd	[223]	PP
$[CAu_3]^+$, [AuCCAu], $[AuCCCAu]^{2+}$	[187]	PP DFT
$[Au_2F_2]$	[227, 228]	PP
$[Au_2X_2]$, X = Cl–I; nearly constant Au–Au	[147]	PP
$[Au_2Cl_2]$	[103]	PP + DFT or MP2
$[Au_2X_2]$, X = F–I	[102]	PP CCSD(T)
$[Au_2X_6]$, X = H,F,Cl; R/NR	[60]	PP + HF
$[Au_2H_6]$	[100]	PP MP2
$[Au_2Cl_6]$; graphite intercalation compound; photoelectric spectra	[647]	DSW
$[Au_2Cl_6]$; structure compared with electron diffraction	[103]	PP + DFT or MP2
$[Au_2X_6]$, X = F–I.	[102]	PP CCSD(T)
$[Au_2I_2]$, $[Au_2I_6]$	[104]	PP + DFT
$[Au_2F_{10}]$, dimerization energy 293 kJ mol^{-1}; $[(F_5Au)\text{–}F\text{–}(SbF_5)]^-$	[233]	PP
[KrF][AuF_6]	[212]	PP
$[(AuCl_3)_2(\mu\text{-}Cl)]^-$; occurs in room-temperature molten salt	[648]	PP
$[Pt_2(PH_3)_4(\mu\text{-}S)(\mu_3\text{-}S)Au(PH_3)]^+$	[649]	PP-DFT
Au^{I} dithioimidodiphosphinato metallacycles	[650]	PP + DFT
Au^{II} porphyrines; bonding, energy levels	[651]	QR-SW
Chemical reactions and solvation effects		
Au speciation in aqueous solution	[365]	PP
$[Au(S_2O_3)_2]^{3-}$ or $[Au(SH)_2]^-$ in COSMO solvent	[367]	PP
decomposition of Au^{I} compounds	[652]	PP
[AuSH], $[Au(SH)_2]^- + H_2S$, H_2O	[368]	PP
H_2 on Au(111); "Why gold is the noblest of all metals"; relativity not mentioned	[6]	PP + DFT
CO on Au(111); simple model for d-band hybridization proposed	[7]	PP + DFT
NO_2 on Au atom, Au clusters.	[75]	DFT + PP
$[Au_2X_2C_2H_2(PH_2)_2]$, X = Cl–I; *cis* has d^{10}–d^{10} photochemistry of *cis*-to-*trans* conversion	[147]	PP
$CO + [Au_n]^q$, $n = 1$–6, $q = -1,0,1$; on-top sites preferred	[573]	PP + DFT
CH_3OH + $[Au_n]$, $n \leq 15$; CO stretch as bonding indicator; the metal cluster is planar for $n = 3,5,7$, nonplanar for $n = 9,15$	[414]	DFT + CP
rearrangements of $[Au_2X_2(\mu\text{-}L)_2]$; X = Cl–I; L = $C_2H_2PH_2$, $C_6H_4PH_2$, $MeC_6H_3PH_2$; Au^{II}–Au^{II} → Au^{I}–Au^{III}, with concomitant C-C coupling	[653]	PP + MP2
$[MCH_2]^+$, M = Ni,Pd,Ir → Au	[654]	DFT
HCN synthesis from methane and ammonia		
Au + ethylene interaction	[76, 77]	PP
Au + H_2O or NH_3 interaction; water weaker	[655]	DK CCSD(T)

 © 2004 Wiley-VCH Verlag GmbH & Co. KGaA, Weinheim

Table 6: (Continued)

System and comments	Reference	Method
$[ClM{=}M'R_2]$, M = Au, M′ = C–Ge; R/NR for Au	[198]	PP + MP2
$[MCH_3]^+$, M = Sc–Cu,La,Hf–Au	[73]	PP
C_6H_6 + M^+, M = Au; prefers η^2 coordination	[86]	PP + DFT,MP2
C_6H_6 + M^+, M = Au; forms $[Au(C_6H_6)_2]^+$; both rings η^2 and *trans*	[656]	PP + DFT.
C_2H_4 + M^+, M = Au; bond analysis	[72]	PP + DFT or CCSD(T)
C_5H_5N + Au^+; prefers planar, N-bound C_{2v}	[87]	PP + MP2/CCSD(T)
Pyridine + Au^+; cibrational frequencies	[88]	PP + DFT
CO + O_2 + $[Au_n]$, $n \leq 20$	[391]	PP + DFT + PW
CO + O_2 + $[Au_{12}]$	[393]	PP + DFT + PW
CO + O_2 + $[Au_2]^-$	[392, 657]	PP + DFT + PW
O_2 + $[Au_n]^q$, $n \leq 11$, $q = -1$, 0	[387]	PP + DFT
O_2 + $[Au_n]^q$, $n \leq 8$, $q = -1$, 0	[384]	PP + DFT + PW
H_2O + Au^+	[658]	PP
$[Au^+(H_2O)_n]$, $n = 1$–4	[83]	PP
$[Au_n]^+$, $n = 1$–15 + CH_3OH	[414]	PP
$[Me_3P\text{-}Au]^+$ + alkyne + alcohol	[373]	PP + MP2/DFT
Photochemistry of *cis*-to-*trans* conversion		
$[Cl_nAuSMe_2]$, $n = 1,3$; inversion at the sulfur atom	[659]	PP
$[\{Cp_2Ti(C{\equiv}CH)_2\}AuR]$	[660]	DFT + PP
$[\{Cl_2Ti(C{\equiv}CH)_2\}MCH_3]$ "tweezers"; M = Cu–Au	[661]	PP
[(Et$_3$P)Au(2-Thiouracil)]	[662]	PP
$[AuPt]^-$, $[Au_2]$, $[AuHg]^+$	[221]	PP
$[AuPt_n] + H_2$, $n = 1,2$	[663]	PP
$[AuPt_2]$, $[Au_2Pt]$ + ethene	[664]	PP
$[(AuPH_3)_6Pt(PH_3)]^{2+}$ + H_2	[665]	DFT + PP
Model for dihydrogen activation		
$[Au(C_2H_4)]$	[77]	PP
$[Au^{III}(C_6H_4S_2)_2]^-$; aromatic Au^{III} dithiolene	[666]	PP
$[Au{-}L]^+$, L = H_2O, CO, NH_3,C_2H_4, etc.	[71, 70, 658, 69, 68]	PP
$[ClAuPH_3]$, $[AuPH_3]^+$	[667]	DFT + PP
$[(F_3As)AuXe]^+$	[209]	PP MP2
$[Au{-}L]^+$, L = adenine, guanine	[95]	PP + MP2
$[Au{-}L]^+$, L = glycine, formate, formamide	[96]	PP
$[Au{-}L]^+$, L = C_2H_4, N_2, HCN, C_2H_2, N_2O, FCN, HCNO, HN_3, HCCF, CH_2N_2, CH_3CN, C_2F_2, FCNO, CH_3CNO	[668]	PP
$[M_2(\mu\text{-}Y)(\mu\text{-}XR)L_4]$, $[M_2(\mu\text{-}XR)_2L_4]$, M = Rh→Pd, Ir→Au, X = O-Te, Y = Cl,S: d^8–d^8	[669, 670]	PP
$[Au(\bar{C}NHCH{=}CHNH)_2Cl_2]^+$, $[Au(\bar{C}NHCH{=}CHNH)_2]^+$; carbenes	[197]	PP
$[Au_3(CH_3N{=}COCH_3)_3]$; solvoluminescent system	[671]	PP + DFT
$[(OC)_5Cr\text{-}(CH_2)C(OMe)(AuPH_3)]$	[672]	PP

py is pyridine.

$[AuI_4]^-$ are known in solution and in compounds. Solid AuI has a zigzag chain structure. The unknown $[Au_2I_6]$ was predicted to be stable. A comparative study of all gold halide molecules at levels up to CCSD(T) was published by Schulz and Hargittai.[102]

Group 18: The $[AuRg]^+$ compounds to rare gases were already discussed in Section 4.4.

4.6. Clusters and Wires

A large amount of experimental and theoretical data exists on gold clusters, see Mingos,[237–240] Pignolet,[241,242] Schwerdtfeger[9] or Steggerda.[243]

Pure clusters: Gas-phase data are available for both cations[244–246] and anions.[247] Rapid isomerization reactions were observed for $[Au_9]^+$ at 140 K, see ref. [246]. The corresponding activation energies were estimated to be 10–20 kJ mol^{-1}. A summary of the calculated structures of $[Au_n]^q$ with $n = 3$–13 and $q = -1$, 0, 1 is given in Table 7. The references for ion-mobility data[245,247] are also given. The neutral clusters are planar up to $n = 7$ or 8.

Experimentally and computationally, the $[Au_n]^-$ anions are planar for $n \leq 11$. For $n = 12$, two isomers are seen and the $n = 13$ is experimentally thought to be nonplanar.[247] This planarity was explicitly attributed by Häkkinen et al.[248] for $n = 7$ to the relativistically induced, stronger 6s–5d hybridization, that lowers the kinetic energy. The ultimate reason can be seen in Figure 1. Recall here the attribution of the gold (100) surface hexagonal reorganization to that relativistic increase by Takeuchi et al.[249]

The $[Au_n]^+$ cations are thought to be planar for $n \leq 7$.[245,250] The experimental evidence is based on collision cross sections for ion mobility. For $n = 8$–10, three-dimensional structures were found, see Figure 12 and Table 7. As to the neutrals, planar trigonal raft structures are found to have the lowest energies up to $n \leq 7$. Note the unusual case of open-shell Au_3, where SO-effects cancel the ground-state

 © 2004 Wiley-VCH Verlag GmbH & Co. KGaA, Weinheim

Table 7: Calculated structures of small $[Au_n]^q$ clusters. The structures chosen in reference [245] are also supported by experimental ion mobility data. The lowest-energy structures are planar up to $n=7$ for the cations and $n=12$ for anions. For latest results, see reference [583]

n	q	Structure	Reference	Comments
3	−1	linear, D_{1h}	[247,556]	
	0	bent, C_{2h}	[556]	No SO
		D_{3h}	[251]	SO effectsincluded
	1	D_{3h}	[245,556]	
4	−1	"Y" and C_{2h} chain[a]	[247,578]	"Y" supported by experiments
	0	rhombic, D_{2h}	[578]	
	1	rhombic, D_{2h}	[245]	
5	−1	C_{2v}, "half-cake" or "W"	[247,578]	
	0	C_{2v}, "half-cake" or "W"	[578]	
	1	planar "X", D_{2h}	[245]	
6	−1	planar D_{3h}	[247,578]	photoelectron spectra support D_{6h} ring[572]
	0	planar D_{3h}	[578]	
	1	planar D_{3h}	[245]	
7	−1	planar C_{2v}	[247]	tricapped square
	0	planar D_{6h}	[578]	
	1	planar D_{6h}	[245]	
8	−1	Planar D_{4h}	[247,248]	tetracapped square
	0	T_d	[578]	
		D_{4h}	[582]	CCSD or BPW/DFT; at MP2 level, 3D
	1	three-dimensional C_s	[245]	
9	−1	planar C_{2v}	[247,248]	bicapped hexagonal ring
	0	C_{3v}	[578]	
	1	C_{2v} capped pyramid	[245]	[b]
10	−1	planar D_{3h} or D_{2h}	[245,248]	experimental favors D_{2h}
	0	C_{2v}	[578]	
	1	quasi-T_d	[245]	[b]; also low-lying C_{2v} capped prism and planar D_{2h} raft found
11	−1	C_s or C_{2v}	[247,248]	experimental favors C_s
	0			
	1	D_{3h}	[245]	
12	−1	D_{3h}	[247]	two experimental isomers seen
	0	C_{3v}	[248]	
	1	C_{2v}	[245]	
13	−1	DFT: planar C_s	[247,583]	experimental: nonplanar
	0		[253,254]	practically disordered
	1	C_{2v}	[245]	[b]
14	−1	DFT: lowest planar C_{2v}. Exp. 3D.	[583]	

[a] Almost degenerate. [b] Fragment of bulk Au.

Jahn–Teller distortion and lead to an equilateral triangular shape. An excited electronic state at 0.2 eV could be experimentally observed.[251]

The cluster structures in Table 7 are thought to be the currently best benchmarks for theoretical calibration runs. Many further calculations on gold clusters, as well as calculations on larger clusters are quoted in Table 6. A rather general conclusion is that for $n \geq 13$, a large amount of amorphous structures with almost the same energy are found for the neutral gold clusters.[252–254] Yet certain magic numbers are quite stable. A notable case is the recently observed, neutral or anionic, tetrahedral $[Au_{20}]$.[255] Its structure is a fragment of *fcc* bulk gold. It has an experimental EA of 2.745 eV and a large HOMO–LUMO gap of 1.77 eV, the largest among all coinage-metal clusters and 0.2 eV larger than the gap in C_{60}. Another case is the $[Au_{55}]$ cluster of unknown effective charge on a silicon surface, that experimentally refuses to react with any oxygen species, including those in atomic plasmas.[256]

Molecular dynamics studies of the melting of gold clusters with up to 459 atoms by Cleveland et al.[257] reveals the existence of icosahedral precursors. Wilson[258] finds that for polyhedral clusters having up to 1500 atoms, icosahedra, and truncated octahedra are particularly stable. Clearly, the conclusions depend on the assumed gold–gold potentials (see Table 3).

Highly-charged clusters: The only way to account for the observation of a gas-phase $[Au_2]^{2+}$ was that it would be a long-lived excited state. Both tight-binding[259] and ab initio[260] calculations exist on this species. As found earlier, the ground state, while being a useful model for the aurophilic attraction, was purely repulsive.[116] In addition to the $[Au_2]^{2+}$ ion, Saunders and Fedrigo also saw in collision-induced fragmentation measurements the species $[Au_n]^{2+}$; $n=3$–5 as well as $[Au_4]^{3+}$.[261]

Doped or covered clusters: In bulk compounds, by 1999, over 300 structurally characterized heteronuclear gold-metal cluster compounds were known.[242] In the gas phase, the $[Na_xAu]$ and $[Cs_xAu]$ bimetallic clusters were studied both experimentally and theoretically by Heiz et al.[262] The Na system could be related to electronic shell models, the Cs systems were rather more ionic. Experimentally, $[Na_3Au]$ and $[Na_9Au]$ were abundant and $[Na_8Au_2]$ very abundant. For Cs, the peaks CsAu and Cs_2Au were strong. The species were created by supersonic expansion of the mixed vapors. After photoionization, the ionic abundancies were determined by a quadrupole mass spectrometer.

As to centred clusters of the type $[X(AuL)_6]^{m+}$; X = B, C, N; L = PR_3, Häberlen et al.[91] found at DFT level that adding the phosphanes lengthened the central X–Au bond in the average by 4 pm. The aurophilic aspects of these species were already discussed in Section 3.3. The six radial covalent bonds can be understood as an eight-electron seven-centre bond of the type $(a_{1g})^2$ $(t_{1u})^6$, the LUMO being a nonbonding e_g. A relativistic bond-length contraction and strengthening of the X–Au and notably the Au–P bonds occurs.

A case with a very short Au–Au bond of 257.5 pm was synthesized by Gabbaï et al.[192] It has an $\{Au_3In_3\}$ core and the short bond occurs along a quasilinear {P-Au-Au-P} axis. The

 © 2004 Wiley-VCH Verlag GmbH & Co. KGaA, Weinheim

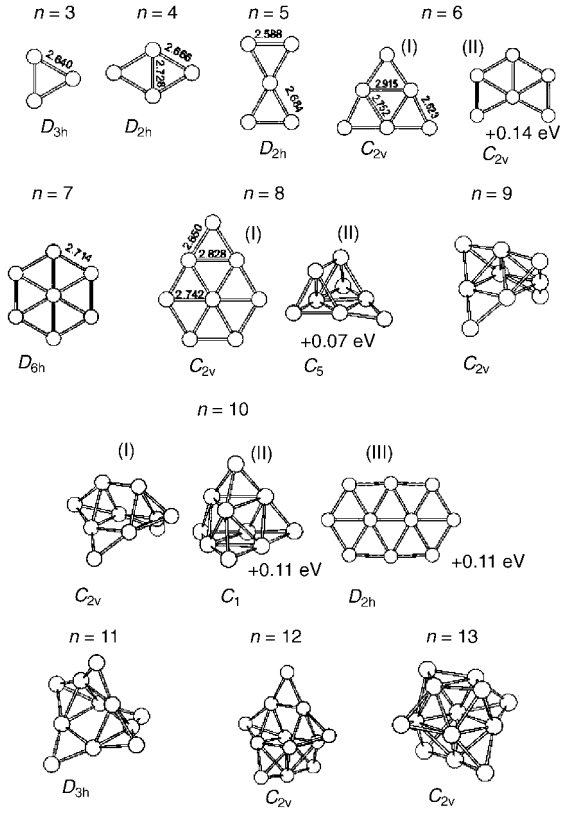


Figure 12. The lowest-energy structures of the $[Au_n]^+$ cations, $n \leq 13$, according to Gilb et al.[245] Copyright 2002 American Institute of Physics.

oxidation state of these gold atoms was assigned to be 0 and that of the third gold atom, +1. DK DFT calculations on $[\{Au_3(PH_3)_4\}L_n]$; $n = 0$–3; L = $InCl_2H_2O$, I were used to gain insight into the bonding.

Electron counts for clusters: In a series of papers, Mingos et al.[137,138,237,239,240,263] have analysed both the general principles of bonding in metal clusters and the electronic structure of pure or doped gold clusters. These discussions take place at the EHT or even more qualitative level. They make the assumption that each gold atom contributes its 6s electron to the bonding and that the 5d electrons would form a lower-lying core band. Thus the icosahedral $[Au_{13}]^{5+}$ system, for instance, would be regarded as an eight-electron closed-shell system. Indeed, it was synthesized in 1981 by the Mingos group[264] as part of $[Au_{13}(PMe_2Ph)_{10}Cl_2][PF_6]_3$. A jellium model has also been used for coinage-metal clusters.[265]

In a different electron-counting system, favored by several other workers, all the valence electrons of the central atom are included (see the corresponding examples given in Table 8.[131,241–243]. The same counting system was reached at ab initio level, when the molecule $[WAu_{12}]$ (Figure 13) was predicted by Pyykkö and Runeberg.[266] In addition to the eight $a_g + t_{1u}$ electrons, the ten h_g electrons were found to participate in the bonding (see also reference [267]). The a_g, t_{1u}, and h_g MOs bond to the 6s, 6p, and 5d shells, respectively, of the central atom. The h_g was the HOMO of $[WAu_{12}]$ or the penultimate MO of $[Au_{13}]^{5+}$, see Figure 14, and not at all an isolated core orbital. Thus these systems were predicted to be particularly stable due to both their 18-electron structure, relativity and the aurophilic attraction. The molecules $[WAu_{12}]$ and $[MoAu_{12}]$ were subsequently experimentally produced by metal evaporation into a helium carrier gas, in the group of Lai-Sheng Wang,[268] who also presented both experimental and theoretical evidence for the I_h structure of the former. Many properties of $[WAu_{12}]$ are predicted by Autschbach et al.[267] Among them the large predicted tungsten chemical shift and gold nuclear quadrupole coupling are noteworthy. Despite the strong radial bonding, the system is highly fluxional.

The 18-electron bonding system should thus be seen as $a_g^2 + t_{1u}^6 + h_g^{10}$ for the group I_h. This single counterexample shows that the Mingos electron count should be taken with a grain of salt. This closed-shell count, especially near the number of 18, is remarkably persistent, see Table 8. Atoms can be omitted from the periphery, if the 18-electron count is maintained, a recent example being $[Au_{11}Cl_3(PPh_3)_7]$.[269] Many such lower-symmetry clusters with $n = 5$–11 are known.[240,242] A Pt-centred 18-e cluster, $[Pt(CO)(AuPPh_3)_8]^{2+}$, was discussed at CNDO level by Boča.[270] The 5d orbitals of the central platinum atom were found to contribute to the Pt–Au bonding.

The rules for site preferences were discussed by Mingos and Lin[271] and by Zhang and Teo.[272] In all known Ag–Au clusters, an Au atom occupies the central or interstitial position. In mixed systems with Pd or Pt, that atom is in the centre. In systems containing Hg, that atom is in the periphery.[242]

Electrochemistry of clusters: After sufficient monodispersity was achieved, Quinn et al.[273] observed experimentally 15 oxidation states of a thiolate-covered $[Au_{147}]$ cluster. The

Table 8: Some experimentally known closed-shell metal clusters.[a]

N	Cluster	Compound	Ref.	Comments
2	$[Au_4]^{2+}$	$Au_4(\mu\text{-}I)_2(PPh_3)_4$ (quasi-T_d)	[237]	empty centre
8	$[CAu_6]^{2+}$ (O_h)	$[C(AuPPh_3)_6]^{2+}$	[106,136,142,143]	
	$[MAu_4]$ (T_d)	MAu_4, M = Ti-Hf,Th	[186]	predicted
18	$[Au_9]^+$	$[Au_9(PR_3)_8]^+$	[673]	bicapped centred chair
	$[Au_{11}]^{3+}$	$[Au_{11}(PPh_3)_7(SCN)_3]$	[138]	tridecahedron.
	$[Au_{13}]^{5+}$ [b]	$[Au_{13}(PMe_2Ph)_{10}Cl_2](PF_6)_3$	[264]	predicted in reference [138]
	$[Au_9Ag_4]^{5+}$ [b]	$[Au_9Ag_4Cl_4(PMePh_2)_8]^+$	[239]	Au at centre. Silvers ordered
	$[PdAu_{12}]^{4+}$ [b]	$[(Ph_3PAu)_6(dppeAu_2)(AuCl)_4Pd]$	[674]	Pd at centre
	$[PtAgHgAu_8]^{3+}$ [b]	$[Pt(Ag)(Hg)(AuPPh_3)_6](NO_3)_3$	[242]	Pt at centre
	$[WAu_{12}]$ (I_h)	$[MAu_{12}]$, M = Mo,W	[268]	Predicted in reference [266]
20	$[MHg_2Au_8]^{2+}$, D_{4d}	$[M(Hg)_2(AuPPh_3)_8]^{2+}$, M = Pd,Pt	[242]	M at centre, Hg axial cap

[a] *N* is the number of valence electrons. For centred clusters, the central atom contributes all its s and d electrons. Peripheral Au atoms contribute one electron. For main-group-centred aurophilic $N = 8$ systems. [b] Approximate icosahedral symmetry.

 © 2004 Wiley-VCH Verlag GmbH & Co. KGaA, Weinheim

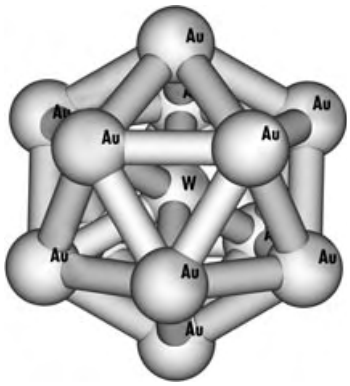


Figure 13. The calculated structure of the $[WAu_{12}]$ molecule.[266]

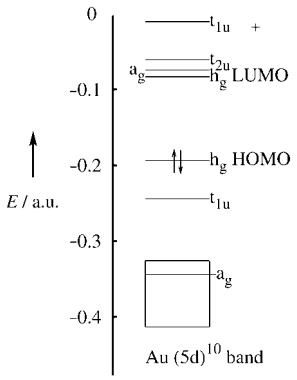


Figure 14. The calculated B3LYP/LANL1DZ orbital energies of the $[WAu_{12}]$ molecule in atomic units.[266]

results were simulated by solving the Poisson equation for a surface-layer model. Theoretical DFT predictions for the HOMO–LUMO gap of that naked cluster in 1997 were of the order of 1.6 V.[274] See also the calculation of the capacitance of $[Au_{38}(SCH_3)_{24}]$ by Häkkinen et al.[30]

Energy decomposition for gold clusters: Non-additivity? For molecular dynamics calculations, interatomic Au–Au potentials are needed. On the basis of an MP2-level calculation, non-additive terms were claimed to be larger than the additive two-body terms. These non-additive terms were suggested as another explanation for the planarity of $[Au_n]$, $n \leq 6$.[275,276]

Fluxionality: As stated by Mingos[237] in 1984, "during the last few years it has become apparent that transition-metal cluster compounds may have alternative structures, which are separated by only small energy differencies". Also the barriers are low, making observations by NMR spectroscopy possible. As an example, $[Au_9(PPh_3)_8]^{3+}$ is stereochemically nonrigid in solution.[277]

"Coupled clusters": polyicosahedral systems**:** The group of Teo has synthesized a series of gold-containing mixed-metal cluster compounds, including dimers, triangular trimers, or tetrahedral tetramers of centered icosahedral 13-atom clusters. The bonding of these "polyicosahedral" systems has been discussed by Zhang and Teo[278] (and references there), who mention their tendency to achieve an 18-electron structure per icosahedron. They also mention relativistic effects and aurophilicity. The first ab initio study of the underlying reasons seems to be the one on monomeric $[WAu_{12}]$.[266]

Doped clusters, ab initio theory: For neutral and anionic clusters $[PdAu_n]$, $n = 1$–4, the lowest-energy structures consisted of Pd-centred triangular rafts.[279] The icosahedral $Au_{12}Pd$ was studied by SW methods.[280]

A particular motif for gold clusters is the triangular $\{Au_3\}^+$, already quoted in Table 7. Compounds with four electrons less, with a formal $\{Pt_2Au\}^{3+}$ core and three bridging diphosphanes, were reported by Toronto et al.[281] The absorption and luminescence spectra were measured and modelled at the QR SW level.

The bimetallic cluster $[Au_4\{Fe(CO)_4\}_4]^{4-}$ and its planar bare-metal framework were studied by Albert et al.[282] at the DFT level. The magnetism induced by the iron atoms was quenched by the carbonyls.

Pure wires: The formation of polyatomic gold wires between a nickel electrode and a gold surface was first predicted by Landman et al.[58] Later simulations on thick wires produce a cylindrical multilayer structure and largest vibrational frequencies approaching 6 THz.[283] These values for wires with radii of roughly 1 nm are above those for bulk gold, or 4.7 THz. All nanowires were found to melt below 1100 K,[284] well below the bulk melting potential of about 1350 K for the potential used.[285]

In an EHT-level study of a helical "7–1" nanowire (one central gold row, seven atoms around it per period), Hasegawa et al.[286] concluded that the outer atoms provide both mechanical stability and electrical conduction. Chiral, seven-strand single-tube nanowires were also found by DFT simulations by Tosatti et al.,[287] in agreement with the observations by Kondo and Takayanagi.[288] No such minimum was found for silver, where the s–d competition leading to surface reconstruction for the (100) surface of an fcc metal to an hexagonal-close-packed arrangement is lacking.[249,289,290] For the latest, electrical conductance evidence on shell structures in gold nanowires, see Díaz et al.[291]

Monoatomic gold wires are wires that are one gold atom thick. Some of them under tension. They form another widely studied topic. As reviewed by Bahn et al.,[292] they were first seen in molecular dynamics simulations and subsequently observed in electron microscope pictures and electrical conductivity measurements.[293,294] In these monoatomic wires, the electric conductivity becomes quantized. The quantum unit is $2e^2h^{-1}$ (in AV^{-1}, corresponding to 1/(12 906 Ohms))* For further references, see Torres et al.[295] Chemical effects on the conductance phenomenon have been studied.[31,296]

The Au−Au distances are of the order of 350–360 pm, before the wire broke under tension. The highest experimental distance claimed is 480 pm. Some possible mechanisms for holding the chain together were enumerated by Torres et al.[295] These included the van der Waals forces, (see Section 3.3). However, no successful aurophilic models have been published. Both experimentally[297] and theoretically,[298] only the late 5d metals (Ir, Pt, Au) form these monoatomic chains.

* For the record, this was written at the end of Ohmstrasse, in Erlangen.

 © 2004 Wiley-VCH Verlag GmbH & Co. KGaA, Weinheim

Smit et al.[297] note that the same metals show surface reconstruction and invoke 6s–5d hybridization.

Ribeiro and Cohen[299] considered both linear and bent monatomic gold chains. A special case of the latter is a flat tape consisting of two parallel chains with 60° bond angles, an extension of the triangular rafts in Figure 12. Nautiyal et al.[300] considered both a linear Au chain and a hexagonal 2D layer.

Doped wire: Another possibility would be that the long, apparently monoatomic gold wires are actually held together by invisible heteroatoms. Novaes et al.[301] find for sulphur impurities an open Au-S-Au angle with Au···Au of about 470 pm under tension of 1.7 nN. Another possibility would be the influence of thiolates.[31,302] The mechanical force on the monoatomic wire can reach about 2 nN before the wire breaks[302] and the process could be seen as "mechanochemistry": feeding in mechanical energy to break a particular chemical bond. Breaking forces of the order of 1–2 nN are commonly obtained.[33,296,301,303–305] Skorodumova and Simak[306] suggest linear {-Au-H-Au-} chains. Bahn et al.[292] consider the incorporation of both O_2 and CO in a monoatomic gold chain.

Gold clusters on other surfaces: A single Au atom was found to bind rather weakly on TiO_2(110) at the DFT level by Giordano et al.[307] Rodriguez et al.[308] found three comparable sites for binding an Au atom: on top of three O atoms, a bridge between two Ti atoms and on top of Ti atoms. Vijay et al.[309] concluded that Au atoms on a five-coordinate Ti atom or atop a bridging O atom had comparable energies, thus suggesting fast diffusion. If the surface was reduced by removing an oxygen atom, a preferential site for Au bonding was created. Substantial charge-transfer to gold occurs. The binding of [Au_2] followed a similar pattern. Wahlström et al.[310] agree with this picture: On a rutile TiO_2(110) surface, [Au_n] clusters were found to bind best to an oxygen vacancy site,[310] with up to three Au atoms per vacancy. The observed positive Au $4f_{7/2}$ core-level shifts of Au atoms on both TiO_2 (110) and MgO (001) surfaces were attributed to the presence of surface O vacancies.[311]

Au atoms on Al(100) were found to bind covalently. The relativistic strengthening and shortening of the bond were explicitly studied.[312] The increase of the work function by Au was entirely attributed to relativistic effects. The core-level shifts in the surface layer were attributed to s–d hybridization. Au atoms on the NaCl(100) surface prefer to sit on top of the cationic sites.[313] For the actual catalytical reactions on such surfaces, see Section 5.3.

Gold clusters and DNA: Ligand-stabilized [Au_{55}] clusters are known to fit into the major grooves of B-DNA. It was found that A-DNA keeps a peeled [Au_{13}] cluster. The system has been modelled at the molecular dynamics (MD) level.[314]

Passivated gold clusters and nanorods: Schiffrin's group[315] exploited phase-transfer catalysis to produce mixtures of large [$Au_N(SR)_M$] clusters by treating aqueous Au salts with hydrophobic thiols at room temperature. Whetten's group[316,317] found ways of selecting by size these passivated clusters. Their structural, electronic, electrochemical, optical, and etching properties have been studied. In the purified forms, N can run from about 20 to 1000 and more. The discussion of their packing structures begins at the level of having structures with a harder "core" and a softer "corona" around the core.[316] Short or moderately long chains (R) yield bcc or fcc superlattices but there are also body-centred tetragonal (bct) structures. Molecular dynamics simulations were reported by Ludtke and Landman.[318] For an example, see Figure 15. The femtosecond dynamics of the gold nanorods have been studied.[319]

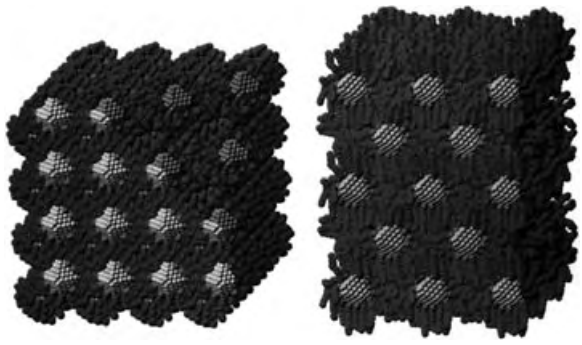


Figure 15. Equilibrium structures of three-dimensional superlattices at 300 K. Left: body-centered cubic superlattice made of [$Au_{140}(C_4H_9S)_{62}$] clusters. A (100) face and a corner-cut exposing a (111) face are shown. Right: a tetragonally distorted face-centered cubic (t-fcc) superlattice made of [$Au_{140}(C_{12}H_{25}S)_{62}$] clusters and an exposed (100) face is shown. Note the preferential aligned molecular bundles and their "interlocking".[318] Copyright 1996 American Chemical Society.

In a study of a passivated, truncated octahedral fcc [$Au_{38}(SCH_3)_{24}$] nanocrystal, Häkkinen et al.[30] determined its electrical capacitance to be 0.084 aF (attofarads), compared to an electrochemical value of 0.13 aF.

The surface atoms in a cluster have fewer neighbors than the bulk atoms, which have twelve. This will lead to an apparent narrowing of both the 5d band and its apparent spin-orbit splitting.[320]

Colors of nanoparticles: The intense red color of colloidal gold nanoparticles is attributed to their surface plasmons, see the review by Link and El-Sayed.[321] They arise from a coherent oscillation of the nearly free conduction electrons. The effects of particle size and shape were treated by using the Mie or Maxwell–Garnett theories. A simple alternative is the model of an electron gas, confined in a box.[322] Palpant et al.[323] used a time dependent (TD)-DFT(LDA) approach to reproduce the optical absorption spectra of 2–4 nm Au clusters in vacuum or in alumina. The "plasmon" peak around 2.4 eV and its size dependence were successfully reproduced.

As discussed by Mafuné and Kondow,[324] the surface plasmon at 450–600 nm is overlapping with an interband transition, peaking in the UV region. Laser irradiation at 355 nm can be used for fragmenting the nanoparticles to the 1.5–2.8 nm range.

A large enhancement of the fluorescence quantum yield, by a factor of more than a million over bulk gold, was observed for the d→sp electronic transitions in gold nanorods encapsulated in micelles.[325] As summarized by Morris et al.,[326] mercury adsorption on the surface of gold nanoparticles leads to a blue shift of the surface plasmon mode.

 © 2004 Wiley-VCH Verlag GmbH & Co. KGaA, Weinheim

4.7. Solids and Surfaces

Pure gold: Some band-structure calculations, explicitly studying the effects of relativity on Au, were already quoted in Table 2. Boettger[327] studied the high-pressure behavior of gold up to 10 Mbar. Above about 3.5–4.1 Mbar gold is predicted to transform from fcc to hcp structure. The results below 3 Mbar are potentially useful for pressure calibration. Several earlier calculations on solid Au are quoted by Boettger. While Ahuja et al.[328] also predicted a hcp phase, Söderlind[329] predicts a bcc structure for the ultimate high-pressure phase above 1.51 Mbar. For high-pressure and high-temperature properties, see Tsuchiya and Kawamura.[330]

Alloys and compounds: Aurides were already listed in Table 5. A sample of other solid-state calculations is given in Table 9. Wang and Zunger[331] noted that the solid 3d–5d compound CuAu was stable while the 3d–4d compound CuAg is not, and attributed this difference to the larger relativistic effects in the 5d case. Both the relativistic radial contraction, the closer 3d–5d energetic distance and the easier s–d hybridization, thus releaving antibonding from the top of the 5d band did help.

Surface reconstruction, adatoms: The role of the facile s–d hybridization in the surface reconstruction of gold, as contrasted to silver, was discussed by Takeuchi et al.,[249,332] by Fiorentini et al.[333] and by Tosatti and Ercolessi,[287,290] who used interatomic potentials with an atomic-density-dependent part, $U(n)$. Typical for gold surfaces, including Au(111), are very strong contractive forces at the surface, combined with rather low shear constants, as indicated by the large ductility and malleability of Au. The role of the 6s–5d hybridization, due to relativistic effects, in leading to surface reconstruction for the (100) surface of a face-centered-cubic metal to an hexagonal-close-packed arrangement was emphasized by both groups. Note that the hexagonal surface layer is incommensurate with the bulk. The energetics of the non-reconstructed Au(100) surface were studied by Eibler et al.[334]

It has been suggested that the hexagonal surface order could even survive on the surface of liquid gold.[335] Note at this point that gold has the next-highest surface tension of all metals. Experimentally the values decrease in the order Cu > Au > Ag > Zn > Cd > Sn > Hg > Pb > Sb > Bi.[336] The experimental γ of gold at 1120–1310 °C is slightly over 1.1 $N\,m^{-1}$, compared for instance with the Hg value of 0.48855 $N\,m^{-1}$ at 25 °C. Cu surpasses Au by a narrow margin. To our knowledge, γ(Au) has not been theoretically calculated.

The diffusion barriers for Au adatoms on Au(100) and Au(111) surfaces were calculated by Boisvert et al.[337] as 0.62(4) and 0.22(3) eV, respectively. The results for Au are now rather higher than lower than those for Ag. The same thing is true for the adsorption energy.

Table 9: Calculations on solids. For aurides, see Table 5.

Authors	Year	Method	System and comments
Weinberger[678]	1982	KKR	$d^n\,s^1$ impurities in Au; $n = 7$–10
Koenig et al.[679]	1984	LMTO	[MAu]; M = Li–Cs. M = Rb, Cs are semiconductors, M = Li–K are metallic; R/NR for CsAu
Davenport et al.[680]	1985	LA-STO	Au; hybridization discussed
Wu et al.[681]	1986		valence levels in AgAu alloys
Qi et al.[682]	1987		Au, [$AuAl_2$]; X-ray absorption; "white lines"
Terakura et al.[683]	1987	ASW	CuAu has ordered phases, Ag/Au is soluble.
Watson et al.[684]	1987	LMTO	alloys of the 5d metals Lu–Pt with Au
Davenport et al.[685]	1988	LA-STO	[Cu_3Au] nonoverlapping 3d and 5d bands; heat of formation
Weinberger et al.[686]	1988		ordered and disordered [Cu_3Au]
Godwal and Jeanloz[687]	1989	LMTO	Au; equation of state
Janiak and Hoffmann[688]	1989	EHT	$[(Au^{I}Cl_2)-(Au^{III}Cl_4)^{2-}]_1$, $[\{(Au^{II}Cl_3)-(Au^{II}Cl_3)\}^{2-}]_\infty$ chain models for halogen-bridged gold chains
Takizawa et al.[689]	1989		AuNi segregates, AuPd forms stable alloys
Arola et al.[690]	1990	KKR	(SO) Disordered $Au_{70}Pd_{30}$.
Arola et al.[691]	1990	KKR	(SO) Disordered $Cu_{75}Au_{25}$.
Krutzen and Inglesfield[692]	1990		calaverite, [$AuTe_2$] incommensurate structure; Te p-Au d hybridization
Weinberger et al.[693]	1990		Fe impurity in Au
Lu et al.[694]	1991	SCPA	Random $Ag_{0.5}Au_{0.5}$. Donation in the direction s(Ag)→s(Au), d(Au)→d(Ag)
Yasui et al.[695]	1991	RAPW	Au; orbital- and SO-induced magnetic susceptibility
Tyson et al.[696]	1992		same conclusion
Weinberger et al.[697,698]	1993	KKR	effective pair interactions in the AuPd system
Weinberger et al.[699]	1994	KKR	electronic and structural aspects of Cu-Au alloys
Bzowski et al.[700]	1995		Au 5d holes in AuM_2, M = Al–In, Sn, Sb, Te; EXAFS experiments
Continenza et al.[701]	1996		optical conductivity of $YbCu_4Au$
Methfessel et al.[702]	2000	LMTO	AuMg; core-level shifts
Philipsen and Baerends[703]	2000	GGA-ZORA	Au; SO increases E_{coh} by 5%, decreases a_0 by −0.4%
Galanakis et al.[794]	2001	LMTO	VAu_4, sign reversal of V orbital moment by ligands
Leiro et al.[704]	2001	SR-LMTO	AuMg, AuZn
Winkler et al.[705]	2001	DFT-PW	$Cs_2Au^{I}Au^{III}Cl_6$ Phase transition to $2Au^{II}$ above 6 GPa
Gauzzi et al.[706]	2002	FLAPW	$Au^{V}S_2$; linear S-Au-S. Hexagonal Au sheets
Godwal et al.[707]	2002	FP-LAPW	$AuIn_2$ $p \leq 10$ GPa.
Hoffmann et al.[708]	2002	TB-LMTO-ASA	LiAuSn, $LiAu_3Sn_4$; planes of condensed Au_3Sn_3 hexagons
Wang et al.[331]	2003		CuAu; stable due to relativity

 © 2004 Wiley-VCH Verlag GmbH & Co. KGaA, Weinheim

Surface states: A spin-orbit-induced splitting of the Shockley-type surface state of Au(111) was observed and explained by Reinert.[338]

Vacancies: The vacancy formation energy for solid gold has been calculated to be of the order of 0.8 eV.[339] The experimental value is 0.93(4) eV.[340]

Atomic mobility in gold and gold clusters: In solid gold, self-interstitial atoms cannot be observed, not even at temperatures as low as 0.01 K, in contrast to Cu and Ag where they exist up to about 38 and 28 K, respectively.[340] Apparently no theory exists for this extreme mobility of Au.

In nanocrystalline gold with grain size of about 20 nm, the activation energy for creep at grain boundaries is measured to be about 0.2 eV or 20 kJ mol^{-1}.[341]

Calculations on solid gold compounds: In addition to the auride work presented in Table 5, one can quote the work on Au_2O_3 by Burdett and Sevov,[224] $Tl_2Au_4S_3$ by Löken et al.[342] For other examples, see Table 9.

Gold-atom impurities in other solids: The case of Au atoms in solid silicon has been modelled by Fazzio et al.[343] The atom is not a simple d^{10} system. In fact it was suggested to be capable of the three charge states Au^+, Au^0, and Au^-. Watkins and Williams[344] considered a substitutional Au^0 in Si. The hyperfine coupling and g tensor were reproduced.

4.8. Optical Properties and Photochemistry

The color of gold and related questions: The optical properties of gold clusters were already discussed. Similarly, the relation of the gap between the top of the 5d band and the Fermi level in the middle of the 6s band[27,345] was already quoted in Table 2. The large relativistic decrease of that gap strongly suggested that the yellow color of gold[25] could be attributed to relativity. The exact combination of this one-particle transition in bulk gold, plasmons, surface states, and relativity, to obtain the "color of gold" has however apparently not yet been worked out. The related question of 5d-hole lifetimes and energies in gold has been addressed by Zhukov et al.[346,347]

Molecules: A large amount of experimental data exists on photoluminescence of gold compounds. Some of these compounds have fascinating phenomena such as solvoluminescence or tribochromism exist. Excited-state covalent bonding has been found. However, rather little theoretical work on this subject, has been carried out so far, see Table 10. For a review on luminescent Au^I compounds, see Gade.[348] The optical properties of molecules can be calculated in wave-function-based calculation at CIS or higher levels. In DFT theories, the TD-DFT approach is a method of choice. One example, $[Tl_2(bipy)_{1.5}(thf)][Au(C_6Cl_5)_2]_2$, is shown in Figure 16.[349] Tetramer chains of the types {Tl-Au-Au-Tl} and {Tl-Au-Tl-Au} were synthesized and modeled (see Figure 17]. TD-DFT calculations exist for the carborane–diphosphanes $[Au\{(PPh_2)_2C_2B_9H_{10}\}PH_3]$.[350]

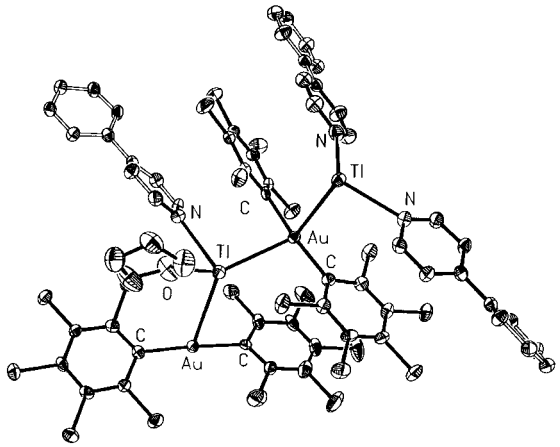


Figure 16. Experimental X-ray crystalographic structure of $[Tl_2(bipy)_{1.5}(thf)][Au(C_6Cl_5)_2]_2$ with a {Tl-Au-Tl-Au} chain.[349] Copyright 2002 American Chemical Society.

Systems with aurophilic attractions: The optical absorption and fluorescence properties of systems with aurophilic pairs or chains have been studied by the group of C. M. Che.[351]

Gold and other metals: For unsupported, infinite Au^I–Tl^I chains, Laguna et al.[155] concluded from TD-DFT model calculations that the excitation has an $\{AuR_2\}\rightarrow Tl^I$ character, whereas the Tl atoms act as fluorophores.

Clusters: Omary et al. found a correlation between the calculated absorption spectra of a naked $[Au_6]$ cluster and the measured vacuum UV spectrum for $[Au_6(PPh_3)_6][BF_4]_2$.[352] No correlation was found for the naked $[Au_6]^{2+}$. For optical properties of gold nanoparticles, see Section 4.6 on clusters.

Nonlinear optical properties of the trinuclear transition-metal clusters $[\{Ph_3PM'\}MS_4\{M'(PPh_3)_2\}]$; M = Mo,W; M′ = Cu–Au were studied by Chen et al.[353]

Table 10: Some calculations of optical properties for molecules or molecular models.

Authors	Year	Method	System and comments
Assefa et al.[709]	1991	REX	$[Au(CN)_2]$ luminescence model
Fernández et al.[710]	2000	TD-DFT	$[Au_2Ag_2(C_6H_5)_4]^n$, $n=1,2$
Sansores et al.[671]	2000	PP+CIS	$[Au_3(CH_3N{=}COCH_3)_3]$ solvoluminescent system
Zhang and Che[351]	2001	PP+CIS	$[Au_2(dpm)_2]^{2+}$ [a]
Fernández et al.[349]	2002	TD-DFT	$[LTlL'][Au(C_6H_5)_2]$, L = py, H_2O
Fernández et al.[155]	2003	TD-DFT	$Tl(OPH_3)_2][Au(C_6H_5)_2]$, its dimer
Pan and Zhang[145]	2003	PP+CIS	$[Au_2(PH_2CH_2S)_2]$and related systems
Xia et al.[154]	2003	PP+CIS	$[PtAu(\mu\text{-}H_2PCH_2PH_2)_2(CN)_2]^+$ and related systems.

[a] dpm = bis(diphosphino)methane. Also with ClO^- counteranions.

4.9. Hyperfine Properties

The gold atom has an experimental magnetic hyperfine splitting of 6099.320184(13) MHz; for a theoretical treatment of this splitting and the isotope shifts of 6s–6p transitions, see the report by Ahmad.[354] Large hyperfine splittings are expected in open-shell systems that contain gold. The

 © 2004 Wiley-VCH Verlag GmbH & Co. KGaA, Weinheim

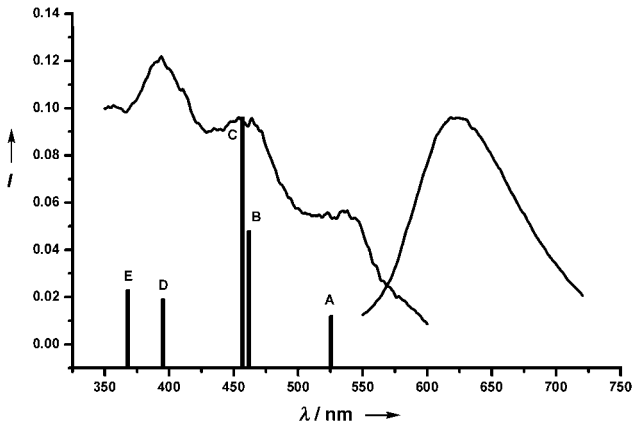


Figure 17. Calculated TD-DFT excitation spectrum (A–E), observed excitation spectrum and observed luminescence spectrum for the tetranuclear Tl-Au-Tl-Au system in Figure 16. From Fernandez et al.[349] Copyright 2002 American Chemical Society.

observed hyperfine splittings have been theoretically calculated based on a C_{2v} structure for $\{Au_3\}$ by using fully relativistic SW methods. [355]

The electric-field gradients (EFG or q) at the gold nucleus can be observed by Mössbauer spectroscopy, which also gives a direct measure of the gold oxidation state through the electron density, seen via the isomer shift. The relativistic effects on the positive EFG of the $[AuX_2]^-$ ions or on the negative EFG of the $[AuX_4]^-$ ions were studied at the SW level.[60]. In the older literature there was a debate whether the q(Au) of AuX_2^- would be dominated by the gold 6p electrons[356] or by 5d holes.[357] The former calculations were relativistic but based on population analysis. The latter were NR DVM calculations on the actual ion. Schwerdtfeger favors the latter sign. [60] In diatomic [AuCl] the q is small and positive.[358] The gold nuclear quadrupole coupling constant in the icosahedral $[WAu_{12}]$ is calculated to be 549 MHz, a typical value for monocoordinated gold.[267]

Magnetic shielding effects: The planar, C_{2v} system $[Au_5Zn]^+$ is characterized as "σ aromatic" and has magnetic screening effects ("nucleus independent chemical shifts", NICS) of the order of 20 ppm inside and above the molecule.[359]

Parity violation effects: These effects are calculated to shift the C–F stretching vibration of $[PH_3AuCHFCl]$ by 0.158 Hz.[360]

4.10. Medical Applications

The experimental biochemistry of gold has been reviewed.[361–364]

4.11. Speciation of Gold

Determining the chemical species in which gold occurs in aqueous solutions is important in geochemistry, metal cycling etc. The broadest study so far for $Au^{I,III}$ in presence of sulfide and chloride has been published by Tossell,[365] unfortunately only at PP HF level. Some attempts were made to include solvent effects.

4.12. Electrochemistry and Solvation

The electrode potentials for a number of electrode reactions in aqueous solution are known.[366] Their theoretical simulation will be a challenge for theory.

Bryce et al.[367] studied Au^I thiosulphate, $[Au(S_2O_3)_2]^{3-}$, including solvent effects through a COSMO continuum model. The calculated Au–S distances were about 236 pm, compared to the values obtained by extended X-ray absorption fine structure (EXAFS) spectroscopy of 229 pm in solution. The calculated Au^I/Au^0 half-reaction energy of $-560\ kJ\,mol^{-1}$ is comparable with the experimental $-592\ kJ\,mol^{-1}$. The complex $[Au(SH)_2]^-(aq)$ was included in the study and exhibited slightly larger stability than the thiosulphate complex. Earlier, less systematic studies of gold thiocomplexes in solvents were reported.[368]

In an experimental context, Li and Gewirth[369] also presented simple DFT cluster models for Bi-modified Au(111) surfaces. Bi–OH and Bi–O species were shown to play a role in electroreduction of hydrogen peroxide.

The electrochemistry of gold clusters was already mentioned in Section 4.6.

4.13. Electron Transport from Gold Electrodes

The case of quantized conductance in monoatomic wires was discussed in Section 4.6.

Damle et al. studied the conductance of a S-(p-C_6H_4)-S group between two gold electrodes.[370] Bauschlicher et al. placed a benzene-1,4-dithiol between electrodes, assumed to have the fcc structure of bulk gold.[371] A tip comprising one Au atom then helped to reduce the current closer to experimental value. Mozos et al.[372] considered the electron transport between carbon nanotubes and gold contacts.

5. Catalysis

5.1. Homogeneous Catalysis

Teles et al. of BASF reported a new, very efficient class of homogeneous Au^I catalysts for the addition of alkohols to alkynes under mild conditions.[373] They were of the type $[LAu]^+$, where L is a phosphane, phosphite or arsane. The catalytic cycle was elucidated by PP calculations at a combined DFT/MP2 level.

For a review on homogeneous gold catalysts in syntheses involving alkynes, see the report by Hashmi.[374] In contrast to Au^I-based catalysts of Teles et al., most applications quoted by Hashmi are based on Au^{III} compounds, notably $Na[AuCl_4]$ or $AuCl_3$.

5.2. Cluster Catalysis

On the experimental side, the catalytical activity of of supported gold clusters was discovered in 1987 by Haruta et al.[375] The oxidation of CO on Au/TiO_2 or Au/Fe_2O_3 took place, down to as low temperatures as 40 K, as found in the group of Goodman.[376] The size of the particles plays a major role, the most active Au particles having diameters of 2–4 nm. For recent reviews, see reference [9, 377–381]. The interaction of O_2 with cationic[245] and anionic[247,382] gold clusters in the gas phase has also been studied. Furthermore, the role of trace amounts of water on gold clusters on the O_2 adsorption, producing adsorbed OH^-, has been studied.[383]

A number of particular theoretical studies exist. The interaction of O_2 with gas-phase gold clusters $[Au_n]^q$; $n \leq 8$; $q = -1, 0$ by Yoon et al.[384] gives the general conclusion that molecular, O_2 adsorption takes place for $n \leq 3$ while dissociative adsorption takes place for $n \geq 4$. The dissociation involves a significant barrier of 1 eV or more and results in a large structural distortion of the host. The anions have a stronger interaction with O_2 and the adsorption prefers even n to odd n. The opposite conclusion was obtained by Mills et al.,[385] but their work may require revision.[386]. The molecular bonding mechanism involves charge transfer to the oxygen molecule with a concomitant activation of the O–O bond to a superoxo-like state. Note that all these clusters were planar. Other studies of the problem do not disagree with this picture.[386–389] Wells et al.[387] went up to $n = 11$ and obtained the largest adsorption energy for $n = 10$ when $q = -1$. Methodologically, Varganov et al.[390] find that DFT would overbind O_2 to $[Au_n]^q$ clusters ($n = 2,3$; $q = -1,0$). At CCSD(T) level, smaller oxygen-binding energies are obtained.

As a counterexample we note that $[Au_{55}]$ clusters on top of silicon wafers were reported to be particularly inert towards oxygen. Not only O_2 but even the oxygen atoms and radicals in plasma failed to react. The observation was attributed to a closed electronic-shell structure,[256] without naming the effective electron number that is expected to fill the shells.

We can then let the adsorbed oxygen react with CO.[391,392,393,394] A possible role for the surface adsorption of the gold cluster to a surface like MgO or TiO_2 is that it will transfer electrons to the gold cluster.[391] This would explain the observed similarities in the reactions of $[Au_n]$, adsorbed on TiO_2, and the gas-phase $[Au_n]^-$ anions.[382] Because the gold wets the titania, flat shapes and large HOMO–LUMO gaps result. For gold particles on MgO(100), Molina and Nørskov[395] find that the CO adsorbs near the junction and then reacts further with adsorbed O_2, which has peroxo character.

The oxidation of CO to CO_2 on a flat $[Au_{10}]$ model was studied by Lopez and Nørskov.[394] This particle was also here found to split O_2 to form a superoxide-like O_2^- state and the adsorbed O was stable in the gas phase. After that, the barrier to CO_2 was low, lower than on a Pt(111) surface. The d levels of the cluster lie higher than those of the surface and this was suggested to strengthen the chemical interactions with adsorbates. Furthermore the particle surface offered corner sites at which the O atom could coordinate to three low-coordinated Au atoms at the same time. The low-coordinated Au atoms had higher-lying d states, which interact more strongly with the adsorbates, a situation noted to favor Au in mixed $[Ag_mAu_n]$ clusters reported in reference[396].

Lopez and Nørskov mention among the suggested reasons behind the catalytic activity of gold:[394] 1) quantum-size effects (with respect to the thickness of the gold islands),[376] 2) charging of the particles by interaction with the defects in the oxide, and 3) availability of low-coordinated sites and strain. Concerning point (1), Mavrikakis et al.[397] found no dependence of the adsorption properties of O_2 and CO on the number of layers in the slab models.

Häkkinen et al. considered the problem of CO oxidation on small gold particles, adsorbed onto a MgO(100) surface.[398] Experimentally, $[Au_8]$ was the smallest particle that catalyzed the reaction. The total binding energies of $[Au_3Sr]$, $[Au_4]$, or $[Au_8]$ clusters to a surface oxygen vacancy (also called surface F centre, FC) were calculated to be in the range of 2.65–4.06 eV. The clusters acquired a small negative charge. Of their three quoted qualitative explanations, the authors found that both 1) dynamic structural fluxionality, 2) quantum-size effects, and 3) impurity-doping effects were there. The effect of point (1)allows the reaction to proceed. The effect of point (2) was behind the splitting of O_2, only if the $[Au_n]$ cluster was big enough. As an example of point (3), although $[Au_4]$ is inactive, $[Au_3Sr]$ does catalyze the reaction. The narrower d band of the smaller $n = 4$ cluster did not reach the O_2 binding levels, whereas those of the $n = 8$ case did.

The entire system of CO interacting with small gold clusters ($[Au_n]$; $n = 1$–3), attached to a TiO_2 slab surface, was studied by Vittadini and Selloni.[399] In contrast to O_2, the CO molecule prefers cationic gold clusters to anionic gold clusters. The lone pair on cationic gold clusters is nucleophilic.

The interaction of an NO_2 molecule with a metal–zeolite model (M = Cu–Au) was discussed by Sierraalta et al.[400] Again the promotion from d^{10} to d^9s^1 was found to favor the interaction between the metal and the NO_2 molecule.

The dissociation of SO_2 on $Au/TiO_2(110)$ was studied by Rodriguez et al.[308] Gold was found to enhance the reactivity of the titania by facilitating the migration of O vacancies from the bulk to the surface. Such oxygen vacancies can also be characterized as surface F centers (FC; i.e., point defects).[398] Periodic gold structures on $TiO_2(110)$ were studied by Lopez and Nørskov.[401] In the absence of defects, the interaction of Au with the support remained weak.

5.3. Surface Adsorption and Heterogeneous Catalysis

Why are gold surfaces "noble"? Hammer and Nørskov[6,402] considered the interaction of a particular ligand, namely, H_2 with a gold (111) surface. Gold was found to have both the highest barrier of dissociation and the least-stable chemisorption state among the metals considered (M = Ni, Cu, Pt, Au). In orbital terms this instability was reduced to the fact that the antibonding $1s_H$-d_M combination is filled for the coinage metals and particularly repulsive for Au among them.

In bulk chemistry, the stability of various compounds will depend on their relative free energies and, apart from the

 © 2004 Wiley-VCH Verlag GmbH & Co. KGaA, Weinheim

influence of the high atomization energy of metallic Au, general, sweeping statements can not and should not be made.[403]

Thiolates on gold: Self-assembled monolayers of alkane thiolates, RS^-, on gold surfaces are widely studied. For a summary of the results of studies on theoretical thiolates, see Table 11. Tachibana et al.[404] find at EHT level that the threefold hollow gives the strongest bond, followed by bridge and on-top sites. Yourdshahyan and Rappe[405] studied thiolate adsorption on an Au(111) surface and found both a physisorbed state of CH_3CH_2SH with an adsorption energy of 0.32 eV at 335 pm from the surface, and lower-lying chemisorption states of CH_3S, with adsorption energies of typically 1.7 eV and Au–S bond lengths of about 250 pm. Bridge sites with two gold atoms were preferred over fcc sites with three gold atoms.The surface lattice of thiolates was also studied.

Larsson et al. found that on an octahedral $[Au_{13}]$ nanoparticle, methanethiol and benzenethiol bind to the threefold site.[406] The gold–gold bond lengths inside the particle increased by as much as 25% on the side bound to the thiolate. Likewise, strong deformations of gold nanoparticles were found by Garzón et al.[407,408]

Molina and Hammer[409] studied the thiol-induced reconstructions on the Au(111) face. Vacances on the gold side were found to cost about 0.6 eV and to favor the thiol adsorption by 0.8 eV, which was predicted to lead to a surface with defects.

Andreoni, Grönbeck et al.[410,411] compared thiolate or disulfide adsorption on Au(111) slab models to that on $[Au_{38}]$ cluster models and found substantial differences between the two. The disulfide dissociated to form thiolates on the surface.

Thiocyanate on gold: Li and Gewirth[412] find that the coordination mode of SCN^- on Au electrodes is dependent on the potential: low potentials favor the N-centred orbitals and high potentials favor the S-centred orbitals. A periodic slab model was used for the gold surface.

Water on gold: Michaelides et al. suggest that a water molecule would bind to close-packed transition-metal surfaces, such as unreconstructed Au(111), by its b_1 MO in a flat or side-on orientation.[413]

Methanol on gold**:** Rousseau et al. studied the adsorption of methanol on $[Au_n]$ clusters.[414] The Au–O stretching frequency was used as an indicator of the interaction.

Ammonia on gold: Bilić et al. studied the adsorption of ammonia on Au(111) by using DFT with a PW91 functional.[415] On-top sites were preferred and a single-molecule adsorption energy of 34 kJ mol^{-1} was obtained.

NO_2 on gold: No_2 was found to have both O-bound and N-bound isomers on cluster models for Au(111).[75]

Alkanes on gold**:** This adsorption process was studied by Fichthorn and Miron as function of the alkane chain length at molecular dynamics level.[416]

Cyanide on gold: The observed shifts of the C–N stretching frequency with electric field were calculated by Liao et al.[417]

Bisulphate on gold: A tripod orientation was found most stable and the bond was characterized as electrostatic.[418]

SO_2 on gold: Corner sites of free clusters were found to bind stronger than bulk Au(100).[419]

Surface adsorption and electron tunneling: The C_{60} fullerene adsorbs on Au(111) surfaces and has been studied by scanning tunneling spectroscopy experiments. The adsorption energy is estimated to be 167–251 kJ mol^{-1} (40–60 kcal mol^{-1}). Electron transfer from the metal to the fullerene LUMO takes place. A theoretical analysis[420] of the tunneling current was given as function of the distance between the microscope tip and the fullerene surface, and as function of voltage.

Heterogeneous catalysis: The work involving the use of cluster models has been discussed above. The adsorption of O and CO on flat and stepped Au(111) surfaces, and a periodic Au_{18} model, was considered by Mavrikakis et al.[397] Two atomic layers suffice for the thickness of the slab. Splitting of CO on the surface was not considered. For earlier work on CO on Au(111) see Hammer et al.[7]

In summary**,** the theoretical treatment of heterogeneous catalysis on metal or metal alloy surfaces (see the review by

Table 11: Studies of alkali thiolates on an Au(111) surface.

Authors	Year	Method	Comments
Sellers et al.[603,604]	1993	PP + MP2	SCH_3, SH on stiff $[Au_n]$ models
Beardmore et al.[602]	1998	DFT	no particular site preferred
Häkkinen et al.[30]	1999	DFT	$[Au_{38}(SCH_3)_{24}]$; capacitance 0.084 aF, agrees with electrochemical measurements
Garzón et al.[407]	2000	DFT	dramatic distortion by thiolates in $[Au_{38}(SCH_3)_{24}]$
Grönbeck et al.[410,411]	2000	DFT	Au(111) slab + SCH_3 [a]
Johansson et al.[675]	2000	PP + HF	PhS- on $[Au_{10}]$
Akinaga et al.[676]	2001	PP-DFT	Au_{18}-SCH_3 model for Au(111); R/NR; relativistic decrease of D_e, for Cl, O, S, OH, SH, SCH_3 but not for H
Garzón et al.[408]	2001	DFT	hybrid DNA-gold
Krüger et al.[32]	2001	PP + DFT, QCISD(T)	$[Au_nSR]$; $n \leq 5$; R = ethyl and propyl more strongly bound than methyl. Au-S-C 103.5–108.7° well-defined.
Molina and Hammer[409]	2002	PP-DFT-PW	vacancies in gold induced.
Tachibana et al.[404]	2002	EHT	$3 > 2 > 1$ [a]
Larsson et al.[406]	2002	DFT	$3 > 2$[a] strong $[Au_{13}]$ deformation by thiolates
Yourdshahyan et al.[405]	2002	DFT-PW	between 3 and 2[a]
Majumder et al.[677]	2003	DFT-PW	thiophene thiol on Au(111) models; $[Au_n]$, $n = 3,24$, slab

[a] Stability order for the given sulfur coordination numbers. Strongest bond first.

 © 2004 Wiley-VCH Verlag GmbH & Co. KGaA, Weinheim

Greeley et al.[421]) has now reached a point that it can be applied to problems, for example, the design of a commercially produced surface alloy catalyst for steam reforming based on high-surface-area gold-nickel alloys.[422] The substitutional alloying of gold to the nickel diminishes the problem of graphite formation. Note that the gold is only needed on the surface.

6. Conclusions

In the theoretical chemistry of gold, two aspects are understood and two not. First, the covalent bonds in small molecules or the electronic structure of bulk metals with simple structures can be calculated with a fair degree of confidence and the role of relativistic effects in them is also understood. Second, it seems that the nature of the "aurophilic" attraction between the d^{10} shells of neighboring gold atoms or ions is now understood as a dispersion effect, with some virtual charge-transfer contribution. Thus a vast domain lies already open for interpretation and prediction.

Based on this understanding at a more approximate level, various molecular dynamics or force-field approaches permit the studies of nanosized systems and surface processes. The Car–Parrinello approach also can be applied to simpler cases.

Two areas that are even more complicated, and not yet thoroughly understood: the nature of the plasma oscillations in gold clusters, which are responsible for their strong colors, in particular their connection with the molecular orbital or band structure; the exact nature of the great fluxionality of gold clusters, gold surfaces, or interstitial atoms in bulk gold. Time will show whether any surprises lie in store there.

Considerable progress is being made in mastering catalysis by systems, wholly or partially based on gold.

Addendum

Between submission and proofs of this Review, about eighty further papers have appeared, which amply demonstrates the current interest in the topic. A few missed references are also included.

In a volume on organic derivatives of Ag and Au, Hoz and Basch[711] review general and theoretical aspects and Liebman et al.[712] thermochemistry. A reduced valence-basis set for use on Au clusters with an SKBJ[437] pseudopotential appeared.[713] A further set of semiempirical atomic potentials was developed.[714]

Section 3.2: The choice of coordination number CN = 2–4 among d^{10} coinage-metal ions was discussed from the perspective of a database analysis and DFT calculations.[715] An energy-partitioning analysis was performed for acetylene and ethylene complexes of gold.[716] Mixed cyanide-halide complexes of Au^{III} and their vibrational spectra were studied at the DFT level.[717] Relativistic effects were explicitly studied in a comparison of η^2 ethylene and P_4 complexes of Au^+.[718] Owing to relativity, Au–P bonds are shorter than those of Ag–P.

Section 3.3: Aurophilic attractions were also shown to exist in Au^{I}-Au^{III} and Au^{III}-Au^{III} pairs.[719,720] O'Grady and Kaltsoyannis[721] raised the question of whether the calculated stronger metallophilicity for Au with respect to Ag would be specific for the MP2 approximation used. They report that higher levels, up to CCSD(T), would give the opposite trend. Wang and Schwarz[722] found purely empirically that local density functionals (LDF) would produce an attraction, which mimicks the aurophilic attraction.

Section 4.2: The analogy between compounds $[MH_n]$ and $[MAu_n]$ (without phosphanes or other ligands on the gold) was tested in several papers. Kiran et al. reported experimental and theoretical studies on gas-phase $[SiAu_4]$,[723] which is analogous to SiH_4 and $[SiAu_n]$, $n = 2,3$, as well as their anions. Gagliardi and Pyykkö found for Group 5 $[MAu_5]$ and Group 6 $[MAu_6]$ molecules that their structures were analogous to those of the $[MH_n]$ hydrides.[724]

Ghanty et al. found that their dimers $[(MAu_4)_2]$, in which M is an element of Group 4, are strongly bonded and not at all van der Waals-like. [725] These systems form a daunting challenge for theory, because neither DFT nor MP2 are adequate levels for a system combining van der Waals-like interactions and dynamic correlation. A relation to bonding in solid $TiAu_4$ may exist.

Section 4.4: The species [KrAuF] was observed in microwave spectroscopy. On basis of observed Kr quadrupole coupling and MP2 calculations, the Kr–Au bond was classified as weakly covalent.[726]

Section 4.5: Among further spectroscopic species, the bent gold dihydride was observed and its X^2B_2 ground state related to the Au atom ^2D state.[727] The molecule lies above $Au(^2S) + H_2$.

Halides: The triatomic dihalides $[AuX_2]^q$; X = Cl,Br; $q = -1,0,+1$ were observed by mass spectroscopy and theoretically characterized by Schröder et al.[728] Note the three formal oxidation states of gold.

Carbonyls: Neutral and cationic $[Au(CO)_n]$, $n = 1,2$ were created at gold field-emitter tips in high electrostatic fields. The situation, including the field, was modelled at the DFT level.[729] The thiocarbonyls [AuCS], $[Au(CS)_2]$ and $[Au_2CS]$ were observed in solid argon and characterized at the DFT level.[730]

Section 4.6, studies on pure $[Au_n]$ clusters: At the quantum mechanical level, a further study of neutral and charged $[Au_4]$ clusters appeared.[731] Two interesting suggestions were made concerning novel structures of medium-sized $[Au_n]$ clusters. Johansson et al. predicted that neutral $[Au_{32}]$ would be a hollow sphere of icosahedral symmetry (an icosahedron outside a dodecahedron) at absolute zero.[732] Both experimentally and theoretically, Häkkinen et al. found that gas-phase $[Au_{55}]^-$ cluster has a low-symmetry, disordered structure, whereas its Cu and Ag analogues are icosahedral.[733] An explicit R/NR comparison showed that this structural change was due to relativistic effects.

Molecular dynamics studies of the melting and freezing of very large clusters ($n \leq 3943$) illustrate the decrease of T_m with decreasing n,[734] originally predicted by Pawlow in 1908.[792] Experimental data on the same phenomenon exist. A structural transformation of the cluster in the 3–14 nm size

 © 2004 Wiley-VCH Verlag GmbH & Co. KGaA, Weinheim

range from icosahedral to decahedral morphology just below the melting point was experimentally observed.[735] Rearrangement collisions between two gold clusters ($n \leq 14$) were modelled.[736] The structures of both pure and methylthiol-passivated gold clusters ($n = 12$–212) were studied by Garzón et al. and some chiral structures were found.[737] The MD studies of passivated gold nanoclusters were reviewed by Landman and Luedtke.[738]

The bimetallic clusters $[Ag_mAu_n]^+$; $m+n<6$ were studied both by experimental collision cross sections in He gas and by DFT calculations.[739] Most of the positive charge resides on silver. The structures were discussed. The $[WAu_{12}]$, mentioned above in chapter 4.6, was placed inside an icosahedral Si_{60} fullerene by Sun et al.[740] Upon geometry optimization, the gold atoms get "stuck" to the Si atoms, instead of the W atom. An experimental study of $[Au_nX]^+$ systems revealed stability maxima at 8 or 18 valence electrons for X = Sc,Ti. For X = V–Ni, the behavior was more complicated.[741] DFT calculations on related $[Au_5X_m]^+$ systems give planar C_{2v} structures.[742]

For pure gold nanowires, da Silva et al. are able to reproduce Au–Au distances in the range of 300–310 pm for monowires by using DFT.[743,744] The chains then have three two-coordinated Au atoms. The other possible explanation for the observation of such distances in electron microscopy it that there are invisible carbon atoms.[745] Monatomic AuMg and AuZn wires were studied by Geng and Kim.[746]

An MD study of local clusters and defects in thicker gold wires was reported by Hui et al.[747]

Section 4.7: Theoretical studies appeared on the lattice dynamics and high-pressure behavior[748] or the structure factor[749] of solid gold. Pressure effects on liquid gold were simulated at the MD level.[750] Band-structure calculations were published on the electronic structure of solid $AuTe_2$ (calaverite).[751] Solid $AuPS_4$ has a chain structure with almost planar $\{AuS_4\}$ groups and the bonding was analyzed.[752]

The various options for reconstruction of Au(110) surfaces were studied by Lozovoi.[753] Honeycomb chains of Au on an Si(111) surface were modelled by Erwin.[754]

Section 4.8: Plasmon excitations of covered nanoparticles have been modelled by TD-DFT calculations by using a jellium model with the electron density of gold.[755]

Jahn–Teller distortions were studied in the excited states of three-coordinate Au^I phosphane complexes.[756] CIS calculations of the optical spectrum of the eight-ring with the ligand combination $[Au_2(dpm)(HSCH_2SH)]^{2+}$ were published by Pan and Zhang.[757] Both DFT and CASSCF calculations were reported for the optical spectra of two Au^I atoms, coupled by a polyacetylide chain.[758] Spin-orbit effects will allow triplet→singlet transitions.

For the tetrahedral $[Au_{20}]$ cluster at the TD-DFT level, a large first hyperpolarizability was found.[759]

Section 4.9: For a review on Mössbauer studies on gold compounds, see Parish.[760] For NMR and ESR, see Shaw.[761]

Section 4.12: The solvation of Au^+ in water was simulated by Armunanto et al.[762] A very labile first hydration shell was found. The second shell also was large.

Section 4.13: In view of potential electronic nanodevices, electron transport through molecules attached to gold, mostly through thiolates, continues to draw attention. Basch and Ratner use pseudopotential methods on several different intervening hydrocarbons and $[Au_4]$ model electrodes.[763–766] They identified the main contributions to the density of states and studied the field-dependence of the electron transport. Other studies exist for benzene dithiolate,[767,768] which was found to act as a bistable electric switch, depending on its conformation.[769] Electron transport through monatomic[770,771] gold nanowires was also studied. All these studies aim at the current–voltage characteristics of the junction.[768] Several other workers concentrated on the interaction between thiolate groups and different models for a gold electrode.[772–776] A comparison of thiolates with different tails on an Au(111) slab model also appeared.[777]

Section 5.1: Homogeneous catalysis, based on Au^I species were reported for *exo*- and *endo*-cyclization of enynes.[778]

Section 5.2: In gas-phase cluster catalysis, or adsorption of molecules onto small clusters, the adsorbants/reactants include molecular hydrogen,[779] oxygen,[780–783] CO,[781,783] HS,[784] methanol[785] and ethanol.[786] The cleavage of the thiolate S–H bond on gold clusters was considered.[775]

Section 5.3: The mechanism for CO oxidation on TiO-supported Au clusters were studied by Liu et al.[787] They suggest that the oxidation takes place at the metal–surface interface. The adsorption of the O atom at the interface is also relevant. Experimentally, Daté et al. have found that moisture plays a vital role in that catalytic process.[788] Guzman and Gates detect both Au^0 and Au^I centers in the working catalyst and find the catalytic sites to have the latter.[789]

Monolayers or partial monolayers of S, Se, or SH on Au(111) were studied by Mankefors et al.[790] The proceedings of the Gold 2003 conference contain a number of articles on gold-based catalysts.[793]

In summary, the status of understanding the catalysis by unsupported clusters in the gas phase, or in particular that by supported clusters on solid surfaces, still appears to be in its infancy.

Acronyms and Symbols

Acronym	Method
α	electric polarizability tensor
AMFI	atomic mean-field SO
β	hyperpolarizability
BSSE	basis-set superposition error
CASSCF	complete active space self-consistent field
CC	coupled cluster approximation
CCSD	coupled clusters with singles and doubles
CCSD(T)	dito, including perturbative triple excitations
CI	configuration interaction (= superposition of configurations)
CIS	configuration interaction with single excitations
CNDO	complete neglect of differential overlap
COSMO	"conductor-like screening model", a dielectric continuum model for solvation
CP	Car–Parrinello: simultaneous solution of

 © 2004 Wiley-VCH Verlag GmbH & Co. KGaA, Weinheim

	the electronic and nuclear problems in a plane-wave basis; uses PP
DF	Dirac–Fock (= relativistic Hartree–Fock = Dirac–Hartree–Fock)
DFT	density functional theory
DK	Douglas–Kroll approximation
Dmol	an all-electron DFT code
DPT	direct perturbation theory
DVM	discrete variational method
EA	electron affinity
ECP	effective core potential (= PP)
EHT	extended Hückel theory
EXAFS	extended X-ray absorption fine structure
GGA	generalized gradient approximation (in DFT)
GVB	generalized valence bond
HF	Hartree–Fock
IP	ionization potential
KKR	Korringa–Kohn–Rostoker band structure method
LDA	local density approximation (in DFT)
LMP2	localized-orbital MP2
μ	electric dipole moment
MBPT	many-body PT
MP*n*	*n*th-order Møller–Plesset
MR	Multireference.
NDO	neglect of differential overlap
NICS	nucleus-independent chemical shifts
OCE	one-centre expansion (of peripheral hydrogen atoms)
PP	pseudopotential (= ECP)
PT	perturbation theory
PW	plane wave basis
QDM	quantum defect method
QED	quantum electrodynamics
QR	quasi-relativistic (= SO-averaged = SR)
RESC	relativistic elimination of the small component
REX	relativistic extended Hückel
SO	SO coupling
SR	scalar relativistic: SO average
SW	scattered wave
TD-DFT	time-dependent DFT
ZORA	zeroth-order regular approximation

This work was supported by The Academy of Finland, project 180437. The author thanks the Alexander von Humboldt Foundation for a Humboldt Research Prize and Professor Bernd Hess and his group for their hospitality at Erlangen. Thanks also to the colleagues who read the manuscript before publication and greatly improved it.

Received: August 11, 2003

[1] *Gold. Progress in Chemistry, Biochemistry and Technology* (Ed.: H. Schmidbaur), Wiley, Chichester, **1999**, p. 894.

[2] M. Jansen, A. V. Mudring in *Gold. Progress in Chemistry, Biochemistry and Technology* (Ed.: H. Schmidbaur), Wiley, New York, **1999**, pp. 747–793.

[3] P. Pyykkö, *Angew. Chem.* **2002**, *114*, 3723–3728; *Angew. Chem. Int. Ed.* **2002**, *41*, 3573–3578.

[4] J. W. Lauher, K. Wald, *J. Am. Chem. Soc.* **1981**, *103*, 7648–7650.

[5] R. Hoffmann, *Angew. Chem.* **1982**, *94*, 725–739; *Angew. Chem. Int. Ed. Engl.* **1982**, *21*, 711–722.

[6] B. Hammer, J. K. Nørskov, *Nature* **1995**, *376*, 238–240.

[7] B. Hammer, Y. Morikawa, J. K. Nørskov, *Phys. Rev. Lett.* **1996**, *76*, 2141–2144.

[8] P. Schwerdtfeger, *Heteroat. Chem.* **2002**, *13*, 578–584.

[9] P. Schwerdtfeger, *Angew. Chem.* **2003**, *115*, 1936–1939; *Angew. Chem. Int. Ed.* **2003**, *42*, 1892–1895.

[10] P. Pyykkö, *Relativistic Theory of Atoms and Molecules, Vol. III*, Springer, Berlin, **2000**, pp. 108–111.

[11] H. Schwarz, *Angew. Chem.* **2003**, *115*, 4580–4593; *Angew. Chem. Int. Ed.* **2003**, *42*, 4442–4454.

[12] N. Bartlett, *Gold Bull.* **1998**, *31*(1), 22–25.

[13] R. Puddephatt, *The Chemistry of Gold*, Elsevier, Amsterdam, **1980**.

[14] R. J. Puddephatt in *Comprehensive Organometallic Chemistry, Vol. 2* (Ed.: G. Wilkinson), Pergamon, Oxford, **1982**, pp. 765–821.

[15] R. J. Puddephatt in *Comprehensive Coordination Chemistry, Vol. 5* (Ed.: G. Wilkinson), Pergamon, Oxford, **1987**, pp. 861–923.

[16] R. J. Puddephatt, J. J. Vittal in *Encyclopedia of Inorganic Chemistry, Vol. 3* (Ed.: R. B. King), Wiley, Chichester, **1994**, pp. 1320–1331.

[17] H. Schmidbaur in *Gmelin Handbuch der Anorganischen Chemie*, 8th ed (Ed.: A. Slawisch), Springer, Berlin, **1980**.

[18] H. Schmidbaur in *Encyclopedia of Inorganic Chemistry, Vol. 3* (Ed.: R. B. King), Wiley, Chichester, **1994**, pp. 1332–1340.

[19] A. Grohmann, H. Schmidbaur, in Comprehensive Organometallic Chemistry II, Pergamon, Oxford, **1995**, pp. 1–56.

[20] It was first shown by Rose et al.[423] that the dominant relativistic effects on the Au 6s level are the direct ones.

[21] P. Pyykkö, M. Tokman, L. N. Labzowsky, *Phys. Rev. A* **1998**, *57*, R689-R692.

[22] L. Labzowsky, I. Goidenko, M. Tokman, P. Pyykkö, *Phys. Rev. A* **1999**, *59*, 2707–2711.

[23] J. P. Desclaux, P. Pyykkö, *Chem. Phys. Lett.* **1976**, *39*, 300–303.

[24] P. Pyykkö, *Adv. Quantum Chem.* **1978**, *11*, 353–409.

[25] P. Pyykkö, J. P. Desclaux, *Acc. Chem. Res.* **1979**, *12*, 276–281.

[26] P. Pyykkö, *Chem. Rev.* **1988**, *88*, 563–594.

[27] N. E. Christensen, B. O. Seraphin, *Phys. Rev. B* **1971**, *4*, 3321–3344.

[28] *Relativistic Electronic Structure Theory. Part I. Fundamentals* (Ed.: P. Schwerdtfeger), Elsevier, Amsterdam, **2002**, p. 935.

[29] *Relativistic Effects in Heavy-Element Chemistry and Physics* (Ed.: B. A. Hess), Wiley, Chichester, **2003**, p. 307.

[30] H. Häkkinen, R. N. Barnett, U. Landman, *Phys. Rev. Lett.* **1999**, *82*, 3264–3267.

[31] H. Häkkinen, R. N. Barnett, U. Landman, *J. Phys. Chem. B* **1999**, *103*, 8814–8816.

[32] D. Krüger, H. Fuchs, R. Rousseau, D. Marx, M. Parrinello, *J. Chem. Phys.* **2001**, *115*, 4776–4786.

[33] D. Krüger, H. Fuchs, R. Rousseau, D. Marx, M. Parrinello, *Phys. Rev. Lett.* **2002**, *89*, 186402, 1–4.

[34] T. Bastug, D. Heinemann, W.-D. Sepp, D. Kolb, B. Fricke, *Chem. Phys. Lett.* **1993**, *211*, 119–124.

[35] P. Pyykkö in *Relativistic Effects in Atoms and Molecules, Vol. 2* (Ed.: S. Wilson), Plenum, New York, **1988**, pp. 137–226 with the ITEREX diskette.

[36] W. A. Shapley, J. R. Reimers, N. S. Hush, *Int. J. Quantum Chem.* **2002**, *90*, 424–438.

 © 2004 Wiley-VCH Verlag GmbH & Co. KGaA, Weinheim

[37] L. A. Cole, J. P. Perdew, *Phys. Rev. A* **1982**, *25*, 1265 – 1271.
[38] T. M. Miller in *CRC Handbook of Chemistry and Physics*, *Vol. 83* (Ed.: D. R. Lide), CRC, Boca Raton, FL, **2002**, chap. 10, pp. 147 – 162.
[39] C. Moore, *Atomic Energy Levels*, *Vol. III*, National Bureau of Standards, Washington, DC, **1958**, circular 467 of the NBS.
[40] S. Bouazza, J. Bauche, *Z. Phys. D* **1988**, *10*, 1 – 11.
[41] D. J. Beideck, L. J. Curtis, R. E. Irving, S. T. Maniak, R. Hellborg, S. G. Johansson, I. Martinson, M. Rosberg, *J. Opt. Soc. Am. B* **1993**, *10*, 977 – 981.
[42] M. Rosberg, J.-F. Wyart, *Phys. Scr.* **1997**, *55*, 690 – 706.
[43] S. S. Churilov, Y. N. Joshi, *Phys. Scr.* **2001**, *63*, 363 – 366.
[44] K. L. Wong, M. J. May, P. Beiersdorfer, K. B. Fournier, B. Wilson, G. V. Brown, P. Springer, P. A. Neill, C. L. Harris, *Phys. Rev. Lett.* **2003**, *90*, 235001, 1 – 4.
[45] T. Beier, P. J. Mohr, H. Persson, G. Plunien, M. Greiner, G. Soff, *Phys. Lett. A* **1997**, *236*, 329 – 338.
[46] P. J. Hay, W. R. Wadt, L. R. Kahn, F. W. Bobrowicz, *J. Chem. Phys.* **1978**, *69*, 984 – 997.
[47] Y. S. Lee, W. C. Ermler, K. S. Pitzer, A. D. McLean, *J. Chem. Phys.* **1979**, *70*, 288 – 292.
[48] U. Kaldor, B. A. Hess, *Chem. Phys. Lett.* **1994**, *230*, 1 – 7.
[49] P. Schwerdtfeger, J. R. Brown, J. K. Laerdahl, H. Stoll, *J. Chem. Phys.* **2000**, *113*, 7110 – 7118.
[50] H.-S. Lee, Y.-K. Han, M. C. Kim, C. Bae, Y. S. Lee, *Chem. Phys. Lett.* **1998**, *293*, 97 – 102.
[51] B. A. Hess, U. Kaldor, *J. Chem. Phys.* **2000**, *112*, 1809 – 1813.
[52] E. van Lenthe, J. G. Snijders, E. J. Baerends, *J. Chem. Phys.* **1996**, *105*, 6505 – 6516.
[53] P. Pyykkö, *Chem. Rev.* **1997**, *97*, 597 – 636.
[54] K. E. Saeger, J. Rodies, *Gold Bull.* **1977**, *10*, 10 – 14.
[55] J. Autschbach, S. Siekierski, M. Seth, P. Schwerdtfeger, W. H. E. Schwarz, *J. Comput. Chem.* **2002**, *23*, 804 – 813.
[56] W. H. E. Schwarz, E. M. van Wezenbeek, E. J. Baerends, J. G. Snijders, *J. Phys. B***1989**, *22*, 1515 – 1530.
[57] E. J. Baerends, W. H. E. Schwarz, P. Schwerdtfeger, J. G. Snijders, *J. Phys. B* **1990**, *23*, 3225 – 3240.
[58] U. Landman, W. D. Luedtke, W. A. Burnham, R. J. Colton, *Science* **1990**, *248*, 454 – 461.
[59] P. Schwerdtfeger, *J. Am. Chem. Soc.* **1989**, *111*, 7261 – 7262 39.
[60] P. Schwerdtfeger, P. D. W. Boyd, S. Brienne, A. K. Burrell, *Inorg. Chem.* **1992**, *31*, 3411 – 3422.
[61] D. Schröder, R. Brown, P. Schwerdtfeger, X.-B. Wang, X. Yang, L.-S. Wang, H. Schwarz, *Angew. Chem.* **2003**, *115*, 323 – 327; *Angew. Chem. Int. Ed.* **2003**, *42*, 311 – 314.
[62] Y. Jiang, S. Alvarez, R. Hoffmann, *Inorg. Chem.* **1985**, *24*, 749 – 757.
[63] P. Pyykkö, F. Mendizabal, *Inorg. Chem.* **1998**, *37*, 3018 – 3025.
[64] V. W.-W. Yam, S. W.-K. Choi, K.-K. Cheung, *Chem. Commun.* **1996**, 1173 – 1174.
[65] J. P. Fackler, Jr., A. A. Mohammed, H. E. Abdou, M. D. Irwin, ACS 125th National Meeting **2003**, INOR, 239.
[66] M. C. Gimeno, A. Laguna in *Comprehensive Coordination Chemistry II*, *Vol. 5* (Eds.: J. A. McCleverty, T. J. Meyer), Elsevier, New York, **2003**.
[67] P. Schwerdtfeger, M. Dolg, W. H. E. Schwarz, G. A. Bowmaker, P. D. W. Boyd, *J. Chem. Phys.* **1989**, *91*, 1762 – 1774.
[68] D. Schröder, H. Schwarz, J. Hrušák, P. Pyykkö, *Inorg. Chem.* **1998**, *37*, 624 – 632.
[69] D. Schröder, J. Hrušák, R. H. Hertwig, W. Koch, P. Schwerdtfeger, H. Schwarz, *Organometallics* **1995**, *14*, 312 – 316.
[70] J. Hrušák, R. H. Hertwig, D. H. Schröder, P. Schwerdtfeger, W. Koch, H. Schwarz, *Organometallics* **1995**, *14*, 1284 – 1291.
[71] R. H. Hertwig, J. Hrušák, D. Schröder, W. Koch, H. Schwarz, *Chem. Phys. Lett.* **1995**, *236*, 194 – 200.
[72] R. H. Hertwig, W. Koch, D. Schröder, H. Schwarz, J. Hrušák, P. Schwerdtfeger, *J. Phys. Chem.* **1996**, *100*, 12253 – 12260.
[73] M. C. Holthausen, C. Heinemann, H. H. Cornehl, W. Koch, H. Schwarz, *J. Chem. Phys.* **1995**, *102*, 4931 – 4941.
[74] J. Hrušák, *S. Afr. J. Chem.* **1997**, *50*, 93 – 101.
[75] X. Lu, X. Xu, N.-Q. Wang, Q.-E. Zhang, *J. Phys. Chem. A* **1999**, *103*, 10969 – 10974.
[76] G. Nicolas, F. Spiegelmann, *J. Am. Chem. Soc.* **1990**, *112*, 5410 – 5419.
[77] F. Mendizabal, *Int. J. Quantum Chem.* **1999**, *73*, 317 – 324.
[78] P. Schwerdtfeger, P. D. W. Boyd, A. K. Burrell, W. T. Robinson, M. J. Taylor, *Inorg. Chem.* **1990**, *29*, 3593 – 3607.
[79] V. Jonas, W. Thiel, *J. Chem. Soc. Dalton Trans.* **1999**, 3783 – 3790.
[80] A. J. Lupinetti, G. Frenking, S. H. Strauss, *Angew. Chem.* **1998**, *110*, 2229 – 2232; *Angew. Chem. Int. Ed.* **1998**, *37*, 2113 – 2116.
[81] A. J. Lupinetti, V. Jonas, W. Thiel, S. H. Strauss, G. Frenking, *Chem. Eur. J.* **1999**, *5*, 2573- 2583.
[82] L. Poisson, F. Lepetit, J.-M. Mestdagh, J.-P. Visticot, *J. Phys. Chem. A* **2002**, *106*, 5455 – 5462.
[83] D. Feller, E. D. Glendening, W. A. de Jong, *J. Chem. Phys.* **1999**, *110*, 1475 – 1491.
[84] R. Kissner, G. Welti, G. Geier, *J. Chem. Soc. Dalton Trans.* **1997**, *1773*–1777.
[85] D. Feller, D. A. Dixon, *J. Phys. Chem. A* **2002**, *106*, 5136 – 5143.
[86] T. K. Dargel, R. H. Hertwig, W. Koch, *Mol. Phys.* **1999**, *96*, 583 – 591.
[87] H.-C. Hsu, F.-W. Lin, C.-C. Lai, P.-H. Su, C.-S. Yeh, *New J. Chem.* **2002**, *26*, 481 – 484.
[88] D.-Y. Wu, B. Ren, Y.-X. Jiang, X. Xu, Z.-Q. Tian, *J. Phys. Chem. A* **2002**, *106*, 9042 – 9052.
[89] O. Crespo, A. Laguna, E. J. Fernández, J. M. López-de-Luzuriaga, P. G. Jones, M. Teichert, M. Monge, P. Pyykkö, N. Runeberg, M. Schütz, H.-J. Werner, *Inorg. Chem.* **2000**, *39*, 4786- 4792.
[90] P. Schwerdtfeger, H. L. Hermann, H. Schmidbaur, *Inorg. Chem.* **2003**, *42*, 1334 – 1342.
[91] O. D. Häberlen, H. Schmidbaur, N. Rösch, *J. Am. Chem. Soc.* **1994**, *116*, 8241 – 8248.
[92] L. J. Larson, E. M. McCauley, B. Weissbart, D. S. Tinti, *J. Phys. Chem.* **1995**, *99*, 7218 – 7226.
[93] T. K. Dargel, R. H. Hertwig, W. Koch, *J. Chem. Phys.* **1998**, *108*, 3876 – 3885.
[94] O. Dietz, V. M. Rayón, G. Frenking, *Inorg. Chem.* **2003**, *42*, 4977 – 4984.
[95] J. V. Burda, J. Šponer, P. Hobza, *J. Phys. Chem.* **1996**, *100*, 7250 – 7255.
[96] H. Basch, T. Hoz in *Supplement B: The Chemistry of Acid Derivatives*, *Vol. 2* (Ed.: S. Patai), Wiley, New York, **1992**, p. 41.
[97] U. Vogel, P. Sekar, R. Ahlrichs, U. Huniar, M. Scheer, *Eur. J. Inorg. Chem.* **2003**, 1518 – 1522.
[98] P. Schwerdtfeger, H. Schmidbaur, *Z. Anorg. Allg. Chem.* **2000**, *626*, 374 – 380.
[99] N. B. Balabanov, J. E. Boggs, *J. Phys. Chem. A* **2001**, *105*, 5906 – 5910.
[100] C. A. Bayse, *J. Phys. Chem. A* **2001**, *105*, 5902 – 5905.
[101] X.-F. Wang, L. Andrews, *J. Phys. Chem. A* **2002**, *106*, 3744 – 3748.
[102] A. Schulz, M. Hargittai, *Chem. Eur. J.* **2001**, *7*, 3657 – 3670.
[103] M. Hargittai, A. Schulz, B. Réffy, M. Kolonits, *J. Am. Chem. Soc.* **2001**, *123*, 1449 – 1458.
[104] T. Söhnel, R. Brown, L. Kloo, P. Schwerdtfeger, *Chem. Eur. J.* **2001**, *7*, 3167 – 3173.
[105] M.-J. Crawford, T. M. Klapötke, *Angew. Chem.* **2002**, *114*, 2373 – 2375; *Angew. Chem. Int. Ed.* **2002**, *41*, 2269 – 2271.
[106] F. Scherbaum, A. Grohmann, B. Huber, C. Krüger, H. Schmidbaur, *Angew. Chem.* **1988**, *100*, 1602 – 1604; *Angew. Chem. Int. Ed. Engl.* **1988**, *27*, 1544 – 1546.

 © 2004 Wiley-VCH Verlag GmbH & Co. KGaA, Weinheim

[107] P. Pyykkö, J. Li, N. Runeberg, *Chem. Phys. Lett.* **1994**, *218*, 133 – 138.
[108] J. J. Rehr, E. Zaremba, W. Kohn, *Phys. Rev. B* **1975**, *12*, 2062 – 2066.
[109] A. Dedieu, R. Hoffmann, *J. Am. Chem. Soc.* **1978**, *100*, 2074 – 2079.
[110] P. K. Mehrotra, R. Hoffmann, *Inorg. Chem.* **1978**, *17*, 2187 – 2189.
[111] J. K. Burdett, O. Eisenstein, W. B. Schweizer, *Inorg. Chem.* **1994**, *33*, 3261 – 3268.
[112] M. J. Calhorda, L. F. Veiros, *J. Organomet. Chem.* **1994**, *478*, 37 – 44.
[113] P. Pyykkö, Y.-F. Zhao, *Angew. Chem.* **1991**, *103*, 622 – 623; *Angew. Chem. Int. Ed. Engl.* **1991**, *30*, 604 – 605.
[114] C. Kölmel, R. Ahlrichs, *J. Phys. Chem.* **1990**, *94*, 5536 – 5542.
[115] P. Schwerdtfeger, *Inorg. Chem.* **1991**, *30*, 1660 – 1663.
[116] J. Li, P. Pyykkö, *Chem. Phys. Lett.* **1992**, *197*, 586 – 590.
[117] P. Pyykkö, N. Runeberg, F. Mendizabal, *Chem. Eur. J.* **1997**, *3*, 1451 – 1457.
[118] L. Magnko, M. Schweizer, G. Rauhut, M. Schütz, H. Stoll, H.-J. Werner, *Phys. Chem. Chem. Phys.* **2002**, *4*, 1006 – 1013.
[119] J. Li, P. Pyykkö, *Inorg. Chem.* **1993**, *32*, 2630 – 2634.
[120] N. Runeberg, P. Pyykkö, *Int. J. Quantum Chem.* **1998**, *66*, 131 – 140.
[121] A. A. Bagatur'yants, A. A. Safonov, H. Stoll, H.-J. Werner, *J. Chem. Phys.* **1998**, *109*, 3096 – 3107.
[122] P. Pyykkö, F. Mendizabal, *Chem. Eur. J.* **1997**, *3*, 1458 – 1465.
[123] P. J. Hay, *New J. Chem.* **1991**, *15*, 735 – 740.
[124] N. Runeberg, M. Schütz, H.-J. Werner, *J. Chem. Phys.* **1999**, *110*, 7210 – 7215.
[125] K. Doll, P. Pyykkö, H. Stoll, *J. Chem. Phys.* **1998**, *109*, 2339 – 2345.
[126] Z. Assefa, B. G. McBurnett, R. J. Staples, J. P. Fackler Jr., B. Assmann, K. Angermaier, H. Schmidbaur, *Inorg. Chem.* **1995**, *34*, 75 – 83.
[127] D. V. Toronto, B. Weissbart, D. S. Tinti, A. L. Balch, *Inorg. Chem.* **1996**, *35*, 2484 – 2489.
[128] B. Weissbart, D. V. Toronto, A. L. Balch, D. S. Tinti, *Inorg. Chem.* **1996**, *35*, 2490 – 2496.
[129] P. M. Van Calcar, M. M. Olmstead, A. L. Balch, *Inorg. Chem.* **1997**, *36*, 5231 – 5238.
[130] P. Pyykkö, K. Angermaier, B. Assmann, H. Schmidbaur, *J. Chem. Soc. Chem. Commun.* **1995**, 1889 – 1890.
[131] Yu. L. Slovokhotov, Yu. T. Struchkov, *J. Organomet. Chem.* **1984**, *277*, 143 – 146.
[132] E. Zeller, H. Beruda, A. Kolb, P. Bissinger, J. Riede, H. Schmidbaur, *Nature* **1991**, *352*, 141 – 143.
[133] H. Schmidbaur, H. Beruda, E. Zeller, *Phosphorus Sulfur Silicon Relat. Elem.* **1994**, *87*, 245 – 255.
[134] R. E. Bachman, H. Schmidbaur, *Inorg. Chem.* **1996**, *35*, 1399 – 1401.
[135] H. Schmidbaur, F. P. Gabbaï, A. Schier, J. Riede, *Organometallics* **1995**, *14*, 4969 – 4971.
[136] P. Pyykkö, T. Tamm, *Organometallics* **1998**, *17*, 4842 – 4852.
[137] D. M. P. Mingos, R. P. F. Kanters, *J. Organomet. Chem.* **1990**, *384*, 405 – 415.
[138] D. M. P. Mingos, *J. Chem. Soc. Dalton* **1976**, 1163 – 1169.
[139] P. Belanzoni, M. Rosi, A. Sgamellotti, E. J. Baerends, C. Floriani, *Chem. Phys. Lett.* **1996**, *257*, 41 – 48.
[140] H. Schmidbaur, *Chem. Soc. Rev.* **1995**, *24*, 391 – 400.
[141] H. Schmidbaur, O. Steigelmann, *Z. Naturforsch. B* **1992**, *47*, 1721 – 1724.
[142] N. Rösch, A. Görling, D. E. Ellis, H. Schmidbaur, *Angew. Chem.* **1989**, *101*, 1410 – 1412; *Angew. Chem. Int. Ed. Engl.* **1989**, *28*, 1357 – 1359.
[143] A. Görling, N. Rösch, D. E. Ellis, H. Schmidbaur, *Inorg. Chem.* **1991**, *30*, 3986 – 3994.
[144] E. I. Smyslova, E. G. Perevalova, V. P. Dyadchenko, K. I. Grandberg, Yu. L. Slovokhotov, Yu. T. Struchkov, *J. Organomet. Chem.* **1981**, *215*, 269 – 279.
[145] Q.-J. Pan, H.-X. Zhang, *J. Chem. Phys.* **2003**, *119*, 4346 – 4352.
[146] P. D. Harvey, *Coord. Chem. Rev.* **1996**, *153*, 175 – 198; T. F. Carlson, J. P. Fackler, Jr., *J. Organomet. Chem.* **2000**, *596*, 237 – 241, suggest that the Au^{II}-Au^{II} case yields two separate *R* versus ν curves for $[Au(CH_2)_2PPh_2]X_2$ and $[(AuMTP)_2]X_2$ (MTP = $CH_2(S)PPh_2$) as function of X = Cl–I.
[147] P. Schwerdtfeger, A. E. Bruce, M. R. M. Bruce, *J. Am. Chem. Soc.* **1998**, *120*, 6587 – 6597.
[148] R.-Y. Liau, T. Mathieson, A. Schier, R. J. F. Berger, N. Runeberg, H. Schmidbaur, *Z. Naturforsch. B* **2002**, *57*, 881 – 889.
[149] P. Pyykkö, W. Schneider, A. Bauer, A. Bayler, H. Schmidbaur, *Chem. Commun.* **1997**, 1111 – 1112.
[150] Z.-J. Tang, A. P. Litvinchuk, H.-G. Lee, A. M. Guloy, *Inorg. Chem.* **1998**, *37*, 4752 – 4753.
[151] S. Canales, O. Crespo, M. C. Gimeno, P. G. Jones, A. Laguna, F. Mendizabal, *Organometallics* **2001**, *20*, 4812 – 4818.
[152] F. Mendizabal, G. Zapata-Torres, C. Olea-Azar, *Chem. Phys. Lett.* 2003, 382, 92 – 99.
[153] E. J. Fernández, J. M. López-de-Luzuriaga, M. Monge, M. A. Rodríguez, O. Crespo, M. C. Gimeno, A. Laguna, P. G. Jones, *Chem. Eur. J.* **2000**, *6*, 636 – 644.
[154] B.-H. Xia, H.-X. Zhang, C.-M. Che, K.-H. Leung, D. L. Phillips, N.-Y. Zhu, Z.-Y. Zhou, *J. Am. Chem. Soc.* **2003**, *125*, 10362 – 10374.
[155] E. J. Fernández, A. Laguna, J. M. L. de Luzuriaga, F. Mendizabal, M. Monge, M. E. Olmos, J. Pérez, *Chem. Eur. J.* **2003**, *9*, 456 – 465.
[156] M. Bardají, A. Laguna, *Eur. J. Inorg. Chem.* **2003**, 3069 – 3079.
[157] P. Pyykkö, N. Runeberg, *J. Chem. Soc. Chem. Commun.* **1993**, 1812 – 1813.
[158] R. Boca, *J. Chem. Soc. Dalton Trans.* **1994**, 2061 – 2064.
[159] W. Schneider, A. Bauer, H. Schmidbaur, *Organometallics* **1996**, *15*, 5445 – 5446.
[160] A. Codina, E. J. Fernández, P. G. Jones, A. Laguna, J. M. L. de Luzuriaga, M. Monge, M. E. Olmos, J. Pérez, M. A. Rodríguez, *J. Am. Chem. Soc.* **2002**, *124*, 6781 – 6786.
[161] F. Mendizabal, P. Pyykkö, N. Runeberg, *Chem. Phys. Lett.* **2003**, *370*, 733 – 740.
[162] R. Wesendrup, P. Schwerdtfeger, *Angew. Chem.* **2000**, *112*, 938 – 942; *Angew. Chem. Int. Ed.* **2000**, *39*, 907 – 910.
[163] A.-V. Mudring, M. Jansen, J. Daniels, S. Krämer, M. Mehring, J. P. Prates Ramalho, A. H. Romero, M. Parrinello, *Angew. Chem.* **2002**, *114*, 128 – 132; *Angew. Chem. Int. Ed.* **2002**, *41*, 120 – 124,.
[164] M.-S. Liao, W. H. E. Schwarz, *Acta Crystallogr. Sect. B* **1994**, *50*, 9 – 12.
[165] A. Bayler, A. Schier, G. A. Bowmaker, H. Schmidbaur, *J. Am. Chem. Soc.* **1996**, *118*, 7006 – 7007.
[166] U. M. Tripathi, A. Bauer, H. Schmidbaur, *J. Chem. Soc. Dalton Trans.* **1997**, 2865 – 2868.
[167] R. E. Bachman, D. F. Andretta, *Inorg. Chem.* **1998**, *37*, 5657 – 5663.
[168] K. Fujisawa, S. Imai, Y. Moro-oka, *Chem. Lett.* **1998**, 167 – 168.
[169] E. J. Fernández, J. M. López-de-Luzuriaga, M. Monge, M. A. Rodríguez, O. Crespo, M. C. Gimeno, A. Laguna, P. G. Jones, *Inorg. Chem.* **1998**, *37*, 6002 – 6006.
[170] D. B. Leznoff, B.-Y. Xue, R. J. Batchelor, F. W. B. Einstein, B. O. Patrick, *Inorg. Chem.* **2001**, *40*, 6026 – 6034.
[171] M.-S. Liao, W. H. E. Schwarz, *J. Alloys Compd.* **1997**, *246*, 2 – 17.
[172] G. A. Bowmaker, H. Schmidbaur, S. Krüger, N. Rösch, *Inorg. Chem.* **1997**, *36*, 1754 – 1757.

 © 2004 Wiley-VCH Verlag GmbH & Co. KGaA, Weinheim

[173] V. Kellö, M. Urban, A. J. Sadlej, *Chem. Phys. Lett.* **1996**, *253*, 383 – 389.
[174] A. Sommer, *Nature* **1943**, *152*, 215.
[175] W. E. Spicer, A. H. Sommer, J. G. White, *Phys. Rev.* **1959**, *115*, 57 – 62.
[176] E. Heymann, H. P. Weber, *Trans. Faraday Soc.* **1938**, *34*, 1492 – 1501.
[177] W. Biltz, F. Weibke, *Z. Anorg. Allg. Chem.* **1938**, *236*, 12 – 23.
[178] F. Hensel, *Z. Phys. Chem. N. F.* **1987**, *154*, 201 – 219.
[179] U. Zachwieja in *Gold. Progress in Chemistry, Biochemistry and Technology* (Ed.: H. Schmidbaur), Wiley, Chichester, **1999**, pp. 495 – 509.
[180] A. Hasegawa, M. Watabe, *J. Phys. F* **1977**, *7*, 75 – 86.
[181] N. E. Christensen, J. Kollar, *Solid State Commun.* **1983**, *46*, 727 – 730.
[182] R. E. Watson, M. Weinert, *Phys. Rev. B* **1994**, *49*, 7148 – 7154.
[183] B. J. Costa Cabral, F. M. S. Silva Fernandes, *AIP Conf. Proc.* **1995**, *330*, 129 – 133.
[184] S. Matsunaga, *J. Phys. Soc. Jpn.* **2000**, *69*, 1712 – 1716.
[185] D. Kędziera, A. Avramopoulos, M. G. Papadopoulos, A. J. Sadlej, *Phys. Chem. Chem. Phys.* **2003**, *5*, 1096 – 1102.
[186] L. Gagliardi, *J. Am. Chem. Soc.* **2003**, *125*, 7504 – 7505.
[187] P. Pyykkö, M. Patzschke, J. Suurpere, *Chem. Phys. Lett.* **2003**, *381*, 45 – 52.
[188] A. Avramopoulos, V. E. Ingamelis, M. G. Papadopoulos, A. J. Sadlej, *J. Chem. Phys.* **2001**, *114*, 198 – 210.
[189] S. Krüger, M. Stener, M. Mayer, F. Nörtemann, N. Rösch, *J. Mol. Struct. (Theochem)* **2000**, *527*, 63 – 74.
[190] P. Schwerdtfeger, P. D. W. Boyd, *Inorg. Chem.* **1992**, *31*, 327 – 329.
[191] S. Hagen, I. Pantenburg, F. Weigend, C. Wickleder, L. Wesemann, *Angew. Chem.* **2003**, *115*, 1539 – 1543; *Angew. Chem. Int. Ed.* **2003**, *42*, 1501 – 1505.
[192] F. P. Gabbaï, S.-C. Chung, A. Schier, S. Krüger, N. Rösch, H. Schmidbaur, *Inorg. Chem.* **1997**, *36*, 5699 – 5705.
[193] M. W. Esterhuysen, H. G. Raubenheimer, *Acta Crystallogr. Sect. C* **2003**, *59*, m286-m288.
[194] A. Avramopoulos, M. G. Papadopoulos, A. J. Sadlej, *Chem. Phys. Lett.* **2003**, *370*, 765 – 769.
[195] K. K. Irikura, W. A. Goddard III, *J. Am. Chem. Soc.* **1994**, *116*, 8733 – 8740.
[196] F. Aguirre, J. Husband, C. J. Thompson, R. B. Metz, *Chem. Phys. Lett.* **2000**, *318*, 466 – 470.
[197] H. G. Raubenheimer, P. J. Olivier, L. Lindeque, M. Desmet, J. Hrušák, G. J. Kruger, *J. Organomet. Chem.* **1997**, *544*, 91 – 100.
[198] C. Boehme, G. Frenking, *Organometallics* **1998**, *17*, 5801 – 5809.
[199] M. Barysz, P. Pyykkö, *Chem. Phys. Lett.* **1998**, *285*, 398 – 403.
[200] M. Barysz, P. Pyykkö, *Chem. Phys. Lett.* **2003**, *368*, 538 – 541.
[201] P. Pyykkö, T. Tamm, *Theor. Chem. Acc.* **1998**, *99*, 113 – 115.
[202] P. Pyykkö, *J. Am. Chem. Soc.* **1995**, *117*, 2067 – 2070.
[203] J. P. Read, A. D. Buckingham, *J. Am. Chem. Soc.* **1997**, *119*, 9010 – 9013.
[204] S. Seidel, K. Seppelt, *Science* **2000**, *290*, 117 – 118.
[205] P. Pyykkö, *Science* **2000**, *290*, 64 – 65.
[206] W.-P. Hu, C.-H. Huang, *J. Am. Chem. Soc.* **2001**, *123*, 2340 – 2343.
[207] S. Berski, Z. Latajka, J. Andrés, *Chem. Phys. Lett.* **2002**, *356*, 483 – 489.
[208] T. Drews, S. Seidel, K. Seppelt, *Angew. Chem.* **2002**, *114*, 470 – 473; *Angew. Chem. Int. Ed.* **2002**, *41*, 454 – 456,.
[209] I.-C. Hwang, S. Seidel, K. Seppelt, *Angew. Chem.* **2003**, *115*, 4528 – 4531; *Angew. Chem. Int. Ed.* **2003**, *42*, 4392 – 4395.
[210] C. J. Evans, A. Lesarri, M. C. L. Gerry, *J. Am. Chem. Soc.* **2000**, *122*, 6100 – 6105.
[211] C. J. Evans, D. S. Rubino-, M. C. L. Gerry, *Phys. Chem. Chem. Phys.* **2000**, *2*, 3943 – 3948.
[212] J. F. Lehmann, G. J. Schrobilgen, *J. Fluorine Chem.* **2003**, *119*, 109 – 124.
[213] http://qcldb2.ims.ac.jp, Quantum Chemistry Literature Database, Version 3.0, Institute for Molecular Science, Okazaki, **2004**.
[214] X.-F. Wang, L. Andrews, *J. Am. Chem. Soc.* **2001**, *123*, 12899 – 12900.
[215] L. Andrews, X.-F. Wang, *J. Am. Chem. Soc.* **2003**, *125*, 11751 – 11760.
[216] X.-F. Wang, L. Andrews, *Angew. Chem.* **2003**, *115*, 5359 – 5364; *Angew. Chem. Int. Ed.* **2003**, *42*, 5201 – 5206.
[217] X.-F. Wang, L. Andrews, L. Manceron, C. Marsden, *J. Phys. Chem. A* **2003**, *107*, 8492 – 8505.
[218] G. S.-M. Tong, A. S.-C. Cheung, *J. Phys. Chem. A* **2002**, *106*, 11637 – 11643.
[219] P. Schwerdtfeger, M. Dolg, *Phys. Rev. A* **1991**, *43*, 1644 – 1647.
[220] W.-J. Liu, C. van Wüllen, *J. Chem. Phys.* **1999**, *110*, 3730 – 3735.
[221] R. Wesendrup, J. K. Laerdahl, P. Schwerdtfeger, *J. Chem. Phys.* **1999**, *110*, 9457 – 9462.
[222] M. Urban, A. J. Sadlej, *Mol. Phys.* **1997**, *92*, 587 – 600.
[223] A. Citra, L. Andrews, *J. Mol. Struct. (Theochem)* **1999**, *489*, 95 – 108.
[224] J. K. Burdett, S. Sevov, *J. Am. Chem. Soc.* **1995**, *117*, 12788 – 12792.
[225] H. Müller-Buschbaum, *Z. Anorg. Allg. Chem.* **2002**, *628*, 2559 – 2584.
[226] F. E. Wagner, S. Haslbeck, L. Stievano, S. Calogero, Q. A. Pankhurst, K.-P. Martinek, *Nature* **2000**, *407*, 691 – 692.
[227] P. Schwerdtfeger, J. S. McFeaters, R. L. Stephens, M. J. Liddell, M. Dolg, B. A. Hess, *Chem. Phys. Lett.* **1994**, *218*, 362 – 366.
[228] P. Schwerdtfeger, J. S. McFeaters, M. J. Liddell, J. Hrušák, H. Schwarz, *J. Chem. Phys.* **1995**, *103*, 245 – 252.
[229] M. Ilia , P. Furdík, M. Urban, *J. Phys. Chem. A* **1998**, *102*, 5263 – 5268.
[230] C. van Wüllen, *J. Chem. Phys.* **1998**, *109*, 392 – 399.
[231] K. G. Dyall, T. Enevoldsen, *J. Chem. Phys.* **1999**, *111*, 10000 – 10007.
[232] M. Seth, F. Cooke, P. Schwerdtfeger, J.-L. Heully, M. Pelissier, *J. Chem. Phys.* **1998**, *109*, 3935 – 3943.
[233] I.-C. Hwang, K. Seppelt, *Angew. Chem.* **2001**, *113*, 3803 – 3805; *Angew. Chem. Int. Ed.* **2001**, *40*, 3690 – 3693,.
[234] T. Söhnel, H. Hermann, P. Schwerdtfeger, *Angew. Chem.* **2001**, *113*, 4511 – 4515; *Angew. Chem. Int. Ed.* **2001**, *40*, 4381 – 4385,.
[235] L. Nalbandian, S. Boghosian, G. N. Papatheodorou, *Inorg. Chem.* **1992**, *31*, 1769 – 1773.
[236] L. Nalbandian, G. N. Papatheodorou, *Vib. Spectrosc.* **1992**, *4*, 25 – 34.
[237] D. M. P. Mingos, *Polyhedron* **1986**, *3*, 1289 – 1297.
[238] D. M. P. Mingos, *Gold Bull.* **1984**, *17*, 5 – 12.
[239] D. M. P. Mingos in *The Chemistry of the Copper and Zinc Triads* (Eds.: A. J. Welch, S. K. Chapman), The Royal Society of Chemistry, Cambridge, **1993**, pp. 189 – 197.
[240] P. J. Dyson, D. M. P. Mingos in *Gold. Progress in Chemistry, Biochemistry and Technology* (Ed.: H. Schmidbaur), Wiley, New York, **1999**, pp. 511 – 556.
[241] L. H. Pignolet, M. A. Aubart, K. L. Craighead, R. A. T. Gould, D. A. Krogstad, J. S. Wiley, *Coord. Chem. Rev.* **1995**, *143*, 219 – 263.
[242] L. H. Pignolet, D. A. Krogstad in *Gold. Progress in Chemistry, Biochemistry and Technology* (Ed.: H. Schmidbaur), Wiley, New York, **1999**, pp. 429 – 493.
[243] J. J. Steggerda, *Comments Inorg. Chem.* **1990**, *11*, 113 – 129.
[244] J. K. Gibson, *J. Vac. Sci. Technol. A* **1998**, *16*, 653 – 659.
[245] S. Gilb, P. Weis, F. Furche, R. Ahlrichs, M. M. Kappes, *J. Chem. Phys.* **2002**, *116*, 4094 – 4101.
[246] P. Weis, T. Bierweiler, E. Vollmer, M. M. Kappes, *J. Chem. Phys.* **2002**, *117*, 9293 – 9297.

 © 2004 Wiley-VCH Verlag GmbH & Co. KGaA, Weinheim

[247] F. Furche, R. Ahlrichs, P. Weis, C. Jacob, S. Gilb, T. Bierweiler, M. M. Kappes, *J. Chem. Phys.* **2002**, *117*, 6982 – 6990.
[248] H. Häkkinen, M. Moseler, U. Landman, *Phys. Rev. Lett.* **2002**, *89*, 033401, 1 – 4.
[249] N. Takeuchi, C. T. Chan, K. M. Ho, *Phys. Rev. B* **1991**, *43*, 14363 – 14370.
[250] K. Sugawara, F. Sobott, A. B. Vakhtin, *J. Chem. Phys.* **2003**, *118*, 7808 – 7816.
[251] R. Guo, K. Balasubramanian, X.-F. Wang, L. Andrews, *J. Chem. Phys.* **2002**, *117*, 1614 – 1620.
[252] I. L. Garzón, K. Michaelian, M. R. Beltrán, A. Posada-Amarillas, P. Ordejón, E. Artacho, D. Sánchez-Portal, J. M. Soler, *Phys. Rev. Lett.* **1998**, *81*, 1600 – 1603.
[253] J. Oviedo, R. E. Palmer, *J. Chem. Phys.* **2002**, *117*, 9548 – 9551.
[254] J.-L. Wang, G.-H. Wang, J.-J. Zhao, *Phys. Rev. B* **2002**, *66*, 035418, 1 – 6.
[255] J. Li, X. Li, H.-J. Zhai, L.-S. Wang, *Science* **2003**, *299*, 864 – 867.
[256] H.-G. Boyen, G. Kästle, F. Weigl, B. Koslowski, C. Dietrich, P. Ziemann, J. P. Spatz, S. Riethmüller, C. Hartmann, M. Möller, G. Schmid, M. G. Garnier, P. Oelhafen, *Science* **2002**, *297*, 1533 – 1536.
[257] C. L. Cleveland, W. D. Luedtke, U. Landman, *Phys. Rev. Lett.* **1998**, *81*, 2036 – 2039.
[258] "The Structure and Dynamics of Noble Metal Clusters": N. T. Wilson, Ph.D. Thesis, Birmingham, UK, **2000**.
[259] S. Mukherjee, G. M. Pastor, K. H. Bennemann, *Phys. Rev. B* **1990**, *42*, 5327 – 5330.
[260] M. Barysz, P. Pyykkö, *Chem. Phys. Lett.* **2000**, *325*, 225 – 231.
[261] W. A. Saunders, S. Fedrigo, *Chem. Phys. Lett.* **1989**, *156*, 14 – 18.
[262] U. Heiz, A. Vayloyan, E. Schumacher, C. Yeretzian, M. Stener, P. Gisdakis, N. Rösch, *J. Chem. Phys.* **1996**, *105*, 5574 – 5585.
[263] D. M. P. Mingos, *J. Chem. Soc. Dalton Trans.* **1996**, 561 – 566.
[264] C. E. Briant, B. R. C. Theobald, J. W. White, L. K. Bell, D. M. P. Mingos, *J. Chem. Soc. Chem. Commun.* **1981**, 201 – 202.
[265] Z. Lin, R. P. F. Kanters, D. M. P. Mingos, *Inorg. Chem.* **1991**, *30*, 91 – 95.
[266] P. Pyykkö, N. Runeberg, *Angew. Chem.* **2002**, *114*, 2278 – 2280; *Angew. Chem. Int. Ed.* **2002**, *41*, 2174 – 2176.
[267] J. Autschbach, B. A. Hess, M. P. Johansson, J. Neugebauer, M. Patzschke, P. Pyykkö, M. Reiher, D. Sundholm, *Phys. Chem. Chem. Phys.* **2004**, *6*, 11 – 22.
[268] X. Li, B. Kiran, J. Li, H.-J. Zhai, L.-S. Wang, *Angew. Chem.* **2002**, *114*, 4980 – 4983; *Angew. Chem. Int. Ed.* **2002**, *41*, 4786 – 4789,.
[269] Y.-Y. Yang, S.-W. Chen, *Nano Lett.* **2003**, *3*, 75 – 79.
[270] R. Boča, *Int. J. Quantum Chem.* **1996**, *57*, 735 – 740.
[271] D. M. P. Mingos, Z. Lin, *Comments Inorg. Chem.* **1989**, *9*, 95 – 122.
[272] H. Zhang, B. K. Teo, *Inorg. Chim. Acta* **1997**, *265*, 213 – 224.
[273] B. M. Quinn, P. Liljeroth, V. Ruiz, T. Laaksonen, K. Kontturi, *J. Am. Chem. Soc.* **2003**, *125*, 6644 – 6645.
[274] O. D. Häberlen, S.-C. Chung, M. Stener, N. Rösch, *J. Chem. Phys.* **1997**, *106*, 5189 – 5201.
[275] G. Bravo-Pérez, I. L. Garzón, O. Novaro, *Chem. Phys. Lett.* **1999**, *313*, 655 – 664.
[276] G. Bravo-Pérez, I. L. Garzón, O. Novaro, *J. Mol. Struct. (Theochem)* **1999**, *493*, 225 – 231.
[277] F. A. Vollenbroek, J. P. van der Berg, J. W. A. van der Velden, J. J. Bour, *Inorg. Chem.* **1980**, *19*, 2685 – 2688.
[278] H. L. Zhang, D. H. Sampson, *At. Data Nucl. Data Tables* **1997**, *65*, 183 – 271.
[279] B. R. Sahu, G. Maofa, L. Kleinman, *Phys. Rev. B* **2003**, *67*, 115420, 1 – 4.
[280] R. Arratia-Pérez, L. Hernández-Acevedo, *Chem. Phys. Lett.* **1999**, *303*, 641 – 648.
[281] D. V. Toronto, A. L. Balch, D. S. Tinti, *Inorg. Chem.* **1994**, *33*, 2507 – 2508.
[282] K. Albert, K. M. Neyman, G. Pacchioni, N. Rösch, *Inorg. Chem.* **1996**, *35*, 7370 – 7376.
[283] G. Bilalbegovic, *Phys. Rev. B* **1998**, *58*, 15142 – 15415.
[284] G. Bilalbegovic, *Solid State Commun.* **2000**, *115*, 73 – 76.
[285] F. Ercolessi, M. Parrinello, E. Tosatti, *Philos. Mag. A* **1988**, *58*, 213 – 226.
[286] A. Hasegawa, K. Yoshizawa, K. Hirao, *Chem. Phys. Lett.* **2001**, *345*, 367 – 371.
[287] E. Tosatti, S. Prestipino, D. Kostlmeier, A. Dal Corso, F. D. Di Tolla, *Science* **2001**, *291*, 288 – 290.
[288] Y. Kondo, K. Takayanagi, *Science* **2000**, *289*, 606 – 608.
[289] N. Takeuchi, C. T. Chan, K. M. Ho, *Phys. Rev. B* **1989**, *40*, 1565 – 1570.
[290] E. Tosatti, F. Ercolessi, *Modern Phys. Lett. B* **1991**, *5*, 413 – 425.
[291] M. Díaz, J. L. Costa-Krämer, E. Medina, A. Hasmy, P. A. Serena, *Nanotechnology* **2003**, *14*, 113 – 116.
[292] S. R. Bahn, N. Lopez, J. K. Nørskov, K. W. Jacobsen, *Phys. Rev. B* **2002**, *66*, 081405, 1 – 4.
[293] H. Ohnishi, Y. Kondo, K. Takayanagi, *Nature* **1998**, *395*, 780 – 783.
[294] A. I. Yanson, G. R. Bollinger, H. E. van den Brom, N. Agraït, J. M. van Ruitenbeek, *Nature* **1998**, *395*, 783 – 785.
[295] J. A. Torres, E. Tosatti, A. Dal Corso, F. Ercolessi, J. J. Kohanoff, F. D. Di Tolla, J. M. Soler, *Surf. Sci.* **1999**, *426*, L441-L446.
[296] H. Häkkinen, R. N. Barnett, A. G. Scherbakov, U. Landman, *J. Phys. Chem. B* **2000**, *104*, 9063 – 9066.
[297] R. H. M. Smit, C. Untiedt, A. I. Yanson, J. M. van Ruitenbeek, *Phys. Rev. Lett.* **2001**, *87*, 266102, 1 – 4.
[298] S. R. Bahn, K. W. Jacobsen, *Phys. Rev. Lett.* **2001**, *87*, 266101, 1 – 4.
[299] F. J. Ribeiro, M. L. Cohen, *Phys. Rev. B* **2003**, *68*, 035423, 1 – 5.
[300] T. Nautiyal, S. J. Youn, K. S. Kim, *Phys. Rev. B* **2003**, *68*, 033407, 1 – 4.
[301] F. D. Novaes, A. J. R. da Silva, E. Z. da Silva, A. Fazzio, *Phys. Rev. Lett.* **2003**, *90*, 036101, 1 – 4.
[302] D. Krüger, R. Rousseau, H. Fuchs, D. Marx, *Angew. Chem.* **2003**, *115*, 2353 – 2355; *Angew. Chem. Int. Ed.* **2003**, *42*, 2251 – 2253.
[303] M. Okamoto, K. Takayanagi, *Phys. Rev. B* **1999**, *60*, 7808 – 7811.
[304] D. Sánchez-Portal, E. Artacho, J. Junquera, P. Ordejón, A. García, J. M. Soler, *Phys. Rev. Lett.* **1999**, *83*, 3884 – 3887.
[305] G. Rubio-Bollinger, S. R. Bahn, N. Agraït, K. W. Jacobsen, S. Vieira, *Phys. Rev. Lett.* **2001**, *87*, 026101, 1 – 4.
[306] N. V. Skorodumova, S. I. Simak, *Phys. Rev. B* **2003**, *67*, 121404, 1 – 4.
[307] L. Giordano, G. Pacchioni, T. Bredow, J. Fernandez Sanz, *Surf. Sci.* **2001**, *471*, 21 – 31.
[308] J. A. Rodriguez, G. Liu, T. Jirsak, J. Hrbek, Z.-P. Chang, J. Dvorak, A. Maiti, *J. Am. Chem. Soc.* **2002**, *124*, 5242 – 5250.
[309] A. Vijay, G. Mills, H. Metiu, *J. Chem. Phys.* **2003**, *118*, 6532 – 6551.
[310] E. Wahlström, N. Lopez, R. Schaub, P. Thostrup, A. Rønnau, C. Africh, E. Laegsgaard, J. K. Nørskov, F. Besenbacher, *Phys. Rev. Lett.* **2003**, *90*, 026101, 1 – 4.
[311] Z.-X. Yang, R.-Q. Wu, *Phys. Rev. B* **2003**, *67*, 081403, 1 – 4.
[312] M. Mayer, G. Pacchioni, N. Rösch, *Surf. Sci.* **1998**, *412*/413, 616 – 624.
[313] J. A. Mejías, *Phys. Rev. B* **1996**, *53*, 10281 – 10288.
[314] Y.-P. Liu, W. Meyer-Zaika, S. Franzka, G. Schmid, M. Tsoli, H. Kuhn, *Angew. Chem.* **2003**, *115*, 2959 – 2963; *Angew. Chem. Int. Ed.* **2003**, *42*, 2853 – 2857.
[315] M. Brust, M. Walker, D. Bethell, D. J. Schiffrin, R. Whyman, *J. Chem. Soc. Chem. Commun.* **1994**, *801*–802.
[316] R. L. Whetten, M. N. Shafigullin, J. T. Khoury, T. G. Schaaff, I. Vezmar, M. M. Alvarez, A. Wilkinson, *Acc. Chem. Res.* **1999**, *32*, 397 – 406.

 © 2004 Wiley-VCH Verlag GmbH & Co. KGaA, Weinheim

[317] T. G. Schaaff, R. L. Whetten, *J. Phys. Chem. B* **2000**, *104*, 2630 – 2641.
[318] W. D. Luedtke, U. Landman, *J. Phys. Chem.* **1996**, *100*, 13323 – 13329.
[319] S. Link, C. Burda, M. B. Mohamed, B. Nikoobaht, M. A. El-Sayed, *Phys. Rev. B* **2000**, *61*, 6086 – 6090.
[320] P. Zhang, T. K. Sham, *Phys. Rev. Lett.* **2003**, *90*, 245502, 1 – 4.
[321] S. Link, M. A. El-Sayed, *Int. Rev. Phys. Chem.* **2000**, *19*, 409 – 453.
[322] S. Bruzzone, G. P. Arrighini, C. Guidotti, *Chem. Phys.* **2003**, *291*, 125 – 140.
[323] B. Palpant, B. Prével, J. Lermé, E. Cottancin, M. Pellarin, M. Treilleux, A. Perez, J. L. Vialle, M. Broyer, *Phys. Rev. B* **1998**, *57*, 1963 – 1970.
[324] F. Mafuné, T. Kondow, *Chem. Phys. Lett.* **2003**, *372*, 199 – 204.
[325] M. B. Mohamed, V. Volkov, S. Link, M. A. El-Sayed, *Chem. Phys. Lett.* **2000**, *317*, 517 – 523.
[326] T. Morris, H. Copeland, E. McLinden, S. Wilson, G. Szulczewski, *Langmuir* **2002**, *18*, 7261 – 7264.
[327] J. C. Boettger, *Phys. Rev. B* **2003**, *67*, 174107, 1 – 7.
[328] R. Ahuja, S. Rekhi, B. Johansson, *Phys. Rev. B* **2001**, *63*, 212101, 1 – 3.
[329] P. Söderlind, *Phys. Rev. B* **2002**, *66*, 176201, 1 – 2.
[330] T. Tsuchiya, K. Kawamura, *Phys. Rev. B* **2002**, *66*, 094115, 1 – 5.
[331] L. G. Wang, A. Zunger, *Phys. Rev. B* **2003**, *67*, 092103, 1 – 4.
[332] N. Takeuchi, C. T. Chan, K. M. Ho, *Phys. Rev. Lett.* **1989**, *63*, 1273 – 1276.
[333] V. Fiorentini, M. Methfessel, M. Scheffler, *Phys. Rev. Lett.* **1993**, *71*, 1051 – 1054.
[334] R. Eibler, H. Reschbaumer, C. Temnitschka, R. Podloucky, A. J. Freeman, *Surf. Sci.* **1993**, *280*, 398 – 414.
[335] F. Celestini, F. Ercolessi, E. Tosatti, *Phys. Rev. Lett.* **1997**, *78*, 3153 – 3156.
[336] in *Gmelins Handbuch der Anorganischen Chemie*, 8th ed., Gold, Systemnummer 62, Verlag Chemie, Weinheim, **1954**, p. 467.
[337] G. Boisvert, L. J. Lewis, M. J. Puska, R. M. Nieminen, *Phys. Rev. B* **1995**, *52*, 9078 – 9085.
[338] F. Reinert, *J. Phys. Condens. Matter* **2003**, *15*, S693-S705.
[339] P. A. Korzhavyi, I. A. Abrikosov, B. Johansson, A. V. Ruban, H. L. Skriver, *Phys. Rev. B* **1999**, *59*, 11693 – 11703.
[340] P. Ehrhart in *Properties and interactions of atomic defects in metals and alloys*, *Vol. 25* (Ed.: H. Ullmaier), Springer, Berlin, **1991**, pp. 88 – 379.
[341] S. Sakai, H. Tanimoto, E. Kita, H. Mizubayashi, *Phys. Rev. B* **2002**, *66*, 214106.
[342] S. Löken, C. Felser, W. Tremel, *Chem. Commun.* **1998**, 1603 – 1604.
[343] A. Fazzio, M. J. Caldas, A. Zunger, *Phys. Rev. B* **1985**, *32*, 934 – 954.
[344] G. D. Watkins, P. M. Williams, *Phys. Rev. B* **1995**, *52*, 16575 – 16580.
[345] N. E. Christensen, *Int. J. Quantum Chem.* **1984**, *25*, 233 – 261.
[346] V. P. Zhukov, F. Aryasetiawan, E. V. Chulkov, I. G. de Gurtubay, P. M. Echenique, *Phys. Rev. B* **2001**, *64*, 195122, 1 – 11.
[347] V. P. Zhukov, E. V. Chulkov, P. M. Echenique, *Phys. Rev. B* **2003**, *68*, 045102, 1 – 7.
[348] L. H. Gade, *Angew. Chem.* **1997**, *109*, 1219 – 1221; *Angew. Chem. Int. Ed. Engl.* **1997**, *36*, 1171 – 1173,.
[349] E. J. Fernández, P. G. Jones, A. Laguna, J. M. L. de Luzuriaga, M. Monge, J. Pérez, M. E. Olmos, *Inorg. Chem.* **2002**, *41*, 1056 – 1063.
[350] O. Crespo, M. C. Gimeno, P. G. Jones, A. Laguna, J. M. López-de-Luzuriaga, M. Monge, J. L. Pérez, M. A. Ramón, *Inorg. Chem.* **2003**, *42*, 2061 – 2068.
[351] H.-X. Zhang, C.-M. Che, *Chem. Eur. J.* **2001**, *7*, 4887 – 4893.
[352] M. A. Omary, M. A. Rawashdeh-Omary, C. C. Chusuei, J. P. Fackler Jr., P. S. Bagus, *J. Chem. Phys.* **2001**, *114*, 10695 – 10701.
[353] X.-H. Chen, K.-C. Wu, J. G. Snijders, C.-S. Lin, *Inorg. Chem.* **2003**, *42*, 532 – 540.
[354] S. Ahmad, *J. Phys. B* **1984**, *17*, L807-L810.
[355] R. Arratia-Pérez, L. Hernández-Acevedo, J. S. Gómez-Jeria, *Chem. Phys. Lett.* **1995**, *236*, 37 – 42.
[356] T. K. Sham, R. E. Watson, M. L. Perlman, *Phys. Rev. B* **1980**, *21*, 1457 – 1461.
[357] D. Guenzburger, D. E. Ellis, *Phys. Rev. B* **1980**, *22*, 4203 – 4214.
[358] M. Pernpointner, P. Schwerdtfeger, B. A. Hess, *Int. J. Quantum Chem.* **2000**, *76*, 371 – 384.
[359] H. Tanaka, S. Neukermans, E. Janssens, R. E. Silverans, P. Lievens, *J. Am. Chem. Soc.* **2003**, *125*, 2862 – 2863.
[360] R. Bast, P. Schwerdtfeger, *Phys. Rev. Lett.* **2003**, *91*, 023001, 1 – 3.
[361] P. J. Sadler, *Struct. Bonding (Berlin)* **1976**, *29*, 171 – 214, see chapter 4.5.
[362] P. J. Sadler, R. E. Sue, *Met.-Based Drugs* **1994**, *1*, 107 – 144.
[363] C. F. Shaw III, *Chem. Rev.* **1999**, *99*, 2589 – 2600.
[364] C. F. Shaw III in *Gold. Progress in Chemistry, Biochemistry and Technology* (Ed.: H. Schmidbaur), Wiley, New York, **1999**, pp. 259 – 308.
[365] J. A. Tossell, *Geochim. Cosmochim. Acta* **1996**, *60*, 17 – 29.
[366] H. G. Raubenheimer, S. Cronje in *Gold. Progress in Chemistry, Biochemistry and Technology* (Ed.: H. Schmidbaur), Wiley, Chichester, **1999**, pp. 557 – 632.
[367] R. A. Bryce, J. M. Charnock, R. A. D. Pattrick, A. R. Lennie, *J. Phys. Chem. A* **2003**, *107*, 2516 – 2523.
[368] A. V. Nemukhin, V. V. Togonidze, V. V. Kovba, R. Y. Orlov, *Zh. Neorg. Strukt.* **1998** *39*, 460 – 463; *J. Struct. Chem.* **1998**, *39*, 372 – 375.
[369] X. Li, A. A. Gewirth, *J. Am. Chem. Soc.* **2003**, *125*, 7086 – 7099.
[370] P. Damle, A. W. Ghosh, S. Datta, *Chem. Phys.* **2002**, *281*, 171 – 187.
[371] C. W. Bauschlicher, Jr., A. Ricca, N. Mingo, J. Lawson, *Chem. Phys. Lett.* **2003**, *372*, 723 – 727.
[372] J. L. Mozos, P. Ordejón, M. Brandbyge, J. Taylor, K. Stokbro, *Adv. Quantum Chem.* **2003**, *42*, 299 – 314.
[373] J. H. Teles, S. Brode, M. Chabanas, *Angew. Chem.* **1998**, *110*, 1475 – 1478; *Angew. Chem. Int. Ed.* **1998**, *37*, 1415 – 1418,.
[374] A. S. K. Hashmi, *Gold Bull.* **2003**, *36*, 3 – 9.
[375] M. Haruta, T. Kobayashi, H. Samo, N. Yamada, *Chem. Lett.* **1987**, *405*–408.
[376] M. Valden, X. Lai, D. W. Goodman, *Science* **1998**, *281*, 1647 – 1650.
[377] M. Haruta, *Catal. Today* **1997**, *36*, 153 – 166.
[378] Y. Iisuka, H. Fujiki, N. Yamauchi, T. Chijiiwa, S. Arai, S. Tsubota, M. Haruta, *Catal. Today* **1997**, *36*, 115 – 123.
[379] M. Haruta, M. Daté, *Appl. Catal. A* **2001**, *222*, 427 – 437.
[380] G. C. Bond, *Catal. Today* **2002**, *72*, 5 – 9.
[381] R. Grisel, K.-J. Weststrate, A. Gluhoi, B. E. Nieuwenhuys, *Gold Bull.* **2002**, *35*, 39 – 45.
[382] Y. D. Kim, M. Fischer, G. Ganteför, *Chem. Phys. Lett.* **2003**, *377*, 170 – 176.
[383] W. T. Wallace, R. B. Wyrwas, R. L. Whetten, R. Mitric, V. Bonacic-Koutecký, *J. Am. Chem. Soc.* **2003**, *125*, 8408 – 8414.
[384] B.-W. Yoon, H. Häkkinen, U. Landman, *J. Phys. Chem. A* **2003**, *107*, 4066 – 4071.
[385] G. Mills, M. S. Gordon, H. Metiu, *Chem. Phys. Lett.* **2002**, *359*, 4493 – 4499.
[386] S. A. Varganov, R. M. Olson, M. S. Gordon, G. Mills, H. Metiu, *Chem. Phys. Lett.* **2003**, *368*, 778 – 779.
[387] D. H. Wells, Jr., W. N. Delgass, K. T. Thomson, *J. Chem. Phys.* **2002**, *117*, 10597 – 10603.
[388] D. Stolcic, M. Fischer, G. Ganteför, Y. D. Kim, Q. Sun, P. Jena, *J. Am. Chem. Soc.* **2003**, *125*, 2848 – 2849.

[389] W. T. Wallace, A. J. Leavitt, R. L. Whetten, *Chem. Phys. Lett.* **2003**, *368*, 774 – 777.
[390] S. A. Varganov, R. M. Olson, M. S. Gordon, H. Metiu, *J. Chem. Phys.* **2003**, *119*, 2531 – 2537.
[391] A. Sanchez, S. Abbet, U. Heiz, W.-D. Schneider, H. Häkkinen, R. N. Barnett, U. Landman, *J. Phys. Chem. A* **1999**, *103*, 9573 – 9578.
[392] H. Häkkinen, U. Landman, *J. Am. Chem. Soc.* **2001**, *123*, 9704 – 9705.
[393] Z.-P. Liu, P. Hu, A. Alavi, *J. Am. Chem. Soc.* **2002**, *124*, 14770 – 14779.
[394] N. Lopez, J. K. Nørskov, *J. Am. Chem. Soc.* **2002**, *124*, 11262 – 11263.
[395] L. M. Molina, B. Hammer, *Phys. Rev. Lett.* **2003**, *90*, 206102, 1 – 4.
[396] V. Bonacic-Koutecký, J. Burda, R. Mitric, M.-F. Ge, *J. Chem. Phys.* **2002**, *117*, 3120 – 3131.
[397] M. Mavrikakis, P. Stoltze, J. K. Nørskov, *Catal. Lett.* **2000**, *64*, 101 – 106.
[398] H. Häkkinen, S. Abbet, A. Sanchez, U. Heiz, U. Landman, *Angew. Chem.* **2003**, *115*, 1335 – 1338; *Angew. Chem. Int. Ed.* **2003**, *42*, 1297 – 1300.
[399] A. Vittadini, A. Selloni, *J. Chem. Phys.* **2002**, *117*, 353 – 361.
[400] A. Sierraalta, R. Añez, M.-R. Brussin, *J. Phys. Chem. A* **2002**, *106*, 6851 – 6856.
[401] N. Lopez, J. K. Nørskov, *Surf. Sci.* **2003**, *515*, 175 – 186.
[402] B. Hammer, J. K. Nørskov, *Surf. Sci.* **1995**, *343*, 211 – 220.
[403] *BildZeitung* **1995**, 12 June. Published in *Nature*, including the front page, the paper by Hammer and Nørskov[6] led, surely without intention of its original authors, to this four-column article, entitled "Künstliches Gold. So einfach geht es" ("Artificial gold. It's so simple.").
[404] M. Tachibana, K. Yoshizawa, A. Ogawa, H. Fujimoto, R. Hoffmann, *J. Phys. Chem. B* **2002**, *106*, 12727 – 12736.
[405] Y. Yourdshahyan, A. M. Rappe, *J. Chem. Phys.* **2002**, *117*, 825 – 833.
[406] J. A. Larsson, M. Nolan, J. C. Greer, *J. Phys. Chem. B* **2002**, *106*, 5931 – 5937.
[407] I. L. Garzón, C. Rovira, K. Michaelian, M. R. Beltrán, P. Ordejón, J. Junquera, D. Sánchez-Portal, E. Artacho, J. M. Soler, *Phys. Rev. Lett.* **2000**, *85*, 5250 – 5251.
[408] I. L. Garzón, E. Artacho, M. R. Beltrán, A. García, J. Junquera, K. Michaelian, P. Ordejón, C. Rovira, D. Sánchez-Portal, J. M. Soler, *Nanotechnology* **2001**, *12*, 126 – 131.
[409] L. M. Molina, B. Hammer, *Chem. Phys. Lett.* **2002**, *360*, 264 – 271.
[410] W. Andreoni, A. Curioni, H. Grönbeck, *Int. J. Quantum Chem.* **2000**, *80*, 598 – 608.
[411] H. Grönbeck, A. Curioni, W. Andreoni, *J. Am. Chem. Soc.* **2000**, *122*, 3839 – 3842.
[412] X. Li, A. A. Gewirth, *J. Am. Chem. Soc.* **2003**, *125*, 11674 – 11683.
[413] A. Michaelides, V. A. Ranea, P. L. de Andres, D. A. King, *Phys. Rev. Lett.* **2003**, *90*, 216102, 1 – 4.
[414] R. Rousseau, G. Dietrich, S. Krückeberg, K. Lützenkirchen, D. Marx, L. Schweikhard, C. Walther, *Chem. Phys. Lett.* **1998**, *295*, 41 – 46.
[415] A. Bilic, J. R. Reimers, N. S. Hush, J. Hafner, *J. Chem. Phys.* **2002**, *116*, 8981 – 8987.
[416] K. A. Fichthorn, R. A. Miron, *Phys. Rev. Lett.* **2002**, *89*, 196103, 1 – 4.
[417] M.-S. Liao, X. Lü, Q.-E. Zhang, *Int. J. Quantum Chem.* **1998**, *67*, 175 – 185.
[418] M. D. Legault, D. E. Bacelo, *J. Phys. Chem. A* **2002**, *106*, 9059 – 9064.
[419] J. A. Rodriguez, M. Pérez, T. Jirsak, J. Evans, J. Hrbek, L. González, *Chem. Phys. Lett.* **2003**, *378*, 526 – 532.
[420] A. J. Pérez-Jiménez, J. J. Palacios, E. Louis, E. SanFabián, J. A. Vergés, *ChemPhysChem* **2003**, *4*, 388 – 392.
[421] J. Greeley, J. K. Nørskov, M. Mavrikakis, *Annu. Rev. Phys. Chem.* **2002**, *53*, 319 – 348.
[422] F. Besenmacher, I. Chorkendorff, B. S. Clausen, B. Hammer, A. M. Molenbroek, J. K. Nørskov, I. Stensgaard, *Science* **1998**, *279*, 1913 – 1915.
[423] S. J. Rose, I. P. Grant, N. C. Pyper, *J. Phys. B* **1978**, *11*, 1171 – 1176.
[424] P. Pyykkö, *J. Chem. Soc. Faraday Trans. 2* **1979**, *75*, 1256 – 1276.
[425] Y. S. Lee, A. D. McLean, *J. Chem. Phys.* **1982**, *76*, 735 – 736.
[426] R. B. Ross, W. C. Ermler, *J. Phys. Chem.* **1985**, *89*, 5202 – 5206.
[427] C. L. Collins, K. G. Dyall, H. F. Schaefer III, *J. Chem. Phys.* **1995**, *102*, 2024 – 2031.
[428] R. Franke, C. van Wüllen, *J. Comput. Chem.* **1998**, *19*, 1596 – 1603.
[429] T. Tsuchiya, M. Abe, T. Nakajima, K. Hirao, *J. Chem. Phys.* **2001**, *115*, 4463 – 4472.
[430] T. Ziegler, J. G. Snijders, E. J. Baerends, *Chem. Phys. Lett.* **1980**, *75*, 1 – 4.
[431] O. D. Häberlen, N. Rösch, *Chem. Phys. Lett.* **1992**, *199*, 491 – 496.
[432] E. van Lenthe, E. J. Baerends, J. G. Snijders, *J. Chem. Phys.* **1994**, *101*, 9783 – 9792.
[433] G. Jansen, B. A. Hess, *Z. Phys. D* **1989**, *13*, 363 – 375.
[434] P. J. Hay, W. R. Wadt, *J. Chem. Phys.* **1985**, *82*, 270 – 283.
[435] P. J. Hay, W. R. Wadt, *J. Chem. Phys.* **1985**, *82*, 299 – 310.
[436] D. Andrae, U. Häussermann, M. Dolg, H. Stoll, H. Preuss, *Theor. Chim. Acta* **1990**, *77*, 123 – 141.
[437] W. J. Stevens, M. Krauss, H. Basch, P. G. Jasien, *Can. J. Chem.* **1992**, *70*, 612 – 630.
[438] S. M. Foiles, M. I. Baskes, M. S. Daw, *Phys. Rev. B* **1986**, *33*, 7983 – 7991.
[439] D. J. Oh, R. A. Johnson, *J. Mater. Res.* **1988**, *3*(3), 471 – 478.
[440] J. G. Ackland, V. Vitek, *Phys. Rev. B* **1990**, *41*, 10324 – 10333.
[441] F. Cleri, V. Rosato, *Phys. Rev. B* **1993**, *48*, 22 – 33.
[442] C. L. Kelchner, D. M. Halstead, L. S. Perkins, N. M. Wallace, A. E. DePristo, *Surf. Sci.* **1994**, *310*, 425 – 435, and references therein.
[443] J. Cai, Y. Y. Ye, *Phys. Rev. B* **1996**, *54*, 8398 – 8410.
[444] G. C. Kallinteris, N. I. Papanicolaou, G. A. Evangelakis, D. A. Papaconstantopoulos, *Phys. Rev. B* **1997**, *55*, 2150 – 2156.
[445] A. Avinc, V. I. Dimitrov, *Comput. Mater. Sci.* **1999**, *13*, 211 – 217.
[446] E. Eliav, U. Kaldor, Y. Ishikawa, *Phys. Rev. A* **1994**, *49*, 1724 – 1729.
[447] P. Neogrády, V. Kellö, M. Urban, A. J. Sadlej, *Int. J. Quantum Chem.* **1997**, *63*, 557 – 565.
[448] C. Elsasser, N. Takeuchi, K. M. Ho, C. T. Chan, P. Braun, M. Fahnle, *J. Phys. Condens. Matter* **1990**, *2*, 4371 – 4394.
[449] M. Henderson, L. J. Curtis, R. Matulioniene, D. G. Ellis, C. E. Theodosiu, *Phys. Rev. A* **1997**, *56*, 1872 – 1878.
[450] G. A. Bishea, M. D. Morse, *J. Chem. Phys.* **1991**, *95*, 5646 – 5659.
[451] R. Hesse in *Advances in the Chemistry of Coordination Compounds* (Ed.: S. Kirschner), MacMillan, New York, **1961**, pp. 314 – 320.
[452] P. G. Jones, *Gold Bull.* **1981**, *14*, 102 – 118; P. G. Jones, *Gold Bull.* **1981**, *14*, 159 – 166, also P. G. Jones, *Gold Bull.* **1983**, *16*, 114 – 124.
[453] M. Melník, R. V. Parish, *Coord. Chem. Rev.* **1986**, *70*, 157 – 257.
[454] M. Jansen, *Angew. Chem.* **1987**, *99*, 1136 – 1149; *Angew. Chem. Int. Ed. Engl.* **1987**, *26*, 1098 – 1110.
[455] H. Schmidbaur, *Gold Bull.* **1990**, *23*, 11 – 21.
[456] C. X. Cui, M. Kertesz, *Inorg. Chem.* **1990**, *29*, 2568 – 2575.
[457] B. Krebs, *Unkonventionelle Wechselwirkungen in der Chemie metallischer Elemente*, VCH, Weinheim, **1992**.

 © 2004 Wiley-VCH Verlag GmbH & Co. KGaA, Weinheim

[458] D. M. P. Mingos, M. J. Watson, *Adv. Inorg. Chem.* **1992**, *39*, 327 – 399.
[459] C. E. Housecroft, *Coord. Chem. Rev.* **1992**, *115*, 117 – 140, **1993**, *127*, 187 – 221; C. E. Housecroft, *Coord. Chem. Rev.* **1995**, *142*, 101 – 121.
[460] S. S. Pathaneni, G. R. Desiraju, *J. Chem. Soc. Dalton Trans.* **1993**, 319 – 322.
[461] A. J. Welch, S. K. Chapman, *The Chemistry of the Copper and Zinc Triads*, Royal Society of Chemistry, Cambridge, **1993**.
[462] A. L. Balch, *Prog. Inorg. Chem.* **1994**, *41*, 239 – 329.
[463] K. I. Grandberg, V. P. Dyadchenko, *J. Organomet. Chem.* **1994**, *474*, 1 – 21.
[464] I. Dance in *The Crystal as Supramolecular Entity* (Ed.: G. R. Desiraju), Wiley, New York, **1996**, pp. 137 – 233.
[465] P. D. Akrivos, H. J. Katsikis, A. Koumoutsi, *Coord. Chem. Rev.* **1997**, *167*, 95 – 204.
[466] J. Vicente, M. T. Chicote, M. D. Abrisqueta, P. González-Herrero, R. Guerrero, *Gold Bull.* **1998**, *31*, 83 – 87; J. Vicente, M. T. Chicote, M. D. Abrisqueta, P. González-Herrero, R. Guerrero, *Gold Bull.* **1998**, *31*, 126 – 130.
[467] M. Bardají, A. Laguna, *J. Chem. Educ.* **1999**, *76*, 201 – 203.
[468] S. R. Collinson, D. W. Bruce in *Transition Metals in Supramolecular Chemistry* (Ed.: J. P. Sauvage), Wiley, Chichester, **1999**, pp. 285 – 369.
[469] G. R. Desiraju, *J. Chem. Soc. Dalton Trans.* **2000**, 3745 – 3751.
[470] D. M. P. Mingos, R. Vilar, D. Rais, *J. Organomet. Chem.* **2002**, *641*, 126 – 133.
[471] V. E. Wood, J. R. Reitz, *J. Phys. Chem. Solids* **1962**, *23*, 229 – 235.
[472] T. L. Liu, H. Amar, *Rev. Mod. Phys.* **1968**, *40*, 782 – 789.
[473] C. Norris, L. Walldén, *Phys. Status Solidi A* **1970**, *2*, 381 – 390.
[474] H. Overhof, J. Knecht, R. Fischer, F. Hensel, *J. Phys. F* **1978**, *8*, 1607 – 1616.
[475] J. Robertson, *Phys. Rev. B* **1983**, *27*, 6322 – 6330.
[476] G. K. Wertheim, R. L. Cohen, G. Crecelius, K. W. West, J. H. Wernick, *Phys. Rev. B* **1979**, *20*, 860 – 866.
[477] G. H. Grosch, K.-J. Range, *J. Alloys Compd.* **1996**, *233*, 30 – 38.
[478] G. H. Grosch, K.-J. Range, *J. Alloys Compd.* **1996**, *233*, 39 – 43.
[479] A.-V. Mudring, J. Nuss, U. Wedig, M. Jansen, *J. Solid State Chem.* **2000**, *155*, 29 – 36.
[480] T. Saue, K. Faegri, T. Helgaker, O. Gropen, *Mol. Phys.* **1997**, *91*, 937 – 950.
[481] O. Fossgaard, O. Gropen, E. Eliav, T. Saue, *J. Chem. Phys.* **2003**, *119*, 9355 – 9363.
[482] T. Ziegler, J. G. Snijders, E. J. Baerends, *J. Chem. Phys.* **1981**, *74*, 1271 – 1284.
[483] J. G. Snijders, P. Pyykkö, *Chem. Phys. Lett.* **1980**, *75*, 5 – 8.
[484] A. D. McLean, Y. S. Lee in " *Current Aspects of Quantum Chemistry 1981*" (Ed.: R Carbo), Elsevier, Amsterdam, **1982**, pp. 219 – 238.
[485] M. Krauss, W. J. Stevens, H. Basch, *J. Comput. Chem.* **1985**, *6*, 287 – 295.
[486] G. L. Malli, N. C. Pyper, *Proc. R. Soc. London Ser. A* **1986**, *407*, 377 – 404.
[487] K. Balasubramanian, P. A. Christiansen, K. S. Pitzer, *Phys. Rev. A* **1991**, *43*, 2581 – 2582.
[488] G. L. Malli, N. C. Pyper, A. F. Ramos, *Phys. Rev. A* **1991**, *43*, 2583 – 2584.
[489] Y. Ishikawa, G. L. Malli, N. C. Pyper, *Chem. Phys. Lett.* **1992**, *194*, 481 – 484.
[490] Y. S. Lee, A. D. McLean, *Bull. Korean. Chem. Soc.* **1987**, *8*, 122 – 126.
[491] G. Ohanessian, M. J. Brusich, W. A. Goddard III, *J. Am. Chem. Soc.* **1990**, *112*, 7179 – 7189.
[492] G. Ohanessian, W. A. Goddard III, *Acc. Chem. Res.* **1990**, *23*, 386 – 392.
[493] V. Kellö, A. J. Sadlej, *J. Chem. Phys.* **1991**, *95*, 8248 – 8253.
[494] A. J. Sadlej, *J. Chem. Phys.* **1991**, *95*, 2614 – 2622.
[495] A. Pizlo, G. Jansen, B. A. Hess, W. von Niessen, *J. Chem. Phys.* **1993**, *98*, 3945 – 3951.
[496] C.-Y. Park, J. E. Almlöf, *Chem. Phys. Lett.* **1994**, *231*, 269 – 276.
[497] V. Kellö, A. J. Sadlej, *Theor. Chim. Acta* **1995**, *92*, 253 – 267.
[498] C. van Wüllen, *J. Chem. Phys.* **1995**, *103*, 3589 – 3599.
[499] V. Kellö, A. J. Sadlej, *Theor. Chim. Acta* **1996**, *94*, 93 – 104.
[500] V. Kellö, A. J. Sadlej, B. A. Hess, *J. Chem. Phys.* **1996**, *105*, 1995 – 2003.
[501] M. Mayer, O. D. Häberlen, N. Rösch, *Phys. Rev. A* **1996**, *54*, 4775 – 4782.
[502] V. A. Nasluzov, N. Rösch, *Chem. Phys. Lett.* **1996**, *210*, 413 – 425.
[503] T. Nakajima, K. Hirao, *Chem. Phys. Lett.* **1999**, *302*, 383 – 391.
[504] T. Nakajima, T. Suzumura, K. Hirao, *Chem. Phys. Lett.* **1999**, *304*, 271 – 277.
[505] T. Suzumura, T. Nakajima, K. Hirao, *Int. J. Quantum Chem.* **1999**, *75*, 757 – 766.
[506] Y.-K. Han, K. Hirao, *Chem. Phys. Lett.* **2000**, *324*, 453 – 458.
[507] H. A. Witek, T. Nakajima, K. Hirao, *J. Chem. Phys.* **2000**, *113*, 8015 – 8025.
[508] T. Yanai, T. Nakajima, Y. Ishikawa, K. Hirao, *J. Chem. Phys.* **2001**, *114*, 6526 – 6538.
[509] H. Gollisch, *J. Phys. B* **1982**, *15*, 2569 – 2578.
[510] M. Harada, H. Dexpert, *C. R. Acad. Sci. Ser. IIb* **1996**, *322*, 239 – 246.
[511] M. Harada, H. Dexpert, *J. Phys. Chem.* **1996**, *100*, 565 – 572.
[512] D.-G. Dai, K. Balasubramanian, *J. Chem. Phys.* **1994**, *100*, 4401 – 4407.
[513] W. C. Ermler, Y. S. Lee, K. S. Pitzer, *J. Chem. Phys.* **1979**, *70*, 293 – 298.
[514] H. Basch, *Faraday Symp. Chem. Soc.* **1980**, *14*, 149 – 158.
[515] Y. S. Lee, W. C. Ermler, K. S. Pitzer, *J. Chem. Phys.* **1977**, *67*, 5861 – 5876.
[516] Y. S. Lee, W. C. Ermler, K. S. Pitzer, *J. Chem. Phys.* **1980**, *73*, 360 – 366.
[517] P. Hafner, P. Habitz, Y. Ishikawa, E. Wechsel-Trakowski, W. H. E. Schwarz, *Chem. Phys. Lett.* **1981**, *80*, 311 – 315.
[518] S. Rabii, C. Y. Yang, *Chem. Phys. Lett.* **1984**, *105*, 480 – 483.
[519] P. A. Christiansen, W. C. Ermler, *Mol. Phys.* **1985**, *55*, 1109 – 1111.
[520] S. P. Walch, C. W. Bauschlicher Jr., S. R. Langhoff, *J. Chem. Phys.* **1986**, *85*, 5900 – 5907.
[521] K. K. Das, K. Balasubramanian, *J. Mol. Spectrosc.* **1990**, *140*, 280 – 294.
[522] H. Partridge, C. W. Bauschlicher Jr., S. R. Langhoff, *Chem. Phys. Lett.* **1990**, *175*, 531 – 535.
[523] D. Strömberg, U. Wahlgren, *Chem. Phys. Lett.* **1990**, *169*, 109 – 115.
[524] D. Andrae, U. Häussermann, M. Dolg, H. Stoll, H. Preuss, *Theor. Chim. Acta* **1991**, *78*, 247 – 266.
[525] H. Basch, *J. Mol. Struct. (Theochem)* **1991**, *234*, 185 – 200.
[526] P. Schwerdtfeger, *Chem. Phys. Lett.* **1991**, *183*, 457 – 463.
[527] U. Wahlgren, B. Schimmelpfennig, S. Jusuf, H. Strömsnes, O. Gropen, L. Maron, *Chem. Phys. Lett.* **1998**, *287*, 525 – 530.
[528] S. Varga, E. Engel, W.-D. Sepp, B. Fricke, *Phys. Rev. A* **1999**, *59*, 4288 – 4294.
[529] T. Nakajima, K. Hirao, *J. Chem. Phys.* **2002**, *116*, 8270 – 8275.
[530] X.-J. Wang, X.-H. Wan, H. Zhou, S. Takami, M. Kubo, A. Miyamoto, *J. Mol. Struct. (Theochem)* **2002**, *579*, 221 – 227.
[531] I. Itkin, A. Zaitsevskii, *Chem. Phys. Lett.* **2003**, *374*, 143 – 150.
[532] T. Saue, H. J. Aa. Jensen, *J. Chem. Phys.* **2003**, *118*, 522 – 536.
[533] V. Kellö, A. J. Sadlej, *J. Chem. Phys.* **1995**, *103*, 2991 – 2999.
[534] V. Pershina, T. Bastug, T. Jacob, B. Fricke, S. Varga, *Chem. Phys. Lett.* **2002**, *365*, 176 – 183.
[535] M. Barysz, M. Urban, *Adv. Quantum Chem.* **1997**, *28*, 257 – 272.
[536] F. Lelj, A. Rosa, *Chem. Phys. Lett.* **1990**, *168*, 417 – 422.

 © 2004 Wiley-VCH Verlag GmbH & Co. KGaA, Weinheim

[537] P. Turski, *Chem. Phys. Lett.* **1999**, *315*, 115 – 118.
[538] P. Turski, M. Barysz, *J. Chem. Phys.* **1999**, *111*, 2973 – 2977.
[539] P. Turski, M. Barysz, *J. Chem. Phys.* **2000**, *113*, 4654 – 4661.
[540] M. Abe, T. Nakajima, K. Hirao, *J. Chem. Phys.* **2002**, *117*, 7960 – 7967.
[541] G. Bravo-Pérez, I. L. Garzón, *J. Mol. Struct. (Theochem)* **2002**, *619*, 79 – 89.
[542] H. Basch, S. Topiol, *J. Chem. Phys.* **1979**, *71*, 802 – 814.
[543] J. K. Laerdahl, T. Saue, K. Faegri, Jr, *Theor. Chem. Acc.* **1997**, *97*, 177 – 184.
[544] L.-J. Baker, R. C. Bott, G. A. Bowmaker, P. C. Healy, B. W. Skelton, P. Schwerdtfeger, A. H. White, *J. Chem. Soc. Dalton Trans.* **1995**, 1341 – 1347.
[545] P. Schwerdtfeger, *Mol. Phys.* **1995**, *86*, 359 – 368.
[546] P. Alemany, L. Bengtsson-Kloo, B. Holmberg, *Acta Chem. Scand.* **1998**, *52*, 718 – 727.
[547] J. R. Brown, P. Schwerdtfeger, D. Schröder, H. Schwarz, *J. Am. Soc. Mass Spectrom.* **2002**, *13*, 485 – 492.
[548] M. Guichemerre, G. Chambaud, H. Stoll, *Chem. Phys.* **2002**, *280*, 71 – 102.
[549] F. S. Legge, G. L. Nyberg, J. B. Peel, *J. Phys. Chem. A* **2001**, *105*, 7905 – 7916.
[550] C. W. Bauschlicher Jr., S. R. Langhoff, *Chem. Phys. Lett.* **1986**, *126*, 163 – 168.
[551] K. Balasubramanian, M. Z. Liao, *J. Chem. Phys.* **1987**, *86*, 5587 – 5590.
[552] C. W. Bauschlicher, Jr., *Chem. Phys. Lett.* **1989**, *156*, 91 – 94.
[553] C. W. Bauschlicher, Jr., S. R. Langhoff, H. Partridge, *J. Chem. Phys.* **1989**, *91*, 2412 – 2419.
[554] K. Balasubramanian, M. Z. Liao, *Chem. Phys.* **1988**, *127*, 313 – 324.
[555] K. Balasubramanian, K. K. Das, *Chem. Phys. Lett.* **1991**, *186*, 577 – 582.
[556] R. Wesendrup, T. Hunt, P. Schwerdtfeger, *J. Chem. Phys.* **2000**, *112*, 9356 – 9362.
[557] R. Arratia-Perez, G. L. Malli, *J. Chem. Phys.* **1986**, *84*, 5891 – 5897.
[558] K. Balasubramanian, P. Y. Feng, M. Z. Liao, *J. Chem. Phys.* **1989**, *91*, 3561 – 3570.
[559] C. W. Bauschlicher, Jr., S. R. Langhoff, H. Partridge, *J. Phys. Chem.* **1990**, *94*, 8378 – 8379.
[560] K. Balasubramanian, K. K. Das, *J. Phys. Chem.* **1990**, *94*, 8379 – 8380.
[561] K. Balasubramanian, K. K. Das, *J. Chem. Phys.* **1991**, *94*, 2923 – 2927.
[562] K. K. Das, K. Balasubramanian, *Chem. Phys. Lett.* **1991**, *176*, 571 – 574.
[563] R. Mitrić, M. Hartmann, B. Stanca, V. Bonačić-Koutecký, P. Fantucci, *J. Phys. Chem. A* **2001**, *105*, 8892 – 8905.
[564] S. Varga, K. Bolton, H. Grönbeck, A. Snis, A. Rosén, B. Fricke, *Eur. Phys. J. D* **2001**, *6*, 29 – 32.
[565] K. Balasubramanian, P. Y. Feng, *Chem. Phys. Lett.* **1989**, *159*, 452 – 458.
[566] K. Balasubramanian, *Relativistic E-ects in Chemistry. Part B. Applications*, Wiley, New York, **1997**, pp. 3 – 46 for coinage-metal molecules.
[567] J. M. Seminario, J. M. Tour, *Int. J. Quantum Chem.* **1997**, *65*, 749 – 758.
[568] C. W. Bauschlicher, Jr., S. R. Langhoff, H. Partridge, *J. Chem. Phys.* **1990**, *93*, 8133 – 8137.
[569] H. Grönbeck, W. Andreoni, *Chem. Phys.* **2000**, *262*, 1 – 14.
[570] R. Arratia-Perez, G. L. Malli, *Chem. Phys. Lett.* **1986**, *125*, 143 – 148.
[571] R. Boca, *Czech. J. Phys.* **1990**, *40*, 629 – 645.
[572] K. Balasubramanian, D.-W. Liao, *J. Chem. Phys.* **1991**, *94*, 5233 – 5236.
[573] X. Wu, L. Senapati, S. K. Nayak, A. Selloni, M. Hajaligol, *J. Chem. Phys.* **2002**, *117*, 4010 – 4015.
[574] D.-W. Liao, K. Balasubramanian, *J. Chem. Phys.* **1992**, *97*, 2548 – 2552.
[575] R. Arratia-Pérez, L. Hernández-Acevedo, *J. Mol. Struct. (Theochem)* **1993**, *282*, 131 – 141.
[576] H. Adachi, *Adv. Quantum Chem.* **1997**, *29*, 49 – 81.
[577] E. van Lenthe, A. van der Avoird, P. E. S. Wormer, *J. Chem. Phys.* **1998**, *108*, 4783 – 4796.
[578] H. Häkkinen, U. Landman, *Phys. Rev. B* **2000**, *62*, R2287 – R2290.
[579] A. F. Ramos, R. Arratia-Perez, G. L. Malli, *Phys. Rev. B* **1987**, *35*, 3790 – 3798.
[580] R. Arratia-Perez, A. F. Ramos, G. L. Malli, *Phys. Rev. B* **1989**, *39*, 3005 – 3009.
[581] L. Lamare, F. Michel-Calendini, *Int. J. Quantum Chem.* **1997**, *61*, 635 – 639.
[582] H. M. Lee, M.-F. Ge, B. R. Sahu, P. Tarakeshwar, K. S. Kim, *J. Phys. Chem. B* **2003**, *107*, 9994 – 10005.
[583] H. Häkkinen, B. Yoon, U. Landman, X. Li, H.-J. Zhai, L.-S. Wang, *J. Phys. Chem. A* **2003**, *107*, 6168 – 6175.
[584] J. Zhao, J.-L. Yang, J. G. Hou, *Phys. Rev. B* **2003**, *67*, 085404, 1 – 6.
[585] C. Y. Yang in *Relativistic E-ects in Atoms, Molecules, and Solids* (Ed.: G. L. Malli), Plenum, New York, **1983**, pp. 335 – 361.
[586] T. X. Li, S. M. Lee, S. J. Han, G. H. Wang, *Phys. Lett. A* **2002**, *300*, 86 – 92.
[587] O. D. Häberlen, S.-C. Chung, N. Rösch, *Int. J. Quantum Chem.* **1994**, *S28*, 595 – 610.
[588] S. Krüger, S. Vent, N. Rösch, *Ber. Bunsen-Ges.* **1997**, *101*, 1640 – 1643.
[589] M. H. McAdon, W. A. Goddard III, *J. Chem. Phys.* **1988**, *88*, 277 – 302.
[590] M. H. McAdon, W. A. Goddard III, *J. Phys. Chem.* **1988**, *92*, 1352 – 1365.
[591] K. Balasubramanian, *J. Mol. Struct. (Theochem)* **1989**, *202*, 291 – 313.
[592] Z. J. Wu, S. H. Zhou, J. S. Shi, S. Y. Zhang, *Chem. Phys. Lett.* **2003**, *368*, 153 – 161.
[593] D. Fischer, W. Andreoni, A. Curioni, H. Grönbeck, S. Burkart, G. Ganteför, *Chem. Phys. Lett.* **2002**, *361*, 389 – 396.
[594] H. Tanaka, S. Neukermans, E. Janssens, R. E. Silverans, P. Lievens, *J. Chem. Phys.* **2003**, *119*, 7115 – 7123.
[595] S. Krüger, M. Stener, N. Rösch, *J. Chem. Phys.* **2001**, *114*, 5207 – 5215.
[596] F. Forstmann, S. Ossicini, *J. Chem. Phys.* **1980**, *73*, 5997 – 6002.
[597] M. G. Ruffolo, S. Ossicini, F. Forstmann, *J. Chem. Phys.* **1985**, *82*, 3988 – 3995.
[598] P. Pyykkö, Y.-F. Zhao, *Chem. Phys. Lett.* **1991**, *177*, 103 – 106.
[599] A. Schweizer, J. M. Weber, S. Gilb, H. Schneider, D. Schooss, M. M. Kappes, *J. Chem. Phys.* **2003**, *119*, 3699 – 3710.
[600] M. J. Calhorda, O. Crespo, M. C. Gimeno, P. G. Jones, A. Laguna, J. M. López-de-Luzuriaga, J. L. Perez, M. A. Ramón, L. F. Veiros, *Inorg. Chem.* **2000**, *39*, 4280 – 4285.
[601] A. Franceschetti, S. J. Pennycook, S. T. Pantelides, *Chem. Phys. Lett.* **2003**, *374*, 471 – 475.
[602] K. M. Beardmore, J. D. Kress, N. Grønbech-Jensen, A. R. Bishop, *Chem. Phys. Lett.* **1998**, *286*, 40 – 45.
[603] H. Sellers, *Surf. Sci.* **1993**, *294*, 99 – 107.
[604] H. Sellers, A. Ulman, Y. Shnidman, J. E. Eilers, *J. Am. Chem. Soc.* **1993**, *115*, 9389 – 9401.
[605] L. De Maria, M. Springborg, *Chem. Phys. Lett.* **2000**, *323*, 293 – 299.
[606] S. Ikeda, T. Nakajima, K. Hirao, *Mol. Phys.* **2003**, *101*, 105 – 110.
[607] T. Ziegler in *Relativistic E-ects in Atoms, Molecules and Solids* (Ed.: G. L. Malli), Plenum, New York, **1983**, pp. 421 – 436.
[608] I. Antes, G. Frenking, *Organometallics* **1995**, *14*, 4263 – 4268.

 © 2004 Wiley-VCH Verlag GmbH & Co. KGaA, Weinheim

[609] D. G. Musaev, K. Morokuma, *Organometallics* **1995**, *14*, 3327 – 3334.
[610] P. Schwerdtfeger, G. A. Bowmaker, *J. Chem. Phys.* **1994**, *100*, 4487 – 4497.
[611] S. Dapprich, G. Frenking, *J. Phys. Chem.* **1995**, *99*, 9352 – 9362.
[612] A. J. Lupinetti, S. Fau, G. Frenking, S. H. Strauss, *J. Phys. Chem. A* **1997**, *101*, 9551 – 9559.
[613] M. Diefenbach, M. Brönstrup, M. Aschi, D. Schröder, H. Schwarz, *J. Am. Chem. Soc.* **1999**, *121*, 10614 – 10625.
[614] N. A. Lambropoulos, J. R. Reimers, N. S. Hush, *J. Chem. Phys.* **2002**, *116*, 10277 – 10286.
[615] K. Balasubramanian, M. Z. Liao, *J. Phys. Chem.* **1988**, *92*, 361 – 364.
[616] P. Schwerdtfeger, *J. Am. Chem. Soc.* **1990**, *112*, 2818 – 2820.
[617] J. A. Tossell, D. J. Vaughan, *Inorg. Chem.* **1981**, *20*, 3333 – 3340.
[618] B. Dai, J.-L. Yang, *Chem. Phys. Lett.* **2003**, *379*, 512 – 516.
[619] R. L. DeKock, E. J. Baerends, P. M. Boerrigter, R. Hengelmolen, *J. Am. Chem. Soc.* **1984**, *106*, 3387 – 3396.
[620] O. D. Häberlen, N. Rösch, *J. Phys. Chem.* **1993**, *97*, 4970 – 4973.
[621] I. Antes, S. Dapprich, G. Frenking, P. Schwerdtfeger, *Inorg. Chem.* **1996**, *35*, 2089 – 2096.
[622] A. Fortunelli, G. Germano, *J. Phys. Chem. A* **2000**, *104*, 10834 – 10841.
[623] C. J. Evans, L. M. Reynard, M. C. L. Gerry, *Inorg. Chem.* **2001**, *40*, 6123 – 6131.
[624] B.-Y. Liang, L. Andrews, *J. Phys. Chem. A* **2000**, *104*, 9156 – 9164.
[625] D. Mandelbaum, M. E. Alikhani, *Theor. Chem. Acc.* **2001**, *105*, 354 – 359.
[626] A. Citra, X.-F. Wang, L. Andrews, *J. Phys. Chem. A* **2002**, *106*, 3287 – 3293.
[627] W. Beck, T. M. Klapötke, P. Klüfers, G. Frenking, C. M. Rienäcker, *Z. Anorg. Allg. Chem.* **2001**, *627*, 1669 – 1674.
[628] P. H. Svensson, J. Rosdahl, L. Kloo, *Chem. Eur. J.* **1999**, *5*, 305 – 311.
[629] E. Miyoshi, Y. Sakai, *J. Chem. Phys.* **1988**, *89*, 7363 – 7366.
[630] F. Mendizabal, *Organometallics* **2001**, *20*, 261 – 265.
[631] K. Mogi, Y. Sakai, T. Sonoda, Q. Xu, Y. Souma, *J. Phys. Chem. A* **2003**, *107*, 3812 – 3821.
[632] F. Cunin, C. Deudon, F. Favier, B. Mula, J. L. Pascal, *Inorg. Chem.* **2002**, *41*, 4173 – 4178.
[633] C. King, J.-C. Wang, M. N. I. Khan, J. P. Fackler, Jr., *Inorg. Chem.* **1989**, *28*, 2145 – 2149.
[634] Z.-M. Su, H.-X. Zhang, C.-M. Che, *Chem. J. Chin. Univ.* **1997**, *18*, 1171 – 1179.
[635] M. Preisenberger, P. Pyykkö, A. Schier, H. Schmidbaur, *Inorg. Chem.* **1999**, *38*, 5870 – 5875.
[636] P. Alemany, J. J. Novoa, L. Bengtsson, *Int. J. Quantum Chem.* **1994**, *52*, 1 – 8.
[637] Y.-F. Zhao, X.-G. Jing, M.-Y. Zhang, *Int. J. Quantum Chem.* **2000**, *80*, 38 – 43.
[638] Y.-F. Zhao, X.-G. Jing, W.-H. Su, *J. Mol. Struct. (Theochem)* **2002**, *587*, 43 – 48.
[639] D. E. Bacelo, S. D. Huang, Y. Ishikawa, *Chem. Phys. Lett.* **1997**, *277*, 215 – 222.
[640] S.-C. Chung, S. Krüger, H. Schmidbaur, N. Rösch, *Inorg. Chem.* **1996**, *35*, 5387 – 5392.
[641] E. J. Fernández, M. C. Gimeno, P. G. Jones, A. Laguna, M. Laguna, J. M. López-de-Luzuriaga, M. A. Rodríguez, *Chem. Ber.* **1995**, *128*, 121 – 124.
[642] S. Canales, O. Crespo, M. C. Gimeno, P. G. Jones, A. Laguna, F. Mendizabal, *Organometallics* **2000**, *19*, 4985 – 4994.
[643] M. J. Calhorda, F. Canales, M. C. Gimeno, J. Jiménez, P. G. Jones, A. Laguna, L. F. Veiros, *Organometallics* **1997**, *16*, 3837 – 3844.
[644] E. J. Fernández, A. Laguna, J. M. L. de Luzuriaga, M. Monge, P. Pyykkö, N. Runeberg, *Eur. J. Inorg. Chem.* **2002**, 750 – 753.
[645] M.-F. Fan, Z.-Y. Lin, J. E. McGrady, D. M. P. Mingos, *J. Chem. Soc. Perkin Trans. 2* **1996**, 563 – 568.
[646] A. Veldkamp, G. Frenking, *Organometallics* **1993**, *12*, 4613 – 4622.
[647] T. Ishii, R. Sekine, T. Enoki, E. Miyazaki, T. Miyamae, T. Miyazaki, *J. Phys. Soc. Jpn.* **1997**, *66*, 3424 – 3433.
[648] E. R. Schreiter, J. E. Stevens, M. F. Ortwerth, R. G. Freeman, *Inorg. Chem.* **1999**, *38*, 3935 – 3937.
[649] Z.-H. Li, Z.-H. Loh, K. F. Mok, T. S. A. Hor, *Inorg. Chem.* **2000**, *39*, 5299 – 5305.
[650] W. C. Herndon, I. Haiduc, *J. Mol. Struct.* **2001**, *598*, 127 – 131.
[651] S. F. Sontum, D. A. Case, *J. Phys. Chem.* **1982**, *86*, 1596 – 1606.
[652] J. A. Tossell, *Chem. Phys. Lett.* **1998**, *286*, 73 – 78.
[653] H. L. Hermann, P. Schwerdtfeger, F. Mohr, S. K. Bhargava, *Organometallics* **2003**, *22*, 2373 – 2377.
[654] C. Heinemann, R. H. Hertwig, R. Wesendrup, W. Koch, H. Schwarz, *J. Am. Chem. Soc.* **1995**, *117*, 495 – 500.
[655] A. Antušek, M. Urban, A. J. Sadlej, *J. Chem. Phys.* **2003**, *119*, 7247 – 7262.
[656] D. Schröder, R. Brown, P. Schwerdtfeger, H. Schwarz, *Int. J. Mass Spectrom.* **2000**, *203*, 155 – 163.
[657] L. D. Socaciu, J. Hagen, T. M. Bernhardt, L. Wöste, U. Heiz, H. Häkkinen, U. Landman, *J. Am. Chem. Soc.* **2003**, *125*, 10437 – 10445.
[658] J. Hrušák, D. Schröder, H. Schwarz, *Chem. Phys. Lett.* **1994**, *225*, 416 – 420.
[659] S. Toyota, M. Oki, *Bull. Chem. Soc. Jpn.* **1995**, *68*, 1345 – 1351.
[660] K. Köhler, S. J. Silverio, I. Hyla-Kryspin, R. Gleiter, L. Zsolnai, A. Driess, G. Huttner, H. Lang, *Organometallics* **1997**, *16*, 4970 – 4979.
[661] A. Kovács, G. Frenking, *Organometallics* **1999**, *18*, 887 – 894.
[662] G. M. Stewart, E. R. T. Tiekink, M. A. Buntine, *J. Phys. Chem. A* **1997**, *101*, 5368 – 5373.
[663] A. Cruz, E. Poulain, G. Del Angel, S. Castillo, V. Bertin, *Int. J. Quantum Chem.* **1998**, *67*, 399 – 409.
[664] A. Cruz, G. Del Angel, E. Poulain, J. M. Martínez-Magadan, M. Castro, *Int. J. Quantum Chem.* **1999**, *75*, 699 – 707.
[665] X. Xu, Y. Z. Yuan, K. Asakura, Y. Iwasawa, H. L. Wan, K. R. Tsai, *Chem. Phys. Lett.* **1998**, *286*, 163 – 170.
[666] N. C. Schiødt, P. Sommer-Larsen, M. Folmer Nielsen, J. Larsen, K. Bechgaard, *Inorg. Chem.* **1995**, *34*, 3688 – 3694.
[667] G. Kickelbick, U. Schubert, *Inorg. Chim. Acta* **1997**, *262*, 61 – 64.
[668] H. Basch, T. Hoz in *Supplement C2: The Chemistry of Triple-Bonded Functional Groups* (Ed.: S. Patai), Wiley, New York, **1994**, pp. 1 – 108.
[669] G. Aullón, G. Ujaque, A. Lledós, S. Alvarez, P. Alemany, *Inorg. Chem.* **1998**, *37*, 804 – 813.
[670] G. Aullón, G. Ujaque, A. Lledós, S. Alvarez, *Chem. Eur. J.* **1999**, *5*, 1391 – 1410.
[671] L. E. Sansores, R. Salcedo, H. Flores, A. Martinez, *J. Mol. Struct. (Theochem)* **2000**, *530*, 125 – 129.
[672] H. G. Raubenheimer, M. W. Esterhuysen, A. Timoshkin, Y. Chen, G. Frenking, *Organometallics* **2002**, *21*, 3173 – 3181.
[673] D. M. P. Mingos, *Chem. Soc. Rev.* **1986**, *15*, 31 – 61.
[674] M. Laupp, J. Strähle, *Angew. Chem.* **1994**, *106*, 210 – 211; *Angew. Chem. Int. Ed. Engl.* **1994**, *33*, 207 – 209.
[675] Å. Johansson, S. Stafström, *Chem. Phys. Lett.* **2000**, *322*, 301 – 306.
[676] Y. Akinaga, T. Nakajima, K. Hirao, *J. Chem. Phys.* **2001**, *114*, 8555 – 8564.
[677] C. Majumder, H. Mizuseki, Y. Kawazoe, *J. Chem. Phys.* **2003**, *118*, 9809 – 9813.
[678] P. Weinberger, *J. Phys. F* **1982**, *12*, 2171 – 2184.
[679] C. Koenig, N. E. Christensen, J. Kollar, *Phys. Rev. B* **1984**, *29*, 6481 – 6488.

 © 2004 Wiley-VCH Verlag GmbH & Co. KGaA, Weinheim

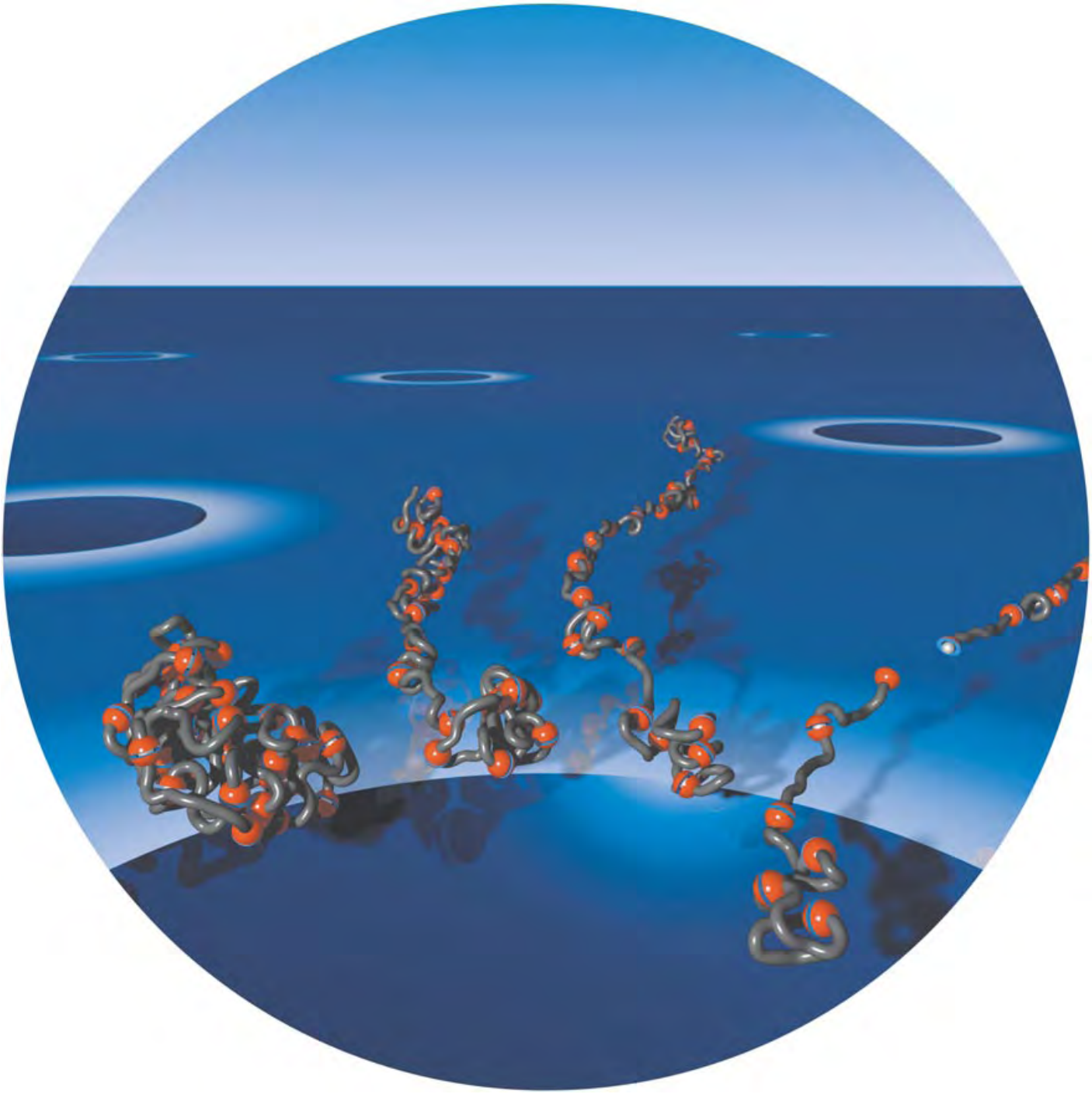
[680] J. W. Davenport, R. E. Watson, M. Weinert, *Phys. Rev. B* **1985**, *32*, 4883 – 4891.
[681] S. C. Wu, Z. Q. Wang, D. Sondericker, J. Sokolov, R. F. Garrett, F. Jona, *Phys. Rev. B* **1986**, *34*, 8418 – 8420.
[682] B.-Y. Qi, I. Perez, P. H. Ansari, F. Lu, M. Croft, *Phys. Rev. B* **1987**, *36*, 2972 – 2975.
[683] K. Terakura, T. Oguchi, T. Mohri, K. Watanabe, *Phys. Rev. B* **1987**, *35*, 2169 – 2173.
[684] R. E. Watson, J. W. Davenport, M. Weinert, *Phys. Rev. B* **1987**, *35*, 508 – 518.
[685] J. W. Davenport, R. E. Watson, M. Weinert, *Phys. Rev. B* **1988**, *37*, 9985 – 9992.
[686] P. Weinberger, A. M. Boring, R. C. Albers, W. M. Temmerman, *Phys. Rev. B* **1988**, *38*, 5357 – 5362.
[687] B. K. Godwal, R. Jeanloz, *Phys. Rev. B* **1989**, *40*, 7501 – 7507.
[688] C. Janiak, R. Hoffmann, *Inorg. Chem.* **1989**, *28*, 2743 – 2747.
[689] S. Takizawa, K. Terakura, T. Mohri, *Phys. Rev. B* **1989**, *39*, 5792 – 5797.
[690] E. Arola, C. J. Barnes, R. S. Rao, A. Bansil, *Phys. Rev. B* **1990**, *42*, 8820 – 8826.
[691] E. Arola, R. S. Rao, A. Salokatve, A. Bansil, *Phys. Rev. B* **1990**, *41*, 7361 – 7369.
[692] B. C. H. Krutzen, J. E. Ingles-eld, *J. Phys. Condens. Matter* **1990**, *2*, 4829 – 4847.
[693] P. Weinberger, J. Banhart, G. H. Schadler, A. M. Boring, P. S. Riseborough, *Phys. Rev. B* **1990**, *41*, 9444 – 9451.
[694] Z. W. Lu, S.-H. Wei, A. Zunger, *Phys. Rev. Lett.* **1991**, *66*, 1753 – 1756.
[695] M. Yasui, T. Takahashi, J. Callaway, *J. Phys. Condens. Matter* **1991**, *3*, 2679 – 2692.
[696] C. C. Tyson, A. Bzowski, P. Kristof, M. Kuhn, R. Sammynaiken, T. K. Sham, *Phys. Rev. B* **1992**, *45*, 8924 – 8928.
[697] P. Weinberger, C. Blaas, B. I. Bennett, A. M. Boring, *Phys. Rev. B* **1993**, *47*, 10158 – 10163.
[698] P. Weinberger, J. Kudrnovsky, J. Redinger, B. I. Bennett, A. M. Boring, *Phys. Rev. B* **1993**, *48*, 7866 – 7871.
[699] P. Weinberger, V. Drchal, L. Szunyogh, J. Fritscher, B. I. Bennett, *Phys. Rev. B* **1994**, *49*, 13366 – 13372.
[700] A. Bzowski, Y. M. Yiu, T. K. Sham, *Phys. Rev. B* **1995**, *51*, 9515 – 9520.
[701] A. Continenza, P. Monachesi, M. Galli, F. Marabelli, E. Bauer, *J. Appl. Phys.* **1996**, *79*, 6423- 6425.
[702] M. Methfessel, V. Fiorentini, S. Oppo, *Phys. Rev. B* **2000**, *61*, 5229 – 5236.
[703] P. H. T. Philipsen, E. J. Baerends, *Phys. Rev. B* **2000**, *61*, 1773 – 1778.
[704] J. A. Leiro, K. Kokko, R. Laihia, *J. Electron Spectrosc. Relat. Phenom.* **2001**, *113*, 167 – 174.
[705] B. Winkler, C. J. Pickard, M. D. Segall, V. Milman, *Phys. Rev. B* **2001**, *63*, 214103, 1 – 4.
[706] A. Gauzzi, E. Gilioli, F. Licci, M. Marezio, G. Calestani, C. Franchini, S. Massidda, *Phys. Rev. B* **2002**, *66*, 085106, 1 – 7.
[707] B. K. Godwal, S. Meenakshi, P. Modak, R. S. Rao, S. K. Sikka, V. Vijayakumar, E. Bussetto, A. Lausi, *Phys. Rev. B* **2002**, *65*, 140101, 1 – 4.
[708] R.-D. Hoffmann, D. Johrendt, Z.-Y. Wu, R. Pöttgen, *J. Mater. Chem.* **2002**, *12*, 676 – 680.
[709] Z. Assefa, F. DeStefano, M. A. Garepapaghi, J. H. LaCasce Jr., S. Ouellete, M. R. Corson, J. K. Nagle, H. H. Patterson, *Inorg. Chem.* **1991**, *30*, 2868 – 2876.
[710] E. J. Fernandez, M. C. Gimeno, A. Laguna, J. M. López-de-Luzuriaga, M. Monge, P. Pyykkö, D. Sundholm, *J. Am. Chem. Soc.* **2000**, *122*, 7287 – 7293.
[711] T. Hoz, H. Basch in *The Chemistry of Organic Derivatives of Gold and Silver* (Eds.: S. Patai, Z. Rappoport, Wiley, New York, **1999**, pp. 1 – 29.
[712] J. F. Liebman, J. Martinho Simões, S. W. Slayden in *The Chemistry of Organic Derivatives of Gold and Silver* (Eds.: S. Patai, Z. Rappoport), Wiley, New York, **1999**.
[713] H. Basch, M. A. Ratner, *J. Comp. Chem.* **2004**, *25*, 899 – 906.
[714] B.-J. Lee, J.-H. Shim, M. I. Baskes, *Phys. Rev. B* **2003**, *68*, 144112.
[715] M. A. Carvajal, J. J. Novoa, S. Alvarez, *J. Am. Chem. Soc.* **2004**, *126*, 1465 – 1477.
[716] M. S. Nechaev, V. M. Rayón, G. Frenking, *J. Phys. Chem. A* **2004**, *108*, 3134 – 3142.
[717] J.-Y. Zhao, Y. Zhang, L.-G. Zhu, *J. Mol. Struct. (Theochem)* **2004**, *671*, 179 – 187.
[718] H.-C. Tai, I. Krossing, M. Seth, D. V. Deubel, *Organometallics* **2004**, *23*, 2343 – 2349.
[719] F. Mendizabal, G. Zapata-Torres, C. Olea-Azar, *Chem. Phys. Lett.* **2003**, *382*, 9299.
[720] F. Mendizabal, P. Pyykkö, *Phys. Chem. Chem. Phys.* **2004**, *6*, 900 – 905.
[721] E. O'Grady, N. Kaltsoyannis, *Phys. Chem. Chem. Phys.* **2004**, *6*, 680 – 687.
[722] S.-G. Wang, W. H. E. Schwarz, *J. Am. Chem. Soc.* **2004**, *126*, 1266 – 1276.
[723] B. Kiran, X. Li, H.-J. Zhai, L.-F. Cui, L.-S. Wang, *Angew. Chem.* **2004**, *116*, 2177 – 2181; *Angew. Chem. Int. Ed.* **2004**, *43*, 2125 – 2129.
[724] L. Gagliardi, P. Pyykkö, *Phys. Chem. Chem. Phys.* **2004**, *6*, 2904 – 2906.
[725] T. K. Ghanty, K. R. S. Chandrakumar, S. K. Ghosh, *J. Chem. Phys.* **2004**, *120*, 11363 – 11366.
[726] J. M. Thomas, N. R. Walker, S. A. Cooke, M. C. L. Gerry, *J. Am. Chem. Soc.* **2004**, *126*, 1235 – 1246.
[727] L. Andrews, X.-F. Wang, L. Manceron, K. Balasubramanian, *J. Phys. Chem. A* **2004**, *108*, 2936 – 2940.
[728] D. Schröder, R. Brown, P. Schwerdtfeger, X.-B. Wang, X. Yang, L.-S. Wang, H. Schwarz, *Angew. Chem.* **2003**, *115*, 323 – 327; *Angew. Chem. Int. Ed.* **2003**, *42*, 311 – 314.
[729] T.-D. Chau, T. Visart de Bocarmé, N. Kruse, R. L. C. Wang, H. J. Kreuzer, *J. Chem. Phys.* **2003**, *119*, 12605 – 12610.
[730] Q.-Y. Kong, A.-H. Zeng, M.-H. Chen, Q. Xu, M.-F. Zhou, *J. Phys. Chem. A* **2004**, *108*, 1531 – 1536.
[731] A. K. Ray, *Comp. Mater. Sci.* **2002**, *25*, 279 – 284.
[732] M. P. Johansson, D. Sundholm, J. Vaara, *Angew. Chem.* **2004**, *116*, 2732 – 2735; *Angew. Chem. Int. Ed.* **2004**, *43*, 2678 – 2681.
[733] M. Häkkinen, M. Moseler, O. Kostko, N. Morgner, M. Astruc Hoffmann, B. von Issendorff, *Phys. Rev. Lett.* **2004**, in press.
[734] Y. G. Chushak, L. S. Bartell, *J. Phys. Chem. B* **2001**, *105*, 11605 – 11614.
[735] K. Koga, T. Ikeshoji, K. Sugawara, *Phys. Rev. Lett.* **2004**, *92*, 115507.
[736] J. Rogan, R. Ramírez, A. H. Romero, M. Kiwi, *Eur. Phys. J. D* **2004**, *28*, 219 – 228.
[737] I. L. Garzón, M. R. Beltrán, G. González, I. Gutíerrez-González, K. Michaelian, J. A. Reyes-Nava, J. I. Rodríguez-Hernández, *Eur. Phys. J. D* **2003**, *24*, 105 – 109.
[738] U. Landman, W. D. Luedtke, *Faraday Discuss.* **2004**, *125*, 1 – 22.
[739] P. Weis, O. Welz, E. Vollmer, M. M. Kappes, *J. Chem. Phys.* **2004**, *120*, 677 – 684.
[740] Q. Sun, Q. Wang, Y. Kawazoe, P. Jena, *Eur. Phys. J. D* **2004**, *29*, 231 – 234.
[741] S. Neukermans, E. Janssens, H. Tanaka, R. E. Silverans, P. Lievens, *Phys. Rev. Lett.* **2003**, *90*, 033401.
[742] E. Janssens, H. Tanaka, S. Neukermans, R. E. Silverans, P. Lievens, *Phys. Rev. B* **2004**, *69*, 085402.
[743] E. Z. da Silva, F. D. Novaes, A. J. R. da Silva, A. Fazzio, *Phys. Rev. B* **2004**, *69*, 115411.
[744] E. Z. da Silva, A. J. R. da Silva, A. Fazzio, *Comp. Mater. Sci.* **2004**, *30*, 73 – 76.

 © 2004 Wiley-VCH Verlag GmbH & Co. KGaA, Weinheim

[745] N. V. Skorodumova, S. I. Simak, *Solid State Commun.* **2004**, *130*, 755 – 757.
[746] W. T. Geng, K. S. Kim, *Phys. Rev. B* **2004**, *67*, 233403.
[747] L. Hui, F. Pederiva, G. H. Wang, B. L. Wang, *J. Chem. Phys.* **2003**, *119*, 9771 – 9776.
[748] C. W. Greeff, M. J. Graf, *Phys. Rev. B* **2004**, *69*, 054107.
[749] I. G. Gurtubay, J. M. Pitarke, I. Campito, A. Rubio, *Comp. Mater. Sci.* **2001**, *22*, 123 – 128.
[750] Y.-N. Zhang, L. Wang, W.-M. Wang, X.-F. Liu, X.-L. Tian, P. Zhang, *Phys. Lett. A* **2004**, *320*, 452 – 458.
[751] R. Caracas, X. Gonze, *Phys. Rev. A* **2004**, *69*, 144114.
[752] S. Jörgens, D. Johrendt, A. Mewis, *Z. Anorg. Allg. Chem.* **2003**, *629*, 2236 – 2239.
[753] A. Y. Lozovoi, A. Alavi, *Phys. Rev. B* **2003**, *68*, 245416.
[754] S. C. Erwin, *Phys. Rev. Lett.* **2003**, *91*, 206101.
[755] R. Baer, D. Neuhauser, S. Weiss, *Nano Lett.* **2004**, *4*, 85 – 88.
[756] K. A. Barakat, T. R. Cundari, M. A. Omary, *J. Am. Chem. Soc.* **2003**, *125*, 14228 – 14229.
[757] Q.-J. Pan, H.-X. Zhang, *J. Mol. Struct. (Theochem)* **2004**, *671*, 53 – 58.
[758] Z.-X. Cao, Q.-E. Zhang, *Chem. Eur. J.* **2004**, *10*, 1920 – 1925.
[759] K.-C. Wu, J. Li, C.-S. Lin, *Chem. Phys. Lett.* **2004**, *388*, 353 – 357.
[760] R. V. Parish in *The Chemistry of Organic Derivatives of Gold and Silver* (Eds.: S. Patai, Z. Rappoport), Wiley, New York, **1999**, pp. 31 – 49.
[761] C. F. Shaw III in *The Chemistry of Organic Derivatives of Gold and Silver* (Eds.: S. Patai, Z. Rappoport), Wiley, New York, **1999**, pp. 67 – 101.
[762] R. Armunanto, C. F. Schwenk, H. T. Tran, B. M. Rode, *J. Am. Chem. Soc.* **2004**, *126*, 2582 – 2587.
[763] H. Basch, M. A. Ratner, *J. Chem. Phys.* **2003**, *119*, 11926 – 11942.
[764] H. Basch, M. A. Ratner, **2003**, *J. Chem. Phys. 119*, 11 94311 950.
[765] H. Basch, M. A. Ratner, *J. Chem. Phys.* **2004**, *120*, 5761 – 5770.
[766] H. Basch, M. A. Ratner, *J. Chem. Phys.* **2004**, *120*, 5771 – 5780.
[767] E. G. Emberly, G. Kirczenow, **2003**, *Phys. Rev. Lett. 91*, 188 301, 14.
[768] Y. Luo, C.-K. Wang, Y. Fu, *J. Chem. Phys.* **2002**, *117*, 10823 – 10290.
[769] K. Stokbro, J. Taylor, M. Brandbyge, J.-L. Mozos, P. Ordejón, *Comp. Mater. Sci.* **2003**, *27*, 151 – 160.
[770] K. Palotás, B. Lazarovits, L. Szunyogh, P. Weinberger, www.arxiv.org Cond-mat/0403282, **2004**.
[771] M. Zhuang, M. Ernzerhof, *J. Chem. Phys.* **2004**, *120*, 4921 – 4926.
[772] R. Di Felice, A. Selloni, *J. Chem. Phys.* **2004**, *120*, 4906 – 4914.
[773] S. Franzen, *Chem. Phys. Lett.* **2003**, *381*, 315 – 321.
[774] Y. Karzazi, X. Crispin, O. Kwon, J. L. Brédas, J. Cornil, *Chem. Phys. Lett.* **2004**, *387*, 502 – 508.
[775] S. Letardi, F. Cleri, *J. Chem. Phys.* **2004**, *120*, 10062 – 10068.
[776] J. Nara, S. Higai, Y. Morikawa, T. Ohno, *J. Chem. Phys.* **2004**, *120*, 6705 – 6711.
[777] S. Higai, J. Nara, T. Ohno, *J. Chem. Phys.* **2004**, *121*, 970 – 972.
[778] C. Nieto-Oberhuber, M. P. Muñoz, E. Buñuel, C. Nevado, D. J. Cardenas, A. M. Echavarren, *Angew. Chem.* **2004**, *116*, 2456 – 2460; *Angew. Chem. Int. Ed.* **2004**, *43*, 2402 – 2406.
[779] S. A. Varganov, R. M. Olson, M. S. Gordon, G. Mills, H. Metiu, *J. Chem. Phys.* **2004**, *120*, 5169 – 5175.
[780] X.-L. Ding, B. Dai, J.-L. Yang, J. G. Hou, Q.-S. Zhu, *J. Chem. Phys.* **2004**, *121*, 621 – 623.
[781] M. L. Kimble, A. W. Castleman Jr., R. Mitri, C. Bürgel, V. Bonačić-Koutecký, *J. Am. Chem. Soc.* **2004**, *126*, 2526 – 2535.
[782] Q. Sun, P. Jena, Y. D. Kim, M. Fischer, G. Ganteför, *J. Chem. Phys.* **2004**, *120*, 6510 – 6515.
[783] D. W. Yuan, Z. Zheng, *J. Chem. Phys.* **2004**, *120*, 6574 – 6584.
[784] I. P. Hamilton, *Chem. Phys. Lett.* **2004**, *390*, 517 – 521.
[785] G. Dietrich, S. Krückeberg, K. Lützenkirchen, L. Schweikhard, C. Walter, *J. Chem. Phys.* **2004**, *112*, 752 – 760.
[786] G. M. Koretsky, M. B. Knickelbein, R. Rousseau, D. Marx, *J. Phys. Chem. A* **2004**, *105*, 11197 – 11203.
[787] Z.-P. Liu, X.-Q. Gong, J. Kohanoff, C. Sanchez, P. Hu, *Phys. Rev. Lett.* **2003**, *91*, 266102.
[788] M. Daté, M. Okumura, S. Tsubota, M. Haruta, *Angew. Chem.* **2004**, *116*, *99*, 2181 – 2184; *Angew. Chem. Int. Ed.* **2004**, *43*, 2129 – 2132.
[789] J. Guzman, B. C. Gates, *J. Am. Chem. Soc.* **2004**, *126*, 2672 – 2673.
[790] S. Mankefors, A. Grigoriev, G. Wendin, *Nanotechnology* **2003**, *14*, 849 – 858.
[791] D. M. P. Mingos, *Pure Appl. Chem.* **1980**, *52*, 705 – 712.
[792] P. Pawlow, *Z. Phys. Chemie* **1909**, *65*, 1 – 35; *Zh. Russk. Fiz.-Khim. Obshch.* **1908**, *40*, 1022 – 1067.
[793] GOLD 2003 Keynote Papers, *Gold Bull.* **2004**, *37(1–2)* 2 – 148.
[794] I. Galanakis, P. M. Oppeneer, P. Ravindran, L. Nordström, P. James, H. Dreysse, O. Eriksson, *Phys. Rev. B* **2001**, *63*, 172405.

 © 2004 Wiley-VCH Verlag GmbH & Co. KGaA, Weinheim

Communications



Ultrasound-induced chain scission in dissolved Pd^{II} coordination polymers is highly selective for the dissociation of phosphane ligands from palladium and therefore reversible. The original molecular weight of the polymer is restored after sonication. See the Communication by J. M. J. Paulusse and R. P. Sijbesma on the following pages for more details.

DOI: 10.1002/anie.200460040
© 2004 Wiley-VCH Verlag GmbH & Co. KGaA, Weinheim

Coordination Polymers

Reversible Mechanochemistry of a Pd^{II} Coordination Polymer**

*Jos M. J. Paulusse and Rint P. Sijbesma**

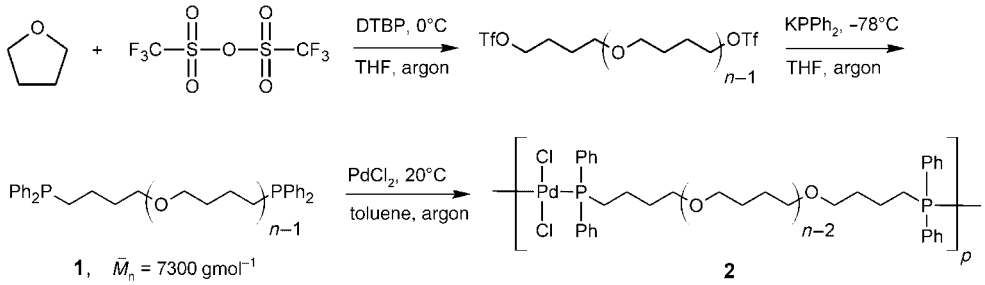
The design and synthesis of appropriate ligands is a well-established, but sometimes cumbersome method for controlling the coordination chemistry of transition-metal complexes. Manipulation of the coordination sphere by mechanical means is an exciting, yet barely explored alternative,[1] which may open up novel avenues in coordination chemistry and catalysis. Although mechanical forces act on even the smallest molecules, the effect of extensional forces is most pronounced in macromolecular species. If these forces act on a coordination polymer[2] of sufficient length, the noncovalent bonds may be broken.[3] Reversibility[4,5] of the coordinative interactions could then result in the continuous reformation of polymer chains until a steady-state degree of polymerization is reached. Irreversible disruption of covalent bonds is known to occur in polymers subject to strong shear forces;[6] it is the basis of some processing technologies, such as the mastication of natural rubber,[7] and even causes undesired degradation of macromolecules in chromatography.[8] Ultrasonication is one of the most efficient methods to induce breakage in polymer chains in homogeneous solution.[9] The shear forces required for chain scission are provided by the collapse of cavitation bubbles created by ultrasound.

Herein, we report on the reversible sonochemistry of high-molecular-weight coordination polymers in dilute solution. The polymeric diphosphane **1** was prepared by the cationic polymerization of tetrahydrofuran initiated by triflic anhydride[10] with subsequent termination by the diphenylphosphane anion ($\bar{M}_n = 7300\ g\,mol^{-1}$; $\bar{M}_w/\bar{M}_n = 1.11$). Linear coordination polymers **2** were obtained by stirring a solution in toluene of ligand **1** with a small excess of palladium dichloride for 2 days (Scheme 1).

Size-exclusion chromatographic (SEC) analysis of the equilibrated samples of **2** at different concentrations (Figure 1a) shows the presence of high-molecular-weight material[11] ($M_{top} = 2.50 \times 10^5\ g\,mol^{-1}$, $\bar{M}_w = 1.70 \times 10^5\ g\,mol^{-1}$, based on polystyrene standards), as well as peaks at 10500 and 23000 $g\,mol^{-1}$, which decrease in intensity relative to the peak for the high-molecular-weight material with increasing concentration. The low-molecular-weight peaks correspond well with the molecular weights of cyclic monomers and dimers (7500 and 15000 $g\,mol^{-1}$). The molecular-weight distributions in Figure 1a show that even at the lowest concentration high-molecular-weight material is present, and the data are in line with an equilibrium between cyclic and linear complexes with a critical polymerization concentration[12] of approximately 0.15 mM.[13]

In linear coordination polymers the degree of polymerization is strongly influenced by any stoichiometric imbalance between the bifunctional ligand and the metal, or by the presence of monofunctional ligands.[4c,5] Indeed, the addition of 1-dodecyl(diphenyl)phosphane (as a palladium dichloride complex to preserve the metal to ligand stoichiometry) to **2** led to a decrease in the molecular weight after equilibration, which confirms the linear nature of the polymer (Figure 1b).

The ultrasound-induced scission of coordination polymer **2** was studied by using a sonication probe in toluene under argon. A 1.5 mM solution, which had been equilibrated for 3 days, was sonicated for 1 h at a constant temperature of 20 °C. Samples were taken during the experiment and analyzed by SEC. The results of the sonication experiment



Scheme 1. Synthesis of the polymeric diphosphane ligand **1** and coordination polymer **2**. DTBP = 2,6-di-*tert*-butylpyridine, Tf = trifluoromethanesulfonyl.

[*] J. M. J. Paulusse, R. P. Sijbesma
Laboratory of Macromolecular and Organic Chemistry
Eindhoven University of Technology
P.O. Box 513, 5600 MB Eindhoven (The Netherlands)
Fax: (+31) 40-2472-655
E-mail: r.p.sijbesma@tue.nl

[**] This work was supported by the Netherlands Research School Combination—Catalysis. The authors thank M. W. A. Kuijpers and Dr. M. F. Kemmere for helpful discussions and assistance with sonication experiments. We thank Dr. K. Pieterse for preparing graphics.

Supporting information for this article is available on the WWW under http://www.angewandte.org or from the author.

are shown in Figure 2a. After sonication for 1 h, the $\bar{M}_w$ had decreased from $1.70 \times 10^5\ g\,mol^{-1}$ to $1.02 \times 10^5\ g\,mol^{-1}$.

^1H NMR, ^{13}C NMR, and ^{31}P NMR spectroscopy showed that no chemical degradation of complex **2** had occurred. Furthermore, when the sample was left for 1 day, the original molecular-weight distribution was restored nearly quantitatively. To test the reversibility of the sonochemical degradation, a 1.5 mM solution was sonicated for 1 h and left to equilibrate for 23 h. This procedure was repeated five times. In Figure 2b, the weight-averaged molecular weight of the sample after each sonication and equilibration period is shown, and there is no sign of irreversible polymer degrada-

 © 2004 Wiley-VCH Verlag GmbH & Co. KGaA, Weinheim DOI: 10.1002/anie.200460040

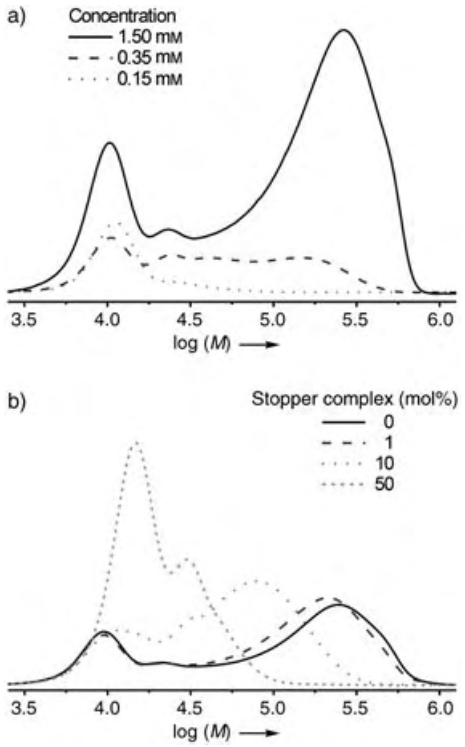


Figure 1. a) Molecular-weight distributions of **2** equilibrated in toluene at different concentrations; b) molecular-weight distributions of **2** (1.5 mM in toluene) equilibrated in the presence of different quantities of [$PdCl_2$(dodecyl(diphenyl)phosphane)$_2$].

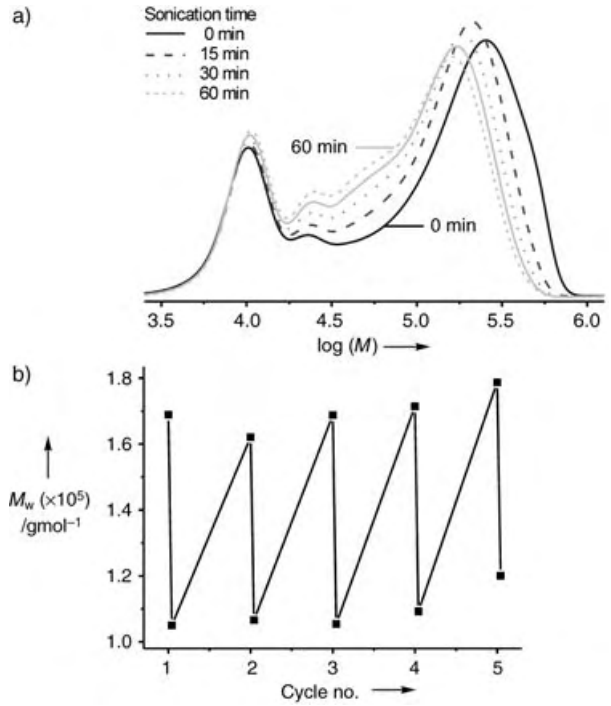


Figure 2. Ultrasound-induced decrease in the molecular weight of **2** (1.5 mM in toluene): a) molecular-weight distribution of samples taken during sonication; b) weight-averaged molecular weight ($\bar{M}_w$) during a reversibility test consisting of five cycles of sonication (1 h) followed by equilibration (23 h).

tion. The reversibility of the effects of sonication shows that no covalent bonds are broken in the process, and that the mechanical degradation is highly selective for the weaker palladium–phosphane coordination bonds.

Although the temperature was kept constant at 20 °C during all sonication experiments, we wanted to confirm that the decrease in molecular weight is indeed brought about by the mechanical action of ultrasound, and not by a trivial heating effect. Therefore, an equilibrated solution of **2** was heated at 80 °C for 3 h and then analyzed at room temperature by SEC. Heating resulted in a much smaller decrease in $\bar{M}_w$ than sonication, from 1.70×10^5 to 1.50×10^5 g mol^{-1}. Moreover, heating led to an increase in lower-molecular-weight material over the whole molecular-weight range, particularly in monomeric cyclic products, whereas sonication led to an increase in polymeric material of a more specific length (after 5 min of sonication the greatest increase was found at $M = 1.90\times10^5$ g mol^{-1}).

In a second control experiment, a solution of complex **2** was equilibrated for 3 days at 0.35 mM. This sample was subsequently concentrated swiftly by partially evaporating the solvent to give a 1.5 mM solution with a molecular-weight distribution corresponding to that of a less concentrated solution. Part of this sample was sonicated and showed a large decrease in molecular weight, whereas the molecular-weight distribution of the rest of the sample shifted towards higher molecular weight (Figure 3). This experiment shows that sonication moves the composition of the solution away from thermodynamic equilibrium.

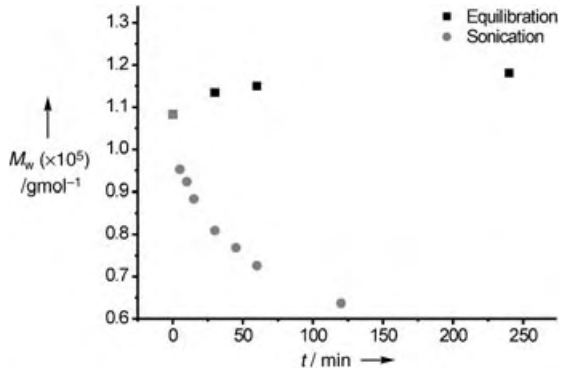
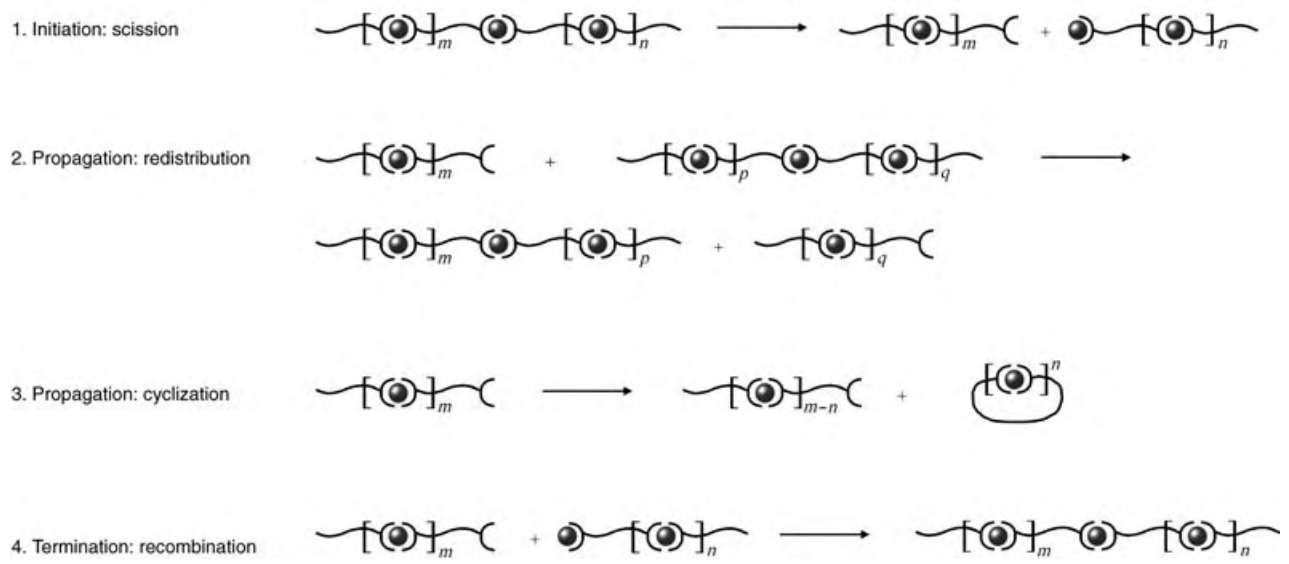


Figure 3. Molecular-weight evolution of equilibrating and sonicated samples of solutions 1.5 mM in **2** of non-equilibrium composition (see text for details).

Ultrasonic chain scission is a nonrandom process that acts preferentially on longer chains.[7,9] In solutions of **2**, this phenomenon is evidenced by the complete disappearance of the highest-molecular-weight polymers after short sonication times (Figure 2a). Several observations suggest a mechanism by which cyclic polymers are formed. For a decrease in molecular weight of any linear polymer, either additional chain ends or rings have to be formed (or a combination of both). Ligand exchange in palladium(II)–phosphane complexes is known to occur predominantly through an associative mechanism and is therefore strongly accelerated by trace

 © 2004 Wiley-VCH Verlag GmbH & Co. KGaA, Weinheim



Scheme 2. Proposed elementary steps upon sonication of **2**.

amounts of free phosphane.[14] Because sonicated solutions of **2** equilibrate at the same rate as non-equilibrium solutions obtained by other means (e.g. by rapidly increasing the concentration), the presence of significant amounts of free phosphane end groups after sonication may be excluded, thus suggesting that the newly formed polymer is mainly cyclic. We propose that the phosphane chain ends formed by cleavage of the polymer react rapidly with a palladium complex either intramolecularly or intermolecularly (Scheme 2). In each case, upon substitution at the palladium center a new reactive phosphane end group is formed and a chain reaction is initiated which terminates when a free phosphane reacts with a coordinatively unsaturated palladium(II) chain end. However, an intermolecular reaction merely results in redistribution to give a statistical (most probable) chain-length distribution and does not change the average molecular weight of the polymer. On the other hand, intramolecular attack of a phosphane end group results in the splitting off of a cyclic compound and a net decrease in molecular weight, as observed for sonicated solutions of **2**.

The results presented herein demonstrate that ultrasound may be used to mechanically induce ligand dissociation from transition-metal complexes, thus making it a novel method for studying and controlling the chemistry of coordination complexes. The creation of vacant coordination sites in combination with the complete reversibility of the process point the way to the application of this principle in transition-metal catalysis. Present efforts are focused on identifying the polymer architecture and experimental conditions required for optimal effectiveness of the sonochemical process, and on studying the reactivity changes induced by ligand dissociation.

Received: March 18, 2004 [Z460040]

Keywords: coordination polymers · macrocycles · phosphanes · supramolecular chemistry · ultrasound

[1] K. S. Suslick, *Adv. Organomet. Chem.* **1986**, *25*, 73.
[2] R. D. Archer, *Coord. Chem. Rev.* **1993**, *128*, 49.
[3] Ultrasound has been used to decrease the size of micellar aggregates; see, for example: J. Massey, K. N. Power, I. Manners, M. A. Winnik, *J. Am. Chem. Soc.* **1998**, *120*, 9533.
[4] a) U. Michelsen, C. A. Hunter, *Angew. Chem.* **2000**, *112*, 780; *Angew. Chem. Int. Ed.* **2000**, *39*, 764; b) J. B. Beck, S. J. Rowan, *J. Am. Chem. Soc.* **2003**, *125*, 13922; c) T. Vermonden, J. van der Gucht, P. de Waard, A. T. M. Marcelis, N. A. M. Besseling, E. J. R. Sudholter, G. J. Fleer, M. A. C. Stuart, *Macromolecules* **2003**, *36*, 7035; d) B. Lahn, M. Rehahn, *e-Polym.* **2002**, *1*, 1.
[5] J. M. J. Paulusse, R. P. Sijbesma, *Chem. Commun.* **2003**, 1494.
[6] a) J. A. Odell, A. Keller, Y. Rabin, *J. Chem. Phys.* **1988**, *88*, 4022; b) T. Q. Nguyen, H. H. Kausch, *Adv. Polym. Sci.* **1992**, *100*, 73.
[7] A. Casale, R. S. Porter, *Polymer stress reactions*, Academic Press, London, **1978**.
[8] H. G. Barth, F. J. Carlin, *J. Liq. Chromatogr.* **1984**, *7*, 1717.
[9] a) T. J. Mason, J. P. Lorimer, *Applied Sonochemistry*, 1st ed., Wiley-VCH, Weinheim, **2002**; b) K. S. Suslick, G. J. Price, *Annu. Rev. Mater. Sci.* **1999**, *29*, 295.
[10] M. F. Dubreuil, N. G. Farcy, E. J. Goethals, *Macromol. Rapid Commun.* **1999**, *20*, 383.
[11] For equilibrated solutions of pure **2**, the top of the high-molecular-weight peak shifts towards higher molecular-weight values with increasing concentration and reaches $2.50 \times 10^5\ g\,mol^{-1}$ at 1.5 mM, which corresponds to a degree of polymerization of 27 units. At even higher concentrations M_{top} does not shift further, although the fraction of cyclic monomers is lower. Based on the assumption that **2** contains a small amount of monophosphane impurities, such as monofunctionalized polymer chains or chains with one oxidized phosphane group, which act as chain ends, the observed ceiling for the concentration-dependent degree of polymerization corresponds to approximately 3.5% impurity in the polymeric ligands.
[12] a) H. Jacobsen, W. H. Stockmayer, *J. Chem. Phys.* **1950**, *18*, 1600; b) G. Ercolani, M. Luigi, P. Mencarelli, S. Roelens, *J. Am. Chem. Soc.* **1993**, *115*, 3901.
[13] Ligand-exchange rates in **2** are slow on the SEC timescale. A lifetime of approximately 13 h was found for the closely related system reported in reference [4].
[14] A. W. Verstuyft, L. W. Cary, J. H. Nelson, *Inorg. Chem.* **1976**, *15*, 3161.

 © 2004 Wiley-VCH Verlag GmbH & Co. KGaA, Weinheim

Photocatalysis

Efficient Photocatalytic Decomposition of Organic Contaminants over $CaBi_2O_4$ under Visible-Light Irradiation**

*Junwang Tang, Zhigang Zou, and Jinhua Ye**

Photocatalysis is a "green" technology for the treatment of all kinds of contaminants, especially for the removal of organic contaminants with solar energy,[1] which mainly includes oxidative decomposition of the volatile organic compounds (VOC) and purification of waste water.[2–10] Photocatalysis has many advantages over other treatment methods, for instance, the use of the environmentally friendly oxidant O_2, the reaction is performed at room temperature, and oxidation of the organics compounds, even at low concentrations.[3,5] To date, TiO_2 has undoubtedly proven to be the most excellent photocatalyst for the oxidative decomposition of many organic compounds under UV irradiation.[4–6,8] However, the relatively wide band gap of 3.2 eV limits further application of the material in the visible-light region ($\lambda > 400$ nm).[7] In view of the efficient utilization of visible light, the largest proportion of the solar spectrum and artificial light sources, the development of a photocatalyst with high activity under a wide range of visible-light irradiation is indispensable.

There are two ways to exploit the photocatalysts responsive to visible-light irradiation: The first involves the modification of TiO_2, the second is the development of a new material. The former has been largely investigated by doping or ion-implanting methods to effect photocatalysis under visible-light irradiation.[2,5,6,9–11] Recent work by Asahi et al. and Kisch et al. is representative of a few successful examples.[2,9] On the other hand, there have only been a few reports on the development of new materials.

We have reported the synthesis of several visible-light-sensitized photocatalytic materials to effect the efficient utilization of solar energy.[12] Herein, we report a novel photocatalyst, $CaBi_2O_4$, which is active in the photocatalytic oxidative decomposition of organic contaminants under visible-light irradiation. Acetaldehyde is known as a key indoor air pollutant and is also largely formed as an intermediate during photocatalytic oxidation of other organic compounds, ranging from alkanes to alcohols. Methylene blue (MB) is a representative of organic dyes in textile effluents. These two organic compounds are often considered as model contaminants in the photocatalytic decomposition of VOC and in the purification of dye waste water, respectively.[2–6,8,10] In the work described herein, they were also selected as model contaminants. The photocatalytic activities of $CaBi_2O_4$ for the decomposition of acetaldehyde and MB were investigated in turn under visible-light irradiation for the same sample. In detail, the $CaBi_2O_4$ photocatalyst was firstly used to decompose acetaldehyde under gaseous phase conditions; the used oxide was then collected and employed again to degrade MB under liquid-phase conditions.

Figure 1 represents the photocatalytic decomposition (versus time) of acetaldehyde over $CaBi_2O_4$ under visible-light irradiation ($\lambda \geq 440$ nm). CO_2 is the final product in the photocatalytic oxidation of organic contaminants.[5] The yield of CO_2, the formed CO_2 divided by the theoretical value of CO_2 for which 100% of the organic compounds would be converted, was used to evaluate the activity of the photocatalyst in the work described herein. It is amazing that 65% of acetaldehyde was photocatalytically oxidized to CO_2 after irradiation for 20 min with visible light over $CaBi_2O_4$. With increasing irradiation time, the conversion of acetaldehyde into CO_2 increased. After irradiation for 2 h, the detected CO_2 yield reached a stable value, 80%. The concentration of acetaldehyde in the reaction system also decreased from the initial 837 ppm to 0 ppm. There seemed to be a discrepancy (~20%) between the acetaldehyde conversion and CO_2 yield. Similar phenomena were also reported in the catalytic decomposition of acetaldehyde over a TiO_2-based photocatalysts under UV irradiation.[6] Possible reasons include: 1) adsorption of intermediates such as formic acid, etc. and

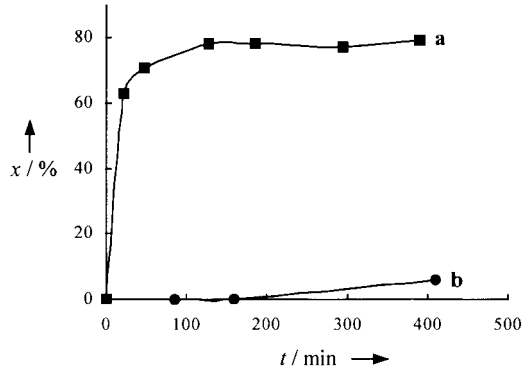


Figure 1. Conversion of acetaldehyde into CO_2 (x) as a function of irradiation time (t) under visible light ($\lambda \geq 440$ nm). a) $CaBi_2O_4$ photocatalyst; b) TiO_2 photocatalyst.

[*] Dr. J. Tang
Ecomaterials Center
National Institute for Materials Science (NIMS)
1-2-1 Sengen, Tsukuba, Ibaraki 305-0047 (Japan)
Dr. J. Ye
Ecomaterials Center
National Institute for Materials Science (NIMS)
1-2-1 Sengen, Tsukuba, Ibaraki 305-0047 (Japan)
and
PRESTO, Japan Science and Technology Agency (JST)
4-1-8 Honcho Kawaguchi, Saitama (Japan)
Fax: (+81) 298-59-2601
E-mail: jinhua.ye@nims.go.jp
Dr. Z. Zou
Photoreaction Control Research Center (PCRC)
National Institute of Advanced Industrial Science and Technology (AIST)
1-1-1 Higashi, Tsukuba, Ibaraki 305-8565 (Japan)

[**] This work was supported by a Grant-in-Aid for the Creation of Innovations through Business–Academic–Public Sector Cooperation, Japan.

 DOI: 10.1002/anie.200353594 © 2004 Wiley-VCH Verlag GmbH & Co. KGaA, Weinheim

deposition of coke-like substances,[4d,6] 2) balance adsorption of formed CO_2 in a closed-cycle system. We checked the products of the photocatalytic reaction and did not find the coke-like substances formed on the surface of $CaBi_2O_4$ after the reaction. Therefore, some intermediates (such as acetic acid, etc.) were possibly formed. These intermediates and some CO_2 were absorbed onto the surface of the photocatalyst and the reaction system. We also confirmed a little amount of CO_2 evolution when heating the photocatalyst in the presence of O_2 after the photocatalytic reaction.

By comparison, acetaldehyde decomposition over TiO_2 was also carried out under the same conditions (Figure 1). The results indicated that TiO_2 was inactive, as reported by Asahi et al.[2] The following experiments were also performed: 1) a dark experiment (without irradiation), 2) blank experiment (in the absence of the photocatalyst), 3) in the absence of oxidant O_2. In any case, CO_2 was hardly detected. Thus it is noteworthy that light irradiation, $CaBi_2O_4$ photocatalyst, and molecular O_2 are all indispensable for the catalytic degradation of acetaldehyde.

The wavelength dependence of the photocatalytic reaction is used to prove if the reaction is really driven by light irradiation.[2,12b,13] The wavelength dependence of acetaldehyde decomposition was investigated with cut-off filters of different wavelengths, and the results are shown in Figure 2.

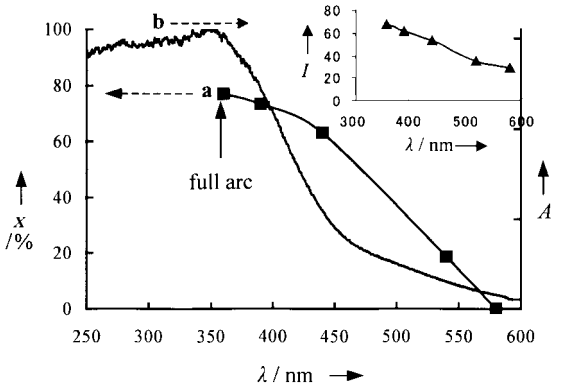


Figure 2. a) Wavelength (λ) dependence of yield of CO_2 (x) from the decomposition of acetaldehyde over $CaBi_2O_4$ upon irradiation with visible light (20 min); b) Relative absorbance (A) of $CaBi_2O_4$ photocatalyst. Insert: wavelength dependence of light intensity (I/mW cm^{-2}) with different cutoff filters.

The intensity variation of the irradiated light when using different cutoff filters is also included in the figure for reference. From Figure 2, clear activity with visible light of a wide range (up to 550 nm) was observed. The light-responsive range is wider than that reported by Asahi et al. for the $TiO_{2-x}N_x$ photocatalyst (500 nm).[2] It can be seen that the yield of CO_2 decreased with increasing wavelength of light, especially in the visible-light region, in good agreement with the optical properties of the photocatalyst as shown in Figure 2. The photocatalyst finally lost its activity when a cutoff of 580 nm (near the absorption edge) was used, although the intensity of the irradiated light at this wavelength was still as strong as 28 mW cm^{-2}. This indicates that the present catalytic reaction is driven by light and that the absorption property of the photocatalyst governs the reaction rate. In other words, the decomposition reaction of acetaldehyde into CO_2 over $CaBi_2O_4$ is a photocatalytic reaction.

Subsequently, the photocatalytic activity of $CaBi_2O_4$ was measured in a liquid medium. Figure 3 represents the variation of MB concentration with irradiation time over

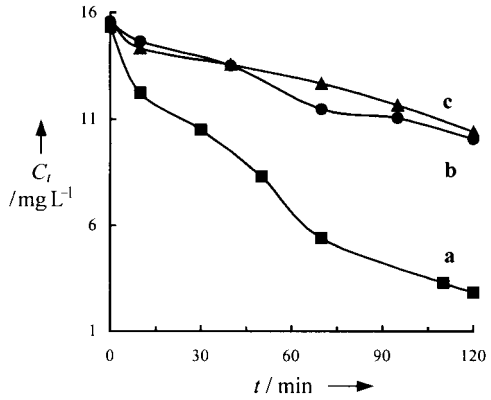


Figure 3. Concentration (C_t) of MB dye as a function of irradiation time (t) under visible light ($\lambda \geq 420$ nm). a) $CaBi_2O_4$ photocatalyst; b) TiO_2 photocatalyst; c) MB photolysis.

$CaBi_2O_4$. As a comparison, MB degradations over TiO_2 and MB photolysis were also performed under the same conditions and are shown in Figure 3. Wu, Zhao, and co-workers reported that many dyes could be degraded over TiO_2 based on the self-photosensitized process of dyes under visible-light irradiation.[7] However, a similar phenomenon was not observed in the degradation of MB over TiO_2 under visible-light irradiation (Figure 3), consistent with the results reported by Li and co-workers[4c] In contrast, the $CaBi_2O_4$ catalyst exhibited a high activity for MB degradation under visible light ($\lambda \geq 420$ nm), although the sample had been employed in the abovementioned photocatalytic acetaldehyde decomposition. The high activity of $CaBi_2O_4$ can also be confirmed from Figure 4, for which the colors of the solutions of MB before and after the photocatalytic reaction over $CaBi_2O_4$ are compared with that over TiO_2.

The photocatalytic oxidation of organic compounds in the presence of oxygen is mainly considered to be controlled by the following processes: 1) the photoelectron transition from the valence band (VB) to the conduction band (CB) of the semiconductor catalyst, 2) the oxidation of the organic compounds by the photohole in the VB or formed OH$^{\bullet}$ radical, 3) the reduction of oxygen by the photoelectron in the CB. Thus the photocatalytic activity of the semiconductor is closely related to its band structure. For the p-block metal-oxide semiconductor with a d^{10} configuration, the VB and CB are the 2p orbital of the oxygen atom and the lowest unoccupied molecular orbital (LUMO) of p-block metal

 © 2004 Wiley-VCH Verlag GmbH & Co. KGaA, Weinheim

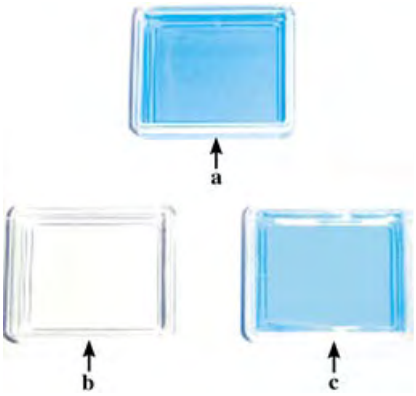


Figure 4. Pictures of solutions of MB: a) before photocatalytic degradation; b) after photocatalytic reaction (120 min) over $CaBi_2O_4$; c) after photocatalytic reaction (120 min) over TiO_2.

center, respectively.[14] For bismuth(III)-based semiconductors, it was also found that the Bi 6s and O 2p levels can form a preferable hybridized VB.[15] In terms of the above depiction, we assumed that the VB of $CaBi_2O_4$ is composed of hybridized Bi 6s and O 2p orbitals, whereas the CB is composed of Bi 6p orbitals, and these bands meet the potential requirements of organic oxidation. An active photocatalyst for the decomposition of the organic compounds must have a VB with strong oxidizing ability and photogenerated holes with high mobility. The hybridized VB of $CaBi_2O_4$ has shown strong oxidative ability in the work described herein. Meanwhile, the hybridization of the Bi 6s and O 2p levels makes the VB largely dispersed, which favors the mobility of photoholes in the VB[16] and is beneficial to the oxidation reaction.

The stability of a photocatalyst is important to its application; doped TiO_2 photocatalysts sometimes suffer from this problem.[2] After each photocatalytic degradation reaction of organic contaminants, the crystal structure of the $CaBi_2O_4$ photocatalyst was checked by X-ray diffraction (XRD) analysis. The analysis showed that $CaBi_2O_4$ belongs to a monoclinic crystal structure (space group: $I2/a$, $a = 1.4002$, $b = 1.1596$, $c = 1.2198$ nm, $\beta = 101.541°$).[17] XRD analysis of the sample also showed that the crystal structure of the photocatalyst was not changed after the photocatalytic reaction. The stability of the photocatalyst will be investigated further in more detail by other characterization methods. The BET (Brunauer–Emmett–Teller) measurement showed that the surface area of the $CaBi_2O_4$ photocatalyst was only $0.6\ m^2g^{-1}$, nearly 1% of the surface area of TiO_2. It is well known that the surface area of a catalyst greatly affects its catalytic activity.[18] The present method for the preparation of the material greatly limits the activity of the photocatalyst. Nano-sized photocatalysts are under investigation and are expected to increase significantly the surface area of the catalyst and therefore the photocatalytic activity.

In summary, the $CaBi_2O_4$ semiconductor was found to be a novel visible-light-driven photocatalyst for the degradation of various organic contaminants. The catalyst exhibits a high photocatalytic activity, not only in the decomposition of acetaldehyde, but also in the degradation of MB dye under wide-ranging visible light irradiation. Furthermore, its activity and crystal structure did not change after a series of continuous investigations under different experimental conditions. Furthermore, this work provides some insight into the design of new green heterogeneous photocatalysts for the degradation of organic contaminants.

Experimental Section

The $CaBi_2O_4$ photocatalyst was prepared by a simple soft chemical method. Stoichiometric amounts of $Ca(NO_3)_2{\cdot}4H_2O$ and $Bi(NO_3)_3{\cdot}5H_2O$ were dissolved in water. The composite was formed by adding a solution of ethylenediaminetetraacetic acid in ammonia and citric acid to the above aqueous solution. A xerogel was then prepared by ageing and drying the composite. The xerogel was calcined at 623 K for 10 h, and crystallized at 1073 K for 12 h in air. The crystal structure of the sample was determined by X-ray diffraction methods (JEOL JDX-3500 Tokyo, Japan). The UV/Vis diffuse reflectance spectrum of $CaBi_2O_4$ was measured on a UV/Vis spectrometer (UV-2500, Shimadzu). The surface area of the material was measured by BET measurements of nitrogen adsorption at 77 K (Micromeritics Automatic Surface Area Analyzer Gemini 2360, Shimadzu). TiO_2 (surface area $50\ m^2g^{-1}$) is commercially available and was used as a reference photocatalyst. The photocatalytic decompositions of acetaldehyde was performed with 1.0 g of the powdered photocatalyst placed at the bottom of a Pyrex glass cell at room temperature in a gas-closed system; the reaction gas mixture (0.5 atm) consisted of 837 ppm CH_3CHO, 21% O_2, and Ar balance gas. The photocatalytic degradation of MB was carried out with 0.3 g of the powdered photocatalyst suspended in a solution of MB ($15.3\ mg\,L^{-1}$, 100 mL), which was prepared by dissolving the MB powder in distilled water in a Pyrex glass cell at room temperature under air. The optical system for the catalytic reaction included a 300 W Xe arc lamp (focused through a shutter window), a cutoff filter (providing visible light of different wavelengths), and a water filter (to prevent IR irradiation). CO_2 and acetaldehyde were detected by GC (CO_2, GC-8A with TCD detector, Shimadzu; acetaldehyde and other organic substances, GC-14B with FID detector, Shimadzu). MB degradation was determined by UV/Vis spectroscopy (UV-2500, Shimadzu).

Received: December 22, 2003
Revised: May 11, 2004 [Z53594]

Keywords: dyes/pigments · green chemistry · heterogeneous catalysis · photochemistry · photooxidation

[1] For relevant reviews, see: a) A. Mills, R. H. Davies, D. Worsley, *Chem. Soc. Rev.* **1993**, *22*, 417; b) M. R. Hoffman, S. T. Martin, W. Choi, D. W. Bahnemann, *Chem. Rev.* **1995**, *95*, 69; c) A. Mills, S. L. Hunte, *J. Photochem. Photobiol. A* **1997**, *108*, 1; d) W. Choi, A. Termin, M. R. Hoffman, *J. Phys. Chem.* **1994**, *98*, 13669; e) A. Linsebigler, G. Lu, J. T. Yates, *Chem. Rev.* **1995**, *95*, 735.

[2] R. Asahi, T. Morikawa, T. Ohwaki, K. Aoki, Y. Taga, *Science* **2001**, *293*, 269.

[3] a) X. Tao, W. Ma, T. Zhang, J. Zhao, *Angew. Chem.* **2001**, *113*, 3103; *Angew. Chem. Int. Ed.* **2001**, *40*, 3014; b) W. Ma, J. Li, X. Tao, J. He, Y. Xu, J. C. Yu, J. Zhao, *Angew. Chem.* **2003**, *115*, 1059; *Angew. Chem. Int. Ed.* **2003**, *42*, 1029.

[4] a) J. M. Herrmann, J. Disdier, P. Pichat, *J. Catal.* **1988**, *113*, 72; b) D. S. Muggli, J. T. McCue, J. L. Falconer, *J. Catal.* **1998**, *173*, 470; c) X. Z. Li, F. B. Li, *Environ. Sci. Technol.* **2001**, *35*, 2381; d) D. S. Muggli, L. Ding, M. J. Odland, *Catal. Lett.* **2002**, *78*, 23.

 © 2004 Wiley-VCH Verlag GmbH & Co. KGaA, Weinheim

[5] J. L. Falconer, K. A. Magrini-Bair, *J. Catal.* **1998**, *179*, 171.
[6] E. Obuchi, T. Sakamoto, K. Nakano, *Chem. Eng. Sci.* **1999**, *54*, 1525.
[7] a) T. Wu, G. Liu, J. Zhao, H. Hidaka, N. Serpone, *J. Phys. Chem. B* **1998**, *102*, 5845; b) T. Wu, G. Liu, J. Zhao, H. Hidaka, N. Serpone, *J. Phys. Chem. B* **1999**, *103*, 4862; c) W. Zhao, C. Chen, X. Li, J. Zhao, H. Hidaka, N. Serpone, *J. Phys. Chem. B* **2002**, *106*, 5022.
[8] a) J. Fernandez, J. Kiwi, C. Lizama, J. Freer, J. Baeza, H. D. Mansilla, *J. Photochem. Photobiol. A* **2002**, *151*, 213; b) A. A. Belhekar, S. V. Awate, R. Anand, *Catal. Commun.* **2002**, *3*, 453; c) T. Tsumura, N. Kojitan, I. Izumi, N. Iwashita, M. Toyoda, M. Inagaki, *J. Mater. Chem.* **2002**, *12*, 1391.
[9] a) H. Kisch, L. Zang, C. Lange, W. F. Maier, C. Antonius, D. Meissner, *Angew. Chem.* **1998**, *110*, 3201; *Angew. Chem. Int. Ed.* **1998**, *37*, 3034; b) S. Sakthivel, H. Kisch, *Angew. Chem.* **2003**, *115*, 5057; *Angew. Chem. Int. Ed.* **2003**, *42*, 4908.
[10] a) A. Houas, H. Lachheb, M. Ksibi, E. Elaloui, C. Guillard, J. M. Herrmann, *Appl. Catal. B* **2001**, *31*, 145; b) F. B. Li, X. Z. Li, *Appl. Catal. A* **2002**, *228*, 15.
[11] M. Anpo, M. Takeuchi, *J. Catal.* **2003**, *216*, 505.
[12] a) Z. Zou, J. Ye, K. Sayama, H. Arakawa, *Nature* **2001**, *414*, 625; b) J. Tang, Z. Zou, J. Yin, J. Ye, *Chem. Phys. Lett.* **2003**, *382*, 175; c) J. Tang, Z. Zou, J. Ye, *Catal. Lett.* **2004**, *92*, 53; d) J. Tang, Z. Zou, J. Ye, *J. Phys. Chem. B* **2003**, *107*, 14265; e) J. Tang, Z. Zou, J. Ye, *Chem. Mater.* **2004**, *16*, 1644.
[13] a) A. Kudo, K. Ueda, H. Kato, I. Mikami, *Cata. Lett.* **1998**, *53*, 229; b) A. Ishikawa, T. Takata, J. N. Kondo, M. Hara, H. Kobayahshi, K. Domen, *J. Am. Chem. Soc.* **2002**, *124*, 13547.
[14] J. Sato, H. Kobayashi, Y. Inoue, *J. Phys. Chem. B* **2003**, *107*, 7970.
[15] a) A. Kudo, K. Omori, H. Kato, *J. Am. Chem. Soc.* **1999**, *121*, 11459; b) M. Wiegel, W. Middel, G. Blasse, *J. Mater. Chem.* **1995**, *5*, 981.
[16] a) W. T. Fu, *Physica C* **1995**, 250, 67; b) M. Oshikiri, M. Boero, J. Ye, Z. Zou, G. Kido, *J. Chem. Phys.* **2002**, *117*, 7313.
[17] T. A. M. Haemers, D. J. W. Ijdo, R. B. Helmholdt, *Mater. Res. Bull.* **1992**, *27*, 1243.
[18] A. T. Bell, *Science* **2003**, *299*, 1688.

 © 2004 Wiley-VCH Verlag GmbH & Co. KGaA, Weinheim

Nanostructures

Artificial Cells: Temperature-Dependent, Reversible Li^+-Ion Uptake/Release Equilibrium at Metal Oxide Nanocontainer Pores**

Achim Müller, Dieter Rehder,* Erhard T. K. Haupt, Alice Merca, Hartmut Bögge, Marc Schmidtmann, and Gabriele Heinze-Brückner*

Dedicated to Professor Martin Jansen on the occasion of his 60th birthday

Whereas a large number of porous materials exist as extended structures, as yet very little is known about well-defined, discrete, stable, and soluble (molecular) nanoporous capsules. These capsules allow the systematic study of processes in solution related to the uptake/release of substrates such as cations, with the possibility of extending such studies to related cation–cation countertransport processes. The prediction of the affinity of *specific* substrates for *specific* areas of the capsule is of particular interest as insight may be gained into a new type of chemistry that could be performed under confined conditions.

This is the case for spherical nanosized capsules based on the rather robust fundamental skeleton $(pent)_{12}(linker)_{30} \equiv \{(Mo^{VI})Mo_5^{VI}O_{21}(H_2O)_6\}_{12}\{Mo_2^{V}O_4(ligand)\}_{30}$, such as in **1**,[1] which is often employed as the starting material for other related compounds as it is easily prepared.[2] The capsules have sizeable pores and finely sculptured interiors inbetween which lie functionalized channels that display unprecedented molecular-scale filter properties.[3a] The size and charge of the capsules can be varied (Figure 1), whereas their affinity for (special) cations depends not only on the charge but also on the nature of the functional groups present inside the cavities.[3b] This allows the transfer of ions in a controlled and specific fashion, reminiscent of the processes that already occur in Nature on a cellular level. With respect to cation-uptake processes and the competitive uptake/release of different cations (countertransport processes), the capsules

[*] Prof. Dr. A. Müller, A. Merca, Dr. H. Bögge, M. Schmidtmann, G. Heinze-Brückner
Lehrstuhl für Anorganische Chemie I
Fakultät für Chemie der Universität
Postfach 100131, 33501 Bielefeld (Germany)
Fax: (+49) 521-106-6003
E-mail: a.mueller@uni-bielefeld.de
Prof. Dr. D. Rehder, Dr. E. T. K. Haupt
Institut für Anorganische und Angewandte Chemie
der Universität Hamburg
Martin-Luther-King-Platz 6, 20146 Hamburg (Germany)
Fax: (+49) 40-42838-2893
E-mail: dieter.rehder@chemie.uni-hamburg.de

[**] The authors gratefully acknowledge the financial support of the Deutsche Forschungsgemeinschaft, the Fonds der Chemischen Industrie, the Volkswagenstiftung, and the European Union (HPRN-CT-1999-00012). A. Merca thanks the "Graduiertenkolleg Strukturbildungsprozesse", Universität Bielefeld, for a fellowship.

 © 2004 Wiley-VCH Verlag GmbH & Co. KGaA, Weinheim DOI: 10.1002/anie.200453762

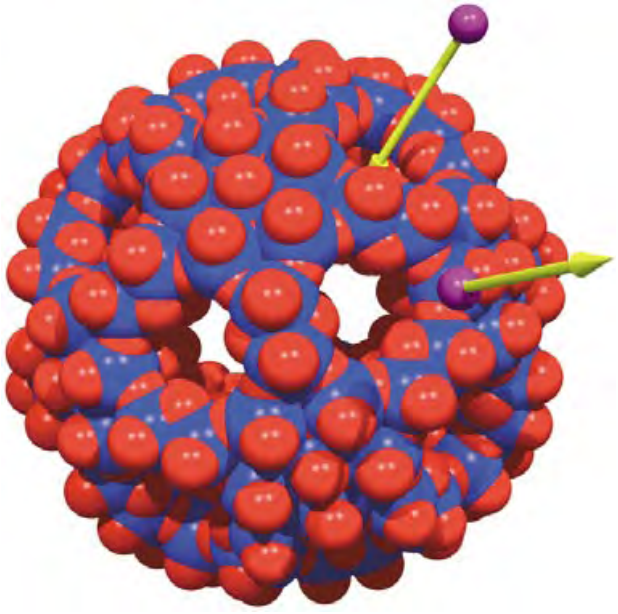


Figure 1. Schematic space-filling representation of the uptake and release of cations such as Li^+ through some of the 20 pores of highly charged anionic capsules of the structure type **2a** (Mo blue, O red).

can be considered formally as artificial cells in as much as they exhibit ion channels[3b,c] and may allow chemistry to be performed on the nanoscale in the future.[3d]

$$(NH_4)_{42}[\{(Mo^{VI})Mo_5^{VI}O_{21}(H_2O)_6\}_{12}\{Mo_2^{V}O_4(CH_3COO)\}_{30}]\cdot \approx [10\,CH_3COONH_4 + 300\,H_2O]\ \ \mathbf{1}^{[1,2]}$$

Herein, we report the stability and the use/applicability of this type of capsule in solution (details about the relative stabilities of capsules with different ligands in different solvents will be published later). A temperature-dependent equilibrium process that involves the uptake/release of Li^+ ions through the capsule pores and channels is also shown to be present. The results bear some relation as a model for Li^+-ion transport processes in clinical chemistry research.

The uptake/release of Li^+ ions was studied by ^7Li NMR spectroscopic analysis of solutions of compound **2**, which comprises the capsule skeleton mentioned earlier. Treatment of an aqueous solution of **1** with Li_2SO_4 in the presence of $[(CH_3)_2NH_2]^+$ cations (to render the compound soluble in DMSO) led to the formation of compound **2**, which was characterized by elemental analysis, thermogravimetry (to determine the amount of water of crystallization), flame photometry (to determine the number of Li^+ cations), redox titrations (to determine the number of Mo^V centers), spectroscopy (IR, Raman, UV/Vis), as well as X-ray single-crystal structure analysis[4] (including bond valence sum calculations), and ^7Li NMR spectroscopy.[5]

$$[(CH_3)_2NH_2]_{44}Li_{28-n}[Li_n \subset \{(Mo^{VI})Mo_5^{VI}O_{21}(H_2O)_6\}_{12}\{Mo_2^{V}O_4(SO_4)\}_{30}]\cdot \approx 250\,H_2O\ \ \mathbf{2}$$

Compound **2** crystallizes in the space group $R\bar{3}$ and is soluble in H_2O and DMSO. Its anionic capsule **2a** contains 20 pores, 20 channels, and a functionalized cavity (see also reference [3a]). The incorporation of Li^+ cations can easily be detected by IR[6a] and especially ^7Li NMR spectroscopy, but is only indirectly detected by X-ray single-crystal structure analysis. Figure 2 shows sections of the crystal structure of **2a**

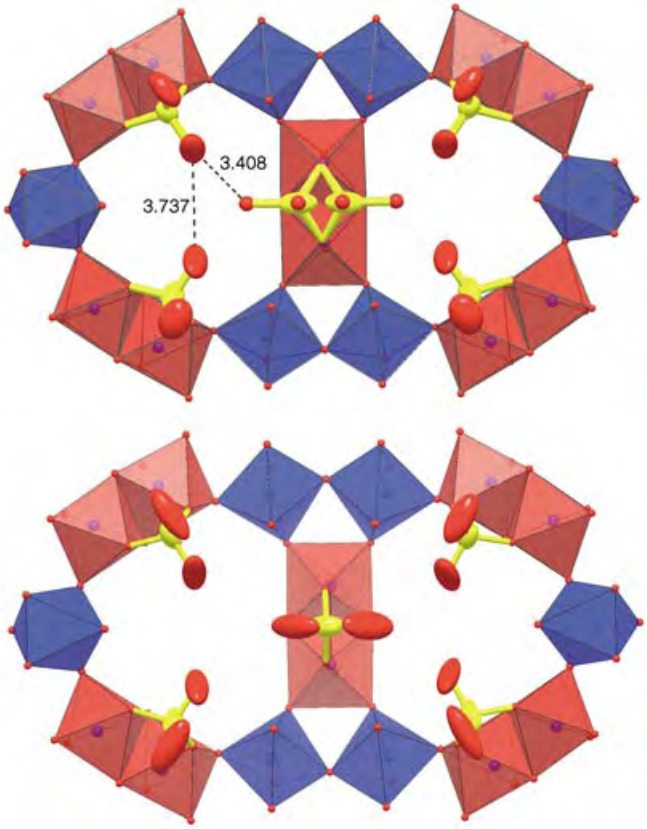


Figure 2. Outline of two of the 20 pores, as well as below-pore sections, of the anions **2a** (bottom) and the related anion **3a** (top).[4] Whereas in the case of **2a**, the disorder could not be resolved for the SO_4^{2-} ligands—although the size and shape of their thermal ellipsoids clearly reflect the influence of Li^+ (bottom)—the disorder was successfully resolved for a sulfate ligand of **3a** (top). Shown are: 1) the MoO_6 polyhedra (binuclear linkers in red) that form two adjacent pores—Mo_9O_9 rings with an average ring-aperture of ≈0.45 nm (for example, see reference [3a]), and 2) the SO_4^{2-} ligands coordinated to the $\{Mo_2\}$ linkers below the pores. The disorder for the SO_4^{2-} ligand coordinated to the "central" $\{Mo_2\}$ group is caused by "directly non-observable" Li^+ cations, giving rise to the respective distances (top).

and of the related structure **3a**, which is abundant in the compound $Li_{65}(NH_4)_7[\{(Mo^{VI})Mo_5^{VI}O_{21}(H_2O)_6\}_{12}\{Mo_2^{V}O_4(SO_4)\}_{30}]\cdot \approx 200\,H_2O$ $\mathbf{3} \equiv Li_{65}(NH_4)_7\cdot\mathbf{3a}\cdot \approx 200\,H_2O$; this material[4] has a higher concentration of Li^+ ions[5] but could not be considered in this case for NMR spectroscopic investigations as it is insoluble in DMSO.

From the present X-ray diffraction study (Figure 2), it is seen that the O···O distances between the three SO_4^{2-} ligands are too large (> 3.7 Å) for a symmetrical coordination of the Li^+ ion to all of the sulfate groups. Consequently, unsymmetrical coordination below the pore channels occurs (Figure 2, top). This is in contrast to the situation encountered with the larger Na^+ cations, which are symmetrically coordi-

 © 2004 Wiley-VCH Verlag GmbH & Co. KGaA, Weinheim

nated to each of the three sulfate groups and which leads to a highly symmetrical $60 = 20 \times 3$ water "cluster" coordinated to the Na^+ cations.[6b] Clearly, this is not possible in the present (unsymmetrical) case with Li^+ ions.

According to the Raman spectra, the capsules with icosahedral symmetry are quite stable in O_2 free solutions in H_2O and DMSO up to $\approx 60\,^{\circ}C$ (Figure 3). As the spectrum

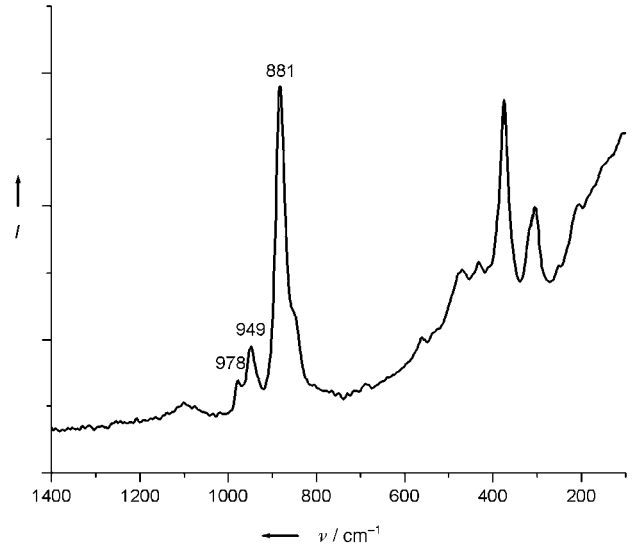


Figure 3. Raman spectrum of **2** in H_2O ($\lambda_{exc} = 1064$ nm), which is practically identical to that of solid **2** and thus supports the reasonable stability of the highly symmetrical capsule **2a** in solution. The most intense band at 881 cm^{-1} corresponds to the totally symmetric A_g breathing vibrations of the capsule which involve predominantly 60 μ_3-O(Mo_3) surface atoms.

consists of only a few lines (note the possible fivefold degeneracy expected for the I_h point group, and that only A_g and H_g type vibrations are Raman allowed) this allows the easy detection of eventual decomposition even for such an extremely large molecular system. The bands are characteristic for the highly symmetrical molybdenum oxide based $\{(Mo^{VI})Mo_5^{VI}\}_{12}\{Mo_2^{V}\}_{30}$ type skeleton.

The ^{7}Li NMR spectrum[7] of **2** dissolved in DMSO/[D_6]DMSO (1:1; $c(Li^+) \approx 50$ mM; Figure 4) measured at room temperature shows two sharp signals at $\delta = -0.78$ and -0.80 ppm (I), which correspond to $[Li(dmso)_n]^+$ in the bulk solution (the peaks are identical to those in the spectrum of Li^+ ions in pure DMSO), and at least three broad (half-width $(W_{1/2}) \approx 80$ Hz) overlapping signals centered at $\delta = -1.67$, -2.18, and -2.56 ppm (II–IV; overall relative intensity $\approx 15\,\%$). These latter peaks are assigned to three different Li^+-ion sites associated with the cluster $Li^+ \subset$ **2a**. The upfield shifts—with respect to $[Li(dmso)_n]^+$, $\delta \approx -0.79$ ppm—reflect the increased complexation of the Li^+ cations to negatively charged ligands such as sulfate, and/or bridging oxo groups such as at the Mo_9O_9 type rings/pores.[8a] This pattern, which is observed immediately after the dissolution of **2**, does not change within several days; that is, the system readily reaches equilibrium and remains rather stable over an extended period of time. Furthermore, the temperature dependence of

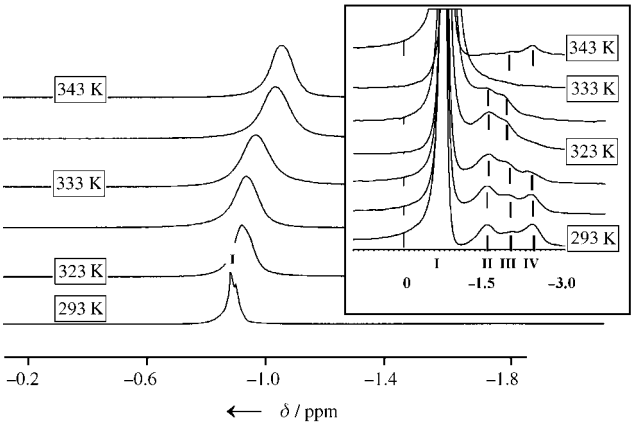


Figure 4. Variable-temperature ^{7}Li NMR spectra of **2** (c(**2**) ≈ 1.8 mM) in DMSO/[D_6]DMSO 1:1. The inset shows the vertical expansion with the uppermost spectrum obtained after cooling back to room temperature. I ($\delta = -0.79$ ppm) corresponds to $[Li(dmso)_n]^+$, whereas II ($\delta = -1.67$ ppm), III ($\delta = -2.18$ ppm), and IV ($\delta = -2.56$ ppm) correspond to Li^+ sites associated with $Li^+ \subset$ **2a**.

the spectral patterns (Figure 4) with respect to both the broadening as well as the shifts (upfield for I, downfield for II, III, and IV) of the bands upon increasing the temperature, clearly indicates an exchange equilibrium between exterior and interior Li^+ ions.[8b] The signal at $\delta = -2.56$ ppm (IV) disappears at about 330 K, whereas a complete coalescence of the signals for the system (signals I, II, III, and IV) occurs at 343 K (average $\delta = -0.96$ ppm) representing very fast exchange within the equilibrium:

$$[Li(dmso)_n]^+ \rightleftharpoons Li^+ \subset \text{capsule}$$

In the temperature range 293–343 K, the exchange process is largely reversible for two of the sites; upon cooling, the signals at $\delta = -2.18$ (III) and -2.56 ppm (IV) are almost restored. However, the signal at $\delta = -1.67$ ppm (II) does not reappear which suggests that one of the Li^+-ion sites is not occupied again. The first of the upfield signals, II, is assigned to Li^+ ions coordinated to the sulfate group which was also proven from crystallographic studies and IR spectroscopic measurements. This site is the furthest distance away from the pore area/cluster periphery and is correspondingly not reoccupied after cooling as the sites closer to the capsule periphery (peaks III and IV) are the first to be reoccupied, which decreases the affinity of the capsule for cations. The more-peripheral sites have a higher electron density (in agreement with a classical Pauling rule) with the consequence that the related peaks are found at higher fields.

Complementary to the temperature-dependent behavior of the signals, the $[Li(dmso)_n]^+$–Li^+(capsule)-exchange process has been confirmed by ^{7}Li–^{2}D exchange spectroscopy (EXSY) of solutions of **2** in DMSO (c(**2**) = 1 mM; $c(Li^+)$ = 30 mM; slow exchange conditions at room temperature and a mixing time of 1.5 s were employed). The EXSY spectrum (not shown here) displays cross-peaks owing to a magnetization transfer between external (signal I) and internal Li^+ ions (signals II–IV) which disappear upon the addition of an

 © 2004 Wiley-VCH Verlag GmbH & Co. KGaA, Weinheim

excess of guanidinium chloride ($c = 30$ mM); guanidinium cations prevent exchange through blockage of the capsule pores (see reference [6c]). Concomitantly, signals II and III almost disappear and a new signal representing 5% of the overall integral intensity appears at $\delta = -3.1$ ppm.

Treatment of a solution of **4** in DMSO with a 20-fold molar excess of LiCl leads to the uptake/incorporation of about 12% of the Li^+ ions as observed from a broad signal at $\delta = -2.03$ ppm for $Li^+ \subset \mathbf{4a}$. This signal is accompanied by the resonance for $[Li(dmso)_n]^+$ at $\delta = -0.82$ ppm with an upfield shoulder at about $\delta = -1.05$ ppm. The situation is comparable to the system $Li^+ \subset \mathbf{2a}$ in as far as the Li^+ ions are apparently taken up by the cluster under changed conditions. In the case of the anionic capsule **4a**, for example, Li^+ competes with NH_4^+ to some extent for the capsule sites.

$(NH_4)_{72-n}[\{(H_2O)_{81-n} + (NH_4)_n\}$
$\subset \{(Mo^{VI})Mo_5^{VI}O_{21}(H_2O)_6\}_{12}\{Mo_2^{V}O_4(SO_4)\}_{30}]\cdot \approx 200\,H_2O$ **4**[6b]

The present study of the uptake/release of cations by a capsule in solution may be extended to investigate nanoscale reactions in solutions (see also reference [3d]) as well as a large variety of cation-transport phenomena (e.g. competition processes) in different solvents[9]; furthermore, unique hydration structures can be investigated under restricted conditions. An important aspect is that the interiors, sizes, and pores of the capsules can be varied to allow different cation-affinity properties. Interestingly, the transport of cations under physiological conditions (e.g. Li^+-ion transmembrane transport and storage) can, in principle, be modeled. Also, there is the possibility to model important transport pathways of medicinal interest, such as the Li^+–Na^+ countertransport process (of interest in hypertension research) in which Na^+ ions enter and Li^+ ions leave erythrocytes in order to maintain the Na^+ ion balance in the cells and the plasma.[10–12]

Experimental Section

2: The pH value of a solution of **1** (2.0 g, 0.068 mmol) and $Li_2SO_4 \cdot H_2O$ (10 g, 78 mmol) in H_2O (80 mL) was adjusted to ≈ 2.2 with aqueous H_2SO_4 (0.5 M), and the solution was stirred for 5 h at room temperature. (The large excess of Li_2SO_4 was necessary first, owing to the large number of functional groups present in the capsule, e.g. 30 SO_4^{2-} groups and 180 Mo_9O_9 type O atoms, and second, to isolate the highly water soluble product **2** as a salt, and third, because of the high affinity of Li^+ to water.) The temperature of the solution was increased to 70 °C over 30 min, then $(CH_3)_2NH_2Cl$ (1.5 g, 18.39 mmol) was added, and the solution was stirred at this temperature for a further 30 min. The hot solution was filtered, then the cooled dark brown filtrate was stored at 20 °C to effect crystallization. After 4 days, the precipitated dark brown, parallelepiped crystals of **2** were isolated by filtration and dried in air (70% based on **1**); elemental analysis: calcd for $C_{88}H_{996}Li_{28}Mo_{132}N_{44}O_{814}S_{30}$: C 3.58, N 2.08, Li 0.65; found: C 3.6, N 2.1, Li (flame photometry) 0.6; IR (KBr): $\tilde{\nu} = 1622$ (m, $\delta(H_2O)$), 1463 (w-m, $\delta_{as}(CH_3)$), 1183 (w), 1137 (m-w), 1053 (w, $\nu_{as}(SO_4)$ triplet), 975 (s), 943 (m, ν(Mo=O)), 860 (s), 802 (vs), 729 (s), 634 (m), 574 cm^{-1} (s); FT-Raman (see Figure 3); UV/Vis (H_2O): $\lambda = 459$ nm.

Received: January 15, 2004
Revised: May 19, 2004 [Z53762]

Keywords: artificial cells · ion channels · lithium · nanostructures · porous materials

[1] For a review, see: A. Müller, P. Kögerler, C. Kuhlmann, *Chem. Commun.* **1999**, 1347–1358.

[2] a) A. Müller, S. K. Das, E. Krickemeyer, C. Kuhlmann, *Inorg. Synth.* **2004**, *34*, 191–200; b) L. Cronin, E. Diemann, A. Müller in *Inorganic Experiments* (Ed.: J. D. Woollins), Wiley-VCH, Weinheim, **2003**, pp. 340–346.

[3] a) A. Müller, S. K. Das, S. Talismanov, S. Roy, E. Beckmann, H. Bögge, M. Schmidtmann, A. Merca, A. Berkle, L. Allouche, Y. Zhou, L. Zhang, *Angew. Chem.* **2003**, *115*, 5193–5198; *Angew. Chem. Int. Ed.* **2003**, *42*, 5039–5044; in all the cases studied therein, the positioning of the cations was clearly understood except for that of Rb^+—this was attributed to the influence of the crystallization process, which does not influence the results in the present solution process. b) An extreme affinity is observed for the sulfate type capsule in the case of Ca^{2+} as 20 of these ions can be positioned at the end of the 20 channels at specific positions where also Na^+ cations, although in a smaller amount, can be positioned[3a]—in doing so, the entrance to the central cavity is completely blocked (unpublished results). In cases where the encapsulated cation positions cannot be determined, the given charge refers to that of the empty capsule[1,2] (see also **3**). c) Interesting cation uptake (and also the uptake of anions and water molecules) under confined conditions has also been observed for nanotube structures, but such a situation does not easily allow an equilibrium study to be performed in solution; see: T. Ohkubo, Y. Hattori, H. Kanoh, T. Konishi, T. Fujikawa, K. Kaneko, *J. Phys. Chem. B* **2003**, *107*, 13616–13622; T. Ohkubo, H. Kanoh, K. Kaneko, *Aust. J. Chem.* **2003**, *56*, 1013–1016; see also: d) "Traps for cations": W. G. Klemperer, G. Westwood, *Nat. Mater.* **2004**, *2*, 780–781.

[4] Crystal data for **2** ($C_{88}H_{996}Li_{28}Mo_{132}N_{44}O_{814}S_{30}$): $M = 29521.49\ g\,mol^{-1}$, rhombohedral, space group $R\bar{3}$, $a = 32.8188(12)$, $c = 74.350(4)$ Å, $V = 69352(5)$ Å^3, $Z = 3$, $\rho = 2.121\ g\,cm^{-3}$, $\mu = 1.908\ mm^{-1}$, $F(000) = 43356$, crystal size $= 0.30 \times 0.25 \times 0.20\ mm^3$; crystals of **2** were removed from the mother liquor and immediately cooled to 188(2) K on a Bruker AXS SMART diffractometer (three cycle goniometer with 1 K CCD detector, $Mo_{K\alpha}$ radiation, graphite monochromator; hemisphere data collection in ω at 0.3° scan width in three runs with 606, 435, and 230 frames ($\phi = 0$, 88, and 180°) at a detector distance of 5.0 cm). A total of 135812 reflections ($1.53 < \Theta < 26.99°$) were collected of which 33506 reflections were unique ($R_{int} = 0.0429$). An empirical absorption correction using equivalent reflections was performed with the program SADABS. The structure was solved with the program SHELXS-97 and refined with SHELXL-97 to $R = 0.0506$ for 25064 reflections with $I > 2\sigma(I)$, $R = 0.0763$ for all reflections; max./min. residual electron density 1.613 and $-1.785\ e\,Å^{-3}$ (SHELXS/L, SADABS from G. M. Sheldrick, University of Göttingen 1997/2001; structure graphics with DIAMOND 2.1 from K. Brandenburg, Crystal Impact GbR, 2001). CCDC 228367 contains the supplementary crystallographic data for this paper. These data can be obtained free of charge via www.ccdc.cam.ac.uk/conts/retrieving.html (or from the Cambridge Crystallographic Data Centre, 12, Union Road, Cambridge CB2 1EZ, UK; fax: (+44) 1223-336-033; or deposit@ccdc.cam.ac.uk). Cell parameters for **3**: monoclinic space group $C2/m$, $a = 44.483(2)$, $b = 40.077(2)$, $c = 31.757(2)$ Å, $\beta = 134.116(1)°$, $V = 40645(5)$ Å^3.

[5] ^{7}Li NMR spectra of solutions were recorded on a Bruker Avance 400 spectrometer (155.51 MHz) in rotating 10-mm diameter tubes; acquisition time 2.1 s, relaxation delay 2 s, pulse width 30°. All data are reported relative to the reference material (9.7 M LiCl in D_2O, according to: R. K. Harris, E. D.

 © 2004 Wiley-VCH Verlag GmbH & Co. KGaA, Weinheim

Becker, S. M. Cabral de Menezes, R. Goodfellow, P. Granger, *Pure Appl. Chem.* **2001**, *73*, 1795–1818). Area calibration was carried out by insertion of a coaxial inset containing LiCl (0.1M in [D$_6$]DMF, $\delta = +0.90$). The Lorentzian line-shape analysis was performed for four lines by using the 'deconvolution 1' feature of the Bruker WINNMR V6.0 program.

[6] a) Compound **2** shows a triplet 1183/1137/1053 cm^{-1} in the IR spectrum which originates from the bidentate coordination of the sulfate anion (ν_{as} mode of the "free" SO_4^{2-} ion lies at ca. 1105 cm^{-1}); see: K. Nakamoto, *Infrared and Raman Spectra of Inorganic and Coordination Compounds*, 5th ed., Wiley, New York, **1997**, Part A, p. 199; Part B, pp. 79–82. As the SO_4^{2-} groups are located *trans* to the Mo=O bonds the coordination is rather weak, with the consequence that the "terminal" sulfate O atoms show a higher electron density than in the case of a stronger ligand coordination. This can strengthen (relatively) the interaction with encapsulated cations, being again stronger for Li^+ ions than in general for Na^+/NH_4^+ ions (note that one Na^+ ion is coordinated to three sulfate ligands in the capsule, whereas Li^+ is predominantly coordinated to one SO_4^{2-} group and so the interaction per sulfate ligand is therefore larger).[6b] In the case of related Na^+/NH_4^+ salts, the two bands at higher energy are observed at nearly the same wavenumbers as the corresponding bands for **2a**, whereas the lower energy band of the triplet occurs at $\approx$1040 cm^{-1} in the Na^+/NH_4^+ salts but at 1053 cm^{-1} in the case of **2a**. The same situation as in the case of the Na^+ and NH_4^+ capsules is found for a compound containing only guanidinium cations, which cannot enter the cavity;[6c] this band consequently is also observed at 1038 cm^{-1}. (The assignment of the respective band for the guanidinium compound was rather difficult as it partially overlaps with the $O_2PH_2^-$-bands.)[6c] The shift of the band in the case of **2a** is influenced by the rather strong interaction with Li^+ ions which partially decreases the negative charge on the sulfate and therefore strengthens the S–O bonds; b) A. Müller, E. Krickemeyer, H. Bögge, M. Schmidtmann, B. Botar, M. O. Talismanova, *Angew. Chem.* **2003**, *115*, 2131–2136; *Angew. Chem. Int. Ed.* **2003**, *42*, 2085–2090; the compound **4** can be obtained more easily and methodically (without the need for heating) by acidification of the solution to protonate the acetate ligands and render them better leaving groups; c) A. Müller, E. Krickemeyer, H. Bögge, M. Schmidtmann, S. Roy, A. Berkle, *Angew. Chem.* **2002**, *114*, 3756–3761; *Angew. Chem. Int. Ed.* **2002**, *41*, 3604–3609.

[7] a) J. W. Akitt in *Multinuclear NMR* (Ed.: J. Mason), Plenum, New York, **1987**, chap. 7; b) C. Detellier in *NMR of Newly Accessible Nuclei*, *Vol. 2* (Ed.: P. Laszlo), Academic Press, New York, **1983**, chap. 5; c) B. Lindmann, S. Forsén in *NMR and the Periodic Table* (Eds.: R. K. Harris, B. E. Mann), Academic Press, New York, **1978**, chap. 6.

[8] a) The notation "increased complexation of Li^+" refers to the dominance of the paramagnetic contribution related to variations in shielding. In other words, paramagnetic shielding is expected to decrease (and overall shielding to increase) with the increasing expansion of the "electron cloud" around Li, to result in an increased covalency of the Li^+–donor interaction as the contact between the Li^+ ion and the donor groups becomes more intimate. The signal IV could be attributed to the complexation of Li^+ ions by the oxo functions of the Mo_9O_9 ring, as this peak disappears the most easily, both upon heating and upon the addition of Na^+ ions. For the crown ether complex $[Li(15C5)]^+$, which may be compared to the coordination of Li^+ ions in the present study, a chemical shift value of $\delta = -1.8$ ppm was noted; see: A. I. Popov, *Pure Appl. Chem.* **1979**, *51*, 101. Importantly,the Mo^V centers in the binuclear unit are spin-coupled upon formation of a metal–metal bond, thereby excluding influences by paramagnetic centers; b) for an *independent resonance signal*, deshielding is expected upon an increase in the temperature as a consequence of the increased paramagnetic-deshielding contributions as the vibronic levels of the ground and excited states become more populated. Concomitantly, if the nucleus is quadrupolar as in the case of ^{7}Li, the resonance should sharpen upon a decrease in the molecular correlation time (decreasing viscosity). In the present case, an increase in the shielding and broadening of the line widths is observed for signal I as the temperature is raised; the spectral patterns clearly indicate an exchange between exterior (I) and interior Li^+ ions (II, III, and IV).

[9] For **2** dissolved in H_2O/D_2O, only one narrow ^{7}Li resonance at $\delta = -0.16$ ppm ($W_{1/2} = 2.3$ Hz) is observed, which corresponds to hydrated Li^+ ions and is indicative of the complete extrusion of Li^+ ions into the aqueous medium. This arises from the higher affinity of Li^+ for water than for the functional capsule sites. Competitive-phenomena studies (e.g. Li^+/Na^+) performed in aqueous media in the presence of electrolytes (to reduce the affinity of the cations for the solvent, and to approximate physiological conditions) are currently underway. As far as the dielectric properties of the medium are concerned, serum and cytosol more closely resemble DMSO than water. Note that more than ten billion proteins are abundant in an animal cell and influence the properties of the water solvent.

[10] Na^+–Li^+ countertransport is an ion-transport process that exchanges sodium ions for lithium ions or other univalent cations. It was brought to clinical attention by Canessa et al., who reported that its activity was enhanced in the erythrocytes of patients with essential hypertension—a finding that was confirmed in many epidemiological and clinical studies thereafter; see: M. Canessa, N. Adragna, H. S. Solomon, T. M. Conolly, D. C. Tosteson, *New Engl. J. Med.* **1980**, *302*, 772–776; P. Strazzullo, A. Siani, F. P. Cappuccio, M. Trevisan, E. Ragone, L. Russo, R. Iacone, E. Farinaro, *Hypertension* **1998**, *31*, 1284–1289. Although the capsule wall of our structure cannot be compared with the red-cell membrane, which perfectly balances the concentrations of cations and water so that the cells do not shrink, nevertheless, it allows fundamental countertransport phenomena to be measured; see: Y. Yawata, *Cell Membrane: The Red Blood Cell as a Model*, Wiley-VCH, Weinheim, **2003**.

[11] Numerous papers are being published on the influence of Li^+ ions on many biochemical and pathobiochemical processes owing to its high positive-charge density, but a complete picture of the medicinal and biochemical properties of Li^+ is not yet available. In any case, Li^+ ions play a key role in the treatment of dipolar disorder (manic depression), the mechanism of which is not known; for examples, see: H. R. Pilcher, *Nature* **2003**, *425*, 118; S. J. Lippard, J. M. Berg, *Bioanorganische Chemie*, Spektrum, Heidelberg, **1995**; *Principles of Bioinorganic Chemistry*, University Science Books, Mill Valley, USA, **1994**. It has been reported that Li^+ ions block the recycling pathway for inositol-1,4,5-triphosphate (IP_3); malfunctions of the inositol system have been linked to a number of illnesses, including manic depression and cancer; see: G. Thomas, *Medicinal Chemistry: An Introduction*, Wiley, Chichester, **2000**.

[12] Preliminary experiments directed towards competition in the uptake/release of Li^+ and Na^+ ions show that for $c(Li^+) = 30$ mM and $c(Na^+) = 15$ mM (in the form of NaBr), almost all of the "capsule-bound" Li^+ ions are replaced by Na^+ ions; that is, about 98% of the Li^+ ions are present in the form of $[Li(dmso)_n]^+$ (signal I), whereas about 70% of the Na^+ are bound to the capsule ($\delta(^{23}Na) = -1.5$ and -12 ppm ($W_{1/2} = 2.6$ kHz) for $[Na(dmso)_n]^+$ and $Na^+\subset$**2a**, respectively). This is a remarkable result that shows the relatively high affinity of the capsule for Na^+ as they block/close the pores/channels[6b] (different aspect in ref. [6]).

Molecular Electronics

Synthesis of Diode Molecules and Their Sequential Assembly to Control Electron Transport**

*Ping Jiang, Gustavo M. Morales, Wei You, and Luping Yu**

Molecular electronics was envisioned to be the ultimate solution to the limit predicted by Moore's law for microelectronic chips. Since Aviram and Ratner proposed the original idea (the AR model) about molecular diodes,[1] many molecules that behave as wires,[2] diodes,[3] and switches[4] have been synthesized and characterized. Despite this progress, however, many challenges still remain to producing true molecular devices. For example, serious challenges exist for the assembly of these molecules into electric circuits, and reliable measurements on electron transport of single molecules in a true circuit configuration are still rare. Although the realization of single molecular electronics cannot be reached in one step, one of the most important steps towards real molecular devices is to control the functions of molecular components, such as rectification, in two-terminal molecules. A number of diode molecules developed by different research groups were based on the AR model and showed possible rectifying effects. However, these molecules could not be assembled into two-terminal circuits with a controlled direction of current flow. Herein, we report that the rectifying direction of diode molecules can be controlled in a two-terminal circuit configuration through a sequential assembly process. To the best of our knowledge, this is the first example in which the electron transport is controlled by the orientation of diode molecules between two electrodes.[5]

Recently, we reported that simple conjugated diblock co-oligomers exhibit pronounced rectification effects.[6] These p-n junction types of molecules incorporate an electron-rich dithiophene segment and an electron-deficient dithiazole segment. These molecular diodes contain only one thiol terminus, which limits their ability to be incorporated between two gold electrodes; it is necessary to equip this thiophene–thiazole diblock oligomer with two different terminal thiol groups that can be sequentially connected to gold electrodes, thereby enabling the molecular orientation between the two electrodes to predetermine the rectifying direction. We synthesized two thiophene–thiazole diblock oligomers with two different thiol-protected end groups. The orientation of the diblock structure between the gold electrodes was controlled through a sequential deprotection and immobilization procedure (deprotection a/self-assembly/deprotection b/adding Au nanoparticles). It was found from electron-transport studies that the rectifying effect of the resulting assembly was indeed controlled by the orientation of the molecules.

The synthetic procedure for the thiophene–thiazole diblock molecule was reported previously.[6] Introducing another thiol group into the compound proved to be not feasible because of tautomerism between the thiol and thione forms. However, we found that thiolation at the 5-position in the thiazole molecule could be achieved. Thus, compounds **6** and **13** were designed and synthesized (Scheme 1). The two thiol-protection groups used are cyanoethyl ($-SCH_2CH_2CN$, CNE) and trimethylsilylethyl ($-SCH_2CH_2SiMe_3$, TMSE). The former can be readily cleaved to the free thiol under basic conditions while the latter is stable even under very basic conditions, such as butyllithium, but labile to fluoride-mediated cleavage.[7] Our synthetic strategy was to take advantage of the inertness of the TMSE protecting group to basic conditions and incorporate it at the beginning, and then add the CNE protection group later in the synthesis. The TMSE-protected thio group was first attached to the dithiophene unit through the dithiophene iodide **1** by using a general method for formation of an aryl–sulfur bond in which a copper(I) salt is used as a catalyst.[8] The diblock molecule **5** with a TMSE protecting group was prepared by Stille coupling of **3** with the dithiazole block **4**. The last step was to introduce the CNE protecting group at the other end to form **6** by using a previously used procedure.[6b]

Originally we planned to deprotect the thio groups in compound **6** by two different sequences so that the diode molecule could be immobilized onto electrodes with different orientations. Experiments showed that initial cleavage of the TMSE group would also simultaneously eliminate the CNE group. However, cleavage of the CNE group first, worked well with the TMSE group remaining intact. Thus, the sequential deprotection procedure (cleavage of the CNE group first and then the TMSE group) was applied. Compound **13** was then synthesized to enable the reverse molecular orientation to be realized between the electrodes. Compound **13** has a similar diblock structure to compound **6**, but with the two different thio-protection groups switched in positions (Scheme 1). Since it is difficult to functionalize the 2-position of the dithiazole unit after protecting the thio group at the 5′-position with TMSE, we chose first to couple dithiazole **4** with one thiophene unit protected at its 2-position to form compound **8**, then attach the TMSE protecting group by using the same coupling reaction described above. Finally another thiophene unit with a built-in CNE-protected thio group was connected through a Stille coupling reaction to make compound **13**. The ^1H and ^{13}C spectra of the compounds are consistent with the expected structures, and the mass spectra show a signal for M^+ at about m/z 604.9 for both **6** and **13**.

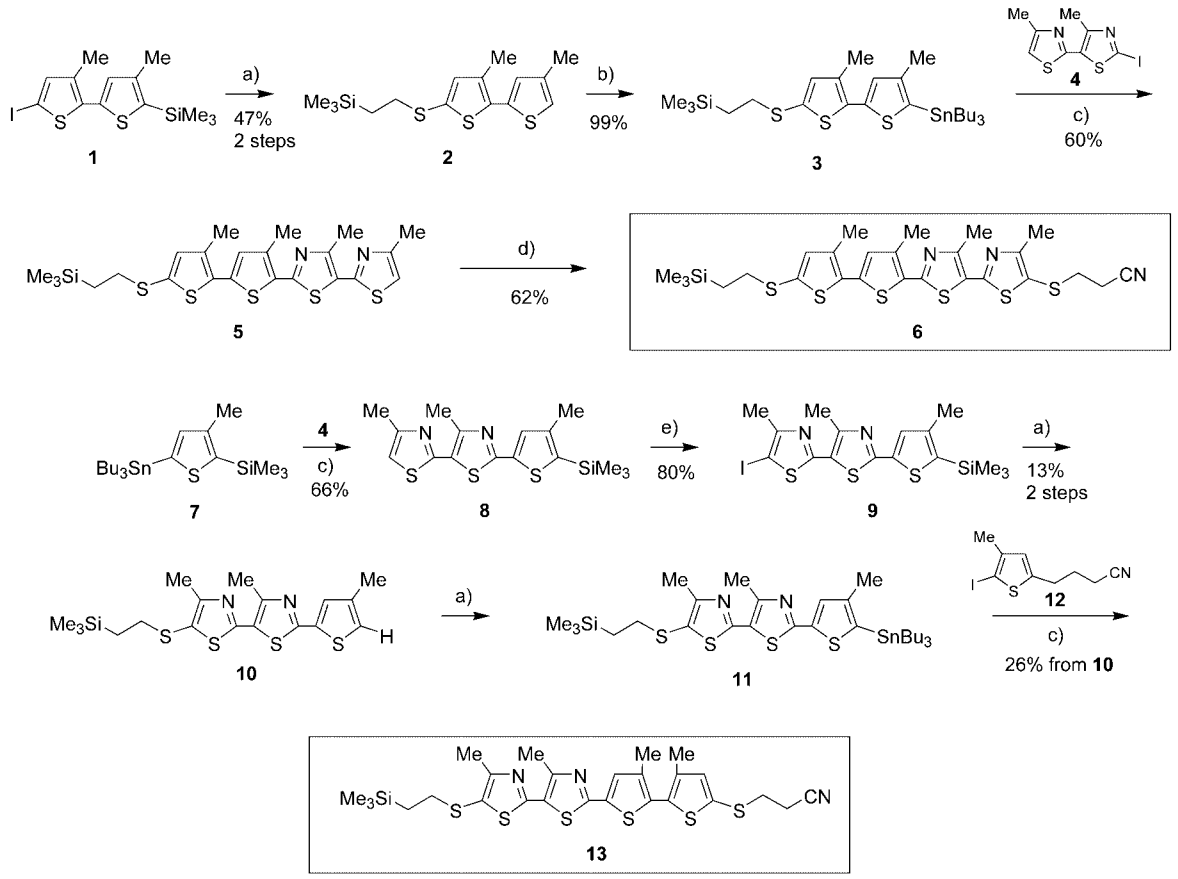
The orientation of the diblock structure between gold electrodes was controlled through a sequential deprotection

[*] P. Jiang, G. M. Morales, W. You, Prof. L. Yu
Department of Chemistry and James Franck Institute
The University of Chicago
5735 South Ellis Avenue, Chicago, Illinois, 60637 (USA)
Fax: (+1) 773-702-0805
E-mail: lupingyu@midway.uchicago.edu

[**] We thank the financial support from the National Science Foundation, the NSF MRSEC program at The University of Chicago, and AFOSR. Partial support for this research was provided by the UC-Argonne Nanoscience Consortium.

Supporting information for this article is available on the WWW under http://www.angewandte.org or from the author.

 DOI: 10.1002/anie.200460110 © 2004 Wiley-VCH Verlag GmbH & Co. KGaA, Weinheim

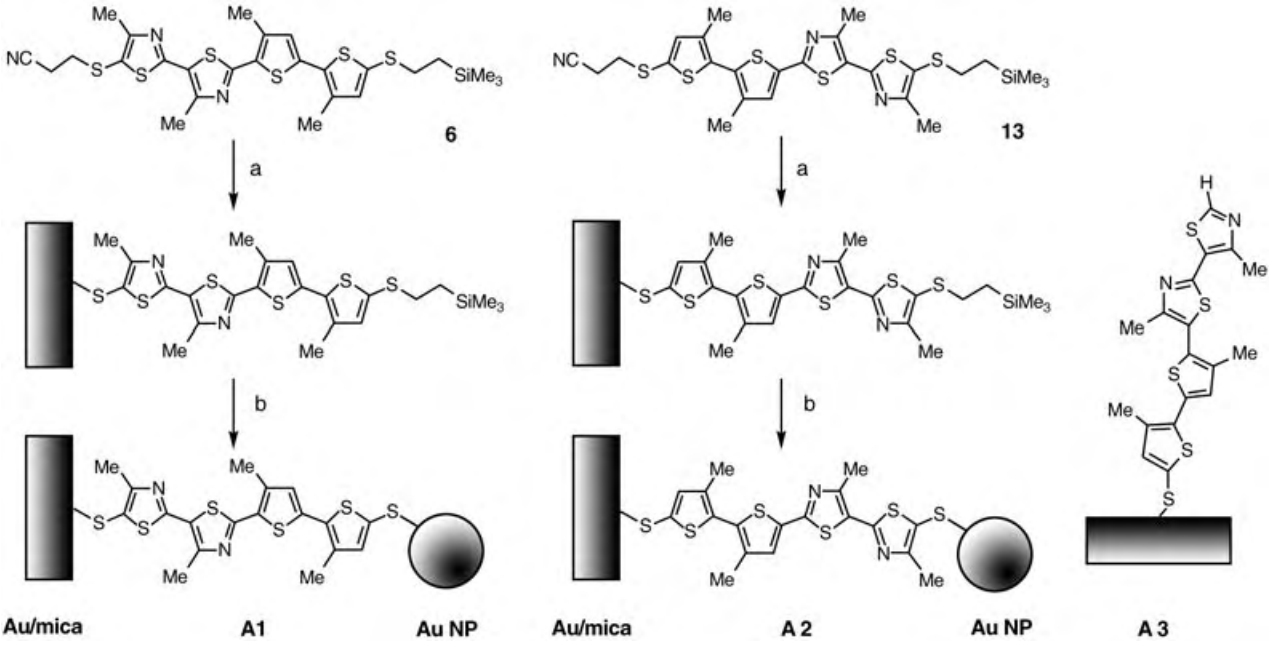


Scheme 1. Syntheses of compound **6** and **13**. a) 1. $Me_3SiCH_2CH_2SH$, CuI, NaO*t*Bu, neocuproine, toluene, 110 °C; 2. TFA; b) 1. *n*BuLi, −78 °C; 2. Bu_3SnCl; c) $[Pd_2(dba)_3]$, PPh_3, Cu_2O, DMF, 130–135 °C; d) 1. *n*BuLi, −78 °C; 2. S_8; 3. $BrCH_2CH_2CN$; e) 1. *n*BuLi, THF, −78 °C; 2. I_2. TFA = trifluoroacetic acid, dba = *trans*,*trans*-dibenzylideneacetone.

and immobilization procedure (deprotection a/self-assembly/deprotection b/add Au nanoparticles) as described in Scheme 2. First, the CNE protecting group was cleaved in situ with sodium ethoxide/ethanol to form a free thiol, and the target molecules were then self-assembled onto the gold substrate. Then the TMSE-protecting group was cleaved with a solution of TBAF in THF and treated with freshly made gold nanoparticles (NP). Thus the diode molecules were connected at both ends to gold electrodes and ready for the electron-transport study. The assemblies **A1** and **A2**, prepared from molecule **6** and **13**, respectively, are shown in Scheme 2.

An investigation of the charge-transport properties of single molecules necessitates monolayers with isolated diode molecules. We utilized a dodecanethiol self-assembled monolayer (DDT SAM) on an Au(111) substrate into which the molecules **6** and **13**, were inserted. Figure 1a shows the STM image of the highly ordered structure of a DDT SAM on an Au(111) surface. High-resolution images (inset in Figure 1a) reveal a hexagonal packing, with an average distance between the nearest and next-nearest-neighbor spacing (represented by *a* and *b*, respectively) of approximately 0.5 and 0.9 nm, which correspond to a characteristic $(\sqrt{3}\times\sqrt{3})$ R30° absorbate overlayer on Au(111).[9] Figure 1b shows an STM image taken on the DDT SAM after insertion of **6**. The bright spot (indicated by a circle) is the constant-current STM image of **6** with the TMSE-protected thio group on the top. The images are reproducible over many scans. The intensity of the bright spots changes sporadically in agreement with the stochastic behavior reported for single molecules inserted in an alkanethiol SAM.[10] The shape and size of the spots are constant and have an average size of about 1.8 nm, which is similar to other single molecules inserted in an alkyl thiol matrix.[11] The bright spots are probably single molecules, but we cannot rule out the possibility of the formation of aggregates. According to literature data the orientation of DDT is defined by a tilt angle of 30°.[9] After removal of the TMSE protecting groups, Au NPs were attached to the exposed terminal thiol groups. Figure 1c shows the STM image of the resulting Au assembly **A1**. The apparent diameter of the Au NP is in the range 9–11 nm. A separate TEM micrograph of the NP showed an average diameter of 8 nm.[12] The enlargement in the size of the single molecules and NPs can be attributed to the combination of electronics factors and tip-convolution effects. Control experiments showed that the nanoparticles were indeed attached to the molecules after cleavage of the TMSE group. First, there were no nanoparticles observed on the STM images of samples prepared under the same conditions without cleavage of the TMSE group or in the absence of inserted target molecules.

 © 2004 Wiley-VCH Verlag GmbH & Co. KGaA, Weinheim



Scheme 2. Preparation of assemblies **A1** and **A2**. a) NaOEt, THF, gold substrate; b) TBAF, THF, Au nanoparticles. For assembly **A3** see ref [5b]. TBAF = tetrabutylammonium fluoride.

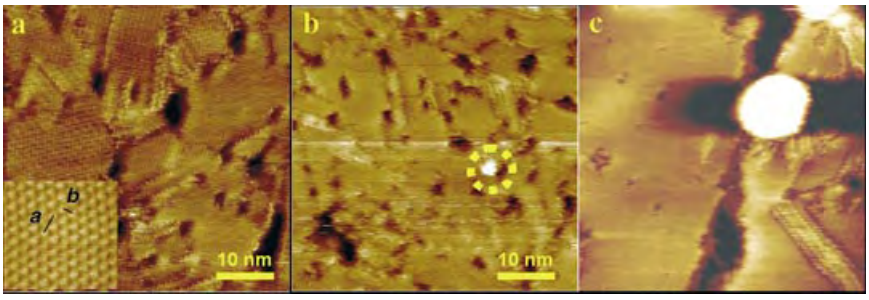


Figure 1. Constant-current STM topography of a dodecanethiol SAM on Au(111)/mica, before (a) and after (b) the insertion of **6**; the molecule is shown as a bright spot and indicated by a circle. c) The image of the surface after attachment of Au nanoparticle to the top termini of **6**. The area shown is 50×50 nm^2, STM imaging conditions: $V_{bias} = +1.0$ V, $I_t = 1$ pA.

Secondly, the density of the nanoparticles observed after step b in Scheme 2 was comparable to that of the bright spots from the molecules with the TMSE-protected thio group after step a in Scheme 2.

Further evidence for the sequential deprotection process was obtained from grazing incidence FTIR. Figure 2 shows the IR spectra in the CH stretching region for a monolayer of **6** following the sequential deprotection. The transmission spectrum of **6** on a KBr plate is shown for comparison (trace a). The inset spectra show the CN stretching region, where disappearance of the CN absorption was clearly observed after the first deprotection step, namely cleavage of the CNE group. The absorption from the CH_2 unit (νCH_2^s symmetric stretching vibration) of the TMSE group remains (indicated by an arrow in trace b),[13] thus indicating the TMSE group was intact. After the second deprotection step (cleavage of the TMSE group), this absorption from the TMSE group disappeared accordingly (trace c).

The electron-transport properties of assemblies **A1** and **A2** were investigated by scanning tunneling spectroscopy (STS). It has been demonstrated that gold NPs can be immobilized on the surface thiol groups in symmetrical alkyl dithiol monolayers assembled on a Au substrate and *I*/*V* properties of the assembly can be readily measured by scanning probe microscopy.[14] Figure 3 summarizes the averaged *I*/V data for assemblies **A1** and **A2** (Scheme 2). The gap conditions used to define the tip–sample separation are −0.5 and −0.1 nA at −1.5 V, respectively. The STS spectra for **A1** clearly showed asymmetric *I*/V behavior, with higher current at a negative bias potential than at a positive one. The average rectification ratio (RR) is 0.19:1 (for easy comparison, 1/RR was used in Figure 3a), where RR is defined as $RR = I(+1.5\text{ V})/I(-1.5\text{ V})$.[15] Opposite rectifying behaviors were found for assembly **A2**, with an average RR value of 4.8:1. The inset histograms show the statistical distribution of 1/RR for **A1** and RR for **A2** for the different NPs measured, thus demonstrating the reproducibility of the *I*/V curves for different NPs on the SAM monolayer. The RR range is 2:1–7:1 for **A1** while the 1/RR range for **A2** is 3:1–7:1. The ranges in both cases can be attributed to different orientations and conformations of the molecules in the SAM defects.[10a,16] The statistical histogram analyses were based on measurements taken on about 50 different immobilized single Au NPs for each assembly. The *I*/*V* data for each NP is the average of about 100 individual *I*/*V* curves, each of which is composed of 256 points, while each point has been averaged 3–5 times by the software.

 © 2004 Wiley-VCH Verlag GmbH & Co. KGaA, Weinheim

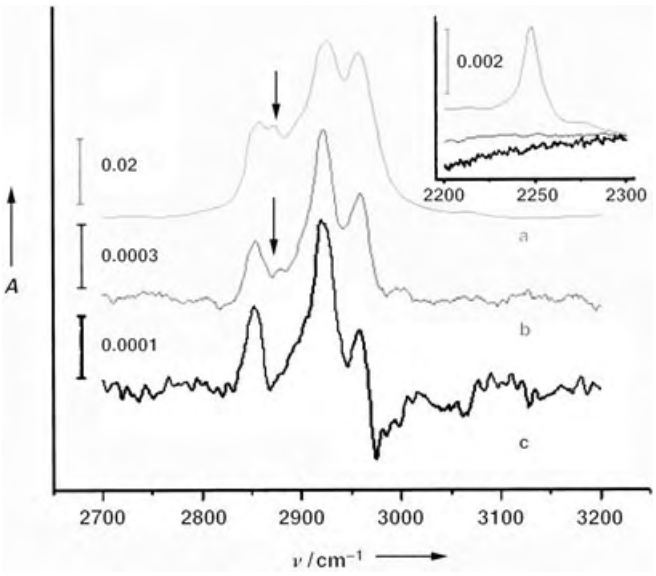


Figure 2. Grazing incidence FTIR spectra in the CH stretching region of a) pure compound **6** in KBr, b) a monolayer of compound **6** on Au after deprotection of the CNE group, and c) after cleavage of the TMSE group. The inset spectra shows the CN stretching region.

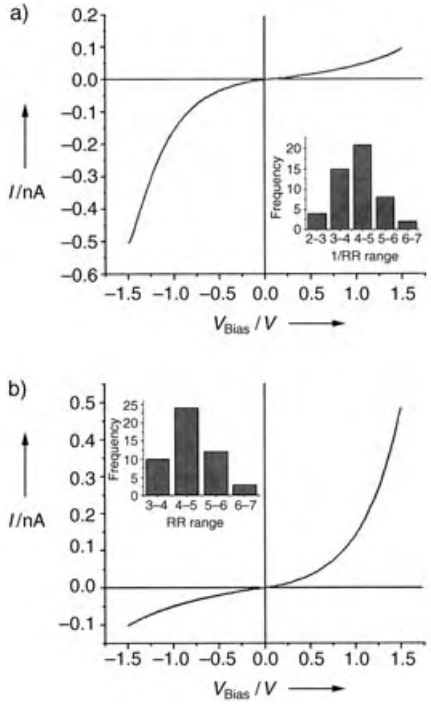


Figure 3. Averaged *I*/*V* curves measured over approximately 50 different gold nanoparticles at $V_{bias} = -1.5$ V for a) **A1** ($I_t = -0.5$ nA) and b) **A2** ($I_t = -0.1$ nA).

We also changed the current set points (distance between the STM tip and the Au NP) to investigate the behavior of the junction under different gap conditions. Figure 4 shows the *I*/*V* curves obtained at different current set points for **A1** and **A2**. The opposite asymmetric *I*/*V* behaviors for **A1** and **A2** were observed consistently with various current set points. Although the interplay of two junctions together with the

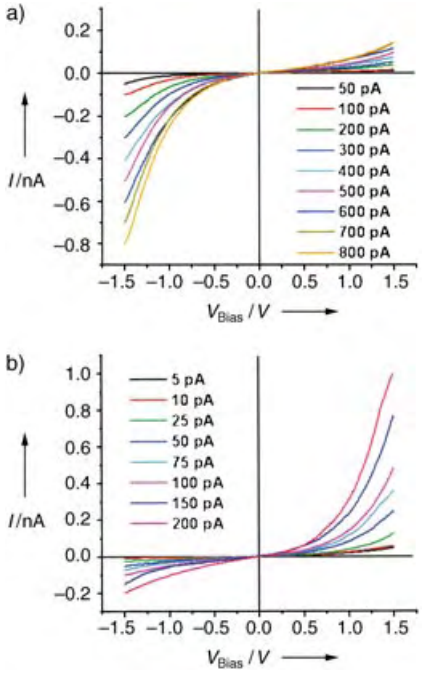


Figure 4. *I*/*V* data taken at different current set points for a V_{bias} of −1.5 V for: a) **A1** and b) **A2**.

charging of the NP can change the symmetry of the *I*/*V* curve,[17] the contribution should be always in the same direction. In our case the opposite asymmetry between **A1** and **A2** ruled out any significant contribution from such an effect.

Since the opposite rectifying behavior for **A1** and **A2** also rules out any contribution in the asymmetry originating from the measurement setup, the rectifying effect observed should be an intrinsic property of the molecules. Although the position of one methyl group on one thiophene ring was different in compounds **6** and **13**, which may affect the twist angle of the conjugation and thus electron delocalization, we believe that the determining factor is the dipole orientation of the thiophene–thiazole diblock rather than the slight difference in the position of the methyl group. The results are consistent with our previous results obtained from **A3** (Scheme 2). Assembly **A3** has the same dipole orientation as **A2**. Preliminary calculations at the HF/G-31G level showed that the component along the molecule axis is 1.68 and 1.54 D for molecules **6** and **13**, respectively.

In summary, we have synthesized new diode molecules with two different terminal thiol groups that are protected differenlt. Sequential deprotection of these groups enables us to assemble the diode molecules with controlled orientations between two gold electrodes. By manipulating the orientations of the diode molecules between electrodes we were able to control the rectification directions. Reproducible results from STS studies clearly support the concept of using diblock conjugated oligomers with opposite electronic demands for a rectifying effect. The results also indicate that the dipole moments may play an important role in determining the rectifying direction and ratio.

 © 2004 Wiley-VCH Verlag GmbH & Co. KGaA, Weinheim

Experimental Section

5: *n*BuLi (1.2 mL, 1.6 M in hexanes) was added dropwise to a solution of **2** (489 mg, 1.5 mmol) in dry THF (15 mL) cooled at −78 °C. The resulting solution was allowed to warm to room temperature over 30 minutes, recooled to −78 °C, and quenched with tributyltin chloride (814 mg, 2.5 mmol). The mixture was stirred at room temperature for 4 h, poured into aqueous sodium carbonate solution, and extracted with diethyl ether. The combined organic extracts were washed with brine, dried (Na_2SO_4), and the solvent was removed in vacuo. The crude organostannane intermediate **3** was obtained in almost quantitatively yield (monitored by ^{1}H NMR spectroscopy). This crude product of **3** and compound **4** (483 mg, 1.5 mmol) were dissolved in anhydrous DMF (20 mL) and a mixture of $[Pd_2(dba)_3]$ (30 mg, 0.03 mmol), PPh_3 (60 mg, 0.23 mmol), and Cu_2O (65 mg, 0.45 mmol) were added in one portion. The resulting mixture was heated at 130–135 °C for 12 h, and then was cooled to room temperature. The DMF was then removed under high vacuum, $CHCl_3$ was added to the residue, and the resulting mixture was filtered through a pad of silica gel. The crude product was purified by column chromatography (silica gel, hexane/ethyl acetate, 10:1, v/v) to afford **5** (468 mg, 60 %) as a pink solid. ^{1}H NMR (500 MHz, $CDCl_3$): $\delta = 0.01$ (s, 9H, $SiMe_3$), 0.94 (t, $J = 8.5$ Hz, 2H, CH_2), 2.37 (s, 3H, Me), 2.47 (s, 3H, Me), 2.49 (s, 3H, Me), 2.68 (s, 3H, Me), 2.88 (t, $J = 8.5$ Hz, 2H, CH_2), 6.82 (s, 1H, Ar-H), 6.88 (s, 1H, Ar-H), 6.91 ppm (s, 1H, Ar-H); ^{13}C NMR (125 MHz, $CDCl_3$): $\delta = -1.8$, 15.8, 16.5, 17.0, 17.5, 17.6, 34.8, 113.5, 126.7, 128.4, 129.4, 131.5, 132.2, 133.9, 135.0, 136.8, 138.0, 150.7, 153.2, 158.1, 158.9 ppm.

6: *n*BuLi (0.4 mL, 1.6 M in hexanes) was added dropwise to a solution of compound **5** (260 mg, 0.5 mmol) in dry THF (10 mL) cooled at −78 °C. The resulting solution was allowed to warm to room temperature for 20 min, recooled to −78 °C, and quenched with sulfur powder (22.4 mg, 0.7 mmol). The mixture was warmed to 0 °C for 20 min, then recooled to −78 °C, and treated with a solution of 3-bromopropionitrile (113 mg, 0.84 mmol) in THF (2 mL). The mixture was stirred at room temperature overnight, poured into water, and extracted with diethyl ether. The combined organic extracts were washed with brine, dried (Na_2SO_4), and the solvent was removed in vacuo. The crude product was purified on silica gel (hexane/ethyl acetate, 4:1, v/v) to afford **6** (202 mg, 62 %). ^{1}H NMR (500 MHz, $CDCl_3$): $\delta = 0.02$ (s, 9H, $SiMe_3$), 0.97 (t, $J = 8.5$ Hz, 2H, CH_2), 2.41 (s, 3H, Me), 2.54 (s, 3H, Me), 2.56 (s, 3H, Me), 2.66 (t, $J = 7.0$ Hz, 2H, CH_2), 2.71 (s, 3H, Me), 2.91 (t, $J = 8.5$ Hz, 2H, CH_2), 3.02 (t, $J = 7.0$ Hz, 2H, CH_2), 6.87 (s, 1H, Ar-H), 6.97 ppm (s, 1H, Ar-H); ^{13}C NMR (125 MHz, $CDCl_3$): $\delta = -1.8$, 15.5, 15.9, 16.5, 17.4, 17.7, 18.0, 33.3, 34.7, 117.5, 119.9, 126.4, 129.3, 130.8, 133.1, 134.1, 135.2, 136.6, 137.7, 138.5, 151.9, 159.0, 159.6, 160.4 ppm; $\lambda_{max} = 421$ nm; MS (CI): calcd mass for $C_{26}H_{31}N_3S_6Si$: m/z 605.06; found: m/z 605.8 $[M+1]^+$.

Further experimental details for the synthesis of all other compounds, assembly preparation, STM, STS, and FTIR measurements can be found in the Supporting Information.

Received: March 24, 2004 [Z460110]

Keywords: electron transport · molecular electronics · monolayers · self-assembly

[1] A. Aviram, M. Ratner, *Chem. Phys. Lett.* **1974**, *29*, 277–283.
[2] J.-P. Launay, *Chem. Soc. Rev.* **2001**, *30*, 386–397.
[3] R. M. Metzger, *Chem. Rev.* **2003**, *103*, 3803–3834.
[4] *Molecular Switches* (Ed.: B. L. Feringa), Weinheim, Chichester, Wiley-VCH, **2001**.
[5] During the preparation of this manuscript, the use of two different protection groups to orientate the molecules on gold wires was reported: S. K. Pollack, J. Naciri, J. Mastrangelo, C. H. Patterson, J. Torres, M. Moore, R. Shashidhar, J. G. Kushmerick, *Langmuir* **2004**, *20*, 1838–1842.
[6] a) M.-K. Ng, L. Yu, *Angew. Chem.* **2002**, *114*, 4750–3753; *Angew. Chem. Int. Ed.* **2002**, *41*, 3598–3601; b) M.-K. Ng, D.-C. Lee, L. Yu, *J. Am. Chem. Soc.* **2002**, *124*, 11862–11863.
[7] M. B. Anderson, M. G. Ranasinghe, J. T. Palmer, P. L. Fuchs, *J. Org. Chem.* **1988**, *53*, 3127–3129.
[8] C. G. Bates, R. K. Gujadhur, D. Venkataraman, *Org. Lett.* **2002**, *4*, 2803–2806.
[9] a) C. A. Widring, C. A. Alves, M. D. Porter, *J. Am. Chem. Soc.* **1991**, *113*, 2805–2810; b) C. A. Alves, E. L. Smith, M. D. Porter, *J. Am. Chem. Soc.* **1992**, *114*, 1222–1227.
[10] a) Z. J. Donhauser, B. A. Mantooth, K. F. Kelly, L. A. Bumm, J. D. Monnell, J. J. Stapleton, D. W. Price, Jr., A. M. Rawlett, D. L. Allara, J. M. Tour, P. S. Weiss, *Science* **2001**, *292*, 2303–2307; b) G. K. Ramachandran, T. J. Hopson, A. M. Rawlett, L. A. Nagahara, A. Primak, S. M. Lindsay, *Science* **2003**, *300*, 1413–1416; c) R. A. Wassel, R. R. Fuierer, N. Kim, C. B. Gorman, *Nano Lett.* **2003**, *3*, 1617–1620.
[11] P. S. Weiss, L. A. Bumm, T. D. Dunbar, T. P. Burgin, J. M. Tour, D. L. Allara, *Ann. N. Y. Acad. Sci.* **1998**, *852*, 145–168.
[12] D. I. Gittins, F. Caruso, *Angew. Chem.* **2001**, *113*, 3089–3092; *Angew. Chem. Int. Ed.* **2001**, *40*, 3001–3004.
[13] The assignment of this absorption band was made by a comparitive study of the IR spectra of different model compounds; for details see the Supporting Information.
[14] a) M. Dorogi, J. Gomez, R. Osifchin, R. P. Andres, R. Reifenberger, *Phys. Rev. B* **1995**, *52*, 9071–9077; b) D. I. Gittins, D. Bethell, D. J. Schiffrin, R. J. Nichols, *Nature* **2000**, *408*, 67–69; c) X. D. Cui, A. Primax, X. Zarate, J. Tomfohr, O. F. Sankey, A. L. Moore, T. A. Moore, D. Gust, G. Harris, S. M. Lindsay, *Science* **2001**, *294*, 571–574.
[15] R. M. Metzger, T. Xu, I. R. Peterson, *J. Phys. Chem. B* **2001**, *105*, 7280–7290.
[16] a) M. T. Cygan, T. D. Dunbar, J. J. Arnold, L. A. Bumm, N. F. Shedlock, T. P. Burgin, L. Jones II, D. L. Allara, J. M. Tour, P. S. Weiss, *J. Am. Chem. Soc.* **1998**, *120*, 2721–2732; b) S. Yasuda, T. Nakamura, M. Matsumoto, H. Shigekawa, *J. Am. Chem. Soc.* **2003**, *125*, 16430–16433; c) L. Patrone, S. Palacin, J. P. Bourgoin, J. Lagoute, T. Zambelli, S. Gauthier, *Chem. Phys.* **2002**, *281*, 325–332.
[17] A. E. Hanna, M. Tinkhan, *Phys. Rev. B* **1991**, *44*, 5919–5922.

 © 2004 Wiley-VCH Verlag GmbH & Co. KGaA, Weinheim

Asymmetric Organocatalysis

Direct Organocatalytic Enantioselective Mannich Reactions of Ketimines: An Approach to Optically Active Quaternary α-Amino Acid Derivatives**

*Wei Zhuang, Steen Saaby, and Karl Anker Jørgensen**

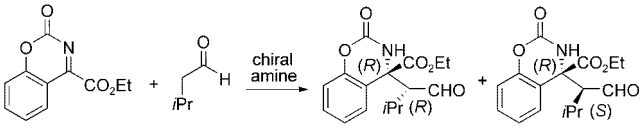
The Mannich reaction is an effective C–C bond-forming process for the construction of nitrogen-containing compounds, such as α- and β-amino acid derivatives, as well as a variety of natural products.[1] The catalytic enantioselective addition of preformed nucleophiles, such as silyl ketene acetals and silyl enol ethers, to imines is well established,[2] but only recently were the first examples of direct enantioselective Mannich reactions reported. By the use of either bifunctional chiral Lewis acid complexes[3] or secondary chiral amines[4] as the catalyst for the reaction of imines with unmodified carbonyl donors, the formation of the corresponding optically active Mannich bases has been reported.

However, despite the tremendous amount of work and effort devoted to the development of efficient and versatile Mannich reactions, the structure of the electrophile has been restricted to imines derived from aldehydes. The organocatalytic enantioselective Mannich reaction of imines derived from ketones (ketimines) is to date unprecedented,[5] although substrates such as α-substituted α-ketimino esters would constitute an interesting template for the synthesis of quaternary α- and β-amino acids.[6,7]

As a result of the tetrasubstituted asymmetric carbon atom, quaternary α-amino acids are considerably more stable than tertiary α-amino acid derivatives, and therefore problems of metabolic degradation, for example, of peptidomimetics, may be avoided. Moreover, α,α-disubstituted α-amino acids exert a remarkable influence on the conformation of peptides into which they are incorporated.[8] Finally, non-natural α-aryl α-alkyl α-amino acid derivatives have shown strong inhibitory effects on aldose reductases, that is, as potential drugs for the treatment of various diabetes-related diseases.[9] Herein the development of the first direct organocatalyzed enantioselective Mannich reaction of ketimines and unmodified aldehydes is presented.

Ketimines are in general less reactive towards nucleophilic additions than aldimines owing to steric hindrance in the C–C bond-forming step, as well as electronic effects. A series of ketimines **1a–f** (see Supporting Information) in which the protecting group on the nitrogen atom is intrinsically bound to an α-aryl substituent of the imine were prepared.[5] The anchoring of the protecting group in this way overcomes the above-mentioned problems by minimizing the degree of rotational freedom and by blocking the *E*/*Z* isomerization of the imine double bond. Consequently, and also as a result of the induced ring strain, ketimines **1a–f** showed high reactivity towards a variety of nucleophiles, in striking contrast to their non-anchored analogues.[5,10] The reaction of ketimine **1a** with isovaleraldehyde (**2a**) was investigated as the model reaction, and a survey of different chiral amines as catalysts was carried out (Table 1).

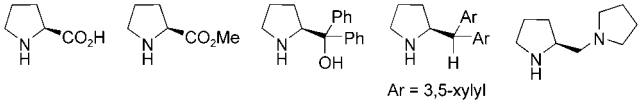
Table 1: Direct organocatalytic asymmetric Mannich reaction of ketimine **1a** with **2a**.



1a **2a** **3a** **4a**

Entry	Catalyst (mol%)	*T* [°C]	**2a** [equiv]	Solvent	Yield[a] [%]	**3a**/**4a**[b]	*ee*[c] [%]
1	**5a** (30)	0	5	CH_2Cl_2	84	1:8	82
2	**5b** (30)	0	5	CH_2Cl_2	11	>20:1	7
3	**5c** (30)	0	5	CH_2Cl_2	trace	>20:1	–
4	**5d** (30)	0	5	CH_2Cl_2	39	>20:1	80
5	**5e** (30)	0	5	CH_2Cl_2	56	15:1	86
6	**5e** (5)	0	5	CH_2Cl_2	73	2:1	88
7	**5e** (5)	0	5	Et_2O	74	19:1	90
8	**5e** (5)	0	2	Et_2O	99	>20:1	91
9	**5e** (5)	−24	2	Et_2O	51	17:1	92
10	**5e** (2)	0	2	Et_2O	93	18:1	91

[a] Combined yield of the two isolated diastereomeric products. [b] The diastereomeric ratio was determined by ^{1}H NMR spectroscopic analysis of the crude product mixture. [c] The *ee* of the major product was determined by HPLC on a Daicel Chiralpak AS column.



5a **5b** **5c** **5d** **5e**

Initial experiments were performed with L-proline (**5a**; 30 mol%) as the catalyst and with 5 equivalents of the aldehyde donor. The reaction proceeded smoothly to afford the desired Mannich products in a combined yield of 84% with a diastereomeric ratio of 1:8 in favor of **4a** (82% *ee*; Table 1, entry 1). The more soluble methyl ester of L-proline also promoted the reaction of ketimine **1a** with **2a**, but the yield dropped to 11%, the diastereoselectivity was inversed (>20:1), and the enantioselectivity was almost completely eroded (7% *ee*) (Table 1, entry 2). The L-proline-derived catalyst **5c** was a poor catalyst for this reaction (Table 1, entry 3). However, the removal of the hydroxy group and introduction of sterically demanding aryl substituents provided the catalyst **5d**, which showed good stereoselectivity

[*] Dr. W. Zhuang, Dr. S. Saaby, Prof. K. A. Jørgensen
The Danish National Research Foundation:
Center for Catalysis
Department of Chemistry, Aarhus University
DK-8000 Aarhus C (Denmark)
Fax: (45) 8619-6199
E-mail: kaj@chem.au.dk

[**] This work was made possible by a grant from The Danish National Research Foundation. We are grateful to Dr. R. G. Hazell for X-ray crystallographic analysis.

Supporting information for this article is available on the WWW under http://www.angewandte.org or from the author.

 © 2004 Wiley-VCH Verlag GmbH & Co. KGaA, Weinheim DOI: 10.1002/anie.200460158

(d.r. > 20:1, 80% *ee*), although it had only a moderate turnover number (39% yield). The chiral diamine (*S*)-1-(2-pyrrolidinylmethyl)pyrrolidine (**5e**) finally proved to be the catalyst of choice, and under the same conditions afforded the Mannich product in 56% yield, with a d.r. of 15:1 and with 86% *ee* for the major diastereomer (Table 1, entry 5). By lowering the amount of catalyst and aldehyde to 5 mol% and 2.0 equivalents, respectively, and changing the solvent to Et_2O, it was possible to prepare **3a** in almost quantitative yield (99%), with excellent diastereoselectivity (> 20:1), and with 91% *ee* (Table 1, entries 6–8). Lowering of the temperature only had a minimal effect on the enantioselectivity (Table 1, entry 9), but the Mannich reaction could be carried out in the presence of only 2 mol% of the catalyst without compromising the yield or enantioselectivity (Table 1, entry 10).

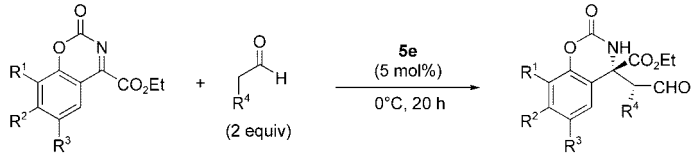
Having optimized the reaction conditions, we investigated the scope of the reaction by treating a series of ketimines **1a–f** with aldehyde donors **2a–c**, as summarized in Table 2. Imines bases **3e**,**f** with 87 and 84% *ee*, respectively (Table 2, entries 5 and 6).

The best results with propionaldehyde (**2b**) as the substrate in the reaction with ketimine **1a** were obtained in CH_2Cl_2. The major diastereomer **3g** (d.r. 5:1) was formed in good yield and with high enantioselectivity (95% *ee*; Table 2, entry 7). Finally, when unsaturated 4-pentenal (**2c**) was used as the aldehyde donor, the Mannich base **3h** was isolated in 82% yield with an excellent optical purity of 98% *ee* (Table 2, entry 8).

It was demonstrated previously that these cyclic carbamates are readily cleaved under basic solvolytic reaction conditions to liberate the phenolic hydroxy group.[5] By this protocol, triflate-substituted aryl compounds are potentially accessible for further elaboration, such as palladium-catalyzed cross-coupling reactions and deoxygenation.

The absolute and relative configuration of the Mannich products **3** and **4** was determined by X-ray crystallography and by comparison of HPLC traces and signs of optical rotation (see Supporting Information). The condensation of **3f** (84% *ee*) with 2,4,6-trichlorophenylhydrazine and subsequent crystallization from acetone provided optically pure crystals of the corresponding chiral hydrazone which were suitable for X-ray crystallographic analysis.

Table 2: Reaction of ketimines **1a–f** with aldehydes **2a–c** under the optimized reaction conditions.



Entry	Imine	Solvent	R^1	R^2	R^3	R^4	Product	Yield [%][a]	**3**/**4**[b]	*ee* [%][c]
1	**1a**	Et_2O	H	H	H	*i*Pr	**3a**	99	> 20:1	91
2	**1b**	Et_2O	H	H	Me	*i*Pr	**3b**	98	6:1	89
3	**1c**	Et_2O	H	H	OMe	*i*Pr	**3c**	95	9:1	86
4	**1d**	Et_2O	H	H	F	*i*Pr	**3d**	97	19:1	83
5	**1e**	Et_2O	H	OMe	H	*i*Pr	**3e**	90	> 20:1	87
6	**1f**	Et_2O	$-C_4H_4-$		H	*i*Pr	**3f**	93	> 20:1	84
7	**1a**	CH_2Cl_2	H	H	H	Me	**3g**	72	5:1	95
8	**1a**	CH_2Cl_2	H	H	H	allyl	**3h**	82	4:1	98

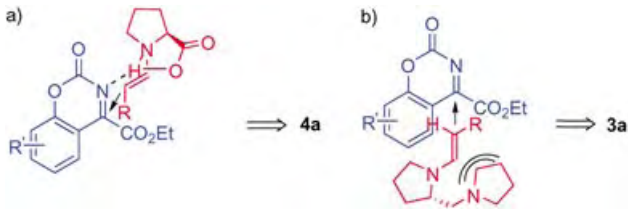
[a] Combined yield of the two isolated diastereomeric products. [b] The diastereomeric ratio was determined by ^{1}H NMR spectroscopic analysis of the crude product. [c] The *ee* value for the major product (with *R* configuration at the quaternary stereocenter) was determined by HPLC on a chiral stationary phase (see Supporting Information for details).

Based on the absolute configuration of the product, attack at the *Si* face of the ketimine was observed for all catalysts **5a–e** tested. However, a very interesting reversal of diastereoselectivity was found when the carboxylic acid functionality of L-proline (**5a**) was substituted for a non-acidic or basic substituent (Table 1, entry 1 versus entries 2–5). The observed stereoselectivity with L-proline as the catalyst is in good agreement with the transition-state models proposed by Córdova and Barbas,[4f] List et al.,[4d] and Bahmanyar and Houk[11] for the catalytic enantioselective Mannich reaction of imines derived from glyoxylic aldehydes. We propose that L-proline directs reaction at the *Re* face of the enamine, and the transition-state model in Scheme 1a may account for the stereochemistry of the Mannich product **4a** observed.

with an electron-donating substituent (a methyl or a methoxy group) in the 4-position underwent a clean reaction with isovaleraldehyde (**2a**) in the presence of the catalyst **5e** (5 mol%). Upon filtration of the reaction mixture through a column of silica gel, the corresponding products **3b**,**c** were isolated in very high yields, with good diastereomeric ratios of 6:1 and 9:1, and with 89 and 86% *ee*, respectively (Table 2, entries 2 and 3). The reaction of the 4-fluoro-substituted ketimine **1d** afforded the Mannich product **3d** in nearly quantitative yield (97%) with excellent diastereoselectivity (19:1) and 83% *ee* (Table 2, entry 4). The 3-methoxy-substituted and 1-naphthol-derived ketimines **1e**,**f** were also successfully employed as substrates in the reaction with aldehyde **2a** to give the diastereomerically pure Mannich

In contrast, when **5e** was used as the catalyst, interactions such as hydrogen bonding between the enamine intermediate and the lone pair of electrons on the nitrogen atom of the ketimine can not occur, as the reaction is conducted under neutral conditions.[12] The concept of intrinsic protecting-group anchoring inherently rules out the possibility of *E*/*Z* isomerization of the ketimine, and a linear transition state in which the *Si* face of the enamine approaches the *Si* face of the imino electrophile may explain the observed stereochemistry

 © 2004 Wiley-VCH Verlag GmbH & Co. KGaA, Weinheim



Scheme 1. A schematic representation of the approach of the ketimine to two enamine intermediates that accounts for the observed diastereoselectivities: a) reaction occurs at the *Si* face of the imine and the *Re* face of the enamine; b) reaction occurs at the *Si* face of the imine and the *Si* face of the enamine.

(Scheme 1b).[13] An *E* geometry of the enamine double bond is anticipated on the basis of energy calculations, and an antiperiplanar approach of the reaction partners would minimize steric repulsions in the C–C bond-forming step.

In conclusion, we have reported the first organocatalytic enantioselective Mannich reaction of ketimines and unmodified aldehydes based on the concept of intrinsic protecting-group anchoring. Under the catalysis of chiral secondary amines (2–5 mol%), optically active quaternary α-amino acid derivatives were formed in high yields (72–99%) with optical purities ranging from 83 to 98% *ee*. Depending on the choice of catalyst, either diastereomer of the Mannich base can be prepared.

Received: March 30, 2004 [Z460158]

Keywords: amino acids · chiral amines · Mannich bases · organocatalysis · quaternary stereocenters

[1] For a review, see: a) E. F. Kleinmann in *Comprehensive Organic Synthesis*, *Vol. 2* (Eds.: B. M. Trost, I. Fleming), Pergamon, Oxford, **1991**, chap. 4.1, p. 893; b) M. Arend, B. Westermann, N. Risch, *Angew. Chem.* **1998**, *110*, 1096–1122; *Angew. Chem. Int. Ed.* **1998**, *37*, 1044–1070.

[2] For leading references, see: a) A. E. Taggi, A. M. Hafez, T. Lectka, *Acc. Chem. Res.* **2003**, *36*, 10–19; b) A. Fujii, E. Hagawara, M. Sodeoka, *J. Am. Chem. Soc.* **1999**, *121*, 5450–5458; c) H. Ishitani, M. Ueno, S. Kobayashi, *J. Am. Chem. Soc.* **2000**, *122*, 8180–8186; d) A. G. Wenzel, E. N. Jacobsen, *J. Am. Chem. Soc.* **2002**, *124*, 12964–12965; e) S. Kobayashi, R. Matsubara, Y. Nakamura, H. Kitigawa, M. Sugiura, *J. Am. Chem. Soc.* **2003**, *125*, 2507–2515, and references therein.

[3] For Lewis acid catalyzed direct asymmetric Mannich reactions, see, for example: a) S. Yamasaki, T. Iida, M. Shibasaki, *Tetrahedron Lett.* **1999**, *40*, 307–310; b) S. Yamasaki, T. Iida, M. Shibasaki, *Tetrahedron* **1999**, *55*, 8857–8867; c) S. Matsunaga, N. Kumagai, S. Harada, M. Shibasaki, *J. Am. Chem. Soc.* **2003**, *125*, 4712–4713; d) B. M. Trost, L. R. Terrell, *J. Am. Chem. Soc.* **2003**, *125*, 338–339; e) K. Juhl, N. Gathergood, K. A. Jørgensen, *Angew. Chem.* **2001**, *113*, 3083–3085; *Angew. Chem. Int. Ed.* **2001**, *40*, 2995–2997; f) L. Bernardi, A. S. Gothelf, R. G. Hazell, K. A. Jørgensen, *J. Org. Chem.* **2003**, *68*, 2583–2591.

[4] For direct organocatalyzed enantioselective Mannich reactions of aldimines, see, for example: a) B. List, *J. Am. Chem. Soc.* **2000**, *122*, 9336–9337; b) K. Sakthivel, W. Notz, T. Bui, C. F. Barbas III, *J. Am. Chem. Soc.* **2001**, *123*, 5260–5267; c) W. Notz, K. Sakthivel, T. Bui, G. Zhong, C. F. Barbas III, *Tetrahedron Lett.* **2001**, *42*, 199–201; d) B. List, P. Pojarliev, W. T. Biller, H. J. Martin, *J. Am. Chem. Soc.* **2002**, *124*, 827–833; e) A. Córdova, W. Notz, G. Zhong, J. M. Betancort, C. F. Barbas III, *J. Am. Chem. Soc.* **2002**, *124*, 1842–1843; f) A. Córdova, C. F. Barbas III, *Tetrahedron Lett.* **2002**, *43*, 7749–7752; g) S. Watanaba, A. Córdova, F. Tanaka, C. F. Barbas III, *Org. Lett.* **2002**, *4*, 4519–4522; h) A. Córdova, S. Watanaba, F. Tanaka, W. Notz, C. F. Barbas III, *J. Am. Chem. Soc.* **2002**, *124*, 1866–1867; i) A. Córdova, C. F. Barbas III, *Tetrahedron Lett.* **2003**, *44*, 1923–1926; j) Y. Hayashi, W. Tsuboi, M. Shoji, N. Suzuki, *J. Am. Chem. Soc.* **2003**, *125*, 11208–11209; k) Y. Hayashi, W. Tsuboi, I. Ashimine, T. Urushima, M. Shoji, K. Sakai, *Angew. Chem.* **2003**, *115*, 3805–3808; *Angew. Chem. Int. Ed.* **2003**, *42*, 3677–3680; l) T. Itoh, M. Yokoya, K. Miyauchi, K. Nagata, A. Oshawa, *Org. Lett.* **2003**, *5*, 4301–4304; m) W. Notz, F. Taneka, S.-i. Watanabe, N. S. Chowdari, J. M. Turner, R. Thaayumanavan, C. F. Barbas III, *J. Org. Chem.* **2003**, *68*, 9624–9634; n) A. Córdova, *Acc. Chem. Res.* **2004**, *37*, 102–112.

[5] For the Lewis acid catalyzed enantioselective Mannich reaction of ketimines, see: S. Saaby, K. Nakama, M. A. Lie, R. G. Hazell, K. A. Jørgensen, *Chem. Eur. J.* **2003**, *9*, 6145–6154.

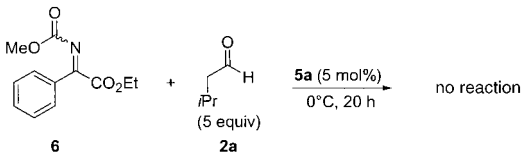
[6] For recent reviews on the asymmetric construction of quaternary carbon centers, see: a) M. Cristoffers, A. Mann, *Angew. Chem.* **2001**, *113*, 4725–4732; *Angew. Chem. Int. Ed.* **2001**, *40*, 4591–4597; b) E. J. Corey, A. Guzman-Perez, *Angew. Chem.* **1998**, *110*, 402–415; *Angew. Chem. Int. Ed.* **1998**, *37*, 388–401.

[7] For a review on the asymmetric synthesis of quaternary α-amino acids, see, for example: C. Cativiela, M. D. Díaz-de-Villegas, *Tetrahedron: Asymmetry* **1998**, *9*, 3517–3599.

[8] a) P. K. C. Paul, M. Sukumar, R. Bardi, A. M. Piazzesi, G. Valle, C. Toniolo, P. Balaram, *J. Am. Chem. Soc.* **1986**, *108*, 6363–6370; b) M. Altorfer, C. Lehmann, P. Schönholzer, K. Müller, *J. Org. Chem.* **1996**, *61*, 4080–4086, and references therein.

[9] See, for example: a) R. Sarges, J. Bordner, B. W. Donimy, M. J. Peterson, E. B. Whipple, *J. Med. Chem.* **1985**, *28*, 1716–1720; b) T. Yamaguchi, K. Miura, T. Usui, R. Unno, Y. Matsumoto, M. Fukushima, K. Mizuno, Y. Kondo, Y. Baba, M. Kurono, *Arzneim.-Forsch.* **1994**, *44*, 344–348; c) H. U. Stilz, B. Jablonka, M. Just, J. Knolle, E. F. Paulus, G. Zoller, *J. Med. Chem.* **1996**, *39*, 2118–2122; d) N. Hotta, T. Touota, K. Matsuoka, Y. Shigeta, R. Kikkiwa, T. Kaneko, A. Takahashi, K. Sugimura, Y. Koike, J. Ishii, N. Sakamoto, *Diabetes Care* **2001**, *24*, 1776–1782.

[10] The ketimine **6**, without intrinsic protecting-group anchoring, did not react with isovaleraldehyde (**2a**) in the presence of 5 mol% of L-proline (**5a**).



[11] S. Bahmanyar, K. N. Houk, *Org. Lett.* **2003**, *5*, 1249–1251.

[12] For an example of the combination of protic acids and chiral diamines as the catalyst, see: S. Saito, M. Nakadai, H. Yamamoto, *Synlett* **2001**, 1245–1248.

[13] See also references [4f,n] for another approach of imines to a related enamine intermediate.

 © 2004 Wiley-VCH Verlag GmbH & Co. KGaA, Weinheim

Biomimetic Catalysis

A C_3-Symmetrical Chiral Trisoxazoline Zinc Complex as a Functional Model for Zinc Hydrolases: Kinetic Resolution of Racemic Chiral Esters by Transesterification**

Clémence Dro, Stéphane Bellemin-Laponnaz, Richard Welter, and Lutz H. Gade**

The key function of the Zn^{2+} cation in the reactive sites of many metalloenzymes is a well-established fact.[1] It normally adopts a tetrahedral coordination geometry and is attached to the protein backbone by three amino acid residues; the fourth coordination site is occupied by a water molecule. In many of the zinc-based peptidases, a tris(histidine)zinc binding site acts as a "tripodal ligand" for the metal ion. These include the Zn-based D-Ala-D-Ala-carboxypeptidase of *Streptomyces albus*[2] and the extensively studied "metzincin" family of endopeptidases.[3,4]

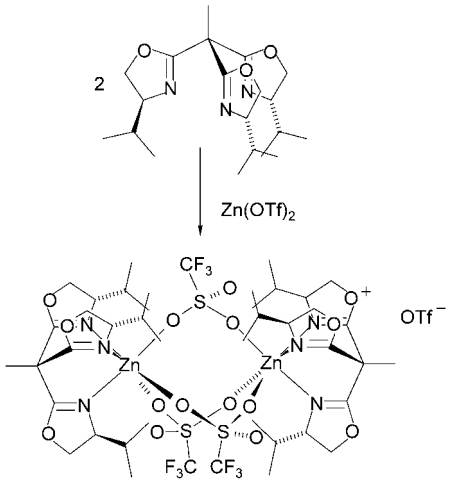
The ubiquity of zinc in metalloenzyme chemistry has been related to its flexible coordination chemistry, substitutional lability, Lewis acidity, intermediate polarizability (and thus moderate softness) combined with a lack of redox activity. Usually, coordination numbers of 4 or 5 are thought to be preferred in enzymes, including bound water molecules, inhibitors or intermediates.[1] To better understand the factors that control the detailed properties of the active sites of zinc enzymes, small molecular models have been studied during the past decade. The extensive work on scorpionate and related tripodal Zn complexes, in particular by the groups of Vahrenkamp and Parkin, has led to the elucidation of key mechanistic features of the activities of Zn enzymes.[5,6] These include biomimetic hydrolyses as well as the modeling of intermediates of peptidase and carboanhydrase catalytic cycles.

[*] C. Dro, Dr. S. Bellemin-Laponnaz, Prof. L. H. Gade[+]
Laboratoire de Chimie Organométallique et de Catalyse
Institut Le Bel
Université Louis Pasteur Strasbourg
4, rue Blaise Pascal, 67000 Strasbourg (France)
Fax: (+33) 390-241-531
E-mail: lutz.gade@uni-hd.de
Prof. R. Welter
Laboratoire DECMET
Institut Le Bel
Université Louis Pasteur Strasbourg
4, rue Blaise Pascal, 67000 Strasbourg (France)
[+] new address:
Institut für Anorganische Chemie
Universität Heidelberg
Im Neuenheimer Feld 270, 69120 Heidelberg (Germany)
Fax: (+49) 6221–545–609

[**] This work was supported by the CNRS, the Institut Universitaire de France and the EU (RTN Network "AC3S"). BASF as well as Degussa AG provided valuable chemicals. We are grateful to the Ministère de L'Education Nationale de la Recherche et de la Technologie for a Ph.D. grant (C.D.) and thank Dr. André De Cian for collecting the X-ray data.

Rendering tripodal metal binding sites chiral may lead to molecular catalysts of C_3 or C_1 symmetry. Their potential in the development of novel enantioselective catalysts remains comparatively underdeveloped.[7] We recently reported a new class of chiral trisoxazoline tripod ligands and have begun studying their properties in asymmetric catalysis.[8] These may be viewed as models emulating both the tris(histidine) binding sites and the chiral environment of the protein skeletal structure. This result provided the opportunity of developing model compounds for hydrolases or transesterases with the potential for stereoselective transformations normally only observed for the enzymatic system. We present herein the first results of this study.

Reaction of the previously reported chiral trisoxazoline ligand 1,1,1-tris{2-[*(S)*-4-isopropyl]oxazolyl}ethane, "*i*Pr-trisox" (**1**)[8b] with $Zn(OTf)_2$ (OTf is trifluoromethanesulfonyl) in dry methanol led to the complete dissolution of the zinc salt and the formation of the *i*Pr-trisox–Zn complex **2a**, which was isolated as a colorless solid and recrystallized from dichloromethane/pentane (Scheme 1).



Scheme 1. Synthesis of the dinuclear complex $[(i\text{Pr-trisox})_2Zn_2(\mu\text{-OTf})_3]OTf$.

Whereas the analytical and ^1H and ^{13}C NMR spectroscopy data are consistent with a tripodal coordination of the trisoxazoline ligand and an overall threefold molecular symmetry, the ESI mass spectrum indicated the presence of a dinuclear complex cation corresponding to the formulation $[(i\text{Pr-trisox})_2Zn_2(\mu\text{-OTf})_3]^+$. A single-crystal X-ray-structure analysis of the salt $[(i\text{Pr-trisox})_2Zn_2(\mu\text{-OTf})_3]OTf$ (**2a**) confirmed this assignment and established the details of the complex structure, which is depicted in Figure 1a.

Compound **2a** crystallizes in the cubic space group $P2_13$ and the dinuclear zinc complex cation is aligned along a crystallographic threefold axis, thus rendering it exactly C_3-symmetric (Figure 1b). Both metal centers are coordinated by the tripodal trisoxazoline ligand and are symmetrically linked by three triflato ligands, an arrangement which is unique for the weakly coordinating triflate anion. While there are very few structurally characterized triflato–zinc com-

 DOI: 10.1002/anie.200460187 © 2004 Wiley-VCH Verlag GmbH & Co. KGaA, Weinheim

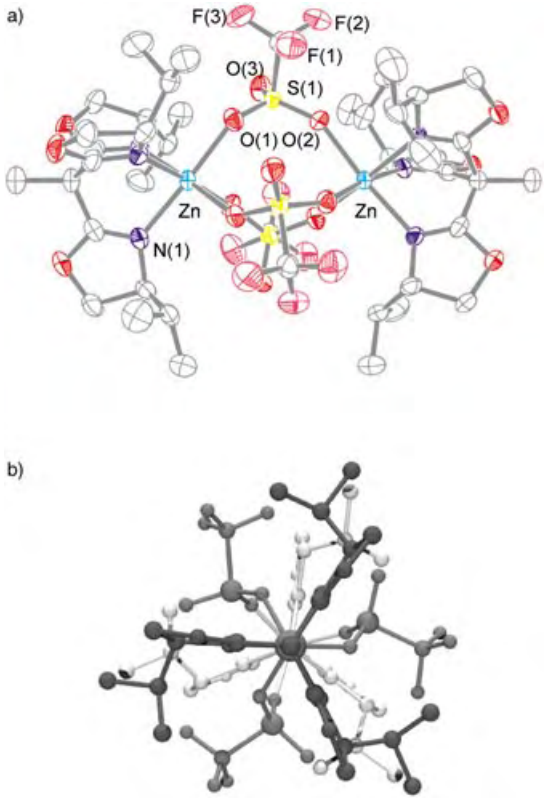
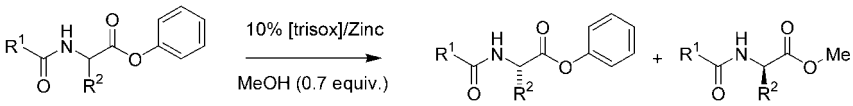


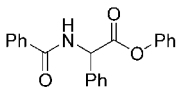
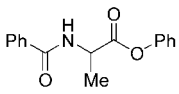
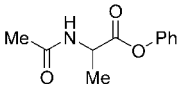
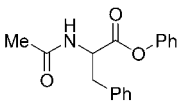
Figure 1. Molecular Structure of the dinuclear zinc complex **2**. a) View perpendicular to the Zn–Zn vector; b) view along the molecular three-fold axis. The principal bond lengths (Å) and angles (°): Zn(1)–N(1) 2.125(4), Zn(2)–N(2) 2.124(4), Zn(1)–O(1) 2.130(4), Zn(2)–O(2) 2.124(4), S(1)–O(1) 1.445(4), S(1)–O(4) 1.444(4), S(1)–O(2) 1.431(4), N(1)-Zn(1)-N(1′) 85.6(2), N(2)-Zn(2)-N(2′) 85.3(2), O(1)-Zn(1)-O(1′) 89.6(2), O(2)-Zn(2)-O(2′) 90.6(2), O(1)-Zn(1)-N(1) 92.6(2), O(1)-Zn(1)-N(1′) 92.1(2), O(4)-Zn(2)-N(2) 87.6(2), O(4)-Zn(2)-N(2′) 96.7(2), O(1)-S(1)-O(4) 113.8(2).

plexes (none of them have the triflate as a bridging ligand),[9] there are several related dinuclear units known in carboxylato–Zn chemistry.[10] We note that bridging triflates have been observed in several other transition-metal complexes, in particular those of the coinage metals.[11] The structural constraints imposed by the relatively rigid tripod ligand lead to a trigonal antiprismatic elongation of the {(*i*Pr-trisox)Zn} unit in the distorted $\{ZnN_3O_3\}$ octahedron [N(1)-Zn(1)-N(1′) 85.6(2), N(2)-Zn(2)-N(2′) 85.3(2) Å], whereas the triflato O atoms are arranged at almost ideal right angles at both Zn centers [O(1)-Zn(1)-O(1′) 89.6(2), O(2)-Zn(2)-O(2′) 90.6(2)°].

We found that the zinc triflate complex **2a** displays catalytic activity in the transesterification of various phenyl esters. It should be noted that the use of non-enzymatic catalysts for asymmetric acylation of substrates is now well-established, in particular, kinetic resolutions by using chiral nucleophilic catalysts have recently proved to be an effective tool in organic synthesis.[12–14] On the other hand, the use of non-enzymatic catalysts for an asymmetric transesterification of activated esters remains, to our knowledge, unexplored.[15,16] This contrasts with the fact that several enzymes have been reported to catalyze the kinetic resolution of carboxylic acid derivatives[17] and the first report of a kinetic resolution by transesterification, with yeast lipase and porcine pancreatic lipase, involved α-halogen-substituted carboxylic acid derivatives.[18]

The chiral zinc complex **2a** showed modest but significant enantioselectivity in the kinetic resolution of various phenyl ester derivatives of *N*-protected amino-acids by transesterification with methanol (Scheme 2). The catalyst is characterized by only modest selectivity factors, in the range of $S = 1.3–2.0$ for substrates listed in Scheme 2.[19] However, upon going from the zinc triflato complex **2a** to the acetate complex **2b** and further to the trifluoroacetate **2c**, there was an increase of the selectivity factor for all the substrates, notably to $S = 5.1$ for entry 3 in the table in Scheme 2. The importance of the tripodal-zinc environment for the observed stereoselectivity is inferred from the observation that the coordination of the classical bidentate dimethyl-bisoxazoline 2,2′-bis[2-((4*S*)-(isopropyl)-1,3-oxazolinyl)]-propane to a zinc salt does not induce kinetic resolution. These first data prove the concept and indicate that non-enzymatic catalysts of this family may prove to be useful in asymmetric transesterifica-



Entry	Substrate	Selectivity factor (s)		
		$Zn(OTf)_2$	$Zn(OAc)_2$	$Zn(OCOCF_3)_2$
1		1.8	3.5	3.8
2		1.3	2.7	3.0
3		2.0	4.5	5.1
4		1.8	2.6	4.3

All reactions were performed in CH_2Cl_2 at room temperature in the presence of 10 mol% of Zinc precursor/ *i*Pr-trisox for 2-3 days.

Scheme 2. Partial kinetic resolution of activated aminoacid esters by stereoselective {trisox–Zn} catalyzed transesterification.

 © 2004 Wiley-VCH Verlag GmbH & Co. KGaA, Weinheim

tion after further development. Ongoing studies are directed at providing mechanistic information, at developing more efficient zinc-based molecular catalysts for this reaction, and at extending the use of these biomimetic systems to other transformations.

Experimental Section

Preparation of complex **2a**: A mixture of *i*Pr-trisox (**1**) (44 mg, 0.12 mmol) and $Zn(OTf)_2$ (40 mg, 0.11 mmol) in methanol (1 mL) was stirred under nitrogen at room temperature for one hour. The solvent was removed in vacuo and the white solid washed with pentane. Recrystallization from dichloromethane/pentane yielded 45 mg (56%) of colorless crystals (suitable for X-ray diffraction). ^{1}H NMR (300 MHz, CD_2Cl_2): $\delta = 4.56$–4.44 (m, 6H), 4.41 (m, 3H), 2.18 (m, 3H), 2.02 (s, 3H), 1.03 (d, $J = 6.9$ Hz, 9H), 0.93 ppm (d, $J = 6.8$ Hz, 9H); ^{13}C NMR (75.5 MHz, CD_2Cl_2): $\delta = 167.3$ (C=N), 119.7 (quad., $J_{(C\text{-}F)} = 318.2$ Hz, CF_3), 71.4 (*C*H*i*Pr), 70.3 (CH_2), 45.1 ($C_{quat.}$), 30.5 ($CH(CH_3)_2$), 17.9 ($CH(CH_3)(CH_3)$, CH_3), 15.2 ppm ($CH(CH_3)(CH_3)$); ^{19}F (282.4 MHz, CD_2Cl_2): $\delta = -78.6$ ppm; HRMS (ESI): *m*/*z* (%): 1305.2194 ($[L_2Zn_2(OTf)_3]^+$; calculated for the most abundant isotopomer: 1305.2186 amu); Elemental analysis (%) calcd. for $C_{44}H_{66}F_{12}N_6O_{18}S_4Zn_2$: C 36.34, H 4.58, N 5.78; found C 36.49, H 4.75, N 5.85.

Complexes **2b** and **2c** were prepared in a similar way. Selected spectroscopic data for **2b**: ^{1}H NMR (300 MHz, $CDCl_3$): $\delta = 4.55$–4.24 (m, 6H), 4.16 (m, 3H), 2.18 (m, 3H), 1.98 (s, 6H), 1.95 (s, 3H), 0.86 (d, $J = 6.9$ Hz, 9H), 0.82 ppm (d, $J = 6.8$ Hz, 9H); ^{13}C NMR (75.5 MHz, $CDCl_3$): $\delta = 179.2$ (C=O), 165.5 (C=N), 70.4 (*C*H*i*Pr), 69.9 (CH_2), 44.3 ($C_{quat.}$), 30.3 ($CH(CH_3)_2$), 22.5 (CH_3-C=O), 18.6 ($CH(CH_3)(CH_3)$), 15.3 ($CH(CH_3)(CH_3)$), 14.0 ppm (CH_3); HRMS (ESI): *m*/*z*: 1035.3877 ($[L_2Zn_2(OAc)_3]^+$; calculated for the most abundant isotopomer: 1035.4025 amu). Selected spectroscopic data for **2c**: ^{1}H NMR (300 MHz, $CDCl_3$): $\delta = 4.45$ (m, 6H), 4.25 (m, 3H), 2.15 (m, 3H), 1.99 (s, 3H), 0.91 (d, $J = 6.9$ Hz, 9H), 0.82 ppm (d, $J = 6.8$ Hz, 9H); ^{13}C NMR (75.5 MHz, $CDCl_3$): $\delta = 166.2$ (C=N), 162.5 (quad., $J_{(C\text{-}F)} = 37.2$ Hz, CO–CF_3), 116.3 (quad., $J_{(C\text{-}F)} = 289.3$ Hz, CF_3), 70.6 (CH_2), 70.4 (*C*H*i*Pr), 44.8 ($C_{quat.}$), 30.6 ($CH(CH_3)_2$), 21.8 (CH_3), 18.4 ($CH(CH_3)(CH_3)$), 15.5 ppm ($CH(CH_3)(CH_3)$); ^{19}F (282.4 MHz, $CDCl_3$): $\delta = -75.4$ ppm; HRMS (ESI): *m*/*z*: 1197.3001 ($[L_2Zn_2(CF_3CO_2)_3]^+$ (calculated for the most abundant isotopomer: 1197.3177 amu).

Crystal data for **2a**: $C_{44}H_{66}F_{12}N_6O_{18}S_4Zn_2$; CF_3O_3S, colorless, crystal dimensions $0.13 \times 0.10 \times 0.08$ mm, $M_r = 1454.01$, cubic, space group $P2_13$, $a = 18.433(2)$ Å, $V = 6263.1(12)$ Å^3, $Z = 4$, $\rho_{calcd} = 1.542$ g cm^{-3}, $\mu = 1.004$ mm^{-1}, $F(000) = 2992$, number of data measure: 5862 ($2.47 < \theta < 30.01°$) at 173(2) K, number of data with $I > 2\sigma(I)$: 3730, number of variables: 260, $R = 0.0678$, $Rw = 0.1617$, GOF = 1.042, largest peak in final difference: 1.42 e Å^{-3}. CCDC-233158 contains the supplementary crystallographic data for this paper. These data can be obtained free of charge via www.ccdc.cam.ac.uk/conts/retrieving.html (or from the Cambridge Crystallographic Data Centre, 12 Union Road, Cambridge CB2 1EZ, UK; fax: (+44) 1223-336-033; or deposit@ccdc.cam.ac.uk).

Representative general procedure for the kinetic resolutions; transesterification of N-benzoyl-phenylglycine phenyl ester: A suspension of zinc triflate (9.0 mg, 0.025 mmol) and *i*Pr-trisox (**1**; 9.5 mg, 0.026 mmol) was stirred in dry methanol (0.5 mL) until complete dissolution of the zinc salt (ca. 1 h). The solvent was then evaporated to dryness and a solution of *rac*-*N*-benzoyl-phenylglycine phenyl ester (83.0 mg, 0.25 mmol) in dry CH_2Cl_2 (1.0 mL) was added followed by dry methanol (7.0 μL, 0.17 mmol). After two days stirring, the mixture was passed through a short plug of silica to separate the esters derivatives from the catalyst. A ^{1}H NMR spectroscopy study showed a conversion of 52% into the methyl ester derivative. HPLC analysis (AD daicel, 95:5 hexane/isopropanol, 0.8 mL min^{-1}) analysis revealed an *ee* of 20.0% for the starting material and 19.5% for the product. These *ee* values correspond to a selectivity factor (s) of 1.8 at 51% conversion.[20]

Received: April 1, 2004 [Z460187]

Keywords: asymmetric catalysis · biomimetic synthesis · chirality · tripodal ligands · zinc

[1] Reviews: a) W. N. Lipscomb, N. Sträter, *Chem. Rev.* **1996**, *96*, 2375; b) D. S. Auld, *Struct. Bonding (Berlin)* **1997**, *89*, 29; c) J. E. Coleman, *Curr. Opin. Chem. Biol.* **1998**, *2*, 222.

[2] O. Dideberg, P. Charlier, G. Dive, B. Joris, J. M. Frère, J. M. Ghuysen, *Nature* **1982**, *299*, 469.

[3] Overview of the chemistry of the "metzincin" endopeptidases: W. Bode, F.-X. Gomis-Rüth, W. Stöcker, *FEBS Lett.* **1993**, *331*, 134.

[4] Trishistidine-zinc reaction centers have been found and studied, amongst others, in the astacins of crayfish: a) W. Bode, F.-X. Gomis-Rüth, R. Huber, R. Zwilling, W. Stöcker, *Nature* **1992**, *358*, 164; in snake venom metalloproteinases: b) J. B. Bjarnason, J. W. Fox, *Methods Enzymol.* **1995**, *248*, 345; adamalysin: c) F.-X. Gomis-Rüth, L. F. Kress, W. Bode, *EMBO J.* **1993**, *12*, 4151; atrolysin C: d) D. Zhang, I. Botos, F.-X. Gomis-Rüth, R. Doll, C. Blood, F. G. Njoroge, J. W. Fox, W. Bode, E. F. Meyer, *Proc. Natl. Acad. Sci. USA* **1994**, *91*, 8447; and in H_2-proteinase: e) T. Kumasaka, M. Yamamoto, H. Moriyama, N. Tanaka, M. Sato, Y. Katsube, Y. Yamakawa, T. Omori-Satoh, S. Iwanaga, T. Ueki, *J. Biochem.* **1996**, *119*, 49.

[5] Reviews: a) H. Vahrenkamp, *Acc. Chem. Res.* **1999**, *32*, 589; b) G. Parkin, *Chem. Commun.* **2000**, 1971; c) G. Parkin, *Chem. Rev.* **2004**, *104*, 699.

[6] Neutral tris(imidazolyl)phosphines: a) C. Kimblin, W. E. Allen, G. Parkin, *J. Chem. Soc. Chem. Commun.* **1995**, 1813; b) C. Kimblin, G. Parkin, *Inorg. Chem.* **1996**, *35*, 6912.

[7] For an overview of C_3-symmetry in catalysis see: C. Moberg, *Angew. Chem.* **1998**, *110*, 210; *Angew. Chem. Int. Ed.* **1998**, *37*, 248.

[8] a) S. Bellemin-Laponnaz, L. H. Gade, *Chem. Commun.* **2002**, 1286; b) S. Bellemin-Laponnaz, L. H. Gade, *Angew. Chem.* **2002**, *114*, 3623; *Angew. Chem. Int. Ed.* **2002**, *41*, 3473.

[9] Structure determinations of zinc triflates: a) D. B. Dell'Amico, D. Boschi, F. Calderazzo, L. Labella, F. Marchetti, *Inorg. Chim. Acta* **2002**, *330*, 149; b) M. Parra-Hake, M. L. Carter, P. Gantzei, G. Aguirre, F. Ortega, R. Somanathan, P. J. Walsh, *Inorg. Chem.* **2000**, *39*, 5400; c) C. Sudbrake, H. Vahrenkamp, *Inorg. Chim. Acta* **2001**, *318*, 23.

[10] Zinc complexes with bridging carboxylates: a) P. Chaudhuri, C, Stockheim, K. Wieghardt, W. Deck, R. Gregorzik, H. Vahrenkamp, B. Nuber, J. Weiss, *Inorg. Chem.* **1992**, *31*, 1451; b) X.-M. Chen, Y.-X. Tong, T. C. W. Mak, *Inorg. Chem.* **1994**, *33*, 4586; c) M. Yamami, M. Tanaka, H. Sakiyama, T. Koga, K. Kobayashi, H. Miyasaka, M. Ohba, H. Okawa, *J. Chem. Soc. Dalton Trans.* **1997**, 4595; d) B. S. Hammes, C. J. Carrano, *Chem. Commun.* **2000**, 1635.

[11] Examples of bridging triflates on transition/coinage metal chemistry: a) P. L. Dedert, T. Sorrell, T. J. Marks, J. A. Ibers, *Inorg. Chem.* **1982**, *21*, 3506; b) D. D. LeCloux, R. Davydiv, S. J. Lippard, *Inorg. Chem.* **1998**, *37*, 6814; c) T. G. Richmond, E. P. Kelson, A. M. Arif, G. B. Carpenter, *J. Am. Chem. Soc.* **1988**, *110*, 2334; d) S. Canales, O. Crespo, A. Fortea, M. C. Gimeno, P. G. Jones, A. Laguna, *J. Chem. Soc. Dalton Trans.* **2002**, 2250; e) G. Paolucci, J. Zanon, V. Lucchini, W.-E. Damrau, E. Siebel, R. D. Fischer, *Organometallics* **2002**, *21*, 1088.

 © 2004 Wiley-VCH Verlag GmbH & Co. KGaA, Weinheim

[12] For an introduction covering the principles of kinetic resolution for asymmetric synthesis, see: H. B. Kagan, J. C. Fiaud, *Top. Stereochem.* **1988**, *18*, 249.
[13] For general reviews on kinetic resolution by using non-enzymatic catalysts, see: a) D. E. J. E. Robinson, S. D. Bull, *Tetrahedron: Asymmetry* **2003**, *14*, 1407; b) M. Keith, J. F. Larrow, E. N. Jacobsen, *Adv. Synth. Catal.* **2001**, *343*, 5; c) G. R. Cook, *Curr. Org. Chem.* **2000**, *4*, 869; d) A. H. Hoveyda, M. T. Didiuk, *Curr. Org. Chem.* **1998**, *2*, 489.
[14] For a review on nucleophilic chiral amines as catalysts, see: a) S. France, D. J. Guerin, S. J. Miller, T. Lectka, T. *Chem. Rev.* **2003**, *103*, 2985; see also: b) G. C. Fu, *Acc. Chem. Res.* **2000**, *33*, 412, and references therein; c) S. Arai, S. Bellemin-Laponnaz, G. C. Fu, *Angew. Chem.* **2001**, *113*, 240; *Angew. Chem. Int. Ed.* **2001**, *40*, 234; d) S. Bellemin-Laponnaz, J. Tweddell, J. C. Ruble, F. M. Breitling, G. C. Fu, *Chem. Commun.* **2000**, 1009; e) B. Tao, J. C. Ruble, D. A. Hoic, G. C. Fu, *J. Am. Chem. Soc.* **1999**, *121*, 5091; f) E. Vedejs, O. Daugulis, J. A. MacKay, E. Rozners, *Synlett* **2001**, 1499; g) E. Vedejs, J. A. MacKay, *Org. Lett.* **2001**, *3*, 535.
[15] Review on catalyzed transesterifications: J. Otera, *Chem. Rev.* **1993**, *93*, 1449.
[16] It should be noted that non-enzymatic catalysts for asymmetric hydrolysis of esters are known, see: M. C. Cleij, W. Drenth, R. J. M. Nolte, *J. Org. Chem.* **1991**, *56*, 3883.
[17] For recent reviews on the use of enzymes for kinetic resolutions, see: a) B. G. Davis, V. Borer, *Nat. Prod. Rep.* **2001**, *18*, 618; b) H. Groger, *Adv. Synth. Catal.* **2001**, *343*, 547; c) S. M. Roberts, *J. Chem. Soc. Perkin Trans. 1* **2001**, 1475; d) M. T. Reetz, *Angew. Chem.* **2001**, *113*, 292; *Angew. Chem. Int. Ed.* **2001**, *40*, 284; e) G. Carrea, S. Riva, *Angew. Chem.* **2000**, *112*, 2312; *Angew. Chem. Int. Ed.* **2000**, *39*, 2226; f) R. D. Schmid, R. Verger, *Angew. Chem.* **1998**, *110*, 1694; *Angew. Chem. Int. Ed.* **1998**, *37*, 1608.
[18] G. Kirchner, M. P. Scollar, A. M. Klibanov, *J. Am. Chem. Soc.* **1985**, *107*, 7072.
[19] Selectivity factor S = (rate of the fast-reacting enantiomer)/(rate of the slow-reacting enantiomer).
[20] Conversion (%) calculated = *ee* (starting material)/[*ee* (starting material) + *ee* (product)]; see reference [12]. The difference between the conversion (%) calculated by this method and the value measured by ^{1}H NMR was less than 2% in all cases.

Supramolecular Chemistry

Stereoselective Synthesis of a Topologically Chiral Molecule: The Trefoil Knot**

Laure-Emmanuelle Perret-Aebi, Alexander von Zelewsky, Christiane Dietrich-Buchecker, and Jean-Pierre Sauvage*

Topological chirality of a molecule is realized when any representation of its graph is topologically distinct from its mirror image, that is, if it cannot be converted into its mirror image by continuous deformation in 3D space.[1] This property implies that the graph of the molecule is nonplanar. Molecular systems with an *intrinsically* nonplanar graph are scarce. Their graphs can be contracted to Kuratowski's graphs K_5 (the complete graph on five vertices) or $K_{3,3}$ (the complete bipartite graph on two sets of three vertices each).[2–4] Many examples of such systems are known, with the 3-rung Möbius strip prepared more than 20 years ago by Walba et al. being a particularly representative example.[5]

Interlocking rings (catenanes) and knots have *extrinsically* nonplanar graphs. As discussed by Schill,[6] an achiral [2]catenane can be desymmetrized by a suitable substitution of its constitutive rings to give a topologically chiral species. Such catenanes, which contain two oriented rings, have been prepared in the past.[7] It has even been possible to resolve them analytically by chiral chromatography.[8] Contrary to a [2]catenane, a trefoil knot is *unconditionally* chiral; the latter object is topologically chiral without having to orient rings. These prototypical nonplanar systems are represented in Figure 1.

Molecular knots were prepared some time ago using a copper(I)-templated strategy.[9] They were resolved and crystallized and their absolute configuration was thereby determined.[10] More recently, another family of molecular knots has been elaborated by Vögtle and co-workers with their synthesis relying on original sets of hydrogen bonds.[11] The enantiomers of some of these knots and their derivatives were also resolved by chiral chromatography in a collaborative project between Vögtle's and Okamoto's groups.[12] Two other examples of synthetic knots have been described,[13–16] including an "open" knotted species constructed around an octahedral metal center as a template.[14]

[*] L.-E. Perret-Aebi, Prof. Dr. A. von Zelewsky
Departement de Chimie, Université de Fribourg
1700 Fribourg (Switzerland)
Fax: (+41) 26-300-9738
E-mail: alexander.vonzelewsky@unifr.ch
Dr. C. Dietrich-Buchecker, Dr. J.-P. Sauvage
Laboratoire de Chimie Organo-Minérale, UMR 7513
Université Louis Pasteur, Institut Le Bel
4 rue Blaise Pascal, 67070 Strasbourg (France)

[**] We thank the Swiss National Science Foundation and the CNRS (CERC3 project on Toplogical Chirality) for financial support.

Supporting information for this article is available on the WWW under http://www.angewandte.org or from the author.

 © 2004 Wiley-VCH Verlag GmbH & Co. KGaA, Weinheim DOI: 10.1002/anie.200460250

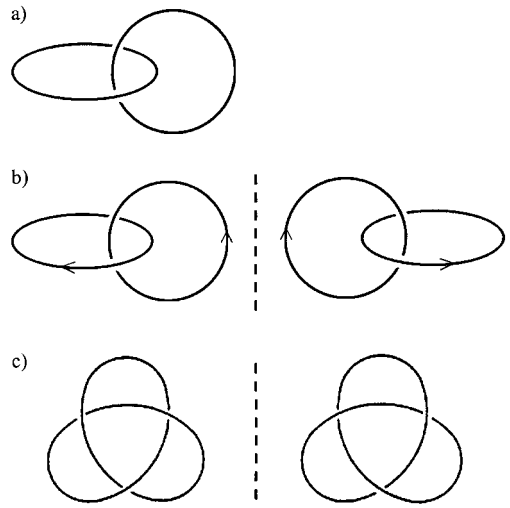


Figure 1. a) A [2]catenane is topologically achiral; b) through orientation of both rings, a chiral object is obtained; c) the trefoil knot is the prototype of topologically chiral objects.

Herein, we report the stereoselective preparation of a topologically chiral compound, a trefoil knot, from two molecular threads that are chiral in the Euclidian sense. The present report is concerned with the conversion of classical (or Euclidian) chirality into topological chirality. The principle of the synthesis is depicted in Figure 2. The trefoil knot is constructed around two copper(I) centers with the chiral ligand 1,3-bis([5′,6′]-pinene-2,2′-bipyridin-2-yl)benzene (**I**),[17] which contains stereogenic carbon centers in the pinene moieties. In principle, two diastereomeric forms are possible upon formation of the trefoil knot. However, our synthesis proceeds completely stereoselectively with only one of the two different topological enantiomers being obtained.

The strategy for the stereoselective preparation of the knot takes advantage of the template effect of copper(I) and of the properties of the bis(pinene-bipyridine) ligand, which induces chirality at the metal centers (Figure 3). The molecular frame for the present trefoil knot is based on the CHIRAGEN family, which is a class of ligands developed by some of us in recent years.[18] The molecule **1**, whose synthesis was reported recently,[17] consists of two 2,2′-bipyridine units connected through a *m*-phenylene bridge. The CH_2 groups in the pinene moieties adjacent to the pyridine rings (indicated by arrows in Figure 3) contain two diastereotopic protons. Alkylation at these position proceeds diastereoselectively to yield the dialkylated ligand **2**.

Ligand **2** forms a double-stranded helix **3** around Cu^I ions in a complexation reaction. As observed by UV/Vis spectroscopy and visually from the formation of a deep red complex, the dinuclear complex **3** is formed rapidly and quantitatively. The ESI mass spectrum shows only one peak at $m/z = 1070.53$. The ^{1}H NMR spectrum indicates a C_2-symmetric arrangement of the ligands (Figure 4a). Furthermore, there is strong deshielding ($\delta = 8.90$–10.19 ppm) of the aromatic proton (a) in the bridge. The presence of only one well-defined peak for this proton indicates a very high percentage (> 95 %) of formation of the double helix **3** (Figure 4).

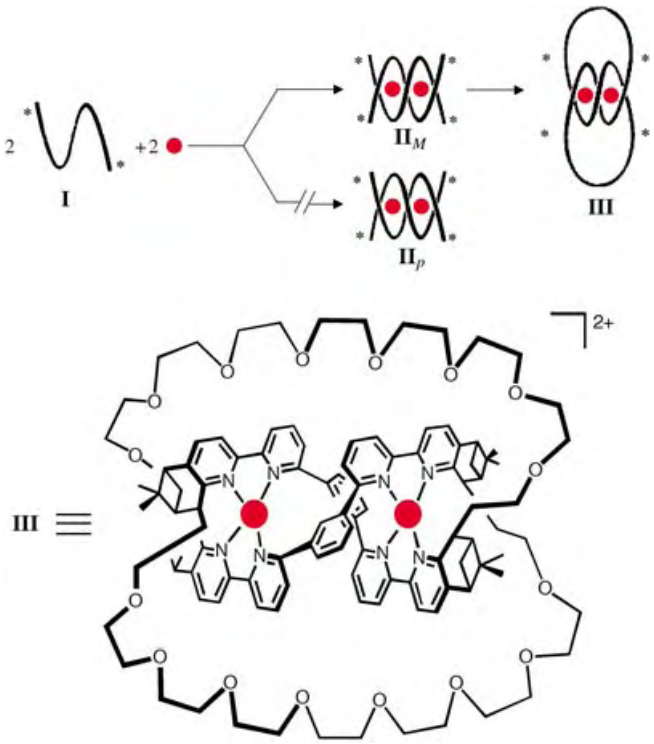


Figure 2. The molecular thread **I** incorporates two bidentate chelating units with each chelate being chiral; the red dot represents the copper(I) atom. In the course of the complexation reaction, only one type of double-stranded helix **II** is formed (with *P* or *M* configuration). The appropriate connections will afford the trefoil knot enantioselectively from **I**. Although **I**, **II**$_M$, and **II**$_P$ are geometrically chiral, they are *topologically achiral*. By contrast, **III** is both geometrically and topologically chiral.

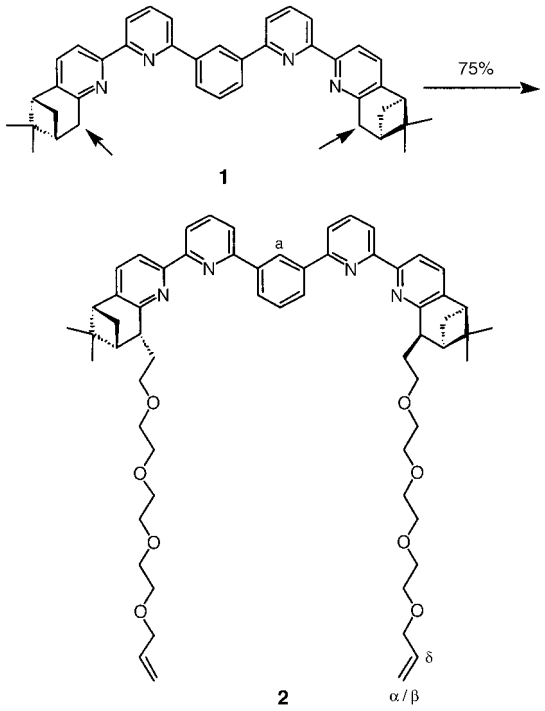


Figure 3. The CHIRAGEN family of ligands used for the construction of the molecular knot (the arrow in **1** indicates the diastereotopic protons).

 © 2004 Wiley-VCH Verlag GmbH & Co. KGaA, Weinheim

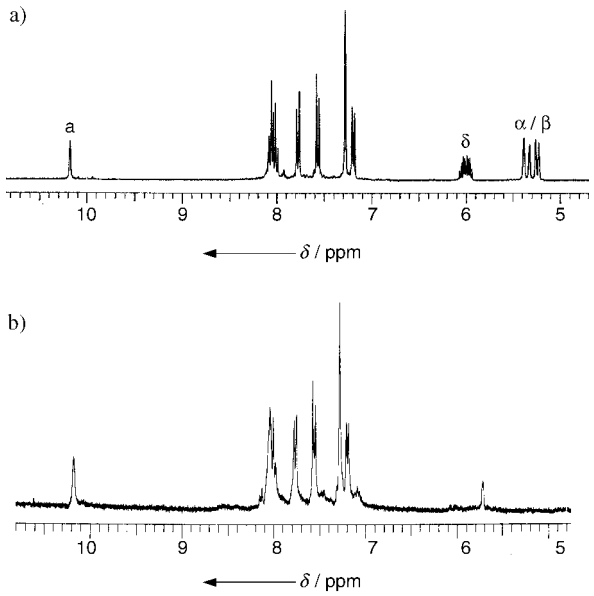


Figure 4. ^{1}H NMR spectra of a) complex **3** and b) the knotted system **4** before hydrogenation. Small impurity signals (intensity ≈ 1%) around $\delta = 10$ ppm are from unidentified side products.

The circular dichroism (CD) spectrum, with a positive exciton-couplet, gives the absolute configuration Λ at the individual copper centers and thus induces an M configuration in the double stranded helix **3**, as expected from Corey–Pauling–Koltun (CPK) molecular models.

A ring-closing metathesis (RCM)[19] reaction is then applied for the formation of the knotted system (Figure 5).

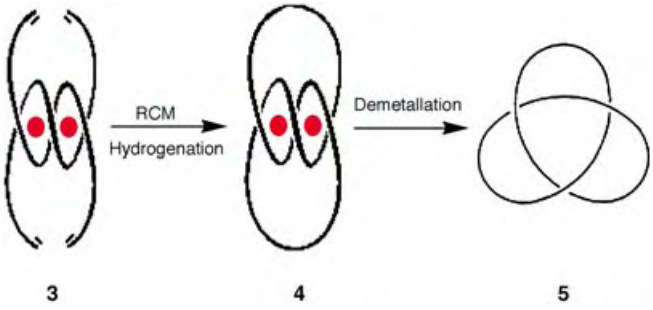


Figure 5. The strategy for the construction of the knot; the knotted system is obtained through a RCM reaction of **3**.

RCM yields three isomers (from E and Z configurations at the double bonds) in 74% total yield. Catalytic hydrogenation (Pd/C (20%), H_2 (3 bar), 16 h) leads to the saturated compound **4** in quantitative yield. The ESI mass spectrum shows one peak at $m/z = 1038.50$. The ^{1}H NMR spectrum again indicates C_2 symmetry and is very similar to that of the open form of the double-helix precursor **3**, except that there are no signals observed for the protons of the double bonds. The CD spectrum of compound **4** is also very similar to that of the open form of the double helix **3** (Figure 6).

Treatment of **4** with a large excess of potassium cyanide in acetonitrile/dichloromethane (1:1) yielded the final product **5** as an almost colorless oil in quantitative yield after 12 h. The

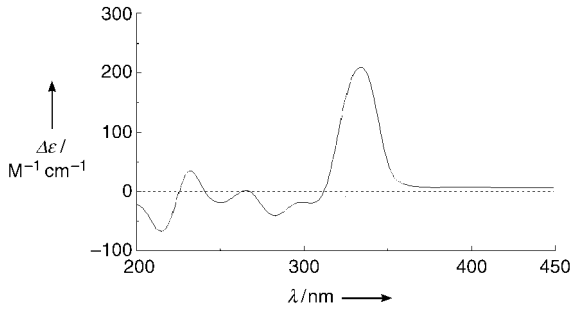


Figure 6. CD spectrum ($\Delta\varepsilon$ = molar circular dichroism) of the left-handed knotted system **4**.

product can be remetallated in a rapid reaction (seconds) to yield a product which is identical to **4**. The ^{1}H NMR spectrum of **5** shows broad signals at room temperature, which we believe is caused by reptation (a snakelike large-scale motion of entangled molecular chains) within the molecule, as observed previously for another molecular trefoil knot.[16] The ESI mass spectrum displays a peak for the molecular ion at $m/z = 1964.22$ as well as a number of fragmentation products. As opposed to the dialkylated ligand **2**, molecule **5** shows a pronounced signal in its CD spectrum in the range 280–340 nm. This arises from a relatively compact arrangement of the bipyridine units which leads to through-space coupling of the π–π* transitions, as with the metallated species.

Unfortunately, we were not able to obtain crystals of either **3** or **4** that were suitable for X-ray crystallographic studies. Nevertheless, the crystal structure of a double helix prepared from **1** and two silver(I) ions[20] was recently obtained. The experimental evidence for the successful synthesis of the trefoil knot **5** and its precursor Cu^I complex **4** is very strong. The mass and chiroptical behavior of **3** and **4** indicate very clearly the presence of the two compounds.

In conclusion, we have demonstrated the stereoselective synthesis of a topologically chiral molecule. The reaction sequence is based on the completely stereoselective formation of a double-stranded helical precursor from two open-chain chelates, which incorporate the appropriate chiral groups.[20] The transformation of the M helix **3** to the left-handed knot **5** corresponds to the conversion of Euclidian chirality into topological chirality.

Received: April 7, 2004 [Z460250]

Keywords: chirality · copper · helical structures · N ligands · template synthesis

[1] D. M. Walba, *Tetrahedron* **1985**, *41*, 3161–3212.
[2] J. C. Chambron, C. Dietriech-Buchecker, J.-P. Sauvage, *Top. Curr. Chem.* **1993**, *165*, 132–162, and references therein.
[3] L. A. Paquette, M. Vazeux, *Tetrahedron Lett.* **1981**, *22*, 291–294; H. E. Simmons III, J. E. Maggio, *Tetrahedron Lett.* **1981**, *22*, 287–290; D. Kuck, A. Schuster, *Angew. Chem.* **1988**, *100*, 1222–1224; *Angew. Chem. Int. Ed. Engl.* **1988**, *27*, 1192–1194.

 © 2004 Wiley-VCH Verlag GmbH & Co. KGaA, Weinheim

[4] C.-T. Chen, P. Gantzel, J. S. Siegel, K. K. Baldridge, R. B. English, D. M. Ho, *Angew. Chem.* **1995**, *107*, 2870 – 2873; *Angew. Chem. Int. Ed. Engl.* **1995**, *34*, 2657 – 2660.
[5] D. M. Walba, R. M. Richards, R. C. Haltiwanger, *J. Am. Chem. Soc.* **1982**, *104*, 3219 – 3221.
[6] G. Schill, *Catenane, Rotaxanes and Knots*, Academic Press, New York, **1971**.
[7] D. K. Mitchell, J.-P. Sauvage, *Angew. Chem.* **1988**, *100*, 985 – 987; *Angew. Chem. Int. Ed. Engl.* **1988**, *27*, 930 – 931; J. C. Chambron, D. K. Mitchell, J.-P. Sauvage, *J. Am. Chem. Soc.* **1992**, *114*, 4625 – 4631.
[8] U. Kaida, Y. Okamoto, J.-C. Chambron, D. K. Mitchell, *Tetrahedron Lett.* **1993**, *34*, 1019 – 1022; C. Yamamoto, J. Okamoto, T. Schmidt, R. Jäger, F. Vögtle, *J. Am. Chem. Soc.* **1997**, *119*, 10546 – 10547.
[9] C. O. Dietrich-Buchecker, J.-P. Sauvage, *Angew. Chem.* **1989**, *101*, 192 – 194; *Angew. Chem. Int. Ed. Engl.* **1989**, *28*, 189 – 192; "Molecular Knots—From Early Attempts to High-Yield Template Syntheses": J.-P. Sauvage, C. Dietrich-Buchecker, G. Rapenne in *Molecular Catenanes, Rotaxanes and Knots* (Eds.: J.-P. Sauvage, C. Dietrich-Buchecker), Wiley-VCH, Weinheim, **1999**, chap. 6, pp. 107 – 139.
[10] L. Hammarström, F. Barigelletti, L. Flamigni, N. Armaroli, A. Sour, J.-P. Collin, J.-P. Sauvage, *J. Am. Chem. Soc.* **1996**, *118*, 11972 – 11973; C. Dietrich-Buchecker, G. Rapenne, J.-P. Sauvage, A. De Cian, J. Fischer, *Chem. Eur. J.* **1999**, *5*, 1432 – 1439.
[11] O. Safarowsky, M. Nieger, R. Fröhlich, F. Vögtle, *Angew. Chem.* **2000**, *112*, 1699 – 1701; *Angew. Chem. Int. Ed.* **2000**, *39*, 1616 – 1618.
[12] F. Vögtle, A. Hünten, E. Vogel, S. Buschbeck, O. Safarowsky, J. Recker, A.-H. Parham, M. Knott, W. M. Müller, U. Müller, Y. Okamoto, T. Kubota, W. Lindner, E. Francotte, S. Grimme, *Angew. Chem.* **2001**, *113*, 2534 – 2537; *Angew. Chem. Int. Ed.* **2001**, *40*, 2468 – 2471; J. Recker, W. M. Müller, U. Müller, T. Kubota, Y. Okamoto, M. Nieger, F. Vögtle, *Chem. Eur. J.* **2002**, *8*, 4434 – 4442.
[13] P. R. Asthon, O. A. Matthews, S. Menzer, F. M. Raymo, N. Spencer, J. F. Stoddart, D. J. Williams, *Liebigs Ann.* **1997**, 2485 – 2494.
[14] C. A. Hunter, P. C. Mayers, *Nature* **2001**, *411*, 763 – 764.
[15] C. Dietrich-Buchecker, J.-P. Sauvage, *Angew. Chem.* **1989**, *101*, 192 – 194; *Angew. Chem. Int. Ed. Engl.* **1989**, *28*, 189 – 201.
[16] O. Lukin, W. M. Müller, U. Müller, A. Kaufmann, C. Schmidt, J. Leszczynski, F. Vögtle, *Chem. Eur. J.* **2003**, *9*, 3507 – 3517.
[17] L.-E. Perret-Aebi, A. von Zelewsky, *Synlett* **2002**, *5*, 773 – 774.
[18] P. Hayoz, A. von Zelewsky, *Tetrahedron Lett.* **1992**, *33*, 5165 – 5168.
[19] G. C. Fu, R. H. Grubbs, *J. Am. Chem. Soc.* **1992**, *114*, 5426 – 5427.
[20] L.-E. Perret-Aebi, A. von Zelewsky, C. Dietrich-Buchecker, J.-P. Sauvage, A. Niels, H. Stoeckli-Evans, unpublished results.

 © 2004 Wiley-VCH Verlag GmbH & Co. KGaA, Weinheim

Quantum Chemistry

Ab Initio NMR Spectra for Molecular Systems with a Thousand and More Atoms: A Linear-Scaling Method**

Christian Ochsenfeld, Jörg Kussmann, and Felix Koziol*

The importance of NMR spectroscopy for modern chemistry and biochemistry cannot be overestimated. Starting with the classical NMR experiments in 1946 by Purcell and Bloch, [1] contributions by numerous scientists have propelled NMR spectroscopy to be an extremely powerful tool in the investigation of structure and dynamics of molecular systems both in solution and in the solid state (e.g., reference [2]). Despite this progress, the understanding and reliable assignment of observed experimental spectra often remains a highly difficult task. Thus, theoretical methods can be extremely useful, which is the focus of this work.

The most reliable way to predict NMR spectra for a specific molecular system is to calculate the NMR chemical shieldings by using quantum-chemical methods. For this purpose an entire hierarchy of methods (and basis sets) exists, which allows the exact result to be systematically approached. The only drawback is, however, the dramatic growth of the computational effort in approaching the exact solution and in increasing the number of atoms in a molecular system. Nevertheless, the hierarchy of ab initio methods allows approximate solutions to be selected and validated, so that error bars can be estimated and the simplest, reliable approximation for studying a specific class of molecular systems can be found.

In recent years there has been much progress with respect to the size of molecular systems that can nowadays be treated by using Hartree–Fock (HF) and density-functional methods, due to a reduction of the scaling of the computational effort to linear. Progress has been made mostly for the calculation of energetics (e.g., see references [3–8]), the optimization of structures by using analytic gradients (e.g., references [9,10]), and for the calculation of molecular properties (e.g., references [6,11]). However, the linear-scaling computation of

[*] Prof. Dr. C. Ochsenfeld, J. Kussmann, Dr. F. Koziol
Institut für Physikalische und Theoretische Chemie
Abteilung für Theoretische Chemie
Universität Tübingen
Auf der Morgenstelle 8, 72076 Tübingen (Germany)
Fax: (+49) 7071-29-5490
E-mail: christian.ochsenfeld@uni-tuebingen.de

[**] We thank Prof. Dr. Reinhart Ahlrichs (Universität Karlsruhe, Germany) for the possibility of using the program TURBOMOLE for the initial comparison of NMR data obtained with our new NMR program. The authors also thank Prof. Dr. Frank-Gerrit Klärner (Universität Essen, Germany) for providing the experimental NMR spectrum of nicotinamide within a molecular clip displayed in the title figure. C.O. further acknowledges financial support by an Emmy Noether research grant of the DFG ("Deutsche Forschungsgemeinschaft"). In addition, the authors thank Sun Microsystems for their financial contribution towards the cost of color reproductions of the cover page and within this work.

 DOI: 10.1002/anie.200460336 © 2004 Wiley-VCH Verlag GmbH & Co. KGaA, Weinheim

NMR chemical shieldings has not been possible so far, so that a particularly important link between experiment and theory for large molecular systems has been missing.

The cost for the calculation of NMR chemical shifts within even the simplest ab initio approximation, the Hartree–Fock (HF) approach, increases conventionally with the third power of the molecular size M ($\mathcal{O}(M^3)$, where $\mathcal{O}()$ stands for the scaling order). Therefore, the computation of NMR chemical shieldings has so far been limited to molecular systems in the order of 100 atoms without molecular symmetry. For larger systems it is crucial to reduce the increase of the computational effort, which is the central goal of this work. We have reduced the scaling of the computational effort to linear so that the computation of NMR shieldings of molecular systems with 1000 atoms becomes possible, while the accuracy and reliability of traditional methods is preserved. In addition, due to the linear-scaling computational cost, any increase of computer speed will now lead to the same increase in the treatable molecular size.

The routine calculation of NMR chemical shifts[12–14] by using quantum-chemical methods has become possible since the introduction of local gauge-origin methods,[15–19] which provide a solution to the gauge-origin problem within approximated schemes. In our formulation we use gauge-including atomic orbitals (GIAO),[17–19] which have proven to be particularly successful.[12] We constrain ourselves to the HF method (GIAO-HF),[18–20] which provides reasonably good results for many molecular systems. For example, in many systems the GIAO-HF method yields ^{1}H NMR chemical shifts with an accuracy of typically 0.2–0.4 ppm.[21–24]

In the first part of our report, we outline briefly our new method for the linear-scaling calculation of NMR shieldings. In the second part, two first examples for applications of our new method are presented, in which we study two systems that are important in the area of molecular recognition and that contain 490 and 1003 atoms (no point-group symmetry). The first example illustrates the new possibilities in assigning solid-state NMR spectra by converging computed shieldings with the solid-state fragment size. The second example shows that our new method allows for the first time the study of solvent effects in an explicit and systematic manner.

NMR chemical shifts are calculated as second derivatives of the energy with respect to the external magnetic field $\boldsymbol{B}$ and the nuclear magnetic spin m_{N_j} of a nucleus N [Eq (1)]:

$$\sigma_{ij}^{N} = \frac{\partial^2 E}{\partial B_i \, \partial m_{N_j}}, \tag{1}$$

in which i, j are x, y, z coordinates. Within HF this leads to [Eq (2)]:

$$\sigma_{ij}^{N} = \sum_{\mu\nu} P_{\mu\nu} \frac{\partial^2 h_{\mu\nu}}{\partial B_i \, \partial m_{N_j}} + \sum_{\mu\nu} \frac{\partial P_{\mu\nu}}{\partial B_i} \frac{\partial h_{\mu\nu}}{\partial m_{N_j}}, \tag{2}$$

in which $P_{\mu\nu}$ represents the one-particle density matrix (with basis functions μ, ν) and $h_{\mu\nu}$ the one-electron matrix. For the calculation of NMR shieldings the perturbed one-particle density matrices $\frac{\partial P_{\mu\nu}}{\partial B_i}$ (short: $\mathbf{P}^{B_i}$) are required, which are obtained by solving the coupled perturbed HF (CPHF) equations. To solve these equations entirely in the molecular-orbital (MO) basis—also necessary for the calculation of vibrational frequencies for example—requires a transformation of the AO two-electron integrals, which leads to an effort scaling with $\mathcal{O}(M^5)$. In the context of NMR shieldings the effort is conventionally reduced to $\mathcal{O}(M^3)$.[19,20] This overall scaling of $\mathcal{O}(M^3)$ for the calculation of NMR chemical shifts hampers the investigation of large molecular systems. To reduce the overall scaling to linear, two key issues need to be tackled: first, the CPHF equations have to be solved with linear-scaling effort and, second, all integral contractions need to be done linearly.

To reduce the scaling of the CPHF equations, we avoid transformations that involve the nonlocal MO coefficient matrix $\mathbf{C}$ entirely and in contrast solve directly for the required (local) derivative density $\mathbf{P}^{B_i}$. We start from our reformulation of CPSCF (CP self-consistent field) theory for the computation of vibrational frequencies within a density matrix-based scheme.[6] The constraints of the idempotency and the number of electrons are preserved through first order by the use of the purification transformation of McWeeny.[25] In the present work, we introduce a new density-based coupled-perturbed method, which allows the density derivatives to be solved directly with respect to the magnetic field. In contrast to our formulation for vibrational frequencies, we exploit the projection properties of $\mathbf{P}$ to solve directly for the required occupied-virtual part of the perturbed density matrix $\mathbf{P}^{B_i}$ [Eq (3)]:

$$\begin{aligned}&\mathbf{FP}^{B_i}\mathbf{SPS} + \mathbf{SPSP}^{B_i}\mathbf{F} - \mathbf{FPSP}^{B_i}\mathbf{S} - \mathbf{SP}^{B_i}\mathbf{SPF} + \mathbf{G}[\mathbf{P}^{B_i}]\mathbf{PS}\\ &+\mathbf{SPG}[\mathbf{P}^{B_i}] - 2\mathbf{SPG}[\mathbf{P}^{B_i}]\mathbf{PS} = \mathbf{FPS}^{B_i} + \mathbf{S}^{B_i}\mathbf{PF}\\ &-\mathbf{FPS}^{B_i}\mathbf{PS} - \mathbf{SPS}^{B_i}\mathbf{PF} - \mathbf{YPS} - \mathbf{SPY} + 2\mathbf{SPYPS},\end{aligned} \tag{3}$$

with:

$$Y_{\mu\nu} = \frac{\partial h_{\mu\nu}}{\partial B_i} + \sum_{\lambda\sigma} P_{\lambda\sigma} \frac{\partial[(\mu\nu|\lambda\sigma) - \frac{1}{2}(\mu\lambda|\nu\sigma)]}{\partial B_i},$$

$$G_{\mu\nu}[P_{\lambda\sigma}^{B_i}] = -\frac{1}{2} \sum_{\lambda\sigma} \frac{\partial P_{\lambda\sigma}}{\partial B_i} (\mu\lambda|\nu\sigma).$$

Mulliken notation is used for two-electron integrals. Our new formulation of the density matrix-based D-CPSCF equations preserves their excellent convergence properties, while offering important advantages for sparse-matrix multiplications. Convergence can be typically achieved within four to six builds of $\mathbf{G}[\mathbf{P}^{B_i}]$, which is similar to the convergence behavior of MO-based theories. The main advantage is of course the reduced scaling of the computational effort of $\mathcal{O}(M)$, since for systems with a nonvanishing HOMO–LUMO gap all matrices scale linearly. For an overall linear-scaling behavior as well all Fock-type matrices ($\mathbf{G}[\mathbf{P}^{B_i}]$ or $\mathbf{Y}$) need to be calculated with linear-scaling effort. This can be done by using extensions of our LinK (linear exchange K) method[8,9] introduced for the formation of exchange contributions to energies and gradients. Since $\mathbf{P}^{B_i}$ is skew-symmetric, the Coulomb part vanishes for $\mathbf{G}$. For the Coulomb-type matrices in $\mathbf{Y}$ we adapt the CFMM (continuous fast multipole method) formulation of White and Head-Gordon.[3] We implemented

 © 2004 Wiley-VCH Verlag GmbH & Co. KGaA, Weinheim

our new method into a development version of the program Q-Chem,[26] in which so far no NMR code existed.

Efficiencies of our new linear-scaling GIAO-HF and the standard method are compared for linear alkanes (6-31G* basis) in Figure 1 for the same accuracies: integral and sparse

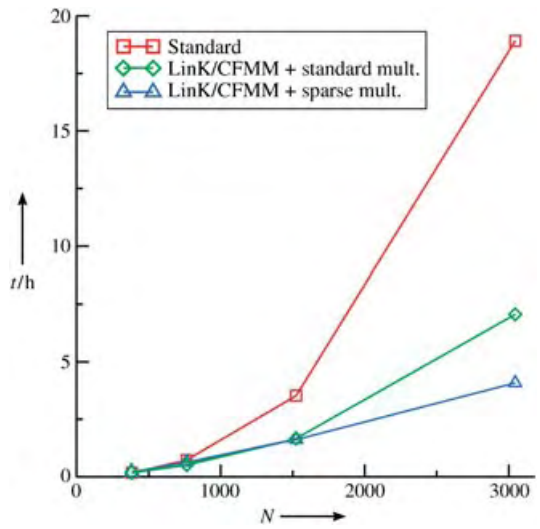


Figure 1. Linear-scaling behavior of the density-matrix based GIAO-HF method with LinK/CFMM and sparse multiplications in comparison to the conventional $\mathcal{O}(M^3)$ scaling by using linear alkanes C_nH_{2n+2} ($n = 20$, 40, 80, 160) within a 6-31G* basis (Itanium II 900 MHz, one processor). In addition, the D-GIAO-HF method with LinK/CFMM but with standard multiplications is plotted. N is the number of basis functions, t is the CPU time required to process the data.

multiplication thresholds are always 10^{-6}. This is sufficient to obtain ^{1}H NMR chemical shifts with accuracies of better than 0.1 ppm within HF/6-31G*. The accuracy can be rigorously controlled by numerical thresholds. Timings were calculated on one processor of an Itanium II 900 MHz; timings for a P4 2.8 GHz computer are listed in parentheses. It has to be stressed that in our present implementation the sparse-matrix multiplications are unusually slow on the Itanium II processor as compared to the P4. For $C_{80}H_{162}$ the overall gain of our preliminary implementation is a factor of 2.2 (2.5) for the total timing and 2.2–4.2 (2.9–4.0) for integral contractions within the D-CPHF scheme. For $C_{160}H_{322}$ the total win is a factor of 4.6; the wins for integral contractions are 3.9–9.1 for the Itanium II. In our preliminary implementation the $\mathcal{O}(M^3)$ matrix multiplications start to become dominant as compared to the integral contractions for alkanes with roughly 2100 (2850) basis functions. The crossover for sparse versus conventional matrix multiplications is in the region of 1400 basis functions for the Itanium II, whereas for the P4 computer the crossover occurs around 1150 basis functions. In addition, our new D-CPSCF scheme allows the reduction of the memory requirements to linear.

As another example, we selected a DNA fragment to investigate the performance of our new method. Here, we obtain for a DNA fragment with four base pairs (GIAO-HF/6-31G*; 280 atoms, 2862 basis functions) a performance win of 1.7–3.6 for integral contractions within our D-CPSCF scheme. In our present implementation we solve the D-CPSCF equations with a minimum number of integral contractions at the expense of more matrix multiplies, which have the smaller prefactor. Nevertheless, sparse matrix multiplies show a later onset of their linear-scaling behavior as compared to integral contractions, so that a good balance becomes important, which we are currently optimizing.

The linear-scaling behavior of our new density matrix-based GIAO-HF method allows for the first time the calculation of molecular systems with 1000 and more atoms without point-group symmetry on one-processor workstations or PCs. We present the first examples of an application below.

Solid-state NMR spectroscopy has evolved into a powerful tool in yielding important statical and dynamical information on molecules.[2] Recently, we demonstrated that some of the difficulties in assigning experimental solid-state NMR spectra can be overcome by using quantum-chemical methods, in which we studied examples of differently substituted hexabenzocoronenes[21,22] and host–guest systems.[23,24] In this way complementary information to X-ray spectroscopy can be obtained, which is particularly important for noncrystalline phases or positions of protons in hydrogen-bonded species. For the simulation of the spectra it is crucial to converge the NMR shieldings with respect to the size of the solid-state fragment to account for influences of neighboring molecules. However, so far both the size of the treatable system and that of the fragment was limited by the strong increase of the computational effort. Therefore one was constrained to relatively small systems and fragments, and it was not possible to avoid small basis sets and incremental approximations.[21,24] In contrast, with our new method we are now able to compute large systems and large fragments of the solid state, so that the size of treatable systems is presently at least increased by an order of magnitude.

As an example, we consider a host–guest complex with a tweezer-shaped host, binding a tetracyano-*p*-quinodimethane (TCNQ) guest used as model system for molecular recognition[27] (Figure 2). We studied similar systems earlier,[23,24] but were strongly limited with respect to the computation of NMR shieldings: for the largest computed system containing three complexes with a total of 276 atoms (guest: dicyanobenzene), we had to use a very small basis (3-21G)[24] at the GIAO-HF level. Since this basis set is too small to provide reliable ^{1}H NMR predictions, an incremental approach was employed.[24] With our new linear-scaling NMR method these problems are solved. For the TCNQ host–guest complex it is now for the first time possible to include the nearest neighbors within a reasonable basis for ^{1}H NMR shifts of the present system (GIAO-HF/6-31G*). The structure is shown in Figure 2 and consists of a total of five complexes (denoted as pentamer; 490 atoms; structure obtained by projecting the HF/6-31G* optimized monomer onto the X-ray solid-state ordering[24]). The calculations show that the accuracy of the ^{1}H NMR chemical shifts for the central complex within the full pentamer calculation (GIAO-HF/6-31G*) is improved by 0.8 ppm as compared to an estimate of these shieldings for the central complex from GIAO-HF/3-21G trimer values, which was the largest system treatable before our new method. The latter estimate has been

 © 2004 Wiley-VCH Verlag GmbH & Co. KGaA, Weinheim

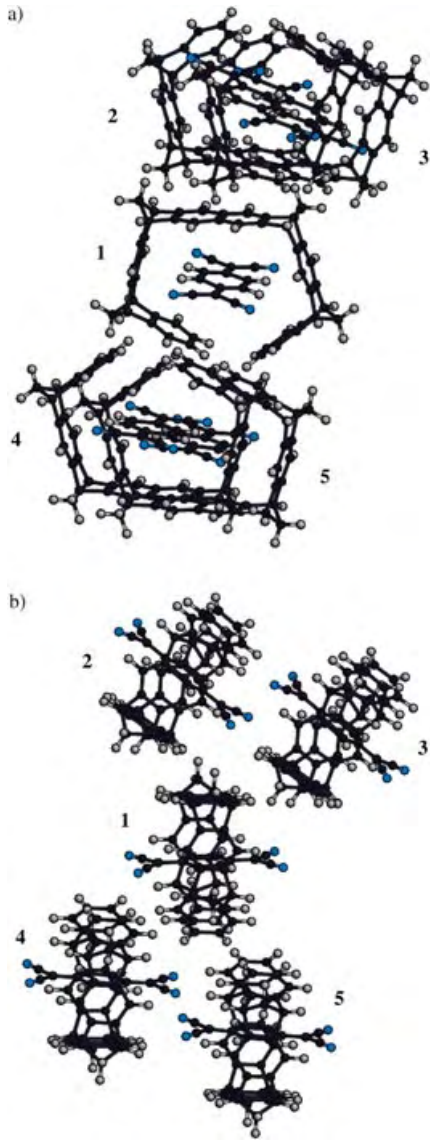


Figure 2. Solid-state fragment of the molecular tweezer host-guest complex (TCNQ guest) with five neighbors (490 atoms): a) front and b) side-on view. C atoms are marked in dark grey, H atoms in light grey, N atoms in blue. N atoms occur only in the four cyano groups of the guest.

obtained by two trimer calculations, in which the influence of units **2**, **3** (Figure 2) and **4**, **5** on the central unit **1** have been added. This error with respect to the full calculation is slightly reduced to 0.7 ppm (the mean error from 0.5 to 0.2 ppm), if the trimer influences (GIAO-HF/3–21G) are added to the GIAO-HF/6-31G* monomer data in an incremental fashion. The calculation for the pentamer avoids the deficiencies of incremental approximations, which illustrates some of the new possibilities with our new linear-scaling method for predicting solid-state NMR spectra.

The second example is focused on an artificial receptor for NAD^+ (NAD is nicotinamide adenine dinucleotide) in water recently presented by the groups of Klärner and Schrader.[28] The form of the host is that of a molecular clip inside which NAD^+ is bound. However, the structure of the host–guest complex remained unclear based on experimental information only. Therefore a comparison of computed and measured NMR chemical shifts is helpful and allows some of the possible binding motifs to be discarded.[29] A complication arises as the NMR measurements have been performed in water. Here, our new method allows for the first time to estimate explicitly the influence of the solvent at the ab initio level, as we are able to treat both the host–guest complex (containing 88 atoms) and neighboring water molecules at the GIAO-HF level: the largest system computed contains 1003 atoms. In this work, our aim is only a proof of principle that we are now able to deal with such large systems and that we can converge the results with respect to the number of surrounding water molecules.

As a first step we performed a classical molecular dynamics simulation of *N*-methyl nicotinamide in a molecular clip[29] within a water surrounding (300 K; MMFF94; 1 ps equilibration; total 20 ps, 1.0 fs time-steps; 2575 water molecules in dielectricum). A snapshot of the MD simulation was selected, for which the water molecules were closest to the center of the guest ring within a radius of 800 pm. Around the host-guest system (88 atoms) different shells of surrounding water molecules were defined (total size: 169, 547, and 1003 atoms). These systems were used to calculate the NMR chemical shifts (GIAO-HF/6-31G**), with the largest system containing 1003 atoms and 8593 basis functions shown in Figure 3. The maximum change with respect to ^{1}H NMR shieldings (protons at the phosphonate groups are not considered in the following) from the isolated host–guest to the 169 atoms system is 1.3 ppm, from 169 to 547 atoms 1.1 ppm, and from 547 to 1003 atoms 0.2 ppm. This result indicates that in the system that contains 1003 atoms, the proton chemical shifts of the host–guest complex are converged to 0.2 ppm. Overall, the maximum influence of the water molecules in the 1003 atom system on host–guest protons is 1.3 ppm and 0.7 ppm if only the aromatic guest protons are considered.

It is clear that for a reliable description of solvent effects not only more extensive MD simulations are necessary but also the NMR shieldings for a multitude of snapshots need to be calculated. Our example application shows that we are now for the first time able to converge the NMR shieldings with respect to the number of surrounding water molecules explicitly, so that the minimum number of water molecules required for an adequate description can be obtained. In addition, the maximum influence of 0.7 ppm calculated for the water-surrounded complex with 1003 atoms presented above is a first hint that complex-induced changes of 6 ppm for guest-proton shieldings calculated in the vacuum for some binding motifs of NAD^+ within a clip,[29] could also be significant in water.

Our new linear-scaling GIAO-HF method allows for the first time the ab initio calculation of NMR chemical shifts for molecular systems with 1000 and more atoms. The accuracy and reliability of conventional methods is fully preserved. Since it is difficult to obtain highly accurate energetics or structural parameters for such large systems due to the large number of energetically close configurations, our new linear-scaling method for the computation of NMR chemical shifts

 © 2004 Wiley-VCH Verlag GmbH & Co. KGaA, Weinheim

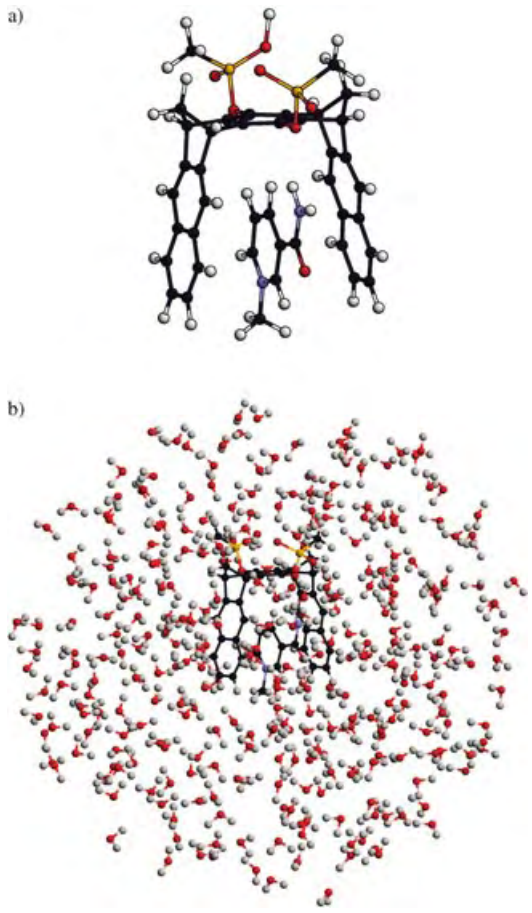


Figure 3. a) Snapshot of *N*-methyl nicotinamide within a molecular clip and b) the same guest-clip system, including the surrounding water molecules comprising 1003 atoms, used to estimate solvent effects on the NMR chemical shifts (GIAO-HF/6-31G*). C atoms are marked in dark grey, H atoms light grey, N atoms blue, O atoms red, and P atoms orange.

opens up the way to a molecular property that allows for a direct interplay with experimental studies as well for large molecular systems. Besides our first two example applications that investigate the convergence of solid-state NMR shieldings and explicit solvent effects, a multitude of new possibilities arise for the study of large molecular systems such as proteins, enzymes, or active centers.

Received: April 15, 2004
Revised: June 1, 2004 [Z460336]

Keywords: ab initio calculations · molecular recognition · NMR spectroscopy · quantum chemistry

[1] a) E. M. Purcell, H. G. Torrey, R. V. Pound, *Phys. Rev.* **1946**, *69*, 37; b) F. Bloch, W. Hansen, M. E. Packard, *Phys. Rev.* **1946**, *69*, 127.
[2] a) K. Wüthrich, *Angew. Chem.* **2003**, *115*, 3462; *Angew. Chem. Int. Ed.* **2003**, *42*, 3340; b) S. P. Brown, H. W. Spiess, *Chem. Rev.* **2001**, *101*, 4125.
[3] C. A. White, M. Head-Gordon, *Chem. Phys. Lett.* **1994**, *230*, 8.
[4] M. Challacombe, E. Schwegler, J. Almlöf, *J. Chem. Phys.* **1996**, *104*, 4685.
[5] M. C. Strain, G. E. Scuseria, M. J. Frisch, *Science* **1996**, *271*, 51.
[6] C. Ochsenfeld, M. Head-Gordon, *Chem. Phys. Lett.* **1997**, *270*, 399.
[7] G. E. Scuseria, *J. Phys. Chem. A* **1999**, *103*, 4782.
[8] C. Ochsenfeld, C. A. White, M. Head-Gordon, *J. Chem. Phys.* **1998**, *109*, 1663.
[9] C. Ochsenfeld, *Chem. Phys. Lett.* **2000**, *327*, 216.
[10] Y. H. Shao, C. A. White, M. Head-Gordon, *J. Chem. Phys.* **2001**, *114*, 6572.
[11] H. Larsen, T. Helgaker, J. Olsen, P. Jorgensen, *J. Chem. Phys.* **2001**, *115*, 10344.
[12] J. Gauss, *Ber. Bunsen-Ges. Phys. Chem.* **1995**, *99*, 1001.
[13] T. Helgaker, M. Jaszunski, K. Ruud, *Chem. Rev.* **1999**, *99*, 293.
[14] "Ab initio NMR Chemical Shift Computation": U. Fleischer, W. Kutzelnigg, C. van Wüllen in *Encyclopedia of Computational Chemistry* (Ed.: P. v. R. Schleyer, N.-L. Allinger, T. Clark, J. Gasteiger, P. A. Kollman, H. F. Schaefer III, P. R. Schreiner), Wiley, Chichester, **1998**, pp. 1827–1835.
[15] W. Kutzelnigg, *Isr. J. Chem.* **1980**, *19*, 193.
[16] A. E. Hansen, T. D. Bouman, *J. Chem. Phys.* **1985**, *82*, 5035.
[17] F. London, *J. Phys. Radium* **1937**, *8*, 397.
[18] R. Ditchfield, *Mol. Phys.* **1974**, *27*, 789.
[19] K. Wolinski, J. F. Hinton, P. Pulay, *J. Am. Chem. Soc.* **1990**, *112*, 8251.
[20] M. Häser, R. Ahlrichs, H. P. Baron, P. Weis, H. Horn, *Theor. Chim. Acta* **1992**, *83*, 455.
[21] C. Ochsenfeld, *Phys. Chem. Chem. Phys.* **2000**, *2*, 2153.
[22] C. Ochsenfeld, S. P. Brown, I. Schnell, J. Gauss, H. W. Spiess, *J. Am. Chem. Soc.* **2001**, *123*, 2597.
[23] S. P. Brown, T. Schaller, U. P. Seelbach, F. Koziol, C. Ochsenfeld, F.-G. Klärner, H. W. Spiess, *Angew. Chem.* **2001**, *113*, 740; *Angew. Chem. Int. Ed.* **2001**, *40*, 717.
[24] C. Ochsenfeld, F. Koziol, S. P. Brown, T. Schaller, U. P. Seelbach, F.-G. Klärner, *Solid State Nucl. Magn. Reson.* **2002**, *22*, 128.
[25] R. McWeeny, *Rev. Mod. Phys.* **1960**, *32*, 335.
[26] J. Kong, C. A. White, A. I. Krylov, C. D. Sherrill, R. D. Adamson, T. R. Furlani, M. S. Lee, A. M. Lee, S. R. Gwaltney, T. R. Adams, H. Daschel, W. Zhang, P. P. Korambath, C. Ochsenfeld, A. T. B. Gilbert, G. S. Keziora, D. R. Maurice, N. Nair, Y. Shao, N. A. Besley, P. E. Maslen, J. P. Dombroski, J. Baker, E. F. C. Byrd, T. v. Voorhis, M. Oumi, S. Hirata, C.-P. Hsu, N. Ishikawa, J. Florian, A. Warshel, B. G. Johnson, P. M. W. Gill, M. Head-Gordon, J. A. Pople, *J. Comput. Chem.* **2000**, *21*, 1532.
[27] F.-G. Klärner, U. Burkert, M. Kamieth, R. Boese, J. Benet-Buchholz, *Chem. Eur. J.* **1999**, *5*, 1700.
[28] C. Jasper, T. Schrader, J. Panitzky, F.-G. Klärner, *Angew. Chem.* **2002**, *114*, 1411; *Angew. Chem. Int. Ed.* **2002**, *41*, 1355.
[29] M. Fokkens, C. Jasper, T. Schrader, F. Koziol, C. Ochsenfeld, J. Polkowska, F.-G. Klärner, submitted.

 © 2004 Wiley-VCH Verlag GmbH & Co. KGaA, Weinheim

Enantioselective Synthesis

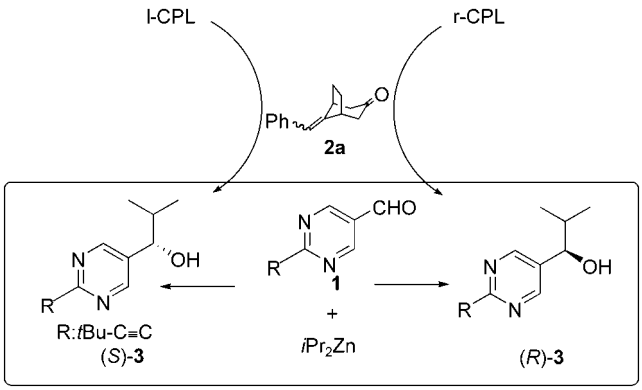
Asymmetric Synthesis Utilizing Circularly Polarized Light Mediated by the Photoequilibrium of Chiral Olefins in Conjunction with Asymmetric Autocatalysis**

*Itaru Sato, Rie Sugie, Yohei Matsueda, Yuri Furumura, and Kenso Soai**

Right- or left-circularly polarized light (r- or l-CPL) has long been proposed as a physical factor in the origin of chirality in organic compounds.[1–4] Asymmetric photolysis,[5] asymmetric photosynthesis,[6] and asymmetric photoequilibrium[7] have been reported to induce only a slight imbalance (< 2% *ee*) in the chirality of organic compounds. The asymmetric photoequilibrium[7] of certain chiral olefins by CPL is of particular importance and has the advantage that the starting material is not consumed in the photoequilibrium. Although the tiny enantioenrichments (< 2% *ee*) of olefins induced by CPL have been correlated with the amplified helicity of polymers[8] and liquid crystals,[7d,9] to the best of our knowledge, chiral olefins[10] with such low *ee* values have never been correlated with a highly enantioenriched compound with a stereogenic center.

We recently reported asymmetric autocatalysis with amplification of enantioselectivity.[11,12] Several chiral molecules with a tiny imbalance of enantiomers work as chiral initiators in the asymmetric autocatalytic system.[11b,c,d,12]

We thought that high enantioselectivity induced by CPL could be realized if combined with asymmetric autocatalysis. Thus, we attempted an asymmetric synthesis by CPL mediated with a chiral olefin (Scheme 1). We employed olefin **2a**[7b] as a switchable chiral mediator for asymmetric autocatalysis. Racemic olefin **2a** was irradiated with r- or l-CPL for 48 hours,[7b] and then diisopropylzinc was treated with 2-alkynyl pyrimidine-5-carbaldehyde (**1**) in the presence of the irradiated olefin **2a** (Scheme 1). A solution of diisopropylzinc in hexane was slowly added to an ice-cooled solution of aldehyde **1** and chiral alkene **2a** in methylcyclohexane. The solution was then diluted with toluene and aldehyde **1** and diisopropylzinc were added portionwise to it. Aqueous workup gave enantiomerically enriched 2-alkynyl-5-pyrimidyl alkanol **3**. As shown in Table 1, the olefin **2a** irradiated with l-CPL gave (*S*)-5-pyrimidyl alkanol **3** in 90–97% *ee* (entries 1, 3, and 5). In contrast, irradiation with r-CPL induced the production of (*R*)-5-pyrimidyl alkanol **3** in 90–93% *ee* (entries 2, 4, and 6). Thus, the reproducibility of the correlation between the direction of CPL and the absolute configuration of pyrimidyl alkanol **3** has been confirmed. It should be noted that the *ee* value of alkanol **3** can be readily increased to > 99.5% *ee* by further asymmetric autocatalysis.[11e]



Scheme 1. Asymmetric synthesis by CPL mediated with a chiral olefin.

Table 1: Highly enantioselective synthesis of 5-pyrimidyl alkanol **3** mediated by chiral alkene **2a** irradiated with CPL.[a]

Entry	Chiral source	5-Pyrimidyl alkanol **3**	
		yield [%]	*ee* [%] (config.)
1	l-CPL	96	97 (*S*)
2	r-CPL	96	93 (*R*)
3	l-CPL	92	91 (*S*)
4	r-CPL	91	90 (*R*)
5[b]	l-CPL	93	90 (*S*)
6[b]	r-CPL	97	90 (*R*)

[a] Unless otherwise noted, aldehyde **1** (1.3 mmol) and diisopropylzinc (2.7 mmol) were added in four portions. Molar ratio of alkene **2a**/pyrimidine-5-carbaldehyde **1**/diisopropylzinc = 0.018/1.0/2.0. [b] Racemic **2a** was prepared independently and used as a mediator. Molar ratio of alkene **2a**/pyrimidine-5-carbaldehyde **1**/diisopropylzinc = 0.046/1.0/2.1.

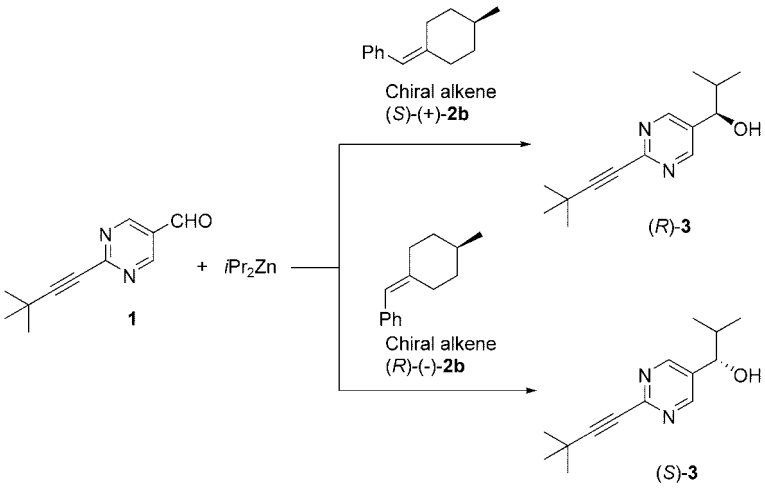
The chiral olefins **2b–e** were also found to act as chiral initiators. Enantioselective addition of diisopropylzinc to pyrimidine-5-carbaldehyde **1** in the presence of chiral [(4-methylcyclohexylidene)methyl]benzene (**2b**) was examined (Scheme 2). The results are summarized in Table 1. When (*S*)-(+)-**2b** was used as a chiral initiator, (*R*)-5-pyrimidyl alkanol **3** was isolated in a yield of 97% and 96% *ee* (entry 1). However, when the opposite enantiomer of the chiral olefin (*R*)-(−)-**2b** was used as a chiral initiator, (*S*)-5-pyrimidyl alkanol **3** was isolated in a yield of 93% and 95% *ee* (entry 2). Thus, the absolute configurations of the produced 5-pyrimidyl alkanols **3** depend on that of the chiral olefin used. The use of chiral olefin **2b** with a moderate enantioenrichment as an inducer gave alkanol **3** with high *ee* values (entries 3 and 4). The 5-pyrimidyl alkanols **3** were obtained in the reaction in 93% and 95% *ee* using chiral olefin **2b** with 60% and 86% *ee*, respectively. Similarly, (+)-[(4-phenylcyclohexylidene)methyl]benzene (**2c**) functioned as a chiral initiator to give (*R*)-**3** in 95% *ee* (entry 5) and (−)-**2c** gave (*S*)-**3** in 96% *ee*

[*] Dr. I. Sato, R. Sugie, Y. Matsueda, Y. Furumura, Prof. Dr. K. Soai
Department of Applied Chemistry
Faculty of Science, Tokyo University of Science
Kagurazaka, Shinjuku-ku, Tokyo 162-8601 (Japan)
Fax: (+81) 3-3235-2214
E-mail: soai@rs.kagu.tus.ac.jp

[**] This work was supported by a Grant-in-Aid from The Ministry of Education, Culture, Sports, Science, and Technology and the New Energy and Industrial Technology Development Organization (NEDO).

Supporting information for this article is available on the WWW under http://www.angewandte.org or from the author.

 © 2004 Wiley-VCH Verlag GmbH & Co. KGaA, Weinheim DOI: 10.1002/anie.200454162



Scheme 2. Enantioselective addition of diisopropylzinc (iPr_2Zn) to pyrimidine-5-carbaldehyde compound **1** in the presence of chiral [(4-methylcyclohexylidene)methyl]-benzene (**2b**).

(entry 6). The conjugation of an olefin to the phenyl group is not essential. Thus, the presence of (*S*)-(−)-(4-phenycyclohexylidene)propane (**2d**) with an ethyl substituent at the double bond gave (*R*)-**3** with 96% *ee* and (*R*)-(+)-**2d** gave (*S*)-**3** with 96% *ee* (entries 7 and 8).

The treatment of chiral olefins with a ketone chromophore was also examined. In the presence of chiral olefin (+)-**2e**, (*R*)-pyrimidyl alkanol **3** was obtained with 91–95% *ee* (entries 9 and 11), while in the presence of (−)-**2e**, (*S*)-**3** (entries 10 and 12) was formed with 90–96% *ee*.

In summary, we have demonstrated that chiral olefins, even with low *ee* values, act as effective chiral inducers in asymmetric autocatalysis to yield products with high *ee* values. Moreover, we have realized a highly enantioselective asymmetric synthesis by CPL mediated with chiral olefins in conjunction with asymmetric autocatalysis. We believe that these results will significantly enhance the use of CPL and the asymmetric photoequilibrium of olefins in the study of the origin of homochirality.

Experimental Section

Representative procedure for the enantioselective synthesis of (*S*)-pyrimidyl alkanol **3** mediated with l-CPL induced olefin **2a**: Racemic **2a** (*ee* was below the detection level) was used after high-performance liquid chromatographic analysis on a chiral stationary phase (Chiralcel OD). A solution of **2a** (5.1 mg, 0.024 mmol) in cyclohexane (3 mL) was degassed by flushing argon through it for 10 min. CPL was produced from a 500-W ultra-high-pressure Hg lamp using a parallel light radiation unit (Ushio). The beam passed through a water cell (10 mm), a 313-nm interference filter, polarizing filter, and quarter-wavelength plate. After irradiation of the solution with l-CPL for 48 h, a CD spectrum was measured ($\Delta\varepsilon_{306} = -0.008\ cm^2 mol^{-1}$). The solution was concentrated and the residue was dissolved in methylcyclohexane (0.5 mL). Aldehyde **1** (4.7 mg, 0.025 mmol) was dissolved in this solution and the solution cooled to 0 °C. A 1.0 M solution of diisopropylzinc (0.08 mmol) in hexane was added at 0 °C over a period of 30 min. The mixture was stirred for 20 h at 0 °C. Toluene (1.9 mL), diisopropylzinc (0.2 mmol, 0.2 mL of a 1.0 M toluene solution), and a solution of aldehyde **1** (1.0 mL, 18.8 mg, 0.10 mmol) in toluene were added successively, and the reaction mixture was stirred for 2 h. Toluene (7.5 mL), diisopropylzinc (0.8 mmol, 0.8 mL of a 1.0 M toluene solution), and a solution of aldehyde **1** (2.0 mL, 75.3 mg, 0.40 mmol) in toluene were then added successively, and the mixture was stirred at 0 °C for additional 5 h. After the addition of toluene (15 mL), diisopropylzinc (1.6 mmol, 1.6 mL of a 1.0 M toluene solution), and a toluene solution of aldehyde **1** (4 mL, 151 mg, 0.80 mmol), the mixture was stirred for 2 h. Hydrochloric acid (6 mL, 1 M) and saturated aqueous sodium hydrogen carbonate (13 mL) were added successively to the mixture. The mixture was filtered through celite, and the filtrate was extracted with ethyl acetate. The combined organic layers were dried over anhydrous sodium sulfate, and evaporated under reduced pressure. Purification of the residue by thin-layer chromatography on silica gel (eluant: hexane/ethyl acetate = 2/1, *v*/*v*) gave (*S*)-5-pyrimidyl alkanol **3** in 97% *ee* in a yield of 96% (294 mg).

Representative procedure for the enantioselective addition of diisopropylzinc to pyrimidine-5-carbaldehyde induced by chiral olefins (Table 2, entry 1): A 1.0 M solution of diisopropylzinc

Table 2: Highly enantioselective synthesis of 5-pyrimidyl alkanol **3** using chiral olefins **2**.[a]

Entry	Alkene **2**			5-Pyrimidyl alkanol	
		ee [%][b]	$[\alpha]_D$ (config.)	Yield [%]	*ee* [%][b] (config.)
1	**2b**	99	+ (*S*)[c]	97	96 (*R*)
2	**2b**	98	− (*R*)[c]	93	95 (*S*)
3	**2b**	60	+ (*S*)[c]	93	93 (*R*)
4	**2b**	86	− (*R*)[c]	89	95 (*S*)
5	**2c**	94	+	94	95 (*R*)
6	**2c**	99	−	94	96 (*S*)
7	**2d**	58	− (*S*)[d]	93	96 (*R*)
8	**2d**	56	+ (*R*)[d]	97	96 (*S*)
9	**2e**	95	+	86	91 (*R*)
10	**2e**	87	−	85	90 (*S*)
11	**2e**	41	+	99	95 (*R*)
12	**2e**	30	−	98	96 (*S*)
13[e]	**2a**	98	+	96	98 (*S*)
14[e]	**2a**	96	−	99	98 (*R*)
15[f]	**2a**	5.0	+	95	97 (*S*)
16[f]	**2a**	5.3	−	97	97 (*R*)
17[f]	**2a**	1.3	+	96	95 (*S*)
18[f]	**2a**	1.8	−	85	97 (*R*)

[a] Unless otherwise noted, aldehyde **1** (0.53 mmol) and diisopropylzinc (1.08 mmol) were added in three portions. Molar ratio of alkene **2**/pyrimidine-5-carbaldehyde **1**/diisopropylzinc = 0.048/1.0/2.0. [b] The *ee* value was determined by high-performance liquid chromatographic analysis with a chiral stationary phase. [c] Absolute configuration was determined by comparison of the sign of the specific rotation to that reported in ref. [13]. [d] Absolute configuration was determined by the derivation from the chiral 3-substituted cyclohexanone. For details, see the Supporting Information. [e] Molar ratio of alkene **2a**/pyrimidine-5-carbaldehyde **1**/diisopropylzinc = 0.019/1.0/2.0. Aldehyde was added in four portions. [f] Molar ratio of alkene **2a**/pyrimidine-5-carbaldehyde **1**/diisopropylzinc = 0.095/1.0/2.0.

 © 2004 Wiley-VCH Verlag GmbH & Co. KGaA, Weinheim

(0.08 mmol) in hexane at 0 °C was added over a period of 30 min to a solution of (*S*)-(+)-[(4-methylcyclohexylidene)methyl]benzene **2b** (4.7 mg, 0.025 mmol) and aldehyde **1** (4.7 mg, 0.025 mmol) in methylcyclohexane (0.5 mL). The mixture was stirred for 12 h at 0 °C. Toluene (1.9 mL), diisopropylzinc (0.2 mmol, 0.2 mL of a 1.0 M toluene solution), and a solution of aldehyde **1** (1.0 mL, 18.8 mg, 0.10 mmol) in toluene were added successively, and the reaction mixture was stirred for 0.5 h. Toluene (7.5 mL), diisopropylzinc (0.8 mmol, 0.8 mL of 1. 0 M toluene solution), and a toluene solution of aldehyde **1** (2.0 mL, 75.3 mg, 0.40 mmol) were then added successively, and the mixture was stirred at 0 °C for another 0.5 h. Saturated aqueous sodium hydrogen carbonate (15 mL) was added to the mixture. The mixture was filtered through celite, and the filtrate was extracted with ethyl acetate. The combined organic layers were dried over anhydrous sodium sulfate, and evaporated under reduced pressure. Purification of the residue by thin-layer chromatography on silica gel (eluant: hexane/ethyl acetate = 3/2, *v*/*v*) gave (*R*)-pyrimidyl alkanol **3** in 96 % *ee* in a yield of 97 % (119 mg).

Received: March 2, 2004
Revised: May 19, 2004 [Z54162]

Keywords: alkenes · asymmetric amplification · asymmetric catalysis · autocatalysis · chirality

[1] a) K. Mislow, *Collect. Czech. Chem. Commun.* **2003**, *68*, 849 – 864; b) A. Eschenmoser, *Science* **1999**, *284*, 2118 – 2124; c) B. L. Feringa, R. A. van Delden, *Angew. Chem.* **1999**, *111*, 3624 – 3645; *Angew. Chem. Int. Ed.* **1999**, *38*, 3418 – 3438; d) H. Zepik, E. Shavit, M. Tang, T. R. Jensen, K. Kjaer, G. Bolbach, L. Leiserowitz, I. Weissbuch, M. Lahav, *Science* **2002**, *295*, 1266 – 1269; e) M. M. Green, J.-W. Park, T. Sato, A. Teramoto, S. Lifson, R. L. B. Selinger, J. V. Selinger, *Angew. Chem.* **1999**, *111*, 3329 – 3345; *Angew. Chem. Int. Ed.* **1999**, *38*, 3139 – 3154; f) J. R. Cronin, S. Pizzarello, *Science* **1997**, *275*, 951 – 955; g) D. K. Kondepudi, K. Asakura, *Acc. Chem. Res.* **2001**, *34*, 946 – 954; h) J. S. Siegel, *Chirality* **1998**, *10*, 24 – 27; i) W. A. Bonner, *Origins Life Evol. Biosphere* **1995**, *25*, 175 – 190.

[2] a) A. Cotton, *Ann. Chim. Phys.* **1896**, *8*, 347; b) W. Kuhn, E. Braun, *Angew. Chem* **1929**, *41*, 296.

[3] a) Y. Inoue, *Chem. Rev.* **1992**, *92*, 741 – 770; b) O. Buchardt, *Angew. Chem.* **1974**, *86*, 222 – 228; *Angew. Chem. Int. Ed. Engl.* **1974**, *13*, 179 – 185.

[4] The star forming region in space has been recognized as a natural source of strong CPL: J. Bailey, A. Chrysostomou, J. H. Hough, T. M. Gledhill, A. McCall, S. Clark, F. Menard, M. Tamura, *Science* **1998**, *281*, 672 – 674.

[5] a) J. J. Flores, W. A. Bonner, G. A. Massey, *J. Am. Chem. Soc.* **1977**, *99*, 3622 – 3625; b) H. Nishino, A. Kosaka, G. A. Hembury, F. Aoki, K. Miyauchi, H. Shitomi, H. Onuki, Y. Inoue, *J. Am. Chem. Soc.* **2002**, *124*, 11618 – 11627.

[6] a) A. Moradpour, J. F. Nicoud, G. Balavoine, H. B. Kagan, G. Tsoucaris, *J. Am. Chem. Soc.* **1971**, *93*, 2353 – 2354; b) W. J. Bernstein, M. Calvin, O. Buchardt, *J. Am. Chem. Soc.* **1972**, *94*, 494 – 498.

[7] a) M. Suarez, G. B. Schuster, *J. Am. Chem. Soc.* **1995**, *117*, 6732 – 6738; b) Y. Zhang, G. B. Shuster, *J. Org. Chem.* **1995**, *60*, 7192 – 7197; c) Y. Inoue, H. Tsuneishi, T. Hakushi, K. Yagi, K. Awazu, H. Onuki, *Chem. Commun.* **1996**, 2627 – 2628; d) N. P. M. Huck, W. F. Jager, B. de Lang, B. L. Feringa, *Science* **1996**, *273*, 1686 – 1688.

[8] J. Li, G. B. Schuster, K.-S. Cheon, M. M. Green, J. V. Selinger, *J. Am. Chem. Soc.* **2000**, *122*, 2603 – 2612.

[9] K. S. Burnham, G. B. Schuster, *J. Am. Chem. Soc.* **1999**, *121*, 10245 – 10246.

[10] E. L. Eliel, S. H. Wilen, L. N. Mander, *Stereochemistry of Organic Compounds*, Wiley, New York, **1994**, Chap. 14.

[11] a) K. Soai, T. Shibata, H. Morioka, K. Choji, *Nature* **1995**, *378*, 767 – 768; b) T. Shibata, J. Yamamoto, N. Matsumoto, S. Yonekubo, S. Osanai, K. Soai, *J. Am. Chem. Soc.* **1998**, *120*, 12157 – 12158; c) I. Sato, K. Kadowaki, K. Soai, *Angew. Chem.* **2000**, *112*, 1570 – 1572; Angew. *Chem. Int. Ed.* **2000**, *39*, 1510 – 1512; d) I. Sato, R. Yamashima, K. Kadowaki, J. Yamamoto, T. Shibata, K. Soai, *Angew. Chem.* **2001**, *113*, 1130 – 1132; *Angew. Chem. Int. Ed.* **2001**, *40*, 1096 – 1098; e) I. Sato, H. Urabe, S. Ishiguro, T. Shibata, K. Soai. *Angew. Chem.* **2003**, *115*, 329 – 331; *Angew. Chem. Int. Ed.* **2003**, *42*, 315 – 317; f) the asymmetric autocatalysis of **3** proceeds with significant amplification of *ee* values in homogeneous solution without any precipitation in toluene using an initial aldehyde concentration of 0.020 M (molar ratio of asymmetric autocatalyst **3**/aldehyde **1**/diisopropylzinc = 0.2/1/2.2); for mechanistic studies by us and other research groups, see g) I. Sato, D. Omiya, K. Tsukiyama, Y. Ogi, K. Soai, *Tetrahedron: Asymmetry* **2001**, *12*, 1965 – 1969; h) I. Sato, D. Omiya, H. Igarashi, K. Kato, Y. Ogi, K. Tsukiyama, K. Soai, *Tetrahedron: Asymmetry* **2003**, *14*, 975 – 979; i) D. G. Blackmond, C. R. McMillan, S. Ramdeehul, A. Schorm, J. M. Brown, *J. Am. Chem. Soc.* **2001**, *123*, 10103 – 10104; j) F. G. Buono, D. G. Blackmond, *J. Am. Chem. Soc.* **2003**, *125*, 8978 – 8979; k) T. Buhse, *Tetrahedron: Asymmetry* **2003**, *14*, 1055 – 1061.

[12] Reviews on asymmetric autocatalysis: a) K. Soai, T. Shibata, I. Sato, *Acc. Chem. Res.* **2000**, *33*, 382 – 390; b) K. Soai, I. Sato, T. Shibata, *Chem. Rec.* **2001**, *1*, 321 – 332; c) C. Bolm, F. Bienewald, A. Seger, *Angew. Chem,* **1996**, *108,* 1767 – 1769; *Angew. Chem. Int. Ed. Engl.* **1996**, *35*, 1657 – 1659; d) M. Avalos, R. Babiano, P. Cintas, J. L. Jiménez, J. C. Palacios, *Chem. Commun.* **2000**, 887 – 892; e) H. Buschmann, R. Thede, D. Heller, *Angew. Chem,* **2000**, *112*, 4197 – 4200; *Angew. Chem. Int. Ed.* **2000**, *39*, 4033 – 4036; f) M. H. Todd, *Chem. Soc. Rev.* **2002**, *31*, 211 – 222; for reviews including both autocatalytic and nonautocatalytic reactions with amplification of *ee* values, see g) C. Girard, H. B. Kagan, *Angew. Chem.* **1998**, *110*, 3088 – 3127; Angew. *Chem. Int. Ed.* **1998**, *37*, 2922 – 2959; h) K. Mikami, M. Yamanaka, *Chem. Rev.* **2003**, *103*, 3369 – 3400.

[13] J. H. Brewster, J. E. Privett, *J. Am. Chem. Soc.* **1966**, *88*, 1419 – 1424.

 © 2004 Wiley-VCH Verlag GmbH & Co. KGaA, Weinheim

Reaction Mechanisms

Mechanistic Studies of a Reaction Promoted by the [YLi$_3$\{tris(binaphthoxide)\}] Complex: Are Three 1,1′-Bi-2-naphthol Units in a Rare-Earth–Alkali-Metal Heterobimetallic Complex Necessary?**

*Noriyuki Yamagiwa, Shigeki Matsunaga, and Masakatsu Shibasaki**

Since the early 1990s,[1a] we have reported series of rare-earth–alkali-metal heterobimetallic complexes that enable various catalytic asymmetric reactions.[1] These complexes, whose structures were determined by X-ray crystallographic analysis, mass spectrometry, and NMR spectroscopy, consist of one rare-earth metal (RE), three 1,1′-2-bi-naphtholate (binol), and three alkali metal (M) parts (Figure 1).[1b,c] Subsequently, independent studies by Aspinall et al. revealed differences in the aqua and anhydrous heterobimetallic

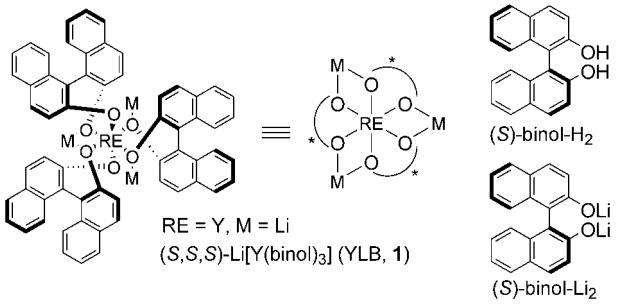


Figure 1. Structure of (*S*,*S*,*S*)-Li$_3$[Y(binol)$_3$] (YLB, **1**), (*S*)-binol-H$_2$, and (*S*)-binol-Li$_2$.

complexes in the solid-phase structures.[2] They also reported preliminary results on the solution-phase structure of heterobimetallic complexes. More recently, Salvadori and co-workers reported a detailed spectroscopic analysis of Yb–alkali-metal heterobimetallic complexes in solution phase, raising the question as to whether the Yb/M/binol = 1:3:3 structure is really an active species or just a precatalyst (Figure 2).[3] They reported that binol in the Yb/K/binol = 1:3:3 heterobimetallic complex is labile (confirmed by an exchange spectroscopy experiment) and proposed that the active species could be generated by dissociation of one binol–Li$_2$ unit, as long as Yb metal was used. Furthermore, the best results in some asymmetric reactions were observed with catalysts prepared from RE/binol/M in a ratio different to 1:3:3. Yb/K/binol = 1:1:3 worked best in a nitro-Mannich-type reaction,[4] and Sc/Li/binol = 1:1:2 in a Strecker-type reaction.[5] The active

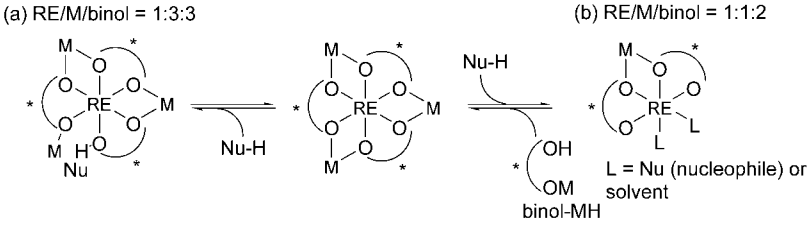
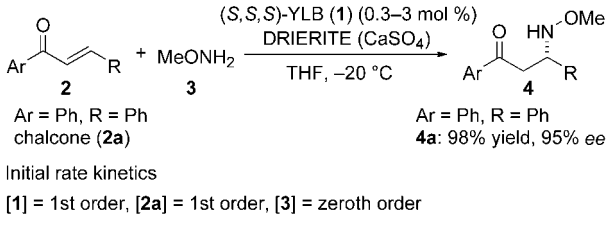


Figure 2. Debated structures of active species of rare-earth–alkali-metal heterobimetallic complexes. a) RE/M/binol = 1:3:3; b) RE/M/binol = 1:1:2. Nu = nucleophile.

species in these reactions has not yet been determined. Mechanistic studies to clarify the composition of the active species of the rare-earth–alkali-metal heterobimetallic complex would facilitate the design and application of bimetallic multifunctional asymmetric catalysis in future research. Although recent detailed spectroscopic analysis of the heterobimetallic complexes by Aspinall et al.[2] and Salvadori and co-workers[3] revealed various new and interesting properties, their behavior during catalytic cycles of asymmetric reactions have not been studied extensively. To elucidate the controversial structure of the active species, investigations based on actual catalytic asymmetric reactions as well as spectroscopic analysis of the heterobimetallic complex are essential. Herein, we report our efforts to determine the active species on the basis of mechanistic studies of a catalytic asymmetric reaction, including various kinetics studies and NMR spectroscopic analysis. Mechanistic studies of the [YLi$_3$\{tris(binaphthoxide)\}] complex (Figure 1, Li$_3$[Y(binol)$_3$], YLB, **1**) and asymmetric 1,4-addition reaction of *O*-methylhydroxylamine catalyzed by YLB (**1**) suggested that the active species of the 1,4-addition reaction requires all three binol units in YLB, although ligand exchange of the YLB complex occurs easily under the reaction conditions (−20 °C).

We selected an asymmetric 1,4-addition of *O*-methylhydroxylamine (**3**) catalyzed by **1** as a target for the mechanistic studies (Scheme 1).[6] Because Aspinall et al. reported detailed spectroscopic data for both the solid-phase and solution-phase structures of YLB (**1**),[2] this reaction was most



Scheme 1. Catalytic asymmetric 1,4-addition of *O*-methylhydroxylamine (**3**) promoted by YLB (**1**) and results of initial rate kinetic experiments.

[*] N. Yamagiwa, Dr. S. Matsunaga, Prof. Dr. M. Shibasaki
Graduate School of Pharmaceutical Sciences
The University of Tokyo
Hongo, Bunkyo-ku, Tokyo 113-0033 (Japan)
Fax: (+81) 3-5684-5206
E-mail: mshibasa@mol.f.u-tokyo.ac.jp

[**] This work was partially supported by a Grant-in-Aid for Specially Promoted Research and a Grant-in-Aid for Encouragement for Young Scientists (B) (for S.M.) from the JSPS and MEXT.

Supporting information for this article is available on the WWW under http://www.angewandte.org or from the author.

 DOI: 10.1002/anie.200454202 © 2004 Wiley-VCH Verlag GmbH & Co. KGaA, Weinheim

suitable to investigate the behavior during the reaction pathway.[7] We first examined the reaction profile of the catalytic asymmetric 1,4-addition of amine **3** to chalcone (**2a**). Initial rate-kinetics studies revealed that several properties of the reaction:

1) first-order dependence on the YLB complex **1**;
2) first-order dependence on chalcone (**2a**);
3) zeroth order dependence on amine **3** (Scheme 1);[8]
4) negligible retro-1,4-addition;
5) only slight product inhibition (the reaction rate decreased by 34% in the presence of as much as 100 equiv of product **4e** (relative to **1**), and the results suggested that product inhibition at the initial stage of the reaction was negligible);
6) retardation of reaction rate upon addition of H_2O;
7) strong, positive, nonlinear effects[9] (Figure 3).

A catalyst with 33% *ee* afforded products with 95% *ee*, which was comparable with that obtained in the presence of an optically pure catalyst (96% *ee*). The reaction rate, however, differed greatly, depending on the optical purity of the catalyst. For example, the reaction rate with catalyst with 33% *ee* was only 1/34 ($v_{33\%\,ee} = 2.98 \times 10^{-4}\,M\,h^{-1}$) of that observed with optically pure catalyst ($v_{100\%\,ee} = 1.01 \times 10^{-2}\,M\,h^{-1}$). The reaction rate with 0% *ee* catalyst was 1/199 ($v_{0\%\,ee} = 5.07 \times 10^{-5}\,M\,h^{-1}$) of that with optically pure catalyst.[8]

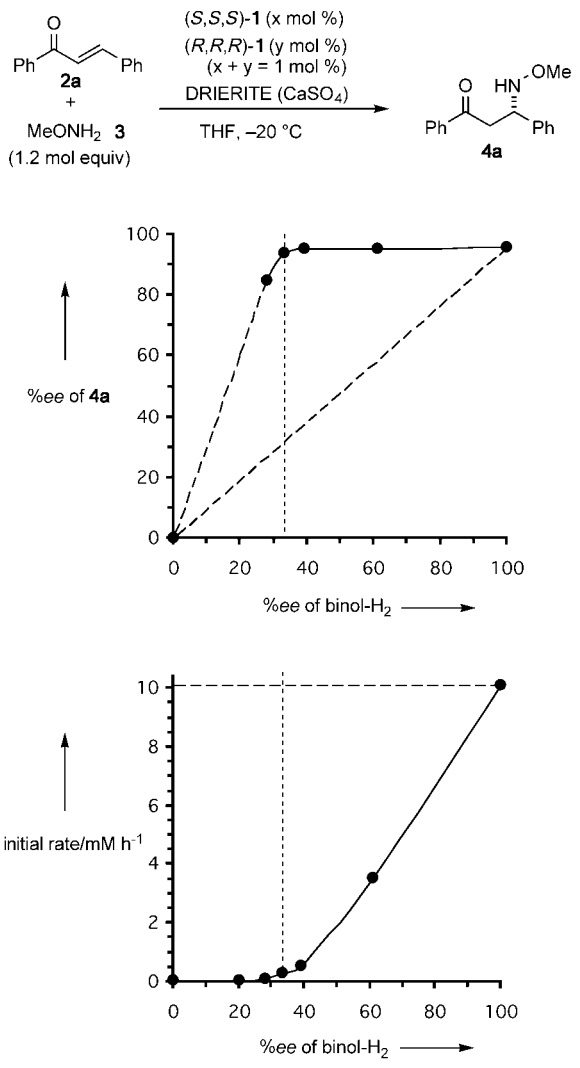


Figure 3. Positive nonlinear effects in catalytic asymmetric 1,4-addition of **3** to **2a** promoted by YLB **1**.

Possible catalytic cycles of the reaction to explain the observed kinetic properties 1)–5) are summarized in Figures 4A–C. In Figure 4A, the active species is postulated to be the Y/Li/binol = 1:3:3 complex coordinated by amine **3**. Formation of active species **A-II** from an amine-free YLB complex **I** should be fast, and the rate-determining step (rds) of the reaction is the 1,4-addition to **2a**. In Figures 4B and C, the active species is postulated to be the Y/Li/binol = 1:1:2 complex. Although the latter complex is thermodynamically unstable,[10] it might exist because of stabilization with amine **3** and/or chalcone (**2a**). In Figure 4B, the amine coordinates to the Y/Li/binol = 1:1:2 complex (**B-II**). The rate-determining step of the reaction is the 1,4-addition to **2a**. In Figure 4C, the active species is postulated to be the Y/Li/binol = 1:1:2 complex coordinated by **2a**. Formation of the active species by replacing one binol-Li_2 unit of YLB with chalcone should be the rate-determining step, and the 1,4-addition of amine is fast. We evaluated the validity of these three possible reaction mechanisms with additional mechanistic experiments.

First, we evaluated the mechanism in Figure 4B. The results of initial rate kinetic studies 1–3 listed above suggested that the formation of active species **B-II** by releasing one binol-Li_2 unit should be favorable ($K_{B1}[\mathbf{3}]/[\mathbf{B\text{-}II}] = [\text{binol-Li}_2]/[\mathbf{I}] \gg 1$) if the mechanism shown in Figure 4B is correct.[11] Thus, the active species would be observed by spectroscopic analysis on the basis of kinetic experiments. NMR spectroscopic analysis of the YLB complex under various conditions (a) (*S*,*S*,*S*)-**1**, b) (*S*,*S*,*S*)-**1** + (*S*)-binol-Li_2 (1 equiv), c) (*S*,*S*,*S*)-**1** + (*S*)-binol-Li_2 (3 equiv), d) (*S*)-binol-Li_2, e) (*S*,*S*,*S*)-**1** + **3** (10 equiv), and f) (*S*,*S*,*S*)-**1** + **3** (10 equiv) + binol-Li_2 (1 equiv) were examined (in b–f, equiv with respect to **1**; NMR spectra are available in the Supporting Information). In b, c, and f, binol-Li_2 was observed independently from peaks derived from YLB. Binol-Li_2, however, was not observed in e). These observations do not support the proposed mechanism in Figure 4B, thus the mechanism in Figure 4B is unlikely. There was no difference in the reaction rate when using 1 mol% of YLB with or without additional binol-Li_2 (1–3 mol%) (Figure 5).[8] The enantioselectivities observed for the product **4a** were 96% *ee* (**1** alone), 96% *ee* (**1** + 1 mol% binol-Li_2), 96% *ee* (**1** + 2 mol% binol-Li_2), 96% *ee* (**1** + 3 mol% binol-Li_2), and 17% *ee* (3 mol% binol-Li_2). The results in Figure 5 also suggested that the mechanism in Figure 4B is incorrect.

In the case of the mechanism shown in Figure 4C, the formation of active species **C-II** by releasing one binol-Li_2 unit should be slow, based on the observed initial rate kinetic properties 1–3 (see list above).[11] Thus, NMR spectroscopic analysis of the active species would be difficult to obtain, because the existence of the active species would be minor and the majority would be in the resting state (Y/Li/binol =

 © 2004 Wiley-VCH Verlag GmbH & Co. KGaA, Weinheim

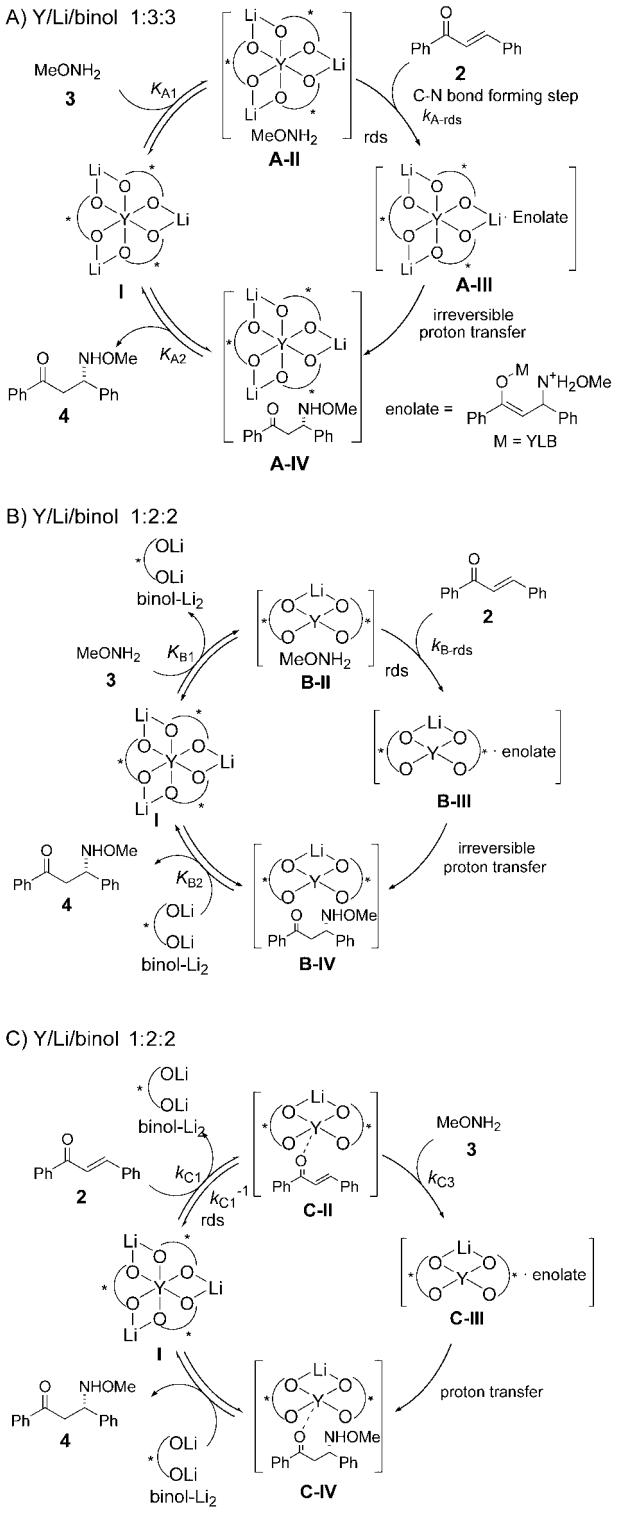


Figure 4. Possible catalytic cycles of catalytic asymmetric 1,4-addition with YLB (**1**). A) with Y/Li/binol = 1:3:3; B) and C) with Y/Li/binol = 1:1.2.

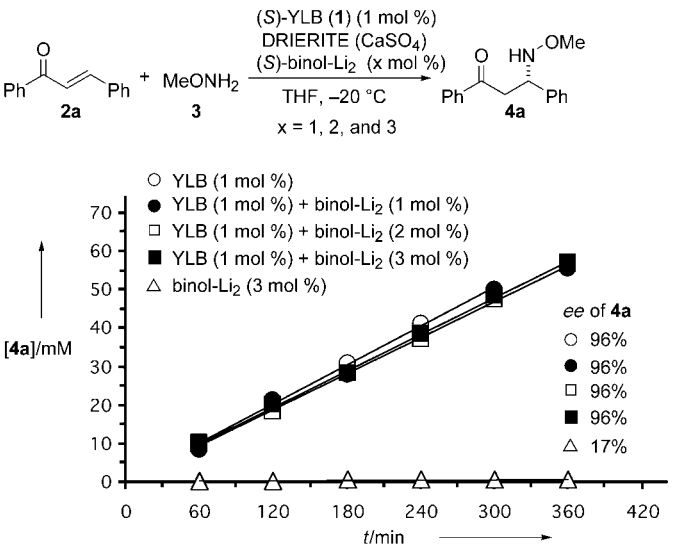


Figure 5. Initial rate kinetics using 1 mol% of (*S,S,S*)-**1** with additional (*S*)-binol-Li_2. (0–3 mol%).

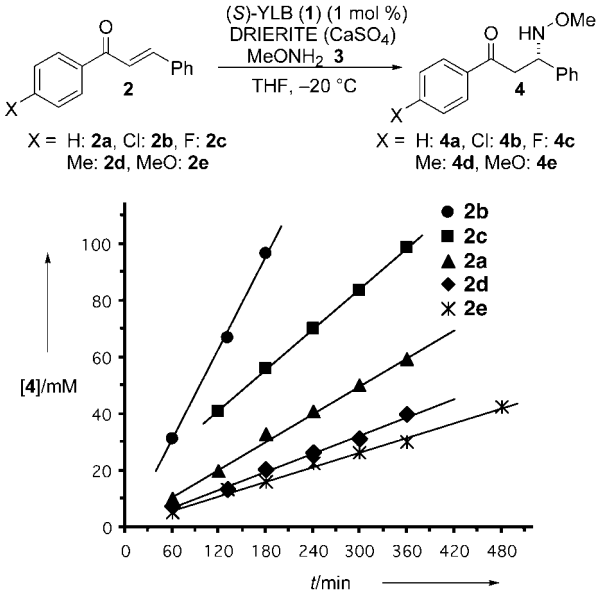


Figure 6. Substituents effects of chalcone **2** on initial rate.

1:3:3). On the other hand, the 1,4-addition step is fast in this mechanism. This mechanism was ruled out, however, when substituent effects on the reaction rate were examined (Figure 6).[8] If the mechanism in Figure 4C were correct, then introduction of an electron-donating group on chalcone **2** would accelerate the reaction, because electron-rich chalcone would accelerate the exchange with binol-Li_2. The tendency shown in Figure 6, however, suggests that the rate-determining step is the 1,4-addition step and not the formation of active species **II-C**.

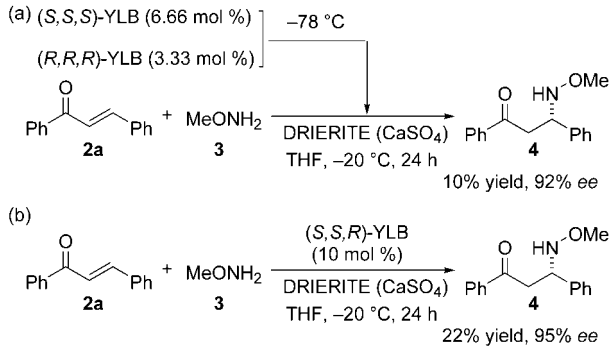
The mechanism shown in Figure 4A is therefore the most probable of the three.[11] The mechanism shown in Figure 4A fits all the observed kinetic profiles 1–6 (see list above) and additional mechanistic studies (NMR spectroscopic analysis, Figure 5, and Figure 6). ^{13}C and ^{1}H NMR spectra of **1** alone and **1** with amine did show small differences, suggesting that amine **3** coordinates to the Y complex without breaking the Y/Li/binol = 1:3:3 framework.[12] Inhibition of the reaction with H_2O (kinetic data 6) is explained by the reversible coordina-

 © 2004 Wiley-VCH Verlag GmbH & Co. KGaA, Weinheim

tion of H_2O to YLB. H_2O would compete with chalcone. NMR spectroscopic analysis supported the reversible coordination of H_2O to **1**.[13] Thus, the properties of **1** are quite different to those of the Yb heterobimetallic complexes reported by Salvadori and co-workers.[3] The mechanism shown in Figure 4A involving a seventh axial ligand would be reasonable in the case of **1**.

To explain the observed nonlinear effects of the present 1,4-addition reaction (Figure 3), we further analyzed YLB complex spectroscopically. Aspinall et al. reported that the (*S*,*S*,*R*)-YLB-type complex is thermodynamically more stable than the (*S*,*S*,*S*)-YLB complex owing to the C–H–π hydrogen bond. Because they synthesized the (*S*,*S*,*R*)-YLB-type complex (together with the (*S*,*R*,*R*)-complex) from racemic-binol, it was uncertain as to whether or not ligand exchange occurs under the 1,4-addition reaction conditions. To observe the lability of binol in **1** under the reaction conditions, we analyzed a YLB solution prepared from (*S*,*S*,*S*)-**1** (2 equiv) and (*R*,*R*,*R*)-**1** (1 equiv) by NMR spectroscopy. The mixed solution revealed only the (*S*,*S*,*R*)-YLB-type complex (> 30:1 ratio when taking the resolution of NMR analysis in consideration: no (*S*,*S*,*S*)-YLB was detected). The spectrum was identical to that reported by Aspinall et al.[2] The results clearly indicated that the ligand exchange between (*S*,*S*,*S*)-**1** and (*R*,*R*,*R*)-**1** occurred smoothly to form a thermodynamically more stable (*S*,*S*,*R*)-YLB-type complex exclusively. On the other hand, the reaction rate when using (*S*,*S*,*S*)-**1** (6.66 mol %) and (*R*,*R*,*R*)-**1** (3.33 mol %) mixed at −78 °C was as slow as that performed with 10 mol % of the preformed (*S*,*S*,*R*)-YLB-type complex (Scheme 2). Product **4a** was obtained in only 10 % yield after 24 h (92 % *ee*). The reaction rate was much slower than that observed with (*S*,*S*,*S*)-**1**. The results indicated that ligand exchange occurs smoothly at least under the 1,4-addition reaction conditions at −20 °C. On the basis of these results, the nonlinear effects and the observed reaction rate tendency in Figure 3 are explained as follows: The (*S*,*S*,*R*)-YLB-type complex is thermodynamically more stable than (*S*,*S*,*S*)-YLB. On the other hand, equilibrium between the (*S*,*S*,*R*)-YLB-type complex and (*S*,*S*,*S*)-YLB would occur under the reaction conditions. The (*S*,*S*,*R*)-YLB-type complex is not active for the 1,4-addition reaction and only trace (*S*,*S*,*S*)-YLB formed in equilibrium and promoted the reaction, when the reaction was performed with ligands with 33 % *ee*.[14] The *ee* value of the product was same with ligands with over 33 % *ee*, whereas the reaction rate increased drastically by increasing the *ee* value of the ligands from 33 to > 99 % *ee*, because the amount of (*S*,*S*,*S*)-**1** increased accordingly (Figure 3).

In summary, various kinetics studies and NMR spectroscopic analysis revealed that the active species in the asymmetric 1,4-addition reaction with YLB as a catalyst is Y/Li/binol = 1:3:3 coordinated with amine **3**, although the binol unit in YLB is labile under the reaction conditions. Our conclusion is different from that proposed by Salvadori and co-workers,[3] probably because the active species differs, depending on the combination of rare earth metal, alkali metal, and nucleophile used. The results reported herein do not necessarily extend to the active species in other reactions. In particular, the active species when using more-acidic nucleophiles such as nitroalkanes and phosphonates, which may or may not be replaced with binol, is the future target of investigation. Further studies based on kinetic studies of other asymmetric reactions are essential to clarify the active species. This project is currently in progress.



Scheme 2. 1,4-Addition reaction: a) with (*S*,*S*,*S*)-YLB (6.66 mol %) + (*R*,*R*,*R*)-YLB (3.33 mol %); b) with preformed (*S*,*S*,*R*)-YLB (10 mol %).

Received: March 6, 2004 [Z54202]

Keywords: asymmetric catalysis · heterobimetallic complexes · kinetics · nonlinear effects · rare-earth metals · yttrium

[1] a) H. Sasai, T. Suzuki, S. Arai, T. Arai, M. Shibasaki, *J. Am. Chem. Soc.* **1992**, *114*, 4418; b) H. Sasai, T. Suzuki, N. Itoh, K. Tanaka, T. Date, K. Okamura, M. Shibasaki, *J. Am. Chem. Soc.* **1993**, *115*, 10372; for reviews, see: c) M. Shibasaki, H. Sasai, T. Arai, *Angew. Chem.* **1997**, *109*, 1290; *Angew. Chem. Int. Ed. Engl.* **1997**, *36*, 1236; d) M. Shibasaki, N. Yoshikawa, *Chem. Rev.* **2002**, *102*, 2187.

[2] a) H. C. Aspinall, J. L. M. Dwyer, N. Greeves, A. Steiner, *Organometallics* **1999**, *18*, 1366; b) H. C. Aspinall, J. F. Bickley, J. L. M. Dwyer, N. Greeves, R. V. Kelley, A. Steiner, *Organometallics* **2000**, *19*, 5416; Review: c) H. C. Aspinall, *Chem. Rev.* **2002**, *102*, 1807.

[3] L. D. Bari, M. Lelli, G. Pintacuda, G. Pescitelli, F. Marchetti, P. Salvadori, *J. Am. Chem. Soc.* **2003**, *125*, 5549.

[4] K. Yamada, S. J. Harwood, H. Gröger, M. Shibasaki, *Angew. Chem.* **1999**, *111*, 3713; *Angew. Chem. Int. Ed.* **1999**, *38*, 3504.

[5] M. Chavarot, J. J. Byrne, P. Y. Chavant, Y. Vallée, *Tetrahedron: Asymmetry* **2001**, *12*, 1147.

[6] N. Yamagiwa, S. Matsunaga, M. Shibasaki, *J. Am. Chem. Soc.* **2003**, *125*, 16178.

[7] YLB (**1**) is also most suitable to investigate the effects of H_2O on reactivity and selectivity of heterobimetallic asymmetric catalysis. Anhydrous YLB was essential for the asymmetric 1,4-addition of amine, whereas aqua YLB was essential for the catalytic asymmetric cyanoethoxycarbonylation reaction. Comparison of these two reactions to clarify the role of H_2O will be reported as a full article. For the use of aqua YLB in the cyanoethoxycarbonylation reaction, see: a) J. Tian, N. Yamagiwa, S. Matsunaga, M. Shibasaki, *Angew. Chem.* **2002**, *114*, 3788; *Angew. Chem. Int. Ed.* **2002**, *41*, 3636; b) J. Tian, N. Yamagiwa, S. Matsunaga, M. Shibasaki, *Org. Lett.* **2003**, *5*, 3021.

[8] For detailed data of kinetic profiles 1–6, nonlinear effects 7, and the reaction profiles in Figures 5 6, see Supporting Information.

[9] For reviews, see: a) C. Girard, H. B. Kagan, *Angew. Chem.* **1998**, *110*, 3088; *Angew. Chem. Int. Ed.* **1998**, *37*, 2922; b) H. B. Kagan,

 © 2004 Wiley-VCH Verlag GmbH & Co. KGaA, Weinheim

Adv. Synth. Catal. **2001**, *343*, 227; for a review discussing kinetic aspects of nonlinear effects, see: c) D. G. Blackmond, *Acc. Chem. Res.* **2000**, *33*, 402.

[10] NMR spectroscopic analysis suggested that YLB (**1**) (1:3:3 complex) forms predominantly even when the Y–Li complex was mixed in a 1:2:2 ratio in THF. Coordination of THF would not be sufficient to stabilize the coordinatively unsaturated Y/Li/binol = 1:1:2 species. When the Y–Li complex was mixed in a 1:1:2 ratio (Y/Li/binol), a complicated NMR spectrum was observed. We speculate that **1** would form, but that other species derived from remaining $Y(HMDS)_3$ and binol-H_2 would also form, thus resulting in the complicated NMR spectrum.

[11] For a more detailed discussion evaluating mechanisms A-C in Figure 4, see Supporting Information.

[12] ^{13}C and ^{1}H NMR spectra of YLB and YLB with amine **3** are shown in the Supporting Information. The difference in chemical shifts is also summarized.

[13] ^{1}H NMR spectra of anhydrous and aqua YLB and experiments to show the reversibility between aqua and anhydrous YLB are summarized in the Supporting Information.

[14] The possibility that the (*S*,*S*,*R*)-YLB-type complex is much less reactive (1/34 of (*S*,*S*,*S*)-YLB), but as enantioselective as (*S*,*S*,*S*)-YLB (95% *ee*) cannot be excluded. Further mechanistic studies are necessary.

 © 2004 Wiley-VCH Verlag GmbH & Co. KGaA, Weinheim

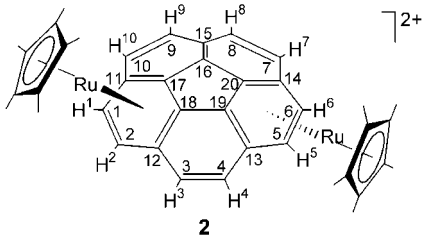
Buckybowls

Synthesis and Structure of a Dimetallated Buckybowl: Coordination of One {Cp*Ru}$^+$ Unit to Each Side of Corannulene**

Paul A. Vecchi, Celedonio M. Alvarez, Arkady Ellern, Robert J. Angelici, Andrzej Sygula, Renata Sygula, and Peter W. Rabideau*

In transition-metal complexes of buckminsterfullerene (C_{60}),[1] the metal atom is bonded to two carbon atoms (η^2) shared by two six-membered rings. On the other hand, curved-surface fragments of C_{60}, called buckybowls, are difficult to prepare and few transition-metal complexes of them have been reported.[2–4] Improved procedures for the synthesis of corannulene[5,6] ($C_{20}H_{10}$, **1**) have led to the preparation of the η^6 complexes [Cp*Ru(η^6-$C_{20}H_{10}$)](O_3SCF_3)[3] and [Cp*Ir(η^6-$C_{20}H_{10}$)](BF_4)$_2$,[4] in which Cp* is η^5-C_5Me_5. Although these complexes have been well-characterized by their NMR spectra, neither has been isolated as the analytically pure solid. Recently, the gas-phase deposition synthesis of [{$Rh_2(O_2CCF_3)_4$}$_m$·($C_{20}H_{10}$)$_n$] (m:n = 1:1 and 3:2), were reported.[2a] Their structures, as determined by X-ray diffraction studies, contain 1D and 2D networks of [$Rh_2(O_2CCF_3)_4$] and corannulene units in which the {Rh_2} groups are η^2-coordinated to both the convex and concave sides of the corannulene. These are the only crystal structures of transition-metal complexes of corannulene. Herein, we report the first X-ray structural characterization of a corannulene that contains η^6-coordinated metal fragments. Of particular interest are the observations that the two {Cp*Ru}$^+$ fragments are on opposite sides of the corannulene bowl, which is significantly flattened as compared to free corannulene.

The reaction of [{Cp*Ru(μ_3-Cl)}$_4$][7] (0.020 mmol) with $AgBF_4$ (for **2a**) or $AgPF_6$ (**2b**) (0.081 mmol) and **1** (0.040 mmol) in a 2:1 ratio of {Cp*Ru}$^+$ to $C_{20}H_{10}$ in CD_3NO_2 under an Ar atmosphere at room temperature gave the dimetallated complex [(Cp*Ru)$_2$(μ_2-η^6,η^6-$C_{20}H_{10}$)]X_2 (X = BF_4^-(**2a**), PF_6^-(**2b**)) (Figure 1). Both **2a** and **2b** are



2

Figure 1. Atom labeling Scheme for compound **2**.

stable in CD_3NO_2 and CH_2Cl_2, very soluble in CD_3NO_2, and moderately soluble in CH_2Cl_2 at room temperature. They are insoluble in diethyl ether and hexanes, and the {Cp*Ru}$^+$ units are displaced from the corannulene when the complex is dissolved in acetone. In the solid state, **2a** and **2b** are stable in dry air for weeks. After 1 week, a solution of **2b** in CD_3NO_2 in dry air decomposed ≈50% to [Cp*Ru(η^6-$C_{20}H_{10}$)]$^+$ with no evidence for free corannulene in the ^{1}H NMR spectrum. Shaking a CD_3NO_2 solution of **2b** with water results in decomposition with the liberation of free corannulene. While the existence of [(Cp*Ru)$_2$(μ_2-η^6,η^6-$C_{20}H_{10}$)]$^{2+}$ was previously proposed on the basis of unspecified NMR data,[3] it was not further characterized.

The ^{1}H NMR spectrum of **2a** in the corannulene region (Figure 2) has signals in the narrow range (δ = 6.87–6.74 ppm) that are shifted upfield with respect to the signal of free corannulene (e.g., δ = 7.85 ppm for **1** in CD_3NO_2). These protons (H1, H2, H5, H6), which are doublets with J_{HH} values of 6 Hz, are assigned to the six-membered rings that are η^6-

[*] P. A. Vecchi, Dr. C. M. Alvarez, Prof. Dr. R. J. Angelici
Department of Chemistry
Iowa State University
Ames, IA 50011 (USA)
Fax: (+1) 515-294-0105
E-mail: angelici@iastate.edu
Dr. A. Ellern
Molecular Structure Laboratory
Iowa State University
Ames, IA 50011 (USA)
Prof. Dr. A. Sygula, R. Sygula, Prof. Dr. P. W. Rabideau
Department of Chemistry
Mississippi State University
Mississippi State, MS 39762 (USA)

[**] This work was supported by the U.S. Department of Energy, Office of Science, Office of Basic Energy Sciences, Chemical Sciences Division, under contract W-7045-Eng-82 with Iowa State University. Cp* is η^5-C_5Me_5.

Supporting information for this article is available on the WWW under http://www.angewandte.org or from the author.

 DOI: 10.1002/anie.200454225 © 2004 Wiley-VCH Verlag GmbH & Co. KGaA, Weinheim

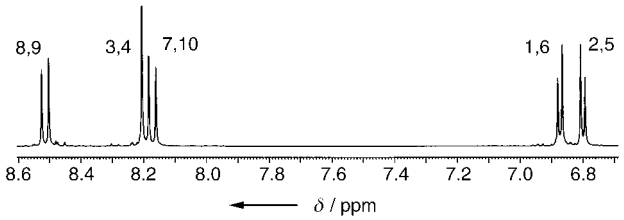


Figure 2. ^{1}H NMR spectrum of the corannulene region of **2A** in CD_3NO_2.

coordinated to the {Cp*Ru}$^+$ units. Such upfield shifts are typical of other [Cp*Ru(η^6-arene)]$^+$ compounds.[7,8] The chemical shifts of the protons on the carbons not bonded to Ru are downfield of free corannulene, as is observed in [Cp*Ru(η^6-$C_{20}H_{10}$)]$^+$[3] and [Cp*Ir(η^6-$C_{20}H_{10}$)]$^{2+}$.[4] These six protons appear as two doublets ($J_{HH} = 9$ Hz) and a singlet. Only one methyl signal is observed in the ^{1}H NMR spectrum, and it integrates to 30H. A COSY NMR experiment was carried out on complex **2a** and used in the assignment of the proton chemical shifts. The $^{13}C\{^1H\}$ NMR spectrum of **2a** shows six carbon signals between $\delta = 98.7$ and 81.1 ppm, which were assigned to the carbons bonded directly to the two Ru atoms. These signals are substantially upfield with respect to the uncoordinated carbon atoms ($\delta = 140.2$–126.7 ppm) and free corannulene ($\delta = 136.3$, 132.0 and 128.2 ppm for **1** in CD_3NO_2), a trend that is also observed in other [Cp*Ru(η^6-arene)]$^+$ complexes.[7,8] The NMR data clearly show that the ruthenium atoms are η^6 coordinated to two of the six-membered rings of corannulene.

Orange crystals of [(Cp*Ru)$_2$(μ_2-η^6,η^6-$C_{20}H_{10}$)][PF_6]$_2$ (**2b**) suitable for an X-ray structure investigation were grown by inverse diffusion of a saturated methylene chloride solution of the complex surrounded by hexanes at −20 °C over a period of one week.[9] The crystals, which contained four molecules of CH_2Cl_2 per unit cell, quickly deteriorated when removed from the methylene chloride solution. The structure reveals that the {Cp*Ru}$^+$ units bind to both the convex and concave sides of the $C_{20}H_{10}$ bowl (Figure 3). Coordination of the two {Cp*Ru}$^+$ cations to the corannulene causes significant structural changes in the shape of the bowl. Differences in bond lengths are observed in the six-membered rings to which the {Cp*Ru}$^+$ groups are coordinated; in these rings, the HC=CH rim bonds are elongated to an average of 1.454(11) Å from 1.402(5) Å in corannulene itself.[10] This elongation releases some strain in the corannulene subunit of **2b** causing a notable flattening of the bowl as compared to **1**. The diminished curvature of the coordinated bowl is clearly demonstrated by a π-orbital axis vector (POAV) analysis.[11] (Figure 4). The pyramidalization angles of the five central carbon atoms and those that are attached to them are on average 4.2° and 1.3°, respectively, in **2b**, whereas the analogous values for corannulene and its derivatives are 8.4° and 3.8°, respectively.[11,12] Thus, the curvature of the corannulene bowl in **2b** is reduced to approximately half of the curvature of corannulene. A closer view of the POAV values shows that they are smaller for the carbon atoms bonded to the convex {Cp*Ru}$^+$ unit (0.8, 3.5, 3.7, 0.5°) than for those bonded to the concave {Cp*Ru}$^+$ unit (2.1, 4.3, 4.4, 1.2°), which indicates that the convex {Cp*Ru}$^+$ causes a greater flattening of the six-membered ring than the concave {Cp*Ru}$^+$. This flattening of the bowl might be expected to

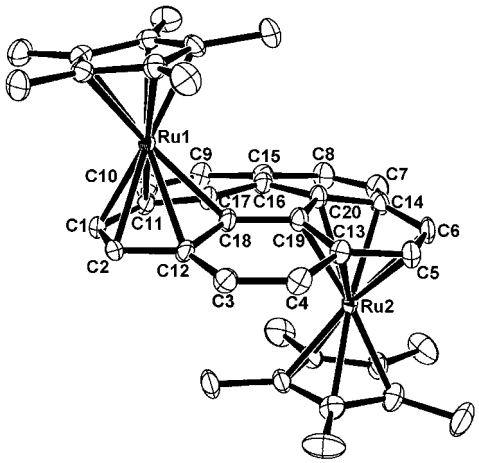


Figure 3. ORTEP drawing of [(Cp*Ru)$_2$(μ_2-η^6,η^6-$C_{20}H_{10}$)][PF_6]$_2$ (**2b**). Ellipsoids are shown at the 30% probability level; hydrogen atoms are omitted for clarity. Selected bond lengths [Å]: Ru1–C1, 2.219(7); Ru1–C2, 2.214(6); Ru1–C12, 2.346(6); Ru1–C18, 2.209(6); Ru1–C17, 2.209(6); Ru1–C11, 2.343(7); Ru2–C5, 2.171(8); Ru2–C6, 2.169(7); Ru2–C14, 2.266(7); Ru2–C20, 2.276(7); Ru2–C19, 2.264(7); Ru2–C13, 2.263(7).

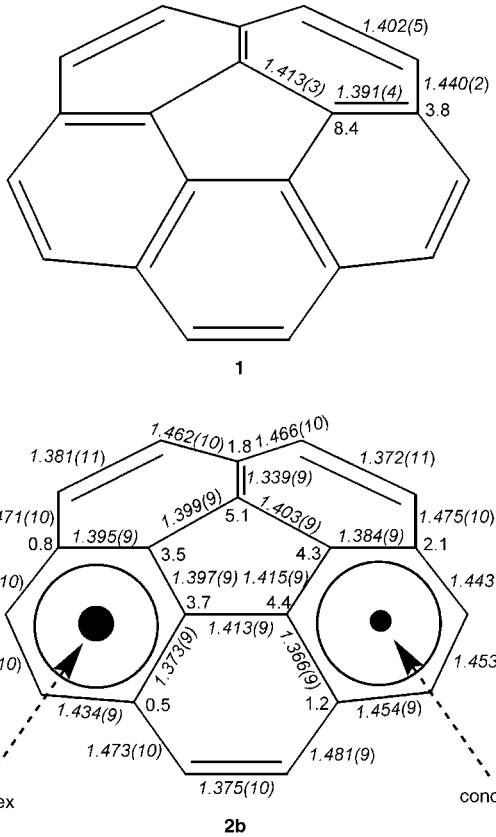


Figure 4. POAV pyramidalization angles and C–C bond lengths (Å; values shown in italics) as found in corannulene (**1**) and [(Cp*Ru)$_2$(μ_2-η^6,η^6-$C_{20}H_{10}$)](PF_6)$_2$·4 CH_2Cl_2 (**2b**). Only the carbon atoms of the corannulene are shown for clarity.

 © 2004 Wiley-VCH Verlag GmbH & Co. KGaA, Weinheim

reduce the barrier to inversion of the $C_{20}H_{10}$ bowl, which is known to have a barrier of 10–11 kcal mol^{-1} in corannulenes functionalized by organic groups on the rim carbon atoms.[13] A previous investigation of corannulene derivatives showed that a flattening of the bowl leads to a decrease in the bowl inversion barrier.[13] The methyl carbon atoms of the two Cp* ligands give a singlet in the room temperature ^{13}C NMR spectrum of **2b** in CD_2Cl_2 indicating rapid inversion of the bowl. Due to the insolubility of **2b** in CD_2Cl_2 at low temperatures, separate resonances for the convex and concave {Cp*Ru}$^+$ groups have not been observed.

Besides the different effects that the concave and convex {Cp*Ru}$^+$ units have on the flattening of the bowl, they also appear to interact with the six-ring carbon atoms differently. The Ru2–C distances for the concave {Cp*Ru}$^+$ unit are significantly shorter to the rim carbon atoms (C5, C6) (2.173(5) Å) than to the other four carbon atoms (C14, C20, C19, C13) (2.267(4) Å). However, the Ru1–C distances for the convex {Cp*Ru}$^+$ group are significantly longer to the atoms C11 and C12 (2.345(5) Å) than to the other four carbon atoms (C1, C2, C18, C17; 2.213(3) Å). Although these results await a theoretical interpretation, it is obvious that the binding of {Cp*Ru}$^+$ is different to the two sides of the bowl. It should be noted that a study of [Cp*Ru(η^6-fluoradene)]$^+$,[8] in which fluoradene ($C_{19}H_{12}$) is another type of curved surface hydrocarbon, showed that {Cp*Ru}$^+$ binds more strongly to the concave side than to the convex side.

In conclusion, complex **2b** is the first structurally characterized compound in which a buckybowl is η^6-coordinated. The {Cp*Ru}$^+$ moieties bind to non-adjacent arene rings on opposite sides of corannulene, and ^{13}C NMR spectroscopic evidence shows that the bowl undergoes rapid inversion at room temperature. Coordination of the {Cp*Ru}$^+$ fragments significantly reduces the overall curvature of the buckybowl; the convex {Cp*Ru}$^+$ group causes a greater flattening than the concave {Cp*Ru}$^+$ unit. These substantial structural effects of the {Cp*Ru}$^+$ units, which contrast with the absence of significant structural changes upon η^2-coordination to $[Rh_2(O_2CCF_3)_4]$,[2a] appear to be caused by the preference of {Cp*Ru}$^+$ for η^6-coordination to a planar arene ring.

Experimental Section

Synthesis and characterization of $[(Cp^*Ru)_2(\mu_2\text{-}\eta^6,\eta^6\text{-}C_{20}H_{10})](X)_2$ (X = BF_4^- **2a**, PF_6^- **2b**)**:** $AgBF_4$ or $AgPF_6$ (0.081 mmol) was added to a solution of $[Cp^*Ru(\mu_3\text{-}Cl)]_4$ (0.022 g, 0.020 mmol) and corannulene (**1**; 0.010 g, 0.040 mmol) in 1 mL of CD_3NO_2. The solution was stirred at room temperature for 1 h, and the AgCl precipitate was removed by filtration. The resulting dark-orange solution was evaporated to dryness under vacuum to give an oily residue of **2a** or **2b**. These reactions are nearly quantitative by NMR spectroscopy. The residue was washed with diethyl ether (2 × 3 mL) and dried under vacuum. After **2a** or **2b** had been dissolved in 1–2 mL of CH_2Cl_2, the resulting solution was added to ≈5 mL of hexanes by cannula to give orange powders (0.034 g, 85 % yield, for **2b**). ^1H NMR (400.13 MHz, CD_3NO_2, RT, **2a**): $\delta = 8.51$ (d, $^3J(H,H) = 9$ Hz, 2 H, H8,9), 8.20 (s, 2 H, H3,4), 8.17 (d, $^3J(H,H) = 9$ Hz, 2 H, H7,10), 6.87 (d, $^3J(H,H) = 6$ Hz, 2 H, H1,6), 6.80 (d, $^3J(H,H) = 6$ Hz, 2 H, H2,5), 1.27 ppm (s, Cp*, 30 H). $^{13}C\{^1H\}$ NMR (100.61 MHz, CD_3NO_2, RT, **2a**): $\delta = 135.1$ (C8,9), 132.2 (C3,4), 128.8 (C7,10), 98.7 (C-Ru), 98.5 (C-Ru), 96.9 (C-Ru), 96.8 (C_5Me_5), 95.6 (C-Ru), 86.9 (C2,5), 85.8 (C1,6), 9.0 (C_5Me_5), 135.6, 132.7 ppm (C15, C16). MS *m/z* 362 ($[(Cp^*Ru)_2(\mu_2\text{-}\eta^6,\eta^6\text{-}C_{20}H_{10})]^{2+}$), electrospray in CD_3NO_2. Anal. Calcd for $[(Cp^*Ru)_2(\mu_2\text{-}\eta^6,\eta^6\text{-}C_{20}H_{10})](PF_6)_2 \cdot 1\,CH_2Cl_2$: C, 44.86; H, 3.86. Found: C, 45.32; H, 3.99. The presence of CH_2Cl_2 in the sample was confirmed by an ^1H NMR spectrum of the compound in CD_3NO_2.

Full details of the synthesis and complete characterization of compounds **2a** and **2b**, including ^1H, $^{13}C\{1H\}$, COSY NMR and mass spectra (**2a**), elemental analysis (**2b**), and thermal ellipsoid drawings and numbering Scheme for **2b** are given in the Supporting Information.

Received: March 9, 2004 [Z54225]

Keywords: aromaticity · corannulenes · ruthenium · structure elucidation

[1] a) A. L. Balch, M. M. Olmstead, *Chem. Rev.* **1998**, *98*, 2123; b) P. J. Fagan, J. C. Calabrese, B. Malone, *Science* **1991**, *252*, 1160; c) H.-F. Hsu, J. R. Shapley, *J. Am. Chem. Soc.* **1996**, *118*, 9192; d) K. Lee, H. Song, B. Kim, J. T. Park, S. Park, M.-G. Choi, *J. Am. Chem. Soc.* **2002**, *124*, 2872.

[2] a) M. A. Petrukhina, K. W. Andreini, J. Mack, L. T. Scott, *Angew. Chem.* **2003**, *115*, 3497; *Angew. Chem. Int. Ed.* **2003**, *42*, 3375; b) R. M. Shaltout, R. Sygula, A. Sygula, F. R. Fronczek, G. G. Stanley, P. W. Rabideau, *J. Am. Chem. Soc.* **1998**, *120*, 835.

[3] T. J. Seiders, K. K. Baldridge, J. M. O'Connor, J. S. Siegel, *J. Am. Chem. Soc.* **1997**, *119*, 4781.

[4] C. M. Alvarez, R. J. Angelici, A. Sygula, R. Sygula, P. W. Rabideau, *Organometallics* **2003**, *22*, 624.

[5] For recent reviews see: a) P. W. Rabideau, A. Sygula, *Acc. Chem. Res.* **1996**, *29*, 235; b) L. T. Scott, *Pure Appl. Chem.* **1996**, *68*, 291; c) G. Mehta, H. S. P. Rao, *Tetrahedron* **1998**, *54*, 13325; d) L. T. Scott, H. E. Bronstein, D. V. Preda, R. B. M. Ansems, M. S. Bratcher, S. Hagen, *Pure Appl. Chem.* **1999**, *71*, 209.

[6] a) L. T. Scott, P.-C. Cheng, M. M. Hashemi, M. S. Bratcher, D. T. Meyer, H. B. Warren, *J. Am. Chem. Soc.* **1997**, *119*, 10963, and references therein; b) T. J. Seiders, E. L. Elliott, G. H. Grube, J. S. Siegel, *J. Am. Chem. Soc.* **1999**, *121*, 7804, and references therein; c) A. Sygula, G. Xu, Z. Marcinow, P. W. Rabideau, *Tetrahedron* **2001**, *57*, 3637, and references therein; d) A. Sygula, S. D. Karlen, R. Sygula, P. W. Rabideau, *Org. Lett.* **2002**, *4*, 3135, and references therein.

[7] P. J. Fagan, M. D. Ward, J. C. Calabrese, *J. Am. Chem. Soc.* **1989**, *111*, 1698.

[8] A. Xia, J. P. Selegue, A. Carrillo, C. P. Brock, *J. Am. Chem. Soc.* **2000**, *122*, 3973.

[9] X-ray crystal data for $[(Cp^*Ru)_2(\mu_2\text{-}\eta^6,\eta^6\text{-}C_{20}H_{10})][PF_6]_2 \cdot 4\,CH_2Cl_2$ (**2b**): Orange single crystals were obtained by slow cooling a saturated CH_2Cl_2 solution of **2b** at room temperature to −77 °C. The crystals decomposed within seconds if contacted with air, and were therefore covered with premixed epoxy glue under the layer of solvent. The sample was immediately mounted under a stream of cold nitrogen and centered in the X-ray beam using a video camera for data collection. $C_{40}H_{40}F_{12}P_2Ru_2 \cdot 4\,CH_2Cl_2$, $M = 1352.50$, triclinic, space group $P\bar{1}$, $a = 11.351(4)$ Å, $b = 12.414(4)$ Å, $c = 19.508(7)$ Å, $\alpha = 89.068(6)°$, $\beta = 74.322(6)°$, $\gamma = 82.114(6)°$, $V = 2620.9(16)$ Å^3, $Z = 2$, $\rho_{calcd} = 1.714$ g cm^{-3}; crystal dimensions 0.30 × 0.20 × 0.20 mm. A total of 23448 reflections (11787 unique, $R_{int} = 0.0398$) were collected using a full-sphere ω-scan routine ($2\theta_{max} = 56.64°$) with Bruker SMART APEX CCD diffractometer, $Mo_{K\alpha}$ radiation ($\lambda = 0.71073$ Å) at $T = 193(2)$ K. Data were corrected for absorption effects by empirical methods using SADABS software (min/max. transmission 0.67). The structure was solved by direct methods and refined using the SHELXTL (version 5.1) software package in full-matrix anisotropic approx-

 © 2004 Wiley-VCH Verlag GmbH & Co. KGaA, Weinheim

imation for all non-hydrogen atoms. Hydrogen atoms were placed at idealized positions and refined using the "riding model". The refinement converged to $R1 = 0.0760$, $wR2 = 0.2048$ for $I > 2\sigma(I)$, and $R1 = 0.1076$, $wR2 = 0.2357$ for all data, and a goodness-of-fit of 1.048. All significant electron density residuals were found approximately 1 Å from Ru atoms. CCDC-236736 contains the supplementary crystallographic data for this paper. These data can be obtained free of charge via www.ccdc.cam.ac.uk/conts/retrieving.html (or from the Cambridge Crystallographic Data Centre, 12, Union Road, Cambridge CB2 1EZ, UK; fax: (+44) 1223-336-033; or deposit@ccdc.cam.ac.uk).

[10] J. C. Hanson, C. E. Nordman, *Acta Crystallogr. Sect. B* **1976**, *32*, 1147. The C–C bond distances are average values of chemically equivalent bonds from two crystallographically independent molecules and two independent sets of data.

[11] a) R. C. Haddon, L. T. Scott, *Pure Appl. Chem.* **1986**, *58*, 137; b) R. C. Haddon, *Acc. Chem. Res.* **1988**, *21*, 243; c) R. C. Haddon, *Science* **1993**, *261*, 1545.

[12] A. Sygula, R. Sygula, A. Ellern, P. W. Rabideau, *Org. Lett.* **2003**, *5*, 2595.

[13] a) L. T. Scott, M. M. Hashemi, M. S. Bratcher, *J. Am. Chem. Soc.* **1992**, *114*, 1920; b) T. J. Seiders, K. K. Baldridge, G. H. Grube, J. S. Siegel, *J. Am. Chem. Soc.* **2001**, *123*, 517; c) A. Sygula, A. H. Abdourazak, P. W. Rabideau, *J. Am. Chem. Soc.* **1996**, *118*, 339; d) Z. Marcinow, A. Sygula, A. Ellern, P. W. Rabideau, *Org. Lett.* **2001**, *3*, 3527; e) G. H. Grube, E. L. Elliott, R. J. Steffens, C. S. Jones, K. K. Baldridge, J. S. Siegel, *Org. Lett.* **2003**, *5*, 713.

 © 2004 Wiley-VCH Verlag GmbH & Co. KGaA, Weinheim

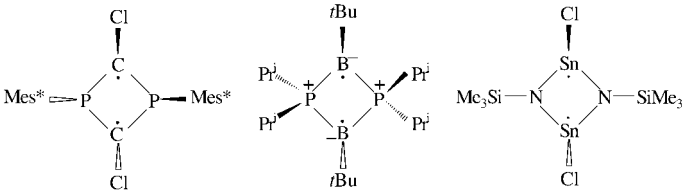
Main-Group Chemistry

A 1,3-Diaza-2,4-distannacyclobutanediide: Synthesis, Structure, and Bonding**

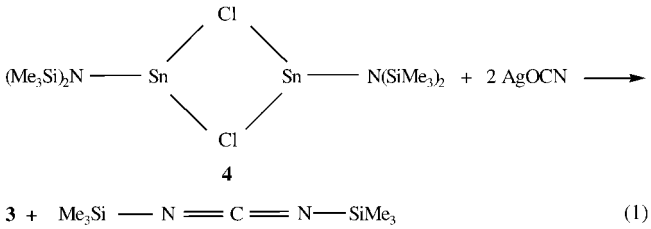
Hazel Cox, Peter B. Hitchcock, Michael F. Lappert,* and Luc J.-M. Pierssens*

There is much current interest in four-membered ring compounds containing heteroatoms that are isoelectronic with a cyclobuta-1,3-dienediide; the first thermally robust parent compound $\{[C(SiMe_3)]_4\}^{2-}$ was only reported in 2000.[1] Homocyclic "aromatic" inorganic compounds include $[E_4]^{2+}$ (E = S, Se, Te),[2] $(\{B(NMe_2)[B(NMe_2)_2]\}_2)^{2-}$,[3] $\{[Al(Cl)(NH_3)]_4\}^{2-}$,[4] and $[Ga_4\{C_6H_3(C_6H_2iPr_3\text{-}2',4',6')\text{-}2,6\}_2\text{-}1,3]^{2-}$.[5] Particular attention has focused on analogues with alternating heteroatoms that have a biradicaloid electronic structure and a feature of interest is the relative stability of the triplet and singlet states; an early example was the labile $[SN]_2$,[6a] a 6π-electron aromatic molecule.[6b] A trigger was the discovery by Niecke et al. of the modestly robust, diamagnetic 1,3-diphosphacyclobutane-2,4-diyl **1**,[7] which was followed by the related compounds $[C(Cl)P(TMP)]_2$,[8a] $[C(H)P(Mes^*)C(SiMe_3)P(Mes^*)]$,[8b] $[C(Cl)P(Mes^*)C(SiMe_3)P(Mes^*)]$,[8b] $[C(SiMe_3)P(Mes^*)C(AlMe_3)P(Mes^*)]^-$,[8c] $[C(Mes^*)P(Me)C(Mes^*)P(tBu)]$,[8d] $[C(SiMe_3)P(Mes^*)]_2$,[8e] and $\{[C(SiMe_3)P]_2\}^{2-}$.[8e] The Group 13/15 isoelectronic system was initially represented by the planar ring compound **2** of Bertrand et al.;[9] puckered ring analogues $[B^-(R)P^+R'_2]_2$ (R, R′ = Dur, *i*Pr; *t*Bu, Ph; Dur, Et; Ph, Ph) were subsequently described.[10a,b] The bonding in compounds of the type **1** and **2** has already been discussed.[11a,b]

Herein we report on the 1,3-diaza-2,4-distanna-cyclobutadienediide **3**. It is unprecedented on two counts: 1) previously reported three-coordinate tin compounds were ionic, free radical, or cluster [as in, for example, $SnCl_3^-$, $[Sn\{Si(Me)tBu_2\}_3]$ (radical or cation),[12a] $[Sn\{N(SiMe_3)_2\}_3]$,[12b] $[(SnR_2)_3Sn_2]$,[12c] $[(SnR_2)_3(SnR)_2Sn_2]$ (R = $C_6H_3Et_2$-2,6)],[12d] or one of the bonds was dative [as in **4**[12e] or $[\{Sn(CH(SiMe_3)_2)_2\}_2]$,[12f]]; 2) it is the first alternating heteroatom analogue of a cyclobuta-1,3-dienediide featuring a 5p-block element.



X-ray-quality crystals of the colorless, diamagnetic (4–298 K) compound **3** were isolated in modest yield from the reaction according to Equation (1); monitoring the reaction



(1)

by ^{119}Sn NMR spectroscopy showed that **3** was the major tin-containing product. It is assumed that Ag and CO_2 had been eliminated.

The above reaction was unexpected in the light of our prior observations on Sn(X)X′/AgY systems. Thus, we had

[*] Dr. H. Cox,[+] Dr. P. B. Hitchcock, Prof. M. F. Lappert, Dr. L. J.-M. Pierssens
Department of Chemistry, School of Life Sciences
University of Sussex, Brighton, BN1 9QJ (UK)
Fax: (+44) 1273 677196
E-mail: h.cox@sussex.ac.uk
m.f.lappert@sussex.ac.uk

[+] Computational studies.

[**] This work was supported by the European Commission (category 20 TMR fellowship for L.J.-M.P.) and EPSRC (Advanced research fellowship for H.C.; Time on the UK computational facilities, Columbus, at RAL for HC). We thank Dr. B. Mahieu (Mössbauer) and Drs. J. Keates and G. A. Lawless (CP-MAS-NMR) for spectral data.

Supporting information for this article is available on the WWW under http://www.angewandte.org or from the author.

 © 2004 Wiley-VCH Verlag GmbH & Co. KGaA, Weinheim DOI: 10.1002/anie.200460039

found: 1) metathetical exchange with (a) **4** + AgOTf, to yield $[\{Sn[N(SiMe_3)_2](\mu\text{-}OTf)\}_2]$ ($OTf = OS(O)_2CF_3$),[13a] (b) SnX_2 + 2 AgOCN, to give $[\{Ag(\mu\text{-}X)\}_4]$ [$X = N(SiMe_3)_2$ or TMP];[13b] 2) oxidative addition to the SnX_2 by AgY to afford $[Sn\{CH(SiMe_3)_2\}_2Y_2]$ (Y = I or NCO) or $[Sn\{2,6\text{-}(NMe_2)_2C_6H_3\}_2Y_2]$ (Y = NCO or NCS);[13c] or (iii) adduct formation between $[Sn\{CH(SiMe_3)_2\}_2]$ + AgY → $[Ag(CN)\{Sn(CH(SiMe_3)_2)_2\}_2]_\infty$ or $[\{Ag(SCN)[Sn(CH(SiMe_3)_2)_2]_2(thf)\}_2]$.[13c] We attribute the driving force of the reaction of **4** with AgOCN to be the oxophilicity of silicon. A common intermediate in each of the above reactions is suggested to be a 1:1 X(X′)Sn→AgY adduct. For X = $N(SiMe_3)_2$, X′ = Cl, and Y = OCN, this leads to a redox reaction, yielding $Me_3SiN{=}C{=}NSiMe_3$ and $[Sn\{N(SiMe_3)\}Cl]$ (which dimerises→**3**) + Ag + Me_3SiOCN. The latter is believed to be transformed into bis(trimethylsilyl) carbodiimide + CO_2, possibly under the catalytic influence of silver. We note that the same carbodiimide has been obtained from $NaN(SiMe_3)_2$ and CO_2 and that Me_3SiOCN was suggested to have been an intermediate.[14]

The NMR spectra of **3** were recorded at 298 K both in solution ($PhMe/C_6D_6$: ^1H, ^{13}C, ^{29}Si, ^{119}Sn) and in the solid state by cross- polarization magic-angle spinning (CPMAS) spectroscopies (^{13}C, ^{29}Si, ^{119}Sn). The ^{119}Sn NMR chemical shift showed that the structure of **3** in $PhMe/C_6D_6$ was temperature-invariant in the range 298 ($\delta = -83$ ppm) to 183 K ($\delta = -104$ ppm). The ^{119}Sn chemical shift at 298 K was solvent-dependent: $\delta = -87$ (C_6D_6), −83 ($PhMe\text{-}C_6D_6$), −102 (CD_2Cl_2), −140 (thf/C_6D_6), −285 ppm ($HMPA/PhMe/C_6D_6$; HMPA is hexamethylphosphoramide). The CPMAS NMR chemical shifts (δ) were observed at lower frequencies than equivalent solution shifts ($PhMe/C_6D_6$; shown in parentheses): δ ^{13}C, −9 (2.62); ^{29}Si, −28 (22.0); ^{119}Sn, −17 (−84). Evidently the "solvent" donates to the Sn centers, consistent with ligating strengths decreasing in the sequence HMPA > thf > CD_2Cl_2 > PhMe > C_6H_6.

The ^{119}Sn-Mössbauer spectra of **3** and **4** were measured.[15] The values of the isomer shift were similar: 3.21 (**3**), 3.28 (**4**) $mm\,s^{-1}$, but those for the quadrupole splitting deviated significantly: 1.76 (**3**), 3.10 (**4**) $mm\,s^{-1}$; this result indicates that **3** and **4** have similar s-electron density at the Sn nucleus, but that their bonding differs.

The molecular structure of **3** shows it to be a monomer (Figure 1 a),[16] with long-range $(Sn\cdots Cl'')_2$ (3.29 Å) contacts (Figure 1 b) to a neighboring molecule.

The monomer has a planar centro-symmetric four-membered $\{(SnN)_2\}$ ring, with *trans*-silicon atoms only 6° out of this plane; the *trans*-chlorine ligands are disposed orthogonally. The Sn–Sn′ separation of 3.398 Å shows that there is no transannular bonding (see the data reported in reference [17] in which the Sn–Sn distance is 2.810 Å in α-tin). The endocyclic bond angles in **3**, as well as the mean Sn–N bond length, are similar to those in the tin(II) complex $[\{Sn^I(\mu\text{-}N{=}PPh_3)\}_2]$ (**5**): 78.3(1) and 101.7° at Sn and N, respectively, and 2.163(4) Å.[18] The Sn–Cl bond length in **3** is significantly shorter than that in the hypothetical chloro-analogue of **5** (about 2.60 Å, which is based on the ionic radii of Cl^- and I^-; l(Sn–I) in **5**, 2.9085(5) Å[18]). The Si–N, Sn–N, and Sn–Cl bond lengths in **3** may be compared with those in **4** (which has a planar $\{(SnCl)_2\}$ ring) of 1.729(3), 2.069(3), and 2.598(1) Å, respectively.[12c]

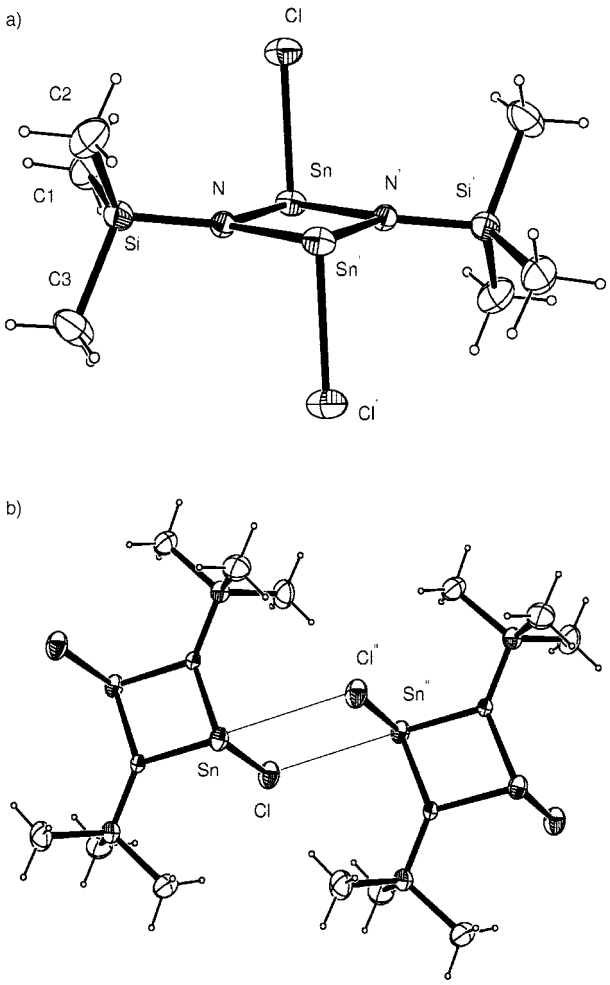


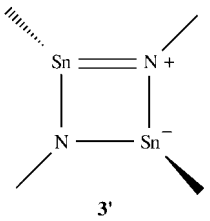
Figure 1. Structure of **3** (H atoms not shown; a) the monomer ; b) showing close Sn···Cl contacts to a neighboring molecule. Selected interatomic distances [Å] and angles [°]: Sn-N 2.120(3), Sn-N′ 2.179(3), Sn-Cl 2.470(2), Si-N 1.666(3), Si-Cl 1.859(5), Sn···Cl″ 3.29, Sn···Sn′ 3.398(1), N-Sn-N′ 75.57(14), N-Sn-Cl 88.71(10), N′-Sn-Cl 91.53(11), Si-N-Sn′ 130.2(2), Sn-N-Sn′ 104.43(14), Sn′-Sn-Cl 90.1

Electronic structure calculations were performed to answer the following questions posed by the experimental results: 1) what is the bonding in **3**, 2) what are the relative energies of the singlet and triplet states, and 3) what is the explanation for the discrepancies between the solid-state and solution NMR spectroscopic data?

The bonding: Geometry optimizations on **3** were performed,[19,20] and in no case was a Sn–Sn′ bond implicated and hence no buckling of the geometry was found. Each N atom and each Sn atom is three-coordinate leaving each N atom to donate two electrons to the ring and each Sn atom one electron. Thus the most appropriate description of **3** is as a pseudo six-π-electron four-center system.

The valence bond structure shown in **3′** (this is one of four resonance structures) is consistent with the calculated molecular orbitals in which three of the four π molecular orbitals, two almost nonbonding orbitals, and a bonding orbital, are

 © 2004 Wiley-VCH Verlag GmbH & Co. KGaA, Weinheim



3'

filled and the antibonding orbital is empty.[2] These four orbitals arising from the four ring atoms consist of combinations of p orbitals on the N atoms (++ and +−) and combinations of sp^3 hybrids on the Sn atoms (again ++ and +−). Of these four orbitals, three are filled: the ++ combination of the tin atoms and both N-centred orbitals. This is in basic agreement with the schematic representation of the π orbitals of a delocalized π complex given by Niecke, et al. for **1**.[7]

Table 1 shows the percentage contribution of N and Sn atoms to the frontier orbitals. As the Sn atom is less electronegative than the N atom, the bonding orbitals have greater N character whilst the antibonding orbitals have greater Sn character.[21]

Table 1: Percentage contribution of nitrogen and tin atoms to the frontier orbitals.

Orbital	Energy [eV]	Atom	s	p_x	p_y	p_z
Lumo	−5.037	Sn	30.36	3.23	10.94	6.56
		N		5.30	16.90	11.40
Homo	−6.201	Sn				
		N		72.22		
Homo-1	−6.343	Sn	34.87	10.59	6.16	4.19
		N	1.80	1.48	1.97	4.62
Homo-2	−6.817	Sn		4.40		
		N		39.22	2.83	

The electronic and geometric structure: Initially, a single-point energy calculation was performed on the X-ray crystal structure (C_i symmetry). However, although SCF convergence was obtained, the filling of the orbitals was non-aufbau: the Sn-centred orbitals, although lower in energy than the lone pair on the nitrogen atoms (−5.81 and −5.67 eV, respectively), were not filled. It was possible to force the electrons into the Sn-centred orbital but this resulted in a destabilization of the Sn orbital and a destabilization of the molecule as a whole. Thus, a full geometry optimization of structure **3** was performed; the results are shown in Table 2, from which it is evident that the singlet state is favored by over 57 kJ mol^{-1} regardless of whether scalar relativistic effects are included or not.* This is in accord with the study by Schoeller, et al.[22] on substituted derivatives of 2,4-diphosphacyclobutane-diyl-1,3, which showed that σ-donating substituents at the phosphorus atom tend to increase the singlet–triplet energy separation.

Surprisingly, however, the optimized geometry differed substantially from the X-ray crystal structure. Selected geometric parameters are compared in the Supporting Information. The Sn–N and N′–Sn bond lengths are reasonably reproduced, within an error of 5%, although this is poor for current density functional methods. However, the Sn′-Sn-Cl bond angle is hugely inaccurate (119.4°) and this, along with the shortening of the Sn–Sn′ bond (3.06 Å), could be responsible for the deviations in the Sn-N-Sn′ and N-Sn-N′ angles (96.1° and 83.9°, respectively). It is pertinent to note that these optimized bond angles are comparable with the bond angles in the isoelectronic $\{C_2P_2\}$ system: P-C-P = 92.2° and C-P-C = 87.8°.[7]

Table 2: Calculated singlet–triplet energy difference (relativistic and nonrelativistic)

	Non-relativistic	Relativistic
Singlet (S) [eV]	−158.832	−158.097
Triplet (T) [eV]	−158.041	−157.505
Δ(T-S) [eV]	0.791	0.592
Δ(T-S) [kJ mol^{-1}]	76.3	57.1

To investigate these substantial differences, a series of single-point energies was performed on the experimental geometry with the Sn′-Sn-Cl bond angle varied at 10° intervals in the range 90° to 130°. A smooth continuous curve was produced with a minimum at 120°, from which a floppy Sn′-Sn-Cl bending mode was estimated. Two alternative methods (the semiempirical method PM3 and the hybrid functional B3LYP with a Gaussian effective core potential[20]) also predicted a Sn′-Sn-Cl bond angle of 120 ± 4°.

However, the X-ray crystal structure revealed close intermolecular Sn···Cl″ contacts (Figure 1b), which may be the cause of the constraint of the Sn′-Sn-Cl bond angle in the X-ray crystal structure.

It was noted by Janssen that out-of-plane distortions factor considerably in the stability of these electron-rich four-membered rings in the free molecule.[23] Thus, an extensive ab initio study was performed to establish whether inorganic six-π-electron four-membered rings (with and without substituents), are more stable than corresponding organic rings. It was concluded that the concept of resonance stabilization, in general, does not fully account for the geometric preferences of six-π-electron four-membered rings that contain atoms from the second-row of the periodic table. Other effects, including σ-bond strengths and especially energy-lowering out-of-plane distortions, are at least of equal importance. Zandwijk, et al.[24] had also shown that low-frequency out-of-plane vibrational modes of substituents on the ring are of major significance for the stability of these electron-rich, six-π-electron, four-membered rings.

NMR chemical-shift calculations: Calculations of the chemical shifts of both the geometry-optimized structure and the X-ray crystal structure were performed. It was proposed that if the electronic-structure calculations were correct and the true relaxed geometry would be that predicted by theory, then this structure would be the most probable in solution in an inert solvent. Thus, the constrained (X-ray) crystal structure would produce different chemical shifts to those of the latter. To test this proposition, NMR chemical shifts were calculated for both the X-ray crystal structure

* Note that all further discussion will refer to the ADF scalar relativistic singlet geometry.

 © 2004 Wiley-VCH Verlag GmbH & Co. KGaA, Weinheim

(single-point energy calculations SPE) and the possible solution (monomeric) structure (optimized geometry).

The calculated relative chemical shifts are compared with the experimental data in Table 3. In each case, the total isotropic shielding constant for each atom in the molecule was calculated and the average was compared to that of the corresponding shift of $SiMe_4$ (for C, H, and Si) and to that of $SnMe_4$ (for Sn) to compare with the experimental relative shifts.

Table 3: Comparison of calculated and experimental chemical shifts

	Average isotropic chemical shifts (ppm)			
		Experimental	Calculated	
	Solid	Solution/C_6D_6/298 K	Expt. geom.	Opt. Geom.
^{13}C	−9	2.62	−3.1	10.8
^{1}H		0.09	−5.6	0.5
^{29}Si	−28	22	−176.1	10.7
^{119}Sn	−17	−84	641.2	740.6

A negative shift indicates that there is more shielding, and a positive number indicates that there is less shielding, in the specified molecule than in the reference molecule. Thus, as expected, there is more shielding in the solid (as evinced by the SPE calculation) than in the solution (to be compared with the optimized geometry). With the exception of Sn, in each case the relative shift follows the trend of the experimental data, and in the case of ^{13}C the shifts are within 8 ppm of the experimental values. This favorable comparison gives credence to the assumption that the relaxed (geometry optimized) structure is indeed the "free" structure that appears in solution, and that in the solid state, intermolecular forces play an important role in fixing the Cl atoms in optimum positions for the interaction with neighboring Sn atoms.

In summary, we have presented the synthesis of the first 1,3-diaza-2,4-distanna-cyclobutanediide [$\overline{N(SiMe_3)\text{-}Sn(Cl)N'(Si'Me_3)Sn'Cl'}$] (**3**) by the unusual reaction between $[Sn\{N(SiMe_3)_2\}(\mu\text{-}Cl)]_2$ and AgOCN. Compound **3** was shown to be diamagnetic in the crystal and in solution. Crystalline **3** has a planar four-membered $\{(SnN)_2\}$ ring with the *trans*-chlorine ligands orthogonal to this plane. There are long range $(Sn\cdots Cl)_2$ contacts between neighboring molecules. The CPMAS NMR ^{13}C, ^{29}Si, and ^{119}Sn chemical shifts were observed at lower frequency than those recorded in PhMe/C_6D_6; and the ^{119}Sn signal was particularly sensitive to solvent, the frequency decreasing in the sequence PhMe/C_6D_6 < CD_2Cl_2 < thf/C_6D_6 ≪ HMPA/PhMe/C_6D_6, attributed to an interaction from the "solvent" donor to the tin atom, probably at the limit disrupting the virtual dimer in the crystal. The computational studies show that the singlet ground state is substantially favored over the triplet. The optimized geometry showed considerable disparity between the calculated and the experimentally determined Sn′-Sn-Cl angle, which is attributed to the constrained geometry of the monomer (Figure 1 a) and does not take into account the intermolecular contacts with the neighboring molecule (Figure 1 b). Calculated ^{13}C- and ^{29}Si-NMR chemical-shift differences as between the solid-state and the PhMe/C_6D_6 solution qualitatively reproduce the experimental observations. Note added in proof: the compound $[\{Ge(R)N(SiMe_3)\}_2]$ [R = $C_6H_3(2,6\text{-}i\text{Pr}_2\text{-}C_6H_3)C_6H_3$] was recently described.[25]

Experimental Section

All manipulations were carried out under vacuum or argon by using Schlenk techniques.

Silver cyanate (2.47 g, 16.5 mmol) was added to a stirring solution of $[Sn\{N(SiMe_3)_2\}(\mu\text{-}Cl)]_2$ (5.18 g, 8.2 mmol) in diethyl ether (150 mL) at room temperature. The brown, cloudy reaction mixture was stirred in darkness for about 16 h. A brown–grey precipitate was removed by filtration and the filtrate concentrated under vacuum. A second filtration and storage of the filtrate at −5 °C yielded a beige solid, which was extracted with refluxing toluene (50 mL). The colorless extract yielded colorless microcrystals of **3** (0.96 g, 24 %), mp 53–56 °C (decomp), which on recrystallization from benzene gave large colorless plates of X-ray quality.

NMR (PhMe + C_6D_6, 303 K): ^{1}H, $\delta = 0.09$ ppm; $^{13}C\{^{1}H\}$, $\delta = 2.62$ ppm; $^{29}Si\{^{1}H\}$, $\delta = 22.0$ ppm; $^{119}Sn\{^{1}H\}$, $\delta = -84$ ppm. CPMAS-NMR: ^{13}C, $\delta = -9$ ppm; ^{29}Si, $\delta = -28$ ppm, ^{119}Sn, $\delta = -17$ ppm. ^{119}Sn Mossbauer (90 K): IS, 3.21 mm s^{-1}; QS, 1.76 mm s^{-1}.

N,*N*′-Bis(trimethylsilyl)carbodiimide, bp 158–162 °C; MS (70 eV, EI): *m*/*z* (%): 180 (10) [M^+], 171 (100) [M−Me]$^+$; IR: $\tilde{\nu}_{max} = 2190$ cm^{-1}, was isolated among the volatile products.

Received: March 18, 2004 [Z460039]

Keywords: density functional calculations · heterocycles · radicals · tin

[1] a) A. Sekiguchi, T. Matsuo, H. Watanabe, *J. Am. Chem. Soc.* **2000**, *122*, 5652; b) T. Matsuo, A. Sekiguchi, *Bull. Chem. Soc. Jpn.* 2004, 77, 211.
[2] See R.J Gillespie, *Chem. Soc. Rev.* **1979**, *8*, 315.
[3] W. Mesbah, C. Präsang, M. Hofmann, G. Geiseler, W. Massa, A. Berndt, *Angew. Chem.* **2003**, *115*, 1758; *Angew. Chem. Int. Ed.* **2003**, *42*, 1717.
[4] a) X. Li, A. E. Kuznetsov, H. F. Zhang, A. I. Boldyrev, L. S. Wang, *Science* **2001**, *291*, 859; b) A. E. Kuznetsov, A. I. Boldyrev, *Inorg. Chem.* **2002**, *41*, 3596.
[5] B. Twamley, P. P. Power, *Angew. Chem.* **2000**, *112*, 3648; *Angew. Chem. Int. Ed.* **2000**, *39*, 3500.
[6] a) C. M. Mikulski, P. J. Russo, M. S. Saran, A. G. MacDiarmid, A. F. Garito, A. J. Heger, *J. Am. Chem. Soc.* **1975**, *97*, 6358; b) Y. Jung, T. Heine, P. v. R. Schleyer, M. Head-Gordon, *J. Am. Chem. Soc.* **2004**, *126*, 3132.
[7] E. Niecke, A. Fuchs, F. Baumeister, M. Nieger, W. W. Schoeller, *Angew. Chem.* **1995**, *107*, 640; *Angew. Chem. Int. Ed. Engl.* **1995**, *34*, 555.
[8] a) O. Schmidt, A. Fuchs, D. Gudat, M. Nieger, W. Hoffbauer, E. Niecke, W. W. Schoeller, *Angew. Chem.* **1998**, *110*, 995; *Angew. Chem. Int. Ed.* **1998**, *37*, 949; b) E. Niecke, A. Fuchs, M. Nieger, *Angew. Chem.* **1999**, *111*, 3213; *Angew. Chem. Int. Ed.* **1999**, *38*, 3028; c) E. Niecke, A. Fuchs, M. Nieger, O. Schmidt, W. W. Schoeller, *Angew. Chem.* **1999**, *111*, 3216; *Angew. Chem. Int. Ed.* **1999**, *38*, 3031; d) H. Sugiyama, S. Ito, M. Yoshifuji, *Angew. Chem.* **2003**, *115*, 3932; *Angew. Chem. Int. Ed*, **2003**, *42*, 3802; e) M. Sebastian, M. Nieger, D. Szieberth, L. Nyulászi, E. Niecke, *Angew. Chem.* **2004**, *116*, 647; *Angew. Chem. Int. Ed*, **2004**, *43*, 637.
[9] D. Scheschkewitz, H. Amii, H. Gornitzka, D. Bourissou, G. Bertrand, *Science* **2002**, *295*, 1880.
[10] a) W. W. Schoeller, A. Rozhenko, D. Bourissou, G. Bertrand, *Chem. Eur. J.* **2003**, *9*, 3611; b) D. Scheschkewitz, H. Amii, H.

 © 2004 Wiley-VCH Verlag GmbH & Co. KGaA, Weinheim

Gornitzka, W. W. Schoeller, D. Bourissou, G. Bertrand, *Angew. Chem.* **2004**, *116*, 595; *Angew. Chem. Int. Ed.* **2004**, *43*, 585.

[11] a) R. A. J. Janssen, *J. Phys. Chem.* **1993**, *97*, 555b) H. Grützmacher, F. Breher, *Angew. Chem.* **2002**, *114*, 4178; *Angew. Chem. Int. Ed.* **2002**, *41*, 4006.

[12] a) A. Sekiguchi, T. Fukawa, V. Ya. Lee, M. Nakamoto, *J. Am. Chem. Soc.* **2003**, *125*, 9250; b) A. Hudson, M. F. Lappert, P. W. Lednor, *J. Chem. Soc. Dalton Trans.* **1976**, 2369; c) L. R. Sita, R. D. Bickerstaff, *J. Am. Chem. Soc.* **1989**, *111*, 6454; d) L. R. Sita, I. Kinoshita, *J. Am. Chem. Soc.* **1992**, *114*, 7024; e) R. W. Chorley, P. B. Hitchcock, B. S. Jolly, M. F. Lappert, G. A. Lawless, *J. Chem. Soc. Chem. Commun.* **1991**, 1302; f) P. J. Davidson, D. H. Harris, M. F. Lappert, *J. Chem. Soc. Dalton Trans.* **1976**, 2268.

[13] a) P. B. Hitchcock, M. F. Lappert, G. A. Lawless, D. M. de Lima, L. J.-M. Pierssens, *J. Organomet. Chem.* **2000**, *601*, 142; b) P. B. Hitchcock, M. F. Lappert, L. J.-M. Pierssens, *Chem. Commun.* **1996**, 1189; c) P. B. Hitchcock, M. F. Lappert, L. J.-M. Pierssens, *Organometallics* **1998**, *17*, 2686.

[14] a) U. Wannagat, J. Pump, H. Bürger, *Monatsh. Chem.* **1963**, *94*, 1013; b) U. Wannagat, H. Kuckertz, C. Krüger, J. Pump, *Z. Anorg. Allg. Chem.* **1964**, *333*, 54.

[15] B. Mahieu, L. J.-M. Pierssens, unpublished work.

[16] X-ray analysis data for **3**: $C_6H_{18}Cl_2N_2Si_2Sn_2$: $a = 6.791(6)$, $b = 6.872(3)$, $c = 9.414(4)$ Å, $\alpha = 84.62(3)$, $\beta = 85.28(5)$, $\gamma = 65.58(6)°$, $Z = 1$, $M_r = 482.7$; triclinic, space group $P\bar{1}$ (No.2), $V = 397.8(4)$ Å^3, $\mu(Mo_{K\alpha}) = 3.60$ mm^{-1}, $T = 173(2)$ K, 2325 independent reflections [$R(\text{int}) = 0.008$], reflections with $I > 2\sigma(I)$ 2155. The structure was solved by direct methods and refined to F^2 anisotropically, the H atoms were included in a riding mode. Final R indices [$I > 2\sigma(I)$]: $R_1 = 0.039$, w$R_2 = 0.104$; R indices (all data): $R_1 = 0.043$, w$R_2 = 0.108$. CCDC-233571 contains the supplementary crystallographic data for this paper. These data can be obtained free of charge via www.ccdc.cam.ac.uk/conts/retrieving.html (or from the Cambridge Crystallographic Data Centre, 12, Union Road, Cambridge CB21EZ, UK; fax: (+44) 1223-336-033; or deposit@ccdc.cam.ac.uk).

[17] J. Thuoliss, A. R. Davey, *Nature* **1954**, *174*, 1011.

[18] S. Chitsaz, B. Neumüller, K. Dehnicke, *Z. Anorg. Allg. Chem.* **1999**, *625*, 1670.

[19] Calculations were performed by using Slater-type orbitals with the BP86 functional as implemented in ADF2000.02 (E. J. Baerends, D. E. Ellis, P. Ros, *Chem. Phys.* **1973**, *2*, 41). The numerical integration procedure applied for the calculations is that of G. te Velde and E. J. Baerends (*J. Comput. Phys.* **1992**, *99*, 84). A triple-ξ Slater-Type-Orbital (STO) basis set with a polarization function was used for describing the valence electrons of Sn (4d 5s 5p), N (2s 2p), Cl (3s 3p) and Si (3s, 3p). A double-ξ STO basis set was used for C (2s 2p) and H, augmented by an extra polarization function. Electrons in lower shells were treated with the frozen core approximation. Energies of **3** were calculated by using the local density approximation (LDA) (S. H. Vosko, L. Wilk, M. Nusair, *Can. J. Phys.* **1980**, *58*, 1200). The non-local exchange of A. D. Becke (A. D. Becke, *Phys. Rev. A* **1988**, *38*, 2398) and the non-local correlation correction of J. P. Perdew (J. P. Perdew, *Phys. Rev. B* **1986**, *33*, 8822) and the scalar relativistic correction (T. Ziegler, V. Tschinke, E. J. Baerends, J. G. Snijders, W. J. Ravenek, *J. Phys. Chem.* **1989**, *93*, 3050) were applied to the LDA density. NMR chemical shifts were calculated by using the implementation by G. Schreckenbach, T. Ziegler, *J. Phys. Chem.* **1995**, *99*, 606.

[20] For confirmation, calculations were carried out by using the Gaussian 98 program. (Gaussian 98 (Revision A.7), M. J. Frisch, G. W. Trucks, H. B. Schlegel, G. E. Scuseria, M. A. Robb, J. R. Cheeseman, V. G. Zakrzewski, J. A. Montgomery, R. E. Stratmann, J. C. Burant, S. Dapprich, J. M. Millam, A. D. Daniels, K. N. Kudin, M. C. Strain, O. Farkas, J. Tomasi, V. Barone, M. Cossi, R. Cammi, B. Mennucci, C. Pomelli, C. Adamo, S. Clifford, J. Ochterski, G. A. Petersson, P. Y. Ayala, Q. Cui, K. Morokuma, D. K. Malick, A. D. Rabuck, K. Raghavachari, J. B. Foresman, J. Cioslowski, J. V. Ortiz, B. B. Stefanov, G. Liu, A. Liashenko, P. Piskorz, I. Komaromi, R. Gomperts, R. L. Martin, D. J. Fox, T. Keith, M. A. Al-Laham, C. Y. Peng, A. Nanayakkara, C. Gonzalez, M. Challacombe, P. M. W. Gill, B. G. Johnson, W. Chen, M. W. Wong, J. L. Andres, M. Head-Gordon, E. S. Replogle, J. A. Pople, Gaussian, Inc., Pittsburgh, PA, **1998**.). The geometries were optimized by using the B3LYP functional and the effective core potential LANL2DZ.

[21] A. J. Bridgman, G. Cavigliasso, L. R. Ireland, J. Rothery, *J. Chem. Soc. Dalton Trans.* **2001**, 2095.

[22] W. W. Schoeller, C. Begemann, E. Niecke, D. Gudat, *J. Phys. Chem. A* **2001**, *105*, 10731.

[23] R. A. J. Janssen, *J. Phys. Chem.* **1993**, *97*, 6384.

[24] G. van Zandwijk, R. A. J. Janssen, H. M. Buck, *J. Am. Chem. Soc.* **1990**, *112*, 4155.

[25] C. Cui, M. Brynda, M. M. Olmstead, P. P. Power, *J. Am. Chem. Soc.* **2004**, *126*, 6510.

 © 2004 Wiley-VCH Verlag GmbH & Co. KGaA, Weinheim

Bioinorganic Chemistry

Biomimetic Oxidation of Chromium(III): Does the Antidiabetic Activity of Chromium(III) Involve Carcinogenic Chromium(VI)?**

*Irma Mulyani, Aviva Levina, and Peter A. Lay**

The proposed role of Cr^{III} ions as an essential human micronutrient, responsible for insulin activation in glucose and fat metabolism,[1] is currently under dispute.[2,3] The most recent mechanistic hypothesis on the biological activity of the Cr^{III} ion assumes the existence of a specific biomolecule that binds Cr^{III} ions, chromodulin, which enhances interactions of insulin with its cellular receptors.[4] No definitive structural information on chromodulin is available as yet,[4] and its isolation procedure is controversial.[3,5] A well-characterized trinuclear oxo–carboxylato complex, $[Cr^{III}_3O(OCOEt)_6(OH_2)_3]^+$ (**1**)[6] has been proposed as a structural and

[*] I. Mulyani, Dr. A. Levina, Prof. P. A. Lay
Centre for Heavy Metals Research
School of Chemistry
University of Sydney
Sydney, NSW 2006 (Australia)
Fax: (+61) 2-9351-3329
E-mail: p.lay@chem.usyd.edu.au

[**] Financial support for this work was provided by an Australian Research Council Discovery grant, including an Australian Professional Fellowship (to P.A.L.). I.M. is grateful to Chemistry Department, Bandung Institute of Technology, Indonesia, for partial funding of her postgraduate studies at the University of Sydney. We thank Dr. Michael Davies (Heart Research Institute, Sydney) for helpful discussions.

Supporting information for this article is available on the WWW under http://www.angewandte.org or from the author.

 © 2004 Wiley-VCH Verlag GmbH & Co. KGaA, Weinheim DOI: 10.1002/anie.200460113

functional mimetic of chromodulin[7] and a safer potential therapeutic agent for Type II diabetes and related disorders[8] than the controversial nutritional supplement, $[Cr^{III}(pic)_3]$ (**2**, pic = picolinato(1−) = pyridine-2-carboxylato(1−)).[9]

Although biological oxidations of Cr^{III} species to genotoxic and carcinogenic Cr^{VI} or Cr^{V} species[3] were previously considered impossible,[10] evidence is mounting for the feasibility of such oxidations under physiologically relevant conditions.[3,11] Herein we propose, for the first time, that the reported insulin-enhancing activities of some Cr^{III} compounds,[1,8] previously attributed to specific interactions of Cr^{III} ions with cellular insulin receptors,[4] are caused by intra- or extracellular oxidations of Cr^{III} to Cr^{V} and/or Cr^{VI} compounds, which act as protein tyrosine phosphatase (PTP) inhibitors by mechanisms similar to those for a well-known insulin mimetic V^{V} species (isoelectronic to Cr^{VI}).[12]

Strong oxidants, such as H_2O_2 and ClO^-, are produced naturally by cells, particularly those involved in the immune response, through the reactions of oxidase enzymes with reductants and O_2.[13] While oxidation of Cr^{III} to Cr^{VI} ions by H_2O_2 in strongly alkaline media is well-known and is widely used in analytical chemistry,[14] only scattered reports exist on the oxidation of some Cr^{III} complexes (with nonbiological ligands) by H_2O_2 or ClO^- in neutral or weakly basic aqueous media (pH 7–9).[15] We chose complex **1** as a main substrate for the systematic studies of the oxidation of Cr^{III} species under physiologically relevant conditions owing to its known biological activity[8] and proposed structural similarity to a purported natural factor that contains Cr^{III} ions.[4,7] Complex **1** can also serve as a representative example of numerous polynuclear species formed on hydrolysis of Cr^{III} complexes in neutral aqueous solutions.[16] It is relatively stable at pH 7.4 and 37 °C, although partial hydrolysis (leading to di- and mononuclear species) occurs on the timescale of hours, as revealed by electrospray mass spectrometry (see the Supporting Information).

Oxidations of **1** by H_2O_2 or ClO^- at pH 7.4 led to the formation of $[Cr^{VI}O_4]^{2-}$, detected from its characteristic absorbance in electronic spectra ($\lambda_{max} = 372$ nm, $\varepsilon_{max} \sim 4.7 \times 10^3\,M^{-1}cm^{-1}$, see the Supporting Information).[14a] Quantitative determination of Cr^{VI} species was performed by the diphenylcarbazide method[17] after the removal of unconverted H_2O_2 by catalase (see the Supporting Information for experimental details), typical results are presented in Table 1.

Micromolar concentrations of Cr^{VI} ions were produced in the reactions of **1** (Cr-ion concentration, 0.10 mM) with sub-mM concentrations of H_2O_2 or ClO^-, as well as with two well-known H_2O_2-producing enzymatic systems, based on glucose oxidase[18] or xanthine oxidase,[19] on the hours timescale at pH 7.0–7.4 and 37 °C (Table 1). This is the first evidence for oxidation of Cr^{III} ions by enzymatic systems. Kinetic studies of the reaction of **1** with the glucose oxidase system showed that the formation of Cr^{VI} species is preceded by the formation of H_2O_2 (see the Supporting Information). Notably, oxidation of **1** by H_2O_2 was efficient in a protein-rich environment and even in undiluted blood serum (buffers *C* and *D* in Table 1). Relatively low but detectable levels of Cr^{VI} species were formed upon the oxidation of **2** or hydrolysed $CrCl_3$ by H_2O_2 (Table 1).[16] No detectable levels of Cr^{V} species (≥ 1 μM, by EPR spectroscopy)[3,11] were formed under the studied conditions (Table 1).

Table 1: Typical conditions and results of Cr^{III} oxidations.

Substrate[a]	Oxidant[b]	Buffer[c]	*t* [h][d]	$[Cr^{VI}]$ [μM][e]
1	H_2O_2 (1.0)	*A*	1.0	12 ± 2
1	H_2O_2 (1.0)	*A*	6.0	33 ± 6
1	H_2O_2 (0.10)	*A*	6.0	4.0 ± 0.7
1	H_2O_2 (1.0)	*B*	6.0	10 ± 1
1	H_2O_2 (1.0)	*C*	6.0	20 ± 1
1	H_2O_2 (1.0)	*D*	1.0[f]	8 ± 2
$CrCl_3$[g]	H_2O_2 (1.0)	*A*	6.0	10 ± 1
2	H_2O_2 (1.0)	*A*	6.0	1.0 ± 0.1
1	ClO^- (0.25)	*B*[h]	6.0	23 ± 2
1	GO[i]	*A*	6.0	14 ± 3
1	XO[j]	*A*	6.0	9 ± 1

[a] In all reactions, $[Cr^{III}]_0 = 0.10$ mM. [b] Concentrations (mM) are given in parentheses. [c] Designations: *A* is 4-(2-hydroxyethyl)-1-piperazineethanesulfonate (HEPES, 0.10 M, pH 7.4); *B* is phosphate (0.10 M, pH 7.4); *C* is tris(hydroxymethyl)aminomethane (Tris, 50 mM, pH 7.0), containing NaCl (0.10 M), ethylenediamine-*N*,*N*,*N*′,*N*′-tetraacetate (EDTA, 0.20 mM), bovine serum albumin (BSA, 1.0 mg mL^{-1}), and Brij 35 (0.001 %); and *D* is fetal bovine serum (undiluted). [d] All the reactions were carried out at 37 °C. [e] Average results and standard deviations of three independent experimental series. [f] Longer reaction times led to partial reduction of the formed Cr^{VI}. [g] Hydrolysis products of $CrCl_3$. [h] No Cr^{VI} formation was observed in buffer *A*, probably because of ClO^- reduction by the buffer. [i] Glucose oxidase (0.10 U mL^{-1}), glucose (5.0 mM), and ambient air O_2. [j] Xanthine oxidase (0.10 U mL^{-1}), xanthine (saturated, ~1 mM), and ambient air O_2.

The abilities of a Cr^{VI} complex, as well as of a model Cr^{V} complex, $[Cr^{V}O(ehba)_2]^-$ (ehba = 2-ethyl-2-hydroxybutanoato(2−)),[20] to inhibit a well-characterized[21] microbial PTP[22] in vitro were comparable to those of V^{V} under the same conditions (Figure 1). The PTP used contained a $Cys(X_5)Arg$ catalytic domain (X is any amino acid), which is common for all the known microbial and mammalian PTPs.[21] The buffer used in the phosphatase reactions (corresponding to *C* in Table 1) contained small amounts of

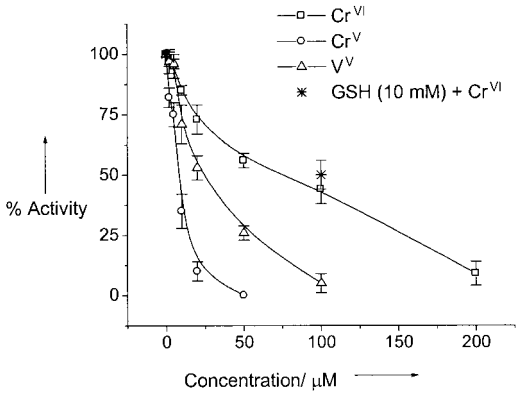


Figure 1. Inhibition of a recombinant *Yersinia enterocolitica* PTP (from Sigma) by Cr^{VI} ions (Na_2CrO_4), Cr^{V} ions ($Na[CrO(ehba)_2]$), or V^{V} ions (Na_3VO_4) in buffer *C* (see note [c] to Table 1), at 37 °C (reaction time 30 min), by using *p*-nitrophenylphosphate (10 mM) as a substrate. Averaged results and standard deviations of three independent experimental series are shown; experimental details are given in the Supporting Information.

 © 2004 Wiley-VCH Verlag GmbH & Co. KGaA, Weinheim

thiols ([RSH] $\approx 7\,\mu M$, see the Supporting Information for details), which helped to maintain the active reduced state of the Cys residue in the catalytic domain of the enzyme.[21] To ensure that the inhibitory effects of Cr^{VI} and Cr^{V} specues were not due to the depletion of the antioxidant thiols in the buffer, the abilities of Cr^{VI} and Cr^{V} complexes to reduce the PTP activity in the presence of excess thiol (dithiothreitol, [RSH] = 1.0 mM) were also demonstrated (see the Supporting Information). Furthermore, the efficiency of PTP inhibition by Cr^{VI} species (0.10 mM) was not significantly decreased in the presence of the most abundant biological reductant, glutathione (GSH) at a high physiological concentration (10 mM, Figure 1).[22] These data suggest that Cr^{VI} and Cr^{V} species are likely to react with PTPs even in the thiol-rich intracellular environment. To our knowledge, this is the first example of inhibition of an isolated PTP by Cr^{VI} or Cr^{V} compounds. No significant ($\geq 20\%$) effects on the PTP activity were observed for Cr^{III} compounds (up to 0.50 mM of **1**, **2**, or $CrCl_3$).[23]

Reactions of $[CrO_4]^{2-}$ ions with PTPs probably involve reversible formation of relatively stable five-coordinate thiolato complexes with Cys residues in the catalytic domains of the enzymes (Figure 2),[24] consistent with the generally

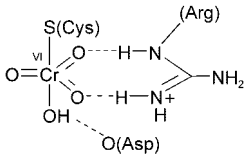


Figure 2. Proposed binding mode of the Cr^{VI} species to the active site of PTP, based on the structures of Cr^{VI} thiolato complexes in aqueous solutions (determined by X-ray absorption spectroscopy)[24] and structures of vanadate-inhibited PTPs (determined by X-ray crystallography).[12b,21b]

accepted mechanism for reactions with $[VO_4]^{3-}$ ions.[12] Reactions of Cr^{V} complexes with Cys residues at the catalytic sites of enzymes, including PTPs, are more likely to lead to their irreversible oxidations,[17b] as was proposed in the mechanism of PTP inhibition by V^{V} peroxo complexes.[12a] Although Cr^{V} species were not detected by EPR spectroscopy during the oxidation of Cr^{III} centers in this work, significant concentrations of such species are likely to form during the reduction of Cr^{VI} centers within the cells or at the cell surface.[3,11] Extracellular oxidation of Cr^{III} to Cr^{VI} ions (e.g., by H_2O_2 or ClO^- released by macrophages)[13] will lead to a dramatic increase in cellular uptake of Cr species.[3,25] Inhibition of PTPs by Cr^{V} and/or Cr^{VI} species is probably responsible for the increased levels of tyrosine phosphorylation in Cr^{VI}-treated cells[26] and for the insulin-mimetic effects of Cr^{VI} species in animals.[27] Such inhibition is likely to lead to disruptions in cell signaling pathways, and to contribute to the Cr^{VI}-induced carcinogenicity.[3]

The relative reactivities of various Cr^{III} complexes towards H_2O_2 (Table 1) may correlate with their reported activities as insulin activators.[1,8] Although both complexes **1** and **2** improve insulin-related metabolic parameters in diabetic rats, only the former complex (which is oxidized more easily, Table 1) is efficient in healthy animals.[8] A stable chelate complex, **2**, is relatively nonreactive in vitro (Table 1); indeed, its stability in gastrointestinal media is one of the main reasons for its use as a nutritional supplement.[1] However, **2** is known to be metabolized by hepatic enzymes with the release of more reactive Cr^{III} species.[28] Rapid hydrolysis of $CrCl_3$ in neutral aqueous media with the formation of insoluble products[16] is a likely reason for its relatively inefficient oxidation to Cr^{VI} (Table 1), as well as for the controversies regarding its biological activity.[1]

In conclusion, the ease of oxidation of **1** to carcinogenic Cr^{VI} under biologically relevant conditions (Table 1) warrants further research into the safety of using **1** (or any other Cr^{III} compound) as a nutritional supplement or therapeutic agent.[8]

Experimental Section

Full details of the used reagents, preparation of reaction solutions and instrumental techniques are given in the Supporting Information.

Received: March 25, 2004 [Z460113]

Keywords: bioinorganic chemistry · biological activity · chromium · enzyme inhibitors · oxidation

[1] R. A. Anderson, *J. Am. Coll. Nutr.* **1998**, *17*, 548–555.
[2] D. M. Stearns, *BioFactors* **2000**, *11*, 149–162.
[3] A. Levina, R. Codd, C. T. Dillon, P. A. Lay, *Prog. Inorg. Chem.* **2003**, *51*, 145–250, and references therein.
[4] a) C. M. Davis, J. B. Vincent, *Biochemistry* **1997**, *36*, 4382–4385; b) L. Jacquamet, Y. Sun, J. Hatfield, W. Gu, S. P. Cramer, M. W. Crowder, G. A. Lorigan, J. B. Vincent, J.-M. Latour, *J. Am. Chem. Soc.* **2003**, *125*, 774–780; c) J. B. Vincent, *J. Trace Elem. Exp. Med.* **2003**, *16*, 227–236.
[5] E. Gaggelli, F. Berti, N. D'Amelio, N. Gaggelli, G. Valensin, L. Bovalini, A. Paffetti, L. Trabalzini, *Environ. Health Perspect.* **2002**, *110*, 733–738.
[6] A. S. Antsyshkina, M. A. Porai-Koshits, I. V. Arkhangel'skii, I. N. Diallo, *Zh. Neorg. Khim.* **1987**, *32*, 2928–2932; Engl. transl.: A. S. Antsyshkina, M. A. Porai-Koshits, I. V. Arkhangel'skii, I. N. Diallo, *Russ. J. Inorg. Chem.* **1987**, *32*, 1700–1703.
[7] The ability of nM concentrations of **1** to enhance the tyrosine kinase activity of β subunits of insulin receptors has been reported (C. M. Davis, A. C. Royer, J. B. Vincent, *Inorg. Chem.* **1997**, *36*, 5316–5320), but our attempts to reproduce these results were not successful.
[8] a) Y. J. Sun, K. Mallya, J. Ramirez, J. B. Vincent, *J. Biol. Inorg. Chem.* **1999**, *4*, 838–845; b) J. B. Vincent, C. M. Davis (University of Alabama), US Patent 6197816, **2001** [*Chem. Abstr.* **2001**, *134*, 207223]; c) Y. J. Sun, B. J. Clodfelder, A. A. Shute, T. Irvin, J. B. Vincent, *J. Biol. Inorg. Chem.* **2002**, *7*, 852–862.
[9] a) D. M. Stearns, W. H. Armstrong, *Inorg. Chem.* **1992**, *31*, 5178–5184; b) D. M. Stearns, S. M. Silveira, K. K. Wolf, A. M. Luke, *Mutat. Res.* **2002**, *513*, 135–142; c) D. D. D. Hepburn, J. Xiao, S. Bindom, J. B. Vincent, J. O'Donnell, *Proc. Natl. Acad. Sci. USA* **2003**, *100*, 3766–3771.
[10] F. L. Petrilli, S. DeFlora, *Mutat. Res.* **1978**, *58*, 167–173.
[11] a) R. Codd, C. T. Dillon, A. Levina, P. A. Lay, *Coord. Chem. Rev.* **2001**, *216–217*, 533–577; b) A. Levina, P. A. Lay, *Coord. Chem. Rev.* **2004**, in press.
[12] a) P. J. Stankiewicz, A. S. Tracey, D. C. Crans in *Metal Ions in Biological Systems*, *Vol. 31* (Eds.: H. Sigel, A. Sigel), Marcel

 © 2004 Wiley-VCH Verlag GmbH & Co. KGaA, Weinheim

Dekker, New York, **1995**, pp. 287 – 324; b) M. Zhang, M. Zhou, R. L. Van Etten, C. V. Stauffacher, *Biochemistry* **1997**, *36*, 15 – 23.
[13] B. Halliwell in *Active Oxygen in Biochemistry* (Eds.: J. S. Valentine, C. S. Foote, A. Greenberg, J. F. Liebman), Blackie Academic and Professional, London, **1995**, pp. 313 – 335.
[14] a) G. W. Haupt, *Natl. Bur. Stand. Circ.* **1952**, *48*, 414 – 423; b) J. E. T. Andersen, *Anal. Chim. Acta* **1998**, *361*, 125 – 131.
[15] a) S. C. Pal, M. T. H. Tarafder, *Indian J. Chem. Sect. A* **1996**, *35*, 960 – 963; b) R. Rajan, B. U. Nair, T. Ramasami, *Inorg. React. Mech.* **2000**, *1*, 247 – 255.
[16] P. A. Lay, A. Levina in *Comprehensive Coordination Chemistry II*, *Vol. 4* (Eds.: J. A. McCleverty, T. J. Meyer), Elsevier, Oxford, UK, **2004**, pp. 313 – 413.
[17] a) *Standard Methods for the Examination of Water and Wastewater*, 16th ed., American Public Health Association, Washington, DC, **1985**, Sect. 312B, pp. 201 – 204; b) A. Levina, A. M. Bailey, G. Champion, P. A. Lay, *J. Am. Chem. Soc.* **2000**, *122*, 6208 – 6216.
[18] J. P. Klinman, *J. Biol. Inorg. Chem.* **2001**, *6*,1 – 13, and references therein.
[19] C. Vorbach, R. Harrison, M. R. Capecchi, *Trends Immunol.* **2003**, *24*, 512 – 517, and references therein.
[20] M. Krumpolc, J. Roček, *J. Am. Chem. Soc.* **1979**, *101*, 3206 – 3209. This complex is widely used as a model for the studies of reactions of Cr^{V} complexes reactions biomolecules in vitro.[3,11a]
[21] a) Z.-Y. Zhang, J. C. Clemens, H. L. Schubert, J. A. Stuckey, M. W. F. Fischer, D. M. Hume, M. A. Saper, J. E. Dixon, *J. Biol. Chem.* **1992**, *267*, 23759 – 23766; b) Z.-Y. Zhang, Y. Wang, L. Wu, E. B. Fauman, J. A. Stuckey, H. L. Schubert, M. A. Saper, J. E. Dixon, *Biochemistry* **1994**, *33*, 15266 – 15270.
[22] Reduction of Cr^{VI} to Cr^{III} ions by GSH at physiological conditions is relatively slow (hours timescale) and leads to the formation of reactive Cr^{V}, Cr^{IV}, and organic radical species, which are likely to contribute to PTP inhibition (A. Kortenkamp, M. Casadevall, S. P. Faux, A. Jenner, R. O. J. Shayer, N. Woodbridge, P. O'Brien, *Arch. Biochem. Biophys.* **1996**, *329*, 199 – 207).
[23] The method for determination of phosphatase activity was similar to that described in: B. J. Goldstein, L. Zhu, R. Hager, A. Zilbering, Y. J. Sun, J. B. Vincent, *J. Trace Elem. Exp. Med.* **2001**, *14*, 393 – 404 (see the Supporting Information for details). Opposite effects (activation by $\approx 50\,\%$ or inhibition by $\approx 70\,\%$) of $CrCl_3$ (0.10 mM) on two recombinant human PTPs, described in this reference, are likely to be due to the changes in protein conformation caused by nonspecific binding of Cr^{III} ions.[3] No significant effects of **1** or chromodulin on human PTPs were found, contrary to the earlier reports.[4,7]
[24] A. Levina, P. A. Lay, *Inorg. Chem.* **2004**, *43*, 324 – 335.
[25] C. T. Dillon, P. A. Lay, A. M. Bonin, M. Cholewa, G. J. F. Legge, *Chem. Res. Toxicol.* **2000**, *13*, 742 – 748.
[26] a) E. J. Yurkow, G. Kim, *Mol. Pharmacol.* **1995**, *47*, 686 – 695; b) Y. Qian, B. Jiang, D. C. Flynn, S. S. Leonard, S. W. Wang, Z. Zhang, J. P. Ye, F. Chen, L. Y. Wang, X. L. Shi, *Mol. Cell. Biochem.* **2001**, *222*, 199 – 204.
[27] a) E. Kim, K. J. Na, *Toxicol. Appl. Pharmacol.* **1991**, *110*, 251 – 258; b) Y. Goto, K. Kida, *Jpn. J. Pharmacol.* **1995**, *67*, 365 – 368.
[28] S. A. Kareus, C. Kelley, H. S. Walton, P. R. Sinclair, *J. Hazard. Mater. B* **2001**, *84*, 163 – 174.

 © 2004 Wiley-VCH Verlag GmbH & Co. KGaA, Weinheim

Coordination Modes

Rhodizonate Metal Complexes with a 2D Chairlike M_6 Metal–Organic Framework: $[M(C_6O_6)(bpym)(H_2O)]\cdot n\,H_2O$**

Chih-Chieh Wang, Chen-Tsung Kuo, Pi-Tai Chou, and Gene-Hsiang Lee*

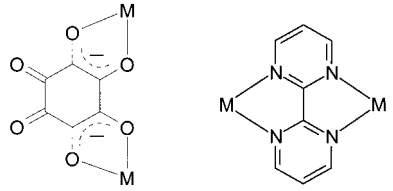
The chronological significance and interesting chemistry of the monocyclic oxocarbon dianions, $C_nO_n^{2-}$ ($n=3$, deltate; $n=4$, squarate; $n=5$, croconate; $n=6$, rhodizonate), which is a nonbenzenoid aromatic system, are well elaborated in numerous books and reviews.[1] Over the past four decades, focus on the whole family of the oxocarbon dianions has been directed towards their aromaticity and molecular symmetry. Theoretical approaches have indicated that the aromaticity decreases as the ring size increases. It is thus expected that rhodizonate ($C_6O_6^{2-}$) has only a small degree of aromatic character.[2] Accordingly, much research has been carried out on the exploitation of squarate ($C_4O_4^{2-}$) and croconate ($C_5O_5^{2-}$) ligands in the construction of versatile coordination polymeric architectures through various binding modes.[3–5] The existence of planar D_{nh} structures has been established on metal salts or complexes chelated by squarate and croconate. Conversely, owing to their relative instability, structural information on complexes by using deltate and rhodizonate as the building ligands is obscure.[6–10] Thus far, just a few rhodizonate salts of $K_2C_6O_6$,[8] $Rb_2C_6O_6$[10] and some inclusion compounds of urea and thiourea[9] have been structurally well characterized. For example, rhodizonate conforms to nonplanar D_{3d} and C_2 molecular geometries coexisting in $K_2C_6O_6$, a D_{6h} geometry in $Rb_2C_6O_6$, $[n\mathrm{Bu_4N}]^+{}_2C_6O_6^{2-}\cdot 4\,\mathrm{PhNHCONH_2}$ and $[n\mathrm{Bu_4N}]^+{}_2C_6O_6^{2-}\cdot 2\,m\text{-}\mathrm{OHC_6H_4NHCONH_2}\cdot 2\,H_2O$, and a planar C_{2v} molecular geometry in $[n\mathrm{Bu_4N}]^+{}_2C_6O_6^{2-}\cdot 2\,\mathrm{NH_2CONHCH_2CH_2NHCONH_2}\cdot 3\,H_2O$.[9] To the best of our knowledge, the crystal structure of a rhodizonate transition-metal complex, unfortunately, has not yet been reported. It is thus both fundamentally and practically important to explore rhodizonate transition-metal complexes and consequently to shed light on their corresponding binding modes and molecular symmetries. Herein, we report the first two rhodizonate

[*] Prof. C.-C. Wang, C.-T. Kuo
Department of Chemistry
Soochow University
Taipei (Taiwan)
Fax: (+886) 2-2881-1053
E-mail: ccwang@mail.scu.edu.tw
Prof. P.-T. Chou
Department of Chemistry
National Taiwan University
Taipei (Taiwan)
G.-H. Lee
Instrumental Center
National Taiwan University
Taipei (Taiwan)

[**] This work was supported by the National Science Council, Taiwan, R.O.C. M = Cd, $n=1$; M = Mn, $n=2$; bpym = 2,2′-bipyrimidine.

 DOI: 10.1002/anie.200460278 © 2004 Wiley-VCH Verlag GmbH & Co. KGaA, Weinheim

transition-metal complexes, $[Cd(C_6O_6)(bpym)(H_2O)]\cdot H_2O$ (**1**) and $[Mn(C_6O_6)(bpym)(H_2O)]\cdot 2H_2O$ (**2**), in which both rhodizonate and 2,2′-bipyrimidine (bpym) act as the bis-bidentate ligands (Scheme 1) to chelate the metal ions, thus forming a novel 2D chairlike M_6 metal–organic framework (MOF).



Scheme 1. The bis-bidentate bridging mode of rhodizonate and bpym.

The preparation of **1** and **2** was carried out by the treatment of $Cd(NO_3)_2\cdot 4H_2O$ (or $MnCl_2\cdot 4H_2O$) with 2,2′-bipyrimidine (bpym) and $Na_2C_6O_6$ in an aqueous solution under acidic conditions (pH ~ 4.4) for a period of several days to yield deep-green crystals. Single-crystal X-ray diffraction studies revealed that the molecular structure of rhodizonate in both complexes has a nonplanar C_2 symmetry. As depicted in Figure 1, all cadmium centers in compound **1** are seven-

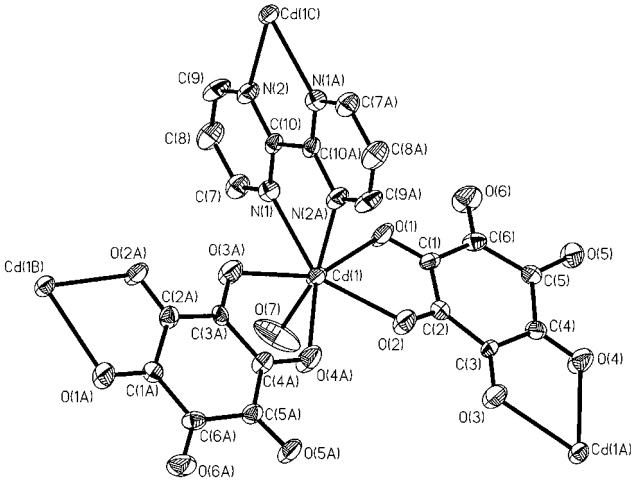


Figure 1. ORTEP drawings of the coordination of the cadimum center in **1** (thermal ellipsoids set at 50% probability, all H atoms and solvated water molecular omitted for clarity).

coordinate.[11] The geometric environment of each Cd atom is in a distorted pentagonal bipyramidal (O(7)-Cd(1)-N(2) 164.3(2)°), coordinated by two nitrogen atoms of bpym ligands, four oxygen atoms of two $C_6O_6^{2-}$ ligands and one water molecule. Each rhodizonate adopts a bis-bidentate (μ_4) bridging mode (Scheme 1) through four adjacent oxygen atoms and links two crystallographically identical Cd ions, thus forming a 1D polymeric zigzag chain (Figure 2a). It is noteworthy that this is the first structure ever reported in which $C_6O_6^{2-}$ acts as a bridging ligand bonded with the metal ion. Adjacent chains are then mutually linked by the bridge of

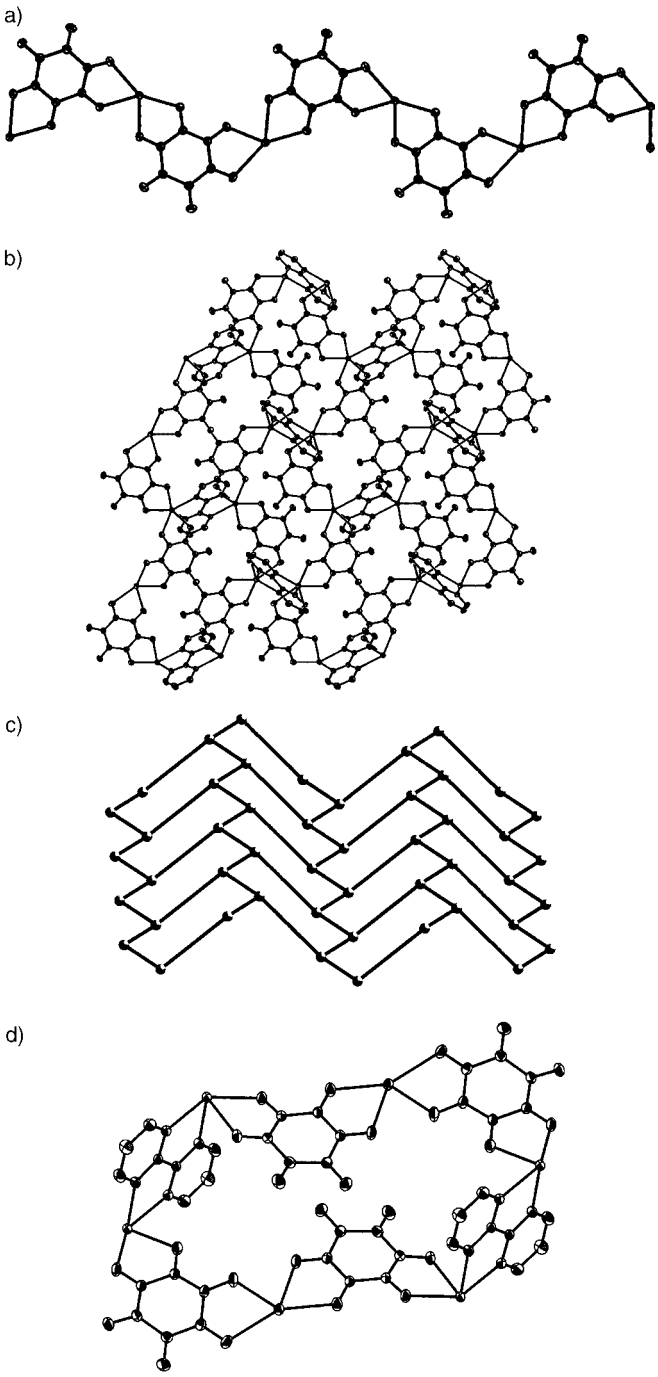


Figure 2. a) A zigzag chain formed by the bridge of Cd with $C_6O_6^{2-}$. b) The 2D metal organic framework through the connectivity of Cd and $C_6O_6^{2-}$, bpym ligands, and c) the schematic representation of chairlike $\{Cd_6\}$ unit, the blue line through bpym bridge and the red line via $C_6O_6^{2-}$ bridge. d) The chairlike building unit composed of six Cd^{II} ions, four $C_6O_6^{2-}$, and two bpym ligands (water molecules omitted for clarity).

bpym ligands that adopt a bis-bidentate binding mode to form a novel 2D MOF (Figure 2b) with a chairlike $\{Cd_6\}$ skeleton as the building unit (Figure 2c). Each $\{Cd_6\}$ unit is composed of six Cd ions, four rhodizonates and two bpym ligands. The Cd···Cd separations through $C_6O_6^{2-}$ and bpym bridges are 7.321(3) and 6.257(1) Å, respectively. Despite the differing

 © 2004 Wiley-VCH Verlag GmbH & Co. KGaA, Weinheim

numbers of lattice water molecules, the molecular structure of compound **2** is almost the same as that of compound **1** and has a 2D chairlike {Mn_6} MOF constructed through the linkages of Mn ions with bis-bidentate (μ_4) bridging the $C_6O_6^{2-}$ and bis-bidentate bpym.[11] The geometric environment of each Mn atom is also in a distorted pentagonal bipyramidal (O(7)-Cd(1)-N(2) 167.77(7)°) coordinated by two nitrogen atoms from bpym ligands, four oxygen atoms from two $C_6O_6^{2-}$ ligands, and an oxygen atom from a water molecule (Figure 3). The Mn···Mn separations through $C_6O_6^{2-}$ and bpym bridges are 7.177(3) and 6.061(1) Å, respectively.

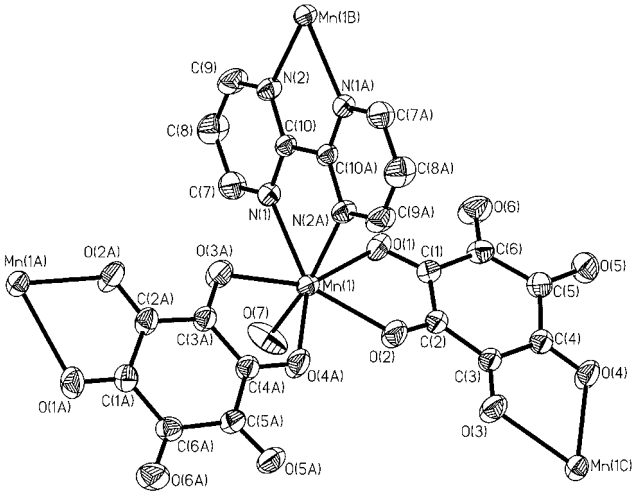


Figure 3. ORTEP drawings of the coordination of manganese ion in **2** (thermal ellipsoids set at 50% probability, all H atoms and solvated water molecular omitted for clarity).

As the bis-bidentate (μ_4) binding mode of rhodizonate found in **1** and **2** is novel, it is of fundamental importance to examine the correlation between molecular symmetry and π-electron delocalization around the six-membered ring. The measured dimensions of the $C_6O_6^{2-}$ species in **1** and **2** conform nearly to a C_2 molecular symmetry, which corresponds to a diketone character (Figure 4). The mean deviations of carbon atoms from planarity are 0.071 and 0.054 Å for **1** and **2**, respectively, which are obviously larger than those of 0.020 and 0.010 Å in the inclusion compounds incorporating tetra-*n*-butylammonium rhodizonate and urea derivatives.[9] Moreover, the deviations of most oxygen atoms (see the numbers shown in Figure 4) in $C_6O_6^{2-}$ are larger than 0.1 Å, thus indicating a nonplanar molecular geometry. Notably, the C–C bond lengths—1.501(7) Å in **1**, 1.492(3) Å in **2**—between two nonbonded C=O groups are close to being single bond in character, and they are also larger than other C–C bond lengths—1.453(7)–1.468(7) Å in **1** and 1.443(3)–1.481(3) Å in **2**—for a C_2 molecular symmetry (Figure 4). This result implies that when $C_6O_6^{2-}$ acts as a bridging ligand, the π-electron delocalization in the six-membered ring of dianion is less extensive than that of its free ion in rhodizonate salts.[7–9] The nonplanar molecular geometry in $C_6O_6^{2-}$ seems to be in accordance with this theoretical prediction.[2] Thus the

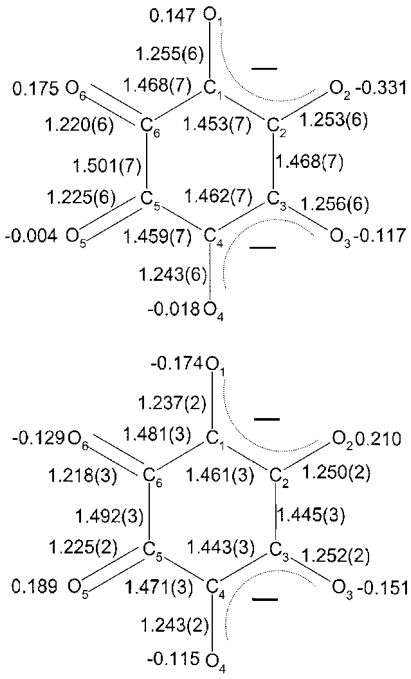


Figure 4. Deviations of the oxygen atoms from the least-square plane of C6, and C–C, C–O bond lengths of the rhodizonate dianion with the C_2 molecular geometry in **1** (top) and **2** (bottom).

present finding provides direct, valuable information on the molecular geometry of rhodizonate when it is being used as a coordinating ligand. Finally, our preliminary results revealed that **1** in DMSO has an absorption band maximized at 490 nm. Upon excitation, **1** gave rise to an emission band maximum at 590 nm with decent quantum efficiency (≈0.05). Thus, the associated luminescence property for both complexes and magnetic phenomena for **2** should be of great interest. Investigations on detailed physical/photophysical properties of these complexes is currently in progress.

Experimental Section

General: All chemicals were of reagent grade and were used as commercially obtained without further purification. Elementary analyses (carbon, hydrogen, and nitrogen) were performed by using a Perkin–Elmer 2400 elemental analyzer. IR spectra were recorded on a KBr disc with a Nicolet Fourier Transform IR, MAGNA-IR 500 spectrometer in the range of 500–4000 cm^{-1}.

Synthesis of $[Cd(C_6O_6)(bpym)(H_2O)]\cdot H_2O$ (**1**): A solution (4 mL) of sodium rhodizonate ($Na_2C_6O_6$, 21.4 mg, 0.1 mmol) was added to a solution (4 mL) of $Cd(NO_3)_2\cdot 4H_2O$ (30.9 mg, 0.1 mmol) and 2,2′-bipyrimidine (15.8 mg, 0.1 mmol) at room temperature to give a dark-brown solution. Deep-green crystals were obtained after several days in a yield of about 23%. IR (KBr pellet): $\tilde{\nu}$ = 3441 (m, br), 3054 (m, sharp), 1648 (m, sharp), 1604 (m, sharp), 1569 (s, sh), 1548 (vs, sharp), 1520 (vs, sharp), 1505 (vs, sharp), 1411 (s, sharp), 1216 (m, sharp), 1093 (m, sharp), 1052 (m, sharp), 1022 (m, sharp), 814 (m, sharp), 755 (m, sharp), 722 (m, sharp), 670 (m, sharp) cm^{-1}. Elemental analysis calcd (%) for $C_{10}H_7CdN_2O_8$ (M_r = 395.58): C 30.33, N 7.07, H 1.76; found: C 29.91, N 6.90, H 1.72.

Synthesis of $[Mn(C_6O_6)(bpym)(H_2O)]\cdot 2H_2O$ (**2**): A solution (2 mL) of sodium rhodizonate ($Na_2C_6O_6$, 21.4 mg, 0.1 mmol) was added to a solution (4 mL) of $MnCl_2$ (19.7 mg, 0.1 mmol) and 2,2′-

 © 2004 Wiley-VCH Verlag GmbH & Co. KGaA, Weinheim

bipyrimidine (15.8 mg, 0.1 mmol) at room temperature to give a dark-brown solution. Red-brown crystals were obtained after several days in a yield of about 34%. IR (KBr pellet): $\tilde{\nu}$ = 3564 (m, sharp), 3509 (m, sharp), 3457 (m, br), 3317 (m, br), 3098 (m, sharp), 1633 (s, sharp), 1568 (s, sharp), 1537 (s, sharp), 1485 (vs, br), 1411 (s, sharp), 1357 (m, sharp), 1216 (m, sharp), 1062 (m, sharp), 1026 (m, sharp), 757 (m, sharp), 671 (m, sharp), 563 (m, sharp) cm^{-1}. Elemental analysis (%) calcd for $C_{10}H_9MnN_2O_9$ (M_r = 356.13): C 33.69, N 7.86, H 2.44; found: C 33.67, N 7.52, H 2.52.

Received: April 9, 2004 [Z460278]

Keywords: cadmium · coordination modes · manganese · O ligands

[1] For example, see: R. West, J. Niu in *Non-benzenoid Aromatics, Vol. I* (Ed.: J. P. Snyder), Academic Press, New York, **1969**, chap. 6; R. West, J. Niu in *The Chemistry of the Carbonyl Group, Vol. II* (Ed.: J. Zabicky), Interscience, London, **1970**, chap. 4; R. West, *Oxocarbons* (Ed.: R. West), Academic Press, New York, **1980**, pp. 1–14; R. West, *Isr. J. Chem.* **1980**, *20*, 300–307; F. Serratosa, *Acc. Chem. Res.* **1983**, *16*, 170–176; G. Seitz, P. Imming, *Chem. Rev.* **1992**, *92*, 1227–1260.

[2] J. Aihara, *J. Am. Chem. Soc.* **1981**, *103*, 1633–1635; P. v. R. Schleyer, K. Najafian, B. Kiran, H. Jiao, *J. Org. Chem.* **2000**, *65*, 426–431.

[3] L. A. Hall, D. J. Williams, S. Menzer, A. J. P. White, *Inorg. Chem.* **1997**, *36*, 3096–3101; K.-J. Lin, K.-H. Lii, *Angew. Chem.* **1997**, *109*, 2166–2167; *Angew. Chem.* **1997**; *Angew. Chem. Int. Ed. Engl.* **1997**, *36*, 2076–2077; S. O. H. Gutschke, M. Molinier, A. K. Powell, P. T. Wood, *Angew. Chem.* **1997**, *109*, 1028–1029; *Angew. Chem. Int. Ed. Engl.* **1997**, *36*, 991–992; D. Braga, F. Grepioni, *Chem. Commun.* **1998**, 911–912; H.-A. Hosein, L. A. Hall, A. J. Lough, W. Desmarais, M. J. Vela, B. M. Foxman, *Inorg. Chem.* **1998**, *37*, 4184–4189.

[4] D. Deguenon, G. Bernardinelli, J.-P. Tuchagues, P. Castan, *Inorg. Chem.* **1990**, *29*, 3031–3037; I. Castro, J. Sletten, J. Faus, M. Julve, Y. Journaux, F. Lloret, S. Alvarez, *Inorg. Chem.* **1992**, *31*, 1889–1894; N. S. Goncalves, P. S. Santos, I. Vencato, *Acta Crystallogr. Sect. C* **1996**, *52*, 622–624; J. Sletten, O. Bjorsvik, *Acta Chem. Scand.* **1998**, *52*, 770–777; J. D. Dunitz, P. Seiler, W. Czechtizky, *Angew. Chem.* **2001**, *113*, 1829–1830; *Angew. Chem. Int. Ed.* **2001**, *40*, 1779–1780; I. Castro, M. L. Calatayud, F. Lloret, J. Sletten, M. Julve, *J. Chem. Soc. Dalton Trans.* **2002**, 2397–2403; T. K. Maji, S. Konar, G. Mostafa, E. Zangrando, T. H. Lu, N. R. Chaudhuri, *J. Chem. Soc. Dalton Trans.* **2003**, 171–175.

[5] C. C. Wang, H. W. Lin, C. H. Yang, C. H. Liao, I. T. Lan, G. H. Lee, *New J. Chem.* **2004**, *28*, 180–182; C. C. Wang, C. H. Yang, S. M. Tseng, G. H. Lee, Y. P. Chiang, H. S. Sheu, *Inorg. Chem.* **2003**, *42*, 8294–8299; C. C. Wang, C. H. Yang, G. H. Lee, *Inorg. Chem.* **2002**, *41*, 1015–1018.

[6] R. West, D. Eggerding, J. Perkin, D. Handy, E. Tuazon, *J. Am. Chem. Soc.* **1979**, *101*, 1710–1714.

[7] R. West, H.-Y. Niu, D. L. Powell, M. V. Evans, *J. Am. Chem. Soc.* **1960**, *82*, 6204–6205.

[8] M. A. Neuman, PhD thesis, University of Wiscosin (USA), **1965**.

[9] C. K. Lam, T. C. W. Mak, *Chem. Commun.* **2001**, 1568–1569; C. K. Lam, T. C. W. Mak, *Angew. Chem.* **2001**, *113*, 3561–3563; *Angew. Chem. Int. Ed.* **2001**, *40*, 3453–3455.

[10] D. Braga, G. Cojazzi, L. Maini, F. Grepioni, *New J. Chem.* **2001**, *25*, 1221–1223.

[11] Crystal data for **1**: $C_{10}H_7CdN_2O_8$, M_r = 395.58, monoclinic, space group $P2_1/n$, a = 7.4250(5), b = 13.9423(9), c = 11.9924(8) Å, β = 93.279(1)°, V = 1239.4(1) $Å^3$, Z = 4, μ = 1.807 mm^{-1}, ρ_{calcd} = 2.120 $g\,cm^{-3}$, $\lambda(Mo_{K\alpha})$ = 0.71073 Å, GOF = 1.244, $R1$ ($wR2$) = 0.0570 (0.1096) [2473 observed ($I > 2\sigma(I)$)] for 2873 (R_{int} = 0.0455) independent reflections out of a total of 11716 reflections with 190 parameters. Crystal data for **2**: $C_{10}H_9MnN_2O_9$, M_r = 356.13, monoclinic, space group $P2_1/n$, a = 8.3746(6), b = 13.6660(9), c = 11.3170(8) Å, β = 94.469(1)°, V = 1291.3(2) $Å^3$, Z = 4, μ = 1.076 mm^{-1}, ρ_{calcd} = 1.832 cm^{-3}, $\lambda(Mo_{K\alpha})$ = 0.71073 Å, GOF = 1.031, $R1$ ($wR2$) = 0.0365 (0.0973) [2676 observed ($I > 2\sigma(I)$)] for 2956 (R_{int} = 0.0258) independent reflections out of a total of 12615 reflections with 199 parameters. Data collection was performed at 298(2) K on a Bruker SMART ApexCCD diffractometer with graphite-monochromated MoKα radiation. The structure was solved by direct methods by using SHELXTL program[12] and extended by using Fourier techniques. CCDC-236318 (**1**) and CCDC-236317 (**2**) contain the supplementary crystallographic data for this paper. These data can be obtained free of charge via www.ccdc.cam.ac.uk/conts/retrieving.html (or from the Cambridge Crystallographic Data Centre, 12, Union Road, Cambridge CB2 1EZ, UK; fax: (+44) 1223-336-033; or deposit@ccdc.cam.ac.uk).

[12] SHELXTL 5.03 (PC-Version), Program Library for Structure Solution and Molecular Graphics; Siemens Analytical Instruments Division: Madison, WI, **1995**.

 © 2004 Wiley-VCH Verlag GmbH & Co. KGaA, Weinheim

Silylenes

The Singlet Excited State of a Stable Dialkylsilylene Is Responsible for Its Photoreactions**

Mitsuo Kira, Shintaro Ishida, Takeaki Iwamoto, Armin de Meijere, Mamoru Fujitsuka, and Osamu Ito*

Silylenes (divalent silicon species)[1] as well as other heavier Group 14 element divalent species are usually singlet at the ground state ($^1A_1$) and should have two low-lying excited states, $^1B_1$ and $^3B_1$, with singlet and triplet 1,1-diradical nature,

[*] Prof. Dr. M. Kira, Dr. S. Ishida, Dr. T. Iwamoto
Department of Chemistry
Graduate School of Science
Tohoku University
Aoba-ku, Sendai 980-8578 (Japan)
Fax: (+81) 22-217-6589
E-mail: mkira@si.chem.tohoku.ac.jp
Prof. Dr. A. de Meijere
Instutut für Organische und Biomolekulare Chemie
Georg-August-Universität Göttingen
Tammannstrasse 2, 37077 Göttingen (Germany)
Dr. M. Fujitsuka, Prof. Dr. O. Ito
Institute of Multidisciplinary Research for Advanced Materials
Tohoku University
1-1, Katahira 2-chome, Aoba-ku, Sendai 980-8577 (Japan)

[**] This work was supported by the Japanese Ministry of Education, Culture, Sports, Science, and Technology [Grant-in-Aid for Scientific Research on Priority Areas (No. 14078203), "Reaction Control of Dynamic Complexes"] (for M.K.) and the Fonds der Chemischen Industrie (for A.d.M.).

Supporting information for this article is available on the WWW under http://www.angewandte.org or from the author.

 © 2004 Wiley-VCH Verlag GmbH & Co. KGaA, Weinheim DOI: 10.1002/anie.200460317

respectively (Figure 1). Little is known, however, about the properties of the excited states of silylenes.[2]

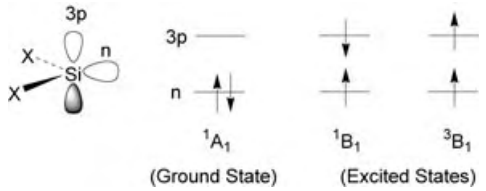
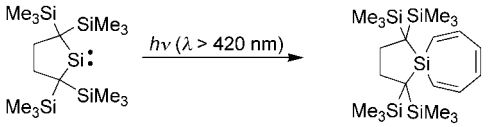


Figure 1. Important electronic states of silylene.

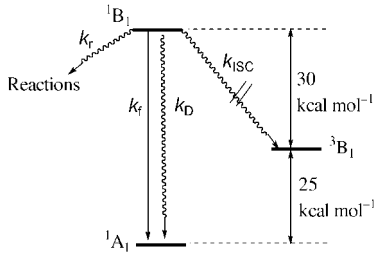
We have recently reported the first intermolecular reactions of an excited silylene with benzene and its derivatives to afford the corresponding adducts.[3] Typically, irradiation of the stable silylene **1**[4] in benzene gave the corresponding silepin in quantitative yield [Eq. (1)].



1 **2** (quant.) (1)

Although all the features of the photoreactions of **1** with benzene derivatives are compatible with a 1,1-diradical nature of the excited silylene, the true multiplicity of the reacting excited state so far could not be proven experimentally. Herein we report that the excited state responsible for the photoreactions of **1** with benzenes and alkenes is a $^1B_1$ state on the basis of the fluorescence quenching behavior of excited **1** by benzene. It is noteworthy that in contrast, similar $^1B_1$ states are rarely encountered in carbene chemistry. The photoreactions should be stepwise but the ring-closure reactions of the intermediate 1-silatrimethylene-1,3-diyl diradicals were estimated to be very fast with rates of more than $10^9\ s^{-1}$ according to the photoaddition modes of silylene **1** to bicyclopropylidene[5] and (*E*)- and (*Z*)-2-butenes.

Broad absorption and fluorescence band maxima of **1** arising from transitions between $^1B_1$ and $^1A_1$ states were observed at 440 nm (ε 500)[4] and 610 nm, respectively, both in hexane and in benzene at room temperature. The spectral features are similar to those for dimethylsilylene, the absorption and fluorescence maxima of which were observed at 450 nm and 650 nm, respectively, at 77 K in a 3-methylpentane glass matrix.[6] As the intersection point of the mirror image absorption and fluorescence spectra, the 0–0 transition energy of **1**, that is, energy gap between $^1A_1$ and $^1B_1$ is estimated to be 55 kcal mol^{-1},[7] the value of which is in excellent agreement with the calculated value for dimethylsilylene at the CISD + Q/DZ(d)//SCF/DZ(d) level of theory (54.2 kcal mol^{-1}).[8] The state diagram for **1** should be similar to that for dimethylsilylene, and hence, can be drawn as shown in Figure 2 using the theoretical energy gap between $^1A_1$ and $^3B_1$ for dimethylsilylene (25.1 kcal mol^{-1});[8] the energy gap between the $^1B_1$ and $^3B_1$ states (ΔE_{ST}) is estimated to be roughly 30 kcal mol^{-1}.



1

Figure 2. Schematic state energy diagram for silylene **1**.

Time-resolved fluorescence spectra of **1** (excited at 440 nm and observed at 610 nm)[7,9] in hexane showed that the fluorescence decay obeyed a first-order rate law with a lifetime of 80.5 ns (τ_0). The fluorescence lifetime in a benzene–hexane mixture (τ) depended on the concentration of benzene according to Equation (2), indicating the effective quenching of the fluorescence by benzene. From the slope of the plot of τ_0/τ versus [benzene] and the τ_0 value, the quenching rate constant k_q was determined as $9.4 \times 10^6\ s^{-1}\,mol^{-1}\,dm^3$.[7] The k_q value would be adequate for the rate constant for the addition of the highly reactive $^1B_1$ state of **1** having a singlet 1,1-biradical nature to benzene, because the rate constant is only twenty times larger than that for the addition of triethylsilyl radical to benzene ($4.6 \times 10^5\ s^{-1}\,mol^{-1}\,dm^3$).[10]

$$\tau_0/\tau = 1 + k_q\,\tau_0\,[\text{benzene}] \qquad (2)$$

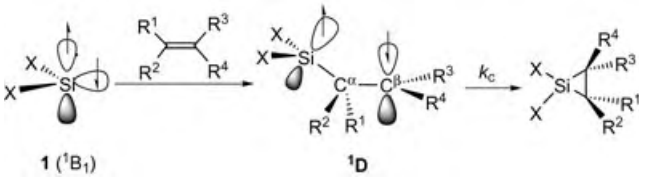
These results imply that though the $^3B_1$ state is more stable than $^1B_1$ (Figure 2), the intersystem crossing of **1** from $^1B_1$ to $^3B_1$ is too slow to compete with other processes such as fluorescence, radiationless decay, and reactions. Neither phosphorescence nor any ESR signals due to the $^3B_1$ state were observed during the irradiation of **1** in a 3-methylpentane glass matrix at 77 K.

No formation of $^3B_1$ from $^1B_1$ is rationalized in terms of the electronic configurations of $^1B_1$ and $^3B_1$ states and ΔE_{ST} in **1**.[11] Because the $^1B_1 \rightarrow {}^3B_1$ transition must involve either a 3p or an n electron spin inversion (Figure 1), the transition should be forbidden according to the El-Sayed rule.[12] In addition, the large ΔE_{ST} value should reduce the rate for the intersystem crossing from $^1B_1$ to $^3B_1$.

Silyl radicals are known to add to alkenes faster than to benzene; the second-order rate constant for the addition of triethylsilyl radical to (*E*)-3-hexene is $9.6 \times 10^5\ s^{-1}\,mol^{-1}\,dm^3$.[10] Consequently, the addition of **1** in its $^1B_1$ state to an alkene is much faster than the intersystem crossing to the $^3B_1$ state, and hence, should give a singlet 1,3-biradical **^{1}D**, the ring closure of which will give the corresponding silacyclopropanes as shown in Scheme 1. The reaction profile is in agreement with that derived theoretically for the addition of the $^1B_1$ state of H_2Si: to ethylene.[13]

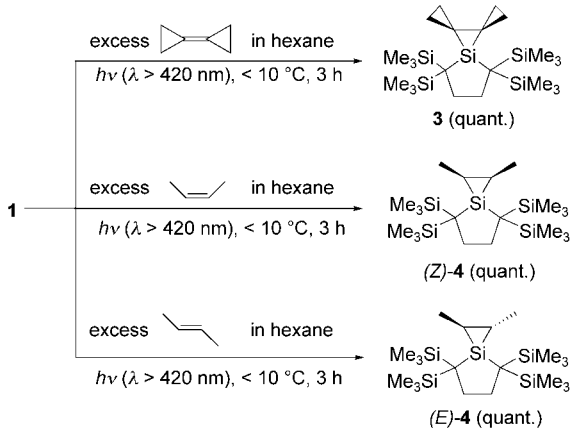
To estimate the rates for the ring closure (k_c), the photochemical reactions of **1** with bicyclopropylidene[5] and (*E*)- and (*Z*)-2-butenes were investigated. Irradiation ($\lambda >$ 420 nm) of a mixture of **1** and excess bicyclopropylidene in

 © 2004 Wiley-VCH Verlag GmbH & Co. KGaA, Weinheim



Scheme 1. Stepwise addition of $^1B_1$ silylene to an alkene.

hexane at $<10\,^{\circ}C$ gave the corresponding silacyclopropane **3** quantitatively (Scheme 2). Similarly, photoreactions of **1** in (*E*)- and (*Z*)-2-butene at $<10\,^{\circ}C$ afforded the corresponding (*E*)- and (*Z*)-2,3-dimethylsilacyclopropanes (*E*)-**4** and (*Z*)-**4**, respectively, in quantitative yields (Scheme 2). The excited state of **1** should be responsible for these reactions, because no reactions of **1** with these alkenes took place in the dark at $<10\,^{\circ}C$.



Scheme 2. Photoadditions of silylene **1** to various alkenes.

The stereospecificity of the addition of a carbene to alkenes has often been used to determine whether the added carbene reacted as a singlet or a triplet species (Skell's rule).[14] However, since Skell's rule is usually applied for the discrimination between $^1A_1$ and $^3B_1$ carbenes, which prefer the stereospecific concerted addition and the two-step addition involving the intermediary formation of a 1,3-diradical followed by ring closure, respectively, this rule may not a priori be used to diagnose the multiplicity of the excited states of silylenes responsible for the addition.

The exclusive formation of **3** in the photoaddition of **1** to bicyclopropylidene as well as the stereospecific photoaddition of **1** to (*E*)- and (*Z*)-2-butenes indicates that the rate constant for the cyclization from ^{1}**D** (k_c) should be more than ten times larger than the rate constants for other competitive processes such as the cyclopropane ring-opening of ^{1}**D** produced in the former reaction and the rotation around the C^{α}–C^{β} bond of ^{1}**D** in the latter reactions. The rate constant for the ring opening of cyclopropylmethyl radical to 3-butenyl radical as a radical clock has been determined to be $1.3\times10^8\ s^{-1}$.[5,15] The rate constants for the rotation around C–C σ bonds are estimated to be larger than $10^8\ s^{-1}$ at 10 °C, if we assume the activation energy for the rotation is less than 6 kcal mol^{-1} with an A factor of $10^{13}\ s^{-1}$.[16] Therefore, the k_c value should be larger than $10^9\ s^{-1}$.

In conclusion, the $^1B_1$ state generated by the irradiation of **1** reacts directly with benzene derivatives and alkenes to give the corresponding singlet 1,3-diradicals ^{1}**D** with the addition rates of around 10^6 mol^{-1} s^{-1} dm^3, and then the ring closures of ^{1}**D** to the corresponding silacyclopropanes occur with rate constants larger than $10^9\ s^{-1}$, while faster radical clocks are required to determine the ring-closure rates more acculately. The $^3B_1$ state of **1** does not participate in the reactions because of the strongly forbidden nature of the intersystem crossing from $^1B_1$ to $^3B_1$ of **1**.

Received: May 14, 2004 [Z460317]

Keywords: carbene homologues · laser spectroscopy · photochemistry · reaction mechanisms · silicon

[1] For a recent review, see: P. P. Gaspar, R. West in *The Chemistry of Organic Silicon Compounds, Vol. 2, Part 3* (Eds.: Z. Rappoport, Y. Apeloig), Wiley, New York, **1998**, Chapter 43, p. 2463.
[2] For reviews on the photochemistry of silylenes, see: a) A. G. Brook in *The Chemistry of Organic Silicon Compounds, Vol. 2, Part 2* (Eds.: Z. Rappoport, Y. Apeloig), Wiley, New York, **1998**, Chapter 21, p. 1233; b) M. Kira, T. Miyazawa in *The Chemistry of Organic Silicon Compounds, Vol. 2, Part 2* (Eds.: Z. Rappoport, Y. Apeloig), Wiley, New York, **1998**, Chapter 22, p. 1311.
[3] M. Kira, S. Ishida, T. Iwamoto, C. Kabuto, *J. Am. Chem. Soc.* **2002**, *124*, 3830.
[4] M. Kira, S. Ishida, T. Iwamoto, C. Kabuto, *J. Am. Chem. Soc.* **1999**, *121*, 9722.
[5] a) A. de Meijere, S. I. Kozhushkov, T. Späth, *Org. Synth.* **2000**, *78*, 142–151; for reviews see: b) A. de Meijere, S. I. Kozhushkov, *Eur. J. Org. Chem.* **2000**, 3809; c) A. de Meijere, S. I. Kozhushkov, A. F. Khlebnikov, *Top. Curr. Chem.* **2000**, *207*, 89.
[6] a) T. J. Drahnak, J. Michl, R. West, *J. Am. Chem. Soc.* **1979**, *101*, 5427; b) C. A. Arrington, K. A. Klingensmith, R. West, J. Michl, *J. Am. Chem. Soc.* **1984**, *106*, 525.
[7] See the Supporting Information for experimental details.
[8] R. S. Grev, H. F. Schaefer III, *J. Am. Chem. Soc.* **1986**, *108*, 5804.
[9] K. Yamanaka, M. Fujitsuka, Y. Araki, O. Ito, T. Aoshima, T. Fukushima, T. Miyashi, *J. Phys. Chem. A* **2004**, *108*, 250.
[10] a) C. Chatgilialoglu, K. U. Ingold, J. C. Scaiano, *J. Am. Chem. Soc.* **1983**, *105*, 3292; b) C. Chatgilialoglu, *Chem. Rev.* **1995**, *95*, 1229.
[11] N. J. Turro, *Modern Molecular Photochemistry*, The Benjamin/Cummings Publishing Co., Inc., Menlo Park, California, **1978**.
[12] a) M. A. El-Sayed, *J. Chem. Phys.* **1962**, *36*, 573; b) M. A. El-Sayed, *J. Chem. Phys.* **1963**, *38*, 2834; c) M. A. El-Sayed, *J. Chem. Phys.* **1964**, *41*, 2462; d) M. A. El-Sayed, *Acc. Chem. Res.* **1968**, *1*, 8; e) S. K. Lower, M. A. El-Sayed, *Chem. Rev.* **1966**, *66*, 199.
[13] C. Lennartz, H. M. Hildebrandt, B. Engels, *J. Phys. Chem. A* **1977**, *101*, 10053.
[14] P. S. Skell, R. C. Woodworth, *J. Am. Chem. Soc.* **1956**, *78*, 4496. See also: P. P. Gaspar, G. S. Hammond in *Carbenes, Vol. 2* (Eds.: R. A. Moss, M. Jones Jr), Wiley, New York, **1975**, Chapter 6.
[15] a) B. Maillard, D. Fonest, K. U. Ingold, *J. Am. Chem. Soc.* **1976**, *98*, 7024; b) D. Griller, K. U. Ingold, *Acc. Chem. Res.* **1980**, *13*, 317.
[16] T. Kawamura, P. Meakin, J. K. Kochi, *J. Am. Chem. Soc.* **1972**, *94*, 8065, and references therein.

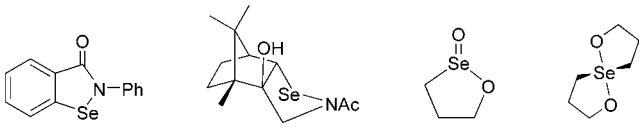
 © 2004 Wiley-VCH Verlag GmbH & Co. KGaA, Weinheim

Selenium Compounds

The Isolation and Crystal Structure of a Cyclic Selenenate Ester Derived from Bis(2,6-diformyl-4-*tert*-butylphenyl)diselenide and its Glutathione Peroxidase-Like Activity**

Sanjio S. Zade, Harkesh B. Singh, and Ray J. Butcher*

Glutathione peroxidase (GPx) is a well-known antioxidant selenoenzyme which protects biomembranes and other cellular components from oxidative stress by catalyzing the reduction of harmful peroxides at the expense of glutathione.[1] Recently, much attention has been directed toward the synthesis of simple organoselenium compounds that mimic the activity of GPx. These include: ebselen (**1**, PZ 51, 2-phenyl-1,2-benzisoselenazol-3(2*H*)-one),[2] ebselen analogues,[3] benzselenazolinones,[4] selenenamide **2** and related derivatives,[5] diaryl diselenides,[6] tellurides and ditellurides,[7] and the synthetic enzyme selenosubtilisin.[8] Diaryl diselenides with intramolecularly coordinating basic amino groups have been studied extensively, since Se···N nonbonded interactions are known to enhance the catalytic capacity of these antioxidants.[6a,d,9]



1 **2** **3** **4**

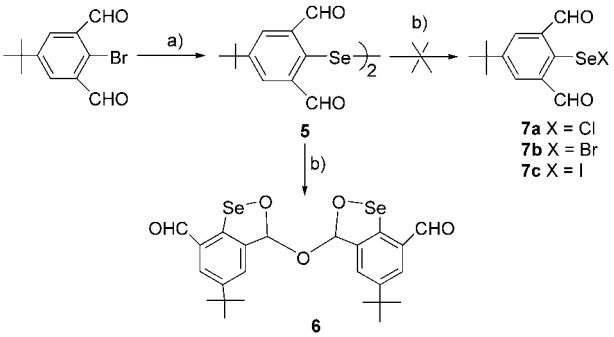
Wirth studied a series of diselenides containing an oxygen atom in proximity to the selenium atoms, and observed that the nonbonded interactions play a role in enhancement of the catalytic activity.[10] Recently, Back et al. reported a seleninate ester **3** and related spirodioxaselenanonane **4** that exhibit remarkable GPx activity.[11] Seleninate **3**, which contains a Se–O bond instead of a Se–N bond, catalyzes the reaction by a different mechanistic pathway than that reported for ebselen and the diselenides. Herein, we report the synthesis and GPx mimetic activity of the diselenide **5** and its cyclic selenenate ester **6**.

[*] S. S. Zade, Prof. H. B. Singh
Department of Chemistry
Indian Institute of Technology
Powai, Bombay 400 076 (India)
Fax: (+91) 22-2572-3480
E-mail: chhbsia@chem.iitb.ac.in
Prof. R. J. Butcher
Department of Chemistry
Howard University
Washington, DC 20059 (USA)

[**] We thank the Department of Science and Technology (DST), India. S.S.Z. would like to thank the Council for Scientific and Industrial Research (CSIR), India, for a fellowship.

Supporting information for this article is available on the WWW under http://www.angewandte.org or from the author.

Synthesis of the diselenide **5** was accomplished by treating 2,6-diformyl-4-*tert*-butyl-1-bromobenzene with disodium diselenide (Scheme 1). In an attempt to synthesize selenenyl

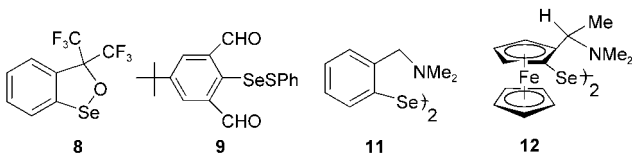


Scheme 1. a) Na_2Se_2, THF, RT, 4 h; b) $SOCl_2$, Br_2, or $I_2/CHCl_3$.

halides **7** (RSeCl, RSeBr, RSeI), diselenide **5** was treated with SO_2Cl_2, Br_2, and I_2, respectively, in $CHCl_3$ under ambient conditions. Interestingly, the isolated product in all cases was an identical yellow crystalline compound along with recovered diselenide. Detailed spectroscopic analysis of the yellow solid and single-crystal structure determination revealed it to be the selenenate ester **6**.

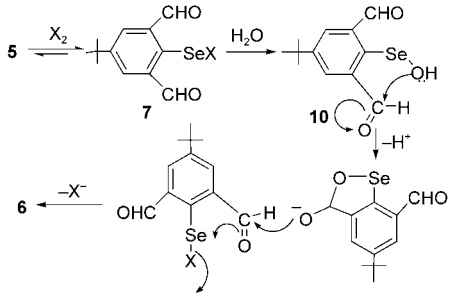
To the best of our knowledge, only one example of the isolated selenenate ester **8** has been reported.[12] However, selenenate **8** was found to be susceptible to hydrolysis and decomposition. Selenenate **6**, in contrast, is stable in air and does not show any decomposition over a year. This extra stability presumably results from the strong intramolecular Se···O interactions. Selenenate **6** contains two chiral centers and can exist as a *meso* compound and a D,L pair. Thus, two sets of signals are expected in the ^{1}H NMR spectrum corresponding to these two diastereomers. The single-crystal X-ray structure clearly shows the D,L pair, which is the major diastereomer. Therefore, the signals at 10.20, 8.00, 7.75, and 6.90 ppm for the D,L pair can be assigned to aldehyde, aromatic, aromatic, and acetal protons, respectively. Next to these signals, at a slightly lower field (10.25, 8.10, and 8.80 ppm), are the corresponding aldehyde and aromatic proton signals for the *meso* diastereomer. There is fortuitous magnetic and chemical equivalency for the more remote signals from the "ether" bridge. However, the "acetal" CH moieties are not equivalent: one projects toward the lone pair of electrons on the ether oxygen atom and the other away from it, and two one-proton singlets are observed. The ratio of the two major *tert*-butyl signals (4:1) is also in accordance with the ratio of other proton signals. All attempts to purify and separate the diastereomers, including chromatographic separation, were unsuccessful. To confirm the purity two equivalents of benzenethiol (PhSH) were added to the solution of selenenate **6** in $CDCl_3$ and the mixture analyzed by ^{1}H NMR spectroscopy. The resulting spectrum indicated clean formation of the selenenyl sulfide **9** with three singlets corresponding to the formyl and *tert*-butyl groups and aromatic protons, respectively. The signal observed at $\delta =$ 1401 ppm in the ^{77}Se NMR spectrum of **6** is shifted upfield

 DOI: 10.1002/anie.200460380 © 2004 Wiley-VCH Verlag GmbH & Co. KGaA, Weinheim



8 9 11 12

relative to that reported for selenenate **8** ($\delta = 1718$ ppm). This shift can be ascribed to the presence of strongly electron-withdrawing CF_3 groups in the five-membered ring in **8**.[12a] Selenenate **6** can be considered as a protected form of the highly unstable selenenic acid **10**. A plausible mechanism for the formation of **6** can be proposed via selenenic acid **10** as an intermediate (Scheme 2).[13]



Scheme 2. Plausible mechanism for the formation of **6**.

The molecular structure of selenenate **6**[14] shows the presence of intramolecular nonbonding Se···O interactions. The distances between the selenium atoms and the formyl oxygen atoms (Se(1A)···O(1A), 2.6042 Å; Se(1B)···O(1B), 2.4647 Å) are considerably smaller than the sum of the van der Waals radii (3.4 Å). The packing diagram of compound **6** reveals the intermolecular hydrogen-bonding interaction between the oxygen atom of the formyl group and the hydrogen atom of the *tert*-butyl group of the other molecule. The crystal packing contains the D,L pair of **6** (Figure 1).

The glutathione peroxidase-like catalytic activity was studied using the method reported by Iwaoka and Tomoda[6d] with PhSH as a glutathione alternative. The initial rates (v_0) for the reduction of H_2O_2 (5 mM) by thiol (0.75 mM) in the presence of catalysts **5** and **6** (0.01 mM) were determined in methanol by monitoring the UV absorption at 305 nm resulting from the formation of diphenyl disulfide. The initial rates for the diselenide **5** and selenenate ester **6** were 202 ± 9 and 167 ± 11 μmol dm^{-3} min^{-1}, respectively. Almost 7- and 6-fold enhancement in the initial reduction rate (v_0) of **5** and **6**, respectively, compared with the catalyst (**11**) reported by Wilson et al.,[6c] and 350- and 300-fold enhancement, respectively, compared with diphenyl diselenide (PhSeSePh) was observed under identical experimental conditions. Also, the v_0 value is roughly $^1/_3$ that of the most active diselenide **12**.[6a,b]

To investigate the mechanistic pathway, ^{77}Se NMR spectroscopic experiments were carried out in a mixture of $CDCl_3$ and CH_3OH (3:1). Four closely related signals were obtained when two equivalents of H_2O_2 were added to a solution of selenenate **6**. These signals can be assigned to the cyclic seleninate **13**.[11] Addition of two equivalents of PhSH resulted in one additional signal corresponding to selenenate **6**. The addition of two more equivalents of PhSH resulted in only the signal corresponding to selenenate **6** being observed. The formation of selenenate **6** can be explained by the opening of the seleninate ring by the thiol,[11] followed by breakdown of the hemiacetal to form thioseleninate **14**. Selenenic acid and PhSSPh were formed on treatment of thioseleninate **14** with a thiol.[15] Selenenic acid affords selenenate **6** (Scheme 2), and the ^{77}Se NMR spectrum of the reaction of **6** with PhSH showed a signal at $\delta = 435$ ppm. This signal can be assigned to the corresponding selenenyl sulfide **9**, formed by ring opening with PhSH. This was further confirmed by ^{1}H NMR studies. No other signals were observed even after addition of an excess of the thiol or H_2O_2 to this solution. However, diselenide **5** and selenenate **6** were isolated after allowing the solution of the selenenyl sulfide containing two equivalents of H_2O_2 to stand for a day. The ^{77}Se NMR studies and the mechanism of Back et al. for catalyst **3** enable the mechanistic pathway for selenenate **6** to be discussed in terms of the oxidation of **6** to seleninate **13**, followed by opening of the ring in **13** by a thiol molecule, and then subsequent steps (Scheme 3).

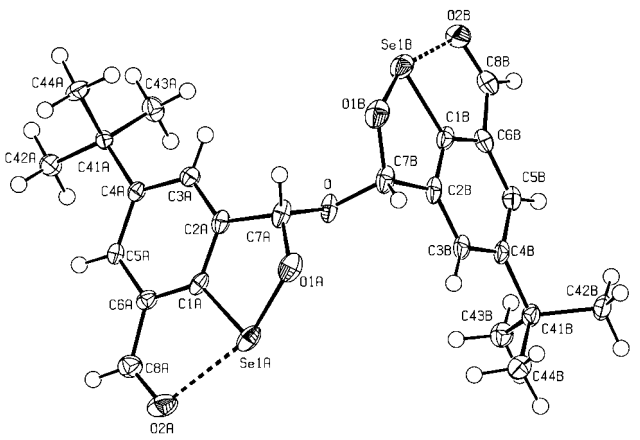
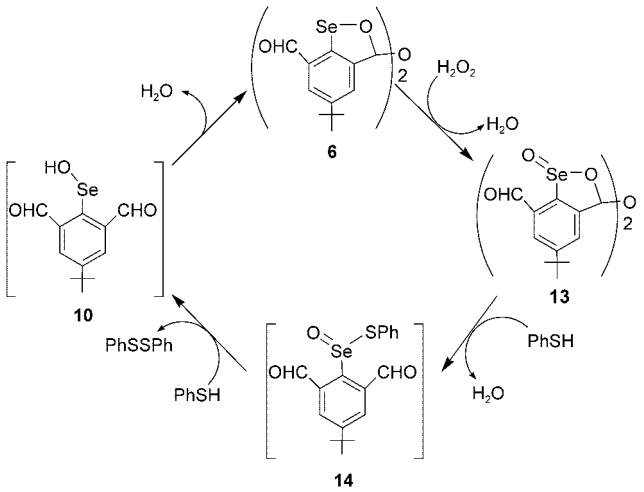


Figure 1. The molecular structure of **6**.



Scheme 3. Catalytic cycle for the GPx-like activity of **6**.

 © 2004 Wiley-VCH Verlag GmbH & Co. KGaA, Weinheim

In summary, diselenide **5**, a GPx mimic with excellent activity, affords the unusual selenenate ester **6** simply by halogenation in the presence of water. The selenenate ester **6** also exhibits excellent catalytic activity. The facile isolation of **6** proved again the role of intramolecular nonbonding interactions between selenium atoms and heteroatoms in the stabilization and isolation of unstable species. This is the first structural report of a selenenate ester. These results corroborate the observations made by Back et al. that compounds containing Se–O bonds can be equally effective catalysts as the commonly studied Se–N derivatives. Further investigation toward the isolation and characterization of intermediates is in progress.

Received: April 20, 2004 [Z460380]

Keywords: enzyme catalysis · esters · halogenation · selenium · structure elucidation

[1] a) G. Mugesh, W.-W. du Mont, H. Sies, *Chem. Rev.* **2001**, *101*, 2125; b) *Selenium in Biology and Human Health* (Ed.: R. F. Burk), Springer, New York, **1994**; c) L. Flohé, *Curr. Top. Cell Regul.* **1985**, *27*, 473; d) A. L. Tappel, *Curr. Top. Cell. Regul.* **1984**, *24*, 87; e) O. Epp, R. Ladenstein, A. Wendel, *Eur. J. Biochem.* **1983**, *133*, 51; f) L. Flohé, G. Loschen, W. A. Günzler, E. Eichele, *Hoppe–Seyler's Z. Physiol. Chem.* **1972**, *353*, 987.

[2] a) A. Müller, E. Cadenas, P. Graf, H. Sies, *Biochem. Pharmacol.* **1984**, *33*, 3235; b) A. Wendel, M. Fausel, H. Safayhi, G. Tiegs, R. Otter, *Biochem. Pharmacol.* **1984**, *33*, 3241; c) M. J. Parnham, S. Kindt, *Biochem. Pharmacol.* **1984**, *33*, 3247; d) A. Wendel, European Patent 0-165-534, **1985**.

[3] P. V. Jacquemin, L. E. Christiaens, M. J. Renson, M. J. Evers, N. Dereu, *Tetrahedron Lett.* **1992**, *33*, 3863.

[4] V. Galet, J.-L. Bernier, J.-P. Hénichart, D. Lesieur, C. Abadie, L. Rochette, A. Lindenbaum, J. Chalas, J.-F. Renaud de la Faverie, B. Pfeiffer, P. Renard, *J. Med. Chem.* **1994**, *37*, 2903.

[5] a) T. G. Back, B. P. Dyck, *J. Am. Chem. Soc.* **1997**, *119*, 2079; b) H. J. Reich, C. P. Jasperse, *J. Am. Chem. Soc.* **1987**, *109*, 5549.

[6] a) G. Mugesh, A. Panda, H. B. Singh, N. S. Punekar, R. J. Butcher, *Chem. Commun.* **1998**, 2227; b) G. Mugesh, A. Panda, H. B. Singh, N. S. Punekar, R. J. Butcher *J. Am. Chem. Soc.* **2001**, *123*, 839; c) S. R. Wilson, P. A. Zucker, R.-R. C. Huang, A. Spector, *J. Am. Chem. Soc.* **1989**, *111*, 5936; d) M. Iwaoka, S. Tomoda, *J. Am. Chem. Soc.* **1994**, *116*, 2557.

[7] a) Y. You, K. Ahsan, M. R. Detty, *J. Am. Chem. Soc.* **2003**, *125*, 4918; b) G. Mugesh, A. Panda, S. Kumar, S. D. Apte, H. B. Singh, R. J. Butcher, *Organometallics* **2002**, *21*, 884; c) L. Engman, D. Stern, I. A. Cotgreave, C. M. Andersson, *J. Am. Chem. Soc.* **1992**, *114*, 9737; d) L. Engman, I. G. Stern, M. Pelcman, C. M. Andersson, *J. Org. Chem.* **1994**, *59*, 1973; e) K. Vessman, M. Ekström, M. Berglund, C. M. Andersson, L. Engman, *J. Org. Chem.* **1995**, *60*, 4461.

[8] a) Z.-P. Wu, D. Hilvert, *J. Am. Chem. Soc.* **1989**, *111*, 4513; b) Z.-P. Wu, D. Hilvert, *J. Am. Chem. Soc.* **1990**, *112*, 5647.

[9] a) G. Mugesh, H. B. Singh, *Chem. Soc. Rev.* **2000**, *29*, 347; b) G. Mugesh, W.-W. du Mont, *Chem. Eur. J.* **2001**, *7*, 1365.

[10] T. Wirth, *Molecules* **1998**, *3*, 164.

[11] a) T. G. Back, Z. Moussa, *J. Am. Chem. Soc.* **2002**, *124*, 12104; b) T. G. Back, Z. Moussa, *J. Am. Chem. Soc.* **2003**, *125*, 13455; c) T. G. Back, Z. Moussa, M. Parvez, *Angew. Chem.* **2004**, *116*, 1288; *Angew. Chem. Int. Ed.* **2004**, *43*, 1268.

[12] a) T. Kawashima, F. Ohno, R. Okazaki, *J. Am. Chem. Soc.* **1993**, *115*, 10434; b) F. Ohno, T. Kawashima, R. Okazaki, *Chem. Commun.* **1997**, 1671; c) N. Kano, Y. Daicho, N. Nakanishi, T. Kawashima, *Org. Lett.* **2001**, *3*, 691.

[13] a) H. J. Reich, W. W. Willis, Jr, S. Wollowitz, *Tetrahedron Lett.* **1982**, *23*, 3319; b) J. L. Kice, F. McAfee, H. Slebocka-Tilk, *Tetrahedron Lett.* **1982**, *23*, 3323; c) J. L. Kice, F. McAfee, H. Slebocka-Tilk, *J. Org. Chem.* **1984**, *49*, 3100; d) J. L. Kice, F. McAfee, H. Slebocka-Tilk, *J. Org. Chem.* **1984**, *49*, 3106.

[14] X-ray crystallographic data for **6**: $C_{12}H_{13}O_{2.50}Se$, $M_r = 276.18$, monoclinic, space group $P\text{-}1$, $a = 8.783(3)$, $b = 8.714(3)$, $c = 14.740(4)$ Å, $V = 1101.3(6)$ Å^3, $T = 93(2)$ K, 9209 reflections collected. CCDC-236477 (**6**) contains the supplementary crystallographic data for this paper. These data can be obtained free of charge via www.ccdc.cam.ac.uk/conts/retrieving.html (or from the Cambridge Crystallographic Data Centre, 12 Union Road, Cambridge CB2 1EZ, UK; fax: (+44) 1223-336-033; or deposit@ccdc.cam.ac.uk).

[15] a) J. L. Kice, T. W. S. Lee, *J. Am. Chem. Soc.* **1978**, *100*, 5094; b) J. L. Kice, D. W. Purkiss, *J. Org. Chem.* **1987**, *52*, 3448.

 © 2004 Wiley-VCH Verlag GmbH & Co. KGaA, Weinheim

Reprogrammable Ligands

Allosteric and Electrostatic Reprogramming of a Ditopic Ligand**

*Christian J. Baylies, Lindsay P. Harding, John C. Jeffery, T. Riis-Johannessen, and Craig R. Rice**

The ability of ligands to partition into different binding domains is instrumental in the formation of transition-metal supramolecular architectures. For this reason ligands are designed and synthesized to contain binding sites of differing nature and number. Hence, on reacting such ligands with metal ions, a desired supramolecular architecture assembles as a result of the particular disposition of the binding sites.[1] The information stored within a ligand strand can lead to a variety of supramolecular species, such as helicates,[2] grids,[3] and cages.[4] Once a ligand has been synthesized the information is permanently stored within it and the ligand can therefore be thought of as being "preprogrammed".[5] Herein, we describe a remarkable new ditopic ligand L^1, whose binding modes can be changed or "reprogrammed" by the addition of barium ions to a crown ether moiety. This is related to the allosteric effect demonstrated by Rebek et al.,

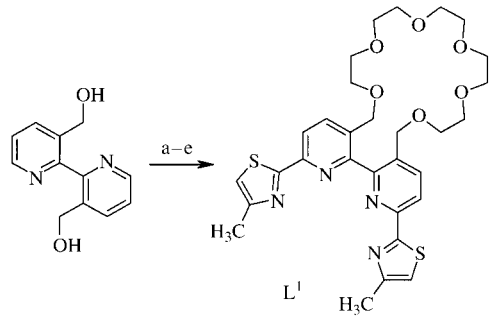
[*] Dr. C. J. Baylies, L. P. Harding, Dr. C. R. Rice
Department of Chemical and Biological Sciences
University of Huddersfield
Huddersfield HD1 3DH (UK)
Fax: (+44) 148-447-2182
E-mail: c.r.rice@hud.ac.uk
Dr. J. C. Jeffery, T. Riis-Johannessen
School of Chemistry, University of Bristol
Cantocks Close, Bristol BS8 1TS (UK)

[**] We thank the EPSRC and the University of Huddersfield for financial support.

 DOI: 10.1002/anie.200460424 © 2004 Wiley-VCH Verlag GmbH & Co. KGaA, Weinheim

who used a derivative of 2,2′-bipyridine in which the twist between the two pyridyl rings was influenced by remote conformational changes in a crown ether fragment joining the backs of the rings.[6] However, in the case of L^1 reported herein, there is a fundamental difference in that the cation that binds to the crown ether moiety changes the gross molecular structure.

The ditopic ligand L^1 was prepared from 2,2′-bipyridine-3,3′-dimethanol as outlined in Scheme 1. L^1 contains a



Scheme 1. Reagents and conditions: a) penta(ethylene glycol) di-*p*-toluenesulfonate, DMF, NaH, 60%; b) *m*CPBA, CH_2Cl_2, 70%; c) TMSCN, PhCOCl, CH_2Cl_2, 83%; d) H_2S, Et_3N, EtOH, 90%; e) chloroacetone, EtOH,76%.

potentially tetradentate pyridyl–thiazole ligand chain and an additional "external" crown ether binding site that connects the two halves of the bipyridyl moiety. On treating L^1 with an equimolar amount of $Hg(ClO_4)_2{\cdot}3H_2O$ in MeCN a colorless solution was produced, and ESI MS showed the formation of a dinuclear double helicate with an ion at *m*/*z* 1924 corresponding to $[Hg_2(L^1)_2](ClO_4)_3^+$. The ^{1}H NMR spectrum of $[Hg_2(L^1)_2]^{4+}$ in CD_3CN shows only three aromatic resonances for the pyridyl–thiazole moiety which is consistent with a highly symmetrical, double-helicate complex. Furthermore, the benzylic -CH_2O- fragment has a diastereotopic methylene group, which, as expected, gives rise to two doublets ($\delta = 4.50$ and 4.39 ppm; Figure 1 a).

Treatment of $[Hg_2(L^1)_2]^{4+}$ with an excess of $NaClO_4$ (3 equiv) followed by crystallization afforded the complex $[Hg_2(L^1)_2Na_2](ClO_4)_6{\cdot}4MeCN$, whose structure has been established by a single-crystal X-ray diffraction studies.[7] In the crystal, the ligand splits into two bis-bidentate binding domains with two Hg^{2+} ions coordinated by two bridging ligands in a double-helicate arrangement (Figure 2). Each of the Hg^{2+} centers has a distorted tetrahedral geometry formed

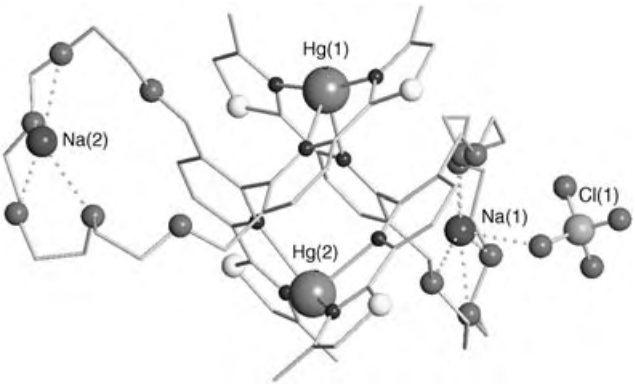


Figure 2. Structure of the complex cation of $[Hg_2(L^1)_2Na_2]^{6+}$.

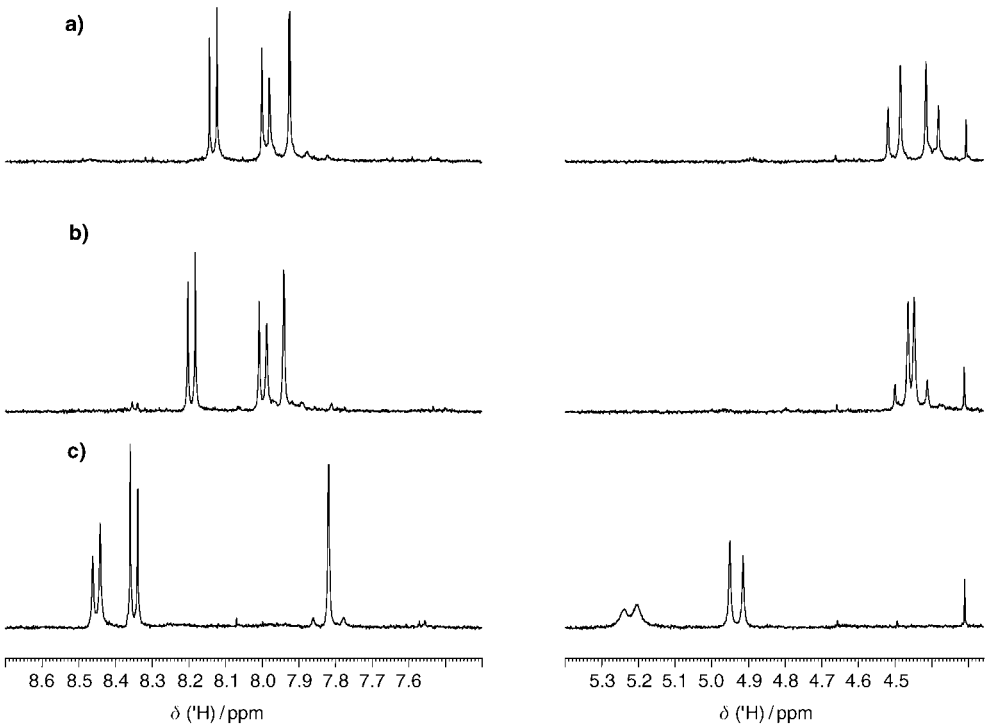


Figure 1. Selected regions of the ^{1}H NMR spectra (CD_3CN) of a) $[Hg_2(L^1)_2]^{4+}$, b) $[Hg_2(L^1)_2]^{4+} + Na^+$, c) $[Hg_2(L^1)_2]^{4+} + Ba^{2+}$.

 © 2004 Wiley-VCH Verlag GmbH & Co. KGaA, Weinheim

by coordination of two thiazole–pyridyl bidentate N-donor units [2.107(5)–2.535(5) Å], one from each ligand. Each ligand is twisted about the central bond between the two pyridyl rings [92.2 and 93.7°]. In theory, L^1 can act as either a bis-bidentate or a tetradentate N-donor ligand. However, in this case, owing to the preference of Hg^{2+} for tetrahedral geometry, the ligand acts as a bis-bidentate donor and forms a dinuclear double helicate.

Both crown ethers partially coordinate sodium ions. In one case the Na^+ is seven-coordinate and bonds to five oxygen atoms (2.351(5)–2.693(5) Å) from the [16]crown-6 fragment, leaving one of the benzylic oxygen atoms uncoordinated. The remaining two coordination sites incorporate an acetonitrile molecule and a perchlorate anion. The other Na^+ ion is five-coordinate and is only coordinated by the four "outer" oxygen atoms (2.319(7)–2.545(6) Å) of the crown ether ring, leaving both benzylic oxygen atoms uncoordinated. A single monodentate perchlorate anion completes the coordination environment. The inability of the sodium ions to coordinate all of the crown oxygen atoms is to be expected, given that a crown-6 type fragment is known to be too big to coordinate optimally to the Na^+ cation.

The weak Na^+ cation binding observed in the solid state is maintained in solution. Thus ESI MS shows ions at m/z 2046 and 2168, which correspond to $[\{Hg_2(L^1)_2Na\}(ClO_4)_4]^+$ and $[\{Hg_2(L^1)_2Na_2\}(ClO_4)_5]^+$, respectively. Similarly, the ^{1}H NMR spectrum of the sodium species in CD_3CN is similar to that of $[Hg_2(L^1)_2]^{4+}$, but in this case a shift in the -CH_2O- region of approximately 0.02 ppm confirms that the crown ether is weakly coordinated to Na^+ in solution (Figure 1b).

In marked contrast, reaction of $[Hg_2(L^1)_2]^{4+}$ with $Ba(ClO_4)_2$ affords a colorless solution for which ESI MS shows only an ion that corresponds to the mononuclear complex $[\{Hg(L^1)Ba\}(ClO_4)_3]^+$. Additionally, the ^{1}H NMR spectrum in CD_3CN showed a marked change in the signals that arise from both the benzylic -CH_2O- and the aromatic regions (Figure 1c). These signals are substantially shifted relative to those for $[Hg_2(L^1)_2]^{4+}$ (-CH_2O- average $\Delta\delta =$ 0.63 ppm) or its Na^+ derivative. Chemical-shift changes of this order in the aromatic region are more indicative of a change in molecular structure rather than the relatively small changes that would be observed with coordinative perturbation of the crown. The formation of the mononuclear species was confirmed by X-ray crystallography,[7] which showed a six-coordinate Hg^{2+} complex with a distorted octahedral environment (Figure 3). The ligand acts as a near-planar tetradentate "equatorial" ligand, with two perchlorate anions acting as bidentate axial ligands. The Hg–N bonds range from 2.24(1) to 2.47(1) Å. The ligand is almost planar but exhibits a shallow helical twist caused by the unfavorable steric interactions between the methylene substituents on the central bipyridyl core (33.1°). The barium ion is ten-coordinate and strongly bonded to all *six* of the crown ether oxygen atoms (2.76(1)–2.90(1) Å), with the oxygen atoms of two perchlorate anions acting as bidentate O-donor ligands. Unlike the sodium analogue, all of the oxygen atoms in the crown ether moiety form bonds to Ba^{2+}, reflecting the good size match between the ion and the crown-6 fragment and the electron-deficient character of the Ba^{2+} dication.

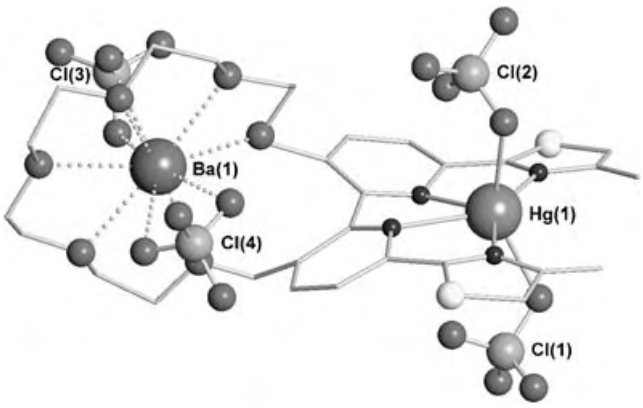


Figure 3. Structure of the complex cation of $[Hg(L^1)Ba]^{4+}$.

Thus, in the presence of Hg^{2+} and Na^+, the ligand L^1 forms a dinuclear double helicate complex, whereas in the presence of Hg^{2+} and Ba^{2+} a mononuclear species is formed exclusively. Such control of self-assembly can be attributed to one of two factors: First, an electrostatic effect as coordination of barium to the helicate would lead to a highly charged 8+ ion. Subsequent disassembly to the mononuclear species would then lower the extent of electrostatic repulsion and increase the entropy of the system. However, the change in structure could also be attributed to an allosteric effect. Thus, in the helicate $[Hg_2(L^1)_2Na_2]^{6+}$ the sodium ions are coordinated by the crown ether moieties but, owing to the poor fit of the Na^+ in the [16]crown-6 fragment, at least one of the benzylic oxygen atoms remains uncoordinated. This poor fit allows the ligand to twist about the central bipyridyl unit, enabling it to partition into two bidentate domains and assemble into a dinuclear double helicate. In contrast, upon reaction with Ba^{2+} the mononuclear species $[Hg(L^1)Ba]^{4+}$ is formed. In this system both benzylic oxygen atoms are coordinated, thus restricting the previously observed conformational mobility of the ligand. This prerequisite for helicate formation being absent means that the ligand does not partition into separate bridging units but instead acts as a simple tetradentate donor.

In an effort to ascertain which effect controls the self-assembly, systematic ^{1}H NMR studies were carried out to monitor the effect of addition of different Group 1 and 2 metal ions to the ditopic helicate $[Hg_2(L^1)_2]^{4+}$. This revealed that dinuclear double helicates are formed in the presence of smaller metal ions of both Group 1 and 2 (i.e. $[Hg_2(L^1)_2M_2]^{6+/8+}$, $M = Li^+$, Na^+, or Mg^{2+}), whereas mononuclear species are formed with Ba^{2+} and Sr^{2+} (i.e. $[Hg(L^1)M]^{4+}$, $M = Ba^{2+}$ or Sr^{2+}). Upon addition of K^+, which is similar in size to Ba^{2+} but only singly charged, a mixture of species is formed ($[Hg_2(L^1)_2K_2]^{6+}/[Hg(L^1)K]^{3+} = 1:2$) whereas with Ca^{2+}, which is doubly charged but is smaller than K^+, a mixture of species is also observed, but the ratios are the reverse of that found with K^+ ($[Hg_2(L^1)_2Ca_2]^{8+}/[Hg(L^1)Ca]^{4+} = 2:1$). Given these results, it would appear that no one factor is dominant in this control of self-assembly and that both electrostatic and allosteric effects play important roles.

So far, this system represents a unique example of how ligand-binding domains can be changed or "reprogrammed" by a combination of electrostatic and allosteric effects.

 © 2004 Wiley-VCH Verlag GmbH & Co. KGaA, Weinheim

Experimental Section

L^1 was prepared in five steps from 2,2′-bipyridine-3,3′-dimethanol (24% overall yield): ^{1}H NMR (400 MHz, $CDCl_3$): $\delta = 8.23$ (2H, d, $J = 8.14$; pyridyl H), 8.11 (2H, d, $J = 8.14$; pyridyl H), 6.91 (2H, s; thiazole H), 4.84 (4H, s; OCH_2), 3.55–3.35 (20H, m; $O(CH_2)_2O$), 1.55 ppm (6H, s; Me); ^{13}C NMR (100.6 MHz, $CDCl_3$): $\delta = 168.6$, 155.3, 154.6, 149.3, 138.3, 135.3, 119.1, 116.5 (pyridyl and thiazole), 71.1, 71.0, 70.7, 70.6, 70.3, 66.3 (CH_2), 17.8 ppm (Me); elemental analysis: calcd for $C_{30}H_{36}N_4O_6S_2$ (%): C 58.8; H 5.9; N 9.1; found: C 58.6, H 5.6, N 8.6; MS ESI: m/z: 613 [MH^+].

Both $[Hg_2(L^1)_2Na_2](ClO_4)_6$ and $[Hg(L^1)Ba](ClO_4)_4$ were prepared in an analogous manner: $Hg(ClO_4)_2 \cdot 3H_2O$ (0.007 g. 0.016 mmol) was added to a suspension of L^1 (0.010 g, 0.016 mmol) in MeCN, and the solution was stirred until dissolution was complete. $NaClO_4$ or $Ba(ClO_4)_2$ (3 equiv) was then added, and the complexes were isolated by slow diffusion of Et_2O.

$[Hg_2(L^1)_2Na_2](ClO_4)_6$ (65% yield): ^{1}H NMR (400 MHz, CD_3CN): $\delta = 8.16$ (d, $J = 8.2$ Hz, 2H; pyridyl-H), 7.96 (d, $J = 8.2$ Hz, 2H; pyridyl-H), 7.90 (s, 2H; thiazole-H), 4.48 (d, $J = 14.3$ Hz, 2H; OCH_2), 4.42 (d, $J = 14.3$ Hz, 2H; OCH_2), 3.7–3.3 (m, (overlapping), 20H; $O(CH_2)_2O$), 2.59 ppm (3H, s, Me); MS ESI: m/z: 2168 [M^+].

$[Hg(L^1)Ba](ClO_4)_4$ (50% yield): ^{1}H NMR (400 MHz, CD_3CN): $\delta = 8.42$ (d, $J = 8.1$ Hz, 2H; pyridyl-H), 8.31 (d, $J = 8.1$ Hz, 2H; pyridyl-H), 7.78 (s, 2H; thiazole), 5.22 (d, $J = 14.5$ Hz, 2H; OCH_2), 4.93 (d, $J = 14.5$ Hz, 2H; OCH_2), 3.8–3.3 (m, (overlapping), 20H; $O(CH_2)_2O$), 2.78 ppm (3H, s, Me); MS ESI: m/z: 1248 [M^+].

Received: April 23, 2004 [Z460424]

Keywords: allosterism · barium · helical structures · mercury · N ligands

[1] J.-M. Lehn, *Supramolecular Chemistry*, VCH, Weinheim, **1995**; J. W. Steed, J. L. Atwood, *Supramolecular Chemistry*, Wiley, Chichester, **2000**.

[2] M. J. Hannon, L. J. Childs, *Supramol. Chem.* **2004**, *16*, 7; M. Albrecht, *Chem. Rev.* **2001**, *101*, 3547; M. Albrecht, *Chem. Soc. Rev.* **1998**, *27*, 281; C. Piguet, G. Bernardinelli, G. Hopfgartner, *Chem. Rev.* **1997**, *97*, 2005; E. C. Constable in *Comprehensive Supramolecular Chemistry*, *Vol. 9* (Ed.: J.-P. Sauvage), Elsevier, Oxford, **1996**, p. 213.

[3] P. Baxter, J.-M. Lehn, A. DeCian, J. Fischer, *Angew. Chem.* **1993**, *105*, 92; *Angew. Chem. Int. Ed. Engl.* **1993**, *32*, 69; M.-T. Youinou, N. Rahmouni, J. Fischer, J. A. Osborn, *Angew. Chem.* **1992**, *104*, 771; *Angew. Chem. Int. Ed. Engl.* **1992**, *31*, 733; S. T. Onions, A. M. Frankin, P. N. Horton, M. B. Hursthouse, C. J. Mathews, *Chem. Commun.* **2003**, 2864.

[4] P. J. Stang, S. R. Seidel, *Acc. Chem. Res.* **2002**, *35*, 972; S. Leininger, B. Olenyuk, P. J. Stang, *Chem. Rev.* **2000**, *100*, 853; Z. R. Bell, L. P. Harding, M. D. Ward, *Chem. Commun.* **2003**, 2432.

[5] R. Krämer, J.-M. Lehn, A. Marquis-Rigault, *Proc. Natl. Acad. Sci. USA* **1993**, *90*, 3114; B. Hasenknopf, J.-M. Lehn, G. Baum, D. Fenske, *Proc. Natl. Acad. Sci. USA* **1996**, *93*, 1397; S. Floquet, M. Borkovec, G. Bernardinelli, A. Pinto, L.-A. Leuthold, G. Hopfgartner, D. Imbert, J.-C. G. Bünzli, C. Piguet, *Chem. Eur. J.* **2004**, *10*, 1091.

[6] J. Rebek, Jr., J. E. Trend, R. V. Wattley, S. J. Chachravorti, *J. Am. Chem. Soc.* **1979**, *101*, 4333; J. Rebeck, Jr., R. V. Wattley, *J. Am. Chem. Soc.* **1980**, *102*, 4853; J. Rebeck, Jr., *Acc. Chem. Res.* **1984**, *17*, 258; for examples of artificial allosteric systems, see: T. Nabeshima, *Coord. Chem. Rev.* **1996**, *148*, 151; S. Shinkai, M. Ikeda, A. Sugasaki, M. Takeuchi, *Acc. Chem. Res.* **2001**, *34*, 494; Y. Kobuke, Y. Satoh, *J. Am. Chem. Soc.* **1992**, *114*, 789; P. D. Beer, A. S. Rothin, *J. Chem. Soc. Chem. Commun.* **1988**, 52; S. K. Dutta, D. Gan, M. W. Perkovic, *Eur. J. Inorg. Chem.* **2003**, 2812; S. A. McFarland, N. S. Finney, *Chem. Commun.* **2003**. 388; T. Nabeshima, Y. Yoshihira, T. Saiki, S. Akin, E. Horn, *J. Am. Chem. Soc.* **2003**, *125*, 28.

[7] Crystal data for $[Hg_2(L^1)_2Na_2](ClO_4)_6 \cdot 4MeCN$: $M = 2433.57$, triclinic, space group $P\bar{1}$, $a = 13.9240(2)$, $b = 18.4535(2)$, $c = 18.6823(2)$ Å, $\alpha = 107.984(1)$, $\beta = 90.519(1)$, $\gamma = 97.451(1)°$, $V = 4521.13(9)$ Å^3, $Z = 2$; $\rho_{calcd} = 1.788$ Mg m^{-3}, $F(000) = 2424$; crystal dimensions $0.1 \times 0.1 \times 0.05$ mm^3; $\mu(Cu_{K\alpha}) = 9.395$ mm^{-1}, $T = 100$ K. A total of 35433 reflections were measured in the range $2.49 \le \theta \le 70.13°$ (*hkl* range indices: $-15 \le h \le 16$, $-22 \le k \le 22$, $-22 \le l \le 22$), 15344 unique reflections ($R_{int} = 0.0576$). The structure was refined on F^2 to $R_w = 0.1053$, $R = 0.0429$ (12005 reflections with $I > 2\sigma(I)$) and GOF = 0.921 on F^2 for 1211 refined parameters, largest difference peak and hole 1.813 and -1.448 e Å^{-3}. Crystal data for $[Hg(L^1)Ba](ClO_4)_4$: $M = 1348.48$, triclinic, space group $P\bar{1}$, $a = 8.785(2)$, $b = 9.619(2)$, $c = 26.409(5)$ Å, $\alpha = 89.95(3)$, $\beta = 88.02(3)$, $\gamma = 77.01(3)°$, $V = 2173.3(8)$ Å^3, $Z = 2$; $\rho_{calcd} = 2.061$ Mg m^{-3}, $F(000) = 1312$; crystal dimensions $0.1 \times 0.1 \times 0.003$ mm^3; $\mu(Mo_{K\alpha}) = 4.858$ mm^{-1}, $T = 100$ K. A total of 20137 reflections were measured in the range $2.17 \le \theta \le 25.03°$ (*hkl* range indices: $-10 \le h \le 10$, $-11 \le k \le 11$, $-31 \le l \le 31$), 20142 unique reflections ($R_{int} = 0.0000$, twinned structure solved with Gemini). The structure was refined on F^2 to $R_w = 0.2220$, $R = 0.0924$ (14866 reflections with $I > 2\sigma(I)$) and GOF = 0.998 on F^2 for 549 refined parameters, largest difference peak and hole 3.390 and -2.141 e Å^{-3}. CCDC-236695 and 236694, respectively, contain supplementary crystallographic data for this paper. These data can be obtained free of charge via www.ccdc.cam.ac.uk/conts/retrieving.html (or from the Cambridge Crystallographic Data Centre, 12, Union Road, Cambridge CB21EZ, UK; fax: (+44) 1223-336-033; or deposit@ccdc.cam.ac.uk). For $[Hg_2(L^1)_2Na_2](ClO_4)_6 \cdot 4MeCN$, the measurements were carried out on a Bruker PROTEUM CCD area-detector diffractometer with a $Cu_{K\alpha}$ rotating anode and Osmic beam focusing ($\lambda = 1.54178$ Å). For $[Hg(L^1)Ba](ClO_4)_4$, data were collected on a Bruker APEX diffractometer with $Mo_{K\alpha}$ radiation (0.71073 Å). Absorption corrections were applied by using SADABS,[8] and the structure was solved by direct methods using SHELXTL.[9] X-ray data collected for crystals of $[Hg(L^1)Ba](ClO_4)_4$ were of sufficient quality to generate a reliable structure solution by using direct methods; however, problems associated with non-merohedral twinning prevented smooth refinement of atomic parameters. Two twin components, related by a 180° rotation about the direct *c* axis, were identified for a complete array of reflections by using the GEMINI Twinning Solution Program Suite.[10] A subsequent decrease from $R = 0.1474$ to 0.0924 was observed on further refinement.

[8] G. M. Sheldrick. *SADABS: A program for absorption correction with the Siemens SMART system*; University of Göttingen (Germany), **1996**.

[9] *SHELXTL program system version 5.1*, Bruker Analytical X-ray Instruments Inc., Madison, WI, **1998**.

[10] GEMINI, Autoindexing Program for Twinned Crystals Vers. 1.02, Release 5/**2000**.

 © 2004 Wiley-VCH Verlag GmbH & Co. KGaA, Weinheim

Nanotechnology

Catalytic Growth of Au Nanoparticles by NAD(P)H Cofactors: Optical Sensors for NAD(P)$^+$-Dependent Biocatalyzed Transformations**

*Yi Xiao, Valeri Pavlov, Semion Levine, Tamara Niazov, Gil Markovitch, and Itamar Willner**

Increasing efforts are directed to the application of metal and semiconductor nanoparticles (NPs) for the development of electronic or optical sensory systems.[1] Metal or semiconductor NPs functionalized with nucleic acids were employed as amplifying labels for the detection of DNA; the dissolution of the nanoparticles was used to follow DNA hybridization events.[2] Also, charge injection from semiconductor nanoparticles into electrodes and the generation of photocurrents was used to follow hybridization processes[3] and biocatalytic transformations.[4] The catalytic deposition of metals onto metal nanoparticles conjugated to DNA-hybridized complexes on surfaces was used as a sensor for DNA through conductivity[5] or microgravimetric quartz crystal microbalance[6] measurements.

The optical detection of processes in the presence of metal and semiconductor NPs has become a common practice in analysis. Besides the use of semiconductor quantum dots as fluorescence labels in sensors,[7] the fluorescence quenching of semiconductor quantum dots has been employed in different sensing paths.[8] The plasmon absorbance of metal nanoparticles, such as Au NPs, and specifically the interparticle-coupled plasmon absorbance of aggregated NPs was extensively used to follow molecular[9] and biomolecular[10] recognition processes. The use of semiconductor or metallic NPs as probes to follow biocatalytic processes is less established, with only a few reports for these applications.[4,11] Nicotinamide adenine dinucleotide (NAD^+)- and nicotinamide adenine dinucleotide phosphate ($NADP^+$)-dependent enzymes are important in biocatalyzed synthesis.[12] Extensive efforts have been directed towards the development of electrochemical sensors based on NAD(P)$^+$-dependent enzymes.[13] Herein, we report the catalyzed growth of gold nanoparticles in the presence of NAD(P)H cofactors. We apply the process to the quantitative optical analysis of NAD(P)H cofactors and to the analysis of NAD(P)$^+$-dependent biocatalyzed reactions in solutions and on surfaces.

[*] Dr. Y. Xiao, Dr. V. Pavlov, S. Levine,[+] T. Niazov, Prof. I. Willner
Institute of Chemistry, The Hebrew University of Jerusalem
Jerusalem 91904 (Israel)
Fax: (+972) 2-652-7715
E-mail: willnea@vms.huji.ac.il
Dr. G. Markovitch
School of Chemistry, Tel-Aviv University
Tel-Aviv 69978 (Israel)
[+] Deceased, April 14, 2004

[**] This research was supported by the Israel Ministry of Commerce and Industry as part of a Nofar project.

The solution for the growth of the particles consisted of citrate-stabilized Au NPs (4.0×10^{-10} M in 13 nm ± 1-nm particles), $HAuCl_4$ (1.8×10^{-4} M), and CTAB (7.4×10^{-2} M) as a surfactant. Figure 1 shows the changes in the UV/Vis spectra

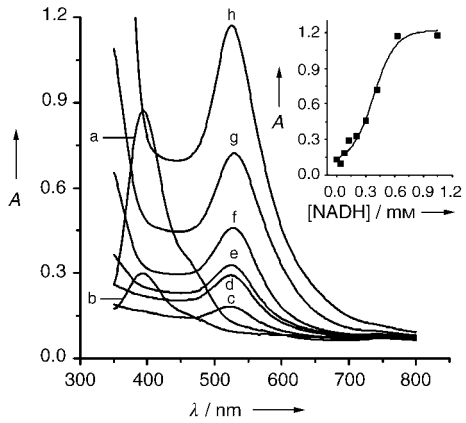


Figure 1. Variation in the absorbance spectra of the Au NP growth solution (4.0×10^{-10} M in Au NPs) at different concentrations of NADH: a) 0 M; b) 4.2×10^{-5} M; c) 8.4×10^{-5} M; d) 12.6×10^{-5} M; e) 21×10^{-5} M; f) 30×10^{-5} M; g) 42×10^{-5} M; h) 63×10^{-5} M. Inset: Variation in the absorbance intensity at $\lambda = 524$ nm of the growth solution upon interaction (30 mins) with variable concentrations of NADH.

of the growth solution upon interaction with different concentrations of NADH. In the absence of NADH, the solution displays an absorbance band at $\lambda = 392$ nm, characteristic of the $AuCl_4^-$ component (Figure 1, curve a). Upon addition of NADH, this band disappears instantaneously and the characteristic orange color of the system is depleted (curve b), and then the slow buildup of the absorbance of the particle plasmon is observed. As the concentration of NADH increases, the absorbance of the Au particles increases and is shifted to longer wavelengths (from 523 to 530 nm; Figure 1, curves c–h). The inset in Figure 1 shows the calibration curve derived from the changes in the absorbance at $\lambda = 524$ nm as the concentration of NADH increases.

Figure 2 shows the changes in the absorbance of the Au NP growth solution upon interaction with different concentrations of the NADPH cofactor. The absorbance of the Au particles increases and is shifted to longer wavelengths as the concentration of the reduced cofactor is increased. Figure 2 inset, shows the calibration curve that corresponds to the absorbance of the Au particles at $\lambda = 524$ nm at different concentrations of NADPH. Control experiments reveal that all of the components of the growth solution are essential for the enhanced growth of the Au particles. Exclusion of the Au NPs from the solution does not yield any gold particles upon the addition of the NAD(P)H cofactors which implies that although the $AuCl_4^-$ salt is reduced to the colorless Au^I species by the NAD(P)H cofactors, the Au NP seeds are required as catalysts for the growth of the particles. The surfactant CTAB is also essential to stimulate the growth of the Au NPs upon the addition of NAD(P)H. Clearly, the enlargement of the Au NP seeds by the NAD(P)H/$AuCl_4^-$ solutions involves two steps: First, the rapid reduction of

 DOI: 10.1002/anie.200460608 © 2004 Wiley-VCH Verlag GmbH & Co. KGaA, Weinheim

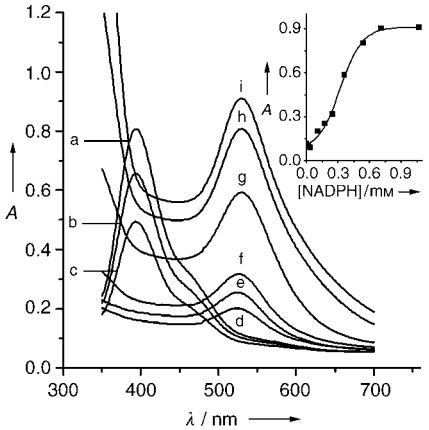


Figure 2. Variation in the absorbance spectra of the Au NP growth solution (4.0×10^{-10} M in Au NPs) at different concentrations of NADPH: a) 0 M; b) 1.79×10^{-5} M; c) 3.57×10^{-5} M; d) 10.7×10^{-5} M; e) 18×10^{-5} M; f) 25×10^{-5} M; g) 36×10^{-5} M; h) 54×10^{-5} M; i) 71×10^{-5} M. Inset: Variation in the absorbance intensity at $\lambda = 524$ nm of the growth solution upon interaction (30 mins) with variable concentrations of NADPH.

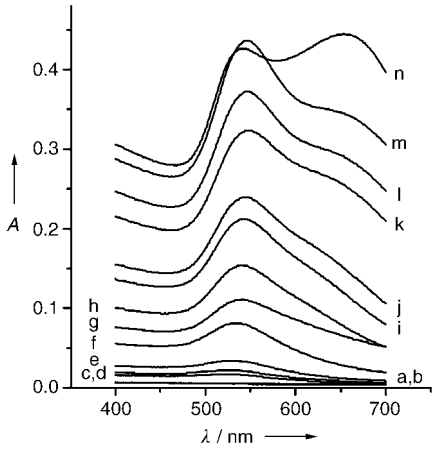


Figure 3. Changes in the absorbance of the Au NP/aminopropylsiloxane-functionalized glass slides upon treatment with the growth solution in the presence of different concentrations of NADH: a) 0 M; b) 14×10^{-5} M; c) 27×10^{-5} M; d) 34×10^{-5} M; e) 41×10^{-5} M; f) 44×10^{-5} M; g) 48×10^{-5} M; h) 51×10^{-5} M; i) 54×10^{-5} M; j) 58×10^{-5} M; k) 61×10^{-5} M; l) 65×10^{-5} M; m) 68×10^{-5} M; n) 1.36×10^{-3} M.

$AuCl_4^-$ by NAD(P)H to the colorless Au^I species takes place as described in Equation (1) (this result is similar to earlier reports[14] in which other reducing agents were employed). Second, the slow catalyzed reduction of the Au^I species by the Au NP seeds to the Au metal particles occurs, [Eq. (2)].

$$AuCl_4^- + NADH \rightarrow Au^I + 4\,Cl^- + NAD^+ + H^+ \quad (1)$$

$$2\,Au^I + NADH \xrightarrow{\text{Au-NP}} 2\,Au^0 + NAD^+ + H^+ \quad (2)$$

The growth of the Au NPs by the NAD(P)H cofactors was also examined on surfaces. Glass slides were functionalized with a 3-aminopropylsiloxane film, and the citrate-stabilized Au-NPs (3 nm ± 1 nm, prepared by reduction with $NaBH_4$ and further stabilized by citrate) were electrostatically bound to the surface.[15] The resulting Au nanoparticle-functionalized glass slides were then treated with the growth solution and different concentrations of the NADH cofactor. Figure 3 depicts the changes in the absorbance spectra of the glass interfaces upon interaction with different concentrations of NADH. Visually, the color of the glass slides turns from red to dark blue depending on the concentration of NADH in solution. As the concentration of NADH is increased, the absorbance spectra of the surfaces reveal an increase in the absorbance band at $\lambda = 535$ nm. At NADH concentrations that are higher than 0.55 mM, the evolution of a second absorbance band at $\lambda = 650$ nm is observed. This absorbance was previously attributed to an interparticle-coupled plasmon exciton that forms upon the aggregation and intimate contact of the Au particles.[16] Thus, at high concentrations of NADH, the growth of the Au NPs on the surface brings the Au particle aggregates into close contact to give rise to the long-wavelength absorbance band.

To understand further the growth mechanism of the Au NP seeds by the $AuCl_4^-$/NADH system, we analyzed the Au NP-functionalized glass surfaces with scanning electron microscopy (SEM). Upon increasing the concentration of NADH from 6.8×10^{-5} to 27×10^{-5} to 41×10^{-5} to 54×10^{-5} M (Figures 4 a–d, respectively), the surface coverage of the enlarged Au particles on the glass surfaces also increases, with the particles exhibiting dimensions of 6 ± 1, 13 ± 2, 18 ± 5, and 40 ± 8 nm, respectively. The SEM images in Figures 4 a–d show isolated, noncontacted particles whose behavior is

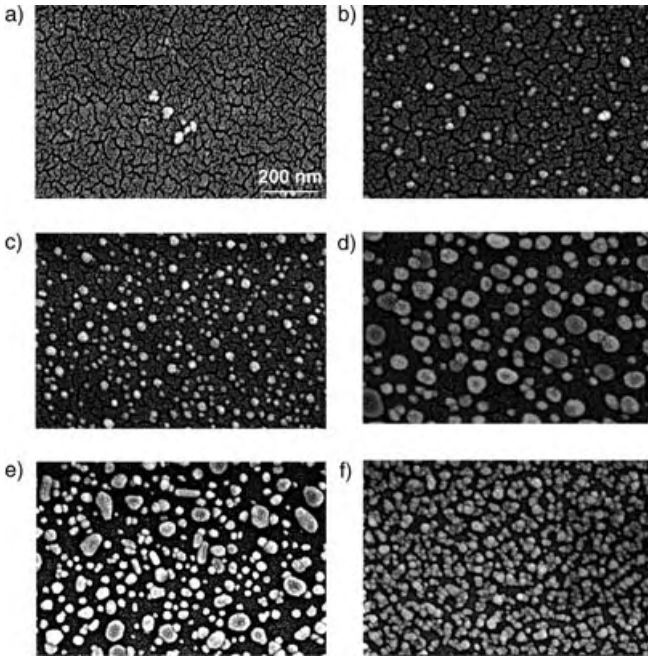


Figure 4. SEM images of enlarged Au particles generated on a Au nanoparticle/3-aminopropylsiloxane interface on a glass support using $AuCl_4^-$ (1.8×10^{-4} M), CTAB (7.4×10^{-2} M), and variable concentrations of NADH: a) 14×10^{-5} M; b) 27×10^{-5} M; c) 41×10^{-5} M; d) 54×10^{-5} M; e) 61×10^{-5} M; f) 1.36×10^{-3} M. All images are on the same scale as indicated in a). All surfaces were coated with a Au/Pt layer (7–8 nm) to enhance the conductivity of the supports.

 © 2004 Wiley-VCH Verlag GmbH & Co. KGaA, Weinheim

consistent with the absorbance features of the respective interface shown in Figure 3, curves b, c, e, and i. At high concentrations of NADH (Figures 4e,f), high surface coverages of the enlarged Au particles are observed. Interestingly, the enlarged particles are of smaller dimensions, $\approx 20 \pm 5$ nm, yet the particles touch one another to form 2D Au particle aggregates. This observation is consistent with the observation of an interparticle-coupled plasmon absorbance band for the aggregated nanoparticles on the surface at high concentrations of NADH (see Figure 3, curves k and n, respectively).

The analysis of surface-enlarged Au particles by SEM provides important information on the growth mechanism of the particles in the presence of the $AuCl_4^-$/NADH system: 1) At low concentrations of NADH, the probability of initiating the catalytic enlargement of the Au NP seeds is low. Once the Au NP seeds are activated, they grow effectively. This explains why at low NADH concentrations the surface coverage of the enlarged particles is low but the particles reach dimensions of 30 ± 20 nm. 2) At high concentrations of NADH, the probability of activating the growth of the Au NPs increases. This facilitates the parallel growth of numerous activated seeds which leads to smaller particles (20 ± 5 nm) with a high surface coverage.

Subsequently, the growth of the Au NP seeds by the NADH/$AuCl_4^-$ system was applied to analyze the substrate coupled to a NAD^+-dependent biocatalyzed process. As the growth of the Au NP seeds proceeds in CTAB-rich acidic medium (pH 4.0) we were forced to compartmentalize the analytical assay to prevent direct contact between the enzyme-active solutions and the Au NP growth systems. Figures 5 and 6 depict the analysis of lactate in the presence of the NAD^+-dependent lactate dehydrogenase (LDH) by using the catalytic growth of the Au NP seeds as a readout method. In one compartment, the LDH-mediated reduction of NAD^+ by different concentrations of lactate was allowed to proceed for a fixed reaction time of 30 mins. The resulting biocatalytic mixture that included the LDH-generated NADH was then introduced into the second compartment, which contained the Au NP seeds in the growth solution (Figure 5). In an alternative procedure, the biocatalytic mixture was added to the Au NP/aminosiloxane-functionalized glass surfaces in the presence of $AuCl_4^-$ (Figure 6).

The spectral changes of the Au NP growth solution upon addition of the LDH-generated NADH in the presence of different concentrations of lactate are shown in Figure 5. As the concentration of lactate increases, the concentration of the generated NADH increases. At low concentrations of lactate, the amount of NADH generated is insufficient to reduce all the $AuCl_4^-$ species to the Au^I species and this leads to a residual absorbance of $AuCl_4^-$ at $\lambda = 392$ nm (Figure 5, curves a–c). At concentrations of lactate higher than 0.45 mM, the generated NADH reduces all the $AuCl_4^-$ species to Au^I, and the seeds are effectively enlarged (curves d–g). Figure 5, inset, shows the variation of the absorbance at $\lambda = 524$ nm with different concentrations of lactate. Figure 6, curves a–h, show the bands that correspond to the enlarged particles on the surface (plasmons) that formed after 60 mins by NADH generated biocatalytically. As the concentration of lactate increases, the plasmon absorbance band increases in intensity and is shifted to longer wavelengths. Thus, at higher concentrations of lactate, more Au NP seeds are activated towards the enlargement process and the resulting particles are larger in dimension.

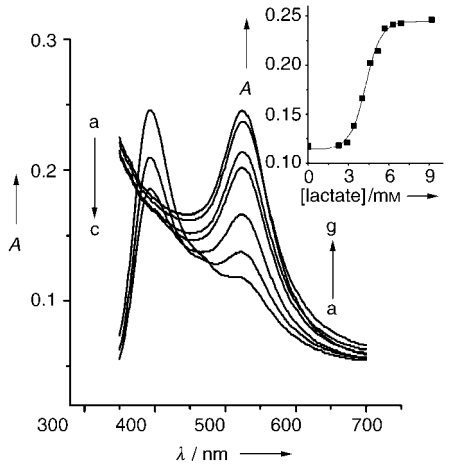


Figure 5. Variation in the absorbance spectra of the growth solution (1.4×10^{-10} M in Au NP seeds) upon the addition of NADH (generated biocatalytically) and variable concentrations of lactate: a) 2.3×10^{-3} M; b) 3.4×10^{-3} M; c) 4.0×10^{-3} M; d) 4.6×10^{-3} M; e) 5.2×10^{-3} M; f) 5.7×10^{-3} M; g) 9.2×10^{-3} M. Inset: Variations in the absorbance of the growth solution as a function of the concentration of lactate in the biocatalysis compartment.

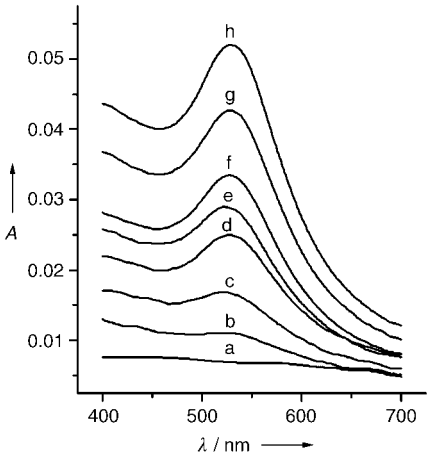


Figure 6. Variation in the absorbance spectra of the Au NP/3-aminopropylsiloxane-functionalized glass slides upon treatment with the growth solution, NADH (generated biocatalytically), and variable concentrations of lactate: a) 0 M; b) 2.9×10^{-3} M; c) 3.6×10^{-3} M; d) 5.1×10^{-3} M; e) 5.8×10^{-3} M; f) 6.6×10^{-3} M; g) 7.3×10^{-3} M; h) 9.8×10^{-3} M.

In conclusion, the present study has demonstrated 1) the enlargement of Au nanoparticles mediated by NADH and 2) an optical readout method based on the absorbance of Au particle-plasmons to monitor biocatalyzed transformations.

Experimental Section

Au NPs (13 ± 2 nm) stabilized with citrate,[17] and Au NPs (3.5 ± 0.5 nm) prepared with $NaBH_4$ and stabilized with citrate[18] were

 © 2004 Wiley-VCH Verlag GmbH & Co. KGaA, Weinheim

prepared according to the literature. The concentration of the Au NPs (13 ± 2 nm) was determined from the absorbance value and the appropriate extinction coefficient at $\lambda = 519$ nm. The solution of the Au NPs was used within 2–5 h after preparation. Growth solutions consisted of $HAuCl_4$ (1.8×10^{-4}), CTAB (7.4×10^{-2} M), and different concentrations of NAD(P)H. For the catalytic growth of the gold nanoparticles, Au NPs (1×10^{-10} M in 13 ± 1-nm particles) were added to the growth solution, and the absorbance spectra were recorded after 30 mins at 30 °C. Glass slides were functionalized with 3-aminopropyl triethoxysilane as described previously[15] and modified accordingly with the citrate-stabilized Au NPs (3.5 ± 0.5 nm). The Au NP-modified glass slides were soaked in the growth solution for 1 h at 30 °C. The absorbance spectra of the resulting modified slides were recorded in water. The LDH-mediated oxidation of lactate in the presence of NAD^+, monitored by the enlargement of the Au NPs (as optical labels), was performed in two steps: 1) A solution of Tris buffer (50 mM; pH 9.0) that contained NAD^+ (1×10^{-3} M), LDH (0.2 mg mL^{-1}), and different concentrations of lactate was allowed to react for 30 mins at 30 °C. 2) A 200-μL aliquot of this mixture was then added to the growth solution (2.5 mL; pH 1.8). Au NPs (1.4×10^{-10} M in 13 ± 1-nm particles) or the Au NP-functionalized slides were then added as seeds to the growth solution. The absorbance spectra of the solutions or of the Au NP-functionalized slides, were then recorded after 30 mins at 30 °C.

Received: May 10, 2004 [Z460608]

Keywords: biosensors · cofactors · enzymes · gold · nanostructures

[1] a) C. M. Niemeyer, *Angew. Chem.* **2001**, *113*, 4643 – 4644; *Angew. Chem. Int. Ed.* **2001**, *40*, 4128 – 4158; b) E. Katz, I. Willner, J. Wang, *Electroanalysis* **2004**, *16*, 19 – 44; c) E. Katz, A. N. Shipway, I. Willner in *Nanoparticles—From Theory to Applications* (Ed.: G. Schmid) Wiley-VCH, Weinheim, **2003**, Chapter 6, pp. 368 – 421.

[2] a) J. Wang, G. D. Liu, A. Merkoci, *J. Am. Chem. Soc.* **2003**, *125*, 3214 – 3215; b) J. Wang, G. D. Liu, Q. Y. Zhu, *Anal. Chem.* **2003**, *75*, 6218 – 6222; c) J. Wang, O. Rincon, R. Polsky, E. Dominguez, *Electrochem. Commun.* **2003**, *5*, 83 – 86; d) J. Wang, R. Polsky, D. K. Xu, *Langmuir* **2001**, *17*, 5739 – 5741.

[3] I. Willner, F. Patolsky, J. Wasserman, *Angew. Chem.* **2001**, *113*, 1913 – 1916; *Angew. Chem. Int. Ed.* **2001**, *40*, 1861 – 1864.

[4] V. Pardo-Yissar, E. Katz, J. Wasserman, I. Willner, *J. Am. Chem. Soc.* **2003**, *125*, 622 – 623.

[5] S. J. Park, T. A. Taton, C. A. Mirkin, *Science* **2002**, *295*, 1503 – 1506.

[6] a) X. C. Zhou, S. J. O'Shea, S. F. Y. Li, *Chem. Commun.* **2000**, 953 – 954; b) F. Patolsky, K. T. Ranjit, A. Lichtenstein, I. Willner, *Chem. Commun.* **2000**, 1025 – 1026; c) I. Willner, F. Patolsky, Y. Weizmann, B. Willner, *Talanta* **2002**, *56*, 847 – 856.

[7] a) X. H. Gao, S. M. Nie, *Trends Biotechnol.* **2003**, *21*, 371 – 373; b) A. P. Alivisatos, *Nat. Biotechnol.* **2004**, *22*, 47 – 52.

[8] a) W. J. Parak, D. Gerion, D. Zanchet, A. S. Woerz, T. Pellegrino, C. Micheel, S. C. Williams, M. Seitz, R. E. Bruehl, Z. Bryant, C. Bustamante, C. R. Bertozzi, A. P. Alivisatos, *Chem. Mater.* **2002**, *14*, 2113 – 2119; b) I. L. Medintz, A. R. Clapp, H. Mattoussi, E. R. Goldman, B. Fisher, J. M. Mauro, *Nat. Mater.* **2003**, *2*, 630 – 638; c) L. Y. Wang, L. Wang, F. Gao, Z. Y. Yu, Z. M. Wu, *Analyst* **2002**, *127*, 977 – 980.

[9] S. O. Obare, R. E. Hollowell, C. J. Murphy, *Langmuir* **2002**, *18*, 10407 – 10410.

[10] J. J. Storhoff, C. A. Mirkin, *Chem. Rev.* **1999**, *99*, 1849 – 1862.

[11] J. W. Liu, Y. Lu, *J. Am. Chem. Soc.* **2003**, *125*, 6642 – 6643.

[12] a) L. G. Lee, G. M. Whitesides, *J. Am. Chem. Soc.* **1985**, *107*, 6999 – 7008; b) I. Willner, D. Mandler, *Enzyme Microb. Technol.* **1989**, *11*, 467 – 483.

[13] a) I. Katakis, E. Dominguez, *Microchim. Acta* **1997**, *126*, 11 – 32; b) A. Bardea, E. Katz, A. F. Bückmann, I. Willner, *J. Am. Chem. Soc.* **1997**, *119*, 9114 – 9119.

[14] J. R. Nikhil, G. Latha, M. J. Catherine, *Langmuir* **2001**, *17*, 6782 – 6786.

[15] A. Doron, E. Katz, I. Willner, *Langmuir* **1995**, *11*, 1313 – 1317.

[16] a) A. N. Shipway, M. Lahav, R. Gabai, I. Willner, *Langmuir* **2000**, *16*, 8789 – 8795; b) M. Quinton, U. Kreibig, *Surf. Sci.* **1986**, *172*, 557 – 577; c) C. G. Blatchord, J. R. Campbell, J. A. Creighton, *Surf. Sci.* **1982**, *120*, 435 – 455; d) C. P. Collier, R. J. Saykally, J. J. Shiang, S. E. Henichs, J. R. Heath, *Science* **1997**, *277*, 1978 – 1981.

[17] K. C. Grabar, R. G. Freeman, M. B. Hommer, M. J. Natan, *Anal. Chem.* **1995**, *67*, 735 – 743.

[18] B. D. Brantley, O. O. Sherine, M. J. Catherine, *Adv. Mater.* **2003**, *15*, 414 – 416.

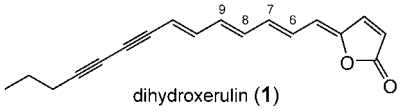
 © 2004 Wiley-VCH Verlag GmbH & Co. KGaA, Weinheim

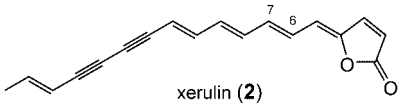
Natural Products Synthesis

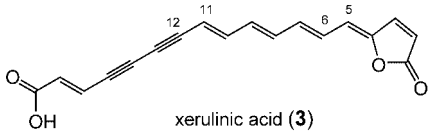
Total Synthesis of Xerulinic Acid**

*Achim Sorg and Reinhard Brückner**

In 1990, Steglich, Anke, and co-workers identified a family of three novel polyenes from the fungus *Xerulina melanotricha* DÖRFELT: dihydroxerulin (**1**), xerulin (**2**), and xerulinic acid (**3**).[1] Dihydroxerulin (**1**) and xerulin (**2**) were characterized



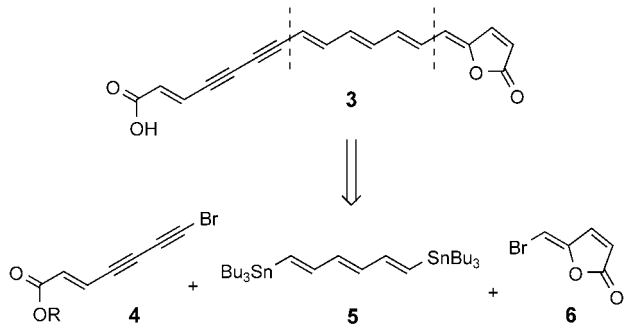




as 90:10–65:35 mixtures, whereas xerulinic acid (**3**) was obtained pure. Each of these compounds inhibited the biosynthesis of cholesterol in HeLa S3 cells by blocking HMG-CoA synthase (EC 4.1.3.5); moreover, in the same cell system, **3** suppressed the synthesis of RNA at $IC_{50} \approx 100$ μM.

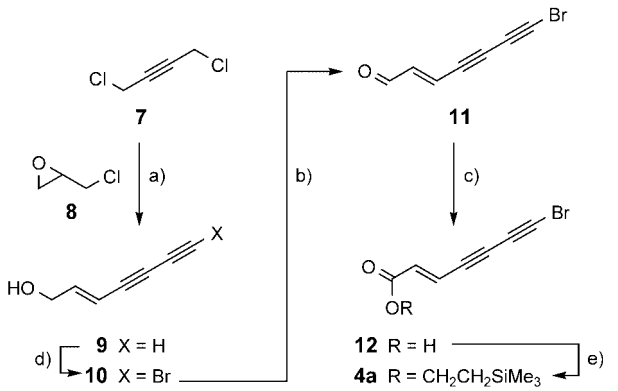
The biological activity and structural uniqueness of the xerulin family stimulated the interest of the synthetic community. The first laboratory syntheses both of dihydroxerulin[2] and xerulin[3] were reported by our group. Rossi et al.[4] completed another synthesis of dihydroxerulin, and Negishi, Alimardanov, and Xu[5] prepared xerulin. Herein we report the first total synthesis of xerulinic acid based on unprecedented disconnections.

Scheme 1 outlines our retrosynthetic analysis. It differs from our routes to dihydroxerulin[2] and xerulin[3] in that we intended to form C–C rather than C=C bonds in the final steps. The latter approach—by Wittig reactions—had been nonstereoselective irrespective of whether the ylides corresponded to the right- or left-hand moiety of the target structure.[2,3] In contrast, the presently adopted approach



Scheme 1. Retrosynthetic analysis of xerulinic acid.

would establish *all* C=C bonds and interconnect them by C–C-forming Stille couplings.[6] This identified the enediyne carboxylate **4**, the hitherto unknown bisstannane **5**, and the novel building block **6**[7]—which ought to be *generally* useful for synthesizing γ-alkylidenebutenolides[8]—as our key precursors. Their syntheses are described in Schemes 2–4,



Scheme 2. a) $LiNH_2$ (6 equiv), NH_3 (l), −35 °C, 15 min; addition of **8**, 3.5 h; →RT, 17% (reference [9]: 21%); b) Dess–Martin periodinane (1.52 equiv), CH_2Cl_2, 0 °C→RT, 2.5 h, 79%; c) $NaClO_2$ (2.1 equiv), KH_2PO_4 (2.5 equiv), 2-methyl-2-butene (3.5 equiv), acetone/H_2O = 3:2, 0 °C, 89%; d) NBS (1.30 equiv), $AgNO_3$ (0.08 equiv), acetone, room temperature, 13 h, 79%; e) $HOCH_2CH_2SiMe_3$ (1.2 equiv), DCC (1.1 equiv), DMAP (0.05 equiv), ethyl acetate, 0 °C→RT, 2 h, 83%. NBS = *N*-bromosuccinimide, DCC = dicyclohexylcarbodiimide, DMAP = 4-dimethylaminopyridine.

respectively, and their coupling to give xerulinic acid (**3**) is shown in Scheme 5.

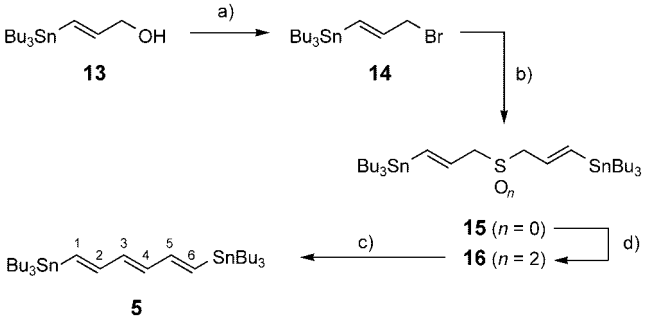
The synthesis of enediyne carboxylate **4a** began with the synthesis of enediynol **9** from epichlorohydrin (**8**) and lithiobutadiyne generated in situ from 1,4-dichlorobut-2-yne (**7**) and excess lithium amide (Scheme 2).[9] Terminal bromination of **9** with NBS/$AgNO_3$[10] led to bromoenediynol **10**.[11] The corresponding aldehyde **11** was generated by a Dess–Martin oxidation[12] of **10** (79% yield) and taken on to the corresponding carboxylic acid **12** by a Lindgren oxidation[13] (89% yield). Esterification with 2-trimethylsilylethanol in the presence of DCC and DMAP provided the unstable ester **4a** in 83% yield.[14]

The synthesis of bisstannane **5** proceeded highly stereoselectively (Scheme 3). It was assembled starting from the tin-

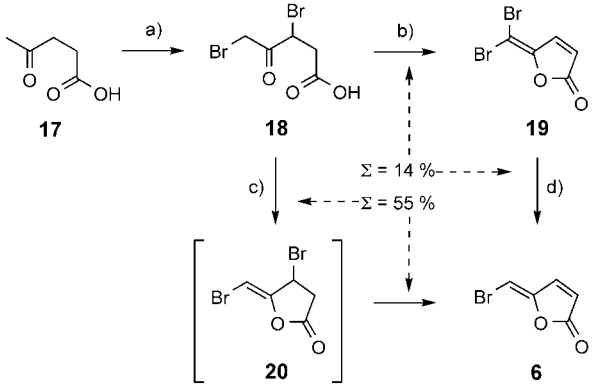
[*] A. Sorg, Prof. Dr. R. Brückner
Institut für Organische Chemie und Biochemie
Universität Freiburg
Albertstrasse 21, 79104 Freiburg (Germany)
Fax: (+49) 761-203-6100
E-mail: reinhard.brueckner@organik.chemie.uni-freiburg.de

[**] This work was financially supported by the Fonds der Chemischen Industrie. We are grateful to Dr. Manfred Keller for valuable spectroscopic support and to Melanie Waldrich for technical assistance.

 DOI: 10.1002/anie.200453729 © 2004 Wiley-VCH Verlag GmbH & Co. KGaA, Weinheim



Scheme 3. a) CBr_4 (1.21 equiv), CH_2Cl_2, 0 °C, addition of PPh_3 (1.10 equiv), 1 h, 82% (reference [16]: 81%); b) Na_2S (0.5 equiv), $Bu_4N^+ HSO_4^-$ (0.7 mol%), H_2O/THF, room temperature, 7 h, 90%; c) KOH (30% on Al_2O_3; 20 equiv), CBr_2F_2 (4 equiv), THF, 0 °C, 30 min, 73%; d) $(NH_4)_6Mo_7O_{24}$ (0.2 equiv), H_2O_2 (10 equiv), EtOH, 0 °C→RT, 1 h, 88%.

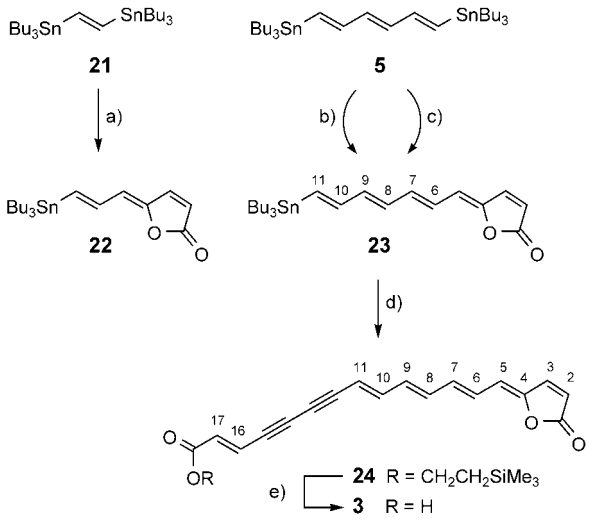


Scheme 4. a) Br_2 (2.1 equiv), CH_2Cl_2, 0 °C→RT, 2 h, 60% (reference [25]: 40%); b) oleum/conc. H_2SO_4 2:1 (v/v), 50–60 °C, 6 min; 28%;[7] c) 1) P_4O_{10} (1.2 equiv), CH_2Cl_2, 0 °C→Δ, 1 h, filtration; 2) NEt_3 (1.03 equiv), CH_2Cl_2, 0 °C→Δ, 1 h, 55%; d) $HSnBu_3$ (1.10 equiv), $[Pd(PPh_3)_4]$ (0.10 equiv), THF, 65 °C, 3 h, 51%.[7]

containing alcohol **13**,[15] which was obtained by cuprostannylation/protonolysis of propargyl alcohol. We transformed compound **13** through nucleophilic attack first into the tin-containing bromide **14** (82%)[16] and subsequently into the tin-containing sulfide **15** (90%).[17] Oxidation with peroxomolybdate provided the corresponding sulfone **16** (88%).[18] Deprotonation of sulfone **16** in the presence of CBr_2F_2 with Al_2O_3-supported KOH[19] induced a Ramberg–Bäcklund reaction[20] to provide triene **5** in 73% yield. The resulting sample of **5** represented a 96:4 mixture of the *trans,trans,trans* and the *trans,cis,trans* isomers. This was inferred from the ratio of the integrals for 2-H and 5-H (*trans,trans,trans*-**5**: $\delta_{2\text{-H}} = \delta_{5\text{-H}} = 6.56$ ppm, *trans,cis,trans*-**5**: $\delta_{2\text{-H}} = \delta_{5\text{-H}} = 7.08$ ppm) and from the magnitudes of the vicinal olefinic H,H coupling constants in the major isomer ($J_{1,2} = J_{5,6} = 18.6$ Hz, $J_{3,4} = 15.1$ Hz).[21] 1,6-Bis(tributylstannyl)hexatriene (**5**) ought to be a valuable conjuctive C_6 reagent in analogy to 1,2-bis(tributylstannyl)ethylene as a conjunctive C_2 reagent[22] and 1,4-bis(methylstannyl)butadiene as a conjunctive C4 reagent.[23,24] The first example of a conjunctive C_6 reagent is provided in the present study (see Scheme 5). Notably, we were able to couple *different* electrophiles at the termini (C1 vs. C6) of **5**. Such a differentiation is more difficult to realize than the C1/C4 differentiation in the single unsymmetrical biscoupling reported for the aforementioned C_4 bisstannane).[23a]

We recently reported the two-step preparation of (bromomethylene)butenolide **6** from dibromolevulinic acid (**18**;[25a] Scheme 4) by oxidative cyclization (→**19**) and stereoselective reduction (→**6**).[7] Since then we have been able to shorten this synthesis by successively treating the same dibromolevulinic acid (**18**) in one pot with two reagents:[26] P_4O_{10} effects a dehydration, presumably giving rise to the enol ester intermediate **20**; thereafter triethylamine (instead of triethylenediamine, which was used in ref. [26]) induces the β-elimination of HBr. This gave four times as much bromobutenolide **6**[27] as our previous synthesis, with the same perfect *Z* selectivity, both of which were prerequisites for **6** to become a viable starting material for our study (we are unaware of previous synthetic applications of this compound[25b]).

To couple bisstannane **5** and butenolide **6** in a 1:1 ratio without too much competitive 1:2 coupling, we considered it safest to perform one Sn→Li exchange per reagent molecule first, a Li→Zn exchange next, and a Negishi coupling[28] thereafter. The model compound 1,2-bis(tributylstannyl)-ethylene (**21**)[22] and butenolide **6** could indeed be combined in this manner, forming 1:1 coupling product **22** in 46% yield (Scheme 5). To our delight, we could extend this procedure to the 1,6-bis(stannyl)hexatriene **5** and butenolide **6** to obtain the desired 1:1 product **23** in 63% yield. By comparison, the combination of the same reagents through a Stille coupling in THF in the presence of $[Pd(dba)_2]$ and $AsPh_3$ led to **23** in only 44% yield. The all-*trans* configuration of **23** was proved by ^1H NMR spectroscopy (499.9 MHz, $CDCl_3$; for the number-



Scheme 5. a) **21** (1.01 equiv), *n*BuLi (1.05 equiv), THF, −78 °C, 70 min; then $ZnCl_2$ (1.05 equiv), →−20 °C, 2 h; then **6**, $[Pd(PPh_3)_4]$ (5 mol%), 0 °C→RT, 45 min, 46%; b) **5** (1.3 equiv), *n*BuLi (1.3 equiv), THF, −78 °C, 20 min; then $ZnCl_2$ (1.3 equiv), 30 min; then **6**, $[Pd(PPh_3)_4]$ (5 mol%), 0 °C, 1 h, 63%; c) **6** (1.1 equiv), $[Pd(dba)_2]$ (5 mol%), $AsPh_3$ (20 mol%) THF, room temperature, 2 h, 44%; d) **4a** (1.08 equiv), $[Pd(dba)_2]$ (6 mol%), $AsPh_3$ (19 mol%), THF, room temperature, 5 h, 73%; e) Bu_4NF (1.5 equiv), THF, 0 °C→RT, 2 h, 61%.

 © 2004 Wiley-VCH Verlag GmbH & Co. KGaA, Weinheim

ing see Scheme 5): $J_{6,7} = 14.9$ Hz, $J_{8,9} = 14.7$ Hz, and $J_{10,11} = 18.7$ Hz.

The carbon skeleton of our target molecule **3** was completed by a Stille coupling[6] ([Pd(dba)$_2$],[29] AsPh$_3$[29]) between the brominated enediyne carboxylate **4a** and the stannylated heptatrienylidenebutenolide **23** (Scheme 5). Provided that exposure to atmospheric oxygen and daylight was avoided, the reaction gave xerulinic acid ester **24**[30] in 73% yield. In the final step, this compound was deprotected by treatment with anhydrous Bu$_4$NF in THF to give **3** in 61% yield. The resulting specimen of synthetic xerulinic acid (**3**) was scrutinized by ^{1}H, ^{13}C, and 2D NMR spectroscopy at the same field strengths (500 MHz/126 MHz) and in the same solvent ([D$_6$]DMSO) as the natural product. The juxtaposition of our data and those from Steglich and co-workers[1,31] unambiguously showed that our compound and the natural product are identical.

In summary, we have completed the first, highly convergent synthesis of xerulinic acid (**3**). Although xerulinic acid is perhaps not "complex", its preparation is by no means simple and its tendency to "polymerize" cannot be overestimated. Our synthetic strategy towards **3** is distinct from previous strategies aimed at the xerulin family of compounds.[32] Bisstannane **5** should open a *general* route to polyunsaturated molecules containing a *trans,trans,trans*-hexatriene moiety and lactone **6** should open a *general* route to γ-alkylidenebutenolides.

Received: January 12, 2004 [Z53729]

Keywords: C–C coupling · inhibitors · lactones · natural products · stereoselective synthesis

[1] D. Kuhnt, T. Anke, H. Besl, M. Bross, R. Herrmann, U. Mocek, B. Steffan, W. Steglich, *J. Antibiot.* **1990**, *43*, 1413–1420.
[2] K. Siegel, R. Brückner, *Synlett* **1999**, 1227–1230.
[3] K. Siegel, R. Brückner, *Chem. Eur. J.* **1998**, *4*, 1116–1122.
[4] R. Rossi, F. Bellina, A. Catanese, L. Mannina, D. Valensin, *Tetrahedron* **2000**, *56*, 479–487.
[5] E.-i. Negishi, A. Alimardanov, C. Xu, *Org. Lett.* **2000**, *2*, 65–67.
[6] For reviews, see: a) J. K. Stille, *Angew. Chem.* **1986**, *98*, 504–519; *Angew. Chem. Int. Ed. Engl.* **1986**, *25*, 508–524; b) V. Farina, G. P. Roth in *Advances in Metal-Organic Chemistry*, *Vol. 5* (Ed.: L. S. Liebeskind), JAI, Greenwich, Connecticut, **1996**, pp. 1–53; c) V. Farina, V. Krishnamurthy, W. J. Scott, *Org. React.* **1997**, *50*, 1–652.
[7] A. Sorg, K. Siegel, R. Brückner, *Synlett* **2004**, 321–325.
[8] a) D. W. Knight, *Contemp. Org. Synth.* **1994**, *1*, 287–315; b) E.-i. Negishi, M. Kotora, *Tetrahedron* **1997**, *53*, 6707–6738; c) R. Brückner, *Chem. Commun.* **2001**, 141–152; d) R. Brückner, *Curr. Org. Chem.* **2001**, *5*, 679–718.
[9] S. R. Landor, E. S. Pepper, *J. Chem. Soc. C* **1966**, 2283–2285.
[10] Prepared by a procedure analogous to that of: T. V. Bohner, R. Beaudegnies, A. Vasella, *Helv. Chim. Acta* **1999**, *82*, 143–160.
[11] All new compounds gave satisfactory ^{1}H and ^{13}C NMR spectra and correct elemental analyses, except acid **12**, unstable ester **4a**, and xerulinic acid (**3**), for all of which, however, correct high-resolution mass spectra were obtained.
[12] D. B. Dess, J. C. Martin, *J. Org. Chem.* **1983**, *48*, 4155–4156.
[13] a) B. O. Lindgren, T. Nilsson, *Acta Chem. Scand.* **1973**, *27*, 888–890 (resorcinol used as hypochlorite scavenger); b) B. S. Bal, W. E. Childers, Jr., H. W. Pinnick, *Tetrahedron* **1981**, *37*, 2091–2096 (2-methyl-2-butene used as hypochlorite scavenger).
[14] Prepared by a procedure analogous to that of: a) N. Jeker, C. Tamm, *Helv. Chim. Acta* **1988**, *71*, 1895–1903; b) G. T. Bourne, D. C. Horwell, M. C. Pritchard, *Tetrahedron* **1991**, *47*, 4763–4774.
[15] Prepared by a procedure analogous to that of: J.-F. Betzer, F. Delaloge, B. Muller, A. Pancrazi, J. Prunet, *J. Org. Chem.* **1997**, *62*, 7768–7780.
[16] A. S.-Y. Lee, C.-W. Wu, *Tetrahedron* **1999**, *55*, 12531–12542.
[17] Method: F. Reimnitz, Ph.D. thesis, Universität Freiburg, **2000**, pp. 71–72, 147–148.
[18] The method is same as that described for the oxidation of heterocycle-substituted sulfides en route to Julia–Lythgoe olefins: P. A. Blakemore, P. J. Kocienski, S. Marzcak, J. Wicha, *Synthesis* **1999**, 1209–1215.
[19] T.-L. Chan, S. Fong, Y. Li, T.-O. Man, C.-D. Poon, *J. Chem. Soc. Chem. Commun.* **1994**, 1771–1772; pure THF was used instead of *t*BuOH/THF (3:1).
[20] For a review, see: L. A. Paquette, *Org. React.* **1977**, *25*, 1–71.
[21] **5**: ^{1}H NMR (499.9 MHz, $CDCl_3$, TMS): $\delta = 0.83$–0.97 (m; $6\times SnCH_2CH_2CH_2CH_3$), overlaps with 0.89 (t, $J_{vic} = 7.3$ Hz; $6\times SnCH_2CH_2CH_2CH_3$), 1.31 (tq, both $J_{vic} = 7.3$ Hz; $6\times SnCH_2CH_2CH_2CH_3$), 1.41–1.58 (m; $6\times SnCH_2CH_2CH_2CH_3$), 6.15 ($m_c$, higher order; 3-H, 4-H), 6.29 (d, $J_{1,2} = J_{6,5} = 18.6$ Hz, each peak flanked by Sn isotope satellites as 2d, $^2J_{^{119}Sn,H} = 70.1$ Hz, $^2J_{^{117}Sn,H} = 67.2$ Hz; 1-H, 6-H), 6.56 ppm (m_c, higher order; 2-H, 5-H); ^{13}C NMR (125.7 MHz, $CDCl_3$): $\delta = 9.6$ (flanked by Sn isotope satellites as 2d, $^1J_{^{119}Sn,C1'} = {}^1J_{^{119}Sn,C1''} = 344.8$ Hz, $^1J_{^{117}Sn,C1'} = {}^1J_{^{117}Sn,C1''} = 329.4$ Hz; $SnCH_2CH_2CH_2CH_3$), 13.7 ($SnCH_2CH_2CH_2CH_3$), 27.3 (flanked by Sn isotope satellites as 1d, $^3J_{^{119}Sn,C3'} = {}^3J_{^{119}Sn,C3''} = {}^3J_{^{117}Sn,C3'} = {}^3J_{^{117}Sn,C3''} = 54.5$ Hz; $SnCH_2CH_2CH_2CH_3$), 29.1 (flanked by Sn isotope satellites as 1d, $^2J_{^{119}Sn,C2'} = {}^2J_{^{119}Sn,C2''} = {}^2J_{^{117}Sn,C2'} = {}^2J_{^{117}Sn,C1''} = 20.6$ Hz; $SnCH_2CH_2CH_2CH_3$), 134.5 (flanked by Sn isotope satellites as 1d, $^3J_{^{119}Sn,C3} = {}^3J_{^{119}Sn,C4} = {}^3J_{^{117}Sn,C3} = {}^3J_{^{117}Sn,C4} = 73.6$ Hz; C3, C4), 135.6 (flanked by Sn isotope satellites as 2d, $^1J_{^{119}Sn,C1} = {}^1J_{^{119}Sn,C6} = 380.0$ Hz, $^1J_{^{117}Sn,C1} = {}^1J_{^{117}Sn,C6} = 363.3$ Hz; C1, C6), 146.9 (flanked by Sn isotope satellites as 1d, $^2J_{^{119}Sn,C2} = {}^2J_{^{119}Sn,C5} = {}^2J_{^{117}Sn,C2} = {}^2J_{^{117}Sn,C5} = 6.4$ Hz; C2, C5); SELINCOR (S. Berger, *J. Magn. Reson.* **1989**, *81*, 561–564; 499.9 MHz/125.7 MHz, $CDCl_3$): $J_{3,4} = 15.1$ Hz, $J_{3,2} = J_{4,5} = 10.1$ Hz; elemental analysis (%): calcd for $C_{30}H_{60}Sn_2$ (656.3): C 54.74, H 9.19; found: C 53.81, H 8.97.
[22] a) K. C. Nicolaou, T. K. Chakraborty, A. D. Piscopio, N. Minowa, P. Bertinato, *J. Am. Chem. Soc.* **1993**, *115*, 4419–4420; b) J. S. Panek, C. E. Masse *J. Org. Chem.* **1997**, *62*, 8290–8291; c) C. E. Masse, M. Yang, J. Solomon, J. S. Panek, *J. Am. Chem. Soc.* **1998**, *120*, 4123–4134; d) P. M. Pihko, A. M. P. Koskinen, *Synlett* **1999**, 1966–1968.
[23] a) A. Kiehl, A. Eberhardt, M. Adam, V. Enkelmann, K. Müllen, *Angew. Chem.* **1992**, *104*, 1623–1626; *Angew. Chem. Int. Ed. Engl.* **1992**, *31*, 1588–1591; b) D. Nozawa, H. Takikawa, K. Mori, *J. Chem. Soc. Perkin Trans. 1* **2000**, 2043–2046.
[24] A fully conjugated 3,8-dimethyl-C$_{10}$-bis(tributylstannane) has also been synthesized and used as a building block: B. Vaz, R. Alvarez, A. R. de Lera, *J. Org. Chem.* **2002**, *67*, 5040–5043.
[25] a) A. J. Manny, S. Kjelleberg, N. Kumar, R. de Nys, R. W. Read, P. Steinberg, *Tetrahedron* **1997**, *53*, 15813–15826. b) The aforementioned authors prepared lactone **6** for the first time but the Experimental Section of their study details no more than a 2% yield of **6** separated chromatographically from a 54%:8%:3%:2%:trace mixture of five compounds; accordingly, **6** becomes a synthetically useful reagent only on the grounds of our two-step synthesis (Scheme 5).
[26] N. Kumar, R. W. Read (Unisearch Limited, Australia), PCT Appl. 20020000639 **2002** [*Chem. Abstr.* **2002**, *136*, 69697].

 © 2004 Wiley-VCH Verlag GmbH & Co. KGaA, Weinheim

[27] **6**: P_4O_{10} (12.62 g, 44.45 mmol, 1.2 equiv) was added to a solution of **18** (10.15 g, 37.04 mmol) in CH_2Cl_2 (150 mL) at 0 °C. After 30 min, the solution was warmed to room temperature and heated at reflux for 1.5 h. After cooling to room temperature, it was filtered and concentrated in vacuo. A solution of the intermediate (8.094 g) in CH_2Cl_2 (75 mL) was cooled to 0 °C, and NEt_3 (5.29 mL, 3.84 g, 38.0 mmol, 1.02 equiv for **18**) was added. After 1 h, the mixture was first warmed to room temperature and then heated at reflux for 1 h. Aqueous NH_4Cl (40 mL) was added, and the mixture was extracted with CH_2Cl_2 (6×20 mL). The combined organic extracts were dried with Na_2SO_4. Evaporation at reduced pressure and flash chromatography (cyclohexane/EtOAc 20:1→2:1) provided **6** (3.54 g, 55 %) as a slightly yellow solid (m.p. 82–84 °C); ^{1}H NMR (300.1 MHz, $CDCl_3$, TMS): $\delta = 6.11$ (s; 1′-H), 6.32 (d, $J_{3,4} = 5.6$ Hz; 3-H), 7.38 ppm (d, $J_{4,3} = 5.6$ Hz; 4-H); ^{13}C NMR (125.7 MHz, $CDCl_3$): $\delta = 92.4$ (C1′), 120.8 (C3), 141.7 (C4), 152.4 (C5), 168.2 ppm (C2); elemental analysis (%): calcd for $C_5H_3BrO_2$ (174.4): C 34.32, H 1.73; found: C 34.20, H 1.61.

[28] For reviews, see: a) E. Erdik, *Tetrahedron* **1992**, *48*, 9577 – 9648; b) E.-i. Negishi, F. Liu, in *Metal-catalyzed Cross-coupling Reactions* (Eds.: F. Diederich, P. J. Stang), Wiley-VCH, Weinheim, **1998**, pp. 1 – 42; c) P. Knochel in *Metal-catalyzed Cross-coupling Reactions* (Eds.: F. Diederich, P. J. Stang), Wiley-VCH, Weinheim, **1998**, pp. 387 – 416.

[29] a) V. Farina, *Pure Appl. Chem.* **1996**, *68*, 73 – 78; b) D. A. Entwistle, S. I. Jordan, J. Montgomery, G. Pattenden, *Synthesis* **1998**, 603 – 612; c) C. Amatore, A. A. Bahsoun, A. Jutand, G. Meyer, A. N. Ntepe, L. Ricard, *J. Am. Chem. Soc.* **2003**, *125*, 4212 – 4222.

[30] **24**: ^{1}H NMR (499.9 MHz, $CDCl_3$, $CHCl_3$ internal standard): $\delta =$ 0.05 (s; $SiMe_3$), 1.03 (m_c; CH_2SiMe_3), 4.26 (m_c; OCH_2), 5.78 (d, $J_{11,10} = 15.4$ Hz; 11-H), 5.89 (d, $J_{5,6} = 11.7$ Hz; 5-H), 6.20 (d, $J_{2,3} =$ 5.4 Hz; 2-H), 6.32 (d, $J_{17,16} = 16.0$ Hz; 17-H), 6.41–6.56 (m; 7-H, 8-H, 9-H), 6.80–6.88 (m; 6-H, 10-H, 16-H), 7.37 ppm (d, $J_{3,2} =$ 5.2 Hz; 3-H); an edited undecoupled HSQC NMR spectrum ("^{1}H-coupled short-range H,C-COSY spectrum"; 499.9 MHz/ 125.7 MHz, $CHCl_3$ and $CDCl_3$ internal standards in $CDCl_3$, respectively) revealed, amongst others: $\delta = 6.44$ ppm (ddd, $^1J_{H,C} = 156.3$ Hz, $J_{9,8} = 12.8$ Hz, $J_{9,10} = 12.0$ Hz; 9-H), $\delta =$ 6.51 ppm (ddd, $^1J_{H,C} = 156.6$ Hz, $J_{8,9} = 14.6$ Hz, $J_{8,7} = 11.6$ Hz; 8-H), $\delta = 6.53$ (ddd, $^1J_{H,C} = 154.3$ Hz, $J_{7,6} = 15.2$ Hz, $J_{7,8} = 11.3$ Hz; 7-H), 6.82 ppm (dd, $^1J_{H,C} = 168.7$ Hz, $J_{16,17} = 16.1$ Hz; 16-H), $\delta =$ 6.85 ppm (ddd, $^1J_{H,C} = 157.6$ Hz, $J_{10,11} = 15.1$ Hz, $J_{10,9} = 11.1$ Hz; 10-H), $\delta = 6.86$ ppm (ddd, $^1J_{H,C} = 159.2$ Hz, $J_{6,7} = 13.7$ Hz, $J_{6,5} =$ 12.3 Hz; 6-H); ^{13}C NMR (125.7 MHz, $CDCl_3$): $\delta = -1.5$ ($Si(CH_3)_3$), 17.3 (C2′), 63.3 (C1′), 78.3, 80.4, 82.5, and 85.3 (C12, C13, C14, C15), 111.1 (C11), 114.4 (C5), 119.1 (C2), 123.6 (C16), 128.4 (C6), 133.0 (C17), 134.6 (C9), 136.6 (C8), 137.5 (C7), 142.5 (C3), 145.3 (C10), 149.7 (C4), 165.5 (C18), 169.2 ppm (C1); elemental analysis (%): calcd for $C_{23}H_{24}O_4Si$ (392.1): C 70.38, H 6.16; found: C 70.15, H 6.13.

[31] W. Steglich, personal communication. We are indebted to Professor Steglich for sending copies of all the original NMR spectra of compound **3**.

[32] A referee suggested that "the possibility of directly obtaining xerulinic acid from xerulin should be commented on". We are unaware of such a possibility; furthermore, during alternative attempts at the synthesis of xerulinic acid, we prepared both the corresponding alcohol ("xerulinol") and aldehyde ("xerulinal") but could not oxidize either to xerulinic acid: K. Siegel, Ph.D. Thesis, Universität Freiburg, **2000**.

Indole Synthesis

A Flexible, Palladium-Catalyzed Indole and Azaindole Synthesis by Direct Annulation of Chloroanilines and Chloroaminopyridines with Ketones

Marc Nazaré, Claudia Schneider, Andreas Lindenschmidt, and David William Will*

The prominent role played by indoles as privileged structures in biological systems[1] has been well documented through a multitude of natural products and bioactive compounds which are indole derivatives and which interact with diverse biological targets.[2] For this reason, the development of simple, general, and especially regioselective synthetic methods for this structural moiety continues to be of tremendous interest.[3] In this context, palladium-catalyzed methods for the construction of the indole scaffold, using *ortho*-alkynylanilines[4] or *N*-acylated *ortho*-alkynylanilines,[5] as well as the reaction of *ortho*-haloanilines and internal alkynes,[6] have been intensively studied. Recently, direct palladium-catalyzed annulation of *ortho*-iodoanilines with ketones by means of enamine formation in situ followed by a Heck reaction has been reported.[7] Not only do 2-iodoanilines have limited commercial availability, but they are also often difficult and expensive to synthesize. The corresponding annulation of 2-chloroanilines does not work under the reported conditions, and to the best of our knowledge has never been investigated. The same applies for heterocyclic derivatives, such as *ortho*-chloroaminopyridines. A procedure for the reaction of 2-chloroanilines, and presumably also 2-bromoanilines, with ketones to give indoles would overcome these limitations. Here we report a very general, mild, one-step palladium-catalyzed annulation procedure for the synthesis of substituted, polyfunctionalized indoles and azaindoles, by reaction of 2-chloroanilines and *ortho*-chloroaminopyridines, respectively, with a variety of ketones.

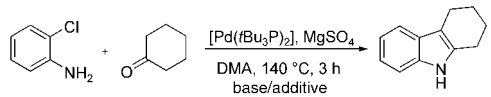
An extensive screening of palladium catalysts and ligands revealed that commercially available $[Pd(t\mathrm{Bu}_3\mathrm{P})_2]$[8] in combination with a base, such as K_3PO_4 or KOAc, and 0.5 equivalents of $MgSO_4$ as a water-binder, was able to catalyze this reaction in dimethylacetamide (DMA) at 140 °C to form indole **3** within 3 h (Table 1). However, variable amounts of side products were formed during the reaction. Investigation of milder, less basic reaction conditions led to the surprising discovery that the addition of 1.5 equivalents of acetic acid to the moderately active base K_3PO_4 was extremely effective and led to a highly selective and almost quantitative

[*] Dr. M. Nazaré, C. Schneider, Dr. A. Lindenschmidt, Dr. D. W. Will
Aventis Pharma Deutschland GmbH
Medicinal Chemistry, DI&A Chemistry
Building G878, 65926 Frankfurt am Main (Germany)
Fax: (+49) 69-331-399
E-mail: marc.nazare@aventis.com

Supporting information for this article is available on the WWW under http://www.angewandte.org or from the author.

 © 2004 Wiley-VCH Verlag GmbH & Co. KGaA, Weinheim DOI: 10.1002/anie.200460122

Table 1: Role of the base and additive in the conversion of 2-chloroaniline with cyclohexanone to indole



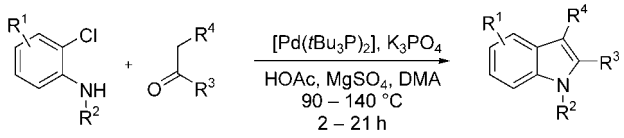
1 **2** **3**

Entry	Base	Additive	Conv. [%][a]
1	Cs_2CO_3	–	63
2	KOAc	–	78
3	K_3PO_4	–	56
4	Cs_2CO_3	1.5 equiv HOAc	83
5	KOAc	1.5 equiv HOAc	70
6	K_3PO_4	1.5 equiv HOAc	88[b]

[a] Conversion by HPLC-MS analysis. [b] Yield of isolated product: 82% with >95% purity by ^{1}H NMR and HPLC.

conversion to the desired product **3**. This effect could also be observed, although to a lesser extent, with Cs_2CO_3 as base, but not with KOAc.[9]

The optimized reaction conditions, using K_3PO_4/acetic acid and [Pd(tBu$_3$P)$_2$], are very broadly applicable and tolerate a wide variety of substitution patterns and functionalities (Scheme 1, Tables 2 and 3). Cyclic ketones with various

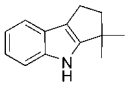
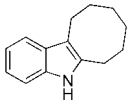
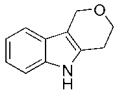
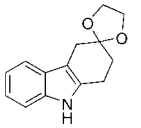
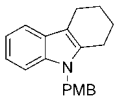
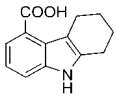
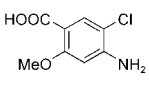
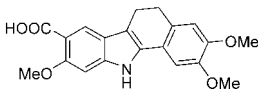
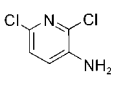
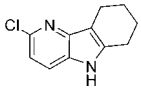
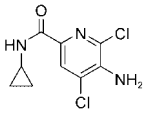
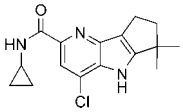
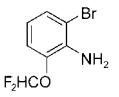
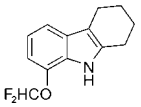


Scheme 1. Annulation of *ortho*-chloroanilines by reaction with ketones. The method can be used with cyclic and acyclic ketones and with bromoanilines as well as chloroaminopyridines (see Tables 2 and 3).

ring sizes and functionalization react with comparable efficiency (Table 2, entries 1–3), and even acid-labile moieties, such as dioxolane, are stable under the reaction conditions (entry 4). The breadth of the 2-chloroaniline substrate spectrum is considerable: both electron-rich and electron-poor 2-chloroanilines are effective substrates. Furthermore, diverse functional groups, such as free acids, amides, methyl and methoxy groups, as well as *N*-alkylated anilines are tolerated (entries 5–7, 10). It should be emphasized that *ortho*-chloroaminopyridines can be cyclized smoothly to give the pharmacologically important azaindoles[10] (entries 8, 9). The reaction is remarkably selective for the *ortho*-chloroaniline moiety. Additional, potentially reactive chloro substituents do not react under these conditions (entries 8, 9). This observation supports the postulated enamine–Heck mechanism,[7] as opposed to a direct α-arylation process of a keto-enolate followed by cyclization.[11] As expected, the corresponding 2-bromoanilines react with similar efficiency (entry 10).

Acetophenones also react under the conditions described, giving the corresponding indoles in good yield (Table 3, entries 1–4). It is remarkable that also in this case *N*-alkylated *ortho*-chloroanilines react as efficiently as their unsubstituted

Table 2: Annulation reaction with cyclic ketones.[a]

Entry	Aryl amine	Indole	t [h]/ T [°C]	Yield [%][b]
1			14/ 125	62
2			2/140	80
3			2/ 90	98
4			2/ 90	96
5			14/ 140	80
6			14/ 140	67
7			14/ 140	73[c]
8			14/ 140	57
9			14/ 140	46
10			14/90	70

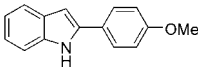
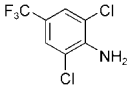
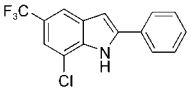
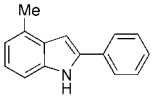
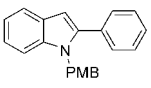
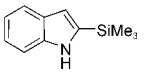
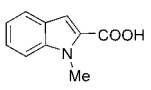
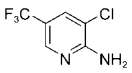
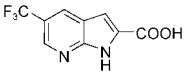
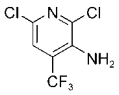
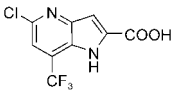
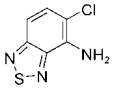
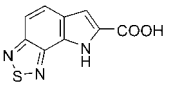
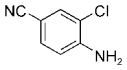
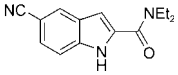
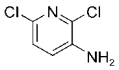
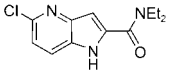
[a] Reaction conditions: 1.0 equiv aniline, 3.0 equiv ketone, 1.3 equiv K_3PO_4, 0.1 equiv [Pd(tBu$_3$P)$_2$], 1.5 equiv acetic acid, 0.5 equiv $MgSO_4$ in DMA. [b] Yields of isolated products with >95% purity by ^{1}H NMR and HPLC. [c] Isolated as a mixture with the oxidation product 2,3,9-trimethoxy-11*H*-benzo[*a*]carbazole-8-carboxylic acid. PMB = *para*-methoxybenzyl.

analogues (entry 4). The synthetically useful intermediate 2-(trimethylsilyl)indole[12,13] can be synthesized in high yield using acetyltrimethylsilane (entry 5). 2-Carboxyindole derivatives, which are valuable scaffolds for the synthesis of biologically active compounds, can be obtained directly using pyruvic acid, or its amides (entries 6–11). Other palladium-catalyzed annulation methods allow only indirect access to these derivatives.[14] Under the mild reaction conditions no decarboxylation of the 2-carboxyindole derivatives is observed.

In conclusion, we have developed a new, mild, and efficient method for the synthesis of polyfunctionalized indoles by direct reaction of substituted 2-chloroanilines with cyclic or acyclic ketones. This procedure is simple to carry out and broadly applicable. It considerably extends the

 © 2004 Wiley-VCH Verlag GmbH & Co. KGaA, Weinheim

Table 3: Annulation reaction with acyclic ketones.[a]

Entry	Aryl amine	Indole	*t* [h]/*T* [°C]	Yield [%][b]
1			21/140	60
2			14/140	65
3			2/90	81
4			14/140	78
5			14/125	80
6			14/140	98
7			4/140	97
8			14/140	71
9			14/140	67
10			14/140	65
11			16/140	60

[a] Reaction conditions: 1.0 equiv aniline, 3.0 equiv ketone, 1.3 equiv K_3PO_4, 0.1 equiv [Pd(*t*Bu$_3$P)$_2$], 1.5 equiv acetic acid, 0.5 equiv $MgSO_4$ in DMA. [b] Yield of isolated products with $>95\%$ purity by ^{1}H NMR and HPLC.

spectrum of products that can be obtained regiospecifically by palladium-catalyzed indole formation starting from easily synthesized or commercially available starting materials. The method described here is thus a useful addition to established synthetic methods and routes to indoles.

Experimental Section

General procedure: The appropriate 2-chloroaniline (4 mmol), ketone (12 mmol), acetic acid (0.3 mL, 6 mmol) and $MgSO_4$ (240 mg, 2 mmol) were suspended in dimethylacetamide (12 mL) in a test tube. The tube was sealed with a septum, and argon was bubbled through the solution for 10 min. K_3PO_4 (1104 mg, 5.2 mmol) and [Pd(*t*Bu$_3$P)$_2$] (202 mg, 0.4 mmol) were added to the solution, and argon was bubbled through the mixture for an additional 5 min. The reaction mixture was heated to the temperature reported for the time reported in a preheated parallel synthesis block (HPLC-MS reaction control). After cooling to room temperature the reaction mixture was filtered, water (30 mL) was added to the filtrate, and the mixture was extracted with ethyl acetate (3 × 50 mL). The combined organic layers were dried over $MgSO_4$ and filtered. After removal of the solvents under reduced pressure the residue was purified either by flash chromatography on silica or by recrystallization.

Received: March 25, 2004
Revised: May 26, 2004 [Z460122]

Keywords: annulation · cyclization · indoles · nitrogen heterocycles · palladium

[1] Reviews: a) A. A. Patchett, R. P. Nargund, J. R. Tata, M.-H. Chen, K. J. Barakat, D. B. R. Johnston, K. Cheng, W. Chan, B. Butler, G. Hickey, T. Jacks, K. Schleim, S.-S. Pong, L.-Y. P. Chaung, H. Y. Chen, E. Frazier, K. H. Leung, S.-H. L. Chiu, R. G. Smith, *Proc. Natl. Acad. Sci. USA* **1995**, *92*, 7001–7005; b) J. S. Mason, I. Morize, P. R. Menard, D. L. Cheney, C. Hulme, R. F. Labaudiniere, *J. Med. Chem.* **1999**, *42*, 3251–3264; c) D. A. Horton, G. T. Bourne, M. L. Smythe, *Chem. Rev.* **2003**, *103*, 893–930.

[2] a) M. Somei, F. Yamada, *Nat. Prod. Rep.* **2003**, *20*, 216–242; b) H.-J. Knölker, K. R. Reddy, *Chem. Rev.* **2002**, *102*, 4303–4427; c) U. Pindur, T. Lemster, *Curr. Med. Chem.* **2001**, *8*, 1681–1698.

[3] Reviews: a) L. S. Hegedus, *Angew. Chem.* **1988**, *100*, 1147–1268; *Angew. Chem. Int. Ed. Engl.* **1988**, *27*, 1113–1226; b) G. W. Gribble, *J. Chem. Soc. Perkin Trans. 1* **2000**, 1045–1075.

[4] a) K. Iritani, S. Maturbara, K. Utimoto, *Tetrahedron Lett.* **1988**, *29*, 1799–1802; b) A. L. Rodriguez, C. Koradin, W. Dohle, P. Knochel, *Angew. Chem.* **2000**, *112*, 2607–2609; *Angew. Chem. Int. Ed.* **2000**, *39*, 2488–2490; c) J. Ezquerra, C. Pedregal. C. Lamas, J. Barluenga, M. Pérez, M. Garcia-Martin, J. Gonzalez, *J. Org. Chem.* **1996**, *61*, 5805–5812.

[5] a) A. Arcadi, S. Cacchi, F. Marinelli, *Tetrahedron Lett.* **1992**, *33*, 3915–3918; b) A. Arcadi, S. Cacchi, V. Carnicelli, F. Marinelli, *Tetrahedron* **1994**, *50*, 437–452; c) J. Barluenga, M. Trincado, E. Rubio, J. González, *Angew. Chem.* **2003**, *115*, 2508–2511; *Angew. Chem. Int. Ed.* **2003**, *42*, 2406–2409.

[6] R. Larock, E. Yum, M. Refvik, *J. Org. Chem.* **1998**, *63*, 7653–7662.

[7] a) C. Chen, D. Lieberman, R. D. Larsen, T. R. Verhoeven, P. J. Reider, *J. Org. Chem.* **1997**, *62*, 2676–2677. For further, multistep palladium-catalyzed procedures involving (2-iodophenyl)enamines or (2-bromophenyl)enamines see: b) K. Koerber-Pié, G. Massiot, *Synlett* **1994**, 759–760; c) T. Sakamoto, T. Nagano, Y. Kondo, H. Yamanaka, *Synthesis* **1990**, 215–218; d) K. Yamazaki, Y. Nakamura, Y. Kondo, *J. Org. Chem.* **2003**, *68*, 6011–6019.

[8] For further applications of [Pd(*t*Bu$_3$P)$_2$] see: a) M. Nishiyama, Y. Yamamoto, Y. Koie, *Tetrahedron Lett.* **1998**, *39*, 617–620; b) C. Dai, G. C. Fu, *J. Am. Chem. Soc.* **2001**, *123*, 2719–2724; c) A. F. Littke, L. Schwarz, G. C. Fu, *J. Am. Chem. Soc.* **2002**, *124*, 6343–6348, and refereces therein.

[9] The control experiment without the addition of base and acetic acid resulted in only negligible conversion to indole **3**.

[10] J.-Y. Mérour, B. Joseph, *Curr. Org. Chem.* **2001**, *5*, 471–506.

[11] a) M. Kawatsura, J. F. Hartwig, *J. Am. Chem. Soc.* **1999**, *121*, 1473–1478; b) J. M. Fox, X. Huang, A. Chieffi, S. L. Buchwald, *J. Am. Chem. Soc.* **2000**, *122*, 1360–1370.

[12] a) R. C. Larock, E. K. Yum, *J. Am. Chem. Soc.* **1991**, *113*, 6689–6690; b) D. M. Ketcha, B. A. Lieurance, D. F. Homan, G. W. Gribble, *J. Org. Chem.* **1989**, *54*, 4350–4356.

[13] a) K. Nakagawa, M. Somei, *Heterocycles* **1994**, *39*, 31–34; b) N. F. Masters, N. Mathews, G. Nechvatal, D. A. Widdowson, *Tetrahedron* **1989**, *45*, 5955–5970.

[14] For indirect palladium-catalyzed routes to 2-carboxyindoles see: a) K. Hiroya, S. Itoh, M. Ozawa, Y. Kanamori, T. Sakamoto, *Tetrahedron Lett.* **2002**, *43*, 1277–1280; b) J. A. Brown, *Tetrahedron Lett.* **2000**, *41*, 1623–1626.

 © 2004 Wiley-VCH Verlag GmbH & Co. KGaA, Weinheim

Bioengineering

Efficient Whole-Cell Biotransformation in a Biphasic Ionic Liquid/Water System**

Holger Pfruender, Maya Amidjojo, Udo Kragl, and Dirk Weuster-Botz**

Whole-cell biocatalysis represents an elegant way of producing fine chemicals.[1] Industrial processes benefit from the high product selectivity, simple catalyst preparation, and, in the case of redox reactions, the recycling system inherent to the cells. Problems arise from substrates and products that are poorly soluble in water and/or display inhibitory or toxic effects on the biocatalyst. Multiphase processes have been established to address these limitations,[2] but the conventional organic solvents used are often, themselves, toxic for the cells, possibly explosive, and environmentally harmful. Green solvents such as supercritical fluids and ionic liquids (ILs) are promising alternatives.[1i,3]

Here we demonstrate the application of ILs as a substrate reservoir and in situ extracting agent in an efficient multiphase process for the whole-cell-catalyzed synthesis of fine chemicals exemplified by the asymmetric reduction of 4-chloroacetophenone to (*R*)-1-(4-chlorophenyl)ethanol with *Lactobacillus kefir*.[4] We have shown for the first time that a cellular cofactor regeneration system is active in the presence of ILs, and consequently high product concentrations can be achieved without cofactor supplements.

Economically interesting whole-cell-catalyzed redox reactions require a solvent that is nontoxic for the biocatalyst, a prerequisite for efficient cofactor regeneration,[1e] and that dissolves poorly water-soluble substrates. We focused on water-immiscible ILs as the second liquid phase because with a virtually nonexistent vapor pressure they are safe and easy to handle, and first reports indicated whole-cell biocatalytic activity in their presence.[3a,b,5] The ILs used in this study were 1-*n*-butyl-3-methylimidazolium hexafluorophosphate (BMIM[PF_6]), BMIM-bis(trifluoromethanesulfonyl)imide (BMIM[Tf_2N]), and methyltrioctylammonium-[Tf_2N] (OMA[Tf_2N]).

In the absence of substrate, the effect of different ILs present at 20% by volume on the *L. kefir* cell membrane, the primary target of solvent toxicity, was determined.[6] The results were compared to those of a spectrum of organic solvents, among which *tert*-butyl methyl ether (MTBE) and diisopropyl ether are known to help stabilize alcohol dehydrogenase from *Lactobacillus brevis*.[7] For organic solvents, membrane integrity clearly depends on their log*P* values (Figure 1), as found earlier.[8,9] For *n*-decane (log*P* = 5.0)

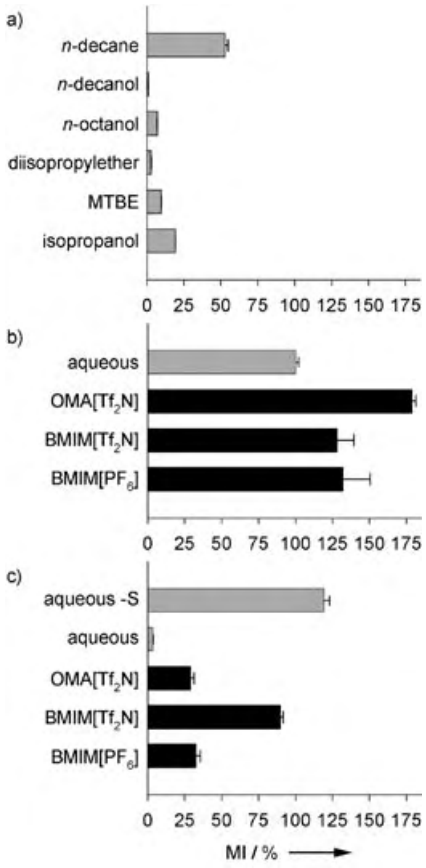


Figure 1. Membrane integrity (MI) of *Lactobacillus kefir* cells after 5 h exposure to biphasic systems consisting of: a) buffer and organic solvents, b) buffer and ionic liquids compared to pure buffer system (aqueous), c) buffer containing glucose and ionic liquids containing 4-chloroacetophenone compared to pure buffer systems containing glucose with ("aqueous") and without ("aqueous -S") dispersed 4-chloroacetophenone.

membrane integrity decreased only to 52.7%. With MTBE (log*P* = 0.9), diisopropylether (1.5), *n*-octanol (3.0), and *n*-decanol (4.6) membrane integrity was 10% or less.

ILs alone do not damage the cell membrane of *L. kefir* (Figure 1b). Membrane integrity rather increases, an effect that can be explained by a change in morphology similar to that observed in growing cells (data not shown). We also investigated the ability of ILs to circumvent substrate and product toxicity. Without the addition of a solvent phase the presence of 150 mM substrate and product led to nearly complete membrane destruction (Figure 1c), whereas whereas with BMIM[Tf_2N] the membrane remained almost intact (89.8%) (Figure 1c). BMIM[PF_6] and OMA[Tf_2N] reduced toxicity to only around 30% although distribution coefficients for the substrate and the product are nearly the

[*] H. Pfruender, M. Amidjojo, Prof. Dr.-Ing. D. Weuster-Botz
Institute of Biochemical Engineering
Munich University of Technology
Boltzmannstrasse 15, 85748 Garching (Germany)
Fax: (+49) 89-289-15714
E-mail: h.pfruender@lrz.tum.de
d.weuster-botz@lrz.tum.de
Prof. Dr. U. Kragl
Department of Chemistry
University of Rostock
Albert-Einstein-Strasse 3a, 18059 Rostock (Germany)

[**] We are grateful to Solvent Innovation for providing us with the ionic liquids. This work was supported by the German Federal Ministry of Education and Research (grant no. 0312737E).

 DOI: 10.1002/anie.200460241 © 2004 Wiley-VCH Verlag GmbH & Co. KGaA, Weinheim

Table 1: Distribution coefficients log *D* of 4-chloroacetophenone and 1-(4-chlorophenyl)ethanol between the aqueous phase and different solvents, chemical yields *Y* of biotransformation reactions in such biphasic systems with different cell densities and product purity (as enantiomeric excess).

	Aqueous	BMIM[PF_6]	BMIM[Tf_2N]	OMA[Tf_2N]	MTBE	*n*-Decane[a]
log *D* (4-Cl-AP)	solubility ≈ 7 mM	2.65(±0.17)	2.71(±0.10)	2.77(±0,.7)	2.73(±0.38)	2.38(±0.16)
log *D* (1-4-Cl-PE)	solubility ≈ 25 mM	1.93(±0.08)	2.03 (±0.09)	1.98(±0.12)	2.54(±0.37)	1.54(±0.10)
Y [%] (25 g L^{-1} cells)	42.1(±6.5)	82.7(±2.1)	89.0(±6.2)	80.1(±17.1)	2.4(±0.0)	n.d.
Y [%] (50 g L^{-1} cells)	46.2(±3.7)	88.2(±4.7)	92.8(±3.4)	88.4(±6.0)	4.2(±0.1)	n.d.
ee [%] (50 g L^{-1} cells)	98.1(±0.2)	99.8(±0.0)	99.7(±0.1)	99.4(±n.d.)	96.3(±0.2)	n.d.

[a] n.d. = not determined.

same (Table 1). Hence, suitability of ILs for whole-cell biocatalytic processes cannot be deduced by their distribution coefficients and biocompatibility in the absence of toxic reactants alone. Tests under the actual process conditions are necessary to choose the right IL for a given system of biocatalyst and reactants.

Equilibrium distribution coefficients of substrate and product are nevertheless interesting with regard to process efficiency. Inter alia, they determine the potential process yield. Due to its low log *D* value for 1-4-Cl-PE (1.54) decane, for example, would reduce the process yield in a 20% solvent setup by about 11.5%, which is the fraction remaining in the aqueous phase (Table 1). With BMIM[Tf_2N] this loss only accounts for 3.7%.

Biotransformation reactions with different solvents were conducted on the 2.8-mL scale to determine the chemical yield and product purity. With 25 g L^{-1} *L. kefir* (dry weight) in the aqueous phase, the reaction proceeded for 6 h and yielded a little less product than reactions with 50 g L^{-1} that were finished after 3 h (Table 1). Employing a pH control did not significantly increase the yield (data not shown). The advantage of ILs used as solvent phase was clearly demonstrated. With BMIM[Tf_2N] the chemical yield of 1-4-Cl-PE was doubled from 46.2% to 92.8% relative to the process with dispersed substrate and product, and the product purity was pushed to an excellent 99.7% *ee*.

Despite the affected cell membranes, the results with BMIM[PF_6] and OMA[Tf_2N] were also very good (Table 1). With MTBE the yield is very low. Cells obviously disintegrate even faster in the presence of MTBE than in the absence of a solvent so that the cofactor regeneration breaks down before significant amounts of product can be formed.

We conducted the reaction as a 200-mL batch process with BMIM[Tf_2N] in a stirred-tank reactor (600 rpm, 2.3 W L^{-1}).[10] The reaction kinetics and process parameters were monitored (Figure 2). The chemical yield (93.8% ± 1.0) and product purity (99.6% *ee* ± 0.1) are identical to those obtained on the 2.8-mL scale. The process yield (88.3% ± 1.4), volumetric productivity (20.4 g L^{-1} h^{-1} ± 0.4), and final product concentration (81.6 g L^{-1} ± 1.6) are much higher than reported so far for whole-cell-catalyzed reductions of ketones in IL.[5d] Furthermore, these key figures are also very good compared to industrial biocatalytic processes.[1b,g] No emulsification of the two-phase medium was observed. Therefore, the phases could be separated easily by sedimentation or centrifugation. For GC analysis, the product was extracted from the ILs with hexane. Quantitative and environmentally benign recovery of product from the IL should be possible by distillation, pervaporation, nanofiltration, or extraction with supercritical fluids.[11] Practically no interfering by-products accumulated in the IL (data not shown). The IL may consequently be recycled. Membrane integrity of the cells at the end of the reaction was 101.7% (±5.8), which indicates that the biocatalyst could potentially be reused. The cofactor turnover number of this process is infinite, as the reaction did not require additional NADPH or other redox equivalents. Thus, overall costs of such a process are estimated to be very competitive.

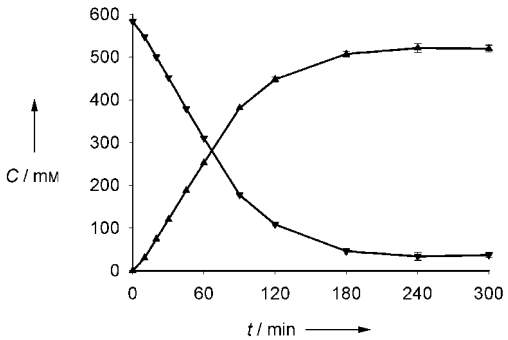


Figure 2. Concentrations of 4-chloroacetophenone (▼) and (*R*)-1-(4-chlorophenyl)ethanol (▲) in BMIM[Tf_2N] during biotransformation with *Lactobacillus kefir* in a biphasic system.

In summary, it could be shown that the ionic liquid BMIM[Tf_2N] exhibits very good solvent properties for 4-chloroacetophenone and its benzyl alcohol reduction product without destructive effects on the cell membranes of *L. kefir*. Therefore, BMIM[Tf_2N] could be used successfully as a substrate reservoir and in situ extracting agent for an efficient whole-cell biocatalytic process with inherent cofactor regeneration. We are currently testing this process design with other reactions in order to evaluate its application range. If positive, it could possibly boost the industrial use of whole-cell catalysts for the production of fine chemicals.

Experimental Section

For biotransformations the IL or organic solvent (20% by volume) containing 600 mM 4-chloroacetophenone, the buffer (0.2 M KP_i, pH 6.5, 0.2 M glucose, 5 mM $MgCl_2$) and *Lactobacillus kefir* DSM20587 cells were combined and stirred in vials (2.8 mL) or in a 200-mL bioreactor, resulting in IL droplets with diameters < 1 mm dispersed in buffer.[10] Reference batches without a solvent phase contained the same amount of substrate dispersed in buffer. Samples were quenched with HCl if necessary, extracted with ethyl acetate or

 © 2004 Wiley-VCH Verlag GmbH & Co. KGaA, Weinheim

hexane, and analyzed by GC on a CP-3800 GC system (Varian) fitted with a chiral BGB-174 column (BGB Analytik AG).

Received: April 6, 2004 [Z460241]

Keywords: asymmetric catalysis · biotransformations · cofactors · ionic liquids · whole-cell methods

[1] a) K. Faber, *Biotransformations in Organic Chemistry: A Textbook,* Springer, Berlin, **1997**, pp. 8–10; b) A. Liese, K. Seelbach, C. Wandrey, *Industrial Biotransformations,* Wiley-VCH, Weinheim **2000**, pp. 25–27; c) A. Liese, M. Villela Filho, *Curr. Opin. Biotechnol.* **1999**, *10*, 595–603; d) B. Schulze, M. G. Wubbolts, *Curr. Opin. Biotechnol.* **1999**, *10*, 609–615; e) A. Schmid, J. S. Dordick, B. Hauer, A. Kiener, M. Wubbolts, B. Witholt, *Nature* **2001**, *409*, 258–268; f) A. Zaks, *Curr. Opin. Chem. Biol.* **2001**, *5*, 130–136; g) A. J. J. Straathof, S. Panke, A. Schmid, *Curr. Opin. Biotechnol.* **2002**, *13*, 548–556; h) R. N. Patel, *Enzyme Microb. Technol.* **2002**, *31*, 804–826; i) M. Bertau, *Curr. Org. Chem.* **2002**, *6*, 987–1014.

[2] a) C. Laane, S. Boeren, K. Vos, C. Veeger, *Biotechnol. Bioeng.* **1987**, *30*, 81–87; b) G. J. Salter, D. B. Kell, *Crit. Rev. Biotechnol.* **1995**, *15*, 139–177; c) R. Leon, P. Fernandes, H. M. Pinheiro, J. M. S. Cabral, *Enzyme Microb. Technol.* **1998**, *23*, 483–500; d) A. J. J. Straathof, A. J. J. *Biotechnol. Prog.* **2003**, *19*, 755–762.

[3] a) K. R. Seddon, *J. Chem. Technol. Biotechnol* **1997**, *68*, 351–356; b) U. Kragl, M. Eckstein, N. Kaftzik in *Ionic Liquids in Synthesis* (Eds.: P. Wasserscheid, T. Welton), Wiley-VCH, Weinheim, **2003**, pp. 336–346; c) R. D. Rogers, K. R. Seddon, *Science* **2003**, *302*, 792–793; d) A. J. Mesiano, E. J. Beckman, A. J. Russell, *Chem. Rev.* **1999**, *99*, 623–633; e) T. Matsuda, T. Harada, K. Nakamura, *Chem. Commun.* **2000**, *15*, 1367–1368; f) S. V. Dzyuba, R. A. Bartsch, *Angew. Chem.* **2003**, *115*, 158–160; *Angew. Chem. Int. Ed.* **2003**, *42*, 148–150.

[4] W. Hummel, *Appl. Microbiol. Biotechnol.* **1990**, *34*, 15–19.

[5] a) M. Freemantle, *Chem. Eng. News* **2003**, *81*, 9; b) B. Jastorff, R. Stormann, J. Ranke, K. Molter, F. Stock, B. Oberheitmann, W. Hoffmann, J. Hoffmann, M. Nuchter, B. Ondruschka, J. Filser, *Green Chem.* **2003**, *5*, 136–142; c) S. G. Cull, J. D. Holbrey, V. Vargas-Mora, K. R. Seddon, G. J. Lye, *Biotechnol. Bioeng.* **2000**, *69*, 227–233; d) J. Howarth, P. James, J. Dai, *Tetrahedron Lett.* **2001**, *42*, 7517–7519.

[6] Membrane integrity determination was based on the viability test kit LIFE/DEAD® *Bac*light (Molecular Probes).

[7] M. Villela Filho, T. Stillger, M. Muller, A. Liese, C. Wandrey, *Angew. Chem.* **2003**, *115*, 3101–3104; *Angew. Chem. Int. Ed.* **2003**, *42*, 2993–2996.

[8] Values for log*P* (*n*-octanol/water) were obtained from http://esc-plaza.syrres.com/interkow/kowdemo.htm (experimental data).

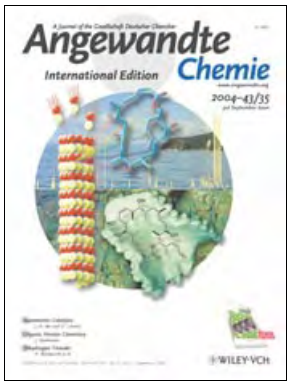
[9] A. Inoue, K. Horikoshi, *J. Ferment. Bioeng.* **1991**, *3*, 194–196.

[10] D. Weuster-Botz, S. Stevens, A. Hawrylenko, *Biochem. Eng. J.* **2002**, *11*, 69–72.

[11] a) L. A. Blanchard, D. Hancu, E. J. Beckman, J. F. Brennecke, *Nature*, **1999**, *399*, 28–29; b) T. Schafer, C. M. Rodrigues, C. A. M. Afonso, J. G. Crespo, *Chem. Commun.* **2001**, *17*, 1622–1623; c) S. H. Schofer, N. Kaftzik, P. Wasserscheid, U. Kragl, *Chem. Commun.* **2001**, *5*, 425–426; d) J. Krockel, U. Kragl, *Chem. Eng. Technol.* **2003**, *26*, 1166–1168.

 © 2004 Wiley-VCH Verlag GmbH & Co. KGaA, Weinheim

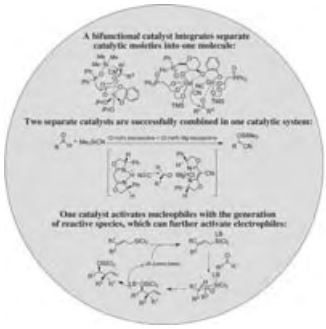
Cover Picture



Ian Paterson,* Robert Britton, Oscar Delgado, Arndt Meyer, and Karine G. Poullennec

Youseung Shin, Jean-Hugues Fournier, Yoshikazu Fukui, Arndt M. Brückner, and Dennis P. Curran*

Sponging off nature is a reliable way to find promising drug leads: (−)-Dictyostatin, which was isolated from the marine sponge *Corallistidae*, is a novel microtubule-stabilizing agent that could be useful against multidrug-resistant tumors. In their Communications on pages 4629 ff. and 4634 ff., the groups of I. Paterson and D. P. Curran describe the total synthesis of this challenging target, thus establishing unequivocally the relative and absolute configuration of the macrolactone and opening the way to useful amounts of the drug and designed analogues. The Photo of the sponge was provided by Harbor Branch Oceanographic Institution.



Asymmetric Synthesis
The advantages of modern dual-activation catalysts with two or more active centers in asymmetric synthesis are discussed by J.-A. Ma and D. Cahard in their Review on page 4566 ff.



Molecular Dynamics Simulations
What sequence of molecular events occurs in the bipropellant monomethylhydrazine/nitrogen tetroxide in the "cold prereaction" before ignition? I. Frank and co-workers address this question with molecular dynamics calculations on page 4586 ff.



Liquid Crystals
The self-organization of rigid rodlike alkali-metal carboxylates into liquid-crystal phases with complex superstructures is described by C. Tschierske and co-workers on page 4621 ff.

Contents

Angewandte EarlyView

The following Communications are available online (in Wiley InterScience). You can find them, as well as forthcoming Reviews, Highlights, and Essays, at www.angewandte.org, under Early View.

S.-X. Liu, C. Tanner, A. Neels, S. Dolder, S. Leutwyler, P. Renaud, P. Bigler, S. Decurtins:*
Tetrathiafulvalenes Acting as Leaving Groups: A Route to Bithiazoles
DOI: 10.1002/anie.200460149
Published online: August 12, 2004

M. Murakami, M. Hasegawa:*
Synthesis and Thermal Ring Opening of *trans*-3,4-Disilylcyclobutene
DOI: 10.1002/anie.200460144
Published online: August 12, 2004

F. Jiao, P. G. Bruce:*
Two- and Three-Dimensional Mesoporous Iron Oxides with Microporous Walls
DOI: 10.1002/anie.200460826
Published online: August 12, 2004

Articles judged by the referees or the editor as being either very important or very urgent are immediately edited, proof-read, and electronically published once the manuscript has arrived in the editorial office in its final form. As long as there is no page number available these articles should be cited in the following manner:

Author(s), *Angew. Chem. Int. Ed.*, online publication date, DOI.

Meeting Review

A Radical Show ——— **4550 – 4551** E. Lacôte

Books

Mass Spectrometry ——— **4552** Jürgen H. Gross *reviewed by M. Hesse*

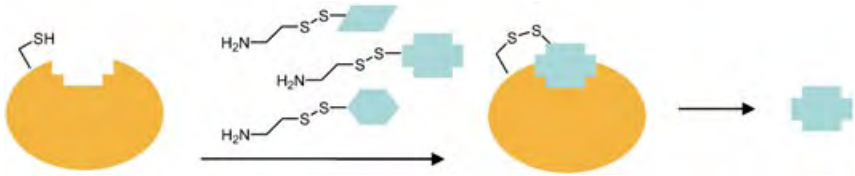
Analysis and Purification Methods in Combinatorial Chemistry ——— **4552** Bing Yan *reviewed by G. Jung*

Highlights

Medicinal Chemistry

J. Rademann* ——— **4554 – 4556**

Organic Protein Chemistry: Drug Discovery through the Chemical Modification of Proteins



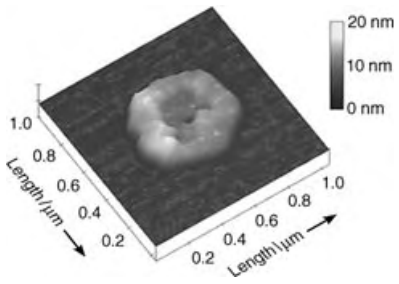
Recent strategies used in the hunt for new active compounds employ chemically modified proteins that are formed by ligation techniques and then transformed chemically. The modified proteins have been successful both as active compounds and in the search for new ligands and binding pockets.

Correspondence

Zeolite Nanoslabs?

H. Ramanan, E. Kokkoli, M. Tsapatsis* ——— **4558 – 4561**

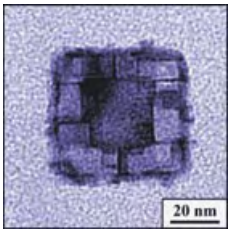
On the TEM and AFM Evidence of Zeosil Nanoslabs Present during the Synthesis of Silicalite-1



Nanoslabs (1): Investigations of the mechanism of formation of tetrapropylammonium (TPA)-silicalite-1 by TEM and atomic force microscopy (AFM) analysis (see picture) are not consistent with the existence of "nanoblocks" or "nanoslabs" previously proposed by J. A. Martens and co-workers

 © 2004 Wiley-VCH Verlag GmbH & Co. KGaA, Weinheim

Nanoslabs (2): Small square domains of lighter contrast observed with TEM on NaCl particles are attributed to tetrapropylammonium-silicalite-1 nanoslabs carefully extracted from a nanoslab suspension (see TEM image).

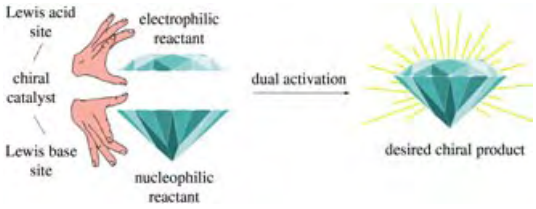


Zeolite Nanoslabs

C. E. A. Kirschhock, D. Liang, A. Aerts, C. A. Aerts, S. P. B. Kremer, P. A. Jacobs, G. Van Tendeloo, J. A. Martens* _____ **4562 – 4564**

Reply

Reviews



Twice as good: The design of new catalysts greatly benefits from the concept of dual activation (see picture) of the electrophile and the nucleophile, which has been increasingly applied in catalytic asymmetric syntheses. This Review gives some examples of spectacular developments in this area; some mechanistic models are also discussed.

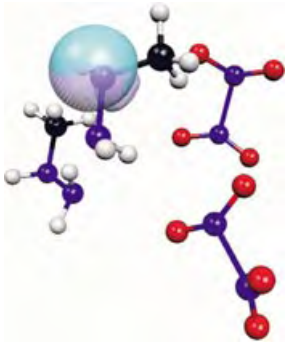
Asymmetric Catalysis

J.-A. Ma, D. Cahard* _____ **4566 – 4583**

Towards Perfect Catalytic Asymmetric Synthesis: Dual Activation of the Electrophile and the Nucleophile

Communications

Highly reactive intermediates, such as that shown, which arise under special conditions in hypergolic mixtures of monomethylhydrazine and nitrogen tetroxide, may trigger uncontrolled reaction behavior. Car–Parrinello molecular dynamics simulations provide an insight into the complex reactions on very short timescales.



Hypergolic Mixtures

C. Nonnenberg, I. Frank,* T. M. Klapötke _____ **4586 – 4589**

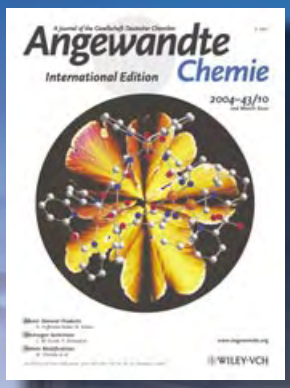
Ultrafast Cold Reactions in the Bipropellant Monomethylhydrazine/Nitrogen Tetroxide: CPMD Simulations

For the USA and Canada:
ANGEWANDTE CHEMIE International Edition (ISSN 1433-7851) is published weekly by Wiley-VCH PO Box 191161, D 69451 Weinheim, Germany. Air freight and mailing in the USA by Publications Expediting Inc. 200 Meacham Ave., Elmont, NY 11003. Periodicals postage paid at Jamaica NY 11431. US POSTMASTER: send address changes to *Angewandte Chemie*, Wiley-VCH, 111 River Street, Hoboken, NJ 07030. Annual subscription price for institutions: Europe € 3430.00/3118.00; outside Europe US$ 4499.00/4090.00 (valid for print and electronic/print or electronic delivery); for individuals who are personal members of a national chemical society, or whose institution already subscribes, or who are retired or self-employed consultants, print only: Europe € 248.00/outside Europe US$ 378.00. Postage and handling charges included. All Wiley-VCH prices are exclusive VAT.

 © 2004 Wiley-VCH Verlag GmbH & Co. KGaA, Weinheim

The best in chemistry –

for more than a hundred years



A Journal of the Gesellschaft Deutscher Chemiker

Angewandte
International Edition **Chemie**

www.angewandte.org

1888: ***The beginning of a success story***

Constant Innovations

1962: *First issue of the International Edition*
1976: *Graphical abstracts*
1979: *Cover pictures*
1988: *Centenary of Angewandte*
1989: *Routine use of color*
1991: *New section: Highlights*
1992: *Computerized editorial tracking system*
1995: *Internet service for readers*
1998: *Regular press service; full-text online*
2000: *New section: Essays; EarlyView: Communications available online ahead of the printed version*
2001: *New section: Minireviews*
2002: *Online submission of manuscripts*
2003: *Weekly publication; new section: News; new layout*
2004: *Backfiles (1962-1997); ManuscriptXpress: Online system for authors and referees*



Angewandte's advisors...

Richard N. Zare
Stanford University

» *Size does matter, as well as shape, motion, composition, and chemical complexity. I read* ***Angewandte Chemie*** *each week to learn about the latest, most exciting developments in the world of chemistry.* «

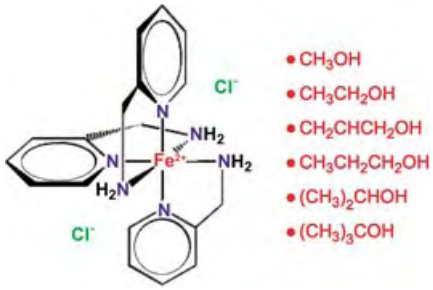
Angewandte Chemie International Edition *is a journal of the German Chemical Society (GDCh)*

GDCh

WILEY InterScience® DISCOVER SOMETHING GREAT

WILEY-VCH

1192104_gu

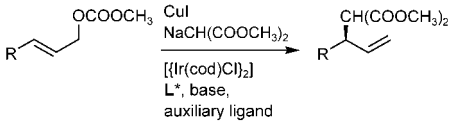


So similar yet so different: The crystal structures of six alcohol solvates of the title compound (see formula) are found to be very similar at 200 K. In contrast, their spin-transition behavior and their structural phase transitions are quite different. Implications of these observations for crystal engineering are discussed.

Crystal Engineering

M. Hostettler, K. W. Törnroos, D. Chernyshov, B. Vangdal, H.-B. Bürgi* ——— **4589 – 4594**

Challenges in Engineering Spin Crossover: Structures and Magnetic Properties of Six Alcohol Solvates of Iron(II) Tris(2-picolylamine) Dichloride

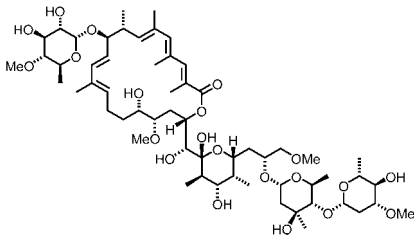


Come together: Successful cooperation of iridium and copper yielded a new catalyst system for allylic alkylation. Branched alkylation products can be obtained rapidly and with high enantioselectivity from simple linear precursors (see scheme; cod = cyclooctadiene).

Allylic Substitution

G. Lipowsky, N. Miller, G. Helmchen* ——— **4595 – 4597**

Regio- and Enantioselective Iridium-Catalyzed Allylic Alkylation with In Situ Activated P,C-Chelate Complexes

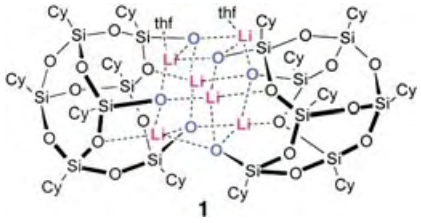


A ring-size-selective macrolactonization and the early introduction of the saccharide portions are the main features of a total synthesis of the 20-membered macrolide apoptolidin (see formula), which induces apoptosis in rat glia cells transformed with oncogenes.

Natural Products Synthesis

H. Wehlan, M. Dauber, M.-T. Mujica Fernaud, J. Schuppan, R. Mahrwald, B. Ziemer, M.-E. Juarez Garcia, U. Koert* ——— **4597 – 4601**

Total Synthesis of Apoptolidin



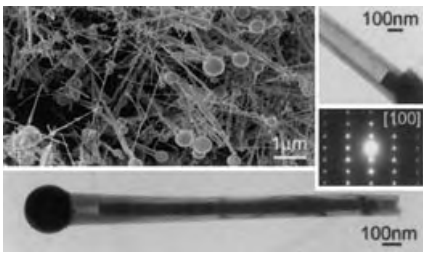
Versatile building blocks for the construction of molecular models for heterogeneous catalysts are readily available in high yields in the form of fully metalated silsesquioxane derivatives, such as dimeric **1**, by using alkali-metal silylamides as deprotonating agents.

Catalyst Models

V. Lorenz, S. Gießmann, Y. K. Gun'ko, A. K. Fischer, J. W. Gilje, F. T. Edelmann* ——— **4603 – 4606**

Fully Metalated Silsesquioxanes: Building Blocks for the Construction of Catalyst Models

A Sn-nanorod-templated process was used for the first synthesis of single-crystalline wurtzite-type ZnS nanotubes. The as-grown ZnS nanotubes are structurally uniform single crystals and are partially filled with Sn (see picture). Most of the tubes are straight with lengths ranging from several to tens of micrometers, diameters of about 150–250 nm, and wall thicknesses of about 50–80 nm.



Nanotubes

J. Hu,* Y. Bando, J. Zhan, D. Golberg ——— **4606 – 4609**

Sn-Filled Single-Crystalline Wurtzite-Type ZnS Nanotubes

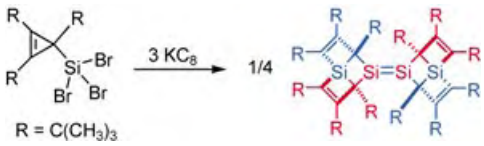
 © 2004 Wiley-VCH Verlag GmbH & Co. KGaA, Weinheim

Contents

Disilenes

S. Matsumoto, S. Tsutsui, E. Kwon, K. Sakamoto* ——— **4610 – 4612**

Formation of a Stable, Lattice-Framework Disilene: A Strategy for the Construction of Bulky Substituents



Bulky protectors: A one-pot reduction of tri(*tert*-butyl)cyclopropenyltribromosilane with potassium graphite yielded a unique lattice-framework disilene in 47% yield (see scheme). The new polycyclic disilene is C_2-symmetric and has a long Si—Si double bond (2.26 Å). Its stability is attributed to the bulky substituents, which act as protecting groups.

Combinatorial Synthesis

A. Clouet, T. Darbre, J.-L. Reymond* ——— **4612 – 4615**

A Combinatorial Approach to Catalytic Peptide Dendrimers

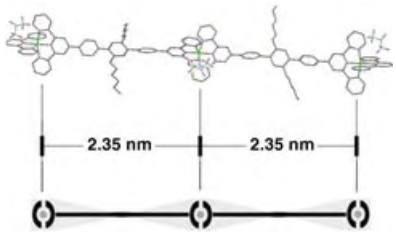
Exploring the structural diversity of peptide dendrimers as synthetic protein models: A 65 536-membered combinatorial peptide-dendrimer library was prepared by split-and-mix techniques on beads (see picture). The library was screened and revealed peptide dendrimers that catalyze fluorogenic ester hydrolysis and peptide dendrimers that bind to vitamin B_{12}.



Noncovalent Interactions

D. Hinderberger, O. Schmelz, M. Rehahn, G. Jeschke* ——— **4616 – 4621**

Electrostatic Site Attachment of Divalent Counterions to Rodlike Ruthenium(II) Coordination Polymers Characterized by EPR Spectroscopy

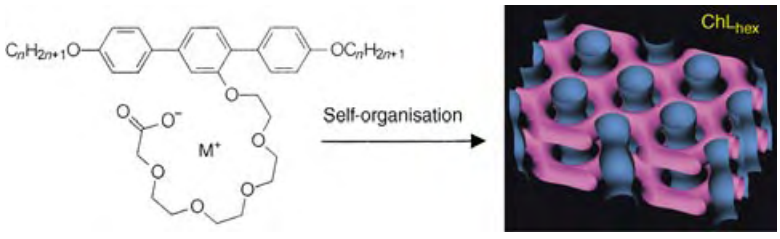


Subnanosecond ion-pair lifetimes have been observed for the electrostatic attachment of divalent spin-carrying counterions to oppositely charged, rodlike Ru^{II} coordination polymers in solution. Continuous wave (CW) EPR and double electron-electron resonance (DEER) spectroscopy show that the spatial distribution of the divalent counterions reflects the spatial distribution of charges on the polyion (see schematic representation).

Liquid Crystals

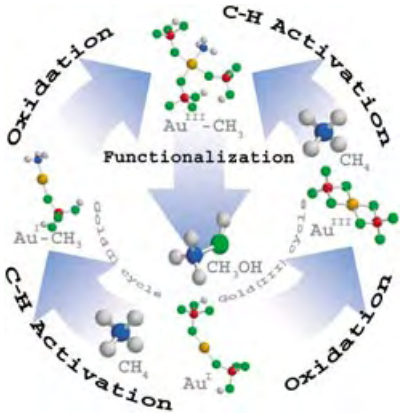
B. Chen, X. B. Zeng, U. Baumeister, S. Diele, G. Ungar, C. Tschierske* ——— **4621 – 4625**

Liquid Crystals with Complex Superstructures



The hexagonal-channeled layer phase (ChL_{hex}; see picture, right) is one of the new liquid-crystalline phases formed by the self-organization of the rigid rodlike alkali-metal carboxylates shown.

Cationic gold catalyzes the title reaction in strong acid solvents with Se^{VI} as the stoichiometric oxidant. At 180 °C and 27 bar of CH_4 turnover numbers of about 30 and methanol concentrations of 0.6 M have been observed with selectivities >90%. DFT calculations indicate that cationic Au^{I} and Au^{III} are both viable catalysts that operate by electrophilic C–H activation and oxidative functionalization (see picture).



Homogeneous Catalysis

C. Jones, D. Taube, V. R. Ziatdinov, R. A. Periana,* R. J. Nielsen, J. Oxgaard, W. A. Goddard III _____ **4626 – 4629**

Selective Oxidation of Methane to Methanol Catalyzed, with C–H Activation, by Homogeneous, Cationic Gold

A flexible and modular approach was used in the convergent and highly stereocontrolled synthesis of the antimitotic agent dictyostatin. This first total synthesis establishes its full stereochemistry and should be amenable to producing useful quantities and designed analogues of this molecule, whose conformation closely resembles that of discodermolide (see overlayed structures).

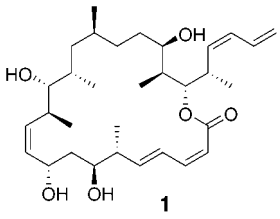


Natural Products Synthesis

I. Paterson,* R. Britton, O. Delgado, A. Meyer, K. G. Poullennec _____ **4629 – 4633**

Total Synthesis and Configurational Assignment of (–)-Dictyostatin, a Microtubule-Stabilizing Macrolide of Marine Sponge Origin

Will the real dictyostatin please stand up? There were five finalists as stereostructures for the potent anticancer agent dictyostatin; ten, if one were to include enantiomers. A total synthesis of (–)-dictyostatin (**1**) has ended the decade-old masquerade and identified the winner as a structure recently proposed by Paterson and Wright.

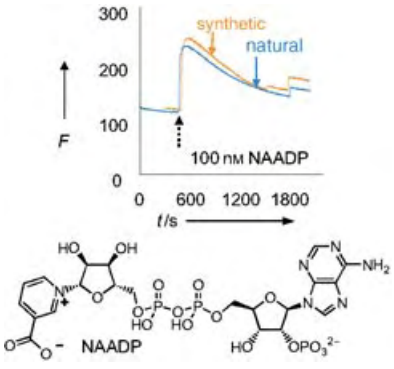


1

Natural Products Synthesis

Y. Shin, J.-H. Fournier, Y. Fukui, A. M. Brückner, D. P. Curran* _____ **4634 – 4637**

Total Synthesis of (–)-Dictyostatin: Confirmation of Relative and Absolute Configurations



Signaling dinucleotides: The first single-isomer synthesis of nicotinamide adenine dinucleotide phosphate (NADP) is reported. Installation and maintenance of sensitive phosphate and pyridinium functionalities were key to success. Significantly, conversion of NADP into the important mammalian second messenger NAADP was achieved. The graph shows the biological evaluation of the activity of the release of Ca^{2+} ions, which confirms the identity of NAADP.

Natural Products Synthesis

J. Dowden,* C. Moreau, R. S. Brown, G. Berridge, A. Galione, B. V. L. Potter _____ **4637 – 4640**

Chemical Synthesis of the Second Messenger Nicotinic Acid Adenine Dinucleotide Phosphate by Total Synthesis of Nicotinamide Adenine Dinucleotide Phosphate

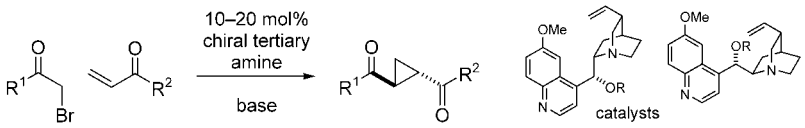
 © 2004 Wiley-VCH Verlag GmbH & Co. KGaA, Weinheim

Contents

Cyclopropanations

C. D. Papageorgiou, M. A. Cubillo de Dios, S. V. Ley, M. J. Gaunt* ——— **4641 – 4644**

Enantioselective Organocatalytic Cyclopropanation via Ammonium Ylides

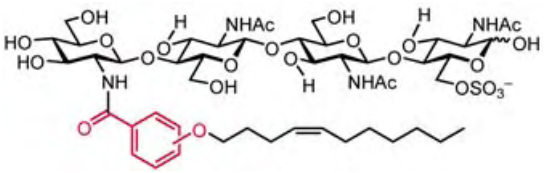


Highly functionalized cyclopropanes can be produced with excellent enantioselectivity through an amine-catalyzed organocatalytic cyclopropanation process (see scheme). Catalytically generated asymmetric ammonium ylides mediate the reaction, and the cyclopropane products can be produced as either enantiomer by using quinine- or quinidine-derived catalysts.

Glycolipid Mimics

N. Grenouillat, B. Vauzeilles, J.-J. Bono, E. Samain, J.-M. Beau* ——— **4644 – 4646**

Simple Synthesis of Nodulation-Factor Analogues Exhibiting High Affinity towards a Specific Binding Protein

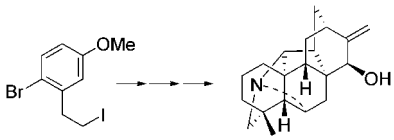


A "Nod" in the right direction: Aromatic analogues of the lipooligosaccharidic nodulation (Nod) factors involved in the symbiosis of *Sinorhizobium meliloti* and legumes are easily assembled from very simple precursors by combining biotechnological and chemical procedures. Some of these analogues (see structure) bind tightly to a specific binding protein and form a new class of glycolipid mimics.

Natural Products Synthesis

H. Muratake,* M. Natsume* ——— **4646 – 4649**

Total Synthesis of (±)-Nominine, a Heptacyclic Hetisine-Type Aconite Alkaloid



1

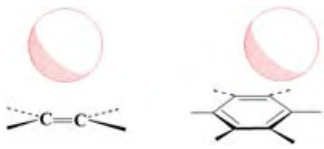
The barrier has finally been lifted to the synthesis of hetisine-type alkaloids with the total synthesis of (±)-nominine (**1**) in 40 steps from 2-bromo-5-methoxyphenethyl iodide. Key steps in the construction of the architecturally complex polycyclic structure of this natural product were a radical cyclization of an enyne and a palladium-catalyzed intramolecular α arylation of an aldehyde.

Charge-Transfer Complexes

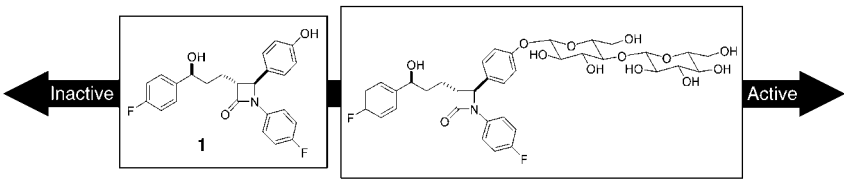
Y. S. Rosokha, S. V. Lindeman, S. V. Rosokha, J. K. Kochi* ——— **4650 – 4652**

Halide Recognition through Diagnostic "Anion–π" Interactions: Molecular Complexes of Cl^-, Br^-, and I^- with Olefinic and Aromatic π Receptors

Intense colorations and new charge-transfer absorption bands are observed upon addition of a halide (Cl^-, Br^-, I^-) to neutral organic π acceptors with electron-deficient olefinic and aromatic centers. These phenomena results from noncovalent anion–π interactions (shown schematically), which were confirmed by X-ray crystallography.



 © 2004 Wiley-VCH Verlag GmbH & Co. KGaA, Weinheim



Giving cholesterol the brush off: An intestinal brush border membrane vesicle assay has been devised for the convenient in vitro testing of small molecules for inhibition of cholesterol absorption. The assay was used to identify new nonhydrolyzable glycosides as potent cholesterol-absorption inhibitors and an oxazolidinone as an effective replacement of the β-lactam scaffold of ezetimibe (**1**).

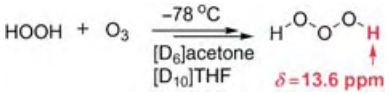
Medicinal Chemistry

L. Kværnø, T. Ritter, M. Werder, H. Hauser, E. M. Carreira* ——— **4653 – 4656**

An In Vitro Assay for Evaluation of Small-Molecule Inhibitors of Cholesterol Absorption

---

Quantifiable amounts of HOOOH can be detected by ^{1}H NMR spectroscopic analysis of the thermal reaction of O_3 and HOOH (see scheme). This first experimental report of a link between these three oxidants suggests that HOOOH may be involved in oxidation reactions that span biological, atmospheric, and environmental systems.

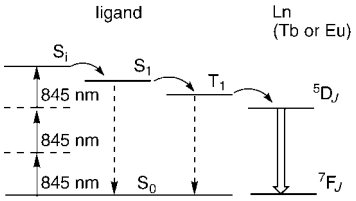


Oxidation

P. T. Nyffeler, N. A. Boyle, L. Eltepu, C.-H. Wong, A. Eschenmoser, R. A. Lerner, P. Wentworth, Jr.* ——— **4656 – 4659**

Dihydrogen Trioxide (HOOOH) Is Generated during the Thermal Reaction between Hydrogen Peroxide and Ozone

---



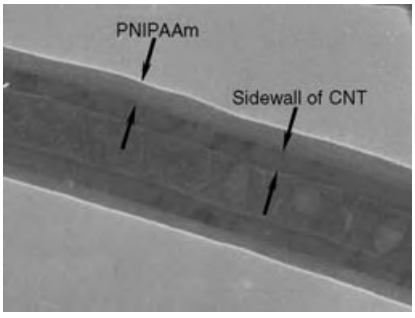
Red light, green light! Emission through three-photon upconversion processes from polymeric organic–lanthanide complexes (lanthanide, Ln = Tb, Eu) was observed upon excitation of the tripodal organic ligand at 845 nm. Multiphoton absorption by the ligand followed by a transfer of energy to Ln (see picture; S = singlet state, T = triplet state) gives rise to characteristic Eu (red) or Tb (green) emission.

Luminescence

K.-L. Wong, W.-M. Kwok, W.-T. Wong,* D. L. Phillips,* K.-W. Cheah* ——— **4659 – 4662**

Green and Red Three-Photon Upconversion from Polymeric Lanthanide(III) Complexes

---



Feeling the heat: Surface-initiated atom transfer radical polymerization was used to modify a film of aligned carbon nanotubes with poly(*N*-isopropylacrylamide) (see TEM image). A distinct temperature responsiveness is found for both the macroscopic (wettability) and the microscopic (the diameter and rigidity of a single carbon nanotube) properties of the resulting film.

Surface Chemistry

T. Sun, H. Liu, W. Song, X. Wang, L. Jiang,* L. Li,* D. Zhu ——— **4663 – 4666**

Responsive Aligned Carbon Nanotubes

VIP Communications labeled with this symbol have been judged by two referees as being "very important papers".

 © 2004 Wiley-VCH Verlag GmbH & Co. KGaA, Weinheim

Deadline for recruitment adverts

39/2004	September 17	Publication date:	October 4
40/2004	September 24	Publication date:	October 11

Angewandte Chemie International Edition
Advertising Sales Department:
Marion Schulz
Phone: 0 62 01 – 60 65 65
Fax: 0 62 01 – 60 65 50
E-Mail: MSchulz@wiley-vch.de

Place an advert in the printed version
and have it made available online for 1 month, free of charge!

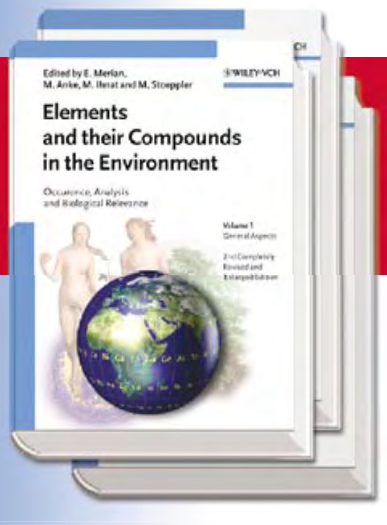
Service

Keywords ____ 4668

Authors ____ 4669

Angewandte's Sister Journals ____ 4670 – 4671

Preview ____ 4673



New ! The Second Edition!

Elements and their Compounds in the Environment

Occurrence, Analysis and Biological Relevance

2nd completely revised and enlarged edition
3 Volume Set

Edited by E. MERIAN, M. ANKE, M. IHNAT and M. STOEPPLER

- The "Merian" is the established standard reference on this topic.
- This new edition is more clearly and concisely structured, with more emphasis on nutritional aspects.
- All contributions are revised and updated to present the current state of knowledge.
- Further elements, including some non-metals of nutritional importance, have been added.
- Essential information for chemists, biologists, geologists, food scientists, toxicologists and physiologists involved in environmental research and remediation, risk assessment, food research and industrial hygiene.

For your order:

3527-30459-2 2004
1774pp with 97 figs and 377 tabs
Hbk
€ 599.00 / £ 355.00 / US$ 550.00

Wiley-VCH,
Customer Service Department,
Fax: +49 (0) 6201 606-184,
E-Mail: service@wiley-vch.de,
www.wiley-vch.de

John Wiley & Sons, Ltd., Customer Services Department, Fax: +44 (0) 1243-843-296,
E-Mail: cs-books@wiley.co.uk,
www.wileyeurope.com

John Wiley & Sons, Inc., Customer Care,
Fax: +1 800-597-3299,
E-Mail: custserv@wiley.com,
www.wiley.com

WILEY-VCH

WILEY

11332403_gu

 © 2004 Wiley-VCH Verlag GmbH & Co. KGaA, Weinheim



A Radical Show**

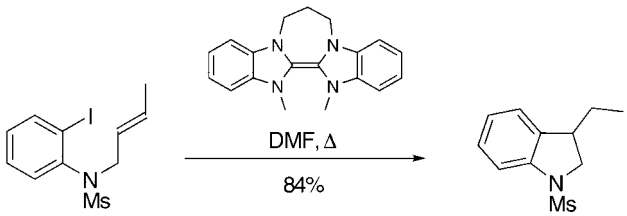
Emmanuel Lacôte

Organic free radicals have been known for more than a century. Initially less popular than polar intermediates, they have gained wide recognition as essential reactive species. The ISOFR conference has played a key role in this acceptance, helping free-radical chemistry reach maturity. The previous meeting was held in Ann Arbor (USA, 2000), the very place where Moses Gomberg first detected the now famous triphenylmethyl radical. This year the conference took place in the coastal resort Porto-Vecchio in the south of Corsica (France) in June. A former Genoese outpost, Porto-Vecchio is situated on a hill overlooking a wide gulf. The conference hall was located next to the city walls, providing the participants with a picturesque setting on one of the finest coasts of France.

The Scientific Committee of C. Chatgilialoglu (CNR Bologna), D. Curran (Pittsburgh), C. Easton (Canberra), H. Fischer (Zürich), B. Giese (Basel), N. Porter (Vanderbilt, Nashville), P. Renaud (Bern), and I. Ryu (Osaka), chaired by M. Malacria (UPMC, Paris) and P. Tordo (Marseille), chose to illustrate the wide scope of free-radical chemistry by starting with a core part devoted to synthesis, then broadening it toward the expanding fields of materials and biochemistry. To further stress the interdependence of the synthetic trunk and its two multidisciplinary branches, the program was not split into three separate sessions, but instead contributions from the different areas were mixed.

Synthetic radical chemistry has witnessed impressive new developments in the discovery of new processes (almost exclusively tin-free), asymmetric synthesis (especially enantioselectivity), the control of more-reactive intermediates, and total syntheses that include radical-mediated key steps, a benchmark of popularity and usefulness in organic chemistry.

The talk of D. Crich (UI Chicago) was partly dedicated to stannane-mediated chain reactions of selenols, which allowed him to greatly improve traditionally difficult radical reactions, such as aryl–aryl coupling. However, because of the toxicity of organostannanes, even very sophisticated processes developed in an academic setting, where tributyltin hydride is used almost universally, are not applied in industry. Thus, the quest for alternative systems is increasingly relevant. L. Fensterbank (UPMC, Paris) reported a new vinylation process based on a titanocene-mediated β elimination of phosphinoyl radicals. U. Jahn (TU Brunswick) presented domino processes combining organometallic and radical steps in which an oxidative trick was used for the crossover process. I. Ryu has further expanded the scope of his trademark multicomponent radical carbonylation by intercalating at will radical and organopalladium species. Similarly, reverse reductive radical–polar crossover strategies have been pursued for several years by J. A. Murphy (Strathclyde, Glasgow). At this meeting he announced that he has gained access to a new generation of TTF-like reagents (TTF: tetrathiafulvalene), which can be used to generate aryl radicals from iodides: usually a very difficult task (Scheme 1). Both J. Kilburn (Southampton) and T. Skrydstrup (Aarhus) reported the use of samarium diiodide. Kilburn was able to synthesize paeonilactone B from a suitable methylenecyclopropane derivative, and Skrydstrup used SmI_2 to selectively introduce side chains onto cyclic peptide strands and to prepare nonnatural amino acids. G. Friestad (Vermont) has explored the use of manganese carbonyl as a replacement for tin reagents. A. Studer (Münster) and L. Engman (Uppsala) showed that microwaves can trigger some radical reactions, such as nitroxide and phenyltelluride group transfer.1. Tin-free radical cyclization from a TTF-like reagent.



Scheme 1. Tin-free radical cyclization from a TTF-like reagent.

One step up the ladder of reactivity control, one runs into problems relating to stereoselectivity. M. Sibi (NDSU Fargo) was the opening lecturer of the meeting. He reported catalytic asymmetric radical Michael additions and illustrated the chiral relay, a concept he introduced together with P. Renaud: that the stereoselectivity of some less selective processes can be increased by inducing a conformational change dynamically through the use of a suitable template. D. Yang (Hong Kong) showed that chiral Lewis acids could catalyze domino group-transfer radical cyclizations with high levels of enantiocontrol. She has used these reactions to create the skeletons of some active agents of traditional Chinese pharmacopeia, such as triptolide. Finally, G. Friestad reported the implementation of a series of diastereo- and enantioselective addition reactions to C=N bonds to prepare chiral amines.

The total synthesis of complex molecules is a good tool to determine whether methodological progress is in fact practical. Along these lines, J. Cossy (ESPCI, Paris) reported the preparation of several bioactive products, such as kainic acid, ptilocaulin, and isoavenaciolide. M. D. Bachi (Weizmann

[*] Dr. E. Lacôte
CNRS and Université Pierre et Marie Curie, Paris (France)
E-mail: lacote@ccr.jussieu.fr

[**] International Symposium on Organic Free Radicals (ISOFR) IX, Porto-Vecchio (France), June 6–11, 2004.

 © 2004 Wiley-VCH Verlag GmbH & Co. KGaA, Weinheim DOI: 10.1002/anie.200461443

Institute, Rehovot) presented some valuable advances in the chemistry of antimalarial cyclic peroxides similar to artemisinin. He was able to prepare a series of these compounds and studied the iron(II)-induced homolytic degradations that are associated with their antiparasitic activity.

This work by Bachi is typical of the broad multidisciplinary nature of free-radical chemistry. A growing number of biological processes have been found to be radical processes, and specialists on molecular organic free radicals have a head start in their elucidation. This facet was covered in several important lectures. It is common knowledge that free radicals are created by oxidative stress, causing damage to our body; but just what kind of damage, how the body deals with it, and the reparative processes employed are important topics.

C. Ferreri (CNR Bologna) reported how thiyl radicals could be involved in the isomerization of phospholipids in lipid bilayers through an addition/elimination pathway, thus adding to the relevance of the type of β-eliminations already mentioned by L. Fensterbank. N. Porter told us about lipid peroxidations and the development of a series of radical clocks to determine rate constants for oxidation reactions. This development was followed logically by the development of a new generation of antioxidants more potent than vitamin E. The quantitative studies of these essential classes of bioactive molecules by Porter and G. Pedulli (Bologna), who delved further into the factors that determine good antioxidant activity, are of considerable significance. The oxidation of LDL (low-density lipoproteins) is believed to be an initiator of atherosclerosis, the major cause of cardiovascular diseases. However, the finding by R. Stocker (New South Wales, Australia) that the inhibition of lipoprotein oxidation does not always result in the attenuation of atherosclerosis was a reminder that real systems are often very sophisticated and that more should be done towards the understanding of in vivo activity.

C. Chatgilialoglu and B. Giese focused on DNA damage. Chatgilialoglu discussed the fate of the hydrated electrons produced under oxidative stress. Guanosine quartets can be very effective in electron transfer. Because of the possible release of a bromide ion, 8-bromo-2′-deoxyguanosine could act as an electron sink. According to Giese, photolesions of DNA are repaired through an electron-catalyzed reaction made possible by electron transport through the heterocyclic bases and aromatic side chains of the biopolymer. A testimony of the breakthrough quality of this discovery is the rate at which it moved from a controversial hypothesis to an established truth with front-page coverage in *Angewandte Chemie*.[1]

Radical enzymatic pathways are attracting increased attention. C. Schöneich (Kansas) reported on the chemistry of Alzheimer's disease, which involves a selective metal-catalyzed oxidation of methionine in a β-amyloid peptide. M. Newcomb (UI Chicago) has evaluated polar catalytic effects on radical reactions of enzymes by laser flash photolysis. In this way, it has been established that B_{12}-dependent enzymes catalyze several isomerization reactions via radical intermediates. Similarly, W. Woggon (Basel) described mimics of P450 enzymes, and showed evidence for the influence of water clusters on such enzymes.

Free radicals are also extremely useful at the other end of the organic continuum. D. Bourissou and G. Bertrand (Toulouse) were able to stabilize diradicals by introducing heteroatoms such as boron and phosphorus. They obtained a compound with a single bond with pure π character, thus opening the way to the preparation of organic materials with magnetic properties.

Most applications of free radicals in materials science are in polymer chemistry. The last few years have witnessed an explosion of new controlled radical polymerizations (CRP). The three main methods for CRP were discussed at this meeting. K. Matyjaszewski (Carnegie Mellon) told us about the potential of metal-mediated atom-transfer radical polymerizations. He showed that polymers of virtually any shape can be obtained by following a preestablished route, in the same way as for synthetic molecules. D. Bertin (Marseille) and A. Studer introduced a nitroxide-mediated polymerization based on the persistent radical effect defined by H. Fischer. Both lectures discussed the synthetic and kinetic aspects of CRP, each with a different highly efficient nitroxide radical. S. Yamago (Osaka) focused on CRP by organotellurium group transfer and described results that complement those of Engman.

During this meeting the important role of physical chemists, who set the theoretical and physical bases on which organic chemists build, was emphasized. V. Barone (Naples) illustrated new quantum-mechanical strategies for the study of complex systems, such as protein radicals, and P. Hiberty (Orsay) discussed the modeling of three-electron bonds. A combination of these two approaches could well be fruitful for the study on Alzheimer's disease presented earlier in the meeting. H. Fischer explained the persistent radical effect, which is a kinetic principle favoring cross-reaction over self-termination and is at the basis of living free-radical polymerization.

Finally, P. Mulder (Leiden) described the search for new thermal sources of iminyl, iminoxyl, and phenoxyl radicals, and the kinetic and thermodynamic factors governing their reactivity and stability.

Overall, the meeting was very well balanced and of a high standard, as was further demonstrated by the high quality of the posters. The breaks and the social dinner, which introduced all participants to Corsican specialties, provided extensive opportunities for scientific and social discussions.

A session was dedicated to the memory of the late Jean-Marie Surzur, who was on the faculty in Marseille. His contribution to the field is an enduring legacy. This conference, which he helped create thirty years ago, is as alive as ever. It will migrate down under to its next location in Australia.

[1] B. Giese, B. Carl, T. Carl, T. Carell, C. Behrens, U. Hennecke, O. Schiemann, E. Feresin, *Angew. Chem.* **2004**, *116*, 1884–1887; *Angew. Chem. Int. Ed.* **2004**, *43*, 1848–1851.

 © 2004 Wiley-VCH Verlag GmbH & Co. KGaA, Weinheim

Medicinal Chemistry

Organic Protein Chemistry: Drug Discovery through the Chemical Modification of Proteins

*Jörg Rademann**

Keywords:
chemical ligation · drug discovery · medicinal chemistry · proteins

For a long time the preparation and transformation of proteins was considered a domain of molecular biology. With modern ligation techniques, however, success has been achieved not only in the de novo preparation of proteins but also in their targeted chemical modification.[1–3] In this way "organic protein chemistry" was founded, which has made an important contribution to the understanding of proteins and to the development of chemical biology. The chemical modification of proteins appears to be a very promising route to new protein-based drugs and low-molecular-weight protein ligands.

Ligation techniques are used preferentially in the chemical transformation of proteins. Chemical ligation is understood to mean synthetic methods for the selective attachment to partially unprotected biopolymers in aqueous buffers under neutral, mild conditions (Figure 1). The starting point for modern ligation techniques was the discovery by Wieland et al. that partially unprotected thioesters of amino acids and peptides form peptide bonds selectively with N-terminal cysteine residues in neutral aqueous solution.[1] In this way an intermediate cysteine thioester initially formed by "thioester exchange" then rearranges into a stable amide bond by means of an S–N acyl shift. Even in the original publication in 1953 it was proposed that a natural synthesis principle for cysteine-containing peptides and proteins had been discovered. In the 1990s this thioester ligation was named a "natural chemical ligation" by Kent's group and was used successfully in the de novo syntheses of proteins in aqueous buffers.[2] The success of thioester ligation has inspired the development of further ligation techniques which have found many applications in the synthesis of proteins and protein mimics (Figure 1).

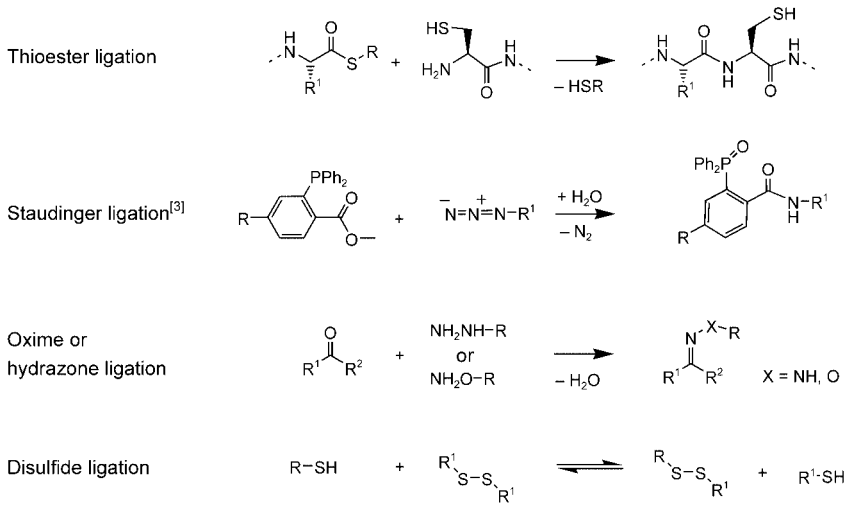


Figure 1. Ligation techniques for de novo synthesis and modification of proteins.

The particular advantage of chemical protein synthesis is the access to chemically modified biopolymers that cannot be obtained with the aid of the methods of molecular biology. With organic synthesis it is possible to produce specifically proteins with new property profiles. The activity, selectivity, and stability of biopolymers become controllable, and proteins can be tailor-made like small organic molecules.

A particularly rewarding target is the construction of chemically modified proteins with increased bioavailability and stability in order to prepare new and improved active peptides and proteins. In this context an important milestone was reached with the chemical preparation of a synthetic, polymer-stabilized erythropoietin.[4] Human erythropoietin (EPO), a glycoprotein hormone, is of considerable interest since it stimulates the growth, differentiation, and maturation of stem cells to erythrocytes. The considerable clinical significance for the therapy of anemia can be appreciated in that the annual EPO turnover exceeds one billion dollars. Unfortunately the action of natural EPO is limited by its short half-life. For this reason a chemical EPO mutant has been prepared which is protected against biodegradation by two

[*] Prof. Dr. J. Rademann
FMP Forschungsinstitut für
Molekulare Pharmakologie
Robert-Rössle-Strasse 10
13125 Berlin (Germany)
and
Institut für Chemie
Freie Universität Berlin
Takustrasse 3
14195 Berlin (Germany)
Fax: (+49) 30-94793-159
E-mail: rademann@fmp-berlin.de

 © 2004 Wiley-VCH Verlag GmbH & Co. KGaA, Weinheim DOI: 10.1002/anie.200460075

branched polyether structures without compromising the stimulating activity on blood cell precursor cells. In rats the synthetic protein has a longer half-life than natural EPO and leads to a greater increase in the hematocrit value.

The chemically modified EPO was prepared by a clever combination of thioester and oxime ligation (Figure 2). A peptide chain of 166 amino acids derived from natural EPO was initially divided into four fragments (A–D) and built up by standard solid-phase methods. Since natural EPO does not contain cysteine side chains in sufficient numbers for ligation, two glutamate residues at the N terminus of fragments C and D were replaced by cysteine. Following ligation these cysteine residues were alkylated with bromoacetic acid to obtain glutamate-like side chains. Fragments B, C, and D thus contained an N-terminal cysteine unit; in fragments B and C this group was protected with an *S*-acetamidomethyl group (Acm). In addition an N^{ε}-levulinyl-lysine was incorporated into both fragments A and D. The keto function contained therein served in each case to couple a branched aminoxy polyether by oxime ligation. The two polyethers were attached to sites in two of the four oligosaccharides present in the natural glycoprotein. Finally the fragments were conjoined by thioester ligation, and after folding and purification a uniform product with a mass of 50825 Da was obtained.[5]

Ketoproteins as starting materials for oxime ligation had previously been prepared by Dixon in 1960 by copper-catalyzed transamination of proteins with glyoxylate.[6] Forty years later this reaction was developed further into a valuable preparative method.[7] More recently ketopeptides with variable side chains were accessible by mild solid-phase acetylation of a cyanophosphorane.[8]

It is even possible to introduce levulinic acid residues into the lysine side chains in defined positions in the protein by de novo formation of the peptide. Alternatively, dithiolane-protected levulinyl residues may be used. The keto functions are released by oxidative cleavage following protein synthesis.[9]

Chemical protein engineering may be used not only for the development of protein-based drugs. The search for low-molecular-weight active compounds is also possible with chemically modified proteins to discover suitable binding pockets and high-affinity ligands for protein surfaces. For some time it has been a standard approach to vary individual amino acids in proteins by targeted mutagenesis in order to understand enzyme mechanisms and to modify them systematically. By means of targeted mutagenesis, attachment sites for chemical ligation techniques can also be produced on protein surfaces. For example, an equilibrium with sulfide exchange exists between cysteine residues and disulfides in aqueous solution (Figure 1). If by specific mutagenesis a cysteine residue is now brought into the immediate proximity of the binding pocket of an enzyme, the "hot spot" of a protein–protein binding surface, preferentially binding residues can be selected from an ensemble of dissolved disulfides and identified by mass spectrometry (LC-MS) of the synthetic protein product. In this way structures active with interleukin-2 could be filtered out of 7000 disulfides.[10]

Ligation on protein surfaces can also be used to discover new interaction regions in addition to known binding pockets that could be used to increase the affinity or selectivity of a ligand. This concept was applied successfully to caspase-3.[11] The caspases are a class of cysteine proteases that play a key role (inter alia in the development of cancer) because of their central function in programmed cell death (apoptosis). The cysteine residue of the active center was chosen for the in situ synthesis of an affinity ligand. (Figure 3). The sulfanyl function of the active center was first alkylated with a known irreversible inhibitor that contained a masked SH function. This second sulfanyl function then reacted with a disulfide library as in the aforementioned in situ ligation. A ligand–linker combination that preferentially occupied a binding pocket outside the active position of the enzyme was selected. For control the structure found was converted into a soluble, reversible inhibitor. However, changes on the linker were necessary to some extent in order to achieve K_i values below 1 μM.

The two examples illustrate the considerable advances in organic protein chemistry. Over and above de novo syntheses of proteins it has become possible to modify the properties of proteins in a targeted manner with

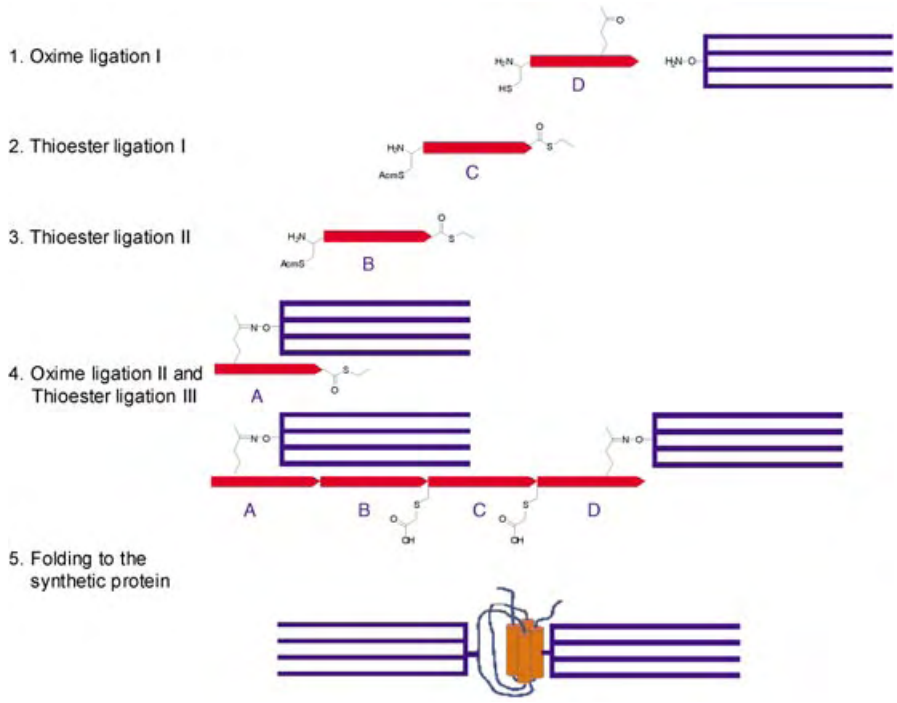


Figure 2. Synthesis of a polymer-modified variant of human erythropoietin by a combination of thioester and oxime ligation. The blue regions denote the polyether units.

 © 2004 Wiley-VCH Verlag GmbH & Co. KGaA, Weinheim

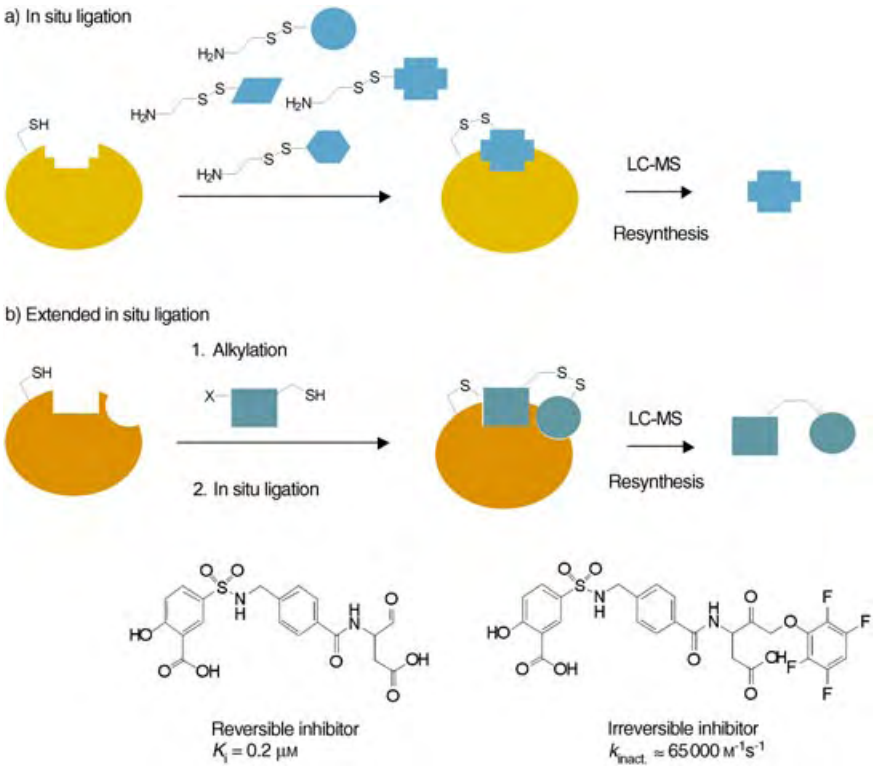


Figure 3. Disulfide ligation on the surface of proteins (in situ ligation) for the identification of high-affinity ligands and new interaction regions outside of the catalytically active binding pocket.

chemical methods. The techniques described can simplify the development of new active proteins, and also the search for new low-molecular-weight active compounds. At the same time it is also evident how important analytical and separation techniques are for the achievement of such demanding targets. Only the extensive availability of high-resolution mass spectrometric and liquid chromatography techniques has made possible the work described. The exact characterization of ligation methods still requires further research. It would be desirable in this context to learn through systematic work more about by-products, the protective groups that may be necessary, and the extent of racemization of the amino acid building blocks in the ligation products.

Published Online: July 20, 2004

[1] T. Wieland, E. Bokelmann, L. Bauer, H. U. Lang, H. Lau, *Justus Liebigs Ann. Chem.* **1953**, *586*, 129–149.

[2] P. E. Dawson, T. W. Muir, I. Clark-Lewis, S. B. H. Kent, *Science* **1994**, *266*, 776–779.

[3] a) E. Saxon, C. R. Bertozzi, *Science* **2000**, *287*, 2007–2010; b) B. L. Nilsson, L. L. Kiessling, R. T. Raines, *Org. Lett.* **2000**, *2*, 1939–1941.

[4] G. G. Kochendoerfer, S. Y. Chen, F. Mao, S. Cressman, S. Traviglia, H. Shao, C. L. Hunter, D. W. Low, E. N. Cagle, M. Carnevali, V. Gueriguian, P. J. Keogh, H. Porter, S. M. Stratton, M. C. Wiedeke, J. Wilken, J. Tang, J. J. Levy, L. P. Miranda, M. M. Crnogorac, S. Kalbag, P. Botti, J. Schindler-Horvat, L. Savatski, J. W. Adamson, A. Kung, S. B. H. Kent, J. A. Bradburne, *Science* **2003**, *299*, 884–887.

[5] Yields of 15–30% were reported for the peptide synthesis and ligation, 30–50% for the oxime ligation, 40–70% for the thioester ligation, and 25–40% for the folding. This gives an overall yield of between 0.072 and 2% without consideration of losses in yield during peptide synthesis.

[6] a) H. B. F. Dixon, *Biochem. J.* **1964**, *90*, 2c–3c; b) H. B. F. Dixon, *Biochem. J.* **1964**, *92*, 661–666.

[7] A. Papanikos, J. Rademann, M. Meldal, *J. Am. Chem. Soc.* **2001**, *123*, 2176–2181.

[8] S. Weik, J. Rademann, *Angew. Chem.* **2003**, *115*, 2595–2598; *Angew. Chem. Int. Ed.* **2003**, *42*, 2491–2494.

[9] D. Tumelty, M. Carnevali, L. P. Miranda, *J. Am. Chem. Soc.* **2003**, *125*, 14238–14239.

[10] M. R. Arkin, M. Randal, W. L. DeLano, J. Hyde, T. N. Luong, J. D. Oslob, D. R. Raphael, L. Taylor, J. Wang, R. S. McDowell, J. A. Wells, A. C. Braisted, *Proc. Natl. Acad. Sci. USA* **2003**, *100*, 1603–1608.

[11] D. A. Erlanson, J. W. Lam, C. Wiesmann, T. N. Luong, R. L. Simmons, W. L. DeLano, I. C. Choong, M. T. Burdett, W. M. Flanagan, D. Lee, E. M. Gordon, T. O'Brien, *Nat. Biotechnol.* **2003**, *21*, 308–314.

 © 2004 Wiley-VCH Verlag GmbH & Co. KGaA, Weinheim

Zeolite Nanoslabs?

On the TEM and AFM Evidence of Zeosil Nanoslabs Present during the Synthesis of Silicalite-1**

*Harikrishnan Ramanan, Efrosini Kokkoli, and Michael Tsapatsis**

Keywords:
nanoblocks · nanoslabs · silicates · zeolites

The mechanism of formation of synthetic zeolite structures has been a subject of many recent investigations.[1–3] One of the commonly studied zeolites is silicalite-1 (siliceous ZSM-5). Recent studies on the synthesis of tetrapropylammonium (TPA) silicalite-1 have reported the formation of zeosil nanoparticles (termed *nanoslabs* or *nanoblocks*) during the early stages of silicalite-1 crystallization.[4–6] The zeosil nanoparticles are believed to agglomerate into larger tablets and eventually form silicalite-1 crystals.[4–6] Transmission electron microscopy (TEM) analysis of samples prepared by evaporation of a clear solution prepared by hydrolyzing tetraethylorthosilicate (TEOS) in the presence of aqueous TPA hydroxide (TPAOH) solution at 20 °C has been claimed to reveal the existence of such nanoparticles.[6] More specifically, TEM images that are provided in ref. [6] are interpreted as "conglomerated" nanosized particles with an average in-plane dimension of 4×4 nm^2 and thickness of approximately 1.2–1.3 nm. It is mentioned that "occasionally larger particles are observed with in-plane dimensions corresponding to multiples of 4 nm", suggesting they are formed through sidewise coalescence of elementary nanoslabs of dimension 4×4 nm^2. Figure 1a and Figure 2a herein are, respectively, Figure 1a and 1b of ref. [6]. It is interesting to note the tetragonal shape of the so-called "conglomerate" and the oriented arrangement of the so-called 4×4 nm^2 nanoblocks with their faces parallel to each other. Such an arrangement indicates oriented aggregation of the nanoslabs by simple evaporation on a TEM grid. Even more interesting is that despite the authors' claim that they are not able to obtain a diffraction pattern from these particles, close inspection of the images in Figure 1a and Figure 2a (Figure 1a and 1b in ref. [6]) clearly shows the presence of approximately 3 Å spaced fringes indicating crystalline order. Optical diffractograms (fast Fourier transform (FFT)) of Figure 1a and Figure 2a (shown in Figure 1b and Figure 2b) clearly show that the entire particle is a single crystal with unambiguous fourfold symmetry. The 3 Å spacing and fourfold symmetry are not discussed in ref. [6]. Such a small spacing and symmetry do not agree with the proposed

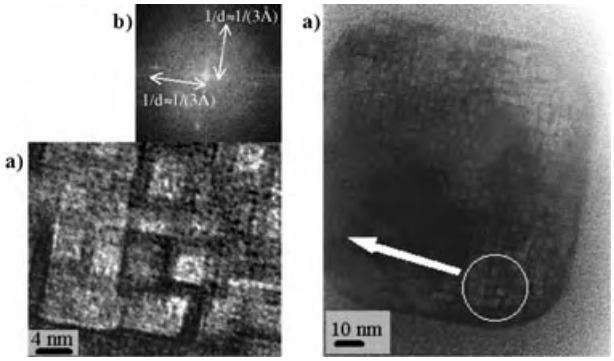


Figure 1. Parts a) Figure 1a in ref. [6], TEM images of nanoslabs prepared from TEOS/TPAOH/water system, b) our FFT of Figure 1a revealing fourfold symmetry with $d \approx 3$ Å.

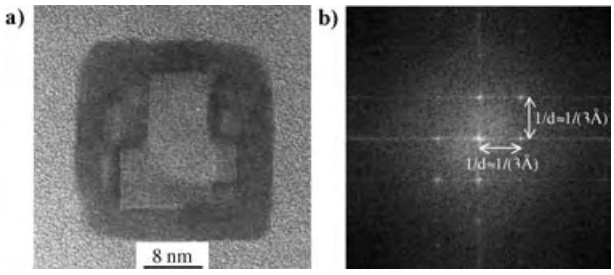


Figure 2. a) Figure 1b in ref. [6], an occasionally observed larger block in nanoslab sample, b) our FFT of Figure 2a confirming crystalline nature of observed particle with $d \approx 3$ Å and fourfold symmetry.

[*] Dr. H. Ramanan, Prof. E. Kokkoli, Prof. M. Tsapatsis
Department of Chemical Engineering and Materials Science
University of Minnesota
151 Amundson Hall
421 Washington Ave SE
Minneapolis, MN 55455-0132 (USA)
Fax: (+1) 612-626-7246
E-mail: tsapatsi@cems.umn.edu

[**] We thank Carol M. Garland of the California Institute of Technology for assistance in the EDX work, Raman Ravishankar and Griselda Bonilla for assistance in the synthesis and gratefully acknowledge the financial support for this work from the National Science Foundation and the Nanoscale Interdisciplinary Research Team (NIRT) grants NSF CTS-0091406 and NSF NIRT CTS-0103010. We acknowledge the W. M. Keck Electron Microscopy facility at the University of Massachusetts, Amherst for the usage of the JEOL JEM 3010 microscope and the Keck Engineering laboratory at the California Institute of technology, Pasadena for the use of the Philips EM 430 microscope. Prof. J. A. Martens and Dr. Christine Kirschhock provided the images shown in Figure 1a and Figure 2a.

 © 2004 Wiley-VCH Verlag GmbH & Co. KGaA, Weinheim DOI: 10.1002/anie.200460376

structure of the nanoslabs. We will show (see below) that the Figure 1a and 1b of ref. [6] are most likely from a small amount of sodium chloride (NaCl) crystals contaminating the extracted material.

Atomic force microscopy (AFM) studies on evaporated suspensions of the extracted silica species reported in ref. [5] were also used to support the discovery of zeosil nanoslabs in ref. [6]. Step sizes determined by AFM were reported to be a multiple of approximately 1.2 ± 0.3 nm and interpreted as nanoslabs present either as single or stacked entities.[6] We also performed AFM measurements to compare our findings with those of ref. [5]. We summarize below our results from the TEM and AFM analysis and compare our findings on the existence of nanoslabs or nanoblocks with earlier studies.[4–6]

The procedure for synthesizing a clear suspension of the nanoparticles and their subsequent isolation or extraction has been adopted from earlier studies.[4–6] Samples prepared from the as-synthesized clear suspension as well as the extracted phase were investigated by TEM imaging, electron diffraction (ED), and energy dispersive X-ray (EDX) analysis. Images and diffraction patterns were captured under conditions of low electron-beam intensity. The as-synthesized clear suspension upon evaporation on a TEM grid forms extended platelike deposits (Figure 3a). Closer examination along the edges of the plates reveals a laminated deposit. In addition to such extended areas with laminated appearance, agglomerates of smaller globular shaped particles approximately 3–5 nm in size (Figure 3b) were also observed, but only rarely. The extended platelike deposits and the globular particles do not exhibit any diffraction. This result, along with the absence of any regular pattern of fringes within the particles confirms their amorphous nature. In contrast to the results reported in ref. [6], no material similar to that shown in Figure 1a and Figure 2a could be found in the powder prepared by evaporation of the as-synthesized suspension though we analyzed a number of representative samples. Note that previous studies, including one report by some of the authors of ref. [6], show similar results,[5] that is,

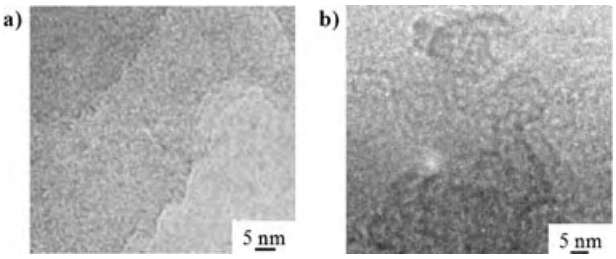


Figure 3. TEM images of amorphous silica powder from as-synthesized clear solution, a) extended laminated deposit, b) globular shaped particles.

evidence of amorphous laminated deposits. The question then remains: what are the particles in Figure 1a and Figure 2a? TEM studies of the powder extracted in the organic phase (tetrahydrofuran (THF)) revealed crystalline particles (Figure 4a and b) that are very similar to the nanoslabs in ref. [6]. Figure 4c shows the FFT of the image in Figure 4b indicating fourfold symmetry and a spacing of 2.8 Å. ED and EDX studies of the crystalline particles confirmed them to be NaCl crystals. Figure 4d shows the ED pattern indexed as a $\langle 001 \rangle$ projection of a face-centered cubic unit cell of NaCl with lattice dimension $a = 5.6$ Å.[7] Figure 4e shows the EDX analysis of the particles with the corresponding Cl (strong) and Na (weak) peaks in agreement with the EDX analysis of a pure NaCl crystal (Figure 4f). The presence of NaCl crystals in the sample extracted from the organic phase indicates that not all the water has been salted out during the extraction stage. In addition to the NaCl particles, large amorphous agglomerates (Figure 5a and 5b) were also found in the extracted sample. The agglomerates appear to be similar to the laminated deposit observed in Figure 3a as well as those in the reported TEM studies (Figure 2 in ref. [5]). The EDX scan of

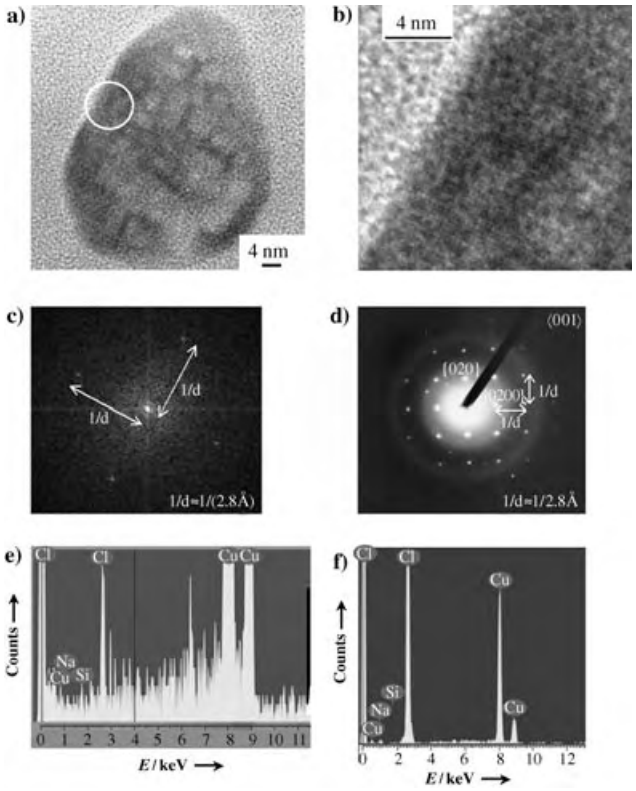


Figure 4. TEM of powder extracted in THF, a) image of particle having the agglomerate appearance reported in ref. [6], b) enlarged view of circled region in (a) revealing lattice fringes spaced at 2.8 Å, c) FFT of image shown in (b) revealing $d \approx 2.8$ Å and fourfold symmetry, d) ED pattern obtained from particle similar to that shown in (a). The fourfold symmetry and $d \approx 2.8$ Å in (c) and (d) are consistent with $\langle 001 \rangle$ projection of NaCl crystals, e) EDX analysis obtained from particle similar to that shown in (a), f) EDX analysis from a sodium chloride standard.

 © 2004 Wiley-VCH Verlag GmbH & Co. KGaA, Weinheim

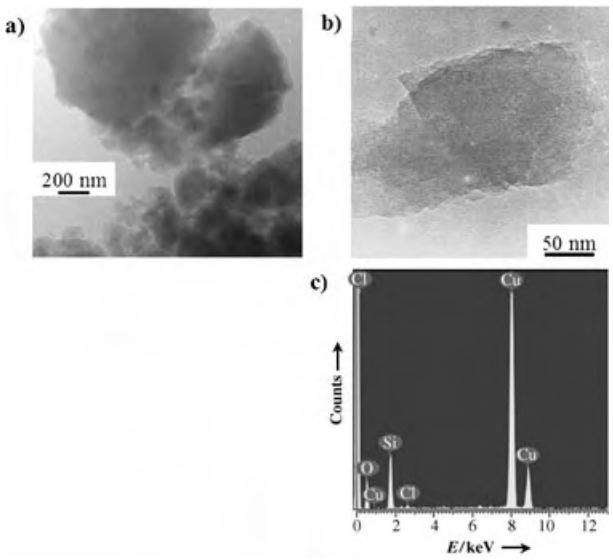


Figure 5. TEM of powder extracted in THF, a) and b) amorphous silica agglomerates, c) EDX analysis of amorphous silica agglomerate.

a representative region of the large agglomerate shown in Figure 5a confirms that the agglomerate is predominantly silica (Figure 5c). The presence of the peak for Cl in the scan suggests that some NaCl particles could be trapped in the amorphous silica (the peak for Na is relatively weak so that it is absent in this scale). The presence of significant peaks for Cu in all the EDX results are due to the use of Cu grids for TEM sample preparation.

The extracted powders were also examined by AFM. Step heights were calculated by analysis of several AFM images such as the ones shown in Figure 6a. The step heights obtained from several representative isolated agglomerates are shown in Figure 6b. Our observance of a step-height distribution centered at about 1.5 nm (Figure 6b) includes the step heights of 1.2 ± 0.3 nm reported by the authors of ref. [5]. However, the distribution measured in our samples is significantly broader and we also observed step heights that do not correspond to multiples of around 1.3 nm or to any other dimensions that have been proposed for the nanoslabs in refs. [5,6] (that is, $2.7 \times 1.0 \times 1.3$, $4 \times 2 \times 1.3$, $4 \times 4 \times 1.3$, and $8 \times 8 \times 1.3$ nm^3). We conclude that AFM analysis of the extracted samples does not confirm the existence of nanoslabs as single or stacked entities as suggested in refs. [5,6].

There are two other more recent published studies that include TEM imaging of nanoslabs.[8,9] In ref. [8], the as-synthesized suspension was used to make thin films on silicon wafers. Although fringes arising from silicon wafers were resolved, the silica–TPA film is featureless. Despite the lack of evidence for the presence of order in these films, the authors call them the thinnest zeolite film synthesized to date based on the assumption that the film is formed predominantly of nanoslabs of silicalite-1. However, this assumption is not supported by their TEM data. In another study,[9] mesoporous materials are claimed to be formed by ordered arrangement (tiling) of nanoslabs. The TEM images provided are typical of mesoporous materials with no clear evidence of order within the wall and especially for the presence of nanoslabs.

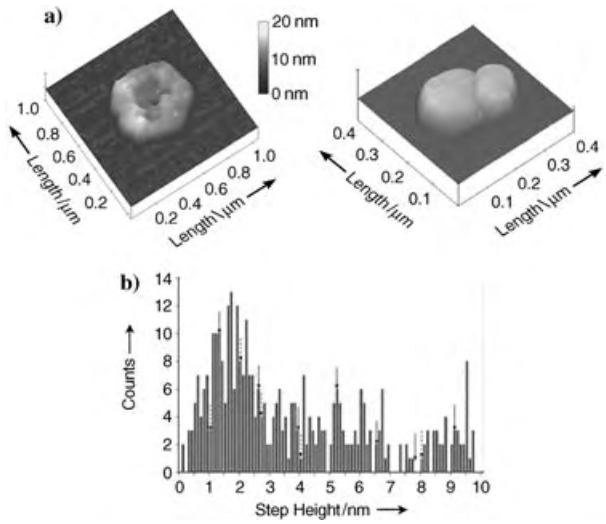


Figure 6. a) AFM images of representative agglomerates on mica substrates taken in air with an oxide-sharpened silicon nitride tip. The images show a 3D representation of the sample-height data and the gray-scale bar indicates the height variations on the topography of the surfaces. b) Histogram of step heights measured from different agglomerates. The graph shows results from 366 measurements. For comparison, arrows with solid lines show multiples of 1.3 nm for the nanoslab thickness from refs. [5,6] and the arrows with dotted lines indicate the nanoslab dimensions (1, 2, 2.7, 4, and 8 nm) from refs. [5,6].

Summarizing, we found that samples prepared by drying the as-synthesized clear suspension contain predominantly amorphous agglomerates of silica along with some nanosized globular particles. Samples prepared by drying of the extracted (by salting out with NaCl) powder in the organic phase contain crystalline NaCl particles as contaminants. Comparing our results with the reported TEM data,[6] we claim that a) NaCl crystals dispersed in the organic-rich phase have been misinterpreted as nanoblocks or nanoslabs and b) no block-shaped nanoparticles could be found in the powder obtained from drying the as-synthesized clear suspension. Our findings do not contradict the existence of nanoscopic entities during the initial stages of silicalite-1 synthesis that has been established by other characterization techniques, such as dynamic light scattering,[2,3] and small angle X-ray scattering.[10] The purpose of the current study is to re-investigate the possible existence of block-shaped nanoparticles with MFI structure during the initial stages of silicalite-1 synthesis as proposed in refs. [4–6]. From the evidence presented herein, we conclude that no such nanoslabs or nanoblocks that could be classified as building blocks for zeolite MFI structure could be unambiguously identified, a situation providing further support to the arguments presented in ref. [11].

Experimental Section

TEM samples for the as-synthesized clear silicate suspension and the extracted phase were prepared as dilute suspensions in ethanol. As the pH of the as-synthesized silicate solution was considerably high (pH > 12), TEM samples were prepared on holey carbon coated Au grids (SPI supplies, Structure Probe Inc.). Alternatively, sample preparation using holey carbon coated Cu grids (Ted Pella Inc.) also gave us identical results

 © 2004 Wiley-VCH Verlag GmbH & Co. KGaA, Weinheim

though we suspected the Cu grids to be affected by the severe pH of the medium. Samples were analyzed on the JEOL JEM 3010 TEM at 300 kV for imaging and electron diffraction (ED) analysis. Energy dispersive X-ray (EDX) analysis was performed on the Philips EM 430 TEM using samples supported on holey carbon coated Cu grids (Ted Pella Inc.).

AFM characterization of the surfaces films was done with a Digital Instruments Nanoscope III system (Digital Instruments, Santa Barbara, CA). Images were obtained in contact mode in air using standard 200 μm V-shaped oxide-sharpened silicon nitride AFM cantilevers with pyramidal tips (Digital Instruments) of nominal radius 5–40 nm and nominal spring constant 0.06 $N m^{-1}$. In order to minimize the drift effects, AFM was warmed up for at least half an hour before an experiment. Samples were prepared for AFM analysis by re-dispersing a few drops of the extracted material originally dispersed in ethanol (same batch used for preparing the TEM samples) in about 10 mL of chloroform and then allowing a drop of this dispersed solution to dry on a mica plate.

Published Online: August 20, 2004

[1] B. J. Schoeman, J. Sterte, J. E. Otterstedt, *Zeolites* **1994**, *14*, 568; A. E. Persson, B. J. Schoeman, J. Sterte, J. E. Otterstedt, *Zeolites* **1994**, *14*, 557; A. E. Persson, B. J. Schoeman, J. Sterte, J. E. Otterstedt, *Abstracts of Papers of the American Chemical Society* **1995**, *209*, 71; S. Mintova, N. H. Olson, V. Valtchev, T. Bein, *Science* **1999**, *283*, 958; S. Y. Yang, A. Navrotsky, *Chem. Mater.* **2002**, *14*, 2803.

[2] B. J. Schoeman, O. Regev, *Zeolites* **1996**, *17*, 447.

[3] V. Nikolakis, E. Kokkoli, M. Tirrell, M. Tsapatsis, D. G. Vlachos, *Chem. Mater.* **2000**, *12*, 845.

[4] R. Ravishankar, C. Kirschhock, B. J. Schoeman, D. De Vos, P. J. Grobet, P. A. Jacobs, J. A. Martens in *Proceedings of the 12th International Zeolite Conference*, *Vol. III* (Eds.: M. M. J. Treacy, B. K. Marcus, M. E. Bisher, J. B. Higgins), Baltimore, Maryland, **1998**, pp. 1825.

[5] R. Ravishankar, C. E. A. Kirschhock, P. P. Knops-Gerrits, E. J. P. Feijen, P. J. Grobet, P. Vanoppen, F. C. De Schryver, G. Miehe, H. Fuess, B. J. Schoeman, P. A. Jacobs, J. A. Martens, *J. Phys. Chem. B* **1999**, *103*, 4960.

[6] C. E. A. Kirschhock, V. Buschmann, S. Kremer, R. Ravishankar, C. J. Y. Houssin, B. L. Mojet, R. A. van Santen, P. J. Grobet, P. A. Jacobs, J. A. Martens, *Angew. Chem.* **2001**, *113*, 2707; *Angew. Chem. Int. Ed.* **2001**, *40*, 2637.

[7] C. Kittel, *Introduction to Solid State Physics*, *7th ed.*, Wiley, New York, **1996**.

[8] S. P. B. Kremer, C. E. A. Kirschhock, A. Aerts, K. Villani, J. A. Martens, O. I. Lebedev, G. Van Tendeloo, *Adv. Mater.* **2003**, *15*, 1705.

[9] A. M. Doyle, G. Rupprechter, N. Pfander, R. Schlögl, C. E. A. Kirschhock, J. A. Martens, H. J. Freund, *Chem. Phys. Lett.* **2003**, *382*, 404.

[10] P. P. E. A. de Moor, T. M. P. Beelen, R. A. van Santen, in *Proceedings of the 12th International Zeolite Conference, Vol. III* (Eds.: M. M. J. Treacy, B. K. Marcus, M. E. Bisher, J. B. Higgins), Baltimore, **1998**, pp. 1529; P. P. E. A. de Moor, T. P. M. Beelen, B. U. Komanschek, L. W. Beck, P. Wagner, M. E. Davis, R. A. van Santen, *Chem. Eur. J.* **1999**, *5*, 2083.

[11] D. D. Kragten, J. M. Fedeyko, K. R. Sawant, J. D. Rimer, D. G. Vlachos, R. F. Lobo, M. Tsapatsis, *J. Phys. Chem. B* **2003**, *107*, 10006; C. T. G. Knight, S. D. Kinrade, *J. Phys. Chem. B* **2002**, *106*, 3329.

 © 2004 Wiley-VCH Verlag GmbH & Co. KGaA, Weinheim

Zeolite Nanoslabs

Reply**

*Christine E. A. Kirschhock, Duoduo Liang, Alexander Aerts, Caroline A. Aerts, Sebastien P. B. Kremer, Pierre A. Jacobs, Gustaaf Van Tendeloo, and Johan A. Martens**

Keywords:
nanoblocks · nanoslabs · silicates · zeolites

In earlier work some of us claimed the existence of nanoslabs at an early stage in the synthesis of silicalite-1 (siliceous ZSM-5) from tetraethylorthosilicate (TEOS), tetrapropylammonium hydroxide (TPAOH), and water.[1] These nanoslabs have discrete sizes, for example, $1.3 \times 4.0 \times 4.0$ nm. The framework connectivity is as in the final zeolite.[1] Nanoslabs can be extracted from suspension and obtained as a powder by neutralization with strong acid, adding hydrogen-bonding organic solvent, salting out by addition of NaCl, and finally evaporation of the organic solvent.[1b,2,3] In recent work by Kragten et al.,[4] an attempt was reported to reproduce the preparation of nanoslab extract. Using those samples, in the preceding correspondence by Ramanan et al.,[5] the observation of the zeosil nanoslabs by transmission electron microscopy (TEM) and atomic force microscopy (AFM) was doubted. We experienced that whereas the preparation of nanoslabs itself is easy, the extraction is much more difficult to achieve. Herein we elaborate the arguments in favor of the observation of nanoslabs with TEM and discuss extraction procedures.

Nanoslab suspension (clear solution) is expected to contain very little NaCl. It is possibly present as an impurity in the TPAOH reagent. Extracted material inevitably contains NaCl. We prepared a new sample of extracted nanoslab (procedure 1 of Table 1) and investigated it with TEM (Figure 1 and Figure 2). The sample contains NaCl cubes, as confirmed by energy dispersive X-ray analysis (EDX; Figure 1b), they appear as single crystalline cubes with dimensions of 50–100 nm (Figure 1 and Figure 2). The NaCl particles exhibit small square domains of lighter contrast. One possible explanation for the presence of these domains is the formation of etch pits in the NaCl introduced by the electron beam. An alternative explanation is that these domains are nanoslabs on top of the NaCl and are stabilized because of the epitaxial relationship with the cubic NaCl. There are several arguments in favor of this latter explanation. Under the electron beam NaCl crystals are damaged and that NaCl is evaporated. We prepared a sample of NaCl using the same procedure as for nanoslab preparation and extraction but omitted the TEOS from the reaction mixture. TEM experiments on these NaCl particles (Figure 3) indeed show severe electron-beam dam-

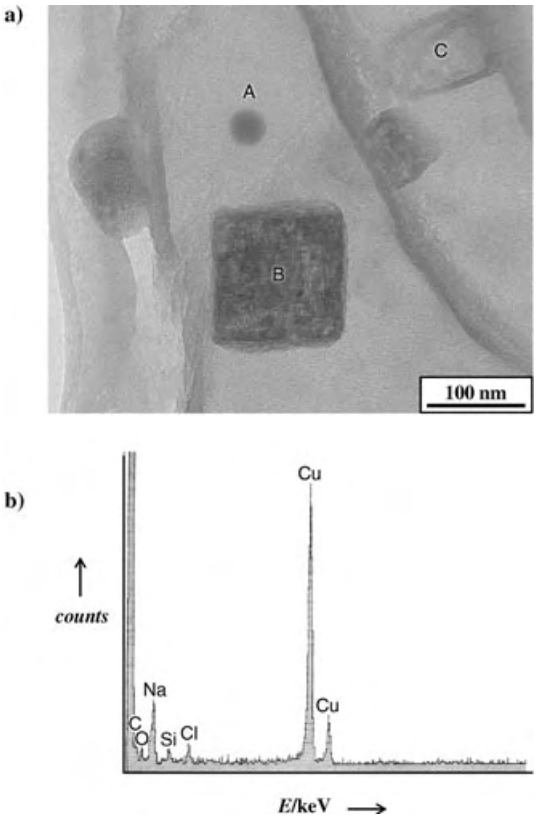


Figure 1. a) TEM image of extracted nanoslab sample prepared according to procedure 1 of Table 1; composition has been measured on the NaCl crystal (region B) and away from it (region A); in region C a NaCl crystal has probably dropped out and only the rim is remaining; b) EDX pattern of region B. Region C is Si/O rich; region A is an EDX contamination spot measured for reference.

[*] Dr. C. E. A. Kirschhock, A. Aerts, C. A. Aerts, Dr. S. P. B. Kremer, Prof. P. A. Jacobs, Prof. J. A. Martens
Centre for Surface Chemistry and Catalysis
Catholic University of Leuven
Kasteelpark Arenberg 23, 3001 Leuven (Belgium)
Fax: (+32) 16-321-998
E-mail: johan.martens@agr.kuleuven.ac.be
D. Liang, Prof. G. Van Tendeloo
Centre for Electron Microscopy for Materials Science
University of Antwerp
Groenenborgerlaan 171, 2020 Antwerpen (Belgium)

[**] J.A.M. and G.V.T. acknowledge the Flemish FWO for a research grant. C.E.A.K acknowledges the Flemish FWO for a postdoctoral fellowship. J.A.M. and P.A.J. acknowledge the Belgian government for financial support in the frame of the IAP-PAI program.

 © 2004 Wiley-VCH Verlag GmbH & Co. KGaA, Weinheim DOI: 10.1002/anie.200460541

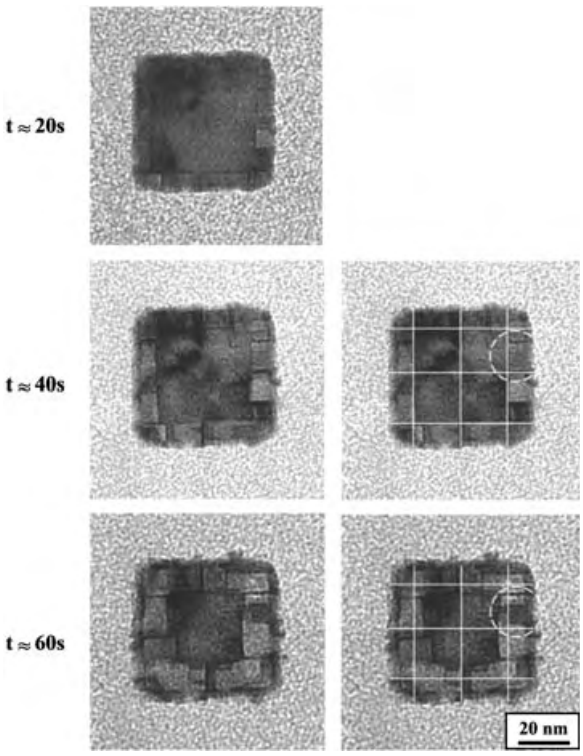


Figure 2. Sequence of TEM images of extracted nanoslab sample prepared according to procedure 1 of Table 1 (the grid superimposed in the right-hand pictures is to aid the eye).

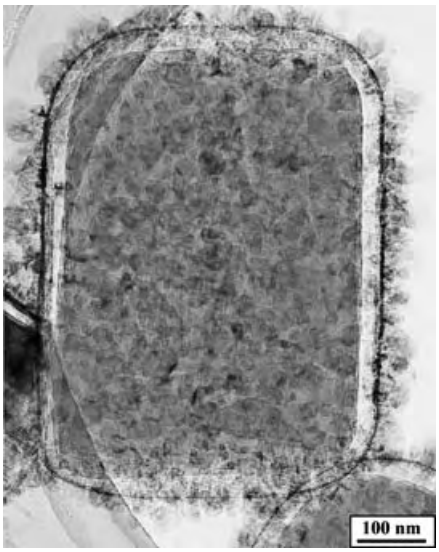


Figure 3. TEM image of a NaCl particle prepared according to procedure 1 of Table 1 in the absence of TEOS from the reaction mixture.

age, evaporation, and re-deposition of material as evidenced by the observation of flakes on the border of the grain. However, this damage does not follow the crystallographic directions as in Figure 1 and Figure 2. In all the TEM pictures of samples supposed to contain nanoslabs, there is a dark rim around the NaCl particles (see for example, Figure 1 a). The area marked C in Figure 1 a, shows a dark contour, where probably a NaCl crystal has evaporated under the electron beam. This contour, according to EDX, is Si/O. Pure NaCl particles, after irradiation, exhibit a bright rim (Figure 3) owing to material being sputtered away from the surface. This rim grows with increased electron irradiation time.

The square domains on top of the NaCl are subject to changes with time (Figure 2). The encircled area in Figure 2 is particularly bright at the beginning of the observation but turns darker in later images. This observation can not be reconciled with the assignment of the domains to etch pits because a white area corresponding to a thinner sample is unlikely to become a black area corresponding to a thicker sample. We are aware that a contrast change in crystalline samples can also be produced by orientation changes. However, since the NaCl particle is single crystalline, then all contrast should reverse and not just the encircled area. This observation therefore strongly suggests that the changes in contrast are linked with changes of the nanoslabs. We believe to have strong arguments for nanoslabs being stabilized on the NaCl crystals, although TEM alone does not provide direct proof. However, the combination of TEM observations with small-angle X-ray scattering and AFM provides the evidence.

The material prepared by Kragten et al. displayed ^{29}Si magic-angle spinning (MAS) NMR and Fourier transform IR spectra similar to that in the original publication,[1b] but the X-ray diffraction (XRD) pattern was different (Figure 4, curves 1 and 3). In the low-angle region, a diffraction peak at $2\theta \approx 2.7°$ was lacking, while an unexpected

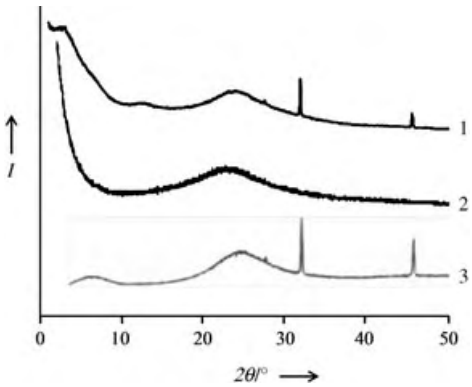


Figure 4. XRD patterns of extracted nanoslab samples prepared according to procedure 1 of Table 1 (curve 1); prepared by us according to the procedure reported by Kragten et al. (procedure 2 of Table 1, curve 2);[4] the spectrum reported by Kragten et al. (curve 3).[4]

diffraction at $2\theta \approx 7°$ was present. Note that the two sharp diffractions at 31.8° and 45.5° are due to NaCl. Redispersion of the extracted material in water[1b] failed with the material prepared by Kragten et al.[4] We revisited the extraction procedures (Table 1) and found the acidification step to be critical. Surface-charge neutralization causes removal of the protective TPA layer from the slabs, rendering them very sensitive towards condensation and degradation reactions. The absence of preferential step heights of 1.2 ± 0.3 nm in the AFM study by Ramanan et al.[5] reflects the poor quality of their extracted material. Our new procedure, involving the use of concentrated HCl (procedure 1 of Table 1) minimizes the damage of the nanoslabs.

Experimental Section

TEM samples for extracted material were prepared as dilute suspensions in methanol. A few drops of suspension were allowed to dry on perforated carbon-coated copper grids. Samples were imaged and analyzed by EDX on a Philips CM20 operating at 200 kV. XRD patterns of extracted powders loaded in capillaries were recorded in Debye-Scherrer mode on a STOE StadiP, equipped with a linear position sensitive detector.

Published Online: August 20, 2004

 © 2004 Wiley-VCH Verlag GmbH & Co. KGaA, Weinheim

Table 1: Nanoslab isolation procedures.

Procedure	Reference	Clear solution, cooled at 0 °C	Acidification		Organic solvent		
		Volume [mL]	Acid, cooled at 0 °C	Quantity [mL] or final pH	Solvent	Volume [mL]	Elimination procedure
1	this work[c]	5	HCl (8.5 M)	15	*t*BuOH	60	evaporation; $T = 20$ °C, $P = 60$ Pa
2	Kragten et al.[c] (ref. [4])	7	HCl (0.5 M)	15[d]	THF[a]	15	evaporation; $T = 60$ °C
3	Schoeman[b] (ref. [3])	?	H-form of ion exchange resin	pH 2	*t*BuOH	?	freeze drying
4	Ravishankar et al.[c] (ref. [1b])	?	HCl (?)	pH 3	*t*BuOH	?	freeze drying
5	Ravishankar et al.[c] (ref. [2])	5	HCl (0.5 M)	15	THF[a]	20	evaporation

[a] Tetrahydrofuran. [b] Molar ratio TEOS:TPAOH:H_2O of 25:9:490. [c] Molar ratio TEOS:TPAOH:H_2O of 25:9:440. [d] 5 mL of clear solution was added to the acid.

[1] a) C. E. A. Kirschhock, V. Buschmann, S. Kremer, R. Ravishankar, C. J. Y. Houssin, B. L. Mojet, R. A. van Santen, P. J. Grobet, P. A. Jacobs, J. A. Martens, *Angew. Chem.* **2001**, *113*, 2707 – 2710; *Angew. Chem. Int. Ed.* **2001**, *40*, 2637 – 2640; b) R. Ravishankar, C. E. A. Kirschhock, P. P. Knops-Gerrits, E. J. P. Feijen, P. J. Grobet, P. Vanoppen, F. C. E. A. De Schryver, G. Miehe, H. Fuess, B. J. Schoeman, P. A. Jacobs and J. A. Martens, *J. Phys. Chem. B* **1999**, *103*, 4960 – 4964.

[2] R. Ravishankar, C. E. A. Kirschhock, B. J. Schoeman, P. Vanoppen, D. De Vos, P. J. Grobet, P. Vanoppen, P. A. Jacobs, J. A. Martens in *Proceedings of the 12th International Zeolite Conference Vol. 3* (Eds.: M. M. J. Treacy, B. K. Marcus, M. E. Bisher, J. B. Higgins), MRS, Baltimore, **1998**, p. 1825.

[3] B. J. Schoeman, *Stud. Surf. Sci. Catal.* **1997**, *105*, 647 – 654.

[4] D. D. Kragten, J. M. Fedeyko, K. R. Sawant, J. D. Rimer, D. G. Vlachos, R. F. Lobo, M. Tsapatsis, *J. Phys. Chem. B* **2003**, *107*, 10006 – 10016.

[5] H. Ramanan, E. Kokkoli, M. Tsapatsis, *Angew. Chem.* **2004**, *116*, DOI:10.1002/ange.200460376; *Angew. Chem. Int. Ed.* **2004**, *43*, DOI:10.1002/anie.200460376.

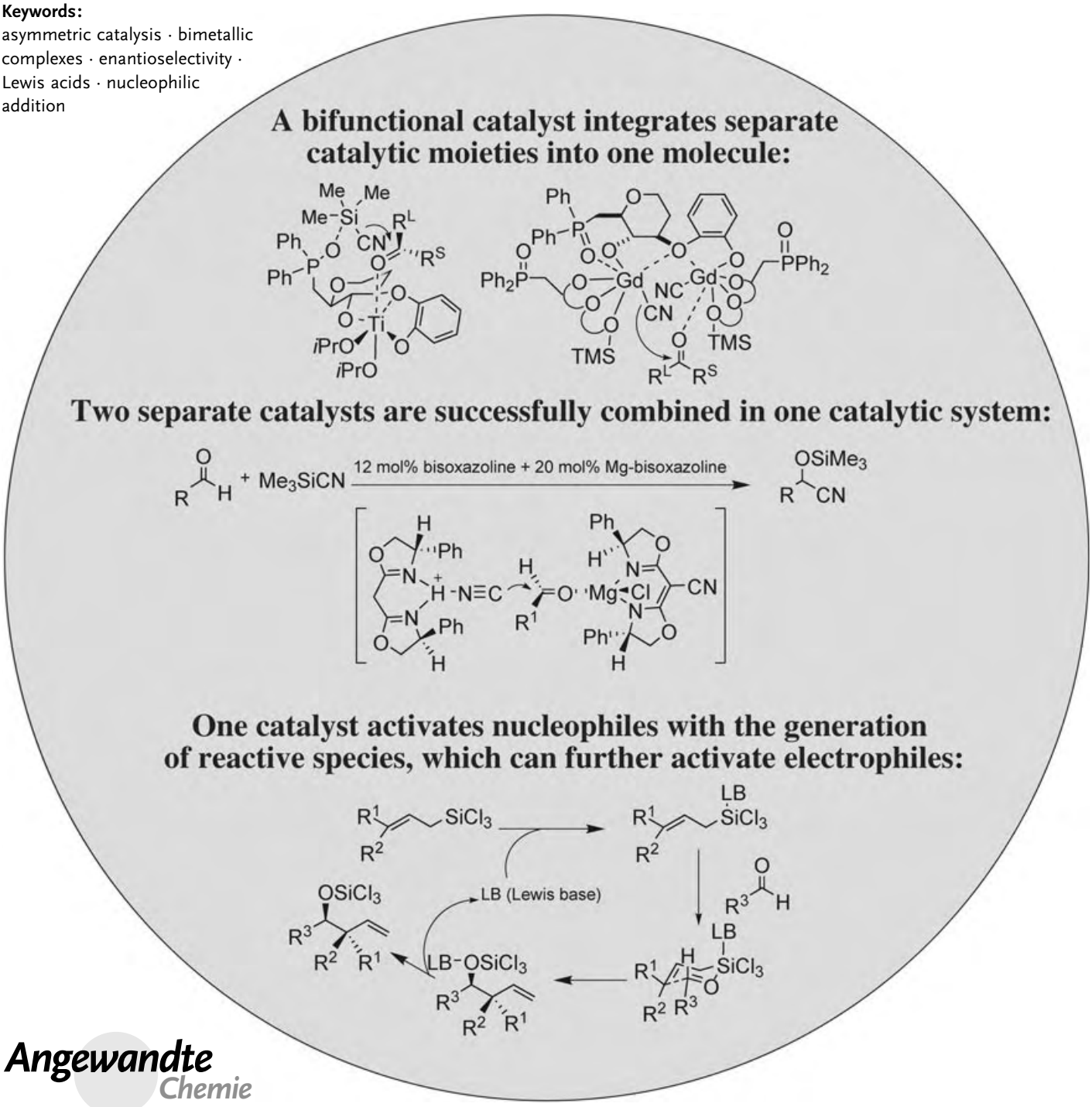
 © 2004 Wiley-VCH Verlag GmbH & Co. KGaA, Weinheim

Asymmetric Catalysis

Towards Perfect Catalytic Asymmetric Synthesis: Dual Activation of the Electrophile and the Nucleophile

*Jun-An Ma and Dominique Cahard**

Keywords:
asymmetric catalysis · bimetallic complexes · enantioselectivity · Lewis acids · nucleophilic addition



© 2004 Wiley-VCH Verlag GmbH & Co. KGaA, Weinheim
DOI: 10.1002/anie.200300635

The design and development of new high-performance catalysts for applications in asymmetric catalytic reactions is of ongoing interest in organic chemistry. The combination of a Lewis acid and a Lewis base working in concert is now considered state of the art in stereoselective syntheses. The synergistic activation by two or more reactive centers allows high reaction rates and excellent transfer of stereochemical information. Despite the self-quenching reaction between Lewis acids and Lewis bases that might lead to an inactive catalyst, considerable effort has been directed towards the development of the dual-activation concept. The ultimate goal is to mimic nature by the discovery of catalytic systems analogous to enzymatic processes that involve metal-ion cocatalysts. With this aim, the dual activation concept greatly broadens the range of artificial catalysts. The most efficient catalytic systems are reviewed, and the mechanisms of action are discussed.

From the Contents

1. Introduction 4567
2. Borane-Mediated Asymmetric Reduction of Carbonyl Compounds 4567
3. Catalytic Asymmetric Additions to Carbonyl Compounds 4568
4. Catalytic Asymmetric 1,4-Addition Reactions 4573
5. Catalytic Asymmetric Aldol Reactions 4575
6. Catalytic Asymmetric Mannich-Type Reactions 4577
7. Catalytic Asymmetric Ring Opening of Epoxides 4578
8. Other Catalytic Asymmetric Reactions 4579
9. Summary and Outlook 4580

1. Introduction

Catalytic asymmetric reactions provide one of the most powerful and economical synthetic approaches to a variety of enantiomerically enriched compounds.[1] The majority of catalytic asymmetric reactions employ chiral complexes based on transition-metal or main-group elements by either of the following methodologies: 1) less-reactive electrophiles are activated by coordination to a chiral Lewis acid, and the nucleophiles react favorably with the resulting electrophile/catalyst complexes to give enantiomerically enriched products; or 2) less-reactive nucleophiles coordinate to a chiral Lewis base, and the corresponding nucleophile/catalyst complexes react smoothly with the electrophiles to yield optically active compounds.[2] There are, however, many reactions whose substrates are too sluggish in reactivity or for which effective enantiomer formations are difficult. Over the past decade, an alternative approach has been developed in catalytic asymmetric synthesis: dual activation of the electrophiles and nucleophiles. For example, catalysts have been reported in which one site involves a Lewis acid moiety that coordinates electrophilic substrates while another site of the catalyst activates nucleophilic reagents. The catalyst positions the two reaction partners in close proximity and with the correct relative geometry, thus facilitating the reaction in a synergistic manner similar to catalysis by enzymes. Although the concept of dual activation has been mentioned in some reviews,[3] the aim of this Review is to provide an up-to-date overview of recent applications in catalytic asymmetric synthesis. Therefore, some early references will be summarized briefly to have all the key information at hand.

Three general strategies of dual activation are known: 1) a bifunctional catalyst integrates separate catalytic moieties into one molecule; 2) two separate catalysts are successfully combined in one catalytic system; 3) one catalyst activates electrophiles (or nucleophiles) with the generation of reactive species that can further activate nucleophiles (or electrophiles). In this Review, the concept of double activation and related strategies will be illustrated with several outstanding recent examples that highlight its utility for obtaining enantiomerically pure compounds. We will concentrate on organometallic-mediated catalysis for asymmetric synthesis. Organocatalysts, supramolecular catalysts, and enzymes are beyond the scope of this Review.

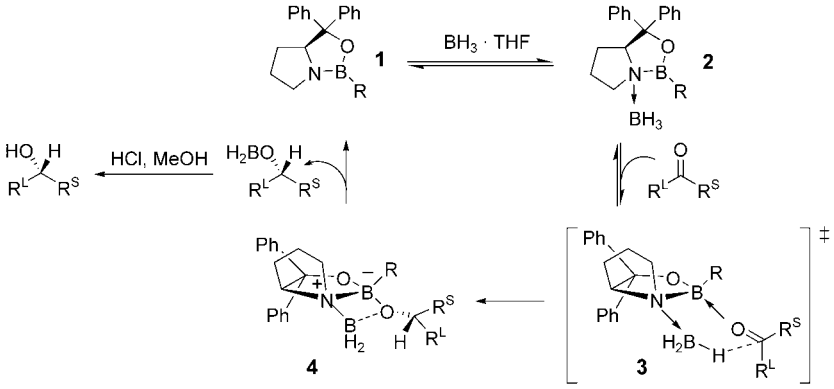
2. Borane-Mediated Asymmetric Reduction of Carbonyl Compounds

The development of borane-mediated enantioselective reduction of ketones was initiated by Itsuno and co-workers in the 1980s.[4] Later, a breakthrough was made with chiral oxazaborolidine catalysts by Corey's group (CBS reduction).[5] The CBS reduction is an excellent example of dual activation: The mechanism proceeds through the rapid

[*] Dr. J.-A. Ma, Dr. D. Cahard
UMR 6014 CNRS de l'IRCOF
Université de Rouen
1 Rue Tesnière, 76821 Mont Saint Aignan Cedex (France)
Fax: (+33) 2-3552-2971
E-mail: dominique.cahard@univ-rouen.fr
Dr. J.-A. Ma
Institute and State Key Laboratory of Elemento-Organic Chemistry
Nankai University
Tianjin 300071 (P.R. China)

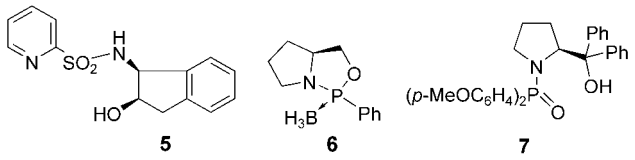
 DOI: 10.1002/anie.200300635 © 2004 Wiley-VCH Verlag GmbH & Co. KGaA, Weinheim

coordination of BH_3 to the Lewis basic nitrogen atom of **1** from the α face to give **2**, resulting in the activation of the borane with simultaneous enhancement of the Lewis acidity of the endocyclic boron atom for activation of the ketone (Scheme 1). The increased electrophilicity of the endocyclic boron atom facilitates the coordination of the ketone substrate at the least sterically demanding lone pair of electrons. The resultant spatial arrangement minimizes the steric interactions between the oxazaborolidine and the ketone and aligns the electron-deficient carbonyl group with the electronically activated boron–hydrogen bond to allow hydride transfer via a six-membered transition state **3**, leading to the formation of the reduction product **4** (Scheme 1).



Scheme 1. Proposed mechanism for the CBS reduction of ketones. R = H, *n*-alkyl, allyl, aryl, 3-phenylpropyl, cyclohexyl, β-branched substituents with or without stereogenic centers, trialkylsilyl methyl.

Since the ground-breaking research work of Corey and co-workers, a number of chiral ligands for the borane-mediated reduction of ketones have been developed. Sibi and co-workers designed a bifunctional catalyst that incorporated an oxazaborolidine moiety as a Lewis acid and the 2-pyridylsulfonamide-tethered Lewis base **5** as a directing group, which led to products with 71–89 % *ee* in the reduction of acetophenone derivatives.[6] Buono and co-workers reported an oxazaphospholidine–borane complex **6**, which mediates enantioselective reductions.[7] A modest selectivity (up to 65 % *ee*) was obtained with 16 mol % of the catalyst, and high enantioselectivities (> 99 % *ee*) were recorded when the catalyst was used in equimolar amounts. Wills and co-workers employed the phosphinamide **7** as a catalyst for the same reaction, and up to 93 % *ee* was observed.[8] Two major advantages of this catalyst are its stability to small amounts of moisture and its facile recovery from the reaction mixture for reuse.



Recently, polymer-supported α,α-diphenyl-L-prolinol was evaluated in the reduction of prochiral ketones with borane.[9] The expected secondary alcohols were obtained in high yields, and with 79–97 % *ee*. Recycling of the polymer-supported catalyst was efficient; indeed, the catalyst was recycled 14 times without loss of stereochemical performance.

3. Catalytic Asymmetric Additions to Carbonyl Compounds

Nucleophilic addition of organometallic reagents (such as alkyl, allyl, and aryl metal reagents, and trimethylsilyl (TMS) cyanide) to carbonyl substrates is one of the most fundamental reactions in organic synthesis. The catalytic asymmetric version offers a convenient approach to create optically active compounds, and the dual-activation approach appears both efficient and elegant.

3.1. Catalytic Asymmetric Alkylation of Carbonyl Compounds

Catalytic asymmetric alkylation of carbonyl compounds is another example of dual activation. In 1986, Noyori's group reported the first example of a highly enantioselective alkylation of aldehydes with diethylzinc, catalyzed by (−)-DAIB (**8**; (−)-3-exo-(dimethylamino)isoborneol) with up to 99 % *ee* (Scheme 2).[10] A bimetallic transition-state model can account for the high catalytic activity and excellent

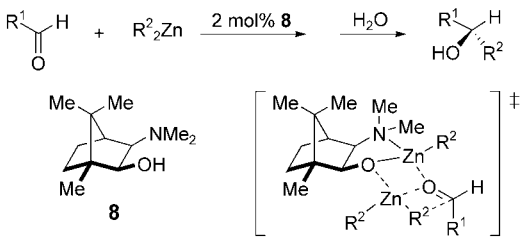


Dominique Cahard was born in 1968 in Fécamp (France). He received his Ph.D. at the University of Rouen with Prof. Pierre Duhamel. He then spent 19 months as a postdoctoral researcher with Prof. Chris McGuigan (Southampton University, UK) then at the Welsh School of Pharmacy (Cardiff, Wales). He also spent a short period of time with Prof. Tadashi Nakata (RIKEN, Tokyo, Japan). In 1996 he joined the CNRS at the University of Rouen where he completed his Habilitation in 2001. His current interests lie mainly in enantioselective synthesis, with an emphasis on electrophilic fluorination and phase-transfer catalysis.



Jun-An Ma was born in Henan (China). He received his B.Sc. from Henan University (1991) and his M.Sc. from Nankai University (1994). He then joined Guangzhou Baihua Flavor & Fragrance Company as a senior research fellow. He completed his Ph.D. under the supervision of Prof. Run-Qiu Huang at Nankai University (1996 to 1999). He remained at Nankai, with Prof. Qi-lin Zhou, before taking up a postdoctoral fellowship with Dr Dominique Cahard at Rouen University. His research interests focus on new methods in asymmetric synthesis, chiral catalysts, bioorganic chemistry, and fluorine chemistry.

 © 2004 Wiley-VCH Verlag GmbH & Co. KGaA, Weinheim



Scheme 2. Chiral aminoalcohol-promoted addition of dialkyl zinc reagents. R^1 = alkyl, aryl, alkenyl; R^2 = alkyl.

enantioselectivity of the reaction: one zinc atom is required for the catalytic cycle and behaves as a Lewis acid; the second zinc atom coordinates to the Lewis basic oxygen atom, which both activates and directs the addition. The successful application of (−)-DAIB resulted in a significant enhancement in ligand design for asymmetric alkylation of carbonyl compounds, and many novel ligands have been developed.[11] Most are believed to proceed by a similar mechanism to that suggested by Noyori and co-workers and other groups.[12]

Recently, Kozlowski and co-workers developed a set of modular bifunctional salen (*N*,*N*′-bis(salicylidene)ethylenediamine) catalysts **9** that contain Lewis acid and Lewis base functionalities; these can be altered independently to control nucleophilic and electrophilic activation of the substrates (Scheme 3).[13] The apical coordination site on the salen metal center acts as a Lewis acid site to activate aldehydes, while the tethered N-donor base independently activates the Et_2Zn nucleophile. The reaction proceeded in the presence of 10 mol% **9a** (M = Zn, X = O, L = no ligand) to obtain secondary alcohols in high yields (78–99%) and with high enantioselectivities (75–91% *ee*).[13a] The authors also reported the first asymmetric addition of dialkyl zinc to α-ketoesters by using bifunctional salen catalyst **9b** (M = Ti, X = CH_2, L = *i*PrO). α-Hydroxyesters with new quaternary stereogenic centers were obtained in high yield (up to 99%) and moderate enantioselectivity (up to 78% *ee*).[13b,c]

Shibasaki and co-workers reported the use of ligand **10** for the enantioselective addition of Me_2Zn to α-ketoesters (Figure 1).[14] The reaction proceeded to give the corresponding products in up to 95% yield with 96% *ee* from aromatic and acetylenic α-ketoesters. Interestingly, slow addition of Me_2Zn and an alcohol as a protic additive were required for high catalyst activity and enantioselectivity.

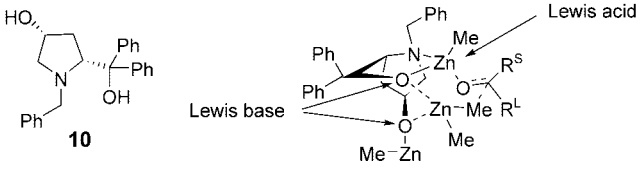
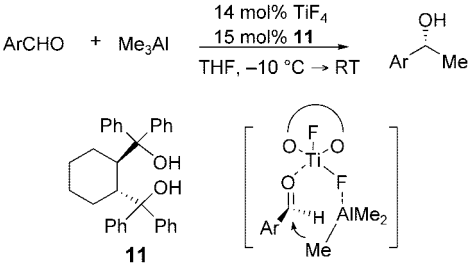


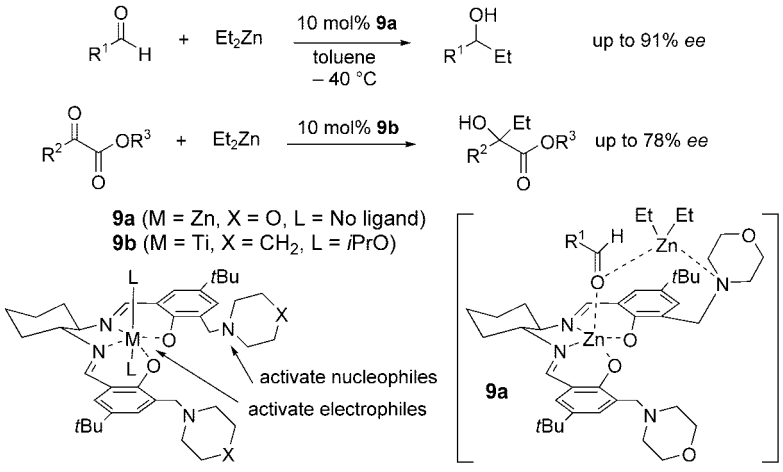
Figure 1. Ligand **10** in the nucleophilic alkylation of α-ketoesters.

A very interesting publication by Carreira's group described the enantioselective addition of trimethylaluminum to aldehydes (Scheme 4).[15] The reaction was carried out in THF



Scheme 4. Fluorotitanium complex in the catalytic asymmetric addition of Me_3Al to aromatic aldehydes.

at −10 °C with TiF_4 (14 mol%) and chiral diol ligand **11** (15 mol%). Given the affinity of aluminum for fluoride,[16] the formation of a fluoride bridge and dual activation were invoked to explain the reactivity and enantioselectivity.



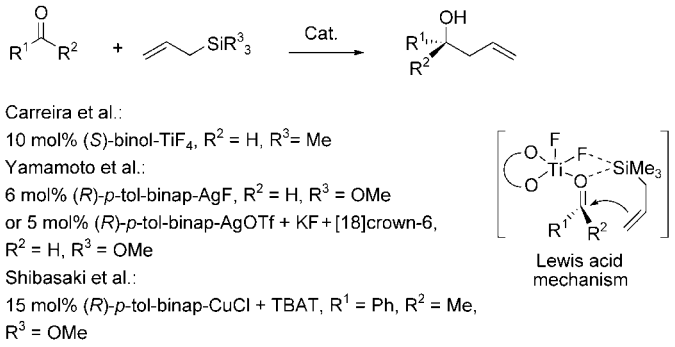
Scheme 3. Salen-derived catalysts for catalytic asymmetric addition of Et_2Zn to aldehydes and α-ketoesters. R^1 = alkyl, cyclohexyl, aryl; R^2 = alkyl, aryl; R^3 = alkyl, benzyl.

3.2. Catalytic Asymmetric Allylation of Carbonyl Compounds

The allylation of carbonyl compounds is a very important carbon–carbon bond-forming reaction because of the versatility of the homoallylic alcohol subunit as a synthetic intermediate. Among various allyl metal reagents, allylsilanes are very useful because of their low toxicity and relative stability. The relatively low reactivity of allylsilanes, however, has limited their synthetic utility. To overcome this drawback, a combination of a Lewis base and a Lewis acid metal to activate allylsilanes and substrates has been designed and used in allylation reactions. Notably, Carreira's group described a catalyst derived from TiF_4 and (*S*)-binol (1,1′-bi-2-naphthol) for the addition of allyltrimethylsilane to aldehydes with up to

 © 2004 Wiley-VCH Verlag GmbH & Co. KGaA, Weinheim

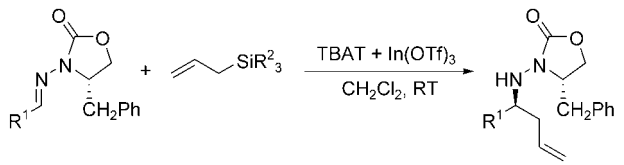
94% *ee*,[17] and Yamamoto and co-workers[18] reported the enantioselective addition of allyltrimethoxysilane to aromatic and α,β-unsaturated aldehydes catalyzed by tol-binap (2,2′-bis(di-*p*-tolylphosphanyl)-1,1′-binaphthyl) and silver(I) fluoride with up to 96% *ee* (Scheme 5). Fluoride ligands exhibit interesting properties as a result of their strong electron-



Scheme 5. Catalytic asymmetric allylation of carbonyl compounds.

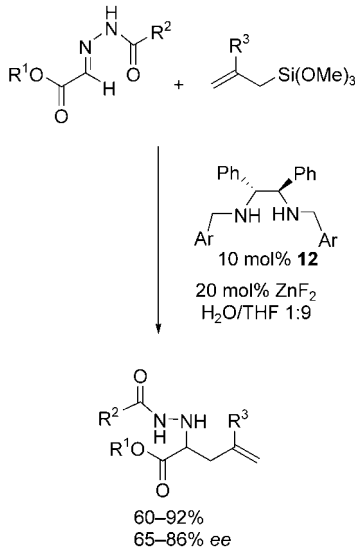
withdrawing nature. This effect renders the metal center more acidic and hence it further activates electrophilic substrates towards nucleophilic attack. In another example illustrating this concept, Shibasaki's group described the enantioselective addition of allyltrimethoxysilane to acetophenone in the presence of tol-binap, CuCl, and tetrabutylammoniumtriphenyldifluorosilicate (TBAT) with a modest 61% *ee*.[19] The detailed reaction mechanism is not established, however the reaction is likely to proceed through a transmetalation or Lewis acid mechanism. Duthaler and Hafner suggested a transition state in which the titanium atom activates the carbonyl compound and the nucleophilic fluorine atom bridged to the silicon center increases the reactivity of the allylsilane.[20]

Friestad and Ding reported highly stereoselective additions of allylsilanes to chiral *N*-acylhydrazones by complementary dual activation of both reactants by a mixture of TBAT and indium(III) trifluoromethanesulfonate ($In(OTf)_3$, Scheme 6).[21] Aromatic and alkenyl aldehyde hydrazones



Scheme 6. Asymmetric addition of allylsilane to hydrazones.

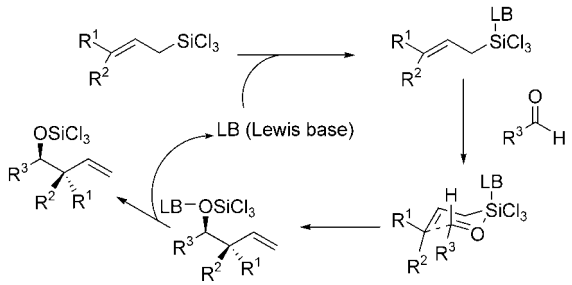
generally gave homoallylic amines in good yield with excellent stereoselectivity (up to 99:1 d.r.), whereas propionaldehyde hydrazone gives modest stereoselectivity (82:18 d.r.). Kobayashi's group presented the asymmetric allylation of acylhydrazone esters in aqueous media by using a catalytic amount of ZnF_2 and a chiral diamine ligand **12** (Scheme 7, e.g., Ar = 2-MeO(C_6H_4), 8-MeO-2-naphthyl).[22] This reaction proceeds with double activation in which the zinc(II) center



Scheme 7. Catalytic asymmetric allylation of acylhydrazones. R^1 = Me, Et; R^2 = Ph, 4-$MeOC_6H_4$, 4-$EtOC_6H_4$; R^3 = H, Me, Ph.

and the fluoride anions simultaneously activate both the acylhydrazones and the allyltrimethoxysilanes. The allylation reaction has been demonstrated to be a versatile method to obtain not only the optically active α-aminoester hydrazine analogues but also *N*-protected α-aminoesters.

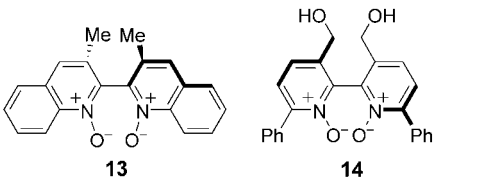
Chiral Lewis base catalyzed addition of allyltrichlorosilanes to aldehydes is a new, conceptually distinct enantioselective process.[23] The reaction involves binding of allyltrichlorosilanes to the Lewis base with the generation of reactive hypercoordinate silicon species, which can then activate the aldehydes. This double-activation mechanism leads to high reaction rates and excellent transfer of stereochemical information because the reactions proceed through a closed assembly of electrophiles, nucleophiles, and chiral catalysts (Scheme 8).



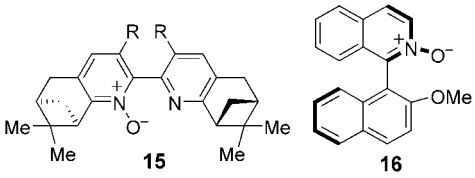
Scheme 8. Dual activation of aldehyde and allylating agent. R^1, R^2 = H, Me; R^3 = Ar, α,β-unsaturated group.

Among the chiral Lewis bases investigated, *N*-oxides have emerged as highly selective catalysts for the addition of allyltrichlorosilanes. The groups of Nakajima[24] and Hayashi[25] prepared bis-*N*-oxides **13** and **14**, respectively, and Kočovský and co-workers reported the use of 2,2′-bipyridyl

 © 2004 Wiley-VCH Verlag GmbH & Co. KGaA, Weinheim



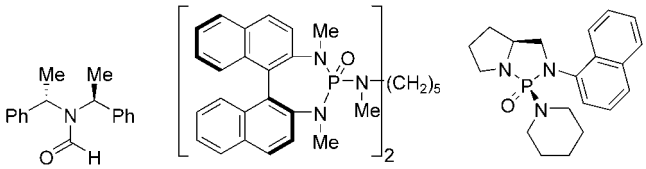
13 14



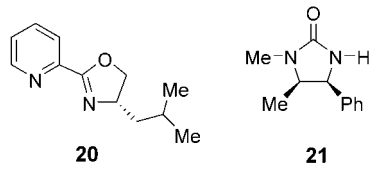
15 16

N-monoxides **15** (R = H, Me) [26] and isoquinoline-*N*-oxide **16**[27] for allylation of aromatic aldehydes with allyltrichlorosilanes. Kočovský found that electron-poor aldehydes afford products with high enantioselectivities and their electron-rich congeners give adducts with low *ee* values. An arene–arene interaction of the electron-rich catalyst with the incoming aldehydes could be the main factor that determines the facial enantioselectivity. Furthermore, the Lewis base catalyzed allylation is strictly limited to aromatic aldehydes since aliphatic aldehydes produce mainly α-chlorosilyl ethers.

Based on the original observation by Kobayashi and co-workers that *N*,*N*-dimethylformamide (DMF) promotes the allylation of aldehydes with allylic trichlorosilanes,[28] Iseki et al. employed chiral formamide **17** for enantioselective



17 18 19



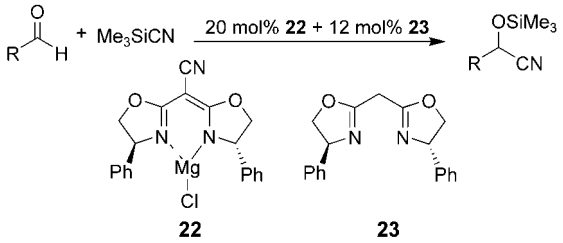
20 21

additions.[29] A stoichiometric amount of **17** catalyzed the allylation of aldehydes to afford the adducts in high yields and modest selectivities. The addition of hexamethyl phosphoramide (HMPA) was beneficial for both the reaction rate and the selectivity, and led to homoallylic alcohol in up to 98% *ee*. Denmark and co-workers pioneered an approach in which dimeric chiral phosphoramides such as **18** (5 mol%) were used as Lewis base catalysts for allylations of aromatic and unsaturated aldehydes in high yields and selectivities.[30] Moreover, the addition of (*E*)- and (*Z*)-crotyltrichlorosilanes gave excellent diastereoselectivity and enantioselectivity (up to 99:1 d.r. and 96% *ee*). Similarly, Iseki and co-workers reported that the chiral phosphoramide **19**, which is derived from (*S*)-proline, also lead to good enantioselectivity; however, catalytic loadings require exceedingly long reaction time.[31] Other chiral Lewis bases such as oxazoline **20**[32] and urea **21**[33] have been developed as promoters for these allylations; however, only modest enantioselectivities have been reported.

3.3. Catalytic Asymmetric Cyanation

3.3.1. Cyanosilylation, Cyanophosphorylation, Cyanoformylation

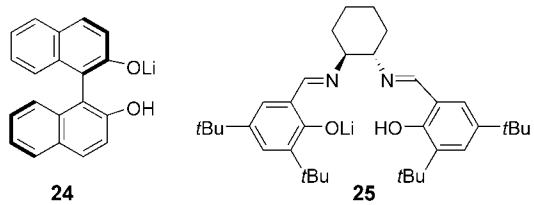
It is well known that the addition of trimethylsilyl cyanide (TMSCN) to carbonyl compounds is catalyzed by Lewis acids or Lewis bases to afford silylated cyanohydrins, which can easily be converted into various important building blocks such as α-hydroxy (or amino) carbonyl derivatives, and β-aminoalcohols.[34] Corey and co-workers reported that the simultaneous use of magnesium bisoxazoline complex **22** and uncomplexed bisoxazoline **23** are a catalytically active system for the asymmetric addition of TMSCN to aldehydes.[35] The magnesium complex **22** behaves as a chiral Lewis acid to activate aldehydes, while bisoxazoline **23** acts as a Lewis base to activate the hydrogen cyanide, which is produced in situ from TMSCN and moisture (Scheme 9). This double activation of both reactants is a key feature in most enantioselective, metal-catalyzed, asymmetric cyanosilylations.



22 23

Scheme 9. Catalytic asymmetric cyanosilylation of carbonyl compounds. R = *n*-alkyl, *t*Bu, cyclohexyl, alkenyl, Ph.

Kagan and co-workers described the addition of TMSCN to aldehydes catalyzed by chiral, nucleophilic monolithium salts **24** and **25**.[36] The reaction is believed to proceed through

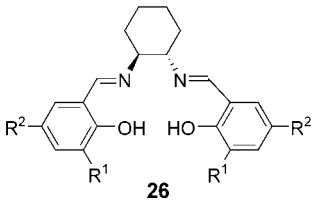


24 25

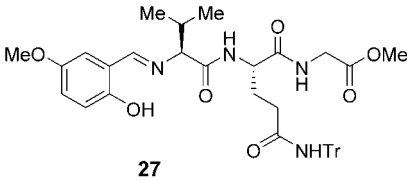
hypervalent silicon intermediates, which can further activate the aldehydes to yield enantiomerically enriched cyanohydrins with up to 97% *ee*.

Chiral titanium complexes catalyze the asymmetric addition of TMSCN to a wide range of carbonyl compounds. Belokon', North, and co-workers studied the titanium complexes of salen ligand **26** (R^1 = H, *t*Bu, Cl; R^2 = H, Me, *t*Bu,

 © 2004 Wiley-VCH Verlag GmbH & Co. KGaA, Weinheim



26



27

OMe, Cl) as catalysts for asymmetric cyanosilylation of aldehydes and ketones.[37] It was found that the bimetallic complex is the actual precatalyst, which simultaneously activates both the carbonyl compound and the TMSCN (Figure 2). The key step is the intramolecular transfer of

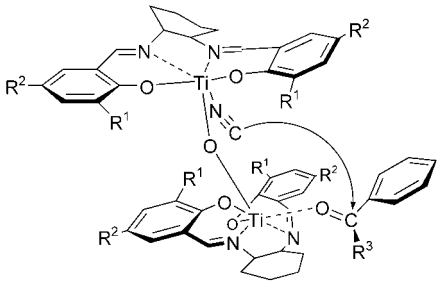
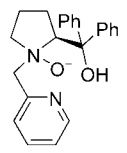


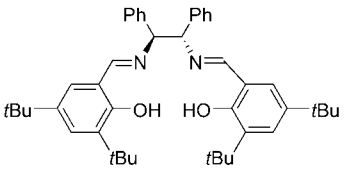
Figure 2. Transition-state model for asymmetric cyanosilylation according to Belokon' and North. R^3 = H, Me, Et, *i*Pr, *t*Bu.

cyanide to the coordinated aldehydes from the *Re* face, thus leading predominantly to the formation of one enantiomer. Snapper, Hoveyda, and co-workers developed peptidic Schiff base ligand **27** (Tr = trityl) complexed to aluminum as a catalyst for the asymmetric cyanation of ketones.[38] As in the case of the titanium-catalyzed Strecker reaction mediated by peptide ligands (see Section 3.3.3), the Al–**27** complex is likely to serve as a bifunctional catalyst that promotes appreciable reactivity and high enantioselectivity.

Feng and Jiang disclosed a bifunctional system for enantioselective cyanosilylation of ketones: A titanium center plays the role of a Lewis acid and the dipolar *N*-oxide **28** acts as a Lewis base to activate the ketone and the TMSCN, respectively.[39a] In this case the reaction gave



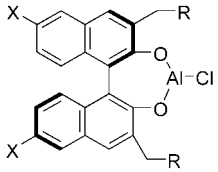
28



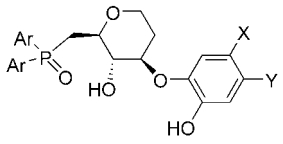
29

cyanohydrin trimethylsilyl ethers with 25–69 % *ee* (20 mol % catalyst). The authors developed an even better combination for double activation, in which electrophiles and nucleophiles are activated by as little as 1 mol % of an achiral Lewis base (*N*,*N*-dimethylaniline *N*-oxide) and 2 mol % of a chiral Lewis acid (Schiff base **29**–titanium complex).[39b]

Shibasaki and co-workers described a new bifunctional catalyst **30a** containing a Lewis acid and a Lewis base for asymmetric cyanosilylation of aldehydes.[40] Cyanohydrins were obtained with 83–98 % *ee*. A limitation of this catalyst system is the need for slow addition of TMSCN for optimal enantioselectivity. Nájera and co-workers prepared catalyst **31** in which the phosphane oxide groups of **30a** were replaced by diethylamino groups as a Lewis base to activate the nucleophile.[41] Complex **31** was found to catalyze the



30 **a** R = $P(O)Ph_2$, X = H
b R = $P(O)(o\text{-Tol})_2$, X = H
c R = $P(O)Ph_2$, X = Br
31 R = NEt_2, X = H



32 **a** X = Y = H, Ar = Ph
b X = COPh, Y = H, Ar = Ph
c X = Y = F, Ar = *p*-MeC_6H_4
d X = Y = F, Ar = Ph

asymmetric addition of TMSCN to aldehydes to give cyanohydrins with modest to excellent enantioselectivities. In contrast to the system of Shibasaki and co-workers, all the reagents could be added at the beginning of the reaction, and the binol ligand could be recovered and reused by a simple acid workup. Both the Shibasaki and Nájera groups employed cyanoformates as alternative reagents for the cyanation,[41b,42] and Nájera and co-workers also reported the first cyanophosphorylation by means of diethyl cyanophosphonate for the enantioselective synthesis of cyanohydrins and derivatives.[41c]

Shibasaki and co-workers extended the concept of joint Lewis acid/Lewis base catalysts to systems other than binol: carbohydrate-derived ligands **32** were synthesized and complexed to different metals.[43] The corresponding titanium complexes were found to be good catalysts. For example, 10 mol % of the titanium complex of **32a** was required to convert several aromatic and aliphatic ketones into *R* cyanohydrins with 69–95 % *ee*. Mechanistic studies suggest that the key features of transition-state structure **A** (Figure 3) are the simultaneous activation of both reaction components through the combined Lewis acid/Lewis base activity of the catalyst and the transfer of cyanide directly from activated TMSCN. Interestingly, the corresponding gadolinium complex of ligand **32a** (the same enantiomer) was used to synthesize the enantiomeric *S* cyanohydrins with 62–97 % *ee*. Shibasaki and co-workers proposed the transition state **B** (Figure 3) to explain this reactivity and selectivity. In this structure, two of the ligands behave as tridentate ligands and the bridging ligand is tetracoordinate. The cyanide ion is activated by coordination to one of the metal ions rather than by the Lewis basic phosphane oxides.

 © 2004 Wiley-VCH Verlag GmbH & Co. KGaA, Weinheim

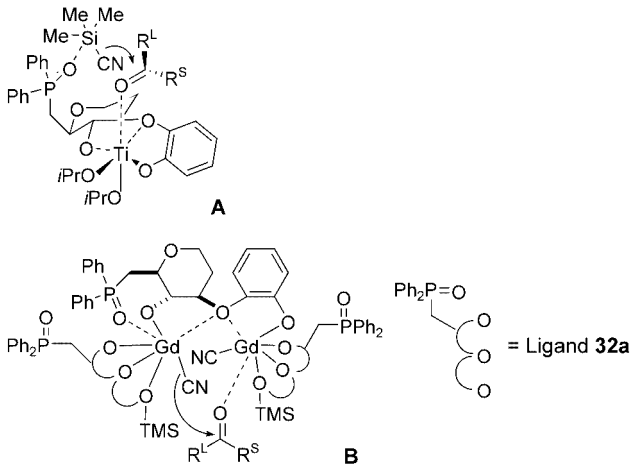
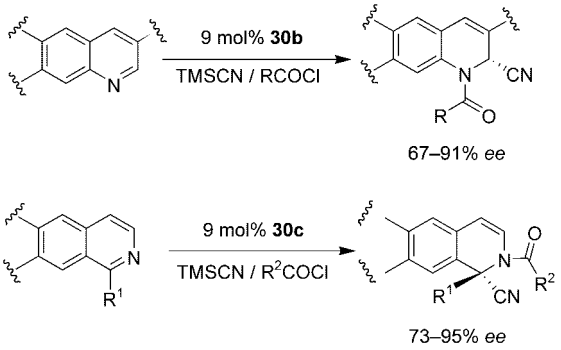


Figure 3. Postulated transition states for Ti–**32a** system and Gd–**32a** system.

3.3.2. *Reissert-Type Reactions*

The asymmetric cyanosilylation of imines (Reissert- and Strecker-type reactions) is of interest as it allows access to biologically important alkaloids and to chiral α-amino acids, respectively. Shibasaki and co-workers developed the first asymmetric Reissert-type reactions in the presence of the bifunctional catalysts **30a–c**.[44] The desired *N*-acylated Reissert products are obtained from quinolines or isoquinolines in high yields (up to 100%) and with high enantioselectivities (up to 95% *ee*) (Scheme 10). Control experiments indicate

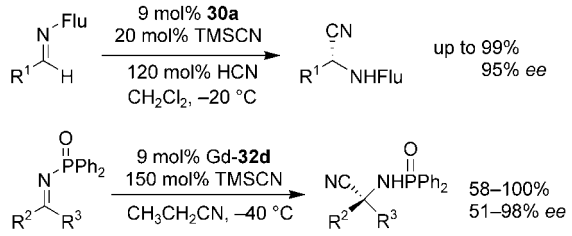


Scheme 10. Catalytic asymmetric Reissert-type reactions according to Shibasaki's group.

that the reactions proceed through dual activation of the acyl quinolinium/acyl isoquinolinium and TMSCN by the Lewis acid and the Lewis base, respectively, of the catalysts.

3.3.3. *Strecker-Type Reactions*

The interesting extension of this concept to the asymmetric Strecker reaction was also reported by Shibasaki and co-workers.[45] The reactions proceed well with various imines, including *N*-aldimines, α,β-unsaturated imines, and ketoimines. Thus, application of the bifunctional catalyst **30a** and the gadolinium complex of ligand **32d** lead to highly asymmetric Strecker-type reactions in good to excellent yields and enantioselectivities (Scheme 11). The products can be successfully converted into the pure amino acids and their derivatives by subsequent cleavage of the protecting groups.



Scheme 11. Catalytic asymmetric Strecker-type reactions according to Shibasaki's group. Flu = 9-fluorenyl.

Inspired by this new concept, Vallée and co-workers synthesized the heterobimetallic catalyst Li[Sc{(*R*)-binol}$_2$] for the enantioselective addition of TMSCN to several imines with up to 95% *ee*.[46] The peptide-based titanium complexes described by Snapper, Hoveyda, and co-workers for the asymmetric cyanation of ketones (see Section 3.3.1.) were first developed as catalysts in the Strecker reaction and led to high enantioselectivities (up to >99%).[47] In a mechanistic study, the authors came to the conclusion that these non-C_2-symmetric catalysts are likely to operate in a bifunctional fashion (Figure 4).[47c]

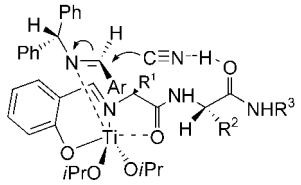


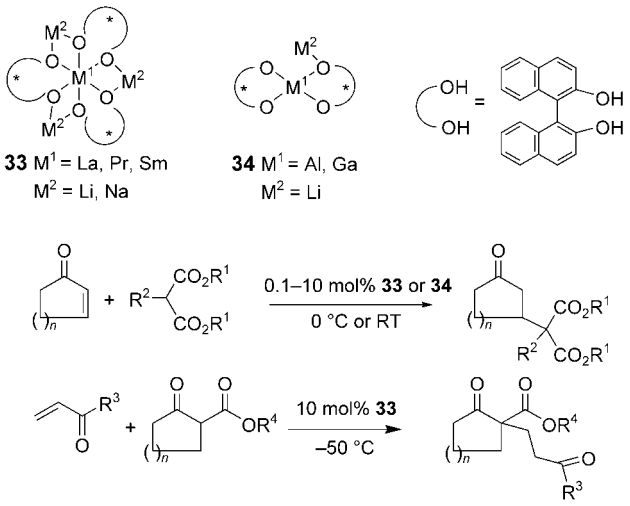
Figure 4. Mechanistic model of enantioselective Ti-catalyzed Strecker reaction.

4. Catalytic Asymmetric 1,4-Addition Reactions

The conjugate addition to acceptor-substituted olefins is a fundamental carbon–carbon bond-forming reaction, which is catalyzed not only by Brønsted bases, but also by a number of metal compounds.[48] The use of chiral multifunctional catalysts containing one Brønsted base center and one Lewis acid center also allows high efficiency and selectivity in conjugate addition reactions. The development by Shibasaki and co-workers of heterobimetallic complexes in which each metal center plays a different role in the enantiodifferentiation represents a real breakthrough in enantioselective conjugate addition reactions. The reaction is promoted mainly by the Brønsted basicity of the catalysts, whereas the Lewis acidity assists the catalysis by controlling the position of the electrophiles as well as activating them. This has been reviewed extensively by Shibasaki and co-workers[3g,40c] and it is briefly treated in this section. Two complexes have been developed, the tris-binol rare-earth complexes **33** and the bis-

 © 2004 Wiley-VCH Verlag GmbH & Co. KGaA, Weinheim

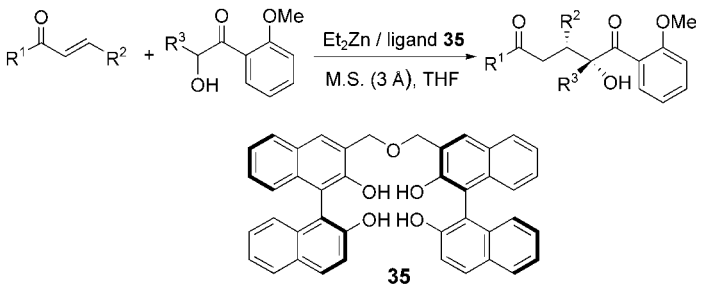
binol complexes **34** with Group IIIA metals.[49] These catalysts currently define the state of the art for the formation of tertiary stereocenters by Michael reactions at room temperature in high yields and with excellent selectivities up to 99% *ee* (Scheme 12). The reaction has been performed in the presence of only 0.1 mol% of **34** (M^1 = Al) at room temperature for the large-scale generation of enantiomerically pure Michael adduct.[49e] A catalytic enantioselective Michael addition of α-nitroesters to α,β-unsaturated ketones in the presence of Al–Li–binol complex **34** was reported by Feringa and co-workers. The enantioselectivity proved to be temperature- and solvent-dependent. Michael adducts were obtained in up to 80% *ee*.[50]



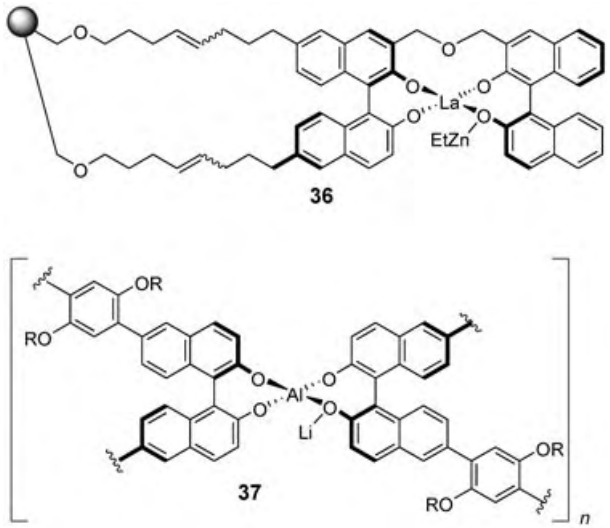
Scheme 12. Catalytic asymmetric Michael additions according to Shibasaki and co-workers. R^1 = Me, Et, benzyl; R^2 = H, Me; R^3 = Me, OMe, OEt; R^4 = Et.

Later, Shibasaki and co-workers developed La complexes with ligand **35** (linked binol), which combine all the desired attributes.[51] This type of catalyst is almost optimal for the synthesis of tertiary stereocenters with regard to stereoselectivity, handling, and reuse; however, these properties do not extend to the formation of quaternary stereocenters. Recently, the same group showed that by complexing ligand **35** to zinc rather than to lanthanum, it is possible to improve the selectivities in 1,4-additions to α-hydroxyketones.[52] Interestingly, a 2:1 complex (Et_2Zn/**35**) was effective for 1,4-addition of β-unsubstituted enones and indenones, and a 4:1 complex (in the presence of 3-Å molecular sieves) was developed to widen the substrate scope and was effective for various β-substituted enones, affording products in up to 99% yield and with 99% *ee*. With the latter complex, ligand loading for the β-unsubstituted enone was decreased to as little as 0.01 mol% (Scheme 13).

Polymer-supported linked-binol–La complex **36** was also synthesized in order to immobilize catalysts with two binol units, which led to products with moderate to good enantioselectivity (up to 78% *ee*).[53] Sasai and co-workers also immobilized poly(Al–Li–binol) catalyst **37**, which led to

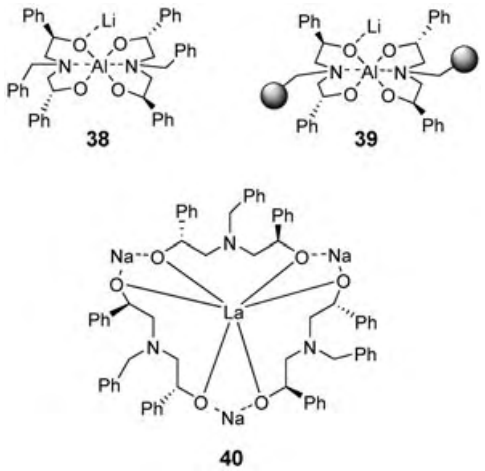


Scheme 13. Catalytic asymmetric Michael reactions (α-hydroxyketones as Michael donors; R^1 = alkyl, aryl; R^2 = H, alkyl, aryl; R^3 = H, Me); the reaction was also carried out with cyclic ketones and indenones.



Michael adducts with high enantioselectivity (93% *ee* for 2-(3-oxo-cyclohexyl)malonic acid dibenzyl ester).[54] Nevertheless, it is clear that the polymer-supported approach is currently unsatisfactory, especially when compared with unsupported catalysts.

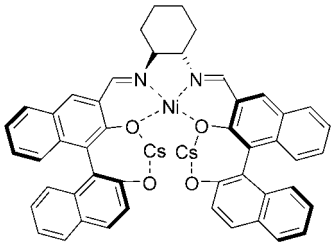
In the meantime, other bifunctional catalyst systems have been discovered. Sundararajan and co-workers reported an asymmetric Michael addition of a variety of malonates to enones in the presence of the aluminium–lithium complex **38**



 © 2004 Wiley-VCH Verlag GmbH & Co. KGaA, Weinheim

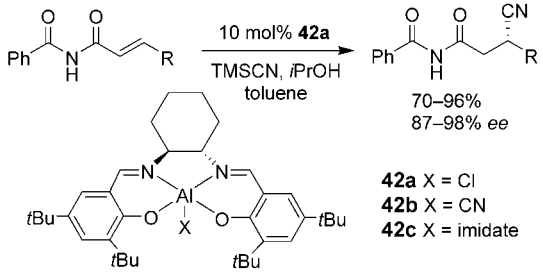
with a C_2-symmetrical chiral aminodiol ligand. The reaction gave the products in good yields and proceeded more rapidly and with comparable to or better enantioselectivities than those in the presence of binol complexes.[55a] The polymer-anchored chiral heterobimetallic catalyst **39** also promotes the Michael addition of several donors in high yields, but with only moderate enantioselectivities.[55b] A lanthanum–sodium–aminodiol heterobimetallic complex **40** was found to be equally efficient.[56]

Kozlowski and co-workers synthesized a binol–salen bimetallic complex that incorporates two chiral binol moieties.[57] Several bifunctional complexes, in which the Lewis acid and Brønsted base portions can be altered independently, were efficient catalysts in the Michael addition of benzyl malonate to cyclohex-2-enone. In particular, the Ni–Cs_2–binol–salen complex **41** exhibits enantioselectivities of up to 90% *ee*.



41

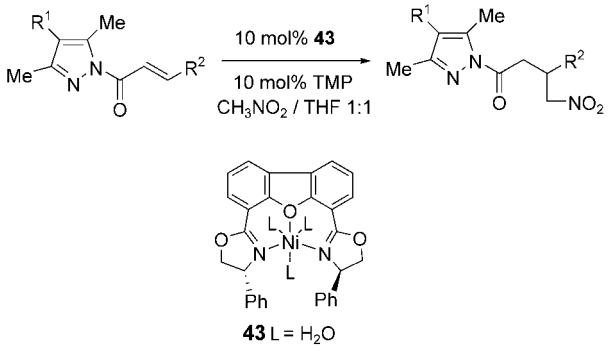
Jacobsen's group provided the first example of asymmetric catalysis in the conjugate addition reactions of cyanide.[58] Chiral salen–aluminum complex **42a** was used as a catalyst, and generally good results were obtained with α,β-unsaturated imide substrates (Scheme 14). Preliminary data show



Scheme 14. Conjugate addition of TMSCN to α,β-unsaturated imides. R = alkyl, CH_2OCH_2Ph.

that a bimetallic, dual-activation mechanism is involved. Upon addition of TMSCN, **42a** is converted into a new complex **42b**, and the addition of imide to this complex results in the formation of a new salen–Al–imidate complex **42c**. Subsequently, the cyanide group is transferred from **42b** to the electrophilic imidate complex **42c**.

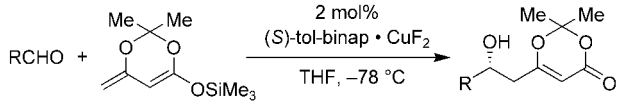
Itoh and Kanemasa developed a new method for the enantioselective Michael addition of nitromethane under catalytic dual activation: The α,β-unsaturated carbonyl acceptors and nitromethane are effectively activated by mixtures of chiral Lewis acid complex **43** and an amine catalyst, respectively.[59] High yields (up to 97%) and enantioselectivities (up to 98% *ee*) were attained (Scheme 15).



Scheme 15. Catalytic asymmetric Michael additions of nitromethane to α,β-unsaturated carbonyl compounds. R^1 = H, Br, I; R^2 = alkyl, cyclohexyl, alkenyl, aryl, MeOOC; TMP = 2,2,6,6-tetramethylpiperidine.

5. Catalytic Asymmetric Aldol Reactions

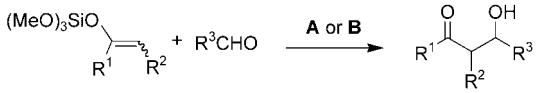
The aldol reaction is generally regarded as one of the most versatile carbon–carbon bond-forming reactions. Many efforts have been directed towards the development of catalytic asymmetric aldol reactions. Carreira and co-workers have shown the utility of chiral copper(II) fluoride complexes as catalysts in the Mukaiyama-type aldol reaction (Scheme 16).[60] Aromatic and α,β-unsaturated aldehydes



Scheme 16. Catalytic aldol reaction of silyl dienolates with aldehydes.

furnished aldol adducts with up to 95% *ee* in 98% yield. A mechanistic study supported the fact that the chiral metal fluoride complex generates a metalloenolate intermediate, which undergoes the enantioselective aldol reaction.

Yamamoto and co-workers described the asymmetric Mukaiyama-type aldol reaction with trimethoxysilyl enol ethers catalyzed by binap–silver(I) fluoride complexes (Scheme 17).[61] Interestingly, high *syn*- and enantioselectivities were attained for both *E* and *Z* silyl enol ethers (> 99:1 *syn*/*anti* and 97% *ee*) with catalyst **A**. With catalyst system **B**,



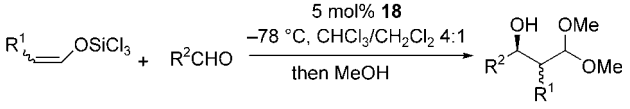
A: 10 mol% (*R*)-*p*-tol-binap • AgF
B: 2 mol% (*R*)-*p*-tol-binap • AgOTf + KF + [18]crown-6

Scheme 17. Catalytic asymmetric aldol reactions of trimethoxysilyl enol ethers with aldehydes. R^1 = H, *t*Bu; R^2 = H, Me; R^3 = aryl, (*E*)-PhCH=CH; $PhCH_2CH_2$. The reaction was also carried out with cyclic enol ethers. Tf = trifluoromethanesulfonyl.

 © 2004 Wiley-VCH Verlag GmbH & Co. KGaA, Weinheim

the *E* silyl enol ether gives the *anti* product, whereas the *Z* silyl enol ether affords the *syn* adduct with high selectivity. These catalyst systems are likely to behave as bifunctional chiral catalysts for asymmetric aldol reactions in which both electrophiles and nucleophiles are activated separately.

The dimeric chiral phosphoramides developed by Denmark and co-workers (see Section 3.2) were also used in a Lewis base catalyzed asymmetric aldol addition, which involves simultaneous activation of the nucleophile and the electrophile within the coordination sphere of the metal center (Scheme 18).[62] Geometrically defined trichlorosilyl



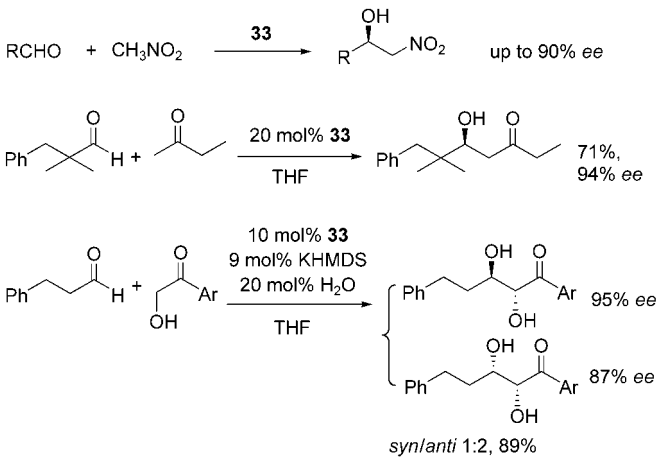
Scheme 18. Chiral Lewis base catalyzed asymmetric aldol reactions of trichlorosilyl enol ethers with aldehydes. R^1 = Me, *n*Pent.

enol ethers of aldehydes undergo high-yielding, diastereoselective additions (*Z* silyl enol ethers afford *syn* products, *E* silyl enol ethers give *anti* adducts) to a wide range of aldehyde acceptors with good, albeit highly variable enantioselectivity.

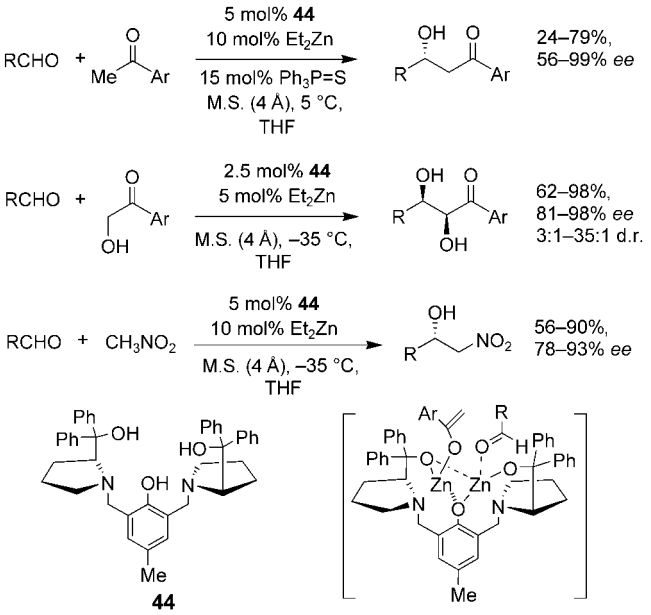
Shibasaki and co-workers first reported a catalytic asymmetric nitroaldol (Henry) reaction in 1992.[63] The chiral heterobimetallic complex $Li_3[La\{(S)\text{-binol}\}_3]$ (**33**) was developed as an efficient asymmetric catalyst for direct aldol reactions of aldehydes and unmodified ketones (Scheme 19). Aldol products are obtained in high yield and with high enantioselectivity.[64] The catalyst **33** also works well for the direct aldol reaction of aldehydes with α-hydroxyketones to provide 1,2-dihydroxyketones with high enantiomeric excesses.[65] The chiral complex [Et_2Zn–**35**] with as little as 0.1 mol% of ligand **35** and 0.4 mol% of Et_2Zn, in the presence of 3-Å molecular sieves efficiently promoted direct aldol reactions to afford diols in good yields (up to 97%) and with high stereoselectivities (up to 98:2 d.r. and 97% *ee*) [66]

Trost and co-workers introduced a novel type of double-activation catalyst, the dinuclear zinc complex with chiral ligand **44**.[67] This complex was successfully applied in enantioselective direct aldol reactions with various aldehyde electrophiles and ketone and nitromethane nucleophiles (Scheme 20). The authors proposed that the role of two proximal zinc species may be to provide both a zinc center to form the requisite enolate and a second zinc center to function as a Lewis acid in the coordination of the aldehyde.

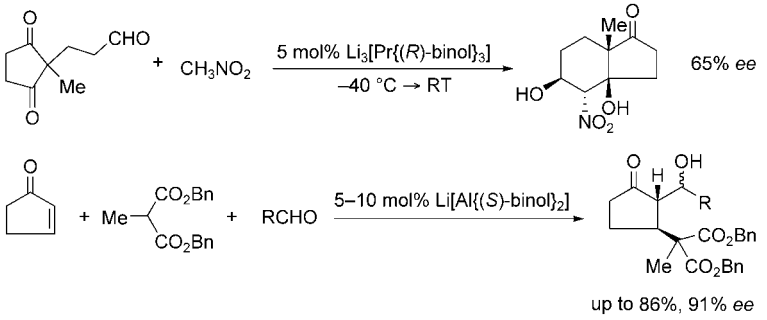
Shibasaki and co-workers employed their multifunctional catalysts for asymmetric tandem inter- and intramolecular nitroaldol reactions and tandem Michael–aldol reactions.[68] Treatment of aldehydes with nitromethane and 5 mol% of **33** (M^1 = Pr, M^2 = Li) gave tandem-reaction products with 65% *ee* (Scheme 21). It was proposed that the praseodymium center acts as a Lewis acid and activates the aldehyde. The Li naphthoxide portion then functions as a Brønsted base and



Scheme 19. $Li_3[La(S\text{-BINOL})_3]$-catalyzed asymmetric aldol reactions according to Shibasaki and co-workers. R = *i*Pr, cyclohexyl, $PhCH_2CH_2$; KHMDS = potassium bis(trimethylsilyl)amide.



Scheme 20. Chiral dinuclear zinc catalyst in asymmetric aldol reactions.

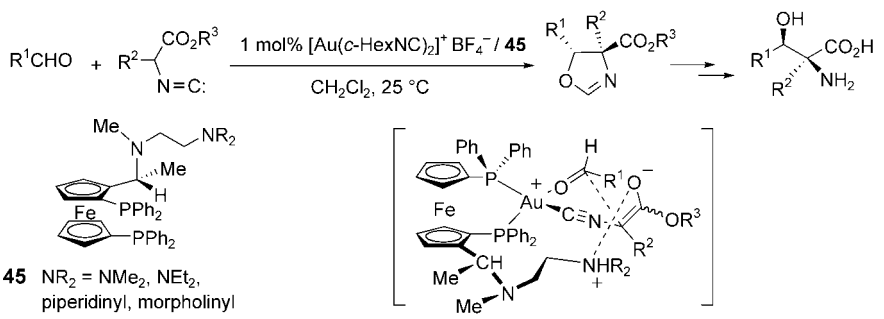


Scheme 21. Catalyzed asymmetric tandem reactions according to Shibasaki's group. R = Ph, $PhCH_2CH_2$, $(CH_2)_5COOMe$.

 © 2004 Wiley-VCH Verlag GmbH & Co. KGaA, Weinheim

deprotonates the nitromethane. Coordination of the aldehyde in the presence of a chiral template and delivery of the nucleophile by the bridging lithium complex render the reaction intramolecular, and thus highly enantioselective. Transfer of a proton from the ligand to the new alkoxide regenerates the catalyst. Selective attack on the diketone moiety is thought to be controlled solely by the configuration at the new hydroxy functionality.[68a] Furthermore, an interesting extension towards a tandem Michael–aldol addition with the multifunctional catalyst **34** (Scheme 21, $M^1 = Al$, $M^2 = Li$) was reported by the same group. The initial lanthanide complexes formed highly reactive enolates that underwent rapid pseudo-intramolecular protonation, thus prohibiting reaction with an external electrophile. It was thought that an aluminum enolate would be more stable and undergo much slower protonation. Indeed, the extended life of the enolate allows the aldol reaction, which proceeds with excellent regiocontrol and considerable selectivity at the new hydroxy group.[68b,c]

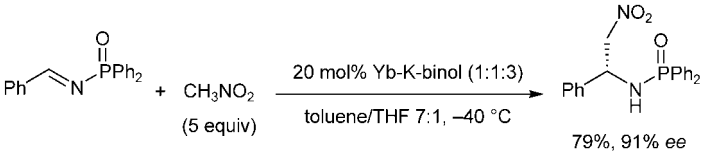
Ito and co-workers reported that the aldol-type reaction of isocyanoacetate with aldehydes is catalyzed by gold complexes of chiral ferrocenyl phosphane ligand **45**, which bears a tertiary amino group at the terminal position of the pendant chain, to give optically active 5-alkyl 2-oxazoline-4-carboxylates with high enantio- and diastereoselectivity (Scheme 22).[3a,69] Both enantio- and diastereoselectivity are remarkably dependant on the length of the tether and the structure of the terminal amino group of the ligand which indicates that the amino group plays a key role in the stereoselectivity. A coordinative interaction of both isocyanide and aldehyde to the gold metal in the transition state was suggested. The terminal amino group of the ligand **45** abstracts one of α-methylene protons of gold-coordinated isocyanoacetate to form an ion pair between the enolate anion and the ammonium cation. Thus, the cooperative interaction ensures a favorable arrangement of the enolate and aldehyde around the gold center in the stereodifferentiating transition state. This method was extended further to the aldol-type condensation of isocyanoacetamide with aldehydes and α-ketoesters,[70a,b] and of (isocyanomethyl)phosphonates with aldehydes;[70c,d] both are useful reactions for the synthesis of different α-aminoesters. Furthermore, the silver-catalyzed asymmetric aldol reaction of isocyanoacetate is also possible when the isocyanoacetate is kept at low concentration throughout the reaction.[71]



Scheme 22. Gold-catalyzed asymmetric aldol reaction of isocyanoacetates with aldehydes. R^1 = alkyl, aryl, alkenyl, ferrocenyl; R^2 = H; R^3 = Me, Et; *c*-HexNC = isocyanocyclohexyl.

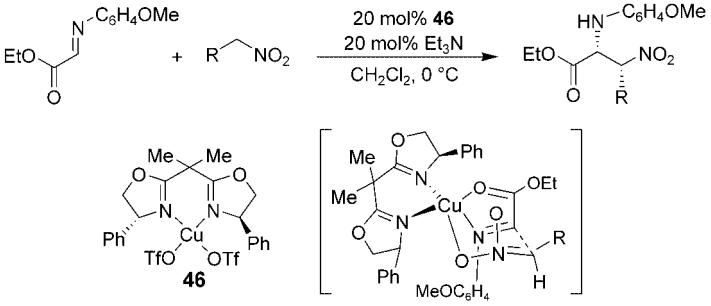
6. Catalytic Asymmetric Mannich-Type Reactions

Catalytic, asymmetric versions of Lewis acid mediated Mannich-type reactions provide useful routes for the synthesis of optically active α- and β-aminoketones or -esters, which are versatile chiral building blocks for the preparation of many nitrogen-containing biologically important compounds. Shibasaki and co-workers developed a catalytic, enantioselective nitro-Mannich-type reaction promoted by the heterobimetallic complex containing both Lewis acid and Brønsted base functionalities (Yb/K/binol 1:1:3) (Scheme 23).[72]



Scheme 23. Nitro-Mannich-type reaction promoted by the Yb–K–binol complex.

Further to this work, Jørgensen and co-workers presented a new and significantly simplified approach to the catalytic stereoselective nitro-Mannich reaction of an *N*-protected α-iminoester with nitro compounds (Scheme 24).[73] The reaction was performed in the presence of bisoxazoline–copper(II) triflate complex **46** and triethylamine at ambient temperature to give β-nitro-α-aminoesters in good yields (38–81%) and with high diastereo- and enantioselectivities (up to 95:5 d.r. and 99% *ee*). The coordination of the nitro group to the copper center facilitates the catalytic deprotonation of the nitro compound with Et_3N to give a cyclohexane-like cyclic

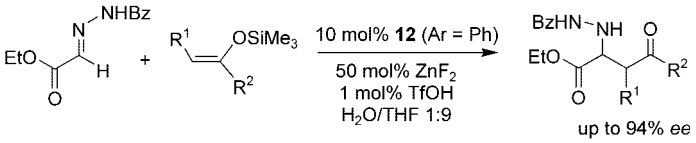


Scheme 24. Nitro-Mannich reaction of iminoesters and nitro compounds according to Jørgensen and co-workers. R = H, Me, Et, pentyl, benzyl, phenyl.

 © 2004 Wiley-VCH Verlag GmbH & Co. KGaA, Weinheim

transition state with additional coordination of the carbonyl group of the electrophile to the copper atom.

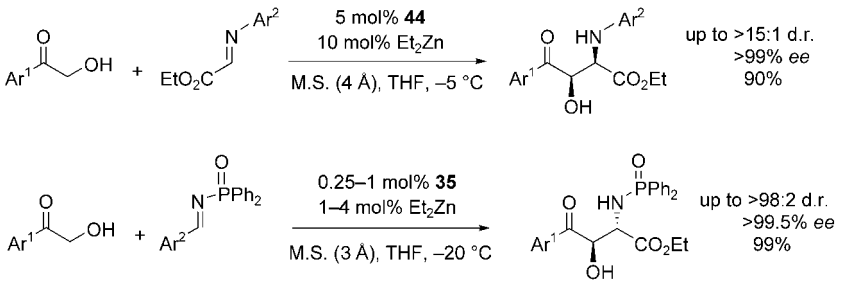
Kobayashi and co-workers reported the catalytic asymmetric Mannich-type reaction of a hydrazonoester with silyl enol ethers in aqueous media with zinc(II) fluoride and chiral diamine ligand **12** (Ar = Ph)(Scheme 25).[74] This reaction



Scheme 25. Catalytic asymmetric Mannich reaction in aqueous media. R^1 = H, Me; R^2 = Ar, *i*Pr.

proceeds with double activation: the zinc center acts as a Lewis acid to activate the hydrazonoester and the fluoride anion functions as a Lewis base to attack the silicon atom of the ether.

Recently, Shibasaki and co-workers and Trost and Tirrell independently applied their trinuclear **35** and dinuclear **44** catalysts, respectively, in asymmetric Mannich-type reactions (Scheme 26).[75,76] Complementary *syn* and *anti* aminoalcohols were obtained in high yields, with stereoselectivities typically >98% *ee*.



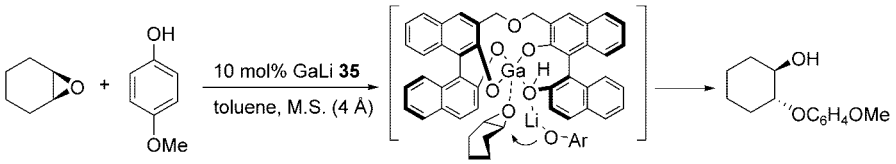
Scheme 26. Direct catalytic asymmetric Mannich-type reactions by Trost and co-workers (top) and Shibasaki and co-workers (bottom).

7. Catalytic Asymmetric Ring Opening of Epoxides

The catalytic ring opening of epoxides has emerged as a powerful method for the asymmetric synthesis of useful chiral 1,2-aminoalcohols, 1,2-diols, and related compounds.[77] The current state of the art for non-enzymatic processes is defined by three catalysts that mediate the delivery of different nucleophiles: heterobimetallic complexes of chiral binol, zirconium complexes of C_3-symmetric trialkanolamine ligands, and chiral salen complexes of chromium.

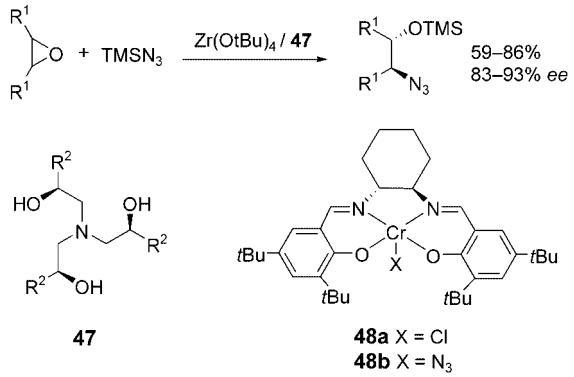
Shibasaki and co-workers applied the multifunctional catalysts to other reactions that benefit from complementary activation and positioning of the electrophile and the nucleophile,[78] such as the catalytic asymmetric ring opening of epoxides with either thiols or phenols.[78g–i] It was found that the heterobimetallic complex derived from gallium and the linked-binol ligand **35** was a more effective catalyst than the unlinked counterpart and led to high yields (up to 72%) and enantioselectivities (up to 91% *ee*) (Scheme 27).[78h,i]

Nugent and co-workers developed zirconium complexes of the C_3-symmetric ligands (+)-(*S*,*S*,*S*)-trialkanolamine **47** for asymmetric ring opening of epoxides with trimethylsilyl azide with up to 93% *ee*,[79] and Jacobsen's group[77b,c] reported enantioselective ring opening of epoxides catalyzed by Cr^{III}– and Co^{III}–salen complexes (Scheme 28). For instance, chiral Cr(III)–salen complexes **48** effectively catalyze the asymmetric ring opening of *meso* epoxides by $TMSN_3$ to give the azido silyl ether products in high yield with high enantiomeric enrichment.[80]



Scheme 27. Catalytic asymmetric ring opening of epoxides by phenols.

Mechanistic studies confirm that the cooperative effect is general in asymmetric epoxide ring opening and that the catalyst plays a dual role, serving both as a Lewis acid to activate the epoxide and as a counterion for the nucleophile.[79c,80c] Bimetallic activation offers an appealing explanation for the mechanism of stereoinduction in the asymmetric ring opening of epoxides, as the two reactants are sandwiched between two chiral catalyst units (Figure 5). Monomeric and dimeric complexes were designed and shown to catalyze the asymmetric ring opening of epoxides with identical enantioselectivity, but the dimeric catalysts exhibit reactivities that are 1–2 orders of magnitude greater than those of the monomeric catalysts. Notably, the enantioselectivity of the catalyst is sensitive to the position of the dimeric tether, therefore implicating



Scheme 28. Asymmetric ring opening of epoxides with trimethylsilyl azide. R^1 = Me. The reaction was also carried out with cyclohexene oxide, cyclopentene oxide, and 7-oxabicyclo[4.1.0]hept-3-ene. R^2 = Me, *t*Bu, cyclohexyl, Ph.

 © 2004 Wiley-VCH Verlag GmbH & Co. KGaA, Weinheim

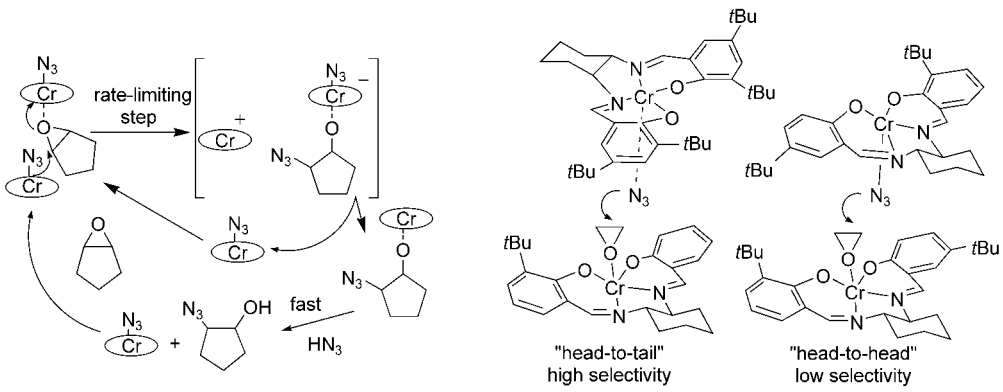
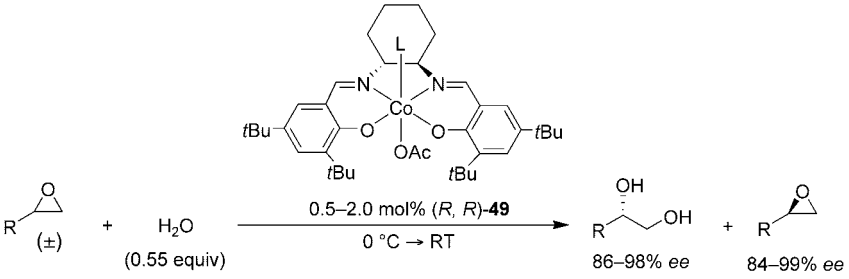


Figure 5. Proposed mechanism and two limiting geometries for the transition state in epoxide ring-opening reactions. Some aromatic substituents are omitted for clarity.

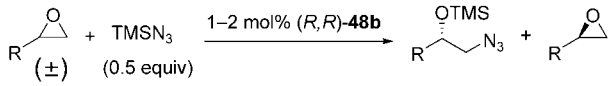
a "head-to-tail" orientation in the stereoselectivity-determining transition state.

The reaction also proceeds with other nucleophiles and catalytic systems: The chiral Co^{III}–salen complex is an effective catalyst for the asymmetric ring-opening of *meso* epoxides with carboxylic acids,[81a] and the chiral complex [(pybox)$YbCl_3$] (pybox = 2,6-bis(oxazoline-2-yl)pyridine) catalyzes the reaction with TMSCN to yield β-trimethylsilyloxynitrile ring-opened products with good enantioselectivities (83–92% *ee*).[81b]



Scheme 30. Catalytic asymmetric hydrolytic kinetic resolution (HKR) of terminal epoxides.

The majority of epoxides (such as terminal epoxides) are in fact chiral and *meso* epoxides constitute a relatively narrow subset of *cis*-disubstituted and tetrasubstituted epoxides. Jacobsen and co-workers disclosed a kinetic resolution of terminal epoxides with Cr^{III}–salen complex **48b** and $TMSN_3$ for accessing β-azidoalcohols based on the asymmetric epoxide-ring-opening reaction involving dual activation of nucleophile and electrophile by two different metal centers (Scheme 29).[82] Several drawbacks, however, limit the utility of this reaction: the maximum yield of 50% based on racemic epoxides, the poor availability of $TMSN_3$, and the heat sensitivity of azides.



Scheme 29. Catalytic asymmetric kinetic resolution of terminal epoxides. R = Me, Et, Bu, CH_2Cl, Bn, cyclohexyl, alkenyl, $CH(OEt)_2$, $CH_2OTBDMS$, CH_2O(1-naphthyl), CH_2CN.

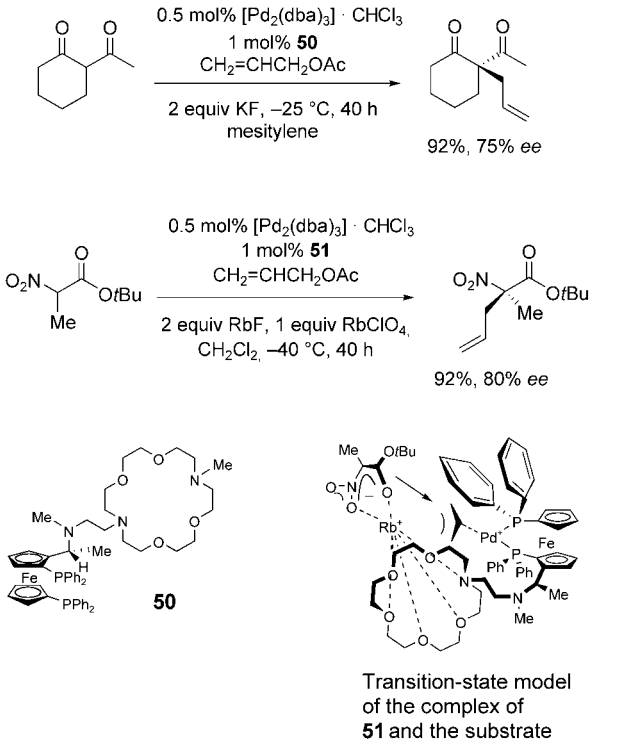
Later, the same group described the hydrolytic kinetic resolution (HKR) of terminal epoxide with cobalt complexes of the same salen framework.[83] HKR is an attractive procedure for the preparation of optically enriched terminal epoxides and 1,2-diols with low catalyst loading (Scheme 30). HKR has proven to be extraordinarily general, not only with all types of terminal epoxides, but also for other classes of nucleophiles.[83c] The reaction followed a second-order dependence on the concentration of catalyst **49**, consistent with a mechanism in which two discrete catalyst molecules cooperate to activate both the electrophile (epoxide) and the nucleophile (water). Thus, Jacobsen and co-workers more recently showed that successful linking of these catalysts as dimeric, polymeric, dendrimeric, or oligomeric frameworks results in catalytic systems with dramatically enhanced reactivity and, in some cases, improved enantioselectivity.[80d,84] However, readily available monomeric catalysts display broad effectiveness for the HKR of terminal epoxides and remain the systems of choice, particularly on a laboratory scale.

8. Other Catalytic Asymmetric Reactions

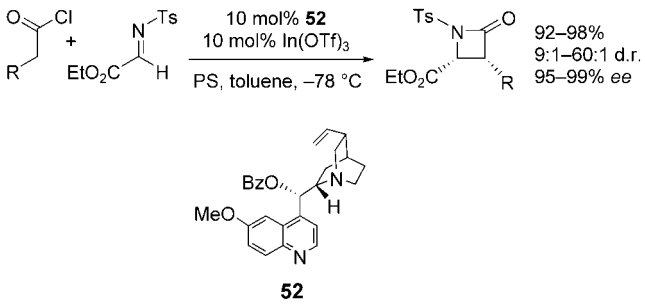
Ito and co-workers described the palladium-catalyzed asymmetric allylation of β-diketone enolates with the aid of a chiral phosphane ligand tethered to an azacrown ether **50**, thus providing double activation: for the electrophile by the palladium center and for the nucleophile by complexation of the cation (Scheme 31).[85] The same group reported the allylation of nitro-group-stabilized carbanions in the presence of ligand **51**, which bears a monoaza[18]crown-6, whose size is complementary to the size of the rubidium cation. Ligand **51** provides high reactivity and selectivity with rubidium enolates of α-nitroesters; a mechanistic model is illustrated in Scheme 31.[86]

Lectka's group developed a bifunctional catalytic system in which a chiral nucleophile **52** is paired with an achiral Lewis acid metal salt for the asymmetric synthesis of β-lactams in high yields and stereoselectivities (Scheme 32).[87]

 © 2004 Wiley-VCH Verlag GmbH & Co. KGaA, Weinheim



Scheme 31. Asymmetric palladium-catalyzed allylations with chiral phosphane ligands bearing an azacrown ether moiety. dba = dibenzylidenacetone.



Scheme 32. Catalytic asymmetric synthesis of β-lactams with benzoylquinine and $In(OTf)_3$ cocatalyst. Ts = *p*-toluenesulfonyl, PS = proton sponge. R = Bn, Ph, CH_2OPh, OPh, OAc, OBn.

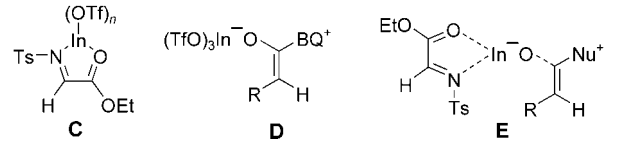


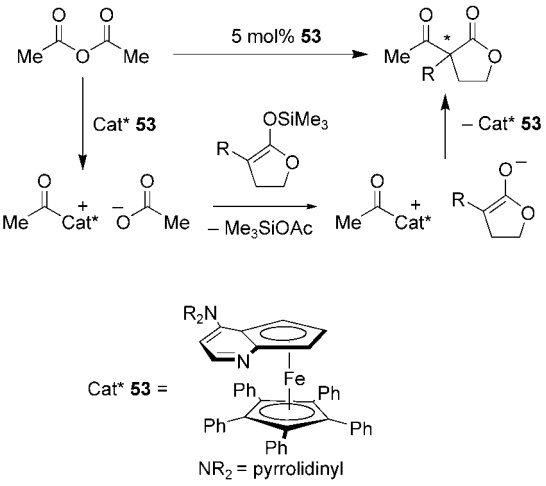
Figure 6. Three mechanistic proposals for the bifunctional Lewis acid/Lewis base catalysts of Lectka and co-workers.

Three plausible mechanistic scenarios account for the dramatic effect of the metal cocatalyst on the reaction (Figure 6): metal-activated imine complex **C**, metal-stabilized zwitterionic enolate **D**, or intermolecular activated complex **E**.

Recently, Fu and Mermerian provided a new process involving a nucleophile-catalyzed intermolecular *C*-acylation of silyl ketene acetals by anhydrides (Scheme 33).[88] The reaction involved dual activation of electrophile and nucleophile: the planar-chiral 4-dimethylaminopyridine (DMAP) derivative catalyst **53** reacts with the anhydride to generate a more-active acylpyridinium ion and an acetate counterion. The Lewis basic acetate then activates the silyl ketene acetal, and the activated components of this new ion pair couple to furnish the desired products in high yield (73–92%) and with high enantioselectivities (76–99% *ee*).

9. Summary and Outlook

Many enzymes are remarkable asymmetric catalysts and promote reactions effectively and selectively. Aspiring to imitate enzymatic synergistic cooperation of multicenters, chemists have succeeded in designing and developing many kinds of multifunctional catalysts for asymmetric synthesis. Several catalytic systems seem to be impressive and promising



Scheme 33. Catalytic enantioselective intermolecular C-acylation of silyl ketene acetals. R = aryl.

(such as CBS reduction, aminoalcohol-mediated addition of dialkylzinc, Shibasaki's hetero- and homobimetallic catalysts, Jacobsen's metal–salen complexes, and Trost's chiral semi-azacrown Zn complex). Despite these excellent developments, there is still a great demand for new multifunctional catalysts, as many organic transformations are still only effective with stoichiometric amounts of chiral reagents. Furthermore, no satisfactory system exists for multicomponent reactions. The use of multifunctional catalysts may overcome these limitations, and further development will pave the way for subsequent industrial application.

Received: October 9, 2003

 © 2004 Wiley-VCH Verlag GmbH & Co. KGaA, Weinheim

[1] a) *Comprehensive Asymmetric Catalysis* (Eds.: E. N. Jacobsen, A. Pfaltz, H. Yamamoto), Springer, Berlin, **1999**; b) *Catalytic Asymmetric Synthesis*, 2nd ed. (Ed.: I. Ojima), Wiley-VCH, Weinheim, **2000**.
[2] S. Woodward, *Tetrahedron* **2002**, *58*, 1017 – 1050.
[3] a) M. Sawamura, Y. Ito, *Chem. Rev.* **1992**, *92*, 857 – 871; b) H. Steinhagen, G. Helmchen, *Angew. Chem.* **1996**, *108*, 2489 – 2492; *Angew. Chem. Int. Ed. Engl.* **1996**, *35*, 2339 – 2342; c) M. Shibasaki, H. Sasai, T. Arai, *Angew. Chem.* **1997**, *109*, 1290 – 1310; *Angew. Chem. Int. Ed. Engl.* **1997**, *36*, 1236 – 1256; d) E. K. van den Beuken, B. L. Feringa, *Tetrahedron* **1998**, *54*, 12985 – 13011; e) G. J. Rowlands, *Tetrahedron* **2001**, *57*, 1865 – 1882; f) H. Gröger, *Chem. Eur. J.* **2001**, *7*, 5246 – 5251; g) M. Shibasaki, N. Yoshikawa, *Chem. Rev.* **2002**, *102*, 2187 – 2209.
[4] a) A. Hirao, S. Itsuno, S. Nakahama, N. Yamazaki, *J. Chem. Soc. Chem. Commun.* **1981**, 315 – 317; b) S. Itsuno, A. Hirao, S. Nakahama, N. Yamazaki, *J. Chem. Soc. Perkin Trans. 1* **1983**, 1673 – 1676; c) S. Itsuno, K. Ito, A. Hirao, S. Nakahama, *J. Chem. Soc. Chem. Commun.* **1983**, 469 – 470.
[5] a) E. J. Corey, R. K. Bakshi, S. Shibata, *J. Am. Chem. Soc.* **1987**, *109*, 5551 – 5553; b) E. J. Corey, C. J. Helal, *Angew. Chem.* **1998**, *110*, 2092 – 2118; *Angew. Chem. Int. Ed.* **1998**, *37*, 1986 – 2012, and references therein.
[6] M. P. Sibi, G. R. Cook, P. Liu, *Tetrahedron Lett.* **1999**, *40*, 2477 – 2480.
[7] a) J. M. Brunel, O. Pardigon, B. Faure, G. Buono, *J. Chem. Soc. Chem. Commun.* **1992**, 287 – 288; b) J. M. Brunel, G. Buono, *Synlett* **1996**, 177 – 178; c) J. M. Brunel, O. Chiodi, B. Faure, F. Fotiadu, G. Buono, *J. Organomet. Chem.* **1997**, *529*, 285 – 294.
[8] a) B. Burns, N. P. King, H. Tye, J. R. Studley, M. Gamble, M. Wills, *J. Chem. Soc. Perkin Trans. 1* **1998**, 1027 – 1038; b) G. Buono, O. Chiodi, M. Wills, *Synlett* **1999**, 377 – 388; c) M. Wills, M. Gamble, M. Palmer, A. Smith, J. Studley, J. Kenny, *J. Mol. Catal. A: Chem.* **1999**, *146*, 139 – 148.
[9] R. J. Kell, P. Hodge, P. Snedden, D. Watson, *Org. Biomol. Chem.* **2003**, *1*, 3238 – 3243.
[10] a) M. Kitamura, S. Suga, K. Kawai, R. Noyori, *J. Am. Chem. Soc.* **1986**, *108*, 6071 – 6072; b) R. Noyori, M. Kitamura, *Angew. Chem.* **1990**, *102*, 34 – 54; *Angew. Chem. Int. Ed. Engl.* **1991**, *30*, 49 – 69; c) M. Kitamura, S. Suga, M. Niwa, R. Noyori, *J. Am. Chem. Soc.* **1995**, *117*, 4832 – 4842.
[11] L. Pu, H.-B. Yu, *Chem. Rev.* **2001**, *101*, 757 – 824, and references therein.
[12] a) M. Yamakawa, R. Noyori, *J. Am. Chem. Soc.* **1995**, *117*, 6327 – 6335; b) M. Yamakawa, R. Noyori, *Organometallics* **1999**, *18*, 128 – 133; c) B. Goldfuss, K. N. Houk, *J. Org. Chem.* **1998**, *63*, 8998 – 9006; d) B. Goldfuss, M. Steigelmann, S. I. Khan, K. N. Houk, *J. Org. Chem.* **2000**, *65*, 77 – 82; e) J. Vazquez, M. A. Pericas, F. Maseras, A. Lledos, *J. Org. Chem.* **2000**, *65*, 7303 – 7309; f) M. Panda, P.-W. Phuan, M. C. Kozlowski, *J. Org. Chem.* **2003**, *68*, 564 – 571; g) M. C. Kozlowski, S. L. Dixon, M. Panda, G. Lauri, *J. Am. Chem. Soc.* **2003**, *125*, 6614 – 6615.
[13] a) E. F. DiMauro, M. C. Kozlowski, *Org. Lett.* **2001**, *3*, 3053 – 3056; b) E. F. DiMauro, M. C. Kozlowski, *J. Am. Chem. Soc.* **2002**, *124*, 12668 – 12669; c) E. F. DiMauro, M. C. Kozlowski, *Org. Lett.* **2002**, *4*, 3781 – 3784.
[14] K. Funabashi, M. Jachmann, M. Kanai, M. Shibasaki, *Angew. Chem.* **2003**, *115*, 5647 – 5650; *Angew. Chem. Int. Ed.* **2003**, *42*, 5489 – 5492.
[15] B. L. Pagenkopf, E. M. Carreira, *Tetrahedron Lett.* **1998**, *39*, 9593 – 9596.
[16] T. Ooi, N. Kagoshima, K. Maruoka, *J. Am. Chem. Soc.* **1997**, *119*, 5754 – 5755.
[17] D. R. Gauthier Jr., E. M. Carreira, *Angew. Chem.* **1996**, *108*, 2521 – 2523; *Angew. Chem. Int. Ed. Engl.* **1996**, *35*, 2363 – 2365.
[18] a) A. Yanagisawa, H. Kageyama, Y. Nakatsuka, K. Asakawa, Y. Matsumoto, H. Yamamoto, *Angew. Chem.* **1999**, *111*, 3916 – 3919; *Angew. Chem. Int. Ed.* **1999**, *38*, 3701 – 3703; b) M. Wadamoto, N. Ozasa, A. Yanagisawa, H. Yamamoto, *J. Org. Chem.* **2003**, *68*, 5593 – 5601.
[19] S. Yamasaki, K. Fujii, R. Wada, M. Kanai, M. Shibasaki, *J. Am. Chem. Soc.* **2002**, *124*, 6536 – 6537.
[20] R. O. Duthaler, A. Hafner, *Angew. Chem.* **1997**, *109*, 43 – 45; *Angew. Chem. Int. Ed. Engl.* **1997**, *36*, 43 – 45.
[21] G. K. Friestad, H. Ding, *Angew. Chem.* **2001**, *113*, 4623 – 4625; *Angew. Chem. Int. Ed.* **2001**, *40*, 4491 – 4493.
[22] T. Hamada, K. Manabe, S. Kobayashi, *Angew. Chem.* **2003** *115*, 4057 – 4060; *Angew. Chem. Int. Ed.* **2003**, *42*, 3927 – 3930.
[23] S. E. Denmark, J. Fu, *Chem. Rev.* **2003**, *103*, 2763 – 2794.
[24] M. Nakajima, M. Saito, M. Shiro, S. Hashimoto, *J. Am. Chem. Soc.* **1998**, *120*, 6419 – 6420.
[25] T. Shimada, A. Kina, S. Ikeda, T. Hayashi, *Org. Lett.* **2002**, *4*, 2799 – 2801.
[26] A. V. Malkov, M. Orsini, D. Pernazza, K. W. Muir, V. Langer, P. Meghani, P. Kočovský, *Org. Lett.* **2002**, *4*, 1047 – 1049.
[27] A. V. Malkov, L. Dufkova, L. Farrugia, P. Kočovský, *Angew. Chem.* **2003**, *115*, 3802 – 3805; *Angew. Chem. Int. Ed.* **2003**, *42*, 3674 – 3677.
[28] a) S. Kobayashi, K. Nishio, *Tetrahedron Lett.* **1993**, *34*, 3453 – 3456; b) S. Kobayashi, K. Nishio, *Synthesis* **1994**, 457 – 459; c) S. Kobayashi, K. Nishio, *J. Org. Chem.* **1994**, *59*, 6620 – 6628.
[29] a) K. Iseki, S. Mizuno, Y. Kuroki, Y. Kobayashi, *Tetrahedron Lett.* **1998**, *39*, 2767 – 2770; b) K. Iseki, S. Mizuno, Y. Kuroki, Y. Kobayashi, *Tetrahedron* **1999**, *55*, 977 – 988.
[30] a) S. E. Denmark, J. Fu, *J. Am. Chem. Soc.* **2000**, *122*, 12021 – 12022; b) S. E. Denmark, J. Fu, *J. Am. Chem. Soc.* **2001**, *123*, 9488 – 9489; c) S. E. Denmark, J. Fu, *J. Am. Chem. Soc.* **2003**, *125*, 2208 – 2216; d) S. E. Denmark, J. Fu, *Chem. Commun.* **2003**, 167 – 170.
[31] a) K. Iseki, Y. Kuroki, M. Takahashi, S. Kishimoto, Y. Kobayashi, *Tetrahedron* **1997**, *53*, 3513 – 3526; b) K. Iseki, Y. Kuroki, M. Takahashi, Y. Kobayashi, *Tetrahedron Lett.* **1996**, *37*, 5149 – 5150.
[32] R. M. Angell, A. G. M. Barrett, D. C. Braddock, S. Swallow, B. D. Vickery, *Chem. Commun.* **1997**, 919 – 920.
[33] I. Chataigner, U. Piarulli, C. Gennari, *Tetrahedron Lett.* **1999**, *40*, 3633 – 3634.
[34] a) M. North, *Tetrahedron: Asymmetry* **2003**, *14*, 147 – 176, and references therein.; b) J.-M. Brunel, I. P. Holmes, *Angew. Chem.* **2004**, *116*, 2810 – 2837; *Angew. Chem. Int. Ed.* **2004**, *43*, 2752 – 2778.
[35] E. J. Corey, Z. Wang, *Tetrahedron Lett.* **1993**, *34*, 4001 – 4004.
[36] a) I. P. Holmes, H. B. Kagan, *Tetrahedron Lett.* **2000**, *41*, 7453 – 7456; b) I. P. Holmes, H. B. Kagan, *Tetrahedron Lett.* **2000**, *41*, 7457 – 7460.
[37] a) Y. Belokon', N. Ikonnikov, M. Moscalenko, M. North, S. Orlova, V. Tararov, L. Yashkina, *Tetrahedron: Asymmetry* **1996**, *7*, 851 – 855; b) Y. Belokon', M. Flego, N. Ikonnikov, M. Moscalenko, M. North, C. Orizu, V. Tararov, M. Tasinazzo, *J. Chem. Soc. Perkin Trans. 1* **1997**, 1293 – 1295; c) Y. N. Belokon', B. Green, N. S. Ikonnikov, M. North, V. I. Tararov, *Tetrahedron Lett.* **1999**, *40*, 8147 – 8150; d) Y. N. Belokon', B. Green, N. S. Ikonnikov, M. North, T. Parsons, V. I. Tararov, *Tetrahedron* **2001**, *57*, 771 – 779; e) Y. N. Belokon', B. Green, N. S. Ikonnikov, V. S. Larichev, B. V. Lokshin, M. A. Moscalenko, M. North, C. Orizu, A. S. Peregudov, G. I. Timofeeva, *Eur. J. Org. Chem.* **2000**, 2655 – 2661.
[38] H. Deng, M. P. Isler, M. L. Snapper, A. H. Hoveyda, *Angew. Chem.* **2002**, *114*, 1051 – 1054; *Angew. Chem. Int. Ed.* **2002**, *41*, 1009 – 1012.
[39] a) Y. Shen, X. Feng, G. Zhang, Y. Jiang, *Synlett* **2002**, 1353 – 1355; b) F. Chen, X. Feng, B. Qin, G. Zhang, Y. Jiang, *Org. Lett.* **2003**, *5*, 949 – 952.

 © 2004 Wiley-VCH Verlag GmbH & Co. KGaA, Weinheim

[40] a) Y. Hamashima, D. Sawada, M. Kanai, M. Shibasaki, *J. Am. Chem. Soc.* **1999**, *121*, 2641 – 2642; b) Y. Hamashima, D. Sawada, H. Nogami, M. Kanai, M. Shibasaki, *Tetrahedron* **2001**, *57*, 805 – 814; c) M. Shibasaki, M. Kanai, K. Funabashi, *Chem. Commun.* **2002**, 1989 – 1999, and references therein.

[41] a) J. Casas, C. Nájera, J. M. Sansano, J. M. Saá, *Org. Lett.* **2002**, *4*, 2589 – 2592; b) J. Casas, A. Baeza, J. M. Sansano, C. Nájera, J. M. Saá, *Tetrahedron: Asymmetry* **2003**, *14*, 197 – 200; c) A. Baeza, J. Casas, C. Nájera, J. M. Sansano, J. M. Saá, *Angew. Chem.* **2003**, *115*, 3251 – 3254; *Angew. Chem. Int. Ed.* **2003**, *42*, 3143 – 3146.

[42] J. Tian, N. Yamagiwa, S. Matsunaga, M. Shibasaki, *Angew. Chem.* **2002**, *114*, 3788 – 3790; *Angew. Chem. Int. Ed.* **2002**, *41*, 3636 – 3638.

[43] a) Y. Hamashima, M. Kanai, M. Shibasaki, *J. Am. Chem. Soc.* **2000**, *122*, 7412 – 7413; b) K. Yabu, S. Masumoto, S. Yamasaki, Y. Hamashima, M. Kanai, W. Du, D. P. Curran, M. Shibasaki, *J. Am. Chem. Soc.* **2001**, *123*, 9908 – 9909.

[44] a) M. Takamura, K. Funabashi, M. Kanai, M. Shibasaki, *J. Am. Chem. Soc.* **2000**, *122*, 6327 – 6328; b) M. Takamura, K. Funabashi, M. Kanai, M. Shibasaki, *J. Am. Chem. Soc.* **2001**, *123*, 6801 – 6808; c) K. Funabashi, H. Ratni, M. Kanai, M. Shibasaki, *J. Am. Chem. Soc.* **2001**, *123*, 10784 – 10785.

[45] a) M. Takamura, Y. Hamashima, H. Usuda, M. Kanai, M. Shibasaki, *Angew. Chem.* **2000**, *112*, 1716 – 1718; *Angew. Chem. Int. Ed.* **2000**, *39*, 1650 – 1652; b) M. Takamura, Y. Hamashima, H. Usuda, M. Kanai, M. Shibasaki, *Chem. Pharm. Bull.* **2000**, *48*, 1586 – 1592; c) H. Nogami, S. Matsunaga, M. Kanai, M. Shibasaki, *Tetrahedron Lett.* **2001**, *42*, 279 – 283; d) S. Masumoto, H. Usuda, M. Suzuki, M. Kanai, M. Shibasaki, *J. Am. Chem. Soc.* **2003**, *125*, 5634 – 5635.

[46] M. Chavarot, J. J. Byrne, Y. Chanant, Y. Vallée, *Tetrahedron: Asymmetry* **2001**, *12*, 1147 – 1150.

[47] a) C. A. Krueger, K. W. Kuntz, C. D. Dzierba, W. G. Wirschun, J. D. Gleason, M. L. Snapper, A. H. Hoveyda, *J. Am. Chem. Soc.* **1999**, *121*, 4284 – 4285; b) J. R. Porter, W. G. Wirschun, K. W. Kuntz, M. L. Snapper, A. H. Hoveyda, *J. Am. Chem. Soc.* **2000**, *122*, 2657 – 2658; c) N. S. Josephsohn, K. W. Kuntz, M. L. Snapper, A. H. Hoveyda, *J. Am. Chem. Soc.* **2001**, *123*, 11594 – 11599.

[48] a) Tetrahedron Organic Chemistry Series, *Vol. 9*: P. Perlmutter, *Conjugate Addition Reactions in Organic Synthesis*, Pergamon, Oxford, **1992**; b) J. Christoffers, *Eur. J. Org. Chem.* **1998**, 1259 – 1266; c) N. Krause, A. Hoffmann-Röder, *Synthesis* **2001**, 171 – 196; d) J. Christoffers, A. Baro, *Angew. Chem.* **2003**, *115*, 1726 – 1728; *Angew. Chem. Int. Ed.* **2003**, *42*, 1688 – 1690.

[49] a) H. Sasai, T. Arai, M. Shibasaki, *J. Am. Chem. Soc.* **1994**, *116*, 1571 – 1572; b) H. Sasai, T. Arai, Y. Satow, K. N. Houk, M. Shibasaki, *J. Am. Chem. Soc.* **1995**, *117*, 6194 – 6198; c) T. Arai, H. Sasai, K. Aoe, K. Okamura, T. Date, M. Shibasaki, *Angew. Chem.* **1996**, *108*, 103 – 105; *Angew. Chem. Int. Ed. Engl.* **1996**, *35*, 104 – 106; d) M. Shibasaki, H. Sasai, T. Arai, *Angew. Chem.* **1997**, *109*, 1290 – 1310; *Angew. Chem. Int. Ed. Engl.* **1997**, *36*, 1236 – 1256; e) Y. Xu, K. Ohori, T. Ohshima, M. Shibasaki, *Tetrahedron* **2002**, *58*, 2585 – 2588.

[50] E. Keller, N. Veldman, A. L. Spek, B. L. Feringa, *Tetrahedron: Asymmetry* **1997**, *8*, 3403 – 3413.

[51] a) Y. S. Kim, S. Matsunaga, J. Das, A. Sekine, T. Ohshima, M. Shibasaki, *J. Am. Chem. Soc.* **2000**, *122*, 6506 – 6507; b) S. Matsunaga, T. Ohshima, M. Shibasaki, *Tetrahedron Lett.* **2000**, *41*, 8473 – 8478; c) N. Kumagai, S. Matsunaga, M. Shibasaki, *Org. Lett.* **2001**, *3*, 4251 – 4254; d) R. Takita, T. Ohshima, M. Shibasaki, *Tetrahedron Lett.* **2002**, *43*, 4661 – 4665; e) S. Matsunaga, T. Ohshima, M. Shibasaki, *Adv. Synth. Catal.* **2002**, *344*, 3 – 15.

[52] S. Harada, N. Kumagai, T. Kinoshita, S. Matsunaga, M. Shibasaki, *J. Am. Chem. Soc.* **2003**, *125*, 2582 – 2590.

[53] S. Matsunaga, T. Ohshima, M. Shibasaki, *Tetrahedron Lett.* **2000**, *41*, 8473 – 8478.

[54] T. Arai, Q.-S. Hu, X.-F. Zheng, L. Pu, H. Sasai, *Org. Lett.* **2000**, *2*, 4261 – 4263.

[55] a) G. Manickam, G. Sundararajan, *Tetrahedron* **1999**, *55*, 2721 – 2736; b) G. Sundararajan, N. Prabagaran, *Org. Lett.* **2001**, *3*, 389 – 392.

[56] N. Prabagaran, G. Sundararajan, *Tetrahedron: Asymmetry* **2002**, *13*, 1053 – 1058.

[57] a) E. F. DiMauro, M. C. Kozlowski, *Org. Lett.* **2001**, *3*, 1641 – 1644; b) V. Annamalai, E. F. DiMauro, P. J. Carroll, M. C. Kozlowski, *J. Org. Chem.* **2003**, *68*, 1973 – 1981.

[58] a) J. K. Myers, E. N. Jacobsen, *J. Am. Chem. Soc.* **1999**, *121*, 8959 – 8960; b) G. M. Sammis, E. N. Jacobsen, *J. Am. Chem. Soc.* **2003**, *125*, 4442 – 4443.

[59] a) K. Itoh, S. Kanemasa, *J. Am. Chem. Soc.* **2002**, *124*, 13394 – 13395; see also the Microreview: b) K. Itoh, S. Kanemasa, *Eur. J. Org. Chem.* **2004**, in press.

[60] a) J. Krüger, E. M. Carreira, *J. Am. Chem. Soc.* **1998**, *120*, 837 – 838; b) B. L. Pagenkopf, J. Krüger, A. Stojanovic, E. M. Carreira, *Angew. Chem.* **1998**, *110*, 3312 – 3314; *Angew. Chem. Int. Ed.* **1998**, *37*, 3124 – 3126.

[61] a) A. Yanagisawa, Y. Nakatsuka, K. Asakawa, H. Kageyama, H. Yamamoto, *Synlett* **2001**, 69 – 72; b) M. Wadamoto, N. Ozasa, A. Yanagisawa, H. Yamamoto, *J. Org. Chem.* **2003**, *68*, 5593 – 5601.

[62] a) S. E. Denmark, R. A. Stavenger, *Acc. Chem. Res.* **2000**, *33*, 432 – 440, and references therein; b) S. E. Denmark, S. K. Ghosh, *Angew. Chem.* **2001**, *113*, 4895 – 4898; *Angew. Chem. Int. Ed.* **2001**, *40*, 4759 – 4762.

[63] H. Sasai, T. Suzuki, S. Arai, T. Arai, M. Shibasaki, *J. Am. Chem. Soc.* **1992**, *114*, 4418 – 4420.

[64] a) Y. M. A. Yamada, N. Yoshikawa, H. Sasai, M. Shibasaki, *Angew. Chem.* **1997**, *109*, 1942 – 1944; *Angew. Chem. Int. Ed. Engl.* **1997**, *36*, 1871 – 1873; b) N. Yoshikawa, Y. M. A. Yamada, J. Das, H. Sasai, M. Shibasaki, *J. Am. Chem. Soc.* **1999**, *121*, 4168 – 4178.

[65] N. Yoshikawa, N. Kumagai, S. Matsunaga, G. Moll, T. Ohshima, T. Suzuki, M. Shibasaki, *J. Am. Chem. Soc.* **2001**, *123*, 2466 – 2467.

[66] a) N. Kumagai, S. Matsunaga, N. Yoshikawa, T. Ohshima, M. Shibasaki, *Org. Lett.* **2001**, *3*, 1539 – 1542; b) N. Kumagai, S. Matsunaga, T. Kinoshita, S. Harada, S. Okada, S. Sakamoto, K. Yamaguchi, M. Shibasaki, *J. Am. Chem. Soc.* **2003**, *125*, 2169 – 2178.

[67] a) B. M. Trost, H. Ito, *J. Am. Chem. Soc.* **2000**, *122*, 12003 – 12004; b) B. M. Trost, H. Ito, E. R. Silcoff, *J. Am. Chem. Soc.* **2001**, *123*, 3367 – 3368; c) B. M. Trost, V. S. C. Yeh, *Angew. Chem.* **2002**, *114*, 889 – 891; *Angew. Chem. Int. Ed.* **2002**, *41*, 861 – 863; d) B. M. Trost, V. S. C. Yeh, H. Ito, N. Bremeyer, *Org. Lett.* **2002**, *4*, 2621 – 2623.

[68] a) H. Sasai, M. Hiroi, Y. M. A. Yamada, M. Shibasaki, *Tetrahedron Lett.* **1997**, *38*, 6031 – 6034; b) T. Arai, H. Sasai, K. Aoe, K. Okamura, T. Date, M. Shibasaki, *Angew. Chem.* **1996** *108*, 103 – 105; *Angew. Chem. Int. Ed. Engl.* **1996**, *35*, 104 – 106; c) K. Yamada, T. Arai, H. Sasai, M. Shibasaki, *J. Org. Chem.* **1998**, *63*, 3666 – 3672.

[69] a) Y. Ito, M. Sawamura, T. Hayashi, *J. Am. Chem. Soc.* **1986**, *108*, 6405 – 6406; b) Y. Ito, M. Sawamura, T. Hayashi, *Tetrahedron Lett.* **1987**, *28*, 6215 – 6218; c) Y. Ito, M. Sawamura, E. Shirakawa, K. Hayashizaki, T. Hayashi, *Tetrahedron Lett.* **1988**, *29*, 235 – 238; d) M. Sawamura, Y. Ito, T. Hayashi, *Tetrahedron Lett.* **1990**, *31*, 2723 – 2726; e) T. Hayashi, M. Sawamura, Y. Ito, *Tetrahedron* **1992**, *48*, 1999 – 2012; see also: f) S. D. Pastor, *Tetrahedron* **1988**, *44*, 2883 – 2886; g) S. D. Pastor, A. Togni, *J. Am. Chem. Soc.* **1989**, *111*, 2333 – 2334; h) A. Togni, R. Hausel, *Synlett* **1990**, 633 – 635; i) S. D. Pastor, A. Togni, *Tetrahedron Lett.* **1990**, *31*, 839 – 840; j) A. Togni, S. D. Pastor, *J. Organomet. Chem.* **1990**, *381*, C21 – C25; k) A. Togni, S. D. Pastor, *J. Org. Chem.* **1990**, *55*, 1649 – 1664.

 © 2004 Wiley-VCH Verlag GmbH & Co. KGaA, Weinheim

[70] a) Y. Ito, M. Sawamura, M. Kobayashi, T. Hayashi, *Tetrahedron Lett.* **1988**, *29*, 6321 – 6324; b) Y. Ito, M. Sawamura, H. Hamashima, T. Emura, T. Hayashi, *Tetrahedron Lett.* **1989**, *30*, 4681 – 4684; c) M. Sawamura, Y. Ito, T. Hayashi, *Tetrahedron Lett.* **1989**, *30*, 2247 – 2250; d) A. Togni, S. D. Pastor, *Tetrahedron Lett.* **1989**, *30*, 1071 – 1072.

[71] T. Hayashi, Y. Uozumi, A. Yamazaki, M. Sawamura, H. Hamashima, Y. Ito, *Tetrahedron Lett.* **1991**, *32*, 2799 – 2802.

[72] a) K. Yamada, S. J. Harwood, H. Gröger, M. Shibasaki, *Angew. Chem.* **1999**, *111*, 3713 – 3715; *Angew. Chem. Int. Ed.* **1999**, *38*, 3504 – 3505; b) K. Yamada, G. Moll, M. Shibasaki, *Synlett* **2001**, 980 – 982; c) N. Tsuritani, K. Yamada, N. Yoshikawa, M. Shibasaki, *Chem. Lett.* **2002**, 276 – 277.

[73] N. Nishiwaki, K. R. Knudsen, K. V. Gothelf, K. A. Jørgensen, *Angew. Chem.* **2001** *113*, 3080 – 3083; *Angew. Chem. Int. Ed.* **2001**, *40*, 2992 – 2995.

[74] S. Kobayashi, T. Hamada, K. Manabe, *J. Am. Chem. Soc.* **2002**, *124*, 5640 – 5641.

[75] S. Matsunaga, N. Kumagai, S. Harada, M. Shibasaki, *J. Am. Chem. Soc.* **2003**, *125*, 4712 – 4713.

[76] B. M. Trost, L. R. Terrell, *J. Am. Chem. Soc.* **2003**, *125*, 338 – 339.

[77] a) I. Paterson, D. J. Berrisford, *Angew. Chem.* **1992**, *104*, 1204 – 1205; *Angew. Chem. Int. Ed. Engl.* **1992**, *31*, 1179 – 1180; b) E. N. Jacobsen, *Acc. Chem. Res.* **2000**, *33*, 421 – 431; c) T. P. Yoon, E. N. Jacobsen, *Science* **2003**, *299*, 1691 – 1693, and references therein.

[78] For several examples of catalytic asymmetric epoxidations of olefins, see: a) M. Bougauchi, S. Watanabe, T. Arai, H. Sasai, M. Shibasaki, *J. Am. Chem. Soc.* **1997**, *119*, 2329 – 2330; b) S. Watanabe, T. Arai, H. Sasai, M. Shibasaki, *J. Org. Chem.* **1998**, *63*, 8090 – 8091; c) T. Nemoto, T. Ohshima, K. Yamaguchi, M. Shibasaki, *J. Am. Chem. Soc.* **2001**, *123*, 2725 – 2732; d) T. Nemoto, T. Ohshima, M. Shibasaki, *J. Am. Chem. Soc.* **2001**, *123*, 9474 – 9475; for examples of catalytic asymmetric hydrophosphonylation and hydrophosphanation, see: e) H. Gröger, Y. Saida, H. Sasai, K. Yamaguchi, J. Martens, M. Shibasaki, *J. Am. Chem. Soc.* **1998**, *120*, 3089 – 3103; f) I. Schlemminger, Y. Saida, H. Gröger, W. Maison, N. Durot, H. Sasai, M. Shibasaki, J. Martens, *J. Org. Chem.* **2000**, *65*, 4818 – 4825; for examples of catalytic asymmetric ring-opening of epoxides, see: g) T. Iida, N. Yamamoto, H. Sasai, M. Shibasaki, *J. Am. Chem. Soc.* **1997**, *119*, 4783 – 4784; h) T. Iida, N. Yamamoto, S. Matsunaga, H. G. Woo, M. Shibasaki, *Angew. Chem.* **1998**, *110*, 2383 – 2386; *Angew. Chem. Int. Ed.* **1998**, *37*, 2223 – 2226; i) S. Matsunaga, J. Das, J. Roels, E. M. Vogl, N. Yamamoto, T. Iida, K. Yamaguchi, M. Shibasaki, *J. Am. Chem. Soc.* **2000**, *122*, 2252 – 2260.

[79] a) W. A. Nugent, *J. Am. Chem. Soc.* **1992**, *114*, 2768 – 2769; b) W. A. Nugent, R. L. Harlow, *J. Am. Chem. Soc.* **1994**, *116*, 6142 – 6148; c) B. W. McCleland, W. A. Nugent, M. G. Finn, *J. Org. Chem.* **1998**, *63*, 6656 – 6666.

[80] a) L. E. Martínez, J. L. Leighton, D. H. Carsten, E. N. Jacobsen, *J. Am. Chem. Soc.* **1995**, *117*, 5897 – 5898; b) J. L. Leighton, E. N. Jacobsen, *J. Org. Chem.* **1996**, *61*, 389 – 390; c) K. B. Hansen, J. L. Leighton, E. N. Jacobsen, *J. Am. Chem. Soc.* **1996**, *118*, 10924 – 10925; d) R. G. Konsler, J. Karl, E. N. Jacobsen, *J. Am. Chem. Soc.* **1998**, *120*, 10780 – 10781.

[81] a) E. N. Jacobsen, F. Kakiuchi, R. G. Konsler, J. F. Larrow, M. Tokunaga, *Tetrahedron Lett.* **1997**, *38*, 773 – 776; b) S. E. Schaus, E. N. Jacobsen, *Org. Lett.* **2000**, *2*, 1001 – 1004.

[82] a) J. F. Larrow, S. E. Schaus, E. N. Jacobsen, *J. Am. Chem. Soc.* **1996**, *118*, 7420 – 7421; b) H. Lebel, E. N. Jacobsen, *Tetrahedron Lett.* **1999**, *40*, 7303 – 7306.

[83] a) M. Tokunaga, J. F. Larrow, F. Kakiuchi, E. N. Jacobsen, *Science* **1997**, *277*, 936 – 938; b) M. E. Furrow, S. E. Schaus, E. N. Jacobsen, *J. Org. Chem.* **1998**, *63*, 6776 – 6777; c) J. M. Ready, E. N. Jacobsen, *J. Am. Chem. Soc.* **1999**, *121*, 6086 – 6087; d) S. E. Schaus, B. D. Brandes, J. F. Larrow, M. Tokunaga, K. B. Hansen, A. E. Gould, M. E. Furrow, E. N. Jacobsen, *J. Am. Chem. Soc.* **2002**, *124*, 1307 – 1315.

[84] a) D. A. Annis, E. N. Jacobsen, *J. Am. Chem. Soc.* **1999**, *121*, 4147 – 4154; b) R. Breinbauer, E. N. Jacobsen, *Angew. Chem.* **2000**, *112*, 3750 – 3753; *Angew. Chem. Int. Ed.* **2000**, *39*, 3604 – 3607; c) J. M. Ready, E. N. Jacobsen, *J. Am. Chem. Soc.* **2001**, *123*, 2687 – 2688; d) J. M. Ready, E. N. Jacobsen, *Angew. Chem.* **2002**, *114*, 1432 – 1435; *Angew. Chem. Int. Ed.* **2002**, *41*, 1374 – 1377; e) D. E. White, E. N. Jacobsen, *Tetrahedron: Asymmetry* **2003**, *14*, 3633 – 3638.

[85] M. Sawamura, H. Nagata, Y. Ito, *J. Am. Chem. Soc.* **1992**, *114*, 2586 – 2592.

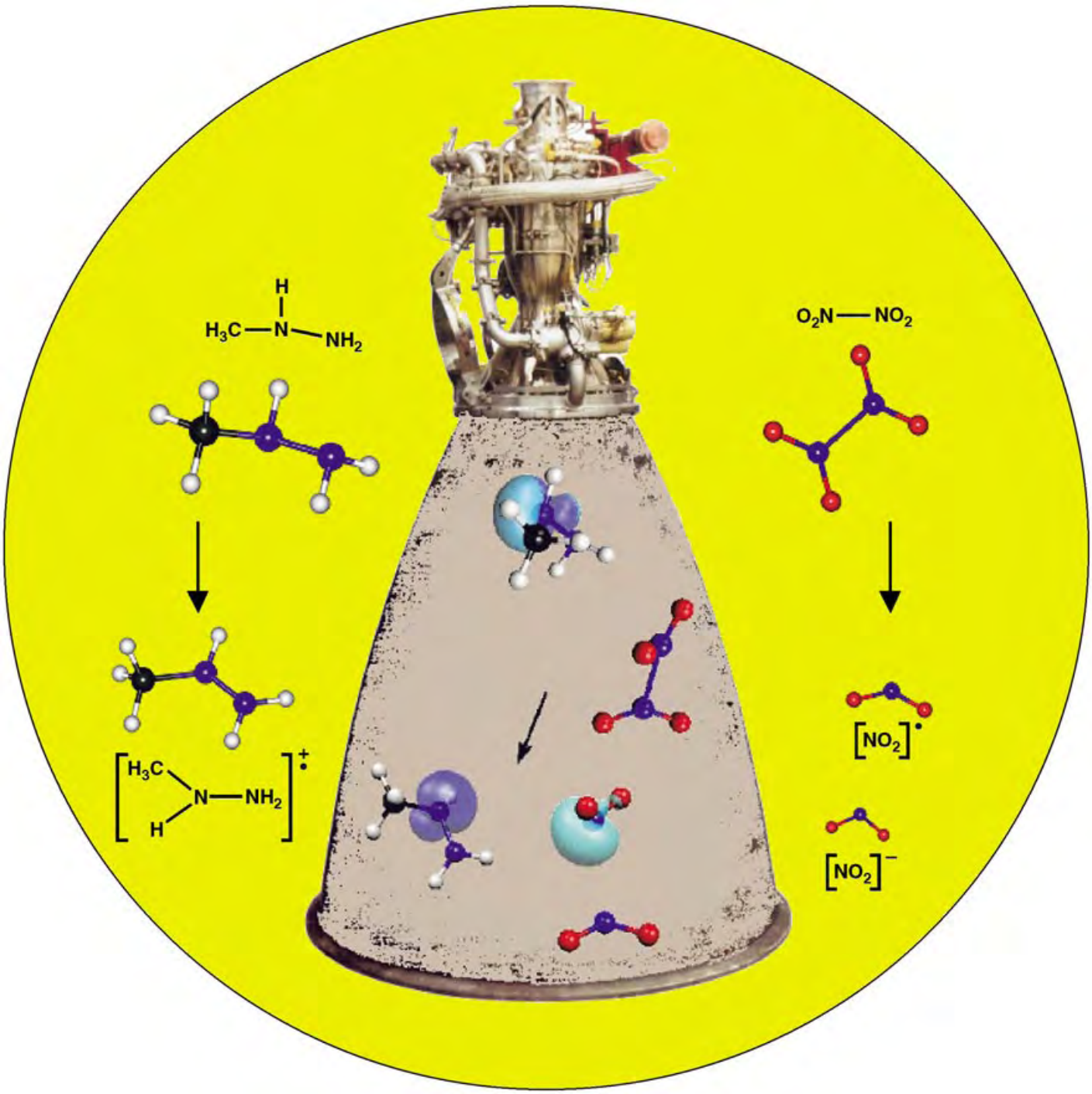
[86] M. Sawamura, Y. Nakayama, W. M. Tang, Y. Ito, *J. Org. Chem.* **1996**, *61*, 9090 – 9096.

[87] a) S. France, H. Wack, A. M. Hafez, A. E. Taggi, D. R. Witsil, T. Lectka, *Org. Lett.* **2002**, *4*, 1603 – 1605; b) A. E. Taggi, A. M. Hafez, H. Wack, B. Young, D. Ferraris, T. Lectka, *J. Am. Chem. Soc.* **2002**, *124*, 6626 – 6635; c) A. E. Taggi, A. M. Hafez, T. Lectka, *Acc. Chem. Res.* **2003**, *36*, 10 – 19.

[88] A. H. Mermerian, G. C. Fu, *J. Am. Chem. Soc.* **2003**, *125*, 4050 – 4051.

 © 2004 Wiley-VCH Verlag GmbH & Co. KGaA, Weinheim

Communications



The bipropellant monomethylhydrazine/nitrogen tetroxide is used as a rocket fuel. Molecular dynamics simulations provide an explanation for the "cold prereaction", which yields methyldiazene and nitrous acid, and for the subsequent explosive reaction via dimethyltetrazane. I. Frank and co-workers give details in the following Communication.

DOI: 10.1002/anie.200454093
© 2004 Wiley-VCH Verlag GmbH & Co. KGaA, Weinheim

Hypergolic Mixtures

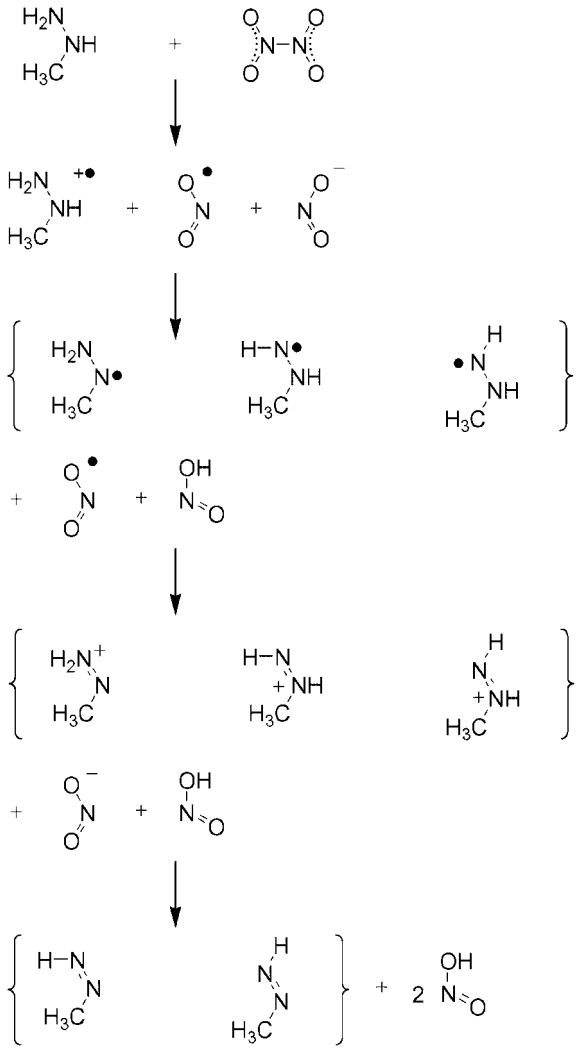
Ultrafast Cold Reactions in the Bipropellant Monomethylhydrazine/Nitrogen Tetroxide: CPMD Simulations**

Christel Nonnenberg, Irmgard Frank, and Thomas M. Klapötke*

The bipropellant monomethylhydrazine (MMH)/nitrogen tetroxide (NTO) has been employed in astronautics for a long time,[1] for example, as fuel for the upper stage engine of the European launch vehicle Ariane 5 and in various U.S. spacecraft engines of the RS series (e.g. RS-21, RS-25, RS-28, RS-41, and RS-42). However, the mixture is unfortunately problematic in its handling and application. In 2001, flight 510 of the Ariane 5 project encountered serious problems due to complications within the upper stage engine.[2]

On contact the components of the mixture react violently, explosively emitting heat and gas, and therefore the mixture is known as hypergolic. However, the mixture does not heat up during the reaction that precedes ignition ("cold prereaction"). Such a fast process is not easy to examine experimentally in full detail, as it is especially difficult to create a well-defined mixture of the reactants. Here theory provides an attractive alternative in terms of molecular dynamics simulations[5–8] within the Car–Parrinello approach,[3,4] where the extreme reactivity of the system is even advantageous. Car–Parrinello Molecular Dynamics (CPMD) allows the simulation of different types of reactions in a system through the description of the electronic structure with the density functional theory approach.[9,10] It is not necessary to predefine a reaction coordinate; rather, all degrees of freedom of the system can be considered. This study does not focus on highly precise computations of properties of isolated molecules. It aims rather at determining the relevant reaction schemes under varying reaction conditions like the ratio of starting materials, temperature, and impurities.

As the first step, an MMH/NTO mixture with a ratio of 1:1 and a density of 0.9 $g\,cm^{-3}$ was simulated (Scheme 1 and Figure 1). At temperatures above 300 K we initially observe electron transfer: an electron is transferred from an MMH molecule to an NTO molecule while the latter dissociates. The resulting ions are neutralized by a consecutive proton transfer. Afterwards a second electron is transferred, and again proton transfer yields neutral products (Scheme 1; details on the energetics are given in the Supporting Information). The oxidation state of the MMH molecule and its products during the molecular dynamics run can easily be determined from



Scheme 1. Redox reaction leading from MMH to methyldiazene as observed in the CPMD simulations.

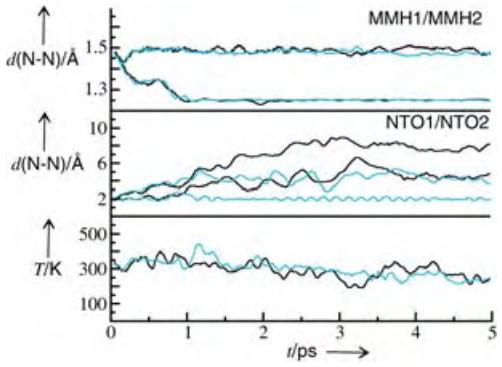


Figure 1. Simulation of a 1:1 mixture of MMH/NTO with a density of 0.9 $g\,cm^{-3}$ (upper panel: N–N distances in the MMH molecules; middle panel: N–N distances in the NTO molecules; lower panel: temperature).

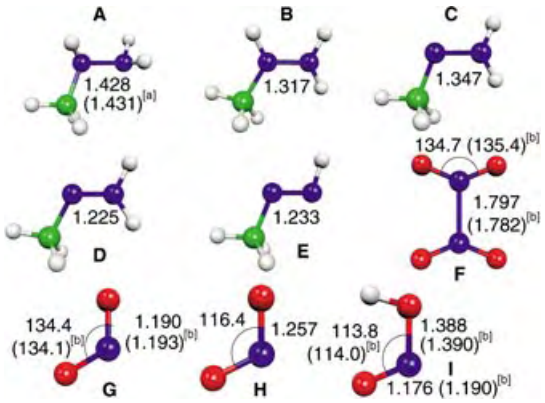
[*] C. Nonnenberg, Dr. I. Frank, Prof. Dr. T. M. Klapötke
Department Chemie und Biochemie
Ludwig-Maximilians-Universität München
81377 München (Germany)
Fax: (+49) 89-2180-77568
E-mail: frank@cup.uni-muenchen.de

[**] We gratefully acknowledge the Deutsche Forschungsgemeinschaft for financial funding and the Leibniz-Rechenzentrum München (HLRB project h0621) for computational resources.

Supporting information for this article is available on the WWW under http://www.angewandte.org or from the author.

 © 2004 Wiley-VCH Verlag GmbH & Co. KGaA, Weinheim DOI: 10.1002/anie.200454093

the N–N distance (see Figure 1 and Scheme 2). Likewise the O-N-O angle of the NO_2 fragment indicates whether it is reduced to an anion after the dissociation of NTO (Scheme 2). The protons may be transferred to an NO_2



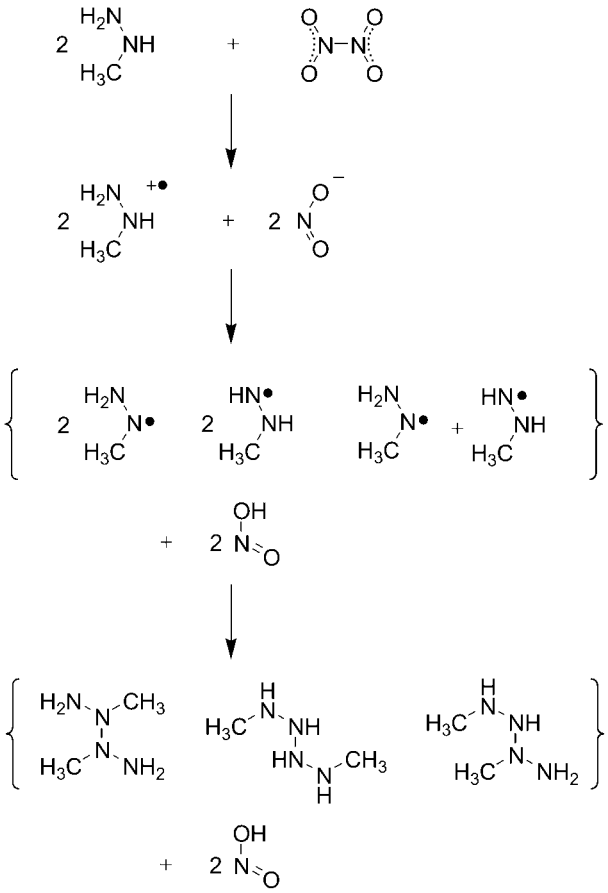
Scheme 2. Calculated structures (B3LYP/cc-pVQZ) of MMH, NTO, and their subsequent products; A: MMH, B: MMH radical cation, C: methylhydrazyl radical, D: protonated methyldiazene, E: *trans*-methyldiazene, F: NTO, G: NO_2 radical, H: NO_2 anion, I: HNO_2. [a] Ref. [11]. [b] Ref. [12].

anion or to another MMH molecule, depending on the actual arrangement of the reactants. The reaction ultimately yields methyldiazene and nitrous acid.

In the next step we checked the effect of impurities on the reaction. Typical by-products of the production process are methylamine, water, and nitric acid. However, simulations of mixtures containing these substances do not show essentially different reaction mechanisms. The impurities may act as proton acceptors, but in the end methyldiazene is formed anyway. Hence, it can be assumed to be the main product even under these conditions.

In further CPMD simulations we investigated whether an ultrafast process may originate from methyldiazene to explain the unstable behavior. Methyldiazene was mixed with NTO, and the relevant impurities as well as the radical and ionic intermediates formed in the prereaction. Even at higher temperatures no reaction was observed. Indeed, studies of the first directly observed monosubstituted diazenes in 1965,[13] and in particular of the isolatable pure methyldiazene,[14] demonstrate a certain kinetic stability. Also the biological chemistry of methyldiazene as an intermediate and a metabolite in chemical carcinogenesis is well known. It reacts directly with hemoglobin[15,16] as does MMH. Furthermore, a reaction with cytochrome P450–Fe^{III} was reported.[17]

We observe in simulations with an excess of MMH that the oxidation is not completed but stops after the oxidation to the methylhydrazyl radical. Partial disproportionation of two methylhydrazyl radicals follows, resulting in the formation of methyldiazene and MMH, as already suggested in experimental studies.[18] However, this reaction sequence does not yield a new intermediate that might lead to a violent reaction, but a recombination of two methylhydrazyl radicals may yield dimethyltetrazane (Scheme 3), a very unstable molecule with a chain of four nitrogen atoms. This recombination reaction

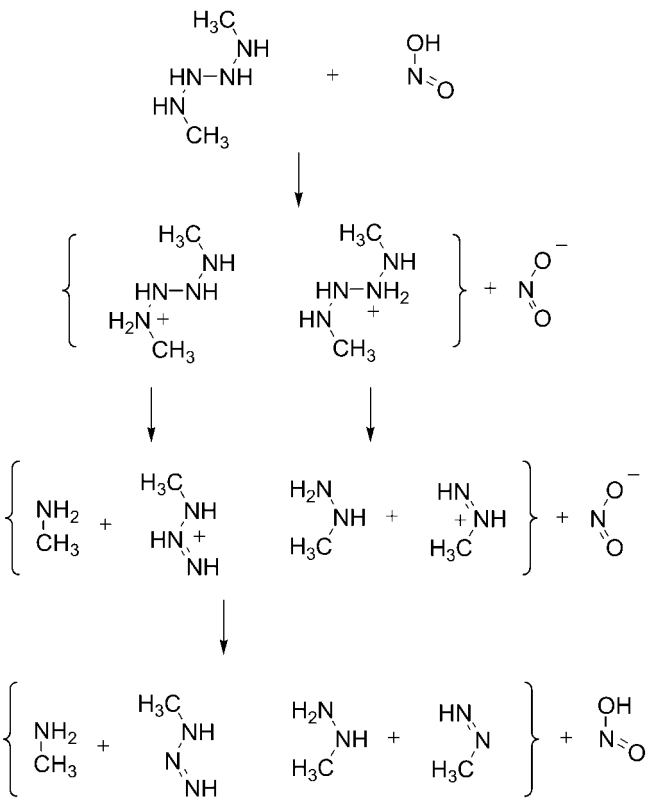


Scheme 3. Reaction scheme for the formation of dimethyltetrazane isomers from an excess of MMH.

shows no or just a very small energy barrier (B3LYP/6-31G*(Gaussian) ≈ 0.1 kcal mol^{-1}, BLYP/6-31G*(Gaussian) = 0.0 kcal mol^{-1}). The formation of tetrazane has already been discussed several times in the literature in the context of the decay of hydrazyl radicals.[19–21] A three-particle collision must occur to cause this exothermic addition reaction in order to dissipate the energy originating from bond formation. Presumably this reaction occurs mostly at the walls of the vessel.

Unsubstituted tetrazane is known to be very unstable in alkaline solutions.[22] The perfluorated methyl-substituted tetrazane derivatives, for example, hexakis(trifluoromethyl)-tetrazane, have been synthesized only recently due to this high reactivity.[23,24] A theoretical study of the thermochemical properties of tetrazane[25] shows that the proton affinity of the nitrogen atoms of tetrazane is higher than that of ammonia or hydrazine. CPMD simulations of dimethyltetrazanes with nitrous acid show on the one hand a protonation of the terminal nitrogen atoms leading to detachment of either methylamine or ammonia, and on the other hand a protonation of a median nitrogen atom resulting in dissociation of the tetrazane derivative to MMH and protonated methyldiazene (Scheme 4). The protonation of a terminal nitrogen atom results in the decomposition reaction that was suggested in experimental studies of unsubstituted tetrazane.[18,20,21] A further decomposition of the resulting methyltriazene was not observed. The molecular dynamics simulations mostly show a

 © 2004 Wiley-VCH Verlag GmbH & Co. KGaA, Weinheim



Scheme 4. Reaction scheme for the decomposition of a dimethyltetrazane isomer in acid–base reactions.

protonation at a terminal sp^2-hybridized nitrogen atom. As for tetrazene,[26] the protonation of the sp^3-hybridized nitrogen might be inhibited because of the interaction of the free electron pair with the π bond of the two other nitrogen atoms. The decomposition in a protic environment to methylated amines or ammonia and nitrogen was proven experimentally.[20,21] The rate of the triazene formation in acidic solutions could not be determined in experiment since the reaction of protonated tetrazane to give triazene is much faster than the decay rate of triazene.[20] Acid is also present in our simulations and results from the reduction of NTO. One-electron oxidation of hydrazine is described in textbooks as a method to form tetrazane, but the proof of dimethyltetrazane formation under these conditions is awkward: the by-product nitrous acid causes immediate decomposition. Experimental detection might be possible spectroscopically or by matrix isolation experiments.

In conclusion with Car–Parrinello Molecular Dynamics simulations we have demonstrated that the cold prereaction in the mixture MMH/NTO can be assigned to an oxidation of monomethylhydrazine to methyldiazene. The mixture does not heat up until this point, and the succeeding reaction to nitrogen is kinetically inhibited. According to our simulations it is plausible to assume that this reaction takes place anyway prior to ignition and does not necessarily trigger an uncontrolled violent reaction. However, uncontrolled behavior could be explained by the reaction sequence involving dimethyltetrazane and methyltriazene. This would correspond to the experimental finding that violent decomposition occurs mainly at low temperatures and with an excess of MMH. With an excess of MMH the reaction can stop after the one-electron oxidation. If two of the resulting radicals meet, low temperatures favor a recombination. The energy released during tetrazane formation and the subsequent decomposition can finally trigger other decomposition reactions.

We could identify the most relevant of the many possible reaction pathways in the MMH/NTO system with Car–Parrinello simulations. According to the simulations a violent reaction prior to ignition is possible by a combination of ultrafast redox, radical, and acid–base reactions.

Computational Procedure

The static calculations of the relative energies and the geometries were performed with the Gaussian package[27] using the hybrid functional B3LYP[28,29] (cc-pVQZ basis set) and with the CPMD package[30] using the BLYP functional[31,29] in the local spin density approximation. A planewave basis set (energy cutoff: 70 Rydberg) and Troullier–Martins pseudopotentials[32] were employed in the CPMD calculations. The molecules were placed in a box of dimensions $8.5 \times 8.5 \times 8.5$ Å^3 and were treated as isolated systems.

The molecular dynamics simulations were performed with the CPMD package using periodic boundary conditions. A timestep of 4 a.u. (0.1 fs) and a fictitious electron mass of 400 a.u. were used. The starting geometries were optimized with molecular dynamics at finite temperatures and afterwards annealed to the desired temperatures. The size of the box was varied from $7.9 \times 7.9 \times 7.9$ Å^3 to $9.5 \times 9.5 \times 9.5$ Å^3 in order to get similar densities for the different ensembles of molecules.

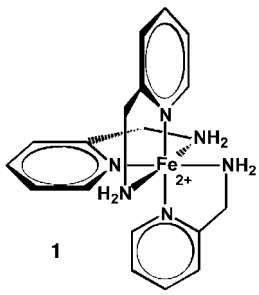
Received: February 24, 2004
Revised: June 15, 2004 [Z54093]
Published Online: August 9, 2004

Keywords: density functional calculations · hypergolic mixtures · quantum chemistry · reactive intermediates

[1] E. W. Schmidt, *Hydrazine and Its Derivatives*, *Vol. 2*, 2nd ed., Wiley, Chichester, New York, **2001**, chap. 6.2, pp. 1475–1539, and references therein.
[2] Launchers.dev, information letter from the CNES Launchers Division, Issue July 2002, CNES, Evry Cedex, France, http://www.cnes.fr.
[3] R. Car, M. Parrinello, *Phys. Rev. Lett.* **1985**, *55*, 2471.
[4] M. Parrinello, *Solid State Commun.* **1997**, *102*, 107.
[5] "Ab Initio Molecular Dynamics: Theory and Implementation" in: D. Marx, J. Hutter in *Modern Methods and Algorithms of Quantum Chemistry*, *Vol. 1* (Ed.: J. Grotendorst), Forschungszentrum Jülich, NIC Series, **2000**, p. 301.
[6] I. Frank, *Angew. Chem.* **2003**, *115*, 1607; *Angew. Chem. Angew. Chem. Int. Ed.* **2003**, *42*, 1569.
[7] S. Reinhardt, C. M. Marian, I. Frank, *Angew. Chem.* **2001**, *113*, 3795; *Angew. Chem. Int. Ed.* **2001**, *40*, 3683.
[8] E. J. Meijer, M. Sprik, *J. Phys. Chem. A* **1998**, *102*, 2893.
[9] P. Hohenberg, W. Kohn, *Phys. Rev.* **1964**, *136*, 864.
[10] W. Kohn, L. J. Sham, *Phys. Rev.* **1965**, *140*, A1133.
[11] N. Murase, K. Yamanouchi, T. Egawa, K. Kuchitsu, *J. Mol. Struct.* **1991**, *242*, 409.
[12] D. R. Lide, *CRC Handbook of Chemistry and Physics* 84th ed., **2003–2004**.
[13] E. M. Kosower, *Acc. Chem. Res.* **1971**, *4*, 193.

 © 2004 Wiley-VCH Verlag GmbH & Co. KGaA, Weinheim

[14] M. N. Ackermann, M. R. Hallmark, S. K. Hammond, N. Roe, *Inorg. Chem.* **1972**, *11*, 3076.
[15] D. Mansuy, P. Battioni, J. P. Mahy, G. Gillet, *Biochem. Biophys. Res. Commun.* **1982**, *106*, 30.
[16] P. Battioni, J. P. Mahy, G. Gillet, D. Mansuy, *J. Am. Chem. Soc.* **1983**, *105*, 1399.
[17] P. Battioni, J. P. Mahy, M. Delaforge, D. Mansuy, *Eur. J. Biochem.* **1983**, *134*, 241.
[18] G. V. Buxton, H. E. Sims, *Phys. Chem. Chem. Phys.* **2000**, *2*, 4941.
[19] F. O. Rice, F. Scherber, *J. Am. Chem. Soc.* **1955**, *77*, 291.
[20] E. Hayon, M. Simic, *J. Am. Chem. Soc.* **1972**, *94*, 42.
[21] J. W. Sutherland, *J. Phys. Chem.* **1979**, *83*, 789.
[22] A. F. Holleman, E. Wiberg, N. Wiberg, *Lehrbuch der Anorganischen Chemie*, 101th ed., Walter de Gruyter, Berlin, **1995**, p. 670.
[23] B. Krumm, A. Vij, R. L. Krichmeier, J. M. Shreeve, H. Oberhammer, *Angew. Chem.* **1995**, *107*, 645; *Angew. Chem. Int. Ed. Engl.* **1995**, *34*, 586.
[24] G. Sarwar, R. L. Kirchmeier, J. M. Shreeve, *Inorg. Chem.* **1990**, *29*, 4255.
[25] D. W. Ball, *J. Phys. Chem.* **2001**, *105*, 465.
[26] B. Kovačević, Z. B. Maksić, P. Rademacher, *Chem. Phys. Lett.* **1998**, *293*, 245.
[27] Gaussian 03 (Revision A.1), M. J. Frisch, G. W. Trucks, H. B. Schlegel, G. E. Scuseria, M. A. Robb, J. R. Cheeseman, J. A. Montgomery, Jr., T. Vreven, K. N. Kudin, J. C. Burant, J. M. Millam, S. S. Iyengar, J. Tomasi, V. Barone, B. Mennucci, M. Cossi, G. Scalmani, N. Rega, G. A. Petersson, H. Nakatsuji, M. Hada, M. Ehara, K. Toyota, R. Fukuda, J. Hasegawa, M. Ishida, T. Nakajima, Y. Honda, O. Kitao, H. Nakai, M. Klene, X. Li, J. E. Knox, H. P. Hratchian, J. B. Cross, C. Adamo, J. Jaramillo, R. Gomperts, R. E. Stratmann, O. Yazyev, A. J. Austin, R. Cammi, C. Pomelli, J. W. Ochterski, P. Y. Ayala, K. Morokuma, G. A. Voth, P. Salvador, J. J. Dannenberg, V. G. Zakrzewski, S. Dapprich, A. D. Daniels, M. C. Strain, O. Farkas, D. K. Malick, A. D. Rabuck, K. Raghavachari, J. B. Foresman, J. V. Ortiz, Q. Cui, A. G. Baboul, S. Clifford, J. Cioslowski, B. B. Stefanov, G. Liu, A. Liashenko, P. Piskorz, I. Komaromi, R. L. Martin, D. J. Fox, T. Keith, M. A. Al-Laham, C. Y. Peng, A. Nanayakkara, M. Challacombe, P. M. W. Gill, B. Johnson, W. Chen, M. W. Wong, C. Gonzalez, J. A. Pople, Gaussian, Inc., Pittsburgh, PA, **2003**.
[28] A. D. Becke, *J. Chem. Phys.* **1993**, *98*, 5648.
[29] C. Lee, W. Yang, R. G. Parr, *Phys. Rev. B* **1988**, *37*, 785.
[30] CPMD, Version 3.4, J. Hutter et al., Max-Planck-Institut für Festkörperforschung and IBM Zurich Research Laboratory (**1995**–**1999**).
[31] A. D. Becke, *Phys. Rev. A* **1988**, *38*, 3098.
[32] N. Troullier, J. L. Martins, *Phys. Rev. B* **1991**, *43*, 1993.



1

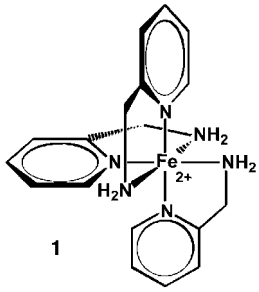
 © 2004 Wiley-VCH Verlag GmbH & Co. KGaA, Weinheim

Crystal Engineering

Challenges in Engineering Spin Crossover: Structures and Magnetic Properties of Six Alcohol Solvates of Iron(II) Tris(2-picolylamine) Dichloride**

*Marc Hostettler, Karl W. Törnroos, Dmitry Chernyshov, Brita Vangdal, and Hans-Beat Bürgi**

"Structure determines properties", this assertion is a central paradigm in materials research as well as in molecular biology. It is a prime reason for the popularity of the notion of crystal engineering, whose goal it is to develop novel materials with predefined and tuned properties.[1] Such engineering necessarily proceeds in two steps: 1) establishing empirical or theoretical relationships between solid-state structure and desired properties, 2) tailoring of the structure by a synthesis process.[2] The property of main interest in spin-crossover compounds is the thermal evolution of magnetic behavior. Herein we report on a serendipitous observation derived from magnetic and structural studies on six different alcohol solvates of iron(II) tris(2-picolylamine) dichloride (**1**),



1

in which the size of the solvating molecules ranges from methanol to *tert*-butyl alcohol. The six crystal structures are either isostructural or polytypic. In spite of evident structural similarity, the spin-transition curves are very different.

[*] Dr. M. Hostettler, Dr. D. Chernyshov,[+] Prof. H.-B. Bürgi
Laboratorium für Kristallographie
Universität Bern
Freiestrasse 3, 3012 Bern (Switzerland)
Fax: (+41) 31-631-3996
E-mail: hans-beat.buergi@krist.unibe.ch
Prof. K. W. Törnroos, B. Vangdal
Department of Chemistry, University of Bergen
Allégt. 41, 5007 Bergen (Norway)
[+] On leave from Petersburg Nuclear Physics Institute
Gatchina (Russia)

[**] This work was supported by the Swiss National Science Foundation and a travel grant from the Norwegian Research Council. We thank the staff of the Swiss Norwegian Beam Lines (SNBL) at the European Synchrotron Research Facility for their support.

Supporting information for this article (syntheses, crystal-structure analysis, and susceptibility measurements) is available on the WWW under http://www.angewandte.org or from the author.

 DOI: 10.1002/anie.200460736 © 2004 Wiley-VCH Verlag GmbH & Co. KGaA, Weinheim

Spin conversion is induced by an external perturbation, such as laser irradiation or a change in temperature or pressure. It manifests itself by changes in crystal properties, such as color, magnetization, volume, average metal–ligand separation, which arise from a collective alteration of the spin states of the individual transition-metal complexes. The change in magnetization is the basis for characterizing the spin crossover in terms of a spin-transition curve relating the concentration of high-spin (HS) molecules, γ_{HS}, to the external perturbation.[3,4] Target properties which are desirable to control in engineering spin-crossover compounds are $T_{1/2}$, the temperature at which half of the molecules are in the HS state, as well as the steepness and hysteresis properties of the transition curve, both of which might be of importance for potential technological applications.[5] Since $T_{1/2}$ depends on metal–ligand bonding, ligand field theory has been—and still is—widely used to understand and anticipate the dependence of $T_{1/2}$ on the nature of ligands.[3,4] The detailed shape of a transition curve depends on the intermolecular interactions between the metal complex, the counterions and the solvate molecules, whose interplay is governed by crystal packing.[3,4] In most theoretical attempts to understand spin crossover[6] the multitude and complexity of such interactions is condensed into a single phenomenological cooperativity parameter modeling the steepness of the transition curve. As illustrated below, such a simplification excludes a detailed understanding of spin crossover at the microscopic level, that is, in terms of the complex interactions within a crystal structure. Because of this problem, systematic manipulation of the shape of spin-transition curves has met with limited success. In spite of big efforts to synthesize and characterize new materials and to derive empirical or theoretical structure–property correlations, no general trends have been formulated as yet.[4,5,7]

Comparison of the crystal structures of the six solvates:[26] The family of iron(II) tris(2-picolylamine) dichloride solvates herein includes the known methanol[9] and ethanol[10] compounds and four new members, namely the 1-propanol, 2-propanol, *tert*-butyl alcohol, and allyl alcohol solvates (see Supporting Information). At 200 K the iron(II) complexes of all solvates are in the HS state. The crystal structures of the six compounds are built from very similar, electroneutral layers with well conserved iron–iron separations, the same two-dimensional network of hydrogen bonds, and the same crystallographic layer group $p1\,2_1/a\,1$.[11] Space-filling plots of these layers for each of the six compounds are shown in Figure 1 (left). It is very difficult to discern differences amongst them, especially after removing the solvent molecules (Figure 1, middle). The layers are stacked into one of two very similar polytypic structures: they are related either by a twofold axis (methanol), an approximate twofold axis (*tert*-butyl alcohol), or an inversion center (ethanol, allyl alcohol, 1-propanol, and 2-propanol).[12] The hydroxy group of the alcohol molecule is always hydrogen bonded into one layer of cations and anions; the hydrophobic part fits into a wedge-shaped cavity formed by two pyridine rings of an iron complex in the neighboring layer, irrespective of the symmetry relationship between consecutive layers (Figure 1, middle).[13] The volumes of the alcohol molecules range from approximately 35 Å^3 for methanol to about 85 Å^3 for *tert*-butyl alcohol, and correspond, respectively, to approximately 6% and 13% of the volume of the unit cell at 200 K.[8] It is striking how the six crystal structures accommodate these widely different volumes in two closely similar molecular packings displaying different space groups.

Of course, there are differences in quantitative detail. They may be examined on the basis of global structural parameters or in terms of the hierarchy of interactions and the way these interactions adapt to the changes in solvent volume. The increase in volume of the solvent molecules expands the unit cell anisotropically (Table 1, Figure 2a). The interlayer distance $d = c\sin\beta$ changes most. Changes in the cell constants a and b are smaller, which is in line with the unchanged topology of the anion–cation network.

There are three types of interactions in the crystal structure: 1) the relatively strong coordinative bonds within the metal complex, 2) the much weaker hydrogen bonds within the layers (Figure 3, dark gray), and 3) the weak van der Waals interactions between successive layers (Figure 3, light gray). Attempts to find correlations between solvent volume and structure parameters were only moderately successful. At 200 K all complexes are in the HS state, as seen from the average iron–nitrogen bond lengths (Table 2). The molecular geometry of the coordination complexes and especially the metal–ligand bond lengths are very similar, if not the same. The alcohol molecules are coupled to the layers of cations and anions through OH···Cl hydrogen bonds ($d4$, Figure 2b), whose lengths do not show any systematic dependence on the volume of the solvent or the pK_a value of the alcohol. The other three hydrogen-bond lengths to the same chloride ions do show some systematic variation ($d1$, $d2$, $d3$, Figure 2c). An increase of the solvent volume opens the NH···Cl···HN angle and shortens the associated separations, thereby flattening the network of hydrogen bonds. Owing to the different sizes and shapes of the solvent molecules differences in the van der Waals interactions are much more difficult to quantify.

Spin conversion and phase transitions:[22] Even though the crystal structures are similar at $T = 200$ K over a substantial range of solvent volumes, the magnetic properties are quite different (Figure 1, right; Table 2). The ethanol, 2-propanol, and allyl alcohol solvates show two-step transitions with different heights of the steps, different degrees of hysteresis, and somewhat different transition temperatures. The methanol solvate shows a continuous, smooth spin crossover, while the 1-propanol and *tert*-butyl alcohol derivatives show no transition at all down to 2 K. Recent variable-temperature diffraction experiments of the ethanol solvate between 12 and 300 K have shown that the step between the isostructural HS and LS phases is associated with an intermediate phase with doubled unit-cell volume, which is stable between 114 and 124 K.[10] In this phase the two solvent molecules and approximately equal fractions of HS and LS states are partially ordered over two, crystallographically different sites. The spin-transition curve of the 2-propanol solvate is more complicated. The small decrease in HS concentration of approximately 2% at 196 K is accompanied by a structural phase transition, which also doubles the unit-cell volume, but

 © 2004 Wiley-VCH Verlag GmbH & Co. KGaA, Weinheim

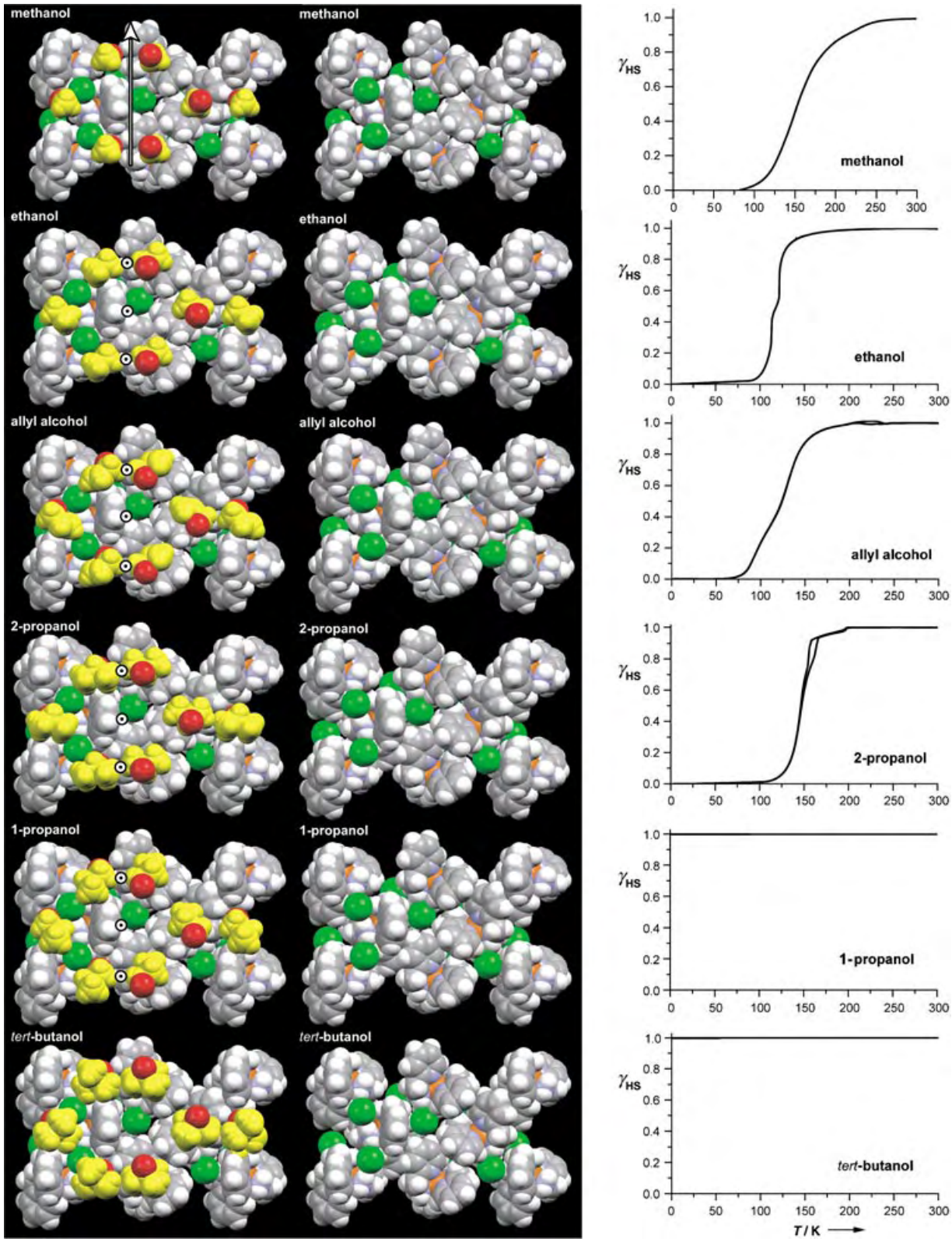


Figure 1. View of the *a*,*b* planes of the six crystal structures (space filling representation). Left: the surfaces of the layers look very similar for all the solvates; yellow = the hydrophobic part of the solvents, red = oxygen atoms, green = chloride ions, gray and white = 2-picolylamine ligands. An arrow indicates the twofold axis and white circles containing a black dot indicate inversion centers. Middle: there is no apparent difference between the structures after removing the solvent molecules. Right: the corresponding spin transition curves are different.

 © 2004 Wiley-VCH Verlag GmbH & Co. KGaA, Weinheim

Table 1: Cell constants (*a*, *b*, *c*, β) and cell volume (*V*) of six solvates of iron(II) tris(2-picolylamine) dichloride (measurement temperature 200 K). Space group symmetries: methanol *Pcan*, *tert*-butyl alcohol $P2_1/a$, all other solvates $B2_1/c$.

Solvate	*a* [Å]	*b* [Å]	*c* [Å]	β [°]	*V* [Å^3]
methanol	11.4517(4)	22.2819(7)	18.7882(6)	90.0	4794.1(3)
ethanol[10]	11.4725(6)	21.9166(12)	19.4189(10)	94.041(4)	4870.5(4)
allyl alcohol	11.5458(15)	22.115(3)	19.658(4)	93.517(12)	5009.8(13)
2-propanol	11.5525(11)	22.056(2)	20.171(3)	96.073(2)	5110.8(9)
1-propanol	11.683(2)	22.127(3)	19.469(3)	92.144(8)	5029.4(13)
tert-butyl alcohol	11.7344(8)	22.3443(14)	20.2083(15)	90.018(6)	5298.6(6)

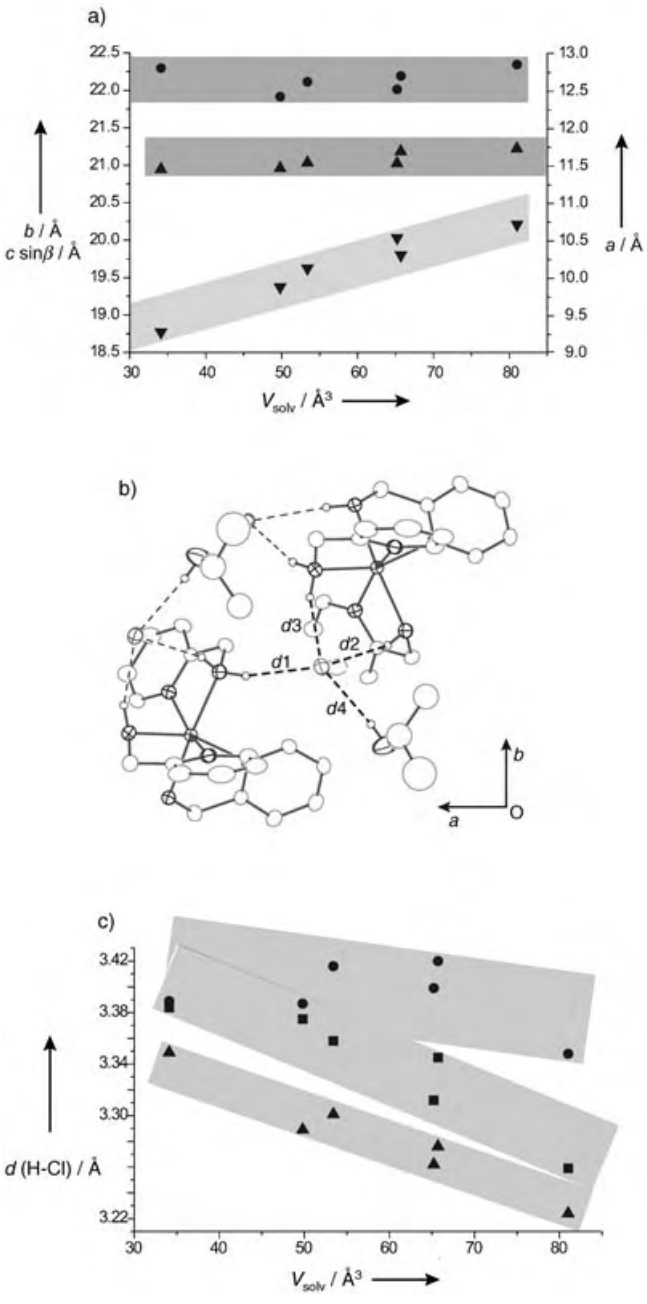


Figure 2. a) Lattice parameters within the *a*,*b* layers (*a*: ▲, *b* ●, highlighted in dark gray) and perpendicular to them (*c* sinβ: ▼, highlighted in light gray) as a function of solvent volume V_{solv}: methanol, ethanol, allyl alcohol, 2-propanol, 1-propanol, *tert*-butyl alcohol. b) Structural fragment showing the hydrogen bonds *d*1, *d*2, *d*3, and *d*4. Ellipsoids are set at 30% probability. c) Lengths of *d*1, *d*2, and *d*3 (squares, circles, and triangles) as a function of solvent volume.

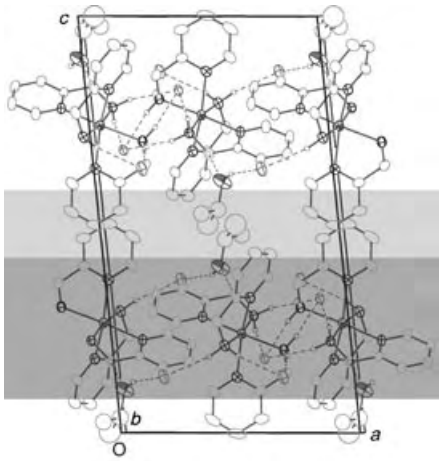


Figure 3. View onto the *a*,*c* plane of the crystal structure of the 2-propanol solvate illustrating the hierarchy of interactions. The 2D network of hydrogen bonds connecting the iron complexes through the ligand nitrogen, anionic chlorine, and alcohol oxygen atoms are indicated by dotted lines and highlighted in dark gray. The van der Waals interactions are highlighted in light gray. Ellipsoids are drawn at the 30% probability level.

in a way that differs from that of the ethanol solvate. One of the two crystallographic sites remains nearly 100% HS, whereas the second site shows a slow, almost linear decrease of the HS concentration down to about 80% at 157 K. The solvent molecules, disordered above 196 K, also occupy two crystallographically independent sites between 196 and 157 K, one of which is now ordered, the other remains disordered. Below 157 K the original unit cell is restored, the solvent molecules become fully ordered, and a sharp drop in the HS fraction is observed until at 90 K more than 99% of the molecules are in the LS state. Upon reheating the sample a triangular hysteresis loop is revealed between 147 and 168 K with indications of an additional, intermediate step. The spin-transition curve of the allyl alcohol derivative is unusual because its plateau region appears closer to a 35% than to a 50% concentration of HS molecules. It shows a gradual decrease of HS concentration towards a first, relatively steep drop-off centered around 131 K then a second, similarly steep drop-off at 92 K; the transition is complete at 70 K. The hysteresis loop between 200 K and 241 K, although narrow, is reproducible. The methanol solvate shows a smooth transition curve centered around 154 K. The *tert*-butyl alcohol solvate shows no spin transition on cooling, but does undergo a structural phase transition somewhere between 200 and 100 K which does not change the cell volume but increases the space

 © 2004 Wiley-VCH Verlag GmbH & Co. KGaA, Weinheim

Table 2: Geometry of the {Fe-N_6} octahedron: average ⟨Fe–N⟩ bond lengths and angle deformation Σ.

Solvate	*T* [K]	Solvent volume [Å^3]	⟨Fe-N⟩ [Å]	Σ [°]	$T_{1/2}$ [K]	Character of transition[b]
methanol[c]	300	34.1	2.195	95.3	150	continuous
ethanol[10]	200	49.8	2.192	100.6	118	2 steps, no hysteresis
allyl alcohol	200	53.4	2.187	100.7	124	2 steps, no hysteresis
2-propanol	200	65.2	2.199	105.5	147	2 steps, with hysteresis
1-propanol	200	65.7	2.198	103.7	–	no transitions
tert-butyl alcohol[d]	200	81.0	2.206	111.3	–	structural, but no spin transition
			2.194	98.9		
averages			2.197	103.6		

[a] $\Sigma = \sum_{i=1}^{12} |90-\theta_i|$. Standard deviations are <0.01 Å for bond lengths and $=1°$ for Σ. [b] Two steps: structural and spin transition. [c] Values are given for 300 K where γ_{HS} is nearly 1 (as for the other compounds); at 200 K γ_{HS} is only about 0.84, which implies that the experimentally determined separation, ⟨Fe-N⟩ = 2.182 Å, does not correspond to a "bond length", but represents an average between the longer HS and the shorter LS bond distances. [d] Two crystallographically independent sites for two molecules in the asymmetric unit.

group symmetry from $P2_1/a$ to *Pcan*.[12] The 1-propanol derivative shows neither spin nor structural transitions down to 2 K.

Related observations have been reported for various other iron(II) complexes. The behavior of the iron(II) hexakis(1-methyl-1*H*-tetrazole) complex with two different anions (triflate or tetrafluoroborate), described by Gütlich and Poganiuch, is probably not too surprising: "Although both complexes … differ only in the anion, their thermal spin crossover behavior differs considerably".[14] In analogy to our results Real et al. find that the two different acetonitrile solvates $[Fe(tap)_2(NCS)_2]\cdot CH_3CN$ and $[Fe(tap)_2(NCS)_2]\cdot{}^1/_2\,CH_3CN$ (tap = 1,4,5,8-tetraazaphenanthrene) "… exhibit drastic different magnetic properties", $[Fe(tap)_2(NCS)_2]\cdot CH_3CN$ shows a gradual transition centered at 168 K, $[Fe(tap)_2(NCS)_2]\cdot{}^1/_2\,CH_3CN$ being "high spin in the whole range of temperature measured".[15] Note, however, that $[Fe(tap)_2(NCS)_2]\cdot CH_3CN$ is triclinic, $[Fe(tap)_2(NCS)_2]\cdot{}^1/_2\,CH_3CN$ monoclinic.

Polymorphs are another case in point. Ozarowski et al. have reported "… two crystalline forms of $[Fe(C_6H_8N_2S_2)_2(NCS)_2]$ and the HS–LS transition that occurs in only one form" (a 2,2′-bi-2-thiazoline complex).[16] Marchivie et al. describe two polymorphs of $[Fe(PMBiA)_2(NCS)_2]$ (PM = *N*-2-pyridylmethylene, BiA = 4-aminobiphenyl): "polymorph (I) shows an extremely abrupt transition at 167 K, while polymorph (II) undergoes a gradual spin conversion centered at 205 K".[17] This collection of examples, although not exhaustive, supports our finding, namely that the spin-transition behavior of a given iron(II) complex depends strongly on subtle chemical changes in its neighborhood. The series of compounds reported herein considerably more extensive than any of the examples listed above and very homogeneous with respect to chemical and isomer composition, stoichiometry, and crystal packing. The series thus seemed particularly well suited to search for structure–property relationships.

The six different alcohol solvates of iron(II) tris(2-picolylamine) dichloride show: 1) very similar crystal structures at 200 K, 2) different structural phase transitions upon changing temperature, and 3) different spin-crossover behavior. First, we would not have predicted that changing the unit cell volume by 7% through the solvent contribution would leave the overall topology of a crystal structure invariant and its main building block, the layer of complex cations and chlorine anions, nearly unchanged. In this respect our view concurs with the opinion of Gavezzotti who argued convincingly for "No" as his one word answer to the question "Are Crystal Structures Predictable?".[18] In our case we would not even entertain a "conditional yes" as proposed by Dunitz.[19]

Second, it came as an additional surprise that the pattern of structural phase transitions is so different, when the crystal structures at 200 K are so similar. We interpret this observation to mean that, in spite of their static similarity, the flexibility of the six crystal structures is quite different, or, in other words, the potential energy surface of this structure type exhibits several secondary minima, which may differ slightly depending on the alcohol. In addition, the vibrational dynamics of each compound appear to sample a different selection of the free energy minima for different compounds. The experimental finding that several minima of potential or free energy coexist within a few kJ mol^{-1} of the global minimum, is reminiscent of analogous computational results obtained during blind tests of structure prediction methods.[20,21]

Third, and in view of the paradigm "structure determines property" the most disturbing result, the spin-transition characteristics of the six solvates are widely different and not correlated in any obvious way to the occurrence and nature of structural phase transitions or to the lack of such transitions. These findings are especially surprising if seen on the background of the only slight differences in crystal structures at 200 K. We conclude that modification of the hydrophobic part of the solvent molecule may affect magnetic behavior as much as a change of ligand and thus of the ligand field. We find these results quite discouraging with respect to the possibility of target-oriented and property-directed synthesis of new materials, at least as far as spin-crossover compounds are concerned.

In general terms the lack of obvious structure–property relationships among spin-crossover compounds may be related to the smallness of the spin conversion energy, which must be of the same order of magnitude as the thermal energy ($\propto k_B T$), but can not be the only factor affecting thermal spin crossover. The presence of structural phase transformations not directly related to spin-crossover shows

 © 2004 Wiley-VCH Verlag GmbH & Co. KGaA, Weinheim

that spin crossover has to compete with changes in the covalent, ionic, hydrogen bonding, and van der Waals interactions between the various components of the crystal lattice. All of these factors influence the collective behavior of the bistable complexes at the microscopic level as well as the enthalpy, entropy, and thus the free energy of the overall process. The quantities appearing in thermodynamic spin-crossover models are—by definition—macroscopic characteristics and provide no direct link to the microscopic structural parameters.[23,24] The single scalar quantity appearing as a cooperativity parameter in microscopic, Ising-like models of spin crossover is deceiving;[6] such models, although physically transparent, merely squeeze many competing interactions into the Procrustes' bed of one phenomenological parameter in an oversimplified model.

In conclusion, the challenges in engineering spin crossover, as we see it, derive from an imbalance between the molecular picture, which emphasizes the "isolated" iron(II) complex, and the notion of the crystal, which also includes molecular packing. The cooperative interactions associated with the complex architecture of a crystal lattice containing counterions and solvent molecules in addition to spin-crossover complexes tend to be oversimplified. Initially we hoped that the homogenous and extensive series of six compounds presented would reveal trends between relevant packing interactions and spin-crossover behavior. In spite of extraordinary structural similarity this expectation was not fulfilled. Desiraju recently noticed that "properties involving mainly cooperative effects of coupling will certainly be the most difficult to access by rational routes, if such a goal is ever achieved".[1] The present results illustrate his dictum and suggest that engineering a spin-transition compound composed of a cationic transition-metal complex, anions, and solvent molecules is not yet within reach. At the present time, classical trial-and-error lead-finding and exhaustive lead-optimization methods involving systematic synthesis and detailed measurements of properties and crystal structures appear to be the most promising strategy towards establishing empirical rules and theoretical models at the microscopic level, from which specific properties can eventually be predicted and corresponding materials synthesized. However, this conclusion should not be generalized without due caution. There are impressive examples of new materials obtained by design, especially in the area of porous framework structures.[25]

Received: May 20, 2004
Published Online: August 9, 2004

Keywords: crystal engineering · magnetic properties · solvate complexes · spin crossover · structure elucidation

[1] G. R. Desiraju, *J. Mol. Struct.* **2003**, *656*, 5.
[2] M. D. Hollingsworth, *Science* **2002**, *295*, 2410.
[3] P. Gütlich, A. Hauser, H. Spiering, *Angew. Chem.* **1994**, *106*, 2109; *Angew. Chem. Int. Ed. Engl.* **1994**, *33*, 2024.
[4] P. Gütlich, Y. Garcia, H. Spiering in *Magnetism: Molecules to Materials IV* (Eds.: J. S. Miller, M. Drillon), Wiley-VCH, Weinheim, **2002**.
[5] O. Kahn, C. J. Martinez, *Science* **1998**, *279*, 44.
[6] For a review see: R. Boča, *Solid State Phenom.* **2003**, *90–91*, 141.
[7] V. Niel, A. L. Thompson, M. C. Muñoz, A. Galet, A. E. Goeta, J. A. Real, *Angew. Chem.* **2003**, *115*, 3890; *Angew. Chem. Int. Ed.* **2003**, *42*, 3760.
[8] Solvent volumes and Connolly surfaces have been calculated with program Cerius2 using a test sphere of diameter 1 Å. Cerius2, Molecular Simulations, San Diego, **1997**.
[9] A. M. Greenaway, E. Sinn, *J. Am. Chem. Soc.* **1978**, *100*, 8080.
[10] D. Chernyshov, M. Hostettler, K. W. Törnroos, H.-B. Bürgi, *Angew. Chem.* **2003**, *115*, 3955; *Angew. Chem. Int. Ed.* **2003**, *42*, 3825.
[11] This is a non-standard setting of layer-group 17 (*International Tables of Crystallography*, *Vol. E*, IUCr & Kluwer, **2002**) chosen to be compatible with the space group symmetries.
[12] The twofold axis relating layers in the methanol solvate combines with the layer group $p12_1/a1$ to the 3D space group $P2/c2_1/a2_1/n$. In the *tert*-butyl alcohol solvate the space group is $P12_1/a1$ as long as the interlayer twofold axis is approximate, but increases to $P2/c2_1/a2_1/n$ once the twofold axis becomes crystallographic after a phase transition at lower temperature. For the other solvates, an interlayer inversion center and the layer group $p12_1/a1$ generate the 3D space group $B12_1/c1$. The latter is the nonstandard setting of space group 14 ($P2_1/c$) that allows for a direct comparison of all unit cells reported herein and elsewhere.[10]
[13] The two different, if very similar packing modes observed in this family of structures may be related to the ellipsoidal shape of the exposed hydrocarbon part of the solvent molecules. Methanol and *tert*-butyl alcohol seem to fit the wedge shaped cavities formed by two pyridine rings of a single complex in the next layer, if successive layers are packed across twofold axes. For all other solvents an optimal fit seems to require stacking of layers across centers of inversion.
[14] P. Gütlich, P. Poganiuch, *Angew. Chem.* **1991**, *103*, 1015; *Angew. Chem. Int. Ed. Engl.* **1991**, *30*, 975.
[15] J. A. Real, M. C. Muñoz, E. Andrés, T. Granier, B. Gallois, *Inorg. Chem.* **1994**, *33*, 3587.
[16] A. Ozarowski, B. R. MacGarvey, A. B. Sarkar, J. E. Drake, *Inorg. Chem.* **1988**, *27*, 628.
[17] M. Marchivie, P. Guionneau, J. F. Létard, D. Chasseau, *Acta Crystallogr. Sect. B* **2003**, *59*, 479.
[18] A. Gavezzotti, *Acc. Chem. Res.* **1994**, *27*, 309.
[19] J. D. Dunitz, *Chem. Commun.* **2003**, 545.
[20] J. P. M. Lommerse, W. D. S. Motherwell, H. L. Ammon, J. D. Dunitz, A. Gavezzotti, D. W. M. Hofmann, F. J. J. Leusen, W. T. M. Mooij, S. L. Price, B. Schweizer, M. U. Schmidt, B. P. van Eijck, P. Verwer, D. E. Williams, *Acta Crystallogr. Sect. B* **2000**, *56*, 697.
[21] W. D. S. Motherwell, H. L. Ammon, J. D. Dunitz, A. Dzyabchenko, P. Erk, A. Gavezzotti, D. W. M. Hofmann, F. J. J. Leusen, J. P. M. Lommerse, W. T. M. Mooij, S. L. Price, H. Scheraga, B. Schweizer, M. U. Schmidt, B. P. van Eijck, P. Verwer, D. E. Williams, *Acta Crystallogr. Sect. B* **2002**, *58*, 647.
[22] Detailed results of these studies will be published elsewhere.
[23] A. B. Koudriavtsev, A. F. Stassen, J. G. Haasnoot, M. Grunert, P. Weinberger, W. Linert, *Phys. Chem. Chem. Phys.* **2003**, *5*, 3666.
[24] A. B. Koudriavtsev, A. F. Stassen, J. G. Haasnoot, M. Grunert, P. Weinberger, W. Linert, *Phys. Chem. Chem. Phys.* **2003**, *5*, 3676.
[25] O. M. Yaghi, M. O'Keeffe, N. W. Ockwig, H. K. Chae, M. Eddaoudi, J. Kim, *Nature* **2003**, *423*, 705.
[26] CCDC-239326–239331 contains the supplementary crystallographic data for this paper. These data can be obtained free of charge via www.ccdc.cam.ac.uk/conts/retrieving.html (or from the Cambridge Crystallographic Data Centre, 12 Union Road, Cambridge CB2 1EZ, UK; fax: (+44) 1223-336-033; or deposit@ccdc.cam.ac.uk).

 © 2004 Wiley-VCH Verlag GmbH & Co. KGaA, Weinheim

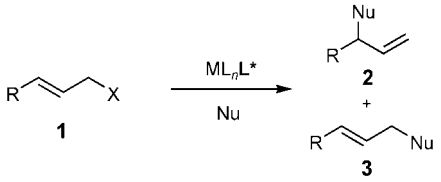
Allylic Substitution

Regio- and Enantioselective Iridium-Catalyzed Allylic Alkylation with In Situ Activated P,C-Chelate Complexes**

*Gunter Lipowsky, Nicole Miller, and Günter Helmchen**

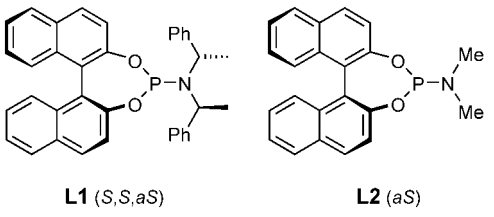
Dedicated to Professor Armin de Meijere on the occasion of his 65th birthday

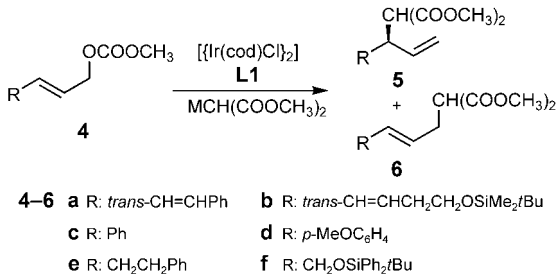
The asymmetric allylic substitution plays an important role in organic synthesis. However, this reaction is still largely limited to symmetrically substituted substrates and palladium catalysts.[1] With the exception of a few examples,[2] the particularly easily accessible monosubstituted allylic substrates **1** (Scheme 1) are not suitable substrates, because in intermolecular reactions using Pd catalysts they yield achiral, linear substitution products **3**. Remarkably, complexes of most of the other transition metals, e.g. Ir, Mo, and Ru, preferentially give rise to the branched, chiral products.[3–5] While Mo and Ru complexes furnished good results only in special cases, Ir catalysts are applicable to reactions with C[6] as well as N[7] and O[8] nucleophiles.[9]



Scheme 1. Allylic substitution (X: leaving group).

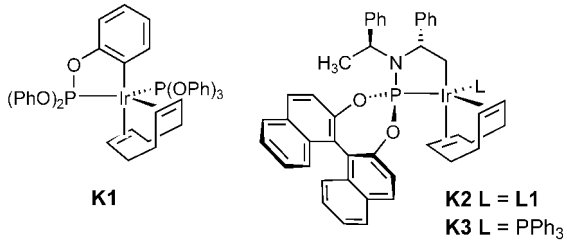
In the case of Ir catalysis, results for alkylations have not been satisfactory so far. Thus, using standard reaction conditions[6b,c] (phosphorus amidites as ligands, [{Ir(cod)Cl}$_2$]/ligand = 1:2, Nu = NaCH(COOCH$_3$)$_2$, THF, 65 °C; cod = cyclooctadiene), we achieved following results: a) with phosphorus amidite[10] **L2** as the ligand regioselectivities (**2**/**3**) of >90:10 were obtained for a broad range of acetates (**1**, X = OAc); however, the *ee* values of the products were low (4–86 %).[11] b) In contrast, with phosphorus amidite **L1** *ee* values ranged from 56 to 94 %, while regioselectivities covered the range from 30:70 up to 91:9.[6c] An improvement of regioselectivities resulted by using carbonates **4** in combination with ligand **L1** according to Scheme 2.[7c] For example, in the case of **4c** the optimum value was found to be **5c**/**6c** = 95:5. However, the enantioselectivity of 86 % *ee* was still below the critical value of 90 % *ee*. Moreover, reaction times of typically several days at room temperature were unsatisfactory; a typical example is the reaction of substrate **4a** (Scheme 2) according to entry 1, Table 1. A slight, but not sufficient improvement resulted with LiCl as additive (Table 1, entry 2).





Scheme 2. Ir-catalyzed allylic substitution with monosubstituted allylic carbonates. M = Na, Li.

We have now developed a new catalyst system that led to very substantial improvement with respect to selectivity and activity for a broad range of substrates. The starting point of the new development was the observation that complexes [Ir(cod)**L**Cl], formed spontaneously upon mixing [{Ir(cod)Cl}$_2$] with a phosphane **L**, do not react with allylic compounds **1** (X = Cl, OAc). An active catalyst is generated by C–H activation only after addition of the typically strongly basic nucleophile (e.g. malonate or amine). Thus, in the case of the achiral ligand P(OPh)$_3$ we identified the complex **K1** as the active species, which is formed by *ortho* C–H activation and elimination of HCl.[6b] Similarly, Hartwig et al. found that complex **K2**, besides other compounds, is formed from **L1** with amines as bases.[7b] The amine, e.g. pyrrolidine, acts as both nucleophile and base.



[*] G. Lipowsky, N. Miller, Prof. Dr. G. Helmchen
Organisch-Chemisches Institut
Universität Heidelberg
Im Neuenheimer Feld 270, 69120 Heidelberg (Germany)
Fax: (+49) 6221-544-205
E-mail: g.helmchen@urz.uni-heidelberg.de

[**] This work was supported by the Deutsche Forschungsgemeinschaft (SFB 623) and by the Fonds der Chemischen Industrie. We thank Markus Krauter for competent experimental assistance, Dr. F. Rominger for the X-ray crystal structure, and Degussa AG for iridium salts.

 DOI: 10.1002/anie.200460016 © 2004 Wiley-VCH Verlag GmbH & Co. KGaA, Weinheim

Table 1: Ir-catalyzed allylic alkylation of carbonate **4a** according to Scheme 2.[a]

Entry	**L1** [mol%]	Additive A[b] ([mol%])	TBD [mol%]	Additive B[c] ([mol%])	t[d] [h]	Yield **5a**+**6a** [%][e]	Ratio **5a**/**6a**[f]	*ee* (**5a**) [%][g] (Abs. config.)
1	4	–	–	–	120	77	89:11	88 (+)(*S*)
2[h]	4	LiCl (100)	–	–	22	87	94:6	90 (+)(*S*)
3	4	–	8	–	4	89	97:3	95 (+)(*S*)
4	8	–	8	–	12	80	97:3	92 (+)(*S*)
5	4	PPh_3 (4)	8	–	140	60	92:8	75 (+)(*S*)
6	4	PPh_3 (4)	8	CuI (4)	2	87	97:3	95 (+)(*S*)
7	4	THT (4)	8	–	6	83	98:2	95 (+)(*S*)
8	4	–	8	CuI (24)	5.5	74	98:2	95 (+)(*S*)
9	4	THT (4)	8	CuI (4)	1.5	83	98:2	96 (+)(*S*)
10	4	THT (20)	12	CuI (20)	1.5	92	98:2	96 (+)(*S*)
11	4	THT (80)	8	CuI (100)	<1	84	99:1	96 (+)(*S*)
12[i]	0.4	THT (5)	1.2	CuI (5)	24	77	98:2	94 (+)(*S*)

[a] Reaction conditions: 1 mmol **4a**, **L1**/[{Ir(cod)Cl}$_2$] = 2:1, 2 equiv NaCH(COOMe)$_2$, 0.25 M in THF, RT. [b] Addition before base and substrate. [c] Addition after substrate. [d] Reaction time. [e] Yield of isolated product. [f] Determined from the ^{1}H NMR spectrum of the crude product. [g] Determined by HPLC on a chiral column (Daicel Chiralcel OJ-H, 250×4.6 mm, 5 μm with guard cartridge OJ-H, 10×4 mm, 5 μm, 0.5 mL min^{-1}): **5a** (*n*-hexane/isopropanol 90:10, 20°C, 254 nm): t_R[(+)(*S*)-**5a**] = 26 min, t_R[(−)(*R*)-**5a**] = 29 min. [h] Reaction temperature: 50°C. [i] 0.2 mol% [{Ir(cod)Cl}$_2$], 0.4 mol% **L1**.

These results suggested that we generate the catalyst before the allylic substitution using a base other than the nucleophile. In our studies on the intramolecular allylic amination,[7d] this concept indeed led to a very active catalyst. This catalyst was prepared by treatment of [Ir(cod)(**L1**)Cl] with 1,5,7-triazabicyclo[4.4.0]undec-5-ene (TBD). In this reaction a species of unknown structure displaying a singlet at 98 ppm (^{31}P NMR) was formed initially. After approximately 2 h the concentration of this compound reached a maximum, and after prolonged reaction time (5–10 h) it was transformed mainly into **K2** (^{31}P NMR signals at 128 and 153 ppm). On the basis of these results it appeared possible to avoid the formation of **K2**, which displays low catalytic activity (Table 1, entry 1) because one coordination site is blocked by **L1**. Indeed, use of the system prepared over a period of only 2 h, largely devoid of **K2**, resulted in very rapid and highly selective alkylation (Table 1, entry 3). For a crosscheck, we increased the amount of **L1** (**L1**:Ir = 2:1); as anticipated, this led to a slow reaction (entry 4).

To explore another possibility for avoiding formation of **K2**, we added a soft, cheap auxiliary ligand **L** (Table 1, additive A) prior to the base, and catalysis was induced with a soft metal ion (Table 1, additive B).[12] PPh_3 was the first auxiliary ligand tested. Treatment of a 1:1:1 mixture of [{Ir(cod)Cl}$_2$], **L1**, and PPh_3 with TBD gave complex **K3** (^{31}P NMR signals at 6 and 152 ppm),[7b] which displayed low catalytic activity (entry 5) as expected, because coordination of PPh_3 to Ir^I is strong. However, if after addition of **4a** an amount of CuI was added equivalent to the amount of Ir, a very active catalyst was obtained (entry 6). In other words, the selective removal of the auxiliary ligand PPh_3 with the cheap CuI as a scavenger is possible.[13]

The continued search for even more suitable auxiliary ligands led to sulfides, in particular tetrahydrothiophene (THT), as the best solution so far. Optimal results were obtained by treatment of a 1:1:5 mixture of [{Ir(cod)Cl}$_2$], **L1**, and THT with TBD for only 2 h, thus, avoiding the formation of **K2**. At this time the species with a singlet at 98 ppm was dominant in the ^{31}P NMR spectrum (see above). Addition of only THT did not affect the activity of the catalyst (cf. entries 7 and 3). Similarly, addition of CuI did not show an effect without additional THT (cf. entries 8, 7 and 3). Increased activity resulted only upon addition of both additives (entry 9). In this case, the signals of **K2** had completely disappeared in the ^{31}P NMR spectrum, and in addition to the signal at 98 ppm there was a broad signal at 130 ppm. The activity of the catalyst could be noticeably increased by using an excess of THT as well as CuI (entries 10, 11; cf. General Procedure). The high activity of the new catalyst allowed Ir-catalyzed allylic alkylations for the first time to be carried out with less than 1 mol% of the iridium catalyst with very good results (entry 12).

The optimal reaction conditions (cf. General Procedure) were applied to further substrates, including the problematic alkyl- and alkoxyalkyl-substituted compounds, in order to investigate the substrate scope of the new catalyst (Table 2). For all examples both very high activity and enantioselectivity were found.

The absolute configuration of dienylic esters such as **5a** and **5b** was not determined previously. We have now prepared the derivative **7** from **5a** (Scheme 3); its absolute configuration could be determined by X-ray crystal structure analysis on account of the two heavy atoms. (Note that the change of the descriptors in Table 2 is only a consequence of the different CIP priorities of the substituents R in **5**.)

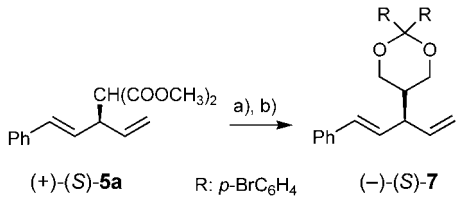
In conclusion, we have developed a highly active in situ catalyst for the iridium-catalyzed enantioselective allylic

Table 2: Ir-catalyzed allylic alkylation of the carbonates **4a**–**4f** according to Scheme 2 under optimal reaction conditions.[a]

Entry	Substrate	t[b] [h]	Yield (**5**+**6**) [%][c]	Ratio **5**:**6**[d]	*ee* (**5**) [%][e] (Abs. config.)
1	**4a**	1.5	92	98:2	96 (+)(*S*)
2	**4b**	1	79	98:2	96 (+)
3	**4c**	1	88	99:1	96 (+)(*R*)
4	**4d**	<1	95	99:1	97 (+)(*R*)
5	**4e**	2	92	81:19	96 (+)(*R*)
6	**4f**	2	88	88:12	97 (+)

[a] M = Na, Table 1, entry 10 and General Procedure. [b] Reaction time. [c] Yield of isolated product. [d] Determined from the ^{1}H NMR spectrum of the crude product. [e] Determined by HPLC on a chiral column; **5b** by determination as 4-bromobenzoate (Daicel Chiralcel OJ-H, 250×4.6 mm, 5 μm with guard cartridge OJ-H, 10×4 mm, 5 μm, 0.5 mL min^{-1}, *n*-hexane/isopropanol 99:1, 28°C, 254 nm): t_R[(+)-**5b**] = 96 min, t_R[(−)-**5b**] = 115 min; **5c** (same HPLC setup as for **5b**, *n*-hexane/isopropanol 97:3, 30°C, 220 nm): t_R[(−)(*S*)-**5c**] = 56 min, t_R[(+)(*R*)-**5c**] = 62 min; **5d** (Daicel Chiralcel OD-H, 250×4.6 mm, 5 μm with guard cartridge OD-H, 10×4 mm, 5 μm, 0.5 mL min^{-1}, *n*-hexane/isopropanol 90:10, 20°C, 220 nm): t_R[(+)(*R*)-**5d**] = 12 min, t_R[(−)(*S*)-**5d**] = 14 min; **5e** (same HPLC setup as for **5b**, *n*-hexane/isopropanol 98:2, 25°C, 220 nm): t_R[(+)(*R*)-**5e**] = 42 min, t_R[(−)(*S*)-**5e**] = 54 min; **5f** (same HPLC setup as for **5d**, *n*-hexane/isopropanol 99:1, 25°C, 220 nm): t_R[(+)-**5f**] = 12.3 min, t_R[(−)-**5f**] = 14.9 min.

 © 2004 Wiley-VCH Verlag GmbH & Co. KGaA, Weinheim



Scheme 3. Synthesis of the acetal (−)(*S*)-**7**; its absolute configuration was determined by X-ray crystal structure analysis. a) Diisobutylaluminum hydride, THF, −78 °C, 1 h, 67%; b) 4,4′-dibromobenzophenone, *p*TsOH (0.3 equiv), toluene, reflux, 20 h, 50%.

alkylation, which by interplay of Ir and Cu allows reaction times of less than an hour at room temperature and *ee* values of 94–97% to be achieved for a broad spectrum of substrates. The ratio of catalyst to substrate could be lowered down to 0.004.[14]

General procedure (corresponding to Table 1, entry 10): Under an atmosphere of argon, a solution of $[\{Ir(cod)Cl\}_2]$ (13.4 mg, 0.02 mmol) and **L1** (21.6 mg, 0.04 mmol) in anhydrous THF (0.5 mL) was treated with tetrahydrothiophene (18 μL, 0.20 mmol) (Table 1, additive A) and TBD (17 mg, 0.12 mmol), and the mixture was stirred for 2 h. Then substrate **4** (1.0 mmol) and subsequently CuI (38 mg, 0.20 mmol) (additive B) as well as a solution of sodium dimethylmalonate (2.0 mmol) in anhydrous THF (4 mL) were added. The mixture was stirred for the time stated in Tables 1 and 2, and conversion was monitored by thin-layer chromatography. When the conversion was complete, Et_2O (5 mL) and saturated NH_4Cl solution (5 mL) were added, and the aqueous phase was extracted with Et_2O (2×20 mL). The organic phases were combined, washed with brine (20 mL), dried over Na_2SO_4, filtered and concentrated in vacuo. The ratio **5**/**6** of the crude product was determined by ^1H NMR spectroscopy. Then the crude product was purified by flash column chromatography (silica, petroleum ether/ethyl acetate 15:1).

Received: March 16, 2004

Keywords: alkylation · allylic substitution · asymmetric catalysis · iridium · phosphorus amidites

[1] a) B. M. Trost, C. Lee in *Catalytic Asymmetric Synthesis*, *2nd Ed.* (Ed.: I. Ojima), Wiley, New York, **2000**, p. 593–649; b) A. Pfaltz, M. Lautens in *Comprehensive Asymmetric Catalysis I–III* (Eds.: E. N. Jacobsen, A. Pfaltz, H. Yamamoto), Springer, Berlin, **1999**, p. 833–884; c) B. M. Trost, M. L. Crawley, *Chem. Rev.* **2003**, *103*, 2921–2943.

[2] a) S.-L. You, X.-Z. Zhu, Y.-M. Luo, X.-L. Hou, L.-X. Dai, *J. Am. Chem. Soc.* **2001**, *123*, 7471–7472, and references therein; b) Vinyl epoxides: B. M. Trost, C. Jiang, *Org. Lett.* **2003**, *5*, 1563–1565, and references therein.

[3] a) Ir: R. Takeuchi, *Synlett* **2002**, 1954–1965; b) First enantioselective reaction: J. P. Janssen, G. Helmchen, *Tetrahedron Lett.* **1997**, *38*, 8025–8026.

[4] Mo: a) B. M. Trost, I. Hachiya, *J. Am. Chem. Soc.* **1998**, *120*, 1104–1105 (arylallyl derivatives); b) B. M. Trost, S. Hildbrand, K. Dogra, *J. Am. Chem. Soc.* **1999**, *121*, 10416–10417 (alkenylallyl derivatives); c) F. Glorius, A. Pfaltz, *Org. Lett.* **1999**, *1*, 141–144 (alkylallyl derivatives).

[5] Ru: B. M. Trost, P. L. Fraisse, Z. T. Ball, *Angew. Chem.* **2002**, *114*, 1101–1103; *Angew. Chem. Int. Ed.* **2002**, *41*, 1059–1061.

[6] a) B. Bartels, G. Helmchen, *Chem. Commun.* **1999**, 741–742; b) B. Bartels, C. Garcia-Yebra, F. Rominger, G. Helmchen, *Eur. J. Inorg. Chem.* **2002**, 2569–2586; c) B. Bartels, C. Garcia-Yebra, G. Helmchen, *Eur. J. Org. Chem.* **2003**, 1097–1103.

[7] a) T. Ohmura, J. F. Hartwig, *J. Am. Chem. Soc.* **2002**, *124*, 15164–15165; b) C. A. Kiener, C. Shu, C. Incarvito, J. F. Hartwig, *J. Am. Chem. Soc.* **2003**, *125*, 14272–14273; c) G. Lipowsky, G. Helmchen, *Chem. Commun.* **2004**, 116–117; d) C. Welter, O. Koch, G. Lipowsky, G. Helmchen, *Chem. Commun.* **2004**, 895–896.

[8] a) F. Lopez, T. Ohmura, J. F. Hartwig, *J. Am. Chem. Soc.* **2003**, *125*, 3426–3427; b) Kinetic resolution: C. Fischer, C. Defieber, T. Suzuki, E. M. Carreira, *J. Am. Chem. Soc.* **2004**, *126*, 1628–1629.

[9] Additionally it has to be noted that the price of iridium is far below that of palladium. The prices per ounce (world market prices, October 2003) are: rhodium $500, palladium $199, iridium $90.

[10] B. L. Feringa, *Acc. Chem. Res.* **2000**, *33*, 346–353.

[11] B. Bartels, unpublished results.

[12] The reason for this demand is the selective coordination of phosphorus in competition with the typically hard nucleophile.

[13] Realization of the obvious possibility of generating the catalyst in the presence of the allylic substrate or another olefin in order to saturate the free coordination site was not successful.

[14] **Note added in proof**: Use of a recently reported dimethoxy derivative of ligand **L1** (compound **3b** in K. Tissot-Croset, D. Polet, A. Alexakis, *Angew. Chem.* **2004**, *43*, 2426–2428) gave the following improved results for the reaction of **4a** according to Table 2, entry 1: reaction time 45 min, yield 80%, regioselectivity 99:1, 98.5% *ee*; the regioselectivity of the reaction according to entry 5 was improved to **5e**/**6e** = 88:12.

 © 2004 Wiley-VCH Verlag GmbH & Co. KGaA, Weinheim

Natural Products Synthesis

Total Synthesis of Apoptolidin**

*Hermut Wehlan, Mario Dauber, M.-Teresa Mujica Fernaud, Julia Schuppan, Rainer Mahrwald, Burkhard Ziemer, M.-Elisa Juarez Garcia, and Ulrich Koert**

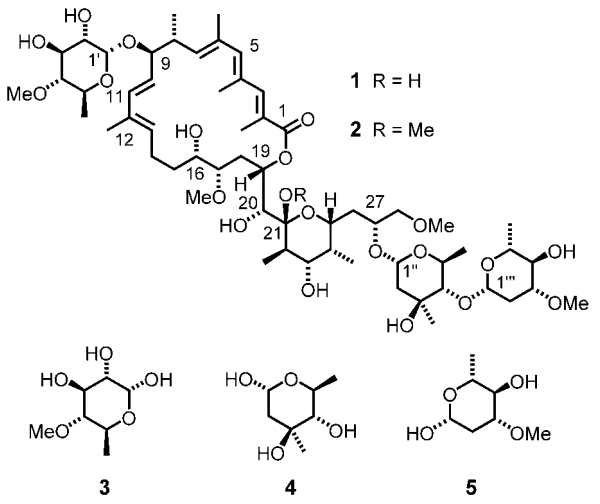
Apoptosis inducers specific for cancer cells are of interest for tumor therapy.[1] Apoptolidin (**1**), isolated from *Nocardiop-*

[*] Dipl.-Chem. H. Wehlan, M. Dauber, Dr. M.-T. Mujica Fernaud, Dr. J. Schuppan, Dipl.-Chem. M.-E. Juarez Garcia, Prof. Dr. U. Koert
Fachbereich Chemie
Philipps-Universität Marburg
Hans-Meerwein-Strasse, 35032 Marburg (Germany)
Fax: (+49) 6421-282-5677
E-mail: koert@chemie.uni-marburg.de
Priv.-Doz. Dr. R. Mahrwald, Dr. B. Ziemer
Institut für Chemie
Humboldt-Universität zu Berlin
Brook-Taylor-Strasse 2, 12489 Berlin (Germany)

[**] This work was supported by Schering AG Berlin and the Fonds der Chemischen Industrie. H.W. thanks the Schering Forschungsgesellschaft for a predoctoral fellowship. The authors thank Prof. Dr. U. Eder for his helpful support.

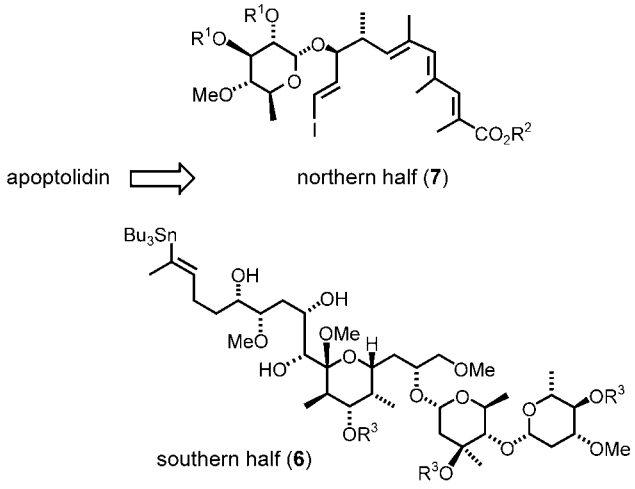
Supporting information for this article is available on the WWW under http://www.angewandte.org or from the author.

 DOI: 10.1002/anie.200460172 © 2004 Wiley-VCH Verlag GmbH & Co. KGaA, Weinheim

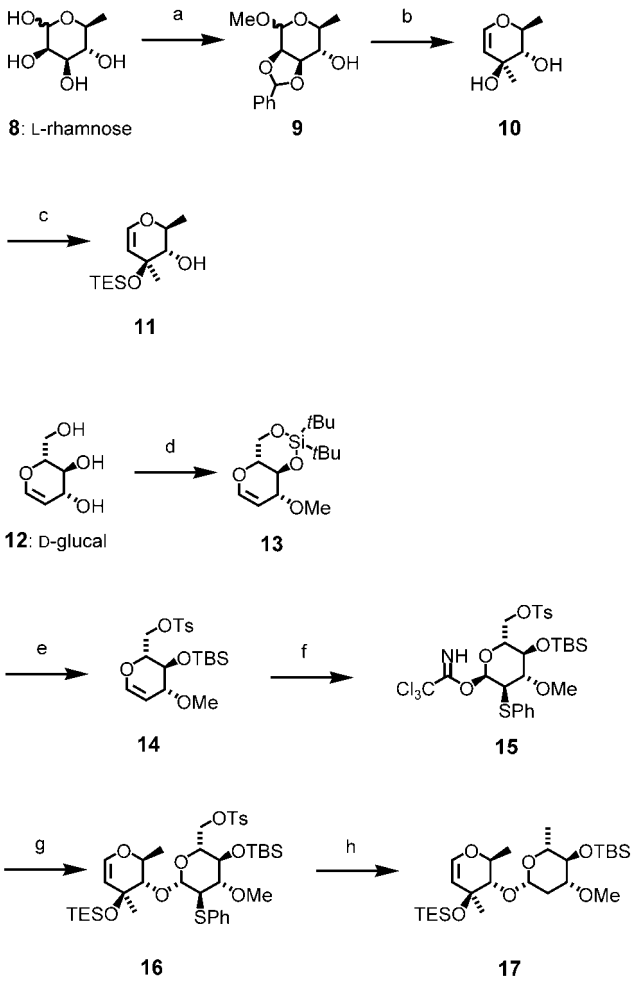


sis sp. by Hayakawa et al., selectively induces apoptosis in rat glia cells transformed with the E1A oncogene (IC_{50} = 11 ng mL^{-1}) but not in untransformed cell lines.[2,3] The apoptotic activity of **1** was correlated with its inhibition of mitochondrial F_0-F_1-ATPase.[4] Apoptolidin (**1**) is a 20-membered macrolactone with a side chain containing a cyclic six-membered hemiketal. 6-Deoxy-4-*o*-methyl-L-glucose (**3**) is attached to O9, and a disaccharide consisting of L-olivomycose (**4**) and D-oleandrose (**5**) is linked to O27. The sugar residues are a prerequisite for the potent bioactivity of **1**. Treatment of **1** with MeOH/Amberlyst-15 produces 21-*o*-methylapoptolidin (**2**).[5] Apoptolidin can rearrange into the 21-membered macrolactone isoapoptolidin by a O19→O20 acyl shift.[6] The noticeable biological activity of apoptolidin (**1**) and its structural challenges make it a prominent synthetic target.[7,8] In continuation of our synthesis of the aglycon apoptolidinone[9] we communicate here the completion of the total synthesis of apoptolidin.

Our synthetic strategy for apoptolidin (Scheme 1) is based on an early introduction of the sugar residues and a late cross-coupling of the fully glycosylated southern half **6** with the glycosylated northern half **7** followed by the macrolactonization. The starting point for the synthesis of the O27 disaccharide portion was L-rhamnose (**8**) which was transformed into the benzylidene-protected methyl acetal **9** (Scheme 2). Treatment of **9** with 6 equiv of methyllithium[10]



Scheme 1. Retrosynthetic analysis of apoptolidin.



Scheme 2. a) 1. MeOH, DOWEX 50WX-8-200; 2. $PhCH(OMe)_2$, *p*TsOH, DMF 58%; b) 6 equiv MeLi, THF, 20°C, 30 h, 43%; c) 1. Ac_2O, Py, DMAP, CH_2Cl_2; 2. TESOTf, lutidine; 3. DIBAH, CH_2Cl_2, −60°C, 71%; d) 1. $tBu_2Si(OTf)_2$, lutidine, DMF/CH_2Cl_2 1:1, −50°C; 2. MeI, Ag_2O, 87%; e) 1. TBAF, THF; 2. *p*TsCl, Py, CH_2Cl_2, 0°C; 3. TBSOTf, lutidine, CH_2Cl_2, 68%; f) 1. PhSCl, CH_2Cl_2; 2. Ag_2CO_3, CH_3CN/H_2O 9:1, 87%; 3. Cl_3CCN, NaH, 91%; g) **11**, TMSOTf, Et_2O, −60→−40°C, 1 h; h) 1. NaI, DMF, 90°C, 2 h; 2. Bu_3SnH, AIBN, toluene, 100°C, 7 h, 70% for three steps. AIBN = 2,2′-azobis(isobutyronitrile), DIBAH = diisobutylaluminum hydride, DMAP = 4-dimethylaminopyridine, TES = triethylsilyl, TMS = trimethylsilyl, TBA = tetrabutylammonium.

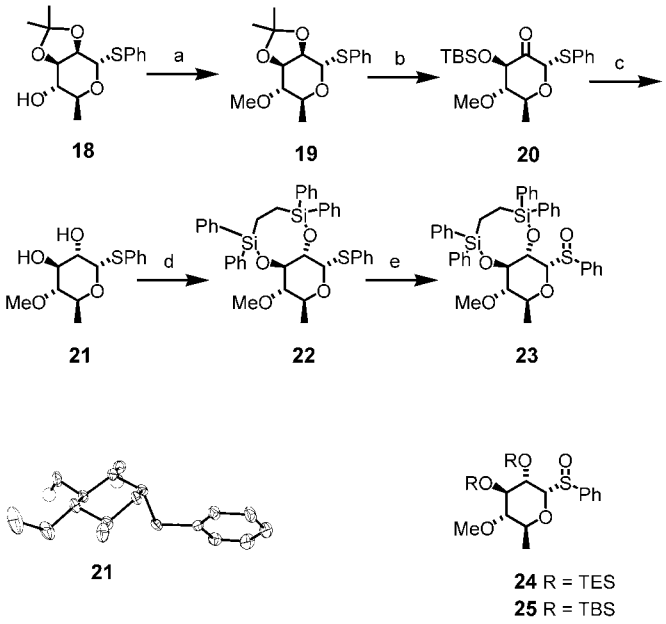
gave via a cyclohexenone intermediate the glycal **10**, which was converted into the protected olivomycal building block **11**. D-Glucal (**12**) was 4,6-silyl-protected and methylated at O3 to give **13**. Desilylation of the latter followed by tosylation of the primary OH group and protection of the secondary alcohol function with a *tert*-butyldimethylsilyl (TBS) group gave **14**. In preparation for a β-selective glycosylation, an auxiliary SPh substituent was introduced at C2 of the D-oleandrose building block.[11] To this end **14** was treated first with PhSCl, then with Ag_2CO_3 in H_2O/CH_3CN, and the

 © 2004 Wiley-VCH Verlag GmbH & Co. KGaA, Weinheim

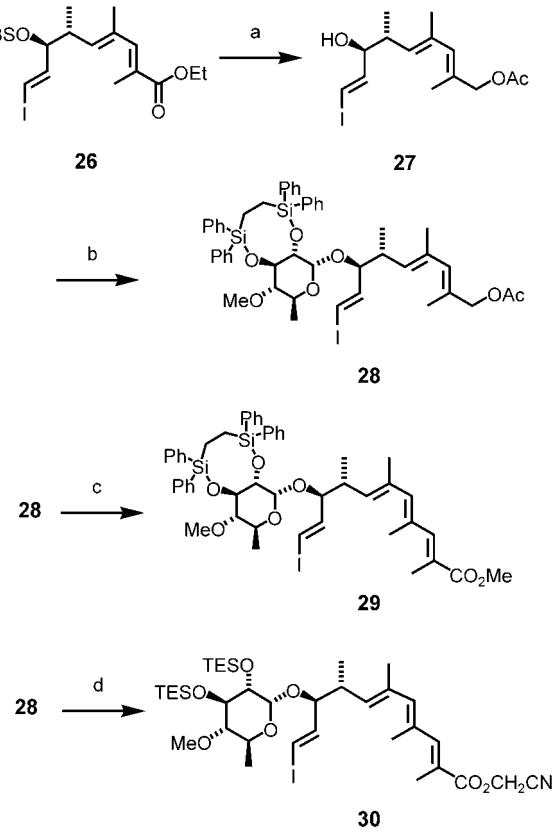
resulting α-anomeric hemiacetal was converted into the trichloroacetimidate **15**. The TMSOTf-mediated glycosylation of **11** and **15** produced the disaccharide **16** with very high β-selectivity (> 95:5). The conversion of the tosylate into an iodide and the combined reductive removal of the iodo and the thio function completed the preparation of the protected 2-deoxydisaccharide building block **17**.

An inversion at C2 converts L-rhamnose into 6-deoxy-L-glucose. Therefore, L-rhamnose is a suitable starting material for the O9 sugar residue of apoptolidin (Scheme 3).[12] The acetonide-protected L-rhamnose thioglycoside **18**[13] was O-methylated to obtain **19**. Acetonide cleavage, TBS protection of O3, and subsequent oxidation of the remaining 2-OH group provided the ketone **20**. A highly stereoselective reduction of **20** with $NaBH_4$ gave the corresponding alcohol, which was desilylated to provide the diol **21**. The relative configuration of **21** was confirmed by X-ray structure analysis (Scheme 3).[14] The following choice of the right O2/O3 L-glucose protecting groups was crucial for the successful glycosylation of the northern half. An α-selective glycosylation required a passive O2 protecting group that can be removed at the end without affecting the highly unsaturated and acid-sensitive target molecule. Silyl ethers should be the best choice. After several unsuccessful glycosylation attempts (trichloroacetimidate, glycosyl fluoride, thioglycoside activation by PhSOTf) we focused on the Kahne glycosylation by means of sulfoxide activation.[15] Initially we prepared and examined the bis(TES)- and bis(TBS)-protected sulfoxides **24** and **25**. However, these glycosyl donors gave unsatisfying glycosylation results (vide infra), which prompted us to develop a new protecting group. Treatment of diol **21** with 1,4-dichloro-1,1,4,4-tetraphenyl-1,4-disilabutane ($SIBACl_2$)[16] gave the disilyl ether **22** in 92% yield. Oxidation of **22** with *m*CPBA led to the desired SIBA-protected glycosyl sulfoxide **23**.

The synthesis of the glycosylated northern half used the unsaturated ester **26**[9] from the aglycone synthesis as a common building block (Scheme 4). Ester **26** was converted into the glycosyl acceptor **27**. Initial attempts to use the bis(TES)-protected glycosylsulfoxide **24** as a glycosyl donor failed due to loss of the TES groups under the reaction conditions (Tf_2O, DTBMP, −80→−35 °C). The more stable bis(TBS)-protected glycosylsulfoxide **25** gave the desired glycoside in 50% yield but with an unacceptably low stereoselectivity (α/β = 66:33). In contrast, the reaction of the SIBA-protected glycosylsulfoxide **23** with **27** gave the expected product **28** in 65% yield with an acceptable stereoselectivity (α/β = 85:15). The final task for the comple-

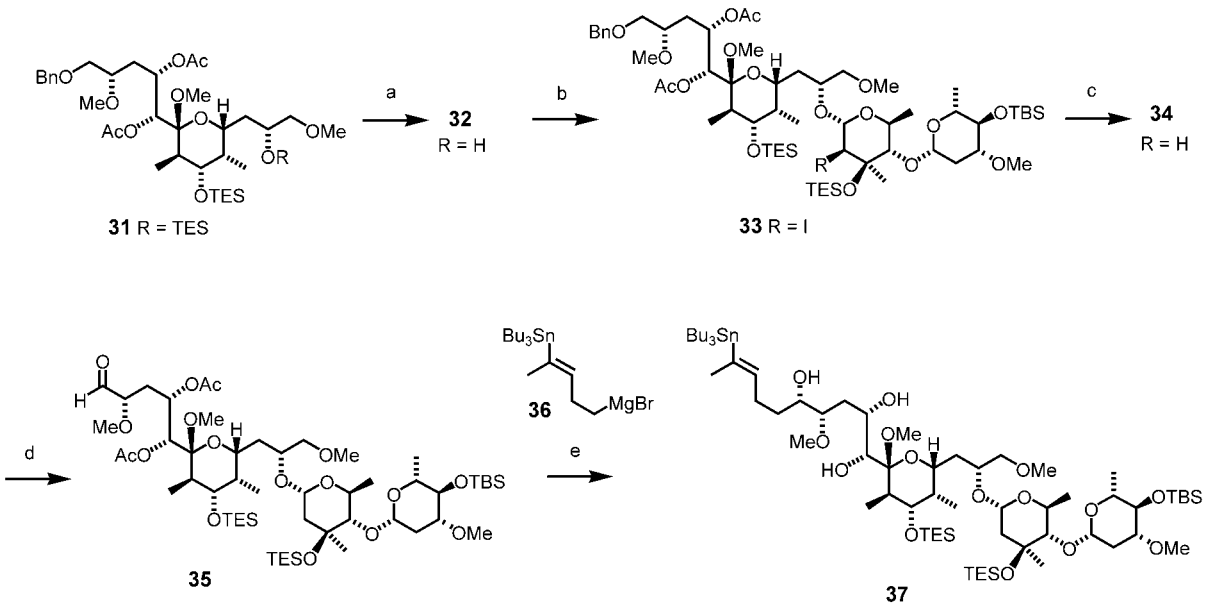


Scheme 3. a) MeI, KOH, DMF, 0 °C, 99%; b) 1. *p*TsOH, MeOH, 89%; 2. TBSCl, imidazole, DMAP, CH_2Cl_2, 91%; 3. Dess–Martin periodinane, 80%; c) 1. $NaBH_4$, MeOH, 0 °C, 15 min, 97%; 2. TBAF, THF, 94%; d) $Ph_2Si(Cl)CH_2CH_2Si(Cl)Ph_2$, imidazole, DMF, 0 °C, 1 h, 92%; e) *m*CPBA, CH_2Cl_2, −78→−20 °C, 2 h, 92%, 2:1 mixture of epimers. *m*CPBA = *meta*-chloroperbenzoic acid.

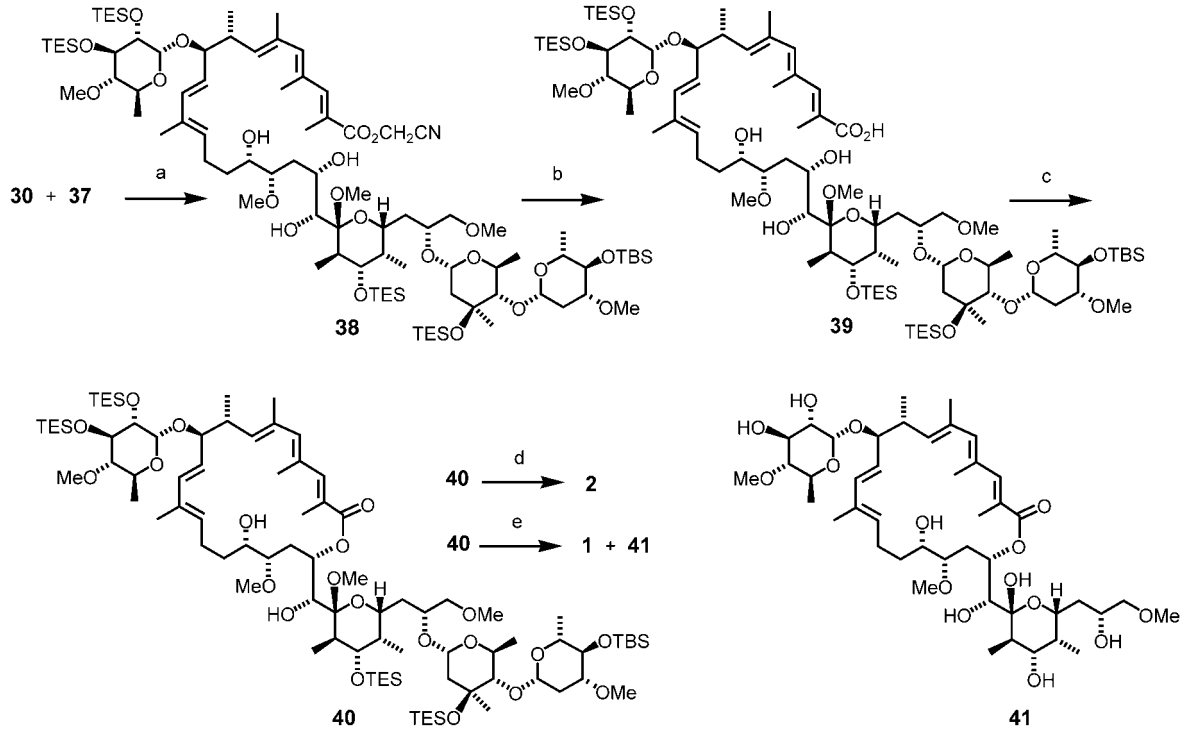


Scheme 4. a) 1. DIBAH, toluene, −78 °C, 98%; 2. Ac_2O, Et_3N, DMAP, CH_2Cl_2, 0 °C; 3. TBAF, THF, 0→20 °C, 92%; b) 1 equiv **23**, 1.5 equiv Tf_2O, DTBMP, −80 °C, 10 min; addition of **27**, −80→−35 °C, 2 h; 65%, α/β = 85:15; c) 1. chromatographic separation of the anomers; 2. $LiEt_3BH$, THF, −50 °C, 1 h, 75%; 3. MnO_2, CH_2Cl_2; 4. $Ph_3P{=}C(CH_3)CO_2Me$, toluene, 90 °C, 44 h, 91%; d) 1. TBAF, THF, 20 °C, 99%; 2. TESCl, imidazole, 20 °C, 99%; 3. LiOH, THF/MeOH/H_2O 2:1:1, 0 °C, 1 h, 83%; 4. MnO_2, CH_2Cl_2, chromatographic separation of the anomers, 78% α-anomer, 13% β-anomer; 5. $(EtO)_2P(O)CH(CH_3)CO_2H$, NaH, THF, 12 °C, 14 h, 87%; 6. $ClCH_2CN$, Et_3N, MeCN, 20 °C, 14 h, 92%. DTBMP = 2,6-di-*tert*-butyl-4-methylpyridine.

 © 2004 Wiley-VCH Verlag GmbH & Co. KGaA, Weinheim



Scheme 5. a) TBAF, THF, 0 °C, 90%; b) **17**, NIS, 4-Å molecular sieves, CH_2Cl_2, 0→20 °C, 72 h, 53%; anomeric ratio >95:5; c) Bu_3SnH, AIBN, toluene, 100 °C, 15 min, 96%; d) 1. H_2, Pd/C, EtOH, 90%; 2. Dess–Martin periodinane, pyridine, CH_2Cl_2, 20 °C, 1 h, 84%; e) 1. Mg, $BrCH_2CH_2Br$, Et_2O, −78 °C, 74%, ds >95:5 ; 2. KCN, MeOH, 40 °C, 16 h, 86%. NIS = *N*-iodosuccinimide.



Scheme 6. a) 3 equiv Cu^{I} thiophenecarboxylate, NMP, 1 h, 0 °C, 89%; b) 3 equiv LiOH, THF/MeOH 3:1, 20 °C, 2 h, 88%; c) 20 equiv 2,4,6-trichlorobenzoyl chloride, 40 equiv Et_3N, THF, 6 h; toluene, 80 equiv DMAP, $c = 3 \times 10^{-4}$ M, 75%; d) HF, pyridine, THF, 20 °C, 5 d, 50%; e) H_2SiF_6 (25% in H_2O), CH_3CN, −40→−20 °C, 2 d, −10 °C, 1 d, 71% **1** and 27% **41**. NMP = *N*-methylpyrrolidone.

tion of the northern half was the introduction of the C1–C3 unsaturated ester fragment. This was accomplished using standard Wittig and Horner—Wadsworth–Emmons procedures to give the methyl ester **29** and the cyanomethyl ester **30**, respectively.

The synthesis of the glycosylated southern half made use of the bis(TES) ether **31** from the aglycone synthesis (Scheme 5).[9] Selective deprotection of the 27-*O*-TES group in **31** gave **32**, which was allowed to react with the disaccharide glycal **17** to produce the glycoconjugate **33**

 © 2004 Wiley-VCH Verlag GmbH & Co. KGaA, Weinheim

with a high α-selectivity of $>95:5$.[17] Reductive removal of the auxiliary iodo function led to the benzyl ether **34**. In order to prevent side reactions with the subsequent hydrogenolysis, it was necessary to remove all tin impurities from **34** by treatment with fluoride at this stage. The corresponding primary alcohol could be oxidized to the aldehyde **35**. The final step for the completion of the southern half was the chelation-controlled addition of the Grignard reagent **36**[9] to **35** to produce the corresponding alcohol with a diastereoselectivity of 96:4. Cleavage of the two acetates led to the triol **37**.

The cross-coupling of either the northern half, **29** or **30,** with the southern half **37** was possible with Cu^I thiophene-2-carboxylate in NMP (Scheme 6).[18] The methyl ester coupling product caused trouble in the subsequent methyl ester hydrolysis. We therefore focused on the cyanomethyl ester coupling product **38**. The cyanomethyl ester function in **38** could be hydrolyzed under very mild conditions (LiOH, 20 °C, 2 h) to the acid **39** without affecting the triene system or the TES protecting groups. A remarkable ring-size-selective macrolactonization of **39** produced the 20-membered lactone **40** in 75% yield. The final deprotection step required a careful examination of reagents and optimization of reaction conditions. The use of HF/pyridine in THF/pyridine at room temperature for 5 d cleaved all silyl ethers but left the methyl ketal intact and gave synthetic 21-o-methyl apoptolidin (**2**) which proved to be identical with **2** derived from natural sources ($[\alpha]_D^{22}=-76$ ($c=0.55$ in $CHCl_3$),[5] $[\alpha]_D^{22}=-67$ ($c=1.28$ in $CHCl_3$); for ^1H and ^{13}C NMR data see the Supporting Information).

We then turned our attention to the complete deprotection of **40** leading to apoptolidin (**1**). Treatment with 25% aqueous H_2SiF_6 in CH_3CN at $-40\rightarrow-10$ °C proved to be effective for cleavage of all silyl ethers[19] and noteworthy the methyl ketal. Apoptolidin (**1**) could be isolated in 71% yield by chromatographic separation on deactivated silica gel[20] with CH_2Cl_2/MeOH. In addition, the cleavage of the 27-*O*-disaccharide was observed and compound **41** was isolated in 27% yield. The physical and spectroscopic data of the synthetic apoptolidin (**1**) matched those published by Hayakawa et al. (m.p. 129–131 °C (MeOH), ref. [2]: 128–130 °C; ($[\alpha]_D^{22}=-4.4$ ($c=0.70$ in MeOH), ref. [2] $[\alpha]_D^{22}=-5.2$ ($c=1.0$ in MeOH); for ^1H and ^{13}C NMR data see the Supporting Information).

In conclusion an efficient, convergent, and stereoselective total synthesis of apoptolidin has been achieved. The distinct features of this synthesis are the early introduction of the sugar residues using a new sugar protecting group (SIBA), a Cu^I-mediated cross-coupling followed by a ring-size-selective macrolactonization, and mild deprotection conditions. This strategy should be applicable to the synthesis of apoptolidin derivatives with potential applications in apoptosis studies and tumor therapy.

Received: March 31, 2004

Keywords: cross-coupling · glycosylation · macrolides · natural products · total synthesis

[1] L. Benitez-Bribiesca in *When Cells Die* (Eds. R. A. Lockshin, Z. Zakeri, J. L. Tilly), Wiley-Liss, New York, **1998**, pp. 453–482.
[2] J. W. Kim, H. Adachi, K. Shin-ya, Y. Hayakawa, H. Seto, *J. Antibiot.* **1997**, *50*, 628–630.
[3] Y. Hayakawa, J. W. Kim, H. Adachi, K. Shin-ya, K. Fujita, H. Seto, *J. Am. Chem. Soc.* **1998**, *120*, 3524–3525.
[4] a) A. R. Salomon, D. W. Voehringer, L. A. Herzenberg, C. Khosla, *Proc. Natl. Acad. Sci. USA* **2000**, *97*, 14766–14771; b) A. R. Salomon, D. W. Voehringer, L. A. Herzenberg, C. Khosla, *Chem. Biol.* **2001**, *8*, 71–80; c) A. R. Salomon, Y. Zhang, H. Seto, C. Khosla, *Org. Lett.* **2001**, *3*, 57–59.
[5] P. A. Wender, O. D. Jankowski, E. A. Tabet, H. Seto, *Org. Lett.* **2003**, *5*, 487–490.
[6] a) P. A. Wender, A. V. Gulledge, O. D. Jankowski, H. Seto, *Org. Lett.* **2002**, *4*, 3819–3822; b) J. D. Pennington, H. J. Williams, A. R. Salomon, G. A. Sulikowski, *Org. Lett.* **2002**, *4*, 3823–3825.
[7] Total syntheses: a) K. C. Nicolaou, Y. Li, K. C. Fylaktakidou, H. J. Mitchell, H. X. Wei, B. Weyershausen, *Angew. Chem.* **2001**, *113*, 3968–3972; *Angew. Chem. Int. Ed.* **2001**, *40*, 3849–3854; b) K. C. Nicolaou, Y. Li, K. C. Fylaktakidou, H. J. Mitchell, K. Sugita, *Angew. Chem.* **2001**, *113*, 3972–3976; *Angew. Chem. Int. Ed.* **2001**, *40*, 3854–3857; c) K. C. Nicolaou, K. C. Fylaktakidou, H. Monenschein, Y. Li, B. Weyershausen, H. J. Mitchell, H. X. Wei, P. Guntupalli, D. Hepworth, K. Sugita, *J. Am. Chem. Soc.* **2003**, *125*, 15433–15442; d) K. C. Nicolaou, Y. Li, K. Sugita, H. Monenschein, P. Guntupalli, H. J. Mitchell, K. C. Fylaktakidou, D. Vourloumis, P. Giannakakou, A. O'Brate, *J. Am. Chem. Soc.* **2003**, *125*, 15443–15454.
[8] Fragment syntheses: a) G. A. Sulikowski, W. M. Lee, B. Jin, B. Wu, *Org. Lett.* **2000**, *2*, 1439–1442; b) K. Toshima, T. Arita, D. Tanaka, S. Matsumura, *Tetrahedron Lett.* **2001**, *42*, 8873–8876; c) W. D. Paquette, R. E. Taylor, *Org. Lett.* **2004**, *6*, 103–106.
[9] a) J. Schuppan, H. Wehlan, S. Keiper, U. Koert, *Angew. Chem.* **2001**, *113*, 2125–2128; *Angew. Chem. Int. Ed.* **2001**, *40*, 2063–2066; b) J. Schuppan, B. Ziemer, *Tetrahedron Lett.* **2000**, *41*, 621–624.
[10] G. Jung, A. Klerner, *Chem. Ber.* **1981**, *114*, 740–745.
[11] a) R. Preuss, R. R. Schmidt, *Synthesis* **1988**, 694–697; b) W. R. Roush, X. F. Lin, *J. Org. Chem.* **1991**, *56*, 5740–5742.
[12] A related route to the 6-deoxy-L-glucose building block was chosen by Nicolaou et al.[7a,c]
[13] I. Bajza, A. Liptak, *Carbohydr. Res.* **1990**, *205*, 435–439.
[14] CCDC 234809 contains the supplementary crystallographic data for this paper. These data can be obtained free of charge via www.ccdc.cam.ac.uk/conts/retrieving.html (or from the Cambridge Crystallographic Data Centre, 12, Union Road, Cambridge CB21EZ, UK; fax: (+44) 1223-336-033; or deposit@ccdc.cam.ac.uk).
[15] D. Kahne, S. Walker, Y. Cheng, D. VanEngen, *J. Am. Chem. Soc.* **1989**, *111*, 6881–6882.
[16] 1,4-Dichloro-1,1,4,4-tetraphenyl-1,4-disilabutane ($SIBACl_2$) was prepared by reaction of 1,2-bis(trichlorosilyl)ethane with phenylmagnesium bromide.
[17] J. Thiem, J. Elvers, *Chem. Ber.* **1980**, *113*, 3049–3057.
[18] G. D. Allred, L. S. Liebeskind, *J. Am. Chem. Soc.* **1996**, *118*, 2748–2749.
[19] A. S. Pilcher, D. K. Hill, S. J. Shimshock, R. E. Waltermire, P. DeShong, *J. Org. Chem.* **1992**, *57*, 2492–2495.
[20] Chromatotrex silicagel MB 100-40/75 from Fuji Silysia Chemical LTD.

 © 2004 Wiley-VCH Verlag GmbH & Co. KGaA, Weinheim

Catalyst Models

Fully Metalated Silsesquioxanes: Building Blocks for the Construction of Catalyst Models**

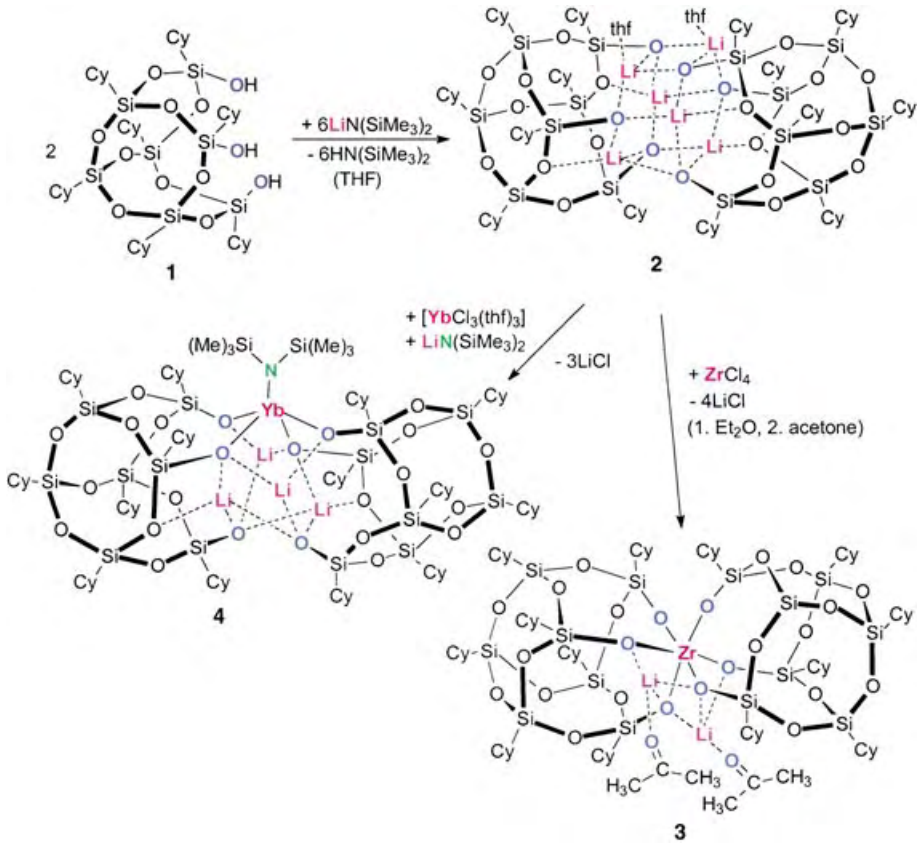
*Volker Lorenz, Stephan Gießmann, Yurii K. Gun'ko, Axel K. Fischer, John W. Gilje, and Frank T. Edelmann**

Dedicated to Professor Gerd-Volker Röschenthaler on the occasion on his 60th birthday

Numerous industrially and commercially important processes such as the production of polyolefins are catalyzed by transition-metal complexes immobilized on silica surfaces.[1] However, due to the heterogeneous nature of these catalysts, full characterization of the catalytically active species is often difficult, and little is known about the reaction mechanisms and the nature of the metal–silica interactions. Surface organometallic chemistry (SOMC), developed by Basset and co-workers, is one suitable approach towards a better understanding of heterogeneous catalytic processes.[2] A different approach uses suitable well-defined homogeneous model systems that provide a coordination environment similar to that of silica surfaces. In recent years, polyhedral metallasilsesquioxanes have been promoted as molecular model compounds which to some extent can provide insight into the scenarios occurring on metal-modified silica surfaces.[3] Feher et al. have established that the incompletely condensed silsesquioxane derivative $Cy_7Si_7O_9(OH)_3$ (**1**, Cy = cyclohexyl, Scheme 1) shares structural similarities with crystalline forms of silica such as β-cristobalite and β-tridymite.[4] Fully metalated silsesquioxane derivatives of the type $Cy_7Si_7O_9(OM)_3$ (M = Li, Na, K) would constitute highly desirable precursors for the construction of catalyst model compounds, including novel heterobimetallic species. However, such alkali metal derivatives of **1** were unknown until recently, and structural information on such materials is still lacking.

There have been contrasting reports in the literature concerning the metalation of **1** by alkali metal reagents. It was reported by Feher et al. that treatment of **1** with three equivalents of NaO*t*Bu resulted in complete breakdown of the silsesquioxane cage.[3a] In contrast, Aspinall and co-workers more recently succeeded in synthesizing $Cy_7Si_7O_9(OLi)_3$ by the reaction of **1** with *n*-butyllithium.[5] $Cy_7Si_7O_9(OLi)_3$ was isolated in virtually quantitative yield as an amorphous, air-stable (!) solid of unknown structure. We report here that with the proper choice of deprotonating agents well-defined, crystalline alkali metal silsesquioxanes are readily available. These represent excellent precursors for the preparation of unprecedented catalyst model compounds.

We found that alkali metal bis(trimethylsilyl)amides are the reagents of choice for achieving smooth and high-yield deprotonation of the incompletely condensed silsesquioxane **1**. Treatment of **1** with $LiN(SiMe_3)_2$ in diethyl ether/THF afforded the crystalline lithium silsesquioxane dimer $[\{(c\text{-}C_6H_{11})_7Si_7O_{12}\}_2Li_6(C_4H_8O)_2]\cdot C_4H_{10}O$ (**2**) in 93% yield



Scheme 1. Synthesis of the metalated silsesquioxanes **2**–**4** (Cy = cyclohexyl).

[*] Dr. V. Lorenz, Dr. S. Gießmann, Dr. A. K. Fischer, Prof. F. T. Edelmann
Chemisches Institut
Otto-von-Guericke-Universität Magdeburg
Universitätsplatz 2, 39106 Magdeburg (Germany)
Fax: (+49) 391-671-2933
E-mail: frank.edelmann@vst.uni-magdeburg.de
Dr. Y. K. Gun'ko
Department of Chemistry
Trinity College
Dublin 2 (Ireland)
Prof. Dr. J. W. Gilje
Chemistry Department
James Madison University
Harrisonburg, VA 22807 (USA)

[**] This work was supported by the Deutsche Forschungsgemeinschaft (Schwerpunktprogramm "Spezifische Phänomene der Silicium-Chemie"), the Fonds der Chemischen Industrie, and the European Commission (contract G1RD-CT-1999-00167 "SAFEGAS").

 DOI: 10.1002/anie.200454094 © 2004 Wiley-VCH Verlag GmbH & Co. KGaA, Weinheim

(Scheme 1). This reaction is not limited to the THF-adduct **2**. The corresponding acetone solvate $[\{(c\text{-}C_6H_{11})_7Si_7O_{12}\}_2Li_6(Me_2CO)_3]$ as well as the dimeric potassium derivative $[\{(c\text{-}C_6H_{11})_7Si_7O_{12}\}_2K_6(dme)_4]$ (dme = dimethoxyethane) have been isolated in a similar manner.[3d,6]

An X-ray diffraction study revealed the dimeric molecular structure of **2** (Figure 1).[7] The central structural unit of **2**

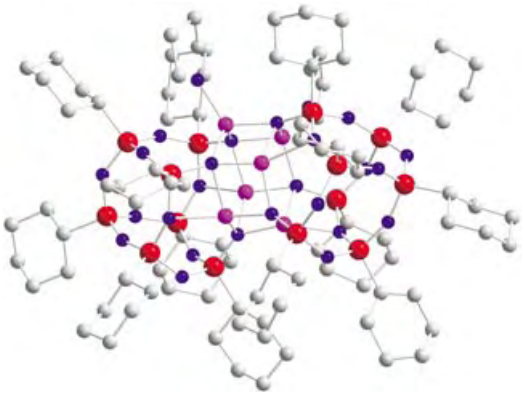


Figure 1. Molecular structure of **2** (● = C, ● = O, ● = Si, ● = Li). Selected bond lengths [Å] and angles [°]: Si-O 1.613(4)–1.662(4), Si-$O_{(Li)}$ 1.584(4)–1.596(4), Li-O 1.889(10)–2.327(10), O-Si-O 105.9(2)–114.0(2), Si-O-Si 131.2(2)–158.4(3), Si-O-Li 85.7(3)–152.9(3).

consists of a box-shaped Li_6O_6 polyhedron. Two lithium ions coordinate to thf ligands, while the other four interact with framework oxygen atoms of the silsesquioxane cages. This bonding situation results in tetracoordination around each lithium center. Structurally related box-shaped Li_6O_6 or Li_6S_6 polyhedra have previously been reported for some hexameric lithium phenoxides or arenethiolates,[8] but are unprecedented in silsesquioxane chemistry. The same structural motif has been established for the closely related molecular structures of $[\{(c\text{-}C_6H_{11})_7Si_7O_{12}\}_2Li_6(Me_2CO)_3]$ and $[\{(c\text{-}C_6H_{11})_7Si_7O_{12}\}_2K_6(dme)_4]$.[3d,6]

With the lithiated silsesquioxane **2** now being readily available in large quantities, we began exploring its derivative chemistry with the aim of synthesizing novel molecular model systems for silica-supported heterogeneous catalysts. For this purpose **2** can be employed as the starting material, but it has been found that the more convenient use of $Cy_7Si_7O_9(OLi)_3$, prepared in situ, in further reactions also gives excellent results. For example, the reaction of $Cy_7Si_7O_9(OLi)_3$ with $ZrCl_4$ in THF/acetone followed by crystallization from acetone afforded the novel heterobimetallic metallasilsesquioxane $[\{[(c\text{-}C_6H_{11})_7Si_7O_{12}]Li(OCMe_2)\}_2Zr]$ (**3**) as a colorless, crystalline material (Scheme 1). The molecular structure of **3** was established by single-crystal X-ray diffraction (Figure 2). The central zirconium atom is encapsulated by two silsesquioxanes cages resulting in an approximate octahedral coordination environment. Two $Li(OCMe_2)$ units are attached to this formally dianionic $\{(c\text{-}C_6H_{11})_7Si_7O_{12}\}_2Zr^{2-}$ moiety. Tetracoordination around each Li ion is achieved through coordinative interaction with three cage oxygen atoms.

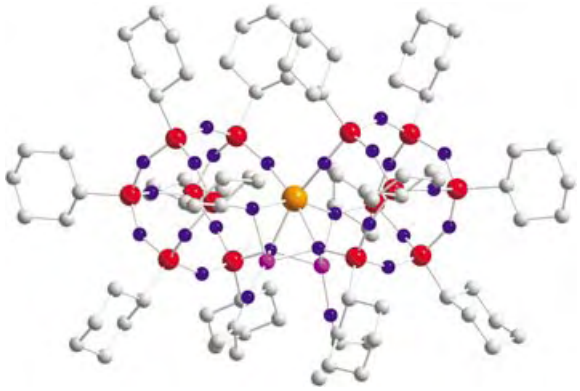


Figure 2. Molecular structure of **3** (● = C, ● = O, ● = Si, ● = Li, ● = Zr). Selected bond lengths [Å] and angles [°]: Zr-O 1.978(3)–2.080(3), Zr-O_{Li} 2.44(4), Si-O 1.607(3)–1.646(3), Li-O 1.895(8)–2.066(9); O_{Li}-Zr-O_{Li} 70.75(11)–79.45(11), O_{Si}-Zr-O_{Si} 96.40(13)–99.64(11), Si-O-Si 107.74(16)–112.12(17).

The most unusual heterometallasilsesquioxane made from **2** thus far is the ytterbium bis(trimethylsilylamide) derivative $[\{[(c\text{-}C_6H_{11})_7Si_7O_{12}]_2Li_4\}YbN(SiMe_3)_2]$ (**4**) which was prepared by reacting **2** (prepared in situ) with anhydrous $YbCl_3$ according to Scheme 1 (51% yield). The structurally characterized ytterbium(III) complex **4** represents a novel type of heterobimetallic metallasilsesquioxane, as it contains an additional functional group at the metal center.[9] Ytterbium is coordinated through oxygen atoms to a lithium silsesquioxane framework made up of two $(c\text{-}C_6H_{11})_7Si_7O_{12}Li_2$ units. Owing to the involvement of cage oxygen atoms in the coordination to the Li ions, there are no additional ligands such as Et_2O or THF present in this molecule. The overall structure with a reactive $[YbN(SiMe_3)_2]$ unit residing on a model silica surface resembles that of typical catalytically active lanthanide metallocenes such as $[(C_5Me_5)_2LnN(SiMe_3)_2]$.[10] In **4** two bulky silsesquioxane cages play the role of the pentamethylcyclopentadienyl ligands in the bent metallocene unit (Figure 3). Most notably, however, the molecular compound

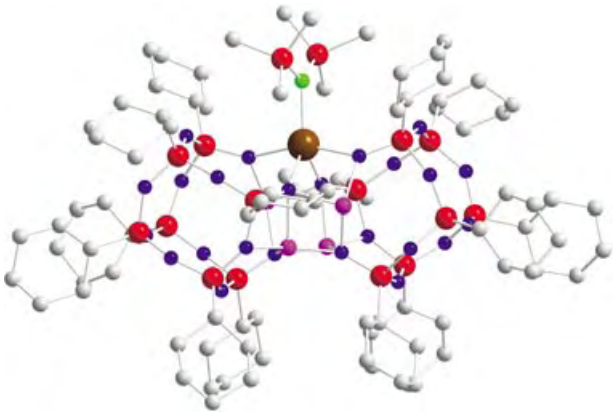


Figure 3. Molecular structure of **4** (● = C, ● = O, ● = Si, ● = N, ● = Li, ● = Yb). Selected bond lengths [Å] and angles [°]: Yb-O 2.194(8)–2.256(9), Yb-N 2.236(3), Si-O 1.606(9)–1.657(10), Li-O 1.96(2)–2.19(2); O_{Li}-Yb-O_{Li} 77.8(3), N-Yb-O 99.9(5)–132.9(6), Si-O-Si 102.5(5)–112.0(5).

 © 2004 Wiley-VCH Verlag GmbH & Co. KGaA, Weinheim

4 represents the first "realistic" model for a reactive lanthanide silylamide species bound to a silica surface. Such lanthanide silylamides grafted on silica or the mesoporous silicate MCM-41 are interesting catalysts which have been investigated in detail by Anwander et al.[11]

In summary, we have demonstrated that fully metalated silsesquioxane derivatives such as dimeric **2** are readily available in high yields by using alkali metal silylamides as deprotonating agents. These fully metalated silsesquioxane derivatives are versatile building blocks for the construction of molecular models for heterogeneous catalysts, including bimetallic species and complexes containing functional groups. As the reactions reported here appear to be quite general, the results are expected to stimulate further research in this area.

Experimental Section

All reactions were carried out under nitrogen and in carefully dried and degassed solvents.

2: Compound **1** (2.0 g, 2.054 mmol) was added to a solution of $LiN(SiMe_3)_2$ (prepared in situ by reaction of *n*-butyllithium (4.13 mL of a 1.6 M solution in diethyl ether) with $HN(SiMe_3)_2$ (1.06 g, 1.40 mL, 6.574 mmol)) in THF (100 mL) at room temperature. The reaction mixture was stirred for 10 h. Compound **2** precipitated almost quantitatively as a white microcrystalline solid after partial removal of solvents. The crude product was isolated by filtration. Colorless crystals of **2** (2.1 g; 93 %) were separated after recrystallization from a mixture of diethyl ether and THF. Correct elemental analysis for $[\{(c\text{-}C_6H_{11})_7Si_7O_{12}\}_2Li_6(C_4H_8O)_2]\cdot C_4H_{10}O$, $C_{96}H_{180}Si_{14}O_{27}Li_6$. ^{1}H NMR (400 MHz, $CDCl_3$, 25 °C): $\delta = 3.77$ (br s, 8H; OCH_2CH_2, thf), 3.34 (q, $^3J(H,H) = 7.0$ Hz 4H; OCH_2CH_3, Et_2O), 1.85 (br s, 8H; OCH_2CH_2, thf), 1.73 (br m, 70H; CH_2, *c*-C_6H_{11}), 1.23 (br m, 70H; CH_2, *c*-C_6H_{11}), 1.08 (t, $^3J(H,H) = 7.0$ Hz 6H; OCH_2CH_3, Et_2O), 0.88 ppm (br m, 14H; Si*CH*, *c*-C_6H_{11}); ^{13}C NMR (101 MHz, $CDCl_3$, 25 °C): $\delta = 68.06$ (OCH_2CH_2, THF), 65.84 (OCH_2CH_3, Et_2O), 28.44, 27.83, 27.75, 27.61, 27.10, 26.97, 26.89, 26.73, 26.65 (CH_2, *c*-C_6H_{11}), 25.59 (OCH_2CH_2, THF), 25.31, 24.83, 23.96, 23.82, 23.23 (Si*CH*, *c*-C_6H_{11}), 15.27 ppm (OCH_2CH_3, Et_2O); ^{29}Si NMR (79.5 MHz, $CDCl_3$, 25 °C): $\delta = -58.22$, -66.98, -67.14 ppm; IR (KBr disc): $\tilde{\nu} = 2925$ (vs, ν_{C-H}), 2848 (vs, ν_{C-H}), 1447 (s, δ_{CH_2}), 1268 (m), 1195 (s), 1130 (vs, $\nu_{as(Si-O-Si)}$), 1110 (vs, $\nu_{as(Si-O-Si)}$), 1083 (vs), 1057 (vs), 1025 (vs), 1010 (vs), 894 (s), 847 (s), 823 (m), 750 (m), 739 (m), 635 (m), 524 (vs, $\nu_{s(Si-O-Si)}$), 410 cm^{-1} (m, $\delta_{(O-Si-O)}$).

3: Compound **1** (3.00 g, 3.081 mmol) was added to a THF solution of $LiN(SiMe_3)_2$ (prepared in situ by reaction of *n*-butyllithium (5.80 mL of a 1.6 M solution in diethyl ether) with $HN(SiMe_3)_2$ (1.50 g, 1.94 mL, 9.243 mmol)). The white slurry was stirred overnight at room temperature. Then $ZrCl_4$ (0.37 g, 1.588 mmol) and acetone (30 mL) were added, followed by stirring for another 48 h. The solvents were evaporated in vacuum. The solid residue was extracted with boiling acetone/diethyl ether for two days, after which **3** was isolated (1.10 g) in 33 % yield. Compound **3** is very poorly soluble in hexane, THF, diethyl ether, and acetone. Crystals suitable for X-ray crystallography were obtained from a saturated acetone/diethyl ether solution at 25 °C after 14 days. Correct elemental analysis for $[\{[(c\text{-}C_6H_{11})_7Si_7O_{12}]Li(OCMe_2)\}_2Zr]$, $C_{90}H_{166}Si_{14}O_{26}Li_2Zr$. ^{1}H NMR (600.1 MHz, [D$_8$]THF, 25 °C): $\delta = 2.02$ (s, 12H; CH_3, acetone), 2.00–1.70 (br m, 70H; CH_2, *c*-C_6H_{11}), 1.55–1.25 (br m, 70H; CH_2, *c*-C_6H_{11}) 0.81–0.74 ppm (br m, 14H; Si*CH*, *c*-C_6H_{11}); ^{13}C NMR (150.9 MHz, [D$_8$]THF, 25 °C): $\delta = 205.68$ (*C*=O), 30.46 (CH_3), 28.69, 28.63, 28.51, 28.42, 28.37, 28.29, 28.05, 28.00, 27.96, 27.93, 27.88, 27.88, 27.81, 27.76, 27.66, 27.45 (CH_2, *c*-C_6H_{11}), 25.69, 25.55, 25.45, 25.29, 24.73, 24.63, 24.47 ppm (Si*CH*, *c*-C_6H_{11}); ^{29}Si NMR (119.2 MHz, [D$_8$]THF, 25 °C): $\delta = -70.89$, -70.90, -71.03, -71.10, -71.63, -71.83, -71.92, -72.75, -72.78, -72.82, -73.04 ppm; IR (KBr disc): $\tilde{\nu} = 2917$ (vs, ν_{C-H}), 2850 (vs, ν_{C-H}), 1637 (w, $\nu_{C=O}$), 1448 (vs, δ_{CH_2}), 1380 (m), 1355 (m), 1346 (m), 1326 (m), 1292 (m), 1268 (s), 1252 (m), 1196 (vs), 1119 (vs, $\nu_{as(Si-O-Si)}$), 942 (vs), 894 (s), 846 (s), 824 (s), 757 (vs), 688 (m), 647 (m), 619 (m), 575 (m), 556 (m), 516 (vs, $\nu_{s(Si-O-Si)}$), 455 (vs), 415 cm^{-1} (m, $\delta_{(O-Si-O)}$).

4: Compound **1** (2.00 g, 2.054 mmol) was added to a THF solution of $LiN(SiMe_3)_2$ (prepared in situ by reaction of *n*-butyllithium (4.50 mL of a 1.6 M solution in diethyl ether) with $HN(SiMe_3)_2$ (1.16 g, 1.50 mL, 7.200 mmol)). The white slurry was stirred overnight at room temperature. Then $[YbCl_3(thf)_3]$ (0.51 g, 1.030 mmol) was added, followed by stirring for another 24 h. The solvents were evaporated in vacuum. The solid residue was extracted with boiling diethyl ether for two days, after which compound **4** was isolated (1.20 g; 51 %) as a white crystalline solid. Crystals suitable for X-ray crystallography were obtained from a saturated diethyl ether solution at 5 °C after seven days. Correct elemental analysis for $[\{[(c\text{-}C_6H_{11})_7Si_7O_{12}]_2Li_4\}YbN(SiMe_3)_2]$, $C_{90}H_{172}Si_{16}NO_{24}Li_4Yb$. NMR: Because of the paramagnetic properties of **4**, it was impossible to obtain NMR data. IR (KBr disc): $\tilde{\nu} = 2922$ (vs, ν_{C-H}), 2850 (vs, ν_{C-H}), 1448 (s, $\delta_{(-CH_2-,\ -CH_3)}$), 1268 (m), 1252 (m), 1196 (s), 1110 (vs, $\tilde{\nu}_{as(Si-O-Si)}$), 1039(vs), 1027(vs), 1009(vs), 942(m), 895 (s), 846 (s), 824 (m), 757 (s), 647 (m), 619 (m), 516 (s, $\nu_{s(Si-O-Si)}$), 492 (m), 456 (s), 418 cm^{-1} (m, $\delta_{(O-Si-O)}$).

Received: February 24, 2004 [Z54094]

Keywords: cage compounds · lithium · silsesquioxanes · ytterbium · zirconium

[1] a) O. Olabisi, M. Atiqullah, W. Kaminsky, *Macromol. Chem. Phys.* **1997**, *C37*, 519; b) J. C. W. Chien, *Top. Catal.* **1999**, *7*, 23; c) M. O. Kristen, *Top. Catal.* **1999**, *7*, 89; d) G. G. Hlatky, *Chem. Rev.* **2000**, *100*, 1347, and references therein; e) G. Fink, B. Steinmetz, J. Zechlin, C. Przybyla, B. Tesche, *Chem. Rev.* **2000**, *100*, 1377; f) C. Merckle, J. Blümel, *Chem. Mater.* **2001**, *13*, 3617.

[2] a) C. Lecuyer, F. Quignard, A. Choplin, D. Olivier, J.-M. Basset, *Angew. Chem.* **1991**, *103*, 1692; *Angew. Chem. Int. Ed. Engl.* **1991**, *30*, 1660; b) F. Quignard, C. Lecuyer, C. Bougault, F. Lefebvre, A. Choplin, D. Olivier, J.-M. Basset, *Inorg. Chem.* **1992**, *31*, 928; c) S. Scott, J.-M. Basset, G. P. Niccolai, C. C. Santini, J.-P. Candy, C. Lecuyer, F. Quignard, A. Choplin, *New J. Chem.* **1994**, *18*, 115; d) J.-M. Basset, F. Lefebvre, C. Santini, *Coord. Chem. Rev.* **1998**, *180*, 1701; e) C. Copéret, O. Maury, J. Thivolle-Cazat, J.-M. Basset, *Angew. Chem.* **2001**, *113*, 2393; *Angew. Chem. Int. Ed.* **2001**, *40*, 2331; f) N. Millot, A. Cox, C. C. Santini, Y. Molard, J.-M. Basset, *Chem. Eur. J.* **2002**, *8*, 1438; g) M. Chabanas, C. Copéret, J.-M. Basset, *Chem. Eur. J.* **2003**, *9*, 971; h) C. Copéret, M. Chabanas, R. Petroff Saint-Arroman, J.-M. Basset, *Angew. Chem.* **2003**, *115*, 164; *Angew. Chem. Int. Ed.* **2003**, *42*, 156.

[3] a) F. J. Feher, T. A. Budzichowski, *Polyhedron* **1995**, *14*, 3239; b) P. G. Harrison, *J. Organomet. Chem.* **1997**, *542*, 141; c) R. Murugavel, A. Voigt, M. G. Walawalkar, H. W. Roesky, *Chem. Rev.* **1996**, *96*, 2205; d) V. Lorenz, A. Fischer, S. Gießmann, J. W. Gilje, Y. Gun'ko, K. Jacob, F. T. Edelmann, *Coord. Chem. Rev.* **2000**, *206–207*, 321; e) R. Duchateau, *Chem. Rev.* **2002**, *102*, 3525; f) R. W. J. M. Hanssen, R. A. van Santen, H. C. L. Abbenhuis, *Eur. J. Inorg. Chem.* **2004**, 675.

[4] F. J. Feher, D. A. Newman, J. F. Walzer, *J. Am. Chem. Soc.* **1989**, *111*, 1741.

[5] J. Annand, H. C. Aspinall, A. Steiner, *Inorg. Chem.* **1999**, *38*, 3941.

[6] V. Lorenz, S. Gießmann, Y. K. Gun'ko, A. K. Fischer, J. W. Gilje, F. T. Edelmann, unpublished results.

[7] X-ray data collection and structure refinement: The measurements on **2**–**4** were performed on a Siemens SMART CCD

 © 2004 Wiley-VCH Verlag GmbH & Co. KGaA, Weinheim

system with $Mo_{K\alpha}$ radiation ($\lambda = 0.71073$ Å) and graphite monochromator. Selected crystals of **2**–**4** were coated with mineral oil, mounted on a glass fiber, and transferred to the cold nitrogen steam (Siemens LT-2 attachment). Full hemispheres of the reciprocal space were scanned by ω in three sets of frames of 0.3°. The SADABS routine was applied as an absorption correction. For structure solution and refinement the programs SHELXS86 and SHELXL97 were used.[12] CCDC-182421 (**2**), CCDC-182423 (**3**), CCDC-182420 (**4**) contain the supplementary crystallographic data for this paper. These data can be obtained free of charge via www.ccdc.cam.ac.uk/conts/retrieving.html (or from the Cambridge Crystallographic Data Centre, 12, Union Road, Cambridge CB21EZ, UK; fax: (+44) 1223-336-033; or deposit@ccdc.cam.ac.uk). **2**: $C_{96}H_{180}Li_6O_{27}Si_{14}$, $M_w = 2201.30\ g\,mol^{-1}$, $T = 173(2)$ K, triclinic, space group $P\bar{1}$, $a = 14.3986(6)$, $b = 18.4236(8)$, $c = 25.6539(4)$ Å, $\alpha = 103.852(3)$, $\beta = 93.379(4)$, $\gamma = 108.523(3)°$, $V = 6197.4(4)$ Å^3, $Z = 2$, $\rho_{calcd} = 1.180\ g\,cm^{-3}$, $\mu = 0.208\ mm^{-1}$, reflections collected: 41313, independent reflections: 29171 ($R_{int} = 0.0523$), final R indices [$I > 2\sigma I$]: $R1 = 0.0912$, $wR2 = 0.2232$, R indices (all data): $R1 = 0.1889$, $wR2 = 0.2861$. **3**: $C_{90}H_{166}Li_2O_{26}Si_{14}Zr$, $M_w = 2162.59\ g\,mol^{-1}$, $T = 143(2)$ K, orthorhombic, space group $Pca2(1)$, $a = 22.1136(10)$, $b = 26.2423(10)$, $c = 19.5055(10)$ Å, $V = 11319.3(9)$ Å^3, $Z = 4$, $\rho_{calcd} = 1.269\ g\,cm^{-3}$, $\mu = 0.311\ mm^{-1}$, reflections collected: 58115, independent reflections: 17109 ($R_{int} = 0.0611$), final R indices [$I > 2\sigma I$]: $R1 = 0.0410$, $wR2 = 0.0989$, R indices (all data): $R1 = 0.0598$, $wR2 = 0.1153$. **4**: $C_{90}H_{172}Li_4NO_{24}Si_{16}Yb$, $M_w = 2302.53\ g\,mol^{-1}$, $T = 173(2)$ K, monoclinic, space group Cc, $a = 27.1505(3)$, $b = 15.5354(9)$, $c = 30.0056(15)$ Å, $\beta = 111.077°$, $V = 11809.5(9)$ Å^3, $Z = 4$, $\rho_{calcd} = 1.295\ g\,cm^{-3}$, $\mu = 1.017\ mm^{-1}$, reflections collected: 39125, independent reflections: 19390 ($R_{int} = 0.0293$), final R indices [$I > 2\sigma I$]: $R1 = 0.0338$, $wR2 = 0.0699$, R indices (all data): $R1 = 0.0457$, $wR2 = 0.0774$.

[8] I. Haiduc, F. T. Edelmann, *Supramolecular Organometallic Chemistry*, Wiley-VCH, Weinheim, **1999**.

[9] A related lanthanide alkoxide species, [{(*c*-C_5H_9)$_7$$Si_7O_9$(O-Li)$_2$(OSiMe$_2$*t*Bu)}$_2$Sm(OC$_6H_3$*t*Bu$_2$-2,6)], has been reported by Arnold et al.: P. L. Arnold, A. J. Blake, S. N. Hall, B. D. Ward, C. Wilson, *J. Chem. Soc. Dalton Trans.* **2001**, 488.

[10] a) K. den Haan, L. L. de Boer, J. H. Teuben, A. L. Spek, B. Kojic-Prodic, G. R. Hays, R. Huis, *Organometallics* **1986**, *5*, 1726; b) W. J. Evans, R. A. Keyer, J. W. Ziller, *Organometallics* **1993**, *12*, 2618; c) M. A. Giardello, V. P. Conticelli, L. Brard, M. R. Gagne, T. J. Marks, *J. Am. Chem. Soc.* **1994**, *116*, 10241, and references therein; d) M. A. Giardello, Y. Yamamoto, L. Brard, T. J. Marks, *J. Am. Chem. Soc.* **1995**, *117*, 3276; e) R. Anwander, *Top. Curr. Chem.* **1996**, *179*, 33.

[11] a) R. Anwander, R. Roesky, *J. Chem. Soc. Dalton Trans.* **1997**, 137; b) R. Anwander, O. Runte, J. Eppinger, G. Gerstberger, E. Herdtweck, M. Spiegler, *J. Chem. Soc. Dalton Trans.* **1998**, 847; c) G. Gerstberger, C. Palm, R. Anwander, *Chem. Eur. J.* **1999**, *5*, 997.

[12] G. M. Sheldrick, SHELXTL, Structure Determination Software Programs, Version 5.03 (PC), Siemens Analytical X-Ray Instruments, Madison, WI, USA, **1995**; G. M. Sheldrick, SHELXL-97, A program for crystal structure refinement, Universität Göttingen, **1997**.

 © 2004 Wiley-VCH Verlag GmbH & Co. KGaA, Weinheim

Nanotubes

Sn-Filled Single-Crystalline Wurtzite-Type ZnS Nanotubes**

Junqing Hu, Yoshio Bando, Jinhua Zhan, and Dmitri Golberg*

Since the discovery of carbon nanotubes,[1] a large number of inorganic solids with layered or nonlayered crystal lattices have been found to form tubular nanostructures.[2] Nowadays, inorganic nanotubes with interesting properties and potential applications constitute an important class of compounds. Among these, Group II–VI semiconductors (e.g., ZnS, ZnSe, CdS, CdSe) are particularly important, and great efforts have been made to fabricate their nanowires, nanorods, and nanoribbons (or nanobelts) by various routes[3] because of their unique optical, electrical, and optoelectronic properties, and potential technological applications.[4] Thus, new synthesis pathways for the formation to nanotubes of these materials are in demand; however, there have been only a few reports on the synthesis of their tubular structures. Rao et al.[5] obtained CdS and CdSe nanotubes by surfactant-assisted synthesis, and these were the first examples of nanotubes made of the Group II–VI semiconductors. Xie and co-workers[6] obtained CdS nanotubes by an in situ micelle–template–interface reaction. Recently, Wang et al.[7] generated ZnS nanotubes by reaction of ZnO nanoribbons (as templates) with H_2S, and Zhu et al.[8] obtained ZnS nanotubes by a high-temperature thermochemical process from ZnS powders. However, the CdS, CdSe, and ZnS nanotubes obtained in these cases are polycrystals, consisting of numerous nanocrystallites, rather than single crystals. This would negatively affect their semiconducting performance in real devices. The synthesis of single-crystalline nanotubes of the Group II–VI semiconductors has not been realized experimentally and still remains a challenge.

Among the many routes for synthesizing tubular structures of nonlayered materials, the template-based method offers a wide range of advantages.[9] Recently, single-crystalline GaN and Si nanotubes were prepared by a template-based process,[10] in which ZnO and ZnS nanowires, respectively, were used as one-dimensional removable templates. We assumed that using an analogous route and a suitable template could provide access to single-crystalline nanotubes of the Group II–VI semiconductors. Indeed we have succeeded in synthesizing single-crystalline wurtzite-type ZnS

[*] Dr. J. Hu, Prof. Y. Bando, Dr. J. Zhan, Dr. D. Golberg
Advanced Materials Laboratory
National Institute for Materials Science (NIMS)
Namiki 1-1, Tsukuba, Ibaraki 305-0044 (Japan)
Fax: (+81) 298-51-6280
E-mail: hu.junqing@nims.go.jp

[**] This work was supported by the Japan Society for the Promotion of Science (JSPS) Fellowship tenable at the National Institute for Materials Science, Tsukuba, Japan.

 © 2004 Wiley-VCH Verlag GmbH & Co. KGaA, Weinheim DOI: 10.1002/anie.200454205

nanotubes for the first time by a novel Sn-nanorod-templated process.

The ZnS nanotubes were synthesized in a horizontal high-temperature resistance furnace at a temperature of 1150 °C by using a mixture of ZnS and SnO powders as starting materials. After the furnace was cooled to room temperature under a stream of N_2, a gray-colored product was collected from the inner wall of the tube downstream, where the temperature was between 180 and 250 °C during heating. As shown in the scanning electron microscopy (SEM) image (Figure 1a),

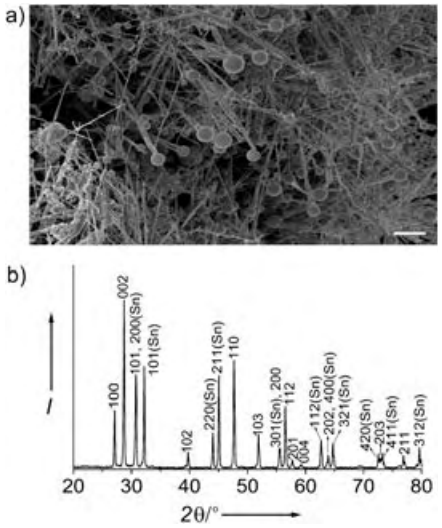


Figure 1. a) SEM image of as-grown ZnS nanostructures. Scale bar: 1 μm. b) XRD spectrum of the product.

numerous one-dimensional nanostructures with spherical particles at their tip ends were formed in the product. Most of them are straight and have lengths ranging from several to tens of micrometers. The X-ray diffraction (XRD) pattern (Figure 1b) of the product presents clear evidence that the nanostructures are composed of two crystalline phases, that is, hexagonal (wurtzite) ZnS (JCPDS: 36-1450; $a = 3.8298$ Å and $c = 6.2573$ Å) and tetragonal Sn (β-Sn) (JCPDS: 04-0673; $a = 5.831$ Å and $c = 3.182$ Å). No characteristic peaks from other impurities, such as ZnO, SnO, and SnO_2 are detected in the XRD pattern.

Transmission electron microscopy (TEM) and X-ray energy-dispersive spectrometry (EDS) reveal that the as-grown structures are in fact ZnS nanotubes filled with Sn. Normally, a Sn-filling occupies more than 70–80% of the entire cavity of a ZnS nanotube. Some of tubes have uniform diameters and wall thicknesses throughout their whole lengths (Figure 2a), and the diameters and wall thicknesses are 150–200 nm and 50–60 nm, respectively. Typically, a given tube is sealed with a Sn-filling at one end (note that each Sn-filling terminates with a spherical Sn particle), whereas the other end and central part of the tube may be open and hollow, respectively. As shown in Figure 2b, the diameters and wall thicknesses of these tubes gradually decrease and become smaller and smaller along their lengths, from 180–250 nm and 60–80 nm at the thicker end to 80–120 nm and 25–

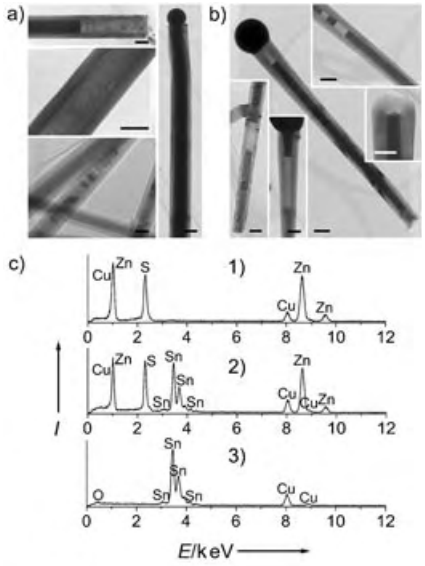


Figure 2. Typical TEM images showing the filling characteristics of Sn inside the ZnS nanotubes. a) ZnS nanotubes with the uniform diameters throughout the whole length. b) ZnS nanotubes for which the diameters gradually decrease along the length. The middle-right inset shows the cross-sectional shape at one end of a Sn-filled ZnS nanotube. Scale bars: 100 nm. c) Energy-dispersive spectra recorded for a tubular sheath or a tube cavity (curve 1), a filling (curve 2), and a spherical Sn particle (3, shown in b) on the end of the tube.

50 nm at the thinner end. Usually, a large spherical Sn particle (several hundred nanometers in diameter) seals the thicker end, and the thinner end is filled with a Sn nanorod, whereas the middle section is a hollow tubular cavity. In some cases, the Sn-fillings divide a tube into independent hollow segments, otherwise the Sn-fillings spread through the entire length, forming a continuous Sn-cored and ZnS-shelled core/shell structure. A quasi-circular cross-sectional shape can easily be viewed at one end of a Sn-filled ZnS nanotube (middle-right inset TEM image, Figure 2b), suggesting that the ZnS nanotube is not a faceted tube, but rather a cylindrical (or taper-like) tube. The energy-dispersive spectra shown in Figure 2c were recorded for a tubular sheath or a tube cavity (curve 1), a Sn-filling (curve 2), and a Sn particle (curve 3) attached to the end of a tube, confirming that the wall has the chemical composition of ZnS, and the filling is metallic Sn.

High-resolution TEM imaging and electron diffraction reveal that all as-grown ZnS nanotubes are structurally uniform single crystals. Figure 3a is an image taken from a tube wall with a uniform thickness along its length. The lattice fringes of the {100} and {001} planes with a d spacing of 0.38 nm and 0.63 nm, respectively, peculiar to the wurtzite ZnS crystal, can be clearly seen. The growth direction of this tube, for example, is parallel to the [120] crystallographic direction of a ZnS crystal, which is perpendicular to the {100} planes. This is a frequent growth characteristic for materials with the wurtzite (hexagonal close-packed, *hcp*) structure, and has been displayed in many one-dimensional forms with the same structure.[3f,11] This can be simply explained in terms of a "low-energy" argument; that is, the (1000) plane is one of

 © 2004 Wiley-VCH Verlag GmbH & Co. KGaA, Weinheim

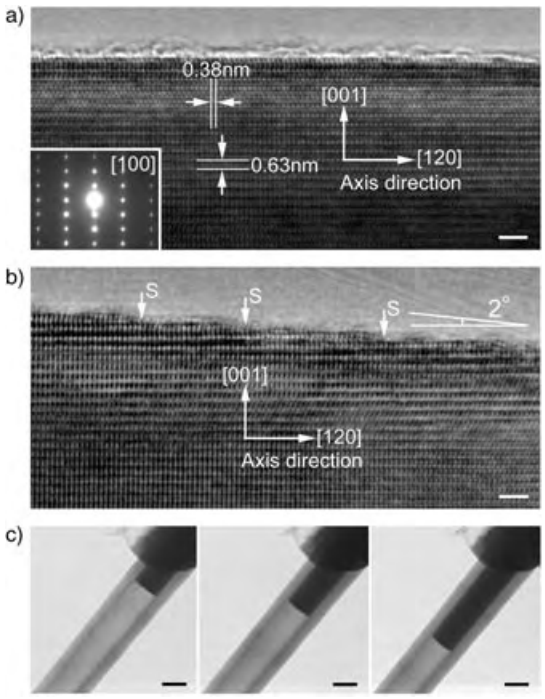


Figure 3. a), b) HRTEM images recorded for the ZnS nanotubes with different wall thicknesses. Scale bars: 2 nm. The lower-left inset in a) shows the corresponding electron diffraction pattern recorded with an incident electron beam along the [100] direction. On the tube surface (shown in b), the atomic steps are marked with "S". c) Consecutive TEM images showing the melting and moving of the Sn-filling in a ZnS nanotube under the slow movement of an electron beam along its length. Scale bars: 100 nm.

the densely arranged planes (it is not the closest stacked plane) in the wurtzite structure, and stacking along [120] thus becomes energetically favorable. As seen from the image, this tube is a structurally uniform single crystal, and no dislocations or other planar defects are observed within it. The edge of the tube is clean and abrupt on an atomic scale, and there are no amorphous layers covering the surface. The corresponding electron diffraction (ED) pattern (the lower-right inset in Figure 3a) can be indexed as the [100] zone axis diffraction pattern of the wurtzite ZnS single crystal. The out-of-focus diffraction pattern also suggests that the long axis or the growth of such a tube occurs along the [120] direction of the ZnS crystal. Careful HRTEM and ED examinations of this tube indicate that the structural uniformity of the single-crystal ZnS tube is maintained throughout the whole length. Figure 3b is an image recorded of a tube whose diameter gradually decreases along its length; it reveals similar imaging characteristics to that of the tube with uniform diameter. In this case, the surface edge is not parallel to the axis of the tube, and a small discrepancy of about 2° is observed with respect to the direction of the tube axis. There are also some atomic steps (marked with "S" on the surface in Figure 3) that are associated with the gradual decrease of the diameter along the length. Research on low melting-point metals confined in carbon nanotubes was pioneered by Ajayan and Iijima,[12] and since then it has attracted considerable attention.[13] In the present work, we found that electron-beam irradiation in the microscope can effectively tailor and adjust the lengths and positions of the Sn-fillings in the ZnS tubes. Figure 3c shows consecutive TEM images recorded on slowly moving an electron beam along the filled tube length; the melting and moving of the Sn-filling within the tube is clearly displayed. A similar phenomenon has been observed previously for encapsulated Sn in carbon nanotubes under electron irradiation.[14] In the present case, it is possible that an increase in temperature occurs upon irradiating the sample, and that a simultaneous thermal expansion due to a very low basic pressure ($\sim 1\times10^{-5}$ Pa) in the TEM chamber favors the movements of the Sn-filling in the ZnS nanotubes.

The present template route for the growth of the Sn-filled ZnS nanotubes was accomplished by combining the decomposition of SnO and the thermal evaporation of ZnS powders. SnO is metastable and will decompose to Sn and SnO_2 at a temperature higher than 300 °C.[15] Moreover, the higher the reaction temperature, the faster is the rate of the decomposition.[16] The as-formed Sn may be in the form of small-sized liquid (Sn: m.p. 232 °C[15]) clusters when reduced from SnO. The Sn clusters are then transported by the carrier gases (N_2) to a lower temperature region in the tube, where they are deposited in the form of a liquid ball on the graphite substrate (Figure 4). The Sn balls provide preferential surface sites for

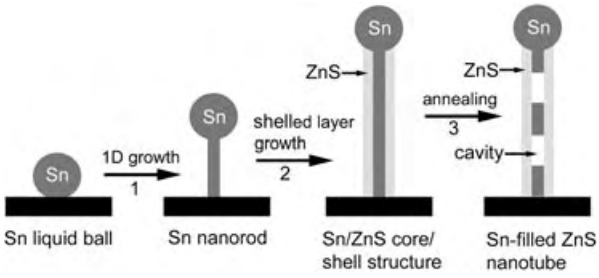


Figure 4. Schematic illustration of the Sn-nanorod-templated process for making single-crystalline ZnS nanotubes. See text for details.

the absorption of the Sn clusters, resulting in the one-dimensional growth of Sn nanorods (Figure 4, step 1). As the processing temperature increases further, the ZnS powders evaporate at a higher rate, producing ZnS vapor. A monocrystalline ZnS thin layer generated upon condensation of the ZnS vapor grows on the Sn nanorod templates, leading to the formation of the Sn/ZnS core/shell structures (Figure 4, step 2). Annealing for a long period partially evaporates the Sn core out of these structures, or melts and moves the Sn nanorods within the structures, whereas the ZnS shell, which has a high melting point (ZnS: m.p. 1722 °C[13]) remains intact. As a result, a partially hollow cavity with a ZnS sheath, namely, a single-crystalline ZnS nanotube, is formed (Figure 4, step 3).

Figure 5 shows comparative room-temperature photoluminescence (PL) spectra of the ZnS nanotubes (curve 1) and a commercial ZnS powder (curve 2). The spectrum for the as-grown ZnS nanotubes exhibits a weak and broad (UV) emission band at 335–355 nm and a strong and stable green emission centered at about 528 nm. The band at 335–355 nm corresponds to a band-gap emission of 3.70–3.49 eV. Thus, the

 © 2004 Wiley-VCH Verlag GmbH & Co. KGaA, Weinheim

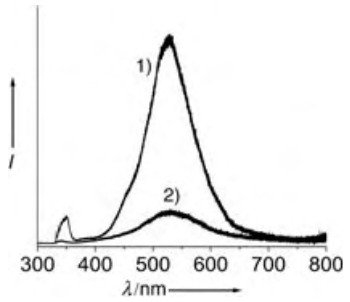


Figure 5. Comparative photoluminescence (PL) spectra of ZnS nanotubes (curve 1) and a commercial ZnS powder (curve 2).

present ZnS nanotubes have a broader energy band gap than that for the bulk material (E_g: ~3.65 eV).[17] The green emission (at ~528 nm) for the ZnS nanotubes is nearly seven times higher in intensity than that for the starting commercial ZnS powders. A similar green emission (at ~534 nm) has been observed in ZnS nanoribbons.[3f] In this case the emission maybe caused by the presence of some self-activated luminescence centers, probably vacancy states or interstitial states related to the peculiar nanostructures.

In summary, we have synthesized single-crystalline wurtzite-type ZnS nanotubes for the first time by using a simple Sn-nanorod-templated evaporation process. The results suggest that this method might be useful for the synthesis of many other single-crystal nanotubes of the Group II–VI semiconductors.

Experimental Section

The ZnS nanotubes were synthesized in a horizontal high-temperature resistance furnace. A graphite crucible containing a mixture of ZnS (1.5 g) and SnO (0.3 g) (or ZnS (1.5 g), SnO (0.3 g), SnO_2 (0.2 g), and activated carbon (0.1 g)) powders was placed in the central zone of a quartz tube. The furnace was heated to 1150 °C at a rate of 10 K min^{-1}, kept at this temperature for 4 h, and then cooled to room temperature. The whole process was carried out under a constant flow of pure N_2 at a rate of 450 mL min^{-1}. The products were collected from the inner wall of the tube and characterized by X-ray diffraction (RINT 2200), scanning electron microscopy (JSM-6700F), and transmission electron microscopy (3000F, equipped with an X-ray energy-dispersive spectrometer (EDS)). The photoluminescence for the as-grown ZnS nanotubes and the starting commercial ZnS powders was measured under the same experimental conditions. The spectra were recorded at room temperature in a spectral range of 300–800 nm using a He–Cd laser line of 325 nm as the excitation source.

Received: March 8, 2004 [Z54205]

Keywords: crystal growth · nanostructures · semiconductors · tin · zinc

[1] S. Iijima, *Nature* **1991**, *354*, 56.
[2] See, for example: a) R. Tenne, L. Margulis, M. Genut, G. Hodes, *Nature* **1992**, *360*, 444; b) E. J. M. Hamilton, S. E. Dolan, C. M. Mann, H. O. Colijn, C. A. Mcdonald, S. G. Shore, *Science* **1993**, *260*, 659; c) Y. Feldman, E. Wasserman, D. J. Srolovitz, R. Tenne, *Science* **1995**, *267*, 222; d) N. G. Chopra, R. J. Luyken, K. Cherrey, V. H. Crespi, M. L. Cohen, S. G. Louie, A. Zettl, *Science* **1995**, *269*, 966; e) L. Pu, X. M. Bao, J. P. Zou, D. Feng, *Angew. Chem.* **2001**, *113*, 1538; *Angew. Chem. Int. Ed.* **2001**, *40*, 1490; f) M. Nath, C. N. R. Rao, *Angew. Chem.* **2002**, *114*, 3601; *Angew. Chem. Int. Ed.* **2001**, *40*, 1490; g) J. H. Jung, H. Kobayashi, K. J. C. van Bommel, S. Shinkai, T. Shimizu, *Chem. Mater.* **2002**, *14*, 1445.
[3] See, for example: a) X. G. Peng, L. Manna, W. D. Yang, J. Wickham, E. Scher, A. Kadavanich, A. P. Alivisatos, *Nature* **2000**, *404*, 59; b) O. Wu, N. Zheng, Y. Ding, Y. Li, *Inorg. Chem. Commun.* **2002**, *5*, 671; c) C. S. Yang, D. D. Awschalom, G. D. Stucky, *Chem. Mater.* **2002**, *14*, 1277; d) Y. W. Wang, G. W. Meng, L. D. Zhang, C. H. Liang, J. Zhang, *Chem. Mater.* **2002**, *14*, 1773; e) C. Ma, D. Moore, J. Li, Z. L. Wang, *Adv. Mater.* **2003**, *15*, 228; f) Y. Jiang, X. M. Meng, J. Liu, Z. Y. Xie, C. S. Lee, S. T. Lee, *Adv. Mater.* **2003**, *15*, 323; g) Y. Jiang, X. M. Meng, J. Liu, Z. R. Hong, C. S. Lee, S. T. Lee, *Adv. Mater.* **2003**, *15*, 1195.
[4] a) B. O. Dabboussi, M. G. Bawendi, O. Onitsuka, M. F. Rubner, *Appl. Phys. Lett.* **1995**, *66*, 1316; b) D. L. Klein, R. Roth, A. K. L. Lim, A. P. Alivisatos, P. L. McEuen, *Nature* **1997**, *389*, 699; c) H. Weller, *Angew. Chem.* **1998**, *110*, 1748; *Angew. Chem. Int. Ed.* **1998**, *37*, 1658; d) J. M. Bruchez, M. Moronne, P. Gin, S. Weiss, A. P. Alivisatos, *Science* **1998**, *281*, 2013; e) X. F. Duan, Y. Huang, R. Agarwal, C. M. Lieber, *Nature* **2003**, *421*, 241.
[5] C. N. R. Rao, A. Govindaraj, F. L. Deepak, N. A. Gunari, M. Nath, *Appl. Phys. Lett.* **2001**, *78*, 1853.
[6] Y. J. Xiong, Y. Xie, J. Yang, R. Zhang, C. Z. Wu, G. A. Du, *J. Mater. Chem.* **2002**, *12*, 3712.
[7] X. D. Wang, P. X. Gao, J. Li, C. J. Summers, Z. L. Wang, *Adv. Mater.* **2002**, *14*, 1732.
[8] Y. C. Zhu, Y. Bando, Y. Uemura, *Chem. Commun.* **2003**, 836.
[9] a) C. J. Brumlik, C. R. Martin, *J. Am. Chem. Soc.* **1991**, *113*, 3174; b) R. Parthasarathy, C. R. Martin, *Nature* **1994**, *369*, 298; c) C. R. Martin, *Science* **1994**, *266*, 1961; d) P. M. Ajayan, O. Stephan, P. Redlich, C. Colliex, *Nature* **1995**, *375*, 564; e) B. B. Lakshmi, P. K. Dorhout, C. R. Martin, *Chem. Mater.* **1997**, *9*, 857; f) J. C. Hulteen, C. R. Martin, *J. Mater. Chem.* **1997**, *7*, 1075.
[10] a) J. Goldberger, R. R. He, Y. F. Zhang, S. Lee, H. Q. Yan, H. -J, Choi, P. D. Yang, *Nature* **2003**, *422*, 599; b) J. Q. Hu, Y. Bando, Z. W. Liu, J. H. Zhan, D. Golberg, *Angew. Chem.* **2004**, *113*, 65; *Angew. Chem. Int. Ed.* **2004**, *43*, 63.
[11] a) J. Q. Hu, Y. Bando, Z. W. Liu, T. Sekiguchi, D. Golberg, J. H. Zhan, *J. Am. Chem. Soc.* **2003**, *125*, 11306; b) Y. Jiang, X. M. Meng, W. C. Yiu, J. Liu, J. X. Ding, C. -S. Lee, S. -T. Lee, *J. Phys. Chem. B* **2004**, *108*, 2784; c) K. M. Ip, C. R. Wang, Q. Li, S. K. Harka, *Appl. Phys. Lett.* **2004**, *84*, 795; d) Y. C. Zhu, Y. Bando, D. F. Xue, D. Dolberg, *Adv. Mater.* **2004**, *16*, 831.
[12] P. M. Ajayan, S. Iijima, *Nature* **1993**, *361*, 333.
[13] a) Y. Y. Wu, P. D. Yang, *Adv. Mater.* **2001**, *13*, 520; b) Y. H. Gao, Y. Bando, *Nature* **2002**, *415*, 599; c) Y. B. Li, Y. Bando, D. Golberg, *Adv. Mater.* **2003**, *15*, 581.
[14] W. K. Hsu, M. Terrones, H. Terrones, N. Grobert, A. I. Kirkland, J. P. Hare, K. Prassides, P. D. Townsend, H. W. Kroto, D. R. M. Walton, *Chem. Phys. Lett.* **1998**, *284*, 177.
[15] *Lange*'s *Handbook of Chemistry, 15th ed.* (Ed.: J. A. Dean), McGraw-Hill, New York, **1999**.
[16] a) D. W. Yuan, R. F. Yan, G. Simkovich, *J. Mater. Sci.* **1999**, *34*, 2911; b) J. Q. Hu, X. L. Ma, N. G. Shang, Z. Y. Xie, N. B. Wong, C. S. Lee, S. T. Lee, *J. Phys. Chem. B* **2002**, *106*, 3823.
[17] N. A. Dhas, A. Zaban, A. Gedanken, *Chem. Mater.* **1999**, *11*, 806.

 © 2004 Wiley-VCH Verlag GmbH & Co. KGaA, Weinheim

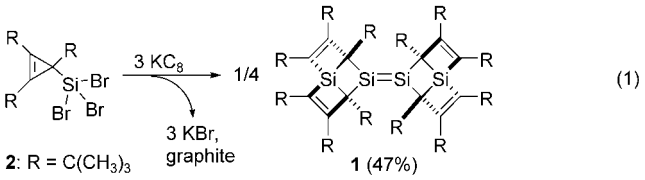
Disilenes

Formation of a Stable, Lattice-Framework Disilene: A Strategy for the Construction of Bulky Substituents**

*Shigeki Matsumoto, Shinobu Tsutsui, Eunsang Kwon, and Kenkichi Sakamoto**

Although multiple-bonded species of carbon such as olefins and acetylenes are very common compounds, it was thought that their heavier homologues, such as Si–Si double-bonded species (disilenes), could not be isolated owing to their high reactivity. However, the steric protection with bulky substituents has been found to be an effective means of isolating labile compounds.[1] To date, trisila- and tristanna-allene derivatives[2,3] as well as the heavier analogues of acetylene[4,5] have been isolated by using various bulky substituents. Evidently, the bulkier a substituent, the higher its protecting ability. However, very bulky substituents cannot be introduced to the target species and their precursors. Herein we show a novel conceptual method for the introduction of such bulky substituents. In the study described herein, we have employed a tri(*tert*-butyl)cyclopropenyl group,[6–9] which becomes an extremely bulky substituent and a good protecting group. The growth is primarily attributed to a spontaneous transformation and combination. This strategy was used to isolate a unique lattice-framework disilene with C_2 symmetry.

Tri(*tert*-butyl)cyclopropenyltribromosilane (**2**)[8,10] was reduced with potassium graphite (KC_8) in 2-MeTHF at approximately −120 °C; the reaction yielded red-orange crystals of the unexpected lattice-framework disilene **1**, which was readily isolated in 47 % yield by recrystallization from hexane [Eq. (1)].



(1)

The structure of **1** was established by using mass spectrometry and ^1H, ^{13}C, and ^{29}Si NMR spectroscopy and was confirmed by X-ray crystallography. As shown in Figure 1, **1** was highly strained; however, it was found to be thermally stable up to 257 °C. The disilene **1** could be manipulated even in air in the crystal form, but gradually

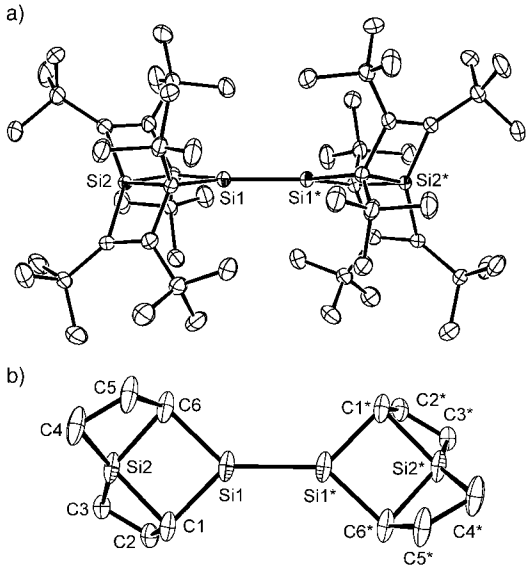
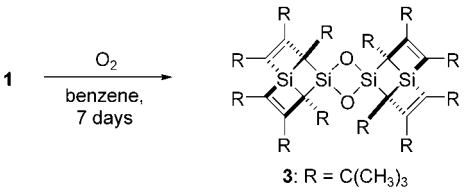


Figure 1. a) Side and b) top ORTEP views of **1**. Thermal ellipsoids are drawn at the 50 % probability level. Hydrogen atoms (a and b) and *tert*-butyl groups (b) were omitted for clarity. Selected bond lengths [Å] and angles [°]: Si1–Si1* 2.2621(15), C1–Si2 1.894(3), C1–Si1 1.958(3), C6–Si2 1.894(3), C6–Si1 1.976(3), C1–C2 1.573(4), C5–C6 1.581(4), C2-C1-Si1 113.07(18), Si2-C1-Si1 88.22(13), C5-C6-Si1 114.9(2), Si2-C6-Si1 87.71(14), C1-Si1-C6 89.77(12), C1-Si1-Si1* 133.97(10), C6-Si1-Si1* 136.26(11), C4-Si2-C3 147.40(12), C1-Si2-C6 94.22(13), C1-Si1-Si1*-C6* 12.08(15).

oxidized in solution.[11] A solution of **1** in benzene under an oxygen atmosphere was stirred at room temperature for a week to yield the 1,3-disila-2,4-dioxetane derivative **3**, which consists of seven four-membered rings [Eq. (2)].[10]



(2)

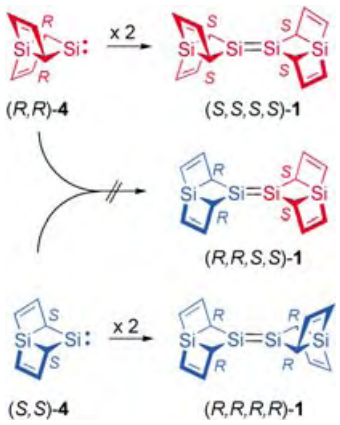
Recently, the reversible tetramerization of a diaminosilylene was reported;[12] **1** is a formal tetramer of tri(*tert*-butyl)cyclopropenylsilylyne. Although the formation pathway of **1** remains uncertain, multistep reactions include the reduction of the silicon–bromine bonds, isomerization,[6,7,13] and condensation to build silylene **4**, which undergoes dimerization to give **1** (Scheme 1).

Compound **1** is the first disilene that has C_2-symmetric chirality through the silicon–silicon double bond, although it was obtained as a racemic mixture of (*S*,*S*,*S*,*S*)-**1** and (*R*,*R*,*R*,*R*)-**1** (Scheme 1). The component silylene **4** is also

[*] S. Matsumoto, Dr. S. Tsutsui, Dr. E. Kwon, Prof. Dr. K. Sakamoto
Photodynamics Research Center
The Institute of Physical and Chemical Research (RIKEN)
519-1399 Aoba, Aramaki, Aoba-ku, Sendai 980-0845 (Japan)
Fax: (+81) 22-228-2017
E-mail: sakamoto@si.chem.tohoku.ac.jp
Prof. Dr. K. Sakamoto
Department of Chemistry, Graduate School of Science
Tohoku University, Aramaki, Aoba-ku, Sendai 980–8578 (Japan)

[**] We thank Dr. Hiromasa Tanaka of RIKEN for valuable discussions.
Supporting information for this article is available on the WWW under http://www.angewandte.org or from the author.

 © 2004 Wiley-VCH Verlag GmbH & Co. KGaA, Weinheim DOI: 10.1002/anie.200460067



Scheme 1. Dimerization of chiral silylene **4** to chiral disilene **1**. *tert*-Butyl groups are omitted for clarity. The absolute configurations of the stereogenic carbon atoms of **4** are formally changed during the dimerization.

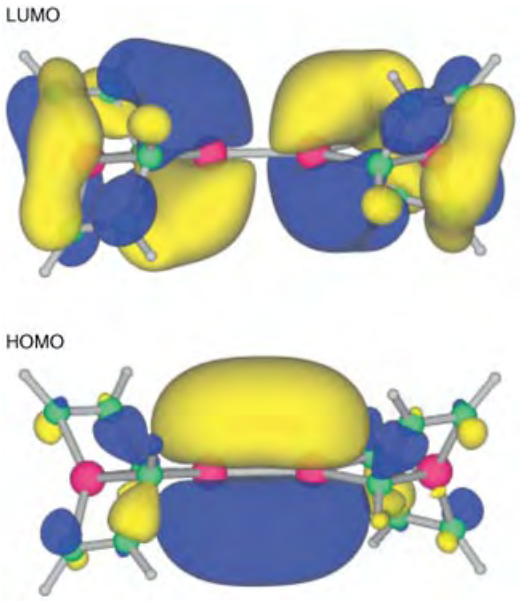


Figure 2. Frontier molecular orbitals of **5** at the B3LYP/6-311+G(d,p) level.

chiral with absolute configurations *R*,*R* and *S*,*S*; (*R*,*S*)-**4** was excluded as a possible structure of **4** because of its large ring strain. The *meso* isomer of the disilene (*R*,*R*,*S*,*S*)-**1** that can be formed by the combination of (*R*,*R*)-**4** and (*S*,*S*)-**4** was not observed, probably as a result of the larger steric repulsion between the heterochiral silylene pair. In other words, the recognition of chirality by the steric hindrance is observed in this system.

The silicon–silicon double-bond length of **1** is 2.26 Å, which is the longest of all the reported carbon-substituted disilenes.[1] Carbon-substituted disilenes generally adopt *trans* bent structures;[14] however, the structure of **1** around the disilene moiety is not bent, but slightly twisted. The unsaturated silicon atom Si1 is not pyramidized and the bent angle defined by Si1* = Si1–Si2 is 177.8°. The central 1,3-disilacyclobutane rings (Si1-C1-Si2-C6) are almost planar (within 0.018 Å from their least-squares plane) and twisted together: the C1-Si1-Si1*-C6* dihedral angle is 12.1°. Notably, the energy levels of the C1–C2 and C5–C6 σ-bonds are raised by the ring strain and the σ bonds are fixed almost perpendicular to the Si=Si bond; the Si1*-Si1-C1-C2 and Si1*-Si1-C6-C5 torsion angles are 96.7 and 102.9°, respectively. Accordingly, the stereoelectronic interactions between the strained C–C σ bonds and the Si–Si π bond become effective.[15]

The UV/Vis absorption maximum of the π→π* transition of **1** occurs at 493 nm. This value indicates that the transition is red-shifted relative to the typical values for the tetraalkyldisilenes: 350 nm for tetramethyldisilene[16] and 393 nm for tetrakis[bis(trimethylsilyl)methyl]disilene.[17] This remarkable red shift is mainly due to the lengthened and twisted Si=Si bond. Also, the stereoelectronic interactions are important.

Theoretical calculations successfully revealed the importance of the stereoelectronic interactions.[18] DFT calculations at the B3LYP/6-311+G(d,p) level were carried out for model compound **5**, in which all the *tert*-butyl groups of **1** were replaced by hydrogen atoms. The optimized structure of **5** did not reproduce the experimental structure of **1**; thus the skeletal structure of **5** was fixed to that of **1**. As shown in Figure 2, the HOMO of **5** consisted not only of the Si–Si π orbitals, but also of the C–C σ orbitals of the strained C1–C2 and C5–C6 bonds. Moreover, we found a substantial contribution from the C–C π orbitals of C2–C3 and the C4–C5 double bonds to the LUMO. The π→π* transition wavelength of **5** was calculated to be 484 nm by using the TDDFT method[19] and was in good agreement with the observed value of **1** (493 nm).

In summary, the one-pot reduction of tri(*tert*-butyl)cyclopropenyltribromosilane with potassium graphite yields a unique lattice-framework disilene **1**, which is a formal tetramer of tri(*tert*-butyl)cyclopropenylsilylyne. We are now applying this strategy to other compounds.

Experimental Section

1: Dry 2-MeTHF (4 mL) was added to a mixture of **2** (98 mg, 0.21 mmol) and KC_8 (92 mg, 0.68 mmol) at −196 °C. After stirring at −120 to −130 °C for 6 h, the resulting mixture was concentrated under reduced pressure at room temperature. Dry hexane (10 mL) was added, and the resulting salt and graphite were removed by decantation. Evaporation of the solvents in vacuo gave a dark red solid. Recrystallization from dry hexane gave **1** (23 mg, 0.024 mmol, 47 %). Red-orange crystals; mp 257.5–260 °C (decomp.); ^{1}H NMR (300 MHz, [D$_6$]benzene, TMS): $\delta = 1.43$ (s, 36H), 1.48 (s, 36H), 1.64 ppm (s, 36H); ^{13}C NMR (75 MHz, [D6]benzene, TMS): $\delta = 34.3$, 34.5, 35.7, 36.0, 36.7, 38.7, 74.3, 164.3, 165.6 ppm; ^{29}Si NMR (59 MHz, [D$_6$]benzene, TMS): $\delta = -36.7$, 102.5 ppm; MS (14 eV): *m*/*z* (%): 941 (9) [M^+], 471 (37), 207 (100); UV/Vis (hexane): λ_{max} (ε) = 359 (6500), 419 (3800), 493 (11 600); Raman (crystals): $\nu_{Si=Si} = 548$ cm^{-1}; elemental analysis: calcd for $C_{60}H_{108}Si_4$ (%): C 76.52, H 11.56; found: C 76.30, H 11.54. Crystal data: $M_w = 941.82$; $T = 123$ K; red-orange plate; orthorhombic; *Pcca*, $a = 28.034(5)$ Å, $b = 19.327(3)$ Å, $c = 10.7343(19)$ Å, $V = 5816.0(17)$ Å^3, $Z = 4$, $\rho_{calcd} = 1.076$ Mg m^{-3}; $0.21 \times 0.18 \times 0.10$ mm^3; independent reflections = 5719; parameters = 307; GOF = 1.027; final $R1 = 0.0618$ [$I > 2\sigma(I)$], $wR2 = 0.1730$ (all data). Intensity data were collected on a Bruker SMART 1000 CCD system with graphite-monochromated $Mo_{K\alpha}$ radiation ($\lambda = 0.71073$ Å). Data

 © 2004 Wiley-VCH Verlag GmbH & Co. KGaA, Weinheim

integration was carried out with the SAINT program. An empirical method was employed for absorption correction with the SADABS program. Subsequent calculations were carried out with the SHELXTL system. CCDC-232428 contains the supplementary crystallographic data for this paper. These data can be obtained free of charge via www.ccdc.cam.ac.uk/conts/retrieving.html (or from the Cambridge Crystallographic Data Centre, 12, Union Road, Cambridge CB21EZ, UK; fax: (+44) 1223-336-033; or deposit@ccdc.cam.ac.uk).

Received: March 21, 2004

Keywords: chirality · disilenes · kinetic stabilization · silicon · small-ring systems

[1] For recent reviews, see: a) R. Okazaki, R. West, *Adv. Organomet. Chem.* **1996**, *39*, 231–273; b) P. P. Power, *Chem. Rev.* **1999**, *99*, 3464–3504; c) M. Kira, T. Iwamoto, *J. Organomet. Chem.* **2000**, *611*, 236–247; d) P. Jutzi, *Angew. Chem.* **2000**, *112*, 3953–3957; *Angew. Chem. Int. Ed.* **2000**, *39*, 3797–3800; e) R. West, *Polyhedron* **2002**, *21*, 467–472; f) M. Weidenbruch, *J. Organomet. Chem.* **2002**, *646*, 39–52; g) M. Weidenbruch, *Angew. Chem.* **2003**, *115*, 2322–2324; *Angew. Chem. Int. Ed.* **2003**, *42*, 2222–2224; h) A. Sekiguchi, V. Y. Lee, *Chem. Rev.* **2003**, *103*, 1429–1447; i) N. Tokitoh, *Acc. Chem. Res.* **2004**, *37*, 86–94.

[2] N. Wiberg, H.-W. Lerner, S.-K. Vasisht, S. Wagner, K. Karaghiosoff, H. Nöth, W. Ponikwar, *Eur. J. Inorg. Chem.* **1999**, 1211–1218.

[3] S. Ishida, T. Iwamoto, C. Kabuto, M. Kira, *Nature* **2003**, *421*, 725–727.

[4] a) M. Stender, A. D. Phillips, R. J. Wright, P. P. Power, *Angew. Chem.* **2002**, *114*, 1863–1865; *Angew. Chem. Int. Ed.* **2002**, *41*, 1785–1787; b) A. D. Phillips, R. J. Wright, M. M. Olmstead, P. P. Power, *J. Am. Chem. Soc.* **2002**, *124*, 5930–5931; c) L. Pu, B. Twamley, P. P. Power, *J. Am. Chem. Soc.* **2000**, *122*, 3524–3525.

[5] N. Wiberg, W. Niedermayer, G. Fischer, H. Nöth, M. Suter, *Eur. J. Inorg. Chem.* **2002**, 1066–1070.

[6] a) M. J. Fink, D. B. Puranik, *Organometallics* **1987**, *6*, 1809–1811; b) M. J. Fink, D. B. Puranik, M. P. Johnson, *J. Am. Chem. Soc.* **1988**, *110*, 1315–1316; c) D. B. Puranik, M. J. Fink, *J. Am. Chem. Soc.* **1989**, *111*, 5951–5952; d) D. B. Puranik, M. P. Johnson, M. J. Fink, *Organometallics* **1989**, *8*, 770–777.

[7] a) G. Maier, J. Neudert, O. Wolf, D. Pappusch, A. Sekiguchi, M. Tanaka, T. Matsuo, *J. Am. Chem. Soc.* **2002**, *124*, 13819–13826; b) G. Maier, A. Kratt, A. Schick, H. P. Reisenauer, F. Barbosa, G. Gescheidt, *Eur. J. Org. Chem.* **2000**, 1107–1112; c) G. Maier, D. Born, I. Bauer, R. Wolf, R. Boese, D. Cremer, *Chem. Ber.* **1994**, *127*, 173–189.

[8] A. Schick, PhD thesis, Universität Giessen, Germany, **1992**.

[9] Transformation reactions of silicon-substituted cyclopropene derivatives were also reported; for hexakis(trimethylsilyl)bicyclopropenyl, see: a) K. Sakamoto, T. Saeki, H. Sakurai, *Chem. Lett.* **1993**, 1675–1678; for cyclopropenylidenesilylene derivatives, see: b) K. Sakamoto, J. Ogasawara, H. Sakurai, M. Kira, *J. Am. Chem. Soc.* **1997**, *119*, 3405–3406; c) K. Sakamoto, J. Ogasawara, Y. Kon, T. Sunagawa, C. Kabuto, M. Kira, *Angew. Chem.* **2002**, *114*, 1460–1462; *Angew. Chem. Int. Ed.* **2002**, *41*, 1402–1404; d) Y. Kon, J. Ogasawara, K. Sakamoto, C. Kabuto, M. Kira, *J. Am. Chem. Soc.* **2003**, *125*, 9310–9311.

[10] For further details on the preparation of **2** and **3**, see Supporting Information.

[11] M. J. Fink, M. J. Michalczyk, K. J. Haller, R. West, J. Michl, *Organometallics* **1984**, *3*, 793–800.

[12] T. A. Schmedake, M. Haaf, Y. Apeloig, T. Müller, S. Bukalov, R. West, *J. Am. Chem. Soc.* **1999**, *121*, 9479–9480.

[13] a) R. T. Conlin, S. Zhang, M. Namavari, K. L. Bobbitt, M. J. Fink, *Organometallics* **1989**, *8*, 571–573; b) M. G. Steinmetz, B. S. Udayakumar, M. S. Gordon, *Organometallics* **1989**, *8*, 530–541.

[14] a) K. Krogh-Jespersen, *J. Phys. Chem.* **1982**, *86*, 1492–1495; b) G. Olbrich, *Chem. Phys. Lett.* **1986**, *130*, 115–119; c) K. Somasundram, R. D. Amos, N. C. Handy, *Theor. Chim. Acta* **1986**, *70*, 393–406; d) H. Teramae, *J. Am. Chem. Soc.* **1987**, *109*, 4140–4142; e) L. Sari, M. C. McCarthy, H. F. Schaefer, P. Thaddeus, *J. Am. Chem. Soc.* **2003**, *125*, 11409–11417.

[15] K. Komatsu, *Bull. Chem. Soc. Jpn.* **2001**, *74*, 407–419.

[16] A. Sekiguchi, I. Maruki, K. Ebata, C. Kabuto, H. Sakurai, *J. Chem. Soc. Chem. Commun.* **1991**, 341–343.

[17] S. Masamune, Y. Eriyama, T. Kawase, *Angew. Chem.* **1987**, *99*, 601–602; *Angew. Chem. Int. Ed. Engl.* **1987**, *26*, 584–585.

[18] Gaussian 98 (Revision A.11), M. J. Frisch, G. W. Trucks, H. B. Schlegel, G. E. Scuseria, M. A. Robb, J. R. Cheeseman, V. G. Zakrzewski, J. A. Montgomery, R. E. Stratmann, J. C. Burant, S. Dapprich, J. M. Millam, A. D. Daniels, K. N. Kudin, M. C. Strain, O. Farkas, J. Tomasi, V. Barone, M. Cossi, R. Cammi, B. Mennucci, C. Pomelli, C. Adamo, S. Clifford, J. Ochterski, G. A. Petersson, P. Y. Ayala, Q. Cui, K. Morokuma, D. K. Malick, A. D. Rabuck, K. Raghavachari, J. B. Foresman, J. Cioslowski, J. V. Ortiz, B. B. Stefanov, G. Liu, A. Liashenko, P. Piskorz, I. Komaromi, R. Gomperts, R. L. Martin, D. J. Fox, T. Keith, M. A. Al-Laham, C. Y. Peng, A. Nanayakkara, C. Gonzalez, M. Challacombe, P. M. W. Gill, B. G. Johnson, W. Chen, M. W. Wong, J. L. Andres, M. Head-Gordon, E. S. Replogle, J. A. Pople, Gaussian, Inc., Pittsburgh, PA, **2001**.

[19] a) R. E. Stratmann, G. E. Scuseria, M. J. Frisch, *J. Chem. Phys.* **1998**, *109*, 8218–8224; b) R. Bauernschmitt, R. Ahlrichs, *Chem. Phys. Lett.* **1996**, *256*, 454–464; c) M. E. Casida, C. Jamorski, K. C. Casida, K. D. R. Salahub, *J. Chem. Phys.* **1998**, *108*, 4439–4449.

 © 2004 Wiley-VCH Verlag GmbH & Co. KGaA, Weinheim

Combinatorial Synthesis

A Combinatorial Approach to Catalytic Peptide Dendrimers**

*Anthony Clouet, Tamis Darbre, and Jean-Louis Reymond**

In de novo protein design one attempts to create artificial proteins with defined structure and function from first principles, usually with the help of trial-and-error procedures

[*] A. Clouet, Priv.-Doz. Dr. T. Darbre, Prof. Dr. J.-L. Reymond
Department of Chemistry and Biochemistry
University of Bern
Freiestrasse 3, 3012 Bern (Switzerland)
Fax: (+41) 31-631-8057
E-mail: jean-louis.reymond@ioc.unibe.ch

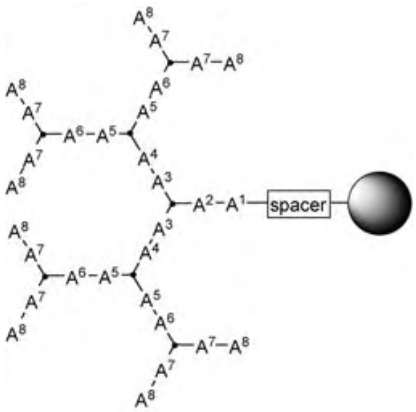
[**] This work was financially supported by the University of Bern and the Swiss National Science Foundation. We thank Mr. Urs Kämpfer of the Protein Analytical Service of the Department of Chemistry and Biochemistry, University of Bern, for performing the amino acid analyses.

Supporting information for this article is available on the WWW under http://www.angewandte.org or from the author.

 © 2004 Wiley-VCH Verlag GmbH & Co. KGaA, Weinheim DOI: 10.1002/anie.200460177

that scan a large number of possible amino acid sequences.[1] Our approach to de novo protein design is based on peptide dendrimers. Dendrimers are treelike structures that adopt a globular or disk-shaped structure as a consequence of topology rather than folding.[2] We have shown that peptide dendrimers that bear histidine residues at the surface catalyze ester hydrolysis in water.[3] Herein we report a combinatorial approach to peptide dendrimers based on split-and-mix synthesis and on-bead screening. The method is exemplified by the discovery of catalytic and binding peptide dendrimers in a 65536-membered library.

As peptide dendrimers are synthesized on solid supports, it should be possible to apply the principles of combinatorial peptide synthesis,[4] which have been exploited successfully for peptide-based and small-molecule catalysts.[5] To achieve this goal, we selected a dendrimeric architecture containing eight variable positions connected by three successive branching diamino acid units (Figure 1). Preliminary experiments showed that the sequence of eleven coupling steps to form such dendrimers gave good chemical yields for single sequences when using 2,3-diaminopropanoic acid as the branching unit.[3b] A split-and-mix library of peptide dendrimers was designed by distributing sixteen proteinogenic amino acids into four groups of four amino acids each. The resulting 65536-member library required splitting in four portions at each variable sequence step, whereby each group of four amino acids would be used at two positions in different branches of the dendrimer. The single-bead sequencing problem was solved by taking advantage of the dendritic structure in which amino acids are present in one, two, four, or eight copies, depending on their placement in the different branches. As each amino acid was present at most at two positions in different branches, the sequence could be unambiguously assigned by quantitative amino acid analysis of the dendrimer.[6]

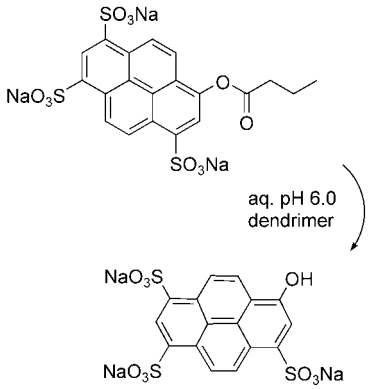


A^8, A^6	A^7, A^5	A^4, A^2	A^3, A^1
His	Pro	Lys	Asp
Glu	Ser	Phe	Ala
Trp	Arg	Ile	Thr
Gly	Leu	Tyr	Val

Figure 1. Combinatorial library of 65536 ($=4^8$) peptide dendrimers obtained by solid-phase split-and-mix synthesis. ● (branching unit) = (*S*)-2,3-diaminopropanoic acid. Spacer = $NH(CH_2)_5CONH$-CH_2CONH-, and $NH(CH_2)_5CONHCH_2CONH_2$ after cleavage from the support for resynthesized dendrimers. The N terminus at position A^8 is either acetylated (esterolysis studies) or free (vitamin B_{12} binding studies). The solid support is tentagel.

The peptide-dendrimer library was prepared from a 400-mg resin batch, which ensured that each sequence would be present in approximately 15 beads. Aromatic, hydrophobic, positively charged, negatively charged, and small amino acids were distributed evenly among the inner positions A^1–A^4 and the outer positions A^5–A^8. Histidine was placed in the outermost layer (A^6 and A^8) as surface placement of this residue was known to favor catalysis.[3] The sequence started with an amino–hexanoyl–glycine spacer to minimize interactions with the solid support. All coupling steps were quantitative, as indicated by the negative TNBS (2,4,6-trinitrobenzenesulfonic acid) staining test. Side-chain protecting groups were removed with trifluoroacetic acid after cleavage of the Fmoc protecting groups and acetylation of the last amino acid, resulting in a functional dendrimer library on beads.

The peptide dendrimer library was screened to find catalytic peptide dendrimers for an ester-hydrolysis reaction. Activity screening was realized by soaking the beads in an aqueous buffered solution of a fluorogenic ester substrate, followed by decantation and spreading the slurry of beads onto a Petri dish. Whereas the solvent quickly evaporated at the glass surface, evaporation inside the beads was slow, so that each bead functioned as a separate microreactor. The procedure was successful for screening the hydrolysis of 8-butyryloxypyrene-1,3,6-trisulfonate, a known fluorogenic lipase substrate (Scheme 1). Approximately 60% of all beads showed low-level fluorescence, among which very few beads (10 beads/40 mg resin) showed an intense green fluorescence that indicated product formation (see Supporting Information). These active beads were picked, washed thoroughly with buffer and water, and subjected to amino acid analysis (Table 1). Two consensus sequences and two original sequences were synthesized as single sequences and purified



Scheme 1. Fluorogenic esterolysis reaction of 8-butyryloxypyrene-1,3,6-trisulfonate catalyzed by peptide dendrimers.

 © 2004 Wiley-VCH Verlag GmbH & Co. KGaA, Weinheim

Table 1: Peptide dendrimer sequences identified by amino acid analysis of active beads from the combinatorial library[6] and the corresponding consensus sequences.[a]

	Dend.	A^8	A^7	A^6	A^5	A^4	A^3	A^2	A^1
Hits for hydrolysis of 8-butyryloxypyrene-1,3,6-trisulfonate[b]	1	W	**S**	***G***	R	**K**	**V**	**I**	A
	2	**H**	L	**H**	***S***	Y	A	**I**	D
	3	**H**	L	***G***	**L**	Y	T	**I**	**V**
	4	**H**	P	***G***	P	**K**	T	**I**	A
	5	E	R	***G***	***S***	***I***	**V**	**I**	**V**
	6	G	R	W	R	***I***	**V**	**I**	A
	7	**H**	**S**	**H**	**L**	F	A	F	D
	8	**H**	**S**	***G***	R	***I***	A	**I**	**V**
	9	**H**	**S**	**H**	P	**K**	**V**	F	**V**
	10	G	R	***G***	P	***I***	**V**	**I**	**V**
consensus sequences	**C11**	**H**	**S**	**H**	**L**	**K**	**V**	**I**	**V**
	C12	**H**	**S**	***G***	***S***	***I***	**V**	**I**	**V**
Hits for binding to vitamin B_{12}[c]	13	**W**	L	H	***S***	***I***	A	***K***	A
	14	E	**P**	**G**	**R**	**Y**	***T***	**Y**	**D**
	15	**W**	**P**	***E***	***S***	**Y**	A	**Y**	**D**
	16	***G***	**P**	W	P	**Y**	**V**	***K***	***V***
	17	***G***	***R***	***E***	**R**	***I***	***T***	I	**D**
	18	H	L	**G**	**R**	K	**V**	***K***	**D**
	19	**W**	***R***	***E***	***S***	***I***	**V**	I	***V***
consensus sequences	**C20**	**W**	**P**	**G**	**R**	**Y**	**V**	**Y**	**D**
	C21	***G***	***R***	***E***	***S***	***I***	***T***	***K***	***V***

[a] Dendrimer structure according to Figure 1. Dendrimers marked bold were resynthesized by Fmoc-SPPS and purified. [b] All N termini *N*-acetylated. Screening conditions: Beads soaked in 20 mM aqueous Bis–Tris buffer containing 80 μM 8-butyryloxypyrene-1,3,6-trisulfonate, 25 °C, 30 min. Hits are green-fluorescent under UV radiation (356 nm). [c] N termini are free amine. Screening conditions: 30 min equilibration in aq. PBS (10 mM phosphate, 160 mM NaCl, pH 7.4) containing 400 μM cyanocobalamin (vitamin B_{12}), followed by washing with PBS and water. Hits are bright orange.

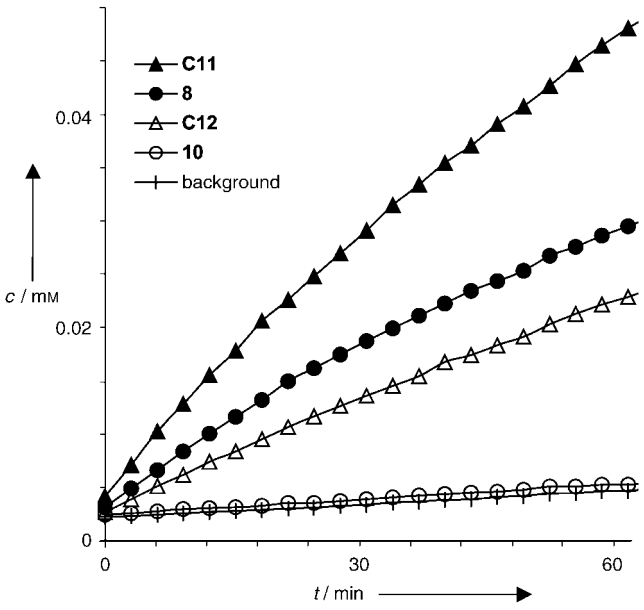


Figure 2. Hydrolysis of 8-butyryloxypyrene-1,3,6-trisulfonate (Scheme 1) catalyzed by peptide dendrimers from the combinatorial library. Conditions: substrate (200 μM), dendrimer (5 μM), aqueous 20 mM Bis–Tris pH 6.0, 25 °C. The reactions were run in 96-well, polystyrene, half-area microtiter plates with subsequent detection on a SpectraMAX fluorescence detector with $\lambda_{exc} = 460$ nm, $\lambda_{em} = 530$ nm. Fluorescence was converted to product concentration by using a calibration curve, which was linear in the concentration range used.

Table 2: Kinetic parameters for esterolytic peptide dendrimers from the combinatorial library.[a]

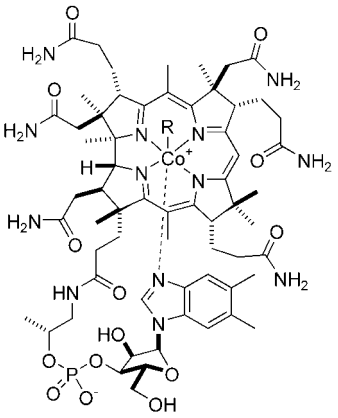
	8	**C11**	**C12**
K_M (mM)	0.065	0.066	0.051
k_{cat} (min^{-1})	0.094	0.14	0.054
k_{cat}/k_{uncat}	2140	3100	1200
$k_{cat}/K_M/k_2$	1800	2540	1300
V_{net}/V_{uncat}	39	51	22

[a] Conditions: 50–800 μM 8-butyryloxypyrene-1,3,6-trisulfonate, 5 μM dendrimer, 20 mM aqueous Bis–Tris pH 6.0, 25 °C. The kinetic constants given are derived from the linear double-reciprocal plots of $1/V_{net}$ versus 1/[S]. V_{net}/V_{uncat} is the apparent rate enhancement observed with S = 200 μM and 2.5 mol% catalytic peptide dendrimer (5 μM). $V_{net} = V_{app} - V_{uncat}$ with V_{app} being the apparent hydrolysis rate in the presence of dendrimer and V_{uncat} the hydrolysis rate in buffer alone ($k_{uncat} = 4.4 \times 10^{-5}\ min^{-1}$). $k_2 = 8.1 \times 10^{-4}\ mM^{-1}\ min^{-1}$ is the catalytic rate constant for hydrolysis by 4-methyl-imidazole under the same conditions.

by preparative HPLC. Dendrimer **10**, which did not contain a histidine residue, was not active and represented a false positive.[7] The three other dendrimers (**8**, **C11**, and **C12**) were catalytically active, and contained histidine at the outermost position A^8 (Figure 2). These dendrimers displayed enzyme-like catalysis for the ester hydrolysis (Table 2) with multiple turnover and rate enhancement k_{cat}/k_{uncat} up to 3000-fold over background and K_M values in the 0.05 mM range. In terms of apparent catalytic effect V_{net}/V_{uncat}, these dendrimers are 2–10 times better than those prepared previously by rational design.[3]

Activity screening of solid-supported combinatorial libraries for binding affinity can be readily carried out by bead staining with a colored ligand.[4a] The dendrimer library was screened for binding to vitamin B_{12}, a corrinoid-type chromophore for which no artificial binding proteins have been described to date (Figure 3). Vitamin B_{12}-containing enzymes hold the vitamin by multiple hydrogen bonds to the carboxamide groups of the corrin ring.[8] Equilibration with vitamin B_{12} in aqueous neutral buffer resulted in staining of two to five beads per experiment (0.01%). The experiment was repeated twice to give a total of seven colored beads, which were subjected to amino acid analysis (Table 1). Two original sequences and two consensus sequence were resynthesized, cleaved from the resin, and purified by preparative HPLC. In each case a small portion of noncleavable synthesis beads were used in the synthesis, and these beads bound vitamin B_{12} as observed during screening. Beads carrying a catalytic sequence were not stained under these conditions. Bead staining by vitamin B_{12} was inhibited in the presence of > 0.5 mM of soluble purified dendrimer **C21**, but not with the same amount of the catalytic dendrimer **C10**, indicating a relatively weak, yet highly selective, binding interaction. While aquocobalamin also bound the dendrimers, there was no binding with cobinamide, which lacks the nucleotide loop, therefore suggesting that this structural element is involved in the dendrimer–vitamin B_{12} interaction (Table 3).

 © 2004 Wiley-VCH Verlag GmbH & Co. KGaA, Weinheim



vitamin B_{12}-cyano (R = CN)
vitamin B_{12}-aquo (R = OH)

Figure 3. Structure of vitamin B_{12}. In cobinamide the 3′-phosphonucleoside is absent and the cobalt center has two cyanide ligands.

Table 3: Interaction between dendrimers and vitamin B_{12} derivatives.[a]

Dendrimer	Vitamin B_{12}-cyano		Vitamin B_{12}-aquo		Cobinamide	
	400 μM	100 μM	400 μM	100 μM	400 μM	100 μM
19	+++	+	+++	++	–	–
14	+++	–	+++	++	–	–
C20	+++	–	+++	++	–	–
C21	+++	–	+++	++	–	–
C11	–	–	–	–	–	–

[a] Intensity of bead staining (orange/red coloration) after equilibration of solid-supported dendrimer with the given concentration of vitamin B_{12} in aqueous phosphate buffer pH 7.4 for 30 min, followed by washing.

The experiments above demonstrate a general approach to functional peptide dendrimers through split-and-mix combinatorial libraries. Library design and the dendritic architecture allow single-bead sequencing by quantitative amino acid analysis, such that bead encoding[9] is not necessary. Selection for catalysis was realized by soaking the beads with fluorogenic substrates and spreading on a dry surface, which allows direct selection for catalytic turnover. The procedure is, to our knowledge, new and is suitable for screening reactions with soluble fluorogenic or chromogenic substrates or sensor systems.[10] The method provides a useful complement to previously reported on-bead screening methods based on the covalent attachment of substrate[11] or sensor[5c] to the beads, the use of precipitating dyes,[5a] or IR thermography.[12] The exploration of focused libraries should enable the refinement and improvement of the properties of the isolated dendrimers, and the exploration of further problems in binding and catalysis.

Received: March 31, 2004

Keywords: cobalamines · combinatorial chemistry · dendrimers · enzyme models · peptides

[1] a) D. A. Moffet, M. H. Hecht, *Chem. Rev.* **2001**, *101*, 3191–3203; b) D. N. Bolon, C. A. Voigt, S. L. Mayo, *Curr. Opin. Chem. Biol.* **2002**, *6*, 125–129.

[2] a) A. W. Bosman, H. M. Janssen, E. W. Meijer, *Chem. Rev.* **1999**, *99*, 1665–1688; b) D. K. Smith, *Tetrahedron* **2003**, *59,* 3797–3798; c) S. Hecht, J. M. J. Fréchet, *Angew. Chem.* **2001**, *113,* 76–94; *Angew. Chem. Int. Ed.* **2001**, *40,* 74–91; d) G. R. Newkome, C. N. Moorefield, F. Vögtle, *Dendritic Molecules: Concepts, Synthesis, Perspectives*, Wiley-VCH, Weinheim, **1996**.

[3] a) A. Esposito, E. Delort, D. Lagnoux, F. Djojo, J. L. Reymond, *Angew. Chem.* **2003**, *115*, 1419–1421; *Angew. Chem. Int. Ed.* **2003**, *42*, 1381–1383; b) D. Lagnoux, E. Delort, C. Douat-Casassus, A. Esposito, J. L. Reymond, *Chem. Eur. J.* **2004**, *10*, 1215–1226.

[4] a) K. S. Lam, S. E. Salmon, E. M. Hersh, V. J. Hruby, W. M. Kazmierski, R. J. Knapp, *Nature* **1991**, *354*, 82–84; b) R. A. Houghten, C. Pinilla, C. , S. E. Blondelle, J. R. Appel, C. T. Dooley, J. H. Cuervo, *Nature* **1991**, *354*, 84–86.

[5] a) A. Berkessel, *Curr. Opin. Chem. Biol.* **2003**, *7*, 409–419; b) C. Gennari, U. Piarulli, *Chem. Rev.* **2003**, *103*, 3071–3100; c) C. A. Evans, S. J. Miller, *Curr. Opin. Chem. Biol.* **2002**, *6*, 333–338; d) B. Linton, A. D. Hamilton, *Curr. Opin. Chem. Biol.* **1999**, *3*, 307–312; e) K. W. Kunz, M. L. Snapper, A. H. Hoveyda, *Curr. Opin. Chem. Biol.* **1999**, *3*, 313–319.

[6] Single dendrimer-containing resin beads were hydrolyzed with aqueous HCl (6 M) at 110 °C for 22 h, and their amino acid composition was determined quantitatively by HPLC after derivatization with phenyl isothiocyanate (PITC). Such amino acid analyses are routine for protein-composition analysis. The analysis detects as little as 5 pmol per amino acid, which is sufficient for single-resin-bead analysis, as these contain 50–200 pmol of dendrimers.

[7] False positives are most likely due to manipulation errors during bead picking. Sometimes more than one bead is transferred to the pipette, and the fluorescence staining is diluted when the beads are washed down the pipette used for picking, which does not allow staining to be rechecked afterwards.

[8] *Chemistry and Biochemistry of B_{12}* (Ed.: R. Banerjee), Wiley, New York, **1999**.

[9] M. H. J. Ohlmeyer, R. N. Swanson, L. W. Dillard, J. C. Reader, G. Asouline, R. Kobayashi, M. H. Wigler, W. C. Still, *Proc. Natl. Acad. Sci. USA* **1993**, *90*, 10922–10926.

[10] a) *Enzyme Assays: A Practical Approach* (Eds.: R. Eisenthal, M. Danson) Oxford University Press, Oxford **2002**; b) S. Gul, S. K. Sreedharan, K. Brocklehurst, *Enzyme Assays: Essential Data*, Wiley, New York, **1998**; c) M. T. Reetz, *Angew. Chem.* **2001**, *113*, 292–320; *Angew. Chem. Int. Ed.* **2001**, *40*, 284–310; d) D. Wahler, J.-L. Reymond, *Curr. Opin. Chem. Biol.* **2001**, *5*, 152–158; e) F. Beisson, A. Tiss, C. Rivière, R. Verger, *Eur. J. Lipid Sci. Technol.* **2000**, 133–153; f) D. Wahler, J.-L. Reymond, *Curr. Opin. Biotechnol.* **2001**, *12*, 535–544.

[11] a) P. Krattiger, C. McCarthy, A. Pfaltz, H. Wennemers, *Angew. Chem.* **2003**, *115*, 1763–1766; *Angew. Chem. Int. Ed.* **2003**, *42*, 1722–1724; b) I. Lingard, G. Bhalay, M. Bradley, *Chem. Commun.* **2003**, 2310–2311.

[12] S. J. Taylor, J. P. Morken, *Science* **1998**, *280*, 267–270.

 © 2004 Wiley-VCH Verlag GmbH & Co. KGaA, Weinheim

Noncovalent Interactions

Electrostatic Site Attachment of Divalent Counterions to Rodlike Ruthenium(II) Coordination Polymers Characterized by EPR Spectroscopy**

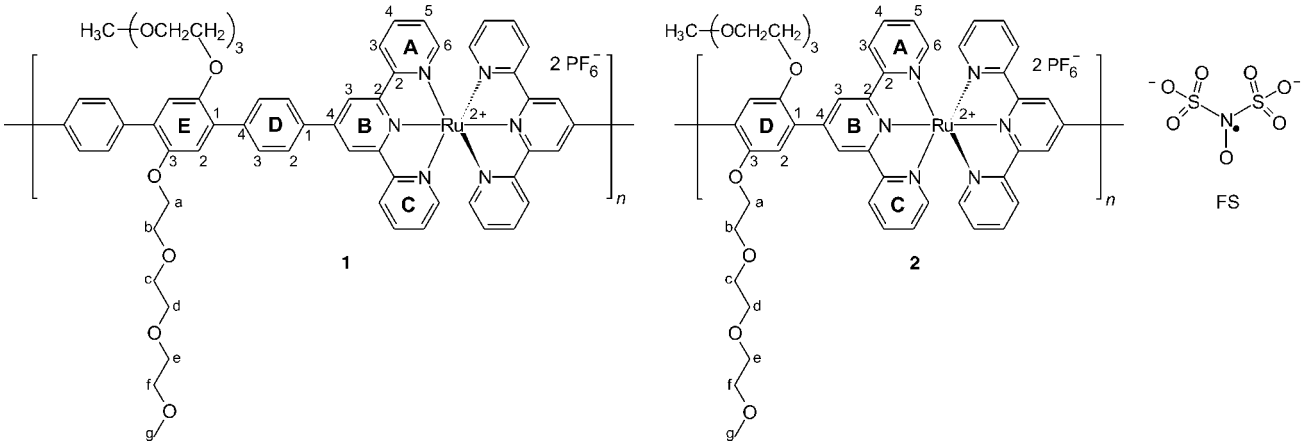
*Dariush Hinderberger, Oliver Schmelz, Matthias Rehahn, and Gunnar Jeschke**

Coordination polymers which are formed from connecting organic bischelating ligand molecules ("ligand monomers") through transition metals have received much attention in the past decade.[1] The use of transition-metal ions such as ruthenium(II) or osmium(II) provides materials with kinetically inert coordinative bonds that are of interest as potential (electro-)optical or magnetic nanomaterials.[1e–h] Such systems are also very well suited as model systems for the study of polyelectrolyte behavior, since they have a well-defined rigid conformation in solution which reduces the complexity of the polyelectrolyte behavior by limiting the conformational degrees of freedom.[2a,b]

Polyelectrolytes are macromolecular substances that are soluble in water or other ionizing solvents.[2] They dissociate into macromolecular ions that carry multiple charges (polyions) together with an equivalent number of ions of small charge and opposite sign. Despite their important role in many fields of scientific research, such as molecular biology (DNA, RNA) and nanotechnology,[3–5] the interplay of electrostatic interactions between macro-ions and counterions is not yet fully understood.[2a,b,6a–6c] Comparison between theoretical and experimental results has proved difficult in the past, as additional complexity is introduced in experiments by solvation effects, specific interaction between counterions and charged groups of the polyelectrolyte, and conformational changes of flexible polymer chains which cannot be separated properly from electrostatic effects.

Herein we consider coordination polymers formed by divalent Ru^{II} ions that are connected by bis(2,2′:6′,2″-terpyridine)-based rigid spacer molecules of variable lengths (Scheme 1) to study the condensation of counterions[6d–g] to a stiff, relatively weakly charged polyion.[6] In the study we use a combination of continuous wave (CW)[7] and pulse[8] EPR spectroscopy on paramagnetic counterions that we have recently used to obtain a local, dynamic picture of counterion condensation to the flexible polyelectrolyte poly(diallyldimethylammonium chloride).[9] For this strongly charged polyelectrolyte we were able to demonstrate that a significant portion of divalent counterions is transiently bound to the quaternary ammonium groups of the polyion with a lifetime that is lower than 1 ns. We call this process dynamic electrostatic attachment.[9]

Herein we raise the question whether such dynamic electrostatic attachment is also observable for a more weakly charged Ru^{II} coordination polymer in which the carriers of the twofold positive charges are sterically shielded by bulky terpyridine ligands. In particular, we use double electron-electron resonance (DEER) spectroscopy[10] to characterize the spatial distribution of dianionic spin probe molecules (Fremy's salt (FS), potassium nitrosodisulfonate, Scheme 1) on a length scale between 1.8 and 5 nm. As this length scale includes the separations of direct and next-neighbor ions of the coordination polymers, such experiments should provide a clear signature of site-attachment[6g] of the counterions along the backbone of the rodlike coordination polymer. By examining distance distributions of the spin-carrying counterions we should also be able to obtain a semiquantitative



Scheme 1. Molecular structures of the spin probe FS (Fremy's salt) and the rodlike coordination polymers containing divalent ruthenium ions as charged groups (**1** and **2**), with the number of repeat units $n = 20–25$.

[*] Dr. D. Hinderberger, Priv.-Doz. Dr. G. Jeschke
Max-Planck-Institut für Polymerforschung
Postfach 3148, 55021 Mainz (Germany)
Fax: (+49) 6131-379-100
E-mail: jeschke@mpip-mainz.mpg.de
O. Schmelz, Prof. Dr. M. Rehahn
Deutsches Kunststoff-Institut (DKI) and
Ernst-Berl-Institut für Technische und Makromolekulare Chemie
Technische Universität Darmstadt
Petersenstrasse 22, 64287 Darmstadt (Germany)

[**] This work was supported by the Deutsche Forschungsgemeinschaft (Schwerpunktprogramm 1051 "High-Field EPR in Biology, Chemistry, and Physics"). We thank Manfred Schmidt for helpful discussions and Christian Bauer for technical support.

 © 2004 Wiley-VCH Verlag GmbH & Co. KGaA, Weinheim DOI: 10.1002/anie.200460500

estimate of the extension of the counterion clouds around the charged groups.

The two ruthenium(II)-based coordination polymers **1** and **2** (Scheme 1) only differ in the separation of the Ru^{2+} centers along the backbone. Each Ru^{2+} center is electrostatically compensated by two PF_6^- counterions. It was estimated from NMR endgroup analysis that both compounds are built up of approximately 25 repeat units, and it was shown that these substances display macroscopic polyelectrolyte properties.[1f,g]

Experiments were performed on solutions of **1** (0.5 mM Ru^{2+} repeat units) and **2** (0.75 mM Ru^{2+} repeat units for pulse EPR, 0.6 mM Ru^{2+} repeat units for CW EPR) that contained an amount of spin-carrying FS counterions (0.5 mM) that approximately matched the number of Ru^{2+} centers. Solutions of **1** had to be prepared with a ternary solvent mixture of 50 vol% DMF and 50 vol% glycerol/water (1:1, v/v) since **1** is not very soluble in water and FS is not very soluble in DMF, while solutions of **2** and FS could be prepared in the binary solvent mixture of 33 vol% glycerol/67 vol% water (for pulse EPR) and 43.5 vol% glycerol/56.5 vol% water (for CW EPR). Addition of glycerol increases the viscosity and thus shifts rotational correlation times for FS dianions closer to the slow-tumbling regime where spectra are more sensitive to specifics of rotational diffusion. Furthermore, glycerol prevents crystallization of the solvent mixture during shock-freezing of the samples, so that glassy samples are obtained and precipitation of the coordination polymer can be avoided.

We first checked for the presence of interspin distances below 2 nm, which would lead to significant broadening in the low-temperature EPR spectra of the nitroxide group. While no such broadening is observed in the field-swept echo-detected EPR spectrum of FS anions in the presence of **1**, broadening in the wings of the spectrum is found in the presence of **2** (data not shown). As the distance between directly neighboring Ru^{2+} ions is longer than 2 nm in **1**, but significantly shorter than 2 nm in **2**, this finding would be consistent with some degree of attachment of FS dianions to the charged groups of the coordination polymers.

To test this hypothesis we have performed DEER experiments. Primary DEER signals of glassy frozen solutions FS with **1** and **2** are presented in Figure 1a and c, respectively. Both time traces clearly cannot be fitted by an exponential decay function (gray curve) as would be expected if the FS dianions were distributed homogeneously throughout the sample. In contrast, a time trace for the coordination monomer with the same spacer as in coordination polymer **2** can be fitted by an exponential decay function (data not shown). Furthermore, the shape of the two signal traces for **1** and **2** differs, which proves that the deviations from the homogeneous distribution are specific signatures of the structure of the coordination polymer.

Indeed the distance distributions obtained from these data by a model-free direct integral transformation[11] both exhibit two marked peaks that are situated at 2.4 and 4.7 nm for **1** (Figure 1b) and 2.9 and 4.5 nm for **2** (Figure 1d) and have approximately Gaussian shape. The additional weaker peak at approximately 3.5 nm in Figure 1b (asterisk) may be a noise artifact, as it is not observed in data with shorter maximum dipolar evolution times (not shown). We nevertheless discuss the data for longer maximum evolution times, as they provide a better estimate of the width of the peak at 4.7 nm.

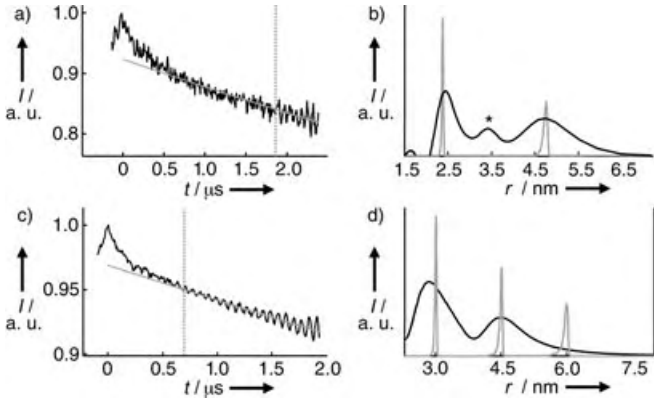


Figure 1. DEER time-domain data (a,c) and extracted distance distributions (b,d) of FS in solutions of **1** (a,b) in 50 vol% DMF/50 vol% glycerol/water and **2** (c,d) in 33 vol% glycerol/67 vol% water. The time traces were recorded at $T = 20$ K and gray lines are exponential fits to the data of FS/**1** between 1.9 and 2.4 μs and FS/**2** between 0.7 and 1.8 μs (both marked by the gray dotted line). The broad distance distributions (black lines) shown in (b) and (d) are obtained by integral transformation,[11] the overlaid gray lines are Ru···Ru distance distributions obtained from an MD simulation as explained in the text. Amplitudes of the MD distributions are scaled by a factor of 0.1. The asterisk in (b) marks a noise artifact.

Remarkably, in both cases the two distances correspond rather nicely to the expected distances between Ru^{2+} centers that are separated by one (peak at 2.4 nm for **1**), two (peak at 4.7 nm for **1** and peak at 2.9 nm for **2**), or three (peak at 4.5 nm for **2**) spacers. The distance of 1.5 nm expected for Ru^{2+} centers separated by one spacer in **2** cannot be reliably detected, as it coincides with an artifact arising from proton modulation.[10,11] This proton modulation is mainly a consequence of solvent protons. Differences in its depth may arise from the different solvent composition, but may also be caused by the slightly different timing of the two experiments. Distances longer than 5 nm cannot be extracted at the experimentally accessible maximum dipolar evolution times. The corresponding part of the distance distribution is suppressed by background correction of the primary data before the integral transformation.[11] This background correction was performed by fitting a monoexponential function to the data at $t > 1$ μs, which corresponds to the assumption of a homogeneous distribution of the FS ions in three dimensions at sufficiently long distances. The slightly stronger background decay for **1** relative to **2** reflects a higher local concentration of FS anions in the former polymer. Deviations from the selected background model cannot definitively be excluded. In particular, it is known that electrostatic repulsion between FS dianions causes an under-representation of short distances.[12] Furthermore, the elongated shape of the polymer chain breaks the spherical symmetry and might cause an admixture of a homogeneous distribution in only one dimension, as we observed earlier on a flexible polyelectrolyte with higher charge density.[9b] However, given the relatively low bulk concentrations, the corresponding contri-

 © 2004 Wiley-VCH Verlag GmbH & Co. KGaA, Weinheim

butions to the decay function are hardly expected to exceed the noise level. When intentionally varying the background decay function we found only minor changes in the distance distribution that do no affect the conclusions drawn above.

The modulation depth obtained after dividing the data by the background function and renormalizing intensity at $t = 0$ contains information on the fraction of FS ions that are close to the coordination polymer. We can estimate that less than 20% of the Ru^{2+} ions have FS counterions attached. A more precise quantification is not possible on the basis of our data, as, in contrast to the distance distribution at $r < 5$ nm, the estimate of the modulation depth is rather sensitive to the choice of background function.

To obtain an estimate for the variation of the distances between the Ru^{2+} centers we performed molecular dynamics simulations in a vacuum for 2 ns of oligomers of both compounds end-capped with terpyridine moieties (**1**: two repeat units and two end caps, **2**: four repeat units and two end caps). The respective distance distributions are shown as solid gray lines in Figure 1 b,d. The theoretically predicted Ru···Ru distance distributions are much narrower than the extracted FS···FS distributions, while the maxima in the distribution (2.35 and 4.7 nm for **1**; 3 and 4.5 nm for **2**) are almost identical to those obtained from the direct DEER transformation.

We consider the latter finding as clear evidence for electrostatic attachment of at least a fraction of FS dianions to the charged groups on the coordination polymers. In the simple picture of (spherically symmetric) Coulomb interaction, such pairing is favored compared to the interaction with the original monovalent counterions of the polyion as it leads to a twofold increase in electrostatic interaction energy, and the replacement of monovalent counterions by divalent counterions is also favored by the gain in entropy for the system as a whole. Nevertheless, it is remarkable that electrostatic site attachment of counterions can be observed for relatively short, weakly charged polyions with approximately 25 repeat units and linear charge densities of the order of 1 nm^{-1}.

The larger width of the peaks in the experimental FS···FS distance distribution compared to the peaks in the theoretically predicted Ru···Ru distance distribution (**1**: full width at half maximum (FWHM) ca. 0.5 nm for the 2.4-nm peak and ca. 1 nm for the 4.7-nm peak; **2**: FWHM ca. 0.6 nm for the 2.9-nm peak and ca. 1 nm for the 4.5-nm peak) can be attributed to the sterical shielding of the Ru^{2+} ions by the terpyridine ligands and to the electrostatic nature of the localized attachment of the counterions. The upper part of Figure 2 shows (using **1** as an example) that if one assumes an octahedral symmetry around a Ru^{2+} center there are at least four equal positions of closest contact for FS counterions. The lower part of Figure 2 gives a schematic plot of the volume around polymer **1** in which FS ions are most likely to reside. Force-field calculations of the structure of both coordination polymers suggest side lengths of about 0.6 nm for the (hypothetical) square "box" that approximates the attachment volume around the Ru^{2+} site, that is, the spatial region in which FS ions can access the oppositely charged Ru^{2+} ions. This attachment volume effectively translates to a degree of

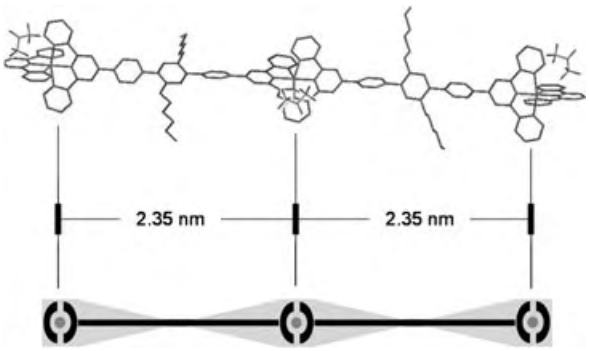


Figure 2. Schematic representation of possible localized binding of FS ions to Ru^{2+} centers in **1**. Top: An end-capped coordination dimer that has been geometry-optimized by force-field calculations (UFF 1.02) as explained in the text. The distinct distances between FS found from DEER data analysis (ca. 2.4 nm and ca. 4.7 nm) agree very well with the distances between Ru^{2+} centers separated by one or two organic spacers, respectively. Bottom: Schematic plot of most probable attachment sites for FS ions (gray area). The relatively broad distribution of spin probe distances can be explained if one accounts for the degrees of freedom of the electrostatic attachment.

freedom for the electrostatic attachment of FS to a Ru^{2+} center, which broadens the FS···FS distribution. Assuming a Gaussian distribution of ions in the attachment volume, such broadening has a square-root dependence on the number of spacers in between the Ru^{2+} centers, which would be consistent with the observed increase in width of the FS distance peak on going to longer distances.

The electrostatic origin of the FS distance distribution also accounts for the fact that FS distance peaks are indeed Gaussian-like and not asymmetric like the theoretical Ru···Ru distance peaks (see Figure 1 b,d). The asymmetry of the latter peaks reflects that the maximum distance upon bending an ideal rigid rod must be that of full linear extension, which is at the same time the most likely distance. Broadening of the peaks by diffuse electrostatic attachment makes this effect unobservable in the FS···FS distance distribution.

To probe the dynamics of the observed attachment process CW EPR spectroscopy was performed on fluid solutions of the same samples. Comparison of the spectra for solutions of only FS (Figure 3 a) and FS and **2** (Figure 3 b, black solid line) reveals a subtle but significant change in the relative intensities of the three lines of the spectrum of the nitroxide group. The same behavior was observed for a solution of **1** (data not shown).

In the spectrum of pure FS (Figure 3 a) the center-field line is the narrowest and has the highest relative amplitude, followed by the low-field line and the high-field line. This pattern is also observed for pure FS in all other solvents. In the spectrum of the solution with added **2** (1.5:1 Ru^{2+}:FS^{2-}), the low-field line is the narrowest and most intense, the center-field line is slightly less intense, and the high-field line is significantly further decreased in intensity. This change indicates that rotational diffusion of the FS dianions is significantly altered by the presence of the coordination polymer. To understand this change in rotational dynamics, spectral simulations were performed by using the program developed by Schneider and Freed[13] which can take into

 © 2004 Wiley-VCH Verlag GmbH & Co. KGaA, Weinheim

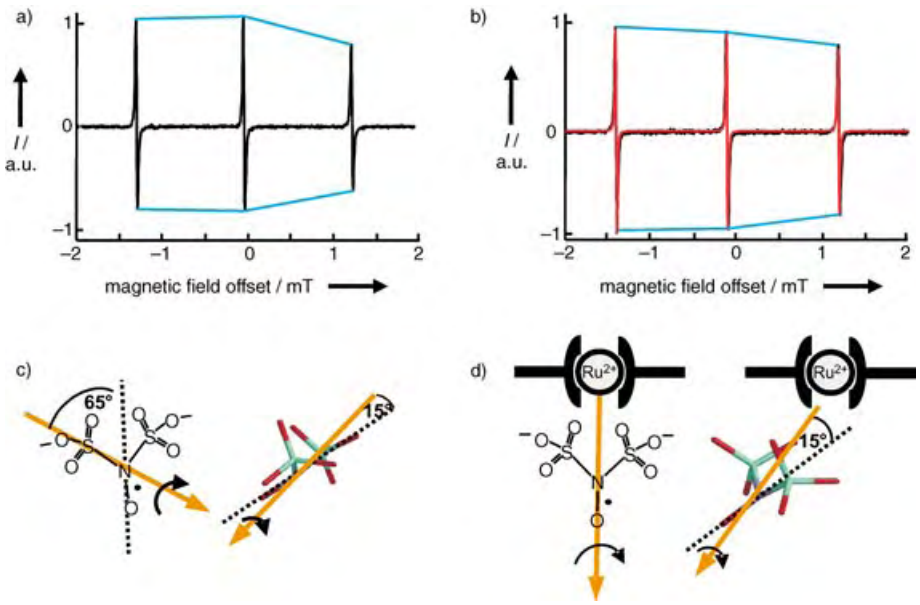


Figure 3. CW EPR spectra (X-band, ca. 9.8 GHz) at room temperature of a) 0.5 mM FS in 43.5 vol% glycerol/56.5 vol% water; b) 0.4 mM FS + 0.6 mM **2** (monomeric units) 43.5 vol% glycerol/56.5 vol% water. A spectral simulation of FS/**2** according to the rotational diffusion tensor explained in the text is shown in red. The blue lines are guides to the eye that pinpoint the change in relative amplitudes of the lines between (a) and (b). c) A visualization of the rotational diffusion tensor for FS in the solvent system 50 vol% glycerol/50 vol% water and d) displays the rotational diffusion tensor for FS with oppositely charged **2** in the same solvent; the orange arrows illustrate the principal axes of fast rotation of FS (c: 65° from the NO bond axis, see projection on the right and 15° out of plane of the plane ONS(2); d: 15° tilted away from the NO-bond axis, in the plane spanned by S(1)NS(2)). The principal values of the rotational diffusion tensor are for a) FS: $d_{\parallel}=30\times10^{9}\ s^{-1}$ (parallel to orange unique axis), $d_{\perp}=6\times10^{9}\ s^{-1}$ (perpendicular to orange axis), and for b) FS/**2**: $d_{\parallel}=30\times10^{9}\ s^{-1}$ (parallel to orange unique axis), $d_{\perp}=0.9\times10^{9}\ s^{-1}$ (perpendicular to orange axis).

account the effect of anisotropies in the rotational diffusion tensor. For simplicity, axial symmetry of the diffusion tensor was assumed.

The best simulation for free FS ions in pure solvents reproduces the lineshape pattern very well (simulation not shown in Figure 3a). It corresponds to a direction of the unique axis of the tensor of rotational diffusion along the N–S bond between the nitroxide group and one of the sulfonate groups (Figure 3c). In contrast, the simulation for the solution containing FS and **2** (red line in Figure 3b, slight deviation arising from phasing problems in the experimental spectrum) corresponds to a unique axis bisecting the two N–S bonds in the FS molecule (Figure 3d). This difference demonstrates that the divalent FS anions preferably interact with the polyion rather than with monovalent counterions, both in frozen solutions and also in fluid solutions.

Remarkably, rotational diffusion of the FS dianion in pure solvents is already slightly but significantly anisotropic, even though the shape of the molecule is almost spherical. The observation that rotation about the axis pointing to one sulfonate group is six times faster than rotation perpendicular to this axis (Figure 3c) can be explained by assuming that dynamic contact ion pairs are formed between one of the sulfonate groups and a counterion (K^+). For short times, the pair might then rotate as a whole about its long axis, which corresponds to the unique axis of the experimentally determined rotational diffusion tensor. The apparent symmetry breaking, that is, the favoring of one of two equivalent N–S bonds would result if on average only one or less contact with a counterion occurs on the timescale of the experiment (less than 1 ns).

This symmetry breaking does not occur in solutions of the coordination polymers where rotational diffusion preferably takes place about an axis bisecting the angle between both sulfonate groups (Figure 3d). Unlike monovalent potassium ions, the divalent Ru^{2+} ion thus appears to interact with both FS sulfonate groups simultaneously. The lifetime of such a "three-center ionic assembly" must be of the same order of magnitude as those of the ion pairs formed with monovalent ions, since the rotational diffusion rates are similar in both cases (about the unique axis $d_{\parallel}=30\times10^{9}\ s^{-1}$, perpendicular to the unique axis $d_{\perp}=0.9\times10^{9}\ s^{-1}$).

In conclusion, by applying two experimental techniques, CW EPR and DEER spectroscopy, to systems of spin-carrying counterions and oppositely charged, rodlike coordination polymers we could demonstrate that divalent counterions interact preferentially with the polyion and that their spatial distribution reflects the spatial distribution of charges on the polyion. We have found that the counterion cloud around bis(terpyridine)-coordinated transition-metal centers has an approximately Gaussian radial distribution with a width of approximately 0.5 nm. The electrostatic self-assembly underlying this spatial heterogeneity is a transient process in which the a lifetime of the electrostatically attached state is less than 1 ns.

Experimental Section

Fremy's salt of technical grade was bought from ICN Biomedicals and used as received.

1: A mixture of 2,5-bis(1,4,7,10-tetraoxaundecanyl)benzene-1,4-diboronic acid[14] (145 mg, 0.295 mmol, 1 equiv) and 4′-(*p*-bromophenyl)-2,2′:6′,2″-terpyridine[15] (229 mg, 0.590 mmol, 2 equiv) were refluxed under nitrogen in a mixture of THF (6 mL), water (6 mL), $NaHCO_3$ (760 mg, 9.047 mmol), and $[Pd(PPh_3)_4]$ (5.0 mg, 0.0043 mmol) for 48 h. After cooling the mixture down to room temperature, it was extracted with $CHCl_3$ (3×25 mL). The combined organic layers were dried ($MgSO_4$), the solvent was removed in vacuum, and the resulting yellowish solid was recrystallized from a mixture of methanol and chloroform (9:1; v/v).

$RuCl_3\cdot3H_2O$ (77.0 mg, 0.294 mmol) was activated by treatment with $AgBF_4$ (175.7 mg, 0.902 mmol) in acetone (25 mL).[11f] After removal of the precipitate (AgCl) by filtration, the solvent was removed in vacuo, and the resulting solid was dissolved in *N*,*N*-dimethylacetamide. The resulting black-violet solution was combined

 © 2004 Wiley-VCH Verlag GmbH & Co. KGaA, Weinheim

with the above ligand monomer and then heated for 72 h at 130 °C. After cooling down the mixture to room temperature, it was poured into a saturated aqueous KPF_6 solution (900 mL). The red precipitate was separated by filtration, washed several times with water and dried in vacuo (P_4O_{10}); yield: 238 mg (57 %). ^{1}H NMR (500 MHz, [D$_6$]DMSO): $\delta = 3.21$ (m, 6H, H^g), 3.46 (m, 4H, H^f), 3.59 (m, 4H, H^e), 3.64 (m, 4H, H^d), 3.69 (m, 4H, H^c), 3.88 (m, 4H, H^b), 4.38 (m, 4H, H^a), 7.33 (m, 4H, H^{A5}), 7.40 (m, 2H, H^{E2}), 7.60 (m, 4H, H^{A6}), 7.97(m, 4H, H^{D3}), 8.14 (m, 4H, H^{A4}), 8.56 (d, 4H, H^{D2}), 9.17 (m, 4H, H^{A3}), 9.57 ppm (m, 4H, H^{B3}).

2: 4′-Bromo-(2,2′:6′,2″)-terpyridine[16] (187 mg, 0.60 mmol, 2 equiv) and 2,5-bis-(1,4,7,10-tetraoxaundecanyl)-phenyl-1,4-diboronic acid[15] (147 mg, 0.3 mmol, 1 equiv) were refluxed under nitrogen in a mixture of ethanol (1 mL), water (2 mL), toluene (3 mL), [Pd(PPh$_3$)$_4$] (10.0 mg, 0.0087 mmol, 1.4 mol %), and Na_2CO_3 (143 mg, 1.35 mmol, 4.5 equiv) for 48 h. After cooling down the mixture to room temperature, it was extracted with CH_2Cl_2 (3 × 25 mL). The combined organic layers were dried ($MgSO_4$) and the solvent was removed in a vacuum. The residue was purified by precipitation from dichloromethane solution using *n*-hexane (3 times). A yellow, highly viscous residue was obtained after drying in vacuum (P_4O_{10}). This ligand monomer was added to a solution of activated ruthenium in *N*,*N*-dimethylacetamide (20 mL), which was prepared as described above from $RuCl_3 \cdot 3H_2O$ (100 mg, 0.383 mmol) and $AgBF_4$ (228 mg, 1.169 mmol) in acetone (30 mL). The mixture was heated to 130 °C for 72 h and then cooled down to room temperature. A red precipitate was obtained by adding saturated aqueous NaCl (100 mL). The solid was isolated by centrifugation, dissolved in water, and precipitated by addition of saturated aqueous NaCl. The polymer was dried in vacuum (P_4O_{10}); yield: 196.3 mg (63.4 %). ^{1}H NMR (500 MHz, [D$_6$]DMSO): $\delta = 3.04$ (m, 6H, H^g), 3.23 (t, 4H, H^f), 3.35 (m, 4H, H^e), 3.53 (m, 4H, H^d), 3.73 (m, 4H, H^c), 4.09 (m, 4H, H^b), 4.71 (m, 4H, H^a), 7.41 (m, 4H, H^{A5}), 7.62 (m, 4H, H^{A6}), 8.07 (m, 4H, H,^{D2}), 8.17 (m, 4H, H^{A4}), 9.03 (m, 4H, H^{A3}), 9.55 ppm (m, 4H, H^{B3}).

Preparation of samples of FS/**1** and FS/**2** for pulse EPR spectroscopy and FS/**1** for CW EPR spectroscopy: Solvent mixtures were made from deionized Milli-Q-water, 87 wt % glycerol/water (Aldrich Chem. Co.) and DMF (Aldrich Chem. Co.). Stock solution of 2 mM FS in water was adjusted to about pH 8.5 by addition of KOH to enhance the stability of the Fremy's salt. This stock solution (25 μL) was added to a mixture of a solution of **1** in DMF (2 mM, 50 μL) and 87 % glycerol/water (25 μL) or to a mixture of a solution of **2** in water (2 mM, 37.5 μL) and 87 % glycerol/water (37.5 μL). In the case of **1**, a precipitate formed from the dark-red solution after a few minutes (this precipitate is assumed to be **1**, thus effectively reducing the concentration of **1**). Separation of the precipitate by use of a centrifuge gave a clear, light-red solution, which was subsequently used for the EPR measurements. No precipitate was found in solutions of FS and **2** in the binary glycerol/water solvent mixture.

Samples of FS/**2** for CW EPR spectroscopy: The same FS stock solution in water (25 μL) was added to a mixture of a 2 mM solution of **2** in water (30 μL) and 87 % glycerol/water (50 μL).

EPR studies: CW EPR spectra in solution ($T = 293$ K) at the X-band (ca. 9.8 GHz) were measured on a Bruker ELEXSYS 580 spectrometer with an AquaX inlet in a rectangular cavity (4103TM, Q values typically 3000). Four-pulse DEER time-domain signals at $T = 20$ K were obtained on the same spectrometer with a Bruker Flexline split-ring resonator (ER 4118X-MS3) with overcoupling to $Q \approx 100$ at a temperature of 20 K. The pulse sequence was $(\pi/2)_{\nu A} - \tau_1 - (\pi)_{\nu A} - t' - (\pi)_{\nu B} - (\tau_1 + \tau_2 - t') - (\pi)_{\nu A} - \tau_2$ echo, with a phase cycle $[(+x) - (-x)]$ applied to the first pulse, and τ_1 was averaged over 8 increments ($\Delta\tau_1 = 8$ ns) to suppress proton modulations.[10c,11] Here, ν_A is the observer frequency (local maximum at the low-field edge of the EPR absorption spectrum) and ν_B the pump frequency (global maximum of the EPR absorption spectrum, $\nu_B = \nu_A - 56$ MHz). The time t' after the first π pulse was incremented, the pulse lengths, and delays were as follows: $(\pi/2)_{\nu A} = 32$ ns, $(\pi)_{\nu A} = 32$ ns, $(\pi)_{\nu B} = 12$ ns, $\tau_1 = 200$ ns, $\tau_2 = 2.4$ μs (**1**) and $\tau_2 = 2$ μs (**2**), $\Delta t' = 8$ ns, $t'_0 = 80$ ns. The pump pulses were generated by feeding the output of a Magnettech OSC 101/1 sweep oscillator to one microwave-pulse-forming unit of the spectrometer. The repetition times were 6 ms (FS/**1**) and 3 ms (FS/**2**).

Data analysis: CW EPR spectral simulations were performed with a program by Schneider and Freed assuming a uniaxial tensor of rotational diffusion.[13] The following magnetic parameters were assumed. G tensor: $g_{xx} = 2.0086$, $g_{yy} = 2.0064$, $g_{zz} = 2.0029$; hyperfine tensor: $A_{xx} = A_{yy} = 0.525$ mT, $A_{zz} = 2.845$ mT; additional linewidth 4.6 μT. DEER time traces were analyzed by direct integral transformation, which has been reviewed elsewhere.[11]

Molecular dynamics simulations: Molecular dynamics simulations were carried out with the program package Cerius2 (version 3.8, Molecular Simulations, Inc.), using the UFF universal force field. The systems were first pre-equilibrated (canonical ensemble in a Berendsen temperature bath, 20000 steps, time step 0.5×10^{-15} s) and then sampled by a 2 ns run (Nosé-Hoover thermostat, 4×10^6 steps, time step 0.5×10^{-15} s). Structures were written to trajectory files in time intervals of 1×10^{-13} s. Time traces of the Ru coordinates were extracted from the trajectory files using the gOpenMol program and converted into histograms of the distance distribution by a home-written Matlab (The MathWorks, Inc.) program.

Received: April 29, 2004
Published Online: August 12, 2004

Keywords: coordination polymers · electrostatic interactions · EPR spectroscopy · noncovalent interactions · self-assembly

[1] a) J.-M. Lehn, *Angew. Chem.* **1990**, *102*, 1347 – 1362; *Angew. Chem. Int. Ed. Engl.* **1990**, *29*, 1303 – 1319; b) J.-M. Lehn, *Supramolecular Chemistry*, Wiley-VCH, Weinheim, **1995**; c) M. Rehahn, *Acta Polym.* **1998**, *49*, 201 – 224; d) H. Chen, J. A. Cronin, R. D. Archer, *Macromolecules* **1994**, *27*, 2174 – 2180; e) J.-P. Sauvage, J. P. Collin, J. C. Chambron, S. Guillerez, C. Coudret, V. Balzani, F. Barigelletti, L. De Cola, L. Flamigni, *Chem. Rev.* **1994**, *94*, 993 – 1019; f) S. Kelch, M. Rehahn, *Macromolecules* **1999**, *32*, 5818 – 5828; g) O. Schmelz, M. Rehahn, *e-Polym.* **2002**, no. 47; h) D. Wöhrle, A. D. Pomogailo, *Metal Complexes and Metals in Macromolecules*, Wiley-VCH, Weinheim, **2003**.

[2] a) J. Bohrisch, C. D. Eisenbach, W. Jaeger, H. Mori, A. H. E. Müller, M. Rehahn, C. Schaller, S. Traser, P. Wittmeyer, *Adv. Polym. Sci.* **2004**, *165*, 1 – 41; b) C. Holm, M. Rehahn, W. Oppermann, M. Ballauff, *Adv. Polym. Sci.* **2004**, *166*, 1 – 27; c) S. Förster, M. Schmidt, *Adv. Polym. Sci.* **1995**, *120*, 51 – 133; d) H. Dautzenberg, W. Jaeger, J. Kötz, B. Philip, C. Seidel, D. Stscherbina, *Polyelectrolytes—Formation, Characterization and Application*, Carl Hanser, Munich, **1994**.

[3] T. Pfohl, Y. Li, J. H. Kim, Z. Wen, G. C. L. Wong, I. Koltover, M. W. Kim, C. R. Safinya, *Colloids Surf. A* **2002**, *198–202*, 613 – 623.

[4] G. Decher, *Science* **1997**, *277*, 1232 – 1237.

[5] J. Kötz, S. Kosmella, T. Beitz, *Prog. Polym. Sci.* **2001**, *26*, 1199 – 1232.

[6] a) V. Vlachy, *Annu. Rev. Phys. Chem.* **1999**, *50*, 145 – 165; b) A. Y. Grosberg, T. T. Nguyen, B. I. Shklovskii, *Rev. Mod. Phys.* **2002**, 74, 329 – 345; c) M. Deserno, A. Arnold, C. Holm, *Macromolecules* **2003**, *36*, 249 – 259; d) G. S. Manning, *J. Chem. Phys.* **1969**, *51*, 924 – 933; e) G. S. Manning, *J. Chem. Phys.* **1969**, *51*, 934 – 938; f) G. S. Manning, *J. Chem. Phys.* **1969**, *51*, 3249 – 3252; g) G. S. Manning, *Acc. Chem. Res.* **1979**, *12*, 443 – 449.

[7] N. M. Atherton, *Principles of Electron Spin Resonance*, Ellis Horwood, New York, **1993**.

 © 2004 Wiley-VCH Verlag GmbH & Co. KGaA, Weinheim

[8] A. Schweiger, G. Jeschke, *Principles of Pulse Electron Paramagnetic Resonance*, Oxford University Press, **2001**.
[9] a) D. Hinderberger, G. Jeschke, H. W. Spiess, *Macromolecules* **2002**, *35*, 9698 – 9706; b) D. Hinderberger, H. W. Spiess, G. Jeschke, *J. Phys. Chem. B* **2004**, *108*, 3698 – 3704; c) D. Hinderberger, H. W. Spiess, G. Jeschke, *Macromol. Symp.* **2004**, *211*, 71 – 86.
[10] a) A. D. Milov, A. G. Maryasov, Y. D. Tsvetkov, *Appl. Magn. Reson.* **1998**, 15, 107 – 143; b) R. G. Larsen, D. J. Singel, *J. Chem. Phys.* **1993**, *98*, 5134 – 5146; c) G. Jeschke, *ChemPhysChem* **2002**, *3*, 927 – 932.
[11] G. Jeschke, A. Koch, U. Jonas, A. Godt, *J. Magn. Reson.* **2002**, *155*, 72 – 82.
[12] A. D. Milov, Y. D. Tsvetkov, *Appl. Magn. Reson.* **2000**, *18*, 217 – 226.
[13] D. J. Schneider, J. H. Freed in *Biological Magnetic Resonance*, *Vol. 8* (Eds.: L. J. Berliner, J. Reuben), Plenum, New York, **1989**, chap. 1.
[14] S. Traser, P. Wittmeyer, M. Rehahn, *e-Polym.* **2002**, no. 32.
[15] P. Korall, A. Börje, P. O. Norrby, B. Åkermark, *Acta Chem. Scand.* **1997**, *51*, 760 – 766.
[16] B. Whittle, S. R. Batten, J. C. Jeffery, L. H. Rees, M. D. Ward, *J. Chem. Soc. Dalton Trans.* **1996**, 4249 – 4255.

 © 2004 Wiley-VCH Verlag GmbH & Co. KGaA, Weinheim

Liquid Crystals

Liquid Crystals with Complex Superstructures**

*Bin Chen, Xiang Bing Zeng, Ute Baumeister, Siegmar Diele, Goran Ungar, and Carsten Tschierske**

The investigation of molecular self-organization is one of the most exciting areas of contemporary chemical research. Significant progress was recently achieved in the field of crystal engineering, especially with coordination polymers.[1] In contrast to these crystalline systems, which once formed are hard to modify, fluid self-organized structures can easily respond to external stimuli and change as a result of changed external conditions. This fundamental principle is used by all biological systems.[2] Liquid-crystalline (LC) systems combine order and mobility and therefore can be regarded as simple model systems in which the driving forces of self assembly can be studied in a systematic and controlled manner. However, the known self-organized structures of LC materials, though of great technological importance,[3] are relatively simple, and are restricted mostly to nematic layered (smectic = Sm) and columnar morphologies (Col).[4] More recently the formation of bicontinuous networks and spherelike aggregates was found to lead to new cubic and noncubic mesophase structures.[5–7] Based on the concept of competitive polyphilicity, elaborated in our laboratories,[8,9] it now seems possible to further increase the complexity of these self-organized fluid systems. This concept was successfully applied first to rodlike bolaamphiphiles with nonpolar lateral chains (see Figure 1), which form honeycomb-like arrays of cylinders and

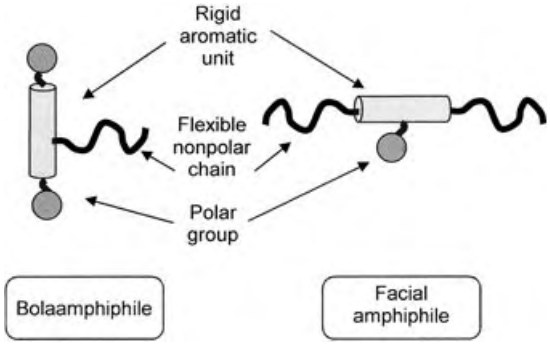


Figure 1. Schematic structures of ternary bolaamphiphiles and facial amphiphiles.

a series of novel layer structures.[8] However, facial amphiphiles, in which the molecular topology is reversed, that is, a polar group is attached to a lateral position on a rigid aromatic core and lipophilic chains are tethered at the termini (see Figure 1), have so far failed to give such complex structures.[10]

Herein we report successful generation of novel soft matter morphologies with facial polyphilic LC molecules of a new type, composed of three incompatible segments. The new LC phases comprise three distinct subspaces, each containing one of the three molecular parts. Two of the incompatible segments, aromatic and aliphatic, form alternating layers. The third segment, which incorporates an ionic group, forms closed spheroidic aggregates, which are distributed either randomly within the aromatic sublayers (filled random-mesh phase) or on an hexagonal net (rhombohedral 3D phase, Rho). These polar ionic groups can also coalesce into infinite columns, which penetrate the layer stacks leading to a completely new type of liquid-crystal organization, characterized by an orthogonal set of layers and columns in one structure, designated as channeled-layer phases (ChL). The first representative of such mesophases, the hexagonal channeled-layer phase (ChL_{hex}) is unambiguously proven by

[*] B. Chen, Prof. Dr. C. Tschierske
Institute of Organic Chemistry
Martin-Luther-University Halle-Wittenberg
Kurt-Mothes-Str. 2, 06120 Halle (Germany)
Fax: (+49) 345-5525-346
E-mail: tschierske@chemie.uni-halle.de
Dr. U. Baumeister, Dr. S. Diele
Institute of Physical Chemistry
Martin-Luther-University Halle-Wittenberg
Dr. X. B. Zeng, Prof. Dr. G. Ungar
Department of Engineering Materials and
Centre for Molecular Materials
University of Sheffield
Robert Hadfield Building, Mappin Street, Sheffield S1 3JD (UK)

[**] This work was supported by the Deutsche Forschungsgemeinschaft, the European Union within the framework of the RTN network LCDD under contract: HPRN-CT-2000-00016 and the Fonds der Chemischen Industrie. We thank A. Gleeson for helping to set up the experiment at Daresbury Synchrotron and CCLRC for granting the beamtime.

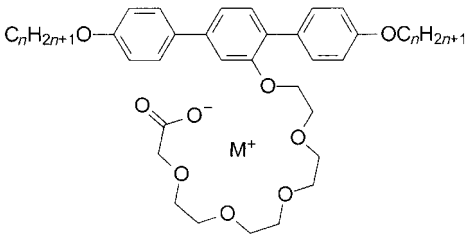
Supporting information for this article is available on the WWW under http://www.angewandte.org or from the author.

 DOI: 10.1002/anie.200460762 © 2004 Wiley-VCH Verlag GmbH & Co. KGaA, Weinheim

electron-density calculation based on high-resolution X-ray diffraction. It is also shown that the transitions between these three new types of LC organization can be tuned by molecular design and triggered by external stimuli.

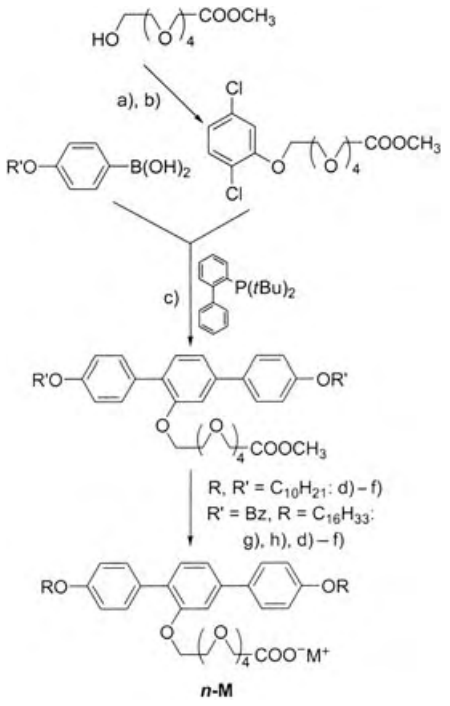
The compounds denoted **16-Na, 16-Cs** and **10-M** (M = Li, Na, K, Cs) were synthesized according to Scheme 1 and the mesophase properties are summarized in Table 1. The sodium salt **16**-Na forms two mesophases. Between 60 °C and the isotropization temperature at 107 °C the X-ray diffraction pattern is characterized by two orders of a meridional-layer reflection, which corresponds to a periodicity of $d_1 = 4.0$ nm (see Figure 2a). The diffuse wide-angle scattering is circular and has two clear maxima centered on the equator (see Figure 2b). This feature indicates a smectic A (SmA) liquid-crystal phase, with the molecules on average perpendicular to the layer plane, but without long-range positional order within the layer. As expected, d_1 is shorter than the length of the extended molecule (L = 5.6 nm), hence the alkyl chains from neighboring layers show some interdigitation. However, in contrast to the conventional SmA phase, even for a highly oriented sample, the diffuse wide angle scattering forms a closed ring (see Figure 2b), and the pattern contains an additional diffuse small angle equatorial maximum, which corresponds to an average distance of $d_2 = 3.2$ nm (see Figure 2a). This diffuse maximum indicates an additional short range periodicity in the layer plane. An explanation of this unique feature can be sought in the T-shaped triblock structure of the molecule. As in other SmA phases the aromatic cores and the alkyl chains are segregated into distinct sublayers. However, the polar groups, fixed to the centers of the terphenyl cores and yet strongly incompatible with them, are forced to cluster mainly within the terphenyl sublayers (see Figure 3a). These clusters are distributed randomly within the aromatic sublayers, with an average distance of $d_2 \approx 3.2$ nm. The polar groups are quite flexible and likely to be orientationally disordered within the aggregates, hence the circular shape of the diffuse wide-angle scattering.

Table 1: Transition temperatures, corresponding enthalpy values, and lattice parameters of the LC phases of the compounds ***n*-M**.[a]



Complex	*n*	M	*T*/°C[b] [ΔH/kJ mol^{-1}][b]	Lattice parameter/nm^{-1}[c]
16-Na	16	Na	Cr_1 37 [17.4] Cr_2 52[d] [42.7] Rho 60 [0.1] SmA_{frm} 108 [2.1] Iso	$d_1 = 4.0$ (90 °C), $a = 3.4$, $c = 12.8$ (50 °C)
16-Cs	16	Cs	Cr_1 37 [35.4] Cr_2 90[d] [14.9] ChL_{hex} 114 [2.0] Iso	$a = 3.9$, $c = 4.1$ (103 °C)
10-Li	10	Li	G 7[e] ChL_{hex} 99 [1.8] Iso	$a = 3.8$, $c = 3.6$ (75 °C)
10-Na	10	Na	G 17[e] ChL_{hex} 105 [1.7] Iso	$a = 3.9$, $c = 3.7$ (70 °C)
10-K	10	K	G 4[e] ChL_{hex} 123 [2.1] Iso	$a = 3.8$, $c = 3.6$ (115 °C)
10-Cs	10	Cs	Cr_1 51[d] [20.3]Cr_2 71[d] [3.3] (G-8) M1 120[f] [–] ChL_{hex} 127 [2.3] Iso	$a = 4.08$, $c = 3.72$ (80 °C)

[a] The analytical data and tables with X-ray data are provided in the Supporting Information; abbreviations: Cr = crystalline solid state; G = glassy state; Iso = isotropic liquid state; Rho = mesophase with a rhombohedral 3D lattice ($R\bar{3}m$), see Figure 3b; SmA_{frm} = filled random-mesh phase, see Figure 3a; ChL_{hex} = channeled-layer phase ($P6/mmm$), see Figure 3c; M1 = low-temperature mesophase. [b] Obtained by differential scanning calorimetry (DSC-7, Perkin Elmer, 10 K min^{-1}) during the second heating scan and confirmed by polarizing microscopy. [c] Obtained from the Guinier pattern, except the values of **10-Cs**, which were taken from the synchrotron small-angle diffraction experiments. [d] Observed only in the first heating scan. [e] Even after storage at 25 °C for about six months no crystallization could be observed. [f] Transition can only be detected in the X-ray diffraction pattern.



Scheme 1. Synthesis of compounds ***n*-M.** a) toluenesulfonyl chloride, pyridine; b) 2,5-dichlorophenol, K_2CO_3; c) $Pd(OAc)_2$, KF, THF;[11] d) NaOH, H_2O; e) HCl, H_2O, Et_2O; f) MOH or Cs_2CO_3 (M is Na–Cs); g) $Pd(OH)_2$, cyclohexene, MeOH; h) $C_{16}H_{33}Br$, K_2CO_3, Bu_4NI.

The layered LC phase can thus be described as a random-mesh phase, in which the holes are filled by the polar lateral groups, that is, by the third incompatible component (filled random-mesh phase, SmA_{frm}). In this respect the mesophase is new and different from conventional smectic phases and from the mesh phases known in lyotropic systems,[12] block copolymers,[13] and rod–coil molecules,[14] in which the holes or dimples within a sublayer are filled not by a third component but by excess material from the two adjacent sublayers.

The rhombohedral phase—a correlated filled hexagonal mesh phase—is described next. Upon cooling the SmA_{frm}

 © 2004 Wiley-VCH Verlag GmbH & Co. KGaA, Weinheim

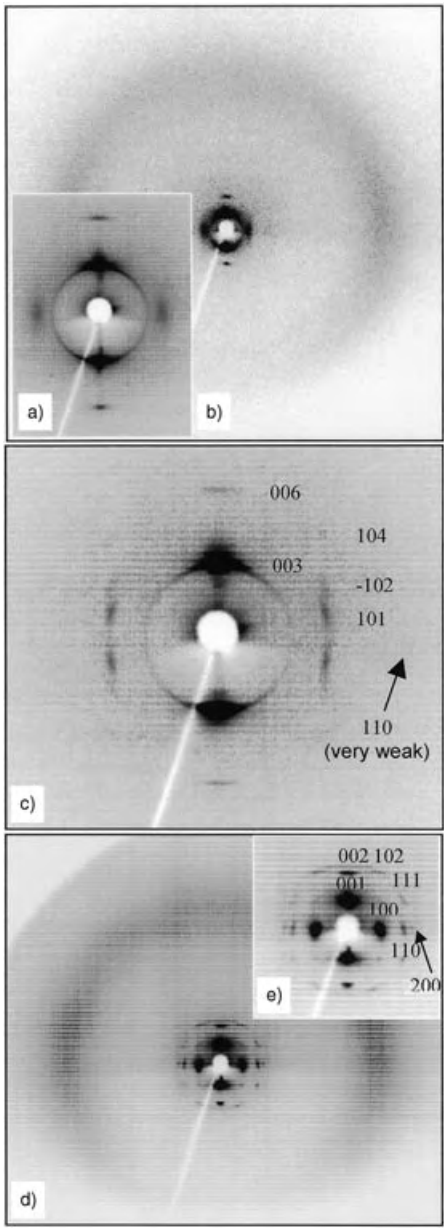


Figure 2. X-ray diffraction pattern of aligned samples of the mesophases. a) Filled random mesh phase (SmA_{frm}) of **16-Na** at 102 °C (small-angle region). b) Same as (a), but wide-angle region. c) Rhombohedral ($R\bar{3}m$) phase of **16-Na** at 50 °C (small-angle region). d) Wide-angle region of the ChL_{hex} ($P6/mmm$) phase of **10-K** at 85 °C. e) Same as (d), but small-angle region. In all diffraction patterns the *c*-axis is vertical, perpendicular to the substrate and the X-ray beam. The samples are disordered around an ∞-fold axis perpendicular to the substrate (fiber geometry).

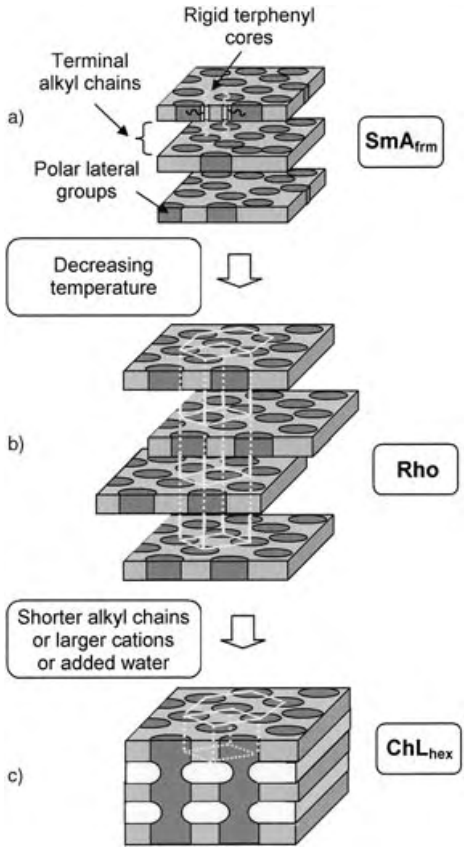


Figure 3. Organization of the facial amphiphiles ***n*-M** depending on the molecular structure and conditions. For clarity, the alkyl chains are not shown in the models and the centers of the unit cells of the 3D lattices are offset vertically from the inversion center by half a sublayer thickness.

phase in **16-Na** below 60 °C, the X-ray diffraction pattern changes significantly. The diffuse small-angle scattering on the equator splits and condenses into a series of row-line Bragg reflections (see Figure 2c). This diffraction pattern can be indexed on a rhombohedral 3D lattice, space group $R\bar{3}m$, with the parameters $a = 3.4$ nm and $c = 12.8$ nm. No significant change can be observed at this phase transition under the polarizing microscope. The fanlike texture of the SmA_{frm} phase remains and also the optically isotropic (homeotropically aligned) regions do not change.[15] Only a significant increase in viscosity is observed. This observation confirms that the mesophase is optically uniaxial, which is consistent with the proposed rhombohedral lattice. To understand the structure of the Rho phase it is reasonable to assume that at the $SmA_{frm} \rightarrow$Rho transition, the polar domains pack on a hexagonal 2D lattice within the aromatic sublayers (filled-hexagonal-mesh layers). The occurrence of this order within the layers is accompanied by long-range positional correlation between layers in an ABC fashion, thus leading to the 3D rhombohedral symmetry $R\bar{3}m$, as shown in Figure 3b. In contrast to the small-angle scattering, the overall appearance of the wide-angle region of the X-ray diffraction pattern does not change at the phase transition, that is, the diffuse ring with distinct equatorial maxima remains. This is in line with the proposed model and indicates that the phase is indeed liquid crystalline with a 3D mesoscale lattice and that it belongs to correlated layer structures.[16] The structure is related to that of the $R\bar{3}m$ mesh phase in some other organized fluids,[12–14] but again unlike in those systems, the holes in the layers are filled with a distinct third component.

The third phase, described below, has a 3D hexagonal structure consisting of layers penetrated by continuous polar channels (channeled-layer phase, ChL_{hex}). It is found in compound **16-Cs**, in which the Na^+ ion of **16-Na** is replaced by

 © 2004 Wiley-VCH Verlag GmbH & Co. KGaA, Weinheim

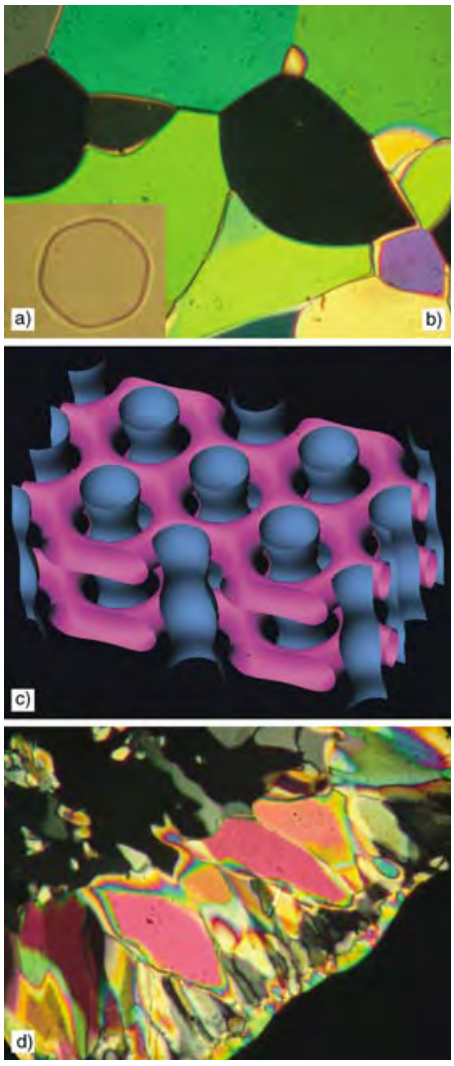


Figure 4. The channeled layer mesophase (ChL_{hex}). a) Growth of an optically isotropic hexagon of the ChL_{hex} phase from the isotropic liquid state at 127 °C. b) Texture of the ChL_{hex} phase of compound **10-Cs** as observed between crossed polarizers at 125 °C (the optically isotropic regions are homeotropically aligned regions). c) Reconstructed electron-density map of the ChL_{hex} mesophase of compound **10-Cs**; the blue isoelectron surfaces enclose the polar channellike domains (high electron density) and the pink surface encloses the low density, that is, aliphatic volume. Texture of the ChL_{hex} phase induced in the contact region between **16-Na** and 5.0 M aqueous NaCl solution at 95 °C. The dark area at the right is the NaCl solution, the dark areas at the left represent homeotropically aligned regions of the ChL_{hex} phase (layers parallel to the substrate).

the larger Cs^+, and also in the series of salts **10-M** (M = Li, Na, K, Cs), in which the length of the two terminal alkyl chains is reduced from hexadecyl to decyl. The common feature of all five compounds is the appearance of a mosaic-like texture with large optically isotropic regions (see Figure 4b) at the transition from the isotropic liquid to the mesophase. The optically isotropic regions grow as rounded hexagons (see Figure 4a). This growth pattern, the optical uniaxiality and the rather high viscosity of the mesophase, are preliminary indications of a 3D hexagonal structure, and such a structure was indeed confirmed by X-ray diffraction. The diffraction pattern of compound **10-K**, obtained with an aligned sample (see Figure 2d and e) shows diffuse wide angle scattering with distinct equatorial maxima. This is very similar to the appearance of the Rho phase, but the positions of the Bragg reflections in the small-angle region are completely different. The reflections can be indexed on a 3D hexagonal lattice, space group *P6/mmm*, with the parameters $a = 3.8$ nm and $c = 3.6$ nm. Similar diffraction patterns were observed for the mesophases of all other **10-M** compounds as well as for **16-Cs**; the lattice parameters are collated in Table 1.

More detailed X-ray investigations were carried out for compound **10-Cs** by using a synchrotron source. Small-angle diffraction intensities were measured from high-resolution powder patterns. The corrected intensities and a description of the electron-density-reconstruction procedure are given in the Supporting Information. The electron-density map of the ChL_{hex} phase of compound **10-Cs** is shown in Figure 4c. The blue surfaces enclose the polar domains (high electron density) and the pink surface encloses the low-density, that is, aliphatic volume. According to the map, the terphenyls are positioned perpendicular to the layer planes (as also indicated by the diffuse wide angle maxima on the equator), thus forming a perforated layer between the perforated alkyl layers. The polar domains form cylinders with undulated profile, arranged on a hexagonal 2D lattice and penetrating the layer structure. At lower temperature additional mesophases were found for the Cs-salt **10-Cs**, which require additional investigations.

From the comparison of compounds **10-Na** and **16-Na** the effect of the length of the terminal alkyl chains is evident. For long chains the aliphatic sublayers are too thick to allow fusion of the polar regions. For such compounds the ABC packing of the layers (Rho phase) allows optimal space filling. In the short-chain compounds the aliphatic sublayers are thinner and fusion of the polar regions is possible. The resulting reduction in interfacial area stabilizes the AAA stacking (ChL_{hex} structure), which allows the formation of continuous polar channels (see Figure 3c). The same change from Rho to ChL_{hex} is observed when the Na^+ ions of **16-Na** are replaced by Cs^+ ions in **16-Cs**. This change could be interpreted in terms of the larger Cs^+ ions increasing the overall volume of polar domains and allowing them to fuse, even across the thick hexadecyl sublayer of **16-Cs**.

The mesophase type can also be influenced by solvents. For example, the addition of a 5.0 M sodium chloride solution to **16-Na** induces a ChL_{hex} phase as indicated by the very typical texture of this mesophase (see Figure 4d). Similar to the effect of large cations, the added aqueous solution is thought to induce fusion of the polar domains by increasing their volume through the coordination of water molecules and/or additional Na^+ ions.

The above results show that competition of multiple-level microsegregation and anisotropic interaction of rodlike molecular segments presents a successful strategy for the design of new and exciting mesophase morphologies. The self-organized structures obtained with the molecules presented here are all quite distinct from conventional thermotropic and lyotropic liquid-crystalline phases of other compounds with low molecular weights and from the mesophases of some LC

 © 2004 Wiley-VCH Verlag GmbH & Co. KGaA, Weinheim

dendrimers[6,17] and main chain polymers.[18] The mesophases we report here represent combinations of spheroids or columns with layers. Hence, a higher-than-usual level of structural complexity is achieved through the presence of three incompatible molecular moieties, instead of two as in more conventional amphiphiles. Though there have been reports of several complex polymer morphologies in triblock copolymers[19] the present morphologies are different with regards to their structure and size. For example, "spheres-on-layer" morphologies were reported for linear ABC block copolymers, whereas the Rho phase represents a "spheres-in-layer" morphology. Similarly, in the ChL_{hex} phase the cylinders are arranged perpendicular to the layer planes, whereas in the "cylinder-on-layer" polymer morphology the columns run parallel to the layers. Additionally, these ordered structures occur at a significantly smaller length scale (3–10 nm) than those of the block copolymers (10 to >100 nm).

In the ChL_{hex} phase reported here, the polar regions represent well defined ion-carrying channels, which can be modified by molecular design and influenced by external stimuli. Hence, these or similar materials might be useful, for example, as components in ion-conducting nanodevices. One can also envisage their use as ion-triggered gate valves, opened (ChL_{hex} phase) by a solution carrying large ions and closed (Rho phase) when small or no ions are present. The study of the current structures may also shed new light on ionic channels in biological systems and on transport across lipid membranes.[20] Being mechanically more robust than columnar liquid crystals and readily surface-aligned,[21] the 3D mesophases may also be used for encapsulating low-molecular and polymeric guests, such as drugs, and electroluminescent[22] or electronically conducting polymers[23] and biopolymers.[24]

Received: May 24, 2004
Published Online: August 19, 2004

Keywords: alkali metals · liquid crystals · mesophases · self-assembly · supramolecular chemistry

[1] B. Moulton, M. J. Zaworotko, *Chem. Rev.* **2001**, *101*, 1629–1658; S. L. James, *Chem. Soc. Rev.* **2003**, *32*, 276–288; C. N. R. Rao, S. Natarajan, R. Vaidhyanathan, *Angew. Chem.* **2004**, *116*, 1490–1521, *Angew. Chem. Int. Ed.* **2004**, *43*, 1466–1496; S. Kitagawa, R. Kitaura, S. Noro, *Angew. Chem.* **2004**, *116*, 2388–2430; *Angew. Chem. Int. Ed.* **2004**, *43*, 2334–2375; S. L. James, *Chem. Soc. Rev.* **2003**, *32*, 276–288.

[2] G. T. Steward, *Liq. Cryst.* **2004**, *31*, 443–471.

[3] P. Kirsch, M. Bremer, *Angew. Chem.* **2000**, *112*, 4384–4405; *Angew. Chem. Int. Ed.* **2000**, *39*, 4216–4235; D. Pauluth, K. Tarumi, *J. Mater. Chem.* **2004**, *14*, 1219–1227.

[4] D. Demus, J. W. Goodby, G. W. Gray, H.-W. Spiess, V. Vill, *Handbook of Liquid Crystals, Vol. 1–3*, Wiley-VCH, Weinheim, **1998**.

[5] K. Borisch, S. Diele, P. Göring, H. Kresse, C. Tschierske, *J. Mater. Chem.* **1998**, *8*, 529–543; C. Tschierske, *Curr. Opin. Colloid Interface Sci.* **2002**, *7*, 69–80.

[6] G. Ungar, Y. Liu, X. Zeng, V. Percec, W.-D. Cho, *Science* **2003**, *299*, 1208–1211; X. Zeng, G. Ungar, Y. Liu, V. Percec, A. E. Dulcey J. K. Hobbs, *Nature* **2004**, *428*, 157–160. V. Percec, C. M. Mitchell, W.-D. Cho, S. Uchida, M. Glodde, G. Ungar, X. Zeng, Y. Liu, V. S. K. Balagurusamy, P. A. Heiney, *J. Am. Chem. Soc.* **2004**, *126*, 6078–6094.

[7] Introduction of chirality is an alternative way to modify mesophase structures, especially of lamellar phases: H.-S. Kitzerow, C. Bahr, *Chirality in Liquid Crystals*, Springer, New York, **2001**.

[8] X. H. Cheng, M. K. Das, S. Diele, C. Tschierske, *Angew. Chem.* **2002**, *114*, 4203–4207; *Angew. Chem. Int. Ed.* **2002**, *41*, 4031–4035; X. H. Cheng, M. Prehm, M. K. Das, J. Kain, U. Baumeister, S. Diele, D. Leine, A. Blume, C. Tschierske, *J. Am. Chem. Soc.* **2003**, *125*, 10977–10996; M. Prehm, S. Diele, M. K. Das, C. Tschierske, *J. Am. Chem. Soc.* **2003**, *125*, 614–615.

[9] C. Tschierske, *J. Mater. Chem.* **1998**, *8*, 1485–1508; C. Tschierske, *J. Mater. Chem.* **2001**, *11*, 2647–2671; C. Tschierske, *Ann. Rep. Progr. Chem., Ser. C* **2001**, *97*, 191–268.

[10] F. Hildebrandt, J. A. Schröter, C. Tschierske, R. Festag, M. Wittenberg, J. H. Wendorff, *Adv. Mater.* **1997**, *9*, 564–567; J. A. Schröter, C. Tschierske, M. Wittenberg, J.-H. Wendorff, *Angew. Chem.* **1997**, *109*, 1160–1163; *Angew. Chem. Int. Ed. Engl.* **1997**, *36*, 1119–1121; R. Plehnert, J. A. Schröter, C. Tschierske, *J. Mater. Chem.* **1998**, *8*, 2611–2626.

[11] J. P. Wolfe, R. A. Singer, B. H. Yang, S. L. Buchwald, *J. Am. Chem. Soc.* **1999**, *121*, 9550–9561.

[12] M. C. Holmes, *Curr. Opin. Colloid Interface Sci.* **1998**, *3*, 485–492.

[13] I. W. Hamley, *The Physics of Block-Copolymers*, Oxford University Press, Oxford, **1998**, pp. 24–130.

[14] M. Lee, B.-K. Cho, W.-C. Zin, *Chem. Rev.* **2001**, *101*, 3869–3892; J.-H. Ryu, N.-K. Oh, W.-C. Zin, M. Lee, *J. Am. Chem. Soc.* **2004**, *126*, 3551–3558.

[15] The optical uniaxiality of this phase is consistent with the terphenyl units having an average orientation perpendicular to the layer planes.

[16] M. Prehm, S. Diele, M. K. Das, C. Tschierske, *J. Am. Chem. Soc.* **2003**, *125*, 614–615.

[17] L. Gehringer, C. Bourgogne, D. Guillon, B. Donnio, *J. Am. Chem. Soc.* **2004**, *126*, 3856–3867; M. Marcos, A. Omenat, J. L. Serrano, *C. R. Chim.* **2003**, *6*, 947–957.

[18] K. Fu, N. Sekine, M. Sone, M. Tokita, J. Watanabe, *Polym. J.* **2002**, *34*, 291–297.

[19] S. Sioula, N. Hadjichristidis, E. L. Thomas, *Macromolecules* **1998**, *31*, 5272–5277; V. Abetz in *Supramolecular Polymers*, (Ed.: A. Ciferri), Marcel Dekker, New York, **2000**, pp. 215–262; J. Beckmann, C. Auschra, R. Stadler, *Macromol. Rapid Commun.* **1994**, *15*, 67–72; H. Hückstädt, A. Göpfert, V. Abetz, *Macromol. Chem. Phys.* **2000**, *201*, 296–307.

[20] D. A. Doyle, J. M. Cabral, R. A. Pfuetzner, A. Kuo, J. M. Gulbis, S. L. Cohen, B. T. Chait, R. MacKinnon, *Science* **1998**, *280*, 69–77.

[21] Between glass substrates (microscope slides), a homeotropic alignment of the ChL_{hex} phases (channels perpendicular to the substrate surfaces) is spontaneously formed by slow cooling from the isotropic melted state. This alignment is indicated by the optically isotropic appearance of the thin films obtained in this way. The homeotropic alignment is found over large areas (several square centimeters), only at the edges and around gas bubbles a birefringent texture (defects) can be found.

[22] Z. N. Bao, K. R. Amundson, A. J. Lovinger, *Macromolecules* **1998**, *31*, 8647–8649.

[23] V. Percec, M. Glodde, T. K. Bera, Y. Miura, I. Shiyanovskaya, K. D. Singer, V. S. K. Balagurusamy, P. A. Heiney, I. Schnell, A. Rapp, H.-W. Spiess, S. D. Hudsonk, H. Duank, *Nature* **2002**, *419*, 384–387.

[24] I. Koltover, T. Salditt, J. O. Radler, C. R. Safinya, *Science* **1998**, *281*, 78–81.

 © 2004 Wiley-VCH Verlag GmbH & Co. KGaA, Weinheim

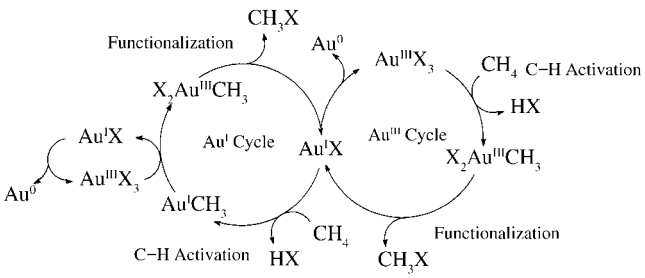
Homogeneous Catalysis

Selective Oxidation of Methane to Methanol Catalyzed, with C–H Activation, by Homogeneous, Cationic Gold**

CJ Jones, Doug Taube, Vadim R. Ziatdinov, Roy A. Periana, Robert J. Nielsen, Jonas Oxgaard, and William A. Goddard III*

Some of the most efficient homogeneous catalysts for the low-temperature, selective oxidation of methane to functionalized products employ a mechanism involving C–H activation[1] with an electrophilic substitution mechanism. Several such systems have been reported based on the cations Hg^{II},[2] Pd^{II},[3] and Pt^{II}.[4] These catalyst systems typically operate by two general steps that involve: A) C–H activation by coordination of the methane to the inner sphere of the catalyst (E^{n+}) followed by cleavage of the C–H bond by overall electrophilic substitution to generate E^{n+}–CH_3 intermediates, and B) oxidative functionalization involving redox reactions of E^{n+}–CH_3 to generate the desired oxidized product CH_3X.[4a] Consequently, efficient catalysts that follow this pathway would be expected to be "soft", highly electrophilic species that form relatively strong covalent bonds to carbon atoms and that are also good oxidants.

We considered that gold cations could be uniquely efficient electrophilic catalysts for methane conversion because, as shown in the conceptual catalytic cycle (Scheme 1), both Au^{I} and Au^{III} oxidation states could be active for heterolytic C–H activation as well as oxidative functionalization; this is likely because Au^{I} (d^{10}, two-coordinate) and Au^{III} ions (d^{8}, square planar) are both "soft" electrophiles that are isoelectronic and isostructural with the neighboring cations (Hg^{II} and Pt^{II}, respectively) that have been shown to be active for electrophilic C–H activation of methane.[2,4] This situation is not common, and in most catalytic systems based on "soft", redox-active electrophiles only one oxidation state of the redox couple is active for C–H activation. Thus, we sought to explore the catalytic chemistry of gold cations for the oxidation of methane. To our knowledge, while gold complexes have been reported to facilitate free-radical reactions of alkanes with peroxides in low yields,[5] no homogeneous gold catalysts that operate by heterolytic C–H activation and oxidative functionalization have been reported for the selective functionalization of alkanes. This is possibly because of the strong propensity for irreversible formation of gold metal, and any attempts to develop redox catalysis based on homogeneous Au cations must address this issue.



Scheme 1. Proposed functionalization catalytic cycles involving C–H activation by Au^{I} and Au^{III} species.

In strong acid solvents such as triflic or sulfuric acid, Au^{III} cations (generated by dissolution[6] of Au_2O_3) react with methane at 180 °C to selectively generate methanol (as a mixture of the ester and methanol) in high yield (Table 1, entries 1 and 2). As expected, the irreversible formation of metallic gold is very evident after these reactions and, unlike reactions with Hg^{II},[2] Pt^{II},[4d] and Pd^{II} [3a] that are catalytic in 96 % H_2SO_4, only stoichiometric reactions (turnover numbers (TONs) < 1) are observed with Au^{III} [Eq. (1)]. Soluble cationic gold is essential for these reactions as no methanol is observed under identical conditions without added Au^{III} ions (entry 3), or in the presence of metallic gold (entry 4) which is not dissolved in hot H_2SO_4.

$$3\,CH_4\ (27\,bar) + 2\,AuX_3 + 3\,H_2O \xrightarrow[180\,^{\circ}C,\ 2\,h]{HX} 3\,CH_3OH + 6\,HX + 2\,Au^0 \qquad X = HSO_4 \qquad (1)$$

Consistent with the known nobility of gold metal, no methanol formed when SO_3 or persulfate ($K_2S_2O_8$) were added as possible oxidants of metallic gold (entries 5 and 6). We considered the use of Se^{VI} ions as a more suitable oxidant. Se^{VI} ions are a more powerful oxidizing agent than S^{VI} ions ($E^{o} = 1.5$ V SeO_4^{2-}/H_2SeO_3, $E^{o} = 0.17$ V SO_4^{2-}/H_2SO_3, respectively) and, critically, the hydrated form, selenic acid (H_2SeO_4), is known to oxidize gold metal.[7] Equally important, selenic acid is also almost as acidic as sulfuric acid,[7,8] and it was anticipated that neither the acid nor the conjugate base ($HSeO_4^-$) would inhibit catalysis with electrophilic, cationic gold by blocking the required coordination of methane to the metal center.[4a]

We now report that a 3 M solution of H_2SeO_4 in 96 % sulfuric acid solvent containing 27 mM metallic gold (added as a 20 mesh powder) leads to catalytic oxidation of methane (27 bar) to methanol at 180 °C [Eq. (2)].[9] Turnover numbers of up to 30 and turnover frequencies of about $10^{-3}\ s^{-1}$ have

$$CH_4 + H_2SeO_4 \rightarrow CH_3OH + H_2SeO_3 \qquad (2)$$

[*] C. Jones, D. Taube, V. R. Ziatdinov, Prof. Dr. R. A. Periana
University of Southern California
Department of Chemistry, Loker Hydrocarbon Institute
Los Angeles, CA 90089 (USA)
Fax: (+) 213-821-2656
E-mail: rperiana@usc.edu
R. J. Nielsen, J. Oxgaard, Prof. Dr. W. A. Goddard III
Materials and Process Simulation Center
Beckman Institute (139-74)
Division of Chemistry and Chemical Engineering
California Institute of Technology, Pasadena, CA 91125 (USA)

[**] This work was supported by NSF Grant CHE-0328121. The computer facilities of the MSC were provided through support from DURIP and MURI. We thank Prof. R. J. Puddephatt for helpful discussion.

 © 2004 Wiley-VCH Verlag GmbH & Co. KGaA, Weinheim DOI: 10.1002/anie.200461055

Table 1: Yield of CH_3OH under different reaction conditions.[a] [9]

Entry	Au source [mM][b]	Additives	t [h]	TON	TOF [s^{-1}]	CH_3OH (% sel)	[CH_3OH] [mM]	CH_4 (% conv)	CO_2 [mol%]
1	Au_2O_3 [50]	–	1	0.8	10^{-3}	>90	60	<2	<1
2	Au_2O_3 [50]	100% CF_3SO_3H	1	0.9	10^{-3}	>90	70	<2	<1
3	–	–	6	0	0	0	0	<1	<1
4	Au^0 [27][c]	–	1	0	0	0	0	<1	<1
5	Au^0 [27][c]	2 wt% SO_3	3	0	0	0	0	<1	<1
6	Au^0 [27][c]	0.1 M $K_2S_2O_8$	2	0	0	0	<5	<1	<2
7	Au^0 [27][c]	3 M H_2SeO_4	2	9	10^{-3}	81	240	11	3
8	Au^0 [5][c]	3 M H_2SeO_4	9	32	10^{-3}	77	178	8	2
9	Au_2O_3 [81]	3 M H_2SeO_4	10	4	10^{-3}	74	350	15	6
10	Au^0 [27][c]	3 M SeO_3 + 6 bar O_2	2	8	10^{-3}	86	215	10	2
11	Au^0 [81][c]	3 M SeO_3 + 2% SO_3	3	15	10^{-3}	94	627	28	2
12	–	3 M H_2SeO_4	6	0	–	68	69	3	<2

[a] Reaction temperature 180°C, 27 bar CH_4 with 96% D_2SO_4 as solvent. [b] Based on in situ generated Au^{III} species assuming complete dissolution of added gold. [c] Added as metallic (20 mesh) gold powder.

been observed in methanol concentrations of up to 0.6 M in sulfuric acid with >90% selectivity, (Table 1, entries 7–11). Both gold and selenic acid are required for the reaction; no methanol is observed in the absence of Se^{VI} ions with or without Au^0 (entries 3 and 4) and only small amounts of methanol are formed in the presence of selenic acid without Au^0 (entry 12). Use of 100% enriched [^{13}C]methane as well as ^{1}H, ^{13}C NMR spectroscopic, and HPLC analyses of the crude reaction mixtures confirmed that methanol is the predominant liquid-phase product generated from methane. As can be seen from an NMR spectrum of the crude reaction mixture (Figure 1), only a small amount of methane selenoic acid (CH_3SeO_3H) is observed in the liquid phase. Very low levels (<5% based on added CH_4) of CO_2 is observed in the gas phase along with recovered CH_4. The observation that addition of O_2 to the reaction mixture (entry 10) has no significant effect on the reaction (compare entry 7) and the high reaction selectivity and reproducibility suggests that free radicals are not involved. Carrying out the stoichiometric reaction with Au_2O_3 at several temperatures between 100 and 200°C leads to an estimated activation barrierof about 30 kcal mol^{-1}.

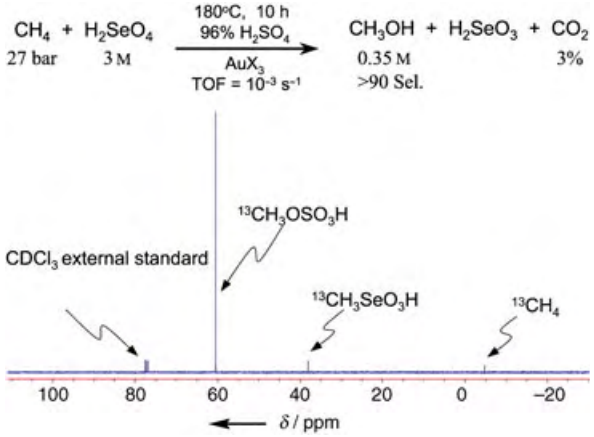


Figure 1. ^{13}C NMR spectrum of the crude reaction mixture resulting from the reaction of $^{13}CH_4$.[10]

Control experiments confirm that selenic acid can dissolve gold metal. Thus, addition of metallic gold powder or gold metal (separately obtained from stoichiometric reactions between Au_2O_3 and methane) to a 3 M solution of selenic acid in 96% sulfuric acid leads to rapid dissolution of the gold metal upon warming to 100°C to generate a clear yellow solution of cationic gold. While we have not obtained kinetic data on the various reaction steps proposed in Figure 1, this visual observation of rapid dissolution at low temperature suggests that the rate-determining step for methane oxidation catalyzed by cationic gold is not Au^0 reoxidation.

We have not been able to determine the exact oxidation state of the dissolved gold, but on the basis of known redox potentials we expect that Au^{III} ions are the major species. However, it is possible that Au^I ions (potentially stabilized to disproportionation by Se anions) could be present. The possibility that both Au^{III} and Au^I ions may be present in solution leads to the challenging question of whether one or both oxidation states (Au^I and Au^{III}) are active for the C–H activation of methane. This is an important point because, as discussed above, both Au^I and Au^{III} ions are potential catalysts. The observation that reactions starting from Au^{III} ions (with Au_2O_3 as the source) lead to stoichiometric conversion of methane into methanol [Eq. (1)] does not require that Au^{III} ions are the active species. The C–H activation reaction could occur with catalytic amounts of Au^I ions, formed by reduction of Au^{III} ions with adventitious reductants, and in both cases the stoichiometry shown in Equation (1) would be expected. As observed with the related Hg^{II},[2] Pt^{II},[4] and Pd^{II}[2] systems, some evidence for the formation of an Au–CH_3 intermediate is the observation that low levels of CH_3D (<2%, which is not produced in the absence of added Au^{III}) are produced when the reactions are carried out in D_2SO_4. So far, attempts at synthesizing likely Au^I–CH_3 or Au^{III}–CH_3 intermediates (without "soft" ligands such as phosphine) have been unsuccessful.

Given the synthetic challenges, we turned to DFT calculations to determine the feasibility of the steps proposed in Scheme 1. B3LYP/LACVP**++,[11] as implemented by the Jaguar 5.5 package,[12] was applied with the basis set for sulfur augmented with an extra, compact d-like polarization shell to

 © 2004 Wiley-VCH Verlag GmbH & Co. KGaA, Weinheim

better describe high oxidation states.[13,14] A dielectric continuum surrounding the models at a probe radius of 2.205 Å represented the sulfuric acid solvent with $\varepsilon = 50$.[15] Enthalpies describe solutes in ideal solution at 175 °C. Entropy changes, which are not accounted for, must be kept in mind as species enter and exit the models. A survey of complexes of gold ions with H_nSO_4 ($n = 0,1,2$) showed that the square planar $Au^{III}(SO_4)_2^-$ ion (**1**) and linear $Au^{I}(HSO_4)_2^-$ ion (**7**) are the most stable Au^{III} and Au^{I} species in solution. However, bidentate sulfate ions, bisulfate ions, and water made similarly strong bonds to gold, so other complexes are most likely present in equilibrium quantities.

Figure 2 illustrates the Au^{III} pathway, by which **1** reacts with methane to produce the $[Au^{III}(CH_3)(HSO_4)_3]^-$ complex **5**. Calculations show that a key role of the acid solvent is the generation of various protonated states of the gold complexes, such as **2**, that are sufficiently labile to allow methane to substitute into the coordination sphere of the metal. C–H activation can proceed through a number of transition states, the most accessible of which is an electrophilic substitution pathway $\mathbf{3}^{\ddagger}$, which features an intramolecular abstraction of a proton from methane by the neighboring bisulfate, with an activation energy of 28.1 kcal mol^{-1}. Alternative mechanisms with slightly higher enthalpies include intermolecular reactions with bisulfate ions in solution. The resulting Au^{III}–CH_3 complex **4** most likely converts into the lowest energy Au^{III}–CH_3 complex **5** before functionalization.

Oxidative functionalization of **5** proceeds with a low energy barrier ($\Delta H = 10.8$ kcal mol^{-1}) through an S_N2 type attack on the methyl group by a free bisulfate ion $\mathbf{6}^{\ddagger}$. This process is facilitated by the dissociation of the ligand *trans* to the CH_3 group. A reductive elimination mechanism was also found, but with a $\Delta H^{\ddagger}$ value of 32.9 kcal mol^{-1}.

Au^{I} species can follow a similar electrophilic substitution C–H activation mechanism (Figure 3) to produce $[Au^{I}(CH_3)(H_2SO_4)]$ (**10**) with an activation energy of 26.2 kcal mol^{-1} from **7**. Interestingly, an oxidative addition mechanism was also found with an activation energy of 21.1 kcal mol^{-1}, somewhat lower than the electrophilic substitution. The resulting Au^{III} species **12** is a stable intermediate, but the compound is acidic enough that deprotonation would rapidly lead to the same Au^{I}–CH_3 complex **10** for the electrophilic substitution pathway.

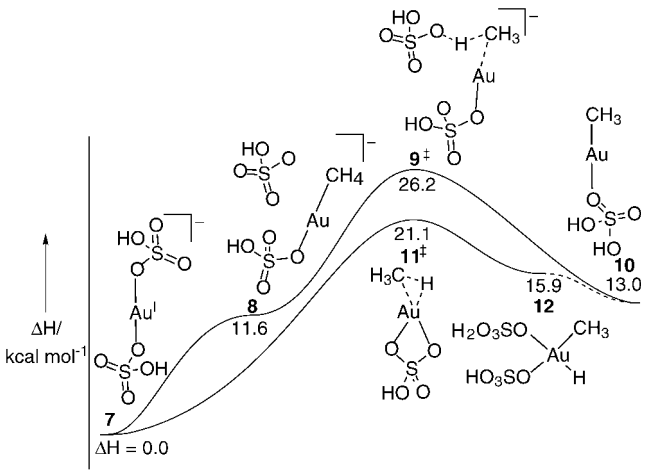


Figure 3. Calculated enthalpies (kcal mol^{-1}) at 175 °C relative to **7**, including solvation by sulfuric acid ($\varepsilon = 50$). For clarity, spectator H_2SO_4 groups have been omitted from some structures. The top curve illustrates electrophilic substitution, while the bottom curve illustrates oxidative addition.

While C–H activation with Au^{I} ions is feasible, direct functionalization from this species is not. Both reductive elimination and nucleophilic substitution yields an $Au^{-I}{\cdot}2\,H_2SO_4$ ion that is calculated to be 37.6 kcal mol^{-1} higher in energy than **10**. However, **10** can most likely be oxidized to the Au^{III} species **5**, either through selenic acid, sulfuric acid, or **1**. Indeed, preliminary calculations show that the redox exchange $\mathbf{10} + \mathbf{1} \rightarrow \mathbf{5} + \mathbf{7}$ is exothermic by about 32 kcal mol^{-1}, and would thus be feasible even for the stoichiometric process.

Based on these results, it appears that oxidative addition to Au^{I} ions is the favored pathway, which is 7.0 kcal mol^{-1} lower in energy than the electrophilic substitution pathway for Au^{III} ions. However, these energetics do not take the relative concentrations of the Au^{III} and Au^{I} cations into account, and the concentration of Au^{I} ions should be significantly lower than Au^{III} ions in the presence of excess oxidant Se^{VI}. A difference of 7.0 kcal mol^{-1} corresponds to a ratio of approximately 2500:1 at 175 °C, and thus if the ratio of Au^{I} to Au^{III} ions is less than 1:2500, the Au^{III} pathway would be favored. Since this is a feasible ratio, both Au^{I} and Au^{III}

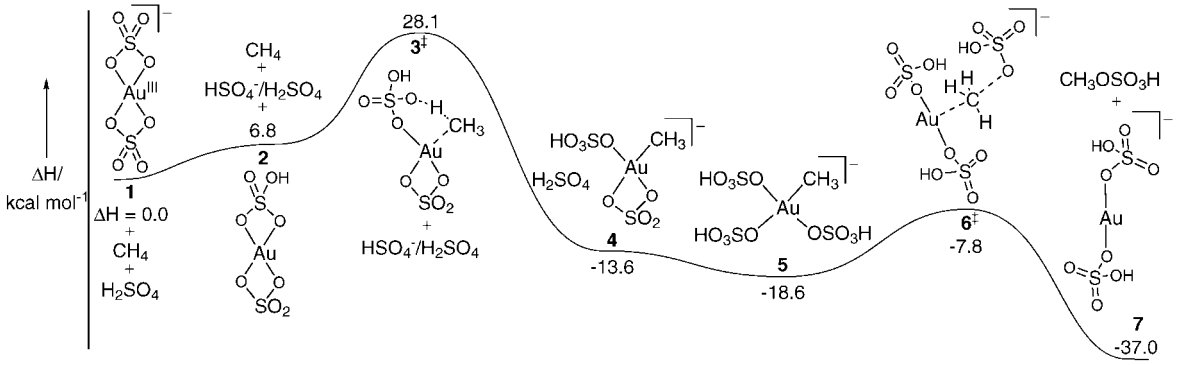


Figure 2. Calculated enthalpies (kcal mol^{-1}) relative to **1**, including solvation by sulfuric acid ($\varepsilon = 50$). Spectator sulfuric acid molecules have been omitted from some structures for clarity.

 © 2004 Wiley-VCH Verlag GmbH & Co. KGaA, Weinheim

remain possible active species, which is in contrast to findings for Pt^{II} [4a] and Hg^{II} ions.[2]

In summary, we report that cationic gold catalyzes the selective, low-temperature, oxidation of methane to methanol in strong acid solvent using Se^{VI} ions as the stoichiometric oxidant. The reaction does not appear to proceed through free radicals and DFT calculations indicate that Au^{I} or Au^{III} species are both viable catalysts that operate by mechanisms involving overall electrophilic C–H activation and oxidative functionalization.

Received: June 23, 2004
Published Online: August 12, 2004

Keywords: C–H activation · gold · homogeneous catalysis · methane · oxidation

[1] a) B. A. Arndtsen, R. G. Bergman, T. A. Mobley, T. H. Peterson, *Acc. Chem. Res.* **1995**, *28*, 154; b) A. E. Shilov, G. B. Shul'pin, *Chem. Rev.* **1997**, *97*, 2879; c) R. H. Crabtree, *J. Chem. Soc. Dalton Trans.* **2001**, *17*, 2437; d) W. D. Jones, *Science* **2000**, *287*, 1942.

[2] R. A. Periana, D. J. Taube, E. R. Evitt, D. G. Loffler, P. R. Wentrcek, G. Voss, T. Masuda, *Science* **1993**, *259*, 340.

[3] a) R. A. Periana, O. Mironov, D. Taube, G. Bhalla, C. J. Jones, *Science* **2003**, *301*, 814; b) A. Sen, *Acc. Chem. Res.* **1998**, *31*, 550.

[4] a) K. X. J. Xu, R. A. Periana, W. A. Goddard III, *Organometallics* **2003**, *22*, 2057; b) J. A. Labinger, J. E. Bercaw, *Nature* **2002**, *507-514*, 507; c) M. Lin, C. Shen, E. A. Garcia-Zayas, A. Sen, *J. Am. Chem. Soc.* **2001**, *123*, 1000; d) R. A. Periana, D. J. Taube, S. Gamble, H. Taube, T. Satoh, H. Fuji, *Science* **1998**, *280*, 560; e) S. Stahl, J. A. Labinger, J. E. Bercaw, *Angew. Chem.* **1998**, *110*, 2298; *Angew. Chem. Int. Ed.* **1998**, *37*, 2180; f) A. E. Shilov, G. B. Shul'pin, *Chem.Rev.* **1997**, *97*, 2879.

[5] a) G. B. Shul'pin, A. E. Shilov, G. Süss-Fink, *Tetrahedron Lett.* **2001**, *42*, 7253; b) G. B. Shul'pin, *J. Mol. Catal. A* **2002**, *189*, 39.

[6] a) M. S. Wickleder, K. Esser, *Z. Anorg. Allg. Chem.* **2002**, *628*, 911; b) M. S. Wickleder, O. Buchner, *Z. Naturforsch. B* **2001**, *56*, 1340.

[7] N. N. Greenwood, A. Earnshaw, *Chemistry of the Elements*, 2nd ed., Butterworth-Heinemann, Oxford, **1997**, p. 782.

[8] a) D. H. McDaniel, L. H. Steinert, *J. Am. Chem. Soc.* **1966**, *88*, 4826; b) S. Wasif, *J. Chem. Soc. A* **1967**, *1*, 142; c) M. A. Hussein, G. M. Iskander, M. M. Nour, S. Wasif, H. M. Zeidan, *J. Chem. Soc. Dalton Trans* **1982**, *9*, 1645.

[9] In a typical reaction, a 50-mL glass-lined, stirred, high-pressure reactor containing 27 mM of 20 mesh, gold powder and 3 M H_2SeO_4 (3 mL) in 96% D_2SO_4 was pressurized with methane to a final pressure of 27 bar. This reaction mixture was vigorously stirred and maintained at 180 °C for 2 h. After cooling the mixture, the reaction gas phase was vented into an evacuated cylinder (to obtained both dissolved and undissolved gases) and analyzed by GC-MS. The liquid phase was analyzed by ^{1}H and ^{13}C NMR spectroscopy and HPLC.[4d]

[10] This NMR spectrum cannot be used to obtain quantitative information nor is it representative of the $^{13}CH_4$ dissolved under reaction conditions. See reference [9].

[11] Relativistic effects are incorporated into the Los Alamos Core-Valence Pseudopotential (LACVP) used for Au (P. J. Hay, W. R. Wadt, *J. Chem. Phys.* **1985**, *82*, 299). The 6-31G** ++ basis was employed for other atoms (M. M. Francl, W. J. Pietro, W. J. Hehre, J. S. Binkley, M. S. Gordon, D. J. DeFrees, J. A. Pople, *J. Chem. Phys.* **1982**, *77*, 3654). In our experience, approximations implied by this finite basis cause average errors of 4 kcal mol^{-1}, which the implicit solvent model will increase.

[12] L. L. C. Schrödinger, Jaguar 5.5, Portland, OR, **1991–2003**.

[13] J. M. L. Martin, *J. Chem. Phys.* **1998**, *108*, 2791.

[14] The d-like polarization shell with exponent $\alpha = 0.65$ was replaced with two shells: a single Gaussian with exponent $\alpha = 0.55$ and a two-Gaussian contraction with exponents $\alpha_1 = 7.5$ and $\alpha_2 = 1.8$ with contraction coefficients $c_1 = 0.2$ and $c_2 = 1.0$.

[15] A high-temperature (175 °C) value was projected assuming the dielectric constant of sulfuric acid decays with temperature at a rate similar to that of water; $-(1/\varepsilon)\ \partial\varepsilon/\partial T = 0.0045$.

 © 2004 Wiley-VCH Verlag GmbH & Co. KGaA, Weinheim

Natural Products Synthesis

Total Synthesis and Configurational Assignment of (−)-Dictyostatin, a Microtubule-Stabilizing Macrolide of Marine Sponge Origin**

Ian Paterson, Robert Britton, Oscar Delgado, Arndt Meyer, and Karine G. Poullennec*

Dictyostatin (**1**, Scheme 1) is a potent cytotoxic macrolide first isolated by Pettit et al.[1] from a marine sponge of the genus *Spongia sp.*, collected in the Republic of Maldives, and, subsequently, isolated by Wright and co-workers[2] from a *lithistida* sponge of the family *Corallistidae,* harvested at great depths off the Jamaican coast. The planar structure of this unsaturated 22-membered macrolactone, featuring 11 stereogenic centers, an endocyclic 2*Z*,4*E* dienoate and a pendant *Z*-diene moiety at C21, was deduced by the Pettit group, primarily on the basis of 2D NMR spectroscopic data.[1] Recently, we proposed a full stereochemical assignment for dictyostatin, as indicated in **1**, based on the use of extensive high-field NMR experiments, including the Murata *J*-based configuration analysis, in combination with molecular modeling.[3] Although it was not possible to ascertain the absolute configuration, our assignment was based on dictyostatin being biogenetically related to discodermolide.[4]

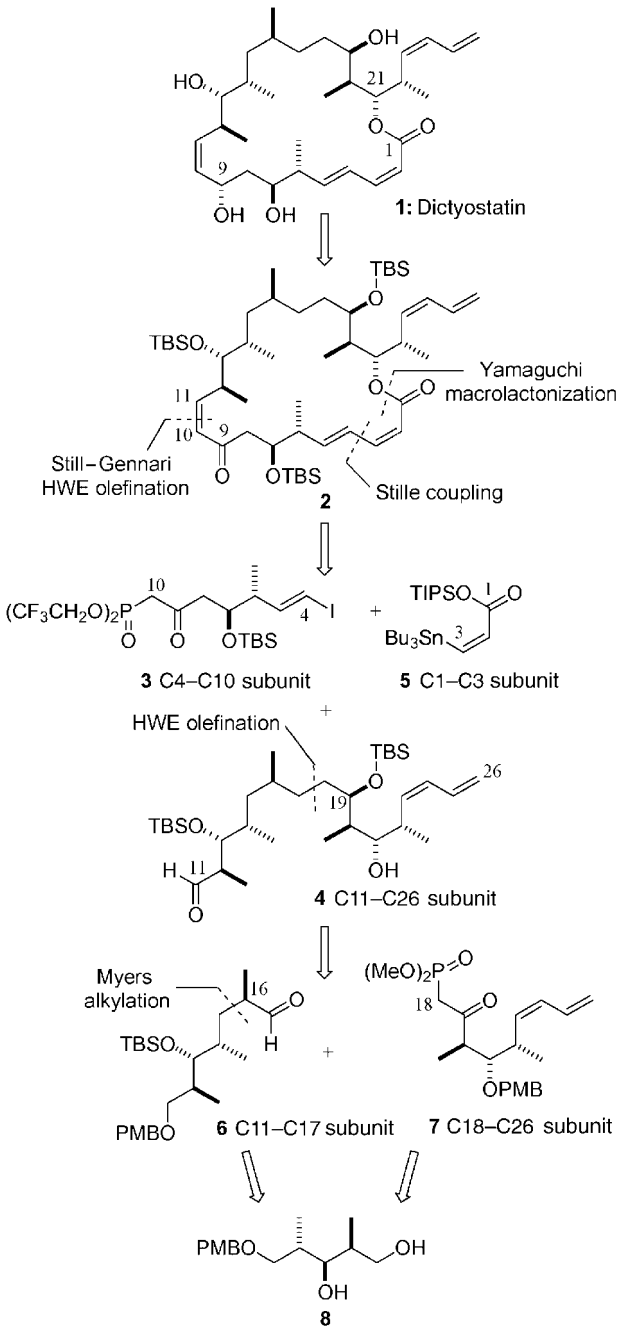
Notably, dictyostatin displays powerful growth-inhibitory activity against a number of murine and human cancer cells at low nanomolar concentrations and, importantly, retains

[*] Prof. Dr. I. Paterson, Dr. R. Britton, Dr. O. Delgado, A. Meyer, Dr. K. G. Poullennec
University Chemical Laboratory
Lensfield Road, Cambridge, CB2 1EW (UK)
Fax: (+44) 1223-336-362
E-mail: ip100@cam.ac.uk

[**] This research was supported by the EPSRC, the NSERC-Canada (R.B.), the Gobierno de Canarias, the Cambridge European Trust (O.D.), the EC (Network HPRN-CT-2000-18 and IE Marie Curie Fellowship to K.G.P.), Novartis Pharma AG, and the Merck Research Council. We thank Dr. Amy Wright (Harbor Branch Oceanographic Institution) for helpful discussions and for providing an authentic sample of dictyostatin, and Kate Ashton (Cambridge) for molecular modeling assistance.

Supporting information for this article is available on the WWW under http://www.angewandte.org or from the author.

 DOI: 10.1002/anie.200460589 © 2004 Wiley-VCH Verlag GmbH & Co. KGaA, Weinheim



Scheme 1. Retrosynthetic analysis for dictyostatin (**1**) leading to key building blocks **3**, **6**, and **7**.

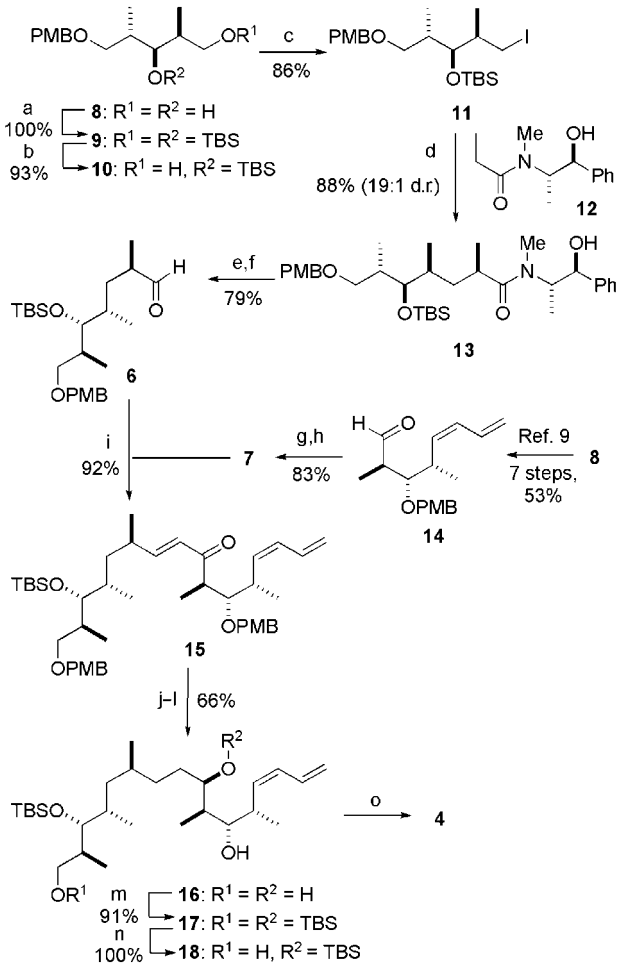
activity against taxol-resistant cancer cells that express active P-glycoprotein. Preliminary studies into the mechanism of action demonstrated that dictyostatin, in a similar manner to taxol (paclitaxel), arrests cells in the G2/M phase by potently inducing tubulin polymerization and suppressing normal microtubule dynamics, leading to apoptosis.[2] Hence, dictyostatin currently represents a promising antimitotic natural product lead for development in cancer chemotherapy, joining an elite group of microtubule-stabilizing polyketides that include laulimalide,[5] peloruside A,[6] and discodermolide.[7] Unfortunately, evaluation of its antitumor properties has been precluded so far by the very low natural abundance.

Herein, we disclose the first total synthesis of dictyostatin (**1**) and establish unequivocally the relative and absolute configuration of this rare polyketide metabolite. Furthermore, the modular synthetic approach employed is flexible, highly convergent, and stereocontrolled, and thus offers the potential to provide useful quantities of dictyostatin as well as a range of structural derivatives to initiate structure–activity relationship studies.

As outlined retrosynthetically in Scheme 1, our approach relies on a late-stage reduction of the enone **2**, controlled by the macrocyclic conformation adopted by the 22-membered ring; molecular modeling studies[8] indicated that hydride addition should occur selectively to install the requisite C9 hydroxyl-bearing stereocenter. The 10*Z* alkene moiety in **2** was planned to arise from a Still–Gennari-type olefination between the β-keto phosphonate **3** and aldehyde **4**, in conjunction with a Stille cross-coupling with vinyl stannane **5** to deliver the 2*Z*,4*E* dienoate. In principle, either of these two reactions could be employed to close the macrocycle as an alternative to a more conventional Yamaguchi macrolactonization, thus offering considerable flexibility in the synthesis. In turn, the C11–C26 subunit **4** should be accessible by a Horner–Wadsworth–Emmons (HWE) coupling between aldehyde **6** and phosphonate **7**, which contains the terminal *Z* diene. As these latter segments share a common stereochemical triad, it was anticipated that both **6** and **7** could be prepared from common intermediate **8**, which is available in multigram quantities through efficient aldol methodology reported previously by our group.[9]

Synthesis of the C11–C26 subunit **4**, as shown in Scheme 2, commenced with conversion of 1,3-diol **8** into bis-TBS ether **9** and liberation of the primary hydroxy group under mildly acidic conditions. The resulting alcohol **10** was readily converted into iodide **11** through a modified Mitsunobu protocol (PPh_3, I_2, imid).[10] Subsequent alkylation of the lithium enolate of the Myers propionamide **12**[11] effected a three-carbon homologation, delivering **13** with excellent diastereoselectivity and yield (19:1 d.r., 88%).[12] Reductive removal of the pseudoephedrine auxiliary ($LiNH_2BH_3$)[11] afforded a primary alcohol, which was, in turn, oxidized with Dess–Martin periodinane to provide aldehyde **6**. The HWE coupling partner **7** was synthesized by addition of $(MeO)_2P(O)CH_2Li$ to aldehyde **14**, which was prepared from 1,3-diol **8** as described previously.[9,13] The resulting epimeric mixture of alcohols was converted into β-ketophosphonate **7** (Dess–Martin periodinane, 83% over two steps). Following a HWE coupling between aldehyde **6** and phosphonate **7**, employing $Ba(OH)_2$ in wet THF, enone **15** was isolated in 92% yield.[14] With the entire C11–C26 backbone assembled, we next focused on the stereocontrolled reduction of the C19 ketone directed by the proximal hydroxy-bearing stereocenter through metal chelation. To this end, conjugate reduction of enone **15** with the Stryker reagent $\{[Ph_3PCuH]_6\}$[15] and oxidative removal of both PMB groups with DDQ provided the intermediate β-hydroxyketone, which underwent 1,3-*syn*-selective reduction when treated with a cold (−30 °C) ethereal solution of $Zn(BH_4)_2$,[16] generating triol **16** (>20:1 d.r.).[17] Finally, the synthesis of subunit **4** was completed by a three-step sequence involving

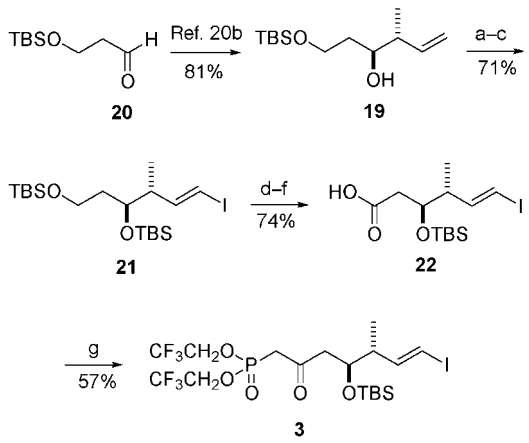
 © 2004 Wiley-VCH Verlag GmbH & Co. KGaA, Weinheim



Scheme 2. Synthesis of C11–C26 subunit **4**. a) TBSOTf, 2,6-lutidine, CH_2Cl_2, 0 °C→RT, 15 min; b) *p*-TSA (30 mol %), 20:1 THF/H_2O, 24 h; c) PPh_3, I_2, imid, PhMe, 0 °C, 15 min; d) 1) **12**, LiCl, LDA, THF, −78 °C→RT; 2) **11**, THF, 0 °C→RT, 18 h; e) 1) LDA, BH_3NH_3, THF, 0 °C; 2) **13**, THF, 0 °C→RT, 18 h; f) DMP, $NaHCO_3$, CH_2Cl_2, 0 °C, 2 h; g) 1) *n*BuLi, $(MeO)_2P(O)Me$, THF, −78 °C, 30 min; 2) **14**, THF, −78 °C ; h) DMP, CH_2Cl_2, room temperature, 10 min; i) 1) **7**, $Ba(OH)_2{\cdot}8H_2O$, THF, 1 h; 2) **6**, 40:1 THF/H_2O, 20 h; j) $[Ph_3PCuH]_6$, PhH, H_2O, room temperature, 2 h; k) DDQ, pH 7 buffer, CH_2Cl_2, 0 °C, 6 h; l) $Zn(BH_4)_2$, Et_2O, −30 °C, 2 h; m) TBSOTf, 2,6-lutidine, −78→0 °C, 30 min; n) TBAF, AcOH, THF, room temperature, 24 h; o) TEMPO, $PhI(OAc)_2$, CH_2Cl_2, room temperature, 18 h. TBS = *tert*-butyldimethylsilyl, Tf = trifluoromethanesulfonyl, *p*-TSA = *p*-toluenesulfonic acid, imid = imidazole, LDA = lithium diisopropylamide, DMP = Dess–Martin periodinane, DDQ = 2,3-dichloro-5,6-dicyano-1,4-benzoquinone, TBAF = tetrabutylammonium fluoride, TEMPO = 2,2,6,6-tetramethyl-1-piperidinyloxy, free radical.

selective TBS protection of the C11 and C19 hydroxy groups over that at C21 (TBSOTf), cleavage (TBAF, AcOH) of the primary TBS ether in **17**, and oxidation of resulting alcohol **18** ($TEMPO/PhI(OAc)_2$).[18]

As our primary objective was an efficient and convergent synthesis of dictyostatin, it was crucial to install the 10*Z* alkene function by employing advanced coupling partners. Although a number of protocols exist to effect such coupling, most require strongly basic conditions. Our concerns regarding the epimerizable center at C12 in aldehyde **4** led us to investigate the mild Still–Gennari modification of the HWE olefination.[19] The requisite F_3CCH_2O-substituted phosphonate **3** was prepared from alcohol **19**, which was obtained with 95 % *ee* and 20:1 d.r. through a Brown asymmetric crotylation of aldehyde **20** (Scheme 3).[20] Silyl ether formation



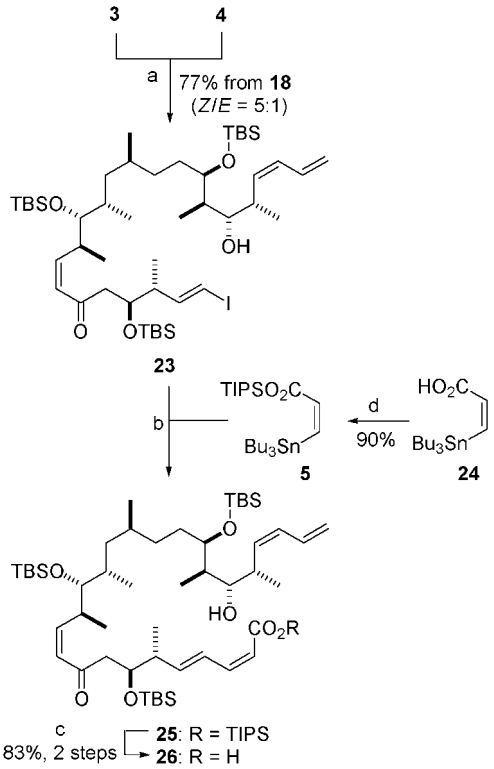
Scheme 3. Synthesis of C4–C10 subunit **3**. a) TBSOTf, 2,6-lutidine, CH_2Cl_2, −78 °C, 30 min; b) 1) O_3, CH_2Cl_2, −78 °C; 2) Ph_3P, −78 °C→RT, 2 h; c) $CrCl_2$, CHI_3, THF, dioxane, 0 °C, 18 h; d) TBAF, AcOH, THF, room temperature, 14 h; e) DMP, py, CH_2Cl_2, room temperature, 3 h; f) $NaClO_2$, NaH_2PO_4, 10:1 *t*BuOH/H_2O, 0 °C, 2 h; g) 1) $Me_2C=C(Cl)NMe_2$, CH_2Cl_2, room temperature, 15 min; 2) $(F_3CCH_2O)_2P(O)CH_2Li$, THF, −100 °C, 1 h.

(TBSOTf), ozonolysis, and Takai methylenation[21] of the intermediate aldehyde provided *E* vinyl iodide **21** in 71 % yield. After selective cleavage of the primary silyl ether, oxidation of the resulting alcohol afforded acid **22**, which was transformed into its acid chloride by using the Ghosez reagent ($Me_2C=C(Cl)NMe_2$).[22] Next, the acid chloride was added to a solution of $(F_3CCH_2O)_2P(O)CH_2Li$ in THF,[23] generated at −100 °C, to afford phosphonate **3** containing the required functionality for the pivotal fragment assembly.

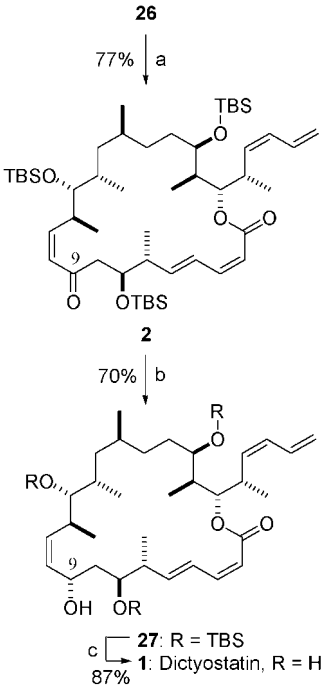
To our delight, when a mixture of aldehyde **4** and phosphonate **3** was subjected to an excess of K_2CO_3 in the presence of [18]crown-6 in toluene (Scheme 4),[19] the HWE coupling proceeded smoothly to produce *Z* enone **23** efficiently, with good levels of selectivity (*Z*/*E* = 5:1, 77 %). Notably, this constitutes one of the first examples of a *Z*-selective *intermolecular* Still–Gennari olefination employing such an elaborate β-ketophosphonate. Construction of the dictyostatin carbon backbone was completed through a copper-mediated, Liebeskind-type Stille coupling[24] (CuTC in NMP) of vinyl iodide **23** and *Z* alkenyl stannane **5**, which is readily accessible from known acid **24**.[25] Finally, TIPS ester **25** was converted into acid **26** (KF, THF/MeOH) in 83 % overall yield.

With **26** in hand, attention was now directed towards the completion of the synthesis, as shown in Scheme 5. Seco acid **26** was subjected to a standard Yamaguchi macrolactonization protocol (2,4,6-trichlorobenzoyl chloride, NEt_3, DMAP, PhMe, 60 °C, 2 h) to furnish the 22-membered macrocycle **2** cleanly in 77 % yield.[26] Next, we investigated the reduction of the C9 ketone, in a bid to exploit macrocyclic stereocontrol.[8]

 © 2004 Wiley-VCH Verlag GmbH & Co. KGaA, Weinheim



Scheme 4. Synthesis of seco acid **26**. a) K_2CO_3 (10 equiv), [18]crown-6 (25 equiv), toluene, room temperature, 48 h; b) CuTC, NMP, room temperature, 1 h; c) KF, THF, MeOH, room temperature, 2 h; d) TIPSCl, Et_3N, CH_2Cl_2, room temperature, 45 min. CuTC = copper(I) thiophenecarboxylate, NMP = 1-methyl-2-pyrrolidinone, TIPS = triisopropylsilyl.



Scheme 5. Completion of the synthesis of dictyostatin (**1**). a) 2,4,6-trichlorobenzoyl chloride, NEt_3, DMAP, PhMe, 60 °C, 2 h; b) $NaBH_4$, $CeCl_3 \cdot 7H_2O$, EtOH, −30 °C; c) HCl (3 N), MeOH, room temperature, 6 h. DMAP = 4-dimethylaminopyridine.

Gratifyingly, Luche reduction of enone **2** ($NaBH_4$, $CeCl_3$, EtOH)[27] provided the expected alcohol **27** (70%). Finally, global deprotection with HCl (3 N) in methanol gave dictyostatin (**1**) in 87% yield. The spectroscopic data of our synthetic material were in complete agreement with those of an authentic sample obtained from the *Corallistidae* sponge source (^{1}H (700 MHz), ^{13}C NMR (125 MHz), MS), and the specific rotation of $[\alpha]_D = -32.7$ ($c = 0.22$, MeOH) agreed with that measured in our laboratory for the authentic sample,[28] thus allowing confident assignment of the relative and absolute configuration of dictyostatin and validating our earlier proposal.[3a]

Significantly, this configurational assignment for dictyostatin is fully consistent with a common biogenesis for the structurally related, but open-chain, polyketide discodermolide (**28**, Figure 1), presently in clinical development as a new-

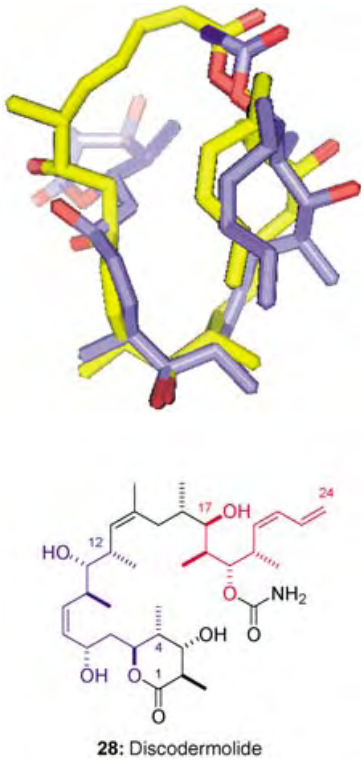


Figure 1. Overlay of preferred solution conformation[3a] of dictyostatin (in yellow, C1/C2 s-*trans* rotamer) in water with conformation of discodermolide (**28**) obtained from the X-ray crystal structure (in blue).

generation microtubule-stabilizing anticancer agent.[29] There is an exact configurational match of the C19–C26 and C6–C14 regions of dictyostatin with those at C17–C24 (shown in red) and C4–C12 (shown in blue) of discodermolide, respectively. As shown by the overlay in Figure 1, the preferred conformation for dictyostatin in solution[3a] resembles closely that determined for discodermolide in the solid state, suggesting that they may interact in a similar fashion with the taxol-binding site on β-tubulin.[30] As a conformationally constrained macrocyclic analogue of discodermolide, dictyostatin represents a highly attractive template for rational drug design.

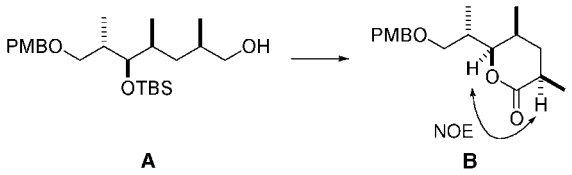
 © 2004 Wiley-VCH Verlag GmbH & Co. KGaA, Weinheim

In conclusion, this expedient total synthesis of (−)-dictyostatin proceeds in 27 steps and 3.8% overall yield (longest linear sequence from the Roche ester[9]) and establishes unequivocally the relative and absolute configuration. Key transformations include an unprecedented Still–Gennari-type HWE coupling with a complex β-ketophosphonate, a Liebeskind-type Stille cross-coupling to install the 2*Z*,4*E* dienoate, a facile Yamaguchi macrolactonization to construct the macrocycle, and subsequent reduction of the C9 ketone under macrocyclic stereocontrol. Importantly, this modular, convergent synthesis should be amenable to producing useful quantities and designed analogues of this novel microtubule-stabilizing agent, enabling extensive exploration of its anticancer properties.

Received: May 7, 2004
Published Online: July 1, 2004

Keywords: antitumor agents · conformation analysis · macrocycles · natural products · total synthesis

[1] G. R. Pettit, Z. A. Cichacz, F. Gao, M. R. Boyd, J. M. Schmidt, *J. Chem. Soc. Chem. Commun.* **1994**, 1111.
[2] R. A. Isbrucker, J. Cummins, S. A. Pomponi, R. E. Longley, A. E. Wright, *Biochem. Pharmacol.* **2003**, *66*, 75.
[3] a) I. Paterson, R. Britton, O. Delgado, A. E. Wright, *Chem. Commun.* **2004**, 632; b) G. R. Pettit, Z. A. Cichacz, WO 5430053, **1995** [*Chem. Abstr.* **1995**,733500; this patent contains a partial stereochemical assignment for dictyostatin that differs significantly from our findings.
[4] The structural similarities between discodermolide and dictyostatin and the scope for preparing hybrid structures have been highlighted before: Y. Shin, N. Choy, R. Balachandran, C. Madiraju, B. W. Day, D. P. Curran, *Org. Lett.* **2002**, *4*, 4443. For an alternative total synthesis of dictyostatin, which independently confirms our earlier stereochemical assignment,[3a] see the following Communication in this issue: Y. Shin, J.-H. Fournier, Y. Fukui, A. M. Brückner, D. P. Curran, *Angew. Chem.* **2004**, *116*, 4734; *Angew. Chem. Int. Ed.* **2004**, *43*, 4634. We thank Professor Curran for the exchange of information.
[5] S. L. Mooberry, G. Tien, A. H. Hernandez, A. Plubrukarn, B. S. Davidson, *Cancer Res.* **1999**, *59*, 653.
[6] K. A. Hood, L. M. West, B. Rouwe, P. T. Northcote, M. V. Berridge, S. J. Wakefield, J. H. Miller, *Cancer Res.* **2002**, *62*, 3356.
[7] a) E. ter Haar, R. J. Kowalski, E. Hamel, C. M. Lin, R. E. Longley, S. P. Gunasekera, H. S. Rosenkranz, B. W. Day, *Biochemistry* **1996**, *35*, 243; b) for a review, see: I. Paterson, G. J. Florence, *Eur. J. Org. Chem.* **2003**, *12*, 2193.
[8] Macromodel (Version 8.0) was used in a 1700-step Monte Carlo search with **2** using the MM2* force field. The accessible low-energy conformations found all had the lower (*Si*) face of the ketone blocked by the bulky TBS ether attached to C7, such that hydride attack was expected from the upper (*Re*) face.
[9] 1,3-Diol **8** was prepared on a multigram scale in five steps and 52% yield from methyl (*S*)-3-hydroxy-2-methylpropionate (Roche ester): I. Paterson, O. Delgado, G. J. Florence, I. Lyothier, J. P. Scott, N. Sereinig, *Org. Lett.* **2003**, *5*, 35.
[10] P. J. Garegg, B. Samuelson, *J. Chem. Soc. Perkin Trans. 1* **1980**, 2866.
[11] A. G. Myers, B. H. Yang, H. Chen, L. McKinstry, D. J. Kopecky, J. L. Gleason, *J. Am. Chem. Soc.* **1997**, *119*, 6496.
[12] The 1,3-*syn* stereochemistry of amide **13** was confirmed by NOE enhancements on lactone **B**, obtained by a two-step sequence (HCl (2N), EtOH; TEMPO, $PhI(OAc)_2$) from alcohol **A**.



A **B**

[13] a) I. Paterson, G. J. Florence, K. Gerlach, J. P. Scott, *Angew. Chem.* **2000**, *112*, 385; *Angew. Chem. Int. Ed.* **2000**, *39*, 377; b) I. Paterson, G. J. Florence, K. Gerlach, J. P. Scott, N. Sereinig, *J. Am. Chem. Soc.* **2001**, *123*, 9535.
[14] I. Paterson, K.-S. Yeung, J. B. Smaill, *Synlett* **1993**, 774.
[15] W. S. Mahoney, D. M. Brestensky, J. M. Stryker, *J. Am. Chem. Soc.* **1988**, *110*, 291.
[16] T. Oishi, T. Nakata, *Acc. Chem. Res.* **1984**, *17*, 338.
[17] The relative stereochemistry of **16** was confirmed unequivocally by NMR spectroscopy experiments performed on the corresponding acetonide.
[18] A. De Mico, R. Margarita, L. Parlanti, A. Vescovi, G. Piancatelli, *J. Org. Chem.* **1997**, *62*, 6974.
[19] W. C. Still, C. Gennari, *Tetrahedron Lett.* **1983**, *24*, 4405.
[20] a) H. C. Brown, K. S. Bhat, R. S. Randad, *J. Org. Chem.* **1989**, *54*, 1570; b) I. Paterson, K. Ashton, R. Britton, H. Knust, *Org. Lett.* **2003**, *5*, 1963.
[21] K. Takai, K. Nitta, K. Utimoto, *J. Am. Chem. Soc.* **1986**, *108*, 7408.
[22] A. Devos, J. Remion, A. M. Frisque-Hesbain, A. Colens, L. Ghosez, *J. Chem. Soc. Chem. Commun.* **1979**, 1180.
[23] C. Patois, P. Savignac, E. About-Jadet, N. Collignon, *Synth. Commun.* **1991**, *21*, 2391.
[24] G. D. Allred, L. S. Liebeskind, *J. Am. Chem. Soc.* **1996**, *118*, 2748.
[25] D. J. Crichter, G. Pattenden, *Tetrahedron Lett.* **1996**, *37*, 9107.
[26] J. Inanaga, K. Hirata, H. Saeki, T. Katsuki, M. Yamaguchi, *Bull. Chem. Soc. Jpn.* **1979**, *52*, 1989.
[27] J. L. Luche, *J. Am. Chem. Soc.* **1978**, *100*, 2226.
[28] In comparison, the specific rotation measured for a natural sample of dictyostatin-1 was $[\alpha]_D = -27.4$ ($c = 0.16$, MeOH), whereas that reported by Pettit et al.[1] was −20 ($c = 0.12$, MeOH). For copies of ^1H and ^{13}C NMR spectra, see the Supporting Information.
[29] For the recent large-scale synthesis of discodermolide, see: S. J. Mickel, D. Niederer, R. Daeffler, A. Osmani, E. Kuesters, E. Schmid, K. Schaer, R. Gamboni, W. Chen, E. Loeser, F. R. Kinder, K. Konigsberger, K. Prasad, T. M. Ramsey, O. Repic, R.-M. Wang, G. J. Florence, I. Lyothier, I. Paterson, *Org. Process Res. Dev.* **2004**, *8*, 122.
[30] Note added in proof: Preliminary biological evaluation suggests that dictyostatin is also a ligand for the taxoid binding site on β.tutublin and binds more strongly than taxol. We thank Dr. Fernando Díaz and Ruben M. Buey (Centro de Investigaciones Biológicas, CSIC, Madrid) for carrying out this study with synthetic dictyostatin.

 © 2004 Wiley-VCH Verlag GmbH & Co. KGaA, Weinheim

Natural Products Synthesis

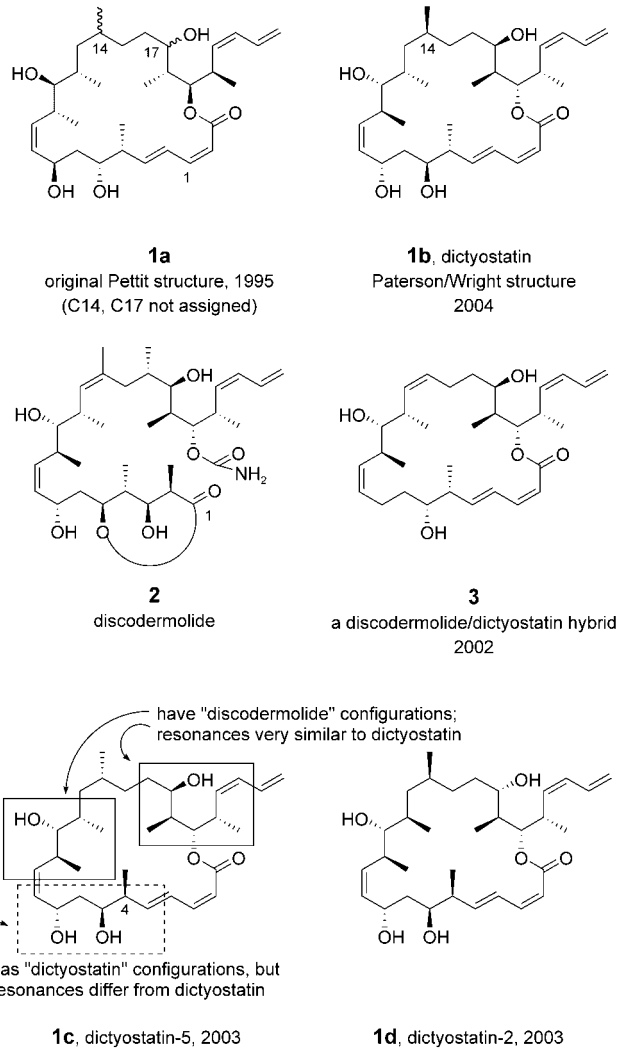
Total Synthesis of (−)-Dictyostatin: Confirmation of Relative and Absolute Configurations**

*Youseung Shin, Jean-Hugues Fournier, Yoshikazu Fukui, Arndt M. Brückner, and Dennis P. Curran**

The macrolactone (−)-dictyostatin was isolated in small quantities from a Maldives marine sponge *Spongia sp.* by Pettit and co-workers in 1994.[1a] Dictyostatin strongly inhibits the growth of human cancer cells with a GI_{50} in the 50 pM to 1 nM range, and in a subsequent patent it was assigned a partial structure **1a** shown.[1b] Wright and co-workers isolated dictyostatin from *Corallistidea* sponges,[2] and showed that it stabilized microtubules in the same way as discodermolide (by preventing the depolymerization to tubulin heterodimers). Studies on taxol-resistant cell lines and other experiments also suggested that dictyostatin could be useful against multidrug-resistant tumors. Despite these exciting results, further study of dictyostatin has been retarded because it is scarce and its structure is not known with certainty.

Dictyostatin is structurally related to discodermolide **2**,[3] and in 2002 we reported the syntheses of the first discodermolide–dictyostatin hybrid molecules and suggested that the absolute configuration of dictyostatin should be inverted so that it more closely resembles discodermolide.[4] The synthesis of hybrids such as **3** taught us how to make the lower dienyl ester chain of the dictyostatins, including the macrolactone ring.

In further work, we began to doubt the relative stereochemical assignments in **1a**.[5] For example, we recently made an isomer of dictyostatin with the structure **1c** ("dictyostatin 5") that has discodermolide-like configurations in the "upper" and "middle" fragments (solid boxes) and the dictyostatin configurations proposed by Pettit and co-workers in the "lower" fragment (dashed box). The resonances of the protons from the "upper" and "middle" fragments resembled those for dictyostatin very closely, but those of the "lower" fragment (especially 3-H–5-H) were very different.[5] Likewise, we made **1d** ("dictyostatin 2"),[5] which is one of the four candidate structures originally proposed; this was not dictyostatin either, and the resonances for its "lower" fragment protons resembled those of **1c**, not dictyostatin.



Very recently, Paterson and Wright conducted a detailed ^{1}H NMR spectroscopic analysis to assign configurations to dictyostatin fragments, and then used molecular modeling to assemble the fragments.[6] They arrived at structure **1b** in which the 10 stereocenters that dictyostatin shares with discodermolide all have the same relative configurations (C14[7] of dictyostatin is not a stereocenter in discodermolide, and was assigned the *S* configuration). We report herein the synthesis of dictyostatin, and confirm that structure **1b** is correct. Concurrently, Paterson and co-workers report their synthesis and have reached the same conclusion.[8]

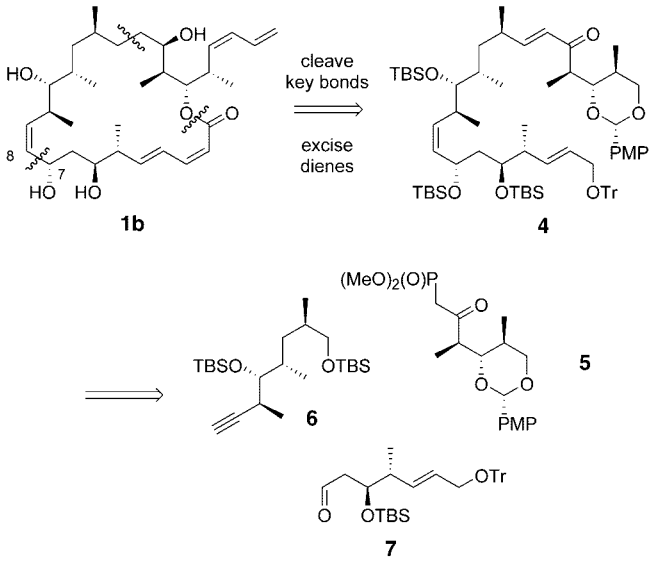
Scheme 1 summarizes key elements of the strategic plan to make **1b**. Because of the uncertainties with configurations, stereochemical flexibility is a key design element.[5] The molecule breaks down into three key fragments as indicated by the wavy lines in **1b**. With the preparation of analogues in mind, we intentionally designed a less convergent synthesis

[*] Y. Shin, Dr. J.-H. Fournier, Dr. Y. Fukui, Dr. A. M. Brückner, Prof. Dr. D. P. Curran
Department of Chemistry
University of Pittsburgh
Pittsburgh, PA 15260 (USA)
Fax: (+1) 412-624-9861
E-mail: curran@pitt.edu

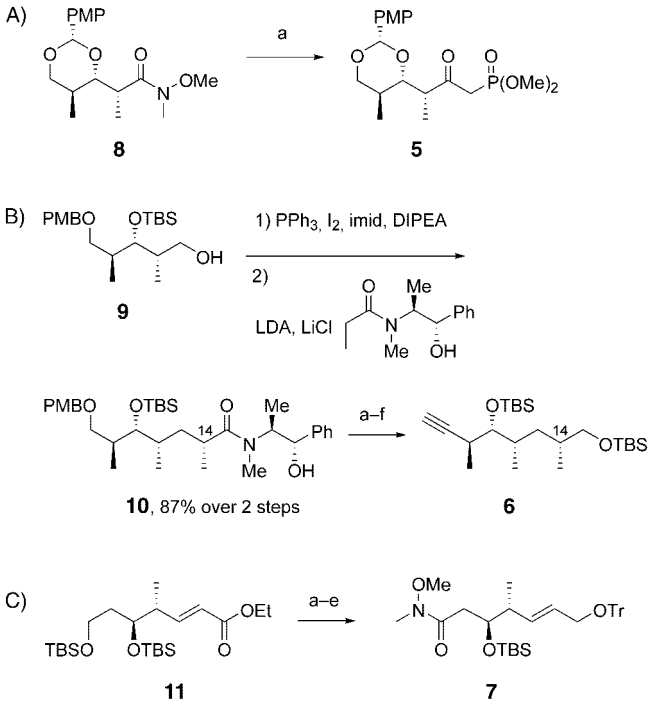
[**] We thank the National Institutes of Health for funding this work, Y.S. thanks the University of Pittsburgh for a Graduate Excellence Fellowship, J.H.F. thanks FCAR, and A.M.B. thanks the German Academic Exchange Service (DAAD) for postdoctoral fellowships. We also thank Professor Billy Day for helpful discussions, Dr. Cherry Herald for spectra of dictyostatin, Dr. Amy Wright for permission to compare samples, and Prof. Ian Paterson for comparing the samples and kindly agreeing to joint publication.

Supporting information for this article (comparison of ^{1}H and ^{13}C NMR spectroscopic data for natural and synthetic samples of dictyostatin) is available on the WWW under http://www.angewandte.org or from the author.

 © 2004 Wiley-VCH Verlag GmbH & Co. KGaA, Weinheim DOI: 10.1002/anie.200460593



Scheme 1. Summary of the synthetic strategy to make **1b**. TBS = *tert*-butyldimethylsilyl, PMP = *p*-methoxyphenyl, Tr = triphenylmethyl.



Scheme 2. A) a) $(MeO)_2P(O)CH_3$, BuLi, −78 °C, 85 %. B) a) LiH_2NBH_3, THF, 96 %; b) TBSCl, imidazole, 4-DMAP, 95 %; c) DDQ, 99 %; d) SO_3·py, Et_3N, DMSO; e) CBr_4, PPh_3, 2,6-lutidine, 73 % over two steps; f) BuLi, THF, 95 %. C) a) DIBAL-H, CH_2Cl_2, 97 %; b) TrCl, 4-DMAP, pyridine; c) HF/py, pyridine, THF, 89 % over two steps; d) 1) SO_3·py, Et_3N, DMSO/CH_2Cl_2; 2) $NaClO_2$, $NaHPO_4$, 2-methyl-2-butene, THF/H_2O; e) NH(Me)(OMe)HCl, DCC, Et_3N, DMAP, CH_2Cl_2, 73 % (three steps). DIPEA = diisopropylethylamine, DMAP = dimethylaminopyridine, DDQ = 2,3-dichloro-5,6-dicyano-1,4-benzoquinone, DMSO = dimethyl sulfoxide, DIBAL-H = diisobutylaluminum hydride, DCC = dicyclohexylcarbodiimide.

that introduces both dienes after coupling of the fragments. Compound **4** became a key intermediate in this strategy and was built from fragments **5**, **6**, and **7**. In turn, the fragments were made by building on prior work in the discodermolide area,[3,9] including our own routes to simplified discodermolide analogues.[10] A key element of the synthesis was our decision to change from a Wittig approach[9] to the synthesis of the C8–C9 *Z* alkene to a more reliable alkyne addition to make the C7–C8 bond.[11]

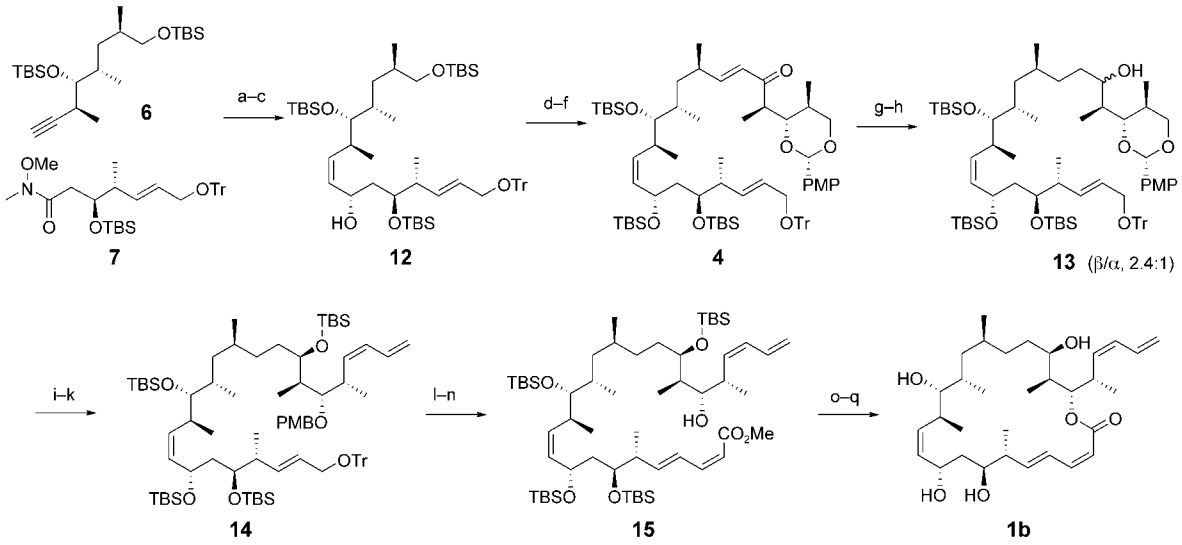
The syntheses of fragments **5**, **6**, and **7** are summarized in Scheme 2. Fragment **5** was prepared from known Weinreb ester **8**[9a,b] by addition of $LiCH_2P(=O)(OMe)_2$. The C14 stereocenter of fragment **6** was introduced by conversion of alcohol **9** into a sensitive iodide,[12] followed by direct Myers alkylation.[13] This gave **10** in 87 % yield as a single stereoisomer. Cleavage of the auxiliary group and protection of the alcohol function were followed by removal of the PMB group, oxidation, Corey–Fuchs olefination, and elimination to install the alkyne on the other end of the backbone. Fragment **7** was prepared by a straightforward sequence of functional-group transformations from the ester **11**.[14]

The union of the fragments and the completion of the synthesis are shown in Scheme 3. Metalation of alkyne **6** and addition of Weinreb ester **7** provided an alkynyl ketone (not shown). The asymmetric reduction of this ketone according to Noyori and co-workers[11,15] followed by Lindlar hydrogenation gave **12** as a single isomer. Protection of the secondary alcohol followed by deprotection of the primary TBS ether, oxidation, and Wittig–Horner coupling with **5** provided key enone **4**. The conjugated double bond of **4** was reduced with nickel boride, and the ketone was then reduced with sodium borohydride to give a readily separable mixture of epimers **13** (β/α 2.4:1).[16] The major β epimer was silylated, the PMP acetal was opened, and the terminal diene was introduced by a standard procedure used in the synthesis of discodermolide[17] to give **14**. Detritylation of **14** followed by oxidation, Still–Gennari olefination,[18] and removal of the PMB group provided the *E*/*Z* dienyl ester **15**.

The final key steps follow directly from our previous syntheses.[4,5] Saponification, Yamaguchi lactonization,[19] and global desilylation provided about 3 mg of **1b** as a white solid after purification by HPLC. Extensive high-field ^{13}C and ^{1}H NMR data are available for both natural samples, and our data match these well.[20] Pettit and co-workers report that natural dictyostatin has an optical rotation of −20 ($c = 0.12$, MeOH),[1] whereas our sample has a rotation of −23 ($c = 0.18$, MeOH). From these data, we conclude that dictyostatin has structure **1b**. The longest linear sequence of 34 steps runs through fragment **6** and provides **1b** in 1 % overall yield from (2*S*)-3-hydroxy-2-methylpropionic acid methyl ester (Roche ester).[9b]

The confirmation of the structure of dictyostatin clears the way for further development in this exciting area. Despite being a macrolactone, dictyostatin presumably has a similar shape to discodermolide, and indeed we had even designed macrocyclic discodermolide analogues before we were aware of dictyostatin.[4] Armed with the knowledge of the structure of dictyostatin, we now know that discodermolide/dictyostatin hybrids such as **3** are much closer to dictyostatin than was originally expected. Our present synthesis is flexible and is

 © 2004 Wiley-VCH Verlag GmbH & Co. KGaA, Weinheim



Scheme 3. a) *n*BuLi, THF, 93%; b) *S,S* Noyori catalyst (20 mol%), *i*PrOH, 79%; c) Lindlar catalyst, H_2 (balloon), toluene, 91%; d) TBSOTf, 2,6-lutidine, CH_2Cl_2, 99%; e) HF/py, pyridine, THF, 0°C, 1 day, 67%; f) 1) Dess–Martin oxidation; 2) $Ba(OH)_2$, **5**, THF/H_2O, 80% (two steps); g) $NiCl_2$, $NaBH_4$, MeOH/THF, 76%; h) $NaBH_4$, MeOH/THF, 70% (β), 29% (α); i) TBSOTf, 2,6-lutidine, CH_2Cl_2, 99%; j) DIBAL-H, CH_2Cl_2, 88%; k) 1) Dess–Martin oxidation; 2) $CH_2=CHCH(TMS)Br$, $CrCl_2$, THF; 3) NaH, THF, 89% (three steps); l) $ZnBr_2$, CH_2Cl_2/MeOH, 69%; m) 1) Dess–Martin oxidation; 2) $(CF_3CH_2O)_2P(O)CH_2CO_2Me$, KHMDS, [18]crown-6, THF, 86% (two steps); n) DDQ, CH_2Cl_2/H_2O, 88%; o) KOH (1 N), EtOH/THF; p) 2,4,6-trichlorobenzoyl chloride, Et_3N, THF then 4-DMAP(10 equiv), toluene, 78% (two steps); q) HCl/MeOH (3 N), THF, 55%. Tf = trifluoromethanesulfonyl, TMS = trimethylsilyl, HMDS = hexamethyldisilazide.

suitable for making other kinds of analogues as well. Increased quantities of dictyostatin are also needed for testing. Although it has two more backbone carbon atoms, dictyostatin lacks three of the stereocenters of discodermolide, therefore it will probably be easier to make in the long run. We are currently investigating ways to increase the convergence of the current synthesis as a prelude to making more dictyostatin.

Received: May 7, 2004
Published Online: July 1, 2004

Keywords: antitumor agents · conformation analysis · macrocycles · natural products · total synthesis

[1] a) G. R. Pettit, Z. A. Cichacz, F. Gao, M. R. Boyd, J. M. Schmidt, *J. Chem. Soc. Chem. Commun.* **1994**, 1111–1112; b) G. R. Pettit, Z. A. Cichacz, *Isolation and structure of dictyostatin*, WO 5430053, **1995** [*Chem. Abstr.* **1995**,733500].

[2] a) A. E. Wright, J. L. Cummins, S. A. Pomponi, R. E. Longley, R. A. Isbrucker, *Dictyostatin compounds for stabilization of microtubules*, WO 0162239, **2001** [*Chem. Abstr.* **2001**, 635882]; b) R. A. Isbrucker, J. Cummins, S. A. Pomponi, R. E. Longley, A. E. Wright, *Biochem. Pharmacol.* **2003**, *66*, 75–82.

[3] a) M. Kalesse, *ChemBioChem* **2000**, *1*, 171–175; b) D. C. Myles, *Annu. Rep. Med. Chem.* **2002**, *37*, 125–132; c) I. Paterson, G. J. Florence, *Eur. J. Org. Chem.* **2003**, 2193–2208; d) S. J. Mickel, G. H. Sedelmeier, D. Niederer, R. Daeffler, A. Osmani, K. Schreiner, M. Seeger-Weibel, B. Berod, K. Schaer, R. Gamboni, *Org. Process Res. Dev.* **2004**, *8*, 92–100, and succeeding papers in that issue.

[4] Y. Shin, N. Choy, R. Balachandran, C. Madiraju, B. W. Day, D. P. Curran, *Org. Lett.* **2002**, *4*, 4443–4446.

[5] a) Y. Shin, unpublished results; syntheses of isomers of dictyostatin will be described in a subsequent full paper; b) D. P. Curran, Y. Shin, N. Choy, B. W. Day, R. Balachandran, C. Madiraju, T. Turner, WO 022552, **2004** [*Chem. Abstr.* **2004**, 220327].

[6] I. Paterson, R. Britton, O. Delgado, A. E. Wright, *Chem. Commun.* **2004**, 632–633.

[7] The numbering system of discodermolide is imposed on dictyostatin in this paper to facilitate comparisons.

[8] See preceding Communication in this issue: I. Paterson, R. Britton, O. Delgado, A. Meyer, K. G. Poullennec, *Angew. Chem.* **2004**, *116*, 4729; *Angew. Chem. Int. Ed.*, **2004**, *43*, 4629.

[9] a) A. B. Smith III, T. J. Beauchamp, M. J. LaMarche, M. D. Kaufman, Y. P. Qiu, H. Arimoto, D. R. Jones, K. Kobayashi, *J. Am. Chem. Soc.* **2000**, *122*, 8654–8664; b) Weinreb amide **8** was made in five steps from (2*S*)-3-hydroxy-2-methylpropionic acid methyl ester (Roche ester) in 39% yield. Roche ester was purchased from Aldrich or Mitsubishi-Rayon.

[10] a) N. Choy, Y. Shin, P. Q. Nguyen, D. P. Curran, R. Balachandran, C. Madiraju, B. W. Day, *J. Med. Chem.* **2003**, *46*, 2846–2860; b) J. M. Minguez, S.-Y. Kim, K. A. Giuliano, R. Balachandran, C. Madiraju, B. W. Day, D. P. Curran, *Bioorg. Med. Chem.* **2003**, *11*, 3335–3354.

[11] J. A. Marshall, M. J. Bourbeau, *Org. Lett.* **2003**, *5*, 3197–3199.

[12] a) R. D. Walkup, R. R. Kane, P. D. Boatman Jr, R. T. Cunningham, *Tetrahedron Lett.* **1990**, *31*, 7587–7609; b) R. D. Walkup, J. D. Kahl, R. R. Kane, *J. Org. Chem.* **1998**, *63*, 9113–9116; c) alcohol **9** was made in five steps from Roche ester in 47% yield.

[13] A. Myers, B. Y. Yang, H. Chen, L. McKinstry, D. J. Kopecky, J. Gleason, *J. Am. Chem. Soc.* **1997**, *119*, 6496–6511.

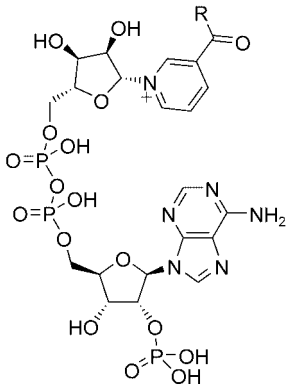
[14] The enantiomer of the methyl ester of **6** is known: a) P. Phukan, S. Sasmal, M. E. Maier, *Eur. J. Org. Chem.* **2003**, 1733–1740; b) M. B. Andrus, A. B. Argade, *Tetrahedron Lett.* **1996**, *37*, 5049–5052; c) ester **11** was made in six steps from 1,3-propanediol in 35% yield.

[15] K. Matsumura, S. Hashiguchi, T. Ikariya, R. Noyori, *J. Am. Chem. Soc.* **1997**, *119*, 8738–8739.

 © 2004 Wiley-VCH Verlag GmbH & Co. KGaA, Weinheim

[16] The nonselective reduction was expressly used to make both isomers because the configuration at this center was at issue.
[17] I. Paterson, G. J. Florence, K. Gerlach, J. P. Scott, N. Sereinig, *J. Am. Chem. Soc.* **2001**, *123*, 9535 – 9544.
[18] W. C. Still, C. Gennari, *Tetrahedron Lett.* **1983**, *24*, 4405 – 4408.
[19] J. Inanaga, H. Kuniko, S. Hiroko, T. Katsuki, M. Yamaguchi, *Bull. Chem. Soc. Jpn.* **1979**, *52*, 1989 – 1994.
[20] Dr. Robert Britton, Cambridge University, kindly recorded 500 MHz NMR spectra of our sample and a natural sample provided by Dr. Amy Wright, Harbor Branch Oceanographic Institute. These spectra are in the Supporting Information.

 © 2004 Wiley-VCH Verlag GmbH & Co. KGaA, Weinheim



1 NAADP; R = OH
2 NADP; R = NH_2

Figure 1. Compounds **1** and **2**.

Natural Products Synthesis

Chemical Synthesis of the Second Messenger Nicotinic Acid Adenine Dinucleotide Phosphate by Total Synthesis of Nicotinamide Adenine Dinucleotide Phosphate**

James Dowden, Christelle Moreau, Richard S. Brown, Georgina Berridge, Antony Galione, and Barry V. L. Potter*

Modulation of intracellular calcium concentration creates signals that control a range of biological pathways. Orchestration of these signals by an array of small molecule second messengers provides the necessary complexity to complement multiple cellular responses, such as activation of the immune system or fertilization.[1] The discovery that nicotinic acid adenine dinucleotide phosphate (NAADP, **1**; Figure 1) potently induces intracellular calcium release in the eggs of sea urchins[2] raised its status, from minor contaminant of nicotinamide adenine dinucleotide phosphate (NADP, **2**), to an important novel second messenger.[3] Recent studies attest to the higher potency of this molecule than the well-known messengers for calcium release [i.e., inositol trisphosphate and cyclic adenosine diphosphoribose (cADPR)] and many of these extend its actions to a wide range of mammalian cells, including cardiac,[4a] skeletal,[4b] T cells,[4c] smooth muscle,[4d] pancreatic acinar[4e] and pancreatic beta cells.[3a,4f,4g]

Compound **1** also appears to play an important role in calcium signaling by triggering and coordinating calcium signals evoked by other calcium-mobilizing messengers. Sensitive radio-receptor assays for tissue measurements of this dinucleotide have been developed,[5] but it is clear that further understanding of its biology will draw heavily on the development of selective molecules to probe this novel signaling pathway and characterize its protein components. A chemo-enzymatic route has so far generated **1** and a small number of analogues from **2** by enzyme-mediated exchange of nicotinamide for nicotinic acid. Clearly, the chemistry that can be performed on this sensitive molecule and compatibility with the enzyme limits the range of available analogues. A synthetic route would provide a wider range of tailored derivatives, such as non-hydrolysable analogues, that could not be achieved by established methods.

We are currently exploring a range of strategies to generate chemical tools with which to interrogate this biological system, including the total synthesis of both dinucleotides. Whitesides and co-workers developed a semisynthetic route to β-nicotinamide adenine dinucleotide (NAD) by using NAD pyrophosphorylase immobilized on polyacrylamide gel, but this relied on a battery of enzymes and reagents to generate stoichiometric quantities of adenosine triphosphate (ATP).[6a] More recently, Lee et al.[6b] reported a practical total chemical synthesis of nicotinamide adenine dinucleotide (NAD) that built upon a much earlier synthesis by Todd and co-workers.[7] Indeed, a number of researchers have developed chemical approaches to NAD derivatives, not least for the preparation of cyclic adenosine 5′-diphosphate ribose.[8] However, the presence of a sensitive 2′-phosphate on a ribose makes the synthesis of **1** or **2** significantly more complex. During early studies Todd and co-workers reported an apparent preparation of **2** inferred from biological evaluation of the complex product mixture but did not successfully isolate the desired coenzyme from the mixture.[7b] Given that this dinucleotide is readily available from commercial sources, it is perhaps not surprising that further developments toward its chemical synthesis are not apparent

[*] Dr. J. Dowden, Dr. C. Moreau, R. S. Brown, Prof. B. V. L. Potter
Wolfson Laboratory of Medicinal Chemistry
Department of Pharmacy & Pharmacology
University of Bath
Claverton Down, Bath BA2 7AY (UK)
Fax: (+44) 1225-386-114
E-mail: j.dowden@bath.ac.uk
G. Berridge, Prof. A. Galione
Department of Pharmacology
University of Oxford (UK)

[**] This research was funded by the Biotechnology and Biology Sciences Research Council and an Engineering and Physical Sciences Research Council (EPSRC) studentship. We acknowledge the use of the EPSRC Chemical Database Service at Daresbury.

Supporting information for this article is available on the WWW under http://www.angewandte.org or from the author.

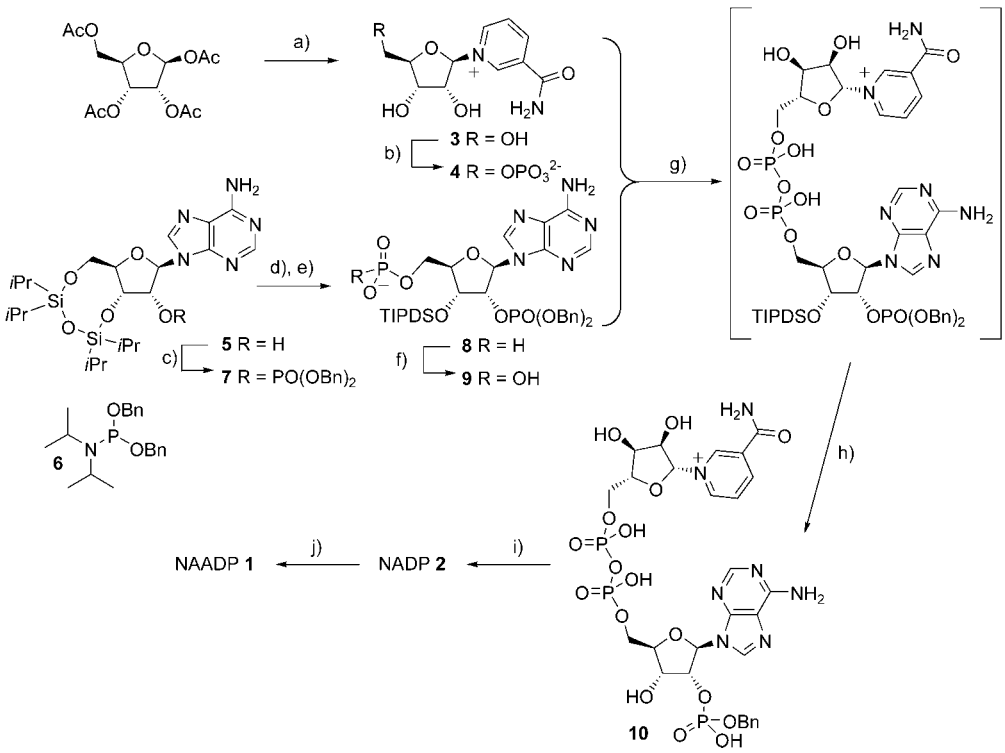
 DOI: 10.1002/anie.200460054 © 2004 Wiley-VCH Verlag GmbH & Co. KGaA, Weinheim

in the general literature. To the best of our knowledge therefore, we describe the first chemical synthesis of **2** as a single isomer, its enzymatic conversion to the potent second messenger **1**, and both chemical characterization and biological proof of the integrity of the latter dinucleotide.

The potentially fragile nature of **2** and its intermediates encouraged a conservative approach that involves the late construction of the pyrophosphate bond by activation of β-nicotinamide mononucleotide (β-NMN, **4**; Scheme 1) and reaction with a suitably decorated adenosine building block. It is known that the 2′-phosphate motif is critical for the activity of **1**[9] and may be involved in its degradation.[10] Structural modifications are likely to be informative and thus we designed a synthesis that was both robust and sufficiently flexible to accommodate future modifications at any position on the NAADP framework.

Compound **4** was generated from tetra-*O*-acetyl-β-D-ribose.[6,11] Reaction between adenosine and 1,3-dichloro-1,1,3,3,-tetraisopropyl disiloxane in pyridine proceeded without complication and lead to simultaneous tethering of the 3′- and 5′-hydroxyls of adenosine, thus permitting unambiguous phosphorylation of the 2′-alcohol. Subsequent elaboration of the 2′-alcohol **5** could be achieved with a range of phosphoramidites, including *bis*(benzyloxy)-*N*,*N*-diisopropylaminophosphane **6** (Scheme 1), to afford the respective phosphate **7** in high yield after oxidation of the intermediate phosphite with *m*-chloroperoxybenzoic acid (*m*CPBA). Imidazolium triflate[12] was used instead of tetrazole to produce a less reactive phosphytilating intermediate that does not react with the purinyl amine, thus saving two steps. Carefully controlled acidic conditions, as previously reported by Scott and co-workers afforded exclusive protodesilylation at the less hindered 5′-position in quantitative yield.[13]

Generally, phosphoramidite chemistry did not proceed in acceptable yields at the 5′-hydroxyl of the precursor, presumably because this position is somewhat crowded. Resorting to the reactive tetrazole-activated phosphoramidites required amine protection and actually led to incorporation of an unwelcome silanol phosphate. It was frustrating that a multitude of protection strategies failed due to unexpected incompatibility with the desired route. Although this chemistry might be optimized to provide acceptable yields of the desired compound, we found that *H*-phosphonate chemistry offered a very effective alternative. Selective 5′-protodesilylation of bis(benzyloxy)phosphate **7**, then treatment of the product with trisimidazolylphosphane, generated in situ from PCl_3 and imidazole, rapidly furnished **8** in quantitative yield (Scheme 1). Oxidation was best achieved by using conditions reported by Sekine and co-workers[14] in a process monitored by ^{31}P NMR spectroscopy, such that the *H*-phosphonate triethylammonium salt ($\delta(^{31}P) = 5.5$ ppm) was treated with *N*,*O*-bis(trimethylsilyl)acetamide (BSA) to afford the bis(trimethysilylphosphonate) ($\delta(^{31}P) = 116$ ppm) after approximately 1 h; the oxidant (1*R*)-(+)-(10-camphorsulfonyl)oxaziridine (CSO) was added to this to generate *bis*(trimethylsilyl)phosphate ($\delta(^{31}P) = -16$ ppm) in about 20 min, which



Scheme 1. a) Nicotinamide, CH_3CN, then TMSOTf, RT; 1.5 h, then MeOH, RT; 1 h; b) $POCl_3$, $PO(OMe)_3$, 0 °C, 4 h; c) **6**, CH_2Cl_2, RT; 3 h, then *m*CPBA, −78 °C, 0.5 h, 98%; d) TFA/H_2O/THF 1:1:4, 0 °C, 3 h, 98%; e) PCl_3, imidazole, Et_3N, THF, 0 °C, 15 mins, then 1 M TEAB aq. pH 7, RT, 15 mins, quant.; f) BSA, $CHCl_3$, RT, 1 h, then CSO, RT, 0.5 h, then MeOH/D_2O, RT, 15 mins, 72%; g) β-NMN, carbonyl diimidazole, Et_3N, DMF, RT, 3 h, then 9, DMF, RT, 16 h; h) 1 M TBAF/THF, AcOH, 0 °C, 1.5 h, 22% i) 10% Pd/C, cyclohexadiene, MeOH/H_2O, RT, 2 h, 77%; j) Nicotinic acid, *Aplysia* ADP-ribosyl cyclase, 1 M NaOAc aq. pH 4, RT, 5 h, 63%.

 © 2004 Wiley-VCH Verlag GmbH & Co. KGaA, Weinheim

slowly hydrolyzed to give the phosphate **9** ($\delta(^{31}P) = 1$ ppm) upon addition of D_2O.

Successful repetition of the approach to NAD reported by Lee and co-workers[6b] encouraged initial exploration of morpholidate activation of the precursor **8**, but attempted conversions were not productive. Production and reaction of the β-NMN imidazolide could be monitored by using ^{31}P NMR spectroscopy ($\delta(^{31}P) = -10.6$ ppm).

Contrary to other reports,[6] we found that bisbenzylphosphate precursor **9** appeared to react with good conversion when monitored by ^{31}P NMR spectroscopy and offered an attractive protecting-group strategy (Scheme 1). Both benzyl groups remained intact during this reaction and the resulting product could not be purified by using our preferred ion-exchange chromatography method. Instead, the crude material was treated with 1M TBAF in THF/AcOH to effect simultaneous cleavage of the silanol ether and one of the benzyl protecting groups to yield monobenzyl NADP **10** after ion-exchange chromatography. Although there was no evidence of migration of the 2′-phosphate, the overall yield of around 22% for these two steps is modest, but is comparable to many literature reports as pyrophosphate bond formation and isolation of the resulting product is generally difficult and yields are highly variable. An alternative route that employs a bis(2-cyanoethyl) protected precursor related to **9** gave yields in the range of 60–80% for the pyrophosphate coupling and we are currently exploring improvements of this route to achieve useful conversion. Nonetheless, transfer hydrogenation of **10** yielded material that was identical to commercial preparations of β-NADP **2** in satisfactory (77%) yield.

With a wider objective in mind we chose to convert synthetic NADP **2** into the target NAADP **1** to test its behavior in a relevant biological system. Base exchange to replace nicotinamide with nicotinic acid was achieved by using an excess of the latter and crude *Aplysia* ADP-ribosyl cyclase [enzyme commission number E.C.3.2.2.5] prepared from *Aplysia* ovotestis[15] to provide NAADP **1** in 63% yield.

The ability of **1** to induce release of Ca^{2+} ions was tested by using a cell-free system derived from the eggs of sea urchins. Aliquots of homogenates of sea-urchin eggs comprise vesicles derived from the intracellular stores that sequester calcium when supplemented with an ATP-regenerating system. Concentration-dependent calcium release is observed when this mixture is challenged with second messengers, such as **1**, which can be measured by using cuvette-based fluorimetry and the calcium reporter dye fluo-3.[16] Synthetic NAADP, carefully quantified by using total phosphate assay prior to evaluation,[17] potently induced calcium release in an identical manner to "authentic" NAADP prepared from commercial NADP (Figure 2). Both preparations display an important characteristic of this signaling pathway that occurs at subthreshold concentrations of NAADP in homogenate of sea-urchin eggs. They both potently deactivate the calcium store in a time dependent manner, so that further challenge with NAADP does not lead to significant calcium release (Figure 3). This property allows competition binding experiments that measure the extent that nonlabeled NAADP displaces subthreshold concentrations of [^{32}P]NAADP (0.2 nM) from the putative receptor (Figure 4).

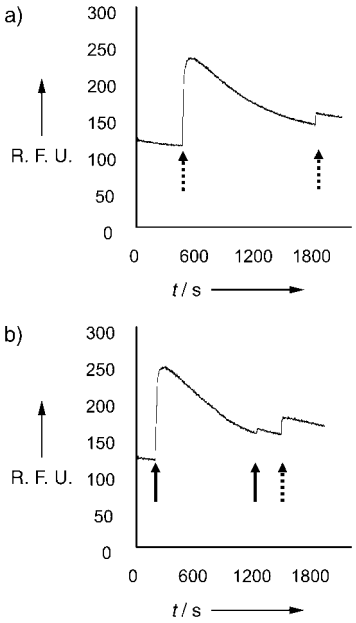


Figure 2. Ca^{2+}-ion release from homogenate of sea-urchin eggs by 100 nM authentic NAADP (dotted arrows) or 100 nM synthetic NAADP, **1** (solid arrows): Samples diluted to 2.5% in GluIM in the presence of regenerating system and kept at 17°C with agitation for 3 h to facilitate Ca^{2+}-ion uptake into stores. Ca^{2+}-ion release determined by an increase of Fluo-3 fluorescence at 526 nm; data expressed as released [Ca^{2+}], determined by fluorescence in arbritrary units; $n = > 3$ for each point. R. F. U. = relative fluorescence units.

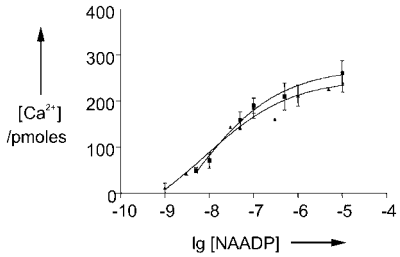


Figure 3. Inhibition of NAADP-induced Ca^{2+}-ion release by authentic NAADP (squares) or synthetic NAADP **1** (triangles) in the homogenate of sea-urchin eggs: Samples diluted to 2.5% in GluIM in the presence of a regenerating system and kept at 17°C with agitation for 3 h to facilitate Ca^{2+}-ion uptake into stores. Ca^{2+}-ion release determined by an increase of Fluo-3 fluorescence at 526 nm; data expressed as pmoles of Ca^{2+}-ions released; $n = > 3$ for each point.

In summary, the strategy of using 1,1,3,3-tetraisopropyl disiloxane protecting groups offers a robust (70%, five steps from adenosine) route to 2′,5′-adenosine diphosphate precursors and the potential to incorporate a range of functionality at these positions. Pyrophosphate formation requires some further development, but affords benzyl protected precursor **10** that, after transfer hydrogenation, leads to the first total chemical synthesis of **2**. This flexible route to 2′-phosphate furnished dinucleotides will allow the development of new chemical tools that probe biological systems at the molecular level. Analogues of **1** are of immediate importance for dissecting this novel and important second

 © 2004 Wiley-VCH Verlag GmbH & Co. KGaA, Weinheim

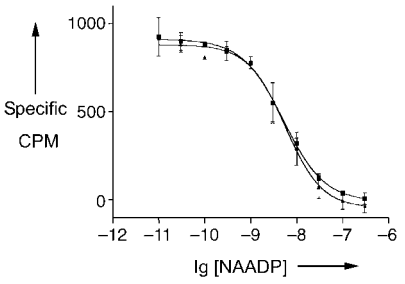


Figure 4. Competitive displacement of [^{32}P]NAADP (0.2 nM) with authentic NAADP (squares) or synthetic NAADP **1** (triangles) from sea-urchin homogenate: Samples diluted in GluIM, then 0.2 nM [^{32}P]NAADP in the presence of increasing NAADP added and incubated at room temperature for 20 mins. Samples filtered through Whatman GF/B filters to separate bound and free [^{32}P]NAADP ligand. Nonspecific binding is defined by incubation of the homogenate in the presence of 10 μM NAADP; $n = 3 \pm$ SEM; data expressed as specific cpm.

messenger pathway. Enzymatic conversion into **1** is confirmed both by identical behavior when evaluated for Ca^{2+}-release properties against sea-urchin-egg homogenate and spectroscopic characterization. Expansion of the route to include suitably protected beta-nicotinic acid mononucleotide (β-NAMN) towards the first total chemical synthesis of **1** and improved isolated yields of pyrophosphate will be reported in due course.

Experimental Section

2: Benzyl NADP **9** (15 mg, 0.018 mmol), 10% Pd/C (15 mg) and cyclohexadiene (100 μL) in a degassed mixture of H_2O:MeOH (3:1, v/v, 2 mL) were stirred at room temperature under an argon atmosphere for 3 h, after which the palladium was filtered and the resulting filtrate subject to ion-exchange chromatography (AG MP-1) by using a 150 mM aqueous TFA gradient. Fractions were combined and lyophilized to yield **2** as a white powder (10 mg, 77%): ^{1}H NMR (400 MHz, D_2O): $\delta = 9.29$ (s, 1H; H_N2), 9.11 (d, $J = 6.3$ Hz, 1H; H_N6), 8.78 (d, $J = 8.2$ Hz, 1H; H_N4), 8.41 (s, 1H; H_A8), 8.23 (s, 1H; H_A2), 8.13 (m, 1H; H_N5), 6.11 (d, $J = 5.9$ Hz, 1H; H_A1'), 6.01 (d, $J = 5.1$ Hz, 1H; H_N1'), 4.96 (m, 1H; H_A2'), 4.49 (m, 1H; H_A3'), 4.44 (br s, 1H; H_N4'), 4.40 (m, 1H; H_N2'), 4.31 (m, 1H; H_N3'), 4.27 (m, 1H; H_A4'), 4.26 (m, 1H; $H_A5'_a$), 4.12 ppm (m, 3H; $H_A5'_b$, H_N5'); ^{31}P NMR (162 MHz, D_2O): $\delta = -0.73$ and -11.42 to -11.84 ppm (br m); MS [FAB+]: *m/z* (%): 744.0 (50) [M^+−H]; found 744.0842 [M^+−H] $C_{21}H_{29}N_7O_{17}P_3$ requires 744.0833.

1: NADP **2** (4 mg 5 mM) and 100 mM nicotinic acid (12 mg) in a 100 mM aqueous AcOH/NaOH (pH 4, 1 mL) were incubated with 5 μL of ADP-ribosyl cyclase at room temperature. After 5 h, HPLC analysis (AG MP-1, aqueous TFA) showed complete consumption of NADP and formation of NAADP ($R_T = 16.8$ mins). The crude mixture was purified on an ion-exchange resin (AG MP-1) by using an aqueous TFA gradient (150 mM), the product eluted at 15% TFA. Combined fractions were evaporated under vacuum at room temperature and lyophilized overnight to afford **1** as a white powder (2.5 mg, 63%): ^{1}H NMR (400 MHz, D_2O): $\delta = 9.32$ (s, 1H; H_N2), 9.17 (d, $J = 5.9$ Hz, 1H; H_N6), 8.87 (d, $J = 8.1$ Hz, 1H; H_N4), 8.45 (s, 1H; H_A8), 8.28 (s, 1H; H_A2), 8.14 (m, 1H; H_N5), 6.14 (d, $J = 5.5$ Hz, 1H; H_A1'), 6.03 (d, $J = 5.1$ Hz, 1H; H_N1'), 4.97 (m, 1H; H_A2'), 4.50 (m, 1H; H_A3'), 4.44 (br, 1H; H_N4'), 4.41 (m, 1H; H_N2'), 4.30 (m, 1H; H_N3'), 4.27–4.22 (m, 2H; H_A4' and $H_A5'_a$), 4.12–4.10 ppm (m, 3H; $H_A5'_b$, H_N5'); ^{13}C NMR (100 MHz, D_2O): $\delta = 165.4$ (CO_2H), 149.8 (C_A4), 148.3 (C_A6), 147.0 (CH_A2), 144.6 (CH_N6), 142.7 (CH_N4), 142.5(CH_A8) 141.8 (CH_N2), 133.8 (C_N3), 128.6 (CH_N5), 118.4 (C_A5), 99.7 (CH_N1'), 86.8 (CH_A4'), 83.9 (CH_A1'), 77.4 (CH_N2'), 76.8 (CH_A2'), 73.8 (CH_N4'), 70.3 (CH_N3'), 69.9 (CH_A3'), 65.1 and 64.8 ppm ($2 \times CH_2$); ^{31}P NMR (162 MHz, D_2O): $\delta = 1.47$ and -9.40 to -9.80 ppm (br m); MS [FAB+] 744.8 [M^+−H]; found 745.0658 [M^+−H $C_{21}H_{29}N_7O_{17}P_3$ requires 745.0673.

Received: March 19, 2004

Keywords: biological activity · calcium · intracellular signaling · nucleotides · total synthesis

[1] M. J. Berridge, M. D. Bootman, H. L. Roderick, *Nat. Rev. Mol. Cell Biol.* **2003**, *4*, 517–529.
[2] H. C. Lee, *Curr. Biol.* **2003**, *13*, R186-R188.
[3] a) R. Masgrau, G. C. Churchill, A. J. Morgan, S. J. H. Ashcroft, A. Galione, *Curr. Biol.* **2003**, *13*, 247–251; b) G. C. Churchill, J. S. O'Neill, R. Masgrau, S. Patel, J. M. Thomas, A. A. Genazzani, A. Galione, *Curr. Biol.* **2003**, *13*, 125–128.
[4] a) J. Bak, R. A. Billington, G. Timar, A. C. Dutton, A. A. Genazzani, *Curr. Biol.* **2001**, *11*, 987–990; b) M. Hohenegger, J. Suko, R. Gscheidlinger, H. Drobny, A. Zidar, *Biochem. J.* **2002**, *367*, 423–431; c) A. H. Guse, *Cyclic ADP-Ribose NAADP* **2002**, 301–318; d) F. X. Boittin, A. Galione, A. M. Evans, *Circ. Res.* **2002**, *91*, 1168–1175; e) J. M. Cancela, G. C. Churchill, A. Galione, *Nature* **1999**, *398*, 74–76; f) J. D. Johnson, S. Misler, *Proc. Natl. Acad. Sci. USA* **2002**, *99*, 14566–14571; g) K. J. Mitchell, F. A. Lai, G. A. Rutter, *J. Biol. Chem.* **2003**, *278*, 11057–11064.
[5] A. Galione, J. M. Cancela, G. C. Churchill, A. A. Genazzani, C. Lad, J. M. Thomas, H. L. Wilson, D. A. Terrar in *Methods in Calcium Signalling* (Ed.: J. W. J. Putney), CRC, Boca Raton, FL, **2000**, pp. 249–296.
[6] a) D. R. Walt, M. A. Findeis, V. M. Rios-Mercadillo, J. Auge, G. M. Whitesides, *J. Am. Chem. Soc.* **1984**, *106*, 234–239; b) J. Lee, H. Churchil, W. B. Choi, J. E. Lynch, F. E. Roberts, R. P. Volante, P. J. Reider, *Chem. Commun.* **1999**, 729–730.
[7] a) L. J. Haynes, N. A. Hughes, G. W. Kenner, A. Todd, *J. Chem. Soc.* **1957**, 3727–3732; b) N. A. Hughes, G. W. Kenner, A. Todd, *J. Chem. Soc.* **1957**, 3733–3738.
[8] V. C. Bailey, J. K. Sethi, S. M. Fortt, A. Galione, B. V. L. Potter, *Chem. Biol.* **1997**, *4*, 51–61.
[9] H. C. Lee, R. Aarhus, *J. Biol. Chem.* **1997**, *272*, 20378–20383.
[10] G. Berridge, R. Cramer, A. Galione, S. Patel, *Biochem. J.* **2002**, *365*, 295–301.
[11] S. Tanimori, T. Ohta, M. Kirihata, *Bioorg. Med. Chem. Lett.* **2002**, *12*, 1135–1137.
[12] Y. Hayakawa, M. Kataoka, *J. Am. Chem. Soc.* **1998**, *120*, 12395–12401.
[13] X. F. Zhu, H. J. Williams, A. I. Scott, *Tetrahedron Lett.* **2000**, *41*, 9541–9545.
[14] T. Wada, A. Mochizuki, Y. Sato, M. Sekine, *Tetrahedron Lett.* **1998**, *39*, 7123–7126.
[15] M. E. Migaud, R. L. Pederick, V. C. Bailey, B. V. L. Potter, *Biochemistry* **1999**, *38*, 9105–9114.
[16] A.Minta, J. P. Y. Kao, R. Y. Tsien, J. Biol. Chem. 1989, 264, 8171–8178
[17] D. Lampe, C. S. Liu, B. V. L. Potter, *J. Med. Chem.* **1994**, *37*, 907–912.

 © 2004 Wiley-VCH Verlag GmbH & Co. KGaA, Weinheim

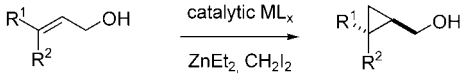
Cyclopropanations

Enantioselective Organocatalytic Cyclopropanation via Ammonium Ylides**

*Charles D. Papageorgiou, Maria A. Cubillo de Dios, Steven V. Ley, and Matthew J. Gaunt**

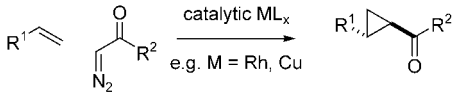
The cyclopropane motif is a common feature in the synthesis of complex molecules and in medicinal chemistry owing to a unique combination of reactivity and structural properties.[1] These properties have made the preparation of cyclopropanes an attractive target for new methodology development. Despite the many processes for the synthesis of functionalized cyclopropanes, there are surprisingly few general catalytic enantioselective methods.[2] Of the methods available, the carbenoid-mediated reactions[2c–e] are most often utilized [Eqs. (1,2)]; however, there are isolated examples of catalytic-ylide-based enantioselective cyclopropanations.[2a,b,e]

Lewis Acid Catalysis: Simmons-Smith type cyclopropanation



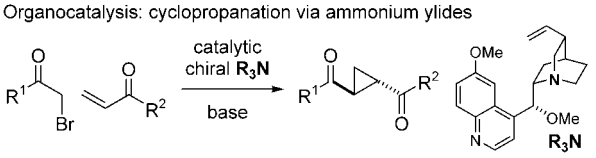
(1)

Metal Catalysis: metallocarbenoid-mediated cyclopropanation



(2)

Organocatalysis: cyclopropanation via ammonium ylides

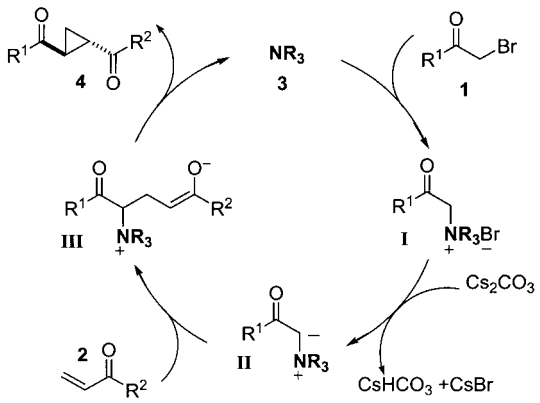


(3)

Recently, we described a cyclopropanation process with a reaction that was mediated by a stoichiometric quantity of a nucleophilic tertiary amine through the formation of an ammonium ylide.[3] We also developed an intramolecular version of this reaction that forms [*n*.1.0]bicyloalkanes as single diastereomers.[3b] Herein, we report the evolution of our studies and the resulting development of a general and practical intermolecular enantioselective organocatalytic cyclopropanation reaction via ammonium ylides. This process produces a range of functionalized molecules with excellent diastereo- and enantioselectivity and as either enantiomer [Eq. (3)].

This enantioselective catalytic cyclopropanation process via ammonium ylides[4] has a number of advantages over its counterparts: There are no transition metals involved in the reaction, and the starting materials are readily available and conveniently handled.[5] Furthermore, the number of known chiral amines represents a significant pool from which potential catalysts can be selected.

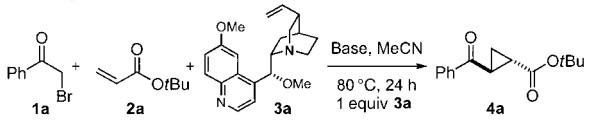
In this system, an α-bromo carbonyl compound **1** undergoes S_N2 displacement with the tertiary amine catalyst **3** to form a quaternary ammonium salt **I**. Deprotonation with mild base forms the ylide **II**, which undergoes conjugate addition to alkene **2** to form **III**. Finally, *3-exo-tet* cyclization generates the cyclopropane **4** and reforms the catalyst (Scheme 1).



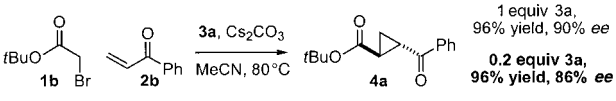
Scheme 1. Proposed catalytic cycle.

To assess the viability of this intermolecular process, reaction conditions were investigated with phenacyl bromide (**1a**), acrylate **2a**, and a stoichiometric quantity of quinine derivative **3a** (Table 1). By screening bases it became apparent that the larger the metal cation (Na→Cs), the better the yield of cyclopropane **4a**, although the enantioselectivity was lower. However, reversing the role of the starting

Table 1: Optimization of reaction conditions.



Entry	Base	Yield [%]	*ee* [%]
1	NaOH	**58**	**94**
2	Na_2CO_3	**19**	**96**
3	Na_2CO_3, [15]crown-5	**57**	**86**
4	K_2CO_3	**61**	**86**
5	Rb_2CO_3	**77**	**74**
6	Cs_2CO_3	**84**	**71**



[*] C. D. Papageorgiou, M. A. Cubillo de Dios, Prof. Dr. S. V. Ley, Dr. M. J. Gaunt
Department of Chemistry
University of Cambridge
Lensfield Road, Cambridge, CB2 1EW (UK)
Fax: (+44) 1223-336-442
E-mail: mjg32@cam.ac.uk

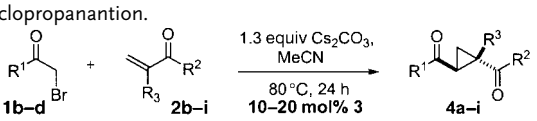
[**] We gratefully acknowledge Pfizer Global Research and Development (Dr. Blanda Stammen, Sandwich (UK)) and the EPSRC for an Industrial Case Award (to C.D.P), Novartis (to S.V.L.), and Magdalene College and Ramsay Memorial Trust (to M.J.G.) for Research Fellowships.

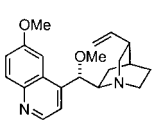
Supporting information for this article is available on the WWW under http://www.angewandte.org or from the author.

 DOI: 10.1002/anie.200460234 © 2004 Wiley-VCH Verlag GmbH & Co. KGaA, Weinheim

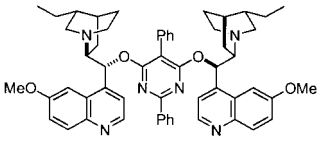
materials so that *tert*-butyl bromoacetate (**1b**) reacted with phenyl enone **2b** in the presence of **3a** resulted in a dramatic change to the outcome of the reaction: cyclopropane **4a** was isolated in 96% yield with 90% *ee* when 1 equivalent of **3a** was used. Most importantly, when the amount of tertiary amine was decreased to 0.2 equivalents, the reaction produced the cyclopropane **4a** in 96% yield with 86% *ee* (same enantiomer as Table 1, entry 6).[6]

Table 2: Enantioselective organocatalytic cyclopropanantion.

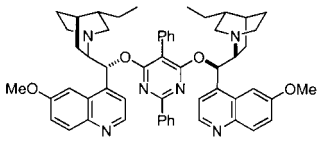




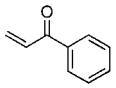
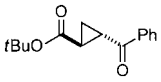
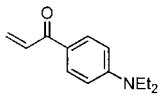
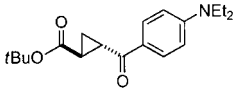
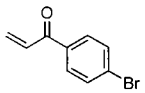
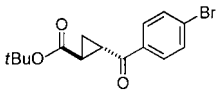
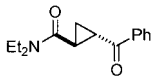
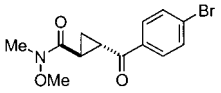
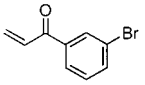
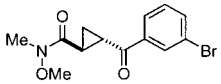
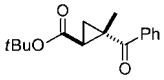
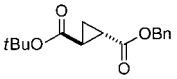
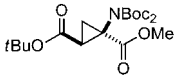
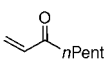
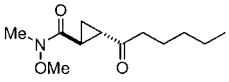
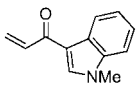
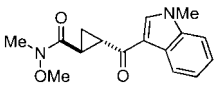
3b



3c



3d

Entry[a]	R^1	Alkene		Product[b]		Catalyst	Yield [%]	*ee* [%]
1	O*t*Bu (**1b**)		**2b**		**4a**	**3a** **3b**	96 92	86 (+) 88 (−)
2	O*t*Bu (**1b**)		**2c**		**4b**	**3a** **3b**	73 73	84 (+) 84 (−)
3	O*t*Bu (**1b**)		**2d**		**4c**	**3a**	83	85 (+)
4	NEt_2 (**1c**)		**2b**		**4d**	**3a** **3b**	94 85	97 (+) 97 (−)
5	NMe(OMe) (**1d**)		**2d**		**4e**	**3c** **3d**	67 74	96 (+) 97 (−)
6	NMe(OMe) (**1d**)		**2e**		**4f**	**3c** **3d**	60 60	96 (+) 97 (−)
7	O*t*Bu (**1b**)		**2f**		**4g**	**3a**	63	92 (+)
8	O*t*Bu (**1b**)		**2g**		**4h**	**3a**	75	80 (+)
9	O*t*Bu (**1b**)		**2h**		**4i**	**3a** **3d** **3a**	90 83 53[c]	97 (+) 90 (−) 96 (+)
10	NMe(OMe) (**1d**)		**2i**		**4j**	**3a** **3d**	65 77	96 (+) 92 (−)
11[d]	NMe(OMe) (**1d**)		**2j**		**4k**	**3c** **3d**	74 84	95 (+) 94 (−)

[a] **1** (1 equiv) and **2** (1.1 equiv) were added to Cs_2CO_3 and **3** (20 mol%) in MeCN (0.25 M) and stirred at 80 °C for 24 h. [b] (+)-enantiomer shown. [c] **3a**: 1 mol%. [d] **1d**: 2 equiv. Boc = *tert*-butoxycarbonyl.

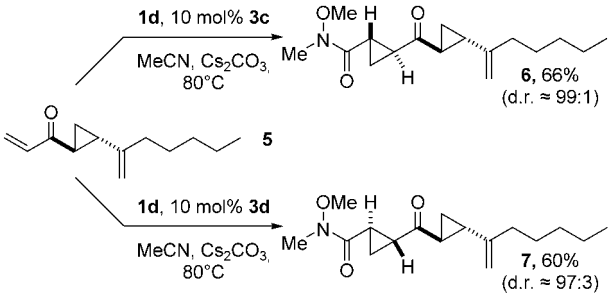
 © 2004 Wiley-VCH Verlag GmbH & Co. KGaA, Weinheim

Having identified an asymmetric process, its scope was investigated with the aim of producing a general catalytic enantioselective cyclopropanation reaction. Table 2 shows the range of cyclopropanes that can be formed by this method. A range of readily available cinchona alkaloids catalyzed the reaction. Importantly, both enantiomers of the cyclopropanes can be accessed in excellent yield and enantioselectivity by using either of the pseudoenantiomeric quinine or quinidine derivatives.[7] Interestingly, the use of alkaloid derivatives **3c** and **3d**[7] (10 mol%) often gave improved yield and enantioselectivity when **3a** or **3b** failed to give good results.

Bromoacetate **1b** reacts with a range of aryl vinyl ketones to form cyclopropanes **4a–c** in good yield and with excellent *ee* in the presence of 20 mol% of catalyst **3a**. The opposite enantiomer is also accessible by using the quinidine-derived catalyst **3b** (Table 2, entries 1–3). The role of these catalysts in the stereochemical outcome of the reaction is currently under investigation. It was also noticed that in some cases the slow addition of **1** and **2** to a solution of the catalyst resulted in higher yields. Changing the bromoacetate reagent **1b** to acetamide **1c** in the reaction with enone **2b** gave cyclopropane **4d** in excellent yield with 93% *ee*. The more versatile Weinreb amide derivative **1d** also produces the cyclopropanes with excellent *ee* values for **4e–f**.[8] High levels of substitution can be incorporated into the cyclopropane by using disubstituted enones or acrylates. For example, trisubstituted cyclopropane **4g** is produced in good yield and with high enantioselectivity. Aminocyclopropane **4i** was also formed in excellent yield and enantioselectivity, thus reflects the power of this process, which generates a high level of functionalization and stereocontrol on the cyclopropane core. The catalyst loading could also be lowered to 1 mol%, producing cyclopropane **4i** in 53% yield (53 catalyst turnovers) after 48 h without compromising the enantioselectivity. Cyclopropanation with bromomethyl alkyl ketones (**1**; R^1 = alkyl) was problematic and produced the cyclopropane in low yields. However, the application of the alkyl-substituted enones, such as **2i**, alleviated this problem, furnishing **4j** in excellent yield and enantioselectivity. Finally, the indole-derived cyclopropane **4k** was formed in good yield and with very high *ee* values, demonstrating the suitability of the reaction for the preparation of medicinally relevant compounds. To the best of our knowledge these results represent the first general intermolecular enantioselective organocatalytic cyclopropanation reaction.

Although it was not possible to form diketocyclopropanes directly by using the described method, they were accessible from the amide **4j**.[6] Thus, enone **5** could be readily generated and subjected to a second cyclopropanation reaction to form structurally and functionally complex biscyclopropanes **6** and **7** through reaction with **1d** (Scheme 2). Interestingly, catalyst **3c** produced **6** as a single diastereomer (d.r. ≈99:1), whereas catalyst **3d** gave only **7** (d.r. 97:3), suggesting that the stereoselectivity is controlled completely by the catalyst.

In summary, we have developed a new enantioselective organocatalytic cyclopropanation reaction. Importantly, the cyclopropanes can be produced as either enantiomer by using the quinine or quinidine series of cinchona alkaloid catalysts. The reaction is applicable to a range of substrates with a variety of versatile functional groups. We are currently investigating expansion of the scope of the reaction and applications to the synthesis of natural and non-natural products.



Scheme 2. Synthesis of biscyclopropanes.

Received: April 6, 2004

Keywords: asymmetric synthesis · cyclopropanation · nitrogen heterocycles · organocatalysis · ylides

[1] a) H.-U. Reissig, R. Zimmer, *Chem. Rev.* **2003**, *103*, 1151; b) J. Pietruszka, *Chem. Rev.* **2003**, *103*, 1051; c) W. A. Donaldson, *Tetrahedron* **2001**, *57*, 8589.

[2] For examples of asymmetric ylide-mediated cyclopropanation reactions, see: a) V. K. Aggarwal, E. Alonso, G. Fang, M. Ferrara, G. Hynd, M. Porcelloni, *Angew. Chem.* **2001**, *113*, 1482; *Angew. Chem. Int. Ed.* **2001**, *40*, 1433; b) W.-W. Lioa, K. Li, Y. Tang, *J. Am. Chem. Soc.* **2003**, *125*, 13030; for examples of carbenoid-mediated processes, see: c) S. E. Denmark, S. P. O'Connor, S. R. Wilson, *Angew. Chem.* **1998**, *110*, 1162; *Angew. Chem. Int. Ed.* **1998**, *37*, 1149, and references therein; d) A. B. Charette, C. Molinaro, C. Brochu, *J. Am. Chem. Soc.* **2001**, *123*, 12168; e) for a review, see: H. Lebel, J.-F. Marcoux, C. Molinaro, A. B. Charette, *Chem. Rev.* **2003**, *103*, 977.

[3] a) C. D. Papageorgiou, S. V. Ley, M. J. Gaunt, *Angew. Chem.* **2003**, *115*, 852; *Angew. Chem. Int. Ed.* **2003**, *42*, 828; b) N. Bremeyer, S. C. Smith, S. V. Ley, M. J. Gaunt, *Angew. Chem.* **2004**, *116*, 2735; *Angew. Chem. Int. Ed.* **2004**, *43*, 2681.

[4] a) S. S. Bhattacargee, H. Ila, H. Junjappa, *Synthesis* **1982**, 301; b) A. Jonczyk, A. Konarska, *Synlett* **1999**, 1085.

[5] a) P. I. Dalko, L. Moisan, *Angew. Chem.* **2001**, *113*, 3840; *Angew. Chem. Int. Ed.* **2001**, *40*, 3726; b) S. P. Brown, M. P. Brochu, C. J. Sinz, D. W. C. MacMillan, *J. Am. Chem. Soc.* **2003**, *125*, 10800; c) P. Chandrakala, H. Linh, N. Vignola, B. List, *Angew. Chem.* **2003**, *115*, 2891; *Angew. Chem. Int. Ed.* **2003**, *42*, 2785, and references therein.

[6] See Supporting Information for full experimental information relating to stereochemical assignment and the determination of *ee* values. General experimental procedure: One-pot method: The catalyst **3a**, **3b** (0.2 equiv) or **3c**, **3d** (0.1 equiv), was added to a solution of the α-bromo carbonyl compound (1.0 equiv), the alkene (1.2 equiv), and Cs_2CO_3 (1.2 equiv) in MeCN (0.25 M) and stirred at 80 °C for 24 h. The reaction was quenched with aqueous HCl (1 M) and extracted three times with Et_2O or EtOAc. The combined organic phases were washed with a saturated aqueous solution of $NaHCO_3$, dried ($MgSO_4$), and concentrated under reduced pressure. The residue was purified by flash column chromatography. Slow addition method: A solution of the α-bromo carbonyl compound (1.0 equiv) and the alkene (1.2 equiv) in MeCN (0.25 M with respect to the α-bromo carbonyl com-

 © 2004 Wiley-VCH Verlag GmbH & Co. KGaA, Weinheim

pound) was added to a solution of the catalyst **3a**, **3b** (0.2 equiv) or **3c**, **3d** (0.1 equiv) and Cs_2CO_3 (1.2 equiv) in MeCN (0.25 M) at 80 °C over 20 h by means of a syringe pump. The syringe was rinsed with MeCN and the reaction mixture stirred for a further 4 h. The reaction was quenched with aqueous HCl (1M) and extracted three times with Et_2O or EtOAc. The combined organic phases were washed with a saturated aqueous solution of $NaHCO_3$, dried ($MgSO_4$), and concentrated under reduced pressure. The residue was purified by flash column chromatography.

[7] For a recent review, see: S. France, D. J. Guerin, S. J. Miller, T. Leckta, *Chem. Rev.* **2003**, *103*, 2985.

[8] The amide derivatives **1c–d** give higher enantioselectivities (5–10%) than reactions with **1b**, although the yields are slightly lower (10–20%).

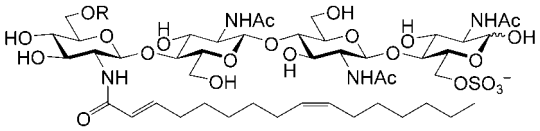
 © 2004 Wiley-VCH Verlag GmbH & Co. KGaA, Weinheim

Glycolipid Mimics

Simple Synthesis of Nodulation-Factor Analogues Exhibiting High Affinity towards a Specific Binding Protein**

*Nathalie Grenouillat, Boris Vauzeilles, Jean-Jacques Bono, Eric Samain, and Jean-Marie Beau**

Rhizobial glycolipids (lipochitooligosaccharides (LCOs), also called nodulation (Nod) factors) are important signaling molecules involved in the establishment of symbiosis with legumes.[1] This association results in the formation of rhizobia-infected nodules on plant roots in which atmospheric nitrogen is reduced to ammonia for the benefit of the plant. These nodulation factors represent a large family of lipo-oligosaccharides consisting of a chitin fragment (three–five *N*-acetyl-D-glucosamine units) with an *N*-acyl chain attached to the nonreducing unit and a variety of additional substituents.[1a] The variations are characteristic of each bacterial strain and define the high degree of specificity in the legume–rhizobia interaction. One of the most studied models is the symbiosis of *Sinorhizobium meliloti* and alfalfa (*Medicago sativa*) in which the major bacterial signal molecule **1** (Scheme 1) contains four D-glucosamine residues with a 6-



1 R = Ac; NodSm-IV (Ac, S)
2 R = H; NodSm-IV (S)

Scheme 1. Structures of the major nodulation factors produced by *Sinorhizobium meliloti*.

O-acetyl group and an *N*-(2*E*,9*Z*)-hexadecadienoyl side chain at the nonreducing residue and an essential 6-*O*-sulfate group at the reducing unit which is the main determinant of the host specificity in *M. sativa*.[2]

Although highly active, signal molecule **2** is approximately ten times less active than the acetylated derivative **1** in morphogenic activity. However, since it is more stable, **2** is more suitable for biological studies. Structure–function relationship studies have shown that the correct nature of the lipid chain, in totally synthetic molecules,[3] is essential for triggering an optimal morphogenic activity in *M. sativa* roots.[4] Moreover, the length and the structure of the lipid chain play a role in the high-affinity binding of LCOs to a Nod factor binding site (NFBS2) characterized in cell suspension cultures of legumes.[5–7]

As a step forward in the search for modified molecules for the study of the Nod factor perception mechanisms by the plant, we now report a simple synthesis of analogues by using metabolically engineered bacterial cells, a method that avoids the complexity of total synthetic approaches from *N*-acetyl-D-glucosamine monomers.[3,8] We further demonstrate that the incorporation of a substituted benzamide (see **B** in Scheme 2) provides new analogues able to interact with a putative LCO receptor at nanomolar concentrations.



Scheme 2. An alkoxybenzamide (X = O) or benzylamine (X = H_2) structure **B** can mimic the natural α,β-unsaturated amide **A**.

The aromatic motif was selected because a) it leads to benzamides that are potentially more stable chemically and metabolically than the natural conjugated amides, b) it makes it possible to introduce a photoactivatable group at a strategic position, and c) it is readily prepared from commercial precursors. Although replacement of unsaturated bonds in lipids by aromatic derivatives is frequently used to produce molecular probes and agonists or antagonists of bioactive molecules, this substitution combining an aromatic motif and

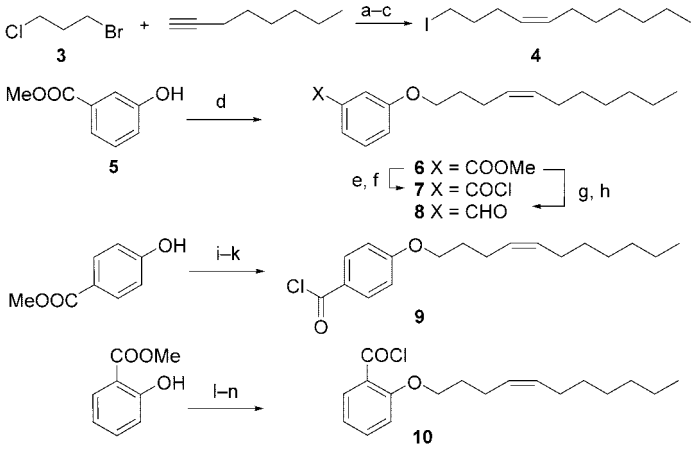
[*] N. Grenouillat, Dr. B. Vauzeilles, Prof. J.-M. Beau
Université Paris-Sud
Laboratoire de Synthèse de Biomolécules
associé au CNRS, Institut de Chimie Moléculaire et des Matériaux
91405 Orsay Cedex (France)
Fax: (+33) 1-6985-3715
E-mail: jmbeau@icmo.u-psud.fr
Dr. J.-J. Bono
Pôle de Biotechnologie Végétale
UMR 5546 CNRS–Université Paul Sabatier
24, Chemin de Borde Rouge, BP 17 Auzeville
31326 Castanet-Tolosan (France)
Dr. E. Samain
Centre de Recherches sur les Macromolécules Végétales
UPR CNRS 5301, BP 53
38041 Grenoble Cedex 9 (France)

[**] We are grateful to Rhone-Poulenc SA (contract no. 041313.00), Aventis CropScience SA, and Bayer CropScience SA for the financial support of this study.

 © 2004 Wiley-VCH Verlag GmbH & Co. KGaA, Weinheim DOI: 10.1002/anie.200460275

a heteroatom to mimic a carbon–carbon double bond *and* a methylene group in the acyclic system has, to our knowledge, never been described.[9]

We started our synthesis by preparing the unsaturated fatty acid analogues **6**, **9**, and **10** as outlined in Scheme 3.

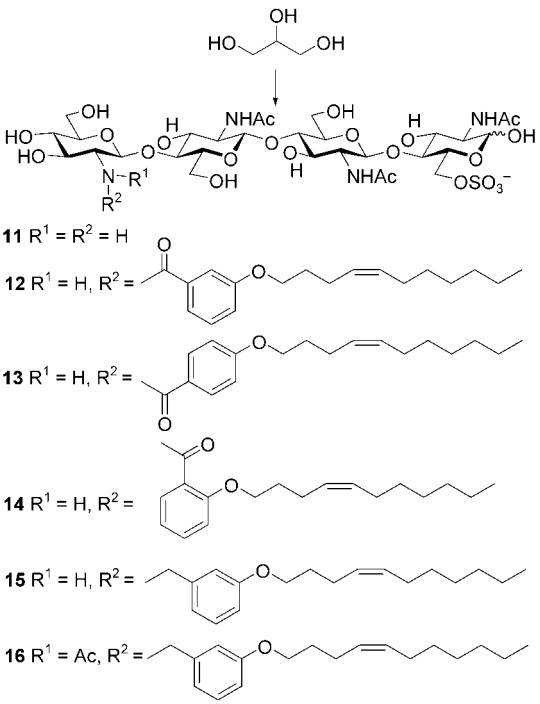


Scheme 3. Synthesis of the side-chain precursors. a) BuLi, HMPA (1 equiv), THF, −78 °C then reflux, 4 h, 80%; b) Lindlar catalyst, quinoline, cyclohexane, H_2, 25 °C, 7 h, 94%; c) NaI (3 equiv), acetone, reflux, 24 h, 89%; d) **4** (1.1 equiv), K_2CO_3 (1.1 equiv), DMF, 90 °C, 4 h, 76%; e) NaOH (2 equiv), MeOH, reflux, overnight, 96%; f) oxalyl chloride, cat. DMF, CH_2Cl_2, 25 °C, 2 h, 99%; g) $LiAlH_4$ (2 equiv), Et_2O, RT, 1.5 h, 99%; h) PCC (2 equiv), CH_2Cl_2, reflux, 1 h, 99%; i) as (d), 7 h, 79%; j) as (e), 98%; k) as (f), 99%; l) as (d), 8 h, 66%; m) as (e), 24 h, 99%; n) as (f), 99%. DMF = *N*,*N*-dimethylformamide, HMPA = hexamethylphosphoramide, PCC = pyridinium chlorochromate.

Coupling of lithiated 1-octyne with commercially available 1-bromo-3-chloropropane (**3**), followed by a Lindlar reduction and a Cl/I exchange gave the expected unsaturated iodide **4**. Alkylation of methyl 3-hydroxybenzoate (**5**) with iodide **4** provided ester **6**, which could be transformed into acid chloride **7** or aldehyde **8**. The *p*- and *o*-isomeric acid chlorides **9** and **10** were also prepared by following the same synthetic sequence from the corresponding *p*- and *o*-substituted phenols.

The carbohydrate segment, the sulfated tetramer **11** (Scheme 4), was easily prepared by cultivating, at high cell density, recombinant *Escherichia coli* strains coexpressing the *nodBC* genes (encoding the chitooligosaccharide synthase and the chitooligosaccharide *N*-deacetylase) and the *nodH* gene (encoding the chitooligosaccharide sulfotransferase) from *Sinorhizobium meliloti*.[10] Glycerol was provided as the carbon source.

The oligosaccharide recovered from the cell extracts by using the published procedure[10b] contained about 25% of the pentamer and was further purified by column chromatography on silica gel. *N*-Acylation of tetrasaccharide **11** with acid chlorides **7**, **9**, and **10** was performed in DMF containing water and provided the corresponding benzamides **12**–**14** in 33, 40, and 48% yields, respectively (60% conversion). Benzyl amine **15** and its *N*-acetyl derivative **16** were also prepared by reductive alkylation of amine **11** with aldehyde **8**.



Scheme 4. Synthesis of nodulation factor analogues (for conditions, see text.)

The synthetic analogues **12**–**15** were tested, and compared with the NodSm-IV(S) molecule (**2**), for their ability to interact with the binding protein NFBS2 associated with a membrane preparation of *M. varia*. The results (Table 1) show that, in comparison with the reference compound **2**, the affinity for NFBS2 of analogues **12**, **13** and **15** was high and in the same 20–30 nM range as the natural signal molecule.

Table 1: Affinity of analogues **12**–**15** for binding site NFBS2, as measured by competitive inhibition of [^{35}S]-NodSm-IV(S) binding, and the chromatographic behavior of the analogues.

Compound	K_i [nM][a]	t_R [min][b]
2	20 (±5%)	17.2
12	35 (±18%)	16.5
13	28 (±7%)	17.9
14	77 (±19%)	13.7
15	22 (±13%)	20.5

[a] K_i = inhibition constant. This is a measure of the affinity for NFBS2. [b] t_R = Retention times on a C18 HPLC column.

The slightly lower affinity exhibited for the *ortho*-substituted benzamide **14** (K_i = 77 nM) probably reflects a very different local geometry close to the nonreducing-end sugar, a geometry that positions the side chain in a different space location. Moreover, compound **14** appeared less hydrophobic than the other analogues, as assumed from its shorter retention time when analyzed by reversed-phase chromatography on a C18 column (Table 1). This observation is in agreement with previous studies on the selectivity of NFBS2, which showed that the overall hydrophobicity of the LCOs,

 © 2004 Wiley-VCH Verlag GmbH & Co. KGaA, Weinheim

mainly due to the structure of the fatty acid chain, was important for high-affinity binding.[6] The morphogenic activity of these benzamide analogues is currently being evaluated for potential agricultural applications, and biological details will be reported in the near future.[11]

Experimental Section

Preparation of **12**: Sodium hydrogencarbonate (2 equiv) and a solution of **7** in THF (0.82 M, 1 equiv) were added to a solution of tetrasaccharide **11** (17 μmol) in DMF/water (2.5:1, 350 μL). The reaction mixture was warmed to 60 °C, then more acid chloride solution (5 equiv) and sodium hydrogencarbonate (6 equiv) were added in six portions over a period of 18 h. Flash chromatography with ethyl acetate/methanol/water (7:2:1) as the eluent and deposition of the reaction residue at the top of the column in dichloromethane/methanol (5:1) gave **12** (6.5 mg, 33 %). The purity of the product was checked by elution at 1 mL min^{-1} on a C_{18} HPLC column with a linear gradient of 28→66 % acetonitrile in 10 mM K_2SO_4 (pH 4.6) and detection at 210 nm; ^{1}H NMR (CD_3OD, 250 MHz): $\delta = 7.48$–7.41 (m, 2H; Ar*H*-2, Ar*H*-6), 7.36 (dd, 1H, $J_{5,6} = 7.8$, $J_{5,4} = 8.1$ Hz; Ar*H*-5), 7.07 (ddd, 1H, $J_{4,2} \approx J_{4,6} = 1.4$ Hz; Ar*H*-4), 5.48–5.33 (m, 2H; C*H*=C*H*), 5.03 (d, 0.8H, $J_{1\alpha,2} = 3.2$ Hz; $H_1\alpha^I$), 4.68/4.59/4.50 (3d, 3H, $J_{1,2} = 8.7$ Hz; $H_1^{II,III,IV}$), 4.56 (d, 0.2H, $J_{1\beta,2} = 7.7$ Hz; $H_1\beta^I$), 4.25–3.30 (m, 26H; CH_2–OAr, other carbohydrate H atoms), 2.25 (td, 2H, $J = 6.7$, 6.2 Hz; CH_2–CH=CH–CH_2), 2.08–1.94 (m, 2H; CH_2–CH=CH–CH_2), 2.03/1.99/1.96 (3s, 9H; 3 × CH_3CO), 1.83 (tt, 2H, $J = 6.7$ Hz; $ArOCH_2CH_2CH_2$), 1.35–1.20 (m, 8H; 4 × CH_2), 0.88 ppm (t, 3H, $J = 7.0$ Hz; CH_3); MS (ES): *m/z*: 1139.4 $[M-Na]^-$.

Binding experiments were performed as previously described.[6] Briefly, microsomal fraction protein (60 μg) was incubated in the presence of 0.8 nM [^{35}S]-NodSm-IV(S) in a binding buffer (total volume 200 μL) with increasing amounts of the different analogues in concentrations ranging between 0.25 nM and 1 μM. The nonspecific binding component was determined in the presence of 2 μM NodSm-IV(S). Incubations were performed for 1 h at 0 °C in 96-well microtiter plates (Nunc), and the steps that followed were as previously described. Binding data were analyzed by the RADLIG software, Version 4 (Biosoft, Cambridge, UK).

Received: April 8, 2004

Keywords: aromatic substitution · glycolipids · lipid analogues · nitrogen fixation · oligosaccharides

[1] a) J. Dénarié, F. Debellé, J.-C. Promé, *Annu. Rev. Biochem.* **1996**, *65*, 503; b) S. R. Long, *Plant Cell* **1996**, *8*, 1885; c) H. P. Spaink, *Annu. Rev. Microbiol.* **1998**, *54*, 257; d) G. E. D. Oldroyd, *Ann. Bot.* **2001**, *87*, 709.

[2] P. Lerouge, P. Roche, C. Faucher, F. Maillet, G. Truchet, J.-C. Promé, J. Dénarié, *Nature* **1990**, *344*, 781; G. Truchet, P. Roche, P. Lerouge, J. Vasse, S. Camut, F. de Billy, J.-C. Promé, J. Dénarié, *Nature* **1991**, *351*, 670; P. Roche, F. Debellé, F. Maillet, P. Lerouge, C. Faucher, G. Truchet, J. Dénarié, J.-C. Promé, *Cell* **1991**, *67*, 1131.

[3] D. Tailler, J.-C. Jacquinet, J.-M. Beau, *J. Chem. Soc. Chem. Commun.* **1994**, 1827.

[4] N. Demont-Caulet, F. Maillet, D. Tailler, J.-C. Jacquinet, J.-C. Promé, K. C. Nicolaou, G. Truchet, J.-M. Beau, J. Dénarié, *Plant Physiol.* **1999**, *120*, 83.

[5] A. Niebel, J.-J. Bono, R. Ranjeva, J. V. Cullimore, *Mol. Plant-Microbe Interact.* **1997**, *10*, 132.

[6] F. Gressent, S. Drouillard, N. Mantegazza, E. Samain, R. A. Geremia, H. Canut, A. Niebel, H. Driguez, R. Ranjeva, J. Culimore, J.-J. Bono, *Proc. Natl. Acad. Sci. USA* **1999**, *96*, 4704; F. Gressent, N. Mantegazza, J. V. Cullimore, H. Driguez, R. Ranjeva, J.-J. Bono, *Mol. Plant-Microbe Interact.* **2002**, *15*, 834.

[7] By using a genetic approach, two genes involved in the perception of Nod factors and encoding transmembrane-receptor-like serine/threonine kinases with extracellular domains containing modules potentially involved in the oligosaccharide binging (LysM motifs) were recently identified: E. Limpens, C. Franken, P. Smit, J. Willemse, T. Bisseling, R. Geurts, *Science* **2003**, *302*, 630; S. Radutoiu, L. H. Madsen, E. B. Madsen, H. H. Felle, Y. Umehara, M. Gronlund, S. Sato, Y. Nakamura, S. Tabata, N. Sandal, J. Stougaard, *Nature* **2003**, *425*, 585; E. B. Madsen, L. H. Madsen, S. Radutoiu, M. Olbryt, M. Rakwalska, K. Szczyglowski, S. Sato, S. Kaneko, S. Tabata, N. Sandal, J. Stougaard, *Nature* **2003**, *425*, 637.

[8] Synthesis of Nod factors from monomers: K. C. Nicolaou, N. J. Bockovich, D. R. Carcanague, C. W. Hummel, L. F. Even, *J. Am. Chem. Soc.* **1992**, *114*, 8701; S. Ikeshita, A. Sakamoto, Y. Nakahara, Y. Nakahara, T. Ogawa, *Tetrahedron Lett.* **1994**, *35*, 3123; L. X. Wang, C. Li, Q. W. Wang, Y. Z. Hui, *J. Chem. Soc. Perkin Trans. 1* **1994**, 621; J. S. Debenham, R. Rodebaugh, B. Fraser-Reid, *J. Org. Chem.* **1996**, *61*, 6478.

[9] Some examples of aromatic derivatives designed to resemble unsaturated lipids: D. W. Snyder, P. R. Bernstein, *Prostaglandins* **1988**, *35*, 903; R. C. Larock, N. H. Lee, *J. Org. Chem.* **1991**, *56*, 6253; H. Hashizume, H. Ito, K. Yamada, H. Nagashima, M. Kanao, H. Tomoda, T. Sunazuka, H. Kumagai, S. Omura, *Chem. Pharm. Bull.* **1994**, *42*, 512; J. P. F. C. Rossi, J. M. Delfino, A. J. Caride, H. N. Fernández, *Biochemistry* **1995**, *34*, 3802.

[10] a) E. Samain, S. Drouillard, A. Heyraud, H. Driguez, R. A. Geremia, *Carbohydr. Res.* **1997**, *302*, 35; b) E. Samain, V. Chazalet, R. A. Geremia, *J. Biotechnol.* **1999**, *72*, 33.

[11] F. Maillet, J. Dénarié, personal communication.

 © 2004 Wiley-VCH Verlag GmbH & Co. KGaA, Weinheim

Natural Products Synthesis

Total Synthesis of (±)-Nominine, a Heptacyclic Hetisine-Type Aconite Alkaloid**

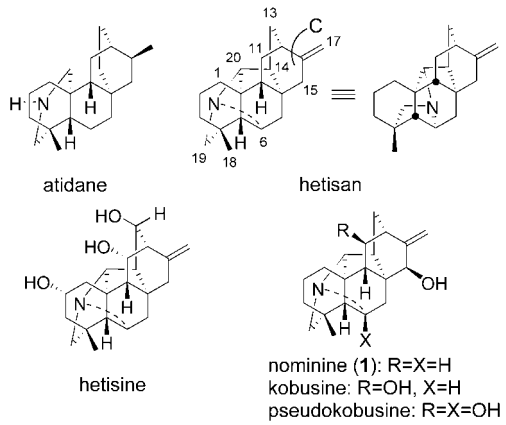
Hideaki Muratake and Mitsutaka Natsume**

Nominine (**1**) is structurally the simplest hetisine-type aconite alkaloid (Scheme 1). It was first isolated as "Nomi-base I" from *Aconitum sanyoense* Nakai, collected at Nomi, Sakyo-ku, Kyoto prefecture in Japan by Ochiai et al. in 1956.[1] Sakai et al.[2] later gave it the name nominine[3] and determined the structure, including the absolute configuration, by chemical correlation with kobusine, whose structure was established

[*] Dr. H. Muratake, Dr. M. Natsume
Research Foundation Itsuu Laboratory
2-28-10 Tamagawa, Setagaya-ku, Tokyo 158-0094 (Japan)
Fax: (+81) 3-3700-5431
E-mail: hmuratake@itsuu.or.jp
mnatsume@itsuu.or.jp

[**] We thank Professor Emeritus Shin-ichiro Sakai and Professor Hiromitsu Takayama of Chiba University for providing a sample of natural nominine.

 © 2004 Wiley-VCH Verlag GmbH & Co. KGaA, Weinheim DOI: 10.1002/anie.200460332

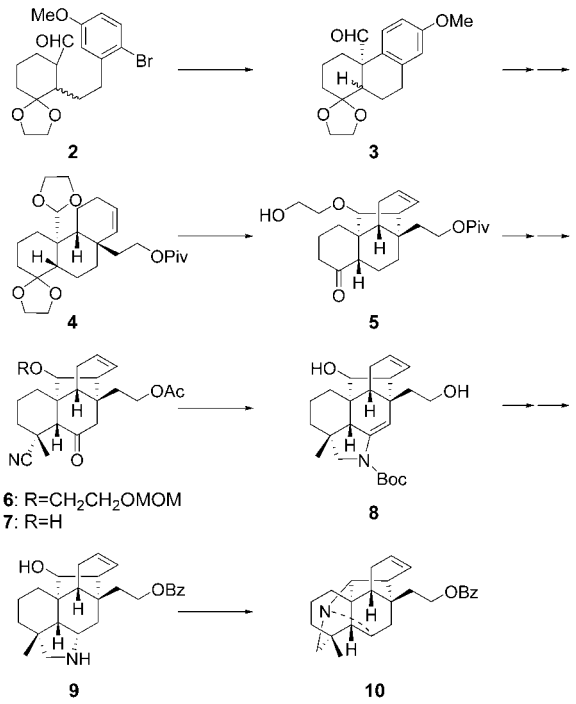


Scheme 1. Atidane and hetisan skeletons, and hetisine-type aconite alkaloids.

unambiguously by X-ray crystal-structure analysis.[4] Our extensive synthetic efforts towards the heptacyclic hetisine-type alkaloids, of which nearly 100 are now known, have culminated in the total synthesis of (±)-nominine (**1**).[5] This constitutes the first total synthesis of a hetisine-type aconite alkaloid.

More than 400 aconite alkaloids have been isolated from plants of the species *Aconitum*, *Delphinium*, *Spiraea*, *Consolida*, and *Thalictrum*. They are generally classified based on their fundamental framework as atidane, veatchane, cycloveatchane, aconitane, or hetisan (the name of which is derived from hetisine) alkaloids.[6,7] Synthetic studies on these pharmacologically important alkaloids during the last approximately 40 years have led to the total synthesis of several alkaloids of the first four of the above skeletal types. [6,7] However, attempts to construct even a simple framework corresponding to the hetisine-type alkaloids, not to mention the total synthesis of one of these alkaloids, have remained unsuccessful until now (Scheme 1). Distinctive structural characteristics of the hetisan framework are the atidane skeleton and the presence of the N–C6 and C14–C20 bonds, which contribute to the difficulty of synthesizing the hetisine-type alkaloids. Shibanuma and Okamoto prepared a pentacyclic compound that contains the N–C6 bond.[8] Two other reports that describe synthetic studies of hetisine-type alkaloids have also appeared.[9]

Previously we reported a palladium-catalyzed intramolecular α arylation reaction of aliphatic ketone, aldehyde (e.g. **2**→**3**), and nitro groups (Scheme 2).[10] As an application of this reaction, we embarked on a project to synthesize hetisine-type alkaloids. Our fundamental synthetic plan was to form the N–C6 and C14–C20 bonds at an early stage of the synthesis, since they greatly restrict the molecular conformation and would become more difficult to form at a later stage. Accordingly, we reported the preparation of a hexacyclic compound **10**, which lacks the C ring of the hetisan framework.[5] Following the transformation of compound **3** into **4**, the C14–C20 bond was created by an intramolecular acetalene reaction to form tetracyclic **5**. The connection between the N atom and C6 was established by utilizing the β-cyanoketone **7**, which was prepared from **5** via **6** and



Scheme 2. Previously reported preparation of the hexacyclic compound **10**. Bz = benzoyl, MOM = methoxymethyl, Piv = pivaloyl.

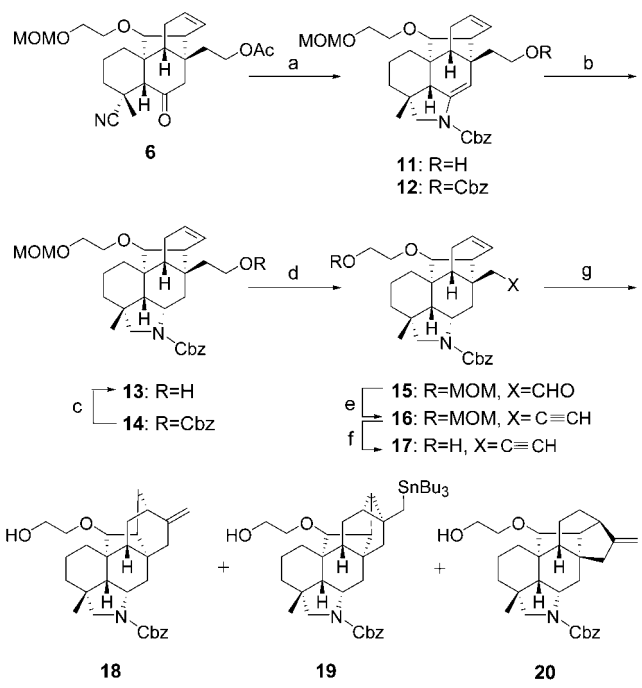
converted into the pentacyclic alkenyl carbamate **8**. The construction of the azabicyclic ring system was completed with the formation of the N–C20 bond upon the treatment of **9** with $SOCl_2$ and pyridine to afford **10**.

At first glance, C-ring formation from compound **10**, followed by functionalization at C15 with a hydroxy substituent in the β orientation, should lead readily to the target nominine (**1**). However, the strong basicity of **10** seriously restricts its versatility as an intermediate. Therefore, we decided to generate the bicyclo[2.2.2]octane ring from the intermediate **6** prior to the creation of the azabicyclic ring system.

The ketone group of **6** was protected as an enol silyl ether, and then the cyano group of the resulting product was reduced with $LiAlH_4$ in THF at reflux (Scheme 3). The careful decomposition of excess $LiAlH_4$ followed by protection of the nitrogen atom with a Cbz group provided the alkenyl carbamate **11** and a small amount of **12**. The Cbz group was employed this time in place of the *tert*-butoxycarbonyl (Boc) group, because we were unable to find suitable reaction conditions to remove the Boc group after the formation of the methylenebicyclo[2.2.2]octane ring system. The alkene bond adjacent to the nitrogen atom of the carbamate group in **11** and **12** was reduced with $NaBH_3CN$ to give **13** and **14**, respectively, and the latter was converted into **13** by methanolysis of the carbonate group. Compound **13** was transformed into the enyne–alcohol **17** via the aldehyde **15** and enyne **16**.[11]

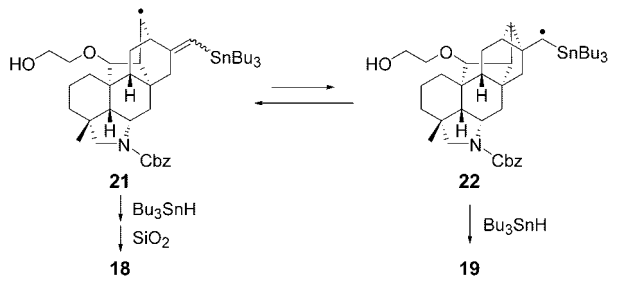
The enyne **17** was the precursor of choice for formation of the C ring through a radical cyclization reaction. A solution of Bu_3SnH (70 mM) in toluene was added slowly (over 1.5 h) to a solution of **17** (5.5 mM) and a catalytic amount of AIBN in

 © 2004 Wiley-VCH Verlag GmbH & Co. KGaA, Weinheim



Scheme 3. Preparation of the intermediate **18** from **6** for the synthesis of (±)-nominine: a) TMSCl, LDA, THF, −78 °C; $LiAlH_4$, THF, reflux; CbzCl, Et_3N, CH_2Cl_2, −18 °C→RT, **11**: 63 %, **12**: 4 %; b) $NaBH_3CN$, aqueous HCl (2.5 %), MeOH, 0 °C→RT, **13**: 90 % from **11**, **14**: 91 % from **12**; c) K_2CO_3 (1 %), MeOH, room temperature, quantitative; d) PCC (20 wt.%)/Al_2O_3, CH_2Cl_2, 0 °C→RT, 84 %; e) dimethyl (1-diazo-2-oxopropyl)phosphonate, K_2CO_3, MeOH, 0 °C→RT, 98 %; f) HCl (5 %), DME/H_2O (3:1), 0 °C→RT, 96 %; g) Bu_3SnH, AIBN, toluene, reflux; SiO_2, CH_2Cl_2, room temperature, **18**: 57 %, **19**: 31 %, **20**: 8 %. AIBN = azobisisobutyronitrile, Cbz = benzyloxycarbonyl, DME = dimethoxyethane, LDA = diisopropylamide, PCC = pyridinium chlorochromate, TMS = trimethylsilyl.

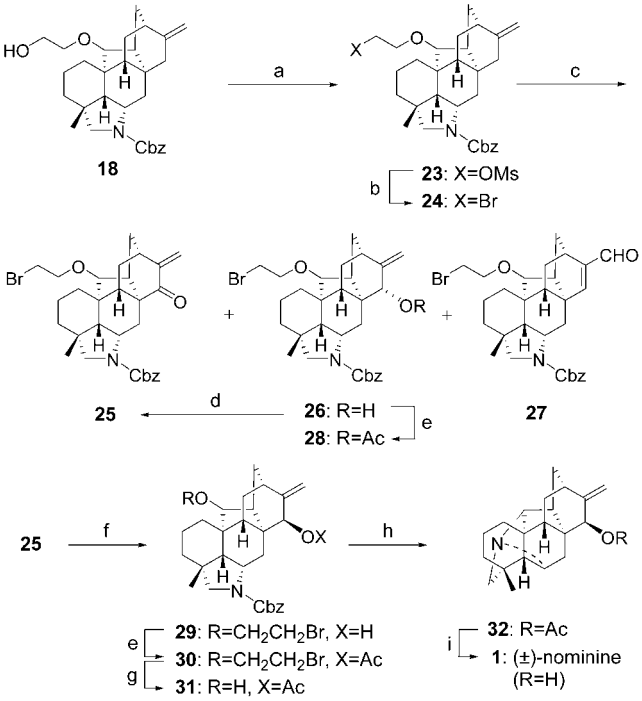
toluene at reflux to secure the desired methylenebicyclo[2.2.2]octane derivative **18** (57 %), the stannyl cyclopropane derivative **19** (31 %), and the methylenebicyclo[3.2.1]octane derivative **20** (8 %) after destannylation of the vinyl stannane products with silica gel.[12] Simple heating of a mixture of **17**, Bu_3SnH, and AIBN in toluene afforded **19** as the major product. Thus, there appears to be an equilibrium between the radical intermediates **21** and **22**, with the former favored thermodynamically (Scheme 4). Similar radical cyclization reactions reported by Toyota et al. afforded mainly bicyclo[2.2.2]octanes or bicyclo[3.2.1]octanes, depending on the substituents of the substrates; no stannyl cyclopropane



Scheme 4. Equilibration between radical intermediates.

derivatives were formed.[13] However, in our case the desired compound **18** and the stannyl cyclopropane **19** were formed as the main products, and the bicyclo[3.2.1]octane derivative **20** was a minor product, probably as a result of the distorted nature of the molecule. The structure of **20** was confirmed by generation of the corresponding cyclopentanone derivative (IR: $\tilde{\nu} = 1730\ cm^{-1}$) by the Lemieux oxidation.

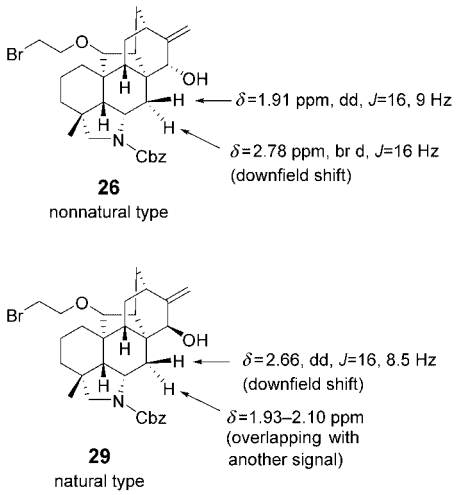
Next, **18** was transformed into the bromide **24** via the mesylate **23** (Scheme 5). Compound **24** underwent allylic



Scheme 5. Synthesis of (±)-nominine (**1**) from **18**: a) MsCl, Et_3N, CH_2Cl_2, −20 °C, 97 %; b) LiBr, acetone, reflux, 90 %; c) *tert*-BuOOH, SeO_2, CH_2Cl_2, 0 °C→RT, **25**: 77 %, **26**: 14 %, **27**: trace; d) MnO_2, CH_2Cl_2, 0 °C→RT, quantitative; e) Ac_2O, pyridine, CH_2Cl_2, room temperature, 93 %; f) $NaBH_4$, $CeCl_3 \cdot 7H_2O$, MeOH, 0 °C, quantitative; g) Zn, NH_4Cl, *i*PrOH/H_2O (14:1), reflux, 97 %; h) Et_3SiH, cat. $Pd(OAc)_2$, cat. Et_3N, CH_2Cl_2, room temperature; $SOCl_2$, pyridine, CH_2Cl_2, 0 °C→RT, 80 %; i) K_2CO_3, MeOH, reflux, 95 %. Ms = methanesulfonyl.

oxidation with aqueous *tert*-BuOOH and SeO_2[14] in CH_2Cl_2 at ambient temperature to afford the enone **25** (77 %), the alcohol 15α-**26** (14 %), and a trace amount of the enal **27**. The 15α-hydroxy product **26**, with the opposite configuration at C15 to the natural product, was oxidized quantitatively to **25** with MnO_2. The enone **25** was reduced with $NaBH_4$ in the presence of $CeCl_3$ to afford the desired 15β-hydroxy compound **29** exclusively. The structures of **26** and **29** were confirmed on the basis of the rule reported by Kawazoe et al. (Scheme 6).[15] Thus, in their ^1H NMR spectra, the signals for 7α-H of **26** and 7β-H of **29** were shifted downfield owing to the influence of the *syn* 15-hydroxy group. Furthermore, upon acetylation of the hydroxy group, the signal for the corresponding hydrogen atom in the resulting compounds **28** and **30** was shifted upfield in accordance with the rule ($\delta = 2.38$–

 © 2004 Wiley-VCH Verlag GmbH & Co. KGaA, Weinheim



Scheme 6. Structural assignment of **26** and **29**.

2.58 ppm for 7α-H of **28** and $\delta \approx 2.0$–2.2 ppm for 7β-H of **30** (overlapping with signals for other hydrogen atoms)). The bromoethyl residue of **30** was removed with zinc and NH_4Cl in 2-propanol/H_2O (14:1) at reflux to give the precursor **31**.

Now the synthesis was in its final stage. The Cbz group was removed with Et_3SiH in the presence of palladium acetate and Et_3N.[16] The resulting amino alcohol was then treated with $SOCl_2$ and pyridine to furnish *O*-acetylnominine (**32**) in good yield. Cleavage of the protecting group completed the total synthesis of (±)-nominine (**1**), which was identical to an authentic specimen (MS, IR, ^1H NMR, ^{13}C NMR).

In summary, we have completed the first total synthesis of (±)-nominine (**1**) in 40 steps and 0.15% overall yield (ca. 85% per step) from 2-bromo-5-methoxyphenethyl iodide.[5] On the basis of the results obtained, further investigations directed towards the total synthesis of other hetisine-type aconite alkaloids, such as kobusine and pseudokobusine, are in progress.

Received: April 15, 2004

Keywords:
radical reactions · alkaloids · natural products · polycycles · total synthesis

[1] E. Ochiai, T. Okamoto, S. Sakai, A. Saito, *Yakugaku Zasshi* **1956**, *76*, 1414–1418.
[2] S. Sakai, I. Yamamoto, K. Yamaguchi, H. Takayama, M. Ito, T. Okamoto, *Chem. Pharm. Bull.* **1982**, *30*, 4579–4582.
[3] The name nominine was also given to an insecticidal indole diterpene: J. B. Gloer, B. L. Rinderknecht, D. T. Wicklow, P. F. Dowd, *J. Org. Chem.* **1989**, *54*, 2530–2532.
[4] S. W. Pelletier, L. H. Wright, M. Gary Newton, H. Wright, *J. Chem. Soc. Chem. Commun.* **1970**, 98–99.
[5] H. Muratake, M. Natsume, *Tetrahedron Lett.* **2002**, *43*, 2913–2917.
[6] a) S. W. Pelletier, S. W. Page, *Nat. Prod. Rep.* **1984**, *1*, 375–386; b) S. W. Pelletier, S. W. Page, *Nat. Prod. Rep.* **1986**, *3*, 452–475; c) M. S. Yunuzov, *Nat. Prod. Rep.* **1991**, *8*, 499–526; d) M. S. Yunuzov, *Nat. Prod. Rep.* **1993**, *10*, 471–486; e) Atta-ur-Rahman, M. I. Choudhary, *Nat. Prod. Rep.* **1995**, *12*, 361–379; f) Atta-ur-Rahman, M. I. Choudhary, *Nat. Prod. Rep.* **1997**, *14*, 191–203; g) Atta-ur-Rahman, M. I. Choudhary, *Nat. Prod. Rep.* **1999**, *16*, 619–635.
[7] a) E. S. Stern in *The Alkaloids*, *Vol. 4* (Eds.: R. H. F. Manske, H. L. Holmes), Academic Press, New York, **1954**, pp. 275–333; b) E. S. Stern in *The Alkaloids*, *Vol. 7* (Ed.: R. H. F. Manske), Academic Press, New York, **1960**, pp. 473–521; c) S. W. Pelletier, L. H. Keith in *The Alkaloids*, *Vol. 12* (Ed.: R. H. F. Manske), Academic Press, New York, **1970**, pp. 1–206; d) S. W. Pelletier, N. V. Mody in *The Alkaloids*, *Vol. 17* (Eds.: R. H. F. Manske, R. G. A. Rodrigo), Academic Press, New York, **1979**, pp. 1–103; e) S. W. Pelletier, N. V. Mody in *The Alkaloids*, *Vol. 18* (Eds.: R. H. F. Manske, R. G. A. Rodrigo), Academic Press, New York, **1981**, pp. 99–216; f) T. Amiya, H. Bando in *The Alkaloids*, *Vol. 34* (Ed.: A. Brossi), Academic Press, New York, **1988**, pp. 95–179; g) F.-P. Wang, X.-T. Liang in *The Alkaloids*, *Vol. 42* (Ed.: G. A. Cordell), Academic Press, New York, **1992**, pp. 151–247; h) F.-P. Wang, X.-T. Liang in *The Alkaloids*, *Vol. 59* (Ed.: G. A. Cordell), Academic Press, New York, **2002**, pp. 1–280.
[8] Y. Shibanuma, T. Okamoto, *Chem. Pharm. Bull.* **1985**, *33*, 3187–3194.
[9] a) J. L. Van der Bean, F. Bickelhaupt, *Recl. Trav. Chim. Pays-Bas* **1975**, *94*, 109–112; b) Y.-S. Kwak, J. D. Winkler, *J. Am. Chem. Soc.* **2001**, *123*, 7429–7430.
[10] a) H. Muratake, M. Natsume, *Tetrahedron Lett.* **1997**, *38*, 7581–7582; b) H. Muratake, H. Nakai, *Tetrahedron Lett.* **1999**, *40*, 2355–2358.
[11] S. Ohira, *Synth. Commun.* **1989**, *19*, 561–564.
[12] G. Stork, F. West, H. Y. Lee, R. C. A. Isaacs, S. Manabe, *J. Am. Chem. Soc.* **1996**, *118*, 10660–10661.
[13] M. Toyota, M. Yokota, M. Ihara, *Tetrahedron Lett.* **1999**, *40*, 1551–1554.
[14] M. A. Umbreit, K. B. Sharpless, *J. Am. Chem. Soc.* **1977**, *99*, 5526–5528.
[15] Y. Kawazoe, Y. Sato, M. Natsume, H. Hasegawa, T. Okamoto, K. Tsuda, *Chem. Pharm. Bull.* **1962**, *10*, 338–344.
[16] a) L. Birkofer, E. Bierwirth, A. Ritter, *Chem. Ber.* **1961**, *94*, 821–824; b) M. Sakaitani, N. Kurokawa, Y. Ohfune, *Tetrahedron Lett.* **1986**, *27*, 3753–3754.

 © 2004 Wiley-VCH Verlag GmbH & Co. KGaA, Weinheim

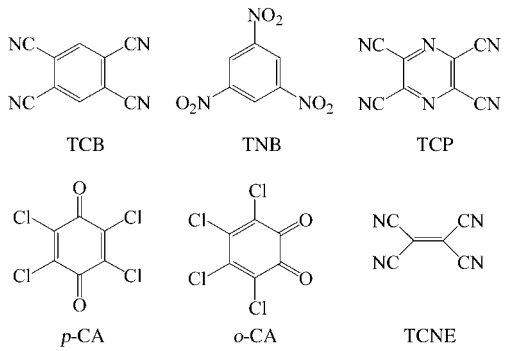
Charge-Transfer Complexes

Halide Recognition through Diagnostic "Anion–π" Interactions: Molecular Complexes of Cl^-, Br^-, and I^- with Olefinic and Aromatic π Receptors

*Yaroslav S. Rosokha, Sergey V. Lindeman, Sergiy V. Rosokha, and Jay K. Kochi**

Noncovalent interactions of anions have become one of the most actively explored areas of supramolecular chemistry.[1,2] Indeed, recent quantum-mechanical calculations suggest the possibility of anion binding to uncharged organic π receptors.[3,4] However, experimental (X-ray) verification of such direct noncovalent interactions is lacking, and the few observations of anion–π bonding are limited to metal coordination compounds.[1,5]

Despite numerous examples of analogous cation–π interactions in a variety of organic and biochemical systems,[6] anion sensing or recognition have heretofore relied primarily on electrostatic binding or hydrogen bonding to the organic receptor.[1,2,7] Thus, to experimentally characterize direct anion–π interactions in the most unambiguous way, we now turn to a series of neutral organic π acceptors with electron-deficient olefinic and aromatic centers (Scheme 1). The



Scheme 1. Neutral organic π acceptors investigated in this study.

recognition of halide anions X^- (X = Cl, Br, I) is established by 1) isolation and X-ray structure determination of a series of well-defined 1:1 salt-admixed complexes, and 2) definitive spectral assignments of each of their diagnostic charge-transfer absorption bands.[8]

[*] Y. S. Rosokha, Dr. S. V. Lindeman, Dr. S. V. Rosokha, Prof. Dr. J. K. Kochi
Chemistry Department
University of Houston
Houston, TX 77204 (USA)
Fax: (+1) 713-743-2709
E-mail: jkochi@uh.edu

Supporting information for this article is available on the WWW under http://www.angewandte.org or from the author.

Typically, an aromatic π acceptor such as tetracyanopyrazine (TCP) shows a characteristic UV/Vis spectrum with a strong absorption at $\lambda = 220$–300 nm (shoulder at 350 nm); in acetonitrile the tetraalkylammonium salts of Cl^-, Br^-, and I^- show no absorption beyond 300 nm. However, when a bromide salt is added to TCP,[9] a new absorption band appears immediately at $\lambda_{max} = 400$ nm and grows with increasing concentration of halide (Figure 1). Job's procedure[10] reveals the 1:1 stoichiometry of the [TCP/Br^-] complex (see the Supporting Information).

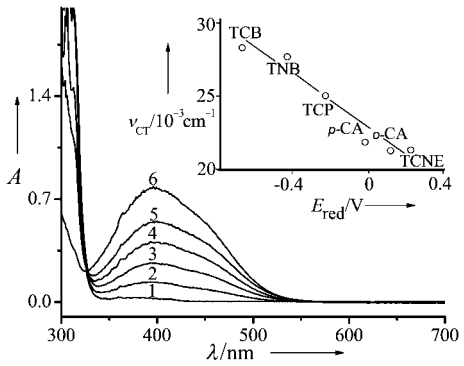


Figure 1. Spectral changes upon incremental addition of $Pr_4N^+Br^-$—0 mM (line 1), 4.9 mM (line 2), 19 mM (line 3), 46 mM (line 4), 83 mM (line 5), 208 mM (line 6)—to the 5 mM solution of TCP in acetonitrile. Inset: Mulliken dependence of the energy of absorption band (ν_{CT}) with the reduction potential of the π acceptor.

Intense colorations are also observed upon addition of chloride and iodide, and these directly relate to the appearance of new absorption bands that are red-shifted for [TCP/I^-] and blue-shifted in [TCP/Cl^-] relative to that of [TCP/Br^-]. Close scrutiny of the spectra of all three complexes reveals that the visible absorption bands consist of two Gaussian components (see the Supporting Information). Most important is the clear Mulliken correlation[8] between the energy of the low-energy band and the oxidation potential of the anion (see the Supporting Information), which establishes the charge-transfer (CT) character of these complexes.[11]

In a similar way, addition of halide to the other π acceptors from Scheme 1 results in a change in color from yellow to red and appearance of new absorption bands in the electronic spectra (see the Supporting Information).[12] The increase in acceptor strength (characterized by a positive shift of the reduction potential) is accompanied by the bathochromic shift of this band, and the Mulliken correlation (inset of Figure 1) further confirms the charge-transfer character of these complexes.

The spectral data thus indicate that halide salts form well-defined electron donor–acceptor complexes with organic π acceptors, as typified by Equation (1). Quantitative analyses of the intensity of the new absorption band as a function of the concentration of bromide and π acceptor (by the Drago procedure[9]) lead to the formation constants $K_{CT} = 1$–$10\ M^{-1}$ and the extinction coefficients $\varepsilon_{CT} = 500$–$5000\ M^{-1}cm^{-1}$ that

 © 2004 Wiley-VCH Verlag GmbH & Co. KGaA, Weinheim DOI: 10.1002/anie.200460337

are typical of charge-transfer complexes (see the Supporting Information).[10,13]

$$Br^- + TCP \overset{K_{CT}}{\rightleftharpoons} [TCP/Br^-] \quad (1)$$

Slow diffusion of hexane into 1:1 mixtures of TCP with Cl^-, Br^-, or I^- (as alkyl ammonium salts) in CH_2Cl_2/CH_3CN results in the formation of yellow to dark-red crystals. The X-ray crystal-structure analysis reveals that the overall stoichiometry of the [TCP/X^-] associates varies from 4:1 to 1:1 (Table 1).[14] For example, if chloride is taken in the form of its

Table 1: Solid-state characteristics of halide associates with π acceptors.

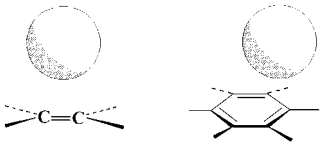
	Molar ratio	Counterion	$X^-\cdots C$ [Å][a]
TCP/Br^-	3:2	Et_4N^+	3.16
	4:1	Pr_4N^+	3.15
TCP/I^-	2:1	Et_4N^+	3.52
	1:1	Bu_4N^+	3.49[b]
TCP/Cl^-	4:1	Bu_4N^+	3.07
TCNE/Br^-	1:2	Et_4N^+	3.20[b]
	1:1	Pr_4N^+	3.11
o-CA/Br^-	1:1	Pr_4N^+	2.93

[a] The $X^-\cdots C$ distance in closest contacts; note that the sums of the van der Waals radii are 3.45 Å ($Cl^-\cdots C$), 3.55 ($Br^-\cdots C$), and 3.68 Å ($I^-\cdots C$). [b] The average of the distances to the two or three neighboring acceptors is given.

Pr_4N^+ salt, the 4:1 [TCP/Cl^-] complex is isolated in which the anion is surrounded by four acceptors and the cation lies outside the cavity. The same structure is found for [TCP/Br^-] when propyl- or butylammonium salts are used. If $Et_4N^+Br^-$ is added, the 3:2 [TCP/Br^-] complex precipitates with anions surrounded by three TCP molecules. Close TCP–X^- contacts with $X^-\cdots C$ distances of up to 0.4 Å shorter than the sum of the van der Waals radii (Table 1) confirm the strong TCP–X^- intermolecular attraction. The solid-state electronic spectra are closely related to those in solution (see the Supporting Information) and thus verify the common charge-transfer nature of the complexes.

In a similar manner, mixtures of the bromide salt and the olefinic acceptors *o*-CA and TCNE in CH_2Cl_2 yield brown-red crystals. The X-ray structure analysis reveals that in the 1:1 complex with *o*-CA, bromide is located over the center of the C–C bond. The $Br^-\cdots C$ contacts are shortened by as much as 0.6 Å relative to the sum of the van der Waals radii (see the Supporting Information). The location of the anion relative to the acceptor varies in bromide complexes with TCNE. Thus, if $Et_4N^+Br^-$ is used, the 1:2 [TCNE/Br^-] complex is isolated in which both anions reside over the olefinic bond, whereas in the 1:1 Pr_4N^+ complex, the bromide is shifted toward the cyano substituents (see the Supporting Information). In both cases, however, short intermolecular separations that are characteristic of π–π bonded CT complexes[13] indicate strong anion–TCNE interactions (Table 1).

The recognition of halides by the π acceptors in Scheme 1 is visually apparent by the color resulting from the diagnostic charge transfer (λ_{CT}, see the Supporting Information). By the same token, the isolation and X-ray crystallography of mixed salts (Table 1) identifies the pertinent separation of the halide donor from the π acceptor, which is responsible for the electronic (charge-transfer) transition. Most importantly, the global Mulliken correlation (inset of Figure 1) underscores the common π-acceptor properties of all the electron-deficient olefinic and aromatic centers. As such, the molecular structure responsible for the color as a result of charge transfer can be gleaned from the X-ray structure data. The composites are schematically presented in Scheme 2 for visualizing the pertinent anion–π interactions.[13d]



Scheme 2. Schematic drawing of the anion–π interactions. The sphere representing the van der Waals radius of bromide (taken as an example) is drawn to scale relative to the electron-deficient olefinic and aromatic centers.

Thus, the general structural feature of the noncovalent (anion–π) interaction with olefinic acceptors holds the bromide ion at roughly 3 Å over the double bond. Similarly, in anion–π interactions of electron-deficient aromatic π acceptors, the bromide ion lies 3 Å over the periphery of the aromatic ring. Indeed, such structures differ from quantum-mechanical calculations that largely show the anion to lie somewhere along the centroid of the aromatic ring in π complexes with 1,3,5-triazine or hexafluorobenzene.[3,15] Furthermore, the possibility of multiple halide–π interactions leads to the formation of three-dimensional solid-state structures in which anions reside in the cavities created by the multiple TCP receptors (Figure 2).

In summary, the formation constants of the halide complexes with neutral π acceptors, together with the intense absorptions and compression of the intermolecular separations found by X-ray structural analysis,[14] indicate the existence of substantial anion–π interactions. Spectral, ther-

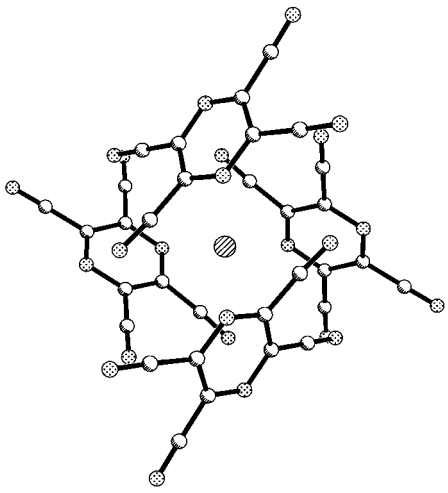


Figure 2. X-ray structure of the 4:1 [TCP/Cl^-] complex (counterions omitted for clarity).

 © 2004 Wiley-VCH Verlag GmbH & Co. KGaA, Weinheim

modynamic, and structural properties of these associates are closely related to those of the classical donor–acceptor complexes,[10,13] which indicates the common charge-transfer origin of the seminal anion–π interactions. The formation of relatively strong complexes together with the distinctive colorations of various anion–π interactions encourage their use in the design of anion-sensing receptors, provided systems with multicentered binding sites are chosen for optimum recognition (compare the Venus fly trap).[16] X-ray crystallography of the halide complexes with TCP (see Figure 2 and the Supporting Information) provides insight into the desirable features of such π receptors.

Received: April 15, 2004

Keywords: anions · charge transfer · halides · pi interactions · UV/Vis spectroscopy

[1] P. D. Beer, P. A. Gale, *Angew. Chem.* **2001**, *113*, 502; *Angew. Chem. Int. Ed.* **2001**, *40*, 487.

[2] *Supramolecular Chemistry of Anion*s (Eds.: A. Bianchi, K. Bowman-James, E. Garcia-España), Wiley-VCH, New York, **1997.**

[3] a) D. Quiñonero, C. Garau, C. Rotger, A. Frontera, P. Ballester, A. Costa, P. M. Deyà, *Angew. Chem.* **2002**, *114*, 3539; *Angew. Chem. Int. Ed.* **2002**, *41*, 3389; b) M. Mascal, A. Armstrong, M. D. Bartberger, *J. Am. Chem. Soc.* **2002**, *124*, 6274; c) I. Alkorta, I. Rozas, J. Elguero, *J. Am. Chem. Soc.* **2002**, *124*, 8593; d) C. Garau, A. Frontera, D. Quiñonero, P. Ballester, A. Costa, P. M. Deyà, *ChemPhysChem* **2003**, *4*, 1344; e) C. Garau, D. Quiñonero, A. Frontera, A. Costa, P. Ballester, P. M. Deyà, *Chem. Phys. Lett.* **2003**, *370*, 7; e) D. Kim, P. Tarakenshwar, K. S. Kim, *J. Phys. Chem. A* **2004**, *108*, 1250.

[4] See also a) C. Garau, A. Frontera, D. Quiñonero, P. Ballester, A. Costa, P. M. Deyà, *Chem. Phys. Lett.* **2003**, *382*, 534; b) S. Demeshko, S. Dechert, F. Meyer, *J. Am. Chem. Soc.* **2004**, *126*, 4508; c) I. Alkorta, J. Elguero, *J. Phys. Chem. A* **2003**, *107*, 9428; d) C. Garau, D. Quinonero, A. Frontera, P. Ballester, A. Costa, P. M. Deyà, *New J. Chem.* **2003**, *27*, 211.

[5] H. Lee, M. Diaz, C. B. Knobler, M. F. Hawthorne, *Angew. Chem.* **2000**, *112*, 792; *Angew. Chem. Int. Ed.* **2000**, *39*, 776, and references therein.

[6] Reviews: a) E. A. Meyer, R. K. Castellano, F. Diederich, *Angew. Chem.* **2003**, *115*, 4254; *Angew. Chem. Int. Ed.* **2003**, *42*, 1210; b) H.-J. Schneider, A. Yatsimirsky, *Principles and Methods in Supramolecular Chemistry*, Wiley, Chichester, **2000**; c) J. C. Ma, D. A. Dougherty, *Chem. Rev.* **1997**, *97*, 1303.

[7] a) J. L. Sessler, D. An, W.-S. Cho, V. Lynch, *Angew. Chem.* **2003**, *115*, 2380; *Angew. Chem. Int. Ed.* **2003**, *42*, 2278; b) F. P. Schmidtchen, M. Berger, *Chem. Rev.* **1997**, *97*, 1609; c) K. J. Wallace, W. J. Belcher, D. R. Turner, K. F. Syed, J. W. Steed, *J. Am. Chem. Soc.* **2003**, *125*, 9699; d) E. M. Kosower, J. C. Burbach, *J. Am. Chem. Soc.* **1956**, *78*, 5838; e) A. Nakahara, J. H. Wang, *J. Phys. Chem.* **1963**, *67*, 491.

[8] a) R. S. Mulliken, W. B. Person, *Molecular Complexes*, Wiley, New York, **1969**; b) although there are a few sporadic reports of charge-transfer absorptions of halide salts,[6c-e] no definitive X-ray structures have been reported; c) G. Briegleb, W. Liptay, R. Fick, *Z. Elektrochem.* **1962**, *66*, 859; d) K. M. C. Davis, *J. Chem. Soc. B* **1967**, 1129 and K. M. C. Davis, *J. Chem. Soc. B* **1969**, 1020; e) J. A. A. de Boer, D. N. Reinhoudt, J. W. H. M. Uiterwijk, S. Harkema, *J. Chem. Soc. Chem. Commun.* **1982**, 194.

[9] In form of the $Pr_4N^+Br^-$ salt; values for $Et_4N^+Br^-$ or $Bu_4N^+Br^-$ are within the error limit (Table S2).

[10] R. S. Drago, *Physical Methods in Chemistry*, Saunders, Philadelphia, **1977**.

[11] a) High-energy components are tentatively assigned to the transition from the subjacent HOMO-1 of the halide since the difference between two components in the [TCP/Br^-] absorption of $3.5\times10^3\,cm^{-1}$ is comparable to the difference ($3.9\times10^3\,cm^{-1}$) between the two highest Br^- levels ($4p_{3/2}$ and $4p_{1/2}$); b) J. Overton, J. P. Hernandes, *Phys. Rev. B* **1973**, *7*, 778.

[12] a) Use of KBr leads to the same absorption maximum for the [TCNE/Br^-] complex (see the Supporting Information); b) if TCNE and $Pr_4N^+Br^-$ are simply ground together under an argon atmosphere, the colorless mixture changes to dark purple. The diffuse reflectance spectrum confirms the presence of [TCNE/Br^-].

[13] a) *Organic Charge-Transfer Complexes* (Ed.: R. Foster), Academic, New York, **1969**; b) *Molecular Complexes* (Ed.: R. Foster), Crane, Russak, **1973**; c) A. V. Vasilyev, S. V. Lindeman, J. K. Kochi, *New J. Chem.* **2002**, *26*, 582; d) for the precise location of the halide anions in the CT complexes, see the Cartesian coordinates in the X-ray (CIF) files.[14]

[14] The intensity data for all compounds were collected with a Siemens SMART APEX diffractometer using $Mo_{K\alpha}$ radiation ($\lambda = 0.71073$ Å) at −150 °C. Structures were solved by direct methods and refined by full matrix least-squares procedure with IBM Pentium and SGI O2 computers. Crystal data for $[(TCP)_4Cl^-]Bu_4N^+$ ($C_{48}H_{36}ClN_{25}$): $M = 998.47$, tetragonal space group $I4$, $a = b = 13.181(1)$, $c = 15.288(1)$ Å, $V = 2656.0(1)$ Å^3, $\rho_{calcd} = 1.248\,g\,cm^{-1}$, $Z = 2$, $2\theta_{max} = 63.71$. Of 14580 reflections measured 4309 were symmetrically nonequivalent. $R1 = 0.057$ and $wR2 = 0.153$ for 4132 reflections with $I > 2\sigma(I)$. For the crystal data of the other complexes from Table 1, see the Supporting Information. CCDC 236236 ($[(TCP)_4Br^-]$-$Pr_4N^+\cdot CH_2Cl_2$), 236237 ($[(o\text{-}CA)Br^-]Pr_4N^+$), 236238 ($[(TCNE)Br^-]Pr_4N^+$), 236239 ($[(TCNE)(Br^-)_2](Et_4N^+)_2$), 236240 ($[(TCP)_3(Br^-)_2](Et_4N^+)_2$), 236241 ($[(TCP)I^-]Bu_4N^+$), 236242 ($[(TCP)_2I^-]Et_4N^+$), 236243 ($[(TCP)_4Cl^-]Bu_4N^+$) contain the supplementary crystallographic data for this paper. These data can be obtained free of charge via www.ccdc.cam.ac.uk/conts/retrieving.html (or from the Cambridge Crystallographic Data Centre, 12, Union Road, Cambridge CB21EZ, UK; fax: (+44) 1223-336-033; or deposit@ccdc.cam.ac.uk).

[15] a) However, the energy difference between the over-ring versus over-center structures in arene π complexes is likely to be small and subject to crystal-packing forces. This has been noted in other donor–acceptor pairs, see: b) S. M. Hubig, S. V. Lindeman, J. K. Kochi, *Coord. Chem. Rev.* **2000**, *200–202*, 831; c) ref [13c] and G. Fukin, S. V. Lindeman, J. K. Kochi, *J. Am. Chem. Soc.* **2002**, *124*, 8329; d) theoretical calculations[3b] of 1,3,5-triazine and fluoride, chloride and azide anions also show this ambiguity.

[16] See, for example, S. V. Rosokha, S. V. Lindeman, R. Rathore, J. K. Kochi, *J. Org. Chem.* **2003**, *68*, 3947.

 © 2004 Wiley-VCH Verlag GmbH & Co. KGaA, Weinheim

Medicinal Chemistry

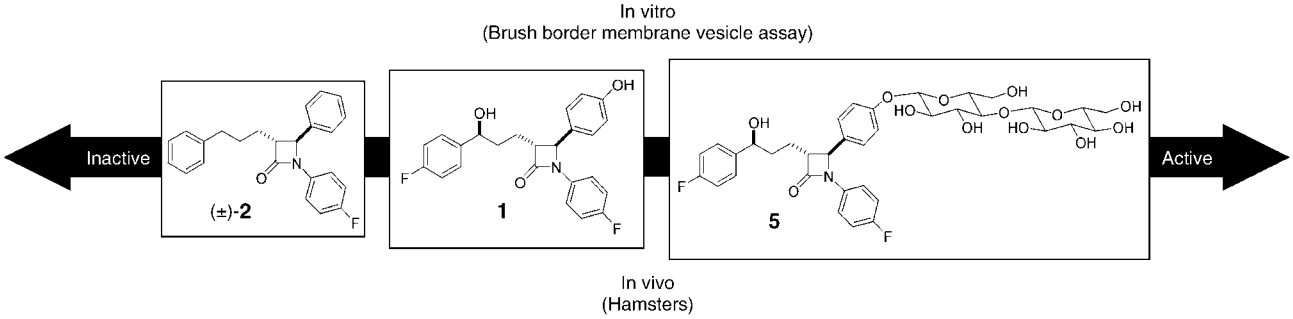
An In Vitro Assay for Evaluation of Small-Molecule Inhibitors of Cholesterol Absorption**

*Lisbet Kværnø, Tobias Ritter, Moritz Werder, Helmut Hauser, and Erick M. Carreira**

Cardiovascular disease is the leading cause of death in the Western industrialized world and claims more lives than the next four causes combined.[1] A major risk factor for this disease is elevated cholesterol levels.[2,3] The current predominant therapy prescribes the use of statins, which lead to inhibition of cholesterol biosynthesis in the liver.[3,4] However, half of all patients undergoing current lipid-lowering treatments fail to reach their cholesterol goals,[3,5] and thus a clear need for the development of new cholesterol-lowering agents remains. Ezetimibe (**1**, Scheme 1) is a recent exciting example of a new class of drugs operating by a different mechanism involving inhibition of intestinal cholesterol absorption. Ezetimibe (**1**) was developed solely by using animal studies.[6] The rapid identification and optimization of new inhibitors would be greatly facilitated with an in vitro assay. In this communication, we introduce the use of intestinal brush border membrane vesicles[7] for the convenient in vitro testing of small molecules for inhibition of cholesterol absorption. We demonstrate the validity of the assay by comparison of the observed in vitro efficacies with published in vivo data (Scheme 1). Moreover, the assay allows us to identify new nonhydrolyzable glycosides as potent cholesterol absorption inhibitors and an oxazolidinone as an effective replacement of the β-lactam scaffold of ezetimibe (**1**).

The actual identity of the intestinal cholesterol transport proteins is still actively debated, with evidence suggesting the involvement of the scavenger receptors SR-BI[7e,f,8] and CD36,[7f,9] the Niemann–Pick C1-like 1 protein,[10] and an Annexin 2/Caveolin 1 complex.[11] Regardless of which proteins are involved, prior work has demonstrated that cholesterol absorption takes place in brush border membrane vesicles made from human or animal small intestines.[7] We thus set out to investigate whether brush border membrane vesicles could be used in the development of an in vitro assay for small-molecule cholesterol absorption inhibitors. For the successful implementation of such an assay, we needed to validate it by synthesizing and examining a number of known ezetimibe analogues for which the corresponding in vivo data were available.

Rabbit brush border membrane vesicles are prepared by shearing the enterocyte brush border membrane region and allowing its reassembly into vesicles with a diameter of 180 nm (Figure 1).[7a,12] Such a preparation can be carried out conveniently in hours, and the vesicles produced can be stored for months. In the experiments, cholesteryl ester is delivered to the brush border membrane vesicles by incorporation into egg phosphatidyl choline small unilamellar vesicles (25 nm diameter) that act as donor particles.[7,13] Direct application of the small-molecule candidates in 1% aqueous dimethylsulfoxide was complicated by their low solubility in water. However, key to the development of the assay was the discovery that these molecules, like the cholesteryl ester, could also be incorporated into the phospholipid small unilamellar vesicles.[14] At a fixed concentration of 9 mol%, corresponding to a nominal concentration of 6 μM, the test substrates were readily incorporated into the vesicles and used in routine inhibition experiments. The cholesterol transfer from donor particles to brush border membrane vesicles was quantified by using radiolabeled [1α,2α(N)-^{3}H]cholesterol oleyl ether (37 Ci mmol^{-1}).[15]



Scheme 1. Correlation between in vitro and in vivo activities with various small molecules.

We selected ezetimibe (**1**),[16] β-lactam (±)-**2**,[17,18] and the *O*-glycosides **3**–**5**[19] as convenient benchmark substrates of the in vitro assay, because in vivo results were available for these compounds (Table 1). In the brush border membrane vesicle assay with rabbit intestine, ezetimibe (**1**) was shown to inhibit cholesteryl ester uptake by 16% when the convenient 9-mol% concentration in the vesicles was used. β-Lactam

[*] L. Kværnø, T. Ritter, Prof. Dr. E. M. Carreira
Laboratorium für Organische Chemie
ETH Hönggerberg, HCI H335
8093 Zürich (Switzerland)
Fax: (+41) 1-632-1328
E-mail: carreira@org.chem.ethz.ch
Dr. M. Werder, Prof. Emeritus Dr. H. Hauser
Institute of Biochemistry
ETH Hönggerberg
8093 Zürich (Switzerland)

[**] This research was supported by a CTI grant (6813.2 BTS-LS) and Lipideon AG. L.K. was supported by a fellowship from The Technical University of Denmark. T.R. thanks the Fonds der Chemischen Industrie for a Kekulé Fellowship.

Supporting information for this article is available on the WWW under http://www.angewandte.org or from the author.

 DOI: 10.1002/anie.200460348 © 2004 Wiley-VCH Verlag GmbH & Co. KGaA, Weinheim

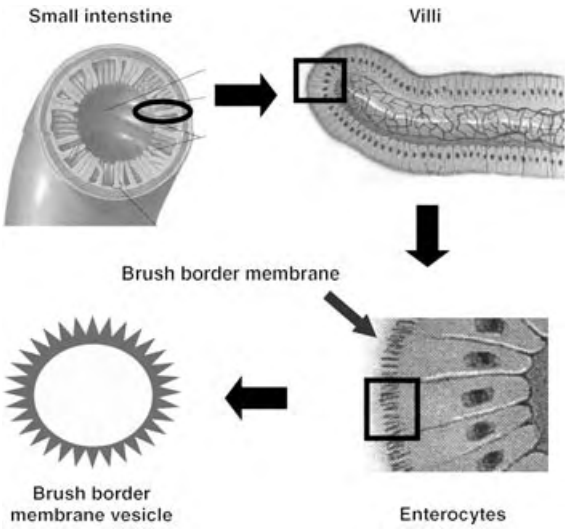
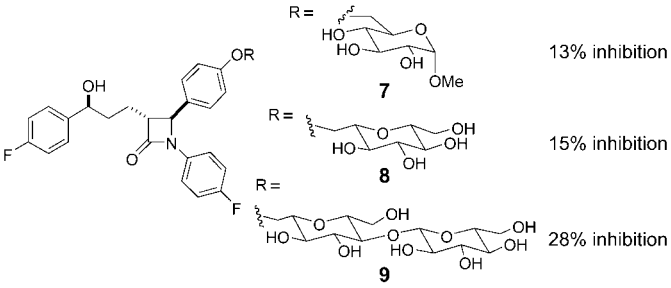


Figure 1. Preparation of brush border membrane vesicles.

(±)-**2** was inactive, a result consistent with the corresponding reported low activity in vivo.[18] Furthermore, the same correlation was observed for the *O*-glycosides as that reported for in vivo studies,[19] wherein cellobioside **5** was significantly more active than glucuronide **3** and glucoside **4**. In the development of ezetimibe (**1**) by using animal studies, the benzylic hydroxy group was shown to be of prime importance for activity.[6c] Likewise in our assay, removal of this hydroxy functionality in **5** to give **6** resulted in a drastic decrease in the in vitro inhibitory activity (3% inhibition for **6** versus 27% for **5**). This molecular editing experiment[21] provides yet another correlation with the in vivo data.

With a validated in vitro assay in hand, we started to address two key issues: 1) the role of glycosylation in inhibitory activity and 2) the use of other ring scaffolds to replace the β-lactam. In vivo, ezetimibe (**1**) has been shown to be rapidly glucuronidated in the intestine to form glucuronide **3** before entering the portal plasma.[22] Rapid metabolic hydrolysis of the *O*-glycosides **3**–**5** and subsequent interconversion between ezetimibe (**1**) and the glucuronide **3** cannot be completely ruled out in the reported animal experiments. Consequently, we designed, synthesized, and examined the structurally related glycosides **7**–**9** with nonhydrolyzable linkages[23] (Scheme 2). These were prepared

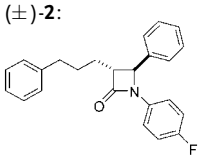
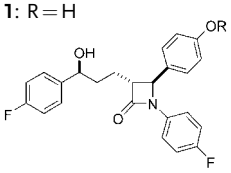
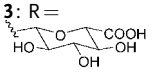
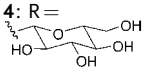
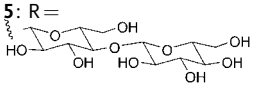
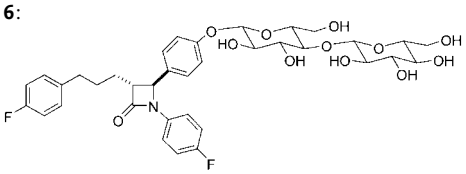


Scheme 2. Nonhydrolyzable glycosides evaluated in the brush border membrane vesicle assay.

by Mitsunobu reactions of **10** with the appropriate primary alcohols, as shown for cellobioside **9** in Scheme 3.

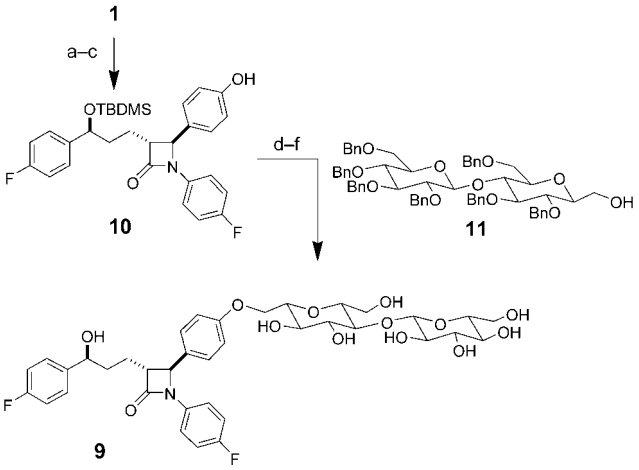
When **7**–**9** were evaluated in the brush border membrane vesicle assay, the glucosides **7** and **8** displayed inhibitions of 13% and 15%, respectively (Scheme 2). The cellobioside **9** (28% inhibition) was clearly more active and was as active an inhibitor as the corresponding *O*-cellobioside **5** (27% inhibition). The activities of the nonhydrolyzable glycosides **7**–**9** indicate that glycosides of ezetimibe (**1**) are indeed capable of being potent cholesterol absorption inhibitors.

Table 1: Activities in the brush border membrane vesicle assay compared to in vivo data.

Inhibitor	In vivo inhibition [mg kg^{-1} day^{-1}][a]	In vitro inhibition [%][b,c]
(±)-**2**: 	low activity[d][18]	2
1: R = H 	0.04[6]	16
3: R = 	0.09[19]	19
4: R = 	0.08[19]	14
5: R = 	0.01[19]	27
6: 	–	3

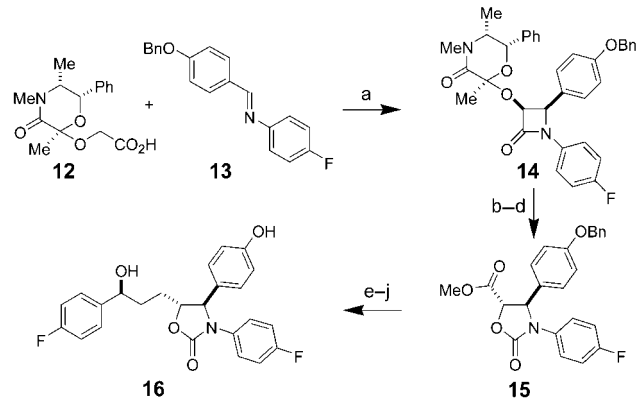
[a] Reported effective dose values for 50% reduction of liver cholesteryl ester level (ED_{50}) in the seven-day cholesterol-fed hamster model.[20] [b] Inhibition in the brush border membrane vesicle assay with rabbit intestine at nominal concentrations of 6 μM. [c] Average standard deviations were ±3% inhibition. [d] At 50 mg kg^{-1} day^{-1}, no ED_{50} value was determined.

 © 2004 Wiley-VCH Verlag GmbH & Co. KGaA, Weinheim



Scheme 3. a) **1**,[16] Ac_2O, NaOH, *i*PrOH, 97%; b) TBDMSCl, imid, DMF, 91%; c) Al_2O_3 (neutral), 70°C, 83%; d) **11**,[24] 1,1′-(azodicarbonyl)dipiperidine, Bu_3P, THF; e) H_2, $Pd(OH)_2/C$, EtOAc/EtOH, 21% over two steps; f) HF·pyridine, pyridine, THF, 62%. Bn = benzyl, DMF = *N*,*N*-dimethylformamide, imid = imidazole, TBDMS = *tert*-butyldimethylsilyl, THF = tetrahydrofuran.

The in vitro assay also allowed us to conveniently examine whether the β-lactam is an integral and essential pharmacophore, as concluded in the early development of ezetimibe (**1**),[18,25] or simply a ring scaffold to appropriately position the required substituents. Thus, oxazolidinone **16**, which closely resembles ezetimibe (**1**) with respect to the positioning of the ring substituents,[25] was synthesized in enantiomerically pure form as outlined in Scheme 4. We were pleased to observe that oxazolidinone **16** showed a similar activity (19% inhibition) to ezetimibe (**1**; 16% inhibition) in the brush border membrane vesicle assay. The notable activity for **16** suggests that an oxazolidinone ring scaffold substituted with the appropriate side chains could effectively replace ezetimibe (**1**).



Scheme 4. a) **12**,[26] **13**,[27] $(Cl_3CO)_2CO$, Et_3N, 0°C→RT, 75%, d.r. = 3:2; b) THF/H_2O, reflux, 50%; c) NaOMe, MeOH; d) $(Cl_3CO)_2CO$, iPr_2NEt, DMAP, CH_2Cl_2, −78°C→23°C, 73% over two steps; e) $NaBH_4$, EtOH; f) $(COCl)_2$, DMSO, Et_3N, CH_2Cl_2, −78°C; g) $pFC_6H_4COCH{=}PPh_3$, CH_2Cl_2, −78°C→23°C, 82% over three steps; h) H_2, Pd/C, EtOH; i) (*R*)-CBS,[28] $BH_3{\cdot}Me_2S$, CH_2Cl_2, −20→0°C; j) H_2, Pd/C, EtOH, 57% over three steps. (*R*)-CBS = *R*-tetrahydro-1-methyl-3,3-diphenyl-1*H*,3*H*-pyrrolo(1,2-C)(1,3,2)oxazaborolidine, DMAP = 4-dimethylaminopyridine, DMSO = dimethylsulfoxide.

In summary, we have used brush border membrane vesicles in the first in vitro assay to evaluate small-molecule cholesterol absorption inhibitors. In comparison with published in vivo data of identical and closely related compounds, consistent in vitro results were obtained. These indicate that both ezetimibe (**1**) and a variety of ezetimibe glycosides are all potent cholesterol absorption inhibitors. The salient feature of the assay is that it permits rapid identification of other useful ring scaffolds for the synthesis of novel cholesterol absorption inhibitors, as exemplified by the oxazolidinone **16**. It should thus be possible to replace tedious, expensive, and lengthy animal experiments by convenient evaluation in the brush border membrane vesicle assay when investigating diverse libraries of small-molecule cholesterol absorption inhibitors.

Received: April 16, 2004

Keywords: cholesterol · inhibitors · medicinal chemistry · membranes

[1] Heart Disease and Stroke. Statistics—2003 Update. Available from The American Heart Association at: http://www.americanheart.org/downloadable/heart/1059017971148 2003HDSStatsBookREV7-03.pdf.
[2] T. Sudhop, K. von Bergmann, *Drugs* **2002**, *62*, 2333.
[3] E. Bruckert, *Cardiology* **2002**, *97*, 59.
[4] D. J. Maron, S. Fazio, M. F. Linton, *Circulation* **2000**, *101*, 207.
[5] Euroaspire II Study Group, *Eur. Heart J.* **2001**, *22*, 554.
[6] a) FDA Drug Approvals List [online]: http://www.fda.gov/cder/foi/label/2002/21445lbl.pdf; b) J. W. Clader, *J. Med. Chem.* **2004**, *47*, 1; c) S. B. Rosenblum, T. Huynh, A. Afonso, H. R. Davis, N. Yumibe, J. W. Clader, D. A. Burnett, *J. Med. Chem.* **1998**, *41*, 973.
[7] a) H. Thurnhofer, H. Hauser, *Biochemistry* **1990**, *29*, 2142; b) S. Compassi, M. Werder, D. Boffelli, F. E. Weber, H. Hauser, G. Schulthess, *Biochemistry* **1995**, *34*, 16473; c) S. Compassi, M. Werder, F. E. Weber, D. Boffeli, H. Hauser, *Biochemistry* **1997**, *36*, 6643; d) G. Schulthess, S. Compassi, D. Boffelli, M. Werder, F. E. Weber, H. Hauser, *J. Lipid Res.* **1996**, *37*, 2405; e) H. Hauser, J. H. Dyer, A. Nandy, M. A. Vega, M. Werder, E. Bieliauskaite, F. E. Weber, S. Compassi, A. Gemperli, D. Boffelli, E. Wehrli, G. Schulthess, M. C. Phillips, *Biochemistry* **1998**, *37*, 17843; f) M. Werder, C. H. Han, E. Wehrli, D. Bimmler, G. Schulthess, H. Hauser, *Biochemistry* **2001**, *40*, 11643.
[8] a) S. F. Cai, R. J. Kirby, P. N. Howles, D. Y. Hui, *J. Lipid Res.* **2001**, *42*, 902; b) L. Cai, E. R. M. Eckhardt, W. Shi, Z. Zhao, M. Nasser, W. J. S. de Villiers, D. R. van der Westhuyzen, *J. Lipid Res.* **2004**, *45*, 253; c) S. W. Altmann, H. R. Davis, X. R. Yao, M. Laverty, D. S. Compton, L. J. Zhu, J. H. Crona, M. A. Caplen, L. M. Hoos, G. Tetzloff, T. Priestley, D. A. Burnett, C. D. Strader, M. P. Graziano, *Biochim. Biophys. Acta* **2002**, *1580*, 77; d) E. Levy, D. Menard, I. Suc, E. Delvin, V. Marcil, L. Brissette, L. Thibault, M. Bendayan, *J. Cell Sci.* **2004**, *117*, 327; e) D. Jourdheuil-Rahmani, M. Charbonnier, N. Domingo, F. Luccioni, H. Lafont, D. Lairon, *Biochem. Biophys. Res. Commun.* **2002**, *292*, 390; f) B. Play, S. Salvini, Z. Haikal, M. Charbonnier, A. Harbis, M. Roussel, D. Lairon, D. Jourdheuil-Rahmani, *Biochem. Biophys. Res. Commun.* **2003**, *310*, 446.

 © 2004 Wiley-VCH Verlag GmbH & Co. KGaA, Weinheim

[9] A. van Bennekum, M. Werder, S. T. Thuahnai, C.-H. Han, D. L. Williams, P. Wettstein, G. Schulthess, M. C. Phillips, H. Hauser, Biochemistry **2004**, submitted.
[10] S. W. Altmann, H. R. Davis, L. J. Zhu, X. R. Yao, L. M. Hoos, G. Tetzloff, S. P. N. Iyer, M. Maguire, A. Golovko, M. Zeng, L. Q. Wang, N. Murgolo, M. P. Graziano, *Science* **2004**, *303*, 1201.
[11] E. J. Smart, R. A. De Rose, S. A. Farber, *Proc. Natl. Acad. Sci. USA* **2004**, *101*, 3450.
[12] H. Hauser, K. Howell, R. M. C. Dawson, D. E. Bowyer, *Biochim. Biophys. Acta* **1980**, *602*, 567.
[13] Cholesteryl ester, instead of free cholesterol, was chosen for the standard inhibition experiments, since passive diffusion is negligible for cholesteryl ester.[7e]
[14] The incorporation into vesicles was shown to be quantitative for representative inhibitors by gel filtration of the vesicles according to established procedures (see G. Schulthess, S. Compassi, M. Werder, C. H. Han, M. C. Phillips, H. Hauser, *Biochemistry* **2000**, *39*, 12623, and references therein) followed by reversed-phase HPLC analysis.
[15] Radiolabeled cholesterol oleyl ether was used as a nonhydrolyzable analogue of cholesterol oleyl ester, since both have been shown to exhibit identical brush border membrane uptake kinetics.[7b]
[16] G. Z. Wu, Y. S. Wong, X. Chen, Z. X. Ding, *J. Org. Chem.* **1999**, *64*, 3714.
[17] M. Browne, D. A. Burnett, M. A. Caplen, 0L. Y. Chen, J. W. Clader, M. Domalski, S. Dugar, P. Pushpavanam, R. Sher, W. Vaccaro, M. Viziano, H. R. Zhao, *Tetrahedron Lett.* **1995**, *36*, 2555.
[18] J. W. Clader, D. A. Burnett, M. A. Caplen, M. S. Domalski, S. Dugar, W. Vaccaro, R. Sher, M. E. Browne, H. R. Zhao, R. E. Burrier, B. Salisbury, H. R. Davis, *J. Med. Chem.* **1996**, *39*, 3684.
[19] W. D. Vaccaro, H. R. Davis, *Bioorg. Med. Chem. Lett.* **1998**, *8*, 313.
[20] a) D. A. Burnett, M. A. Caplen, H. R. Davis, R. E. Burrier, J. W. Clader, *J. Med. Chem.* **1994**, *37*, 1733; b) R. Schnitzerpolokoff, D. Compton, G. Boykow, H. Davis, R. Burrier, *Comp. Biochem. Physiol. Part A* **1991**, *99*, 665.
[21] a) A. M. Rouhi, *Chem. Eng. News* **2003**, *81*, 104; for recent examples of successful molecular editing of epothilones, see: b) T. C. Chou, H. J. Dong, A. Rivkin, F. Yoshimura, A. E. Gabarda, Y. S. Cho, W. P. Tong, S. J. Danishefsky, *Angew. Chem.* **2003**, *115*, 4910; *Angew. Chem. Int. Ed.* **2003**, *42*, 4761; c) K. C. Nicolaou, P. K. Sasmal, G. Rassias, M. V. Reddy, K. H. Altmann, M. Wartmann, A. O'Brate, P. Giannakakou, *Angew. Chem.* **2003**, *115*, 3639; *Angew. Chem. Int. Ed.* **2003**, *42*, 3515.
[22] M. van Heek, C. Farley, D. S. Compton, L. Hoos, K. B. Alton, E. J. Sybertz, H. R. Davis, *Br. J. Pharmacol.* **2000**, *129*, 1748.
[23] W. D. Vaccaro, R. Sher, H. R. Davis, *Bioorg. Med. Chem. Lett.* **1998**, *8*, 35.
[24] S. J. Spak, O. R. Martin, *Tetrahedron* **2000**, *56*, 217.
[25] S. Dugar, M. P. Kirkup, J. W. Clader, S. I. Lin, R. Rizvi, M. E. Snow, H. R. Davis, S. W. McCombie, *Bioorg. Med. Chem. Lett.* **1995**, *5*, 2947.
[26] B. A. Shinkre, V. G. Puranik, B. M. Bhawal, A. Deshmukh, *Tetrahedron: Asymmetry* **2003**, *14*, 453.
[27] T. Kambara, K. Tomioka, *J. Org. Chem.* **1999**, *64*, 9282.
[28] a) E. J. Corey, R. K. Bakshi, S. Shibata, *J. Am. Chem. Soc.* **1987**, *109*, 5551; b) E. J. Corey, R. K. Bakshi, S. Shibata, C. P. Chen, V. K. Singh, *J. Am. Chem. Soc.* **1987**, *109*, 7925.

 © 2004 Wiley-VCH Verlag GmbH & Co. KGaA, Weinheim

Oxidation

Dihydrogen Trioxide (HOOOH) Is Generated during the Thermal Reaction between Hydrogen Peroxide and Ozone**

*Paul T. Nyffeler, Nicholas A. Boyle, Laxman Eltepu, Chi-Huey Wong, Albert Eschenmoser, Richard A. Lerner, and Paul Wentworth, Jr.**

In memory of Bernard (Bernie) M. Babior

The reaction between HOOH and O_3 has fascinated scientists for almost a century.[1–3] The reactivity of O_3 is markedly increased by the presence of HOOH, although a clear mechanistic understanding of this phenomenon has thus far eluded researchers.[4–8] In modern times, the reaction between HOOH and O_3 has received industrial utility and has been named both the peroxone process and an advanced oxidation reaction.[9,10] It is one of the most potent antibacterial processes known and is a powerful chemical remediation tool utilized to treat soil, groundwater, and wastewater contaminated with polycyclic aromatic hydrocarbons, polychlorinated biphenyls (PCBs), methyl *tert*-butyl ether (MTBE), benzene, toluene, ethylbenzene and xylene (BTEX), trinitrotoluene (TNT), and other persistent organic pollutants.[10]

Recently, the reaction between HOOH and O_3 has become of biological interest. It has been discovered that all antibodies have the ability to catalyze the oxidation of water by singlet oxygen ($^1\Delta_g$), with the postulated intermediacy of HOOOH, to generate HOOH and detectable amounts of an oxidant with the chemical signature of O_3.[11–13] The proposition of HOOOH as a key intermediate in the antibody-catalyzed reaction has led to an interest in the study of thermally accessible routes to HOOOH that may utilize biologically relevant components.

[*] P. T. Nyffeler, Dr. N. A. Boyle, Dr. L. Eltepu, Prof. C.-H. Wong, Prof. R. A. Lerner, Prof. P. Wentworth, Jr.
Department of Chemistry &
The Skaggs Institute for Chemical Biology
The Scripps Research Institute
10550 N. Torrey Pines Rd., La Jolla, CA92037 (USA)
Fax: (+1) 858-784-2590
E-mail: paulw@scripps.edu

Prof. P. Wentworth, Jr.
Oxford Glycobiology Institute
Department of Biochemistry, University of Oxford
South Parks Rd., Oxford, OX1 3QU (UK)

Prof. A. Eschenmoser
Laboratorium für organische Chemie
Eidgenössische Technische Hochschule (ETH)
Hönggerberg HCl-H309
Universitaetstrasse 16 8093 Zürich (Switzerland)

[**] This work was supported by the Skaggs Institute for Chemical Biology. P.W. thanks the members of The Scripps Research Institute NMR facility, especially Dr. D. Huang and Dr. L. Pasternack, for expert assistance during this study.

 © 2004 Wiley-VCH Verlag GmbH & Co. KGaA, Weinheim DOI: 10.1002/anie.200460457

A rigorous kinetic examination of the reaction between O_3 and HOOH was first performed by Rothmund and Burgstaller in 1917.[1] Weiss[14] first proposed a free-radical mechanism for this process, and subsequently Bray[3] concluded that either free radicals, ·OH and hydroperoxyl (HO_2·), or HOOH were necessary to explain the observed kinetics of the process. Taube and Bray[2] in 1940 then established the role of ·OH and HO_2· as chain-initiating intermediates in a complex radical cascade (Table 1, entries 1–4). Subsequent detection of ·OH, the superoxide anion (O_2·$^-$), and the ozonide radical anion (O_3·$^-$) as intermediates in this process supported the free-radical mechanism proposed by Weiss.[15–17] Thus, the contemporary view is that a common free-radical mechanism may account for the decomposition of O_3 by HOOH under all conditions, with the potential involvement of HOOOH being largely ignored. Recently however, HOOOH has been thrust into center stage as a plausible intermediate in the photochemical peroxone process. Engdahl and Nelander[18] observed that mixing HOOH and O_3 in an argon matrix results in a complex that, when photolyzed at 266 nm, produces HOOOH. However, there is no report of HOOOH being detected from the strictly thermal peroxone reaction.

Herein we demonstrate the direct observation of HOOOH formed during the thermal reaction between HOOH and O_3. Passage of a stream of ozone/oxygen gas through a solution of aqueous hydrogen peroxide (ca. 96% w/w), generated either by vacuum distillation of commercially available HOOH (containing stabilizers) or pure HOOH generated by reduction of O_2,[19] in [D_6]acetone or [D_{10}]tetrahydrofuran at −78 °C produced an intermediate that could be characterized by ^{1}H NMR analysis (−60 °C) as having a typical OOOH resonance at $\delta = 13.6 \pm 0.2$ ppm relative to tetramethylsilane (Figure 1b).

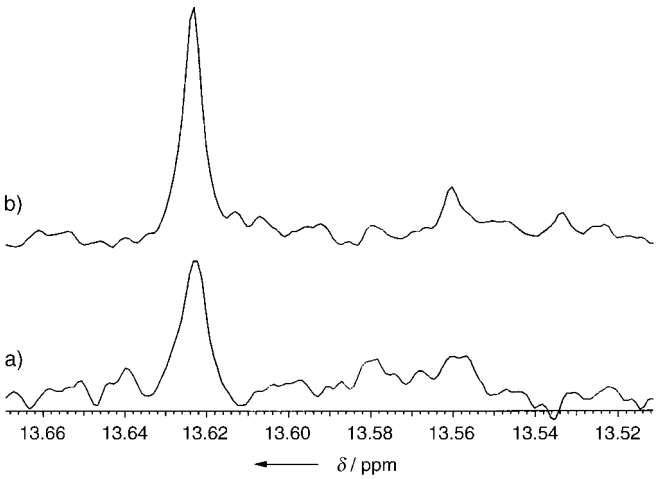


Figure 1. ^{1}H NMR spectra (600 MHz recorded at −60 °C) of the peroxone reaction between $\delta = 13.50$ and 13.70 ppm downfield from phenyltrimethylsilane (PhTMS) in [D_4]methanol (99%, external reference). a) $H_2O_2 + O_3/O_2$ (20 s), b) $H_2O_2 + O_3/O_2$ (20 s) + H_2O_3 (authentic sample). The authentic HOOOH used as an additive in (b) was generated by the ozonation of a resin-supported 1,2-diphenylhydrazine (hydrazobenzene) derivative.[19] An aliquot of this HOOOH solution (100 μL) was added with a glass syringe and needle to the teflon-valved NMR tube at −60 °C. Note that no signal at about 13.60 ppm was present in the following control NMR spectra: 1) After O_3/O_2 was bubbled through [D_6]acetone (99.9%) for 20 s and 2) HOOH (28 M) in [D_6]acetone (99.9%).

Table 1: Selected equations from the reaction between ozone and hydrogen peroxide (in aqueous media unless otherwise stated).

Entry	Equation	Comment
1[a]	$O_3 + H_2O_2 \rightarrow$ ·OH + HO_2· + O_2	$k_1 = 6.5 \times 10^{-2}$ M^{-1} s^{-1}
2[b]	O_3 + ·OH → HO_2· + O_2	$k_2 = 1.1 \times 10^8$ M^{-1} s^{-1}
3[c]	$O_3 + {}^-O_2$· + $H^+ \rightarrow$ ·OH + 2 O_2	$k_3 = 1.6 \times 10^9$ M^{-1} s^{-1}
4[d]	H_2O_2 + ·OH → HO_2· + H_2O	$k_4 = 2.7 \times 10^7$ M^{-1} s^{-1}
5[e]	$O_3 + H_2O_2 \rightarrow H_2O_3 + {}^3O_2$	$\Delta H_r = -32.3$ kcal mol^{-1}
6[f]	$O_3 + HO_2^- \rightarrow HO_3^- + O_2$	$k_6 = 2.8 \times 10^6$ M^{-1} s^{-1}
7[g]	$H_2O_3 \rightarrow {}^1O_2 + H_2O$	$\Delta H_r = -16.2$ kcal mol^{-1}, ΔH_a(0 H_2O) = 45.1 kcal mol^{-1}[h] ΔH_a(1 H_2O) = 12.7 kcal mol^{-1} ΔH_a(2 H_2O) = 0.2 kcal mol^{-1}

[a] Ref. [2, 33]. [b] Ref. [34]. [c] Ref. [35]. [d] Ref. [36, 37]. [e] Gas-phase calculation: Ref. [31]. [f] Ref. [32]. [g] Ref. [21, 38]. [h] The number of water molecules (in parentheses) signifies the molar equivalents of water participating as a catalyst in the reaction.

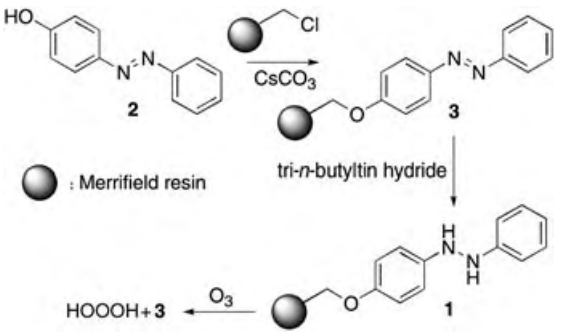
This signal disappeared upon warming the [D_6]acetone and [D_{10}]tetrahydrofuran solutions to room temperature and did not reappear upon recooling. The ^{1}H NMR chemical shift and thermal instability of this intermediate are both in line with the wealth of physical data available for HOOOH.[18,20–23]

To add support to the notion that this ^{1}H NMR resonance at $\delta = 13.6 \pm 0.2$ ppm in the peroxone reactions corresponds to HOOOH, an authentic solution of HOOOH in [D_6]acetone was required as a control. Neither of the two main chemical routes for the preparation of HOOOH (pulsed radiolysis of air-saturated perchloric acid solutions[24,25] or reduction of ozone by reducing agents such as 2-ethylanthrahydroquinone[20] and 1,2-diphenylhydrazine[20,21,23]) were suitable for this control sample. The lifetime of HOOOH in acid solutions (ca. 200 ms in perchlorate pH 2) precludes the pulsed radiolysis method as being viable for NMR analysis (a single pulse sequence in a typical ^{1}H NMR experiment shown in Figure 1 is > 25 s). Plesnicar et al.[26] have shown that HOOOH is always contaminated with a number of oxidation products of 1,2-diphenylhydrazine and HOOH when the low-temperature ozonation of 1,2-diphenylhydrazine in an organic solvent is employed. Therefore a new methodology was required for the generation of a pure solution of HOOOH.

The development of polymer-supported methodologies to facilitate solution-phase chemistry has exploded over the past decade in response to the stringent requirements of high-throughput solution-phase combinatorial and parallel synthesis.[27–30] We rationalized that HOOOH could be prepared free of the contamination products arising from the oxidation of 1,2-diphenylhydrazine (1,2-DPH) if the 1,2-DPH was on a

 © 2004 Wiley-VCH Verlag GmbH & Co. KGaA, Weinheim

resin support. Thus, resin-supported 1,2-DPH derivative **1** was prepared (Scheme 1).[19]



Scheme 1. Preparation of resin-bound diphenylhydrazine **1** and its use to prepare HOOOH from O_3.

The resin-supported hydrazine **1** was prepared in two steps by an initial addition of 4-phenylazophenol (**2**) to low cross-linked (1% divinylbenzene) chloromethylpolystyrene followed by reduction of the orange azo resin derivative **3** with tri-*n*-butyltin hydride in refluxing toluene. Low-temperature ozonation (−78 °C) of resin-1,2-DPH **1** in [D_6]acetone or [D_{10}]tetrahydrofuran with a stream of ozone/oxygen led to the formation of HOOOH in solution, with the only contaminant being HOOH (Figure 2). The oxidized resin turns bright orange during the ozonation, as it becomes oxidized in part to **3**, and can then be removed by filtration.

Addition of the solution of HOOOH in [D_6]acetone (generated by ozonation of **1**) to the NMR tube containing the peroxone reaction resulted in an increase in the area of the OOOH resonance (13.6 ± 0.2 ppm, Figure 1a), thus strengthening the hypothesis that the unknown resonance corresponds to HOOOH.

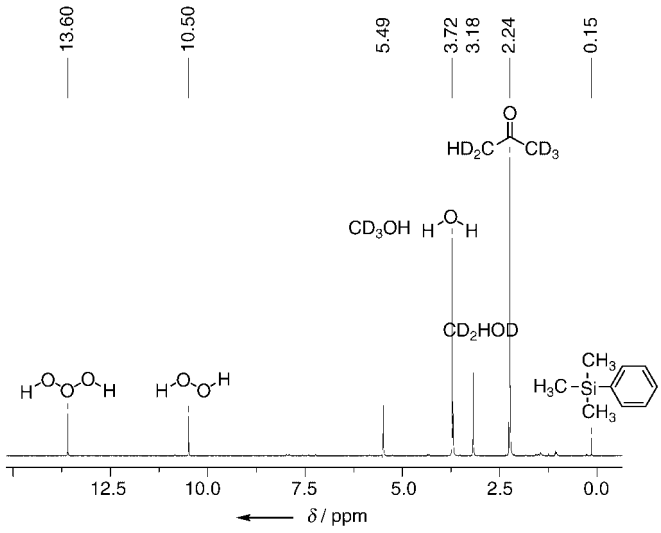


Figure 2. ^{1}H NMR spectrum (600 MHz recorded at −60 °C) of the filtrate following low-temperature ozonation (−78 °C) of resin-**1**. Note PhTMS in [D_4]methanol is present as an external standard for quantification of HOOOH.

The amount of HOOOH generated during the peroxone reaction was determined from an analysis of the relationship between the area of the OOOH resonance (13.6 ± 0.2 ppm) and the amount of HOOOH present in the NMR sample. This relationship was determined by a standard method involving interpolation of the ratio of the peak areas of the OOOH resonance at 13.6 ± 0.2 ppm and the methyl protons of an external standard (phenyltrimethylsilane) to a standard calibration curve. This analysis revealed that approximately 29 μmol of HOOOH (corresponding to a concentration of 2.9 mM in the [D_6]acetone solution) was formed in this specific peroxone reaction (10 mL reaction volume). This quantity of H_2O_3 was reproducibly generated when the peroxone reaction was repeated under identical conditions of HOOH concentration and O_3 flow. This amount of H_2O_3 generated in the peroxone process is significant, and therefore the chemistry of the peroxone reaction may now have to be revised to not only consider ozone and HOOH chemistry, but also that of H_2O_3.

There are at least two mechanistically viable possibilities for the origin of HOOOH in the peroxone reaction. By using quantum chemical methods Xu and Goddard[31] have calculated that the enthalpy of reaction (ΔH_r) for the thermal reaction of HOOH and O_3 to yield HOOOH and $^3O_2$ in the gas phase is −32.3 kcal mol^{-1}, with the highest enthalpy of activation (ΔH_a) being 4.8 kcal mol^{-1} (Table 1, entry 5). The process involves two sequential single electron transfer reactions that is formally the redox reaction between O_3 and HOOH. Xu and Goddard[31] have proposed that the reaction proceeds via a planar seven-membered-ring biradical intermediate (with the spin multiplicity of the triplet and singlet states being almost degenerate) to yield HOOOH and $^3O_2$ (Figure 3 and Table 1, entry 5). More recently, to explain hydrogen isotope effects on the reaction kinetics of the peroxone reaction in water, Lesko et al.[32] have concluded that HO_3^-, the conjugate base of H_2O_3, may be generated from a reaction between the anion of hydrogen peroxide and O_3 (Table 1, entry 6).

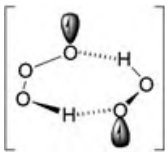


Figure 3. Postulated seven-membered-ring triplet biradical intermediate on the pathway from H_2O_2 and O_3 into H_2O_3 and $^3O_2$.

The observation that HOOOH is generated in the thermal peroxone reaction in low-water-content organic solvents at low temperature brings with it clear questions. These include the as yet, unknown generation of HOOOH under totally aqueous conditions at room temperature of a peroxone mixture. Bielski[24,25] has shown that HOOOH, detected chemically and spectroscopically, is quasistable under totally aqueous conditions ($t_{1/2}$ = ca. 2 s at pH 1.5, 298 K). Koller and Plesnicar[21] and Xu and Goddard[31] have independently calculated that HOOOH decomposes to yield $^1O_2$ and H_2O in a water-catalyzed reaction (Table 1 entry 7). Thus, although not yet reported, $^1O_2$ may well be generated during the peroxone reaction in aqueous systems from the known decomposition of H_2O_3. In addition, further reactions of HOOOH with either itself, HOOH, $^1O_2$, or O_3 to yield, as yet, undefined products will add further complexity to this rich and complex reaction process.

 © 2004 Wiley-VCH Verlag GmbH & Co. KGaA, Weinheim

Experimental Section

Reaction between O_3 and HOOH: All samples were prepared as solutions in $[D_6]$acetone (99.9%) or $[D_{10}]$tetrahydrofuran (99.9%, 10 mL). The experiments were carried out by using Schlenk techniques. In brief, a stream of O_3 in O_2 was bubbled through an HOOH solution (28 M) in $[D_6]$acetone (99.9%) or $[D_{10}]$tetrahydrofuran (99.9%, 10 mL) precooled to −78 °C for 20 s. The hydrogen peroxide used in these studies was prepared either by the resin method described in the Supporting Information or by vacuum distillation of an aqueous H_2O_2 (50% w/v containing stabilizers) solution to approximately one-third volume. These ozonolyzed solutions were then degassed briefly by bubbling argon through the solution of H_2O_2 and transferred to a teflon-valved NMR tube. The samples were then warmed to −60 °C and ^{1}H NMR spectra were measured. Each experiment was repeated at least twice and gave essentially the same amount of HOOOH.

Generation of HOOOH in $[D_6]$acetone with **1**: Resin-supported 1,2-diphenylhydrazine **1** was suspended in $[D_6]$acetone (5 mL) and cooled to −78 °C. A stream of ozone/oxygen gas was passed through the suspension for 2 min. The resin was then removed by filtration under argon and the filtrate was quickly transferred to an NMR tube under a positive argon pressure.

Received: April 26, 2004
Published Online: August 12, 2004

Keywords: deuterium · hydrogen peroxide · oxidation · ozone · solid-phase synthesis

[1] V. Rothmund, A. Burgstaller, *Monatsh. Chem.* **1917**, *38*, 295.
[2] H. Taube, W. C. Bray, *J. Am. Chem. Soc.* **1940**, *62*, 3357.
[3] W. C. Bray, *J. Am. Chem. Soc.* **1938**, *60*, 82.
[4] C.-H. Kuo, L. Zhong, M. E. Zappi, A. P. Hong, *Can. J. Chem. Eng.* **1999**, *77*, 473.
[5] R. J. Spanggord, D. Yao, T. Mill, *Environ. Sci. Technol.* **2000**, *34*, 450.
[6] M. Elovitz, U. von Gunten, *Ozone Sci. Eng.* **1999**, *21*, 239.
[7] M. Elovitz, U. von Gunten, H. Kaiser, *Ozone Sci. Eng.* **2000**, *22*, 123.
[8] J. L. Acero, U. von Gunten, *Ozone Sci. Eng.* **2000**, *22*, 305.
[9] R. Brunet, M. M. Bourbigot, M. Dore, *Ozone Sci. Eng.* **1984**, *6*.
[10] J. Prousek, *Chem. Listy* **1996**, *60*, 229.
[11] P. Wentworth, Jr., L. H. Jones, A. D. Wentworth, X. Zhu, N. A. Larsen, I. A. Wilson, X. Xu, W. A. Goddard III, K. D. Janda, A. Eschenmoser, R. A. Lerner, *Science* **2001**, *293*, 1806.
[12] P. Wentworth, Jr., J. McDunn, A. D. Wentworth, C. Takeuchi, J. Nieva, K. D. Janda, A. Eschenmoser, R. A. Lerner, *Science* **2002**, *298*, 2195.
[13] P. Wentworth, Jr., A. D. Wentworth, X. Zhu, I. A. Wilson, K. D. Janda, A. Eschenmoser, R. A. Lerner, *Proc. Natl. Acad. Sci. USA* **2003**, *100*, 1490.
[14] J. Weiss, *Trans. Faraday Soc.* **1935**, *31*, 668.
[15] K. Sehested, H. Corfitzen, J. Holcman, E. J. Hart, *J. Phys. Chem. A* **1998**, *102*, 2667.
[16] J. Staehelin, R. E. Buhler, J. Hoigne, *J. Phys. Chem.* **1984**, *88*, 5999.
[17] R. E. Buhler, J. Staehelin, J. Hoigne, *J. Phys. Chem.* **1984**, *88*, 2560.
[18] A. Engdahl, B. Nelander, *Science* **2002**, *295*, 482.
[19] See Supporting Information for full details.
[20] J. Cerkovnik, B. Plesnicar, *J. Am. Chem. Soc.* **1993**, *115*, 12169.
[21] J. Koller, B. Plesnicar, *J. Am. Chem. Soc.* **1996**, *118*, 2470.
[22] B. Plesnicar, J. Cerkovnik, T. Tuttle, E. Kraka, D. Cremer, *J. Am. Chem. Soc.* **2002**, *124*, 11260.
[23] B. Plesnicar, J. Cerkovnik, T. Tekavec, J. Koller, *Chem. Eur. J.* **2000**, *6*, 809.
[24] B. H. J. Bielski, *J. Phys. Chem.* **1970**, *74*, 3213.
[25] B. H. J. Bielski, H. A. Schwartz, *J. Phys. Chem.* **1968**, *72*, 3836.
[26] B. Plesnicar, T. Tuttle, J. Cerkovnik, J. Koller, D. Cremer, *J. Am. Chem. Soc.* **2003**, *125*, 11553.
[27] C. Spanka, P. Wentworth, K. D. Janda, *Comb. Chem. High Throughput Screening* **2002**, *5*, 233.
[28] P. Wentworth, Jr., K. D. Janda, *Curr. Opin. Biotechnol.* **1998**, *9*, 109.
[29] P. Wentworth, Jr., K. D. Janda, *Chem. Commun.* **1999**, 1917.
[30] P. Wentworth, Jr., *Trends Biotechnol.* **1999**, *17*, 448.
[31] X. Xu, W. A. Goddard, *Proc. Natl. Acad. Sci. USA* **2002**, *99*, 15308.
[32] T. M. Lesko, A. J. Colussi, M. R. Hoffman, *J. Am. Chem. Soc.* **2004**, *126*, 4432.
[33] K. Sehested, H. Corfitzen, J. Holcman, E. J. Hart, *J. Phys. Chem.* **1992**, *96*, 1005.
[34] K. Sehested, J. Holcman, E. Bjergbakke, E. J. Hart, *J. Phys. Chem.* **1984**, *88*, 4144.
[35] NDRL/NIST Solutions Kinetics Database, NIST Standard Reference Database 40, http://kinetics.nist.gov/solution/index.php, **2002**.
[36] H. Christensen, K. Sehested, H. Corfitzen, *J. Phys. Chem.* **1982**, *86*, 1588.
[37] G. V. Buxton, C. L. Greenstock, W. P. Helman, A. B. Ross, *J. Phys. Chem. Ref. Data* **1988**, *17*, 513.
[38] X. Xu, P. R. Muller, W. A. Goddard III, *Proc. Natl. Acad. Sci. USA* **2002**, *99*, 3376.

 © 2004 Wiley-VCH Verlag GmbH & Co. KGaA, Weinheim

Luminescence

Green and Red Three-Photon Upconversion from Polymeric Lanthanide(III) Complexes**

Ka-Leung Wong, Wai-Ming Kwok, Wing-Tak Wong, David Lee Phillips,* and Kok-Wai Cheah**

In the last decade, there has been significant interest in the nonlinear luminescence from organic–lanthanide complexes owing to their potential applications in three-dimensional

[*] K.-L. Wong, Dr. W.-M. Kwok, Prof. Dr. W.-T. Wong, Prof. Dr. D. L. Phillips
Department of Chemistry, The University of Hong Kong
Pokfulam Road, Hong Kong (P. R. China)
Fax: (+852) 2547-2933
E-mail: wtwong@hkucc.hku.hk
phillips@hku.hk

Dr. K.-W. Cheah
Department of Physics, Hong Kong Baptist University
Kowloon Tong, Hong Kong, (P. R. China)
Fax: (+852) 3411-5882
E-mail: kwcheah@hkbu.edu.hk

[**] The authors acknowledge the financial support of the Hong Kong Research Grants Council (HKU 1/01C), The University of Hong Kong, and the Hong Kong Baptist University. We thank The University of Hong Kong for a postgraduate studentship (K.L.W.) and a postdoctoral fellowship (W.M.K.).

Supporting information for this article is available on the WWW under http://www.angewandte.org or from the author.

 DOI: 10.1002/anie.200460576 © 2004 Wiley-VCH Verlag GmbH & Co. KGaA, Weinheim

fluorescence imaging, optical data storage, lithographic microfabrication, and laser device fabrication.[1] Multiphoton (e.g. indirect three-photon) processes allow the excitation of fluorophores in a lower energy spectral region—this is useful for optical communications (such as three-dimensional data storage) and is particularly important for imaging and therapy as longer wavelength radiation is less harmful to the body's tissues and cells and allows efficient penetration with less damage.[2] Multiphoton excitation allows molecules that typically absorb in the ultraviolet region to be excited with red or near-infrared light. The photoluminescence processes from organic–lanthanide complexes are usually induced by an organic chromophoric ligand that absorbs light and transfers this excitation energy to the lanthanide ion.[2] A large number of complexes of lanthanide (Ln) ions with organic chromophores have been synthesized and their two-photon upconversion photophysical properties investigated.[3] Complexes of Eu^{III}, Tb^{III}, Dy^{III}, Er^{III}, Nd^{III}, Sm^{III}, and Yb^{III} ions with fluorescent chelators, and complexes of Eu^{III} and Tb^{III} ions with nucleic acids and proteins have been reported.[4]

Until now, only a few multiphoton processes have been observed owing to the limitations of experimental measurements, but with recent advances in technology experimentation has coalesced with theory to allow direct three-photon excitation. Stimulated emission following direct three-photon excitation has only been observed for one organic chromophore,[5] and reports of three-photon upconversion processes from organic–lanthanide complexes are very scarce.[6] Herein, we demonstrate a direct three-photon upconversion process in organic–lanthanide complexes (Ln = Eu, Tb) upon excitation at 845 nm.

The tripodal ligand *N*-[2-(bis{2-[(2-methoxybenzoyl)amino]ethyl}amino)ethyl]-2-methoxybenzamide (**1**)[7] was treated with terbium and europium nitrate salts to give the complexes $[Tb(\mathbf{1})(NO_3)_3]$ and $[Eu(\mathbf{1})(NO_3)_3]$. Single crystals of both complexes were isolated through the slow evaporation of a solution of the respective complex in acetonitrile at room temperature over a few days. The crystal structures of both complexes were determined by X-ray crystallography; the structure of $[Tb(\mathbf{1})(NO_3)_3]$ is shown in Figure 1. The Ln ion is coordinated by three amide groups from two ligands, which function as bridges to give a one-dimensional covalent (linear polymeric) chain (Figure 2). The distances between the two

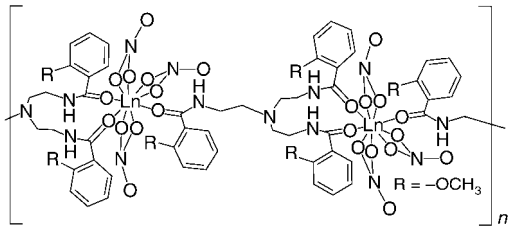


Figure 2. Schematic drawing of the polymeric structure of the complexes $[Ln(\mathbf{1})(NO_3)_3]$ (Ln = Tb or Eu).

neighboring Ln^{3+} ions in the homometallic complexes are 9.443 Å for Ln = Tb and 9.465 Å for Ln = Eu along the *c* axis.

The UV/Vis absorption spectrum of the ligand displays three intense bands at $\lambda \sim 220$, 280, and 330 nm (see Figure 3) which are attributed to benzyl π–π* and carbonyl transitions of the benzoate groups of the ligand. Upon complexation of the ligand to the lanthanide ions, the absorption bands undergo small shifts to longer wavelengths.[8,9] The ligand and complexes do not display absorption bands in the spectral range from 400 to 845 nm. However, the blue, green, and red upconversion luminescence emissions from the ligand and the Tb and Eu complexes, respectively, were observed upon excitation at 845 nm (with a Ti:sapphire laser). It can be seen from Figure 3a that at least three photons are required to promote the ligand to the excited state when it is irradiated at 845 nm. Figure 3b shows the nonlinear f→f emission spectra of $[Eu(\mathbf{1})(NO_3)_3]$ and $[Tb(\mathbf{1})(NO_3)_3]$ recorded in the solid state upon excitation at 845 nm. The structured emission

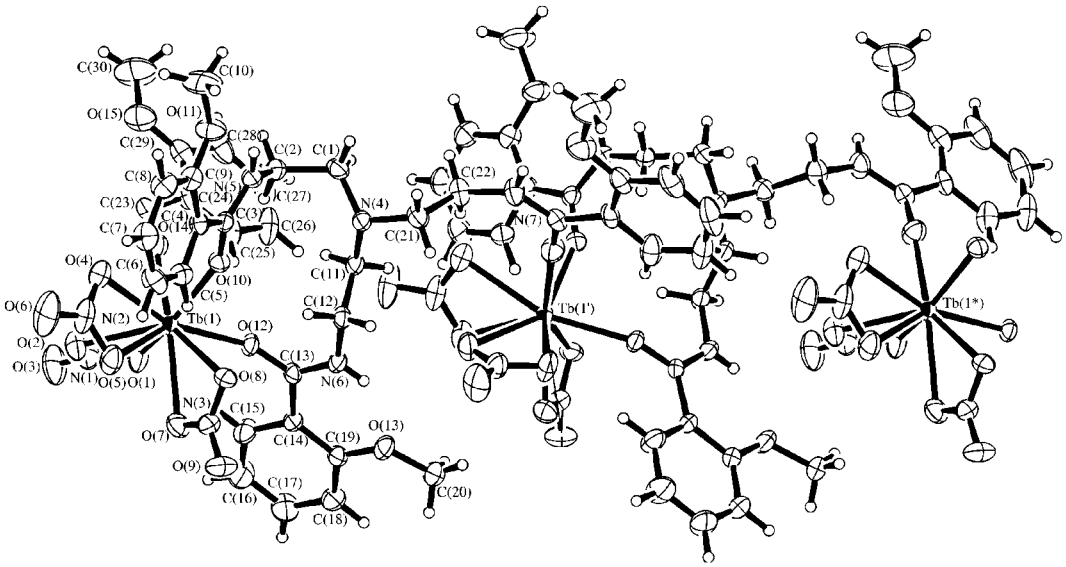


Figure 1. ORTEP drawing of $[Tb(\mathbf{1})(NO_3)_3]$.

 © 2004 Wiley-VCH Verlag GmbH & Co. KGaA, Weinheim

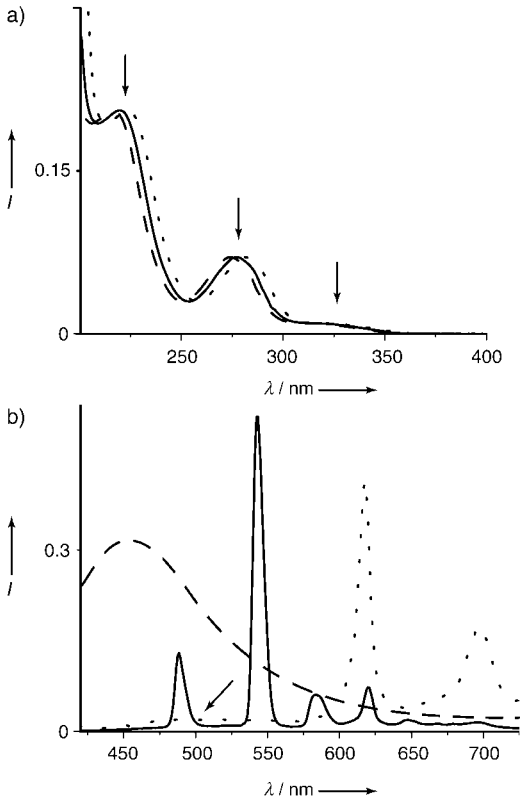


Figure 3. a) UV/Vis absorption spectra of **1**, $[Tb(\mathbf{1})(NO_3)_3]$, and $[Eu(\mathbf{1})(NO_3)_3]$ (1.0×10^{-5} M in MeOH); b) the three-photon-induced upconversion emission of **1**, $[Tb(\mathbf{1})(NO_3)_3]$, and $[Eu(\mathbf{1})(NO_3)_3]$ in the solid state (room temperature, $\lambda_{ex}=845$ nm). – – – = **1**, —— = $[Tb(\mathbf{1})(NO_3)_3]$, ----- = $[Eu(\mathbf{1})(NO_3)_3]$.

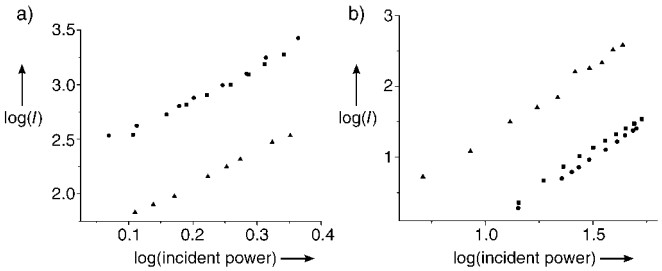


Figure 4. Power dependence of the emission intensities of a) three-photon ($\lambda_{ex}=845$ nm) and b) two-photon ($\lambda_{ex}=650$ nm) upconversion processes of **1** (▲; $\lambda_{em}=450$ nm; $S_1\rightarrow S_0$), $[Tb(\mathbf{1})(NO_3)_3]$ (■; $\lambda_{em}=545$ nm; $^5D_4\rightarrow{}^7F_5$), and $[Eu(\mathbf{1})(NO_3)_3]$ (●; $\lambda_{em}=620$ nm; $^5D_0\rightarrow{}^7F_2$).

bands that arise from transitions of $^5D_4\rightarrow{}^7F_J$ ($J=6$–3) states in $[Tb(\mathbf{1})(NO_3)_3]$ and $^5D_0\rightarrow{}^7F_J$ ($J=1$, 2, 4) states in $[Eu(\mathbf{1})(NO_3)_3]$ are shown. A weak emission from the ligand in $[Eu(\mathbf{1})(NO_3)_3]$ is detected between 400 and 550 nm (as indicated by the arrow in Figure 3b) In a control experiment, the inorganic terbium and europium nitrate salts were also directly excited under the same experimental conditions. Emission through upconversion processes was *not* observed which implies that the three-photon nonlinear energy-transfer emission is induced by the ligand.

Furthermore, two-photon emission was observed when the complexes were excited at 650 nm (with a nanosecond Nd:YAG laser) yet emission was not observed when the sample was excited at 845 nm with the same source (emission was only observed upon excitation at 845 nm with a Ti:sapphire femtosecond laser source). The power output from a femtosecond laser is ten thousand times stronger than that from a nanosecond laser and consequently, the quantum efficiency of the three-photon process is therefore much lower than the two-photon process. To confirm further the nonlinear processes of the ligand and the complexes, the evolution of the intensities of the peaks were plotted as a function of the incident power[10] at 845 and 650 nm (Figures 4a and b, respectively). The results obey the equation derived by Soga and co-workers,[11] whereas the slopes derived from the experimental data for the ligand and the complexes (≈3.0 at $\lambda_{ex=}845$ nm; ≈2.0 at $\lambda_{ex=}650$ nm) are in good agreement with the upconversion processes; that is, three photons are absorbed at 845 nm.

The pathway of the three-photon upconversion process for the ligands and complexes is proposed in Figure 5. First,

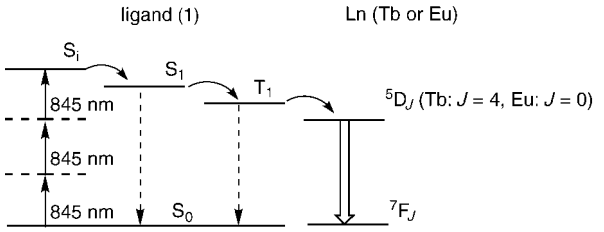


Figure 5. The proposed mechanism for the three-photon excitation and emission process. S_i is a higher energy singlet state; S_1 is the radiative lower singlet state; T_1 is the lowest energy triplet excited state; S_0 refers to the ground state. Linear arrows indicate radiative energy-transfer processes and curly arrows represent nonradiative energy-transfer processes.

upon excitation with either visible or near-infrared pulses, the ligand absorbs three photons and is excited from the ground singlet state S_0 to a higher energy singlet state S_i. Then, the electrons in S_i relax to the lowest energy singlet state S_1 from where they relax further through intersystem crossing to the lowest triplet excited state T_1.[5,12] A photophysical study of the analogous Gd complex $[Gd(\mathbf{1})(NO_3)_3]$ showed that the transfer of energy from the ligand to the metal takes place from the triplet state of the ligand as opposed to the singlet state (recently, it has been shown that lanthanide luminescence can also be sensitized through energy transfer from the singlet state of an appropriate ligand.[13]) As the ligand is coordinated to a 'heavy' atom (Ln), the ($S_1\rightarrow T_1$) intersystem-crossing rate is enhanced.[12,13] Finally, energy is transferred from the triplet state of the ligand to Tb^{III} or Eu^{III} through either a nonresonant phonon-assisted or resonant process. This leads to the excitation of Tb^{III} to the $^5D_4$ state and Eu^{III} to the $^5D_0$ state; upon relaxation from these states, they emit their characteristic green and red luminescence, respectively.

In summary, we have demonstrated the indirect, three-photon-induced sensitization of terbium and europium complexes through an upconversion process. Tris(2-methoxybenz-

 © 2004 Wiley-VCH Verlag GmbH & Co. KGaA, Weinheim

amide)triethylamine **1** is a good ligand for the multiphoton nonlinear photoluminescence of the lanthanides and may serve in future designs of new three-photon materials and in the development of organic–lanthanide complexes as biological probes.

Experimental Section

Ligand **1** was prepared according to the literature.[7] $Ln(NO_3)_3{\cdot}6H_2O$ (47 mmol; Ln = Tb or Eu) and **1** (47 mmol) were dissolved in acetonitrile (15 mL) and the mixture was heated at reflux for 24 h. Colorless single crystals of $Ln(\mathbf{1})(NO_3)_3$ were obtained by slow evaporation of the solution. $[Tb(\mathbf{1})(NO_3)_3]$ (65%); elemental analysis: calcd for $C_{30}H_{38}N_7O_{16}Tb$ (%): C 39.47, H 4.17, N 10.75; found: C 39.46, H 4.18, N 10.74; FAB-MS: *m/z*: 831 $[M-NO_3-H_2O]^+$, 770 $[M-2NO_3-H_2O]^+$, 708 $[M-3NO_3-H_2O]^+$, 549 $[M-3NO_3-H_2O-Tb]^+$. $[Eu(\mathbf{1})(NO_3)_3]$ (60%); elemental analysis: calcd for $C_{30}H_{38}N_7O_{16}Eu$ (%): C 40.63, H 4.06, N 11.06; found: C 39.77, H 4.19, N 11.82; FAB-MS: *m/z*: 825 $[M-NO_3-H_2O]^+$, 763 $[M-2NO_3-H_2O]^+$, 701 $[M-3NO_3-H_2O]^+$, 549 $[M-3NO_3-H_2O-Eu]^+$.

Crystal data for $[Tb(\mathbf{1})(NO_3)_3]$: $C_{30}H_{38}N_7O_{16}Tb$, $M = 911.59$, monoclinic, $P2_1/c$, $a = 9.922(2)$, $b = 20.738(3)$, $c = 18.849(3)$ Å, $V = 3775.9(11)$ Å^3, $T = 298$ K, $Z = 4$, $\mu(Mo_{K\alpha}) = 1.948$ cm^{-1}, 23674 reflections measured of which 8761 were unique ($R_{int} = 0.048$), 4861 observed reflections [$I > 2\sigma(I)$] were used in all calculations, $R(F) = 0.039$, $R_w = 0.039$. Crystal data for $[Eu(\mathbf{1})(NO_3)_3]$: $C_{30}H_{38}N_7O_{16}Eu$, $M = 904.63$, monoclinic, $P2_1/c$, $a = 9.987(4)$, $b = 20.783(7)$, $c = 18.893(7)$ Å, $V = 3822.6(25)$ Å^3, $T = 298$ K, $Z = 4$, $\mu(Mo_{K\alpha}) = 1.813$ cm^{-1}, 23452 reflections measured of which 8741 were unique ($R_{int} = 0.034$), 6096 observed reflections [$I > 2\sigma(I)$] were used in all calculations, $R(F) = 0.034$, $R_w = 0.039$. CCDC 237876 ($[Tb(\mathbf{1})(NO_3)_3]$) and 237877 ($[Eu(\mathbf{1})(NO_3)_3]$) contain the supplementary crystallographic data for this paper. These data can be obtained free of charge via www.ccdc.cam.ac.uk/conts/retrieving.html (or from the Cambridge Crystallographic Data Centre, 12, Union Road, Cambridge CB2 1EZ, UK; fax: (+44) 1223-336-033; or deposit@ccdc.cam.ac.uk).

UV/Vis absorption spectra (200–1100 nm) were recorded on a HP UV-8453 spectrophotometer. The 845-nm pump excitation sources were generated from the fundamental of a femtosecond modelocked Ti:Sapphire laser system (output beam ~150-fs duration, 1-kHz repetition rate). The lasers were focused through a 10-cm lens onto the sample and the pumping peak intensity at the sample point was ≈3 to 0.5 GW cm^{-1}. The third harmonics, 325-nm line of a Nd:YAG laser (Quantel Brillant B) was used to pump the OPO (Opotek MagicPrism VIR) system to provide a tunable laser source from 650 nm with a pulse width of ≈4 ns. The emitted light was collected with a backscattering configuration into a 0.5-m spectrograph and detected with a liquid nitrogen-cooled CCD detector.

Received: May 7, 2004

Keywords: energy transfer · lanthanides · luminescence · tripodal ligands · upconversion

[1] a) X.-M. Wang, D. Wang, W.-L. Jiang, M.-H. Jiang, *Opt. Mater.* **2002**, *20*, 217–223; b) R. Sivaraman, S. J. Clarson, B. K. Lee, A. J. Steckl, B. A. Reinhardt, *Appl. Phys. Lett.* **2000**, *77*, 328–330.

[2] a) H. C. Aspinall, *Chem. Rev.* **2002**, *102*, 1807–1850; b) G. F. Sá, O. L. Malta, C. Mello Dongeá, A. M. Simas, R. L. Longo, P. A. SantaCruz, E. F. Silva, Jr., *Coord. Chem. Rev.* **2000**, 196, 165–195; c) S. I. Klink, H. Keizer, F. C. J. M. van Veggel, *Angew. Chem.* **2000**, *112*, 4489–4491; *Angew. Chem. Int. Ed.* **2000**, *39*, 4319- 4321; d) O. L. Malta, H. F. Brito, J. F. S. Menezes, F. R. Gonçalves de Silva, C. de Mello Donegá, S. Alves, Jr., *Chem. Phys. Lett.* **1998**, *282*, 233–238; e) M. Latva, H. Takalo, V. M. Mukkala, C. Matachescu, J. C. Rodriguez-Ubis, J. Kankare, *J. Lumin.* **1997**, *75*, 149–169.

[3] a) M. N. Bochkarev, *Chem. Rev.* **2002**, *102*, 2089–2117; b) C.-F. Liao, J.-L. Lai, J.-A. Chen, H.-T. Chen, H.-L. Cheng, G.-R. Her, J.-K. Su, Y. Wang, G.-H. Lee, M.-K. Leung, C.-C. Wang, *J. Org. Chem.* **2001**, *66*, 2566–2571; c) K.-Z. Wang, C.-H. Huang, D.-J. Zhou, G.-X. Xu, Y. Xu, Y. Q. Liu, D.-B. Zhu, X.-S. Zhao, X.-M. Xie, *Solid State Commun.* **1995**, *93*, 189–191; d) J. R. Peterson, *J. Alloys Compd.* **1995**, *225*, 11–14; e) J. Sztucki, W. Strek, *Chem. Phys.* **1990**, *143*, 347–357; f) K.-F. Li, J.-X. Meng, K.-W. Cheah, *Chem. Phys. Lett.* **2004**, in press.

[4] a) F. Auzel, *Chem. Rev.* **2004**, *104*, 139–174; b) S. Petoud, S. M. Cohen, J.-C. G. Bünzli, K. N. Raymond, *J. Am. Chem. Soc.* **2003**, *125*, 13324–13325; c) W. P.-W. Lai, W.-T. Wong, B. K.-F. Li, K.-W. Cheah, *New J. Chem.* **2002**, *26*, 576–581; d) G. Piszczek, I. Gryczynski, B. P. Maliwal, J. R. Lakowicz, *J. Fluoresc.* **2002**, *12*, 15–17; e) G. Piszczek, B. P. Maliwal, I. Gryczynski, J. Dattelbaum, J. R. Lakowicz, *J. Fluoresc.* **2001**, *11*, 101–107; f) S. Wang, W. Huang, T. Zhang, H. Yang, Q. Gong, Y. Okuma, M. Horokri, Y. F. Miura, *Appl. Phys. Lett.* **1999**, *75*, 1845–1847.

[5] G.-S. He, P. P. Markowlez, T.-C. Lin, P. N. Prasad, *Nature* **2002**, *415*, 767–770.

[6] J. S. Shirk, J. R. Lindle, F. J. Bartoll, M. E. Boyle, *J. Phys. Chem.* **1992**, *96*, 5847–5852.

[7] S. M. Cohen, M. Meyer, K. N. Raymond, *J. Am. Chem. Soc.* **1998**, *120*, 6277–6286.

[8] M. Rumi, J. E. Ehrlich, A. A. Heikal, J. W. Perry, S. Barlow, Z.-Y. Hu, D. McCord-Maughom, T. C. Parker, H. Röckel, S. Thayumanavan, S. R. Marder, D. Beljonne, J. L. Brédas, *J. Am. Chem. Soc.* **2000**, *122*, 9500–9510.

[9] N. Sabbatini, M. Guardigli, J.-M. Lehn, *Coord. Chem. Rev.* **1993**, *123*, 201–208.

[10] a) J. L. Adam, N. Duhausl-Hery, J. Y. Allas, *J. Non-Cryst. Solids* **1997**, *213*, 245–250; b) M. Pollnau, D. R. Gamelin, S. R. Lüthi, H. U. Güdel, M. P. Hehlen, *Phys. Rev. B* **2000**, *61*, 3337–3346.

[11] S. Tanabe, K. Tamai, K. Hirao, N. Soga, *Phys. Rev. B* **1993**, *47*, 2507–2514.

[12] G. S. Maciel, K.-S. Kim, S.-J. Chung, J. Swiatkiewicz, G.-S. He, P. N. Prasad, *J. Phys. Chem. B* **2001**, *105*, 3155–3157.

[13] C. Yang, L.-M. Wang, J.-P. Zhang, W.-T. Wong, X.-C. Ai, Y.-F. Qiao, B.-S. Zou, L.-L. Gui, *Angew. Chem.* **2004**, in press; *Angew. Chem. Int. Ed. Engl.* **2004**, in press.

 © 2004 Wiley-VCH Verlag GmbH & Co. KGaA, Weinheim

Surface Chemistry

Responsive Aligned Carbon Nanotubes**

Taolei Sun, Huan Liu, Wenlong Song, Xi Wang, Lei Jiang, Lin Li,* and Daoben Zhu*

Aligned carbon nanotubes (ACNTs)[1] have aroused great interest because of their ability to align and their easy integration into microdevices. Surface modification of ACNTs by responsive molecules is still a challenge, but it could help to obtain better control over their properties and thus may bring about more opportunities for their application. Wettability[2] is a basic property of solid surfaces and is important in both fundamental research and industrial applications. We have reported previously superhydrophobicity on ACNT films[3] as well as control over the wettability of the films by controlling the tropism of the carbon nanotubes (CNT) and adjusting the structural parameters.[4] Herein, we report the modification of ACNT films with poly(*N*-isopropylacrylamide) (PNIPAAm),[5] a temperature-responsive polymer, through surface-initiated atom transfer radical polymerization (SI-ATRP),[6] a method which can be easily extended to modification with other responsive polymers. Both the macroscopic and the microscopic properties of the modified ACNTs exhibit remarkable responsiveness. On the macroscopic scale the ACNT film shows distinct temperature-sensitive wettability, while on the microscopic scale atomic force microscopy (AFM) studies indicate that a single CNT on this film is also temperature responsive—its diameter and rigidity can change with variation of the temperature. This responsiveness is important in applications of ACNTs, including in intelligent microdevices.[7]

[*] Dr. T. Sun, H. Liu, W. Song, Prof. Dr. L. Jiang, Prof. Dr. D. Zhu
Key Laboratory of Organic Solids
Institute of Chemistry
The Chinese Academy of Sciences
Beijing 100080 (P. R. China)
Fax: (+86) 10-8262-7566
E-mail: jianglei@iccas.ac.cn

X. Wang, Prof. Dr. L. Li
Joint Laboratory of Polymer Science and Materials
Institute of Chemistry
Beijing 100080 (P. R. China)
Fax: (+86) 10-82619830
E-mail: lilin@iccas.ac.cn

Dr. T. Sun, Prof. Dr. L. Jiang
National Center for Nanoscience and Technology
Beijing 100080 (P. R. China)

W. Song
Department of Chemistry
Jilin University
Changchun 130023 (P. R. China)

[**] This work was supported by the National Nature Science Foundation of China (20374054, 90306011, and 20125102) and the Outstanding Youth Fund (Grant No. 20325414).

Supporting information for this article is available on the WWW under http://www.angewandte.org or from the author.

The SI-ATRP technique provides a "graft-from" approach to fabricate a polymer film on a solid surface, and has been applied in the functionalization[8] of multiwall CNT surfaces.[8c,d] In this study we used this technique to achieve PNIPAAm modification of ACNTs that had been deposited on a silicon substrate by chemical vapor deposition (CVD). The experiments involve four steps: 1) ACNTs functionalized with carboxy groups[3a,8c,8d] were obtained by immersing an ACNT film in hot (80 °C) concentrated nitric acid (63 %) for about two hours; 2) NH_2 groups were introduced onto the ACNT surface by refluxing the carboxy-functionalized ACNT film in a solution of aminopropyltrimethoxysilane in toluene; 3) initiators were anchored onto the surface by reaction of bromoisobutyryl bromide with the NH_2 groups; and 4) *N*-isopropylacrylamide was polymerized by SI-ATRP, which resulted in the PNIPAAm-modified ACNTs.

Comparison of the X-ray photoelectron spectra (see Supporting Information) of the ACNTs after the polymerization process with those of the fresh ACNTs, as well as the FTIR spectrum of the modified ACNTs (also see Supporting Information), show that PNIPAAm had been successfully coated onto the ACNT surface by the SI-ATRP process. The scanning electron microscopic (SEM) images for ACNT film with PNIPAAm modification (Figure 1a,b) indicate that

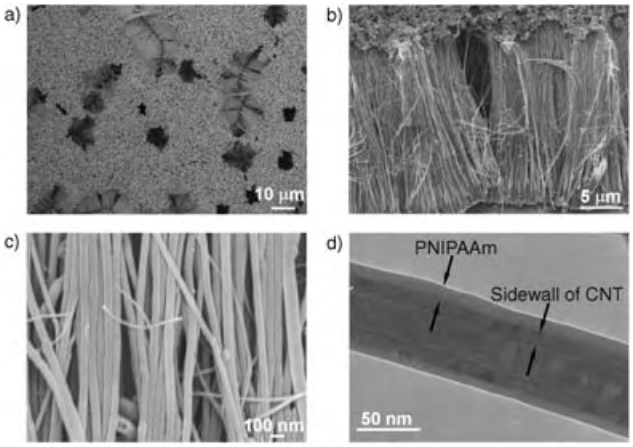


Figure 1. SEM and TEM images of PNIPAAm-modified ACNTs. SEM images viewed from the a) top and b) side. c) The magnified image of (b). d) TEM image of a single CNT taken from the ACNT film with PNIPAAm modification.

although there is some aggregation of the ACNTs (as shown by the holes in Figure 1a), the aligned structure remains virtually intact after polymerization. The magnified image (Figure 1c) of Figure 1b shows a clear increase of about 15 nm in the average diameter of the CNTs relative to the fresh ACNTs, the diameter of which is about 15–50 nm (average value: ca. 39.7 nm). The transmission electron microscopy (TEM) image (Figure 1d) of a single CNT taken from the PNIPAAm-modified ACNT film reveals a distinct layer of PNIPAAm with an average thickness of about 9.3 ± 2.0 nm compared to the TEM images (see Supporting Information) of fresh CNTs. This observation is consistent with the SEM results and further confirms the

 DOI: 10.1002/anie.200460774 © 2004 Wiley-VCH Verlag GmbH & Co. KGaA, Weinheim

successful grafting of PNIPAAm. More interestingly, both the SEM and TEM images show that the modification layer is homogeneous and almost free of defects, thus indicating the good reliability of this polymerization method. Furthermore, this SI-ATRP technique can be easily extended to the modification of ACNTs with other responsive polymers; for example, we have modified the ACNTs with the electrosensitive polymer poly(2-acrylamido-2-methylpropane sulfonic acid) by a similar process, and will be reported later.

PNIPAAm-modified solid surfaces are reported to exhibit responsive wettability,[9] which is considered to result from the competition between intermolecular and intramolecular hydrogen bonding below and above the lower critical solution temperature of about 32–33 °C.[10] For example, we demonstrated previously[11] a reversible switching between superhydrophilicity and superhydrophobicity in a temperature range of about 10 °C on a PNIPAAm-modified rough substrate. Thus, the wettability on a PNIPAAm-modified ACNT film was also expected to be responsive to variation in temperature.

The wettability of the ACNT films with and without PNIPAAm modification was investigated by measurement of the contact angle (CA). The fresh ACNT film shows a superhydrophobicity with a contact angle of $159.5 \pm 2.2°$, while after functionalization with NH_2 groups and initiator molecules the film is much more hydrophilic, with CA values of 0 and $36.0 \pm 2.4°$, respectively; no temperature-responsive behavior was observed for any of these contact angles. Figure 2 shows the spreading behavior of a water droplet on a

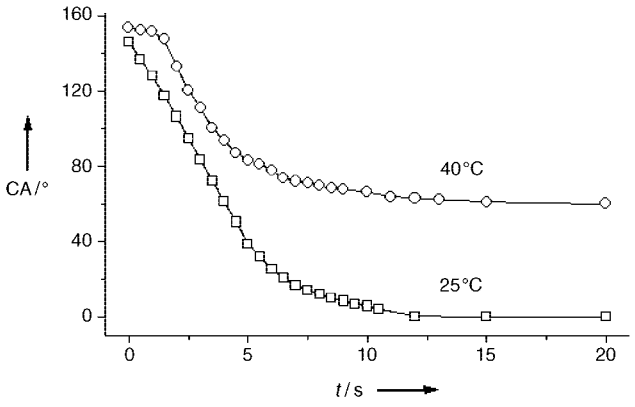


Figure 2. The spreading behavior of a water droplet on a PNIPAAm-modified ACNT film under different temperatures.

PNIPAAm-modified ACNT film under low (25 °C) and high (40 °C) temperatures. The water droplet spreads out quickly at low temperature, and superhydrophilicity with a contact angle of about 0° could be reached in about 10 seconds. At a higher temperature, however, the film remained superhydrophobic with a contact angle of about 150° for about 1.5 seconds before the water droplet started to spread to give a CA value of $63.7 \pm 1.8°$ (after about 10 seconds). This result indicates that this film is temperature-responsive and that the wettability can be controlled by variation of the temperature. More importantly, good reproducibility and reversibility of this effect was observed in experiments with repeated cycling of the temperature from 25 °C to 40 °C, and the recovery process is quick (less than 5 minutes, depending on the time needed for the water droplet to dry on the slice), thus indicating that the responsive wettability can be controlled. In contrast with the wettability switching on a PNIPAAm-modified rough silicon substrate,[11] the modified ACNT film did not show a superhydrophobic property at high temperatures, but was relatively hydrophilic. We consider this property occurs because of the looser configuration of the PNIPAAm chains as a result of the low concentration of the surface-bonded initiator (see Supporting Information) and the structural factors of the film, for example, the partial loss of roughness induced by PNIPAAm grafting.

The intermolecular and intramolecular hydrogen-bonding interactions between the PNIPAAm chains lead to an extended and a compact configuration of the PNIPAAm chains, respectively, which can result in another important property of PNIPAAm: the temperature-induced swelling and shrinkage of the volume. For example, Jones et al.[12] reported a volume change of about 30 % for a surface-modified layer of PNIPAAm when the temperature was raised from 25 to 35 °C. The microscopic properties of a single CNT form the foundation of the macroscopic properties of the ACNT film. Therefore, to confirm the temperature responsiveness of the PNIPAAm-modified ACNTs we carried out further experiments to investigate the temperature-induced contraction of the PNIPAAm layer on a single CNT by using an AFM apparatus equipped with a high-temperature facility.[13] Figure 3 a,b shows the AFM images of a single CNT taken from the PNIPAAm-modified ACNT film at temperatures of 25 and 40 °C, respectively. A clear reduction in the diameter of the nanotube, which is about 4.3 ± 0.3 nm, can be observed with an increase of temperature. The images indicate a contraction of 21–25 % in the film thickness of the PNIPAAm-modification layer compared to that of the original thickness, as determined by TEM. The corresponding phase images (Figure 3 c,d) also show a distinct change when the temperature is changed from 25 to 40 °C. The PNIPAAm-modified CNT exhibits a phase difference of about 15.4° relative to the surrounding silicon substrate at 25 °C, while this difference changes to only about 7.4° at 40 °C, thus indicating that the rigidity of the PNIPAAm layer increases with the increase in temperature. This result can be explained by the PNIPAAm chains becoming denser with the elevation of temperature. These effects further confirm the temperature responsiveness of the PNIPAAm-modified ACNTs, and are also very important for both CNTs and ACNTs in applications as intelligent microdevices, for example, as a transducer for temperature control in a microsystem.

In conclusion, we successfully grafted PNIPAAm onto ACNTs by using an SI-ATRP method and observed the temperature responsiveness of the resulting surface. A water droplet exhibits different spreading behaviors on the film surface, which shows different wettability under low and high temperatures. The good reproducibility of this effect shows a high degree of control over the responsive wettability of the ACNT film. Correspondingly, a distinct reduction in the diameter of the modified CNT, as well as a clear increase in the rigidity of its surface can be observed with an increase of

 © 2004 Wiley-VCH Verlag GmbH & Co. KGaA, Weinheim

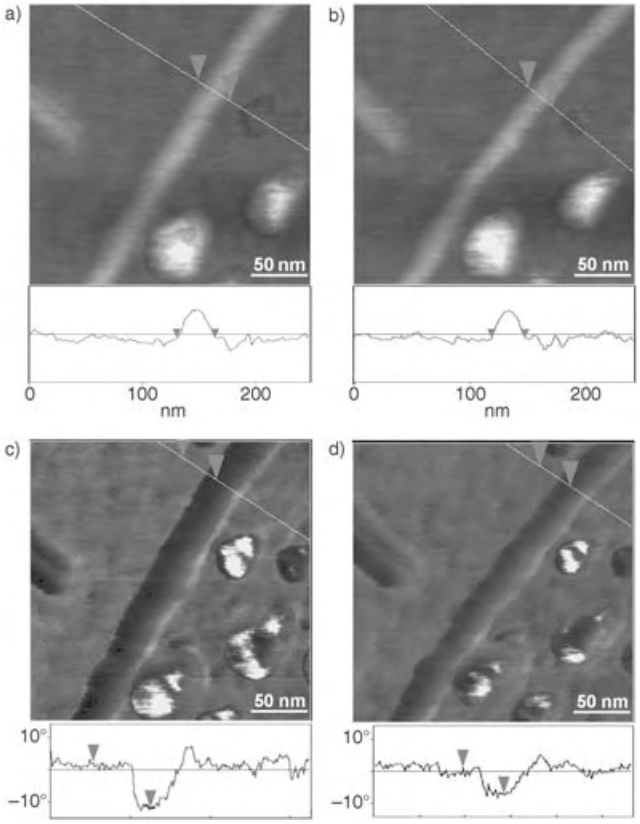


Figure 3. AFM images of a single CNT taken from the PNIPAAm-modified ACNT film under different temperature. a, b) Morphological images; c, d) corresponding phase images; a), c) 25 °C; b), d) 40 °C.

temperature, which is the result of the temperature-induced contraction of the PIPAAm modification layer. This responsiveness of ACNTs may help to obtain better control over their properties, and thus extend their range of applications.

Experimental Section

Preparation of an ACNT film on a silicon substrate: These were prepared by pyrolysis of iron phthalocyanines (FePc) containing both the metal catalyst and carbon source required for the growth of the nanotube. The pyrolysis of FePc was performed under an Ar/H_2 (1:2 v:v) flow of 50–60 $cm^3 min^{-1}$ at 600–900 °C on a 1×1 cm^2 cleaned silicon template in a flow reactor consisting of a quartz glass tube and a furnace fitted with an independent temperature controller. The pyrolysis time was 1 h.

Modification of PNIPAAm on ACNTs: The ACNT film was firstly left to stand for at least one week and then put in a high-vacuum chamber (for example, the high-vacuum chamber of a SEM apparatus) for about 3 h before further treatment to gain better stability of the aligned structures of the ACNTs in the subsequent experiments. The ACNT film was immersed in hot (80 °C) concentrated nitric acid (63 %) for at least 2 h to generate hydrophilic groups, such as carboxy or hydroxy, on the ACNT surface. After washing the film with copious amounts of double-distilled water, it was dried in a vacuum oven at room temperature. It was then refluxed in a solution of aminopropyltrimethoxysilane in toluene at a concentration of about 5 wt % for about 6 h to obtain a NH_2-functionalized ACNT film. The subsequent polymerization of PNIPAAm was carried out for 3 h by using the method previously reported.[11]

Water contact angle, SEM, and TEM measurements: The water contact angle was measured on a SCA20 system (Dataphysics) with a super-thermostat. The measurement was conducted under saturated humidity. The SEM images were obtained on a field emission SEM apparatus (JSM-6700F, JEOL). The CNTs were scratched from the ACNT film and then dispersed in water by super-sonication, after which a droplet of water containing CNTs was dropped onto a copper mesh containing 400 grids. The TEM images were obtained on a JEM-100CXII (JEOL).

AFM studies: The CNTs were scratched from the ACNT film and then dispersed in water by super-sonication, after which a droplet of water containing CNTs was dropped onto a hydrophilic silicon wafer. The AFM images and the corresponding phase images of a single CNT were obtained in the tapping mode on a NanoScope IIIA MultiMode AFM (Digital Instrument) with a hot stage, at temperatures in the range of 20–50 °C.

Received: May 25, 2004

Keywords: carbon nanotubes · electron microscopy · polymers · surface chemistry · wettability

[1] a) Z. F. Ren, Z. P. Huang, J. W. Xu, J. H. Wang, P. Bush, M. P. Siegal, P. N. Prevencio, *Science* **1998**, *282*, 1105 – 1107; b) X. B. Wang, Y. Q. Liu, D. B. Zhu, *Appl. Phys. A* **2000**, *71*, 347 – 348; c) B. Q. Wei, R. Vajtai, Y. Jung, J. Ward, R. Zhang, G. Ramanath, P. M. Ajayan, *Nature* **2002**, *416*, 495 – 496; d) H. Liu, S. Li, J. Zhai, H. Li, Q. Zheng, L. Jiang, D. Zhu, *Angew. Chem.* **2004**, *116*, 1166 – 1169; *Angew. Chem. Int. Ed.* **2004**, *43*, 1146 – 1149.

[2] See, for example, a) T. Onda, S. Shibuichi, N. Satoh, K. Tsujii, *Langmuir* **1996**, *12*, 2125 – 2127; b) S. Shibuichi, T. Onda, N. Satoh, K. Tsujii, *J. Phys. Chem.* **1996**, *100*, 19512 – 19517; c) W. Chen, A. Y. Fadeev, M. C. Hsieh, D. Öner, J. Youngblood, T. J. McCarthy, *Langmuir* **1999**, *15*, 3395 – 3399; d) T. J. McCarthy, D. Öner, *Langmuir* **2000**, *16*, 7777 – 7782; e) L. Feng, S. Li, H. Li, J. Zhai, Y. Song, L. Jiang, D. Zhu, *Angew. Chem.* **2002**, *114*, 1269 – 1271; *Angew. Chem. Int. Ed.* **2002**, *41*, 1221 – 1223; f) H. Y. Erbil, A. L. Demirel, Y. Avci, O. Mert, *Science* **1977**, *299*, 1377 – 1380.

[3] a) H. Li, X. Wang, Y. Song, Y. Liu, Q. Li, L. Jiang, D. Zhu, *Angew. Chem.* **2001**, *113*, 1793 – 1796; *Angew. Chem. Int. Ed.* **2001**, *40*, 1743 – 1746; b) S. Li, H. Li, X. Wang, Y. Song, Y. Liu, L. Jiang, D. Zhu, *J. Phys. Chem.* **2002**, *106*, 9274 – 9276.

[4] T. Sun, G. Wang, H. Liu, L. Feng, L. Jiang, D. Zhu, *J. Am. Chem. Soc.* **2004**, *125*, 14996 – 14997.

[5] a) H. G. Schild, *Prog. Polym. Sci.* **1992**, *17*, 163 – 249; b) Z. Hu, Y. Chen, C. Wang, Y. Zheng, Y. Li, *Nature* **1998**, *393*, 149 – 152.

[6] a) X. Huang, M. J. Wirth, *Anal. Chem.* **1997**, *69*, 4577 – 4580; b) X. Huang, M. J. Wirth, *Macromolecules* **1999**, *32*, 1694 – 1696; c) D. M. Jones, W. T. S. Huck, *Adv. Mater.* **2001**, *13*, 1256 – 1259; d) X. Kong, T. Kawai, J. Abe, T. Iyoda, *Macromolecules* **2001**, *34*, 1837 – 1844.

[7] See, for example, a) P. G. Collins, A. Zettle, H. Bando, A. Thess, R. E. Smalley, *Science* **1997**, *278*, 100 – 103; b) A. Bachtold, P. Hadley, T. Nakanishi, C. Dekker, *Science* **2001**, *294*, 1317 – 1320; c) S. Ghosh, A. K. Sood, N. Kumar, *Science* **2003**, *299*, 1042 – 1044.

[8] a) B. R. Martin, S. K. St. Angelo, T. E. Mallouk, *Adv. Funct. Mater.* **2002**, *12*, 759 – 765; b) N. I. Kovtyukhova, T. E. Mallouk, L. Pan, E. C. Dickey, *J. Am. Chem. Soc.* **2003**, *125*, 9761 – 9769; c) H. Kong, C. Gao, D. Yan, *J. Am. Chem. Soc.* **2004**, *126*, 412 – 413; d) D. Baskaran, J. W. Mays, M. S. Bratcher, *Angew. Chem.* **2004**, *116*, 2190 – 2194; *Angew. Chem. Int. Ed.* **2004**, *43*, 2138 – 2142.

 © 2004 Wiley-VCH Verlag GmbH & Co. KGaA, Weinheim

[9] a) Y. G. Takei, T. Aoki, K. Sanui, N. Ogata, Y. Sakurai, T. Okano, *Macromolecules* **1994**, *27*, 6163 – 6166; b) L. Liang, P. C. Rieke, G. E. Fryxell, J. Liu, M. H. Engelhard, K. L. Alford, *J. Phys. Chem. B* **2000**, *104*, 11667 – 11673; c) L. Liang, P. C. Rieke, J. Liu, G. E. Fryxell, J. S. Young, M. H. Engelhard, K. L. Alford, *Langmuir* **2000**, *16*, 8016 – 8023.
[10] S. Lin, K. Chen, R. Liang, *Polymer* **1999**, *40*, 2619 – 2624.
[11] T. Sun, G. Wang, L. Feng, B. Liu, Y. Ma, L. Jiang, D. Zhu, *Angew. Chem.* **2004**, *116*, 361 – 364; *Angew. Chem. Int. Ed.* **2004**, *43*, 357 – 360.
[12] D. M. Jones, J. R. Smith, W. T. S. Huck, C. Alexander, *Adv. Mater.* **2002**, *14*, 1130 – 1134.
[13] a) Y. Jiang, X. -G. Jin, C. C. Han, L. Li, *Langmuir* **2003**, *19*, 8010 – 8018; b) Y. Jiang, D.-D. Yan, X. Gao, C. C. Han, X.-G. Jin, L. Li, *Macromolecules* **2003**, *36*, 3652 – 3655.

Life's Simple Pleasures!



13280407_gu

No need to waste precious time looking for the right information – Register now for the free **Wiley-VCH Alerting Service.**

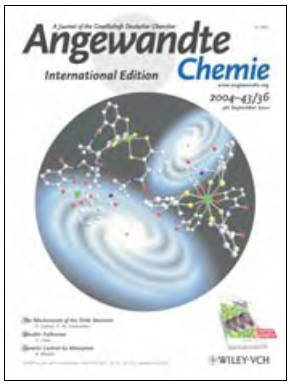
It's simple – and it's fast.

To receive regular news per e-mail tailored precisely to your needs and interests, just fill in the registration form at **www.wiley-vch.de/home/pas/**

WILEY-VCH

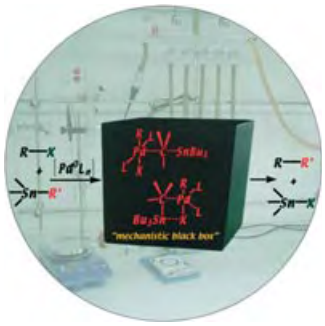
 © 2004 Wiley-VCH Verlag GmbH & Co. KGaA, Weinheim

Cover Picture

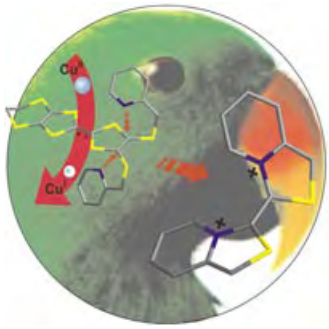


F. Ekkehardt Hahn,* Christian Schulze Isfort, and Tania Pape

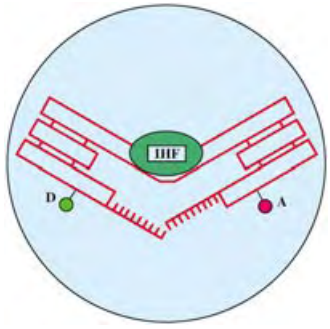
Helices are a universal structure. They are found in all sizes from molecular species to spiral nebula. The cover picture shows a dinuclear, triple-stranded helicate containing a novel ligand with a catecholato and an *o*-benzenedithiolato donor group. Only the regioisomer with a parallel orientation of the ligands is formed and from only one pair of enantiomers. For more information, see the Communication by F. E. Hahn et al. on page 4807 ff.



Reaction Mechanisms
P. Espinet and A. M. Echavarren have gone through the mechanism of the Stille coupling reaction with a fine-tooth comb. See their Review on page 4704 ff. to find out which factors determine the intermediates formed in the individual reaction steps.



Heterocycle Synthesis
Tetrathiafulvalene acts as a leaving group in the oxidative cyclization reactions leading to a new bithiazole-type ring assembly. The synthesis and properties of this heterocycle are described by S. Decurtins and co-workers on page 4738 ff.



Nanomechanical DNA Devices
Nanomechanical devices are promising probes for performing measurements at the molecular level. N. C. Seeman and co-workers explain on page 4750 ff. the structure and function of a "DNA machine" obtained by linking two triple-helical DNA motifs with a shaft of conventional DNA.

Contents

Angewandte EarlyView

The following Communications are available online (in Wiley InterScience). You can find them, as well as forthcoming Reviews, Highlights, and Essays, at www.angewandte.org, under Early View.

G. Férey, C. Serre, C. Mellot-Draznieks, F. Millange, S. Surble, J. Dutour, I. Margiolaki:*
A Hybrid Solid with Giant Pores Prepared by a Combination of Targeted Chemistry, Simulation, and Powder Diffraction
DOI: 10.1002/anie.200460592
Published online: August 30, 2004

Y. Zhou, D. Yan:*
Supramolecular Self-Assembly of Giant Polymer Vesicles with Controlled Sizes
DOI: 10.1002/anie.200460325
Published online: August 30, 2004

P. Yin, H. Yan, X. G. Daniell, A. J. Turberfield,* J. H. Reif*:*
A Unidirectional DNA Walker That Moves Autonomously Along a Track
DOI: 10.1002/anie.200460522
Published online: August 30, 2004

Articles judged by the referees or the editor as being either very important or very urgent are immediately edited, proof-read, and electronically published once the manuscript has arrived in the editorial office in its final form. As long as there is no page number available these articles should be cited in the following manner:

Author(s), *Angew. Chem. Int. Ed.*, online publication date, DOI.

News

Honorary Doctorate for H. Brunner **4687**

C. T. Walsh Receives Boehringer Ingelheim Award **4687**

Books

Molecular Clusters of the Main Group Elements — Matthias Driess, Heinrich Nöth — *reviewed by M. Ruck* **4688**

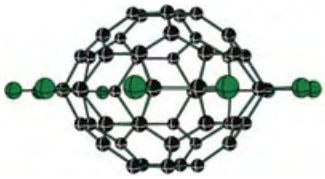
Encyclopedia of Molecular Cell Biology and Molecular Medicine — Robert A. Meyers — *reviewed by H. Kubinyi* **4689**

Highlights

Fullerene Derivative

Z. Chen* **4690 – 4691**

The Smaller Fullerene C_{50}, Isolated as $C_{50}Cl_{10}$

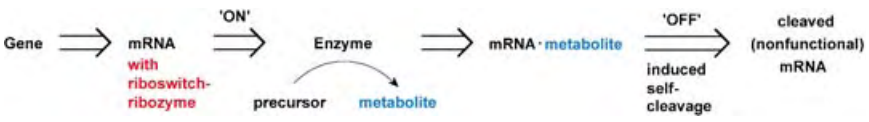


A second fullerene "Saturn", $C_{50}Cl_{10}$, has been prepared in a graphite arc-discharge process conducted with small amount of CCl_4 in the inert-gas atmosphere. This is the first stable smaller fullerene derivative to be prepared and fully characterized (see structure). Its existence has implications for the mechanism of fullerene formation.

Gene Regulation

R. Micura* **4692 – 4694**

Genetic Control by a Natural Metabolite-Responsive Ribozyme



Another striking example for the functional diversity of RNA is represented by the recently discovered riboswitch ribozyme in the leader sequence of bacterial mRNAs. A simple mechanism is responsible for controlling expression of the corresponding gene (see scheme) and demonstrates that gene regulation is no longer a domain necessarily assisted by proteins.

Correspondence

Diamond Synthesis

H. Sachdev* ——— **4696 – 4699**

Diamonds from the Pressure Cooker—Science or Science Fiction?

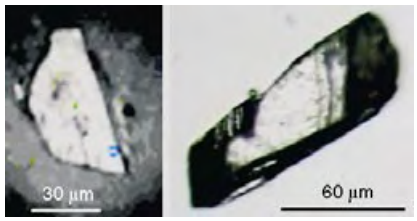
Questions are raised about some of the arguments and methods described by Q. Chen and co-workers in their reports on the synthesis of diamonds under mild conditions: Are the data provided sufficient proof of a new synthetic method? Where is the evidence of the proposed reaction intermediates? Is there another cause for the formation of diamond?

Diamond Synthesis

Z. Lou, Q. Chen* ——— **4700 – 4701**

Reply to Comment on "Growth of Large Diamond Crystals by Reduction of Magnesium Carbonate with Metallic Sodium"

In reply, some of the large diamonds synthesized in CO_2/Na and $MgCO_3$/Na systems are irregular in shape (see picture), and therefore different from diamonds made by high-pressure high-temperature techniques or by chemical vapor deposition. In addition, the Raman spectra of diamonds prepared from the new systems have features that do not appear in those of diamonds obtained by other techniques, thus indicating that the diamonds have different origins.

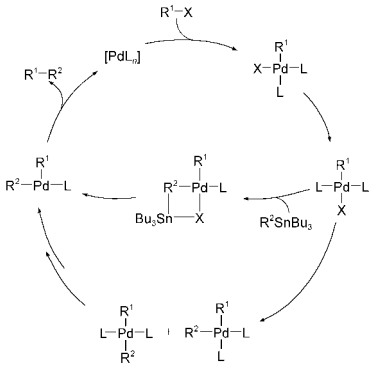


Reviews

C–C Coupling

P. Espinet,*
A. M. Echavarren* ——— **4704 – 4734**

The Mechanisms of the Stille Reaction



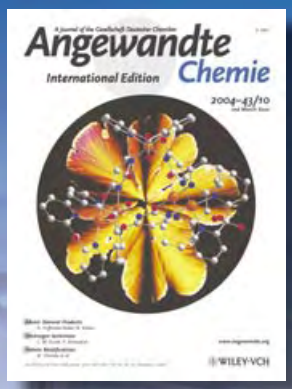
Who could imagine modern organic chemistry without the reliable and general Stille coupling reaction? But what are the requirements for this transformation to proceed smoothly and selectively? This Review shows which reactive intermediates form during the course of these coupling reactions (see scheme for a more general mechanistic view of the coupling reaction).

For the USA and Canada:
ANGEWANDTE CHEMIE International Edition (ISSN 1433-7851) is published weekly by Wiley-VCH PO Box 191161, D 69451 Weinheim, Germany. Air freight and mailing in the USA by Publications Expediting Inc. 200 Meacham Ave., Elmont, NY 11003. Periodicals postage paid at Jamaica NY 11431. US POSTMASTER: send address changes to *Angewandte Chemie*, Wiley-VCH, 111 River Street, Hoboken, NJ 07030. Annual subscription price for institutions: Europe € 3430.00/3118.00; outside Europe US$ 4499.00/4090.00 (valid for print and electronic/print or electronic delivery); for individuals who are personal members of a national chemical society, or whose institution already subscribes, or who are retired or self-employed consultants, print only: Europe € 248.00/outside Europe US$ 378.00. Postage and handling charges included. All Wiley-VCH prices are exclusive VAT.

 © 2004 Wiley-VCH Verlag GmbH & Co. KGaA, Weinheim

The best in chemistry –

for more than a hundred years



A Journal of the Gesellschaft Deutscher Chemiker

Angewandte International Edition **Chemie**

www.angewandte.org

1888: ***The beginning of a success story***

Constant Innovations

- **1962:** *First issue of the International Edition*
- **1976:** *Graphical abstracts*
- **1979:** *Cover pictures*
- **1988:** *Centenary of Angewandte*
- **1989:** *Routine use of color*
- **1991:** *New section: Highlights*
- **1992:** *Computerized editorial tracking system*
- **1995:** *Internet service for readers*
- **1998:** *Regular press service; full-text online*
- **2000:** *New section: Essays; EarlyView: Communications available online ahead of the printed version*
- **2001:** *New section: Minireviews*
- **2002:** *Online submission of manuscripts*
- **2003:** *Weekly publication; new section: News; new layout*
- **2004:** *Backfiles (1962-1997); ManuscriptXpress: Online system for authors and referees*



Angewandte's advisors...

Daniel Bellus
Ciba Specialty Chemicals, Basel

*» For the past thirty years **Angewandte Chemie** has continued to be my primary source of inspiration and self-education. In each new issue I find a real gem of chemistry, capable of further nurturing the innovation process. It is my pleasure to inject my industrial R&D experience into the International Advisory Board. «*

***Angewandte Chemie International Edition** is a journal of the German Chemical Society (GDCh)*

GDCh

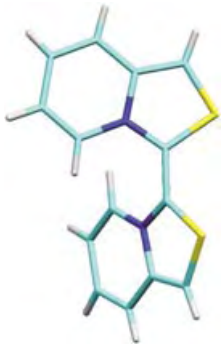
WILEY InterScience® DISCOVER SOMETHING GREAT

WILEY-VCH

1180140d_gu

Communications

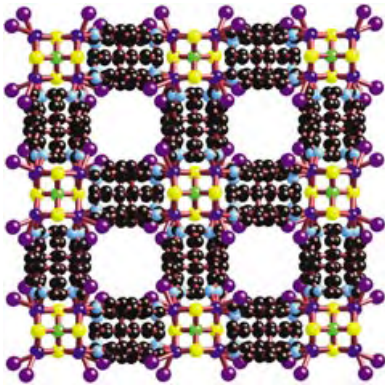
They are still out there—original heterocycles like the bithiazole-type assembly shown (N: dark blue, S: yellow). The two linked bicyclic heterocycles form simultaneously when functionalized tetrathiafulvalene acts as a leaving group. The mechanistic pathway involving oxidative cyclization reactions provides an entry to this class of fused-ring systems.



Heterocycle Synthesis

S.-X. Liu, C. Tanner, A. Neels, S. Dolder, S. Leutwyler, P. Renaud, P. Bigler, S. Decurtins* _____ 4738 – 4741

Tetrathiafulvalenes Acting as Leaving Groups: A Route to Bithiazoles

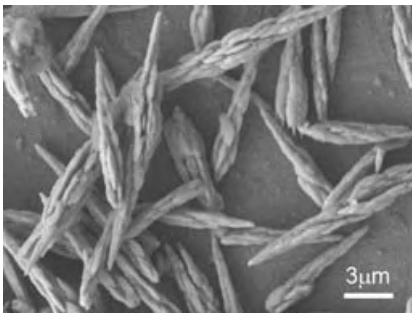


An unusual supramolecular compound $\{[WS_4Cu_4(4,4'\text{-bpy})_4][WS_4Cu_4I_4(4,4'\text{-bpy})_2]\}_\infty$ (see picture) was obtained from the self-assembly of a preformed mixed-metal sulfide cluster, $[NEt_4]_4[WS_4Cu_4I_6]$. The product consists of four interpenetrating diamond-type nets (two cationic and two anionic) and has large open channels that are lined with "receptor sites" for guest iodine molecules. 4,4′-bpy = 4,4′-bipyridyl.

Supramolecular Compounds

J.-P. Lang,* Q.-F. Xu, R.-X. Yuan, B. F. Abrahams* _____ 4741 – 4745

$\{[WS_4Cu_4(4,4'\text{-bpy})_4][WS_4Cu_4I_4(4,4'\text{-bpy})_2]\}_\infty$—An Unusual 3D Porous Coordination Polymer Formed from the Preformed Cluster $[Et_4N]_4[WS_4Cu_4I_6]$

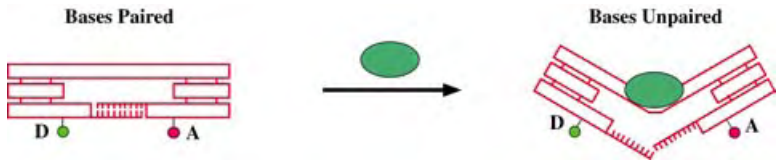


Crystal gazing: A mild solution route has been designed for the controlled synthesis of lead tungstate microcrystals with high crystal symmetry, in which the cationic surfactant, pH value, and temperature play key roles. Helix- (see TEM image), spindle-, chainlike, and dendritic structures can be produced by varying the reaction conditions.

Crystal Growth

B. Liu, S.-H. Yu,* L. Li, Q. Zhang, F. Zhang, K. Jiang _____ 4745 – 4750

Morphology Control of Stolzite Microcrystals with High Hierarchy in Solution



A DNA nanomechanical device was constructed by linking two triple-helical DNA motifs with a shaft of conventional DNA bearing the binding site for the integration host factor (IHF, shown as green ellipse in the picture). Binding of IHF to this site causes marked shaft bending, which can be monitored by fluorescence resonance energy transfer between donor (D) and acceptor (A) dyes.

DNA Devices

W. Shen, M. F. Bruist, S. D. Goodman, N. C. Seeman* _____ 4750 – 4752

A Protein-Driven DNA Device That Measures the Excess Binding Energy of Proteins That Distort DNA

 © 2004 Wiley-VCH Verlag GmbH & Co. KGaA, Weinheim

Contents

Cluster Compounds

N. Zheng, X. Bu, P. Feng* — **4753 – 4755**

Pentasupertetrahedral Clusters as Building Blocks for a Three-Dimensional Sulfide Superlattice

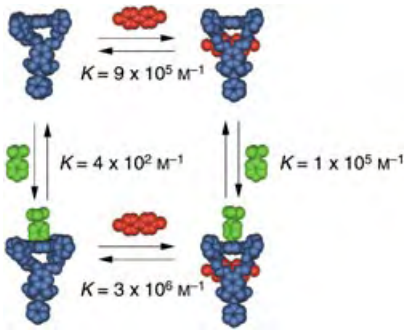


Highly mobile extra-framework cations encapsulated in the 3D open-framework architecture of ICF-26 result in remarkably high ion conductivity. The framework is composed of $Li_4In_{22}S_{44}^{18-}$ clusters, which represent the second member of a series of pentasupertetrahedral clusters P*n*. The P2 cluster reported here is the largest member of the P*n* series so far. In the crystal, each P2 cluster shares all four corners with adjacent P2 clusters (see picture).

Supramolecular Chemistry

P. Thordarson,* R. G. E. Coumans, J. A. A. W. Elemans, P. J. Thomassen, J. Visser, A. E. Rowan,* R. J. M. Nolte — **4755 – 4759**

Allosterically Driven Multicomponent Assembly

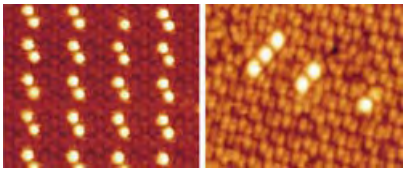


Bound to cooperate: Binding of dimethylviologen in the cavity of a Zn porphyrin host dramatically increases the affinity of the host for N-donating ligands and vice versa (see scheme). These positive heterotropic allosteric effects are exploited to direct complex equilibrium mixtures towards a single self-assembled species. This allosteric magnification was used to obtain a pentameric sandwich architecture from a complex mixture of components.

Self-Assembly on Surfaces

D. Bonifazi, H. Spillmann,* A. Kiebele, M. de Wild, P. Seiler, F. Cheng, H.-J. Güntherodt, T. Jung,* F. Diederich* — **4759 – 4763**

Supramolecular Patterned Surfaces Driven by Cooperative Assembly of C_{60} and Porphyrins on Metal Substrates

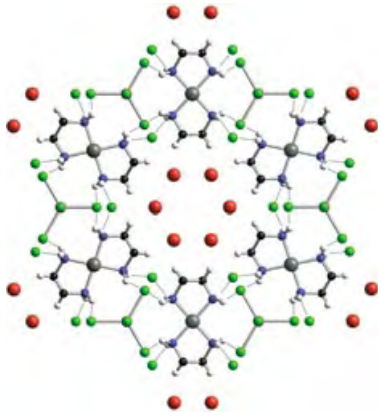


Plenty of room on top: Unprecedented one- and two-dimensional fullerene patterns were obtained upon evaporation of pristine C_{60} onto pre-organized porphyrin monolayers on silver surfaces following a bottom-up approach. The arrangement of the fullerene molecules on the patterned layer can be controlled by the porphyrin structure (see scanning tunneling microscopy images).

Charge-Transfer Complexes

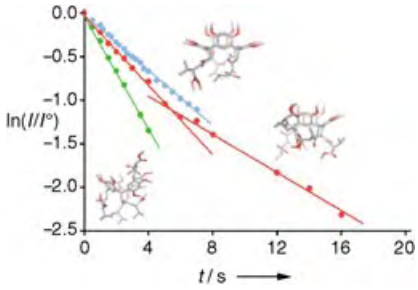
M. Yamashita,* D. Kawakami, S. Matsunaga, Y. Nakayama, M. Sasaki, S. Takaishi, F. Iwahori, H. Miyasaka, K.-i. Sugiura, Y. Wada, H. Miyamae, H. Matsuzaki, H. Okamoto, H. Tanaka, K. Marumoto, S. Kuroda — **4763 – 4767**

$[\{[Pt(en)_2][PtX_2(en)_2]\}_3]$-$[\{(MX_5)X_3\}_2]\cdot 12\,H_2O$: Quasi-One-Dimensional Halogen-Bridged Pt^{II}–Pt^{IV} Mixed-Valence Compounds with Magnetic Counteranions



Attractive complexes: Hexagonal micropores similar to zeolites have been observed in mixed-valence Pt^{II}–Pt^{IV} compounds with magnetic counteranions (see X-ray crystal structure). The micropores contain 12 water molecules per molecular unit which can be desorbed by heating the complexes to 100 °C and re-adsorbed by cooling to 20 °C without affecting the skeletal structure.

The dramatic effects of the size and hydrophilic/hydrophobic properties of cavities on the intrinsic reaction kinetics and dynamics is shown by the gas-phase reaction of (*R*)-(−)-2-butylamine and complexes of stereoisomeric amido[4]resorcinarene hosts with aromatic amino acids. The graph shows the kinetic plots of the base-induced loss of L-Phe (green), L-Tyr (red), and L-dopa (blue).

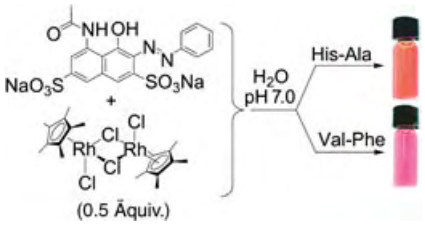


Host–Guest Systems

B. Botta, D. Subissati, A. Tafi, G. Delle Monache, A. Filippi, M. Speranza* ——— 4767 – 4770

Cavity Effects on the Enantioselectivity of Chiral Amido[4]resorcinarene Stereoisomers

---

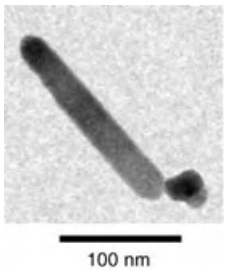


Detected by the naked eye: An indicator-displacement assay that comprises an organometallic rhodium complex and the indicator azophloxine can be used to selectively detect histidine- or methionine-containing peptides in water at neutral pH (see picture).

Chemosensors

A. Buryak, K. Severin* ——— 4771 – 4774

An Organometallic Chemosensor for the Sequence-Selective Detection of Histidine- and Methionine-Containing Peptides in Water at Neutral pH

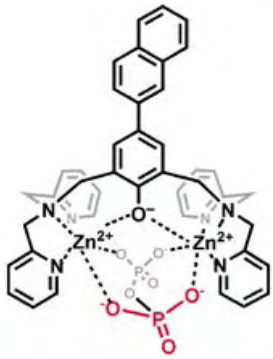


Head–tail-like nanoheterostructures consisting of ZnO nanorods and silver nanoparticles (see picture) are assembled by site-specific photoreduction of silver ions at the surface of pre-formed ZnO nanorods. Several mechanisms for this process are discussed.

Nanomaterials

C. Pacholski, A. Kornowski, H. Weller* ——— 4774 – 4777

Site-Specific Photodeposition of Silver on ZnO Nanorods



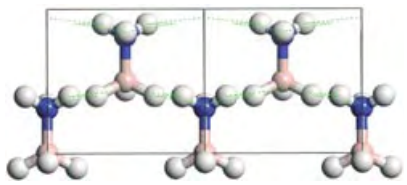
High affinity and selective detection for PPi is exhibited by a new fluorescent sensor based on a naphthalene–dpa system (see picture). The binuclear zinc complex is remarkably selective toward PPi over other anions. For example, PPi can be detected at micromolar concentrations in the presence of a large excess of ATP. PPi = pyrophosphate, ATP = adenosine triphosphate, dpa = bis(2-pyridylmethyl)amine.

Fluorescent Sensors

D. H. Lee, S. Y. Kim, J.-I. Hong* ——— 4777 – 4780

A Fluorescent Pyrophosphate Sensor with High Selectivity over ATP in Water

---



How strong is the H···H bond in solid BH_3NH_3? Insight from periodic density functional calculations predicts an average value of 12.7 kJ mol^{-1}, reassigning the interaction towards the lower end of the dihydrogen bond strength spectrum.

Density Functional Calculations

C. A. Morrison,* M. M. Siddick ——— 4780 – 4782

Dihydrogen Bonds in Solid BH_3NH_3

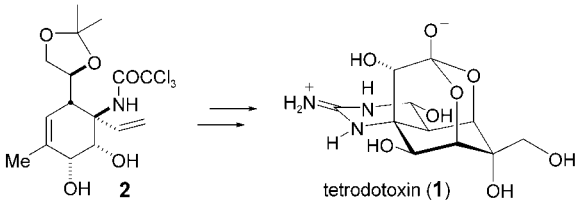
 © 2004 Wiley-VCH Verlag GmbH & Co. KGaA, Weinheim

Contents

Natural Product Synthesis

T. Nishikawa, D. Urabe, M. Isobe* ——— **4782 – 4785**

An Efficient Total Synthesis of Optically Active Tetrodotoxin

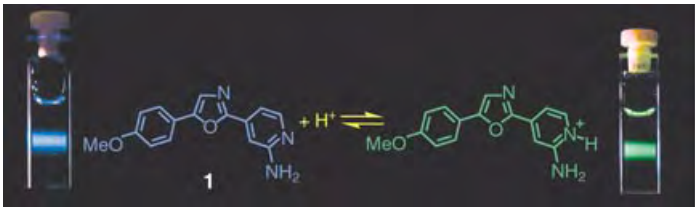


The toxic principle of puffer-fish poison, (−)-tetrodotoxin (**1**), has been recognized as a formidable synthetic target since its structure elucidation in 1964. An efficient total synthesis of **1** via the intermediate **2**, which was used previously for the synthesis of 11-deoxytetrodotoxin, is described.

pH Sensors

S. Charier, O. Ruel, J.-B. Baudin, D. Alcor, J.-F. Allemand, A. Meglio, L. Jullien* ——— **4785 – 4788**

An Efficient Fluorescent Probe for Ratiometric pH Measurements in Aqueous Solutions

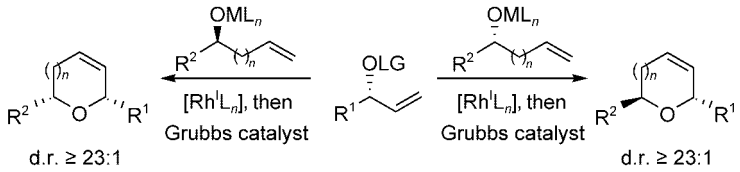


Just as litmus paper changes from red to blue with an increase in pH, so the fluorescence emission of the oxazole derivative **1** shifts from green to blue. Ratiometric measurements of the fluorescence emissions of the two species, after one- or two-photon excitation, allow **1** to be employed as a pH sensor over the mid-pH range.

Cyclic Ethers

P. A. Evans,* D. K. Leahy, W. J. Andrews, D. Uraguchi ——— **4788 – 4791**

Stereodivergent Construction of Cyclic Ethers by a Regioselective and Enantiospecific Rhodium-Catalyzed Allylic Etherification: Total Synthesis of Gaur Acid

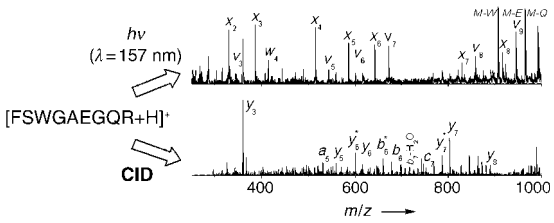


A dramatic enhancement of the stereospecificity of the title reaction was observed with trimethylphosphite-modified copper(I) alkoxide reagents. The combination of this reaction with ring-closing metathesis provides a direct approach to *cis*- and *trans*-disubstituted cyclic ethers (see scheme). A seven-step total synthesis of the natural product gaur acid highlighted the potential of this methodology. LG = leaving group.

Mass Spectrometry

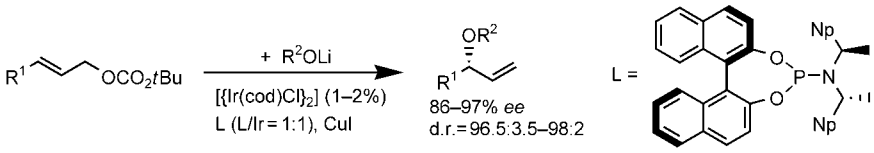
M. S. Thompson, W. Cui, J. P. Reilly* ——— **4791 – 4794**

Fragmentation of Singly Charged Peptide Ions by Photodissociation at $\lambda = 157$ nm



A study in contrasts: Mass spectra of singly protonated peptide ions excited with 157-nm light show unorthodox fragmentation patterns in comparison to those obtained by collision-induced dissociation (CID). Observations are consistent with an initial photochemical cleavage of α-C–CO bonds in the peptide backbone by a Norrish Type I reaction to create radical precursor ions followed by one of three elimination processes that form ion fragments with even numbers of electrons.

 © 2004 Wiley-VCH Verlag GmbH & Co. KGaA, Weinheim

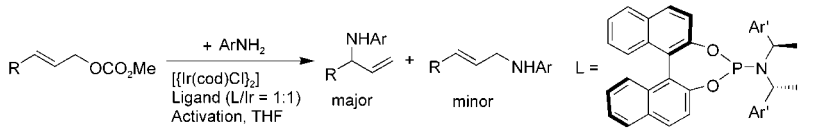


Synthesis of Allylic Ethers

C. Shu, J. F. Hartwig* ____ 4794 – 4797

Iridium-Catalyzed Intermolecular Allylic Etherification with Aliphatic Alkoxides: Asymmetric Synthesis of Dihydropyrans and Dihydrofurans

Hindered chiral ethers with one or two stereocenters are now readily available by allylic etherification of primary and secondary alkoxides (see reaction). When an Ir–phosphoramidite complex is used as the catalyst, the reaction proceeds with high regio-, enantio-, and diastereoselectivity. Np = 1-naphthyl.

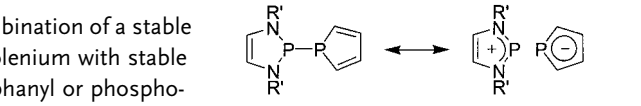


Synthesis of Allylic Amines

C. Shu, A. Leitner, J. F. Hartwig* ____ 4797 – 4800

Enantioselective Allylation of Aromatic Amines after In Situ Generation of an Activated Cyclometalated Iridium Catalyst

Highly regio- and enantioselective allylation of aromatic amines is observed when a cyclometalated Ir–phosphoramidite complex is generated in situ (see scheme). The active catalyst can be formed from [{Ir(cod)Cl}$_2$] and ligand L with a volatile alkylamine prior to addition of the reagents or upon use of a tertiary amine additive.

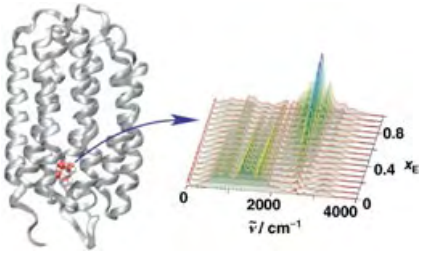


Polarized P—P Bonds

S. Burck, D. Gudat,* M. Nieger ____ 4801 – 4804

Diphosphanes with Polarized and Highly Reactive P—P Bonds

Uneven split: The combination of a stable cationic diazaphospholenium with stable anionic diphenylphosphanyl or phosphoryl fragments affords diphosphanes with a polarized P—P bond (see scheme). This results not only in interesting molecular structures, but also in the chemical activation of the P—P bond in addition reactions.

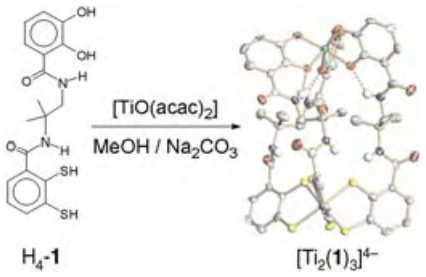


Ab Initio Molecular Dynamics

R. Rousseau, V. Kleinschmidt, U. W. Schmitt, D. Marx* ____ 4804 – 4807

Assigning Protonation Patterns in Water Networks in Bacteriorhodopsin Based on Computed IR Spectra

Car–Parrinello simulations were used to study two types of protonated hydrogen-bonded networks inside the proton pump bacteriorhodopsin (see picture). The computed infrared spectra exhibit complementary absorption continua, a finding that could possibly open the door to time-resolved spectroscopic probes of proton transport on the molecular level.



Helical Structures

F. E. Hahn,* C. Schulze Isfort, T. Pape ____ 4807 – 4810

A Dinuclear, Triple-Stranded Helicate with a Diamide-Bridged Catechol/Benzenedithiol Ligand

Three of a kind: The directional O–O/S–S heterodonor ligand H$_4$-**1** reacts with Ti^{IV} to give the triple-stranded dinuclear tetraanion [Ti$_2$(**1**)$_3$]$^{4-}$ (see picture, acac = 2,4-pentanedione). The reaction yields exclusively the regioisomer with a parallel orientation of the ligands and only one pair of enantiomers is obtained.

VIP Communications labeled with this symbol have been judged by two referees as being "very important papers".

 © 2004 Wiley-VCH Verlag GmbH & Co. KGaA, Weinheim

Sources

Product and Company Directory

You can start the entry for your company in "Sources" in any issue of *Angewandte Chemie*.

If you would like more information, please do not hesitate to contact us.

Wiley-VCH Verlag – Advertising Department
Tel.: 0 62 01 - 60 65 65
Fax: 0 62 01 - 60 65 50
E-Mail: MSchulz@wiley-vch.de

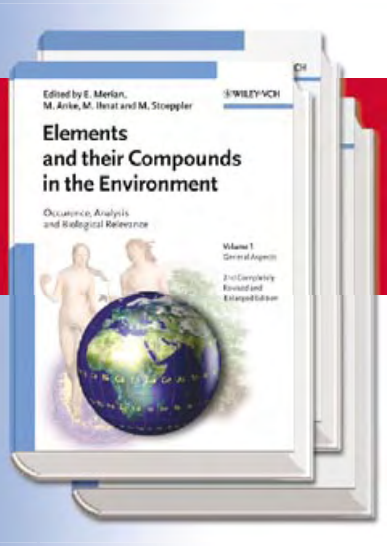
Service

Keywords ____ *4812*

Authors ____ *4813*

Vacancies ____ *A59*

Preview ____ *4815*



New ! The Second Edition!

Elements and their Compounds in the Environment

Occurrence, Analysis and Biological Relevance

2nd completely revised and enlarged edition
3 Volume Set

Edited by E. MERIAN, M. ANKE, M. IHNAT and M. STOEPPLER

- The "Merian" is the established standard reference on this topic.
- This new edition is more clearly and concisely structured, with more emphasis on nutritional aspects.
- All contributions are revised and updated to present the current state of knowledge.
- Further elements, including some non-metals of nutritional importance, have been added.
- Essential information for chemists, biologists, geologists, food scientists, toxicologists and physiologists involved in environmental research and remediation, risk assessment, food research and industrial hygiene.

For your order:

3527-30459-2 2004
1774pp with 97 figs and 377 tabs
Hbk
€ 599.00 / £ 355.00 / US$ 550.00

Wiley-VCH,
Customer Service Department,
Fax: +49 (0) 6201 606-184,
E-Mail: service@wiley-vch.de,
www.wiley-vch.de

John Wiley & Sons, Ltd., Customer Services Department, Fax: +44 (0) 1243-843-296,
E-Mail: cs-books@wiley.co.uk,
www.wileyeurope.com

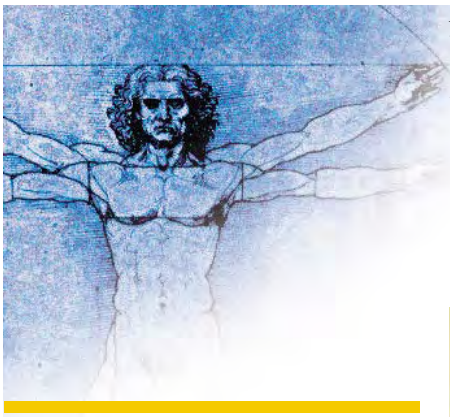
John Wiley & Sons, Inc., Customer Care,
Fax: +1 800-597-3299,
E-Mail: custserv@wiley.com,
www.wiley.com

WILEY-VCH

WILEY

1332403_gu

 © 2004 Wiley-VCH Verlag GmbH & Co. KGaA, Weinheim



Honorary Doctorate for H. Brunner



The chemistry department of the Technische Universität München (Germany) has awarded Henri Brunner of the Universität Regensburg (Germany) an honorary doctorate. This distinction was awarded in recognition of "his trend-setting research in organometallic chemistry and homogeneous catalysis, with which he has paved the way to modern enantioselective methods for the preparation of chiral fine chemicals and precursors to pharmaceutically active compounds".

Brunner completed his PhD in 1963 at the Universität München under the guidance of E. O. Fischer (Nobel Prize in Chemistry, 1973). After a postdoctoral year at the University of California, Los Angeles in the research group of H. D. Kaesz, he returned to München, where he completed his habilitation in 1969. In 1971 he accepted the chair for inorganic chemistry at the Universität Regensburg, which he held until he received emeritus status in 2004. He has been awarded many prizes for his work, including the Carl Duisberg Memorial Award of the Gesellschaft Deutscher Chemiker (German Chemical Society, GDCh) in 1970, the Horst Pracejus Award of the GDCh in 1999, and the Humboldt Research Award for German–French Cooperation in 1993. Brunner was a member of the Editorial Board of *Angewandte Chemie* from 1989 to 1997 (Chairman 1993–97). He is the author of three Reviews on asymmetric transition-metal catalysis in *Angewandte Chemie*[1] and of a popular book on chirality: "Rechts oder links—In der Natur und anderswo" (Wiley-VCH, **1999**).

Photo: Uli Benz

C. T. Walsh Receives Boehringer Ingelheim Award



Christopher T. Walsh majored in biology at Harvard College (Cambridge, MA, USA) and completed his PhD in the research group of Fritz Lipmann at The Rockefeller University in New York. He carried out postdoctoral research from 1970 to 1972 with R. H. Abeles, then took up a position at Massachusetts Institute of Technology (MIT, Cambridge, USA) to study enzymatic reactions. Focal points of his research included the design of inhibitors and enzymatic catalysis of the Baeyer–Villiger oxidation.[2a] After 15 years he left MIT to become Professor of Biological Chemistry and Molecular Pharmacology at Harvard Medical School. There he investigates enzymes of therapeutic relevance and the mechanism of action of antibiotics, such as vancomycin.[2b,c]

Walsh is the recipient of the Boehringer Ingelheim Award 2004 of the Division of Chemical Toxicology of the American Chemical Society (ACS) for his work on the mechanism of action of xenobiotic chemicals, in particular antibiotics, in living organisms, and on antibiotic resistance. Walsh is the author of several books, including *Antibiotics* (ASM Press, **2003**) and *Enzymatic Reaction Mechanisms* (Freeman, **1978**). Walsh is a member of the Editorial Advisory Board of *ChemBioChem*.

[1] Most recently: H. Brunner, *Angew. Chem.* **1999**, *111*, 1248; *Angew. Chem. Int. Ed.* **1999**, *38*, 1194.

[2] a) C. T. Walsh, Y.-C. J. Chen, *Angew. Chem.* **1988**, *100*, 342; *Angew. Chem. Int. Ed. Engl.* **1988**, *27*, 333; b) C. T. Walsh, *ChemBioChem* **2000**, *1*, 99; c) B. K. Hubbard, C. T. Walsh, *Angew. Chem.* **2003**, *115*, 752; *Angew. Chem. Int. Ed.* **2003**, *42*, 730.

Editorial Note: Diamond Synthesis in Doubt

Last year in *Angewandte Chemie* and in the *Journal of the American Chemical Society* Quianwang Chen et al. reported diamond syntheses from $MgCO_3$-Na and CO_2-(Li, Na, K), respectively.[1,2] The authors have apologized for failing to cross-reference the papers and for manipulation of some of the data (see the second paragraph in the Correspondence from Z. Lou and Q. Chen on page 4700).

In addition, the results reported in both publications are heavily criticized by H. Sachdev in the Correspondence on page 4696:[3] The details of the reaction conditions are not reported in sufficient detail for the work to be repeated and the characterizations (or even proof) of the final products are not without doubt; furthermore, the characterization of intermediate products, important for the postulated reaction mechanism, is missing. Even if a diamond synthesis is, in principle, possible under the conditions presumably present in the reaction system used by Chen et al. then its actual realization remains doubtful. Chen and Lou give a series of arguments in their Reply[4] in order to support their diamond synthesis, however, they close with the comment "we could produce diamonds *from time to time* in $MgCO_3$-Na and CO_2-(Li, Na, K) system" (italicized by me), which naturally casts doubts about the reproducibility. Hopefully this Note and the two Correspondences[3,4] will lead to a rapid resolution of the problem of whether or not diamonds can be prepared by the method of Chen et al.[1,2]

Peter Gölitz

[1] Z. S. Lou, Q. W. Chen, W. Wang, Y. T. Qian, Y. F. Zhang, *Angew. Chem.* **2003**, *115*, 4639; *Angew. Chem. Int. Ed.* **2003**, *42*, 4501.

[2] Z. S. Lou, Q. W. Chen, Y. F. Zhang, W. Wang, Y. T. Qian, *J. Am. Chem. Soc.* **2003**, *125*, 9302.

[3] H. Sachdev, *Angew. Chem.* **2004**, *116*, 4800, *Angew. Chem. Int. Ed.* **2004**, *43*, 4696.

[4] Z. S. Lou, Q. W. Chen, *Angew. Chem.* **2004**, *116*, 4804, *Angew. Chem. Int. Ed.* **2004**, *43*, 4700.

DOI: 10.1002/anie.200461702

© 2004 Wiley-VCH Verlag GmbH & Co. KGaA, Weinheim

Fullerene Derivative

The Smaller Fullerene C_{50}, Isolated as $C_{50}Cl_{10}$**

*Zhongfang Chen**

Keywords:
fullerenes · materials science · reaction mechanisms · reactive intermediates

Smaller isolable fullerenes have long been sought since the discovery of C_{60}.[1] However, fullerenes smaller than C_{60} should be highly reactive due to their condensed pentagons and increased strain. Although smaller fullerenes can be generated in trace amounts by the traditional Krätschmer–Huffman method,[2] in which graphite rods are vaporized by arc-discharge under a low-pressure inert-gas atmosphere, they have not been extracted from the raw soot. The high reactivity also precludes their more conventional chemical syntheses by procedures that gave C_{60}[3] and its key segments, for example, $C_{20}H_{10}$,[4] $C_{36}H_{12}$,[5] and sumanene.[6]

Production of the smaller fullerene C_{36} in macroscopic quantities by DC arc discharge has been claimed, and it was suggested that a fullerene-like C_{36} cage exists as a covalently bonded cluster assembly in the solid state.[7] However, the definite characterization of a C_{36}-based solid is in doubt since no signals for sp^3 carbon atoms were found in the ^{13}C NMR spectrum. Various attempts to reproduce the production of C_{36} by arc discharge have not been successful. The synthesis, purification, and identification of $C_{36}H_6$ and $C_{36}H_6O$ have also been reported, but the detailed structures are still not clear.[8] Due to its high reactivity, $C_{36}H_6$ forms oligomers or other products immediately after removal of the solvent.

[*] Dr. Z. Chen
Department of Chemistry and
Center for Computational Chemistry
University of Georgia
Athens, GA 30602 (USA)
Fax: (1) 706-542-0406
E-mail: chen@chem.uga.edu

[**] The author's work in this field was supported by the National Science Foundation (Grant CHE-0209857).

The viability of the smallest fullerene C_{20} was established experimentally by its production in the gas phase and its characterization by anion photoelectron spectroscopy.[9] However, the tremendously reactive C_{20} has only a fleeting existence in the condensed phase. Recently, it has been reported that a crystallized solid form of C_{20} was prepared in ultrahigh-molecular-weight polyethylene samples during Ar^+ ion beam irradiation;[10] computations have been performed to assist the characterization.[11]

Two important hints to the capture of smaller fullerenes are given by the experience with C_{36} and C_{20}: 1) When generated, smaller fullerenes have to be stabilized, for example, by partial saturation as in $C_{36}H_6$. 2) Less strained, larger cages are better targets for production and isolation. Following these two guidelines, Xie and co-workers have now reported the landmark achievement of $C_{50}Cl_{10}$ (Figure 1),[12] the first isolated and fully characterized stable smaller fullerene derivative.

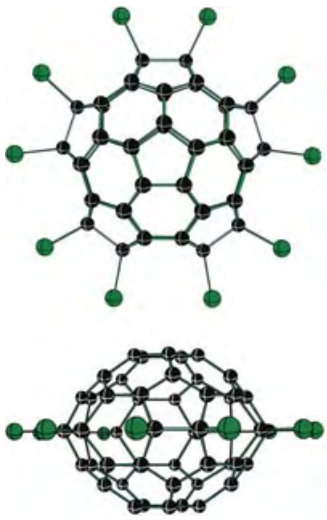


Figure 1. The B3LYP/6-31G* optimized structure of $C_{50}Cl_{10}$ (D_{5h}).

C_{50} itself is distinguished from other smaller fullerenes. First, it has a completely filled electron shell and is thus highly aromatic.[13] Second, it is the smallest cluster for which a cage can be constructed without triplets of directly or sequentially fused pentagons; it contains only isolated singlet and doublet pentagon configurations. The expected enhanced abundance of C_{50}[14] has been confirmed experimentally[15] in the gas phase by mass spectrometry.

Xie and his co-workers prepared $C_{50}Cl_{10}$ by a graphite arc-discharge process modified by introducing a small amount of carbon tetrachloride (CCl_4) in the helium atmosphere.[12] Chlorine not only stabilizes the reactive smaller fullerenes but also is known to catalyze fullerene formation.[16] The availability of samples in milligram quantities facilitated a definite structural assignment. Extensive characterization by mass spectrometry, ^{13}C NMR, infrared absorption, Raman, UV-Vis absorption, and fluorescence spectroscopies, and theoretical computations established the D_{5h} structure. The elegant architecture of $C_{50}Cl_{10}$ is the second fullerene "Saturn" after $C_{60}F_{20}$,[17] which also has a halogen "ring".

The C_{50} core in $C_{50}Cl_{10}$ consists of two C_{20} caps and five C_2 units around the equator. The local strain of C_{50}, as assessed by the pyramidalization angle (θ_p),[18] for the carbon atoms of the C_{20} caps (10.7–12.8°) is comparable to that of C_{60} (11.6°). However, a larger pyramidalization angle (15.5°) is responsible for the higher strain of the equatorial C atoms and their readiness to form exohedral adducts. Such structural features result in the instability of a bare C_{50} cage and the stability of $C_{50}Cl_{10}$.

 © 2004 Wiley-VCH Verlag GmbH & Co. KGaA, Weinheim DOI: 10.1002/anie.200401764

Oligomerization of bare C_{50} can occur easily; one- and two-dimensional solids can form by covalent bonding at the atoms around the equator. However, as in C_{60}, the C_{20} caps of C_{50} will interact only very weakly with each other; thus, layered solid structures can be expected. Upon heating, $C_{50}Cl_{10}$ might lose its chlorine atoms and form a bare C_{50} cluster, but this would be subject to oligomerization and formation of carbon solids.

Exohedral derivatives of fullerenes are attractive as structural templates and building blocks for supramolecular architectures and nanomaterials. The $C_{50}Cl_{10}$ offers ten reactive C–Cl sites for further chemical functionalization. Solvolysis reactions with methanol have already shown that the chlorine atoms in $C_{50}Cl_{10}$ can be replaced by methoxy groups to form a series of C_{50} derivatives, $C_{50}Cl_{10-n}(OCH_3)_n$ $(n = 1–4)$.[12] Similar to $C_{60}X_n$ and $C_{70}X_n$ (X = F, Cl), $C_{50}Cl_{10}$ may react easily with a variety of functional groups to form a wide range of derivatives with potential applications.

The preparation of $C_{50}Cl_{10}$ provides a practical method for the synthesis of smaller fullerene derivatives in isolable amounts. $C_{54}Cl_8$ and $C_{56}Cl_{10}$ were obtained as side products of $C_{50}Cl_{10}$, and various chloro derivatives of smaller clusters were also formed. Most likely these chlorides also have fullerene structures, although some could be deep bowls. Extension and development of Xie's method will hopefully result in their macroscopic synthesis and structural characterization in the very near future. One interesting and promising target is fullerene C_{32}, which has also a closed electronic shell and is a magic cluster in the gas phase.[15] The future isolation of smaller fullerene chlorides will undoubtedly instigate thorough investigations, for example, of the physical properties and potential applications.

The stabilization and characterization of smaller fullerenes as derivatives will provide evidence for the mechanism of fullerene formation. Almost two decades after the discovery of C_{60}, this is still an unsolved puzzle. Various speculative scenarios explain the formation of fullerenes, including the "Pentagon Road" (carbon clusters in the 25–50 range are open graphitic cups or bowls to which C_2 and other small carbon fragments add until the cage closes),[19] the "Fullerene Road" (similar to Pentagon Road, but intermediates with 30–58 carbon atoms are fullerene cages),[20] and the "Coalescence/Annealing Scheme" (C_{60} formation occurs through ring coalescence and annealing of medium-sized carbon clusters such as C_{18}, C_{24}, and C_{30}, rather than gradual addition of C_2 and C_3 particles).[21] However, very little detailed information supports any of the proposed scenarios. The trapping of C_{50} from the graphite arc-discharge soot at least provides experimental evidence for the existence of the closed cage structure smaller than C_{60}, but this is consistent with all three mechanistic proposals. Further experiments, such as the reaction between C_{50} and small carbon clusters (e.g., C_2, C_4…) will help to elucidate this long pending question. In principle, such experiments should now be possible, using $C_{50}Cl_{10}$ to produce clean gas-phase samples of C_{50}, in the same manner that Prinzbach et al.[9] used to produce clean C_{20} in the gas phase from $C_{20}Br_{20}$.

Xie's preparation of $C_{50}Cl_{10}$[12] provides a route to the bulk synthesis of the smaller fullerenes and their derivatives and provides new insights into the mechanism of fullerene formation. Hopefully routine investigations of the properties and applications of smaller fullerenes will become possible in the very near future.

Published Online: August 20, 2004

[1] H. W. Kroto, J. R. Heath, S. C. O'Brien, R. F. Curl, R. E. Smalley, *Nature* **1985**, *318*, 162 – 163.

[2] W. Krätschmer, L. D. Lamb, K. Fostiropoulos, D. R. Huffman, *Nature* **1990**, *347*, 354 – 358.

[3] L. T. Scott, M. M. Boorum, B. J. McMahon, S. Hagen, J. Mack, J. Blank, H. Wegner, A. de Meijere, *Science* **2002**, *295*, 1500 – 1503.

[4] L. T. Scott, M. M. Hashemi, D. T. Meyer, H. B. Warren, *J. Am. Chem. Soc.* **1991**, *113*, 7082 – 7084.

[5] L. T. Scott, M. S. Bratcher, S. Hagen, *J. Am. Chem. Soc.* **1996**, *118*, 8743 – 8744.

[6] H. Sakurai, T. Daiko, T. Hirao, *Science* **2003**, *301*, 1878 – 1878.

[7] C. Piskoti, J. Yarger, A. Zettl, *Nature* **1998**, *393*, 771 – 774.

[8] a) A. Koshio, M. Inakuma, T. Sugai, H. Shinohara, *J. Am. Chem. Soc.* **2000**, *122*, 398 – 399; b) A. Koshio, M. Inakuma, Z. W. Wang, T. Sugia, H. Shinohara, *J. Phys. Chem. B* **2000**, *104*, 7908 – 7913.

[9] H. Prinzbach, A. Weiler, P. Landenberger, F. Wahl, J. Wörth, L. T. Scott, M. Gelmont, D. Olevano, B. von Issendorff, *Nature* **2000**, *407*, 60 – 63.

[10] Z. Wang, X. Ke, Z. Zhu, F. Zhu, M. Ruan, H. Chen, R. Huang, L. Zheng, *Phys. Lett. A* **2001**, *280*, 351 – 356.

[11] Z. Chen, T. Heine, H. Jiao, A. Hirsch, W. Thiel, P. von R. Schleyer, *Chem. Eur. J.* **2004**, *10*, 963 – 970.

[12] S. Y. Xie, F. Gao, X. Lu, R. B. Huang, C. R. Wang, X. Zhang, M. L. Liu, S. L. Deng, L. S. Zheng, *Science* **2004**, *304*, 699.

[13] a) A. Hirsch, Z. Chen, H. Jiao, *Angew. Chem.* **2000**, *113*, 4079 – 4081; *Angew. Chem. Int. Ed.* **2000**, *39*, 3915 – 3917; b) Z. Chen, H. Jiao, A. Hirsch, W. Thiel, *J. Mol. Model.* **2001**, *7*, 161 – 163.

[14] H. W. Kroto, *Nature* **1987**, *329*, 529 – 531.

[15] For example, H. Kietzmann, R. Rochow, G. Ganteför, W. Eberhardt, K. Vietze, G. Seifert, P. W. Fowler, *Phys. Rev. Lett.* **1998**, *81*, 5378 – 5381.

[16] F. Gao, S. Y. Xie, R. B. Huang, L. S. Zheng, *Chem. Commun.* **2003**, 2676 – 2677.

[17] O. V. Boltalina, V. Yu. Markov, P. A. Troshin, A. D. Darwish, J. M. Street, R. Taylor, *Angew. Chem.* **2001**, *112*, 809 – 811; *Angew. Chem. Int. Ed.* **2001**, *40*, 787 – 789.

[18] R. C. Haddon, *J. Phys. Chem. A* **2001**, *105*, 4164 – 4165.

[19] R. E. Smalley, *Acc. Chem. Res.* **1992**, *25*, 98 – 105.

[20] J. R. Heath. *ACS Symp. Ser.* **1991**, *24*, 1 – 23.

[21] S. W. McElvany, M. M. Ross, N. S. Goroff, F. Diederich, *Science* **1993**, *259*, 1594 – 1596.

 © 2004 Wiley-VCH Verlag GmbH & Co. KGaA, Weinheim

Gene Regulation

Genetic Control by a Natural Metabolite-Responsive Ribozyme**

*Ronald Micura**

Keywords:
gene expression · nucleotides · riboswitches · ribozymes · RNA

Gene expression is a complex issue for all living organisms, with hundreds of genes to be controlled at the same time. Therefore, it is not surprising that nature has ingeniously created a great diversity of different tools and mechanisms to control and regulate these processes. The classical examples for gene regulation are transcription and translation attenuation in bacteria.[1,2] A common principle behind gene regulation is that some external event associated with the metabolic state of the cell triggers the formation of mutually dependent mRNA secondary structures and consequently either terminates transcription, or sequesters the Shine–Dalgarno (SD) sequence to hamper translation initiation. For a long time, this type of gene regulation was believed to be a domain of protein factors, as the external event usually involves a protein that senses the accumulation of a certain metabolite, then binds to the corresponding mRNA, thus inducing the structural change and the genetic on/off response.

However, in the past two years, it has been found that specialized domains within certain mRNAs directly bind metabolites in a selective and concentration-dependent manner and hence control gene expression without the need for protein factors.[3] These RNA domains are generally referred to as riboswitches, with the general organization of a natural aptamer domain and an expression platform in the untranslated leader region. Upon interaction with the small-molecule ligand, riboswitch mRNAs undergo a structural reorganization that results in the modulation of expression of the genes they precede. The first representative of a riboswitch was discovered by Ronald Breaker and co-workers from Yale University and concerned the regulation of cobalamine transport in bacteria.[4] Soon thereafter, a number of prokaryotic riboswitches that sense the metabolites thiamine pyrophosphate (TPP),[5] flavine mononucleotide (FMN),[6] *S*-adenosylmethionine (SAM),[7] guanine[8] and adenine[9] were ascertained for the regulation of other important biochemical processes.

The most recent findings in this exciting research area again comes from Ronald Breaker's laboratories. His team has now discovered a novel ribozyme that acts as a metabolite-responsive genetic switch in Gram-positive bacteria.[10] The ribozyme motif is located in the 5′-untranslated leader region (UTR) of the *glmS* mRNA. The *glmS* gene encodes the enzyme glutamine-fructose-6-phosphate amidotransferase, which uses fructose-6-phosphate (Fru6P) and glutamine to generate glucosamine-6-phosphate (GlcN6P), a compound that is critical for cell-wall biosynthesis. When GlcN6P accumulates, it binds to the ribozyme motif. The binding event triggers the ribozyme to cleave itself into two; the production of the amidotransferase is terminated, the synthesis of GlcN6P is suspended, and consequently the level of GlcN6P decreases. Notably, the cleavage event leaves the coding region of the mRNA intact, so that either the RNA is destabilized and subject to degradation, or its ability to be translated by the ribosome is hampered (Figure 1).

Experimental evidence for this new class of ribozymes arose from detailed biochemical studies on a 246-nucleotide RNA (246-*glmS*) that carried most of the highly conserved portion of the intergenic region preceding the *glmS* gene in *B. subtilis*. First, "in-line probing" assays of the RNA fragment indicated the preference for a specific cleavage site. It was then found that the self-cleavage of the 246-*glmS* RNA proceeds significantly faster within only 60 s when incubated in the presence of micromolar amounts of GlcN6P. The cleavage rate is 1000-fold faster than in the absence of metabolite. As an aside, Mg^{2+} in near-physiological concentrations is also required for the activation of the ribozyme by GlcN6P, but can be substituted by other divalent metal ions. Moreover, the ribozyme responds linearly to increasing ligand concentrations, such that a tenfold increase in metabolite concentration produces a tenfold increase in the cleavage rate. This behavior is consistent with a 1:1 complex between metabolite and ribozyme. Furthermore, most analogues of GlcN6P, such as GlcP6, GlcP1, or Glc are discriminated by the 246-*glmS* RNA, demonstrating the high specificity of the ribozyme. The 246-*glmS* RNA responds instantaneously to the addition of GlcN6P, indicating that this RNA serves as a rapid switch that forms its active structure without high-energy barriers for the required structural rearrangement. It has not yet been specified whether GlcN6P might take on a direct chemical role in the RNA cleavage event by constituting a part of the active

[*] Prof. Dr. R. Micura
University of Innsbruck, Institute of Organic Chemistry
Innrain 52a, 6020 Innsbruck (Austria)
Fax: (+43) 512-507-2892
E-mail: ronald.micura@uibk.ac.at

[**] The author acknowledges the Austrian Science Fund (FWF) for generous funding.

 © 2004 Wiley-VCH Verlag GmbH & Co. KGaA, Weinheim DOI: 10.1002/anie.200460233

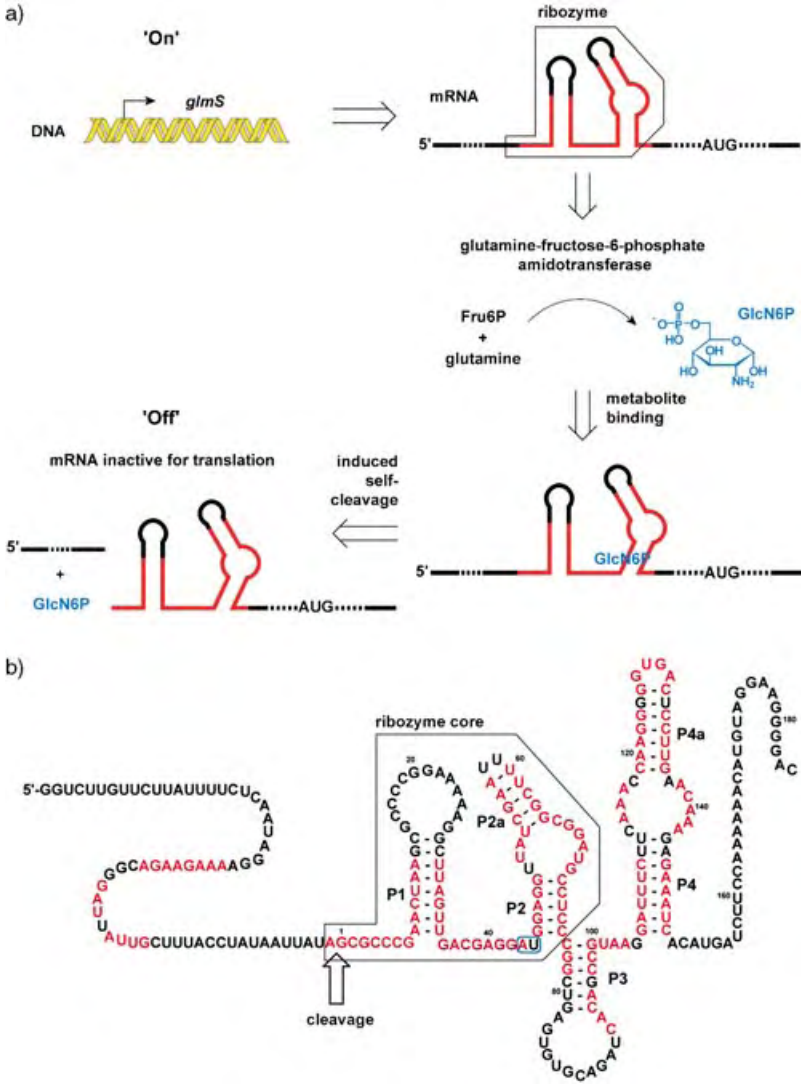


Figure 1. a) Repression of a gene at the RNA level by metabolite-activated ribozyme cleavage. The *glmS* mRNA encodes the enzyme glutamine-fructose-6-phosphate amidotransferase, which is involved in the synthesis of glucosamine-6-phosphate (GlcN6P). In the 5′-untranslated leader sequence, this mRNA contains a ribozyme motif with self-cleavage activity that is significantly enhanced when micromolar concentrations of GlcN6P are reached. Ribozyme self-destruction renders the *glmS* mRNA nonfunctional and inhibits further synthesis of GlcN6P. b) Investigated 246-nucleotide RNA comprising the novel ribozyme fold from *glmS* mRNA of *B. subtilis*. Red nucleotides match the consensus sequence and secondary structure of the *glmS* motif based on 18 representatives. The AUG start codon begins 245 nucleotides downstream from the cleavage site. Nucleotides 43 and 44 (blue circle) show altered spontaneous cleavage rates in the presence of GlcN6P, thereby suggesting close proximity to the metabolite binding site

site. However, the authors argue that the chemical mechanism of cleavage most likely resembles self-cleavage of other small ribozymes, such as the hammerhead or hairpin ribozyme. This mechanism proceeds by nucleophilic attack of the ribose 2′-OH at the adjacent phosphorus center, resulting in a 2′,3′-cyclic phosphate moiety at the termini of the 5′-cleavage products which were also observed in the case of *glmS* ribozyme. The minimal size of the active ribozyme was determined by testing a series of truncated RNA constructs and consists of roughly 75 nucleotides comprising stems P1 and P2; the loss of stems P3 and P4, however, results in decreased activity. Moreover, a series of mutants was investigated by testing their functions as self-cleaving ribozymes in vitro and as genetic control elements in vivo. It was found that mutations adjacent to the cleavage site are not tolerated. The *glmS* ribozyme element was also placed upstream of an unrelated β-galactosidase "reporter" gene. The inverse relationship between ribozyme activity in vitro and β-galactosidase activity in vivo documents the modular and transplantable nature of this novel metabolite-responsive functional RNA.

Remarkably, prior to the discovery of this natural riboswitch ribozyme, several groups—including Breaker and co-workers—were engaged in the engineering of allosterically triggered ribozymes.[11] The successful realization of such artificial molecular switches that consist of an aptamer selected in vitro directly adjoined to a ribozyme domain, may have paved the way for the successful search for a naturally occurring counterpart.

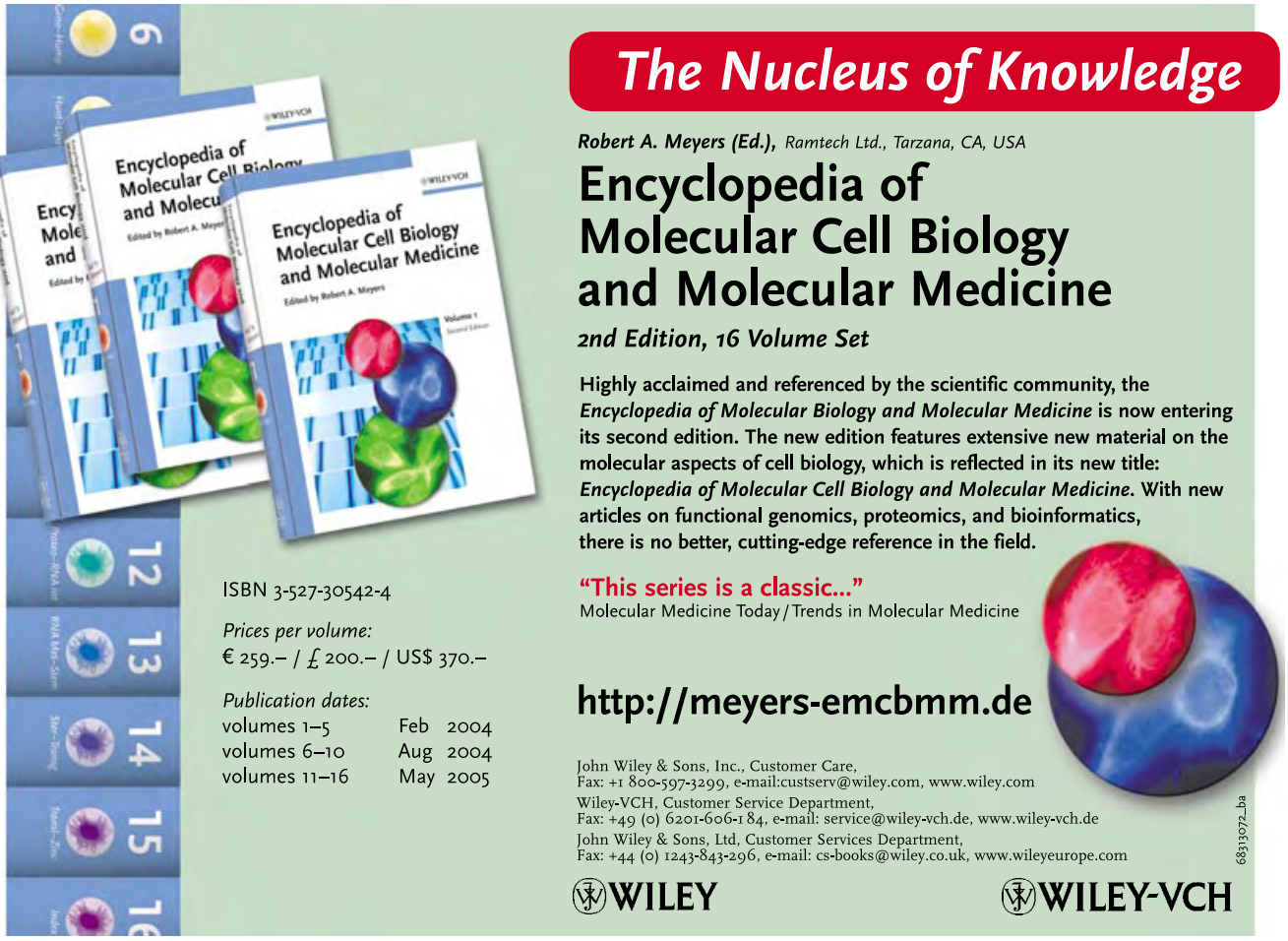
The discovery of the metabolite-responsive ribozyme should also have an impact on those who seek to understand how life evolved from primitive to more complex forms. This ribozyme might well stand for a surviving concept of regulative mechanisms in ancient organisms. It will be a challenge to elucidate whether this type of regulation is widespread and also existent in higher organisms.

Published Online: August 4, 2004

[1] J. Stülke, *Arch. Microbiol.* **2002**, *177*, 433–440.
[2] P. Romby, M. Springer, *Trends Genet.* **2003**, *19*, 155–161.
[3] W. C. Winkler, R. R. Breaker, *ChemBioChem* **2003**, *4*, 1024–1032.
[4] A. Nahvi, N. Sudarsan, M. S. Ebert, X. Zou, K. L. Brown, R. R. Breaker, *Chem. Biol.* **2002**, *9*, 1043–1049.
[5] W. C. Winkler, A. Nahvi, R. R. Breaker, *Nature* **2002**, *419*, 952–956.
[6] a) W. C. Winkler, S. Cohen-Chalamish, R. R. Breaker, *Proc. Natl. Acad. Sci. USA* **2002**, *99*, 15908–15913; b) A. S. Mironov, I. Gusarov, R. Rafikov, L. E. Lopez, K. Shatalin, R. A. Kreneva, D. A. Perumov, E. Nudler, *Cell* **2002**, *111*, 747–756.
[7] a) B. A. McDaniel, F. J. Grundy, I. Artsimovitch, T. M. Henkin, *Proc. Natl. Acad. Sci. USA* **2003**, *100*, 3083–3088; b) W. C. Winkler, A. Nahvi, N. Sudarsan, J. E. Barrick, R. R. Breaker, *Nat. Struct. Biol.* **2003**, *10*, 701–707; c) V. Epshtein, A. S. Mironov, E. Nudler,

 © 2004 Wiley-VCH Verlag GmbH & Co. KGaA, Weinheim

Proc. Natl. Acad. Sci. USA **2003**, *100*, 5052 – 5056.
[8] M. Mandal, B. Boese, J. E. Barrick, W. C. Winkler, R. R. Breaker, *Cell* **2003**, *113*, 577 – 586.
[9] M. Mandal, R. R. Breaker, *Nat. Struct. Biol.* **2004**, *11*, 29 – 35.
[10] W. Winkler, A. Nahvi, A. Roth, J. A. Collins, R. R. Breaker, *Nature* **2004**, *428*, 281 – 285.
[11] R. R. Breaker, *Curr. Opin. Biotechnol.* **2002**, *13*, 31 – 39.



Diamond Synthesis

Diamonds from the Pressure Cooker—Science or Science Fiction?**

*Hermann Sachdev**

Keywords:
chemical vapor deposition · correspondence · diamond synthesis · high-pressure chemistry · Raman spectroscopy · synthetic methods

Recently, a diamond synthesis was reported by Chen and co-workers under conditions of diamond being metastable,[1,2] and both publications deal with the synthesis of diamond by reduction of carbon dioxide or carbonates with sodium metal at about 460–500 °C/800–860 atm, thus being quite comparable methods. Each of the papers is based on conclusions made from an interpretation of similar experimental data (one powder diffraction pattern (XRD spectrum), one Raman spectrum, and SEM pictures), all displaying only characteristics of the product. The authors do not present any experimental data regarding reaction intermediates in the publications or as supporting information, nor do they argue about similarities to already existing diamond-formation processes, although they claim to have characterized the intermediates.[2] In the case of the reduction of magnesium carbonate[2] the authors explain their results with the following reactions [Eq (1)–(3)]:

$$MgCO_3 \rightarrow MgO + CO_2 \quad (1)$$

$$CO_2 + 4\,Na \rightarrow 2\,Na_2O + C \quad (2)$$

$$Na_2O + CO_2 \rightarrow Na_2CO_3 \quad (3)$$

In the experimental section, the authors argue that they have characterized the intermediates MgO and Na_2CO_3 besides graphite and diamond by XRD. In the case of the neat reduction of carbon dioxide[1] similar argumentations are made. No diamond formation was reported so far from alkali metal or alkaline earth metal carbides under the pressure/temperature conditions given by the authors in the concerned publications. It is known that the primary reaction of alkali metals (M) with carbon dioxide leads to oxalates by single electron transfer (SET) reactions [(Eq. (4), (5)]:[3]

$$M + CO_2 \rightarrow M^+\,CO_2^{*-} \quad (4)$$

$$2\,M^+\,CO_2^{*-} \rightarrow M_2C_2O_4 \quad (5)$$

The oxalates are prone to disproportionation at elevated temperatures and form the corresponding carbonates and carbon monoxide [Eq. (6)] (standard calibration of thermal gravimetric–differential thermal analysis (TG–DTA) devices by, for example, CaC_2O_4 decomposition):

$$M_2C_2O_4 \rightarrow M_2CO_3 + CO \quad (6)$$

From a chemical point of view, a reduction of carbon dioxide or carbonates by sodium metal may form the corresponding oxalates, which finally decompose at higher temperatures to carbon monoxide. Carbon formation thus can occur by disproportionation of carbon monoxide to carbon and carbon dioxide [(Eq. (7)]. Therefore, it has to be considered whether a diamond formation from carbon monoxide is feasible.

$$2\,CO \rightarrow CO_2 + C_{(graphite,\ diamond)} \quad (7)$$

The diamond formation in the ternary C/H/O system under metastable conditions involving CO in the gas phase is well documented,[4] but not mentioned by Chen et al. In chemical vapor deposition (CVD) syntheses of diamond (performed at the pressure/temperature domain in which the diamond is metastable), usually the carbon–hydrogen system is used to deposit crystalline diamond. However, it is also possible to obtain well-grown diamond in the ternary C/H/O system. A diamond formation in a reductive system of carbon dioxide (e.g., sodium and carbon dioxide or sodium and carbonates), as presented by Chen et al.[1,2] in a pressure/temperature regime of diamond being metastable can not be excluded in principle and might be feasible, especially if traces of water are present. But it has to be considered whether the presented measurements and the spectroscopic data prove that the presented reactions have taken place and whether the experimental procedures are reproducible and consistent with the descriptions and interpretations.

The most critical points in these publications[1,2] will be discussed to evaluate the results claimed by the authors. In reference [1]

- no reference of the XRD interpretation of Figure 1 is given and no description of the XRD spectrometer is mentioned. The formation of graphite is based on the interpretation of a single diffraction peak in

[*] PD Dr. H. Sachdev
Anorganische Chemie 8.11
Universität des Saarlandes
66041 Saarbrücken (Germany)
Fax: (+49) 681-302-3995
E-mail: h.sachdev@mx.uni-saarland.de

[**] Comments to the "Growth of Large Diamond Crystals by Reduction of Magnesium Carbonate with Metallic Sodium"

 © 2004 Wiley-VCH Verlag GmbH & Co. KGaA, Weinheim DOI: 10.1002/anie.200460689

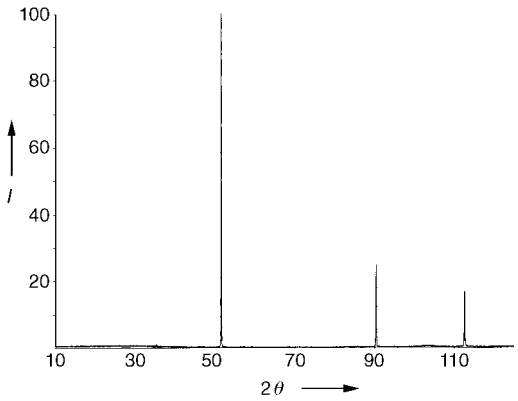


Figure 1. XRD spectrum of natural diamond grit displaying the 111, 220, and 311 reflections (measured with $Co_{K\alpha}$ radiation). I = relative intensity.[7]

the XRD spectrum of Figure 1, whereas no other diffraction peaks of graphite are present.

- the Raman spectrum displays additional features at about 1600 cm^{-1}, which are not discussed
- the crystal morphologies shown in Figure 3 a, b and Figure 4 do not match (important note: similar magnification!): Figure 3 displays solid material that is not facetted and resembles dissolutive or broken material, whereas Figure 4 clearly shows an octahedral-shaped, facetted material of growth-type morphology. The morphological features of these "typical sample pictures" do not correspond with the described "diamond growth" and no explanation is given for this significant and obvious fact. Additionally, SEM pictures may display diamond but these cannot prove that diamond is present.
- supporting information is of no significance (a picture of an octahedral crystal).

With regard to reference [2] it is noted—besides the correspondence of the XRD pattern in Figure 1 with the spectrum shown in reference[1]—that:

- The XRD pattern in Figure 1 is referenced with a Joint Committee on Powder Diffraction Standards (JCPDS) file 75–0623, which actually is a calculated spectrum displaying explicitly only two calculated 2θ values (for the 111 and 220 reflections), whereas the calculated value for the 311 reflection is not mentioned. Thus it makes no sense to correlate this JCPDS card to the three diffraction peaks of the "obtained diamond spectrum" of Figure 1. Also, the legend of Figure 1 is in contradiction to the text and experimental section "XRD … of *as-prepared* diamond…" In this case, the reaction intermediates would also have to be present in the XRD spectrum, since it is referred to an "as-prepared" sample.

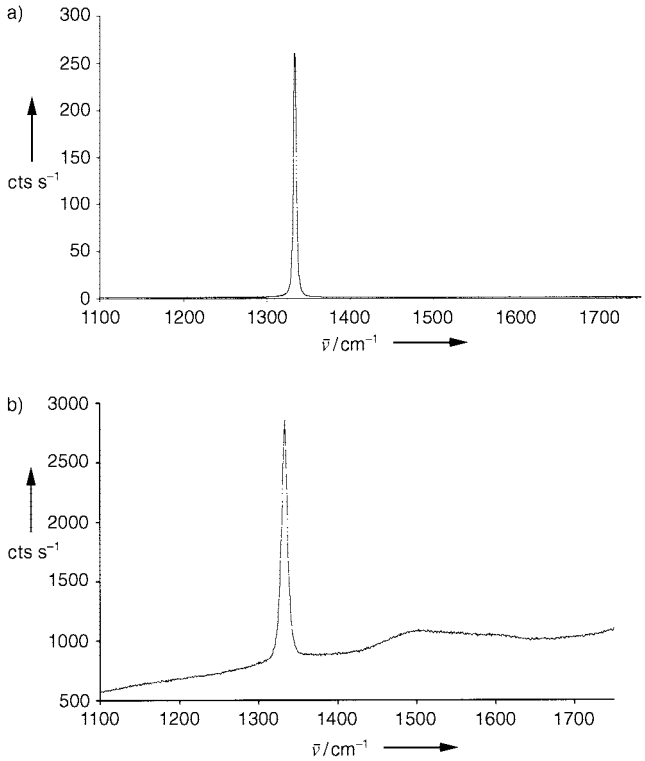


Figure 2. Raman spectra of diamond samples.[8] a) Raman spectrum of HPHT diamond (diamond peak at 1332 cm^{-1}). b) Raman spectrum of CVD diamond with traces of sp^2-type carbon (diamond peak at 1332 cm^{-1}, graphitic broad D- and G-modes centred at about 1350 and 1500–1600 cm^{-1}). Cts = counts.

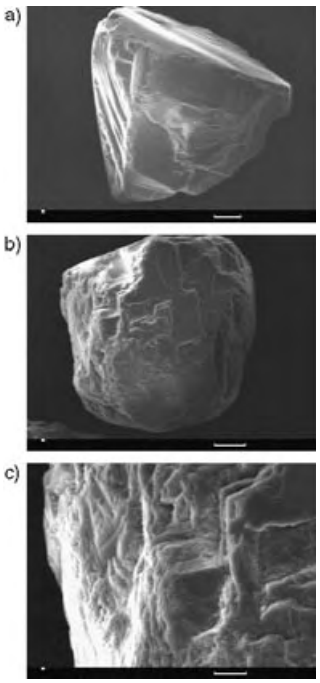


Figure 3. a)–c) SEM pictures displaying the morphology of natural diamond grit (broken, dissolutive) in the range of 200 μm. The bar in (a) and (b) is 30 μm long and 10 μm long in (c).

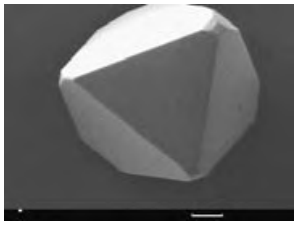


Figure 4. SEM picture displaying the morphology of a growth type HPHT diamond crystal. The bar is 30 μm long.

 © 2004 Wiley-VCH Verlag GmbH & Co. KGaA, Weinheim

- The Raman spectrum in Figure 2 is from a diamond sample and exhibits a broad structure in the region of 2000 cm^{-1}. The authors do not mention this aspect or possible origin of this feature in the text.
- The SEM in Figure 3 displays a sample of solid material of broken or dissolutive nature. How does this crystal morphology correlate with diamond growth as claimed in the text?
- Regarding the experimental setup, from the presented data it is not evident how the pressure/temperature conditions were measured or maintained in the autoclave or recorded as described in the Experimental Section. No heating device or temperature-control unit is mentioned or depicted or referenced. The detailed experimental setup was never referenced or displayed properly in both publications. Furthermore, stainless steel will be severely corroded by the mentioned reaction parameters and may cause side reactions that initiate carbon formation.
- In their communication the authors themselves mention in the Experimental Section that their main identified products by XRD were "diamond, graphite, Na_2CO_3, and MgO". They state that they have detected Na_2CO_3 and MgO in the product mixture by XRD analysis and formulate the Equations (1)–(3). Neither in the publications nor in any supporting information were such XRD files or XRD spectra of any "as-prepared sample" presented.
- In the experimental section: perchloric acid ($HClO_4$) is mentioned as a reagent to dissolve graphite, but this procedure is also not cited and referenced. No concentration is mentioned. Reaction conditions, such as temperature or duration for the dissolution, are missing. A reaction of perchloric acid is strongly dependent on the concentration and finally may lead to a distinctive intercalation and oxidation product (graphite perchlorate), which itself has a crystalline nature (and might be detected by XRD), but graphite is not really being dissolved as described by the authors. No reaction parameters are given either.

In addition to these more specific points there are important general remarks with respect to both publications:[1,2] Neither publication gives detailed references for the experimental setup nor describes the autoclave, pressure and temperature measurements, which are the most critical parameters in these reactions, thus, the results can not be reproduced in a proper manner. Even if it is stated that the pressure is autogenic, how were the corresponding pressure/temperature values obtained and measured (e.g., 500 °C/860 atm in reference [2] 440 °C/800 atm in reference [1])? Furthermore, the materials used as described in the autoclave synthesis are highly corrosive at temperatures about 500–700 °C and thus can cause severe damage or corrosion to the described stainless-steel autoclave, which will lead to contamination of the reaction mixture, thus additional compounds may affect or catalyze the formation of carbon. In general, the experimental description is not sufficient to clarify or validate the claimed results. A total yield of carbonic material was not given for either reaction.

Are the presented analytical data (XRD, Raman, SEM) a sufficient proof of a new synthetic method as published by the authors? Broken natural or artificial high-pressure high-temperature (HPHT) diamond samples or CVD samples lead to similar XRD, Raman, and SEM data as presented by the authors in both articles,[1,2] especially if the crystal quality is quite good. Irrespective of how the XRD spectra in Figures 1 of both publications were obtained, the standard XRD spectra of natural, HPHT, or CVD diamond samples are rather similar and can not be distinguished by simple diffraction methods.

Such diamond samples exhibit almost identical XRD patterns under standard routine measurement conditions, especially if the diamond quality is good. The same argument is also valid for the Raman spectra[5,6] of Figure 2 of the concerned publications.

The presence of signals from sp^2-hybridized carbon atoms in the Raman spectrum may be due to surface reconstruction, additional carbonic matter on grain boundaries, or graphitic inclusions within the diamond crystal. In general, the Raman cross section of sp^2-hybridized carbon atoms is about 10^2 times higher than of sp^3-hybridized carbon atoms (depending on the excitation wavelength), therefore the presence of signals of sp^2-hybridized carbon atoms in the Raman spectra is no proof for the formation of crystalline graphite, which might be detected by XRD. The SEM pictures might be taken from any material, and no energy-dispersive X-ray (EDX) analyses are presented to proof the presence of carbon or any other element. Most of the SEM pictures display nonfacetted, dissolutive material although diamond growth is mentioned by the authors, the issue of the fragmented material is not discussed.

The spectra and pictures displayed in Figures 1–Figure 4 from diamond samples of different origin indicate that the conclusions drawn by Chen and co-workers[1,2] can not be solely based on their presented data, as there is no experimental support for the proposed reaction mechanism provided by the authors.

Even if it is assumed that the data presented by Chen and co-workers[1,2] are correct, they cannot be used as a unique and significant proof of the reported diamond synthesis as it is not possible to distinguish the presented analytical data (XRD, Raman spectrum, SEM micrograph) from other (crushed, broken) artificial or natural diamond samples of the same size and morphology.

When a new reaction pathway is claimed, the characterization and presentation of intermediates is necessary and mandatory in a communication, even if a full and thorough scientific interpretation cannot be given in the first instance. The mentioned reaction intermediates in the publications were not presented by the authors although the authors claimed several times to have identified them by XRD.[2]

The most critical parameters for diamond formation by any method are the pressure and temperature conditions. The experimental descriptions[1,2] do not allow a straightforward reproduction of the procedures, since there are no details of how the temperature/

 © 2004 Wiley-VCH Verlag GmbH & Co. KGaA, Weinheim

pressure values were obtained. There are also other significant factors that may severely affect the reaction (e.g., moisture incorporated by weighing the solid carbon dioxide, influence of iron from the autoclave, etc.). From the way of handling the XRD and other data by the authors, together with the above raised aspects, there are severe doubts that both approaches of the diamond syntheses are based on the experiments as described by the authors,[1,2] even if they are not contradictory to the current models of diamond formation and might be feasible. At this stage the authors failed to prove their reported syntheses and their interpretation is not supported by the presented analytical data.

Published Online: August 20, 2004

[1] Z. Lou, Q. Chen, Y. Zhang, W. Wang, Y. Qian, *J. Am. Chem. Soc.* **2003**, *125*, 9302 – 9303.
[2] Z. Lou, Q. Chen, W. Wang, Y. Qian, Y. Zhang, *Angew. Chem.* **2003**, *115*, 4639 – 4641; *Angew. Chem. Int. Ed.* **2003**, *42*, 4501 – 4503.
[3] A. F. Holleman, E. Wiberg, *Lehrbuch der Anorganischen Chemie* (Ed.: N. Wiberg),Walter de Gruyter, Berlin, **1996**, p. 100 – 105.
[4] P. K. Bachmann, D. Leers, H. Lydtin, *Diamond Relat. Mater.* **1991**, *1*, 1 – 12 and plenty of other reports in the same journal up to now.
[5] J. Wilks, E. Wilks, *Properties and Applications of Diamond*, Butterworth-Heinemann, Oxford, **1991**.
[6] J. E. Field, *The properties of natural and synthetic diamond*, Academic Press, London, **1992**.
[7] STOE STADI-P XRD diffractometer.
[8] S.A. T64000 Raman spectrometer [excitation wavelength: 514 and 488 nm (2 μm spot size, 8 mW power at sample), backscattering geometry].
[9] CamScan 44FE Field emission scanning electron microscope.

Life's Simple Pleasures!



No need to waste precious time looking for the right information – Register now for the free **Wiley-VCH Alerting Service.**

It's simple – and it's fast.

To receive regular news per e-mail tailored precisely to your needs and interests, just fill in the registration form at **www.wiley-vch.de/home/pas/**

WILEY-VCH

 © 2004 Wiley-VCH Verlag GmbH & Co. KGaA, Weinheim

Diamond Synthesis

Reply to Comment on "Growth of Large Diamond Crystals by Reduction of Magnesium Carbonate with Metallic Sodium"**

*Zhengsong Lou and Qianwang Chen**

Keywords:
chemical vapor deposition · correspondence · diamond synthesis · high-pressure chemistry · Raman spectroscopy · synthetic methods

First, thanks to Dr. Hermann Sachdev who has commented on our work. The comments were thoughtful.

We should have cited reference [1] paper in our communication in reference [2] because the latter paper reported progress related to the former, we apologize for having not done so. We also apologize for a mistake made during handing the X-ray diffraction data for reference [2]. The original XRD paper was recorded on chart paper, which was then scanned into the computer as a BMP format file and subsequently digitized. In this process, our technician responsible for treating the X-ray data made an error and used, after polishing, a similar BMP format file obtained from a another sample synthesized in our lab.

We appreciate the analysis of Sachdev: diamonds might be generated from carbon monoxide or formed in a C/H/O system. In our synthesis, diamond was not found in the $K_2C_2O_4$/Na and CoC_2O_4/Na systems (not published), and carbon nanotubes were formed by using carbon suboxide as carbon source.[3] In both of these cases, carbon monoxide is present during the reaction.

Chemical vapor deposition (CVD) is a low-pressure synthetic process, which normally requires that the substrate be maintained at a temperature in the range of 1000–1400 K and that the precursor gas be diluted in an excess of hydrogen (typical CH_4 mixing ratio $\approx$ 1–2 vol %).[4] In our process, diamond particles about 250 μm long formed in the CO_2/Na system; the volume of hydrogen in the gas phase could not have reached the levels required to produce diamonds in the CVD system, even though traces of water are present in dry ice. In addition, the $MgCO_3$/Na system, which has considerably less water present, also produces diamonds. The intense, sharp peaks found in the Raman spectra at 1332 cm^{-1} show that the diamonds are highly crystalline. [1,2]

Indeed, most diamond particles generated in our process appear with irregular morphologies (see Supporting Information). The particles in the scanning electron micrographs (SEM) images were picked up from products under an optical microscope, which were already confirmed to be diamond by Raman analysis. Sachdev observed that Figure 3 of reference [1] displayed solid material that was not facetted and resembled dissolutive material, whereas Figure 4 in reference [1] clearly showed facetted material of growth type. In fact, we have no idea what the appearance of our diamond should be. We are also aware of this difference as discussed in reference [1]: Octahedral diamond particles were observed in the CO_2/Na system when the particles were rather small (only several micrometers), and an increase in the particle size led to the disappearance of the octahedral shape. Octahedral particles of around 4.3 μm were also observed in CO_2/Li system under SEM and TEM, which were confirmed to be diamonds by electron diffraction.[5] It is true that energy-dispersive spectroscopy (EDS) analyses can provide information of elemental composition, and can further confirm whether a particle is diamond, as suggested by Sachdev. We have performed EDS analysis under SEM on a particle that was produced in the $MgCO_3$/Na system followed by treatment with aqueous HF solution to remove α-SiO_2, which shows that the particle contains 93.05 % carbon with F, Na, Mg, and Si contaminations (see Supporting Information).

Graphite and amorphous carbon were removed by treating the solid precipitate with aqueous perchloric acid ($HClO_4$; 4.0 M) at 140 °C for about 10 hrs.[6] In some cases, large particles were picked out from the treated sample for Raman and SEM analysis. A particle separated by this process is shown in the inset of Figure 1. This particle has an irregular shape, but it was confirmed to be diamond by Raman spectroscopy (Figure 1).

With regard to diamond characterization, the synthesized diamonds were usually characterized by electron diffraction,[7] X-ray diffraction (XRD), Raman spectroscopy, and SEM.[8] These common tools for diamond character-

[*] Z. Lou, Q. Chen
Structure Research Laboratory and Department of Materials Science & Engineering
University of Science & Technology of China
Hefei 230026 (China)
Fax: (+86) 551-360-7292
E-mail: cqw@ustc.edu.cn

[**] This work was supported by the National Natural Science Foundation of China.

Supporting information for this article is available on the WWW under http://www.angewandte.org or from the author.

 © 2004 Wiley-VCH Verlag GmbH & Co. KGaA, Weinheim DOI: 10.1002/anie.200460857

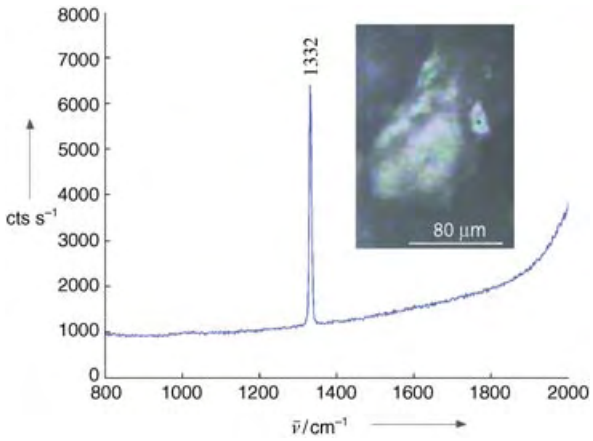


Figure 1. Raman spectrum and image of a diamond particle produced in $MgCO_3$/Na system, the image was taken by an optical microscope attached to a Raman spectrometer. Cts = counts.

ization were also used in our characterization, which provides enough evidence that diamonds were indeed produced in our synthesis.

In the early stage of this research, it was our aim to get pure diamonds, therefore the XRD patterns were measured on the products after appropriate treatments. In reference [2] graphite and other crystalline impurities were completely removed by treating the sample with ethanol, HCl (2.0 M), distilled water, and $HClO_4$ (4.0 M). As the reaction was performed in a new cell, no significant amount of silicon oxide and iron-based compounds were detected. Therefore, the XRD pattern only shows peaks from diamond, although there are some amorphous impurities. These details should have been included in reference [2].

We agree with Sachdev that the characterization of reaction intermediates is important for a new process and could help us to understand the diamond-growth process in the system. It was found that impurities were also formed during the reaction, which depend upon the material of the cell wall (that is, whether a new cell or old cell was used), the starting materials, and reaction conditions. For example, $FeCO_3$ and graphite were found to be present as by-products in CO_2/K system.[5] In addition to graphite, Na_2CO_3, MgO, α-SiO_2, and iron-based compounds were also found in the product mixture along with diamonds in $MgCO_3$/Na system when the reaction was carried out in an old cell (see Supporting Information). Some impurities (Si, Fe) may originate from the wall of the stainless-steel cell.

In Figure 2 of reference [1], the Raman spectrum displays a strong peak at 1332 cm^{-1}, which is characteristic peak of cubic diamond. It also contains an additional broad feature at about 1600 cm^{-1} (between 1582 cm^{-1} of E_{2g} mode of graphite and 1620 cm^{-1} of microcrystalline graphite). We agree that this one may be assigned to sp^2 hybridized carbon atom. We also wished to know whether this feature arises from an sp^2 hybridized carbon atom present as inclusion in the diamond particles or originates from surface reconstruction. In reference [2], the feature at about 2000 cm^{-1} might originate from strong fluorescence of carbon materials, which has also been observed in the spectrum of other diamond materials.[9] However the above features do not appear in the Raman spectrum of high-pressure high-temperature (HPHT) and CVD diamonds referred to by Sachdev, which also indicates that our diamonds have different origins. The detail reason about these features needs to be investigated.

Our reaction cell was not commercial and was heated in an oven. The temperature was measured by a temperature controller linked to a thermocouple, while the pressure is autogenic and calculated for high temperatures. The growth of diamonds is dependent on many parameters, some of which are: temperature, pressure, cell material, and starting reactants. Therefore, the reproduction experiments need to be carried out in a careful manner. Even so, we could produce diamonds from time to time with the $MgCO_3$/Na and CO_2/M (M = Li, Na, K) systems.

Published Online: August 20, 2004

Please note: Minor changes have been made to this manuscript since its publication in *Angewandte* Early View. The Editor.

[1] Z. S. Lou, Q. W. Chen, Y. F. Zhang, W. Wang, Y. T. Qian, *J. Am. Chem. Soc.* **2003**, *125*, 9302 – 9303.

[2] Z. S. Lou, Q. W. Chen, W. Wang, Y. T. Qian, Y. F. Zhang, *Angew. Chem.* **2003**, *115*, 4639 – 4641; *Angew. Chem. Int. Ed.* **2003**, *42*, 4501 – 4503.

[3] M. W. Shao, D. B. Wang, G. H. Yu, B. Hu, W. C. Yu, Y. T. Qian, *Carbon* **2004**, *42*, 183 – 185.

[4] P. W. May, *Endeavour* **1995**, *19*, 101 – 106.

[5] Z. S. Lou, Q. W. Chen, Y. F. Zhang, Y. T. Qian, W. Wang, *J. Phys. Chem. B* **2004**, *108*, 4239 – 4241.

[6] Y. C. Guo, Z. H. Li, G. Y. Zheng, *Man made diamond and applications*, *Chinese edition*, Science Press, Beijing, **1984**.

[7] Y. Gogotsi, S. Welz, D. A. Ersoy, M. J. Mcnallan, *Nature* **2001**, *411*, 283 – 287.

[8] A. V. Palnichenko, A. M. Jonas, J. C. Charlier, A. S. Aronin, J. P. Issi, *Nature* **1999**, *402*, 162 – 165.

[9] A. Greshake, T. Kenkmann, R. T. Schmitt, *63rd Annual Meteoritical Society Meeting, In Situ Raman Spectroscopy Of Diamond In The Ureilite Hammadah Al Hamra 126*, Institut für Mineralogie, Museum für Naturkunde, Invalidenstr. 43, 10115 Berlin, Germany.

[10] The Raman measurements were performed on a LABRAM-HR confocal laser microRaman spectrometer with an excitation wavelength of 514.3 nm. Optical photograph of diamonds taken from a LABRAM-HR Confocal Laser MicroRaman Spectrometer, the spot size is about 8 μm and scanning time is 3 seconds. X-ray diffraction patterns were performed on a Rigaku D/max-rA X-ray diffractometer with CuKα radiation.

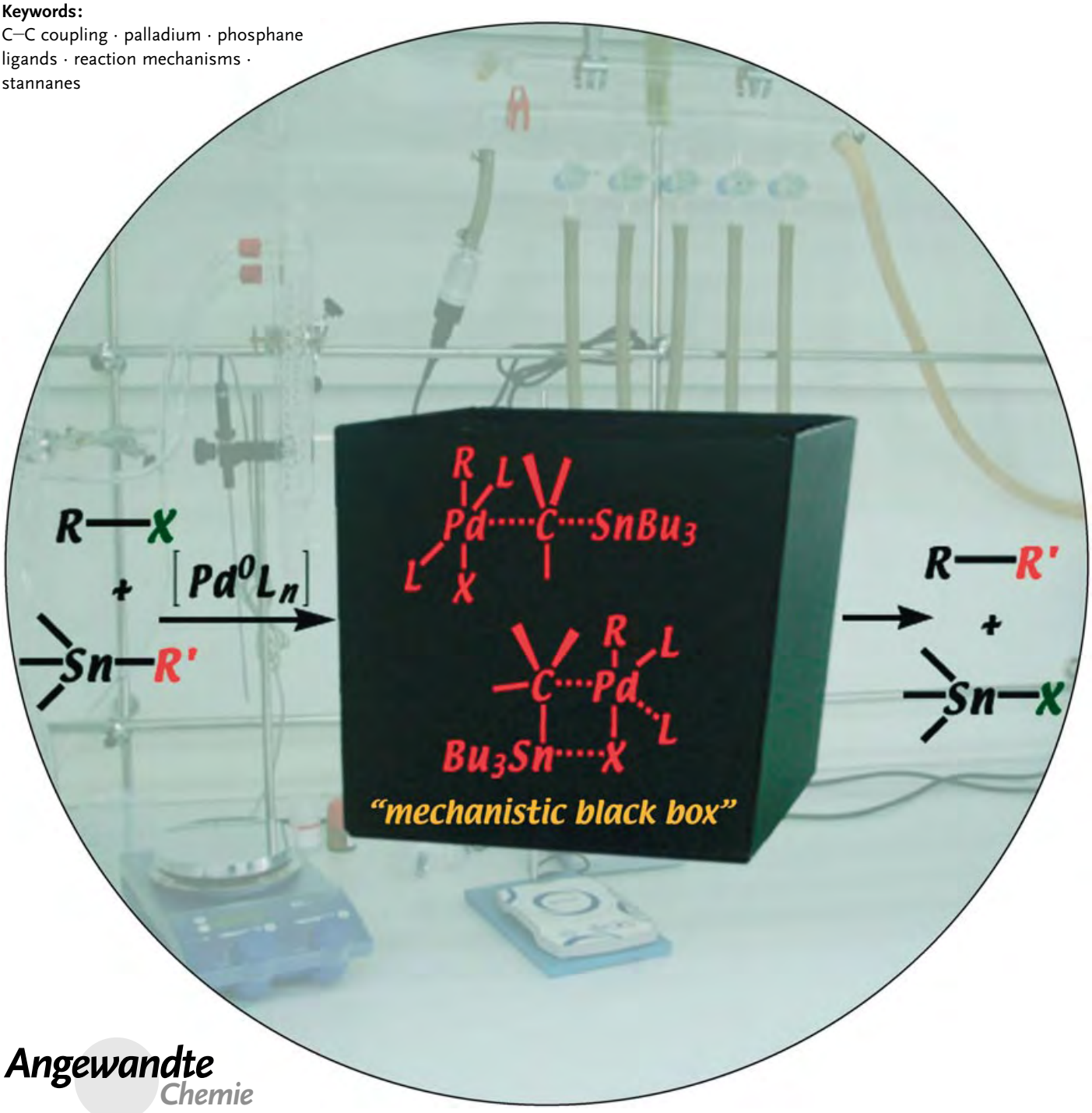
 © 2004 Wiley-VCH Verlag GmbH & Co. KGaA, Weinheim

C–C Coupling

The Mechanisms of the Stille Reaction

Pablo Espinet and Antonio M. Echavarren**

Keywords:
C–C coupling · palladium · phosphane ligands · reaction mechanisms · stannanes



 © 2004 Wiley-VCH Verlag GmbH & Co. KGaA, Weinheim DOI: 10.1002/anie.200300638

Eighteen years ago in Angewandte Chemie John K. Stille reviewed a novel methodology, which eventually became known by his name, for the coupling of organostannanes with organic electrophiles. Since then that seed has blossomed into a multifaceted methodology full of hidden possibilities to explore, discover, and enjoy. Very recent modifications are making synthetic wishes come true that were only dreamed of a few years ago. Moreover, as important advances are being made in the understanding of the mechanistic details of the process, it is becoming increasingly possible to apply this essential reaction and its new variants in a less empirical way. The purpose of this Review is to give a critical account of this progress.

From the Contents

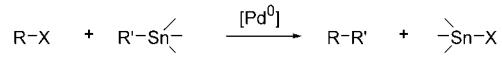
1. Introduction	4705
2. The Oxidative Addition	4707
3. The Transmetalation	4714
4. The Reductive Elimination	4723
5. Scrambling of Substituents and Homocoupling	4724
6. Unorthodox Mechanisms	4724
7. Copper Effects	4726
8. Summary and Outlook	4727

> *Why with the time do I not glance asideTo new-found methods...?*
>
> W. Shakespeare, Sonnet LXXVI

1. Introduction

1.1. Palladium-Catalyzed Cross-Coupling Reactions

The Stille reaction has established itself as one of the two most general and most selective palladium-catalyzed cross-coupling reactions (Scheme 1),[1–3] along with the Suzuki



Scheme 1. The Stille coupling.

cross-coupling of organoboron compounds.[4] The first examples of the coupling of organostannanes with organic electrophiles were disclosed during the period 1976–1977 by the research groups of Eaborn[5] and Kosugi,[6,7] but it was the extensive synthetic and mechanistic work carried out by Stille and co-workers from 1978[8] that made this reaction a standard method in organic synthesis.[9]

The Stille and Suzuki reactions rank today amongst the more general transformations in organic synthesis.[10] For the synthesis of complex molecules,[11] the Stille coupling is usually superior, displaying high selectivity and broad scope. Its tolerance towards most functional groups makes the Stille coupling particularly effective for transformations of highly functionalized molecules. In fact it has been applied successfully to the construction of a variety of ring systems bearing sensitive functional groups.[12] Notable examples are the syntheses of dynemicin A by Danishefsky and co-workers[13] and rapamycin by Nicolaou and co-workers,[14] in which double couplings are used for the formation of two C–C bonds are formed in a single step.

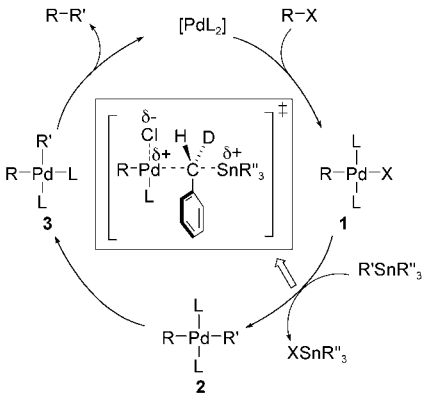
The Stille reaction is related to other cross-coupling reactions based transmetalations of a variety of hard or soft organometallic nucleophiles.[15] Besides the two prominent members already mentioned, the family of palladium-catalyzed cross-coupling reactions includes the Hiyama,[16–18] Sonogashira,[19] Kumada,[20] and Negishi reactions,[21] and related reactions.[22,23] Cross-coupling reactions are also somewhat related to the Heck reaction (the alkenylation of organic electrophiles).[24] However, although the first step in both processes is identical (activation of the organic electrophile by oxidative addition to Pd), there is no transmetalation step in the Heck reaction, in which the C–C bond is formed through an insertion step, followed by a β-hydride elimination to form the substituted alkene product.

1.2. Original Mechanistic Proposal

In his influential Review of 1986,[1] Stille proposed a mechanism for the Stille reaction based primarily on data obtained from the coupling of benzoyl chloride with tributyl(phenyl)stannane.[1] In the generalized mechanism, the active catalytic species was assumed to be a $[PdL_2]$ ($L = PPh_3$) complex, which reacts with the organic electrophile R–X to

[*] Prof. Dr. P. Espinet
Química Inorgánica
Facultad de Ciencias, Universidad de Valladolid
47005 Valladolid (Spain)
Fax: (+34) 983-423-013
E-mail: espinet@qi.uva.es
Prof. Dr. A. M. Echavarren
Institute of Chemical Research of Catalonia (ICIQ)
43007 Tarragona (Spain) and
Departamento de Química Orgánica
Universidad Autónoma de Madrid
28049 Madrid (Spain)
Fax: (+34) 977-920-225
E-mail: aechavarren@iciq.es

DOI: 10.1002/anie.200300638
© 2004 Wiley-VCH Verlag GmbH & Co. KGaA, Weinheim

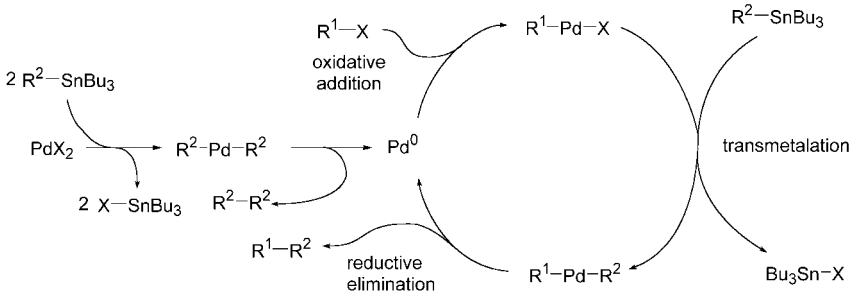


Scheme 2. The original proposal for the mechanism of the Stille reaction.

form complex **1** (Scheme 2). The latter complex was the only observable species in the catalytic cycle, even in the presence of excess organostannane, which demonstrated that the slow step was the transmetalation reaction with the organostannane. The transmetalation was believed to lead to complex **2**. A *trans* to *cis* isomerization to give **3**, thought to be very fast, was then required for the reductive elimination to give the organic product R–R′.

In that Review, Stille considered that the oxidative-addition and reductive-elimination sequences were reasonably well understood, whereas the transmetalation step was much less so.[1] He pointed out that the existing data for the transmetalation supported an electrophilic cleavage of the Sn–C bond (S_E2), with the Pd^{II} complex **1** acting as the electrophile. (Looking at the reaction from the point of view of the metal undergoing the attack, this is a nucleophilic attack (S_N2), which is convenient to have in mind to see the relationship with the ligand substitution reactions discussed later). From his studies on the $[Pd(CH_2Ph)Cl(PPh_3)_2]$-catalyzed coupling of benzoyl chloride with (*S*)-PhCHDSnBu$_3$, which took place "certainly with more than 65% net inversion",[1] Stille proposed for the S_E2 transmetalation step the open transition state shown in the center of Scheme 2. This early mechanistic interpretation of the Stille reaction has been very fruitful in the hands of Farina and co-workers, who have been able to improve the practical application of the reaction considerably by using different ligands L from the commonly used triphenylphosphane, such as trifurylphosphane[25,26] and triphenylarsane.[27–29]

Interestingly, although the mechanism in Scheme 2 was proposed by Stille as a working model,[1] it seems to have been taken for granted. Moreover, it is not unusual for some details shown clearly in Scheme 2 to be oversimplified in papers and reviews focused on the synthetic applications of the Stille reaction, and to be systematically overlooked by practitioners of the process. For example, Scheme 3 shows a simplified catalytic cycle as published in a recent thorough and valuable



Scheme 3. A recent simplified representation of the Pd-catalyzed coupling of stannanes with organic electrophiles.

synthesis-focused review. This scheme is more detailed than average in that it offers details about the formation of Pd^0 from a Pd^{II} precursor.[7] However, as is often the case in books and articles, it fails to provide any information about the geometry at the Pd center in the complexes or about the ligands; only the fragments arising from the two organic reagents are depicted. Thus, the need for a *trans–cis* isomerization step to give **3**, preceding the coupling step, is omitted. In our view, neglect of the coordination sphere of the palladium center can be detrimental to a more rational application of the process.

Although the use of the Stille coupling in synthesis is frequently empirical, the achievements are remarkable. The



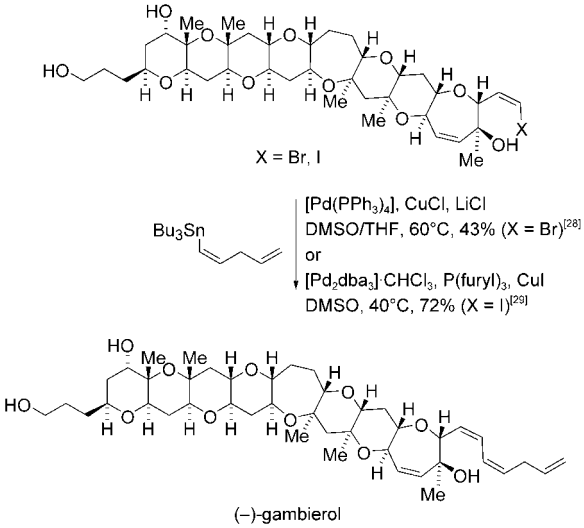
Pablo Espinet, born in Borja (Spain) in 1949, completed his PhD at the University of Saragossa with Prof. R. Usón in 1975. After one year at San Sebastián (Spain) and a postdoctoral period with Prof. P. M. Maitlis in Sheffield (UK), he became a lecturer at Saragossa in 1979. In 1986 he moved to the University of Valladolid as Professor of Inorganic Chemistry. His research interests range from the mechanisms of transition-metal-catalyzed reactions to organometallic and coordination complexes in molecular materials. In 2001 he received the prestigious prize IBERDROLA for science and technology.



Antonio M. Echavarren, born in Bilbao (Spain) in 1955, completed his PhD at the Universidad Autónoma de Madrid (UAM) in 1982 with Prof. F. Fariña. After postdoctoral studies at Boston College with Prof. T. R. Kelly, he became assistant professor at the UAM (1984–86), then a NATO fellow at Colorado State University with Prof. J. K. Stille. He moved from the CSIC in Madrid to the UAM in 1992 as Professor of Organic Chemistry. Since March 2004 he has been at the ICIQ in Tarragona. He investigates new synthetic methods and the organometallic chemistry of late transition metals.

 © 2004 Wiley-VCH Verlag GmbH & Co. KGaA, Weinheim

recent syntheses of gambierol by the groups of Sasaki[30] and Yamamoto[31] illustrate the advanced state of the art in this field. Both syntheses take advantage of the Stille coupling reaction to construct the *Z*,*Z* 1,3-diene functionality in the last step (Scheme 4), whereby it is not necessary to protect the hydroxy groups. These selective couplings were achieved under quite different conditions (see conditions in Scheme 4),[32] but in both cases the addition of a Cu^I salt was required to facilitate the transmetalation.[33]



Scheme 4. The Stille coupling in the synthesis of (−)-gambierol.

The success of the coupling reactions depicted in Scheme 4 relies on recent work aimed at improving the transmetalation step, which has been deemed as the rate-determining step in the coupling cycle. Thus, the addition of CuI or the use of $P(furyl)_3$ in place of PPh_3 is meant to facilitate the dissociation of one ligand and the formation of a [PdRXL] or [PdRXL(S)] intermediate ((S) = solvent molecule) prior to the formation of the putative transition state shown in Scheme 2.[25–27]

There are many indications that the original mechanistic model needs revision and completion. For example, both inversion[34] and retention[35] of the configuration of alkyl stannanes with a stereogenic C^α center have been observed. These results need to be accommodated in the mechanistic model. Similar stereoselectivity was found in the coupling of silanes.[36] Furthermore, it is not clear that the *trans–cis* isomerization of $[PdR_2L_2]$ complexes is always fast.[37] Actually, some isomerization reactions studied for isolated $[PdR_2L_2]$ complexes are slow,[38] or even extremely slow.[39] Therefore, intermediates of the type *trans*-$[PdRR'L_2]$ (**2** in Scheme 2) might be expected to be quite long-lived, but they have never been detected under catalytic conditions.[40] The effects of additives, such as Cu^I halides and alkaline salts, and the influence of the organic electrophile and the solvent are not yet well understood.

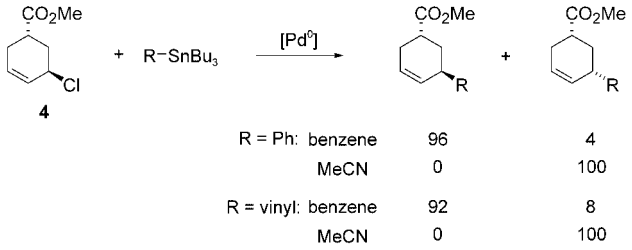
The purpose of this Review is to present a more complete and complex mechanistic picture of the reaction, including the interpretation of new experimental findings. It is hoped that this will help to emphasize the capital importance of the coordination sphere of the metal center, and will offer some hints for a more rational selection of reaction conditions. Selectivity, scope,[1,9] and other synthetic aspects of the reaction[41,42] that have already been covered in recent reviews are not dealt with in detail. Herein the different steps are discussed as they occur in the catalytic cycle. However, since the different factors that influence the course of the reaction are difficult to separate, this order is interrupted occasionally.

2. The Oxidative Addition

2.1. Inversion versus Retention

The oxidative addition of organic electrophiles (halides, sulfonates, and related compounds)[43] to Pd^0 is the first step in cross-coupling and Heck reactions.[24] The oxidative addition of $C(sp^3)$–X to Pd^0 complexes $[PdL_4]$ (L = phosphane) is usually an associative bimolecular process (S_N2 reaction). The leaving anion then adds to the metal center to give the product. The expected inversion at stereogenic centers was confirmed by the studies of Stille on the oxidative addition of chiral benzyl derivatives to Pd^0 coordinated to phosphane ligands.[50,51]

The stereochemical course of the oxidative addition of allyl halides depends on the nature of the solvent and the metal-bound ligands. Thus, the coupling of **4** with $RSnBu_3$ occurred with overall retention of configuration when the reactions were performed in benzene with a Pd^0 complex made in situ from $[Pd(\eta^3\text{-}C_3H_5)Cl]$ and maleic anhydride (Scheme 5). The configuration of the product is a conse-



Scheme 5. The effect of the polarity of the solvent on stereoselective coupling reactions.

quence of the oxidative addition step, which occurs with complete or predominant retention of configuration in less coordinating solvents, such as benzene, CH_2Cl_2, THF, or acetone.[44,45] However, complete or nearly complete inversion was observed in more polar, coordinating solvents, such as MeCN or DMSO.[44] The results of theoretical studies on the oxidative addition of CH_3Cl to ligand-free Pd^0 support a three-center transition state involving the Pd atom and the C–Cl bond, which should lead to retention of configuration at a stereogenic carbon atom.[46] Oxidative addition in a *syn* sense has also been reported for related substrates.[47] However, with $[Pd(PPh_3)_4]$ the usual inversion of configuration in the oxidative addition was observed.[44,48,49]

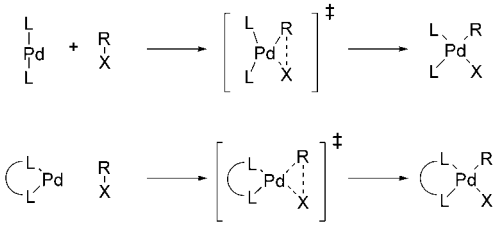
Much work has been carried out on the mechanisms of the oxidative addition of aryl and alkenyl halides and triflates (electrophiles $C(sp^2)$–X), the most common organic electro-

 © 2004 Wiley-VCH Verlag GmbH & Co. KGaA, Weinheim

philes in the Stille reaction.[50,51] These studies have shown that this transformation is not as simple as it appears in simplified general mechanistic schemes.[1]

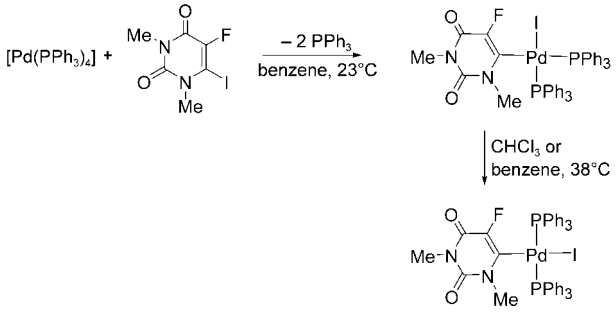
2.2. cis *Complexes in the Oxidative Addition*

As the intermediates observed in the catalytic cycle of the Stille reaction are *trans*-[$PdRXL_2$] complexes, this led to the widespread belief that these complexes are the primary products of the oxidative addition. However, the mechanism of the oxidative addition (at least for the most common electrophiles C(sp^2)–X) has been proposed to proceed by a concerted interaction of a reactive [PdL_2] or [Pd(L-L)] (L-L = diphosphane) species with R–X in a three-center transition state. This process should lead to *cis*-[$PdRXL_2$] complexes (Scheme 6). In the case of complexes with monodentate phosphane ligands, the initially formed *cis*-[$PdRXL_2$] complexes can isomerize to form the more stable *trans*-[$PdRXL_2$] complexes.



Scheme 6. Formation of *cis* complexes by oxidative addition to [PdL_2] or [Pd(L-L)] (L-L = diphosphane).

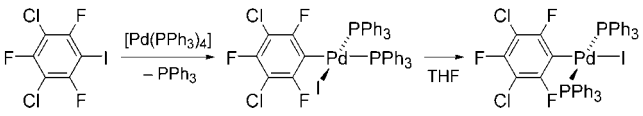
In fact *cis* complexes are observed to result from the oxidative addition reaction in a few cases with C(sp^2) electrophiles. The reaction of an iodouracil with [$Pd(PPh_3)_4$] leads initially to a *cis* Pd^{II} complex, which subsequently isomerizes to the more stable *trans* complex (Scheme 7).[52] A



Scheme 7. Formation of a stable *cis* complex through oxidative addition.

few other *cis* complexes have also been reported as the kinetic products of oxidative addition to Pd.[53]

The *cis–trans* isomerization process has been analyzed in detail for the complex formed by the oxidative addition of $C_6Cl_2F_3I$ to [$Pd(PPh_3)_4$] (Scheme 8).[54] It takes place by four



Scheme 8. Model reaction for the *cis–trans* isomerization.

major parallel pathways. The two main pathways involve direct and solvent-assisted associative replacement of PPh_3 by an iodo ligand of a second palladium complex, thus leading to the mono-iodo-bridged intermediate *cis*-[$Pd(C_6Cl_2F_3)I(PPh_3)(\mu\text{-}I)\text{–}\{Pd\}$], which then rearranges to *trans*-[$Pd(C_6Cl_2F_3)I(PPh_3)(\mu\text{-}I)\text{–}\{Pd\}$]. The two minor routes involve Berry pseudorotations on pentacoordinated species.

It is quite general that complexes with a phosphane ligand and an R group in a *trans* relationship (usually the kinetic product of the oxidative addition) are unstable, as a result of the mutual destabilizing effect associated with the high *trans* influence of these ligands. Often they isomerize to the *cis* product (the thermodynamic product). The destabilizing interaction between pairs of ligands (in this case a phosphane ligand and a *trans* C-donor ligand) in Pd^{II} complexes has been named transphobia,[55] an effect that results in the enhanced kinetic reactivity of such complexes in ligand substitution reactions.[56]

A recent study on the oxidative addition of a series of aryl iodides with different Hammet parameters to [$Pd(PPh_3)_4$] confirmed that in all cases the oxidative addition step initially gives *cis*-[$PdArI(PPh_3)_2$].[57] These *cis* complexes undergo isomerization to *trans*-[$PdArI(PPh_3)_2$] at very different rates, and sometimes extremely fast. When the isomerization is too fast, the putative initial product of the oxidative addition, *cis*-[$PdArI(PPh_3)_2$], can not be observed. Under the standard reaction conditions for the Stille coupling, the isomerization of the initial *cis* complex to the thermodynamically favored *trans* isomer appears to be very fast relative to the transmetalation. Thus, for most *practical* purposes the intermediates *cis*-[$PdRXL_2$] need not be considered.

2.3. Regioselectivity of the Oxidative Addition.

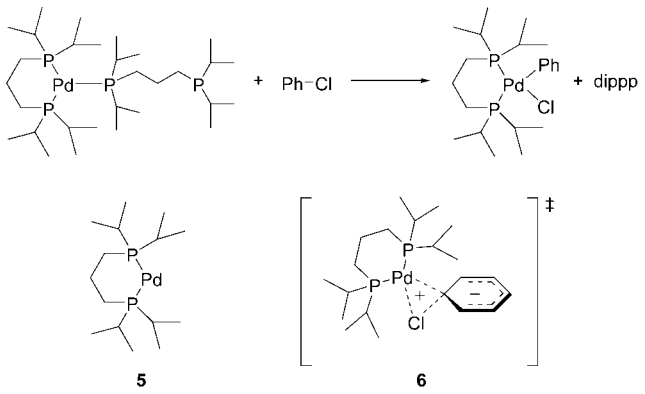
The regioselectivity of the oxidative addition has not yet been systematically investigated. However, it was reported recently that the coupling of *p*-$BrC_6H_4CH_2Br$ with tributyl(vinyl)tin catalyzed by *cis*-[$PdBr(N\text{-succinimido})(PPh_3)_2$] yields a mixture of *p*-$BrC_6H_4CH_2CH{=}CH_2$ (84%) and *p*-$CH_2{=}CHC_6H_4CH_2Br$ (7%). This selectivity must be traced back to the oxidative addition step.[58] Another example of regioselectivity, which is induced by the addition of copper salts, is discussed in Section 7.

2.4. The Role of Bidentate Ligands

The results of an early study on the mechanism of the oxidative addition of aryl iodides to [PdL_2] were consistent with an aromatic nucleophilic substitution.[59] Accordingly, electron-withdrawing substituents on aryl electrophiles lead

 © 2004 Wiley-VCH Verlag GmbH & Co. KGaA, Weinheim

to rate acceleration.[60] Similar conclusions were drawn by Portnoy and Milstein for the oxidative addition of aryl chlorides to [Pd(L-L)$_2$] (Scheme 9).[61] In this study, the kinetic data suggested that the oxidative addition was



Scheme 9. Oxidative addition of chlorobenzene to [Pd(dippp)$_2$] (dippp = 1,3-bis(diisopropylphosphanyl)propane).

preceded by a ligand dissociation to form the 14-electron complex **5**. On the other hand, the results of a Hammett study and the activation parameters for the oxidative addition supported the charged transition state **6** (Scheme 9). It was also found that on increasing the bite angle of the ligand by exchanging 1,3-bis(diisopropropylphosphanyl)propane for 1,4-bis(diisopropropylphosphanyl)butane, the rate of the oxidative addition decreased.[61,62] Note that these diphosphanes have bulky substituents, and ligands of this type have some unusual features (see Section 2.7).

2.5. Oxidative Addition with [Pd$_2$(dba)$_3$]

Complexes [Pd$_2$(dba)$_3$]·(S) (dba = dibenzylideneacetone, (S) = dba or solvent molecule)[63,64] have been used as source of Pd^0 in palladium-catalyzed reactions.[10] Early work by Roundhill and co-workers suggested that the dba ligands are not completely substituted in the reactions of [Pd$_2$(dba)$_3$]·(S) with P,N bidentate ligands under mild conditions.[65] The equilibrium established upon the addition of different phosphanes and diphosphanes has been studied in detail by Amatore, Jutand, and co-workers.[66–68]

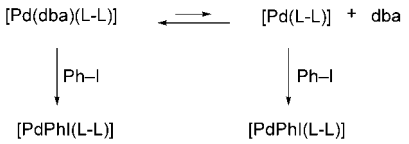
On the basis of ^{31}P NMR spectroscopy and voltammetric studies it was suggested that upon the mixing of [Pd$_2$(dba)$_3$] and PPh$_3$, [Pd(dba)(PPh$_3$)$_2$] is formed in equilibrium with [Pd(PPh$_3$)$_3$] (Scheme 10).[65,67b,69] The equilibrium constant of $K_0 = 0.14$ determined in THF indicates that dba is a better ligand for PPh$_3$ than [Pd(PPh$_3$)$_2$]. In monomeric [Pd(dba)L$_2$] complexes dba coordinates to the palladium center as a monodentate, two-electron-donor ligand. Similar equilibria were found for tri-2-furylphosphane (TFP)[70] and triphenylarsane.[71,72] [Pd(dba)(AsPh$_3$)$_2$] was found to be more stable than analogous phosphane complexes [Pd(dba)L$_2$] (L = PPh$_3$ or TFP).



Scheme 10. Ligand-exchange equilibrium in the system [Pd$_2$(dba)$_3$]/PPh$_3$.

Interestingly, the oxidative addition of PhI to a 1:2 [Pd$_2$(dba)$_3$]/PPh$_3$ mixture proceeds at an overall rate approximately 10 times lower than for [Pd(PPh$_3$)$_4$]. A similar effect was observed in the oxidative addition of PhI to [Pd(PPh$_3$)$_4$] or to the anionic complex [Pd(OAc)(PPh$_3$)$_3$]$^-$ in the presence of an alkene (styrene, methyl acrylate),[73] as well as in the Heck reaction of PhOTf and methyl acrylate catalyzed by [Pd$_2$(dba)$_3$]/dppf (dppf = 1,1′-bis(diphenylphosphanyl)ferrocene).[74] In coupling reactions with alkenyl stannanes catalyzed by [Pd$_2$(dba)$_3$]/AsPh$_3$, η^2-coordination of the alkene[75] slows down the oxidative addition because the concentration of the active complex [Pd(AsPh$_3$)$_2$] or [Pd(AsPh$_3$)$_2$(S)] decreases.[71]

Amatore, Jutand, and co-workers compared the effect of the ligands diop (diop = 2,3-*O*-isopropylidene-2,3-dihydroxy-1,4-bis(diphenylphosphanyl)butan), dppf, and binap (binap = 2,2′-bis(diphenylphosphanyl)-1,1′-binaphthyl) on the oxidative addition of iodobenzene (Scheme 11), and observed the



Scheme 11. Oxidative addition of iodobenzene to [Pd(dba)(L-L)] and [Pd(L-L)].

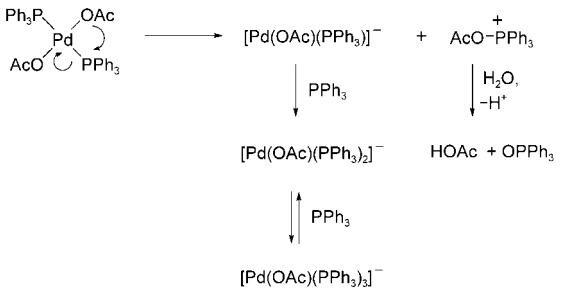
slowest oxidative addition with binap, which is the ligand with the smallest bite angle.[76,77] This result is opposite to that previously observed by Milstein and Portnoy.[61] However, Portnoy and Milstein used ligands of very different basicity to those used by Amatore and Jutand.[78] All the systems with bidentate ligands investigated are less reactive than [Pd$_2$(dba)$_3$]+2 PPh$_3$. Coordinatively saturated [Pd(L-L)$_2$] complexes were found to be unreactive in the oxidative addition with iodobenzene.[76]

2.6. The Role of Anionic Ligands

In a series of studies combining electrochemistry and ^{31}P NMR spectroscopy, Amatore and Jutand established the important role played by anionic ligands in oxidative addition reactions.[79] They concluded that in the presence of acetate or chloride anions, tricoordinated anionic complexes [Pd(OAc)L$_2$]$^-$ or [PdClL$_2$]$^-$ are the actual species that undergo oxidative addition, rather than the neutral [PdL$_2$] complex usually postulated (see below). These anions will be present in the reaction mixture whenever Pd^{II} salts (e.g. Pd(OAc)$_2$) or complexes (e.g. [PdCl$_2$L$_2$]; L = MeCN, PhCN, PPh$_3$, etc.) are used as the catalyst precursor.

Mixtures of Pd(OAc)$_2$ and PPh$_3$ rapidly lead to [Pd(OAc)$_2$(PPh$_3$)$_2$],[80,81] which undergoes slow intramolecular reduction to form a Pd^0 complex (Scheme 12). This reduction is facilitated by electron-withdrawing substituents

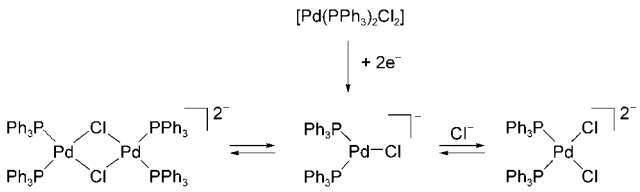
 © 2004 Wiley-VCH Verlag GmbH & Co. KGaA, Weinheim



Scheme 12. Formation of Pd^0 species in the system $Pd(OAc)_2/PPh_3$.

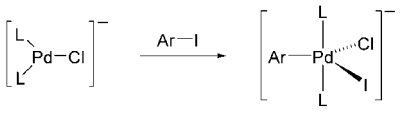
at the *para* position of the aryl groups on the phosphane.[81,82] Even in the presence of excess PPh_3, anionic Pd^0 complexes with acetate as a ligand are formed. The anionic complex $[Pd(OAc)(PPh_3)_2]^-$ is the reactive species undergoing oxidative addition.[83] The reaction of $Pd(OAc)_2$ with diphosphanes can be more complex. Thus, with dppe (dppe = 1,2-bis(diphenylphosphanyl)ethane) $[Pd(dppe)_2](OAc)_2$ is formed as the kinetic product, which slowly undergoes conversion into the thermodynamically favored monochelate $[Pd(OAc)_2(dppe)]$. In the presence of 2 equivalents of dppp (dppp = 1,3-bis(diphenylphosphanyl)propane), water, and a base (NEt_3), the hemioxide of dppp and the stable anionic complex $[Pd(OAc)(dppp)]^-$ are formed.[84] In this instance, the oxidative addition of PhI is mechanistically complex, as both dimeric and monomeric Pd^0 complexes ligated by AcO^- can be involved as reactive species.[85]

Many cross-coupling reactions are carried out with catalysts generated from $[PdCl_2L_2]$ or similar complexes. In the presence of chloride ions, anionic Pd^0 complexes are also formed.[86,87] For example, the reduction of $[PdCl_2(PPh_3)_2]$ in THF affords three anionic complexes, including one dimer (Scheme 13).[88,89]



Scheme 13. Pd^0 complexes that form during the reduction of $[PdCl_2(PPh_3)]$.

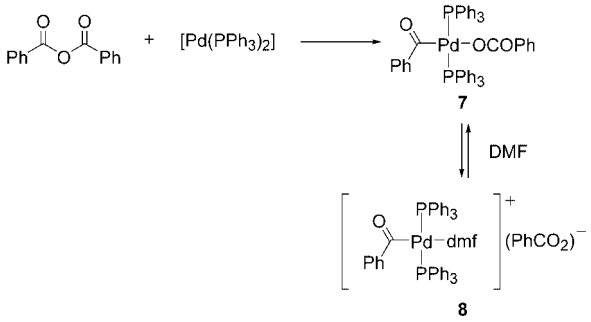
Under the usual conditions, the major Pd^0 complex generated by the reduction of $[PdX_2(PPh_3)_2]$ is $[PdX(PPh_3)_2]^-$, with the order of stabilization of the halide X^- on the anionic Pd^0 species: $I^- > Br^- > Cl^-$.[89] The oxidative addition reaction of PhI to $[PdCl(PPh_3)_2]^-$ affords *trans*-$[PdPhI(PPh_3)_2]$ as expected. However, after shorter reaction times an intermediate anionic species was detected, which was proposed to be the 18-electron complex $[PdPhClI(PPh_3)_2]^-$ (Scheme 14).[90] It was also proposed that this pentacoordinated intermediate was involved in the transmetalation reaction, but this view seems to have found little echo.[90] Related anionic $[PdAr(PPh_3)_2]^-$ species have



Scheme 14. Oxidative addition to $[PdClL_2]^-$ (L = PPh_3) proceeds via a five-coordinate intermediate.

also been postulated as key intermediates in the palladium-catalyzed homocoupling of aryl halides.[91]

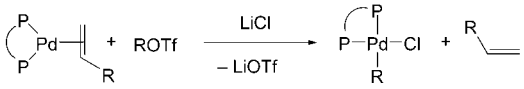
The oxidative addition of benzoic anhydride to $[Pd(PPh_3)_4]$ was proposed by Jutand et al.[92] to follow a pathway similar to that observed earlier for aryl halides and triflates (Scheme 15).[69,93] The reaction of benzoic anhydride



Scheme 15. Solvolysis equilibrium following the oxidative addition of benzoic anhydride to $[Pd(PPh_3)_2]$. DMF = *N*,*N*-dimethylformamide.

with $[Pd(PPh_3)_2]$ yields a *trans* complex **7**, in agreement with previous results of Grushin and Alper,[94] and Yamamoto and co-workers.[95] Complex **7** is in equilibrium with the cationic complex **8**, which results from benzoate displacement by the solvent DMF.

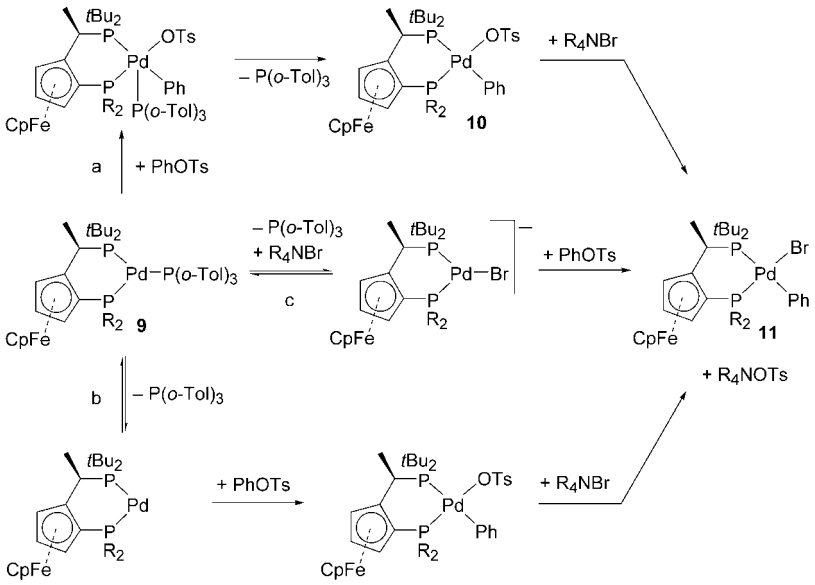
The oxidative addition of C_6F_5OTf to $[PdL_4]$ complexes proceeds well for L = PPh_3, but requires the addition of LiCl for L = $AsPh_3$. Thus, for L = $AsPh_3$ the oxidative addition becomes rate determining in the absence of an added halide, and the Stille coupling is hindered.[96] Similarly, the oxidative addition of C_6F_5OTf to complexes [Pd(dppe)(olefin)] extremely slow, but can be accelerated very efficiently by adding LiCl, which promotes the ready formation of [PdRCl(dppe)] (Scheme 16).[97]



Scheme 16. Oxidative addition of ROTf in the presence of LiCl. P–P = dppe.

A recent study showed that the oxidative addition of alkenyl triflates to $[Pd(PPh_3)_4]$ in DMF gives $[Pd(\eta^1\text{-alkenyl})(PPh_3)_2(dmf)](TfO)$ under stoichiometric conditions (Tf = trifluoromethanesulfonyl).[98] The following reactivity order was established: alkenyl–OTf ≫ vinyl–Br > PhBr and vinyl–OTf ≫ PhOTf.

Roy and Hartwig studied in detail the oxidative addition of aryl tosylates to the Pd^0 complex **9** (Scheme 17).[99] The



Scheme 17. Oxidative addition of PhOTs in the presence of R_4NBr. Tol = tolyl, Ts = *p*-toluenesulfonyl.

results offer new views on the role of added salts. The reaction in benzene of **9** with aryl tosylates at room temperature affords the isolable complex **10**, which reacts fast with $(n\text{-}C_8H_{17})_4NBr$ to give **11**. The oxidative addition of the tosylate is faster if R_4NBr is present from the beginning and gives **11**. The reaction shows positive kinetic order in PhOTs, inverse order in P(*o*-Tol)$_3$, and positive order in the bromide, thus eliminating path a. In the absence of the bromide, the kinetics are consistent with path b. Taken alone, the acceleration of the reaction by the bromide might be considered to support path c, in accordance with the related results of Amatore and Jutand. However, an even higher acceleration was found in the presence of Bu_4NPF_6 or in polar solvents. This was interpreted to imply that in this case the acceleration by R_4NBr is due to the creation of a more polar medium and not to the direct coordination of this ion to Pd^0.[99]

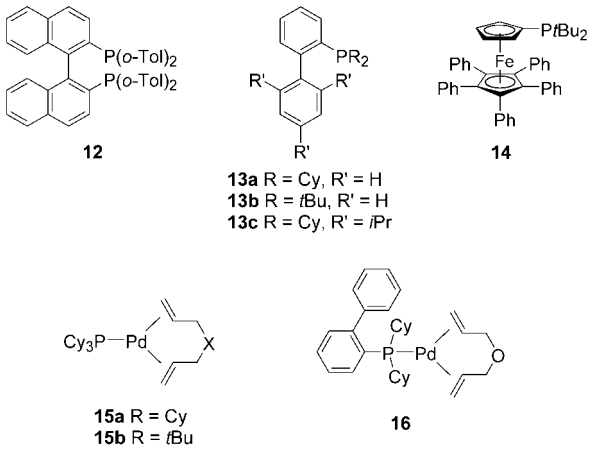
2.7. Cross-Coupling Reactions in the Presence of Bulky Phosphanes

In the last few years the use of bulky phosphanes has revolutionized the scope of cross-coupling reactions, particularly for the coupling of less reactive organic substrates, such as aryl chlorides[100,101] and alkyl electrophiles.[102] Since bulky phosphanes make a big difference in the oxidative addition step, they are treated in this section.

Aryl chlorides usually react more sluggishly in cross-coupling reactions than the corresponding bromides, iodides, and triflates, as a result of their reluctance to undergo oxidative addition to Pd^0.[103] Early on it was noted that the use of sterically hindered, chelating ligands could help to overcome this problem. Thus, Milstein and co-workers reported that [Pd(dippp)$_2$] (Scheme 9) was an efficient catalyst for carbonylation, formylation, and Heck reactions of aryl chlorides.[61,104]

The research groups of Buchwald and Hartwig also demonstrated the activity of a variety of sterically hindered chelating phosphanes in palladium-catalyzed transformations. In particular, the amination and etherification of aryl electrophiles,[105] as well as processes for the arylation of ketones and malonates,[106–108] benefit greatly from the use of ligands such as **12**.[109] Other bulky bidentate ferrocenyl diphosphanes allow Kumada and amination reactions with unactivated aryl tosylates at room temperature (see Scheme 17).[99] Bulky P,O chelating ligands also facilitate Suzuki coupling reactions of a wide variety of aryl boronic acids and aryl chlorides, bromides, and iodides.[110,111]

Monodentate bulky phosphane ligands also promote the coupling of less reactive substrates under relatively mild conditions. This accelerating effect on the oxidative addition had already been demonstrated in

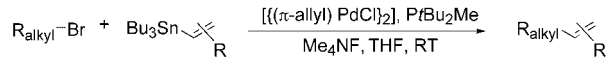


the context of the formation of η^3-allyl palladium complexes.[112] Particularly useful for the activation of aryl chlorides are palladium complexes of the bulky phosphane P(*t*Bu)$_3$,[113–117] which is readily available.[118] Even bulkier phosphanes, such as P(1-Ad)*t*Bu$_2$ (Ad = adamantyl), have also been used in the palladium-catalyzed arylation of malonates and cyanoesters.[119] The biphenylphosphanes **13** (Cy = cyclohexyl) were employed by Buchwald and co-workers in the palladium-catalyzed reaction of amines with aryl bromides, chlorides, and triflates,[120] and in Suzuki coupling reactions.[120a,121] In particular, ligand **13c** was found to be extremely effective in the Suzuki coupling and enolate arylation of aryl arene sulfonates.[122] Ligand **14** has been used for Suzuki coupling reactions and C–N or C–O bond-forming reactions.[123] Beller and co-workers showed that a series of [Pd(1,6-diene)L] (L = phosphane) complexes, such as **15** and **16**, catalyze efficiently the Suzuki coupling of aryl chlorides with phenylboronic acid.[124,125] The [Pd(1,6-diene)L] complexes were found to be more effective catalysts

 © 2004 Wiley-VCH Verlag GmbH & Co. KGaA, Weinheim

for these reactions than mixtures of the phosphanes and $Pd(OAc)_2$ or $[Pd_2(dba)_3]$.[126]

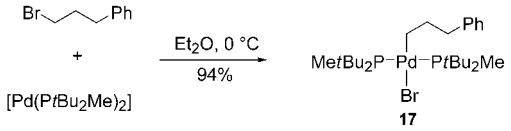
The Stille coupling at room temperature of alkenyl stannanes with alkyl bromides that possess β hydrogen atoms is also possible with similar catalysts (Scheme 18),[127]



Scheme 18. Stille coupling of alkyl electrophiles catalyzed by a palladium complex with the bulky, monodentate phosphane ligand $PtBu_2Me$.

although it was necessary to add a fluoride salt to promote the reactivity of the stannane. With the diaminophosphane ligand $PCy(pyrrolidinyl)_2$ the reaction can be extended to the coupling of aryl stannanes.[128]

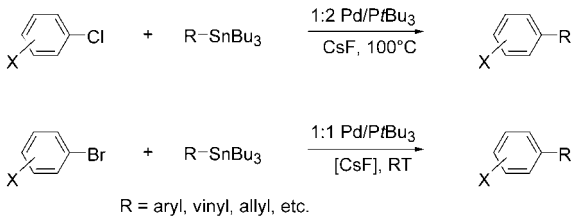
In reactions with $Pd/PtBu_2Me$, the complex that undergoes oxidative addition by the alkyl halide is $[Pd(PtBu_2Me)_2]$, and the activation parameters correspond to an S_N2 process with a large negative activation entropy.[129] Consequently, the oxidative addition is very sensitive to steric hindrance on the alkyl halide. The product of the oxidative addition of an alkyl bromide to the active complex $[Pd(PtBu_2Me)_2]$ has been isolated and structurally characterized (Scheme 19):[130] The



Scheme 19. Oxidative addition to give the structurally characterized product **17**.

complex **17** was formed readily at 0 °C and was found to react with *o*-$TolB(OH)_2$ at room temperature to give the coupling product. Alkyl electrophiles also couple with other organometallic reagents.[131]

The $Pd/PtBu_3$ system is also useful in the Stille reaction with aryl electrophiles (Scheme 20).[132] Thus, the coupling of

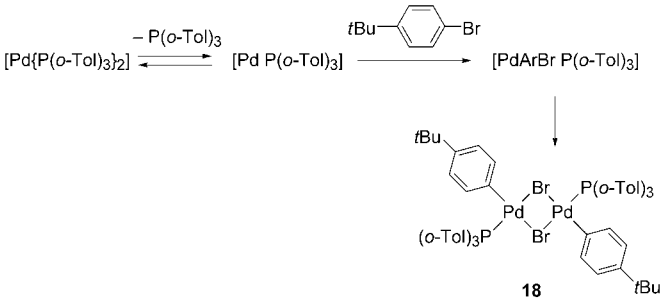


Scheme 20. CsF can have an activating effect in the coupling of aryl chlorides and aryl bromides with stannanes.

aryl chlorides with organostannanes can be performed at 100 °C, and in some cases even at room temperature, with a catalyst prepared from $[Pd_2(dba)_3]/PtBu_3$ (1:2) or with $[Pd(P(tBu)_3)_2]$. CsF was used to activate the stannane. It is suggested that the fluoride anion coordinates to tin to afford a pentacoordinated tin species with enhanced reactivity towards transmetalation.[133] Aryl bromides could also be coupled at room temperature, although in this case a 1:1 ratio of phosphane to Pd was necessary. In the coupling of aryl bromides, CsF was only required with less reactive organostannanes. Again, aryl chlorides underwent coupling more readily than aryl triflates. Preliminary mechanistic studies suggested that a palladium monophosphane complex [PdL] is the active catalyst in the cross-coupling of aryl halides.[132]

Although, as usual, aryl iodides undergo oxidative addition more rapidly than aryl bromides, the rate-limiting transmetalation of the resulting $[PdArI(PtBu_3)]$ complex is slower than the transmetalation of $[PdArBr(PtBu_3)]$.[132] Similar conclusions were reached for Suzuki reactions catalyzed by $Pd(OAc)_2/PPh_3$.[134]

Hartwig and co-workers proposed that the oxidative addition of an aryl bromide to $[Pd\{P(o\text{-}Tol)_3\}_2]$ involved prior dissociation of a phosphane ligand to give the 12-electron complex $[Pd\{P(o\text{-}Tol)_3\}]$ (Scheme 21).[135–137] In a related



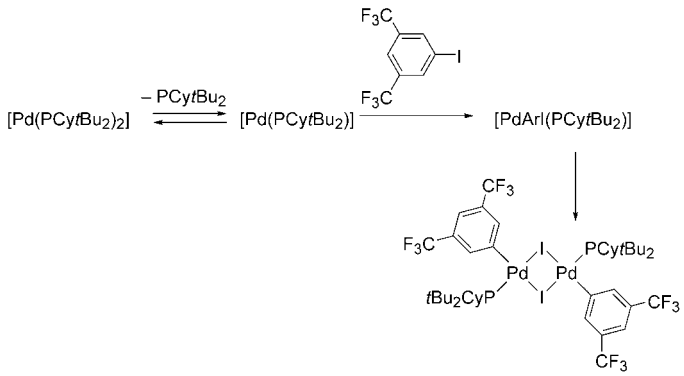
Scheme 21. Predissociation of a $P(o\text{-}Tol)_3$ ligand before the oxidative addition of an aryl bromide.

system it was concluded from kinetic measurements that the oxidative addition of ArBr to $[Pd(PtBu_3)]$ is faster than coordination of a new $PtBu_3$ ligand to the highly uncoordinated $[Pd(PtBu_3)]$ intermediate.[138] The addition of $PtBu_3$ to dimeric complexes of type **18** promotes the reductive elimination with formation of ArX. This process was proposed to involve irreversible dissociative ligand substitution (a very unusual mechanism, presumably induced by the steric properties of the ligands involved) and cleavage to the monomers, prior to reductive elimination.[139]

The thermodynamics of the reductive elimination from $[PdArX(PtBu_3)]$ complexes parallels the strengths of the Ar–X bonds (Cl > Br > I) and is most favorable for X = Cl.[138] However, the kinetic trend is the opposite, and the reductive elimination of ArCl is actually the slowest. It was suggested that the stability of the transition state depends critically on the softness of the halide.

Brown, Jutand, and co-workers reported that $[Pd(PCy_3)_2]$ reacts with PhOTf by an associative mechanism.[140] The reaction of PhI with $[Pd(PCy_3)_2]$ or $[Pd(PCy_2tBu)_2]$ also proceeds associatively. In contrast, $[Pd(PCytBu_2)_2]$ (Scheme 22) and $[Pd(PtBu_3)_2]$, with bulkier phosphane ligands, behave like $[Pd\{P(o\text{-}Tol)_3\}_2]$, which requires ligand dissociation to a [PdL] complex prior to oxidative addition.

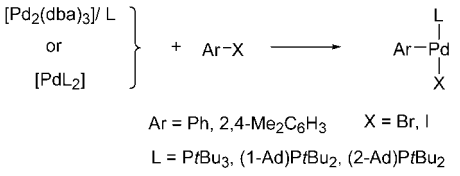
 © 2004 Wiley-VCH Verlag GmbH & Co. KGaA, Weinheim



Scheme 22. Predissociation of a $PCyt Bu_2$ ligand before the oxidative addition of an aryl iodide. Cy = cyclohexyl.

X-ray crystal-structure analysis of $[Pd\{P(o\text{-}Tol)_3\}_2]$[135] and $[Pd(PPht Bu_2)_2]$[141] showed that they have linear or near-linear geometries. However, the $[PdL_2]$ complex with the ligand **13b** differs from these complexes and displays an unusual P1-Pd-P2 angle of 154.82(4)° and η^1-π coordination of the *ortho* carbon atom of the unsubstituted phenyl ring of the ligand to the Pd center.[142]

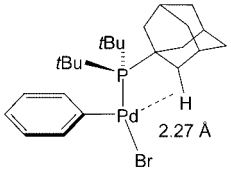
Hartwig and co-workers also reported the isolation of so-called tricoordinated, T-shaped, Pd^{II} complexes resulting from the oxidative addition of Ar–X to $[PdL_2]$ or [Pd(dba)L] complexes bearing very bulky phosphane ligands (Scheme 23).[143] The resulting species are *cis* complexes with



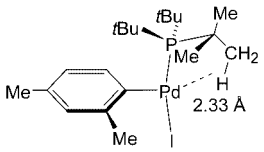
Scheme 23. The oxidative addition of Ar–X to Pd complexes with bulky phosphane ligands leads to apparently three-coordinate products. Ad = adamantyl.

an apparently open coordination site *trans* to the aryl group.[55,56]

Two of these apparently three-coordinate complexes, $[PdPhBr\{P(1\text{-}Ad)t Bu_2\}]$ (**19**) and $[Pd(2,4\text{-}Me_2C_6H_3)I(Pt Bu_3)]$ (**20**), were structurally characterized. In both complexes there are agostic interactions between the Pd center and the C–H bonds of the phosphane.[143] Therefore, it would be more correct to consider them as four-coordinate distorted square-planar Pd^{II} complexes. However, the intrinsic weakness of the agostic bond is an important difference with respect to regular tetracoordinated complexes.



19
P-Pd-Br angle = 162.6°



20
P-Pd-I angle = 164.6°

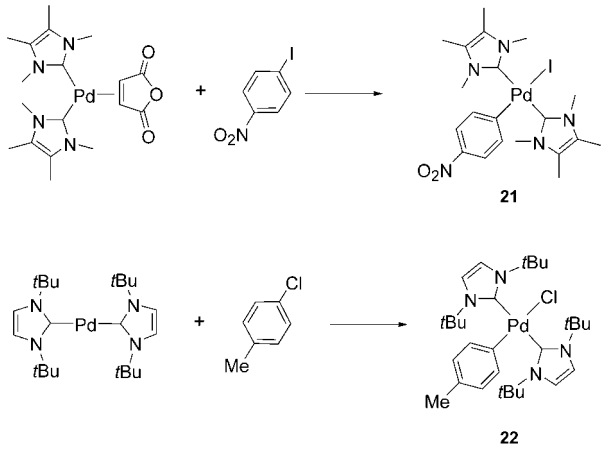
Recently, Blackmond, Buchwald, and co-workers carried out kinetic studies by using reaction calorimetry under synthetically relevant conditions to study the mechanism of the amination of bromobenzene with primary and secondary amines. The catalysts were $[Pd_2(dba)_3]$/binap mixtures, as well as preformed [Pd(binap)(dba)], [Pd(*p*-Tol)Br(binap)], and $[Pd(binap)_2]$ complexes.[144] The significant induction period observed for the reaction was attributed to the slow activation of the catalytic precursor, resulting in an increase in the concentration of active species within the catalytic cycle. It was also confirmed that $[Pd(binap)_2]$ does not play a direct catalytic role.[76] Both a pathway involving oxidative addition of the aryl halide to [Pd(binap)] as the first step and a pathway initiated by addition of the amine to the catalyst were proposed.

In a more radical approach in the quest for coordinatively unsaturated palladium catalysts "ligandless conditions" are used,[145–149] based on the pioneering work of Beletskaya and co-workers.[150] Thus, in the absence of phosphanes and other common ligands, palladium nanoparticles are formed.[151] Details of the mechanism in the context of Stille reactions under these conditions are lacking,[152] although the results of studies on a Heck reaction under very similar conditions are available.[153]

2.8. Heterocyclic Carbenes as Ligands

N-Heterocyclic carbenes have demonstrated their utility as ligands in a variety of cross-coupling reactions, including the Stille reaction.[154–157] Recent mechanistic work has shown that the oxidative addition of aryl halides to $[PdL_2]$ (L = heterocyclic carbene = NHC) furnishes the expected *trans* square planar complexes (e.g. **21** and **22**, Scheme 24).[158–160]

Very bulky *N*-heterocyclic carbene ligands lead to substantial rate increases,[161] which might be attributed to the inhibition of dimer formation[162] and enhancement of the rate



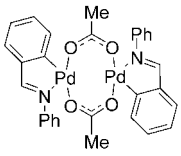
Scheme 24. Oxidative addition of aryl halides to Pd complexes with sterically demanding N-heterocyclic ligands.

 © 2004 Wiley-VCH Verlag GmbH & Co. KGaA, Weinheim

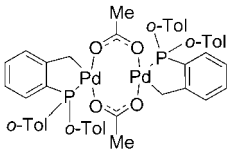
of the reductive elimination step.[157] In the context of the catalytic amination of aryl chlorides, the oxidative addition to $[PdL_2]$ (L = NHC) has been shown to be rate determining.[163] The oxidative addition proceeded dissociatively and the expected acceleration by electron-withdrawing substituents on the aryl chloride was observed.

2.9. Palladacycles as Catalysts

Many palladacycles have been described as active catalysts for cross-coupling and related reactions.[164–172] Strong evidence has been accumulated that indicates that the palladacycles actually act as a reservoir for Pd^{II}, which must undergo reduction to Pd^0 to enter the catalytic cycle.[169–171,173] Thus, in a detailed study of a Heck reaction with the palladacycles **23** and **24** as precatalysts, Blackmond, Pfaltz,



23



24

and co-workers concluded that the resting state of the catalyst within the catalytic cycle was the product of oxidative addition $[PdRXL_2]$. The majority of the palladium remained outside the catalytic cycle as the dimer $[(\mu\text{-}X)_2Pd_2R_2L_2]$, which is in equilibrium with $[PdRXL_2]$.[173]

3. The Transmetalation

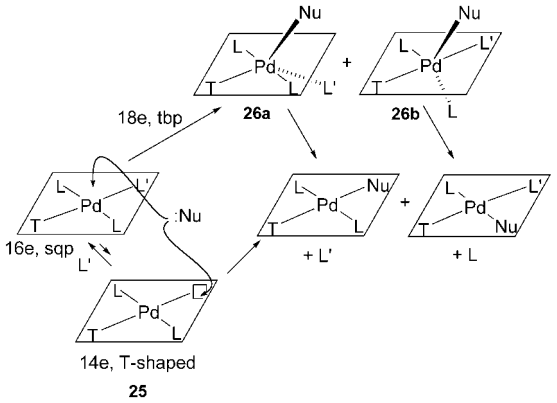
3.1. The Intricate Step That Makes the Difference

All Pd-catalyzed cross-coupling processes have in common a sequence that, starting with Pd^0, involves oxidative addition, transmetalation, and reductive elimination steps (as well as isomerization steps when needed). One of the reasons for the popularity of the Stille reaction in modern organic synthesis is the fact that trialkyl organotin species are readily available, quite air and moisture stable, and tolerate many functional groups.[1,9,174] These properties are mostly due to the low polarity of the Sn–C bond. In this respect, the Stille reaction differs from others with more polar organometallic reagents (e.g. Grignard reagents in the Kumada reaction[175] or zinc derivatives in the Negishi reaction) and is more similar to those in which boron (Suzuki coupling) or silicon (Hiyama coupling) derivatives are used. It can be assumed that the polarity of the organometallic nucleophile is important in determining the mechanism of the transmetalation, and some similarities are expected for the all processes involving nucleophiles with M–C bonds of moderate polarity. Consequently, insight gained into the transmetalation step of the Stille reaction has the added value that it may be relevant to the Suzuki and Hiyama coupling reactions.

The mechanisms proposed for the transmetalation should be able to explain satisfactorily the experimental observations. Improvements in the ability to detect intermediates and in kinetic studies have led to an increasingly complex mechanistic picture. Each variable in the reaction (the electrophile, the nucleophile, the ancillary ligands, the solvent, and the presence of additives) seems to be able to produce dramatic changes in the process.

3.2. The Transmetalation: A Ligand Substitution at Pd^{II}

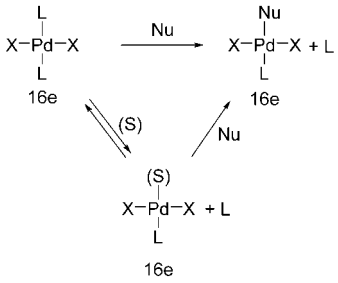
Some background mechanistic comments on palladium are pertinent before we proceed to review the studies on transmetalation. It is interesting to realize from the beginning that the very nature of the transmetalation is that of a ligand substitution on a Pd^{II} complex.[176] These complexes are usually tetracoordinated square-planar 16-electron species and can undergo ligand-substitution processes by the two pathways depicted in Scheme 25.[177,178] The dissociative path-



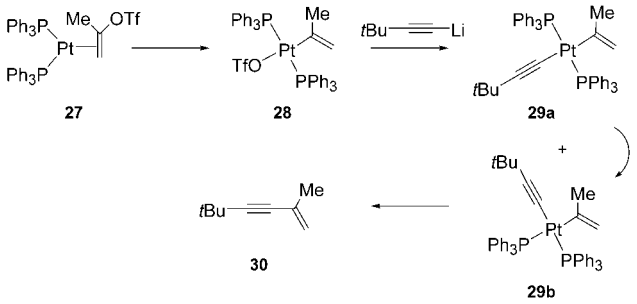
Scheme 25. Possible reaction pathways for the transmetalation.

way involves a 14-electron T-shaped intermediate **25**, and the position at which the substitution occurs is determined by the ligand with the highest *trans* influence, which weakens the bond *trans* to it and determines the dissociation equilibrium. The associative pathway goes through an 18-electron trigonal bipyramidal complex **26** as an intermediate or transition state, and the position at which the substitution occurs is determined by the ligand with the highest *trans* effect, which determines the lowest-energy transition state. In both pathways the substituted ligand is eventually released. It is frequently said, cursorily, that the ligand has dissociated, but this expression should be avoided because it can lead to confusion with a dissociative pathway.

Often the associative mechanism includes two parallel pathways: direct substitution and solvent-assisted substitution (Scheme 26). The two pathways contribute to the rate of substitution, and the reaction kinetics become more complex. Note that in the solvent-assisted pathway both the substitution of L for (S) and that of (S) for Nu are associative. Note also that a coordinating solvent is simply a ligand and contributes two electrons to the complex. Thus, a [PdRXL(S)]



Scheme 26. Direct and solvent-assisted substitution of L by Nu. (S) = solvent molecule.



Scheme 27. Transmetalation and coupling in a Pt model system. Tf = trifluoromethanesulfonyl.

complex is a 16-electron species. Olefins, adventitious water, and agostic bonds can play a similar role as ligands.

In the frequently used halo-bridged $[PdR_2(\mu\text{-}X)_2L_2]$ complexes the dissociative mechanism should involve direct cleavage of the bridges, whereas an associative cleavage involves associative substitution of the bridging ligand at one Pd atom by the entering ligand. The bridging X is then transformed into a terminal X ligand.

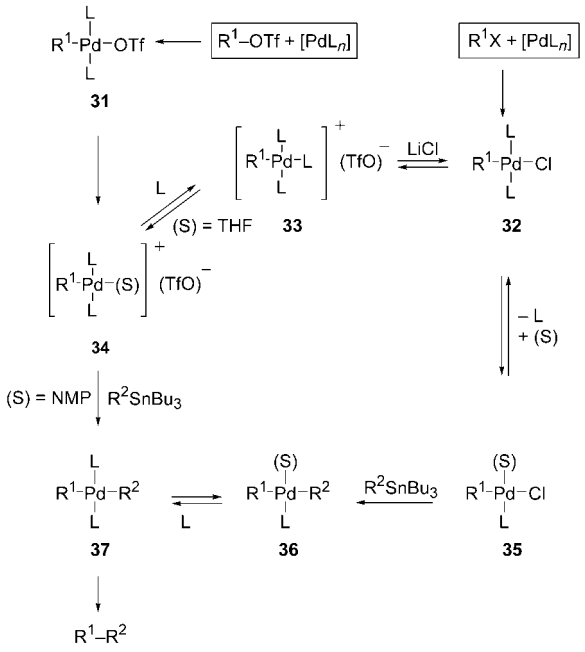
Although dissociative mechanisms apparently play a role in isomerization, β-H elimination, reductive elimination, and other processes involving Pd^{II} complexes (three-coordinate species were "observed" in kinetic studies on the rotation of some fluoroaryl compounds),[179] they are a rarity in ligand substitutions.[180] There is convincing support for dissociative ligand substitution in the case of relatively electron-rich platinum complexes $[PtR_2L_2]$ (with fairly good σ donors R),[181,182] but all ligand substitutions on the more electrophilic $[PdRXL_2]$ complexes seem to follow an associative pathway.[183]

These background comments on ligand substitution should in principle hold for the transmetalation with stannanes, in which the role of the nucleophile is played by the carbon atom undergoing transmetalation (in the case of alkynyl, vinyl, or aryl stannanes the π-electron density can facilitate the initial coordination). The differences are that stannanes are weak nucleophiles relative to typical two-electron ligands, and that the transmetalation with stannanes requires formal heterolytic cleavage of a C–Sn bond and release of R_3Sn^+.

3.3. Landmarks in the Study of the Transmetalation Mechanisms

The results of early mechanistic work aimed at ascertaining key aspects of cross-coupling and Heck reactions were in agreement with the original proposal advanced by Stille. A model study carried out by Stang et al. on the coupling of alkynes with vinyl triflates in the presence of $[Pt(PPh_3)_4]$ showed that the oxidative addition proceeded by the rate-determining formation of the (η^2-alkene)Pt complex **27**.[184] The reaction of **28** with lithium *tert*-butylacetylide (Li/Pt transmetalation) afforded a 4:1 mixture of *trans* and *cis* Pt^{II} complexes **29a** and **29b**, respectively (Scheme 27).[185,186] It was suggested that the *trans* and the *cis* isomer were in equilibrium with one another through ligand dissociation via T-shaped intermediates, and that reductive elimination from the *cis* isomer led to the enyne product **30**. Although some of the complexes in Scheme 27 are likely intermediate types in the Stille reaction, it should be kept in mind that Pd and Pt can be very different kinetically, and that the nucleophilicity of lithium organometallic compounds is very different from that of tin organometallic compounds.

The initial kinetic studies by Farina and others on the overall catalytic cycle of the Stille reaction, for which the transmetalation was assumed to be rate determining, confirmed that the reactions with organic halides (usually iodides, R^1I) showed a first-order dependence on [Sn] and [Pd], and an inverse dependence on [L].[29,27,187] These results were interpreted in terms of a dissociative preequilibrium of *trans*-$[PdR^1XL_2]$ to form $[PdR^1XL]$, which can be represented indistinctly as such or as a "solvent-stabilized" complex $[PdR^1XL(S)]$ (e.g. **35**, Scheme 28). This intermediate should undergo transmetalation to exchange X for R^2 and give the intermediate **36**. It is not clear why the subsequent coordination of L and coupling from that *trans* complex was proposed, since the complex needs to isomerize to the *cis* isomer before



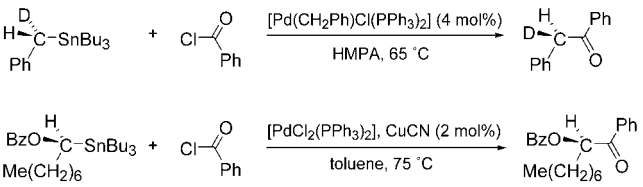
Scheme 28. Course of the transmetalation of halo and triflato complexes with R^2SnBu_3.

 © 2004 Wiley-VCH Verlag GmbH & Co. KGaA, Weinheim

the coupling product can form. Based on the observed inverse dependence on the concentration of the ligand, Farina and co-workers proposed the use of less coordinating ligands ($AsPh_3$, $P(furyl)_3$) to facilitate the transmetalation step, a strategy that has had a very positive impact on synthesis.

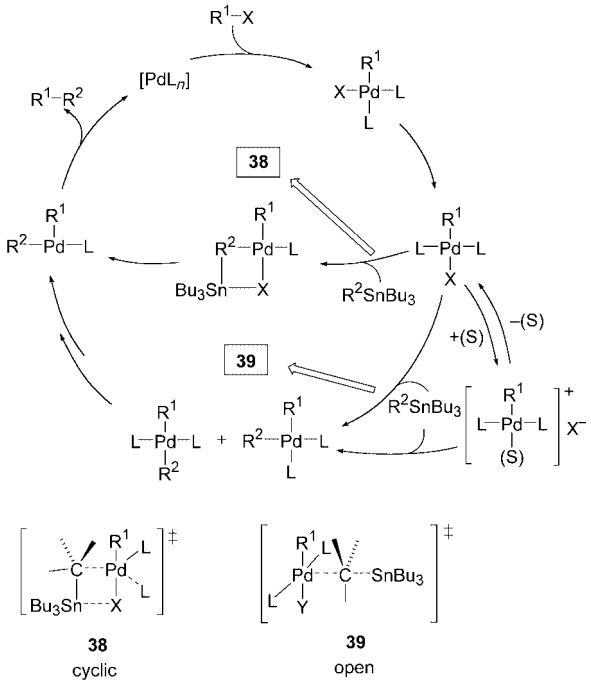
Farina and Roth also noted that reactions with organic triflates show some distinct characteristics, and proposed for them a different pathway (Scheme 28).[29] In this case the triflato complex **31** formed upon oxidative addition would react to give a cationic solvento complex **34** by substitution of the triflate group by a molecule of a coordinating solvent (e.g. *N*-methyl-2-pyrrolidinone (NMP)). The failure of organic triflates to react in less coordinating solvents (e.g. THF) was attributed to the instability of the triflato complex. This problem could be overcome by adding LiCl. This additive was proposed to transform the triflato complex into the chloro complex **32**, which then enters the catalytic cycle discussed above for organic halide complexes. Although some of these proposals have since been shown not to be fully correct, the use of LiCl often has a positive effect.

The studies mentioned so far did not provide a detailed picture of how the interaction between the palladium complex and the stannane brings about transmetalation. It is also clear that these mechanistic proposals can not accommodate the fact that the transmetalation of chiral stannanes can take place with retention or with inversion of configuration. There are two reports in the literature that provide stereochemical information on the transmetalated carbon center: Stille and Labadie found the reaction to proceed with predominant inversion of configuration (Scheme 29, top),[34] whereas Falk and co-workers reported complete retention of configuration in a related process (Scheme 29, bottom).[35]



Scheme 29. Inversion (top) and retention (bottom) of the configuration at the α carbon atom in the Stille coupling. HMPA = hexamethyl phosphoramide. Bz = benzoyl.

The need to explain the different stereochemical outcome of the reactions in Scheme 29 and consideration of quantitative results on transmetalation rates led to the proposal by Espinet and Casado of a dual catalytic cycle with two different transition states, one cyclic and one open, **38** and **39**, respectively (Scheme 30).[96,188] The upper cycle in Scheme 30 depicts the cyclic transmetalation as an associative process assisted by the formation of a Pd–X–Sn second bridge. This mechanism leads to the exchange of L (and not X) for R^2, forces retention (and not inversion) of the configuration at C^{α}, and leads to a *cis* (rather than a *trans*) $[PdR^1R^2L_2]$ complex, from which coupling is immediate. All these features differ from the previous proposals.



Scheme 30. Catalytic cycles for the transmetalation with the cyclic and open transition states **38** and **39**, respectively. Y = (S) or X, (S) = L or solvent molecule.

The lower cycle includes and expands on open mechanisms. It is not excluded that open mechanisms can also operate on halide-containing complexes (leading to the replacement of any of the ligand on palladium), provided that a sufficiently electrophilic complex (e.g. a solvento complex) or a sufficiently nucleophilic stannane (e.g. an alkynyl stannane) makes the rate of such a process competitive. This is further elaborated below.

These studies also revealed clearly that, although the transmetalation is often rate determining, this is not always the case. In some instances it is the oxidative addition[96] or the reductive elimination[97] that controls the rate of the reaction.

The general representation $[PdR^1XL_2]$ (Scheme 30) stands for neutral compounds with a potentially bridging X ligand (to assist Pd–X–Sn formation), including chelate complexes $[PdR^1X(L\text{-}L)]$ (in which case the complex is necessarily *cis*), $[PdR^1XL(S)]$ (formed by the substitution of one ligand L by a solvent or water molecule (S)), $[PdR^1X(L\text{-}H_{agostic})]$, and other species.

The actual Pd species in solution can be different from those introduced initially as a catalyst or formed directly in the oxidative addition, as discussed below. Studies have shown the formation of cationic complexes by the replacement of coordinated OTf groups or halides with ligands or coordinating solvent molecules,[96] neutral solvento complexes by the replacement of one or more ligands with coordinating solvent molecules,[96,176] and dimers by the replacement of weakly coordinating ligands with the terminal halide of the monomer.[176] It is difficult to ascertain which species undergoes faster transmetalation even by kinetic studies, because the kinetic equations show similar dependences on the concentration of the reagents. Whereas in some cases it

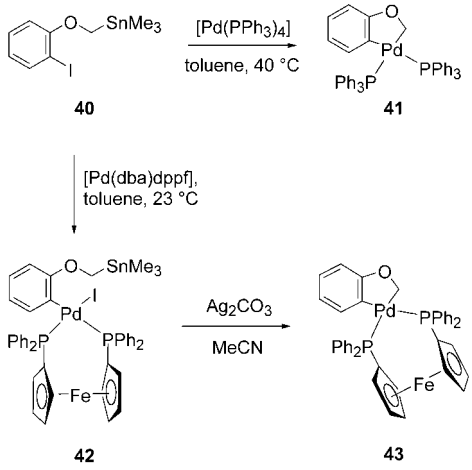
 © 2004 Wiley-VCH Verlag GmbH & Co. KGaA, Weinheim

seems clear that the associative transmetalation occurs on the dominant $[PdR^1XL_2]$ complex,[188] Amatore, Jutand, and co-workers showed in a nice study that in certain other cases the reaction mainly proceeds by associative substitution on the solvento complex $[PdR^1XL(S)]$ ((S) *trans* to L), even when the concentration of this solvento complex is kept very low through the addition of L.[189] However, a substitution of (S) for R^2 (as in the modern Scheme 30) rather than of X for R^2 (as in Schemes 2 and 28) is still proposed.

Thus, Scheme 30 is fairly comprehensive, and most experimental observations, including the stereochemical outcome of the transmetalation can be rationalized satisfactorily within this framework (retention of configuration implies a cyclic pathway, inversion an open pathway). A different mechanism is proposed for a few exceptional cases (see Section 6).

3.4. Isolation of the Transmetalation Step

There have been a number of observations made and studies carried out on the transmetalation as an isolated step, in instances in which the reductive elimination is slow. Thus, Echavarren and co-workers studied an intramolecular version of the transmetalation step with systems **40**, which undergo oxidative addition to $[Pd(PPh_3)_4]$ followed by transmetalation to form palladacycles **41** (Scheme 31).[190] These are stable species that do not undergo reductive elimination because of the high ring strain of the four-membered heterocyclic ring that would form.

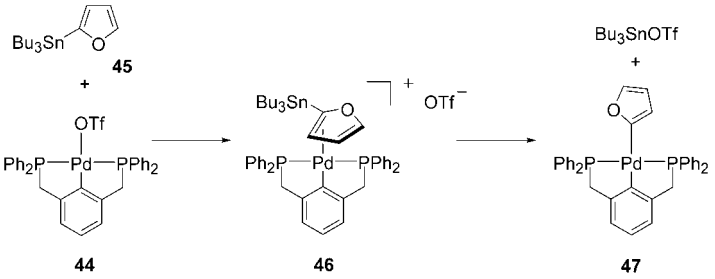


Scheme 31. Stable cyclic transmetalation products: **41** and **43**.

Intermediate **42** was isolated from the oxidative addition of **40** to the complex [Pd(dba)dppf]. Presumably, the chelating dppf ligand disfavors a cyclic transmetalation (Section 3.6). However, a smooth transmetalation was observed in the presence of Ag_2CO_3 to form palladacycle **43**.[190b] Under these conditions, the formation of a cationic acetonitrile complex upon extraction of the iodide with the silver salt might facilitate transmetalation through an open transition state.

The concept outlined in Scheme 31 was also extended to the study of the transmetalation of silanes (the key step of the Hiyama cross-coupling reaction) isolated from the oxidative addition and reductive elimination steps,[191] and to the related transmetalation of stannanes with Pt^{II}.[192]

The reaction between the pincer triflato complex **44** and 2-tributylstannyl furan (**45**) led to transmetalation product **47** as a stable compound (Scheme 32).[193,194] When the reaction



Scheme 32. The transmetalation of the stannyl furan **45** with the pincer complex **44** afford the stable product **47**.

was performed at low temperature, an intermediate cationic complex **46** was observed, with the furan ligand η^2-coordinated to the palladium center. Intermediate **46** is a model for the transmetalation of vinyl stannanes. Transmetalation intermediates [Pd(aryl)(heteroaryl)] have been detected by electrospray mass spectrometry in the Suzuki coupling of bromopyridines with aryl boronic acids.[195]

Under certain conditions, the transmetalation of tributyl(vinyl)stannane with $[Pd(C_6Cl_2F_3)(PPh_3)_3]BF_4$ (**48**, Figure 1) gives rise to significant concentrations of the

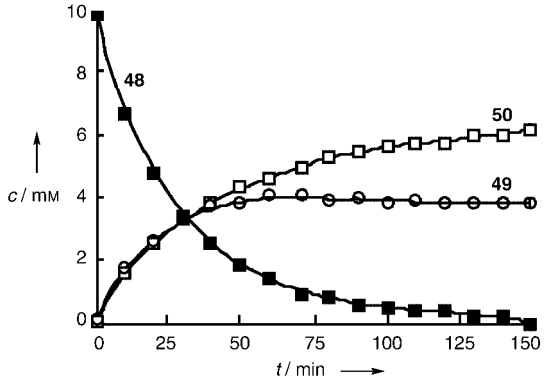


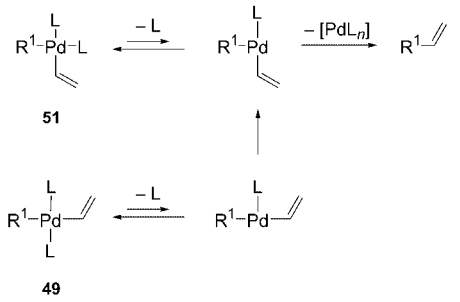
Figure 1. Concentration profiles of the reaction between $[PdR^1(PPh_3)_3]BF_4$ (**48**) and $Bu_3SnCH{=}CH_2$ in CH_2Cl_2, as determined by ^{19}F NMR spectroscopy; *trans*-$[PdR^1(CH{=}CH_2)L_2]$ (**49**) and the coupling product $R^1{-}CH{=}CH_2$ (**50**) were observed. ($R^1 = C_6Cl_2F_3$).

intermediate *trans*-$[PdR^1(CH{=}CH_2)L_2]$ (**49**), which has a noticeably long lifetime (even at 50 °C) but eventually generates the coupling product $R^1{-}CH{=}CH_2$ (**50**; $R^1 = C_6Cl_2F_3$).[96] Complex **49** is the result of a *trans* transmetalation via an open transition state. There is also, in competition, a *cis* transmetalation via an open transition state, which leads to

 © 2004 Wiley-VCH Verlag GmbH & Co. KGaA, Weinheim

substitution of the PPh_3 ligand *cis* to the R^1 group in $[PdR^1L_3]^+$ to give a putative intermediate *cis*-$[PdR^1(CH{=}CH_2)(PPh_3)_2]$. (The same competition can be found with iodide instead of a stannane as the nucleophile, which affords a kinetic mixture of *cis*- and *trans*-$[PdR^1I(PPh_3)_2]$; this establishes a perfect correlation between a typical ligand substitution and an open transmetalation.) Complex *cis*-$[PdR^1(CH{=}CH_2)(PPh_3)_2]$ couples immediately and was not observed directly, but could be inferred kinetically from its effect on the rate of formation of the coupling product **50**, which is initially much faster than could be expected from the (very slow) decomposition of the *trans* complex **49** alone.

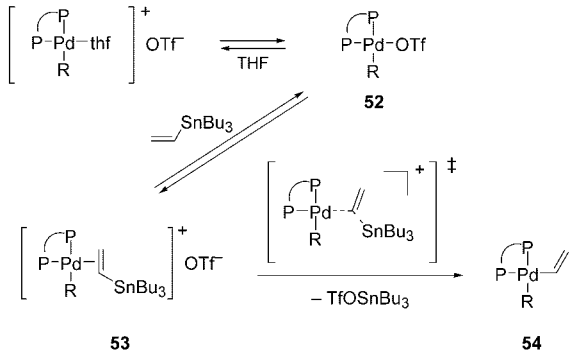
Assuming that the coupling takes place from a *cis* three-coordinate species (Scheme 33), the proposed *cis* intermediate **51** needs only to undergo the dissociation of L (if even



Scheme 33. Different pathways for the reductive elimination of *cis* and *trans* vinyl palladium complexes **51** and **49**, respectively. Three-coordinate *trans* complexes must isomerize to the corresponding *cis* complex before elimination of the product can occur.

that) for the coupling to occur. The *trans* isomer **49** must undergo isomerization into a three-coordinate species, which has been shown to be the highest barrier towards coupling in closely related complexes. Consequently, the *cis* complex produces the coupling product much faster than the *trans* isomer[196] and is not observed.

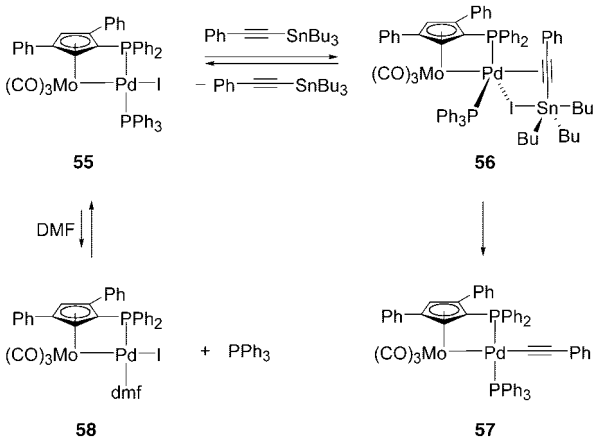
The reductive elimination is also slow when allyl groups (see Section 5.2)[197] or chelating ligands are involved (as in **52**, Scheme 34), enabling the observation of *cis* transmetalation products. Thus, by using dppe as the ligand, Espinet and co-workers observed the key intermediates in the catalytic cycle



Scheme 34. The mechanism of the transmetalation can be investigated by using chelate complexes.

for the coupling of an aryl triflate with tributyl(vinyl)stannane,[97] including the transmetalation product $[PdR(CH{=}CH_2)(dppe)]$ (**54**). The reaction proceeds as outlined in Scheme 34 via an S_E(open) transmetalation on complex **53**.

Lo Sterzo and co-workers detected spectroscopically the pentacoordinated palladium complex **56** in the transmetalation of complex **55** with an alkynyl stannanes (Scheme 35).[198]



Scheme 35. Complex **56** as a model for the transition state of the cyclic transmetalation.

This reaction is an example of palladium-catalyzed metal–carbon bond formation.[198–201] Complex **56** is a model of the transition state for the cyclic transmetalation and was shown to evolve to give **57** by first eliminating PPh_3.

Complex **55** exchanged a PPh_3 ligand in DMF to form complex **58** and the corresponding iodo-bridged palladium dimer (Scheme 35).[198] The involvement of this complex in a parallel transmetalation with the organostannane is another example of the competition of open and cyclic mechanisms.[198]

3.5. Proposals for Dissociative Mechanisms

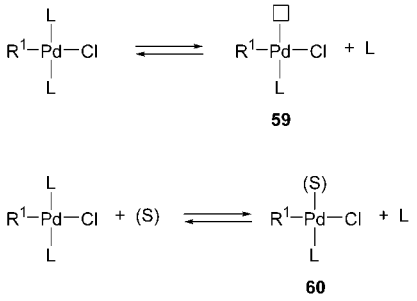
As stated above, the fact that the addition of a neutral ligand L retards the coupling[28,187] was initially taken as an indication that the dissociation of L from **32** (see Scheme 28) was a key step in the transmetalation. However, as discussed in Section 3.3, it is unlikely that transmetalations at Pd should proceed through true dissociative mechanisms involving 14-electron Pd intermediates.

Although supposed evidence for the involvement and observation of a 14-electron T-shaped complex, $[PdPhI(AsPh_3)]$, was reported,[71] a reexamination of the issue revealed that the species observed differed depending on the solvent and whether or not excess ligand was present.[176] At a $Pd/AsPh_3$ ratio of 1:2 in $CHCl_3$ the species initially thought to be T-shaped was actually the dimeric complex $[Pd_2Ph_2(\mu\text{-}I)_2(AsPh_3)_2]$.[176] In the more coordinating solvent DMF, the species detected was in fact the 16-electron tetracoordinated complex $[PdPhI(AsPh_3)(dmf)]$. In a later publication the authors of the original report reexamined thoroughly their system and acknowledged this reinterpreta-

tion.[189] The reformulation of the nature of these complexes also affects some earlier definitions of "$[ArPd(PPh_3)_2]^+$" complexes with triflate as the counterion.[93] In coordinating solvents these complexes are most likely the solvent-coordinated (rather than "solvated") complexes $[ArPd(PPh_3)_2(S)](TfO)$ ((S) = dmf), whereas in THF an equilibrium between $[ArPd(PPh_3)_2(S)](TfO)$ and $[ArPd(PPh_3)_2(TfO)]$ would exist, as found in related cases.[96] In less coordinating solvents, such as toluene, or in the solid state, these complexes should exist as covalent triflato derivatives $[PdAr(TfO)(PPh_3)_2]$, rather than as ion pairs.

The rate equations for dissociative transmetalation on $[PdR^1XL]$ (formed by the fast dissociation of L), on $[PdR^1XL(S)]$ (formed by a fast associative ligand substitution preequilibrium) with replacement of (S), and for associative transmetalation on $[PdR^1X(L)_2]$ with replacement of L display similar qualitative concentration dependence (Scheme 30).[176,188] Only with complete quantitative data would it be possible to decide whether the value of the concentration of $[PdR^1XL(S)]$ that would mathematically account for the reaction rate observed is a plausible value or not.

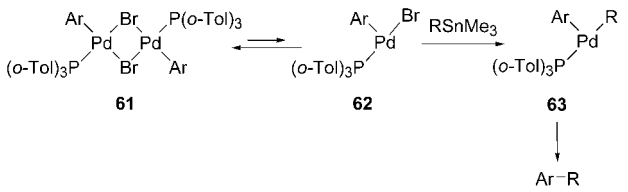
In the publication in which these issues were reexamined it was noted that ligand substitutions at Pd^{II} are usually associative (via pentacoordinated intermediates) and that the S_N2 transmetalation, whether through an open or a cyclic mechanism, is not an exception, except, perhaps, in special cases.[176] Since the concentration of the three-coordinate species is negligible in conventional systems, the transmetalation must involve associative displacement of one ligand (L, (S), or X) by the entering R^2 from R^2SnR_3. Thus, independent of the formulation of the complexes in the original literature, we regard herein those processes described as *dissociative* in the literature as *solvent-assisted associative*, and the dissociation equilibria to give three-coordinate species **59** (Scheme 36, top) as solvolysis reactions to give solvento



Scheme 36. Three-coordinate intermediates **59** and four-coordinate solvento complexes **60**.

four-coordinate complexes **60** (Scheme 36, bottom). The corresponding literature will be discussed in Sections 4.4 and 4.5 on associative transmetalation.

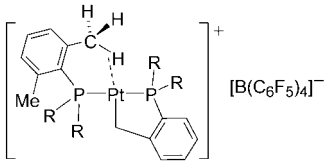
There are, however, a few possible exceptions. The best candidate for a true observation of transmetalation at a T-shaped 14-electron complex is the report by Louie and Hartwig on the behavior of **61** (Scheme 37).[187] This complex



Scheme 37. Apparently three-coordinate intermediates such as **62** can be stabilized through agostic interactions. Ar = *p*-Tol.

undergoes stoichiometric transmetalation with organotin aryl, thiolate, and amide compounds. Hartwig found that the transmetalation rate depends on the square root of the concentration of the dimer,[187] which is consistent with a dissociation of the dimer. Therefore, T-shaped monomers **62** were proposed to react with the organostannane to form **63**, from which the coupled product Ar–R forms.

The properties of complex **61** were rather unique at that time: The addition of $P(o\text{-Tol})_3$ does not lead to cleavage of this complex nor to retardation of the transmetalation (retardation is usually observed for catalysts with conventional ligands), thus showing that the formation of $[PdArBr\{P(o\text{-Tol})_3\}_2]$ is severely hindered. The monomer formed is unlikely to be $[PdArBr\{P(o\text{-Tol})_3\}(S)]$, as the solvent (toluene) is noncoordinanting. However, another possibility for the stabilization of the monomer as a 16-electron complex was not considered in the original publication: the formation of an agostic complex. It is plausible that the monomeric species **62** might be stabilized by an agostic interaction involving the empty orbital on Pd and the electron pair of the C–H bond of a methyl group. Since this intermediate is not observed spectroscopically because of its very low concentration, this hypothesis can not be proven, but the recent X-ray crystal structures of apparently three-coordinate Pd complexes with bulky phosphane ligands (complexes **19** and **20**) indeed reveal the existence of agostic interactions at the "vacant" coordination site.[143] A recent example from platinum chemistry also illustrates that apparently three-coordinate aryl Pt^{II} complexes **64a** and **64b** are in fact square planar complexes stabilized through an agostic interaction with one of the methyl groups of the phosphane ligand.[202]



64a R = Ph
64b R = Cy

Since it was recognized that complexes with bulky ligands can catalyze the Stille and other coupling reactions with less active organic nucleophiles, such as chlorides or triflates (see Section 2.6), the number of examples of such complexes has increased.[203,204] From a practical point of view, a formally 16-electron agostic complex, with very high nucleophilicity and

 © 2004 Wiley-VCH Verlag GmbH & Co. KGaA, Weinheim

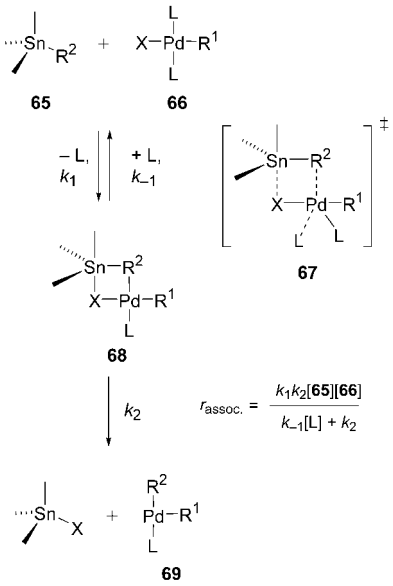
reactivity, is probably the stabilized intermediate that is functionally most similar to a T-shaped 14-electron species. Ligands that produce these agostic interactions might be considered an extreme case of hemilabile ligands. Because of the very poor donation from the agostic bond, these complexes have a highly electrophilic metal center.

In practice complexes stabilized by agostic bonds may be functionally equivalent to three-coordinate complexes. True T-shaped three-coordinate complexes were characterized recently in the solid state for electron-rich Pd complexes bonded to a very basic bulky phosphane, an amido group, and an aryl or thienyl group. The examples include one case of the coexistence of three-coordinate and agostic-bond-stabilized square-planar-coordinated isomers in the same crystal, thus showing the proximity in stability of the two systems and the extremely weak nature of agostic bonds to electron-rich centers.[205]

3.6. The Cyclic Associative Transmetalation

In the mechanistic proposals of Stille and Farina (Schemes 2 and 28, respectively) it was assumed that the transmetalation involved a preequilibrium to release one ligand, which explained the inverse dependence of the rate of reaction on the concentration of L.[1,29] It was also thought, in analogy with transmetalation reactions of organometallic compounds of main-group elements, that the *trans* geometry of the starting complex *trans*-$[PdR^1XL_2]$ was preserved in the reaction to give a *trans*-$[PdR^1R^2L_2]$ complex.[206] Since it is well established that the reductive elimination of R^1–R^2 occurs from *cis* derivatives,[1] a fast *trans* to *cis* isomerization is needed (Scheme 2).

The observed inverse dependence on the ligand concentration was recently found to be perfectly compatible with the rate expression for an associative mechanism (Scheme 38).[188]



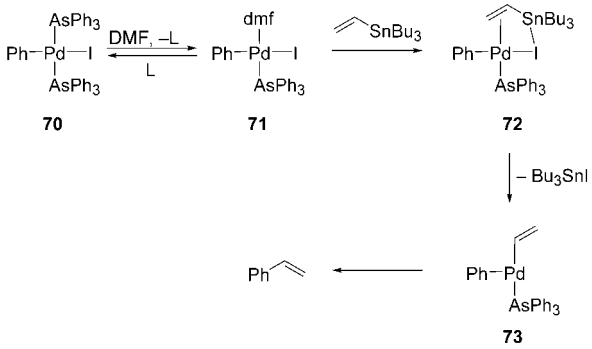
Scheme 38. The cyclic associative transmetalation.

This result led to the proposal of an additional transmetalation pathway via the cyclic structure **67**.

Importantly, this transmetalation pathway involves an associative substitution of L for R^2 via the bridged intermediate **68**[207,208] to give directly the complex **69** with R^1 and R^2 in a *cis* rather than a *trans* arrangement from which the coupled product will eliminate immediately. Moreover, the mechanism in Scheme 38 accounts for the retention of the configuration at C^α observed in some reactions,[35] which is difficult to account for by any other mechanism. Similar activated complexes have been proposed by Hatanaka and Hiyama for the palladium-catalyzed coupling of organosilicon compounds with the aid of fluoride ions.[36]

In coordinating solvents this mechanism can operate on $[PdR^1XL_2]$ or $[PdR^1XL(S)]$ complexes. Since these complexes obey rate laws with qualitatively similar kinetic dependence on the reagents, detailed studies are needed to distinguish between these possibilities. For the coupling in THF of 3,5-dichloro-2,4,6-trifluoro-1-iodobenzene ($C_6Cl_2F_3I$) and tributyl(vinyl)tin catalyzed by *trans*-$[Pd(C_6Cl_2F_3)I(AsPh_3)_2]$, the coupling rate observed would require the formation of 12% *trans*-$[Pd(C_6Cl_2F_3)I(AsPh_3)(thf)]$ if the transmetalation took place on this intermediate. At such a high concentration this complex could not escape detection by ^{19}F NMR spectroscopy. Since only *trans*-$[Pd(C_6Cl_2F_3)I(AsPh_3)_2]$ was observed, any kinetically relevant participation by *trans*-$[Pd(C_6Cl_2F_3)I(AsPh_3)(thf)]$ was excluded. The transmetalation takes place in this case on *trans*-$[Pd(C_6Cl_2F_3)X(AsPh_3)_2]$, and the rate increases with increasing electrophilicity of the metal center in the order $X = I < Br < Cl$.[188]

In contrast, in the coupling of PhI with tributyl(vinyl)tin in the presence of $[Pd(dba)(AsPh_3)_2]$ in DMF,[189] the species on which the transmetalation takes place is not *trans*-$[PdPhI(AsPh_3)_2]$ (**70**), but *trans*-$[PdPhI(AsPh_3)(dmf)]$ (**71**; Scheme 39). The alkenyl stannane then substitutes the dmf ligand to form **72**, which evolves to the transmetalation product **73**. An elegant kinetic study showed that even in the presence of excess $AsPh_3$ (when the concentration of **71** is very low) the associative transmetalation still mainly takes place on the solvento complex. Although the authors state that these findings confirm Farina's proposal for reactions in THF, in fact the sequence of reaction that they propose involves the substitution of a neutral ligand for R, as proposed



Scheme 39. An example of the influence of the solvent on the transmetalation.

 © 2004 Wiley-VCH Verlag GmbH & Co. KGaA, Weinheim

by Espinet, rather than a substitution of I for R as proposed by Farina. Moreover, it is clear that under the conditions of Farina (PhI, $(CH_2{=}CH)SnBu_3$, and $AsPh_3$ in THF) the substitution does not occur on *trans*-[PdPhI($AsPh_3$)(thf)]. As calculated by Casado and Espinet, the rate of reaction observed should require 40% solvolysis to *trans*-[PdPhI($AsPh_3$)(thf)], which is not observed.[29,188] The complexes detected experimentally in a solution of *trans*-[PdPhI($AsPh_3$)$_2$] in THF, in the absence of added $AsPh_3$, are [PdPhI($AsPh_3$)$_2$] and [$Pd_2Ph_2(\mu\text{-}I)_2(AsPh_3)_2$],[176] whereas those observed in DMF are [PdPhI($AsPh_3$)$_2$] and [PdPhI($AsPh_3$)(dmf)].[176,189] These observations emphasize the important influence of the solvent on the transmetalation mechanism, and serve as a warning on the risk of giving conclusions drawn for a particular system universal value.

In summary, although the operation of a cyclic mechanism with exchange of L for R^2 (or (S) for R^2) now seems to be well established, it is also clear that the exact complex undergoing the transmetalation can change as a function of the solvent, R^1, L, and X.

3.7. The Open Associative Transmetalation

Until recently open transmetalation pathways were the only mechanisms considered in the literature (although within the misconception of dissociation). Most reactions probably do proceed by open mechanisms (but associatively), which explains the fact that the transmetalation step can be very fast in the absence of any potential bridging ligand, and that inversion at the α carbon atom sometimes occurs.[34]

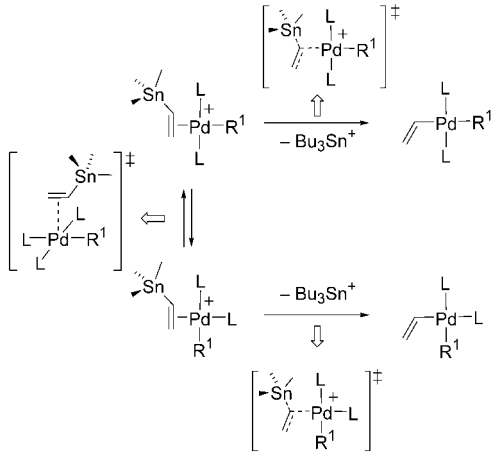
The main products of the oxidative addition of ArOTf to [PdL_n] complexes are not neutral complexes [PdAr(OTf)L_2], but cationic complexes [PdAr(S)L_2](OTf), with a molecule of solvent (e.g. THF, DMF) or water coordinated to the palladium center.[93,96,209] Simplified representations, such as [PdAr(PPh_3)$_2$]$^+$, which ignore the coordination of the solvent, have most often been formuated.

For the coupling of organostannanes with vinyl[210] and aryl triflates,[211,212] LiCl has been used as an additive. Iodide salts have also been shown to promote other coupling reactions with aryl triflates.[213] Farina and co-workers found both accelerating and retarding effects for added LiCl,[27,29] depending on the solvent (NMP or THF), the organic triflate (R^1 = aryl or vinyl), and the neutral ancillary ligand (L = $AsPh_3$ or PPh_3). Based on results for related platinum systems,[184] it was postulated that the intermediates formed upon the oxidative addition of organic triflates to Pd^0 in the absence of LiCl are cationic complexes, such as [PdR^1(S)L_2]$^+$ and [PdR^1L_3]$^+$. The solvento complexes could be the active species in the subsequent transmetalation step.[28] In solvents such as THF, in which these species were inactive, the neutral complex [PdR^1ClL_2] would be formed in the presence of LiCl, and the reaction would continue from this point by ligand "dissociation", transmetalation to a *trans* complex, and coupling (Scheme 28).[29]

This proposal is not correct, and the coupling of aryl triflates is mechanistically more complex.[96,97] Thus, the addition of LiCl favors the coupling of C_6F_5I with stannanes catalyzed by [$Pd(AsPh_3)_4$] in THF.[96] In this case, LiCl promotes the very slow rate-determining oxidative addition of the aryl triflate by converting [$Pd(AsPh_3)_4$] into more electron rich [$PdCl_n(AsPh_3)_m$]$^{n-}$ complexes, which give *trans*-[$PdRClL_2$] as the product of the oxidative addition. In contrast, with the more nucleophilic [$Pd(PPh_3)_4$], the Stille coupling is retarded by the addition of LiCl. In this case, the oxidative addition takes place readily in the absence of LiCl. In the presence of chloride ions the complex *trans*-[$PdRClL_2$] is formed rapidly. In their absence *trans*-[PdR(OTf)(PPh_3)$_2$] and [$PdR(PPh_3)_3$]$^+$, which undergo transmetalation faster, are formed. Therefore, the overall process is retarded in the presence of LiCl.[96] The recent proposal of Roy and Hartwig that the acceleration of the oxidative addition step by LiX is due in some cases to an increase in the polarity of the reaction medium may explain why this promoter is not needed in polar solvents.[99]

In general, the transmetalation in the absence of LiCl occurs on *trans*-[PdR^1(OTf)L_2], [PdR^1L_3]$^+$, or *trans*-[PdR^1L_2(S)]$^+$. Studies of the transmetalation of [PdR^1L_3]$^+$ as an isolated step (Section 3.4, Figure 1) showed that the transmetalation gives rise to a significant concentration of the intermediate *trans*-[$PdR^1(CH{=}CH_2)L_2$]. *cis*-[$PdR^1(CH{=}CH_2)L_2$] is also formed, but is not detected because of its high reactivity. The *trans* complexes have a long lifetime in solution, whereas the *cis* complexes undergo coupling very rapidly and are not observed, unless they are stabilized by chelating ligands. These results reveal competitive *cis* and *trans* ligand substitution in palladium complexes (both via open transition states), in proportions controlled by the different *trans* effects of the ligands (see Section 3.4). The process is illustrated for a cationic [PdR^1L_3]$^+$ complex and a vinyl stannane in Scheme 40. Similar results were obtained for *trans*-[PdR^1(OTf)L_2],[96] as well as in the coupling of an aryl triflate with tributyl(vinyl)tin with dppe as the ligand (see Scheme 34).[97]

In the case of alkyl stannanes and other derivatives with sp^3-configured α carbon atoms, the transmetalation leads to inversion of configuration. As the nucleophilicity of the α carbon atoms of alkyl stannanes is very low, an efficient

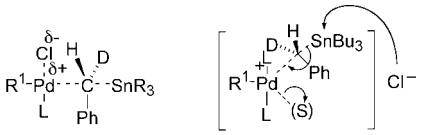


Scheme 40. Formation pathways of the complexes *cis*- and *trans*-[$PdR^1(CH{=}CH_2)L_2$] in the transmetalation with a vinyl stannane.

 © 2004 Wiley-VCH Verlag GmbH & Co. KGaA, Weinheim

transmetalation will probably require a highly electrophilic metal center. A cationic complex $[PdR^1L_2(S)]^+$ would therefore be expected to be a more favorable intermediate than the neutral $[PdClR^1L(S)]$ ((S) = hmpa) initially suggested by Stille for the transformation shown in Scheme 29 (top).[34] In fact, in strongly coordinating and solvating HMPA the complexes $[PdR^1XL^2]$ (X = Cl, Br, I) are fully converted into $[PdR^1L_2(hmpa)]X$.[96]

Thus, solvents exert a very important influence on the transmetalation and can displace both neutral and anionic ligands, including halides. This behavior has very important stereochemical consequences, as the contradictory stereochemical results reported in the literature (Scheme 29) can now be understood. Thus, Falck and co-workers reported 98% retention of configuration in the coupling of chiral stannanes bearing an α-alkoxy substituent with acyl chlorides in toluene.[35] These conditions should strongly favor reaction via a cyclic transition state, because the transmetalation will take place on *trans*-$[Pd(acyl)Cl(PPh_3)_2]$.[96] Labadie and Stille found ≥65% inversion in the coupling of a chiral benzylic stannane with an acyl chloride in the highly polar solvent HMPA.[34] These conditions should favor reaction via an open transition state, which is probably **75**, arising from attack on $[Pd(acyl)(PPh_3)_2(hmpa)]^+$, rather than the neutral form **74** proposed by Stille.[96] Interestingly, the latter result shows that



74 **75**

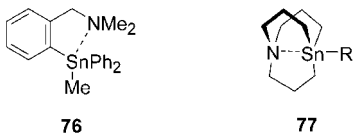
the S_E2(open) mechanism may be preferred even in the presence of a halide, provided that the solvent used is polar enough to provide good stabilization of the polar transition state **75**. This may explain the early observation of a significant rate acceleration in the presence of coordinating polar solvents, such as HMPA.[1]

In summary, the S_E(open) transmetalation mechanism is the only possible pathway in the absence of bridging ligands, but it can also operate in the presence of such ligands under appropriate conditions. It implies overall replacement of X for R^2 or L for R^2 at the Pd center, with competitive formation of *cis* and *trans* intermediates, and leads to inversion of configuration at the α carbon atom. This mechanism should be favored by the use of polar, coordinating, nonbridging solvents and for nonbridging anionic ligands that are readily cleaved.

3.8. Enhancement of Stannane Nucleophilicity by Additives

As mentioned in Section 2.6, fluoride additives enhance the reactivity of organostannanes.[132,133,214] Hydroxide ions[215] have a similar effect. Hydroxo ligands also play a major role in the transmetalation step of the Suzuki coupling reaction[4,216] and in other catalytic transformations of organoboranes.[217]

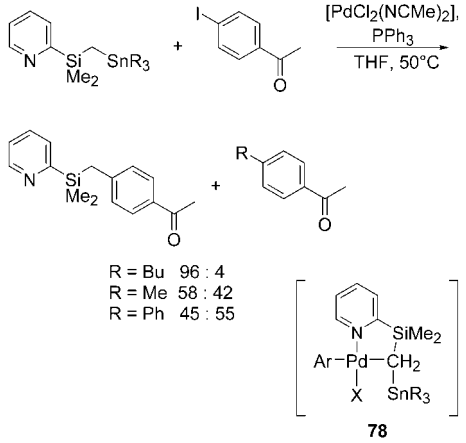
Particularly effective is the coordination of the nitrogen atom in benzyl amines such as **76**[218] and stannatrane derivatives **77**,[219–221] which allows the selective transfer of



76 **77**

the R group in Stille coupling reactions. The activation of stannanes by fluoride ions is particularly effective[133] and can be carried out in situ for the coupling of certain monoorganostannanes with alkenyl and aryl triflates.[133d]

The selective transfer of a substituted alkyl group in $RSnMe_3$ is difficult. Thus, in the palladium-catalyzed coupling of $Me_3SiCH_2SnMe_3$ with aryl triflates, the methyl group is transferred selectively.[211a] However, Yoshida and co-workers have demonstrated that when the silane is substituted with a 2-pyridyl ring (2-Py), selective transfer of the silylmethyl group takes place (Scheme 41).[222] A new concept is involved



78

Scheme 41. Selective transfer of a silylmethyl group. Taking into account the 2-pyMe_2SiCH_2/R ratio of 1:3 on the organotin reagent, the relative ratios for the transfer of the two groups are 99:1 (R = Bu), 81:19 (R = Me), and 71:29 (R = Ph).

in this selective coupling, as the coordination of the pyridyl nitrogen atom to the tin center should favor the transfer of R, whereas coordination to the palladium(II) center should favor the intramolecular transmetalation via an S_E2(cyclic) intermediate **78**.

Although not strictly an additive, it is very likely that in many cases the solvent acts as a ligand for the stannane in solution, enhancing its nucleophilicity. This behavior can also contribute to the rate acceleration observed in the presence of solvents such as HMPA.[1] Although no detailed study has been carried out specifically on this important aspect, recent theoretical calculations on the transmetalation of $[Pd(C{\equiv}CH)Br(PH_3)_2]$ with tetraethynylstannane in the presence of

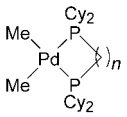
ammonia as a nucleophilic assistant support the hypothesis that coordination expansion at tin plays an important role in facilitating the transmetalation.[223]

4. The Reductive Elimination

An excellent review on reductive elimination is available. For this reason only a few examples are discussed herein.[224]

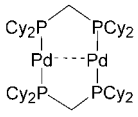
4.1. The Effect of Bidentate Ligands

As stated above, the formation of T-shaped intermediates [PdRR′L] greatly accelerates the reductive elimination of [PdRR′(L)$_2$] complexes.[40] The same is true for complexes bearing bidentate diphosphane ligands.[37,38,40] The reductive elimination of a series of complexes [PdMe$_2$(L-L)] (**79**, L-L = Cy$_2$P(CH$_2$)$_n$PCy$_2$; n = 1–4) revealed that only Cy$_2$PCH$_2$PCy$_2$,



n = 1–4

79a–d



80

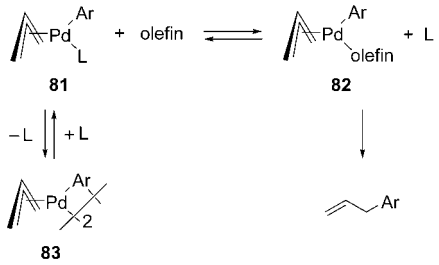
the ligand with the smallest bite angle, leads to a smooth elimination of ethane. Reductive elimination from these complexes is probably preceded by the dissociation of one of the diphosphane arms to form a T-shaped intermediate.[225] The resulting Pd^0 complex [Pd(L-L)] undergoes dimerization to form complex **80**. The complexes with more stable chelates (n = 2–4) do not eliminate ethane under mild conditions.

On the other hand, the fastest elimination for a series of complexes [PdMe$_2$(L-L)] with L-L = dppp, dppf, and 1,1′-bis(diphenylphosphanyl)ruthenocene (dppr) was observed with the ligand with the largest bite angle.[226,227] This effect on the reductive elimination was also found by Hayashi et al.[228] and van Leeuwen and co-workers[229] in the palladium-catalyzed cross-coupling reaction of Grignard reagents with aryl halides. In this process, the highest initial turnover frequencies were observed with ligands with large bite angles.

4.2. Coupling with Allylic Electrophiles: The Slow Reductive Elimination

The rate-determining step in the coupling of aryl halides or triflates with aryl or alkenyl stannanes can either be the transmetalation or the oxidative addition, depending on the exact reaction conditions.[97,188] On the other hand, in the coupling of allylic electrophiles, the reductive elimination step might become rate determining, since the C–C coupling is slower for allyl–R than for aryl–aryl or vinyl–aryl coupling.[224]

In fact, Schwartz and co-workers have shown that the coupling of allylic halides with allylic organometallic reagents does not proceed unless an electron-withdrawing olefin, such as maleic anhydride, is added.[230,231] The reductive elimination in allyl aryl palladium complexes of type **81** was studied by Kurosawa and co-workers (Scheme 42), who also noted



Scheme 42. Electron-poor olefins accelerate the reductive elimination of allylic arenes through the formation of complexes such as **82**.

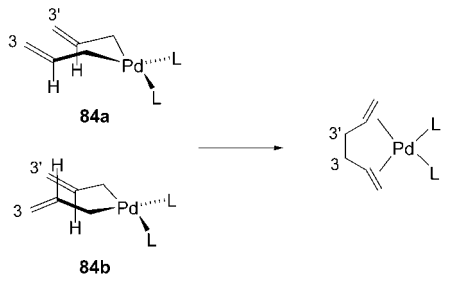
this promoting effect of olefins with electron-withdrawing substituents.[232] Kinetic studies supported by theoretical work suggest that the reductive elimination occurs from an η^3-allyl palladium complex **82** with a coordinated olefin. This species was detected by NMR spectroscopy at low temperature.[232d] These results have been used to improve some catalytic coupling reactions by adding olefins with electron-withdrawing substituents (often maleic anhydride).[230,233,234]

It is remarkable that palladium-catalyzed coupling reactions of allyl halides with aryl stannanes are more efficient than the stoichiometric allyl–aryl reductive coupling on isolated allyl aryl palladium complexes. The stoichiometric transmetalation of η^3-allyl palladium complexes with an aryl stannane (Ar = C$_6$F$_5$) gives allyl aryl palladium complexes **81** and **82** (Scheme 42).[197] Reductive elimination from these complexes does not occur in the absence of additives. For an efficient coupling, the coordination of a promoter of reductive elimination, such as 1,4-benzoquinone or another electron-withdrawing olefin, is needed. Under catalytic conditions, the allyl electrophile itself acts as the electron-withdrawing olefin,[197] which explains why the catalytic coupling proceeds fairly well despite the resistance of complexes **81** or **83** to reductive elimination.

The coupling of allyl stannanes with allyl carboxylates[235,236] or allyl bromides[237,238] allows the synthesis of 1,5-dienes.[239] Bis(η^3-allyl) palladium complexes do not show any tendency to undergo reductive elimination.[240,241] In the presence of phosphane ligands, η^1-allyl η^3-allyl palladium complexes are formed,[242,243] which can decompose to form dinuclear Pd^I derivatives.[244] On the other hand, the addition of diphosphanes leads to bis(η^1-allyl) palladium diphosphane complexes,[245] which undergo smooth reductive elimination at low temperatures.[246]

That the most favorable pathway for the reductive elimination involves bis(η^1-allyl) palladium complexes bearing two phosphane ligands is supported by calculations (Scheme 43).[247] Interestingly, regardless of whether the allyl moieties are in a *syn* (**84a**) or an *anti* (**84b**) arrangement, the formation of a C3–C3′ bond (E_a = 11.1 and 8.5 kcal mol^{-1}, respectively, for L = PH$_3$) is favored significantly over the

 © 2004 Wiley-VCH Verlag GmbH & Co. KGaA, Weinheim

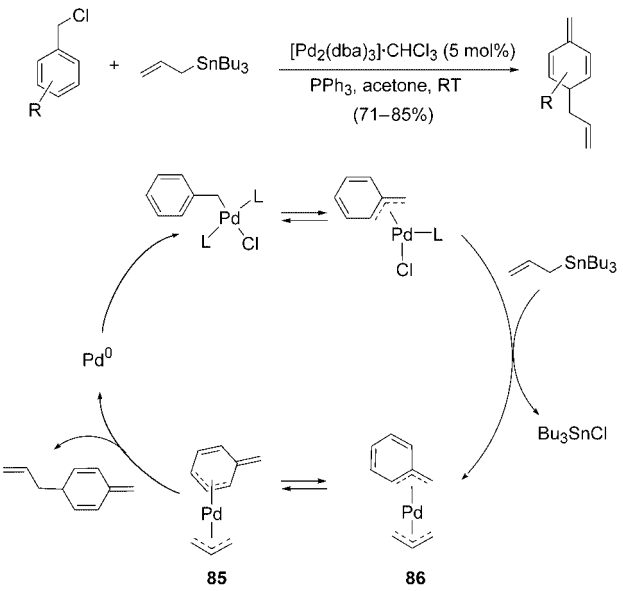


Scheme 43. Favored 3,3′ coupling of two allyl ligands.

formation of a C1–C1′ or a C1–C3′ bond ($E_a = 20.9$ and 22.8 kcal mol^{-1}, respectively).

4.3. Allyl–Benzyl Coupling

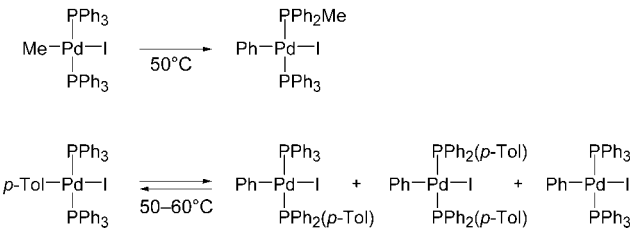
The recently discovered coupling of allyl stannanes with benzyl chlorides, resulting in the dearomatization of the aryl ring, is synthetically and mechanistically remarkable (Scheme 44).[248] Although the mechanism of this transformation has not been studied, the overall process probably involves isomerization of an η^3-allyl η^3-benzyl palladium complex **85** to give **86**, which could undergo reductive elimination to form the dearomatized product.[248]



Scheme 44. Mechanism of the dearomatizing coupling of benzyl chlorides with allyltributylstannane.

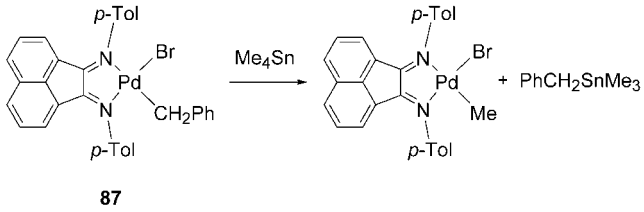
5. Scrambling of Substituents and Homocoupling

The exchange of R groups between the palladium center and the phosphane can take place under very mild conditions.[249–251] Investigations into the Me/Ph and the Ar/Ph exchange led to contradictory mechanistic results. In the first study (Scheme 45, top),[249] the rate was not affected by added PPh_3. However, in the second example (Scheme 45, bottom), the rearrangement was almost completely inhibited by PPh_3.[250] This contradiction was addressed by Novak and co-workers,[252] who showed that the aryl–aryl exchange reaction of $[PdArL_2X]$ proceeds first through a reductive elimination to form a phosphonium salt, followed by the oxidative addition of a different phosphorous–carbon bond.[253,254] Homocoupling processes resulting from an intermolecular Ar/Ar exchange between different Pd^{II} complexes have also been documented.[39b,255–257]



Scheme 45. Exchange of organic groups between the Pd center and the phosphane ligand.

Occasionally, instead of the expected transmetalation, the organostannane may undergo exchange reactions with the organic group in the oxidative-addition product, a process that can result in the formation of homocoupled derivatives.[256,258] This process has been studied by van Asselt and Elsevier with complexes such as **87** containing rigid bidentate nitrogen ligands (Scheme 46).[259]



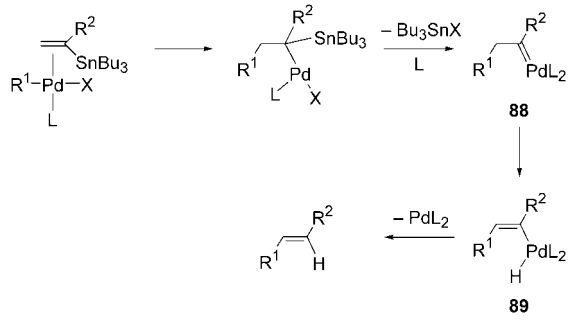
Scheme 46. Exchange of organic groups between the Pd complex **87** and tetramethyltin.

6. Unorthodox Mechanisms

Although the classical mechanistic sequence for the Stille coupling reaction (oxidative addition, transmetalation, reductive elimination) is reasonably reliable, some significant exceptions are known.

6.1. Reactions via Palladium Carbenes

Sterically hindered alkenyl stannanes might react by a different mechanism, which results in the formation of cine-substitution products.[260] Mechanistic studies carried out by Busacca et al.[260c] and Farina and Hossain[260d] suggest the participation of palladium carbenes **88** as intermediates,[261] which are formed by a Heck-type reaction involving olefin insertion and elimination of Bu_3SnX (Scheme 47). β-Hydride



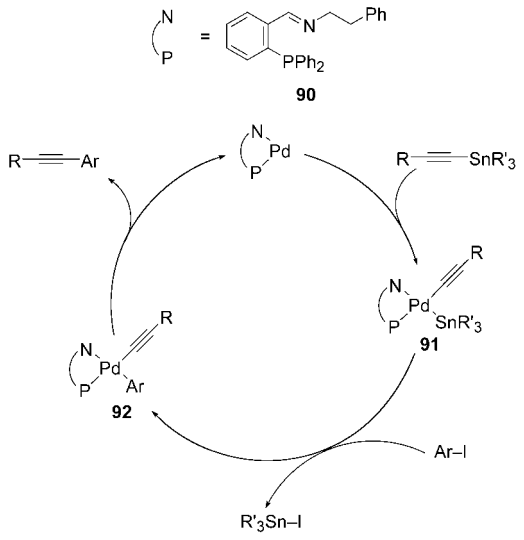
Scheme 47. Synthesis of 1,2-disubstituted alkenes via the palladium complex **88**.

elimination of the intermediate carbenes[262] gives complexes **89**, which undergo reductive elimination to form 1,2-disubstituted alkenes as the final products.

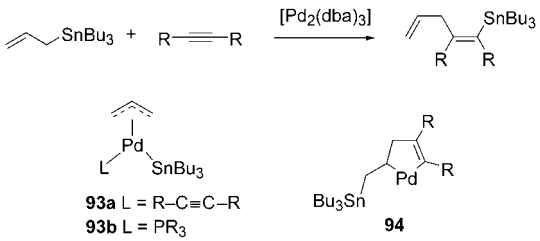
6.2. Reactions Initiated by the Oxidative Addition of Stannanes to Pd^0

The oxidative addition of some types of stannanes to Pd^0 complexes also appears to be an alternative pathway to the classical Stille sequence. Thus, Shirakawa et al. found that alkynyl stannanes react with certain Pd^0 complexes by oxidative addition.[263] Whereas aryl iodides react with alkynyl stannanes by the usual Stille pathway in the presence of Pd^0 complexes bearing phosphane ligands, the reaction proceeds via the complex **91** in the presence of a Pd^0 complex with the ligand **90** (Scheme 48).[263,264] Subsequent reaction with the aryl iodide was proposed to give **92**, which undergoes reductive elimination to form the C–C bond.

Allyl stannanes add to Pd^0 complexes to give η^3-allyl palladium complexes **93** (Scheme 49), which react with alkynes to afford allylstannylated derivatives.[265] An intramolecular version of this reaction has also been developed.[266]



Scheme 48. Example of a mechanism involving oxidative addition of the organotin reagent to a Pd^0 complex.



Scheme 49. Addition of allyltributylstannane to alkynes.

Complexes **93b** have also been proposed as intermediates in the Pd^0-catalyzed carboxylation of allyl stannanes with CO_2.[267] Similar complexes are probably formed by the transmetalation of η^3-allyl palladium complexes with hexamethyldistannane.[268]

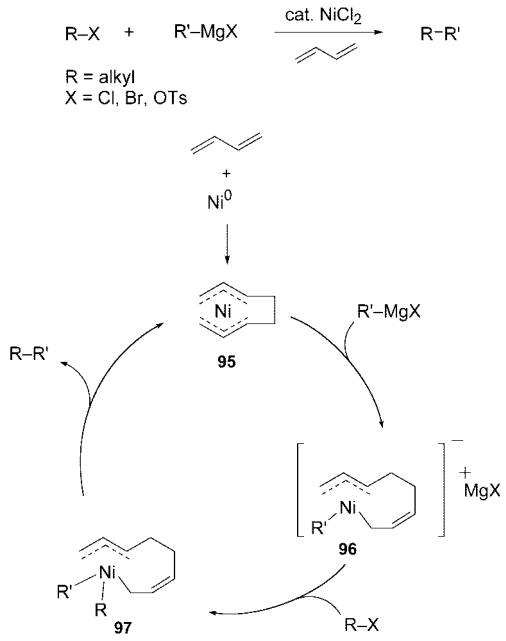
For the allylstannylation reaction, an alternative process involving an oxidative cyclometalation to form a palladacyclopentene complex **94** seems less likely on the basis of recent theoretical calculations, which support the smooth oxidative addition of allyl stannanes to Pd^0.[266]

6.3. A New Catalytic Cycle Based on Pd^{II}/Pd^{IV}?

Although a Pd^{II}/Pd^{IV} catalytic cycle has not yet been proposed for the Stille reaction, there are hints that this possibility should be kept in mind when considering mechanisms of Pd-catalyzed coupling processes. There is strong evidence for the formation of Pd^{IV} intermediates by the oxidative addition of alkyl halides to Pd^{II} complexes.[269] Other d^8 organometallic compounds, such as $[IrCl(CO)L_2]$ (Vaska-type complexes) and certain Pt^{II} complexes, react readily with alkyl halides.[270,271] However, electrophiles $C(sp^2)$–X, such as aryl halides, are much less reactive in the oxidative addition to Pd^{II} complexes, and the formation of Pd^{IV} species from these electrophiles is therefore less likely. Indeed, there is no experimental evidence for such a process in the organometallic chemistry of Pd^{II} complexes,[272,273] although Pd^{IV} complexes $[PdArX_3(L\text{-}L)]$ ($Ar = C_6F_5$; X = Cl, Br), obtained by the oxidative addition of X_2 to [PdArX(L-L)], are known.[274]

The nickel-catalyzed coupling of alkyl halides and tosylates with Grignard reagents discovered by Kambe and coworkers is probably a genuine example of a coupling reaction under M^{II}/M^{IV} catalysis with a Group 10 metal (Scheme 50).[275] The active nickel complex is generated in situ by reaction of $NiCl_2$ and the Grignard reagent in the presence of 1,3-butadiene or isoprene. Although reduction of $NiCl_2$ by the Grignard reagent undoubtedly takes place under the reaction conditions, it was demonstrated that Ni^0 complexes are not the active catalysts. The requirement of a diene suggests that a bis(η^3-allyl) nickel(II) complex **95** is formed by oxidative dimerization,[276] and that **95** reacts subsequently with the Grignard reagent to form **96**. The oxidative addition of the alkyl halide or tosylate to the electron-rich complex **96** would then give a Ni^{IV} complex **97**. Reductive elimination should lead to the formation of the C–C bond and regeneration of the active Ni^{II} complex.

 © 2004 Wiley-VCH Verlag GmbH & Co. KGaA, Weinheim



Scheme 50. The proposed catalytic cycle proceeds via Ni^{II} intermediates **95** and **96**, and Ni^{IV} intermediates **97**.

7. Copper Effects

A remarkable phenomenon in Stille coupling reactions is the effect of the addition of CuI or other Cu^{I} salts, which accelerate couplings catalyzed by $[PdL_4]$ with variable success.[27,29,35,277–281] This so-called "copper effect" was first studied by the research groups of Farina and Liebeskind.[282] Assuming a predissociation mechanism for the transmetalation, they concluded that the role of CuI in systems with "strong" ligands, such as PPh_3, was to scavenge free ligand. It was also suggested that for "soft ligands" (such as $AsPh_3$) ligand dissociation from Pd^{II} is not a problem, and therefore the addition of CuI leads to minimal rate acceleration.

The "copper effect" can be rationalized within the new framework of the associative mechanism. Accordingly, CuI does not promote the dissociation of L from *trans*-$[PdR^1IL_2]$, but it captures part of the neutral ligand L released during the oxidation of $[PdL_4]$ to *trans*-$[PdR^1IL_2]$, the species that actually undergoes the transmetalation. Thus, the effect of CuI is to mitigate the "autoretardation" by free L of the rate-determining associative transmetalation.[283] The effect is strong for PPh_3 and weak for $AsPh_3$ for two reasons: 1) The autoretardation is much more effective for $L = PPh_3$ (Figure 2), and 2) CuI is a more effective scavenger of PPh_3 than of $AsPh_3$.

In their initial study, Farina, Liebeskind and co-workers[282] proposed that in very polar solvents another phenomenon, a Sn/Cu transmetalation, was taking place. Thus, organocopper species were participating in the reaction.[284] An effective coupling system was later developed based on this proposal. Piers and Wong demonstrated that the intramolecular coupling of alkenyl iodides with alkenyl stannanes can be carried out in the presence of a stoichiometric amount

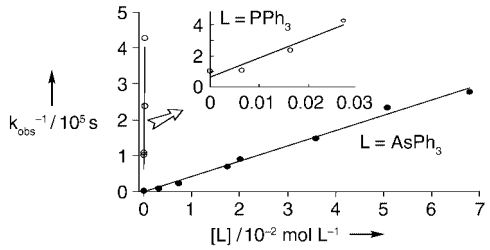
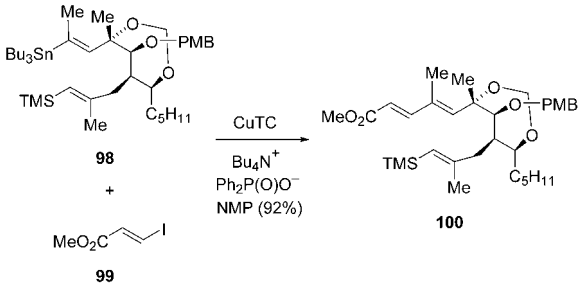


Figure 2. Inhibition by added L of the coupling of $C_6Cl_2F_3I$ with $Bu_3SnCH{=}CH_2$ catalyzed by *trans*-$[PdC_6Cl_2F_3)IL_2]$, represented as k_{obs}^{-1} versus [L]. $[C_6Cl_2F_3I] = [Bu_3SnCH{=}CH_2] = 0.2$ mol L^{-1}, THF, 322.6 K.

of CuCl.[285,286] Better results were later obtained with other Cu^{I} salts under catalytic conditions.[287–291] As an illustration, the cross-coupling of **98** and methyl (*E*)-β-iodoacrylate (**99**) promoted by copper(I) thiophene-2-carboxylate (CuTC) furnished **100** (Scheme 51), an intermediate in the synthesis of

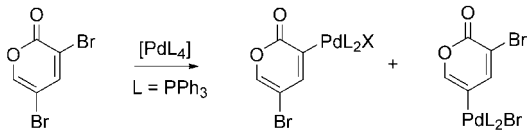


Scheme 51. Copper-catalyzed coupling of the alkenyl stannane **98** with the alkenyl iodide **99**. PMB = 4-methoxybenzyl, TMS = trimethylsilyl.

formamicinone.[292] Recently, the Stille coupling of heteroaromatic thioethers as the electrophiles was achieved in the presence of CuBr[293] or copper(I) 3-methylsalicylate.[294]

Finally, a new effect of the addition of copper salts was noted recently: The regioselectivity of Stille coupling reactions of 3,5-dibromo-2-pyrone (**101**) changes in the presence of CuI in DMF as the solvent, leading to the Pd^{II} complex **103** (Table 1).[295]

Table 1: Regioselectivity of the coupling of **101** in the presence and absence of CuI, in toluene and DMF.



Entry	Conditions	**102/103**
1	toluene, 100 °C	100:0
2	toluene, 100 °C, CuI (1 equiv)	100:0
3	DMF, 50 °C	100:0
4	DMF, 50 °C, CuI (1 equiv)	30:70

 © 2004 Wiley-VCH Verlag GmbH & Co. KGaA, Weinheim

8. Summary and Outlook

Recent studies on the mechanism of the Stille reaction are uncovering a complex picture (Scheme 30), rich in possibilities. Each step can be rate determining, depending on the reaction variables. However, it is now better understood how each step can be accelerated. The transmetalation appears particularly complex, as it can operate on different Pd^{II} species in solution. These species change depending on the solvent, the reagents, and the catalyst. The nucleophilicity of the tin reagent can also be influenced by the solvent or by additives. The use of complexes with sterically demanding ligands as catalysts has recently made it possible to carry out the reaction with electrophiles that were unreactive when conventional ligands were used. Finally, a unified view seems to be emerging for transmetalations to palladium, whether with organotin compounds (Stille coupling), fluoride-activated silanes (Hiyama coupling), or other nucleophilic organometallic compounds: Some reactions occur with retention of configuration at the carbon atom that is transmetalated and probably proceed by an S_E2(cyclic) substitution of L for R at the Pd center. Other reactions occur with inversion of configuration by an S_E2(open) mechanism. This behavior, common to tin and silicon organometallic compounds, strongly suggests that under appropriate conditions similar dual reaction pathways might be found in reactions involving other organometallic reagents with the less electropositive metals, such as the Suzuki coupling.

We thank the Ministerio de Ciencia y Tecnología for support (projects BQU2001-2015 and BQU2001-0193-C02-01).

Received: October 23, 2003
Revised: March 19, 2004
Published Online: August 27, 2004

[1] J. K. Stille, *Angew. Chem.* **1986**, *98*, 504 – 519; *Angew. Chem. Int. Ed. Engl.* **1986**, *25*, 508 – 524.
[2] V. Farina in *Comprehensive Organometallic Chemistry II*, *Vol. 12* (Eds.: E. W. Abel, F. G. A. Stone, G. Wilkinson), Pergamon, Oxford, **1995**, chap. 3.4.
[3] a) T. N. Mitchell, *Synthesis* **1992**, 803 – 815; b) T. N. Mitchell in *Metal-Catalyzed Cross-Coupling Reactions* (Eds.: F. Diederich, P. J. Stang), Wiley-VCH, New York, **1998**, chap. 4.
[4] For a review on Suzuki cross-coupling reactions, see: N. Miyaura, A. Suzuki, *Chem. Rev.* **1995**, *95*, 2457 – 2483.
[5] D. Azarian, S. S. Dua, C. Eaborn, D. R. M. Walton, *J. Organomet. Chem.* **1976**, *117*, C55 – C75.
[6] a) M. Kosugi, K. Sasazawa, Y. Shimizu, T. Migita, *Chem. Lett.* **1977**, 301 – 302; b) M. Kosugi, Y. Shimizu, T. Migita, *Chem. Lett.* **1977**, 1423 – 1424.
[7] For a historical account of the Stille reaction, see: M. Kosugi, K. Fugami, *J. Organomet. Chem.* **2002**, *653*, 50 – 53.
[8] D. Milstein, J. K. Stille, *J. Am. Chem. Soc.* **1978**, *100*, 3636 – 3638.
[9] V. Farina, V. Krishnamurthy, W. K. Scott, *Organic Reactions*, *Vol. 50*, Wiley, New York, **1997**.
[10] J. Tsuji, *Palladium Reagents and Catalysts*, Wiley, Chichester, **1995**.
[11] a) K. C. Nicolaou, E. J. Sorensen, *Classics in Total Synthesis*, VCH, Weinheim, **1996**; b) K. C. Nicolaou, S. A. Snyder, *Classics in Total Synthesis II*, Wiley-VCH, Weinheim, **2003**.
[12] M. A. J. Duncton, G. Pattenden, *J. Chem. Soc. Perkin Trans. 1* **1999**, 1235 – 1246.
[13] M. D. Shair, T. Y. Yoon, K. K. Mosny, T. C. Chou, S. J. Danishefsky, *J. Am. Chem. Soc.* **1996**, *118*, 9509 – 9525.
[14] a) K. C. Nicolaou, T. K. Chakraborty, A. D. Piscopio, N. Minowa, P. Bertinato, *J. Am. Chem. Soc.* **1993**, *115*, 4419 – 4420; b) K. C. Nicolaou, A. D. Piscopio, P. Bertinato, T. K. Chakraborty, N. Minowa, K. Koide, *Chem. Eur. J.* **1995**, *1*, 318 – 323.
[15] E.-I. Negishi, *J. Organomet. Chem.* **2002**, *653*, 34 – 40.
[16] For reviews, see: a) Y. Hatanaka, T. Hiyama, *Pure Appl. Chem.* **1994**, *66*, 1471; b) Y. Hatanaka, T. Hiyama, *Synlett* **1991**, 845 – 853; c) T. Hiyama in *Metal-Catalyzed Cross-Coupling Reactions* (Eds.: F. Diederich, P. J. Stang), Wiley-VCH, Weinheim, **1998**, chap. 10; d) T. Hiyama, E. Shirakawa, *Top. Curr. Chem.* **2002**, *219*, 61 – 85.
[17] S. E. Denmark, R. F. Sweis, *Acc. Chem. Res.* **2002**, *35*, 835 – 846.
[18] The related coupling of organogermanes has been less explored: a) M. Kosugi, T. Tanji, Y. Tanaka, A. Yoshida, K. Fugami, M. Kameyama, T. Migita, *J. Organomet. Chem.* **1996**, *508*, 255 – 257; b) see also: T. Nakamura, H. Kinoshita, H. Shinokubo, K. Oshima, *Org. Lett.* **2002**, *4*, 3165 – 3167.
[19] For reviews, see: a) K. Sonogashira, *J. Organomet. Chem.* **2002**, *653*, 46 – 49; b) R. R. Tywinski, *Angew. Chem.* **2003**, *115*, 1604 – 1606; *Angew. Chem. Int. Ed.* **2003**, *42*, 1566 – 1568; c) see also reference [21].
[20] a) K. Tamao, K. Sumitani, M. Kumada, *J. Am. Chem. Soc.* **1972**, *94*, 4374 – 4376; b) M. Yamamura, I. Moritani, S.-I. Murahashi, *J. Organomet. Chem.* **1975**, *91*, C39-C42; c) J. F. Fauvarque, A. Jutand, *Bull. Soc. Chim. Fr.* **1976**, 765 – 770; d) A. Sekiya, N. Ishikawa, *J. Organomet. Chem.* **1976**, *118*, 349 – 354.
[21] a) E. Negishi, *Acc. Chem. Res.* **1982**, *15*, 340 – 348; b) E. Negishi, M. Qian, F. Zeng, L. Anastasia, D. Babinski, *Org. Lett.* **2003**, *5*, 1597 – 1600, and references therein; c) E. Negishi, L. Anastasia, *Chem. Rev.* **2003**, *103*, 1979 – 2017.
[22] For leading references on palladium-catalyzed coupling reactions of organoindium compounds, see: a) I. Pérez, J. P. Sestelo, L. A. Sarandeses, *J. Am. Chem. Soc.* **2001**, *123*, 4155 – 4160; b) K. Takami, H. Yorimitsu, H. Shinokubo, S. Matsubara, K. Oshima, *Org. Lett.* **2001**, *3*, 1997 – 1999; c) U. Lehmann, S. Awasthi, T. Minehan, *Org. Lett.* **2003**, *5*, 2405 – 2408; d) P. Ho Lee, S. W. Lee, D. Seomoon, *Org. Lett.* **2003**, *5*, 4963 – 4966.
[23] For iron-catalyzed cross-coupling reactions of alkyl Grignards reactions, see: a) A. Fürstner, A. Leitner, *Angew. Chem.* **2002**, *114*, 632 – 635; *Angew. Chem. Int. Ed.* **2002**, *41*, 609 – 612; b) A. Fürstner, A. Leitner, M. Méndez, H. Krause, *J. Am. Chem. Soc.* **2002**, *124*, 13856 – 13863.
[24] a) A. de Meijere, F. E. Meyer, *Angew. Chem.* **1994**, *106*, 2473 – 2506; *Angew. Chem. Int. Ed. Engl.* **1994**, *33*, 2379 – 2411; b) I. P. Beletskaya, A. V. Cheprakov, *Chem. Rev.* **2000**, *100*, 3009 – 3066; c) G. T. Crisp, *Chem. Soc. Rev.* **1998**, *27*, 427 – 436; d) M. T. Reetz in *Transition Metal Catalyzed Reactions* (Eds.: S. G. Davis, S.-I. Murahashi), Blackwell Science, Oxford, **1999**; e) J. T. Link, L. E. Overman in *Metal-Catalyzed Cross-Coupling Reactions* (Eds.: F. Diederich, P. J. Stang), Wiley-VCH, Weinheim, **1998**, chap. 6; f) S. Bräse, A. de Meijere in *Metal-Catalyzed Cross-Coupling Reactions* (Eds.: F. Diederich, P. J. Stang), Wiley-VCH, Weinheim, **1998**, chap. 3.
[25] V. Farina, S. R. Baker, D. A. Benigni, C. Sapino, *Tetrahedron Lett.* **1988**, *29*, 5739 – 5742.
[26] For a review on 2-furyl phosphanes, see: N. G. Andersen, B. A. Keay, *Chem. Rev.* **2001**, *101*, 997 – 1030.
[27] V. Farina, B. Krishnan, *J. Am. Chem. Soc.* **1991**, *113*, 9585 – 9595.

 © 2004 Wiley-VCH Verlag GmbH & Co. KGaA, Weinheim

[28] V. Farina, B. Krishnan, D. R. Marshall, G. P. Roth, *J. Org. Chem.* **1993**, *58*, 5434 – 5444.

[29] a) V. Farina, G. P. Roth, *Adv. Met.-Org. Chem.* **1996**, *5*, 1 – 53; b) V. Farina, *Pure Appl. Chem.* **1996**, *68*, 73 – 78.

[30] a) H. Fuwa, N. Kainuma, K. Tachibana, M. Sasaki, *J. Am. Chem. Soc.* **2002**, *124*, 14983 – 14992; b) H. Fuwa, M. Sasaki, M. Satake, K. Tachibana, *Org. Lett.* **2002**, *4*, 2981 – 2984.

[31] a) I. Kadota, H. Takamura, K. Sato, A. Ohno, K. Matsuda, Y. Yamamoto, *J. Am. Chem. Soc.* **2003**, *125*, 46 – 47; b) I. Kadota, H. Takamura, K. Sato, A. Ohno, K. Matsuda, M. Satake, Y. Yamamoto, *J. Am. Chem. Soc.* **2003**, *125*, 11893 – 11899.

[32] For a Review on salt effects, see: K. Fagnou, M. Lautens, *Angew. Chem.* **2002**, *114*, 26 – 49; *Angew. Chem. Int. Ed.* **2002**, *41*, 26 – 47.

[33] For conditions developed for similar alkenyl–alkenyl couplings, see: X. Han, B. M. Stolz, E. J. Corey, *J. Am. Chem. Soc.* **1999**, *121*, 7600 – 7605.

[34] J. W. Labadie, J. K. Stille, *J. Am. Chem. Soc.* **1983**, *105*, 6129 – 6137.

[35] a) J. Ye, R. K. Bhatt, J. R. Falck, *J. Am. Chem. Soc.* **1994**, *116*, 1 – 5; b) J. Ye, R. K. Bhatt, J. R. Falck, *Tetrahedron Lett.* **1993**, *34*, 8007 – 8010.

[36] Y. Hatanaka, T. Hiyama, *J. Am. Chem. Soc.* **1990**, *112*, 7793 – 7794.

[37] K. Tatsumi, R. Hoffmann, A. Yamamoto, J. K. Stille, *Bull. Chem. Soc. Jpn.* **1981**, *54*, 1857 – 1867.

[38] F. Ozawa, T. Ito, Y. Nakamura, A. Yamamoto, *Bull. Chem. Soc. Jpn.* **1981**, *54*, 1868 – 1880.

[39] a) D. Minniti, *Inorg. Chem.* **1994**, *33*, 2631 – 2634; b) A. L. Casado, J. A. Casares, P. Espinet, *Organometallics* **1997**, *16*, 5730 – 5736.

[40] A. Gillie, J. K. Stille, *J. Am. Chem. Soc.* **1980**, *102*, 4933 – 4941.

[41] For an aryl–aryl coupling, see: J. Hassan, M. Sévignon, C. Gozzi, E. Schulz, M. Lemaire, *Chem. Rev.* **2002**, *102*, 1359 – 1470.

[42] For a review of the synthesis of stannanes by palladium-catalyzed coupling reactions, see: J. A. Marshall, *Chem. Rev.* **2000**, *100*, 3163 – 3185.

[43] a) For a Minireview on the use of anhydrides, esters, and carbonic acid derivatives as substrates for the oxidative addition to Pd^0, see: A. Zapf, *Angew. Chem.* **2003**, *115*, 5552 – 5557; *Angew. Chem. Int. Ed.* **2003**, *42*, 5394 – 5399; b) for the Stille coupling of sulfonyl chlorides, see: S. R. Dubbaka, P. Vogel, *J. Am. Chem. Soc.* **2003**, *125*, 15292 – 15293.

[44] a) H. Kurosawa, S. Ogoshi, Y. Kawasaki, S. Murai, M. Miyoshi, I. Ikeda, *J. Am. Chem. Soc.* **1990**, *112*, 2813 – 2814; b) H. Kurosawa, H. Kajimura, S. Ogoshi, H. Yoneda, K. Miki, N. Kasai, S. Murai, I. Ikeda, *J. Am. Chem. Soc.* **1992**, *114*, 8417 – 8424.

[45] A. Vitagliano, B. Åkermark, S. Hansson, *Organometallics* **1991**, *10*, 2592 – 2599.

[46] A. Diefenbach, F. M. Bickelhaupt, *J. Chem. Phys.* **2001**, *115*, 4030 – 4040.

[47] I. Stary, P. Kocovsky, *J. Am. Chem. Soc.* **1989**, *111*, 4981 – 4982.

[48] B. M. Trost, T. R. Verhoeven, *J. Am. Chem. Soc.* **1980**, *102*, 4730 – 4743.

[49] C. Amatore, S. Gamez, A. Jutand, G. Meyer, M. Moreno-Mañas, L. Morral, R. Pleixats, *Chem. Eur. J.* **2000**, *6*, 3372 – 3376.

[50] a) J. K. Stille in *The Chemistry of the Metal-Carbon Bond*, *Vol. 2* (Eds.: F. R. Hartley, S. Patai), Wiley, Chichester, **1985**, chap. 9; b) J. K. Stille, K. S. Y. Lau, *Acc. Chem. Res.* **1977**, *10*, 434 – 442.

[51] "Fundamentals of Molecular Catalysis": S. Komiya, M. Hirano in *Current Methods in Inorganic Chemistry*, *Vol. 3* (Eds.: H. Kurosawa, A. Yamamoto), Elsevier, Amsterdam, **2003**, chap. 3.

[52] H. Urata, M. Tanaka, T. Fuchikami, *Chem. Lett.* **1987**, 751 – 754.

[53] a) N. J. Kermode, M. F. Lappert, B. W. Skelton, A. H. White, *J. Organomet. Chem.* **1982**, *228*, C71 – C75; b) H. Urata, H. Suzuki, Y. Moro-oka, T. Ikawa, *J. Organomet. Chem.* **1989**, *364*, 235 – 244; c) V. N. Kalinin, F. M. She, V. N. Khandozhko, P. V. Petrovskii, *Russ. Chem. Bull.* **2001**, *50*, 525 – 530; d) A. Füstner, G. Seidel, D. Kremzow, C. W. Lehmann, *Organometallics* **2003**, *22*, 907 – 909; e) T. Aoki, Y. Ishii, Y. Mizobe, M. Hidai, *Chem. Lett.* **1991**, 615 – 618; f) J.-F. Carpentier, Y. Castanet, J. Brocard, A. Mortreux, F. Rose-Munch, C. Susanne, E. Rose, *J. Organomet. Chem.* **1995**, *493*, C22 – C24.

[54] A. L. Casado, P. Espinet, *Organometallics* **1998**, *17*, 954 – 959.

[55] J. Vicente, A. Arcas, D. Bautista, P. G. Jones, *Organometallics* **1997**, *16*, 2127 – 2138.

[56] a) J. Vicente, A. Arcas, M. A. Blasco, J. Lozano, M. C. Ramírez de Arellano, *Organometallics* **1998**, *17*, 5374 – 5383; b) J. Vicente, M. T. Chicote, C. Rubio, M. C. Ramírez de Arellano, P. G. Jones, *Organometallics* **1999**, *18*, 2750 – 2759; c) J. Vicente, J. A. Abad, A. D. Frankland, M. C. Ramírez de Arellano, *Chem. Eur. J.* **1999**, *5*, 3067 – 3075; d) J. Vicente, J. A. Abad, A. D. Frankland, J. López-Serrano, M. C. Ramírez de Arellano, P. G. Jones, *Organometallics* **2002**, *21*, 272 – 282; e) J. Vicente, J. A. Abad, E. Martínez-Viviente, *Organometallics* **2002**, *21*, 4454 – 4467.

[57] M. A. F. Hernandez-Gruel, P. Espinet, unpublished results.

[58] a) C. M. Crawforth, S. Burling, I. J. S. Fairlamb, R. J. K. Taylor, A. C. Whitwood, *Chem. Commun.* **2003**, 2194 – 2195; b) C. M. Crawforth, I. J. S. Fairlamb, R. J. K. Taylor, *Tetrahedron Lett.* **2004**, *45*, 461 – 465.

[59] J.-F. Fauvarque, F. Pflüger, M. Troupel, *J. Organomet. Chem.* **1981**, *208*, 419 – 427.

[60] A. Jutand, A. Mosleh, *Organometallics* **1995**, *14*, 1810 – 1817.

[61] a) M. Portnoy, D. Milstein, *Organometallics* **1993**, *12*, 1655 – 1664; b) M. Portnoy, D. Milstein, *Organometallics* **1993**, *12*, 1665 – 1673.

[62] For a review on the effect of the ligand bite angle, see: P. W. N. M. van Leeuwen, P. C. J. Kamer, J. N. H. Reek, P. Dierker, *Chem. Rev.* **2000**, *100*, 2741 – 2769.

[63] Very often, this complex is described as $[Pd(dba)_2]$; however, its formulation as the dimetallic complex $[Pd_2(dba)_3{\cdot}dba]$ is more precise: Y. Takahashi, T. Ito, S. Sakai, Y. Ishii, *Chem. Commun.* **1970**, 1065 – 1066; after recrystallization, the solvento complexes $[Pd_2(dba)_3]{\cdot}(S)$ ((S) = CH_2Cl_2, $CHCl_3$, benzene, toluene) are obtained: T. Ukai, H. Kawazura, Y. Ishii, J. J. Bonnet, J. A. Ibers, *J. Organomet. Chem.* **1974**, *65*, 253 – 266; M. C. Mazza, C. G. Pierpont, *J. Chem. Soc. Chem. Commun.* **1973**, 207; M. C. Mazza, C. G. Pierpont, *Inorg. Chem.* **1974**, *13*, 1891 – 1895; see also: A. M. Echavarren, J. K. Stille, *J. Organomet. Chem.* **1988**, *356*, C35 – C37; tris(dibenzylideneacetone)palladium(0), $[Pd(dba)_3]$, has been prepared by heating $[Pd(dba)_2]$ with excess dba in benzene: M. C. Mazza, C. G. Pierpont, *Inorg. Chem.* **1973**, *12*, 2955 – 2959.

[64] The rates of oxidative addition are probably different depending on whether $[Pd_2(dba)_3{\cdot}dba]$ or $[Pd_2(dba)_3]{\cdot}(S)$ is used as the starting complex, as an excess of dba can retard the reaction. However, the actual solvento complex used in catalytic transformations is probably not very important. Herein we refer to these complexes as $[Pd_2(dba)_3]$.

[65] S. Park, D. Hidden, A. L. Rheingold, D. M. Roundhill, *Organometallics* **1986**, *5*, 1305 – 1311.

[66] For reviews, see: a) C. Amatore, A. Jutand, *Coord. Chem. Rev.* **1998**, *178–180*, 511 – 528; b) A. Jutand, *Eur. J. Inorg. Chem.* **2003**, 2017 – 2040.

[67] a) C. Amatore, G. Broeker, A. Jutand, F. Khalil, *J. Am. Chem. Soc.* **1997**, *119*, 5176 – 5185; b) C. Amatore, A. Jutand, G. Meyer, *Inorg. Chim. Acta* **1998**, *273*, 76 – 84.

[68] H. S. Sørensen, J. Larsen, B. S. Rasmussen, B. Laursen, S. G. Hansen, T. Skrydstrup, C. Amatore, A. Jutand, *Organometallics* **2002**, *21*, 5243 – 5253.

[69] C. Amatore, A. Jutand, F. Khalil, M. A. M'Barki, L. Mottier, *Organometallics* **1993**, *12*, 3168 – 3178.
[70] C. Amatore, A. Jutand, G. Meyer, H. Atmani, F. Khalil, F. O. Chahdi, *Organometallics* **1998**, *17*, 2958 – 2964.
[71] C. Amatore, A. Bucaille, A. Fuxa, A. Jutand, G. Meyer, A. N. Ntepe, *Chem. Eur. J.* **2001**, *7*, 2134 – 2142.
[72] See also: A. D. Burrows, N. Choi, M. McPartlin, D. M. P. Mingos, S. Tarlton, R. Vilar, *J. Organomet. Chem.* **1999**, *573*, 313 – 322.
[73] C. Amatore, E. Carré, A. Jutand, Y. Medjour, *Organometallics* **2002**, *21*, 4540 – 4545.
[74] A. Jutand, K. K. Hii, M. Thornton-Pett, J. M. Brown, *Organometallics* **1999**, *18*, 5367 – 5374.
[75] For a study on the rate of exchange of alkene ligands in Pd^0 complexes, see: S. S. Stahl, J. L. Thorman, N. de Silva, I. A. Guzei, R. W. Clark, *J. Am. Chem. Soc.* **2003**, *125*, 12 – 13.
[76] C. Amatore, G. Broeker, A. Jutand, F. Khalil, *J. Am. Chem. Soc.* **1997**, *119*, 5176 – 5185.
[77] W. J. Marshall, V. V. Grushin, *Organometallics* **2003**, *22*, 555 – 562.
[78] For the rate of the oxidative addition of allyl acetates to palladium phosphane complexes [Pd(L-L)] and [PdL_2], the following order was observed: dppb > dppf > PPh_3: C. Amatore, S. Gamez, A. Jutand, *Chem. Eur. J.* **2001**, *7*, 1273 – 1280.
[79] C. Amatore, A. Jutand, *Acc. Chem. Res.* **2000**, *33*, 314 – 321.
[80] C. Amatore, A. Jutand, M. M'Barki, *Organometallics* **1992**, *11*, 3009 – 3013.
[81] C. Amatore, E. Carré, A. Jutand, M. M'Barki, *Organometallics* **1995**, *14*, 1818 – 1826.
[82] A mixture of $Pd(OAc)_2$ and tppts (*m*-sulfonated triphenylphosphane) affords a Pd^0 complex: C. Amatore, E. Blart, J. P. Genêt, A. Jutand, S. Lemaire-Audoire, M. Savignac, *J. Org. Chem.* **1995**, *60*, 6829 – 6839.
[83] C. Amatore, E. Carré, A. Jutand, M. M'Barki, G. Meyer, *Organometallics* **1995**, *14*, 5605 – 5614.
[84] a) C. Bianchini, A. Meli, W. Oberhauser, *Organometallics* **2003**, *22*, 4281 – 4285; b) A. Marson, A. B. van Oort, W. P. Mul, *Eur. J. Inorg. Chem.* **2002**, 3028 – 3031.
[85] C. Amatore, A. Jutand, A. Thuilliez, *Organometallics* **2001**, *20*, 3241 – 3249.
[86] E.-i. Negishi, T. Takahashi, K. Akiyoshi, *J. Chem. Soc. Chem. Commun.* **1986**, 1338 – 1339.
[87] M. T. Reetz, G. Lohmer, R. Schwickardi, *Angew. Chem.* **1998**, *110*, 492 – 495; *Angew. Chem. Int. Ed.* **1998**, *37*, 481 – 483.
[88] C. Amatore, M. Azzabi, A. Jutand, *J. Organomet. Chem.* **1989**, *363*, C41 – C45.
[89] C. Amatore, M. Azzabi, A. Jutand, *J. Am. Chem. Soc.* **1991**, *113*, 8375 – 8384.
[90] C. Amatore, A. Jutand, A. Suarez, *J. Am. Chem. Soc.* **1993**, *115*, 9531 – 9541.
[91] C. Amatore, E. Carré, A. Jutand, H. Tanaka, Q. Ren, S. Torii, *Chem. Eur. J.* **1996**, *2*, 957 – 966.
[92] A. Jutand, S. Négri, J. G. de Vries, *Eur. J. Inorg. Chem.* **2002**, 1711 – 1717.
[93] A. Jutand, A. Mosleh, *Organometallics* **1995**, *14*, 1810 – 1817.
[94] V. V. Grushin, H. Alper, *J. Am. Chem. Soc.* **1995**, *117*, 4305 – 4315.
[95] a) K. Nagayama, F. Kawataka, M. Sakamoto, I. Shimizu, A. Yamamoto, *Chem. Lett.* **1995**, 367 – 368; b) K. Nagayama, F. Kawataka, M. Sakamoto, I. Shimizu, A. Yamamoto, *Bull. Chem. Soc. Jpn.* **1999**, *72*, 573 – 580; c) A. Yamamoto, Y. Kayaki, K. Nagayama, I. Shimizu, *Synlett* **2000**, 925 – 937.
[96] A. L. Casado, P. Espinet, A. M. Gallego, *J. Am. Chem. Soc.* **2000**, *122*, 11771 – 11782.
[97] A. L. Casado, P. Espinet, A. M. Gallego, J. M. Martínez-Ilarduya, *Chem. Commun.* **2001**, 339 – 340.
[98] A. Jutand, S. Négri, *Organometallics* **2003**, *22*, 4229 – 4237.
[99] a) A. H. Roy, J. F. Hartwig, *J. Am. Chem. Soc.* **2003**, *125*, 8704 – 8705; b) A. H. Roy, J. F. Hartwig, *Organometallics* **2004**, *23*, 194 – 202.
[100] For a Review of cross-coupling reactions of aryl chlorides, see: A. F. Littke, G. C. Fu, *Angew. Chem.* **2002**, *114*, 4350 – 4386; *Angew. Chem. Int. Ed.* **2002**, *41*, 4177 – 4211.
[101] The Stille coupling of activated aryl fluorides was recently found to be possible with [$Pd(PPh_3)_4$] as the catalyst: Y. M. Kim, S. Yu, *J. Am. Chem. Soc.* **2003**, *125*, 1696 – 1697.
[102] For Highlights on the coupling of alkyl electrophiles, see: a) D. J. Cárdenas, *Angew. Chem.* **1999**, *111*, 3201 – 3203; Angew. *Chem. Int. Ed.* **1999**, *38*, 3018 – 3020; b) D. J. Cárdenas, *Angew. Chem.* **2003**, *115*, 398 – 401; Angew. *Chem. Int. Ed.* **2003**, *42*, 384 – 387.
[103] V. V. Grushin, H. Alper, *Chem. Rev.* **1994**, *94*, 1047 – 1062.
[104] a) Y. Ben-David, M. Portnoy, D. Milstein, *J. Am. Chem. Soc.* **1989**, *111*, 8742 – 8743; b) Y. Ben-David, M. Portnoy, D. Milstein, *J. Chem. Soc. Chem. Commun.* **1989**, 1816 – 1817; c) Y. Ben-David, M. Portnoy, M. Gozin, D. Milstein, *Organometallics* **1992**, *11*, 1995 – 1996.
[105] a) For reviews of the palladium-catalyzed amination of aryl electrophiles, see: J. F. Hartwig, *Angew. Chem.* **1998**, *110*, 2154 – 2177; *Angew. Chem. Int. Ed.* **1998**, *37*, 2046 – 2067; b) M. Yamashita, J. V. Cuevas Vicario, J. F. Hartwig, *J. Am. Chem. Soc.* **2003**, *125*, 16347 – 16360, and references therein.
[106] a) B. C. Hamann, J. F. Hartwig, *J. Am. Chem. Soc.* **1997**, *119*, 12382 – 12383; b) B. C. Hamann, J. F. Hartwig, *J. Am. Chem. Soc.* **1998**, *120*, 7369 – 7370; c) B. C. Hamann, J. F. Hartwig, *J. Am. Chem. Soc.* **1998**, *120*, 3694 – 3703; d) M. Kawatsura, J. F. Hartwig, *J. Am. Chem. Soc.* **1999**, *121*, 1473 – 1478.
[107] J. F. Hartwig, *Acc. Chem. Res.* **2003**, *36*, 234 – 245.
[108] a) M. Palucki, S. L. Buchwald, *J. Am. Chem. Soc.* **1997**, *119*, 11108 – 11109; b) J. Åhman, J. P. Wolfe, M. V. Troutman, M. Palucki, S. L. Buchwald, *J. Am. Chem. Soc.* **1998**, *120*, 1918 – 1919.
[109] A recent mechanistic study on the palladium-catalyzed amination of chloroarenes in the presence of bulky ligands, such as **13c**, shows that the high reactivity of the catalysts formed in situ correlates with the steady-state concentration of active Pd and the ligand size: E. R. Strieter, D. G. Blackmond, S. L. Buchwald, *J. Am. Chem. Soc.* **2003**, *125*, 13978 – 13980.
[110] a) X. Bei, H. W. Turner, W. H. Weinberg, A. S. Guram, *J. Org. Chem.* **1999**, *64*, 6797 – 6803; b) X. Bei, T. Uno, J. Norris, H. W. Turner, W. H. Weinberg, A. S. Guram, J. L. Petersen, *Organometallics* **1999**, *18*, 1840 – 1853; c) X. Bei, A. S. Guram, H. W. Turner, W. H. Weinberg, *Tetrahedron Lett.* **1999**, *40*, 1237 – 1241.
[111] a) X. Bei, T. Crevier, A. S. Guram, B. Jandeleit, T. S. Powers, H. W. Turner, T. Uno, W. H. Weinberg, *Tetrahedron Lett.* **1999**, *40*, 3855 – 3858; b) X. Bei, H. W. Turner, W. H. Weinberg, A. S. Guram, J. L. Petersen, *J. Org. Chem.* **1999**, *64*, 6797 – 6803.
[112] a) T. Yamamoto, O. Saito, A. Yamamoto, *J. Am. Chem. Soc.* **1981**, *103*, 5600 – 5602; b) T. Yamamoto, M. Akimoto, A. Yamamoto, *Chem. Lett.* **1983**, 1725 – 1726; c) T. Yamamoto, M. Akimoto, O. Saito, A. Yamamoto, *Organometallics* **1986**, *5*, 1559 – 1567.
[113] For Suzuki cross-coupling reactions, see: A. F. Littke, G. C. Fu, *Angew. Chem.* **1998**, *110*, 3586 – 3587; *Angew. Chem. Int. Ed.* **1998**, *37*, 3387 – 3388.
[114] For Heck reactions, see: a) A. F. Litke, G. C. Fu, *J. Org. Chem.* **1999**, *64*, 10 – 11; b) A. F. Litke, G. C. Fu, *J. Am. Chem. Soc.* **2001**, *123*, 6989 – 7000.
[115] For the amination of aryl bromides and aryl chlorides with [$Pd(PtBu_3)_2$], see: a) M. Nishiyama, T. Yamamoto, Y. Koie, *Tetrahedron Lett.* **1998**, *39*, 617 – 620; b) T. Yamamoto, M. Nishiyama, Y. Koie, *Tetrahedron Lett.* **1998**, *39*, 2367 – 2370; c) J. F. Hartwig, M. Kawatsura, S. I. Hauck, K. H. Shaughnessy,

 © 2004 Wiley-VCH Verlag GmbH & Co. KGaA, Weinheim

L. M. Alcazar-Roman, *J. Org. Chem.* **1999**, *64*, 5575 – 5580; d) R. Kuwano, M. Utsunomiya, J. F. Hartwig, *J. Org. Chem.* **2002**, *67*, 6479 – 6486.

[116] For other related phosphanes for the activation of aryl chlorides, see: a) G. Y. Li, *J. Org. Chem.* **2002**, *67*, 3643 – 3650; b) G. Y. Li, G. Zheng, A. F. Noonan, *J. Org. Chem.* **2001**, *66*, 8677 – 8681; c) G. Y. Li, *Angew. Chem.* **2001**, *113*, 1561 – 1564; *Angew. Chem. Int. Ed.* **2001**, *40*, 1513 – 1516; d) A. Zapf, A. Ehrentraut, M. Beller, *Angew. Chem.* **2000**, *112*, 4315 – 4317; *Angew. Chem. Int. Ed.* **2000**, *39*, 4153 – 4155; e) S.-Y. Liu, M. J. Choi, G. C. Fu, *Chem. Commun.* **2001**, 2408 – 2409; f) S. Urgaonkar, M. Nagarajan, J. G. Verkade, *Tetrahedron Lett.* **2002**, *43*, 8921 – 8924.

[117] a) Water-soluble palladium complexes of di-*tert*-butylphosphinous acid (tBu$_2$P(OH)) catalyze the Stille coupling of aryl chlorides in water: C. Wolf, R. Lerebours, *J. Org. Chem.* **2003**, *68*, 7551 – 7554; b) see also: C. Wolf, R. Lerebours, E. H. Tanzini, *Synlett* **2003**, 2069 – 2073.

[118] Trialkyl phosphonium salts are practical alternatives to air-sensitive phosphanes: M. R. Netherton, G. C. Fu, *Org. Lett.* **2001**, *3*, 4295 – 4298.

[119] a) S. R. Stauffer, N. A. Beare, J. P. Stambuli, J. F. Hartwig, *J. Am. Chem. Soc.* **2001**, *123*, 4641 – 4642; b) N. A. Beare, J. F. Hartwig, *J. Org. Chem.* **2002**, *67*, 541 – 555.

[120] a) D. W. Old, J. P. Wolfe, S. L. Buchwald, *J. Am. Chem. Soc.* **1998**, *120*, 9722 – 9723; b) J. P. Wolfe, S. L. Buchwald, *Angew. Chem.* **1999**, *111*, 2570 – 2573; *Angew. Chem. Int. Ed.* **1999**, *38*, 2413 – 2416; c) M. C. Harris, S. L. Buchwald, *J. Org. Chem.* **2000**, *65*, 5327 – 5333.

[121] J. P. Wolfe, R. A. Singer, B. H. Yang, S. L. Buchwald, *J. Am. Chem. Soc.* **1999**, *121*, 9550 – 9561.

[122] H. N. Nguyen, X. Huang, S. L. Buchwald, *J. Am. Chem. Soc.* **2003**, *125*, 11 118 – 11 819.

[123] N. Kataoka, Q. Shelby, J. P. Stambuli, J. F. Hartwig, *J. Org. Chem.* **2002**, *67*, 5553 – 5566.

[124] M. Gómez Andreu, A. Zapf, M. Beller, *Chem. Commun.* **2000**, 2475 – 2476.

[125] For Suzuki coupling reactions with Pd^0 complexes of 15-membered macrocyclic trienes, see: a) J. Cortès, M. Moreno-Mañas, R. Pleixats, *Eur. J. Org. Chem.* **2000**, 239 – 243; b) A. Llobet, E. Masllorens, M. Moreno-Mañas, A. Pla-Quintana, M. Rodríguez, A. Roglans, *Tetrahedron Lett.* **2002**, *43*, 1425 – 1428.

[126] Recently, [PdL$_2$(ma)] (L = σ-donor ligands, ma = maleic anhydride) complexes were prepared as useful catalyst precursors: A. M. Kluwer, C. J. Elsevier, M. Bühl, M. Lutz, A. L. Spek, *Angew. Chem.* **2003**, *115*, 3625 – 3628; *Angew. Chem. Int. Ed.* **2003**, *42*, 3501 – 3504.

[127] K. Menzel, G. C. Fu, *J. Am. Chem. Soc.* **2003**, *125*, 3718 – 3719.

[128] H. Tang, K. Menzel, G. C. Fu, *Angew. Chem.* **2003**, *115*, 5233 – 5236; *Angew. Chem. Int. Ed.* **2003**, *42*, 5079 – 5082.

[129] I. D. Hills, M. R. Netherton, G. C. Fu, *Angew. Chem.* **2003**, *115*, 5927 – 5930; *Angew. Chem. Int. Ed.* **2003**, *42*, 5749 – 5752.

[130] J. H. Kirchhoff, M. R. Netherton, I. D. Hills, G. C. Fu, *J. Am. Chem. Soc.* **2002**, *124*, 13 662 – 13 663.

[131] a) For the Sonogashira coupling of alkyl electrophiles in the presence of carbene ligands, see: M. Eckhardt, G. C. Fu, *J. Am. Chem. Soc.* **2003**, *125*, 13 642 – 13 643; b) for the palladium-catalyzed cross-coupling of alkyl electrophiles with organozirconium reagents under "ligandless" conditions, see: S. L. Wiskur, A. Korte, G. C. Fu, *J. Am. Chem. Soc.* **2004**, *126*, 82 – 83; c) for the coupling of secondary halides with organozinc reagents in the presence of nickel catalysts, see: J. Zhou, G. C. Fu, *J. Am. Chem. Soc.* **2004**, *126*, 14 726 – 14 727.

[132] A. F. Littke, L. Schwarz, G. C. Fu, *J. Am. Chem. Soc.* **2002**, *124*, 6343 – 6348.

[133] For coupling reactions with fluorostannates, see: a) A. García-Martínez, J. O. Barcina, Á. de Fresno Cerezo, L. R. Subramanian, *Synlett* **1994**, 1047 – 1048; b) A. García-Martínez, J. O. Barcina, M. R. Colorado Heras, Á. de Fresno Cerezo, *Org. Lett.* **2000**, *2*, 1377 – 1378; c) E. Fouquet, M. Pereyre, A. L. Rodriguez, *J. Org. Chem.* **1997**, *62*, 5242 – 5243; d) E. Fouquet, A. L. Rodriguez, *Synlett* **1998**, 1323 – 1324.

[134] G. B. Smith, G. C. Dezeny, D. L. Hughes, A. O. King, T. R. Verhoeven, *J. Org. Chem.* **1994**, *59*, 8151 – 8156.

[135] F. Paul, J. Patt, J. F. Hartwig, *Organometallics* **1995**, *14*, 3030 – 3039.

[136] F. Paul, J. Patt, J. F. Hartwig, *J. Am. Chem. Soc.* **1994**, *116*, 5969 – 5970.

[137] J. F. Hartwig, F. Paul, *J. Am. Chem. Soc.* **1995**, *117*, 5373 – 5374.

[138] A. H. Roy, J. F. Hartwig, *J. Am. Chem. Soc.* **2003**, *125*, 13 944 – 13 945.

[139] A. H. Roy, J. F. Hartwig, *J. Am. Chem. Soc.* **2001**, *123*, 1232 – 1233.

[140] E. Galardon, S. Ramdeehul, J. M. Brown, A. Cowley, K. K. Hii, A. Jutand, *Angew. Chem.* **2002**, *114*, 1838 – 1841; *Angew. Chem. Int. Ed.* **2002**, *41*, 1760 – 1763.

[141] S. Otsuka, T. Yoshida, M. Matsumoto, K. Nakatsu, *J. Am. Chem. Soc.* **1976**, *98*, 5850 – 5858.

[142] S. M. Reid, R. C. Boyle, J. T. Mague, M. J. Fink, *J. Am. Chem. Soc.* **2003**, *125*, 7816 – 7817.

[143] J. P. Stambuli, M. Bühl, J. F. Hartwig, *J. Am. Chem. Soc.* **2002**, *124*, 9346 – 9347.

[144] U. K. Singh, E. R. Strieter, D. G. Blackmond, S. L. Buchwald, *J. Am. Chem. Soc.* **2002**, *124*, 14 104 – 14 114.

[145] Y. Mori, M. Seki, *J. Org. Chem.* **2003**, *68*, 1571 – 1574.

[146] B. M. Choudary, S. Madhi, N. S. Chowdari, M. L. Kantam, B. Sreedhar, *J. Am. Chem. Soc.* **2002**, *124*, 14 127 – 14 136.

[147] For Suzuki coupling reactions in the absence of ligands, see: a) T. I. Wallow, B. M. Novak, *J. Org. Chem.* **1994**, *59*, 5034 – 5037; b) I. Fenger, C. Le Drian, *Tetrahedron Lett.* **1998**, *39*, 4287 – 4290; c) S.-B. Jang, *Tetrahedron Lett.* **1997**, *38*, 1793 – 1796; d) D. Badone, M. Baroni, R. Cardamone, A. Ielmini, U. Guzzi, *J. Org. Chem.* **1997**, *62*, 7170 – 7173; e) S. Wendeborn, S. Berteina, W. K.-D. Brill, A. De Mesmaeker, *Synlett* **1998**, 671 – 675; f) R. Narayanan, M. A. El-Sayed, *J. Am. Chem. Soc.* **2003**, *125*, 8340 – 8347.

[148] Intriguingly, the Suzuki reaction of aryl iodides and aryl bromides with some aryl boronic acids has been carried out in the absence of a metal as a catalyst in water at 150 °C (microwave irradiation): a) N. E. Leadbeater, M. Marco, *Angew. Chem.* **2003**, *115*, 1445 – 1447; *Angew. Chem. Int. Ed.* **2003**, *42*, 1407 – 1409; b) N. E. Leadbeater, M. Marco, *J. Org. Chem.* **2003**, *68*, 5660 – 5667; c) Sonogashira coupling reactions also take place under similar palladium-free conditions: N. E. Leadbeater, M. Marco, B. J. Tominack, *Org. Lett.* **2003**, *5*, 3919 – 3922; d) for a comment and mechanistic proposal, see: C.-J. Li, *Angew. Chem.* **2003**, *115*, 5004 – 5006; *Angew. Chem. Int. Ed.* **2003**, *42*, 4856 – 4858.

[149] A. H. M. de Vries, J. M. C. A. Mulders, J. H. M. Mommers, H. J. W. Henderickx, J. G. de Vries, *Org. Lett.* **2003**, *5*, 3285 – 3288, and references therein.

[150] a) N. A. Bumagin, I. G. Bumagina, I. P. Beletskaya, *Dokl. Akad. Nauk SSSR* **1984**, *274*, 1103 – 1106; b) I. P. Beletskaya, *J. Organomet. Chem.* **1982**, *250*, 551 – 564.

[151] M. Moreno-Mañas, R. Pleixats, *Acc. Chem. Res.* **2003**, *36*, 638 – 643.

[152] For a recent leading reference on the mechanism of the Heck reaction with palladium metal, see: J. Le Bars, U. Specht, J. S. Bradley, D. G. Blackmond, *Langmuir* **1999**, *15*, 7621 – 7625.

[153] A. C. Albéniz, P. Espinet, B. Martín-Ruiz, D. Milstein, *J. Am. Chem. Soc.* **2001**, *123*, 11 504 – 11 505.

[154] For reviews, see: a) W. A. Herrmann, *Angew. Chem.* **2002**, *114*, 1342 – 1363; *Angew. Chem. Int. Ed.* **2002**, *41*, 1290 – 1309; b) L. Jafarpour, S. P. Nolan, *Adv. Organomet. Chem.* **2001**, *46*, 181 –

222; c) D. Bourissou, O. Guerret, F. P. Gabbaï, G. Bertrand, *Chem. Rev.* **2000**, *100*, 39 – 92; d) W. A. Herrmann, C. Köcher, *Angew. Chem.* **1997**, *109*, 2256 – 2282; *Angew. Chem. Int. Ed. Engl.* **1997**, *36*, 2162 – 2187.

[155] a) C. Zhang, J. Huang, M. L. Trudell, S. P. Nolan, *J. Org. Chem.* **1999**, *64*, 3804 – 3805; b) for recent applications of Suzuki coupling reactions, see: O. Navarro, R. A. Kelly, S. P. Nolan, *J. Am. Chem. Soc.* **2003**, *125*, 16194 – 16195, and references therein.

[156] K. Selvakumar, A. Zapf, A. Spannenberg, M. Beller, *Chem. Eur. J.* **2002**, *8*, 3901 – 3906.

[157] Y. Ma, C. Song, W. Jiang, Q. Wu, Y. Wang, X. Liu, M. B. Andrus, *Org. Lett.* **2003**, *5*, 3317 – 3319.

[158] a) D. S. McGuinness, M. J. Green, K. J. Cavell, B. W. Skelton, A. H. White, *J. Organomet. Chem.* **1998**, *565*, 165 – 178; b) D. S. McGuinness, K. J. Cavell, *Organometallics* **1999**, *18*, 1596 – 1605.

[159] S. Caddick, F. G. N. Cloke, P. B. Hitchcock, J. Leonard, A. K. de K. Lewis, D. McKerrecher, L. R. Titcomb, *Organometallics* **2002**, *21*, 4318 – 4319.

[160] J. Pytkowicz, S. Roland, P. Mangeney, G. Meyer, A. Jutand, *J. Organomet. Chem.* **2003**, *678*, 166 – 179.

[161] For reductive elimination reactions of σ-aryl palladium complexes stabilized by N-heterocyclic carbenes, see: W. J. Marshall, V. V. Grushin, *Organometallics* **2003**, *22*, 1591 – 1593.

[162] Known palladium–NHC complexes are μ_2-bridged dimers: a) M. S. Viciu, R. M. Kissling, E. D. Stevens, S. P. Nolan, *Org. Lett.* **2002**, *4*, 2229 – 2231; b) C. W. K. Gstöttmayr, V. P. W. Bohm, E. Herdtweck, M. Grosche, W. A. Herrmann, *Angew. Chem.* **2002**, *114*, 1421 – 1423; *Angew. Chem. Int. Ed.* **2002**, *41*, 1363 – 1365.

[163] A. K. K. Lewis, S. Caddick, F. G. N. Cloke, N. C. Billingham, P. B. Hitchcock, J. Leonard, *J. Am. Chem. Soc.* **2003**, *125*, 10066 – 10073.

[164] J. Dupont, M. Pfeffer, J. Spencer, *Eur. J. Inorg. Chem.* **2001**, 1917 – 1927.

[165] R. B. Bedford, *Chem. Commun.* **2003**, 1787 – 1796.

[166] A. Schnyder, A. F. Indolese, M. Studer, H.-U. Blaser, *Angew. Chem.* **2002**, *114*, 3820 – 3823; *Angew. Chem. Int. Ed.* **2002**, *41*, 3668 – 3671.

[167] a) D. A. Alonso, C. Nájera, M. C. Pacheco, *Org. Lett.* **2000**, *2*, 1823 – 1826; b) D. A. Alonso, C. Nájera, M. C. Pacheco, *J. Org. Chem.* **2002**, *67*, 5588 – 5594; c) D. A. Alonso, C. Nájera, M. C. Pacheco, *Adv. Synth. Catal.* **2002**, *344*, 172 – 183; d) L. Botella, C. Najera, *Angew. Chem.* **2002**, *114*, 187 – 189; *Angew. Chem. Int. Ed.* **2002**, *41*, 179 – 181.

[168] a) M. Beller, H. Fischer, W. A. Herrmann, K. Öfele, C. Brossmer, *Angew. Chem.* **1995**, *107*, 1992 – 1993; *Angew. Chem. Int. Ed. Engl.* **1995**, *34*, 1848 – 1849; b) S. Gibson, D. F. Foster, G. R. Eastham, R. P. Tooze, D. J. Cole-Hamilton, *Chem. Commun.* **2001**, 779 – 780; c) D. A. Albisson, R. B. Bedford, S. E. Lawrence, P. N. Scully, *Chem. Commun.* **1998**, 2095 – 2096; d) R. B. Bedford, S. L. Welch, *Chem. Commun.* **2001**, 129 – 130; e) R. B. Bedford, S. M. Draper, P. N. Scully, S. L. Welch, *New J. Chem.* **2000**, *24*, 745 – 746; f) D. Zim, A. S. Gruber, G. Ebeling, J. Dupont, A. L. Monteiro, *Org. Lett.* **2000**, *2*, 2881 – 2884; g) H. Weissman, D. Milstein, *Chem. Commun.* 1999, 1901 – 1902.

[169] I. P. Beletskaya, A. N. Kashin, N. B. Karlstedt, A. V. Mitin, A. V. Cheprakov, G. M. Kazankov, *J. Organomet. Chem.* **2001**, *622*, 89 – 96.

[170] M. P. Muñoz, B. Martín-Matute, C. Fernández-Rivas, D. J. Cárdenas, A. M. Echavarren, *Adv. Synth. Catal.* **2001**, *343*, 338 – 342.

[171] C. S. Consorti, M. L. Zanini, S. Leal, G. Ebeling, J. Dupont, *Org. Lett.* **2003**, *5*, 983 – 986.

[172] C. Rocaboy, J. A. Gladysz, *New J. Chem.* **2003**, *27*, 39 – 49.

[173] a) T. Rosner, J. Le Bars, A. Pfaltz, D. G. Blackmond, *J. Am. Chem. Soc.* **2001**, *123*, 1848 – 1855; b) T. Rosner, A. Pfaltz, D. G. Blackmond, *J. Am. Chem. Soc.* **2001**, *123*, 4621 – 4622.

[174] A. S.-Y. Lee, W.-C. Dai, *Tetrahedron* **1997**, *53*, 859 – 868, and references therein.

[175] A Grignard reagent with an asymmetric α carbon atom was shown to undergo the Kumada coupling in the presence of Pd^0 or Ni^0 catalysts with full retention of configuration. However, the use of $[Fe(acac)_3]$ or $[Co(acac)_2]$ led to extensive racemization: B. Hölzer, R. W. Hoffmann, *Chem. Commun.* **2003**, 732 – 733.

[176] J. A. Casares, P. Espinet, G. Salas, *Chem. Eur. J.* **2002**, *8*, 4843 – 4853.

[177] a) R. Cross, *Ligand substitution reactions of square-planar molecules*, The Royal Society of Chemistry, London, **1985**; b) R. Cross, *Adv. Inorg. Chem.* **1989**, *34*, 219 – 292.

[178] R. Romeo, *Comments Inorg. Chem.* **1990**, *11*, 21 – 57.

[179] J. A. Casares, S. Coco, P. Espinet, Y.-S. Lin, *Organometallics* **1995**, *14*, 3058 – 3067.

[180] J. Burguess, C. D. Hubbard, *Adv. Inorg. Chem.* **2003**, *54*, 71 – 155.

[181] U. Frey, L. Helm, A. E. Merbach, R. Romeo, *J. Am. Chem. Soc.* **1989**, *111*, 8161 – 8165.

[182] R. Romeo, A. Grassi, L. Monsù Scholaro, *Inorg. Chem.* **1992**, *31*, 4383.

[183] This observation is true at least for conventional ligands. See, however, the reports by Roy and Hartwig for complexes with hindered alkyl phosphanes,[138,139] in which the high basicity of the phosphane and the high axial protection that it exerts on the Pd center seem to induce dissociative ligand substitution. For a change of mechanism to dissociative substitution associated with axial protection of the Pd center, see: C. Bartolomé, P. Espinet, J. M. Martín-Álvarez, F. Villafañe, *Eur. J. Inorg. Chem.* **2004**, 2326 – 2337.

[184] P. J. Stang, M. H. Kowalski, M. D. Schiavelli, D. Longford, *J. Am. Chem. Soc.* **1989**, *111*, 3347 – 3356.

[185] P. J. Stang, M. H. Kowalski, *J. Am. Chem. Soc.* **1989**, *111*, 3356 – 3362.

[186] For the transmetalation of *trans*-$[PtPhFL_2]$ ($L = PPh_3$, PMe_2Ph) with $PhSnMe_3$, see: P. Nilsson, F. Plamper, O. F. Wendt, *Organometallics* **2003**, *22*, 5235 – 5242.

[187] J. Louie, J. F. Hartwig, *J. Am. Chem. Soc.* **1995**, *117*, 11598 – 11599.

[188] A. L. Casado, P. Espinet, *J. Am. Chem. Soc.* **1998**, *120*, 8978 – 8985.

[189] C. Amatore, A. A. Bahsoun, A. Jutand, G. Meyer, A. N. Ntepe, L. Ricard, *J. Am. Chem. Soc.* **2003**, *125*, 4212 – 4222.

[190] a) D. J. Cárdenas, C. Mateo, A. M. Echavarren, *Angew. Chem.* **1994**, *106*, 2529 – 2531; *Angew. Chem. Int. Ed. Engl.* **1994**, *33*, 2445 – 2447; b) C. Mateo, D. J. Cárdenas, C. Fernández-Rivas, A. M. Echavarren, *Chem. Eur. J.* **1996**, *2*, 1596 – 1606.

[191] C. Mateo, C. Fernández-Rivas, A. M. Echavarren, D. J. Cárdenas, *Organometallics* **1997**, *16*, 1997 – 1999.

[192] For platinum catalysts in Suzuki-type reactions, see: R. B. Bedford, S. L. Hazelwood, D. A. Albisson, *Organometallics* **2002**, *21*, 2599 – 2600.

[193] W. D. Cotter, L. Barbour, K. L. McNamara, R. Hechter, R. J. Lachicotte, *J. Am. Chem. Soc.* **1998**, *120*, 11016 – 11017.

[194] For an earlier observation of diaryl palladium(II) complexes, see: G. W. Parshall, *J. Am. Chem. Soc.* **1974**, *96*, 2360 – 2366.

[195] a) A. O. Aliprantis, J. W. Canary, *J. Am. Chem. Soc.* **1994**, *116*, 6985 – 6986; b) see also: M. A. Aramendia, F. Lafont, M. Moreno-Mañas, R. Pleixats, A. Roglans, *J. Org. Chem.* **1999**, *64*, 3592 – 3594.

[196] In closely related $[PdR_2L_2]$ systems, the main barrier to *cis–trans* isomerization is not the dissociation of L, but the *cis–trans*

 © 2004 Wiley-VCH Verlag GmbH & Co. KGaA, Weinheim

topomerization of the three-coordinate species: A. L. Casado, J. A. Casares, P. Espinet, *Inorg. Chem.* **1998**, *37*, 4154 – 4156.
[197] A. C. Albéniz, P. Espinet, B. Martín-Ruiz, *Chem. Eur. J.* **2001**, *7*, 2481 – 2489.
[198] A. Ricci, A. Angelucci, M. Bassetti, C. Lo Sterzo, *J. Am. Chem. Soc.* **2002**, *124*, 1060 – 1071.
[199] a) C. Lo Sterzo, M. M. Miller, J. K. Stille, *Organometallics* **1989**, *8*, 2331 – 2337; b) C. Lo Sterzo, J. K. Stille, *Organometallics* **1990**, *9*, 687 – 694; c) C. Lo Sterzo, G. Bocelli, *J. Chem. Soc. Dalton Trans.* **1991**, 1881 – 1885; d) C. Lo Sterzo, *Organometallics* **1990**, *9*, 3185 – 3188; e) C. Lo Sterzo, G. Bandoli, A. Dolmella, *J. Chem. Soc. Dalton Trans.* **1992**, 697 – 701.
[200] a) R. Crescenzi, C. Lo Sterzo, *Organometallics* **1992**, *11*, 4301 – 4305; b) E. Viola, C. Lo Sterzo, R. Crescenzi, G. Frachey, *J. Organomet. Chem.* **1995**, *493*, 55 – 59; c) E. Viola, C. Lo Sterzo, R. Crescenzi, G. Frachey, *J. Organomet. Chem.* **1995**, *493*, C9 – C13; d) E. Viola, C. Lo Sterzo, F. Trezzi, *Organometallics* **1996**, *15*, 4352 – 4354; e) A. Buttinelli, E. Viola, E. Antonelli, C. Lo Sterzo, *Organometallics* **1998**, *17*, 2574 – 2582.
[201] a) L. Spadoni, C. Lo Sterzo, R. Crescenzi, G. Frachey, *Organometallics* **1995**, *14*, 3149 – 3151; b) P. Cianfriglia, V. Narducci, C. Lo Sterzo, E. Viola, G. Bocelli, T. A. Kodenkandath, *Organometallics* **1996**, *15*, 5220 – 5230; c) S. Tollis, V. Narducci, P. Cianfriglia, C. Lo Sterzo, E. Viola, *Organometallics* **1998**, *17*, 2388 – 2390; d) F. Angelucci, A. Ricci, C. Lo Sterzo, D. Masi, C. Bianchini, G. Bocelli *Organometallics* **2002**, *21*, 3001 – 3008.
[202] W. Baratta, S. Stoccoro, A. Doppiu, E. Herdtweck, A. Zucca, P. Rigo, *Angew. Chem.* **2003**, *115*, 109 – 113; *Angew. Chem. Int. Ed.* **2003**, *42*, 105 – 108.
[203] a) M. R. Netherton, M. R. C. Dai, K. Neuschütz, G. C. Fu, *J. Am. Chem. Soc.* **2001**, *123*, 10099 – 10100; b) A. C. Frisch, N. Shaikh, A. Zapf, M. Beller, *Angew. Chem.* **2002**, *114*, 4218 – 4221; *Angew. Chem. Int. Ed.* **2002**, *41*, 4056 – 4059; c) M. R. Netherton, G. C. Fu, *Angew. Chem.* **2002**, *114*, 4066 – 4068; *Angew. Chem. Int. Ed.* **2002**, *41*, 3910 – 3912; d) J.-Y. Lee, G. C. Fu, *J. Am. Chem. Soc.* **2003**, *125*, 5616 – 5617; e) J. Zhou, G. C. Fu, *J. Am. Chem. Soc.* **2003**, *125*, 12527 – 12530.
[204] Q.-S. Hu, Y. Lu, Z.-Y. Tang, H.-B. Yu, *J. Am. Chem. Soc.* **2003**, *125*, 2856 – 2857.
[205] M. Yamashita, J. F. Hartwig, *J. Am. Chem. Soc.* **2004**, *126*, 5344 – 5345.
[206] K. Osakada, T. Yamamoto, *Coord. Chem. Rev.* **2000**, *198*, 379 – 399.
[207] Both the ability of Sn^{IV} to increase its coordination number and the formation of single-bridged compounds are well documented: a) A. G. Davies in *Comprehensive Organometallic Chemistry II*, *Vol. 2* (Eds.: E. W. Abel, F. G. A. Stone, G. Wilkinson), Pergamon, Oxford, **1995**, chap. 6.4 and 6.5; b) P. G. Harrison in *Comprehensive Coordination Chemistry*, *Vol. 3* (Eds.: G. Wilkinson, R. D. Gillard, J. A. McCleverty), Pergamon, Oxford, **1987**, chap. 26.3.4; c) A. G. Davies, P. J. Smith in *Comprehensive Organometallic Chemistry*, *Vol. 2* (Eds.: G. Wilkinson, F. G. A. Stone, E. W. Abel), Pergamon, Oxford, **1982**, chap. 11.4.4.2.
[208] For R-bridging structures characterized by X-ray diffraction, see: a) R. Usón, J. Forniés, L. R. Falvello, M. Tomás, J. M. Casas, A. Martín, F. A. Cotton, *J. Am. Chem. Soc.* **1994**, *116*, 7160 – 7165; b) R. Usón, J. Forniés, M. Tomás, J. M. Casas, F. A. Cotton, L. R. Falvello, X. Feng, *J. Am. Chem. Soc.* **1993**, *115*, 4145 – 4154; c) R. Usón, J. Forniés, M. Tomás, J. M. Casas, P. Navarro, *J. Chem. Soc. Dalton Trans.* **1989**, 169 – 172; d) R. Usón, J. Forniés, M. Tomás, J. M. Casas, *Organometallics* **1988**, *7*, 2279 – 2285.
[209] J. M. Brown, K. K. Hii, *Angew. Chem.* **1996**, *108*, 679 – 682; *Angew. Chem. Int. Ed. Engl.* **1996**, *35*, 657 – 659.
[210] W. J. Scott, J. K. Stille, *J. Am. Chem. Soc.* **1986**, *108*, 3033 – 3040.
[211] a) A. M. Echavarren, J. K. Stille, *J. Am. Chem. Soc.* **1987**, *109*, 5478 – 5486; b) J. K. Stille, A. M. Echavarren, R. M. Williams, J. A. Hendrix, *Org. Synth.* **1993**, *71*, 97 – 106.
[212] However, LiCl retards some intramolecular couplings: a) E. Piers, R. W. Friesen, B. A. Keay, *J. Chem. Soc. Chem. Commun.* **1985**, 809 – 810; b) E. Piers, R. W. Friesen, *J. Org. Chem.* **1986**, *51*, 3405 – 3406.
[213] N. A. Powell, S. D. Rychnovsky, *Tetrahedron Lett.* **1996**, *37*, 7901 – 7904.
[214] For the transmetalation of hypercoordinated aryl trialkyl silanes and aryl trialkyl stannanes with Pd^{II} and Pt^{II} complexes, see: P. Steenwinkel, J. T. B. H. Jastrzebski, B.-J. Deelman, D. M. Grove, H. Kooijman, N. Veldman, W. J. J. Smeets, A. L. Spek, G. van Koten, *Organometallics* **1997**, *16*, 5486 – 5498, and references therein.
[215] a) A. I. Roshchin, N. A. Bumagin, I. P. Beletskaya, *Tetrahedron Lett.* **1995**, *36*, 125 – 128; b) R. Rai, K. B. Aubrecht, D. B. Collum, *Tetrahedron Lett.* **1995**, *36*, 3111 – 3114.
[216] K. Matos, J. A. Soderquist, *J. Org. Chem.* **1998**, *63*, 461 – 470.
[217] T. Hayashi, M. Takahashi, Y. Takaya, M. Ogasawara, *J. Am. Chem. Soc.* **2002**, *124*, 5052 – 5058, and references therein.
[218] J. M. Brown, M. Pearson, J. T. B. H. Jastrzebski, G. van Koten, *J. Chem. Soc. Chem. Commun.* **1992**, 1440 – 1441.
[219] E. Vedejs, A. R. Haigt, W. O. Moss, *J. Am. Chem. Soc.* **1992**, *114*, 6556 – 6558.
[220] a) M. S. Jensen, C. Yang, Y. Hsiao, N. Rivera, K. M. Wells, J. Y. L. Chung, N. Yasuda, D. L. Hughes, P. J. Reider, *Org. Lett.* **2000**, *2*, 1981 – 1984; b) H. L. Sebahar, K. Yoshida, L. S. Hegedus, *J. Org. Chem.* **2002**, *67*, 3788 – 3795.
[221] Intramolecular coordination by an amine also facilitates the transmetalation of less reactive organobismuth compounds with aryl bromides: S. Shimada, O. Yamazaki, T. Tanaka, M. L. N. Rao, Y. Suzuki, M. Tanaka, *Angew. Chem.* **2003**, *115*, 1889 – 1892; *Angew. Chem. Int. Ed.* **2003**, *42*, 1845 – 1848.
[222] K. Itami, T. Kamei, J. Yoshida, *J. Am. Chem. Soc.* **2001**, *123*, 8773 – 8779.
[223] E. Napolitano, V. Farina, M. Persico, *Organometallics* **2003**, *22*, 4030 – 4037.
[224] J. M. Brown, N. A. Cooley, *Chem. Rev.* **1988**, *88*, 1031 – 1046.
[225] P. Dierkes, P. W. N. M. van Leeuwen, *J. Chem. Soc. Dalton Trans.* **1999**, 1519 – 1530.
[226] a) J. M. Brown, P. J. Guiry, *Inorg. Chim. Acta* **1994**, *220*, 249 – 259; b) J. S. Calhorda, J. M. Brown, N. A. Cooley, *Organometallics* **1991**, *10*, 1431 – 1438.
[227] The same effect has been observed in other reductive eliminations: a) G. Mann, D. Baranano, J. F. Hartwig, A. L. Rheingold, I. A. Guzei, *J. Am. Chem. Soc.* **1998**, *120*, 9205 – 9219; b) J. E. Marcone, K. G. Moloy, *J. Am. Chem. Soc.* **1998**, *120*, 8527 – 8528.
[228] For earlier studies, see: a) T. Hayashi, K. Tamao, Y. Katsuro, I. Nakae, M. Kumada, *Tetrahedron Lett.* **1979**, 1871 – 1874; b) T. Hayashi, M. Konishi, Y. Kobori, M. Kumada, T. Higuchi, K. Hirotsu, *J. Am. Chem. Soc.* **1984**, *106*, 158 – 163.
[229] M. Kranenburg, Y. E. M. van der Burgt, P. C. J. Kamer, P. W. N. M. van Leeuwen, *Eur. J. Inorg. Chem.* **1998**, 155 – 157.
[230] a) A. Goliaszewski, J. Schwartz, *Organometallics* **1985**, *4*, 417 – 419; b) A. Goliaszewski, J. Schwartz, *J. Am. Chem. Soc.* **1984**, *106*, 5028 – 5030; c) J. S. Temple, M. Riediker, J. Schwartz, *J. Am. Chem. Soc.* **1982**, *104*, 1310 – 1315; d) A. Goliaszewski, J. Schwartz, *Tetrahedron Lett.* **1985**, *26*, 5779 – 5789.
[231] R. Bertani, A. Berton, G. Carturan, R. Campostrini, *J. Organomet. Chem.* **1988**, *349*, 263 – 268.
[232] a) S. Numata, H. Kurosawa, *J. Organomet. Chem.* **1977**, *131*, 301 – 308; b) H. Kurosawa, K. Shiba, K. Hirako, K. Kakiuchi, I. Ikeda, *J. Chem. Soc. Chem. Commun.* **1994**, 1099 – 1100; c) H. Kurosawa, M. Emoto, Y. Kawasaki, *J. Organomet. Chem.* **1988**, *346*, 137 – 146; d) H. Kurosawa, M. Emoto, H. Ohnishi, K. Miki,

 © 2004 Wiley-VCH Verlag GmbH & Co. KGaA, Weinheim

N. Kasai, K. Tatsumi, A. Nakamura, *J. Am. Chem. Soc.* **1987**, *109*, 6333 – 6340.

[233] H. Kurosawa, H. Kajimaru, M.-A. Miyoshi, H. Ohnishi, I. Ikeda, *J. Mol. Catal.* **1992**, *74*, 481 – 488.

[234] R. Sutsman, J. Lau, M. Zipp, *Tetrahedron Lett.* **1986**, *27*, 5207 – 5210.

[235] a) B. M. Trost, E. Keinan, *Tetrahedron Lett.* **1980**, *21*, 2595 – 2598; b) E. Keinan, M. Peretz, *J. Org. Chem.* **1983**, *48*, 5302 – 5309.

[236] Allyl phosphates also couple with stannanes: M. Kosugi, K. Ohashi, K. Akuzawa, T. Nazazoe, H. Sano, T. Migia, *Chem. Lett.* **1987**, 1237 – 1238.

[237] J. Godschalx, J. K. Stille, *Tetrahedron Lett.* **1980**, *21*, 2599 – 2602.

[238] For the palladium-catalyzed carboxylative coupling of allyl stannanes with allyl chlorides, see: R. J. Franks, K. M. Nicholas, *Organometallics* **2000**, *19*, 1458 – 1460.

[239] For a review on allyl–allyl coupling, see: M. Méndez, A. M. Echavarren, *Eur. J. Org. Chem.* **2002**, 15 – 28.

[240] H. Nakamura, K. Aoyagi, J.-G. Shim, Y. Yamamoto, *J. Am. Chem. Soc.* **2001**, *123*, 372 – 377.

[241] K. J. Szabó, *Chem. Eur. J.* **2000**, *6*, 4413 – 4421.

[242] B. Henc, P. W. Jolly, R. Salz, S. Stobbe, G. Wilke, R. Benn, R. Mynott, K. Seevogel, R. Goddard, C. Kruger, *J. Organomet. Chem.* **1980**, *191*, 419 – 475.

[243] O. Kuhn, H. Mayr, *Angew. Chem.* **1999**, *111*, 356 – 358; *Angew. Chem. Int. Ed.* **1999**, *38*, 343 – 346.

[244] J. Krause, R. Goddard, R. Mynott, K.-R. Pörschke, *Organometallics* **2001**, *20*, 1992 – 1999, and references therein.

[245] P. W. Jolly, *Angew. Chem.* **1985**, *97*, 279 – 291; *Angew. Chem. Int. Ed. Engl.* **1985**, *24*, 283 – 295.

[246] J. Krause, W. Bonrath, K.-R. Pörschke, *Organometallics* **1992**, *11*, 1158 – 1167.

[247] M. Méndez, J. M. Cuerva, E. Gómez-Bengoa, D. J. Cárdenas, A. M. Echavarren, *Chem. Eur. J.* **2002**, *8*, 3620 – 3628.

[248] M. Bao, H. Nakamura, Y. Yamamoto, *J. Am. Chem. Soc.* **2001**, *123*, 759 – 760.

[249] D. K. Morita, J. K. Stille, J. R. Norton, *J. Am. Chem. Soc.* **1995**, *117*, 8576 – 8581.

[250] K.-C. Kong, C.-H. Cheng, *J. Am. Chem. Soc.* **1991**, *113*, 6313 – 6315.

[251] B. E. Segelstein, T. W. Butler, B. L. Chenard, *J. Org. Chem.* **1995**, *60*, 12 – 13.

[252] F. E. Goodson, T. I. Wallow, B. M. Novak, *J. Am. Chem. Soc.* **1997**, *119*, 12441 – 12453.

[253] V. V. Grushin, *Organometallics* **2000**, *19*, 1888 – 1900.

[254] See also: a) J. Vicente, A. Arcas, D. Bautista, A. Tiripicchio, M. Tiripicchio-Camellini, *New J. Chem.* **1996**, *20*, 345 – 356; b) J. Vicente, J. A. Abad, E. Martínez-Viviente, M. C. Ramírez - de Arellano, P. G. Jones, *Organometallics* **2000**, *19*, 752 – 760.

[255] A. L. casado, P. Espinet, *Organometallics* **1998**, *17*, 3677 – 3683.

[256] a) F. Ozawa, M. Fijimori, T. Yamamoto, A. Yamamoto, *Organometallics* **1986**, *5*, 2144 – 2149; b) F. Ozawa, T. Hidaka, T. Yamamoto, A. Yamamoto, *J. Organomet. Chem.* **1987**, *330*, 253 – 263; c) F. Ozawa, K. Kurihara, M. Fijimori, T. Hidaka, T. Toyoshima, A. Yamamoto, *Organometallics* **1989**, *8*, 180 – 188.

[257] a) T. Yagyu, M. Hamada, K. Osakada, T. Yamamoto, *Organometallics* **2001**, *20*, 1087 – 1101; b) Y. Suzaki, K. Osakada, *Organometallics* **2003**, *22*, 2193 – 2195.

[258] D. Milstein, J. K. Stille, *J. Am. Chem. Soc.* **1979**, *101*, 4981.

[259] R. van Asselt, C. J. Elsevier, *Organometallics* **1994**, *13*, 1972 – 1980.

[260] a) K. Kikukawa, H. Umekawa, T. Matsuda, *J. Organomet. Chem.* **1986**, *311*, C44 – C46; b) G. Stork, R. C. A. Isaacs, *J. Am. Chem. Soc.* **1990**, *112*, 7399 – 7400; c) C. A. Busacca, J. Swestock, R. E. Johnson, T. R. Bailey, L. Musza, C. A. Rodger, *J. Org. Chem.* **1994**, *59*, 7553 – 7556; d) V. Farina, M. A. Hossain, *Tetrahedron Lett.* **1996**, *37*, 6997 – 7000; e) S.-H. Chen, *Tetrahedron Lett.* **1997**, *38*, 4741 – 4744; f) T. Choshi, S. Yamada, J. Nobuhiro, Y. Mihara, E. Sugino, S. Hibino, *Heterocycles* **1998**, *48*, 11 – 14; g) P. Quayle, J. Wang, J. Xu, *Tetrahedron Lett.* **1998**, *39*, 489 – 492; h) A. Flohr, *Tetrahedron Lett.* **1998**, *39*, 5177 – 5180; i) W. Shen, L. Wang, *J. Org. Chem.* **1999**, *64*, 8873 – 8879.

[261] E. Fillion, N. J. Taylor, *J. Am. Chem. Soc.* **2003**, *125*, 12700 – 12701.

[262] For evidence for the involvement of palladium carbene or carbenoid intermediates, see: E. Fillion, N. J. Taylor, *J. Am. Chem. Soc.* **2003**, *125*, 12700 – 12701.

[263] a) E. Shirakawa, H. Yoshida, T. Hiyama, *Tetrahedron Lett.* **1997**, *38*, 5177; b) E. Shirakawa, T. Hiyama, *J. Organomet. Chem.* **1999**, *576*, 169; c) E. Shirakawa, H. Yoshida, T. Kurahashi, Y. Nakao, T. Hiyama, *J. Am. Chem. Soc.* **1998**, *120*, 2975 – 2976; d) H. Yoshida, E. Shirakawa, T. Kurahashi, Y. Nakao, T. Hiyama, *Organometallics* **2000**, *19*, 5671 – 5678; e) E. Shirakawa, Y. Murota, Y. Nakao, T. Hiyama, *Synlett* **1997**, 1143 – 1144; f) E. Shirakawa, Y. Nakao, Y. Murota, T. Hiyama, *J. Organomet. Chem.* **2003**, *670*, 132 – 136.

[264] Density functional calculations on the oxidative addition of alkynyl stannanes to [PdL_2]: a) T. Matsubara, K. Hirao, *Organometallics* **2002**, *21*, 4482 – 4489; b) T. Matsubara, K. Hirao, *Organometallics* **2003**, *22*, 4286 – 4296.

[265] a) E. Shirakawa, K. Yamasaki, H. Yoshida, T. Hiyama, *J. Am. Chem. Soc.* **1999**, *121*, 10221; b) E. Shirakawa, H. Yoshida, Y. Nakao, T. Hiyama, *Org. Lett.* **2000**, *2*, 2209 – 2211.

[266] B. Martín-Matute, E. Buñuel, D. J. Cárdenas, M. Méndez, C. Nieto-Oberhuber, A. M. Echavarren, *J. Organomet. Chem.* **2003**, *687*, 410 – 419.

[267] a) M. Shi, K. M. Nicholas, *J. Am. Chem. Soc.* **1997**, *119*, 5057 – 5058; b) see also: R. J. Franks, K. M. Nicholas, *Organometallics* **2000**, *19*, 1458 – 1460.

[268] a) N. A. Bumagin, A. N. Kasatkin, I. P. Beletskaya, *Izv. Akad. Nauk SSSR Ser. Khim.* **1984**, 636 – 642; b) O. A. Wallner, K. Szabó, *Org. Lett.* **2002**, *4*, 1563 – 1566.

[269] a) A. J. Canty, *Acc. Chem. Res.* **1992**, *25*, 83 – 90; b) A. J. Canty, *Platinum Metals Rev.* **1993**, *37*, 2 – 7.

[270] L. M. Rendina, R. J. Puddephatt, *Chem. Rev.* **1997**, *97*, 1735 – 1754.

[271] C. R. Baar, H. A. Jenkins, J. J. Vittal, G. P. A. Yap, R. J. Puddephatt, *Organometallics* **1998**, *17*, 2805 – 2818.

[272] The X-ray crystal structure of a Pd^{IV} complex formed by oxidative addition of PhI to a Pd^{II} complex was published. This structure included several improbable features: a) J. M. Brunel, M.-H. Hirlemann, A. Heumann, G. Buono, *Chem. Commun.* **2000**, 1869 – 1870; b) Corrections to reference [272a]: J. M. Brunel, M.-H. Hirlemann, A. Heumann, G. Buono, *Chem. Commun.* **2001**, 1869; J. M. Brunel, M.-H. Hirlemann, A. Heumann, G. Buono, *Chem. Commun.* **2001**, 2298. The authors later retracted this communication (*Chem. Commun.* **2002**, May 16).

[273] Theoretical work on a hypothetical mechanism for the Heck reaction based on Pd^{II}/Pd^{IV} suggests that the oxidative addition of PhI to Pd^{II} is the rate-determining step: A. Sundermann, O. Uzan, J. M. L. Martin, *Chem. Eur. J.* **2001**, *7*, 1703 – 1711.

[274] a) R. Usón, J. Forniés, R. Navarro, *J. Organomet. Chem.* **1975**, *96*, 307 – 312; b) R. Usón, J. Forniés, R. Navarro, *Synth. React. Inorg. Met.-Org. Chem.* **1977**, *7*, 235 – 241.

[275] J. Terao, H. Watanabe, A. Ikumi, H. Kuniyasu, N. Kambe, *J. Am. Chem. Soc.* **2002**, *124*, 4222 – 4223.

[276] R. Benn, B. Büssemeier, S. Holle, P. W. Joly, R. Mynott, I. Tkatchenko, G. Wilke, *J. Organomet. Chem.* **1985**, *279*, 63 – 86.

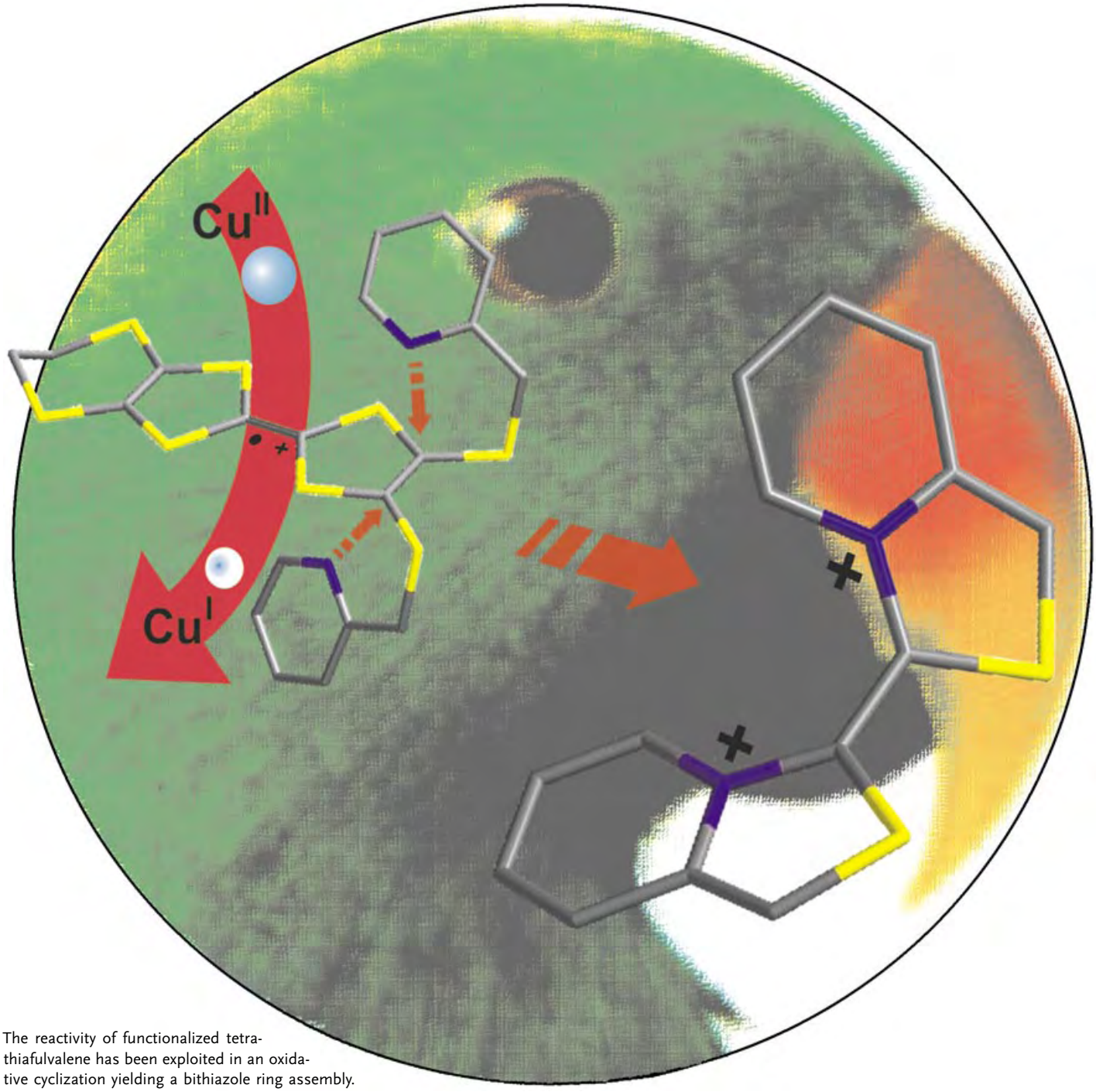
[277] a) L. S. Liebeskind, R. W. Fengl, *J. Org. Chem.* **1990**, *55*, 5359 – 5364; b) L. S. Liebeskind, S. W. Riesinger, *J. Org. Chem.* **1993**, *58*, 408 – 413.

 © 2004 Wiley-VCH Verlag GmbH & Co. KGaA, Weinheim

[278] E. Gómez-Bengoa, A. M. Echavarren, *J. Org. Chem.* **1991**, *56*, 3497 – 3501.
[279] J. M. Saá, G. Martorell, *J. Org. Chem.* **1993**, *58*, 1963 – 1966.
[280] R. D. Mazzola, S. Giese, C. L. Benson, F. G. West, *J. Org. Chem.* **2004**, *69*, 220 – 223.
[281] a) In the palladium-catalyzed coupling of aryl chlorides with alkynes, copper has been found to inhibit product formation: D. Gelman, S. L. Buchwald, *Angew. Chem.* **2003**, *115*, 6175 – 6178; *Angew. Chem. Int. Ed.* **2003**, *42*, 5993 – 5996; b) see also: A. Soheili, J. Albaneze-Walker, J. A. Murry, P. G. Dormer, D. L. Hughes, *Org. Lett.* **2003**, *5*, 4191 – 4194.
[282] V. Farina, S. Kapadia, B. Krishnan, C. Wang, L. S. Liebeskind, *J. Org. Chem.* **1994**, *59*, 5905 – 5911.
[283] A. L. Casado, P. Espinet, *Organometallics* **2003**, *22*, 1305 – 1309.
[284] A new variant of the Stille reaction in which CuI and CsF are used as additives is based on this concept: S. P. H. Mee, V. Lee, J. E. Baldwin, *Angew. Chem.* **2004**, *116*, 1152 – 1156; *Angew. Chem. Int. Ed.* **2004**, *43*, 1132 – 1136.
[285] E. Piers, T. Wong, *J. Org. Chem.* **1993**, *58*, 3609 – 3610.
[286] See also: T. Takeda, K. I. Matsunaga, Y. Kabasawa, T. Fukiwara, *Chem. Lett.* **1995**, 771 – 772.
[287] a) J. R. Falck, R. K. Bahtt, J. Ye, *J. Am. Chem. Soc.* **1995**, *117*, 5973 – 5982; b) S. Mohapatra, A. Bandyopadhyay, D. K. Barma, J. H. Capdevila, J. R. Falck, *Org. Lett.* **2003**, *5*, 4759 – 4762.
[288] R. J. Linderman, J. M. Siedlecki, *J. Org. Chem.* **1996**, *61*, 6492 – 6493.
[289] a) G. D. Allred, L. S. Liebeskind, *J. Am. Chem. Soc.* **1996**, *118*, 2748 – 2749; b) S. Zhang, D. Zhang, L. S. Liebeskind, *J. Org. Chem.* **1997**, *62*, 2312 – 2313; c) R. Wittenberg, J. Srogl, M. Egi, L. S. Liebeskind, *Org. Lett.* **2003**, *5*, 3033 – 3035.
[290] For coupling reactions catalyzed by Cu^{I} or Mn^{II}, see: S.-K. Kang, J.-S. Kim, S.-C. Choi, *J. Org. Chem.* **1997**, *62*, 4208 – 4209.
[291] R. Wittenberg, J. Srogl, M. Egi, L. S. Liebeskind, *Org. Lett.* **2003**, *5*, 3033 – 3035.
[292] B. M. Savall, N. Blanchard, W. R. Roush, *Org. Lett.* **2003**, *5*, 377 – 379.
[293] F.-A. Alphonse, F. Suzenet, A. Keromnes, B. Lebret, G. Guillaumet, *Org. Lett.* **2003**, *5*, 803 – 805.
[294] M. Egi, L. S. Liebeskind, *Org. Lett.* **2003**, *5*, 801 – 802.
[295] W.-S. Kim, H.-J. Kim, C.-G. Cho, *J. Am. Chem. Soc.* **2003**, *125*, 14288 – 14289.

 © 2004 Wiley-VCH Verlag GmbH & Co. KGaA, Weinheim

Communications



The reactivity of functionalized tetrathiafulvalene has been exploited in an oxidative cyclization yielding a bithiazole ring assembly. The electronic properties of this new chromophore and dichroitic behavior of single crystals can be rationalized by a nearly pure HOMO→LUMO transition of the ππ* type, which is polarized perpendicular to the molecular and crystallographic C_2 axes. For more information, see the Communication by S. Decurtins and co-workers on the following pages.

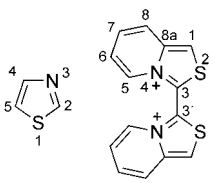
DOI: 10.1002/anie.200460149
© 2004 Wiley-VCH Verlag GmbH & Co. KGaA, Weinheim

Heterocycle Synthesis

Tetrathiafulvalenes Acting as Leaving Groups: A Route to Bithiazoles**

*Shi-Xia Liu, Christian Tanner, Antonia Neels, Stefan Dolder, Samuel Leutwyler, Philippe Renaud, Peter Bigler, and Silvio Decurtins**

The five-membered heterocyclic 1,3-thiazole ring system is found in many natural products,[1–3] and alkylbithiazole oligomers have also been tested for organic electronic applications.[4] Here, we consider the extension of monocyclic heterocycles to bicyclic systems. The annulation of a benzene ring to a heterocycle generally results in change of properties, depending on the annulation topology. Specifically, in the case of thiazoles, the annulation of a benzene ring by means of the established cyclocondensation of *ortho*-aminothiophenols with carboxylic acids or aldehydes yields benzo[*d*]thiazoles. Two notable examples of thiazoles fused at face *d* (at the 4,5 bond) are thiazole orange, a powerful intercalator dye with base-stacking ability,[5] and luciferin, which causes bioluminescence in insects.[6] In contrast, however, there are few reports on thiazoles fused at face *c* (at the 3,4 bond),[7] and there are, to our knowledge, no structural reports of the thiazolo[3,4-*a*]pyridinium ring system. Here, the facile conversion of a tetrathiafulvalene (TTF) derivative into 3,3′-bithiazolo[3,4-*a*]pyridinium (**1**), a stable heterocyclic 10+10 π electron system, is particularly noteworthy because it extends the synthetic utilities of TTFs and it provides a new and straightforward entry to a particular class of fused-ring systems.



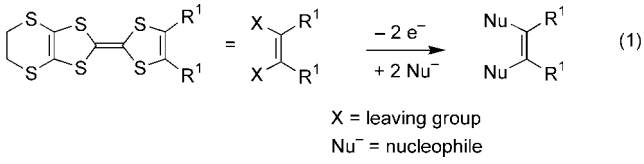
1

The well-known TTFs π-donor form stable radical cation species which in combination with acceptor molecules give rise to conducting and superconducting materials.[8] Current activities in this research field comprise the functionalization of the TTF backbone. As an example, functionalization with ligating groups such as pyridine aims at binding metal ions to the organic donor unit which, consequently, leads to organic/inorganic hybrid materials.[9] During this work we discovered that the pyridine-functionalized redox-active TTF ligand 4,5-bis(2-pyridylmethylsulfanyl)-4′,5′-ethylenedithiotetrathiafulvalene (ET-2Py)[9a] underwent ring transformation to give a 3,3′-bithiazolo[3,4-*a*]pyridinium. It must be noted that the synthesis of a parent, nonfused dithiadiazafulvalene (DTDAF) has been reported.[10] In contrast to the pyridine-fused bithiazole compound (**1**), DTDAFs are air-sensitive but can be trapped, for example, as a charge-transfer salt, due to their good electron-donor properties.

Herein we describe the synthesis, the single-crystal X-ray structure, the photophysical properties, and a theoretical investigation of the electronic structure of the dicationic, bis(bicyclic) ring assembly **1**. Thus the reaction of ET-2Py, or alternatively its Ni^{II} complex $[NiCl_2(ET\text{-}2Py)]$,[9c] with $Cu(ClO_4)_2$ gave yellow needlelike single crystals of $\mathbf{1}(ClO_4)_2$.[11] The Cu^{II}-mediated oxidative cyclization may proceed through the mechanistic pathway outlined in Scheme 1. One-electron oxidation of the TTF moiety affords an electrophilic radical cation **2** that reacts intramolecularly by means of a 5-*exo*-trig cyclization with the nucleophilic pyridyl residue.[12] After fragmentation of the intermediate spirocyclic compound **3**, a dihydrothiazolopyridinium derivative **4** is formed. Oxidation of the 1,3-dithiol-2-yl radical gives the cation **5**, which undergoes a second nucleophilic 5-*exo*-trig cyclization. β Fragmentation of the dithioate residue in **6** furnishes 1*H*,1′*H*-3,3′-thiazolo[3,4-*a*]pyridin-4-ium (**7**). Finally, aromatization of the thiazole moiety under oxidative conditions affords the observed final product **1**.

Interestingly, in this reaction, the TTF moiety acts as a pair of bis-vicinal leaving groups bonded to an ethylene residue that can be triggered by two one-electron oxidation processes. To the best of our knowledge, this reactivity of TTF has not been exploited and could be general for the transformation depicted in Equation (1).[13] A detailed examination of the rearrangement by replacing the pyridinyl groups on the the TTF ligands with functional groups such as pyrazinyl and quinolinyl is now under investigation.

The single-crystal structure of $\mathbf{1}(ClO_4)_2$ comprises dicationic ring assemblies and perchlorate anions in a 1:2 ratio. The compound crystallizes in the tetragonal crystal system,



(1)

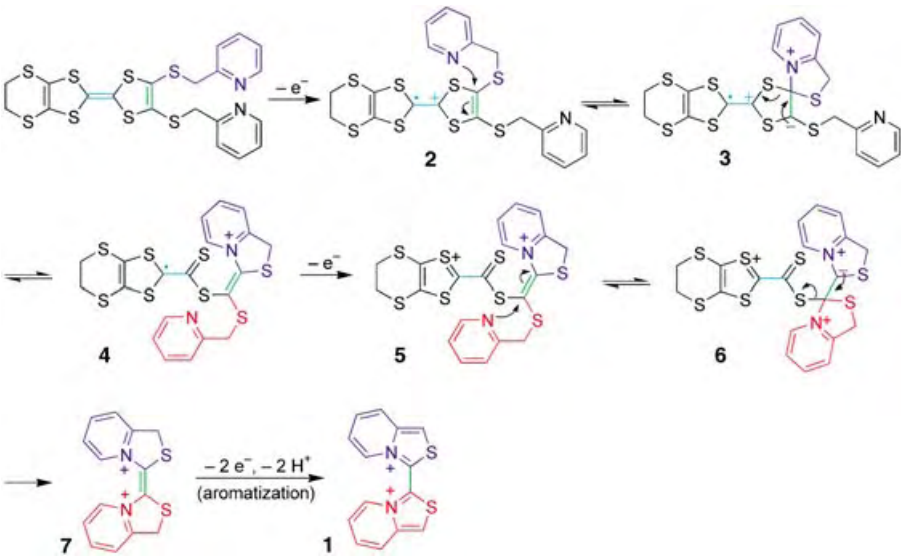
X = leaving group
Nu^- = nucleophile

polar space group $I\bar{4}cd$. The yellow crystals have a needle-shaped morphology, in which the *c* axis lies parallel to the needle axis. In the structure of the ring assembly (Figure 1) the asymmetric unit is one half of the molecule, and the other half is generated by rotation about a crystallographic twofold axis that bisects the C3–C3′ bond. Each fused bicyclic heterocycle is virtually planar (rms deviation from a least-squares plane through all atoms amounts to only 0.023 Å;

[*] Dr. S.-X. Liu, C. Tanner, S. Dolder, Prof. S. Leutwyler, Prof. P. Renaud, Prof. P. Bigler, Prof. S. Decurtins
Departement für Chemie und Biochemie
Universität Bern
Freiestrasse 3, 3012 Bern (Switzerland)
Fax: (+41) 31-631-3995
E-mail: decurtins@iac.unibe.ch
Dr. A. Neels
Institut de Chimie
Université Neuchâtel
Av. de Bellevaux 51
2007 Neuchâtel (Switzerland)

[**] This work was supported by the Swiss National Science Foundation (project no. 200020-100432). We thank Dr. Stefan Schürch for his assistance in the MS investigation and Dr. Hans-Martin Frey for fluorescence lifetime measurements.

 © 2004 Wiley-VCH Verlag GmbH & Co. KGaA, Weinheim DOI: 10.1002/anie.200460149



Scheme 1. Proposed mechanistic pathway for **1**.

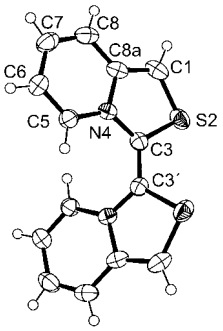


Figure 1. X-ray crystal structure of **1** in $\mathbf{1}(ClO_4)_2$ (ORTEP, thermal ellipsoids set at the 50% probability level). For bond lengths see Table 1; selected bond angles [°]: C1-S2-C3 92.47(11), S2-C3-N4 111.56(15), C3-N4-C8a 113.24(18), N4-C8a-C1 111.2(2), C8a-C1-S2 111.48(18), N4-C3-C3′ 126.08(16), S2-C3-C3′ 122.28(11).

maximum deviation for C1: 0.037 Å); the molecule has a *cis* arrangement about the central C3–C3′ bond with a dihedral angle of 54.4°. The compound exists in its most stable conformation as a chiral molecule; however, both enantiomeric forms are present in the solid state in equal amounts.[14]

With regard to the electronic structure of **1**, the individual bond lengths are of interest. For the annulated six-membered heterocycle, distinct C–C bond-length alternations are observed (Table 1), indicating some dienic character. The ratio of the C5–C6 (1.345 Å) and C6–C7 (1.426 Å) bond lengths, 0.94, clearly diverges from unity. In pyridine, which may serve as a reference for aromaticity, the ratio of the C2–C3 (1.395 Å) and C3–C4 (1.394 Å) bond lengths is practically unity. Moreover, the C–N bond in pyridine is considerably shorter (1.340 Å) than those within the fused bicyclic systems (Table 1), which agrees with the expectation that annulation affects the bond lengths with an appreciable increase in the length of the C–N bond. The C–S bonds (Table 1) are slightly shorter than cited values of a thiazole derivative (av 1.705 Å)[15] and therefore, they may be involved in resonance. For the central C3–C3′ bond linking the two bicyclic residues, a length of 1.430 Å is found, indicating its predominantly σ character. The bond angles of the six-membered ring are found to be 120° to within 1.2°; the C1-S2-C3 angle (92.47°) lies within the expected range.[15]

Figure 2a highlights the mutual arrangement of the bis(bicyclic) dications. A noticeable feature is the parallel orientation of the ring assemblies along the *c* axis which, of course, is related to their C_2 symmetry and is also expressed through the polar space group of the crystal structure. There are several C–H···O contacts in the crystal packing with the following donor···acceptor distances: C1···O1 3.153(4), C8···O1 3.351(4), C5···O3 3.277(4) Å. Figure 2b displays the hydrogen-bonding pattern of the crystal structure of $\mathbf{1}(ClO_4)_2$.

Ab initio calculations of **1** in the electronic ground state were performed at the correlated level using the Gaussian 98 package.[16] The calculated bond lengths are in very good agreement with the experimental values and are typically 0.0–0.02 Å longer than those observed (Table 1). A calculation for a constrained structure (twist angle 54.4°) gave no significant changes in bond lengths. However, the calculated twist angle θ around the central C3–C3′ bond (the N4-C3-C3′-N4′ dihedral angle)

Table 1: Bond lengths [Å] and twist angles [°] of **1** observed and calculated by the MP2/6-31G(d,p) method for a fully relaxed structure.

Bonds and angle	Obsd.	Calcd.	Δ (obsd.–calcd.)
N4–C5	1.384(3)	1.379	+0.005
C5–C6	1.345(3)	1.369	−0.024
C6–C7	1.426(4)	1.416	+0.010
C7–C8	1.345(4)	1.376	−0.031
C8–C8a	1.410(3)	1.411	−0.001
C8a–N4	1.398(3)	1.401	−0.003
C8a–C1	1.381(3)	1.398	−0.017
C1–S2	1.684(3)	1.680	+0.004
S2–C3	1.683(2)	1.706	−0.023
C3–N4	1.353(3)	1.387	−0.034
C3–C3′	1.430(4)	1.435	−0.005
N4-C3-C3′-N4′	54.4	76.4	−22.0

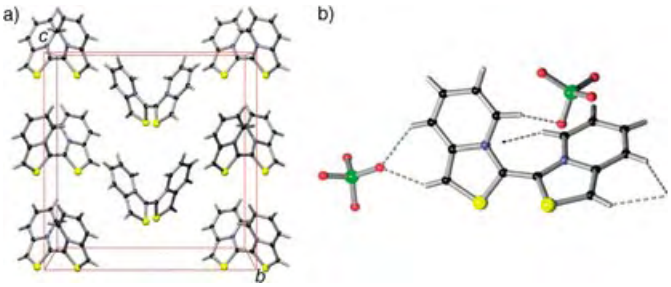
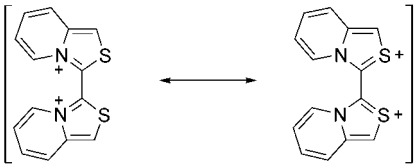


Figure 2. a) [100] Projection of $\mathbf{1}(ClO_4)_2$, accentuating the alignment of the bis(bicycle)s. ClO_4^- ions are omitted. b) Hydrogen-bonding pattern of $\mathbf{1}(ClO_4)_2$.

 © 2004 Wiley-VCH Verlag GmbH & Co. KGaA, Weinheim

is 76.4°, which is 22° larger than that measured in the crystal structure. That can be ascribed to crystal packing and hydrogen-bonding effects. Further details of the energy dependence on θ are discussed below.

The atomic charges were obtained by fitting the electrostatic potential (ESP) to atom-centered monopoles using the Merz–Singh–Kollmann (MSK)[17,18] and CHelpG[19] schemes. The ESP charges predict that the positive charge is equally distributed between N and S atoms. The CHelpG method produces qualitatively the same results as the MSK fit but with the positive charge less evenly distributed between N and S. In terms of valence-bond structures, the formal positive charges are either on the nitrogen or on the sulfur atoms (Scheme 2). Comparison with the calculated atomic charges leads us to conclude that both resonance structures in Scheme 2 contribute to the electronic structure of **1**.



Scheme 2. Resonance structures of **1**.

The chromophore **1** strongly absorbs at the violet end of the visible region as evidenced by its yellow color. The solution (MeCN) spectrum displays an intensive, broad absorption band around 377 nm with a ε value of $8\times10^3\,\mathrm{L\,mol^{-1}\,cm^{-1}}$ (Figure 3). The chromophore also shows a

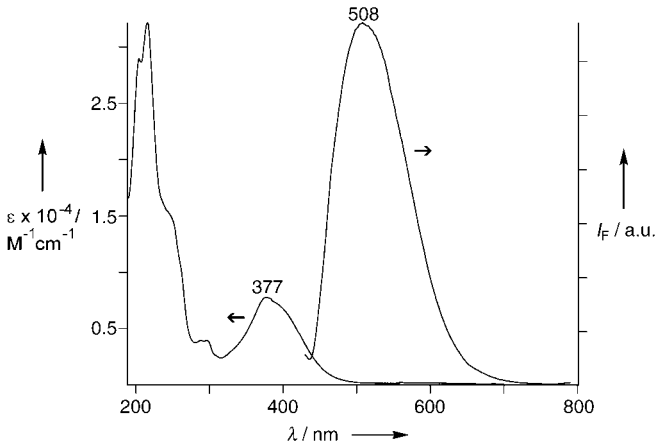


Figure 3. Electronic absorption and emission fluorescence spectra of $\mathbf{1}(ClO_4)_2$ in acetonitrile solution at 298 K ($\lambda_{exc}=420$ nm).

strongly Stokes-shifted fluorescence emission in acetonitrile solution. The chromophore shows an emission maximum of 508 nm when it is excited at 420 nm (Figure 3). Furthermore, the excitation spectrum between 470 and 300 nm (emission at 510 nm) compares well with the corresponding absorption profile. The fluorescence lifetime in MeCN was determined as $\tau=2.8\pm0.1$ ns.

To rationalize the electronic properties of the first excited state of **1**, CIS/6-31G(d,p) calculations were performed for the MP2/6-31G(d,p) ground-state geometry constrained to the experimental twist angle ($\theta=54.4°$). The predicted $S_1\leftarrow S_0$ absorption energy is 3.483 eV (356 nm), with a high oscillator strength $f=0.608$ ($f_{obs}=0.22$). The transition corresponds to a nearly pure HOMO→LUMO transition (89%) of the $\pi\pi^*$ type. The $S_1\leftarrow S_0$ transition dipole moment transforms as B in the point group C_2. Thus, the polarization of the absorption is perpendicular to the molecular and crystallographic C_2 axes (Figure 4), which is in perfect agreement with the dichroitic behavior of single crystals of $\mathbf{1}(ClO_4)_2$. The needlelike crystals appear yellow when examined with light polarized perpendicular to the needle axis (c axis) and colorless with polarization along the needle axis.



Figure 4. Orientation of the $S_1\leftarrow S_0$ transition dipole moment.

Comparison of the HOMO and LUMO shows that $S_1\leftarrow S_0$ electronic excitation induces a considerable charge flow from the six-membered ring to the S and N atoms, and increases the double-bond character of the central C3–C3′ bond. Despite the large twist angle θ between the two halves of the molecule there is a noticeable π-electronic overlap of helicoidal shape in both HOMO and LUMO. As θ goes to 90° this overlap drops to zero.

The calculated barrier for torsion around the angle θ is 30.1 kJ mol^{-1} at the SCF level and decreases to 25.5 kJ mol^{-1} at the MP2 correlated level. This barrier is not high enough to separate the two enantiomeric forms at room temperature, although interconversion of the two rotamers is not fast due to the large masses involved in the movement.

In summary, **1** is the first isolated and structurally characterized thiazolo[3,4-*a*]pyridinium ring assembly. In particular, the reactivity of functionalized tetrathiafulvalene has been exploited which, in turn, opens a straightforward synthetic entry to a particular class of fused-ring systems. A full photophysical analysis of the chromophoric ring assembly will be reported elsewhere.[20] A detailed examination of the synthetic pathway linking TTF and thiazole chemistry is now in progress.

Received: March 29, 2004

Keywords:
structure elucidation · cyclization · fluorescence · heterocycles · tetrathiafulvalene

[1] *The Merck Index*, 13th ed, Merck Research Laboratories, Whitehouse Station, NJ, USA, **2001**.

 © 2004 Wiley-VCH Verlag GmbH & Co. KGaA, Weinheim

[2] a) R. R. Gupta, M. Kumar, V. Gupta, *Heterocyclic Chemistry II*, Springer, Berlin, **1999**; b) P. Vicini, A. Geronikaki, M. Incerti, B. Busonera, G. Poni, C. A. Cabras, P. La Colla, *Bioorg. Med. Chem.* **2003**, *11*, 4785 – 4789.
[3] J. Kasparkova, O. Novakova, N. Farrell, V. Brabec, *Biochemistry* **2003**, *42*, 792 – 800.
[4] a) A. B. Koren, M. D. Curtis, A. H. Francis, J. W. Kampf, *J. Am. Chem. Soc.* **2003**, *125*, 5040 – 5050; b) J. Cao, J. W. Kampf, M. D. Curtis, *Chem. Mater.* **2003**, *15*, 404 – 411.
[5] a) O. Köhler, O. Seitz, *Chem. Commun.* **2003**, 2938 – 2939; b) A. N. Glazer, H. S. Rye, *Nature* **1992**, *359*, 859 – 861.
[6] T. Toya, M. Takagi, T. Kondo, H. Nakata, M. Isobe, T. Goto, *Bull. Chem. Soc. Jpn.* **1992**, *65*, 2604 – 2610.
[7] a) D. G. Jones, G. Jones, *J. Chem. Soc. C* **1969**, 707 – 710; b) J. N. Shah, B. D. Tilak, *Indian J. Chem. Sect. B* **1979**, *18*, 486 – 487.
[8] a) J. L. Segura, N. Martin, *Angew. Chem.* **2001**, *113*, 1417 – 1455; *Angew. Chem. Int. Ed.* **2001**, *40*, 1372 – 1409; b) M. B. Nielsen, C. Lomholt, J. Becher, *Chem. Soc. Rev.* **2000**, *29*, 153 – 164.
[9] a) S-X. Liu, S. Dolder, E. B. Rusanov, H. Stoeckli-Evans, S. Decurtins, *C. R. Chim.* **2003**, *6*, 657 – 662; b) J. O. Jeppesen, J. Becher, *Eur. J. Org. Chem.* **2003**, 3245 – 3266; c) S-X. Liu, S. Dolder, P. Franz, A. Neels, H. Stoeckli-Evans, S. Decurtins, *Inorg. Chem.* **2003**, *42*, 4801 – 4803; d) F. Setifi, L. Ouahab, S. Golhen, Y. Yoshida, G. Saito, *Inorg. Chem.* **2003**, *42*, 1791 – 1793.
[10] N. Bellec, D. Lorcy, A. Robert, R. Carlier, A. Tallec, C. Rimbaud, L. Ouahab, R. Clerac, P. Delhaes, *Adv. Mater.* **1997**, *9*, 1052 – 1056.
[11] **1**$(ClO_4)_2$: (*Caution!* Perchlorate salts can be explosive and must be handled with care). A layer diffusion between $NiCl_2$(ET-2Py)[9c] or ET-2Py[9a] (1.2×10^{-3} M) in CH_2Cl_2 and $Cu(ClO_4)_2\cdot6H_2O$ (1.2×10^{-2} M) in MeOH afforded within three weeks yellow single crystals suitable for X-ray analysis. Yield: 17 %. m.p. >300 °C (decomp.); IR (KBr): $\tilde{\nu}=1638$, 1518, 1457, 1333, 1265, 1101 cm^{-1} (ClO_4^-); ^1H NMR (D_2O): $\delta=7.76$ (m, 1H), 7.94 (m, 1H), 8.42 (m, 2H), 9.46 ppm (s, 1H); ^{13}C NMR (D_2O): $\delta=143.2$, 144.8, 146.9, 147.2, 150.4, 151.7, 164.7 ppm; ESI-MS (*m*/*z*): 135.02 $[C_{14}H_{10}N_2S_2]^{2+}$ (in CH_3CN), 136.01 $[C_{14}H_8D_2N_2S_2]^{2+}$ (in D_2O).
[12] T. Linker, M. Schmittel, *Radikale und Radikalionen in der Organischen Synthese*, Wiley-VCH, Weinheim, **1998**, pp. 315 – 373.
[13] The proposed transformation has also been confirmed successfully with the reaction of a $CoCl_2$ complex of 4,5-bis(2-pyridylmethylsulfanyl)-4′,5′-bis(methylthio)tetrathiafulvalene with $CuBr_2$ resulting in **1**·($CoBr_4$) showing a transoid conformation.
[14] Supplementary crystallographic data for this paper are available from the IUCr electronic archives. CCDC-230147 contains the supplementary crystallographic data for this paper. These data can be obtained free of charge via www.ccdc.cam.ac.uk/conts/retrieving.html (or from the Cambridge Crystallographic Data Centre, 12, Union Road, Cambridge CB2 1EZ, UK; fax: (+44) 1223-336-033; or deposit@ccdc.cam.ac.uk).
[15] C. Rodriguez de Barbarin, S. Bernès, F. Sanchez-Viesca, M. Berros, *Acta. Crystallogr. Sect. C* **2003**, *59*, o360-o362.
[16] Gaussian 98 (Revision A.7), M. J. Frisch, G. W. Trucks, H. B. Schlegel, G. E. Scuseria, M. A. Robb, J. R. Cheeseman, V. G. Zakrzewski, J. A. Montgomery, R. E. Stratmann, J. C. Burant, S. Dapprich, J. M. Millam, A. D. Daniels, K. N. Kudin, M. C. Strain, O. Farkas, J. Tomasi, V. Barone, M. Cossi, R. Cammi, B. Mennucci, C. Pomelli, C. Adamo, S. Clifford, J. Ochterski, G. A. Petersson, P. Y. Ayala, Q. Cui, K. Morokuma, D. K. Malick, A. D. Rabuck, K. Raghavachari, J. B. Foresman, J. Cioslowski, J. V. Ortiz, B. B. Stefanov, G. Liu, A. Liashenko, P. Piskorz, I. Komaromi, R. Gomperts, R. L. Martin, D. J. Fox, T. Keith, M. A. Al-Laham, C. Y. Peng, A. Nanayakkara, C. Gonzalez, M. Challacombe, P. M. W. Gill, B. G. Johnson, W. Chen, M. W. Wong, J. L. Andres, M. Head-Gordon, E. S. Replogle, J. A. Pople, Gaussian, Inc., Pittsburgh, PA, **2001**.
[17] B. H. Besler, K. M. Merz, Jr., P. A. Kollman, *J. Comput. Chem.* **1990**, *11*, 431 – 439.
[18] U. C. Singh, P. A. Kollman, *J. Comput. Chem.* **1984**, *5*, 129 – 145.
[19] C. M. Breneman, K. B. Wiberg, *J. Comput. Chem.* **1990**, *11*, 361 – 373.
[20] Details will be reported in a full paper.

 © 2004 Wiley-VCH Verlag GmbH & Co. KGaA, Weinheim

Supramolecular Compounds

$\{[WS_4Cu_4(4,4'\text{-bpy})_4][WS_4Cu_4I_4(4,4'\text{-bpy})_2]\}_\infty$—An Unusual 3D Porous Coordination Polymer Formed from the Preformed Cluster $[Et_4N]_4[WS_4Cu_4I_6]$**

Jian-Ping Lang, Qing-Feng Xu, Rong-Xin Yuan, and Brendan F. Abrahams**

In recent years, the assembly of supramolecular structures from preformed metal clusters has been the focus of intense research.[1] So far, several preformed metal clusters have been successfully incorporated into infinite assemblies to produce materials with fascinating properties.[1g,h,2–5] For example, Yaghi and co-workers synthesized frameworks that show promise as hydrogen-storage materials by using tetrazinc carboxylate clusters as 6-connecting nodes.[2] Shriver and co-workers employed hexanuclear clusters that contain the octahedral $[Mo_6(\mu_3\text{-}Cl)_8]^{4+}$ core to generate microporous xerogels for size-selective ion exchange.[3] The importance of Mo(W)/Cu(Ag)/S clusters[6] in biological systems[7a] and materials science[7b-d] as well as their unique structure

[*] Dr. B. F. Abrahams
School of Chemistry
University of Melbourne
Victoria 3010 (Australia)
Fax: (+61) 3-9347-5180
E-mail: bfa@unimelb.edu.au
Prof. J.-P. Lang, Dr. Q.-F. Xu
Key Laboratory of Organic Synthesis of Jiangsu Province
School of Chemistry and Chemical Engineering
Suzhou University
1 Shizi Street, Suzhou 215006, Jiangsu (China)
Fax: (+86) 512-6522-4783
E-mail: jplang@suda.edu.cn
Prof. Dr. R.-X. Yuan
Department of Chemistry
Changshu Institute of Technology
Changshu 215500, Jiangsu (China)

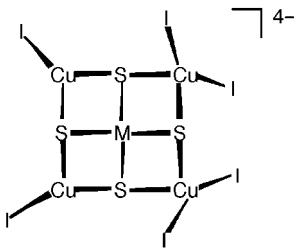
[**] This work was supported by the NNSF of China (No. 20271036), the NSF of the Education Committee of Jiangsu Province (No. 02 KJB150001), and the State Key Laboratory of Structural Chemistry of FJIRSM (No. 030066). 4,4′-bpy = 4,4′-bipyridyl.

Supporting information for this article is available on the WWW under http://www.angewandte.org or from the author.

 DOI: 10.1002/anie.200460076 © 2004 Wiley-VCH Verlag GmbH & Co. KGaA, Weinheim

prompted our interest in using such species in the assembly of cluster-containing supramolecular compounds. To date, there have only been a few reports on the use of Mo(W)/Cu(Ag)/S clusters as building blocks for supramolecular assemblies.[8]

After careful consideration of cluster geometry and chemical behavior, we believed the cluster $[Et_4N]_4[WS_4Cu_4I_6]$ (**1**)[9] to be a very good candidate for inclusion into an



1

extended network. The tetraanion of **1** has a saddle-shaped cluster framework in which two copper centers are each coordinated by two terminal iodides while each of the other two are coordinated to a single terminal iodide. Given the geometry of **1**, we anticipated that the full or partial substitution of the coordinated iodides with the bridging ligand would give rise to novel structural arrays. Herein, we report the synthesis, structure, and absorption properties of an unusual 3D porous coordination polymer, assembled from **1** and 4,4′-bpy.

Crystals of the compound $\{[WS_4Cu_4(4,4'\text{-bpy})_4][WS_4Cu_4I_4(4,4'\text{-bpy})_2]\}\cdot 8\,CH_3CN$ (**2**·8 CH_3CN) were obtained by the reaction of **1** with 2.5 equivalents of 4,4′-bpy in solution in DMF/MeCN. The crystals rapidly lose acetonitrile; however, **2** is stable in air and moisture, and is insoluble in common organic solvents. X-ray crystallographic analysis revealed that the asymmetric unit of **2**·8CH_3CN consists of one quarter of the $[WS_4Cu_4(4,4'\text{-bpy})_4]^{2+}$ dication and one quarter of the $[WS_4Cu_4I_4(4,4'\text{-bpy})_2]^{2-}$ dianion.[10] The oxidation states of the tungsten and copper centers in **1** (+6 and +1, respectively) are retained in **2**. Although the dianion and dication contain a saddle-shaped $[WS_4Cu_4]$ core structure similar to that found in **1**, the Cu centers have different coordination environments. Each Cu atom in the dication of **2** is coordinated by two μ_3-S and two N atoms, whereas in the dianion the Cu atom is tetrahedrally bound by one I, one N, and two μ_3-S atoms. The W···Cu separations in the dication and dianion are 2.673 and 2.719 Å, respectively, which are similar to that found for **1** (av. 2.673 Å).[9]

As indicated in Figure 1, the cationic cluster is coordinated by eight bridging 4,4′-bpy ligands. Four pairs of ligands extend to four crystallographically equivalent clusters that lie at the corners of a distorted tetrahedron. The W atom lies on a site of 222 symmetry. From a topological perspective, each cluster serves as a 4-connecting center in an infinite cationic 3D network. The topology of the net is the same as that found for diamond, with the WS_4Cu_4 clusters serving as tetrahedral nodes. The adamantane-type unit is a characteristic feature of the diamond net, and such a unit within **2** is represented in Figure 2 A. The relationship of the unit represented in

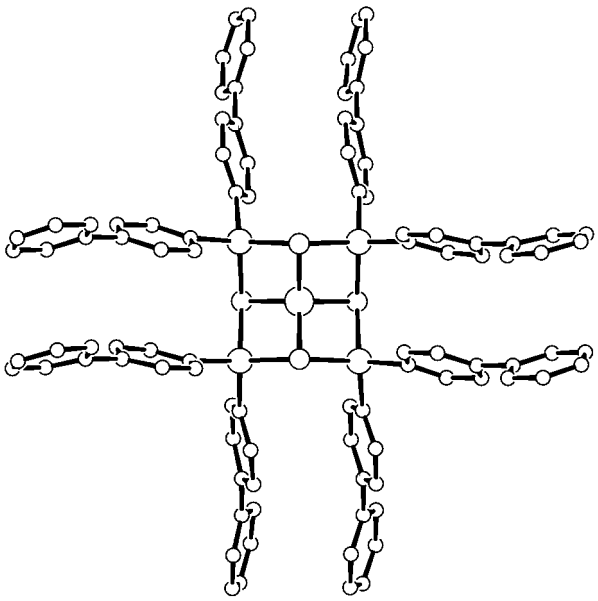


Figure 1. Part of the cationic network within **2** showing the double 4,4′-bpy ligands that extend to equivalent WS_4Cu_4 clusters; hydrogen atoms have been omitted for clarity.

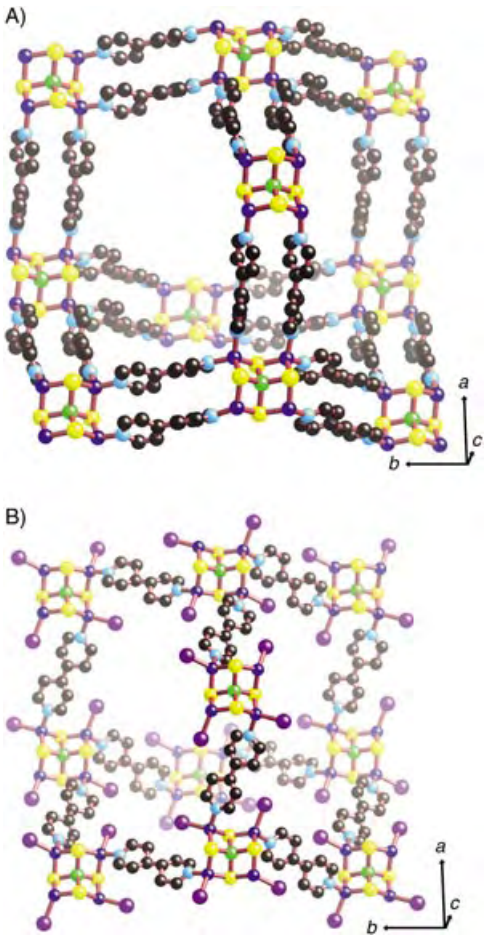


Figure 2. Adamantane-type units within A) the cationic network of **2** and B) the anionic network of **2** viewed from a position just off the *c* axis. Atom color code: W green, Cu royal blue, S yellow, N pale blue, C black; hydrogen atoms have been omitted for clarity. The interpenetrating networks stack along the *c* direction.

 © 2004 Wiley-VCH Verlag GmbH & Co. KGaA, Weinheim

Figure 2A with adamantane is highlighted in the Supporting Information. The crystal contains two independent cationic diamond nets that interpenetrate.

In contrast to the cation, the WS_4Cu_4 cluster in the anion retains four iodide ions from the starting material **1** and has its remaining coordination sites occupied by nitrogen atoms from four bridging 4,4′-bpy ligands. The W atom in this case lies on a site of $\bar{4}$ symmetry. The ligands link a cluster to four equivalent clusters that lie at the vertices of a distorted tetrahedron. As with the cation, a diamond-type network results, but now the bridges between clusters are single 4,4′-bpy ligands. An adamantane-related unit is represented in Figure 2B. In the anion, the bridging ligand is inclined to the W···W vector of the linked clusters, whereas in the cation the 4,4′-bpy ligands are parallel to the W···W vector. In the anionic network the 4,4′-bpy makes close contact with a coordinated iodide ion bound to an adjacent Cu center. We consider that this steric clash leads to disorder and slight distortion of the 4,4′-bpy ligands of the anionic network. Within the crystal there are two independent, interpenetrating, anionic diamond networks.

The interpenetration of the four diamond nets (two cationic and two anionic) is remarkable, given that the cationic and anionic nets are so different. Views of the interpenetration of four adamantane units are presented in the Supporting Information. For interpenetration to occur, the spacing of network voids in one network needs to match perfectly the spacing of network nodes in the other and as a consequence, interpenetration is normally observed in crystals that contain identical open networks. Not surprisingly, the occurrence of two different interpenetrating diamondlike nets in the same compound is unusual but not unprecedented.[11]

Although it was not possible to identify solvent molecules in the crystal structure, it was considered likely that large intraframework regions are occupied by solvent molecules. On the basis of the "void" volumes, the formula of the crystal was estimated as **2**·8 CH_3CN. Most of this solvent appears to be lost when the sample is exposed to the atmosphere. Thermogravimetric analysis (TGA) of the compound (see Supporting Information) reveals a weight loss of 2.3% in the region 30–110 °C, consistent with the loss of a small amount of residual acetonitrile from the channels. The compound is stable until ~180 °C; above this temperature a series of decomposition steps commence.

In **2**, the four independent diamondlike networks stack evenly along a direction parallel to the unique *c* axis in such a manner that channels of approximate circular cross-section extending in the *c* direction are produced (Figure 3). Allowing for the van der Waals size of the 4,4′-bpy atoms that line the surface of the channel, it is estimated[12] that each channel has a volume of approximately 880 $Å^3$ over the *c* cell length of the tetragonal unit cell. This corresponds to an average cross-sectional area of ~31 $Å^2$. The channel volume (van der Waals free space) represents 20% of the crystal volume.

When the crystals are dried in vacuo, they fail to diffract as single crystals. However, analysis of the powder diffraction pattern (see Supporting Information) reveals that the framework remains intact upon loss of solvent from the channels.

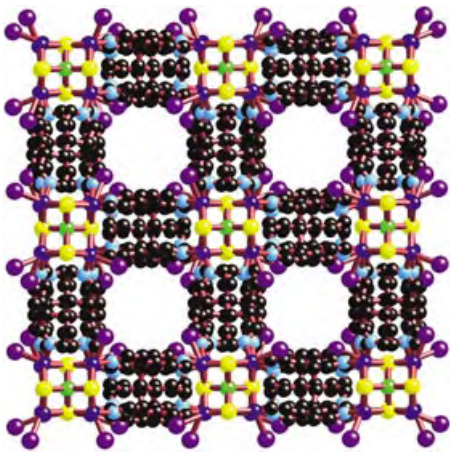


Figure 3. The structure formed from the interpenetration of the four diamond networks (two cationic and two anionic). See Figure 2 for color code; hydrogen atoms have been omitted for clarity. The channels that result from the interpenetration extend in the *c* direction.

The retention of the network structure upon loss of solvent prompted an investigation of whether guest molecules such as I_2 could be incorporated into the channels of the crystal.[13] When crystals are transferred directly from the mother liquor to a CCl_4 solution of I_2, the crystals darken considerably within a matter of minutes to a deep red-brown color, consistent with absorption of iodine. A suitable crystal was transferred directly to protective oil and placed on a diffractometer, where it was cooled to 193 K under a stream of nitrogen. Crystal-structure analysis indicated that the crystal was essentially identical to the parent crystal, except for the fact that I_2 guest molecules were now included in the channels.[10] The crystal formula was found to be **2**·2 I_2. Although the channels are large enough to hold CCl_4, the channels preferentially absorb I_2. The crystal-structure analysis revealed that the iodine is associated with the coordinated iodide. The I_2 molecule slots neatly into a space between coordinated iodide ions of two bridged clusters of an anionic net to form a Cu-I-I-I-I-Cu bridge that runs parallel to the 4,4′-bpy bridge. As indicated in Figure 4, the iodine atoms in this bridge are not evenly spaced and, in fact, may be considered as an I_2 molecule that forms interactions with a pair of coordinated iodide ions. A representation of the channels showing the I_4^{2-} bridges is presented in the Supporting Information. Examples of M-I-I-I-I-M bridges are well known[14,15] (M = a wide variety of metals), and

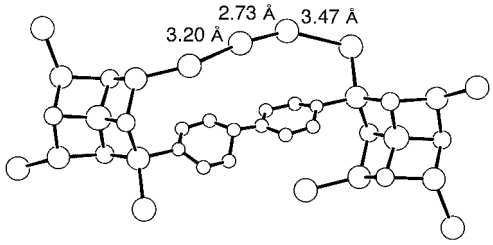


Figure 4. The I_4^{2-} link between two clusters of the anionic network in **2**·2 I_2; hydrogen atoms have been omitted for clarity.

 © 2004 Wiley-VCH Verlag GmbH & Co. KGaA, Weinheim

although there is some variation in the geometry of the I_4^{2-} ion, most examples seem to have a short separation between the central iodine atoms, with longer contacts to the terminal iodides. The Raman spectrum of **2**·2 I_2 (see Supporting Information) shows a band at 175 cm^{-1}, which is absent in the spectrum of **2**, and is presumably due to the incorporation of iodine. In the compound $CrPcI_2 \cdot I_2$ (H_2Pc = phthalocyanine), in which iodine molecules are held between coordinated iodides, the vibrational band is at 180 cm^{-1}.[16] Pure I_2 has a vibrational band at 185 cm^{-1}.

As indicated earlier, precautions need to be taken to protect the crystals from iodine loss. If the crystals are exposed to the atmosphere then some iodine is lost relatively easily to form crystals of formula **2**·0.9 I_2 (See Supporting Information). These crystals can withstand washing with solvents (carbon tetrachloride and diethyl ether) without further loss of I_2, however the single-crystal character appears to be affected in the transition from **2**·I_2 to **2**·0.9 I_2. TGA indicates that **2**·0.9 I_2 starts to lose iodine (not the coordinated iodide) at $\approx$60 °C (see Supporting Information), and the mass loss is consistent with the chemical analysis. Following the loss of the iodine, the TGA results are similar to those of the parent compound. Although it may be reasonably argued that the relative ease with which at least half the iodine is lost from **2**·2 I_2 indicates only a weak association, it is clear that the coordinated iodide ions belonging to neighboring clusters of a single net provide a simple and effective receptor site for a guest iodine molecule. Not only are the crystals capable of absorbing iodine from solution, but they can also absorb iodine vapor to form a more deeply colored material (see Supporting Information for photograph). The successful inclusion of the iodine prompted an investigation of whether other guests could be accommodated within the channels. When crystals are placed in neat aniline, the crystals absorb the aniline to form a compound of formula **2**·4.2 aniline. TGA measurements show the loss of $\approx$13 % mass which corresponds to the loss of aniline from the host crystal (see Supporting Information). The incorporation of the aniline despite the absence of a specific receptor site suggests that a range of suitably sized guests may be incorporated into channels.

In summary, we have demonstrated herein a facile synthesis of a novel supramolecular compound through the reaction of a preformed cluster, **1**, with 4,4′-bpy. A particularly novel feature of **2** is its ability to bind guest iodine molecules between a pair of coordinated iodide ions. Although the host properties of a wide range of coordination polymers have been previously investigated, this present work provides strong encouragement that specific receptor sites can be included in coordination polymers. We consider that there is a rich variety of finite and infinite networks that may be constructed by linking copper thiotungstate clusters with a range of ligand bridges. Work is continuing in this area.

Experimental Section

2: A "buffer band" of CH_3CN (3 mL) was carefully added to a zigzag glass tube (60 mm in diameter) containing a red solution of **1** (0.037 g, 0.02 mmol) in DMF (1 mL). This was followed by the slow addition of a solution of 4,4′-bpy (0.009 g, 0.05 mmol) in CH_3CN (2.5 mL). Finally, diethyl ether (2 mL) was carefully layered onto the solution. The glass tube was sealed and left to stand at room temperature; red prisms of **2** contaminated with some red precipitate formed in the glass tube after 5 days. Crystals for single-crystal structure analysis were transferred directly to protective oil. The prisms **2** were mechanically separated from the precipitate under a microscope. Crystals of **2** were washed thoroughly with CH_3CN and Et_2O and dried in vacuo. Yield: 6.2 mg, 24 %. Elemental analysis: calcd for $C_{60}H_{48}Cu_8I_4N_{12}S_8W_2$ (%): C 27.96, H 1.88, N 6.52, I 19.71, Cu 19.73, W 14.27; found: C 27.89, H 1.86, N 6.64, I 19.41, Cu 19.52, W 13.78; IR (KBr pellet): $\tilde{\nu} = \nu$(W-S_{br}), 439 (s) cm^{-1}.

2·2 I_2: Crystals of **2** were transferred from the mother liquor to a solution of iodine in CCl_4 and left immersed for several minutes. A suitable crystal was transferred to protective oil and placed in a stream of nitrogen at 193 K on a single-crystal diffractometer. The crystal analysis showed the formation of $[WS_4Cu_4(4,4'\text{-bpy})_4][WS_4Cu_4I_4(4,4'\text{-bpy})_2]\cdot 2\,I_2$.

2·0.9 I_2: Desolvated **2** (45.9 mg) was immersed in a solution of I_2 (80 mg) in CCl_4 (20 mL) in a closed tube for one week and then filtered. The solid was washed thoroughly with carbon tetrachloride and diethyl ether. Yield: 49.2 mg. Thermogravimetric analysis of **2**·0.9 I_2 (Supporting Information) showed a first weight loss of 8.17 %, which corresponds to 0.9 I_2 per formula unit and is consistent with the formulation: $[WS_4Cu_4(4,4'\text{-bpy})_4][WS_4Cu_4I_4(4,4'\text{-bpy})_2]\cdot 0.9\,I_2$. Subsequent weight losses follow that found for the desolvated compound. Elemental analysis: calcd for $C_{60}H_{48}Cu_8I_{5.8}N_{12}S_8W_2$ (%) C 25.68, H 1.73, N 5.99, I 26.23; found: C 25.53, H 1.69, N 5.84, I 26.17.

2·4.2 aniline: Desolvated crystals (52 mg) of **2** were added to freshly distilled aniline (20 mL) in a 20-mL Erlenmeyer flask, which was capped. The mixture was stirred for 10 min and allowed to stand at 0 °C for approximately one week. The solid, $[WS_4Cu_4(4,4'\text{-bpy})_4][WS_4Cu_4I_4(4,4'\text{-bpy})_2]\cdot 4.2\,NH_2C_6H_5$ was washed with acetonitrile and diethyl ether. Yield: 60.4 mg. Elemental analysis: calcd for $[WS_4Cu_4(4,4'\text{-bpy})_4][WS_4Cu_4I_4(4,4'\text{-bpy})_2]\cdot 4.2$ aniline (**2**·4.2 aniline) (%): C 34.47, H 2.63, N 7.65, I 17.01, Cu 7.13, W 12.39; found: C 34.63, H 2.72, N 7.98, I 16.35, Cu 6.87, W 11.88.

Received: March 22, 2004
Revised: June 4, 2004

Keywords: cluster compounds · coordination polymers · copper · sulfur · supramolecular chemistry · tungsten

[1] a) O. M. Yaghi, H. L. Li, C. Davis, D. Richardson, T. L. Groy, *Acc. Chem. Res.* **1998**, *31*, 474; b) S. R. Batten, R. Robson, *Angew. Chem.* **1998**, *110*, 1558; *Angew. Chem. Int. Ed. Engl.* **1998**, *37*, 1460; c) M. Fujita, *Chem. Soc. Rev.* **1998**, *27*, 417; d) S. Leininger, B. Olenyuk, P. J. Stang, *Chem. Rev.* **2000**, *100*, 853; e) B. J. Holliday, C. A. Mirkin, *Angew. Chem.* **2001**, *113*, 2035; *Angew. Chem. Int. Ed.* **2001**, *40*, 2022; f) F. A. Cotton, C. Lin, C. A. Murillo, *Acc. Chem. Res.* **2001**, *34*, 759; g) M. V. Bennett, L. G. Beauvais, M. P. Shores, J. R. Long, *J. Am. Chem. Soc.* **2001**, *123*, 8022; h) S. R. Seidel, P. J. Stang, *Acc. Chem. Res.* **2002**, *35*, 972; i) H. D. Selby, B. K. Roland, Z. P. Zheng, *Acc. Chem. Res.* **2003**, *36*, 933.

[2] N. L. Rosi, J. Eckert, M. Eddaoudi, D. T. Vodak, J. Kim, M. O'Keeffe, O. M. Yaghi, *Science* **2003**, *300*, 1127.

[3] R. L. Bain, D. F. Shriver, D. E. Ellis, *Inorg. Chim. Acta* **2001**, *325*, 171.

[4] S. Jin, F. J. DiSalvo, *Chem. Mater.* **2002**, *14*, 3448.

[5] J. S. Seo, D. Whang, H. Lee, S. I. Jun, J. Oh, Y. J. Jeon, K. A. Kim, *Nature* **2000**, *404*, 982.

[6] a) A. Müller, E. Diemann, R. Jostes, H. Bögge, *Angew. Chem.* **1981**, *93*, 957; *Angew. Chem. Int. Ed. Engl.* **1981**, *20*, 934; b) Y. Jeannin, F. Sécheresse, S. Bernes, F. Robert, *Inorg. Chim. Acta*

 © 2004 Wiley-VCH Verlag GmbH & Co. KGaA, Weinheim

1992, *198–200*, 493; c) X. T. Wu, P. C. Chen, S. W. Du, N. Y. Zhu, J. X. Lu, *J. Cluster Sci.* **1994**, *5*, 265; d) H. W. Hou, X. Q. Xin, S. Shi, *Coord. Chem. Rev.* **1996**, *153*, 25; e) J. P. Lang, S. J. Ji, Q. F. Xu, Q. Shen, K. Tatsumi, *Coord. Chem. Rev.* **2003**, *241*, 47.

[7] a) G. N. George, I. J. Pickering, E. Y. Yu, R. C. Prince, S. A. Bursakov, O. Y. Gavel, I. Moura, J. J. G. Moura, *J. Am. Chem. Soc.* **2000**, *122*, 8321; b) S. Shi, W. Ji, S. H. Tang, J. P. Lang, X. Q. Xin, *J. Am. Chem. Soc.* **1994**, *116*, 3615; c) S. Shi in *Optoelectronic Properties of Inorganic Compounds* (Eds.: D. M. Roundhill, J. P. Fackler, Jr.), Plenum, New York, **1998**, p. 55; d) C. M. Che, B. H. Xia, J. S. Huang, C. K. Chan, Z. Y. Zhou, K. K. Cheung, *Chem. Eur. J.* **2001**, *7*, 3998.

[8] a) J. P. Lang, H. Kawaguchi, K. Tatsumi, *Chem. Commun.* **1999**, 2315; b) Q. F. Zhang, Y. Y. Niu, W. H. Leung, Y. L. Song, I. D. Williams, X. Q. Xin, *Chem. Commun.* **2001**, 1126; c) J. P. Lang, Q. F. Xu, Z. N. Chen, B. F. Abrahams, *J. Am. Chem. Soc.* **2003**, *125*, 12683; d) W. J. Zhang, X. T. Wu, B. Wu, S. Y. Yu, G. Santoni, D. Rehder, *Inorg. Chem.* **2003**, *42*, 1130.

[9] J. P. Lang, G. Q. Bian, J. H. Cai, B. S. Kang, X. Q. Xin, *Transition Met. Chem.* **1995**, *20*, 376.

[10] Crystal data for solvated **2**·8 CH_3CN (and **2**·2 I_2 in brackets): $0.30\times0.30\times0.20$ mm^3, ($0.15\times0.15\times0.15$ mm^3), tetragonal (tetragonal), $I4_1/acd$ ($I4_1/acd$), $a=24.803(1)$ (24.803(2)), $c=28.170(2)$ (28.412(3)) Å, $V=17329.3(19)$ (17479(2)) Å^3, $\rho_{calcd}=2.227$ (2.344) g cm^{-3}, $2\theta_{max}=55.0$ (50.0)°, $\lambda=0.71070$ (0.71070) Å, $T=193$ (193) K, no. of measured and independent reflections: 87303, 4952 (147604, 4277), no. of reflections included in the refinement: 2950, $I>3\sigma(I)$ (2333, $I>3\sigma(I)$), multiscan absorption corrections applied to both crystals, $\mu=6.242$ (7.588) mm^{-1}, min./max. transmission 0.216/0.287 (0.371/0.468), structure solved by using heavy-atom methods[17] (direct methods[18]), both structures were refined against F,[19] no. of parameters 240 (228), H atoms on 4,4′-bpy ligands included at geometrically estimated positions, $R=0.052$ (0.080), $wR=0.065$ (0.087), max./min. residual electrons density 1.57/−1.25 (3.00/−2.90) e Å^{-3}. In the case of **2**·8 CH_3CN, disordered CH_3CN solvent molecules could not be identified in the large channels: however, given the size of the channels it is estimated the channels hold 64 CH_3CN molecules per unit cell. In both cases, the difference map indicated that the 4,4′-bpy unit belonging to the anionic nets exhibits some disorder. Two atoms of the asymmetric unit, which includes one half of the 4,4′-bpy ligand, were modeled over two sites each with 50% occupancy. CCDC-233039 (**2**·8 CH_3CN) and -233040 (**2**·2 I_2) contain the supplementary crystallographic data for this paper. These data can be obtained free of charge via www.ccdc.cam.ac.uk/conts/retrieving.html (or from the Cambridge Crystallographic Data Centre, 12, Union Road, Cambridge CB2 1EZ, UK; fax: (+44) 1223-336-033; or deposit@ccdc.cam.ac.uk).

[11] a) A. W. Sleight, *Inorg. Chem.* **1968**, *7*, 1704; b) K. W. Kim, M. G. Kanazidis, *J. Am. Chem. Soc.* **1992**, *114*, 4878.

[12] Volumes were estimated by using the PLATON program. PLATON: A. L. Spek, *Acta Crystallogr. Sect A* **1990**, *46*, C34.

[13] B. F. Abrahams, M. Moylan, S. D. Orchard, R. Robson, *Angew. Chem.* **2003**, *115*, 1892; *Angew. Chem. Int. Ed.* **2003**, *42*, 1848.

[14] N. N. Greenwood, A. Earnshaw, *Chemistry of the Elements*, 2nd ed., Butterworth Heinemann, Oxford, **1997**.

[15] For examples, see: E. Dubler, L. Linowsky, *Helv. Chim. Acta* **1978**, *61*, 2604; M. F. Belicchi, G. G. Fava, C. Pelizzi, *Acta Crystallogr. Sect. B* **1981**, *37*, 924; L. R. Gray, D. J. Gulliver, W. Levason, M. Webster, *Inorg. Chem.* **1983**, *22*, 2362; P. H. Svensson, J. Rosdahl, L. Khoo, *Chem. Eur. J.* **1999**, *5*, 305; P. H. Svensson, L. Khoo, *Inorg. Chem.* **1999**, *38*, 3390.

[16] J. Janczak, Y. M. Idemori, *Inorg. Chem.* **2002**, *41*, 5059.

[17] *DIRDIF99*: P. T. Beurskens, G. Admiraal, G. Beurskens, W. P. Bosman, R. de Gelder, R. Israel, J. M. M. Smits, *The DIRDIF-99 program system*, *Technical Report of the Crystallography Laboratory*, University of Nijmegen, The Netherlands, **1999**.

[18] G. M. Sheldrick, SHELX97-*Programs for Crystal Structure Analysis*, Göttingen, Germany, **1998**.

[19] D. J. Watkin, C. K. Prout, J. R. Carruthers, P. W. Betteridge, CRYSTALS, Issue 10, Chemical Crystallography Laboratory, Oxford, UK, **1996**.

 © 2004 Wiley-VCH Verlag GmbH & Co. KGaA, Weinheim

Crystal Growth

Morphology Control of Stolzite Microcrystals with High Hierarchy in Solution**

Biao Liu, Shu-Hong Yu, Linjie Li, Qiao Zhang, Fen Zhang, and Ke Jiang*

The shape, phase, and size of inorganic nanocrystals are important elements in varying their electrical, optical, and other properties,[1] so rational control over these elements has become a hot research topic in recent years.[2] Much effort has been made in the design of rational methods for synthesizing one-dimensional nanostructures such as nanorods, nanowires,[3] nanobelts,[4] and nanotubes.[5] Self-assembled hierarchical and repetitive superstructures are also fascinating because of their promising complex functions.[6] Chemical vapor deposition (CVD),[4,7] laser-assisted catalytic growth (LCG),[8] the use of hard templates,[9] electrochemical deposition, and controlled solution growth at elevated temperature or pH value are general synthesis routes.[5] Application of organic additives,[10] self-assembled organic superstructures, and templates with complex functionalization patterns[11] to direct the growth of inorganic material is also attractive, as controlled morphologies and architectures can be obtained under near-natural conditions.[12]

Lead tungstate ($PbWO_4$) has attracted intense interest for its scintillator applications in high-energy physics.[13] This crystal has a density of 8.2 $g\,cm^{-3}$, a short decay time (less than

[*] B. Liu, Prof. Dr. S.-H. Yu, L. Li, Q. Zhang, F. Zhang, K. Jiang
Department of Nanomaterials and Nanochemistry
Hefei National Laboratory for Physical Sciences at Microscale
Structure Research Laboratory of CAS and
Department of Materials Science and Engineering
University of Science and Technology of China
Hefei 230026 (P. R. China)
Fax: (+86) 551-360-3040
E-mail: shyu@ustc.edu.cn

[**] This work was supported by special funding from the Centurial Program of the Chinese Academy of Sciences, the Distinguished Youth Fund (Contract No. 20325104), the Distinguished Team (Grant No. 20321101), and Contract No. 50372065 from the Natural Science Foundation of China.

Supporting information for this article is available on the WWW under http://www.angewandte.org or from the author.

 DOI: 10.1002/anie.200460090 © 2004 Wiley-VCH Verlag GmbH & Co. KGaA, Weinheim

10 ns for 85% of light output), and high resistance to radiation damage (10^7 rad for undoped material and 10^8 rad for La-doped $PbWO_4$).[14] Since 1994 it has been used as a scintillating medium for a new-generation crystal calorimeter in the Large Hadron Collider (LHC) project at CERN.[15] Moreover, $PbWO_4$ is promising as an active medium in laser and stimulated Raman scattering.[16]

A lot of effort has been made to synthesize $PbWO_4$ crystals. Single crystals are usually grown from the melt by the Czochralski[13] and Bridgeman[14] methods, whereas a hydrothermal route results in $PbWO_4$ crystals with poorly defined shapes.[17] Recently, $CdWO_4$ and $PbWO_4$ nano- and microcrystals with various morphologies such as rods, spindles, and pagodas were synthesized by a wet chemical route.[18,19] Nitsch et al. synthesized $PbWO_4$ with a scheelite structure from a gel at low temperature.[20]

Herein, we introduce a facile and mild solution method for preparing $PbWO_4$ crystals with controlled morphologies and special optical properties. Tetragonal stolzite with hierarchical microstructures can be easily synthesized on a large scale by controlling the reaction conditions, such as pH value, surfactant, and temperature.

Figure 1 shows the X-ray diffraction (XRD) patterns of the as-prepared products at different temperatures and pH values with the same initial concentrations (the concentrations of Pb^{2+}, WO_4^{2-}, and cetyltrimethylammonium bromide (CTAB) were all 0.0333 mol L^{-1}). The reflection peaks of the different products can be indexed as a pure tetragonal scheelite structure with cell parameters $a = 5.46$ and $c = 12.04$ Å, which is in good agreement with the literature values (JCPDS Card Number 86-0843). However, on comparing the peak intensities we found that the relative intensity of the peaks corresponding to the (004) and (200) planes varied significantly from the literature value, which indicates the different tropism of the crystals.

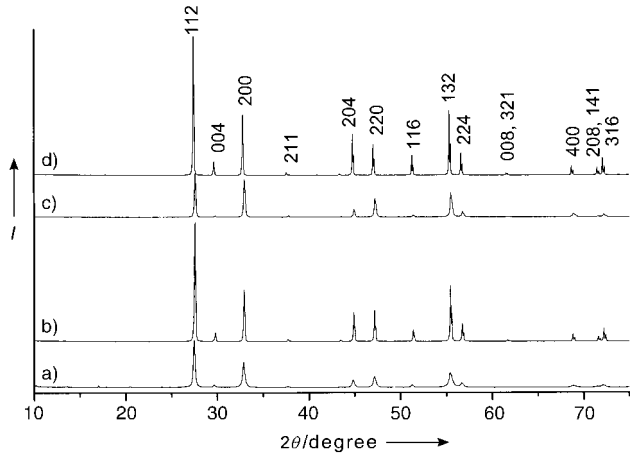


Figure 1. XRD patterns of the $PbWO_4$ obtained under different conditions: a) aging at 60 °C for 60 h, pH 4.0; b) aging at 60 °C for 18 h, pH 7.0; c) aging at 160 °C for 12 h, pH 4.0; d) aging at 160 °C for 12 h, pH 7.0. The initial concentrations of CTAB, Pb^{2+}, and WO_4^{2-} were all 0.0333 mol L^{-1}.

Figure 2a is a typical SEM image of the sample (Figure 1a) obtained after aging at 60 °C for 60 hours, which shows that the product consists of homogeneous spindlelike microrods of diameter 0.8–1.5 μm at the center and length more than 10 μm. High-magnification SEM images (Figure 2b–d) clearly reveal that the microrods are constructed from ellipsoidal particles with a diameter of about 100 nm and length of about 1 μm. It is interesting that these ellipsoidal nanoparticles are highly directed to form arrays in a somewhat helical manner (see the arrows in Figure 2b,c). Our proposed schematic illustration for such complex structures is depicted in Figure 2d.

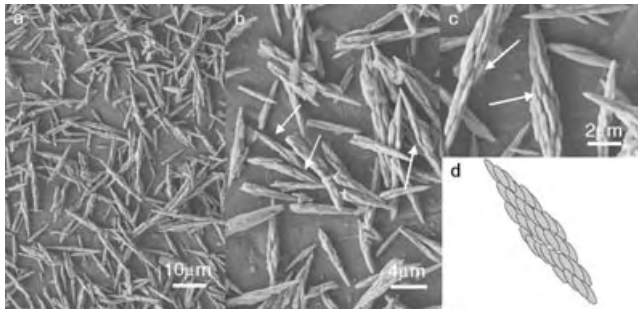


Figure 2. a)–c) SEM images of the $PbWO_4$ helixlike structures obtained by aging at 60 °C for 60 h; the concentrations of Pb^{2+}, WO_4^{2-}, and CTAB were all 0.0333 mol L^{-1}, pH 4.0. The arrows show helixlike structures which are composed of arrayed ellipsoidal particles. d) A schematic illustration of the helixlike structures.

The growth process of these helical structures was carefully followed by time-dependent experiments. The TEM image in Figure 3a shows that some spindles and chainlike structures occur. These structures are composed of directly arrayed nanopolyhedrons (Figure 3b,d) that are attached to each other in an interesting parallel and scalariform way, rather than in a simple parallel manner. Selected-area electron diffraction (SAED) and high-resolution TEM (HRTEM) were used to investigate how the nanopolyhedrons are attached to each other. Figure 3c shows the electron diffraction (ED) patterns recorded from the whole chainlike structure (Figure 3b), which can be indexed to tetragonal-phase $PbWO_4$ viewed along the $[28\bar{1}]$ direction. Similarly, the ED patterns (Figure 3d) recorded from the whole spindle constructed from assembled nanopolyhedrons (Figure 3e) can be indexed to tetragonal-phase $PbWO_4$ viewed along the $\langle 1\bar{1}0 \rangle$ direction. The ED patterns are similar from whichever direction they are viewed or from whichever congeries in the samples they are recorded, which underlines the fact that the attached nanoparticles share the same crystal direction. This observation was further confirmed by a careful HRTEM study. Therefore, the early stage in the formation of such helixlike structures still agrees well with that of the final stage (Figure 2).

The two-dimensional crystal-lattice patterns are the same even though they are obtained from the "subunits" of the crystals, that is, different nanopolyhedrons (Figure 3e–h). The fringe spacing along the different directions was determined

 © 2004 Wiley-VCH Verlag GmbH & Co. KGaA, Weinheim

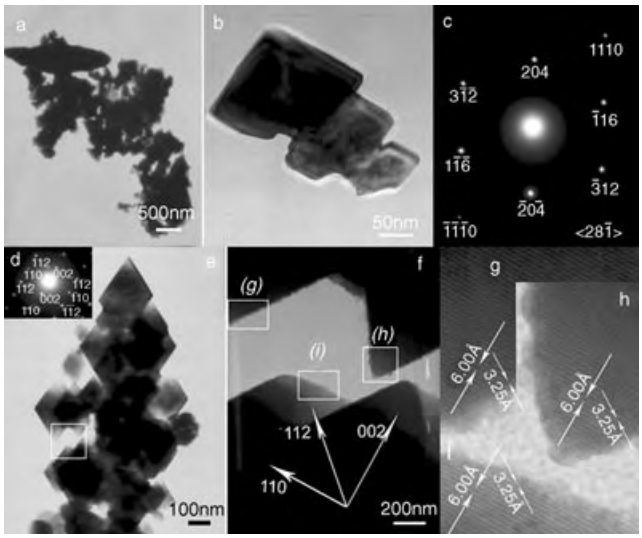


Figure 3. TEM images, ED patterns, and HRTEM images of the sample obtained in the early stages of forming $PbWO_4$ helical structures by mixing $Na_2WO_4{\cdot}2H_2O$, $PbAc_2$, and CTAB solution. The concentrations of Pb^{2+}, WO_4^{2-}, and CTAB were all kept at 0.0333 mol L^{-1}, pH 4.0. a) The general morphology of the sample. b) The chainlike structure formed by nanopolyhedrons assembled in a scalariform manner, which is observed frequently in the sample. c) The ED pattern recorded from the whole chainlike structure shown in (b). d) The ED pattern recorded from the whole spindlelike particle shown in (e). e) A typical spindlelike particle which is constructed from assembled nanopolyhedrons, showing the scalariform ordered assembly. f) A HRTEM image taken from the area marked by the pane in (e). g)–i) HRTEM images magnified from (f); the areas are indicated by the panes marked with *(g)*, *(h)*, and *(i)*.

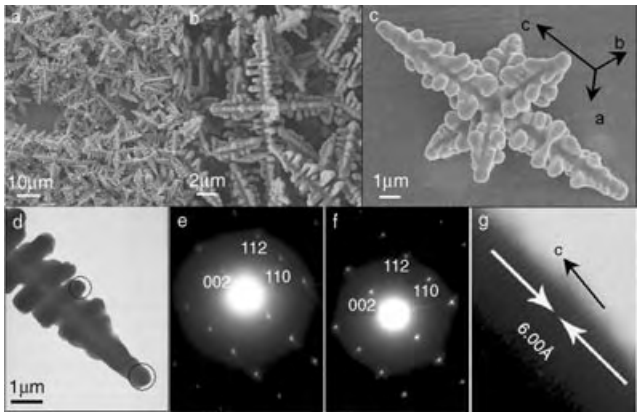


Figure 4. SEM images, TEM images, and ED patterns of the $PbWO_4$ dendrites obtained after aging at 60 °C for 18 h. The initial concentrations of Pb^{2+}, WO_4^{2-}, and CTAB were all 0.0333 mol L^{-1}, pH 7.0. a) A general view of the sample; b) a higher magnification SEM image; c) a typical single dendrite; d) a magnified TEM image showing part of the dendrite; e) ED pattern recorded from the branched part marked with circles in (d); f) ED pattern recorded from the tip of the trunk circled in (d); g) a typical HRTEM image taken from the tip of the branch.

as 3.25 and 6.00 Å for the (112) and (002) planes, respectively. It can be concluded that the elongated helical structures evolved from such aggregates, which grew preferentially along the *c* axis after aging for some time. The nanopolyhedrons were formed quickly after the reagents were mixed, and the spindles with hierarchical structures evolved from the nanopolyhedrons by the oriented attachment process accompanying Ostwald ripening. Such events are consistent with previous reports[21–23] of a so-called "oriented attachment" process that controls the initial stages in the formation of these unusual structures. However, the Ostwald ripening process also contributes to the formation of such structures, by "shearing" the nanopolyhedrons into the blunt ellipsoidal particles identified in their ripened final stage.

The morphology of the products varied greatly when the pH value was increased to 7.0 and the other conditions were kept the same. All the samples are homogeneous dendritic structures (Figure 4 a,b), which are quite similar to that reported for cubic PbS microstructures.[24,25] However, the individual $PbWO_4$ dendrite with three-dimensional structure displays more complex features than that previously reported for PbS.[24,25] There are two shorter trunks and a longer one; three crossed trunks construct the framework in a perfect perpendicular manner. Four branches grow vertically on each trunk in two perpendicular directions, which are similar to the growth directions of the other two trunks, and ordered microrods parallel to each other form the branches. The length of the longer trunk is about 20 μm and that of the two branches is about 9 μm. The ratio of the lengths of the three main trunks is equal to the ratio of the cell parameters $c/a = c/b = 2.2{:}1$; therefore, it is believed that the longer trunk grew in the *c* direction and the two shorter ones, in the *a* or *b* direction (Figure 4 c). The dimensions of such high hierarchical structures finely reflect the outside embodiment of the intrinsic cell structure of stolzite quite well. Further optimization of the growth conditions could make it possible to obtain perfect hierarchical structures.

The structural characteristics of the crystal were further elucidated by TEM and ED techniques. The SAED patterns taken from the branch and main trunk areas marked by the circles in Figure 4 d (Figure 4 e,f, respectively) are identical, which indicates that they share the same crystal direction along the *c* axis. We also investigated some other crystals in the sample and found that this observation is universal for all dendritic crystals. A typical HRTEM image recorded from the tip of a branch is shown in Figure 4 g. The fringe spacing was about 6.00 Å, which corresponds to the lattice spacing for the (002) faces. This result confirmed the supposition of the growth direction of the dendritic crystal.

The temperature was found to significantly affect the shape of the particles. The shape when the temperature was increased to 160 °C and the other conditions were kept constant was completely different from that observed at low temperature. After hydrothermal treatment for 12 hours at 160 °C (pH 4.0), the products are dendritic structures (Figure 5 a,b), whose length ranges from several micrometers to more than 10 μm. Unlike the sample obtained at 60 °C for 60 hours, the individual $PbWO_4$ dendrite has only one trunk and four shrunken branches. The branches are perpendicular to the trunk and they are built up of parallel-arrayed particles. The sample was transformed into peanutlike microrods with certain crystal faces exposed (Figure 5 c,d) after hydrothermal treatment for 12 hours at pH 7.0.

 © 2004 Wiley-VCH Verlag GmbH & Co. KGaA, Weinheim

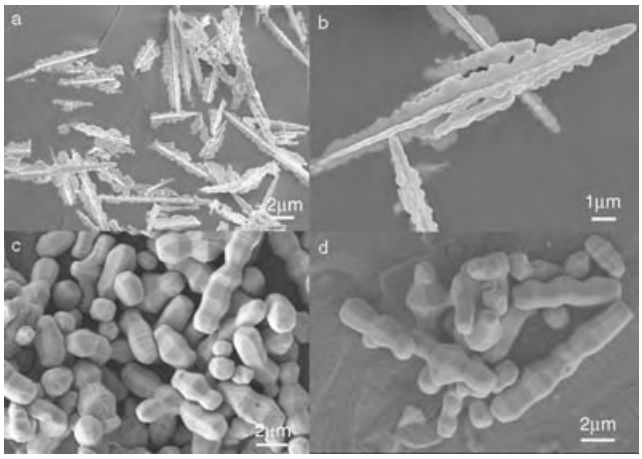


Figure 5. The influence of the pH value on the shape of $PbWO_4$ crystals. SEM images of: a),b) dendrite structures obtained at pH 4.0; c),d) rodlike and crosslike structures obtained at pH 7.0. Both of these samples were hydrothermally treated at 160 °C for 12 h, and the initial concentrations of Pb^{2+}, WO_4^{2-}, and CTAB were all 0.0333 mol L^{-1}.

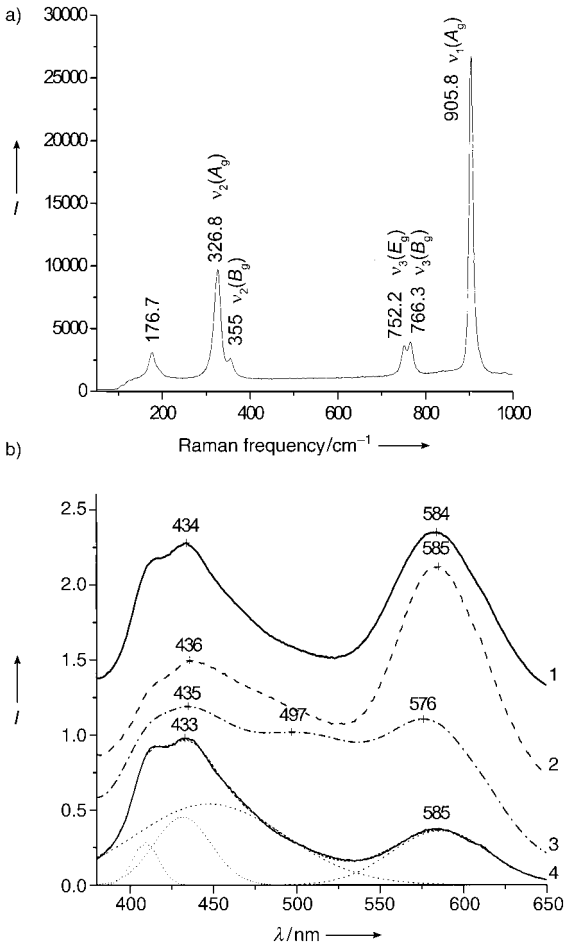


Figure 6. Optical properties of $PbWO_4$ crystals. a) Raman spectrum of the dendritic crystals with three trunks. b) Photoluminescence spectra. Curve 1 corresponds to the helical-array structure (Figure 2). Curve 2 corresponds to the dendritic structure with three trunks (Figure 4) and curve 3, to the dendritic crystals with only one trunk (Figure 5 a,b). Curve 4 corresponds to the peanutlike crystals (Figure 5 c,d) and is decomposed into four Gaussian components with peaks located at 410, 431, 454, and 485 nm (dotted lines). The excitation wavelength was 350 nm and all the spectra were recorded at room temperature.

Furthermore, the surfactant CTAB plays an important role in controlling the morphology of $PbWO_4$. If the other conditions are kept the same but with no added CTAB, or the concentration of CTAB is increased from 0.0333 to 0.2333 mol L^{-1}, only irregular particles are obtained (see Supporting Information). This observation can be explained if CTAB is adsorbed on specific facets of the $PbWO_4$ crystal and changes their surface energy if the amount of CTAB is appropriate. In contrast, the nonadsorbed facets will grow rapidly, as identified in the synthesis of TiO_2 nanocrystals controlled by a surfactant.[23] If the concentration of CTAB is too high, all the facets will have adsorbed surfactant such that it loses the ability to control the morphology of the growing crystals (see Supporting Information). We assume that the influence of the temperature and pH value on the growth of the crystals may lie in three aspects: affecting the adsorption of CTAB to different facets, changing the relative energy of the different facets, and affecting the controlling growth mechanism. More careful investigation is still needed.

The optical properties of these complex structures were also studied. The Raman spectrum of the stolzite helical structure (Figure 6 a) shows six bands in the range 100–1000 cm^{-1}. The peaks located at 905.8, 766.3, 752.2, 355, and 326.8 cm^{-1} correspond to the vibration modes $\nu_1(A_g)$, $\nu_3(B_g)$, $\nu_3(E_g)$, $\nu_2(B_g)$, and $\nu_2(A_g)$, respectively, which are consistent with those reported by Frost and co-workers.[26] However, a peak at 176.1 cm^{-1} was observed, which was not reported previously.[26] This peak is not assigned by Ross,[27] but it could be assigned as the translation mode analogous to that for $CdMoO_4$.[26] The two bands at 752.2 and 766.3 cm^{-1} are of almost identical intensity, which could be a consequence of identical crystal growth along the *a* and *b* axes. The Raman spectra of stolzite crystals with other shapes (Figure 5 and Supporting Information) are similar to that of the stolzite with hierarchical structures (Figure 2 and Figure 4).

Figure 6 b shows the room-temperature photoluminescence spectra of the different microstructures. Curves 1–4 correspond to the helical-array structures (Figure 2), the dendritic structures with three trunks (Figure 4), the dendritic structures with one trunk (Figure 5 a,b), and the peanutlike structures (Figure 5 c,d), respectively. All the curves have two main peaks: one is located at about 435 nm, which is similar to the reported value for the blue emission component;[13,28] the other is at about 585 nm and has never been observed previously in the bulk stolzite by other authors. The existence of the orange emission peak (at about 585 nm) may be related to the surface defects of the stolzite crystals, since it was observed in all the crystals with different structures as their size decreased to the micrometer scale but not in bulk crystals. Meanwhile, the relative intensities of the two broadening emission peaks seem closely related to the surface/volume ratio. The dendritic structures with three trunks have the biggest surface/volume ratio, and the relative intensity of the peak at 585 nm is highest. In contrast, the relative intensity of the emission peak at 585 nm for peanutlike structures, which

 © 2004 Wiley-VCH Verlag GmbH & Co. KGaA, Weinheim

have the smallest surface/volume ratio, is the lowest. As described previously,[27a] the peaks at about 435 nm can be decomposed into several Gaussian components with peaks at 410, 431, 454, and 500 nm. The relative intensity of these decomposed peaks differed according to the particular crystal structure. For example, only the dendritic structures with one trunk give a strong peak at about 500 nm, and the helical-array structures give a stronger peak than the other structures at 435 nm. These results could indicate that the special structures might have some significant influence on the optical properties of tetragonal $PbWO_4$ crystals, which could be adopted in fine-tuning the surface-defect-related optical properties of this material.

In summary, we have successfully synthesized tetragonal $PbWO_4$ microcrystals with special hierarchical structures by controlling the solution reaction conditions, such as the amount of cationic surfactant CTAB, pH value, and temperature. The formation of helixlike structures has been investigated, and the oriented attachment process clearly contributes to the creation of such structures. Novel dendrites with hierarchical structures and exhibiting high crystal symmetry can be synthesized by further varying the pH value of the solution. Each dendritic crystal is composed of three main trunks on which four branches of arrayed nanorods start to grow. The CTAB and the temperature play important roles in controlling the morphology.

The optical properties of these hierarchical tetragonal $PbWO_4$ microcrystals differ from those of the bulk crystals, which could be related to their structural complexity and specialty. Further detailed characterization of this relationship is needed. Lead tungstate has an important role as a functional material, and thus the rational design of its complex structures could be of significance in scintillator applications. This synthesis method has demonstrated that it is possible to design complex and hierarchical structures by a facile, mild solution approach, which could be extended to the morphogenesis of other inorganic crystals with complex forms.

Experimental Section

Analytical grade $Na_2WO_4{\cdot}2H_2O$, $Pb(CH_3COO)_2$ ($PbAc_2$), and cetyltrimethylammonium bromide (CTAB) were purchased from Shanghai Chemical Industrial Company and were used without further purification. The reaction was carried out in a 60-mL teflon-lined stainless-steel autoclave or a 100-mL glass jar, and the temperature was regulated by a digital-type temperature-controlled oven.

Typical procedure: $Na_2WO_4{\cdot}2H_2O$ (2 mmol) and $PbAc_2$ (2 mmol) were placed in separate beakers, distilled water (25 mL) was added, and the contents were magnetically stirred to form homogeneous solutions at room temperature. The $PbAc_2$ solution was added slowly to the Na_2WO_4 solution under strong magnetic stirring to form a mixture containing amorphous particulates. The pH was adjusted to a specific value using NaOH or acetic acid solution (1 mol L^{-1}). The resulting precursor suspension was transferred to a teflon-lined stainless-steel autoclave (reaction temperature higher than 100 °C) or glass jar (reaction temperature lower than 100 °C). The container was sealed and maintained at a certain temperature for the desired reaction time, then allowed to cool slowly to room temperature. The products were collected by filtration, washed several times with distilled water and absolute ethanol, and finally dried in a vacuum at 60 °C for 4 h.

The products were characterized by X-ray diffraction (XRD), recorded on a MAC Science Co. Ltd. MXP 18 AHF X-ray diffractometer with monochromatized CuK_α radiation ($\lambda =$ 1.54056 Å). Microscopy was performed with a Hitachi (Tokyo, Japan) H-800 transmission electron microscope (TEM) at an accelerating voltage of 200 kV, and a JEOL-2010 high-resolution TEM, also at 200 kV. Raman spectra were recorded on a Jobin Yvon (France) LABRAM-HR confocal laser micro-Raman spectrometer at room temperature and an excitation wavelength of 514.5 nm. The photoluminescence spectra were recorded on a Fluorolog3-TAU-P instrument at room temperature.

Received: March 23, 2004

Keywords: self-assembly · crystal growth · helical structures · lead · tungsten

[1] a) C. M. Lieber, *Solid State Commun.* **1998**, *107*, 607; b) A. P. Alivisatos, *Science* **1996**, *271*, 933.
[2] Y. Xia, P. Yang, Y. Sun, Y. Wu, B. Mayer, B. Gates, Y. Yin, F. Kim, H. Yan, *Adv. Mater.* **2003**, *15*, 353.
[3] S. H. Yu, B. Liu, M. S. Mo, J. H. Huang, X. M. Liu, Y. T. Qian, *Adv. Funct. Mater.* **2003**, *13*, 639.
[4] Z. W. Pan, Z. R. Dai, Z. L. Wang, *Science* **2001**, *291*, 1947.
[5] X. Wang, X. M. Sun, D. Yu, B. S. Zou, Y. Li, *Adv. Mater.* **2003**, *15*, 1442.
[6] a) H. Yang, N. Coombs, G. A. Ozin, *Nature* **1997**, *386*, 692; b) G. A. Ozin, H. Yang, I. Sokolov, N. Coombs, *Adv. Mater.* **1997**, *9*, 662; c) S. Mann, *Angew. Chem.* **2000**, *112*, 3532; *Angew. Chem. Int. Ed.* **2000**, *39*, 3392; d) S. H. Yu, M. Antonietti, H. Colfen, J. Hartmann, *Nano Lett.* **2003**, *3*, 379.
[7] J. Y. Lao, J. G. Wen, Z. F. Ren, *Nano Lett.* **2002**, *2*, 1287.
[8] a) J. T. Hu, T. W. Odom, C. M. Lieber, *Acc. Chem. Res.* **1999**, *32*, 435; b) A. M. Morales, C. M. Lieber, *Science* **1998**, *279*, 208; c) X. F. Duan, C. M. Lieber, *Adv. Mater.* **2000**, *12*, 298.
[9] a) J. Goldberger, R. R. He, Y. F. Zhang, S. W. Lee, H. Q. Yan, H. J. Choi, P. D. Yang, *Nature* **2003**, *422*, 599; b) R. Fan, Y. Y. Wu, D. Y. Li, M. Yue, A. Majumdar, P. D. Yang, *J. Am. Chem. Soc.* **2003**, *125*, 5254.
[10] a) Z. R. Tian, J. A. Voigt, J. Liu, B. Mckenzie, M. J. Mcdermott, *J. Am. Chem. Soc.* **2002**, *124*, 12954; b) D. Kuang, A. Xu, Y. Fang, H. Liu, C. Frommen, D. Fenke, *Adv. Mater.* **2003**, *15*, 1747.
[11] a) W. A. Lopes, H. M. Jaeger, *Nature* **2001**, *414*, 735; b) X. Chen, Z. Chen, N. Fu, G. Lu, B. Yang, *Adv. Mater.* **2003**, *15*, 1413.
[12] a) D. D. Archibald, S. Mann, *Nature* **1993**, *364*, 430; b) S. Mann, G. A. Ozin, *Nature* **1996**, *382*, 313; c) for a review, see: H. Cölfen, S. Mann, *Angew. Chem.* **2003**, *115*, 2452; *Angew. Chem. Int. Ed.* **2003**, *42*, 2350 and references therein; L. A. Estroff, A. D. Hamilton, *Chem. Mater.* **2001**, *13*, 3227.
[13] K. Nitsch, M. Nikl, S. Ganschow, P. Reiche, R. Uecker, *J. Cryst. Growth* **1996**, *165*, 163.
[14] K. Tanji, M. Ishii, Y. Usuki, M. Kobayashi, K. Hara, H. Takano, *J. Cryst. Growth* **1999**, *204*, 505.
[15] a) P. Lecoq, I. Dafinei, E. Auffray, M. V. Korzhik, V. B. Pavlenko, A. A. Fedorov, A. N. Annencov, V. L. Kostyllev, V. D. Ligun, *Nucl. Instrum. Methods Phys. Res. Sect. A* **1995**, *365*, 291.
[16] A. A. Kaminskii, H. J. Eichler, K. Ueda, N. V. Klassen, B. S. Redkin, L. E. Li, J. Findeisen, D. Jaque, J. Garcia-Sole, J. Fernandez, R. Balda, *Appl. Opt.* **1999**, *38*, 4533.
[17] C. H. An, K. B. Tang, G. Z. Shen, C. R. Wang, Y. T. Qian, *Mater. Lett.* **2002**, *57*, 565.
[18] S. H. Yu, M. Antonietti, H. Cölfen, M. Giersig, *Angew. Chem.* **2002**, *114*, 2462; *Angew. Chem. Int. Ed.* **2002**, *41*, 2356.

 © 2004 Wiley-VCH Verlag GmbH & Co. KGaA, Weinheim

[19] X. L. Hu, Y. J. Zhu, *Langmuir* **2004**, *20*, 1521.
[20] K. Nitsch, M. Nikl, M. Rodova, S. Santucci, *Phys. Status Solidi A*, **2000**, *179*, 261.
[21] a) R. L. Penn, J. F. Banfield, *Geochim. Cosmochim. Acta* **1999**, *63*, 1549; b) R. L. Penn, J. F. Banfield, *Science* **1998**, *281*, 969.
[22] Z. Y. Tang, N. A. Kotov, M. Giersig, *Science* **2002**, *297*, 237.
[23] Y. W. Jun, M. F. Casula, J. H. Sim, S. Y. Kim, J. Cheon, A. P. Alivisatos, *J. Am. Chem. Soc.* **2003**, *125*, 15981.
[24] D. Kuang, A. Xu, Y. Fang, H. Liu, C. Frommen, D. Fenske, *Adv. Mater.* **2003**, *15*, 1747.
[25] Y. Ma, L. Qi, J. Ma, H. Cheng, *Cryst. Growth Des.* **2004**, *2*, 351.
[26] M. Crane, R. L. Frost, P. A. Williams, J. T. Kloprogge, *J. Raman Spectrosc.* **2002**, *33*, 62.
[27] S. D. Ross, *Inorganic Infrared and Raman Spectra*, McGraw-Hill, Maidenhead, **1972**.
[28] a) K. Polak, M. Nikl, K. Nitsch, M. Kobayashi, M. Ishii, Y. Usuki, O. Jarolimek, *J. Lumin.* **1997**, *72–74*, 781; b) M. Nikl, P. Strakova, K. Nitsch, V. Petricek, V. Mucka, O. Jarolimek, J. Novak, P. Fabeni, *Chem. Phys. Lett.* **1998**, *291*, 300.

 © 2004 Wiley-VCH Verlag GmbH & Co. KGaA, Weinheim

DNA Devices

A Protein-Driven DNA Device That Measures the Excess Binding Energy of Proteins That Distort DNA**

*Wanqiu Shen, Michael F. Bruist, Steven D. Goodman, and Nadrian C. Seeman**

Nanomechanical devices hold the promise of controlling structure and performing exquisitely fine measurements on the molecular scale. We previously have reported three nanoscale devices that were built from DNA. The first device[1] extrudes or withdraws a portion of a DNA cruciform from a cyclic molecule in response to the presence of an intercalator. The second device is powered by the B–Z transition:[2] it switches a DNA domain from one side of a double-helical shaft to the other in response to the presence or absence of $[Co(NH_3)_6]^{3+}$ in its environment. The third device is sequence-dependent;[3] it changes structure as a function of DNA strands that are in solution with it. All of these devices change their states in response to an external stimulus, but they do not report new information about any other molecular system. Here we describe a new DNA device that changes shape when a DNA-distorting protein is added to the system. In this case, we used *E. coli* integration host factor (IHF), which bends DNA significantly when it binds to an appropriate recognition site.[4] Thus, we have developed a nanomechanical device for which the stimulus is a protein. However, this device does not merely have a different kind of activation signal. A second part of the device contains a series of nucleotide pairs that must be disrupted when the device is distorted by IHF. Consequently, this is a measuring device that enables us to estimate the amount of additional work that the protein can do when it binds to DNA.

Our IHF-activated device is illustrated schematically in Figure 1. This diagram does not illustrate the part of the device involved in measuring the work, but, for simplicity, shows just the way in which the binding of IHF to its target site can distort the relationship between two DNA triple crossover (TX) motifs that flank the binding site. The upper panel shows the DNA molecule in the absence of IHF: two previously characterized TX molecules[5] are connected by a DNA double-helical shaft; each TX molecule creates a stiff domain that rigidly transmits motions of the shaft on one side to the dyes on the other side. The shaft contains the λH1

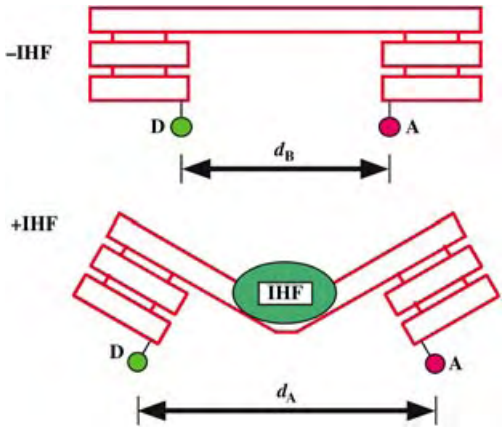


Figure 1. The action of the nanomechanical device. Double-helical DNA is shown as rectangular boxes. The triple crossover motifs (TX) are shown as three fused rectangular boxes. The upper domain connects the two TX motifs with the binding site for IHF. IHF is shown as a green ellipse, and in the lower panel its binding distorts the connecting shaft. For clarity, the 160° bend[4] is reduced to 45° here. A donor dye (D, fluorescein) and an acceptor dye (A, Cy3) are shown as a green and a magenta circle, respectively. The fluorescence resonance energy transfer reported by this pair decreases upon IHF binding, as the distance between the dyes increases from d_B to d_A.

[*] Dr. W. Shen, Prof. N. C. Seeman
Department of Chemistry
New York University
New York, NY 10003 (USA)
Fax: (+1) 212-260-7905
E-mail: ned.seeman@nyu.edu
Prof. M. F. Bruist
Department of Chemistry
University of the Sciences in Philadelphia
Philadelphia, PA 19104 (USA)
Prof. S. D. Goodman
Department of Molecular and Computational Biology
University of Southern California
Los Angeles, CA 90089-0641 (USA)

[**] We thank Dr. Paul Rothemund, Dr. Bruce Demple, and Dr. Alexander Vologodskii for valuable suggestions, and Dr. John SantaLucia for generously giving us prepublication estimates of stacking free energies. This research has been supported by grants GM-29554 from NIGMS, N00014-98-1-0093 from ONR, grants DMI-0210844, EIA-0086015, DMR-01138790, and CTS-0103002 from the NSF, F30602-01-2-0561 from DARPA/AFSOR to N.C.S. and GM-055392 from NIGMS to S.D.G.

 © 2004 Wiley-VCH Verlag GmbH & Co. KGaA, Weinheim DOI: 10.1002/anie.200460302

binding site[6] for IHF; the binding site is completely contained on the shaft, and does not extend past it to the TX molecules. Pendent from the bottom domains of the TX molecules are a pair of fluorescent dyes that are close enough (distance d_B) for energy to transfer between them, thus leading to a fluorescence resonance energy transfer (FRET) signal. The lower panel illustrates the effect of binding IHF to the molecule: it is distorted, which leads to an increase in the distance between the dyes (d_A) and a corresponding decrease in the FRET signal. This system is similar to that used in the B–Z device reported earlier, except that the change in energy transfer is now a consequence of DNA bending, rather than rotary displacement of a DNA double-crossover (DX) molecule.

Figure 2 illustrates the operation of the measuring device. The system is similar to that shown in Figure 1, but the lower domains of the TX portions of the device are now connected by a pair of cohesive strands (upper panel). The cohesion is broken when IHF binds to its recognition site on the top domain (lower panel). If an excess of free energy is available when IHF binds, it can disrupt the base pairs and bind normally. By using a range of cohesive lengths, each with a different free energy of association, one can use the nanodevice to estimate the amount of work of which IHF is capable when it binds to DNA. Figure 3 shows the sequence of the device. All devices used in this study migrate identically on nondenaturing gels, with mobilities similar to that of a topologically closed standard (data not shown).[7]

Figure 4 contains bar graphs that show the results of our experiments monitoring energy transfer from donor quenching; similar results are obtained from acceptor fluorescence (data not shown). In the first experiment, we took a given sequence of DNA [5′-TGCATCAC/TC-3′, where the slash

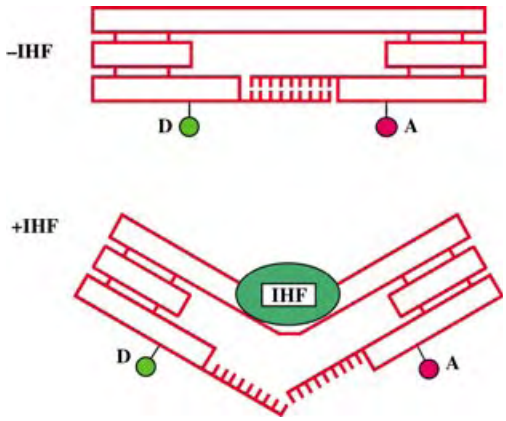


Figure 2. The TX-based measuring device. The diagram is similar to Figure 1, and the conventions there apply. However, the bottom domains have been extended towards each other, and they are connected by a cohesive tract. IHF must do work to separate the two strands in proportion to the length of the cohesive tract. Increasing the length of the cohesive tract leads to a decreasing ability of IHF to break the base pairs within it.

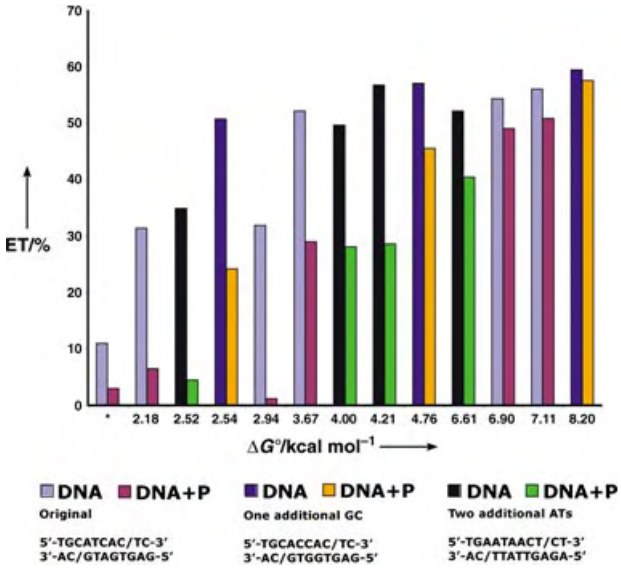


Figure 4. Donor energy transfer for molecules bound by IHF. The pairs of colored bars indicate the difference in energy transfer (ET) between unbound (DNA, left bar) and IHF-bound (DNA+P, right bar) forms. Three different overlap regions were used. The abscissa shows the estimated standard molar free energy available, based on a nearest-neighbor approximation.[8] Loop entropy was neglected. The differences are minimal at about 7–8 kcal mol^{-1}.

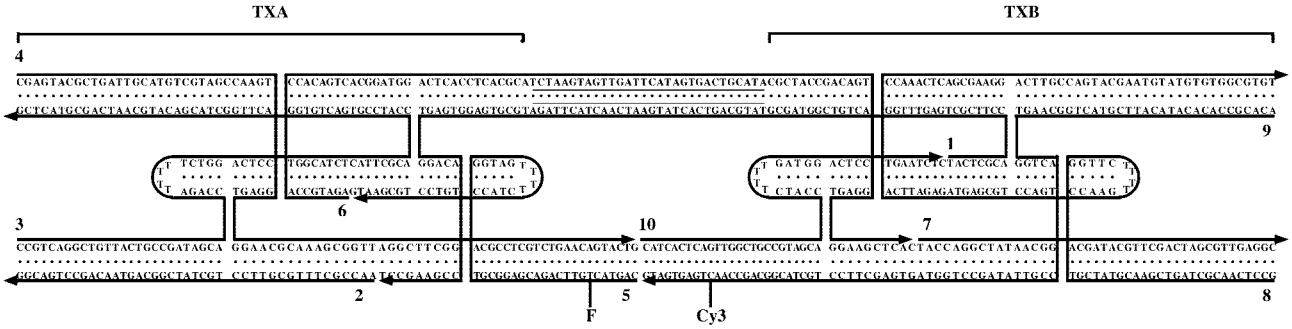


Figure 3. Sequence of the TX device used here. The ten individually numbered strands are indicated; arrowheads indicate the 3′ ends of the strands. The individual TX molecules are also indicated, and the IHF binding sequence is shown on strands 4 and 9 between them as an underlined region in the top helix. The site of fluorescein is indicated by F and that of Cy3 is shown similarly. Crossovers between strands are drawn as connections. A blunt-ended stack is shown in the bottom domain, but moving the nicks in the 3′ direction leads to the series of molecules used for the measurements. Variation of the sequence enables interpolation of values.

 © 2004 Wiley-VCH Verlag GmbH & Co. KGaA, Weinheim

indicates a nick] and changed the length of the overlap region systematically over a range of one to six nucleotide pairs. The donor energy transfers are plotted as light blue bars (before IHF binding) and light red bars (after IHF binding,). The abscissa corresponds to the standard free energy of the overlap region, using the parameters of ref. [8], plus others for the nicks, generously supplied by John SantaLucia. Each measurement was performed at least twice. Upon addition of IHF, the signal reporting energy transfer evolved for two minutes, and remained constant thereafter. We used two modifications of the basic sequence to supplement the values available from the initial sequence: data for [5′-TGCACCAC/TC-3′], containing one additional GC for AT substitution are shown in royal blue (unbound) and orange (bound), and those for [5′-TGAATAACT/CT-3′], containing two additional AT for GC substitutions, in black (unbound) and green (bound). We ascribe the relatively small amount of transfer before addition in the low-energy measurements to fraying of the small cohesive ends present. Nevertheless, it is clear that the energy transfer observed following addition of IHF increases as we increase the number of pairs holding the device together. The transition appears to be complete at about 7–8 kcal mol^{-1}, as indicated by the similar rates of energy transfer with and without IHF. We interpret the data for higher values of ΔG to indicate that the cohesion is too strong for the transition to occur.

The structures with a strand-disruption energy of less than 3 kcal mol^{-1} show little energy transfer when IHF is bound, while the structures with a disruption energy of 3–5 kcal mol^{-1} have an intermediate value for energy transfer in the presence of IHF. It is unlikely that this intermediate level comes from partial conversion of a device; these signals are more likely the average of a mixed population of completely disrupted molecules and intact molecules to which IHF was unable to bind. Once more than 7–8 kcal mol^{-1} is needed to disrupt the cohesive strands, essentially none of the devices are bent by IHF. Rather than selecting the midpoint of the measurement for our estimate of the amount of work that IHF can do, we selected the endpoint of the transition. The DNA base-pairing free energies provide only a crude indication of the energy. Yang and Nash[6] estimated the dissociation constant for IHF from the λH1 binding site to be 5.5 nM, a value for a system with no sticky ends to disrupt. Our measurement is independent of the value, and is the first estimate of the work IHF can do when it binds DNA.

We used IHF as a model DNA-bending protein to demonstrate that it is possible to use this nanomechanical device to perform the measurements described here. It is evident that this same system could be used to characterize the amount of work that can be done by other DNA-bending proteins. However, for proteins that bend in the opposite direction, such as TATA binding protein (TBP),[9] motifs with more than three coplanar helices may be needed. The question arises whether it would be possible to measure the amount of work available from proteins that introduce other distortions of DNA, such as twisting. We intentionally made this device sensitive to the relatively small spatial displacements associated with rotations. Thus, we replaced the DX units we used in the related B–Z device[2] with TX units; consequently, a twisting displacement as small as 60° leads to a change in distance (observed as a change in FRET) as large as that associated with the 180° rotation of the B–Z device. For example, the postulated twisting of SoxR[10] could be examined if its iron sulfur cluster did not quench the dyes.

Experimental Section

DNA sequences were designed with SEQUIN,[11] synthesized by standard phosphoramidite techniques,[12] and purified from denaturing gels. Cy3 labeling was done by filling-in Cyanine 3-dCTP (PerkinElmer) with Klenow Fragment (NEB) polymerase, by following a protocol suggested by the supplier. IHF was prepared as described previously.[13] 50 μM IHF stock solutions were added to aliquots of 100 μL of 100 nM DNA device complexes up to a final IHF concentration of 300 nM and incubated for 10 min before each measurement. Steady-state fluorescence measurements were performed with an AMINCO BOWMAN Series 2 spectrometer at room temperature. The emission spectra were corrected for instrument response, lamp fluctuations, and buffer contributions; energy transfer was performed as described previously.[2]

Received: April 13, 2004

Keywords: DNA structures · fluorescent probes · molecular devices · proteins

[1] X. Yang, A. Vologodskii, B. Liu, B. Kemper, N. C. Seeman, *Biopolymers* **1998**, *45*, 69–83.
[2] C. Mao, W. Sun, Z. Shen, N. C. Seeman, *Nature* **1999**, *397*, 144–146.
[3] H. Yan, X. Zhang, Z. Shen, N. C. Seeman, *Nature* **2002**, *415*, 62–65.
[4] P. A. Rice, S. W. Yang, K. Mizuuchi, H. A. Nash, *Cell* **1996**, *87*, 1295–1306.
[5] T. LaBean, H. Yan, J. Kopatsch, F. Liu, E. Winfree, J. H. Reif, N. C. Seeman, *J. Am. Chem. Soc.* **2000**, *122*, 1848–1860.
[6] S. W. Yang, H. A. Nash, *EMBO J.* **1995**, *14*, 6292–6300.
[7] W. Shen, PhD Thesis, New York University, **2004**.
[8] J. SantaLucia, *Proc. Natl. Acad. Sci. USA* **1998**, *95*, 1460–1465, and references therein.
[9] Y. C. Kim, J. H. Geiger, S. Hahn, P. B. Sigler, *Nature* **1993**, *365*, 512–520.
[10] E. Hidalgo, B. Demple, *EMBO J.* **1997**, *16*, 1056–1065.
[11] N. C. Seeman, *J. Biomol. Struct. Dyn.* **1990**, *8*, 573–581.
[12] M. H. Caruthers, *Science* **1985**, *230*, 281–285.
[13] S. D. Goodman, S. C. Nicholson, H. A. Nash, *Proc. Natl. Acad. Sci. USA* **1992**, *89*, 11910–11914.

 © 2004 Wiley-VCH Verlag GmbH & Co. KGaA, Weinheim

Cluster Compounds

Pentasupertetrahedral Clusters as Building Blocks for a Three-Dimensional Sulfide Superlattice**

*Nanfeng Zheng, Xianhui Bu, and Pingyun Feng**

Chalcogenides are becoming increasingly important in the development of new solid-state materials for technological applications. Chalcogenide clusters with well-defined size and composition represent the lower limit of semiconducting nanoparticles and serve to span the size gap between quantum dot structures and molecular species in solution.[1] Moreover, these large clusters can be used as building blocks to construct supramolecular assemblies with unique properties. Among chalcogenide clusters with various geometrical features,[2–4] tetrahedral clusters are of particular significance because they can act as pseudotetrahedral building blocks for the construction of zeolite-like open architectures.[5–9] Unfortunately, even though a number of superlattices built from supertetrahedral clusters have been reported,[10–13] relatively little progress has been made with other types of tetrahedral clusters.

Here we report a three-dimensional open-framework material (denoted ICF-26) built from an unusual tetrahedral cluster. ICF-26 was prepared from the Ca–Li–In–S quaternary system in a procedure mimicking the preparation of natural zeolites by using alkali and alkaline earth metal cations as structure-directing agents.[14] Organic species are not needed as either surface-stabilizing ligands or extraframework structure-directing agents, in contrast to other recent work that relies heavily on the use of organic compounds.[15–21] The highly mobile extraframework cations results in the ionic conductivity of ICF-26 being higher than that of any previously known crystalline lithium compound at room temperature.[22,23]

ICF-26 is built from a tetrahedral cluster denoted P2 (Figure 1). The P2 cluster (that is, $Li_4In_{22}S_{44}^{18-}$) is the second member of a mathematical series of pentasupertetrahedral clusters P*n*, thus termed because they can be conceptually constructed by coupling four supertetrahedral clusters onto the faces of an antisupertetrahedral cluster of the same order (Figure 1). Supertetrahedral clusters are regular tetrahedron-shaped fragments of the cubic ZnS type lattice and are denoted as T*n*, where *n* is the number of metal layers.[10] An antisupertetrahedral cluster is defined here as having the same geometrical features as a supertetrahedral cluster with the positions of cations and anions being exchanged.

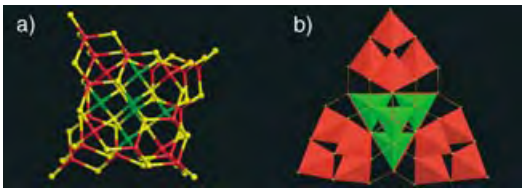


Figure 1. a) Ball-and-stick view of the P2 cluster $Li_4In_{22}S_{44}^{18-}$. Red: In^{3+}, green: mixed In^{3+}/Li^+ sites, yellow: S^{2-}. b) Four supertetrahedral T2 clusters (red) are covalently bonded to one antisupertetrahedral T2 cluster (green) to form a pentasupertetrahedral P2 cluster in ICF-26.

Thus, the P1 cluster consists of four T1 clusters (MX_4) at the corners and one anti-T1 cluster (XM_4) at the core, resulting in the composition $(MX_4)_4(XM_4)$ (namely, M_8X_{17}). Examples of P1 clusters include $[SCd_8(SBu)_{12}](CN)_{4/2}$, $K_{10}M_4Sn_4S_{17}$ (M = Mn, Fe, Co, Zn), and $[M_4(Se)(SnSe_4)_4]^{10-}$ (M = Zn, Mn).[24–26] The P2 cluster contains four T2 clusters (M_4X_{10}) and one anti-T2 cluster (X_4M_{10}), thus giving the composition $(M_4X_{10})_4(X_4M_{10})$ (namely, $M_{26}X_{44}$; Figure 1). The P3 cluster (not yet synthesized) consists of four T3 clusters ($M_{10}X_{20}$) and one anti-T3 cluster ($X_{10}M_{20}$) with the composition $(M_{10}X_{20})_4(X_{10}M_{20})$ (namely, $M_{60}X_{90}$). The same procedure can be used to derive the composition of other P*n* clusters.

A pentasupertetrahedral cluster is considerably larger than a supertetrahedral cluster of the same order, and hence it is difficult to prepare open-framework materials with pentasupertetrahedral clusters larger than P1. Even though supertetrahedral clusters as large as T5 are known,[12] the P2 cluster reported herein represents the largest known cluster of the P*n* series.

While all metal cations of each P2 cluster adopt tetrahedral coordination, sulfur atoms can be two-, three-, or four-coordinate. There are a total of four tetrahedrally coordinated sulfur atoms. They are tetrahedrally distributed around the geometrical center of the P2 cluster and are in fact the anionic core of the anti-T2 cluster. To satisfy Pauling's electrostatic valence rule,[12,27] each tetrahedral S^{2-} site is surrounded by two Li^+ and two In^{3+} sites to give a bond valence sum of +2, which is consistent with the valence of S^{2-}. There are three statistically equivalent ways to achieve this when two In^{3+} and four Li^+ cations are placed at six core cationic sites. As a result, all six metal sites of the anti-T2 clusters are disordered with each site occupied by 2/3 Li^+ cations and 1/3 In^{3+} cations (Figure 1). This leads to an overall cluster formula of $Li_4In_{22}S_{44}^{18-}$. The corner sharing of S sites results in the overall framework composition being $Li_4In_{22}S_{42}^{14-}$, which is consistent with both the elemental analysis and the crystallographic occupancy refinement.[14] The crystallographically determined formula is $Li_{4.13}In_{21.9}S_{42}$. Similar tetrahedral coordination of Li to S is known in a number of other sulfides such as Li_2S (2.47 Å), $KLiMnS_2$ (2.44 Å), and $LiGaS_2$ (2.29–2.59 Å).[28–30] The Li–S bond length in the tetrahedral

[*] N. Zheng, Prof. P. Feng
Department of Chemistry
University of California
Riverside, California 92521 (USA)
Fax: (+1) 909-787-4713
E-mail: pingyun.feng@ucr.edu
Prof. X. Bu
Department of Chemistry and Biochemistry
California State University
1250 Bellflower Blvd.
Long Beach, CA 90840 (USA)

[**] We are grateful for the support of CSULB (X.B.), the National Science Foundation (DMR-0349326, P.F.), Beckman Foundation (P.F.), and the donors of the Petroleum Research Fund (administered by the ACS, P.F.). P.F. is an Alfred P. Sloan research fellow.

 DOI: 10.1002/anie.200460386 © 2004 Wiley-VCH Verlag GmbH & Co. KGaA, Weinheim

environment matches well with the In–S distance in these clusters (about 2.4 Å).

The topological type of ICF-26 resembles that of the cubic ZnS lattice (Figure 2). Even with the formation of two interpenetrating lattices, the framework of ICF-26 is still highly open. More than half of the crystal volume (58.8%) is occupied by extraframework species in ICF-26, as calculated with the program PLATON.[31] The ring size, which is defined as the number of tetrahedral metal atoms, is 30.



Figure 2. Three-dimensional framework of ICF-26. Red and green represent two interpenetrating diamond-type lattices.

One of the most prominent properties of ICF-26 is its fast ion conductivity. The specific conductivity is as high as 0.15 $\Omega^{-1}cm^{-1}$ at 27°C under 100% relative humidity (RH) (Figure 3), which is significantly higher than that of other well-known crystalline lithium conductors at room temperature. Prior to our work, the highest conductivity for a crystalline lithium compound was about $10^{-3}\,\Omega^{-1}cm^{-1}$ at room temperature.[23] The ionic conductivity of ICF-26 increases with increasing relative humidity. At about 26°C, the conductivity ranges from 0.011 $\Omega^{-1}cm^{-1}$ at 29.8% RH to 0.15 $\Omega^{-1}cm^{-1}$ under 100% RH (Figure 3). This property is potentially useful in electrochemical sensors.

The optical properties of ICF-26 were studied with solid-state diffuse reflectance UV/Vis–NIR spectroscopy. It showed a clear optical transition with a band gap of 3.51 eV (Figure 4). The transition is likely a result of charge transfer from the S^{2-}-dominated valence band to the In^{3+}/Li^{+}-dominated conduction band. When excited at 375 nm at room

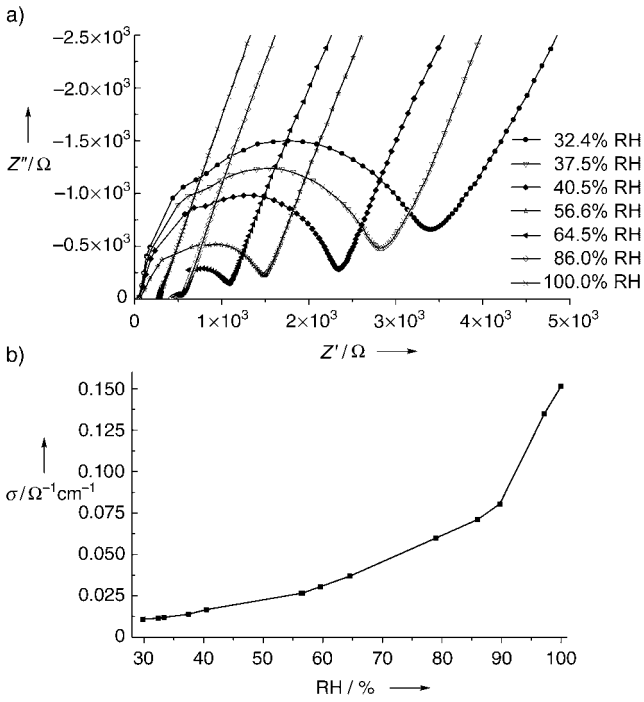


Figure 3. a) The ac impedance plots of ICF-26 at room temperature and different relative humidities. b) Ionic conductivity of ICF-26 at different relative humidities. Ionic conductivities were measured on a single crystal (cross section: 0.37×0.43 mm, length: 0.63 mm) by the ac impedance method with a Solatron 1260 frequency response analyzer. The resistance decreased from $3.590\times10^3\,\Omega$ at 29.8% RH to $2.614\times10^2\,\Omega$ at 100% RH.

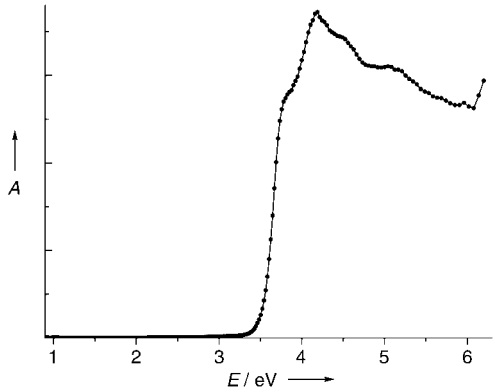


Figure 4. Optical absorption spectra of ICF-26. The absorption data were calculated from reflectance data by using the Kubelka–Munk function. $BaSO_4$ powder was used as a reference (100% reflectance). UV/Vis–NIR diffuse reflectance spectra were measured on a Shimadzu UV 3101PC double-beam, double-monochromator spectrophotometer. *A* = absorbance.

temperature, ICF-26 exhibits strong photoluminescence with the maximum wavelength centered at 440 nm.

In conclusion, the second member of a rare series of chalcogenide tetrahedral clusters ($Li_4In_{22}S_{44}^{18-}$) has been synthesized as the building block for a three-dimensional chalcogenide open-framework superlattice. The geometric features of the cluster can be simply described as the coupling

 © 2004 Wiley-VCH Verlag GmbH & Co. KGaA, Weinheim

between four peripheral supertetrahedral clusters and one core antisupertetrahedral cluster. The highly mobile extra-framework cations lead to extraordinary humidity-dependent fast ion conductivity at room temperature.

Received: April 20, 2004

Keywords: cluster compounds · hydrothermal synthesis · indium · microporous materials · sulfur

[1] V. N. Soloviev, A. Eichhöfer, D. Fenske, U. Banin, *J. Am. Chem. Soc.* **2001**, *123*, 2354 – 2364.
[2] W. S. Sheldrick, M. Wachhold, *Angew. Chem.* **1997**, *109*, 214 – 233; *Angew. Chem. Int. Ed. Engl.* **1997**, *36*, 206 – 224.
[3] B. Krebs, G. Henkel, *Angew. Chem.* **1991**, *103*, 785 – 804; *Angew. Chem. Int. Ed. Engl.* **1991**, *30*, 769 – 788.
[4] I. Dance, K. Fisher, *Prog. Inorg. Chem.* **1994**, *41*, 637 – 803.
[5] P. Behrens, G. D. Stucky in *Comprehensive Supramolecular Chemistry*, *Vol. 7* (Eds.: J. L. Atwood, J. E. D. Davies, D. D. MacNicol, F. Vögtle, J.-M. Lehn, S. V. Ley), Pergamon, Oxford, **1996**, pp. 721 – 772.
[6] T. Vossmeyer, G. Reck, L. Katsikas, E. T. K. Haupt, B. Schulz, H. Weller, *Science* **1995**, *267*, 1476 – 1479.
[7] E. M. Flanigen in *Introduction to Zeolite Science and Practice* (Eds.: H. van Bekkum, E. M. Flanigen, J. C. Jansen), Elsevier, New York, **1991**, pp. 13 – 34.
[8] M. E. Davis, *Nature* **2002**, *417*, 813.
[9] A. K. Cheetham, G. Férey, T. Loiseau, *Angew. Chem.* **1999**, *111*, 3466 – 3492, *Angew. Chem. Int. Ed.* **1999**, *38*, 3268 – 3292.
[10] H. Li, A. Laine, M. O'Keeffe, O. M. Yaghi, *Science* **1999**, *283*, 1145 – 1147.
[11] C. L. Cahill, J. B. Parise, *J. Chem. Soc. Dalton Trans.* **2000**, 1475 – 1482.
[12] X. Bu, N. Zheng, Y. Li, P. Feng, *J. Am. Chem. Soc.* **2002**, *124*, 12646 – 12647.
[13] N. Zheng, X. Bu, B. Wang, P. Feng, *Science* **2002**, *298*, 2366 – 2369.
[14] $In(NO_3)_3{\cdot}H_2O$ (0.3196) and Li_2S (0.2048 g) were mixed in water (1.0667 g) and stirred until a clear solution formed. $CaCl_2$ (0.2228 g) was then added to the solution and a cloudy gel mixture formed within minutes. The mixture was placed in a 23 mL autoclave and kept at 150 °C for 3 days. Large crystals of ICF-26 formed in about 30 % yield. Crystallographic data for ICF-26: $Ca_{1.5}Li_{11}(In_{22}Li_4S_{42}){\cdot}44\,H_2O$, *Pbca*, $a = 28.172(4)$, $b = 29.183(4)$, $c = 40.0949(6)$ Å, $V = 32962(8)$ Å^3, $Z = 8$, $Mo_{K\alpha}$, $T = 150$ K, $2\theta_{max} = 40°$, $R(F) = 8.25\,\%$, $wR(F^2) = 19.6\,\%$ for 757 parameters and 15348 reflections with $I > 2\sigma(I)$, $R(F) = 13.9\,\%$, $wR(F^2) = 26.3\,\%$ for all data. Elemental analysis (%) found (calcd): Li 2.24 (2.16), Ca 1.23 (1.24), In 52.26 (52.30). Further details on the crystal structure investigations may be obtained from the Fachinformationszentrum Karlsruhe, 76344 Eggenstein-Leopoldshafen, Germany (fax: (+49) 7247-808-666; e-mail: crysdata@fiz-karlsruhe.de), on quoting the depository number CSD-413961.
[15] N. Herron, J. C. Calabrese, W. E. Farneth, Y. Wang, *Science* **1993**, *259*, 1426 – 1428.
[16] A. Eichhöfer, D. Fenske, *J. Chem. Soc. Dalton Trans.* **2000**, 941 – 944.
[17] G. B. Gardner, D. Venkataraman, J. S. Moore, S. Lee, *Nature* **1995**, *374*, 792.
[18] B. Chen, M. Eddaouli, S. T. Hyde, M. O'Keeffe, O. M. Yaghi, *Science* **2001**, *291*, 1021.
[19] R. L. Bedard, S. T. Wilson, L. D. Vail, J. M. Bennett, E. M. Flanigen in *Zeolites: Facts, Figures, Future. Proceedings of the 8th International Zeolite Conference* (Eds.: P. A. Jacobs, R. A. van Santen), Elsevier, Amsterdam, **1989**, p. 375.
[20] S. Dhingra, M. G. Kanatzidis, *Science* **1992**, *258*, 1769 – 1772.
[21] R. W. J. Scott, M. J. MacLachlan, G. A. Ozin, *Curr. Opin. Solid State Mater. Sci.* **1999**, *4*, 113 – 121.
[22] N. Zheng, X. Bu, P. Feng, *Nature* **2003**, *426*, 428 – 432.
[23] M. Murayama, R. Kanno, M. Irie, S. Ito, T. Hata, N. Sonoyama, Y. Kawamoto, *J. Solid State Chem.* **2002**, *168*, 140 – 148.
[24] G. S. H. Lee, D. C. Craig, I. Ma, M. L. Scudder, T. D. Bailey, I. G. Dance, *J. Am. Chem. Soc.* **1988**, *110*, 4863 – 4864.
[25] O. Palchik, R. G. Iyer, J. H. Liao, M. G. Kanatzidis, *Inorg. Chem.* **2003**, *42*, 5052 – 5054.
[26] S. Dehnen, M. K. Brandmayer, *J. Am. Chem. Soc.* **2003**, *125*, 6618 – 6619.
[27] H. Li, J. Kim, T. L. Groy, M. O'Keeffe, O. M. Yaghi, *J. Am. Chem. Soc.* **2001**, *123*, 4867 – 6868.
[28] E. Zintl, A. Harder, B. Dauth, *Z. Elektrochem.* **1934**, *40*, 588 – 593.
[29] D. Schmitz, W. Bronger, *Z. Anorg. Allg. Chem.* **1987**, *553*, 248 – 260.
[30] J. Leal-Gonzalez, S. S. Melibary, A. J. Smith, *Acta Crystallogr. Sect. C* **1990**, *46*, 2017 – 2019.
[31] A. L. Spek, *Acta Crystallogr. Sect. A* **1990**, *46*, C34.

 © 2004 Wiley-VCH Verlag GmbH & Co. KGaA, Weinheim

Supramolecular Chemistry

Allosterically Driven Multicomponent Assembly**

Pall Thordarson, Ruud G. E. Coumans, Johannes A. A. W. Elemans, Paul J. Thomassen, Johan Visser, Alan E. Rowan,* and Roeland J. M. Nolte*

Cooperative interactions play a ubiquitous role in Nature and are utilized not only to construct discrete assemblies such as the tobacco mosaic virus (TMV), but also to transfer information, crucially exemplified in the binding of oxygen

[*] Dr. P. Thordarson, R. G. E. Coumans, Dr. J. A. A. W. Elemans, P. J. Thomassen, J. Visser, Dr. A. E. Rowan, Prof. R. J. M. Nolte
Department of Organic Chemistry, NSRIM Institute
University of Nijmegen
Toernooiveld, 6525 ED Nijmegen (The Netherlands)
Fax: (+31)24-3652929
E-mail: p.thordarson@chem.usyd.edu.au
rowan@sci.kun.nl

Dr. P. Thordarson
Australian Key Centre for Microscopy and Microanalysis
School of Chemistry, Madsen Building
The University of Sydney
NSW 2006 (Australia)
Fax: (+61)2-93517682

[**] This research was supported by the NRSCC, an EC Marie Curie Fellowship to P.T. (Contract No. HPMF-CT-2000-01053), and an NWO Vidi grant to A.E.R.

Supporting information for this article is available on the WWW under http://www.angewandte.org or from the author.

 DOI: 10.1002/anie.200460398 © 2004 Wiley-VCH Verlag GmbH & Co. KGaA, Weinheim

to hemoglobin.[1,2] Cooperative interactions also play a critical role in gene transcription; for instance, cyclic AMP has a strong cooperative effect upon the binding of the gene-transcription-regulating cAMP receptor protein (CRP) to DNA.[3] In the latter two examples, the binding event at one site in a multivalent host causes a discrete, reversible alteration in the structure of the host which is transmitted to another binding site and is called an allosteric interaction.[4] In the case of hemoglobin, the binding of oxygen can be described as positively homotropic, whereas the allosteric interactions in the cAMP/CRP/DNA can be described as positively heterotropic.

The area of artificial allosteric interactions is of great general interest[5–7] not only because of its crucial role in Nature, but also because it may help in the construction of functional nanoscale objects. Towards understanding these complex processes, we recently developed a double-cavity porphyrin that displays very strong negative homotropic allosteric behavior.[8] As a continuation of this research, we present herein a positively heterotropic synthetic allosteric system based on a combination of host–guest and metal–ligand interactions.[9] This system was constructed from a monocavity-appended porphyrin host **ZnP**[10,11] by using various combinations of 4-*tert*-butylpyridine (tbpy), 1,4-diazabicyclo[2.2.2]octane (dabco), dimethylviologen (V), and *meso*-tetrakis(4-pyridyl)porphyrin (py_4por) as the ligands or substrates (Figure 1). The choice of ligands was based on

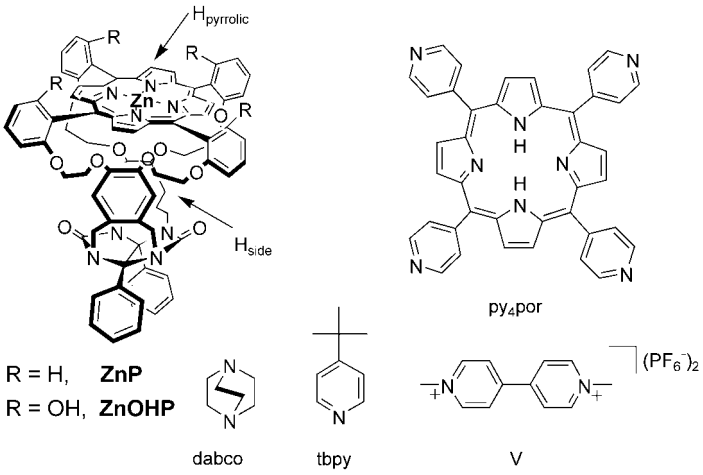


Figure 1. Molecules used in this study.

earlier work in which it was demonstrated that **ZnP** binds V very strongly in its cavity ($K_{ass} > 10^5\,M^{-1}$) and the bulky ligands tbpy and py_4por outside its cavity (Figure 2a).[12]

The binding between tbpy and **ZnP** was studied by a ^1H NMR titration (Figure 2b), both in the absence and presence of 1 equivalent of V as the allosteric substrate (Table 1). A clear positive heterotropic allosteric effect was observed: The K_{ass} for the binding of tbpy to **ZnP** is more than two orders of magnitude larger in the presence of V than in its absence. In a system in which a host interacts with two different guests, ligand L and substrate R (Figure 2a), the allosteric magnification ${}^{R}AM_{L}$ caused by R on binding of the ligand L to the host can be defined as:

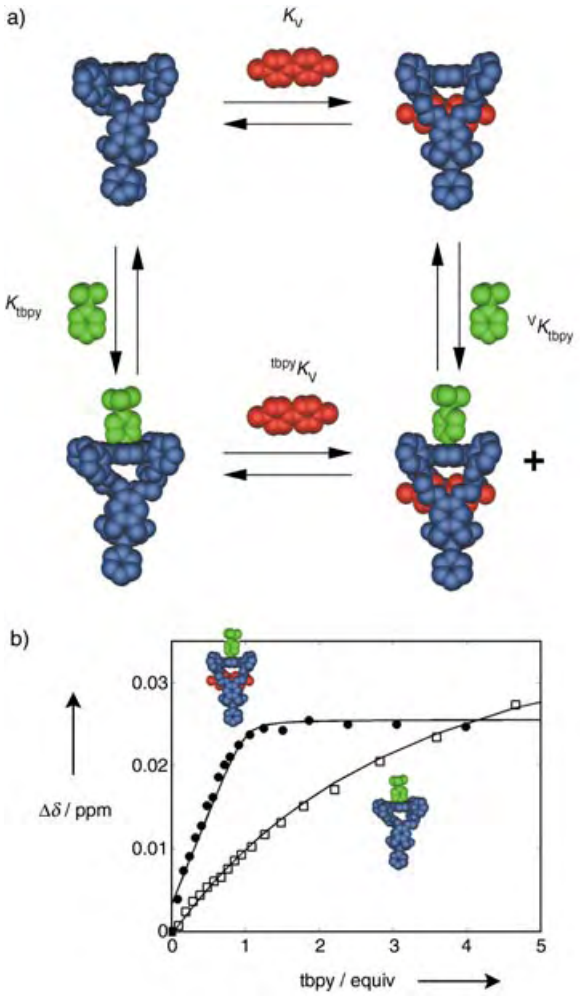


Figure 2. a) Schematic representation of the possible interactions between a host, ligand L, and substrate R, with **ZnP**, tbpy, and V, respectively, as an illustrative example. The + sign indicates the positive cooperativity between the neighboring ligands (guests). b) ^1H NMR titration of the **ZnP** host with the tbpy ligand showing the chemical shifts changes ($\Delta\delta$) for H_{side} (Figure 1) in the absence (□) and presence (●) of 1 equivalent of V. Also shown are the calculated binding isotherms (——) obtained by nonlinear regression (assuming a 1:1 binding model).

$$ {}^{R}AM_{L} = \frac{K_{ass}\text{ for L in the presence of R}}{K_{ass}\text{ for L in the absence of R}} \qquad (1) $$

This results in a ${}^{V}AM_{tbpy}$ of 250 for the aforementioned system, and corresponds to a $\Delta\Delta G$ of $-14\,kJ\,mol^{-1}$. To investigate the reverse effect, that is, the effect of tbpy on the binding of V, a fluorescence titration was carried out in which V was added to **ZnP** both in the absence and presence of 500 equivalents of tbpy. An allosteric magnification ${}^{tbpy}AM_{V} = 3$ was observed (Table 1), revealing that the binding of tbpy also enhances the binding of V. It can be calculated that at the concentrations used ($\sim 10^{-6}$ M) about 17% of **ZnP** is bound to tbpy before the addition of V, but this portion rises to >98% after 1 equivalent of V has been added. In a perfect three-component system, as assumed here, the thermodynamic cycle has to follow Hess's law and balance: ${}^{R}AM_{L}$ should be equal to ${}^{L}AM_{R}$.[13] The observation that ${}^{V}AM_{tbpy}$ is not equal to ${}^{tbpy}AM_{V}$ highlights the fact that additional subtle effects also

 © 2004 Wiley-VCH Verlag GmbH & Co. KGaA, Weinheim

Table 1: Association constants K [M^{-1}] and binding free energies ΔG [kJ mol^{-1}] for the complexation of **ZnP** and **ZnOHP** to various ligands L in the absence and presence of substrates R at 298 K.

Host	L	R	Without R		With R		$\Delta\Delta G$[b]	$^{R}AM_{L}$[c]
			K_1[a]	ΔG	K_1[a]	ΔG		
ZnP[d]	tbpy	V (1 equiv)	4×10^{2}	−15	1×10^{5}	−29	−14	250
ZnP[e]	V	tbpy (500 equiv)	9×10^{5}	−34	3×10^{6}	−37	−3	3
ZnP[f]	V	tbpy (500 equiv)	3×10^{5}	−31	1×10^{6}	−34	−3	3
ZnP[g]	dabco	V (10 equiv)	5×10^{4}	−27	4×10^{5}	−32	−5	8
ZnP[f]	V	dabco (10 equiv)	3×10^{5}	−31	9×10^{5}	−34	−3	3
ZnP[h]	py_4por	V (1 equiv)	2×10^{2}	−13	3×10^{3}	−20	−7	15
ZnOHP[i]	dabco	V (10 equiv)	n.d.	n.d.	2×10^{6}	−34	n.d.	n.d.

[a] Measurements in duplicate or triplicate. Estimated errors: 50%. [b] $\Delta\Delta G = (\Delta G$ for L with R$) - (\Delta G$ for L without R). [c] Defined as $^{R}AM_{L} = (K_1$ of L with R$)/(K_1$ of L without R). [d] In $CDCl_3/CD_3CN$ (4:1, v/v) measured by ^{1}H NMR titration. [e] In $CHCl_3/CH_3CN$ (4:1, v/v) measured by fluorescence titration. [f] In $CHCl_3/CH_3CN$ (1:1, v/v) measured by fluorescence titration. [g] In $CDCl_3/CD_3CN$ (1:1, v/v) measured by ^{1}H NMR (without R) and in $CHCl_3/CH_3CN$ (1:1, v/v) measured by UV/Vis titration (with R). An interaction cooperativity parameter α ($4K_2/K_1$) = 0.05–0.07 for dabco is used, see text for details. [h] In $CDCl_3/CD_3CN$ (1:1, v/v) measured by ^{1}H NMR titration. [i] In $CHCl_3/CH_3CN$ (1:1, v/v) measured by UV/Vis titration.

play a role. Inspection of the thermodynamic cycle shown in Figure 2a and Table 1 shows that the actual calculated free-energy gain in the anticlockwise direction is −52 kJ mol^{-1}, whilst in the clockwise direction the energy gain is −63 kJ mol^{-1}. The difference of only −12 kJ mol^{-1} is however significantly greater than the experimental errors and would appear to violate Hess's law, as in a complete thermodynamic cycle both directions should be equal. Our binding model, as used in the model studies, does not take into account a competitive effect from the solvent molecules. These third competitive species are the acetonitrile solvent or residual water molecules, (although extreme care was taken to avoid the latter solvent), both of which are known to bind strongly within the cavity. In a complete cycle, however, this competitive behavior should also balance out if all measurements are carried out at the same concentration. The discrepancy arises from the fact that the complete cycle is not measured at one concentration; owing to the extremely high association constant of the bipyridine within the host, binding studies were carried out at 10^{-6} M, whereas the binding of *tert*-butyl pyridine was measured at 10^{-3} M. The combination of the solvent effect and the different concentrations are thought to be responsible for the incomplete thermodynamic cycle. It is only when the whole thermodynamic cycle is measured that these additional factors become apparent.

We investigated whether the allosteric effect could be utilized in the directed self-assembly of a larger supramolecular complex, from a multicomponent solution consisting of a **ZnP** host and a tetradentate ligand py_4por, again with V as an allosteric cofactor (Figure 3). This system would be a very simple analogue to the natural cAMP/CRP/DNA allosteric system. **ZnP** and py_4por can form complexes with varying stochiometry. To calculate the K_{ass} values between **ZnP** and py_4por, each *meso*-4-pyridyl group on py_4por was treated as an independent ligand (the results from the NMR titrations showed no signs of cooperativity). In the presence of 1 equivalent of V per **ZnP** molecule a strong positive heterotropic allosteric effect was found: $^{V}AM_{py4por} = 15$, $\Delta\Delta G = -7$ kJ mol^{-1} (Table 1). From the K_{ass} values it can be calculated that in a mixture of **ZnP** and py_4por (4:1, [py_4por] = 1 mM) in the absence of V only 1% of the ligand is completely surrounded by four **ZnP** molecules, whilst in the presence of V about 34% of the py_4por ligands form a 1:4 complex with **ZnP**. The above results clearly illustrate how, in principle, allosteric magnification can drive complex equilibrium mixtures towards a more discrete architecture.

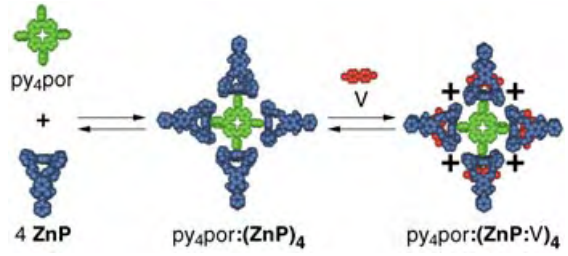


Figure 3. Schematic representation showing how 4 equivalents of **ZnP** assemble around the py_4pyr ligand either with or without V as a substrate, the + signs indicate the positive cooperativity between the neighboring ligands (guests).

The allosteric effect that V showed on the binding of the noncooperative ligands tbpy and py_4por was also investigated on the binding of the cooperative bidentate ligand dabco. Anderson and Taylor have shown[14] that dabco binds to zinc(II) porphyrins with negative cooperativity, with an interaction cooperativity parameter[15] ($\alpha = 4K_{2ass}/K_{1ass}$) that varies between 0.01 and 0.2, depending on the solvent. When **ZnP** was titrated with dabco, a similar negative cooperativity was observed. The cooperativity parameter α was estimated to be approximately 0.05, with the association constant $K_{1ass} = 5\times10^{4}$ M^{-1}.[16] Upon the addition of V, K_{1ass} was found to increase by one order of magnitude ($K_{1ass} = 4\times10^{5}$ M^{-1}) (Table 1, Figure 4). The differences in binding affinity of dabco for **ZnP** in the presence and absence of V were most clearly observed in the ^{1}H NMR spectra. The porphyrin resonances of **ZnP** bound and unbound to dabco underwent fast exchange on the NMR timescale when V was absent, but only slow exchange upon the addition of V. The latter observation allowed us to measure directly the ratio between the ternary V:**ZnP**:dabco complex ($\delta_{dabco} = 0.87$ and −2.88 ppm) and the pentameric V:**ZnP**:dabco:**ZnP**:V complex ($\delta_{dabco} = -4.74$ ppm) and thus measure the K_{1ass}/K_{2ass} ratios.[17] A cooperativity interaction parameter $\alpha = 0.07$, which is similar to the value found in the absence of V was calculated. The allosteric magnification observed in this case has a pronounced effect on the distribution of species present

 © 2004 Wiley-VCH Verlag GmbH & Co. KGaA, Weinheim

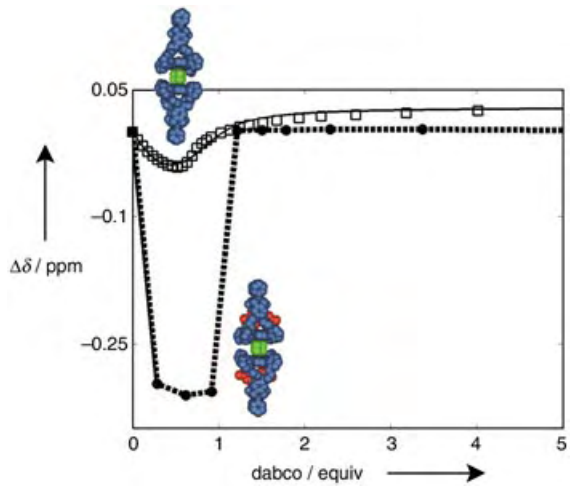


Figure 4. ^{1}H NMR titration of the **ZnP** host with the dabco ligand showing the chemical shifts changes ($\Delta\delta$) for $H_{pyrrolic}$ (Figure 1) in the absence of V (□) together with the calculated binding isotherm (——) obtained by nonlinear regression (assuming a 1:2 binding between **ZnP** and dabco and $\alpha = 0.05$). Also shown are the chemical shifts changes ($\Delta\delta$) for the same $H_{pyrrolic}$ in **ZnP** in the presence of 1 equivalent of V upon addition of dabco. In this case, the observed complexes do not undergo fast exchange, so that the data points shown (•••••) illustrate only the dominating species at any given point of the titration.

in the solution (Figure 5). Calculations with the measured association constants and with [**ZnP**] = 1 mM and [dabco] = 0.5 mM showed that the sandwich species **ZnP**:dabco:**ZnP** accounts for only 22% of **ZnP** present in solution. Upon the addition of V (and based on the assumption that **ZnP**, V:**ZnP**:dabco and V:**ZnP**:dabco:**ZnP**:V are the only species in the mixture), 57% of **ZnP** is calculated to be in the sandwich complex, thus illustrating how the binding of V promotes the assembly of **ZnP** around the dabco ligand. However, it does not drive the equilibrium through to the pentameric complex owing to the negative cooperativity of dabco.[18]

To form the desired pentameric architecture, a **ZnP** cavity was synthesized with 4 hydroxy functions positioned on the *meso* phenyl rings which might serve as additional interactive elements (**ZnOHP**, Figure 1).[8] As indicated by molecular modeling, the OH functions of **ZnOHP** are 3 Å apart when two molecules of this compound are self-assembled with dabco. These OH functions can form hydrogen bonds upon dimerization, possibly overcoming the negative cooperativity of dabco. Initial studies revealed that in the presence of V, the ditopic ligand dabco binds with $K_{1ass} = 2 \times 10^6\,M^{-1}$ and $K_{2ass} = 9 \times 10^6\,M^{-1}$, resulting in an α value of 17, which points to an exceptionally positive cooperative assembly process. A consequence of the cooperative process is that at concentrations of [**ZnOHP**] = 1 mM and [dabco] = 0.5 mM, a remarkable 98.5% of **ZnOHP** is involved in the pentameric sandwich complex (Figure 6). This indicates that the addition of an extra factor, namely, the OH-groups in **ZnOHP**, combined with the allosteric magnification that V exerts on the binding of dabco, results in the assembly of a single species from a complex equilibrium mixture.

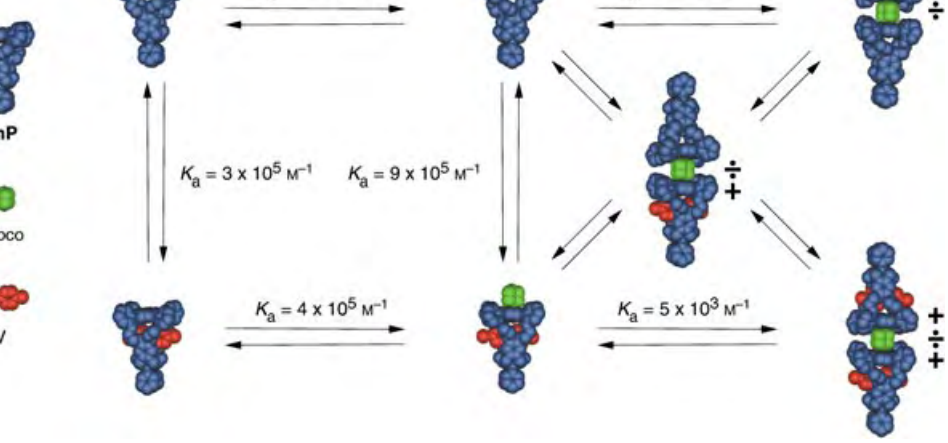


Figure 6. Molecular models of **ZnOHP** and the pentameric sandwich complex.

Figure 5. Schematic representation summarizing all the possible complexes of **ZnP** with dabco in the presence or absence of V, together with the relevant association constants obtained in this study. The +/÷ signs indicate the positive or negative cooperativity between the neighboring ligands (guests), respectively.

Allosterically controlled assembly, as demonstrated herein, opens up numerous possibilities for directing complex equilibrium mixtures to a

 © 2004 Wiley-VCH Verlag GmbH & Co. KGaA, Weinheim

desired product that mimics the hierarchical self-assembly processes found in Nature. The manganese derivatives of the above-mentioned systems have the added property of catalytic activity.[12] Current research is directed at the construction of allosteric nanometer-sized assemblies with unique catalytic properties.

Received: April 21, 2004

Keywords: allosterism · cooperative phenomena · porphyrins · self-assembly · supramolecular chemistry

[1] A. Klug, *Angew. Chem.* **1983**, *95*, 579; *Angew. Chem. Int. Ed. Engl.* **1983**, *22*, 585.
[2] a) G. K. Ackers, M. L. Doyle, D. Myers, M. A. Daugherty, *Science* **1992**, *255*, 54; b) Y. Huang, M. L. Doyle, G. K. Ackers, *Biophys. J.* **1996**, *71*, 2094; c) M. L. Johnson, *Methods Enzymol.* **2000**, *323*, 124.
[3] J. G. Harman, *Biochim. Biophys. Acta* **2001**, *1547*, 1.
[4] J. Monod, J. Wyman, J. P. Changeux, *J. Mol. Biol.* **1965**, *12*, 88.
[5] a) J. Rebek, Jr., *Acc. Chem. Res.* **1984**, *17*, 258; b) I. Tabushi, *Pure Appl. Chem.* **1988**, *60*, 581; c) R. P. Sijbesma, R. J. M. Nolte, *J. Am. Chem. Soc.* **1991**, *113*, 6695.
[6] S. Shinkai, M. Ikeda, A. Sugasaki, M. Takeuchi, *Acc. Chem. Res.* **2001**, *34*, 494.
[7] M. Takeuchi, M. Ikeda, A. Sugasaki, S. Shinkai, *Acc. Chem. Res.* **2001**, *34*, 865.
[8] P. Thordarson, E. J. A. Bijsterveld, J. A. A. W. Elemans, P. Kasák, R. J. M. Nolte, A. E. Rowan, *J. Am. Chem. Soc.* **2003**, *125*, 1186.
[9] Positive heterotropic allosteric behavior has been demonstrated in synthetic ion-ligand systems: a) M. H. Al-Sayah, N. R. Branda, *Chem. Commun.* **2002**, 178; b) A. Lützen, O. Hass, T. Bruhn, *Tetrahedron Lett.* **2002**, *43*, 1807; c) examples listed in references [6] and [7].
[10] A. E. Rowan, P. P. M. Aarts, K. W. M. Koutstaal, *Chem. Commun.* **1998**, 611.
[11] J. A. A. W. Elemans, M. B. Claase, P. P. M. Aarts, A. E. Rowan, A. P. H. J. Schenning, R. J. M. Nolte, *J. Org. Chem.* **1999**, *64*, 7009.
[12] a) J. A. A. W. Elemans, E. J. A. Bijsterveld, A. E. Rowan, R. J. M. Nolte, *Chem. Commun.* **2000**, 2443; b) P. Thordarson, E. J. A. Bijsterveld, A. E. Rowan, R. J. M. Nolte, *Nature* **2003**, *424*, 915.
[13] E. Di Cera, Q. Dang, Y. Ayala, A. Vindigni, *Methods Enzymol.* **1995**, *259*, 127.
[14] P. N. Taylor, H. L. Anderson, *J. Am. Chem. Soc.* **1999**, *121*, 11538.
[15] a) K. A. Connors, *Binding Constants*, Wiley, New York, **1987**; b) K. A. Connors, A. Paulson, D. Toledo-Velasquez, *J. Org. Chem.* **1988**, *53*, 2023.
[16] Only binding of dabco to the "outside" of **ZnP** was observed, as seen for tbpy. We attribute this to the bulkiness of dabco, which cannot be easily accommodated within the cavity in **ZnP**.
[17] H. L. Anderson, C. A. Hunter, M. N. Meah, J. K. M. Sanders, *J. Am. Chem. Soc.* **1990**, *112*, 5780.
[18] It is proposed that a structural rearrangement of the host and/or electrostatic interactions occur upon binding of V and these alterations are responsible for the observed allosteric effect. Current investigations are focused on high-level molecular-modeling studies to obtain further insight into the processes reported herein.

 © 2004 Wiley-VCH Verlag GmbH & Co. KGaA, Weinheim

Self-Assembly on Surfaces

Supramolecular Patterned Surfaces Driven by Cooperative Assembly of C_{60} and Porphyrins on Metal Substrates**

Davide Bonifazi, Hannes Spillmann, Andreas Kiebele, Michael de Wild, Paul Seiler, Fuyong Cheng, Hans-Joachim Güntherodt, Thomas Jung,* and François Diederich**

Systems that spontaneously self-organize through selective interactions into extended supramolecular entities offer a number of powerful approaches for the development of functional-molecule-based devices.[1] Selective noncovalent interactions have been widely exploited both in solution and in the solid state to prepare extended assemblies in one (polymolecular chains and fibers),[2,3] two (arrays, layers, and membranes),[3,4] and three dimensions.[5] Recently this concept has been extended to the surface engineering of multidimensional assemblies[6] stabilized by hydrogen-bonding,[7] dipole–dipole,[8] donor–acceptor,[9] and van der Waals[10] interactions.

π-Conjugated molecules such as fullerenes and porphyrins with tunable electronic properties are appealing building blocks for the construction of functional materials with exceptional electrochemical and photophysical properties.[11] One of the most interesting aspects of C_{60} and porphyrins is that they spontaneously attract each other mainly through orbital interactions, as experimentally determined in so-

[*] Dr. H. Spillmann, A. Kiebele, Dr. M. de Wild, Prof. Dr. H.-J. Güntherodt
NCCR Nanoscale Science
Department of Physics, University of Basel
Klingelbergstrasse 82, 4056 Basel (Switzerland)
Fax: (+41) 61-267-3784
E-mail: h.spillmann@unibas.ch

Dr. T. Jung
Laboratory for Micro- and Nanotechnology
Paul Scherrer Institute
5232 Villigen PSI (Switzerland)
Fax: (+41) 56-310-2646
E-mail: thomas.jung@psi.ch

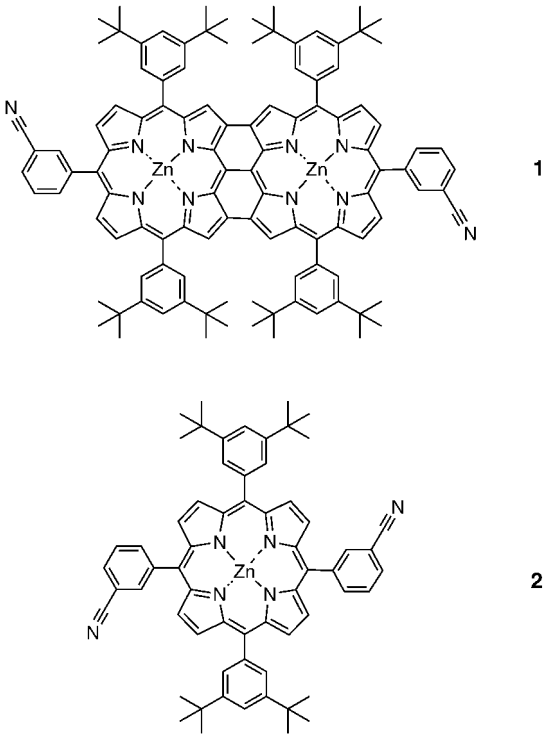
D. Bonifazi, Dr. P. Seiler, Dr. F. Cheng, Prof. Dr. F. Diederich
Laboratorium für Organische Chemie
ETH-Hönggerberg, HCI
8093 Zürich (Switzerland)
Fax: (+41) 1-632-1109
E-mail: diederich@org.chem.ethz.ch

[**] We gratefully acknowledge the financial support from the Swiss National Science Foundation, the NCCR "Nanoscience", and the Swiss Federal Commission for Technology and Innovation (KTI). We also thank Nanonis Inc. for their fruitful collaboration on the data acquisition and molecular positioning system.

Supporting information (X-ray crystal structure of **2**, STM studies on monolayers of a triply fused diporphyrin with two 4-cyanophenyl residues, and movies illustrating dynamic processes) for this article is available on the WWW under http://www.angewandte.org or from the author.

 DOI: 10.1002/anie.200460562 © 2004 Wiley-VCH Verlag GmbH & Co. KGaA, Weinheim

lution[12] and in the solid state,[13] and confirmed by high-level calculations.[14] In earlier reports we evidenced that the attractive C_{60}–porphyrin interaction substantially affects the conformational, electrochemical, and photophysical properties of covalent conjugates.[15–17] However, the study of the C_{60}–porphyrin interaction on solid surfaces is largely unexplored.[18] The formation of self-assembled molecular layers that are weakly physisorbed on surfaces provides the conceptional basis to engineer addressable fullerene–porphyrin architectures in which both chromophores are proximally assembled by noncovalent interactions. Herein we report on the bottom-up fabrication of patterned surfaces based on unprecedented two-dimensional (2D) supramolecular assemblies composed of porphyrins and C_{60}. The first scanning tunneling microscopy (STM) studies on monolayers of triply fused and monomeric porphyrins show that **1**[17,19] and **2** (Scheme 1) self-organize into ordered molecular bilayers upon co-deposition with C_{60}. Repositioning experiments[20] conducted with the STM tip demonstrate that the C_{60} molecules are weakly adsorbed onto the porphyrin monolayers and they can be easily relocated without disrupting the underlying layer.



Scheme 1. Chemical structure of the porphyrin derivatives prepared according to the synthetic protocols recently reported.[17]

The first step in the formation of the self-assembled patterned surfaces is the deposition of the porphyrin macrocycles onto an Ag(100) surface under ultrahigh vacuum (UHV).[21] High-resolution STM images taken on an Ag(100) substrate covered with a 0.2–0.5 monolayer of diporphyrin **1** showed the coexistence of two phases: 2D ordered islands in dynamic equilibrium with a 2D gas phase. Evidence for this 2D molecular gas phase was obtained from the fluctuation of the borders of the condensed islands in time-lapse imaging sequences (see the Supporting Information).[22] The individual molecules in the STM images are represented as groups of four lobes arranged in a slightly distorted square shape (Figure 1 a, left). According to earlier experiments conducted on tetra-arylated porphyrins,[18] each lobe in the STM image results from preferential tunneling transport through the 3,5-di(*tert*-butyl)phenyl substituents.[23] The observed size of the four-lobed shape is about $1.1 \times 0.8\ nm^2$, which is consistent with the molecular dimensions of **1**, as estimated by PM3-

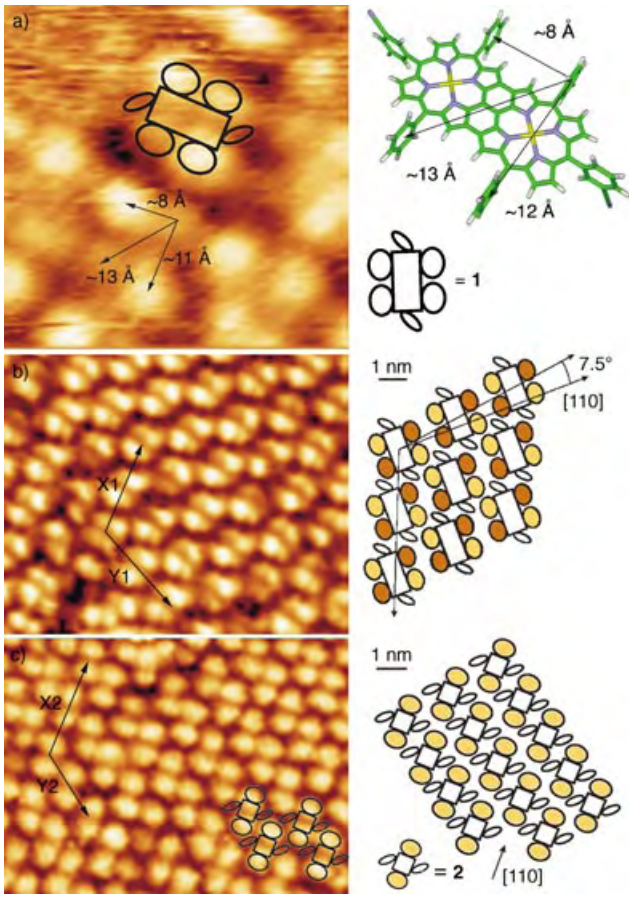


Figure 1. a) Left: STM image (scan range: $5.0 \times 5.0\ nm^2$, $V_{bias} = 2.57$ V, $I_t = 21$ pA, $T = 298$ K) of a single molecule of diporphyrin **1** sublimed on Ag(100) in proximity to a 2D mobile molecular phase.[22] Right: optimized molecular structure of porphyrin **1** generated by PM3 calculations implemented within Spartan (the *tert*-butyl functionalities have been omitted for clarity). b) Left: STM image (scan range: $15.8 \times 11.9\ nm^2$, $V_{bias} = 2.5$ V, $I_t = 72$ pA, $T = 298$ K) of a full-coverage monolayer of **1** sublimed on Ag(100); the distance between the centers of two neighboring molecules is 2.2 ± 0.1 nm along the X1 direction and 2.3 ± 0.1 nm along the Y1 direction; the molecular rows cross each other at an angle of $120 \pm 5°$ along the direction X1 and Y1. Right: proposed surface pattern of the self-assembled monolayer on Ag(100) (the yellow and brown lobes reflect the heights attributed to the different conformation adopted by the 3,5-di(*tert*-butyl)phenyl legs as displayed by the dissimilar intensity tunneling current). c) Left: STM image (scan range: $12.2 \times 9.1\ nm^2$, $V_{bias} = 2.80$ V, $I_t = 72$ pA, $T = 298$ K) of a full-coverage monolayer of porphyrin **2** sublimed on Ag(100); the distance between the centers of two neighboring molecular subunits is 2.4 ± 0.1 nm along the X2 direction and 1.5 ± 0.1 nm along the Y2 direction; the molecular rows along the direction X2 and Y2 cross each other at an angle of $126 \pm 5°$. Right: proposed surface pattern of the self-assembled molecular layer on Ag(100).

 © 2004 Wiley-VCH Verlag GmbH & Co. KGaA, Weinheim

based geometry optimization (Figure 1a, right). Although the rotation of the 3,5-di(*tert*-butyl)phenyl substituents about the phenyl–porphyrin σ bond is sterically hindered at small interplanar angles, they still have a certain degree of freedom to partially rotate without affecting each other. Therefore, the reason why the four protrusions appear with distinct heights is attributable to a different conformation being adopted by the four 3,5-di(*tert*-butyl)phenyl moieties.[23] To confirm such conformational arguments a triply linked diporphyrin bearing two 4-cyanophenyl substituents was also synthesized as a reference compound, and the results are consistent with our interpretations (see the Supporting Information). At higher coverage (ca. 1.0 monolayer), diporphyrin **1** self-organizes in regular molecular rows that are clearly distinguishable in the STM images (Figure 1b, left), which are characterized by a high packing density.

Compound **2** was also sublimed on Ag(100) under the same conditions. Each molecule is represented as two aligned lobes which correspond to the 3,5-di(*tert*-butyl)phenyl substituents (Figure 1c, left). The distance between two bright lobes is about 1.1 nm, which is in agreement with the intramolecular distance between the 3,5-di(*tert*-butyl)phenyl moieties as measured in the crystal structure of **2** (see the Supporting Information). In analogy to **1**, the porphyrin central core and the 3-cyanophenyl residues are not visible on a single-molecule image. Again a 2D gas phase was observed in equilibrium with the ordered islands, thus showing that the porphyrin–substrate and porphyrin–porphyrin interactions at 298 K are similar for both compounds **1** and **2**. At complete surface coverage (ca. 1.0 monolayer) the molecules arrange themselves into rows along the ⟨110⟩ direction of the underlying Ag(100) substrate (Figure 1c, right). In contrast to **1**, all the lobes appear with the same height, which suggests that the interplanar angle between the 3,5-di(*tert*-butyl)phenyl moiety and the porphyrin plane is equal for all molecules within the monolayer.

Sublimation of an approximately 0.02 monolayer of C_{60} on top of a full monolayer of **1** on Ag(100) resulted in the predominant formation of unidirectional chains of various lengths composed of several bright protrusions (Figure 2a, left).[24] Each protrusion has a height of 4.4 ± 0.2 Å (measured with respect to the porphyrin layer). These protrusions can clearly be identified from their spherical appearance in the STM data as single C_{60} molecules.[25] The longest chains (ca. 15.5 nm) are composed of eight C_{60} molecules with an intermolecular $C_{60}\cdots C_{60}$ distance of about 2.2 nm. Surprisingly, no 2D islands composed of C_{60} have been detected. The superstructure of the bimolecular C_{60}–diporphyrin assembly (Figure 2a, left) which best fits the experimental data is also depicted (Figure 2a, right). Despite the large surface area of the fused macrocyclic core (ca. 1 nm^2), the fullerene-based chains are formed by molecules which are located outside of the porphyrin macrocycles, precisely on top of the 3-cyanophenyl substituents.

To exclude the possibility that the C_{60} molecules are embedded in the porphyrin domains as self-intermixed phase, for example, such as in subphthalocyanine and C_{60} assemblies,[26] single-molecule repositioning experiments of the carbon spheres were performed. Figure 2b shows the STM

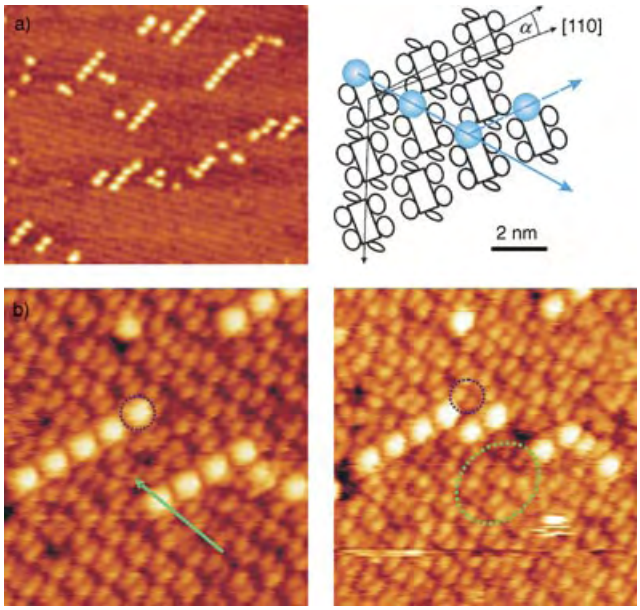


Figure 2. STM images of **1**–C_{60} assembly. a) Left: STM images showing the preferential direction of the chainlike assembly of C_{60} on a previously deposited monolayer of **1** (scan range: 77×65 nm^2, $I_t = 22$ pA, $V_{bias} = 2.59$ V). Right: proposed model for the chainlike assembly (α = ca. 7.5°); the C_{60} molecules (blue spheres) are located between the diporphyrin molecules approximately on top of the 3-cyanophenyl residues; the solid blue and dashed blue arrow indicates the major and minor growth direction, respectively. b) Detailed view before (left) and after (right) manipulation sequence of the C_{60} molecule on a layer of **1** (scan range: 21×21 nm^2, $I_t = 11$ pA, $V_{bias} = 3.01$ V). The green arrow traces the lateral displacements of the STM tip during the manipulation (tunneling parameters: $I_t = 214$ pA, $V_{bias} = 1.43$ V, $V_{tip} = 5$ $nm\,s^{-1}$) and the green ellipse indicates the intact layer of **1** after repositioning of the C_{60} molecule; the blue circle denotes a C_{60} molecule that vanished during the repositioning experiment.

images recorded before (left) and after (right) C_{60} repositioning on a full monolayer of **1**. After the relocation sequence, the former fullerene site (green ellipse in Figure 2b, right) is clearly occupied only by **1**, thus proving that the C_{60} molecules sit on top of the monolayer. Interestingly all attempts toward the formation of square islands composed of four carbon spheres failed, but led to the abstraction of a C_{60} molecule, as evident with the fullerene molecule positioned at the end of the left chain (blue circle in Figure 2b). The latter observation hints at an intrinsic property of such layers of **1**: condensed 2D phases composed of C_{60} molecules are energetically unfavored and only chainlike phases are preferred.

Deposition of an approximately 0.14 monolayer of C_{60} onto a preadsorbed approximately 0.85 monolayer of **2** on an Ag(111) substrate resulted in the formation of two segregate molecular domains: 1) $2\sqrt{3} \times 2\sqrt{3}$ R30° islands[27,28] of C_{60} and 2) a condensed phase composed of **2**. Thermal annealing (453 K) of samples containing such segregate domains afforded the unprecedented porphyrin–C_{60} assembly shown in Figure 3 as the main phase. The carbon spheres are arranged in vertically aligned pairs (intrapair $C_{60}\cdots C_{60}$ distance of 2.3 nm) which are separated by about 6.0 nm. This paired line pattern is repeated every 7.3 nm in the horizontal direction and results in exceptionally large domains (up to

 © 2004 Wiley-VCH Verlag GmbH & Co. KGaA, Weinheim

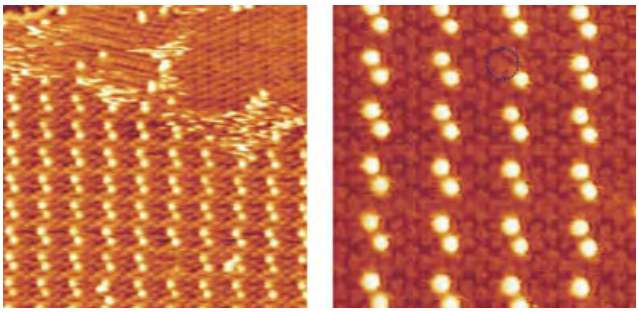


Figure 3. STM image of **1**–C_{60} assembly. Left: STM image of the 2D arrangement of C_{60} on a monolayer of **2** (scan range: 68×68 nm^2, $I_t = 64$ pA, $V_{bias} = 1.97$ V). Right: detailed view (scan range: 30×30 nm^2, $I_t = 16$ pA, $V_{bias} = 2.67$ V); the blue circle indicates a C_{60} vacancy.

50×100 nm^2). Notably the presence of an undistorted monolayer of **2** in the proximity of the fullerene vacancy (blue circle in Figure 3, right), supports the assumption that the C_{60} molecules are accommodated on top of the porphyrin layer. In the upper part of Figure 3 (left), isolated domains of **2** on Ag(111) with some loose C_{60} molecules are visible (see also the Supporting Information). Noisy areas consisting of spikes with an apparent height similar to that of C_{60} molecules at the boundary of the porphyrin domains are indicative of loosely bound C_{60} molecules which are moving on the porphyrin layer at a frequency similar to the one of the STM tip.[22] The shape and apparent height of such bright protrusions (4.8 ± 0.3 Å) are very similar to those found for the C_{60} spheres on top of the layer of **1**. While the monolayer of **1** does not reorder upon deposition of C_{60}, the monolayer of **2** reorganizes upon formation of the hybrid **2**–C_{60} assembly (see top part on Figure 3 (left) and Supporting Information).

Notably while the assembly of C_{60} and **1** is disrupted at 423 K, the assembly of C_{60} and **2** is formed at 453 K. The C_{60} molecules do not diffuse within both assemblies at 298 K. This observation indicates that the energy barrier for diffusion of the C_{60} molecules is larger than the thermal energy at 298 K. The large $C_{60}\cdots C_{60}$ distance in both superstructures excludes the presence of any significant contribution from the cohesive $C_{60}\cdots C_{60}$ energy, which is of the order of 31 kcal mol^{-1} at a separation of about 1 nm.[29] Moreover, in agreement with previous studies in solution,[17] any strong fullerene–porphyrin interactions are absent in the assembly of diporphyrin **1**, since the C_{60} molecules are not located directly above the macrocyclic cores and can be repositioned without altering the underlying porphyrin layer (see Figure 2 b).

Evidence for a unique type of interplay can be deduced by time-lapsed series of STM images of a full-coverage monolayer of a tetra-arylated porphyrin (see the Supporting Information). Fluctuating bright/dim patterns which are attributed to rotations of the 3,5-di(*tert*-butyl)phenyl substituents of neighboring molecules were observed. These conformational changes are most likely based on van der Waals interactions and propagate within the monolayer from one molecule to its neighbors. The same interpretation can be assigned to the formation of chains of C_{60} molecules on a monolayer of **1**. In this assembly, C_{60}-induced conformational changes of the 3,5-di(*tert*-butyl)phenyl substituents propagate in the underlying porphyrin layer, thus directing the formation of fullerene chains on top of it.

In contrast to the chainlike assembly, we could not precisely estimate the location of the C_{60} molecules with respect to the underlying monolayer of **2** within the **2**–C_{60} assembly. Nevertheless, the high thermal stability and the long-range order accounts for a strong interaction within the assembly that we tentatively ascribe to the rather high porphyrin–fullerene interaction energy (of the order of 16–18 kcal mol^{-1} for monomeric porphyrin).[14] These conclusions are in agreement with our recent results obtained in solution, which show that monomeric porphyrins such as **2** undergo much stronger interchromophoric interactions with C_{60} than triply fused diporphyrins such as **1**.[15,17]

In summary, the first example of addressable supramolecular architectures was obtained by self-assembly of fullerenes and porphyrins on surfaces. The arrangement of the fullerene molecules on the patterned layer can be controlled by the porphyrin structure. The observed mode of self-assembly results from a delicate balance between the fullerene–porphyrin interaction and the conformational motion within the underlaying porphyrin layer. In addition to the exceptional molecular properties that can be embedded on the surface, such systems offer a valid alternative toward the construction of identical addressable molecular architectures. This is hardly imaginable by using established miniaturizing methods, such as the "lithographic" techniques, and provides an exceptional example of the potential of the supramolecular approach for the fabrication of laterally addressable molecular devices.

Received: May 5, 2004

Keywords: fullerenes · porphyrinoids · scanning probe microscopy · self-assembly · surface chemistry

[1] J.-M. Lehn, *Science* **2002**, *295*, 2400–2403.
[2] O. Ikkala, G. ten Brinke, *Science* **2002**, *295*, 2407–2409.
[3] D. N. Reinhoudt, M. Crego-Calama, *Science* **2002**, *295*, 2403–2407.
[4] G. M. Whitesides, B. Grzybowski, *Science* **2002**, *295*, 2418–2421.
[5] a) M. D. Hollingsworth, *Science* **2002**, *295*, 2410–2413; b) T. Kato, *Science* **2002**, *295*, 2414–2418.
[6] F. C. De Schryver, S. De Feyeter, *Chem. Soc. Rev.* **2003**, *32*, 139–150.
[7] a) M. Furukawa, H. Tanaka, K. Sugiura, Y. Sakata, T. Kawai, *Surf. Sci.* **2000**, *445*, L58–L63; b) J. A. Theobald, N. S. Oxtoby, M. A. Phillips, N. R. Champness, P. H. Beton, *Nature* **2003**, *424*, 1029–1031; c) J. Weckesser, A. D. Vita, J. V. Barth, C. Cai, K. Kern, *Phys. Rev. Lett.* **2001**, *87*, 096101; d) M. Böhringer, W.-D. Schneider, R. Berndt, *Surf. Rev. Lett.* **2000**, *7*, 661–663; e) S. De Feyter, M. Larsson, N. Schuurmans, B. Verkuijl, G. Zoriniants, A. Gesquiere, M. M. Abdel-Mottaleb, J. van Esch, B. L. Feringa, J. van Stam, F. De Schryver, *Chem. Eur. J.* **2003**, *9*, 1198–1206.
[8] a) T. Yokoyama, S. Yokoyama, T. Kamikado, Y. Okuno, S. Mashiko, *Nature* **2001**, *413*, 619–621; b) K. Morgenstern, E. Laegsgaard, I. Stensgaard, F. Besenbacher, M. Böhringer, W.-D. Schneider, R. Berndt, F. Mauri, A. D. Vita, R. Car, *Appl. Phys. A* **1999**, *69*, 559–663.

 © 2004 Wiley-VCH Verlag GmbH & Co. KGaA, Weinheim

[9] a) P. Samori, X. M. Yin, N. Tchebotareva, Z. H. Wang, T. Pakula, F. Jackel, M. D. Watson, A. Venturini, K. Mullen, J. P. Rabe, *J. Am. Chem. Soc.* **2004**, *126*, 3567 – 3575; b) M. Stöhr, T. Wagner, M. Gabriel, B. Weyers, R. Möller, *Adv. Funct. Mater.* **2001**, *11*, 175 – 178.

[10] a) M. Schunack, L. Petersen, A. Kühnle, E. Lægsgaard, I. Stensgaard, I. Johannsen, F. Besenbacher, *Phys. Rev. Lett.* **2001**, *86*, 456 – 459; b) M. Böhringer, K. Morgenstern, W.-D. Schneider, R. Berndt, F. Mauri, A. D. Vita, R. Car, *Phys. Rev. Lett.* **1999**, *83*, 324 – 327.

[11] R. E. Martin, F. Diederich, *Angew. Chem.* **1999**, *111*, 1440 – 1469; *Angew. Chem. Int. Ed.* **1999**, *38*, 1350 – 1377.

[12] a) J. Xiao, M. E. Meyerhoff, *J. Chromatogr. A* **1995**, *715*, 19 – 29; b) M. Ayabe, A. Ikeda, Y. Kubo, M. Takeuchi, S. Shinkai, *Angew. Chem.* **2002**, *114*, 2914 – 2916; *Angew. Chem. Int. Ed.* **2002**, *41*, 2790 – 2792.

[13] a) D. Sun, F. S. Tham, C. A. Reed, P. D. W. Boyd, *Proc. Natl. Acad. Sci. USA* **2002**, *99*, 5088 – 5092; b) D. Y. Sun, F. S. Tham, C. A. Reed, L. Chaker, P. D. W. Boyd, *J. Am. Chem. Soc.* **2002**, *124*, 6604 – 6612.

[14] Y.-B. Wang, Z. Lin, *J. Am. Chem. Soc.* **2003**, *125*, 6072 – 6073.

[15] N. Armaroli, G. Marconi, L. Echegoyen, J. P. Bourgeois, F. Diederich, *Chem. Eur. J.* **2000**, *6*, 1629 – 1645.

[16] D. Bonifazi, F. Diederich, *Chem. Commun.* **2002**, 2178 – 2179.

[17] D. Bonifazi, M. Scholl, F. Y. Song, L. Echegoyen, G. Accorsi, N. Armaroli, F. Diederich, *Angew. Chem.* **2003**, *115*, 5116 – 5120; *Angew. Chem. Int. Ed.* **2003**, *42*, 4966 – 4970.

[18] J. K. Gimzewski, T. A. Jung, M. T. Cuberes, R. R. Schlitter, *Surf. Sci.* **1997**, *386*, 101 – 114.

[19] A. Tsuda, H. Furuta, A. Osuka, *Angew. Chem.* **2000**, *112*, 2649 – 2652; *Angew. Chem. Int. Ed.* **2000**, *39*, 2549 – 2551.

[20] T. A. Jung, R. R. Schlitter, J. K. Gimzewski, H. Tang, C. Joachim, *Science* **1996**, *271*, 181 – 184.

[21] The porphyrins as well as C_{60} were deposited on the metal substrates in a standard UHV chamber ($P_{base} = 2 \times 10^{-10}$ mbar). Flat Ag(100) and Ag(111) terraces (up to 200 nm of width) separated by monoatomic steps were prepared by repeated cycles (ca. 15 min) of Ar^+ sputtering and thermal annealing (ca. 870 K). All molecules were transferred onto the silver surfaces (kept at 298 K) by organic molecular beam deposition from a Knudsen-cell-type evaporator with a deposition rate of about 0.3 monolayer min^{-1}. The rate was controlled by a quartz microbalance which was calibrated with STM images of ordered areas. Room-temperature STM experiments employing constant current mode were performed in situ after the deposition of the molecular layer with a chemically etched tungsten tip and with an in-house built microscope (comparable to the OMICRON design). Typical scan rates were in the range of 2–4 Hz per scanline. The chemical composition of the layers was confirmed by X-ray photoelectron spectroscopy.

[22] S. Berner, M. de Wild, L. Ramoino, S. Ivan, A. Baratoff, H.-J. Güntherodt, H. Suzuki, D. Schlettwein, T. A. Jung, *Phys. Rev. B* **2003**, *68*, 115410.

[23] a) T. A. Jung, R. R. Schlitter, J. K. Gimzewski, *Nature* **1997**, *386*, 696 – 698; b) J. Kuntze, X. Ge, R. Berndt, *Nanotechnology* **2002**, *15*, S337-S340.

[24] Chains consisting of a maximum of three C_{60} molecules tilted at an angle of $120 \pm 4°$ (dashed blue arrow in Figure 2a, right) with respect to the main direction of the fullerene chains (blue arrow in Figure 2a, right) have also been observed in the STM images.

[25] The C_{60} molecules appear with a diameter of approximately 1.5 nm (van der Waals diameter of C_{60} is ca. 1 nm) because of the tip–molecule convolution that broadens the lateral dimensions of single objects in STM.

[26] M. de Wild, S. Berner, H. Suzuki, H. Yanagi, D. Schlettwein, S. Ivan, A. Baratoff, H.-J. Güntherodt, T. A. Jung, *ChemPhysChem* **2002**, *3*, 881 – 885.

[27] E. I. Altman, R. J. Colton, *Phys. Rev. B* **1993**, *48*, 18244 – 18249.

[28] C. Ton-That, A. G. Shard, S. Egger, V. R. Dhanak, M. E. Welland, *Phys. Rev. B* **2003**, *67*, 155415.

[29] a) C. Pan, M. P. Sampson, Y. Chai, R. H. Hauge, J. L. Margrave, *J. Phys. Chem.* **1991**, *95*, 2944 – 2946; b) X. Shi, W. B. Caldwell, K. Chen, C. A. Mirkin, *J. Am. Chem. Soc.* **1994**, *116*, 11598 – 11599.

 © 2004 Wiley-VCH Verlag GmbH & Co. KGaA, Weinheim

Charge-Transfer Complexes

$[\{[Pt(en)_2][PtX_2(en)_2]\}_3][\{(MX_5)X_3\}_2]\cdot 12H_2O$: Quasi-One-Dimensional Halogen-Bridged Pt^{II}–Pt^{IV} Mixed-Valence Compounds with Magnetic Counteranions**

Masahiro Yamashita, Daisuke Kawakami, Satoshi Matsunaga, Yoshio Nakayama, Mari Sasaki, Shinya Takaishi, Fumiyasu Iwahori, Hitoshi Miyasaka, Ken-ichi Sugiura, Yoshiki Wada, Hiroshi Miyamae, Hiroyuki Matsuzaki, Hiroshi Okamoto, Hisaaki Tanaka, Kazuhiro Marumoto, and Shin-ichi Kuroda*

Quasi-one-dimensional, halogen-bridged mixed-valence compounds (MX chains) have recently attracted much

[*] Prof. M. Yamashita, D. Kawakami, S. Matsunaga, Y. Nakayama, M. Sasaki, Dr. S. Takaishi, Dr. F. Iwahori, Dr. H. Miyasaka, Prof. K.-i. Sugiura
Department of Chemistry
Graduate School of Science
Tokyo Metropolitan University and CREST(JST)
1-1 Minamiosawa, Hachioji, Tokyo 192-0397 (Japan)
Fax: (+81) 426-77-2525
E-mail: yamashit@comp.metro-u.ac.jp

Dr. Y. Wada
Advanced Materials Laboratory
National Institute for Materials Science
1-1 Namiki, Tsukuba, Ibaraki 305-0044 (Japan)

Prof. H. Miyamae
Faculty of Science
Josai University
1-1 Keyakidai, Sakado, Saitama 350-0295 (Japan)

Dr. H. Matsuzaki, Prof. H. Okamoto
Department of Advanced Materials Science
Graduate School of Frontier Science
The University of Tokyo
Kashiwa, Chiba 277-8561 (Japan)

Dr. H. Tanaka, Dr. K. Marumoto, Prof. S. Kuroda
Department of Applied Physics
Graduate School of Engineering
Nagoya University
Furocho, Chikusa-ku, Nagoya, Aichi 464-8603 (Japan)

[**] This work was partly supported by a Grant-in Aid for Creative Scientific Research from the Ministry of Education, Culture, Sports, Science, and Technology. We are grateful to Dr. Noboru Kishi of the Rigaku Corporation for measuring the temperature dependence of the X-ray powder-diffraction patterns. en = ethylenediamine; M = Co^{2+}, Mn^{2+}, and Fe^{2+}; X = Cl^- and Br^-.

 DOI: 10.1002/anie.200460580 © 2004 Wiley-VCH Verlag GmbH & Co. KGaA, Weinheim

attention because they show very interesting physical properties, such as intense and dichroic intervalence charge-transfer bands, overtone progression of resonance-Raman spectra, luminescence spectra with large Stokes shifts, large third-order nonlinear optical properties, mid-gap absorptions attributable to solitons and polarons, etc., and because they are one-dimensional model compounds of high-critical-temperature (T_c) copper oxide superconductors.[1–9] Theoretically, these MX chains are considered as Peierls–Hubbard systems where the electron–phonon interaction (S), the electron transfer (T), and the intra- and intersite Coulomb repulsion energies (U and V, respectively) compete or cooperate with each other.[10,11] Platinum and palladium compounds form charge-density-wave (CDW) states or M^{II}–M^{IV} mixed-valence states as a result of electron–phonon interactions (S), where the bridging halogen atoms are displaced from the midpoint between the two neighboring metal ions. Accordingly, the half-filled metallic band splits into an occupied valence band and an unoccupied conduction band with finite Peierls energy gaps. Therefore, these compounds belong to class II in the Robin–Day classification of mixed-valence complexes.[1] In these MX chain compounds the CDW amplitudes can be tuned by varying the metal ions, bridging halogen atoms, in-plane ligands, and counteranions.[12] Although more than 200 mixed-valence platinum compounds have been synthesized so far, all these MX chain compounds have closed-shell or nonmagnetic counteranions such as ClO_4^-, BF_4^-, or halogen ions. In this study we have succeeded in synthesizing the novel Pt^{II}–Pt^{IV} mixed-valence complexes $[\{[Pt(en)_2][PtX_2(en)_2]\}_3][\{(MX_5)X_3\}_2]\cdot 12\,H_2O$ ($M = Co^{2+}$, Mn^{2+}, and Fe^{2+}; $X = Cl^-$ and Br^-; en = ethylenediamine) with magnetic counteranions. At the same time, a unique packing motif as well as an interesting adsorption–desorption of water molecules has been observed. Herein, we describe the syntheses, crystal structures, thermogravimetric analysis (TGA), temperature dependence of X-ray powder-diffraction patterns, single-crystal reflectance spectra, resonance-Raman spectra, and electron spin resonance (ESR) spectra of these complexes.

Single-crystal X-ray structural determinations were carried out for $[\{[Pt(en)_2][PtCl_2(en)_2]\}_3][\{(MnCl_5)Cl_3\}_2]\cdot 12\,H_2O$. Figure 1 shows two perspective views of this complex. The planar $\{Pt(en)_2\}$ units are bridged by halogen ions which are disordered at positions away from the midpoints between two neighboring Pt ions with half occupancies, thus forming linear chain Pt^{II}–Pt^{IV} mixed-valence structures (one of the distorted Cl ions has been omitted for clarity). The Pt···Pt distance and Pt^{IV}–Cl and Pt^{II}···Cl bond lengths are 5.303 Å, 2.325 Å, and 2.978 Å, respectively, while those in $[\{Pt(en)_2\}\{PtCl_2(en)_2\}](ClO_4)_4$ are 5.403 Å, 2.318 Å, and 3.085 Å, respectively.[13] Therefore, the degrees of distortions of the bridging halogen atoms from the midpoints between two neighboring Pt ions, defined as $d(Pt^{IV}–Cl)/d(Pt^{II}\cdots Cl)$, are 0.78 for the former compound and 0.75 for the latter, thus indicating that the oxidation state of the magnetic counteranion complex is closer to Pt^{III}, namely a Robin–Day class III complex, than the ClO_4^- compound.[1] The magnetic $MnCl_5$ counterions have a trigonal-bipyramidal structure. The Mn–Cl bond lengths range from 2.457 Å in the plane to 2.495 Å along the axis. The Cl_3 ions form a triangular structure, with a Cl···Cl distance in this triangle of 6.051 Å. These MCl_5 and Cl_3 ions stack alternately along the main Pt^{II}–Pt^{IV} chains. Hydrogen bonds between the H atoms of the en ligands and the

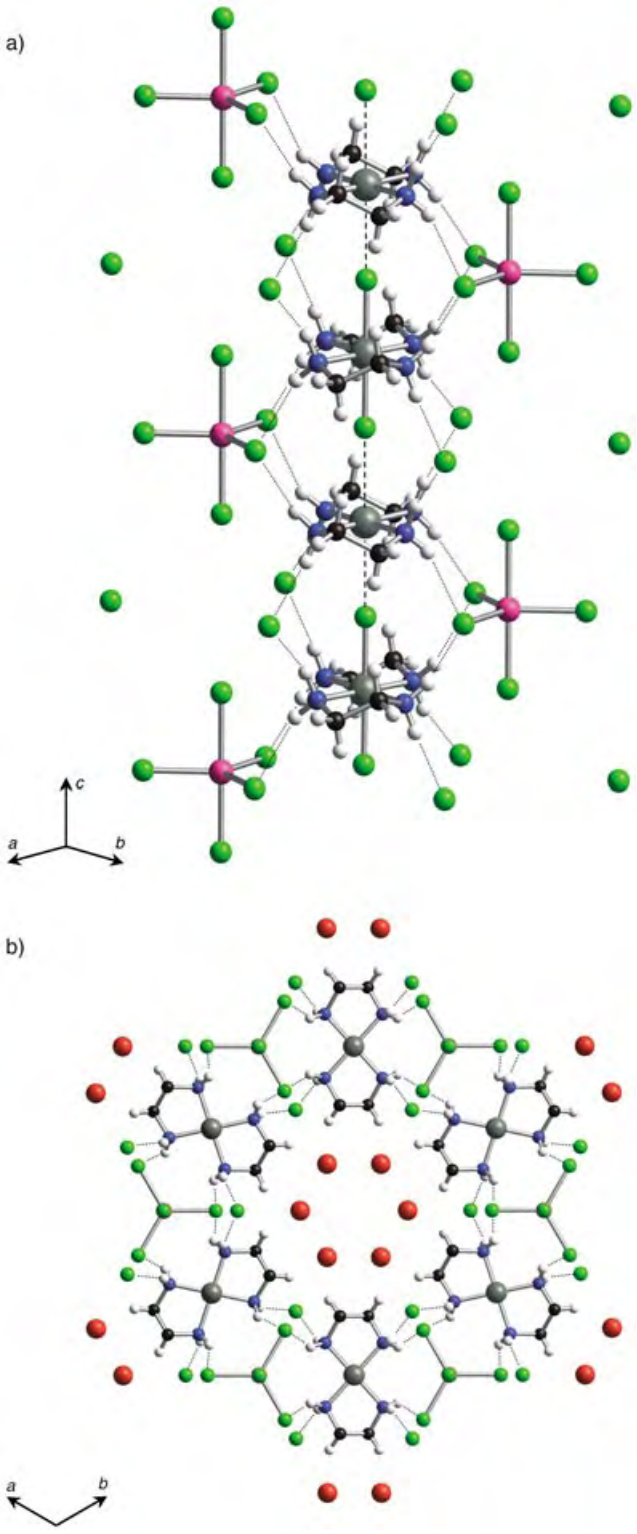


Figure 1. Perspective views of the 3D packing of $[\{[Pt(en)_2][PtCl_2(en)_2]\}_3][\{(MnCl_5)Cl_3\}_2]\cdot 12\,H_2O$; H white, C black, N blue, O red, Mn pink, Cl green, Pt gray. One of the disordered Cl ions has been omitted for clarity. Dotted and broken lines represent hydrogen bonds and Pt^{II}···Cl interactions, respectively.

 © 2004 Wiley-VCH Verlag GmbH & Co. KGaA, Weinheim

Cl atoms of $MnCl_5$ are observed (H···Cl = 2.526 Å), as are hydrogen bonds between these H atoms and the Cl atoms of the Cl_3 unit (H···Cl = 2.471 Å). As shown in Figure 1b, the Pt chains and counteranions form hexagonal spaces, which are filled with water molecules. Although only six water molecules are observed in the crystal structure, the presence of 12 water molecules per molecular unit was confirmed by thermogravimetric analysis (TGA) and elemental analysis (see below). All 12 water molecules were observed in the solid-state structure of $[\{[Pt(en)_2][PtBr_2(en)_2]\}_3][\{(MnBr_5)Br_3\}_2]\cdot 12H_2O$. A preliminary structure determination of the other compounds was also carried out. Although they have not been completely solved, their essential structures are the same as that of $[\{[Pt(en)_2][PtCl_2(en)_2]\}_3][\{(MnCl_5)Cl_3\}_2]\cdot 12H_2O$.

To clarify the desorption behavior of the water molecules a TGA study was performed on $[\{[Pt(en)_2][PtCl_2(en)_2]\}_3][\{(MnCl_5)Cl_3\}_2]\cdot 12H_2O$ (Figure 2). Upon heating the sample

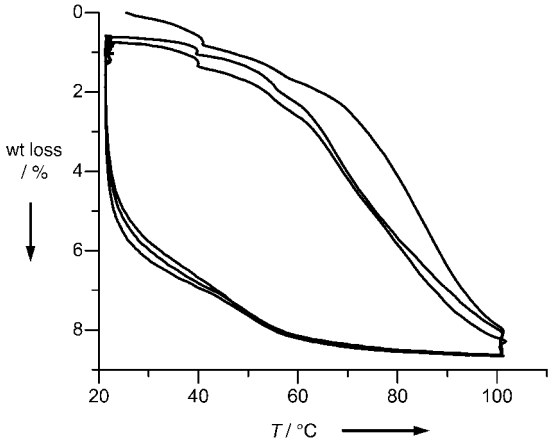


Figure 2. TGA plots of $[\{[Pt(en)_2][PtCl_2(en)_2]\}_3][\{(MnCl_5)Cl_3\}_2]\cdot 12H_2O$.

from 20 to 100 °C, at a rate of 3 °C min^{-1}, the sample weight gradually decreased. This weight loss of approximately 8% can be attributed to the loss of water molecules, and is in good agreement with the desorption of 12 water molecules per molecular unit (7.2%). After keeping the temperature at 100 °C for 60 min, the sample was cooled down to 20 °C at a rate of 3 °C min^{-1}. The weight of the sample gradually increased and became almost the same as that of the initial sample. This result indicates that the 12 desorbed water molecules can re-enter the crystals reversibly. We confirmed this reversibility by repeating the process three times. The weight loss during the first heating stage is a little larger than those during the second and third stages. This can be accounted for by desorption of impurities from the crystal surface.

Temperature-dependent X-ray powder-diffraction patterns were measured in order to confirm that the crystal structure is maintained even in the absence of water molecules. Figure 3 shows X-ray powder-diffraction patterns of $[\{[Pt(en)_2][PtCl_2(en)_2]\}_3][\{(MnCl_5)Cl_3\}_2]\cdot 12H_2O$ at various temperatures. The peaks of these patterns remain sharp and their positions do not change during the heating and cooling

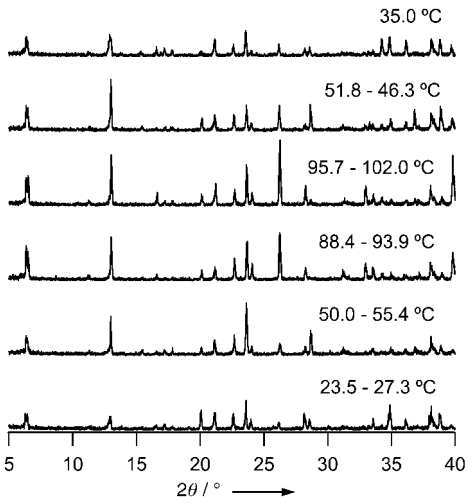


Figure 3. Temperature dependence of the X-ray powder-diffraction patterns in $[\{[Pt(en)_2][PtCl_2(en)_2]\}_3][\{(MnCl_5)Cl_3\}_2]\cdot 12H_2O$.

processes, thus indicating that the crystal structure is sustained even in the absence of water molecules.

The single-crystal reflectance spectra of $[\{[Pt(en)_2][PtCl_2(en)_2]\}_3][\{(MnCl_5)Cl_3\}_2]\cdot 12H_2O$ and $[\{[Pt(en)_2][PtBr_2(en)_2]\}_3][\{(MBr_5)Br_3\}_2]\cdot 12H_2O$ (M = Mn and Co) were measured at room temperature. Their optical conductivities obtained from the Kramers–Kronig transformation are shown in Figure 4. The Cl- and Br-bridged compounds show

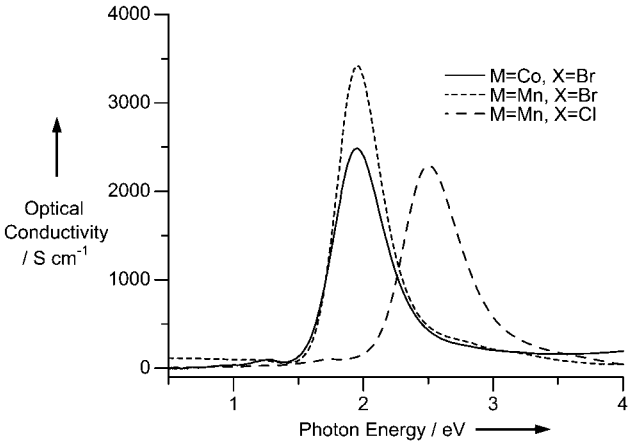


Figure 4. Optical conductivity spectra of $[\{[Pt(en)_2][PtCl_2(en)_2]\}_3][\{(MnCl_5)Cl_3\}_2]\cdot 12H_2O$ and $[\{[Pt(en)_2][PtCl_2(en)_2]\}_3][\{(MnBr_5)Br_3\}_2]\cdot 12H_2O$ (M = Mn and Co).

dichroic, intense bands at 2.50 eV and 1.95 eV, respectively. These are attributable to the charge-transfer (CT) transition from the Pt^{II} species to the Pt^{IV} species along the chain. According to theoretical studies,[14,15] the energy position of the CT bands in mixed-valence compounds can be given by $2S-U$ if T and V are neglected. The lower CT energy of the Mn compound than the ClO_4 compound (2.72 eV) could be a consequence of a decrease of S, thus indicating that the charge delocalization of this compound is greater than that of the

 © 2004 Wiley-VCH Verlag GmbH & Co. KGaA, Weinheim

ClO_4 compound; this proposal is consistent with the X-ray crystal structures. The CT energies of the Br-bridged compounds are lower than those of the Cl-bridged compounds because of their greater charge delocalization.

Overtone progressions attributable to the Pt^{IV}–X stretching modes are observed in the resonance-Raman spectra, where the stretching modes of the Cl- and Br-bridged compounds occur at about 310 cm^{-1} (310.1 cm^{-1} for Mn and Fe) and 175 cm^{-1} (177.1 cm^{-1} for Mn, 175.7 cm^{-1} for Fe, and 175.7 cm^{-1} for Co), respectively. The lower value of the stretching mode of $[\{[Pt(en)_2][PtCl_2(en)_2]\}_3][\{(MnCl_5)Cl_3\}_2]\cdot 12H_2O$ than that of the ClO_4 compound (311.3 cm^{-1}) could be the result of an increase in the anharmonicity of the potential energy surface, thus indicating that electronic delocalization of the Mn compound is greater than that of the ClO_4 compound, as predicted in a previous theoretical study.[15] This fact is consistent with the crystal structure and the optical-conductivity results.

Temperature-dependent (M = Co, X = Br) and angle-dependent (M = Mn, X = Cl) ESR spectra are shown in Figure 5. Polycrystalline samples of the Co salt were used. The ESR spectra depend highly on the metal species, and their intensity decreases with increasing temperature following the Curie law. The nearly symmetrical line-shape for the Co salt with a mean g value of about 4.9 indicates that the g factor is nearly isotropic—the magnetic-field difference arising from the anisotropic g values for polycrystalline samples is less than the linewidth. In general, the free Co^{2+} ion has a ^4F state ($S = {}^3/_2$) and the orbital triplet becomes the lowest state in the cubic crystal-field symmetry. However, these degenerate levels are split both by a lower symmetry of the crystal field, such as tetragonal or trigonal, and spin–orbit coupling. As a result, six Kramer's doublets ($S = {}^1/_2$) are created and each level can be represented by a "fictitious spin $^1/_2$".[16,17] In this case, the inter-level mixing with the excited states lying close to the ground-state Kramer's doublet causes the large g shift from the free-electron g value (2.0023); the broadening of the spectrum as the temperature is raised is a consequence of the shortening of the spin–lattice relaxation time (Figure 5a). In the case of the Mn salt the ESR spectrum is spread over a wide magnetic-field range with several splittings; the spectral shape is almost unchanged within the measured temperature range. Such a situation may be caused by the zero-field splitting of the high-spin Mn^{2+} ion ($S = {}^5/_2$). We also note that the total span of the signal splitting is a maximum at 0 and 180° from the chain axis, thus indicating that the axis of the dipolar interaction coincides with the chain direction. The ESR signals for the Co and Mn salts are ascribed to the M sites, which confirms the successful synthesis of the 1D electronic system with magnetic counteranions.

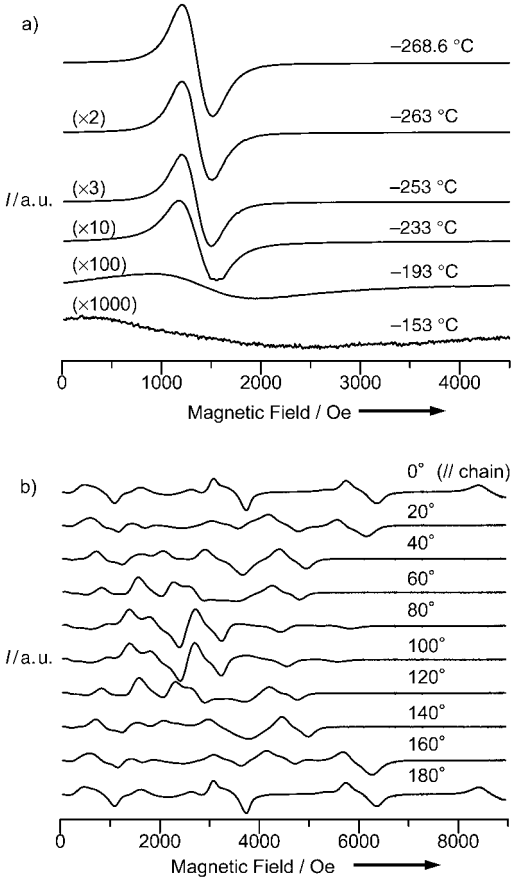


Figure 5. Temperature- and angle-dependence of the ESR spectra of $[\{[Pt(en)_2][PtX_2(en)_2]\}_3][\{(MX_5)X_3\}_2]\cdot 12H_2O$: a) M = Co^{2+}, X = Br; b) M = Mn^{2+}, X = Cl.

In summary, we have succeeded in synthesizing mixed-valence Pt^{II}–Pt^{IV} compounds with magnetic counteranions. These magnetic MX_5 counterions (M = Mn^{2+}, Fe^{2+}, Co^{2+}; X = Cl^-, Br^-) have an unusual trigonal-bipyramidal structure. The complexes have hexagonal micropores, similar to zeolites, which contain 12 water molecules per molecular unit. These water molecules can be desorbed by heating the complexes to 100 °C whilst maintaining the skeletal structure; they can be adsorbed again by cooling to 20 °C. The ESR spectra reflect the variety of the spin species in the counteranions.

Experimental Section

The compounds were synthesized by adding 150 mg (0.76 mmol) of MX_2 and 1.5 ml HX to an aqueous solution (1 ml) containing 100 mg (0.26 mmol) $[Pt(en)_2]X_2$ and 120 mg (0.26 mmol) $[PtX_2(en)_2]X_2$. Lustrous, needle-shaped crystals were obtained after a week. The elemental analyses are as follows: calcd for $C_{24}H_{120}Cl_{22}Mn_2N_{24}O_{12}Pt_6$: C 9.62, H 4.03, N 11.21; found: C 9.52, H 3.75, N 11.07; calcd for $C_{24}H_{120}Cl_{22}Fe_2N_{24}O_{12}Pt_6$: C 9.61, H 4.03, N 11.21; found: C 9.41, H 3.69, N 11.08; calcd for $C_{24}H_{120}Br_{22}Mn_2N_{24}O_{12}Pt_6$: C 7.25, H 3.04, N 8.46; found: C 7.11, H 2.94, N 8.23; calcd for $C_{24}H_{120}Br_{22}Fe_2N_{24}O_{12}Pt_6$: C 7.25, H 3.04, N 8.45; found: C 7.08, H 2.79, N 8.17; calcd for $C_{24}H_{120}Br_{22}Co_2N_{24}O_{12}Pt_6$: C 7.24, H 3.04, N 8.44; found: C 7.03, H 2.84, N 8.34.

X-ray crystallographic analyses of $[\{[Pt(en)_2][PtX_2(en)_2]\}_3][\{(MX_5)X_3\}_2]\cdot 12H_2O$ (M = Co^{2+}, Mn^{2+}, and Fe^{2+}; X = Cl^- and Br^-) were performed with a Rigaku RAXIS-RAPID imaging plate diffractometer equipped with graphite monochromated $Mo_{K\alpha}$ radiation ($\lambda = 0.7107$ Å). Crystal data of $[\{[Pt(en)_2][PtX_2(en)_2]\}_3][\{(MnCl_5)Cl_3\}_2]\cdot 6H_2O$: $C_{24}H_{108}Cl_{22}Mn_2N_{24}O_6Pt_6$, $M_r = 2889.60$, hexagonal, $P6_3/mmc$ (no. 194), $T = 156 \pm 1$ K, $a = 16.0035(6)$, $b = 16.0035(6)$, $c = 10.9333(5)$ Å, $\gamma = 120°$, $V = 2424.0(2)$ Å^3, $Z = 1$, $\rho_{calcd} = 2.078$, final $R = 0.030$, $wR = 0.029$, GOF = 0.985 with $I > 3.00\sigma(I)$. CCDC-238001 contains the supplementary crystallographic data for this paper. These data can be obtained free of charge at www.ccdc.cam.ac.uk/conts/retrieving.html [or from the Cambridge

 © 2004 Wiley-VCH Verlag GmbH & Co. KGaA, Weinheim

Crystallographic Data Centre, 12 Union Road, Cambridge CB2 1EZ, UK; Fax: (+44) 1223-336-033; E-mail: deposit@ccdc.cam.ac.ukTGA was performed with a Rigaku DSC 8230L calorimeter. X-ray powder diffraction measurements were recorded with a Rigaku RINT UltimaII + DSC equipment. ESR spectra were measured with a Bruker EMX spectrometer equipped with a gas-flow type cryostat Oxford ESR 900.

Received: May 7, 2004

Keywords: bridging ligands · charge transfer · EPR spectroscopy · mixed-valent compounds · zeolite analogues

[1] M. B. Robin, P. Day, *Adv. Inorg. Chem. Radiochem.* **1967**, *10*, 247–297.
[2] H. Tanino, K. Kobayashi, *J. Phys. Soc. Jpn.* **1983**, *52*, 1446–1456.
[3] A. R. Bishop, B. L. Swanson, *Los Alamos Sci.* **1993**, *21*, 133–143.
[4] R. J. H. Clark, *Adv. Infrared Raman Spectrosc.* **1983**, *11*, 95–132.
[5] H. Okamoto, M. Yamashita, *Bull. Chem. Soc. Jpn.* **1998**, *71*, 2023–2039.
[6] M. Yamashita, T. Manabe, T. Kawashima, H. Okamoto, H. Kitagawa, *Coord. Chem. Rev.* **1999**, *190–192*, 309–330.
[7] N. Kuroda, M. Sakai, Y. Nishina, M. Tanaka, S. Kurita, *Phys. Rev. Lett.* **1987**, *58*, 2122–2125.
[8] H. Okamoto, T. Mitani, K. Toriumi, M. Yamashita, *Phys. Rev. Lett.* **1992**, *69*, 2248–2251.
[9] R. J. Donohoe, L. A. Worl, C. A. Arrington, A. Bulou, B. I. Swanson, *Phys. Rev. B: Condens. Matter* **1992**, *45*, 13185–13195.
[10] D. Baeriswyl, A. R. Bishop, *J. Phys. C: Solid State Phys.* **1988**, *21*, 339–356.
[11] A. Mishima, K. Nasu, *Phys. Rev. B: Condens. Matter* **1989**, *39*, 5758–5762.
[12] H. Okamoto, K. Toriumi, K. Okaniwa, T. Mitani, M. Yamashita, *Mater. Sci. Eng.* **1992**, *B13*, L9–L14.
[13] H. Okamoto, M. Yamashita, *Bull. Chem. Soc. Jpn.* **1998**, *71*, 2023–2039.
[14] K. Prassides, P. Shatz, K. Wong, P. Day, *J. Phys. Chem.* **1986**, *90*, 5588–5597.
[15] K. Prassides, P. Shatz, *Chem. Phys. Lett.* **1991**, *178*, 227–234.
[16] A. Abragam, M. H. L. Pryce, *Proc. R. Soc. London* **1951**, *206*, 173–191.
[17] S. Kuroda, M. Motokawa, M. Date, *J. Phys. Soc. Jpn.* **1978**, *44*, 1797–1803.

 © 2004 Wiley-VCH Verlag GmbH & Co. KGaA, Weinheim

Host–Guest Systems

Cavity Effects on the Enantioselectivity of Chiral Amido[4]resorcinarene Stereoisomers**

*Bruno Botta, Deborah Subissati, Andrea Tafi, Giuliano Delle Monache, Antonello Filippi, and Maurizio Speranza**

Enzyme catalysis plays a crucial role in all biochemical processes. Natural and artificial enzymes normally exhibit a high enantioselectivity toward chiral molecules as a consequence of shape-specific noncovalent attractive and repulsive intermolecular interactions.[1–5] An important step toward the elucidation of enzyme mechanisms requires a comprehensive kinetic study using simplified models under conditions, such as the gas phase, where the molecule/receptor interactions are not perturbed by medium effects.[6]

Calixarenes lend themselves to this task since they are synthetic macrocycles endowed with a cavity-shaped architecture, which can be made asymmetric by the presence of chiral pendant groups. A peculiar feature of calixarene macrocycles is their nonplanar cyclophane structure, which may give rise to relatively stable stereoisomeric and conformational forms. A pertinent case is that of 2,8,14,20-tetrakis(L-valinamido)[4]resorcinarene (**1**), which can display at least four stable stereoisomeric structures, that is, flattened cone ($\mathbf{1a_L}$), 1,2-alternate ($\mathbf{1b_L}$), chair 1 ($\mathbf{1c_L}$) (Figure 1), and chair 2.[7] Its stereoisomerism allows the tailoring of variously shaped cavities, which can be probed to evaluate their effect on ion or molecular recognition.[8,9]

Herein, we report the first comparative gas-phase study along these lines. The intrinsic enantioselectivity of the $\mathbf{1a_L}$, $\mathbf{1b_L}$, and $\mathbf{1c_L}$ diastereomeric structures was checked by introducing their proton-bonded complexes with the pure D and L enantiomers of some aromatic amino acids (A), such as phenylalanine (Phe), tyrosine (Tyr), and 3,4-dihydroxyphenylalanine (dopa), into the cell of a Fourier-transform ion cyclotron resonance mass spectrometer (FT-ICR-MS) and measuring the exchange rate of the amino acid A with

[*] Prof. B. Botta, Dr. D. Subissati, Dr. A. Filippi, Prof. M. Speranza
Dipartimento di Studi di Chimica e Tecnologia
delle Sostanze Biologicamente Attive
Università "La Sapienza", 00185 Roma (Italy)
Fax: (+39) 06-4991-3602
E-mail: maurizio.speranza@uniroma1.it
Prof. A. Tafi
Dipartimento Farmaco Chimico Tecnologico
Università di Siena, 53100 Siena (Italy)
Dr. G. Delle Monache
Istituto Chimica del Riconoscimento Molecolare
Università Cattolica del Sacro Cuore, 00168 Roma (Italy)

[**] This work was supported by the Ministero dell'Istruzione dell'Università e della Ricerca (MIUR) and the Consiglio Nazionale delle Ricerche (CNR). The authors express their gratitude to F. Angelelli for technical assistance.

Supporting information for this article is available on the WWW under http://www.angewandte.org or from the author.

 DOI: 10.1002/anie.200460663 © 2004 Wiley-VCH Verlag GmbH & Co. KGaA, Weinheim

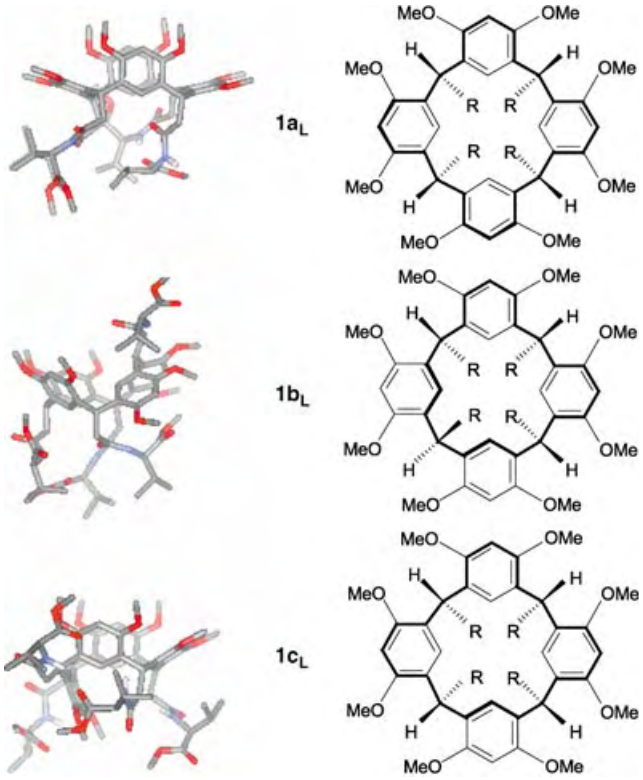


Figure 1. Formulas and side views of local minimum geometry of 2,8,14,20-tetrakis(L-valinamido)[4]resorcinarene (R = L-CH_2CONH-CH(*i*Pr)COOEt) in the flattened-cone **1a**$_L$, 1,2-alternate **1b**$_L$, and chair 1 **1c**$_L$ structures.

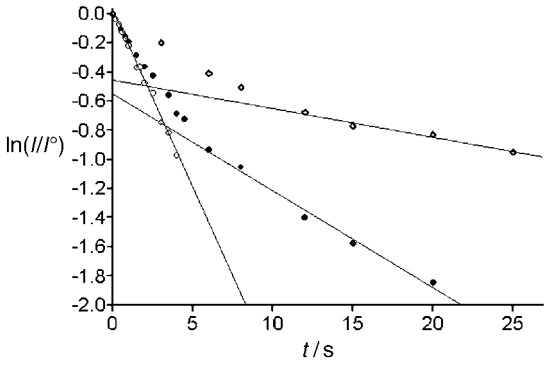


Figure 2. Kinetic plots for the gas-phase reaction between (*R*)-(−)-2-butylamine (B_R) and $[(\mathbf{1c}_L)\cdot H\cdot A]^+$ (A = L-Phe (open circles; $P(B_R) = 4.1\times10^{-8}$ mbar); L-Tyr (solid circles; $P(B_R) = 6.2\times10^{-8}$ mbar); L-dopa (diamonds; $P(B_R) = 2.6\times10^{-7}$ mbar)).

(*S*)-(+)- and (*R*)-(−)-2-butylamine (B_S and B_R, respectively) [Eq. (1)].

$$[\mathbf{1}\cdot H\cdot A]^+ + B \rightarrow [\mathbf{1}\cdot H\cdot B]^+ + A \qquad (1)$$

The rate constants k' for the reaction defined in Equation (1) were obtained from the slopes of the pseudo-first-order rate plots ($\ln(I/I_0)$ versus t), where I is the abundance of complex $[\mathbf{1}\cdot H\cdot A]^+$ at the delay time t and I_0 is the sum of the abundances of $[\mathbf{1}\cdot H\cdot A]^+$ and $[\mathbf{1}\cdot H\cdot B]^+$. Irrespective of the configurations of A and B, linear rate plots are invariably observed with all $[\mathbf{1}\cdot H\cdot A]^+$ complexes except those with **1c**$_L$, Tyr; **1a**$_L$, dopa; and **1c**$_L$, dopa (see Figure 2 and Supporting Information).

The bimodal kinetics shown by these latter systems reveal the presence of several stable isomeric $[\mathbf{1}\cdot H\cdot A]^+$ structures. Above a certain reaction time, for example 6 s for $[(\mathbf{1c}_L)\cdot H\cdot$(L-Tyr)$]^+$ and 12 s for $[(\mathbf{1c}_L)\cdot H\cdot$(L-dopa)$]^+$ (Figure 2), the bimodal curves become linear (correlation coefficient $r^2 = 0.990$ and 0.976, respectively) which indicates that, at that delay time, only the less-reactive isomer $[\mathbf{1}\cdot H\cdot A]^+_{slow}$ is present. The time dependence of the more-reactive fraction $[\mathbf{1}\cdot H\cdot A]^+_{fast}$ can be inferred from the overall $[\mathbf{1}\cdot H\cdot A]^+$ decay after subtracting the first-order decay of the $[\mathbf{1}\cdot H\cdot A]^+_{slow}$ fraction. The good linearity of the resulting curve ($r^2 = 0.998$ and 0.991, respectively) suggests that only a single isomer is present in the more reactive $[\mathbf{1}\cdot H\cdot A]^+_{fast}$ fraction. Its y intercept, as well as that of the linear $[\mathbf{1}\cdot H\cdot A]^+_{fast}$ decay curve, provides an estimate of the relative distribution of $[\mathbf{1}\cdot H\cdot A]^+_{fast}$ and $[\mathbf{1}\cdot H\cdot A]^+_{slow}$, respectively (Table 1).

Table 1: Percent distribution of isomeric $[\mathbf{1}\cdot H\cdot A]^+$ structures.

Host (**1**)	Guest (A)	$[\mathbf{1}\cdot H\cdot A]^+_{fast}$	$[\mathbf{1}\cdot H\cdot A]^+_{slow}$
1a$_L$	D-dopa	20 ± 4	80 ± 4
	L-dopa	19 ± 3	81 ± 3
1c$_L$	D-Tyr	42 ± 3	58 ± 3
	L-Tyr	44 ± 2	56 ± 2
1c$_L$	D-dopa	48 ± 2	52 ± 2
	L-dopa	39 ± 3	61 ± 3

The second-order rate constants k, calculated from the corresponding $k'/[B]$ ratios, are listed in Table 2. Their values, compared with the relevant collision rate constants (k_{coll}),[10] provide a measure of the efficiency of the reaction (eff = k/k_{coll}, figures in parentheses in Table 2). The enantioselectivity factor ρ is defined as the ratio of the k value for the reaction of a given base B with the $[\mathbf{1}\cdot H\cdot A_D]^+$ complex and that for the same reaction with the $[\mathbf{1}\cdot H\cdot A_L]^+$ complex. The enantioselectivity factor ξ is defined as the ratio of the k value for the reaction of a given $[\mathbf{1}\cdot H\cdot A]^+$ complex with (*R*)-(−)-2-butylamine and that for the same reaction with (*S*)-(+)-2-butylamine. The $\rho < 1$ terms of Table 2 indicate that the $[\mathbf{1}\cdot H\cdot A_L]^+$ complex is more reactive than its $[\mathbf{1}\cdot H\cdot A_D)]^+$ diastereomer toward the same base B. The reverse is true when $\rho > 1$. The $\xi > 1$ terms of Table 2 indicate that (*R*)-(−)-2-butylamine is more reactive than (*S*)-(+)-2-butylamine toward the same $[\mathbf{1}\cdot H\cdot A]^+$ complex. The reverse is true when $\xi < 1$.

Comparative analysis of the kinetic data reported in Tables 1 and 2 shows the strict relationship between the structural features of the selected stereoisomeric hosts and their kinetic enantioselectivity toward a given chiral guest. In a previous study,[9] a structure (denoted as *up*) was assigned to the $[(\mathbf{1a}_L)\cdot H\cdot(dopa)]^+_{fast}$ isomer in which the guest is located on the hydrophobic aromatic rim of the host. Conversely, in the $[(\mathbf{1a}_L)\cdot H\cdot(dopa)]^+_{slow}$ structure (denoted as *down*), the guest is

 © 2004 Wiley-VCH Verlag GmbH & Co. KGaA, Weinheim

Table 2: Exchange rate constants ($k \times 10^{-10}$ cm^3 molecule^{-1} s^{-1}).

Host (**1**)	Guest (A)	(*R*)-(−)-$C_4H_9NH_2$ *k*	eff	(*S*)-(+)-$C_4H_9NH_2$ *k*	eff	ξ
1a$_L$	D-Phe	3.60 ± 0.03	(0.32)	3.56 ± 0.04	(0.32)	1.01 ± 0.02
	L-Phe	2.20 ± 0.03	(0.20)	2.28 ± 0.04	(0.20)	0.96 ± 0.03
		ρ = 1.64 ± 0.03		1.56 ± 0.05		
	D-Tyr	0.86 ± 0.02	(0.08)	1.42 ± 0.02	(0.13)	0.61 ± 0.02
	L-Tyr	1.07 ± 0.02	(0.10)	1.36 ± 0.02	(0.13)	0.79 ± 0.02
		ρ = 0.80 ± 0.04		1.04 ± 0.03		
	D-dopa$_{fast}$	2.28 ± 0.06	(0.20)	1.26 ± 0.05	(0.11)	1.81 ± 0.12
	L-dopa$_{fast}$	3.00 ± 0.09	(0.27)	1.82 ± 0.20	(0.16)	1.65 ± 0.24
		ρ = 0.76 ± 0.04		0.69 ± 0.11		
	D-dopa$_{slow}$	$0.07_3 \pm 0.00_8$	(0.00_6)	$0.06_4 \pm 0.00_8$	(0.00_6)	1.14 ± 0.28
	L-dopa$_{slow}$	$0.10_0 \pm 0.00_8$	(0.00_9)	$0.07_9 \pm 0.00_9$	(0.00_7)	1.27 ± 0.25
		ρ = 0.73 ± 0.13		0.81 ± 0.19		
1b$_L$	D-Phe	4.06 ± 0.09	(0.36)	5.15 ± 0.06	(0.46)	0.79 ± 0.02
	L-Phe	3.78 ± 0.07	(0.34)	4.93 ± 0.06	(0.44)	0.77 ± 0.02
		ρ = 1.07 ± 0.05		1.04 ± 0.03		
	D-Tyr	2.29 ± 0.04	(0.21)	2.93 ± 0.03	(0.26)	0.78 ± 0.02
	L-Tyr	3.06 ± 0.06	(0.27)	3.81 ± 0.06	(0.34)	0.80 ± 0.03
		ρ = 0.75 ± 0.03		0.77 ± 0.02		
	D-dopa	1.57 ± 0.06	(0.14)	1.91 ± 0.06	(0.17)	0.82 ± 0.02
	L-dopa	1.47 ± 0.05	(0.13)	1.55 ± 0.05	(0.14)	0.95 ± 0.03
		ρ = 1.07 ± 0.07		1.23 ± 0.08		
1c$_L$	D-Phe	3.67 ± 0.04	(0.33)	3.61 ± 0.04	(0.32)	1.02 ± 0.02
	L-Phe	3.20 ± 0.05	(0.29)	3.25 ± 0.04	(0.29)	0.98 ± 0.04
		ρ = 1.15 ± 0.03		1.11 ± 0.03		
	D-Tyr$_{fast}$	3.39 ± 0.08	(0.30)	3.95 ± 0.11	(0.35)	0.86 ± 0.04
	L-Tyr$_{fast}$	3.24 ± 0.06	(0.29)	3.00 ± 0.13	(0.27)	1.08 ± 0.07
		ρ = 1.05 ± 0.04		1.32 ± 0.09		
	D-Tyr$_{slow}$	0.90 ± 0.03	(0.08)	0.97 ± 0.04	(0.09)	0.93 ± 0.06
	L-Tyr$_{slow}$	0.58 ± 0.03	(0.05)	0.61 ± 0.03	(0.06)	0.95 ± 0.09
		ρ = 1.55 ± 0.14		1.59 ± 0.13		
	D-dopa$_{fast}$	1.27 ± 0.03	(0.11)	0.87 ± 0.10	(0.08)	1.45 ± 0.23
	L-dopa$_{fast}$	0.47 ± 0.04	(0.04)	1.12 ± 0.10	(0.10)	0.42 ± 0.08
		ρ = 2.68 ± 0.30		0.78 ± 0.09		
	D-dopa$_{slow}$	$0.09_4 \pm 0.00_6$	(0.00_8)	$0.09_5 \pm 0.03_4$	(0.00_9)	0.99 ± 0.64
	L-dopa$_{slow}$	$0.04_1 \pm 0.00_5$	(0.00_4)	$0.04_6 \pm 0.00_8$	(0.00_4)	0.86 ± 0.35
		ρ = 2.30 ± 0.44		2.08 ± 1.33		

located at the hydrophilic rim of the host among the four chiral R pendant groups (Figure 1). The relative abundance of these isomeric structures (20 ± 4 versus 80 ± 4 %; Table 1) qualitatively conforms to their computed stability difference (20 kJ mol^{-1}).[9] The loss of dopa from the *up* structure of $[(\mathbf{1a_L})\cdot H\cdot(dopa)]^+_{fast}$ is promoted by the uptake of base B into the chiral hydrophilic rim of the host. This accounts for the high ξ values (1.81 ± 0.12 (D-dopa); 1.65 ± 0.24 (L-dopa)) in Table 2. A similar uptake is prevented in the *down* structure of $[(\mathbf{1a_L})\cdot H\cdot(dopa)]^+_{slow}$ by the presence of the guest in the hydrophilic cavity of the host. In this case, the amine B can only interact from outside the chiral cavity of the host, which can then exert only in part its asymmetry toward it (ξ = 1.14 ± 0.28 (D-dopa); 1.27 ± 0.25 (L-dopa); Table 2).

Similarly, the comparatively more level distribution of the isomeric $[(\mathbf{1c_L})\cdot H\cdot(dopa)]^+_{fast}$ and $[(\mathbf{1c_L})\cdot H\cdot(dopa)]^+_{slow}$ structures (48 ± 2 versus 52 ± 2 % (D-dopa); 39 ± 3 versus 61 ± 3 % (L-dopa); Table 1) indicates that their stability difference is somewhat reduced by the orientation of the chiral hydrophilic R pendant groups, not only along the *down*-like cavity of the host but also near its *up*-like region. This effect is also mirrored by the reduced difference in reaction rates of $[(\mathbf{1c_L})\cdot H\cdot(dopa)]^+_{fast}$ and $[(\mathbf{1c_L})\cdot H\cdot(dopa)]^+_{slow}$ relative to that of the $[(\mathbf{1a_L})\cdot H\cdot(dopa)]^+_{fast}$/$[(\mathbf{1a_L})\cdot H\cdot(dopa)]^+_{slow}$ pair (Table 2). The size and physical properties of the *up*-like and *down*-like regions of the chair stereoisomer **1c**$_L$ are markedly different from those of the *up* and *down* regions of the flattened cone stereoisomer **1a**$_L$. This may account for their opposite enantioselectivity toward dopa (ρ factors in Table 2). The diverse orientation of the incoming base B toward $[\mathbf{1}\cdot H\cdot(dopa)]^+$ ($\mathbf{1} = \mathbf{1a_L}, \mathbf{1c_L}$) may play a role as well, as suggested by the appreciable differences in the corresponding ξ terms (Table 2).

The apparently linear rate plots associated with the attack by base B on the diastereomeric $[(\mathbf{1b_L})\cdot H\cdot(dopa)]^+$ complexes can be correlated not only with the occurrence of a single complex structure, but also with the occurrence of different structures having comparable reactivity toward base B. Although no clear-cut evidence is presently available,[11] the reaction patterns shown by the ($[\mathbf{1}\cdot H\cdot(dopa)]^+$ (W = **1a**$_L$; **1c**$_L$) stereoisomers lend support to the latter hypothesis. This view conforms well with the ρ and ξ enantioselectivity values of the $[(\mathbf{1b_L})\cdot H\cdot(dopa)]^+$ complexes, which are in the middle of those of their $[\mathbf{1}\cdot H\cdot(dopa)]^+$ ($\mathbf{1} = \mathbf{1a_L}, \mathbf{1c_L}$) analogues (Table 2).

The general enantioselectivity picture shown by the $[\mathbf{1}\cdot H\cdot(dopa)]^+$ complexes finds some confirmation in their $[\mathbf{1}\cdot H\cdot(Tyr)]^+$ analogues. Although here the unequivocal assignment of two stable isomeric structures is limited only to the $[(\mathbf{1c_L})\cdot H\cdot(Tyr)]^+$ complex (Table 1), nevertheless the same ρ value trend is observed for both the $[\mathbf{1}\cdot H\cdot(Tyr)]^+$ and $[\mathbf{1}\cdot H\cdot(dopa)]^+$ series, which increases in the order: $\mathbf{1a_L} \leq \mathbf{1b_L} < \mathbf{1c_L}$ (Table 2). However, the complete absence of phenolic OH groups in Phe has a remarkable effect on the enantioselectivity of the reaction between base B and the corresponding $[\mathbf{1}\cdot H\cdot(Phe)]^+$ complexes. In contrast to their $[\mathbf{1}\cdot H\cdot(Tyr)]^+$ analogues, the $[\mathbf{1}\cdot H\cdot(Phe)]^+$ complexes invariably exhibit $\rho > 1$ values which increase in the reverse order: $\mathbf{1c_L} \sim \mathbf{1b_L} < \mathbf{1a_L}$. This selectivity picture finds some analogies with that observed in the gas-phase reaction of base B with

 © 2004 Wiley-VCH Verlag GmbH & Co. KGaA, Weinheim

diastereomeric $[(\mathbf{1a_L})\cdot H\cdot A]^+$ (A = alanine (Ala) and serine (Ser)) complexes.[8,9] Indeed, $\rho > 1$ values have been measured for $[(\mathbf{1a_L})\cdot H\cdot(Ala)]^+$, whereas the $[(\mathbf{1a_L})\cdot H\cdot(Ser)]^+$ analogues invariably display $\rho < 1$ values. This opposite enantioselectivity is attributed to the different structures of $[(\mathbf{1a_L})\cdot H\cdot(Ala)]^+$ and $[(\mathbf{1a_L})\cdot H\cdot(Ser)]^+$, the first having the Ala guest located outside the host cavity in proximity to two adjacent pendant groups, and the latter having the Ser guest preferentially located inside the host cavity among the four pendant groups (the *down* structure).[9]

In conclusion, chiral recognition of the selected aromatic amino acids markedly depends on the structural features of the tetrakis(L-valinamido)[4]resorcinarene receptor, and mainly on the spatial orientation of its chiral R pendant groups. The flattened cone structure $\mathbf{1a_L}$ is characterized by a hydrophobic achiral (*up*) and a hydrophilic chiral (*down*) region. Dopa and Tyr, with OH functionalities on their aromatic ring, are preferentially hosted in the *down* region. Base-induced removal of their L enantiomers is faster than that of the D forms. The reverse is true for Phe where OH phenolic groups are absent. Two adjacent pendant groups lean outward from both the *up*-like and *down*-like cavities of $\mathbf{1c_L}$, and the other two lean over its *down*-like region. Both $\mathbf{1c_L}$ cavities seem capable of hosting the dopa and Tyr guests. In this case, base-induced removal of their L enantiomers is slower than that of the D enantiomers. Only one pendant group leans over the *up*-like structure of the 1,2-alternate stereoisomer $\mathbf{1b_L}$. The others form a sort of chiral *down* niche, which may accommodate better the selected amino acid guests. This may explain why the $[(\mathbf{1b_L})\cdot H\cdot A]^+$ complexes apparently exhibit only a single structural regioisomer, and why the base-induced removal of their amino acid guest displays the lowest measured enantioselectivity as regards both the configuration of the leaving guest and that of the incoming base.

Experimental Section

Optically pure $\mathbf{1a_L}$, $\mathbf{1b_L}$, and $\mathbf{1c_L}$ were coproduced from the $BF_3\cdot Et_2O$-catalyzed cyclization of the L enantiomer of (*E*)-*N*-[1-carboxyethyl)-2-methylpropyl]-2,4-dimethoxycinnamamide and isolated according to established procedures.[7] The D and L enantiomers of the amino acids (A) were obtained from Aldrich Co. and used without further purification. The same source provided the (*R*)-(−) (B_R) and (*S*)-(+) (B_S) enantiomers of 2-butylamine, which were purified in the vacuum manifold with several freeze–thaw cycles.

The experiments were performed at room temperature in an APEX 47e FT-ICR mass spectrometer equipped with an ESI source (Bruker Spectrospin) and a resonance cell ("infinity cell") situated between the poles of a superconducting magnet (4.7 T). Stock solutions of **1** (1×10^{-5} M) in 1:3 H_2O/CH_3OH, which contained a fivefold excess of the appropriate amino acid A, were electrosprayed through a heated capillary (130 °C) into the external source of the FT-ICR mass spectrometer. The resulting ions were transferred into the resonance cell by a system of potentials and lenses and thermalized by collisions with methane pulsed into the cell through a magnetic valve.[12] Abundant signals, which corresponded to the natural isotopomers of the proton-bound complex $[\mathbf{1}\cdot H\cdot A]^+$, were monitored and isolated by broad-band ejection of the accompanying ions. The $[\mathbf{1}\cdot H\cdot A]^+$ family was then allowed to react with the chiral amine B present in the cell at a fixed pressure of 4×10^{-8} to 3×10^{-7} mbar. Accurate measurement of the amine B pressure in the resonance cell necessitated the use of an ion gauge whose sensitivity was dependent on the nature of the chemical species. The correction of the ionization gauge reading was achieved by first determining the rate constant of the reaction between the $CH_4^{\cdot+}$ radical cation and CH_4 in the FT-ICR instrument at a given nominal methane pressure, and then comparing the result obtained with the average value of the rate constants reported for this process (1.13×10^{-9} cm^3 molecule^{-1} s^{-1}).[13] Subsequently, the correction factor needed for amine B was estimated by using the method based on an indicated linear dependence of the response of the ionization gauge with the polarizability of the base in question.[14]

Received: May 14, 2004

Keywords: enantioselectivity · enzyme models · host–guest systems · kinetics · macrocycles

[1] F. Diederich, *Angew. Chem.* **1988**, *100*, 372; *Angew. Chem. Int. Ed. Engl.* **1988**, *27*, 362.
[2] J.-M. Lehn, *Angew. Chem.* **1988**, *100*, 91; *Angew. Chem. Int. Ed. Engl.* **1988**, *27*, 89.
[3] D. Cram, *Angew. Chem.* **1988**, *100*, 1041; *Angew. Chem. Int. Ed. Engl.* **1988**, *27*, 1009.
[4] K. S. Jeong, J. Rebek, Jr., *J. Am. Chem. Soc.* **1988**, *110*, 3327, and references therein.
[5] N. Pant, A. D. Hamilton, *J. Am. Chem. Soc.* **1988**, *110*, 2002.
[6] For recent reviews on gas-phase enantioselectivity, see: a) M. Speranza, *Adv. Phys. Org. Chem.* **2004**, *39*, 147; b) M. Speranza, *Int. J. Mass Spectrom.* **2004**, *232*, 277.
[7] B. Botta, G. Delle Monache, P. Salvatore, F. Gasparrini, C. Villani, M. Botta, F. Corelli, A. Tafi, E. Gacs-Baitz, A. Santini, C. Carvalho, D. Misiti, *J. Org. Chem.* **1997**, *62*, 932.
[8] B. Botta, M. Botta, A. Filippi, A. Tafi, G. Delle Monache, M. Speranza, *J. Am. Chem. Soc.* **2002**, *124*, 7658.
[9] B. Botta, A. Tafi, M. Botta, G. Delle Monache, A. Filippi, M. Speranza, *Chem. Eur. J.* **2004**, *10*, 4126.
[10] T. Su, *J. Chem. Phys.* **1988**, *88*, 4102–4103, 5355.
[11] Careful inspection of Figures in the Supporting Information does not exclude the possibility of bimodal reaction kinetics between base B and the diastereomeric $[(\mathbf{1b_L})\cdot H\cdot(dopa)]^+$ complexes.
[12] Observation of the same time dependence of $[\mathbf{1}\cdot H\cdot A]^+$ when unquenched or collisionally quenched by methane in the FT-ICR cell indicates that the $[\mathbf{1}\cdot H\cdot A]^+$ complexes are translationally and vibrationally thermal when reacting with base B.
[13] Y. Ikezoe, S. Matsuoka, M. Takebe, A. A. Viggiano, *Gas-Phase Ion–Molecule Reaction Rate Constants Through 1986*, Maruzen Company, Tokyo, **1987**.
[14] J. E. Bartmess, R. M. Georgiadis, *Vacuum* **1983**, *33*, 149.

 © 2004 Wiley-VCH Verlag GmbH & Co. KGaA, Weinheim

Chemosensors

An Organometallic Chemosensor for the Sequence-Selective Detection of Histidine- and Methionine-Containing Peptides in Water at Neutral pH**

*Andrey Buryak and Kay Severin**

A synthetic receptor, which is bound through noncovalent interactions to an indicator, can function as a chemosensor. The fundamental requirement is that the displacement of the indicator by an analyte results in a change in its optical properties.[1] An indicator-displacement assay (IDA) of this kind has been used to detect analytes such as citrate,[2] tartrate,[3] gallic acid,[4] heparin,[5] phosphates,[6] carbonate,[7] and amino acids.[8] Relative to "classical" chemosensors with integrated binding and signaling components, IDAs have two major advantages: 1) they are easy to generate because the signaling unit is attached by noncovalent interactions, and 2) the physical properties of the indicator (color, affinity for the host, solubility) as well as the indicator–receptor ratio[9] can be varied according to specific needs.

To attach the indicator to the binding site of the host, electrostatic interactions, hydrogen bonding, and/or metal–ligand interactions have been employed. The latter mode of attachment has the advantage that it is able to provide sufficiently high association constants, even in polar solvents such as water. So far, 3d transition-metal ions have been used almost exclusively for this purpose.[10] At first glance, 4d and 5d transition metals appear to be less suited because they generally display slower exchange kinetics. On the other hand, they may show very high binding constants which would allow the detection of analytes at low concentrations. Furthermore, they preferentially bind to ligands with "soft" donor groups (e.g. amines) which may be of interest for certain analytes. Herein, we demonstrate that the combination of an organometallic Cp*Rh^{III} complex **1** with the indicator azophloxine (**2**) comprises an IDA, which allows the selective detection of histidine- and methionine-containing peptides.

In continuation of our studies of organometallic receptors,[11,12] we have investigated whether half-sandwich complexes of rhodium(III) can be reversibly attached to indicators to build a sensing ensemble as described above. The Cp*Rh complex **1** appeared to be well suited for this purpose because it is soluble in water and because the exchange kinetics for the three facial coordination sites opposite to the π ligand are fast.[13] The screening of a number of commercially available indicators showed that the dye azophloxine (**2**) undergoes a strong color change upon complexation to Cp*Rh. The UV/Vis absorption spectrum of **2** (25 μM) after the addition of increasing amounts of **1** in aqueous phosphate buffer solution (100 mM, pH 7.0) is shown in Figure 1.

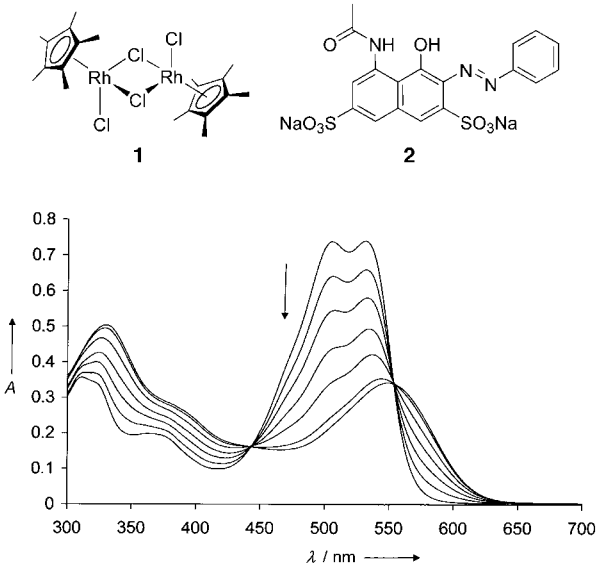


Figure 1. UV/Vis absorption spectra of a solution of **2** (25 μM) in aqueous phosphate buffer solution (100 mM, pH 7.0) upon addition of complex **1** (final Rh concentration: 0, 4.8, 9.6, 14.4, 19.2, 24.0 and 26.4 μM). The spectra were recorded after equilibration.

The complexation of the indicator to the rhodium complex results in a pronounced decrease in the absorption in the region of 500 nm with a new local maximum observed at $\lambda = 549$ nm. Clear isosbestic points are observed at $\lambda = 554$ and 443 nm which indicate that a single species is formed. It appears likely that the indicator is attached to the metal through the diazo and the phenolate groups as Cp*Rh complexes are known to form stable N,O-chelates with azophenolates.[14] At room temperature, the reaction between **1** (12.5 μM) and **2** (25 μM) proceeds with a half-life of $t_{1/2} = 2.5$ min; at 50 °C, the reaction is complete within 5 min. The interaction between the indicator and the rhodium complex is very strong: fitting of the titration data to a 1:1 binding algorithm yielded a binding constant of $3.2(\pm 1.0) \times 10^7\ M^{-1}$.[15,16]

Having confirmed that the indicator **2** is able to bind to the Cp*Rh complex with a strong concomitant change in color, we investigated whether a mixture of **1** and **2** could be employed to detect histidine- or methionine-containing peptides. The coordination chemistry of organometallic half-sandwich complexes with amino acids and peptides is well established.[17] It has been demonstrated that peptides preferentially bind to Cp*Rh^{III}, Cp*Ir^{III}, and (arene)Ru^{II} fragments through their terminal amino groups and deprotonated amide bonds. For histidine and methionine, a further interaction between the N- or S-donor group of the sidechain and the metal is generally observed. To determine whether this latter interaction allows a differentiation between pep-

[*] A. Buryak, Prof. K. Severin
Institute of Chemical Sciences and Engineering
Swiss Federal Institute of Technology Lausanne (EPFL)
1015 Lausanne (Switzerland)
Fax: (+41) 21-693-9305
E-mail: kay.severin@epfl.ch

[**] This work was supported by a PhD fellowship from the doctoral program of the EPFL (A.B.).

 DOI: 10.1002/anie.200460808 © 2004 Wiley-VCH Verlag GmbH & Co. KGaA, Weinheim

tides, we first examined competition experiments with **1**, **2**, and the dipeptides His-Ala or Val-Phe. Upon introduction of one equivalent of His-Ala to a mixture of **1** and **2** ([Rh] = [**2**] = 50 μM) in buffered aqueous solution, the original red color of the free indicator **2** reappeared. On the other hand, no color change was observed if the indicator **2** was added to a solution of **1** and His-Ala. This showed that the stability of the complex between Cp*Rh and His-Ala is considerably higher than that of the adduct between **1** and **2**. With Val-Phe instead of His-Ala, the purple color of the adduct between the receptor **1** and the indicator **2** was observed (Figure 2).[18] The affinity of Val-Phe to the Cp*Rh complex is thus not sufficient to displace the indicator **2** to a significant extent.



Figure 2. "Naked-eye" detection of the dipeptide His-Ala by an indicator-displacement assay (IDA) by using a solution of receptor **1** (50 μM), the indicator **2** (100 μM), and the respective dipeptide (100 μM) in aqueous phosphate buffer solution (100 mM, pH 7.0).

A more detailed analysis of competition experiments was performed by using UV/Vis spectroscopy to determine the relative binding constants $K_r = K_{peptide}/K_{indicator}$ of the Cp*Rh complex **1** to various peptides.[19] A variable amount of the respective peptide (final concentration: 0–26 μM) was mixed with the receptor (final Rh concentration: 12 μM) and the indicator (final concentration: 50 μM). After equilibration (50 °C, 10 min), the amount of free indicator was determined by using a calibration curve and the resulting data were fitted to calculate K_r.[16,20] The results are summarized in Table 1.

Upon addition of peptides that contain either His or Met residues in positions one or two from the N terminus, near complete replacement of the dye was observed ($K_r \geq 740$, entries 1–6). This holds true even for peptides such as Leu-His-Leu, in which the His residue is flanked by amino acids with sterically demanding side chains (entry 4). It is reasonable to assume that for peptides with His/Met residues at (or directly adjacent to) the N terminus, a simultaneous coordination of the amino acid and the respective sidechain occurs.[21] For tri- or longer peptides with His/Met residues in the middle or at the C terminus, this is less favorable and consequently lower relative binding constants are observed (entries 7–10). From the values observed for Gly-Gly-His and Gly-Gly-Met (entries 7 and 10), the interaction of the imidazole sidechain of histidine with the Cp*Rh complex seems to be stronger than the interaction of the thioether sidechain of methionine.[22] Five peptides without His/Met residues were also investigated (including dipeptides with basic and acidic sidechains),[23] and they all showed a very low relative binding constant. Remarkably, the substitution of a single His residue with an Ala residue results in a drop in affinity of more than five orders of magnitude (entries 1 and 12).

The high selectivity of the Cp*Rh receptor allows IDAs to be performed for the quantitative detection of peptides that contain His/Met residues close to the N terminus. For the detection of His-Ala, for example, the receptor **1** (final Rh concentration: 12 μM) and the indicator **2** (final concentration: 50 μM) were added successively to a solution that contained a variable amount of peptide (0–10 μM).[24] The resulting mixture was tempered for 10 min at 50 °C, and then the absorption at 580 nm was determined.[25] The corresponding calibration curve is depicted in Figure 3. The detection limit of this assay was found to be 0.3 μM.[26] In similar experiments with Val-Phe in place of His-Ala, no significant change in absorption was observed. This pronounced selectivity allows (low) micromolar concentrations of His-Ala to be detected in the presence of a 100-fold excess of Val-Phe (Figure 3).

A unique advantage of IDAs is that the indicator–receptor ratio can be adjusted for specific sensing problems.[9] It is thus

Table 1: Relative binding constants $K_r = K_{peptide}/K_{indicator}$ of the Cp*Rh complex **1** to various peptides.

Entry	Peptide	K_r[a]
1	His-Ala	$>1\times10^3$
2	His-Gly-Gly	$>1\times10^3$
3	Gly-His-Gly	$>1\times10^3$
4	Leu-His-Leu	$>1\times10^3$
5	Gly-Met-Gly	$>1\times10^3$
6	Met-Leu-Phe	$7.4\times10^2(\pm1.5\times10^2)$
7	Gly-Gly-His	$1.6\times10^1(\pm0.2\times10^1)$
8	Tyr-Gly-Gly-Phe-Met-Arg-Phe	6.9(±0.2)
9	Ala-Ser-His-Leu-Gly-Leu-Ala-Arg	$9.1\times10^{-1}(\pm0.2\times10^{-1})$
10	Gly-Gly-Met	$1.7\times10^{-1}(\pm0.2\times10^{-1})$
11	Val-Gly-Gly	$7.4\times10^{-2}(\pm0.2\times10^{-2})$
12	Ala-Ala	$2.2\times10^{-3}(\pm0.3\times10^{-3})$
13	Pro-Glu	$<1\times10^{-3}$
14	Val-Phe	$<1\times10^{-4}$
15	Lys-Tyr	$<1\times10^{-4}$

[a] Conditions: phosphate buffer (100 mM), pH 7.0.

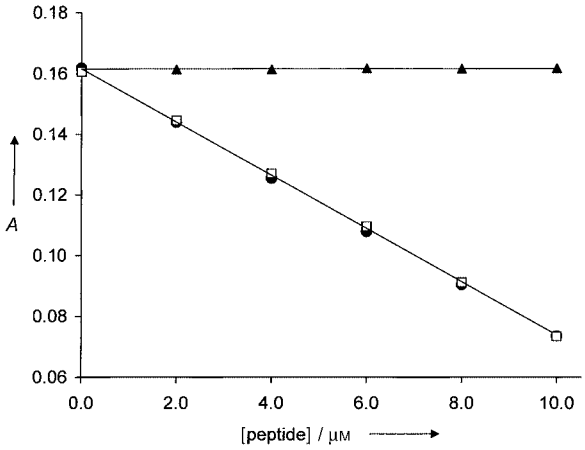


Figure 3. Absorbance at 580 nm for solutions containing receptor **1** (6 μM), the indicator **2** (50 μM), and different amounts of His-Ala (●), Val-Phe (▲), or His-Ala in the presence of a 100-fold excess of Val-Phe (□). The data points represent the average values of three independent experiments; the errors are less than 2%.

 © 2004 Wiley-VCH Verlag GmbH & Co. KGaA, Weinheim

possible to quantify *and* distinguish the tripeptides His-Gly-Gly and Gly-Gly-His in two sets of experiments. Assuming that the peptides are present in concentrations between 0 and 10 μM, one would first have to perform an IDA with excesses of receptor and indicator ([Rh] = 50 μM; [**2**] = 60 μM). Under these conditions, the near-quantitative displacement of the indicator by both peptides is observed which allows their concentration to be determined without knowing their identity. In a second experiment, the concentration of the receptor is decreased to the value determined in the first experiment. Because of the excess of the indicator, only the high affinity analyte His-Gly-Gly completely displaces the indicator, whereas for the lower affinity analyte Gly-Gly-His, the UV/Vis response is much smaller. On the basis of these data, it is possible to identify the two peptides. The experimental values for peptide concentrations of 5 μM are given in Table 2.

Table 2: Differences in the absorbance at 504 nm for solutions of the dipeptides His-Gly-Gly and Gly-Gly-His after addition of various amounts of receptor **1** and indicator **2**.

Peptide	[Peptide][a]	[**1**][a]	[**2**][a]	ΔA
His-Gly-Gly	5.0 μM	25 μM	60 μM	0.108
Gly-Gly-His	5.0 μM	25 μM	60 μM	0.103
His-Gly-Gly	5.0 μM	2.5 μM	60 μM	0.108
Gly-Gly-His	5.0 μM	2.5 μM	60 μM	0.057

[a] Final concentrations are given.

In summary, we have shown that an organometallic 4d transition-metal complex can be used to build an IDA for the sequence-specific detection of histidine- and methionine-containing peptides in water at neutral pH. Although the assay is not suited for real-time measurements, it can be completed within a few minutes. The following characteristics make this new system especially appealing: a) the receptor **1** and the indicator **2** are both commercially available; b) the interaction of the receptor with the analyte is very strong which allows peptides with His/Met residues close to the N terminus to be detected at concentrations as low as 0.3 μM; c) the receptor displays a very high selectivity, which allows the analysis to be performed in the presence of phosphate buffer (100 mM) and in the presence of a large excess of competing peptides.

Received: May 27, 2004

Keywords: amino acids · peptides · rhodium · sensors · uv/vis spectroscopy

[1] For reviews, see: a) S. L. Wiskur, H. Aït-Haddou, J. J. Lavigne, E. V. Anslyn, *Acc. Chem. Res.* **2001**, *34*, 963 – 972; b) L. Fabbrizzi, M. Licchelli, A. Taglietti, *Dalton Trans.* **2003**, 3471 – 3479; c) C. Sukasai, T. Tuntulani, *Chem. Soc. Rev.* **2003**, *32*, 192 – 202.

[2] a) S. C. McCleskey, A. Metzger, C. S. Simmons, E. V. Anslyn, *Tetrahedron* **2002**, *58*, 621 – 628; b) A. Metzger, E. V. Anslyn, *Angew. Chem.* **1998**, *110*, 682 – 684; *Angew. Chem. Int. Ed. Engl.* **1998**, *37*, 649 – 652.

[3] J. J. Lavigne, E. V. Anslyn, *Angew. Chem.* **1999**, *111*, 3903 – 3906; *Angew. Chem. Int. Ed.* **1999**, *38*, 3666 – 3669.

[4] S. L. Wiskur, E. V. Anslyn, *J. Am. Chem. Soc.* **2001**, *123*, 10109 – 10110.

[5] Z. Zhong, E. V. Anslyn, *J. Am. Chem. Soc.* **2002**, *124*, 9014 – 9015.

[6] a) S. L. Tobey, E. V. Anslyn, *Org. Lett.* **2003**, *5*, 2029 – 2031; b) Z. Zhong, E. V. Anslyn, *Angew. Chem.* **2003**, *115*, 3113 – 3116; *Angew. Chem. Int. Ed.* **2003**, *42*, 3005 – 3008; c) M. S. Han, D. H. Kim, *Angew. Chem.* **2002**, *114*, 3963 – 3965; *Angew. Chem. Int. Ed.* **2002**, *41*, 3809 – 3811; d) L. Fabbrizzi, N. Marcotte, F. Stomeo, A. Taglietti, *Angew. Chem.* **2002**, *114*, 2665 – 2668; *Angew. Chem. Int. Ed.* **2002**, *41*, 3811 – 3814; e) K. Niikura, A. Metzger, E. V. Anslyn, *J. Am. Chem. Soc.* **1998**, *120*, 8533 – 8534.

[7] L. Fabbrizzi, A. Leone, A. Taglietti, *Angew. Chem.* **2001**, *113*, 3156 – 3159; *Angew. Chem. Int. Ed.* **2001**, *40*, 3066 – 3069.

[8] a) M. A. Hortalá, L. Fabbrizzi, N. Marcotte, F. Stomeo, A. Taglietti, *J. Am. Chem. Soc.* **2003**, *125*, 20 – 21; b) K. E. S. Deam, G. Klein, O. Renaudet, J.-L. Reymond, *Bioorg. Med. Chem. Lett.* **2003**, *13*, 1653 – 1656; c) H. Aït-Haddou, S. L. Wiskur, V. M. Lynch, E. V. Anslyn, *J. Am. Chem. Soc.* **2001**, *123*, 11296 – 11297; d) G. Klein, J.-L. Reymond, *Angew. Chem.* **2001**, *113*, 1821 – 1823; *Angew. Chem. Int. Ed.* **2001**, *40*, 1771 – 1773.

[9] A. M. Piątek, Y. J. Bomble, S. L. Wiskur, E. V. Anslyn, *J. Am. Chem. Soc.* **2004**, *126*, 6072 – 6077.

[10] For details about an IDA for nitric oxide which is based on a rhodium complex, see: S. A. Hilderbrand, M. H. Lim, S. J. Lippard, *J. Am. Chem. Soc.* **2004**, *126*, 4972 – 4978.

[11] a) Z. Grote, M.-L. Lehaire, R. Scopelitti, K. Severin, *J. Am. Chem. Soc.* **2003**, *125*, 13638 – 13639; b) M.-L. Lehaire, R. Scopelitti, H. Piotrowski, K. Severin, *Angew. Chem.* **2002**, *114*, 1477 – 1480; *Angew. Chem. Int. Ed.* **2002**, *41*, 1419 – 1421; c) H. Piotrowski, K. Severin, *Proc. Natl. Acad. Sci. USA* **2002**, *99*, 4997 – 5000; d) H. Piotrowski, G. Hilt, A. Schulz, P. Mayer, K. Polborn, K. Severin, *Chem. Eur. J.* **2001**, *7*, 3196 – 3208; e) H. Piotrowski, K. Polborn, G. Hilt, K. Severin, *J. Am. Chem. Soc.* **2001**, *123*, 2699 – 2700.

[12] K. Severin, *Coord. Chem. Rev.* **2003**, *245*, 3 – 10.

[13] F. A. Dunand, L. Helm, A. E. Merbach, *Adv. Inorg. Chem.* **2003**, *54*, 1 – 69.

[14] F. Hintermaier, F. Kühlwein, C. Robl, W. Beck, *Z. Anorg. Allg. Chem.* **1996**, *621*, 829 – 836.

[15] The titrations were performed with **2** (12.0 μM) and **1** (0–20 μM) in aqueous phosphate buffer solution (100 mM) at pH 7.0.

[16] The data were fitted with the help of the Gepasi program, version 3.30 using a preinstalled Levenberg–Marquardt algorithm; a) P. Mendes, *Comput. Appl. Biosci.* **1993**, *9*, 563 – 571; b) P. Mendes, *Trends Biochem. Sci.* **1997**, *22*, 361 – 363.

[17] K. Severin, R. Bergs, W. Beck, *Angew. Chem.* **1998**, *110*, 1722 – 1743; *Angew. Chem. Int. Ed. Engl.* **1998**, *37*, 1635 – 1654, and references therein.

[18] For the "naked-eye" detection of histidine-containing peptides, the required minimum concentration is approximately 20 μM.

[19] $K_{peptide}$ is defined as: $K_{peptide}$ = [Cp*Rh—peptide complex]/[Cp*Rh(L_n)][peptide] with L_n being aqua, chloro, and/or phosphate ligands. $K_{indicator}$ is defined accordingly.

[20] To estimate K_r for peptides without His/Met residues, a large excess of the respective peptide (final concentration: 300–500 μM) was mixed with the receptor (final concentration: 25 μM) and the indicator (final concentration: 25 μM).

[21] Besides the N-terminal amino group and the sidechain, an amide group can potentially participate in coordination.

[22] The thermodynamic preference for the coordination of N-donor ligands in competition to S-donor ligands has also been observed for a Zn^{II}-containing receptor and is in accordance with

 © 2004 Wiley-VCH Verlag GmbH & Co. KGaA, Weinheim

theoretical studies of Pt^{II} complexes; a) A. T. Wright, E. V. Anslyn, *Org. Lett.* **2004**, *6*, 1341 – 1344; b) D. V. Deubel, *J. Am. Chem. Soc.* **2004**, *126*, 5999 – 6004.

[23] Redox-active Cys-containing peptides were not included in our study.

[24] Stock solutions were employed for the receptor and the indicator.

[25] The largest relative changes in absorption are observed at 599 nm but owing to reasons of sensitivity (larger absolute changes) it is advantageous to perform the assay at 504 nm or at ~580 nm (see Figure 1).

[26] The detection limit was assumed to be $3\,s_{blank}$ (s = standard deviation). The limit for the quantitative detection is approximately 1.0 μM ($10\,s_{blank}$); see: J. C. Miller, J. N. Miller, *Statistics for Analytical Chemistry*, Ellis Horwood Limited, Chichester, **1984**, pp. 96 – 100.

 © 2004 Wiley-VCH Verlag GmbH & Co. KGaA, Weinheim

Nanomaterials

Site-Specific Photodeposition of Silver on ZnO Nanorods**

*Claudia Pacholski, Andreas Kornowski, and Horst Weller**

In recent years the optical and electronic properties of semiconductor and metal nanoparticles were intensively investigated and their functionality was improved by forming hybrid materials.[1–3] Great progress was made in coating nanoparticles with an appropriate material to increase the stability and to control the properties.[3–7] These nanocomposites have proven to be useful for a lot of applications such as biolabels, electroluminescent displays, memory devices, photochemical solar cells, and sensors.[8–12]

The combination of semiconductor and metal nanoparticles is particularly interesting for catalytic applications. Both the photochemical removal of contaminants from waste stream water and the optimization of the water-splitting reaction require high photocatalytic activity of the nanoparticles.[13] In general the photocatalytic efficiency is limited by the fast recombination of the photogenerated charge carriers. In semiconductor/metal nanocomposites the photoinduced charge carriers are trapped by the noble metal, which promotes interfacial charge-transfer processes.[14,15] Thus, the photocatalytic performance was improved by deposition of metal or metal islands on TiO_2 or ZnO nanoparticles.[16]

In addition to the preparation of core/shell particles, the construction of complex nanostructures by self-organization also expands the scope of composite nanoclusters to a wide range of applications.[17] Strategies for the formation of superlattices and macroscopic solids consisting of two- or three-dimensional periodic structures include the utilization of electrostatic interactions between positively and negatively charged nanoparticles, covalent linkage of particles, magnetic forces, as well as interparticle van der Waals forces. In the latter case colloidal crystals from CdSe, FePt, and $CoPt_3$ with sizes of up to 200 μm could be prepared by using the method of controlled oversaturation. The growth of the crystals was induced by slow diffusion of a non-solvent into a concentrated solution of nanocrystals.[18,19] A very promising approach is the biomolecule-driven assembly of nanoparticles that were functionalized with, for example, single-stranded DNA or biotin prior to the self-assembly process.[20] In the most advanced form this concept requires anisotropic nanoparticles, which can be functionalized with different molecular recognition groups at specific positions on the nanoparticles. Such anisotropic microrods encoded with sub-μm stripes of metals and molecules were synthesized by sequential electrochemical depositions inside porous templates and have been immobilized on Au films through selective DNA hybridization.[21,22]

In contrast, the utilization of the intrinsic properties of nanocrystals for their assembly has so far not been investigated in detail even though the dependence of both the adsorption of molecules on bulk surfaces and the different reactivity of the crystallographic facets is well known in surface science.[23,24] First attempts to transfer this knowledge from surface science to nanoparticles led to promising results. For example, the synthesis of CdSe nanorods is based on the different adsorption behavior of ligands on the crystallographic facets and the resulting differences in the growth rates.[25,26] El-Sayed et al. have demonstrated laser-induced shape changes of colloidal gold nanorods. This behavior of the gold particles was explained by the different stability of the crystallographic facets.[27,28] Comparable results were achieved by Murphy et al. who investigated the effect of nanoparticle shape on their chemical behaviour. The results indicated that gold spheroids are more stable than spheres and nanorods with regard to their dissolution.[29]

We report here a novel method for the formation of a nanoheterostructure consisting of a ZnO nanorod with an attached spherical Ag particle at one end. This material is easily accessible by the anisotropic photoreduction of Ag^+ ions at the ZnO.

The electronic structure of semiconductors such as zinc oxide is characterized by a valence band, which is filled with electrons, and an empty conduction band. Upon light absorption an electron is promoted from the valence band into the conduction band. The generated hole in the valence band and the conduction band electron can react with electron donors and electron acceptors adsorbed on the semiconductor surface, respectively.[30,31] Thus, irradiation of a

[*] Dr. C. Pacholski, Dipl.-Ing. A. Kornowski, Prof. Dr. H. Weller
University of Hamburg
Institute of Physical Chemistry
Grindelalle 117, 20146 Hamburg (Germany)
Fax: (+49) 40-42838-3452
E-mail: weller@chemie.uni-hamburg.de

[**] This work was partially funded by the European Commission through the IST-FET Nanotechnology Information Devices initiative, BIOAND project IST-1999-11974.

Supporting information for this article is available on the WWW under http://www.angewandte.org or from the author.

 © 2004 Wiley-VCH Verlag GmbH & Co. KGaA, Weinheim DOI: 10.1002/anie.200453880

solution of ZnO nanoparticles in ethanediol/water containing metal ions leads to metal nanoparticle formation by reduction by the conduction band electrons, and concomitantly to an oxidation of the alcohol by valence band holes.

Figure 1a shows a TEM image of the solution after irradiation. The silver particles can clearly be distinguished from the ZnO nanorods by shape and contrast. In all cases the

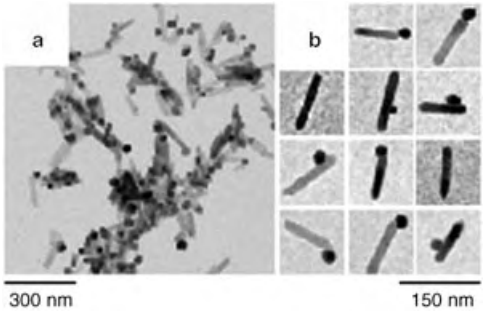


Figure 1. TEM images of Ag^+-containing ZnO nanorod solutions after irradiation. a) ZnO nanorods with deposited silver particles. b) Irradiation experiment with poly(ethylenimine) as stabilizer.

silver particles are quite polydisperse; prolonged irradiation increases the polydispersity. A detailed inspection of the image shows that not more than one Ag particle per ZnO rod is formed, and the Ag particles are preferentially located at one end of the ZnO nanorods. The latter finding is more clearly seen in the case of longer ZnO rods. To achieve a better separation of the ZnO/Ag nanocomposites on the TEM grid a stabilizer (poly(ethylenimine)) was added to the reaction solution before irradiation.[32] The corresponding TEM images are depicted as a gallery of typical selected area images in Figure 1b and also in the Supporting Information. These images strongly suggest that the photoreduction preferentially occurs at one end of the ZnO nanorods and that once a Ag nucleus is formed further reduction of Ag at this nucleus is clearly favored over nucleation.

These results can be explained in different ways. The most trivial explanation is based on drying effects during the preparation of the TEM grids. In this case silver particles would be formed homogeneously in solution and a specific interaction between the crystalline facets and the bottom or the top of the nanorod would lead to the observed nanoheterostructures. However, Figure 1b strongly contradicts this hypothesis since the images were taken at low coverage. Further evidence against this mechanism was also found in absorption and fluorescence investigations during Ag formation. Figure 2 shows the absorption spectra of ZnO nanorods (20 nm × 6 nm) at different times after reduction of silver ions. One clearly recognizes that the typical ZnO absorption becomes more and more superimposed by the growing silver plasmon band with a maximum around 440 nm. The corresponding fluorescence spectra are displayed in the inset of Figure 2. The luminescence is more and more quenched on increasing the amount of silver. Since the absorbance at the excitation wavelength (340 nm) does not significantly change during the silver reduction and the absorbance of silver is

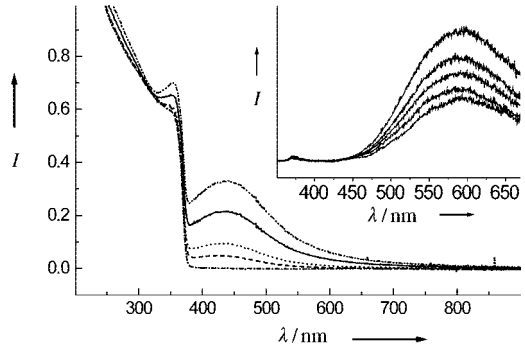


Figure 2. Evolution of the absorption spectra of an Ag^+-containing ZnO solution during irradiation. Nanorods: length 20 nm, width 6 nm. The inset shows the appropriate fluorescence spectra of the mixture.

negligible in the spectral range of the ZnO fluorescence, the quenching of the trapped emission must be due to electron transfer from ZnO to silver particles.[14]

Another explanation for the site-selective deposition of silver involves a preferentially small lattice mismatch of silver on ZnO at the respective crystallographic plane. In this case tiny Ag clusters could be formed at various sites on the ZnO nanorod, whereas nucleation of Ag particles would occur in a consecutive step at the energetically favored plane after surface diffusion. Indeed, several high-resolution TEM images show almost epitaxial growth of single-crystalline Ag particles on the ZnO nanorod substrate (Figure 3a, b). Ag particles on the ZnO moieties can clearly be distinguished by the different contrast. The lattice distances are in accord with silver and ZnO. Unfortunately, even tilt experiments in the TEM did not allow the respective crystallographic planes at

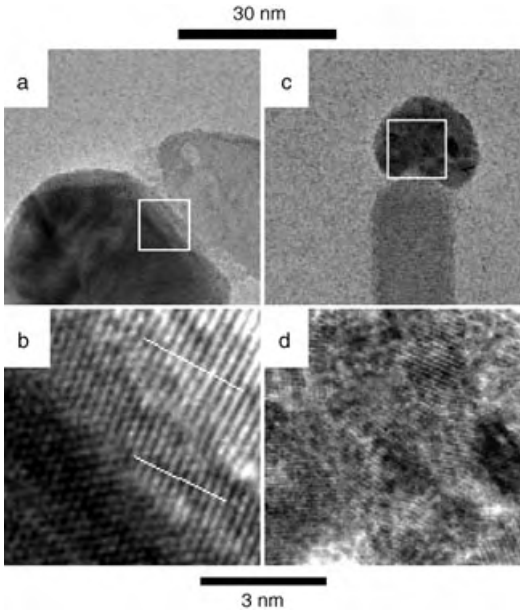


Figure 3. HRTEM images of the interface of Ag particles and ZnO nanorods. a) Epitaxially grown single-crystalline silver particle on ZnO, and b) corresponding high-resolution TEM image of the interface, c) and d) polycrystalline silver particle deposited on ZnO.

 © 2004 Wiley-VCH Verlag GmbH & Co. KGaA, Weinheim

the interface of ZnO and Ag to be identified unambiguously, and therefore this mechanism remains speculative. In addition the formation of polycrystalline Ag particles at the top of the ZnO nanorods was also observed (Figure 3c, d). In this case, the epitaxial growth model is of course completely hypothetical.

Reduction of Ag at preferential crystallographic planes could also be explained by specific adsorption of Ag^+ ions at the respective plane. Literature data for aqueous solutions containing additional stabilizer molecules such as citrate and poly(ethylenimine) are, however, not available and our attempts to analyze the Ag content at the respective ZnO sites prior to the photoreduction step by energy-dispersive X-ray (EDX) and wavelength-dispersive X-ray (WDX) experiments failed due to the limited stability of the sample under intense electron illumination.

Finally one might discuss a localization of the electrons at the ends of the ZnO nanorods prior to the electron transfer step. This charge separation might be supported by an intrinsic dipole moment along the *c* axis, that is the growth direction of the rods or an asymmetric band bending along the *c* axis.[33–35] Electron density calculations of excited ZnO nanorods would be required to get further evidence for this mechanism. Which of the discussed processes is responsible for the obtained results can not be decided at this stage.

The presented results provide a rational approach for the bottom-up assembly of complex nanostructures. Indeed the here presented structure represents electronically a fully self-assembled 2D quantum-confined semiconductor with an in-built Schottky barrier. Furthermore, the chemical anisotropy might serve as branching centers for a more complex architecture of nanohybrid materials, which should have favorable charge-transport properties as compared to conventional nanoparticle solids. Also site-specific building of different ligands and molecular recognition groups such as single-stranded DNA oligonucleotides or peptides should become possible with the presented Ag/ZnO nanocomposite particles. The further development of this concept could lead to the custom-made construction of electronic and optical devices.

Experimental Section

ZnO nanorods were prepared according to a method described earlier. Briefly, zinc acetate dihydrate (29.5 g, 0.13 mol) was dissolved in methanol (125 mL) at 60 °C. Then, a solution of potassium hydroxide (14.8 g, 0.23 mol) in methanol (65 mL) was subsequently added under vigorous stirring. The size of the resulting nanorods was controlled by refluxing the reaction mixture for different times at 60 °C. Lengthening the reaction time led to a considerable increase in length along the *c* axis of the crystals, whereas the width of the rods is only slightly enlarged. Because of precipitation of the ZnO particles during the synthesis they could be easily isolated from the reaction mixture by centrifugation. Washing of the precipitated particles with methanol was necessary to remove the excess ions. After centrifugation (5500 U min^{-1}, 30 min) the resulting gel was redispersed in chloroform. For optical measurements the nanoparticles were diluted with a mixture of ethyleneglycol/water (2:1).

Silver deposition was carried out photocatalytically in quartz cells using a 450-W xenon lamp in combination with a monochromator and a band-edge filter (320 nm). A mixture of ethanediol/water (2:1, v:v; 2670 μL), ZnO nanorods (300 μL) in ethanediol/water (c = 0.01 mol L^{-1}) and $AgNO_3$ (30 μL) in water (c = 0,1 mol L^{-1} or 0.01 mol L^{-1}) was illuminated with monochromatic light (λ = 340 nm) under stirring. To separate the silver/ZnO nanocomposites on the TEM grid, a diluted poly(ethylenimine) solution (30 μL) in water was added. All experiments were carried out in degassed solutions to avoid oxygen reduction by the conduction band electrons, although significantly different results were not observed in the presence of oxygen.

Received: January 29, 2004 [Z53880]

Keywords: photochemistry · quantum dots · semiconductors · silver · zinc oxide

[1] A. Eychmüller, *J. Phys. Chem. B* **2000**, *104*, 6514–6528.
[2] S. Link, M. A. El-Sayed, *J. Phys. Chem. B* **1999**, *103*, 8410–8426.
[3] P. Mulvaney, *Langmuir* **1996**, *12*, 788–800.
[4] A. Dawson, P. V. Kamat, *J. Phys. Chem. B* **2001**, *105*, 960–966.
[5] I. Pastoriza-Santos, D. S. Koktysh, A. A. Mamedov, M. Giersig, N. A. Kotov, L. M. Liz-Marzán, *Langmuir* **2000**, *16*, 2731–2735.
[6] A. Wood, M. Giersig, P. Mulvaney, *J. Phys. Chem. B* **2001**, *105*, 8810–8815.
[7] S. Haubold, M. Haase, A. Kornowski, H. Weller, *ChemPhysChem* **2001**, *2*, 331.
[8] Jr. M. Bruchez, M. Moronne, P. Gin, S. Weiss, A. P. Alivisatos, *Science* **1998**, *281*, 2013–2016.
[9] A. Schroedter, H. Weller, R. Eritja, W. E. Ford, J. M. Wessels, *Nano Lett.* **2002**, *2*, 1363.
[10] M. C. Schlamp, X. Peng, A. P. Alivisatos, *J. Appl. Phys.* **1997**, *82*, 5837–5842.
[11] W. U. Huynh, J. J. Dittmer, A. P. Alivisatos, *Science* **2002**, *295*, 2425–2427.
[12] Y. Nakato, K. Ueda, H. Yano, H. Tsubomura, *J. Phys. Chem.* **1988**, *92*, 2316.
[13] D. W. Bahnemann, D. Bockelmann, R. Goslich, M. Hilgendorff in *Photocatalytic detoxification of polluted aquifers: Novel catalysts and solar applications, Vol. 1* (Eds.: D. W. Bahnemann, D. Bockelmann, R. Goslich, M. Hilgendorff) Lewis Publishers, Boca Raton, Ann Arbor, London, Tokyo, **1994,** pp. 349–367.
[14] V. Subramanian, E. E. Wolf, P. V. Kamat, *J. Phys. Chem. B* **2003**, *107*, 7479–7485.
[15] M. Jakob, H. Levanon, P. V. Kamat, *Nano Lett.* **2003**, *3*, 353.
[16] T. Abe, E. Suzuki, K. Nagoshi, K. Miyashita, M. Kaneko, *J. Phys. Chem. B* **1999**, *103*, 1119–1123.
[17] A. N. Shipway, E. Katz, I. Willner, *ChemPhysChem* **2000**, *1*, 18–52.
[18] D. V. Talapin, E. V. Shevschenko, A. Kornowski, N. Gaponik, M. Haase, A. L. Rogach, H. Weller, *Adv. Mater.* **2001**, *13*, 1868–1871.
[19] E. V. Shevchenko, D. V. Talapin, A. Kornowski, F. Wiekhorst, J. Kötzler, M. Haase, A. L. Rogach, H. Weller, *Adv. Mater.* **2002**, *14*, 287–290.
[20] R. C. Mucic, J. J. Storhoff, C. A. Mirkin, R. L. Letsinger, *J. Am. Chem. Soc.* **1998**, *120*, 12674–12675.
[21] D. J. Pena, B. Razavi, P. A. Smith, J. K. Mbindyo, M. J. Natan, T. S. Mayer, T. E. Mallouk, C. D. Keating, *Mater. Res. Soc. Symp. Proc.* **2001**, *636*, D4.6.1-D4.6.6.
[22] B. D. Reiss, J. N. K. Mbindyo, B. R. Martin, S. R. Nicewarner, T. E. Mallouk, M. J. Natan, C. D. Keating, *Mater. Res. Soc. Symp. Proc.* **2001**, *635*.
[23] P. A. M. Hotsenpiller, J. D. Bolt, W. E. Farneth, J. B. Lowekamp, G. S. Rohrer, *J. Phys. Chem. B* **1998**, *102*, 3216–3226.
[24] O. Dulub, L. A. Boatner, U. Diebold, *Surf. Sci.* **2002**, *519*, 201–217.

 © 2004 Wiley-VCH Verlag GmbH & Co. KGaA, Weinheim

[25] X. Peng, L. Manna, W. Yang, J. Wickham, E. Scher, A. Kadavanich, A. P. Alivisatos, *Nature* **2000**, *404*, 59 – 61.
[26] L. Manna, E. C. Scher, A. P. Alivisatos, *J. Am. Chem. Soc.* **2000**, *122*, 12700 – 12706.
[27] S. Link, C. Burda, B. Nikoobakht, M. A. El-Sayed, *J. Phys. Chem. B* **2000**, *104*, 6152 – 6163.
[28] Z. L. Wang, R. P. Gao, B. Nikoobakht, M. A. El-Sayed, *J. Phys. Chem. B* **2000**, *104*, 5417 – 5420.
[29] N. R. Jana, L. Gearheart, S. O. Obare, C. J. Murphy, *Langmuir* **2002**, *18*, 922 – 927.
[30] D. W. Bahnemann, *Isr. J. of Chem.* **1993**, *33*, 115 – 136.
[31] S. Chen, U. Nickel, *J. Chem. Soc. Faraday Trans.* **1996**, *92*, 1555 – 1562.
[32] A. Henglein, *Chem. Mater.* **1998**, *10*, 444 – 450.
[33] S. A. Empedocles, M. G. Bawendi, *Science* **1997**, *278*, 2114 – 2117.
[34] V. L. Colvin, A. P. Alivisatos, *J. Chem. Phys.* **1992**, *97*, 730 – 733.
[35] M. Shim, P. Guyot-Sionnest, *J. Chem. Phys.* **1999**, *111*, 6955 – 6964.

 © 2004 Wiley-VCH Verlag GmbH & Co. KGaA, Weinheim

Fluorescent Sensors

A Fluorescent Pyrophosphate Sensor with High Selectivity over ATP in Water**

*Dong Hoon Lee, Soon Young Kim, and Jong-In Hong**

Recently, considerable attention has been focused on the design of receptors and sensors that have the ability to bind and sense biologically important anions selectively through electrochemical and optical responses.[1] Anions such as pyrophosphate ($P_2O_7^{4-}$, PPi) and adenosine triphosphate (ATP) play an important role in energy transduction in organisms and control metabolic processes by participation in enzymatic reactions.[2,3] ATP hydrolysis with the concomitant release of PPi is central to many biochemical reactions, such as DNA polymerization and the synthesis of cyclic adenosine monophosphate (AMP) catalyzed by DNA polymerase and adenylate cyclase, respectively.[2] Therefore, the detection and discrimination of these anions has been the main focus of the efforts of several research groups. Although traditional methods of anion sensing such as the use of ion-selective electrodes continue to hold their ground, there is an increasing incentive to find alternative means of analysis, including those based on the use of selective chemosensors.[1b,4] Among the various chemosensors, fluorescent chemosensors present many advantages, as they benefit from high sensitivity, low cost, easy detection, and versatility.[1,5] Unfortunately, few, if any, fluorescent anion sensors exist that display both high PPi/ATP selectivities and function in aqueous solution over a wide range of pH values.[6,7] Herein, we present a new fluorescent PPi sensor based on a naphthalene–dpa system (dpa = bis(2-pyridylmethyl)amine), which exhibits high sensitivity and selectivity over a wide range of pH values for PPi ions relative to other anions, including ATP and ADP (which are structurally similar to PPi in aqueous solution).

A fluorescent reporting naphthalene group was easily introduced into the sensor by a Suzuki coupling reaction. Compound **1** was obtained in 35% overall yield from acetonide.[8] Zn^{II} complexation with the dpa moieties generates an anion-binding site through the formation of a well-known phenoxo-bridged binuclear metal complex (Scheme 1):[9] Sensor **1**·2Zn, a binuclear Zn^{II} complex of compound **1**, was easily formed by the addition of a methanolic solution of **1** to an aqueous solution of $Zn(NO_3)_2$ (2 equiv).

First, the effect of anions (sodium salts) on the absorption spectrum of sensor **1**·2Zn (30 μM) was examined in an aqueous solution of HEPES buffer (0.01M, pH 7.4) (HEPES = 2-[4-(2-hydroxyethyl)-1-piperazinyl]-ethanesulfonic acid) at 25°C (Figure 1). In the absence of an anion guest, the absorption spectrum of sensor **1**·2Zn is characterized by an intense band centered at 305 nm. Upon the addition of PPi in increasing amounts, the peak at 305 nm decreases and a new peak appears at 316 nm. The degree of absorption change is not affected even by the addition of more than 1 equiv of PPi (Figure 1a). Unlike the large 11-nm red shift observed with PPi, relatively small red shifts are seen with ATP (5 nm) and ADP (2 nm) upon complexation. Furthermore, sensor **1**·2Zn does not exhibit any clear spectral change upon addition of AMP, HPO_4^{2-}; other monovalent anions such as $CH_3CO_2^-$, F^-, HCO_3^-, and Cl^- do not affect the spectrum, even when present in excess (up to 100 equiv). The degree of red shift was determined to be PPi ≫ ATP > ADP > AMP ≈ HPO_4^{2-}. These results suggest that sensor **1**·2Zn has a higher selectivity for PPi over other anions.

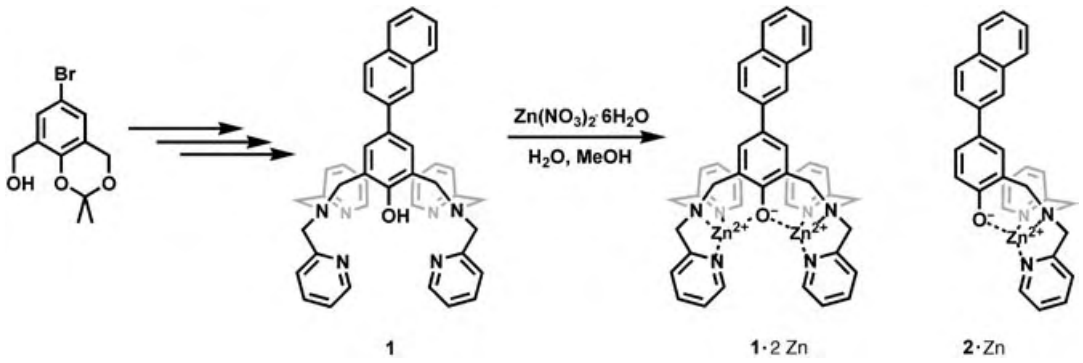
The optical sensing of anions was more drastically demonstrated by virtue of the fluorescent response of **1**·2Zn to complex formation. The effect of anions (sodium salts) on the fluorescent emission spectrum of sensor **1**·2Zn (6 μM) was investigated in an aqueous solution of HEPES buffer (0.01M, pH 7.4) at 25°C (Figure 2). When PPi was added to an aqueous solution of **1**·2Zn, the fluorescent emission spectrum shifted in a dose-dependent manner toward longer wavelengths. As shown in Figure 2a, the λ_{max} shifted from 436 nm to 456 nm. An increase in the PPi concentration up to 1 equiv resulted in a 9.5-fold fluorescence enhancement. However, the addition of more than 4 equiv of ATP shows only twofold

[*] D. H. Lee, S. Y. Kim, Prof. Dr. J.-I. Hong
Department of Chemistry, College of Natural Sciences
Seoul National University
Seoul 151-747 (Korea)
Fax: (+82) 2-889-1568
E-mail: jihong@plaza.snu.ac.kr
Prof. Dr. J.-I. Hong
Center for Molecular Design and Synthesis
KAIST, Daejon 305-701 (Korea)

[**] Support for this work in the form of a grant from the Basic Research Program of the KOSEF (Grant No. R02-2003-000-10055-0) is gratefully acknowledged. D.H.L. and S.Y.K. thank the Ministry of Education for the award of a BK 21 fellowship. ATP = adenosine triphosphate.

Supporting information for this article is available on the WWW under http://www.angewandte.org or from the author.

 DOI: 10.1002/anie.200453914 © 2004 Wiley-VCH Verlag GmbH & Co. KGaA, Weinheim



Scheme 1. Synthetic strategy for sensors **1**·2 Zn and **2**·Zn.

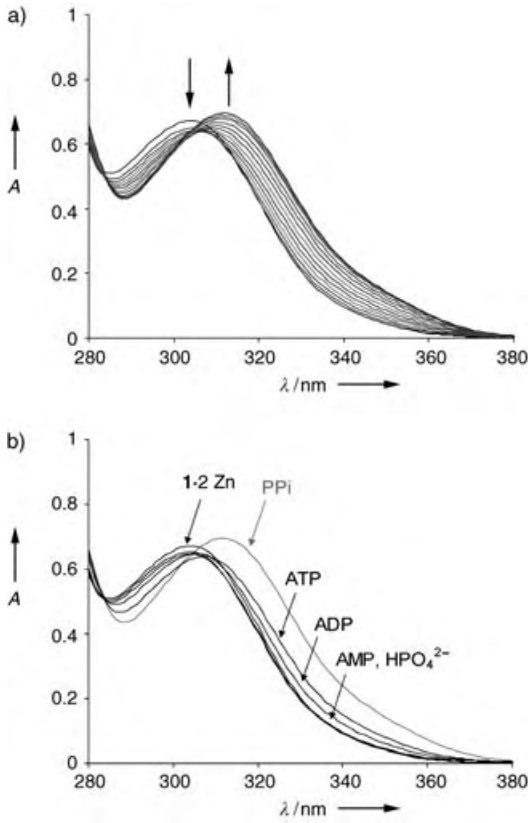


Figure 1. a) Change in absorbance for sensor **1**·2 Zn (30 μM) upon addition of PPi (sodium salt): [PPi] = 0, 3, 6, 9, 12, 15, 18, 21, 24, 27, 30, 32, 34, 36, 38 μM. The spectra were measured in an aqueous solvent of HEPES buffer (10 mM, pH 7.4) at 25 °C. b) UV/Vis spectra of sensor **1**·2 Zn (30 μM) in HEPES buffer (0.01 M, pH 7.4) at 25 °C in the presence of various anions (30 μM).

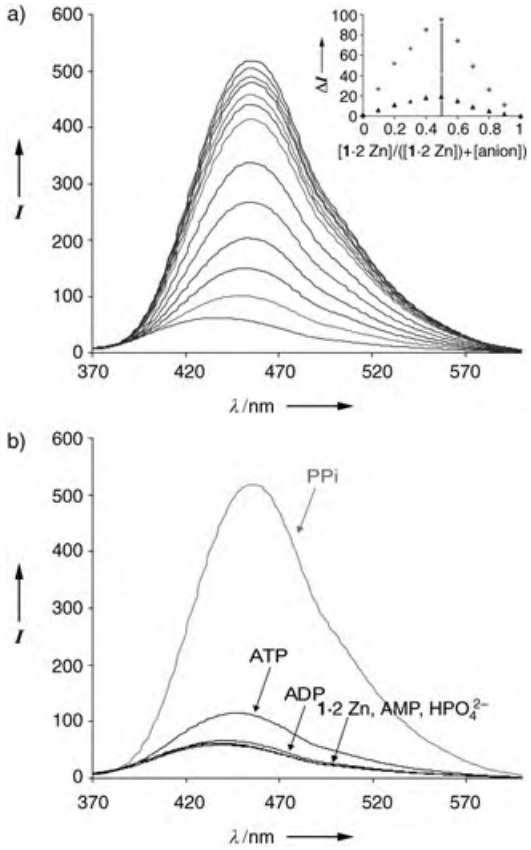


Figure 2. a) Change in fluorescence emission for sensor **1**·2 Zn (6 μM) upon addition of PPi (sodium salt): [PPi] = 0, 0.6, 1.2, 1.8, 2.4, 3.0, 3.6, 4.2, 4.8, 5.4, 6.0, 6.6, 7.2 μM. The spectra were measured in an aqueous solvent of HEPES buffer (0.01 M, pH 7.4) at 25 °C. (Inset: Job plot of **1**·2 Zn and anions: ◆ PPi, ▲ ATP.) b) Fluorescence emission spectra of sensor **1**·2 Zn (6 μM) in HEPES buffer (10 mM, pH 7.4) at 25 °C in the presence of various anions (8 μM). *I* = Intensity (arbitrary units).

enhancement accompanied by a 12-nm red shift. In the case of ADP, sensor **1**·2 Zn shows only a subtle emission change (1.5-fold increase) upon addition of a 50-fold excess of ADP. The addition of AMP and HPO_4^{2-} does not lead to an emission enhancement, even after the addition of 100 equivalents of each anion (Figure 2b).

The Job plot for the binding between **1**·2 Zn and anions (PPi and ATP) shows a 1:1 stoichiometry (inset of Figure 2a). The apparent association constant (K_a) was determined to be $(2.9 \pm 0.7) \times 10^8\,M^{-1}$ for PPi–**1**·2 Zn by a standard algorithm for competitive binding in the presence of excess HPO_4^{2-} in an aqueous solvent of HEPES buffer (0.01 M, pH 7.4) at 25 °C.[8,10] By the same method, K_a for ATP–**1**·2 Zn was found to be $(7.2 \pm 1.0) \times 10^6\,M^{-1}$, which is 40-fold lower than for PPi–**1**·2 Zn. This observation means that **1**·2 Zn can even detect PPi at nanomolar concentrations in water.

 © 2004 Wiley-VCH Verlag GmbH & Co. KGaA, Weinheim

The same selectivity trend found in the absorbance spectra (Figure 1b) is observed in the fluorescence spectra (Figure 2b). However the signal difference is greatly enhanced because of the high sensitivity of fluorescence spectroscopy in favor of PPi. This selectivity enables PPi detection by fluorescence, even in the presence of a large excess of ATP (Figure 3). Figure 3 shows that **1**·2Zn can

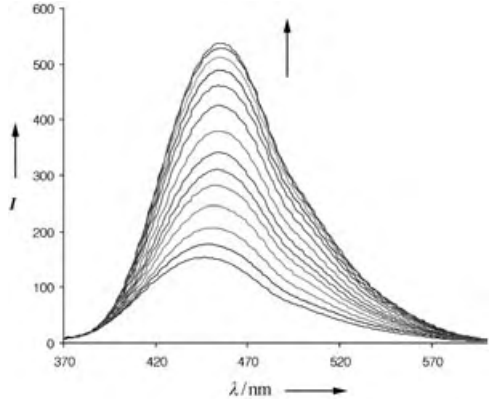
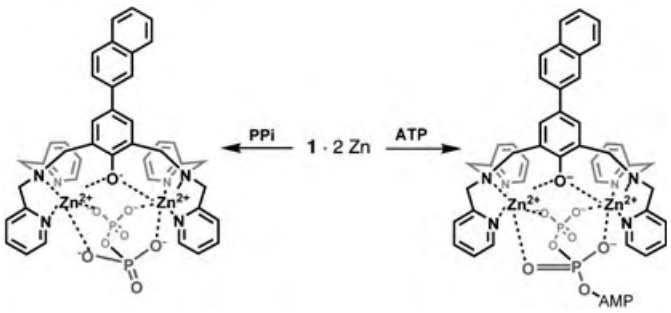


Figure 3. a) Change in fluorescence emission for sensor **1**·2Zn (6 μM) in the presence of ATP (300 μM) upon addition of PPi (sodium salt): [PPi] = 0, 1.2, 2.4, 3.6, 4.8, 6.0, 8.0, 11, 17, 24, 34, 45, 65, 85 μM. The spectra were measured in a pure aqueous solution of HEPES buffer (0.01 M, pH 7.4) at 25 °C. *I* = Intensity (arbitrary units).

detect less than 1 equivalent of PPi even in the presence of a 50- to 250-fold excess of ATP (based on the amount of PPi detected). In other words, **1**·2Zn can selectively detect PPi in an aqueous solution with remarkable selectivity over ATP with a detection limit at micromolar concentrations. This is significant in view of the fact that there are many biochemical reactions in which PPi is released in the presence of ATP. An efficient PPi sensor for bioanalytical applications requires that PPi be detected in small amounts in the presence of a large excess of ATP,[8] thus making our sensor suitable for bioanalytical applications.

The binding mode for PPi–**1**·2Zn is illustrated in Scheme 2, which is based on our previous work involving a structurally similar sensor and its X-ray crystal structure.[11] The proposed complex shows that the two sets of oxygen anions on each P atom of PPi bind to the binuclear zinc



Scheme 2. Proposed mechanism for the complexation of sensor **1**·2Zn with PPi and ATP.

complex by bridging the two metal ions to give rise to two hexacoordinated Zn^{II} ions in **1**·2Zn.[11] PPi induces a pronounced red shift of λ_{max} of **1**·2Zn because the weakening of the bond between the phenolate oxygen atom and Zn^{II} induces a more-negative charge characteristic on the phenolate oxygen atom and thus the bathochromic shift of λ_{max} of **1**·2Zn occurs. Simultaneously, an increased charge characteristic on the phenolate oxygen atom induces a fluorescence enhancement.

The selectivity for PPi over ATP can be understood on the basis of the structure of the guest and the charge density of four O-P oxygen atoms of the guest involved in the complexation. The total anionic charge density of the four O-P oxygen atoms involved in the complexation of ATP with **1**·2Zn is relatively smaller than that of the four O-P oxygen atoms of PPi (Scheme 2). Therefore, the binding affinity of ATP is drastically reduced, and the degree of fluorescence change becomes smaller relative to PPi binding.

A control sensor, mononuclear **2**·Zn (Scheme 1), does not show emission λ_{max} shift and fluorescence enhancement upon addition of PPi. This result means that the cooperative action of two Zn^{II}–dpa units is required for the selective sensing of PPi. Finally, to check for the working pH range for sensing, the effect of the pH value of the medium on the PPi sensing was investigated. Fortunately, fluorescence emission changes shown in Figure 2b were also observed over a wide range of pH values (6.5–10.1) with a similar tendency. This result shows that even if the external pH value is disturbed, sensor **1**·2Zn can still detect PPi.[8]

In summary, we have developed a naphthalene-based fluorescent sensor that selectively detects PPi with high affinity in aqueous solution over a wide pH range. This system shows remarkable selectivity for PPi over other anions, including strong competitors such as HPO_4^{2-} and ATP. This system can be applied for biochemical and analytical enzyme assays involving ATP and PPi.

Received: February 3, 2004
Revised: June 25, 2004 [Z53914]

Keywords: binuclear complexes · fluorescent probes · molecular recognition · pyrophosphates · zinc

[1] a) Z. Brzózka in *Comprehensive Supramolecular Chemistry*, *Vol. 10* (Eds.: J. L. Atwood, J. E. D. Davies, D. D. MacNicol, F. Vögtle, K. S. Suslick), Pergamon, Oxford, **1996**, pp. 187–212; b) *Chemosensors of Ion and Molecular Recognition* (Eds.: J.-P. Desvergne, A. W. Czarnik), Kluwer, Dordrecht, **1997**; c) F. P. Schmidtchen, M. Berger, *Chem. Rev.* **1997**, *97*, 1609–1646; d) P. D. Beer, *Acc. Chem. Res.* **1998**, *31*, 71–80; e) *Supramolecular chemistry of anions* (Eds.: K. Bianchi, K. Bowman-James, E. García-España), Wiley, New York, **1997**; f) J.-M. Lehn, *Supramolecular chemistry, Concepts and Perspectives*, VCH, Weinheim, **1995**; g) R. Martínez-Máñez, F. Sancenón, *Chem. Rev.* **2003**, *103*, 4419–4476; h) P. D. Beer, P. A. Gale, *Angew. Chem.* **2001**, *113*, 502–532; *Angew. Chem. Int. Ed.* **2001**, *40*, 486–516.

[2] a) W. N. Limpcombe, N. Sträter, *Chem. Rev.* **1996**, *96*, 2375; b) P. Nyrén, *Anal. Biochem.* **1987**, *167*, 235–238; c) T. Tabary, L. Ju, *J. Immunol. Methods* **1992**, *156*, 55–60.

 © 2004 Wiley-VCH Verlag GmbH & Co. KGaA, Weinheim

[3] a) D. J. McCarty, *Arthritis Rheum.* **1976**, *19*, 275 – 285; b) A. Caswell, D. F. Guilland-Cumming, P. R. Hearn, M. K. McGuire, R. G. Russell, *Ann. Rheum. Dis.* **1983**, *42* (Suppl. 1), 27 – 37; c) M. Doherty, *Ann. Rheum. Dis.* **1983**, *42* (Suppl. 1), 38 – 44.

[4] a) Y. Kubo, S. Maeda, S. Tokita, M. Kubo, *Nature* **1996**, *382*, 522 – 523; b) K. Niikura, A. Metzger, E. V. Anslyn, *J. Am. Chem. Soc.* **1998**, *120*, 8533 – 8534; c) J. J. Lavigene, E. V. Anslyn, *Angew. Chem.* **1999**, *111*, 3903 – 3906; *Angew. Chem. Int. Ed.* **1999**, *38*, 3666 – 3669; d) L. Fabbrizzi, M. Licchelli, G. Rabioli, A. Taglietti, *Coord. Chem. Rev.* **2000**, *205*, 85 – 108; e) Z. Zhong, E. V. Anslyn, *J. Am. Chem. Soc.* **2002**, *124*, 9014 – 9015; f) F. Sancenón, A. B. Descalzo, R. Martínez-Máñez, M. A. Miranda, J. Soto, *Angew. Chem.* **2001**, *113*, 2710 – 2713; *Angew. Chem. Int. Ed.* **2001**, *40*, 2640 – 2643.

[5] a) L. Fabbrizzi, A. Poggi, *Chem. Soc. Rev.* **1995**, *24*, 197 – 202; b) B. I. Valeur, Leray, *Coord. Chem. Rev.* **2000**, *205*, 3 – 40; c) E. V. Anslyn, *Curr. Opin. Chem. Biol.* **1999**, *3*, 740; d) L. Fabbrizzi, M. Licchelli, P. Pallavicini, L. Parodi, A. Taglietti in *Transition Metals in Supramolecular Chemistry*, Wiley, New York, **1999**, p. 93; e) J. R. Lakowicz in *Principles of Fluorescence Spectroscopy*, Plenum, New York, **1999**.

[6] For PPi sensors in aqueous solution, see: a) D. H. Vance, A. W. Czarnik, *J. Am. Chem. Soc.* **1994**, *116*, 9397 – 9398; b) A. W. Czarnik, *Acc. Chem. Res.* **1994**, *27*, 302 – 308; c) S. Mizukami, T. Nagano, Y. Urano, A. Odani, K. Kikuchi, *J. Am. Chem. Soc.* **2002**, *124*, 3920 – 3925; d) L. Fabbrizzi, N. Marcotte, F. Stomeo, A. Taglietti, *Angew. Chem.* **2002**, *114*, 3965 – 3968; *Angew. Chem. Int. Ed.* **2002**, *41*, 3811 – 3814.

[7] For PPi sensors in MeOH and aqueous CH_3CN, see: a) S. Nishizawa, Y. Kato, N. Teramae, *J. Am. Chem. Soc.* **1999**, *121*, 9463 – 9464; b) P. Anzenbacher, Jr., K. Jursíková, J. L. Sessler, *J. Am. Chem. Soc.* **2000**, *122*, 9350 – 9351.

[8] For a detailed synthesis, fluorescence data, and pH dependence of sensor **1**·2 Zn, see Supporting Information.

[9] a) M. Suzuki, H. Kanatomi, I. Murase, *Chem. Lett.* **1981**, 1745 – 1748; b) B. P. Munch, F. C. Bradley, P. D. Boyle, V. Papaefthymiou, L. Que, Jr., *J. Am. Chem. Soc.* **1987**, *109*, 7993 – 8003; c) S. S. Jin, N. D. Sung, R. C. Hynes, J. Chin, *Inorg. Chem.* **1996**, *35*, 7472 – 7473; d) S. Torelli, C. Belle, I. Gautier-Luneau, J. L. Pierre, E. Saint-Aman, J. M. Latour, L. Le Page, D. Luneau, *Inorg. Chem.* **2000**, *39*, 3526 – 3536; e) M. S. Han, D. H. Kim, *Angew. Chem.* **2002**, *114*, 3963 – 3965; *Angew. Chem. Int. Ed.* **2002**, *41*, 3809 – 3811; f) P. Molenveld, J. F. J. Engbersen, D. N. Reinhoudt, *Chem. Soc. Rev.* **2000**, *29*, 75 – 86.

[10] K. A. Connors in *Binding Constants, The Measurement of Molecular Complex Stability*, Wiley, New York, **1987**, pp. 175 – 183.

[11] D. H. Lee, J. H. Im, S. U. Son, Y. K. Chung, J.-I. Hong, *J. Am. Chem. Soc.* **2003**, *125*, 7752 – 7753.

 © 2004 Wiley-VCH Verlag GmbH & Co. KGaA, Weinheim

Density Functional Calculations

Dihydrogen Bonds in Solid BH_3NH_3**

Carole A. Morrison and Muhammad M. Siddick*

The "dihydrogen bond" $D{-}H^{\delta+}\cdots^{\delta-}H{-}E$—where D is a typical electrostatic atom such as nitrogen or oxygen, and E is a transition metal or boron—was first described by Crabtree and co-workers.[1] Both inter- and intramolecular versions of this bond have been cited, and with typical energies in the range of 12–28 kJ mol^{-1},[2] they are comparable in strength to conventional hydrogen bonds. In particular, the $N{-}H^{\delta+}\cdots^{\delta-}H{-}B$ intermolecular contact in solid-state BH_3NH_3 has received special attention.[1–4] The absence of nonbonding valence electrons on boron negates a possible $H^{\delta+}\cdots^{\delta-}E$ interaction that could arise if E were a d-block element. Thus, for BH_3NH_3 the H···H contact must result from a sigma-type interaction.

To date, all computational studies investigating properties of this unusual intermolecular bond refer to isolated dimer (i.e., gas-phase) models, which do not resemble the crystal structure all that closely (Figure 1 a,b). The global minimum calculated by Crabtree and co-workers contains two H···H contacts (PCI-80/B3LYP, Figure 1 c), which are each assigned an average bond strength of 25.5 kJ mol^{-1} (no basis set superposition error (BSSE) or zero-point energy (ZPE) corrections applied).[2] This value has been described as being "surprisingly large" by the authors, and places the N–H···H–B contact at the upper end of the energy range quoted for dihydrogen bonds. Li et al. cite a different structure comprising four dihydrogen bonds (Figure 1 d), with an average bond strength of 11.6 kJ mol^{-1} (after BSSE and ZPE correction; 6-31++G*/MP2), that is, at the lower end of the dihydrogen bond energy spectrum.[3] Popelier characterized the intermolecular interaction on the basis of the calculated electron density for a third dimer containing three dihydrogen bonds (Figure 1 e), with an average bond energy of 18.3 kJ mol^{-1} (although bond

[*] Dr. C. A. Morrison
School of Chemistry
University of Edinburgh
The King's Buildings
West Mains Road, Edinburgh, EH9 3 JJ (UK)
Fax: (+44) 131-650-4743
E-mail: c.morrison@ed.ac.uk

M. M. Siddick
School of Chemistry and School of Physics
University of Edinburgh
The King's Buildings
Mayfield Road, Edinburgh, EH9 3 JZ (UK)

[**] C.A.M. gratefully acknowledges The Royal Society for the award of a University Research Fellowship and the University of Edinburgh (School of Chemistry) for financial support. M.M.S. is grateful to the University of Edinburgh (Schools of Chemistry and Physics) for the award of a Research Studentship.

Supporting information for this article is available on the WWW under http://www.angewandte.org or from the author.

 © 2004 Wiley-VCH Verlag GmbH & Co. KGaA, Weinheim DOI: 10.1002/anie.200460096

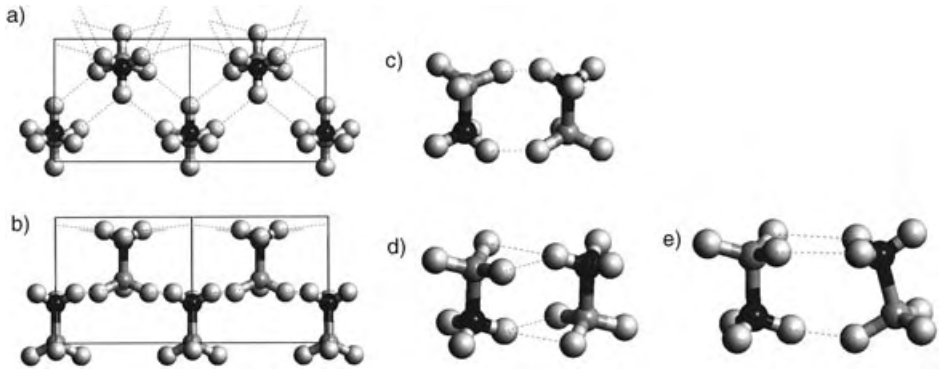


Figure 1. Crystal structure of BH_3NH_3 showing the dihydrogen intermolecular bonding network as viewed along the *c* (a) and *b* axes (b). Dimer models used by Crabtree and co-workers. (c), Li et al. (d), and Popelier (e) to investigate properties of the H···H contacts.

Table 1: Selected parameters for BH_3NH_3.

Parameters	Experimental		Calculated				
	solid[a]	gas[b]	solid	not relaxed	relaxed	supercell dimer	monomer, relaxed
lattice							
a [Å]	5.395(2)	–	5.366	10.0	10.0	12.0	12.0
b [Å]	4.887(2)	–	4.914	10.0	10.0	12.0	12.0
c [Å]	4.986(2)	–	5.100	10.0	10.0	12.0	12.0
α, β, γ [°]	90	–	90	90	90	90.0	90.0
Z	2	–	2	1	1	2	1
volume [Å^3]	131.5(16)	–	134.5	1000.0	1000.0	1728	1728
space/point group	$Pmn2_1$	–	$Pmn2_1$	*P*1	*P*1	C_{2h}	C_{3v}
geometry							
*r*B–N [Å]	1.58(2)	1.6576(16)	1.580	1.580	1.624	1.606	1.624
*r*H···H(1) [Å]	2.02(3)	–	1.909	1.909	–	1.940	–
*r*H···H(2) [Å]	2.23(4)	–	2.174	2.174	–	–	–
*r*H···H(3) [Å]	2.21(4)	–	2.271	2.271	–	–	–
total energy [eV]	–	–	−896.43917	−447.39887	−447.43142	−895.50251	−447.41750
lattice energy [kJ mol^{-1}][c]	–	–	–	79.2	–	–	–
sublimation energy [kJ mol^{-1}][d]	–	–	–	–	76.0	–	–
H-bond strength [kJ mol^{-1}]	–	–	–	–	12.7[e]	–	16.1[f]

[a] Neutron diffraction study.[7] [b] Microwave spectroscopy study.[8] [c] $\Delta H_{lattice}$ (0 K) $= E_{unit\,cell}/Z - E_{supercell\,(not\,relaxed)}$. [d] ΔH_{sub} (0 K) $= E_{unit\,cell}/Z - E_{supercell\,(relaxed)}$. [e] H-bond strength $= \Delta H_{sub}$/(intermolecular bond order = 6). [f] H-bond strength $= [(E_{dimer}/2 - E_{monomer\,(relaxed)})]$/(intermolecular bond order = 2)]

ellipticities indicate that not all bonds are of equal strength; 6-31G*/MP2, no BSSE or ZPE correction applied).[4]

Given that the dimer models do not mimic the crystal structure all that closely, it is now timely to revisit the dihydrogen bond found in solid BH_3NH_3 using a periodic quantum mechanical modeling approach, where the full crystallographic unit cell is used as the model for calculation. An optimized structure (unit cell and atomic positions) has been obtained with plane-wave density functional theory (PW-DFT) and the energy per molecule in the crystal lattice calculated. Deleting all but one molecule from the crystal lattice, and stretching the unit cell parameters (i.e., creating a pseudo-isolated molecule) effectively takes us to the gas phase. As the same basis set and level of theory are used in both calculations, comparison of the energies obtained gives the interaction energy, from which the average hydrogen bond strength can be obtained. (A full discussion of the computational methods is available in the Supporting Information.) We have recently demonstrated the success of this method for the test systems ammonia and urea.[5]

The results obtained from the PW-DFT calculations are given in Table 1. Although the simulation slightly overestimates the volume of the unit cell (+2%), this is commonly observed with generalized gradient approximation (GGA) DFT functionals and translates to an increase in lattice parameters of no more than 0.1 Å. Similarly, all bond distances are reproduced to within approximately 0.1 Å. In the supercell calculation (i.e. pseudo-isolated molecule) the

 © 2004 Wiley-VCH Verlag GmbH & Co. KGaA, Weinheim

B–N bond lengthens by 0.044 Å, which is consistent with experimental values (Δ0.078 Å in going from the solid state to the gas phase).

Comparing the energy per molecule from the crystal lattice with that from the supercell calculation (with one molecule still in the crystal geometry, that is, no atom relaxation at this stage) enables the lattice energy[6] at 0 K for the crystal to be determined (79.2 kJ mol^{-1}). Taking atomic relaxation for the isolated molecule into account gives a value of 76.0 kJ mol^{-1} for the sublimation energy[6] at 0 K.[†] As each BH_3NH_3 molecule in the crystal lattice is connected by twelve intermolecular dihydrogen bonds to its neighbours (that is, an intermolecular bond order of six, see Figure 1 a) we estimate the average value for the dihydrogen bond present in the crystal structure to be 12.7 kJ mol^{-1}.[††]

To demonstrate that the PW-DFT supercell method can reliably calculate binding energies for this system, we have also performed calculations for the dimer structure obtained by Li et al. (see Figure 1 d and Table 1) for direct comparison with the results obtained from ab initio molecular orbital calculations.[3] Comparing the energies of the dimer and monomer structures located in the center of a 12 × 12 × 12 Å supercell, we calculate the total binding energy (per molecule) to be 32.2 kJ mol^{-1}, thus giving a dihydrogen bond strength for this complex of 16.1 kJ mol^{-1}. This is largely consistent with Li's value of 13.4 kJ mol^{-1} (after BSSE correction, ZPE correction not applied for consistency with our calculations). We note that our optimized structure exhibits a slightly shorter H···H interaction (1.94 versus 2.04 Å obtained by Li et al.), and this may explain why our simulations return a slightly stronger bond.

In conclusion, we have performed PW-DFT calculations to investigate the strength of the dihydrogen bond in the solid-state structure of BH_3NH_3. The initial parameters used in our periodic calculations are taken directly from the experimental crystallographic coordinates and unit cell, thus bypassing the need to construct a dimer model to mimic features of the solid-state geometry. Our simulations predict an average value of 12.7 kJ mol^{-1} (no ZPE correction) for the interaction in solid BH_3NH_3, thus reassigning it towards the lower end of the dihydrogen bond strength spectrum.

Received: March 23, 2004
Revised: May 28, 2004

Keywords: boron · density functional calculations · dihydrogen bonds · solid state structures

[†] This value does not include a ZPE correction, which would require the full set of vibrational modes to be averaged over all of k-space. This calculation is currently beyond our computational resources. Unfortunately there is no experimental sublimation energy available in the literature for comparison.

[††] As the PW basis set is by its very nature delocalized, no correction for BSSE is necessary.
The current generation of DFT functionals cannot account for nonlocal dispersion interactions. However, such contacts are likely to be of minimal importance for the first row element compound BH_3NH_3.

[1] T. B. Richardson, S. de Gala, R. H. Crabtree, P. E. M. Siegbahn, *J. Am. Chem. Soc.* **1995**, *117*, 12875.
[2] R. H. Crabtree, P. E. M. Siegbahn, O. Eisenstein, A. L. Rheingold, T. F. Koetzle, *Acc. Chem. Res.* **1996**, *29*, 348.
[3] J. Li, F. Zhao, F. Jing, *J. Chem. Phys.* **2002**, *116*, 25.
[4] P. L. A. Popelier, *J. Phys. Chem. A* **1998**, *102*, 1873.
[5] C. A. Morrison, M. M. Siddick, *Chem. Eur. J.* **2003**, *9*, 628.
[6] In this work we take the definitions of lattice and sublimation energies from L. L. Shipman, A. W. Burgess, H. A. Scheraga, *J. Phys. Chem.* **1976**, *80*, 52.
[7] W. T. Klooster, T. F. Koetzle, P. E. M. Siegbahn, R. B. Richardson, R. H. Crabtree, *J. Am. Chem. Soc.* **1999**, *121*, 6337.
[8] L. R. Thorne, R. D. Suenram, F. J. Lovas, *J. Chem. Phys.* **1983**, *78*, 167.

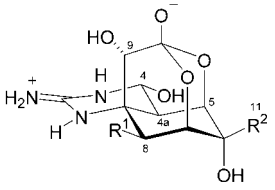
 © 2004 Wiley-VCH Verlag GmbH & Co. KGaA, Weinheim

Natural Product Synthesis

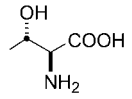
An Efficient Total Synthesis of Optically Active Tetrodotoxin**

*Toshio Nishikawa, Daisuke Urabe, and Minoru Isobe**

Tetrodotoxin (TTX, **1**), a toxic principle of puffer-fish poison, is one of the most famous natural products because of its novel structure coupled with its potent biological activity.[1] The structure was revealed by Hirata, Goto, and co-workers,



1 R^1 = OH R^2 = CH_2OH
2 R^1 = OH R^2 = Me
3 R^1 = H R^2 = Me
4 R^1 = OH R^2 =



[*] Dr. T. Nishikawa, D. Urabe, Prof. M. Isobe
Graduate School of Bioagricultural Sciences
Nagoya University
Chikusa, Nagoya 464-8601 (Japan)
Fax: (+81) 52-789-4111
E-mail: isobem@agr.nagoya-u.ac.jp
Dr. T. Nishikawa
PRESTO, Japan Science and Technology Agency (JST)
4-1-8 Honcho, Kawaguchi, Saitama, 332-0012 (Japan)

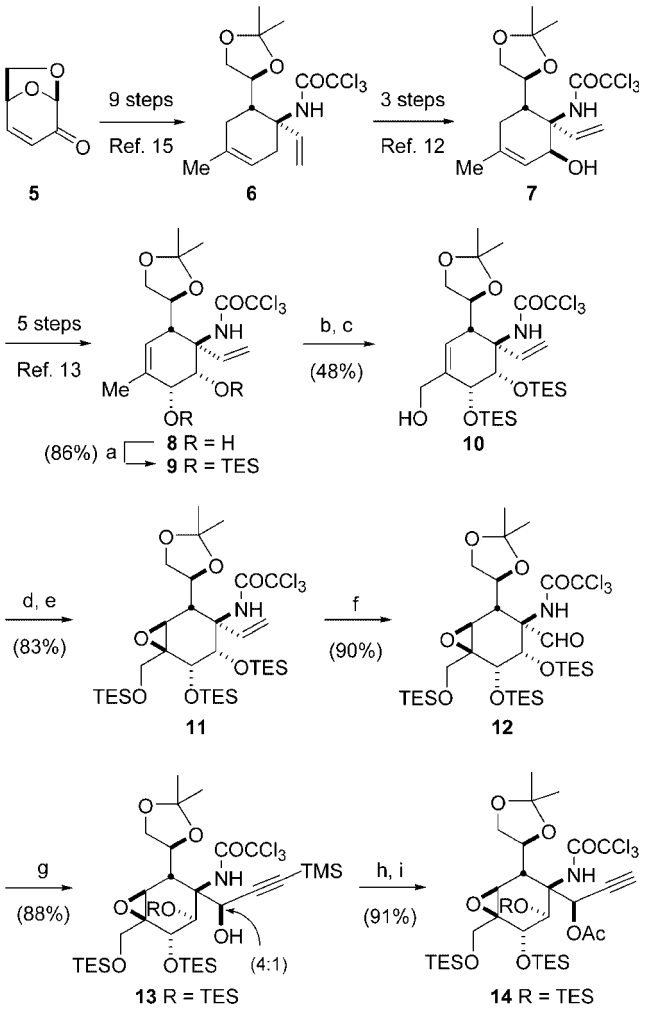
[**] This work was supported financially by a Grand-in-Aid for Scientific Research and the 21st Century COE grant from MEXT, PRESTO of the Japan Science and Technology Agency (JST), and the Naito Foundation. We thank Dr. Masanori Asai for carrying out some preliminary experiments.

Supporting information for this article is available on the WWW under http://www.angewandte.org or from the author.

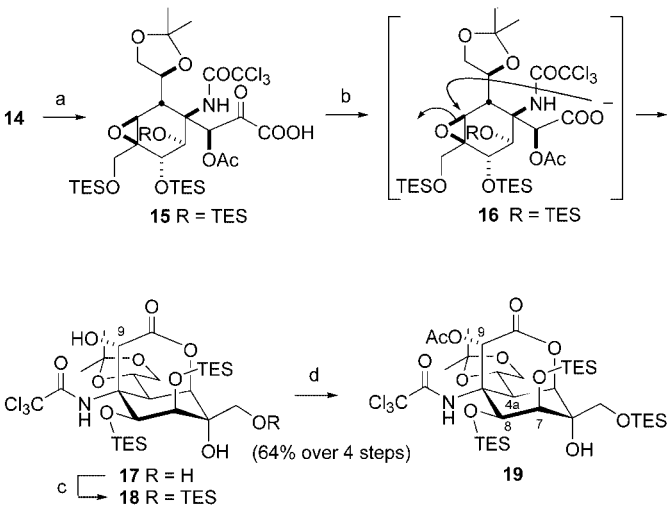
 © 2004 Wiley-VCH Verlag GmbH & Co. KGaA, Weinheim DOI: 10.1002/anie.200460293

Tsuda et al., and Woodward in the 1960s[2] to be an unprecedented multifunctional structure that includes a polyhydroxylated dioxaadamantane unit with an ortho ester and a cyclic guanidine unit with a hemiaminal. The discovery that this toxin acts as a specific blocker of voltage-dependent sodium channels has led to its widespread use as a biochemical tool in neurophysiology.[3] The highly functionalized cage structure and unusual chemical properties of (−)-tetrodotoxin (**1**) had hindered efforts towards its synthesis[4] until our recent total synthesis,[5] although Kishi and co-workers had already reported the total synthesis of racemic tetrodotoxin in 1972.[6] Another total synthesis of **1** was reported by Hinman and Du Bois in 2003.[7] Over the last few decades, a variety of analogues of tetrodotoxin, such as 11-deoxytetrodotoxin (**2**), 5,6,11-trideoxytetrodotoxin, and chiriquitoxin (**4**), have been isolated not only from puffer fish, but from many other organisms living in oceanic and fresh water, as well as from terrestrial animals.[8] These new findings have raised several interesting issues, such as questions about the biosynthesis of tetrodotoxin and the organisms that produce it,[9] as well as about the resistance mechanism and the actual biological function of tetrodotoxin in puffer fish.[10,11] During the course of our synthetic studies on tetrodotoxin with the aim of analyzing such problems, we have reported the total synthesis of several naturally occurring and nonnatural tetrodotoxin analogues, such as 5,11-dideoxytetrodotoxin,[12] 11-deoxytetrodotoxin (**2**),[13] and 8,11-dideoxytetrodotoxin (**3**),[14] from a common synthetic intermediate **6** (Scheme 1).[15] We describe herein an efficient total synthesis of (−)-tetrodotoxin (**1**) on the basis of an alternative strategy to that used for the first total synthesis of **1** in our laboratory.[5]

The synthesis commenced with the hydroxylation of the vinylic methyl group of an intermediate **8** in our synthesis of 11-deoxytetrodotoxin.[13] This intermediate was prepared in 17 steps from the chiral starting material levoglucosenone (**5**) through the common intermediate **6**[15] and an intermediate **7** for 5,11-dideoxytetrodotoxin[12] (Scheme 1). Following protection of the diol as the bis(triethylsilyl) ether **9**, the allylic oxidation of **9** was carried out with selenium dioxide and pyridine *N*-oxide (PNO)[16] to give the corresponding unsaturated aldehyde, which was reduced under the Luche conditions to the allylic alcohol **10** in moderate overall yield. The protection of the resulting primary alcohol with a TES group was followed by treatment with *m*-chloroperbenzoic acid (MCPBA) to afford a single epoxide **11** in high yield. In analogy with the previous syntheses of tetrodotoxin analogues,[12–14] the vinyl group was cleaved by ozonolysis followed by in situ reduction with Et_3N to yield the aldehyde **12**, which was subjected to the stereoselective addition of acetylide as a carboxylic acid equivalent. In this case, the alkynyl magnesium bromide prepared from (trimethylsilyl)-acetylene and EtMgBr in THF was found to be the best reagent, and these conditions led to a 4:1 mixture of **13** from



Scheme 1. Reagents and conditions: a) TESOTf, pyridine, CH_3CN, room temperature; b) SeO_2, PNO, dioxane, reflux; c) $NaBH_4$, $CeCl_3 \cdot 7H_2O$, MeOH, 0 °C; d) TESOTf, 2,6-lutidine, CH_2Cl_2, 0 °C; e) MCPBA, Na_2HPO_4, CH_2Cl_2, room temperature; f) O_3, CH_2Cl_2, −78 °C, then Et_3N; g) TMS−C≡CH, EtMgBr, THF, 0 °C; h) Ac_2O, DMAP, pyridine, room temperature; i) TBAF, THF, −10 °C. TBAF = tetrabutylammonium fluoride, DMAP = 4-dimethylaminopyridine, TES = triethylsilyl, Tf = trifluoromethanesulfonyl, TMS = trimethylsilyl.



Scheme 2. Reagents and conditions: a) $KMnO_4$, $NaIO_4$, $NaHCO_3$, *t*BuOH, H_2O, 50 °C; b) H_2O_2 (30%), $NaHCO_3$, MeOH, room temperature; c) TESOTf, 2,6-lutidine, CH_2Cl_2, −40 °C; d) Ac_2O, pyridine, room temperature.

 © 2004 Wiley-VCH Verlag GmbH & Co. KGaA, Weinheim

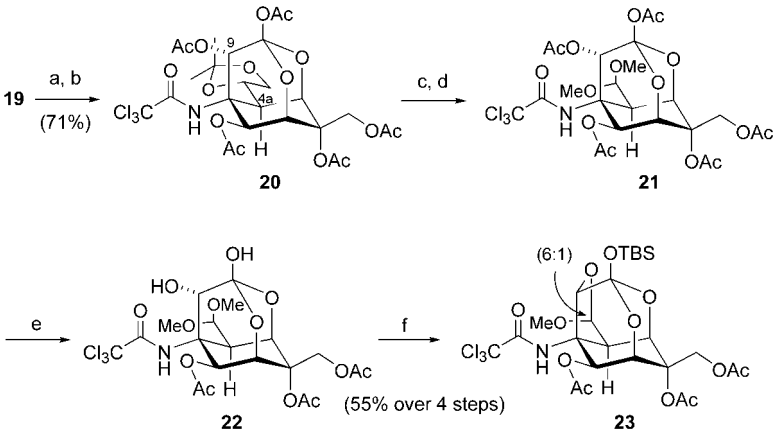
which the desired product was isolated in 70% yield.[17] The major product **13** was transformed by acetylation and removal of the TMS group into the propargyl acetate **14**, which was set for oxidative cleavage of the acetylenic moiety.

The attempted cleavage of the acetylenic moiety of **14** with ruthenium oxide, which had been employed in our previous syntheses of deoxytetrodotoxin analogues, failed to give the expected α-acetoxycarboxylic acid or lactone. The product obtained was instead found to be the α-keto acid **15**,[18] thus indicating steric congestion around the acetylenic moiety. Further experiments led us to find that $KMnO_4$ and $NaIO_4$ were the most efficient oxidants[19] of **14** to the α-keto acid **15**, which was cleaved with alkaline hydrogen peroxide to furnish a mixture of the desired lactone **18** and a partially desilylated product **17** (Scheme 2). The treatment of the crude reaction mixture with TESOTf and 2,6-lutidine effected resilylation to give **18**. Acetylation of the hydroxy group at C9 gave **19**, which contains a fully functionalized cyclohexane ring with the correct stereochemistry.

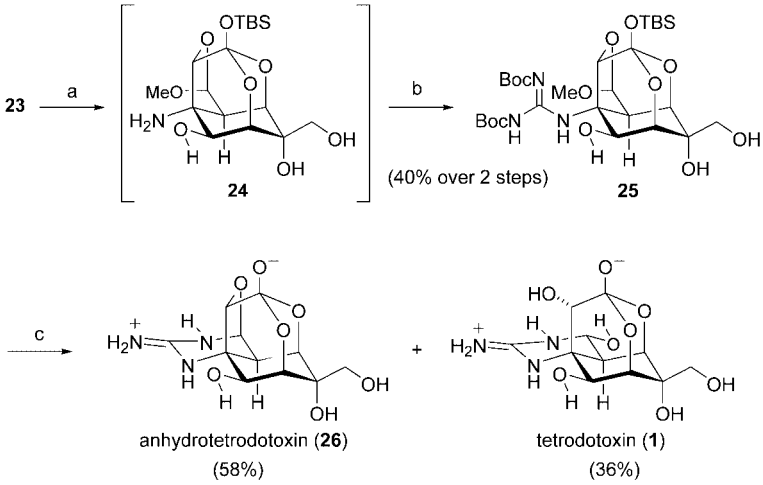
The remaining tasks in the total synthesis of tetrodotoxin were the cleavage of the 1,2-diol protected as an acetonide and the installation of the guanidine functionality. Major difficulties encountered at this stage were epimerization at C9 and the low nucleophilicity of the amino group obtained from the trichloroacetamide. After extensive investigations of protective-group strategies for hydroxy groups, we eventually found the following successful route via the key intermediate **23**, which contains an acetal and an ortho ester (Scheme 3). Thus, prior to cleavage of the acetonide with periodic acid, it was necessary to exchange the acid-sensitive TES protective groups for acetate groups. The removal of all TES groups in **19** with TBAF was followed by peracetylation to give pentaacetate **20**[20] in the form of an ortho ester.[21] Attempted desilylation of **18** (with a free 9-hydroxy group) under the same conditions resulted in exclusive deprotection of the 11-hydroxy group without epimerization, thus indicating that the presence of the acetate group on the 9-hydroxy group might be crucial for deprotection of TES groups at the 7- and 8-positions. The 1,2-acetonide was cleaved with periodic acid to give an aldehyde, which was immediately protected as the dimethylacetal **21**. Reductive cleavage of the trichloroacetamide with DIBAL-H[14,22] required protection of the ortho ester with a silyl group. Fortunately, we found that the treatment of **21** with aqueous ammonia in MeOH afforded **22** exclusively. Compound **22** was treated with an excess of TBSOTf to give a 6:1 inseparable mixture of the acetal **23**.[21,23]

All acyl protecting groups in **23** were removed with DIBAL-H at −40 °C for 8 h (Scheme 4).[24] The resulting amine **24** was then guanidinylated with bis(Boc-(*S*)-methylisothiourea) in the presence of mercuric chloride[25] to give **25**, a suitably protected precursor of tetrodotoxin. Exposure of **25** to aqueous TFA caused global deprotection and subsequent formation of the cyclic guanidine moiety to furnish tetrodotoxin (**1**) and 4,9-anhydrotetrodotoxin (**26**) in 36 and 58% yield, respectively, after purification by HPLC on an ion-exchange resin. The synthetic material **1** proved to be identical in all respects to natural tetrodotoxin.

In summary, the total synthesis of tetrodotoxin from **8** has been accomplished in a highly concise manner, which should enable us to supply a variety of tetrodotoxin derivatives that are not readily accessible from natural products for biochemical studies.



Scheme 3. Reagents and conditions: a) TBAF, CH_3CN, 0 °C; b) Ac_2O, pyridine, room temperature; c) HIO_4, AcOMe, room temperature; d) CSA, $HC(OMe)_3$, MeOH, room temperature; e) aqueous NH_3, MeOH, 0 °C; f) TBSOTf, 2,6-lutidine, CH_2Cl_2, 0 °C. CSA = camphor sulfonic acid, TBS = *tert*-butyldimethylsilyl.



Scheme 4. Reagents and conditions: a) DIBAL-H, CH_2Cl_2, −40 °C; b) BocN=C(SMe)NHBoc, $HgCl_2$, Et_3N, DMF, room temperature; c) TFA, H_2O, room temperature. Boc = *tert*-butoxycarbonyl, DIBAL-H = diisobutylaluminum hydride, DMF = *N*,*N*-dimethylformamide, TFA = trifluoroacetic acid.

Received: April 12, 2004

Keywords: guanidine · ion channels · natural products · tetrodotoxin · total synthesis

 © 2004 Wiley-VCH Verlag GmbH & Co. KGaA, Weinheim

[1] For a review, see: "Tetrodotoxin, Saxitoxin, and the Molecular Biology of the Sodium Channel" (Eds.: C. Y. Kao, S. Lovinson), *Ann. N. Y. Acad. Sci.* **1986**, *479*.

[2] a) T. Goto, Y. Kishi, S. Takahashi, Y. Hirata, *Tetrahedron* **1965**, *21*, 2059–2088; b) K. Tsuda, S. Ikuma, M. Kawamura, R. Tachikawa, K. Sakai, C. Tamura, O. Amakasu, *Chem. Pharm. Bull.* **1964**, *12*, 1357–1374; c) R. B. Woodward, *Pure. Appl. Chem.* **1964**, *9*, 49–74.

[3] a) T. Narahashi, J. W. Moore, W. R. Scott, *J. Gen. Physiol.* **1964**, *47*, 965–974; b) F. Hucho, *Angew. Chem.* **1994**, *106*, 23; *Angew. Chem. Int. Ed. Engl.* **1995**, *34*, 39–50.

[4] For leading references, see: a) Y. Ohtani, T. Shinada, Y. Ohfune, *Synlett* **2003**, 619–622; b) T. Itoh, M. Watanabe, T. Fukuyama, *Synlett* **2002**, 1323–1325; c) B. Noya, M. D. Paredes, L. Ozores, R. Alonso, *J. Org. Chem.* **2000**, *65*, 5960–5968; d) B. Fraser-Reid, C. S. Burgey, R. Vollerthun, *Pure Appl. Chem.* **1998**, *70*, 285–288; e) K. Sato, Y. Kajihara, Y. Nakamura, J. Yoshimura, *Chem. Lett.* **1991**, 1559–1562; f) R. J. Nachman, M. Hönel, T. M. Williams, R. C. Halaska, H. S. Mosher, *J. Org. Chem.* **1986**, *51*, 4802–4806; g) J. F. W. Keana, J. S. Bland, P. J. Boyle, M. Erion, R. Hartling, J. R. Husman, R. B. Roman, *J. Org. Chem.* **1983**, *48*, 3621–3627; J. F. W. Keana, J. S. Bland, P. J. Boyle, M. Erion, R. Hartling, J. R. Husman, R. B. Roman, *J. Org. Chem.* **1983**, *48*, 3627–3631.

[5] N. Ohyabu, T. Nishikawa, M. Isobe, *J. Am. Chem. Soc.* **2003**, *125*, 8798–8805.

[6] a) Y. Kishi, M. Aratani, T. Fukuyama, F. Nakatsubo, T. Goto, S. Inoue, H. Tanino, S. Sugiura, H. Kakoi, *J. Am. Chem. Soc.* **1972**, *94*, 9217–9219; b) Y. Kishi, T. Fukuyama, M. Aratani, F. Nakatsubo, T. Goto, S. Inoue, H. Tanino, S. Sugiura, H. Kakoi, *J. Am. Chem. Soc.* **1972**, *94*, 9219–9221.

[7] A. Hinman, J. Du Bois, *J. Am. Chem. Soc.* **2003**, *125*, 11510–11511.

[8] a) M. Yotsu-Yamashita, *J. Toxicol. Toxin Rev.* **2001**, *20*, 51–66; b) K. Miyazawa, T. Noguchi, *J. Toxicol. Toxin Rev.* **2001**, *20*, 11–33.

[9] The biosynthetic precursors and pathway are completely unknown, whereas tetrodotoxin-producing bacteria have been identified; see: a) T. Yasumoto, D. Yamamura, M. Yotsu, T. Michishita, A. Endo, Y. Kotaki, *Agric. Biol. Chem.* **1986**, *50*, 793–795; b) T. Noguchi, J.-K. Jeon, O. Arakawa, H. Sugita, Y. Deguchi, Y. Shida, K. Hashimoto, *J. Biochem.* **1986**, 99, 311–314; c) Y. Shimizu, *Ann. N. Y. Acad. Sci.* **1986**, *479*, 24–31.

[10] a) T. Matsui, K. Yamamori, K. Furukawa, M. Kono, *Toxicon* **2000**, *38*, 463–468; b) M. Yotsu-Yamashita, A. Sugimoto, T. Terakawa, Y. Shoji, T. Miyazawa, T. Yasumoto, *Eur. J. Biochem.* **2001**, *268*, 5937–5946.

[11] K. Matsumura, *Nature* **1995**, *378*, 563–564.

[12] a) T. Nishikawa, M. Asai, N. Ohyabu, N. Yamamoto, M. Isobe, *Angew. Chem.* **1999**, *111*, 3268–3271; *Angew. Chem. Int. Ed.* **1999**, *38*, 3081–3084; b) M. Asai, T. Nishikawa, N. Ohyabu, N. Yamamoto, M. Isobe, *Tetrahedron* **2001**, *57*, 4543–4558.

[13] T. Nishikawa, M. Asai, M. Isobe, *J. Am. Chem. Soc.* **2002**, *124*, 7847–7852.

[14] a) T. Nishikawa, D. Urabe, K. Yoshida, T. Iwabuchi, M. Asai, M. Isobe, *Org. Lett.* **2002**, *4*, 2679–2682; b) T. Nishikawa, D. Urabe, K. Yoshida, T. Iwabuchi, M. Asai, M. Isobe, *Chem. Eur. J.* **2004**, *10*, 452–462.

[15] T. Nishikawa, M. Asai, N. Ohyabu, N. Yamamoto, Y. Fukuda, M. Isobe, *Tetrahedron* **2001**, *57*, 3875–3883.

[16] K. A. Parker, A. Dermatakis, *J. Org. Chem.* **1997**, *62*, 6692–6696.

[17] The configuration of the major product could not be determined at this stage.

[18] The structure was confirmed by the methylation of **15** with TMS–CHN_2.

[19] P. A. Grieco, D. L. Flynn, R. E. Zelle, *J. Am. Chem. Soc.* **1984**, *106*, 6414–6417.

[20] The configuration at C9 was established based on the long-range coupling ($J = 1$ Hz) between 9-H and 4a-H.

[21] The structure of the ortho ester was confirmed by ^{13}C NMR spectroscopy; $\delta = 108.2$ ppm for compound **20**, $\delta = 108.5$ ppm for compound **23**.

[22] T. Oishi, K. Ando, K. Inomoya, H. Sato, M. Iida, N. Chida, *Org. Lett.* **2002**, *4*, 151–154.

[23] The configuration of the acetal was determined as shown in Scheme 3 based on the coupling constant for 4-H and 4a-H; see reference [13].

[24] The temperature was important for obtaining the amine in good yield. At an elevated temperature (around 0 °C) the product was obtained in very low yield.

[25] a) K. S. Kim, L. Qian, *Tetrahedron Lett.* **1993**, *34*, 7677–7680; b) R. J. Bergeron, J. S. McManis, *J. Org. Chem.* **1987**, *52*, 1700–1703.

 © 2004 Wiley-VCH Verlag GmbH & Co. KGaA, Weinheim

pH Sensors

An Efficient Fluorescent Probe for Ratiometric pH Measurements in Aqueous Solutions

*Sandrine Charier, Odile Ruel, Jean-Bernard Baudin, Damien Alcor, Jean-François Allemand, Adrien Meglio, and Ludovic Jullien**

The development of new powerful microscopy approaches,[1–4] as well as the availability of various synthetic and natural fluorescent molecules,[5–7] has made fluorescence microscopy an essential tool for cellular biology. Fluorescent labels that specifically target molecules or organelles are currently used to investigate the structures and functions of cells. In particular, fluorescent probes have been developed to locally measure the concentrations of important metabolites, such as ions that are involved in signaling and energy transduction. Despite their significance in many essential biological processes, protons have not been studied as much as other ions (e.g. Ca^{2+}) by fluorescence microscopy;[8] a possible explanation for this is the absence of entirely satisfactory fluorescent indicators to measure pH in the relevant range (4.5–7.4).[9] In fact, pH does not significantly alter the emission spectra of most current fluorescent indicators, for instance, fluorescein

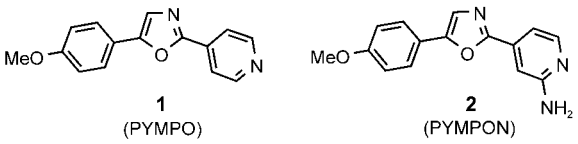
[*] S. Charier, Dr. O. Ruel, Dr. J.-B. Baudin, D. Alcor, Dr. J.-F. Allemand, A. Meglio, Prof. Dr. L. Jullien
Département de Chimie (C.N.R.S. U.M.R. 8640)
École Normale Supérieure
24, rue Lhomond, 75231 Paris Cedex 05 (France)
Fax: (+33) 1-4432-3325
E-mail: Ludovic.Jullien@ens.fr
Dr. J.-F. Allemand
Département de Physique (C.N.R.S. U.M.R. 8550)
École Normale Supérieure
24, rue Lhomond, 75231 Paris Cedex 05 (France)

 DOI: 10.1002/anie.200460557 © 2004 Wiley-VCH Verlag GmbH & Co. KGaA, Weinheim

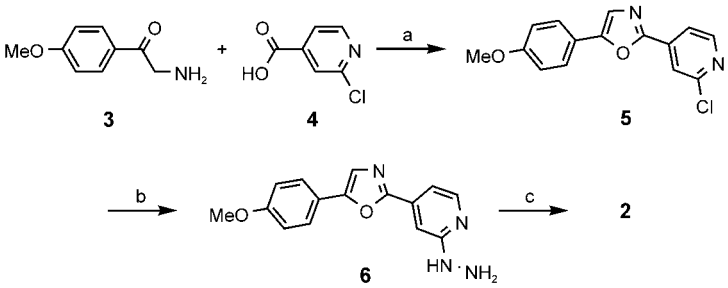
and pyranin, other than to modify the intensity of their fluorescence emission. To measure pH by fluorescence spectroscopic techniques is a delicate process and requires preliminary calibrations. Herein, we report a new fluorescent indicator designed to measure pH in the range of 5–7 in aqueous solution by means of a ratiometric method that relies on fluorescence emission after one- and two-photon excitation.

To measure pH by a ratiometric fluorometric method, both the acidic and basic states of the indicator should ideally be fluorescent and exhibit shifted absorption and emission spectra. In principle, this is the case when either the electron-donor or the -acceptor moiety of a donor–acceptor fluorophore exhibits acid or base properties. However, in practice, numerous pathways compete with fluorescence emission for the relaxation of the excited state in donor–acceptor chromophores; for example, basic donor amino groups can act as fluorescence quenchers.[6,7] An important constraint is thus to have similar quantum yields of fluorescence for the acidic and basic states of the pH indicator. Furthermore, the pK_a values of the ground and excited states are prone to be significantly different in many donor–acceptor molecules owing to the redistribution of the electron density about the molecule upon light absorption. This feature may complicate the analysis.[10–12]

A 2-(4-pyridyl)-5-aryloxazole backbone was chosen to engineer the donor–acceptor fluorescent pH probe. A series of oxazole derivatives was originally investigated to develop laser dyes[13] owing to the favorable photophysical features exhibited after one-photon excitation: $\varepsilon \approx 3\times10^4\,\text{M}^{-1}\text{cm}^{-1}$ at $\lambda \approx 350$ nm and strong fluorescence emission ($\Phi_F \approx 1$) at $\lambda \approx 500$ nm. 2-(4-pyridyl)-5-(4-methoxyphenyl)oxazole (PYMPO, **1**) has already been reported to be an attractive fluorescent probe to measure pH,[8,14] but its use is restricted to the most acidic cellular compartments as it has a low pK_a value (p$K_a \approx 4$). A related boronic acid probe with a larger pK_a value (≈ 8)[15] was sensitive to interference from solutes other than protons.[16] Our design relied on the introduction of substituents on the pyridine ring of **1** to induce a shift in its pK_a value without altering too strongly its favorable photophysical features or its solubility in water. The 2-aminopyridyl derivative **2** (PYMPON) was hence prepared—the pK_a value of 2-aminopyridine is 6.9 at 20 °C whereas that of pyridine is 5.3 at the same temperature.[17]



PYMPON **2** was obtained in three steps (Scheme 1): The oxazole **5** was prepared in 88% yield by the condensation of 4-methoxyphenacylamine (**3**) with 2-chloroisonicotinic acid (**4**) and was subsequently converted into the hydrazine **6** in 41% yield. Reduction of the hydrazine moiety in the latter compound yielded the aniline derivative **2** (PYMPON) in 51% yield. Figure 1 displays the absorption and emission



Scheme 1. Pathway for synthesis of the target compound PYMPON **2**. a) $POCl_3$, Δ, 8 h; b) NH_2NH_2, H_2O, Δ, 16 h; c) Raney Ni, EtOH, H_2 (1 bar), room temperature.

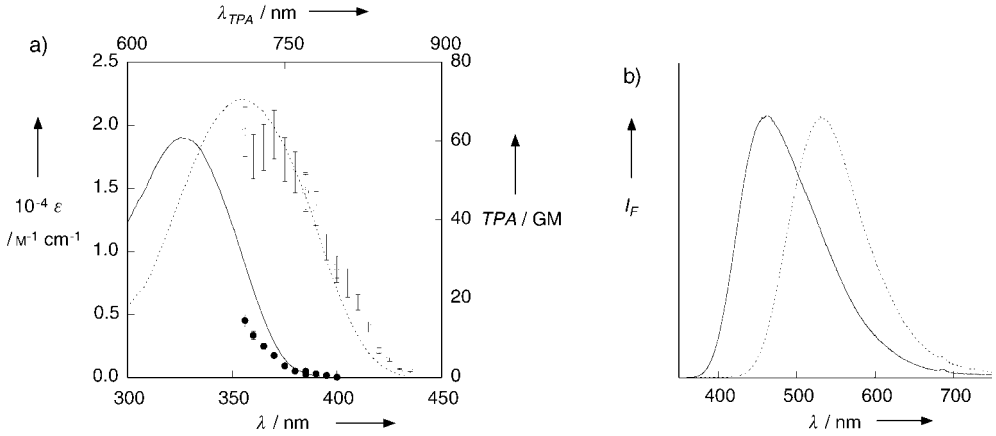


Figure 1. Photophysical properties of PYMPON **2** (in Britton–Robinson buffer)[20] at different pH values at 298 K; a) single-photon absorption (molar absorption coefficient ε in $\text{M}^{-1}\text{cm}^{-1}$; solid line = pH 8, dotted line = pH 3) and two-photon absorptivity (TPA, ● = pH 9, ○ = pH 2) spectra; b) normalized steady-state fluorescence emission I_F after one-photon excitation at $\lambda = 335$ nm (solid line = PYMPON **2**, dotted line = **2**H^+). 1 GM = 10^{-50} $\text{cm}^4\,\text{s}\,(\text{photon molecule})^{-1}$

 © 2004 Wiley-VCH Verlag GmbH & Co. KGaA, Weinheim

spectra of **2**, as well as its excitation spectra after two-photon excitation at pH 3 and pH 8. PYMPON **2** exhibits a large one-photon absorption band ($\varepsilon \approx 2 \times 10^4\,\text{M}^{-1}\,\text{cm}^{-1}$) at $\lambda_{max} = 355$ nm (pH 3) and at $\lambda_{max} = 326$ nm (pH 8); (Figure 1a). The bathochromic shift observed upon decreasing the pH value is in line with the increase in the electron-withdrawing power of the pyridine ring upon protonation of the pyridyl nitrogen atom. PYMPON is highly fluorescent at 298 K (Figure 1b): At pH 3, the fluorescence emission maximum of the protonated PYMPON species $\mathbf{2H^+}$ is located at 530 nm with a quantum yield $\Phi_F = 0.7$. At pH 8, the emission maximum of **2** lies at 465 nm with $\Phi_F = 0.8$.

Figure 1a also displays the two-photon excitation spectra of PYMPON **2** recorded at pH 2 and 9 at 298 K. The power-squared dependence of two-photon-excited fluorescence was checked at several wavelengths in the investigated range and revealed satisfactory behavior over the 0–60 mW range. The two-photon absorption spectra compared well with the one-photon absorption spectra after division of the wavelength by a factor of 2: This suggests that the same excited states are reached regardless of the excitation mode. Such an observation is in agreement with other reports that make use of a comparable technique with unsymmetrical donor–acceptor compounds.[18,19] In the present case with **2**, the maximum two-photon absorptivity at 710 nm ($\delta_{max}(710)$) is 60 ± 10 GM at pH 2 and 15 ± 3 GM at pH 9 (1 GM $= 10^{-50}\,\text{cm}^4\,\text{s}\,(\text{photon-molecule})^{-1}$). These values compare well with the corresponding values for commonly employed pH probes (fluorescein at pH 11: $\delta_{max}(780) = 35$ GM, $\Phi_F = 0.9$; pyranin backbone: $\delta_{max}(750) = 4$ GM, $\Phi_F = 0.54$[19]).

The evolution of the fluorescence emission after one-photon excitation of an aqueous solution of PYMPON **2** (100 nM) as a function of pH is shown in Figure 2. The acid–base reaction depicted in Equation (1) yields $pK_a(\mathbf{2H^+}) = 5.7 \pm 0.1$ at 298 K; the same value was extracted from the pH-dependence of the one-photon absorption spectrum. The pK_a value confirms the earlier observation from the photophysical studies, that is, protonation of PYMPON **2** occurs at the nitrogen atom of the pyridine ring. The $pK_a(\mathbf{2H^+})$ value is shifted by $+1.7$ units relative to that of PYMPO ($pK_a(\mathbf{1H^+}) \approx 4$): this difference is similar to the corresponding shift in the pyridine series (pK_a(pyridine) $= 5.3$, pK_a(2-amino-pyridine) $= 6.9$[17]). Furthermore, one anticipates much lower pK_a values for acids that result from protonation of either the nitrogen atom of the oxazole ring ($pK_a \approx 0$) or the amino group on the pyridine ring ($pK_a < 0$).[17]

$$\text{PYMPON H}^+ \rightleftharpoons \text{PYMPON} + \text{H}^+ \qquad (1)$$

Figure 2b shows that PYMPON **2** can serve as a fluorescent probe to measure pH values in the range 3–8 by a ratiometric method by tuning the excitation and emission wavelengths [Eq. (3), see Experimental Section]. When one-photon excitation is performed at the isobestic point (339 nm), the ratio $\rho^{e,1}_{550/430}$ of the fluorescence emissions at 550 nm and at 430 nm varies by one order of magnitude in the pH 3.5–6.5 range. The same behavior is observed for $\rho^{e,2}_{550/430}$ after two-photon excitation at 712 nm between pH 4.5–7.5.

In conclusion, the present study suggests that the PYMPON platform **2** is appropriate to measure pH values in the range 3–8 by a ratiometric method that relies on fluorescence emission. This is especially attractive when two-photon excitation is used as it would allow local addressing on the femtoliter scale. Its similarity to the PYMPO backbone **1**, which was used to design an efficient probe,[8] suggests that derivatives of PYMPON **2** could find useful applications as intracellular pH meters.

Experimental Section

2: ^{1}H NMR (400 MHz, $CDCl_3$, 25 °C, TMS): $\delta = 8.19$ (d, $^3J = 5.4$ Hz, 1H), 7.65 (AA′XX′, $^3J = 8.8$ Hz, 2H), 7.36 (s, 1H), 7.29 (dd, $^3J = 5.4$ Hz, $^4J = 1.4$ Hz, 1H), 7.16 (m, 1H), 6.98 (AA′XX′, $^3J = 8.8$ Hz, 2H), 3.87 ppm (s, 3H); ^{13}C NMR (100.6 MHz, $CDCl_3$, 25 °C, TMS): $\delta = 160.19$, 158.88, 158.61, 152.27, 148.90, 136.07, 126.02, 122.34, 120.34, 114.48, 110.55, 104.65, 55.40 ppm; HRMS: calcd for $C_{15}H_{14}N_3O_2$: 268.1086; found: 268.1084.

UV/Vis absorption and fluorescence spectra were recorded on a Kontron Uvikon-940 spectrophotometer and a Photon Technology International LPS 220 spectrofluorimeter, respectively. The two-photon excitation spectra were recorded with a homebuilt setup[18] by using the reported excitation spectrum of fluorescein for calibration.[19] All experiments were performed at 293 K in Britton–Robinson buffer solution (0.1 mol L^{-1}) prepared according to the literature.[20]

Theoretical expressions of the ratios of the absorbances and of the fluorescence emissions at two wavelengths with pH: Denoting AH for PYMPON H$^+$ and A for PYMPON, the ratio $\rho^{\alpha^i,i}_{\lambda_1,\lambda_2}$ of the absorbances of PYMPON solutions at two different wavelengths λ_1 and λ_2 after one ($i = 1$, $\alpha^i = \varepsilon$) or two ($i = 2$, $\alpha^i = \delta$) photon excitation can be written:

$$\rho^{\alpha^i,i}_{\lambda_1,\lambda_2} = \frac{\alpha^i_{AH}(\lambda_1)10^{-pH} + \alpha^i_{A}(\lambda_1)10^{-pK_a}}{\alpha^i_{AH}(\lambda_2)10^{-pH} + \alpha^i_{A}(\lambda_2)10^{-pK_a}} \qquad (2)$$

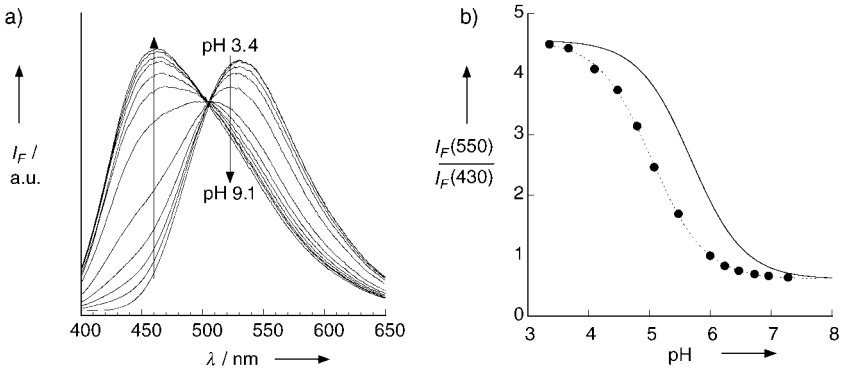


Figure 2. a) Dependence of the emission spectrum of PYMPON **2** (100 nM in Britton-Robinson buffer, 298 K) on pH: from acidic to basic conditions: pH 3.4, 4.5, 4.8, 5.1, 5.5, 6.0, 6.2, 6.5, 6.7, 7.0, 7.3, 9.1. b) Evolution of the ratio of the fluorescence emissions at 550 and 430 nm after one- ($\rho^{e,1}_{550/430}$, $\lambda_{exc} = 339$ nm; dotted line) and two- ($\rho^{e,2}_{550/430}$, $\lambda_{exc} = 712$ nm; solid line) photon excitations. Experimental data: ●; theoretical predictions: dotted and solid lines (calculated from Eq. (3) by using the parameter values measured during the present study).

 © 2004 Wiley-VCH Verlag GmbH & Co. KGaA, Weinheim

At a given excitation wavelength λ_{exc}, the ratio $\rho^{e^l,i}_{\lambda_1,\lambda_2}$ of the fluorescence emissions of PYMPON solutions at two different wavelengths λ_1 and λ_2 can be written:

$$\rho^{e^l,i}_{\lambda_1,\lambda_2} = \frac{I_{AH*}(\lambda_1)\phi_{AH*}\alpha^i_{AH}(\lambda_{exc})10^{-pH} + I_{A*}(\lambda_1)\phi_{A*}\alpha^i_{A}(\lambda_{exc})10^{-pK_a}}{I_{AH*}(\lambda_2)\phi_{AH*}\alpha^i_{AH}(\lambda_{exc})10^{-pH} + I_{A*}(\lambda_2)\phi_{A*}\alpha^i_{A}(\lambda_{exc})10^{-pK_a}} \quad (3)$$

The terms ϕ and $I(\lambda)$ designate the quantum yield of fluorescence and the normalized emission spectrum of the considered species, respectively ($\int_0^\infty I(\lambda)d\lambda = 1$). The experimental curves were analyzed with Specfit software to extract the pK_a values.

Received: May 5, 2004

Keywords: acidity · basicity · fluorescent probes · nitrogen heterocycles · sensors

[1] W. Denk, J. H. Strickler, W. W. Webb, *Science* **1990**, *248*, 73 – 76.
[2] C. Xu, W. Zipfel, J. B. Shear, R. M. Williams, W. W. Webb, *Proc. Natl. Acad. Sci. USA* **1996**, *93*, 10763 – 10768.
[3] R. M. Williams, W. R. Zipfel, W. W. Webb, *Curr. Opin. Chem. Biol.* **2001**, *5*, 603 – 608.
[4] S. W. Hell, *Nat. Biotechnol.* **2003**, *11*, 1347 – 1355.
[5] T. Förster, *Fluoreszenz Organischer Verbindungen*, Vandenhoeck & Ruprecht, Göttingen, **1951**.
[6] J. R. Lakowicz, *Principles of Fluorescence Spectroscopy*, Plenum, New York, **1999**.
[7] B. Valeur, *Molecular Fluorescence: Principles and Applications*, Wiley-VCH, Weinheim, **2002**.
[8] Z. Diwu, C.-S. Chen, C. Zhang, D. H. Klaubert, R. P. Haugland, *Chem. Biol.* **1999**, *6*, 411 – 418.
[9] D. E. Metzler, *Biochemistry: The Chemical Reactions of Living Cells*, *Vol. 1*, 2nd ed., Harcourt Academic Press, San Diego, **2001**, p. 295.
[10] T. Förster, *Z. Elektrochem.* **1950**, *54*, 42 – 46.
[11] a) A. Weller, *Z. Elektrochem.* **1952**, *56*, 662 – 668; b) A. Weller, *Z. Phys. Chem. Neue Folge* **1955**, *3*, 238 – 254; c) A. Weller, *Z. Phys. Chem. Neue Folge* **1958**, *17*, 224 – 245.
[12] S. G. Schulman, *Molecular Luminescence Spectroscopy: Methods and Applications*, *Part 2*, Wiley-Interscience, New York, **1988**.
[13] J. H. Hall, J. Y. Chien, J. M. Kaufman, P. T. Litak, J. K. Adams, R. A. Henry, R. A. Hollins, *J. Heterocycl. Chem.* **1992**, *29*, 1245 – 1273.
[14] R. G. Haugland, *Handbook of Fluorescent Probes and Research Products*, 9th ed., Molecular Probes Inc, Eugene, **2002**.
[15] N. DiCesare, J. R. Lakowicz, *Chem. Commun.* **2001**, 2022 – 2023.
[16] S. Yamaguchi, T. Shirasaka, S. Akiyama, K. Tamao, *J. Am. Chem. Soc.* **2002**, *124*, 8816 – 8817.
[17] D. D. Perrin, *Dissociation Constants of Organic Bases in Aqueous Solution: Supplement 1972*, Butterworths, London, **1972**.
[18] E. Cogné-Laage, J.-F. Allemand, O. Ruel, J.-B. Baudin, V. Croquette, M. Blanchard-Desce, L. Jullien, *Chem. Eur. J.* **2004**, *10*, 1445 – 1455.
[19] The cross-section for two-photon absorption of the pyranin backbone was deduced from the product $\delta_{max} \times \Phi_F$ by Xu and Webb by using the quantum yield of the related 'Cascade Blue' derivative (Molecular Probes Inc.) under comparable conditions; C. Xu, W. W. Webb, *J. Opt. Soc. Am. B* **1996**, *13*, 481 – 491.
[20] C. Frugoni, *Gazz. Chim. Ital.* **1957**, *87*, 403 – 407.

 © 2004 Wiley-VCH Verlag GmbH & Co. KGaA, Weinheim

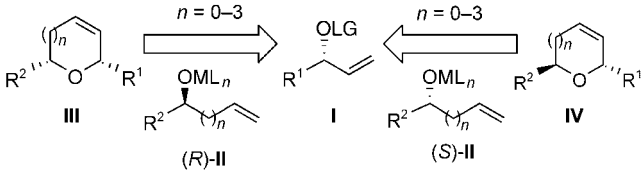
Cyclic Ethers

Stereodivergent Construction of Cyclic Ethers by a Regioselective and Enantiospecific Rhodium-Catalyzed Allylic Etherification: Total Synthesis of Gaur Acid**

P. Andrew Evans, David K. Leahy, William J. Andrews, and Daisuke Uraguchi*

The transition-metal-catalyzed intermolecular allylic etherification is a fundamentally important cross-coupling strategy for the construction of enantiomerically enriched allylic ethers.[1] Although there are numerous examples of the use of simple primary alcohols as nucleophiles, secondary or tertiary alcohols have been used in relatively few studies,[2] partially because of the poor nucleophilicity of these alcohols and the high basicity of the corresponding alkali-metal alkoxides. In response to these underlying problems, we recently reported a regioselective and enantiospecific rhodium-catalyzed allylic etherification with copper(I) alkoxides as nucleophiles.[3] The transmetalation of an alkali-metal alkoxide served to diminish its basicity, thereby promoting the etherification of a soft metal–allyl electrophile.[4]

Herein, we now describe a two-step stereodivergent synthesis of cyclic ethers. The stereospecific etherification of the acyclic enantiomerically enriched allylic carbonate **I** with secondary alkenyl alcohols (*R*)- and (*S*)-**II** followed by ring-closing metathesis (RCM) affords the *cis*- and *trans*-disubstituted cyclic ethers **III** and **IV**, respectively (Scheme 1; $n = 0$–3).[5–7] The inherent advantage of this approach is the ability to vary both ring size and relative configuration as a direct



Scheme 1. General approach for the stereodivergent construction of cyclic ethers. LG = leaving group.

[*] Dr. P. A. Evans, D. K. Leahy, W. J. Andrews, Dr. D. Uraguchi
Department of Chemistry
Indiana University
Bloomington, IN 47405 (USA)
Fax: (+1) 812-855-8300
E-mail: paevans@indiana.edu

[**] We sincerely thank the National Institutes of Health (GM58877) for generous financial support. We also thank Johnson and Johnson for a Focused Giving Award, Pfizer GRD for the Creativity in Organic Chemistry Award, and the Japan Society for the Promotion of Sciences for a JSPS Research Fellowship for Young Scientists (D.U.). We acknowledge Dr. James E. Oliver, who also recently completed a total synthesis of gaur acid, for providing spectroscopic and optical-rotation data for this compound.

Supporting information for this article is available on the WWW under http://www.angewandte.org or from the author.

 © 2004 Wiley-VCH Verlag GmbH & Co. KGaA, Weinheim DOI: 10.1002/anie.200460612

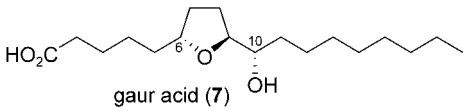
function of the alkenyl alcohol nucleophile employed in the cross-coupling reaction.[8] This strategy was then applied to the total synthesis of the natural product gaur acid to establish its absolute configuration.[9,10]

Table 1 outlines the development of the stereospecific allylic etherification by using the secondary copper(I) alkoxides derived from (*R*)-**2** ($n=1$). Although we had demonstrated previously that primary copper(I) alkoxides derived from copper(I) chloride facilitate the enantiospecific etherification, the allylic etherification with the secondary copper(I) alkoxide proved problematic irrespective of the copper(I) halide employed (Table 1, entries 1 and 2).[3] Hence, we decided to screen a variety of rhodium catalysts with the expectation that the stereospecificity could be improved by either a decrease in the rate of π–σ–π isomerization or an increase in the rate of nucleophilic attack.

Preliminary screening of the catalyst derived from μ-dichlorotetraethylene dirhodium(I), in which there is no free triphenylphosphane from the in situ ligand exchange, with trimethylphosphite demonstrated slightly diminished stereospecificity. This result was intriguing given that the same catalyst is presumably formed through its in situ modification as that formed with the Wilkinson catalyst.[11] We reasoned that the difference could be attributed to the absence of residual triphenylphosphane from the in situ ligand exchange in the latter case; the triphenylphosphane presumably modifies and thereby activates the copper(I) alkoxide. To test this hypothesis, the copper(I) alkoxide derived from (*R*)-**2** ($n=1$) was treated with an equimolar amount of triphenylphosphane, with the expectation that this would improve the stereospecificity. Gratifyingly, an increase in the specificity was observed (Table 1, entry 4), which prompted the screening of additional ligands. This study demonstrated trimethylphosphite to be the optimal ligand in terms of the regioselectivity and enantiospecificity of the catalyst (Table 1, entry 5). Thus, it appears that the phosphite ligand activates the copper(I) alkoxide so that it alkylates the rhodium–allyl electrophile stereospecifically prior to π–σ–π isomerization. To rule out the possibility that the rhodium catalyst is further modified with the additional trimethylphosphite, the reaction was performed with the phosphite-ligated copper(I) alkoxides in the presence of an unmodified Wilkinson catalyst (Table 1, entry 6). This led to poor turnover and modest stereospecificity, thus indicating minimal transfer of trimethylphosphite from the copper(I) alkoxide to the rhodium catalyst.

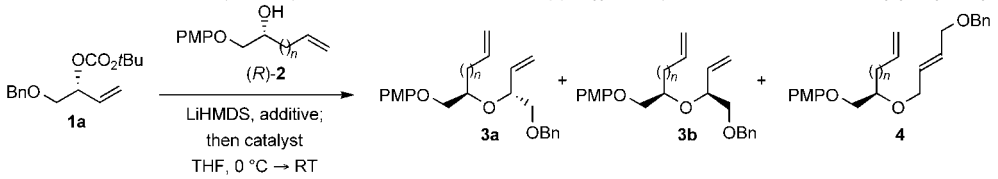
The rhodium-catalyzed allylic etherification with the copper(I) alkoxide derived from the alkenyl alcohols (*R*)- and (*S*)-**2** was studied in combination with subsequent ring-closing metathesis to furnish the *cis*- and *trans*-disubstituted cyclic ethers **5** and *ent*-**6** (Table 2).[5–7] This study demonstrates that excellent regioselectivity and enantiospecificity is observed irrespective of which enantiomer of the alkenyl copper(I) alkoxide is employed (Table 2, entries 1–8). Moreover, ring-closing metathesis with the Grubbs catalyst proceeds to furnish the cyclic ethers in good to excellent yield. However, the construction of the oxocine **5d** and *ent*-**6d** required the use of the Grubbs N-heterocyclic carbene catalyst and very high dilution for efficient cyclization (Table 2, entries 7–8). Overall, the ability to form cyclic ethers in this manner is impressive not only in terms of the excellent stereospecificity, but also because of the minimal conformational bias present for the formation of medium-ring ethers.[12]

Gaur acid (**7**) was recently isolated from the oily secretion of the gaur (*B. frontalis*), a wild ox in Asia, by Oliver et al.[9,10] This 18-carbon acid is thought to serve as a landing and feeding deterrent for the yellow-fever mosquito (*Aedes aegypti*). Although the relative configuration of **7** was assigned, the absolute configuration of this agent had not been established. We envisaged that the rhodium-catalyzed allylic etherification in conjunction with ring-closing metathesis would provide a stereospecific route to the *trans*-2,5-



gaur acid (**7**)

Table 1: Optimization of the rhodium-catalyzed allylic etherification with the copper(I) alkenyl alkoxide derived from (*R*)-**2** ($n=1$).[a]

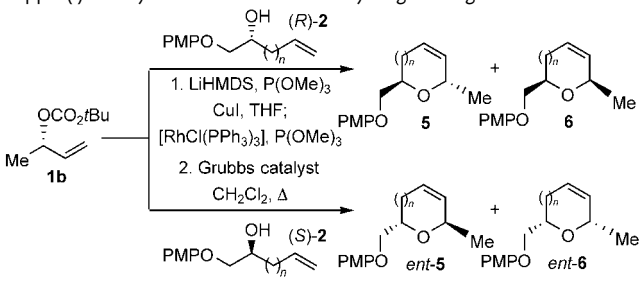


Entry	Catalyst	Additive	**3**/**4**[b,c]	d.r. **3a**/**3b**[b]	Yield [%][d]
1	$[RhCl(PPh_3)_3]/P(OMe)_3$	CuCl	9:1	2:1	20
2	$[RhCl(PPh_3)_3]/P(OMe)_3$	CuI	11:1	4:1	63
3	$[\{RhCl(C_2H_4)\}_2]/P(OMe)_3$	CuI	13:1	3:1	63
4	$[RhCl(PPh_3)_3]/P(OMe)_3$	CuI/PPh_3	13:1	7:1	46
5	**$[RhCl(PPh_3)_3]/P(OMe)_3$**	**$CuI/P(OMe)_3$**	**49:1**	**≥99:1**	**72**
6	$[RhCl(PPh_3)_3]$	$CuI/P(OMe)_3$	24:1	10:1	15

[a] All reactions (0.25 mmol) were carried out with 10 mol% of the catalyst in tetrahydrofuran with 1.9 equivalents of the copper alkoxide. [b] Diastereomeric ratios were determined by capillary GLC on aliquots of the crude reaction mixture. [c] Authentic standards were prepared independently by using copper cyanide as an additive. [d] Yields of the isolated products. Bn = benzyl, HMDS = hexamethyldisilazide, PMP = *p*-methoxyphenyl, RT = room temperature.

 © 2004 Wiley-VCH Verlag GmbH & Co. KGaA, Weinheim

Table 2: Scope of the rhodium-catalyzed allylic etherification with the copper(I) alkenyl alkoxides **2** followed by ring-closing metathesis.[a,b]

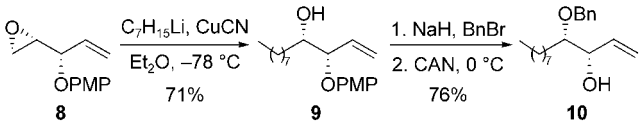


Entry	Config. of **2**	*n*	d.r.[c]	Yield of addition product [%][d]	Cyclic ether	Yield [%][d]
1	*R*	0	53:1	74	**5a**	94
2	*S*	0	1:50	78	*ent*-**6a**	99
3	*R*	1	23:1	77	**5b**	85
4	*S*	1	1:23	76	*ent*-**6b**	98
5	*R*	2	27:1	77	**5c**	85
6	*S*	2	1:26	77	*ent*-**6c**	93
7	*R*	3	29:1	77	**5d**	73[e]
8	*S*	3	1:39	77	*ent*-**6d**	82[e]

[a] All allylic etherification reactions (0.25 mmol) were carried out with 10 mol% of the catalyst in tetrahydrofuran with 1.9 equivalents of the copper alkoxide. The regioselectivity (2°/1°) observed for the addition of the copper alkoxide was ≥99:1 in all cases. (Authentic standards were prepared independently by using copper cyanide as an additive.) [b] All ring-closing metathesis reactions were carried out on a 0.1-mmol scale with 5–10 mol% of the Grubbs catalyst in dichloromethane (0.1 M). [c] Ratios of regio- and diastereoisomers were determined by capillary GLC on aliquots of the crude reaction mixture. [d] Yields of the isolated products. [e] The Grubbs N-heterocyclic carbene catalyst (0.001 M) was used at reflux.

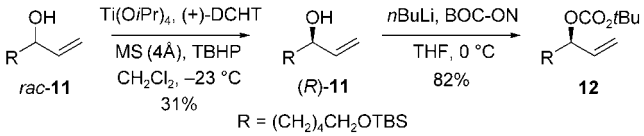
disubstituted tetrahydrofuran present in this potentially biologically important agent, and thereby enable the determination of the absolute configuration.

The allylic alcohol **10** was prepared by the three-step sequence outlined in Scheme 2. Regioselective ring-opening of the known epoxide **8** with the cuprate derived from *n*-



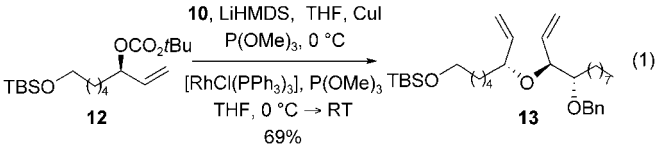
Scheme 2. Preparation of the enantiomerically enriched allylic alcohol nucleophile. CAN = cerium(IV) ammonium nitrate.

heptyllithium and copper(I) cyanide at −78 °C, gave the desired alcohol **9** in 71% yield.[13,14] Benzyl protection of the secondary alcohol **9**, followed by oxidative cleavage of the *p*-methoxyphenyl group, furnished the allylic alcohol **10** in 76% yield (two steps).[15] The enantiomerically enriched allylic carbonate **12** was prepared by an initial Sharpless kinetic resolution of the allylic alcohol *rac*-**11**, followed by acylation of the product (*R*)-**11** (≥99% *ee*) with BOC-ON (Scheme 3).[16]

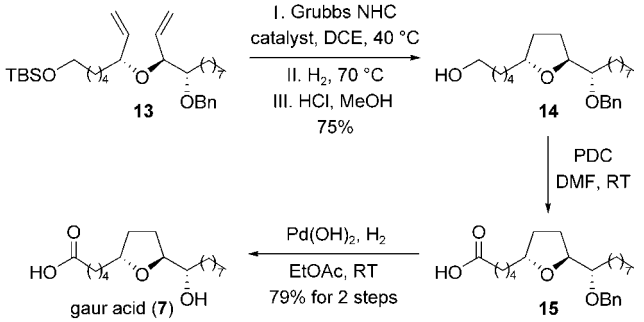


Scheme 3. Preparation of the enantiomerically enriched allylic carbonate electrophile. BOC-ON = 2-(*tert*-butoxycarbonyloxyimino)-2-phenylacetonitrile, DCHT = dicyclohexyl tartrate, MS = molecular sieves, TBHP = *tert*-butyl hydroperoxide, TBS = *tert*-butyldimethylsilyl.

The stereospecific allylic etherification was carried out under analogous reaction conditions to those outlined in Table 2.[17] Treatment of the allylic carbonate **12** with the trimethylphosphite-modified Wilkinson catalyst and the copper(I) alkoxide derived from the allylic alcohol **10**, afforded the diene **13** in 69% yield with excellent regioselectivity and enantiospecificity [≥19:1 by NMR spectroscopy, Eq. (1)].



The synthesis of gaur acid (**7**) was then completed as illustrated in Scheme 4. Treatment of the diene **13** with the Grubbs N-heterocyclic carbene catalyst at 40 °C gave the



Scheme 4. Completion of the synthesis of gaur acid (**7**). DCE = 1,2-dichloroethane, DMF = *N*,*N*-dimethylformamide, NHC = N-heterocyclic carbene, PDC = pyridinium dichromate.

desired cyclic ether, which was reduced in situ and deprotected with acid to afford the primary alcohol **14** in 75% overall yield.[18] The hydrogenation of the alkene in the metathesis product was necessary at this juncture because of its propensity to undergo oxidation. Oxidation of the primary alcohol **14** by pyridinium dichromate,[19] followed by palladium-catalyzed hydrogenation of the benzyl ether, furnished gaur acid (**7**) in 79% yield (two steps). Although the spectroscopic data of the synthetic sample of **7** is identical in all respects to those of the natural substance (^{1}H/^{13}C NMR, IR, and MS), the optical rotation has the opposite sign ($[\alpha]_D^{25}$ −7.5 (c = 1.1, $CDCl_3$); lit.:[9,10] $[\alpha]_D^{26}$ +7.0 (c = 7.1,

$CDCl_3$)), thus indicating the absolute configuration of the natural product to be 6*S*, 9*R*, 10*R*.[20]

In conclusion, the stereospecific rhodium-catalyzed allylic etherification with secondary alkenyl alcohols in conjunction with ring-closing metathesis provides a direct approach to *cis*- and *trans*-disubstituted cyclic ethers. This study demonstrated that a dramatic enhancement of the stereospecificity is possible through the modification of the copper(I) alkoxide with trimethylphosphite, which presumably promotes the rapid nucleophilic attack of the rhodium–allyl intermediate prior to the π–σ–π isomerization. Finally, the potential of this methodology was highlighted through a seven-step total synthesis of gaur acid (**7**), whereby the absolute configuration of **7** was established.

Received: May 10, 2004

Keywords: allylation · asymmetric synthesis · cyclic ethers · metathesis · rhodium

[1] For recent reviews on metal-catalyzed allylic substitution, see: a) J. Tsuji in *Palladium Reagents and Catalysts*, Wiley, New York, **1996**, chap. 4, pp. 290–404; b) B. M. Trost, C. Lee in *Catalytic Asymmetric Synthesis*, 2nd ed. (Ed.: I. Ojima), Wiley-VCH, New York, **2000**, chap. 8, pp. 593–649, and references therein.

[2] For related references on intermolecular metal-catalyzed allylic etherification reactions with metal alkoxides, see: a) E. Keinan, M. Sahai, Z. Roth, A. Nudelman, J. Herzig, *J. Org. Chem.* **1985**, *50*, 3558–3566; b) B. M. Trost, A. Tenaglia, *Tetrahedron Lett.* **1988**, *29*, 2931–2934; c) B. M. Trost, E. J. McEachern, F. D. Toste, *J. Am. Chem. Soc.* **1998**, *120*, 12702–12703; d) H. Kim, C. Lee, *Org. Lett.* **2002**, *4*, 4369–4371, and references therein.

[3] P. A. Evans, D. K. Leahy, *J. Am. Chem. Soc.* **2002**, *124*, 7882–7883.

[4] G. M. Whitesides, J. S. Sadowski, J. Lilburn, *J. Am. Chem. Soc.* **1974**, *96*, 2829–2835.

[5] For recent reviews on ring-closing metathesis, see: a) R. H. Grubbs, S. Chang, *Tetrahedron* **1998**, *54*, 4413–4450; b) A. Fürstner, *Angew. Chem.* **2000**, *112*, 3140–3172; *Angew. Chem. Int. Ed.* **2000**, *39*, 3012–3043; c) A. Deiters, S. F. Martin, *Chem. Rev.* **2004**, *104*, 2199–2238, and references therein.

[6] G. C. Fu, R. H. Grubbs, *J. Am. Chem. Soc.* **1992**, *114*, 5426–5427.

[7] For recent examples of the synthesis of cyclic ethers by ring-closing metathesis, see: a) M.-P. Heck, C. Baylon, S. P. Nolan, C. Mioskowski, *Org. Lett.* **2001**, *3*, 1989–1991; b) K. C. Nicolaou, J. A. Vega, G. Vassilikogiannakis, *Angew. Chem.* **2001**, *113*, 4573–4577; *Angew. Chem. Int. Ed.* **2001**, *40*, 4441–4445; c) K. Fujiwara, S.-I. Souma, H. Mishima, A. Murai, *Synlett* **2002**, 1493–1495; d) A. E. Sutton, B. A. Seigal, D. F. Finnegan, M. L. Snapper, *J. Am. Chem. Soc.* **2002**, *124*, 13390–13391; e) M. W. Peczuh, N. Snyder, *Tetrahedron Lett.* **2003**, *44*, 4057–4061; f) M. T. Crimmins, M. T. Powell, *J. Am. Chem. Soc.* **2003**, *125*, 7592–7595.

[8] For an explanation of the effect of copper(I) halide salts on the stereospecificity of the rhodium-catalyzed allylic etherification reaction with copper(I) alkoxides, see: P. A. Evans, D. K. Leahy, L. M. Slieker, *Tetrahedron: Asymmetry* **2003**, *14*, 3613–3618.

[9] For the isolation of the same agent from sheep wool, see: S. Ito, K. Endo, S. Inoue, T. Nozoe, *Tetrahedron Lett.* **1971**, 4011–4014.

[10] J. E. Oliver, P. J. Weldon, K. S. Peterson, W. F. Schmidt, M. Debboun, *Abstracts of Papers*, 225th ACS National Meeting, New Orleans, LA, USA, March 23–27, **2003**.

[11] a) M. L. Wu, M. J. Desmond, R. S. Drago, *Inorg. Chem.* **1979**, *18*, 679–686; b) L. A. Watson, D. K. Leahy, P. A. Evans, K. G. Caulton, unpublished results.

[12] a) J. S. Clark, J. G. Kettle, *Tetrahedron Lett.* **1997**, *38*, 127–130; b) R. J. Linderman, J. Siedlecki, S. A. O'Neill, H. Sun, *J. Am. Chem. Soc.* **1997**, *119*, 6919–6920; c) M. T. Crimmins, A. L. Choy, *J. Org. Chem.* **1997**, *62*, 7548–7549.

[13] S. L. Schreiber, T. S. Schreiber, D. B. Smith, *J. Am. Chem. Soc.* **1987**, *109*, 1525–1529.

[14] P. A. Evans, J. Cui, S. J. Gharpure, A. Polosukhin, H.-R. Zhang, *J. Am. Chem. Soc.* **2003**, *125*, 14702–14703.

[15] T. Fukuyama, A. A. Laird, L. M. Hotchkiss, *Tetrahedron Lett.* **1985**, *26*, 6291–6292.

[16] H. C. Kolb, M. S. VanNieuwenhze, K. B. Sharpless, *Chem. Rev.* **1994**, *94*, 2483–2547.

[17] This rather demanding cross-coupling reaction required a higher catalyst loading (30 mol%) for efficient and complete conversion.

[18] J. Louie, C. W. Bielawski, R. H. Grubbs, *J. Am. Chem. Soc.* **2001**, *123*, 11312–11313.

[19] E. J. Corey, G. Schmidt, *Tetrahedron Lett.* **1979**, *20*, 399–402.

[20] This result contradicts the original stereochemical assignment made by Ito et al. for the same agent isolated from sheep wool, by analogy with a C_{16} derivative.[9]

 © 2004 Wiley-VCH Verlag GmbH & Co. KGaA, Weinheim

Mass Spectrometry

Fragmentation of Singly Charged Peptide Ions by Photodissociation at $\lambda = 157$ nm**

*Matthew S. Thompson, Weidong Cui, and James P. Reilly**

Bond-selective chemistry has been a goal of photochemists for decades, particularly since the development and proliferation of tunable laser light sources. Nevertheless, for relatively large molecules, this goal has been elusive. Rapid intramolecular vibrational relaxation appears to redistribute energy throughout large molecules on timescales faster than dissociation so that any selectivity that may be injected by an excitation process is lost. The fragmentation of peptide ions activated by blackbody radiation,[1] IR multiphoton excitation,[2] UV laser excitation,[3–5] and collisions with gas-phase molecules or surfaces[6,7] involves vibrational excitation of precursor ions and consequently, production of similar types of daughter ions. The latter are primarily *b*- and *y*-type fragments as defined by the standard nomenclature shown in

[*] M. S. Thompson, W. Cui, Prof. J. P. Reilly
Department of Chemistry
Indiana University
Bloomington, IN 47405 (USA)
Fax: (+1) 812-855-8300
E-mail: reilly@indiana.edu

[**] This work has been supported by NIH grant GM61336, NSF grant CHE00945479, the Indiana Genomics Initiative, and Inproteo.

 DOI: 10.1002/anie.200460788 © 2004 Wiley-VCH Verlag GmbH & Co. KGaA, Weinheim

Figure 1 a.[8,9] In sharp contrast, electron capture dissociation (ECD)[10] and electron transfer dissociation (ETD)[11] apparently involve the capture of an electron by a multiply

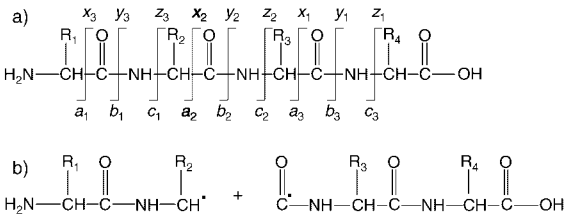


Figure 1. a) Standard nomenclature of peptide fragmentation; b) products of homolytic radical cleavage of a sample peptide. Note that the location of the added proton is not specified.

protonated protein ion, leading to charge reduction and the formation of a hydrogen atom that subsequently induces cleavage between the backbone nitrogen and α-carbon atoms. These techniques induce localized excitation, and dissociation apparently occurs before the internal energy is randomized, producing *c*- and *z*-type fragment ions with high sequence coverage. We now report another unorthodox fragmentation phenomenon in which 157-nm light excitation induces unusual backbone cleavage in singly protonated peptide ions.

Theoretical and spectroscopic studies suggest that small polypeptides absorb rather strongly in the vacuum ultraviolet, and the chromophore involved in the process is associated with the peptide backbone amides.[12] One absorption band occurs near 190 nm.[13] This transition can be excited using 193-nm ArF laser light. Disappointingly, photodissociation experiments at this wavelength have generated a combination of thermal ion fragments and a few fragments that are similar to those produced by high-energy collision-induced excitation.[4,5,14] Small model compounds such as *N*-acetylglycine absorb near 160 nm.[15,16] Theoretical studies of polyamides predict several charge-transfer bands in the 150- to 175-nm region, and an interaction between the excited states of the carboxyl terminus and the backbone amides has been inferred.[17] Robin suggested that one of the absorption bands in this wavelength region might be associated with an $n_o \rightarrow \sigma^*$ transition.[18] In order to investigate whether excitation of these electronic states would lead to novel dissociation products, the present study was undertaken (for details see the Experimental Section).

Tandem mass spectra of the peptide FSWGAEGQR generated with four sources of excitation are displayed in Figure 2. Collision-induced dissociation (CID) and post-source decay (PSD) generate primarily *y* fragments from this peptide, although several *b* and *a* fragments are also observed. Photodissociation with 157-nm light generates a completely different fragmentation pattern dominated by *x*-, *v*-, and *w*-type fragments. The appearance of y_3 and y_6 is probably associated with the enhancement of already intense PSD ions. Ions labeled *x* correspond to cleavage of the backbone bond between the α-carbon and the carbonyl carbon with the charge remaining on the C-terminal fragment. *v* ions are high-energy C-terminal fragments that

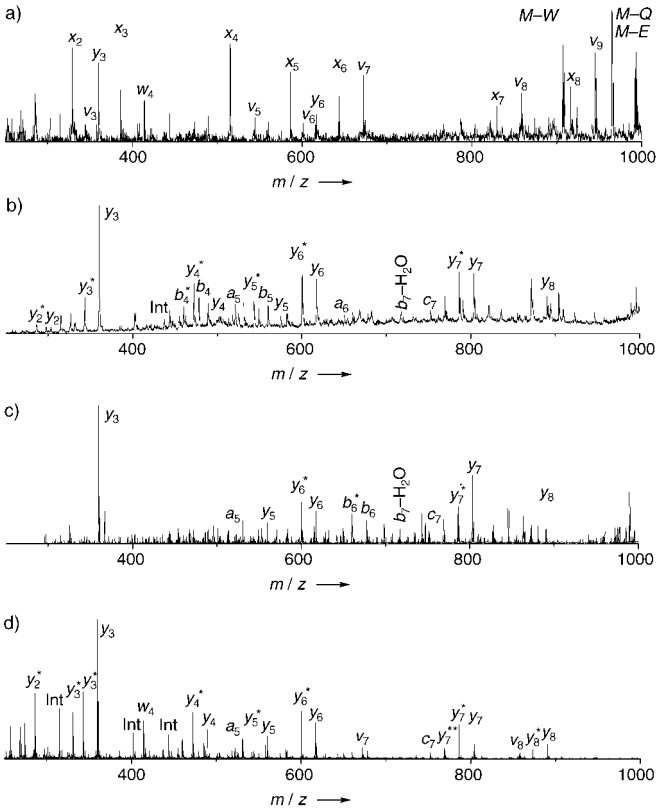


Figure 2. MALDI tandem mass spectra of peptide FSWGAEGQR obtained by: a) 157-nm photodissociation using 2,5-dihydroxybenzoic acid as matrix, b) PSD using α-cyano-4-hydroxycinnamic acid as matrix, c) AP MALDI CID, d) 2-keV TOF-TOF CID. Peaks labeled Int are internal fragments. The * and ** labels represent the loss of one and two NH_3 groups, respectively.

completely lose an adjacent amino acid side chain. Certain amino acids produce *w* ions from partial side-chain loss, with cleavage occurring between the β and γ carbon atoms. Losses of the side chains of some amino acids that would be expected to absorb 157-nm light are also observed and labeled *M*−*X*.

We propose that x_n+1 ions are initially generated by homolytic radical cleavage as shown in Figure 1 b. *x*, *v*, and *w* ions with even numbers of electrons[9] are formed following subsequent loss of H atoms or radicals. Ultraviolet-light-induced homolytic radical cleavage of small amides by means of a Norrish Type I mechanism is well known,[19] but this reaction has not been reported for larger molecules such as peptides. The initially formed radical ions subsequently lose an H atom to form x_n ions, CO and a side-chain radical to form v_n ions, or HN=C=O and part of a side chain to form w_n ions. Biemann and co-workers have suggested that v_n ions can be produced from x_n+1 precursor ions following high-energy peptide excitation.[9]

A number of peptides with basic residues at their C termini were fragmented using 157-nm photodissociation, and four typical mass spectra are shown in Figure 3. Every spectrum is dominated by *x*, *v*, and *w* fragments. *w* fragments are usually observed at leucine residues, rendering them distinguishable from isoleucine. Although *b*- and *y*-type ions occasionally appear in these spectra, they generally corre-

 © 2004 Wiley-VCH Verlag GmbH & Co. KGaA, Weinheim

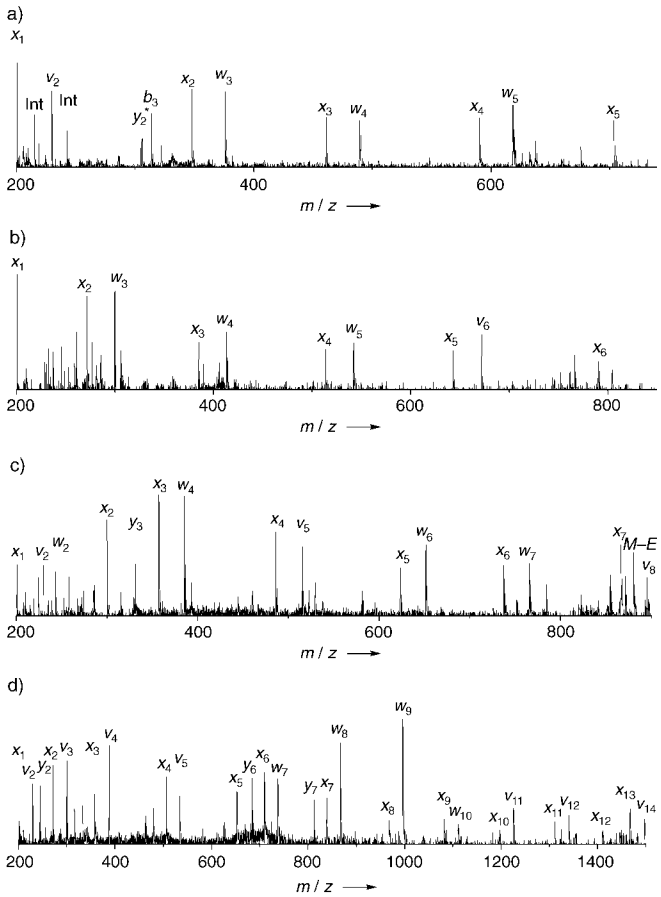


Figure 3. MALDI 157-nm photodissociation tandem time-of-flight mass spectra of a series of peptides containing C-terminal arginine. A) ALELFR; B) LFEELAR; C) IENHEGVR; D) EGVNDNEEGFFSAR. Peaks labeled Int are internal fragments. The * label represents the loss of one NH_3 group.

spond to intense PSD fragments that were not completely eliminated with background subtraction.

Other experiments, for which the data are not shown, were performed on peptides having N-terminal arginines. 157-nm light is found to cleave the backbone bond between the α-carbon and the carbonyl carbon as discussed above. In these cases, the N-terminal arginines sequester the charge, resulting in spectra dominated by *a*-type daughter ions. Whereas *a*-type ions are observed with other peptide-ion fragmentation techniques, we observe high sequence coverage and similar fragment-ion intensities just as with peptides having C-terminal arginines. This is consistent with the Norrish Type I photochemical cleavage model described previously.

Thus far we have photodissociated over two dozen peptide ions using 157-nm light. All peptides with C-terminal arginines yield predominantly *x*, *v*, and *w* ion fragments. This simple and well-defined product distribution apparently results from excitation of a dissociative electronic state by the 157-nm light. Thus, despite the relatively large size of the molecules investigated, at least the initial fragmentation step must be occurring without electronic-to-vibrational relaxation. Prompt dissociation may precede intramolecular vibrational relaxation in the excited electronic state. Alternatively, dissociation may take place from a vibrationally randomized excited electronic state. As our experiment does not provide time-dependence information but simply offers evidence of a novel fragmentation mechanism, it is not possible to rule out either of these possibilities.

The relative similarity of the intensities of many photofragment-ion peaks together with the fact that the charge always remains on the fragment containing arginine suggests that the charge is not involved in the fragmentation mechanism. Observation of *a* ions from peptides with R near the N terminus and *x* ions from peptides with R near the C terminus suggests that the role of the charge is simply to make the fragments detectable. This is in contrast with low-energy peptide fragmentation in which the mobility (or lack of mobility) of a proton usually has a dramatic effect on the observed spectra.[20]

Most peptides generated by digesting proteins with the enzyme trypsin have the basic residues arginine or lysine at their C termini. However, lysine does not sequester protons as effectively as arginine, and we have preliminary evidence that it should be guanidinated[21] to produce *x*-, *v*-, and *w*-type fragments. This is currently under investigation. Since tryptic digests are widely used, 157-nm photodissociation may interface well with protein identification experiments. The rapid timescale and charge conservation obtained with 157-nm photodissociation make it complementary to ECD and ETD, since it is compatible with singly protonated MALDI ions and TOF mass analyzers. The high sequence coverage observed and potential predictability of ion fragmentation patterns may facilitate peptide de novo sequencing. Because light is not affected by electric or magnetic fields, photofragmentation should be compatible with various mass analyzers and ion sources. Further studies of this phenomenon will involve 157-nm photodissociation of singly and multiply protonated peptide and protein ions generated by atmospheric pressure ion sources and will further probe the mechanism through which this fragmentation occurs.

Experimental Section

Experiments were performed on a homebuilt MALDI tandem time-of-flight instrument. Its design is similar to tandem time-of-flight instruments that employ collision cells[22,23] except that ion fragmentation is induced by 157-nm VUV light from an F_2 laser. Precursor ions are separated in a linear TOF apparatus, and those of interest are selected by an ion gate. An unfocused 10-ns, 2-mJ laser pulse with a cross section of 5 mm × 10 mm interacts with the selected ions. Precursor and fragment ions are then reaccelerated, separated, and detected in a reflectron TOF analyzer. Spectra with and without photodissociation are recorded on alternating shots so that the post-source decay contribution can be subtracted away. For comparison, high-energy collision-induced dissociation data were recorded on an Applied Biosystems (Foster City, CA) 4700 Proteomics Analyzer using 2-keV fragmentation energy with air as the collision gas. Low-energy CID was performed on a ThermoFinnigan LCQ Deca XP (Waltham, MA) using an atmospheric pressure MALDI ionization source.

Received: May 26, 2004
Published Online: August 20, 2004

 © 2004 Wiley-VCH Verlag GmbH & Co. KGaA, Weinheim

Keywords: mass spectrometry · peptides · photochemistry · proteomics · radical ions

[1] W. D. Price, P. D. Schnier, E. R. Williams, *Anal. Chem.* **1996**, *68*, 859.
[2] J. A. Zimmerman, C. H. Watson, J. R. Eyler, *Anal. Chem.* **1991**, *63*, 361.
[3] W. D. Bowers, S. S. Delbert, R. L. Hunter, R. T. McIver, Jr., *J. Am. Chem. Soc.* **1984**, *106*, 7288.
[4] S. A. Martin, J. A. Hill, C. Kittrell, K. Biemann, *J. Am. Soc. Mass Spectrom.* **1990**, *1*, 107.
[5] D. C. Barbacci, D. H. Russell, *J. Am. Soc. Mass Spectrom.* **1999**, *10*, 1038.
[6] D. F. Hunt, W. M. Bone, J. Shabanowitz, J. Rhodes, J. M. Ballard, *Anal. Chem.* **1981**, *53*, 1704.
[7] E. R. Williams, K. D. Henry, F. W. McLafferty, J. Shabanowitz, D. F. Hunt, *J. Am. Soc. Mass Spectrom.* **1990**, *1*, 413.
[8] P. Roepstorff, J. Fohlman, *Biomed. Mass Spectrom.* **1984**, *11*, 601.
[9] R. S. Johnson, S. A. Martin, K. Biemann, *Int. J. Mass Spectrom. Ion Processes* **1988**, *86*, 137.
[10] R. A. Zubarev, N. L. Kelleher, F. W. McLafferty, *J. Am. Chem. Soc.* **1998**, *120*, 3265.
[11] J. E. P. Syka, J. J. Coon, M. J. Schroeder, J. Shabanowitz, D. F. Hunt, *Proc. Natl. Acad. Sci. USA* **2004**, *101*, 9528.
[12] J. W. Preiss, R. Setlow, *J. Chem. Phys.* **1956**, *25*, 138.
[13] D. L. Peterson, W. T. Simpson, *J. Am. Chem. Soc.* **1957**, *79*, 2375.
[14] M. S. Thompson, W. Cui, J. P. Reilly, *Proceedings of the 51st ASMS Conference on Mass Spectrometry and Allied Topics* (Montreal, QC, June 8–12, 2003), **2003**.
[15] R. W. Woody, A. Koslowski, *Biophys. Chem.* **2002**, *101–102*, 535.
[16] L. B. Clark, *J. Am. Chem. Soc.* **1995**, *117*, 7974.
[17] X. G. Chen, P. Li, J. S. W. Holtz, Z. Chi, V. Pajcini, S. A. Asher, L. A. Kelly, *J. Am. Chem. Soc.* **1996**, *118*, 9716.
[18] M. Robin, *Higher Excited States of Polyatomic Molecules, Vol. II*, Academic Press, Orlando, **1975**.
[19] G. H. Booth, R. G. W. Norrish, *J. Chem. Soc.* **1952**, 188.
[20] V. H. Wysocki, G. Tsaprailis, L. L. Smith, L. A. Breci, *J. Mass Spectrom.* **2000**, *35*, 139.
[21] R. L. Beardsley, J. A. Karty, J. P. Reilly, *Rapid Commun. Mass Spectrom.* **2000**, *14*, 2147.
[22] D. Suckau, A. Resemann, M. Schuerenberg, P. Hufnagel, J. Franzen, A. Holle, *Anal. Bioanal. Chem.* **2003**, *376*, 952.
[23] K. F. Medzihradszky, J. M. Campbell, M. A. Baldwin, A. M. Falick, P. Juhasz, M. L. Vestal, A. L. Burlingame, *Anal. Chem.* **2000**, *72*, 552.

 © 2004 Wiley-VCH Verlag GmbH & Co. KGaA, Weinheim

Synthesis of Allylic Ethers

Iridium-Catalyzed Intermolecular Allylic Etherification with Aliphatic Alkoxides: Asymmetric Synthesis of Dihydropyrans and Dihydrofurans**

*Chutian Shu and John F. Hartwig**

Elimination and racemization limit the synthesis of sterically hindered ethers,[1] such as α-chiral ethers, by the Willamson synthesis. Enantioselective transition-metal-catalyzed allylic substitution[2–6] could be used to prepare these materials from achiral or racemic allylic electrophiles, but intermolecular enantioselective reactions of allylic acetates or carbonates with alkoxides are limited. Enantioselective reactions of phenoxides are well documented,[7–9] but no metal catalyzes intermolecular enantioselective allylations of alkoxides with broad scope.[10–13]

Lee and Kim[14] as well as Evans and Leahy[15] demonstrated that zinc and copper alkoxides were more reactive for allylic substitution with achiral palladium and rhodium catalysts than alkali metal alkoxides. The palladium-catalyzed reactions generated achiral ethers, but the rhodium-catalyzed reactions formed branched chiral ethers. Reactions of primary alkoxides with optically active allylic acetates occurred with predominant retention of configuration, but reactions of secondary and tertiary alkoxides were conducted with racemic allylic electrophiles. Because the products from reactions of primary alkoxides can be formed by alkylation of an optically active alcohol, but products from reactions of secondary alkoxides cannot, a catalyst that forms optically active products from hindered alkoxides and allylic carbonates is synthetically valuable. We report herein enantioselective reactions of primary, secondary, and tertiary alkoxides with achiral allylic carbonates to form branched chiral allylic ethers in high yields and with high stereoselectivity in the presence of an iridium catalyst containing a phosphoramidite ligand (Scheme 1).[16–22]

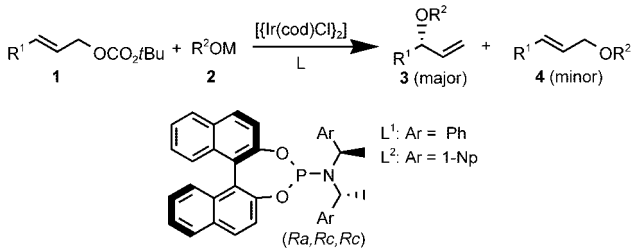
To optimize the conditions for the allylation of aliphatic alkoxides with iridium–phosphoramidite catalysts, we studied the reactions of cinnamyl carbonate with benzyloxides (Table 1). Careful selection of carbonate, alkoxide counterion, and nitrogen substituents in the ligand was essential for high yields. Cinnamyl carbonates with small alkyl groups underwent transesterification in competition with etherification, but *tert*-butyl cinnamyl carbonate (**1a**) provided the

[*] Dr. C. Shu, Prof. Dr. J. F. Hartwig
Department of Chemistry
Yale University
P.O. Box 208107, New Haven, CT 06520-8107 (USA)
Fax: (+1) 203-432-6144
E-mail: john.hartwig@yale.edu

[**] We thank Merck Research Laboratories and Boehringer Ingelheim for unrestricted gifts.

Supporting information for this article is available on the WWW under http://www.angewandte.org or from the author.

 © 2004 Wiley-VCH Verlag GmbH & Co. KGaA, Weinheim DOI: 10.1002/anie.200460214



Scheme 1. The synthesis of chiral allylic ethers. The ratio L/Ir was 1:1. cod = cycloocta-1,5-diene, 1-Np = 1-naphthyl.

Table 1: Effect of ligands and nucleophiles on the regio- and enantioselective allylic etherification with aliphatic alkoxides (Scheme 1).[a]

Alkoxide **2**	L (mol%)	Yield [%]	**3**/**4**	*ee* [%]
$Zn(BnO)_2$ (**2a**)	L^1 (4)	45	75:25	93
LiOBn + CuCl (**2b**)	L^1 (4)	56	92:8	70
LiOBn + CuBr (**2c**)	L^1 (4)	65	96:4	73
LiOBn + CuI (**2d**)	L^1 (4)	68	95:5	93
$Zn(BnO)_2$ (**2a**)	L^2 (2)	72	90:10	94
LiOBn + CuI (**2d**)	L^2 (2)	92	99:1	94

[a] In all cases *tert*-butyl cinnamyl carbonate (**1a**, R^1 = Ph) was used.

desired product in high yields. Alkali metal alkoxides did not form the ether, but zinc[14] and copper[15] alkoxides did; reactions in the presence of copper iodide furnished the products in the highest yields.[23] Reactions conducted with an iridium catalyst generated from $[\{Ir(cod)Cl\}_2]$ and phosphoramide L^1 found the branched ethers in low yields, but reactions conducted with the catalyst bearing L^2,[24,25] which contains a bis(naphthethylamino) group instead of the bis(phenethylamino) group (Scheme 1), formed this ether in high yields. With this catalyst and the above conditions, LiOBn (Bn = benzyl) and CuI reacted with *tert*-butyl cinnamyl carbonate to form the allylic ether in 92% yield with a branched-to-linear regioselectivity of 99:1 and 94% *ee*.[26]

The scope of the allylation of copper alkoxides in the presence of $[\{Ir(cod)Cl\}_2]$ and L^2 is summarized in Table 2. Allylic ethers were formed in high yield and enantioselectivity from reactions of primary alkoxides. For example, methyl-substituted allylic carbonate **1b** reacted with alkoxide **2d** to afford the branched ether, with a branched-to-linear (B/L) ratio of 95/5, in 80% yield and 97% *ee* (entry 1).

More important, secondary alkoxides reacted with a variety of allylic carbonates in the presence of 4 mol% iridium to form allylic ethers with excellent regio- and enantioselectivities. Reaction yields varied from moderate to excellent (entries 2–8). Copper alkoxides derived from simple secondary alcohols (**2e, 2f**) reacted with cinnamyl carbonate (**1a**) to give the branched ethers in high yields, as well as high regio- and enantioselectivities (entries 2, 3). Reactions of secondary alkoxides containing an accompanying tert-butoxycarbonyl (Boc) group formed the allylic ether in lower yield, but the regio- and enantioselectivities remained high (entry 4). The etherification with secondary alkoxides encompassed both aromatic and aliphatic carbonates. The reactions between alkyl-substituted allylic carbonates **1b**, **1c**, and alkoxide **2g**, and the reactions between aryl-substituted allylic carbonates **1d**, **1e**, and alkoxide **2f** all proceeded with excellent regio- and enantioselectivities.

Reactions with tertiary alkoxides also formed the allylic ether products in good yields. However, the reactions were slower and the enantioselectivities were lower than for reactions of secondary alkoxides (entry 9). Although the reason for the lower enantioselectivity is not clear at this time, slow attack of a tertiary alkoxide may allow epimerization of the allyl intermediate and erosion of stereoselectivity established during the addition of the allylic carbonate.

Optically active ethers with two chiral centers adjacent to the central oxygen atom are important structural motifs in a number of biologically important natural products.[27] A metal-catalyzed diastereoselective addition of chiral, nonracemic secondary alcohols to allylic carbonates could provide a versatile route to these compounds. An achiral catalyst would be unlikely to generate the product diastereoselectively because of the distance between the newly forming and existing stereocenters. However, a catalyst for enantioselective allylic etherification of allylic carbonates could provide diastereocontrol in the formation of chiral ethers with two stereocenters.

Table 2: Enantioselective allylic etherification of allylic carbonates with aliphatic copper alkoxides catalyzed by the complex formed from $[\{Ir(cod)Cl\}_2]$ and L^2 (Scheme 1).[a]

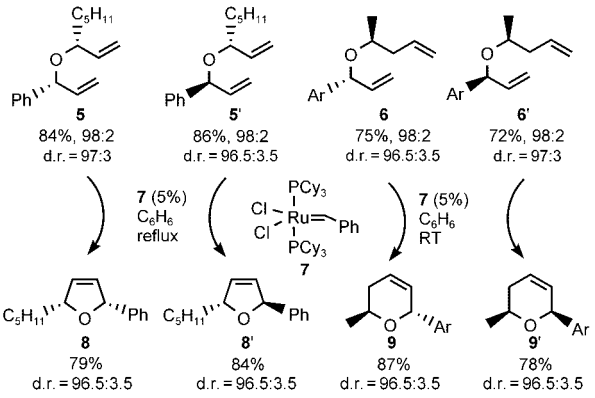
Entry	R^1 (**1**)	R^2 (**2**)	**3**/**4**[b]	Yield [%][c]	*ee* [%][d]
1[e]	Me (**1b**)	Bn (**2d**)	95:5	80	97
2	Ph (**1a**)	iPr_2CH (**2e**)	99:1	86	96
3	**1a**	1-cyclohexyl (**2f**)	97:3	79	94
4	**1a**	*N*-Boc-4-piperidinyl (**2g**)	98:2	70[f]	95
5	**1b**	**2g**	97:3	56[f]	94
6	*n*Pr (**1c**)	**2g**	92:8	66[f]	93
7[g]	*p*-$NO_2C_6H_4$ (**1d**)	**2f**	94:6	59	86
8[g]	*p*-$MeOC_6H_4$ (**1e**)	**2f**	99:1	86	95
9[h]	**1a**	*t*Bu (**2h**)	96:4	80	63
10	**1a**	(*S*)-1-(2-Np)-1-ethyl (**2i**)	99:1	90	95 de
11[i]	**1a**	**2i**	99:1	91[j]	93 de
12	*E*-$CH_3CH{=}CH$ (**1f**)	**2i**	98:2	90	96 de
13[i]	**1f**	**2i**	98:2	88[j]	96 de

[a] All reactions were conducted with 0.5 mmol of **1** and 1.0 mmol of **2** (prepared by treating $LiOR^2$ with 1.05 equiv of CuI) in THF (2.0 mL) in the presence of 0.010 mmol of $[\{Ir(cod)Cl\}_2]$ and 0.020 mmol of (R_a,R_c,R_c)-L^2 (L:Ir = 1) for 12–16 h unless specified otherwise. [b] Determined by ^1H NMR spectroscopy of the crude reaction mixtures. [c] Average of two yields of isolated **3** and **4** unless specified otherwise. [d] Determined by chiral HPLC. [e] The reaction was conducted with 0.005 mmol of $[\{Ir(cod)Cl\}_2]$ and 0.01 mmol of (R_a,R_c,R_c)-L^2. [f] Average of two yields of isolated **3**. [g] The reactions were conducted with 3.0 mL THF. [h] The reaction time was 48 h. [i] The ligand (S_a,S_c,S_c)-L^2 was used. [j] The major product is the opposite diastereomer of that from the reaction conducted with (R_a,R_c,R_c)-L^2.

 © 2004 Wiley-VCH Verlag GmbH & Co. KGaA, Weinheim

Indeed, reactions of the alkoxide derived from (*S*)-1-(2-naphthyl)ethanol (**2i**) with allylic carbonates (**1a, 1f**) catalyzed by iridium complexes containing opposite enantiomers of ligand L^2 formed the opposite diastereomers of the allylic ether with excellent yields, regio- and diastereoselectivities (entries 10–13). The reaction was not constrained by a match and mismatch of the substrate and catalyst chirality.

The control of enantio- and diastereoselectivity is applicable to the synthesis of *cis*- and *trans*-2,5-disubstituted dihydrofurans and *cis*- and *trans*-2,6-disubstituted dihydropyrans[28,29] with control of absolute and relative stereochemistry with readily available, enantioenriched allylic[30,31] and homoallylic alcohols[32,33] (Scheme 2). For example, **1a** and **1e**



Scheme 2. Synthesis of disubstituted dihydrofurans and dihydropyrans. Ar = *p*-$MeOC_6H_4$, Cy = cyclohexyl.

reacted with alkoxides derived from (*R*)-1-octen-3-ol and (*S*)-4-penten-2-ol, respectively, in the presence of catalysts derived from the two enantiomers of L^2 to form the branched allylic ethers **5, 5′** and **6, 6′** with excellent yields and regio- and diastereoselectivities. Ring-closing metathesis[34] with the Grubbs catalyst **7**[35] proceeded smoothly to give the corresponding cyclic ethers **8, 8′** and **9, 9′** in high yields and with retention of configuration.[36]

In summary, we have developed the first general and highly selective allylic etherification with both primary and secondary aliphatic alkoxides. The ability of the catalyst to control the new stereocenter generated from the reaction of chiral secondary alkoxides makes possible highly enantioselective and diastereoselective routes to ethers and oxygen heterocycles that have been challenging to prepare in uncatalyzed reactions.

Experimental Section

Representative procedure. In a drybox, lithium alkoxide (1.00 mmol) and CuI (200 mg, 1.05 mmol) were mixed in a screw-capped vial. THF (1.0 mL) was added, and the suspension was stirred for 30 min. To this suspension was added a solution of $[\{Ir(cod)Cl\}_2]$ (3.4 mg, 0.0051 mmol for primary alkoxides; 6.7 mg, 0.010 mmol for secondary and tertiary alkoxides) and (*Ra,Rc,Rc*)-L^2 (6.4 mg, 0.010 mmol for primary alkoxides; 12.8 mg, 0.020 mmol for secondary and tertiary alkoxides) in THF (0.5 mL for primary alkoxides; 1.0 mL for secondary and tertiary alkoxides). A magnetic stir bar was added, and the vial was sealed with a cap containing a PTFE septum and removed from the drybox. The vial was placed in an ice-water bath, and *tert*-butyl carbonate (0.50 mmol) was added to the reaction mixture by syringe. The reaction mixture was slowly warmed to room temperature over 4 h. After the reaction was complete (determined by GC and TLC) the crude mixture was passed through a pad of silica gel (EtOAc/hexanes 10:90), and the resulting solutions were concentrated. The ratio of regioisomers was determined by ^1H NMR spectroscopy of the crude sample. The mixture was then purified by flash column chromatography on silica gel to give the desired product.

Received: April 3, 2004
Revised: May 18, 2004

Keywords: alkoxides · allylations · asymmetric synthesis · iridium · P ligands

[1] H. Feuer, J. Hooz in *The Chemistry of Ether Linkage* (Ed.: S. Patai), Interscience, London, UK, **1967**, p. 445.
[2] B. M. Trost, C. Lee in *Catalytic Asymmetric Synthesis 2nd Edition* (Ed.: I. Ojima), Wiley-VCH, New York, **2000**, Ch. 8.
[3] B. M. Trost, M. L. Crawley, *Chem. Rev.* **2003**, *103*, 2921.
[4] J. Tusji, *Palladium Reagents and Catalysis*, Wiley, New York, **1996**.
[5] L. Acemoglu, J. M. J. Williams in *Handbook of Organopalladium Chemistry for Organic Synthesis*, *Vol. 2* (Ed.: E.-I. Negishi), Wiley, New York, **2002**, p. 1945.
[6] A. Pfaltz, M. Lautens in *Comprehensive Asymmetric Catalysis I-III*, *Vol. 2*, Springer, New York, **1999**, p. 833.
[7] A. Iourtchenko, D. Sinou, *J. Mol. Catal. A* **1997**, *122*, 91.
[8] B. M. Trost, F. D. Toste, *J. Am. Chem. Soc.* **1998**, *120*, 815.
[9] C. Fisher, C. Defieber, T. Suzuki, E. M. Carreira, *J. Am. Chem. Soc.* **2004**, *126*, 1628.
[10] C. Thorey, J. Wilken, F. Henin, J. Martens, T. Mehler, J. Muzart, *Tetrahedron Lett.* **1995**, *36*, 5527.
[11] B. M. Trost, E. J. McEachern, F. D. Toste, *J. Am. Chem. Soc.* **1998**, *120*, 12702.
[12] L. Jiang, S. D. Burke, *Org. Lett.* **2002**, *4*, 3411.
[13] E. Keinan, M. Sahai, Z. Poth, A. Nudelman, J. Herzig, *J. Org. Chem.* **1985**, *50*, 3558.
[14] H. Kim, C. Lee, *Org. Lett.* **2002**, *4*, 4369.
[15] P. A. Evans, D. K. Leahy, *J. Am. Chem. Soc.* **2002**, *124*, 7882.
[16] T. Ohmura, J. F. Hartwig, *J. Am. Chem. Soc.* **2002**, *124*, 15164.
[17] F. Lopez, T. Ohmura, J. F. Hartwig, *J. Am. Chem. Soc.* **2003**, *125*, 3426.
[18] C. A. Kiener, C. Shu, C. Incarvito, J. F. Hartwig, *J. Am. Chem. Soc.* **2003**, *125*, 14272.
[19] J. P. Janssen, G. Helmchen, *Tetrahedron Lett.* **1997**, *38*, 8025.
[20] B. Bartels, G. Helmchen, *Chem. Commun.* **1999**, 741.
[21] B. Bartels, C. Garcia-Yebra, G. Helmchen, *Eur. J. Org. Chem.* **2003**, 1097.
[22] G. Lipowsky, G. Helmchen, *Chem. Commun.* **2004**, 116.
[23] P. A. Evans, D. K. Leahy, L. M. Slieker, *Tetrahedron: Asymmetry* **2003**, *14*, 3613.
[24] L. A. Arnold, R. Imbos, A. Mandoli, A. H. M. De Vries, R. Naasz, B. L. Feringa, *Tetrahedron* **2000**, *56*, 2865.
[25] A. Alexakis, S. Rosset, J. Allamand, S. March, F. Guillen, C. Benhaim, *Synlett* **2001**, 1375.
[26] The absolute configuration of the product was established by comparison with the *R* configured ether prepared from commercial (*R*)-1-phenylpropanol.
[27] J. Buckingham, *Dictionary of Natural Products*, University Press, Cambridge, MA, **1994**.
[28] W. Friedrichsen in *Comprehensive Heterocyclic Chemistry*, *Vol. 2* (Ed.: C. W. Bird), Elsevier, Oxford, UK, **1996**, p. 386.

 © 2004 Wiley-VCH Verlag GmbH & Co. KGaA, Weinheim

[29] J. D. Hepworth, C. D. Gabbutt, B. M. Heron in *Comprehensive Heterocyclic Chemistry II*, *Vol. 5* (Ed.: A. McKillop), Elsevier, Oxford, **1996**, p. 382.
[30] Y. Gao, J. M. Klunder, R. M. Hanson, H. Masamune, S. Y. Ko, K. B. Sharpless, *J. Am. Chem. Soc.* **1987**, *109*, 5765.
[31] K. Burgess, L. D. Jennings, *J. Am. Chem. Soc.* **1990**, *112*, 7434.
[32] W. R. Roush, K. Ando, D. B. Powers, A. D. Palkowitz, R. L. Halterman, *J. Am. Chem. Soc.* **1990**, *112*, 6339.
[33] W. R. Roush, A. D. Palkowitz, K. Ando, *J. Am. Chem. Soc.* **1990**, *112*, 6348.
[34] A. Fürstner, *Angew. Chem.* **2000**, *112*, 3140; *Angew. Chem. Int. Ed.* **2000**, *39*, 3012.
[35] P. Schwab, M. B. France, J. W. Ziller, R. H. Grubbs, *Angew. Chem.* **1995**, *107*, 2179; *Angew. Chem. Int. Ed. Engl.* **1995**, *34*, 2039.
[36] M. T. Crimmins, A. L. Choy, *J. Org. Chem.* **1997**, *62*, 7548.

 © 2004 Wiley-VCH Verlag GmbH & Co. KGaA, Weinheim

Synthesis of Allylic Amines

Enantioselective Allylation of Aromatic Amines after In Situ Generation of an Activated Cyclometalated Iridium Catalyst**

*Chutian Shu, Andreas Leitner, and John F. Hartwig**

Aromatic amines with a stereocenter α to the nitrogen atom are important structural motifs in a number of biologically active compounds.[1] Many of approaches to such structures have been investigated, but each method has limitations. Thus, a highly enantioselective procedure to prepare optically active aromatic amines would be valuable, and an enantioselective route to *N*-aryl allylic amines would be particularly useful because of the dual functionality in these compounds.

Allylic substitution catalyzed by transition metals has emerged as a powerful tool for enantioselective formation of C–C, C–N, and C–O bonds.[2–4] However, aromatic amines have not been used commonly in allylic amination,[5–7] presumably because they are less nucleophilic than the more commonly used benzylamine or stabilized anionic nitrogen nucleophiles. A general and highly enantioselective reaction between an aromatic amine without an activating group on the nitrogen atom and an achiral allylic ester or a racemic branched allylic electrophile has not been reported.

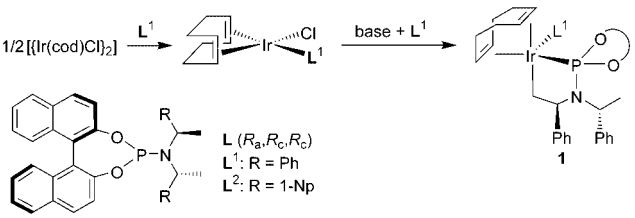
[*] Dr. C. Shu, Dr. A. Leitner, Prof. Dr. J. F. Hartwig
Department of Chemistry
Yale University
P.O. Box 208107, New Haven, CT 06520-8107 (USA)
Fax: (+1) 203-432-6144
E-mail: john.hartwig@yale.edu

[**] We thank Merck Research Laboratories and Boehringer Ingelheim for unrestricted support. A.L. thanks the FWF Austria for an Erwin Schrödinger fellowship.

Supporting information for this article is available on the WWW under http://www.angewandte.org or from the author.

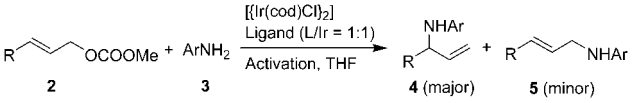
Catalysts based on metals other than palladium[8–16] and its congeners often form the more hindered, branched product from nucleophilic substitution with unsymmetrical monosubstituted allylic esters.[17–20] This reactivity complements the regioselectivity of palladium catalysts, which tend to form the linear products. We previously reported asymmetric allylic substitution of achiral allylic carbonates with aliphatic amines and phenoxides to form branched allylic amines and ethers with high regio- and enantioselectivities in the presence of an iridium complex with a phosphoramidite ligand.[21,22] Reactions of aromatic amines did not occur under the conditions developed originally.

Our mechanistic studies have shown that the cyclometalated complex **1**, generated in situ by treatment of $[\{Ir(cod)Cl\}_2]$ (cod = cycloocta-1,5-diene) and the ligand L^1 with an alkylamine base (Scheme 1), is likely to be the true catalyst in the allylic amination.[23] Reactions conducted with the isolated complex **1** as catalyst occurred faster and with broader scope than those with the combination of $[\{Ir(cod)Cl\}_2]$ and L^1.



Scheme 1. Synthesis of **1**; 1-Np = 1-naphthyl.

We proposed that the initial system failed to catalyze reactions of anilines because aromatic amines are not basic enough to induce cyclometalation, not because aromatic amines are too weakly nucleophilic to react with the iridium allyl intermediate.[23] If so, then the reactions of aniline should occur with a catalyst generated in situ by the action of a separate additive. Herein we report two convenient methods to generate the active catalyst in situ and the use of this catalyst to develop a general reaction of allylic carbonates with aromatic amines.[24] These reactions occur with a broad range of achiral, linear allylic carbonates to give branched chiral allyl aryl amines in excellent yields and with high regio- and enantioselectivities (Scheme 2).



Scheme 2. Amination of allylic carbonates **2** with aniline.

The cyclometalated complex **1** was generated in pure form by reaction of $[\{Ir(cod)Cl\}_2]$ and L^1 with an unhindered secondary amine, such as pyrrolidine (Scheme 1). We reasoned that the addition of a volatile primary amine prior to addition of aniline or a tertiary aliphatic amine would induce

 DOI: 10.1002/anie.200460276 © 2004 Wiley-VCH Verlag GmbH & Co. KGaA, Weinheim

cyclometalation without interfering with the reaction of the aniline.

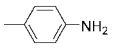
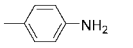
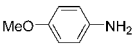
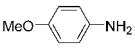
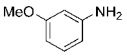
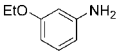
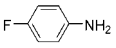
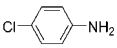
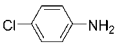
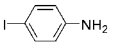
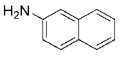
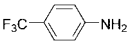
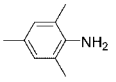
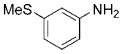
Thus, one procedure (method A) involved heating [{Ir(cod)Cl}$_2$] and L^1 with propylamine at 50 °C for 20 min. After evaporation of the volatile materials, the crude yellow solid **1** was dissolved in THF, and a portion or all of this solution was used as catalyst for the reactions of aromatic amines. As shown in Table 1, reactions of allylic carbonates with electron-rich as well as electron-neutral anilines in the presence of 2 mol % iridium catalyst occurred within 2–2.5 h, with high regioselectivities and enantioselectivities up to 98 %. Aromatic (**2a**) and aliphatic allylic carbonates (**2b**) reacted similarly.

Alternatively, the reaction was conducted at room temperature with a tertiary amine additive. We tested the reaction of methyl cinnamyl carbonate with aniline in the presence of tertiary amine additives (Table 2). The reaction in the presence of the relatively unhindered 1,4-diazabicyclo[2.2.2]octane (DABCO) gave the desired branched amine in high yield and with 92 % *ee*. The amount of DABCO influenced the reaction rate but did not significantly affect the enantioselectivity.

Table 2: Optimization of the reaction conditions with a tertiary amine base as additive.

Ligand	Additives (equiv)	*t* [h]	Conv. [%]	Yield [%]	**3**/**4**	*ee* [%]
L^1 (2 %)	NEt_3 (0.50)	24	0	–	–	–
L^1 (2 %)	DABCO (0.50)	24	100	72	>99:1	92
L^2 (1 %)	DABCO (0.50)	2	100	77	>99:1	95
L^2 (1 %)	DABCO (0.10)	6	100	80	>99:1	96

Table 1: Allylic amination of methyl cinnamyl carbonate (**2a**) and the methyl carbonate derived from (*E*)-2-hexen-1-ol (**2b**) with aromatic amines (see Scheme 2).

Entry	Carbonate **2**	Amine **3**	*t* [h]	**4**	Yield [%]	**4**/**5**	*ee* [%]	Method[a]
1	**2a**		6	**4b**	76	99:1	94	B
2	**2b**		2	**4c**	94	96:4	93	A
3	**2a**		4	**4d**	91	98:2	95	B
4	**2b**		2	**4e**	95	95:5	95	A
5	**2a**		4	**4f**	82	97:3	96	B
6	**2a**		2.5	**4g**	86	97:3	96	A
7	**2a**		10	**4h**	90	98:2	94	B
8	**2a**		10	**4i**	89	98:2	96	B
9	**2a**		2.5	**4i**	80	95:5	96	A
10	**2a**		10	**4j**	92	98:2	96	B
11	**2a**		10	**4k**	83	97:3	95	B
12	**2a**		10	**4l**	89	99:1	95	B
13	**2a**		16	**4m**	72	94:6	96	C
14	**2a**		16	**4n**	66	93:7	94	B
15	**2a**		2	**4o**	82	97:3	96	B
16	**2a**		2.5	**4p**	85	97:3	96	A
17	**2a**		2	**4q**	90	99:1	95	B
18	**2a**		2	**4r**	89	97:3	96	B

[a] Method A: The catalyst was generated from propylamine (3.6 mmol) upon heating with [{Ir(cod)Cl}$_2$] and L^1 at 50 °C for 20 min. The reactions were conducted on a 1.0-mmol scale in THF (0.5 mL) with a molar ratio for **2a**/**3**/[{Ir(cod)Cl}$_2$]/L^1 of 1:1.2:0.01:0.02. Method B: The catalyst was generated in situ with DABCO as additive. The reactions were conducted on a 1.0-mmol scale in THF (0.5 mL) at room temperature with a molar ratio for **2a**/**3**/DABCO/[{Ir(cod)Cl}$_2$]/L^2 of 100:125:10:0.5:1. Method C: The reactions were conducted as for method B, but with a molar ratio for **2a**/**3**/DABCO/[{Ir(cod)Cl}$_2$]/L^2 of 100:125:10:1:2.

We tested the reaction of methyl cinnamyl carbonate with aniline in the presence of the catalyst generated from L^2 occurred with 96 % *ee*, while the same reaction occurred with 92 % *ee* when the catalyst was generated from L^1.

The results with methods B and C show that the scope of the reaction of aromatic amines with aromatic and aliphatic carbonates with DABCO as additive is broad (Table 1). Electron-rich and electron-neutral aromatic amines reacted with allylic carbonates to generate the branched *N*-aryl allylic amines in high yields and with excellent regio- and enantioselectivities (entries 1, 3, 5, 7, 8, 10–12). Unhindered aromatic amines or sterically hindered primary aromatic amines, such as 2,4,6-trimethylaniline, reacted in high yields with excellent selectivities (entries 14, 15). The reaction of *o*-bromoaniline is noteworthy because the *ortho*-bromo substituent can be used for further transformations.[25] Cyclic secondary aromatic amines also reacted to give the branched *N*-allylamine in excellent yields (entries 17, 18), but acy-

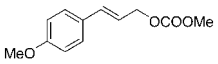
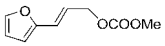
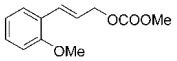
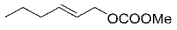
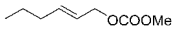
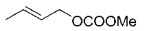
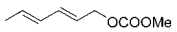
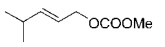
 © 2004 Wiley-VCH Verlag GmbH & Co. KGaA, Weinheim

clic secondary aromatic amines reacted with regioselectivities that ranged from 4:1 (in favor of the branched isomer) to 1:1.

Some electron-deficient aromatic amines required longer reaction times and higher catalyst loadings but formed the substitution product in acceptable yield and high enantioselectivity (Table 1, entries 13, 14). More electron-deficient anilines like *p*-cyanoaniline, did react, but in low yield and regioselectivity. The extremely electron-deficient *p*-nitroaniline did not react.

The scope of electrophile used encompassed both aromatic and aliphatic allylic carbonates (Table 3). In addition to the parent cinnamyl carbonate (**2a**), *p*-methoxy cinnamyl carbonate and the 2-furyl-substituted allylic carbonate reacted to give the branched products in excellent yields and selectivities (entries 1, 2).

Table 3: Amination of allylic carbonates **2** with aniline (Scheme 2, Ar = Ph).

Entry	Carbonate **2**	*t* [h]	**4**	Yield [%]	*ee* [%]	b/l **4/5**	Method[a]
1		10	**4s**	88	96	97:3	B
2		10	**4t**	81	90	94:6	B
3		10	**4u**	91	74	99:1	B
4		3	**4v**	87	95	98:2	B
5		2.5	**4v**	93	92	92:8	A
6		3	**4w**	72	95	97:3	B
7		3	**4x**	87	97	98:1:1[b]	B
8		16	**4y**	83	97	97:3	D[c]

[a] For conditions of methods A–C see footnote [a] to Table 1. [b] The ratio of α-branched/γ-branched/linear product. [c] Method D: The reaction was conducted with the catalyst generated in situ with DABCO as additive. The reaction was carried out on a 1.0-mmol scale in THF (0.5 mL) at room temperature with a relative mole ratio for **2a**/**3**/DABCO/[{Ir(cod)Cl}$_2$]/L^2 of 100:125:5:0.5:1.

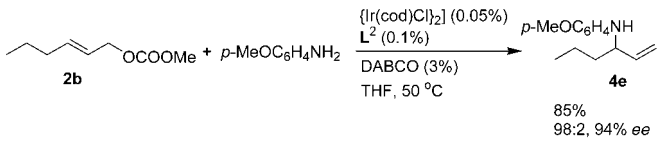
In contrast to most previous systems for allylic substitution, reactions of aliphatic allylic carbonates in the presence of the iridium-phosphoramidite catalyst occurred in high yield and with high regio- and enantioselectivities. Furthermore, the aliphatic carbonates reacted even faster than the aromatic carbonates. Thus, reactions of the methyl carbonates derived from (*E*)-2-hexen-1-ol and (*E*)-2-buten-1-ol with aniline were complete in 3 h and required only 5% DABCO additive (Table 3, entries 4, 6). In contrast, the reaction of methyl cinnamyl carbonate with aniline required 10 h under otherwise identical conditions. The methyl carbonate derived from (*E*,*E*)-2,4-hexadien-1-ol, a substrate recently explored by Helmchen and Lipowsky in allylic amination with alkyl and benzyl amines,[26] reacted with aniline to form the α-substituted **4x** with excellent regio- and enantioselectivities (entry 7).

Even aliphatic allylic carbonates with branching points α to the allyl unit reacted with high regio- and enantioselectivities. The branched allylic carbonate derived from (*E*)-4-methyl-2-penten-1-ol gave mostly linear product upon rhodium-catalyzed allylic amination. In contrast, reaction of the linear isomer of this allylic ester with aniline in the presence of 1 mol% of the iridium catalyst and 3 mol% DABCO formed the branched allylic amine **4y** with 97% *ee* and a branched-to-linear ratio of 97:3 (Table 3, entry 8).[27]

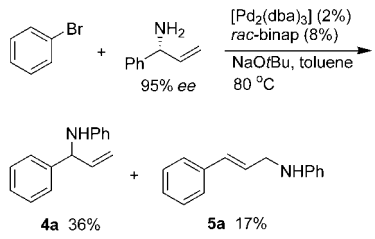
The unusually fast amination of aliphatic allylic carbonates allowed reactions of these substrates to be conducted with low catalyst loadings. For example, the reaction of carbonate **2b** with *p*-anisidine in the presence of 0.1 mol% of iridium catalyst afforded the allylic amine **4e** in 85% yield and with 94% *ee* (Scheme 3).

In contrast to these examples, *ortho*-methoxy cinnamyl carbonate reacted with aniline to give the substitution product with the same enantiomeric excess (74% *ee*) that was observed for reactions of this carbonate with aliphatic amines and phenoxides. Thus far, we have not solved the problem of enantioselective reactions of *ortho*-substituted allylic carbonates (Table 3, entry 3).

In principle, Pd-catalyzed cross-coupling[28–30] of an aromatic halide with an enantiopure α-chiral primary or secondary amine could be used to form the same α-chiral amines as those generated by this allylic substituiton. To compare aromatic amination to allylic amination as a method to prepare these materials, we conducted the reaction between phenyl bromide and an enantioenriched primary allylic amine (95% *ee*) catalyzed by a combination of [Pd$_2$(dba)$_3$] and (±)-binap (Scheme 4), which was shown previously[31] to couple an aryl bromide with optically active phenethylamine without racemization. In contrast to reactions of



Scheme 3. Reaction of carbonate **2b** with *p*-anisidine in the presence of iridium catalyst to afford the allylic amine **4e**.



Scheme 4. Reaction of PhBr with an enantioenriched primary allylic amine catalyzed by a combination of [Pd$_2$(dba)$_3$] and (±)-binap; dba = *trans*,*trans*-dibenzylidenacetone, binap = 2,2′-bis(diphenylphosphanyl)-1,1′-binaphthyl.

 © 2004 Wiley-VCH Verlag GmbH & Co. KGaA, Weinheim

phenethylamine, reaction of the allylic amine formed a 2:1 mixture of branched **4a** (83% *ee*) and linear **5a** products in a moderate combined yield (53%). Presumably, isomerization and partial racemization of the branched allylic amine by the Pd catalyst occurred before or after coupling. Thus, the allylic amination appears to be a superior method for the synthesis of *N*-aryl allylic amines.

In conclusion, we have developed the first convenient and highly selective allylic amination with "electron-neutral" aromatic amines that lack an activating group on the nitrogen atom. This process was developed by conversion of an iridium precatalyst into an active cyclometalated catalyst in the presence of an appropriate additive. This catalyst activation was either conducted in situ prior to addition of the aromatic amine or with DABCO additive in the presence of aniline. This reaction occurs with electron-neutral and electron-rich aromatic amine nucleophiles as well as aromatic or aliphatic allylic carbonates, and displays remarkable catalyst efficiency. Further studies on the reaction mechanism, as well as applications in synthesis, will be reported in due course.

Received: April 9, 2004
Revised: May 18, 2004

Keywords: allylations · aminations · asymmetric catalysis · iridium · regioselectivity

[1] J. S. Glasby, *Encyclopedia of the Alkaloids*, *Vol. 1–5*, Plenum, New York, NY, **1975**.
[2] B. M. Trost, M. L. Crawley, *Chem. Rev.* **2003**, *103*, 2921.
[3] J. Tusji, *Palladium Reagents and Catalysis*, Wiley, New York, **1996**.
[4] A. Pfaltz, M. Lautens in *Comprehensive Asymmetric Catalysis I–III*, *Vol. 2*, Springer, New York, **1999**, p. 833.
[5] S.-C. Yang, C.-W. Hung, *J. Org. Chem.* **1999**, *64*, 5000.
[6] F. Ozawa, H. Okamoto, S. Kawagishi, S. Yamamoto, T. Minami, M. Yoshifuji, *J. Am. Chem. Soc.* **2002**, *124*, 10968.
[7] R. Takeuchi, N. Ue, K. Tanabe, K. Yamashita, N. Shiga, *J. Am. Chem. Soc.* **2001**, *123*, 9525.
[8] B. M. Trost, I. Hachiya, *J. Am. Chem. Soc.* **1998**, *120*, 1104.
[9] B. M. Trost, P. L. Fraisse, Z. T. Ball, *Angew. Chem.* **2002**, *114*, 1101; *Angew. Chem. Int. Ed.* **2002**, *41*, 1059.
[10] G. C. Lloyd-Jones, A. Pfaltz, *Angew. Chem.* **1995**, *107*, 534; *Angew. Chem. Int. Ed. Engl.* **1995**, *34*, 462.
[11] P. A. Evans, J. D. Nelson, *J. Am. Chem. Soc.* **1998**, *120*, 5581.
[12] R. Takeuchi, M. Kashio, *Angew. Chem.* **1997**, *109*, 268; *Angew. Chem. Int. Ed. Engl.* **1997**, *36*, 263.
[13] R. Takeuchi, M. Kashio, *J. Am. Chem. Soc.* **1998**, *120*, 8647.
[14] R. Takeuchi, *Synlett* **2002**, 1954.
[15] B. Bartels, C. Garcia-Yebra, F. Rominger, G. Helmchen, *Eur. J. Inorg. Chem.* **2002**, 2569.
[16] B. Bartels, C. Garcia-Yebra, G. Helmchen, *Eur. J. Org. Chem.* **2003**, 1097.
[17] For selective formation of branched products with palladium catalysts, see refs [18–20].
[18] I. D. G. Watson, S. A. Styler, A. K. Yudin, *J. Am. Chem. Soc.* **2004**, *126*, 5086.
[19] C. E. Anderson, L. E. Overman, *J. Am. Chem. Soc.* **2003**, *125*, 12412.
[20] T. Hayashi, M. Kawatsura, Y. Uozumi, *J. Am. Chem. Soc.* **1998**, *120*, 1681.
[21] T. Ohmura, J. F. Hartwig, *J. Am. Chem. Soc.* **2002**, *124*, 15164.
[22] F. Lopez, T. Ohmura, J. F. Hartwig, *J. Am. Chem. Soc.* **2003**, *125*, 3426.
[23] C. A. Kiener, C. Shu, C. Incarvito, J. F. Hartwig, *J. Am. Chem. Soc.* **2003**, *125*, 14272.
[24] C. Welter, O. Koch, G. Lipowsky, G. Helmchen, *Chem. Commun.* **2004**, 896.
[25] E. I. Negishi in *Handbook of Organopalladium Chemistry for Organic Synthesis*, *Vol. 1* (Ed.: E. I. Negishi), Wiley Interscience, New York, NY, **2002**, p. 215.
[26] G. Lipowsky, G. Helmchen, *Chem. Commun.* **2004**, 116.
[27] P. A. Evans, J. E. Robinson, K. K. Moffett, *Org. Lett.* **2001**, *3*, 3269.
[28] J. F. Hartwig in *Modern Arene Chemistry* (Ed.: D. Astruc), Wiley-VCH, Weinheim, **2002**, p. 107.
[29] J. F. Hartwig in *Handbook of Organopalladium Chemistry for Organic Synthesis*, *Vol. 1* (Ed.: E. I. Negishi), Wiley-Interscience, New York, **2002**, p. 1051.
[30] B. H. Yang, S. L. Buchwald, *J. Organomet. Chem.* **1999**, *576*, 125.
[31] S. Wagaw, R. A. Rennels, S. L. Buchwald, *J. Am. Chem. Soc.* **1997**, *119*, 8451.

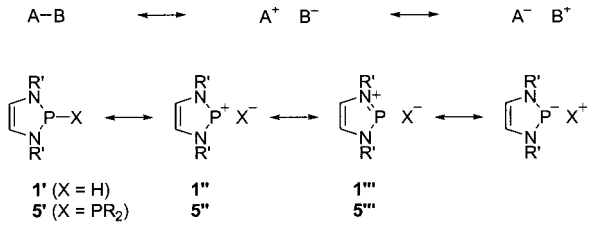
 © 2004 Wiley-VCH Verlag GmbH & Co. KGaA, Weinheim

Polarized P–P Bonds

Diphosphanes with Polarized and Highly Reactive P–P Bonds

Sebastian Burck, Dietrich Gudat, and Martin Nieger*

Single bonds are described in the valence-bond (VB) model in terms of resonance between covalent and ionic canonical structures (Scheme 1).[1] Whereas the covalent canonical structure is dominant for homoatomic bonds (A–B), the weight of the appropriately polarized ionic canonical structure prevails for heteroatomic bonds with a large electronegativity difference ($\chi A \ll \chi B$). As a result, this leads to a lower covalent bond order and a substantial bond polarity ($A^{\delta+}$–$B^{\delta-}$).

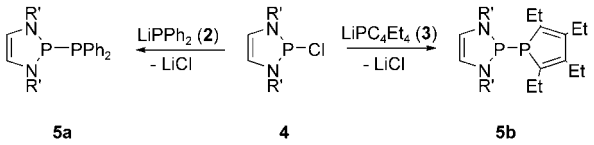


Scheme 1. R′ = Mes, *t*Bu.

We reported in 2000 on the hydride reactivity of 2-hydridodiazaphospholenes **1**, and interpreted this behavior as a consequence of a polarization $P^{\delta+}$–$H^{\delta-}$ of the P–H bond that can be explained in terms of a hyperconjugation between the six π electrons in the C_2N_2 moiety and the σ*(P–H) orbital.[2] In the frame of the VB model, this indicates that ionic canonical structures contribute, regardless of the low electronegativity difference (χ^{AR}(H) 2.2, χ^{AR}(P) 2.06), significantly to the bonding. The cause of this effect lies in the high cation stability of the diazaphospholenium fragment which yields an energetic stabilization of canonical structures such as **1**″ and **1**‴, and provides, for example, the driving force for the increased tendency towards dissociation of *P*-halogeno-1,3,2-diazaphospholenes.[3] Following this principle, a combination of a diazaphospholenium with a stable anionic phosphanide fragment should likewise render the polarization of the homoatomic P–P bond of a diphosphane feasible. Herein we describe the synthesis and characterization of such derivatives, and the unusual reactivity of the P–P bond resulting from the polarization will be demonstrated.

[*] Dipl. Chem. S. Burck, Prof. Dr. D. Gudat
Anorganisch-Chemisches Institut
Universität Stuttgart
Pfaffenwaldring 55, 70550 Stuttgart (Germany)
Fax: (+49) 711-685-4241
E-mail: gudat@iac.uni-stuttgart.de
Dr. M. Nieger
Anorganisch-Chemisches Institut
Universität Bonn
Gerhard-Domagk Strasse 1, 53121 Bonn (Germany)

First attempts at the synthesis of *P*-phosphanyldiazaphospholenes were made starting from lithium diphenylphosphanide (**2**) or lithium tetraethyl phospholide (**3**),[4] whose high anion stability offer particularly suitable conditions for a dipolar polarization of the P–P bond. The reaction of **2** or **3** with an equivalent of the *P*-chlorodiazaphospholene **4** in THF yielded cleanly the target compounds **5a**,**b**, which were isolated after workup as yellow, crystalline solids that are sensitive to hydrolysis and were characterized by means of spectroscopic and analytical studies (Scheme 2).



Scheme 2. R′ = Mes.

Whereas the spectroscopic data are not very unusual,[5] X-ray crystal structural studies[6] furnished clear evidence for a weakening of the P–P bond that is expected as the result of an increased weight of ionic canonical structures such as **5**‴. The P1–P2 bond length in **5a** (2.334(1) Å, Figure 1) is substantially longer than typical P–P distances in diphosphanes

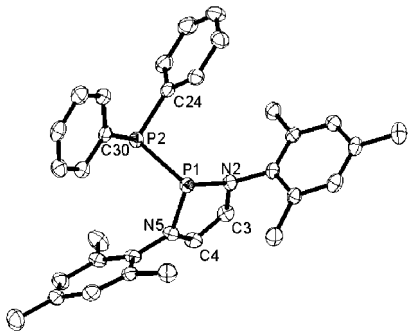


Figure 1. Molecular structure of **5a** in the crystal (H atoms omitted for clarity; 50% probability thermal ellipsoids). Selected distances [Å] and angles [°]: P1-P2 2.334(1), P1-N2 1.710(2), P1-N5 1.734(2), N5-C4 1.402(2), C3-N2 1.419(2), C3-C4 1.325(3); N2-P1-N5 90.3(1), N5-P1-P2 99.5(1), P2-P1-N2 104.0(1), P1-P2-C30 93.6(1), C24-P2-P1 99.6(1), C24-P2-C30 102.5(1).

(2.217 ± 0.08 Å[8]) and exceeds even the distances in the sterically overcrowded $[\{(Me_3Si)_2CH\}_2P]_2$ (2.310 Å),[9] which dissociates easily under homolytic cleavage of the P–P bond to give two radicals, and in the 1,1-diaminodiphosphane $(iPr_2N)_2P$–PPh_2 (2.250 Å),[10] for which, owing to the significantly lower cation stability of $(iPr_2N)_2P^+$ as compared to a diazaphospholenium cation,[3] a less pronounced dipolar polarization of the P–P bond is expected.

Compound **5b** (Figure 2a) is notable not only for the further elongation of the P–P bond to 2.484(1) Å, but also for the contraction of the P1-P2-C24(C27) bond angles to 81–82°. As a consequence of this effect, the P1 atom lies above the planar phosphole ring (Figure 2b), and the sum of all bond angles at the phosphanyl P atom decreases from 295.6° (**5a**) to

 DOI: 10.1002/anie.200460003 © 2004 Wiley-VCH Verlag GmbH & Co. KGaA, Weinheim

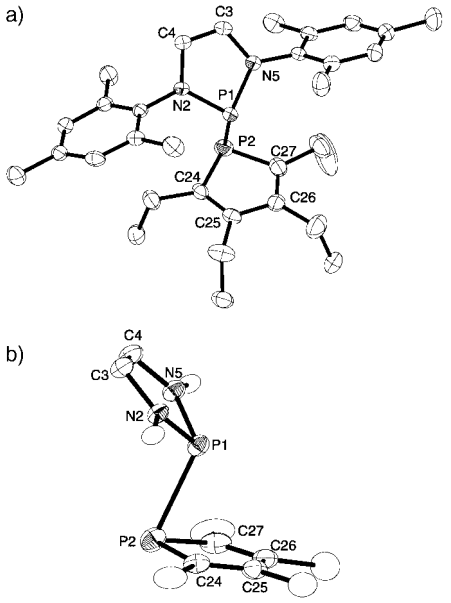
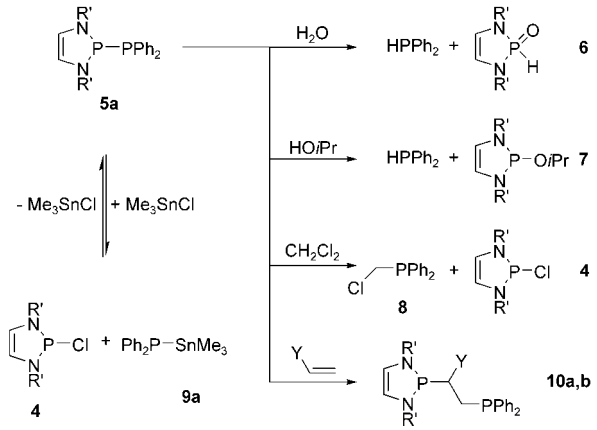


Figure 2. Complete (a) and reduced view (b, all atoms that are not directly adjacent to one of the five-membered rings were omitted) of the molecular structure of **5b** in the crystal (H atoms omitted for clarity; 50% probability thermal ellipsoids). Selected distances [Å] and angles [°]: P1-P2 2.484(1), P1-N5 1.716(2), P1-N2 1.722 (2), N2-C3 1.404(2), C3-C4 1.327(3), C4-N5 1.397(3), P2-C27 1.788(2), P2-C24 1.789(2), C24-C25 1.371(3), C25-C26 1.446(3), C26-C27 1.371(3); N5-P1-N2 87.1(1), N5-P1-P2 110.9(1), N2-P1-P2 109.7(1), C27-P2-C24 90.5(1), C27-P2-P1 81.9(1), C24-P2-P1 81.1(1).

253.5° (**5b**). The P–C and C–C bonds in the phosphole ring are comparable to the known values (P–C 1.79 ± 0.07 Å, C=C 1.36 ± 0.07 Å, C–C 1.46 ± 0.06 Å[11]) in phospholes and in η^1-phospholyl complexes. The distances within the diazaphospholene rings of **5a**,**b** are similar to the values found for the P-H derivative **1b** (Scheme 1, R′ = Mes).[2]

Both the lengthening of the P–P bonds and the unusual bond angle deformations in **5b** are in principle confirmed by DFT calculations[12] on the model compound **5c** (Scheme 1; **5c**: R′ = H; X = H_4C_4P; P–P 2.522 Å; C-P-P 83.7°; numerical differences between computed and experimental bond lengths of similar magnitude were also observed for **4**[3]). The assumption of significant ionic bonding contributions and a low covalent bond order for **5c** is further emphasized by natural bond order (NBO)/natural resonance theory (NRT) analyses,[13] which attest contributions by ionic canonical structures such as **5**″ or **5**‴, respectively,[14] of 28%, a significant charge transfer of −0.33 electrons from the diazaphospholene to the phosphole ring, and a very low value of 0.56 for the Wiberg bond index of the P–P bond. A detailed inspection of the non-localizable fraction of the electron density in the phospholyl fragment of **5c** suggests further that the bonding situation can be described, in good accordance with the unusual molecular geometry, in terms of a hybrid between a diphosphane with a localized P–P bond and a $\pi(\eta^3)$-phospholyl complex of a diazaphospholenium ion.[15]

That the ionic polarization implied by the elongation of the P–P bond in connection with the theoretical findings leads to a significant chemical activation, as in the case of the hydridodiazaphospholenes **1**,[2] is confirmed by a series of reactions that proceed by metathesis or by insertion into the P–P bond (Scheme 3).



Scheme 3. R′ = Mes; Y = CN (**10a**), CO_2Me (**10b**).

In contrast to white phosphorus, which is, regardless of its high reactivity, chemically inert against pure water, **5a** reacts with H_2O within a few minutes at 20 °C quantitatively under cleavage of the P–P bond to give diphenylphosphane and the 2-oxodiazaphospholene **6**.[16] A slower reaction to yield $HPPh_2$ and the alkoxydiazaphospholene **7**[16] is observed with *i*PrOH.[16] The cleavage of **5a** by CH_2Cl_2 at 40–60 °C to give **4** and (chloromethyl)diphenylphosphane (**8**)[17] follows the known pattern of reactions of diphosphanes with perfluoroalkyl iodides or CCl_4,[18] but is noteworthy because of the mild reaction conditions. Noteworthy is the reaction of **5a** with Me_3SnCl to give an equilibrium mixture that is dynamic on the NMR time scale and contains, beside the starting materials (ca. 10%), the chlorodiazaphospholene **4** and diphenyl(trimethylstannyl)phosphane (**9a**)[17] as main products.[19] The reaction pathway represents in essence a reversal of the dechlorostannylation that has been established as a smooth synthetic route to oligophosphanes,[20] and may be regarded to provide an experimental clue for a comparatively low P–P bond energy in **5a**. Analogous reactions to those for **5a** were also observed for **5b**.

In addition to the metathesis reactions with polar E–H or E–Cl single bonds, the diphosphanes **5** exhibit likewise an interesting reactivity towards olefins, which provides a surprisingly simple route to 1-phosphanyl-2-diazaphospholenylethane derivatives with electronically different donor centers. As first examples we studied the reactions of **5a** with acrylonitrile or methyl acrylate, respectively, which proceed under mild conditions (50 °C) by chemo- and regioselective addition to the C=C double bond to give the products **10a** and **10b**, respectively. Both compounds were isolated in yields of 31% (**5a**) and 63% (**5b**) and were identified by spectroscopy.[16] Unsymmetrical and potentially chiral phosphanes of this type, which are of current interest in catalysis,[21] have as yet not been prepared from diphosphanes.[22] The reaction described here displays close anal-

 © 2004 Wiley-VCH Verlag GmbH & Co. KGaA, Weinheim

ogies to the recently reported "non-oxidative" insertion of a metal atom into the P–C bond of a phosphenium–carbene adduct.[23]

Remarkably, unlike tetraaminodiphosphanes that may easily decay into two phosphanyl radicals,[24] **5a,b** fail to react with P_4 under addition to a P–P bond even in boiling toluene; possibly, this may indicate a certain complementary nature of reactions involving radical ($R_2P\cdot\cdot PR_2$) or ionic ($R_2P^+\ ^-PR_2$) activation of a P–P bond.

In summary, we have described the synthesis and characterization of diphosphanes with a polarized P–P bond. The molecules display not only an interesting bonding situation, but also allow a variety of synthetically valuable transformations which are, together with coordination chemical studies, currently under investigation.

Experimental Section

5a,b: A solution of $LiPPh_2$ (10 mmol) in THF (20 mL) or $LiPC_4Et_4$ (10 mmol)[4] in THF (50 mL) was added dropwise to a cooled (−78 °C) solution of **4** (10 mmol) in THF (100 mL). The mixture was then allowed to warm to ambient temperature, and stirred for one additional hour. The solvent was removed in vacuum, the residue extracted with hexane (100 mL), and filtered over Celite. The filtrate was concentrated to 30 mL, and the product crystallized at −20 °C.

5a: M.p. 193 °C, yield 77 %. ^{1}H NMR (C_6D_6): $\delta = 7.22$ (m, 4H, *o*-H_{Ph}), 6.80–6.77 (m, 6H, *m*/*p*-H_{Ph}), 6.61 (br, 4H, *m*-H_{Mes}), 5.78 (d, 2H, $^3J_{P,H} = 1.5$ Hz, N-CH), 2.40 (br, 12H, *o*-CH_3), 2.07 ppm (s, 6H, *p*-CH_3); ^{13}C{^{1}H} NMR (C_6D_6): $\delta = 136.7$ (dd, $^1J_{P,C} = 25.7$ Hz, $^2J_{P,C} = 12.7$ Hz, *i*-C_{Ph}), 135.8 (dd, $^2J_{P,C} = 10.4$ Hz, $^3J_{P,C} = 1.3$ Hz, *i*-C_{Mes}), 133.3 (br, *o*-C_{Mes}), 133.3 (d, $^5J_{P,C} = 2.0$ Hz, *p*-C_{Mes}), 132.7 (dd, $^3J_{P,C} = 15.5$ Hz, $^4J_{P,C} = 4.8$ Hz, *m*-C_{Ph}), 128.2 (br, *m*-C_{Mes}), 126.4 (d, $^4J_{P,C} = 6.1$ Hz, *o*-C_{Ph}), 125.6 (s, *p*-C_{Ph}), 118.4 (dd, $^2J_{P,C} = 7.6$ Hz, $^3J_{P,C} = 1.0$ Hz, N-CH), 19.0 (d, $^6J_{P,C} = 1.0$ Hz, *p*-CH_3), 18.4 ppm (br s, *o*-CH_3); ^{31}P{^{1}H} NMR (C_6D_6, 303 K): $\delta = 131.0$ (d, $^2J_{P,P} = 259$ Hz, PN_2), −28.8 ppm (d, $^2J_{P,P=}259$ Hz, PPh_2); MS (EI, 70 eV, 410 K): *m*/*z* (%): 508(0.1) $[M]^+$, 323(100) $[PN_2C_{20}H_{24}]^+$, 185(17) $[PPh_2]^+$; correct elemental analysis.

5b: m.p. 97 °C, yield 65 %. ^{1}H NMR (C_6D_6): $\delta = 6.77$ (s, 4H, *m*-CH), 5.85 (d, 2H, $^3J_{P,H} = 0.5$ Hz, N-CH), 2.45 (s, 12H, *o*-CH_3), 2.34 (q, 4H, $^3J_{H,H} = 7.5$ Hz, CH_2), 2.12 (s, 6H, *p*-CH_3), 1.73 (br dq, 4H, $^3J_{H,H} = 7.5$ Hz, $J_{P,H} = 9.3$ Hz, CH_2), 1.07 (t, 6H, $^3J_{H,H} = 7.5$ Hz, CH_3), 1.06 ppm (t, 6H, $^3J_{H,H} = 7.5$ Hz, CH_3); ^{13}C{^{1}H} NMR (C_6D_6): $\delta = 152.2$ (dd, $^2J_{P,C} = 8.9$ Hz, $^3J_{P,C} = 2.6$ Hz, PCC), 143.4 (dd, $^1J_{P,C} = 22.4$ Hz, $^2J_{P,C} = 14.6$ Hz, PC), 136.9 (dd, $^2J_{P,C} = 7.4$ Hz, $^3J_{P,C} = 1.7$ Hz, *i*-C), 136.1 (d, $^5J_{P,C} = 2.0$ Hz, *p*-C), 135.5 (dd, $^3J_{P,C} = 3.3$ Hz, $^4J_{P,C} = 1.6$ Hz, *o*-C), 129.5 (d, $^4J_{P,C} = 1.1$ Hz, *m*-C), 120.9 (dd, $^2J_{P,C} = 8.8$ Hz, $^3J_{P,C} = 1.2$ Hz, N-CH), 21.0 (dd, $J_{P,C} = 22.5$, 0.9 Hz, CH_2), 20.9 (d, $J_{P,C} = 1.6$ Hz, CH_2), 20.5 (d, $^6J_{P,C} = 0.8$ Hz, *p*-CH_3), 19.7 (dd, $^4J_{P,C} = 6.2$ Hz, $^5J_{P,C} = 3.2$ Hz, *o*-CH_3), 18.3 (dd, $^3J_{P,C} = 5.7$ Hz, $^4J_{P,C} = 2.4$ Hz, CH_3), 16.6 ppm (d, $^4J_{P,C} = 1.1$ Hz, CH_3); ^{31}P{^{1}H} NMR (C_6D_6, 303 K): $\delta = 147.1$ (d, $^1J_{P,P} = 188$ Hz, PN_2), 23.1 ppm (d, $^1J_{P,P} = 188$ Hz, $P_{phosphole}$); MS (EI, 70 eV, 380 K): *m*/*z* (%): 518(0.1) $[M]^+$, 323(100) $[PN_2C_{20}H_{24}]^+$, 196(14) $[PC_{12}H_{20}]^+$; correct elemental analysis.

Received: March 15, 2004

Keywords: addition reactions · bond polarization · insertions · phosphanes · phosphorus heterocycles

[1] G. A. Gallup , *Valence Bond Methods—Theory and Applications*, Cambridge University Press, Cambridge, **2002**.

[2] D. Gudat, A. Haghverdi, M. Nieger, *Angew. Chem.* **2000**, *112*, 3211; *Angew. Chem. Int. Ed.* **2000**, *39*, 3084.

[3] D. Gudat, A. Haghverdi, H. Hupfer, M. Nieger, *Chem. Eur. J.* **2000**, *6*, 3414.

[4] X. Sava, L. Ricard, F. Mathey, P. Le Floch, *Inorg. Chim. Acta* **2003**, *350*, 182.

[5] A VT-NMR study showed a significant temperature dependence of the values of $^1J_{P,P}$ in **5a,b** (**5a**: $^1J_{P,P} = 255$ Hz (203 K) to 264 Hz (363 K); **5b**: $^1J_{P,P} = 177$ Hz (203 K) to 204 Hz (363 K)). The precise origin of this effect, which is likewise known for other diphosphanes and has been explained by temperature-dependent equilibria between conformers (cf. J. G. Verkade, L. D. Quin, *P-31 NMR-Spectroscopy in Stereochemical Analysis*, VCH, Deerfield Beach, **1987**, p. 450f), is currently being intensively investigated.

[6] Crystal structure analyses: Nonius KappaCCD diffractometer, $T = 123(2)$ K, $Mo_{K\alpha}$ radiation ($\lambda = 0.71073$ Å), SHELX97 program package[7] for structure solution (direct methods) and refinement (full-matrix, least-squares refined against F^2). The positions of the hydrogen atoms were refined with a riding model. **5a**: yellow crystals, $C_{32}H_{34}N_2P_2$, $M_r = 508.6$, crystal size $0.45 \times 0.30 \times 0.20$ mm, triclinic, space group $P\bar{1}$ (no. 2), $a = 8.1758(2)$, $b = 10.6220(3)$, $c = 17.1208(7)$ Å, $\alpha = 96.601(2)$, $\beta = 100.350(2)$, $\gamma = 106.349(2)$°, $V = 1381.75(8)$ Å^3, $Z = 2$, $\mu(Mo_{K\alpha}) = 0.181$ mm^{-1}, $T = 123(2)$ K, $F(000) = 540$, $\theta_{max} = 25$°, 10884 reflections, of which 4866 were independent ($R_{int} = 0.043$), $R_1 = 0.039$ (for $I > 2\sigma(I)$), w$R_2 = 0.089$ (all data). **5b**: yellow crystals, $C_{32}H_{44}N_2P_2$, $M_r = 518.6$, crystal size $0.50 \times 0.40 \times 0.30$ mm, triclinic, space group $P\bar{1}$ (no. 2), $a = 8.1305(2)$, $b = 8.9507(2)$, $c = 20.5590(5)$ Å, $\alpha = 96.269(1)$, $\beta = 90.165(1)$, $\gamma = 94.510(1)$°, $V = 1482.50(6)$ Å^3, $Z = 2$, $\mu(Mo_{K\alpha}) = 0.169$ mm^{-1}, $F(000) = 560$, $\theta_{max} = 25$°; 13028 reflections, of which 5220 were independent ($R_{int} = 0.034$); $R_1 = 0.044$ (for $I > 2\sigma(I)$), w$R_2 = 0.125$ (all data). CCDC-232847 (**5a**) and CCDC-232848 (**5b**) contain the supplementary crystallographic data for this paper. These data can be obtained free of charge via www.ccdc.cam.ac.uk/conts/retrieving.html (or from the Cambridge Crystallographic Data Centre, 12, Union Road, Cambridge CB2 1EZ, UK; fax: (+44) 1223-336-033; or deposit@ccdc.cam.ac.uk).

[7] a) G. M. Sheldrick, *Acta Crystallogr. Sect. A* **1990**, *46*, 467; b) G. M. Sheldrick, SHELXL-97, University of Göttingen, **1997**.

[8] Average value ±3 standard deviations as result of a query in the CCSD data base for P–P distances in diphosphanes R_2P–PR_2 (R = nonmetal substituent).

[9] S. L. Hinchley, C. A. Morrison, D. W. H. Rankin, C. L. B. Macdonald, R. J. Wiacek, A. Voigt, A. H. Cowley, M. F. Lappert, G. Gundersen, J. A. C. Clyburne, P. P. Power, *J. Am. Chem. Soc.* **2001**, *123*, 9045.

[10] H. R. G. Bender, E. Niecke, M. Nieger, H. Westermann, *Z. Anorg. Allg. Chem.* **1994**, *620*, 1194.

[11] Average ±3 standard deviations as result of a query in the CCSD data base for P–C and C–C distances in phospholes.

[12] All computations were carried out at the B3LYP/6-31g(d)-level with the Gaussian program package: Gaussian 98 (Rev. A.7), M. J. Frisch, G. W. Trucks, H. B. Schlegel, G. E. Scuseria, M. A. Robb, J. R. Cheeseman, V. G. Zakrzewski, J. A. Montgomery, R. E. Stratmann, J. C. Burant, S. Dapprich, J. M. Millam, A. D. Daniels, K. N. Kudin, M. C. Strain, O. Farkas, J. Tomasi, V. Barone, M. Cossi, R. Cammi, B. Mennucci, C. Pomelli, C. Adamo, S. Clifford, J. Ochterski, G. A. Petersson, P. Y. Ayala, Q. Cui, K. Morokuma, D. K. Malick, A. D. Rabuck, K. Raghavachari, J. B.Foresman, J. Cioslowski, J. V. Ortiz, B. B. Stefanov, G. Liu, A. Liashenko, P. Piskorz, I. Komaromi, R. Gomperts, R. L. Martin, D. J. Fox, T. Keith, M. A. Al-Laham, C. Y. Peng, A. Nanayakkara, C. Gonzalez, M. Challacombe, P. M. W. Gill, B. G. Johnson, W. Chen, M. W. Wong, J. L. Andres, M. Head-Gordon, E. S. Replogle, J. A. Pople, Gaussian, Inc., Pittsburgh PA, **1998**.

[13] NBO 5.0: E. D. Glendening, J. K. Badenhoop, A. E. Reed, J. E. Carpenter, J. A. Bohmann, C. M. Morales, F. Weinhold, Theo-

 © 2004 Wiley-VCH Verlag GmbH & Co. KGaA, Weinheim

retical Chemistry Institute, Univ. of Wisconsin, Madison, WI, **2001**; http://www.chem.wisc.edu/~nbo5.

[14] In addition to **5″** and **5‴**, further ionic canonical structures were found which feature delocalization of the negative charge within the phospholyl fragment.

[15] A quite similar bonding situation was established for cyclopentadienyl phosphenium or arsenium ions, respectively; see: D. Gudat, M. Nieger, E. Niecke, *J. Chem. Soc. Dalton Trans.* **1989**, 693; P. Jutzi, T. Wippermann, C. Krüger, H.-J. Kraus, *Angew. Chem.* **1983**, *95*, 244; *Angew. Chem. Int. Ed. Engl.* **1983**, *22*, 250.

[16] Characteristic spectroscopic data: ^{31}P NMR (161.9 MHz, C_6D_6): $\delta = 0.4$ ppm (dt, $^1J_{P,H} = 650$ Hz, $^3J_{P,H} = 16.4$ Hz); ^{1}H-NMR (250 MHz, C_6D_6): $\delta = 8.72$ (dt, 1H, $^1J_{P,H} = 650$ Hz, $^4J_{H,H} =$ 1.5 Hz, P(O)H), 6.94 (m, 2H, *m*-CH), 6.91 (m, 2H, *m*-CH), 5.89 (dd, $^3J_{P,H} = 16.4$ Hz, $^4J_{H,H} = 1.5$ Hz, N-CH), 2.47 (s, 6H, *p*-CH_3), 2.28 (s, 6H, *o*-CH_3), 2.26 ppm (s, 6H, *o*-CH_3). **7**: ^{31}P{^{1}H} NMR: $\delta = 113.3$ ppm (s) ; ^{1}H-NMR (C_6D_6): $\delta = 6.87$ (m, 2H, *m*-CH), 6.83 (m, 2H, *m*-CH), 5.80 (d, 2H, $^3J_{P,H} = 2.1$ Hz, N-CH), 3.96 (dsept, 1H, $^3J_{P,H} = 7.6$ Hz, $^3J_{H,H} = 6.2$ Hz, POCH), 2.51 (s, 6H, *o*-CH_3), 2.44 (s, 6H, *o*-CH_3), 2.15 (s, 6H, *p*-CH_3), 0.82 ppm (d, 6H, $^3J_{H,H} = 6.2$ Hz, $CH(CH_3)_2$). **10a**: ^{31}P{^{1}H} NMR: $\delta = 99.5$ (d, $^3J_{P,P} = 17.9$ Hz, PN_2), −15.5 ppm (d, $^3J_{P,P} = 17.9$ Hz, PPh_2); ^{1}H NMR (C_6D_6): $\delta = 7.20$–7.13 (m, 4H, H_{Ph}), 6.95–6.85 (m, 6H, H_{Ph}), 6.71 (s, 2H, *m*-CH), 6.63 (s, 2H, *m*-CH), 5.61 (dd, 1H, $^3J_{H,H} = 2.5$ Hz, $^3J_{P,H} = 2.4$ Hz, N-CH), 5.56 (dd, 1H, $^3J_{H,H} =$ 2.5 Hz, $^3J_{P,H} = 2.5$ Hz, N-CH), 2.50 (s, br, 6H, *o*-CH_3), 2.35 (dddd, 1H, $^3J_{H,H} = 11.1$ und 4.9 Hz, $^{2/3}J_{P,H} = 7.8$ und 7.8 Hz, CN-CH), 2.28 (s, 6H, *o*-CH_3), 2.04 (6H, *p*-CH_3), 1.98 (dddd, 1H, $^2J_{H,H} = 13.7$ Hz, $^3J_{H,H} = 11.1$ Hz, $^{2/3}J_{P,H} = 2.0$ and 6.6 Hz, CH_2), 1.86 ppm (ddd, 1H, $^2J_{H,H} = 13.7$ Hz, $^2J_{H,H} = 4.9$ Hz, $^nJ_{P,H} = 7.0$ Hz, CH_2). **10b**: ^{31}P{^{1}H} NMR: $\delta = 102.6$ (d, $^3J_{P,P} = 11.8$ Hz, PN_2), −13.4 ppm (d, $^3J_{P,P} = 11.8$ Hz, PPh_2); ^{1}H NMR (C_6D_6): $\delta = 7.35$ (m, 2H, H_{Ph}), 7.18 (m, 2H, H_{Ph}), 7.05–6.90 (m, 6H, H_{Ph}), 6.73 (s, 4H, *m*-CH), 5.73 (dd, 1H, $^3J_{H,H} = 2.9$ Hz, $^3J_{P,H} = 2.0$ Hz, N-CH), 5.57 (dd, 1H, $^3J_{H,H} = 2.9$ Hz, $^3J_{P,H} = 2.1$ Hz, N-CH), 3.57 (dddd, 1H, $^3J_{H,H} = 12.3$ and 8.5 Hz, $^{2/3}J_{P,H} = 2.6$ and 0.8 Hz, C(O)-CH), 3.26 (s, 3H, *o*-CH_3), 2.49 (dddd, 1H, $^2J_{H,H} = 13.6$ Hz, $^3J_{H,H} =$ 12.3 Hz, $^{2/3}J_{P,H} = 5.2$ and 1.9 Hz, CH_2), 2.49 (s, 6H, *o*-CH_3), 2.36 (s, 6H, *o*-CH_3), 2.13 (s, 3H, *p*-CH_3), 2.08 (s, 3H, *p*-CH_3), 1.91 ppm (dddd, 1H, $^2J_{H,H} = 13.6$ Hz, $^3J_{H,H} = 8.5$ Hz, $^{2/3}J_{P,H} = 2.5$ and 0.3 Hz, CH_2). The regiochemistry in **10a,b** was unequivocally established from 2D-NOESY spectra.

[17] Identified by comparison of ^{31}P and ^{1}H NMR data with those of authentic samples.

[18] G. Elsner, *Methoden Org. Chem. (Houben-Weyl) 4th ed.*, *Vol. 13/E1*, **1980**, 129 ff.

[19] In the analogous reaction of **5a** with Me_3SiCl, formation of traces $\ll 1\%$ of the silylphosphane **9b** was likewise established from ^{31}P{^{1}H} and ^{1}H,^{31}P HMQC NMR spectra.

[20] M. Baudler, B. Makowka, *Angew. Chem.* **1984**, *96*, 976; *Angew. Chem. Int. Ed. Engl.* **1984**, *23*, 987; M. Baudler, L. De Riese-Meyer, *Z. Naturforsch. B* **1986**, *41*, 399.

[21] G. Fries, J. Wolf, M. Pfeiffer, D. Stalke, H. Werner, *Angew. Chem.* **2000**, *112*, 575; *Angew. Chem. Int. Ed.* **2000**, *39*, 564.

[22] Additions of symmetrical diphosphanes to olefins are possible under drastic conditions, but have hardly gained any relevance (cf. ref. [18]).

[23] N. J. Hardman, M. B. Abrams, M. A. Pribisko, T. M. Gilbert, R. L. Martin, G. J. Kubas, R. T. Baker, *Angew. Chem.* **2004**, *116*, 1989; *Angew. Chem. Int. Ed.* **2004**, *43*, 1955.

[24] J. P. Bezombes, P. B. Hitchcock, M. F. Lappert, J. E. Nycz, *J. Chem. Soc. Dalton Trans.* **2004**, 499.

Ab Initio Molecular Dynamics

Assigning Protonation Patterns in Water Networks in Bacteriorhodopsin Based on Computed IR Spectra**

*Roger Rousseau, Volker Kleinschmidt, Udo W. Schmitt, and Dominik Marx**

Bacteriorhodopsin (bR) is a prototypical light-driven ion pump that converts a photon flux into a proton gradient across cell walls.[1] Currently, a dynamic picture of how its photocycle operates on the atomistic level is beginning to emerge.[2] Contrary to the traditional paradigm that amino acid side chains are mainly responsible for vectorial proton translocation and release, evidence is accumulating that water networks[3–7] inside bR are actively involved. Much evidence is coming from broad continua in infrared absorption[8,9] believed to be caused by polarizable hydrogen bonds[10] in a protonated water network.[11,12] In particular, changes in continuum absorbance between 1800 and 1900 cm^{-1} could be measured by time-resolved FT-IR difference spectroscopy and correlated with the kinetics of proton release in the L-to-M transition.[8] The protonated water cluster causing this continuum consists of a $H_5O_2^+$ or larger complex,[8] which is stabilized by the nearby residues Glu194 and Glu204 as supported by pK_a calculations.[11] Above 2700 cm^{-1}, an additional broad continuum band was reported and associated with polarizable hydrogen bonds possibly belonging to another water (sub)network.[9]

Making use of hybrid quantum/classical (QM/MM) Car–Parrinello simulations[13,14] in conjunction with a realistic model for bR embedded in a fully hydrated palmitoyloleyl phosphatidylcholine (POPC) membrane, we computed IR spectra of protonated water networks close to the L-to-M transition. Although bR may be called a "simple model system", it turns out to be fairly complex from the viewpoint of an atomistic computer simulation since the electronic structure must be invoked in several crucial events during the pumping cycle. These difficulties are apparent by the rather scarce literature on bR and related prototypical G-protein-coupled seven-helix receptors such as rhodopsin where both quantum mechanics and protein dynamics are included (see, e.g. references [20–25] and references therein). To cope with this complexity, we treated as a first step the protonated water

[*] Dr. R. Rousseau, Dipl.-Phys. V. Kleinschmidt, Dr. U. W. Schmitt, Prof. Dr. D. Marx
Lehrstuhl für Theoretische Chemie
Ruhr-Universität Bochum
44780 Bochum (Germany)
Fax: (+49) 234-321-4045
E-mail: office@theochem.rub.de

[**] We are grateful to Alessandro Laio and Ursula Röthlisberger for help with their interface software, Axel Kohlmeyer for technical assistance, and Klaus Gerwert for fruitful discussions. The simulations were carried out at BOVILAB@RUB (Bochum) and at NIC (Jülich). Finally, we thank the DFG (FOR 436) and the FCI for financial support.

 © 2004 Wiley-VCH Verlag GmbH & Co. KGaA, Weinheim DOI: 10.1002/anie.200453857

network (QM part) here within density functional theory, whereas the biomatrix (MM part) was described by established force fields by using the Car–Parrinello molecular dynamics CPMD/GROMOS QM/MM interface.[13,14]

Unfortunately, the number of internal water molecules is still not exactly known from experiment,[4,6,12] although roughly four to five were found in the large hydrophilic pocket. Given this situation, we attempted to embed water networks that are representative of two important protonation topologies well-known from both gas-phase clusters[19] and from excess protons in liquid water[16,17] and ice.[18] Thus, a symmetrically solvated Zundel complex $H_5O_2^+ \cdot (H_2O)_4$ ("shared proton" between two H_2O molecules),[19] and an Eigen complex $H_3O^+ \cdot (H_2O)_3$ ("localized proton" at one H_2O molecule) were embedded in an appropriate wildtype bR intermediate[26] with a deprotonated Schiff base and a 13-*cis*,15-*anti*-retinal conformation (see Figure 1). The initial positions of the water molecules were based on recent crystallographic assignments as reviewed in reference [6] subject to protonation. This bR monomer was inserted into a fully solvated POPC membrane.[27]

The overall scheme is very realistic and enables the performance, after a cascade of careful MM and QM/MM relaxation steps and classical preequilibration on the nanosecond range at 300 K, of stable QM/MM molecular dynamics simulations on the 10-ps timescale. IR spectra can be computed by Fourier-transforming the dipole autocorrelation function, which is obtained directly from the total dipole moment of the protonated network. We note in passing that "electron spill-out" at the QM/MM interface, which is established here by hydrogen bonds between solvating water molecules of the $H_5O_2^+$ and H_3O^+ cores and residues, is taken care of by using the renormalized Coulomb potential previously introduced and tested for hydrogen bonding.[13] As a result, fully coupled anharmonic IR spectra of protonated water networks in bR at room temperature are accessible without reducing the dimensionality of this complex system. Note that the location of the networks including their hydrogen bonding to the nearby residues was a result of careful MM and QM/MM relaxation.

The reliability of this approach in particular for anharmonic floppy motion is demonstrated in Figure 2 (inset). Here the computed spectrum of an isolated $H_5O_2^+$ gas-phase complex[19] is compared with the one recently measured.[28] All calculations relied on the use of the BLYP density functional, Troullier–Martins pseudopotentials, 70 Rydberg planewave cutoff, 30 a.u. finite cubic box, compensating charge background, 300 K, and 10 ps equilibrated trajectory (see references [14,15] for further technical details).

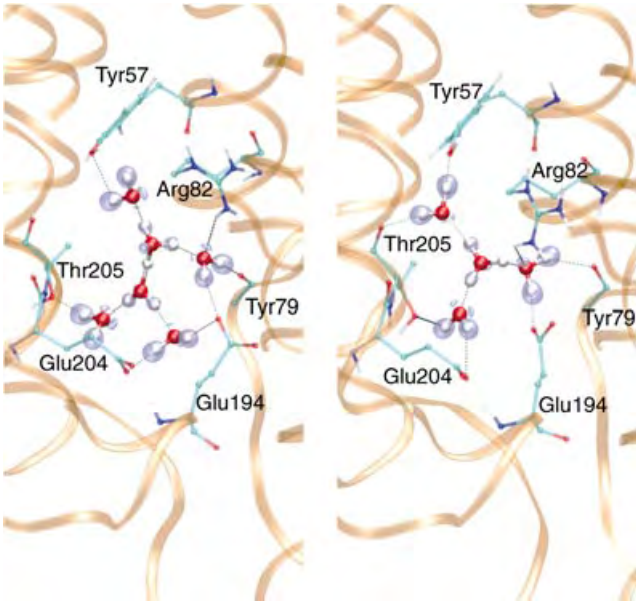


Figure 1. Representative snapshots of solvated Zundel-type (left) and Eigen-type (right) protonated water networks in bR at 300 K. Hydrogen bonds are represented schematically by thin broken lines, some key residues are labeled, and parts of the bR backbone are sketched as ribbons. The electronic structure is visualized in terms of the electron localization function (ELF, blue) superimposed on the nuclear skeleton; ELF is large in regions of space with pronounced electron pairing, such as in covalent OH bonds and lone electron pairs. Note that the excess proton is shared symmetrically between two neighboring water molecules in the solvated Zundel network yielding a "symmetrized hydrogen bond" in the $H_5O_2^+$ core, whereas in the Eigen network the proton is localized at a particular water molecule, forming a solvated hydronium core H_3O^+.

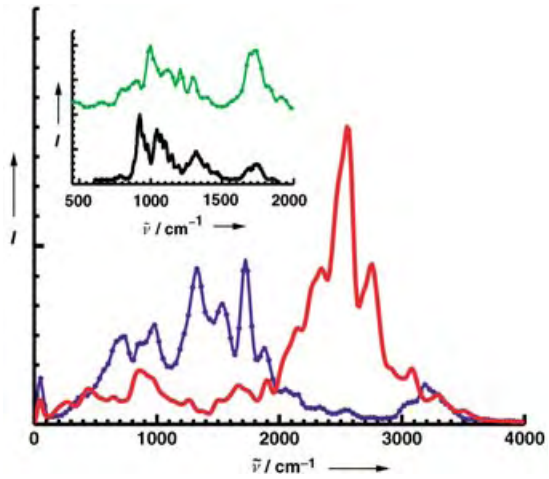


Figure 2. IR spectra computed for solvated Zundel (blue line with dots) and Eigen (red line without dots) networks in bR. Inset: Computed (upper green curve with dots) vs. measured[28] (lower black curve without dots) IR spectrum of bare $H_5O_2^+$ in the gas phase.

In the QM/MM simulations, the symmetrized hydrogen bond of the solvated Zundel-type complex was kept as symmetric as possible by connecting the four terminal hydrogens of the $H_5O_2^+$ core to the oxygens of the solvating water molecules by distance constraints. Spontaneous formation of hydrogen bonds with, for example, Glu194, Glu204, Arg82, and Tyr57 was observed. The asymmetric Eigen-type network was unconstrained and turned out to form hydrogen bonds to the same set of residues. This result (see Figure 1) is in line with X-ray crystallographic data,[3,5,6] which established that several water molecules are hosted inside bR, including

 © 2004 Wiley-VCH Verlag GmbH & Co. KGaA, Weinheim

the hydrophilic cavity surrounded by these residues. The calculated room-temperature IR spectra of these two protonated water networks are shown in Figure 2. Note that in view of the timescale accessible to QM/MM dynamics these spectra are representative for a given bR configuration and are not averaged over large-amplitude protein fluctuations.

Most interestingly, the simulated spectra of the Zundel- and Eigen-type networks in bR are complementary, similar to their gas-phase spectra (apart from the high-frequency OH stretch and low-frequency torsional and wagging mode regions, which are not of interest here). In particular, there is only one prominent resonance of the Eigen complex, which extends from about 2000 to 3000 cm^{-1} and can be explained in terms of linear combinations of symmetric and antisymmetric stretching modes of the central H_3O^+ moiety. In contrast, the solvated Zundel network does not have much spectral density in the 2000–3000-cm^{-1} window but instead a very broad feature covering the entire range from roughly 500 up to 2000 cm^{-1}. This band is clearly associated with both the large-amplitude floppy motion of the symmetric hydrogen bond and the bending motion of the two terminal water molecules that share the central "Zundel proton" (which leads to an isolated peak around 1700–1800 cm^{-1} in case of the bare Zundel cation $H_5O_2^+$ in the gas phase, see inset of Figure 2). The solvation-shell constraint used to stabilize a symmetric hydrogen bond in the core of the solvated Zundel complex does not much affect the IR spectrum in the region of interest (as assessed by comparing such constrained and unconstrained complexes in the gas phase).

Stimulated by this observed complementarity, we were intrigued to see how a composite spectrum would change upon variation of the concentration of the two network types. This is in essence what is measured by time resolution in difference FT-IR experiments[8,9] by scanning from about 20 ns up to seconds, but this is obviously not possible in QM/MM simulations. In the computed total spectrum in Figure 3 one can observe three important isosbestic points around 480, 1950, and 3150 cm^{-1}. Thus, the relative spectral density in the resulting two regions can be integrated and plotted vs. concentration of, for example, the Eigen network (see Figure 3, inset). Clearly, the lower and upper frequency regimes are dominated by the Zundel- and Eigen-type topologies, respectively.

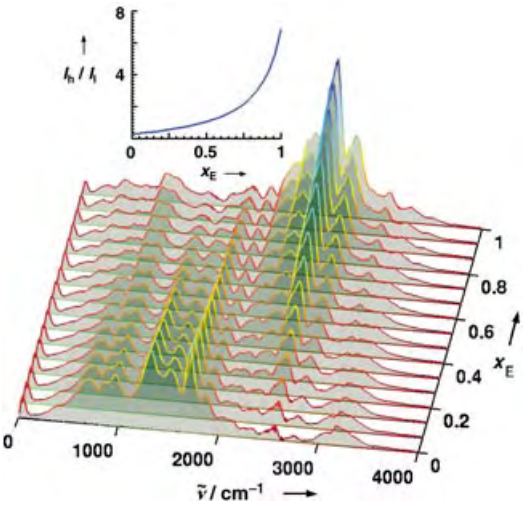


Figure 3. Concentration dependence of a linear superposition of solvated Zundel and Eigen spectra in bR as a function of the relative mole fraction x_E of the Eigen-like contribution. Inset: I_h/I_l as a function of x_E, where I_h and I_l are the integrated total intensities in the low- and high-frequency spectral windows, 480–1950 and 1950–3150 cm^{-1}, respectively, as defined by isosbestic points.

Most intriguingly, changes in the continuum absorption band at 1800–1900 cm^{-1} discovered in transient step-scan FT-IR experiments[8] were tentatively rationalized based on pK_a calculations[11] in terms of the minimal model for a protonated water network, that is, the Zundel cation $H_5O_2^+$ itself. This interpretation is consistent with the present observation that spectral changes up to about 2000 cm^{-1} are mainly due to the solvated Zundel network in bR. On the other hand, the presence of additional broad continua at high frequencies might indicate transient passage through local Eigen-type protonation patterns, that is, a proton localized in a H_3O^+ core which is stabilized by hydrogen bonds. This is suggested by the changes observed in the entire frequency range from 2100 up to 3150 cm^{-1} (Figure 3). This interesting finding clearly requires further experimental and theoretical clarification.

The comparison of these results to our reference simulations in the gas phase also suggests that the spectral features of protonated water networks attached to residues will be determined mainly by their local protonation pattern and thus overall topology, rather than by their precise location in the protein. Thus, by extending the experimental time resolution to the picosecond regime, it should be possible to follow transformations between network topologies characterized by localized or shared excess protons corresponding to Eigen- and Zundel-type topologies even in situ. Finally, these simulations, in concert with recent IR and X-ray experiments, support the paradigm that protonated water (sub)networks are actively participating in vectorial proton transfer throughout bR by storing and releasing an excess proton, in particular a water cluster close to the extracellular exit.

Received: January 27, 2004
Revised: April 7, 2004 [Z53857]

Keywords: biophysics · density functional calculations · ion channels · IR spectroscopy · molecular dynamics · proton transport

[1] U. Haupts, J. Tittor, D. Oesterhelt, *Annu. Rev. Biophys. Biomol. Struct.* **1999**, *28*, 367–399.
[2] W. Kühlbrand, *Nature* **2000**, *406*, 569–570.
[3] H. Luecke, B. Schobert, H.-T. Richter, J.-P. Cartailler, J. K. Lanyi, *Science* **1999**, *286*, 255–260; see also R. B. Gennis, T. G. Ebrey, *Science* **1999**, *286*, 252–253.
[4] H. Kandori, *Biochim. Biophys. Acta* **2000**, *1460*, 177–191.
[5] N. A. Dencher, H. J. Sass, G. Büldt, *Biochim. Biophys. Acta* **2000**, *1460*, 192–203.
[6] H. Luecke, J. K. Lanyi, *Adv. Protein Chem.* **2003**, *63*, 111–130.
[7] J. Baudry, E. Tajkhorshid, F. Molnar, J. Phillips, K. Schulten, *J. Phys. Chem. B* **2001**, *105*, 905–918.
[8] R. Rammelsberg, G. Huhn, M. Lübben, K. Gerwert, *Biochemistry* **1998**, *37*, 5001–5009.
[9] J. Wang, M. A. El-Sayed, *Biophys. J.* **2001**, *80*, 961–971.

 © 2004 Wiley-VCH Verlag GmbH & Co. KGaA, Weinheim

[10] G. Zundel, H. Metzger, *Z. Phys. Chem. (N. F. Frankfurt)* **1968**, *58*, 225 – 245; G. Zundel, *Adv. Chem. Phys.* **2000**, *111*, 1 – 217.
[11] V. Z. Spassov, H. Luecke, K. Gerwert, D. Bashford, *J. Mol. Biol.* **2001**, *312*, 203 – 219.
[12] C. Kandt, J. Schlitter, K. Gerwert, *Biophys. J.* **2004**, *86*, 705 – 717.
[13] A. Laio, J. Van de Vondele, U. Rothlisberger, *J. Chem. Phys.* **2002**, *116*, 6941 – 6947.
[14] D. Marx , J. Hutter in *Ab Initio Molecular Dynamics: Theory and Implementation* in *Modern Methods and Algorithms of Quantum Chemistry*, *Vol. 1* (Ed.: J. Grotendorst), NIC, FZ Jülich, **2000**, pp. 301 – 449; see www.theochem.rub.de/go/cprev.html; J. Hutter et al., CPMD, Max-Planck-Institut für Festkörperforschung Stuttgart and IBM Zurich, **1995–1999**; W. F. van Gunsteren et al., GROMOS96, BIOMOS b.v. ETH, Zürich, **1996**.
[15] R. Rousseau, V. Kleinschmidt, U. W. Schmitt, D. Marx, *Phys. Chem. Chem. Phys.* **2004**, *6*, 1848 – 1859.
[16] D. Marx, M. E. Tuckerman, J. Hutter, M. Parrinello, *Nature* **1999**, *397*, 601 – 604; see also J. T. Hynes, *Nature* **1999**, *397*, 565 – 567.
[17] U. W. Schmitt, G. A. Voth, *J. Chem. Phys.* **1999**, *111*, 9361 – 9381.
[18] C. Kobayashi, S. Saito, I. Ohmine, *J. Chem. Phys.* **2000**, *113*, 9090 – 9100; C. Kobayashi, S. Saito, I. Ohmine, *J. Chem. Phys.* **2001**, *114*, 1440 – 1440.
[19] M. E. Tuckerman, D. Marx, M. L. Klein, M. Parrinello, *Science* **1997**, *275*, 817 – 820.
[20] S. Hayashi I. Ohmine, *J. Phys. Chem. B* **2000**, *104*, 10678 – 10691.
[21] A. Warshel, Z. T. Chu, *J. Phys. Chem. B* **2001**, *105*, 9857 – 9871.
[22] S. Hayashi, E. Tajkhorshid, K. Schulten, *Biophys. J.* **2002**, *83*, 1281 – 1297; S. Hayashi, E. Tajkhorshid, K. Schulten, *Biophys. J.* **2003**, *85*, 1440 – 1449.
[23] U. F. Röhrig, L. Guidoni, U. Rothlisberger, *Biochemistry* **2002**, *41*, 10799 – 10809 and unpublished results.
[24] Y.-S. Lee, M. Krauss, *J. Am. Chem. Soc.* **2004**, *126*, 2225 – 2230.
[25] M. Sugihara, V. Buss, P. Entel, J. Hafner, A. N. Bondar, M. Elstner, T. Frauenheim, *Phase Transitions* **2004**, *77*, 31 – 45.
[26] A. Royant, K. Edmann, T. Ursby, E. Pebay-Peyroula, E. M. Landau, R. Neutze, *Nature* **2000**, *406*, 645 – 648; see also comment "*e*" in Table I of reference [6].
[27] H. Heller, M. Schaefer, K. Schulten, *J. Phys. Chem.* **1993**, *97*, 8343 – 8360.
[28] K. R. Asmis, N. L. Pivonka, G. Santambrogio, M. Brümmer, C. Kaposta, D. M. Neumark, L. Wöste, *Science* **2003**, *299*, 1375 – 1377. Note, however, the controversy about the assignment of the measured spectrum: J. Dai, Z. Bačić, X. Huang, S. Carter, J. M. Bowman, *J. Chem. Phys.* **2003**, *119*, 6571 – 6580.

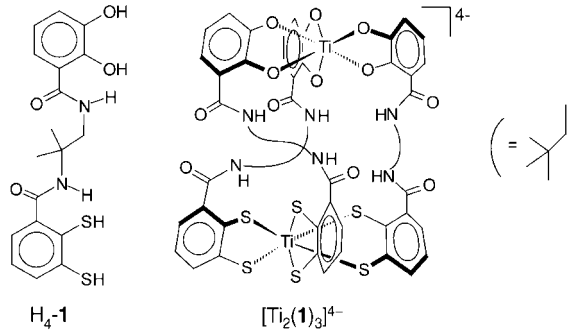
 © 2004 Wiley-VCH Verlag GmbH & Co. KGaA, Weinheim

Helical Structures

A Dinuclear, Triple-Stranded Helicate with a Diamide-Bridged Catechol/Benzenedithiol Ligand**

F. Ekkehardt Hahn, Christian Schulze Isfort, and Tania Pape*

The spontaneous self-organization of coordination compounds has been studied intensively over the last few years.[1] One area of particular interest are the triple-stranded helicates with catecholato donor groups.[2] Much less is known about helicates with thiolato donor groups, only bis(benzenedithiol) ligands[3] and their dinuclear nickel complexes have been reported.[4] Herein we present the synthesis of the first catechol/benzenedithiol (O–O/S–S) ligand H_4-**1** and the molecular structure of the triple-stranded *Λ*,*Λ*-helicate $Na(PNP)_3[Ti_2(\mathbf{1})_3]$ (PNP^+ = bis(triphenylphosphoranylidene)-ammonium).



H_4-**1** $[Ti_2(\mathbf{1})_3]^{4-}$

Triple-stranded helicates containing donor atoms from the second period (O, N) contain two metal centers coordinated in an octahedral fashion. However, under certain conditions, macrobicyclic tris(catecholato) ligands can enforce a trigonal-prismatic coordination environment in mononuclear complexes.[5] In contrast, tris(benzenedithiolato) complexes can be pseudo-octahedral (e.g. $[W^V(bdt)_3]^-$, bdt = benzene-1,2-dithiolate)[6] or trigonal-prismatic (e.g. $[W^{VI}(bdt)_3]$),[7] depending on the oxidation state of the coordinated metal center. The connection of a catechol and an *o*-benzenedithiol donor group in the same ligand and the preparation of triple-stranded dinuclear complexes with such ligands was of interest to us. A parallel orientation of the ligands would

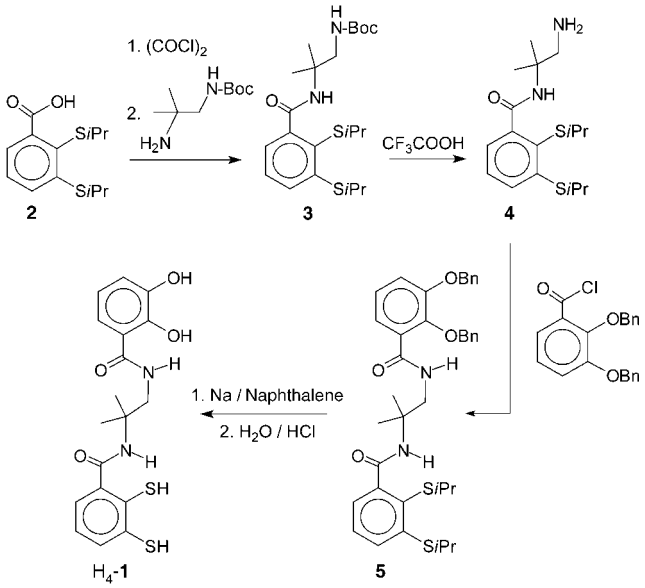
[*] Prof. Dr. F. E. Hahn, Dipl.-Chem. C. Schulze Isfort, T. Pape
Institut für Anorganische und Analytische Chemie
Westfälische Wilhelms-Universität Münster
Wilhelm-Klemm-Strasse 8, 48149 Münster (Germany)
Fax: (+49) 251-833-3293
E-mail: fehahn@uni-muenster.de

[**] Financial support for this work was provided by the Deutsche Forschungsgemeinschaft (GRK 673). We thank Dr. Klaus Bergander for recording of the NMR spectra.

 DOI: 10.1002/anie.200460188 © 2004 Wiley-VCH Verlag GmbH & Co. KGaA, Weinheim

allow the coordination geometry of the *o*-benzenedithiolato-coordinated metal center and thus the helicity of the complex to be switched by varying the oxidation state of this $\{MS_6\}$ metal center.

The preparation of ligand H_4-**1** starts from 2,3-di(isopropylsulfanyl) benzoic acid (**2**, Scheme 1).[8] This acid was converted into the acid chloride, followed by the reaction with the single *tert*-butoxycarbonyl (Boc) protected diamine[9] and subsequent removal of the Boc protecting group. The primary amine **4** reacts with 2,3-di(benzyloxy)benzoic acid chloride[10] to give the ligand precursor **5**. All the protecting groups were simultaneously removed with Na/naphthalene in THF.[4,8] After protonation with H_2O/HCl ligand H_4-**1** was obtained in about 59% yield (relative to **2**) as a light yellow solid.



Scheme 1. Synthesis of ligand H_4-**4**.

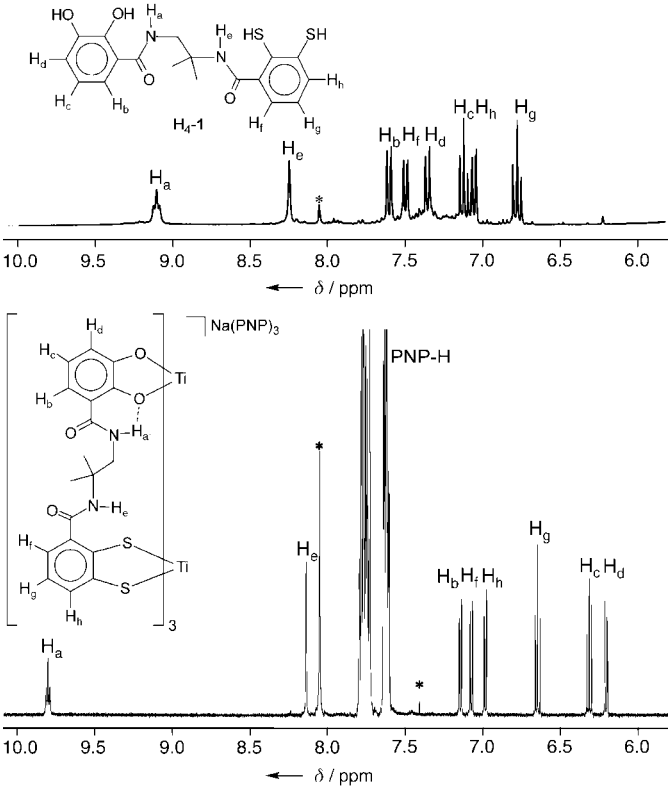


Figure 1. ^{1}H NMR spectra (in $[D_7]$DMF, $\star$ = DMF resonances) of H_4-**1** (top) and $Na(PNP)_3[Ti_2(\mathbf{1})_3]$ (bottom).

The ^{1}H NMR spectrum of H_4-**1** (Figure 1, top) shows two resonance signals for the N–H protons (H_a, t, 9.10 ppm and H_e, s, 8.25 ppm), which based on their multiplicity were assigned to the catechol- and *o*-benzenedithiol-bound amide groups. In addition, six well resolved resonance signals were observed for the protons of the aromatic rings.

Only a few helical complexes with asymmetrical donor groups derived from functionalized benzene are known.[11] Albrecht et al. reported a tetradentate, directional ligand containing an aminophenol and a catechol unit.[12] In addition, directional ligands are known which have identical donor groups but an asymmetric spacer between them.[13] The orientation of directional ligands in dinuclear complexes (parallel or antiparallel[14]) is of special interest since not only complexes with stereoisomeric metal centers (Λ, Δ) but also as regioisomeric complexes can form.

The directional catechol/aminophenol ligand[12] reacts with Ga^{III} or Ti^{IV} to give a dinuclear complex with parallel orientation of the ligands, while the reaction with a mixture of Ga^{III} and Ti^{IV} (1:1) gives a dinuclear complex with an antiparallel orientation of the ligands. The reaction of a directional phenylalanine-bridged di(catechol) ligand with Ti^{IV} gives a mixture of products containing a total of seven double-stranded dinuclear stereoisomeric (Λ, Δ) and regioisomeric (parallel and antiparallel) complexes.[13b,c]

Ligand H_4-**1** shows directionality based on the two different donor groups (O–O/S–S) and on the asymmetric CMe_2CH_2 spacer between them. The reaction of three equivalents of H_4-**1** with two equivalents of $[TiO(acac)_2]$ in the presence of Na_2CO_3 in methanol gives a red-brownish complex which dissolves well in methanol. Addition of PNPCl and diffusion of diethyl ether into a saturated methanol solution of the product gives the dinuclear complex $Na(PNP)_3[Ti_2[(\mathbf{1})_3]$ as red-brown crystals. The NMR spectra of $Na(PNP)_3[Ti_2[(\mathbf{1})_3]$ show a surprisingly small number of signals (Figure 1, bottom). The aromatic protons of the benzenedithiolato and the catecholato groups are detected as one triplet ($\delta = 6.65\,(H_g)$ and $6.32\,(H_c)$ ppm) and two doublets ($\delta = 7.08\,(H_f)$, $6.98\,(H_h)$ ppm, and $\delta = 7.15\,(H_b)$, $6.21\,(H_d)$ ppm) for each ring. This result demonstrates that the three ligands are oriented in an identical, parallel manner.

The downfield shift of the triplet H_a for the N–H proton of the catechol-bound amide ($\Delta\delta = 0.70$ ppm, Figure 1) is remarkable. This shift indicates the formation of a planar six-membered ring and a strong N–H···O hydrogen bond between the amide proton H_a and the *o*-catecholato oxygen atom (Figure 1). This type of hydrogen bond has been observed for helicates with amide-bridged catecholato donor groups[15] and for other catechoylamide complexes and has often been shown to be structure determining.[5,16]

 © 2004 Wiley-VCH Verlag GmbH & Co. KGaA, Weinheim

The chemical shift for the amide protons next to the benzenedithiolato group changes only marginally upon complex formation indicating the presence of no or only very weak N–H···S hydrogen bonds.

All the NMR data indicate the presence of the parallel regioisomer and only one pair of enantiomers in solution. However, the NMR data do not allow the determination which pair of enantiomers *Λ*,*Δ*/*Δ*,*Λ* or *Λ*,*Λ*/*Δ*,*Δ* is present.[17] Slow diffusion of diethyl ether into a methanol solution of the complex gave single crystals of $Na(PNP)_3[Ti_2(\mathbf{1})_3]\cdot CH_3OH\cdot H_2O\cdot Et_2O$ suitable for an X-ray diffraction analysis.[18]

The structure analysis revealed, that indeed the triple-stranded helicate $[Ti_2(\mathbf{1})_3]^{4-}$ had formed (Figure 2). The three ligands are oriented in a parallel manner, as expected. One

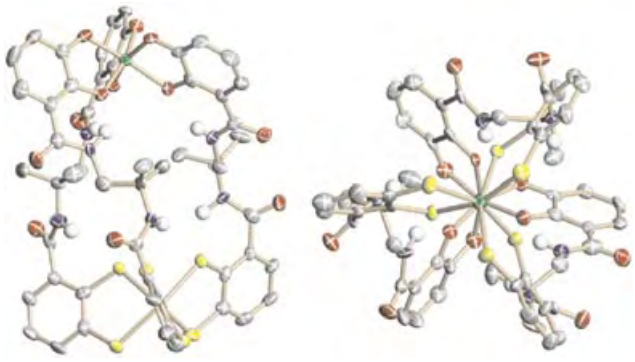


Figure 2. Molecular structure of the tetraanion $[Ti_2(\mathbf{1})_3]^{4-}$ in a side-view (left) and along the Ti–Ti axis (right). Selected bond lengths [Å] and angles [°]: Ti-S 2.381(3)–2.436(3), Ti-O 1.904(6)–2.010(6), in one donor group S-Ti-S 81.64(9)–81.94(9), O-Ti-O 78.9(2)–80.9(3); the Ti–S or Ti–O bonds to the donor atoms in 2-position at the aromatic ring are always slightly longer than the bonds to donor atoms at the 3-positions at the aromatic rings.

titanium atom is coordinated in a distorted octahedral fashion by the six oxygen atoms of three catechoylamide groups. The Ti–O bond lengths fall in the range reported for other Ti^{IV} tris(catecholato) complexes.[19] The second titanium atom is surrounded by six sulfur atoms from three benzenedithiolato groups in a strongly distorted octahedral fashion. The Ti–S bond lengths vary only slightly and are comparable to bond lengths reported for tris(*o*-benzenedtihiolato) Ti^{IV} complexes.[20] The helical twist between two titanium centers measures 65.6°.

The unit cell contains one $[Ti_2(\mathbf{1})_3]^{4-}$ ion, three PNP cations, one sodium cation, and one molecule each of water, methanol, and (disordered) diethyl ether. The PNP cations maintain no contacts to the $[Ti_2(\mathbf{1})_3]^{4-}$ ion whereas the Na^+ ion acts as a bridge between the $[Ti_2(\mathbf{1})_3]^{4-}$ ions and this leads to indefinite chains in the crystal lattice. The Na^+ ion completes its coordination sphere by the coordination of one molecule each of methanol and water (Figure 3).

Both metal centers in $[Ti_2(\mathbf{1})_3]^{4-}$ in the crystal under investigation assume the same configuration, namely *Λ*. Since the complex crystallized in the acentric space group *P*1 and the CD spectrum of the reaction product shows no Cotton effect, crystals of the *Δ*,*Λ* enantiomer must also have formed.

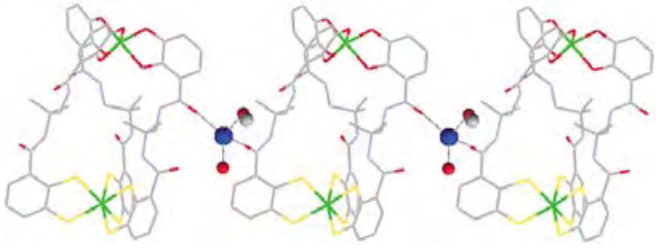


Figure 3. Section of the crystal structure of $Na(PNP)_3[Ti_2(\mathbf{1})_3]\cdot CH_3OH\cdot H_2O\cdot Et_2O$, for clarity the PNP cations and the diethyl ether molecule are not shown.

A similar spontaneous resolution of stereoisomers upon crystallization was first described for triple-stranded Ni^{II} complexes with oligobipyridine ligands.[21] Since the NMR spectra show the formation of only one pair of enantiomers, the formation of helicates of the *Λ*,*Λ* and *Δ*,*Δ* type, can be excluded.

Currently we can only speculate about the driving force for the formation of the parallel triple-stranded helical complex $[Ti_2(\mathbf{1})_3]^{4-}$. With the related directional ligand containing catechol/aminophenol donor groups reported by Albrecht et al. only the antiparallel ligand orientation was observed for homobinuclear complexes,[12] which leads to the smallest possible charge separation in the complex.[22] Ligand H_4-**1** was expected to behave similarly. However, H_4-**1** is directional with respect the donor groups and with respect the spacer between them. Upon formation of the triple-stranded helicate a distorted $\{TiS_6\}$ octahedron and a smaller $\{TiO_6\}$ octahedron are obtained. It is reasonable to expect, that the sterically more demanding (CMe_2) part of the spacer CMe_2CH_2 is oriented towards the larger $\{TiS_6\}$ octahedron thereby causing the parallel orientation of the ligands. This orientation allows the formation of three stable N–H···O hydrogen bridges (length H···O 1.824–2.039 Å) and of three almost planar N–H···O-C-C-C(O) rings within the catechoylamide groups at the $\{TiO_6\}$ octahedron (Figure 2). Similarly strong N–H···S hydrogen bonds were not observed (distance H···S 2.444–2.701 Å) and the benzenedithiolato groups are not coplanar with their amide groups. We therefore propose a structure-determining influence of the sterically unsymmetrical CMe_2CH_2 spacer for the formation of the parallel regioisomer. This postulate is corroborated by the observation that a ligand isomeric to H_4-**1** with a symmetrical CH_2CH_2 spacer forms dinuclear Ti^{IV} complexes of the known structural type[13b,c] $[Ti_2(L)_2(OMe)_2]^{2-}$ with an antiparallel orientation of the ligands.[23]

The structure-determining influence of the unsymmetrical spacer in ligand H_4-**1** will be more prominent in the synthesis of heterobimetallic triple-stranded helicates, where the preferences of the donor groups for different metal ions will be a factor. We expect that the reaction of H_4-**1** with a mixture (1:1) of Ti^{IV} and W^V will yield a triple-stranded helicate with parallel ligand orientation containing $\{TiO_6\}$ and $\{WS_6\}$ octahedra. Such investigations are currently underway as well as attempts to remove the helicity in such heterobimetallic complexes by oxidation of the $\{W^VS_6\}$ octahedron to give the trigonal-prismatic $\{W^{VI}S_6\}$ coordination polyhedron.

 © 2004 Wiley-VCH Verlag GmbH & Co. KGaA, Weinheim

Experimental Section

All synthetic manipulations were carried out under argon in Schlenk flasks. Solvents were dried, distilled, and stored under argon. Correct elemental analyses (C, H, N, S) were obtained for all compounds.

H_4-**1**: Yield 59% relative to **2**. ^{1}H NMR (300 MHz, [D$_7$]DMF, assignment of signals given in Figure 1): $\delta = 10.44$ (s, br, 2H, OH), 9.10 (t, 1H, H_a), 8.25 (s, 1H, H_e), 7.60 (d, $^3J = 7.8$ Hz, 1H, H_b), 7.49 (d, $^3J = 8.2$ Hz, 1H, H_f), 7.35 (d, $^3J = 7.8$ Hz, 1H, H_d), 7.12 (t, $^3J = 7.8$ Hz, 1H, H_c), 7.05 (d, $^3J = 8.2$ Hz, 1H, H_h), 6.78 (t, $^3J = 8.2$ Hz, 1H, H_g), 5.59 (s, br, 2H, SH), 3.82 (d, 2H, CH_2), 1.56 ppm (s, 6H, CH_3); ^{13}C NMR (75 MHz, [D$_7$]DMF): $\delta = 171.40$ (C=O), 169.93 (C=O), 150.58, 147.51, 137.56, 133.98, 131.59, 130.63, 126.09, 125.63, 119.55, 118.83, 118.03, 116.07 (C_{Ar}), 56.12 ($CH_2C(CH_3)_2$), 48.39 ($CH_2C(CH_3)_2$), 24.87 ppm ($CH_2C(CH_3)_2$); MALDI-MS (positive ions): m/z (%): 393 (100) $[M+H]^+$.

Na(PNP)$_3$[Ti$_2$[(**1**)$_3$] was prepared by stirring ligand H_4-**1** (104 mg, 0.26 mmol), [TiO(acac)$_2$] (45 mg, 0.17 mmol), and Na_2CO_3 (18 mg, 0.17 mol) in methanol at room temperature for 72 h. Subsequently, the solvent was removed and the solid obtained was redissolved in methanol. After addition of bis(triphenylphosphoranylidene)ammonium chloride (PNPCl) (98 mg, 0.17 mmol) of the reaction mixture was filtered. Slow diffusion of diethyl ether into the filtrate yielded 60 mg (0.06 mmol, 23%) of red-brown crystals of (PNP)$_3$Na[Ti$_2$(**1**)$_3$]·CH_3OH·H_2O·Et_2O. ^{1}H NMR (500 MHz, [D$_7$]DMF, solvent-free compound, assignment of signals given in Figure 1): $\delta = 9.80$ (t, br, 3H, H_a), 8.14 (s, br, 3H, H_e), 7.80–7.60 (m, 90H, H_{Ar}, PNP), 7.15 (d, $^3J = 7.8$ Hz, 3H, H_b), 7.08 (d, $^3J = 7.5$ Hz, 3H, H_f), 6.98 (d, $^3J = 7.5$ Hz, 3H, H_h), 6.65 (t, $^3J = 7.5$ Hz, 3H, H_g), 6.32 (t, $^3J = 7.8$ Hz, 3H, H_c), 6.21 (d, $^3J = 7.8$ Hz, 3H, H_d), 4.81 (s, br, 6H, CH_2), 1.38 ppm (s, br, 18H, CH_3); ^{13}C NMR (125 MHz, [D$_7$]DMF, solvent-free compound): $\delta = 169.41$ (C=O), 167.44 (C=O), 161.81, 161.40, 155.24, 152.05, 135.63 (C_{Ar}, 1), 134.34, 133.08, 133.03, 132.98, 130.24, 130.19, 130.11, 128.48, 128.46, 127.62 (C_{Ar}, PNP), 128.22, 123.03, 121.85, 117.86, 116.47, 115.56, 112.29 (C_{Ar}, **1**), 54.98 ($CH_2C(CH_3)_2$), 49.46 ($CH_2C(CH_3)_2$), 25.16 ppm (br, $CH_2C(CH_3)_2$); MS (ESI, negative ions): m/z (%): 630.7 (100) $[Ti_2(\mathbf{1})_3 + 2H]^{2-}$.

Received: April 1, 2004

Keywords: chirality · helical structures · O,S ligands · supramolecular chemistry · titanium

[1] a) J. M. Lehn, *Supramolecular Chemistry: Concepts and Perspectives*, VCH, Weinheim, **1995**, Chapter 9; b) C. Piguet, G. Bernardinelli, G. Hopfgarten, *Chem. Rev.* **1997**, *97*, 2005 – 2062; c) C. A. Schalley, A. Lützen, M. Albrecht, *Chem. Eur. J.* **2004**, *10*, 1072 – 1080.

[2] M. Albrecht, *Chem. Soc. Rev.* **1998**, *27*, 281 – 287.

[3] a) F. E. Hahn, W. W. Seidel, *Angew. Chem.* **1995**, *107*, 2938 – 2941; *Angew. Chem. Int. Ed. Engl.* **1995**, *34*, 2700 – 2703; b) W. W. Seidel, F. E. Hahn, T. Lügger, *Inorg. Chem.* **1998**, *37*, 6587 – 6596; c) W. W. Seidel, F. E. Hahn, *J. Chem. Soc. Dalton Trans.* **1999**, 2237 – 2241.

[4] H. V. Huynh, C. Schulze Isfort, W. W. Seidel, T. Lügger, R. Fröhlich, O. Kataeva, F. E. Hahn, *Chem. Eur. J.* **2002**, *8*, 1327 – 1335.

[5] a) T. J. McMurry, M. W. Hosseini, T. M. Garrett, F. E. Hahn, Z. E. Reyes, K. N. Raymond, *J. Am. Chem. Soc.* **1987**, *109*, 7196 – 7198; b) T. M. Garrett, T. J. McMurry, M. W. Hossaini, Z. E. Reyes, F. E. Hahn, K. N. Raymond, *J. Am. Chem. Soc.* **1991**, *113*, 2965 – 2977.

[6] T. E. Burrow, R. H. Moras, A. Hills, D. L. Hughes, R. L. Richards, *Acta Crystallogr.* **1993**, *C49*, 1591 – 1594.

[7] H. V. Huynh, T. Lügger, F. E. Hahn, *Eur. J. Inorg. Chem.* **2002**, 3007 – 3009.

[8] H. V. Huynh, W. W. Seidel, T. Lügger, R. Fröhlich, B. Wibbeling, F. E. Hahn, *Z. Naturforsch. B* **2002**, *57*, 1401 – 1408.

[9] J.-F. Pons, J.-L. Fauchère, F. Lamaty, A. Molla, R. Lazaro, *Eur. J. Org. Chem.* **1998**, 853 – 859.

[10] W. H. Rastetter, T. J. Erickson, M. C. Venuti, *J. Org. Chem.* **1981**, *46*, 3579 – 3590.

[11] M. Albrecht, *Chem. Rev.* **2001**, *101*, 3457 – 3497.

[12] M. Albrecht, R. Fröhlich, *J. Am. Chem. Soc.* **1997**, *119*, 1659 – 1661.

[13] a) M. J. Hannon, S. Bunce, A. J. Clarke, N. W. Alcock, *Angew. Chem.* **1999**, *111*, 1353 – 1355; *Angew. Chem. Int. Ed.* **1999**, *38*, 1277 – 1278; b) M. Albrecht, M. Napp, M. Schneider, P. Weis, R. Fröhlich, *J. Chem. Soc. Chem. Commun.* **2001**, 409 – 410; c) M. Albrecht, M. Napp, M. Schneider, P. Weis, R. Fröhlich, *Chem. Eur. J.* **2001**, *7*, 3966 – 3975.

[14] E. C. Constable, F. Heirtzler, M. Neuburger, Z. Zehnder, *J. Am. Chem. Soc.* **1997**, *119*, 5606 – 5617.

[15] a) E. J. Enemark, T. D. P. Stack, *Angew. Chem.* **1995**, *107*, 1082 – 1084; *Angew. Chem. Int. Ed. Engl.* **1995**, *34*, 996 – 998; b) B. Kersting, M. Meyer, R. E. Powers, K. N. Raymond, *J. Am. Chem. Soc.* **1996**, *118*, 7221 – 7222; c) C. Brückner, R. E. Powers, K. N. Raymond, *Angew. Chem.* **1998**, *110*, 1937 – 1940; *Angew. Chem. Int. Ed.* **1998**, *37*, 1837 – 1839.

[16] a) T. D. P. Stack, T. B. Karpishin, K. N. Raymond, *J. Am. Chem. Soc.* **1992**, *114*, 1512 – 1514; b) T. B. Karpishin, T. D. P. Stack, K. N. Raymond, *J. Am. Chem. Soc.* **1993**, *115*, 182 – 192; c) T. B. Karpishin, T. D. P. Stack, K. N. Raymond, *J. Am. Chem. Soc.* **1993**, *115*, 6115 – 6125; d) T. B. Karpishin, T. M. Dewey, K. N. Raymond, *J. Am. Chem. Soc.* **1993**, *115*, 1842 – 1851.

[17] The term *meso*-helicate, which is often used in the literature, is not applicable here owing to the two different stereocenters {TiS_6} and {TiO_6} present.

[18] X-ray diffraction study: Crystals of Na(PNP)$_3$[Ti$_2$(**1**)$_3$]·CH_3OH·H_2O·Et_2O were obtained by diffusion of diethyl ether into a methanol solution of Na(PNP)$_3$[Ti$_2$(**1**)$_3$], $C_{167}H_{154}N_9NaO_{15}P_6S_6Ti_2$, $M_r = 3023.96$, red crystal, $0.10 \times 0.07 \times 0.04$ mm^3, $P1$, $a = 13.594(3)$, $b = 17.190(4)$, $c = 18.900(4)$ Å, $\alpha = 66.722(4)$, $\beta = 79.188(4)$, $\gamma = 82.523(4)°$, $V = 3977.6(15)$ Å^3, $\rho_{calcd} = 1.262$ g cm^{-3}, $\mu = 0.306$ mm^{-1}, semi-empirical absorption correction ($0.9701 \le T \le 0.9879$), ω- and ϕ-scans, 24856 measured intensities ($2.4° \le 2\theta \le 45.2°$), 20191 independent ($R_{int} = 0.0583$) and 13406 observed ($I \ge 2\sigma(I)$) intensities, $\lambda = 0.71073$ Å, $T = 123(2)$ K, $Z = 1$, $R = 0.0771$, $wR^2 = 0.1645$ (refinement against $\langle F^2 \rangle$ with H atoms on calculated positions). The diethyl ether molecule in the unit cell is disordered, positional parameters for the hydrogen atoms of the water and methanol OH protons were not determined. CCDC 234748 contains the supplementary crystallographic data for this paper. These data can be obtained free of charge via www.ccdc.cam.ac.uk/conts/retrieving.html (or from the Cambridge Crystallographic Data Centre, 12 Union Road, Cambridge CB2 1EZ, UK; fax: (+44) 1223-336-033; or deposit@ccdc.cam.ac.uk).

[19] a) B. A. Borgias, S. R. Cooper, Y. B. Koh, K. N. Raymond, *Inorg. Chem.* **1984**, *23*, 1009 – 1016; b) F. E. Hahn, S. Rupprecht, K. H. Moock, *J. Chem. Soc. Chem. Commun.* **1991**, 224 – 225.

[20] M. Könemann, W. Stüer, K. Kirschbaum, D. M. Giolando, *Polyhedron* **1994**, *13*, 1415 – 1425.

[21] R. Krämer, J.-M. Lehn, A. De Cian, J. Fischer, *Angew. Chem.* **1993**, *105*, 764 – 767; *Angew. Chem. Int. Ed. Engl.* **1993**, *32*, 703 – 706.

[22] R. Krämer, J. M. Lehn, A. Marquis-Rigault, *Proc. Natl. Acad. Sci. USA* **1993**, *90*, 5394 – 5398.

[23] F. E. Hahn, C. Schulze Isfort, R. Fröhlich, unpublished results.

 © 2004 Wiley-VCH Verlag GmbH & Co. KGaA, Weinheim